International Beam Instrumentation Conference IBIC

11 - 15 September 2016 Barcelona

Organised by: ALBA

www.ibic2016.org


Est
International Beam Instrumentation Conference IBIC

Dear Colleagues,

the 2016 International Beam Instrumentation Conference, ***IBIC 2016***, was held in Barcelona (Spain) between September 11th and 15th 2016, and it was hosted by the ALBA Synchrotron Light Source. IBIC is a fruitful and successful gathering of the world's beam instrumentation community and it is dedicated to exploring the physics and engineering challenges of beam diagnostic and measurement techniques for particle accelerators.

The conference took place in the World Trade Center, set right on the Barcelona harbor (Port Vell), in the heart of the city and surrounded by a wide offer of hotels, restaurants, and a wonderful cultural heritage that could be enjoyed by all the participants. In addition, Barcelona is one of the leading technological centers of south Europe, and a visit to the ALBA synchrotron was organized.

The 3.5 day programme of the 2016 IBIC conference included 15 invited and 15 contributed talks, 2 seminars and 1 public lecture. The Conference celebrated for its first time the "Speakers Corner", a successful initiative in which the participants could come up to stage for 5 minutes and present any innovative concepts that could potentially interest the audience. Furthermore, 239 posters were presented in the 3 poster sessions, and a 3 day long vendor exhibition with 32 exhibitors could be visited during the conference. In total, **349 participants** coming from 24 countries gather around during the 3.5 days of the conference. To all of them, the Organizing Committee is pleased to thank them for their enthusiastic participation.

Not only to the participants, we would like to explicitly express our gratitude to all those who have contributed to this conference: the Scientific Committee for forming a balanced and interesting programme, the Editorial Team for working hard to enable us to present these proceedings, and last but not least, the Local Organisation Committee for turning this conference into reality.

Francis Pérez
IBIC 2016 Conference Chair

Ubaldo Iriso
IBIC 2016 Scientific Chair

Scientific Programme Committee

Chair

Ubaldo Iriso, ALBA-CELLS

Members

Mark Boland, ASLS
Alessandro Cianchi, INFN
Friederike Ewald, ESRF
Mario Ferianis, ELETTRA
Peter Forck, GSI
Dave Gassner, BNL
Kuotung Hsu, NSRRC
Andreas Jansson, ESS
Kevin Jordan, JLAB
Yongbin Leng, SSRF
Steven Lidia, FRIB (IBIC17 chair)
Hirokazu Maesaka, SPring-8
Sergio Marques, LNLS
Toshiyuki Mitsuhashi, KEK
Francis Pérez, ALBA-CELLS
Guenther Rehm, DIAMOND
Hermann Schmickler, CERN
James Sedillo, LANL
Kay Wittenburg, DESY

Local Organizing Committee

Chair Francis Pérez, ALBA-CELLS
Scientific Chair Ubaldo Iriso, ALBA-CELLS
Editor in Chief Isidre Costa, ALBA-CELLS
Poster Andriy Nosych, ALBA-CELLS
Industrial Ángel Olmos, ALBA-CELLS
Secretary & Speakers Daimí Pérez, ALBA-CELLS

JACoW Editorial Team

Ivan Andrian, Elettra
Isidre Costa, ALBA-CELLS
Caitlin Marie Hoffman, BNL
Amy McCausey, FRIB
Maggie Montes-Loera, SLAC
Raphael Müller, GSI

JACoW External Help

Ronny Billen, CERN (SPMS Support)
Jan Chrin, PSI (JACoW File Server)
Volker RW Schaa, GSI (JACoW Scripts)

Contents

DIAGNOSTICS AT THE MAX IV 3 GeV STORAGE RING DURING COMMISSIONING

Å. Andersson†, J. Breunlin, B. N. Jensen, R. Lindvall, E. Mansten, D. Olsson, J. Sundberg, P. F. Tavares, S. Thorin, MAX-IV Laboratory, Lund University, Lund, Sweden

Abstract

The MAX IV 3 GeV storage ring based on a multibend achromat lattice allows for horizontal emittances from 330 pm rad down to 180 pm rad, depending on the number of insertion devices. The diagnostics used during commissioning will be described, with emphasis on the emittance diagnostics. This will involve two diagnostic beam lines to image the electron beam with infrared and ultraviolet synchrotron radiation from bending magnets, in order to determine also beam energy spread. The scheme for horizontal emittance measurements looks promising also for an order of magnitude lower emittance. Bunch lengthening with harmonic cavities is essential for the low emittance machine performance. We have used a radiation-based sampling technique to verify individual bunch distributions.

THE MAX IV FACILITY

The MAX accelerator facility is shown in Fig. 1. A more detailed description can be found in [1]. As an injector, a 3 GeV S-band linac has been chosen. Admittedly, a booster synchrotron is a more economical choice as a ring injector, but a linac injector opens up for Short-Pulse Facility (SPF) operation [2] and also paves the way for possible Free-Electron Laser operation [3]. A smaller ring at 1.5 GeV, MAX V, was also introduced at the laboratory to increase the spectral range of high-quality undulator radiation. This ring has just started (fall 2016) to be commissioned.

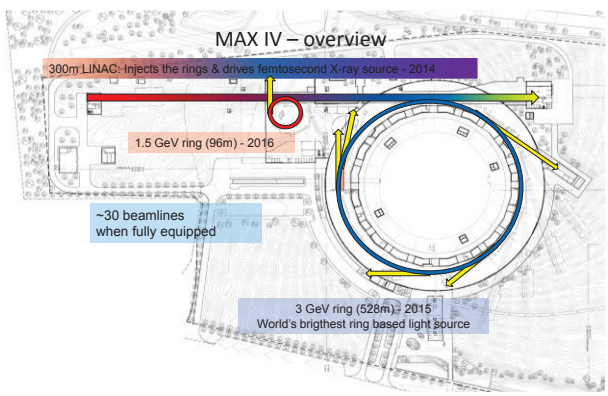

Figure 1: The MAX IV facility.

THE LINAC INJECTOR AND ITS MAIN DIAGNOSTICS FOR INJECTION

The 3 GeV injector linac is described in more detail in [1] and [4]. Two electron guns are used; one thermionic RF gun used for injections into the rings and one photo-cathode RF gun for short pulse operation for the SPF. Our experience with the former is positive regarding robustness and long cathode lifetime. However, recent experience with the photo-cathode gun operation exceeds the expectations, and in future it might be used as injector gun as well. In this paper we limit the description to the diagnostics relevant for ring injections.

Linac commissioning started in August 2014 when the installation of the MAX IV 3 GeV ring started. After one year the linac commissioning was completed and the 3 GeV ring commissioning started. Some parameters for the MAX IV linac can be found in Table 1.

Table 1: Injector Linac Parameter Values

End energy	3 GeV
RF	2.9985 GHz
Field gradient	17 MV/m
Acc cell length	5.2 m
No of structures	39
Bunch compressors	Double achromats

Current Transformers

The beam current and the electron bunch train envelope are resolved by twelve current transformers (CTs). Three of them are strategically placed after the RF thermionic gun, just after the chopper system [5], and just after an energy filter designed to cut away the low energy tail of the emitted pulse. Examples of these pulses are shown in Fig. 2. The chopper system efficiently creates a 100 MHz time structure, matching the ring RF, or a 500 MHz structure for maximum ring BPM sensitivity. Further, two CTs surround each bunch compressor achromats, and two CTs are placed at the beginning and at the end of each transfer line going up to the two rings. The CT signals are used continuously by the radiation protection system generating alarms in case of non-acceptable losses.

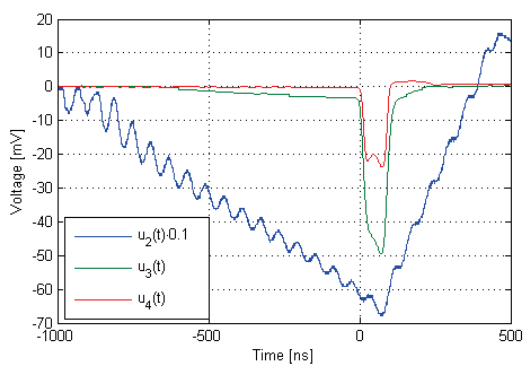

Figure 2: CT signals (Z=1 Ω) after thermionic gun (blue), chopper system (green) and energy filter (orange).

ISBN 978-3-95450-177-9

Beam Position Monitors (BPMs)

The BPMs are of quarter wave strip-line type in order to have a good sensitivity to beam displacement even at low currents. The read out is performed with Libera Brilliance "Single pass" commercial electronics (without channel equalization). The standard deviation in position determination is of the order 0.1 mm at a few pC. The BPM offset values were determined with beam based calibration methods, and seldom the offset values exceeded 1 mm, which point on an acceptable alignment and cable phase length determination. BPMs located either in the bunch compressors, or in the transfer lines are used for energy measurements of the linac beam.

Screens

Screens are placed in the vicinity of the chopper system and after the energy filter, in transfer lines and in the bunch compressors. The screens are of YAG-type with thickness 100 microns, in order to keep the depth-of-field contribution sufficiently small. Some YAG screens, especially those at low energy, are covered with a thin conducting layer, to avoid charge build-up. A YAG screen at maximum dispersion, in the transfer line up to the 3 GeV ring, has capability to resolve individual S-band bunches. The most important screen regarding ring injection has shown to be the one situated just after the septum magnet in the ring. If something is largely detuned in the linac and/or the transfer line, it is usually seen on this screen. The thermionic RF gun delivers a transverse normalized beam emittance that has been measured to be in the order of 10 mm*mrad. This was achieved with quadrupole scans before the first bunch compressor at 260 MeV. Thus, the beam size that should be resolved at the screen position in the 3 GeV ring is in the order of 150 microns. However, this measurement is still to be confirmed.

THE MAX IV STORAGE RING AND ITS MAIN DIAGNOSTICS

The 3 GeV storage ring is described in detail in [1], [6] and [7]. In short, the 3 GeV storage ring was designed to meet the requirements of state-of-the-art insertion devices (IDs) for the generation of high-brightness hard x-rays. Its lattice was therefore based on a novel compact multibend achromat (MBA) delivering 328 pm rad bare lattice emittance in a circumference of 528 m [5-7]. 20 MBAs provide 19 long straights (4.6 m) for IDs and 40 short straights (1.3 m) for RF and diagnostics. The MAX IV achromat is a 7-bend achromat with 5 unit cells (3°) and 2 matching cells (1.5°). All bends contain a transverse gradient for vertical focusing. The matching cell dipoles have a longitudinal gradient as well. Since the vertical focusing is performed by the gradient bends, only horizontally focusing quadrupoles are contained in the unit cells. The optics for one achromat is displayed in Fig.3 and storage ring parameters are given in Table 2.

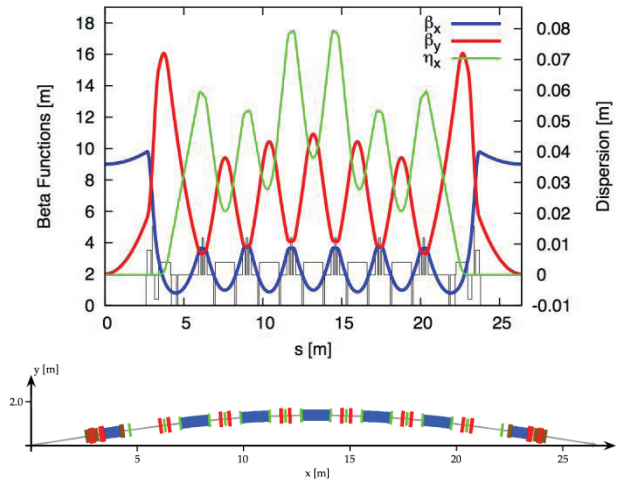

Figure 3: MAX IV 3 GeV achromat and optics.

Table 2: MAX IV 3 GeV Storage Ring Parameters

Operating energy	3 GeV
Circulating current	500 mA
Circumference	528 m
Horizontal emittance (bare lattice)	328 pm rad
Horizontal emittance (incl. IDs)	179 pm rad
Vertical emittance	2 – 8 pm rad
Total beam lifetime at 500 mA	>10 h
Q_x, Q_y	42.20, 16.28
ξ_x, ξ_y (natural)	-50.0, -50.2
Momentum compaction factor	3.06×10^{-4}
Required momentum acceptance	>4.5 %

Beam Position Monitors

The ring BPMs, amounting to 200 units (10/achromat), constitutes the backbone of the ring diagnostics. Here, the Libera Brilliance "+" units are used, which allow read-out in either single pass mode (injected beam) or integrating mode (stored beam). However, for initial commissioning, the BPMs are not used as indication of beam position, but rather they are the first diagnostic tool used to detect any (tiny) charge finding its way into the storage ring. Actually, in our case, we used the combined sum signal from all four buttons of the first BPM unit after the injection point. After verifying one or two turns, the buffer size in the read-out was enlarged, making it easy to adjust carefully some corrector magnets and follow the increasing number of turns achieved.

Once a beam is stored, the BPMs can be calibrated in positon relative to magnet centres, with help of a beam based technique [8]. In our case, we have introduced what we call "trim coils" in every sextupole and octupole magnets. For BPM calibration these coils are one by one excited in an upright quadrupole mode of quite tiny

ISBN 978-3-95450-177-9

strength. The beam is displaced horizontally and vertically, and for each position the trim coil is excited. Observing the beam position readout in the nearby BPM for which the excitation has minimum influence on the beam closed orbit, gives the x and y offset values for that BPM. The novelty in our scheme is that the beam is centred in the non-linear magnetic elements, while traditionally the centring was towards the quadrupoles.

The BPM units are clamped into the magnetic blocks, with a bellow on one side in order to relax material stress. Seven magnetic blocks, encompassing several individual magnets, constitutes the entire achromat. BPM physical movements will follow the magnet blocks. Therefore, in long time scales, we are not monitoring the physical BPMs, but rather we will monitor the magnetic blocks. In short time scales, the resolution of the vertical beam positions enclosing the straight sections are the most critical. The goal is less movement than 10% of the rms beam size, which corresponds to 0.4 microns initially, and eventually 0.2 microns. A major monitor campaign has started to analyse the short term data in order to track any vibration sources.

Strip-lines for Tune Measurements

Considering our commercial BPM read-out system, one could contemplate measuring the machine betatron tunes with turn-by-turn data from a single BPM unit, by exciting the beam with an extra (in our case) vertical pinger magnet, and the horizontal injection kicker magnet. However, we found so far higher accuracy in tune measurements where a spectrum analyser (SA) is exciting a pair of strip-lines, inducing a tiny beam displacement, which is detected at an ordinary BPM in integration mode, connected to the SA.

Monitoring Machine Functions

With the equipment mentioned above, there are two ways of monitoring possible. Using the well-known LOCO approach [9], where the response matrix, 200 times 200 horizontal and vertical beam movements are measured for 200*190 horizontal and vertical corrector kicks. This huge amount of data is processed in an adequate model of the ring magnets, and the outcome is the horizontal and vertical beta functions. The dispersion function is monitored by RF changes, resulting in off-energy orbits. However, we have additionally used our trim coils (see above), and monitored induced tune shifts. This gives the beta function values in the non-linear magnets in which the trim coils are situated. Looking at Figure 3, where those are indicated with green and brown colours, we see that quite a dense sampling of the beta functions is possible. However, so far not all our trim coils are equipped with its own power supply. Additionally, we must admit that more commissioning work is needed, since the two methods still have discrepancies sometimes over 20 %, which is not acceptable. Both a LOCO model not converging properly, and an uncertainty in trim coil settings, are investigated as possible error sources.

Bunch-by-bunch Feedback System

At currents up to 120 mA, the 3 GeV ring has been operated stably, with a bunch-by-bunch feedback system with signal processors delivered by Dimtel [10]. Two 30 cm long strip-line pairs are used as transverse actuators, and a standard button BPM chamber is used as the detector. Figure 4 shows the vertical strip-line pair. One of the strip-line pairs is simultaneously used as a weak longitudinal kicker by feeding a common mode signal to its two electrodes. A waveguide overloaded cavity that will be dedicated for longitudinal feedback is currently being developed. This cavity is operating at 625 MHz ±25 MHz and will probably be installed in early 2017. The relatively low centre frequency is chosen since the form factor of the ring bunches drop rapidly at higher frequencies due to the long bunches.

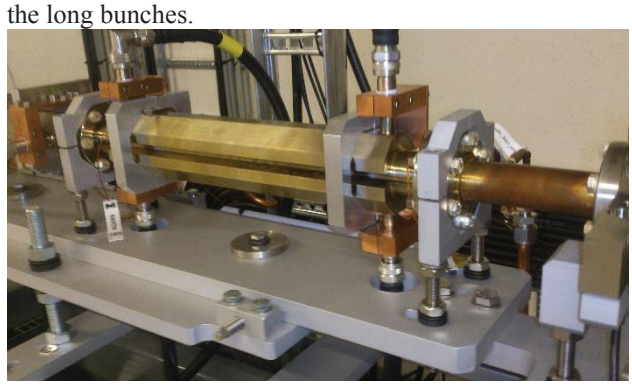

Figure 4: A 30 cm vertical strip-line pair. The horizontal pair is at left side, and the BPM is at right side.

The bunch-by-bunch system provides an efficient way to diagnose the potentially dangerous coupled bunch mode instabilities (CBI), so far mainly driven by higher order modes in the cavities. When aiming for higher currents, we use the system for instability growth rate measurements, which guides us in the temperature tuning of the individual cavities.

Vacuum Diagnostics and Scrapers

Because of the small radius vacuum chamber, r = 11 mm, almost the whole ring vacuum system is NEG-coated. Ion pumps and vacuum gauges are only placed in the short straights, and in the long straights not yet equipped with insertion devices (ID). Thus their read-out values only represent a minor part of the whole rest-gas volume encountered by the beam. It therefore becomes extra interesting to evaluate the pressure encountered by the beam, with help of scraper measurements. A vertical scraper scan, while observing the total lifetime, is shown in Fig. 5.

With the aid of in total five rest gas analyzers in the ring, capable to read-out also with beam in the ring, a fairly good estimate of the rest-gas composition could be made at around 100 mA: H2 79 %, CO 12%, CH4 (and dissociates) 5%, O2 0.6% and CO2 0.5%. Assuming this is also the composition experienced by the beam, the total pressure has been estimated at different current values, where scraper scans were performed. The result after

ISBN 978-3-95450-177-9

several scans in the region up to 100 mA (at roughly 40 Ah integrated dose) was:

P [nTorr] = 1.156 + 0.028*I[mA]

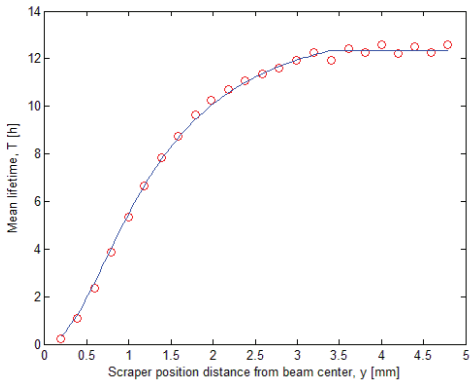

Figure 5: A vertical scraper scan. Rings are measurements and line is fitted curve.

At 50 mA both the elastic and inelastic scattering lifetimes are measured to be around 100 h. Rest gas compositions and vertical scraper scans are planned to continue for increasingly higher integrated doses. So far, these derived pressures tend to be higher than the gauge read-outs, but lower than the ion-pump read-outs.

Emittance Diagnostics

The emittance diagnostic at the MAX IV storage rings is based on imaging the beam with synchrotron radiation (SR) in the near-visible spectral range from dipoles [11]. Employing two beam lines for each ring with source points at different horizontal dispersions will enable measurements also of the beam energy spread. In the 3 GeV storage ring a diagnostic beam line imaging the beam in the first dipole at horizontal dispersion close to zero has been installed and is under commissioning. Installations for another beam line in the sixth dipole (though in another achromat), where the dispersion is roughly 27 mm, is scheduled for 2017. The source points can be imagined in Fig. 3, where the dipoles are indicated in blue. These beam lines are for the moment the only dipole source beam lines in the entire 3 GeV ring, the reason being that it is quite difficult to guide the light out through the magnet blocks, which can be seen in Fig. 6.

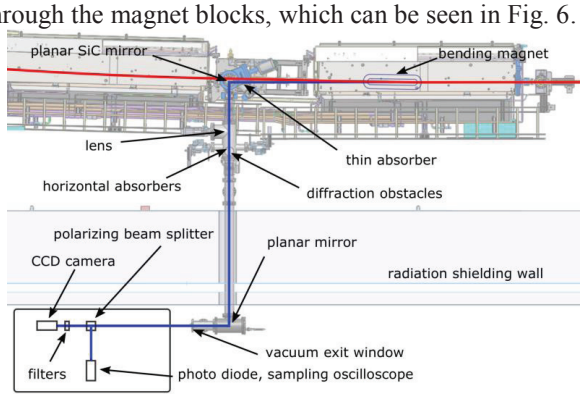

Figure 6: Schematic beam line layout. Electron path in red and SR path in blue. The distance from the center of the dipole to the first mirror is 1.85 m.

Images of the electron beam at near-visible wavelengths are dominated by diffraction that is inherent to the synchrotron radiation emitted into a narrow cone around the particle trajectory. In the MAX IV 3 GeV ring diagnostic beam lines, however, we make use of these diffraction effects by deriving both transverse beam sizes from the fringe contrast of the diffraction dominated images. Numerical simulations from a beam line modeled in the Synchrotron Radiation Workshop (SRW) [12], [13], thereby provide the relation between the fringe contrast and the horizontal and vertical beam size. SRW provides an accurate treatment of the synchrotron radiation emission process along the curved trajectory of the ultra-relativistic beam in a dipole magnet in the near-field regime as well as the propagation of SR through optical components like apertures and a thin lens.

Vertical Beam Size Measurements Established at the Swiss Light Source for resolving low vertical emittance beams, the imaging of pi-polarized SR in the near-UV [14] will be applied, as well as the obstacle diffractometer method, in which a fringe pattern is intensified in a predictable way by a horizontal obstacle in the path of the SR beam [15], (see Fig. 7).

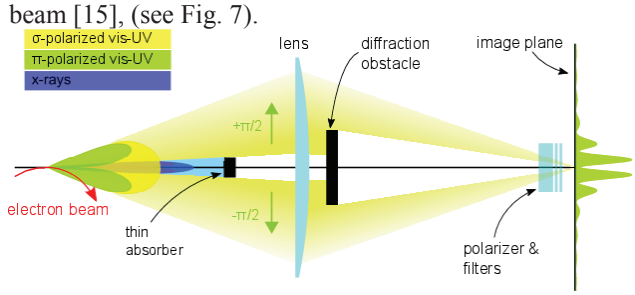

Figure 7: Schematic side-view of the obstacle diffractometer technique.

Measurements on an uncorrected beam in the 3 GeV storage ring at a vertical beam size of approximately 11.5 µm, corresponding to a vertical emittance of approximately 6.4 pm rad have been achieved to study the imaging quality of the first operational diagnostic beam line. In Fig. 8, a vertical profile of pi-polarized SR is shown with a diffraction pattern intensified by an inserted diffraction obstacle.

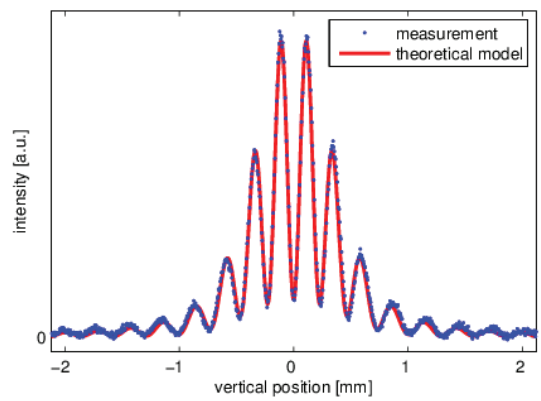

Figure 8: Vertical profile of imaged pi-polarized SR with a 9 mm diffraction obstacle at 488 nm wavelength. The measured profile (blue) is compared to a SRW calculated profile of the same fringe contrast.

ISBN 978-3-95450-177-9

For vertical beam sizes in the 10 µm range the utilized imaging wavelength of 488 nm is sufficient. A reduction in vertical emittance and beam size to the 0.3 pm rad and 2.2 µm level, respectively, (corresponding to an emittance ratio of 1 ‰) will require shorter wavelengths down to 266 nm, for which the beam lines have been designed.

Horizontal Beam Size Measurements In the 3 GeV storage ring the expected horizontal beam sizes of approximately 22 to 24 µm are resolved by imaging SR in the near infrared. We make use of an interference effect originating in the longitudinally extended source of SR, emitted by the electron beam along its trajectory in the dipole magnet. For a wide horizontal acceptance angle of up to 18 mrad enabled by the design of the beam lines, an asymmetric fringe pattern is formed in the image plane from which, by evaluation of the fringe contrast, the horizontal beam size is derived. In Fig. 9 the sensitivity of the diffraction pattern is demonstrated. Preliminary measurements indicate a horizontal beam size of 24.5±1.5 µm. The betax is still to be determined (see sub-section on machine functions), but using the design betax places the horizontal emittance at 400 pm rad. Further improvement of the experimental condition as well as the numerical model are, however, necessary.

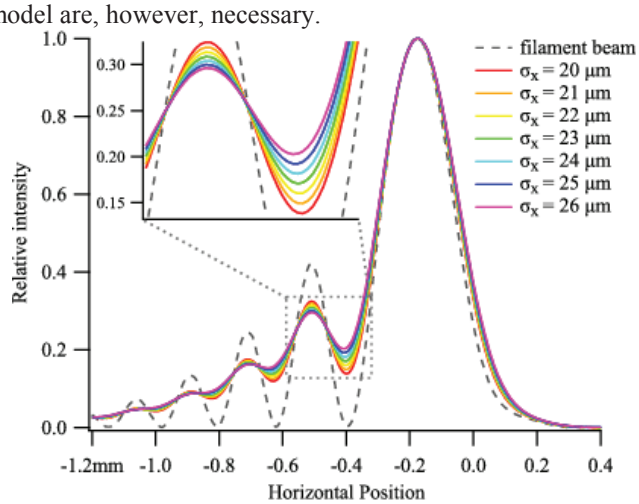

Figure 9: Horizontal profiles of sigma polarized SR calculated in SRW. The wavelength is 930 nm and the horizontal acceptance angle of the beam line is 15 mrad.

We would like to emphasize that introducing a double slit scheme, could have a beneficial effect on the resolution in this region of beam size. However, Fig. 9 indicates clearly that for future planned storage ring light sources with horizontal emittances for example at 50 pm rad, and a horizontal beta-function around a few meters, the resolution possibilities are actually higher than in the present case. In such case, or for even lower horizontal emittances, one would simply go to visible wavelengths, and image the beam without obstacles similar, in principle, to the pi-polarization method in the vertical case.

Longitudinal Bunch Shape Measurements In the same diagnostic beam line as described above, we use a Glan-Tayler polarizer for choosing the desired polarization. The discarded polarization we guide to an optical sampling oscilloscope. We have performed bunch shape measurements up to 8 mA in single bunch, verifying at low currents the natural bunch length and at increasing currents the potential well distortion. Studies to reveal the Intra Beam Scattering (IBS) onset are planned. In multi-bunch mode the bunch-by-bunch feedback system must be used in parallel with the measurements, to ensure the longitudinal stability.

REFERENCES

[1] The MAX IV Detailed Design Report, available at http://www.maxlab.lu.se/maxlab/max4/index.html
[2] S. Werin, S. Thorin, M. Eriksson and J. Larsson, “Short Pulse Facility for MAX-lab”, NIM-A **601** (2009) 98-107.
[3] Anders Nilsson et al, “The Soft X-Ray Laser@MAX IV, A Science Case for SXL”, Stockholm University, to be published
[4] J. Andersson et al, "Initial commissioning results of the MAX IV injector", TUP036, FEL2015, Daejeon, Korea, p.448.
[5] D. Olsson et al, "A chopper system for the MAX IV thermionic pre-injector", NIM-A **759** (2014) 29-35.
[6] S.C. Leemann et al., "Beam dynamics and expected performance of Sweden’s new storage-ring light source: MAX IV", Phys. Rev. ST Accel. Beams **12**, 120701 (2009).
[7] P. F. Tavares et al., “The MAX IV storage ring project” J. Synchrotron Rad. **21**, 862-877 (2014).
[8] P. Röjsel, "A beam position measurement system using quadrupole magnets magnetic centra as the position reference”, NIM-A **343** (1994) 374-382.
[9] J. Safranek, "Experimental determination of storage ring optics using orbit response measurements”, NIM-A **388** (1997) 27-36.
[10] URL: http://www.dimtel.com/
[11] J. Breunlin and Å. Andersson, "Emittance diagnostics at the MAX IV 3 GeV storage ring", WEPOW034, IPAC2016, Busan, Korea, p.2908.
[12] O. Chubar and P. Elleaume, "Accurate and efficient computation of synchrotron radiation in the near field region", EPAC1998, Stockholm, Sweden, p. 1177.
[13] http://www.esrf.eu/Accelerators/Groups/InsertionDevices/Software/SRW
[14] Å. Andersson et al, "Determination of a small vertical electron beam profile and emittance at the Swiss Light Source", NIM-A **591** (2008) 437-446.
[15] J. Breunlin et al, "Methods for measuring sub-pm rad vertical emittance at the Swiss Light Source", NIM-A **803** (2015) 55-64.

ISBN 978-3-95450-177-9

BEAM COMISSIONING OF SuperKEKB RINGS AT PHASE 1

M. Tobiyama*, M. Arinaga, J. W. Flanagan, H. Fukuma, H. Ikeda, H. Ishii, K. Mori, E. Mulyani[1], M. Tejima, KEK Accelerator Laboratory, 1-1 Oho, Tsukuba 305-0801, Japan
[1]also at SOKENDAI (The Graduate University for Advanced Studies), 1-1 Oho, Tsukuba, Japan
G.S. Varner, U. Hawaii, Dept. Physics and Astronomy, 2505 Correa Rd., Honolulu HI 96822 USA
G. Bonvicini, Wayne State U., 135 Physics Bldg., Detroit MI 48201, USA

Abstract

The Phase 1 commissioning of SuperKEKB rings without superconducting final focus magnets or Belle-II detector began in Feb., 2016. A total of 1010 mA (LER) and 870 mA (HER) stored beam has been achieved close to the design emittance and x-y coupling. Most of the beam diagnostics, including new systems such as gated turn-by-turn monitors and X-ray beam size monitors, have been commissioned with beam and proved to be essential to the success of machine commissioning. The results of the beam commissioning, including the evaluation and difficulties of the beam diagnostics are shown.

INTRODUCTION

The KEKB collider has been upgraded to the SuperKEKB collider with a final target of 40 times higher luminosity than that of KEKB. It consists of a 7 GeV high energy ring (HER, electrons) and a 4 GeV low energy ring (LER, positrons). About 2500 bunches per ring will be stored at total beam currents of 2.6 A (HER) and 3.6 A (LER) in the final design goal.

The first stage of commissioning (Phase 1 operation) without the Belle-II detector started in Feb. 2016 and continued until the end of June [1]. The major purposes of this operation were start-up of each hardware components, establishment of beam operation software and tools, low-emittance and x-y coupling tuning, and background studies with the BEAST detector. The Belle-II group requested an integrated beam dose of 360 to 720 Ah to achieve a very low beam-gas background when the Belle-II detector is installed at Phase 2.

The beam instrumentation has played a very important role at each step of commissioning, such as establishing the circulating orbit in the very early stage of commissioning, accumulating large beam currents, and so on. At the same time the performance of the beam instrumentations has been evaluated by the beam.

In this paper we describe the results of the beam commissioning of SuperKEKB rings with the obtained performance of the beam instrumentations. The main parameters of the Phase 1 operation of SuperKEKB HER/LER and the types and number of main beam instrumentations are shown in Table 1.

OUTLINE OF THE COMMISSIONING

Figure 1 shows the Phase 1 commissioning history [2].

Table1: Main Parameters and Beam Instrumentations of SuperKEKB HER/LER in Phase 1 Operation

	HER	LER
Energy (GeV)	7	4
Circumference(m)	3016	
Max. Beam current (mA)	1010	870
Max. Number of bunches	2455	2363
Single bunch current (mA)	1.04	1.44
Min. bunch separation(ns)	4	
Bunch length (mm)	5	6
RF frequency (MHz)	508.887	
Harmonic number (h)	5120	
Betatron tune (H/V)	44.54/46.56	45.54/43.56
Synchrotron tune	0.02	0.018
T. rad. damping time (ms)	58	43
L. rad. damping time (ms)	29	22
x-y coupling (%)	0.27	0.28
Natural emittance (nm)	3.2	4.6
Beam position monitor	486	444
BPM Displacement sensor	110	108
Gated turn-by-turn monitor	58	59
Transverse FB system	2	2
Longitudinal FB system	0	1
Visible SR size monitor	1	1
X-ray size monitor	1	1
Betatron tune monitor	2	2
DCCT	1	1
CT	1	1
Bunch current monitor	1	1

The commissioning started with the tuning of the beam transfer lines. Injection to the LER started on Feb. 8th and beam was successfully stored on the 10th. The HER

* email address: makoto.tobiyama@kek.jp

ISBN 978-3-95450-177-9

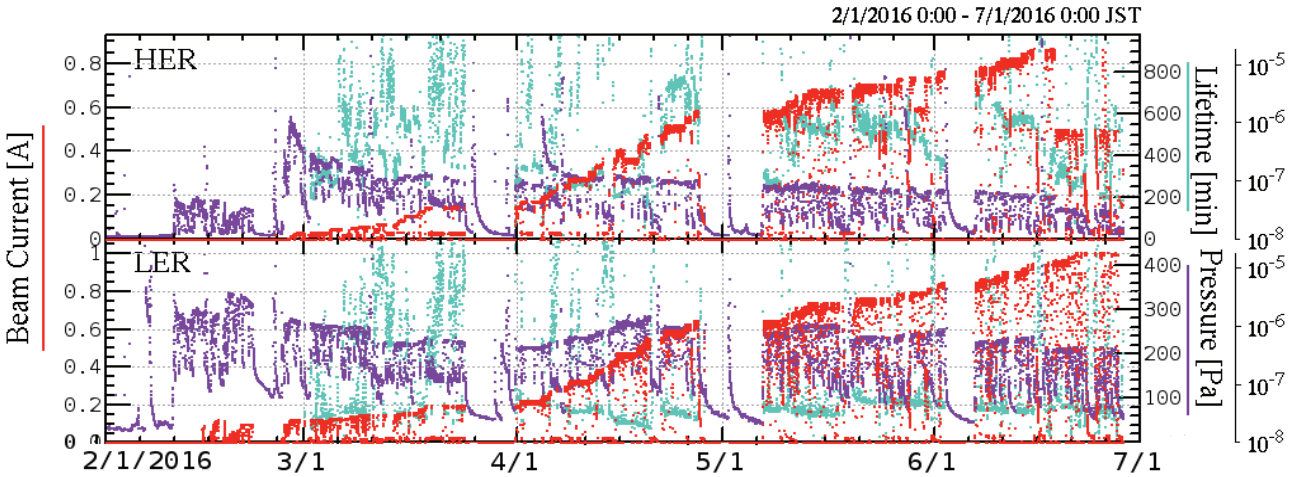

Figure 1: Beam history of Phase 1 operation of SuperKEKB rings. Red: Beam current, Purple: Average vacuum pressure (Pa), Cyan: Beam lifetime (min).

injection tuning started on Feb. 22nd and the beam was stored on the 25th. After the successful beam storage of both rings, we checked the BPM response, corrected the beam optics to reduce deviations from the design, then fairly conservatively increased the beam current, about 20 mA/day while carefully monitoring the status of vacuum components. Maximum beam currents of 1010 mA and 870 mA in LER and HER have been achieved. The integrated beam dose amounted to 768 Ah and 658 Ah for LER and HER, respectively, which fulfil the requirements from the Belle-II Group.

BEAM POSITION MONITORS

Though most of the vacuum chambers including BPM chambers of HER are the same as used in KEKB, we have replaced most of the LER vacuum chambers with an antechamber structure to suppress electron cloud build-up. As the cutoff frequency of the chamber became lower than the detection frequency (1 GHz) of the old narrowband detector used at KEKB [3], we have developed 509 MHz narrowband detectors, and separated the LER and HER detection systems. We have also developed gated turn-by-turn monitors [4,5] inserted between the buttons and the narrowband detectors, which are selectable by the optics group. Figure 2 shows the block diagram of the BPM systems.

Cable connections from BPM heads to the detectors at local control rooms have been checked using the beam. In total, 25 misconnections have been found and one damaged SMA connector has been found. The misconnections have been repaired at the maintenance time during Phase-1 operation. The damaged SMA connector was also replaced after operation.

Button Electrode and BPM Chamber

Most of the BPM chambers and button electrodes in the HER have been reused from KEKB, with the diameter of the button of 12 mm, and the N-type connector. For LER and new HER chambers, a button electrode with a diameter of 6 mm and with reverse-SMA connector has been developed with a flange type structure [6]. The rotation angles of the BPM chambers were measured prior to operation and the RMS value was 0.62 mrad and 0.78 mrad for HER and LER, respectively. This data has been included in the position calculation of the narrowband systems.

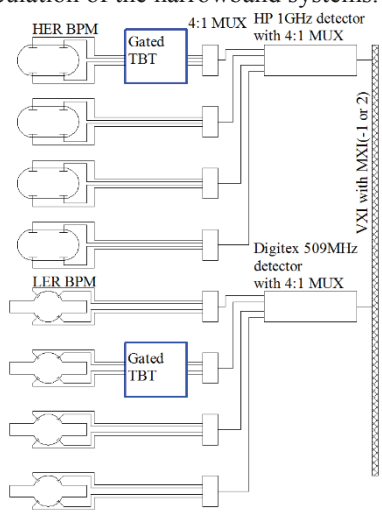

Figure 2: Block diagram of beam position monitors.

Narrowband Systems

The KEKB detectors were 1 GHz super-heterodyne detectors with the form factor of VXI-C. They are re-used in most of the HER BPMs and some of the LER BPMs at RF sections. For new chambers with a lower cut off frequency, new 509 MHz super-heterodyne detectors have been developed and installed.

In the early stage of the commissioning, we have observed an anomalous increase of the detected signal level of 1 GHz detectors around the RF section without beam, which might be caused by leakage fields from the RF high power stations. In the 509 MHz detector, no such signal has been observed, which shows the much better RF shielding characteristics of the new system.

ISBN 978-3-95450-177-9

The gain differences between the four electrodes have been calibrated using the beam with the gain mapping method [7]. Figure 3 shows an example of the result of gain mapping of LER relative to electrode A. Since most of the LER electrodes are installed on the monitor chamber with a flange connection, it shows a somewhat worse distribution than that of the HER, where electrodes were brazed to the monitor chambers. The change of the gains has been monitored by using the "consistency calculation method" where the rms of four beam positions solved by using combination of 3 electrodes were checked. The HER BPM showed worse behaviour where old N-type connectors have been used.

The BPM centers relative to the adjacent quadrupole magnetic centers have been measured by the beam based alignment method. The rms values of the offset (x, y) were 0.570 mm/0.222 mm in LER, and 0.505 mm/0.392 mm in HER. After the correction of the gain and the real center of the BPM, the optics group successfully corrected the beam optics with correction magnets prepared using the model assumptions.

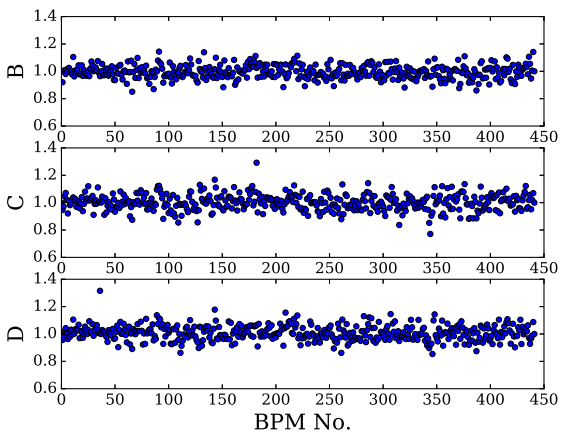

Figure 3: Example of BPM gain mapping of LER relative to electrode A.

The resolution of the narrowband BPM has been measured with the "3-bpm method," which measures correlations of the orbit among three BPMs. Obtained resolution is better than 3 μm and 5 μm in the LER and HER, respectively, for most of the BPMs. As the result will be affected by beam movement between the switching interval of the multiplexer, and as the amplitude of observed real beam motion around 9 Hz was of the order of a few μm, this rather larger value does not representing the real performance of the detector. We have also measured the current dependence of the resolution from 20 mA to 80 mA and found almost no dependence.

Gated Turn-by-Turn Monitor

We have developed the gated turn-by-turn monitor (GTBT) mainly to measure the beam optics (phase advance between the BPMs) during the collision using non-colliding bunch without feedback, and to measure the injection beam orbit [4, 5]. It has four independent channels, each of them consisting of a fast RF switch, a log-ratio beam signal detector, and a 14-bit ADC. A photo of the GTBT is shown in Fig. 4.

Since it is almost impossible to adjust the timing of the GTBTs before the beam circulation of the rings, we at first struggled to adjust the ADC timing with the injection beam with the signal gate fully opened. Also very unfortunately, as the distribution of the GTBT was not dense enough around the injection point, we needed to connect fast oscilloscopes to several BPMs to see the injection beam before the next GTBT. After most of the ADC timings were roughly adjusted, they contributed to tuning injection, especially in the HER where the betatron tune fell into the stopband, preventing longer beam circulation. Figure 5 shows an example of intensity and position of the injected beam in the HER. After beam storage, we adjusted fine ADC and gate timing. The optics measurement with GTBTs using single-bunch beam excitation was also attempted. The analysis is in progress.

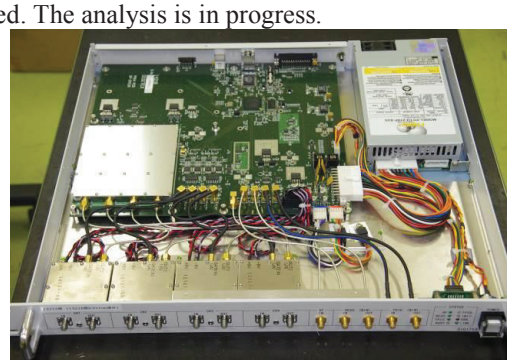

Figure 4: Photo of the gated turn-by-turn detector.

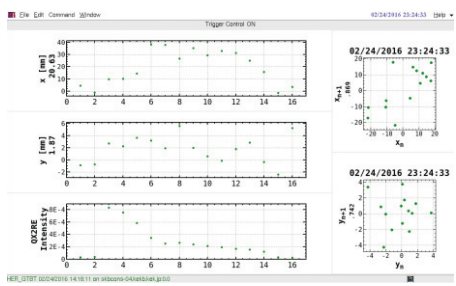

Figure 5: Example of turn-by-turn data at HER injection.

Low frequency beam oscillation was measured in several BPMs with long-duration recording (1.3 s) of the GTBTs. Figure 6 shows an example of an FFT of the vertical beam position of a BPM at a normal arc section. At lower frequency two peaks (9.1 Hz and 16.68 Hz) exist with an amplitude of around 5 μm.

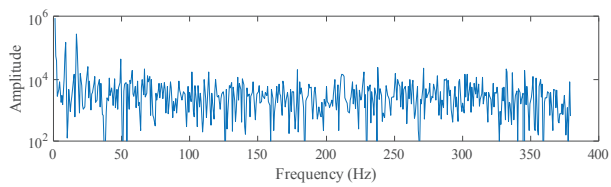

Figure 6: FFT of vertical beam position. Amplitude at 16.68 Hz was about 5 μm.

ISBN 978-3-95450-177-9

BUNCH FEEDBACK SYSTEMS

Figure 7 shows the block diagram of the bunch-by-bunch feedback systems installed in SuperKEKB rings [8]. The system consists of position detection systems, high-speed digital signal processing systems with a base clock of 509 MHz (iGp12 [9]), and wide-band kickers fed by wide-band, high-power amplifiers.

In the very early stage of the commissioning of both rings, we encountered very strong transverse coupled-bunch instabilities which limited the maximum beam currents. We have roughly adjusted the feedback timing including one-turn delay, feedback gain and feedback phase by seeing the beam response on an oscilloscope, then closed one loop per plane on each ring. The instability was successfully suppressed and the beam current was increased fairly smoothly, which contributed greatly to vacuum scrubbing.

During the scrubbing of the LER with a current of more than 660 mA, we encountered an unexpected longitudinal broadband coupled-bunch instability. We quickly tuned the longitudinal feedback system of LER. Though the fine tuning was not optimized, we successfully suppressed the instability up to the maximum beam current of the LER.

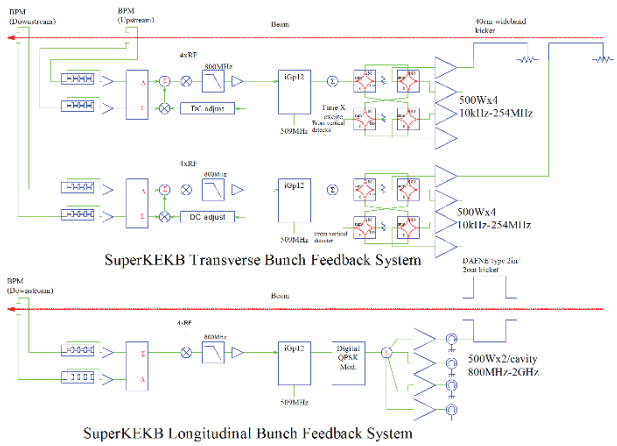

Figure 7: Block diagram of the transverse and longitudinal bunch feedback systems.

After fine-tuning all the feedback components, we made transient-domain measurements of the system [10]. Figure 8 shows an example of the evolution of unstable modes in a grow-damp experiment at the LER with a by-2 filling pattern where the total recording time, FB-off start and FB-off time are 24.72 ms, 2ms and 8ms, respectively. The unstable modes and exponential growth suggest this instability comes from electron-cloud instabilities.

In the HER, the growth time of the instability seemed to be governed by the vacuum condition, not only the mean vacuum pressure but also the worst vacuum pressure in the ring. The slowing-down behaviour of evolution of unstable modes suggests it is caused by ions, such as a fast ion instability. The nominal feedback damping time at the beam current of near 1 A was about 0.5 ms in both rings.

By using the bunch feedback technology, we have prepared the following instrumentation: the bunch current monitor (BCM), the bunch oscillation recorder and the betatron tune monitor. In the BCM, we stopped the recoding with the injection trigger. The ADC data are also written to a reflective memory which automatically transfers the data to the connected board at the bucket selection system, which selects the next injection bucket within 20 ms. With this bunch current equalizer, very flat filling pattern have been realized during Phase 1 operation.

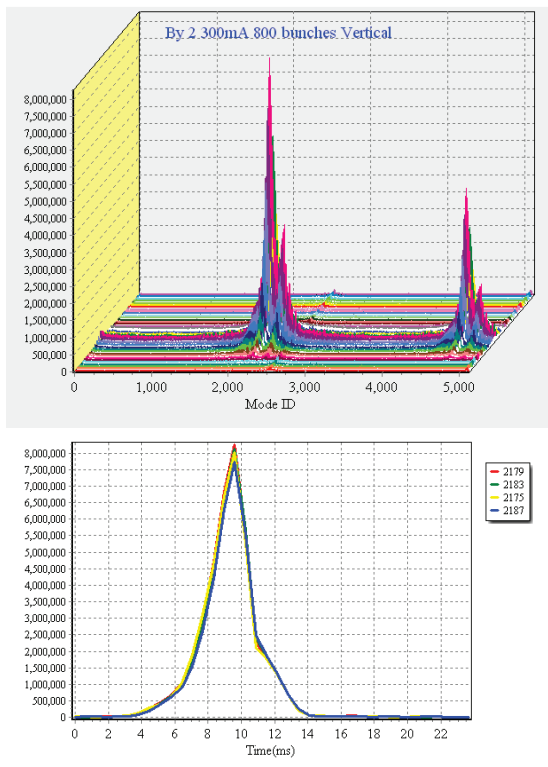

Figure 8: Evolution of vertical unstable modes with by-2 pattern in LER at a current of 300 mA. The growth time constant of mode 2179 was about 1.2 ms and the feedback damping time was about 1.1 ms.

For the betatron tune measurement, during the low beam current, we excite all bunches using the feedback kicker with the frequency down-converted from the tracking generator of a spectrum analyser while monitoring the beam signal from a feedback button electrode. This response becomes wider with the feedback damping so it is not applicable in high beam current conditions of, for example, larger than 50 mA.

In the single bunch measurement, we use an iGp12 to close the phase-locked loop excitation for a selected bunch without feedback damping. The betatron frequency is directly measured by the excitation frequency of the loop.

During operation, we found an increase in the reflected power from several rods of the transverse feedback kickers, which might be the result of rod damage in the kicker. Since the feedback damping was sufficient in the Phase 1 operation, we temporarily changed the power line from amplifier to high power attenuator, and continued the operation. After the end of Phase 1 running we inspected all the

ISBN 978-3-95450-177-9

components by TDR and found loosely connected N-connectors, and damaged high power attenuators. No suspicious symptoms have been found in the kicker and cables. Nevertheless, we are planning to open the kickers to inspect them directly.

PHOTON MONITORS

X-ray Monitor

X-ray monitors (XRMs) are installed in both rings, primarily for vertical beam size measurements. Three sets of optical elements, made of gold masking on diamond substrates, are available at each ring: a single 33 μm slit, a multi-slit coded aperture, and a URA coded aperture [11]. From Phase 2 of SuperKEKB operations, a fast pixel detector for bunch-by-bunch, turn-by-turn measurements is planned. For Phase 1 of SuperKEKB operations, the detector consists of a YAG:Ce scintillator observed by a CCD camera, with which commissioning of the x-ray beam lines and calibration studies [12] were carried out, as well as bunch- and turn-averaged emittance measurements and electron-cloud blow-up studies. Figure 9 shows an example of electron-cloud blow-up data taken at the LER. For details on the calibration studies carried out, see [12], elsewhere in these proceedings. Detailed analysis of calibration data taken during Phase 1 is still underway.

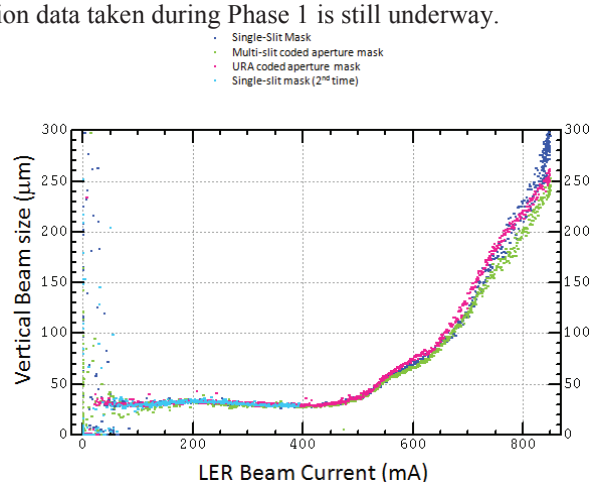

Figure 9. LER Vertical beam size as function of beam current, showing electron-cloud blow-up above 450 μm. Different colors represent data taken with different x-ray optical elements.

Synchrotron Radiation Monitor

The synchrotron radiation monitors (SRMs) use visible synchrotron radiation for use by interferometers, primarily for horizontal beam size measurement, and streak cameras, for bunch length measurement. The visible light lines were commissioned and aligned during Phase 1. Figure 10 shows an example of bunch lengths measured as functions of LER and HER bunch currents.

Large-Angle Beamstrahlung Monitor

A Large-Angle Beamstrahlung Monitor (LABM) has been installed to measure the polarization components of the synchrotron-like radiation emitted by beam-beam collisions, from which mismatches in beam sizes, offsets and orientations can be detected for luminosity tuning. There were no beam collisions in Phase 1, but the LABM system was tested and successfully observed synchrotron radiation that passed through the interaction point from bending magnets upstream of the IP.

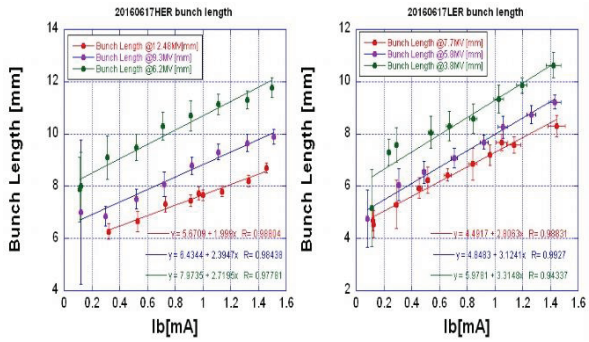

Figure 10: Bunch lengths as functions of bunch currents at HER (left) and LER (right) for different RF voltages. Measurements were made using streak cameras.

SUMMARY

Beam instrumentation systems for SuperKEKB rings have been constructed and commissioned. All the system has shown excellent performance and helped to realize fairly smooth beam commissioning of the rings.

The authors would like to express their sincere appreciation to Dr. A. Drago for his deep contributions of the commissioning. They thank the commissioning group of SuperKEKB for their help in the operation.

REFERENCES

[1] Y. Funakoshi, *et al.*, in proceedings of IPAC 2016, TUOBA01, 2016, Busan, Korea.
[2] Y. Funakoshi, private communication.
[3] M. Arinaga, *et al.*, Prog. Theor. Exp. Phys. (2013) 03A007.
[4] M. Tobiyama, *et al.*, in proceedings of IBIC 2013, MOPF32, 2013, Oxford, GB.
[5] M. Tobiyama, in proceedings of IBIC 2014, WEPD05, 2014, Monterey, CA, U.S.A.
[6] M. Tobiyama, *et al.*, in proceedings of BIW10, TUPSM041, Santa Fe, NM, U.S.A.
[7] M. Tejima, in proceedings of IBIC 2015, TUBLA01, 2015, Melbourne, Australia.
[8] M. Tobiyama, *et al.*, in proceedings of 13th Annual Meeting of Particle Accelerator Society of Japan, TUOM06, Makuhari, 2016, Japan.
[9] DimTel, `http://www.dimtel.com`
[10] J. D. Fox, *et al.*, in proceedings of the 1999 PAC, New York, NY, p.636.
[11] E. Mulyani and J.W. Flanagan, in proceedings of IBIC 2015, Melbourne, p.377 (2015).
[12] E. Mulyani and J.W. Flanagan, TUPG72, in proceedings of IBIC 2016, Barcelona, Spain.

ISBN 978-3-95450-177-9

DIAGNOSTIC SYSTEMS FOR THE PAL-XFEL COMMISSIONING

Changbum Kim*, Sojeong Lee, Gyujin Kim, Bonggi Oh, Haeryong Yang, Juho Hong, Hyo-Jin Choi, Geonyeong Mun, Soungyoul Baek, Dongchul Shin, Youngjin Suh, Byoung Ryul Park, Jihwa Kim, Heung-Sik Kang, and In Soo Ko
Pohang Accelerator Laboratory, POSTECH, Pohang 790-834, Korea

Abstract

In 2011, an X-ray Free-Electron-Laser project was started in the Pohang Accelerator Laboratory (PAL-XFEL). The construction of the PAL-XFEL was finished at the end of 2015, and the commissioning was started from April 2016. The electron beam energy of 10 GeV was achieved at the end of April and the bunch compression was tried in May. The undulator commissioning was started from June. During the commissioning process, various kinds of instruments were used for the beam parameter monitoring including beam position monitors, beam profile monitors, beam charge monitors, beam arrival-time monitors, and beam loss monitors. This work will introduce the PAL-XFEL diagnostic system which was used in the commissioning process.

INTRODUCTION

The PAL-XFEL is a fourth-generation light source to produce hard X-ray radiation with a femto-second pulse width by using the Self Amplification of Spontaneous Emission (SASE) [1]. In the PAL-XFEL, electron beams with 200 pC can be generated from a photocathode RF gun and accelerated to 10 GeV energy by using a 780 m long linear accelerator. After the linear accelerator, the electron beam passes through a 250 m long undulator section to produce hard X-ray of 0.1 nm wavelength. Finally, the FEL radiation come into the beamline of which length is 80 m long. Figure 1 shows a bird's eye view of the PAL site. The PAL-XFEL is shown as a long line in the left and the storage ring of the PLS-II is shown in the right.

The PAL-XFEL building construction was started from September 2012 and it was finished in December 2014. After that, the installation of the linac, the undulator, and the beamline components were continued to the end of 2015 as shown in Fig. 2. The RF conditioning started from November 2015 and it was continued about six months. The commissioning was started in the mid of April 2016, and 10 GeV electron beam was achieved in the end of April. The first spontaneous radiation of the undulator was obtained on 12th of June, and the first SASE FEL was observed on 14th of June 2016. The wavelength of the SASE FEL radiation was 0.5 nm with the electron beam energy of 4 GeV.

For the successful commissioning of the PAL-XFEL, various kinds of diagnostics along the linac and undulator section were used to measure beam parameters such as the beam position, the beam charge, the beam size, the bunch length, et cetera. These parameters for the beam operation and instruments for measurements of them are listed in Table 1. In this paper, diagnostic system of the PAL-XFEL will be presented. It will include the beam position monitor, the beam profile monitor, the beam charge monitor, the beam arrival-time monitor, and the beam loss monitor.

Figure 1: A bird's eyes view of the PAL. The PAL-XFEL and the PLS-II are shown in the left and the right, respectively.

PAL-XFEL DIAGNOSTICS

Beam Position Monitor

Figure 3 shows the stripline Beam-Position-Monitor (BPM) pickup of the PAL-XFEL. For the beam operation of an accelerator, it is important that the electron beam passes through the center of the quadrupole magnet to keep the beam shape symmetrically, and to make the orbit close to the ideal one as much as possible. In the PAL-XFEL, stripline BPMs were installed along the linear accelerator to monitor the beam position inside the vacuum chamber. The measured resolution of the stripline BPM was 3 μm. For the BPM

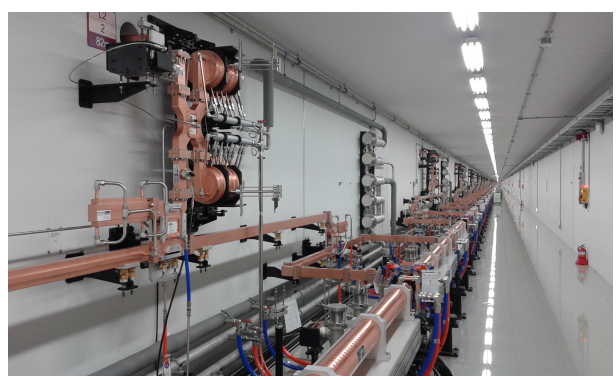

Figure 2: Accelerating structures inside the PAL-XFEL linac tunnel.

* chbkim@postech.ac.kr

ISBN 978-3-95450-177-9

Table 1: Operation Parameters and Measurement Instruments for the PAL-XFEL

Parameter	Instrument
Beam Position	Stripline BPM
	Cavity BPM (Undulator)
Beam Size	Screen Monitor
	Wire Scanner
Bunch Length	Transverse Deflecting Cavity
	Coherent Radiation Monitor
Beam Charge	Turbo-ICT
Beam Arrival Time	Beam Arrival-Time Monitor
Beam Loss	Beam Loss Monitor (Undulator)

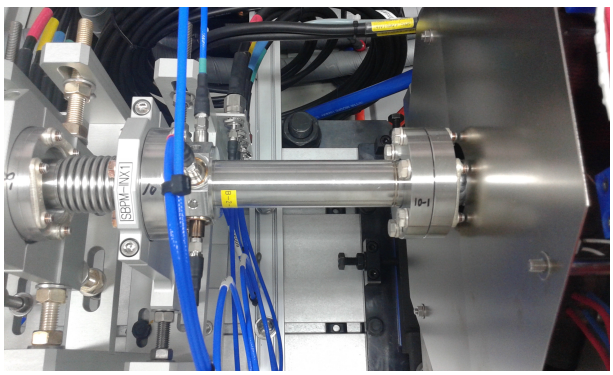

Figure 3: A stripline BPM of the PAL-XFEL linac.

electronics, μTCA-based digital electronics were prepared under the collaboration with the SLAC [2].

In the undulator section, cavity BPMs were installed because of their good resolution. The resolution of the cavity BPM is less than 1 μm so that it can be used for the beam alignment in the undulator section where the electron beam and the radiation should be overlapped, precisely. The PAL and the SLAC have been collaborated for the development of the X-band cavity BPM since 2013 [3]. The cavity BPM pickup was developed in the PAL and the electronics was made in the SLAC. Figure 4 shows a cavity BPM pickup in the PAL-XFEL [4].

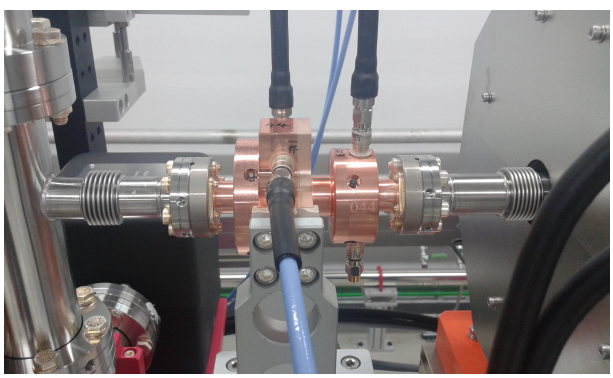

Figure 4: A cavity BPM of the PAL-XFEL undulator section.

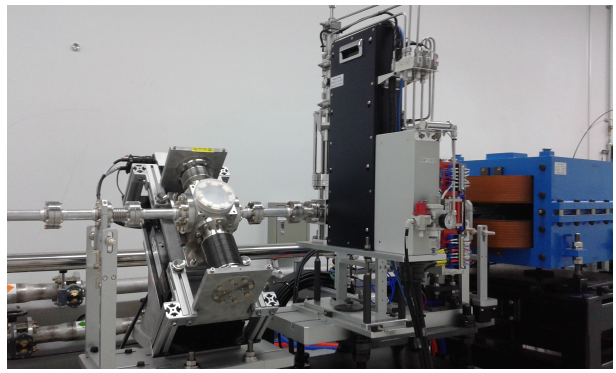

Figure 5: A wire scanner (left) and a screen monitor (right) to measure the transeverse beam profile.

Transverse Profile Monitor

Figure 5 shows a wire scanner (left) and a screen monitor (right) for the transverse profile measurement. In the screen monitor, a two-step pneumatic actuator was used to inject the target holder to the electron beam trajectory. Two kinds of target can be mounted in the target holder for the beam profile imaging. One is a YAG:Ce scintillator and the other is an Al-foil OTR target. The target size is one inch and the thickness is 100 μm and 1 μm for the YAG:Ce and Al-foil, respectively.

The target holder was specially designed to remove the Coherent-Optical-Transition-Radiation (COTR) by using a method developed in the SwissFEL and the European XFEL [5]. The OTR has a very small opening angle with the high energy electron beam, so that the OTR can be avoided if the reflection mirror is miss aligned slightly from the OTR propagation direction. The scintillation light from the YAG:Ce target without the OTR can be reflected to the CCD camera.

In the wire scanner, a tungsten (18 μm thickness) and carbon (34 μm thickness) wires were used in the linac and the undulator section, respectively. The wire is fixed on a frame which is mounted on a 45° tilted translation stage. A linear motor is used in the translation stage to minimize the vibration while the translation stage moving. Simple optical fibers, which were connected to Photo Multiplier Tubes (PMTs), were installed for detectors downstream of the wire scanner.

Longitudinal Profile Monitor

For the bunch length measurement, transverse deflecting cavities, from the RadiaBeam Technologies and the VITZROTECH, were installed after bunch compressors as shown in Fig. 6. The transverse deflecting cavity looks like a normal accelerating column, however, it can generate a transverse kick to the electron beam instead of a longitudinal one. Because of the transverse kick, the head and the tail of the electron beam moves to the plus and the minus direction of the vertical axis, respectively. In this way, time information of the bunch length can be converted to space information of the beam size, and the electron beam makes

ISBN 978-3-95450-177-9

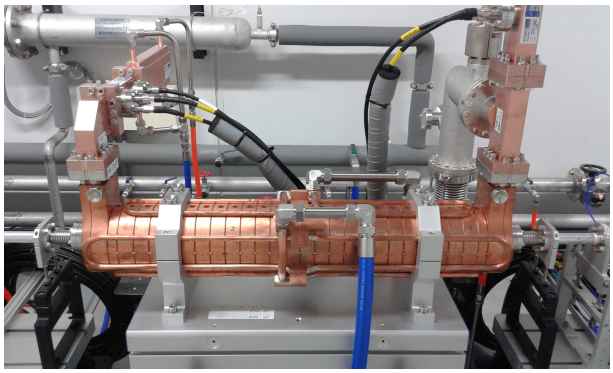

Figure 6: A deflecting cavity for the measurement of the longitudinal bunch length.

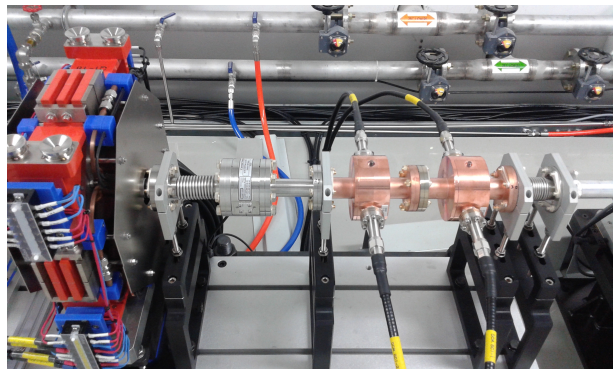

Figure 7: A Turbo-ICT and beam arrival-time monitors of the PAL-XFEL linac.

a long profile image which is corresponding to the bunch length.

Even though the transverse deflecting cavity can measure the absolute bunch length, one should kick the electron beam to the vertical direction and block it to get the beam image for the bunch length measurement. For a non-destructive monitoring of the bunch length, coherent radiation monitors were installed after bunch compressors to measure the relative bunch length.

After the bunch compressor, one can find several kinds of radiation, such as synchrotron radiation, edge radiation, diffraction radiation, et cetera, and their intensities are inversely proportional to the bunch length. Thus, the relative bunch length can be obtained by monitoring the radiation intensity.

A gold coated mirror was installed inside the vacuum chamber after the last bending magnet of the bunch compressor. Reflected radiation is guided into a detector chamber and focused into a pyro detector by using a parabolic mirror. The pyro detector can measure the radiation intensity in the range of the infrared wavelength.

Beam Charge Monitor

Turbo Integrated-Charge-Transformers (Turbo-ICTs) from the Bergoz Instrumentation were installed for the beam charge measurement. The Turbo-ICT has less than 1 pC resolution and showed a good performance for the PAL-XFEL commissioning. Figure 7 shows a Turbo-ICT and beam arrival-time monitors of the PAL-XFEL linac.

Beam Arrival-Time Monitor

One of the advantage of the PAL-XFEL is that a pump-prove experiment is possible. The laser pump excite the sample and the FEL prove can detect the change of the sample. In that case, beam arrival time relative to the reference trigger is important information for the experiment.

The beam arrival-time monitor has a simple cavity structure. When the electron beam passes through it, S-band resonance signal can be generated and IF signal is obtained after a mixing with the reference signal. The IF frequency comes into an Analog Digital Converter (ADC) to analyze the phase and the amplitude. If the electron beam is synchronized with the reference signal exactly, then the phase of the IF signal will remain constant. In this way, the phase jitter gives us information of the arrival time jitter with a 20 fs resolution.

Beam Loss Monitor

Continuous exposure to high energy electron beams can change the magnetic property of the undulator permanent magnet. Thus, we installed a beam loss monitor before every undulator to monitor the beam loss. The beam loss monitor consists of two acrylic (Polymethyl methacrylate, PMMA) rods and two PMT modules. Two rods were transversely installed above and below the vacuum chamber and Cherenkov radiation can be generated in the case of the beam loss. The amplitude of Cherenkov radiation is amplified with the PMT module and measured by using an ADC.

SUMMARY

The PAL-XFEL project was started 2011 and finished at the end of 2015. The commissioning was started in April 2016 and the first SASE FEL was observed at the end of June. For the successful commissioning, various kinds of diagnostic instruments were installed in the PAL-XFEL to measure the beam position, the beam charge, the beam size and the bunch length. The beam arrival time and the beam loss were monitored as well.

REFERENCES

[1] H.S. Kang, K.-W Kim, I.S. Ko, in proceedings of IPAC2015, Richmond, VA, USA, 2439 (2015).

[2] C. Xu, S. Allison, S. L. Hoobler, D.J. Martin, J.J. Olsen, T. Straumann, A. Young, H.-S. Kang, C. Kim, S.J. Lee, G. Mun, in proceedings of IBIC2014, Monterey, CA, USA, 680 (2014).

[3] A. Young, J. Dusatko, S. Hoobler, J. Olsen, T. Straumann, C. Kim, in Proceedings of IBIC2013, Oxford, UK, 735 (2013).

[4] S. Lee, Y. J. Park, C. Kim, S. H. Kim, D. C. Shin, J.-H. Han, I. S. Ko, NIMA, **827**, 107 (2016).

[5] R. Ichebeck, E. Prat, V. Thominet, and C. O. Loch, Phys. Rev. ST Accel. Beams **18**, 082802 (2015).

ISBN 978-3-95450-177-9

FIRST EXPERIENCE WITH THE STANDARD DIAGNOSTICS AT THE EUROPEAN XFEL INJECTOR

D. Lipka*, A. Affeldt, R. Awwad, N. Baboi, R. Barret, B. Beutner, F. Brinker, W. Decking, A. Delfs, M. Drewitsch, O. Frank, C. Gerth, V. Gharibyan, O. Hensler, M. Hoeptner, M. Holz, K. Knaack, F. Krivan, I. Krouptchenkov, J. Kruse, G. Kube, B. Lemcke, T. Lensch, J. Liebing, T. Limberg, B. Lorbeer, J. Lund-Nielsen, S. Meykopff, B. Michalek, J. Neugebauer, Re. Neumann, Ru. Neumann, D. Noelle, M. Pelzer, G. Petrosyan, Z. Pisarov, P. Pototzki, G. Priebe, K. Rehlich, D. Renner, V. Rybnikov, G. Schlesselmann, F. Schmidt-Foehre, M. Scholz, L. Shi, P. Smirnov, H. Sokolinski, C. Stechmann, M. Steckel, R. Susen, H. Tiessen, S. Vilcins, T. Wamsat, N. Wentowski, M. Werner, C. Wiebers, J. Wilgen, K. Wittenburg, R. Zahn, A. Ziegler,
DESY, Hamburg, Germany
O. Napoly, C. Simon, CEA Saclay, France
A. Ignatenko, DESY, Zeuthen, Germany
R. Baldinger, R. Ditter, B. Keil, W. Koprek, R. Kramert, G. Marinkovic, M. Roggli, M. Stadler, D. M. Treyer, PSI, Villigen, Switzerland†
A. Kaukher, European XFEL, Hamburg, Germany

Abstract

The injector of the European XFEL started beam operation in December 2015. Besides the gun and the accelerating section, containing a 1.3 and a 3.9 GHz accelerating module, it contains a variety of standard diagnostics systems specially designed for this facility. With very few exceptions, all types of diagnostics systems of the whole XFEL are installed in the injector. Therefore the injector operation allows validating and proving of the diagnostics performances for the entire facility. Most of the standard diagnostics have been available from the very beginning of the beam operation and have been used for the monitoring of the first beam. In the following months the diagnostics have been optimized and used for improvements of beam quality. In this contribution, the first results and the operation experience of the standard beam diagnostics of the European XFEL are reported.

INTRODUCTION

The European X-ray Free-Electron Laser (E-XFEL) [1] is the 3.4 km long international facility, running from DESY in Hamburg to the town of Schenefeld (Schleswig-Holstein) in Germany. To construct and operate the E-XFEL, international partners agreed on the foundation of an independent research organization – a non-profit limited liability company under German law named the European XFEL GmbH. DESY is leading the accelerator construction consortium and will be in charge of the accelerator operation.

The accelerator is based on superconducting TESLA Radio-Frequency (RF) technology. Within one RF pulse of up to 600 μs length, a train with up to 2700 bunches will be generated. This results in a bunch minimal spacing of 222 ns. The repetition rate of the RF pulses is 10 Hz, so that a maximum number of 27000 X-ray pulses per second can be produced. The operation charge varies from 20 pC to 1 nC to provide different characteristics of the output radiation, i. e. the average power or the bunch length, as requested by the users. Therefore diagnostics components have to monitor the beam properties within this dynamic range.

Beam operation of the photocathode gun started already in February 2015, the complete injector became operable in December 2015. In this first accelerator part of the facility, several diagnostics systems are installed, commissioned and have been optimized for the measurement of the electron beam properties. This paper focuses on standard electron beam diagnostics for the E-XFEL injector. Special and higher-order mode diagnostics systems are described in [2–8].

STANDARD DIAGNOSTICS FOR THE EUROPEAN XFEL

The standard diagnostics contains a variety of position, charge and loss monitors and screen stations. It is also planned to use wire scanners at positions with high electron energies. The full list of monitoring systems is given in Table 1. A description of the different systems with results of their laboratory and beam tests can be found in [9–24].

Table 1: Diagnostics System Numbers for the Complete E-XFEL and for the Gun with Injector

System	Total number	Gun and injector
BPMs	~460	14
Charge monitors	~50	10
Screens	~70	11
Wire scanners	12	0
Loss monitors	~490	20

* dirk.lipka@desy.de
† This work was partially funded by the Swiss State Secretariat for Education, Research and Innovation SERI

ISBN 978-3-95450-177-9

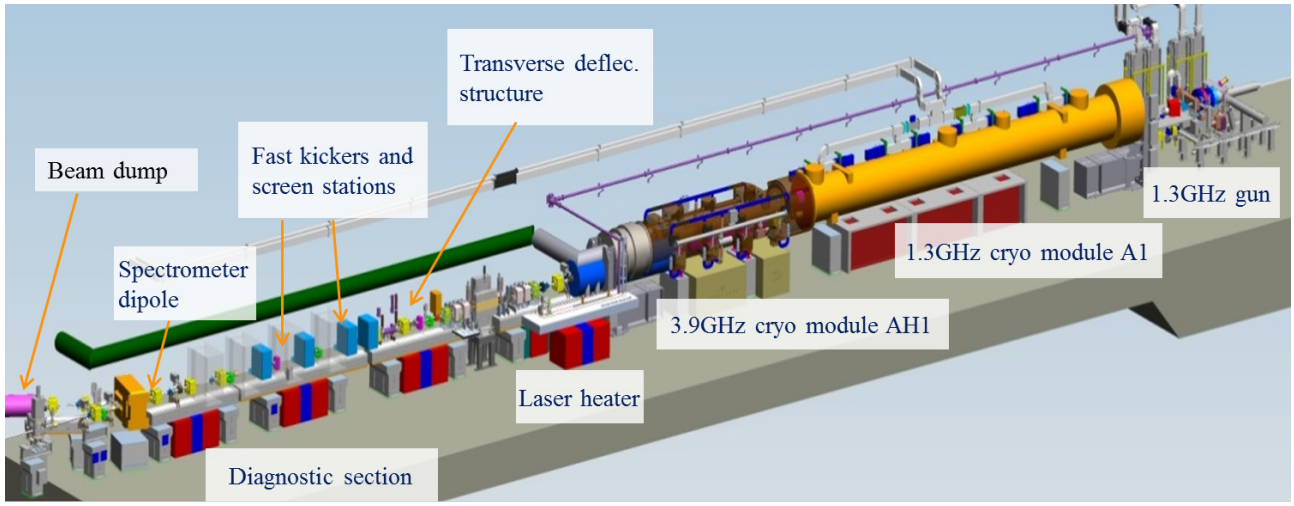

Figure 1: Scheme of the E-XFEL injector and its subsystems. The beam starts at the gun on the right and is stopped in the injector beam dump on the left. Total length of the shown section is 41m.

All sub systems are installed and used in the E-XFEL injector, except wire scanners. Therefore the commissioning and validation of the diagnostics systems in the real environment is possible before the commissioning of the entire facility.

THE INJECTOR

The E-XFEL injector consists of a normal conducting photocathode RF-gun followed by a standard 1.3 GHz XFEL superconducting module, as shown in Fig. 1. The module contains 8 Niobium cavities and accelerates the beam to about 150 MeV/c. Between gun and module, a first section with gun diagnostics is installed, containing 3 Beam Position Monitors (BPMs), a Toroid, a dark current monitor, 3 screen stations, 4 Faraday cups and beam loss monitors. The 1.3 GHz module is followed by a superconducting 3.9 GHz module, which is used to optimize the longitudinal phase space [25, 26]. In the standard setting it decelerates the beam by 20 MeV, so that the final electron energy from the injector is 130 MeV. In each module a *cold* BPM is installed. The *cold* section is followed by a diagnostics section, see Fig. 1. The diagnostics section allows measuring the complete 6-dimensional phase space properties of the electron bunch. More details of the injector can be found in [27].

Chronological Order of Beam Commissioning

The operation of the photocathode RF-gun started in the end of 2013 with a conditioning process. On usual working days the installation of the gun diagnostics and following components continued. The first standard diagnostics system of the E-XFEL, which has detected field-emitted electrons along the RF pulse in 2014, was the dark current monitor (DaMon) [17]. Also the screen stations could identify the dark current. The first beam operation started February 2015, with operating the Toroid and the BPM systems, such that the charge and the position of the beam could be monitored immediately. The beam was transmitted to a dispersive section that provides a dump in the gun area, with screen station, BPM and Faraday cup to measure the beam momentum.

In 2015, the installation of the injector continued with the cooling down of the modules and it accomplished on December 15th, with all accelerator cavities tuned to resonance on December 18th. On the same day, the beam was transmitted to the injector dump within few hours. Even this first transmission was detected by the diagnostics systems, with the Toroids and the BPMs available from the first shot. Three days later the first emittance measurement was performed with the screen stations. Until July 2016, the operation continued for the full characterization and optimization of the beam properties. Currently the injector is switched off and is warmed up to prepare the cryo system for the cooling down of the entire facility.

Diagnostics Setup and Experience from the Injector Commissioning and Optimization

Beam Position Monitors Button and cavity BPMs [10–15] with single-bunch detection are used, such that each bunch with 222 ns spacing can be measured. Button BPMs with an aperture of 40.5 mm are the *working horse* along the E-XFEL beamline. Variants with apertures between 34 mm and 200 mm are used to adapt to the adjacent beam pipes. Cavity BPMs are used in the undulator intersection with 10 mm aperture and at dedicated positions where a better resolution is requested, e. g. for the intra-bunch feedback system [28], with the standard 40.5 mm aperture. Inside of each superconducting module, BPMs with aperture of 78 mm are installed, where 30 % of these *cold* BPMs are of reentrant type [14], and the others are button BPMs. The complete BPM system including electronics is an in-kind contribution of CEA Saclay, DESY and PSI [29]. The pick-ups are developed at DESY (buttons and cavities) and CEA (reentrant cavities); the electronics, firmware and software for all BPMs is developed at PSI, except for the reentrant front-end electronics provided by CEA. The information

ISBN 978-3-95450-177-9

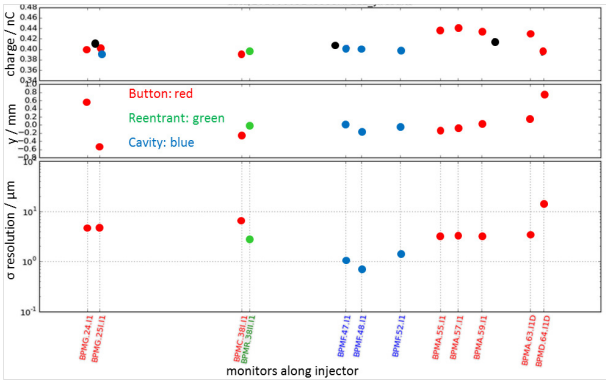

Figure 2: Measured charge values, positions and single bunch position resolution of the BPMs along the E-XFEL injector. The gun is on the left and the dump on the right side. The resolution was obtained by correlating the readings for 1000 bunches; the error bars are covered by the symbols. Therefore, a very stable operation is observed. Beam pipe apertures: BPMG 34 mm; BPMC, BPMR 78 mm; BPMF, BPMA 40.5 mm; BPMD 100 mm. The BPMG signals are attenuated by 6 dB remnant needed to protect the electronics during early gun tests.

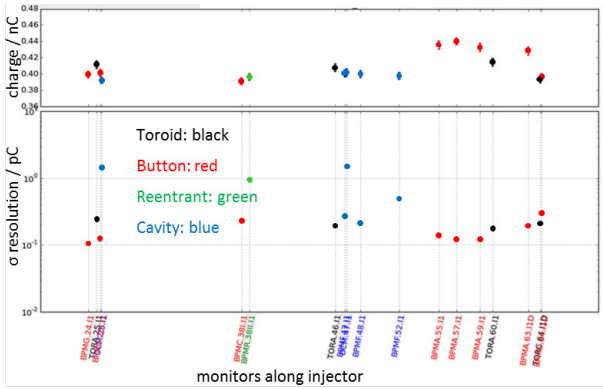

Figure 3: Measured charge values and single bunch charge resolutions from non-destructive charge monitors along the E-XFEL injector, the gun is on the left and the dump on the right side. The resolution was obtained by correlating the readings for 1000 bunches; the error bars are covered by the symbols. The data from cavity BPMs and DaMons are shown in blue.

about the position and charge from a BPM system is read by µTCA crates via a FPGA-to-FPGA bridge using optical fibers. The timing signals are connected by optical fibers as well. For the first beam the BPMs are used in self-trigger mode: if the ADC amplitude exceeds a given threshold, the data is treated as signal and the bunch is detected. In this mode, the first beam can be monitored independently of the timing system. Once the delay between beam and timing signal is measured (by the BPM electronics itself), the externally-triggered mode is used to improve the performance of the BPMs. Cavity BPMs need more adjustment for better performances (phase matching between signals from reference and dipole resonators). A pre-calibration of the front ends is made beforehand in the laboratory, and for cavities also by beam measurements at FLASH, such that all BPM are well-configured and operational before the first beam appears [10, 12, 15]. The BPM performance has been verified by cross correlation of each BPM to all the others, as depicted in Fig. 2, for details see [30]. In this example at a charge of about 0.4 nC, the position resolution is below 7 μm for button BPMs (except the last one in the dump line with larger aperture of 100 mm), for the reentrant BPM it is about 3 μm and for the cavity BPMs the resolution reaches about 1 μm.

Charge Monitors Thirty-five Toroids are distributed along the E-XFEL beamline, 4 of them are installed in the injector [16]. These are conventional current transformers, consisting of a ferrite core with windings around a ceramic gap in the pipe. The calibration is performed with additional windings and test signals; that can be used for self-test too. Like the BPMs the Toroids can run in self-trigger mode, and provide a measurement of the beam delay with respect to the timing system trigger. Like for the BPMs, first beam detection in self-triggered mode was successfully used. In addition, 9 dark current monitor (DaMon) systems [17] are distributed along the E-XFEL to measure the transmission of the dark current (2 of them in the injector); this device is able to detect the beam charge as well. Four destructive Faraday cups are installed in the gun diagnostics section. In Fig. 3, the resolutions of Toroids, BPMs and DaMons are shown. The reason of the charge difference is caused by non-perfect calibration of the devices. The resolutions are mostly below 1 pC, therefore these devices are capable to measure charges down to this level. Within the first half year of the operation in 2016, an integrated charge of 3 C was transmitted to the dump, mainly in some long bunch train runs, to test operation with 27000 bunches per second.

Beam Loss and Halo Monitors A beam loss monitor (BLM) is based on 4 scintillator pieces read out by photomultipliers [22]. The 490 BLMs are distributed along the electron beamline of the E-XFEL. These monitors are capable to detect the dark current and single bunch losses. In case the signal exceeds a threshold, an alarm is sent to the machine protection system (MPS). The analog signal processing and analog-to-digital conversion is performed in a rear transition module of a μTCA board. Various alarms are processed using fast digital signal processing in an FPGA AMC board that is connected to the MPS system. For safety reasons, an analog comparator based alarm is provided too. Fig. 4 shows an example of a BLM signal. The shown signals are mostly produced by dark current, one exceeds the threshold and indicates an (integration) alarm. Beam Halo monitor (BHM) consists of four diamond and four sapphire sensors operating as solid-state ionization chambers [23]. A BHM is installed in the injector dump section, three more

ISBN 978-3-95450-177-9

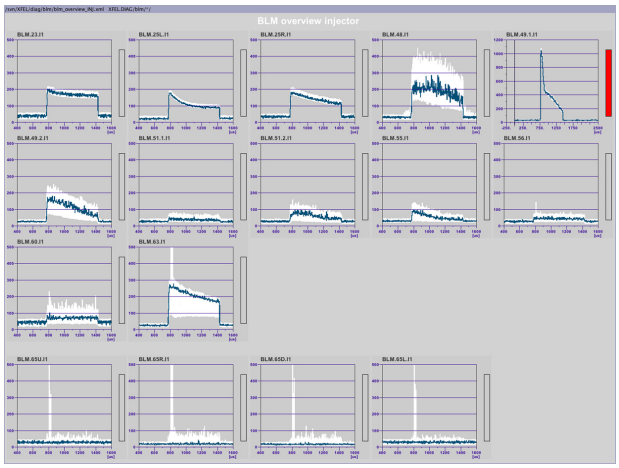

Figure 4: Display of the beam loss monitors during beam operation. Most of the monitors show the continuous dark current background, one BLM.49 produces an alarm (indicated in red). The BLMs in the dump line (bottom row) show in white color history data from previous trains.

BHMs are at the main dumps. They are capable to detect both beam losses on a bunch-by-bunch basis and dark current. Diamond sensors provide higher sensitivity, whereas sapphire sensors remain operational at higher intensities of impinging particles. The signal processing and electronics are similar to those of the BLMs.

Dosimetry The γ radiation is measured due to RadFets with rack-internal and external sensors [24]. The internal sensors are hosted on plug-in readout modules according to FPGA Mezzanine Card (FMC) standard. These modules are directly connected to the FMC carrier slots of the MPS μTCA electronics or the PSI BPM electronics. Online radiation monitors are distributed in critical sections along the accelerator. The external sensors are distributed at dedicated position along the E-XFEL and are connected via field bus system. The majority of sensors are installed in the undulator, where two sensors are fixed at the entrance of the magnetic structure. This system has the option of extension by Neutron dosimetry. During the E-XFEL injector operation, few sensors showed the integrated radiation at dedicated positions.

Screens The scintillating screen with 200 μm thick LYSO:Ce targets are oriented such that coherent optical transition radiation generated at the screen boundaries will geometrically be suppressed by an observation angle of 45 °. An additional feature is that the imaging optics operates in Scheimpflug condition, thus adjusting the plane of sharp focus with respect to the CCD chip. This significantly increases the apparent depth of field and the well-focused field of view. At each motorized station one full and one half filled screen (on- and off-axis) can be inserted. A grid for calibration is mounted on the screen mover too. Depending on the requirements, different optical systems are used for the screen stations. One provides 1:1 imaging, the other one reduces the screen image by a factor of two. Basler Aviator cameras are installed for good image resolution. The main system with 1:1 imaging reaches a resolution $\leq$10 μm [18]. In the following, measurements with these screen stations are described.

Highlights: Emittance along Bunch Train and TDS Operation

The emittance is measured through analysis of the beam images using the screen stations. Four stations within a FODO lattice with on-axis screens and quadrupole scans are used. Further, in order to perform the emittance measurements during long bunch train operation, a single bunch can be deflected from the train towards the off-axis screens by using fast kickers. This is demonstrated in Fig. 5. This offers additional possibility of emittance measurements during user operation, since a single bunch of one train and the train evolution can be investigated. The measurement can be performed at 2.5 Hz repetition rate. These measurements have been successfully performed routinely during the long bunch train operation of the injector.

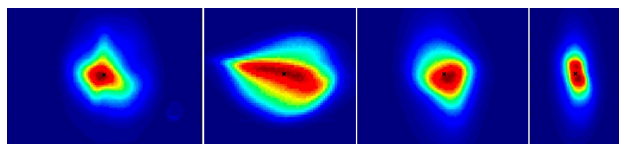

Figure 5: Four transverse images of kicked beams to off-axis screens for emittance measurements.

The main tool for longitudinal phase space diagnostics is the Transverse Deflecting Structure (TDS) [4]. A single bunch of a train is streaked and in the following kicked towards the off-axis screens. As a result, one axis on the image corresponds to the longitudinal dimension of the bunch. Several measurements were performed during E-XFEL injector operation in June and July 2016 such that the slice emittance could be measured and optimized.

SUMMARY

The standard diagnostics of the E-XFEL injector has been ready for beam property measurements since the first day of beam operation and the beam properties are investigated. All design values of the standard diagnostics could be achieved. BPMs and Toroids can be used in self-trigger as well as in externally-triggered mode for better performance. The resolution requirements are fulfilled. The dark current monitors are useful to measure both, dark current and beam charge. Online monitors of beam loss, halos and radiation dose are installed and operational. Screen stations are used with on- and off-axis screens. The latter one is useful during long bunch train operation to prove the beam properties during user operations by observing one bunch out of the whole train.

ISBN 978-3-95450-177-9

OUTLOOK

The E-XFEL installation in the main accelerator tunnel is nearly finished. The electronics installation and technical commissioning of the linac should be finished in September 2016. BPMs and charge monitors are laboratory-calibrated and the results are compared with those in injector-operation. These devices will start in self-triggered mode to detect the first beam, with later usage in the triggered-mode to improve their performance. All screen stations are being installed and calibrated. BLM, BHM and dosimetry are ready for online monitoring using default thresholds. Cooling down of the superconducting modules is scheduled for October 2016, with first beam expected end of 2016. Remaining parts of the beamlines will be commissioned in the beginning of 2017. First lasing will be possible in April 2017.

ACKNOWLEDGEMENT

The authors thanks all colleagues who contributed to this project.

REFERENCES

[1] M. Altarelli *et al.*, "The European X-Ray Free-Electron Laser", technical design report, 2007, http://www.xfel.eu/en/documents/

[2] C. Gerth, "Electron Beam Diagnostics for the European X-Ray Free-Electron Laser", proceedings of DIPAC 2007, http://accelconf.web.cern.ch/AccelConf/d07/papers/moo2a02.pdf

[3] M. Roehrs and C. Gerth, "Electron Beam Diagnostics with Transverse Deflecting Structures at the European X-Ray Free Electron Laser", proceedings of FEL 2008, http://accelconf.web.cern.ch/AccelConf/FEL2008/papers/mopph049.pdf

[4] J. Wychowaniak *et al.*, "Design of TDS-based Multi-screen Electron Beam Diagnostics for the European XFEL", proceedings of FEL 2014, http://accelconf.web.cern.ch/AccelConf/FEL2014/papers/thp075.pdf

[5] M. K. Czwalinna *et al.*, "New Design of the 40 GHz Bunch Arrival Time Monitor Using MTCA.4 Electronics at FLASH and for the European XFEL", proceedings of IBIC 2013, http://accelconf.web.cern.ch/AccelConf/IBIC2013/papers/wepc31.pdf

[6] C. Gerth *et al.*, "MicroTCA.4 Based Optical Frontend Readout Electronics and Its Applications", these proceedings 2016, MOPG14

[7] M. Yan and C. Gerth, "Single-bunch Longitudinal Phase Space Diagnostics in Multi-bunch Mode at the European XFEL", proceedings of IBIC 2013, http://accelconf.web.cern.ch/AccelConf/IPAC2013/papers/mopme012.pdf

[8] N. Baboi *et al.*, "HOM Characterization for Beam Diagnostics at the European XFEL Injector", these proceedings 2016, WEPG03

[9] D. Lipka *et al.*, "Standard Electron Beam Diagnostics for the European XFEL", proceedings of FEL 2011, http://accelconf.web.cern.ch/AccelConf/FEL2011/papers/thpa25.pdf

[10] M. Stadler *et al.*, "Low-Q Cavity BPM Electronics for E-XFEL, FLASH-II and SwissFEL", proceedings of IBIC 2014, http://accelconf.web.cern.ch/AccelConf/IBIC2014/papers/wepd12.pdf

[11] D. Lipka *et al.*, "Development of Cavity BPM for the European XFEL", proceedings of LINAC 2010, http://accelconf.web.cern.ch/AccelConf/LINAC2010/papers/tup094.pdf

[12] D. M. Treyer *et al.*, "Design and Beam Test Results of Button BPMs for the European XFEL", proceedings of IBIC 2013, http://accelconf.web.cern.ch/AccelConf/IBIC2013/papers/wepc21.pdf

[13] C. Simon *et al.*, "New Electronics Design for the European XFEL Re-entrant Cavity Monitor", proceedings of IBIC 2012, http://accelconf.web.cern.ch/AccelConf/IBIC2012/papers/mopa15.pdf

[14] C. Simon *et al.*, "Production Process for the European XFEL Re-Entrant Cavity BPM", proceedings of IBIC 2014, http://accelconf.web.cern.ch/AccelConf/IBIC2014/papers/tupf05.pdf

[15] C. Simon *et al.*, "Design and Beam Test Results of the Reentrant Cavity BPM for the European XFEL", these proceedings 2016, TUPG17

[16] M. Werner *et al.*, "A Toroid Based Bunch Charge Monitor System with Machine Protection Features for FLASH and XFEL", proceedings of IBIC 2014, http://accelconf.web.cern.ch/AccelConf/IBIC2014/papers/wepf02.pdf

[17] D. Lipka *et al.*, "Dark Current Monitor for the European XFEL", proceedings of DIPAC 2011, http://accelconf.web.cern.ch/AccelConf/DIPAC2011/papers/weoc03.pdf

[18] C. Wiebers *et al.*, "Scintillating Screen Monitors for Transverse Electron Beam Profile Diagnostics at the European XFEL", proceedings of IBIC 2013, http://accelconf.web.cern.ch/AccelConf/IBIC2013/papers/wepf03.pdf

[19] G. Kube *et al.*, "Transverse Beam Profile Imaging of Few-Micrometer Beam Sizes Based on a Scintillator Screen", proceedings of IBIC 2015, http://accelconf.web.cern.ch/AccelConf/IBIC2015/papers/tupb012.pdf

[20] T. Lensch *et al.*, "Wire Scanner Installation into the MicroTCA Environment for the European XFEL", proceedings of IBIC 2014, http://accelconf.web.cern.ch/AccelConf/IBIC2014/papers/mopf13.pdf

[21] V. Gharibyan *et al.*, "Twisting Wire Scanner", proceedings of IBIC 2012, http://accelconf.web.cern.ch/AccelConf/IBIC2012/papers/thcb02.pdf

[22] A. Kaukher *et al.*, "XFEL Beam Loss Monitor System", proceedings of BIW 2012, http://accelconf.web.cern.ch/AccelConf/BIW2012/papers/mopg007.pdf

[23] A. Ignatenko *et al.*, "Beam Halo Monitor for FLASH and the European XFEL", proceedings of IPAC 2012, http://accelconf.web.cern.ch/AccelConf/IPAC2012/papers/moppr018.pdf

[24] F. Schmidt-Foehre *et al.*, "Commissioning of the New Online-Radiation-Monitoring-System at the New European XFEL Injector with First Tests of the High-

ISBN 978-3-95450-177-9

Sensitivity-Mode for Intra-Tunnel Rack Surveillance", proceedings of IBIC 2015, http://accelconf.web.cern.ch/AccelConf/IBIC2015/papers/wecla02.pdf

[25] C. Maiano *et al.*, "Status of the Fabrication of the XFEL 3.9 GHz Cavity Series", proceedings of IPAC 2014, http://accelconf.web.cern.ch/AccelConf/IPAC2014/papers/wepri018.pdf

[26] P. Pierini *et al.*, "Preparation of the 3.9 GHz System for the European XFEL Injector Commissioning", proceedings of SRF 2015, http://accelconf.web.cern.ch/AccelConf/SRF2015/papers/tupb018.pdf

[27] F. Brinker *et al.*, "Commissioning of the European XFEL Injector", proceedings of IPAC 2016, http://accelconf.web.cern.ch/AccelConf/ipac2016/papers/tuoca03.pdf

[28] B. Keil *et al.*, "Status of The European XFEL Transverse Intra Bunch Train Feedback System", proceedings of IBIC 2015, http://accelconf.web.cern.ch/AccelConf/IBIC2015/papers/tupb064.pdf

[29] B. Keil *et al.*, "The European XFEL Beam Position Monitor System", proceedings of IPAC 2010, http://accelconf.web.cern.ch/AccelConf/IPAC10/papers/mope064.pdf

[30] N. Baboi *et al.*, "Resolution Studies at Beam Position Monitors at the FLASH Facility at DESY", AIP Conf. Proc. 868, 227, 2006, http://dx.doi.org/10.1063/1.2401409

ISBN 978-3-95450-177-9

LHC ONLINE CHROMATICITY MEASUREMENT - EXPERIENCE AFTER ONE YEAR OF OPERATION

K. Fuchsberger, G.H. Hemelsoet (CERN, Geneva, Switzerland)

Abstract

Hardware and infrastructural requirements to measure chromaticity in the LHC were available since the beginning. However, the calculation of the chromaticity was mostly made offline. This gap was closed in 2015 by the development of a dedicated application for the LHC control room, which takes the measured data and produces estimates for the chromaticity values immediately online and allows to correct chroma and tune accordingly. This tool proved to be essential during commissioning as well as during every injection phase of the LHC. It became particularly important during the intensity ramp up with 25ns where good control of the chromaticity became crucial at injection. This paper describes the concepts and algorithms behind this tool, the experience gained as well as further plans for improvements.

INTRODUCTION

A very good control of chromaticity is critical for LHC operation to counteract instabilities and resulting emittance blowup. During standard operation a big part of this is achieved by model based feed-forward during injection and ramp [1, 2]. However, in numerous operational scenarios (e.g. commissioning periods, machine development, non-standard cycles), a manual way for the operations crew to check and correct chromaticity is indispensible.

Additionally, the measurement data for the feed-forward and for tuning the models have to be qualified and at the beginning of each filling of the LHC, the chromaticity is systematically checked by the operations team. Therefore, such means have to be quick and simple in order reduce turnaround time and operational mistakes, respectively.

Already in LHC run 1, a simple online chroma display was available, based on radial modulation. At the start of run 2, with the big amount of software changes on different layers, this display became dysfunctional and was not maintained anymore. To fill this gap, a more integrated application was introduced, which not only allowed measuring and tracking chroma through the cycle, but also allowed direct calculations of corrections and sending them to the hardware.

The following sections are describing the principles and features of this application, its usage and future improvements as well as some more general outlook on the future of LHC online chroma measurement.

FEATURES AND OVERVIEW

Figure 1 shows a screenshot of the LHC chroma application displaying traces of measured chroma during a ramp. The top panel of this application shows the actually measured chroma values, allows to set target values, calculate

Figure 1: LHC Chroma Application, showing chroma traces throughout a ramp, dedicated chroma measurement.

corrections and send them to the hardware. The bottom panel of the application can display various traces of input- and calculated data:

- raw tunes,
- raw RF modulation signal,
- fits to both (see below) and
- calculated chroma values.

Further, the same application also allows to trim tune values (placed on a second tab).

Since no direct measurement of the chromaticity is yet available at the LHC, the chroma app follows the 'usual procedure' as if measuring the chroma manually: Changing the RF frequency (corresponding to an energy change) and measuring the tune change resulting from this energy change. Therefore, two signals are required: The frequency change (wrt the centered frequency) and the actual tune of the machine.

Raw Data Flow

While the RF frequency is a direct input to the machine and can therefore directly be acquired from the RF systems in high precision, the tune has to be derived (measured) from the transverse beam motions. The state-of-the-art devices to accomplish a high sensitivity tune signals are the so-called BBQ devices [3], which deliver a very good tune signal under various different conditions. Without going into the detailed complexity of the full LHC tune acquisition chain, we only want to mention here, that these are the same systems which are also used for the LHC tune realtime feedback systems. Several instances of such BBQ devices are available, which are pre-configured for different scenarios (mainly driven by

ISBN 978-3-95450-177-9

beam intensities). The different devices are selected by the control system during the different phases of operation and the feedback system feeds-through the signals of the actually selected device. For this reason, it proved to be a good choice to take the tune signal from the feedback system to be used in the chroma measurement application, since then always the 'good' signal is automatically selected. Figure 2 shows a sketch illustrating this concept.

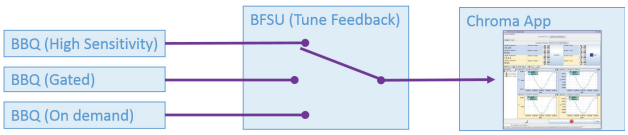

Figure 2: Overview of the tune data flow from the tune measurement devices up to the chroma measurement GUI.

In addition to the 'signal switching' the feedback device also provides functionality to easily modulate the RF frequency with a sine function. From the beginning, this was used in LHC run 1 already for an online chroma display. Another idea was also to have feedback based on these principles. However, this never became operational because a continuous shaking of the beam is undesirable. However, at injection, using pilot bunches, this concept proved to be useful as described in the following.

ALGORITHMS

The chromaticity Q' of the machine dictates a tune change ΔQ resulting from a momentum deviation $\Delta p/p$:

$$\Delta Q = Q' \frac{\Delta p}{p}. \tag{1}$$

The energy change $\Delta p/p$ is given by

$$\frac{\Delta p}{p} = \frac{\frac{\Delta f}{f}}{\eta}, \tag{2}$$

with

$$\eta = \frac{1}{\gamma_r} - \alpha_C. \tag{3}$$

where Δf is the change in RF frequency, f denotes the on-momentum RF frequency, γ_r the relativistic gamma and α_C the momentum compaction factor of the ring. For reference, the relevant parameter values for the LHC are given in Table 1.

Table1: Relevant Machine Parameters for Chroma Calculation in LHC

parameter	unit	value
α_C	[1]	$3.225 \cdot 10^{-4}$
f	[Hz]	400 788 860
γ_r (injection)	[1]	479.6

Version 0 - The Naive Approach

The simplest way to calculate the chroma is the inversion of Eq. (1). Using $Q(t) = Q_{\text{om}} + \Delta Q(t)$, this results in

$$Q(t) = Q_{\text{om}} + Q' \frac{\Delta p}{p}(t). \tag{4}$$

$Q(t)$ denotes the tune signal over time, and Q_{om} the on-momentum tune. In the initial version of the chroma application, an algorithm was implemented which, for each acquired tune value, calculated the momentum offset from the actual frequency and performed a linear fit to Eq. (4), using Q_{om} and Q' as free parameters. Figure 3 shows an example of such a fit.

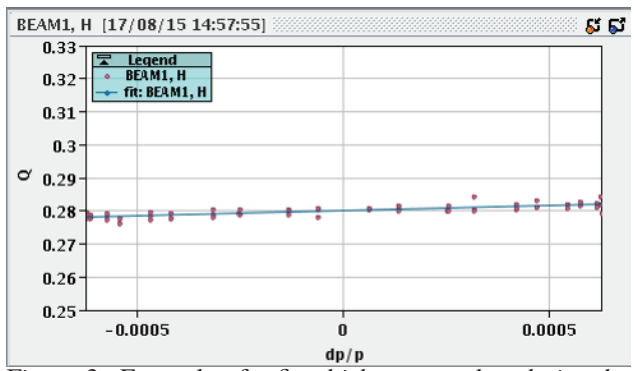

Figure 3: Example of a fit which was used to derive the chromaticity from the tune-slope.

This algorithm worked well as a first iteration and had the advantage that it was independent of the way how the RF frequency was changed (e.g. momentum trims in steps or automatic modulation). Nevertheless, it showed problems due to technical particularities in the acquisition chain: In cases where there were delays in acquiring either the RF frequency or the tune signal and thus the signals were misaligned in the order of a second, the derived chroma could not be trusted.

Version 1 - Sine Fits

To be independant of misalignments in time of the tune- and RF- modulation, the following algorithm based on harmonic fits was implemented: When using the RF modulation functionality, both the RF frequency and the tune signal follow harmonic oscillations:

$$\frac{\Delta p}{p}(t) = A_p \sin(\omega t + \varphi_p) + B_p, \tag{5}$$

$$Q(t) = A_Q \sin(\omega t + \varphi_Q) + B_Q. \tag{6}$$

A_p and A_Q denote the amplitudes of the $\Delta p/p$ and tune oscillations, respectively, φ_p and φ_Q the phases, B_p and B_Q an offset and ω the frequency of the modulation[1]. Hereby B_p corresponds to an 'artificial' energy offset which can come from small RF trims at injection to center the orbit and B_Q corresponds to the on-momentum tune. The 4 parameters

[1] Typical parameters for modulating the RF frequency during a chroma measurement are e.g. $f = \omega/2\pi = 0.08$ Hz and $A_p = 0.0003$.

ISBN 978-3-95450-177-9

($A_{...}$, ω, $\varphi_{...}$ and $B_{...}$) for each of the above equations are determined by corresponding fits. Figure 4 shows example data for the evolution of the tune signal, together with its corresponding fit.

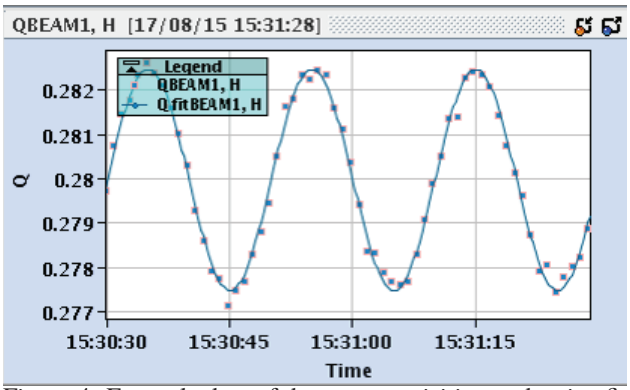

Figure 4: Example data of the tune acquisition and a sine fit to it.

Since the frequency ω is by definition the same in Eq. (6) and Eq. (6) and the RF signal is very precise, the value for ω from the fit to the $\Delta p/p$ evolution is used as an initial guess to the fit of the Q evolution.

Finally, the chroma Q' can simply be calculated as

$$Q' = \frac{A_Q}{A_p} \cdot \mathrm{sgn}(Q') \tag{7}$$

with $\mathrm{sgn}(Q')$, the sign of Q' being estimated as

$$\mathrm{sgn}(Q') := \begin{cases} +1 & \text{if} \quad \Delta\varphi = 0 \pm \varphi_{\mathrm{lim}}, \\ -1 & \text{if} \quad \Delta\varphi = \pi \pm \varphi_{\mathrm{lim}}. \end{cases} \tag{8}$$

Hereby, $\Delta\varphi$ is simply the absolute difference between the two fitted phases, $\Delta\varphi = \mathrm{abs}(\varphi_Q - \varphi_p)$ and φ_{lim} an (experimentaly determined) tolerance[2].

Potential Improvements

The described algorithm proved to be stable in general. The most relevant improvement to be introduced in the near future is the proper automatic treatment of measurement outliers. The planned approach is to do a second fit, which would only include data points which are within a certain distance to the initial fit (e.g. below 3σ).

Another (similar) option which is considered is a second fit, taking into account again all data points but using weighting factors inversely proportional to the distance to the initial fit.

ARCHITECTURE AND TECHNOLOGY

The application is written in the java programming language as all the rest of the LHC control system GUI parts. While the user interface part is still written using swing technology, which is already deprecated at the time of writing, the backend part uses state of the art technologies and served as a usecase to probe several new technologies for their usage in further software projects. The most promising of them turned out to be RxJava [6].

RxJava allows provides a concept called 'reactive streams', which allows to implement dataflows within the application as streams which can be transformed and combined. This approach leads to a very clean, data-focused approach. Generalization of these concepts is currently ongoing and we are planning to reuse the same approach in new developments and restructurings within the LHC control system.

Another design principle which is consistently followed in the application is so-called dependency injection [7], using the spring framework [8]. The main concept of dependency injection is that collaborators of certain 'clients' (objects that use the collaborators) are injected into the clients by a framework, instead of the clients looking up their collaborators. This allows to inject different collaborators in different situations (contexts), e.g. for development, testing or production.

Testing

One big advantage of the abovementioned dependency injection principle is that the resulting code is nicely decoupled and testable. The reason for this is that e.g. mocked or stubbed collaborators can injected for testing purposes.

In the case of the chroma application, the same principle is also used to start up an instance of the GUI which uses a self-consistent simulation layer, which allows to try and test the application fully without beam. Similar principles are applied in the meantime also to several other software projects and we are planning to generalize these concepts to make them more easily usable [9].

EXPERIENCE AND OUTLOOK

The chroma app proved to be very reliable and the fit algorithms to be robust. The application is used systematically in every fill to check and trim chroma and tune. Up to now, it never caused problems which would have contributed to unavailability of the LHC. Since there are several other applications (automatic laslett feed-forward application, coupling correction, injection phase) which have to be used while filling the LHC, it will be useful for the future to combine these applications into one.

THE FUTURE: LHC SCHOTTKY

As mentioned in the beginning, the described procedures require 'shaking' the beam with the RF frequency, which is undesirable and even dangerous for high intensity beams. The only device which could potentially derive a direct chroma signal from the particle beam is a schottky monitor. Figure 5 shows a typical FFT spectrum of the schottky monitor from which several beam parameters can be extracted. Efforts in this direction are ongoing and gave first good results recently [4, 5]:

- The tune can already be nicely derived from the signal. In contrast to the BBQ devices, this even works on

[2] In the current version we are using $\varphi_{\mathrm{lim}} \approx 30\,\mathrm{deg}$.

ISBN 978-3-95450-177-9

bunches which are strongly affected by the transverse damper. The corresponding algorithm is already implemented in the device itself and is therefore running online on the frontend computer and prepared for first tests in an operational environment.

- An algorithm to extract chromaticity was developed offline and shows promising results. As an example, Fig. 6 shows data from a machine development session at injection energy, where the chroma was trimmed deliberately from about 4 units up to about 15 units; the plot compares the chromaticity derived from the schottky monitor and the one derived from RF modulation and shows a very good agreement of the two.

The chroma signal processing is already working very well at injection energy; work is still ongoing to also push the signal quality to a similar level during ramp and flat top. Despite those current limitations, it is planned to implement the chroma algorithm in the device itself still before the end of this year. Integrating these signals then into the chroma application will make it possible to easily compare them, get first operational experience of the signal quality and even use them as source for calculating corrections. Later, this would in principle allow continuous chromaticity measurements throughout the whole cycle and would eliminate (or reduce) the need for dedicated cycles to perform the measurements for the chromaticity feed-forward.

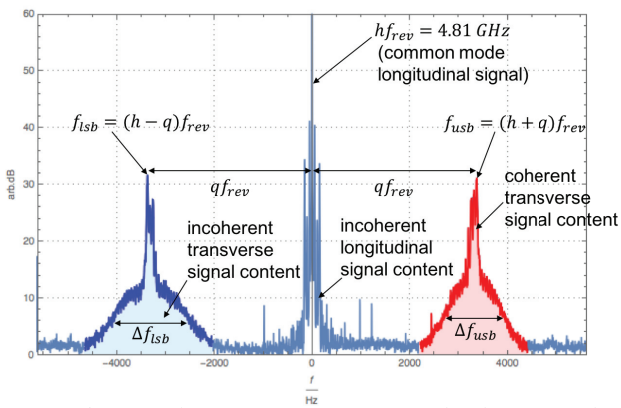

Figure 5: Typical Beam Spectrum as seen by the LHC schottky monitor (Courtesy: M. Wendt, M. Betz).

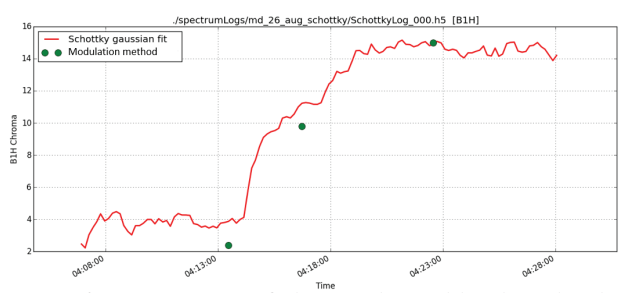

Figure 6: Comparison of chroma derived by the schottky monitor (red line) and chroma as derived with the modulation method (green dots) (Courtesy: M. Wendt, M. Betz).

SUMMARY

The online chroma measurement application turned into a robust tool which was used systematically during filling of the LHC during the first year of LHC Run 2. Next to different measurement algorithms it also allows to calculate corrections and send them directly to the hardware. Planned improvements include better handling of data outliers and integration with tools dealing with other parameters which have to be checked and corrected when filling the LHC.

Particularly promising are the good results from recent tests of the LHC Schottky monitor. The integration of this device into the operational landscape will eventually allow to measure chromaticity and other beam parameters continuously, without shaking the beam with RF modulation. Until then, the RF modulation method will serve as an useful calibration standard during the development of the Schottky data extraction algorithms.

ACKNOWLEDGEMENTS

The authors would like to thank in particular M. Betz and M. Wendt for their contributions related to the Schottky Monitor. Furthermore, a lot of thanks to all our colleagues in the operations group for all the valuable feedback and suggestions.

REFERENCES

[1] M. Schaumann et al., "Tune and Chromaticity Control durning Snapback and Ramp in 2015 LHC Operation", *Proc. IPAC 2016*, Busan, Korea.

[2] M. Schaumann et al., "Feed-Forward Corrections for Tune and Chromaticity Injection Decay during 2015 LHC Operation", *Proc. IPAC 2016,* Busan, Korea.

[3] M. Gasior, R. Jones, "High Sensitivity Tune Measurement by Direct Diode Detection", *Proceedings of DIPAC'05*, Lyon, France.

[4] M. Wendt et al.,"Upgrade of the LHC Schottky Monitor, Operational Experience and First Results", *Proc. IPAC 2016*, Busan, Korea.

[5] M. Wendt et al., "Improvements of the LHC Schottky Monitors", presented at *IBIC2016*, Barcelona, Spain, this conference.

[6] https://github.com/ReactiveX/RxJava

[7] http://martinfowler.com/articles/injection.html

[8] https://projects.spring.io/spring-framework

[9] A. Calia, K. Fuchsberger, M. Hostettler, "Testing the Untestable: A Realistic Vision of Fearlessly Testing (Almost) Every Single Accelerator Component Without Beam and Continuous Deployment Thereof", presented at *IBIC2016,* Barcelona, Spain, this conference.

ISBN 978-3-95450-177-9

HARMONICALLY RESONANT CAVITY AS A BUNCH LENGTH MONITOR

B. Roberts, M. Pablo, Electrodynamic 4909 Paseo Del Norte Ne suite D, Albuquerque, NM 87113
E. Forman, J. Grames, F. Hannon, R. Kazimi W. Moore, M. Poelker, Thomas Jefferson National Accelerator Facility, 12000 Jefferson Ave., Newport News, VA 23606,
M. M. Ali,' Department of Physics, Old Dominion University, Norfolk, Virginia 23529

Abstract

A compact, harmonically-resonant cavity with a fundamental resonant frequency of 1497 MHz was used to evaluate the temporal characteristics of electron bunches produced by a 130 kV dc high voltage spin-polarized photoelectron source at the Continuous Electron Beam Accelerator Facility (CEBAF) photoinjector, delivered at 249.5 and 499 MHz repetition rates and ranging in width from 45 to 150 picoseconds (FWHM). The cavity's antenna was attached directly to a sampling oscilloscope that detected the electron bunches as they passed through the cavity bore with a sensitivity of ~ 1 mV/μA. The oscilloscope waveforms are a superposition of the harmonic modes excited by the beam, with each cavity mode representing a term of the Fourier series of the electron bunch train. Relatively straightforward post-processing of the waveforms provided a near-real time representation of the electron bunches revealing bunchlength and the relative phasing of interleaved beams. The non-invasive measurements from the harmonically-resonant cavity were compared to measurements obtained using an invasive rf-deflector-cavity technique and to predictions from particle tracking simulations [1].

THE HARMONIC CAVITY

The Harmonic cavity was designed to resonate at many harmonic TM_{0N0} modes, and to suppress or displace TE and non-axially symmetric TM modes within or beyond its operational bandwidth. The shallow saucer-shaped cavity (Fig 1) has a mode spectrum free of TE modes for several tens of GHz because TE modes resonate at frequencies greater than $c/2h$ where c is the speed of light and h is the cavity length along the beam's direction of motion. Radial slits cut into the cavity walls do not affect the TM_{0N0} modes which have purely radial wall currents while the TM_{MNP} modes with azimuthal mode numbers, M, less than the number of discontinuities are suppressed. Finally, the shape of the cavity was tuned to yield harmonic TM0N0 modes. This was accomplished in the design phase by iteratively modifying the cavity geometry and solving for the TM_{0N0} mode frequencies with the field solver POISSON/Superfish [2]. The TM_{0N0} cavity modes are axially symmetric and have a field maximum on the cavity axis, i.e., along the direction of the electron beam motion.

Electron bunches at a pulse repetition rate w_0 can be described using a Fourier series expansion:

$$i_{beam}(t) = a_1 \cos(w_o t + \theta_1) + a_2 \cos(2w_o t + \theta_2) \ldots + a_n \cos(nw_o t + \theta_n) \quad (1)$$

where a_n and θ_n describe the relative amplitudes and phases of each contributing harmonic term. The non-invasive bunchlength monitor cavity was designed to measure each term of the Fourier series expansion:

$$v_{detected}(t) = a_{TM_{010}} \cos(w_0 t + \theta_{010}) + a_{TM_{020}} \cos(2w_0 t + \theta_{020}) \ldots + a_{TM_{0n0}} \cos(nw_0 t + \theta_{0n0}) \quad (2)$$

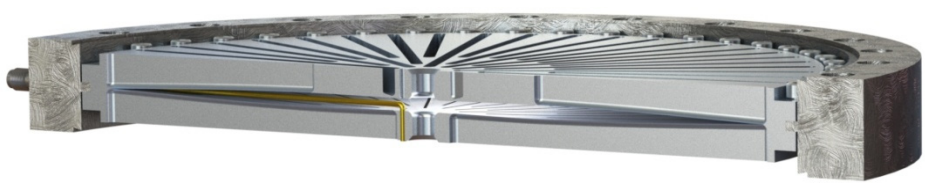

Figure 1: (top) A cut-away drawing of the harmonically-resonant cavity showing the antenna and the curvature of the cavity surfaces. (bottom) A photograph of the cavity nested inside the bore of a 10" double-sided knife edge Conflat flange. Two additional 10" Conflat flanges attach to either side to form the UHV-compatible vacuum vessel.

ISBN 978-3-95450-177-9

where a_{TM0N0} and θ_{0N0} describe the relative amplitudes and phases of each detected cavity mode. If the harmonically-resonant cavity were perfect, with infinite bandwidth and with all modes perfectly harmonic and equally coupled to the antenna, the amplitude coefficients and phase terms of both equations would be identical (barring a scale factor). However, the cavity and antenna do not have infinite bandwidth and manufacturing imperfections result in some modes being slightly displaced from the intended resonant frequencies. Similarly, the cavity antenna does not couple identically to all modes. In sections below, we describe how these imperfections can be corrected with a post process that multiplies the individual terms of the detected waveform's Fourier series expansion with the cavity's transfer function. In principle, the cavity transfer function can be calculated by dividing equation 1 by equation 2, but this requires that the electron bunch profile be precisely known. In this work, the cavity transfer function was determined empirically via blind deconvolution [3, 4].

Bunchlength Measurements Using the Harmonically-Resonant Cavity

After making invasive bunchlength measurements using the rf-deflector technique, non-invasive measurements were made using the harmonically resonant cavity at a location upstream of the rf-deflecting cavity using the photogun's "laser 1" operating at 499 MHz and with 45 ps optical pulsewidth. A Tektronix SD-30, 40 GHz sampling head was directly attached to the sma-vacuum feedthrough of the harmonically resonant cavity and connected to a 11801B digital sampling oscilloscope with an extender cable. Figure 2 (a) shows an oscilloscope measurement of a 10 μA beam, (red) and an estimate of the true shape of the electron bunches that induced the measurement (blue). The "distortions" seen in the detected waveform stem from small imperfections in the cavity geometry, and imperfect antenna coupling to all cavity modes. Slightly off-resonant cavity modes, combined with non-uniform antenna coupling, result in phase and amplitude differences between the measured response of each cavity mode and the Fourier series of the beam that induced it. The amplitude differences in the harmonic spectrum of both waveforms are shown in Fig.2 (b).

If the resonant frequency of an individual cavity mode is slightly off design, the beam can still excite this mode provided the beam's Fourier term is not outside the mode's resonance curve. But driving a cavity mode off the resonance peak causes a decrease in detected amplitude, and it introduces a phase shift between the beam and the excited mode. The error associated with this mode can be corrected using a single complex multiplier that "un-shifts" the phase offset and scales the detected amplitude. A series of complex multipliers - one for each cavity mode - can be created. This series expansion has a functional form similar to equation 1 and it is called the cavity transfer function. The beam's true Fourier series representation can be obtained by multiplying each term of the Fourier series of the detected signal by each term of the cavity transfer function.

The challenge associated with this approach relates to the fact that the cavity transfer function is not explicitly known, rather it must be deduced in a sensible manner. However, once the transfer function is known, it can then be used to correct the cavity systematic errors for all subsequent data, independent of new bunch shapes.

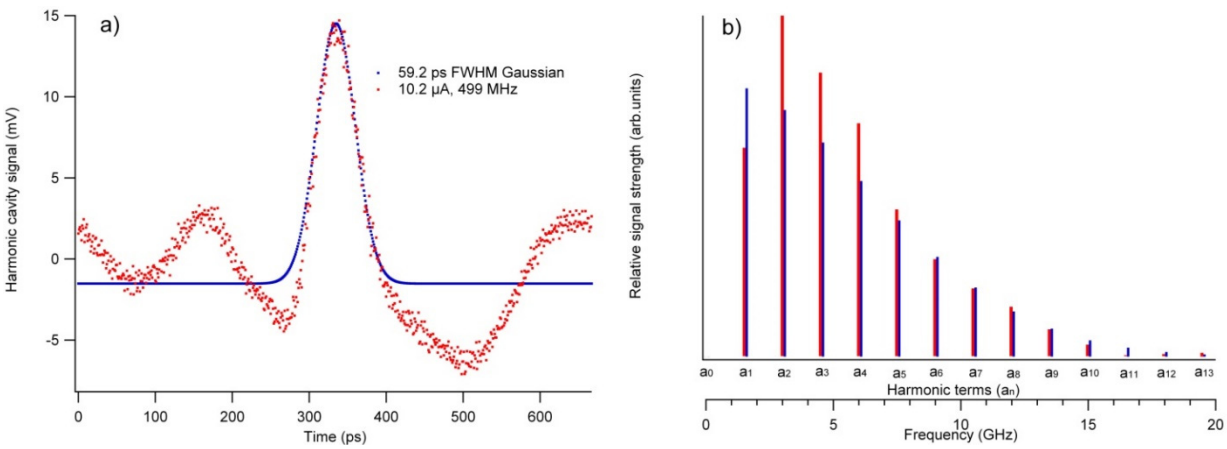

Figure 2: (a) A raw oscilloscope trace of a 10 μA beam made using laser 1 as it passed through the harmonically-resonant cavity (red), and an estimate of the bunch profile that induced it (blue). These waveforms were used to create a transfer function that transformed measurements of higher current beams with the minimum signal outside the central bunch. (b) The signal strength of each resonant mode of the harmonically-resonant cavity as measured (red), and the response of an ideal harmonic cavity (blue).

ISBN 978-3-95450-177-9

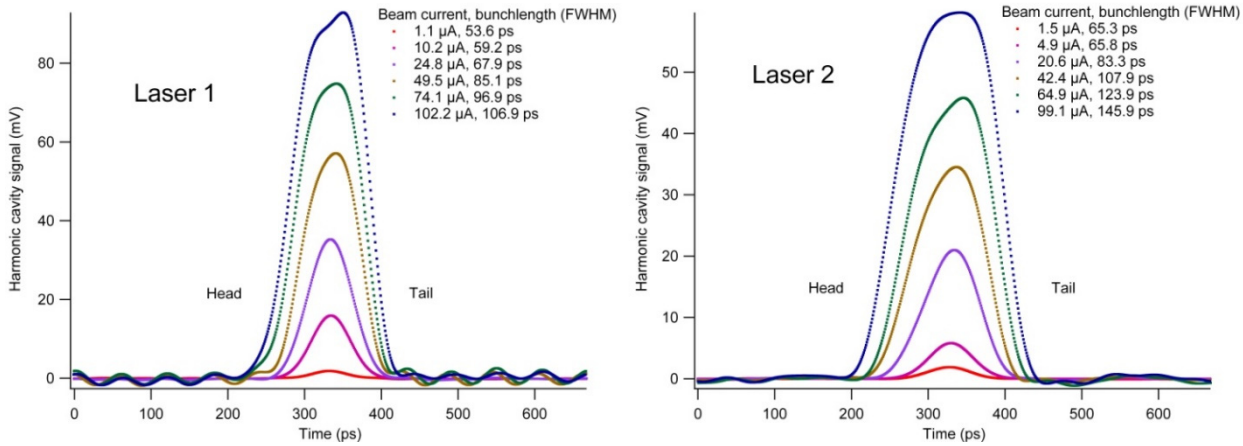

Figure 3: Bunchlength measurements made with the harmonically-resonant cavity of 499 MHz electron beams using "laser 1" with 45 ps optical pulsewidth FWHM (top), and 249.5 MHz beams using "laser 2" with 60 ps optical pulsewidth FWHM (bottom), for different extracted beam currents. These plots were obtained by transforming the raw oscilloscope waveforms using an estimate of the harmonic cavities transfer function.

To generate a sensible cavity transfer function, the method of blind deconvolution [3, 4] was employed. A low-current waveform obtained using "laser 1" operating at 499 MHz and with 45 ps optical pulsewidth was selected because space charge forces were less likely to influence the shape of the bunch. Fourier series were created for "guessed" Gaussian bunchlengths ranging from 40 to 60 ps, in 2 ps increments. Candidate transfer functions were then calculated by dividing the Fourier series of the guessed profiles by the Fourier series of the actual measured waveform. Each of these candidate transfer functions was then used to correct the waveforms of measurements of longer bunches arriving at the harmonically resonant cavity. Most of these transfer functions did a poor job of correcting waveform distortions, particularly at higher currents. The transfer function deemed most accurate was one that generated the least amount of signal outside the central bunch. It produced the corrected waveforms shown in Figure 3 (a), where distortions and oscillations outside the central bunch were effectively minimized. The same methodology was employed for measurements obtained using "laser 2" shown in Fig. 3 (b).

CONCLUSION

A novel non-invasive bunchlength measurement technique was validated against a traditional invasive rf-deflector cavity technique, and particle tracking simulations. The compact harmonically-resonant cavity provided near-real time evaluation of electron bunches as short as 35 ps and phase information of interleaved beams. Future plans include making design and manufacturing improvements to increase the harmonic cavities bandwidth and antenna coupling uniformity, and developing an algorithm to more accurately determine the harmonically resonant cavities transfer function. It was shown that the harmonic cavity provides very practical information on the relative phasing of interleaved pulse trains, a feature that will reduce the setup time of the CEBAF photoinjector. It is possible this feature could be exploited at other locations at CEBAF, for example, where beams at higher energy are combined for recirculation through the linac.

Authored by Jefferson Science Associates under U.S. DOE Contract No. DE-AC05-84ER40150 and with funding from the DOE Office of High Energy Physics and the Americas Region ILC R&D program. The U.S. Government retains a non-exclusive, paid-up, irrevocable, worldwide license to publish or reproduce this manuscript for U.S. Government purposes.

Electrodynamic is funded by the DOE's SBIR program DE-SC0009509

REFERENCES

[1] B. Roberts, F. Hannon , M.M. Ali E. Forman, J. Grames R.Kazimi, W. Moore, M. Pablo, M. Poelker, , A.Sanchez, and D.Speirs " Harmonically Resonant cavity as a bunch-length monitor", Phys. Rev. ST Accel. Beams **19** , 052801 (2016)

[2] K. Halbach and R. F. Holsinger, ″SUPERFISH -- A Computer Program for Evaluation of RF Cavities with Cylindrical Symmetry″, Particle Accelerators 7 (4), 213-222 (1976)

[3] M. Cannon, "Blind deconvolution of spatially invariant image blurs with phase", IEEE Trans. Acoust. Speech Signal Process. ASSP-24, 58 - 63 (1976);

[4] E. Y. Lam and J. W. Goodman "Iterative statistical approach to blind image deconvolution", J. Opt. Soc. Am. A Vol. 17, Issue 7, pp. 1177-1184 (2000)

ISBN 978-3-95450-177-9

DESIGN, PRODUCTION AND TESTS OF BUTTON TYPE BPM FOR TAC-TARLA IR FEL FACILITY

M. T. Gundogan, O. Yavas, Dept. of Engineering Physics, Ankara University, Ankara, Turkey
A.Aydin, E.Kasap, Dept. of Physics, Gazi University, Ankara, Turkey
C.Kaya, Institute of Accelerator Technologies, Ankara University, Ankara, Turkey

Abstract

Turkish Accelerator and Radiation Laboratory in Ankara (TARLA) facility is an IR FEL and Bremsstrahlung facility as the first facility of Turkish Accelerator Center (TAC) that is under construction in Golbasi Campus of Ankara University. TARLA is proposed to generate oscillator mode FEL in 3-250 microns wavelengths range and Bremsstrahlung radiation. It will consist of normal conducting injector system with 250 keV beam energy and two superconducting RF accelerating modules in order to accelerate the beam 15-40 MeV. The electron beam will be in both continuous wave (CW) and macro pulse (MP) modes. The bunch charge will be limited by 77pC and the average beam current will be 1 mA.

To detect electron beam position, BPM (Beam Position Monitor) has to use through beam line. Wall current monitor based system button type TARLA BPM are briefly mentioned.

In this study, simulation results of design in CST, production and test studies for button type TARLA BPM are presented. Mechanical and electronic design, antenna simulations, and the latest testing procedures are given for a button type BPM.

INTRODUCTION

The Turkish Accelerator Center (TAC) Collaboration is established in 2006 as an inter-university collaboration with 12 Turkish Universities under the coordination of Ankara University by support of Ministry of Development of Turkey. Main aim of the collaboration is to study on technical design and construction of proposed accelerator facilities in Turkey for accelerator based scientific research and technological developments in basic and applied sciences [1].

Turkish Accelerator and Radiation Laboratory in Ankara (TARLA) facility is under construction as a first facility of TAC which is proposed to generate infrared FEL beams in 3-250 micrometers wavelength range based on superconducting electron linac with 15-40 MeV beam energy [2]. TARLA electron source is a thermionic DC gun with 250 keV energy. It is planned that the TARLA facility will provide electron beam in continuous wave (CW) and macro pulse (MP) modes based on SRF modules. Longitudinal electron bunch length will be change between 6ps and 0.4 ps along to accelerator. Repetition rate of electron bunches will be 13 MHz. The bunch charge will be limited by 77pC and the average beam current will be 1 mA. The schematic diagram of TARLA facility is shown in Figure 1 [3].

The facility will contain also IR FEL and Bremsstrahlung radiation production halls and experimental stations. It is planned that the facility will produce two FEL beams by two different undulator magnets U25 and U90 with 2.5 cm and 9 cm period lengths, respectively. The main aim of the facility is to use IR FEL beams for research and application in material science, nonlinear optics, semiconductors, biotechnology, medicine and photochemical processes. In addition, a bremsstrahlung station is planned for nuclear spectroscopy studies up to 35 MeV. The main parameters of TARLA Facility are given in Table 1[3].

Table 1: The Main Parameters of TARLA Facility

Parameters	Value
Energy [MeV]	15-40
Bunch charge [pC]	77
Average beam current [mA]	1.0
Bunch repetition rate [MHz]	13 (16.25)
Bunch length [ps]	0.4-6
Norm. RMS trans. emit. [mm mrad]	< 16
Norm. RMS long. emittance. [keV.ps]	< 100
Macro pulse duration [μs]	50 - CW
Macropulse reputation rate [Hz]	1- CW
Wavelength [μm]	U25:3-20 U90:18-250

BEAM POSITION MONITORS FOR TARLA

Beam diagnostics is an essential part for all types of accelerators; because it should be known different beam characteristics such as beam position, beam current, beam charge etc. Beam characteristics have been kept under control by diagnostic devices. Beam position monitors are one of important online diagnostics devices to measure the position of the beam in the beam line. They are designed in order to provide reliable and accurate beam position readings. Typical BPM is composed of four opposite mounted plates called electrodes or antenna.

The difference of signal from opposite electrodes gives information about the beam position and average beam current in the beam line and report it to the control system [4].

ISBN 978-3-95450-177-9

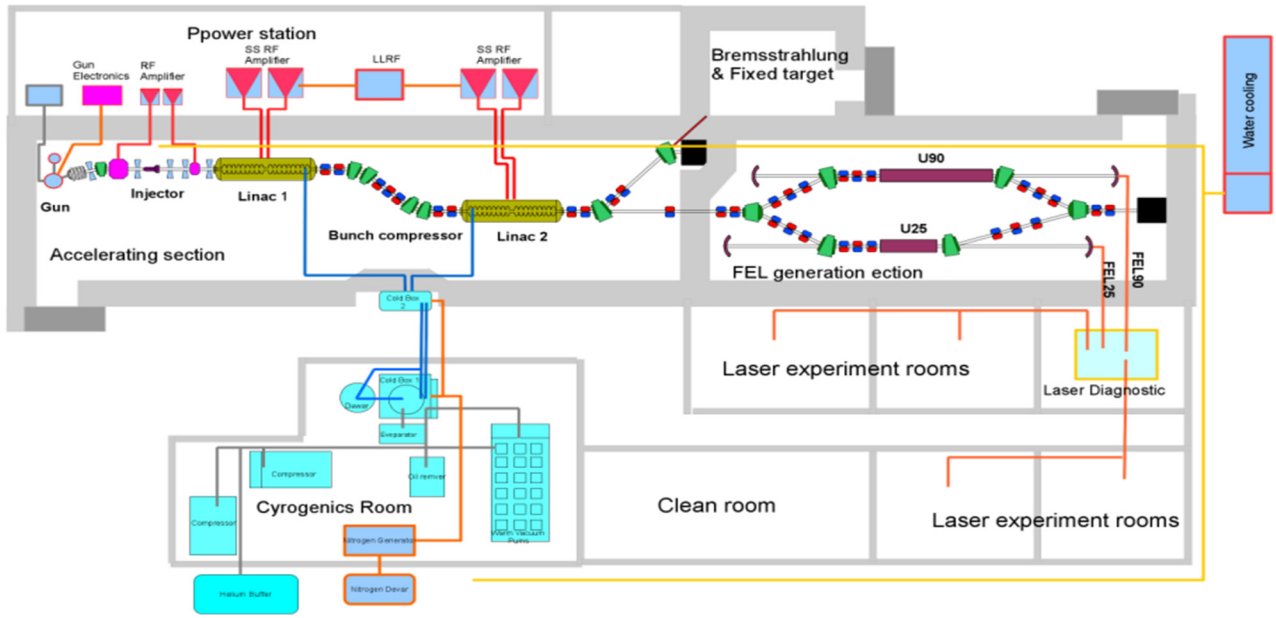

Figure 1: The hardware installation plan of TARLA facility.

There are different types of BPMs to detect signal for different purposes; such as button, stripline and cavity type BPM etc. Design ideas of button type BPMs are detect electro static radiations of bunches. Stripline type monitors are used traveling wave of bunches. Button type monitors have a good resolution more than stripline type BPMs. But signal strength of a button type monitor is lower than stripline type. A Cavity type BPM requires different design. They are more complex than the others [5].

Button and stripline type BPMs will be used in TARLA facility. Because, TARLA beam repetition frequency and average beam current are high enough to give suitable signal on electrodes of monitors. It is planned that, 16 button and 10 stripline type BPMs will be used in TARLA.

DESIGN AND SIMULATION STUDIES FOR BUTTON TYPE BPM

In this study, a licenced CST (Computer Simulation Technology) Particle Studio code was used to design most effective geometry of electrodes [6]. The geometry of BPM antennas are shown in Figure 2. Four antennas were located as mutually. Distance between opposed button electrodes are 28 mm. An electron beam bunch passes through the four antennas.

1 pC Gaussian bunch and 0.99c (c is speed of light) velocity along the z axis are used in simulation studies (Figure 3).

Output signal is expected to be Fourier transform of input signal. The output signals are observed from second and fourth antenna wave ports. BPM calculated output voltages in time domains are shown in Figure 4.

We performed numerical simulations of a button electrode with wake-field solver on a hexahedral mesh. Electrical field energy (E) of electron bunch is given by CST EM Studio (E= 6.21x10^{-13} Joule). The capacitance (C) is calculated using the Equation 1

$$E = \frac{1}{2}CV^2 \quad (1)$$

where V is the voltage applied to electrodes that is applied as 1V.

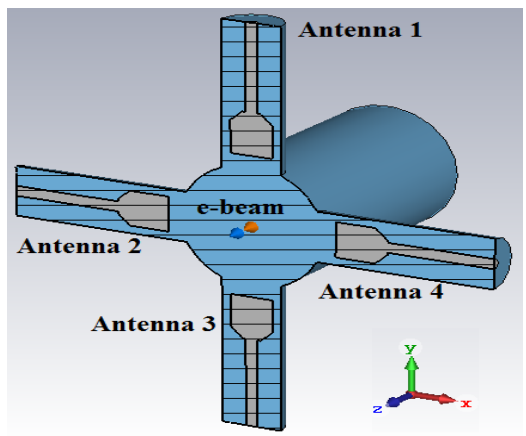

Figure 2: A view of button type BPM by CST.

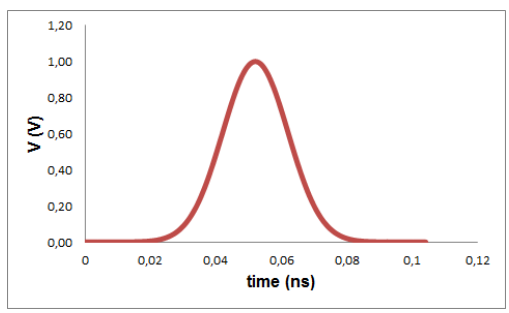

Figure 3: BPM input voltage in time domain.

For the button BPM with radius 3.5 mm the capacitance C is calculated 1.24 pF. Equivalent circuit of BPM is shown in Figure 5.

ISBN 978-3-95450-177-9

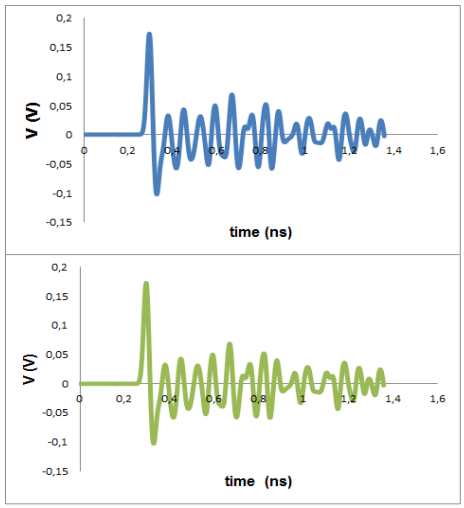

Figure 4: BPM output voltages from second (up) and fourth (down) antennas in time domain.

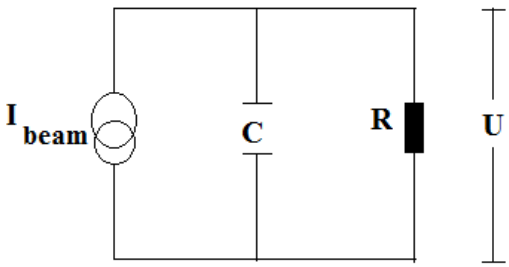

Figure 5: Equivalent circuit of BPM.

For all type electrodes, the general quantity of longitudinal transfer impedance (Z_t) is defined in the frequency domain according to Ohm's low (Equation 2).

$$U = Z_t . I_{beam} \quad (2)$$

Absolute value of the transfer impedance is shown in Figure 6. The impedance is dependent on frequency (w), on the velocity of the beam particles (β) and on geometrical factors (the area of button plate A and distance of two opposite buttons a).

$$Z_t = \frac{1}{\beta c}\frac{1}{C}\frac{A}{2\pi a}\frac{w/w_{cut}}{\sqrt{1+w^2/w^2{}_{cut}}} \quad (3)$$

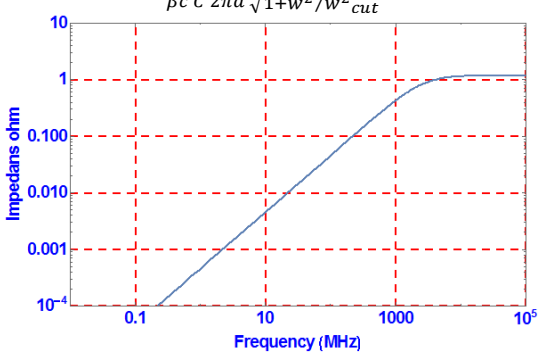

Figure 6: Antenna impedance distribution versus of the frequency.

The results of resolution were calculated by CST and the value is 150 mV/mm that is shown in Figure 7.

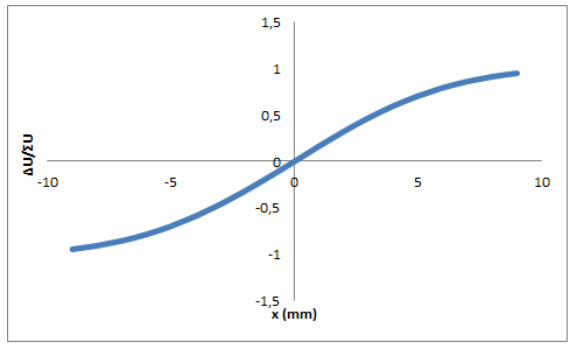

Figure 7: The resolution curve of designed BPM.

PRODUCTION AND TEST STUDIES FOR BUTTON TYPE BPM

After completed simulation, our own design of button type BPM was manufactured by NTG (Neue Technologien GmbH) Company (Germany). They are cupper coated and have a 3.5 mm radius. The picture of manufactured BPM is shown in Figure 8.

Figure 8: The picture of button type BPM produced by NTG Company.

Tests of BPM was made in the test setup in TARLA. The test setup is shown in Figure 9.

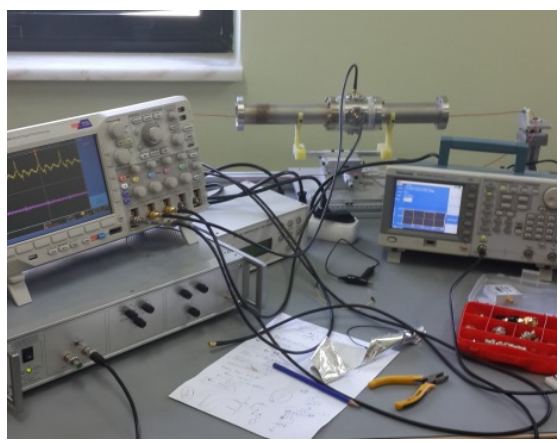

Figure 9: The BPM test setup.

The test setup consists of a signal generator (Tektronics AFG3101), pulse source (Avtech) and a scope (Agilent 500 MHz). 13 MHz of external clock was used as a trigger

ISBN 978-3-95450-177-9

signal to lock pulse source. Output signal amplitude of pulser was 70V and pulse repetition was 77ns. 70V pulses were applied to thin wire. Wire was installed inside of monitor and 100 ohm resistor was used to block electronic reflections in monitor. The block diagram of test setup is shown in Figure 10.

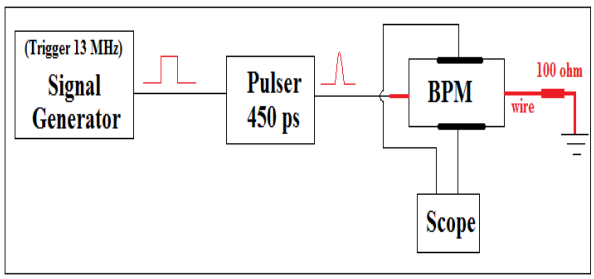

Figure 10: The block diagram of the test setup.

Output voltages of BPM electrodes were measured by scope. The position of wire was changed in the beam line with range of 0.5 mm then voltages were measured step by step for each location of wire. The resolution in x-axis was calculated using Equation 4.

$$\frac{\Delta U}{\sum U} = \frac{U_2 - U_4}{U_2 + U_4} \quad (4)$$

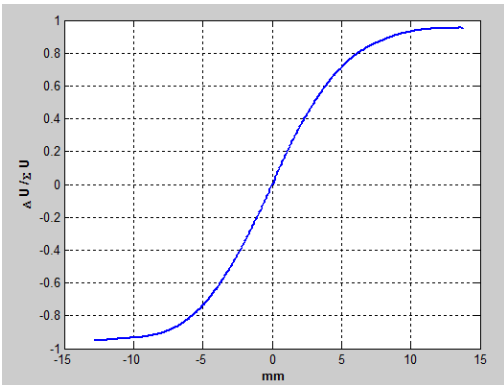

Figure 11: The resolution curve of test setup.

The resolution curve for a 28 mm button radius is shown in Figure 11. The slope of the linear fit function of resolution curve gives position sensitivity factor. Resolution was calculated as 150 mV/mm.

CONCLUSION

A Button type BPM was designed and manufactured for Turkey's TAC-TARLA Facility. Design of TARLA button type BPM antenna performance was numerically simulated with CST Particle Studio. The resolution of designed BPM is obtained 150 mV/mm by simulation. The resolution of produced button BPM is obtained 150 mV/mm by test measurements. Simulation and experiment results are matched each other. TARLA beam line radius is 40mm, therefore to make effective measurements we need to work on different type of BPMs with large beam line radius. It is planned that, 16 pieces button BPM will be used in TARLA Facility. The stripline BPM and cavity type BPM studies will be keep going for TARLA facility.

ACKNOWLEDGEMENT

This work is supported by Ministry of Development of Turkey with grant no DPT2006K-120470

REFERENCES

[1] http://thm.ankara.edu.tr

[2] https://tarla.org.tr

[3] The Technical Design Report of Turkish Accelerator and Radiation Laboratory at Ankara (TARLA), Ankara University, Institute of Accelerator Technologies, 2015.

[4] P. Forck et al., DITANET School, London, 2009.

[5] R.E. Shafer, Beam Position Monitoring, AIP Conference Proceedings, vol. 212, 1989, pp. 26 –58.

[6] https://www.cst.com

ISBN 978-3-95450-177-9

INVESTIGTION OF TRANSVERSE BEAM INSTABILITY INDUCED BY AN IN-VACUUM UNDULATOR AT SPEAR3*

K. Tian†, J. Sebek, J. L. Vargas, SLAC National Accelerator Laboratory, Menlo Park, USA

Abstract

Vertical beam instabilities have been observed at SPEAR3 when a newly installed in-vacuum undulator (IVUN) is operated at a set of narrow gap settings. The source of the instabilities is believed to be vertically deflecting trapped modes inside the IVUN tank that are excited by the beam. We have used beam-based measurements to characterize the frequencies and strengths of the excited modes using both our bunch-by-bunch feedback system and a spectrum analyzer. Using numerical simulations of our IVUN structure, we have found modes with high shunt impedance near the measured frequencies. Recently, we have successfully measured these IVUN modes during our current downtime. In this paper, we will report on the measurements, simulations, and plans to damp these modes.

INTRODUCTION

Transverse beam instabilities at intermittent IVUN pole gap positions have previously been reported by other facilities [1-3]. However, the sources of the instabilities have never been well understood. Recently, we have observed similar beam instabilities associated with one of our IVUNs, the BL15 insertion device (ID).

The 2-meter-long BL15 insertion device in SPEAR3 is the second IVUN in the storage ring and is still under commissioning for full user operation. The undulator period is 22 mm with 86 full strength periods and 2 end periods with reduced strength. When in operations, it will close down to a minimum 6.82 mm pole gap. During early commissioning tests of BL15 ID, we encountered several problems. We found that the injection efficiency of the storage ring degraded significantly when the ID gap was closed to the minimum gap. Therefore, we temporarily raised the lower limit of the ID gap to 8 mm in the control system. Later, we found that the beam size blew up when the gap was set to 8.4 mm during 500mA operation. Upon further investigation, we have discovered that these problems are likely caused by vertical beam instabilities that have occurred at these and other intermittent pole gaps.

The cross section of the ID chamber is shown on the left of Fig. 1. As a standard means of decreasing the resistive wall impedance of the ID, two 70mm wide nickel-plated copper foils (current sheets) are attached to both the top and bottom rows of the magnets through the magnetic attractive force of the nickel to the pole pieces. Since the electron beam is shielded by the current sheet, we can simplify the complicated ID chamber assembly by approximating it by a round ridge waveguide shown on the right of Fig. 1. The width and height of the narrow gap at the center of the ridge waveguide represent the width of the current sheets and the pole gap, respectively. Based on the theory of the ridge waveguide [4], the cutoff frequency of the waveguide will decrease with the gap height. Because the ID gap opens up to 34 mm at the end of the transition, a small gap means that the cut-off frequency for the cross-sections of the central part of the ID will be lower than that for the cross-sections at the ends of the ID. As a result, the beam can excite low frequency modes which are trapped inside the ID chamber. We believe that these trapped modes are the sources of the beam instabilities we observed at SPEAR3. In the following, we will present the results from beam based measurements, numerical simulations, and RF measurements to support our theory.

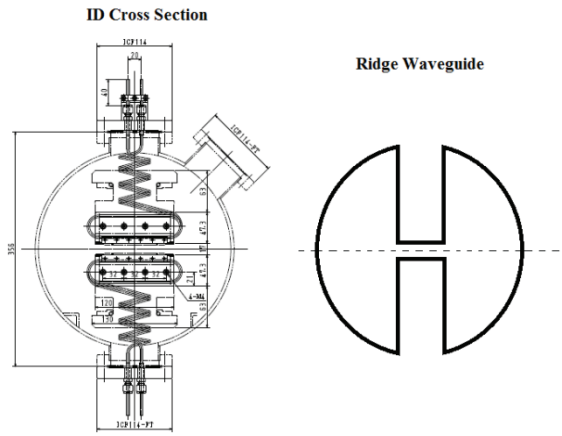

Figure 1: Cross section of SPEAR3 BL15 ID (left) and a round ridge waveguide (right).

BEAM BASED MEASURMENT

To reveal all the instability modes at different gaps, we scanned the ID gap from 6.82mm to 8.6mm at 10 μm per step. Then we conducted modal analysis using the bunch-by-bunch (BxB) data taken by the feedback system [5] to characterize the mode number and potential frequencies of the modes at different ID gaps. The results are shown in Table 1. The pole gap in the table is the rough midpoint for each instability mode. For the transverse beam instability, the lower betatron sideband drives the instability while the upper sideband damps it [6], so the instability modes and frequencies shown in the table all correspond to the lower sideband of the lowest potential driving frequency. Starting from 6.82mm, we observed a series of instability modes, each of which covered ~100 μm gap range and was separated by ~300 μm from its neighbors. This indicates that the resonant frequency of the problematic mode in the ID chamber reduces by one

* Work supported by DOE contract DE-AC02-76SF00515
† email address: ktian@slac.stanford.edu

ISBN 978-3-95450-177-9

revolution frequency about every 300 μm of gap closure, i.e. ~4.3 MHz/mm.

Table 1: BL15 Pole Gap vs Instability Modes

Pole Gap(mm)	Peak Mode	Freq.(MHz)
6.82	156	199.51
7.10	157	200.79
7.43	158	202.07
7.77	159	203.35
8.10	160	204.63
8.40	161	205.91

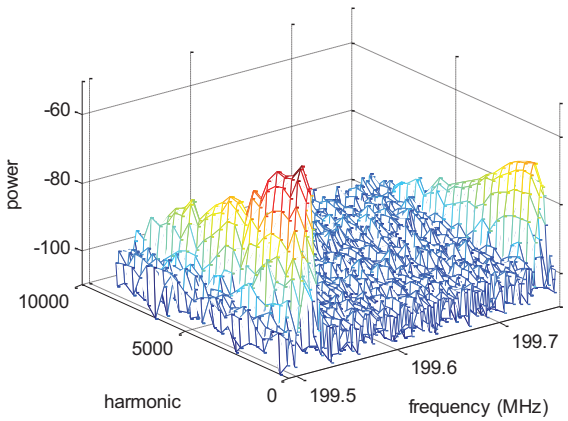

Figure 2: Spectrum analyzer data: pole gap at 6.82mm.

The frequencies of the beam instability modes at different pole gaps were also verified with an HP8563 spectrum analyzer monitoring a beam position monitor (BPM) button. During the experiment, we uniformly filled all RF buckets in order to suppress the revolution harmonics. For each instability mode, we set the analyzer span to just cover the revolution harmonic and the lower/upper side bands. Then we shifted the center frequency by the ring RF frequency, 476 MHz, to measure the same mode at the next higher candidate frequency. We continued these measurements up to about 10 GHz. Fig. 2 shows the results for mode 156 with the pole gap of 6.82mm and stored beam current of 191mA. In the figure, all frequencies have been aliased to the base band with the lower sidebands near 199.5 MHz and the revolution harmonics at 199.7 MHz. The lower sideband is obviously stronger than the revolution harmonic and the upper sideband (not shown here). These plots clearly show the unstable mode. However, from these measurements, we were unable to determine which of the aliased frequencies drove the instability.

NUMERICAL SIMULATIONS

Numerical simulations for the possible modes causing the beam instabilities have been carried out using a parallel code, Omega3P [7], running on the super computer, Edison, at the National Energy Research Scientific Computing Center (NERSC) [8]. The solid model was build and meshed using CUBIT [9] and the data visualization was done with ParaView [10].

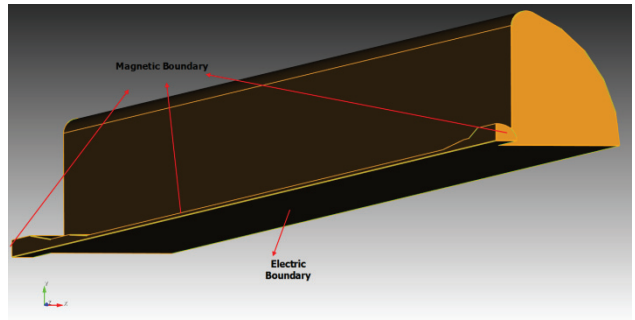

Figure 3: Solid model for the simulations.

Fig. 3 shows the solid model for the simulation, which is a quarter of the whole volume. The model is about 2.6 m long including 2 m of the ID length with transitions at both ends and about 60 cm for elliptical beam pipes having similar size as the standard SPEAR3 vacuum chamber. The full pole gap in this model is initially set to 7 mm. The center plane of the pole gap was set as an electric boundary so that only the TE modes were solved. Partitioning this problem into 22 run, we have spanned the spectrum up to 8 GHz and have found 4600 modes, with the computing time for each run from 10 minutes to 25 minutes.

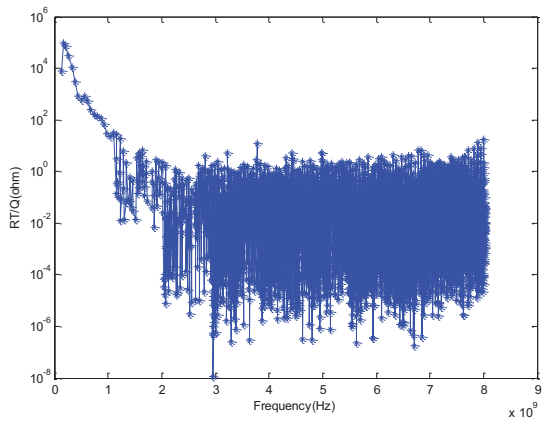

Figure 4: Transverse R/Q up to 8GHz at 7mm gap

As shown in Fig. 4, the transverse R/Q of the modes above 1GHz are more than 4 orders of magnitude lower than those of the first 5 modes, which are all below 400 MHz. The results indicate that the trapped mode in the ID chamber causing the instability should be one of the low frequency modes and should have the same frequency as the instability mode. We have listed the transverse R/Q, Q, and the resonant frequencies for the first 6 modes in Table 2. In the simulation model, we did not include the ID magnets and other supporting mechanical structures, which can contribute significantly to the power dissipations of the resonant modes. As a result, the numerical solutions of the Q may have large discrepancies from the actual values. However, we still expect the mode frequencies and transverse R/Q to be reasonably accurate. At pole gap of 7 mm, our beam-based measurement tells us that the frequency of the instability mode is about 200 MHz. Therefore, Mode 3 in Table 2 is most likely to be the responsible mode because

ISBN 978-3-95450-177-9

it has a high transverse R/Q and is the closest resonant frequency to our measured value. Only Mode 2 showed a higher R/Q in the numerical simulations, but we did not observe instability at this Mode in SPEAR3.

Table 2: Simulation Results for the First 6 Modes

Mode ID	$(R/Q)_T$(ohm)	Q	Freq.(MHz)
1	4.44085e+03	7439	136.48
2	6.15448e+04	4096	167.02
3	5.54048e+04	3127	212.38
4	2.52495e+04	2869	266.75
5	9.16657e+03	2860	325.91
6	2.80429e+03	2967	386.99

Figure 5: RF fields distribution of the 3rd mode. Top: E_y; Middle: B_z; Bottom B_x.

In the pole gap, the electromagnetic fields are dominated by the vertical electric field E_y and the horizontal magnetic field B_x. Elsewhere, in the vast volume of the rest of the ID chamber; the primary field is the longitudinal magnetic field B_z. For each Mode N in Table 2, the longitudinal variation of the RF fields goes through N/2 periods in the chamber.

In Fig. 5, we illustrate the field distributions of the 3rd mode. Both E_y and B_z have a maximum at the longitudinal center while B_x has a null there. These symmetries also hold true for all the modes with odd numbers. For the even-numbered modes, the symmetries are exactly opposite: E_y and B_z vanish at the longitudinal center while B_x has its maximum there. The knowledge of the longitudinal RF field distributions of these modes is helpful for designing methods of coupling their power out of the chamber in an attempt to damp the unstable modes.

We then modified the model to change the pole gap to 6mm and 8mm, respectively, before repeating the simulation for the low frequency modes. The results are shown in Fig. 6. When varying the pole gap from 6mm to 8mm, the frequency of Mode 3 is varied by about 12 MHz, consistent with our beam-based measurements.

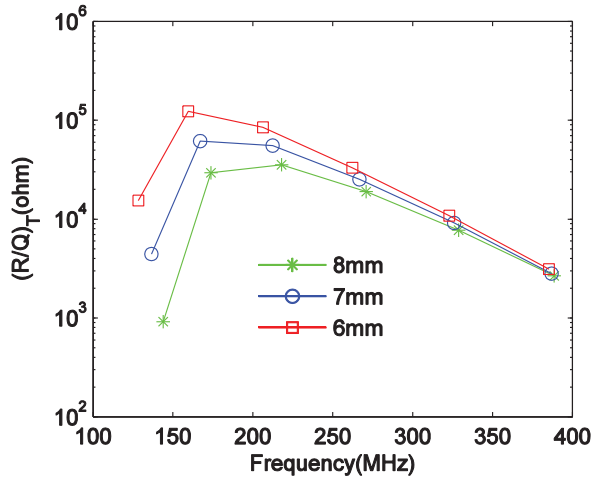

Figure 6: Simulation results at different gaps: 6mm, 7mm, and 8mm.

RF MEASUREMENT

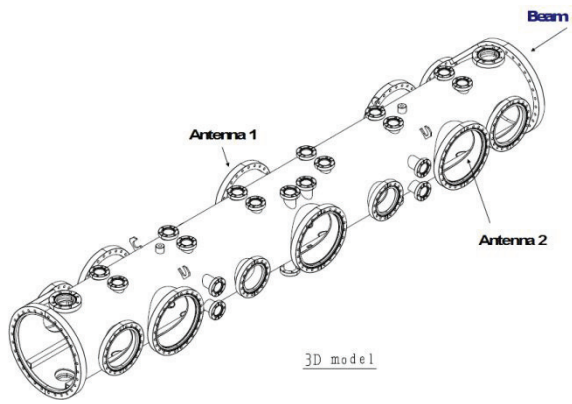

Figure 7: ID chamber and antennas locations.

During the recent SPEAR3 shutdown maintenance period, we conducted S parameter measurements of the BL15 chamber with an Agilent 8753ES network analyzer. We installed two loop antennas into the chamber, so that we could perform both S_{11} and S_{21} measurements. As shown in Fig. 7, one antenna is at the center port of the ID chamber and the other one is at an upstream port about 64.8 cm away. Both antennas are identical; each has a 94mm diameter loop connected to an N-type feedthrough. The loop size was maximized to have the coupling to the chamber as large as possible. However, for an RF frequency of about 200 MHz, the calculated free space radiation impedance from the antenna is only about 0.3 Ω, so we would expect relatively weak coupling for this measurement. Because, for Mode 3, the vacuum chamber is filled with nearly uniformly distributed longitudinal magnetic fields at the longitudinal center, the loop was placed vertically to maximize the coupling.

First we set the BL15 ID gap to 6.82mm and measured the return loss by monitoring the S_{11} at both ports. After scanning a wide range of frequency from 100 MHz to about 400 MHz, we found two dips at the center port corresponding to two modes. The first one was at 109 MHz with less than 0.1 dB return loss and the second one

ISBN 978-3-95450-177-9

was at about 200 MHz with about 0.2 dB return loss. Repeating the S_{11} measurement at the upstream port, the first dip became indistinguishable, but the dip at 200 MHz still remained. In addition another mode showed up at about 148 MHz. As indicated in the simulation, the longitudinal magnetic field has a maximum at the center of the ID chamber for Modes 1 and 3, but has a notch for Mode 2. Comparing the resonant frequency with the first three modes solved in Omega3P shown in Table 2, the discrepancy is reasonable. Therefore, we can conclude that the three modes we observed from the S_{11} measurements correspond to the first three modes in the numerical simulations.

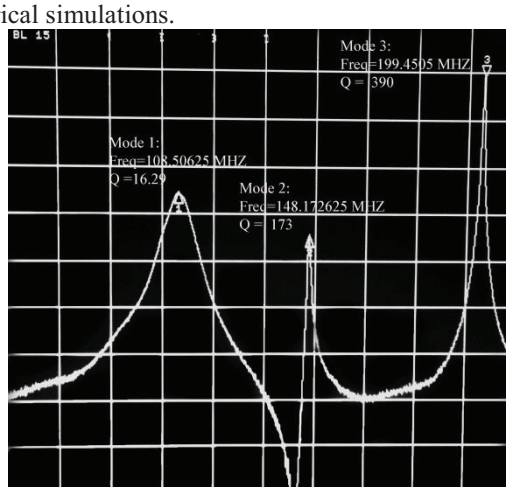

Figure 8: S21 measurement at two ports with 5dB/div

As shown in Fig. 8, the first three resonant modes were all resolved clearly in the S_{21} measurements using both ports. By zooming into each peak, we can measure the Q for each mode as shown in Table 3.

Table 3: S21 Measurement Results for the First 3 Modes

Mode #	Q	Freq. (MHz)
1	16	108.51
2	173	148.17
3	390(0º)/388(45º)/380(90º)	199.45

For mode 3, we rotated the antenna at the center port from vertical orientation (90º) to diagonal (45º) and horizontal (0º) orientation. One should note that the rotation was not done precisely, so an error of several degrees can be expected. At 0º, the antenna had its weakest coupling to the mode, so the measured Q was close to the intrinsic Q. Table 3 shows that, at 90º (maximum coupling), the loaded Q only dropped by 10, less than 3% from the intrinsic Q, which suggests that the power coupled out of the chamber by the antenna is only a small fraction of the power loss inside the chamber. As a result, the antenna we installed for measurements will likely not be effective for coupling the trapped mode out of the chamber during the operation. Fig 9 shows the measured resonant frequency of Mode 3 at various pole gaps from 6.82mm to 10mm at an interval of 0.1mm. The results fit a quadratic curve extremely well (following Slater's perturbation theory [11]) and also agree well with the frequencies of the beam instability mode.

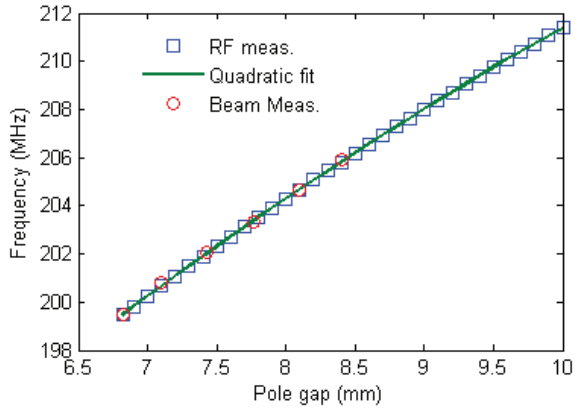

Figure 9: Frequency of Mode 3 at different gaps.

CONCLUSION

After comprehensive studies on the beam instabilities induced by the BL15 ID, we believe that we have identified the trapped mode leading to the instabilities. We are working on the details of an engineering solution to damp the modes sufficiently for stable beam operation at SPEAR3. The results from the study will be useful for future IVUN development in SPEAR3.

ACKNOWLEDGMENT

We want to thank Z. Li, J. Safranek, X. Huang, and A. Ringwall for useful discussions. We also want to thank members of the SSRL vacuum team and the SPEAR3 core team for their support in our RF measurements.

REFERENCES

[1] D. J. Peake *et al.*, "Preliminary Operational Experiences of a Bunch-by-bunch Transverse Feedback System at the Australian Synchrotron", in *Proc. IPAC'10*, Kyoto, Japan, May 2010.

[2] R. Dowd *et al.*, "Investigations of Trapped Resonant Modes in Insertion Devices at The Australian Synchrotron", in *Proc. IPAC'16*, Busan, Korea, May 2016.

[3] R. Bartolini *et al.*, "Analysis of Multi-bunch Instabilities at the Diamond Storage Ring", in *Proc. IPAC'16*, Busan, Korea, May 2016.

[4] S. B. Cohn, "Properties of Ridge Wave Guide", in *Proceedings of the IRE* 35(8), 1947.

[5] Dimtel, San Jose, USA, http://www.dimtel.com

[6] A. Chao, *Physics of Collective Beam Instabilities in High Energy Accelerators,* John Wiley & Sons, Inc., 1993

[7] L.-Q. Lee *et al.*, "Omega3P: A Parallel Finite-Element Eigenmode Analysis Code for Accelerator Cavities", SLAC-PUB-13529, 2009.

[8] NERSC website: http://www.nersc.gov

[9] CUBIT code website: https://cubit.sandia.gov

[10] ParaView code website: http://www.paraview.org

[11] J. C. Slater, Microwave Electronics, Van Nostrand Company, Inc., 1950.

ISBN 978-3-95450-177-9

TRANSIENT STUDIES OF THE STRIPLINE KICKER FOR BEAM EXTRACTION FROM CLIC DAMPING RINGS

C. Belver-Aguilar, M.J. Barnes, CERN, Geneva, Switzerland

Abstract

Stripline kickers are generally assumed to have equal contributions from the electric and magnetic field to the total deflection angle, for ultra-relativistic beams. Hence parameters of the striplines, such as the characteristic impedance, the field homogeneity and the deflection angle are typically determined by simulating the striplines from an electrostatic perspective. However recent studies show that, when exciting the striplines with a trapezoidal current pulse, the magnetic field changes during the flat-top of the pulse, and this can have a significant effect upon the striplines performances. The transient solver of Opera2D has been used to study the magnetic field, for the striplines to be used for beam extraction from the CLIC Damping Rings (DRs), when exciting the electrodes with a pulse of 1 μs flat-top and 100 ns rise and fall times. The time dependence of the characteristic impedance, field homogeneity and deflection angle are presented in this paper. In addition, two solutions are proposed to improve the flatness of the magnitude of the magnetic field throughout the flat-top of the pulse, and the predicted results are reported.

STUDIES IN THE TIME DOMAIN

DRs for high energy e^+e^- colliders, such as CLIC, have a significant role for achieving high luminosity at the interaction point. Two RF baselines are considered for the CLIC DR operation: 1 GHz and 2 GHz RF systems. The injection and extraction process from the DRs will be carried out using one injection and one extraction system, respectively, in each ring, with only one pulse stored in the rings per cycle: this pulse contains either one single train of 156 bunches with 1 GHz RF structure, or two trains of 312 bunches with 2 GHz RF structure. For the extraction system, a pulse of 560 ns rise/fall time and 900 ns pulse flat-top is required for the 1 GHz baseline, whereas the 2 GHz RF system demands a pulse of 1 μs rise/fall time and 160 ns flat-top [1].

Inductive adders will be used to generate the pulses for the striplines for the CLIC DRs [2]. In order to limit the electrical and thermal stresses on the system, the goal is to achieve output current pulse rise and fall times of approximately 100 ns.

The deflecting field of the striplines has been previously studied considering only an electrostatic field [3] and an AC magnetic field [4]. Now, transient simulations with Opera2D [5] have been carried out, and a pulse of 100 ns rise and fall time and 1 μs flat-top has been considered (values close to the 1 GHz RF system goals). The prototype electrodes are made of aluminium Al6063, with an electrical conductivity $\sigma = 3.03 \times 10^7$ S/m. The magnetic field at the centre of the striplines aperture has been calculated and the results are shown in Fig. 1. For these simulations terminating resistors of 50 Ω are assumed, which results in a nominal current of ± 250 A with ± 12.5 kV driving voltage.

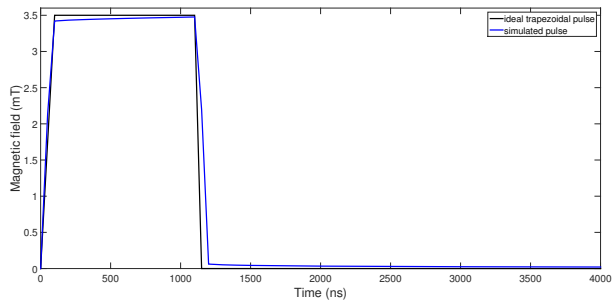

Figure 1: Magnetic field calculated with Opera2D (blue line), compared with an ideal trapezoidal current pulse (black line).

The odd mode characteristic impedance, field inhomogeneity and deflection angle have been studied when considering ideal trapezoidal voltage and current pulses. The characteristic impedance is calculated from inductance and capacitance: these quantities are derived from predicted stored magnetic and electrostatic energy, respectively. The odd mode characteristic impedance increases from 40.57 Ω at the beginning of the flat-top to 41.01 Ω at the end of the flat-top, corresponding to an increase of 1.1%. The field inhomogeneity at 1 mm radius, from the centre of the striplines aperture, increases from ±0.0028% to ±0.0112%, which is close to the maximum limit imposed by beam dynamics requirements (±0.01%). The total deflection angle increases from 1.3597 mrad to 1.3697 mrad, as shown in Fig. 2, which corresponds to an increase of 0.73%.

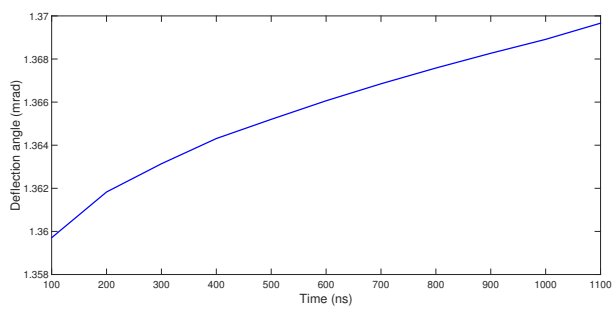

Figure 2: Total (sum of electric and magnetic) deflection angle, during the pulse flat-top.

The increase of the characteristic impedance and hence the increase of the magnetic field and deflection angle, during the pulse flat-top, is greater than specified. In an attempt to flatten the "flat-top" field two proposals are pre-

ISBN 978-3-95450-177-9

sented in the following: (1) using a thin silver coating on the electrodes, and (2) modulate the driving pulses to compensate for the variations in the field flat-top.

SILVER COATING

To improve the flatness of the deflection pulse, the electrodes could be coated by a thin layer of silver in order to increase the electrical conductivity. Opera2D does not presently permit a thin layer of silver to be modelled on top of the aluminium electrodes. Hence, to evaluate the influence of silver, the electrical conductivity of the electrodes has been changed to that of silver ($\sigma = 6.3 \times 10^7$ S/m). A comparison of the magnetic field, during the pulse flat-top, when considering solid aluminium or solid silver electrodes is shown in Fig. 3.

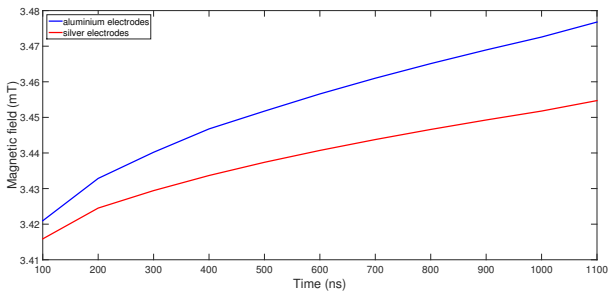

Figure 3: Flat-top magnetic field when considering electrodes made of aluminium (blue line) and silver (red line).

When modelling silver electrodes, the magnetic field at the beginning and at the end of the flat-top is 3.416 mT and 3.455 mT, respectively: hence the increase of the magnetic field during the pulse flat-top is reduced from 1.63% (aluminium electrodes) to 1.14%. Also the field inhomogeneity improves, with a maximum value at the end of the flat-top of ±0.0078%. In addition, the odd mode characteristic impedance ranges from 40.52 Ω to 40.84 Ω during the pulse flat-top: hence the increase of the odd mode characteristic impedance is reduced from 1.1 % (aluminium electrodes) to 0.8%. The total deflection angle, for silver electrodes, changes from 1.359 mrad to 1.366 mrad during the pulse flat-top, as shown in Fig. 4, which corresponds to an increase of 0.5%.

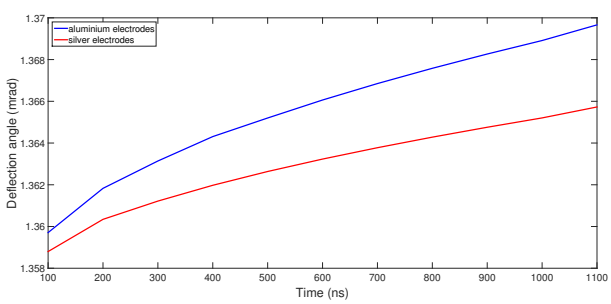

Figure 4: Flat-top deflection angle when considering electrodes made of aluminium (blue line) and silver (red line).

PULSE MODULATION

The variation of the magnetic field, and therefore the total field during the pulse flat-top, can theoretically be compensated, as shown in Fig. 5, by modulating the driving current/voltage, of the electrodes, during the flat-top of the pulse.

The inductive adder has a modulation layer and hence this layer could be used to achieve the required waveforms. The "ideal" current and voltage waveforms have been calculated by considering the total compensation required to achieve a flat deflection angle pulse. To verify the derived waveforms, these are modelled in Opera2D as the driving current and voltage waveforms, assuming ideal terminating resistors on the output of the electrodes.

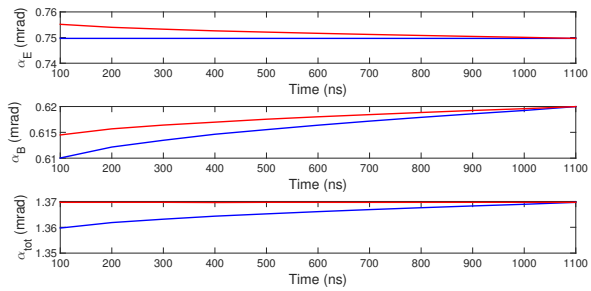

Figure 5: Flat-top electrostatic, magnetic and total deflection angle before modulation (blue line) and after modulation (red line), for aluminium electrodes and considering 50 Ω terminating resistors.

Modelling the derived, modulated, waveform in Opera2D, the increase of the total deflection angle during the flat-top is reduced by more than a factor 100: from 0.73% to 0.006%. The modulation is such as to appropriately increase the magnitude of the start of the flat-top driving voltage/current: the flat-top then decreases in value until it is equal to the original value at the end of the flat-top: Fig. 6 shows a zoom of the required "flat-top" of the voltage/current, for ideal 50 Ω terminating resistors.

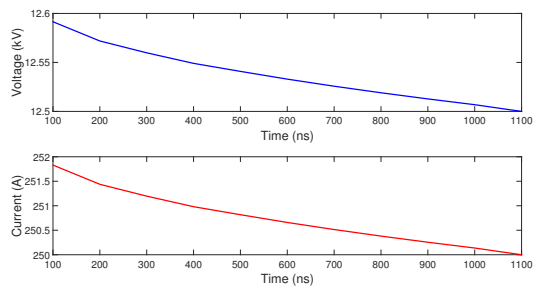

Figure 6: "Flat-top" voltage (blue) and current (red), in order to obtain a “constant” deflecting field (50 Ω terminators).

The voltage and current pulses shown in Fig. 6 have been specified as the flat-top of the driving waveforms in

ISBN 978-3-95450-177-9

Opera2D electrostatic and transient magnetic analyses, respectively, to predict the deflection angle shown in Fig. 5: these waveforms assume ideal 50 Ω terminating resistors. When considering 40.5 Ω terminating resistors, the ideal driving waveforms are shown in Fig. 7.

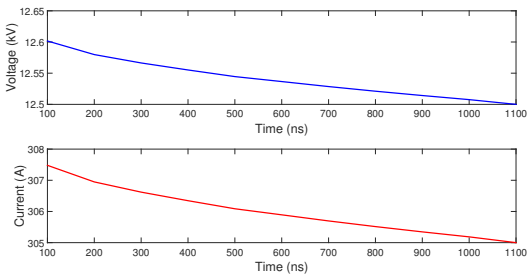

Figure 7: "Flat-top" voltage (blue) and current (red), in order to obtain a "constant" deflecting field (40.5 Ω terminators).

The deflection angles, following the current and voltage pulse modulation, have been calculated: results are shown in Fig. 8.

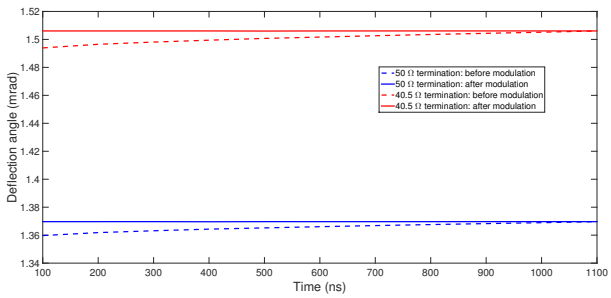

Figure 8: Total deflection angle after voltage/current modulation, for 50 Ω terminating resistors (blue line) and 40.5 Ω terminating resistors (red line).

With 50 Ω terminating resistors the total deflection angle, in the present configuration (aluminium plates, unmodulated waveform), increases during the flat-top from 1.3597 mrad to 1.3697 mrad, which corresponds to an increase of 0.73%. When modulating the pulse current, the predicted stability of the deflection angle is within specification: however the total deflection angle is still 8.7% less than the required 1.5 mrad. Considering 40.5 Ω terminating resistors and modulating the pulse current, the stability of the total flat-top deflection angle is within specification. In addition, the deflection angle of 1.5 mrad is as required for the extraction kicker from the CLIC DRs.

SUMMARY OF THE RESULTS

Driving the striplines with trapezoidal waveforms and considering the electrodes to have an electrical conductivity equal to that of silver, rather than aluminium, improves the flat-top stability of the total deflection angle from 0.73% to 0.52%: however this is still outside the specification of ±0.01%. Appropriately modulating the driving waveforms theoretically results in the required flatness of the total deflection angle.

Table 1: Comparison of the Relative Variation of the Deflection Angle (α), Field Homogeneity (FH) and Odd Mode Characteristic Impedance (Z_{odd}), when Considering Silver Coating and Pulse Modulation

	Al6063 electrodes, (unmodulated pulse)	Silver electrodes, (unmodulated pulse)	Al6063 electrodes, (modulated pulse)
$\Delta\alpha$	0.73%	0.52%	$\ll$ 0.01%
FH	±0.0112%	±0.0078%	±0.0112%
ΔZ_{odd}	1.1%	0.8%	1.1%

CONCLUSIONS

Transient simulations have been carried out in order to consider the effects of 100 ns rise/fall time driving pulses, with a flat-top of 1 μs, upon the predicted characteristic impedance and hence the total deflection angle. The magnetic field, and therefore the magnetic field contribution to the deflection angle is not constant during the flat-top of a trapezoidal current pulse. Two means of improving the flatness of the total deflection angle have been proposed: coating the electrodes with silver or modulating the pulse created by the inductive adder - silver electrodes give the required field homogeneity but do not result in the flat-top stability specifications being met. From the studies, the required output pulse shape from the inductive adder, to compensate the time dependence of the impedance of the striplines, has been derived for both 50 Ω and 40.5 Ω terminating resistors: these waveforms theoretically give the required flat-top of the total deflection pulses. However the field homogeneity is close to, but slightly outside, the specification of ±0.01%. Termination resistors of 40.5 Ω provide the required deflection angle of 1.5 mrad, with a 12.5 kV driving voltage: to achieve the 1.5 mrad with 50 Ω terminating resistors requires that the nominal driving voltage is increased to 13.7 kV. With 40.5 Ω terminating resistors it is not necessary to increase the nominal drive voltage, except for modulation. PSpice simulations to study reflections with 40.5 Ω and 50 Ω terminating resistors will be carried out next.

REFERENCES

[1] CLIC Conceptual Design Report (CDR), Volume 1, www.project-clic-cdr.web.cern.ch/project-clic-cdr/CDR-Volume1.pdf, 2012.

[2] J. Holma, M.J. Barnes, L. Ducimitière, "Measurements on Magnetic Cores for Inductive Adders with Ultra-flat Output Pulses for CLIC DR Kickers", *Proceedings of IPAC 2016*, TH-PMW032.

ISBN 978-3-95450-177-9

[3] C. Belver-Aguilar, "Development of Stripline Kickers for Low Emittance Rings: Application to the Beam Extraction Kicker for CLIC Damping Rings", PhD thesis, 2015.

[4] C. Belver-Aguilar, M.J. Barnes, L. Ducimitière, "Review on the Effects of Characteristic Impedance Mismatching in a Stripline Kicker", *Proceedings of IPAC 2016,* THPMW034.

[5] Opera2D User Guide, Version 17R1. Cobham Technical Services, Vector Fields Software, Oxfordshire, 2014.

ISBN 978-3-95450-177-9

FIRST BEAM TESTS OF THE APS MBA UPGRADE ORBIT FEEDBACK CONTROLLER*

N. S. Sereno†, N. Arnold, A. Brill, H. Bui, J. Carwardine, G. Decker, B. Deriy, L. Emery, R. Farnsworth, T. Fors, R. Keane, F. Lenkszus, R. Lill, D. Paskvan, A. Pietryla, H. Shang, S. Shoaf, S. Veseli, J. Wang, S. Xu, B. X. Yang,
ANL, Argonne, IL, USA 60439

Abstract

The new orbit feedback system required for the APS multi-bend acromat (MBA) ring must meet challenging beam stability requirements. The AC stability requirement is to correct rms beam motion to 10 % the rms beam size at the insertion device source points from 0.01 to 1000 Hz. The vertical plane represents the biggest challenge for AC stability which is required to be 400 nm rms for a 4 micron vertical beam size. In addition long term drift over a period of 7 days is required to be 1 micron or less at insertion device BPMs and 2 microns for arc bpms. We present test results of the MBA prototype orbit feedback controller (FBC) in the APS storage ring. In this test, four insertion device BPMs were configured to send data to the FBC for processing into four fast corrector setpoints. The configuration of four bpms and four fast correctors creates a 4-bump and the configuration of fast correctors is similar to what will be implemented in the MBA ring. We report on performance benefits of increasing the sampling rate by a factor of 15 to 22.6 kHz over the existing APS orbit feedback system, limitations due to existing storage ring hardware and extrapolation to the MBA orbit feedback design. FBC architecture, signal flow and processing design will also be discussed.

INTRODUCTION

Figure 1 shows the layout of the "4x4-test" in sectors 27 and 28 of the APS storage-ring (SR). In green are shown the new orbit feedback hardware including the new FBC to process bpm data and generate corrector setpoints. Four insertion device A:P0 and B:P0 bpms are connected to commercial Libera Brilliance+ (LB+) bpm electronics from Instrumentation Technologies, Solkan, Slovenia to obtain beam position for processing in the FBC. The FBC receives the turn-by-turn (TBT) or 271 kHz beam position data, decimates it by twelve to 22.6 kHz and processes it to obtain corrector setpoints. The corrector setpoints are then applied using an interface (CMPSI-2) between the FBC and the existing fast corrector power supply (PS) controls. The four horizontal and vertical fast correctors used are the A:HV3s and B:HV4s in sectors 27 and 28. In addition the FBC is able to send its bpm and corrector data to a data acquisition system (DAQ) which allows the data to be captured and provides a convenient interface to perform step response measurements (at the 22.6 kHz corrector update rate).

* Work supported by the U.S. Department of Energy, Office of Science, under Contract No. DE-AC02-06CH11357

† sereno@aps.anl.gov

Additional diagnostics shown in the figure include the mechanical motion system (MMS) system [1] and the next generation, grazing incidence insertion device (GRID) XBPM [2]. In these tests, we were most concerned with seeing what is required of the system to meet the AC stability specification so the MMS system data was not used by the FBC to correct for long term drift of the bpms. The GRID, also was not used but is presently used in the APS operations orbit feedback system. Table 1 lists the AC and long term beam stability requirements for the MBA ring.

To begin each study, the SR was filled to 102 mA in 324 equally spaced single bunches. Use of this bunch pattern is twofold: first, the LB+ bpms will have a clean, nearly CW signal at their rf inputs and hence all ADC samples in one turn can be used to compute the average beam position; second, this fill pattern has the longest lifetime (60 h) and there is no need for top-up. During top-up injection transients were expected to corrupt some of the data. Every so often, usually when the beam current dropped below 90-95 mA, we would do a fill-on-fill to 102 mA in the 324 bunch fill pattern.

We used the LB+ with its switching feature off so as to not corrupt the fast data stream (at TBT rates as sent to the FBC) with switching noise. The LB+ was operated in its time-domain processing (TDP) mode so as to reduce the latency as much as possible for data processing and transmission through the device (latency is 2 turns in this mode compared to its digital down-conversion (DDC) processing mode where the latency is 4 turns). Toward the end of the testing program reported here, we also implemented notch filtering to eliminate LB+ switching noise and a low-pass (LP) anti-alias filter in the LB+ to remove switching transients and prevent aliasing of signals above 11.3 kHz. The experiments reported in this note were all performed in the horizontal plane since the vertical plane response matrix was ill-conditioned when using all four singular values (SVs) to construct the inverse response matrix (irm).

FEEDBACK CONTROLLER SIGNAL FLOW, PROCESSING, CONTROL AND HARDWARE

Figure 2 shows the signal flow from bpm data to processed and applied fast corrector setpoints. After forming the bpm error by subtracting the orbit setpoint, the bpm data is multiplied by an irm calculated using standard SR high level software tools. The corrector errors can then be filtered and sent through a PID regulator to produce corrector

ISBN 978-3-95450-177-9

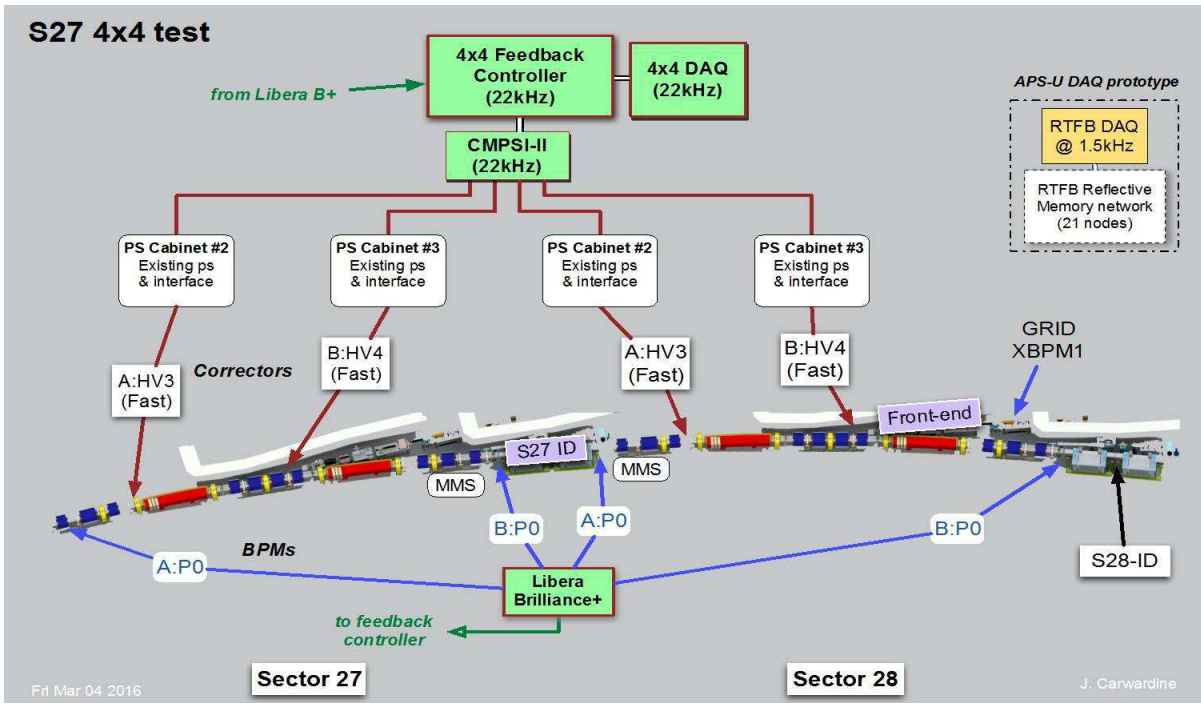

Figure 1: Four corrector, four BPM "4x4-test" layout in sectors 27 and 28 of the APS storage ring. New signal processing hardware is indicated in green.

Table 1: Beam Stability Requirements for the MBA Ring

Plane	**AC Motion (0.01-1000 Hz)** Position (rms)	**AC Motion (0.01-1000 Hz)** Angle (rms)	**Long-term Drift (>100 s)** Position (rms)	**Long-term Drift (>100 s)** Angle (rms)
Horizontal	1.7 μm	0.26 μrad	1.0 μm	0.6 μrad
Vertical	0.4 μm	0.17 μrad	1.0 μm	0.5 μrad

delta values which are then added to the corrector DC setpoint and applied to the corrector CMPSI-2 interface. Main goals for the test are to demonstrate all hardware functioning together, increase the sampling rate by a factor of 15 over the existing real time feedback system (RTFB) to 22.6 kHz from 1.5 kHz, and demonstrate closed-loop bandwidth increase at the four P0 bpms in the loop above the 80-100 Hz closed-loop bandwidth of the present RTFB system. Initial testing reported here used no filtering of the bpm TBT data for closed-loop testing (only decimation by a factor of 12 to 22.6 kHz).

Figure 2 also shows pictures of the hardware used in the test. We used a microTCA-based CommAgility AMC-V7-2C6678 as the FBC which uses a Xilinx Virtex 7 FPGA to route data to two TMS320C6678 DSPs each with eight cores. We implemented the feedback algorithm shown in the figure on one core on one of the DSPs. This offered the flexibility of implementing the feedback algorithm in C code and allowed easy reuse of code from our existing RTFB system which is presently running a previous generation TMS320 DSP. Additional flexibility is afforded by the DSP hardware since additional processing of the same bpm and corrector data can be done on the other 15 remaining DSP cores. The FPGA is used to receive TBT LB+ BPM data and send it to the DSP and receive processed corrector setpoints at 22.6 kHz (every 12 turns) from the DSP and send to the CMPSI-2. The CMPSI-2 consists of a Xilinx Zynq FPGA and is used to convert DSP corrector setpoints to the format used by the existing APS fast corrector interface. The DSP can also generate a step input using the bpm or corrector setpoints. In this way, step response measurements can easily be done. We measured step responses using this functionality to assess the latency in the existing fast corrector system and identify where latency reductions should be made in the future full integrated test in sectors 27 and 28 planned in fall of 2016.

A long term plan for the MBA ring is to implement the FBC system using a modular approach in a microTCA crate (the existing RTFB system uses VME). We anticipate using the present double-sector feedback architecture where each FBC has access to two sectors worth of bpms and correctors. The FBCs communicate via fast fiber links to adjacent FBCs. TBT bpm data will allow flexibility to test different feedback algorithms such as the ability to perform local

ISBN 978-3-95450-177-9

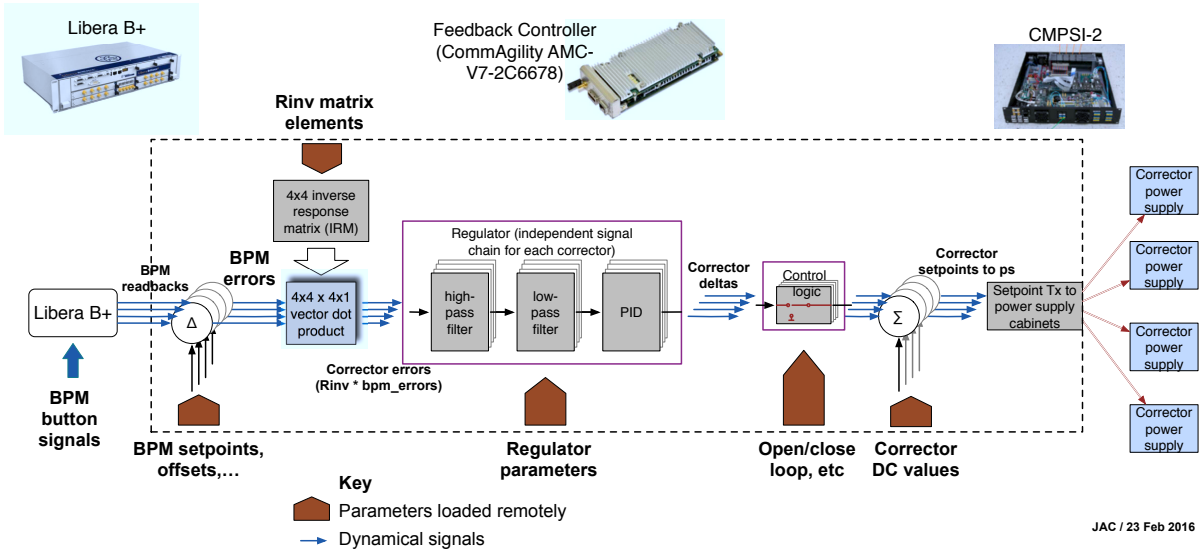

Figure 2: FBC signal flow diagram starting with bpm data on the left to fast corrector setpoints on the right. Shown at the top of the figure are pictures of the new hardware including: commercial BPM electronics (LB+) available from Instrumentation Technologies, the FBC CommAgility AMC-V7-2C6678 microTCA board and the CMPSI-2 which uses a Xilinx Zinq FPGA used to convert corrector setpoints at 22.6 kHz to the existing CMPSI interface for the APS fast corrector power supplies.

fast correction (using only local TBT bpm data is used to compute local fast corrector setpoints) before the full bpm vector is available to each FBC for full correction of the orbit. Other FBC star-type architectures for the system are also being considered where TBT bpm data transfer latency reduction is a primary goal.

CLOSED-LOOP BANDWIDTH AND RMS MOTION MEASUREMENTS

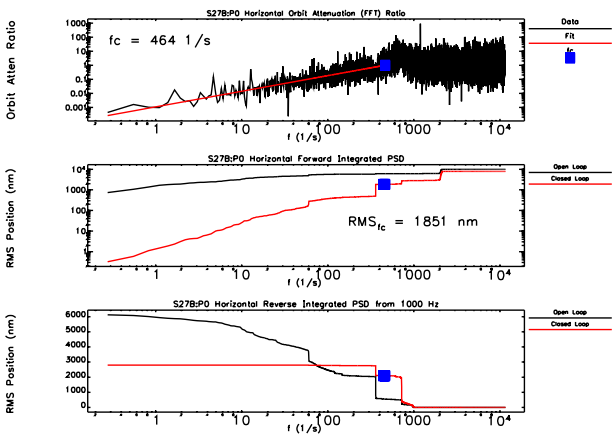

Figure 3: Orbit attenuation and closed-loop bandwidth plot for S27B:P0 (upstream ID P0 bpm). Top plot: Orbit attenuation showing closed-loop bandwidth cutoff frequency of 464 Hz. Middle plot: forward integrated PSD. Bottom plot: reverse integrated PSD starting at 1000 Hz. The closed-loop bandwidth shown in the figure did not change when we tested notch filtering and anti-alias LP filtering in the LB+.

Figure 3 shows the results of the closed-loop bandwidth test as measured at the S27B:P0 bpm (the bpm upstream of the sector 27 ID). The top plot shows the orbit attenuation as a function of frequency as the ratio of the FFT of the data closed-loop vs open-loop (approximately 5 seconds of data at 22.6 kHz sampling rate was taken to generate the plots). One clearly sees that near DC three orders of magnitude of attenuation (60 dB) is achieved. The curve crosses unity at a cutoff frequency of approximately fc = 464 Hz indicating the closed-loop bandwidth. This closed-loop bandwidth is a factor of 5 above that achieved by RTFB in the present machine. The middle plot shows the total rms (square-root of the forward-integrated PSD) motion of 1851 nm at the cutoff frequency compared to closed-loop. The bottom plot shows the square-root of the reverse-integrated PSD starting from 1000 Hz showing amplification of the line at 720 Hz and attenuation at 360 Hz. The data shown in fig. 3 were obtained using only proportional and integral control and no filtering. Frequency domain data closed-loop at the other three P0 bpms was similar to that shown in fig. 3.

FAST CORRECTOR STEP RESPONSE MEASUREMENTS

The FBC was used to perform both closed and open-loop step response measurements by changing bpm or corrector setpoints in a single 22.6 kHz clock tick of 44.2 μs. Comparing closed-loop step response for the 4x4-test and a similar configuration of 4 bpms and 4 fast correctors configured for use by the operations RTFB system showed an increase in speed by a factor of 2.5 when using integral control only for each system. In addition, open-loop step response measurements of the fast correctors were obtained by using an

ISBN 978-3-95450-177-9

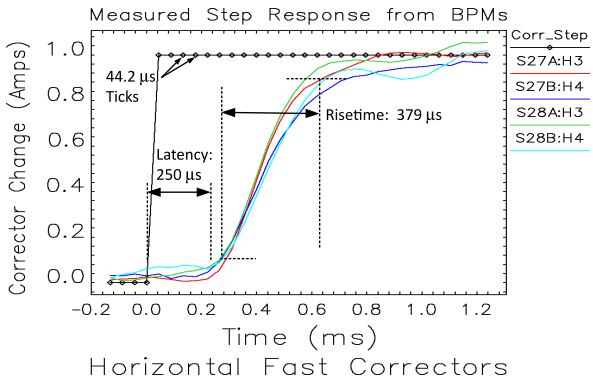

Figure 4: Open-loop horizontal fast corrector step response measurements inferred from P0 bpm step response data and the inverse response matrix.

inverse response matrix on bpm data when each fast corrector was stepped in turn. Figure 4 shows the results for the horizontal correctors. Vertical corrector step responses were similar. Note the plot shows the measured total latency in the system. The plot shows large 250 μs latency where no output from the fast corrector is observed. After this initial latency, the risetime from 10 to 90 % full value is 379 μs.

Due to the large corrector latency, one would not expect to be able to achieve 1000 Hz closed-loop bandwidth since alone, 250 μs implies 90 degrees of the total phase margin at 1000 Hz. Other latencies in the system were tabulated and found to be mostly due to the fast corrector PS including setpoint data transmission, DAC and regulator delay and the 22.6 kHz clock tick. The LB+ was found to have negligible latency of 7 μs in its time-domain processing (TDC) mode (with no filtering) by comparison. We expect the large corrector latency to be much reduced for the MBA ring by careful design of PS controllers, fast corrector power supplies and magnets and vacuum chambers.

CONCLUSION

We have demonstrated first closed-loop test of new orbit feedback hardware at a 22.6 kHz update rate using four bpms and four correctors configured as a "4x4" bump. We have demonstrated closed-loop orbit attenuation at the bpms up to 464 Hz and step response improvement of a factor of 2.5 over the existing orbit feedback system. These results will be used to optimize the system for the full integrated test this fall. In the integrated test, latencies in the PS will be minimized by using MBA upgrade PS hardware including a new PS corrector setpoint switch, controllers and fast corrector power supplies. In addition, a fully unified fast and slow corrector feedback algorithm will be used [3,4]. It is expected that ultimately the limiting factor to achiving the 1000 Hz closed-loop bandwidth will be the fast corrector magnet and vacuum chamber which has been measured to have a 3dB bandwidth of approximately 750 Hz. In addition, notch filtering for LB+ switching transients and anti-alias filtering will be added to the TBT data to eliminate aliased and switching transient signals. Additional closed-loop bandwidth testing will be done to assess the impact of additional latency due to filtering in the LB+ (or when as planned this filtering is moved to the FBC). Additional filtering latency will be offset to a large degree by using MBA upgrade fast corrector power supplies, controllers and setpoint transfer switch which should save at least $\approx 200\mu$s.

Finally MMS and GRID diagnostics will be brought to bear on assessing how well the prototype FBC can meet the demanding long-term beam stability goals in table 1. The 4x4-test was an important stepping stone that was used to develop and test the first version of the prototype FBC and bpm hardware. In addition, software tools were developed for control room evaluation of FBC performace which will be upgraded and modified going forward into integrated feedback system testing in the fall of 2016.

ACKNOWLEDGMENT

The authors thank V. Sajaev and A. Xiao for helpful discussions and comments on orbit feedback. Many thanks go to the technicians from the various technical groups who assembled and tested hardware for the 4x4-test. We also appreciate help from the APS main control room operators during the course of the 4x4-test machine studies.

REFERENCES

[1] R. Lill, N. Sereno and B. X. Yang, "BPM Stability Studies for the APSMBAUpgrade," proceedings of IBIC16.

[2] B. X. Yang, etal. "Performance Test of the Next Generation X-Ray Beam Position Monitor System for the APS Upgrade," proceedings of IBIC16.

[3] J. Carwardine, APS Upgrade Feedback Workshop, May, (2013).

[4] N. S. Sereno, etal. "Beam Stability R&D for the APS MBA Upgrade," IPAC15, Richmond, Va. (2015).

ISBN 978-3-95450-177-9

FIRST OPERATIONAL EXPERIENCE WITH THE LHC DIODE ORBIT AND OSCILLATION (DOROS) SYSTEM

M. Gasior, G. Baud, J. Olexa, G. Valentino, CERN, Geneva, Switzerland

Abstract

The LHC started high-energy operation in 2015 with new tertiary collimators, equipped with beam position monitors embedded in their jaws. The required resolution and stability of the beam orbit measurements linked to these BPMs were addressed by the development of a new Diode ORbit and OScillation (DOROS) system. DOROS converts the short BPM electrode pulses into slowly varying signals by compensated diode detectors, whose output signals can be precisely processed and acquired with 24-bit ADCs. This scheme allows a sub-micrometre orbit resolution to be achieved with robust and relatively simple hardware. The DOROS system is also equipped with dedicated channels optimised for processing beam oscillation signals. Data from these channels can be used to perform betatron coupling and beta-beating measurements. The achieved performance of the DOROS system triggered its installation on the beam position monitors located next to the LHC experiments for testing the system as an option of improving the beam orbit measurement in the most important LHC locations. After introducing the DOROS system, its performance is discussed through both, beam and laboratory measurements.

INTRODUCTION

The Diode ORbit and OScillation (DOROS) system has been primarily designed and optimised for processing signals from the beam position monitors (BPMs) embedded into the jaws of the LHC collimators [1-3]. The system provides orbit readings used for the automatic positioning of the collimator jaws symmetrically around the beam, which reduces drastically the time needed to set-up the collimators and ensures that the collimation hierarchy is always maintained [4].

The DOROS processing for one BPM electrode pair is schematically shown on the block diagram in Fig. 1. It contains four main parts, namely RF processing, orbit processing, oscillation processing and the FPGA controller. The role of the RF processing is to deliver signals with sufficiently large amplitudes to the orbit processing, whose key components are the compensated diode detectors [1]. The detectors convert the amplitude of RF beam pulses into DC voltages which can be measured with very high resolution by the system ADCs. As the orbit processing does not have sufficient bandwidth to cope with signals at LHC betatron frequencies (around 3 kHz), the system is also equipped with a dedicated circuitry optimised for beam oscillation signals.

The RF processing starts with 80 MHz non-reflective filters to reduce the peak amplitudes of the BPM signals, followed by an isolation RF transformer. The transformer cuts ground loops between the LHC machine and the racks where DOROS front-ends are installed, allowing a very clean transmission of the BPM signals. The signals then pass through a calibration switch, which periodically swaps the BPM electrode signals. This way each electrode

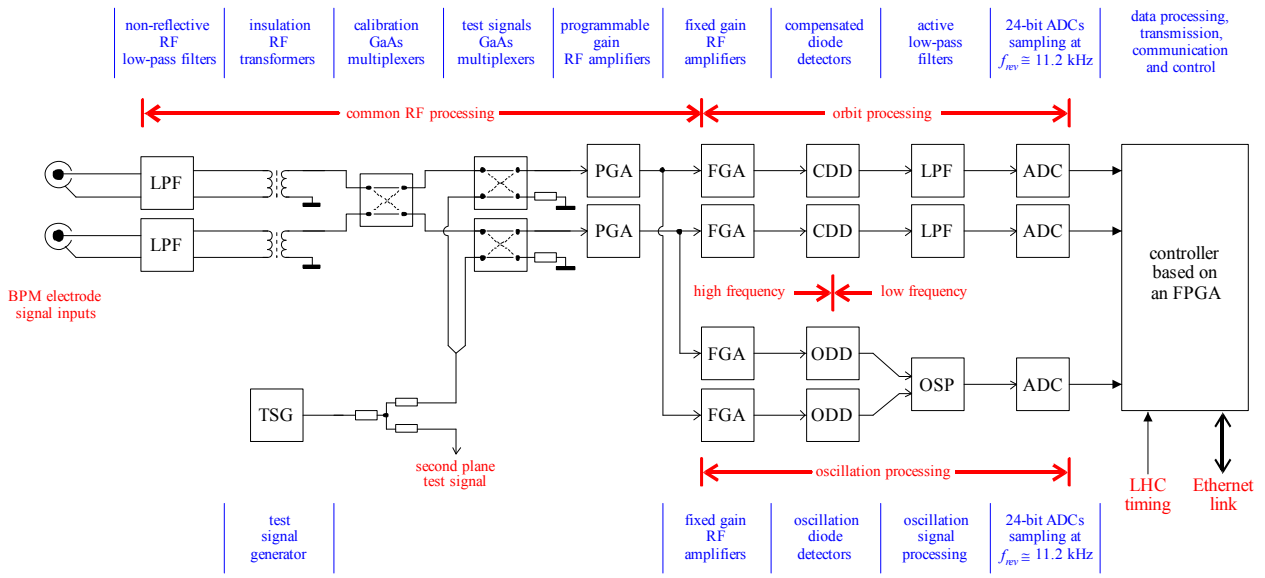

Figure 1: Block diagram of two channels of a DOROS front-end processing signals from one pair of BPM electrodes. LPF – low-pass filter, TSG – test signal generator, PGA – programmable gain amplifier, FGA – fixed gain amplifier, CDD – compensated diode detector, ODD – oscillation diode detector, OSP – oscillation signal processing.

ISBN 978-3-95450-177-9

signal is measured twice in either configuration of the switch. The resulting amplitudes are combined to make the calculated beam position independent of the residual asymmetry between both channels [5].

The test multiplexers allow injection of locally generated signals used to check the functionality of the system without beam. They are followed by programmable gain amplifiers, whose gain can be changed from −15 to +50 dB in 1dB steps. The gain is automatically set according to the actual beam intensity by the system FPGA controller to maintain optimal signals on the diode detectors.

The orbit processing starts with fixed gain amplifiers driving the compensated diode detectors. Their output signals go through 100 Hz low pass filters prior to being digitised by the ADC sampling at the LHC revolution frequency (f_{rev}, about 11.2 kHz). For orbit processing the ADC samples are filtered in IIR filters implemented in the system FPGA, decimated and transmitted over Ethernet as UDP packets.

The oscillation part implements signal processing similar to tune measurement systems based on diode detectors [6]. It starts with fixed gain amplifiers driving the oscillation diode detectors. They are followed by oscillation signal processing, consisting of amplifying and filtering the differential detector signal to the bandwidth 0.05–0.5 f_{rev}, which is then digitised at f_{rev} synchronously to the orbit signals. The oscillation ADC samples are processed in the system FPGA, resulting in amplitudes and phases, which are sent in the common UDP packets [7].

The oscillation part requires special timing and synchronisation circuitry to relate the beam oscillation signals acquired with many DOROS front-ends distributed around the LHC ring [8]. A detailed description of the DOROS system and of its performance can be found in a Ph.D. thesis [9].

DOROS SYSTEMS

The DOROS processing is implemented in front-ends built as 1U 19” modules. Each front-end can process signals from four BPM electrode pairs. This typically means the upstream and downstream single-plane BPMs of two collimators or the horizontal and vertical electrode pairs of two stripline BPMs. All DOROS front-ends are identical and transmit both the amplitudes of BPM electrode signals and beam oscillation data. The front-ends continuously send data as UDP packets every 40 ms upon triggers received over optical fibre distributing the LHC beam synchronous timing. A dedicated DOROS server receives this data and converts it into beam parameters, based on the geometry and location of the corresponding BPMs. The server also sends control commands to the DOROS front-ends, performs data logging and monitors the proper operation of the front-ends.

Each DOROS front-end is declared in the CERN Ethernet network as an independent device identified by a programmable 16-bit ID. This ID also defines the front-end MAC address, allowing for an easy exchange of the front-ends, as the new front-end gets the same ID and MAC address as its predecessor.

The system FPGA runs permanent system checks and is able to reboot its hosting front-end autonomously. The reboot is done by switching off the power of all front-end components, except for a robust passive power supply and simple watchdog circuitry. This way the front-end can recover from a latch-up caused by a radiation-induced single even upset. The system server also checks data consistency and can trigger a reboot of a malfunctioning front-end by sending a reset UDP command.

DOROS front-ends can store in a local memory both orbit and oscillation ADC samples for a few millions of turns, which can be read-out for off-line analysis upon user requests. The front-ends also have a dedicated post-mortem buffer transmitted for analysis after each beam dump.

There are currently three separate DOROS systems installed, each connected to its dedicated server. The first system consists of 10 DOROS front-ends connected to the BPMs of 18 LHC collimators. The second contains 11 front-ends connected to 21 stripline BPMs located next to the LHC experiments, with the signals split between DOROS and the regular LHC BPM electronics [10]. The third system contains a few development front-ends located in both the LHC and the SPS accelerators.

ORBIT MEASUREMENTS

The quality of DOROS orbit measurements is presented in Fig. 2, showing typical orbit drifts from the upstream and downstream BPMs of a collimator, logged during an 11-hour LHC physics fill. The distance between the two BPMs embedded into the collimator jaws is about 1 m. There is a very good correlation between the orbits measured by both BPMs indicating that the observed drifts, in the order of 10 μm, are indeed caused by the beam. The two abrupt position changes are related to orbit scans performed to optimise the LHC collisions.

The stability of the DOROS orbit measurements can be assessed from the difference between the orbit readings of the upstream and downstream BPMs. This variation can be seen to be of the order of 0.5 μm, as shown in red curve of Fig. 2. The 0.1 μm granularity of the variation is defined by the resolution of the logging database from which the orbit data was taken. The resolution of the DOROS orbit measurements is about an order of magnitude better [3].

DOROS system works very well with the collimator BPMs for which it was designed, where the beam is always quite close to the BPM centre resulting in similar signals on the opposing electrodes. For the standard BPMs it is not generally the case, especially for the stripline BPMs installed next to the LHC experiments, where both beam travel in the same beam pipe with an intentional separation between them. Artificial orbit drifts in the order of a few tens of micrometres have been observed on these stripline BPMs during typical LHC physics fills. The drifts are caused by the combination of a large beam offset, the residual nonlinearity of the compensated diode detectors

ISBN 978-3-95450-177-9

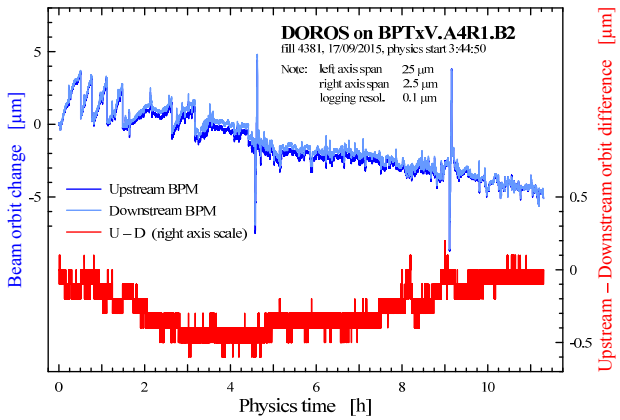

Figure 2: Orbit measurements on two BPMs embedded in the jaws of a collimator.

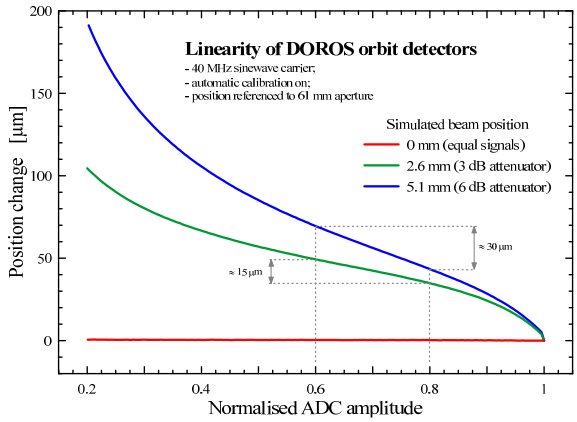

Figure 3: Position change caused by the nonlinearity of the compensated diode detectors (laboratory).

and the beam intensity decay during the physics fill. This effect can be reproduced and has been studied in the laboratory. Figure 3 shows measurements performed by operating a DOROS front-end using a generator signal with a linearly decreasing amplitude to simulate the beam intensity change. The signal was split between the two channels and attenuated to produce signals with different amplitude ratios, simulating three different beam positions. As the position calculation involves signal normalisation, the quality of the generator signal was not critical for the measurements.

The plot shows three measurements with the simulated positions referenced to a stripline with 61 mm aperture, the same as for the LHC BPMs equipped with the DOROS electronics. It can be seen that for the centred beam the nonlinearity of the detectors has little influence, as it is common to both signals. This is why the collimator BPMs work very well. However, for an offset position significant orbit drifts are observed as the beam intensity decreases.

During typical physics fills the LHC intensity can halve, causing a proportional drop in the BPM signals. Most of this drop is compensated automatically by increasing the gain of the DOROS RF amplifiers. The gain can be increased in 1 dB steps (some 12 %) and is controlled by an automatic algorithm (switched off for the measurements of Fig. 2) to maintain the amplitudes measured by the ADCs within a certain window. To estimate the orbit error due to the intensity decay with an offset position one can assume that the larger electrode signal is maintained between 0.6 and 0.8 of the ADC full scale. Variations within this window would result in an orbit error of up to 15 µm for a beam offset by 2.6 mm and 30 µm for a beam offset of 5.1 mm. The orbit drifts observed with beam are compatible with this estimate. These drifts currently prevent the use of DOROS for orbit feedback to maintain optimal collisions. Dedicated studies are therefore ongoing to precisely characterise the nonlinearity of the orbit detectors, with the aim of performing adequate software corrections on the system server prior to calculating the beam orbits.

An example of the use of the orbit data stored in the DOROS local memory is presented in Fig 4. The plot shows magnitude spectra calculated from 1 million turns of orbit data. The data was acquired from a BPM located next to the LHC ATLAS experiment. Two spectra are shown, one where the beta function at the BPM is relatively small (flat top) and one after the beta squeeze, where the beta function is much larger (physics). Comparing these spectra allows deducing the origin of the oscillations observed on the beam, with those originating from the mechanical vibration of the quadrupole magnets of the experimental insertions expected to be enhanced with the change in machine optics. This knowledge is crucial both for optimising the machine and for the design of the next generation of focusing quadrupoles foreseen for the high-luminosity LHC upgrade.

OSCILLATION MEASUREMENTS

Due to optimisation of the orbit detectors for stability and resolution their bandwidth is limited to some 100 Hz. To analyse beam motion at higher frequencies one can use data from the oscillation processing. A comparison of the vertical plane magnitude spectra calculated from DOROS oscillation data with that from the standard LHC BPM electronics is presented in Fig. 5. Both systems were connected to the same stripline BPM, to compare their relative sensitivities for a single pilot bunch. The beam excitation with the amplitude of some 20 μm_{RMS} was provided by the transverse damper system.

The spectral line corresponding to the vertical excitation at $0.32\,f_{rev}$ is visible in the spectra from both systems. However, the much smaller line corresponding to the horizontal excitation at $0.27\,f_{rev}$, present in the vertical spectrum due to the betatron coupling, is only seen with the DOROS system, whilst it is completely immersed in the noise when measured with the standard BPM electronics. With the order of magnitude higher sensitivity shown by the DOROS system it is hoped that on-line local coupling and optics measurement with LHC physics beams might become a reality [11]. Such measurements currently rely on the standard BPM system, requiring excitation at the millimetre level, which can only be used with few bunches in the machine.

ISBN 978-3-95450-177-9

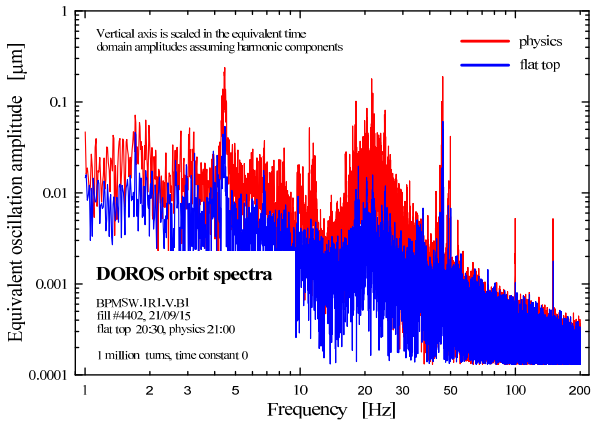

Figure 4: Low frequency vertical beam spectra calculated from DOROS orbit data.

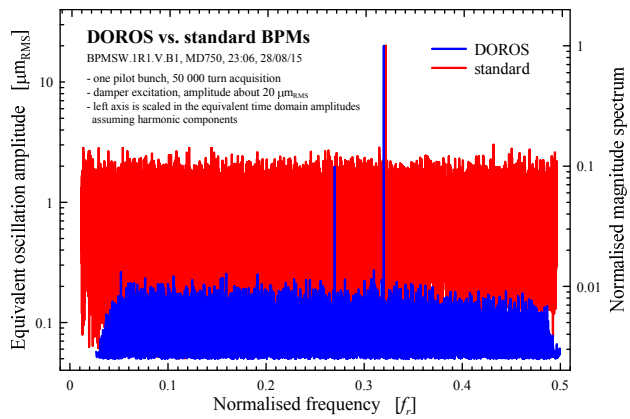

Figure 5: Comparison of vertical beam spectra from the DOROS and standard BPM electronics.

CONCLUSIONS AND OUTLOOK

The DOROS system was designed for measuring beam orbits in the BPMs embedded in the LHC collimators jaws. The goal of achieving sub-micrometre orbit resolution and micrometre stability was achieved with relatively simple and robust hardware, despite the relatively low signal amplitudes available from the small button electrodes of the collimator BPMs. The system is now operationally used for automatic positioning of the collimator jaws and for the continuous monitoring of the beam position at the collimator locations [4]. Further developments involving the generation of beam interlocks from collimator BPMs are ongoing.

The same system was installed on some 20 LHC BPMs located around the LHC interaction regions for comparison with the standard LHC BPM system. It was found that the residual nonlinearity of the orbit diode detectors causes systematic orbit errors at the level of tens of micrometres when the beam has large orbit offsets or when the beam intensity varies. Extensive studies are currently being carried out to linearize the detector characteristics.

The DOROS system can also be used for observing beam spectra and deriving beam parameters from driven beam oscillations. Beam spectra in the frequency range from DC to some 100 Hz can be analysed using DOROS orbit data while the range from 0.5 to 5 kHz can be covered with the oscillation data.

The most advanced application of DOROS oscillation data is for local coupling measurement, which has been demonstrated with very small beam excitation. In the future it is also planned to use DOROS for beta-beating measurements using the synchronous detection implemented in the DOROS FPGAs [7].

The DOROS principle is planned to be implemented in the new SPS BPM electronics and in the longer term it is considered also as a candidate for orbit processing of new LHC BPM electronic. Recent studies have also shown that using BPM electronics based on diode detectors may improve the orbit measurement accuracy in stripline BPMs working with counter-propagating beams [12].

REFERENCES

[1] M. Gasior, R.J. Steinhagen, “High resolution beam orbit measurement electronics (…)”, Proceedings of BIW 2010, Santa Fe, NM, USA, CERN-BE-2010-009.

[2] M. Gasior, J. Olexa, R.J. Steinhagen, “A high resolution diode-based orbit measurement system (…)”, Proceedings of DIPAC 2011, Hamburg, Germany, CERN-BE-2011-024.

[3] M. Gasior, J. Olexa, R.J. Steinhagen, “BPM electronics based on compensated diode detectors – results from development systems”, Proceedings of BIW 2012, Newport News, VA, USA, CERN-ATS-2012-247.

[4] G. Valentino et al., “First operational experience with embedded collimator BPMs in the LHC”, Proceedings of IPAC2016, Busan, Korea, 10.18429/JACoW-IPAC2016-WEPMW034.

[5] M. Gasior, “Calibration of a non-linear beam position monitor electronics (…)”, Proceedings of IBIC 2013, Oxford, UK, CERN-ACC-2013-0295.

[6] M. Gasior, “(…) High sensitivity tune measurement using direct diode detection”, Proceedings of BIW 2012, Newport News, VA, USA, CERN-ATS-2012-246.

[7] J. Olexa et al., “Prototype system for phase advance measurements (…)”, Proceedings of MAREW 2013, Pardubice, Czech Republic, CERN-ATS-2013-038.

[8] M. Gasior, J. Olexa, “Synchronisation of the LHC betatron coupling and phase advance measurement system”, Proceedings of IBIC 2014, Monterey, CA, USA, CERN-BE-2014-001.

[9] J. Olexa “Signal processing and synchronisation of the novel LHC diode orbit and oscillation system”, Ph.D. thesis, Faculty of Electronics and Information Technology, Slovak University of Technology, Bratislava, to be published.

[10] E. Calvo-Giraldo et all, “The LHC Beam Position System (…)”, Proceedings of DIPAC 2011, Hamburg, Germany, CERN-BE-2011-010.

[11] T. Persson et al., “Experience with DOROS BPMs (…)”, Proceedings of IPAC2016, Busan, Korea, 10.18429/JACoW-IPAC2016-MOPMR029.

[12] D. Draskovic al., “Impact of the directivity of a stripline pickup on the accuracy of the beam position monitor systems (…)”, to be published in Journal of Instrumentation.

ISBN 978-3-95450-177-9

BEAM POSITION MONITORS FOR LEReC*

Z. Sorrell†, P. Cerniglia, R. Hulsart, K. Mernick, R. Michnoff
Brookhaven National Laboratory, Upton, NY, USA

Abstract

The operating parameters for Brookhaven National Laboratory's Low Energy RHIC Electron Cooling (LEReC) project create a unique challenge. To ensure proper beam trajectories for cooling, the relative position between the electron and the ion beams needs to be known to within 50µm. In addition, time of flight needs to be provided for electron beam energy measurement. Various issues have become apparent as testing has progressed, such as mismatches in cable impedance and drifts due to temperature sensitivity. This paper will explore the difficulties related to achieving the level of accuracy required for this system, as well as the potential solutions for these problems.

INTRODUCTION

The LEReC project has strict requirements for position and phase measurements. The ion beam has a repetition rate of 9 MHz and the electron beam has a repetition rate of 704 MHz. Two sets of electronics are planned for handling the low frequency and high frequency signals. The typically operation will have 704 MHz bunch trains to overlap the ion beam (Fig. 1). For the electrons to properly cool the ion beam they must be travelling at the same speed with an angle of less than 100 µrad between the beams [1]. To ensure sufficient cooling, the difference between the electron beam and the ion beam must be measured with 50 um accuracy. The challenge with this level of accuracy is the difference between the frequencies of the two beams which creates disparate responses in signal processing. Due to difficulties associated with absolute calibration of BPM electronics, a relative measurement between the two beams is planned.

. During the initial testing, the BPM system will also be responsible for making phase measurements that can be used to calculate the energy of the electron beam. These phase measurements must have a resolution of 0.25 degrees at 704 MHz to give the necessary 1ps resolution for time of flight between BPMs placed several meters apart, in order to provide the required energy resolution of roughly 2E-4 at 400KeV [1].

Several design challenges exist including, synchronous phase measurements across all BPMs, unacceptable errors due to temperature sensitivity of the cables which affect attenuation and cable delays, and matching the high and low frequency signal responses for relative position measurements.

* Work supported by BSA under DOE contract DE-AC02-98CH10886
† zsorrell@bnl.gov

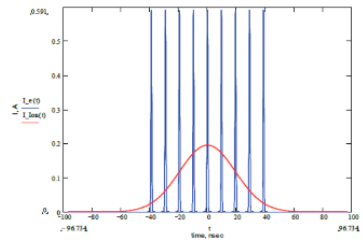

Figure 1: Electron bunches (blue) overlapping with ion bunches (red). [2]

HARDWARE ARCHITECTURE

The LEReC BPM pickups use 9mm, 15 mm and 28mm buttons oriented along the x and y planes of the machine [2]. The electronics for processing the data from the buttons will be located in a nearby equipment building and will require cable lengths greater than 200 feet, partially routed outdoors. The long cable lengths introduce severe attenuation of the higher frequency 704 MHz electron signal.

Due to the difficulties associated with accurately measuring electron and ion beam signals with different base frequencies, two different analog front ends planned to be used to pre-process the signals. The most significant difference between the two sets of analog front ends is the filters. For low frequency ion and electron measurements a 39 MHz low pass filter will be used and for electrons a 707 MHz band pass filter will be used (Fig. 2). The 9 MHz macrobunch structure of the electron beam signal creates a strong response when the signal is processed at 9 MHz, allowing the electron and ion beam signals to be processed with the same electronics. Diplexers will be mounted in the racks to separate the low and high frequency signals. There will be an RF switch module mounted in the tunnel, the purpose of this module will be explained later in the paper.

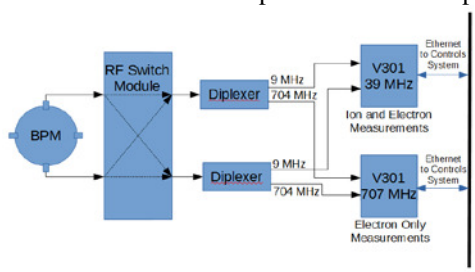

Figure 2: The basic configuration showing how BPM signals are connected to the processing electronics. The 39 MHz electronics measures both electrons and ions.

Libera BPM electronics from a previous project will process the signals in the transport section of the electron beam line. The remaining BPM signals will be processed using in-house designed V301 modules, which are based

ISBN 978-3-95450-177-9

on a ZYNQ SoC containing an FPGA and a microprocessor on the same die. This architecture provides an incredible amount of flexibility for processing data [3].

PHASE MEASUREMENT TECHNIQUE

Achieving the desired one picosecond resolution for time of flight requires a phase measurement with a resolution of approximately 0.25 degrees. Phase measurements with this resolution must be made at multiple BPMs with a common reference in order to be useful.

One common method for measuring phase is to down convert relative to a distributed reference signal. The BPM electronics that are being used for LEReC were not initially designed with phase measurements in mind. However, a solution has been found. A digital recreation of the 704 MHz RF clock will be produced in each V301 module to provide a common reference for phase. The RF clock for LEReC is generated using a 100 MHz master clock and a direct digital synthesizer driving a 400 MHz digital to analog converter. By converting the 100 MHz reference clock to 400 MHz to drive both the analog to digital converters and the direct digital synthesizer, the RF clock can be accurately reproduced. The phase of the electron beam at a BPM relative to this RF clock can then be calculated using IQ demodulation (Fig. 3). The phase is then the inverse tangent of the in-phase and quadrature components of the output of the demodulator.

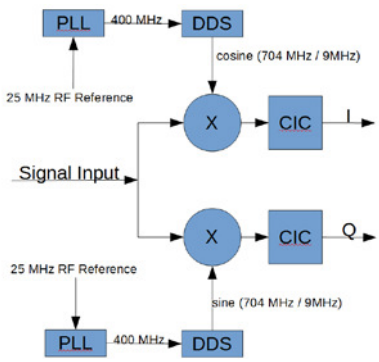

Figure 3: Block diagram of the digital IQ demodulator. Both direct digital synthesizers (DDS) blocks refer to the same synthesizer with sine and cosine outputs. The cascaded integrator comb filters (CIC) decimate the signal by a factor of 512.

Demodulation using a common clock does not provide a sufficient measurement by itself. The BPMs have different cable lengths between the pickups and the electronics. Although the length of each cable can be measured, the overall time of flight on the cable is not actually required. Instead, a function generator can be placed at the far end of the cables sending the same signal to multiple channels. A phase offset can then be introduced in the BPM electronics to zero the phase relative to the sine wave produced by the function generator. Zeroing all electronics against the same function generator using the same master clock while including the different cable delays ensures that the observed phase difference between the BPMs is the actual change in phase of the electron beam relative to the RF clock.

PHASE MEASUREMENT TEST

To test the quality of the phase measurements that can be achieved using the above described technique a test signal needed to be created that would be respectably similar in nature to the expected electron signal. To generate this signal, two function generators, an Agilent 8448C and a Tektronix AFG3202, were use alongside a Model 3600 impulse generator from Picosecond Pulse Labs (Fig. 4). The Agilent function generator was used to generate a 700 MHz sinusoidal signal to clock the impulse generator, while other Tektronix function generator was used to "gate" the impulse generator to simulate the 9MHz macrobunch structure. The impulse generator output from this setup was a 700 MHz train of 70ps bunches with a 9MHz structure (Fig. 4).

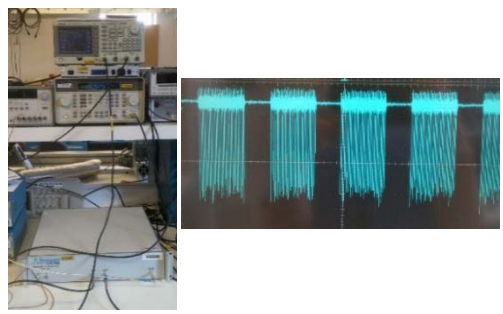

Figure 4: The picture on the left shows the test setup used to generate the 704 MHz pulse train test signal with 9MHz macrobunch structure. The picture on the right shows the resulting test signal.

The simulated signal was split, with one output of the splitter connected directly to the input of the V301. The other splitter output was passed through a coaxial phase shifter. The phase shifter was used to delay one input of the V301 so that the phase difference between the two channels would be tuneable. The delay at the output of the phase shifter changes by 2.45 degrees per turn, with a precision of 0.35 degrees. The output of this variable delay line was then inserted into another channel of the V301.

The goal was to measure the change in relative phase between the two channels.

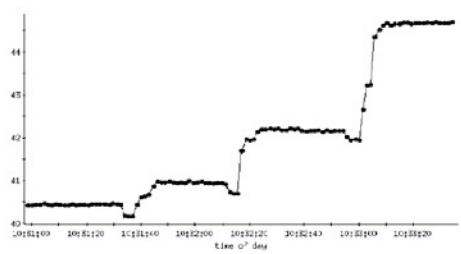

Figure 5: Phase difference in degrees between two channels of the electronics as the delay on one channel was increased.

ISBN 978-3-95450-177-9

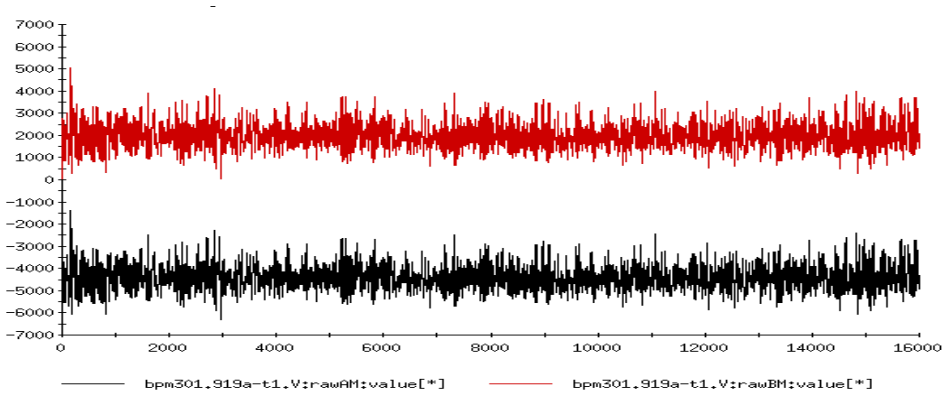

Figure 6: Raw phase measurements from two channels of the V301. The peak to peak is approximately 4000 counts, which equates to 110 degrees.

The results of this test showed that the phase could be measured to within 0.1 degrees when using multiple channels on the same module (Fig. 5). However, phase measurements of a single channel are quite noisy. The noise in the phase measurement is common to both channels, so the noise is completely eliminated when one channel is subtracted from the other (Fig. 6).

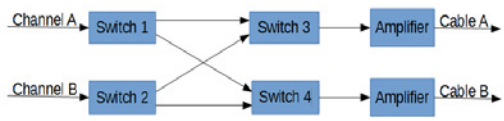

Figure 7: A block diagram of the switch configuration. In the default switch position, switch 1 is connected to switch 3 and switch 2 is connected to switch 4. A logic high connects switch 1 to switch 4 and switch 2 to switch 3.

The ultimate goal for phase measurements is to observe the relative phase measured by two different sets of electronics. This will require a single phase measurement with low noise that can then be compared with a phase measurement from another set of electronics. The phase measurements of different channels from the same BPM can be averaged together over a sufficiently long period of time to improve the quality of the phase measurements before delivering the data.

DRIFT CORRECTION

One of the challenges regarding position measurements for LEReC are the changes in the cable losses as temperature changes for a 704 MHz signal. Due to their length, the cables connecting the BPM buttons to the electronics introduce significant attenuation for the high frequency electron signal of approximately 20 decibels. By itself, this problem can be solved by using amplifiers, but changes in temperature throughout the day slightly change the losses in the cables. The change of attenuation in a cable is typically not the same as the change of attenuation of any other cable. This asymmetrical change in cable losses creates an offset in position that can change throughout the day. An amplitude imbalance of +/- 0.05 dB equates to a position shift of 50 microns. The small changes in the cable losses are enough to create errors greater than 50 microns.

To counteract this effect, switches will be placed in the tunnel near the pickups (Fig. 7). These switches will swap signal pairs from a single plane. If no offsets exist downstream of the switch, then the position in that plane should be equal and opposite. When an amplitude imbalance exists downstream of the switch, the position will instead reflect around a nonzero point that can be found by averaging the position before switching with the position after switching. The value of this average is the position offset created by the amplitude imbalance. This offset can then be eliminated by either scaling one or both of the channels, or by subtracting the offset value from the final position measurement.

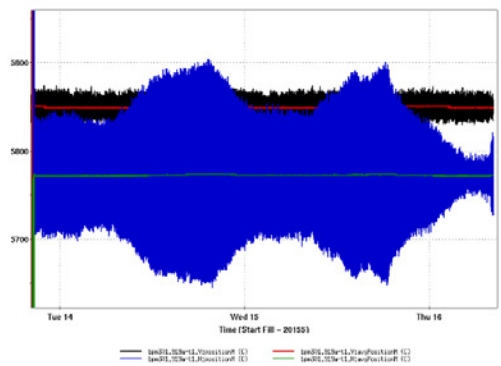

Figure 8: The blue and black show positions calculated from a pair of cables that were actively being switched. The envelope of the blue represents the changes due to temperature. The green and red are the average positions.

By automating the control of these switches using the V301 electronics, the switching can be performed at regular intervals with the cable offsets removed seamlessly (Fig. 8).

ISBN 978-3-95450-177-9

MATCHING LOW AND HIGH FREQUENCY RESPONSES

To measure both the ion and electron signals from the same BPM pickups, the signal will be diplexed and sampled with V301 modules with different RF front ends. The lower frequency 9 MHz ion and electron train signals can be oversampled with a 400 MS/s sampling rate with all additional processing taking place digitally. The 704 MHz electron signal is bandpass filtered with a 707 MHz saw filter before being sampled at the same 400 MS/s rate. The position of the 704 MHz electron can be calculated using the same IQ demodulation process required by the phase measurement. The magnitude of each channel is the square root of the sum of the squares of the in-phase and quadrature signals. From the magnitude, the position is simply the difference divided by the sum.

The ion signal will be processed using a similar method. However, the electron beam has a 9MHz macrobunch structure which will affect the amplitude measurement of the ion beam. This macrobunch structure can interfere with the ion measurements, but it can also be used to cross-calibrate the high and low frequency electronics. The response of the low frequency electronics after filtering with a narrow band digital filter will be similar between the ion and electron signals owing to the 9 MHz component of the electron signal. In the absence of an ion signal, the electrons can be measured with both sets of electronics to determine the calibration coefficients required to match their responses. The 9 MHz component of the electron beam will also prevent accurate ion measurements, so the electron beam will need to be shut off periodically to allow the ion signals to be measured without interference.

CONCLUSION

Various methods have been outlined that will enable the BPM system to meet the requirements for LEReC. IQ demodulation with a synchronous reference will be used for phase measurements. Switching modules will be installed in the tunnel to remove errors introduced by temperature variations. The 9 MHz and 704 MHz responses of the electron beam signal will be used to cross-calibrate the electronics.

The solutions discussed for correcting drift and measuring phase have limitations, and further development is necessary. There is a significant amount of jitter associated with the phase measurements using IQ demodulation. To compare the phase measurements made by two different sets of electronics will require longer averaging to eliminate jitter before the data can be delivered.

The proposed method for eliminating observed position drifts also has limitations. The switches have transients with durations greater than 50 ns. Although short, the position measurements are affected for 5 µs. This is an undesirable effect of the switches as it does not allow us to meet the requirements for the MPS system. Several additional solutions need to be explored, including reducing the switching transients by subtracting the transients from two switches as was done at SuperKEKB [4].

With some additional development, the beam position monitoring system is expected to be on track to satisfy the requirements for LEReC.

ACKNOWLEDGEMENTS

The authors would like to acknowledge the contributions of M. Blaskiewicz, and S. Seletskiy for their input on relative position measurements, as well as N. Baer, A. Curcio, J. Jackson, and J. Kelly for assembling the switch and amplifier electronics that were used in testing.

REFERENCES

[1] T. Miller et al. "LEReC Instrumentation Design and Construction," *IBIC 2016*, Barcelona, Spain (2016), paper TUPG35.

[2] A.V. Fedotov et al. "Bunched Beam Electron Cooler for Low-energy RHIC Operation," *NA-PAC 2013*, Pasadena, USA (2013), paper TUOAA1.

[3] R. Hulsart, et al., "A Versatile BPM Signal Processing System Based on the Xilinx Zynq SoC," *IBIC 2016*, Barcelona, Spain (2016), paper WEPG12.

[4] H. Fukuma et al. "Beam Instrumentation for the SuperKEKB Rings," *IBIC 2012*, Tsukuba, Japan (2012), paper MOCB01.

ISBN 978-3-95450-177-9

THE ORBIT CORRECTION SCHEME OF THE NEW EBS OF THE ESRF

E. Plouviez †, F. Uberto, ESRF, Grenoble, France

Abstract

The ESRF storage ring is going to be upgraded into an Extremely Bright Source (EBS). The orbit correction system of the EBS ring will require 320 BPMs and 288 correctors instead of 224 BPMs and 96 correctors for the present ring. On the new ring, we are planning to reuse 192 *Libera Brilliance* [1] electronics and 96 fast corrector power supplies and the 8 FPGA controllers of the present system and to add 128 new BPMs electronics and 196 new corrector power supplies. These new BPM electronics and power supplies will not have the fast 10 KHz data broadcast capability of the components of the present system. So we plan to implement a hybrid slow/ fast correction scheme on the SR of the EBS in order to reuse the present fast orbit correction system on a reduced set of the BPMs and correctors and combine this fast orbit correction with an orbit correction performed at a slower rate using the full set of BPMs and correctors. We have made simulations to predict the efficiency of this scheme for the EBS and tested on the present ring a similar orbit correction scheme using only 160 BPMs and 64 correctors for the fast correction. We present the results of our simulations and experiments.

ISSUES

We aim at achieving a horizontal orbit stability consistent with the 100 pm horizontal emittance of the new ring (instead of 4 nm for the present storage ring). One cell of the new lattice including BPMs and correctors is shown on Figure 1.

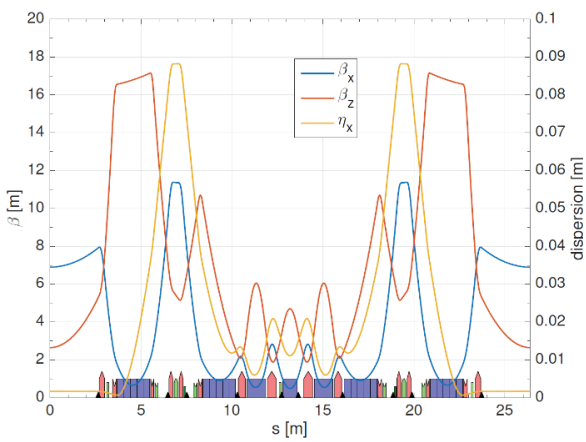

Figure 1: BPMs and correctors in the EBS lattice.
Black triangle: BPM
Small green rectangle: fast corrector
Large green rectangle: slow corrector (sextupole)

The orbit distortion in the frequency range going from .1Hz to 1Hz will come from changes of the parameters (gap and phase) of the ID insertion devices if they are not perfectly corrected against field integral defects. In the 1 Hz to 100Hz range the distortion will first come from the ground vibration filtered by the girder supporting the magnets. We expect that the frequency of the first resonance of the girder will be above 40Hz. The other source of orbit distortion are the spurious fields at the AC mains frequencies (50Hz and its harmonics) and the spurious fields coming from the booster operation (250ms ramp). The correction of these orbit distortions requires operating the orbit correction system in a wide bandwidth. The present fast orbit correction system cannot be easily upgraded to include the larger number of BPMs used on the new ring. Concerning the correctors, among the 288 correctors, 192 correctors will be embedded in the sextupoles; the core of the sextupoles will not be laminated; this will limit drastically the bandwidth of these correctors; the 96 others correctors will have laminated core and will be able to achieve a bandwidth of 500Hz and can reuse the power supplies of the present system. Given the tight time schedule of the project we wanted to avoid as much as possible any unnecessary risky development for the implementation of this fast orbit correction system. For this reason, we are testing an orbit correction scheme using the components of the fast orbit correction system working at 10 KHz of the present ring [1] combined with extra BPMs and correctors power supplies operated at a lower rate. The layout is shown on figure 2.

ORBIT CORRECTION LAYOUT

The orbit control of the new EBS ring will use 10 BPMs and 9 correctors per cell in order to get a closed orbit, averaged in a bandwidth of a fraction of Hertz, close enough to the ideal orbit to allow the required lifetime and coupling control (this orbit correction is not perfect but only optimal since the number of correctors is less than the number of BPMs); the corrector settings for this optimal correction are obtained by multiplying the orbit distortion vector by a correction matrix M_{cors} obtained by inverting the M_{res} response matrix of the system using the SVD method. The 320 BPM pickups will be connected to two types of electronics: 192 *Libera Brillance* electronics of the type used on our present orbit correction system which will used be both for the slow and fast orbit correction; the others 108 BPMs will be connected to new and simpler electronics. The design of these new BPM electronics will most likely be an evolution of the simple *Spark* electronics [2] already used on the BPMs of our booster. Two types of magnets will be used for the orbit correction: 96 dedicated corrector magnets which will be driven by the power supplies used on the present system with a bandwidth of about 500Hz for

ISBN 978-3-95450-177-9

small signals and 192 correctors which will be embedded in the sextupoles and driven by new power supplies. So among these BPMs and correctors, a subset of 192 fast BPMs and 96 fast correctors which are already used for the slow correction can also get position data and produce corrections at a rate of 10 KHz. The position data from these electronics are broadcast at a slow rate on the Ethernet network, to be used by the slow orbit correction and on a dedicated fast network using the *Communication Controller* protocol [3] at a rate of 10 KHz. A set of 8 FPGA power supply controller boards are also connected to this network; these FPGAs compute the $CorX_f$ and $CorZ_f$ fast correctors setting vectors and apply these settings to the fast correctors input using serial lines. The fast correctors setting are obtained using a reduced correction matrix M_{corf} obtained using the same SVD method to invert the response matrix of the reduced set of BPMs to the reduced set of correctors. The multiplication of the correction matrix M_{corf} by the error position vector is done at the rate of 10 KHz. The results of these multiplications are then iterated in order obtain the combination of a PID corrector with a bandwidth of 120Hz and a narrow bandwidth damping around 50Hz of the AC mains related position oscillation. The fast correctors have a dual control: the full range of the power supply can be controlled with Ethernet at a slow rate; a fast trim current can be added at 10 KHz over a dynamic range of 10% of the full range to provide the fast orbit correction. So the current delivered by the fast correctors is the sum of a slow setting $CorX_s$ and $CorZ_s$ applied by the slow orbit correction and a fast setting $CorX_f$ and $CorZ_f$ applied at 10 KHz by the fast orbit correction.

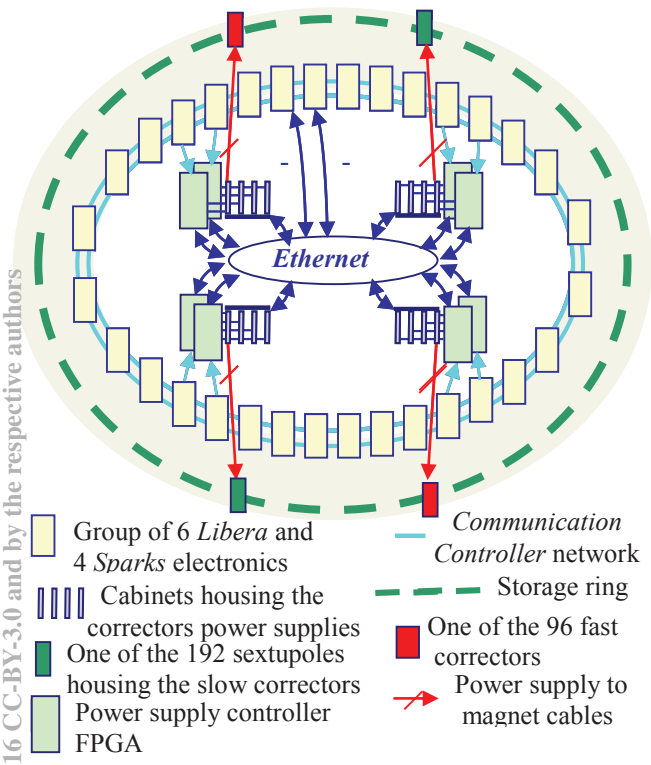

Figure 2: Layout of the EBS orbit correction system.

Residual Orbit Distortion

The rms amplitude of the residual orbit distortion is determined by the number of BPMs and correctors and by the frequency of the distortion that we want to damp. As mentioned above we are using the combination of PID corrector with a band width of 120Hz and a narrow bandwidth damping of the 50 Hz position oscillation. The left plot of Fig.3 shows the damping of the orbit distortion achieved by our present system as function of the frequency (PID only, 50 Hz notch inactive). The right plot shows the overall effect of the correction on our present ring, which is a reduction by roughly a factor of 2 of the fast orbit distortion from 1 Hz to 1 KHz; it is obvious that the residual orbit distortion above a few Hz is mostly due to the limited bandwidth of the PID corrector; so it does not make any significant difference if the full set or a reduced set of BPMs or correctors are used.

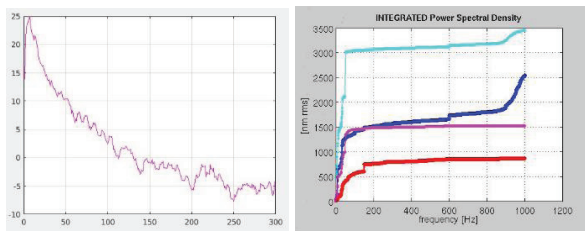

Figure 3: Left plot: fast PID correction effect versus frequency in dB Right plot: integrated spectrum of the orbit distortion; Light blue/horizontal without feedback, dark blue/horizontal with feedback, purple/vertical without feedback, red vertical with feedback.

To illustrate this point, we have simulated for the EBS the orbit correction efficiency seen by the 320 BPMs when using only 192 fast BPMs and 96 fast correctors for the correction, for different patterns of orbit distortion (random quadrupole motion and ID defects). The damping efficiency is still very good as shown on Fig. 4, 5 and 6, so the effect of using a reduced set of BPMs and correctors for the fast orbit correction is negligible compared to the effect of the limited bandwidth of the fast orbit correction.

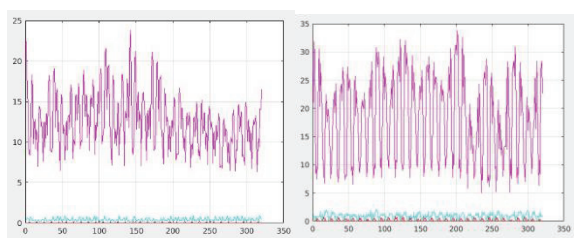

Figure 4: Orbit distortion rms due to random quadrupole displacements (purple) and rms of orbits corrected using the full (red) or reduced set (blue) of BPMs and correctors

Left: vertical, right: horizontal

H scale: BPM number, V scale: μm

ISBN 978-3-95450-177-9

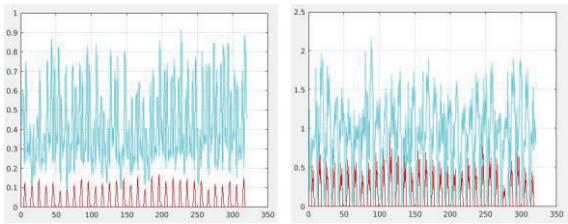

Figure 5: Detail of the corrected orbits rms of Figure 4.

The quality of the correction in the case of a distortion caused by kicks located inside the straight section (caused by badly corrected IDs) shown on Figure 5 is even better due to the availability of two fast correctors immediately upstream and downstream of the orbit perturbation

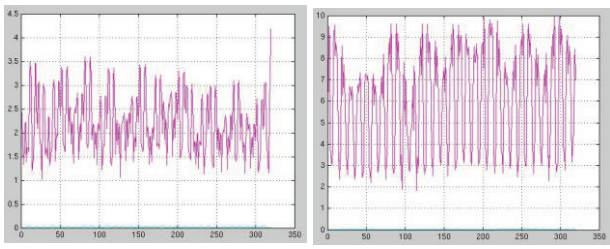

Figure 6: rms effect of kicks in the straight sections.

Left: vertical, right: horizontal

Purple: distorted orbit, blue: corrected orbit

H scale: BPM number, V scale: mm

COMBINATION OF THE SLOW AND FAST CORRECTION

The fast and slow correction orbit control when operating in parallel must exchange data in order to converge toward the same closed orbit and avoid generating corrections aiming at opposite orbit changes [4].

Principle of the Data Transfer Between the Slow and Fast System

We are using the scheme implemented first at the ALS [5]. The position data vectors X_s and Z_s used by the slow system are the position obtained from the 320 BPMs without any trim; the position data vectors X_f and Z_f used by the fast system are the sum of the direct position reading from the 192 fast BPMs plus the offset vectors X_{off} and Z_{off}. The system starts with orbit set using the slow correction system only; When the fast system starts operating, the offsets are set in order to start the fast correction with $X_f=0$ and $Z_f=0$; in this way the fast correction will not modify the average closed orbit set by the slow correction and will only damp the fast variation of the orbit with respect with this average orbit. Since the optimal average corrected orbit set by the slow system will slightly change depending on the evolution of the sources of the orbit distortion, the offset vectors X_{off} and Z_{off} must also be slightly modified accordingly. The sequence to update the slow correctors and fast BPMs offsets settings is the following:

- Add the average over 1 s of $CorX_f$ and $CorZ_f$ to the settings $CorX_s$ and $CorZ_s$ in order to suppress the contribution of the fast correction to the DC correction.
- Measure the orbit X_s and Z_s using the 320 BPMs.
- Get the optimal settings $CorX_s$ and $CorZ_s$ of the slow correctors using the full matrix M_{cors}
- Get the orbit change ΔX_s and ΔZ_s that would result from the application of the new corrector settings, if the fast orbit correction was not active.
- Add ΔX_s and ΔZ_s to the offsets X_{off} and Z_{off} in order to get $X_f=0$ and $Z_f=0$ with the new X_s and Z_s orbit which will prevent the fast correction from interfering with the slow correction.
- Apply the new settings $CorX_s$ and $CorZ_s$

TEST OF THE COMBINED SLOW AND FAST ORBIT CORRECTION ON THE PRESENT ESRF STORAGE RING

We have tested the orbit correction scheme described above on our present ring; the orbit correction system of this ring can use 224 BPMs and 96 correctors which can be used in a slow or fast correction scheme as shown on Figure 5. For our test we have set up our system to provide a fast orbit correction at a rate of 10 KHz using 160 fast BPMs and 64 fast correctors in parallel with a slow orbit correction using 224 BPMs and 96 correctors at a rate of .1Hz.

The resolution of the BPMs and correctors data are detailed below:

- Slow position data: 1nm/32bits
- Fast position data: 256nm/16bits
- Orbit offset data: 16nm/16bits
- Fast correction: 3nrad /16bits
- Slow corrections: 30nrad/16bits

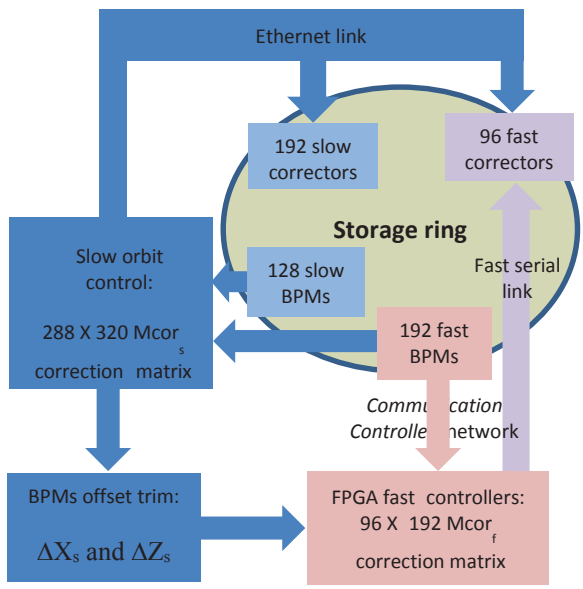

Figure 5: Layout of the control of the orbit correction system used for the test.

ISBN 978-3-95450-177-9

Test Result

We wanted to check the following points:

1. Long term stability of the loop
2. Quality of the correction at high frequency (above 1Hz)
3. Quality of the correction at low frequency

Concerning the points 1 and 2 there is no difference between the effect of the fast correction using the 224 BPMs and 96 correctors and the effect of the hybrid fast/slow system. The figure 6 shows the spectrum of the orbit distortion observed on our ring without fast orbit correction and with the hybrid correction scheme that we were testing. There is no observable difference compared to the damping obtained using the full set of BPMs and correctors.

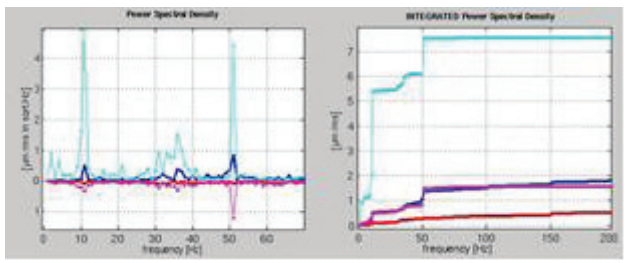

Figure 6: Spectrum of the orbit distortion (left plot). Integrated spectrum of the orbit distortion (right plot). Light blue/horizontal without feedback, dark blue/horizontal with feedback, purple/vertical without feedback, red vertical with feedback

Concerning the point 3, a slight degradation of the stability can still be observed as shown on figure 7. Figure 7 shows the difference between the position measured at 2 Hz by the *Liberas* "slow acquisition" outputs and the rolling average over 60s of the same positions. The right part of the plots shows the stability observed when the full set of BPMs and correctors is used for the fast and slow correction; the left part of the plots shows the stability observed when the full set of 224 BPMs and 96 correctors is used for the fast correction. The central red part of the display corresponds to the switching time between the two orbit correction modes, when the orbit correction is inactive. The slow correction and the corresponding trim of the offset vectors of the fast correction position data was done every 45 seconds. We have not yet found the reason of the slight horizontal orbit drifts observable with a periodicity of 16 around the ring circumference (16 being the number of super periods of our lattice). However, the amplitude of these drifts is only a fraction of micron.

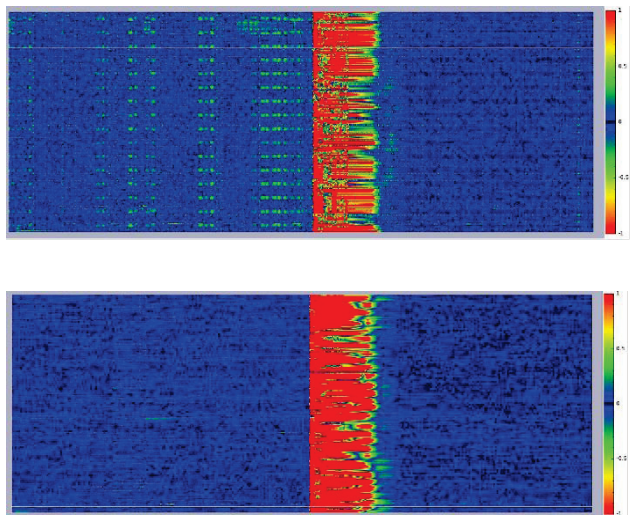

Figure 7: Display of the stability of the orbit stability with the hybrid slow/fast correction scheme (left part) and the normal correction scheme (right part).

Horizontal full scale: 500 s.

Upper/lower plot: horizontal/vertical stability display.

Vertical full scale: +/- 1 µm (red on the colour scale)

CONCLUSION

We have tested that we will be able to implement an orbit correction system on the storage ring of the EBS using the components of the system working on our present ring. The extra components required for the orbit control of the new ring which will use 320 BPMs instead of 224 BPMs and 288 correctors instead of 96 correctors will be controlled at a slow rate so their integration in the control of the orbit correction will be straightforward. The orbit stability achieved during our tests meets the stability requirement of the new EBS ring.

REFERENCES

[1] E. Plouviez *et al.*, 'The New Fast Orbit Correction System of the ESRF Storage Ring", *Proceeding of DIPAC 2011*, Hamburg, Germany, paper MOPD74.

[2] G. Jug *et al.*, "Development of Compact Electronics Dedicated to Beam Position Monitors in Injectors and Boosters", *Proceeding of IBIC 2013*, Oxford, UK, paper WEPC18.

[3] S. Uzun *et al.*, "Initial Design of the Fast Orbit Feedback System for Diamond Light Source", *Proceedings of ICALEPCS 2005*, Geneva, paper PO2.030-2 (2005).

[4] N. Hubert *et al.*, "Global Fast Orbit Feedback System Down To DC using Fast and Slow Correctors", *DIPAC 2009*, Basel, Switzerland, paper MOOC01.

[5] C. Steier *et al.*, "Operational Experience Integrating the Slow and Fast Feedbacks at the ALS", *Proceedings of EPAC 2004*, Lucerne, Switzerland, paper THPLT141.

ISBN 978-3-95450-177-9

BPM STABILTIY STUDIES FOR THE APS MBA UPGRADE*

R. Lill, N. Sereno, B. Yang
Advanced Photon Source, Argonne National Laboratory, Argonne, IL 60439 USA

Abstract

The Advanced Photon Source (APS) is currently in the preliminary design phase for the multi-bend achromat (MBA) lattice upgrade. Beam stability is critical for the MBA and will require long term drift, defined as beam motion, over a seven-day timescale to be no more than 1 micron at the insertion device locations and beam angle change of no more than 0.25 micro-radian. Mechanical stability of beam position monitor (BPM) pickup electrodes mounted on insertion device vacuum chambers place a fundamental limitation on long-term beam stability for insertion device beamlines. We present the design and implementation of prototype mechanical motion system (MMS) instrumentation for quantifying this type of motion, specifically in the APS accelerator tunnel and experiment hall floor under normal operating conditions. The MMS presently provides critical position information on the vacuum chamber and BPM support systems. Initial results of the R&D prototype systems have demonstrated that the chamber movements far exceed the long-term drift tolerance specified for the APS Upgrade MBA storage ring.

INTRODUCTION

In order to achieve the MBA beam stability requirements, an extensive R&D program has been planned and is presently being implemented. The beam diagnostics required for the APS MBA are driven largely from a small electron beam size and the requirements for those systems are outlined in Table 1. The minimum beam size for the MBA lattice is expected to approach 4 microns at the insertion device (ID) source points. AC rms beam stability requirements are defined as 10% the minimum source size at the ID in the band 0.01-1000 Hz. The vertical plane stability requirement is the most ambitious, requiring a stability of 400 nm at the ID source point. In addition, long term drift, defined as motion over a seven-day timescale, can be no more than 1 micron.

Table 1: MBA Beam Stability Requirements

Plane	AC rms Motion (0.01-1000 Hz)	Long-term Drift (100s-7 days)
Horizontal	1.7 μm 0.25 μrad	1.0 μm 0.6 μrad
Vertical	0.4 μm 0.17 μrad	1.0 μm 0.5 μrad

* Work supported by U.S. Department of Energy, Office of Science, under Contract No. DE-AC02-06CH11357.

BEAM STABILITY R&D OVERVIEW

We have approached the MBA diagnostics R&D in two phases. The first phase, outlined in Figure 1, prototypes new, higher risk diagnostics and their interfaces. This R&D includes an MMS, BPM electronics, Grazing Incidence Insertion Device (GRID) X-Ray BPM [1], and new feedback processing electronics [2]. This phase is presently near completion and has provided the foundation for the next phase of R&D [3].

The MMS system shown on the lower section of Figure 1 will be discussed in greater detail in the paper. This diagnostic has been designed to monitor critical in-tunnel beam position monitoring devices. The mechanical motion generated from changes in chamber cooling water temperature, tunnel air temperature, beam current, and undulator gap position causes erroneous changes in beam position measurements, creating drift in the x-ray beam position. Research to quantify mechanical motion specifically for the APS accelerator tunnel has been ongoing for over five years [4,5].

The second phase of the R&D effort advances the design and integrates all systems required to qualify beam stability. The integrated beam stability testing will require 16 new rf BPMs and 8 new corrector power supplies and interfaces. The integrated beam stability effort will be required to operate transparent to normal APS operation and is planned to start in the late summer of 2016. This testing will greatly reduce risks and qualify many diagnostic systems and their related interfaces.

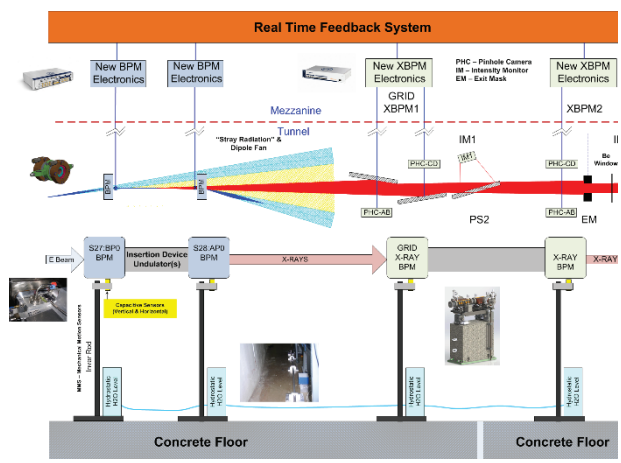

Figure 1: APS-U beam stability R&D.

ISBN 978-3-95450-177-9

MMS SYSTEM DESIGN

In order to achieve long-term beam stability goals, a mechanical motion system (MMS) has been developed. The need for this development started in early 2010 when periodic 15-minute duration beam motion was reported on many ID locations during user operations [4]. It was determined that the periodic beam position motion was correlated to the cooling water cycle for the aluminium vacuum chamber. Experiments conducted confirmed that thermal distortion of the vacuum chamber leads to movements of the BPMs up to 10 μm/°C. This distortion was incompatible with the present operations of APS and with the new beam stability requirements for the planned MBA upgrade. Improvements to the aluminium water regulation system has greatly reduced these negative effects. Further studies of the ID BPM detectors have identified nonlinear mechanical movement of the BPM detectors that change with tunnel air temperature, and beam current. All sources of mechanical motion of critical in-tunnel beam position monitoring devices are presently being carefully evaluated and appropriately addressed.

The MMS instruments' critical ID and X-ray bpm locations with sensors are shown in the lower section of Figure 1. These diagnostics measure the mechanical movements of the detectors and the ground motion of the floor supporting the detectors. The ID and X-ray BPM detector locations are instrumented with commercial high-resolution non-contact capacitive detectors by Micro-Epsilon [6]. The capacitive detectors are mounted on super invar low expansion support systems. The Micro-Epsilon CapaNCDT 6200 is a multi-channel measuring system that is entirely modular and can support up to four synchronized channels with integrated Ethernet interface. A parallel plate capacitor is formed between the sensor and the BPM vacuum chamber. If a constant alternating current flows through the sensor capacitor, the amplitude of the alternating voltage on the sensor is proportional to the distance between the capacitor electrodes. Any change in the capacitance, due to a change in its area or spacing, is demodulated and presented as a dc signal. The range of measurement is 500 microns with a resolution of 10 nanometres. The capacitive detection electronics must be installed in the tunnel in a shielded enclosure.

Figure 1 illustrates the design Hydrostatic Level System (HLS) where the floor is measured at critical support locations. The fundamental principle of HLS is based on the communicating vessels principle. The baseline design uses Fermi Lab Budker design sensors [7]. Argonne has worked with Micro-Epsilon to combine their expertise in capacitive detection with the Budker HLS design concept and has developed and built prototypes presently being evaluated. The sensors have two main components: the water reservoir and the capacitive pick-up. The reactance of the capacitor changes in direct proportion to the water level. The electronics are similar to the capacitive detector described earlier.

Another capability that we added is the ability to precisely move the support system for the BPM detectors. The thermal expansion of the steel supports can be controlled using a 300-watt electric heater in an effort to regulate vertical height of the BPM. The MMS output is used in a feedback loop controlling the heater duty cycle holding the mechanical position of the BPM constant. The vertical drift of the BPM detector that typically moves 14 microns per degree Celsius can be regulated to less than 300 nanometre peak to peak. This test demonstrated the feasibility of regulating the steel support to compensate for many systematic effects altering the vertical position of the BPM.

PROTOTYPE TESTING

A rigorous test plan is presently being implemented for the MBA prototype diagnostics. The MBA R&D plan prototypes— the rf BPMs, GRID-XBPMs, MMS, and feedback system— will demonstrate compliance to the MBA requirements for beam stability. This testing has added new capacities to make precision mechanical movements of the bpm support system which enables cross calibration between beam diagnostic systems. Cross calibration tests can now be made using the local BPM and MMS. The BPM can be removed from being used in the orbit control feedback and then physically moved with the heater actuators vertically while stable beam is present. This presents a direct calibration of the BPM system with a known beam position movement. This data has been useful during the test and commissioning of the new bpm system installed.

To demonstrate the impact of mechanical motion for ID BPMs, we ran an experiment using the heater actuators where we moved each end of the ID supports. This was accomplished while the ID BPM on both sides of the 5-m ID chamber were being used in feedback to hold position constant to observe the movement on the GRID X-ray bpm 16-m further from the downstream end of the ID chamber. This experiment demonstrates the impact of bpm mechanical motion on beam stability during machine studies. First we moved the downstream bpm up by 5 μm (shown in Figure 2) at approximately 10 minutes shown on horizontal scale. This resulted in the X-ray beam moving approximately 20 μm as measured by the GRID (top plot). Next, the beam is deliberately steered by approximately 5 μm at the downstream bpm, thereby returning the X-ray bpm position back to the starting point as measured at the GRID at approximately 20 minutes. At approximately the 30 and 60-minute marks we repeat the experiment using the upstream BPM and steer the x-ray beam down by 15 μm at the XBPM with identical results. This experiment demonstrates the impact that a 5-micron thermally driven movement of the ID bpm can have on the x-ray beam 20 meter downstream. It also provides a cross-correlation calibration between the rf BPMs, MMS, and GRID BPMs used for this experiment.

In another example of how the mechanical motion system has improved the APS today, we discovered a step change of 60 microns vertically on the MMS when the undulator gap approaches the minimum gap. It turns out that the spring force of the limit switch plunger is strong enough to deflect the ID chamber and move the rf BPM. This problem has since been noted in other insertion device

ISBN 978-3-95450-177-9

locations. Based on this discovery, design changes are being made to minimize this adverse effect.

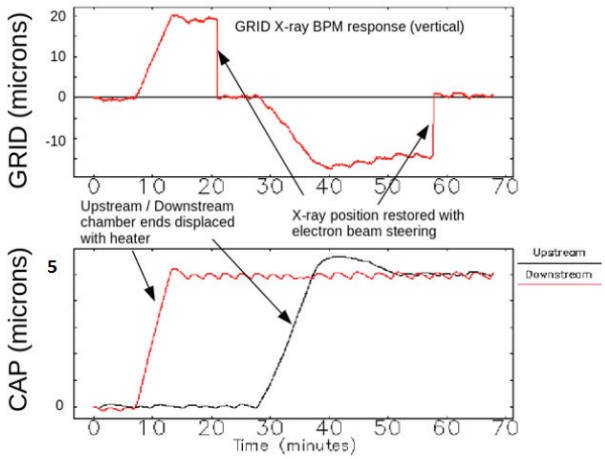

Figure 2: Impact of mechanical motion for ID BPMs.

The HLS, shown in Figure 1, measures the relative ground motion between the IDVC BPMs in the APS accelerator tunnel and the beamline x-ray BPM locations. Studies have been conducted to quantify this type of motion specifically for the APS accelerator tunnel. These studies are providing data under normal machine operating conditions necessary to develop a strategy for measurement and correction of this drift.

A common measure of diffusive ground motion over extended time periods is the so-called ATL law, whereby the mean square amount of ground motion taking place over a time period, T, between two points separated by a displacement, L, is proportional to their product, with proportionality constant, A [8]. Estimates of diffusive ground motion between the two IDVC BPMs separated by 5 meters can be expected to be up to 7 microns in a 5-day time period, using the constants provided in Ref. [7] for Fermi Laboratory Tevatron collider HLS. The ground motion at APS sector 27 ID typically measures about 1-micron peak to peak over a five-day period shown in figure 3.

The other ground motion observation shown in Figure 3 is an approximate 12-hour cycle. This 12-hour cycle can be correlated directly to tidal effects. The APS storage ring is also effected by tidal motion. The horizontal beam position is measured and the variation of the ring diameter is compensated by changing the rf frequency. The effective circumference change of the 1105-meter storage ring is 3 microns for the same five-day period shown in Figure 3.

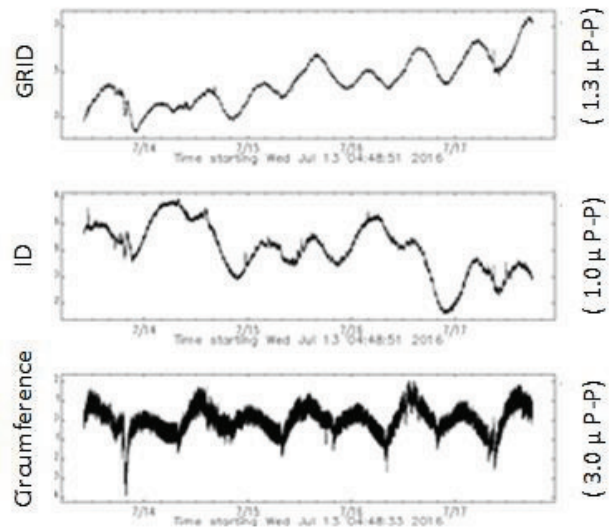

Figure 3: HSL and APS ring diameter change.

MBA SYSTEM DESIGN

The MBA upgrade will require instrumenting 35 ID BPMs and 35 X-ray BPMs for a total of 280 channels of capacitive detectors. These detectors will provide measurement information which will be used in a feed forward compensation loop to remove any residual mechanical motion for the bpm measurements. There will also be 140 hydrostatic detectors located at the ID and GRID BPM locations. These detectors will measure ground motion and be used to compensate for localized ground motion in each of the 35 locations.

The MMS has provided design insight on the vacuum chamber and beam position monitor support systems. The MBA design for the ID BPMs have recently been changed from a vacuum chamber mounted button to the bellows isolated BPM shown in Figure 4. The BPM will now be isolated from the negative effect of the chamber cooling water and additional vibrations when mounted directly to the vacuum chamber. The integration of the MMS system to the new bpm design is ongoing at this time.

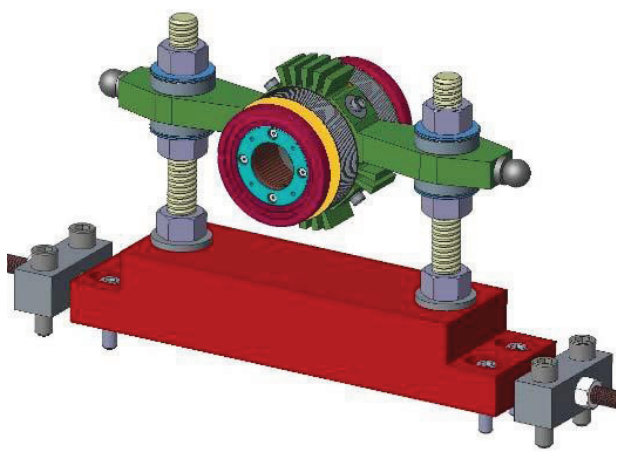

Figure 4: Bellows isolated BPM.

ISBN 978-3-95450-177-9

The supports for the ID bpm will also be changed from a steel support system to the concrete support system shown in Figure 5. This support system promises a greatly improved mechanical stability.

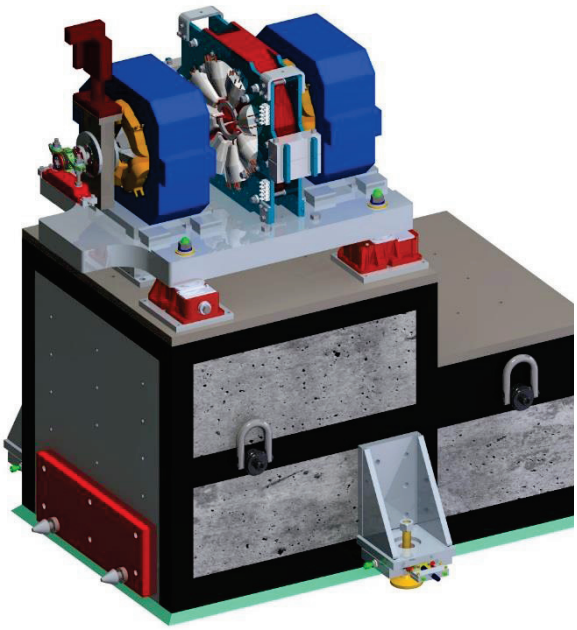

Figure 5: ID BPM concrete support system.

The MMS has also provided critical information on the accelerator cooling water and air handling systems' effects on beam stability. These systems have been proven to have significant impact on mechanical bpm detector stability. The MMS provides real time data to inform improvements of these systems and incremental improvements of the water and air handing regulation systems have been accomplished. These improvements presently benefit the current APS machine operations and also promise to ensure the MBA meets these very difficult beam stability requirements.

CONCLUSION

It is imperative that the MBA upgrade have world class beam stability performance. The MBA upgrade will instrument 35 ID BPM locations and 35 GRID X-ray BPM locations with high-resolution, non-contact capacitive detectors. The floors in these locations will be instrumented with a HLS system. The HLS will provide a reliable reference frame, which is not easily distorted, and MMS will link the position of the BPMs to the reference plane so their positions are known in real time. Only with the confidence of the physical locations of the diagnostics themselves will their position information be truly meaningful.

Having the access to study APS beam stability in the existing machine provides the great advantage of being able to prove and test designs for the new MBA machine. It also promises improvements to the existing machine.

ACKNOWLEDGMENTS

The authors would like to acknowledge the project support of Glenn Decker and John Carwardine. The authors would like to thank Steve Shoaf for his controls interface support, and thank Ron Blake, Randy Zabel, and Lester Erwin for all their help with building and testing the prototypes.

REFERENCES

[1] B. Yang *et al.*, "Design and Development for The Next Generation X-ray Beam Position Monitor System at the APS," *IPAC 2015*, Richmond, VA, USA (2015), paper MOPWI014.

[2] N. Sereno *et al.*, "Beam Stability R&D for the APS MBA Upgrade," *IPAC 2015*, Richmond, VA, USA (2015), paper MOPW011.

[3] N. Sereno *et al.*, "First Beam Tests of the APS MBA Upgrade Orbit Feedback Controller," presented at *IBIC 2016*, Barcelona, Spain (2016), paper MOPG06.

[4] R. Lill *et al.*, "Studies of APS Storage Ring Vacuum Chamber Thermal Mechanical Effects and their Impact on Beam Stability," in Proceedings of the *14th Beam Instrumentation Workshop*, Santa Fe, NM, USA (2010), paper TUPSM050.

[5] R.M. Lill *et al.*, "Design and Development of a Beam Stability Mechanical Motion System Diagnostic for the Aps MBA Upgrade," *IPAC 2015*, Richmond, VA, USA (2015), paper MOPWI010.

[6] Micro-Epsilon, micro-epsilon.com

[7] J. Volk *et al.*, "Hydrostatic Level Sensors as High Precision Ground Motion Instrumentation for Tevatron and Other Energy Frontier Accelerators," INST **7** (2012) P01004.

[8] V. Shiltsev, "Observations of Random Walk of the Ground in Space and Time," PRL **104**, 238501 (2010).

ISBN 978-3-95450-177-9

BEAM COMMISSIONING OF TPS FAST ORBIT FEEDBACK SYSTEM

P. C. Chiu, Y. S. Cheng, K. T. Hsu, K. H. Hu, C.H. Huang
NSRRC, Hsinchu 30076, Taiwan

Abstract

TPS (Taiwan Photon Source) is a 3 GeV synchrotron light source which had be successfully commissioning with SRF up to 500 Amp in 2015 and Phase I beamline commissioning have followed soon. It has been scheduled to open user operation in 2016. To provide stable and reliable beam, the fast orbit feedback system is indispensable. Due to the vacuum chamber material made of aluminum with higher conductivity and lower bandwidth, extra fast correctors mounted on bellows will be used for FOFB correction loop and DC correction of fast correctors would be transferred to slow ones and avoid fast corrector saturation. Besides, the path length compensation by RF feedback is also tested. This report summarizes the infrastructure of the FOFB and the preliminary beam test is also presented.

INTRODUCTION

The TPS is a state-of-the-art synchrotron radiation facility which consists of a 150 MeV S-band linac, linac to booster transfer line (LTB), 0.15–3 GeV booster synchrotron, booster to storage ring transfer line (BTS), and 3 GeV storage ring. This synchrotron machine featuring ultra-high photon brightness with low emittance [1] requires beam position stability less than 1/10 beam size. FOFB is therefore implemented to achieve sub-micron orbit stability and it has been tested together with beamline commissioning since 2015. The orbit stability had been effectively improved with FOFB and it showed that the suppression bandwidth could achieve 250 Hz in both horizontal and vertical plane. This had been considered quite helpful for beamline commissioning, especially that TPS had strong 3 Hz booster ramping disturbance and 60 Hz power line noise. After applying RF feedback and resolving long-term reliability related problem, FOFB would be officially operated in September 2016.

FOFB INFRASTRUCTURE

The design of the TPS storage ring has 24 cells, each cell is equipped with 7 BPMs and 7 horizontal/vertical correctors winding on the sexupoles. These kinds of slow correctors could provide about 500 μrad kick while their bandwidth could be limited only several tens of Hertz due to the eddy effect of the alumina vacuum chamber. This bandwidth is not sufficient to eliminate perturbation with frequency above several hundreds of hertz. Therefore, extra four horizontal/vertical correctors per cell are installed on the bellows site to obtain higher correction bandwidth. These horizontal/vertical correctors have fast response but smaller kick strength around 100/50 μrad. Thus the orbit feedback system would adopt two kinds of correctors simultaneously. The DC component of the fast correctors will transfer from fast to slow correctors smoothly and avoid saturation of the fast correctors as well as provide capability to suppress orbit disturbance. The overall infrastructure of FOFB is as Fig. 1. It is mainly implemented by three parts: BPM, feedback computation unit and corrector power supply control interface. TPS BPM electrical system will adopt the latest I-tech product: Brilliance+ [2]. It also offers a large playground for custom- written applications with VirtexTM 5, Virtex 6 in the gigabit data exchange module (GDX) to be used as orbit feedback computation. The corrector power-supply controller (CPSC) is designed for FOFB corrector control interface. This module is embedded with Intel XScale IOP and Xilinx Spartan-6 FPGA which will interface the fast setting from feedback engines. It was contracted to D-TACQ [3].

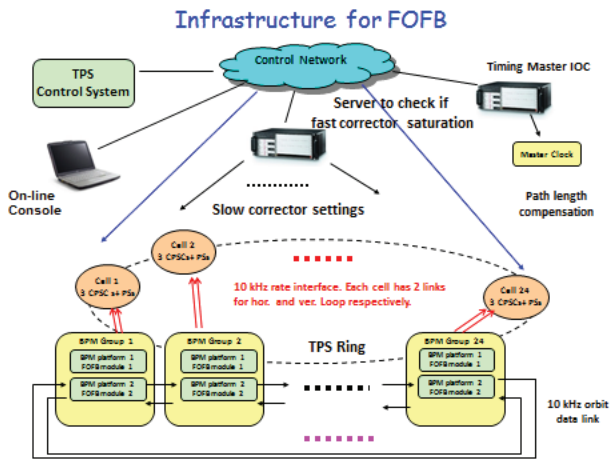

Figure 1: FOFB infrastructure.

BPM and GDX Interface

The TPS BPM electronics had commission with TPS beam commissioning in 2014 [4, 5]. It consists of four kinds of modules: The timing module for clock locking and trigger; up to four BPM modules for receiving button pick-ups and signal processing, the inter-connection board (ICB) module for SW and HW interface; the GDX (Gigabit data exchange) module as Fig. 2 shown for FA data grouping and FOFB computation which could support at most 256 BPMs and 128 correctors feedback computation. The magnet correction output is transmitted to CPSC (corrector power supply controller) based on AURORA protocol of Xilinx. It also provides 10 kHz BPM grouping data through Gigabit Ethernet to support the angle interlock functionalities of TPS. The functional block of FOFB is shown as Fig. 3.

ISBN 978-3-95450-177-9

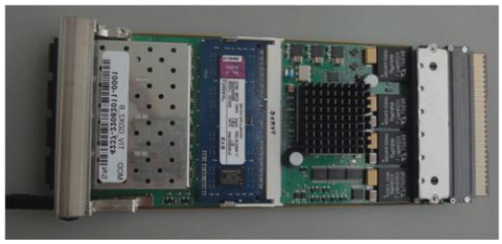

Figure 2: GDX module for FA data grouping and FOFB computation. There are 4 SFP ports provided: two SFP ports for FA data grouping; one SFP for magnet output; one SFP for BPM grouping data output (Gigabit Ethernet).

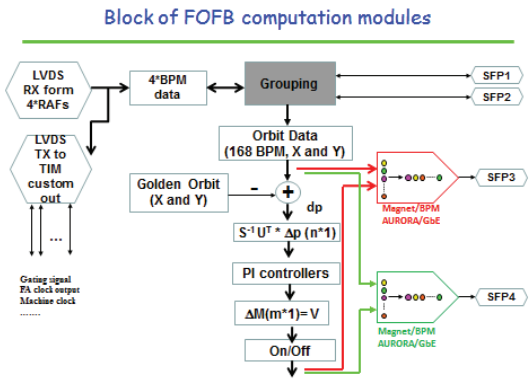

Figure 3: Functional block of FOFB computation module.

Corrector Power Supply Controller Interface

To support diverse functionalities of fast orbit feedback [6], booster ramping, compensations for insertion device and skew quadrupoles, the CPSC for TPS corrector power supply is proposed. CPSC is installed into the center slot of power supply rack as Fig. 4. It was contracted to D-TACQ and consists of four moulds of boards: IOP, ADC unit, DAC unit and FPGA for summing of FOFB fast setting and EPICS slow setting. This functional block is shown as Fig. 5. It is embedded with EPICS IOC for slow access of the EPICS clients and its FPGA supports fast settings from GDX modules via fibre link based on Aurora protocol.

Figure 4: Power supply rack. CPSC is plugged in the center slot and could controller 8 channels of power supplies.

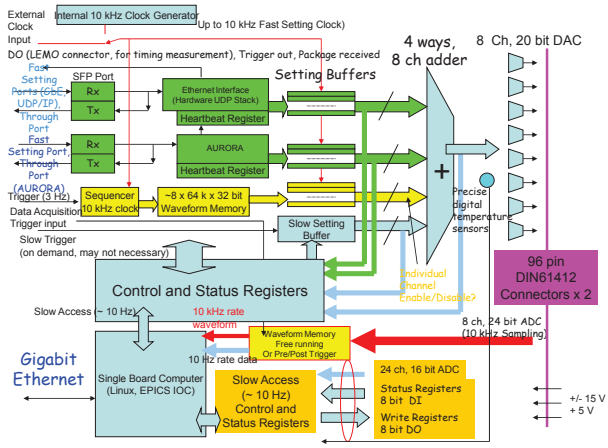

Figure 5: Functional block diagram of the corrector power supply controller module. The EPICS channel access is via a dedicated embedded IOC. The fast setting from feedback engines would sum with the EPICS CA slow setting.

ORBIT STABILITY IMPROVED WITH FOFB

FOFB has continuous tested and operated with beamline commissioning since 2016 February both for horizontal and vertical planes. It has been proven to suppress the noise from DC to 200 Hz effectively.

For beam position stability of the raw TPS machine without FOFB, as Fig. 6 shown, most of horizontal position disturbance (blue line) is contributed from mechanical vibration which is excited by cooling water majorly [7], distributed below 80 Hz. There is also strong 3 Hz up to tens of micron meter from field leakage during booster power supply ramping. For the vertical position plane, there were also very strong 60 Hz powerline noises which were later identified as contribution from grounding problem of RF system.

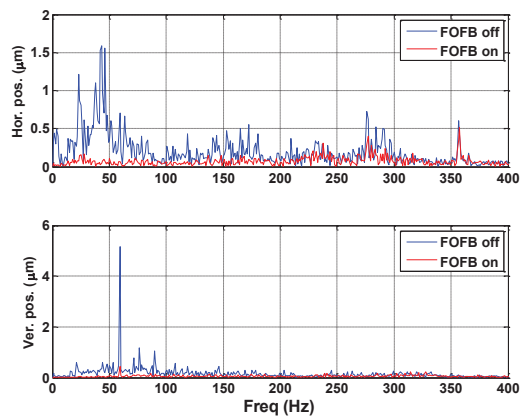

Figure 6: Beam Spectrum (no booster power supply ramping).

With FOFB applied, it could be observed that beam stabilities of horizontal and vertical planes are both much

ISBN 978-3-95450-177-9

improved. The integrated displacement of the straight line BPM from DC to 200 Hz could achieve 0.5 um for both of horizontal and vertical planes and it is satisfied the one tens of beam size stability as Fig. 7(a) shown. Besides, the overall BPM 10 Hz data RMS comparison of FOFB on and off is also presented as Fig. 7(b). The overall orbit stability is improved one order of magnitude.

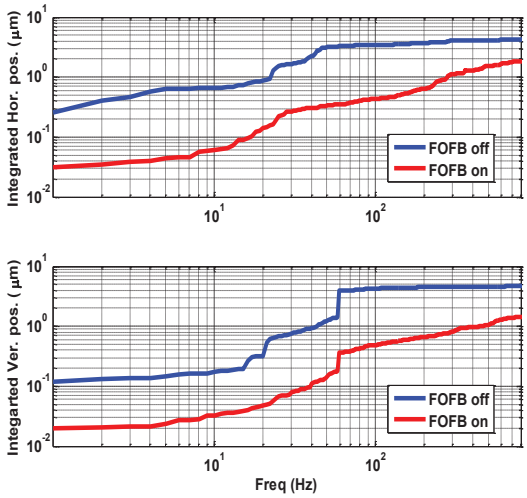

(a) Integrated BPM position displacement

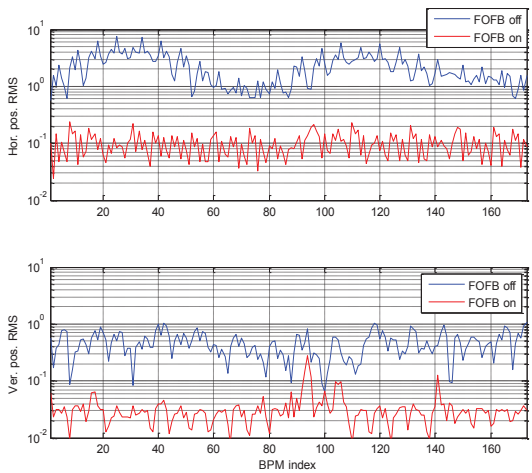

(b) BPM 10 Hz data RMS comparison.

Figure 7: BPM orbit stability comparison between FOFB on and off.

The estimated bandwidth of FOFB is around 250 Hz for horizontal plane and 300 Hz for vertical plane as Fig. 8 shown. It could suppress ten times of noise around 50 Hz which is the major noise source of TPS. FOFB would also amplify noise around 400~700Hz while the beamline experiments would not be concerned about these frequency range. The parameter optimization of which BPMs and eigenmodes selected and PI coefficient weighting adjustment would be based on beam condition. The performance and reliability should be both considered and it would be required further studied.

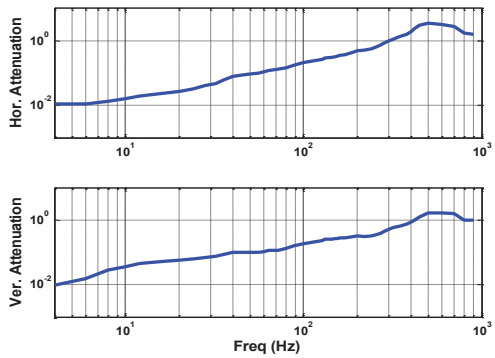

Figure 8: The measured bandwidth of FOFB. Horizontal is around 250Hz and vertical around 300 Hz.

FAST ORBIT FEEDBACK WITH SLOW CORRECTOR COMPENSATION

Since the slow correctors' bandwidth would be limited much less than 100 Hz due to the TPS alumni vacuum chamber, the fast corrector would be used only for feedback correction to suppress various disturbance form DC to 300 Hz [8, 9]. A process which flow chart is shown as Fig. 9 would check the fast corrector output current periodically and transfer DC part correction to the nearby slow correctors when accumulating greater than acceptable value to avoid saturation. According the experience, FOFB operation would cause maximum 2~3 Amp accumulating value of the fast correctors since beam current injection from 30 mA to 500 mA. And after thermal equilibrium reached at top-up mode, the drift could be controlled below 0.5 Amp with RF feedback but could be over 4 mA without RF feedback.

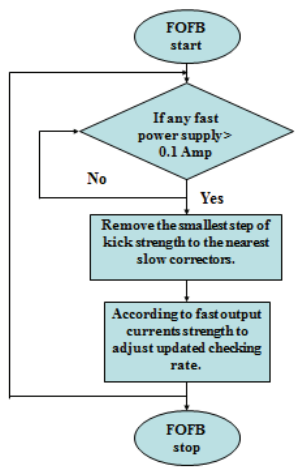

Figure 9: FOFB with slow corrector compensation to avoid fast corrector saturation.

RF FEEDBACK FOR PATH LENGTH COMPENSATION

RF feedback is used to minimize the effects of path length change mainly caused by temperature drift. Although FOFB could compensate some parts of the path

ISBN 978-3-95450-177-9

length change, there are still some residual orbit difference remained up to several tens of microns during 24 hours operations. Furthermore, this difference would be amplified ten times observed at the beamline XBPM where it was unacceptable. The RF feedback thus was soon implemented and applied with FOFB. The orbit drift could be controlled and limited less than 1 um for one day operations as shown in Fig. 10. There are some spikes observed due to injection around every 5 minutes. The RF feedback process would poll the horizontal correctors' current ΔI at 0.1 Hz, convert it to the corresponding orbit deviation by response matrix R, and then dispersion function D is used to calculate the required RF frequency change ΔRF.

$$\Delta RF = D^{+} R \Delta I$$

where D^{+} is pseudo-inverse of D. The longer orbit stability test with FOFB and RF feedback would be done after long shut down of TPS.

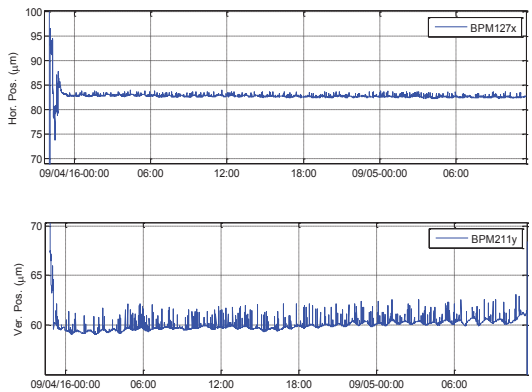

Figure 10: Horizontal and vertical orbit with FOFB and RF feedback during 36 hours of operations. There are some spikes due to injection around every 5 minutes.

CONCLUSION

BPM electronics and integrated orbit feedback system combined with slow and fast correctors of the TPS are summarized. All major components were tested and verified its functionalities. Testing is on-going and long-term reliability would be continuously improved. There are 170 BPMs and 96 fast correctors used in FOFB loop. The proper BPM selected would be adjusted according to the beamline experiments and the optimization would be the next efforts.

REFERENCE

[1] TPS Design Handbook, version 16, June 2009.
[2] http://www.i-tech.si
[3] http://www.d-tacq.com
[4] Pei-Chen Chiu, *et al.*, "TPS BPM Performance Measurement and Statistics", Proceeding of *IBIC 2012*, Tsukuba, Japan.
[5] Pei-Chen Chiu, et al., "Commissioning of BPM System for the TPS Project", Proceeding of IBIC 2015, Melbourne, Australia.
[6] K. B. Liu, et al., "TPS Correct Magnet Power Converter", Proceedings of IPAC'10, WEPD073, Kyoto, Japan.
[7] C. H. Huang, et al., "Vibration Measurement of the Magnets in the Storage Ring of TPS", IPAC2015, Richmond, USA.
[8] Pei-Chen Chiu, et al., "Fast Orbit Scheme and Implementation for TPS", Proceeding of IPAC2013, Shanghi, China.
[9] C. H. Kuo, et al., "The Design Strategy of Orbit Feedback System in the TPS", Proceeding of IBIC 2013, Oxford, UK.

ISBN 978-3-95450-177-9

A WIRE-BASED METHODOLOGY TO ANALYSE THE NANOMETRIC RESOLUTION OF AN RF CAVITY BPM

S. Zorzetti[1*], K. Artoos, F. N. Morel, P. Novotny, D. Tshilumba, M. Wendt
CERN, Geneva, Switzerland
L. Fanucci, University of Pisa, Pisa, Italy
[1]also at University of Pisa, Pisa, Italy

Abstract

Resonant Cavity Beam Position Monitors (RF-BPMs) are diagnostic instruments capable of achieving beam position resolutions down to the nanometre scale. To date, their nanometric resolution capabilities have been predicted by simulation and verified through beam-based measurements with particle beams. In the frame of the PACMAN project at CERN, an innovative methodology has been developed to directly observe signal variations corresponding to nanometric displacements of the BPM cavity with respect to a conductive stretched wire. The cavity BPM of this R&D study operates at the TM110 dipole mode frequency of 15GHz. The concepts and details of the RF stretched wire BPM testbench to achieve the best resolution results are presented, along with the required control hardware and software.

INTRODUCTION

The CLIC experiment at CERN is an international study of a future Compact LInear Collider. The main purpose is to achieve both high efficiency and luminosity at the Interaction Point (IP) at a beam energy up to 1.5 TeV. Therefore, the required beam size at the IP is in the range of a few nanometres. To achieve this, the beam emittance needs to be maintained over the whole 30 km length of the main linac, implying Beam Position Monitor (BPM) technologies capable of measuring nanometric displacements and a precise alignment between the main accelerator components in the micrometric range. In this scenario, the PACMAN project [1], funded by the European Union's Seventh Framework Programme, aims to prove the feasibility of innovative, high precision alignment methods for BPMs, quadrupoles and accelerating structures, based on stretched and vibrating wire technologies.

CLIC CAVITY BPM AND TESTS

The CLIC cavity BPM design is based on the combination of a monopole TM010 mode reference cavity and a dipole TM110 position cavity, resonating at ~ 15 GHz (a 3D model of the position cavity and pickups is shown in Fig. 1). The initial design in stainless steel was studied through beam measurements in the CLIC Test Facility (CTF3) at CERN and it was later improved to achieve an higher Q value through a copper construction. Five cavity BPM prototypes of the new design are now being studied at CERN. Three BPMs are installed in CTF3 [2] and two others are used by the PACMAN project in a laboratory environment to test stretched-wire methods.

* silvia.zorzetti@cern.ch

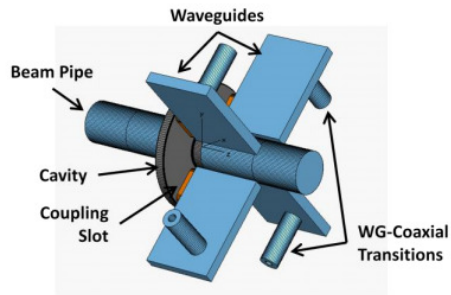

Figure 1: BPM moodel.

The BPM resolution depends on many factors. A relevant signal deterioration is caused by manufacturing imperfections, leading to monopole mode leakage to the position cavity, asymmetries between the lateral pickup ports, or cross coupling between adjacent ports. To avoid a significant degradation of the performances and accuracy, the fabrication tolerances were set very tight. Taking into account the weakest manufacturing aspects, RF simulations of the BPM design anticipated a 50 nm spatial resolution, for 50 ns measurement time with beam [3].
So far, cavity BPM resolution results have mainly been achieved through beam-based techniques. The traditional approach is to pre-align three BPMs in a straight line on a common support, and to predict the position of the central BPM out of the position of the other two. The resolution is extrapolated by the residuals' standard distribution, returned by the difference between the measured position and the calculated one [4].

BPM experiments using particle beams are essential tests for calibrations purposes, e.g. analysing the sensitivity of the cavity as a function of the beam position or the number of charges. However, RF tests, without requiring beam, present a simple way for characterizing first prototypes and pre-align the BPM and its associated quadrupole. The proposed stretched-wire analysis is particularly valuable for finding the electrical center of the position cavity or analysing its high spacial resolution capability.

STRETCHED-WIRE SETUP

To study the BPM resolution, a standalone test bench has been assembled. The main bench components, and measurement procedure are shown in Fig.2, 3. A Vector Network Analyser (VNA) is added for signal read-out. The scattering parameters acquired through this setup allow the measure

ISBN 978-3-95450-177-9

of the relative displacement between the wire and the electrical center of the cavity. We found that the most sensitive information is returned by the phase between adjacent ports (e.g. $\angle S14$[1]), which demonstrates a linear behaviour around the electrical center of the cavity [5].

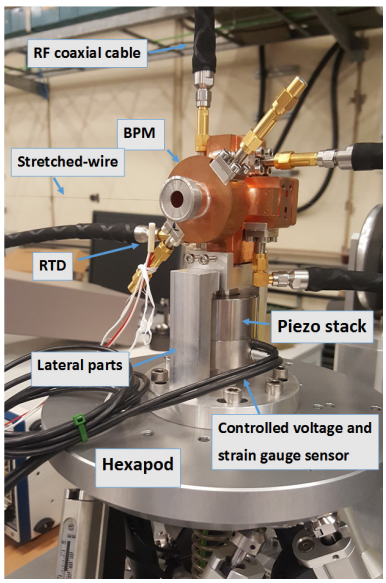

Figure 2: BPM test bench with hexapod and piezo stages.

Laboratory Environment

Environmental tests have been carried out to verify the stability of the laboratory in terms of temperatures and vibrations.

Temperature The resonant frequency of the position cavity versus temperature has a gradient of $-359 kHz/^\circ$ C [6]. As a drift in resonant frequency or Q-factor also affects the stability of the measurements, it is important that the temperature of the laboratory is stable. In this laboratory, the recorded temperature drift is less than 0.3° C over ~ 12 hours (Fig.4). The signal phase, as measured by the VNA, shows a linear dependence from the temperature Fig.5. It is necessary to underline that the temperature was monitored on the complete coaxial assembly, composed of both the BPM and the stretched wire, therefore a change of temperature was impacting not only on the BPM position cavity but on the entire installation.

Vibrations The test bench is mounted on an active optical table to damp vibrations. The chosen model is a Vision IsoStation from Newport, ensuring a reduction of vibration transmission to the vertical and horizontal axis of 85% above 5 Hz and 95% above 10 Hz. Vibration measurements of the ground, the table and the hexapod were performed in order to estimate their possible effect on the wire position measurements. The results are presented in Fig.6 and depend on the period of the day measured: lower vibrations are registered during the night than during the day. However the parameter of interest is the relative motion between the table and the hexapod, as the wire is attached to the table via holders and the hexapod moves relatively to this wire. This always remains below 4 nm [2]. It is necessary to remark that these measurements characterize only the dynamic behaviour of the BPM measuring system and do not provide any information about possible drift or very low frequency vibrations.

Actuators and Sensors

Actuators Two types of actuators are used, a Hexapod for pre-positioning the BPM with respect to the wire (with sub-micrometer minimum incremental motion on 6-DOF [3]), and a piezo to move the BPM with respect to the wire with a finer step size.
The piezoelectric actuator is a high voltage pre-loaded piezo stack P-225 from Physik Instrumente (PI). The actuator has an embedded strain gauge sensor to measure its elongation during operation, with 0.3 nm resolution. The actuator is powered by an E-508 amplifier module and it is driven by an E-509 servo module from the same company. The piezo is operated in closed loop to cancel hysteresis and improve linearity. The input signal to drive the actuator is fed to the control port of the piezo amplifier by a voltage generator, providing DC voltage levels. An input voltage of 10V corresponds to $15 \mu m$ displacement.
The actuator is mounted on the hexapod and drives the BPM in a single direction (vertical axis). The BPM center of gravity was positioned on the axis of the actuator. Due to the small mass (0.7 kg) of the BPM with respect to the high load actuator (12.5 kN), no external linear guidance was used for this simple setup. This was considered sufficient as of the measurement campaign consists of a rather static process. Two lateral parts were used to align around the vertical axis.

Sensor A Copper beryllium wire of 0.1 mm diameter is stretched through the BPM cavity to simulate the particle beam. The choice of the wire is mainly driven by the compatibility with magnetic measurements for the Final PACMAN Bench [7]. In this case it acts as a passive probe, sensing the dipole electric field excited into the cavity. The wire is fixed and mounted to two lateral stretching devices, installed on the table.

Software Automation and VNA Setup

The measurements procedure is completely automated through a controller software developed in LabVIEW (interface in Fig.7), with a state machine to synchronize the different steps.

1 The *hexapod* is moved to prepositioned coordinates. This predetermined point is close to the electrical center and has high sensitivity;

[1] Signal phase acquired exciting from $Port4$ and reading from $Port1$ - Reference to cavity depicted in Fig.3

[2] $x_{\Delta_{RMS}} = \sqrt{x_1^2 - x_2^2}$

[3] three linear axis and three angular ones

ISBN 978-3-95450-177-9

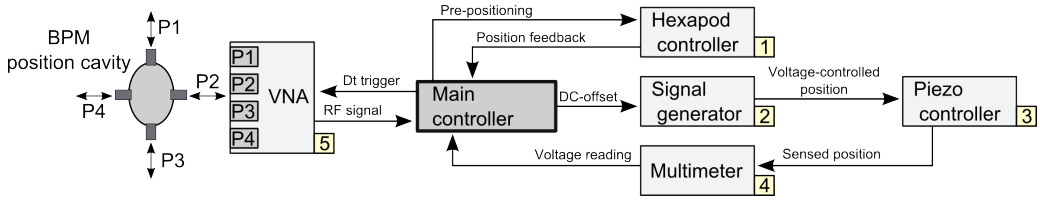

Figure 3: Schematic view of the test bench for resolution nanometric measurements.

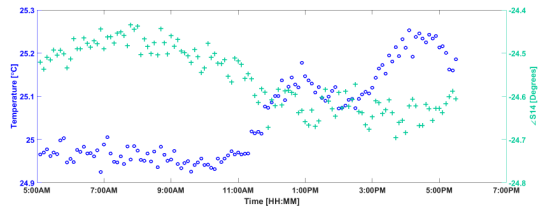

Figure 4: Temperature and cross-section's phase trends.

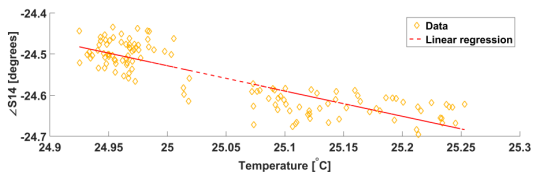

Figure 5: Temperature vs cross-section's phase.

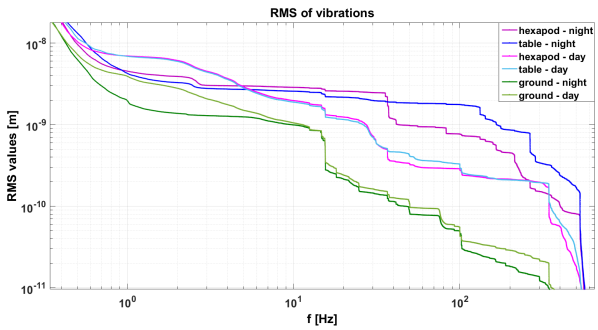

Figure 6: RMS vibrations of the bench.

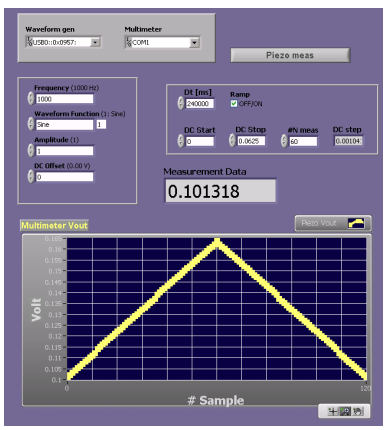

Figure 7: LabVIEW interface, piezo controller.

2 The main controller provides the voltage value to the *signal generator*;

3 The *piezo actuator* is controlled in voltage by the signal generator's output;

4 After the movement of the piezo, a sensed position is sent in closed loop for voltage reading to the *multimeter*;

5 A trigger to a VNA is generated every *Dt* (a user-defined time constant);

6 The *VNA*, connected to the four BPM ports, performs RF magnitude and phase measurements in frequency sweep. The lower the frequency of the sweep (IFBW), the higher the time constant *Dt* needs to be. In the present experiment $IFBW$=70 Hz, with a sweep centered around the position cavity's resonant frequency ($\sim$ 15 GHz). Moreover, before taking data, the VNA was calibrated and a phase offset has been applied to center the BPM signal phase in a 0° to ±180° range.

NANOMETRE RESOLUTION RESULTS THROUGH STRETCHED-WIRE MEASUREMENTS

The signal generator is programmed by the LabVIEW interface to sweep in a DC voltage range for a number of steps. After every movement of the piezo, the VNA acquires magnitude and phase data. With this experiment we intend to demonstrate that a few nanometres resolution could be resolved in a static conditions process.
Fig.8a shows the linear dependence between piezo elongation (resulting in wire displacement with reference to the center of the position cavity) and the adjacent ports phase ($\angle S14$). The position displacement is $\Delta l = 25nm$, from a DC voltage offset driving the piezo of $\Delta V \simeq 33.33mV$. A finer DC offset voltage sweep ($\Delta V \simeq 2mV$) shows, with less accuracy, the outstanding BPM sensitivity and ability to detect position displacements of $\sim 3nm$ (Fig.8b).

Impact of Environmental Characteristics

The rather high acquisition time (Dt = 240000 ms) results in a very low sampling frequency f_s = 4 mHz. Possible sources of noise at frequencies above f_s, such as air flows or vibrations (4 nm at 1 Hz in Fig. 6) could be considered removed. Although, practical experiences may still be affected by environmental changes over a long time scale (e.g. wire tension or ambient temperature) as they were performed during different time slots and days. To reduce their impact, tests were repeated several times and averaged.

Gradient Distribution

Plots in Fig. 8 show the result of the experience. We observe a dependence between the phase and the piezo elongation expressed in a linear form: $y = ax + b$, where a is the

ISBN 978-3-95450-177-9

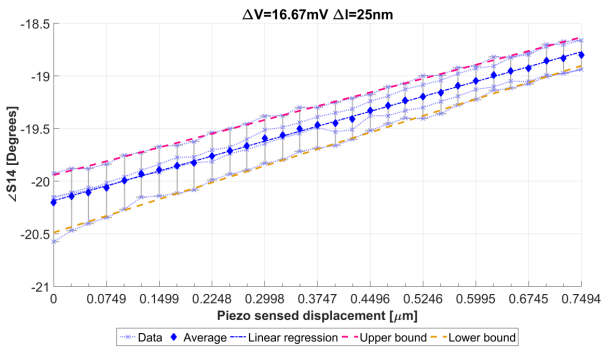

(a) $\angle S14$ resolution results at 25 nm piezo step size.

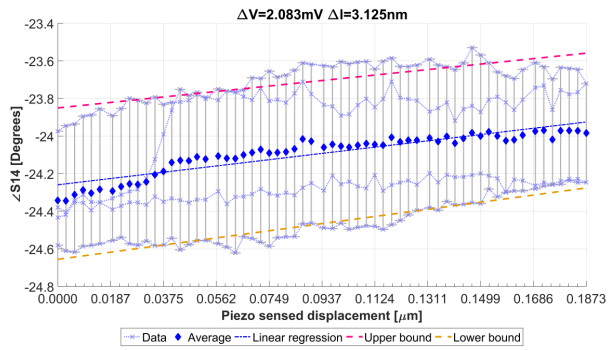

(b) $\angle S14$ resolution results at 3.125 nm piezo step size.

Figure 8: BPM nanometre resolution results.

gradient (angular coefficient) and b the line offset. The table below summarizes those parameters for the mean, upper and lower lines, calculated with the mean squared fit method.

Table 1: Gradients and Offsets

Parameter	Upper error	Mean	Lower error
Gradient - 25 nm [Degrees/μm]	1.7472	1.8881	2.1145
Gradient - 3 nm [Degrees/μm]	1.5556	1.7842	2.0283
Offset - 25 nm [Degrees]	-19.9416	-20.1856	-20.4879
Offset - 3 nm [Degrees]	-23.8501	-24.2595	-24.6557

The gradient distribution between every couple of samples ($\frac{\Delta\angle S41}{\Delta l}$) is shown in Fig. 9. The mean (μ) gradient value, presenting a higher probability of occurrence, is close to the computed average value in Table 1. The high variance depends mainly on the impact of environmental characteristics drifts at very low frequencies ($\ll f_s$), as well as from the limited number of observations recorded.

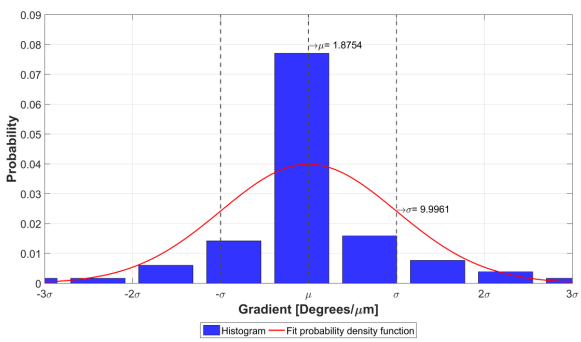

Figure 9: Histogram of gradient values.

CONCLUSION

A test bench to perform static nanometric stretched-wire measurements was developed and first results achieved. The presented experiences demonstrated the mechanical capability of the BPM position cavity of acquiring with nanometric sensitivity the position of a floating conductive stretched-wire, out of its coupling with the electrical field excited by the attached waveguides in the position resonant cavity. This result can be seen as an upper resolution limit for beam-based tests.

REFERENCES

[1] H. Mainaud Durand et al., "Status of the PACMAN project", in *Proc. IBIC'15*, Melbourne, Asutralia, September 2015, pp. 483–486.

[2] J. R. Towler et al., "Development and Test of High Resolution Cavity BPMs for the CLIC Main Beam", in *Proc. IBIC'15*, Melbourne, Asutralia, September 2015, pp. 474–478.

[3] A. Lunin et al., "Design of a submicron resolution cavity BPM for the CLIC main linac", Rep. TD-09-028, December 2009.

[4] S. Walston et al., "Performace of a nanometer resolution BPM system", in *Proc. EPAC'06*, Edinburgh, United Kingdom, June 2006, pp. 1256–1258.

[5] S. Zorzetti et al., "Stretched-Wire Techniques and Measurements for the Alignment of a 15GHz RF-BPM for CLIC", in *Proc. IBIC'15*, Melbourne, Asutralia, September 2015, pp. 487–491.

[6] F. Cullinan et al., "A prototype cavity BPM position monitor for the CLIC main beam", in *Proc. IBIC'12*, Tsukuba, Japan, October 2012, pp. 1–3.

[7] C. Sanz et al., "Characterization and measurement to the sub-micron scale of a reference wire position", in *Proc. CIM'15*, Paris, France, September 2015, Article Number 13005.

ISBN 978-3-95450-177-9

MICROTCA.4 BASED OPTICAL FRONTEND READOUT ELECTRONICS AND ITS APPLICATIONS

K. Przygoda†, L. Butkowski, M. K. Czwalinna, H. Dinter, C. Gerth, E. Janas, F. Ludwig, S. Pfeiffer, H. Schlarb, C. Schmidt, M. Viti, Deutsches Elektronen-Synchrotron, Hamburg, Germany
R. Rybaniec, Warsaw University of Technology, Warsaw, Poland

Abstract

In the paper the MicroTCA.4 based optical frontend readout (OFR) electronics and its applications for beam arrival time monitor (BAM) and fast beam based feedback (BBF) is presented. The idea is to have a possibility to monitor the modulation density of the optical laser pulses by the electron bunches and apply this information for the BBF. The OFR composed of double width fast mezzanine card (FMC) and advanced mezzanine card (AMC) based FMC carrier. The FMC module consists of three optical channel inputs (data and clock), two optical channel outputs (beam arrival time), 250 MSPS ADCs, clock generator module (CGM) with integrated 2.8 GHz voltage control oscillator (VCO). The optical signals are detected with 800 MHz InGaAs photodiodes, conditioned using 2 GHz current-feedback amplifiers, filtered by 3.3 GHz differential amplifiers and next direct sampled with 16-bit 900 MHz of analog bandwidth ADCs. The CGM is used to provide clock outputs for the ADCs and for the FMC carrier with additive output jitter of less than 300 fs rms. The BAM application has been implemented using Virtex 5 FPGA and measured with its performance at Free Electron LASer in Hamburg (FLASH) facility.

INTRODUCTION

The Micro Telecommunication Computing Architecture (MicroTCA) is a standard in Telecommunication from several years. Nowadays more often high energy physics research centres are trying to migrate from commonly used Versa Module Europa (VME) to more compact, modular, redundant solutions offered by MicroTCA, especially generation four of the standard. The Deutsches Elektronen-Synchrotron (DESY) in Hamburg in Germany is a leading institute which developing, designing, testing and even commercializing general purpose and application specific modules using this modern technology. Moreover, the next generation light sources such FLASH and European X-Ray Free Electron Laser (E-XFEL) accelerators have been decided to be fully controlled and monitored with its crucial parameters by MicroTCA.4 [1].

The scope of the paper is to summarise the several year research and development (R&D) program on developing direct sampling OFR electronics [2]. The OFR electronics have been optimized to get the best achievable performance when considering the optical to RF conversion of the laser pulses, ADC stability and fast data processing by FPGA's. Fast digital feedback information can be sent out using small form-factor pluggable (SFP) optical modules allowing data transfers up to 10 Gbps. The OFR electronics can be efficiently applied for several applications. Within the paper we are presenting its usage for BAM and BBF experiments.

† konrad.przygoda@desy.de

BEAM ARRIVAL MONITOR AND BEAM BASED FEEDBACK APPLICATIONS

The BAM signal creation, detection and analysis in the electron bunch arrival time monitor is split into several subsystems, each fulfilling a particular function as shown in Fig. 1.

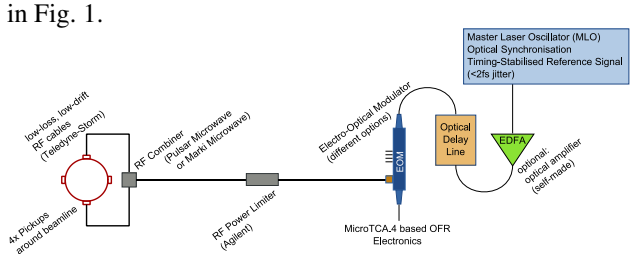

Figure 1: The block diagram of BAM detector.

The RF module which consists of four broadband pickups mounted in the beam tube is applied in order to capture the electric field induced by the passing electron bunches. The signals of opposite pickups are combined for a reduced position dependence of the measurement, resulting in two independent RF channels for the arrival time detection: course and fine. Than the electro-optical modulator (EOM) unit is introduced mainly for translating the RF signals into an amplitude modulation of time-stabilized, ultra-short laser pulses provided by the Master Laser Oscillator (MLO) synchronization system in order to achieve a high temporal sensitivity. The optical frontend electronics need to be installed at the end of the system for signal processing and control of the individual subsystems [3].

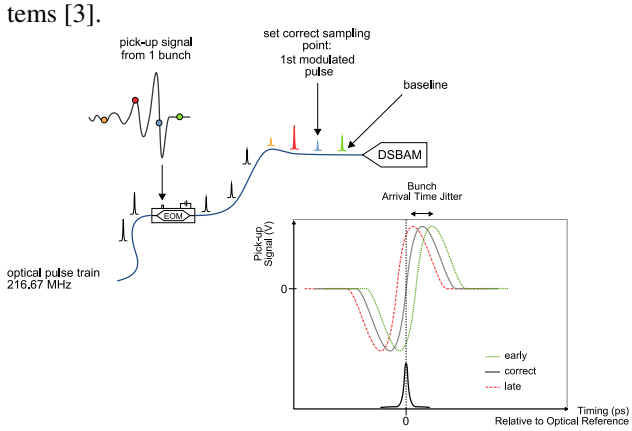

Figure 2: The block diagram of BAM signal detection and calibration.

The beam arrival time is calculated using peak and baseline values of the first modulated (mod) and first unmodu-

ISBN 978-3-95450-177-9

lated (unmod) laser pulses according to the following formula:

$$BAM = \frac{Peak_{mod} - Baseline_{mod}}{Peak_{unmod} - Baseline_{unmod}}. \quad (1)$$

The search of the correct BAM signal operating point (zero-crossing region) is done by a change of the position in time of the laser pulses using motorized delay stage (see Fig. 2).

The RF field stability is one of the major components which determine the beam stability. The path to improve this is certainly to use the beam itself as a detection mechanisms and feedback the information to the corresponding RF station. Here one can distinguish between two time scenarios in a pulsed machine. First to compensate for drifts induced to the machine due to environmental influences of other subsystems as well as the regulating RF station itself. The information of the arrival time from the previous pulses can be used to correct the actual one. At FLASH this is meant to be the slow RF feedback. With the current repetition rate this feedback can achieve a maximum frequency of 10 Hz. In order to compensate for stochastically and fast fluctuations appearing from pulse to pulse an intra train feedback is required, acting on the bunches of the same pulse by information of the previous bunches of the same train. Depending on the delay and bandwidth of the feedback system disturbances up to a few hundred kHz can be compensated. In order to illustrate the functionality in Fig. 3 a functional block diagram is given.

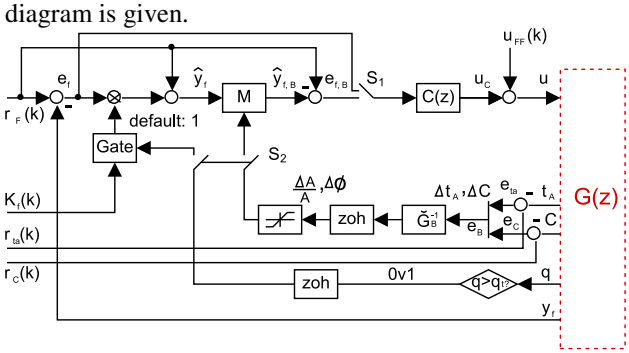

Figure 3: Functional block diagram for the intra-train beam based feedback.

The system itself is described as G(z). As an input to the system, the RF drive given as u is a function of the measured RF field y_F and the arrival time t_A. For further details we refer to [4]. Beside the arrival time also the compression signals are processed in the loop which is necessary in terms of coupling between those two signals with the manipulation of amplitude and phase settings of the RF field. Further coupling of arrival time and compression changes between different RF stations along a linac with several bunch compression and drift sections has to be also taken into account. Coupling and distribution of fast feedback data is foreseen.

OFR HARDWARE OVERVIEW

The OFR electronics are composed of double width FMC module and supporting AMC based carrier as shown in Fig. 4 [5]. The DFMC-DSBAM adapter is equipped with 3 optical inputs and 2 optical outputs placed on the front side of the module. The optical inputs are used to provide data and clock signals directly obtained from optical laser pulses. The idea is to provide each of data channel into two independent ADC channels using single-ended to differential buffers. The optical signal conversion to its electrical representation is performed using photodiode and transimpedance amplifier. In order to avoid problems with optical cables mismatch and different length, the programmable attenuators have been introduced. The main concept is to have a possibility to make remote calibration of each of data input channels with respect to the fact that ADC buffers have maximum possible gain. The heart of the system is CGM module that synthesizes optical input clock into 4 LVPECL and 4 LVDS clock outputs. The LVPECL and LVDS clock outputs are grouped into pairs. The each pair is equipped with its individual frequency dividers. In addition LVDS outputs are equipped with ramping capacitors that can be configured for different ramping current values and as a result allowing additional fine delays of each output individually.

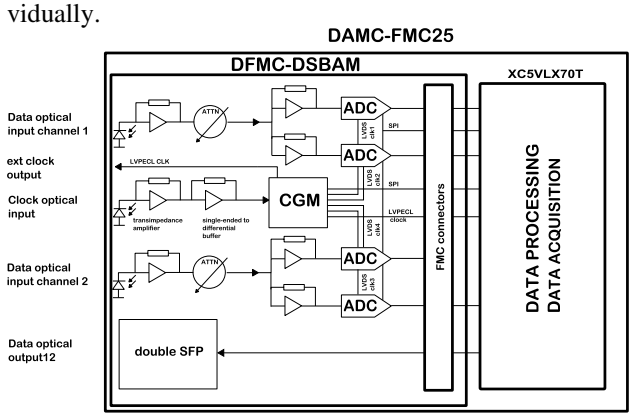

Figure 4: The block diagram of MTCA.4 based OFR electronics.

For the BAM application the optical input clock period is 4.6 ns. The CGM module is than phase locked with 216 MHz input using built-in phase locked loop (PLL) equipped with VCO operated at 2.592 GHz. The direct output of the PLL is divided by 2 giving a possibility to provide 1.296 GHz reference frequency driving one of the LVPECL outputs. Finally each of ADC clock can be shifted by 6 independent coarse steps of 800 ps each. The fine delay allows making 48 individual steps of 16 ps each. The ADC chips have been equipped with self-testing procedures implemented by manufacturer. The proper operation of the chips can be easily verified without any optical signal connection for the data channels. The LVDS data outputs of each ADC are fed to the carrier using both available FMC connectors. The information of operating voltage of FMC module is stored inside field replaceable unit (FRU). The voltage record is read by the

ISBN 978-3-95450-177-9

carrier using module management controller (MMC) and then the proper voltage level is adjusted. The each FMC module has its unique identification (ID) number together with sensor data records (SDR) filled out with temperature meters. The raw data from ADCs are processed by the FPGA device ported to DAMC-FMC25 carrier. The data are next sent back to the FMC module using fast serial links connected to built-in multi-gigabit transceivers (MGTs) on the FPGA side and to the SFP modules on the FMC module side.

FIRMWARE AND SUPPORTED SOFTWARE

The OFR electronics firmware is processing two independent bunch arrival monitor (BAM) channels. The peak and baseline of the optical pulse are digitized by two ADCs. FIFO memories store ADC data using the 216 MHz ADC data clock (DCLK). IODELAY component allows shifting of the input clock to match the data lines from the ADC. The 216 MHz system clock is also applied to the second port of the FIFO. The 1024 data points are stored in the BRAM memory in the FPGA with full 216 MSPS acquisition frequency for PLL delay adjustments. The SYNCH block synchronizes the data from the FIFO to align them with the input TRIGGER and match with the electron bunches. The BAM component uses information from two SYNCH blocks (two pairs of unmodulated and modulated pulses) to compute the bunch arrival time (BAT). Computed BAT is then sent to the RF field controller via a 3.125 Gbps fiber link using the proprietary LLL protocol. The BAT so as the other variables are stored in the data acquisition (DAQ) block for the post-processing with the high level software (HLS). The HLS also provides the configuration parameters by the PCIe bus. Internal registers in the FPGA are addressed using the internal bus (IBUS) [6]. Internal PLL in the FPGA synthesizes the divided 108 MHz clock which is used for components outside of the processing pipeline which do not require low latency operation. The block diagram of BAM firmware is shown in Fig. 5.

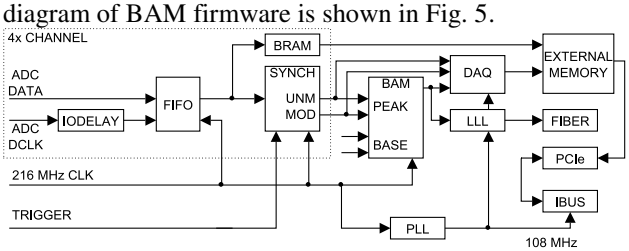

Figure 5: The block diagram of supporting firmware for BAM application.

The BBF firmware first computes the difference between RF field set-point (SP) and vector sum (VS). The resulting field error is scaled by BBF Gain, which is one in case of no beam, otherwise a user defined value. Next the field error is modulated by the beam error (AMP CORR and PHS CORR), which is done around the SP. The beam error is computed from bunch arrival monitor and bunch compression set-points (BAM SP). The beam scaling factor is a part of the transformation matrix whose elements correspond to the weighting of bunch arrival time and bunch compression measurements, respectively. A limiter for beam related amplitude and phase is implemented to avoid undesired large field changes if one of the beam measurements is corrupted. Within the limits, the input is fed through to the output, while the output is truncated in case of reached predefined limits. Furthermore, the set-point correction is done by a manipulation of the predefined RF field set-point, leading to a beam based correction (BBF error) as shown in Fig. 6.

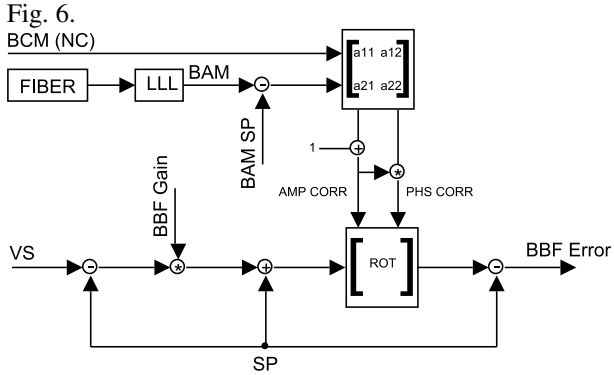

Figure 6: The block diagram of supporting firmware for BBF application.

The high level software for the data acquisition system and slow control is written using the distributed object oriented control system (DOOCS) framework [7]. The state machine for the high level software is show in Fig. 7.

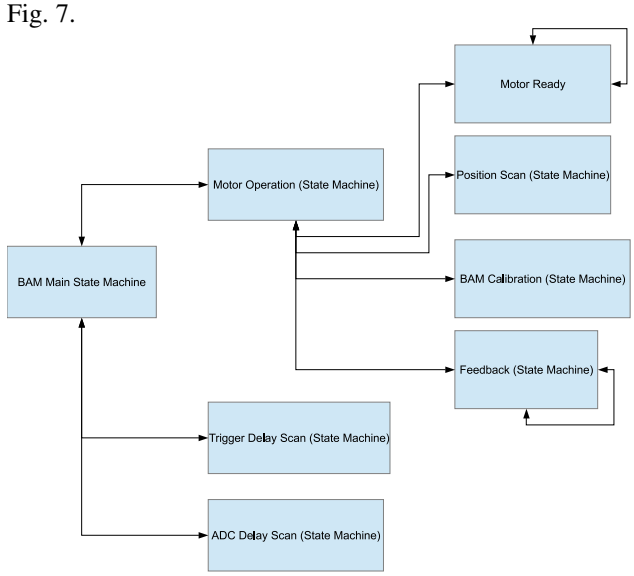

Figure 7: The HLS software state machines to control BAM application.

The default state for the Main State machine is Motor Operation which is as a State Machine as well and the default state for the Motor Operation State Machine is simply Motor Ready. The system remains in this state until an external trigger causes a transition. A transition may occur internally the Motor Operation State Machine to Position Scan or BAM Calibration or Feedback which are State Machines as well. The first is used to find the working point during initialization and configuration of

ISBN 978-3-95450-177-9

the BAM system, BAM Calibration to determine the parameters to transform modulation in femtosecond and Feedback to provide slow feedback. The system can remain indefinitely in Feedback state. An external trigger maybe cause also a transition inside the BAM Main State Machine, from Motor Operation to the states Trigger Delay or ADC Delay Scan. Both are State Machines as well and they are used to configure the BAM System.

EXPERIMENTAL RESULTS AND CONCLUSIONS

The OFR electronics have been installed inside 12 slot Schroff MTCA.4 crate at injector hutch in FLASH and connected to 3DBC2 BAM detector located after first accelerating modules (ACC1 and ACC39) but before first bunch compressor. The OFR electronics have been connected with optical fiber cable to LLRF controller of ACC1 module.

The optical laser pulses have been adjusted with their optical power level using laser driver current of 200 mA in order to not saturate the monitoring ADCs. Next the peak and baseline values of the first modulated and none modulated laser pulses have been captured at 14e3 and -5e3, respectively. During the process absolute value calculation (peak minus baseline of the laser pulse) the ADC raw data stability performance has been measured as shown in Fig. 8.

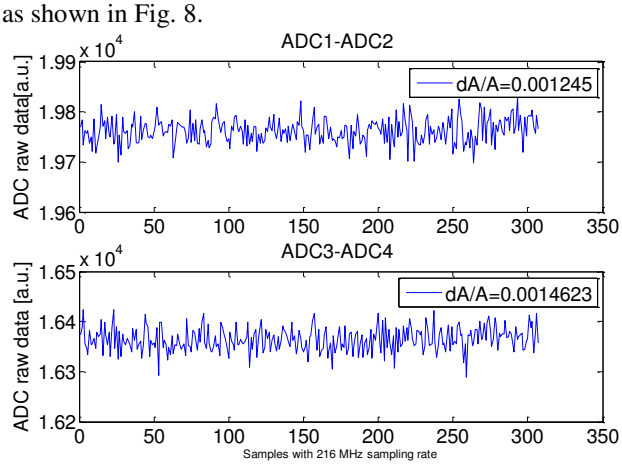

Figure 8: ADC stability measurements for the BAM signals detection of 3DBC2 detector.

Finally, the beam arrival time has been estimated to be of order of 4 ps of the mean value over several tens of measurements. The BBF controller has been setup with its basic functionality excluding bunch compression information (not available yet). During feedback controller operation the rms value of beam time arrival over more than 100 measurements has been recorded for 200 bunches along the bunch train repeated with 1 MHz (see Fig. 9).

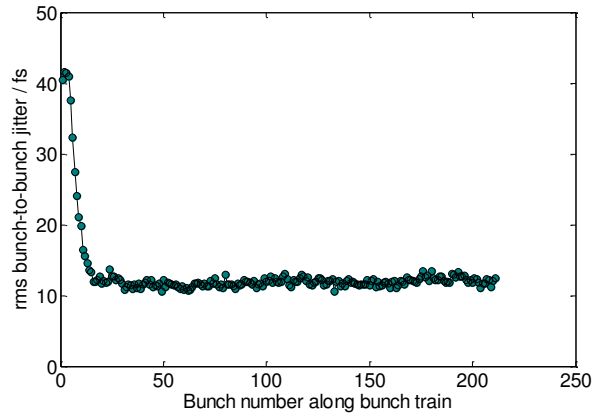

Figure 9: The BAM and BBF application performance at 3DBC2 BAM at FLASH.

The designed OFR electronics have been successfully demonstrated for beam arrival time and fast beam based feedback experiments. The achieved bunch to bunch jitter has been reduced from 40 fs (without BBF) up to 12 fs (with BBF) when considering in-loop measurements (the same detector used as a sensor). The permanent system installation is scheduled and its regular operation supporting beam acceleration efficiency (i.e. SASE) is foreseen.

ACKNOWLEDGEMENT

We would like to express special thanks to our colleagues for all their valuable comments, especially to V. Ayvazyan, C. Sydlo, M. Felber, F. Zumack, M. Fenner from Deutsches Elektronen-Synchrotron (DESY) as well as S. B. Habib, G. Boltruczyk, S. Korolczuk and J. Szewinski from Warsaw University of Technology (WUT).

REFERENCES

[1] J. Branlard *et al.*, in *Proc. IPAC'12*, pp. 55-57.

[2] J. Szewinski, "Zastosowanie Cyfrowego Sprzezenia Zwrotnego do Stabilizacji Wiazki Elektronowej w Liniowych Akceleratorach Nadprzewodzacych", Ph.D. thesis, Warsaw University of Technology, Warsaw, Poland, 2013.

[3] H. Dinter *et al.*, in *Proc. FEL'15*, pp. 478-482.

[4] S. Pfeiffer, "Symmetric Grey Box Identification and Distributed Beam-Based Controller Design for Free-Electron Lasers", Ph.D. thesis, Technische Universität Hamburg-Harburg, Hamburg, Germany, 2014.

[5] J. Szewinski, S. Korolczuk, S.B. Habib and D. Sikora, in *Proc. MIXDES'12*, pp. 147-151.

[6] L. Butkowski *et al.*, in *Proc. ICALEPS2015*, pp. 1-5.

[7] DOOCS, http://tesla.desy.de/doocs/doocs.html

ISBN 978-3-95450-177-9

THE USE OF SINGLE-CRYSTAL CVD DIAMOND AS A POSITION SENSITIVE X-RAY DETECTOR

E. Griesmayer†, P. Kavrigin, C. Weiss, CIVIDEC Instrumentation, Vienna, Austria
C. Bloomer, Diamond Light Source Ltd, Didcot, UK

Abstract

Synchrotron light sources generate intense beams of X-ray light for beamline experiments, and the stability of these X-ray beams has a large impact on the quality of the experiments that can be performed. User experiments increasingly utilise micro-focus techniques, focusing the X-ray beam size to below 10 microns at the sample point, with beamline detectors operating at kHz bandwidths. Thus, there is a demand for non-invasive diagnostic techniques that can reliably monitor the X-ray beam position with sub-micron accuracy in order to characterise X-ray beam motion, at corresponding kHz bandwidths. Reported in this paper are measurements from single-crystal CVD diamond detectors, and a comparison with the previous-generation of polycrystalline CVD diamond detectors is offered. Single-crystal diamond is shown to offer superior uniformity of response to incident X-rays, and excellent intensity and position sensitivity. Measurements from single-crystal diamond detectors installed at Diamond Light Source are presented, and their use in feedback routines in order to stabilise the X-ray beam at the sample point is discussed.

INTRODUCTION

Diamond radiation detectors typically utilise diamond films or plates, some 50 µm thick. Electrodes are deposited on opposite surfaces of the plate (the "front" and "back" of the device), with wire-bonded connections to a PCB frame or holder for the diamond. Standard lithography techniques allow the size and shape of the electrodes to be controlled: dots, quadrants, strips, and pixels can all be realised on the diamond surface. Figure 1 shows a typical arrangement.

Sufficiently energetic incident radiation absorbed by carbon atoms promote electrons from the valence band into the conduction band, forming electron hole pairs. Under the influence of a bias voltage these charge carriers travel to one of the electrodes, where this current can be amplified and measured.

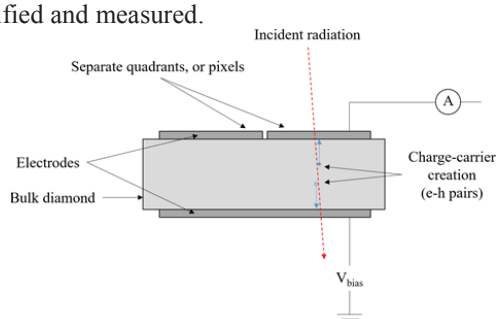

Figure 1: A schematic layout of a diamond X-ray detector

† erich.griesmayer@cividec.at

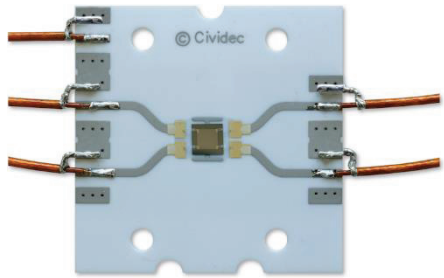

Figure 2: A photograph of the single-crystal diamond detector tested at DLS. The detector is a 4.5 mm x 4.5 mm square diamond in the centre of the image, and is mounted on a ceramic PCB.

Experiments carried out at Diamond Light Source Ltd. (DLS) have been performed to evaluate the performance single-crystal diamond X-ray detectors. Maintaining the spatial stability of the X-ray beam relative to the sample point for the duration of user data collection is vitally important for synchrotron beamlines. Sub-micrometer beamsizes at the sample point are increasing common, and the typically required beam stability is some 10% of beamsize [1]. Reliable X-ray diagnostics are essential during beamline commissioning, during routine "start-up", and during data collection itself as, increasingly, beamline detectors at DLS operate in the kHz regime. Single-crystal diamond detectors offer the ability to make correspondingly high precision position measurements at these bandwidths.

Results presented in this paper are from quadrant detectors, with four square electrodes (metallised "quadrants", or "pads" on the surface of the diamond, less than 100 nm thick) deposited onto one face of the diamond, and a single electrode deposited onto the opposite face of the diamond. These sensors can be used to provide both spatial and intensity measurements. Commonly, this type of detector is referred to as an X-ray Beam Position Monitor (XBPM).

SIGNAL LINEARITY VS INCIDENT FLUX

The signal produced by diamond detectors is typically a current of a few nanoamps to microamps. The signal produced (i.e. the number of charge carriers created in the bulk diamond) is directly proportional to the number of absorbed photons, and thus proportional to the incident light. Signal-crystal diamond has been shown to exhibit a linear signal response to incident flux over many orders of magnitude.

The I04 beamline at DLS has the ability to attenuate the incident light using a series of calibrated absorption materials, inserted into the X-ray beam path. In this way, the

ISBN 978-3-95450-177-9

incident flux can be highly controlled, and the flux reaching the detector can be accurately adjusted over several orders of magnitude.

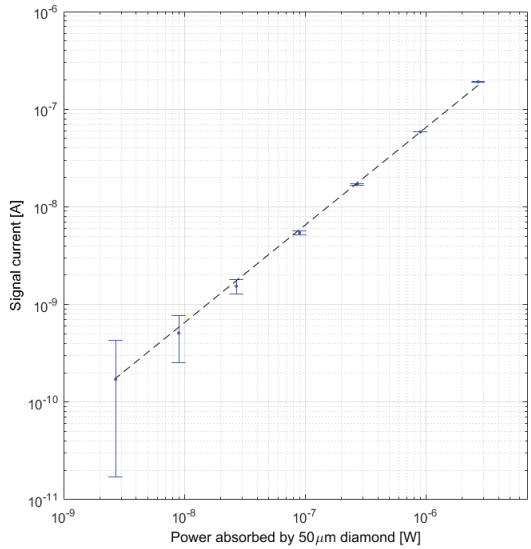

Figure 3: The linearity of signal response from a 50µm thick single-crystal diamond detector.

Figure 3 shows the linearity of the detector to incident flux ("absorbed power") for incident light at 12.7 keV. The amount of incident flux (determined by the absorption materials inserted into the beam path) is independently established using a calibrated diode. Measured noise on the signal is as low as 0.52% of the detected signal at 1 kHz bandwidth.

SIGNAL UNIFORMITY ACROSS THE DETECTOR FACE

Polycrystalline diamond can be used as a detector of ionizing radiation, however the resolution of the sensor is limited by the size of the crystal grains, and single-crystal diamond is known to produce a superior detector [2, 3]. In order to measure the uniformity of a diamond detector a focussed X-ray beam is used to illuminate the sensor surface and the resulting signal currents are measured. A calibrated diode is mounted behind the detector in order to provide an independent measure of the incident beam intensity (referred to as an "*i0*" measurement). The diamond detector is mounted on a precision motion stage, capable of sub-micron movements in the horizontal and vertical direction. The signals from each of the four detector channels are recorded as a 2D raster scan of the detector through the incident beam is performed. As a raster scan of this nature takes some considerable time (some ~30 minutes) the measured signal from the diamond detector quadrants must be normalised to the *i0* measurement in order to remove the effects of top-up and other variations in incident beam intensity over this period.

The results of such a scan using a 25 µm (RMS) Gaussian beam of 12.7 keV photons are shown in Figure 4, where the sum of the signal currents from each of the four quadrants is presented.

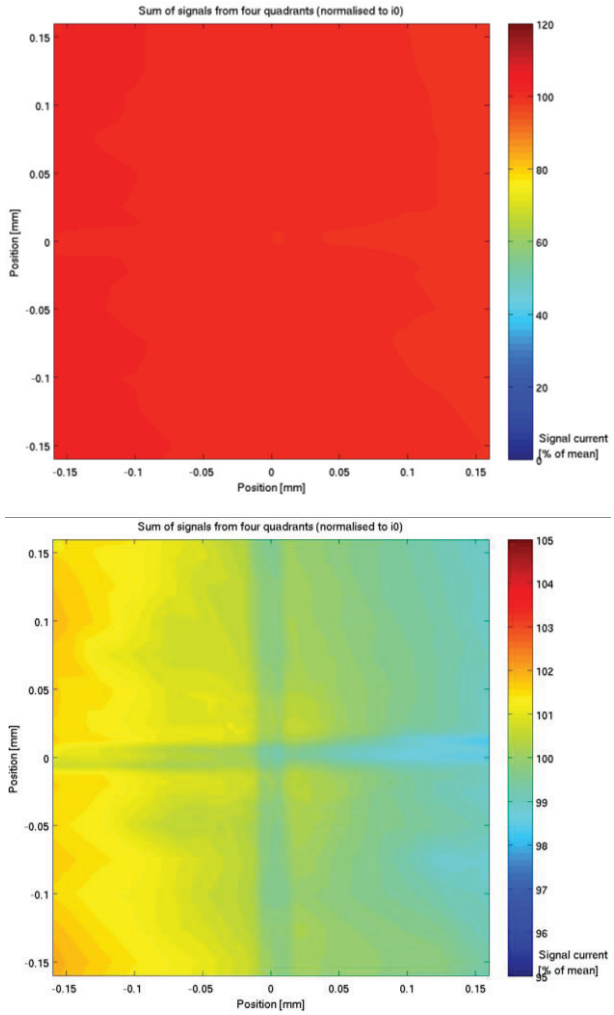

Figure 4: (Top) The measured uniformity of response to incident X-rays over the position-sensitive region at the centre of the detector. The signal current from all four quadrants is summed and displayed. (Bottom) The same measured signal, scaled in order to small changes in sensitivity over the surface of the detector.

These results show a uniform response to signal to within a few percent. There is however a measurable change in the measured signal between the left and the right of the detector (as viewed in this plot). This is due to the polishing of the diamond resulting in a wedge shape. Where the diamond is thickest (at the left of the image) it absorbs more of the incident light and thus a higher signal current is produced.

The gap between the quadrants is visible on the uniformity plot, seen as a "cross" on the image. The thickness of this cross in the plot is a convolution of the size of the insulating gap between neighbouring quadrants, 2 µm, and the incident X-ray beam size, 25 µm.

That the measured signal current appears weaker in this gap region is due to an artefact with the *i0* normalisation.

ISBN 978-3-95450-177-9

The metallised electrodes, despite being less than 100 nm thick, absorb a portion of the incident light. However, there Figure 5 show the individual measured signal currents from each of the four quadrants (labelled A, B, C, and D) as the X-ray beam is moved across the face of the detector shown in Figure 4.

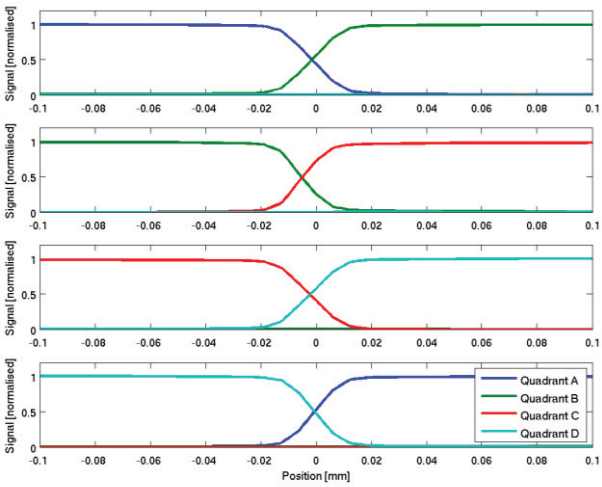

Figure 5: The results of 1D scans of the X-ray beam moving across the face of the detector is shown, demonstrating the uniformity of the signal currents seen as the beam passes from one quadrant into the neighbouring quadrants. The top plot shows the signal seen as the beam moves from quadrant A into quadrant B; the second shows the beam moving from quadrant B into quadrant C; and so on.

The measured signal currents from four 1D scans are presented. Each scan is 200 µm long scan as the X-ray beam passes from one quadrant into the next. Quadrant A is located in the top left of the detector shown in Figures 2 and 4; quadrant B is top right; and naming continues in a clockwise direction. The top plot of Figure 5 shows the signals measured during a scan starting at coordinate (X = -0.1 mm, Y = 0.1 mm) and moving horizontally to (X = 0.1 mm, Y = 0.1 mm); the second plot shows the results from a scan starting at (X = 0.1 mm, Y = 0.1 mm) and moving vertically to (X = 0.1 mm, Y = -0.1 mm); and so on.

THE EFFECTS OF CHANGING BIAS VOLTAGE

The bias voltage that is applied to the detector has an impact on the velocity at which the charge carriers will travel through the bulk diamond. This has previously been examined elsewhere [4], and it is recognised that the sensitivity of single-crystal diamond detectors can be influenced by the magnitude of the bias used.

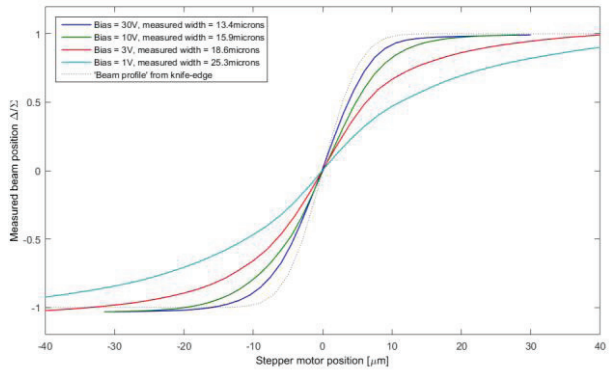

Figure 6: The recorded 1D X-ray beam spatial profile using a single-crystal diamond detector with different bias voltages applied.

Figure 6 shows the measured beam position (calculated as the difference of quadrants located on opposite sides of the device divided by the sum of all four quadrants, Δ/Σ) during a scan of the detector across the incident X-ray beam, for various bias voltages on the I24 beamline at DLS. The beam size is independently measured using a knife-edge scan to be 10.0 µm (RMS) in size. The incident light is 12.7 keV photons, and the flux is measured to be 2.5e9 photons / s.

It is seen that the apparent X-ray beam profile is dependent on the bias voltage used. It is hypothesized that at higher bias voltages the velocity of the charge carriers is greater, and so there is less time for diffusion of the charge carries through the material to occur before they eventually reach the electrode. Thus, at higher bias voltages the measured profile from the detector signal currents more closely matches the "real" X-ray beam profile obtained from a traditional knife-edge measurement.

RF READOUT AT 2 GHZ

A CIVIDEC 2 GHz Broadband Amplifier was used for RF readout of the single-crystal diamond detector in order to make observations of the bunch train at DLS. The ring mode used was so-called "hybrid mode", consisting of a train with 686 1 nC electron bunches, and a single 1 nC "hybrid bunch" in the remaining gap. Figure 7 shows the measured signals, recorded by a 13 GHz oscilloscope. The repeating train itself (top), as well as the 2 ns bunch separation and single bunch (middle and bottom) are easily distinguishable. It should be noted that the actual measured synchrotron bunch length measured at Diamond Light Source was ~20 ps (as recorded by streak camera measurement), meaning that these measurements are many orders of magnitude away from being able to resolving the actual DLS bunch length itself, however they are encouraging in that they offer the potential to distinguish individual bunches. This provides the possibility to develop bunch-by-bunch beam position and intensity measurements in the future.

ISBN 978-3-95450-177-9

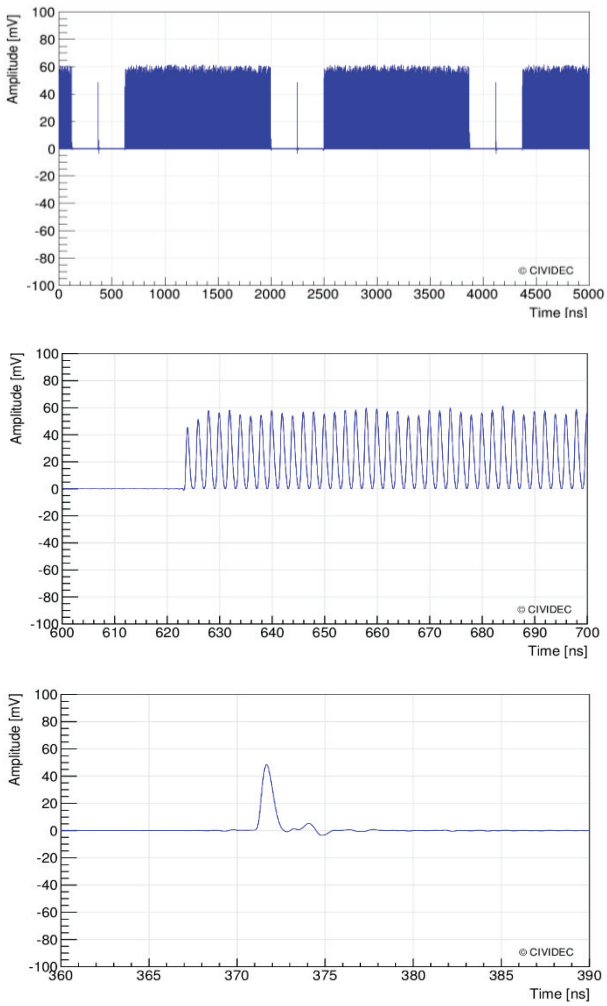

Figure 7: Measurements of the bunch train at DLS. (Top) the repeating bunch train with a single "hybrid bunch" in the gap is seen. (Middle) The 2 ns bunch structure can be resolved. (Bottom) The single 1 nC "hybrid bunch" can be observed.

CONCLUSIONS

Single-crystal diamond X-ray beam position monitors are shown to perform excellently as a non-destructive monitor for synchrotron X-ray beamlines. The transparency of single-crystal diamond makes it a suitable detector material for beamlines operating above 4 keV photon energy.

Accurate and repeatable beam intensity measurements at kHz bandwidths are obtained as long as care is taken that the incident X-ray beam is positioned at the centre of the four quadrants so that the effects of a slight "wedge" of the diamond plate can be mitigated. The RMS noise observed on such intensity measurements has been shown to be as low as 0.52% of the observed signal at 1 kHz bandwidth. The corresponding position measurement resolution is estimated to better than 1% of the beamsize. This corroborates data published elsewhere, demonstrating better than 1% of beamsize position noise at kHz bandwidths, even during unusually low flux measurement conditions, and it has previously been shown that, particularly for low-flux conditions, single-crystal diamond offers offer superior performance when compared to other X-ray diagnostics [3]. The results published in this paper offer further evidence of the advantages of these diamond detectors.

The first permanent beamline installations of single-crystal diamond radiation detectors at DLS occurred early in 2016, and further single-crystal diamond XBPMs are due to be installed imminently. Early results in using these XBPMs as part of routine beamline commissioning and "start-up" have been extremely encouraging, and simple feedback routines in order to maintain a beam position at the sample point have been developed and employed.

The challenge remains to develop technologies that would allow non-destructive X-ray beam monitoring below 4 keV photon energies, where even 50 µm thick plates of diamond absorb too many user photons. Refinements to traditional mechanical polishing techniques allow for plates down to some 10 µm – 20 µm thick to help alleviate this problem. Elsewhere, novel techniques have been explored offering the potential for diamond membranes just a few µm thick [5]. Such very thin devices may also offer additional advantages for XFEL machines with higher photon fluxes and higher power densities.

REFERENCES

[1] R.O. Hettel, "Beam stability at light sources", Review of Scientific Instruments, 73, 2002

[2] J. Morse, "Progress on single crystal diamond beam position monitors for synchrotron X-ray beams", LIST-CEA data presented at ADAMAS workshop, Darmstadt, 2012

[3] C. Bloomer, "An Experimental Evaluation of Monochromatic X-ray Beam Position Monitors at Diamond Light Source", Proceedings of the Synchrotron Radiation Instrumentation Workshop, 2015.

[4] J. Bohon, "Development of diamond-based X-ray detection for high-flux beamline diagnostics", Journal of Synchrotron Radiation, 17, 2010.

[5] K. Desjardins, "Ultra-thin optical grade scCVD diamond as X-ray beam position monitor", Journal of Synchrotron Radiation, 21, 2014.

ISBN 978-3-95450-177-9

BPM ELECTRONICS FOR THE ELBE LINEAR ACCELERATOR - A COMPARISON

U. Lehnert, A. Büchner, B. Lange, R. Schurig, R. Steinbrück
Helmholtz Center Dresden-Rossendorf, PF 510119, 01328 Dresden, Germany

Abstract

The ELBE linear accelerator supports a great variety of possible beam options ranging from single bunches to 1.6 mA CW beams at 13 MHz bunch repetition rate. Accordingly high are the dynamic range requirements for the BPM system. Recently, we are testing the Libera Spark EL electronics to supplement our home-built BPM electronics for low repetition rate operation. Here, we discuss the advantages and disadvantages of the two completely different detection schemes. For integration of the Libera Spark EL into our accelerator control system we are implementing an OPC-UA server embedded into the device. The server is based on the free Open62541 protocol stack which is available as open source under the LGPL.

THE HZDR BPM ELECTRONICS

Figure 1: The HZDR BPM electronics comes in a 1U 19" rack-mount enclosure.

The BPM electronics currently used at ELBE is an in-house design which has been presented at IBIC2013 [1]. It's RF front-end detects the fundamental frequency of 1.3 GHz from the $\lambda/4$ strip-line sensors used at ELBE. This signal after some filtering and amplification/attenuation (see Fig. 2) is mixed down to a 19.5 MHz intermediate frequency. The IF signal is sampled and digitized at 52 MS/s rate. The digital signal is then processed with an I/Q-demodulation over 512 samples yielding a system bandwidth of 95 kHz. This bandwidth was chosen to give a sufficiently fast response but at the same time to integrate the least possible amount of noise in order to reach a high signal-to-noise ratio and dynamic range. A difference-over-sum formula is used to convert the measured signal amplitudes into a position information.

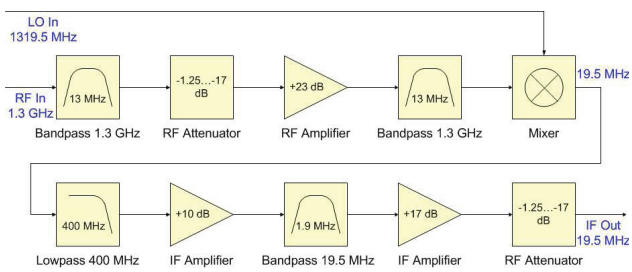

Figure 2: The analog front-end of the HZDR BPM electronics.

ELBE ist mostly run at 13 MHz bunch repetition rate but frequencies down to 100 kHz or single pulses with arbitrary repetition rates are available. At all frequencies above 100 kHz more than a single bunch is detected in every acquisition frame. The according averaging effect further improves the signal-to-noise ratio. This signal processing, however, is not optimized for low bunch repetition rates. The duration of a single-bunch signal is less than 1 μs according to the 1.9 MHz bandwidth of the analog front-end while the noise is integrated over the full 10 μs duration of the sample frame.

THE LIBERA SPARK EL BPM ELECTRONICS

Figure 3: The Libera Spark EL BPM Electronics.

The Libera Spark EL [2] manufactured by Instrumentation Technologies in the tests reported here was connected to an identical strip-line pickup mounted back-to-back with the one used for the HZDR electronics. This device uses a rather different analog front-end and detection scheme. Right at the input the signal is filtered with a SAW resonator centered at a frequency of 500 MHz. The filtered and amplified/attenuated signal is then directly sent to an ADC with a fast sample-and-hold input stage. Sub-sampling at 117 MS/s the signal is mirrored to a 32 MHz base-band frequency. The signal amplitude is then determined by integrating over a fixed number of samples including a few pre-trigger samples. We have chosen 100 post-trigger samples to capture the waveform shown in Fig. 4. Again, we use a linear difference-over-sum formula to derive the position information from the 4 channel amplitudes.

The bandwidth of the whole system is solely determined by the filter bandwidth which is specified in the datasheet to 8 MHz full width. The time-domain approach to the signal detection is very well suited to the measurement of single bunches at low repetition rates. One may note that actually no harmonic of the 13 MHz bunch repetition rate falls into

ISBN 978-3-95450-177-9

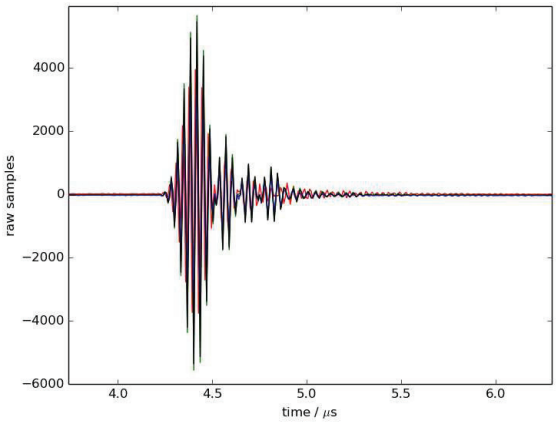

Figure 4: The Libera Spark single-bunch waveforms.

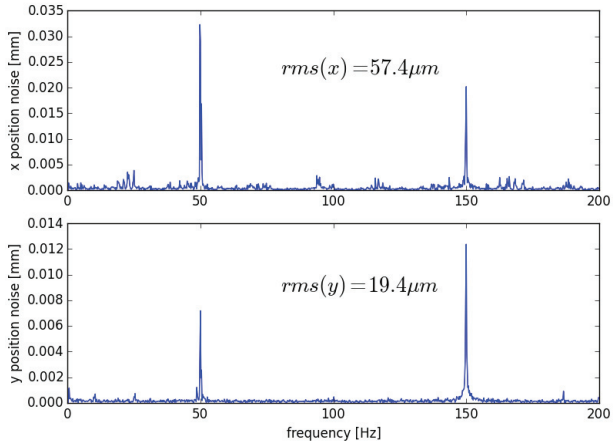

Figure 6: Spectral distribution of the measured beam position noise.

the input filter bandwidth. This surely impairs the results of the measurements shown here. We have recently received a customized version of the instrument with an adapted input filter with 416 MHz central frequency but we didn't have time to test it yet.

NOISE MEASUREMENTS

For comparative measurements the two electronics were connected to two strip-line pickups mounted back-to-back at the ELBE linac1 beamline. This setup does not allow a distinction between the noise contributions carried by the beam and those introduced by the devices but a third sensor could not be mounted. The beam shows a position fluctuation dominated by power-line frequencies. The corresponding signal frequencies have been filtered out in the measurements shown here.

At 13 MHz bunch repetition rate (see Fig. 5) both devices show a quite similar position noise. The acquisition time of the Libera instrument was increased to 1000 samples for this measurement to have a direct comparison to our device. Very likely the noise floor at 10 μm was caused by the beam itself – both devices have shown a <5 μm resolution in other measurements. Also Fig. 6 indicates that there are more spurious noise frequencies modulated onto the beam. The resolution obtained for the Libera Spark EL for single bunches quite well matches the values published by Instrumentation Technologies [3] given the pulse amplitude of 0.3 V we are measuring from our strip-line pickups at 70 pC bunch charge. At 100 kHz (see Fig. 7) the Libera Spark EL demonstrates the superiority of the bandwidth-matched time-domain data evaluation for evaluation of single bunches. A similar algorithm is under development for our device but has not yet been tested with the beam.

CONTROL SYSTEM ACCESS BASED ON OPC-UA

OPC Unified Architecture (UA) is an industry standard communication protocol developed for M2M interoperability. It provides a cross-platform service-oriented architecture using secure communication channels. The standard was released in 2010/2011 under IEC-62541 [4]. There exist many different implementations of the OPC UA standard. APIs for C/C++, .NET, Java or Python are available, LabView,

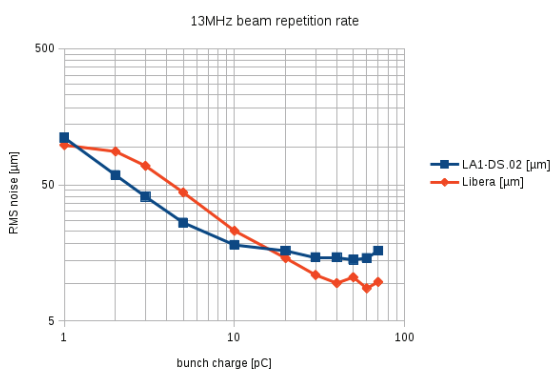

Figure 5: Measured beam position noise at 13 MHz bunch repetition rate.

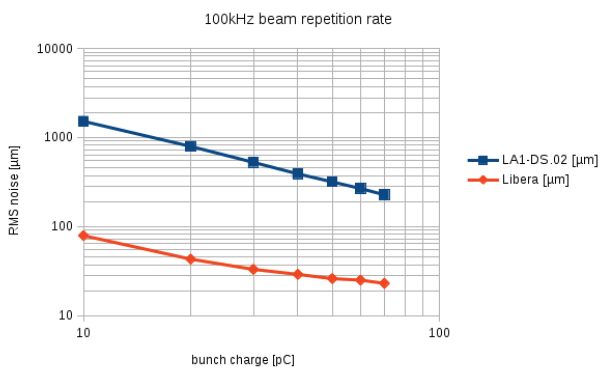

Figure 7: Measured beam position noise at 100 kHz bunch repetition rate.

ISBN 978-3-95450-177-9

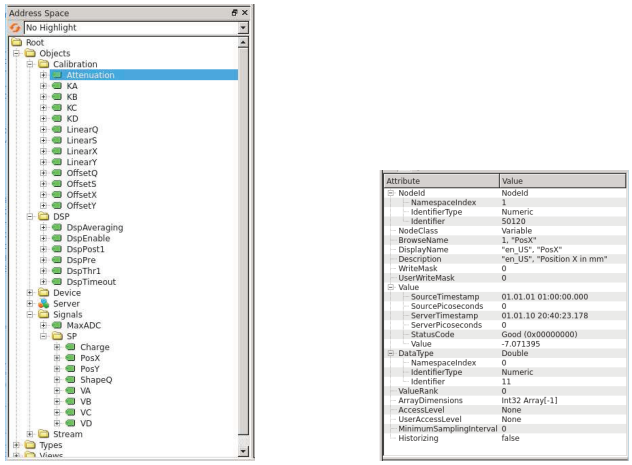

Figure 8: The OPC information model presents itself as a hierarchy of folders, items and properties. All nodes possess attributes delivering meta-data and diagnostic information in addition to the payload data.

EPICS and other control systems also support OPC UA. The standard guarantees interoperability between all the different implementations across all supported platforms (see Fig. 8 on information model). There exist protocol stacks with low resource usage to allow an implementation into embedded devices.

We have chosen an open-source free protocol stack implemented in C and licensed under the LGPL with static linking exception [5] to create a server application embedded into the Libera Spark EL operating system. This allows direct access with the Siemens PLCs and the WinCC control system used at the ELBE facility. Specialized operator panels generated with LabView or programmed in Python can be used in parallel. In addition to that, the server provides a low-latency UDP data stream of the position data for feedback applications.

REFERENCES

[1] A. Büchner, B. Lange: "A New High-dynamic Range BPM for ELBE with Integrated Differential Current Monitor (DCM)", IBIC2013, MOPC22 (2013).

[2] Instrumentation Technologies, `http://www.i-tech.si`

[3] M. Znidarcic, M. Cargnelutti, E. Janezic: "Compact Single-Pass BPM", IPAC2015, MOPTY039, Richmond (2015).

[4] IEC TR 62541-1 (2010).

[5] open62541: An open source and free implementation of OPC UA, `http://open62541.org`

ISBN 978-3-95450-177-9

PERFORMANCE TEST OF THE NEXT GENERATION X-RAY BEAM POSITION MONITOR SYSTEM FOR THE APS UPGRADE*

B.X. Yang, Y. Jaski, S.H. Lee, F. Lenkszus, M. Ramanathan, N. Sereno, F. Westferro
Advanced Photon Source, Argonne National Laboratory, Argonne, IL 60439 USA

Abstract

The Advanced Photon Source is developing its next major upgrade (APS-U) based on the multi-bend achromat lattice. Improved beam stability is critical for the upgrade and will require keeping short-time beam angle change below 0.25 μrad and long-term angle drift below 0.6 μrad. A reliable white x-ray beam diagnostic system in the front end will be a key part of the planned beam stabilization system. This system includes an x-ray beam position monitor (XBPM) based on x-ray fluorescence (XRF) from two specially designed GlidCop A-15 absorbers, a second XBPM using XRF photons from the Exit Mask, and two white beam intensity monitors using XRF from the photon shutter and Compton-scattered photons from the front end beryllium window or a retractable diamond film in windowless front ends. We present orbit stability data for the first XBPM used in the feedback control during user operations, as well as test data from the second XBPM and the intensity monitors. They demonstrate that the XBPM system meets APS-U beam stability requirements.

INTRODUCTION

The Advanced Photon Source (APS) storage ring will receive a major upgrade based on multi-bend achromat lattice [1]. The storage ring emittance will be under 70 pm-rad and the x-ray beam divergence will be dominated by the natural opening angle of the undulator radiation, as expected from a diffraction-limited source. The angular beam stability tolerance is chosen to be a fraction of the beam angular spread. For example, the long-term drift tolerance is 0.6 μrad RMS. For an XBPM at 20 m from the source, this specification translates to an x-ray beam position tolerance of 12 μm. We can assign 70% of this value, 8.5 μm, to the XBPM's total error budget. Table 1 lists the XBPM tolerance for RMS AC beam motion (0.01 – 1000 Hz) and long-term drift (7 days) derived in this manner from the beam stability specifications of the new storage ring.

The first XBPM system designed with these specifications were installed in Sector 27 of the APS storage ring in 2014 [2]. Figure 1 shows the XBPM system which includes the following components: (A) The first XBPM (XBPM1) measures the transverse x-ray beam positions at 18.6 m from the source, which is dominated by the angular motion of the e-beam; (B) the first intensity monitor (IM1) measures the beam intensity when the photon shutter (PS2) is closed; (C) the second XBPM (XBPM2) measures the x-ray beam position at the Exit Mask; and (D) the second intensity monitor (IM2) measures the beam intensity entering the user beamline. The two intensity monitors are used as alignment aids.

* Work supported by U.S. Department of Energy, Office of Science, under Contract No. DE-AC02-06CH11357.

In this work, we will present the performance data of the XBPM1 in user operations, and discuss the design and performance of the XBPM2, IM1 and IM2.

Table 1: APS-U XBPM Tolerance (Z = 20 m)

	Plane	AC motion	Long-term drift
X-ray beam position tolerance	X	5.3 μm	12 μm
	Y	3.4 μm	10 μm
Total XBPM error budget	X	3.7 μm	8.5 μm
	Y	2.4 μm	7.1 μm

GRID-XBPM PERFORMANCE

The first XBPM is a grazing-incidence insertion-device XBPM (GRID-XBPM) based on XRF from two GlidCop absorbers. Since it is sensitive only to hard x-rays, the bend magnet background is less than 3% of the XBPM signal at the maximum undulator gap (30 mm) or minimum undulator power ($K \sim 0.4$) for user operations. In the vertical plane, the XBPM calibration is independent of the undulator gap due to pinhole camera geometry used in x-ray readout optics. In the horizontal plane, the calibration is gap dependent but the offset is small due to symmetry in XBPM design [3,4].

Figure 2 shows the beam stability performance during user operations, as measured by the XBPM1. The data includes 60-days of operations in Summer 2015:

- In the week of June 30, only RFBPMs are used in the orbit feedback control and the x-ray beam is stabilized within +10 μm and −5 μm range, a reasonably good performance.
- After the July 4, the XBPM1 is added into the feedback loop. The black traces show 324-bunch mode of operations where the storage ring is filled twice daily. In these two weeks, we can see small saw tooth shape representing beam motion of 2 μm when the stored current decays from 102 mA to approximately 85 mA.
- After July 21, the blue trace shows operations in 24-bunch top-up mode, and the ring is filled every 2 – 3 minutes. The fuzzy traces represent the beam motion excited by the top-up shots. The severe reduction of the motion amplitude shows the effect of heavy filtering of the XBPM data in signal processing.
- When the XBPM is in the feedback loop, the x-ray beam motion is well within the boundary defined by the red and green lines, which represents the tolerance specifications in Table 1.
- No big jumps of beam positions are found in the gaps on Tuesday machine study days. This indicates that the XBPM helps the beam position return after studies, a feature important to beamline users.

ISBN 978-3-95450-177-9

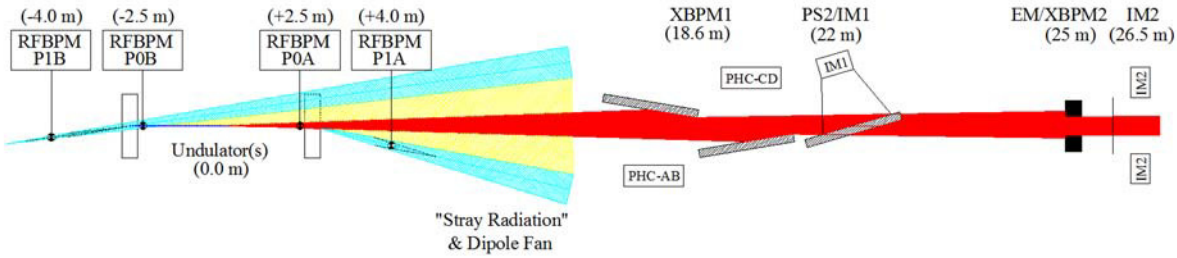

Figure 1: APS 27-ID RFBPM and XBPM system components for orbit controls.

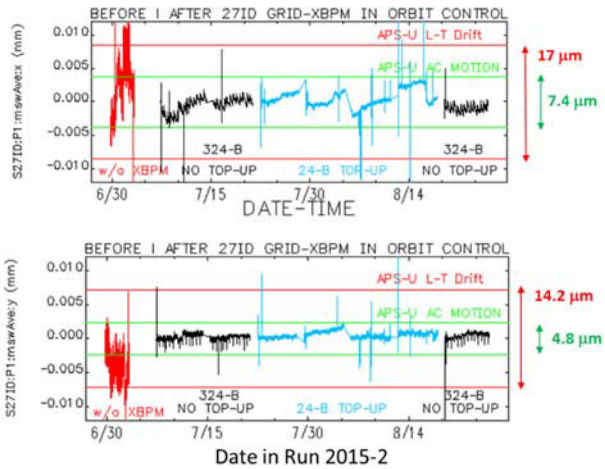

Figure 2: S27-ID GRID-XBPM data taken in 60-days of user operations: The upper panel is for the horizontal x-ray beam positions at 18.6 m from the undulator source and the lower panel is for the vertical beam positions.

SECOND X-RAY BPM

The second XBPM (XBPM2) derives its beam position information from the XRF from the front end Exit Mask (EM). Figure 3 shows its design: Two vertical apertures are placed at both sides of the EM entrance. Each aperture images the XRF photons from the opposite side onto two silicon PIN diodes located further upstream in the pumping chamber. If the beam moves down, more photons passes through aperture to reach the top PIN diode, and vice versa. The difference-over-sum of the two diode signal is proportional to the vertical beam position at the Mask. At the same time, the horizontal beam position can be derived from XRF intensities from two opposing sides of the Mask.

Since the horizontal aperture of the upstream XBPM1 is only 1.6 mm, only a small section of the Mask is illuminated by the beam during normal operations. If we use orbit control to hold beam position at the XBPM1, we can scan the orbit by changing set points of RFBPM P1B. Figure 4 shows the horizontal signal intensity ratio as a function of undulator gap for five different horizontal set points in P1B. Using the known geometry in Figure 1, we can calculate the x-ray beam positions at the Exit Mask, and calibrate the XBPM2.

Figure 5 shows the horizontal calibration constants and offsets for 27-ID XBPM2 as functions of undulator gap. The calibration constant is nearly gap independent. This is likely due to the nearly constant size of the beam passing XBPM1, resulting a constant area of Exit Mask being exposed to the x-ray beam. The offset changes less than 5 µm over the entire undulator gap range. The change may come from the instrument error or from the source motion induced by undulator steering. Regardless of its origin, such a minute change is unlikely to be significant to user operations.

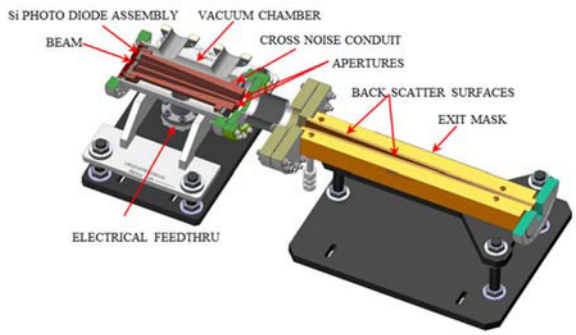

Figure 3: The second XBPM uses the XRF from the Exit Mask to monitors positions of the x-ray beam before it enters the beamline.

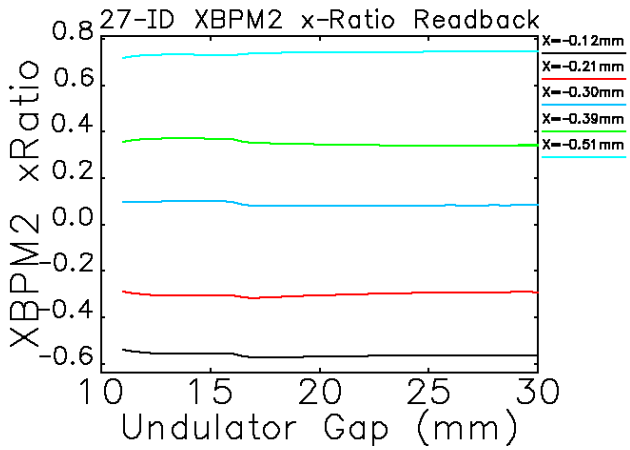

Figure 4: Vertical XBPM2 beam position signals (Δ/Σ) as functions of undulator gap for different x-ray beam positions on the Exit Mask.

FIRST INTENSITY MONITOR

The first intensity monitor (IM1) measures the XRF intensity from the photon shutter (PS2). Figure 6 shows the cross section of IM1. When the shutter is closed, it intercepts the beam on the outboard wall (upper right in the figure). The copper XRF photons will travel back upstream

ISBN 978-3-95450-177-9

through the imaging aperture and reach the silicon PIN diode. Since the length of shutter surface receiving the beam is long compared to the propagation distance, the XRF signal originating from an upstream point may be stronger than from the downstream point due to shorter distance to the diode. In order to get a signal truly proportional to XRF intensity and independent of beam spot location, the silicon PIN diode has a special mask shown in the inset of Fig. 6. The solid angle of the exposed detector surface is made independent of the beam spot position on the shutter.

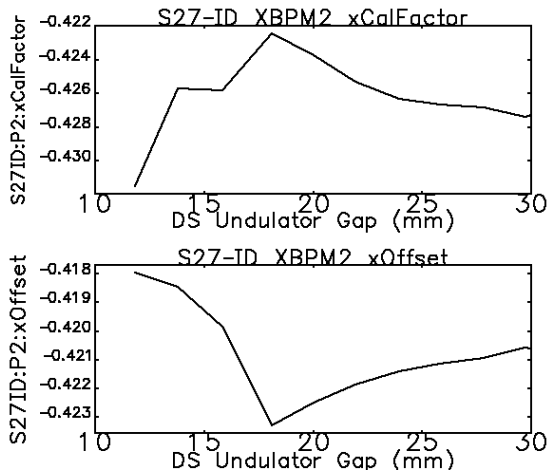

Figure 5: XBPM2 horizontal calibration constant (upper panel) and offset (lower panel) as functions of undulator gap.

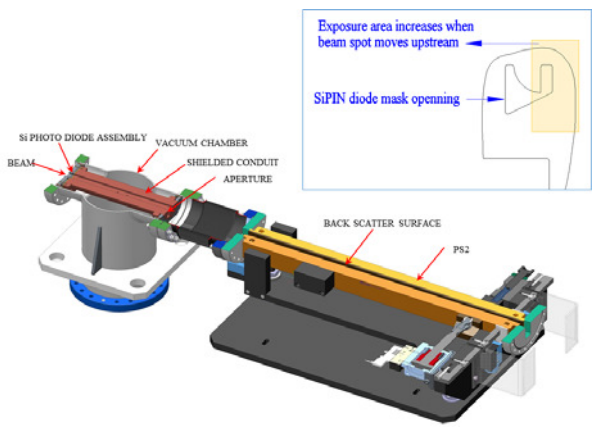

Figure 6: The first intensity monitor uses the XRF photons from the photon shutter (PS2) to monitors the beam intensity at the shutter.

Figure 7 shows the IM1 signal as functions of undulator gaps for upstream, downstream, and both undulators. We can see that two undulators generate the strongest signal and the upstream undulator the weakest one. For two 30-mm period undulator installed, the first harmonic reaches the copper K-edge near the gap of 16 mm, producing the spectral features in that region. Figure 8 shows the IM1 current as functions of horizontal x-ray beam position (projected to 20 m from source) for several undulator gap settings. For first harmonic well above copper K-edge, G > 20 mm, the horizontal profile has a well-defined single peak. After the first harmonic goes below the K-edge, the profile starts to broaden into a flat top and eventually into a tween peak shape. For longer period undulators such as U33, the maximum K may be as high as 2.85 and we will be able to see triple peaked profiles.

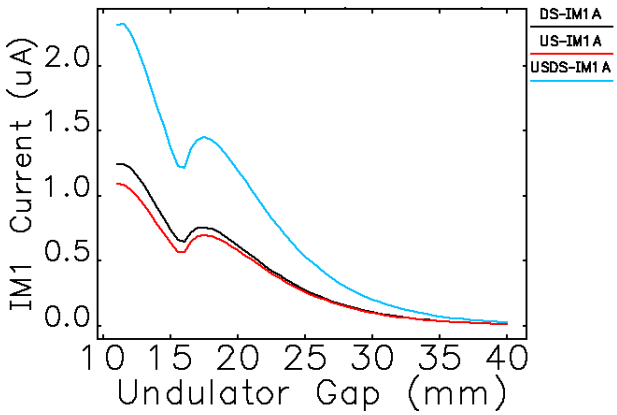

Figure 7: IM1 signal current as functions of the undulator gap for upstream (US), downstream (DS) and both undulators (USDS), respectively.

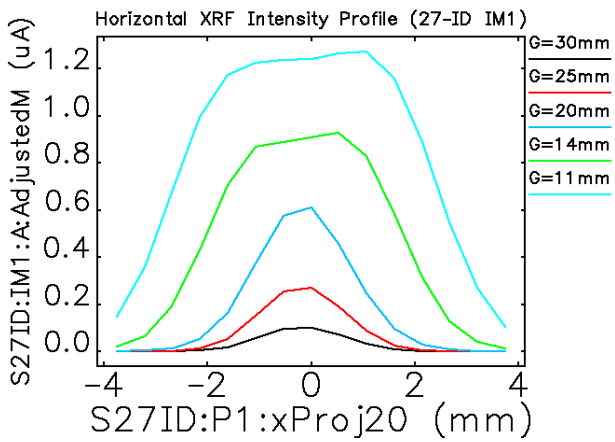

Figure 8: IM1 signal as functions of horizontal beam positions for selected undulator gaps.

SECOND INTENSITY MONITOR

For front ends with windows, the second intensity monitor (IM2) uses the front end Be window to intercept the beam [2]. For front ends without windows, IM2 uses a retractable, water-cooled diamond disc to intercept the beam. Figure 9 shows the windowless design in 27-ID.

Each IM2 can be used in two different modes. In Compton mode, the gold-plated photocathode facing the diamond film is biased negatively, its current signal is from the photoemission of the gold surface generated by (primarily Compton) scattered x-ray photons from the diamond disc. In photoemission mode, on the other hand, the gold-coated plate is biased positively to collect electrons in vacuum, its current is most likely derived from the photoemission from the diamond film.

Figure 10 compares the IM2 currents as functions of the undulator gap for different modes. Current from Compton mode is about three times higher than photoemission current, probably because the uncoated diamond film is not a

ISBN 978-3-95450-177-9

good photocathode. We choose Compton mode as our standard mode of operation.

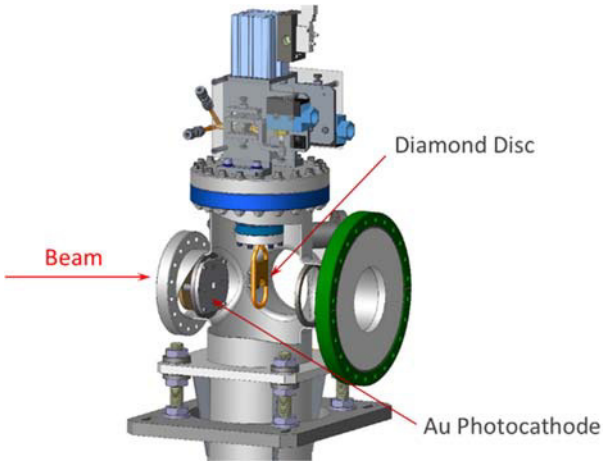

Figure 9: Cross section of IM2 for windowless front end.

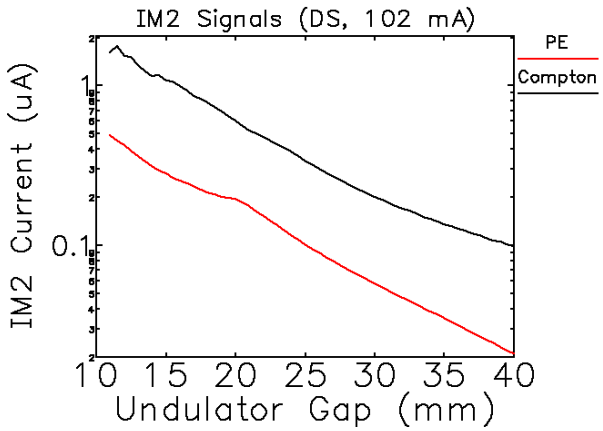

Figure 10: Absolute value of the IM2 current as functions of undulator gap for Compton and photoemission mode, respectively.

Figure 11 shows IM2 current for a horizontal beam angle scan for gap = 25 mm. This curve can be used for aligning white x-ray beam through two upstream apertures, a 1.6 mm horizontal gap for XBPM1 at 18.6 m, and 2 mm wide hole for the Exit Mask at 25 m. A deviation of ±0.5 mm (20 μrad) would results in approximately 6% changes in signal. For users seeking to align the beam to ±10 μrad accuracy, the IM2 signal level reduces only ~1.5% on each side. Users in 27-ID occasionally used this device for aligning the white x-ray beam or confirming proper operation of front end.

An ideal intensity monitor is expected to be independent of photon energies and insensitive to the undulator beam angle since the undulator spectrum depends on the angle from the beam axis. Figure 12 shows undulator gap scan data for five slightly different orbit angle settings. It shows that the IM2 spectra are very sensitive to beam angles in the gap region of 15 – 23 mm. This indicates that IM2 is quite sensitive to the x-ray energies and its data in 15 – 23 mm gaps range should be used with caution.

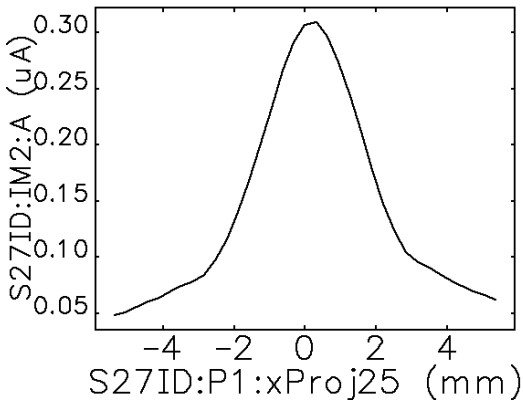

Figure 11: The normalized IM2 currents as functions of horizontal beam position for undulator gap of 25 mm.

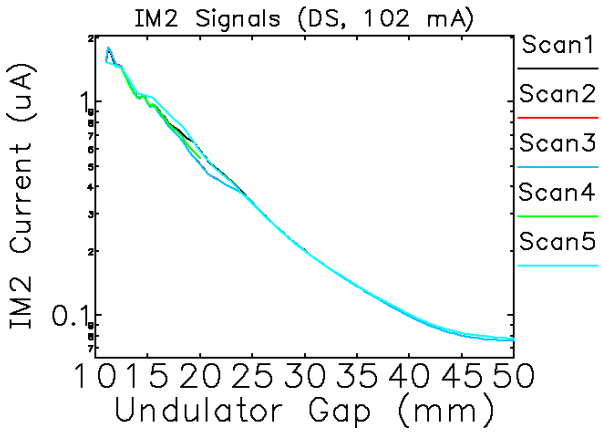

Figure 12: IM2 current as functions of undulator gap for five different small deviations in orbit angles.

CONCLUSION

The GRID-XBPM for in APS 27-ID high heat load front end showed that it has met the specifications for the APS Upgrade, with a possible long-term beam stability in the range of ±3 μm (±120 nrad). In the horizontal plane, the second XBPM based on the Exit Mask has a gap-independent calibration and an insignificant gap-dependent offset. The first and the second intensity monitors (IM1 and IM2) are calibrated with undulator beam and used occasionally for beam alignment.

REFERENCES

[1] M. Borland, V. Sajaev, Y. Sun, A. Xiao, Hybrid Seven-Bend-Achromat Lattice for the Advanced Photon Source Upgrade, IPAC 2015, pp. 1776 – 1779 (2015).

[2] B.X. Yang, G. Decker, J. Downey, Y. Jaski, T. Kruy, S. H. Lee, M. Ramanathan and F. Westferro, Advanced x-ray beam position monitor system design at the APS, NAPAC 2013, pp. 1079 – 1081.

[3] B. X. Yang, et al, High-power beam test of the APS grazing-incidence insertion device x-ray beam position monitor, BIW (2012), 235 – 237.

[4] B. X. Yang, et al, Design and development for the next generation x-ray beam position monitor system at the APS, IPAC 2015, 1175 – 1177.

ISBN 978-3-95450-177-9

DIAMOND MONITOR BASED BEAM LOSS MEASUREMENTS IN THE LHC

C. Xu*, B. Dehning, F. S. Domingues Sousa, CERN, Geneva, Switzerland
E. Griesmayer, CIVIDEC Instrumentation, Vienna, Austria

Abstract

Two pCVD Diamond based Beam Loss Monitors (dBLM) are installed near the primary collimators of the LHC, with a dedicated, commercial readout-system used to acquire their signals. The system is simultaneously able to produce a high sampling rate waveform and provide a real-time beam loss histogram for all bunches in the machine. This paper presents the data measured by the dBLM system during LHC beam operation in 2016.

INTRODUCTION

Diamond detectors with nanosecond time resolution and high dynamic range have been successfully tested and used in the LHC [1, 2]. Two diamond detectors are installed next to the primary collimators in the insertion region 7 (IR7) of the LHC for both beam1 (B1) and beam2 (B2).

The initial acquisition system used oscilloscopes to digitize the output of these diamond detectors, however, due to the lack of dedicated software, the beam loss measurements performed with this set-up was neither systematically logged nor analysed since the start of LHC Run2.

A dedicated commercial readout-system was therefore installed in order to better utilize the high time resolution provided by the diamond detectors. The data acquisition software was developed so that automatic data logging would be possible, and the system could provide valuable multi-purpose data for accelerator studies.

SYSTEM DESCRIPTION

Diamond Beam Loss Monitor

The diamond based detector system is comprised of poly-crystalline diamond detectors (CIVIDEC Instrumentation GmbH) with a size of 10 mm × 10 mm × 0.5 mm [3]. Each detector is connected to an AC-DC splitter, where the AC-part of the signal is amplified by a current amplifier with 40 dB gain and bandwidth of 2 GHz (both the AC-DC splitter and the preamplifier are provided by CIVIDEC Instrumentation GmbH). The detector system is mounted on a metal panel on top of the beam pipe, 6 meters downstream of the primary collimators (TCP) in IR7 (shown in Fig. 1). The coaxial cable which connects the detector system to the read-out system is about 250 m long. The diamond detectors are operated with a bias voltage of 500 V.

Readout System

The detector signals are read out by the ROSY® data acquisition system also provided by CIVIDEC Instrumentation GmbH. The ROSY® system comes with all the acquisition and triggering functionalities of a digital oscilloscope. In addition, an integrated FPGA provides dead-time-free online signal processing. The ROSY® system has an embedded Linux operating system and provides a programmable interface to control the system and transfer the acquired data. This system is installed in the LHC service tunnel and is connected to the CERN technical network via an Ethernet cable.

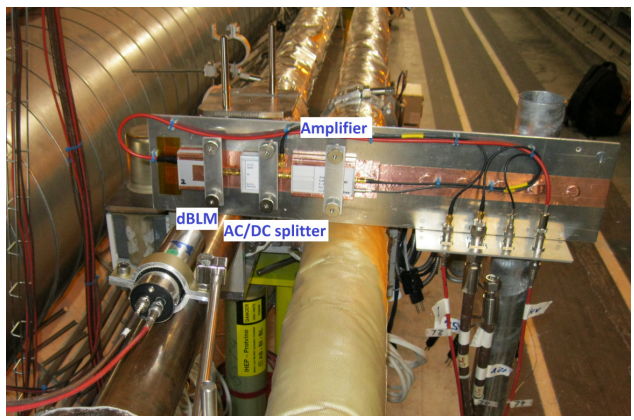

Figure 1: dBLM installation in the LHC IR7.

The ROSY® system is simultaneously able to produce a high sampling rate waveform and provide a real-time beam loss time histogram. In the histogram mode, the system synchronizes to the LHC turn clock and increases the corresponding bin when the loss signal exceeds a user defined threshold. The bin width is 1.6 ns. Figure 2 explains the operational principle of the histogram mode.

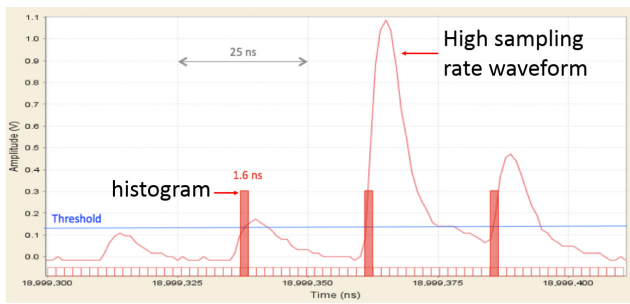

Figure 2: Beam loss signals exceeding a threshold causes the corresponding bin to increase in value [4]. The data is captured using the post-mortem application from CIVIDEC Instrumentation GmbH.

The ROSY® system has 4 analog input channels for the waveform measurement, each channel having a maximum

* chen.xu@cern.ch

ISBN 978-3-95450-177-9

sampling rate of 5 GS/s (when using all 4 channels). A maximum buffer size of 1×10^9 samples is available to store the data from all 4 channels. The system's dead-time for transferring the data to the client application varies de-pending on the number of samples acquired. The 8-bit ADC has a vertical range from ±100 mV to ±5 V. Data acquisition is edge-triggered by one of the 4 channels, configurable before the acquisition is started.

DAQ Software

A Python script has been developed to configure the ROSY® system and store the detector data from both types of measurement for offline analysis. The script utilizes the PyJapc library [1] to obtain LHC machine status parameters, starting and stopping the data acquisition automatically depending on the machine status. The detector data are compressed and uploaded to the CERN EOS file system [5] for long term storage. An independent graphical user interface (GUI) has been developed to provide online monitoring and a quick review of the detector data without interrupting the data acquisition process. Figure 3 shows a screenshot of the GUI software, in which the time loss histogram is visible in the top plot and beam loss signal waveforms from multiple LHC turns are shown in the bottom plot. In this particular case both data sets were simultaneously acquired during an LHC beam injection in 2016.

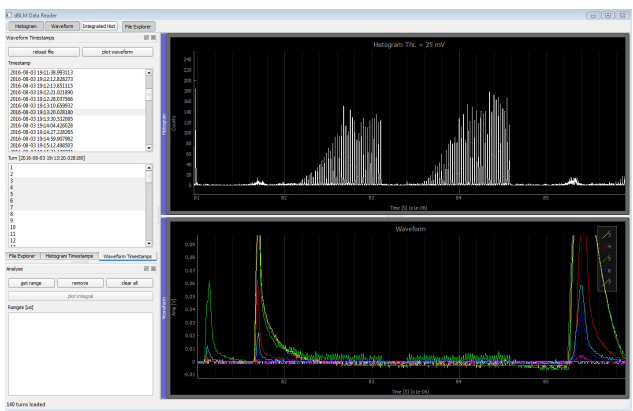

Figure 3: A screenshot of the GUI software for online monitoring of the dBLM data acquired by the ROSY® system.

BEAM LOSS MEASUREMENT

Time Loss Histogram

As described previously, the time loss histogram accumulates the static beam loss over multiple turns for each 1.6 ns of the 88.9 μs LHC turn period.

Figure 4 shows a time loss histogram of beam1 acquired during the stable beam period of one particular fill, when the beams are colliding for physics. The time structure of the LHC beam can clearly be resolved from the histogram. The total width of the histogram corresponds to the 88.9 μs LHC turn period. During this fill, there were in total 2076 bunches in the machine, constructed of one 12-bunch train, one 48-bunch train and 21 96-bunch trains. The gaps between the bunch trains correspond to the LHC injection gaps, required to accommodate the risetime of the injection kickers. The large, 3 μs gap preceding the 12-bunch train is the beam abort gap, required to accommodate the risetime of the LHC beam dump extraction kickers.The losses visible in the beam abort gap mainly come from crosstalk with the other beam, with its 96-bunch time structure clearly visible during this period.

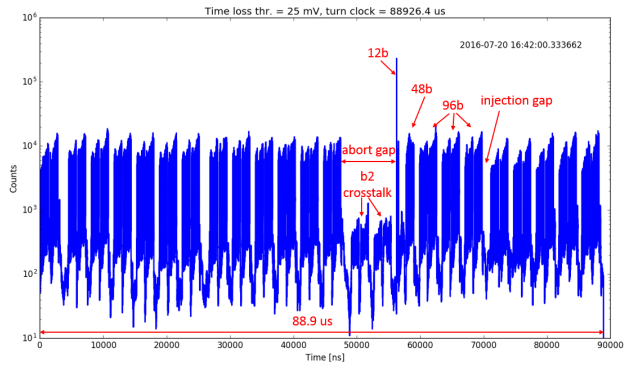

Figure 4: Time loss histogram of beam1 during physics operation in stable beam.

Figure 5 shows a zoom-in view of the 12-bunch train from the same histogram. It shows that beam loss from a single bunch is contained within 4 bins, corresponding to 6.4 ns. The 25 ns bunch spacing can clearly be resolved from this histogram.

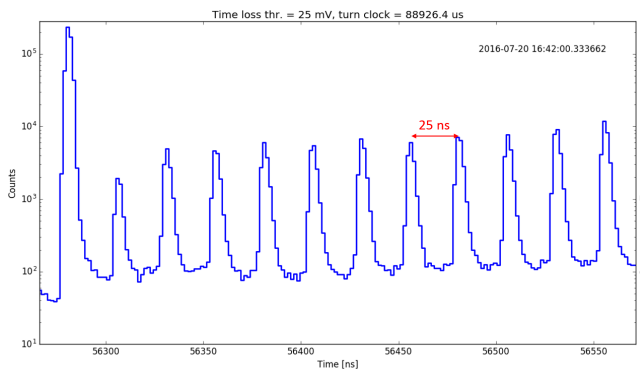

Figure 5: Zoom-in view of the 12-bunch train.

The evolution of the time loss histogram can give information about changing beam loss patterns or rates. In order to be able to calculate beam loss variations through changes to the time loss histogram, the DAQ software records the evolution of the histogram every second.

On July 20th 2016, a time loss histogram was acquired parasitically during an end of fill machine development (MD) experiment intended to measure the transverse beam halo population. During the experiment, a primary collimator

[1] PyJapc is a python interface to CERN Java API for Parameter Control, developed by the CERN Beam-Instrumentation department.

ISBN 978-3-95450-177-9

(TCP) in IR7 was moved towards the beam core to scrape away any beam halo. Higher than normal beam loss was therefore created when the beam halo was intercepted by the TCP jaws. Figure 6 shows the beam loss recorded by a standard ionization chamber BLM at the same location as the dBLM during this process.

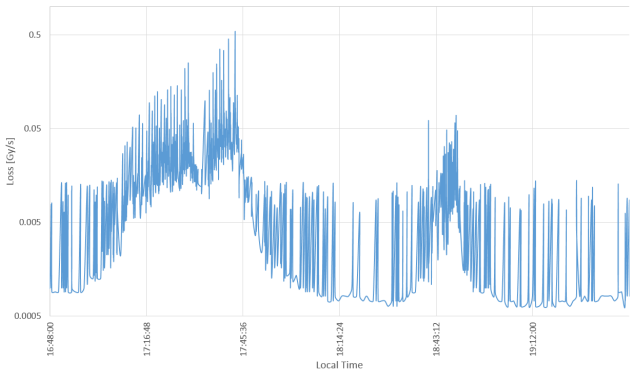

Figure 6: Beam loss recorded by an ionisation chamber BLM at the same location as the dBLM during halo scraping.

The top plot of Fig. 7 shows the time loss histogram recorded by the dBLM system during the same time period. By integrating the bin contents of the 12-bunch and 48-bunch trains separately and plotting the integrated counts as a function of time, the beam loss evolution corresponding to the two separate bunch trains can be obtained (as shown in the bottom plot of Fig. 7). The result indicates that losses from the 12-bunch train are significantly larger than from the 48-bunch train. It is worth noting that the loss evolution calculated from the evolution of the time loss histogram does not directly correspond to the total loss seen by the ionisation chamber. This can be explained by the fact that the histogram does not take into account the size of the loss, increasing as long as the loss signal from the beam exceeds the threshold, regardless of the amplitude.

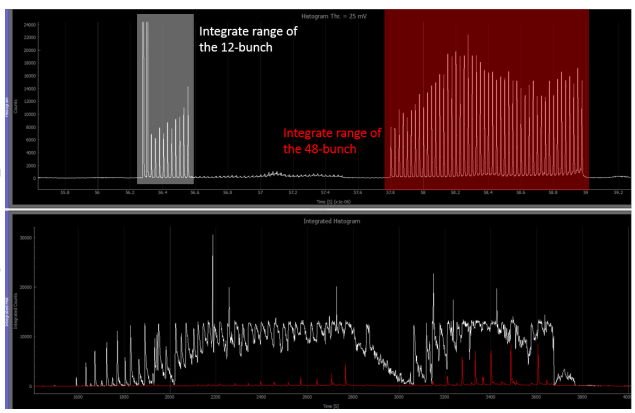

Figure 7: Time loss histogram of beam1 during a halo scraping experiment. Snapshot of the 12-bunch and 48-bunch train histogram (top) and loss evolution of each train (bottom).

Waveform

Two channels of the ROSY® system are used to record the dBLM detector signal and LHC turn clock respectively. The LHC turn clock is used to align the waveform signal from the dBLM to the beam time structure that is resolved by the time loss histogram data. In this way, the beam loss amplitude can be associated to a single bunch on consecutive turns with an uncertainty of ±1 bin.

The bottom plot of Figure 8 shows the waveform data acquired during eight consecutive turns after the injection of 96 bunches (2 closely spaced trains of 48 bunches) into a machine with 48 bunches already circulating. In the same figure, the top plot shows the time loss histogram accumulated during the whole injection process. Using the LHC turn clock, the beam loss signature shown in the waveform can be associated to the location of the loss within the 88.9 μs revolution period. The large beam loss signal before and after the bunch train in the waveform corresponds to the beam out of the main buckets from the SPS injector which is injected into the LHC during the rise or fall time of the LHC injection kicker (referred to as the recaptured beam in [2]). While most of this beam is intercepted by collimators in the injection region, their loss signature near the primary collimator in IR7 can be seen to last up to 100 turns. The first loss signal in the waveform data is due to the tail of the circulating beam being affected by the injection kicker field.

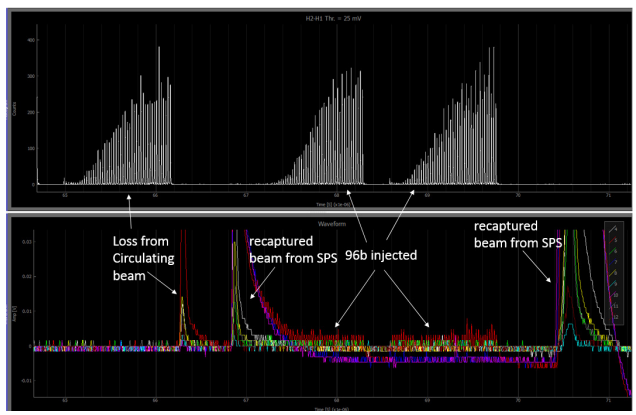

Figure 8: LHC injection loss recorded by the dBLM in IR7.

SUMMARY

The dBLM and its associated DAQ software has shown that it is capable of achieving the goal of providing useful data for further understanding beam dynamics in the LHC and optimizing its operation. The system can automatically configure and start the acquisition for predefined periods of interest, and logs the data for offline analysis. Further development is now underway to fully integrate the system into the LHC control and logging infrastructure.

ISBN 978-3-95450-177-9

ACKNOWLEDGEMENT

The author would like to thank G. Valentino and F. Burkart for their helps in understanding the dBLM data, and R. Jones for proofreading the paper and his valuable inputs.

REFERENCES

[1] F. Burkart et al. , "Diamond particle detector properties during high fluence material damage tests and their future applications for machine protection in the LHC," in proceedings of IPAC14, Shanghai, China

[2] F. Burkart et al. , "Investigation of injection losses at the LHC with diamond based particle detectors," in proceedings of IPAC16; Busan, Korea

[3] CIVIDEC Instrumentation GmbH, http://www.cividec.at

[4] H. Frais-Kölbl et al. , "A prototype readout system for the diamond beam loss moni-tors at LHC," in proceedings of IBIC13, Oxford, UK

[5] CERN EOS, https://eos.readthedocs.io

ISBN 978-3-95450-177-9

OPTIMIZED BEAM LOSS MONITOR SYSTEM FOR THE ESRF

B.K. Scheidt, F.Ewald, ESRF, Grenoble, France
P.Leban, Instrumentation Technologies, Solkan, Slovenia

Abstract

Monitoring of the 6 GeV electron losses around the ESRF storage ring is presently done by a hybrid system consisting of ionization chambers and scintillators. It allows a rough localization of the losses, but has numerous limitations: size, weight, time-resolution, sensitivity, versatility, and costs. A new system was developed consisting of a detector head (BLD) and the electronics for signal acquisition and control (BLM). The BLD is compact, based on a scintillator coupled to a small photo-multiplier module. The BLM controls 4 independent BLDs and acquires data with sampling rates up to 125 MHz Measurements performed on different configurations of BLD prototypes have lead to an optimized design that allows, together with the flexible signal processing performed in the BLM, to cover a wide range of applications: measurement of fast and strong losses during injection is just as well possible as detection of very small variations of weak losses during the slow current decay. This paper describes the BLD/BLM design, its functionality and performance characteristics, and shows results from prototypes installed in the injection zone and in close vicinity to in-vacuum undulators.

PURPOSES AND APPLICATIONS OF BEAMLOSS MONITORING

Historic Situation

The ESRF produces synchrotron light for its 40 beamlines by operating as its source a 6GeV electron beam in a Storage Ring of 844m circumference. The nominal values for the current and the emittances are respect. 200mA and 4nm (hor.) & 5pm (vert.). The typical lifetime of the electron beam is about 50hrs, meaning an electron loss rate of about 20 million/sec.

The localization of these losses is monitored & surveyed since long by different systems: A total of 64 ionization chambers of 2 different kinds, and a further set of (also 64) detectors that are based on a scintillator, optically coupled to a photo-multiplier-tube [1]. This total of 128 detectors is positioned identically in the ring structure with its 32 cells, i.e. the 4 detectors have the same position in each cell. For the bulky and heavy ionization chambers this is on the floor underneath each of the 64 dipoles, while the scintillator based detectors are placed at the beam height, radially about 40cm on the internal side of each dipole, and roughly in the middle of the dipole length. Each type of the above detectors employ a 1cm thick lead shielding to avoid detecting the inevitable scattered X-rays inside the tunnel.

Essential Diagnostic Tool in the Storage Ring

This comprehensive set of BLDs has been very helpful in the history of the ESRF in rapidly, and unambiguously, detecting and localizing any excessive electron losses. It is to be noted that the usual loss pattern does not show 128 values of roughly equal values: the loss values among these 128 units can have strong deviations due to numerous non-regular structures in the ring like e.g. the injection-zone elements (septum), scrapers, insertion device vacuum chambers with small apertures, especially for in-vacuum undulators, chambers for different modules of RF-cavities, etc.

In general, the 3 most common causes of strong or excessive losses are:

-1- Aperture-limiting effects by e.g. a miss-aligned chamber, or a non-optimum trajectory of the injected beam.

-2- A locally poor vacuum quality by e.g. a vacuum leak or a reduced conductance (e.g. a newly installed chamber with a different UHV pumping structure), or a poorly conditioned chamber (after its installation).

-3- The characteristics of the electron beam itself (variations in dynamic aperture, resonances, Touschek scattering, etc.)

These, more or less drastic, changes in the loss pattern can occur at different moments. For those mentioned under 1) it is often after installation work in the ring, so directly at the restart after a shut-down period. Those linked with vacuum leaks are obviously occurring when such leaks develop, and usually soon afterwards confirmed by the increase of the pressure gauges in the affected zone. The variations induced by beam dynamics are numerous and these variations in the beamloss readings are directly correlated with other measurements on the beam's lifetime, emittance and injection efficiency.

For all of the above uses the data rate of all these loss detectors was low, in the order of 1Hz. This speed limitation is imposed by both (some of the used) detectors, their cables for signal transmission and in particular their electronics for signal treatment and digitization. Although the detectors posses a gain control that can be set to low gain at e.g. time of injection, it is insufficient to verify that no saturation occurs in the early stage (and fast outputs) of these detectors.

IMPROVEMENTS WITH THE NEW AND OPTIMIZED SYSTEM

One of the main aims of the new system was to drastically improve the speed and bandwidth up to a time resolution of sub-orbit time (2.816us). This concerns both the BLD detector (and notably its photon-detection-electronics) and the acquisition electronics (BLM).

ISBN 978-3-95450-177-9

For the new BLD detector it was decided to keep the concept of using a scintillator for the conversion of the products in the electro-magnetic shower (resulting from a crash of a 6GeV electron into the vacuum chamber etc.) into visible light photons, and to convert these photons into an electric signal by means of a photo-multiplier-tube (PMT). That concept had been applied in the 64 old units and shown reliable and robust behaviour during nearly 20 years of use.

Also, both the different versions of suitable scintillators and the most suitable PMTs offer the required detection speeds & bandwidth. All these components are commercially 'off-the-shelve' available. [2, 3, 4]

The other aim was to make these new BLDs much more compact than the present devices. The presently used ionization chamber based system weighs 64 Kg and have a volume of >110 litres, and the scintillator based system weighs 13 Kg with a 4 litres volume. For both systems the volume and weight is dominated by the 1cm thick lead shielding (and housing) that encapsulates the whole of the detector. In comparison, and as described here below, the new BLD detector will be less than 1 Kg of weight and about 0.3 litres in volume.

Cherenkov versus Gamma Detection

The need for lead shielding is to stop scattered synchrotron radiation being detected by the BLD. It is stressed here that these X-rays have no relation with electron losses but are continuously produced with an overall flux that is proportional to the stored current, and with a geometrical pattern in the tunnel that is strongly determined by the position of the numerous X-ray absorbers in the UHV ring which take care of the heat-load that they present.

The detection of an electron loss can be effected by so-called Cherenkov radiators that are insensitive to the above X-rays and gamma radiation. The visible light generated in such a radiator is caused by particles with mass only, which are also strongly present in the shower caused by a 6GeV electron loss. This type of detector could (in principle) have a significant advantage with respect to the so-called gamma scintillator in avoiding that additional external and heavy lead shielding. We decided to construct different prototypes based on both types of scintillators /radiators. In both cases the concept of visible photon detection was identical, i.e. with a PMT coupled to the cylindrical rod of either the Cherenkov radiator (typically quartz glass) or the scintillator. For the latter we used EJ-200, which is an inexpensive plastic scintillator that is easy to handle and can also be machined to good optical quality. We tested quartz from two different manufacturers, in comparison to the EJ-200 scintillator and also to the old perspex material used in the old BLDs with a massive volume. Such measurements were done for different thicknesses of lead shielding (for the gamma scintillators only).

The first 2 main purposes were: 1) comparing the visible light-flux produced by a Cherenkov radiator with respect to the gamma-scintillator. 2) minimizing the lead thickness for the gamma detectors without becoming sensitive to X-rays.

Another characteristic needed to be verified: the compatibility of the PMT coping with very strong light levels of ultra-short duration, typically 100ps: the length of an electron bunch. In total 4 different types of PMT were tested.

Test Bench in the Injection Zone for Prototypes

These BLD prototypes are all devices that can be installed and connected-up quickly and easily at a very suitable location : The Cell-4 injection zone. This zone offers the following possibilities and features :

-1- obtaining strong & fast losses at the time of injection during (normal user operation)

-2- creating a (very) small variation of the weak & slow losses by closing slightly a scraper in this same zone, during the normal user operation time. The sensitivity of all the prototypes is so high that such scraper induced losses were not affecting the lifetime of the electron beam.

-3- injecting different levels of beam current (from the injector) entirely & directly into this same scraper so to create massive losses and to assess the PMT's capacity of handling these more or less linearly.

We could install numerous prototypes at nearly identical positions, with only a slight displacement to avoid that one would be in the shadow of the other one. Typically a set of 4 prototypes were within 0.5 m maximum distance from each other. This allowed a direct comparison of their results and behaviour under identical conditions of imposed beamlosses. Any modifications to be made (e.g. changing the thickness of the lead shielding) could be done at a weekly basis, during the usual day of accelerator maintenance with tunnel access.

Main Conclusions of Tests for and Optimized BLD

The flux produced by the Cherenkov radiators was at least one order of magnitude below that of the EJ-200 scintillators (for comparable volumes).

Also, the 2 mm thick lead shielding proved sufficient to be immune against the scattered X-rays, provided that (known) hot points of such scattering are avoided for the location of the BLD.

Consequently, we see no advantages of pursuing a Cherenkov based BLD since the (quartz) material is more expensive while less sensitive, and the only 2mm lead shielding has little impact on the size, weight and compactness of the final BLD.

The 4 PMTs under test showed important differences in coping with very strong & ultra-fast losses. The PMT module of Hamamatsu H10721-110 offered a satisfactory behaviour in both regimes of extreme uses like fast and strong losses (with the PMT connected to a 50 Ω impedance) and the slow and weak losses (now connected to a Hi-Z load).

It is finally remarked that the 425 nm of peak-emission in the spectra of the EJ-200 scintillator is well suited for the photo-cathode characteristics of the PMT.

ISBN 978-3-95450-177-9

Other Aspects of Optimizing the BLD Design

The sensitivity depends on the volume of the scintillator/radiator and then the efficiency of transmitting these generated visible photons to the photo-cathode of the PMT. The H10721-110 device has an 8mm circular area of the effective photo-cathode. Coupling the light produced in a cylindrical rod of 100 mm length and 22 mm diameter with a maximum possible efficiency to a window of only 8 mm needed a suitable adaptation. But the assessment of the efficiency of the various possible configurations needed an experimental determining that was done by exposing these different configurations to a radio-active source (Cesium 137, 600 KeV gamma emitter) at close distance. For each configuration we used the same EJ-200 material and a calibrated PMT. This method allowed us to also detect that the quality of the surface finishing of the rod is very important.

These tests concluded that wrapping the rod in highly-reflective aluminium foil, on all sides except the 8mm diameter on the face in contact with the PMT, was the most effective way of optimizing the sensitivity.

ELECTRONICS FOR THE CONTROL AND SIGNAL ACQUISITION (BLM)

The BLDs' output signal is sent over a standard 50 Ω coax cable. This is typically a unipolar pulse or train of pulses with negative polarity in the case of fast/strong losses, or a rather weak and close to DC signal in the case of slow/weak losses without any rapid variations. It is important to set the input impedance to 50 Ω in case of measuring these fast/strong losses (at e.g. injection) while the Hi-Z impedance is much more suitable for the weak/slow loss measurement. The BLM device offers the possibility to acquire the signals of 4 BLDs (see table 1). Each of these 4 input channels can be configured fully independently for input impedance and for analog gain. For the analog-to-digital conversion a DC-coupled dual-channel 125 MHz ADC with 14-bit granularity is used. The sampling frequency is configurable within a 80-125 MHz range and common for the 4 channels, as is a trigger signal that defines the start of buffer filling.

Table 1: Hardware Properties of the BLM

Property	Description
Input channel connector	SMA-female
Max. input amplitude	±5 V CW at 50 Ω ±1.25 V CW at 1 MΩ
A/D converter	14-bit, dual channel
Sampling rate	80-125 MHz
Measurement bandwidth @ 50 Ω input termination	35-50 MHz depending on signal amplitude
Variable Attenuation	31 dB, 1 dB step
Trigger input	LEMO, LVTTL

The ADC-buffers (up to 1 mega-samples in size, is ~8ms) are the fastest data available with 8 ns time resolution (when at 125 MHz sampling). The limitation of the analogue bandwidth to 50 MHz is still fast enough to clearly detect and measure losses of individual bunches when in e.g. the 16 bunch filling mode with 176 ns separation between these bunches (=22 ADC_samples).

In many cases the user wants to obtain information of the losses on a different (slower) time-scale, e.g. at turn-by-turn rate. In that case a SUM buffer is available in which the sum of a user-defined number (SUM_DEC) of ADC samples is stored. In the case of the ESRF this number is set to 352 (352x8 ns=2.816 us=orbit revolution time). An additional so-called ADC_mask makes it possible to define a window on the raw ADC data in which only samples within this mask are summed-up in that SUM buffer. This allows to precisely put a time-domain filter on e.g. a single bunch in the ring and to effectively measure the turn-by-turn losses of that bunch only.

Data samples from the SUM buffer are additionally averaged and stored to the AVG buffer that is again conveniently configurable with a selectable decimation value (AVG_DEC). All the above buffers need either a trigger signal, or can be self-triggered by setting a threshold level on the input signal that is continuously monitored for detecting a signal above that threshold and then subsequently starting the filling of the buffer(s).

In addition to these triggerable buffers there is also a continuous data stream (SA_stream) available with its selectable SA_DEC parameter.

In addition to the here above type of 'integrating-mode', the processing in this BLM device offers a 'counter-mode' : the ADC data is continuously processed and checked for the "count" threshold. Every ADC sample that exceeds the count threshold increments the counter value. The "data rate set" parameter specifies the read interval (e.g. 0.1 second). It subsequently results in a 'Counter stream', as shown in the upper part of the below Figure 1.

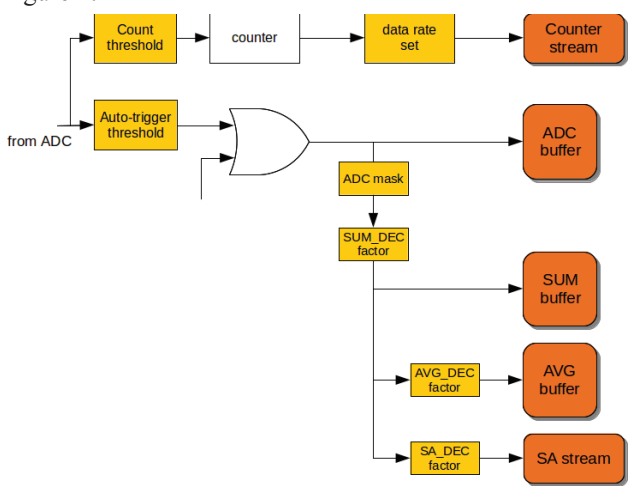

Figure 1: Numeric processing modes in the BLM.

ISBN 978-3-95450-177-9

To make the combined system of BLD and BLM as simple and straight-forward as possible in its practical installation and use, the Libera BLM can provide the power supplies and gain control signals to each of the 4 BLDs. The maximum output current per channel (power supply + gain control) is limited to 30mA. Power supply voltage can be selected by a dip switch (±5, ±10, ±12, ±15 V). The gain control voltage can be set with 12-bit granularity through the software interface. The limit is still set by a dip switch (1, 2, 5 or 12 V). Connections between the BLM and the 4 BLDs are made with the low-cost RJ-25 6p6c connectors and with a 6-wire cable. The BLM instrument itself is powered by Power-over-Ethernet (consuming less than 15 W in total).

This BLM acquisition and control electronics was developed in cooperation with the Instrumentation Technologies company and realised by them and is now commercially available under the name Libera-BLM [5].

The detailed functionalities were defined by the ESRF and then implemented in the Libera BLM's FPGA and CPU. The top-layer interface is TANGO compatible.

RESULTS AT INJECTION

The BLD prototypes have been tested under numerous conditions of the stored beam in the storage ring, and very different conditions of the injected beam. Initially we only had these prototypes in the injection zone, but later we installed 2 units each just down-stream two different in-vacuum undulators (ID27 and ID31). Examples of the fast data that they yield at injection are shown in the below Figures 2 and 3. The ADC buffer shows the strongly varying loss level of the 5 injected bunches, within one turn, and from turn-to-turn. The vertical scale is mV and the horizontal scale in samples (at 125MHz, meaning 352 samples per turn (green lines), and 22 samples between the bunches).

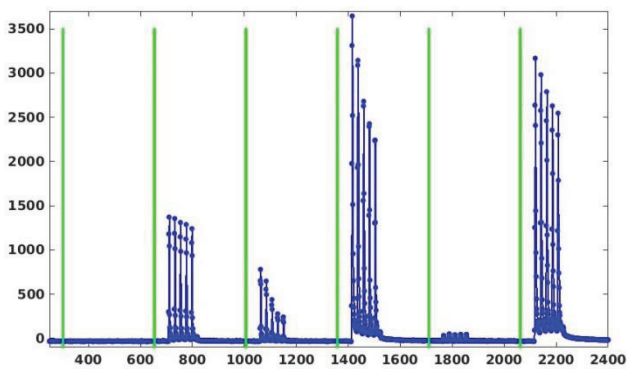

Figure 2: The ADC buffer at injection, showing the injection of the 5 bunches over 6 consecutive turns.

The SUM buffer shows losses at orbit-turn sample rate and allows seeing the signature of phase and energy oscillations of that injected beam. By a change of 30 degrees (red-curve) with respect to the nominal value (blue) the time structure of the synchrotron oscillations appears with a stronger amplitude.

The above results are obtained with a moderate gain (GCV) setting of the PMT, typically 0.5 V for 1 V maximum, so still offering an increase of sensitivity by two orders of magnitude.

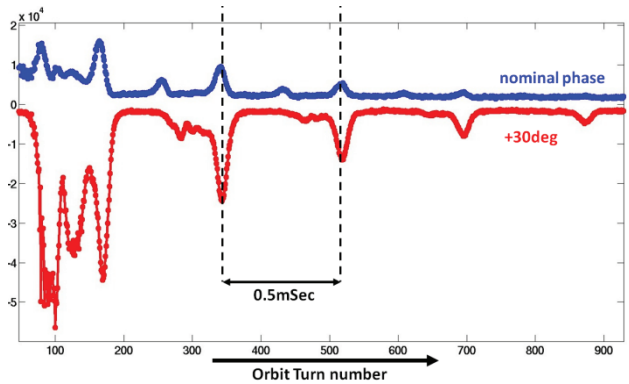

Figure 3: BLD signal at injection, with injected beam at 2 different phases: blue = nominal, red = -30 (plot inversed)

CONCLUSION AND PROSPECTS OF FULL INSTALLATION IN 2017

The optimized beam loss detector system of the ESRF is based on an EJ-200 scintillator rod of 100x22mm, coupled to a compact PMT-module and housed in a 190x25x25mm simple housing with convenient SMA and RJ-25 connectors. It is a low-cost device with compact dimensions that allows a straight-forward installation in various locations in the ring tunnel, also at points with limited access or free space.

The BLD device is capable of both detecting and transmitting the fast signals caused by fast losses at e.g. injection, and detecting very small variations of losses. In both cases the transmitted signals are fully exploited by a performing and versatile acquisition (Libera-BLM) with flexible digital signal processing and also providing the full control of power supplies and PMT gains for the four BLD units.

The ESRF is now procuring about 160 of such BLDs and 40 associated BLMs for their signal acquisition and control. They will be installed progressively from early 2017 onwards in the present storage ring to gain full experience with them in all modes of use and functionality in the two remaining years before dismantling that storage ring. They will then be recovered (early 2019) and re-installed for the new EBS storage ring to provide an essential tool in the commissioning of EBS (early 2020) and well beyond.

REFERENCES

[1] B.Joly *et al.*, "BeamLoss Monitors at the ESRF", DIPAC-99, Chester, UK, pp. 3-6.

[2] Scionix, http://scionix.nl/

[3] ELJEN, http://www.eljentechnology.com/index.php

[4] Hamamatsu, http://www.hamamatsu.com/eu/en/index.html

[5] Instrumentation Technologies, http://www.i-tech.si/

ISBN 978-3-95450-177-9

DEVELOPMENT OF A METHOD FOR CONTINUOUS FUNCTIONAL SUPERVISION OF BLM SYSTEMS

C. F. Hajdu, CERN, Geneva, CH; Budapest University of Technology and Economics, HU
C. Zamantzas, CERN, Geneva, Switzerland
T. Dabóczi, Budapest University of Technology and Economics, Hungary

Abstract

It is of vital importance to provide a continuous and comprehensive overview of the functionality of beam loss monitoring (BLM) systems, with particular emphasis on the connectivity and correct operation of the detectors. At CERN, a new BLM system for the pre-accelerators of the LHC is currently at an advanced stage of development. This contribution reports on a new method which aims to automatically and continuously ensure the proper connection and performance of the detectors used in the new BLM system.

INTRODUCTION

At CERN, the scheme for machine protection and optimization relies heavily on beam loss monitors (BLMs). Therefore, a continuous functional supervision of the BLM system is essential. To our knowledge, no particle accelerator in the world has this feature at present.

Currently, one of the most advanced solutions for supervising the functionality of a BLM system is in operation at the LHC. This method enforces a connectivity check of each detector channel every 24 hours, which can only be executed while the accelerator is offline.

The LHC Injectors Upgrade (LIU) project, presently underway at CERN, is a major accelerator upgrade project targeting the pre-accelerators of the LHC. Among other activities, this program mandates the deployment of an upgraded BLM system with extended functionality in the injectors, which is at an advanced stage of development at the time of writing.

This paper reviews the present state of a project aimed at building on LHC experience to develop a process capable of ensuring an uninterrupted supervision of the entire beam loss monitor signal chain from the detector to the acquisition electronics.

DETECTOR CONNECTIVITY CHECKS AT THE LHC

Ionization chambers are the most frequently used detector type in the LHC BLM system [1]. The bias high voltage applied to the chamber gives rise to an output current proportional to the energy deposited in the volume of the chamber by incident ionizing radiation. This current is acquired and digitized by the front-end electronics [2], then further processed by the back-end electronics [3] responsible for deciding whether the machine is operating under safe conditions. These modules can trigger the safe extraction of circulating beams or inhibit further injections as required.

At the LHC, the method for checking the connectivity of the detectors relies on inducing a sinusoidal modulation at a frequency on the order of 50 mHz in the bias high voltage. The chamber responds as a capacitor and a corresponding sinusoidal signal is generated in its output current, which can then be digitized through the standard signal acquisition chain. The signal is then detected in the time domain using a matched filtering algorithm executed on an FPGA device.

The absence of the modulation in the digitized data stream indicates a defective cabling connection, while variations in the amplitude and the phase of the modulation have been shown to correspond to various other degradations of the signal chain. The connectivity check thus also acts as a component integrity survey [4,5]. Such a check is performed without beam before the start of each physics fill.

SYSTEM SUPERVISION AT THE INJECTORS

System Architecture in Brief

The new BLM system under development will be common to all injectors. These accelerators impose widely varying requirements, thus the acquisition frequency and input dynamic range of the new system must surpass those of its predecessors. In most locations, ionization chambers will be employed but the use of other detector types such as Cherenkov monitors, diamond detectors and secondary emission monitors is also foreseen. Therefore, the system needs to be able to handle all these various types of detectors [6].

These considerations imply that a new acquisition front-end module had to be designed for the new BLM system. It can digitize input currents ranging from 10 pA to 200 mA using a novel measurement method based on a fully differential integrator [7]. The digitized samples are forwarded to the back-end processing and triggering (BLEPT) modules at 500 ksps for further processing. These modules calculate several moving window integrals referred to as running sums for the digitized current of each detector and are responsible for revoking the beam circulation permit if required.

The Suggested Method

For checking the integrity of the main ionization chamber beam loss monitoring system of the injectors, a modulation-based scheme like the one used in the LHC might be a viable option. However, that scheme requires the accelerator to be offline as the checks, lasting about 6 minutes, are executed during the injection preparation phase, i.e. long periods with no beam characterizing the operation of the LHC. In

ISBN 978-3-95450-177-9

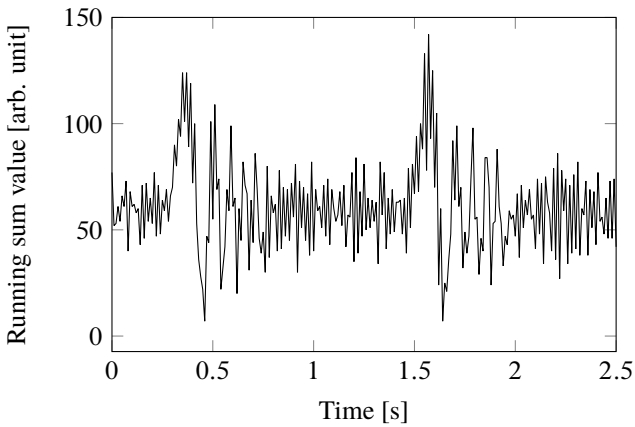

Figure 1: Acquisition made in the PSB system with a linear chirp excitation. Frequency sweep: 0 Hz to 20 Hz. The running sum window length is 10 ms to ensure a good visualization of the features of the signal. Note the reduction in the amplitude of the modulation as the frequency increases, due to the length of the cables connected to the detector.

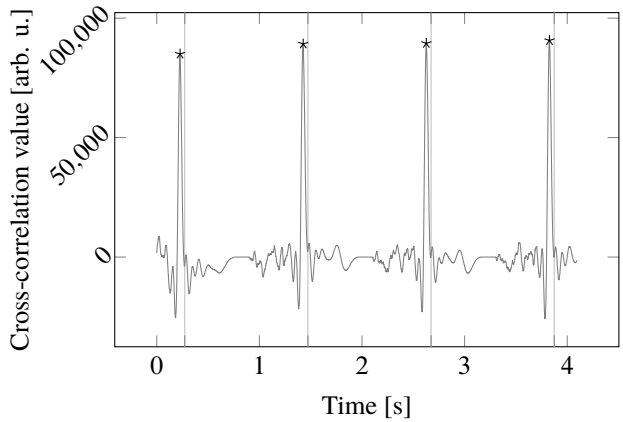

Figure 2: Cross-correlation waveform acquired in the PSB, using the 1 ms running sum with a linear chirp signal sweeping from 0 Hz to 20 Hz. Windowing and average suppression features active. The vertical grid lines represent the moment the Beam In timing strobe signal is asserted. The maxima detected by the logic ($\star$) take place about 50 ms before the strobe signal.

contrast, the operation of the injectors is practically uninterrupted and our goal is to provide continuous supervision. As revealed by previous measurements [8], the frequency range usable for modulation in the new BLM system far exceeds that available in the LHC, due to architectural differences between the two systems. This, combined with the fact that the injectors operate in a pulsed mode, allow us to exploit the gaps between the pulses for the execution of our checks.

At present, two installations of the new system are almost complete, at the Proton Synchrotron Booster (PSB) and LINAC4 accelerators. For both, the basic period of the pulsed operation is 1.2 seconds. In every basic period, there is beam in the LINAC4 for less than 1 ms, and in the PSB for only about 0.7 s, allowing over 0.5 s for checks without beam in both cases.

According to our measurements, by setting up the modulation signal to start and end at the steady-state value of the high voltage, all transients can be avoided when enabling or disabling the modulation. Additionally, the high voltage power supplies providing the bias voltage are capable of producing a swept-frequency modulation. We considered a linear swept frequency sine (chirp) signal, sweeping from 0 Hz to $10 - 100$ Hz. Fig. 1 shows a sample acquisition.

This configuration offers the following advantages:

- The operational measurement and the modulation related to the connectivity checks are executed in distinct time intervals, thus any mutual interference can be avoided.
- The swept-frequency sine signal produces a unique signature and can easily be detected in the time domain by matched filtering, even in noisy environments.

The high voltage power supplies are controlled by an FPGA on the Combiner and Survey (BLECS) module installed in the back-end crate. We developed a firmware for the BLECS card capable of producing arbitrary modulation waveforms of a duration up to 0.5 s. In order to emit the modulation only in periods without beam, the functionality is triggered by the Beam Out signal from the accelerator timing.

The detection of the corresponding signal in the output current of the detectors is done on one of the FPGAs of the BLEPT back-end module. The cross-correlation of the acquired signal to the samples of the excitation signal can be calculated using simple fixed-point arithmetic. Our tests in MATLAB showed that detection is possible using the digitized data at the full sampling rate of 500 ksps, but the resource cost of this implementation would be too high for the FPGA at hand and it is not necessary for the frequency range we are targeting. Instead, we resorted to using the 1 ms running sum readily available in the back-end processing firmware.

Typically, the signal amplitudes related to actual beam loss events are much higher than the amplitude of the modulation. In order to eliminate any disturbing influence in the cross-correlation waveforms, we apply windowing to the input signal: we set all samples to 0 when beam might be present. Since an offset current is injected into the input of the front-end card in order to stabilize it and the steady-state value of the input current is not zero, this manipulation causes abrupt jumps and spurious peaks in the cross-correlation waveform at the edges of the window. In order to mitigate this phenomenon, we calculate the average value of 512 samples in the beam-free part of each basic period by accumulating them and simply applying a bit shift, then subtract the resulting number from all non-windowed sample values. Despite its simplicity and low resource use, this method reduces spurious peaks considerably.

ISBN 978-3-95450-177-9

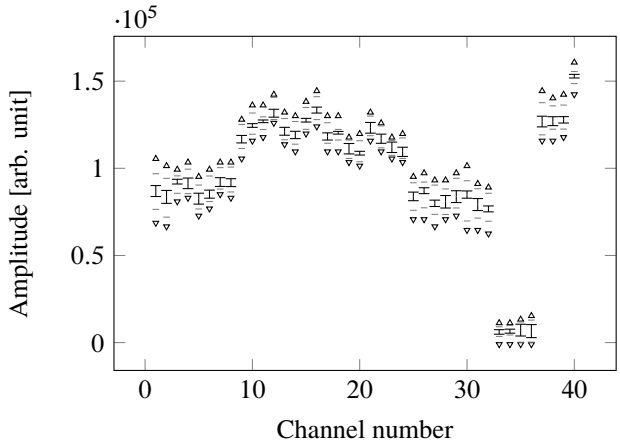

(a) Cross-correlation peak amplitude statistics and acceptance limits per channel. Note that channels with longer cables (channels 1-8, 25-32) tend to have lower amplitudes with higher standard deviations. Disconnected channels (channels 33-36) exhibit amplitudes in a completely separate, lower range.

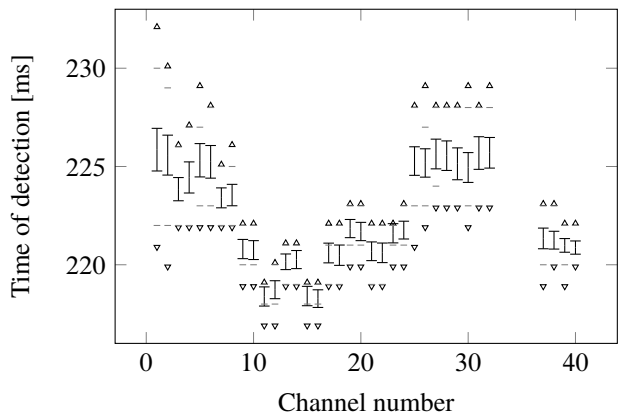

(b) Cross-correlation peak detection time statistics and acceptance limits per channel. Channels with shorter cables (channels 9-24) tend to have shorter delays with lower standard deviations. The detection time is unpredictable in disconnected channels (channels 33-36), thus these are omitted here.

Figure 3: Cross-correlation peak amplitude and detection time statistics for 1024 contiguous samples (about 20 minutes) acquired in all available channels at the PSB. The mean values and corresponding standard deviations per channel are represented by error bars, while the minima and maxima of these samples are shown by ⁻. ▿ and ▵ represent the low and high acceptance limits, respectively. The acceptance limits are unique per detector and the values shown in the plot were adjusted further with respect to the ones established based on this acquisition, since our subsequent acquisitions over longer time periods showed a non-negligible amount of outlier points.

The maximum of the resulting cross-correlation waveform is identified in each basic period, as demonstrated in Fig. 2. The firmware then checks if the corresponding amplitude and sample number values are within the acceptance window established through calibration, and a decision whether the modulation is present can then be made automatically.

After a series of acquisitions from all 40 detector channels currently available at the PSB accelerator (Fig. 3), we found that the minimum cross-correlation amplitude recorded in presence of the modulation on a correctly working channel is about 4 times higher than the maximum amplitude recorded on an unconnected channel, which provides a satisfactory margin for detection. However, fluctuations in amplitude may be as high as 25-35 %, thus the acceptance windows need to be fairly wide in general. Nevertheless, over a basic period of 1.2 s, the maximum variation in the measured time of the maximum is quite low, at ± 10 samples (10 ms).

Failure Cases Covered

In our tests in the laboratory and at LINAC4, this method allowed us to detect all possible cable disconnection scenarios correctly: disconnection of the high voltage or signal cables, either at the acquisition electronics or at the detector.

In the LHC implementation, variations in the value of the filter capacitor at the input of the ionization chambers were found to cause phase shifts in the recorded modulation signal. These variations may reveal faulty soldering or the degradation of the capacitor due to radiation [5]. We tried reproducing this behavior with our implementation, both through simulation by adapting a previous model [9] and laboratory testing. The simulation was intended as a qualitative study of the phenomena. The results, shown in Fig. 4, suggest that in the frequency range we are targeting, changes in the value of the capacitor don't produce phase shifts but result in changes in the amplitude of the output current. This behavior was confirmed by test measurements. However, the acceptance windows currently required to detect disconnection are quite wide in terms of amplitude (see Fig. 3), which results in a reduced sensitivity to the deterioration of the filter capacitance. Nonetheless, sufficiently high variations such as a disconnected filter capacitor remain detectable.

CONCLUSIONS

We presented a promising method for continuous functional supervision of the BLM system currently being developed for the injectors. The procedure takes advantage of the non-presence of beam between injection cycles.

It is desirable to refine the acceptance windows currently used, since narrower windows, especially in terms of amplitude, would improve the sensitivity of the method for the detection of non-conformities.

In the future, we'd also like to assess whether this method can be used to detect other failure cases, such as the connection of a wrong detector type or a leaky ionization chamber.

ACKNOWLEDGMENTS

Csaba F. Hajdu would like to express his gratitude to William Viganò for all his help in the execution of this project, both in theory and in practice.

ISBN 978-3-95450-177-9

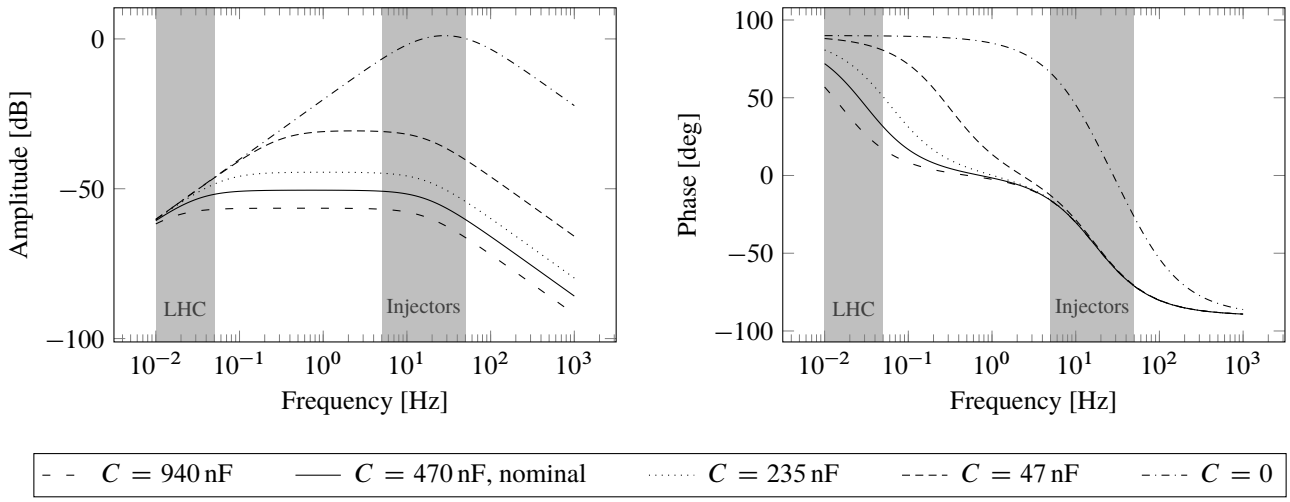

Figure 4: Bode plot of the input current digitized by the front-end card for different values of the filter capacitor at the input of the ionization chamber. The curves were obtained using a simulation model adapted from our earlier work [9], assuming cable lengths of 100 m. The excitation is a sine wave with an amplitude of 5 V superimposed onto a DC component of 1500 V. These simulations underpin that the behavior changes substantially between the frequency ranges targeted in the two systems (highlighted). In the new BLM system, variations in the value of the filter capacitor are to be expected to cause changes in the amplitude of the output signal while having a very limited effect in terms of phase behavior.

Tamás Dabóczi acknowledges the support of ARTEMIS JU and the Hungarian National Research, Development and Innovation Fund in the frame of the R5-COP project.

REFERENCES

[1] B. Dehning, E. Effinger, J. Emery, G. Ferioli, G. Guaglio, E. B. Holzer, D. Kramer, L. Ponce, V. Prieto, M. Stockner, and C. Zamantzas. The LHC Beam Loss Measurement System. In *Proc. 22nd Particle Accelerator Conference (PAC07)*, pages 4192–4194, Albuquerque, NM, USA, Jun 2007. URL: `http://epaper.kek.jp/p07/PAPERS/FRPMN071.PDF`.

[2] E. Effinger, C. Zamantzas, G. Ferioli, G. Gauglio, J. Emery, and B. Dehning. The LHC beam loss monitoring system's data acquisition card. In *Proceedings of the 12th Workshop on Electronics for LHC and Future Experiments*, pages 108–112, Valencia, Spain, Sep 2006. URL: `https://cds.cern.ch/record/1027422/files/p108.pdf`.

[3] C. Zamantzas, B. Dehning, E. Effinger, J. Emery, and G. Ferioli. An FPGA Based Implementation for Real-time Processing of the LHC Beam Loss Monitoring System's Data. In *2006 IEEE Nuclear Science Symposium Conference Record*, volume 2, pages 950–954, San Diego, CA, USA, Oct–Nov 2006. `doi:10.1109/NSSMIC.2006.356003`.

[4] J. Emery, B. Dehning, E. Effinger, G. Ferioli, C. Zamantzas, H. Ikeda, and E. Verhagen. LHC BLM Single Channel Connectivity Test using the Standard Installation. In *Proc. 9th European Workshop on Beam Diagnostics and Instrumentation for Particle Accelerators (DIPAC09)*, pages 354–356, Basel, Switzerland, May 2009. URL: `http://epaper.kek.jp/d09/papers/tupd26.pdf`.

[5] J. Emery, B. Dehning, E. Effinger, A. Nordt, M. G. Sapinski, and C. Zamantzas. First experiences with the LHC BLM sanity checks. *Journal of Instrumentation*, 5(12):C12044, Dec 2010. `doi:10.1088/1748-0221/5/12/C12044`.

[6] C. Zamantzas, M. Alsdorf, B. Dehning, S. Jackson, M. Kwiatkowski, and W. Viganò. System Architecture for measuring and monitoring Beam Losses in the Injector Complex at CERN. In *Proc. 1st International Beam Instrumentation Conference (IBIC2012)*, pages 347–350, Tsukuba, Japan, Oct 2012. URL: `http://accelconf.web.cern.ch/AccelConf/IBIC2012/papers/tupa09.pdf`.

[7] W. Viganò, M. Alsdorf, B. Dehning, M. Kwiatkowski, G. G. Venturini, and C. Zamantzas. 10 orders of magnitude current measurement digitisers for the CERN beam loss systems. *Journal of Instrumentation*, 9(02):C02011, Feb 2014. `doi:10.1088/1748-0221/9/02/C02011`.

[8] C. F. Hajdu, T. Dabóczi, and C. Zamantzas. On-line system supervision of beam loss monitoring systems with sinusoidal excitation. In *XXI IMEKO World Congress – Full Papers*, pages 1176–1180, Prague, Czech Republic, Sep 2015. URL: `https://www.imeko.org/publications/wc-2015/IMEKO-WC-2015-TC10-237.pdf`.

[9] C. F. Hajdu, T. Dabóczi, and C. Zamantzas. Possibilities for On-line Detector Connectivity Checks in Beam Loss Monitoring Systems. *Periodica Polytechnica Electrical Engineering and Computer Science*, in press, 2016.

ISBN 978-3-95450-177-9

STUDIES AND HISTORICAL ANALYSIS OF ALBA BEAM LOSS MONITORS

A. A. Nosych, U. Iriso, ALBA-CELLS, Barcelona, Spain

Abstract

During 5 years of operation in the 3 GeV storage ring of ALBA, the 124 beam loss monitors (BLMs) have provided stable measurements of relative losses around the machine, with around 10% breakdown of units. We have analyzed these BLM failures and correlated the integrated received dose with any special conditions of each BLM location which might have led to their breakdown.

We also show studies of beam losses in the insertion devices, with particular attention to the results in the multipole wiggler (MPW), where the vacuum chamber is (suspected to be) misaligned and high BLMs counts are detected.

INTRODUCTION

ALBA is a 3 GeV 3rd-generation synchrotron light source, operational since 2011. Currently it is running in top-up mode with beam current of up to 150 mA and the horizontal emittance of 4.6 nmrad. During 5 years of operation the 124 beam loss monitors have been generally doing a very good service in measuring the loss distribution around the 269 m storage ring (SR). Nevertheless, several units did get out of order, some others did get detuned and some more did change their positions over time. A campaign to re-organize the BLM units and understand their health state has been conducted.

LAYOUT OF ALBA BLMS

Common to other synchrotrons [1], the beam loss detection system of ALBA consists of a pair of compact PIN-diode Bergoz BLMs connected to a two-channel beam signal conditioner (BSC). The BSC provides electrical power and signal readout to- and from- the BLMs. The BLMs are evenly spread around the storage ring at approximately every 2.5 m, coinciding with BPM locations. For maximum sensitivity the active part of BLMs has been positioned in the beam orbit plane and is perpendicular to the beam direction. Besides, placed in the inner side of the ring, they are subjected from the X-ray background.

In total there are 66 BSCs and 124 corresponding BLMs spread around 16 sectors of the machine: 7 or 8 per sector (depending on sector type), plus a few additional units around the injection line from booster. A typical 8-BLM connectivity schematic per sector is shown in Fig. 1.

The BLM detector is sensitive to minimum ionizing particles (MIP) produced when an accelerated particle hits the vacuum chamber [2]. The detector is composed of two PIN-diodes mounted face to face to form a 2-channel coincidence detector. When an ionizing particle hits a PIN-diode, an electric charge is produced, and a bias voltage allows collection of this charge. A particle energy of > 700 keV is required to get the PIN-diode ionized and it is detected with an efficiency of > 30%. MIPs cause ionization in both PIN-diodes, while photons do not, which excludes BLMs from being affected by synchrotron radiation.

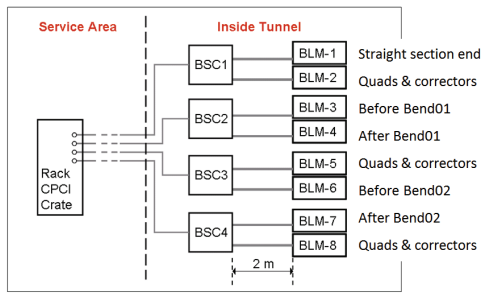

Figure 1: Beam loss detection system of ALBA per storage ring sector.

The size of the PIN-diodes mounted on the circuit determines the detector's solid angle. The coincidence scheme effectively rejects the spurious noise from each channel well below 1 counts per second (cps). The amplification gain of each channel is adjusted with a potentiometer [2].

Beam Loss Monitors in Operation

The nominal counts in the majority of BLM locations during SR operation is around 10-20 cps, which slightly rise during injections, reaching some 10s and 100s in the vicinity of the booster-to-storage transfer line and the injection kickers.

Figure 2 shows a typical loss distribution map around the ring during decay and injection modes, updated at 1 Hz rate. In each sector the lowest losses correspond to the beginning/end of the sector (straight sections), while the highest are systematically read downstream of both dipoles in each sector.

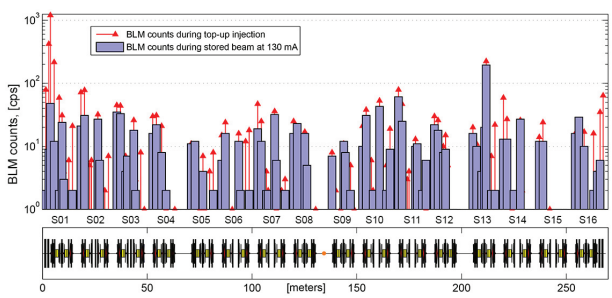

Figure 2: Operational beam loss distribution (log scale) on the ALBA storage ring as observed in the control room.

ISBN 978-3-95450-177-9

HISTORIC BLM DATA ANALYSIS

Since the installation of the storage ring in 2009, through its commissioning in March 2011, and after 5 years of operation by the end of 2015, we have made an attempt to analyze the evolution of BLM readings and estimate the degradation and survival rate of the physical BLM units. We look for possible correlation between BLM mortality, various operational conditions, and total received counts.

Evolution of Dark Counts, 2009-2015

The dynamic range of a PIN-diode BLM is determined by the spurious noise of the detector and the maximum count rate. The spurious noise is below 1 cps in the absence of any background. The detector recovers 100 ns after a hit, leading to 10 MHz maximum count rate.

The Bergoz BLM circuits are shipped pre-calibrated for a spurious count rate of 10 kHz. By forcing one PIN-diode to be always True (i.e. always reading a hit), the spurious counts calibration of the other PIN-diode can be checked. The control system of ALBA allows simultaneous switching of all available BLM PIN-diodes to False-False (FF) operational mode, and True-False (TF) or False-True (FT) calibration modes. The readings in two latter modes are called "dark counts".

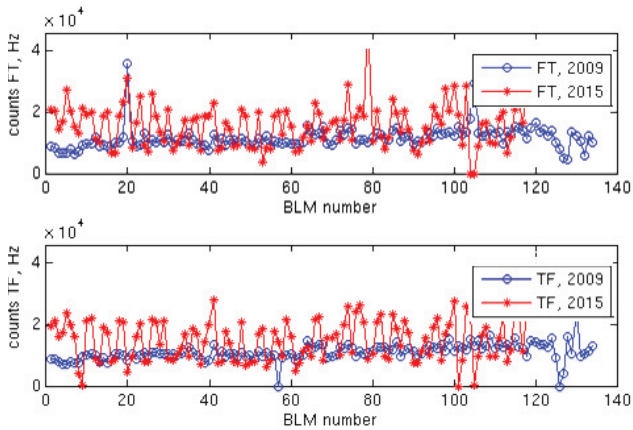

Figure 3: Dark counts in TF and FT calibration modes: 2009 vs. 2015 (without beam).

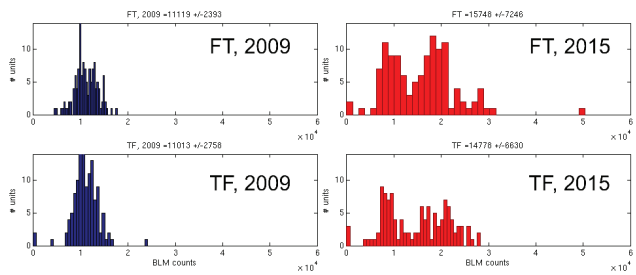

Figure 4: Histograms of dark count measurements in TF and FT modes in Fig 3: 2009 vs. 2015 (without beam).

When a BLM shows zero or extraordinarily high or low counts, most likely it has been detuned. Its PIN-diodes can be re-calibrated back to 10 kHz by adjusting the potentiometers and measuring the dark counts.

Figure 3 compares the dark counts of all SR BLM units after installation in 2009 with the ones measured in the end of 2015 without beam. There is a clear increase in TF and FT modes for some BLMs, possibly those receiving higher radiation doses leading to their slow detuning over time.

In Fig. 4 the histograms highlight an increase in the spread (more units read more spurious counts) and in the average (more units read higher spurious counts than average) of dark count measurements in 2015 versus 2009.

By doing periodic checks we regularly monitor BLM calibrations and tune the potentiometers if needed.

Integrated Counts of ALBA BLMs, 2011-2015

We calculate and analyze the total amount of counts received by each BLM location and correlate the results with BLM failures.

The data archiver of ALBA control system logs the BLM counts at 0.1 Hz rate. Since the SR commissioning there are 13 million data points recorded for each of the 124 BLM locations (not for particular BLM unit). Integrating over these points gives an estimate of the total counts received in 5 years. They are shown in Fig. 5, where the intermediate values corresponding to FT/TF modes, as well as those taken with beam current < 1 mA, have been filtered out.

The overall amount of counts for the majority of BLM locations since 2011 are < 10 million, with only a couple of them exceeding this dose (BLM-0103: 15M counts, BLM-1609: 60M counts) for unknown reason.

The locations of 9 failed BLM units are also highlighted, together with the color-coded failure type and detuned units: 2 fatal (red, non-repairable), 7 with failed on-board electronics (black, repairable), and 8 detuned (green, repaired in-situ). In particular, among the units with failed electronics, 4 had lost video amplifiers, one had lost an inductor, and one more - a transistor [3].

Unfortunately, by comparing the total amount of counts with the BLM failure type no correlation could be established: the high amount of received counts does not lead a loss of BLM unit.

To cross-check further, we super-impose the operational counts at 1 Hz (during stored beam and a top-up injection) with the total integrated counts, Fig. 6. However, again we see no correlation between the operational counts and BLM failures: no indication of constant high-loss region systematically affecting the BLMs in the area.

Furthermore, comparing the dark counts (taken during beamtime) with the total integrated counts in Fig. 7, neither reveals any correlation between these data sets and particular BLM failure locations.

Finally, we correlate the BLM unit failures with some location specifics around the ring: the high radiation environment around the RF plants and the injection sector, Fig. 8. The majority of failed (7/9) and half of the detuned (4/8) BLM units were located in the highlighted areas, which can hint on their degradation.

ISBN 978-3-95450-177-9

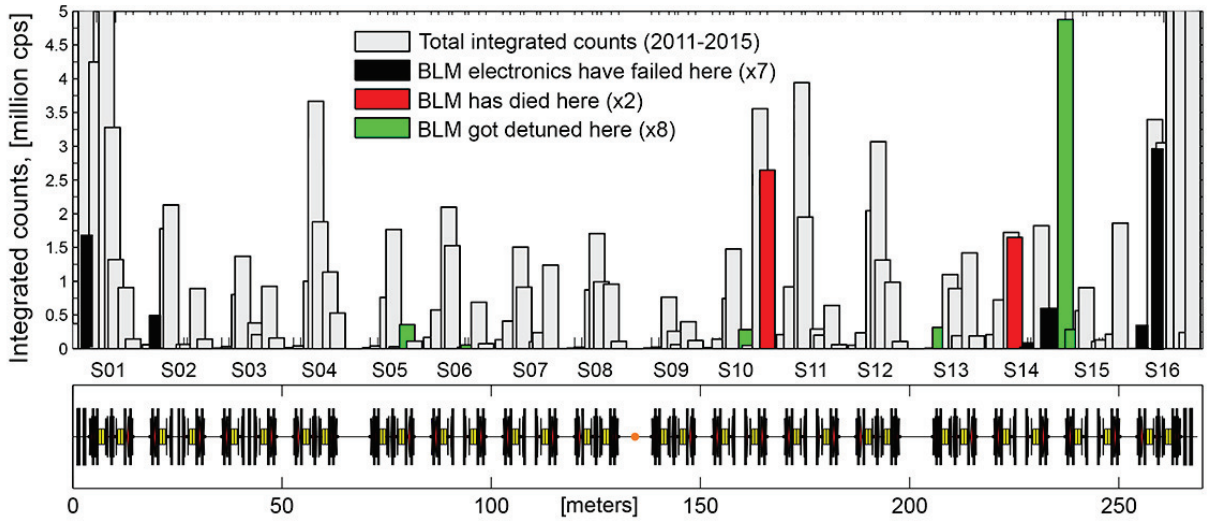

Figure 5: Overall integrated counts (2011-2015) for every BLM location vs. BLM failures.

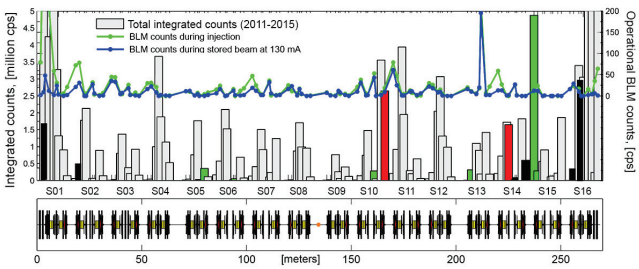

Figure 6: Overall integrated counts vs. loss patterns during injection and stored beam.

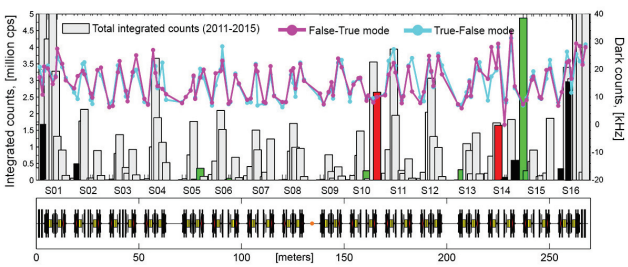

Figure 7: Overall integrated counts vs. operational dark counts pattern during beam time.

MISALIGNMENT DIAGNOSTICS WITH BLMS

The ALBA storage ring operates several insertion devices (IDs) to produce high-brilliance X-rays for its 6 beamlines (plus two beamlines using bending dipoles). These IDs are the multi-pole wiggler (MPW), the super-conducting wiggler, two in-air elliptic undulators (EU), and two in-vacuum undulators.

The MPW, in particular, is placed in a straight section between two sectors. The 2 m long vacuum chamber of MPW is elliptic, machined in an 8 mm thick rectangular aluminum block. It is attached to an upstream and downstream SR vacuum chambers (28 mm thick) with the so-called *distributed absorbers*, which bear the octagonal-to-elliptic transitions. Figure 9 shows the distribution of all these elements.

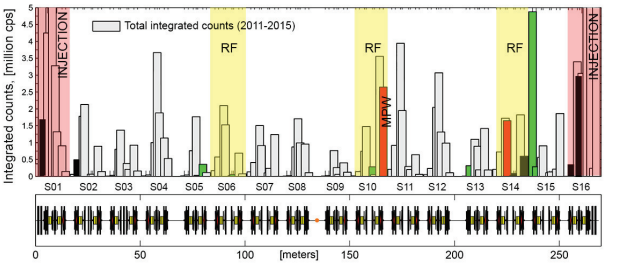

Figure 8: Overall integrated counts vs. location specifics.

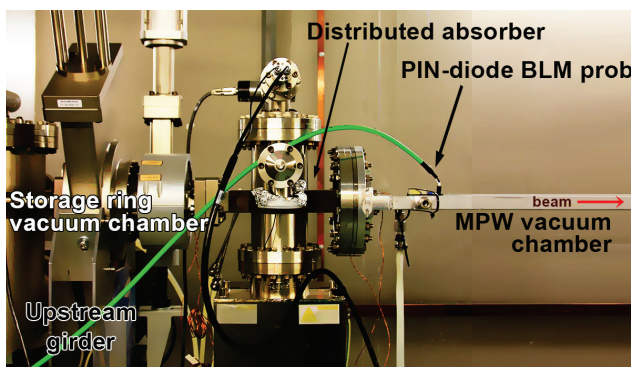

Figure 9: Side view of the storage ring vacuum chamber connection with the MPW straight section.

An alignment survey had indicated that the SR girder, upstream of the MPW, is misaligned by 0.8 mm downwards with respect to the downstream girder. A BLM was placed on top of the MPW vacuum chamber (Fig. 10) to monitor beam losses, possibly induced by electrons interacting with misaligned vacuum chambers or the absorber.

ISBN 978-3-95450-177-9

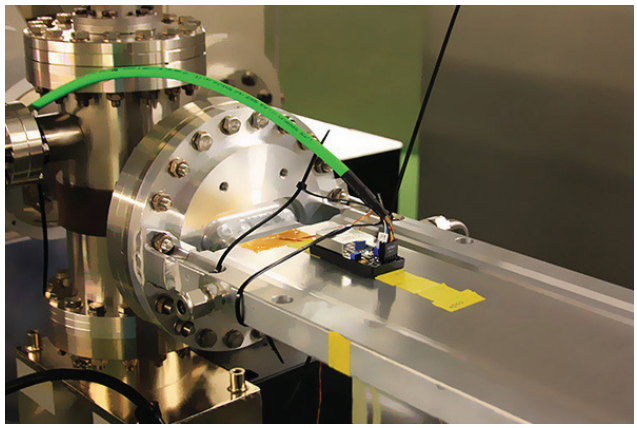

Figure 10: Beam loss monitor placed on top of the MPW vacuum chamber to study losses induced by misaligned storage ring sections.

Very high loss counts, shown in Fig. 11, were indeed detected. The losses on top of the MPW chamber appear to be highly beam current-dependent, rising drastically from 1000 cps at 120 mA to 6000 cps at 150 mA. The losses also appear to be very sensitive to top-up injections.

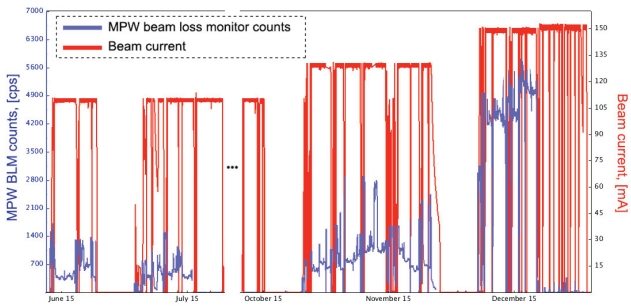

Figure 11: Beam losses measured on top of the MPW vacuum chamber throughout part of 2015, indicating a drastic dependence on beam current.

A BLM placed under the MPW beam pipe did also detect some losses, but less than on top. Another unit did not measure any losses on the side of the beam pipe in the horizontal plane, confirming the vertical plane misalignment theory.

Figure 12 shows the simultaneous measurement of losses above and under the MPW beam pipe at two longitudinal BLM positions: both BLMs at 5 and 10 cm away from the distributed absorber transition. The counts above decrease as the BLM gets farther from the misaligned region, while the counts below stay constant.

As of September 2016 the current state of loss distribution in the ALBA storage ring is shown in Fig. 13. Here one can see several locations with high losses, which are possibly related to misalignment issues of ID vacuum chambers: the MPW (CLAESS beamline), the EU62 (CIRCE beamline)

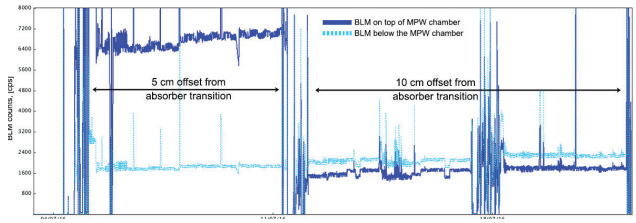

Figure 12: Longitudinal scanning of beam losses on top and bottom of the MPW vacuum chamber.

and the recently installed vacuum chamber of another EU for the future LOREA beamline to be commissioned in 2017. The losses in the latter one combine also the losses induced by vacuum conditioning (unknown to-date).

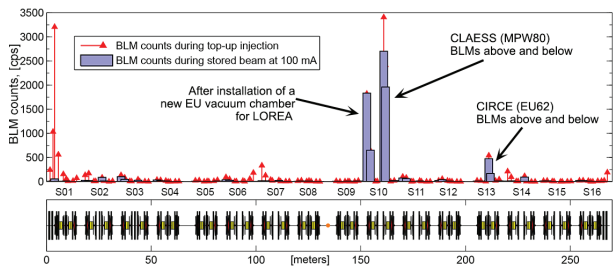

Figure 13: Up-to-date beam loss distribution map of the ALBA storage ring, showing high-loss regions (02.09.2016).

CONCLUSION

We have made an attempt to correlate the BLM failures occurring in the last 5 years with the total counts received by each BLM location, as well as with other BLM-specific measurements. We conclude that the BLMs seem to be having some problems with integrated electronics, mostly failing in the areas of high radiation background. Across 5 years of operation 9 failed BLM units (out of 124) do not make such bad statistics after all.

The PIN-diode BLMs are useful tools in studying vacuum chamber misalignment issues, especially in the regions of vacuum chamber transitions. They are able to indicate the misalignment direction and magnitude. As of end of 2016 we continue monitoring beam losses related to misaligned insertion device vacuum chambers.

REFERENCES

[1] F. Perez, et al., "Studies using Beam loss monitors at ANKA", Proceedings of EPAC 2004, Lucerne, Switzerland

[2] Bergoz Instrumentation, Beam Loss Monitor User's Manual, http://www.bergoz.com

[3] Private communication with J. Bergoz

ISBN 978-3-95450-177-9

INDUSTRIALISATION OF CAVITY BPMS

E. Yamakawa*, S. Boogert, A. Lyapin,
John Adams Institute at Royal Holloway, University of London, Egham, UK
S. Syme, FMB Oxford, Oxford, UK

Abstract

The industrialisation project of a cavity beam position monitor (CBPM) has been commissioned aiming at providing reliable and economical CBPM systems for future Free Electron Lasers (FEL) and similar linac-based facilities. The first prototype of a CBPM system was built at Versatile Electron Linear Accelerator (VELA) in Daresbury Laboratory. We report on the measurement results from the first prototype of our system at VELA and current developments of CBPMs, down-converter electronics and Data Acquisition (DAQ) system.

INTRODUCTION

CBPMs have gradually moved from an exotic extreme spatial resolution tool designed for use in final focus collider systems [1] to an FEL workhorse [2, 3] providing sub-micrometre resolutions even at low, typically less than 100 pC bunch charge. An industrialisation project had been started jointly by the John Adams Institute (at Royal Holloway, University of London), FMB-Oxford and Daresbury Laboratory in 2014 with support by the Science and Technology Facilities Council (STFC) Innovations Partnership Scheme (grant number ST/L00013X/1). The aim of the project is to design a low-cost, easy in operation and reliable CBPM system that could be deployed even in smaller high brilliance light facilities with no direct access to the required expertise.

A basic CBPM system typically consists of 2 cavities: one position (dipole) and one reference (monopole) cavity for charge and phase normalisation, a set of down-converter electronics, high-speed digitisers for data acquisition and digital processing. In order to kick-start the project, cavity, electronics, DAQ and processing development, as well as setting up the beam experiment started in parallel, with an existing cavity [4] used as a test subject to set up the beam measurements while the new cavities are still in development. The beam test has been set up at STFC Daresbury Laboratory in VELA test facility.

CBPM TEST SYSTEM AT VELA

We built the first prototype of CBPM system at VELA in Daresbury Laboratory. Currently, the system includes one position and one reference cavity, and is planned to be extended to 3 position cavities plus reference in 2017. There are 2 precision position stages moving a single CBPM horizontally and vertically with respect to the beam (Fig.1). The motion stages are controlled remotely via a MINT motion controller coupled with a PC running LabVIEW code. Three channels of homodyne down-converting electronics reduce the frequency of the signal down to about 20 MHz (Fig. 2).

Two Red Pitaya [5] open source SoC (system on a chip) boards are deployed for DAQ. Red Pitaya hosts a single processor plus FPGA (field-programmable gate array) chip, two 125 MHz 14-bit ADC and 2 DAC channels and a number of GPIO pins. The native code has been modified in order to acquire signals with external trigger and include EPICS (Experimental Physics and Industrial Control System) API modules for seamless interfacing with VELA for DAQ and control.

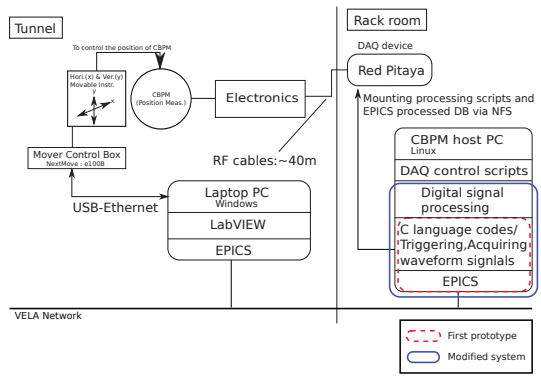

Figure 1: The layout of CBPM system in VELA.

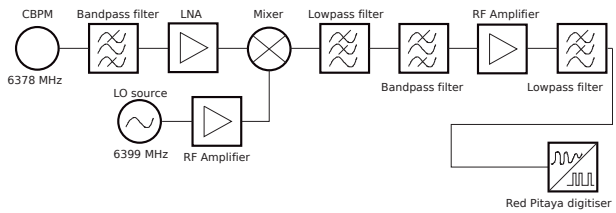

Figure 2: Schematic of the signal down-converting electronics for the C-band system.

In the first instance, we installed a single existing position cavity (Fig. 3) to commission the test system and start working on the electronics and DAQ, the data were taken on the 8th of July 2015.

We measured CBPM signals while moving the stages first in horizontal and then in vertical in order to measure the sensitivity of the cavity in hand. The digitised waveform signal was processed by the digital down-conversion (DDC) algorithm [6] on the host PC to detect the amplitude of the signal using a digital LO (Local Oscillator) of the same frequency as the incoming CBPM signal. A Gaussian filter was applied to remove the noise and up-converted component of the IF signal. For measuring the sensitivity of the cavity, the maximum amplitude of the demodulated signal

* Emi.Yamakawa@rhul.ac.uk

ISBN 978-3-95450-177-9

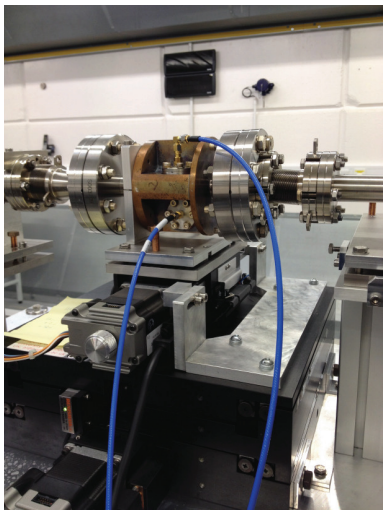

Figure 3: C-band BPM located on the VELA beam line. The CBPM is on the stepping motor which can move horizontally and vertically.

was sampled and propagated back to the cavity output using bench-measured conversion factors. Finally, the amplitude was normalised by the beam charge measured by VELA's wall current monitor. The measurement is shown in Fig. 4. We applied a fitting function $a|x-b|+c$ to the data, and the fitted position sensitivity (coefficient a of the fit) is consistent with the prediction of 1 mV/pC/mm calculated using the results of a 3D electromagnetic simulation with GdfidL [7].

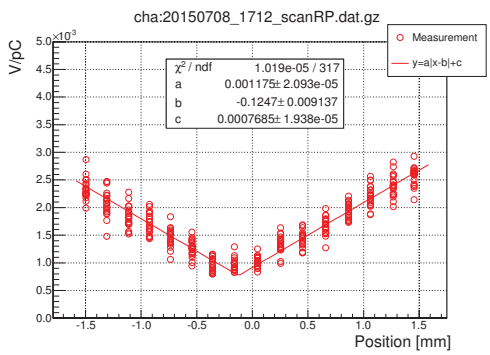

Figure 4: The normalised DDC amplitude vs. the CBPM horizontal position.

CURRENT DEVELOPMENTS

The CBPM hardware has been developed as following subsystems: position and reference cavities, signal processing electronics and DAQ system. Each subsystem is described in turn in the following sections.

Position and Reference Cavity Design

Both position and reference cavities are being developed. A reference cavity operates the monopole mode to provide the charge and phase normalisation of the offset signal, which otherwise depends on the charge and beam arrival time. The first prototype of the developed reference cavity is currently in the VELA beam line awaiting the next beam for testing (Fig. 5). A position cavity senses the beam offset via the dipole mode, which has a crest at the symmetry axis of the cavity and grows with the offset from it. The mechanical design of the position cavity is currently being finalised and is foreseen to be tested on a triplet of cavities in VELA beam line. The design draws on experience of manufacturing braze-free reference cavities. As a measure towards cost reduction, a thorough tolerance analysis has been carried out in simulation with the cavity dimensions varied in frequency and asymmetries introduced in cross-coupling studies.

Figure 5: Reference CBPM manufactured and assembled at FMB oxford.

Signal Down-Converter Electronics

The cavity signals are down-converted for digitisation. In this case, we deployed the classical heterodyne scheme, which is convenient for lowering the frequency of the signal close to the source for transmitting it to the digitisers outside of the accelerator enclosure, with the capability of high gain and efficient filtering at the intermediate frequency (IF), in this case 500 MHz. In the second stage of downconversion the frequency is lowered further to around 20 MHz, which is easy to convert with high bit resolution. The prototypes of the RF front-end and IF sections printed circuit boards (PCB) are shown in Figs. 6 and 7. They demonstrated the basic RF functionality in terms of the gain and noise characteristics as per cascaded system simulations. The next steps will include packaging these boards in a user-friendly format, where 2 possibilities are considered at the moment: standalone rack-mounted units with several channels per unit or single channel modules in a popular chassis format.

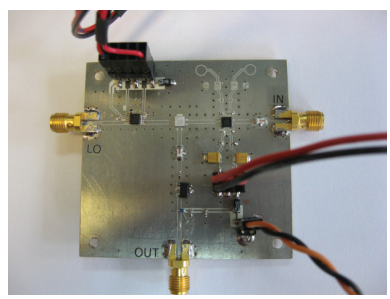

Figure 6: RF front-end PCB.

ISBN 978-3-95450-177-9

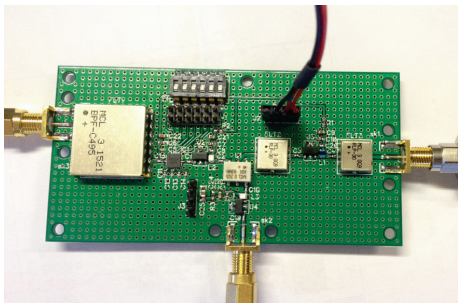

Figure 7: IF section PCB.

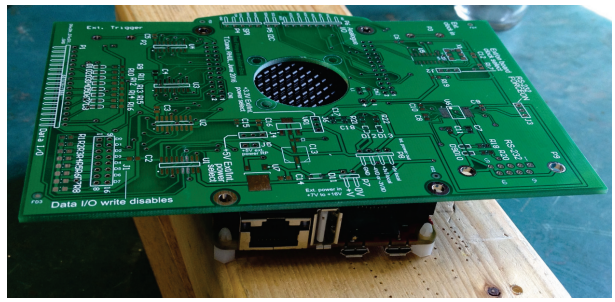

Figure 8: Extension PCB (unpopulated) on top of a Red Pitaya board.

DAQ System

The baseline DAQ system is based on Red Pitaya boards, which are built around a SoC processor combined with an FPGA. Notably, the boards have 2 channels of 14 bit 125 MHz ADC, as well as 2 channels of DAC and GPIO lines. The sampling frequency and resolution are similar to that of a typical CBPM system, while GPIO lines can be used for control and monitoring. A faster version of the CBPM processing code may be implemented on FPGAs, in which case the DAC outputs can be used for generating feedback signals.

Insofar, EPICS channel access client API has been added to stock software as well as digital processing code for CBPM signals. Running processing on Red Pitaya is much more efficient with the external clock as many channels can be synced and the same phase reference used for all position channels. This requires minor hardware modifications, so an extension board is being developed for easy excess to the external clock and other features of the board (Fig. 8). Digital processing, currently running on the processor, will later be moved to FPGA part of the chip allowing for higher repetition rates.

Alternatively, the signal processing code can be executed on a centralised server, either on a rack controller hosting the digitisers or an external PC. This may be preferable when standard DAQ solutions exist locally.

CONCLUSION

The industrialisation of CBPMs has started, several subsystems have been tested, and a beam test prepared for position cavity prototypes. Most effort is now being put into manufacturing a test series of position cavities, with beam tests expected in 2017. Work on other subsystems will continue towards industrialising the developed designs into user-friendly robust systems. The whole system is expected to be tested at VELA and its performance characterised in various beam conditions.

REFERENCES

[1] Nuc. Inst. Meth. A, 578, 2007, pp. 1–22.

[2] Nuc. Inst. Meth. A, 696, 2012, pp. 4366–4368.

[3] Proc. of PAC07, FRPMN111, 2007, pp. 66–74.

[4] Proc. of Beam Inst. Workshop, TUPSM026, 2010, pp. 168–172.

[5] Red Pitaya `http://redpitaya.com`

[6] Phys. Rev. Special Topics - Accelerator and Beams, 15, 2012, 042801.

[7] GdfidL `http://www.gdfidl.de`

ISBN 978-3-95450-177-9

THE DESIGN, CONSTRUCTION AND OPERATION OF THE BEAM INSTRUMENTATION FOR THE HIGH INTENISTY AND ENERGY UPGRADE OF ISOLDE AT CERN

W. Andreazza, E. Bravin, E.D. Cantero, S. Sadovich, A.G. Sosa, R. Veness,
CERN, Geneva, Switzerland
J. Carmona, J. Galipienzo, P. Noguera Crespo, AVS, Elgoibar, Spain

Abstract

The High Intensity and Energy (HIE) upgrade to the online isotope separation facility (ISOLDE) facility at CERN is currently in the process of being commissioned. The very tight space available between the superconducting acceleration cavities used and a challenging specification led to the design of a compact 'diagnostic box' (DB) with a number of insertable instruments on a common vacuum chamber. The box was conceived in partnership with the engineering firm AVS and produced as a completed assembly in industry. 14 diagnostic boxes have been installed and are now operational. This paper will describe the design, the construction and first results from operation of these HIE-ISOLDE diagnostic boxes.

INTRODUCTION

The High Intensity and Energy (HIE) ISOLDE project is a major upgrade of the ISOLDE and REX-ISOLDE facilities at CERN. The aim of the HIE-ISOLDE project is to greatly expand the physics programme compared to that of REX-ISOLDE. The energy of the post-accelerated radioactive beams will be increased from 3 MeV/u to 10 MeV/u. At the same time the intensity of the source will be increased with higher beam power on the production target, from 2 kW to 10 kW.

The HIE-ISOLDE diagnostic boxes are installed in the Linac between the cryomodules and in the High Energy Beam Transport (HEBT) line, between the quadrupoles of the doublet transport channel, in the dispersive sections of the double-bend achromats and before the experimental target positions.

BEAM DIAGNOSTIC REQUIREMENTS

The beam diagnostic system must provide a wide range of possibilities for measuring properties of the beam during set-up and operation of the HIE-ISOLDE facility, specifically: measurement of beam intensity using a Faraday cup; measurement of beam transverse profile and beam position using a Faraday cup in parallel with a scanning slit; collimation of the beam using collimator slits; charge-state cleaning using stripping foils; measuring energy and longitudinal profile using silicon detectors [1].

DESIGN

The design of the diagnostic boxes (DB) was driven by the very tight space available between the superconducting acceleration cavities installed in the LINAC (Fig. 1 & 2). Two cryomodules have been installed so far with four more units planned to be added over the next few years. The LINAC layout allowed a maximum inter-cryomodule distance of 250 mm, where the DBs are located. Two different versions of boxes were designed and produced, equipped with various selections of the same instruments. Five so-called "short DBs" are installed in the HIE-ISOLDE LINAC and eight "long DBs" provide beam instruments in the HIE-ISOLDE experimental lines.

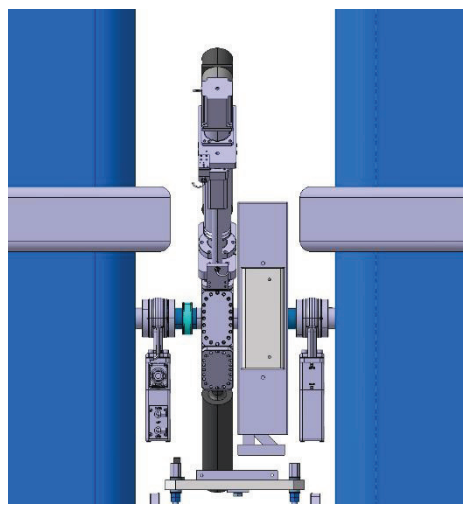

Figure 1: Schematic of the inter-cryomodule region with a short diagnostic box installed.

The design had to allow for installation of the following ultra-high vacuum (UHV) compatible instruments:

- Faraday cup
- Scanning slit
- Collimating slit
- Silicon detector
- Stripping foil

Two edge welded bellows allow the diagnostic box to be aligned with the surrounding components, with a permanently installed survey target used for fiducialisation.

ISBN 978-3-95450-177-9

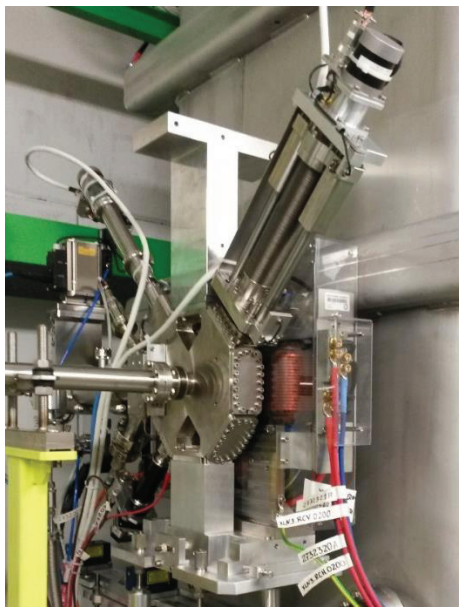

Figure 2: A short DB containing a faraday cup, a scanning slit and a collimating slit installed beside a cryomodule.

DB MAIN BODY

The strict constraints for space, flexibility, UHV compatibility and precision led to the development of a very compact unit where the main structure is an octagonal shaped tank made out of austenitic stainless steel with six ports available for the insertion of the instruments (Fig. 3). Two edge welded bellows with conflat flanges are welded on both sides.

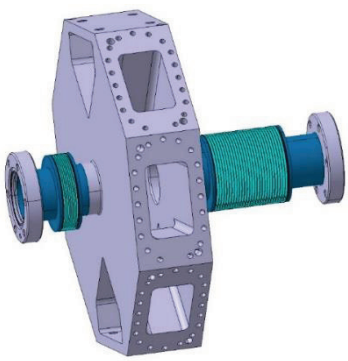

Figure 3: 3D image of the DB main body.

FARADAY CUP

A very compact Faraday cup (Fig. 4) was designed and tested to cope with the very limited space available. The length of both the collector plate and the repeller were severely reduced compared to a standard Faraday cup and optimised to keep a good accuracy [2]. A first version of the short FC was tested and did not achieve the expected results. A second iteration led to a newer, more elegant design which significantly reduced secondary particle loss. The structure materials were also all selected with their both their mechanical and electrical properties kept in mind. This design was built at CERN and tested at the TRIUMF facility in Canada. Although the geometry of the HIE short FC is very different to that used in standard cups, these differences were shown to have only a minor effect on the overall performance. The current ranges from 1 to 100 pA for stable beams while for radioactive beams it can range from a few pA down to a few particles per second.

The Faraday cup is mounted on a UHV linear feedthrough in order to allow its insertion and extraction from the beam line. The Faraday cup can be used together with either the scanning or the collimating slits.

In the initial design, the material for the insulator was polyimide. However, this was later changed to MACOR®, a machinable ceramic, to minimise the chance of contaminating the nearby superconducting cavities.

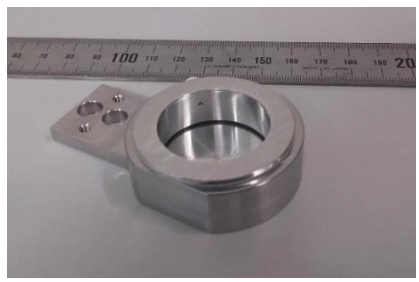

Figure 4: Short Faraday cup.

SCANNING SLIT

In order to measure the transverse position and beam profile a customized UHV Linear Shift Mechanism was developed (Fig. 5) to precisely move a scanning slit located in front of a faraday cup or silicon detector. It consists of a metallic blade with a V shaped slit of 1 mm width that moves at 45° across the beam to allow reconstruction of both the horizontal and vertical profiles. The required accuracy for the measurement of the transverse position was 100 µm. A first prototype with an in-vacuum guiding system and a commercial linear motion actuator did not pass a stress test (10000 cycles) and the decision was taken to develop a customised linear motion actuator. The system has a stroke of 135 mm with guiding rods surrounding a high precision ball bearing screw connected to a stepper motor.

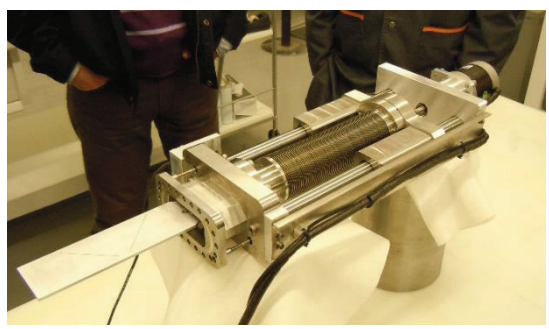

Figure 5: A scanning slit fully assembled.

An acceptance test of the new prototype was performed at the AVS headquarters in February 2014. A special blade with a slit and six holes of 0.1 mm was built for the test. The test consisted of tracking the position of the drilled

ISBN 978-3-95450-177-9

holes for different blades position, either with the blade fixed or while moving, using a system with an illuminator and a camera (Fig. 6). When the scanning blade crossed the beam aperture the light passing through the holes (or the slit) was detected by the camera. By analysing the size and position of the light spots frame by frame, the displacements of the blade due to mechanical vibrations were determined (Fig. 7). Results showed that the position variation was less than 20 μm [3]. With the instrument performing to specification the design was approved for production.

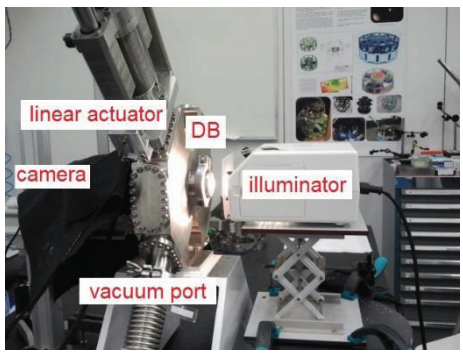

Figure 6: Scanning slit acceptance test set up [3].

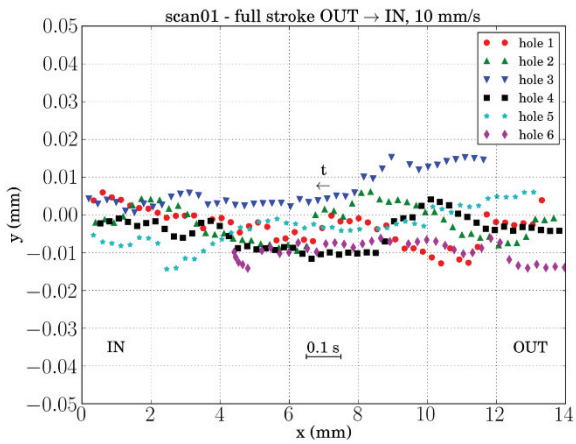

Figure 7: Tracking of the hole positions in the x-y (camera) plane. The blade speed was 10 mm/s, and the movement was from the fully OUT to the fully IN positions.

COLLIMATING SLITS

Two types of collimating slits were designed to fulfil the requirement for supplementary fixed position aperture measurement. These devices are used to reproducibly define the beam position in one or both planes when tuning the accelerator, to clean halo produced by off-axis or off-momentum particles, or to measure the energy spread in the dispersion section when a thin slit is placed at the spectrometer entrance. All measurements are performed in combination with a faraday cup.

Two different collimating slits are installed. Type I (fig. 8) with four circular holes (from 2.5 mm to 20 mm) is mainly used for quick centring and tight collimation of the beam while type II (four vertical slits with widths from 2 mm to 15 mm) is used for position determination for energy measurement.

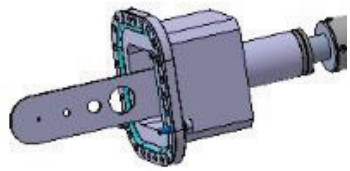

Figure 8: 3D image of a Type I collimating slit.

SILICON DETECTOR

A silicon detector is used to optimise the operational settings of the accelerator by measuring the energy of the beam after each accelerating structure for different values of the RF phase. The silicon detector can also be used to measure the beam energy and the beam purity as well as to analyse the time structure of the beam.

It consists of a commercial Passivated Implanted Planar Silicon (PIPS) detector installed onto a UHV linear feedthrough in order to allow its insertion and extraction from the beam line. The silicon detector can be used together with either the scanning or the collimating slits.

STRIPPING FOILS

Lightweight carbon stripping foils of varying thicknesses in the range of tens or hundreds of μg/cm^2 are needed for beam charge-state cleaning. The instrument consists of a metallic blade with 2 holes of diameter 30 mm over which the foils are mounted using a separate frame (Fig. 9). The blade is attached to a linear motion feedthrough that allows movement of the different foils onto the beam. The foils need to be “in beam” together with Faraday cup.

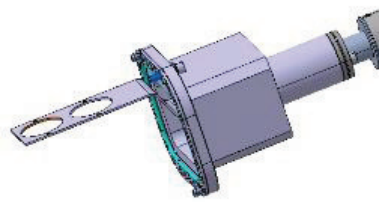

Figure 9: 3D model of a stripping foil mechanism.

OPERATIONAL EXPERIENCE

After a first period of commissioning the DBs have shown that their behaviour is within the required specification and have been used during regular machine operation since the summer of 2015. Some examples of their use are described below.

Figure 10 shows beam profiles obtained by scanning the scanning slit in front of the Faraday cup. The vertical axis shows the intensity of the beam that impinges on the FC after passing through the slits, while the x axis shows the

ISBN 978-3-95450-177-9

position of the blade. The profile on the left corresponds to the vertical plane while the one on the right to the horizontal plane.

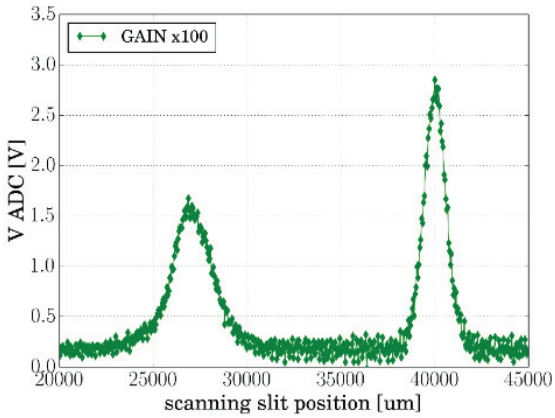

Figure 10: Beam profile measurement.

Figure 11 shows the energy spectrum of the beam for two different operational configurations measured with the silicon detector. The blue curve shows the spectrum obtained when the ISOLDE target is irradiated with protons while the red curve is obtained when the proton beam is turned off. The picture shows that when protons hit the ISOLDE target the beam is made predominantly of $^{76}Zn^{22+}$, while the main contaminant (protons off) is $^{38}Ar^{11+}$. Such measurements can be used to study and optimise the composition and purity of the beams.

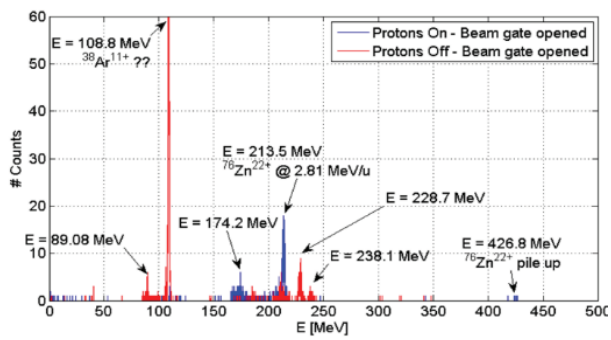

Figure 11: Particle energy spectrum.

Histograms of the particle energy as function of the phase of the RF in a superconducting cavity are shown in Figure 12. Each colour refers to a particular phase setting, while the different peaks of each trace correspond to different particle species (the probe beam used contains several elements). It is evident how the average beam energy changes as function of the RF phase. This type of measurements is routinely used to adjust the RF phase to the most appropriate value.

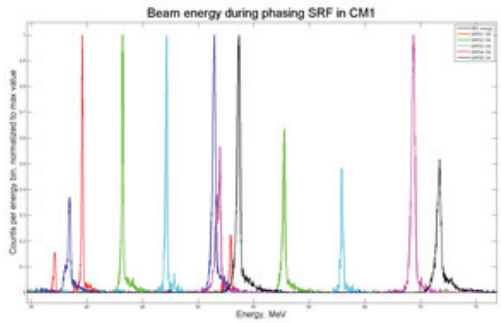

Figure 12: RF cavity phasing.

CONCLUSIONS

Two types of diagnostic boxes were designed and produced in collaboration with private industry with a total of 14 units now installed at the HIE-ISOLDE facility. The beam instrumentation provided by these diagnostic boxes have shown very good accuracy and reliability and have been essential for both commissioning and everyday operation.

REFERENCES

[1] M. Fraser *et al.*, "Beam Diagnostic boxes for HIE-ISOLDE", *HIE-BDB-ES-0001*, CERN, Geneva, Switzerland.

[2] E. Cantero *et al.*, "HIE-ISOLDE Faraday cups tested with ion beams at TRIUMF", *HIE-BDB-NOT-0006*, CERN, Geneva, Switzerland.

[3] E. Cantero *et al.*, "Acceptance test for the linear motion actuator for the scanning slit of the HIE-ISOLDE short diagnostic boxes", *HIE-BDB-NOT-0003*, CERN, Geneva, Switzerland.

ISBN 978-3-95450-177-9

THE BROOKHAVEN LINAC ISOTOPE PRODUCTION (BLIP) FACILITY RASTER SCANNING SYSTEM FIRST YEAR OPERATION WITH BEAM*

R. Michnoff#, Z. Altinbas, P. Cerniglia, R. Connolly, C. Cullen, C. Degen, R. Hulsart, R. Lambiase, L. Mausner, W. Pekrul, D. Raparia, P. Thieberger, Brookhaven National Laboratory, Upton, NY

Abstract

Brookhaven National Laboratory's BLIP facility produces radioisotopes for the nuclear medicine community and industry, and performs research to develop new radioisotopes desired by nuclear medicine investigators. A raster scanning system was recently completed in December 2015 and fully commissioned in January 2016 to provide improved beam distribution on the targets, allow higher beam intensities, and ultimately increase production yield of the isotopes. The project included the installation of horizontal and vertical dipole magnets driven at 5 kHz with 90 deg phase separation to produce a circular beam raster pattern, a beam interlock system, and several instrumentation devices including multi-wire profile monitors, a laser profile monitor, beam current transformers and a beam position monitor. The first year operational experiences will be presented.

INTRODUCTION

The purpose of the recently completed raster system at BNL's BLIP facility is to "paint" the proton beam on the target in a circular pattern in order to provide a more even distribution of beam on the target material. At IBIC 2014 we reported on the overall system architecture and presented specific details for each system component [1]. This report will focus on results with beam during the first year of operation with the new system.

The beam instrumentation devices were installed in the fall of 2014 and commissioned with beam during the 2015 beam run from January to July 2015. The raster magnet and associated power supplies were installed during the fall of 2015, and full system commissioning was quickly completed in January 2016, four months ahead of the schedule that was already shortened by one year. The system was reliably operated with beam for the entire 2016 beam run from January to July 2016.

The new BLIP beam-line layout is shown in figure 1.

BEAM RASTER PATTERNS

The horizontal and vertical raster magnets are driven continuously with sine waves at 5 kHz and 90 deg. phase separation to provide a circular or elliptical beam pattern [2]. The amplitude of the magnet current controls the amplitude of the beam motion.

The raster pattern is programmed using a circular table of horizontal and vertical magnet current amplitudes. The output current changes to the next amplitude in the table after each 450 μs long Linac beam pulse, which occurs every 150 ms. The table size can contain more than 100 values and the amplitudes of the horizontal and vertical values do not need to be equal, thus allowing both circular

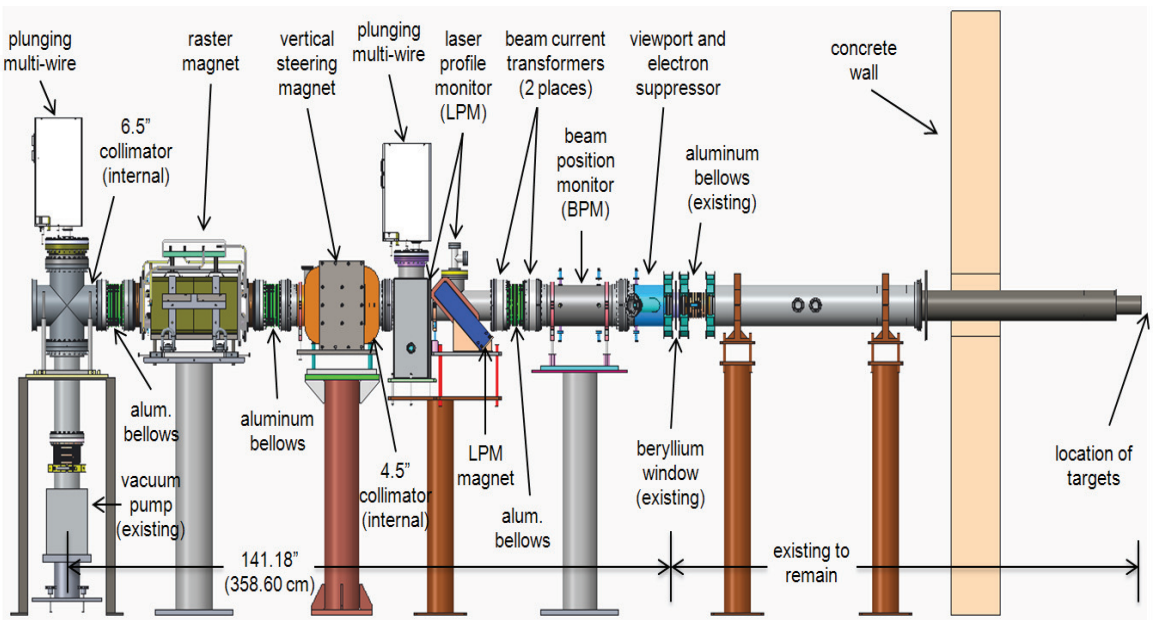

Figure 1: New BLIP beam-line layout.

* Work supported by Brookhaven Science Associates, LLC under Contract No. DE-AC02-98CH10886 with the U.S. Dept. of Energy

#michnoff@bnl.gov

ISBN 978-3-95450-177-9

and elliptical patterns. With a Linac pulse length of 450 μs and 5 kHz sine wave raster frequency, the beam makes about 2.25 rotations per beam pulse. A photo of the raster magnet installed in the beam-line is provided in figure 2.

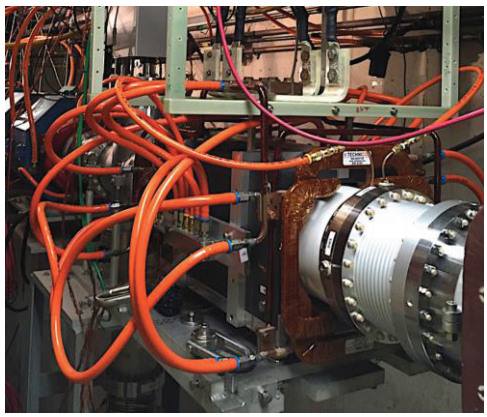

Figure 2: Photo of raster magnet installed in beam-line.

Based on early simulations, the anticipated repeating raster pattern was 3 consecutive beam pulses at 19.5 mm radius followed by one beam pulse at 6.5 mm radius. However, the actual beam size in terms of full width half max (FWHM) and full width tenth max (FWTM) is significantly larger than the beam size used in the early simulations. Therefore, in order to limit beam spill off the target, the maximum large radius used for production has been limited to 12.5 mm (Fig. 3).

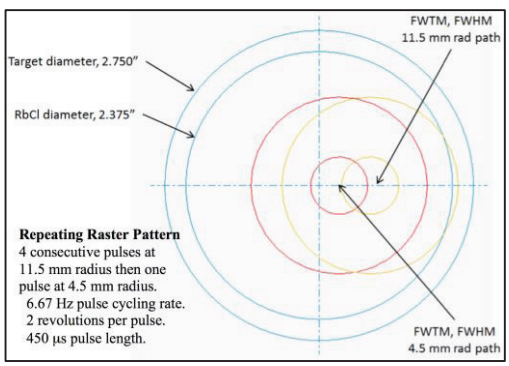

Figure 3: Diagram of beam images on target plotted at the right most positions for each radius of the circular raster pattern used during 117 MeV ^{82}Sr production from January 2016 to March 22, 2016. On March 22, 2016 the 117 MeV beam size was reduced from 13 mm FWHM and 40 mm FWTM to 10 mm FWHM and 23 mm FWTM, and the raster pattern was changed to the repeating pattern of 4 beam pulses at 12.5 mm radius and 1 beam pulse at 5.5 mm radius.

Figure 4 compares rastered and non-rastered beam profiles on the target. Although the non-rastered beam widths vary with different beam conditions including energy, a 2-radius pattern has proven to be quite adequate for providing good beam distribution. Optimum raster patterns will continue to be explored.

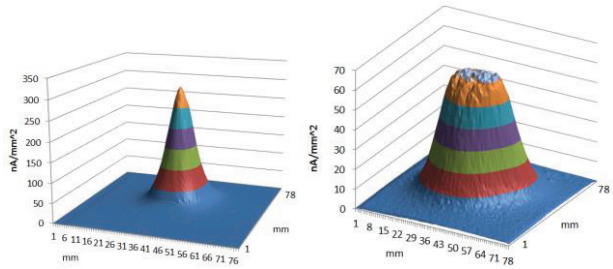

Figure 4: Beam profile on target without raster (left) and with repeating raster pattern of 4 Linac pulses at 11.5 mm radius and 1 Linac pulse at 4.5 mm radius (right), 117 MeV, 100 μA, Dec. 24, 2015. The integral of the beam distribution is equivalent for both profiles. Note that the y-scale for the non-rastered profile is about 5 times the y-scale for the rastered profile.
Non-rastered beam FWHM: 13 mm, FWTM: 40 mm
Rastered beam FWHM: 32 mm, FWTM: 60 mm

BEAM INSTRUMENTATION

All of the new beam instrumentation devices have been successfully operating as expected with beam and are providing reliable, high quality measurements. These new devices have proven to be directly attributable to improved beam stability. Figures 5-8 provide plots of beam data from each of the new devices.

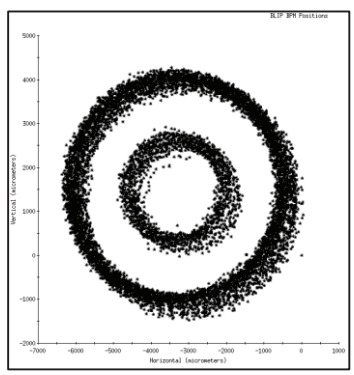

Figure 5: Beam position monitor data [3], horizontal vs. vertical (~100 points per beam pulse), March 30, 2016, 117 MeV beam and repeating raster pattern radii of 12.5 mm and 5.5 mm at the target. The actual positions at the BPM are about 1.8 times that shown in the plots.

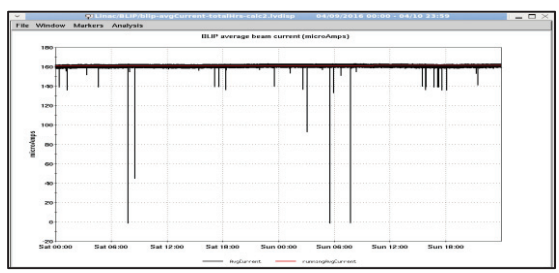

Figure 6: A 48-hour period (April 9-10, 2016) of the average beam current for 117 MeV ^{82}Sr production with the raster system on. Note that the average beam current is nearly steady at 160 μA for the entire period.

ISBN 978-3-95450-177-9

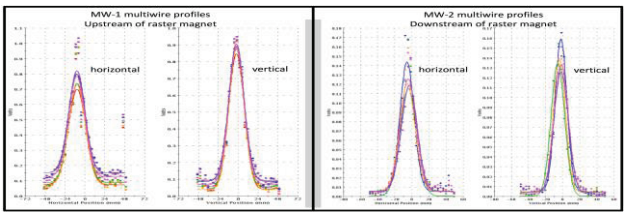

Figure 7: BLIP horizontal and vertical multi-wire profile measurements for MW-1 (left) and MW-2 (right). Profiles for six beam pulses are overlaid in each plot. The y-scale is the integrated signal strength for each wire. The wire spacing is 3.175 mm and each plane has 32 wires. These profiles were taken with 117 MeV and with the raster on. Note that all overlaid profiles for MW-1 (which is located upstream of the raster magnet) are well aligned, while the overlaid profiles for MW-2 (which is located downstream of the raster magnet) are shifted with respect to each other. This is the expected beam raster behavior.

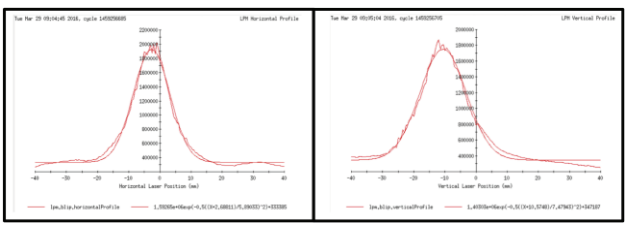

Figure 8: Horizontal (left) and vertical (right) BLIP laser profile monitor data with curve fits, with raster on. The y-scale is arbitrary units and is proportional to the number of electrons collected at each laser position. In these scans, the distance between each data point is 0.5 mm. A total number of 161 laser positions are provided. Each position value is the average of 24 points, where each point is a narrow slice of one beam pulse.

BEAM INTERLOCK SYSTEM

The beam interlock system defined in Ref. 1 has been implemented and has proven to be very reliable for machine and target protection. If the raster magnet power supply currents or magnetic field measurements indicate that the raster system is not operating as expected, then the beam is inhibited to protect the targets. The algorithm is fairly complex to allow a variety of raster radius patterns while ensuring that for example, a small radius does not continue for longer than an acceptable period of time.

Several other interlocks can also inhibit the beam to provide the required protection, including high beam current, plunging multi-wire device in mid-travel position, collimator temperature high and raster magnet water flow error.

ISOTOPE PRODUCTION RESULTS

In previous years with the non-rastered Gaussian beam profile, targets such as RbCl melted only in the region of highest beam intensity. This caused a large local density reduction leading to reduced and erratic production yield. The rastered beam distribution has resulted in higher yield of isotopes, especially the critical isotope ^{82}Sr.

In addition, improved beam distribution on targets with the raster system has allowed higher integrated beam current levels to be applied to the targets. In previous years integrated current levels were limited to about 135 μA; and in 2016 with the raster system operational and with the implementation of other Linac upgrades, the typical integrated current applied to the targets was 160 μA. Figure 9 compares total beam currents to BLIP for the 6-year period from 2011 to 2016.

The higher total current on target directly translates to higher production yields, and the improved distribution of beam on the target with the raster system has been calculated to improve the yield (in mCi/μAh) by an additional 9%.

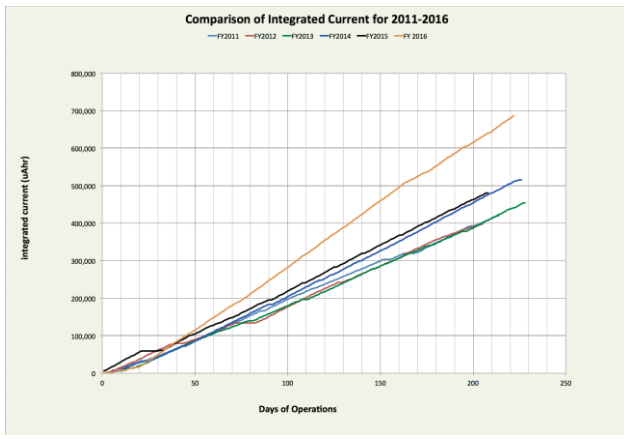

Figure 9: Plot of annual BLIP integrated currents from 2011 to 2016. The total integrated current increased 48% from 2015 to 2016.

ACKNOWLEDGEMENTS

The authors would like to thank the large group of technicians, engineers, and physicists who helped make this very important project a great success. We would also like to thank BNL management for their support, the DOE Office of Nuclear Physics for funding the project and Marc Garland and Michelle Shinn from the DOE for their continued overall guidance and project support.

REFERENCES

[1] R. Michnoff, *et al.*, "The Brookhaven LINAC Isotope Production Facility (BLIP) Raster Scanning Upgrade," IBIC 2014, Monterey, CA, USA (2014)

[2] Z. Altinbas, R. Lambiase, C. Theisen, "BLIP Scanning System Power Supply Control," IBIC 2016, Barcelona, Spain (2016).

[3] R. Hulsart, *et al.*, "A Versatile BPM Signal Processing System Based on the Xilinx Zynq SoC," IBIC 2016, Barcelona, Spain (2016).

ISBN 978-3-95450-177-9

BEAM DIAGNOSTICS DESIGN FOR A COMPACT SUPERCONDUCTING CYCLOTRON FOR RADIOISOTOPE PRODUCTION*

R. Varela†, P. Abramian, J. Calero, P. Calvo, M. Domínguez, A. Estévez, L. García-Tabarés, D. Gavela, P.Gómez, A. Guirao, J.L Gutierrez, J.I. Lagares, D. López, L. M. Martínez, D. Obradors, C. Oliver, J.M. Pérez, I. Podadera, F. Toral, C. Vázquez, CIEMAT, Madrid, Spain

Abstract

The aim of the AMIT cyclotron is to deliver an 8.5 MeV, 10 μA CW proton beam to a target to produce radioisotopes for PET diagnostics. Such a small cyclotron poses some challenges to the diagnostics design for commissioning and normal operation due to its small size, so miniaturized devices should be built in order to fit in the available space. Two sets of diagnostics have been designed, each one aiming at a different phase of the machine lifecycle. During normal operation the stripping foil and the target will be used to measure the current, a dual transverse profile monitor based on a scintillating screen will be used for interceptive measurements and a Fluorescence Profile Monitor will measure the beam position and the horizontal profile without intercepting the beam. During first stages of commissioning the dual transverse profile monitor and the target will be substituted by an emittance monitor based on a pepperpot to characterize the beam at the cyclotron exit. Also a movable interceptive Beam Probe will be located inside the cyclotron to give information about the beam during acceleration. Additionally, a test bench for the characterization of the beam right after the exit of the ion source has been built with different instruments to measure the beam current and the transverse profile. In this paper the present status of the design, simulation and tests of the diagnostics for the AMIT cyclotron are described.

INTRODUCTION

The use of PET as a diagnostic tool in the cancer diagnostic field has rised the demand of suitable radionuclides. Some of the most used radioactive atoms have relatively short lifetimes (few hours at max), which constrains the distance of the medical diagnoses centers to the radioisotope producing facilities. To overcome this limitation a compact cyclotron provides a good solution to this problem, because its small size makes it easy to allocate in small medical centers, allowing the distribution of the radioisotopes to cover as much area as possible.

The AMIT cyclotron (Fig. 1) tries to improve the size and cost efficiency limitations by a careful study of the beam dynamics [1] and the electromagnetic design [2]. It uses two superconducting coils to provide the 4 T magnetic field and a 180º Dee attached to the RF cavity to accelerate H- ions produced by a cold cathode Penning Ion Source. The machine aims to deliver a 10 uA beam of 8.5 MeV protons to irradiate two different targets (one at a time) in order to produce the required amount of ^{11}C and ^{18}F.

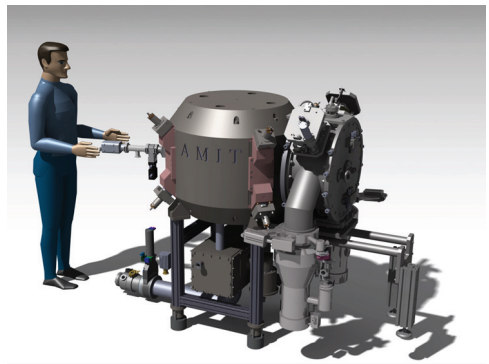

Figure 1: CAD design of AMIT cyclotron.

MACHINE OPERATION

The main challenge of this cyclotron with respect to the beam diagnostics is compactness. At 4 T and 8.5 MeV the proton bending radius is about 10 cm, limiting enormously the beam diagnostics which can fit inside the cyclotron. Different sets of diagnostics were proposed for the cyclotron's different phases [3]:

1. **Phase 1: Ion Source Characterization.** In this first stage a special test bench (Fig. 2) has been constructed to measure different beam parameters right after the exit of the ion source. This will help to verify and optimize the ion source prior to the assembly in the cyclotron.

2. **Phase 2: Beam Commissioning.** This phase consists of a few subphases, corresponding each one of them at different energy ranges:

   (a) Low energy: In this phase the proper operation of the ion source and the correct alignment between puller and source and first turns is checked.

   (b) Intermediate energy: Optimization of the acceleration from the injection up to the stripping foil.

   (c) Beam delivery at target: Comissioning of the stripping foil and beam transport up to the target and its commissioning.

3. **Phase 3: Operation.** Normal run of the machine with the continuous production of the required radioisotopes.

* This work has been funded by the Spanish Ministry of Economy and Competitiveness under project FIS2013-40860-R.

† rodrigo.varela@ciemat.es

ISBN 978-3-95450-177-9

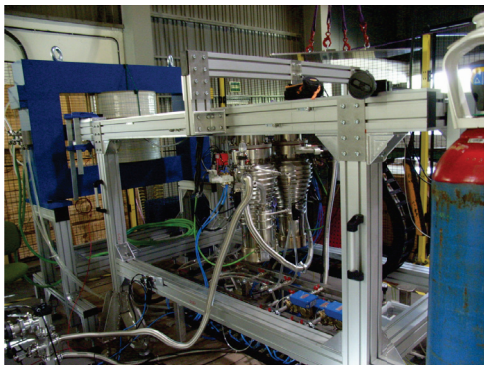

Figure 2: Test bench built for Phase 1 in order to characterize the Ion Source.

DIAGNOSTIC LAYOUT

The diagnostic layout of **Phase 1** consists of an intercepting beam probe (Fig. 3) to measure the total beam current and a wire scanner to measure both the vertical and horizontal profiles of the beam. The current readings are performed simultaneously by a Keithley 6485 Picoammeter and with the measure of the voltage drop in a shunt resistor. Due to the low beam power (less than 1 W) no special thermomechanical requirements are needed , hence a simple stainless steel probe and copper wires are used. During this phase we have been steadily increasing the voltage extraction and the beam current. So far more than 100 μA have been extracted at 1.8 kV and continuous progress is been made.

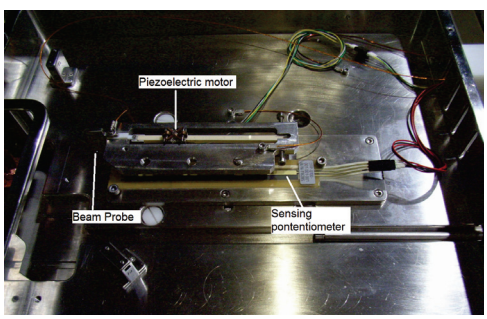

Figure 3: First mechanical test of the beam probe in Phase 1. The final design of the system for the cyclotron improves accuracy and reduces the size.

During **Phase 2** the only possible diagnostic to employ is the moveable beam probe inside the cyclotron . The mechanical design of the probe is similar to the one shown in Fig. 3, albeit with a few changes to improve the design tested in Phase 1. Graphite has been chosen for the probe in order to withstand the 85 W continuous beam power in an area of few square millimeters and keep its activation as low as possible for easy maintenance. Simulations of the maximum temperature over time performed with ANSYS show that the probe should withstand CW operation mode although the RF system is capable of pulsed mode. Results are shown in Fig. 4.

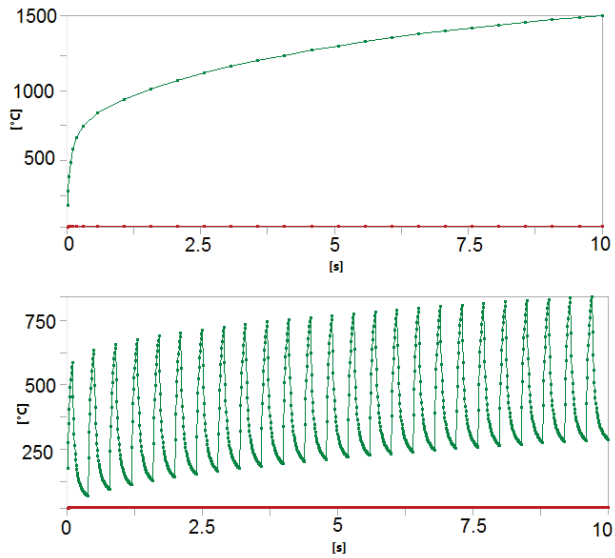

Figure 4: Max temperature with a step pulse at nominal power (top) and maximum temperature evolution with a pulsed beam of 400 ms period and 25% DC (bottom).

After the H- complete acceleration, it is stripped of its two electrons by means of a carbon foil. Another current measurement is integrated in this stripping foil to measure the beam current deposited in the foil. Just after the exit of the cyclotron is located the Compact Diagnostic Line (CDL). This short beamline (Fig. 5) will be installed in both **Phase 2 and Phase 3**, being interchanged with the energy monitor during the former and left alone during the later phase.

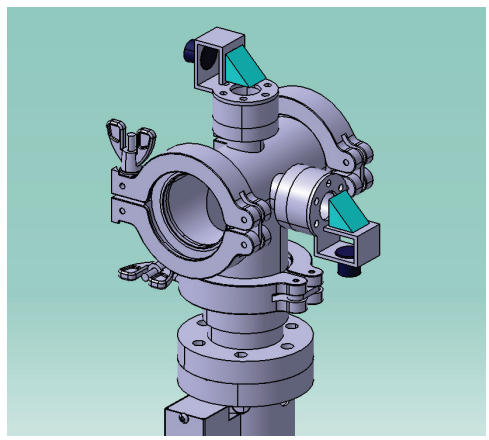

Figure 5: CAD design of the CDL. The prisms (in turquoise) reflect the fluorescence light to the micro video lenses (black) wich are attached to the image fibers (not shown) and will be covered to avoid stray light getting into the system. The device in the bottom is the pneumatic actuator which moves the Al_2O_3 screen.

The current and energy measurements will come from a dedicated energy monitor . With this information we will be able to evaluate the beam loses in the transport from the stripping foil to the target and the position.

ISBN 978-3-95450-177-9

A pepperpot based emittance measurement device has been chosen to characterize the beam during commissioning. In its design the same considerations of the Beam Probe were taken into account, albeit it is expected to activate less the the BP due to its use only during commissioning.

The transverse profile is given by two independent methods, an Al_2O_3 fluorescent screen and a Fluorescent Profile Monitor. Both of them share the same optical system, although they are intended for different uses. The screen is dedicated to the commissioning phase and initial tuning during normal operation and the FPM intended to monitor the beam during the irradiation. Due to the small available space for diagnostics the compactness of the diagnostics was a very strong requirement that influenced all the design process, for this reason we choose an approach based on image fiber bundles and micro video lenses, which are capable of delivering the images where camera lies down. Because of the small light output of the residual gas fluorescence [4] a detector based on an image intensifier and a CID camera was chosen, with the possibility to install a gas leak valve to use different gases to enhance both the light output and profile accuracy [4]. It has been also foreseen the possibility to install an optical filter wheel to select different transitions. In our case a rough estimation of the signal strength interpolating the results obtained in [5] gives a cross section about 10^{-18} cm^2, which results in a photon yield in our nominal conditions about 10^9 photons generated per second in one meter length. It is not a very high number after taking into account the transmittance losses and the aperture of our optical system, which justifies our decision of using a gas leak valve to enhance the S/N ratio of our detector.

Additionally, two beam loss monitors are going to be installed during commissioning and normal operations to check the radiation levels, one of them for gamma rays detection and the other aiming at the neutrons.

CONCLUSIONS

A set of diagnostics has been designed and constructed to be installed in the AMIT cyclotron. It includes interceptive devices which are very reliable and are well established in the field with non-interceptive ones which can provide information without affecting the beam. Although the size requirements are very strict the designed instruments fit into the specifications and provide measurements of the beam parameters during commissioning and normal operation.

REFERENCES

[1] C. Oliver et al., "Optimizing the Radioisotope Production with a Weak Focusing Compact Cyclotron", Cyclotrons'13, 2013.

[2] D. Gavela et al., "Calculation and design of a RF Cavity for a Novel Compact Superconducting Cyclotron for Radioisotope Production (AMIT)", IPAC'15, 2015.

[3] I. Podadera et al., "Beam Diagnostics for Commissioning and Operation of a Novel Compact Cyclotron for Radioisotope Production", IBIC'13, 2013.

[4] J. M. Carmona et al., "First Measurements of non-interceptive fluorescence profile monitor prototypes using 9 MeV deuterons", Phys. Rev. Special Topics – Accelerators and Beams 15, 072801 (2012).

[5] A. Variola et al., "Characterization of a nondestructive beam profile monitor using luminescent emission", Phys. Rev. Special Topics – Accelerators and Beams 10, 122801, 2007.

ISBN 978-3-95450-177-9

BEAM DIAGNOSTICS FOR THE MULTI-MW HADRON LINAC IFMIF/DONES *

I. Podadera †, B. Brañas, A. Guirao, A. Ibarra, D. Jiménez, E. Molina,
J. Molla, C. Oliver, R. Varela, CIEMAT, Madrid, Spain
P. Cara, Fusion for Energy, Garching, Germany

Abstract

In the frame of the material research for future fusion reactors, the construction of a simplified facility of IFMIF [2], the so-called DONES (Demo-Oriented Neutron Early Source) [1], is planned to generate sufficient material damage for the new design of DEMO . DONES will be a 40 MeV, 125 mA deuteron accelerator. The 5 MW beam will impact in a lithium flow target to yield a neutron source. The detailed design of the DONES accelerator is being pushed forward within EUROFUSION-WPENS project. One of the most critical tasks of the accelerator will be to identify the layout of beam diagnostics along the accelerator. This instrumentation shall guarantee the high availability of the whole accelerator system and the beam characteristics and machine protection. This contribution will describe the beam diagnostics selected along the accelerator, focusing on the High Energy Beam Transport line, in charge of shaping the beam down to the high power target. The main open questions will be analyzed and the path to obtain the detailed design by the end of the project described.

ACCELERATOR DESCRIPTION

The linear accelerator for the DONES facility [1] will serve as a neutron source for the assessment of materials damage in future fusion reactors. Unlike the two coupled accelerators for the final IFMIF [2], DONES will be one accelerator, instead of two, accelerating deuterons up to 40 MeV at full CW current of 125 mA (Tab. 1). DONES is divided in three major systems: the particle accelerator, the target and the experimental area. The accelerator system is based on the design of LIPAC [3], which is currently in its commissioning phase [4]. The main sections are (Fig. 1):

- A Low Energy Beam Transport (LEBT) section at 100 keV to guide the low energy ions up to the RadioFrequency Quadrupole (RFQ) and match its injection acceptance.
- An RFQ to accelerate the ions from 100 keV up to 5 MeV.
- A Medium energy Beam Transport Line (MEBT) to match the RFQ extracted beam to the injection of the SRF Linac. It will also be used for matching the RFQ beam with the requirements of the Diagnostics Plate during the RFQ commissioning.
- An SRF Linac to bring the energy of the deuterons up to 40 MeV. It is made of four cryomodules, bringing the energy from 5 MeV up to 9 / 14.5 / 26 and 40 MeV respectively at the exit of each cryomodule.
- A High Energy Beam Transport (HEBT) lines to transport the beam from SRF Linac towards the lithium target or the beam dump transport line (BDTL, in pulse mode).
- A Diagnostics Plate (DP) to commission the beam at medium and high energies. It will be located at the exit of the RFQ and SRF LINAC cryomodules during each beam commissioning stage.

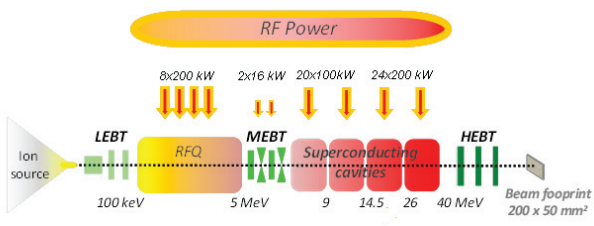

Figure 1: Layout of the DONES accelerator system.

Table 1: DONES Main Beam Parameters

Peak current	125 mA
RF frequency	175 MHz
Beam energy	0.1/5/9/14.5/26/40 MeV
β	0.01/0.073/0.097/0.12/0.165/0.2

BEAM DIAGNOSTICS REQUIREMENTS

The requirements of DONES pose several challenges to the beam diagnostics [5]. The normal operation mode of the accelerator will be in continuous (CW) mode, with an average beam current of 125 mA at a bunch frequency of 175 MHz. An additional pulsed mode operation must be taken into account during the commissioning. The use of special interceptive diagnostics is required for this case (e.g. wire scanners, Faraday cups…). A 0.1 % duty factor is estimated for the pulsed mode, with a minimum pulse of 50 µs and a maximum one of 200 µs, as defined for LIPAC. The present plan assumes the operation with deuterons from the earliest stage. However a preliminary operation with protons is highly probable/almost mandatory, as it has been

* This work has been carried out within the framework of the EUROfusion Consortium and has received funding from the Euratom research and training programme 2014-2018 under grant agreement No 633053
† ivan.podadera@ciemat.es

ISBN 978-3-95450-177-9

found/estimated beneficial at LIPAC. First of all, the availability of the accelerator system [6] is very important to guarantee the irradiation dose rate to the material samples. The monitors should be robust enough to monitor continuously and with high reliability the important beam parameters used to control and protect the machine during operation and tuning status. Therefore, the monitors should withstand the severe environment conditions of the beamline, especially regarding the high neutron and gamma radiation. On the other hand, due to the compactness of the design, special beam diagnostics devices cannot be integrated along the beamline.Therefore, the beam cannot be fully characterized once the accelerator is fully assembled. As a consequence of this design decision, it is of highly importance to well characterise each acceleration stage prior to move forward.

BEAM DIAGNOSTICS LAYOUT

The beam diagnostics design is based on the monitors designed and installed for LIPAC. In the injector [7], the MEBT [8] and the first cryomodule of the SRF Linac [8, 9], the diagnostics integrated should be in principle identical to the ones used there.

High Energy Beam Transport Line

The distribution of the monitors along the HEBT is based on the beam dynamics design [10]. The beamline can be divided in three sections (Fig. 2): a section S1 before the dipole which directs the beam to the target, a section S2 which transforms the beam phase-space using octupoles and dodecapoles, and a section S3 which makes the beam imping in the right spot. This section passes through two separate rooms: the Radiation Isolation Room (RIR) and the Target Isolation Room (TIR), before colliding with the target. Along section S1 the monitors are focused in monitoring the beam from the SRF Linac. The following properties should permanently monitored to be sured the right beam is delivered to the target: DC current, mean energy and transverse size. In section S2 it is very important to control the profile and position of the beam at each multipole magnet. In section S3 the essential points are: 1) to point the beam to the center of the target. This can be achieved by using RF pickups tuned to the fundamental frequency, 2) to control the size and uniformity of the transverse profile.

PRELIMINARY DESIGN OF MONITORS

Beam Position

BPM's in the HEBT will be longer than in LIPAC, due to the higher energy, and a bigger longitudinal space should be reserved in the beamline. In the last section of the HEBT, at least three beam position monitors should be located to steerer the beam into the target. In addition, due to the big beampipe aperture (at least 300 mm) and the high debunching effect in this area, the measurement of the position will be challenging. First studies have been carried out in order to check the feasibility of BPM's in this area, without any need of installing a re-buncher cavity. Fig. 3 shows the signals in the electrodes simulated for a BPM in the last HEBT section. Using the real BPM stimulus, an output of around 20 mV is obtained, which should be enough for a reliable measurement. Once the distance to the acquisition electronics is set, it should be taken into account to evaluate the impact on the signal strength.

Mean Energy

Figure 4 plots the accuracy of the energy measurement as function of the distance between pickups 1 and 2. A phase accuracy of 2° and a distance accuracy of 100 µm is assumed. With pickup separations above 0.5 m, the error is kept below 1 %, which represents 50 keV at 5 MeV beam energy and 400 keV at 40 MeV. To get smaller values at high energy, the diagnostics plate should be longer than in LIPAC. A length between BPM's of 2.5-3 m is proposed for the Diagnostics Plate during the commissioning. With 3 m length, the error is kept below 50 keV for a phase accuracy of 2 % and a length accuracy of 100 µm.

Transverse Profile

One of the most specific instrumentation for DONES is the development of a transverse beam profile close to the 40 MeV lithium target, at the TIR of the HEBT at 40 MeV. There, the DONES beam profile must have a rectangular shape of 20 cm wide and 5 cm height or alternatively 10 cm wide and 5 cm height. A non-interceptive monitor was already studied in the frame of EFDA-IFMIF activities [11]. The non-interceptive profiler should monitor permanently the square size of the target, the edges of the rectangular shape, and the flatness of the profile. At the moment two are the most promising candidates: a monitor based on the residual gas fluorescence [12], and one based in the residual gas ionization [13]. Both monitors are being installed in the HEBT beamline of LIPAC for comparison and feedback. In parallel, more experiments are planned to advance in the verification of the use of those monitors in DONES.

CONCLUSIONS AND OUTLOOK

A complete list of the beam diagnostics for DONES has been elaborated and presented as a basis for the detailed design of the accelerator system. The list has taken into account all the important aspects of the accelerator: the availability and reliability of the system, the radiation resistance, the beam dynamics requirements, and the mechanical integration. For the more critical devices several simulations and calculations have been performed before validating the complete system.

Future activities will include the assessment of beam loss monitors along all the accelerator system, especially in the RIR/TIR areas. A very important work will be detailing the requirements and design of the beam profile diagnostics in the TIR. Feedback from the beam commissioning from LIPAC is of utmost importance for considering any change in the list and type of diagnostics proposed. Unlike LIPAC, there should be a risk assessment of the beam diagnostics

ISBN 978-3-95450-177-9

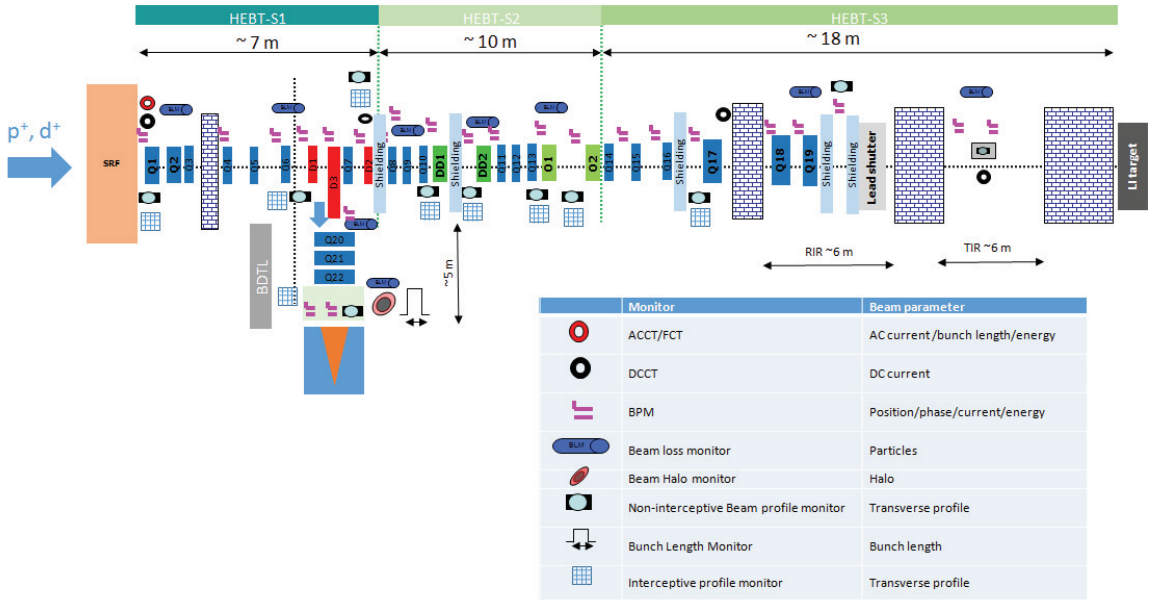

Figure 2: Preliminary schematic of the beam diagnostics proposed at the exit of the cryomodule.

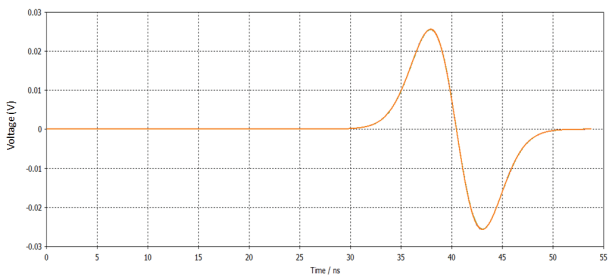

Figure 3: Simulation of the response of the last BPM in the TIR.

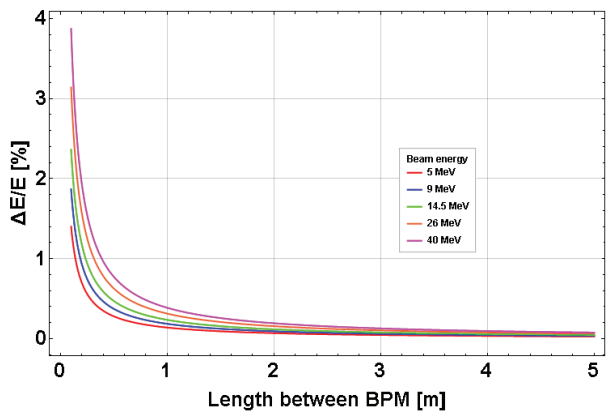

Figure 4: Accuracy of the mean energy measurement vs the distance between phase monitors for the different commissioning stages of the accelerator facility.

proposed all along the accelerator, but especially inside the SRF Linac. Last but not least, a preliminary mechanical design of the more critical areas shal be elaborated in order to validate the integration of the diagnostics proposed.

DISCLAIMER

Views and opinions expressed herein do not necessarily reflect those of Fusion for Energy.

REFERENCES

[1] A. Ibarra *et al.*, "DONES Conceptual Design Report", Apr. 2014

[2] A. Ibarra *et al.*, "IFMIF Intermediate Engineering Design report", Broader Approach, Rep. 23VD38, Jun. 2013

[3] P. Cara *et al.*, "The Linear IFMIF Prototype Accelerator (LIPAc) design development under the European-Japanese collaboration", Proc. of IPAC 2016, Busan, Korea.

[4] J. Knaster *et al.*, "The installation and Start of Commissioning of the 1.1 MW Deuteron Prototype Linac for IFMIF", Proc. of IPAC 2014, Shanghai, China.

[5] J. Marroncle *et al.*, "IFMIF-LIPAc Diagnostics and its Challenges", Proc. of IBIC 2012, Tsukuba, Japan, 2012.

[6] J.M. Arroyo *et al.*, "Hardware availability calculations and results of the IFMIF accelerator facility", Fus. Eng. Design 89, 9-10, pp. 2388-2392, 2014.

[7] B. Bolzon *et al.*, "Beam Diagnostics of the LIPAC Injector With a Focus on the Algorithm Developed for Emittance Data Analysis of High Background Including Species Fraction Calculation ", TUPB008, Proc. of IBIC 2015, Melbourne, Australia, 2015.

[8] I. Podadera *et al.*, "Status of the Beam Position Monitors for LIPAc", MOPC019, Proc. of IBIC 2013, Oxford, UK, 2013.

[9] J. Marroncle *et al.*, "R&D on Micro-Loss Monitors for High Intensity Linacs like LIPAc's ", Proc. of HB2016, Malmo, Sweden, 2016.

[10] C.Oliver *et al.*, "Phase-Space Transformation for a Uniform Target Irradiation at DONES", LINAC 2016, 2016.

ISBN 978-3-95450-177-9

[11] E. Surrey *et al.*, "A beam profile monitor for IFMIF reference", EFDA TW5-TTMI-001, 2006

[12] J.M. Carmona *et al.*, "Measurements of noninterceptive fluorescence profile monitor prototypes using 9 MeV deuterons", Phys. Rev. ST Accel. Beams 15, 072801, 2012.

[13] J. Egberts, "IFMIF-LIPAc Beam Diagnostics. Profiling and Loss Monitoring Systems", PhD Thesis, IRFU-CEA Saclay, 2012.

ISBN 978-3-95450-177-9

DESIGN OF RISP RFQ COOLER BUNCHER

R. Boussaid†, S. Kondrashev, Young-Ho. Park
Rare Isotope Sciences Project, Institute for Basic Science, Republic of Korea

Abstract

Under RISP project, wide variety of intense rare isotope ion beams will be provided. An EBIS charge breeder has been designed to charge breed these beams. Its optimum operation requires injection of bunched beam with small emittance and energy spread. An RFQCB is designed to meet these requirements. In this respect, the RFQCB should efficiently accept high intensity continuous beams and deliver to EBIS bunched beams with emittance around 3 π.mm.mrad, energy spread < 10 eV and short bunch width (~10 μs). A new design concept to be implemented in this RFQCB have been developed, including a novel injection/extraction electrodes geometry with improved differential pumping system. Simulations have shown high efficiency of transmission more than 93 % of incoming ions for beam intensities up to 1 μA with improved beam quality. A set of beam diagnostics tools including Faraday cups, pepper-pot emittance-meter with MCP based detector are designed to characterize the ionbeams.

RISP PROJECT

A heavy ion accelerator facility called RAON [1] is being designed to produce various rare isotopes under the Rare Isotope Science Project (RISP) [2]. Using the ISOLand IFbeam production methods [3], as well as a combination of these methods RAON will provide wide variety of intense rare isotope ion beams [4] for nuclear physics experiments and applied science.

An efficient and cost effective acceleration of rare isotope beams requires utilization of charge breeder as an interface between ion source and linear accelerator to convert a singly-charged ion beam into the highly-charged ion beam. An Electron Beam Ion Source (EBIS) charge breeder (CB) has been designed [5] and is being built to charge breed rare isotope ion beams for further acceleration. EBIS CB is preferable choice for the most ongoing projects, including RISP, because of its high breeding efficiency, short breeding time, and in particular, high purity of charge bred ion beams. The optimum operation of EBIS CB requires injection of bunched beam with small emittance and low energy spread. An RFQ Cooler/Buncher (RISP-RFQCB) is designed to meet these requirements.

RFQ COOLER-BUNCHER

At present, RFQCB is operational at multiple rare isotope facilities like CARIBU, ISCOOL, NSCL and others [6]. In order to meet requirements of modern ISOL facilities, it is necessary to increase the beam intensity limit of such device from typically several tens of pico-amperes (~10^6 pps) to several tens of nano-amperes (~10^9 pps) and to accumulate the ions during time determined by the required EBIS charge breeding time (~10-1000ms). As the existing devices are not able neither to handle high beam current nor to accumulate ions for long period of time, a new RISP-RFQCB device is being developed. In order to meet the EBIS beam requirements, the RISP-RFQCB should efficiently accept high intensity continuous beams from ISOL ion source and deliver to the EBIS charge breeder bunched ion beams with small emittance (~3 π.mm.mrad), low energy spread (<10 eV) and short bunch width (~10 μs).

The RISP-RFQCB is designed to handle intense ion beams with large emittances and wide range of ion masses (6-180 a.m.u), and to deliver bunches with high rep-rate (1-100 Hz). A new design concept to be implemented in the RISP RFQCB have been developed, including a novel injection/extraction electrodes geometry. An overview of the RISP RFQCB design concept will be presented. Simulated performance of the device and design of different sub-systems will be presented and discussed as well.

Optics Design

The RFQCB must accept up to few tens nAmps continuous beam with energy <=60keV and transverse emittance going up to 40 π.mm.mrad over a mass range between 6 and 180 uma. It must also deliver bunched beams in agreement with EBIS injection beam requirements. To conform a conceptual design capable of satisfying these requirements, several ion optical simulations were performed using SIMION 8.1 to model ion optics, including RF/DC fields, buffer gas and space charge effects.

As for all RFQCB devices, ion optical system of the present device can be divided into three sections [7]: injection section, cooling section and extraction section. These sections have to ensure an efficient transmission of the input beams. To efficiently cool RISP beams, the injection energy that will bring the ions to the cooling section should be of ~20-100 eV. Therefore, the relatively high energy of beam should be decreased using a DC electric field. The deceleration can be done by the injection plate electrode setting at high voltage (HV) platform and grounded input electrode, Figure 1. Other injection electrodes provide a fine-tuning of beam transmission. The cooling section consists of the main RFQCB chamber placed at HV platform. This chamber is filled with helium buffer gas and it accommodate the radiofrequency quadrupole (RFQ). It is devoted to trap efficiently the injected beam and to cool it progressively with the buffer gas. To guide the ions along the RFQ up to the extraction section, the RFQ electrodes are segmented and a DC potentials are applied to these segments. The structure is 800 mm in length and is separated into 27 segments of various length. Several electrodes are placed at RFQCB exit to extract and accelerate cooled and bunched ion beam back to the same energy as that of the

†nounaramzi@ibs.re.kr

ISBN 978-3-95450-177-9

injected beam. Extraction section structure and geometry are similar to structure and geometry of the injection section, Figure 1. Numerical simulations, done by SIMION [8], were carried out to design this system. The beam is extracted from the cooling section through the extraction aperture. Once it passes through this aperture, it is strongly accelerated by the DC electric field created between the extraction aperture and the ground electrode. Two conical electrodes are used to prevent ion losses. Multiple simulations were undertaken to confirm the design of the RISP-RFQCB. The simulations were done for a uniform circular distribution of one thousands of 133Cs+ ions in helium buffer gas. The ions initial conditions were determined for ion beam with 60 keV energy, 40 π.mm.mrad transverse emittance, 10 mm diameter and 10 eV energy spread.

Once the ions are successfully injected into the RFQ, they progressively undergo the cooling process and then released in short bunches [9]. The cooling will occur over 750 mm through the RFQ and the bunching will be done using the 26th segment. Simulations of the bunching and extraction section were carried out to understand operating parameters to be used in experiments. Several parameters that may involve the cooling effects are evaluated in SIMION including the gas pressure, input beam energy, ion mass, ion charge, guiding DC voltages and RF voltage. Simulations were performed with various operating parameters and only the optimal results will be presented.

The described device is designed to be used either as a cooler (DC mode) or as a cooler buncher. In DC mode the ions are guided via DC potential distribution up to the RFQ output where they are extracted and accelerated to their initial beam energy before entering RFQCB. Simulation results showed more than 95 % of incoming ions can be transmitted through the extraction section with an energy spread ~ 2 eV and a beam emittance ~2.9 π.mm.mrad for 10 nA beam current. With higher beam currents the space charge effect becomes considerable on the beam features. This was well depicted in the progressive beam growth reaching ~ 3.4 eVenergy spread and ~4 π.mm.mrad emittance (Figure 2)for 1 μA input beam current. The transmission remains above 95 % in spite of the significant contribution of the space charge effect.

In our case, the RFQCB will be operated in bunched mode, collecting ions of interest for some amount of time, bunching, and ejecting them in a tight packet. Simulations of emittance, ion pulse duration and energy spread for 10 nA beam current and 10 ms cooling time were performed with the same parameters as for DC mode described above. The extracted beam has the following parameters in this case: an emittance of 3.1 π.mm.mrad, an ion bunch duration of 1.9 μs and an energy spread of 2.2 eV (Figure 3).

RFQ CB Beamline

The entire RFQ CB beamline consists of five sections (Figure 4): Pre-injection section (1), Injection section (2), RFQ cavity (3), Extraction section (4), Post-extraction section (5). These sections are connected via CF-160 flanges and consists of stainless steel vacuum chambers. All sections are pumped by Turbo-molecular pumps (TMP). Buffer gas is injected into the RFQ section and diffuse to other sections as well. All vacuum components are chosen to be standard commercial when it is possible. Stainless steel is used for manufacture of all electrodes and ceramic-for most of insulators. The gap between various electrodes were chosen to avoid breakdowns.

RFQ chamber is filled with 0.5-3 mbar of helium. There are several differential pumping stages between RFQCB chamber and other sections of the RFQCB.

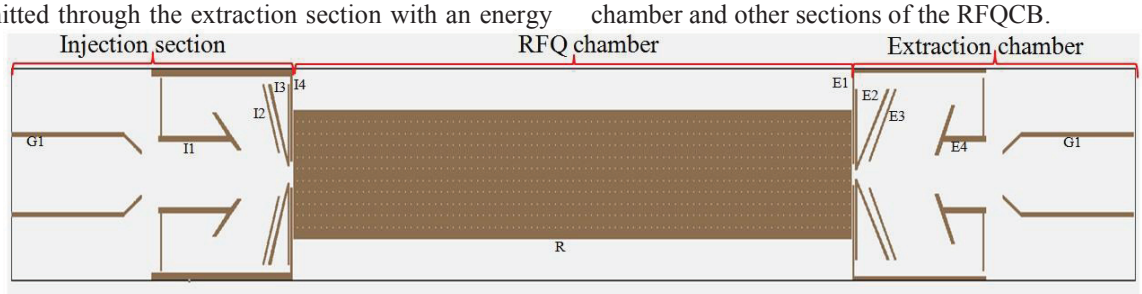

Figure 1: Optics design of the RFQ CB and overview of the three sections forming its optics system: Ground electrode(G1), 1st injection electrode(I1), 2nd injection electrode (I2), 3rd injection electrode(I3), injection plate(I4), RFQ section(R), extraction plate(E1), 1st extraction electrode(E2), 2nd extraction electrode(E3), 3rd extraction electrode(E4).

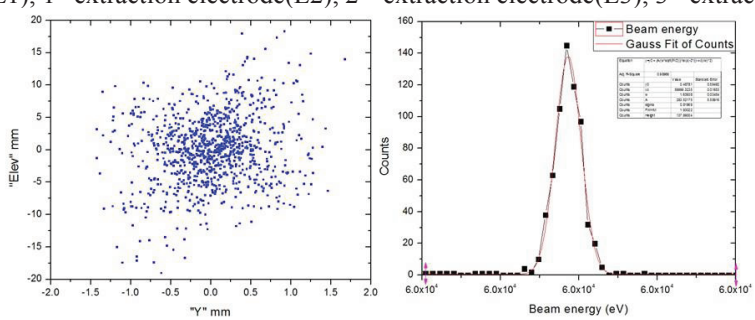

Figure 2: Extracted DC beam parameter (simulations are performed with buffer gas pressure of 2.6 Pa, RF voltage amplitude and frequency of 5 kV and 5MHz, a guiding field of 0.14 V/mm): beam emittance (left) and beam energy spread (right).

ISBN 978-3-95450-177-9

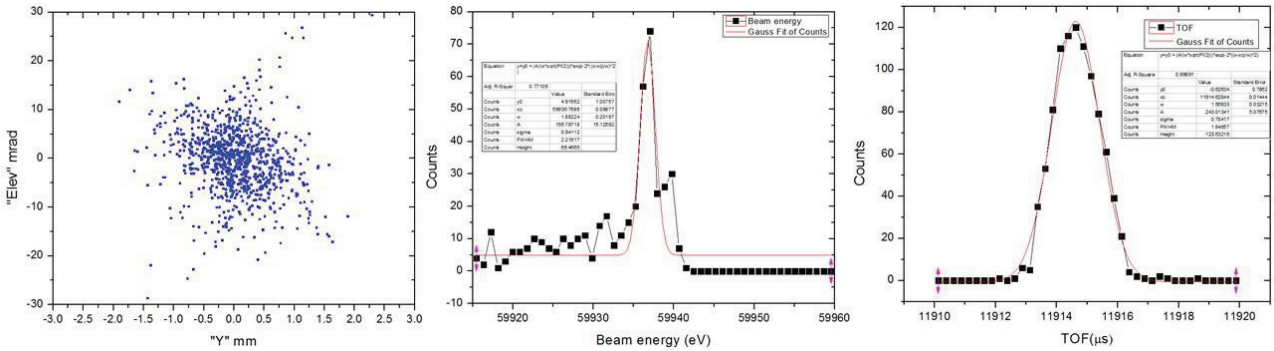

Figure 3: Simulated parameters of extracted beam in bunching mode: beam emittance (left), energy spread (middle) and bunch width (right).

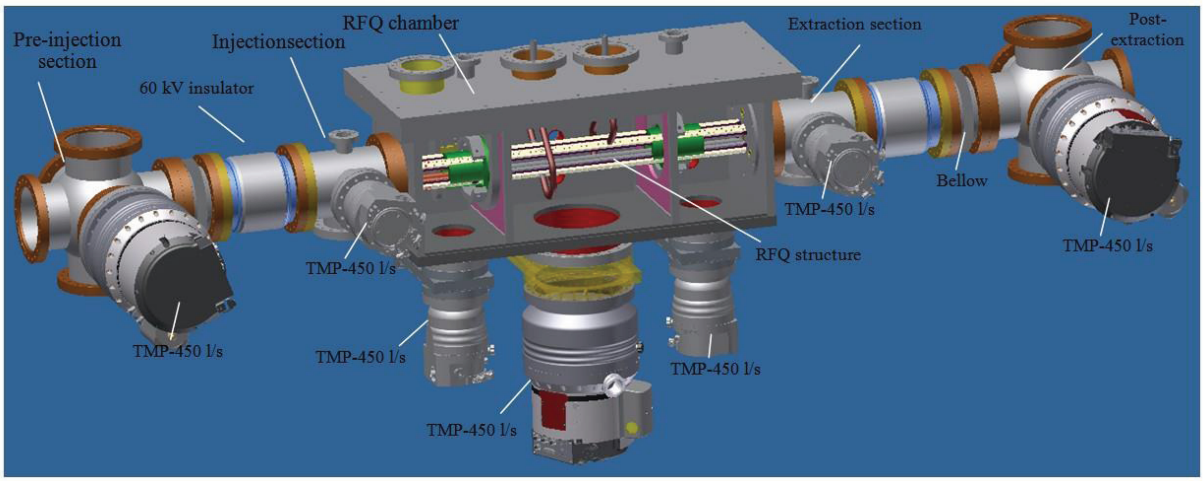

Figure 4: Engineering model of the RISP RFQ Cooler-Buncher.

BEAM DIAGNOSTIC

Efficiency RFQCB, output beam emittance, energy spread and bunch width will be measured and optimized during off-line commissioning.

The transmission is the ratio of the beam current extracted from RFQCB and injected into RFQCB. These currents will be measured by two identical Faraday cups placed at the input and output of RFQCB. Emittance of output beam will be measured by pepper-pot emittance meter. Measurement of beam energy spread is very important for understanding the cooling process of intense beam. The measurements of the transmission as a function of the DC retarding potential, applied to the last segment of the RFQ, will be used to determine the longitudinal energy spread using the width (FWHM) of its derivative. The bunch width will be measured using fast MCP detector. Some details of these beam diagnostic tools are described below.

Faraday Cup

The 3D model of Faraday cup is presented in Figure 5. Faraday cup is with 47 mm input aperture is driven by air stroke. It stops all beam particles and the resulting signal is measured to obtain information on the beam intensity. The accuracy of the method depends on the noise level present in the system and the charge collection efficiency. Low-energy beams can be easily stopped in a metal plate, but backscattered and secondary particles can carry the charge away. For ions, it is resolved with additional suppression by means of an electric field.

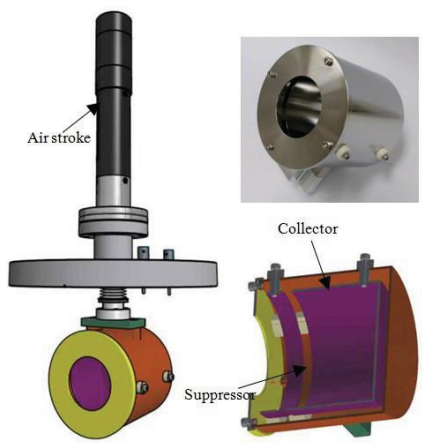

Figure 5: Faraday cup system. (Left) Faraday cup attached to air stroke, (right) sketch of its collector and suppressor.

Emittance Meter

The pepper-pot method is a common way to determine the transverse beam emittance. The pepper-pot mask consists of an even plate with a 2D array of holes in it. Ion beam which passes the pepper-pot mask through its holes

ISBN 978-3-95450-177-9

gets separated into several beamlets which hit a scintillating screen (MCP-chevron type) located further downstream. Design of pepper-pot meter is based on one described in [10]. It has the following parameters: an MCP active area of 40 mm, a mask aperture of 40 mm, mask holes separation/size 1mm/20 um. The distance between the MCP and the mask is adjustable from 5 to 50 mm, to provide optimization for non-overlapping beamlet images with maximum diameter. The rms transverse beam emittance can be calculated from the position, size, and shape of these images. The geometric transverse emittance can then be deduced from the rms emittance where it is defined at 90% of the action volume.

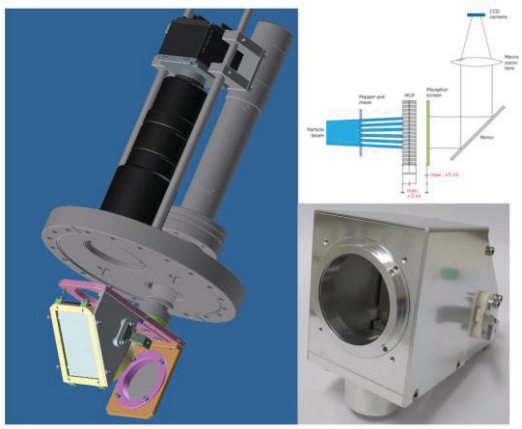

Figure 6: Emittance meter system. (Left) 3D model Schematic of the pepper-pot emittance meter. (Right) scheme of the ion beam imaging system [11].

MCP Detector

The MCP (Micro Channel Plate) detector consists of a MCP screenbacked by a P46 phosphor screen spaced by few millimeters gap. The MCP screen is a matrix of thousands of miniature electron multipliers oriented parallel to one another and fabricated on a lead glass. The length to diameter ratio of each channel is typically around 60, and the channel axis is normally biased at a small angle to the MCP input surface. Thus the incident particle can strike out a large number of secondary electrons when a typical voltage of 1 kV is applied between the two sides of the MCP. With a typical gain of several 10^4 it provides the capability to detect single ion. Since this detector is fast, it is also used for obtaining the time-of-flight information on ions. An assembly of two MCPs is often used to enhance the signal multiplication. An Einzel lens and an attenuator can be mounted in front of the MCP screen for high-sensitivity detection.

As each ion reaches the MCP detector plane, its arrival time is binned appropriately, creating a time of flight histogram for each extracted ensemble that simulates the experimental ion signal recorded by the MCP detector. These signals imitate the temporal distribution of extracted cooled beam and possible contaminants.

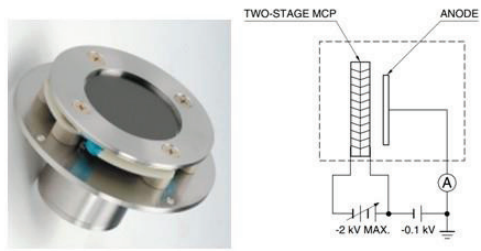

Figure 7: MCP detector system. (Left) schematic of the MCP, (right) MCP bias diagram of MCP when detecting positive ions [12].

CONCLUSION

RFQCB capable to handle high intensity rare isotope DC ion beams has been designed for future RAON facility. Based on the RFQ CB design presented in this paper, the manufacturing of the various subsystems (electric system, vacuum system, control system, (DAQ) has been started. Described ion beam diagnostic tools will be used for RFQCB off-line commissioning.

REFERENCES

[1] D-O-Jeon, "Status of RAON accelerator systems", RISP Workshop on Accelerator Systems, 19 May 2013, http://indico.risp.re.kr/indico/conferenceOtherViews.py?view=standard&confId=2

[2] S-K.Kim, "Status of rare isotope science project", RISP Workshop on Accelerator Systems, May 2013, http://indico.risp.re.kr/indico/conferenceOtherViews.py?view=standard&confId=2

[3] S. Jeong, "Progress of the RAON Heavy Ion Accelerator Project in Korea", *7th Int. Particle Accelerator Conf. (IPAC'16)*, Busan, Korea, May 2016, paper MOAB01.

[4] I.-S.Hong *et al.*,*Nucl. Instrum. Meth. B 317* (2013) 248-352,http://dx.doi.org/10.1016/j.nimb.2013.08.047

[5] S.Kondrashev*et al.*,"Advance EBIS Charge Breeder for Rare Isotope Science Project", Proceeding of *IPAC2016*, ISBN 978-3-95450-147-24, Busan, Korea.

[6] R.Boussaid *et al.*, *Phys. Rev. ST. Accel. Beams 18*, 072802(2015), DOI: http://dx.doi.org/10.1103/PhysRevSTAB.18.072802

[7] M. D. Lunney and R. B. Moore, Int. J. Mass Spectrom.190/191,153(1999). http://dx.doi.org/10.1016/S1-3873806(99)0000-93

[8] D.A. Dah 2000 Simion 3D V8.0 User Manual, Idaho National Engineering Laboratory, Idaho Falls U.S.A.

[9] A. Jokinen *et al.*, Nucl. Instrum. Meth. B204 86 (2003) http://dx.doi.org/10.1016/S0-168583X(02)01894-3

[10] S.Kondrashev *et al.*,"Emittance measurement for stable and radioactive ion beams", proceeding of LINAC2010, TUP086, Tsukuba, Japan.

[11] R. Boussaid, Study and development of buffer gas RFquadrupole cooler for radioactive and very intense ion beams, Ph.D. thesis, Caen Basse-normandie University, France, 2012. https://tel.archivesouvertes.fr/tel00787132/document

[12] Technical report, MCP assembly, HAMAMATSU Inc.,http://www.triumf.ca/sites/default/files/Hamamatsu%20MCP%20guide.pdf

ISBN 978-3-95450-177-9

SINGLE PULSE SUB-PICOCOULOMB CHARGE MEASURED BY A TURBO-ICT IN A LASER PLASMA ACCELERATOR

F. Stulle*, J. Bergoz, Bergoz Instrumentation, Saint-Genis-Pouilly, France
W.P. Leemans, K. Nakamura, Lawrence Berkeley National Laboratory, Berkeley, CA 94720, USA

Abstract

Experiments at the Berkeley Lab Laser Accelerator (BELLA) verified that the Turbo-ICT allows high resolution charge measurements even in the presence of strong background signals. For comparison, a Turbo-ICT and a conventional ICT were installed on the BELLA petawatt beamline, both sharing the same vacuum flanges. We report on measurements performed using a gas-jet and a capillary-discharge based laser plasma accelerator. In both setups the Turbo-ICT was able to resolve sub-picocoulomb charges.

INTRODUCTION

Imaging plates and scintillating screens are widely used in laser plasma accelerators (LPAs) for beam diagnostics [1-3]. They allow accurate measurements of the transverse profiles and the bunch charges even in the presence of strong background signals, which often accompany the beam signal due to the LPA working principle. For example, the laser – plasma interaction creates a strong electromagnetic pulse. However, plates and screens are obstacles for the particle beam, degrading beam quality or even capturing particles. And they are susceptible to X-rays. Complementing them by non-destructive charge diagnostics would be highly desirable.

One possibility would be to use integrating current transformers (ICTs) [4]. Previous studies comparing an ICT to a scintillating screen at a gas-jet based LPA [5] have shown that an ICT can provide accurate charge information for this type of accelerators [6]. However, the measurement setup needed to be carefully arranged to reduce the detrimental influence of electromagnetic pulses and other background signals. Capillary-discharge based LPAs [7-10] create even stronger background signals. Consequently, the beam diagnostic must be even less sensitive to such influences.

Examples of ICT signals recorded at a gas-jet based LPA and a capillary-discharge based LPA are shown in Fig. 1 and 2. Note that the background signals were highly variable.

At the gas-jet based LPA the background is a mostly constant offset. For the deduction of the charge a constant background is irrelevant. At the capillary-discharge based LPA the background contributes higher frequency components to the measured signal. This background signal has an important impact on the deduction of the charge.

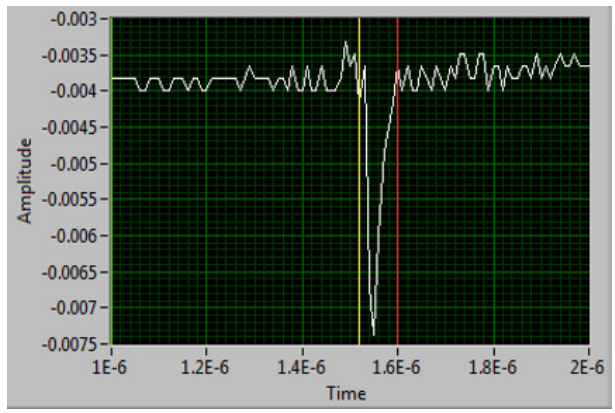

Figure 1: ICT signal recorded in a gas-jet based LPA. The peak between the yellow and red lines is the signal induced by a 10 pC bunch. The constant offset is irrelevant for the deduction of the charge.

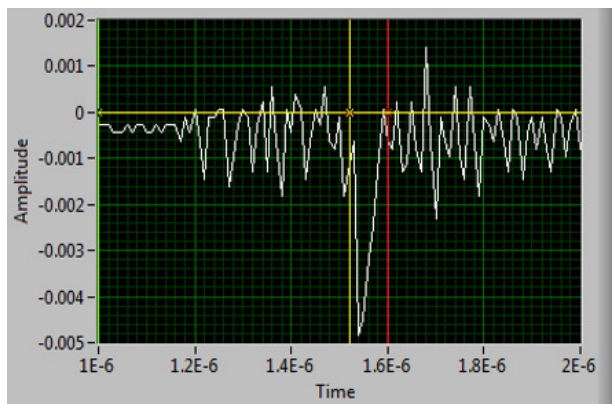

Figure 2: ICT signal recorded in a capillary-discharge based LPA. The peak between the yellow and red lines is the signal induced by a 18 pC bunch.

The Turbo-ICT current transformer and the corresponding BCM-RF electronics have been developed to address the requirements of X-ray free-electron lasers (X-FELs) and LPAs. Thanks to narrow band-pass filtering at a high center frequency, typically 180 MHz, they show little susceptibility to background signals, including electromagnetic pulses, dark current and long particle bunch tails.

To demonstrate the Turbo-ICT advantages for LPAs, a Turbo-ICT was installed in the Berkeley Lab Laser Accelerator (BELLA) petawatt beamline at the Lawrence Berkeley National Laboratory [10]. For comparison, a normal ICT was included in the same vacuum flanges as the Turbo-ICT.

*stulle@bergoz.com

ISBN 978-3-95450-177-9

In this paper we compare experimental results obtained by the Turbo-ICT and the ICT. Measurements were performed using a gas-jet target and a capillary-discharge based target. A comparison including measurements by a scintillating screen was reported in [11].

EXPERIMENTAL SETUP

The BELLA petawatt beamline could be operated using a gas-jet target or a capillary-discharge target. In these targets the plasma was created and the interaction with the laser took place. Since the particle beam created at the laser – plasma interaction point could contain particles of high angular divergence, the beam was collimated before reaching the diagnostics instruments. After passing a spectrometer, the beam was dumped.

A simplified sketch of the experimental setup is shown in Figure 3. More details about the experiments and the BELLA petawatt beamline can be found in [11] and [12].

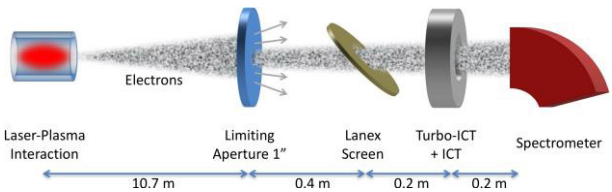

Figure 3: Schematic of the measurement setup

Using two kinds of laser targets allowed to compare the charge diagnostics under considerably different noise conditions. The background signals not only differed in amplitude but also in spectrum. The capillary-discharge based LPA produced a stronger background reaching to higher frequencies.

The ICT was sensitive to the low frequency part of the beam spectrum ranging from about a kHz to above 10 MHz. Its output pulse had a FWHM of about 30 ns. Integrating this pulse over a short time interval resulted a value proportional to the input pulse charge. Unfortunately, in LPAs the frequency range covered by the ICT has been found to be prone to strong noise contributions [2, 6].

The Turbo-ICT was sensitive to higher frequencies of the beam spectrum. Its response was centered around 180 MHz with a bandwidth of 15 MHz. By using such a frequency band its output signal was not a pulse but a resonance. The apex of this resonance was proportional to the input pulse charge.

Figure 4 shows the expected output resonance of the Turbo-ICT installed at BELLA. This signal was reconstructed from vector network analyzer measurements performed in the laboratory prior to installation. To be comparable to the oscilloscope measurements (Tektronix DSO3054, 500 MHz bandwidth, 2.5 GS/s) performed during the experiments, the influence of cable losses and oscilloscope bandwidth was estimated and taken into account for the calculation of the signal shown.

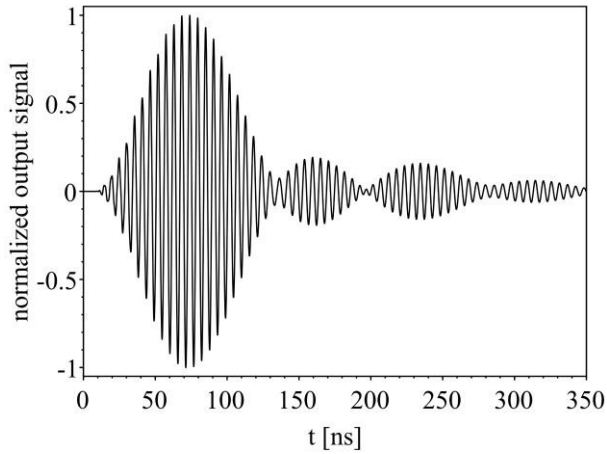

Figure 4: Normalized Turbo-ICT output signal as deduced from laboratory measurements and taking into account the influence of the experimental setup.

The Turbo-ICT bandwidth was similar to the ICT bandwidth. But working at higher frequencies had the advantage of avoiding many sources of random noise or systematic background signals.

If the spectra of the background signals are known prior to Turbo-ICT production, its center frequency can be shifted to a quiet band. A detailed description of Turbo-ICT and BCM-RF is given in [13].

During the experiments, the signal of the ICT was recorded by a 100 MS/s digitizer (National Instruments NI-USB 5133). Digitizing its output waveform allowed to compensate for the influence of low frequency background signals. The resulting waveform was integrated. Cable attenuation was not relevant for these measurements.

The Turbo-ICT signal was detected using the BCM-RF electronics, which created a DC voltage logarithmically proportional to input charge. This DC voltage was also recorded by above-mentioned digitizer. Turbo-ICT and BCM-RF were connected by 90 ft of LMR-200 coax cable. The cable attenuation at the Turbo-ICT resonance frequency was estimated to be 4.3 dB, which was taken into account for the deduction of the charge.

ICT, Turbo-ICT and BCM-RF were calibrated prior to installation using their respective calibration procedures. Thanks to sharing the same vacuum flanges, ICT and Turbo-ICT simultaneously measured exactly the same electron beam. That means, in average they should result the same charge readings. Only their respective noise should differ.

RESULTS USING A GAS-JET TARGET

For the gas-jet based LPA, Figure 5 shows the charge measured by the ICT versus the charge measured by Turbo-ICT. The plot reveals a very good linear correlation between the two diagnostics systems. Fitting a line to the data results:

$$Q_{\mathrm{fit}} = 0.88\, Q_{\mathrm{Turbo-ICT}} + 0.13\ \mathrm{pC}\,.$$

ISBN 978-3-95450-177-9

The major contribution to the data scatter around the fit line can be addressed to the noise present in the ICT measurements. This fact can be deduced from the distribution of the data points. After removing the linear correlation, the standard deviation of the data points is:

$$\sigma_{\mathrm{ICT}} = 1.3\ \mathrm{pC}\,.$$

The standard deviation varies from 1.0 pC at low charge to 2.4 pC at high charge. The noise of the Turbo-ICT measurements is too small to have a relevant impact. It must be well below 1 pC.

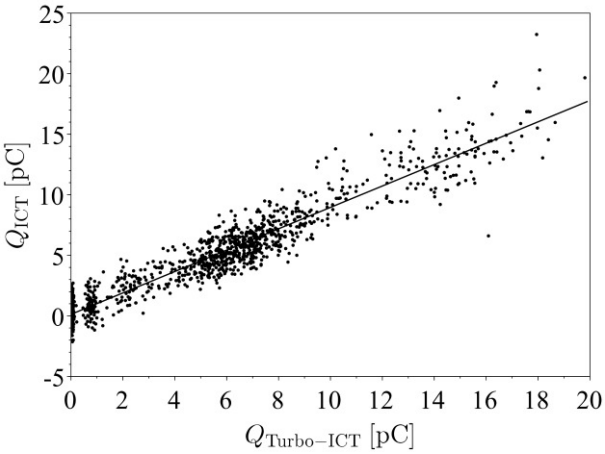

Figure 5: For the gas-jet based LPA, charge measured by the ICT versus charge measured by the Turbo-ICT. The line is a linear fit to the data.

That the fit slope does not equal unity means a small systematic error must have been present during the measurements. Possible causes are errors in the experimental setup, e.g. insufficiently compensated cable attenuation, errors in the data analysis, e.g. the calculation of charge from the digitized ICT signal, or the influence of a systematic background signal proportional to charge.

The small fit offset of 0.13 pC is not relevant, because it is well below the ICT noise level. Such a small offset could have been induced by many effects. It does not even have a high statistical significance.

Turbo-ICT Output Signal

The noise immunity of the Turbo-ICT was further examined by measuring the Turbo-ICT output signal directly on an oscilloscope, i.e. without using the BCM-RF (Figure 6).

The measured response agrees very well with the expected Turbo-ICT output signal deduced from vector network analyzer data and assuming an infinitely short input pulse (compare Figure 4).

Minor differences are visible. But the contribution of noise remains irrelevant, i.e. at the level of the oscilloscope accuracy and noise. Note that only the signal around the resonance apex is relevant for the determination of the input charge.

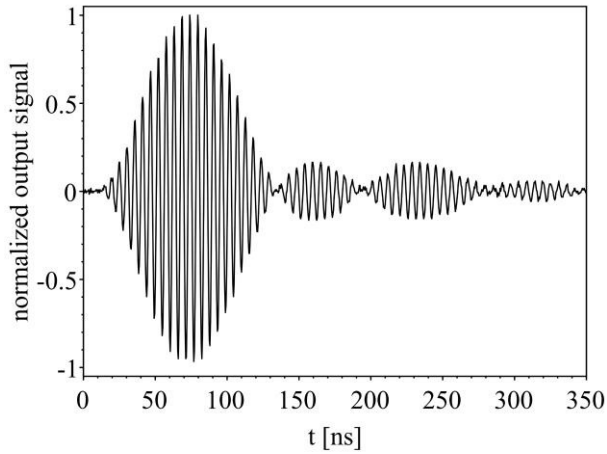

Figure 6: Normalized Turbo-ICT output signal measured on an oscilloscope.

RESULTS USING A CAPILLARY-DISCHARGE TARGET

For the capillary-discharge based LPA, Figure 7 shows the charge measured by the ICT versus the charge measured by Turbo-ICT. The data still exhibits a linear correlation. But the data scatter is considerably stronger. Furthermore, the data consists of two parallel bands of similar properties with an offset of about 30 pC. Linear fits to these two bands result:

$$Q_{\mathrm{fit1}} = 0.83\ Q_{\mathrm{Turbo-ICT}} + 26.6\ \mathrm{pC}$$
$$Q_{\mathrm{fit2}} = 0.82\ Q_{\mathrm{Turbo-ICT}} - 3.75\ \mathrm{pC}\,.$$

Their respective standard deviations are:

$$\sigma_1 = 8.5\ \mathrm{pC}$$
$$\sigma_2 = 8.2\ \mathrm{pC}\,.$$

Since the banding was only recognized during data analysis, its cause could not be investigated in detail. In the experimental data at hand no clear correlation to other measured quantities was found. A possible explanation could be timing jitter between the beam and a short background signal sometimes falling within the ICT integration window and sometimes not.

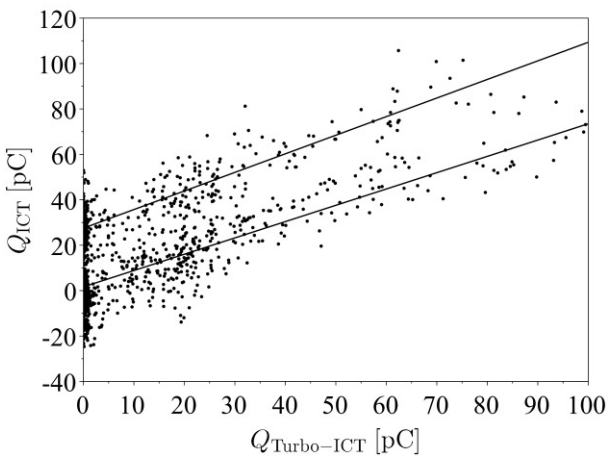

Figure 7: For the capillary-discharge based LPA, charge measured by the ICT versus charge measured by the Turbo-ICT. The data splits into two parallel bands. The lines are linear fits to these bands.

ISBN 978-3-95450-177-9

As for the gas-jet measurements, the noise captured by the ICT contributed most to the data scatter. Without banding the standard deviation of the ICT measurements would be:

$$\sigma_{\mathrm{ICT}} = 8.4\ \mathrm{pC}\,.$$

Calculating the standard deviation over the full data set, i.e. including banding, results in:

$$\sigma_{\mathrm{ICT}} = 16.9\ \mathrm{pC}\,.$$

The quality of the data is only sufficient to deduce an upper limit for the Turbo-ICT noise of a few pC.

The fit slopes of 0.83 and 0.82, respectively, are very similar to the fit slope of 0.88 obtained with the gas-jet target. This fact signifies that most likely errors in the experimental setup or data analysis caused the slope deviating from unity. The experimental setup and data analysis remained unchanged except for the laser target. But the background signals changed considerably. Hence, the fit slopes should have differed more between gas-jet measurements and capillary-discharge measurements if background signals would have had a major influence.

On the other hand, the strong offsets of the two bands of 26.6 pC and -3.75 pC, respectively, must have been caused by background signals impacting the ICT measurements.

CONCLUSION

Experiments have been carried out at the BELLA petawatt beamline to examine the suitability of a Turbo-ICT current transformer and the corresponding BCM-RF electronics for accurate charge measurements at LPAs.

For comparison, a Turbo-ICT and a conventional ICT were installed inside the same vacuum flanges, ensuring that they measure the same particle beams. To test the charge diagnostics under different noise conditions, the LPA was operated using a gas-jet target and a capillary-discharge target.

For both LPA targets, Turbo-ICT and ICT measurements correlated linearly. But the ICT measurements contained a considerable amount of noise, reaching $\sigma_{\mathrm{ICT}} = 1.3\ \mathrm{pC}$ for the gas-jet target and $\sigma_{\mathrm{ICT}} = 8.4\ \mathrm{pC}$ for the capillary-discharge target. On the other hand, the noise of the Turbo-ICT measurements was at such small levels that its contribution remained invisible in the data.

Consequently, the ICT and the Turbo-ICT proved to be useful charge diagnostics for gas-jet based LPAs. But only the Turbo-ICT allows to resolve sub-picocoulomb charges.

For capillary-discharge based LPAs, the ICT provides useful information only after careful setup and if the beam charge is at least of the order of a few 10 pC, while the Turbo-ICT still resolves at least picocoulomb pulses.

ACKNOWLEDGMENTS

This work was performed as part of a collaboration between the BELLA Center, Lawrence Berkeley Laboratory, and Bergoz Instrumentation. The work by the BELLA Center scientists and staff was supported by Office of Science, Office of HEP, US DOE under Contract DE-AC02-05CH11231 and the National Science Foundation.

The authors gratefully acknowledge the contributions from J. Daniels, A.J. Gonsalves, H.-S. Mao, D. Mittelberger and C. Toth and the technical support from A. Deshmukh, D. Evans, M. Kirkpatrick, A. Magana, G. Mannino, J. Riley, K. Sihler, T. Sipla, D. Syversrud and N. Ybarrolaza.

REFERENCES

[1] K.A. Tanaka et al., “Calibration of imaging plate for high energy electron spectrometer”, *Rev. Sci. Instrm* . vol. 76, 013507, 2005.

[2] Y. Glinec et al., “Absolute calibration for a broad range single shot electron spectrometer”, *Rev. Sci. Instrm.* vol. 77, 103301, 2006.

[3] B. Hidding et al., “Novel method for characterizing relativistic electron beams in a harsh laser-plasma environment”, *Rev. Sci. Instrum.* vol. 78, 083301, 2007.

[4] K.B. Unser, “Design and preliminary tests of a beam intensity monitor for LEP”, Proc. of *Particle Accelerator Conference* (PAC’89), Chicago, USA, 1989, paper , pp. 71-73.

[5] M. Krishnan et al., “Electromagnetically driven, fast opening and closing gas jet valve”, *Phys. Rev. ST Acc. Beams* vol. 14, 033502, 2011.

[6] K. Nakamura et al., “Electron beam charge diagnostics for laser plasma accelerators”, *Phys. Rev. ST Acc. Beams* vol. 14, 062801, 2011.

[7] D.J. Spence, S.M. Hooker, “Investigation of a hydrogen plasma waveguide”, *Phys. Rev.* E vol. 63, 015401, 2001.

[8] W.P. Leemans et al., “GeV electron beams from a centimeter-scale accelerator”, *Nat. Phys.* vol. 2, 2006, pp. 696-699.

[9] A.J. Gonsalves et al., “Tunable laser plasma accelerator based on longitudinal density tailoring”, *Nat. Phys.* vol. 7, 2011, pp. 862-866.

[10] W.P. Leemans et al., “Multi-GeV electron beams from capillary-discharge-guided subpetawatt laser pulses in the self-trapping regime”, *Phys. Rev. Lett.* vol. 113, 245002, 2014.

[11] K. Nakamura et al., “Pico-coulomb charge measured at BELLA to percent-level precision using a Turbo-ICT”, *Plasma Physics and Controlled Fusion* vol. 58, no. 3, 2016.

[12] A.J. Gonsalves et al., “Generation and pointing stabilization of multi-GeV electron beams from a laser plasma accelerator driven in a pre-formed plasma waveguide”, Phys. of Plasmas vol. 22, 056703, 2015

[13] F. Stulle, J. Bergoz, “Turbo-ICT pico-coulomb calibration to percent-level accuracy”, Proc. of *Free Electron Laser Conference* (FEL’15), Daejeon, South Korea, 2015, paper MOP041.

ISBN 978-3-95450-177-9

TIMING WINDOW AND OPTIMIZATION FOR POSITION RESOLUTION AND ENERGY CALIBRATION OF SCINTILLATION DETECTOR

Jing Zhu, Meihau Fang, Jing Wang, Zhiyong Wei§,
Nanjing University of Aeronautics and Astronautics, Nanjing 210016, P. R. China

Abstract

We studied fast plastic scintillation detector array. The array consists of four cuboid bars of EJ200， each bar with PMT readout at both ends. The geometry of the detector, energy deposition in the scintillator， signal generation and energy response have been simulated based on Monte Carlo. The detection efficiency and the real events selection have been obtained while the background noise has been reduced by using two-end readout timing window coincidence. We developed an off-line analysis code, which is suitable for massive data from the digitizer. We set different coincidence timing windows, and did the off-line data processing respectively. It can be shown that the detection efficiency increases as the width of the timing window increases, and when the width of timing window is more than 10 ns, the detection efficiency will slowly grow until it reaches saturation. Therefore, the best timing window parameter τ as 16 ns is obtained for the on-line coincidence measurement. When exposure to ^{137}Cs γ -ray irradiation, a 12 cm position resolution can be achieved while reaching the timing resolution of 0.9 ns. The pulse integration of signals of the detector is in proportion to the energy of incident particles. Furthermore, the geometrical mean of the dual-ended signals, which is almost independent of the hit position, could be used as the particle energy. Therefore, this geometrical mean as the energy of incident particle is calibrated via the Compton edges of ^{60}Co source, ^{137}Cs source and the natural ^{40}K, ^{208}Tl, and the reliability of the calibration results has been improved. Besides, the energy response is linear.

INTRODUCTION

When an incident particle interacts in a scintillator, it can cause ionization and excitation of the atoms and molecules of the scintillator. The energy of the incident particle is deposited in the scintillator [1]. The decay of excited atoms and molecules back to their ground states results in a emission of photons with two decay components: the fast one with decay time less than a nanosecond， and the slow one has decay time of hundreds of nanoseconds. The photons are collected on photocathode of the photomultiplier tube (PMT), and then these photons are converted to photoelectrons and amplified. The output signals of the scintillation detector depend on both the energy and the hit position of the incident particle. Besides, false signals come from the dark current and noise also. When the dual-ended readout is taken, we need methods to get hit position and energy of the particles, and also need to select the real events [2]. In this paper, we got real events from incident particles with the background noise reduced by using two-end readout timing window coincidence.

EJ-200 plastic scintillation detector array and its data acquisition system have been set up for radiation measurement in our laboratory. The scintillation detector array consists of four EJ-200 plastic scintillators which have dual-ended PMTs. The EJ-200 plastic scintillator combines two main benefits of long optical attenuation length and fast timing. On the basis of coincidence measurement, we picked out the real events from the timing window of signals, and optimized the timing resolution, position resolution and energy response of the detector.

SCINTILLATION DETECTION AND DATA ACQUISITION SYSTEM

The plastic scintillator used in this work was provided by the ELJEN Enterprises, USA. The scintillator (denoted by the ELJEN number EJ-200) had dimensions: 5 cm × 5 cm × 125 cm. The decay time of the scintillator is at the level of ns, and the rise time is less than 1 ns. The EJ-200 plastic scintillator was coupled to an ET Enterprises 9813B PMT. A VME bus system was used in our laboratory, and a schematic diagram of the detection system is shown in Fig. 1.

The DT5751 is a 4 channels 10 bit 1 GS/s Desktop Waveform Digitizer with 1 Vpp input dynamic range on single ended MCX coaxial connectors. The DT5751 Waveform Digitizer, which is taken in on-line coincidence measurement, has replaced some complex modules in the traditional coincidence circuits.

The V6533 is a 6 channels High Voltage Power Supply in 1 unit wide VME 6U module.

The online Digital Pulse Processing for Pulse Shape Discrimination firmware (DPP-PSD) was used in this study. Under the frame of DPP-PSD, we got the on-line waveforms and the energy histograms. Besides, the lists for the on-line data were obtained from the digitizer, and were further processed by ROOT, an off-line data-analysis software.

§ email address: wzy_msc@nuaa.edu.cn

ISBN 978-3-95450-177-9

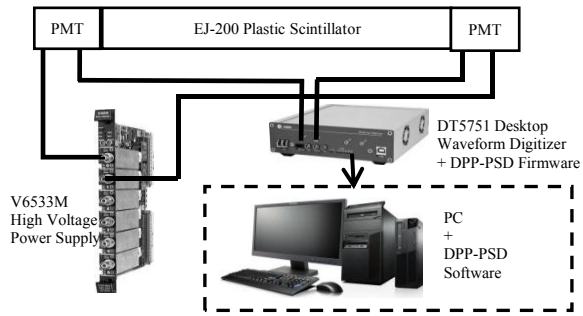

Figure 1: Schematic diagram of the experimental setup.

SIMULATION AND ITS RESULTS

The core idea of the coincidence measurement is to pick out the real event according to the timing window of signals. The key technical parameter of the coincidence circuits is the coincidence timing window τ. See in Fig. 2, if x, the distance between the hit position and the left side of the scintillator, corresponds to time t_1, and L-x, the distance between the hit position and the right side of the scintillator, corresponds to time t_2, then, the timing window of signals can be represented by $\tau = |t_1 - t_2|$. If the incident particles hit in the middle of the detector, $|t_1 - t_2| = 0$; If the incident particles hit in either end of the detector, $|t_1 - t_2|$ is up to the maximum value of the timing window. The true events take place in the span of $|t_1 - t_2|$. When the time interval between two pulses is less than τ, it outputs the coincidence pulse; otherwise it rejects. The timing window parameter can be used both in on-line analysis and off-line analysis.

The detector has been simulated based on Monte Carlo, including its geometry and particle interactions in the scintillator.

In Fig. 2, x, the distance between the hit position and the left side of the scintillator, is shown, and Δt, the time difference between the signals at both ends of the detector, is shown in Fig. 3, then, the $\Delta t - x$ curve is simulated in Fig. 4.

In Fig. 4, the time difference of signals at both ends of the scintillator is linear to the distance x, and $\Delta t - x$ is linear up to 9 ns. Considering the transit-time jitter of the PMT, which is determined as 1.17 ns, then, the maximum time difference in case of a true event is estimated to be 11 ns.

We developed an off-line analysis code, which is suitable for massive data from the digitizer, in order to find a reasonable timing resolution window for on-line experiment. The detection efficiency $\varepsilon_c(t)$ can be expressed as the ratio between the number of the coincidence particles(denoted by N_c) and the number of the particles produced by the radiation source during detection (denoted by N), which as shown in Eq. (1):

$$\varepsilon_c(t) = \frac{N_c}{N} \times 100\% \quad . \qquad (1)$$

The simulations based on the ^{137}Cs γ-ray source were done. The experiment time is 1000 s. Set different coincidence timing windows, and do the off-line data processing respectively. Detection efficiency versus coincidence timing window is given in Fig. 5. The black dots in the figure stand for experiment data and the curve is a fitted curve obtained by the off-line programs based on ROOT. It can be observed that detection efficiency is changing over the value of the coincidence timing window, and the width of timing window is more than 10 ns, the detection efficiency will slowly grow until it reaches about 20%. Therefore, this paper sets the best timing window parameter τ as 16 ns for the on-line coincidence measurement.

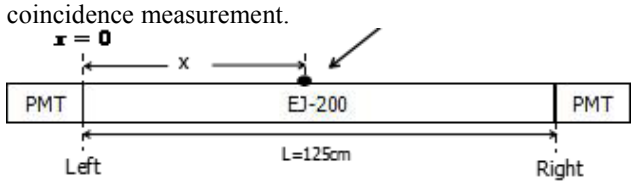

Figure 2: Schematic diagram of the distance between the hit position and the left side of the scintillator.

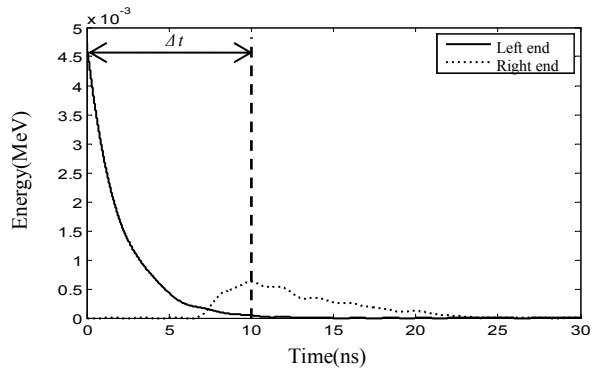

Figure 3: Schematic diagram of the time difference between the signals at both ends of the detector (x=0).

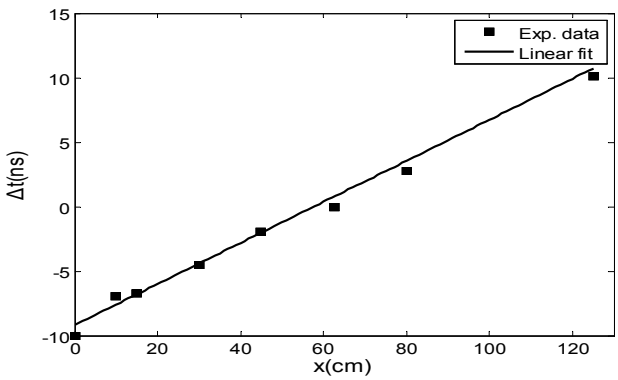

Figure 4: Δt (ns) , time difference of signals at both ends of the detector vs. x (cm), the distance between the hit position and the left side of the scintillator.

POSITION RESOLUTION AND ENERGY RESPONSE

This paper finds the best coincidence timing window parameter as 16 ns for the on-line coincidence measurement, see Fig. 5.

ISBN 978-3-95450-177-9

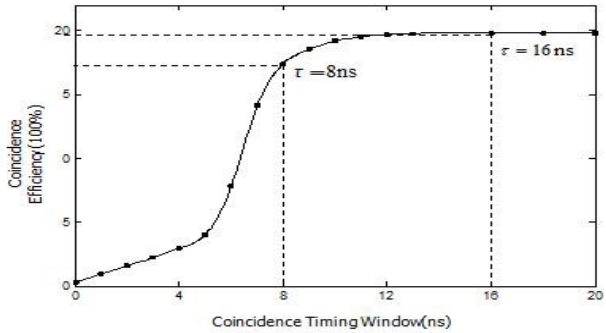

Figure 5: Detection efficiency vs. the coincidence timing window for the scintillation detector.

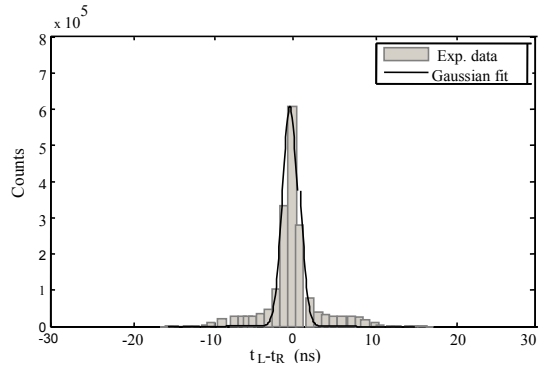

(a) in the middle

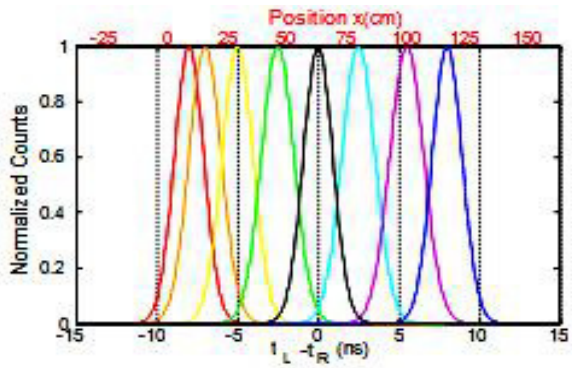

(b) on different positions

Figure 6: Time difference of signals generated from real events at both ends of the scintillator through Gaussian fitting with the ^{137}Cs source (a) in the middle of the scintillator and (b) on different positions.

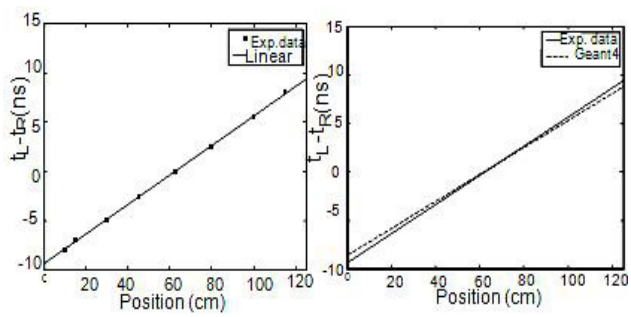

Figure 7: Time difference versus the position of the radiation source : experiment results (left) and simulation results by Geant4 code (right).

Since the two PMTs at both end of the plastic scintillation detector studied in this work are nearly the same, the timing resolution of the detector, σ_t , can be defined as Eq. (2):

$$\sigma_t^2 = \sigma_1^2 + \sigma_2^2 . \quad (2)$$

Where σ_1 and σ_2 represent the timing resolution at each end of the detector, respectively. Besides, if the scintillator used in this work has the intrinsic timing resolution (denoted by σ_s) and substituting the transit-time spread of the PMT, σ_{PMT} , for its timing resolution [3], and then σ_t , the timing resolution of the scintillation detector in this work can be represented by Eq. (3):

$$\sigma_t^2 = \sigma_s^2 + 2\sigma_{PMT}^2 . \quad (3)$$

The effective transmission speed of the signals in the scintillator is represented by c_{eff} [4]. Furthermore, it has been concluded that the integral charge of the signals at both ends, $\ln(Q_L/Q_R)$, is linearly associated with x. Therefore, the position resolution σ_x is shown as Eq. (4):

$$\sigma_x = \sigma_t \times c_{eff} . \quad (4)$$

By exposing the scintillation detector to the ^{137}Cs γ -ray source, a timing resolution of 0.9 ns is reached (when the best coincidence timing window $\tau = 16$ ns), see Fig. 6. Time difference of signals, which is generated from real events at both ends of the scintillator, and the position of the radiation source is near to a linear relationship (see Fig. 7), which fits the simulation results by Geant4. In Fig. 7, the slope of the fit line is 0.15, and the position resolution of the detector reaches 12 cm. The pulse integration of signals of the detector is in proportion to the energy of incident particles [5]. Furthermore, the geometrical mean of the dual-ended signals, which is almost independent of the hit position, could be used as the particle energy (see Eq. (5)):

$$Q_{GM} = \sqrt{Q_L Q_R} . \quad (5)$$

Where Q_{GM} represents the the geometrical mean of the dual-ended signals, and Q_L (or Q_R) represents the integral charge of the signals at the left (or right) end of the detector .

Therefore, this geometrical mean as the energy of incident particle is calibrated via the Compton edges of ^{60}Co source, ^{137}Cs source and the natural ^{40}K, ^{208}Tl, and the reliability of the calibration results has been improved. The gamma ray energy, E_γ, Compton edges, E_0, the ADC number of the photopeak, ch_p, the standard deviation of the photopeak, σ, the ADC number of the Compton edges,

ISBN 978-3-95450-177-9

ch_c, are listed in Table 1. The energy calibration of the detector see Fig. 8. It is shown that the energy response is linear within the lower energy range.

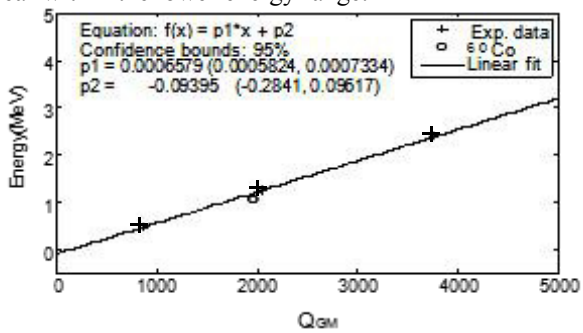

Figure 8: The energy calibration of the detector : crosses are experimental data and the curve represents the best-fitting.

Table 1: The Compton Edges of Different Radioactive Sources

γ	$E_{\gamma(MeV)}$	$E_{0(MeV)}$	ch_p	σ	ch_c
^{60}Co	1.173 1.333	1.0408	1603	312	1968
^{137}Cs	0.662	0.4777	679	154	860
^{40}K	1.461	1.2435	1710	289	2048
^{208}Tl	2.614	2.3812	3148	520	3756

CONCLUSION

The real event selection, timing resolution, position resolution and energy response of the EJ-200 plastic scintillation detector have been analyzed using timing window coincidence measurement. The detector was simulated based on Monte Carlo, including its geometry, energy deposition in the scintillator, photon collection and signal generation. The decay time of the pulse of scintillator is at the level of ns, and the rise time is less than 1 ns. Theoretical derivation and simulation results showed that Δt , time difference of signals at both ends of the detector, was linear with x, distance between the hit position and the left side of the scintillator, and Δt -x curve was linear up to 9 ns. Besides, time and position response have been measured by exposing to a ^{137}Cs γ -ray source. The best coincidence timing window parameter is 16 ns, and the position resolution is up to 12 cm. Since the pulse integration of signals of the detector is in proportion to the energy of incident particles, the geometrical mean of the dual-ended signals, which is almost independent of the hit position, could be used as the particle energy to calibrate the energy response of the detector via the Compton edges of ^{60}Co source, ^{137}Cs source and the natural ^{40}K, ^{208}Tl. The reliability of the calibration results has been improved. It was shown that the energy response of the detector was linear within the experimental energy range.

REFERENCES

[1] A. V. Kuznetsov *et al.*, “Position-sensitive neutron detector”, *Nuclear Instruments and Methods in Physics Research A*, vol. 477, pp. 372–377, 2002.

[2] Wu, Zhihua *et al.*, *The research methods of nuclear physics,* Beijing: Atomic Energy Press, 1997.

[3] Liu,Yang *et al.*, ”Measurement of TTS of Fine-Mesh PMT with Cherenkov Light”, *Journal of University of Science and Technology of China*, vol. 35, no. 5, pp. 608-612, 2005.

[4] L. Lüdemann, K. Knoche *et al.*, ”A Large-area Position-sensitive Detector for Fast Neutrons”, *Nuclear Instruments and Methods in Physics Research A*, vol. 334, pp. 495-503, 1993.

[5] L. Karsch, A. Bohm *et al.*, ”Design and Test of A Large-area Scintillation Detector for Fast Neutrons ” , *Nuclear Instruments and Methods in Physics Research A*, vol. 460, pp. 362-367, 2001.

ISBN 978-3-95450-177-9

COMPARATIVE STUDY OF MAGNETIC PROPERTIES FOR CERN BEAM CURRENT TRANSFORMERS

S. Aguilera[1,*] , H. Hofmann[1], P. Odier
CERN, Geneva, Switzerland
[1]also at École Polytechnique Fédérale de Lausanne, Lausanne, Switzerland

Abstract

At CERN, the circulating beam current measurement is provided by two types of transformer, the Direct Current Current Transformer and the Fast Beam Current Transformer. Each transformer is built based on toroidal cores made from a soft magnetic material. Depending on the type of measurement to be performed these cores require different magnetic characteristics for parameters such as permeability, coercivity and the shape of the magnetisation curve. In order to study the effect of changes in these parameters on the current transformers, several interesting raw materials based on their as-cast properties were selected. The materials have been characterised to determine their crystallisation, melting and Curie Temperatures in order to determine suitable annealing processes to tailor their properties. They have been analysed by several techniques including Electron Microscopy and X-ray Diffraction. As-cast magnetic properties such as the permeability, the B-H curve and Barkhausen noise have also been measured to enable the study of the effect of thermal treatment in the microstructure of the alloys, and the correlation of this with the change in the magnetic properties.

INTRODUCTION

The total electrical charge of the beam circulating in CERN's accelerators is measured by a family of devices that include current transformers, such as the DC Current Transformers (DCCT) and Fast Beam Current Transformers (FBCT) [1]. This measurement is especially crucial for tuning the beam transfer efficiency between accelerators, monitoring beam losses leading to possible radiation-related issues, assessing beam lifetime, as well as for safety measures to be taken based on the readings. There are a total of 96 transformers at CERN out of which 22 are DCCTs and 74 are FBCTs, coming in various sizes in order to adapt to different vacuum chamber dimensions.

The transformer cores are made out of wound ribbons of soft magnetic material which couple to the electro-magnetic fields accompanying the motion of the charged particle beams. Each type of transformer requires different magnetic materials in terms of permeability, coercivity and the shape of the magnetisation curve to obtain an optimal response for the differing beam parameters of each machine. The choice of material and the associated magnetic characteristics affects transformer parameters such as resolution in the case of the DCCT and bandwidth in case of the FBCT.

* silvia.aguilera@cern.ch

The study of commercially available soft magnetic materials, including physical properties such as crystallisation and melting temperatures, and magnetic properties like their Curie temperature and the magnetisation curve, will determine their suitability for each kind of instrument. With this information, a suitable annealing procedure can then be designed for each material. Thermal or thermo-magnetic annealing can drastically change the magnetic properties of the raw materials. The time and heating rate of annealing are the two key parameters that play a crucial role in the final result, enabling for example, the fabrication of nanocrystalline material. By being able to fabricate different cores, it is possible to study how these properties affect the final beam response of such systems in order to find the best solution for each type of application.

MATERIALS USED

For this study, the materials used were iron-based amorphous and nanocrystalline alloys and cobalt-based amorphous alloys. Two iron-based alloys were purchased from Qinhuangdao Yanqin Nano Science & Technology Co., Ltd., Nanocrystalline 107A1 and amorphous 2065, with the Iron-based amorphous alloy FINEMET® FT-3 bought from Hitachi Metals Europe GmbH. The amorphous cobalt-based materials were purchased from Nanostructured & Amorphous Materials (Nanoamor), Inc., VACUUMSCHMELZE GmbH & Co. KG as VAC 6025 G40 Z and alloy Metglas 2705M from Hitachi Metals. Several cores made out of iron-based nanocrystalline material NANOPERM® were also bought from MAGNETEC GmbH, to be used as a reference material in the study.

MATERIAL CHARACTERISATION

In order to thermally anneal the samples properly and understand the changes in their magnetic properties, it is first necessary to thoroughly characterise the alloys. Magnetic measurements like permeability, B-H curve and Barkhausen Noise will give an indication of the final performance of the material when in use in the instrument. Repeating these measurements after the annealing process then allows us to understand how the magnetic properties change during the treatment. The main goal being to tune the final magnetic properties through annealing.

Permeability and B-H Curve Measurements

The relative complex permeability was calculated from the impedance measured with the Agilent Vector Impedance Analyser 4294 in the range of 40 Hz to 110 MHz. Cores of

ISBN 978-3-95450-177-9

40 mm external diameter were used. The real and imaginary parts of permeability were derived from the in-series inductance and resistance of the core (following reference [2]) and uncertainty was calculated following [3]. The results are summarised in Table 1, where it can be seen that the iron-based materials (Yanqin and Finemet) have a lower permeability than the cobalt-based materials. All results have an uncertainty below 10 %.

Table 1: Maximum Relative Complex Permeability (μ_R) summary.

Sample	μ_R
Yanqin amorphous	1171
Yanqin nanocrystalline	697
Finemet FT-3	1219
VAC 6025 G40	165626
Nanoamor	158110
Metglas 2705M	250802

B-H curve measurements were performed at a frequency of 212 Hz on the same cores. Table 2 shows a summary of the coercivity and saturation derived from these measurements, where it can be seen that the cobalt-based alloys present a lower coercivity than the iron-based alloys.

Table 2: Coercivity (H_C) [A m^{-1}] and Saturation (B_{sat}) [T] for all Samples.

Sample	H_C [A m^{-1}]	B_{sat} [T]
Yanqin amorphous	14.98	0.27
Yanqin nanocrystalline	19.43	0.62
Finemet FT-3	14.37	0.18
VAC 6025 G40	7.62	0.50
Nanoamor	4.47	0.45
Metglas 2705M	9.63	0.59

Curie Temperature

The Curie temperature (T_C) is a key parameter for the annealing process. Above this, the material loses its magnetic properties. This makes the rearrangement of magnetic domains possible during the thermal treatment, which can therefore mean a change in the magnetic properties of the sample. Annealing over T_C, but below the crystallisation point also allows the sample to relax internal stresses generated during the fabrication process without changing the microstructure.

The Curie temperature was measured with a Thermo gravimetric Analysis Instrument (PerkinElmer TGA 4000) in a magnetic field. The PerkinElmer 4000 has an oven temperature uncertainty of 1.8 °C, and a sample temperature uncertainty of ±0.8 °C at 300 °C and ±1.5 °C at 900 °C. The balance uncertainty is ±0.03 % [4]. The total uncertainty for the measurement is ±2.6 °C. Table 3 shows the results for the heating curve at 10 °C min^{-1}.

Table 3: Curie Temperature (T_C) at 10 °C min^{-1}. Uncertainty for all measurements is ±2.6 °C

Sample	T_C [°C]
Yanqin amorphous	319
Yanqin nanocrystalline	405
Finemet FT-3	319
Magnetec	565
VAC 6025 G40	222
Nanoamor	223
Metglas 2705M	361

Crystallisation and Melting Point Characterisation

Crystallisation and melting temperatures are characteristic of each alloy that change with composition. They are therefore not only essential input for the annealing process, but also as a means to compare various alloys. The crystallisation temperature becomes the key parameter when the amorphous samples are to be transformed into nanocrystalline materials.

These measurements were performed with alumina pans in a Netzsch DSC 404 C under an argon atmosphere at 10 °C min^{-1}. All the curves were started from room temperature, as will be the case when the material are annealed in an oven. Table 4 summarises the onset and peak crystallisation temperatures found.

Table 4: Onset Crystallisation Temperature (T_O), Peak Crystallisation Temperature (T_P) and Area of the Curve (A) at 10 °C min^{-1}.

Sample	T_O[°C]	T_P[°C]	A[J g^{-1}]
Yanqin amor.	507.8	529.5	63.4
	686.0	700.0	19.3
Yanqin nano.	498.1	507.7	43.1
	540.3	544.8	67.7
Finemet FT-3	507.5	527.4	61.8
	695.1	703.8	26.2
Magnetec	681.4	693.3	16.4
	718.1	730.0	3.3
VAC 6025 G40	546.3	552.3	65.2
	613.1	638.4	33.7
Nanoamor	548.2	549.1	73.6
	597.4	626.4	7.9
Metglas 2705M	511.6	529.1	-
	-	554.2	72.3
	638.2	656.2	30.2

The onset melting temperatures (T_M) and their standard deviation (σ) are summarised in Table 5. It can be seen that the cobalt-based alloys have a melting temperature of about 100 °C lower than the iron-based alloys.

ISBN 978-3-95450-177-9

Table 5: Melting Temperatures

Sample	T_M [°C]	σ[°C]
Yanqin amor.	1102.4	0.2
Yanqin nano.	1139.1	0.5
Finemet FT-3	1102.6	0.5
Magnetec	1104.2	0.0
VAC 6025 G40	1011.7	1.0
Nanoamor	1007.6	1.4
Metglas 2705M	1007.1	2.6

X-ray Diffraction (XRD) Analyses

The XRD studies are a useful tool to check for the presence of ordered regions (crystals) in the samples. Changes in the microstructure of the alloy, being amorphous, nanocrystalline or completely crystalline, entirely changes its magnetic and mechanical properties. It is therefore important to know what state the material is in in its as-cast state and how it evolves under thermal treatment. A High-Energy XRD study will show the microstructure of the as-cast sample, while a High-Temperature in-situ XRD (HT-XRD) allows the evolution of the sample during thermal treatment to be studied.

For the High-Energy XRD the samples were analysed by Phase Solutions Co. Ltd. at the ESRF (European Synchrotron Radiation Facility), after pulverisation. The diffraction images were recorded at room temperature using an incident X-ray beam with a cross-section of 3 mm by 3 mm.

It can be seen from Table 6 that all of the samples present a certain degree of crystallinity. Only the Magnetec sample can be considered nanocrystalline (with crystals larger than 5 nm), as it has an average crystal size of 14.3 nm.

Table 6: Average Crystal Size and Standard Deviation (σ) Measured by HE-XRD

Sample	Average crystal size $\pm\sigma$ [nm]
Yanqin amorphous	1.6 ± 0.2
Yanqin nanocrystalline	1.5 ± 0.2
Finemet FT-3	2.0 ± 0.2
Magnetec	14.3 ± 0.2
VAC 6025 G40	2.0 ± 0.2
Nanoamor	2.2 ± 0.2
Metglas 2705M	1.9 ± 0.2

The HT-XRD experiments were performed in the Swiss Center for Electronics and Microtechnology (CSEM) in Neuchâtel. Samples were heated at a rate of 10 °C min^{-1} under a nitrogen atmosphere. Table 7 shows the crystallisation temperature results and the proposed crystalline composition of the samples studied up to now. The results are consistent both with the composition and the crystallisation temperature characterisation.

Table 7: Crystallisation Temperatures (T_X) and Crystal Composition Detected by HT-XRD

Sample	T_X [°C]	Crystal composition
Finemet FT-3	550 - 575	Co_2Si
Nanoamor	550 - 575	Co_2Si, $Co_{21}Mo_2B_6$
Metglas 2705M	550 - 575	Fe_3Si

Transmission Electron Microscopy (TEM)

TEM was used in Bright-Field (BF) and Dark-Field (DF) mode. In the BF mode, the electrons from the microscope interact with the sample and give a darker projection where the sample is thicker or denser or where there are heavier atoms, so giving information on the composition. To obtain a DF image, the Diffraction Pattern (DP) of the sample is first obtained. Then, a point in the DP can be selected for observation and this gives the DF image. The bright areas will be the ones diffracting in that particular direction. DF images can give information on defects or particle sizes in the samples.

TEM measurements were taken with a TECNAI OSIRIS microscope and an 11 Megapixel Gatan Orius CCD camera. This TEM has 0.24 nm point resolution and a 0.14 nm information limit. Figure 1 shows the bright field of the Magnetec sample. It can be seen that there are crystals of about 20 nm in size, which is consistent with the XRD analyses. The rest of the samples show crystalline regions of much smaller size as measured by XRD.

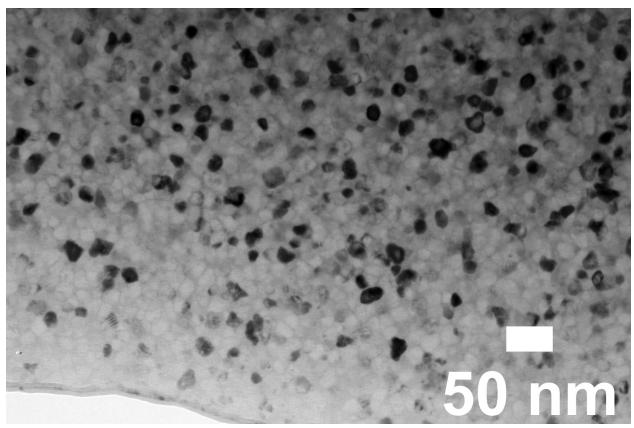

Figure 1: Bright-Field image of the Magnetec sample.

Figure 2 shows the DF image for the Magnetec sample and the DP in the insert. It can be seen that the diffracting crystals in this case are up to 25 nm in size, slightly bigger than the ones measured by XRD.

Barkausen Noise (BN) Measurements

Barkhausen noise measurements were performed using a setup based on that described in [5]. This was improved by additional common-mode chokes in order to limit the sensitivity of the setup to stray fields, and using a 30 mHz, 8 V peak-peak filtered triangular current for the driving solenoid.

ISBN 978-3-95450-177-9

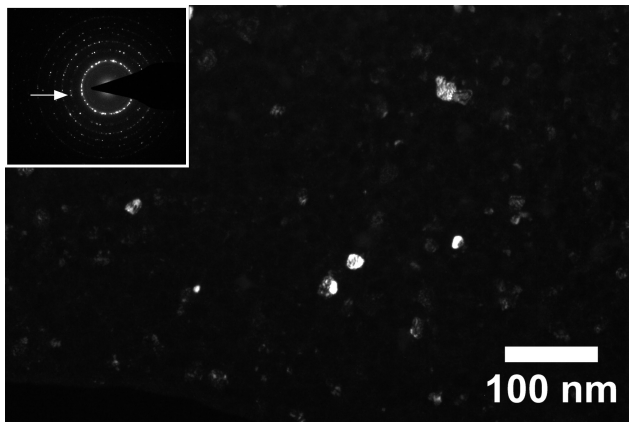

Figure 2: Dark-Field image of the Magnetec sample, the Diffraction Pattern can be seen in the insert.

50 averages were performed for each measurement. Figure 3 shows the BN measurement for Finemet (top) and the excitation signal (bottom). What can be seen is the voltage induced in the secondary coil surrounding the magnetic sample while it is subjected to the driving current. The voltage drops to zero when the sample is saturated.

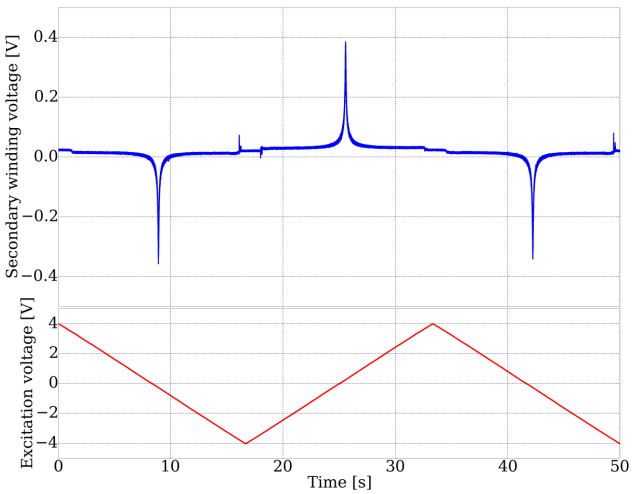

Figure 3: BN measurement for Finemet FT-3 (top) and excitation signal (bottom).

Figure 4 shows the BN (proportional to the secondary winding voltage) for VAC 6025. Once measured as-cast, the samples where annealed for half an hour above their T_C before being re-measured. As can be seen, the BN in this case decreases after annealing. A similar reduction in BN was found for Yanqin amorphous and Nanoamor, with Finemet showing an increase after annealing and Yanqin nanocrystalline and Metglas 2705M showing no significant change. Further XRD and magnetic domain visualisation studies of the annealed samples are being performed in order to understand these results, which may be caused by stress relaxation, dislocation displacement and crystal growth.

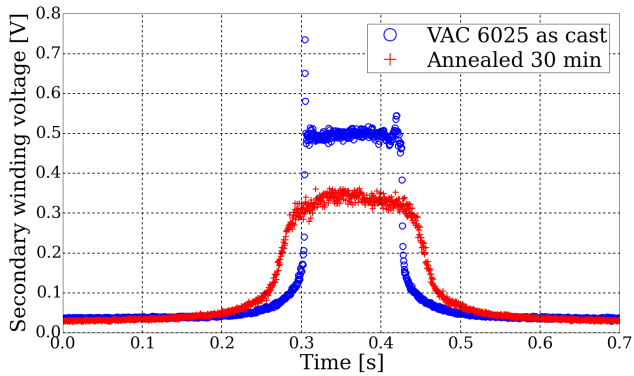

Figure 4: BN for VAC 6025 before and after annealing.

CONCLUSIONS

Taking into account the measured magnetic properties of many different materials, it can be seen that there is a great difference between the iron-based and cobalt-based alloys. The latter present better as-cast properties in their amorphous state for use as transformer cores. However, the former could potentially be good materials in their nanocrystalline state, as nanocrystalline iron-based materials are known for their good magnetic properties and Finemet FT-3 is extensively used for building cores. Materials VAC 6025 and Nanoamor were found to have very similar properties and therefore only one needs to be maintained for further study. This leaves three materials to be studied in-depth for final exploitation as beam current transformer cores: Finemet FT-3, VAC 6025 and Metglas 2705M.

ACKNOWLEDGMENTS

The authors would like to thank Michał Krupa, Jacques Longo, Dr. Emad Oveisi, Romain Ruffieux, Dr. Olha Sereda and Dr. Jérémy Tillier for their contribution to the results in this paper.

REFERENCES

[1] S. Aguilera, P. Odier and R. Ruffieux, "Magnetic Materials for Current Transformers", in Proc. International Beam Instrumentation Conference 2013 (IBIC2013), Oxford, UK, paper MOPF24, pp. 263-266, [Online], Available: http://www.ibic2013.org/prepress/papers/mopf24.pdf

[2] Agilent Technologies, *Application Note 1369-1*, 2008, p. 17

[3] "Agilent 4294A Precision Impedance Analyzer Operation Manual." Agilent Technologies Japan Ltd., Hyogo, Japan, 2003, p. 469.

[4] "Technical Specifications for the TGA 4000 Thermogravimetric Analyzer", PerkinElmer Inc., 2009, [Online], Available: http://www.perkinelmer.com/CMSResources/Images/46-74807SPC_TGA4000.pdf

[5] D. Spasojević, S. Bukvić, S. Milošević and H.Stanley, "Barkhausen noise: Elementary signals, power laws, and scaling relations", Phys. Rev. E, 3, Vol. 54, 1996, pp. 2531-2546.

ISBN 978-3-95450-177-9

CHARACTERIZATION AND SIMULATIONS OF ELECTRON BEAMS PRODUCED FROM LINAC-BASED INTENSE THz RADIATION SOURCE

N. Chaisueb†, N. Kangrang, S. Rimjaem, J. Saisut, Plasma and Beam Physics Research Facility, Department of Physics and Materials Science, Faculty of Science, Chiang Mai University, Chiang Mai 50200, Thailand

Abstract

Electron beams with a maximum kinetic energy of around 2.5 MeV and a macropulse current of about 1 A are produced from an S-band thermionic cathode RF-gun of the linear accelerator system at the Plasma and Beam Physics (PBP) Research Facility, Chiang Mai University (CMU), Thailand. An RF rectangular waveguide input-port and a side coupling cavity of the PBP-CMU RF gun introduce asymmetric electromagnetic field distribution inside the gun cavities. To investigate the effect of the asymmetric field distribution on electron beam production and acceleration, measurements and simulations of the electron beam properties were performed. In this study we use well calibrated current transformers, alpha magnet energy slits, and a Michelson interferometer to measure the electron pulse current, the beam energy, and the bunch length, respectively. This paper presents the measurement data of the electron beam properties at various location along the beam transport line and compares the results with the beam dynamic simulations by using the particle tracking program ELEGANT. Moreover, the RF field feature and the cathode power were optimized in order to achieve the high qualities of the electron beam produced from the RF gun. This result implies and correlates to the electron back-bombardment effect inside the gun cavities.

INTRODUCTION

The electron linear accelerator at the Plasma and Beam Physics Research Facility (PBP-CMU Linac), Chiang Mai University, Thailand, is used to generate short electron bunches for generation of intense coherent THz radiation in forms of transition radiation and undulator radiation [1-4]. The PBP-CMU Linac transport line consists of two main parts that are the Gun-to-Linac (GTL) section and the Linac-to-Experimental station (LTE) section. In the GTL section, electron bunches are produced from a thermionic RF-gun and are transported to an alpha magnet by using three quadrupoles and two pairs of steering magnets to focus and guide the beam to centre of the alpha magnet entrance.

The alpha magnet is used as a magnetic bunch compressor and also as an energy measuring instrument by utilizing high and low energy slits installed inside its vacuum chamber. Furthermore, the energy slits are used to filter out low energy electrons in order to decrease the energy spread before the beam is post-accelerated in an S-band travelling-wave linear accelerator (linac) structure. In the LTE section, relativistic electron bunches exiting from the post-accelerated linac are currently used to generate the coherent THz radiation at the transition radiation station. To measure the electron beam energy after the linac acceleration, the beam is guided through a 60^{o} dipole magnet and a beam dump equipped with a Faraday cup at the end of the beam transport line.

Various beam diagnostic instruments are installed along the PBP-CMU Linac system to measure and analyse electron beam properties. Firstly, the current and pulse length of the electron macropulse were monitored with a non-destructive device called a current transformer. This device consists of a ferrite-core toroid with a ceramic tube enclosing the electron beam path and a loaded resistor. Secondly, the electron beam energy and energy spread were measured by using the alpha magnet energy slits and the current transformer for the beam after the RF-gun acceleration and a combination of a dipole magnet, a view screen, and a Faraday cup for the beam after the linac acceleration. Thirdly, a screen station, which consists of a phosphor screen and a CCD camera, is used to capture the transverse distribution of the electron beam. The beam image is then analysed with MATLAB code to obtain the transverse size and profile. Lastly, the bunch length measurement is performed by using an autocorrelation technique with a Michelson interferometer and a pyroelectric detector.

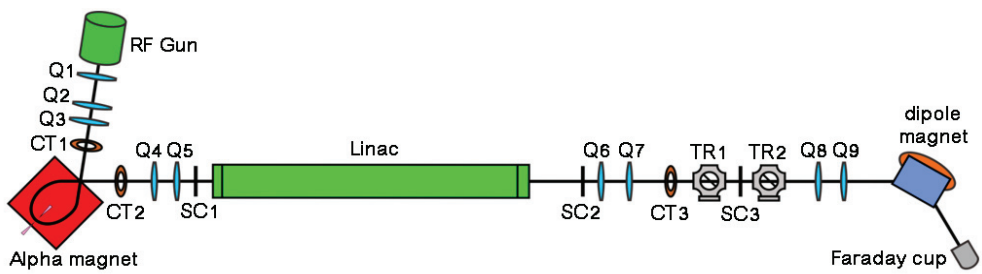

Figure 1: Schematic setup of the PBP-CMU linac system and the beam transport line. The letters Q, CT, SC and TR represent quadrupole magnets, current transformers, screen stations and transition radiation stations.

† Corresponding author: natthawut_chai@cmu.ac.th

ISBN 978-3-95450-177-9

GUN-TO-LINAC

Experimental Results

The electron beam performance in the Gun-to-Linac (GTL) section corresponds significantly to the RF-field feature inside the RF-gun such as RF pulse length, RF power, and RF waveform. When the RF pulse length is longer, the RF peak power gets higher and the flat top of waveform is longer due to the imperfection of the RF pulse production and power amplification. The RF pulse length of the PBP-CMU RF-gun can be varied up to 8 μs (FWHM). However, the long RF pulse is avoided since the effect of electron back-bombardment is large, which is a well-known disadvantage of the thermionic RF-gun. This effect leads to instability of the beam output, breakdown of the RF-gun operation and reduction of the electron energy gain due to the beam loading effect. The RF pulse length of 2.8 μs FWHM with the forward power of 3.65 MW at the proper gun temperature of 27ºC was used for the experiments presented in this paper in order to minimize the dark current and the electron back-bombardment effect.

After the electron beam exits the RF gun, a macropulse current is measured at the first current transformer (CT1) with the maximum macropulse current of about 1 A (as shown in Fig. 2). The electron macropulse has a triangular-like pulse shape with a FWHM pulse width of around 1-2.5 μs depending on the cathode temperature. A fraction of low energy electrons is filtered out with the low energy slit in the alpha magnet vacuum chamber. About 30% of the beam with high energy electrons exits the alpha magnet and is observed at the second current transformer (CT2) with the maximum macropulse current of about 0.35 A.

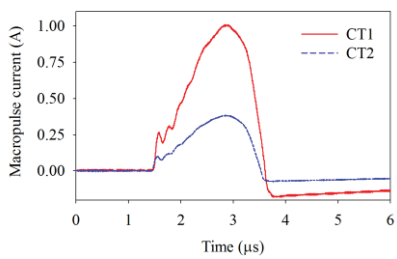

Figure 2: Electron macropulse currents at the gun exit (CT1) and at the exit of the alpha magnet (CT2).

The dependence of electron charge on the cathode temperature for different RF powers is shown in Fig. 3. It illustrates that electrons started to emit from the cathode at lower cathode temperature, when higher RF power was used. This indicates the more effect of the electron back-bombardment at higher RF power. For all RF powers, the number of electrons is low at high cathode temperature due to the back-bombardment phenomena.

The electron macropulse current, pulse width and maximum kinetic energy were measured at various cathode powers by using the current transformer CT1 and the alpha magnet energy slits. The measurement results at the RF peak power of 3.65 MW are plotted in Fig. 4 and Fig. 5. According the experimental results, electrons start to emit from the cathode when the cathode power is above 13 W. The maximum kinetic energy and the beam pulse width decrease quickly when the cathode power above 13.2 W. For the cathode power in the range of 13.2 W to 16.5 W, the beam energy reduces from 2.6 MeV to 0.5 MeV and the beam pulse width shortens from 2.8 μs to 1 μs. Contradictory, at these cathode powers the beam pulse current increases immediately up to 1 A and then decreases gradually to about 0.9 A when the cathode power is higher than 14.2 W. This is clearly due to the result of back-bombardment effect.

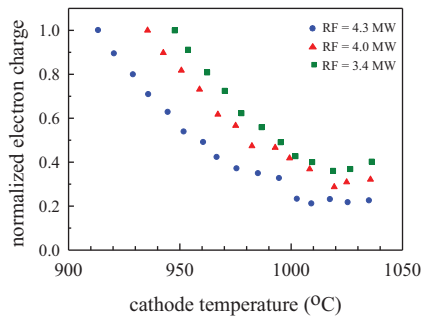

Figure 3: Normalized electron charge at the gun exit as a function of cathode temperature for three RF powers.

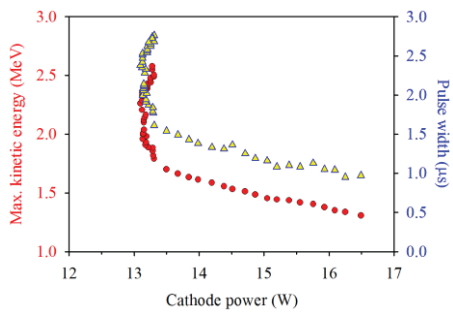

Figure 4: Maximum kinetic energy (dots) and pulse width (triangles) of electron beam as a function of cathode power.

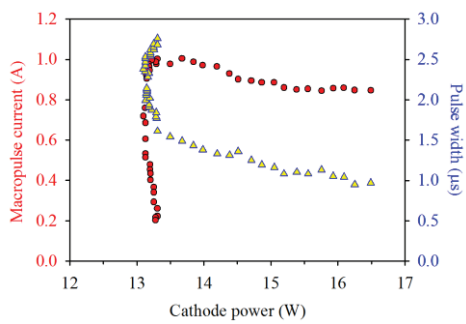

Figure 5: Electron macropulse current (dots) and macropulse width (triangles) as a function of cathode power.

The alpha magnet energy slits were used to measure the energy spectrum of electron beams produced from the RF-gun for three different cathode temperatures; 945, 950 and 960ºC. The experimental results are shown in Fig. 6. For the temperature of 950ºC, the integrated charge is higher than other two temperatures. Furthermore, the main part of electrons has more uniform energy in the high energy range with the maximum charge per energy

ISBN 978-3-95450-177-9

bin. Therefore, the cathode temperature of 950ºC is the most optimal condition for electron production. Experimental experience also showed that the RF-gun had stable operation at this temperature.

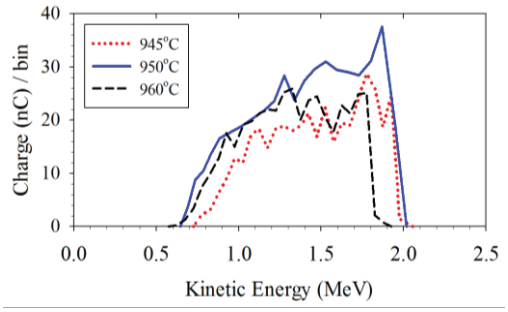

Figure 6: Energy spectra of electron beams produced at the cathode temperatures of 945, 950 and 960ºC.

The transverse image of electron beam with the maximum total energy of around 2.5 MeV was measured prior the linac entrance at the screen station SC1, which can be used to analyze the transverse intensity distribution and the transverse beam size as shown in Fig. 7. Both horizontal and vertical beam profiles were fitted with a Gaussian distribution. The results show that the horizontal and vertical beam sizes are 3.1 mm and 3.4 mm, respectively.

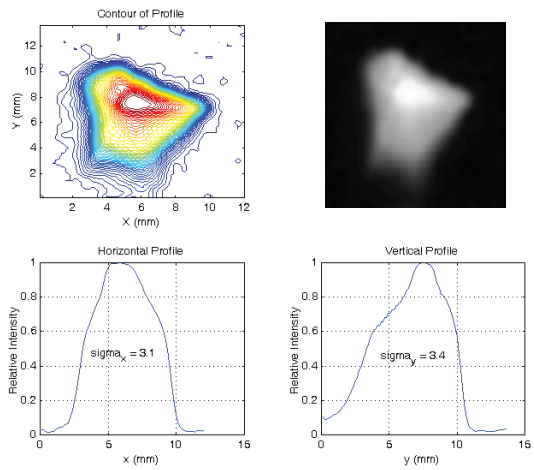

Figure 7: Intensity contour, beam image and relative horizontal and vertical beam profiles for the 2.5 MeV electron beam measured at the screen station SC1.

Simulation Results

The electron beam dynamic simulation inside the RF-gun was done by using the code PARMELA [5] and the results were reported in [6]. In this study, the particle tracking program ELEGANT [7] was used to investigate the electrons' motion along the beam transport line from the gun exit to the experimental station. Electron beam transverse distributions at different positions in the GTL section are shown in Fig. 8. The electron bunch exits the RF-gun with off-axis centroid position on both horizontal and vertical axes, which is the result of the asymmetric electromagnetic field distribution inside the gun cavities.

As discussed in [6], the electron bunch produced from the RF-gun with asymmetric field distribution has larger emittance value than the electron bunch produced from the symmetric RF-gun. This leads to the increase of the electron transverse size and the off-axis distance from the reference trajectory when the electron bunch arrives the entrance of the alpha magnet as shown in Fig. 8 (b). The steering magnets were used to guide the beam to enter the centroid of the alpha magnet entrance. The electron beam downstream the alpha magnet has smaller beam size in y-axis, which indicates that the alpha magnet has the focusing property in vertical direction. Then, the electron bunch was focused with the quadrupoles before traveling to the linac.

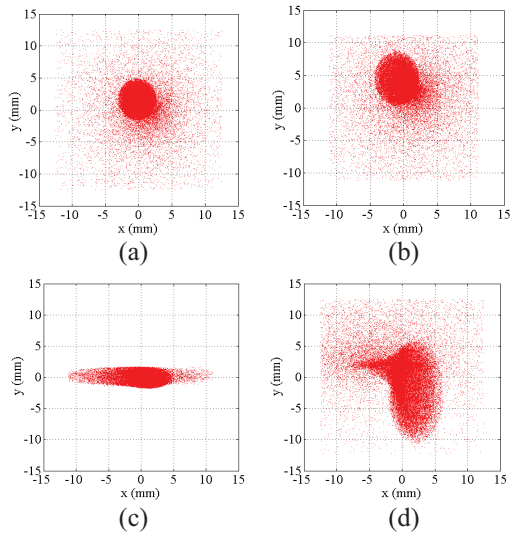

Figure 8: Beam transverse distributions at (a) the gun exit, (b) upstream the alpha magnet, (c) downstream the alpha magnet, and (d) the linac entrance.

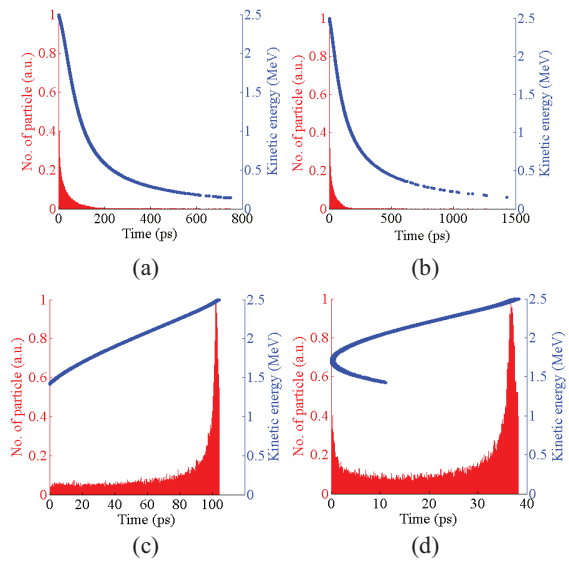

Figure 9: Longitudinal particle distributions at (a) the gun exit, (b) upstream the alpha magnet, (c) downstream the alpha magnet, and (d) the linac entrance.

The longitudinal distributions of the electron bunch at different locations in the GTL section are shown in Fig. 9.

ISBN 978-3-95450-177-9

In this study, the maximum kinetic energy and average energy of electron bunch are 2.5 MeV and 2.2 MeV, respectively. After exiting the RF-gun, the high energy electrons move to the alpha magnet before the low energy ones. When the electrons depart from the alpha magnet, the low energy electrons are in the head of the bunch leading to the bunch compression. The FWHM length of the electron bunch at the alpha magnet exit is about 10 ps compared to about 100 ps at the gun exit. The main fraction of electrons at the linac entrance has the FWHM bunch length of about 3 ps.

LINAC-TO-EXPERIMENTAL STATION

The electron beam with a kinetic energy range of 1.42 to 2.5 MeV was selected by using the energy slits before transporting it to the linac. The beam with a macropulse current of 350 mA and a pulse width of 1.3 μs was measured at CT2. The performance of the linac acceleration involves an input RF power and RF phase, which were optimized to obtain electron beam with maximum energy gain and minimum energy spread. The beam macropulse current after the linac acceleration measured at CT3 was 150 mA with a pulse width of 0.8 μs.

The energy spectrum of the beam measured with the dipole magnet and the Faraday cup in Fig. 10 reveals that the average electron beam energy is 9.8 MeV with energy spread of about 1.08 MeV. Therefore, the energy gain from accelerating in the linac was 7.3 MeV resulting in the linac acceleration gradient of 2.4 MeV/m. The result of the electron bunch length measurement with Michelson interferometer implies that the FWHM length of the electron bunch is calculated to be 124 μm [8].

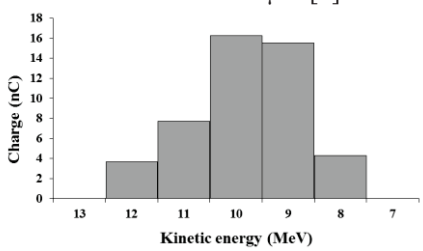

Figure 10: Energy spectrum of the electron beam after the linac acceleration.

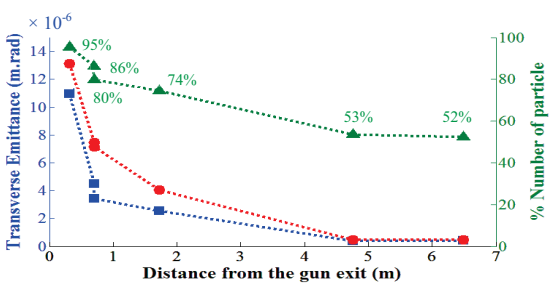

Figure 11: Transverse emittances in x axis (squares) and y axis (dots) with percentage of particle number (triangles) along the PBP-CMU beamline.

Simulation results from program ELEGENT in Fig. 11 and Table 1 suggest that at the experimental station the electron beam with a bunch charge of 27 pC has the geometric emittance of 0.43 mm.mrad.

Table 1: Simulated Electron Beam Properties at the Experimental Station

Parameters	Value
x/y beam size	4.52 / 4.67 mm
x/y emittance	0.41 / 0.45 mm.mrad
Average energy	9.82 MeV
Energy spread	0.24 MeV

CONCLUSION

The RF characteristics and the cathode temperature are the most important parameters for electron beam production of the thermionic RF gun. The effect of the electron back-bombardment is a limitation of the thermionic RF-gun, which affects the macropulse current, the pulse length, and the kinetic energy of the electron beam. The cathode power of around 13.2 W or equivalent to the cathode temperature of 950ºC is the optimal condition for achieving the electron pulses of 2.0-2.5 μs with the maximum energy of 2.0-2.5 MeV and the beam pulse current of 1 A at the gun exit. The simulation results show that the transverse emittance decreases, when the electron bunch arrives at the experimental station. This is the result of the increase of the beam energy and the loss of electrons. The beam emittance will be measured in the future by using the multi-quadrupole scan technique to compare with the simulated result.

ACKNOWLEDGEMENTS

The authors would like to acknowledge the supports by the Department of Physics and Materials Science, the Faculty of Science, Chiang Mai University, the CMU Junior Research Fellowship Program, the Science Achievement Scholarship of Thailand and the Thailand Center of Excellence in Physics (ThEP Center).

REFERENCES

[1] S. Rimjaem *et al.*, "Femtosecond Electron Bunches from an RF-gun", *Nucl. Instr. Meth.*, vol. 533, pp. 62-75, 2004.

[2] C. Thongbai *et al.*, "Femtosecond Electron Bunches, Source and Characterization", *Nucl. Instr. Meth.*, vol. 587, pp. 258-269, 2006.

[3] N. Chaisueb, S. Rimjaem, "Study on undulator radiation from femtosecond electron bunches", in *Proc. 37th Int. Free-Electron Laser Conf. (FEL'15)*, Daejeon, Korea, Aug. 2015, paper WEP062, pp. 702-706.

[4] N. Chaisueb *et al.*, "Optimization of electron beam properties for generation of coherent THz undulator radiation at PBP-CMU linac laboratory", in *Proc. 7th Int. Particle Accelerator Conf. (IPAC'16)*, Busan, Korea, May. 2016, paper TUPOW026, pp. 1803-1805.

[5] L.M. Young, J. H. Billen, "PARMELA", Los Alamos, NewMexico, USA, Los Alamos National Laboratory TechnicalNote LA-UR-96-1835, 2002.

[6] S. Rimjaem *et al.*, "RF study and 3-D simulations of a sidecoupling thermionic RF-gun", *Nucl. Instr. Meth. A*, vol. 736, pp. 10–21, 2014.

[7] ELEGANT, `http://www.aps.anl.gov`

[8] J. Saisut *et al.*, "Construction of the magnetic bunch compressor", *Nucl. Instr. Meth.*, vol. 637, pp. 99-106, 2011

ISBN 978-3-95450-177-9

UPGRADE OF THE LHC BUNCH BY BUNCH INTENSITY MEASUREMENT ACQUISITION SYSTEM

D. Belohrad*, D. Esperante Pereira, J. Kral, S. B. Pedersen, CERN, Geneva, Switzerland

Abstract

The fast beam intensity measurement systems for the LHC currently use an analogue signal processing chain to provide the charge information for individual bunches. This limits the possibility to use higher level correction algorithms to remove systematic measurement errors coming from the beam current transformer and the associated analogue electronics chain. In addition, the current measurement system requires individual settings for different types of beams, implying the need for continuous tuning during LHC operation. Using modern technology, the analogue measurement chain can be replaced by an entirely digital acquisition system, even in the case of the short, pulsed signals produced by the LHC beams. This paper discusses the implementation of the new digital acquisition system and the calculations required to reconstruct the individual LHC bunch intensities, along with the presentation of results from actual beam measurements.

INTRODUCTION

The existing beam intensity measurement system for the LHC was designed some 15 years ago and fully operational at the LHC start-up in 2008. At this time, the available analogue-to-digital (ADC) converters did not have the analogue bandwidth, sampling speed and precision to directly convert short, pulsed signals from LHC beams. Using such ADCs to provide data for the digital integration would have resulted in a much lower measurement accuracy than using analogue integration. Hence the existing system uses an integrator ASIC. The chip integrates the incoming signal at 40 MHz using two integrators working in multiplexed manner. Even if both integrators share the same silicon die, the manufacturing process causes them perform slightly differently when exposed to the same signal. Offset, gain, and the time of integration have to be compensated for each individual integrator. This is done in the FPGA once the integrated data stream has been converted to the digital domain.

Analogue integration also causes a loss of information as the baseline of the signal is integrated together with the beam signal. Once the integrated signal is converted into the digital domain, the algorithm restoring the DC component is unable to separate the baseline from the total integrated value, making it bunch pattern dependent.

The continued progress in ADC technology now enables us to investigate whether fast ADCs can now be used to sample the LHC bunched beam signals, so the complete bunch-by-bunch intensity measurement is performed in the digital domain. This would not only avoid complicated compensation techniques to reduce the problems associated with the integrator ASIC, but it would also allow the use of more sophisticated base-line restoration methods and bunch apex tracking, making the measurement technique more robust.

Further studies confirmed, that when using two dynamic ranges, an ADC with ENOB better than 10.5 bits and sampling rate greater than 500 MHz is needed to limit single shot digital integration error to 1% when a full scale signal is applied. For circulating beam measurements averaging can be used to reduce the ENOB requirements of the ADC.

IMPLEMENTATION

Hardware Layer

Several requirements have to be satisfied in order to achieve the desired measurement precision:

1. the bandwidth and the impulse response of the measurement device has to be sufficient to fully contain the bunch signal within the 25 ns spacing between LHC bunches (Bandwidth≥800 MHz, Impulse response≪25 ns),

2. the analogue front-end has to shape the bunch signal such that it entirely fills the 25 ns spacing between LHC bunches, but decaying fully to zero before the next bunch signal arrives,

3. the amplitude of the shaped signal must be adapted to optimally use the ADC dynamic range. This involves injection of an offset voltage V_{ofs} and gain optimisation to increase the measured signal amplitude to cover ≈80% of the ADC dynamic range.

The final requirements for this signal shaping can be seen in Fig. 1.

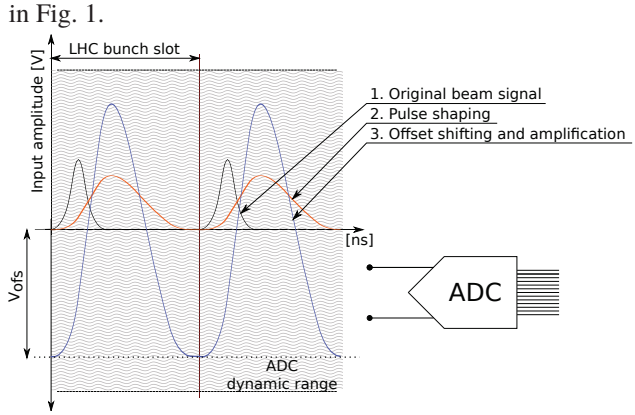

Figure 1: The BCTW signal shaping.

The first condition, concerning the bandwidth and impulse response, could not be satisfied using the original fast beam current transformers (FBCT) installed in the LHC due to the leakage of signal from one bunch into that of a neighbouring bunch slot, and the fact that the signal obtained was position

* david.belohrad@cern.ch

ISBN 978-3-95450-177-9

dependent [1]. Hence an upgrade of the FBCTs to a CERN developed Wall Current Transformer (BCTW, [2]) was performed during the annual end-of-year CERN shutdown in 2015-2016.

The other signal shaping conditions were satisfied by designing an analogue front-end to the BCTWs. An 8^{th} order 80 MHz Gaussian low-pass filter was used to shape the BCTW signal, and the signal amplitude was adapted to use the same two dynamic ranges as the existing system (full scale of 2×10^{10} and 2×10^{11} ch/b). This also simplified the comparison of measurements performance between the digital and analogue systems. For the time being, the offset voltage V_{ofs} is set to zero and hence the ADC dynamic range is not fully optimised.

The main challenged was in finding a suitable sampling module. The module had to satisfy following criteria:

- an ADC with 10.5 bits ENOB, DC coupled, having an analogue bandwidth greater than 800 MHz and sampling rate ≥500 MSPS,
- a high-pin count FMC form factor compatible with the newly developed CERN beam instrumentation group VME motherboard (VFC-HD, [3])

A market survey show, that an FMC module satisfying all those criteria does not currently exist. Lowering the requirements of the ENOB to ≈9.5 bits the FMC-1000 module from Innovative Integration could be used. Its two channel 14-bit, 1.25 GSPS, ADC allows parallel data acquisition of both dynamic ranges.

The maximum sampling rate of the FMC-1000 connected to the VFC-HD is 650 MSPS. This limitation comes from the speed of the Arria V (GX) transceivers used in the VFC-HD. For the purpose of the intensity measurements, however, the sampling rate is fully sufficient.

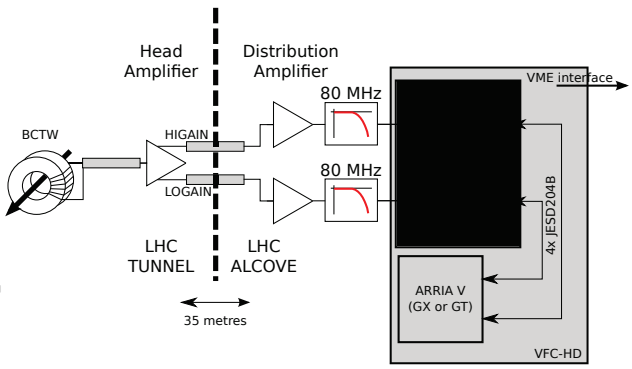

Figure 2: The BCTW analogue front-end overview.

In 2016, three complete acquisition chains (Fig. 2) were installed to measure the intensity of the circulating particle bunches in the LHC. These systems are currently running in parallel with the analogue systems used for the LHC operation.

Firmware Layer

The FPGA data processing flow is shown in Fig. 3. The analogue signal is converted to the digital domain at a rate

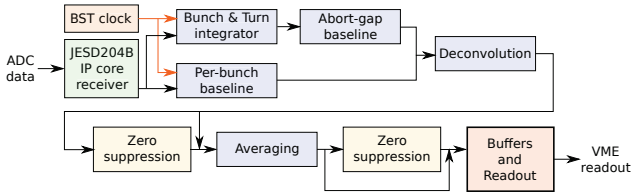

Figure 3: The FPGA data processing flow.

of 650 MSPS. The raw data of both ADC channels are transported to the FPGA through four 6.55 GbPS serial links (VFC-HD equipped with Arria V GX FPGA). An Altera JESD204B IP core is used to de-serialise the data streams on the FPGA side. A successful test was carried out to prove that a 1 GSPS sampling could be used with a custom deserialiser and the VFC-HD equipped with Arria V GT.

An internal 40 MHz clock, synchronous with the beam synchronous timing (BST), is generated, with its phase continuously adjusted using a digital delay such that there is a constant phase shift between the clock's rising edge and a bunch apex. A bunch boundary is then identified by the rising edge of this clock.

Such an implementation allows the system to track the clock frequency changes during the acceleration cycle. Using a peak-finding algorithm, a measurement of one LHC lead ion fill showed that a total phase shift of ≈1.5 ns has to be accommodated (Fig. 4). This corresponds to a displacement of the bunch boundary by approximately 1 ADC sample.

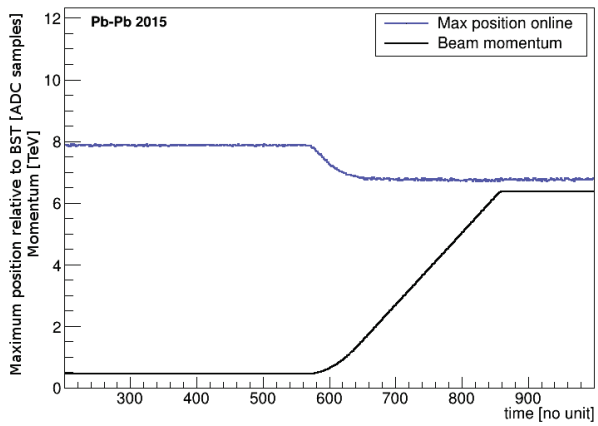

Figure 4: Evolution of the phase between the bunch apex and the BST clock during the acceleration of lead ions in the LHC. The blue trace shows the measured phase while the black trace shows the beam energy.

Once identified the bunch boundaries permit bunch by bunch digital integration to be performed. In addition, a total per-turn integral is provided as the sum of all the bunch intensities within a turn.

Both integrals have to be corrected for a DC component. Two correction algorithms were implemented to compare their performance: baseline correction using extraction kicker abort gap, and a per-bunch baseline correction.

- The abort gap baseline correction uses the 3μs LHC abort gap (which in principle does not contain any particles) to estimate the DC value of the beam signal. Each

ISBN 978-3-95450-177-9

turn, the *average DC component* of the beam signal can be estimated by calculating a mean value of the integrals of the empty bunch slots in the abort gap. To correct for the baseline, the DC component is added to the bunch and turn integrals at the end of each turn.

- The per-bunch baseline is calculated on the fly as an interpolation of the beam signal captured at two consecutive bunch boundaries. The interpolated bunch baseline is subtracted from each bunch integral individually.

The abort gap baseline correction algorithm is easier to implement compared to the per-bunch algorithm. The average baseline is calculated from the bunch integrals and can hence run at low clock speed (40 MHz). The disadvantage of this algorithm lies in its inefficiency to cope with fast baseline drifts. This is seen in Fig. 5 where the red trace shows a zoom of a typical signal produced by LHC proton bunches, while the blue trace shows the average baseline calculated by the abort gap algorithm.

These baseline drifts are caused by the non-uniform bunch filling pattern, and the only way to eliminate them is to lower the low-frequency cut-off of the BCTW. The difference in the average DC value with respect to the actual one in any given bunch slot might exceed 1% when using the BCTW with a low-frequency cut-off of 500 Hz.

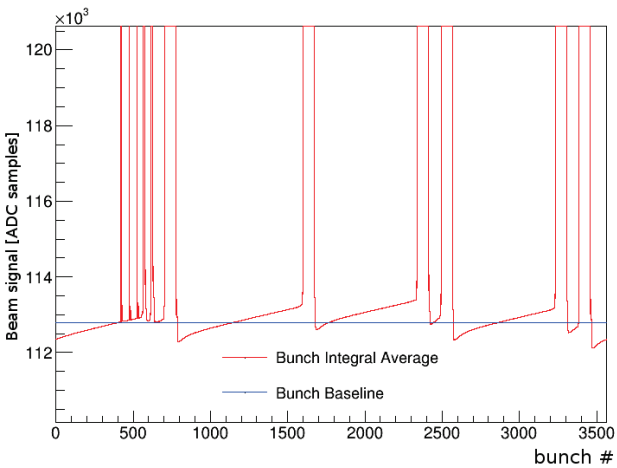

Figure 5: The abort gap baseline reconstruction.

Figure 6 shows an example of the per-bunch baseline restoration performed on 12 LHC proton bunches. The green bars identify the bunch boundaries while the blue trace depicts the raw ADC data and the black trace shows the result of the baseline correction. Compared to the abort gap algorithm, the per-bunch algorithm is more precise as it can calculate the baseline with a higher temporal resolution. The mandatory condition for this algorithm to work is that the analogue signal must return to zero before the start of the next bunch slot. This is a condition which in this particular case was not achieved as these data were taken using a 6^{th} order Gaussian low-pass filter with only a 60 MHz cut-off frequency.

The deconvolution algorithm is applied on the integrated data. It corrects the response of the measurement device

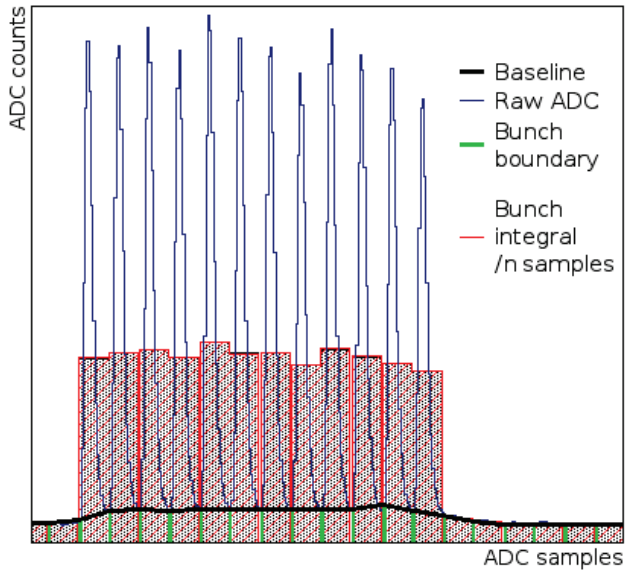

Figure 6: The per-bunch baseline reconstruction.

(BCTW, FBCT) in the case where signal generated by one bunch leaks into the adjacent bunch slot.

The bunch and turn intensities are averaged over 224 turns (20 ms) to improve the rejection of the 50 Hz component in the signal spectra.

To increase the measurement precision of low-intensity beams, two zero-suppression blocks are implemented. They act as noise filters, setting the bunch integral to zero when it is lower than a defined threshold. The first zero-suppression module filters the data at the output of the integrator, while the second one processes the averaged integrals. Both filters can be bypassed.

Software Layer

Integrated data are transported from the internal memory of each sampling system to the operational memory of a MEN A20 CPU using an interrupt-driven DMA VME transfer. The CPU runs the Linux operational system. It is patched to provide a scheduler allowing hard real-time applications to be run. Dedicated real-time and server classes [4] were written to perform the data transport, data processing and calibration, and to expose the measurement device's application interface (API) to the standard CERN controls infrastructure.

Bunch and turn integrals are logged in the CERN logging database. An expert graphical interface (Fig. 7) is available to visualise the measured data in real-time, as well to change the operational parameters of the measurement.

MEASUREMENTS

The digital intensity measurement systems is currently being commissioned and compared in terms of stability and performance to the old analogue and the LHC DC current transformers (DCCT) systems.

One such comparison is shown in Fig. 8. The top graph shows the total beam intensity measurement of the LHC fill number 5076 (beam 1). Three measurement methods are

ISBN 978-3-95450-177-9

Figure 7: The expert graphical interface captured during the LHC filling with proton bunches.

compared: the digital (VFC), the analogue (DAB), and the DCCT measurements. To highlight the differences, the bottom graph depicts a ratio of the fast intensity measurements (DAB and VFC) to the DCCT measurement. All three measurement methods agree at start of acceleration (where there is no unbunched beam in the machine) within a fraction of a percent. In the figure, the higher ratio at the injection is caused by a slow rise time of the DCCT measurement. Beam debunching is believed to be the source of the increasing deviation of the fast intensity measurements with time as both the bunch by bunch systems deviate from the DCCT measurement in the same way.

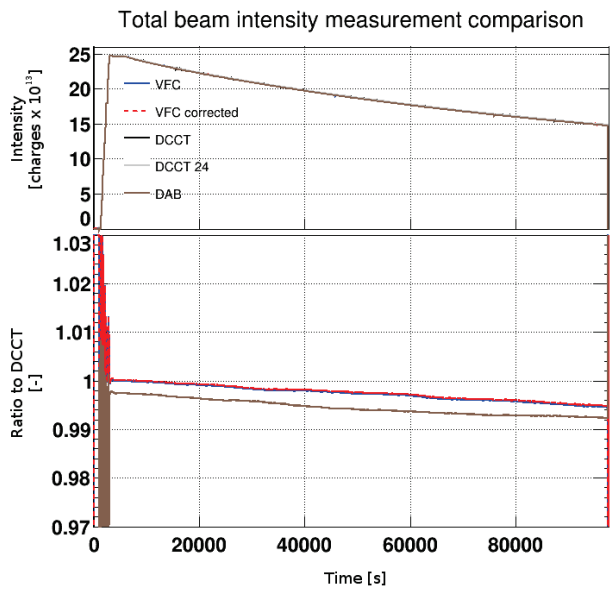

Figure 8: Comparison of the digital intensity measurement method with the DCCT and analogue measurements.

Fig. 9 shows a noise distribution on the total intensity as measured by the three measurement methods. It can be seen, that even when not fully using the ADC's dynamic range ($V_{ofs} = 0$), the digital acquisition system exhibits the same noise performance as the analogue (DAB) measurements.

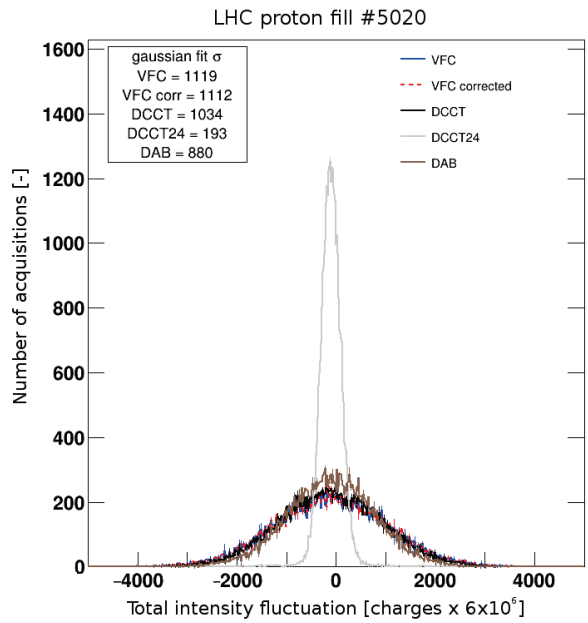

Figure 9: Noise performance of different intensity measurement systems.

OUTLOOK

While still in a commissioning phase, the new digital measurement systems are now fully operational, and for the moment working in parallel to the operational analogue systems. It has been shown that they already provide measurements of the same quality as the old analogue systems, while guaranteeing a more robust functioning, and the possibility for even more advanced signal processing in the future. At the end of the commissioning phase, the digital intensity measurement system will replace the old analogue system, which will permit further optimisation to be performed on the analogue front end.

REFERENCES

[1] D. Belohrad, M. Gasior, M. Krupa, T. Lefevre, L. Soby, "Summary of LHC MD398: Verification of the dependence of the BCTF measurements on beam position and bunch length", in *CERN Internal Note CERN-ACC-Note-2015-0031*, CERN, Geneva, Switzerland, October 2015.

[2] M. Krupa, M. Gasior, "The Wall Current Transformer – a new sensor for precise bunch-by-bunch intensity measurements in the LHC", in *Proc. of IBIC16*, Barcelona, Spain, September, 2016.

[3] A. Boccardi et al., "A Modular Approach to Acquisition Systems for the Future CERN Beam Instrumentation Developments", in *Proc. of ICALEPCS 2015*, Melbourne, Australia, October 2015.

[4] M. Arruat et al., "Front-End Software Architecture", in *Proc of ICALEPCS07*, Knoxwille, Tennessee, USA, March, 2007.

ISBN 978-3-95450-177-9

PERFORMANCE STUDIES OF A SINGLE VERTICAL BEAM HALO COLLIMATION SYSTEM AT ATF2

N. Fuster-Martínez, IFIC (CSIC-UV)*, Valencia, Spain
A. Faus-Golfe, IFIC (CSIC-UV), Valencia, Spain and LAL, Université Paris-Sud,Orsay, France
P. Bambade, R. Yang, S. Wallon, LAL, Université Paris-Sud, Orsay, France
I. Podadera, F. Toral CIEMAT, Madrid, Spain
K. Kubo, N. Terunuma, T. Okugi, T. Tauchi, KEK and SOKENDAI, Tsukuba, Japan

Abstract

In order to reduce the background that could limit the precision of the diagnostics located in the ATF2 post-IP beamline a single vertical beam halo collimation system was installed and commissioned in March 2016. In this paper, we present the measurements done in March and May 2016 in order to characterize the collimation system performance. Furthermore, the collimator wakefield impact has been measured and compared with theoretical calculations and numerical simulations in order to determine the most efficient operation mode of the collimation system in terms of halo cleaning and negligible wakefield impact.

INTRODUCTION

ATF2 is a scaled-down version of the Beam Delivery System (BDS) of the Future Linear Colliders (FLCs) Final Focus System (FFS) [1] built after the ATF Damping Ring (DR) (see Fig. 1). The ATF2 main objective is to achieve a vertical beam size at the virtual IP of 37 nm within a nanometer level stability.

The control and reduction of the beam halo distribution that could be intercepted by different components in the beamline producing undesired background is a crucial aspect for the FLCs and also for ATF2. In ATF2 the beam halo is formed mainly in the ATF DR and goes into the ATF2 beamline hitting at some locations the beam pipe. The most critical regions are the IP and post-IP were a Shintake monitor (IPBSM) is located used for measuring the nanometer vertical beam size (see Fig. 1). The IPBSM measures the modulation pattern photons produced in the interaction of a laser with the electron beam. Additional background photons in this region may be mixed with the IPBSM signal and limit its precision. Experimentally and by means of tracking simulations the vertical aperture of the last bending magnet (BDUMP) has been identified as the main source of background photons limiting the IPBSM signal to noise ratio. A transverse beam halo collimation system feasibility and design study for reducing the background in ATF2, specially in the last bending magnet, was done and reported in [2]. In March 2016, the vertical beam halo collimation system was installed and commissioned [3].

In this paper, we present the performance studies carried out in the ATF2 spring run. Secondly, we present the comparison of these measurements with realistic tracking simulations performed with the tracking code BDSIM [4]. Furthermore, the collimator wakefield impact on the orbit has been measured using the cavity BPMs system of ATF2 in order to verify the wakefield impact induced, to determine the optimum operation mode of the system and to perform benchmarking between analytical calculations, numerical simulations and measurements. These measurement are relevant for the FLCs because the ATF2 collimator design is based on a first mechanical design of the International Linear Collider (ILC) [5] spoilers. In addition, these measurements could be crucial to understand the discrepancies observed between measurements and predictions for similar geometries in the past experiments performed at ESA [6].

* Work supported by IDC-20101074, FPA2013-47883-C2-1-P and ANR-11-IDEX-0003-02

COLLIMATION EFFICIENCY STUDIES

The vertical collimation system was constructed and first tested at LAL without beam at the end of 2015. Then, in March 2016 the system was installed in ATF2 (see Fig. 2). More details about the installation and commissioning can be found in [3].

In the March and May 2016 runs the performance of the vertical collimation system with beam has been studied. First, beam halo measurements were performed with the post-IP Wire Scanner (WS) and the Diamond Sensor (DS) [7] located in the post-IP region to study the beam-jaws movement and alignment (see Fig. 1). During these runs the beam energy was 1.3 GeV, the intensity ranging from 0.1-1 $\times 10^{10}$ electrons per bunch and the optics configuration used was the $(10\beta_x^* \times 1\beta_y^*)$ being β_x^* and β_y^* the value of the nominal betatron functions at the IP. Fig. 3 shows the vertical beam halo distribution measured with the vertical DS with the collimator opened and close to 3 mm half aperture. The DS is located after the BDUMP as can be seen in Fig. 1. The DS measurements are limited by the BDUMP elliptical full aperture which is 26 mm in the vertical plane and 56 in the horizontal one. In order to observe the effect of the collimator on the DS we need to close the collimator at least to 4 mm.

The ATF2 studies required different beam and machine conditions. Because of that, the relative efficiency of the vertical collimation system has been studied for different beam intensities, DR vacuum pressures and ATF2 optics. The intensity ranging from 0.1-1 $\times 10^{10}$, the DR vacuum pressures was changed from $4.99 \times 10^{-7} Pa$ to $1.06 \times 10^{-6} Pa$ and the optics used were the nominal one $(10\beta_x^* \times 1\beta_y^*)$ and the

ISBN 978-3-95450-177-9

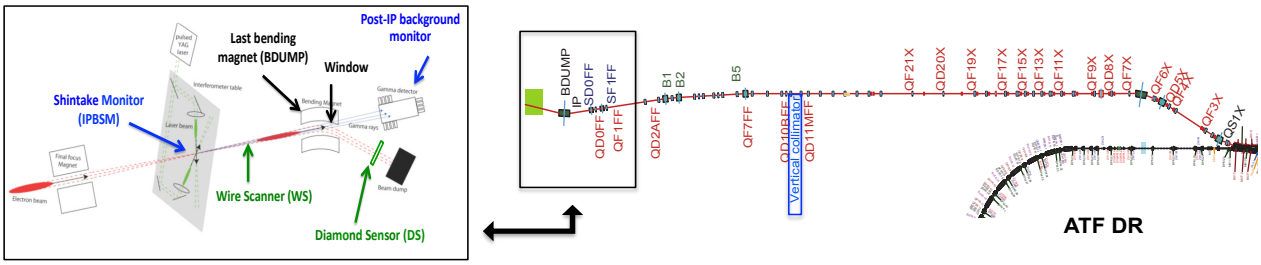

Figure 1: ATF and ATF2 layout with a zoom of the ATF2 post-IP beamline.

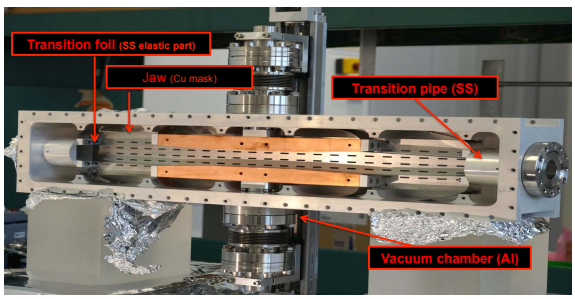

Figure 2: Vertical collimation system installed in ATF2.

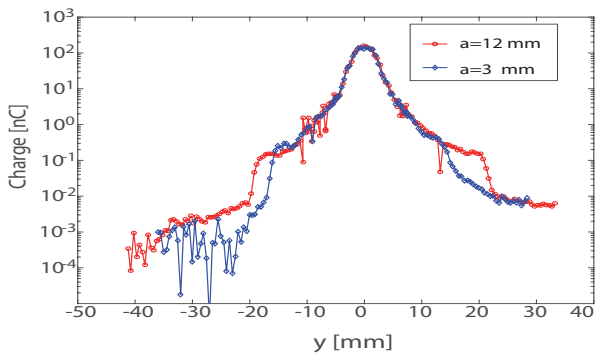

Figure 3: DS vertical beam halo distribution measurement.

so-called low beta optics ($10\beta_x^* \times 0.5\beta_y^*$). Measurements with the post-IP background monitor (CsI scintillator) and the post-IP Cherenkov monitor (used by the IPBSM monitor for beam size measurements) have been taken for different collimator apertures (both detectors are located in the post-IP beamline after the BDUMP as can be sen in Fig. 1). In all these scenarios the relative efficiency has been calculated in a relative way as the reduction of background photons as we close the collimator respect to the measured background level when the collimator is completely opened (vertical half aperture of 12 mm). In Fig. 4 is shown the relative reduction of background photons averaged over 100 pulses measured with the post-IP background monitor as a function of the half aperture of the collimator. The top plot of Fig. 4 shows the relative efficiency for three different intensities being the difference between the highest and the lowest intensity a 30 %, the middle plot shows the efficiency for the two DR vacuum pressures and the bottom plot the comparison for the two different optics studied. Notice that the negative values of the relative efficiency are due to the background fluctuations that can be caused by the interaction of the beam halo with other components along the beamline.

From these measurements we could conclude that for a variation of the intensity of about 30% the efficiency does not change. In the case of the DR vacuum pressure, for a worst vacuum scenario we observed a highest level of collimation relative efficiency. This is consistent with the DS transverse beam halo measurements performed in 2016 [8] showing an increase of the beam halo density and a change on the parametrization. In the case of the comparison for the two optics operation modes the difference observed on the relative efficiency is due to the increase of the beam size by a factor $\sqrt{2}$ in all the FFS.

Comparison with Realistic Simulations

Beam halo tracking simulations have been performed with MADX [9] and PLACET [10] tracking codes in order to optimize the location and study the efficiency of the vertical collimation system, the results were presented in [2]. These studies have been completed using the tracking code BDSIM an extension toolkit of Geant4 in order to study the efficiency of the collimator taking into account the emission of secondary particles and beam halo regeneration due to Electro Magnetic (EM) processes. The main goal of this study is to quantify the efficiency of the collimator in the reduction of photons that can reach the gamma detector of the IPBSM. The background generated by the collimator itself has also been studied in order to verify that the EM shower produced by the collimator does not generate additional background photons in the IP region. No additional background is expected at the IP and this is in agreement with the observations. More details can be found in [2] .

For the BDSIM simulations the ATF2 FFS line has been considered with ($10\beta_x^* \times 1\beta_y^*$) optics. A gaussian transverse beam halo distribution (x, x', y, y') with 10^6 electrons of 1.3 GeV has been generated from $\pm 3\sigma_{x,y}^{core}$ (only the beam halo tails are considered in these studies) with $\sigma_x^{halo} = 5\sigma_x^{core}$ and $\sigma_y^{halo} = 10\sigma_y^{core}$. No coupling between x-y planes has been taken into account. For the longitudinal distribution a gaussian model has been used with an energy spread of 0.08%. Multipoles and misalignments have not been taken into account. In Fig. 5 is shown the relative reduction of background photons generated in the BDUMP for different collimator half apertures at the BDUMP window for photons simulated and compared with the measurements performed

ISBN 978-3-95450-177-9

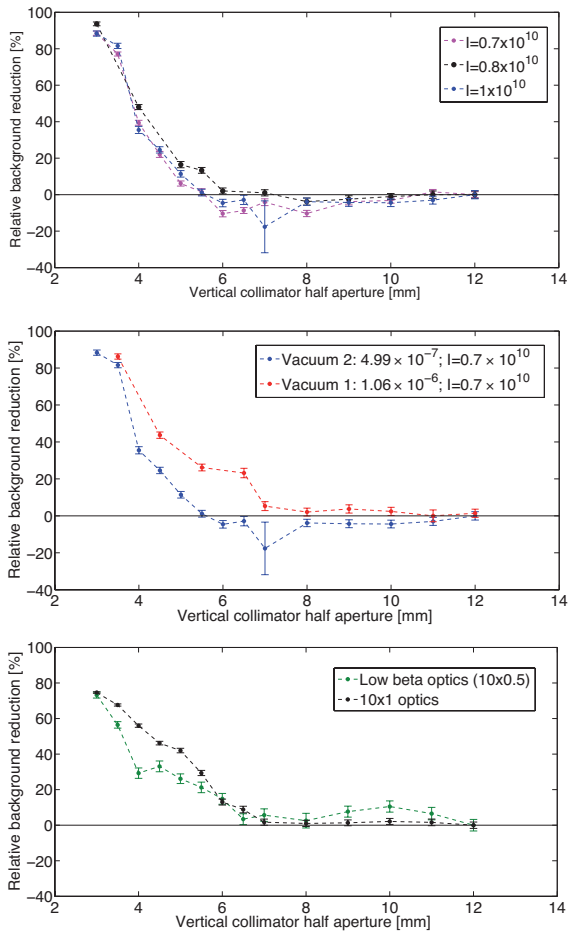

Figure 4: Relative efficiency for different intensities (top), DR vacuum pressures (middle) and optics (bottom).

with the background monitors. The comparison is compatible within the associated error for the two period runs (with the same beam and machine conditions) and the two detectors used.

It has been demonstrated that by adjusting the half aperture of the collimation system to a smaller aperture than 5 mm one can improve the IPBSM signal to noise ratio. However the collimator wakefield impact induced has to be considered when reducing the aperture of the collimator. In order to clarify this aspect and verify that we understand the wakefield impact induced by the collimator a measurements campaign have been carried out and the results are shown in the next section.

ORBIT COLLIMATOR WAKEFIELD IMPACT MEASUREMENTS

The wakefield impact induced in the vertical collimation system has been studied by means of analytical calculations, 3D EM simulations using CST PS [11] and tracking studies using a modified version of PLACET [12]. In order to complete the study the wakefield impact induced by the collimator on the beam orbit has been measured using the ATF2

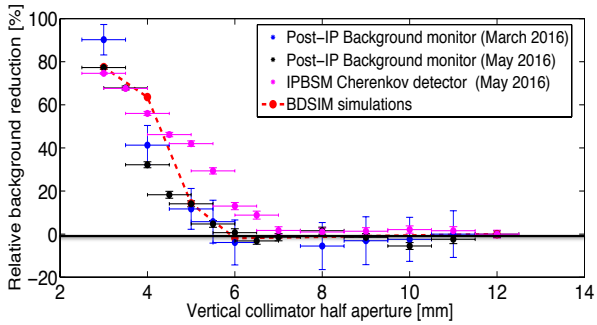

Figure 5: Comparison of the measured relative background reduction in the Post-IP region with the BDSIM simulations.

beam position monitors system formed by 45 C-band BPMs with 200 nm resolution in $\pm$ 1 mm range with 20 dB attenuation. In May 2016 run, orbit data have been taken for a fix collimator half aperture of 4 mm and different collimator offsets respect to the beam. Prior to the data analysis a study has been performed to select at which BPMs we expect to be able to observe a correlation between the measured beam position and the collimator offset. This selection is based on the BPMs resolution measured and the expected orbit variation, Δy, at each BPM using the kick factor calculated from the CST PS numerical simulations. The analysis of the orbit data have been performed following the procedure detailed in [13]. In order to subtract the orbit jitter, which is at the level of the expected collimator wakefield impact, the correlation between the collimator upstream and downstream BPMs has been calculated, X. Then, the residuals, $R = A'X - B'$, are calculated for each collimator offset where A' is the upstream BPMs readings, B' is the downstream BPMs readings. From the linear fit of the correlation between the collimator offset and the orbit change at each BPMs, R, the collimator wakefield kick, κ_T, can be estimated as [12]:

$$\kappa_T[\frac{V}{pCmm}] = \frac{p}{R_{34}[mm]}\frac{E[eV]}{eq[pC]} \quad (1)$$

where p is the slope of the linear fit, R_{34} is the corresponding transfer matrix element, E is the nominal ATF2 beam energy and eq is the measured charge of the beam.

Measurements have been taken in three different days in May 2016. During these runs the beam energy was 1.3 GeV, the intensity ranging from 0.9-0.95 $\times 10^{10}$ electrons per bunch and the optics configuration ($10\beta_x^* \times 1\beta_y^*$). An example of the correlation observed at QF7FF C-BPM is depicted in Fig. 6. The resulting kick obtained at the different BPMs is depicted in Fig. 7 for the run on the 27th of May 2016. In green the expected value calculated using the analytical models is indicated and in red the one calculated from the numerical simulations. The bunch length was also measured using a Streak camera installed in the ATF DR in order to reduce uncertainties enabling the comparison of these results with simulations and analytical models which are bunch length dependent.

ISBN 978-3-95450-177-9

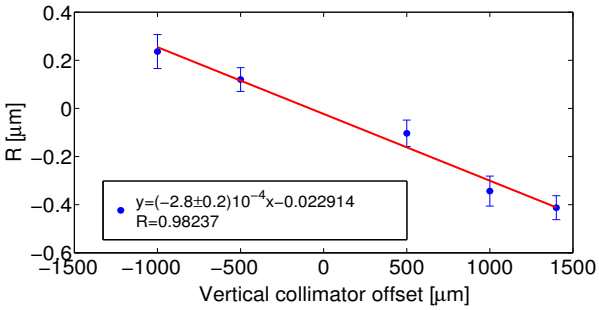

Figure 6: Residuals as a function of collimator offset from the 27th of May run at QF7FF.

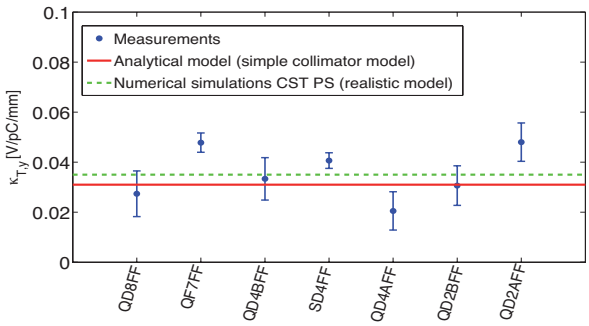

Figure 7: $\kappa_{T,y}$ reconstructed at different C-BPMs from the 27th of May run.

The weighted mean, $\bar{\kappa}_{T,y}$, of the three sets of measurements taken on the 22th, 25th and 27th of May is shown in Table 1 in comparison with the corresponding analytical and numerical calculation. These first measurements are compatible with

Table 1: Average $\bar{\kappa}_{T,y}$ and Comparison with Analytical and Numerical Calculations.

σ_z [mm]	$\kappa_{T,y}$ [V/pC/mm]		$\bar{\kappa}_{T,y}$ [V/pC/mm]
	Analytic	CST PS	Measured
9.6	0.031	0.035	0.038±0.002

the numerical simulations performed with CST PS within a 9 % and with the analytical calculation within a 23% for a bunch length of 9.6 mm. Notice here the difference on the model considered on the analytical calculations where only the jaws are considered while in the CST PS a realistic model has been simulated taken into account also de transition parts of the system and the connection to the beam pipe.

SUMMARY AND FUTURE WORK

A vertical collimation system has been installed in the ATF2 beamline. The efficiency of the collimator has been demonstrated by measuring the background photons with the post-IP background monitor. Furthermore, the relative efficiency has been studied and characterized under different beam intensities, DR vacuum pressures and ATF2 optics. The relative background photons reduction measured in the post-IP region as a function of the collimator half aperture is compatible with the simulations performed with the tracking code BDSIM. In addition, a first campaign of collimator wakefield impact measurements on the orbit has been carried out for 4 mm half aperture. The wakefield kick obtained from these first measurements is compatible with the numerical simulations within a 9 % and with the analytical calculation within a 23%. A second campaign of wakefield measurements is planned in the fall run in order to confirm these results.

ACKNOWLEDGMENTS

We gratefully acknowledge J. Snuverink, L. Nevay and S. Boogert for their contribution with the BDSIM and the wakefield kick analysis. Also we would like to thanks G. White, A. Schuetz, and M. Stanitzki for their help on the experimental tests performed at ATF2.

REFERENCES

[1] G. R. White et al., “Experimental Validation of a Novel Compact Focusing Scheme for Future Energy Frontier Linear Lepton Colliders”, Phys. Rev. Lett. 112,034802, 2014

[2] N. Fuster-Martínez, A. Faus-Golfe, J. Resta-López, P. Bambade, S. Liu, S. Wallon, F. Toral, I. Podadera, K. Kubo, N. Terenuma, T. Okugi, T. Tauchi,“Design study and construction of a transverse halo collimation system”, IPAC15, WEPMN059

[3] N. Fuster- Martínez, A. Faus-Golfe, J. Resta- López, P. Bambade, R. Yang, S. Wallon. F. Toral, I. Podadera, K. Kubo, N. terunuma, T. Okugi, T. Tauchi. Commissioning and first performance studies of a single vertical beam halo collimation system at ATF2”, IPAC16, THPOR030

[4] `http://twiki.ph.rhul.ac.uk/twiki/bin/view/PP/JAI/BdSim`

[5] TDR, ILC-TDREPORT-2013

[6] J. L. Fernandez-Hernando, , S. Molloy, J.D.A. Smith, N. K. Watson, “Measurements of collimator wakefields at End Station A”, EPAC08, WEPP163

[7] S. Liu, P. Bambade,F. Bogard, P. Cornebise, V. Kubytskyi, C. Sylvia, A. Faus-Golfe, N. Fuster-Martinez, T. Tauchi, N. Terenuma,“Investigation of beam halo using in vacuum diamond sensor at ATF2”, IPAC15, THPOR030

[8] R.J. Yang, P. Bambade, V. Kubytskyi, A. Faus-Golfe, N. Fuster-Martínez T. Naito, “Modeling and Experimental Studies of Beam Halo at ATF2”, IPAC16, MOPMB008,

[9] `http://mad.web.cern.ch/mad`

[10] A. Latina, Y. Levinsen, D. Schulte, J. Snuverink, “Evolution of the tracking code Placet", IPAC13, MOPWO053

[11] https://www.cst.com/products/cstps

[12] N. Fuster-Martínez, A. Faus-Golfe, A. Latina, J. Snuverink, “Geometric wakefield regimes study of a rectangular tapered collimator for ATF2”, ATF2-01-2016

[13] J. Snuverink, R. Ainsworth, S.T. Boogert, F. J. Cullinan, A. Lyapin, Y. I, Kim, K. Kubo, T. Okugui, T. Tauchi, N. Terunuma, J. Urakawa, G. R. White, “Simulations and measurements of wake fields at the Accelerator Test Facility 2”, PRST-AB submitted to be published

ISBN 978-3-95450-177-9

A NEW WALL CURRENT MONITOR FOR THE CERN PROTON SYNCHROTRON

J.M. Belleman*, W. Andreazza, CERN, Geneva, Switzerland
A.A. Nosych, ALBA-CELLS Synchrotron, Cerdanyola del Vallès, Spain

Abstract

Wall Current Monitors are the devices of choice to observe the instantaneous beam current in proton accelerators. These entirely passive transformers deliver a high-fidelity image of the beam intensity in a bandwidth spanning from about 100kHz up to several GHz. They serve as a signal source for a diverse set of applications including Low Level RF feedback and longitudinal diagnostics such as bunch shape measurements and phase-space tomography. They are appreciated for their excellent reliability, large bandwidth and unsurpassed dynamic range. We describe the design of a new Wall Current Monitor for the CERN Proton Synchrotron with a useful bandwidth of 100kHz to 4GHz. Two such devices have been installed in the PS machine and are now used in regular operation. Some usage examples will be shown.

THE CERN PROTON SYNCHROTRON

CERN's Proton Synchrotron is a 628 m circumference, 26 GeV accelerator operating since 1959. Over the years, it has served to accelerate protons and electrons and their anti-particles, as well as several ion species. Today it is an important part of the CERN injector complex, delivering both protons and lead ions to the Large Hadron Collider via the Super Proton Synchrotron, as well as serving many other clients with its dedicated experimental area.

WALL CURRENT MONITOR PRINCIPLE

As a beam of particles travels through a conducting vacuum tube, it is accompanied by an image charge of equal magnitude but opposite sign flowing along the inside wall of the tube [1]. This co-moving wave of charge constitutes a localised current. If we were to cut the vacuum tube and place an impedance across the gap, this current would develop a voltage which is an accurate replica of the beam current.

To confine signal currents to a well-defined geometry, the gap is surrounded by a conducting shell. In this design the gap is empty, so the shell also holds the vacuum. Inside the shell are ferrite toroid cores that increase the WCM inductance and thereby extend the lower cut-off frequency downwards (Fig. 1). The whole arrangement is basically a single-turn transformer with the beam in the role of the primary 'winding', the conducting shell and the inner chamber as the secondary and the ferrite toroids as the core (Fig. 2).

* jeroen.belleman@cern.ch

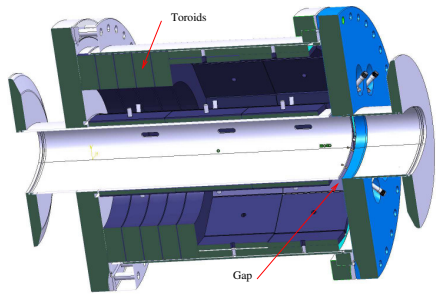

Figure 1: Cut-away view of the Wall Current Monitor.

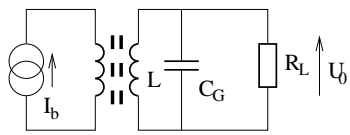

Figure 2: Simplified WCM equivalent circuit.

The WCM's low frequency cut-off is $\omega_L = \frac{R_L}{L}$, with L the inductance of the ferrite toroids and R_L the gap load resistance. The ferrite toroids are Ferroxcube T240/160/20-8C11, with a single-turn inductance of about 2 μH. Five toroids supply a total of about 10 μH. With the gap load resistance of 6 Ω, this yields a lower cut-off frequency of about 100 kHz.

The inner surfaces of the shell, as well as the outer surface of the beam pipe, are covered in Ferroxcube 4S60 absorptive ferrite tiles. This does not contribute substantially to the transformer inductance, but it muffles the EM energy propagating into the space between the shell and the beam pipe, which would otherwise look like a coaxial shorted stub in parallel with the gap load resistance.

Despite the liberal use of absorptive ferrite, the high frequency response is dominated by various EM wave effects —cavity resonances— well before it finally drops off because of the gap capacitance C_G. A lower gap load resistance would widen the WCM's bandwidth at both ends of the frequency response, but reduce the output signal for a given beam intensity.

Since the ferrites are installed inside the vacuum, they were all subjected to chemical degreasing, followed by a bake-out at 1000 °C in air. The bake-out does not discernably affect the ferrite properties [1]. The main residual gas source was adsorbed water. Although the outgassing rate is not enormous, a WCM has a dedicated ion pump.

ISBN 978-3-95450-177-9

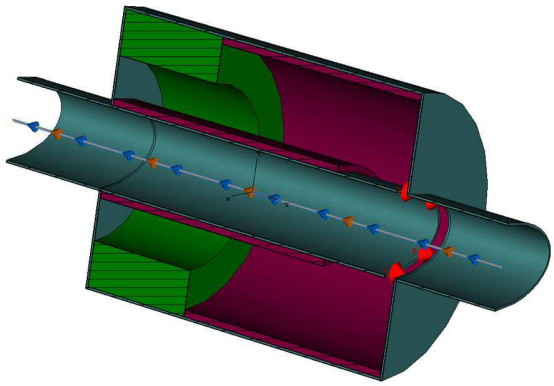

Figure 3: WCM simulation model.

SIMULATION

Simulation models were used to sort out WCM architecture variants. This also helped to decide on details of the WCM construction: whether or not to use oval-to-cylindrical transitions, how to position the feedthroughs, probe geometry, where to put absorbing ferrites, etc. We converged on the model shown in Fig. 3 as being best. Inductive ferrite is green, absorptive ferrite is bordeaux red and the gap loads are represented by the little bright red cones. To avoid burdening the model with details, some specific parts, such as the feedthroughs, were simulated separately.

To make the best of the high-frequency response, the gap is free of any dielectric material. Eight coaxial 50 Ω probes bridge the gap. Each of these probes is brought out via a vacuum-tight controlled-impedance feedthrough (Fig. 4) with an SMA connector on the outside. The feedthroughs are made by Times Microwave Systems from an original Fermilab design.

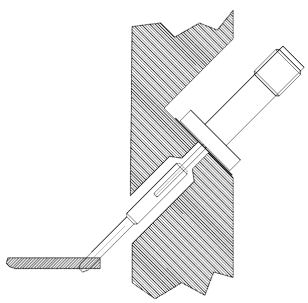

Figure 4: Probe and feedthrough geometry.

The cross-section of the CERN Proton Synchrotron vacuum chamber is oval and the distribution of the image current is therefore not homogeneous, even for a perfectly centred beam. The probes are spaced to sit at equal angular distances seen from the central axis (Fig. 5). Each thus collects a similar fraction of the image current for a centred beam. The eight partial outputs are then combined into one on the outside of the WCM.

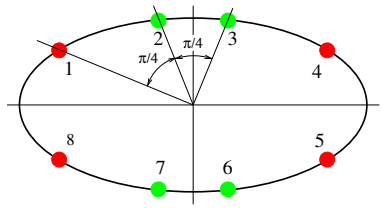

Figure 5: Distribution of probe positions around the gap perimeter.

COMBINERS

A tree of elementary passive star combiners merges the eight outputs of the wall current monitor into two identical, approximately position-independent, output signals (Fig. 6) [2, 3]. Matched-length 50 Ω coax cables are used for the interconnections. The blocks marked 'T' are coaxial terminators. Attenuators serve to spread-out signal power to prevent overload damage, or to enhance the damping of transients. The attenuators are rated for 15 W average. The *peak* power in each individual attenuator approaches 2 kW for the most intense beams, albeit fortunately at tiny dutycycles.

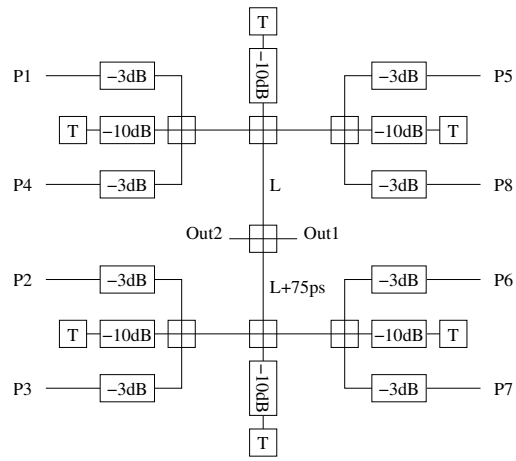

Figure 6: Combiner tree.

Each elementary star combiner is a simple junction of four coaxial transmission lines (Fig. 7). Seven are needed for a complete tree. Despite their apparent simplicity, these devices have some subtleties in their behaviour. Let's consider the case of a simple four-port combiner:

Figure 7: An elementary four-port star combiner.

ISBN 978-3-95450-177-9

As shown in Fig. 8, suppose all ports are terminated in their characteristic impedance Z_0. Ideally, two identical input signals travel from the sources towards the junction, are superimposed with the resultant sum divided over the two outputs. In practice, the input signals may not be exactly equal and the source impedances aren't necessarily equal to Z_0, nor even the same.

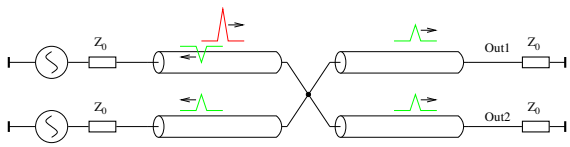

Figure 8: Model of an elementary four-port star combiner.

A signal propagating on a transmission line with impedance Z_0 reflects on a discontinuity with impedance Z according to:

$$\Gamma = \frac{Z - Z_0}{Z + Z_0} \tag{1}$$

From the point of view of a single signal incident on the junction (red in Fig. 8), $Z = \frac{Z_0}{3}$, so there is a reflection of $\Gamma = -\frac{1}{2}$ of the incident signal travelling back to its source, while $+\frac{1}{2}$ travels towards each of the three other ports (green in Fig. 8). If we have two identical incident signals, the reflection of each is exactly cancelled by the forward travelling contribution from the other input, and all energy ends up in the output loads on the right.

If the two incident signals are *not* equal, half of the difference is reflected back to each of the inputs. Now, if the source impedances are equal to Z_0, these reflections are absorbed and we're done. If the source impedances are the same but *not* equal to Z_0, new reflections depart once more towards the junction. These reflections are exactly complementary, so at the junction they cancel and nothing shows up in the outputs. All energy is returned once more to the sources. This repeats until all energy is dissipated in the source impedances.

If the source impedances are *not* equal, the secondary reflections do not cancel when they reach the junction again and some energy *does* end up in the output. This then repeats until all energy is dissipated, this time in both the source impedances and the output loads. This latter situation yields an exponentially decaying tail of afterpulses, piling up into a single trailing messy transient. Clearly this is a very undesirable result.

For a WCM in a cylindrical vacuum pipe, it's easy to make sure that all ports have the same source impedance. However, the PS has an oval chamber, as does this WCM. Even for a perfectly centred beam, it has two sets of outputs with different output signals and different source impedances.

For off-centre beams, the signal levels will differ even within one set. Measurements have shown that the return loss of the WCM ports is in the range of 5 to 10 dB. Signal energy bouncing back and forth between the ports will be damped relatively slowly. It is therefore beneficial to add attenuators between the ports and the combiners. This reduces the mismatch between ports and provides a faster means of dissipating multiple reflections. The WCM fortunately provides enough signal to make this acceptable.

LAB TEST SETUP

In this section, rather than showing smooth progress from concept to result, we choose to expose some of the nitty-gritty laboratory work.

To simulate the passage of a beam in the lab, the WCM is mounted between a pair of short pieces of standard PS vacuum pipe and a ⊘ 6 mm rod is strung through the centre, thus forming a coaxial line. A pulse generator injects signals onto this line (Fig. 9). The rod's characteristic impedance is 160 Ω. It is important that the rod present the smoothest impedance possible. Any discontinuity causes reflections, complicating the interpretation of measurements and placing additional uncertainties on the current flowing on the line.

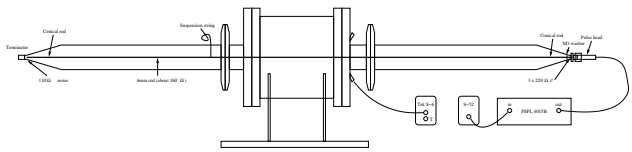

Figure 9: Lab test setup.

We went to considerable effort to smooth out any impedance variations. To keep the rod from sagging under its own weight, it was suspended near the centre with a simple piece of string. Padding resistors match both ends of the rod to 50 Ω. This is a great opportunity to discover that resistors are not just resistive, and that different resistors have different parasitic capacitances and inductances. For example, low-value 1206 SMD chip resistors are predominantly capacitive at high frequency, whereas 1206 MELF resistors are inductive. We used MELFs, combined with capacitive shims to tune out the inductance. The first and last few decimeters of the chamber and the rod are constant-ratio cones, narrowing down from the full size pipe to diameters compatible with standard N-connectors.

The vacuum flanges at each end of the WCM resonate at 2.5 GHz. This was reduced by inserting RF springs in the gaps between the flanges.

Some residual reflections cannot be avoided. The time-domain reflection plot of Fig. 10 shows what could finally be achieved. The vertical scale is normalised to the incident step. The tallest reflections are about 4 %.

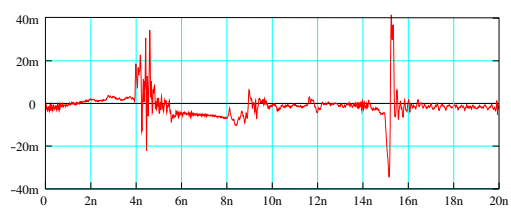

Figure 10: Beam simulation rod TDR plot.

ISBN 978-3-95450-177-9

The reflections around 4 ns and 15 ns in Fig. 10 are from the ends of the rod. The small reflections at 8 ns and 12 ns are the vacuum flanges at either end of the WCM. The step at 9 ns is the gap of the WCM itself. These measurements were taken using a Tektronix S-52 pulse generator and an S-6 sampler, having a 30 ps risetime, or equivalently a 10 GHz bandwidth.

Despite the effort invested in simulating the main structure of the WCM, several surprises cropped up, resulting from seemingly innocent mechanical details. For example, the absorbing ferrites along the outside wall are mounted on two aluminium hoops that are held in place by a narrow steel retainer ring. The hoops and the ring have some play within the WCM container to allow for mechanical tolerances and moved around every time the WCM was handled. This led to mysterious multi-GHz resonances that were never the same twice. Springs and RF gaskets were added to ensure that these parts would stay put.

Another intermittent several-GHz resonance was traced to the probe pins shown in Fig. 4. The pins have split tips designed to engage with some spring force in their sockets in the edge of the vacuum chamber across the gap. Sometimes, one of the prongs wouldn't touch the socket. From an EM point of view, the free prong is a little antenna resonating at a frequency where its length is $\frac{1}{4}\lambda$, at around 4 GHz. The problem was solved simply by splaying the prongs a little.

Both time domain and frequency domain reflectometry on the WCM output ports were indispensable to detect such problems.

PERFORMANCE MEASUREMENTS

Figure 11 shows the measured risetimes on individual ports. Since the ports closer to the centre of the beam pipe collect charge over a smaller section of the circumference, the signal rises much faster than for the ports farther away.

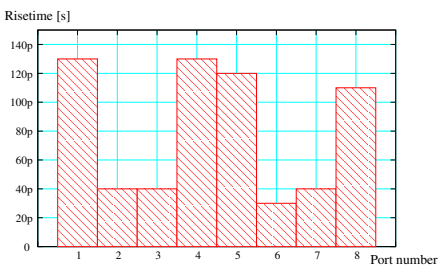

Figure 11: Risetimes measured on individual ports.

The final step response output signal, Fig. 12, has a risetime of 60 ps. The nicks near 13 ns and 17 ns are reflections from the end of the beam simulation rod and would not exist for real beams.

APPLICATION RESULTS

In the PS, the WCMs deliver signals for three main applications: low-level RF feedback, beam shape measurement and longitudinal phase space tomography (Fig: 13) [4]. The Tomoscope is an intensively used diagnostic tool in the PS control room and the better signal quality and greater bandwidth of these WCMs have significantly improved the clarity of the tomograms.

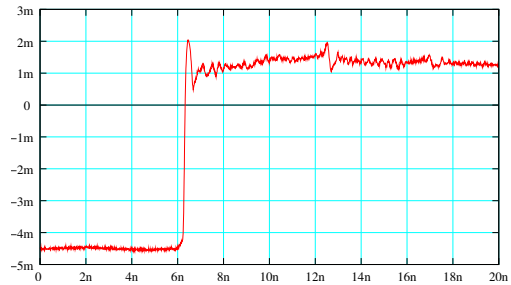

Figure 12: Overall combined output signal has a 60 ps step response risetime.

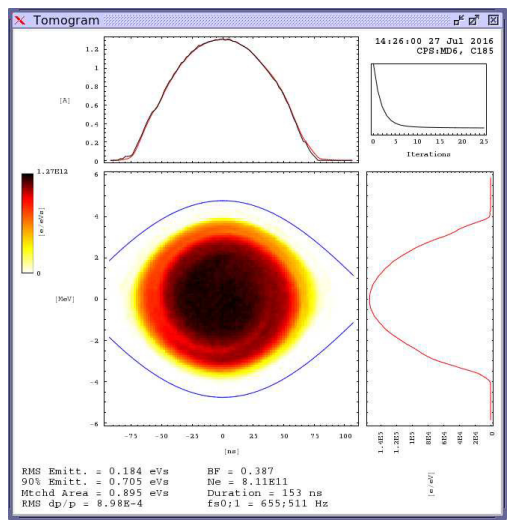

Figure 13: A longitudinal phase space tomogram of a proton bunch in the PS.

ACKNOWLEDGEMENTS

We gratefully acknowledge the cooperation of the CERN vacuum group and mechanical workshops in the successful conclusion of this project.

REFERENCES

[1] T.P.R. Linnecar, "The high frequency longitudinal and transverse pick-ups used in the SPS", CERN-SPS-ARF-78-17, CERN, Geneva, Switzerland.

[2] J. Durand, "Combining wideband signals from a wall current monitor", PS-LP-Note-94-14-Tech, CERN, Geneva, Switzerland.

[3] P. Odier, "A new wide band wall current monitor", CERN-AB-2003-063-BDI, CERN, Geneva, Switzerland.

[4] S. Hancock, P. Knaus, M. Lindroos, "Tomographic Measurements of Longitudinal Phase Space Density", CERN-PS-98-030-RF, CERN, Geneva, Switzerland.

ISBN 978-3-95450-177-9

TEST RESULTS FROM THE ATLAS HYBRID PARTICLE DETECTOR PROTOTYPE*

C.A. Dickerson#, B. DiGiovine, L.Y. Lin, Argonne National Laboratory, Lemont, IL 60439, USA
D. Santiago-Gonzalez, Louisiana State University, Baton Rouge, LA 70806, USA

Abstract

At the Argonne Tandem Linear Accelerator System (ATLAS) we designed and built a hybrid particle detector consisting of a gas ionization chamber followed by an inorganic scintillator. This detector will aid the tuning of low intensity beam constituents, typically radioactive, with relatively high intensity (>100x) contaminants. These conditions are regularly encountered during radioactive ion beam production via the in-flight method, or when charge breeding fission fragments from the CAlifornium Rare Isotope Breeder Upgrade (CARIBU). The detector was designed to have an energy resolution of ~5% at a rate of 10^5 particles per second (pps), to generate energy loss and residual energy signals for the identification of both Z and A, to be compact (retractable from the beamline), and to be radiation hard. The combination of a gas ionization chamber and scintillator will enable the detector to be very versatile and be useful for a wide range of masses and energies. Design details and testing results from the prototype detector are presented in this paper.

INTRODUCTION

At the Argonne Tandem Linear Accelerator System (ATLAS) we built and tested a fast, compact particle detector to aid the tuning of low intensity beam constituents with relatively high intensity (>100x) contaminants. These conditions are regularly encountered during radioactive ion beam production via the in-flight method, or when charge breeding fission fragments from the CAlifornium Rare Isotope Breeder Upgrade (CARIBU). The in-flight method of RIB production at ATLAS generally produces beams of interest with energies 5-15 MeV/u and masses less than 30 AMU, while reaccelerated fission fragments from CARIBU, 80 < A < 160, are typically accelerated to energies of 4-10 MeV/u. Our goal is to achieve ~5% energy resolution at a total rate of 10^5 pps over these energy and mass ranges without significant performance degradation after extended use.

The detector combines a gas ionization chamber (IC) with an inorganic scintillator, Fig. 1, to generate energy loss, ΔE, and residual E signals, which enable the identification of both the Z and the A of the beam constituents. The IC configuration followed designs for similar Tilted Electrode Gas Ionization Chambers (TEGIC) [1-2] – closely spaced parallel grids normal to the beam direction. Resolutions of ~4% and ~2% were reported for A and Z identification, respectively. GSO:Ce, the chosen scintillator, is the most radiation hard of any well characterized scintillator [3], has a 60 ns decay time, and 3-5% energy resolution for heavy ions [4-5]. The scintillator will provide residual E for particles not stopped in the gas, and enables the flexibility to tune the gas properties for the best signal while largely ignoring the gas' stopping power. An avalanche photo diode (APD) was selected as the photoelectric device mainly due to the device's compactness. A more detailed discussion of the design considerations was previously reported [6].

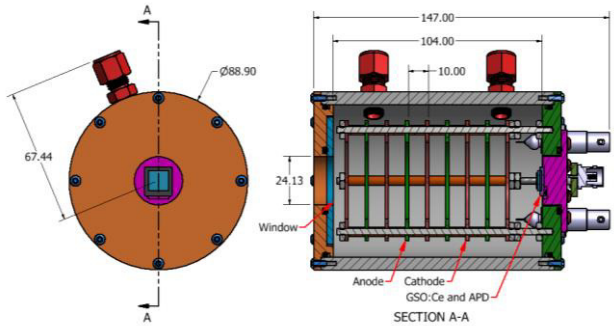

Figure 1: A model of the ATLAS hybrid detector. Dimensions are in mm.

EXPERIMENT

For the results reported here the scintillator and the gas IC were tested separately; the GSO:Ce was not incorporated into the assembly of the IC. Additionally, an insertion mechanism and vacuum chamber for the hybrid detector have not been designed yet, so the front plate of the IC was adapted to fit directly on a 6 in. CF flange at the end of the beamline.

The ion beam used in these tests was a cocktail of 7.28 MeV/u $^{18}O^{4+}$, $^{27}Al^{6+}$, and $^{36}Ar^{8+}$, corresponding to 131 MeV ^{18}O, 197 MeV ^{27}Al, and 262 MeV ^{36}Ar. The ^{36}Ar and ^{18}O were injected into the ECR source via gas metering valves, and were delivered at similar intensities. The ^{27}Al was a contaminant from the ECR plasma chamber walls, thus it was much less intense and only identified upon analysis.

The gas IC window was 1.14 mg/cm^2 (8 μm) Kapton epoxied to an aluminum window mount to facilitate replacement in the event a window broke, Fig. 2.a. The electrical grids were made using ø20 μm gold plated W wire spaced 1 mm apart, Fig. 2.a, which allowed ~98% transmission. The grid frames are printed circuit boards with the appropriate solder traces to mount the grid wire and solder pads to make inter-grid connections. Kapton

*Work supported by U.S. Department of Energy, Office of Nuclear Physics, under contract DE-AC02-06CH11357
#cdickerson@anl.gov

ISBN 978-3-95450-177-9

coated wire was used to electrically connect grids, and the electrodes were configured into two 40 mm long sections, each consisting of two anodes and four cathode-anode gaps, Fig. 2.b. The cathode grids were commonly connected, and grounded to the chamber.

A bias of 350 V was applied to the anodes, and with 450 Torr of CF_4 supplied to the IC a normalized electric field of 0.78 V/(Torr-cm) was present. At this field the electron drift velocity in pure CF_4 was $9x10^6$ cm/μs [7]. Ortec 142B preamplifiers and 572 spectroscopy amplifiers set to 0.5 μs shaping times conditioned and amplified the anode signals, then a 12 bit ADC digitized the pulses before recording. A Hamamatsu S8664-1010 APD with a gain of 50 converted and amplified photons from the scintillator. Electrical signals from the APD were conditioned and recorded in the same manner as the IC signals.

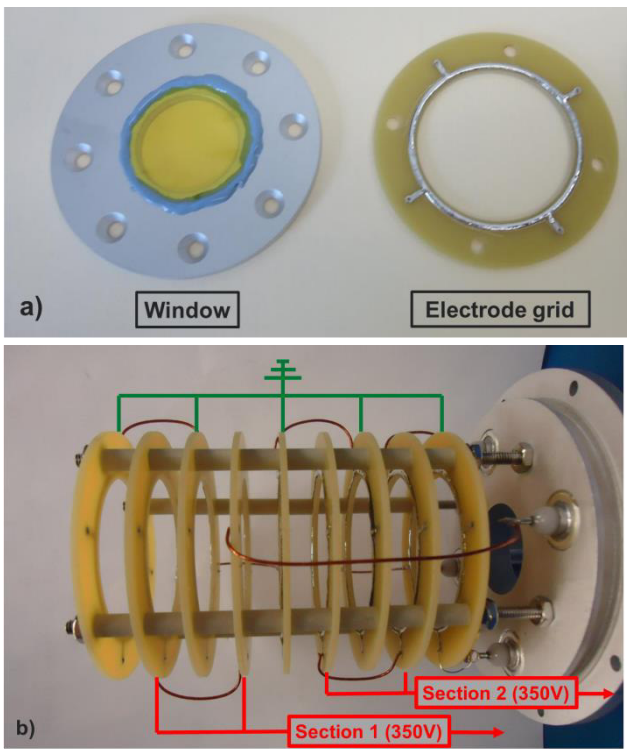

Figure 2: a) IC assembly components: 1.14 mg/cm^2 (8 μm) Kapton window epoxied to an aluminum mount, and an electrode grid of ø20 μm gold plated W wire soldered to a printed circuit board frame. b) The assembled electrode grids configured in two 40 mm long sections.

RESULTS

Signal amplitudes corresponded to the amount of energy deposited in the given section. All the ions in the beam made it through section 1, so these signals corresponded to energy loss, ΔE, signals. The ^{18}O and ^{27}Al also punched through section 2 and produced additional ΔE signals, while the ^{36}Ar stopped in section 2, resulting in residual E signals. The raw data was calibrated with energy loss calculations from LISE++ [8] using the appropriate thicknesses of the various energy loss regions: the window, the dead zone between the window and the first cathode, section 1, and section 2.

Section 1 signals were converted to represent the Z of the ions, since $\Delta E \propto Z^2/v^2$, and the velocities of the ions from the linac were identical, $\Delta E \propto Z^2$ in this case. Energy signals from both sections could be added to indicate the total deposited ion energy. Summing the calibrated energy loss from section 1 and the residual energy from section 2 for ^{36}Ar, the only ion completely stopped in the gas, indicated the mass (A) resolution of the detector since the total energy is directly proportional. Figure 3 shows the results of a typical IC spectrum acquired at a rate of 0.7 kpps. Artifacts from the wire grids are seen as intense, discreet spots along the same ordinate values as identified ions, and striations near ^{18}O are attributed to reaction products from interactions with the window.

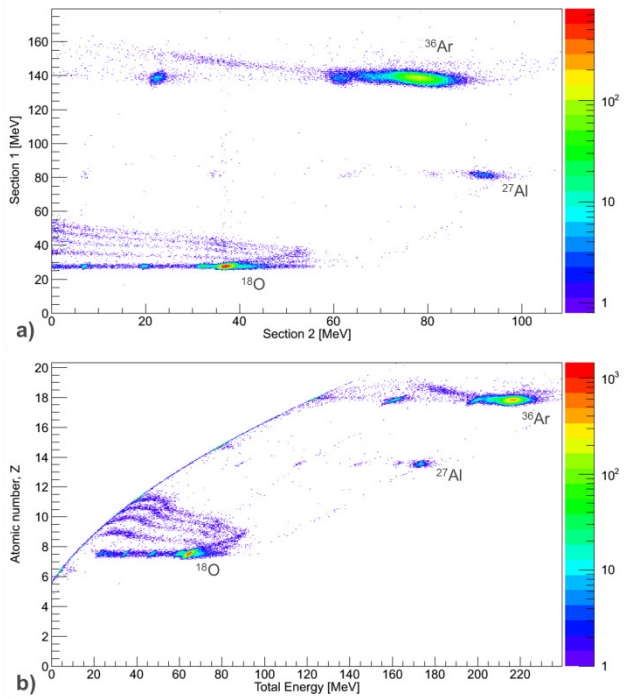

Figure 3: a) Energy loss in section 1 vs section 2, calibrated with energy loss calculations. b) Energy loss signals were converted to Z and total energy loss to measure Z and A resolutions.

Figure 4 shows the achievable Z and A resolutions for a variety of incident particle rates. The expected resolutions of ≤ 5% and ≤ 2% in A and Z, respectively, at 10^5 pps were not realized. Only at rates ≤ 2.4 x 10^4 pps were these resolutions achievable, so additional efforts, discussed below, will be made to increase the range at which this detector's resolution is sufficient.

The resolutions of the ^{18}O and ^{36}Ar peaks (3.5% and 4.8%, respectively) in the GSO:Ce are shown in Fig. 5, a typical spectrum acquired at 1.8 kpps. Possible evidence of quenching is seen in Fig. 5; the ratio of centroid channel numbers between the ^{36}Ar peak and the ^{18}O peak is 1.5 (1050/700), but should be 2, considering ^{36}Ar had

ISBN 978-3-95450-177-9

twice the energy as ^{18}O. Evidence of rate dependent peak positions, not presented here, was also observed. These features, quenching and rate dependence, may be problematic for particle identification and require additional investigation.

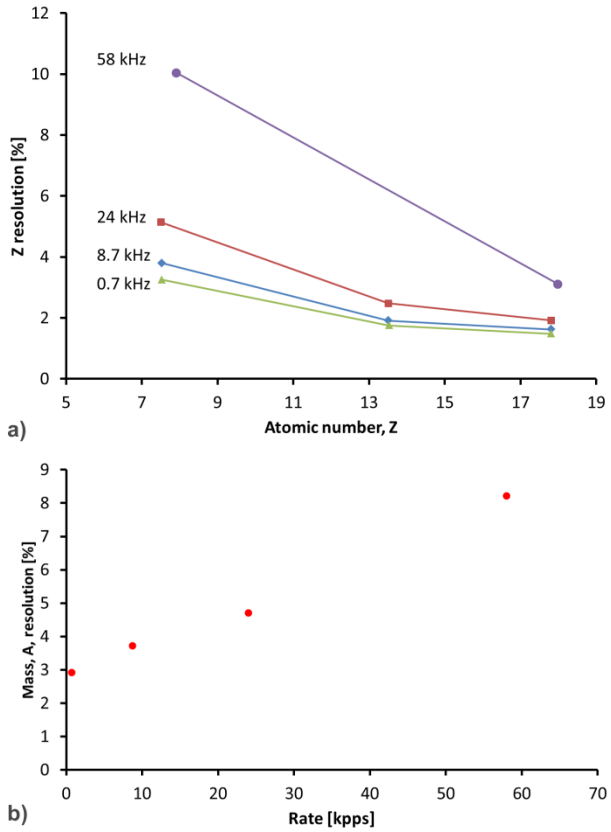

Figure 4: a) Z resolution vs. Z and rate in the IC. b) Mass, A, resolution vs. rate for ^{36}Ar deposited into the IC.

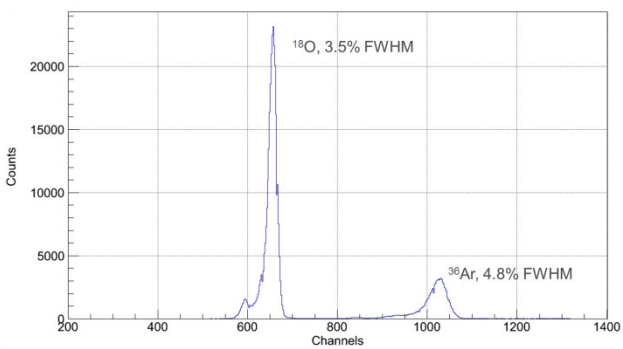

Figure 5: Typical GSO:Ce spectrum acquired at 1.8 kpps.

FUTURE WORK

Significant resolution degradation occurred by 5.8 x 10^4 pps in the IC, which is at a lower rate than we expected. Two potential factors influencing this performance were the ion beam density and the electron drift velocity. The ion beam was delivered directly from the linac, so the quality was relatively good and could be focused well. This most likely resulted in a high ion-gas interaction density along the beam axis while not utilizing much of the IC volume. Recombination was likely significant for these conditions. To lower the beam density in the future we will either defocus the beam or use a scattering foil up stream of the detector.

The electron drift velocity can be increased by ~30% by increasing the normalized field to ~3 V/(cm-Torr) for pure CF_4, or by mixing 20% CF_4 with 80% Ar. [7]. The preamplifiers are limited to a bias of 1000 V, so we will investigate the rate dependence of the detector performance with a gas mixture. The potential drawback is that the gas stopping power decreases significantly, so the scintillator is required to produce residual energy signals even for ion masses of ~50 at ~10 MeV/u.

SUMMARY

Optimizing ATLAS for the delivery of radioactive ion beams requires a detector capable of distinguishing a low intensity species of interest from a high intensity background. The combination of a gas ionization chamber and scintillator was designed, constructed, and tested to assess the detector's ability to perform the needed separation and particle identification. The gas IC chamber performance was promising up to a rate of 2.4 x 10^4 pps; mass resolution was 4.7% and Z resolution was 1.9% for $Z \geq 18$. Measures will be taken to minimize the beam density in the IC and increase the electron drift velocity to achieve similar performance up to a rate of 10^5 pps. The performance of the GSO:Ce was also promising – mass resolutions of 3.5% and 4.8% for 18O and 36Ar, respectively – but not without issues; potential influences of quenching and rate dependent peak positioning were observed and will be investigated further.

REFERENCES

[1] K. Kimura et al., "High-rate particle identification of high-energy heavy ions using a tilted electrode gas ionization chamber," *Nucl. Instr. Meth. A*, vol. 538, p. 608-614, 2005.

[2] K.Y. Chae et al., "Construction of a fast ionization chamber for high-rate particle identification," *Nucl. Instr. Meth. A*, vol. 751, p. 6-10, 2014.

[3] V.V. Avdeichikov et al., "Light output and energy resolution of CSI, YAG, GSO, BGO, and LSO scintillators for light ions," *Nucl. Instr. Meth. A*, vol. 349, p. 216-224, 1994.

[4] M. Kobayashi et al., "radiation hardness of cerium-doped gadolinium silicate GD2SiO3:Ce against high energy protons, fast and thermal neutrons," *Nucl. Instr. Meth. A*, vol. 330, p. 115-120, 1993.

[5] G. Miersch et al., "Fast scintillators as radiation resistant heavy ion detectors," *Nucl. Instr. Meth. A*, vol. 369, p. 277-283, 1996.

[6] C. Dickerson et al., "A fast, compact particle detector for tuning radioactive beams at ATLAS," in *Proc. HIAT'15*, Yokohama, Japan, Sep. 2015, paper MOPA29, pp. 107-109.

[7] L.G. Christophorou et al., "Fast gas mixtures for gas-filled particle detectors," *Nucl. Instr. Meth*, vol. 163, p. 141-149, 1979.

[8] LISE++, http://lise.nscl.msu.edu/lise.html

ISBN 978-3-95450-177-9

BEAM TUNING FOR LONGITUDINAL PROFILE AT J-PARC LINAC

A. Miura†
J-PARC Center, Japan Atomic Energy Agency, Tokai, Ibaraki, JAPAN
Y. Liu, T. Maruta, T. Miyao
J-PARC Center, High Energy Accelerator Research Organization, Tsukuba, Ibaraki, JAPAN

Abstract

Using bunch shape monitors (BSMs), we measured the longitudinal bunch lengths of negative hydrogen ion beams in the J-PARC linac. A BSM was installed between two linacs, separate-type drift tube linac (SDTL) and an annular-ring-coupled structure linac (ACS), having acceleration frequencies of 324 and 972 MHz, respectively. We used radio-frequency amplitude modulation of bunches in the beam transport between the SDTL and ACS to minimize emittance growth and beam loss. We conducted amplitude scanning and compared the results with the twiss-parameters obtained from the transverse profiles. In this paper, we discuss the results of amplitude tuning of the buncher cavity at the point of beam loss and emittance. We also discuss the measurement results for various equipartitioning settings of quadrupole magnets.

INTRODUCTION

At the energy upgrade project in the J-PARC linac, we installed an annular-ring-coupled structure linac (ACS) whose acceleration frequency of 972 MHz can be used to obtain beam energies ranging from 191 to 400 MeV downstream of the separate-type drift tube linac (SDTL). The acceleration frequency of the ACS is three times that of the SDTL; as this frequency jump may lead to beam loss owing to longitudinal (phase spread) mismatch, conducting phase-width matching between the SDTL and ACS sections is critical. To implement this matching strategy, we developed bunch shape monitors (BSMs) to follow the beam behavior in the two ACS-type buncher cavities. A tuning method involving phase-width matching of the three BSMs along with transverse profile matching was proposed. To establish equipartitioning conditions that would meet the beam dynamics design of the J-PARC linac, we use both the transverse profile and the phase width. In this paper, we explain and discuss the measurement results for the various equipartitioning settings.

BUNCH SHAPE MONITOR IN J-PARC LINAC

Bunch Shape Measurement

In collaboration with the Institute for Nuclear Research of the Russian Academy of Sciences (INR/RAS), a device for the beam phase width measurement was designed based on the observation of secondary electrons from a single wire intersecting a beam. After a series of beam bunches under measurement intersect a target wire having a diameter of 0.1 mm, low-energy secondary electrons are emitted owing to the beam–wire interaction [1, 2]. The wire is held at a negative potential of typically −10 kV. The secondary electrons move almost radially and enter a radio frequency (RF) deflector through collimators. An RF field with the same frequency as the accelerating RF (324 MHz) is applied to deflect the excess secondary electrons by an angle that depends on the phase of the deflecting field. By adjusting the deflecting field phase with respect to the accelerator RF reference, the phase widths of the bunches can be obtained.

Installation Layout

Three BSMs were installed upstream of the ACS section and two ACS-type bunchers were installed between the SDTL and ACS sections, as shown in Fig. 1. We implemented a tuning method involving phase-width matching using the three BSMs along with transverse profile matching. During the BSM measurements, the two 972-MHz ACS-type buncher cavities served as control knobs for phase-width matching [3]. Later, all three BSMs were removed and disassembled for out-gas conditioning. Currently, only one BSM has been reinstalled in front of the ACS01 cavity using additional vacuum pumps [4]. In this study, we used all three BSMs for amplitude scanning of the two ACS type-bunchers, while the single reinstalled BSM in front of the ACS01 was primarily used for an equipartitioning study. We set the longitudinal direction as the direction for phase spreading.

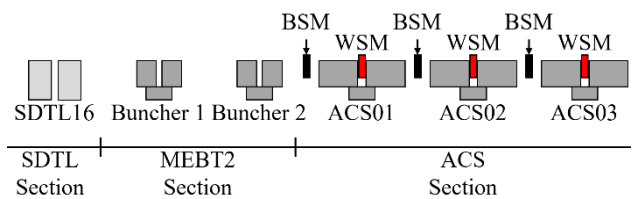

Figure 1: BSM and WSM layout around the upstream ACS section. Positions of WSMs and BSMs are indicated with arrows.

BUNCH SHAPE MEASUREMENT

During BSM calibration, a full scan was performed wherein the RMS beam width was measured as a function of SDTL15 cavity amplitude and compared with simulations performed using IMPACT and TraceWin. The results for the most upstream BSM (BMS#1) in Fig. 1, which was used further to measure emittance, can be seen in Fig. 2, wherein a close agreement between simulation and measurement is observed.

With the synchronous phase of SDTL15 set to bunching mode (−90°), the root-mean-square (RMS) phase width was measured at the BSMs as a function of the cavity

† akihiko.miura@j-parc.jp

ISBN 978-3-95450-177-9

amplitude. The resulting beam profiles measured for the J-PARC linac can be seen in Fig. 2, which shows the phase width for the entire pulse duration. The phase-width emittance measurement was performed at the SDTL–ACS transition using one BSM. The emittance and twiss-parameters at SDTL15 were then calculated by performing a three-parameter scan to fit the measured beam widths. The fitting was performed by particle tracking using IMPACT simulation assuming a Gaussian distribution at SDTL15 [5].

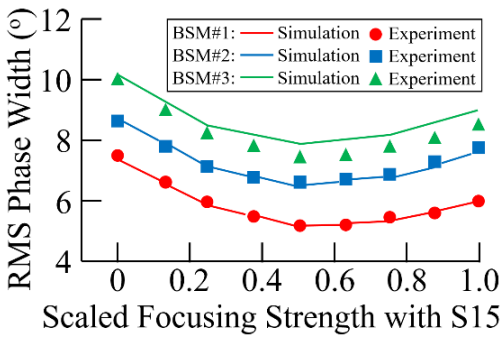

Figure 2: Measured RMS beam phase width versus focusing strength of last SDTL cavity (SDTL15) and corresponding simulation results.

BEAM STUDY FOR EQUIPARTITIONING

To study the space-charge-driven transverse–longitudinal (phase spread) coupling resonance, we used the BSMs to measure the emittance of phase width. The results are expected to contribute to the design of the beam operational parameters for the energy-upgraded linac. The high-intensity linac design follows the equipartitioning (EP) condition, namely, that strict control of the transverse and longitudinal tune ratios throughout the linac is considered to be important. To ensure space-charge-driven resonance, emittance exchange between the longitudinal and transverse planes should be minimized, as indicated in the tune ratio diagram (Hofmann's stability charts). Using BSMs, experimentally measuring this resonance phenomenon was possible [6] by simultaneously monitoring the transverse and longitudinal emittances for the first time.

When the J-PARC project was being designed, there was sufficient evidence from the pioneering works of I. Hofmann, R. A. Jameson et al, [7] and data based on experience from the Spallation Neutron Source (SNS) at Oak Ridge National Laboratory in the United States that EP-conditioned lattices offer a natural solution for emittance conservation in such high-intensity hadron accelerators. Fortunately, the J-PARC linac could find its EP solution as a baseline design without sacrificing hardware efficiency. The J-PARC linac can also be used in a wide range of off-EP conditions. As such, there is an opportunity not only for investigating basic beam physics principles but also for further optimizations of machine operation.

Normally, it can be assumed that $T_x = T_y$, where T_x, T_y, and T_z represent the horizontal, vertical, and longitudinal temperatures, respectively. As shown in Fig. 3, it is within the existing hardware capability to set the DTL, SDTL, and ACS to operate at a wide range the horizontal-to-longitudinal-temperature ratio (T_x/T_z). It is also equivalent to the ratio of oscillation energies in the transverse and longitudinal planes, as given as follows:

$$T_x/T_z = r_x^2 k_x^2 / r_z^2 k_z^2 = \varepsilon_x k_x / \varepsilon_z k_z \quad , \qquad (1)$$

where r is the radius of the beam RMS envelope, ε is the RMS emittance, and the degree of focusing is proportional to the wave number k (with current) and k_0 (zero current). For instance, the settings to the left in Fig. 3 represent reduced transverse focusing or increased longitudinal focusing. The EP condition generates the largest stable area for beam propagation.

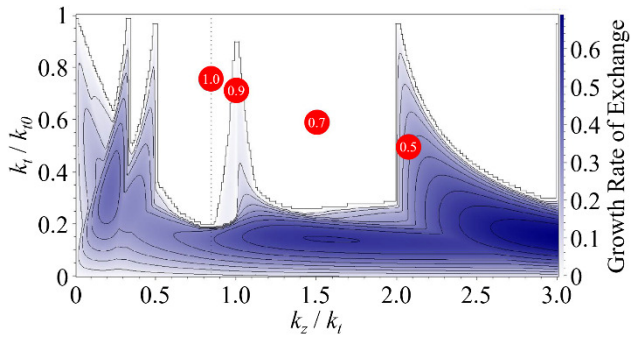

Figure 3: Hoffman's stability chart for J-PARC linac with emittance ratio $\varepsilon_z/\varepsilon_t = 1.2$ [9].

Four working points at temperature ratios of 1.0, 0.9, 0.7, and 0.5 were assessed, as shown in Fig. 3. To avoid any uncertainty from matching into the DTL, only the SDTL section was modified for each test case; this was done by adjusting the quadrupole gradients so that the beam stayed on the resonance, thus, enhancing the effect. The front-end and DTL settings were kept constant for all measurements. The beam current was set at 15 mA, which is the operating value.

The experimental procedure followed several steps. First, the quadrupole settings in the SDTL section were changed to bring the working point to the desired value. Transverse matching was then achieved at the DTL–SDTL transition with an array of wire scanner monitors (WSMs) and quadrupoles. Next, the WSMs were used to measure the transverse emittance at the ACS entrance. Finally, the BSMs at the ACS entrance were used to evaluate the longitudinal emittance (details of the SDTL–ACS section are shown in Fig. 1). This procedure was repeated for each of the working points. The gradients of four quadrupoles in DTL–SDTL transition were varied, and the beam size was measured using four periodically placed wire WSMs. Matching involved the use of an envelope over several quadrupole tuning iterations until the RMS beam widths became equal.

By determining the phase advance between the wire scanners, the emittance and twiss-parameters could be obtained by applying a parameter fitting routine to the measured RMS beam widths. For this, a three-dimensional

ISBN 978-3-95450-177-9

envelope model of the machine used during the operation was developed using Open XAL [5, 8].

The phase width measurement results are shown in Fig. 4, and the emittance evolution throughout the linac for the four cases is summarized in Fig. 5 and Table 1, which shows some emittance exchange for the case $T = 0.9$ ($k_z/k_t = 1$) and a much stronger exchange for $T = 0.5$ ($k_z/k_t = 2$), but no exchange for the cases $T = 1.0$ or 0.7. It is also interesting to note that there is a strong longitudinal emittance growth between the end of the SDTL and BSM locations, which is caused by the absence of longitudinal focusing in this section and is the reason that multiparticle tracking is required to estimate the emittance.

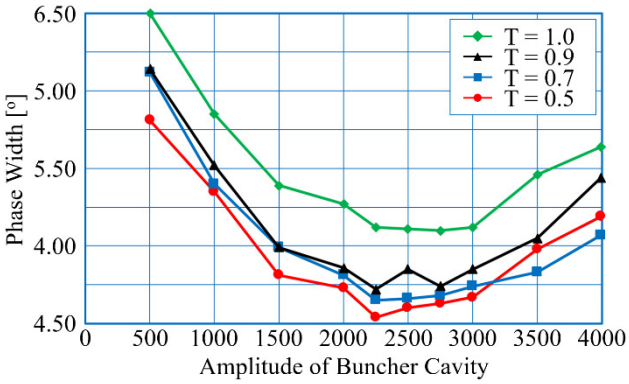

Figure 4: Measured phase-width in the linac for the four tested working points.

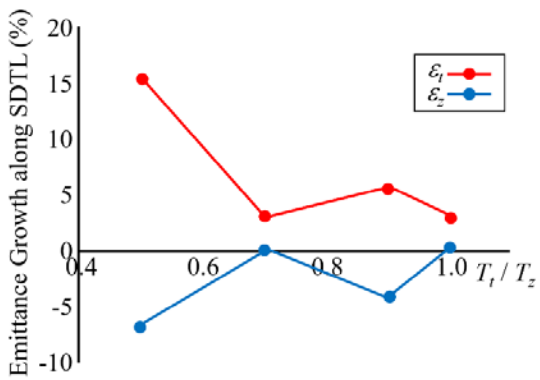

Figure 5: Simulated emittance growth in the linac for the four tested working points.

Table 1: Measured J-PARC Linac Emittance Values for the Four Working Points Tested [9].

T_t/T_z	DTL output [π.mm.mrad]	
	ε_t	ε_z
1.0	0.216	0.269
0.9	0.229	0.233
0.7	0.253	0.223
0.5	0.293	0.160

As explained above, the transverse emittance was measured at the SDTL output using a set of WSMs at the beginning of the ACS section. The longitudinal emittance was estimated using the RMS beam phase lengths measured by BSM1.

A clear increase in transverse emittance coupled with a decrease of longitudinal one was observed for the case $T = 0.5$. This is the first experimental observation of emittance exchange in a linac driven by the $k_z/k_t = 2$ resonance; it is also the first emittance exchange measurement in a proton linac with emittance ratios close to 1. Additionally, an unexpected halo was transversely measured, as indicated by the long tails in Fig. 6. Some exchanges were also measured for the case T = 0.7, which, as it has neither been numerically predicted nor by theory, was unexpected.

Although the first experimental evidence for emittance exchange at $k_z/k_t = 2$ in a proton linac with emittance ratios close to 1 is certainly encouraging in terms of the prospects for EP tuning, questions still remain. Efforts are being made to quantify our measurement limitations and fully understand the results. The unexpected emittance exchange seen at $T = 0.7$ should also be studied further.

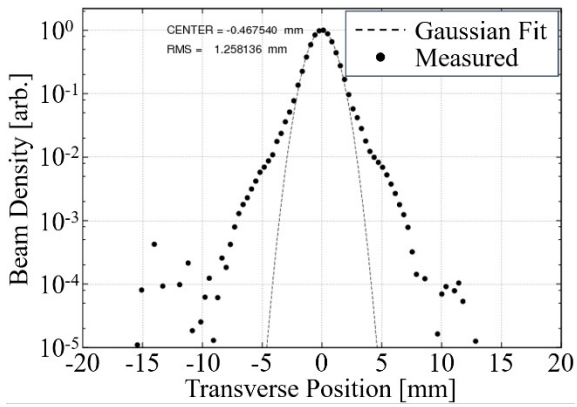

Figure 6: Measured transverse beam profiles in the ACS section at $T_t / T_z = 0.5$.

CONCLUSION

Experiments to determine the beam dynamics of the J-PARC linac design, which follows the EP condition, were conducted by measuring the longitudinal bunch length to produce Hofmann's stability charts indicating a region of space-charge driven transverse–longitudinal coupling resonance. The results supported this chart and the condition for avoiding the resonant region was estimated using the operational settings.

BSM measurements have the advantage of being able to measure longitudinal emittance; in this study, the accuracy of both transverse and longitudinal emittance measurements was verified. This method brings the discussion back to the choice of working point (i.e., using the EP set-point or not) and the use of stability charts in linac design.

The implications of these results for future linac designs are clear. Based on this experiment, there is now sufficient experimental and theoretical evidence to support the avoidance of the $k_z/k_t = 1$ and $k_z/k_t = 2$ stopbands. From our analysis, it is clear that a design procedure based on the EP criterion does not necessarily equate to the absence of emittance growth and halo development. It is also clear that safe working points do exist outside of EP; to avoid the

ISBN 978-3-95450-177-9

growth of intra-beam-stripping, setting a larger T point as a safe working position outside of the EP region is possible.

REFERENCES

[1] A. V. Feschenko, "Methods and Instrumentation for Bunch Shape Measurements", in *Proc. Particle Accelerator Conf. (PAC 2001)*, Chicago, USA, 2001, p. 517.

[2] A. Miura, *et al.,* "Bunch Shape Measurement of 181 MeV Beam in J-PARC Linac", Conf. Proc. Journal of the Physical Society of Japan (JPS), No. 8, 011003, (2015).

[3] A. Miura *et al.,* "Bunch Length Analysis of Negative Hydrogen Ion Beam in J-PARC Linac", in *Proc. the 4th Int. Beam Instrumentation Conf. (IBIC 2015)*, Melbourne, Australia, 2015, TUPB027.

[4] A. Miura *et al.,* "Vacuum Improvement of Bunch Shape Monitor for J-PARC Linac", in *Proc. the 3rd Int. Beam Instrumentation Conf. (IBIC 2014)*, Monterey, California, USA, 2014, TUPD09.

[5] Y. Liu *et al.,* "Stability Studies for J-PARC Linac Upgrade to 50 mA/400 MeV", *Proc. the sixth Int. Particle Accelerator Conf. (IPAC15),* Richmond, Virginia, USA, 2015, THPF039.

[6] I. Hofmann *et al.,* "Space Charge Resonances in Two and Three Dimensional Anisotropic Beams", Physical Review Special Topics Accelerator and Beams 6, 024202 (2003).

[7] R. A. Jameson, "Equipartitioning in Linear Accelerators", *Proc. 1981 Linear Accelerator Conf.*, Santa Fe, New Mexico, USA, 1981, pp. 125.

[8] T. Pelaia II, "Open XAL Status Report 2013", *Proc. 4th Int. Particle Accelerator Conf. (IPAC2013),* Shanghai, China, 2013, MOPWO086.

[9] C. Plostinar, *et al.,* "Summary of the 2012 J-PARC Space Charge Resonance Experiment", in private communication, 2015.

ISBN 978-3-95450-177-9

SNS RFQ VOLTAGE MEASUREMENTS USING X-RAY SPECTROMETER

A.P. Zhukov, ORNL, Oak Ridge, TN 37830, USA

Abstract

Absolute measurement of vane voltage is essential to understand RFQ transmission. We used a non-intrusive technique of bremsstrahlung X-ray measurement. Several windows were installed in different locations of the RFQ to allow measurement of the X-ray spectrum. A CdTe spectrometer was used to estimate spectrum cutoff energy that corresponds to the vane voltage. Different device setups are described as well as measurement accuracy and interpretation of experimental data.

INTROUDUCTION

An RFQ is a crucial part of the SNS accelerator. It's performance directly affects beam power on target. The history of RFQ detuning issues [1] increased importance of full understanding and extensive characterization of RFQ parameters. These issues are identified as critical for successful upgrades of the SNS accelerator. The Beam Test Facility (BTF) has been constructed for validation of the new spare RFQ [2]. One of the key parameters is the actual RFQ vane voltage. X-ray spectra measurement is a common technique used to obtain vane voltage independently, not relying on design parameters and magnetic field probes [3, 4]. We first reported the preliminary results of such measurements in 2014 [5].

EXPERIMENTAL SETUP

Theory of Operation

There is always a stream of electrons between RFQ vanes due to the field emission. These emitted electrons are accelerated to the energy corresponding to RFQ voltage and bombard the copper vane. Electrons produce radiation in the form of X-rays with energy spectrum extending up to the energy of an incident electron. Thus measuring the maximum energy of bremsstrahlung X-rays one can obtain the vane voltage.

X-ray Spectrometer

We use an off the shelf X-123 CdTe X-ray spectrometer [6]. Spectroscopy is the main application of this device so one of the main parameters is FWHM (Full Width at Half Maximum). The spectrometer has an internal amplifier that has to be calibrated for a particular energy range. We used Am-241 source for calibration. It has a peak at 69.5 keV that is close enough to maximum expected energy of X-rays – around 80 keV. The FWHM contributes to error of our measurements and is close to 0.8 keV for this energy. The amplifier's settings were optimized to allow binning in 1024-channel MCA with maximum energy 90 keV. The calibration error was estimated to be 0.5 keV at 100 keV for spectrum shown on Fig. 1.

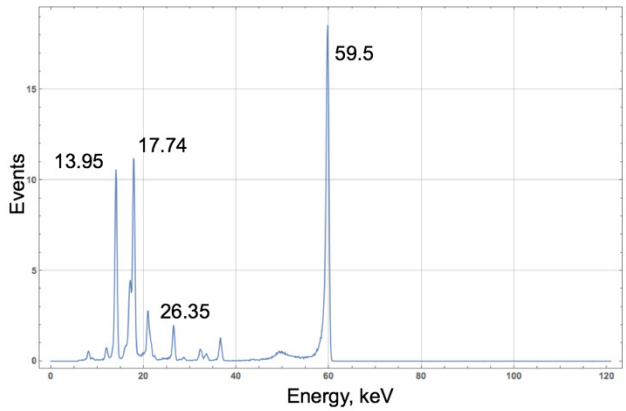

Figure 1: Spectrometer calibration with Am-241 source.

RFQ Ports

Special quartz windows were added to RFQ to allow X-rays reach the spectrometer that is mounted outside of the port looking at the window. The production RFQ that is currently used at the SNS accelerator has four windows. We used one spectrometer and attached it to different

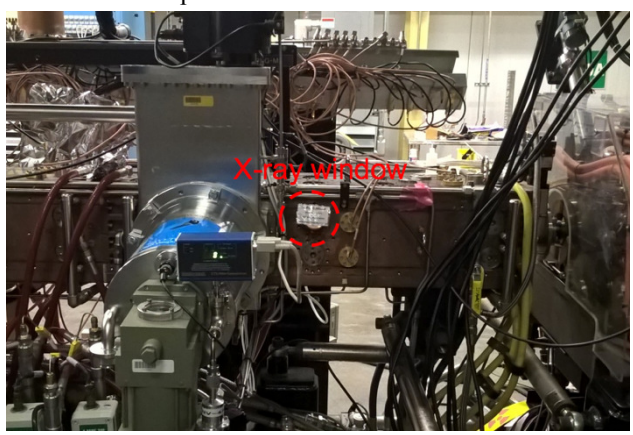

Figure 2: Quartz X-ray window installed in RFQ.

Proof of Principle Measurements

The first set of measurements was done without any shielding enclosure, using vendor calibration and the main goal was to observe correlation of RFQ set point (proportional to vane voltage) and X-rays spectrum. The Fig. 3 shows typical spectrum.

There are different ways of quantifying the cut-off energy [3, 4]. To obtain cut-off energy of the tail we used following procedure: the tail consisting of 0.5% of total events was considered background (shaded grey on Fig. 3), the adjacent 1.5% events were selected and the spectrum was linearized for this part (green shading and red line), intersection of the line with X – axis is called the maximum energy of this distribution.

ISBN 978-3-95450-177-9

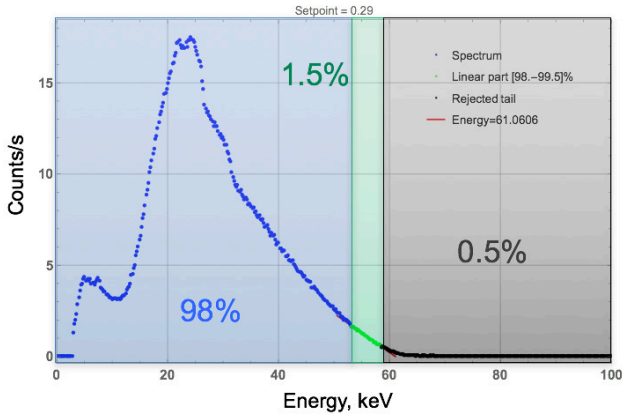

Figure 3: Typical spectrum measured by unshielded spectrometer.

The same procedure was applied to spectra obtained with different RFQ set points and plotted measured energy vs set point value as shown on Fig. 4.

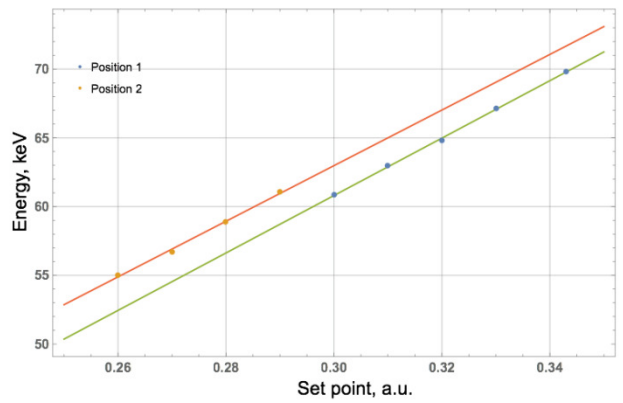

Figure 4: Measured X-ray energy vs RFQ set point taken in two different positions: orange – facing directly the window, green – moved 30 cm away and slightly misaligned.

It's clearly seen that the experimental data is well fitted by a straight line for measurements taken at the same position but there is a significant shift when two positions are compared. Thus, although the technique itself is working, there is no way to measure absolute value of the vane voltage with required accuracy (1-2 keV). Also the resulting energy for production set point appeared to be too low: less than 73 keV, such voltage would not provide RFQ efficiency that we observe in production.

Another issue we encountered is the total amount of radiation at different set points. Since field emission drops significantly with voltage decrease, the counting intensity is different, so we had to move the spectrometer closer for lower field set point. On the other hand, the spectrum is dominated by low energy peak and the spectrometer is saturated when it faces the window directly and the RFQ field is high.

Shielding and Collimation

The SNS front end has many sources of X-rays: the ion source has several high voltage lenses (~ 40 kV) and 65 kV extraction voltage, MEBT RF structures are capable of procuring X-rays with energies up to 100 keV. Since we are interested in X-rays from RFQ only, all other sources are considered background that needs to be filtered out. Since the spectrum by itself is not an objective of the measurement, we are not interested in low energy X-rays coming from RFQ, we have to measure the tail only.

Some filtering is achieved by spatial orientation of the spectrometer. But it appeared to be not enough because levels of radiation from the RFQ itself can vary greatly (10-300 mRem/h) and the radiations levels from rebunchers can vary independently. To alleviate this problem, we came up with a shielding enclosure, shown on Fig. 5, a set of collimators and screens placed in front of the detector's window – Fig. 6.

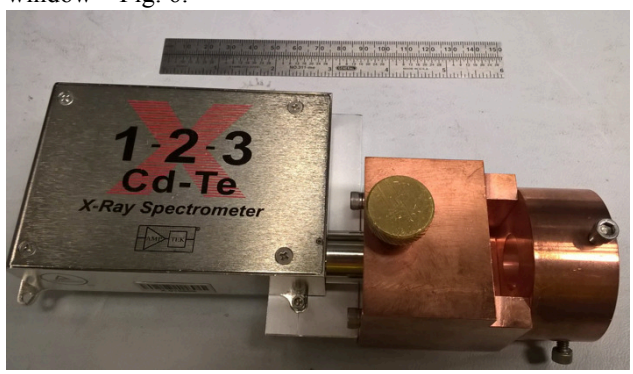

Figure 5: Spectrometer inside copper enclosure.

The outer shielding decreases input from background sources, the collimation makes sure that the source is actually vane's tip, and screen removes low energy part of the spectrum.

Figure 6: Set of collimators and screens.

Data Acquisition

We used the standard AmptekDpp [6] software that came with the spectrometer. It has an extensive set of parameters, that allow adjusting for different MCA thresholds, amplification settings and pulse shaping. We started with a standard spectroscopic configuration and then tailored them for high energy measurements: increased fast threshold to maximum. Since these settings are somewhat extreme we made sure that the peaks of calibration spectrum shown at Fig.1 is still reproducible with these settings.

ISBN 978-3-95450-177-9

RESULTS FOR SNS PRODUCTION RFQ

Considered the issues mentioned above we tested different collimation and shielding configurations and settled down on having a 2 mm pin hole behind 3 mm of copper shield. The enclosure itself has at least 1.5 cm of copper shielding around the detector, see Fig. 5. We also performed in house calibration with a radioactive source. Such modifications significantly changed the shape of observed spectra and absolute value of cut off energy Fig. 7 shows spectra measured at different ports. The spectrometer was attached directly to ports.

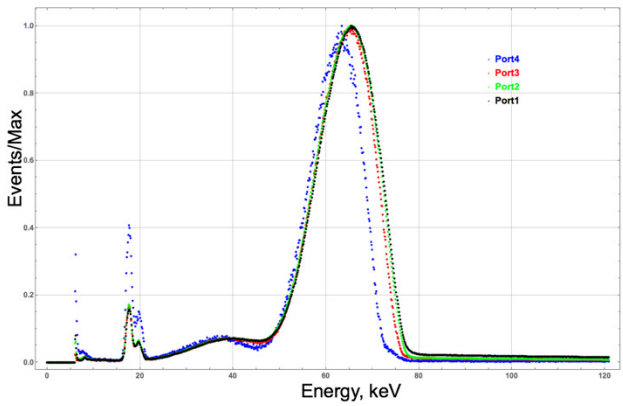

Figure 7: X-ray spectra at different ports, normalized over peak maximum.

As expected the low energy part was suppressed by the shield in front of the collimator. The port 4 (blue plot on Fig.7, the most downstream location) is significantly different from the other three ports. It's important to mention that its main high energy peak is shifted, while the bimodal peak below 20 keV seems to be in the same place (due to MCA nature of measurement the relative error is higher for lower energies, since the histogram bin width is constant). Also the ratio of main peak's maximum to low energy peak's maximum is constant for Ports 1-3, but is different for Port 4. And the most important difference demonstrates itself in the tail region. The "end" of the distribution comes to the same point, although the peaks are really different. Unfortunately applying the linearization technique described above gives different values of energy: 72.3 keV for port 4 and 75.9 keV for other ports, which is expected since the shape is different and the technique works fine for similar shapes. The absolute values measured for ports 1-3 are within 76-77 keV and are much closer to expected values.

CONCLUSION

We performed an extensive set of measurements trying to quantify the edge of X-ray spectrum caused by field emission in RFQ vanes. We successfully proved that the described linearization method works well for spectra with similar shape. A special collimated enclosure was designed and built to filter out X-rays from irrelevant sources. We were able to estimate the vane voltage of SNS RFQ within 2.5 keV (76 keV for field set point 0.323).

Spectra were measured for different ports and show similarity in shape for ports 1-3 and is different for port 4.

Future Plans

The RFQ parameters are known to change over time due to different reasons, so it will be beneficial to have several spectrometers to measure different ports simultaneously. The set of collimators allows to measure background with no pin-hole and subtract it from the measurement with a pin-hole. Such approach is not straightforward because of the pulse pile-up effects. Pile-up affects the artificial tail of the spectrum and is dependent on radiation intensity. Bringing down total number of counts per second (to avoid pile up) will require a significant time of measurement, so there should be a carefully designed trade off.

We also plan to have similar measurements for the spare RFQ after it is commissioned. There will be less background radiation and we will have more opportunities for measuring at different field settings.

ACKNOWLEDGMENT

ORNL is managed by UT-Battelle, LLC, under contract DE-AC05-00OR22725 for the U.S. Department of Energy. This research was supported by the DOE Office of Science, Basic Energy Science, Scientific User Facilities.

REFERENCES

[1] J. Galambos, "SNS Performance and the Next Generation of High Power Accelerators" in *proceedings of NA-PAC2013*, Pasadena, CA, USA, paper FRYAA1.

[2] Y.W. Kang et al., "Development and Tests of Beam Test Facility with New Spare RFQ for Spallation Neutron Source", in *proceedings of IPAC2016*, Busan, Korea, paper TUPOW023.

[3] P.N. Ostroumov et al., "High Power Test of a 57-MHz CW RFQ", in *proceedings of LINAC2006*, Knoxville, TN USA, paper THP079.

[4] J.P. Duke et al.,"Measurements of RF Cavity Voltages by X-ray Spectrum Measurements," in proceedings of XX International Linac Conference, Monterey, CA USA (2000), paper MOC08.

[5] A.Aleksandrov et al., "Status of New 2.5 MeV Test Facility at SNS", in *proceedings of LINAC2014,* Geneva, Switzerland, paper THPP108.

[6] Ametek http://amptek.com

ISBN 978-3-95450-177-9

BETA FUNCTION MEASUREMENT FOR THE AGS IPM*

H. Huang†, L. Ahrens, C. Harper, F. Meot, V. Schoefer
Brookhaven National Laboratory, Upton, New York, 11973, USA

Abstract

Emittance control is important for polarization preservation of proton beam in the Alternative Gradient Synchrotron (AGS). For polarization preservation, two helical dipole partial Siberian snake magnets are inserted into the AGS lattice. In addition, the vertical tune has to run very high, in the vicinity of integer. These helical dipole magnets greatly distort the optics, especially near injection. The beta functions along the energy ramp have been modeled and measured at the locations of the Ion Profile Monitor (IPM). For the measurements to be valid, the betatron tune, dipole current and orbit responses have to be carefully measured. This paper summarize the experiment results and comparison with the model. These results will lead to understanding of emittance evolution in the AGS.

INTRODUCTION

Emittance control is important for high luminosity in colliders. For polarized proton operation in Relativistic Heavy Ion Collider (RHIC), emittance preservation is advantageous due to its link to polarization preservation. In general, larger emittance results in larger depolarizing resonance strength and consequently, larger polarization loss. Several techniques have been employed in the AGS to preserve polarization, such as dual partial snakes [1], horizontal tune jump quadrupoles [2] and harmonic orbit corrections. To further reduce polarization loss in the accelerator chain, it is necessary to control the emittance growth. As the first step, we need to measure emittance reliably.

The main device in the AGS to measure emittance is the ion collecting IPM [3], which has been put in use for more than 20 years. They are installed at β_{max} locations to measure both horizontal and vertical emittances. The device shows that vertical emittance increases four times in the AGS during polarized proton acceleration. However, some reported emittance growth is not real. There are several problems with this measurement. First, polarized proton operation requires two partial snake magnets which are helical dipole magnets with constant fields during the whole AGS cycle. The high magnet field near injection causes significant optical distortion. Several compensation quadrupoles have been installed on both sides of each helical dipole to mitigate the optical effect but their effects are limited. The expected beta beating may distort the reported emittance values at low energies. Second, the space charge of bunched beam is stronger at higher energy due to smaller beam size which causes larger reported emittance [4]. The profiles obtained from the AGS IPM has known effects from space charge of bunched beam, which can only be mitigated at a flattop by turning off RF cavities.

The real currents of all active magnets and other beam radius can be logged for each AGS cycle. The AGS can be modeled by MAD-X with these input information. Using the lattice model with the helical magnets included, the beta functions at the IPM locations can be calculated along the AGS magnet ramp. One example of measured emittance for polarized protons with the modeled beta functions in both vertical and horizontal in AGS magnet cycle is shown in Fig. 1. Polarized protons are injected into the AGS at 150ms from the start of the magnet cycle (AGS T0) and is ramped immediately. The acceleration is finished at 582ms and about one second at flattop is used for extraction manuevers. For the measurement shown in Fig.1, the RF cavity was shut off at 1000ms and beam was debunched after 1000ms. The drop of reported emittance at 1000ms indicates the effects of space charge. The distortion of the beam profile is due to space charge force and is mitigated with RF off. The bunch intensity for these measurements was 2×10^{11}. The modeled vertical beta function near injection is less than half of the value at flattop. There are fluctuations in the measurements, but it is clear that the vertical emittance seems doubled from injection to the flattop, even taking into account the new beta functions and removing the space charge effect. On the other hand, the horizontal emittance growth is not so strong, if any. Since the helical dipole partial snake magnets

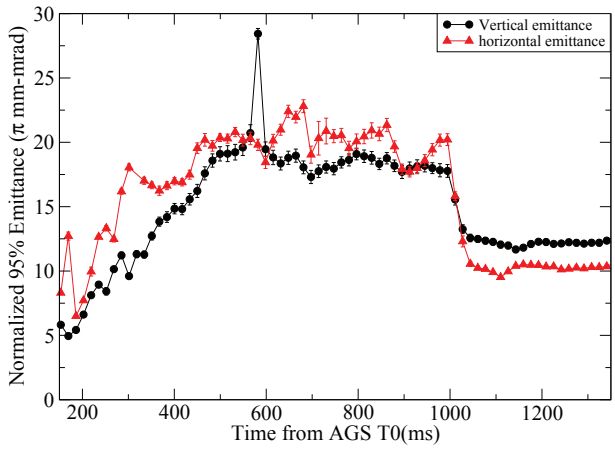

Figure 1: The normalized 95% emittance of both planes along the AGS magnet cycle. The energy ramp finishes at 582ms. The RF cavities are shut off at 1000ms and the "true" emittance at flattop is reported after that.

are hard to model, there is some doubt if the model gives the correct beta functions along the energy ramp. At higher energies, as the beam rigidity is higher, the effect from the helical dipoles are smaller. The model predicts that with

* Work supported by Brookhaven Science Associates, LLC under Contract No. DE-AC02-98CH10886 with the U.S. Department of Energy.
† huanghai@bnl.gov

ISBN 978-3-95450-177-9

helical dipoles inserted, the vertical beta function near injection is only half of the nominal beta function value. To check the model and to get true emittance evolution along the energy ramp, the beta functions have to be measured along the ramp.

There are two other devices in the AGS which can measure emittance. First one is the polarimeter [5], which measures polarization by using silicon detectors to measure the recoil scattering particles between proton beam and a very thin carbon filament target(50μm×30nm×25mm). The drawback of the device is that the ultra thin target could be stretched due to beam heating and deform during motion. The obtained profile is then distorted and often overestimated. This method can only give an upper limit of emittance. In addition, it takes about 20-30ms to fly through beam, so it can only provide the beam profiles at flattop. The second one is the electron collecting IPM, which is expected to have no space charge effect. It has RF noise issues due to the noisy AGS environment and is still under commissioning [6].

β FUNCTION MEASUREMENT

The beta function can be learned by distorting the equilibrium orbit of a functioning machine - by adding a dipole kick - and measuring the orbit motion at the dipole. This measurement is model-independent. One needs position-measuring capability at the dipole, and one only learns the beta function at the dipole. With a dipole magnet right at the IPM, the centroid of the ion beam profile from the IPM provides the position measurement.

The beam position change due to a dipole kick is related to the local beta function, kick strength and the betatron tune. Beam position shift ΔY due to a known kick (with kick strength k) is given by

$$\Delta Y = \frac{1}{2} k\beta \cot(\pi Q) \tag{1}$$

where Q is betatron tune and β is the beta function in the corresponding plane. The kick strength is given as

$$k = \frac{Bdl}{B\rho} \tag{2}$$

where $Bdl = IT$ denotes the integrated magnetic fields of the dipole corrector, $B\rho$ is the magnetic rigidity of beam, I is the dipole corrector current and T is the transfer function of the dipole correctors. The shift in measured position of the beam centroid at IPM (ΔY_{IPM}) and the known dipole kick (k) can be used to calculate the beta function:

$$\beta = 2\frac{\Delta Y_{IPM}}{IT} B\rho \tan(\pi Q) \tag{3}$$

In the above equation, betatron tune and beam position shift are measured with tune meter and IPM, respectively. The dipole corrector current is set to have maximum position shift without beam loss. The transfer function is known as 2.8×10^{-4} T-m/Amp.

Dipole correctors have been installed at the locations of both the vertical and horizontal IPM in the AGS. They are used to generate a cusp in the closed orbit at the IPM. These are all standard beam and machine parameters. The measurements would seem straightforward. In reality, there are many subtleties for the measurement.

DATA QUALITY CONTROL

The emittance can be learned by measuring the width of the beam, and then translating that into an emittance by using the beta function at the measuring instrument. A straightforward measurement turned out to be a difficult and challenging one. To reach a benchmark error bar of 5%, we need to know following quantities well in the AGS magnet cycle: B field , betatron tune, beam centroid and readback current. It is necessary to estimate the errors for these calculated betas. From Eq. (3), taking partial derivatives, the dependence to each input can be calculated. For B field, taking the middle field 5kG on the ramp as example, 5% error means to know the B field down to 250G, which is easy to achieve. Polarized proton operation requires vertical tune near integer along the energy ramp (higher than 8.98) [1]. For betatron tune, the 5% error means that the betatron tune error needs to be less than 0.0005 for $\nu_y = 8.99$, or 0.001 for $\nu_y = 8.98$. These requirements can still be met for real measurement.

The dipole current readback at first was corrupted by beam noise. To alleviate this, filters were added to these signals on all dipole correctors associated with IPM. Once this was done, we were able to sufficiently determine that the functions were properly being followed and the current was known. The data was logged and they followed the set values within the 1%. The bottom line is that we need well controlled error for these quantities (B field, betatron tune, beam centroid, and read back dipole current (1kHz).

The IPM individual channel gains can also affect the results. The centroid and beam sigmas are affected by the channel gain correction at 4-7% level. If these are not properly calibrated/understood, it could exceed the 5% error for emittance measurement. The channel gain calibration was done and the emittance data shown are with the proper channel gains.

AGS BETA FUNCTION RESULTS

Proton beam is injected into AGS 150ms after the AGS magnet cycle starts(or from AGS T0). The beam is then accelerated and reaches a flattop energy of 25GeV at 582ms. There is a flattop of one second for extraction maneuver. The transition is crossed around 315ms from AGS T0. To preserve beam polarization, the vertical tune has to be pushed high (above 8.98) on the acceleration part. Ideally, the vertical tune should be pushed high right at the beginning of acceleration. However, the significant optics distortion introduced by the partial Siberian snakes results in large beta function beating at lower energies. The vertical tune has to stay low for beam survival. After that, the ver-

ISBN 978-3-95450-177-9

tical tune needs to be pushed high as soon as possible so that it is higher than 8.98 before the first major depolarizing resonance, which is located around 262ms from AGS T0.

The dipole kick current for the beta function measurement needs to move the beam as far as possible without scraping - to improve signal to noise both for beam displacement and for dipole current. Given the tune variation this is a challenge. Big changes between minimum and maximum currents make the slopes less sensitive to small underlying machine drifts. For each point, the bipolar dipole was fired in both positive and negative signs to get several position changes. The measurement was repeated several times and the average was used in beta function calculation.

The measured vertical tunes for AGS with partial Siberian snake on and the measured vertical beta functions are shown in Fig. 2. Several features are worth noting. First,

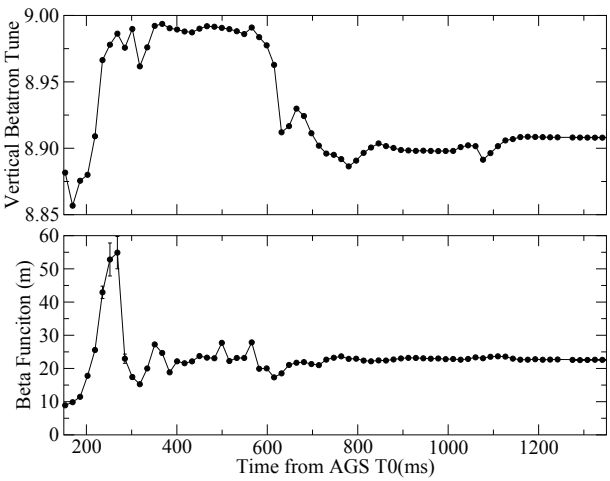

Figure 2: AGS vertical tunes (top) and vertical beta function(bottom) in an AGS cycle for AGS partial Siberian snakes on. The error bars are statistical errors only.

the measured beta function near injection is indeed less than half of the values at flattop. The optics near injection is distorted by the helical partial Siberian snake magnets, even in the presence of the compensating quadrupoles. The distortion effect diminishes quickly as beam energy goes up and the effect is negligible after 400ms. Second, the vertical betatron tune has to be pushed higher as soon as the ramp starts. The fast tune swing is associated with a large beta function swing. This large beta function variation is likely due to the helical dipole magnets and compensation quadrupoles, instead of high vertical tune. The high vertical tune after 300ms is still associated with beta function around 20 meters.

The vertical tunes in the AGS for partial Siberian snakes on and off are shown in Fig. 3. The beta function measurements for partial Siberian snake on case were done several times over a few sessions. The tunes plotted are the average of the measured tune over several months. So it is not surprising for a few points the tune values have changed quite a bit, which resulted in larger error bars. As these large error bars are with tunes lower than 8.98, the impact on beta function measurement is not significant.

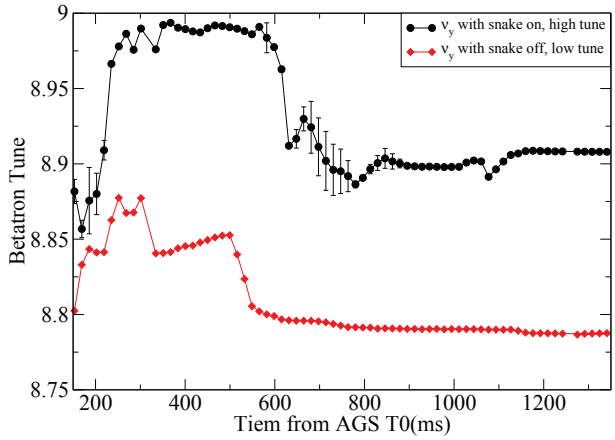

Figure 3: AGS vertical tunes in an AGS cycle for AGS partial Siberian snakes on and off. The error bars are statistical errors only.

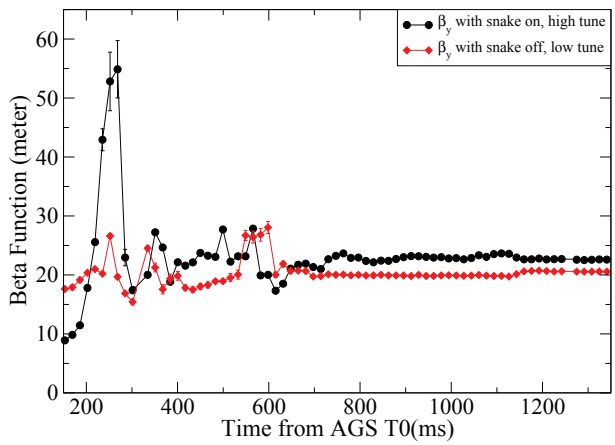

Figure 4: The measured vertical beta function for one AGS cycle. The flattop is reached at 582ms from the AGS T0. Transition is crossed around 300ms.

The measured beta functions with partial Siberian snakes on and off are shown in Fig. 4. For the optics without partial Siberian snakes, the beta functions at the IPM location is expected to be around 23m (β_{max}) from model. The measured beta functions vary around 20m through the AGS cycle. There are some fluctuations which could be from systematic errors. For the optics with partial Siberian snakes, the beta functions at the IPM location is expected to be around 25m at flattop, when the partial Siberian snake effect is small (but still visible for slightly larger beta function). At injection, the model predicts that the beta function should be less than half of the value at flattop. The measurements confirmed that overall trend.

In addition, there is a systematic difference between the beta functions from measurements and model. The measurement results are smaller by about 14%. The transfer function was one we don't have much information about

ISBN 978-3-95450-177-9

its accuracy. It is very possible that this number is off by 14%. The partial snake on and off data were taken on different years. However, the difference between model and measurements at flattop for both sets are the same. After multiplying the measurements with a factor 1.137, the beta functions from the measurements and model are plotted in Fig.5. For the partial Siberian snake on case, the small fluctuations in the modeled beta function on the ramp is due to the jump quadrupoles on, which adds to discrepancy as the jump quadrupoles were off during beta function measurement. Besides the large deviations during the vertical tune swing (between 200-300ms), the agreement in other portion is fine, for both near injection and at flattop. This may imply that the fudge factor 1.137 is reasonable. The model beta function also shows a beta function swing between 200-300ms, but in a much smaller scale. It should be noted that the γ_{tr} quadrupoles were not in this model. Although these γ_{tr} quadrupoles are in the lattice and their transfer functions are available, they are timed on Gauss clock (magnetic field) instead of real time. Currently, they could not be included in the real time MAD-X model. Some work is needed to include them in the model. For the partial Siberian snake off case, the model predicts a more or less flat beta function through AGS cycle. The measured beta functions has some fluctuations around that. Nevertheless, the modeled beta functions at flattop match the measurements after the fudge factor.

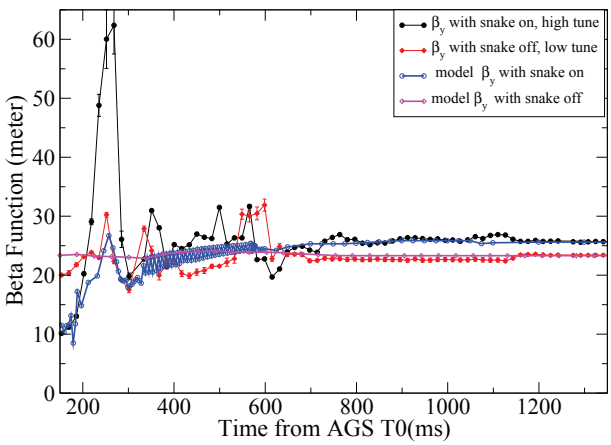

Figure 5: The measured vertical beta function for AGS with and without partial snakes. The flattop is reached at 582ms from the AGS T0. Transition is crossed around 300ms.

The horizontal beta function at the IPM can be measured with the same procedure. However, the location of horizontal IPM is between the two BPMs used by the RF system for the radial loop. To measure the beta function there, the RF system has to switch to phase loop so that the radius can be moved by dipole correctors. The RF system has to be on radial loop around transition crossing (300ms) but can be on phase loop during the rest period. The horizontal beta function measurement with RF system at phase loop has been tested but more beam time is needed to get this working.

SUMMARY

The Siberian partial snakes required for proton polarization preservation and near integer vertical tune(8.98-8.99) complicate the optics in the AGS. To understand if the observed emittance growth is real and where is the growth, the vertical beta functions at IPM locations are needed. Careful attentions have been put into betatron tune, dipole current and orbit response measurements. With these quantities measured, the vertical beta functions have been measured along the AGS ramp with partial Siberian snakes on and off. The modeled and measured beta functions agreed with each other at AGS flattop and near injection for partial Siberian snakes on and off case. The measured big swing of beta functions between 200-300ms for partial Siberian snakes on case requires more modeling work. So far the model does not give the same level of beta function variation. However, the measured and modeled vertical beta function near injection and in the later part of the AGS cycle already suggest that some vertical emittance growth is real, as much as 100%, but the source is not fully understood. Emittances have also been measured with beam debunched at flattop to eliminate the space charge effect. The horizontal beta function measurement has been worked on and but more beam time is needed to get this working. The modeled horizontal beta function implies not much horizontal emittance growth. The horizontal beta function measurement will be taken in the future.

REFERENCES

[1] H. Huang, *et al.*, Phys. Rev. Lett. **99**, 184501 (2007).

[2] H. Huang, *et al.*, Phys. Rev. ST AB. **17**, 0810001 (2014).

[3] H. Weisberg, *et al.*, Proceedings of PAC'83, Santa Fe, NM, USA, p. 2179.

[4] R.E. Thern, Proceedings of PAC'87, Washington, DC, USA, p. 646.

[5] H. Huang, *et al.*, Proceedings of IBIC2013, Oxford, UK, p. 492.

[6] R. Connolly, *et al.*, Proceedings of IBIC2014, Monterey, CA, USA, p. 39.

ISBN 978-3-95450-177-9

OPTIMIZED CRYOGENIC CURRENT COMPARATOR FOR CERN'S LOW-ENERGY ANTIPROTON FACILITIES

M. Fernandes*, The University of Liverpool, U.K. & CERN, Geneva, Switzerland
A. Lees, D. Alves, T. Koettig, E. Oponowicz, J. Tan, CERN, Geneva, Switzerland
C. Welsch, Cockcroft Institute & The University of Liverpool, U.K
R. Geithner, R. Neubert, T. Stöhlker, Friedrich-Schiller-Universität &
Helmholtz Institute Jena, Jena, Germany
M. Schwickert, GSI, Darmstadt, Germany

Abstract

Non-perturbative measurement of low-intensity charged particle beams is particularly challenging for beam diagnostics due to the low amplitude of the induced electromagnetic fields. In the low-energy Antiproton Decelerator (AD) and the future Extra Low ENergy Antiproton (ELENA) rings at CERN, an absolute measurement of the beam intensity is essential to monitor operational efficiency and provide important calibration data for all AD experiments. Cryogenic Current Comparators (CCC) based on Superconducting QUantum Interference Device (SQUID) have in the past been used for the measurement of beams in the nA range, showing a very good current resolution. However these were unable to provide a measurement of short bunched beams, due to the slew-rate limitation of SQUID devices and their strong susceptibility to external perturbations. Here, we present the measurements and results obtained during 2016 with a CCC system developed for the Antiproton Decelerator, which has been optimized to overcome these earlier limitations in terms of current resolution, system stability, the ability to cope with short bunched beams, and immunity to mechanical vibrations.

CURRENT MEASUREMENT OF LOW-INTENSITY BEAMS

Low-intensity charged particle beams present a considerable challenge for existing beam current diagnostic devices. This is particularly true for beams with average currents below 1 µA which is the resolution limit of standard DC Current Transformers [1]. Other monitors, such as AC Current Transformers or Schottky monitors are able to measure low-intensity beam currents, but neither can simultaneously provide an absolute measurement, with a high current and time resolution, which at the same time is independent of the beam profile, trajectory and energy.

At CERN's low-energy antiproton ($\bar{p}$) decelerators, the AD and ELENA (currently under construction) rings, both bunched and coasting beams of antiprotons circulate with average currents ranging from 300 nA to 12 µA. The AD cycle consists of alternate phases of deceleration, where the beam is bunched, and beam cooling, when the beam is debunched and its velocity is kept constant. The beam is also bunched at injection and extraction. The AD current profile during the whole deceleration and cooling cycle along with the maximum slew-rate during phases where the beam is bunched is shown in Fig 1. The $\bar{p}$'s are injected in the AD with a momentum of 3.5 GeV corresponding to $\beta = 0.967$, and are extracted with 100 MeV and $\beta = 0.106$.

Having a current measurement able to cope with these characteristics would greatly help the optimisation of the machine operation. To meet these requirements, a low-temperature SQUID-based Cryogenic Current Comparator (CCC) system is currently under development [2]. Similar devices have already been developed for electrical metrology [3], and have already been used for beam current measurements in particle accelerator [4]. The current project, is a collaboration between CERN, GSI, Jena University and Helmholtz Institute Jena to develop this technique further.

The main design specifications for the monitor are: beam current resolution < 10 nA; and a measurement bandwidth of 1 kHz.

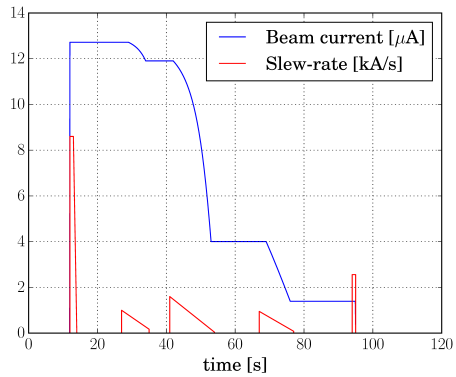

Figure 1: Nominal beam current during an AD cycle, and maximum beam current slew-rate in bunched beam phases.

OVERVIEW OF THE FUNCTIONING PRINCIPLE OF THE CCC

The CCC (see schematic in Fig. 2) works by measuring the magnetic field induced by a charged particle beam. This field is concentrated in a high-permeability ferromagnetic pickup core, from which it is coupled into the SQUID sensor via a superconducting flux transformer. The SQUID's are highly sensitive magnetic flux sensors that permit the measurement of the weak fields created by the beam. The superconducting magnetic shield structure around the pickup-core

* e-mail: miguel.fernandes@cern.ch

ISBN 978-3-95450-177-9

renders the coupled magnetic field nearly independent of the beam position and also shields the system against external magnetic field perturbations [5]. The feedback loop in the SQUID read-out implements a so called Flux Locked Loop (FLL) [6], increasing the dynamic range of the SQUID, but imposing a stability limit on the maximum slew-rate of the input signals.

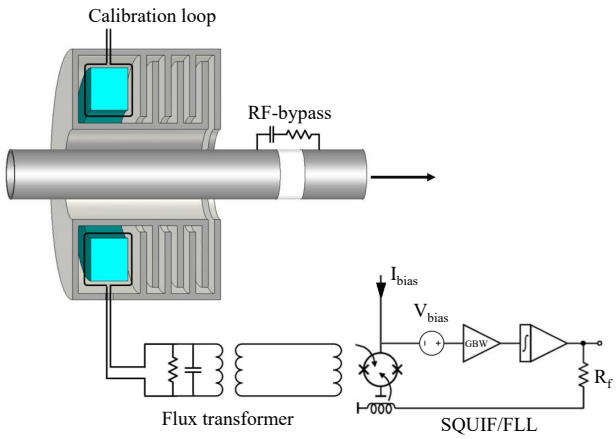

Figure 2: Schematic of the CCC.

The unique advantage of the CCC monitor is its ability to measure the average current of both coasting and bunched beams with nA resolution. Previous installations of the CCC for beam current measurements were, however, usually restricted to slowly extracted beams in transfer lines. When measuring bunched beams, the high slew-rate soon becomes a limiting factor [7] as is the case in the AD (see Fig 1). In order to reduce the slew-rate of the signal coupled to the SQUID, a filter has been implemented in the coupling circuit [8]. The CCC is also very sensitive to mechanical and electromagnetic interference, which represent an additional limitation when operating in an accelerator environment.

CRYOSTAT DESIGN

To house the CCC monitor a LHe-bath cryostat fed by a pulse-tube reliquefier was designed and manufactured. As shown in Fig. 3 the cryostat is composed of three main parts: helium vessel (HV), thermal radiation shield (TS) and vacuum vessel (VV). The VV beam tube has a diameter of 103 mm, leaving enough space to fit the inner walls of the TS and HV beam tubes between the VV beam tube and the 185 mm inner diameter of the CCC monitor. To prevent the mirror currents induced by the AD beam from shielding the beam's magnetic field from the CCC, electrically insulating ceramic isolators are integrated into the inner walls of the HV and VV with a 4 mm gap integrated into the TS beams tube. The SQUID cables are routed to their data acquisition equipment through a dedicated feedthrough on the HV.

The main design challenge was to optimize the thermal and mechanical performance of the cryostat to retain a stable amount of liquid helium while minimizing the transmission of vibrations to the CCC. The masses of the HV (145 kg

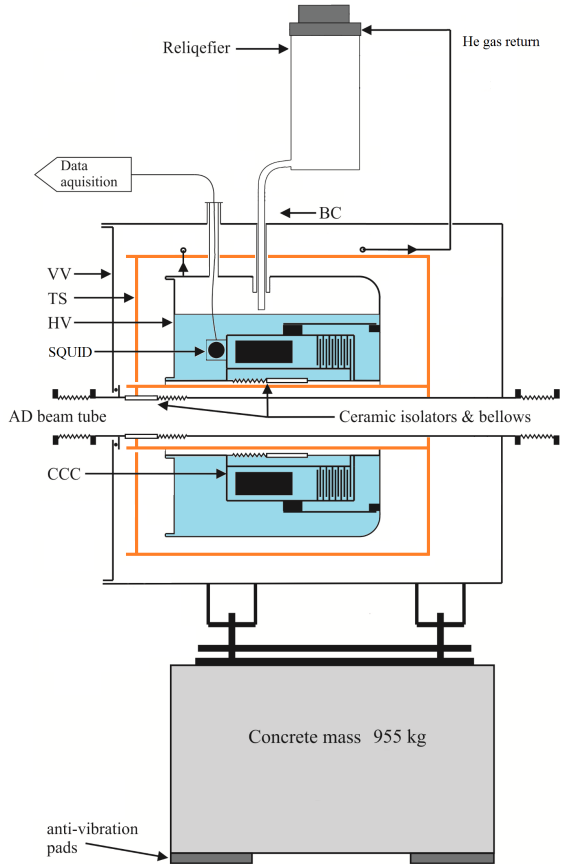

Figure 3: CCC cryostat schematic.

including 55 kg for the CCC) and TS (55 kg) are supported using independent sets of twelve titanium support rods which are dimensioned to increase the resonant frequencies of the HV and TS above 50 Hz. Titanium was used due to its low stiffness to thermal conductivity ratio. To isolate the CCC from vibrations an external Cryomech® PT415 helium reliquefier was used and connected to the cryostat using a flexible bayonet connection (BC) designed to mechanically isolate the two systems. To isolate the 850 kg cryostat assembly from ground vibration it is mounted on a 955 kg concrete mass and four Apsopur® anti-vibration mats a configuration which is calculated to isolate 92 % of vibrations at 50 Hz. A detailed description of the cryostat design and first performance measurements obtained during the 2015 run can be found in [9].

A PLC-based system has been implemented to monitor and control the cryostat status and is independent of the CCC beam diagnostic acquisition and control system.

ACQUISITION AND CONTROLS

The data acquisition system used for control and measurements is based on the VME standard and comprised of a MEN-A20 CPU card, a VD80 ADC card, and a CTRV CERN timing receiver. The CPU card hosts a dual core INTEL Core 2 Duo L7400 64-bit processor running at 1.5 GHz

ISBN 978-3-95450-177-9

with 4 GB of RAM. The VD80 ADC card enables the simultaneous sampling of 16 channels (16 MB per channel) with a 16-bit resolution, an input range of ±10 V (differential) and a maximum acquisition frequency of 200 kHz. The currently used sampling rate is set to 1 kHz. The CTRV is a CERN timing receiver used to provide information and triggers, for both software actions and TTL hardware outputs, on the arrival of accelerator timing events.

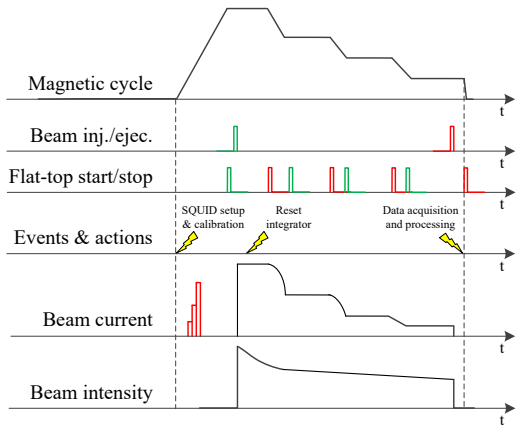

Figure 4: Actions and events during the AD cycle acquisition.

The time diagram representing the main events, triggers and actions performed during an AD cycle are depicted in Fig. 4. The acquired time markers register the TTL output signal of the CTRV card at beam injection, at the start of each magnetic cycle flat-top and at the end of each magnetic flat-top. The injection event is used in real-time for re-setting the SQUID integrator in order to ensure a zero offset and guarantee sufficient dynamic range for the current measurement. Furthermore, the flat-top markers are subsequently used to automatically detect the beginning and the end of each phase time window for which intensity measurements are particularly relevant for the operators.

A real-time server, running on the VME-based CPU card, has been developed in order to automate the configuration, calibration, acquisition and publishing of the measurements. The software architecture of this server is based on the CERN Front-End Software Architecture (FESA) C++ framework [10]. The SQUID and the current source used for the calibration support a serial communication interface. This serial interface to both devices is currently proxied using a serial device server converting to TCP-based socket communication. The FESA server implements the instruction protocols used to configure these devices according to the user settings. These settings include important SQUID configuration parameters such as the bias current, bias voltage, gain bandwidth and feedback resistance when running in FLL mode (see Fig. 2), to name a few. It also allows the expert to configure and trigger the precision current source used for the automatic calibration of the system, something that is performed at the beginning of each cycle of the AD machine.

The FESA server also implements the post-processing algorithms which entail offset correction, the detection of the current calibration steps, the linear fit to estimate the calibration factor, the computation of the revolution frequency based on the magnetic cycle and the computation of the number of charges from the current measurement and the inferred revolution frequency. These results are then made available to experts and operators via CERN's standard controls middleware infrastructure.

BEAM MEASUREMENTS

The first AD beam measurements with the CCC were obtained during the 2015 run [8]. Two main limitations in the beam current measurement were observed. The current resolution was limited to ~ 300 nA, mainly due to strong perturbations at 50 Hz and harmonics, and an offset jump was seen to occur at injection, due to the SQUID/FLL feedback loop locking to a different working point. This latter effect be caused by a combination of excessive slew-rate of the input signal and excessive flux noise/perturbations coupled to the SQUID [2, 6].

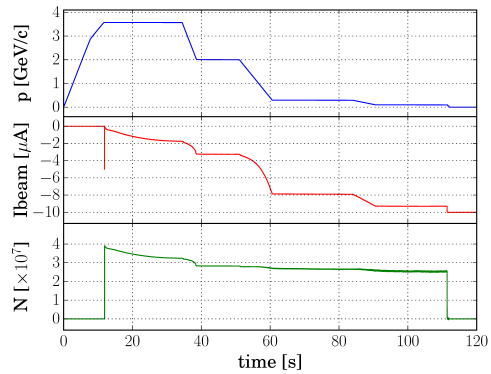

Figure 5: Measurement of the AD cycle beam current in red (middle) and intensity in green (bottom), with the particle momentum shown in blue (top).

It was suspected that the excess noise and perturbations could be due to currents passing through the RF-bypass installed in the ceramic gap of the beam pipe (see Fig 2). This was originally included in order to improve the SQUID/FLL stability by reducing the beam signal slew-rate. For the 2016 run the RF-bypass was removed leaving an isolated ceramic gap. This resulted in a significant reduction in the noise, enabling current measurements with a resolution as low as ~ 3 nA to be achieved. This allowed for a total dynamic range of 85 dB. Consequently, the beam intensity measurement was also improved showing a resolution of $0.0012 \times 10^7\ \bar{p}$ when $\beta = 0.967$, and $0.013 \times 10^7\ \bar{p}$ when $\beta = 0.106$. An example of the measurement of an AD cycle with this improved performance is shown in Fig. 5. The flux-jump at injection, however, still occurs. In order to compensate for this a reset of the SQUID/FLL is performed right after injection. This way it is possible to obtain a relative measurement of the cycle efficiency in real-time while the

ISBN 978-3-95450-177-9

absolute measurement is obtained after the cycle is complete by calculating the zero current baseline after beam ejection.

With the acquisition and control system for the CCC in place, it was possible to consistently acquire data for many AD cycles, making it available to perform a first statistical analysis of the CCC measurement parameters. Fig. 6 shows the histogram of current resolution $\sigma(I_{\mathrm{beam}})$ for more than 4500 cycles. It can be seen that for the majority of the acquired cycles $\sigma(I_{\mathrm{beam}}) < 10\,\mathrm{nA}$, with a peak at $\sim 3\,\mathrm{nA}$. The principal cause for the large tail in $\sigma(I_{\mathrm{beam}})$ was seen to be the noise from pressure fluctuations in the HV caused by thermoacoustic oscillations. This can eliminated by proper adjustment of the cryostat settings. An analysis of the baseline variation during a cycle was also performed by looking at cycles where no beam was injected. A histogram of the maximum drift of the baseline within a cycle is shown in Fig. 7. Except for a small number of cycles, the baseline drifts by $< 50\,\mathrm{nA}$. These long-term variations are again thought to be mainly caused by variations of the pressure in the HV of the cryostat.

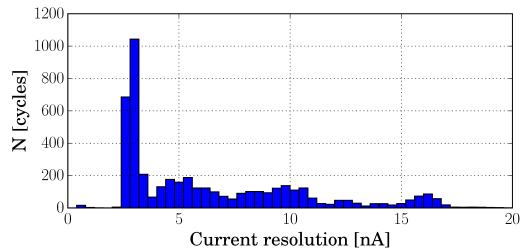

Figure 6: Distribution of the current resolution for 4685 acquired cycles.

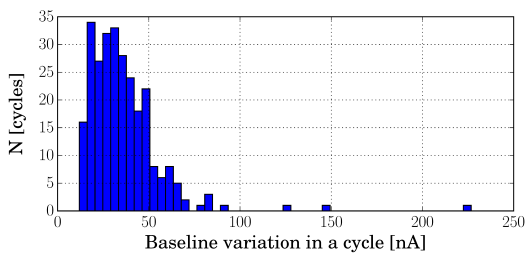

Figure 7: Distribution of the baseline drift for 271 acquired cycles where no beam was injected.

CONCLUSIONS

A CCC monitor with complete acquisition system has been developed and installed in the AD. Beam measurements obtained during the first half of 2016 show significant improvements in the current resolution when compared to results obtained in 2015. The current implementation of the CCC monitor has been able to provide a beam current measurement with resolutions down to 3 nA. This performance was possible even with the cryocooler reliquifier running and supplying LHe to the cryostat. This was only possible due to the careful design of the cryostat to suppress most mechanical vibrations. This is the first fully operational CCC system able to continuously measure both bunched and coasting beams in a synchrotron accelerator.

Statistical analysis of the monitor performance reveals that the drift of the baseline may have a considerable contribution to overall accuracy, with correction techniques needed to compensate for this, e.g. by implementing a deconvolution for effects of pressure and temperature variations. These signals are already being acquired by the acquisition system. It should, however, be noted that for many of the cycles acquired for this analysis, the settings in the cryostat were still being tested and adjusted, and that steady-state functioning had not yet been reached.

ACKNOWLEDGEMENT

The authors acknowledge the outstanding work of CERN's Central Workshop (EN-MME), Cryogenic group (TE-CRG), Vacuum group (TE-VSC) and AD operations (BE-OP) who assisted in the design, manufacture, assembly and installation of the CCC cryostat. Fruitful discussions with Patrick Odier, Jeroen Belleman, Manfred Wendt, Henry-Jobes Barthelmess and Dietmar Drung are gratefully acknowledged.

This project has received funding from the European Union's Seventh Framework Programme for research, technological development and demonstration under grant agreement number 289485.

REFERENCES

[1] P. Odier, CARE-CONF-2004-023-HHH. P. Odier, "DCCT technology review," C04-12-01.1, Proceedings of CARE-HHH-ABI.

[2] M. Fernandes *et al.*, "A Cryogenic Current Comparator for the Low Energy Antiprton Facitilities at CERN," in *Proc. IBIC'14*, Monterey, CA, USA, paper WEPF04, 2014.

[3] I.K. Harvey, *Rev. Sci. Instrum.* 43 (1972) 1626.

[4] A. Peters *et al.*, "A cryogenic current comparator for the absolute measurement of nA beams," BIW98, Standford, May 1998, (p. 163), AIP conference proceedings.

[5] K. Grohmann *et al.*, *Cryogenics* 16(10) (1976) 601.

[6] D. Drung, "High-performance DC SQUID read-out electronics," *Physica C: Superconductivity*, Vol. 368, Issues 14, 1 March 2002, 134-140.

[7] R. H. Koch, "Maximum theoretical bandwidth and slewrate of a dc SQUID feedback system," *IEEE Transactions on Applied Superconductivity* 7(2), p. 3259 (1997).

[8] M. Fernandes *et al.*, "Cryogenic Current Comparator for Low-Energy Antiproton Facilities at CERN," in *Proc. IBIC'15*, Melbourne, Australia, paper MOPB043, 2015.

[9] A. Lees *et al.*, "Design and optimisation of low heat load liquid helium cryostat to house cryogenic current comparator in antiproton decelerator at CERN," ICEC 2016 Conference, 9-P2-111, New Delhi, India, 2016.

[10] M. Arruat *et al.*, "Front-End Software Architecture," in *Proc. ICALEPCS'07*, Knoxville, TN, USA, paper WOPA04, 2007.

ISBN 978-3-95450-177-9

A PRECISE PULSED CURRENT SOURCE FOR ABSOLUTE CALIBRATION OF CURRENT MEASUREMENT SYSTEMS WITH NO DC RESPONSE

M. Krupa*[1], M. Gasior
CERN, Geneva, Switzerland
[1] also at Lodz University of Technology, Lodz, Poland

Abstract

Absolute calibration of systems with no DC response requires pulsed calibration circuits. This paper presents a precise pulsed current source designed primarily for remote calibration of a beam intensity measurement system. However, due to its simple and flexible design, it might also prove interesting for other applications. The circuit was designed to drive a load of 10 Ω with current pulses lasting a few hundred microseconds with an amplitude of 1 A and precision in the order of 0.01 %. The circuit is equipped with a half-bridge for precise determination of the absolute output current using the 0 V method. This paper presents the circuit topology and discusses in detail the choice of the critical components along with their influence on the final achieved accuracy. The performance of the built prototype of the current source is presented with laboratory measurements.

INTRODUCTION

Many modern measurement systems have no low-frequency response so that their calibration cannot be achieved with DC signals. One of the available possibilities to calibrate such systems is to use a circuit generating long pulses with a well-defined and stable amplitude.

The pulsed current calibration unit described in this paper consists of two main circuits: a current source generating the calibration current and a half-bridge circuit for measuring the current with high accuracy. Similar circuitry was developed in the past for the inductive beam position monitors of the CERN CLIC Test Facility (CTF3) [1].

This paper describes the principle of operation and discusses the choice of the most critical components. A brief description of additional features, extending the field of potential applications, is also given.

All measurements shown in this paper were obtained with a prototype circuit built and optimised for calibrating the new bunch-by-bunch intensity measurement system of the Large Hadron Collider (LHC) [2, 3]. The source was designed to deliver a current pulse of 1 A into 10 Ω load for a few hundred microseconds. However, the system can easily be adapted for other values of the current and a wide range of loads by simply adjusting the values of a handful of components.

* michal.krupa@cern.ch

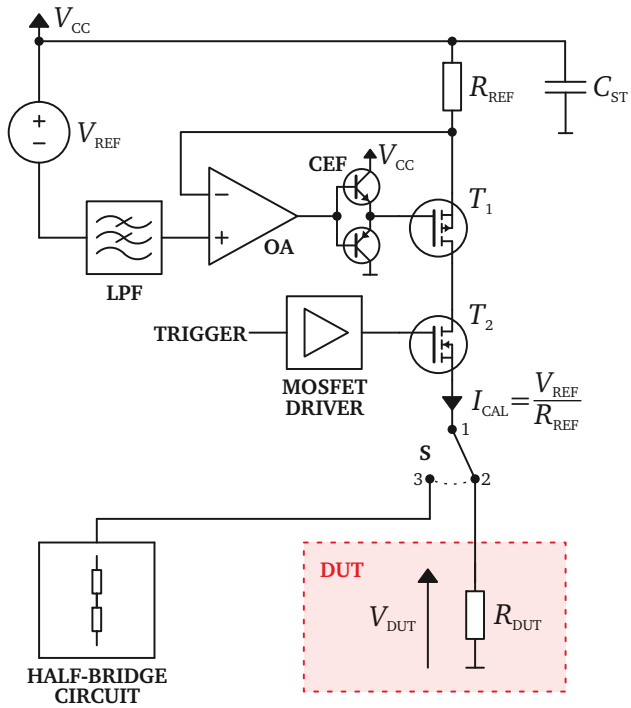

Figure 1: A simplified circuit diagram of the current source. LPF - Low-Pass Filter; OA - Operational Amplifier; CEF - Complementary Emitter Follower; DUT - device being calibrated

CURRENT SOURCE

The principle of operation of the current source can be explained using the circuit diagram shown in Fig. 1. During normal operation the switch S is in position 1-2 to send the calibration current I_{CAL} to the grounded load R_{DUT} of the device to be calibrated.

The value of I_{CAL} is determined by the ratio of the reference voltage V_{REF} and the reference resistance R_{REF}, both being part of the regulation loop. The non-inverting input of the operational amplifier (OA) is set to $V_{CC} - V_{REF}$ and additionally filtered by a low-pass filer (LPF). OA regulates its output voltage such that its inverting input virtually matches the voltage of the non-inverting input. Hence, the voltage at the inverting input of OA also equals $V_{CC} - V_{REF}$ which in turns yields a voltage drop of V_{REF} across the reference resistor R_{REF}. The complementary emitter-follower (CEF) buffers the output of OA to drive the large gate capacitance of the top p-channel MOSFET T_1 to improve the response time

ISBN 978-3-95450-177-9

of the loop. The capacitor C_{ST} provides a low-impedance storage for the charge necessary to generate the current pulse.

The regulation loop can operate only when the bottom n-channel MOSFET T_2 is switched on. Hence, T_2 is used to gate the output current and produce pulses of the required length. When T_2 is switched off, the OA output reaches its negative rail making T_1 switch on. The gate of T_2 is connected to a dedicated MOSFET driver designed for the fast driving of large gate capacitance. The length of the TRIGGER input pulse defines the length of the generated current pulse.

In its other position 1-3, the switch S directs the output current to the half-bridge circuit used for the precise measurements of the output current.

The maximum allowed value of R_{DUT} is limited by the compliance voltage of the current source i.e. the maximum output voltage V_{DUT} for which the source can deliver constant current I_{CAL}. For the designed source $V_{CAL,max} \approx V_{CC} - V_{REF}$, hence:

$$R_{DUT} < \frac{V_{CC} - V_{REF}}{I_{CAL}} \quad (1)$$

The quality of the generated current is directly linked to the quality of the voltage reference V_{REF} and therefore the reference should be exceptionally stable and clean. Due to the topology of the current source, a two-pin voltage reference was used to refer it directly to the positive power supply rail. A number of such integrated circuits are available on the market. The precision voltage reference used in the prototype has an initial voltage accuracy of 0.05 %, temperature coefficient of 4 ppm/°C and low-frequency noise in the order of 7 ppm_{pp}. Nevertheless, additional filtering by the LPF with a cut-off frequency of 2 Hz was required to further reduce the low-frequency fluctuations. The LPF was built with a precision operational amplifier in a follower configuration in which the output voltage is independent of the value of the resistors used. For the prototype a V_{REF} of 5 V was used to set the inputs of OA far enough from the power supply rails to ensure its proper operation.

The other critical component of the source is the reference resistor R_{REF}. Once V_{REF} is set, the value of R_{REF} directly determines the value of I_{CAL}. There are a number of high-precision 4-terminal current-sensing resistors available commercially and two identical resistors were used in parallel to achieve the desired R_{REF} of 5 Ω. Each of the resistors has a tolerance of 0.01 %, thermal coefficient of 0.05 ppm/°C and power coefficient of 4 ppm/W.

An important feature of the design is that the tolerances on the absolute value of V_{REF} and R_{REF} are not as critical as their stability and drifts, as I_{CAL} can be precisely measured with the half-bridge circuit.

The operational amplifier used has a very small input bias current of 0.5 pA to minimise the error introduced by the inverting input bias current flowing through R_{REF}. A precision, low-noise, JFET-input operational amplifier with 120 µV input offset voltage, 250 nV_{pp} low-frequency noise and slew rate of 20 V μs^{-1} was used.

Due to the limited output impedance of the power supply, most of the output current must come from the local storage capacitor C_{ST} when the current source is turned on. It can be assumed that the supply voltage V_{CC} decreases at the same rate as the voltage across C_{ST}. For the designed source C_{ST} of 5 mF was chosen to limit the drop of V_{CC} to 100 mV for the nominal current of 1 A and the maximum pulse length of 500 µs as calculated from:

$$\Delta V_{CC} = \frac{I_{ST} \cdot t}{C_{ST}} \quad (2)$$

The output current pulse of the prototype is shown in Fig. 2 with a zoom on the initial 5 µs shown in Fig. 3. The source was triggered with pulses of 250 µs every 100 ms.

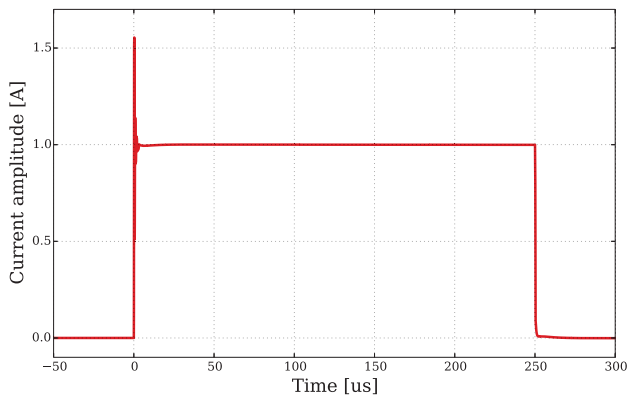

Figure 2: Output current of the current source.

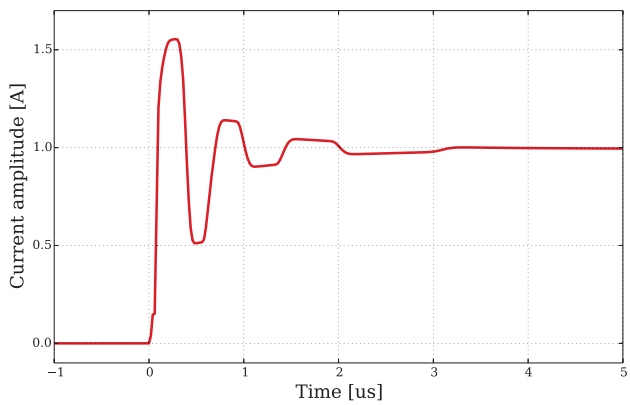

Figure 3: The first 5 µs of the pulse shown in Fig. 2.

The output current oscillates for approximately 3.5 µs before reaching its nominal value of 1 A within 0.1 % accuracy. After an additional 30 µs it attains an accuracy of ±0.01 %.

The initial oscillation of the output current illustrates the operation of the regulation loop of the current source. When the current source output is switched off by T_2, the operational amplifier OA is saturated at its negative rail. At the beginning of the pulse the output current reaches the maximum possible value as T_2 can be turned on much faster than the regulation loop starts working. The regulation then kicks in to stabilise the output current at the nominal value.

ISBN 978-3-95450-177-9

HALF-BRIDGE CIRCUIT

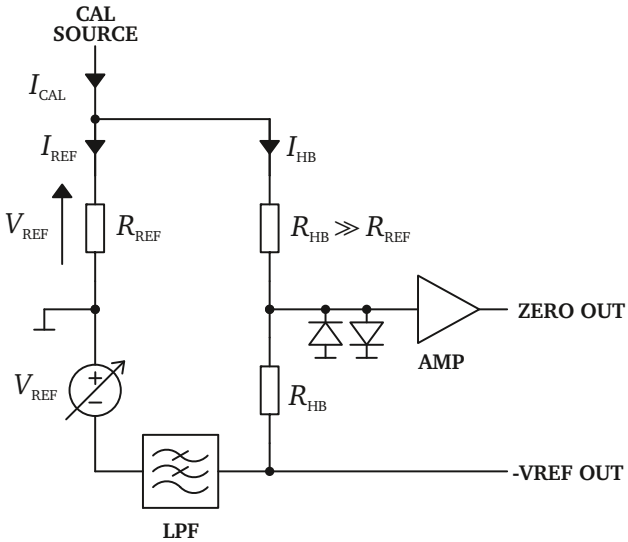

Figure 4: A simplified circuit diagram of the internal half-bridge.

When the switch S of the circuit diagram in Fig. 1 is in position 1-3, the pulsed current I_{CAL} is sent to the half-bridge circuit shown schematically in Fig. 4. The pulsed calibration current I_{CAL} is converted into a voltage which is compared to a DC voltage of the opposite sign. Hence, the value of the pulsed I_{CAL} can be accurately determined with DC measurements.

The calibration current I_{CAL} is converted into voltage across the reference resistor R_{REF}. If the adjustable V_{REF} is set such that $V_{REF} = I_{REF} \cdot R_{REF}$ then the potential at the common node between the two half-bridge resistors R_{HB} is 0 V.

The two precision resistors R_{HB} have equal values, much larger than R_{REF}, to make the half-bridge current I_{HB} negligibly small with respect to I_{REF}.

Assuming that the value of R_{REF} is known, the value of $I_{REF} \approx I_{CAL}$ can be indirectly measured as V_{REF}/R_{REF} after adjusting V_{REF} such that the potential at the common node of the half-bridge is 0 V. To improve the stability of the circuit, V_{REF} can be low-pass filtered.

For the prototype V_{REF} can be adjusted by two means: a precision trimming potentiometer and a remotely controlled Digital to Analogue Converter (DAC). Each of these can independently regulate V_{REF} by ±0.2 %.

In nominal conditions the potential at the common node of the half-bridge is very close to 0 V. To increase the resolution of the measurement this signal is amplified with a relatively large gain. This also decreases the influence on the measurement accuracy of the offset voltage of the digitiser used to determine the 0 V conditions.

For the developed prototype, the amplification factor was chosen such that 1 mV at the output translates to 1 ppm of deviation from the nominal current. Clamping diodes are used to keep the amplifier out of saturation when there is no I_{CAL} sent to the half-bridge.

If required, the half-bridge current I_{HB} can be taken into account for a more precise determination of I_{CAL}:

$$I_{CAL} = I_{REF} \cdot \frac{R_{REF} + R_{HB}}{R_{HB}} = V_{REF} \cdot \frac{R_{REF} + R_{HB}}{R_{REF} \cdot R_{HB}} \quad (3)$$

Similarly to the current source, R_{REF} and V_{REF} should be very stable. However, contrary to the current source circuit, the absolute accuracy of the components used in the half-bridge circuit is critical. The 5 V voltage reference used in the half-bridge circuit was the same as the one used in the current source. $R_{REF} = 10\,\Omega$ consisted of a single resistor of the same type as the R_{REF} used in the current source. Since the value of R_{REF} was twice as high as in the current source, V_{REF} also had to be increased by a factor of two. A $V_{REF} = -10$ V was achieved by amplifying the output of the voltage reference with an operational amplifier and implementing low-pass filtering with a cut-off frequency of 2 Hz. This apparent complication has, in reality, a few advantages. The same types of resistor and voltage reference are shared by the current source and the half-bridge circuit which simplifies selection of components and makes potential drifts more coherent. Moreover, the R_{REF} of the half-bridge is exactly the same as the R_{DUT} of the device being calibrated so the current source operates at the same output voltage, minimising the impact of the output impedance of the source on the calibration quality.

The set value of V_{REF} can be directly monitored with 50 ppm accuracy using a precision multimeter. The value of R_{REF} can be known with a tolerance of 100 ppm. Hence, using the half-bridge circuit built with the components described and accounting for I_{HB}, the absolute accuracy for determining I_{CAL} is at the level of 150 ppm.

The output signal of the half-bridge circuit of the prototype is shown in Fig. 5 with a zoom to the area of interest around 0 V shown in Fig. 6. The source was triggered with 250 µs pulses every 100 ms.

The measurements indicate that the output current of the source is within 200 ppm of its nominal value 22 µs after triggering and within 100 ppm after additional 10 µs and attains its nominal value after approximately 130 µs with some subsequent decay.

PROTOTYPE

A picture of the prototype calibration circuit is shown in Fig. 7. The source can be seen in the lower left-hand side with the half-bridge in the upper left-hand side.

The stability of the prototype was measured with the half-bridge circuit over a 24-hour period with the source triggered by 250 µs pulses every 100 ms. A histogram of the results is presented in Fig. 8 showing the average deviation from the nominal current for a 10 µs period of the half-bridge output measured 120 µs after triggering the source. The measurements follow a Gaussian distribution with a standard

ISBN 978-3-95450-177-9

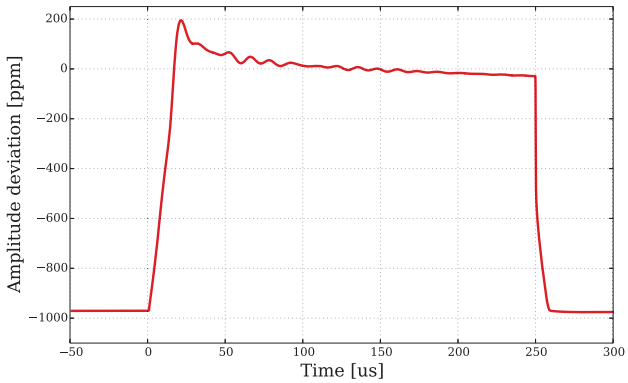

Figure 5: Full output of the half-bridge circuit.

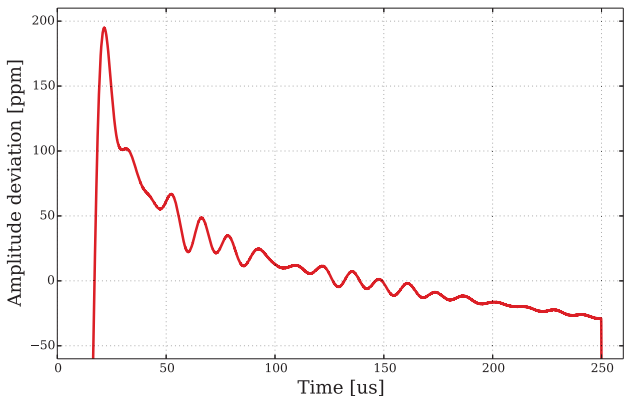

Figure 6: Output of the half-bridge circuit as the source current stabilises.

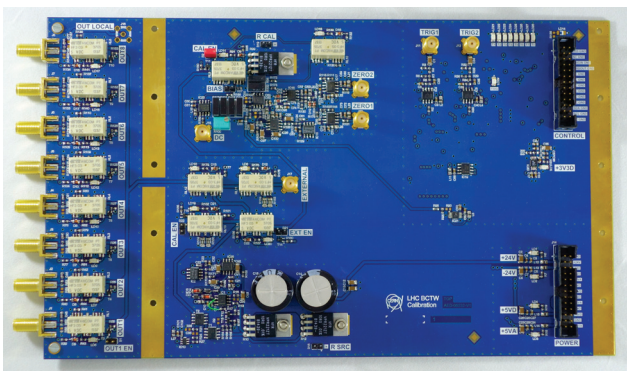

Figure 7: A photograph of the prototype.

deviation of 4.7 ppm. The largest measured deviation from the nominal current was 18.5 ppm

The prototype also includes additional features to accommodate the needs of the LHC bunch-by-bunch intensity measurement system. There are eight selectable output relays to allow a single source to calibrate multiple devices. The source can be triggered using one of the eight available trigger inputs, some of which have timings predefined on the hardware level. In order to protect the devices being calibrated from excessive power sent to their calibration inputs, each of the trigger signals passes through a hardware duty-cycle protection circuit which limits the average output current to 0.1 % of the nominal current. To allow the calibration of different sensitivity ranges of the acquisition system, the prototype also includes an input for an external source and supports daisy-chaining multiple current sources.

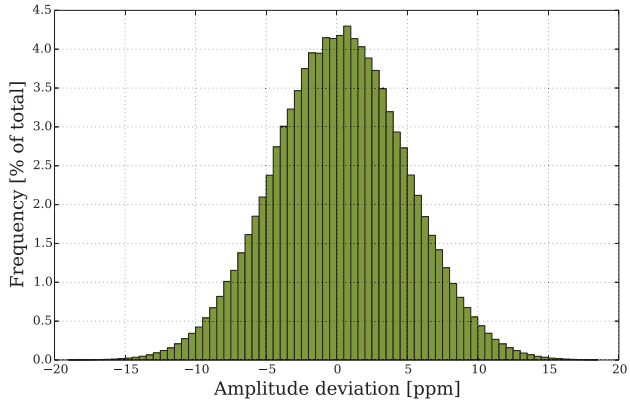

Figure 8: Current source stability measured with the half-bridge over a 24-hour period.

CONCLUSIONS

The pulsed current calibration circuitry described in this paper was originally optimised for calibrating the new bunch current measurement system in the LHC.

Laboratory measurements of a prototype show that the achieved absolute accuracy is limited to approximately 200 ppm (0.02 %) by tolerances of the components used and the decay of the output current, but is nevertheless exceptionally stable. The shot-to-shot stability has a standard deviation of only 4.7 ppm and the output current within 100 ppm of the nominal current after 32 µs.

The current source and half-bridge circuits were optimised to be simple, stable and precise yet flexible enough so that the calibration current can be easily adjusted by replacing a few components. The number of performance-critical components was minimised making it an interesting choice for applications requiring a precise pulsed current generator.

ACKNOWLEDGEMENTS

The authors would like to thank their colleague Jeroen Belleman from the CERN Beam Instrumentation Group for his help in the development of the pulsed current source.

REFERENCES

[1] M. Gasior, “Hardware of the CTF3 Beam Position Measurement System”, CERN Note CERN-CTF3-Note-053, Geneva, Switzerland 2003.

[2] M. Krupa, M. Gasior, “The Wall Current Transformer – a new sensor for precise bunch-by-bunch intensity measurements in the LHC”, presented at IBIC2016, Barcelona, Spain, paper WEAL02, this conference.

[3] D. Belohrad, D. Esperante Pereira, J. Kral and S. Bart Pedersen, “Upgrade of the LHC Bunch by Bunch Intensity Measurement Acquisition System”, presented at IBIC2016, Barcelona, Spain, paper MOPG39, this conference.

ISBN 978-3-95450-177-9

DEFLECTING CAVITY DYNAMICS FOR TIME-RESOLVED MACHINE STUDIES OF SXFEL USER FACILITY*

M. Song, H. Deng†, B. Liu, D. Wang, SINAP, Shanghai, 201800, China

Abstract

Radio frequency deflectors are widely used for time-resolved electron beam energy, emittance and radiation profile measurements in modern free electron laser facilities. In this paper, we present the beam dynamics aspects of the deflecting cavity of SXFEL user facility, which is located at the exit of the undulator. With a targeted time resolution around 10 fs, it is expected to be an important tool for time-resolved commissioning and machine studies for SXFEL user facility.

INTRODUCTION

Free electron laser (FEL) in the X-ray spectral region is a highly fruitful field ranging from ultra-fast scale probe to molecular biology, and from material science to medical science. Currently, the first X-ray FEL (8.8 nm) facility in China driven by 840 MeV LINAC is under construction at Shanghai, namely SXFEL test facility [1-2]. A soft X-ray user facility [3] has been proposed on the basis of SXFEL test facility. With a straightforward beam energy upgrade to 1.5 GeV, the FEL wavelength will extend to 2.0 nm and fully cover the water-window region [3]. In order to guarantee the FEL lasing performance at short wavelength, besides cascading HGHG [4], EEHG [5] and PEHG [6], a SASE [7] undulator line which consists of in-vacuum undulator and the insertion is also raised up.

For such an ultra-short bunch required for excellent FEL performance, one of the great challenges is the measurement and diagnosis with high temporal resolution. Up to now, many techniques have been developed, including zero RF phasing and streak camera. Transverse RF deflecting cavity is introduced to diagnose longitudinal profile of the electron bunch and FEL radiation, which is capable of resolving the temporal structure as short as sub-fs level under the circumstance of high deflecting voltage and frequency [8]. Since this method can effectively convert time-correlated longitudinal profile into the transverse profile, thus the bunch could be revealed and analysed in more detail. In terms of high efficiency and resolution, this technique would become key diagnostic system in the future. Therefore, a pair of X-band RF deflectors is planned at the exit of the undulator section of SXFEL user facility.

DIAGNOSTIC BEAMLINE OPTIMIZATION

The preliminary designed deflector beamline of SXFEL user facility is shown in Fig. 1. Four quadruple magnets can be used for the beam optics optimization within the system, in which, one quadruple magnet downstream the RF deflecting cavity can be used for additional beam focusing in case of relative large beam size on the screen. The bending magnet located about 6 m downstream the undulator exit, is used for beam momentum and spread measurement. The transverse deflecting structure (TDS) installed in the beam line provide the performance to measure the longitudinal phase space, and thus the longitudinal bunch distribution.

The main goal of the whole TDS beamline is achieving high temporal resolution and allowing precious longitudinal measurement of ultra-short bunch. When the electron bunch passes through the RF deflecting cavity with the bunch centre at the zero-phase, the high frequency and time-resolved deflecting fields will kick the bunch and broaden its transverse size on the screen. According to the basics of the deflecting concept, the analytical formula of resolution can be deduced as follows [9]:

$$\Delta_s = \frac{c(E/e)}{\omega V_0}\frac{\sqrt{\varepsilon_x}}{\sqrt{\beta_d \sin\Delta\psi\cdot\gamma}} \qquad (1)$$

On the basis of the formula, it is found that the resolution not only depends on the beam emittance and TWISS parameters but also influenced by the phase advance and deflecting force induced by the RF deflecting. Considering the time-resolved ability and the intrinsic beam profile, the beamline optimization could be achieved by adjusting four quadruple magnets gradient with ELEGANT [10] simulation under the condition that β function at the screen ranging from 2 m to 4 m. The main parameters of TDS and optimized beamline are summarized in Table 1. It should be pointed out that the parameters are tentative and still need to be optimized.

Table 1: Main Parameters of TDS and Optimized Beamline

RF deflecting frequency	f	11.424	*GHz*
RF deflector voltage	V_0	10	*MV*
RF deflector length	L	1	*m*
RF deflector number		2	
Nominal beam size	σ_{x0}	31.5	μm
Beam size with TDS on	σ_x	971.6	μm
Beta at TDS	β_d	8.8	*m*
Beta at screen	β_s	2.9	*m*
Phase advance	$\Delta\varphi$	79	*degree*
Normalized emittance	ε_n	1.015	μm
RMS bunch length	σ_z	55.797	μm

*Work supported by Natural Science Foundation of China (11475250 and 11322550) and TenThousand Talent Program.

†denghaixiao@sinap.ac.cn

ISBN 978-3-95450-177-9

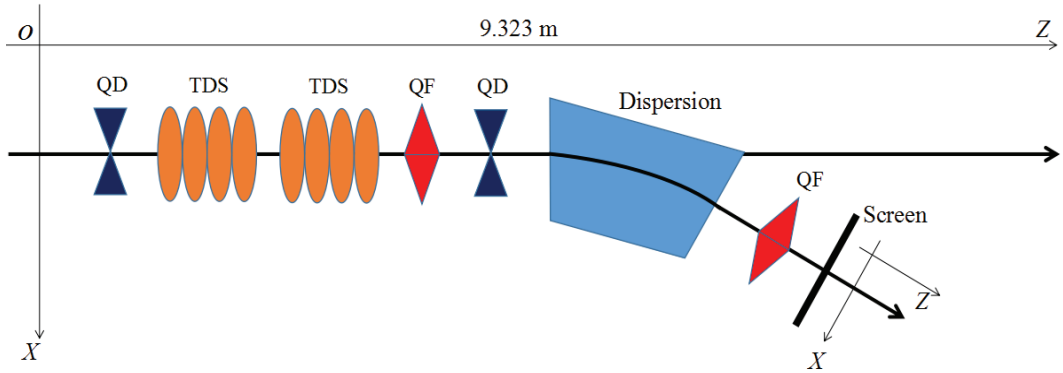

Figure 1: Layout of the TDS beamline downstream the undulator section.

According to the main parameter from Table 1 and analytical formula, the best time resolution can be achieved is approximately 6.6 fs with two RF deflectors of this type, which is pretty enough to measure 180 fs electron bunch in SXFEL user facility.

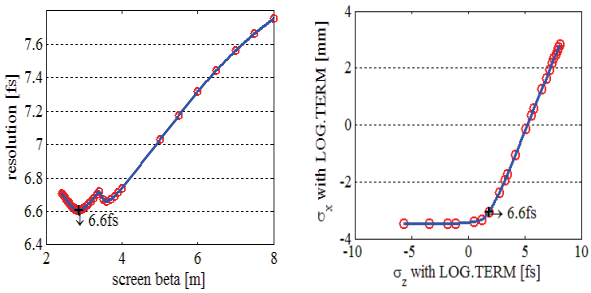

Figure 2: Resolution optimization & simulation results.

Figure 2 presents the resolution results from different method, the left shows the resolution distribution versus screen beta through adjusting four quadruple with regarding screen beta as target, then the computed phase advance and beta at deflector substituted into analytical formula will generate the resolution profile, it is obvious to find the minimum resolution approaches nearly 6.6 fs. The right shows the case on the basis of the optimized lattice from former method, in this sense, RMS bunch length was increased from almost zero to 1 mm. It is deserved noting that the horizontal RMS beam sizes on the screen approximately keep constant at first, while with the growth of bunch length, the beam size will experience a linear relationship with bunch length. According to the resolution definition and Fig. 2 (b), the transverse beam size at the screen is square root of two times of initial size when the RMS bunch length reaches about 6.6 fs, which also corresponding to the best resolution value and verifying the correction of previous lattice optimization.

LONGITUDINAL PHASE SPACE & BUNCH PROFILE MEASUREMENT

The bunch length and longitudinal profile measurements performed by the RF deflecting cavities installed at the SXFEL user facility diagnostic beamline need horizontal focus on the downstream screen. As a result, the beam longitudinal profile can be reconstructed by the horizontal image on the screen.

TDS Calibration

The horizontal position of bunch on the screen at the end of beamline wholly depends on the RF deflecting phase at which bunch experiences. In order to reconstruct longitudinal profile one needs to know the deflecting parameter which could be measured in an experiment, here also could be obtained through ELEGANT simulation [10]. It is assumed that TDS RF phase is earlier or later than the zero-phase at which bunch propagates. Thus the electron bunch at the previous position will experience an off-axis shift due to transverse kick. As a result, considering shifted length and deriving it in terms of phase delay, the deflecting parameter can be written as follows:

$$D = K * 360^{\circ} * f / (\beta * c) \qquad (2)$$

Here K is slope of the linear line with f the deflecting frequency. For the SXFEL user facility diagnostic beamline, the simulation result of TDS calibration is shown in Fig. 3.

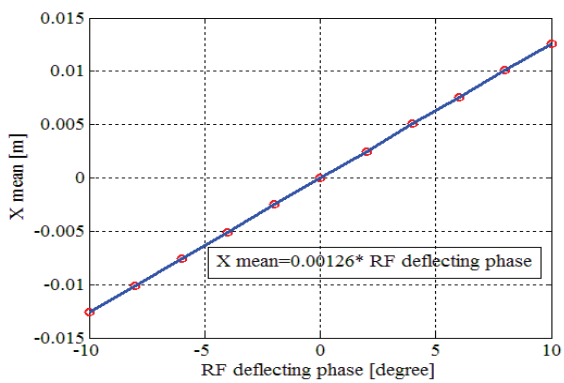

Figure 3: TDS calibration at the observation screen at the end of beamline. The horizontal beam centre shows a dependence on RF deflecting phase with red circle points, the blue line represents the linear fit.

ISBN 978-3-95450-177-9

On the basis of the eleven groups of simulation results one can obtain the slope of linear fit is 0.00126 m/degree, thus for user facility diagnosis parameter with a frequency of f=11.424 *GHz* and relativistic velocity equal to one. Equation (2) can calculate the deflecting parameter as 17.273.

Longitudinal Phase Space Reconstructed

In future measurements of longitudinal phase space at the SXFEL user facility could be done with the combination of RF deflecting cavity and dipole magnet as well as to achieve higher resolution. As aforementioned, the diagnostic beamline should be optimized along with deflecting parameter measured to allow for such measurement. In addition, a more detailed schematic layout of the measurement items related to longitudinal phase space has shown in Fig. 1.

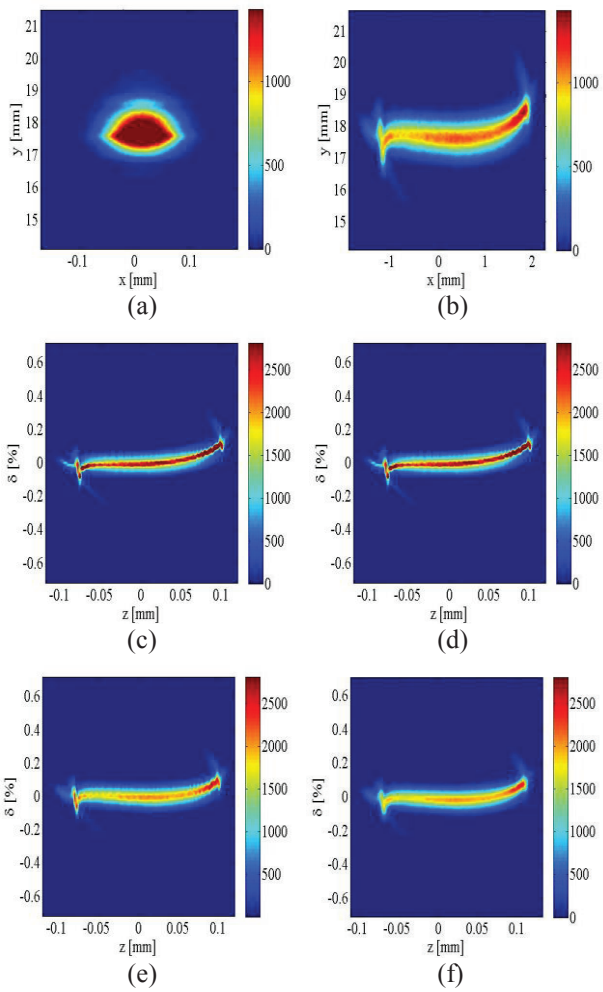

Figure 4: Simulated screen beam images with TDS off (a) and TDS on (b). Simulated longitudinal phase space along the beamline: (c) the original phase space, (d) in front of the RF deflecting cavity, (e) in front of the dipole magnet, (f) reconstructed phase space at the screen.

Simulated images on the observation screen are presented in Fig. 4. The picture in Fig. 4 (a) shows the beam image on the observation screen when the RF deflecting cavity is switched off. While the Fig. 4 (b) presents beam image with TDS switched on and this will give a longitudinal resolution of 6.6 fs. It is obvious to find that two RF deflecting cavities operated in X-band give the electron bunch a strong horizontal kick. Simulation consequences of longitudinal phase space are presented in Fig. 4 with electron bunch charge 500 pC. The plot (c) shows the original electron bunch longitudinal phase space. Moreover, the plot (d) expresses the longitudinal phase space in front of RF deflecting cavity. Furthermore, the plot (e) presents the longitudinal phase space downstream the TDS while upstream the dispersion section. In the final, the plot (f) represents the reconstructed longitudinal phase space located at the observation screen, which derived from Fig. 4 (b).

From the longitudinal phase space evolution along the diagnostic beamline, one can find that the reconstructed one shown in Fig. 4 (f) becomes wider and has a slightly different shape from input electron bunch profile. This effect can be explained by the additional increased TDS energy spread.

Longitudinal Bunch Profile Reconstructed

The reconstructed longitudinal profile is shown in Fig. 5 resulted from Fig. 4 (f), which scaled screen image size with deflecting parameter of 17.273. The longitudinal profile obtained through ELEGANT [10] particle tracking are also shown. The Fig. 5 shows a good agreement between reconstructed profile and initial one.

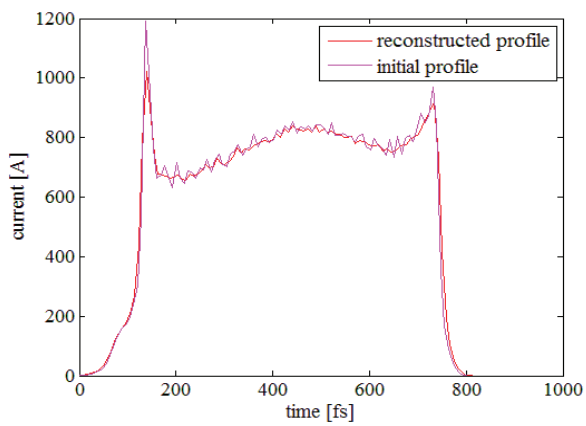

Figure 5: Comparison between the tracked current profile (pink curve) and the reconstructed profile (red curve).

FEL PROFILE RECONSTRUCTION

The direct application of RF deflecting cavity is the longitudinal phase space observation of the electron beam. As demonstrated at LCLS [8], under the verification of simulated results of reconstructed longitudinal bunch profile compared with given distribution, the SXFEL diagnostic beamline has the capability to measure the X-ray pulse temporal distribution.

As presented in Fig. 6, the longitudinal profile of the X-ray FEL pulse are simulated and reconstructed, which illustrates that the electron beam experience a two-stage HGHG lasing, by comparing the longitudinal phase with

ISBN 978-3-95450-177-9

FEL lasing-off, the FEL pulse duration and shape can be retrieved as shown in Fig. 6 (b). On the basis of the temporal profile, on can find an approximately 1.5 GW radiation power generated at the first stage HGHG along with a nearly 400 MW X-ray power produced at the second stage HGHG.

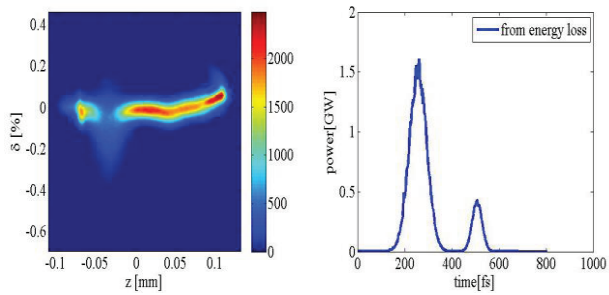

(a) (b)

Figure 6: FEL temporal profile reconstruction. The electron bunch charge is 500 pC with electron energy of 1.5 GeV. The simulated results are shown in: (a) Reconstructed FEL lasing downstream the TDS, (b) Reconstructed X-ray pulse duration and shape.

CONCLUSION & OUTLOOK

The schematic layout of TDS beamline for SXFEL user facility was described and optimized in this paper. With the installation of X-band RF deflecting cavities, measurements of the longitudinal electron beam phase space and the X-ray FEL pulse profile can be carried out. Simulation results confirm that the beamline allows one to measure the electron bunch with a time resolution of 6.6 fs, which can be further enhanced by the transverse gradient undulator compensation [11]. In addition, besides the capabilities shown in this paper, other potential applications, for instance, studies of micro-bunching instability and slice energy spread can be carried out in the future.

REFERENCES

[1] Soft X-ray FEL Concept Design Report, Shanghai, 2015.

[2] M. Song *et al.*, *Nucl. Instr. and Meth.* A822, 71, 2016.

[3] M. Song*et al.*,in: Proceedings of IPAC16, Busan, Korea, 2016.

[4] L.H. Yu, *Phys. Rev. A* 44, 5178(1991).

[5] G. Stupakov, *Phys. Rev. Lett.* 102, 074801, 2009.

[6] H. Deng, C. Feng, *Phys. Rev. Lett.* 111**,** 084801, 2013.

[7] A. Kondratenko, E. Saldin, Part Accel. 10, 207, 1980.

[8] C. Behrens *et al.*, Nature Communication 5, 3762, 2014.

[9] R. Akre *et al.*, SLAC-PUB-8864, June, 2001.

[10] M. Borland *et al.*, Elegant: A Flexible SDDS-compliant Code for Accelerator Simulation, Argonne National Lab, IL, US, 2000 (unpublished).

[11] G. Wang *et al.*,Time-resolved Electron Beam Diagnostics with Sub-femtosecond Resolution, arXiv: 1510.06111.

ISBN 978-3-95450-177-9

ELECTRON BEAM LONGITUDINAL DIAGNOSTIC WITH SUB-FEMTOSECOND RESOLUTION

G. Andonian[1], M. Harrison, F. O'Shea, A. Ovodenko, RadiaBeam Technologies, Santa Monica, CA, USA
M. Fedurin, K. Kusche, I. Pogorelsky, M. Polyanski,
C. Swinson, Brookhaven National Laboratory, Upton, NY, USA
M. Weikum, DESY, Hamburg, Germany
J. Duris, J. Rosenzweig, N. Sudar, UCLA, Los Angeles, CA, 90095
[1] also at UCLA, Los Angeles, CA 90095

Abstract

In this paper, we describe the status of prototype development on a diagnostic for high brightness electron beams, that has the potential to achieve sub-femtosecond longitudinal resolution. The diagnostic employs a high-power laser-electron beam interaction in an undulator magnetic field, in tandem with a rf bunch deflecting cavity to impose an angular-longitudinal coordinate correlation on the bunch which is resolvable with standard optical systems. The fundamental underlying angular modulation that is the basis of this diagnostic has been tested experimentally at the Brookhaven National Laboratory Accelerator Test Facility (BNL ATF) with a high-brightness electron beam and >100GW IR laser operating in the TEM_{10} mode. Here we provide an update on the status of the experimental program with details on the undulator testing, and initial results that include a study of the effects of the laser mode, and energy, on the beam angular projection.

INTRODUCTION

The precise characterization of the longitudinal profile of high-brightness electron beams is crucial for applications in light source development and advanced accelerator applications. Current techniques to measure the beam bunch profile include rf zero phasing methods, pulse reconstruction using interferometry of beam-based coherent radiation [1], and transverse deflecting cavities [2]. Deflecting cavities are very attractive because the presently attainable resolution with modern cavities in the x-band is on the order of a few fs. This paper describes a method to further enhance the resolution of the transverse deflecting cavity with the addition of an orthogonal transverse angular modulation on the beam correlated to the longitudinal coordinate. The correlation is generated by an interaction of the electron beam with a high-power laser in a resonant undulator. The interaction, similar to a higher-order inverse free-electron laser interaction, provides a correlated angular modulation that is resolvable on a distant screen with standard diagnostics and is schematically pictured in Fig. 1.

The interaction of the TEM_{10} laser mode, operating at high power and an electron beam in an undulator field yields an angular modulation on the beam. The detailed physical description is presented in Ref. [3]. For the system sketched in Fig. 1, the total angular modulation $\Delta x'$ is a function of

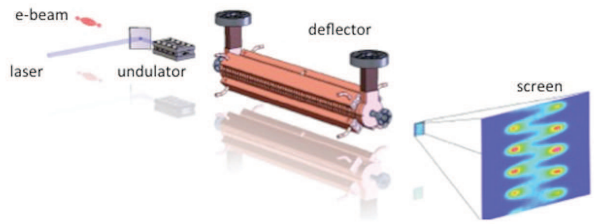

Figure 1: The electron beam interacts with a high-power, IR laser in the TEM_{10} mode, in a resonant undulator to provide a "fast", sinusoidal transverse angular modulation. The deflecting cavity provides a "slow" streak in the orthogonal dimension. The resultant combined downstream pattern yields information on the bunch profile with enhanced longitudinal resolution.

the longitudinal coordinate, s, and is given by the expression [4],

$$\Delta x' = Ak\sin(ks + \phi) \tag{1}$$

where k is the wavenumber of the driving laser, ϕ is the relative phase, and the amplitude of the oscillation, A, is proportional to

$$A \sim \frac{2K}{\gamma^2}\sqrt{\frac{P_L}{P_0}}[JJ] \tag{2}$$

In the expression for the amplitude A, K is the scaled undulator parameter, γ is the beam Lorentz factor, P_L is the laser power, and the coupling factor $[JJ] = J_0(K^2/(4+2K^2)) - J_1(K^2/4+2K^2))$. For application as a bunch length diagnostic, it is important to maximize this amplitude because the angular modulation projection on a downstream profile monitor is the direct observable. From the expression above, it is clear the oscillation amplitude scales as the $\sqrt{P_L}$ and inversely with γ^2. Therefore the interaction favors high power, long wavelength lasers, and low-moderate energy beams. Based on this scaling, an experiment was designed for the Brookhaven National Laboratory Accelerator Test Facility (BNL ATF). The BNL ATF has a long history in experiments based on laser-electron beam interactions due to the availability of a high-brightness beam and high-power, CO_2 based IR laser. The expected interaction based on relevant BNL ATF parameters for the electron beam (ϵ_n=1mm-mrad, E=48MeV, Q=300 nC) and high power laser operations ($\lambda = 10.6\mu m$, P_L= 100GW) is shown in Fig. 2 using

ISBN 978-3-95450-177-9

a resonant undulator (described in the next section) and a x-band rf defelecting cavity [5] (f=11.6 GHz, V_0=8MV). Results of Elegant [6] simulations for the BNL ATF parameters are shown below.

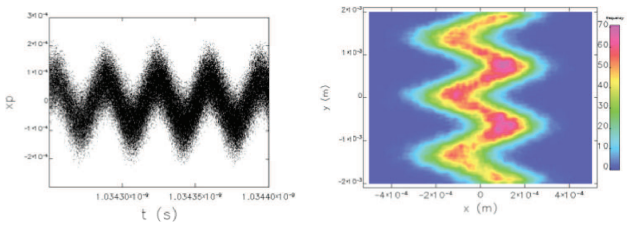

Figure 2: Simulations of angular beam modulation versus longitudinal coordinate after interaction in undulator (left) and transverse profile on diagnostic imaging screen 1m downstream.

UNDULATOR DEVELOPMENT

The design undulator parameter was K=2.49 with a period of 4cm to satisfy the resonant wavelength (10.6μm for the BNL ATF CO_2 laser). The undulator length was constrained by the available space on the beamline of the BNL ATF for the 10 period undulator (total length 40cm) and is shown in Fig. 3 - top. The undulator poles are composed of Neodymium-Iron-Boron (NdFeB) magnets which were procured, individually characterized and sorted, then epoxied into tightly toleranced holders. The undulator mechanical design is based on the principles of total access from one side to allow for a Hall probe measurement. The tuning of the magnets occurs from the top (or bottom) allowing flexibility for quick on-the-fly tuning if necessary. The distance of the individual magnets from the center plane is adjusted via the screw that holds the magnet in place. The undulator has variable height endplates, which are readily adaptable to the BNL ATF beamline for alignment. The mounting plate has the capability for fine positional and angular adjustments in the transverse dimensions; the 5-axis degree of freedom stage allows for control of roll.

The undulator fields were characterized using two complimentary methods. First, a Hall probe scan was used to determine some of the magnetic field features directly. The Hall probe scan was performed on the RadiaBeam magnetic measurement station. The first measurement performed is a longitudinal scan of the undulator on-axis. The results of the scan at 33 points/period are shown in Fig. 3 - bottom, where the line represents the simulation performed using Radia, and the dots are the measured field showing good agreement within tolerance.

Second, a pulse wire measurement was performed to measure the effect of the undulator on electron beam transport. For the pulsed-wire measurement, a small current-carrying wire is passed through the magnetically active area of the undulator. The wire displacement is measured by a laser diode detector. In this method, both the first (angle offset) and second (position offset) integral can be measured and tuned out appropriately prior to installation.

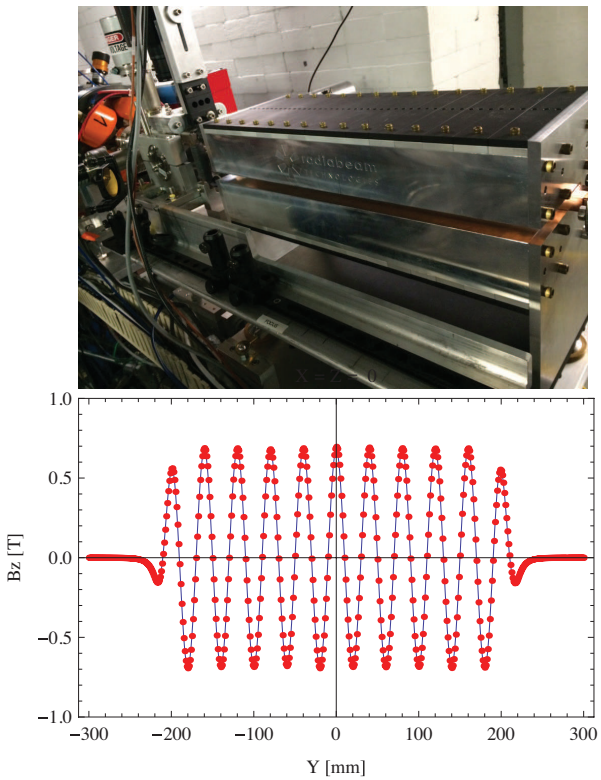

Figure 3: Top: Photograph of the undulator fabricated and installed at the BNL ATF beamline. Bottom: Field profile of undulator as measured on test bench prior to installation.

INITIAL MEASUREMENTS

The challenges of operation at high laser power, necessitate the minimal use of transmissive optics for the purpose of shaping the initial Gaussian laser mode into a higher-order TEM_{10} mode. The generation of the appropriate laser mode is accomplished by a simple interferometer setup. The initial pulse is split in two equal intensity parts and sent through equal length transport arms. The delay between the two arms is controlled by precision micrometer. The two pulses are then recombined at a very shallow angle to produce an interference pattern with the same characteristics as desired. An example of the pattern is shown in Fig. 4 for low-power on the test bench using a pyrocam detector. This interferometric method accurately produces a pulse profile that is characteristically similar to a pure TEM_{10} mode.

Synchronization between the laser pulse and electron beam is critical to observe the interaction. Course synchronization is accomplished by comparing the laser signal on a silicon photodiode and the electron beam at an rf pickup. For further precision, the electron beam transmission through a thin germanium foil with the IR laser is monitored [7]. Ultimately, the observation of the interaction determines the synchronization at the ps time scale.

ISBN 978-3-95450-177-9

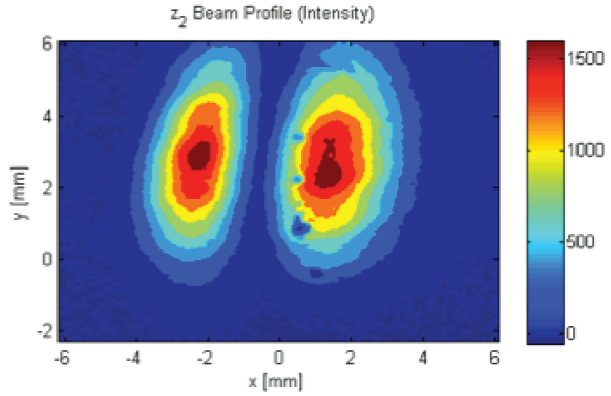

Figure 4: The laser pulse profile of the TEM_{10} mode converter at low power on the test bench.

The first studies employing the undulator and laser interaction were conducted without the deflecting cavity to test the concept feasibility. In this case the main observable is the increase in angular modulation due to increased laser power. The transverse trace space output from the undulator would show an an increase in the projected horizontal beam spread. Fig. 5 shows a qualitative example from simulation for the beam rms transverse size increase in cases of laser driver energy of 10-100GW in the laser modulator section.

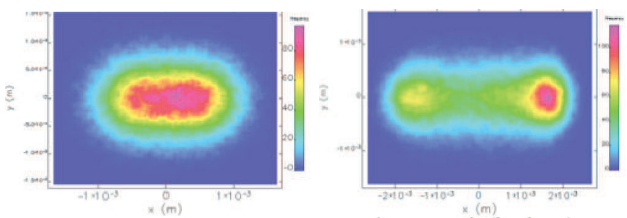

Figure 5: Simulations for the electron beam profile with a 10GW driving laser (left) and 100GW driving laser power (right) shows increase in projected horizontal beam size.

The first beam tests with the interaction at the BNL ATF were conducted prior to installation and commissioning of the x-band transverse deflecting cavity. In these runs, the laser was operated at a power of ~100GW in the higher order mode configuration. The focus of the laser spot was placed at approximately the center of the undulator. The electron beam and laser spatial overlap was determined using beam profile monitors and a co-aligned optical wavelength laser. The electron beam profile was imaged on a screen 1.2 m downstream of the undulator exit. Fig. 6 shows the beam profile on the screen for two cases; first when the laser is off (left), and for the laser powered to 100GW (right). An approximate 25% increase in the horizontal spread (the undulator direction) is seen for the case when the laser is turned on. The increase in the projected rms beam size is an indication of the interaction effect. These results agree with the initial simulations but further work is ongoing on the data analysis to precisely characterize the effect.

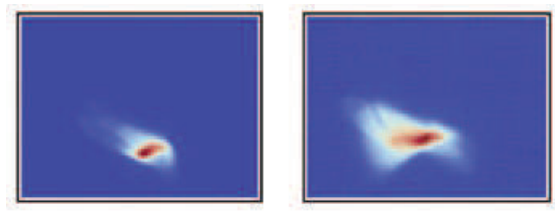

Figure 6: Raw data (uncalibrated) of the electron beam transverse profile at the BNL ATF after traversing through the undulator (left) and when the laser is turned on (right).

CONCLUSIONS

The development of a bunch profile diagnostic with sub-fs resolution has made significant progress in the last year. The initial results without the use of the rf deflecting cavity, presented here, demonstrate the angular modulation of the electron beam from a higher-order laser mode interaction in the resonant undulator. The final results are awaiting the installation and commissioning of the transverse deflecting cavity at the BNL ATF. The complete experiment also has demanding requirements on the electron beam in terms of emittance and energy spread, achievable by the BL ATF. Parallel efforts are also being undertaken to develop analysis tools to directly infer the bunch profile from the screen image for given laser and undulator parameters. In addition, future experiments are being considered to measure the submicron scale microbunching of the beam from an upstream laser modulator using the sub-fs diagnostic. The results are scalable to higher energy beams and optical wavelength lasers and are the subject of continuing and upcoming work.

ACKNOWLEDGMENT

This work is supported by U.S. DOE Grant No. DE-SC0007701.

REFERENCES

[1] R. Lai and A. J. Sievers, Phys. Rev. E 50, R3342 (1994).

[2] R. Akre et al., in Proceedings of the 19th Particle Accelerator Conference, Chicago, Illinois, 2001 (IEEE, Piscataway, NJ, 2001), p. 2353.

[3] G. Andonian, et al., Phys. Rev. ST Accel. and Beams 14, 072802 (2011).

[4] A. Zholents and M. Zolotorev, New J. Phys. 10, 025005 (2008).

[5] M. Fedurin, presented at these proceedings.

[6] M. Borland, Tech. Report Advanced Photon Source LS-287 (2000).

[7] J. Duris, et al., Nat. Comm. 5:4928 (2014).

ISBN 978-3-95450-177-9

SIMULATION OF THz STREAK CAMERA PERFORMANCE FOR FEMTOSECOND FEL PULSE LENGTH MEASUREMENT

I. Gorgisyan*, PSI, Villigen, Switzerland, EPFL, Lausanne, Switzerland
R. Ischebeck, P. Juranic, E. Prat, S. Reiche, PSI, Villigen, Switzerland

Abstract

Extremely bright short-pulsed radiation delivered by the free electron laser (FEL) facilities is used in various fields of science and industry. Most of the experiments carried out using FEL radiation are dependent on the temporal durations of these photon pulses. Monitoring the FEL pulse lengths during these experiments is of particular importance to better understand the measurement results. One of the methods to measure the temporal durations of the FEL pulses is the THz streak camera. This contribution presents simulation of the THz streak camera concept that allows better understanding of the measurement technique and estimating measurement accuracies achievable with this method.

INTRODUCTION

The ultrashort pulses of FEL radiation are used to study the dynamic processes in ultrafast temporal domain. The advancement of the FEL technologies enables delivery of photon pulses with durations in the femtosecond region or shorter. Measuring the lengths of the photon pulses is useful both for the users performing measurements at FEL facilities and the machine operators to monitor the performance of the accelerator itself.

Various techniques are currently used in different facilities to measure the temporal duration of the FEL pulses [1–6]. Among these methods is THz streak camera [2, 7–10] that is able to measure the pulse durations of FEL pulses with photon energies from UV to hard X-ray. To better understand the performance of THz streak cameras, to estimate the possible measurement accuracy of this method and to optimize the data analysis method used to retrieve the pulse lengths from the THz streaking measurements, a Matlab code was developed to simulate the streaking effect and the pulse length calculation procedure. The results delivered by the simulation demonstrate that the THz streak camera method is able to measure the length of the FEL pulses with an accuracy of about a femtosecond and indicate ways towards achieving sub-femtosecond accuracies. More comprehensive information about the simulation procedure and the obtained results is provided in [11].

CONCEPT

The theory of the THz streak camera is presented in detail in [7, 12]. The idea of the method is to encode the temporal duration of an FEL pulse into the energy spectra of the photoelectrons produced by this pulse. This is done by ionizing the electrons in presence of an external THz radiation. Depending on the time of the ionization, the created electron experiences different phase of the THz pulse. Due to the interaction of the electron with the electric field of the THz pulse, its final kinetic energy changes. This change is dependent on the phase of the THz at the moment of the ionization. Electrons created by different parts of a photon pulse have different ionization times and, therefore, experience different energy shifts due to the interaction with the external streaking field. As a result, the energy spectrum of the streaked electrons is the convolution of the non-streaked electron spectrum and the temporal profile of the photon pulse. In case of convolution the rms widths of the two profiles add quadratically, meaning that the spectral width of the streaked photoelectrons can be written in the following form:

$$\sigma_{st}^2 = \sigma_0^2 + \tau_X^2(s^2 \pm 4cs). \quad (1)$$

Here σ_0 is the rms width of the non-streaked spectrum, τ_X is the duration of the ionizing pulse and s is the streaking strength of the THz pulse. The term c in equation 1 represents the linear energy chirp along the photon pulse. The sign ± corresponds to the electrons traveling along the electric field of the THz and opposite to it. By comparing the two streaked spectra of the electrons to their non-streaked spectra, one can calculate the spectral broadening $\Delta\sigma_\pm$ due to streaking in opposite directions. Using these two amounts of broadening, it is possible to exclude the chirp from equation 1 and obtain the pulse duration as

$$\tau_X = \sqrt{\frac{\Delta\sigma_+^2 + \Delta\sigma_-^2}{2s^2}}. \quad (2)$$

This expression is used in the simulation process to retrieve the rms lengths of FEL pulse using the photoelectron spectra.

SIMULATION PROCEDURE

The simulation procedure uses energy spectra and temporal profiles of different FEL pulses generated by code Genesis [13] to reproduce the ionization of the electrons and their consequent streaking by the THz pulse. Once the non-streaked spectrum and the two streaked spectra of the electrons are obtained, the pulse lengths are calculated using equation 2. The reconstructed rms durations of the pulses are compared to the rms lengths of the input FEL pulses, and the accuracy and the precision of the calculations are estimated for each of the FEL pulses.

Overall, 178 FEL pulses were generated using the Genesis code. The pulse lengths were in range from about 1 fs up to 40 fs. The pulses of lengths from 1 fs to 15 fs were in the hard X-ray radiation range with photon energies of 12.4 keV,

* ishkhan.gorgisyan@psi.ch

ISBN 978-3-95450-177-9

while the pulses with the lengths from 20 fs to 40 fs were in the soft X-ray region with photon energies of 1.24 keV. The generated FEL pulses corresponded to various operation modes of SwissFEL [14], a free electron laser facility that is currently under commissioning at PSI.

During the simulation the properties of the THz pulse and the electron time-of-flight (eTOF) spectrometers were chosen based on the experimental setup previously used in THz streaking measurements [10, 15, 16]. For such configuration, the main contribution of the uncertainties comes from the measurement accuracy of the eTOFs and from the statistical fluctuations of the electron spectra because of the finite number of the registered photoelectrons.

The simulation procedure assumes that the number of photoelectrons produced by the FEL pulse is proportional to the duration of the pulse. For this reason, different number of electrons are generated in the simulation depending on the length of the input FEL pulses. The electrons are created, and energy values are assigned to them using a Monte Carlo method called acceptance-rejection (rejection sampling) [17]. The energy of a non-streak electron that is measured by the eTOF is given by the following formula:

$$K(t_i) = K_0 + R_n(\sigma_{eTOF}) + ct_i, \quad (3)$$

where K_0 is defined by subtracting the ionization potential of the electron from the central energy of the photon pulse, c is the linear chirp introduced in equation 1 and t_i is the temporal position of the ionizing photon along the FEL pulse. The function R_n in equation 3 generates random values from a normal distribution with an rms width of σ_{eTOF} . This term in the equation is responsible for the uncertainty caused by the limited resolution of the eTOFs σ_{eTOF}. Using formula 3, a number of electrons is generated that constitute the non-streak spectrum measured by the eTOF. The energy values assigned to the streaked electrons are obtained from the following formula:

$$K_{st}(t_i) = K_{ch}(t_i) + R_n(\sigma_{eTOF}) \pm \sqrt{8U_p K_{ch}(t_i)}sin(\omega_{THz}t_i). \quad (4)$$

The term $K_{ch}(t_i)$ here is the non-streak energy with the effect of chirp taken into account. The last term of the right-hand-side gives the amount of the energy shift caused by the interaction of the electron with the external THz field, with U_p being the ponderomotive potential and ω_{THz} being the frequency of the THz field.

Once the non-streaked spectrum and the two streaked spectra of the electrons are reconstructed for a certain FEL pulse, the rms duration of this pulse is calculated from the spectral widths using equation 2. The rms widths of the energy spectra are obtained by either fitting Gaussian profiles to them or by calculating directly the rms spread of the simulated spectra. The results of the simulations indicate which of these two methods are preferable for different FEL pulses.

RESULTS

The results provided by the simulations using Gaussian fitting for the spectral width evaluation are shown in table 1 for 10 different photon pulses. The first column shows the photon energy of the FEL pulse, the second one gives the rms length of the input pulses, while the third and the forth columns correspond to the calculated mean pulse lengths with the standard deviations and their absolute accuracies, respectively. One can see from the table that the accuracies

Table 1: Fitting Gausian

Phot. en.	Input len. [fs]	Calc. len. [fs]	Acc. [fs]
12.4 keV	1.5	8.6 ± 3.8	7.1
	1.6	7.9 ± 3.2	6.3
	5.6	6.8 ± 2.2	1.2
	11.3	11.2 ± 1.6	0.1
	16.5	16.9 ± 0.8	0.4
1.24 keV	19.4	20.3 ± 6.4	0.9
	22.2	21.8 ± 5.5	0.4
	26.3	26.1 ± 4.9	0.2
	30.2	31.0 ± 3.4	0.8
	35.8	36.7 ± 3.0	0.9
	39.1	40.3 ± 2.6	1.2

of the calculated average pulse lengths are in range from about 7 fs down to 0.1 fs. For the short pulses, the distribution of the obtained pulse length values has a cutoff at 0, and the average pulse length is shifted towards larger values. For this reason, the obtained average values for the short pulses (about 1.5 fs) serve as a higher limit estimate of the pulse lengths. As for the pulses longer than 5 fs, the accuracies are about 1 fs or better. The accuracy gets worse for the longer pulses as they correspond to photoelectron energy spectra that are not perfectly Gaussian (more flat-top), and the fitting process induces additional uncertainties. The standard deviations of the calculated pulse lengths per input pulse (precision of the calculation) vary from about 6 fs down to sub-femtosecond. The precision of the measurements improves with longer pulse lengths as they correspond to a larger number of measured photoelectrons and, therefore, smaller statistical fluctuations of the energy spectra. Table 1 also shows that the precision is better in case of the hard X-ray FEL pulses. This is caused by the fact that the higher photon energies correspond to more energetic photoelectrons that are streaked more by the THz field (equation 4). This corresponds to a bigger value of the streaking strength s from equation 2, which reduces the uncertainties in the pulse length calculation.

The results obtained by using the direct rms widths of the spectral distributions are shown in table 2. Similar to the Gaussian fitting method, the values obtained for the short pulses in this case show only the upper limit of the lengths. Meanwhile, the average pulse lengths calculated for the FEL pulses of 5 fs and longer, have accuracies of sub-femtosecond. The precision of the calculations is in range from 4.8 fs down to 0.6 fs and improves with longer photon pulses and higher photon energies. Comparing the results presented in tables 1 and 2, one can see that in average the

ISBN 978-3-95450-177-9

Table 2: Calculating rms Widths

Phot. en.	Input len. [fs]	Calc. len. [fs]	Acc. [fs]
12.4 keV	1.5	6.1 ± 3.1	4.6
	1.6	6.4 ± 2.6	4.8
	5.6	6.2 ± 2.2	0.6
	11.3	11.1 ± 1.1	0.2
	16.5	16.5 ± 0.6	<0.1
1.24 keV	19.4	19.1 ± 4.8	0.3
	22.2	21.7 ± 4.0	0.5
	26.3	26.3 ± 2.7	<0.1
	30.2	30.1 ± 2.2	0.1
	35.8	35.8 ± 1.8	<0.1
	39.1	39.2 ± 1.8	0.1

second calculation method provides slightly better accuracy and precision. Such a result is caused by the fact that the calculations using the Gaussian fitting method include additional uncertainties caused by the fitting process.

CONCLUSION

A number of simulations have been performed to better understand the performance of the THz streak camera photon pulse length measurement method. The simulations are based on an experimental setup used for streaking measurements. During the pulse length calculation two different methods of evaluating the spectral widths have been tested. The results revealed that the direct calculation of the rms spread of the simulated energy spectra corresponds to better accuracy and precision. The simulation results showed that the THz streak camera technique is capable of measuring the duration of FEL pulses with accuracies of about 1 fs both in soft X-ray and hard X-ray regions.

REFERENCES

[1] M. Drescher *et al.*, "X-ray pulses approaching the attosecond frontier", *Science*, vol. 291, p. 1923–1927, 2001.

[2] U. Frühling *et al.*, "Single-shot terahertz-field-driven X-ray streak camera", *Nat. Photonics*, vol. 3, p. 523–528, 2009.

[3] Y. Ding *et al.*, "Femtosecond x-ray pulse temporal characterization in free-electron lasers using a transverse deflector", *PRST-Acc. and Beams*, vol. 14, p. 120701, 2011.

[4] S. Düsterer *et. al*, "Femtosecond x-ray pulse length characterization at the Linac Coherent Light Source free-electron laser", *New J. Phys.*, vol. 13, p. 093024, 2011.

[5] Y. Inubushi *et. al*, "Determination of the pulse duration of an X-ray free electron laser using highly resolved single-shot spectra", *Phys. Rev. Let.*, vol. 109, p. 144801, 2012.

[6] R. Riedel *et. al*, "Single-shot pulse duration monitor for extreme ultraviolet and X-ray free-electron lasers", *Nat. Communications*, vol. 4, p. 1731, 2013.

[7] J. Itatani, F. Quéré, G. L. Yudin, M. Y. Ivanov, F. Krausz and P. B. Corkum, "Attosecond streak camera", *Phys. Rev. Lett.*, vol. 88, p. 173903, 2002.

[8] I. Grguraš *et al.*, "Ultrafast X-ray pulse characterization at free-electron lasers", *Nat. Photonics*, vol. 6, p. 852–857, 2012.

[9] W. Helml *et al.*, "Measuring the temporal structure of few-femtosecond free-electron laser X-ray pulses directly in the time domain", *Nat. Photonics*, vol. 8, p. 950–957, 2014.

[10] P. N. Juranić *et al.*, "A scheme for a shot-to-shot, femtosecond-resolved pulse length and arrival time measurement of free electron laser x-ray pulses that overcomes the time jitter problem between the FEL and the laser", *J. Inst.*, vol. 9, p. P03006, 2014.

[11] I. Gorgisyan, R. Ischebeck, E. Prat, S. Reiche, L. Rivkin and P. Juranić, "Simulation of FEL pulse length calculation with THz streaking method", *J Synch. Rad*, vol. 23, p. 643–651, 2016.

[12] F. Quéré, Y. Mairesse and J. Itatani, "Temporal characterization of attosecond XUV fields", *J. Mod. Opt.*, vol. 52, p. 339–360, 2005.

[13] S. Reiche, *Nucl. Instr. Meth. Phys. Res. A: Acc., Spec., Det. Assoc. Eq.*, vol. 429, p. 243–248, 1999.

[14] R. Ganter *et al.*, "SwissFEL-Conceptual design report", PSI, Villigen, Switzerland, Rep. 42006326, 2010.

[15] P. N. Juranić *et al.*, "High-precision x-ray FEL pulse arrival time measurements at SACLA by a THz streak camera with Xe clusters", *Opt. Exp.*, vol. 22, p. 30004–30012, 2014.

[16] F. Ardana-Lamas *et al.*, "Temporal characterization of individual harmonics of an attosecond pulse train by THz streaking", *Phys. Rev. A*, vol. 93, p. 043838, 2016.

[17] W. Gilks and P. Wild, "Adaptive rejection sampling for Gibbs sampling", *App. Stat.*, p. 337–348, 1992.

ISBN 978-3-95450-177-9

ELECTRON BEAM PROBE DIAGNOSTIC FOR BESSY II STORAGE RING

D. Malyutin, A. Matveenko, Helmholtz-Zentrum Berlin, Berlin, Germany

Abstract

A low energy electron beam can be used to characterize the high energy ultra-relativistic bunches. This technique allows one to obtain the bunch transverse profiles as well as the bunch length within a non-destructive single shot measurement.

In this paper the bunch length measurement technique based on the interaction of the low energy electron beam with an ultra-relativistic bunch is described. Results of numerical simulations of measurements related to BESSY II are presented. A possible setup of such diagnostic system for BESSY II and in future for BESSY VSR is proposed.

INTRODUCTION

For better understanding of the beam dynamics in particle accelerators detailed bunch characterization is required. This includes, for example, the bunch length measurements.

The bunch length can be measured, for example, using a standard method with a streak camera which analyses a synchrotron light from a dipole magnet [1, 2] or using a low energy electron beam crossing the electron bunch trajectory in the accelerator [3]. Both methods are non-destructive, i.e. does not affect the bunch, and therefore they can be used during the standard routine operation at user facilities or at others accelerators where destructive diagnostic methods cannot be used. Each method has its own advantages and disadvantages.

Streak Camera

A streak camera measures length and structure of an ultra-fast light signal by representing it as a two-dimensional image. In particle accelerators the light comes, for example, from the synchrotron radiation or optical transition radiation.

A light pulse hits the photocathode causing it to emit a bunch of photoelectrons, Fig. 1 [4]. The time structure of this bunch is identical to the structure of the light pulse.

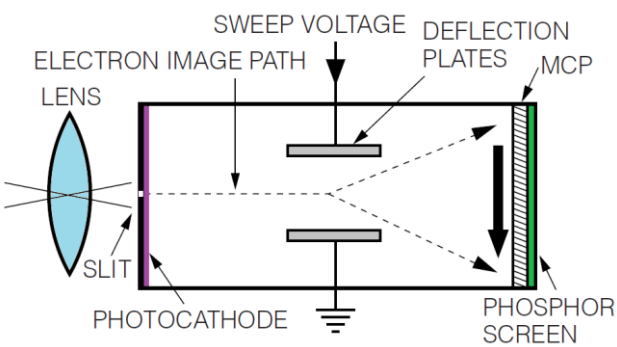

Figure 1: Streak camera basics [4].

These electrons are accelerated and then deflected by a ramped transverse electric field between the deflection plates. Afterwards the number of electrons is multiplied by the microchannel plate (MCP) and imaged on the phosphor screen. The resulted transverse profile of the screen image will represent the temporal profile of the light pulse. The minimal achieved resolution by available commercial streak cameras is in the order of 200 fs [4, 5].

Electron Beam Probe

Electron beam probe diagnostic is based on interaction of the low energy electrons with the strong electric and magnetic fields of the relativistic bunch. Measuring the result of such interaction the bunch length or transverse bunch profile can be obtained [3].

A probe electron beam (3) is generated and accelerated in the electron gun (1) up to about 100 keV energy, Fig. 2.

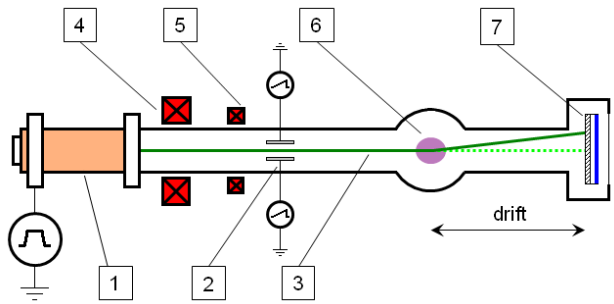

Figure 2: Electron Beam Probe layout: 1 – electron gun, 2 – horizontal deflecting plates, 3 – probe electron beam, 4 – focusing solenoid, 5 – magnetic correctors, 6 – electron bunch to be measured, 7 – detector (MCP and phosphor screen).

The beam is focused by the lens (4) and adjusted vertically and horizontally by a two-coordinate corrector (5). Time correlation in the beam is introduced by horizontal deflecting plates (2). After interaction with the ultra-relativistic bunch (6) the beam is projected on the observation screen (7). The horizontal axis on the screen will correspond to the time and the vertical axis will contain information about the bunch length. In Fig.2 the orientation of the deflecting plates is misleading: they are drown as the view from the top and all others components are drown as the side view.

The additional amplification scheme for the electron detection is required due to the low electron density of the probe beam on the observation screen. It can be realized as an electron-optical assembly of a microchannel plate (MCP) and a phosphor screen, in a similar way as it is done for the streak camera. The resulting image of the probe beam on the phosphor screen is recorded by a CCD camera. The vertical deflection angle is calculated from the image vertical size divided by the drift length, Fig. 2.

The maximal deflection angle of the probe electrons can be a parameter which can be used to characterize the bunch length. The deflection angle depends on the distance from

ISBN 978-3-95450-177-9

the probe electrons to the electron bunch, so called impact parameter. For the case of ultra-relativistic axial symmetric bunch with Gaussian transverse distribution the vertical deflection angle θ_y can be described by the following equation [6]:

$$\theta_y(\rho,x)=\frac{2\rho r_e}{\gamma\beta}\int_{-\infty}^{+\infty}\frac{n(z)dz}{\rho^2+(x+\beta z)^2}\left(1-e^{-\frac{\rho^2+(x+\beta z)^2}{2\sigma_\perp^2}}\right), \quad (1)$$

where ρ is the impact parameter, r_e is the classical electron radius, γ und β are the probe electron relativistic parameters, $n(z)$ is the longitudinal particle distribution of the bunch, x is the relative electron coordinate in the probe beam, $\sigma_\perp$ is the transverse root mean square (RMS) size of the bunch.

Each electron in the probe beam will receive a different deflection after interaction with the relativistic bunch. Electrons with $x = 0$ will get a maximal vertical deflection for the case of symmetrical bunch longitudinal distribution $n(-z) = n(z)$ and maximum at $z = 0$.

For the case of the flat bunch like in storage ring, where the vertical bunch size is much smaller than the horizontal one due to synchrotron radiation damping, the deflecting angle can be calculated as a sum of the deflection from axial symmetric Gaussian bunches. A non-symmetric Gaussian transverse distribution can be represented as a sum of the 2*N*+1 symmetric Gaussian distributions with $\sigma_x = \sigma_y$ and different amplitudes with a horizontal step of two sigma:

$$n(x,y)=A\cdot e^{-\frac{y^2}{2\sigma_1^2}}\sum_{i=-N}^{N}e^{-\frac{(x-2\cdot\sigma_1\cdot i)^2}{2\sigma_1^2}}\cdot e^{-\frac{(2\cdot\sigma_1\cdot i)^2}{2\sigma_2^2}}, \quad (2)$$

where A is the normalization coefficient, σ_1 is the RMS size of the axially symmetric bunch and σ_2 is the desired horizontal RMS size of the flat bunch ($\sigma_2 \gg \sigma_1$). Comparison with the Gaussian distribution having RMS size of σ_2 is shown in Fig. 3 for $N = 15$ and $\sigma_2 = 10 \cdot \sigma_1$.

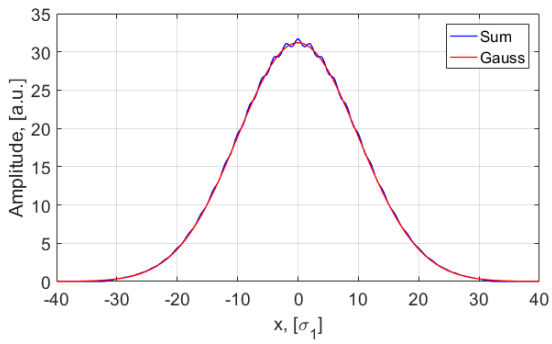

Figure 3: Representation of the long Gauss as a sum of the short ones – the blue curve, see Eq. (2), and Gaussian distribution – the red curve.

The difference with the original Gauss distribution is negligible and is in order of 1%. Making the step in Eq. 1 of one sigma will remove this difference, but it will require two times more elements in the sum and in result will double the calculation time.

Dependence of the maximal deflection angle of the probe electrons versus the bunch length is shown in Fig. 4 for horizontal and vertical bunch orientations. The vertical bunch orientation here means that the probe beam sees the relativistic bunch whose vertical size is bigger than horizontal one. For the horizontal bunch orientation all the way around: the probe beam sees that the vertical size is smaller. For the experiment these two orientations mean that the diagnostic can be installed not only horizontally but also vertically relative to the storage ring plane.

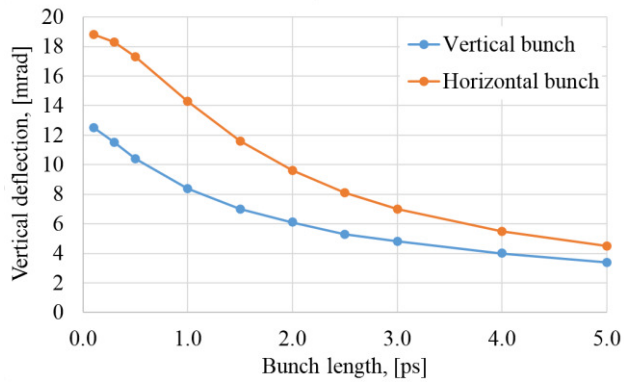

Figure 4: Maximal vertical deflection angle θ_y of the probe electrons as a function of the bunch length for vertical and horizontal bunch orientations.

This example was calculated for bunch charge of 144 pC and RMS sizes of 17 and 170 µm respectively. Horizontal bunch orientation is preferable as it produces higher deflecting angles to the probe electrons, which in turn is increasing the method resolution.

NUMERICAL SIMULATIONS

Particle tracking simulations were performed in analytical fields for an axially symmetric ultra-relativistic bunch. Space charge forces of the probe beam were not taken into account. The bunch has Gaussian charge distributions: 17 µm vertical RMS size and 170 µm horizontal size. Probe beam electrons have an energy of 100 keV, particles distributed uniformly inside a cylinder with transverse size of 0.6 mm and duration of 50 ps. Trajectories of the probe beam and the bunch are crossing – the probe beam electrons have impact parameter in the range from –0.3 mm to +0.3 mm.

Figure 5 shows simulated images of the probe electron beam on the observation screen after interaction with two consequent bunches of 15 (left) and 1.7 ps (right) long with 1.4 and 0.6 nC charge respectively and with 2 ns delay between them. The drift length after interaction is 10 cm and image grid size is 2x2 mm. Bunch parameters were taken from the standard operation mode of BESSY VSR [7].

ISBN 978-3-95450-177-9

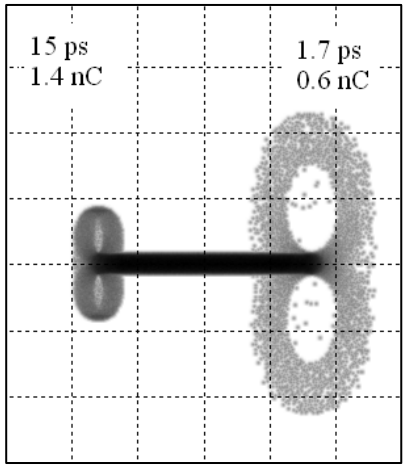

Figure 5: The probe electron beam images on the observation screen for 15 (left) and 1.7 ps (right) long bunch, bunch charges are 1.4 and 0.6 nC respectively (standard BESSY VSR mode); grid size is 2 mm.

The upper half of the image shows probe electrons with a positive impact parameter (their trajectory is above the bunch trajectory) – they are deflecting up, the lower half shows probe electrons with a negative impact parameters – they are deflecting down. The longer bunch gives as a result a smaller size of the image despite the larger bunch charge in this case: +/- 1.8 mm for 15 ps long bunch and +/- 4.4 mm for 1.7 ps long bunch.

Simulation for the case of the low alpha operation mode at BESSY VSR is shown on Fig. 6. Two consequent bunches have 3 (left) and 0.3 ps (right) length, 33 and 30 pC charge respectively, the drift length after interaction is 40 cm and the image grid size is 2 mm. The energy of the probe beam was decreased to 50 keV to have higher deflection angles. The big difference for these two bunches can be seen for the vertical deflection of the probe beam: about +/- 1.3 mm for 3 ps bunch and +/- 2.2 mm for 0.3 ps bunch.

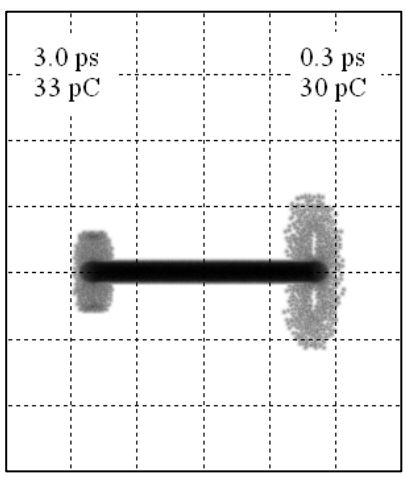

Figure 6: The probe electron beam images on the observation screen for 3.0 (left) and 0.3 ps (right) long bunch, bunch charges are 33 and 30 pC respectively (low alpha BESSY VSR mode); grid size is 2 mm.

Measurements of the bunch length bellow 0.3 ps for such small charge of 30 pC requires the deflection angle resolution better than 0.2 mrad.

In general case, the probe beam energy can be adjusted in such a way that the image of the deflected beam is occupying the full vertical size of the effective area of the MCP and the phosphor screen. This in result will give the best deflection angle resolution. Lower and higher borders come from the electron gun specification and the reasonable numbers are from 30 to 100 kV [6].

Bunch Length Measurement Errors

The measurements errors for all sets of bunches at BESSY II and for future BESSY VSR [7] are presented in Table 1.

Table 1: Bunch length measurement errors.

	Bunch type	Length, ps	Charge, nC	Err1, ps	Err2, ps
BESSYII	Bunch train (1x300)	15	0.7	±3	±1
	Camshaft (x1)	27	4.0	±5	±1
	Slicing (x3)	27	4.0	±1	±0.1
	Bunch train (1x300)	3.0	0.04	±1	±1
	Booster (1x5)	60	1.0	±10	±2
BESSY VSR	Long bunch (2x75)	15	1.32	±3	±1
	Long bunch (2x75)	1.1	0.144	±0.3	±0.2
	Short bunch (x1)	1.7	0.64	±0.5	±0.3
	Camshaft (x1)	27	8.0	±5	±1
	Slicing (x3)	3.7	4.0	±1	±0.1
	Long bunch (2x75)	3.0	0.036	±1	±1
	Short bunch (2x75)	0.3	0.032	±0.5	±1

The Err1 is calculated assuming the bunch transverse size error of 20% and the Err2 is calculated for the case of deflection angle measurement error ±1 mrad.

Better knowledge of the transverse bunch size at the interaction point will significantly improve the resolution of this method. Also with the good optical readout system the angle resolution can reach ±0.2 mrad, which will greatly reduce the Err2.

CONCLUSION

Two non-destructive bunch length measurements have been discussed. A diagnostic based on the interaction of a low energy electrons with the fields of the ultra-relativistic bunch has been comprehensively studied. The achievable resolution is strongly dependent on how precise the transverse bunch size is known, depends on the readout optics resolution and in general can reach sub-picosecond range.

More detailed and sophisticated analysis of the electron beam image on the screen may allow this technique to get even the full longitudinal profile of the bunch like the streak camera [6]. But still there are several advantages compare to streak camera: the single shot measurement, it doesn't require synchrotron light (this is important for low energy accelerators <50 MeV or injectors, e.g. bERLinPro) and lower costs for the case of sub-picosecond bunch length ranges.

ISBN 978-3-95450-177-9

REFERENCES

[1] Mitsuru Uesaka *et al.,* "Precise measurement of a sub-picosecond electron single bunch by the femtosecond streak camera", *Nucl. Instr. Meth. A*, vol. 406 p. 371, 1998.

[2] A. M. MacLeod *et al.,* "Subpicosecond Electro-optic Measurement of Relativistic Electron Pulses", *Phys. Rev. Lett.*, vol. 85, p. 3404, 2000.

[3] D. Malyutin, A. Matveenko, "Electron Beam Probe for the bunch length measurements at bERLinPro", *in Proc. IPAC'16,* Busan, Korea, May 2016, paper MOPMB009.

[4] http://www.hamamatsu.com

[5] K.Scheidt, "Review of Streak Cameras for Accelerators: Features, Applications and Results", *in Proc. EPAC'00,* Vienna, Austria, paper WEYF202.

[6] P. V. Logachev, D. A. Malyutin, and A. A. Starostenko, "Application of a low energy electron beam as a tool of nondestructive diagnostic of intense charged-particle beams", *Instruments and Experimental Techniques,* Vol. 51, No. 1, pp. 1–27, 2008.

[7] A. Jankowiak, J. Knobloch, P. Goslawski, N. Neumann, editors, "BESSY VSR – Technical Design Study", Helmholtz-Zentrum Berlin, 2015

ISBN 978-3-95450-177-9

LASER-BASED BEAM DIAGNOSTICS FOR ACCELERATORS AND LIGHT SOURCES*

C.P. Welsch#, Cockcroft Institute and The University of Liverpool, UK
on behalf of the LA³NET Consortium

Abstract

The Laser Applications at Accelerators network (LA³NET) was selected for funding within the European Union's 7th Framework Programme. During its 4 year duration the project has successfully trained 19 Fellows and organized numerous events that were open to the wider laser and accelerator communities. The network linked research into lasers and accelerators to develop advanced particle sources, new accelerating schemes, and in particular beyond state-of-the-art beam diagnostics. This paper summarizes the research results in laser-based beam diagnostics for accelerators and light sources. It discusses the achievable resolution of laser-based velocimeters to measure the velocity of particle beams, the resolution limits of bunch shape measurements using electro-optical crystals, position resolution of laser wire scanners, and limits in energy measurements using Compton backscattering at synchrotron light sources. Finally, it also provides a summary of events organized by the network and shows how an interdisciplinary research program can provide comprehensive training to a cohort of early career researchers.

OVERVIEW

The primary aim of the LA³NET project [1] was to train 19 early stage researcher within a multidisciplinary network of academic and research-focused organizations across Europe. The network was awarded 4.6 M€ by the European Commission in 2011 and joined more than 30 institutions from around the world. The secondary aim was to establish a sustainable network and generate new knowledge through the research carried out by the Fellows. The LA³NET Fellows were hosted by 11 partner institutions all over Europe and although their work focuses on research, they are provided not only with scientific supervision and opportunities of secondments to other institutions involved in the project, but also complementary training through network-wide events. This includes international schools and topical workshops, as well as a final project conference and numerous outreach events. Through the involvement of almost 30 associated and adjunct partners the project gains an interdisciplinary dimension including strong links to industry. In the following section examples of research results from across the consortium in the beam diagnostics work package are given.

* This project has received funding from the European Union's Seventh Framework Programme for research, technological development and demonstration under grant agreement no 289191.
# c.p.welsch@liverpool.ac.uk

RESEARCH

The Fellows carried out research within one out of five thematic work packages. These are particle sources, beam acceleration, beam diagnostics and instrumentation, system integration and detector technology.

Laser Velocimeter

Pencil or curtain-shaped neutral gas jet targets are important for a number of accelerator-based experiments, either as cold targets or for example for diagnostic purposes [2]. However, only very few studies have addressed the optimization of these jets towards their respective application. The development of a laser velocimeter for an in-detail characterization of the gas jet and investigations into the jet dynamics, probing simultaneously its density, velocity, and temperature, was the aim of an ESR project at University of Liverpool [3]. For this purpose, laser self-mixing has been developed by Alexandra Alexandrova. The theoretical and experimental analysis of factors influencing the performance of the self-mixing laser diode sensor was compared. Variables that influence the resulting spectrum were investigated, primarily the velocity of the target, and the concentration of the seeders to assess the performance of the sensor. It has been shown that the spectrum of the signal directly depends on these factors. Experiments have demonstrated the possibility to use the self-mixing technique for measuring the velocity of fluids up to 1.5 m/s with a low level of seeders from 0.03% which would provide sufficient feedback of light. It has also been shown that increasing the target velocity reduces the amplitude of the peak of the spectrum and broadens the peak itself [4]. Analysis of the spectrum allows information to be obtained of the distribution of the velocities within the volume of the flow illuminated by laser light. The outlook of the project focused on characterization of different gas jets, studies into 3D position and motion detection in an UHV environment, using different lasers and benchmarking of numerical studies.

Laser Emittance Meter

The optimum exploitation of the LHC ultimately depends on the quality and availability of the beams prepared in the injector complex. To set up new machine and achieve the best performance, it is important to measure the transverse emittance of the beam as it exits LINAC4 [5, 6]. A new technique has been proposed, based on the "slit & grid" technique, but using a laser beam rather than a physical slit. The project based at CERN was focused on the development of a laser emittance meter and carried out by Thomas Hofmann. Photo-detachment of electrons in an H- ion beam provides an interesting way of non-

ISBN 978-3-95450-177-9

invasive, reliable and maintenance-free diagnostics [7, 8]. Since the reduction of accelerator downtime is a major target for any accelerator and in particular for high current accelerators this technique can help to maximize machine efficiency. He used a 1080 nm laser with 154 µJ pulse energy, 80 ns pulse length (FWHM), 60 kHz repetition frequency and an M^2 of 1.8. Due to its comparatively low pulse energy, the laser can be efficiently delivered to the accelerator by means of a long optical fiber. The laser is focused into the vacuum vessel with a final diameter of approximately 150 µm. Due to the quasi-monomode beam quality the laser diameter remains almost constant when colliding with the millimeter-size particle beam. Vertical scanning of the laser is performed by a remote controlled stage. A CCD camera and a fast photodiode are used to continuously monitor the laser beam quality. To detect the neutralized H^0 atoms a 20 mm x 20 mm polycrystalline diamond detector with 5 strip channels was used. Fig. 1 shows the resulting emittance values, measured with both a laser-diamond detector system, as well as with a 'classic' slit/grid reference system as a function of the applied threshold.

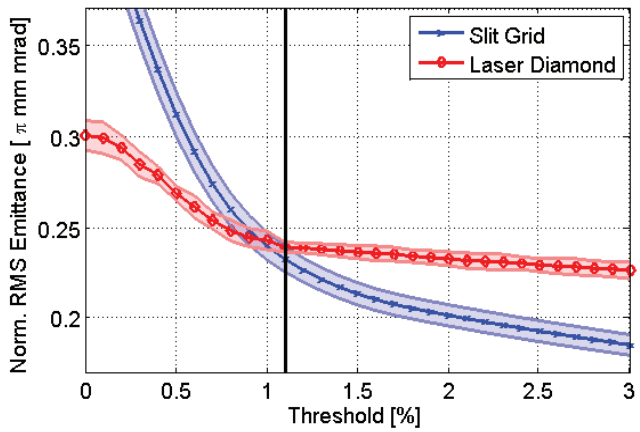

Figure 1: Normalized emittance resulting from both instruments as a function of threshold used for noise suppression.

The characteristic kink in this curve marks the spot where the noise is largely suppressed and the sampled signal starts to originate from impinging particles. It can be seen that for the laserwire system this point is quite well-defined at 1.1%. The equivalent position for the slit/grid is not so clearly defined but can be marked down in the same region. Assuming the same threshold of 1.1% for both systems the resulting emittance values are 0.232 π mm·mrad for the slit/grid system and 0.239 π mm·mrad for the laserwire. It is planned to use a modified version of the instrument during LINAC4 commissioning at 50 MeV and 100 MeV with the aim to measure the detached electrons and reconstruct the beam profile in a non-invasive manner [9]. In preparation for permanent operation the electrode design of the diamond detector and its data acquisition readout chain are being re-designed to provide even higher angular resolution and faster emittance measurements.

Longitudinal Bunch Shape Measurements Using Electro-optical Techniques

To generate highly intense coherent synchrotron radiation in the THz range, the synchrotron ANKA is frequently operated in an optics mode with a reduced momentum compaction factor. The characteristics of the emitted THz radiation depends heavily on the exact length, shape and substructure of the individual electron bunches. A broad research program into the characterization of coherent THz radiation, as well as on the properties of the low alpha mode was established at the ANKA facility, including both, single particle dynamics issues, as well as collective effects. An ESR project at KIT covered the measurement of the bunch shape with electro-optical sampling in an electron accelerator. The linear accelerator FLUTE is currently under construction at KIT and it is expected to have a longitudinal bunch length detection system incorporated. During the development of a bunch profile monitor a set of simulation studies has been performed to make the best possible design for the specific beam parameters of the machine. Within the project, the laser for electro-optical detection system has been assembled at DESY in collaboration with the colleagues from FLUTE. The whole system will be installed at FLUTE to further the understanding of beam dynamics effects.

Electron Beam Energy measurements with Compton-backscattered Laser Photons

The second ESR project at KIT covered the precision determination of the momentum compaction factor with Compton backscattered laser photons at ANKA and was completed by Cheng Chang. Compton Back-Scattering (CBS) has some significant advantages for non-invasive beam energy measurements as compared to other techniques such as spin depolarization, reduced measurement times and that a polarized beam is not required. Several facilities have reported energy measurements based on CBS using a head-on collision geometry with relative accuracies reaching 10^{-4} to a few 10^{-5} [10, 11].

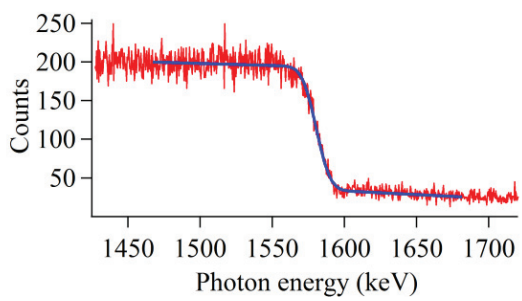

Figure 2: Measured CBS spectrum at 1.3 GeV with fit to determine the Compton edge energy.

Cheng Chang and his co-workers have developed a CBS geometry that applies a transverse configuration (φ=π/2). This setup has several advantages: It is very compact and can therefore be used at rings with restricted space. Furthermore, the transverse setup reduces the energy of Compton edge photons by a factor of two which

ISBN 978-3-95450-177-9

either makes measurements and detector calibration easier or enlarges the measurable range of a specific setup. They have used a High Purity Germanium (HPGe) spectrometer to determine the energy of the emitted photons [12]. Fig. 2 shows a typical spectrum that was acquired from a 1.3 GeV electron beam over 120 seconds. The mechanical centers of two quadrupoles were used as the reference line and the laser direction measured relative to this line with a laser tracker and a camera. The collision angle φ was determined from this measurement and yielded an average value of the beam energy of 1287.0 MeV ± 0.2 MeV. As compared to conventional CBS methods for energy measurement, a compact setup based on a transverse scheme has been successfully tested at ANKA. These measurements have been extended to beam energies of 0.5 GeV, 1.6 GeV and 2.5 GeV and gave promising initial results. It was shown that longer acquisition times can help further reduce statistical uncertainties in the Compton edge and hence beam energy.

Electro-Optics Bunch Time Monitor

An advanced electro-optic bunch time profile monitor for the CERN CLIC Project - development of novel materials and techniques was a project completed by Mateusz Tyrk. This project aimed at pushing the limits of electro-optic (EO) techniques to measure relativistic electron bunches with a time resolution better than 20 femtoseconds. The ability to measure electron bunches with this time resolution have a significant impact on coherent light sources like LCLS or X-FEL, since the generation of coherent X-ray beams from these machines depends critically on maintaining an ultrashort bunch length and direct measurement is not currently feasible. Measurements were carried out in the University of Dundee, with a range of novel nanostructured metamaterials based on metal-glass nanocomposites (MGN). These silver-doped glass nanocomposites were processed using a picosecond laser system in order to change the structure and shape of embedded nanoparticles. This process resulted in a higher efficiency of the nonlinear optical properties of the samples. Tests were also carried out with mechanically stretched MGNs where the shape of previously spherical nanoparticles of silver changed into highly elongated ellipsoids. Measurements at STFC Daresbury Laboratory were performed for further nonlinear optical characterization as well as for EO based characterization of samples, with the conclusion that they could in principle solve many of the problems associated with 'classical' materials like ZnTe and GaP.

TRAINING EVENTS

LA^{3}NET serves as an example of the benefits of network training built on project-based research within an international consortium. The fundamental core of the training was a dedicated cutting edge research project for each researcher. The individual research projects were complemented by a series of network-wide events that included external participation and were open to the wider scientific community. Amongst those were two international Schools on Laser Applications at Accelerators which were held at GANIL, France in 2012 [13] and at the Spanish Pulsed Lasers Centre (CLPU) in Salamanca, Spain [14]. Each school attracted more than 70 participants and all course material remains available via the event indico page. In addition, LA^{3}NET has also organized a number of targeted scientific workshops at venues across Europe. These lasted 2-3 days and focused on expert topics within the network's scientific work packages. The network will continue this activity and will organize Topical Workshops on 'Novel Accelerators' [15], as well as on 'Laser Ion Sources' [16], between 24 - 26 October 2016 in Paris, France. The network also held an international Conference on Laser Applications at Accelerators on Mallorca, Spain [17] and an international Symposium on Lasers and Accelerators for Science & Society with delegates comprising 100 researchers from across Europe and 150 local A-level students and teachers [18].

SUMMARY

LA^{3}NET successfully trained 19 Fellows in an interdisciplinary area and organized numerous events for the wider scientific community. This paper summarized the research results by LA^{3}NET Fellows in the beam diagnostics work package. Whilst the project has formally ended in 2015, the consortium continues a number of key activities, including communication of research outcomes and the organization of events for the wider scientific community.

REFERENCES

[1] LA^{3}NET, http://www.la3net.eu
[2] V. Tzoganis, C. P. Welsch, *Applied Physics Letters* 104, 204104 (2014).
[3] A. Alexandrova, *et al.*, *Optical Engineering* 54(3), 034104 (2015).
[4] A. Alexandrova, *et al.*, *Nucl. Instr. Meth. A* 830 (2016)
[5]. T. Hofmann, *et al*, *Proc. IPAC*, Shanghai, China (2013), paper MOPME075.
[6] T. Hofmann, *et al.*, "Experimental Results of the Laserwire Emittance Scanner for LINAC4", Phys. Procedia (2015).
[7] W. B. Cottingame, *et al.*, "Non-interceptive Techniques for the Measurement of Longitudinal Parameters for Intense H$^-$ beams." *IEEE NS-32*, 1985.
[8] Y. Liu, e*t al.*, *Nucl. Instr. and Meth. A 612*, 241, (2010).
[9] T. Hofmann, *et al.*, "Design of a Laser Based Profile-Meter for LINAC4 Commissioning at 50 Mev", *Proc. IBIC*, Melbourne, Australia (2015).
[10] R. Klein, *et al.*, *Nucl. Instr. Meth. A* 384, 293 (1997).
[11] C. Sun, *et al.*, *Phys. Rev. STAB* 12, 062801 (2009).
[12] C. Chang, *et al.*, "First Results of Energy Measurements with a Compact Compton Backscattering Setup at ANKA", *Proc. IPAC*, Richmond, USA (2015).
[13] http://indico.cern.ch/event/177701/
[14] http://indico.cern.ch/event/285698
[15] http://indico.cern.ch/event/527727/
[16] http://indico.cern.ch/event/546015/
[17] http://indico.cern.ch/event/340381/
[18] http://indico.cern.ch/event/368273/

ISBN 978-3-95450-177-9

STREAK CAMERA CALIBRATION USING RF SWITCHES

U. Iriso, M. Alvarez, A.A. Nosych, ALBA-CELLS, Barcelona, Spain
A. Molas, Universitat Autónoma de Barcelona, Spain

Abstract

The streak camera has been used to measure the bunch length since the ALBA storage ring commissioning in 2011. Previously, we developed an optical calibration system based on the Michelson interferometry. In this report, we show the electronic calibration system based on the work in DLS [1], and compare both calibration systems. Finally, we show measurements of the longitudinal impedance obtained with the new calibration.

INTRODUCTION

ALBA is equipped with a beam diagnostics beamline (BL34- Xanadu) that uses the visible part of the synchrotron radiation to characterize both longitudinal and transversely the electron beam profile [2, 3]. In the longitudinal plane, the key instrumentation is the Streak Camera (SC), which allows precise bunch length measurements and longitudinal beam dynamics studies. The camera is the Optronis SC-10 model, with a synchroscan frequency working at 250 MHz to distinguish the beam bunches spaced by 2 ns [4].

In order to perform precise measurements using the streak camera, it is necessary to determine the calibration factor that provides the relationship between the number of pixels and the corresponding time units. Moreover, Ref. [2] shows that depending on the speed sweep unit of the streak camera, this calibration might not be completely linear and a multi-linear calibration is required. This is especially the case for the slowest synchroscan speed of 50 ps/mm, while the speeds of 25 and 15 ps/mm show a very linear behaviour.

At ALBA, this factor was calibrated in 2012 using an optical set-up based on the Michelson interferometry [2]. The goal in those experiments was to include an optical delay of a known amount in the path of the synchrotron radiation, and measure it using the streak camera. This solution faces two main limitations: on one side, it is not easy to assemble the calibration setup (proper alignment of the optical systems); and secondly, it only provides calibration in the fast (in our case, vertical) sweep speeds.

Instead, the solution developed at Diamond Light Source [1] is based on delaying the reference RF signal used for the fast sweep unit with respect to the synchrotron radiation. This is achieved using RF switches, which change the path length of the RF signal by a known amount. Moreover, since the switching frequency is also known, a calibration pattern for the slow (in our case, hor) scale is also given.

ELECTRONIC CALIBRATION KIT

The layout of the calibration kit is shown in Fig. 1. The $f_{\mathrm{rf}}/2$=250 MHz reference signal is introduced in the crate, where two RF switches alternate the signal path between

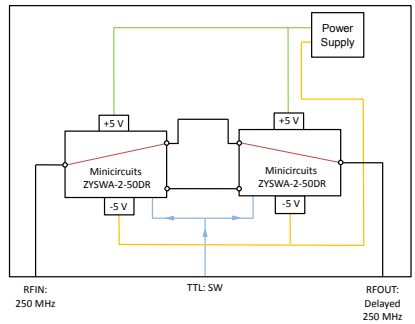

Figure 1: Schematic illustration of the crate used in order to introduce a delay in the 250MHz signal using the PIN diodes switching with a frequency set by the TTL signal and two cables with a certain different length.

a longer or a shorter way, whose difference is called $\Delta\tau$. By precisely measuring the difference in the path length, we can calibrate the streak camera. The RF switches are triggered by an Event Receiver producing TTL square waves, whose switching frequency f_{sw} can be changed at will. The calibration process is disabled if we disable the output on the Event Receiver.

The image obtained in the SC when the calibration kit is in use has the zigzag shape shown in Fig. 2. The image has a symmetry top/bottom, since the SC sends odd bunches to the top half of the image, and bottom bunches to the bottom.

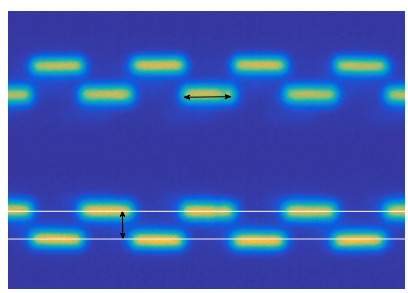

Figure 2: Output image of the streak camera after performing the delay of the 250MHz signal with the RF switches.

Note that:

- The horizontal scale is calibrated using the distance between streaks, which corresponds to $0.5/f_{\mathrm{sw}}$ (see horizontal arrow in Fig. 2).
- The vertical scale is calibrated using the distance between the zigzag streaks, which corresponds to the time delay given by the cable difference, $\Delta\tau$ (see vertical arrow in Fig. 2).

ISBN 978-3-95450-177-9

Delay Characterization

We use the VNA Agilent E5071B (300 kHz – 8.5 GHz) to measure the time difference between the cables in Fig. 1. The measurement is performed from the phase difference measured on a 250 MHz signal with the RF switches on. An example of this measurement is shown in Fig.3 for a switching frequency of 10 Hz. The measured delay between cables is (77.298 ± 0.015) ps.

The delay between the cables are measured using different switching frequencies, spanning from 10 Hz to 4 kHz. The variation of the length difference changes only by ∼ 0.5%, so we conclude that the average value of the delay is: $\Delta\tau$ **= 77.420 ± 0.080 ps**.

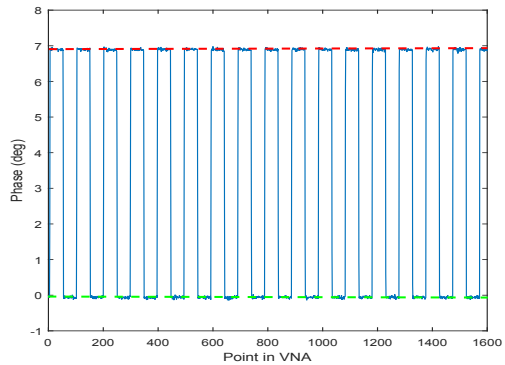

Figure 3: Phase delay between the long and short cables for a 10 Hz switching frequency.

CALIBRATION RESULTS

Horizontal (Slow) Time Unit

The horizontal calibration for the different sweeps speeds of the deflection unit are listed in Table 1. In general, the theoretical factor is always smaller than the measured one by about 10%. The sweep speed in the horizontal time unit is constant and so it is properly characterized by a simple linear factor. (This is not the case for the slowest sweep speeds in the vertical deflection – see next).

Table 1: Horizontal Calibration Factor Measured for Different (Not All) hor Sweep Speeds of the SC

Sweep Speed	Cal. Factor, $\frac{\mu s}{pix}$	Theo. Factor, $\frac{\mu s}{pix}$
5 ms/mm	75.0 ± 0.5	70
1 ms/mm	15.6 ± 0.2	14
500 μs/mm	7.56 ± 0.15	7
100 μs/mm	1.60 ± 0.04	1.4
50 μs/mm	0.790 ± 0.02	0.7
10 μs/mm	0.163 ± 0.005	0.14
5 μs/mm	(76.8 ± 1.8)×10^{-3}	70×10^{-3}
1 μs/mm	(16.2 ± 0.6)×10^{-3}	14×10^{-3}
250 ns/mm	(3.8 ± 0.1)×10^{-3}	3.5×10^{-3}

Vertical (Fast) Time Unite

Since the signal at the vertical deflection unit is sinusoidal, the relation between the pixel position and time is only linear near the center. While the linear approximation for the faster vertical sweep speeds is valid, for the slowest speed (50 ps/mm) the calibration needs to take into account the non-linear effects. For this reason, a piecewise linear aproximation (or *multi-linear* calibration) is used. Since most of our measurements are done using the 50 ps/mm speed, in the following we focus our results on this case.

Figure 4 plots the pixel vs time for different horizontal sweep speeds of the SC. Identical curves are found for sweep speeds between 5 ms/mm to 5μs/mm. On the other hand, the calibration curve using the optical delay described in Ref. [2] is slightly different. While the systematic errors related to the optical system set-up are difficult to evaluate, the errors associated to the calibration kit are below 0.5%.

In the following, the measurements are performed using the results provided by the rf switches calibration kit, considering only a single multi-linear calibration for all horizontal sweep speeds.

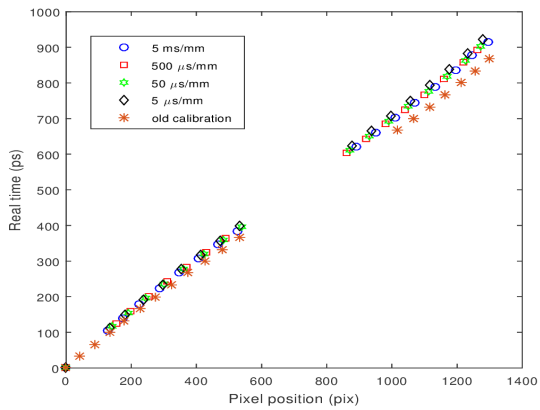

Figure 4: Multilinear calibration for different sweep speeds and using the old calibration from the Michelson interferometry [2]. For the sweep speeds from 5ms/mm to 5μs/mm the multilinear calibration is almost identical.

RECOVERING AN RF PLANT

When one of the 6 RF cavities at ALBA trips, the available voltage decreases and the phase in the rest of the 5 cavities decreases to provide the beam with the necessary energy per turn. This is translated with an increase of the bunch length σ and a shift of the beam centroid ϕ. An example of this case is shown in Fig. 5, which shows the centroid and bunch length evolution during the recovery of an rf cavity. In total, the voltage changes from 2.25 MV to 2.6 MV.

The top plot in Fig. 5 shows the evolution of the difference in the bunch centroid for odd and even bunches as measured in the SC. From the average of this centroid difference, we infer a phase change of $\Delta\phi^{SC}$ = (3.2 ± 0.20)°. On the other hand, the phase measured from the rf power is $\Delta\phi^{RF}$ = (3.76 ± 0.60)° – see Ref. [5]. Although the results differ by

ISBN 978-3-95450-177-9

~15%, we can conclude the results are consistent if we take into account the associated error bars.

The evolution of the bunch length is shown in Fig. 5 (bottom plot). When the rf cavity is recovered, the bunch length ratio σ_2/σ_1 follows:

$$\frac{\sigma_2}{\sigma_1} = \sqrt{\frac{V_1 \cos\phi_1}{V_2 \cos\phi_2}} \,. \tag{1}$$

While the bunch length ratio is σ_2/σ_1=1.08±0.01, the voltage ratio (rhs of Eq. 1) is 1.092 ± 0.005 corresponding to a disagreement around 1%, from where we conclude that the results are very consistent and the calibration is very good.

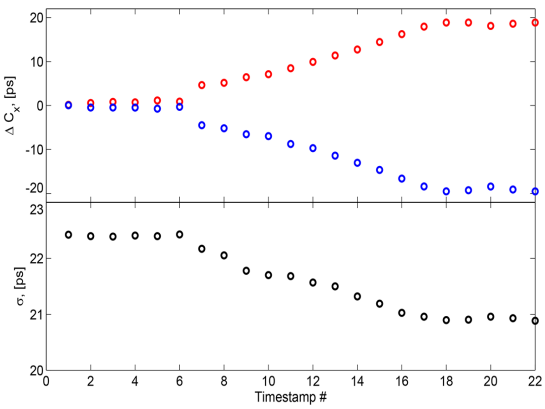

Figure 5: Centroid position (top) and bunch length (bottom) evolution during an RF cavity recovery. The RF voltage goes from 2.3 MV to 2.6 MV in about 5 min, and each timestamp corresponds to approximately 14 sec.

LONG. IMPEDANCE MEASUREMENTS

In order to characterize the ALBA longitudinal impedance, single bunch measurements are carried out at two different voltages, V_0=2.6 MV and V_0=2.35 MV.

Bunch Length Measurements

The longitudinal impedance $\mathrm{Im}(Z_0^{\parallel}/n)_{\mathrm{eff}}$ is determined by measuring the variation in the bunch length σ with single bunch current I_B. Away from the MW-instability, the bunch length parametrisation is:

$$\left(\frac{\sigma}{\sigma_0}\right)^3 - \left(\frac{\sigma}{\sigma_0}\right) = \frac{\alpha_c \mathrm{Im}(Z_0^{\parallel}/n)_{\mathrm{eff}}}{\sqrt{2\pi}(E/e)Q_{s0}^2(\omega_0\sigma_0)^3} \cdot I_B \,, \tag{2}$$

where α_c is the momentum compaction factor, σ_0 is the bunch length in the limit $I_B = 0$, E/e is the beam energy (in eV), and Q_{s0} is the synchrotron frequency.

The bunch profile for different intensities are shown in Fig. 6. Although the profile for low currents is well approximated by a Gaussian shape, the bunch starts to deform with increasing currents. In order to infer the proper value of the bunch length σ, one should solve the so-called Haissinsky equation [6]. This process is currently on-going, and therefore we cannot show exact results of $\mathrm{Im}(Z_0^{\parallel}/n)_{\mathrm{eff}}$.

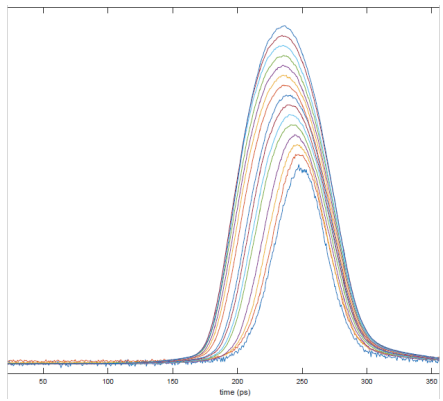

Figure 6: Mountain range plot while increasing the bunch intensity from 0.5 mA (lower trace) to 8 mA (top).

For illustrative purposes, we infer the bunch length σ just by fitting a Gaussian shape to the profiles shown in Fig. 6. This is shown in Fig. 7, where the bunch length increases with increasing current approximately with a I_B dependence. The injection was stopped at 8 mA for safety purposes.

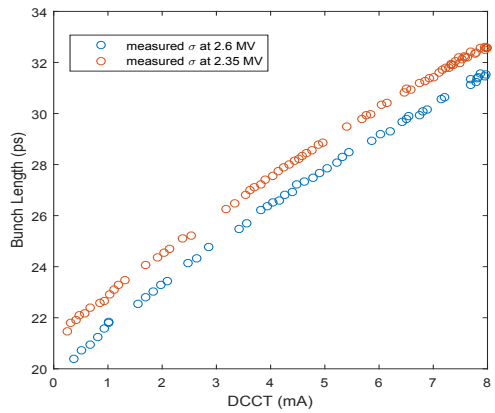

Figure 7: Change of the bunch length during the injection in single bunch mode. The profiles in Fig. 6 are fitted to a simple Gaussian curve.

Centroid Measurements

The loss factor $k_{\parallel}$ of a storage ring relates the energy transfer ΔE per revolution from the beam bunch to the machine vacuum chamber as:

$$\Delta E = k_{\parallel} \cdot Q_B^2 \,, \tag{3}$$

where Q_b is the beam bunch charge. When the beam bunch transfers this energy to the machine, it needs to ride higher on the rf wave to recover this loss and the synchrotron phase ϕ_s shifts. In time domain, the phase shift is expressed as [7]:

$$\Delta T_C = \frac{T_{\mathrm{rf}}}{2\pi} \frac{k_{\parallel} T_0}{V_0 \cos\phi_s} I_B \,, \tag{4}$$

where $T_{\mathrm{rf}} = 1/f_{\mathrm{rf}}$ is the rf period and T_0 is the revolution period. Thus, the loss factor $k_{\parallel}$ is inferred by measuring the

ISBN 978-3-95450-177-9

Table 2: ALBA Parameters and Results during Single Bunch Measurements

mom. comp. factor, α_c	0.0088	
revolution period, T_0[ns]	896	
rf frequency, f_{rf}[MHz]	499.649	
energy, E[GeV]	2.987	
rf voltage, V_0[MV]	2.6	2.35
sync. phase, ϕ_s[°]	152.9	154.2
sync. tune,	0.0071	0.0066
bunch length, σ_0[ps]	18.75	20.26
loss factor, $k_{\|\|}$[V/pc]	14.1± 0.4	13.12 ±0.05
resistance, R[Ω]	935 ± 25	940 ± 5
Re($Z_0^{\|\|}/n$) [mΩ]	127±4	136±1

centroid displacement with respect to the single bunch intensity, which is shown in Fig. 8 for two different rf voltages, 2.35 and 2.6 MV. From the fit in Fig. 8 and using the measured values shown in Table 2, the loss factor is inferred as $k_{\|} = 14.2 \pm 0.4$ (for 2.6 MV), and $k_{\|} = 13.12 \pm 0.03$ V/pC (for 2.35 MV).

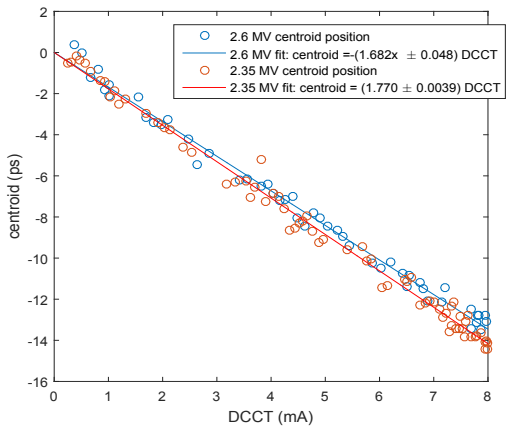

Figure 8: Centroid displacement during an injection in single bunch mode for V_0=2.5 MV and V_0=2.35 MV.

The complete expression of the loss factor for Gaussian bunches is given by:

$$k_{\|} = \frac{1}{2\pi}\int_{-\infty}^{+\infty} \mathrm{Re}\, Z_0^{\|}(\omega)\cdot e^{-(\sigma\omega)^2} d\omega, \qquad (5)$$

where $Z_0^{\|}$ is the longitudinal impedance, σ is the temporal bunch length and ω is the angular frequency. If one approximates the impedance by a constant resistance R, the loss factor can be simplified by:

$$k_{\|} = \frac{R}{2\sqrt{\pi}\sigma_0}, \qquad (6)$$

With this assumption, the resistance of ALBA is R=935±25 Ω (2.6 MV), and 940±5 Ω (2.35 MV), which is consistent with values found in other machines [7, 8]. Furthermore, we can approximate:

$$\mathrm{Re}\left(Z_0^{\|}\right)_{\mathrm{eff}} \approx R\cdot(\sigma\omega), \qquad (7)$$

which provides a value of $\mathrm{Re}\left(Z_0^{\|}\right)_{\mathrm{eff}}$ ~130 mΩ (see Table 2), consistent with the expectations. Again, a more precise way to tackle this calculation is by solving the Haissinsky equation.

CONCLUSIONS

We have implemented a calibration kit for our Streak Camera based on the electrical delay between two different cables, whose length is precisely measured with a VNA. The calibration kit allows almost on-line calibration in both the slow (horizontal) and fast unit (vertical). While the horizontal values are typically ~10% larger than the theoretical ones, in the vertical direction we found most convenient to use the slowest sweep speed (50 ps/mm) with a multi-linear calibration whose spread is very small (~0.5%).

Several machine measurements are presented using the calibration results presented in this report. The bunch length evolution during the recovery of an rf cavity at ALBA showed a good agreement with the expectations. Moreover, longitudinal impedance measurements showed values consistent with other machines, although a more careful analysis of the result is foreseen in the near future.

ACKNOWLEDGEMENTS

The authors would like to thank B. Bravo for useful discussions regarding RF issues and T. Guenzel for guiding the impedance calculations.

REFERENCES

[1] L.M. Bobb, A.F.D. Morgan, G. Rehm, *Streak Camera PSF Optimisation and Dual Sweep Calibration for Sub-ps Bunch Length Measurement*, IBIC'15, Melbourne (Australia), 2015.

[2] U. Iriso and F. Fernández, *Streak Camera Measurements at ALBA: Bunch Length and Energy Matching*, IBIC'12, Tsukuba (Japan), 2012.

[3] L. Torino and U. Iriso, *Limitations and Solutions of Beam Size Measurements via Interferometry at ALBA*, IBIC'15, Melbourne (Australia), 2015.

[4] Optronis GmbH, `http://www.optronis.com`

[5] B. Bravo et al, *Calibration of the acceleration voltage of six normal conducting cavities at ALBA*, Proc. of IPAC15.

[6] J. Haissinski, Nuovo Cimento B, 18 (1973).

[7] R.Dowd et al, *Single bunch studies at the Australian Synchrotron*, TUPC010, Proc. of EPAC08.

[8] J.C. Bergstrom, *Jack's Book on Beam Instabilities*, Canadian Light Source Internal Note, 5.17.38.1 (2006)

ISBN 978-3-95450-177-9

DEVELOPMENT OF ACCELERATOR SYSTEM AND BEAM DIAGNOSTIC INSTRUMENTS FOR NATURAL RUBBER AND POLYMER RESEARCH

E. Kongmon†, N. Kangrang, S. Rimjaem, J. Saisut, C. Thongbai, Plasma and Beam Physics Research Facility, Department of Physics and Materials Science, Faculty of Science, Chiang Mai University, Chiang Mai 50200, Thailand
M.W. Rhodes, Thailand Center of Excellence in Physics, Commission on Higher Education, Bangkok 10400, Thailand
P. Wichaisirimongkol, Science and Technology Research Institute, Chiang Mai University, Chiang Mai 50200, Thailand

Abstract

This research aims to design and develop an electron linear accelerator system and beam diagnostic instruments for natural rubber and polymer research at the Plasma and Beam Physics Research Facility, Chiang Mai University, Thailand. The accelerator consists of a DC thermionic electron gun and an S-band standing-wave linac. The system can produce electron beams with the energy range of 0.5 to 4 MeV for the pulse repetition rate of 30 to 200 Hz and the pulse duration of 4 μs. Commissioning of the accelerator system and development of beam diagnostic instruments to measure electron beam energy, electron pulse current and electron dose are underway. This contribution presents and discusses on the RF commissioning progress as well as status of design and construction of the beam diagnostic system.

INTRODUCTION

A linear accelerator (linac) system for electron beam irradiation on natural rubber and polymeric materials is developed at the Plasma and Beam Physics Research Facility, Chiang Mai University, Thailand. The system consists of a Pierce-type DC gun with a flat circular thermionic cathode with diameter of 4.86 mm, a 5-cell standing-wave linac structure equipped with a driven radio-frequency (RF) system, electron beam diagnostic instruments and an irradiation apparatus. It is foreseen that the irradiation system composes of a beam sweeper with a vacuum horn chamber and a movable stage for the sample container. The layout of the accelerator and irradiation system is shown in Fig. 1.

The electron beam diagnostic instruments are under design and construction. A Faraday cup and an integrated current transformer will be used to measure the electron charge and pulse current. A dipole magnet and phosphor screen equipped with a CCD camera readout system will be utilized for an electron beam energy measurement. The results from the current and energy measurement can be used to estimate the electron dose produced from the accelerator system. The transverse beam size and transverse electron distribution at the sample container location will be observed via an outside vacuum screen station. The electron depth and dose distribution will also be measured with dosimeter [1]. In this paper, we present the results of the RF commissioning, electron beam dynamic simulations and status of preparation for the beam diagnostic instruments.

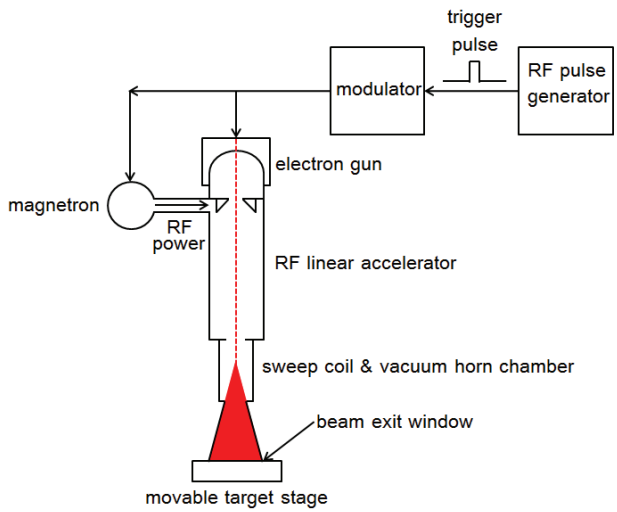

Figure 1: Layout of electron linear accelerator, a related RF power system and an irradiation apparatus.

HIGH POWER RF COMMISSIONING

The linac system can be used to accelerate electron beam to reach the average kinetic energy of 0.5 to 4 MeV depending on the supplied RF peak power, which can be varied from 0.66 to 2 MW. A diagram of the RF generator and measurement systems are shown in Fig.2. The main components of the RF generator are a high voltage power supply with a variac for voltage variable (VAC), a pulse forming network (PFN) and a pulse modulator system. The RF signal amplitude is generated and amplified by a magnetron to reach the MW level. Then, the RF wave is transported from the magnetron to the linac via a WR-284 rectangular waveguide system with a ceramic RF window to separate the SF_6 pressurized part and the vacuum part. A forward and reflected RF powers are measured at a directional coupler prior the ceramic RF window.

As shown in Fig. 2, the forward and reflected RF ports of the directional coupler have the attenuation values of -60 dB. The forward and reflected RF power ports are connected to the cables and the attenuators with total attenuation values of -96.66 dB and -97.89 dB, respectively. The RF signals are converted to analog

†Corresponding author: Ekkachai_kon@cmu.ac.th

ISBN 978-3-95450-177-9

signals by using crystal detectors, which can be measured with a digital oscilloscope.

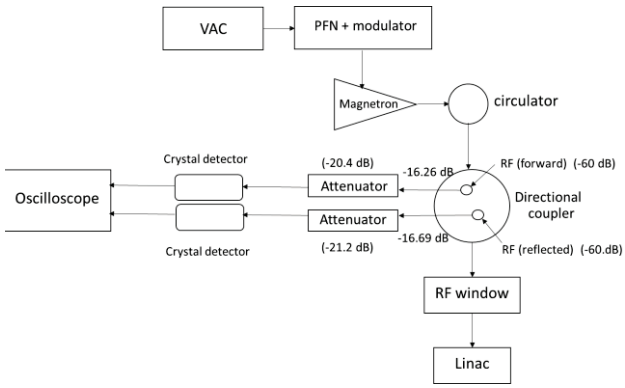

Figure 2: Schematic layout of the RF system.

During the RF commissioning, an operating temperature of 35°C, an RF pulse width of 4 μs and a current of the magnetron filament of 0.42 A were used. The variac (VAC) was adjusted from 70% to 85% with 5% for each step in order to vary the high voltage value and also the RF peak power. The result of this measurement in Fig. 3 shows that the RF peak power increases almost linearly from 0.9 MW to 2 MW for the high voltage value of 5 to 6.8 kV.

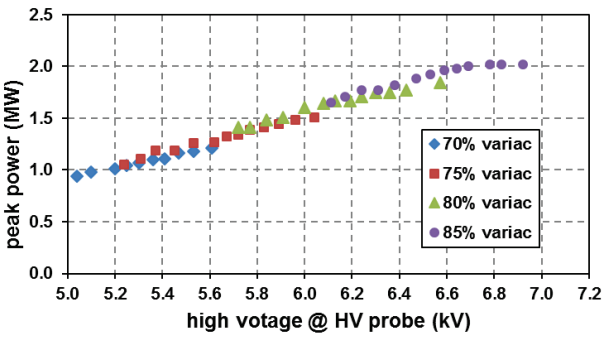

Figure 3: Relationship between the high voltage value and the peak power of the forward RF signal.

The average power of the RF wave can be calculated by using the following equation

$$P_{average} = (\tau)(pps)(P_{peak}), \quad (1)$$

where τ is the RF pulse width, which is equal to 4 μs. Here, pps is the pulse repetition rate, which was adjusted from 30 to 200 Hz in this experiment and P_{peak} is the RF peak power. The relationship between the pulse repetition rate and the average power for each variac level is shown in Fig. 4. An example of the measurement result of forward and reflected RF signals at the pulse repetition rate of 200 Hz are shown in Fig. 5. In this measurement, the forward peak power is 1.65 MW and the reflected RF power is 0.38 MW. Thus, the absorb RF power in this case is 1.27 MW. In the high power RF measurement, the resonant frequency of the linac structure was measured to be 2997.103 GHz, while the measured value for the low-power RF measurement with the S-parameter network analyser was 2996.816 MHz. The frequency difference of 187 kHz is probably due to the resolution of the frequency measurement with the spectrum analyzer in the high power measurement. The RF commissioning results are summarized in Table 1.

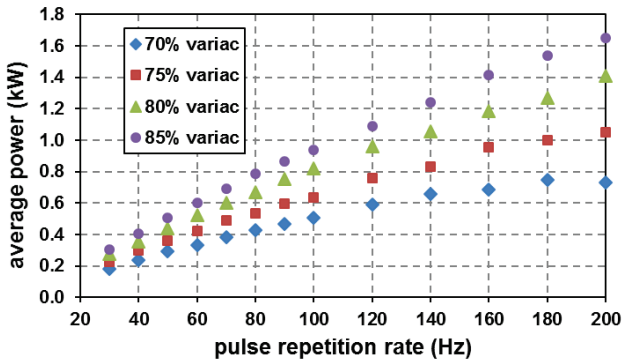

Figure 4: Relationship between the pulse repetition rate and the average power.

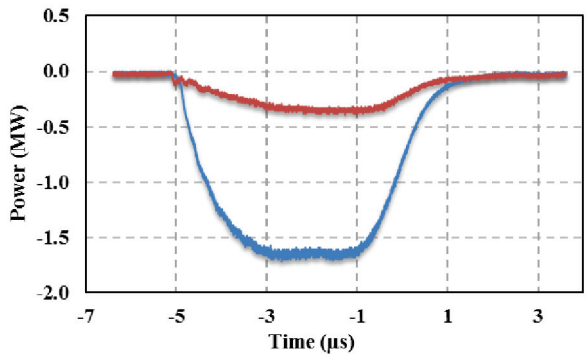

Figure 5: Forward (blue-line) and reflected (red-line) RF signals of 85% VAC at the pulse repetition rate of 200 Hz.

Table 1: Summary of RF Commissioning Results

Parameter	Value
Resonant frequency	2997.103 MHz
Resonant temperature	35°C
RF peak power	0.9 - 2 MW
Maximum pulse duration	4 μs
Pulse repetition rate	25-200 Hz

ELECTRON BEAM DYNAMIC STUDY

Electron beam dynamic study inside the linac structure was performed by using A Space Charge Tracking Algorithm ASTRA [2] program. The initial on-axis electric field distribution in the linac cavities (Fig. 6) used in ASTRA simulations was obtained from bead pull measurements. The measured effective length of the electric field in the linac is 0.2215 m. A conflat flange (CF) with titanium foil will be connected to the linac exit, which is 0.06 m downstream the end of the electric field effective length, to separate the vacuum environment and the ambient air. Thus, the interested positions in this study are at the end of the field and at the titanium foil window.

ISBN 978-3-95450-177-9

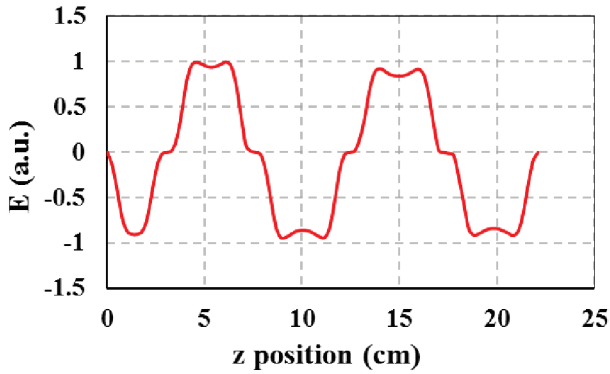

Figure 6: Normalized electric field as a function of longitudinal distance in the linac structure.

In this research, the electron beam energy and current will be varied. In order to vary the beam energy, the peak power of the RF field will practically be adjusted. This results in the different accelerating gradients in the linac structure. Table 2 and Fig. 7 show the results of the output beam energy for four different accelerating gradients. For maximum acceleration, the accelerating gradient of the linac is 41.7 MV/m. This leads to the average kinetic energy of 4.016 MeV and 3.995 MeV at the end of the field and at the titanium window, respectively. A tiny different of the average energy at the two locations can be due to the space charge effect.

Table 2: RF Accelerating gradient (E) and average beam kinetic energy (E_k) at the end of field and at the titanium window

E (MV/m)	E_k at end of field (MeV)	E_k at titanium window (MeV)
16.0	1.032	1.025
20.5	1.962	1.961
29.0	3.028	3.025
41.7	4.016	3.995

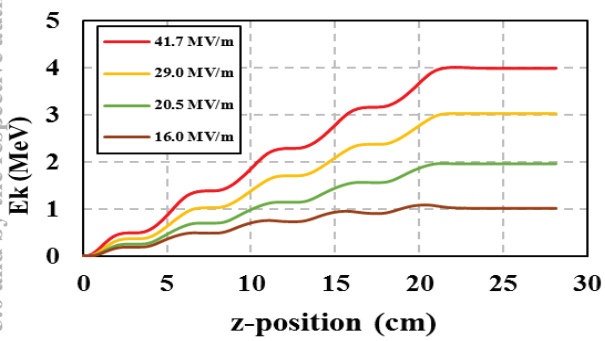

Figure 7: Electron beam kinetic energy as a function of longitudinal (z-position) along the linac structure for four different accelerating gradients.

The simulation results in Fig. 8 show the transverse distributions of electron bunch at the end of field (0.2215 m) and at the titanium window (0.2815 m), respectively. The simulated distributions suggest that the beam diverts with the geometric emittance of 10.15 π mm·mrad at the titanium window. Summary of parameters from ASTRA simulation for the case of maximum acceleration at the end of field and at the titanium window are listed in Table 3.

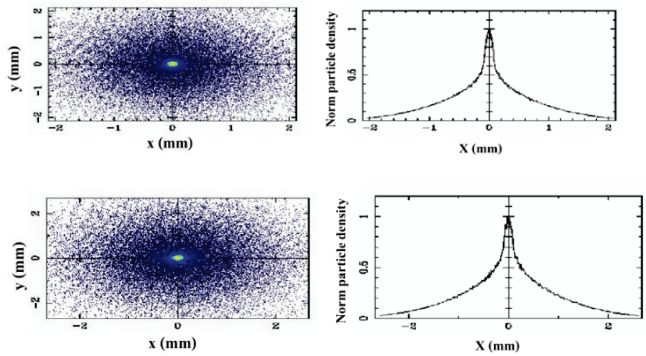

Figure 8: Transverse particle distributions and profiles at the end of field or z = 0.2215 m (top row) and at the titanium window or z = 0.2815 m (bottom row).

Table 3: Results of ASTRA Simulation for the Case of Maximum Acceleration with the Accelerating Gradient of 41.7 MV/m at the end of Field and at the Titanium Window

Parameter	End of field	Titanium window
Average energy	4.016 MeV	3.995 MeV
rms transverse size	0.848 mm	1.070 mm
Bunch charge	300 pC	300pC
rms norm. emittance	9.588 π mm·mrad	10.15 π mm·mrad

DIAGNOSTIC INSTRUMENTS

Design and construction of the electron beam diagnostic instruments of the linac for rubber vulcanization are ongoing. A Faraday cup and an integrated current transformer will be used to measure the electron charge and macropulse current. A dipole magnet, a phosphor screen and a CCD camera will be utilized for an electron beam energy measurement. The transverse beam size and transverse electron distribution at the sample container location will be observed via an in air vacuum screen station.

Charge and Current Measurements

A macropulse current of electron beams produced from this accelerator is measured after the titanium window by using a current transformer (CT) as shown in Fig.9. The current transformer has been designed for the measurement of electron beam with a macropulse width of 4 μs and the current of electron beam can be calculated from

$$I_b = \frac{NV_0}{R}, \quad (2)$$

ISBN 978-3-95450-177-9

where I_b is the current of electron beam, N is the number of wiring turns, V_0 is the voltage across R, and R is the resistant of the load. From the test results, the current transformer has N = 16 and R= 50 Ω. Furthermore, a Faraday cup will be installed downstream the current transformer to measure the electron charge. Both signals from the current transformer and the Faraday cup are observed by a digital oscilloscope.

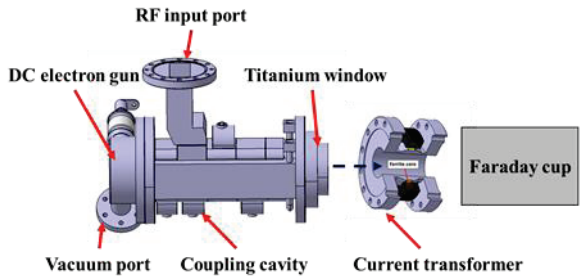

Figure 9: Schematic setup to measure the electron macropulse current and the electron charge.

Energy Measurement

A dipole magnet, a phosphor screen and a CCD camera will be used to measure the electron beam energy after exiting the linac. The energy measurement will be performed in ambient air. The dipole magnet with the magnetic field of 183.63 mT can bend 4 MeV electron beam with a bending angle of 60°. Then, the energy of the electron beam can be calculated from

$$\frac{1}{\rho[\mathrm{m}]} = 0.2998 \frac{\mathrm{ZB_0[T]}}{\beta \mathrm{E[GeV]}} \qquad (3)$$

where ρ is the bending radius, Z is the charge multiplicity, B_0 is the magnetic intensity, E is the electron beam energy in GeV.

The setup of the electron beam energy measurement is shown in Fig. 10. The diameter of the titanium foil window is 5 cm. In this setup, the dipole magnet will be placed as close as possible to the titanium window exit to avoid the loss of the electron beam in air.

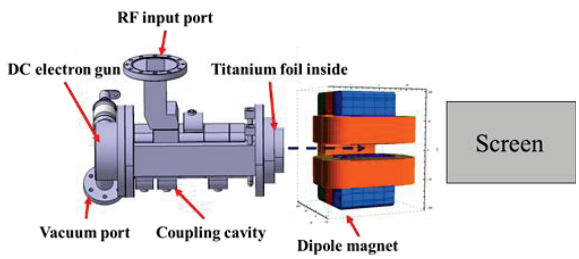

Figure 10: Schematic setup of electron beam energy measurement.

CONCLUSION

In this paper, we present the progress of development on the electron linear accelerator system and beam diagnostic instruments for natural rubber and polymer researches. The high power RF commissioning results show that the resonant frequency of the linac structure is 2997.103 MHz at the operating temperature of 35°C. The maximum RF pulse duration is 4 μs with 200 Hz of pulse repetition rate. This experimental information gives an average RF power of 1.32 kW. From beam dynamic study with the accelerating gradient of 41.7 MV/m, the simulated electron beam average energy at the titanium window is 3.995 MeV. The rms transverse beam size equals to 0.848 mm and 1.070 mm at the end of field and at the titanium window, respectively.

Currently, electron beam diagnostic instruments to measure electron macropulse current, electron charge, beam energy, transverse beam size and transverse beam distribution are under design and construction. The current transformer and the faraday cup will be used to measure the electron beam pulse current and charge. The dipole magnet with screen station has been designed to measure the electron beam energy after passing the titanium window. Furthermore, parameters of electron beams after exiting the titanium window and at the sample irradiation location will be simulated by using the Monte Carlo simulation program GEANT4. [3,4] The beam parameters will be measured to compare with the simulation prediction.

ACKNOWLEDGEMENTS

The authors would like to acknowledge the supports by the Department of Physics and Materials Science, the Faculty of Science, Chiang Mai University, the Science Achievement Scholarship of Thailand, the Thailand Center of Excellence in Physics (ThEP Center) and the Science and Technology Park Chiang Mai University (CMU STeP).

REFERENCES

[1] Gex Corportion; Colorado: Gex Corporation the Dosimetry Company. Available on: [cited 2016 Sep. 06], http://gexcorporation.com/pro-dosimetry-system.php

[2] K. Flottman, ASTRA particle tracking code, http://www.desy.de/mpyflo/.

[3] S. Agostinelli, J. Allison, K. Amako, J. Apostolakis, H. Araujo, P. Arce *et al.,* Nucl. Instrum. Methods A 506 (2003) 250-303.

[4] J. Allison, J. Amako, K. Apostolakis, J. Araujo, H. Dubois, P.A. Asai *et al.*, IEEE Trans. Nuc. Sci. 53 (2006) 270-278.

ISBN 978-3-95450-177-9

TEMPERATURE AND HUMIDITY DRIFT CHARACTERIZATION OF PASSIVE RF COMPONENTS FOR A TWO-TONE CALIBRATION METHOD

E. Janas[1,2,*], K. Czuba[1], U. Mavrič[2], H. Schlarb[2]
[1] ISE, Warsaw University of Technology, Poland
[2] DESY, Hamburg, Germany

Abstract

Femtosecond-level synchronization is required for various systems in modern accelerators especially in fourth generation light sources. In those high precision synchronization systems the phase detection accuracy is crucial. However, synchronization to a low noise electrical source is corrupted by a phase detection error originating in the electrical components and connections due to thermal and humidity-related drifts. In future, we plan to implement calibration methods to mitigate these drifts. Those methods require a calibration signal injection, called second tone, into the system. Intrinsically, the injection circuit remains uncalibrated therefore it needs to be drift-free. We performed drift characterization of a set of RF components, which could serve for implementation of a signal injection circuit, namely selected types of couplers and splitters. We describe the measurement setup and discuss the challenges associated with this kind of measurement. Finally, we provide a qualitative and quantitative evaluation of the measurements results.

MOTIVATION

A two-tone calibration method bases on an additional signal injection to the electronics circuits, which should get calibrated; in our case it is a phase detector for synchronization of a laser. Because the second signal properties are known, a drift arising in phase detector circuit can be measured. On this base a drift for an effective signal (being a subject of detection) can be estimated. Naturally, the second signal should be distinguishable from the effective one, therefore slightly apart in frequency. From the other hand, it should also be close enough to allow for comparison of the phase change between the two. A thorough analysis for a proper frequency choice has been presented in [1] and in essence shows, that the smaller the offset, the better calibration. More detailed description or another view on the method can also be found for example in [2, 3].

The injection of a calibration signal requires auxiliary hardware, which consist of at least a small section, where the effective and the calibration signal would not share the same path. An example would be a passive RF combiner, where its two arms are separate for each signal. Consequently, this piece of a circuit remains uncalibrated and introduces an error. In this paper, measurements of drift between two inputs of a combiner are presented, which allow for a rough comparison of different selected components.

* Ewa.Janas@desy.de

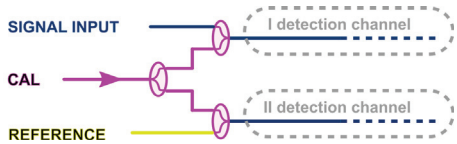

Figure 1: Phase calibration scheme.

APPLICATION

In our case, the method will be used in a bit more complex setup, where additionally a complete second channel is introduced, injected with a reference signal. As the reference is intrinsically drift-free, it allows, that the drifts of the circuits can also be observed at the original frequency, possibly further improving the drift calibration. The drawback of this additional calibration method is, that the circuits are made equal, but are not very same; there are natural differences between them. These include for example PCB traces lengths inaccuracies or ambient temperature differences. The errors can be reduced by a proper PCB routing and placing both channels close to each other, but they can never be completely removed. Therefore both methods could be seen as supplementary to each other. However, the injection circuit in case of combined methods becomes bigger. Effectively, it has a structure depicted in Fig. 1. The splitters/combiners shown here can be as well implemented by couplers; the most important is, that the arrangement remains symmetrical.

In this configuration, the effective phase difference between the laser and the reference $\Delta\phi_{Eff}$ (which is present at the entrance of a phase detection module, that is yet devoid of parasitic drifts from the detector circuits) is defined by a following equation [1]:

$$\Delta\phi_{Eff} = \Delta\phi_{EffMeas} - A * \Delta\phi_{CalMeas}$$

where:

$\Delta\phi_{EffMeas}$ – phase difference measured by a phase detector between the input signal at the first channel and the reference at the second channel

$\Delta\phi_{CalMeas}$ – phase difference measured by a phase detector between both channels at the calibration signal

$A = \frac{f_{Eff}}{f_{Cal}}$ – coefficient to translate the drift at the calibration frequency into phase difference at the frequency of the measured signal

Besides phase stability, another crucial requirement for the injection circuit components to assure a decent level of calibration, is good isolation. This allows to avoid refer-

ISBN 978-3-95450-177-9

ence signal leaking into the information channel or crosstalk between the calibration signals - both would distort the measurement. For same reasons, special care has to be taken for proper matching to avoid reflections. It might be inevitable to use ancillary attenuators, but they introduce more drifts and aggravate SNR. If the part does not provide proper isolation due to its design, then the required attenuator has to be accordingly bigger.

Besides above listed general requirements, there are also few attributes to consider regarding the specific application. Usually, the synchronization of pulsed lasers takes effect at one of the higher harmonics of the repetition rate to improve accuracy. But the base harmonic of the laser should also be detected to define the right RF-bucket, so that there is no ambiguity and the locking occurs at the correct phase/timing. This means, that the laser synchronization takes place in 2 steps: first coarse synchronization at the base harmonic (without any drift correction) followed by the fine synchronization at the higher harmonic. This is then also a subject for calibration, and its frequency should conform with the reference. If the external laser signal splitting to get both signals should be avoided, a combiner for the main input (1st detection channel in Fig.1) has to transmit both base and higher laser harmonic. To keep the symmetry, the combiner at the 2nd channel should be the same. In consequence, the part should be dual-band or wideband. Wideband leaves the detector more flexible, as different lasers with different base repetition rates can be handled. Another important factor not to be forgotten is the size of the components. The best is, if they can be integrated on a PCB.

Considering all requirements listed above, the following parts have been selected and measured:

1. CBR16-0006 Marki Microwave 200 kHz - 6 GHz coupler. It is very wideband, but its form factor does not fit onto PCB. Nevertheless, it is small enough to consider it as an external part to the board, giving not too much mechanical stress when hanging on the PCB connectors. Its isolation is 38 dB by 16 dB coupling.

2. Resistive splitter. Very wideband, simple and small, but shows nearly no isolation. Therefore it has been measured also in the version equipped with 30 dB attenuators, which corresponds to a relative good isolation of a Wilkinson splitter. For test purpose, the part has been designed and fabricated on a RO4003 laminate, of good thermal and humidity stability. The resistors have been selected to have low (in the range of 15-25) ppm/°C value, which promises low temperature drift. The attenuators have been implemented on the same PCB; the 30dB attenuator again with the same low ppm/°C values, the 0 dB attenuator has been made out of 100 ppm/°C 0 Ohm resistors.

3. S 802-4-1.900-M02 MECA Wilkinson splitter. According to the previous tests that is the lowest drift splitter we know. Therefore it is a good reference to other measurements.

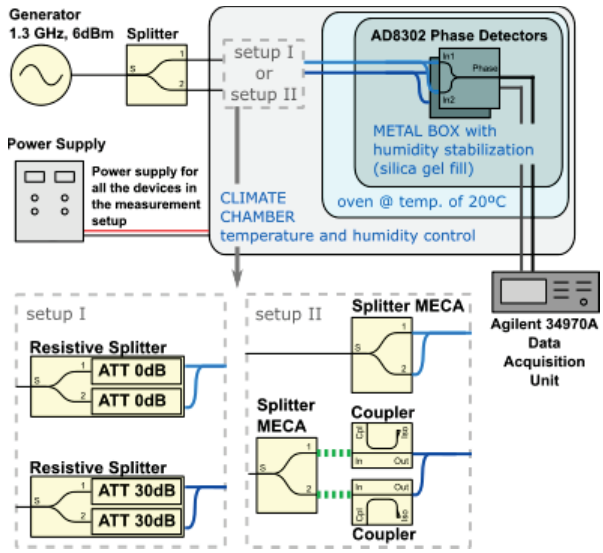

Figure 2: Measurement setup schematic.

MEASUREMENT SETUP

The measurement setup is illustrated in Fig. 2. First bunch of components characterized, called 'Setup I', included resistive splitters in version with and without attenuators. The second set of parts, described as 'Setup II', were MECA splitters and couplers. The detectors have been placed in a humidity stabilized box. The box with the phase stable cables connecting DUTs with the phase detectors, all together, have been enclosed in an oven, which allows for temperature regulation. The equipment did not allow, in terms of available space, for a measurement of more than 3 DUTs at once, that is why they were divided into two groups. The measurement required, for its precision, very low drift cables of exact lengths. These include:

- 2 cables of same lengths, short and low drift, for connection between MECA splitter and the couplers (marked in green in 'Setup II'). Here a Teledyne Phase Master190E of length 13 cm has been used.

- 4 cables of Teledyne Phase Master 160, A64 type. Each of 50 cm length, which allowed, very tightly, to connect the phase detectors box and the measured components, which were placed outside the stabilized area, but within the climate chamber to experience controlled environmental change.

In the section that follows, the measurements conducted in this setup will be presented.

MEASUREMENT RESULTS

The temperature drift has been measured with the temperature profile depicted in Fig. 3 (and in Fig. 6) by dashed green line. The temperature has been changed from 17°C to 25°C in steps of 2°C, and back to 17°C. After each step the stable conditions were left for 8 hours. There are 2 more temperature readings: from the box with phase detectors

ISBN 978-3-95450-177-9

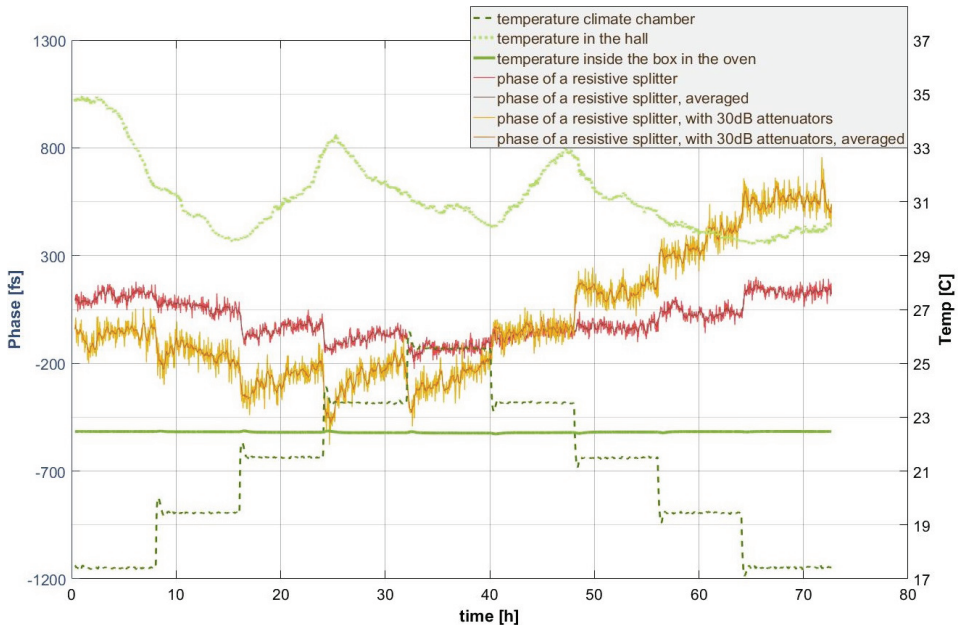

Figure 3: Setup I. Phase difference measured at 1.3 GHz between the outputs, and environmental temperature vs. time.

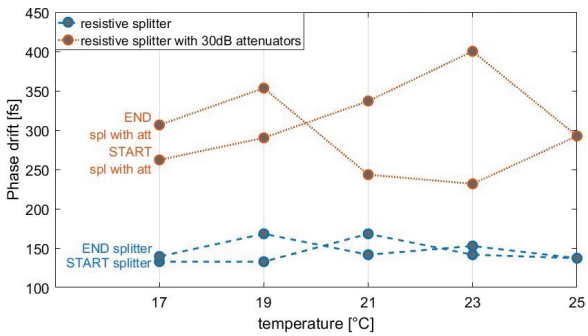

Figure 4: Setup I. Peak-peak drifts within each step.

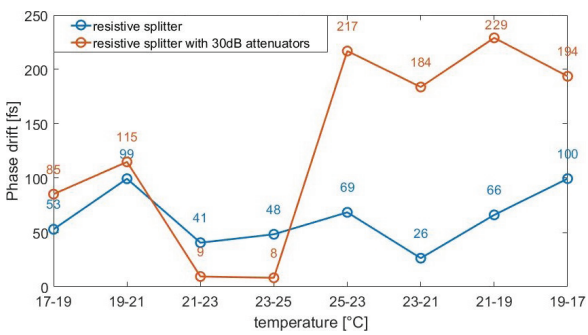

Figure 5: Setup I. Drift per 2°C steps (between mean values of each step).

and from outside the climate chamber, in the hall where it is located. While doing preceding measurements, the phase detectors were placed in the free air outside climate chamber and the hall temperature fluctuation had a great effect on the measurements results. Here can be observed, that the influence, if exists, is marginal, so that no correlated effect is present. The figures 3 - 5 show different measurements from 'Setup I', i.e. the setup with resistive splitters. It can already be observed, that the phase fluctuations within each step, i.e. where the conditions are kept constant and the phase ideally would not change, is much smaller for the resistive splitter without attenuators. This is more clearly shown in Fig. 4. Here, there are usually 2 values for each temperature - one when the temperature was rising and one when falling. The less hysteresis visible, the more reliable the measurement, proving the correlation of the drift only to the induced environmental conditions. The measurement proves, that the peak-to-peak fluctuations for the resistive splitter with the 30 dB attenuators are bigger, approximately by a factor of 2. It also reveals, that apparently another effect of unknown origin contributes to the measurement of the splitter with 30 dB attenuators. This was definitely not the humidity around the splitters or the phase detectors, which readings were also followed, but not shown in the figures for clarity. The drifts had no correlation with humidity, besides the measurement of the resistive splitter. Unfortunately, there the dependence was also not very clear and coefficient determination impossible; no phase jump was present when making a humidity step. Only the phase drift direction changed according to humidity steps direction (humidity rising or falling) and the phase drifted by about 300 fs per 20 % humidity change (in both directions the same). This measurement has been done for step lengths of 12 hours and probably even longer periods were needed to see any convincing correlations.

The temperature coefficient, so the phase change corresponding to the temperature change, is depicted in Fig. 5. The already mentioned effect is also manifested here, as a strong asymmetry of the plot. It lowers the drift when the temperature is rising and increases, when the temperature goes down. The most representative would be probably the value between 'flat' steps of the yellow plot in Fig. 3,

ISBN 978-3-95450-177-9

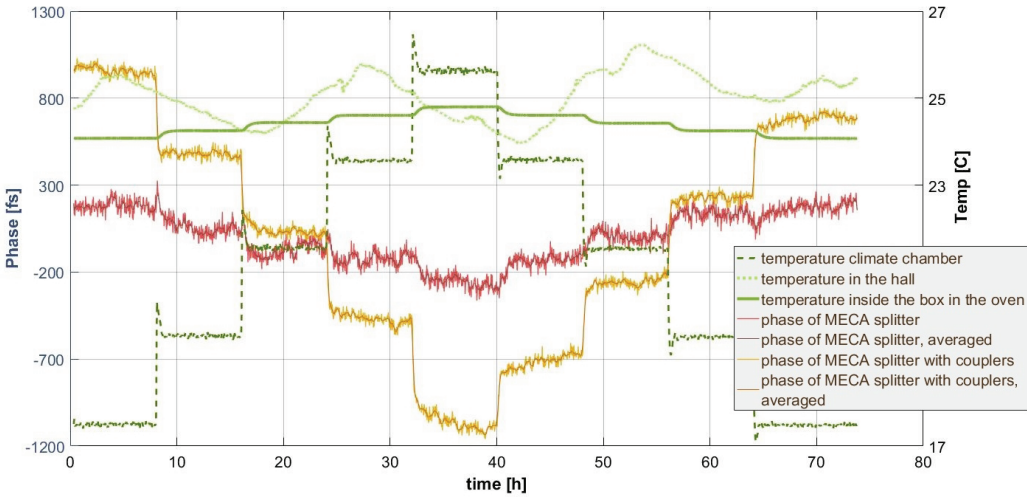

Figure 6: Setup II. Phase difference measured at 1.3 GHz between the outputs, and environmental temperature vs. time.

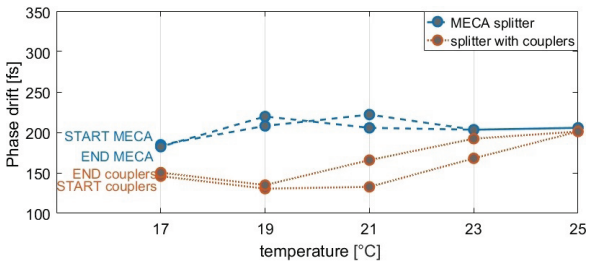

Figure 7: Setup II. Peak-peak drifts within each step.

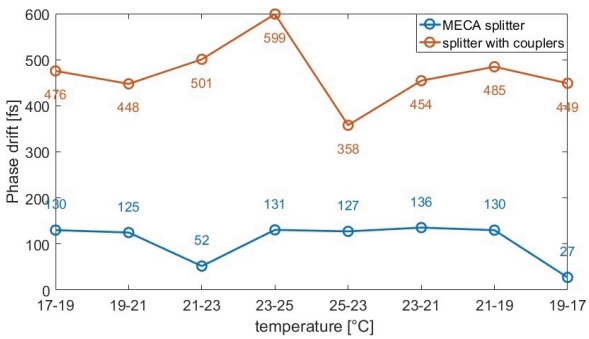

Figure 8: Setup II. Drift per 2°C steps (between mean values of each step).

which is a step from 23 °C to 21 °C. The readings is around 180 fs/2 °C giving the coefficient of 90 fs/°C. The coefficient for the splitter with 0 dB attenuators is about 30 fs/°C (calculated from the mean of the values shown in the plot).

Figures 6-8 show the same measurements for Setup II. The splitter with couplers reveals slightly lower peak-to-peak drift within each step than the splitter alone. In turn, it is much more sensitive to temperature. The coefficient is 240 fs/°C in comparison to the 50 fs/°C of the MECA splitter alone.

Conclusions and Outlook

Temperature coefficients of all the parts are relatively high taking in the account the required precision of our phase detector, which should be on the level of tens of femtoseconds. On the other hand, the measurement setup contributes to the drift and an integrated version of the measured components should reveal better performance. Surprisingly, the best component is the self-made resistive splitter, which shows 140 fs pk-to-pk drifts within 8 hours in stable conditions, and 30 fs/°C temperature coefficient, so both even better than for a low drift MECA splitter with an additional advantage of being closed in a housing (which could act as a low pass filter for any temperature effects) . The limitation of the resistive splitter is a necessary attenuator, which makes the phase inaccuracy between the outputs distinctly bigger. One of the solutions relaxing the requirements would be a selection of a very high isolation splitter for a calibration signal. As it does not have to be wideband, the design of this part could be concentrated more on the isolation attribute.

The commercial couplers occured to be very drifty and together with their inconvenient form factor, it yields to exclusion from this project.

REFERENCES

[1] S. Jablonski, “A Fiber-Optic System Using a Continuous-Wave Laser for Providing Phase-Stable Radio-Frequency Signals to Remote Locations”, Ph.D. thesis, Warsaw University of Technology, 2016.

[2] G. Huang et al., “Signal processing for high precision phase measurements”, Proc. BIW10, TUPSM082.

[3] E. Janas et al., “MTCA.4 phase detector for femtosecondprecision laser synchronization”, Proc. FEL2015, TUP045.

ISBN 978-3-95450-177-9

COHERENT DIFFRACTION RADIATION IMAGING METHODS TO MEASURE RMS BUNCH

R.B. Fiorito†, C. P. Welsch, Cockcroft Institute, University of Liverpool, Daresbury, UK
A.G. Shkvarunets, IREAP, University of Maryland, College Park, MD USA,
C. Clarke, A. Fisher, SLAC National Accelerator Laboratory, Menlo Park, CA

Abstract

The measurement of beam bunch length with high resolution is very important for the latest generation light sources and also a key parameter for the optimization of the final beam quality in high gradient plasma accelerators. In this contribution we present progress in the development of novel single shot, RMS bunch length diagnostic techniques based on imaging the near and far fields of coherent THz diffraction radiation (CDR) that is produced as a charged particle beam interacts with a solid foil or an aperture. Recent simulation results show that the profile of a THz image of the point spread function (PSF) of a beam whose radius is less than the image produced by a single electron, is sensitive to bunch length and can thus be used as a diagnostic. The advantages of near (source) field imaging over far field imaging are examined and the results of recent high energy (20 GeV) CDR THz experiments at SLAC/FACET are presented. Plans for experiments to further validate and compare these imaging methods for both moderate and high energy charged particle beams are discussed.

INTRODUCTION

In previous studies we have shown that the angular distribution (AD) of CDR from a slit or aperture is sensitive to RMS bunch length [1]. The AD can be calculated from the integrated spectral angular density of DR from single electron multiplied by the longitudinal form factor of the pulse integrated over a frequency band in which the integrand is appreciable [2]. Typically this band is limited at low frequencies by the outer radius or boundary of the radiator. At high frequencies it is truncated by the fall off of the longitudinal bunch form factor and, if the radiator is an aperture, by the aperture size. The AD is given by

$$\frac{dI_{bunch}^{CDR}}{d\Omega} \approx N_e^2 \int_{\Delta\omega} \frac{d^2 I_e^{DR}}{d\omega d\Omega} S_z(\sigma_z, \omega) d\omega$$

where I_e is the intensity of the CDR from a single electron, N_e is the number of electrons, S_z is the longitudinal form factor, σ_z is the RMS longitudinal size of the bunch, $\omega=2\pi f$ is the angular frequency, and $d\Omega$ is the solid angle of observation.

In a proof of principle experiment, the AD projected on a plane normal to the direction of the CDR from a plate and a slit were observed using a scanning Golay cell at PSI's 100 MeV injector linac for various bunch lengths. The latter was varied by a compressor chicane in the range of 0.5-2 psec. The bunch lengths were inferred fitting scans of the angular distribution obtained from the equation above to the data. The inferred bunch lengths were also compared with those obtained independently with an electro-optical sampling method and were found to be in excellent agreement with the AD measurements in all cases studied.

OBSERVING THE CDR PSF

According to the virtual photon paradigm [3] the properties of radiation produced by relativistic particles interacting with materials or fields follow those of real photon interactions. For example, when a relativistic charged particle passes through an aperture, diffraction radiation is produced with properties similar to those observed when real photons diffract from the aperture. Applying this paradigm to CDR, the spatial distribution of CDR from a transversely coherent source, i.e. the PSF of the radiation from a coherent source such as a bunch of electrons radiating at a wavelength close to the bunch size, should be related by Fourier transformation to the AD of the photons observed. Then since the AD is related to the longitudinal bunch size, the PSF should also be likewise sensitive to the bunch length.

To observe the PSF, i.e. the spatial form of the CDR from a "single" electron, the transverse size of the beam must be much smaller than the PSF observed of a single electron. In this case the CDR is fully transversely coherent and the CDR PSF will be observed. The PSF of coherent transition radiation (CTR) has been similarly observed in the optical band [4], and under similar beam size conditions should be observable in the THz regime as well (note that CDR and CTR for a finite radiator are closely related via Babinet's principle [5]).

To test this hypothesis we have developed a simulation code to calculate the CDR PSF and explore its sensitivity to bunch length. The CDR produced as an electron passes through a finite sized radiator is intercepted by a lens positioned in the far field of the source which focuses the radiation onto the image plane of the lens.

Simulation results for a 100 MeV beam, interacting with a simple annular aperture oriented normal to the beam are shown in Figure 1 for various bunch sizes in the range of 1-3 picoseconds in the wave band (1-600 GHz). In this example the transverse beam size of the frequency integrated PSF from a single electron has a FWHM ~ 10-20mm (see Figure 1). Note that each of the PSFs shown is

†ralph.fiorito@cockcroft.ac.uk

ISBN 978-3-95450-177-9

scaled in amplitude by a different factor A for each bunch length.

The advantages of observing and using the PSF over the AD of CDR to determine the bunch length are: 1) the former is less susceptible to upstream source contamination than the latter, which is especially important at high energies, where the coherence length of any radiation

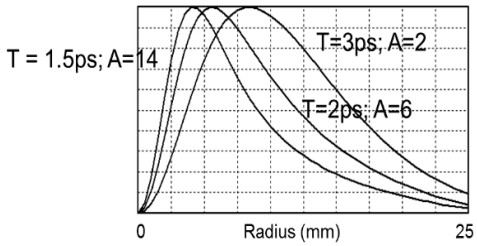

Figure 1: Theoretical CDR PSF distributions produced by a 100 MeV beam interacting with an annular radiator (R_{out}=25mm, R_{in}=5mm) for various bunch lengths.

driven by the beam is very long, i.e. $L \sim \gamma^2 \lambda$ - in this case upstream sources, e.g. CSR synchrotron radiation or another source of CDR within L can strongly interfere with and distort the CDR produced by the primary source; 2) the PSF image can be more easily focused to produce a high number of photons per detector pixel for the source image in comparison to the AD image.

Note that the AD is commonly observed in the focal plane of the lens (focus at infinity). However, in this plane the AD from all upstream sources will also be in focus along with that of the CDR. In contrast, the PSF of the designated source is uniquely observed in the image plane when the focal and image plane are well differentiated. Thus, by carefully choosing the focal length of the lens and the object distance, the PSF from the desired CDR source can be readily distinguished from other sources, i.e. upstream sources will be out of focus and will only create a diffuse background in the image plane.

CDR EXPERIMENTS AT FACET

Setup

Observations of the AD and PSF of CDR were made using the FACET facility at SLAC in the first half of 2016 before its shutdown at the end of April.

The FACET electron beam used in our experiments had the following properties: E = 20 GeV, Q ~ 1.1 nC, bunch rep rate f = 10 Hz; transverse beam size ~100 micron, available bunch lengths = 60 - 80 microns FWHM; observed THz wavelength band: 18-200 mm (0.15-2 THz).

A schematic of the experimental setup is shown in Figure 2. A two foil laser based alignment system is used to overlap incoherent OTR generated by the electron beam with a HeNe laser. The laser and OTR are observed using two CCD cameras, which can be remotely inserted into the optical path. The laser is first used to align the optics used to transport the CDR produced by the radiator to two 7 inch focal length off axis parabolic mirrors arranged in a confocal periscope arrangement, then to a flat remotely rotatable mirror and finally to a 250 mm focal length Teflon lens. Two detectors: a Pyrocam pyroelectric array consisting of 128 x 128, 85micron square pixels and a Gentec single, 6 mm square, pyroelectric detector were employed. Each of these detectors can be positioned via a linear translator to the focal plane or the image plane of the final lens in the optical train. Either the AD or PSF could be scanned across the Gentec via the rotating mirror. A one mm diameter iris was inserted in front of the Gentec detector to create a high resolution line scan in either the horizontal or vertical direction.

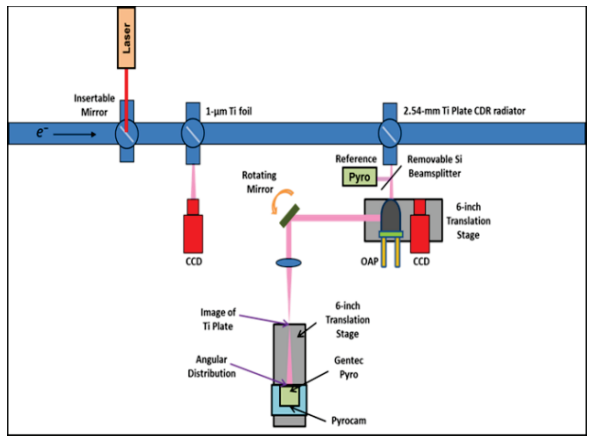

Figure 2: AD and PSF imaging system at FACET.

The CDR radiator is a flat, polished, rectangular Titanium plate (31mm wide, 0.2 inch thick, 4.7 inches long) with a 5 mm circulator aperture located about 2 inches from the bottom of the radiator. Either the flat portion of the radiator or the circular hole could be vertically positioned to intercept the electron beam.

Preliminary Results

Imaging of the PSF of CDR was not possible with the Pyrocam due to experimental difficulties. However, line scans of the radiation observed in the image plane of the Teflon lens were obtained using the Gentec detector with the 1 mm iris.

Figure 3a shows a theoretical horizontal line scan (inverted) obtained using the CDR code described above for a beam with bunch length equal to 60 microns (FWHM), the value measured independently by a transverse deflecting cavity monitor at FACET. The transverse beam size for our experiment was 250 microns, which is much less than the FWHM of the single electron CDR PSF calculated for the FACET parameters.

Figure 3b shows a line scan corresponding to 4a, measured using the rotating mirror and Gentec detector covered with the 1mm iris. Note that this measured scan has the same qualitative shape as the theoretical distribution. However, the measured distribution is about a factor of two wider than the theoretical prediction (see e.g. the peak to peak separation).

The cause of this discrepancy is currently being investigated. It may be due to a calibration error or distortion

ISBN 978-3-95450-177-9

of the CDR distribution due to improper focusing of the THz radiation in the transport optics. The latter is the most likely problem since, in the later stages of the experiment, little time was available to thoroughly test and check the focus of the optics, in particular the image plane of final Teflon lens. We are in the process of comparing our calculations of the PSF with other available codes and studying the effect of defocusing on the image distribution to better understand our results.

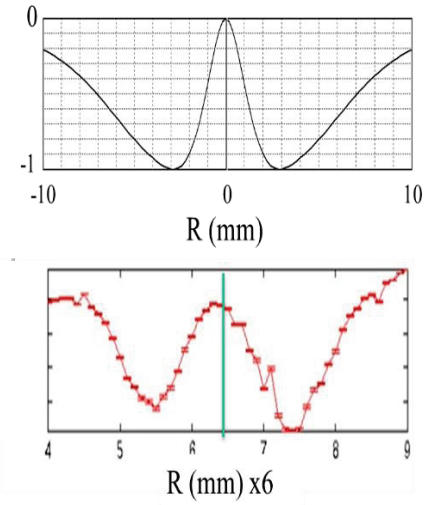

Figure 3: a) theoretical normalized horizontal line scan of the PSF of CDR from a flat rectangular radiator; b) measured normalized line scan of CDR distribution.

CONCLUSIONS

We have developed a new method to measure the RMS bunch length using the PSF of CDR generated in the THz regime. Simulations have shown that the CDR PSF can be observed for a beam with transverse dimensions that are much smaller than the FWHM of the PSF produced by a single electron and thus similar to what has been observed in the optical regime with COTR. A preliminary experiment to image the CDR PSF using the SLAC FACET facility has been done and the results obtained qualitatively agree with predictions. However, a discrepancy of about a factor of two in the scaling of the data is still present and remains to be explained. We are currently examining the issue of image defocusing in the optical system as well as comparing our CDR simulations with other available codes.

Further experiments under more controlled conditions are also being planned at 100 MeV (PSI) and a possible follow up experiment at SLAC using LCLS is under consideration.

ACKNOWLEDGEMENT

Work supported by the EU under grant agreement 624890, the STFC Cockcroft Institute Core Grant No. ST/G008248/1 and DOE Contract DE-AC02-76SF00515.

REFERENCES

[1] A. Shkvarunets, R. Fiorito, F. Mueller and V. Schlott, "Diagnostics of the Waveform of Coherent Sub-mm Transition and Diffraction Radiation", Proc. of DIPAC07, 2007.

[2] A. Shkvarunets and R. Fiorito, Phys. Rev. ST Accel. and Beams 11, 012801 (2008).

[3] M. Termikaelian, "High Energy Electromagnetic Processes in Condensed Media", J. Wiley-Interscience, New York, 1972.

[4] H. Loos, R. Akre, A. Brachmann, et. al.,"Observations of Coherent Transition Radiation in the LCLS Linac", THBAU01, Proc. of FEL08, 2008; and SLAC-PUB-13395, Sept. 2008.

[5] R. Fiorito, "Transition, Diffraction and Smith Purcell Diagnostics for Charged Particle Beams", WE10TI001, Proc. of BIW08, 2008.

ISBN 978-3-95450-177-9

TIME CORRELATED SINGLE PHOTON COUNTING USING DIFFERENT PHOTON DETECTORS

L. Torino, U. Iriso, ALBA-CELLS, Cerdanyola del Vallès, Spain

Abstract

Time Correlated Single Photon Counting (TCSPC) is used in accelerators to measure the filling pattern and perform bunch purity measurements. The most used photon detectors are photomultipliers (PMTs), generally used to detect visible light; and Avalanche Photo-Diodes (APDs), which are often used to detect X-rays. At ALBA synchrotron light source, the TCSPC using a standard PMT has been developed and is currently in operation. Further tests have been performed using an APD. This work presents the experimental results using both detectors, and compares their performances.

INTRODUCTION

The Time Correlated Single Photon Counting (TCSPC) is largely used in several accelerators to perform Filling Pattern (FP), and Bunch Purity measurements [1, 2]. The technique allows real time, and non-destructive FP measurements using the synchrotron radiation and providing high dynamic ranges.

The TCSPC is based on the fact that the number of photons produced when the beam is passing through a bending magnet is directly proportional to the number of electrons in the beam. Therefore, the FP can be obtained by measuring the temporal distribution of the synchrotron radiation, which corresponds to the one of the electron beam.

At ALBA the TCSPC using visible light has been successfully tested (see [3] for details), and more recently, a final setup for the routine operation has been developed. Moreover an Avalanche Photo-Diode (APD) has been also tested to perform TCSPC using x-rays.

The final setup for the visible light, and the new setup for the x-rays are presented in this work, together with a discussion on the obtained results.

Table 1: Manufacturer specification of the PMT and the APD. The Transit Time Spread that is measured in house.

	PMT H10721-210	APD C5658
Photocathode Material	Ultra Bialkali	Silicon
Spectral Response	230-700 nm	200-1100 nm
Dark Current	10 nA	0.1 nA
Rise Time	0.57 ns	0.5 ns
Transit Time Spread	0.2281 ns	0.47 ns

TCSPC USING VISIBLE LIGHT

The photon-detector used to perform TCSPC in the visible range at ALBA is a Hamamatsu photomultiplier (PMT) H10721-210. The main characteristics of the device are collected in Table 1, and preliminary tests are shown in [3].

The final TCSPC setup has been moved for operation stability reasons inside the tunnel. The light is extracted using the copper absorber located at the end of visible light diagnostic frontend. This is possible since the synchrotron light reaching the ALBA diagnostic beamline Xanadu is extracted through an "half-mirror" which selects only the upper lobe of the radiation generated. In this way the central and the lower lobe reach the copper absorber, which is oriented at 45°with respect to the incident light. Even if the absorber is not polished, it is still able to reflect the visible light which is extracted through an extraction window, after which the PMT is located. A sketch of the light path at the end point of FE01 is presented in Fig. 1.

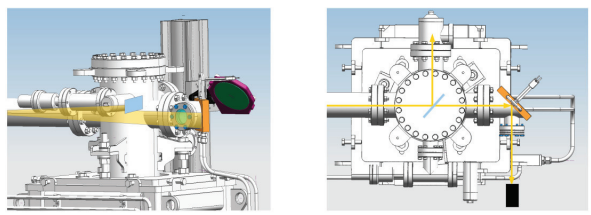

(a) *Front view.* (b) *Top view, the black box represent the PMT.*

Figure 1: Layout of FE01 endpoint and sketch of the light path.

In order to avoid the contaminations from the visible ambient light in the tunnel, a container has been designed to accommodate the TCSPC final setup. The container is a black box fixed on a support, and is directly connected to the secondary extraction window of FE01.

The PMT is contained in a small box in order to make the cabling easier (see Fig. 2(a)). On the front part of the box a c-mount lens tube is mounted, holding a Neutral-Density (ND) filter and a 633 nm band pass filter in order to shield the radiation and low the flux to less than one photon per revolution period, as required from the TCSPC. In front of the PMT box, a motor allows to introduce a gradual ND filter (from 0 to 10^5) to control the photon flux.

Lead sheets have been located around the PMT to reduce the noise produced by particle losses and to slow down the device aging process.

Figure 2 shows two pictures of the setup. In the first the container is open and all the components are visible, while in the second the box is closed and is mounted in the tunnel at the FE01 location.

The power supply and the required electronics to properly control the components in the container (PMT and motor) are located outside the tunnel. The PMT signal is connected to a Picoharp300, which acquires the data and send them to

ISBN 978-3-95450-177-9

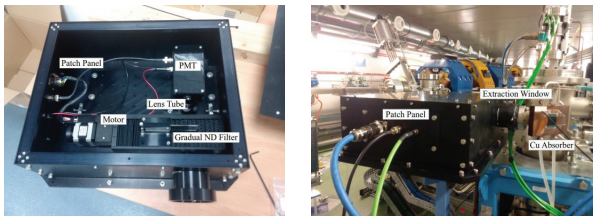

(a) *Container open.* (b) *Container mounted.*

Figure 2: Final setup for TCSPC using visible light.

the ALBA control system where an on-line data analysis is performed [3]. A Tango version of the Picoharp300 software has been developed in house [4].

Filling Pattern Measurements

TCSPC using visible synchrotron radiation is nowadays used routinely at ALBA for FP monitoring during machine operation, where 130 mA of current are distributed in the 10-trains with 32 bunches each. The integration time used to perform TCSPC is 10 s, with a bin width for the Picoharp300 of 16 ps.

The typical raw data are presented in Fig. 3. In the top plot all the ten trains of the ALBA FP are presented: the horizontal scale is a machine period. The bottom plot is the zoom of the first train of the the FP. The peaks have a modulation of 2 ns, which corresponds to the 32 train bunches. The number of photon counted each 2 ns is proportional to the amount of current per bunch.

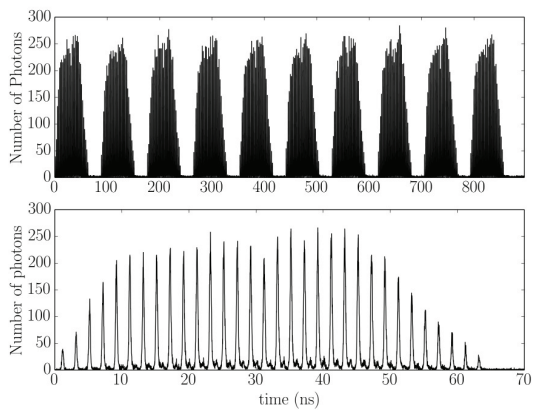

Figure 3: Results form TCSPC using visible light. The top plot is the whole beam while the bottom plot is a zoom on the first train.

Single Bunch Measurements

Single bunch measurements were also performed using this configuration. A single bunch of 5 mA was injected at the bucket 3 (around 6 ns), and some spurious counts appeared at bucket 12 (around 24 ns), as presented by the black line of black line in Fig. 4. Not being sure of the nature of the spurious counts we applied the bunch cleaning. The result is given by the red line in the same Figure, where the spurious counts disappears. The bunch cleaning has also been applied to the surrounding buckets but no improvements were observed.

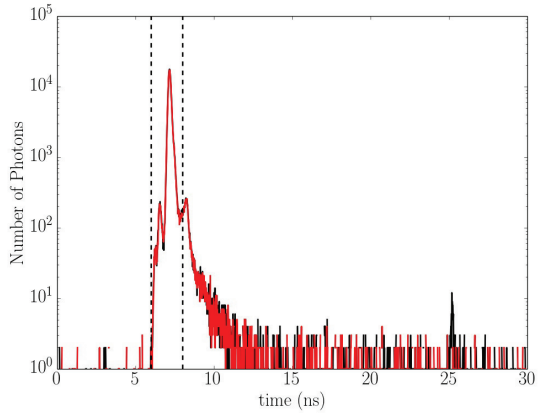

Figure 4: TCSPC to measure a single bunch of 5 mA using the PMT. Data were acquired for 15 s. Horizontal dashed lines represent the bucket length.

More in general, the response of the PMT presents a sharp peak, with a maximum of roughly 10^4 counts per bin, centered within one bucket (from 6-8 ns, dashed vertical lines in Fig. 4). The PMT signal decays of two order of magnitudes in the 2 ns delimiting the bucket length, which define a dynamic range of 10^2. On the other side the PMT has been able to detect in a separate bucket very small amount of current that only produced around 10 counts. This provide a dynamic range of 10^3.

It is worth to notice that during standard operation FP measurements, since we are not interested in the bunch purity, the maximum number of photon counted per bin is in the order of a few hundred (see Fig. 3). In this count range the profile of the single bunch stays within one bucket and photons coming from different bunches are not mixed, minimizing the effect on the linearity of the measurement.

TCSPC USING X-RAYS

The device chosen to perform TCSPC at ALBA is the APD module C5658 by Hamamatsu [5]. The silicon detector included in the module is the Hamamatsu Si APD S12023-02 [6], the effective area has a diameter of 0.2 mm. The full integrated module also contains a bias power supply and a low noise amplifier. The gain of the module is set to 50 (for light in the visible range), and the detection limit is up to 1 GHz. In order to guarantee a stable operation of the APD, a thermosensor and a temperature-compensated bias power supply are also present in the integrated module.

This kind of detector is thought to detect visible light in a range from 200 to 1100 nm, but since the APD will be used for x-ray detection, the foreseen borosilicate window has been removed. The main specifications of the module and the silicon detector are listed in Table 1. Note that

ISBN 978-3-95450-177-9

all the parameters (but the Transit Time Spread which is measured in house) refers to the behavior of the detector when measuring visible light pulses.

Following experiments at other machines [1,7,8], the goal is to use the secondary x-rays produced from the collision between the synchrotron radiation beam and a metal, such as copper, to measure the FP. When copper is bombarded with hard x-rays some electrons transitions to the innermost K shell from a $2p$ orbital of the second, or L shell are exited, and soft x-rays (about 8 keV) are emitted. Figure 5 (top) shows the position of the peaks for this kind of transition in copper. The so called K_α and K_β transitions are very fast (order of 10 ps) so they can be used to detect indirectly the arrival time of the photons [9]. Moreover the fluorescence yield is around 50% for copper, as shown in the rightmost plot in Fig. 5 (bottom). This means that roughly half of the x-rays that are absorbed will produce the transition and generate softer x-rays, while the others will generate Augers electrons.

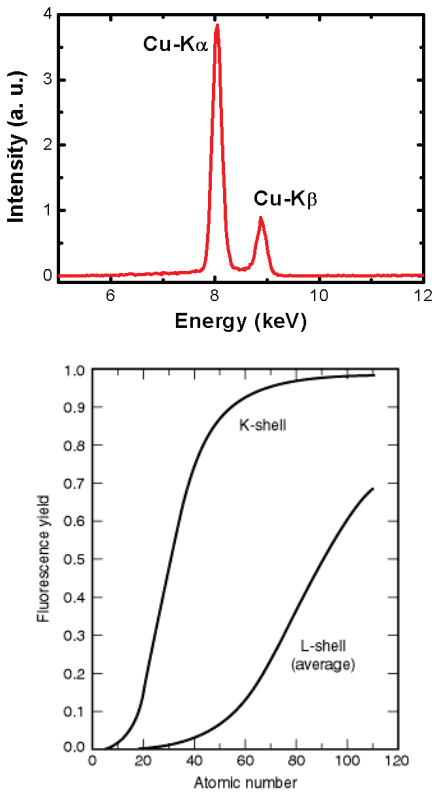

Figure 5: Intensity of the K_α and K_β transition of copper and fluorescence yield for metals [9]. The copper atomic number is 29.

To exploit the K_α transition, the APD has been located looking at the copper filter used for the x-rays pinhole at Front-End 34 (FE34), as presented in Fig. 6. A bending magnet generates the synchrotron radiation, X-rays are extracted through a 1 mm aluminum window selecting photons with an energy larger than 1 keV. A copper filter, with a thickness of 0.5 mm, selects x-rays with an energy larger than 12 keV to perform pinhole imaging avoiding diffraction limitation.

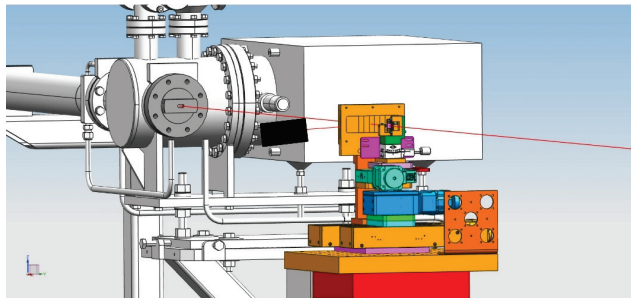

Figure 6: FE34: the x-rays (red line) are extracted through the aluminum window and filtered by a copper absorber (orange parallelepiped). Red line outgoing from the filter represent part of the K_α transition reaching the APD (black rectangle).

The filter can be used as source of K_α. Note that only x-rays absorbed in the first 20 µm of Cu provide suitable K_α photons, being 20 µm the attenuation length for photons of this energy in the material.

The APD C5658 provides a positive pulse with an amplitude that depends on the energy of the x-ray detected. To make the signal compatible with the Picoharp300, which only accepts negative pulses, a delay generator DG645 [10] has been used to invert the signal. The pulse from the APD is given as input trigger to the DG645, which finally produces a squared pulse of negative amplitude (-600 mV) and short enough rise time ($<$ 1 ns). The threshold used to fire the trigger has been set to 40 mV. This pulse is then connected to the Channel 1 of Picoharp300 to measure the photons temporal distribution, using the same setting as for the PMT.

Filling Pattern Measurements

Measurements of the same FP shown in Fig. 3 has been performed using the APD to detect x-rays. The result is presented in Fig. 7.

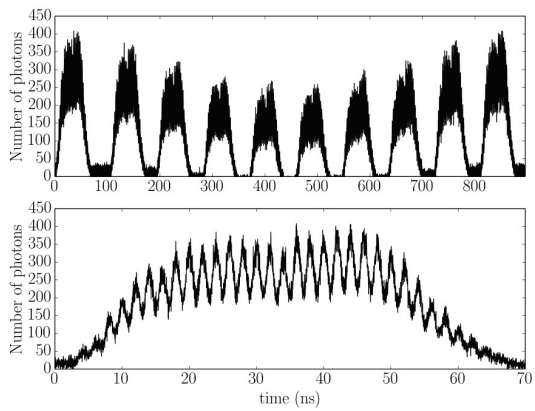

Figure 7: Results form TCSPC using the APD to detect x-rays. The top plot is the whole beam while the bottom plot is a zoom on the first train.

ISBN 978-3-95450-177-9

The APD measurements looks noisier and that the shape of the FP measured is not the same. When measuring with the APD the central trains looks less filled with respect to the "lateral" ones. This may be due to the response of the device when detecting x-rays at high repetition rate. The effect is currently under investigation because not fully understood.

Moreover the Temporal Time Spread of the device is not as good as the one of the PMT, and consecutive bunches are mixed up. This also contribute to the distortion of the measured FP. This effect is corrected in other machines using a dedicated algorithm [2].

Single Bunch Measurements

Single bunch measurements using the APD has been also performed. Data were acquired for 200 s and a bunch of 3.5 mA was placed at bucket 3 (6 ns). Results are presented by the black line of Fig. 8. Also in this case the vertical dashed lines delimit the bucket length.

To have an estimation of the sensitivity of the detector, we filled with a few shots the bucket 4 (red line of Fig. 8): it is clear that the APD is measuring the small amount of current in the bucket as an excess of counts with respect to the single bunch curve. Other shots were injected in buckets 0, 1, 2, 4, 5, and 6 changing the linac gun-level to inject less and less current [11]. Results shows that the APD was able to resolve a very low amount of particles.

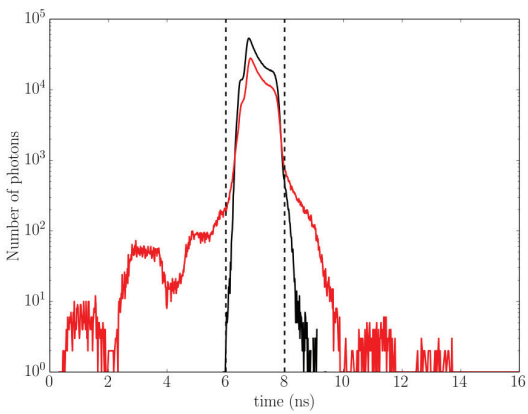

Figure 8: TCSPC to measure a single bunch of 5 mA. Horizontal dashed lines represent the bucket length.

In the APD case the signal decays of almost 3 order of magnitude in the bucket length leading to an estimated dynamic range of 10^3. On the other hand no noise is surrounding the main bunch. Moreover the it has been proved that a modification of the signal shape can be appreciated when injecting few current in the bucket following the main one. Finally the device is also sensitive to very low amounts of current injected in further buckets, providing a dynamic range in this conditions better than 10^4.

CONCLUSION

In this report we presented the setup and the results obtained for the TCSPC using visible light and x-rays at ALBA synchrotron light source.

From the measurements it is clear that a standard PMT using visible light is preferable to perform routine operation FP measurements since the shape of the pulse is reasonably contained within the 2 ns of a single bucket. This is not the case of the APD, for this reason, when performing multi-bunch measurements the consecutive buckets are mixed. Moreover a strange behavior of the trains trend makes the results nor fully reliable. The effect is still under investigations.

On the other side, the APD detecting x-rays seems much more sensitive when measuring single bunch showing an high dynamic range, better than the PMT.

As a consequence to this measurements the PMT has been chosen to measure the FP during routine operations, while the APD will be further investigated for bunch purity applications.

ACKNOWLEDGMENTS

We would like to thanks S. Blanch for the effort with the software, and R. Muñoz for for the help with the linac single bunch operation. Many thanks to the operation group for the indispensable help during the tests.

REFERENCES

[1] C.A. Thomas et al. "Bunch Purity Measurements for DIAMOND" Nucl.Instum.Meth., A 566 (2006) 762-766.

[2] A. Jeff "A Longitudinal Density Monitor for the LHC" PhD thesis, Liverpool U., 2012-12-11.

[3] L. Torino, et al. " Filling Pattern Measurements at ALBA using Time Correlated Single Photon Counting" IPAC 2014, Dresden (Germany), THPME162 (2014).

[4] S. Blanch `https://github.com/srgblnch/PicoHarp300`

[5] "APD module C5658 series Data Sheet" (Hamamatsu) `http://www.hamamatsu.com/resources/pdf/ssd/c5658_kacc1023e.pdf`

[6] "Si APD S12023 series Data Sheet" (Hamamatsu) `http://www.hamamatsu.com/resources/pdf/ssd/s12023-02_etc_kapd1007e.pdf`

[7] S. Kishimoto "Bunch-purity measurements of synchrotron X-ray beams with an avalanche photodiode detector" Nucl. Instr. Meth. Phys. Res. A, Volume 351, Pag. 554 - 558 (1994).

[8] Hubert, N. "Purity measurement at SOLEIL" Talk for DEELS 2014, Grenoble (France).

[9] A. Thompson et al. "X-ray data booklet" DouglasEditors (2001).

[10] "DG645 — Digital delay and pulse generator (4 or 8 channels)" (Stanford Research Systems) `http://www.thinksrs.com/downloads/PDFs/Catalog/DG645c.pdf`

[11] R. Muñoz et al. "Status and Operation of the ALBA Linac" Linac 16, East Lansing (USA).

ISBN 978-3-95450-177-9

DEVELOPMENT, CALIBRATION AND APPLICATION OF NEW-GENERATION DISSECTOR WITH PICOSECOND TEMPORAL RESOLUTION

*O. I. Meshkov[1], O. V. Anchugov, V. L. Dorokhov, G. Ya. Kurkin, A. N. Petrozhitsky, D. V. Shvedov, E. I. Zinin, BINP SB RAS, Novosibirsk, 630090, Russia
P.B. Gornostaev, M.Ya. Schelev, E.V. Shashkov, A.V. Smirnov, A.I. Zarovskii, GPI RAS, Moscow, 119991, Russia
[1]also at NSU, Novosibirsk, 630090, Russia

Abstract

A dissector is an electron-optical device designed for measurement of periodic light pulses of subnanosecond and picosecond duration. LI-602 dissector developed at BINP SB RAS is widely used for routine measurements of a longitudinal profile of electron and positron beams at BINP electron-positron colliders and other similar installations [1-3]. LI-602 dissector is a part of many optical diagnostic systems and provides temporal resolution of about 20 ps. Recently a new generation of picosecond dissectors were created on the basis of the PIF-01/S1 picosecond streak-image tube designed and manufactured at the GPI Photoelectronics Department [4, 8-10]. The results of the measurements of instrument function of the new dissector based on PIF-01/S1, which were carried out in the static mode [5], showed that temporal resolution of the dissector can be better than 3-4 ps (FWHM). The results of temporal resolution calibration of the new-generation picosecond dissector carried out at the specialized set-up based on a femtosecond Ti:sapphire laser and recent results of longitudinal beam profile measurements at BINP damping ring are given in this work.

BASIC PRINCIPLES OF DISSECTOR OPERATION

The detailed description of the detector operation can be found in [3, 6]. We will remind just very common ideas of the device operation. The layout of a dissector is shown in Fig. 1. The image section of dissector consists of a photocathode, electron lens, deflection plates and slit aperture.

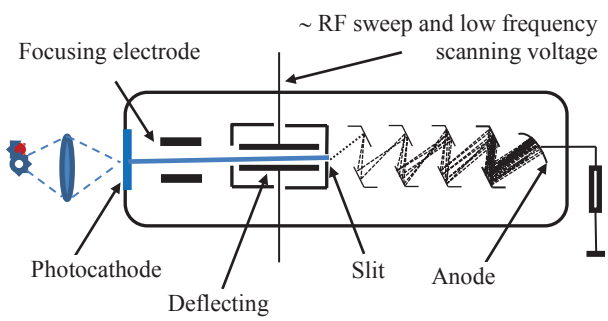

Figure 1: The simplified layout of the dissector.

*O.I.Meshkov@inp.nsk.su

Let the point-like image of a pulse radiation source be projected onto the photocathode of such a device. If radiation pulses and RF deflection voltage are strictly synchronized, then a stationary electron image $Q(x)$ appears on the slit plane (Fig. 2). The typical frequency of RF sweep voltage $U_{sw}(t)$ is tens of MHz. The image $Q(x)$ reproduces the time structure of the object under observation.

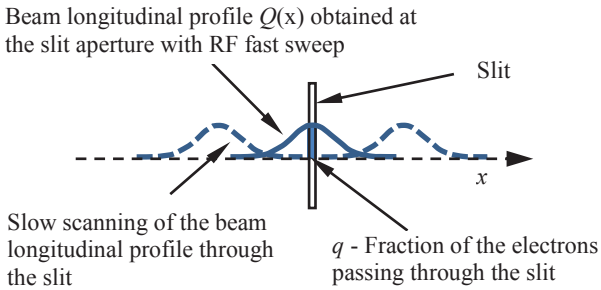

Figure 2: The scheme of slow scanning of $Q(x)$ distribution transversely through the slit.

Only the electrons with charge q, which pass through the slit, reach the secondary electron multiplier. The average anode current of the secondary electron multiplier is proportional to this charge q and is proportional to the luminosity of the process at the given moment. The beam image is scanned transversely through the slit with velocity $V_{sl} << V_{sw}$. When distribution $Q(x)$ is scanned, the anode signal of the secondary electron multiplier repeats the shape of the observed signal.

TIME SCALE OF THE DISSECTOR

A simple way to define a time scale is an important advantage of the dissector. It is achieved with permanent point-like source of the light focused on the photocathode of the dissector. The space distribution $Q_p(x)$, as it is represented in Fig.3, periodically appears on the slit aperture plane and is read out during slow scanning. As a result, the space scale transforms into time scale. The space interval and the corresponding time interval T_l between two distinct marks at the calibration curve depend on U_0 at fixed RF frequency ν_{RF}. The same signal appears at the anode of the dissector if to scan slowly this distribution with linear ramp voltage applied to the deflecting plates.

The upper plot in Fig. 3 is an experimental curve obtained for temporal calibration of the dissector. The sweep velocity as well as the time scale of the dissector

ISBN 978-3-95450-177-9

are obviously non-linear and varies within the period of RF sweep. The shape of the calibration curve depends on the relation between technical resolution of the dissector (see below) and the RF sweep span [3, 6].

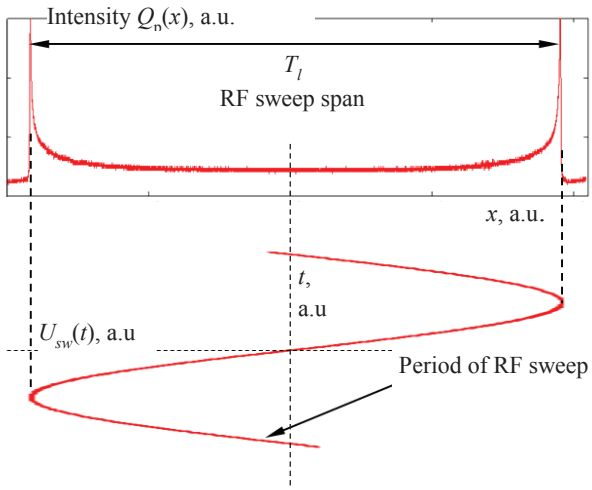

Figure 3: The temporal calibration of dissector with a permanent point-like light source.

The restrictions of accuracy of calibration caused by non-linearity of the scan are described in [6]. The temporal interval corresponding to the labels is $T = 2/\omega_{RF} = T_{RF}/\pi$, ω_{RF} is an angular velocity of RF sweep. We define a technical resolution as an instrumental function of the tube, which depends just on the quality of electron optics of the device.

The measured pulse should be placed at the center of the sweep where non-linearity is negligible. It is achieved with a change of a phase shift between the measured signal and the RF sweep.

FEATURES OF THE DISSECTOR OPERATION

The precise measurements of bunch length with LI-602 dissector can be done at single-bunch mode of operations of accelerator. A dissector must operate at N harmonic of revolution frequency (N>>1).

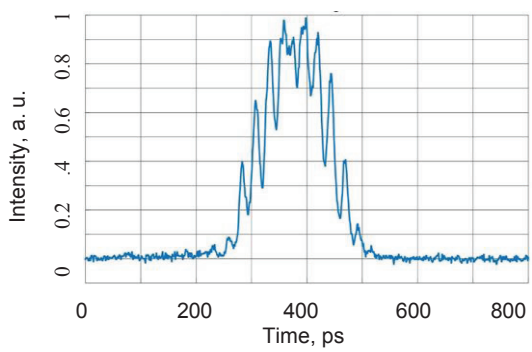

Figure 4: Distortions of the signal of the dissector caused by synchrotron oscillations.

It means that signals from different bunches will overlap for multi-bunch beam. For example, SIBERIA-2 storage ring has 75 separatrices. The LI-602 dissector is applied for beam length measurements and operates at 15 harmonic of revolution frequency [7]. Due to that the signal of the dissector contains 5 peaks and each of them is a sum of signals from 5 separatrices. The new version of the dissector has an electrons shutter which may select a chosen separatrix.

Another feature of the dissector is a high sensitivity to the phase oscillations of the beam. Phase oscillations appear at SIBERIA-2 at the beam current less than 2 mA at the energy of injection. It takes place because of decrease of a feedback between the beam and accelerating RF cavity. It distorts an operation of the dissector (Fig. 4). On the other hand a Fourier transform of the dissector signal enables us to determine a synchrotron frequency (Fig. 5).

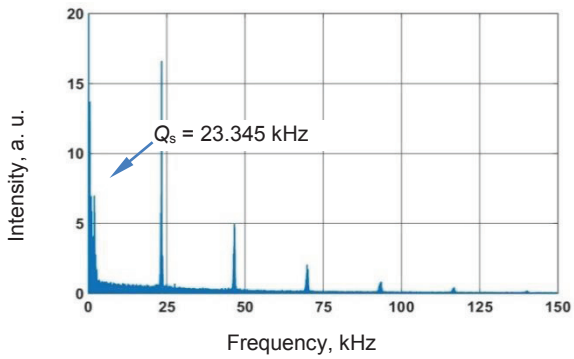

Figure 5: Synchrotron frequency obtained by Fourier transform of the dissector signal.

DIRECT TEMPORAL-RESOLUTION CALIBRATION OF THE DISSECTOR

The direct measurements of the dissector temporal resolution were carried out at the laser set-up (specially created at the GPI Department of Photoelectronics) for testing technical parameters of the picosecond dissectors being under development by means of synchronous electron-optical chronography method (Fig. 6), [11]. The Ti:sapphire laser generated light pulses at the wavelength of 0,81 microns with a 30-femtosecond duration at the frequency of 75,3 MHz.

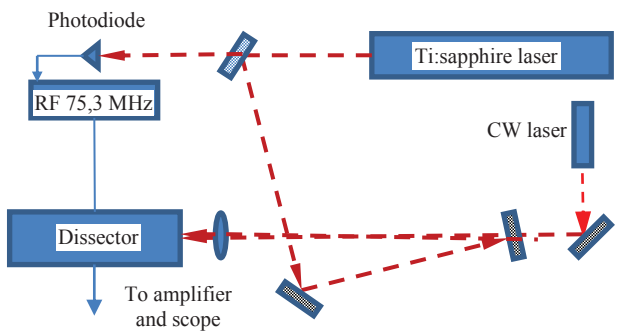

Figure 6: The scheme of the experiment for direct measurement of the temporal resolution of the dissector.

Thus, the pulse duration was much shorter than the expected temporal resolution of the dissector and can be neglected at measurements. Radiation of the laser, re-

ISBN 978-3-95450-177-9

flected from two surfaces of the plane-parallel glass plate, was focused on the dissector photocathode by a lens. As a result, a pair of pulses separated by the time interval $\tau = 2dn/c$ (where d is thickness of the glass plate, $n = 1{,}51$ is glass refraction index) came to the dissector with a frequency of 75 MHz. We used four plates with the thicknesses creating a time interval between pulses of 100; 52,1; 25,4 and 9,7 ps (Fig. 7).

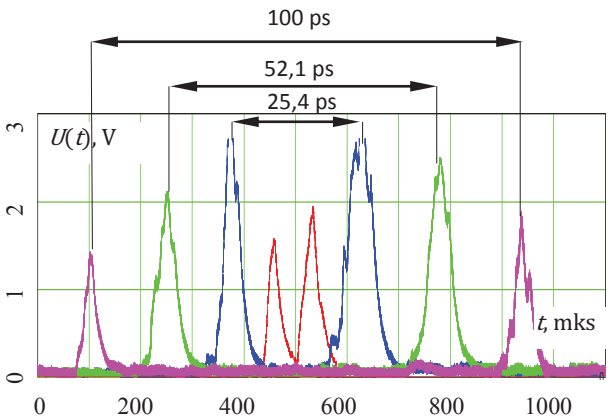

Figure 7: Pairs of the laser pulses acquired by the dissector at different time intervals between them.

RF voltage with a frequency of 75,3 MHz and with a total amplitude up to 1500 V and scanning saw-tooth voltage with a frequency of 50 Hz and with an amplitude up to 750 V were simultaneously applied to the deflecting plates of the dissector.

It should be noted that to achieve the ultimate temporal resolution, light should be focused on the dissector photocathode in a spot with a size not exceeding the width of the slit at the EMT input, which in our case is s = 0,04 mm. The expected value of temporal resolution is [4, 12]: $t_{tr}(s) = (s(mm)\cdot M)/(2\pi\nu_{RF}(Hz)\cdot U_{RF}(V)\cdot\xi\ (V/mm)) \approx 3$ ps, where $\xi = 0.07$ mm/V is an efficiency of the deflecting plates for PIF-01/S1, M =1,5 is coefficient of electron-optical magnification.

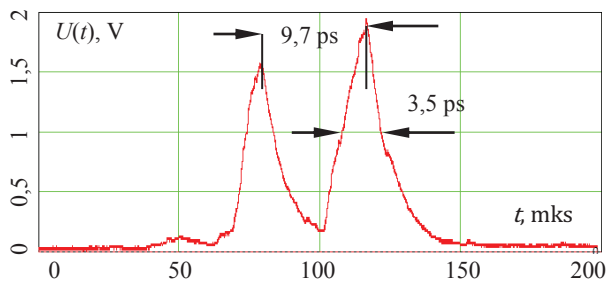

Figure 8: The two laser pulses separated by a 10-ps time interval acquired by the dissector.

The best temporal resolution of 3,5 ps (FWHM) was measured for the 10-ps interval, as shown in Fig 8. The average value for all pairs of pulses is 4,5±0,6 ps.

APPLICATON OF THE DISSECTOR AT THE DUMPING RING

The dissector with temporal resolution of about 4 picoseconds has recently started operating at the BINP damping ring. The beam stored at accelerator contains several bunches separated by time interval of 1,2 ns.

The comparison of data obtained with streak camera PS-1/S1 and the dissector is presented in Fig. 9. A good agreement of two methods can be observed.

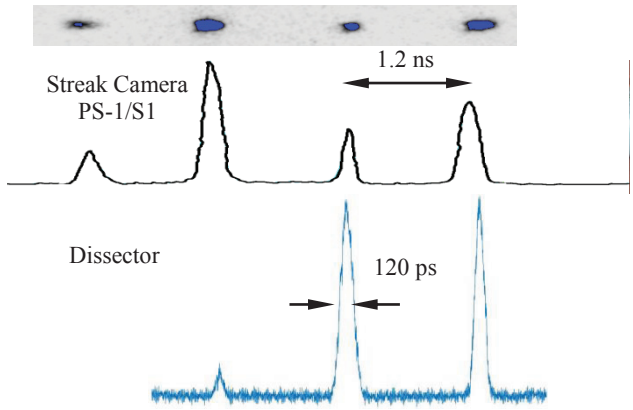

Figure 9: The longitudinal bunches profiles acquired by streak camera PS-1/S1 and the dissector.

CONCLUSION

We have showed the possibility to achieve temporal resolution within picosecond range by means of the dissector created based on the PIF-01/S1 picosecond streak tube developed earlier at GPI RAS. The set-up, created at the GPI Department of Photoelectronics for measurement and calibration of temporal resolution of new-generation picosecond dissectors, which uses radiation of the femtosecond Ti:sapphire lasers, has showed efficiency and reliability at testing of the dissectors in the continuous scanning mode with the highly-stable 75-MHz generator, also developed by the participants of the present Russian Science Foundation Project. The dissector was successfully tested at damping ring of BINP.

ACKNOWLEDGMENTS

The presented experimental results were implemented due to financial support of the Russian Science Foundation (Projects N 14-29-00295). Experimental samples of picosecond dissector based on PIF-01 streak tube was designed and manufactured at the Department of Photoelectronics of A.M. Prokhorov General Physics Institute, Russian Academy of Sciences. The authors wish to thank all the Department members and especially the members of its technological chain, namely, G.P. Levina, V.A. Makushina, S.R. Ivanova, Yu.M. Mikhal'kov. The authors are grateful to P. A. Molyavin for technical assistance.

ISBN 978-3-95450-177-9

REFERENCES

[1] L. N. Vyacheslavov, M. V. Ivantzivskiy, O. I. Meshkov *et al.*, *Phys. At. Nucl.,* 43, 451 (2012).

[2] E. I. Zinin *et al., At. Energ.,* 20, 320 (1966).

[3] E. I. Zinin *et al., Nucl. Instrum. Methods*, 208, 439 (1983).

[4] V. P. Degtyareva, Yu. V. Kulikov, M. A. Monastyrsky *et al.*, in *Proc. SPIE,* 491, 239 (1984).

[5] E.I. Zinin and O.I. Meshkov, "Optical dissector for longitudinal beam profile measurement", *JINST*, 2015 1748-0221 10 P10024 doi:10.1088/1748-0221/10/10/P10024.

[6] V.Smaluk, *Particle beam diagnostics for accelerators - Instruments and methods*, Saarbrucken: VDM Publishing, 2009, 276 p. ill.

[7] V. Dorokhov et al., "Recent Results from New Station for Optical Observation of Electron Beam Parameters at KCSR Storage Ring", *IBIC 2016*, Barcelona, Spain, paper TUPG60.

[8] E.I. Zinin, O.V. Anchugov, V.L. Dorokhov *et al.*, "Direct temporal-resolution calibration of new-generation dissector", *JINST*, 2016 1748-0221 11 T03001 doi:10.1088/1748-0221/11/03/T03001.

[9] A. M. Prokhorov, N. S. Vorob'ev, V. I. Lozovoi, *et al.*, *Quantum Electron*., 32, 283 (2002).

[10] S. G. Garanin, S. A. Bel'kov, G. S. Rogozhnikov *et al.*, *Quantum Electron*., 44, 798 (2014).

[11] M.Ya. Schelev, "Pico-femto-attosecond photoelectronics: looking through the lens of a half-century", *Phys. Usp*. **55** (6) (2012).

[12] E. K. Zavoisky and S. D. Fanchenko, "Image Converter High-Speed Photography with 10^{-9}–10^{-14} sec Time Resolution", *Applied Optics,* Vol. 4, Issue 9, pp. 1155-1167 (1965*)*.

ISBN 978-3-95450-177-9

AXD MEASUREMENTS AT SOLEIL

M. Labat, M. El Ajjouri, N. Hubert, D. Pedeau, M. Ribbens, M.A. Tordeux, Synchrotron SOLEIL, 91 191 Gif-sur-Yvette, France

Abstract

A first prototype of in-Air X-ray Detector (AXD) has been installed on the SOLEIL storage ring. An AXD simply consists of a scintillator, an objective and a camera installed in air behind the absorber of the bending magnet's synchrotron radiation layer. The radiation vertical profile analysis easily enables to retrieve the vertical beam size of the electron beam at the source point. This simple diagnostics opens large perspectives of beam size measurement all around the ring for an accurate characterization of the beam and improvement of its stability survey.

INTRODUCTION

An in Air X-ray Detector (AXD) has been installed at SOLEIL in August 2016 for vertical electron beam position and size measurements. An AXD consists of a scintillator and an imaging system [1] as illustrated in Figure 1. When the electron beam passes in the ring dipole field, it produces synchrotron radiation (SR) over a wide spectral range including hard X-rays. The synchrotron radiation in the X-ray range can pass through the absorber and the dipole vacuum chamber to reach the air in the tunnel. The X-ray SR layer distribution is then transformed into a visible light distribution by a scintillator. Finally, an imaging system enables to record this distribution on a camera. The analysis of the vertical profile of the light distribution enables to retrieve the vertical dimension at the source point, i.e. in the ring dipole. This paper summarizes the design and installation of the AXD at SOLEIL and presents its first measurements obtained in September 2016.

AXD SOURCE POINT

AXD Location

The AXD has been installed behind the second dipole of cell 12 at SOLEIL (C12-D2). The geometry of the C12-D2 vacuum chamber enables to mount the scintillator only 1.3 m downstream the source point inside the dipole (see Figure 2).

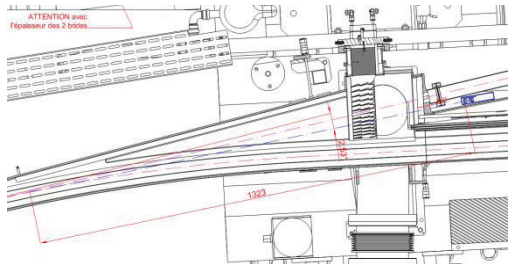

(a) Chamber drawing. Scintillator in blue.

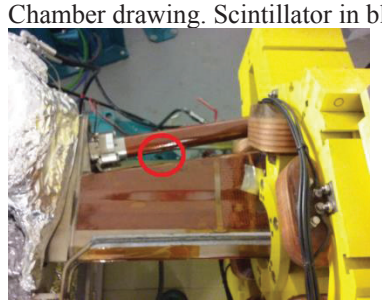

(b) Chamber picture before AXD installation. Red circle: expected scintillator location.

Figure 2: C12-D2 vacuum chamber.

Beam Parameters at Source Point

The scintillator is in fact in between two vacuum chamber exit branches: the one for the 0° radiation and the one for the electron beam exit, corresponding to an extraction angle of 2.53°. The electron beam parameters at the 2.53° source point are given in Table 1.

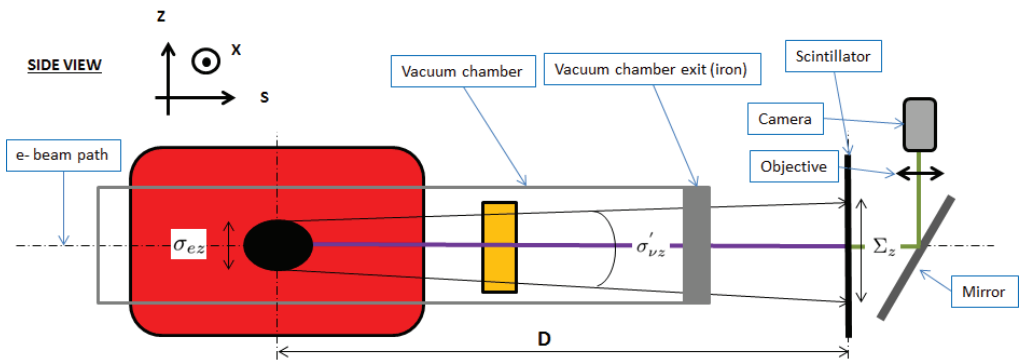

Figure 1: AXD schematic.

ISBN 978-3-95450-177-9

Table 1: Beam Parameters at the 2.53° Exit of C12-D2

Parameter	Symbol	Unit	Value
Energy	E_e	GeV	2.75
Hor. Emitance	ε_x	nm.rad	4.0
Energy dispersion	σ_e	-	0.001025
Vert. beta function	β_z	m	12.026
Vert. alpha function	α_z	m	0.552
Vert. beam size	σ_{ez}	µm-rms	21.93
Vert. beam divergence	σ'_{ez}	µrad-rms	2.08

The Absorber

Inside the SOLEIL dipole vacuum chambers are installed absorbers to block the synchrotron radiation which is not used by a beamline. Those copper absorbers, called crotchs, do not present a constant thickness of copper. They are made of series of teeth (see Figure 3a) to optimize the power deposition, which results into a periodic shape of the transverse thickness (see Figure 3b). The thickness varies between 6 and 22 mm along the X axis. For the following calculations, we will assume that the copper density is 8.96 g/cm^3.

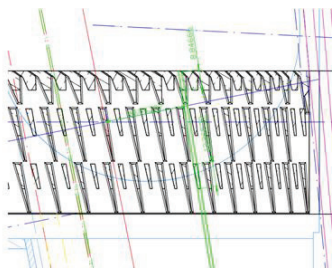

(a) Crotch drawing in the XS orbit plane. Top view.

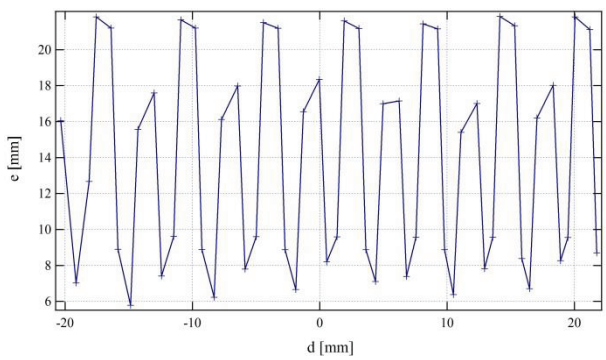

(b) Crotch thickness profile along X.

Figure 3: Characteristics of SOLEIL absorbers (crotch).

The Vacuum Chamber Exit

The AXD is located in the middle of the dipole vacuum chamber, where a gap appears between the 0° exit branch and the electron beam exit branch. The dipole vacuum chamber is made of stainless steel, i.e. essentially iron. For the following calculations, we will assume that the chamber is only made of iron, with a density of 7.874 g/cm^3. The thickness of the chamber on the SR path towards the AXD is changing rapidly in the transverse direction as shown in Figure 4. We will assume that at the scale of the scintillator, i.e. 10 mm, it is constant and equal to 20 mm. The left part of the X-rays will also intercept the 0° branch exit flange. It is there 25 mm thick and is also made of iron.

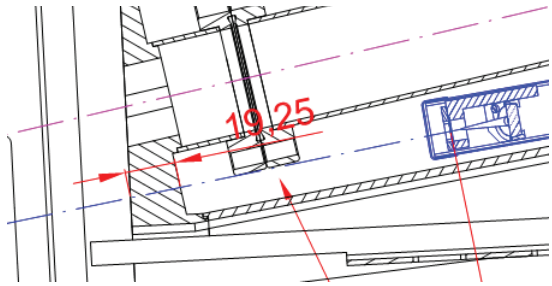

Figure 4: Dipole chamber exit. Scintillator in blue.

SIMULATION OF THE AXD

Analytical Calculations

The synchrotron radiation layer rms vertical size at scintillator can be calculated analytically according to the following formula:

$$\Sigma_z = \sqrt{\sigma_{ez}{}^2 + D^2(\sigma'_{\upsilon z}{}^2 + \sigma'_{ez}{}^2)} \qquad (1)$$

σ_{ez} and σ'_{ez} are respectively the electron beam vertical size and divergence (rms) and $\sigma'_{\upsilon z}$ the photon beam vertical divergence (rms). D is the distance between source point and scintillator. For a photon energy E_υ of 100 keV: Σ_z = 46.3 µm.

SRW Simulations

The analytical calculation assumes that the photon beam is mono energetic, which is far from being the case. SRW simulation enables to simulate the 3D radiation distribution emitted by the dipole which should provide a much more accurate estimate of the expected vertical size.

The electron beam is simulated using parameters of Table 1. The dipole field is simulated using its longitudinal profile with a plateau at 1.71 T. The 3D radiation distribution (E_υ, X, Z) is extracted at the scintillator location, i.e. at 1323 mm downstream the 2.53° exit of the dipole. The 3D distribution is then filtered in E_υ using the transmission profile of the crotch, of the vacuum chamber, and the absorption of the scintillator.

Integrating over E_υ, we obtain the 2D distribution of the visible light at the exit of the scintillator, as illustrated in Figure 6. The width of the field of view corresponds to the scintillator width. Three teeth should be visible on the scintillator. Their absolute position on the scintillator is not known, since we don't know the relative position between the crotch teeth and the 2.53° axis.

ISBN 978-3-95450-177-9

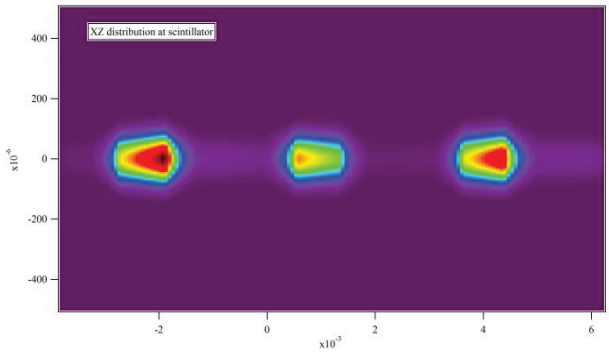

Figure 5: 2D distribution at the scintillator location. XZ grid: 151 x 151 over 10 x 1 mm. Initial photon distribution: 100 photons from 50 up to 200 keV. Fe thickness: 20 mm.

Integrating over XZ, we obtain the average spectrum of the X-rays transmitted to the scintillator, and the average spectrum of the light absorbed in the scintillator (see Figure 7). This gives an indication of the central wavelength of the X-rays that contributed to the visible pattern.

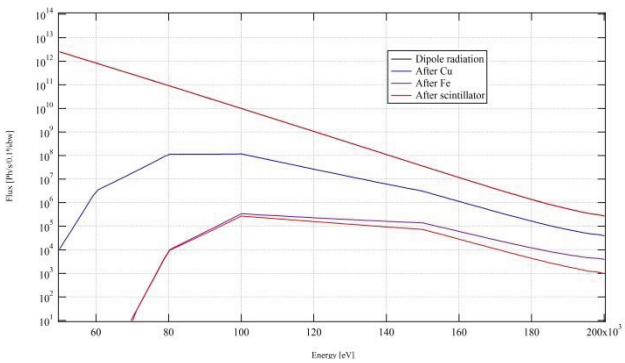

Figure 6: SR spectrum at various stages of the process. Integration over the 10 x 1 mm transverse window at the scintillator location. Fe thickness: 20 mm.

In the case of 45 mm iron thickness (case with the flange), the distribution is peaked at 130 keV (100 keV with 20 mm). It was difficult to predict how many teeth would be in the shade of the flange. But the teeth behind the flange should be significantly less intense than the others since the photon flux is more than one order of magnitude lower.

Expected Measurements

The crotch thickness changes the output spectrum of the radiation. At maximum thickness (22 mm approximately) the radiation reaching the scintillator will be of higher energy than at the minimum thickness (6.6 mm approximately). This means that the crotch thickness changes along the X axis the divergence of the photons reaching the scintillator and the scintillator response. To retrieve the electron beam size σ_{ez} from the layer size Σ_z, the vertical profile must be done on a narrow band for which we know the corresponding copper thickness.

For instance, the simulation in the case of 45 mm iron thickness gives:

- Σ_z = 41.29 µm at minimum crotch thickness (6.6 mm)
- Σ_z = 40.16 µm at maximum crotch thickness (21.6 mm)

The analytical calculation of Σ_z gives:

- Σ_z = 40.63 µm at 150~keV
- Σ_z = 41.6 µm at 140~keV
- Σ_z = 47.2 µm at 100~keV

Those results are in good agreement with the estimate from the average spectra of a median photon energy of 150 keV.

The crotch thickness changes sharply from "very thick" to "very thin". But it also changes within the "very thick/thin" regions. Inside a tooth ("very thin" region), the variation of copper thickness is typically of 2 mm per mm along X. According to the simulation, with an iron thickness of both 20 and 45 mm, the resulting Σ_z variation is about 1%, i.e. negligible. Consequently, to measure the electron beam size from Σ_z, we can use the vertical profile obtained from the projection in Z over one tooth. Of course, if the signal is enough, one should favour narrower integration in X.

DETECTOR DESIGN

The scintillator is a CdW04 crystal provided by Saint-Gobain. Its dimensions are 10 x 10 x 0.5 mm.

The camera is a CCD from Basler, model Scout Series scA640-70gm, 494 x 659 pixels of 7.4 microns.

The specifications on the optics are the following:

- To locate the teeth, we first need a field of view of 10 mm, i.e. a magnification of 0.4.
- To measure the vertical layer size, we will need a resolution of Σ_z / 10, i.e. a magnification up to 1.8.

For high quality imaging, we chose to use an objective: a MVL6X12Z (6.5X) from Navitar. The magnification is variable from 0.26 to 1.69, which fits the requirements.

The mechanics of the detector is illustrated in Figure 8:

- The scintillator is hold between an aluminium piece and a peek piece.
- A 1/2 inch broadband metallic mirror is hold in an aluminium support to deflect the light upward.
- The camera is fixed on a motorized translation stage to enable remote controlled focussing.
- A manual stage enables to adjust the camera position in X within a +/- 3 mm range to select the zoomed area.
- The whole detector is hold by a massive post.

ISBN 978-3-95450-177-9

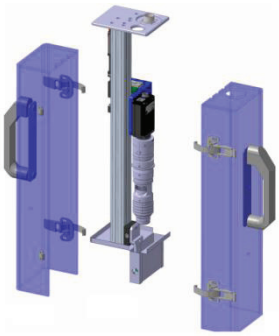

Figure 7: 3D view of the detector and its mechanics.

Shielding

The camera and the stage will be installed in a high radiation environment, requiring a heavy shielding. The whole detector is enclosed into a 5 mm thick lead box made of two pieces (see Figure 8).

AXD FIRST MEASUREMENTS

Figure 8: AXD on C12-D2 (August 2016).

The AXD was installed in August 2016 (see Figure 8). And the first AXD observation was performed in September 2016. The magnification factor was set to 0.35 in order to visualize the whole scintillator area, and we could observe immediately at the machine restart one tooth on the scintillator. On the 5th of September, we increased the magnification coefficient up to 0.78 and therefore zoomed on the observed tooth (see Figure 9). We measured Σ_z = 50 µm-rms, i.e. slightly above the expected value probably because of the system resolution. Unfortunately we could not increase further the magnification due to mechanical constraints. We plan to modify the support by the end of October in order to reach the expected final magnification of 1.69.

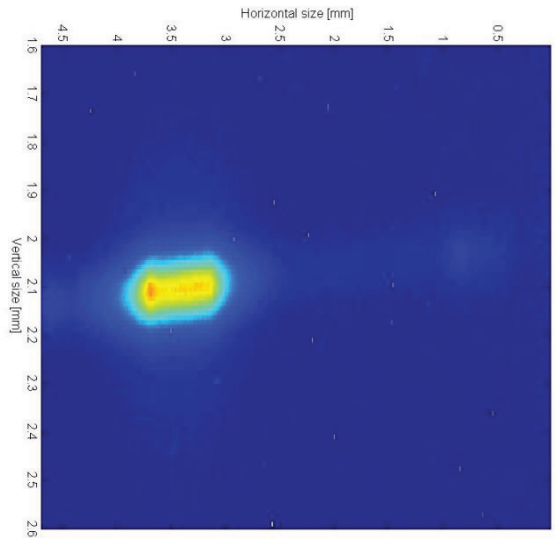

(a) AXD image (part of the full field).

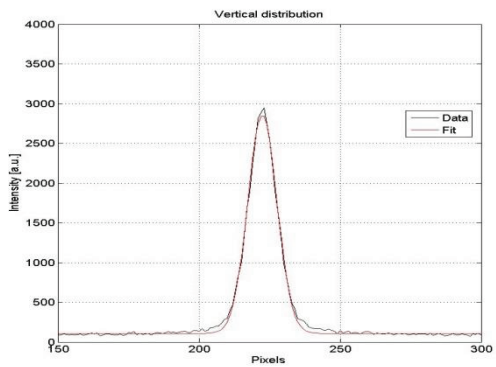

(b) Vertical profile.

Figure 9: AXD record of the 05/09/2016.

CONCLUSION

An AXD has been installed on C12-D2 at SOLEIL. It aims at the vertical position and size measurements of the electron beam inside one of SOLEIL's dipole ring. According to simulations, the AXD should be an accurate diagnostic once taken into account the peculiar geometry of the SOLEIL's absorber. The first measurements performed in September 2016 are very encouraging.

REFERENCES

[1] K. Scheidt, "Detection of hard X-rays in air for precise monitoring of the vertical position and emittance in the ESRF dipoles", Proc. of DIPAC'05, Lyon, France, May 2005, pp. 238-2.

ISBN 978-3-95450-177-9

NOVEL GRATING DESIGNS FOR A SINGLE-SHOT SMITH-PURCELL BUNCH PROFILE MONITOR

A. J. Lancaster*, G. Doucas, H. Harrison, I. V. Konoplev,
John Adams Institute, Department of Physics, University of Oxford, Oxford, OX1 3RH, UK

Abstract

Smith-Purcell radiation has been successfully used to perform longitudinal profile measurements of electron bunches with sub-ps lengths [1]. These measurements require radiation to be generated from a series of gratings to cover a sufficient frequency range for accurate profile reconstruction. In past systems the gratings were used sequentially and so several bunches were required to generate a single profile, but modern accelerators would benefit from such measurements being performed on a bunch by bunch basis. To do this the radiation from all three gratings would need to be measured simultaneously, increasing the mechanical complexity of the device as each grating would need to be positioned individually and at a different azimuthal angle around the electron beam. Investigations into gratings designed to displace the radiation azimuthally will be presented. Such gratings could provide an alternative to the rotated-grating approach, and would simplify the design of the single-shot monitor by reducing the number of motors required as all of the gratings could be positioned using a single mount.

INTRODUCTION

Modern and future particle accelerators provide challenges for longitudinal beam profile monitors by producing short bunches with highly variable profiles. A successful monitor will have to resolve sub-ps bunches in a non-destructive manner on a single-shot (bunch-by-bunch) basis. Possible techniques which could enable such a monitor include electro-optic measurements [2] and the use of coherent radiation spectroscopy [3] [4]. This paper presents a preliminary conceptual design for a single bunch profile monitor based on coherent Smith-Purcell radiation (cSPR), with an emphasis on changes to the design of the metallic grating used to generate the radiation.

SMITH-PURCELL RADIATION

Smith-Purcell radiation arises when a charged particle bunch travels near to a periodic metallic structure. The electric field of the particles induces a surface charge on the surface of the structure which then follows the particles, giving rise to a surface current. Discontinuities in the structure result in changes to the current and so to the emission of radiation. Each period will emit radiation in the same way, giving rise to a far field dispersion relation which links the wavelength of the radiation to angle of emission.

* andrew.lancaster@physics.ox.ac.uk

To use cSPR as a beam diagnostic it is necessary to predict the intensity of the radiation which will be generated, which requires several functions to be understood. The first step is to calculate the radiation produced by a single particle travelling above a single period of the grating. The effect of the grating periodicity can then be incorporated to give the expected intensity distribution from a single particle travelling above the full Smith-Purcell grating. It is at this stage that the dispersion relation becomes apparent.

The particle bunch must then be modelled. Assuming that the transverse bunch profile remains constant throughout we can describe the charge distribution as $T(x, y)Z(z, t)$, and the intensity of the cSPR is then found to be proportional to the Fourier transform of the longitudinal bunch profile. This means that by measuring the intensity of the cSPR along with other relevant beam parameters it is possible to retrieve the frequency components of the particle bunch and determine the longitudinal profile [5].

Coherent Smith-Purcell radiation has already been used to perform longitudinal bunch profile measurements at FACET, SLAC [1]. The E203 experiment sequentially measured three gratings with different periods, with three additional blank measurements to perform background subtraction. Each grating provided 11 frequency measurements, giving 33 measurement points in total. These measurements had to be taken over an extended period of time as the gratings were mounted on a carousel. As each accelerator will have different measurement requirements 33 frequency measurements has been taken as the target for the design of the single-shot device. The key constraints on the monitor are that background subtraction needs to be performed without the use of blanks and that the device must be compact.

The first constraint can be addressed by taking advantage of the high degree of polarization of Smith-Purcell radiation, which is predicted by theory and has been confirmed experimentally [6]. Previous measurements have shown the background signal to be broadly unpolarized [1]. This means that cSPR will be split asymmetrically by a polarizer but the background radiation will be evenly split. By using a pair of detectors it would therefore be possible to subtract the background radiation from the cSPR signal on a bunch-by-bunch basis. Such a detector layout is shown in Fig. 1.

The second constraint can be met by rotating the three gratings azimuthally around the particle beam. By positioning the three gratings at ϕ=0° and ±60° there is enough space for the three sets of detectors to be positioned in a compact region along the beam pipe. The layout, shown in Fig. 2, is approximately 160 mm longer than the E203

ISBN 978-3-95450-177-9

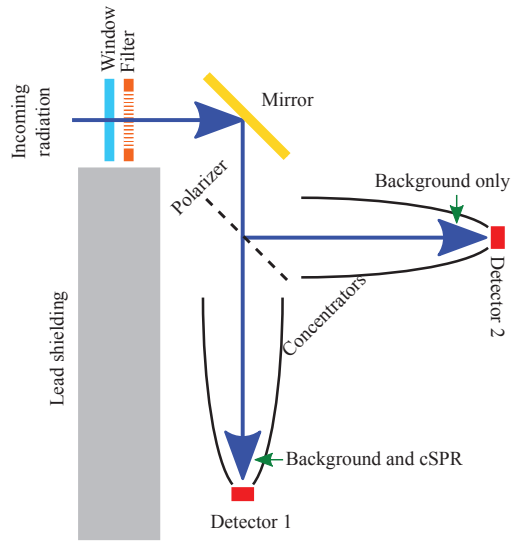

Figure 1: Two detector system to enable background subtraction on a shot-by-shot basis. By subtracting the signal from detector 2 from the signal from detector 1 it is possible to extract the SPR signal without backgrounds (assuming that it is perfectly polarized).

system which has been deemed to be reasonable until constraints from specific accelerators are determined.

Other components (such as vacuum windows, band-pass filters and mirrors) are expected to be similar to the E203 system, with the notable exception of the detectors. The E203 experiment used pyroelectric detectors because their broad frequency response meant that they could be used with all three gratings, but in a single-shot device this is no longer necessary. This enables more sensitive devices with narrow frequency ranges, such as Schottky barrier diodes, to be used. The specific choice of detector architecture would be linked to the requirements of each application.

MODIFYING THE GRATING DESIGN

A key factor in the performance of a cSPR longitudinal profile monitor is the number of radiation frequencies which can be sampled, although the choice of frequencies is also important. To sample a single frequency requires two detectors in the proposed system, meaning that the cost of detectors will be a major factor in the design of a final device. The cost of the rest of the system should be minimized to either compensate for the cost of the detectors or to enable more to be incorporated into the device.

The obvious approach to simplifying the system would be to reduce the number of motors and vacuum feedthroughs required to position the three gratings. It is not possible to mount three gratings in the orientations shown in Fig. 2 on a single mount without modifying their design, because variations in the beam position would asymmetrically change the beam-grating separation, leaving some gratings with optimal separation and others either too close or too far from the beam.

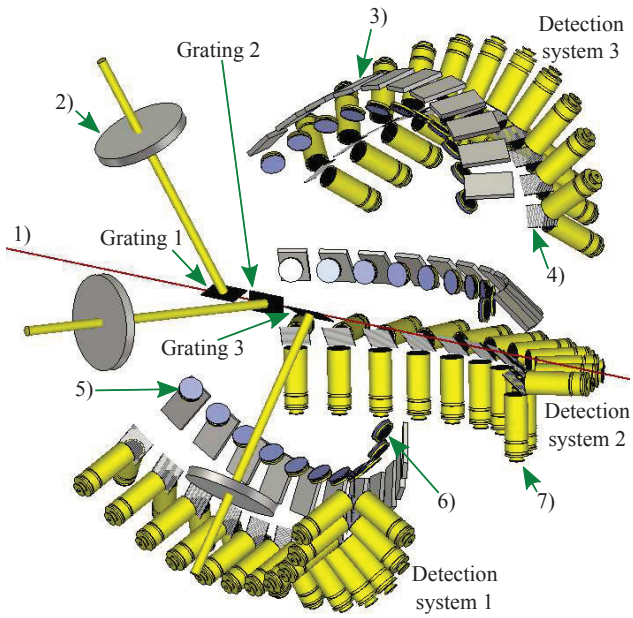

Figure 2: The proposed layout of a single-shot longitudinal profile monitor. The components are: 1) beam path, 2) vacuum feedthroughs, 3) mirrors, 4) polarizers, 5) vacuum windows, 6) filters and 7) concentrators and detectors. Grating 1 illuminates detection system 1. Components are to scale. Schematic drawn using CST Microwave Studio [7].

A possible solution to this problem is to angle the rulings of the gratings with respect to the direction of travel of the beam. This has been studied by Sergeeva et. al. [8] who investigated Smith-Purcell radiation generated by an infinitely wide gratings with the electron beam travelling at non-normal incidence to the facets, which causes the Smith-Purcell radiation to be emitted at non-zero azimuthal angles and so provides a mechanism to distribute the radiation while ensuring the gratings have a consistent beam-grating separation.

To take advantage of this effect it is necessary to make radiation intensity predictions for a grating with a finite width. A program based on the NAG libraries [9] is in development to achieve this using the surface current model. An electron propagates in the $\hat{\mathbf{z}}$ direction at a fixed height above the grating. The grating is modelled as a flat sheet of perfect conductor with gaps consisting of vacuum. The user defines the shape of a single facet and the number of facets which make up the grating. At the current stage we assume that the electron is ultra-relativistic and so the electric field (and so the surface current) is only calculated directly below the electron. This assumption means that the model provides qualitative distributions but does not currently provide quantitative results.

Two example grating facets and their associated intensity distributions (as calculated by the program) are shown in Fig. 3. Grating A is a standard (normal incidence) 0.5 mm

ISBN 978-3-95450-177-9

period grating, and grating B has the same physical period but its rulings are rotated by 30° with respect to the direction of particle propagation, which increases the facet length by a factor of $1/(\cos\delta)$ where δ is the angle of rotation. The gratings have 120 facets, meaning that the plots show the intensity associated with the wavelength given by the Smith-Purcell dispersion relation at each angle.

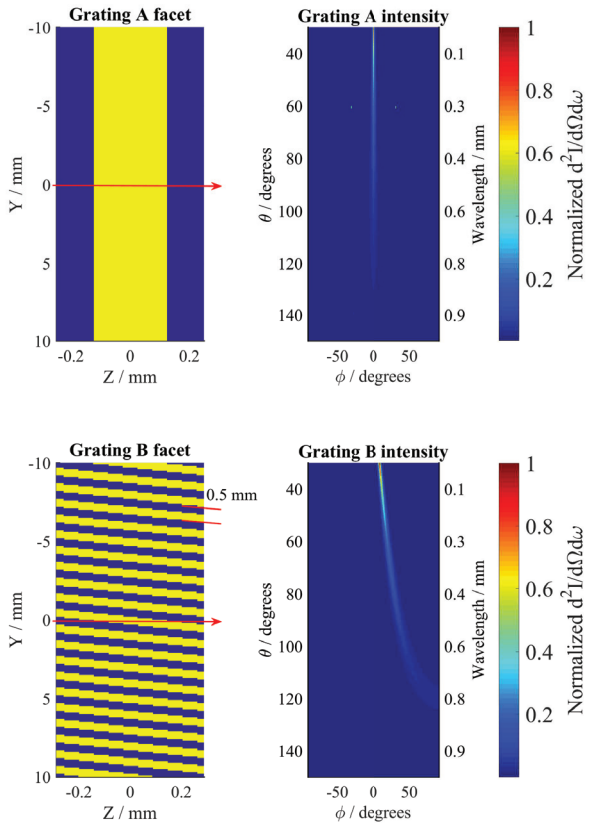

Figure 3: Two example grating facets and their associated intensity distributions. Yellow indicates conductor and blue indicates vacuum. Grating A is a "standard" grating, whereas grating B has been rotated with respect to the direction of beam propagation ($\hat{\mathbf{z}}$), shifting the ϕ position of the peak of the intensity distribution. Note that the Y-axis covers 20 mm but the Z-axis only covers around 0.5 mm which exaggerates the effect of the rotation. The beam propagation direction is shown by the red arrows.

It is clear that the radiation from grating A is emitted along ϕ=0°, whereas the radiation distribution for grating B is displaced from the ϕ axis, with a minimum value of ϕ=9° at θ=30°. The position of the maximum of the intensity distribution can be predicted by considering the system as a pair of coupled diffraction gratings, one in the direction of beam propagation and a second perpendicular to it. The first gives the SPR dispersion relation, where λ is the emitted wavelength, l is the grating period, n is the radiation order, β is the particle speed as a fraction of the speed of light and θ is the emission angle where 0° is the beam direction and 90° is perpendicular to the grating surface, with the addition of the $\cos\delta$ term to model the stretch of the period as the grating is rotated (Eq. 1). The perpendicular periodicity of each facet can be viewed as a standard diffraction grating, meaning that the radiation peak can be predicted using the relation given in Eq. 2 for order m. By equating the wavelengths it is possible to predict the ϕ-position of the peak of the intensity distribution, as given in Eq. 3.

$$\lambda = \frac{l}{n\cos\delta}\left(\frac{1}{\beta} - \cos(\theta)\right) \quad (1)$$

$$\lambda = \frac{l}{m\sin\delta}\sin\theta\sin\phi \quad (2)$$

$$\sin\phi = \frac{m\tan\delta}{n\sin\theta}\left(\frac{1}{\beta} - \cos(\theta)\right) \quad (3)$$

The ϕ values predicted by Eq. 3 (see Fig. 4) agree with the results of the calculation program to within the resolution of the simulation. By using three gratings with different values of δ it should be possible to spatially distribute the radiation without needing to change the ϕ positions of the gratings and therefore correct changes in beam-grating separation for all three gratings simultaneously.

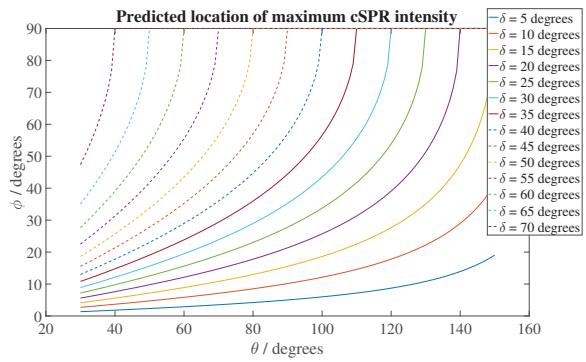

Figure 4: Predicted locations of peak cSPR intensity according to Eq. 3 for a particle beam with γ=39000 and n = m = 1.

A further improvement would be to combine the three gratings into one, as shown in Fig. 5 which combines a grating with a facet length of 1.5 mm and δ = 0° with a grating with a facet length of 0.75 mm and δ=20° and a third grating with 0.5 mm facet length and δ=−20°. The grating was 60 mm long, meaning that there were 40 0° facets, 80 20° facets and 120 −20° facets. The predicted radiation intensity distributions for each facet length in Fig. 5 show that the radiation is either spatially or chromatically separated, with the highest intensities distributed either at ϕ=0° or at +ve or -ve ϕ angles. The spatial distributions may cause difficulties when manufacturing the vacuum chamber because of the variations in ϕ-angle with θ, so designs should be sought which alleviate this problem.

CONCLUSION

A preliminary concept for a single-shot cSPR longitudinal bunch profile monitor has been developed. Novel grat-

ISBN 978-3-95450-177-9

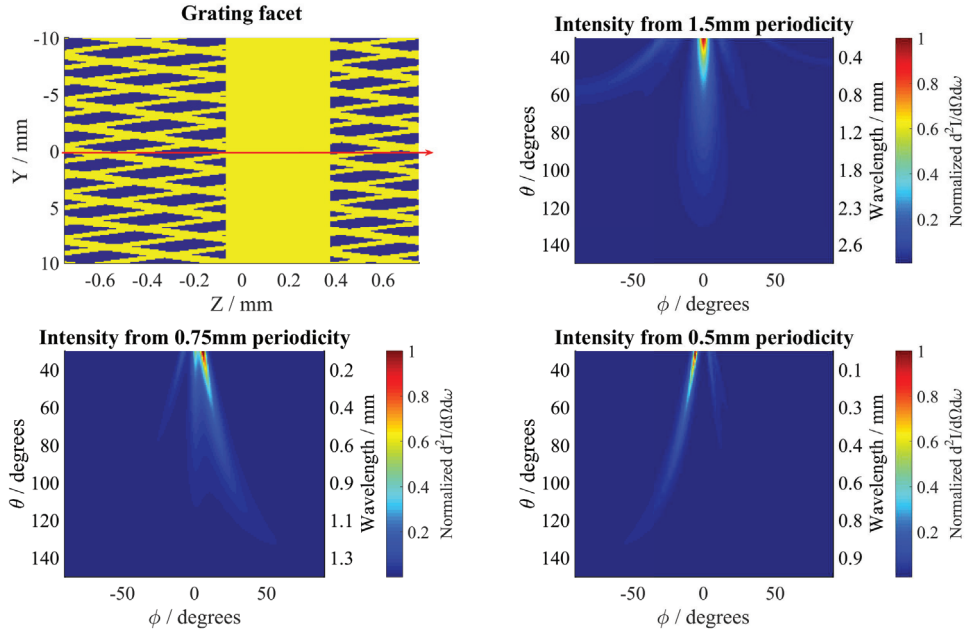

Figure 5: A facet which combines three gratings of different periodicities into a single grating. Yellow indicates conductor, blue indicates vacuum and the beam propagation direction is shown by the red arrow. The calculated intensity distributions associated with each periodicity predict that the radiation should be spatially and spectrally separated.

ings could be selected to spatially disperse the radiation at a reduced cost, enabling higher performance for given financial constraints. Rotated gratings are currently under study, although the intention is to use more complex designs to allow f or easier manufacturing of the vacuum chamber. The grating simulations require further development to move beyond qualitative distributions. The radiation intensity from any novel grating design would require extensive experimental testing before it could be used in a bunch profile monitor.

ACKNOWLEDGEMENTS

This work was supported by the UK Science and Technology Facilities Council (STFC UK) through grant ST/M003590/1 and studentship ST/M50371X/1, the Leverhulme Trust through International Network Grant IN–2015–012 and by the John Adams Institute of Accelerator Science (University of Oxford). We also thank P. Huggard (STFC, RAL) and the RAL Space Millimetre-Wave Technology Group for useful discussions on THz detectors.

REFERENCES

[1] H. L. Andrews *et al.*, "Reconstruction of the time profile of 20.35 GeV, subpicosecond long electron bunches by means of coherent Smith-Purcell radiation", *Phys. Rev. ST Accel. Beams*, vol. 17, no. 5, p. 052802, May 2014.

[2] G. Berden *et al.*, "Time resolved single-shot measurements of transition radiation at the THz beamline of flash using electro-optic spectral decoding", in *Proc. EPAC'06*, Edinburgh, Scotland, May 2006, paper TUPCH027, pp. 1058–1060.

[3] S. Wesch *et al.*, "A multi-channel THz and infrared spectrometer for femtosecond electron bunch diagnostics by single-shot spectroscopy of coherent radiation", *Nucl. Instrum. Meth. Phys. Res. A*, vol. 665, p. 40–47, Feb. 2011.

[4] A. D. Debus *et al.*, "Electron Bunch Length Measurements from Laser-Accelerated Electrons Using Single-Shot THz Time-Domain Interferometry", *Phy. Rev. Lett.*, vol. 104, no. 8, p. 084802, Feb. 2010.

[5] J. H. Brownell *et al.*, "Spontaneous Smith-Purcell radiation described through induced surface currents", *Phys. Rev. E*, vol. 57, no. 1, p. 1075–1080, Jan. 1998.

[6] H. Harrison *et al.*, "Novel approach to the elimination of background radiation in a single-shot longitudinal beam profile monitor", presented at IBIC'16, Barcelona, Spain, Sep. 2016, paper TUPG5, this conference.

[7] *CST Studio Suite 2015*, CST Computer Simulation Technology AG., `www.cst.com`

[8] D. Yu. Sergeeva *et al.*, "Conical diffraction effect in optical and x-ray Smith-Purcell radiation", *Phys. Rev. ST Accel. Beams*, vol. 18, no. 5, p. 052801, May 2015.

[9] *The NAG Library*, The Numerical Algorithms Group (NAG), Oxford, United Kingdom, `www.nag.com`

ISBN 978-3-95450-177-9

RECENT BEAM SIZE MEASUREMENT RESULT USING SYNCHROTRON RADIATION INTEFEROMETER IN TPS

M.L. Chen, H.C. Ho, K.H. Hsu, D.G. Huang, C.K. Kuan, W.Y. Lai, C.J. Lin, S.Y. Perng, C.W. Tsai, T.C. Tseng, H.S. Wang
NSRRC, Hsinchu, Taiwan

Abstract

Taiwan Photon Source (TPS) was under commissioning operation in 2015. An optical diagnostic beam line was constructed in TPS 40th beam port for the diagnostics of the electron beam properties. A synchrotron radiation interferometer, one instrument of this diagnostic beam line, operates for monitoring the beam size. In the beginning, the interferogram of the vertical beam is usually distorted. We found the stray light affected the vertical interferogram obviously while the beam current was raised. This paper describes the problems we met and how to eliminate the stray light for better beam size estimation. In the normal course of events, TPS is driven in 300mA and the horizontal beam size is 56um and the vertical beam size is 32um. The beam current of TPS is maximumly driven to 518mA in June, 2016. This paper also presents the trend of beam size during current running up.

INTRODUCTION

Taiwan Photon Source (TPS) was commissioned in 2015. The electron beam has stored in the storage ring of current 518 mA and energy 3 GeV in June 2016. The beam is operated at 300 mA for normal operation and the current is also rising up to 518mA for machine study.

To measure the transverse beam size, two monitors are adopted in TPS 40th beam port. One is an X-ray pinhole camera and the other is a synchrotron radiation interferometer (SRI). [1] The X-ray pinehole camera is installed in the vacuumed chamber inside the shielding wall. And the beam line is also extended to the experiment area by using several folding mirrors to transport light to pass through the shielding wall. The SRI is installed on an optical table in a hutch lab outside of shielding wall.

In this paper we present the resent beam size measurement result and the relation of measurement result between two beam size monitors. We also present the problems we met and our countermeasures.

PRINCIPAL OF SYNCHROTRON RADIATION INTERFEROMETER

The synchrotron radiation interferometer, presented by Dr. T. Mitsuhasi in KEK, is widely applied to monitor beam size of synchrotron light sources [2,3,4].The basic principle of a SR interferometer is to measure the profile of a small beam through the spatial coherency of light, and is known as the Van Citter-Zernike theorem. The distribution of intensity of the object is given by the Fourier transform of the complex degree of first-order spatial coherence. The intensity of interferogram pattern, I, is shown as the function of position,y_1,

$$\mathrm{I}(\mathrm{y1}) = I_0\left[sinc(\tfrac{2\pi a}{\lambda R}y_1)\right]^2\left[1+|\gamma(v)|\cos\tfrac{2\pi D}{\lambda R}\,y_1+\varphi\right] \quad (1)$$

Where λ denotes the wavelength, R denotes the distance from the light source to the double slit, and D denotes the double slit separation, and a denotes half-height of slits. The visibility γ is related to the complex degree of coherence.

$$\gamma = \left(\frac{2\sqrt{I_1.I_2}}{I_1+I_2}\right)\left(\frac{I_{max}-I_{min}}{I_{max}+I_{min}}\right) \quad (2)$$

The beam size is given by

$$\sigma_{beam} = \frac{\lambda \mathrm{R}}{\pi \mathrm{D}}\sqrt{\frac{1}{2}\ln(\frac{1}{\gamma})} \quad (3)$$

According to the above equation (3), the beam size is observed by the visibility of the interferogram.

MONITOR SYSTEM SETUP

The SRI beam-size monitor is installed at TPS 40th beam port. The beam line structure is shown as fig1. The radiation produced at the dipole magnet propagates 19.2 m to pass through the shielding wall.

The main error of the visible SR interferometer arises from the distortion of the mirror by the radiation power [5]. So the first mirror of the beam line is a cooled beryllium mirror, which was adopted to prevent distortion. After beryllium mirror, the light passes the extraction window and an aluminium reflection mirror, and then it transports through the shielding wall. In the outside of the shielding wall, two folding aluminium mirrors are used to connect the synchrotron light to the optical table in hutch. Synchrotron light is separated to three channels by two beam splitter. 50% light is delicate for SR interferometer and the other 50% light is for streak camera monitoring.

The SRI beam size monitoring system is constructed by a diffraction-limited high-quality lens for focusing; the focusing length of this lens is 2 m; the wavefront error is less than $\frac{1}{10}\lambda$. A polarizer and a band-pass filter are used to obtain quasi-monochromatic light. The centre wavelength of the bandpass filter is 500 nm with 10 nm bandwidth. An eyepiece is applied to magnify the

ISBN 978-3-95450-177-9

interferogram on CCD; Two CCDs are applied to observe the horizontal and vertical interferograms respectively. [6]

The distances from the source point to the horizontal and vertical double slits are 22 m and 22.5m respectively.

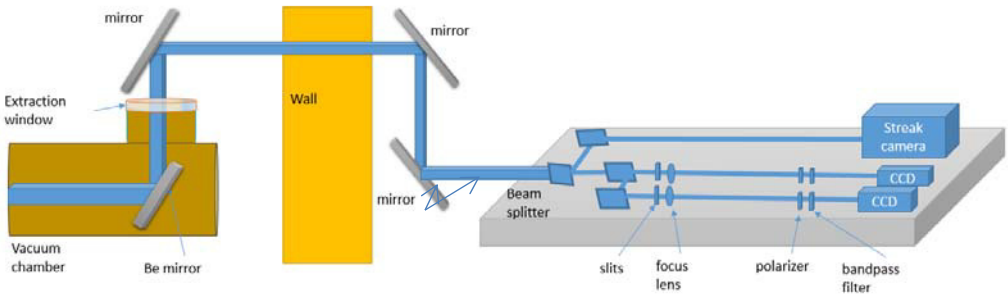

Figure 1: The optical architecture of monitors on optical table.

TESTS AND RESULTS

Stray light effect of vertical interferogram

The photons of the SR produce an interferogram after pass through a double slit, a focusing system, a band-pass filter, and a polarizer. By equation (3), the beam size of SRI is estimated from visibility of intereferogram.

If the interferogram of beam is distorted, the beam size cannot be evaluated correctly. During the experiment, the interferogram pattern of the vertical direction is very sensitive to the position of the double slit; somewhere it becomes disordered, and the visibility fitting comes with huge error.

For high resolution, the half of the slit height of the double slit (a) set as 0.5mm and slit separation (D) set as 60mm at first. Since the slit separation is large, the spatial frequency of fringe of the interferogram is quite high, and the fringes are destroyed by background noise seriously, shown as fig2.

In order to find out the background noise, we change the vertical double slits to the horizontal channel. No matter horizontal slit at which channel, the pattern of horizontal interferogram is always intact. But the pattern of vertical interferogram is still fragmented. The stray light in background doesn't come from the optics.

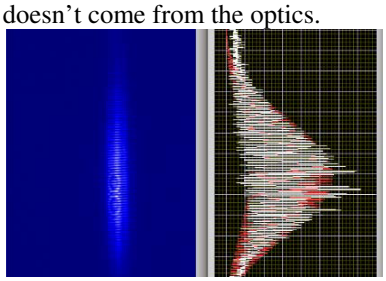

Figure 2: the vertical interferogram fringes and envelope of fringe are destroyed by stray light.

The ray trace is done for checking the optical system. The result is shown as fig3. Firstly we found the color band appears in the up and down edges of the synchrotron entrance light. The separated synchrotron lights passing through the slits of the double slit are also chromatic. Closing to the focus plane, an un-expected light spot point appears under the double slit light spot. The coming synchrotorn light is not as parallel as designed light source.

The wild angle light is produced during light propagation and has the interference with the edge of vacuum pipe. The focus point of the edged light with wide angle is not same as the main point.

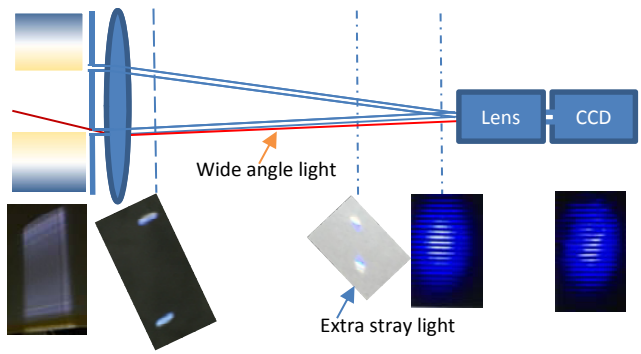

Figure3: The light distribution of ray tracing in different positions.

Several countermeasures are induced for stray light elimination. We change the vertical double slit to prevent stray light passing firstly. In order to find the most suitable coefficient of double slit, the vertical slit separation (*D*) and half opening (*a*) were tested with varied size. We enlarge the half opening (*a*) of the vertical double slit to enhance the intensity of slit entrance light and the stray light noise level is declined. Not only increasing the SN ratio, the envelope width of the vertical interferogram is minimized when the half-height of slit opening is enlarged, shown as fig4. The magnification of eyepiece lens is increased to lower the spatial frequency of interference fringe on CCD. Eventually the half opening (a) is chosen as 1.5 mm.

Then for eliminating the wide angle stray light, the vertical slit separations (*D*) can't open too wide. The color band must be blocked for preventing entering the SRI monitor. When the slit separation was enlarged to 70 mm, the coherence of light source is poor and the interferogram is destroyed. By checking the entrance synchrotron light

ISBN 978-3-95450-177-9

which is reflected by an aluminium mirror, the width of white light without chromatic light is smaller than 50mm. The most suitable slit separation is less than 50mm. By reference to beam size error function, the recommend visibility is in the range of 0.2 to 0.8. [3] At 30um beam size level, the best separation value (D) is 40mm for system resolution compensation.

Finally, several stops were installed to decrease the stray light in the light path. The system stray light was totally blocked.

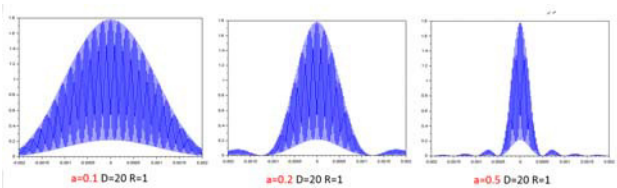

Figure 4: The interferogram variation by enlarging the half- height of the slit (a) of double slit.

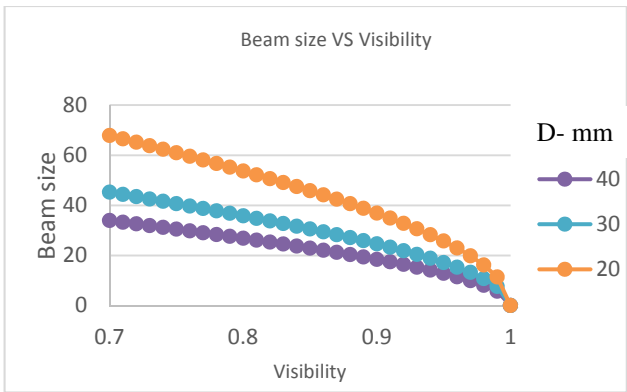

Figure 5: Beam size and visibility correlation for various double slit separation (D).

Beam size variation for high current operation

For a horizontal beam size monitor, the slit separation (*D*) is 20 mm and the half opening (*a*) is 0.5 mm. For a vertical beam size, the slit separation (*D*) is 50 mm and the half opening (*a*) is 1.5 mm. The horizontal beam size is 57.5μm and the vertical beam size is 35.8μm during 300mA operation.

The beam current of TPS is maximumly driven to 518mA in June, 2016. The trend of horizontal and vertical beam size during current run-up is shown as fig7 and fig 8. The measurement result of SRI has good correlation to X-ray pinehole camera.

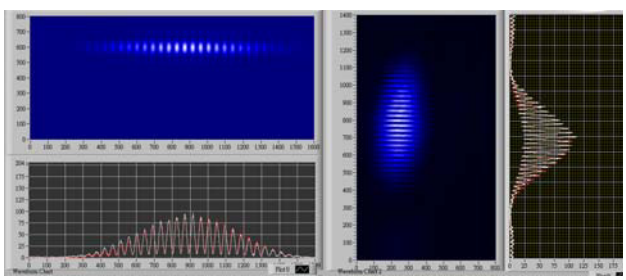

Figure 6: The horizontal and vertical interferogram image at normal operation 300mA.

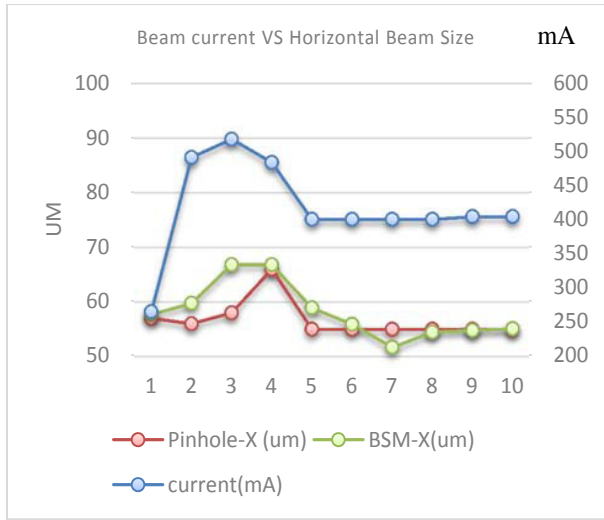

Figure 7: The horizontal beam size variation during various operation currents

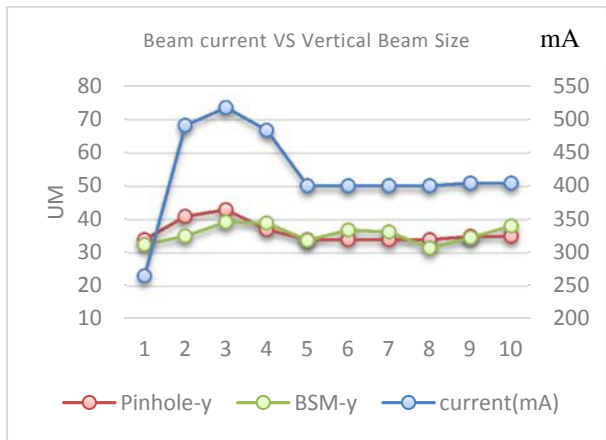

Figure 8: The vertical beam size variation during various operations current.

CONCLUSION

A SRI beam size monitor was installed and operated in NSRRC TPS from Sep, 2015. To minimize the measurement error of the vertical beam size, the stray light is eliminated by minimization the separation of the slit and enlarging the half-height of slit.

Since TPS starts operation, the SRI keeps monitoring the horizontal and the vertical beam sizes, the measurement result of SRI has good correlation to another instrument, pinehole camera. For improving the resolution, the intensity imbalance of the light path of the SR interferometer will be introduced to reduce the effect of the measurement error in the future.

REFERENCES

[1] C.K. Kuan et al, “Beam size monitor for TPS”, Proceedings of IBIC2012(MOPB88) ,pp.1-3, Tsukuba, Japan.

[2] T. Mitsuhashi, “Recent trends in beam size measurements using the spatial coherence of visible synchrotron radiation”, IPAC2015(THYC2) , pp. 3662-3667 , Richmond, VA, USA.

ISBN 978-3-95450-177-9

[3] T.Naito et al, “Very small beam-size measurement by a reflective synchrotron radiation interferometer”, Physical Review Special Topics- Accelerator and Beams, 9, 122802 (2006).
[4] T.Naito et al, “Improvement of the operation of a SR interferometer at KEK-ATF damping ring”, Proceedings of IPAC10(MOPE009) ,pp.972-974, Kyoto, Japan.
[5] T.C. Tseng et al, “The SRI beam-size monitor developed at NSRRC”, pp.3465-3467, Proceedings of 2005 Particle Accelerator Conference, Knoxville, Tennessee USA.
[6] M.L. Chen et al, “Measurement of Beam Size with a SR interferometer in TPS”, IPAC2016(MOPMR032) , pp. 313-315, Busan Korea

ISBN 978-3-95450-177-9

FRASCATI BEAM-TEST FACILITY (BTF) HIGH RESOLUTION BEAM SPOT DIAGNOSTICS

P. Valente, INFN – Sezione di Roma, P.le Aldo Moro 2, I-00185 Rome, Italy.
B. Buonomo, C. Di Giulio, L. G. Foggetta, INFN – Laboratori Nazionali di Frascati, Via Enrico Fermi 40, I-00044 Frascati (Rome), Italy.

Abstract

The DAFNE Beam Test Facility (BTF) is operational in Frascati since 2003, hosting tens of experimental groups for an average of more than 200 beam-days each year. In the last years the beam diagnostics tools have been completely renewed and the services for the users have been largely improved.

We describe here the new transverse beam diagnostics based on GEM compact time projection chambers (TPC) and MEDIPIX Silicon pixel detectors, the upgraded data acquisition and the data caching system based on MEMCACHED, allowing a straight-forward integration of existing and new sub-systems in the renewed data logging. Results on the optimization of the transverse beam spot and divergence are reported, as well as the real-time diagnostics and feed-back user experience.

INTRODUCTION

The beam parameters of the Beam Test Facility, operational at the Frascati laboratories since 2004 [1], cover a wide range in terms of intensity (from 10^{10} particles/pulse down to the single particle regime) and energy (from 30 to 750 MeV), while the transverse beam spot can be adjusted with beam-line optics and collimators [2].

This requires a high-resolution, efficient, robust, reliable, fast, easily manageable transverse diagnostics detector, with online readout capability in order to be effective in the beam setup phases. As additional requirement, the thickness of the detector should be kept at an acceptable level in order not to spoil the beam spot or alternatively the detector should be easily removable from the beam-line.

TRANSVERSE DIAGNOSTICS

The transverse diagnostics of the BTF beam is an essential tool for the users, especially for detector characterization and calibration purposes.

We have developed both a very light diagnostics, based on micro-pattern gas detectors, namely a compact time-projection chamber (TPC) based on a triple Gas Electron Multiplier (GEM), and a thicker, but higher resolution system based on Silicon pixel detectors with integrated readout.

The two different systems have different limitations and advantages, so that we can choose the best solution depending on the beam parameter required by the users.

GEM TPC

In the framework of the AIDA EU project a triple-GEM TPC has been developed, with the idea of having a very compact and light device, capable of reconstructing in 3D the particle tracks, even though with different resolutions in the three coordinates: if the beam passes in the drift space between the cathode and the first GEM foil, one of the two transverse coordinates will correspond to the drift direction, so that the time of arrival measurement will allow reaching a resolution of the order of 100 μm (limited by the longitudinal diffusion in the drift gap). In our case we have chosen a 4 cm drift length and a standard Ar-CO_2-CF_4 mixture. The other two coordinates are measured by the 128 pads, 3×6 mm^2 over an active area of 50×50 mm^2, smaller with respect to the GEM foils, cathode and anode planes, with standard dimensions 100×100 mm^2, in order to avoid the effect of electric field lines distorsion at the edges, even though we have introduced a thin kapton foil with Copper surface all around the drift space as Faraday-cage for a better shaping of he field.

A FPGA allows to easily readout the 128 pad times and quickly transfer the data via Ethernet interface. The online display of the GEM TPC acquired beam profiles is shown in Fig. 1.

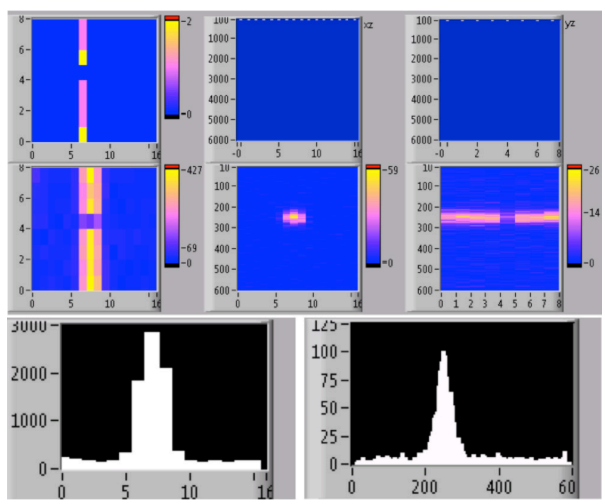

Figure 1: 477 MeV electron beam imaged by the GEM TPC; online display of the six planes view (top) and the two transverse projections (bottom).

ISBN 978-3-95450-177-9

FitPIX Silicon Pixel Detectors

In order to achieve a better resolution in both the transverse coordinates, we have implemented MEDIPIX-like Silicon pixel detector with WIDEPIX FitPIX® Kit electronic.

The FitPIX is a 300 μm thick Silicon detector with 256×256, 55 μm pitch pixels, for an active area of approximately 14×14 mm^2. The readout is performed with USB interface; we have used the standard PIXETPRO software but we have also developed a suite of custom software packages, in order to reach the maximum readout speed of about 80 frames/s, so that we can real-time read and reconstruct beam profiles at the full 50 Hz rate of the BTF beam.

Moreover, in order to have a completely arbitrary access to live data at the maximum frame-rate, we have implemented a new software architecture with a typical producer-consumer layout, implementing data caching on MEMCACHED server, to allow more than one different consumers at the same time. A more detailed description of the hardware and software of our custom implementation is given in [3].

An example of real-time acquisition and display (using a custom LabVIEW interface) of FitPIX detectors, retrieving data at the full 49 Hz rate, is shown in Fig. 2 for a typical BTF beam (intermediate intensity, 450 MeV electrons, approximately 1% momentum spread, about σ_y=0.5 mm spot, almost flat horizontal distribution) is shown in Fig. 2.

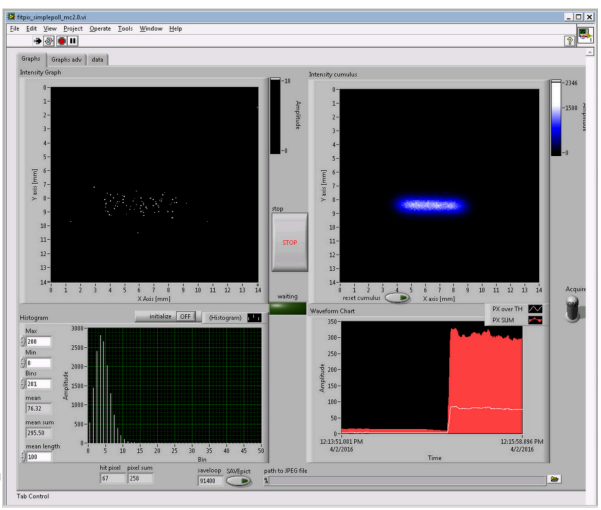

Figure 2: Example of real-time display with a LabVIEW interface of a FitPIX with a typical 450 MeV, intermediate "single electron" beam. Top: on the left a single frame is displayed, while on the right the cumulative beam spot distribution is shown; bottom: the multiplicity distribution and the pulse-by-pulse particle count are displayed.

Up to three FitPIX devices are routinely used in the facility (as shown in Fig. 3), in general the up-stream one is permanently mounted on a linear stage, remotely controlled, in order to be easily moved in and out of the beam for a quick feedback to the users.

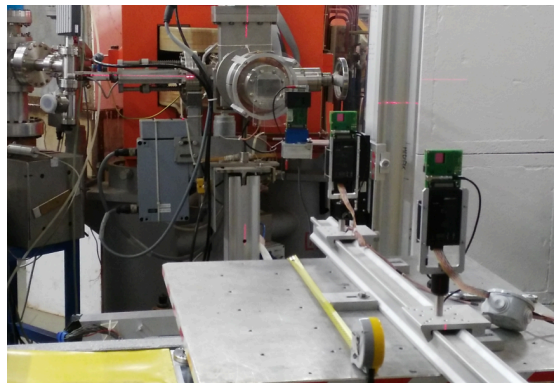

Figure 3: Three FitPIX detectors mounted on the BTF beam line for the transverse spot characterization and tracking tests.

The development of the track reconstruction software with multiple FitPIX detectors is under way, in order to realize an easily manageable Silicon pixel tracking system, even though with the limitation of a significant multiple scattering effect due to the not negligible amount of material (at least 1 mm of Silicon plus approximately 1 m of air), as described in the following section.

BEAM SPOT CHARACTERIZATION AND OPTIMIZATION

We have performed a number of studies of transverse beam spot in a wide range of beam parameters, e.g. at different selected energies and by optimizing the beamline optics according to different requirements: "pencil" beam, e.g. the smallest possible spot; low-divergence; round beam; highest possible uniformity "flat" beam, very elongated aspect-ratio "knife" beam; etc.

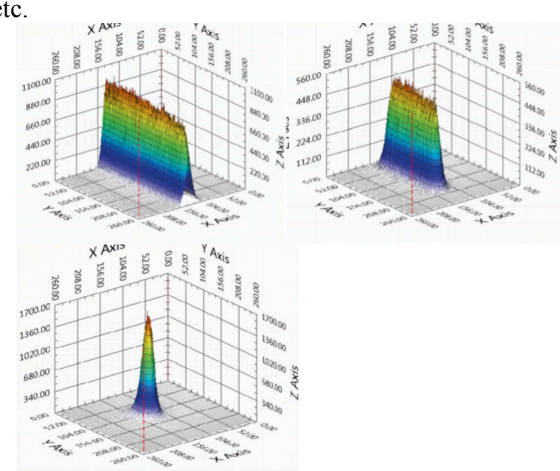

Figure 4: FitPIX display of 450 MeV electron beam for different beam energy spread, translating in different horizontal beam sizes due to the dispersion introduced by the last transport dipole in the BTF line.

As an example, in Fig. 4 the effect of the dispersion introduced by the last BTF line dipole on the beam size is shown: a larger momentum spread of the beam (due to different settings in the collimator system [1]) translates in a larger beam spot in the bending coordinate (in this case the horizontal one). This effect is very easily

ISBN 978-3-95450-177-9

and precisely measured by means of the FitPIX diagnostics.

Thanks to our custom software, we have the possibility of reconstructing the beam profiles on a pulse by pulse basis, running the FitPIX acquisition at full frame rate and storing the live data on the MEMCACHED system. With a simple LabVIEW interface we can the display in real-time the main spot parameters (average position, size, etc.), as shown in Fig. 5.

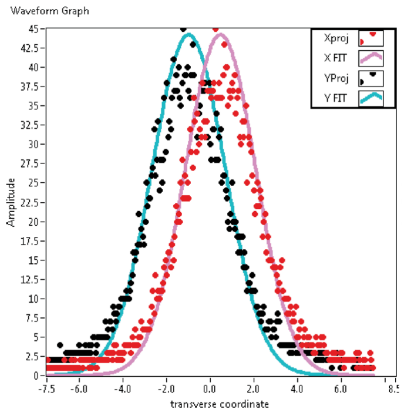

Figure 5: Real-time reconstructed transverse profiles and Gaussian fit for a 100 MeV electron beam.

With high-statistics data acquisition we can also study the tails of the electron or positron beam, in the different configuration, this is particularly relevant for instance for the PADME experiment [4-5], demanding a small spot (<1 mm), low divergence beam (<1 mrad), with the lowest possible halo. As an example, in Fig. 6 the distribution of an optimized beam, 700 MeV electrons, is shown (in logarithmic scale), showing the effect of a lower energy tail on one side in the bending coordinate.

The most important contribution to the beam size and divergence is the multiple scattering on the 0.5 mm thick Beryllium window at the exit of the BTF vacuum beam-pipe. This can be seen measuring the beam spot at different beam energies, given that we can keep constant the beam momentum spread, in order not to change the horizontal size due to the effect of the last dipole dispersion described above.

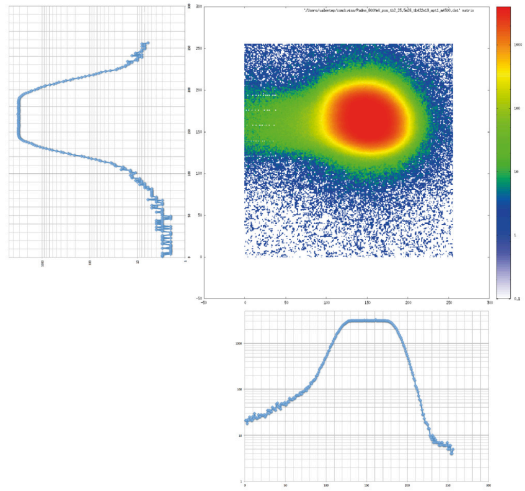

Figure 6: High statistics image of a 700 MeV electron beam in the transverse coordinates (logarithmic scale).

The 2D beam spots with horizontal (x) and vertical (y) profiles with Gaussian fits at 30, 60, 90, 120 and 150 MeV electron energies are shown in Fig. 7, while in Fig. 8 we show the fitted transverse size $\sigma=\sqrt{(\sigma_x^2+\sigma_y^2)}$, as a function of the momentum, together with the calculation of the multiple scattering contribution due to the Be window material only.

Low energy beams are also required for electron irradiation, with the additional requirement of keeping an uniform intensity (within 10%) over a large (order of few cm^2) area. Even though a single FitPIX active area is limited to 2 cm^2, thanks to the full efficiency we can obtain real-time maps of the irradiation field, as shown in Fig. 9, where a 1.7×10^6 electrons/s, 50 MeV beam is shown in a ±25% intensity range.

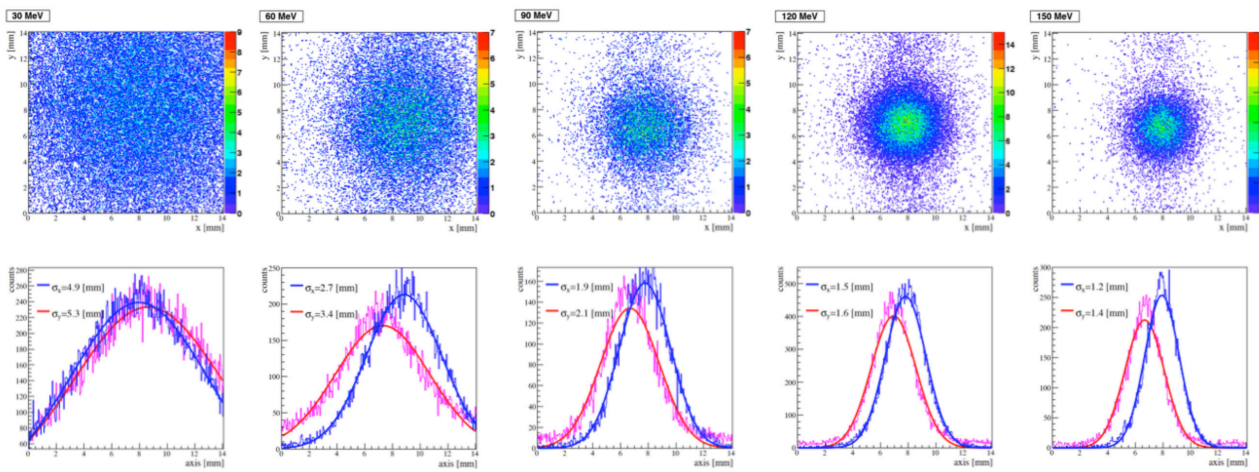

Figure 7: Beam transverse spot imaged by a FitPIX detector at different beam energies, from left to right 30, 60, 90, 120 and 150 MeV electrons (online display).

ISBN 978-3-95450-177-9

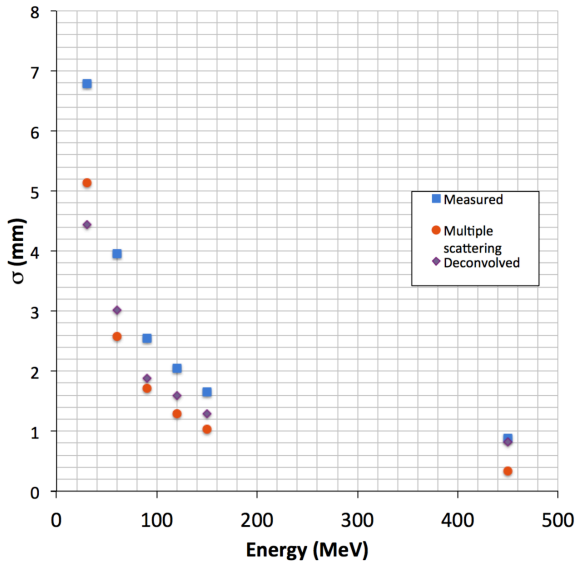

Figure 8: Measured beam transverse size $\sigma=\sqrt{(\sigma_x^2+\sigma_y^2)}$ as a function of the electron beam energy. The computed contribution of the multiple scattering on the Beryllium window is also shown.

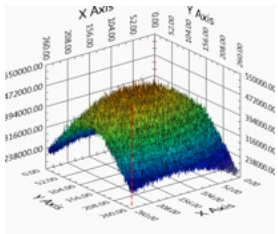

Figure 9: Beam distribution of 50 MeV electrons, 3.5×10^3/pulse, during a test BTF irradiation run.

CONCLUSIONS

The transverse beam spot diagnostics developed in the last years is a fundamental tool for characterizing and optimizing the BTF beam, and for quickly responding to the users requirements in terms of beam spot size, position, divergence, etc. The constant improvement of both the detectors hardware and software now allow us a reliable, real-time, full-speed readout of multiple FitPIX devices.

ACKNOWLEDGEMENT

This work is supported by the H2020 project AIDA-2020, GA no. 654168.

REFERENCES

[1] G. Mazzitelli, A. Ghigo, F. Sannibale, P. Valente and G. Vignola, *Nucl. Instrum. Meth. A* 515 (2003) 524-542.

[2] B. Buonomo, C. Di Giulio, L. G. Foggetta and P. Valente, "The Frascati LINAC Beam-Test Facility (BTF) Performance and Upgrades", Proceedings of IBIC 2016, Barcelona, Spain, TUPG29.

[3] B. Buonomo, C. Di Giulio, L. G. Foggetta and P. Valente, "A Hardware and Software Overview on the New BTF Transverse Profile Monitor", Proceedings of IBIC 2016, Barcelona, Spain, WEPG73.

[4] M. Raggi and V. Kozhuharov, *Adv. High Energy Phys.* 2014 (2014) 959802.

[5] M. Raggi, V. Kozhuharov and P. Valente, *EPJ Web Conf.* 96, 01025 (2015).

ISBN 978-3-95450-177-9

DESIGN AND EXPERIMENTAL TESTS OF THE SwissFEL WIRE-SCANNERS

G.L.Orlandi*, R.Ischebeck, C.Ozkan Loch, V.Schlott,
Paul Scherrer Institut, 5232 Villigen PSI, Switzerland
M. Ferianis, G. Penco
Elettra Sincrotrone Trieste, 34149 Basovizza, Trieste, Italy

Abstract

The SwissFEL wire-scanner (WSC) composes of an in-vacuum beam-probe - motorized by a stepper motor - and an out-vacuum pick-up of the wire-signal. In SwissFEL, WSCs will absolve two main tasks: high precision measurement of the beam profile for determining the beam emittance as a complement to view-screens; routine monitoring of the beam profile under FEL operations. In order to fulfill the aforementioned tasks, the design of the in-vacuum component of the SwissFEL WSCs followed the guidelines to ensure a mechanical stability of the scanning wire at the micrometer level as well as a significative containment of the radiation-dose release along the machine thanks to the choice of metallic wires with low density and Atomic number. Beam-loss monitors have been suitably designed to ensure a sufficient sensitivity and dynamics to detect signals from scanned beams in the charge range 10-200 pC. The design, the prototyping phases, the bench and electron-beam tests - performed at SITF (Paul Scherrer Institut) and FERMI (Elettra, Trieste) - of the entire SwissFEL WSC set-up will be presented.

PREMISE

The proceeding contents are an extract of an article recently accepted for publication in Physical Review Accelerators and Beams [1]. Aim of the present proceeding is to outline the most relevant aspects of the work done for the development of the SwissFEL WSC which the reader can examine in depth in [1]. The introductory and conclusive sections of the proceeding directly descend from [1].

INTRODUCTION

SwissFEL will provide coherent X-rays light in the wavelength region $7-0.7\ nm$ and $0.7-0.1\ nm$ [2]. Electron bunches with charge of 200/10 pC and transverse normalized slice emittance of 0.4/0.2 $\mathrm{mm.mrad}$ will be emitted by a S-band photocathode gun at a repetition rate of $100\ \mathrm{Hz}$ according to a two-bunches structure with a temporal separation of $28\ \mathrm{ns}$. The electron beam will be then accelerated up to $330\ \mathrm{MeV}$ by a S-band RF booster and, finally, to $5.8\ \mathrm{GeV}$ by a C-band RF linac. Thanks to an off-crest acceleration in the RF Booster, the electron beam will experience a longitudinal compression in two magnetic chicanes from an initial bunch length of $3/1\ \mathrm{ps}$ (rms) down to $20/3\ \mathrm{fs}$ (rms). Two X-band RF cavities will compensate the quadratic distortion of the longitudinal phase space due to the off-crest acceleration of the beam and the non-linear contribution of the magnetic dispersion [3]. In the booster section, a laser-heater will smooth down possible micro-structures affecting the longitudinal profile of the beam [4, 5]. Finally, thanks to a RF kicker - placed after the second bunch-compressor - and a magnetic switch-yard, the second electron bunch of the beam train will be shifted from the main beam line to a secondary one so that the SwissFEL linac, after a further acceleration stage of the two bunches, will supply two distinct undulator chains at a repetition rate of $100\ \mathrm{Hz}$: the hard X-rays line Aramis and the soft X-rays line Athos [2].

In a FEL (Free Electron Laser) driver linac, WSCs are currently used to monitor the transverse profile of the electron beam [6, 7, 8, 9, 10, 11, 12, 13, 14] when the view-screen imaging of the beam is hampered by coherent radiation emission due to microbunching. In SwissFEL, WSCs will be complementary to view-screens for emittance measurements and, thanks to the barely invasive feature, also used for routine monitoring of the transverse profile of the electron beam during FEL operations. Moreover, the beam imaging at SwissFEL being performed by means of YAG:Ce screens [15], only WSCs will be able to discriminate the profile of each single bunch in two-bunches operations. In SwissFEL, the WSC in-vacuum hardware consists of a planar wire fork which can be inserted 45^o with respect to the vertical direction into the vacuum chamber by means of a UHV linear-stage driven by a stepper motor, see Fig.(1). The wire-fork is designed to be equipped with two wire triplets, the spare triplet being possibly composed of wires of different material and/or diameter. Each wire of the triplet will separately scan the beam profile along a given direction: the vertical wire (X-scanning, horizontal-scanning), the horizontal wire (Y-scanning, vertical-scanning) and the diagonal wire (XY-coupling). During a WSC measurement, the single wire scanning the beam at a constant speed produces - at every RF shot - a shower of primary scattered electrons and secondary emitted particles in proportion to the fraction of the beam sampled by the wire. In SwissFEL, the forward - high energy and small scattering angle - component of the particle shower (wire-signal) will be out-vacuum detected by means of Beam-Loss-Monitors (BLMs). The beam-loss sensitive material of the SwissFEL BLMs is a scintillator fiber (Saint Gobain BCF-20, decay time 2.7 ns) wrapped

* gianluca.orlandi@psi.ch

ISBN 978-3-95450-177-9

around the vacuum pipe. The scintillator fiber is matched by means of a Plastic Optical Fiber (POF) to a photomultiplier (PMT) having a remotely adjustable gain in the range $5 \times 10^3 - 4 \times 10^6$. The PMT signal is finally digitized and integrated in time by an ADC unit. The SwissFEL BLMs are designed to detect the wire-signal from $10 - 200$ pC bunches and to have a sufficient time-response to discriminate the 28 ns time structure of the SwissFEL beam in two-bunches operations [16]. In SwissFEL, the wire-scanned profile of the electron beam will be reconstructed thanks to the beam-synchronous acquisition (BSDAQ) of the encoder read-out of the wire-position and of the signal read-out of the BLM at every RF shot. Furthermore, thanks to the BSDAQ readout of the beam charge and the transverse position of the beam centroid provided by Beam Position Monitors (BPMs) [17] placed immediately downstream and upstream the WSC, possible errors due to the beam jitter can be corrected in the reconstructed beam profile.

In the present work, technical details on the design of the SwissFEL WSCs will be presented as well as the main results of the bench and electron-beam tests of the entire WSC set-up. Laboratory tests aimed at determining the mechanical stability of the in-vacuum hardware of the WSC and, in particular, the stepper-motor induced vibration of the wire in the speed range of interest of SwissFEL were carried out. e-Beam tests of a prototype of the SwissFEL WSC - in-vacuum and out-vacuum components - were performed: (1) at low charge and energy - 10 pC and 250 MeV - at SITF [19] and (2) at high charge and energy - 700 pC and 1.5 GeV - at FERMI [20, 21]. Thanks to the e-beam tests, the issue of the necessary detection sensitivity and dynamics of the SwissFEL BLM in the beam charge range $10 - 200$ pC was clarified as well as the issue of the optimum distance of the BLM from the WSC as a function of the beam energy. The question of the choice of the most suitable wire solution (material and diameter) was also positively defined thanks to the e-beam tests. The robustness of wires of different materials and diameters was tested on electron beams. The relative measurement accuracy and the radiation-dose release along the machine during a WSC measurement was also determined for different wire-solutions. In particular, a comparative study of the scanning performances - relative measurement accuracy and radiation-dose release - of a Al(99):Si(1) wire with a diameter of 12.5 μm and a tungsten (W) wire with a diameter of 5 μm was carried out at FERMI at a beam energy of 1.325 GeV and at a charge of 700 pC.

SWISSFEL WIRE-SCANNER (WSC), MEASUREMENT GOALS

The SwissFEL WSC are requested to absolve the following tasks:
(1a) monitor the transverse profile of beams having a size of 5-500 μm (rms), charge of 10-200 pC and energy of 0.340-5.8 GeV;
(2a) resolve the beam transverse profile of the SwissFEL two-bunches train: time structure, 100Hz repetition rate and 28ns time separation;
(3a) measure the beam transverse profile and emittance as a complement to view screens and as a further option in case the view-screen imaging of the beam will be hampered by possible microbunching induced effects of coherent radiation emission;
(4a) routine monitoring of the beam transverse profile during FEL operations.

SWISSFEL WSC, DESIGN CRITERIA

The design criteria of the SwissFEL wire scanners followed the below indicated guidelines:
(1b) use a single UHV linear stage motorized by a 2-phase stepper motor to scan the beam profile in the vertical plane along the X,Y and X-Y directions, see Figs.(1, 2);
(2b) wire-fork designed to be equipped with two triplets of wires of different material and diameter, see Figs.(1, 2);
(3b) wire-fork equipped with multiple pin-slots to fix the wires of each triplet at different relative distances (wire-vertex from vacuum-chamber axis: 8, 5.5, 3 mm);
(4b) 1^{st} wire-triplet: 5 μm Tungsten wire for high resolution measurement of the beam emittance (1.3 μm geometrical resolution of the wire);
(5b) 2^{nd} wire-triplet: 12.5 μm Al(99):Si(1) wire for routine scanning of the beam profile during FEL operations;
(6b) wire-scanner signal: forward shower of primary scattered electrons and secondary emitted particles in proportion to the fraction of the beam charge sampled by the wire;
(7b) wire-scanner signal (particle shower) detected by beam-loss-monitors (BLMs) composed of a scintillator fiber wrapped around the beam pipe and matched by means of a POF (Plastic Optical Fiber) to a photomultiplier (PMT gain $5 \times 10^3 - 4 \times 10^6$);
(8b) beam transverse profile reconstructed thanks to the Beam-Synchronized-Acquisition (BS-ACQ) of the motor encoder and BLM readouts;
(9b) correction of the beam charge fluctuation and transverse jitter of the beam centroid thanks to the BS-ACQ of the signals (beam charge and position) of the closest beam position monitors (BPMs) placed downstream and upstream the WSC.

SWISSFEL WSC, EXPERIMENTAL RESULTS

The experimental work on the SwissFEL WSC was carried out at the 250MeV SwissFEL Injector Test Facility (SITF, 200MeV, 10-200 pC, 10 Hz) and at FERMI (300-700 pC, 1.3-1.5 GeV, 10 Hz). The work of WSC characterization focused on:
I) determination of the wire stability under motion [wire-vibration measurements on test-bench, see Fig.(3)];
II) e-Beam resistance tests of wires of different material and diameter at high charge (700 pC, 10Hz) and energy (1.3-1.5 GeV);

ISBN 978-3-95450-177-9

III) determination of the optimum distance WSC-BLM as a function of the beam energy (0.200-1.5 GeV);
IV) study of the BLM sensitivity at low charge (10pC);
V) comparative studies WSC vs. OTR: compared to OTR, WSC measurements of emittance at FERMI characterized by a higher resolution and a significative speed-up and improvement of the matching procedure of the magnetic optics to the design lattice;
VI) comparative studies of the WSC performances (5 μm Tungsten wires vs. 12.5 μm Al(99):Si(1) wires): study of the measurement accuracy and determination of the radiation dose release along the machine.

Achievements and expected performances:
(1c) wire-vibration measurements: measured wire-vibration below the tolerance limit of 1.3 μm in the stepper motor velocity range 0.1 - 3.0 mm/s. Anomalous wire-vibration of 2.1-1.6 μm in the velocity range 0.5 - 0.6 mm/s (stepper motor resonance velocity), see Fig.(3);
(2c) spatial resolution and accuracy features: wire-geometrical resolution $\rightarrow$ $1.3\mu m$ (5 μm Tungsten); motor encoder resolution $\rightarrow$ $0.1\mu m$; jitter of the encoder BS-ACQ readout $\rightarrow$ $0.1ms$;
(3c) optimum distance WSC-BLM scaling up between 3-6m in the beam energy range 0.200-1.5 GeV;
(4c) BLM sensitivity sufficient to scan 10 pC beam with 5 μm Tungsten wire and detector dynamics sufficient to cover the charge range 10-200 pC;
(5c) FEL operations (FERMI) almost transparent to wire-scanning with Tungsten;
(6c) comparison of the wire-scanning performances 5 μm Tungsten vs. 12.5 μm Al(99):Si(1), experimental results (FERMI):
i) same measurement accuracy in scanning beam profiles with a size of 35 μm;
ii) compared to Tungsten, reduction by a factor 11 of the radiation dose released along the FERMI FEL1 undulator chain when scanning the beam with Al(99):Si(1).

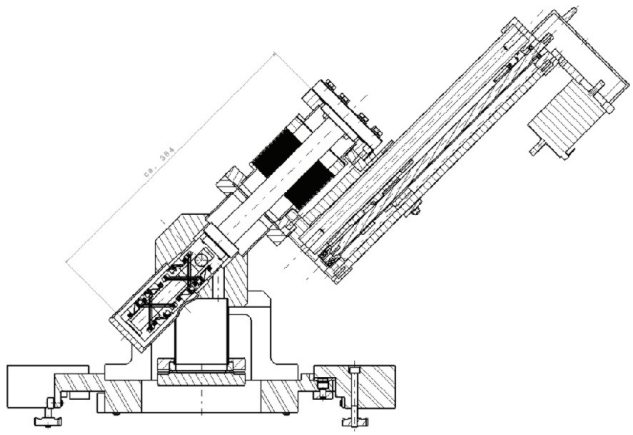

Figure 1: View of the transverse section of the in-vacuum set-up of the SwissFEL WSC: CF16 vacuum chamber, motorized UHV-Linear-Stage and wire fork. The SwissFEL wire-fork can be equipped with two triplets of wires. Thanks to a system of multiple pin-slots, the horizontal and the vertical wires of each triplet can be set, respectively, at a distance from the center of the vacuum chamber of either 8 mm or 5.5 mm or 3 mm, see also Fig.(2). In order to outline this feature of the SwissFEL wire-fork - in both Figs.(1,2) - all the three pin-slots are virtually provided with wires. In the real wire-fork of SwissFEL, only one wire is fixed along the horizontal direction by means of one of the three possible pin-slots (the same for the vertical direction).

CONCLUSIONS

The design features and the main prototyping steps of the SwissFEL wire-scanners have been presented as well as the results of bench and electron-beam tests of the entire WSC set-up [1, 22]. Electron beam tests were carried out at SITF and FERMI. The experimental characterization of the mechanical stability of the WSC confirmed that, in the motor-speed range of interest of SwissFEL ($0.1 - 3.0$ $\mathrm{mm/s}$), the wire-vibration stays largely below the tolerance limit of 1.3 μm (rms). According to the results of electron beam tests carried out at SITF, the detection set-up of the wire-signal showed a sufficient sensitivity to reconstruct the beam profile of a 10 pC beam scanned by a 5 μm tungsten wire and, in general, a sufficient large dynamics to cover the beam charge range $10 - 200$ pC. Furthermore, thanks to the electron beam tests carried out at SITF and FERMI, the optimum distance between WSC and wire-signal detector was estimated to scale up between 3 and 6 m in the beam energy range $0.250 - 1.5$ GeV. Several solutions of metallic wires of different material and diameter have been tested on the electron beam at different conditions of charge and energy. In particular, comparative tests of the scanning performance of a 5 μm tungsten wire and of 12.5 μm Al(99):Si(1) wire were carried out at FERMI at a beam energy of 1.325 GeV and charge of 700 pC. The results of this comparative study demonstrated a satisfactory robustness of the Al(99):Si(1) wire to the beam loading as well as a comparable accuracy of the two wire-solutions in measuring an electron beam size of about 35 μm. In addition, the radiation-dose measured at the FEL1 undulator chain of FERMI when scanning the beam with a 12.5 μm Al(99):Si(1) was about a factor 11 smaller than the one measured with a 5 μm tungsten wire. On the basis of the outcome of the electron beam tests, the SwissFEL WSC forks - being designed to be equipped with two distinct triplets of metallic wires - will be provided with 5 μm tungsten wires - for high precision measurements of the beam profile and emittance - and with 12.5 μm Al(99):Si(1) wire for routine monitoring of the transverse profile of the electron beam during FEL operations. The prototyping and experimental characterization phases of the SwissFEL WSC being accomplished, WSC commissioning and operations in SwissFEL are expected to start by Summer 2016.

ISBN 978-3-95450-177-9

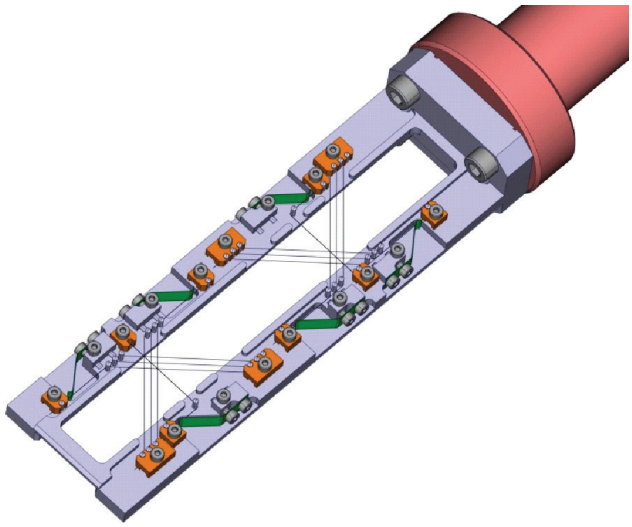

Figure 2: Technical drawing of the SwissFEL wire-fork. Thanks to a system of multiple pin-slots, the vertex of each wire-triplet can be set at three different distances (8, 5.5 and 3 mm) from the center of the vacuum chamber. In order to outline such a flexibility feature of the design of the SwissFEL wire-fork - in the present technical drawing - all the three pin-slots are shown to be provided with horizontal and vertical wires. In reality, only one of the three possible pin-slots will be equipped with a wire so that each of the two wire triplets of the SwissFEL wire-fork will be composed of: one single horizontal wire; one single vertical wire; one single wire for XY coupling.

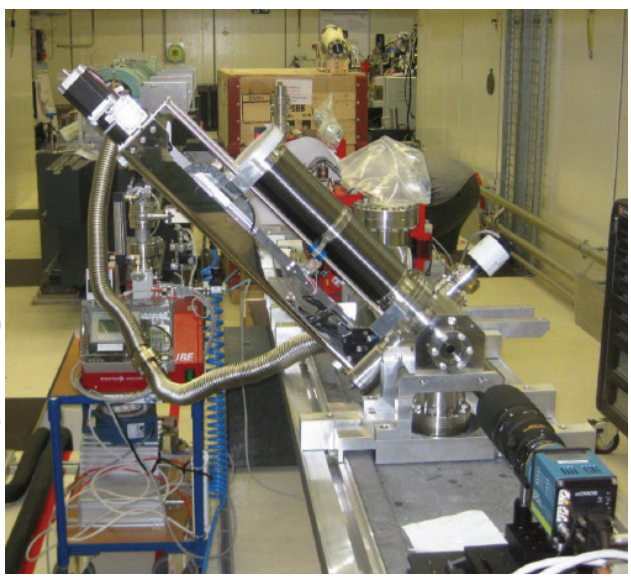

Figure 3: Image of a prototype of the SwissFEL WSC installed onto a girder together with the measurement set-up of the stepper-motor induced vibrations of the wire.

REFERENCES

[1] G.L. Orlandi, M. Ferianis, P. Heimgartner, R. Ischebeck, C. Ozkan Loch, G. Penco, S. Trovati, P. Valitutti, V. Schlott, Design and experimental tests of free electron laser wire scanners, accepted for publication in Physical Review Accelerators and Beams.

[2] SwissFEL Conceptual Design Report, PSI Bericht Nr. 10-04 April 2012.

[3] P. Emma, J. Frisch, P. Krejcik, LCLS-TN-00-12.

[4] Z. Huang, K. J. Kim, PRST-AB, **5**, 074401 (2002).

[5] E.L. Saldin, E.A. Schneidmiller, M.V. Yurkov, Nucl. Instr. Meth. in Phys. Res. A **528**, 355-359 (2004).

[6] R. Fulton, J. Haggerty, R. Jared, R. Jones, J. Kadyk, C. Field, W. Kozanecki, W. Koska, Nucl. Instr. Meth. in Phys. Res. A **274** (1989) 37-44.

[7] M.C. Ross, J. T. Seeman, E. Bong, L. Hendrickson, D. McCormick, L. Sanchez-Chopitea, Particle Accelerator Conference (PAC) 1991.

[8] C. Field, Nucl. Instr. Meth. in Phys. Res. A **360** (1995) 467-475.

[9] P. Tenenbaum and T. Shintake, Annu. Rev. Nucl. Part. Sci. 1999. 49:12562.

[10] H.-D. Nuhn, P.J. Emma, G.L. Gassner, C.M. LeCocq, F. Peters, R.E. Ruland, *Electron Beam Alignment Strategy in the LCLS Undulators*, SLAC-PUB-12098 (2006).

[11] H. Loos, et al., *Operational Performance of LCLS Beam Instrumentation*, SLAC-PUB-14121.

[12] J. Wu, P. Emma, and R.C. Field *Electron Signal Detection for the Beam-Finder Wire of the Linac Coherent Light Source Undulator*, SLAC-PUB-12120 LCLS-TN-06-7, April 2006.

[13] K. Wittenburg, Report No. TESLA2000-18 (2000).

[14] U. Hahn, N.v. Bargen, P. Castro, O. Hensler, S. Karstensen, M. Sachwitz, H. Thom, Nuclear Instruments and Methods in Physics Research A 592 (2008) 189196.

[15] R. Ischebeck, P. Eduard, T. Vincent, C. Loch Ozkan, Physical Review Special Topics - Accelerators and Beams **18**, 082802 (2015).

[16] C. Ozkan Loch, et al., Proceedings of IBIC2015, Melbourne, Australia, September 2015 (MOPB051).

[17] B. Keil, et al., Proceedings of IBIC2015, Melbourne, Australia, September 2015 (TUPB065).

[18] T. Moore, N. I. Agladze, I. V. Bazarov, A. Bartnik, J. Dobbins, B. Dunham, S. Full, Y. Li, X. Liu, J. Savino, and K. Smolenski, Physical Review Special Topics - Accelerators and Beams **17**, 022801 (2014).

[19] SwissFEL Injector Conceptual Design Report, PSI Bericht Nr. 10-05 July 2010.

[20] C. Bocchetta et al., FERMi@Elettra Conceptual Design Report, Tech Report No. ST/F-TN-07/12 (2007).

[21] S. Di Mitri, et al., Nucl. Instr. Meth. in Phys. Res. A **608**, 19-2 (2009).

[22] G.L. Orlandi, et al., Proceedings of FEL2014, Basel, Switzerland (2014) 948-951.

ISBN 978-3-95450-177-9

DEVELOPMENT AND COMMISSIONING OF THE NEXT GENERATION X-RAY BEAM SIZE MONITOR IN CESR *

N.T. Rider, S.T. Barrett, M.G. Billing, J.V.Conway, B. Heltsley, A. Mikhailichenko, D.P. Peterson, D. Rubin, J.P. Shanks, S. Wang, CLASSE, Cornell University, Ithaca, NY 14853, U.S.A

Abstract

The CESR Test Accelerator (CESRTA) program targets the study of beam physics issues relevant to linear collider damping rings and other low emittance storage rings. This endeavour requires new instrumentation to study the beam dynamics along trains of ultra-low emittance bunches. A key element of the program has been the design, commissioning and operation of an x-ray beam size monitor capable, on a turn by turn basis, of collecting single pass measurements of each individual bunch in a train over many thousands of turns. The x-ray beam size monitor development has matured to include the design of a new instrument which has been permanently integrated into the storage ring. A new beam line has been designed and constructed which allows for the extraction of x-rays from the positron beam using a newly developed electro magnet pair. This new instrument utilizes custom, high bandwidth amplifiers and digitization hardware and firmware to collect signals from a linear InGaAs diode array. This paper reports on the development of this new instrument and its integration into storage ring operation including vacuum component design, electromagnet design, electronics and capabilities.

INTRODUCTION

The Cornell Electron Storage Ring (CESR) provides electron and positron beams which are used for accelerator research and as a synchrotron light source. Both of these applications require diagnostic equipment and instrumentation to maintain particle beam and x-ray quality. The Next Generation x-Ray Beam Size Monitor (NGXBSM) is part of a suite of instrumentation developed for this purpose. The NGXBSM is a natural evolution of the instrument which was developed during the early stages of the CESRTA program. This instrument images x-rays from a bending magnet through a pinhole optical element on to a 32x1 pixel linear array detector. Figure 1 shows the basic concept of beam size measurement using x-rays.

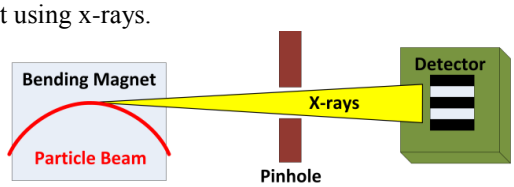

Figure 1: XBSM concept.

The development program has thus far leveraged the existing beam line and support structure of the experimental hutches at the Cornell High Energy Synchrotron Source (CHESS). While this arrangement was convenient, it was also temporary. The instrument was disassembled at the end of every CESRTA run and reinstalled, aligned and calibrated at the beginning of the next run. This prevented the use of the instrument during normal CHESS operations and limited development opportunities. The instrument provides valuable beam tuning information and an effort was undertaken to design and build a permanently installed instrument in CESR. The new instrument is a simplified application of the first generation technology. It provides vertical beam size measurements on a bunch by bunch and turn by turn basis. The available optical elements include a 35 micron vertical pinhole, a 200 micron vertical pinhole and an unlimited opening. These were chosen to support the typical operating energies of CESR, 2.085 GeV and 5.3 GeV. The instrument is capable of operating with CESR beam energies down to 1.8 GeV. First generation data acquisition electronics and software have been utilized to capture and process the x-ray images.

ACCELERATOR INTEGRATION

In order to reduce the risk to the accelerator vacuum system, it was decided to pursue a windowed beam line design with the optical elements and detector outside of the CESR beam pipe. A beryllium window provides physical separation between the CESR and NGXBSM beam pipes. Usable x-ray intensity across the energy range of the accelerator is maintained by utilizing multiple x-ray sources. At 5.3 GeV an existing normal bend magnet is used as the x-ray source. At 2.085 GeV, a new two pole source magnet has been designed and constructed to provide the x-ray source. This new magnet is required to provide sufficient x-ray flux through the beryllium window at lower CESR beam energies. The spatial requirements of the new beam line coupled with the requirement for the installation of a new source magnet, limited potential instrument locations in the CESR tunnel. The location chosen for this new instrument forced an overall reduction in length of the x-ray path from optical element to detector when compared to the first generation instrument. Since the instrument is effectively a pinhole camera, this serves to reduce the effective magnification from source to detector. In order to offset this effect, the detector has been tilted at a 60 degree angle to functionally reduce the pixel height and increase resolution. The present configuration has a distance from source to optic of 4.4m or 6.76m, depending on which source is used, and a distance from optic to detector of 4.4m. Motorized stages are used to allow for precision alignment of the optical elements and the detector. Figure 2 shows a functional overview of the instrument and key CESR components.

*Work supported by NSF grant PHY-0734867 and DOE grant DE-FC02-08ER41538

ISBN 978-3-95450-177-9

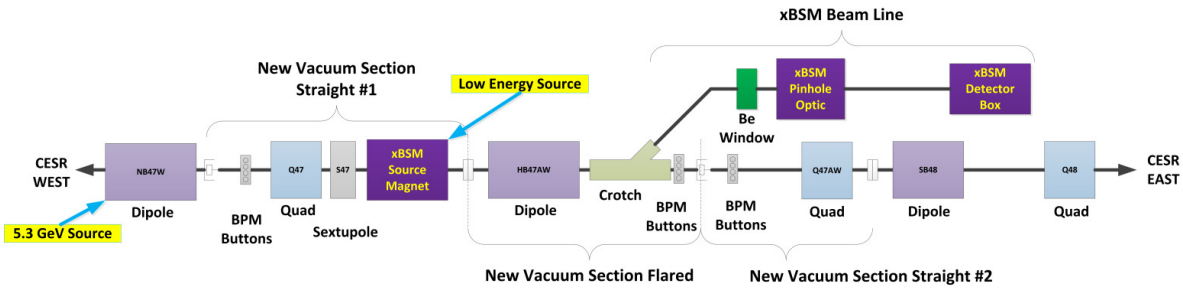

Figure 2: NGXBSM functional diagram.

VACUUM COMPONENTS

In order to transfer the x-rays from CESR to the detector, a flared vacuum chamber, beam line crotch, beryllium window and dedicated beam line have been designed and installed in CESR. The flared vacuum chamber is installed inside of a standard CESR hard bend magnet and has a large flange which mates with the beam line crotch. The beam line crotch is a water cooled copper device which absorbs the fan of synchrotron radiation while allowing the particle beam and the x-rays to pass down their respective lines. The shape of the crotch was carefully designed to absorb the synchrotron radiation energy across all operating parameters for CESR. The beryllium window is 200 microns thick, 38 mm in diameter and allows for the x-rays to pass from CESR vacuum into the NGXBSM beam line. The NGXBSM beam line is rough pumped and backfilled with helium. This provides a clean medium which minimizes x-ray scatter and contamination. The window provides vacuum isolation and filters out low energy x-rays. All vacuum components are cooled with 85 degree Fahrenheit water which is supplied from the main CESR cooling loop. Figure 3 shows these new components as installed.

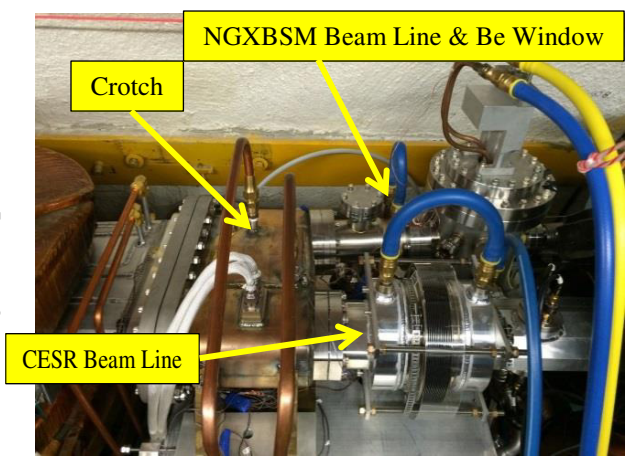

Figure 3: NGXBSM vacuum components.

LOW ENERGY SOURCE MAGNET

The normal bend magnet which is used as a source at 5.3 GeV has a field strength of 0.972 kG when CESR is operated at 2.085 GeV. This is not sufficient to provide usable x-rays. Therefore an electro-magnet pair has been designed and constructed to support operation at low energy. This pair, in conjunction with an additional CESR magnet, provides the horizontal beam trajectory necessary to generate x-rays which are of useful energy and direction. This trajectory requires a minimum of three poles to close the horizontal orbit bump which is created at the source point.

The new magnet was limited to two poles due to spatial constraints. An additional trim winding, which is part of a normal CESR bending magnet, is used to close the beam orbit disturbance created by the NGXBSM source magnet. Maximum horizontal beam orbit displacement within the source magnet is calculated to be 5.2 mm radially outward.

The two magnet poles are powered by a common 60 Volt, 300 Amp switched power supply. The current provided by the supply is controlled via the CESR control system. This allows for a design field of 4.5 kG in the shorter pole and 1.5 kG in the longer pole. The ratio between these two magnet poles provides the proper CESR beam trajectory for x-ray transmission. A 25 Amp active shunt is connected around the long pole and allows for precision adjustment of this ratio. The x-ray source point is provided by the short pole. Figure 4 shows the magnet as installed. The design magnetic field characteristics for the new source magnet are shown in Figure 5.

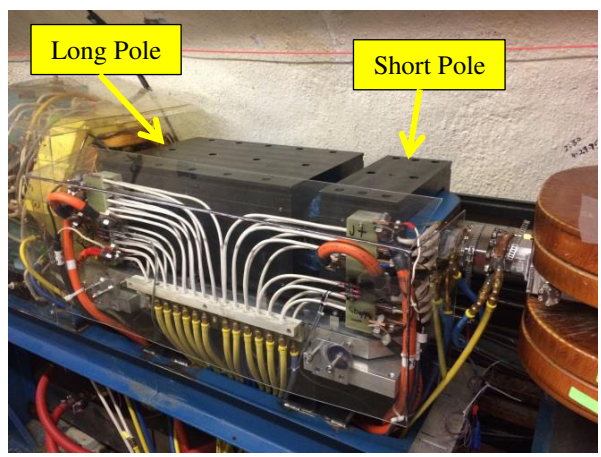

Figure 4: NGXBSM source magnet.

ISBN 978-3-95450-177-9

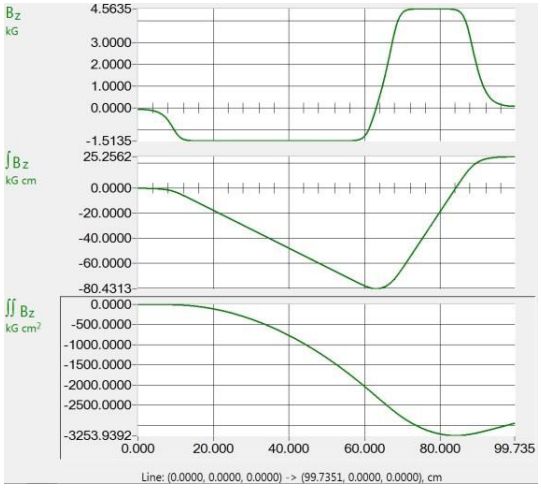

Figure 5: Magnetic field map of NGBSM magnet.

X-RAY SPECTRUM

The NGXBSM utilizes the same detector as the original instrument. This detector was used in conjunction with an existing hard bend magnet in CESR with a field of 5.1 kG at 5.3 GeV and 2.0 kG at 2.1 GeV. The detector response has been extensively studied over the course of the CESRTA program. Figure 6 shows the inferred detector response as well as the transmission characteristics of the 200 micron beryllium window. The detector response was determined empirically by using a variety of filters with a constant x-ray source.

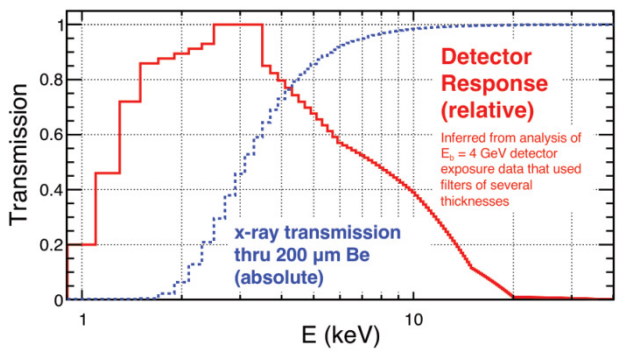

Figure 6: Detector response and be window transmission.

For CESR operations at 2.085 GeV the new source magnet has a calculated output spectrum as shown in Figure 7. For CESR operations at 5.3 GeV, the existing bend magnet has a calculated output spectrum as shown in Figure 8. Here, intensity is defined to be electromagnetic energy per unit time per unit area per unit current perpendicular to the x-ray beam in arbitrary units which are the same for both cases. A 1.5 mm aluminium filter is required at 5.3 GeV to lower the intensity so as to not saturate the detector. This filter is removable for operation at lower CESR beam energies.

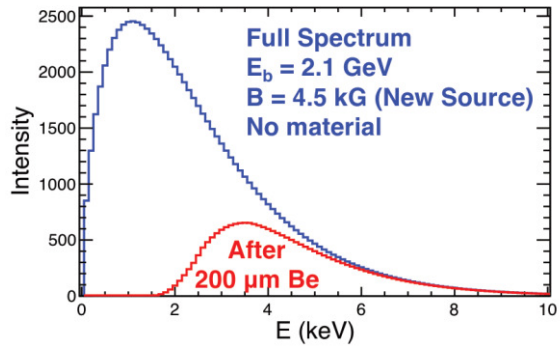

Figure 7: 2.085 GeV x-ray spectrum.

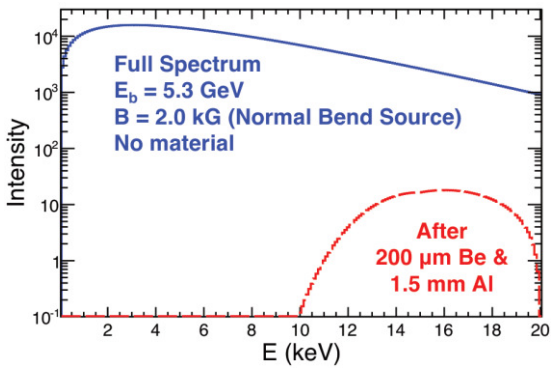

Figure 8: 5.3 GeV x-ray spectrum.

ACCELERATOR OPTICS

In order to create enough physical space in CESR for the installation of the new source magnet, several quadrupole magnets were moved. These changes coupled with the effect of the two pole source magnet at 2.085 GeV forced a redesign of the CESR magnetic optics. The trim winding of the closest CESR bending magnet is used to close the horizontal bump which is introduced by the two pole source magnet. After correction, we are left with an RMS orbit ripple of 111 microns and an RMS horizontal dispersion ripple of 1.9 mm. This results in an increase in horizontal emittance of 1.5% in our low emittance optics. This increase is deemed acceptable.

At 5.3 GeV the existing normal bend magnet is used with no impact on beam characteristics for CHESS operations.

MEASUREMENTS

At this point in the project, x-rays have been delivered to the detector at both 2.085 GeV and 5.3 GeV. The pinhole optical elements have been manufactured but have not yet been used to image the beam. During alignment, a digital camera was used to capture the x-ray beam position on the aluminium flag. Figure 9 shows the x-ray fluorescence on the aluminium filter at 5.3 GeV.

ISBN 978-3-95450-177-9

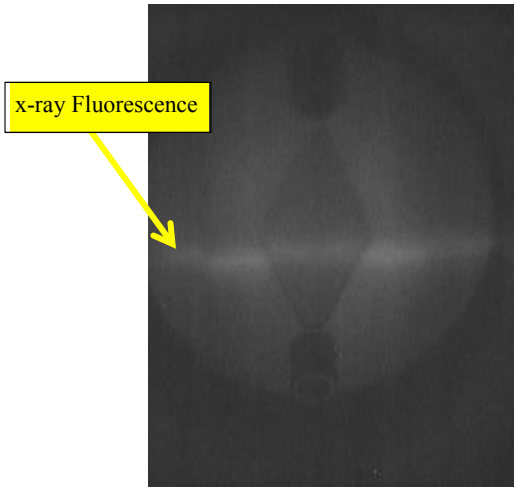

Figure 9: X-ray fluorescence at 5.3 GeV.

Once basic alignment was achieved, the detector and accompanying electronics were used to capture an x-ray profile of the straight through beam. Careful timing calibrations were performed to align the sampling electronics with the revolving bunch in CESR. This calibration positions the sampling point on the peak of the induced signals produced by each diode segment. Typical alignment procedures produce temporal alignment within 50 picoseconds. Figure 10 shows the detector response of straight through beam at 2.085 GeV.

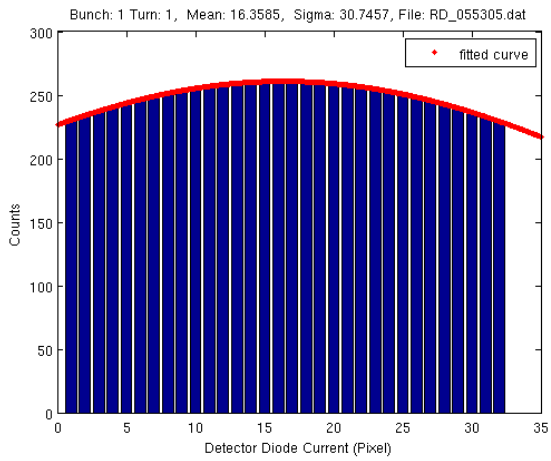

Figure 10: Straight through beam Image at 2.085 GeV.

FUTURE EFFORTS

The motorized pinhole stage has been completed and will be installed prior to the CESR accelerator start up in October 2016. It is expected that alignment will be completed and measurements at 5.3 GeV will be made using the 35 and 200 micron pinhole optics. Figure 11 shows the pinhole stage prior to installation.

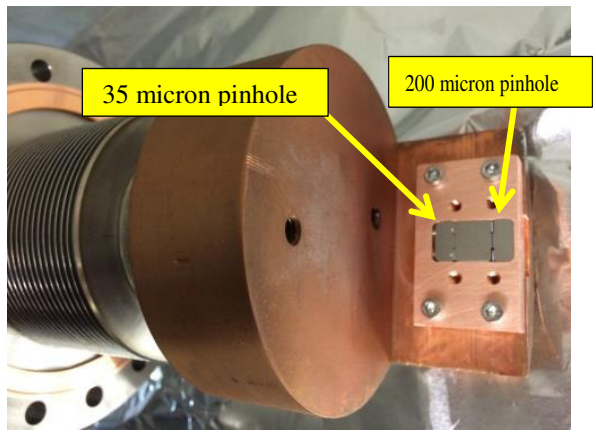

Figure 11: NGXBSM pinhole stage.

The instrument will then be used for experimental measurements as part of normal CHESS operations. 2.085 GeV alignment and measurements will be made during the December 2016 CESRTA run. Additional efforts to improve the quality of the detector itself are being planned.

CONCLUSION

The transition of the xBSM instrument from temporary prototype to permanently installed instrument has required significant intellectual and physical investment. New hardware, software and operating procedures have been developed and are presently being tested. It is expected that the instrument will be commissioned and placed into regular operation by the end of 2016.

ACKNOWLEDGMENT

The NGXBSM development team would like to thank the staff at CESR and CHESS for assisting in the development of the NGXBSM. Without the riggers, surveyors, technicians, operators and craftspeople this work would not be possible.

REFERENCES

[1] J.P Alexander et al, "Vertical beam size measurement in the CESR-TA e^+e^- storage ring using x-rays from synchrotron radiation", *Nuclear Instruments and Methods in Physics* , vol. 767, p 467-474, Dec 2014.

[2] J.P Alexander et al, "Design and performance of coded aperture optical elements for the CESR-TA x-ray beam size monitor ", *Nuclear Instruments and Methods in Physics*, vol. 767, p 467-474, Dec 2014.

[3] J.P Alexander et al, "Operation of the CESR-TA vertical beam size monitor at E_b=4GeV", *Nuclear Instruments and Methods in Physics*, vol. 798, p 127-134, Oct 2015.

ISBN 978-3-95450-177-9

STUDY OF YAG EXPOSURE TIME FOR LEREC RF DIAGNOSTIC BEAMLINE

S. Seletskiy †, T. Miller, P. Thieberger
BNL, Upton, USA

Abstract

The LEReC RF diagnostic beamline is supposed to accept 250 us long bunch trains of 1.6 MeV – 2.6 MeV (kinetic energy) electrons. This beamline is equipped with a YAG profile monitor. Since we are interested in observing only the last bunch in the train, one of the possibilities is to install a fast kicker and a dedicated dump upstream of the YAG screen and related diagnostic equipment. This approach is expensive and challenging from an engineering point of view. Another possibility is to send the whole bunch train to the YAG screen and to use a fast gated camera to observe the image from the last bunch only. In this paper we demonstrate the feasibility of the last approach, which significantly simplifies the overall design of the RF diagnostic beamline.

LEREC RF DIAGNOSTIC BEAMLINE

The LEReC accelerator [1, 2] includes a dedicated RF diagnostic beamline (Fig. 1). This beamline will be utilized for fine-tuning of the RF required to produce electron bunches with energy spread better than $5 \cdot 10^{-4}$.

The beamline consists of a bending magnet creating dispersion at the location of the YAG screen and a deflecting cavity "crabbing" electron bunches in time domain. Thus, the beam image on the YAG screen represents the longitudinal phase space of the beam.

The temporal structure of the bunch train sent to the diagnostic beamline is as follows. There are N=30 (100 ps long) electron bunches, with nominal charge Q=130 pC, spaced by 1.4 ns and forming a single macro-bunch. The macro-bunches are separated by Δt=110 ns and form the train of any chosen length. The schematic of e-beam temporal structure is shown in Fig. 2.

The overall length of the bunch train required for RF diagnostic is determined by stabilization time of the RF system. It was determined [3] that bunch train of length t=250 us is sufficiently long to study the beam-loading effects in LEReC RF cavities.

We plan to send the whole bunch train to the YAG screen and to use a fast gated camera (such as Imperex B0610 with trigger jitter under 60ns [4]) to observe the image from the last macro-bunch only.

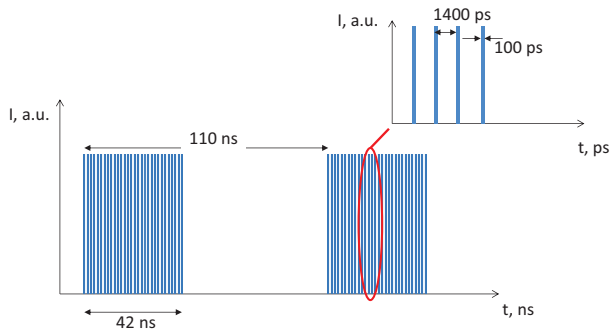

Figure 2: Temporal structure of electron beam.

In this paper we will consider two connected questions of YAG screen performance for the described bunch train.

First, we will study the instantaneous temperature jump in YAG crystal due to deposition of a single bunch train.

Second, we will find the steady-state temperature of YAG screen for various e-beam repetition rates.

YAG SCREEN PERFORMANCE

The best, known to us, test of YAG screen performance under temperature stress is the RHIC electron lens operation. In this test 5 keV, 97 mA DC beam "chunks" as long as 1.2 ms were deposited on the YAG screen.

The crystal response still was linear for such parameters and the Gaussian transverse distribution with σ=0.133 cm was still observed on the YAG screen.

We calculated that due to deposition of each shot YAG temperature had to jump by 194 K. Numerous shots with 3-5 s repetition rate were sent to YAG crystal without damaging it.

The test [5] of the dependence of YAG crystal performance on temperature corroborates that it is safe to heat the YAG screen up to 200 C.

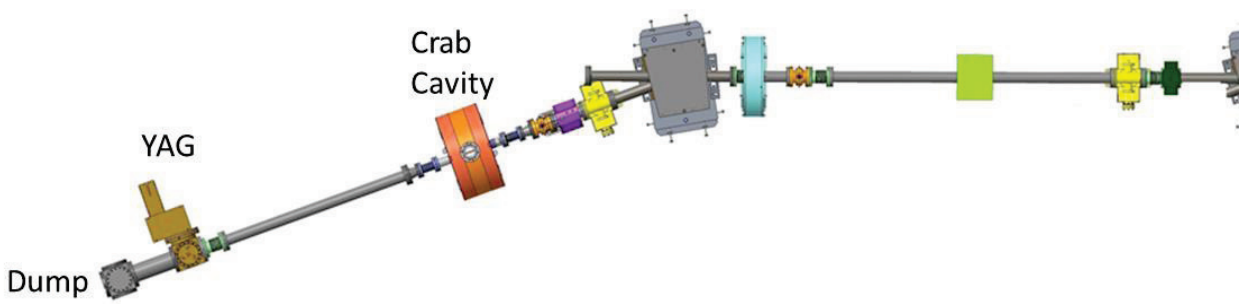

Figure 1: LEReC RF diagnostic beamline layout.

† seletskiy@bnl.gov

ISBN 978-3-95450-177-9

INSTANTANEOUS TEMPERATURE RISE FOR YAG SCREEN

YAG stopping power per electron with 2.1 MeV energy is p=1.46 MeV cm^2/g [6] (in our energy range it changes only slightly). Therefore, the energy loss per electron in YAG screen of width w=100 um is:

$$\Delta E = p \cdot w \cdot \rho = 0.066 \text{ MeV} \quad (1)$$

where $\rho = 4.55 \text{ g}/cm^3$ is YAG density.

The total number of electrons interacting with YAG screen is:

$$N_e = N \frac{Q}{e} \frac{t}{\Delta t} = 5.54 \cdot 10^{13} \quad (2)$$

where e is charge of electron.

Thus, from (1) and (2), the total energy deposited on YAG crystal by the bunch train is:

$$E_{tot} = N_e \Delta E = 0.59 \text{ J} \quad (3)$$

The typical beam profile on YAG screen is shown in Fig. 3. For the sake of energy density calculation we can substitute real beam profile with a homogenous ellipse with 0.11 cm and 1.79 cm semi-axes.

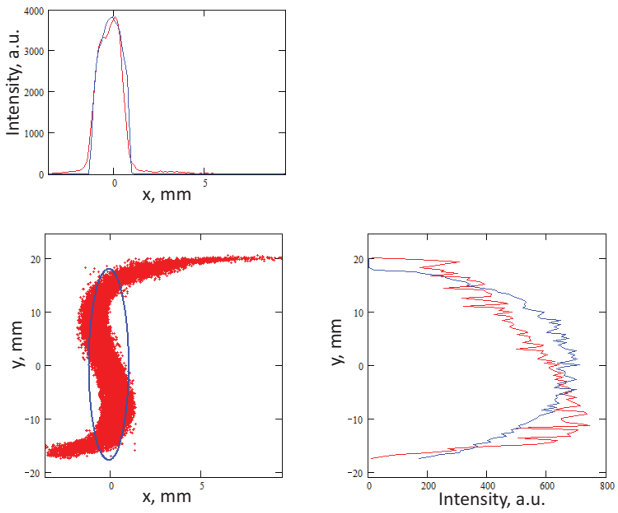

Figure 3: Typical beam profile on YAG screen (red) and equivalent ellipse (blue) homogeneously filled with the same number of particles. For the ellipse, only the outline is shown on the plot.

Since, the specific heat capacity of YAG is c_s=590 J/kg/K, the heat capacity of YAG heated by electron beam is C=0.017 J/K.

Finally, an instantaneous increase in YAG temperature due to deposition of a single bunch train is:

$$\Delta T = \frac{E_{tot}}{C} = 35.5 \text{ K} \quad (4)$$

Apparently, such small (as compared to electron lens experience) temperature jump will not degrade YAG performance.

STEADY STATE TEMPERATURE OF YAG SCREEN

Assuming that the main mechanism of YAG cooling is radiation we find from black-body radiation formula that the steady state temperature is given by:

$$T = \left(\frac{E_{tot} f}{A \sigma_{SB}}\right)^{\frac{1}{4}} \quad (5)$$

Here A is the area covered by the beam image; f is the repetition rate of the beam trains, and Stefan-Boltzmann constant $\sigma_{SB} = 5.67 \cdot 10^{-8} \text{ W/m}^2/\text{K}^4$. We assume 100% emissivity for the YAG crystal in (5).

The result of application of formula (5) to our case is shown in Fig. 4. It is obvious that the safe repetition rate can be at least one shot per 5 seconds.

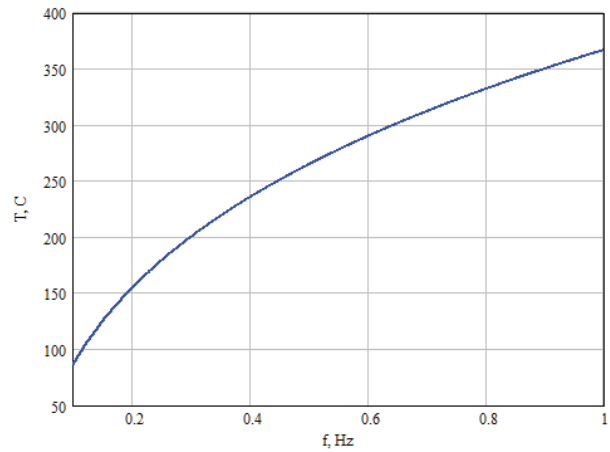

Figure 4: Steady state temperature of YAG crystal depending on e-beam repetition rate.

More precise simulations of YAG cooling take into account crystal emissivity ($\epsilon = 0.8$). To increase the YAG emissivity we plan to coat the back side of the crystal with a layer of carbon on top of the 100nm of aluminum.

In our simulations we assume that over time period dt the crystal is cooled by temperature:

$$dT = \frac{\sigma_{SB} \epsilon (T^4 - T_{room}{}^4) dt}{c_s \rho w} \quad (6)$$

where $T_{room} = 300$ K is room temperature.

Results of simulations for bunch train repetition rate of 0.2 Hz are shown in Fig. 5.

The average steady state temperature of YAG screen for bunch trains arriving with 5 s period is about 170 C and the maximum observed temperature is 186 C.

Notice that by not exceeding 194 C threshold for steady state temperature we create a rather large safety margin since average steady state temperature in electron lens test

ISBN 978-3-95450-177-9

had to be about 400 C (calculations for e-lens parameters were performed using (1)-(6)).

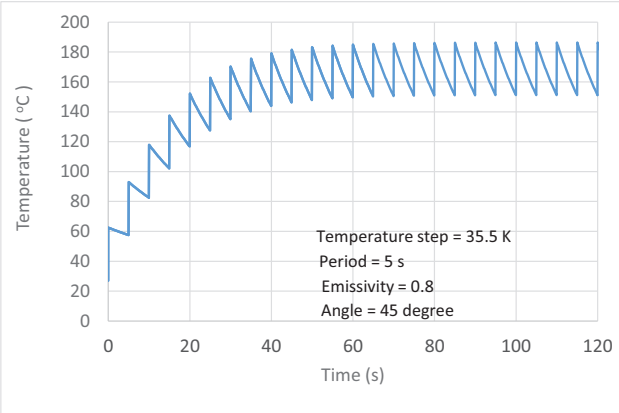

Figure 5: Simulations of steady state temperature.

Finally, one can measure longer than 250 us bunch trains by increasing the period between the trains. Figure 6 shows the period between the bunch trains of various length required to guarantee that YAG steady state temperature does not exceed 186 C (maximum temperature for nominal 250 us long bunch train arriving every 5 s).

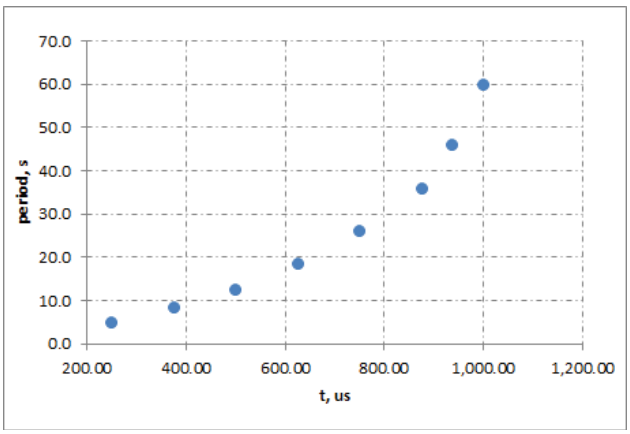

Figure 6: Period between bunch trains depending on train length. For each case YAG steady state temperature does not exceed 186 C.

CONCLUSION

We considered performance of the YAG screen in RF diagnostic beamline of the Low Energy RHIC Electron Cooler for the case of high power (250 us long) bunch trains directed to the YAG screen.

We determined that it is safe to operate such diagnostic with the bunch trains repetition rate of 0.2 Hz.

In case we need to measure the longer bunch trains, the trains' repetition rate can be farther decreased.

Our findings allow us to cut the cost and simplify the design of the RF diagnostic beamline by eliminating a necessity of a fast kicker and a dedicated dump at the beginning of the beamline.

REFERENCES

[1] A. Fedotov, "LEReC project", COOL'15, 2015.

[2] T. Miller *et al.*, "LEReC instrumentation design & construction", presented at the IBIC'16, Barcelona, Spain, Sept. 2016, paper TUPG35.

[3] Private conversations with K. Smith, K. Mernick, A. Zaltsman.

[4] T. Naito, T.M. Mitsuhashi, TUPD08, Proceedings of IBIC2014, Monterey, CA, USA.

[5] Reported by Crytur in email correspondence.

[6] http://physics.nist.gov/PhysRefData/Star/Text/ESTAR-u.html

ISBN 978-3-95450-177-9

TRANSVERSE BEAM PROFILING AND VERTICAL EMITTANCE CONTROL WITH A DOUBLE-SLIT STELLAR INTERFEROMETER*

J. Corbett†, X. Huang and J. Wu, SLAC National Accelerator Laboratory, Menlo Park, USA
C.L. Li, East China University of Science and Technology, Shanghai, China
T. Mitsuhashi, KEK, Tsukuba, Japan
Y.H. Xu, Donghua University, Shanghai, China
W.J. Zhang, East China University of Science and Technology, Shanghai, China
and the University of Saskatchewan, Saskatoon, Canada

Abstract

Double-slit interferometers are useful tools to measure the transverse the cross-section of relativistic charged particle beams emitting incoherent synchrotron radiation. By rotating the double-slit about the beam propagation axis, the transverse beam profile can be reconstructed including beam tilt at the source. The interferometer can also be used as a sensitive monitor for vertical emittance control. In this paper we outline a simple derivation of the Van Cittert-Zernike theorem, present results for a rotating double-slit measurement and demonstrate application of the interferometer to vertical emittance control using the Robust Conjugate Direction Search (RCDS) optimization algorithm.

INTRODUCTION

The concept of a double-slit visible light SR interferometer for charged-particle beam size measurement was first developed at KEK [1] and has since been widely used at many accelerator facilities [2]. Compared with an optical telescope, the double-slit interferometer has the advantage of removing aperture diffraction effects thereby improving spatial resolution.

Perhaps the most well-known application of the stellar interferometer was Michelson's measurement of the 0.047" angle subtended by α-Orionis [3]. Subsequently the field of stellar interferometry has advanced to include telescope configurations with sophisticated aperture synthesis [4] and non-redundant aperture arrays which have also been applied to measure charged particle beam cross-sections using synchrotron radiation [5].

SPEAR3 has a dedicated SR diagnostic beam line designed to characterize properties of the electron beam. Within the beam line, unfocused visible light travels 16m to an optical bench where it has a rectangular cross-section of 60mm x 100mm. The vertical acceptance of ±3mrad is sufficient to pass almost all of the 500nm wavelength component with measureable edge diffraction around the perimeter of the beam (Fig. 1, inset).

Figure 1 shows a schematic of the beamline including the interferometer optics. At the dipole source point, the electron beam cross-section is approximately 120μm x 20μm depending on the lattice configuration. A stationary ±0.6mrad beam stop at the accelerator midplane protects the Rhodium-coated SR beam extraction mirror from the high heat flux of the primary x-ray beam. Typical interferometer slit separations for horizontal and vertical beam size measurements are 15 mm and 50 mm, respectively [6]. Both the double-slit mask and the CCD camera can be mounted on rotatable stages to enable measurement at arbitrary angles relative to the beam axis.

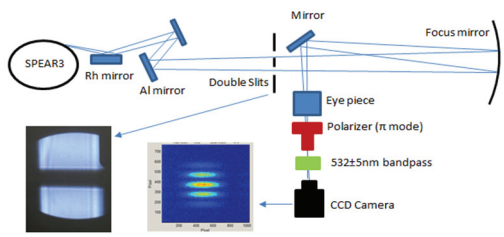

Figure 1: Stellar interferometer on the SPEAR3 visible light diagnostic beam line.

In this paper we first provide a simplified 'conceptual' derivation of the Van Cittert-Zernike theorem to demonstrate the Fourier transform nature of a stellar interferometer operating in the far-field regime. Axial rotation of the interferometer slits about the beam propagation axis is shown to yield the transverse electron beam profile and corresponding beam coherence ellipse in reciprocal space. As an application to machine tuning, vertical interferometer slits are used with a robust optimization program to control vertical beam emittance.

VAN CITTERT-ZERNIKE THEOREM

Analysis of the fringe pattern from a double-slit interferometer in the far field of an incoherent radiating source is often based on the Van Cittert-Zernike theorem [7,8]. In short, the theorem states that under proper paraxial and monochromatic light conditions the fringe contrast evaluated as a function of spatial frequency defined by the slits is the Fourier transform (FT) of the incoherent intensity distribution of the source, $I(x,y)$:

$$\Gamma(f_x, f_y) = \iint I(x,y) e^{-2\pi i(f_x x + f_y y)} dx dy \qquad (1)$$

In practice, by measuring the fringe contrast Γ as a function of slit separation (spatial frequencies f_x ,f_y), one can deduce the source profile $I(x,y)$ via the inverse FT.

* Work supported by US Department of Energy Contract DE-AC03-76SF00515, Office of Basic Energy Sciences and the China Scholarship Council.
† corbett@slac.stanford.edu

ISBN 978-3-95450-177-9

The application to synchrotron radiation opened the door high-resolution transverse beam profile measurements for charged particle accelerators [1,2]. In this section we present a brief history and a conceptually simple version of the Van Cittert-Zernike theorem that highlights the FT relation.

In the late 19th century A.A. Michelson recognized the double-slit interferometer fringe visibility $\frac{I_{max}-I_{min}}{I_{max}+I_{min}}$ produced from an incoherent source could be used to measure the angular diameter of a star [3]. Later, P.H. Van Cittert calculated partition functions [7], and F. Zernike formalized Michelson's result by integrating over statistically independent radiators in the source and introduced the concept of 'degree of coherence' [8]. This work was re-iterated and expanded by Goodman [9] and Born & Wolf [10] who re-cast the theory in the form of 'Fourier optics', i.e. the source distribution can be represented as a continuous spectrum of plane waves.

Goodman in particular refers to the Van Cittert-Zernike theorem as 'one of the most important theorems of modern optics' and demonstrated the FT nature of the theorem in terms of the propagation of mutual intensity in the far-field.

Born and Wolf stressed time-averaging of the ergodic process in taking the sum over statistically uncorrelated point radiators at the source, and introduced the concept of 'mutual coherence' as the FT of the source intensity in the far-field region. Both developments emphasized that the coherent field component mathematically corresponds to the cross-correlation of the fields evaluated at the two interferometer slits. The derivations hold for rather general conditions and consequently contain intricate mathematical nomenclature.

Here we present simplified steps to illuminate a one-dimensional FT relation between fringe contrast and source profile. Referring to Fig. 2, a classical field *E(y)* emitted from a single point on the y axis to the left generates an interference pattern with a modulated intensity profile along the y'-axis to the right. The fields arriving at point y' through apertures p_1 and p_2 are

$$E_1(y,y') = \frac{E(y)}{r_1+r_1'}e^{-ik(r_1+r_1')} \quad (2a)$$

$$E_2(y,y') = \frac{E(y)}{r_2+r_2'}e^{-ik(r_2+r_2')} \quad (2b)$$

where $E(y)$ statistically fluctuates in amplitude and phase. The light *intensity* at y' is

$$I(y,y') = 2I(y) + 2Re\left\{E^*(y)E(y)e^{-ik(r_1-r_2)}e^{-ik(r_1'-r_2')}\right\} \quad (3)$$

where *I(y)* is the intensity per unit radiator and $Re\{\ \}$ indicates 'real part'. Distance factors are suppressed in the denominator. The cross term on the right is perfectly correlated when fields through slit 1 and 2 originate from the same infinitesimal radiator. The time average of the cross-correlation term is identically zero when the fields originate from different radiators.

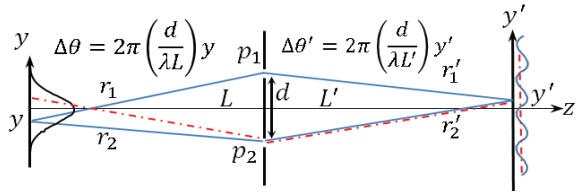

Figure 2: Far-field phase differentials $\Delta\theta = k(r_1 - r_2)$ and $\Delta\theta' = k(r_1' - r_2')$, respectively. Like radiators interfere (blue) and unlike radiators do not interfere (blue and red-dash).

At this point several approximations are typically made prior to integration over the extended source:

a) the intensity pattern is evaluated in the far-field
b) statistically independence (separate points along the y-axis radiate incoherently and do not interfere)
c) quasi-monochromatic light.

Using the far-field approximation, the phase differentials seen in Fig. 2 are [9,10,11]

$$e^{-ik(r_1-r_2)} \sim e^{-2\pi i\left(\frac{d}{\lambda L}\right)y} \quad (4a)$$

$$e^{-ik(r_1'-r_2')} \sim e^{-2\pi i\left(\frac{d}{\lambda L'}\right)y'} \quad (4b)$$

Substituting Eq. 4 into 3

$$I(y,y') = 2I(y) + 2Re\left\{E^*(y)E(y)e^{-2\pi i\left(\frac{d}{\lambda L}\right)y}e^{-2\pi i\left(\frac{d}{\lambda L'}\right)y'}\right\} \quad (5)$$

Taking the time average over the ensemble of statistically uncorrelated radiators at the source and integrating over source coordinate y gives the total light intensity at observation point y':

$$I(y') = 2I_o\left(1 + Re\left\{\int \frac{I(y)}{I_o}e^{-2\pi i\left(\frac{d}{\lambda L}\right)y}\,dy \cdot e^{-2\pi i\left(\frac{d}{\lambda L'}\right)y'}\right\}\right). \quad (6)$$

with $I(y) = E^*(y)E(y)$ and I_0 is the total intensity at each interferometer slit. The exponential term in the FT 'visibility integral' accounts for the phase shift in the fringe pattern from each independent radiator along the y-axis, $I(y)$. Re-writing in more familiar form

$$I(y', f_y) = 2I_o\left(1 + \gamma(f_y)\cos\left(2\pi f_y' y'\right)\right) \quad (7)$$

where $\gamma(f_y) = \frac{1}{I_0}\int I(y)e^{-2\pi i f_y}\,dy$ is the normalized degree of coherence [10], $f_y = \frac{d}{\lambda L}$ is the spatial frequency defined by the slits, and the cosine term produces fringe modulation on the screen. Thus, in the monochromatic far-field approximation, the incoherent source distribution and fringe visibility form a Fourier transform pair with y and f_y the conjugate Fourier transform variables.

ISBN 978-3-95450-177-9

DOUBLE SLIT ROTATION

In two dimensions the Van Cittert-Zernike relation can be written

$$\Gamma(f_x, f_y) = \iint I(x,y) e^{-2\pi i(f_x x + f_y y)} dx dy \qquad (8)$$

where the configuration-space axes (x,y) and spatial frequencies (f_x,f_y) are referenced to an x-y Cartesian coordinate system. From Eq. 8 a bi-Gaussian beam profile

$$I(x,y) = I_o e^{-\left(\frac{x^2}{2\sigma_x^2} + \frac{y^2}{2\sigma_y^2}\right)} \qquad (9)$$

has a Gaussian degree of coherence function

$$\Gamma(f_x, f_y) = \Gamma_o e^{-\left(\frac{f_x^2}{2\sigma_{\gamma,x}^2} + \frac{f_y^2}{2\sigma_{\gamma,y}^2}\right)} \qquad (10)$$

The expression in the exponent of Eq. 10 indicates the coherence function $\gamma(f_x, f_y)$ is a continuum of concentric ellipses conjugate to the electron beam intensity profile.

Experimentally it is possible to rotate the double-slit system to measure the SR beam coherence as a function of slit observation angle θ. Relative to the x-axis, the projected spatial frequencies become $f_x = \frac{d}{\lambda L} cos\theta$ and $f_y = \frac{d}{\lambda L} sin\theta$. For an upright Gaussian beam profile (Eq. 9), the coherence function becomes

$$\Gamma(f_x, f_y, \theta) = \Gamma_o e^{-\left(\frac{\left(\frac{d}{\lambda L} cos\theta\right)^2}{2\sigma_{\gamma,x}^2} + \frac{\left(\frac{d}{\lambda L} sin\theta\right)^2}{2\sigma_{\gamma,y}^2}\right)} \qquad (11)$$

To measure angular dependence, a double slit with separation d=16.94 mm was rotated in the unfocused beam from 0 to 180 degrees with a step size of 5 degrees. Figure 3 shows the variation in fringe contrast when the double slit and CCD camera were rotated synchronously around the SR beam axis and the polarizer angle held fixed. In this case the slits were placed in the lower half of the SR beam below the cold finger. The double slit separation distance was a compromise between RMS values for the θ=0° and θ=90° contrast curves of $\sigma_{\gamma,x}$~15 mm and $\sigma_{\gamma,y}$~50 mm, respectively.

Four data sets corresponding to different values of x-y betatron coupling are plotted in Fig. 3. The displacements in the data along the rotation angle axis correspond to electron beam rotations of θ_0=0°, 9°, 16° and 27°. The theoretical curves according to Eq. 11 are superimposed in the plot. The RMS beam size as measured along the minor axis of the beam ellipse was determined to be σ_{minor}=20, 35, 53 and 69 um.

Figure 4 plots the transverse RMS electron beam profile at the source point with the x-y beam ellipses derived from the fringe contrast data shown in Fig. 3. The electron beam eigen-axes are clearly rotated by coupling of the betafunctions.

BEAM SIZE CONTROL WITH RCDS

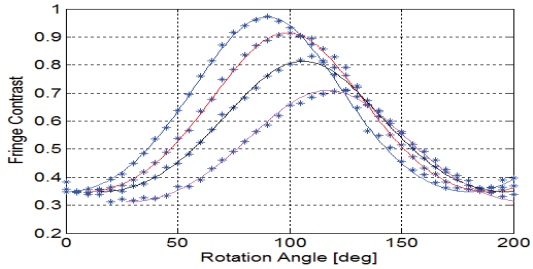

Figure 3: Contrast measured with double-slit rotation for 4 betatron coupling conditions.

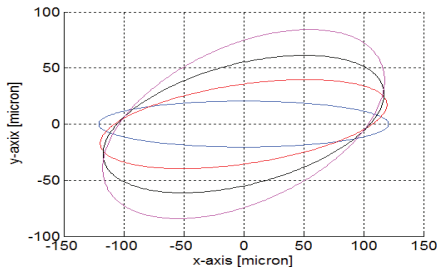

Figure 4: RMS electron beam cross-section color coded for beam coupling conditions in Figure 3.

Optimum accelerator performance frequently requires tuning the magnet lattice with manual or computer-controlled knobs to change machine parameters. In general, accelerator tuning is a multi-variable, nonlinear optimization problem. Most optimization algorithms are not suitable for *online* applications because they are designed to work with smooth mathematical models. Noise in the objective function can cause incorrect steps and hence fail to approach the true optimum.

An algorithm specifically designed for online applications, the *Robust Conjugate Direction Search* (RCDS) [12] overcomes this difficulty. In this section we demonstrate how RCDS was used to control vertical beam size in SPEAR3. Technically, the RCDS algorithm combines the power of Powell's conjugate direction method [12] with a robust, noise-resistant line optimizer. The result is an optimization algorithm for noisy, on-line applications to control multi-variable, non-linear processes.

The RCDS algorithm was initially demonstrated at SPEAR3 by minimizing the betatron coupling using 13 independent skew quadrupoles with the Touschek-dominated beam loss rate as the objective function [12]. Despite the relatively large noise component in the measurements, the algorithm found an optimal solution starting from all skew quadrupole fields set to zero.

For the RCDS applications reported here, the objective function was vertical beam size as measured by the double-slit interferometer. Thirteen skew-quads were again used to control x-y betatron coupling. Referring to Fig. 5, both the interferometer and an x-ray pinhole camera report online values of vertical beam size to the EPICS database. The RCDS algorithm reads these values and performs the

ISBN 978-3-95450-177-9

optimization procedure to control the vertical beam size at the interferometer or pinhole camera.

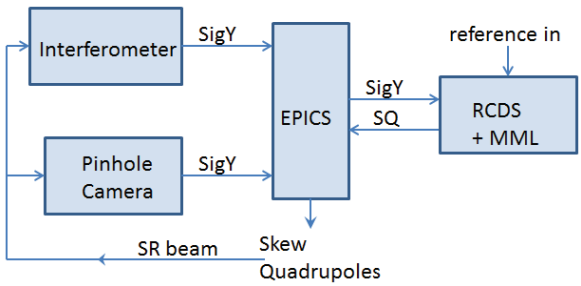

Figure 5: Architecture for RCDS optimization software to control vertical beam size in SPEAR3.

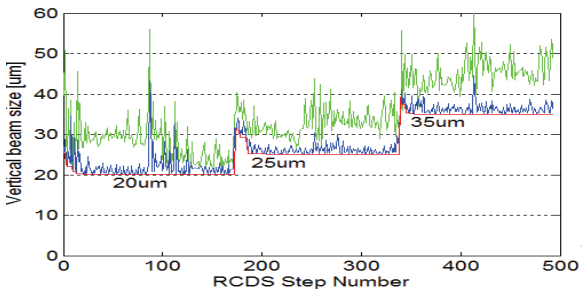

Figure 6: Vertical beam size reference set to 20um, 25um and 30um for the interferometer (blue) and resulting pinhole camera values (red). The two source points have different values for β_y.

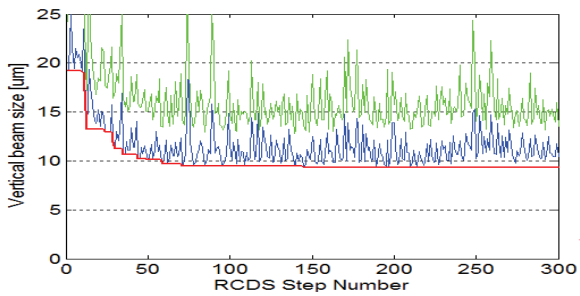

Figure 7: Convergence to minimum vertical beam size with interferometer objective function set to '0'.

The updated skew-quad power supply setpoint values are reported back to EPICS and applied to the lattice magnets.

Figure 6 shows data when the RCDS reference value was set to 20um, 25um and 35um as measured by the interferometer. For each new reference value, the skew quad power supplies were initially set to zero and the algorithm converged within a few minutes. The 'jumps' seen midway along each new search correspond less-than-optimal conditions as the RCDS algorithm explores the phase-space of skew quad eigenvector combinations.

Comparisons were made using the individual skew quads as independent variables against 13 skew quad eigenvector patterns extracted from the Jacobian of the orbit response matrix with respect to each skew quad setting. For each run the eigenvector method converged more quickly because the eigenvectors are inherently more orthogonal than the individual skew quad supplies.

Figure 7 shows the case where the RCDS reference was set to zero (minimum coupling). The red line underlying the data indicates conditions with minimum objective function value. Application of the corresponding skew quad power supply settings produced a minimum value of σ_y=9.5um as measured at the interferometer. Further tests using electron beam Touschek lifetime are planned to determine whether σ_y=9.5um is the minimum resolution limit of the interferometer or the minimum achievable coupling value with only 13 skew quadrupoles.

CONCLUSION

In this paper we report on application of a double-slit interferometer in use at SPEAR3 A simplified derivation of the Van Cittert-Zernike theorem is provided to demonstrate the origin of the Fourier transform relation between incoherent source distribution and fringe contrast evaluated as a function of spatial frequency. Rotation of the double-slit system with respect to the beam axis yields a modulates the fringe visibility and can be used as a tomographic 'slicing' tool to extract the x-y beam intensity profile in agreement with theory. The interferometer was then applied as a measurement tool to control vertical electron beam size using the Robust Conjugate Directional Search algorithm (RCDS).

ACKNOWLEDGMENTS

The authors would like to thank the China Scholarship Council and members of the SPEAR3 operations team for support of this work.

REFERENCES

[1] T.M. Mitsuhashi, 'Beam Profile and Size Measurements by SR Interferometers,' in Beam Measurements, Joint US-CERN-Japan-Russia School, Montreaux, Switzerland, World Scientific (1998).

[2] T.M. Mitsuhashi, "Recent Trends in Beam Size Measurements Using Spatial Coherence of Visible Synchrotron Radiation", *IPAC15*, Richmond, VA, USA (2015), paper THYC2.

[3] A.A. Michelson and F.G. Pease, "Measurement of the Diameter of α-Orionis with the Interferometer", *Astrophysical Journal*, 249-258 (1921).

[4] A. Labeyrie, *et al.*, "An Introduction to Optical Stellar Interferometry", *Cambridge University Press* (2006).

[5] P. Skopintsev, *et al.*, "Characterization of spatial-coherence of synchrotron radiation with Non-Redundant Arrays of Apertures", JSR 21 (2014).

[6] C.L. Li, et al, "Double-slit Interferometer Measurements at SPEAR3', *IPAC16* (2016), paper MOPMR054.

[7] P.H. Van-Cittert, Physica 1, 2001 (1934).

[8] F. Zernike, 'The Concept of Degree of Coherence and Application to Optical Problems', Physica, 5 (1938).

[9] J. Goodman, 'Statistical Optics', Wiley & Sons (1985).

[10] M. Born and E. Wolf, "Principles of Optics", Sixth Edition, Pergamon Press (1980).

[11] J. Peatross and M.Ware, "Physics of Light and Optics," Brigham Young University, unpublished, (2008).

[12] X. Huang, *et al.*, "An Algorithm for Online Optimization of Accelerators", NIM A 726 77-83 (2013), and references therein.

ISBN 978-3-95450-177-9

POLARIZATION MEASUREMENT AND MODELING OF VISIBLE SYNCHROTRON RADIATION AT SPEAR3*

C. L. Li†, East China University of Science and Technology, Shanghai, China
J. Corbett, SLAC National Accelerator Laboratory, Menlo Park, USA
Y. H. Xu, Donghua University, Shanghai, China
W.J. Zhang, East China University of Science and Technology, Shanghai, China
and the University of Saskatchewan, Saskatoon, Canada

Abstract

Synchrotron radiation from dipole magnets is linearly polarized in the plane of acceleration and evolves toward circular polarization with increasing vertical observation angle. The intensity of the x-y field components can be modeled with Schwinger's theory for the angular-spectral power distribution. Combined with Fresnel's laws for reflection at a mirror surface, it is possible to model field polarization of visible SR light in the laboratory. The polarization can also be measured with a polarizer and quarter wave plate to yield Stokes' parameters S_0-S_3. In this paper we present measurements and modeling of the visible SPEAR3 SR beam in terms of Stokes' parameters and plot on the results on the Poincaré sphere.

INTRODUCTION

Synchrotron radiation (SR) has the unique property of a high degree of field polarization. The SR beam from a dipole magnet, for instance, is linearly polarized in the transverse acceleration plane, and changes to elliptical and finally circular polarization as the vertical observation angle increases [1]. Polarized SR in the UV or X-ray regime is frequently used to probe structural properties of matter [2]. Visible SR, with a relatively large opening angle, provides a unique opportunity to study the SR beam polarization state.

According to Schwinger's theory for synchrotron radiation, the σ- and π mode power density distributions produced from a dipole magnet can be accurately modeled. By combining with Fresnel's equations for reflection of electromagnetic radiation at a material interface, the beam polarization at the SR source and at the optical bench can be modeled.

For this work we constructed an optical measurement system composed of a bandpass filter, field-discriminating polarizer and quarter wave plate (QWP) to characterize the beam polarization state in terms of Stokes's parameters [3,4]. The measurement system is mounted on a continuous-scan vertical stage to record the beam intensity as a function of vertical observation angle and polarizer rotation angle. Preliminary results have been presented in references [5,6]. In this paper, we extend the analysis to a Stokes' parameter representation, extract beam polarization ellipse parameters and display the results on the Poincaré sphere.

* Work supported by US Department of Energy Contract DE-AC03-76SF00515, Office of Basic Energy Sciences and the China Scholarship Council.
† Corresponding author: chunlei520@gmail.com

THE SPEAR3 DIAGNOSTIC BEAMLINE

As shown in Fig. 1, the unfocused visible SR beam first encounters a Rhodium-coated extraction mirror at an incidence angle of 81 degrees to the surface normal. The beam is then reflected by two near-normal Al mirrors onto the optical bench. An image of the unfocused SR beam at a distance ~16m from the source is seen to the right. A 'cold finger' x-ray beam stop shadows a range of ±0.6 mrad at the accelerator midplane to protect the extraction mirror from high heat loads at 500mA electron beam current.

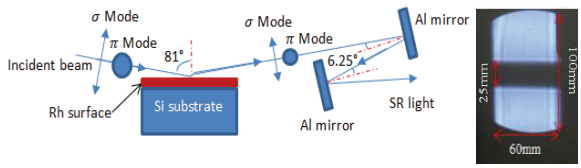

Figure 1: Schematic diagram of the visible-light SR beam transport line at SPEAR3.

Table 1: Reflection Properties of the Rh-coated Mirror

Parameters	Value
Wavelength (nm)	532
Refractive index (n_r)	2.633
Extinction index (k_i)	3.306
Reflection coefficient r_s(π mode)	0.957
Reflection coefficient r_p (σ mode)	0.508
Intensity ratio $I_p/I_s=(r_p/r_s)^2$	0.2818
π mode phase shift $\Delta\emptyset_S$	-176.726°
σ mode phase shift $\Delta\emptyset_P$	119.555°
Phase difference $\Delta\emptyset_{S-P}$	above=153.6°

The visible SR beam extraction mirror was manufactured with 600Å Rhodium deposited on a monolithic Si block [7]. As a result, the refractive index n_r and extinction index k_i exhibit 'thin film' properties as found in [8]. The corresponding reflection coefficients listed in Table 1 were calculated using Fresnel's laws [9] with a complex index of refraction $n=n_r+ik_i$. The grazing-incidence reflection angle in combination with the thin-film Rh mirror surface properties results in ~75% power loss of the horizontal beam polarization component (σ-mode radiation). The normal-incidence Al mirrors have only a small effect.

Stokes' parameters for the unfocused beam were measured using the continuous-scan data acquisition system to systematically probe the vertical observation

ISBN 978-3-95450-177-9

angle and rotate the polarizer transmission axis [10,11]. A typical elevation/rotation scan contains 240360 points and requires ~8 hours to acquire.

SCHWINGER'S EQUATIONS

Schwinger's equations can be used to calculate the vertical SR beam intensity profile as a function of radiation frequency. The single-particle intensity distribution for the σ and π polarization components from a dipole magnet can be written in compact form as [1]

$$F_\sigma = \left(\frac{3}{2\pi}\right)^3 \left(\frac{\omega}{2\omega_c}\right)^2 (1+\gamma^2\psi^2)^2 K_{\frac{2}{3}}^2 \left(\frac{\omega}{2\omega_c}(1+\gamma^2\psi^2)^{\frac{3}{2}}\right) \quad (1)$$

$$F_\pi = \left(\frac{3}{2\pi}\right)^3 \left(\frac{\omega}{2\omega_c}\right)^2 \gamma^2\psi^2(1+\gamma^2\psi^2)^2 K_{\frac{1}{3}}^2 \left(\frac{\omega}{2\omega_c}(1+\gamma^2\psi^2)^{\frac{3}{2}}\right) \quad (2)$$

where ω=2πf is the angular frequency of the light, ψ is the vertical observation angle, γ is the relativistic Lorentz factor for the radiating charges and ω_c is the 'critical frequency' characteristic of the radiated power spectrum. $K_{1/3}^2$ and $K_{2/3}^2$ are modified Bessel functions. By inspection F_σ is finite at the orbit midplane and F_π has a null at the midplane where $\gamma\psi=0$. The functional arguments ω/ω_c and $\gamma\psi$ are normalized so the equations for SR emission are valid over a range different magnetic fields and charged particle beam energies.

For visible light, it is of interest to experimentally validate these expressions in the regime where $\omega << \omega_c$ by comparing with measured results. The key observation parameters for SPEAR3 are defined in Table 2.

Table 2: SPEAR3 Experiment Parameters at 3GeV

Parameter	Value
Observation wavelength	532 nm
Observation angle (ψ)	-3.5 to +3.5 mrad
Lorentz factor (γ)	5860.8
Crit. Energy ($h\nu_c$,ω/ω$_c$)	7.6keV, 3x10^{-4}

STOKES' PARAMETERS AND THE BEAM POLARIZATION ELLIPSE

Stokes' parameters are often used to describe the polarization state of light. The four parameters S_0-S_3 define measurable beam intensity quantities that can be obtained using a field polarizer and a quarter waveplate (QWP) [3,4]. Stokes' parameters are valid for unpolarized light, partially polarized light and fully polarized light, in the latter case synchrotron radiation.

Mathematically, two orthogonal components for monochromatic polarized light can be represented by [4]

$$E_x = E_{ox}\cos(\omega t - kz + \delta_x) = E_{ox}e^{i(\omega t - kz + \delta_x)} \quad (3)$$

$$E_y = E_{ox}\cos(\omega t - kz + \delta_y) = E_{oy}e^{i(\omega t - kz + \delta_y)} \quad (4)$$

As shown in Fig. 2, these equations can be combined to define a 'beam polarization ellipse' by eliminating the common propagation factor $\omega t - kz$:

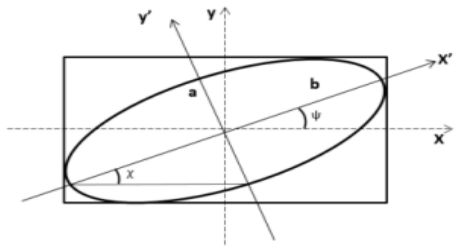

Figure 2: Typical beam polarization ellipse.

$$\frac{E_x^2(t)}{E_{ox}^2} + \frac{E_y^2(t)}{E_{oy}^2} - 2\frac{E_x(t)}{E_{ox}}\frac{E_y(t)}{E_{oy}}\cos\delta = \sin^2\delta \quad (5)$$

Mathematically, the electric field transmitted through a phase-shifting 'wave plate' which delays E_x by φ followed by a polarizer oriented at angle θ to the x-axis can be expressed as

$$E = E_x e^{-i\varphi}\cdot\cos\theta + E_y\cdot\sin\theta\,. \quad (6)$$

In 1852 G.G. Stokes' demonstrated that by squaring Eq. 6 (E^*E) and using trigonometric double-angle formulas the beam intensity can be written in terms of *measureable* quantities [3]:

$$I(\theta,\varphi) = \mathrm{E}\cdot E^* = \frac{1}{2}\big[(E_{ox}^2 + E_{oy}^2) + (E_{ox}^2 - E_{oy}^2)\cos 2\theta + (2E_{ox}E_{oy}\cos\delta)\cos\varphi\sin 2\theta + (2E_{ox}E_{oy}\sin\delta)\sin\varphi\sin 2\theta\big] \quad (7)$$

where $\delta = \delta_x - \delta_y$ and time averages are implied.

In terms of Stokes' parameters S_0-S_3, Eq. 7 can be expressed as

$$I(\theta,\varphi) = \frac{1}{2}[S_0 + S_1\cos 2\theta + S_2\cos\varphi\sin 2\theta + S_3\sin\varphi\sin 2\theta] \quad (8)$$

where

$$S_0 = I(0^\circ,0^\circ) + I(90^\circ,0^\circ) = E_{ox}^2 + E_{oy}^2 \quad (8a)$$

$$S_1 = I(0^\circ,0^\circ) - I(90^\circ,0^\circ) = E_{ox}^2 - E_{oy}^2 \quad (8b)$$

$$S_2 = I(45^\circ,0^\circ) - I(135^\circ,0^\circ) = 2E_{ox}E_{oy}\cos\delta \quad (8c)$$

$$S_3 = I(45^\circ,90^\circ) - I(135^\circ,90^\circ) = 2E_{ox}E_{oy}\sin\delta \quad (8d)$$

The beam polarization ellipse shown in Fig. 2 has a rotation angle ψ and a characteristic ellipticity angle χ where tan χ=±a/*b* that can be expressed either in terms of field parameters $\{E_{ox}, E_{oy}, \delta\}$, or Stokes' parameters:

$$\tan 2\Psi = \frac{2E_{ox}E_{oy}\cos\delta}{E_{ox}^2 - E_{oy}^2} = \frac{S_2}{S_1} \quad (10)$$

$$\sin 2\chi = \frac{2E_{ox}E_{oy}\sin\delta}{E_{ox}^2 + E_{oy}^2} = \frac{S_3}{S_0} \quad (11)$$

The relation between Stokes' parameters and the beam polarization ellipse parameters ψ and χ can be re-written

$$S_2 = S_1\tan 2\Psi \quad (12)$$

$$S_3 = S_0\sin 2\chi \quad . \quad (13)$$

ISBN 978-3-95450-177-9

For a fully-polarized beam, Stokes' parameters obey

$$S_0^2 = S_1^2 + S_2^2 + S_3^2 \quad . \qquad (14)$$

Substituting Eqs. 12 and 13 into Eq. 14, we obtain

$$S_1 = S_0 \cos 2\chi \cos 2\Psi \qquad (15a)$$

$$S_2 = S_0 \cos 2\chi \sin 2\Psi \qquad (15b)$$

$$S_3 = S_0 \sin 2\chi \qquad (15c)$$

By analogy, standard spherical coordinates {r, θ, φ} are related to the Cartesian coordinate axes {x, y, z} by

$$x = r \sin\theta \cos\phi \qquad (16a)$$

$$y = r \sin\theta \sin\phi \qquad (16b)$$

$$z = r \cos\theta \qquad (16c)$$

S_1, S_2, S_3 in Eqs. 15 may therefore be identified with Cartesian coordinate axes provided

$$\theta = 90° - 2\chi \quad \text{and} \quad \phi = 2\psi \, .$$

As first demonstrated by Poincaré [4], the polarization state of light can be plotted in terms of ellipse parameters ψ and χ on the 'Poincaré sphere' illustrated in Fig. 3. In the equatorial plane (S_3=0) the field is linearly polarized and at the poles the field is circularly polarized. All states between the equator and the two poles represent elliptical polarization. Interestingly, nearby points on the sphere represent similar polarization states and therefore have the potential to produce interference fringes.

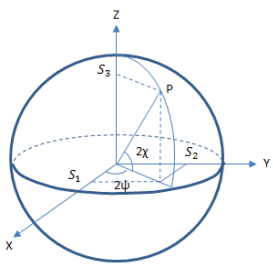

Figure 3: Poincaré sphere for field polarization.

MEASUREMENT AND MODEL

Intensity profiles were first measured along the vertical observation axis for the E_{0x}^2 and E_{0y}^2 SR field components at λ=532nm. Stokes' parameters S_0 and S_1 were then calculated by substituting the data into Eqs. 8a and 8b and plotted in Figs. 4 and 5. The solid red lines are the theoretical values from Schwinger's equations taking account attenuation at the Rh-coated beam extraction mirror (Table 1) [6].

S_2 was measured by rotating the polarizer to 45° and 135° relative to the horizontal axis and calculating the intensity difference from Eq. 8c. The measured data is plotted in Fig. 6. The theoretical solid red curve was obtained from Eq. 8c where E_{ox} and E_{oy} are the scaled Schwinger equations and the relative phase δ=153.56° (see Table 1). To improve the model, the black curve retains Schwinger intensity profiles but introduces the *measured* phase shift at the mirror derived from Eq. 8c [6]. The natural phase

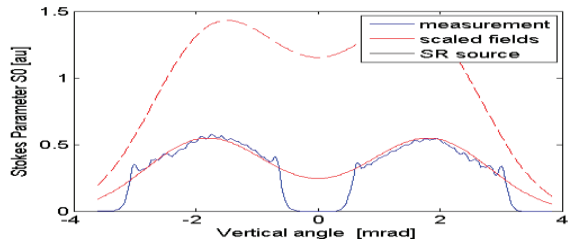

Figure 4: S_0 profile - blue=measured, red=model with mirror attenuation, red-dash=SR source.

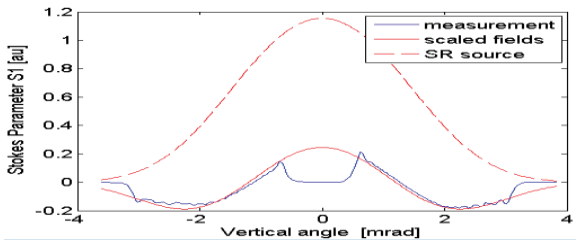

Figure 5: S_1 profile - blue=measured, red=model with mirror attenuation, red-dash=SR source.

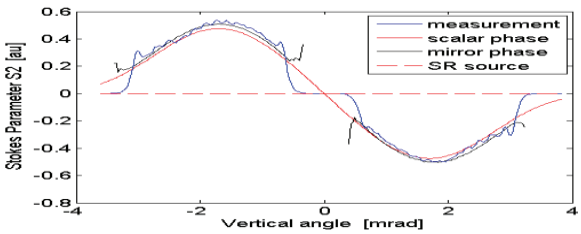

Figure 6: S_2 profile - blue=measured, red=model phase shift, black=measured phase, dash=SR source.

difference at the SR source point is δ=±90°.

In practice the phase shift induced by the extraction mirror evaluated along the vertical observation axis is important for modeling the beam polarization state. As seen in Fig. 7, the model for the ellipticity angle χ is inaccurate when a fixed scalar value is used for the phase shift. If the *measured* phase profile is used in the model, the agreement between measured and modeled ellipticity angle improves significantly.

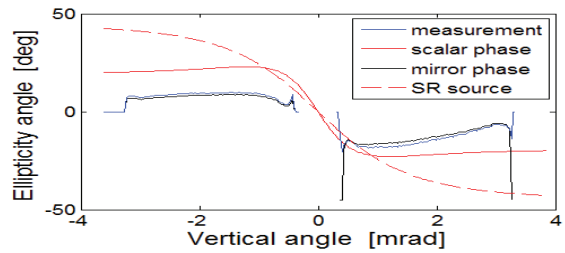

Figure 7: Profile for ellipticity angle - blue=measured, red=model phase shift, black=measured phase shift, red dash=SR source.

Stokes' parameter S_3 yields the 'handness' of helically polarized light. S_3 was measured by inserting the QWP upstream of the polarizer with the fast axis oriented vertically and again setting the polarizer to 45° and 135°, respectively. Figure 8 shows the measured S_3 profile (blue) and the calculated value after the Rh-mirror (solid red). The black curve is the result of using the measured

ISBN 978-3-95450-177-9

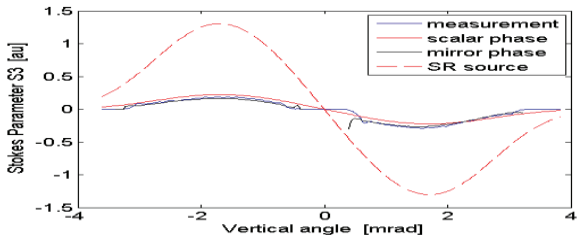

Figure 8: S_3 profile - blue=measured, red=model phase shift, black=measured phase, dash=SR source.

phase profile. The red-dashed line represents S_3 at the SR source. The reduction in magnitude of S_3 demonstrates that the Rh extraction mirror converts helically-polarized light to much more linearly-polarized light.

Figure 9 shows the Poincaré sphere representation of the normalized beam polarization state as a function of vertical observation angle. The axes of the Poincaré sphere represent Stokes' parameters $\{S_1\ S_2\ S_3\}$. The ellipticity angle χ corresponds to lattitude and the ellipse rotation angle ψ corresponds to longitude (Fig. 3). For the SPEAR3 data, the upper half of the sphere contains the SR beam below the accelerator midplane while the lower half shows the beam above the midplane.

The blue line in Fig. 9 shows the theoretical variation in beam polarization state at the SR source – the light is linearly polarized at the midplane (S_3=0) with increasing ellipticity and no ellipse rotation angle ψ (natural dipole SR lies entirely in the S_1-S_3 plane). The green line shows the measured polarization trajectory. The field is significantly more 'linearly' polarized than at the source due to the phase shift at the extraction mirror. The presence of the cold finger is evident in the data (accelerator midplane).

The red line shows the calculated polarization state after the extraction mirror when a fixed scalar value is used for phase shift at the mirror, The trajectory is slightly offset in 2χ from the measured data. When the measured phase is used in the calculation the agreement between measurement and model is good (magenta model curve on top of blue measured data).

CONCLUSIONS

Field polarization measurements of an unfocused visible SR beam are presented and modeled using Schwinger's equations to calculate vertical elevation dependence and the Stokes' parameters to represent the polarization state. Fresnel's equations were used to simulate reflection from the Rh-coated beam pick-off mirror. The data is plotted on the Poincaré sphere to yield a compact representation of the variation in beam polarization with vertical observation angle. The close agreement between measurement and model confirms Schwinger's theory in the visible light regime ($\omega << \omega_c$) and demonstrates the thin-film Rh-coated beam pick-off mirror has a significant influence on the extracted light.

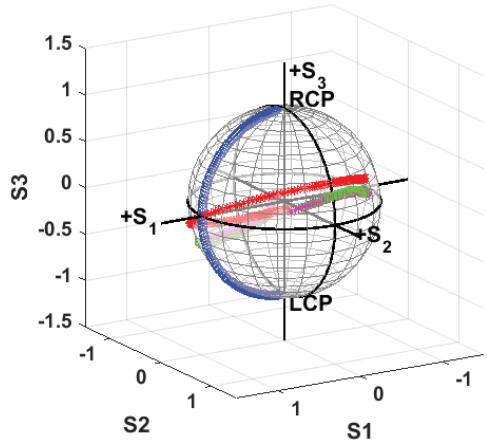

Figure 9: Poincaré sphere representation of SR beam polarization. Red=model, green=measured, magenta=measured phase shift, blue=SR source.

ACKNOWLEDGMENTS

The authors would like to thank the China Scholarship Council, D.Van Campen and SPEAR3 staff for support of this work.

REFERENCES

[1] A. Hofmann, "*The Physics of Synchrotron Radiation*", Cambridge University Press, (2004).

[2] J.Stöhr, *et al.*, "*Element specific magnetic microscopy with circularly polarized X-ray*", Science, Vol. 259, p.658 (1993).

[3] G.G.Stokes, "*On the composition and resolution of streams of polarized light from different sources*", Trans. Camb. Phil. Soc., Vol. IX, p.399 (1852).

[4] E.Collett, "*Polarized Light: Fundamentals and Applications*", Marcel Dekker, Inc., NY,p.34-49 (1992).

[5] J.Corbett, C.L.Li, et al., "*Characterization of Visible SR at SPEAR3*", IPAC15, Richmond, VA (2015).

[6] C.L.Li, J.Corbett, J., T.Mistuhashi, "*Characterization of the visible beam polarization state at SPEAR3*", IBIC2015, Melbourne, Australia (2015).

[7] C.Limborg, *et al.*, "*An Ultraviolet Light Monitor for SPEAR3*", EPAC02, Paris, France (2002).

[8] D.P.Arndt, *et al.*, "*Multiple determination of the optical constants of thin film coating materials*", Applied Optics, 23, No. 20, p.3594, (1984).

[9] E.Hecht, *Optics*, 2nd Edition, Addison-Wesley (1987).

[10] C.L.Li *et al.*, "*Investigation of Continuous Scan Methods for Rapid Data Acquisition*", IPAC15, Richmond, VA (2015).

[11] C.L.Li, *et al.*, "*Continuous scan capability at SSRL and application to X-ray diffraction*", J. Synchrotron Radiation 23, p.912 (2016).

ISBN 978-3-95450-177-9

DIAGNOSTIC TEST-BEAM-LINE FOR THE INJECTOR OF MESA*

I. Alexander†, K. Aulenbacher
Institut für Kernphysik, Johannes Gutenberg-Universität, D-55099 Mainz, Germany

Abstract

With the test-beam-line it is possible to measure the two transverse phase-spaces and the temporal distribution of the electron bunches. It is also possible to investigate the emittance close to the source. The beam-line components will be introduced and a selection of the results will be presented.

INTRODUCTION

MESA will be a multi-turn Energy Recovery Linac (ERL) which can be operated in two different modes. An ERL Mode (105 MeV) or an External Beam (EB) Mode (155 MeV) [1]. The source will be a 100 kV dc photo gun which delivers polarized electrons with a current of 150 µA and an unpolarized electron beam with a beam current of 1 mA in stage-1 and 10 mA in stage-2. The goal is to operate in c.w.-mode which means a bunch charge (Q_b) of 0.8 pC in stage-1 and 8 pC in stage-2. More details on the MESA project and the current status can be found in [1–3].

The task of the diagnostic test-beam-line is to determine if the photo electron source (PES) can deliver a smaller normalized emittance (ϵ_n) than the acceptance of the accelerator with a sufficient safety margin - for all Q_b - which requires that $\epsilon_n \leq 1\,\mu m$. For the operation of MESA the source should be reliable and deliver a high extractable charge with a long lifetime.

Semiconductor photo-cathodes have some properties that should be taken into account. When excited with photon energies close to the band gap energy it is possible to create spin polarized electrons with circular polarized photons. However, when operating in this mode one suffers from low quantum efficiency (QE) and reduced cathode lifetime. If high currents, but no spin-polarization, are desired it is advantageous to use higher photon energies, since the QE is almost an order of magnitude larger and the lifetime is longer. At around 400 nm the photo-cathodes can have a QE of 10% ≙ 32mA/W. For higher photon energies not only the QE increases but also the thermal emittance does. This is because of the fact, that the stimulated electrons have not enough time to thermalize while they are traveling through the semiconductor and end up with a wider energy distribution. This additional energy spread gets transferred into larger transverse momenta which leads to a larger thermal emittance [4].

The source in the diagnostic test-beam-line has delivered 700 C [5] within one charge-lifetime at average currents exceeding 1 mA. The experiment needs average current of 1(10) mA corresponding to an extracted charge of 3.6(36) C/h. Therefore, the transmission from PES to target should be as big as possible, to allow long continuous runtimes. To achieve this requirement a RF-synchronized laser must excite photo-emission. We will capture the so-produced bunches by a harmonic buncher system which can accept bunches with an extension of about 160° [6]. This leads to the requirement that the emitted intensity - which is the convolution of the temporal laser intensity profile and the response of the photo-cathode - must fit into this interval. Fractions outside the interval may be suppressed by a chopper system to provide very clean operating conditions for MESA. In the setup described here one of the circular deflecting cavities which were developed for the chopper system of MESA is used as temporal diagnostic instrument - see below.

COMPONENTS

Beam Line

A schematic overview of the beam-line setup is given in Fig. 1. In the upper left side there is the dc photo gun with a load-lock system and a potential of −100 kV. After the excitation of the electrons by laser light they are accelerated in the vertical direction. 1 m downstream of the source the first analyzing stage (scanner 1) is placed followed by an α-magnet which bends the electrons 270° from the vertical to the horizontal direction. Between the both α-magnets the second analyzing stage (scanner 2) is mounted. Here the evolution of ϵ_n with respect to the position of scanner 1 can be studied. If the second α-magnet is switched off investigations of the temporal distribution (TD) of the electron beam can be done with a deflecting cavity [7, 8] and a Ce:YAG screen. If the second α-magnet is switched on the electrons pass by the third analyzing stage (scanner 3) where it is possible to take a closer look to the beam halo with two perforated Ce:YAG screens. Behind scanner 3 there is a Wien-Filter for spin manipulation and a double scattering Mott polarimeter. This device is currently under test and promises to yield very precise polarization measurements [9] for the experiments (P2 [10] and MAGIX [11]) foreseen at MESA. It is, however, not relevant for the contents discussed here. All components between the source and the second α-magnet/scanner 3 are UHV compatible and bakeable. There are focusing elements like quadrupoles (blue) and solenoids (green) as well as several steering magnets which are not shown in Fig. 1.

The laser system (LS) for unpolarized high average electron current is installed close to the source chamber to create a minimized beam spot on the photo-cathode.

* Work supported by the German Science Foundation (DFG) under the Cluster of Excellence PRISMA
† alexand@kph.uni-mainz.de

ISBN 978-3-95450-177-9

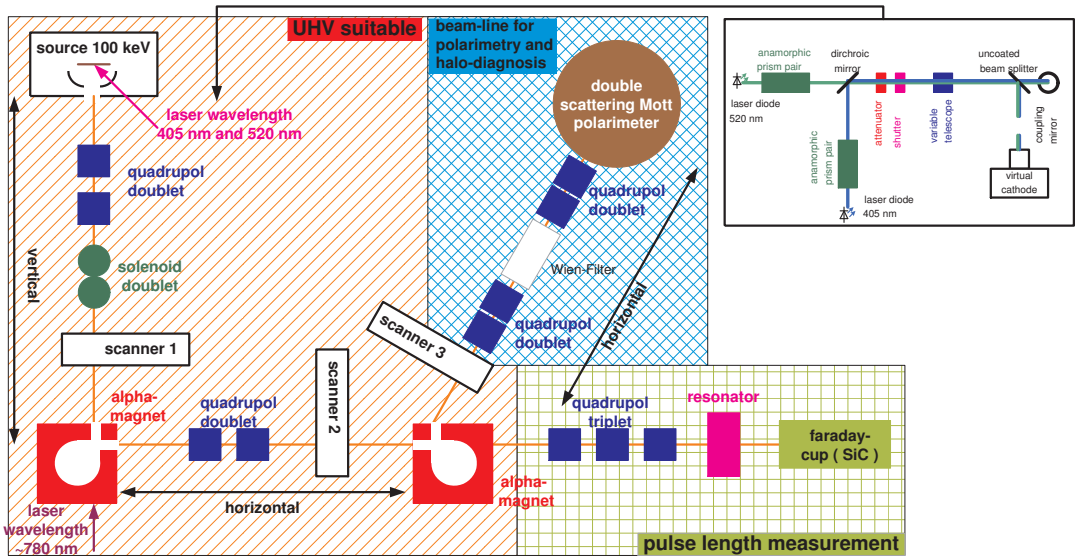

Figure 1: Schematic overview of the beam-line setup and the laser system (top right).

Laser System

The *LS* used for the presented results consists of two laser diodes (*LD*) with different wavelengths (λ_L) of 405 nm and 520 nm respectively and illuminates the cathode through a view-port on the bottom of the source chamber. A schematic sketch is illustrated in Fig. 1 (top right). At short distance after both *LD*s there is an anamorphic prism pair to compensate the astigmatism of the diodes. After the prism pair a dichroic mirror to combine both λ_L is installed, followed by a remotely controlled attenuator and shutter. The next element is a variable telescope to create different beam spot sizes (*BSS*) on the photo-cathode. The penultimate element is an uncoated beam splitter which couples out 3% of the laser power (P_L) and brings it onto a CCD-camera which works as virtual cathode to determine the *BSS* of the laser. The rest of P_L is reflected onto the photo-cathode via a mirror. An example of the laser spot shape at the waist is given in Fig. 2 for both λ_L. These 2D plots show the normalized intensity over the pixels of the camera which have a size of 6.6 µm.

The irregular patterns (in particular of the green *LD*) in Fig. 2 and the temporal distribution (at aspired Q_b) presented below in Fig. 8 illustrate the inferiority of *LD*s in comparison to a dedicated *LS* such as fiber based MOPA's [12]. However, for our purposes, these lasers, which are cheap and reliable, are adequate.

The *LS* can be operated in c.w. or in pulse train mode (*PTM*). For both modes the injection current of the laser diode driver (*LDD*) is superimposed by a RF power (P_{RF}) of 1.7 W with $\nu_{RF} = 1.3$ GHz. P_{RF} can be adjusted by an attenuator to optimize the operating parameters to different *LD* types. In *PTM* the *LDD* is supplied by rectangular shaped pulses with a length of $\tau \geq 300$ µs and a repetition rate $\nu \geq 5$ Hz from a pulse generator. The *PTM* is used to minimize the thermal load on the screens with respect to

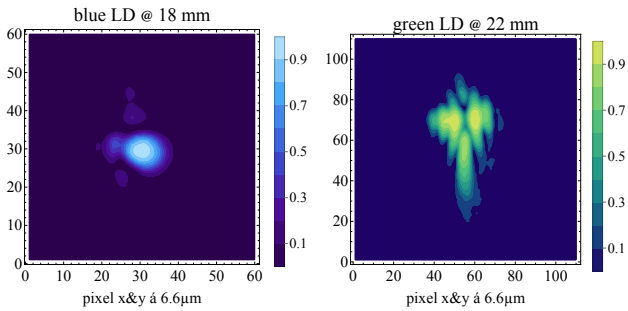

Figure 2: Examples for the normalized intensity of the *BSS* on the virtual cathode for the blue *LD* (left) and the green *LD* (right). In the plot title is also indicated the telescope setting.

high Q_b measurements. In the figures 5, 6 the Q_b is replaced by an equivalent average current which would occur in c.w. operation. Investigations with the deflecting cavity in the test-beam-line have clarified that the RF synchronized pulses within the pulse train are stable, which is depicted in Fig. 3. Here are taken four examples of the *TD* within a 300 µs long pulse train and it can be seen that the blue *LD* produces a double pulse with a RF phase length of $\vartheta_{RF,b} < 120°$ (left) and the green *LD* generates single pulses with $\vartheta_{RF,g} < 100°$ (right). Additional information on the *LS* can be found in [13].

The reason for the two different λ_L is to check the influence of it on ϵ_n and because both *LD*s show different pulsing behavior which are illustrated in Fig. 3 and thus, these measurements enables to consider the influence of the pulse shape on the ϵ_n growth for higher Q_b.

Scanner Devices

All three scanners have at least one Ce:YAG screen with a $\emptyset = 25$ mm to optimize the beam trajectory and to make

ISBN 978-3-95450-177-9

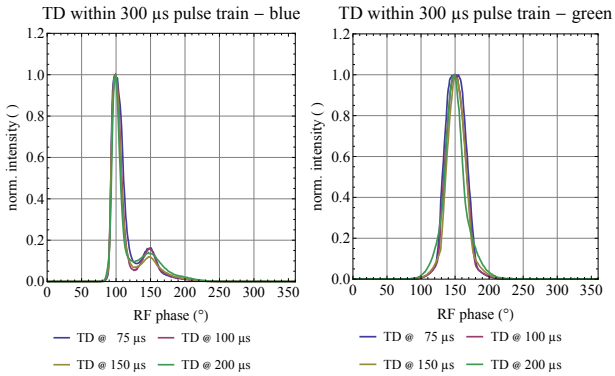

Figure 3: Examples for the RF synchronized pulses within a 300 µs pulse train for the blue *LD* (left) and the green *LD* (right). Over 4σ of both distributions lie within $\vartheta_{RF} = 120°$.

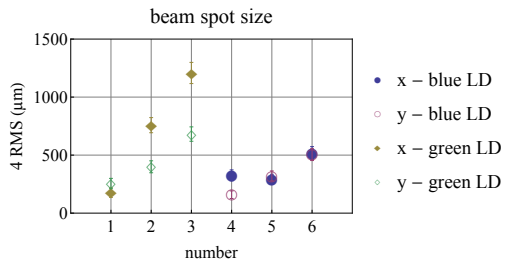

Figure 4: Overview of the *BSS*s generated by the telescope for small, medium and big laser spot.

emittance measurements by quadrupole scans. The electron facing side of the Ce:YAG screens is coated with *Al* to take the charge away and to avoid image distortion by charging of the surface. Scanner 1 and 2 also contain *W* wires with a $\emptyset = 40$ µm for emittance measurements and to investigate the halo distribution because of the higher dynamic range of a PMT-scintillator setup in comparison to a CCD-camera. Furthermore, scanner 1 has two slit arrays which are oriented perpendicular to each other. They have a slit width of 25 µm and a spacing of 250 µm to make emittance measurements complementary to quad scan results. In scanner 2 the slits are replaced by a hole mask (pepper pot) with 21 x 21 holes with a $\emptyset = 25$ µm and a spacing of 250 µm in both directions. The purpose of scanner 3 is halo investigations and for that there are mounted two additional perforated Ce:YAG screens with a 2 mm or a 3 mm hole. Here the observing direction is the same as the incident electrons come from and thus, the screens are coated with ITO in addition.

RESULTS

Quad Scan

For the quad scan the focusing strength k of one quadrupole is varied in small steps and the beam profile is obtained from a Ce:YAG screen with a CCD-camera. The dimensions of the *BSS*s are shown in Fig. 4 and in Fig. 5 are presented some results of ϵ_n for the blue *LD* (left) and for the green one (right). The legends indicate the I_e dependent slope of ϵ_n and the used *BSS*. These results clarify a dependence on the *BSS* and show that the requirements for MESA stage-1 could be fulfilled with the medium spot size for both *LD*s.

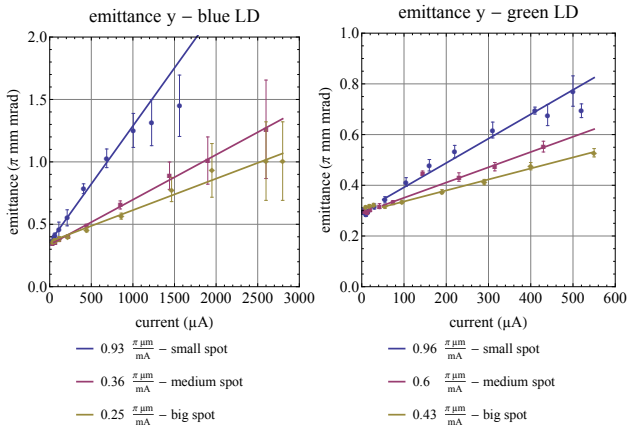

Figure 5: ϵ_n results from quad scan for the blue *LD* (left) and the green *LD* (right) plotted over I_e.

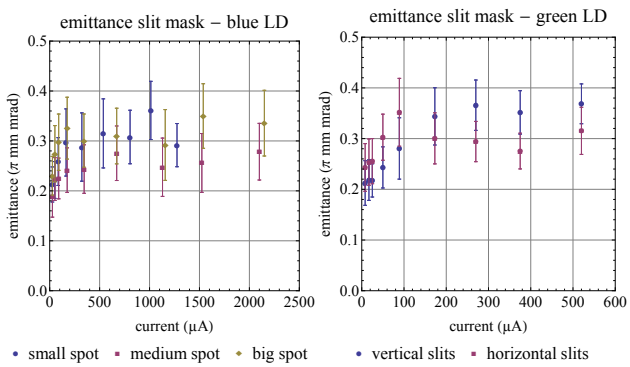

Figure 6: ϵ_n results from the slit mask measurements plotted over I_e for the blue *LD* (left) and the green *LD* (right).

Slit Mask

In the slit mask emittance measurement method small slices of the beam are cut-out. With the width, the displacement and the amplitude of each beamlet it is possible to reconstruct the phase-space distribution. More details of the slit mask method can be seen in [14]. Furthermore, with these parameters ϵ_n can be calculated. In Fig. 6 are introduced some results for the blue *LD* (left) and for the green one (right). This data also represents the 1σ–ϵ_n.

If Fig. 5 and Fig. 6 are compared it strikes that the results for ϵ_n from the slit mask does not show a dependence on I_e for currents > 100 µA for both λ_L. The values scatter around $\epsilon_n \simeq 0.3\,\pi$ µm. This could be explained with the fact, that the phase-space distribution is curved with increasing I_e and if an ellipse is used to describe this distribution ϵ_n becomes larger to capture the same proportion of particles as in case of the slit mask. This should not be the case for the slit mask measurements which capture the true (conserved)

ISBN 978-3-95450-177-9

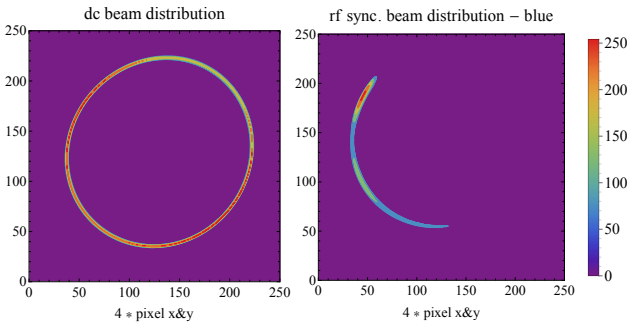

Figure 7: Example intensity distribution for a dc (left) and a c.w. (right) beam behind the deflecting cavity.

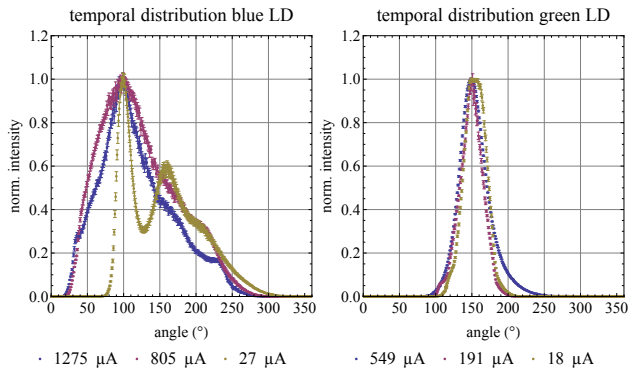

Figure 8: Selection of the I_e dependent evolution of the TD for the blue LD (left) and the green LD (right). The corresponding I_e is indicated in the legend.

emittance area. Our measurements (Fig. 6) seem to support this assumption.

Temporal Distribution

The deflecting cavity works with the MESA RF and is synchronized to the LS. Over the applied RF field in the cavity the beam is deflected circular and thus, the TD is transformed into a transverse one which can be observed with a CCD-camera and a Ce:YAG screen. The analyzed pictures are a superposition of many synchronous bunches and an example for a dc (left) and c.w. (right) beam of the blue LD is given in Fig. 7.

Due to the long drift space between the PES and the deflector ($\sim$ 4.5 m) strong modifications of the TD by space-charge can be expected. Investigations have been done for both λ_L and for different I_e up to the mA region. Fig. 8 is representing a selection of TDs for both LDs and the corresponding I_e are indicated in the legends. The LDs used here are an easy means to demonstrate the performance of the analysis systems at the relevant Q_b for MESA.

SUMMARY

The collected experience with the diagnostic test-beam-line have shown that it is a powerful tool to investigate the transverse ϵ_n and the TD for different bunch shapes up to the mA ($\sim$ 1 pC/bunch) region. Investigations of the two transverse phase-spaces with quadrupole scan technique and the determination of the beam profile with a screen or with wires are possible. The beam-line gives the possibility of a cross check between quad scan and slit mask measurements.

The test-beam-line setup has a similar length compared to the one foreseen for MESA, where the necessities of spin manipulation increase the size by about 1.5 m. The presented results indicate that MESA stage-1 parameters can be achieved, whereas stage-2 parameters probably require a shorter distance between PES and injector (at the expense of spin manipulation flexibility) and/or a PES with larger accelerating gradient and potential.

REFERENCES

[1] R. Heine, ERL2015, Stony Brook, USA, WEIBLH1049

[2] T. Stengler, K. Aulenbacher et al., IPAC'16, Busan, Korea, WEPMB009

[3] R. Heine, K. Aulenbacher et al., IPAC'16, Busan, Korea, TUPOW002

[4] I. V. Bazarov, Journal Of Applied Physics 103, 054901 (2008)

[5] K. Aulenbacher, I. Alexander et al., J. Phys. Conf. Series 298 (2011) 012019

[6] P. Heil, Diploma thesis, JGU Mainz, Germany (2015)

[7] V. Bechthold, Diploma thesis, JGU Mainz, Germany (2013)

[8] B. Ledroit, Bachelor thesis, JGU Mainz, Germany (2014)

[9] A. Gellrich, J. Kessler,Phys. Rev. A 43, 204 (1991)

[10] N. Berger, K. Aulenbacher et al., PhiPsi15, USTC, China (2015)

[11] A. Denig, APS April Meeting (2015), Baltimore, USA

[12] D. G. Ouzounov et al., PAC07, Albuquerque, USA, MPOAS044

[13] I. Alexander, K. Aulenbacher et al., ERL2015, Stony Brook, USA, THIALH2069

[14] M. Zhang, FERMILAB-TM (1988)

ISBN 978-3-95450-177-9

TRANSVERSE BEAM SIZE DIAGNOSTICS USING BROWNIAN NANOPARTICLES AT ALBA

M. Siano*, B. Paroli, M. A. C. Potenza, Dipartimento di Fisica,
Università degli Studi di Milano and INFN Sezione di Milano, via G.Celoria ,16 ,20133 Milano ,Italy
U. Iriso, A. Nosych, L. Torino, ALBA-CELLS, Cerdanyola del Vallès, Spain
A. N. Goldblatt, S. Mazzoni, G. Trad, CERN, Geneva, Switzerland

Abstract

In this work we describe a novel beam diagnostic method based on coherence characterization of broad-spectrum bending magnet radiation through the Heterodyne Near Field Scattering (HNFS) technique. HNFS is a self-referencing technique based on the interference between the transmitted beam and the spherical waves scattered by each particle of a colloidal suspension. The resulting single-particle interferogram shows circular interference fringes modulated by the spatio-temporal Complex Coherence Factor (CCF) of the radiation. Superposition of a number of these patterns results in a stochastic speckle field, from which spatial and temporal coherence information can be retrieved in near field conditions. Here we describe the basics of this technique, the experimental setup mounted along the hard X-ray pinhole at the ALBA synchrotron light source, and the possibility of transverse electron beam size retrieval from the spatial coherence function of the emitted dipole radiation. We also show preliminary results concerning power spectral density of visible synchrotron radiation as obtained from temporal coherence.

INTRODUCTION

In the ALBA storage ring, electrons are kept circulating to produce hard X-ray synchrotron radiation through bending dipoles and other insertion devices. Transverse beam size measurements are routinely performed with an X-ray pinhole camera [1], while parallel reliable measurements are provided by classical Young interferometry for visible synchrotron radiation in the Xanadu beamline [2]. A novel approach to access the full 2D coherence map and hence the 2-dimensional beam profile, also suitable for X-ray wavelengths, is given by the Heterodyne Near Field Speckle technique (HNFS) [3–5]. It has already been successfully applied to visible (λ = 402 nm) SASE FEL radiation at SPARC_LAB, Laboratori Nazionali di Frascati [4] and to soft X-ray (λ = 0.1 nm) undulator radiation at ESRF, Grenoble [5]. Recently [6], we have overcome monochromatic requirements and extended the technique to broadband visible radiation. The aim of this work is to describe applicability of HNFS to hard X-ray spatial and temporal coherence measurements at ALBA and to discuss the related transverse beam size diagnostics.

The paper is organized as follows: we first provide the reader with an overview of the HNFS technique and its extension to broadband radiation; then we describe the ALBA facility and the related HNFS diagnostics; we show experimental results regarding temporal coherence measurements of visible synchrotron radiation along the Xanadu beamline; finally, we collect our conclusion.

* mirko.siano@unimi.it

HETERODYNE NEAR FIELD SPECKLE TECHNIQUE

Fundamentals of the Technique

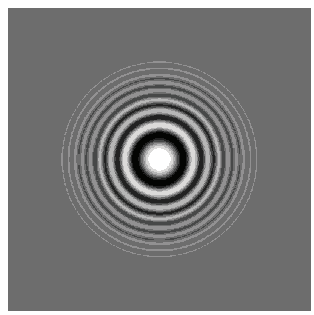

Figure 1: Single particle interferogram described by Eq. 2. Interference fringes have been modulated with a Gaussian coherence factor $e^{-2\left[(x-x_i)^2+(y-y_i)^2\right]/\sigma^2}$ with a coherence area of linear dimension σ = 200 μm. Mesh size 500×500, parameters used for the computation are λ = 632.8 nm, z = 5mm, frame dimension 0.7 mm.

Heterodyne Near Field Scattering (HNFS) is a self-referencing interferometric technique based on the superposition of the strong transmitted incident beam (E_0) and the weak spherical waves scattered by each particle of a colloidal suspension (E_s). The resulting intensity distribution is given by [7]

$$I = |E_0 + E_s|^2 = |E_0|^2 + 2Re\{E_0^* E_s\} \qquad (1)$$

where in the last equality we have neglected the term $|E_s|^2$ accounting for multiple scattering and the interference between different scattered spherical waves (heterodyne conditions). The term $2Re\{E_0^* E_s\}$ describes the superposition of many single-particle interferograms, each showing circular interference fringes of the form

$$I_i(x,y) \propto cos\left[\frac{k}{2z}\left[(x-x_i)^2 + (y-y_i)^2\right]\right] \qquad (2)$$

being $k = 2\pi/\lambda$, λ the radiation wavelength, (x, y) the transverse coordinates on the detection plane at a distance z from

ISBN 978-3-95450-177-9

the sample and (x_i, y_i) the transverse coordinates of the i-th particle inside the colloidal sample. Partial coherence of the incident beam (either spatial or temporal or both) prevents the formation of higher order fringes, as shown in Fig. 1. The Complex Coherence Factor (CCF) of the incoming radiation could in principle be obtained from fringe visibility, as in standard interferometric devices. However, due to the random positions of the particles within the suspension, the superposition of many of these patterns generates a stochastic speckle field in which information about fringe position is lost (Fig. 2).

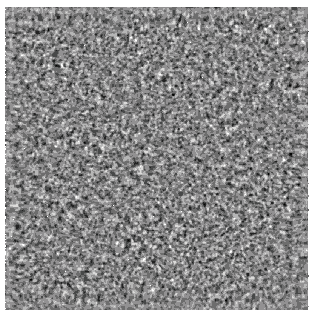

Figure 2: Heterodyne speckle field simulated as a sum over 10000 single-particle interferograms. Mesh size 500×500, parameters used in the simulation are $\lambda = 632.8$ nm, $z =$ 5mm, frame dimension 1.75 mm.

Despite coherence properties cannot be accessed in direct space, the squared modulus of the radiation CCF can be measured via spatial frequency analysis of near field speckle fields. By calling the reciprocal space coordinates as $\vec{q} = \left(q_x, q_y\right)$, it can be shown [3, 5] that power spectra of near field speckle fields can be written as

$$I(q) = S(q)T(q)C(q)H(q) + P(q) \tag{3}$$

where $q = |\vec{q}|$. The function

$$T(q) = sin^2\left[\frac{zq^2}{2k}\right] \tag{4}$$

describes power spectra fluctuations known as Talbot oscillations [3,8,9] whose amplitude is modulated by the squared modulus of the radiation CCF ($C(q)$), as shown in Fig. 3.

It is worth noting here that the Talbot transfer function and the single-particle interferogram form a Fourier transform pair. For completeness, the other terms describe power spectra contributions arising from the particle form factor ($S(q)$), the response function of the detection system ($H(q)$) and spurious and shotnoise signals ($P(q)$). Finally, in order to express the radiation CCF as a function of transverse coordinates, we apply the near field scaling law [5]

$$\Delta r = \frac{zq}{k} \tag{5}$$

that allows to directly convert Fourier wavevectors into transverse displacements. As a further consequence, performing measurements at different distances will cause all

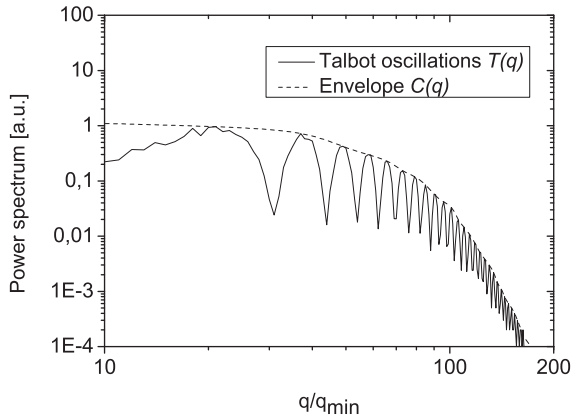

Figure 3: Typical radial profile of speckle power spectra showing Talbot oscillations (solid line) enveloped by the squared modulus of the radiation CCF (dashed line). Reduced wavevectors have been reported on the X-axis, being $q_{min} = \frac{2\pi}{D}$ where D is the effective frame dimension.

power spectra to collapse under the same enveloping curve (the squared modulus of the radiation CCF) upon the described scaling.

Advantages of the Technique

Since Talbot oscillations are reminiscent of the 2-dimensional single particle interferogram, Fourier analysis of single speckle images provides the full 2-D coherence map of the impinging radiation. This result also relies on the self-referencing scheme of the technique, which allows to directly measure field correlation functions. Exploiting the dynamical nature of colloidal suspensions, averages over many different speckle fields can be performed to greatly improve the finesse of the technique. The full bi-dimensional source profile can then be retrieved by applying the Van Cittert-Zernike's theorem [10, 11], thus making the technique a promising and powerful 2D diagnostics tool. Further advantages arise at X-ray wavelengths, since the technique does not require any dedicated X-ray optics nor alignment constraints, contrarily to other interferometric methods.

HNFS with Broadband Radiation

In case of radiation endowed with a broad spectrum, Talbot oscillations are generally modulated by the spatio-temporal coherence function of the impinging radiation, since a given scattering angle corresponds to a certain time delay between the transmitted beam and the wavefront of the scattered spherical wave. Close to the sample, the optical path difference associated to the angle subtended by coherence areas is much larger than the longitudinal coherence length. As a consequence, the envelope of Talbot oscillations together with the scaling law [6]

$$\Delta t = \frac{zq^2}{2k^2c} \tag{6}$$

ISBN 978-3-95450-177-9

allows to reconstruct the temporal coherence function of the radiation. Similarly to source profile retrieval, the emitted power spectral density can then be recovered by applying the Wiener-Khintchine's theorem [10, 11]. A peculiar behavior is observed under the near field scaling: power spectra measured at different distances, besides collapsing under the same enveloping curve, exactly superimpose one on the other. Spatial coherence can still be measured either by inserting a monochromator or by detecting speckle fields at larger distances (as long as near field conditions are fulfilled), since the angle subtended by coherence patches would be small enough to neglect temporal effects. The main limitations of the latter approach may be the minimum distance at which optical path differences become negligible (it must satisfy near field requirements) and the decay of the scattered signal due to the term $1/z$ of spherical waves.

ALBA FACILITY AND THE HNFS DIAGNOSTICS

The ALBA facility is a high flux, high brilliance synchrotron light source consisting of a 100 MeV Linac followed by a Booster that accelerates electrons to their final energy of 3 GeV before they are transferred into the Storage Ring. The main electron beam parameters are summarized in Table 1.

Table 1: Main Beam Parameters at ALBA

Hor beam size	$\sigma_{el,x}$	60 μm
Ver beam size	$\sigma_{el,y}$	30 μm
-	β_x (at pinhole)	0.3 m
-	β_y (at pinhole)	25.08 m
Dispersion (at pinhole)	D	0.0387 m
Emittance	ϵ	4.6 nm rad
Coupling	-	0.53 %
Beam current	I_{beam}	130 mA

The HNFS diagnostic will be installed alongside the already existing hard X-ray pinhole camera beamline. An Aluminum vacuum window and a Molybdenum filter select the hard X-ray part of the synchrotron radiation emitted by a bending dipole. A Copper filter with variable thickness (triangular profile) can be inserted to narrow the broad spectrum down to a Full Width at Half Maximum (FWHM) of 20 keV at a mean energy of 40 keV (Fig. 4), corresponding to a mean wavelength $\lambda = 0.3$ Å.

The optical bench will be installed at 15 m from the source, where coherence areas are expected to have dimensions of $\sigma_{coh,x} \approx \lambda z/\sigma_{el,x} = 6.9$ μm and $\sigma_{coh,y} \approx \lambda z/\sigma_{el,y} = 13.7$ μm. It hosts two step-motor for transverse and longitudinal movements of the sample. The longitudinal screw motor is a 1m-long stage that allows to perform measurements at different distances and monitor Talbot collapse. Transverse motor is used to select the sample since three different scattering cells can be supported. Speckle fields are acquired through a 0.1 mm thick

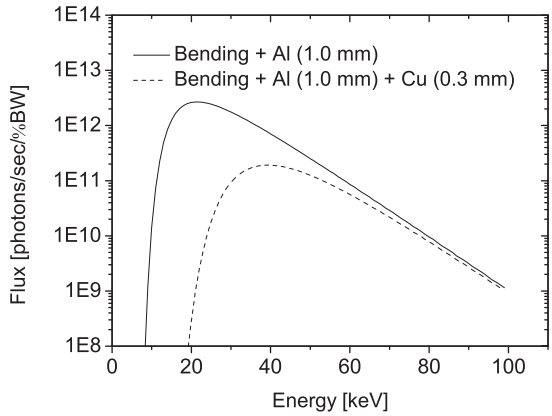

Figure 4: Power spectral density of the synchrotron radiation emitted by the bending dipole without (solid line) and with (dashed line) the Copper filter.

YAG:Ce phosphor screen with diameter of 6 mm coupled to a Basler scA1300-32cm/gc CCD camera through a 10x infinite-conjugated microscope objective. The minimum distance between the sample and the scintillator is set to 4 cm due to mechanical issues. A 45 degrees mirror deflects visible light arising from the scintillator in order to avoid sensor damage from the transmitted X-ray photons. An additional transverse motor allows to switch from the speckle diagnostics to the pinhole camera by simply moving out the sample and inserting the pinhole, thus allowing direct comparison of the experiments. Images are then acquired and processed remotely.

The chosen samples are monodispersed water suspensions of calibrated silica nanospheres with diameters of 100 nm and 500 nm at a nominal concentration of 0.1 w/w contained in a 1mm thick quartz cell. When compared with polystyrene nanoparticles usually employed in similar experiments with visible light, the X-ray scattered signal is enhanced due to the higher refractive index mismatch [12]. Calculation of the scattering cross section and forward scattering amplitude were performed with the Rayleigh-Gans approximation of the Mie theory, always valid at X-ray wavelengths [13].

Preliminary tests aimed at detecting speckle fields generated by broadband hard X-ray synchrotron light are scheduled in September. Simulations are in progress to optimize distances and spectral bandwidth in order to maximize detected signal (enhance speckle contrast with respect to background and CCD noise). Furthermore, feasibility of spatial coherence measurements at large sample-detector distances, as explained earlier, will be check both in terms of scattered radiation (the most demanding issue at such high photon energies) and near field conditions.

TEMPORAL COHERENCE RESULTS

ALBA is also equipped with a diagnostic beamline (Xanadu) where a classical double pinhole Young setup is

ISBN 978-3-95450-177-9

mounted to perform spatial coherence measurements at visible wavelengths through interferometry [2]. Eight extraction mirrors select the visible part of the spectrum and deflect and transfer light into the experimental hall. Due to the larger wavelength, coherence areas have transverse dimensions $\sigma_{coh} \approx \lambda z/\sigma_{el}$ of the order of a few centimeters. Regarding HNFS experiments, this means that fully coherent radiation impinges on the sample, thus making spatial coherence measurements not feasible. We took advantage of such large coherence areas to perform temporal coherence measurements aimed at retrieving the power spectral density of the emitted radiation. We used a colloidal suspension of polystyrene spheres with concentration $\approx 10^{-5}$ w/w and diameter of 1 μm.

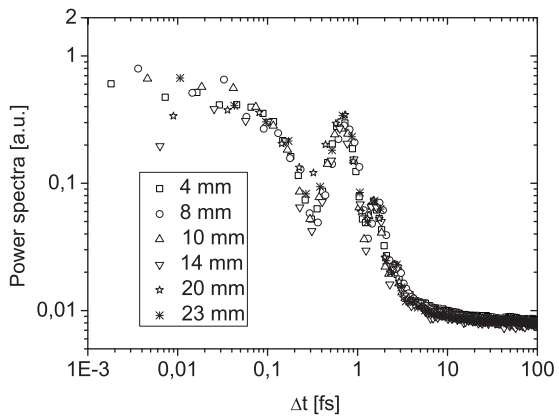

Figure 5: Collapse of speckle power spectra under the scaling $\Delta t = \frac{zq^2}{2k^2c}$, probing the limited temporal coherence of visible synchrotron radiation.

The peculiar Talbot collapse was probed for a longitudinal scan from 4 mm to 24 mm and is shown in Fig. 5. From the measured temporal coherence factors, the power spectral density of the visible synchrotron radiation has been calculated by virtue of the Wiener-Khintchine's theorem. Results are in fair agreement with independent measurements performed with a spectrometer and are summarized in Fig. 6.

CONCLUSION

We have described the fundamentals of the Heterodyne Near Field Speckle technique and shown how it can be applied to measure spatial and temporal coherence properties of synchrotron radiation emitted by a bending dipole. Attention has also been devoted to the advantages of the technique over other interferometric methods for coherence characterization of X-ray radiation. We have described the experimental setup that will be installed at ALBA synchrotron light source alongside the existing hard X-ray pinhole camera. We have also reported on results obtained on a visible line regarding measurements of temporal coherence and power spectral density with the HNFS technique.

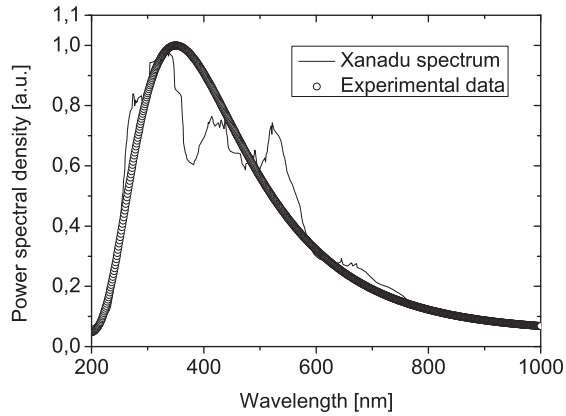

Figure 6: Comparison between the power spectral density of visible synchrotron radiation as retrieved with the HNFS technique via Wiener-Khintchine's theorem (open circles) and as independently measured along Xanadu beamline (solid curve).

The good accordance with independent measurements of the emitted spectrum shows the powerfulness of the technique as a beam diagnostics tool.

ACKNOWLEDGMENTS

The authors would like to acknowledge the ALBA Team for their substantial help in installing the HNFS diagnostics in the X-ray pinhole camera beamline and X. Rodriguez for the engineering support.

REFERENCES

[1] U. Iriso and F. Perez, *Synchrotron Radiation Monitors at ALBA*, Proc. of EPAC 2006.

[2] L. Torino, U. Iriso, and T. Mitsuhashi, *Beam Size Measurements using Synchrotron Radiation Interferometry at ALBA*, Proc. of IBIC 2014.

[3] R. Cerbino, L. Peverini, M. A. C. Potenza, A. Robert, P. Bosecke, and M. Giglio, *X-ray scattering information obtained from near field speckle*, Nature Phys, **4** (2008).

[4] M. D. Alaimo et al., *Mapping the transverse coherence of the self amplified spontaneous emission of a free electron laser with the heterodyne speckle method*, Opt. Express, **22** (24) (2014).

[5] M. D. Alaimo, M. A. C. Potenza, M. Manfredda, G. Geloni, M. Sztucki, T, Narayanan, and M. Giglio, *Probing the transverse coherence of an undulator X-ray beam using brownian nanoparticles*, Phys. Rev. Lett., **103**, 194805 (2009).

[6] M. Siano, B. Paroli, E. Chiadroni, M. Ferrario, and M. A. C. Potenza, *Measurement of the power spectral density of brod-spectrum visible light with heterodyne near field scattering and its scalability to betatron radiation*, Opt. Express, **23** (26) (2016).

[7] F. Ferri, D. Magatti, D. Pescini, M. A. C. Potenza, and M. Giglio, *Heterodyne near-field scattering: a technique for complex fluids*, Phys. Rev. E, **70**, 041405 (2004).

ISBN 978-3-95450-177-9

[8] M. A. C. Potenza, K. P. V. Sabareesh, M. Carpineti, M. D. Alaimo, and M. Giglio, *How to measure the optical thickness of scattering particles from the phase delays of scattered waves: application to turbid samples*, Phys. Rev. Lett., **105**, 193901 (2010).

[9] S. Mazzoni, M. A. C. Potenza, M. D. Alaimo, S. J. Veen, M. Dielissen, E. Leussink, J. L. Dewandel, O. Minster, E. Kufner, G. Wegdam, and P. Schall, *SODI-COLLOID: a combination of static and dynamic light scattering on board the International Space Station*, Rev. Sci. Instrum., **84**, 043704 (2013).

[10] J. W. Goodman, *Statistical Optics* (Wiley-Interscience, New York, 2000).

[11] M. Born and E. Wolf, *Principles of Optics* (Cambridge University Press, Cambridge, England, 1999).

[12] M. Siano, B. Paroli, E. Chiadroni, M. Ferrario, and M. A. C. Potenza, *Nanosecond LED-based source for optical modeling of scintillators illuminated by partially coherent X-ray radiation*, submitted to Rev. Sci. Instrum.

[13] H. C. Van de Hulst, *Light Scattering by Small Particles* (Dover, NY, 1957).

ISBN 978-3-95450-177-9

DESIGN AND PERFORMANCE OF CORONAGRAPH FOR BEAM HALO MEASUREMENTS IN THE LHC

A. Goldblatt*, E. Bravin, F. Roncarolo, G. Trad, CERN, Geneva, Switzerland
T. Mitsuhashi, KEK, Ibaraki, Japan

Abstract

The CERN Large Hadron Collider is equipped with two Beam Synchrotron Radiation systems (BSR), one per beam. These systems are used to monitor the transverse distribution of the beam, its longitudinal distribution and the abort gap population. During the 2015-2016 winter shut-down period, one of the two BSR systems was equipped with a prototype beam halo monitor, based on the Lyot coronagraph, classically used in astrophysics telescopes to observe the sun's corona. The system design, as well as part of the optics, was taken from the coronagraph used in the KEK Photon Factory, adapted in order to satisfy the LHC BSR source constraints. This project is in the framework of the HL-LHC project, for which there is the requirement to monitor the beam halo at the level of 10^{-6} of the core intensity. This first prototype has been designed as a demonstrator system aimed at resolving a halo-core contrast in the 10^{-3} to 10^{-4} range. After illustrating the design of the LHC coronagraph and its technical implementation, this contribution presents the result of the first tests with beam and the planned system upgrades for 2017.

PRINCIPLE OF THE CORONAGRAPH

The coronagraph is an instrument developed in the first half of 20th century by Bernard Lyot, a French astrophysicist, in order to observe the halo of the sun. A sketch of the Lyot coronagraph can be seen in Fig. 1.

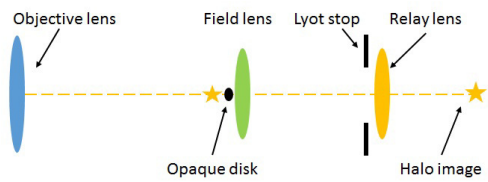

Figure 1: Sketch of the Lyot coronagraph optical layout.

A real image of the object is created by an objective lens. An opaque disk located at the image plane of this lens masks the bright core of the object in order to make the halo visible.
Such a system is however limited by the light diffracted from the limited aperture of the objective lens, which creates a diffraction pattern at the image plane, perturbing the observation of the halo.
Lyot's solution consisted of adding a field lens, which images the objective lens and thus shifts the diffraction fringes out of the center, as shown in Fig. 2.
By placing a well dimensioned aperture stop, the "Lyot stop", at the location where the diffraction fringes are re-imaged, the fringes are blocked and can't propagate to the final image plane, where the halo is observed. [1–4]
A relay lens creates the final image of the beam with a magnification suitable for the camera sensor.

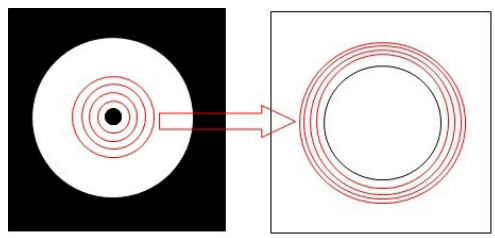

Figure 2: Sketch of diffraction pattern at the objective lens (left) and field lens (right) image planes.

The performance of the coronagraph is defined by its contrast, that is to say the ratio of the halo intensity with respect to the core intensity at image plane. It is limited by the background noise, which has mainly two sources: the first is the diffraction "leakage" to the image plane (i.e. diffraction fringes which are not blocked by the Lyot stop), which depends of the objective lens aperture, the mask size and the Lyot stop aperture. The second is Mie scattering, which is generated mainly by small particles on the optical elements located before the objective lens, and leads to a uniform increase of the background level. The Mie scattering depends on the size of the scattering particles and their distance to the objective lens. Mie scattering after the mask doesn't have a strong impact, since the light is by then strongly attenuated.
These limitations and the expected performance of the LHC coronagraph are quantified in the next section.

LHC HALO MONITOR DESIGN

Layout

The prototype beam halo monitor installed in the LHC during the winter shut down 2015-2016 is based on the same design and re-uses the optics of the Photon Factory coronagraph tested at KEK. Some modifications were introduced in order to fulfill the specific conditions of the LHC synchrotron light source and mechanical constraints. [5–7]
The coronagraph is designed to be used both at injection and top energy (450GeV and 7TeV respectively).

* Aurelie.Goldblatt@cern.ch

ISBN 978-3-95450-177-9

At injection energy, the synchrotron light in the visible range is generated by an undulator magnet located 27.2m before the extraction mirror, which sends the light through a viewport to an optical table. At top energy, the visible light comes from a superconducting dipole located 26m from the mirror. The expected beam emittance is around 2um, corresponding to beam sizes varying from 1.2mm (at injection energy) to 200um (at top energy).

The coronagraph optics is composed of three sections:

The first section consists of a finely polished plano-convex objective lens of f=2000mm, located 27.5m after the dipole magnet. It creates an image of the beam with a magnification of 0.077 and 0.08 for injection and top energy respectively. A motorized rectangular slit with a 30x30mm opening is placed just before the objective lens, in order to control the aperture.The diffraction pattern of the aperture thus has a cross shape, which turns into square fringes at the Lyot stop plane.

The mask is placed at the first image plane, with a size of 5 beam sigmas required to block the beam core. In order to cover the different beam sizes, the mask is made of a 3 inch glass substrate with 12 opaque disks ranging from 100um to 650um in diameter, made by chromium deposition and etching. The mask is motorized in order to select and center the appropriate disk.

The second stage of the coronagraph is composed of the field lens, which creates an image of the objective lens with a magnification of 0.6 and the Lyot stop, located at the field lens image plane.

The field lens is an apochromat of f=816mm and 102mm diameter. The Lyot stop is a motorized rectangular slit of the same model as the one used for defining the objective lens aperture.

The third stage contains the relay lens, which is an apochromat lens of f=500mm placed just after the Lyot stop, and a telescope eyepiece of f=18mm, which is set to adjust the final image with a magnification of 30, in order to achieve a beam size on the camera of about 1.5 times the real beam size.

The Fig. 3 shows the layout of the coronagraph.

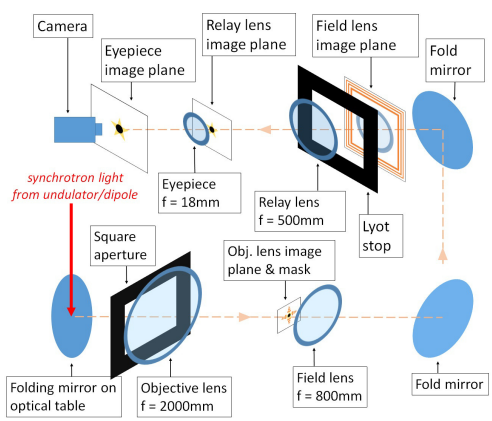

Figure 3: Layout of the LHC coronagraph.

Expected Performance

Some analysis and simulations were performed to estimate the background coming from diffraction leakage and Mie scattering. The method and results are detailed in [1].

The diffraction leakage is estimated to be 3.7 10^{-4}, while the Mie scattering should be in the order of 10^{-4} to 10^{-5} with respect to the beam core intensity.

Considering these calculations, the contrast of the beam halo monitor in LHC is expected to be of 10^{4} with respect to the beam core.

Implementation

The LHC beam halo monitor shares the light source, in-vacuum mirror and optical table with the Beam Synchrotron Radiation system (BSR), used to measure the transverse and longitudinal distribution of the beam, and the abort gap population.

The implementation of the different elements on the optical table was studied with Catia CAD software.

In order to operate the coronagraph remotely (since the LHC tunnel is not accessible while the machine is running), many of the optical components are motorized. This gives the possibility to adjust at any time the alignment, the aperture, the different focusing stages as well as the mask position and the Lyot stop size.

The whole system is enclosed in shielding boxes, in order to protect it from parasitic light and dust. In particular, the space between the objective lens to it's image plane is enclosed in a telescope tube containing baffle plates, in order to minimize the parasitic reflections and thus the background noise.

For the laboratory tests and the commissioning with beam, a simple USB CCD camera was used, with the control of the integration time used to determine the contrast. It is planned to replace the camera with an intensified scientific CMOS camera in the near future, which would allow bunch by bunch halo measurements to be performed, gating on a single bunch at any one time.

Fig. 4 shows a 3D drawing of the BSR optical table with the coronagraph installed, but without the light shielding boxes.

LHC HALO MONITOR TEST BENCH

Before the installation of the halo monitor in the LHC, a test of the complete instrument was conducted in order to check mechanical aspects (assembly, motors, etc.) and measure its performance.

In order to reproduce as accurately as possible the LHC conditions, the test included a 27m long drift line, mimicking the distance between LHC light source and the in-vacuum extraction mirror. A spare of the in-vacuum mirror was used to reproduce its contribution to the Mie scattering.

A 200um pinhole illuminated by a broadband fiber lamp was used as a light source. A piece of transparent plastic could be inserted in front of the pinhole in order to create an artificial halo.

ISBN 978-3-95450-177-9

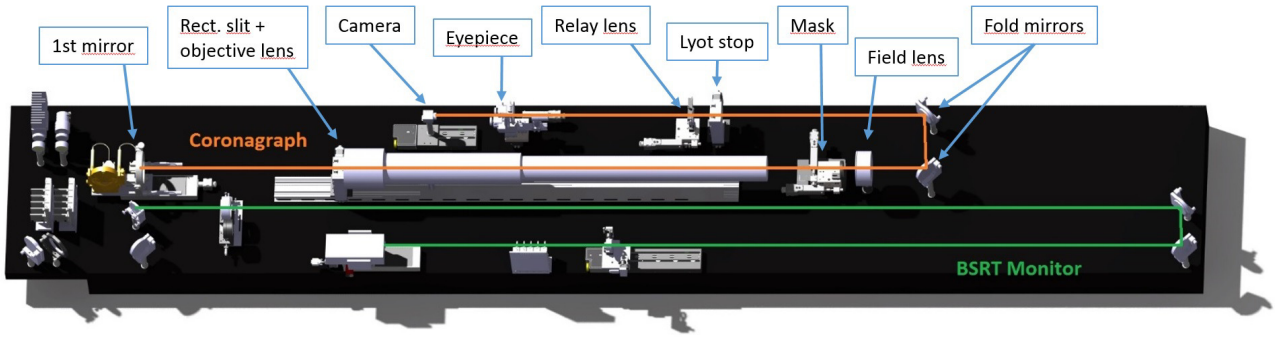

Figure 4: 3D drawing of the LHC halo monitor.

The first step of the test consisted of precisely locating the objective lens image plane in order to place the mask.
The second step was then to adjust the objective lens aperture and the Lyot stop. The diffraction pattern at the Lyot stop location depends on the objective lens aperture and the mask size, but it has to be considered that a small objective lens and Lyot stop aperture deteriorates the image resolution by increasing the point spread function. An objective lens aperture of 20x20mm was finally selected with the Lyot stop adjusted by optimizing the final image.
The contrast was measured with the following procedure. Images of the object without the mask were acquired, adjusting the camera exposure time in order to reach a maximum intensity value at the light core near (but below) saturation. The mask was then inserted and the exposure time increased until a maximum halo intensity of the same value as that of the core without mask was achieved. The ratio between the halo exposure time and the core exposure time gives the contrast.
Fig. 5 shows images obtained with a 800um mask. It was possible to observe light with a contrast of 10^7. The results on the test bench were promising: the surface quality of the in-vacuum mirror appears to be sufficient to allow the halo observation.

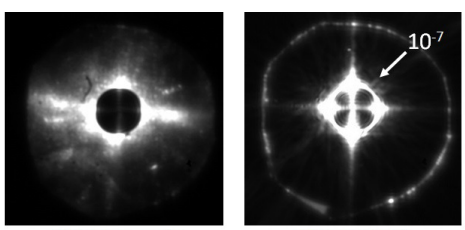

Figure 5: Images acquired with different camera exposure time.

LHC HALO MONITOR COMMISSIONING

The beam-halo monitor was installed in the LHC during the winter shutdown 2015-2016, and commissioned in April 2016, at the 2016 LHC top energy of 6.5TeV.
The same procedure as the one described in the test bench section of this paper was carried out for finding the objective lens image plane and setting the aperture.
A test to quantify the diffraction leakage was then performed. At top energy, the aperture available for beam imposed by the collimation system is 3.5x4.5mm. This implies that at the objective lens image plane, where the magnification is 0.08, the light produced by the beam should be confined in a 280x360um area. Thus, with the biggest size of mask (650um) placed in front of the core, all observable light on the image can be considered as diffraction leakage and Mie scattering. The Fig. 6 shows an image obtained during this test. A light spot of intensity 10^{-4} with respect to the beam core is clearly visible on the right side of the mask only, whose origin appears to be independent of the objective lens and Lyot stop size apertures. Its intensity makes the observation of the beam halo impossible in the present state.

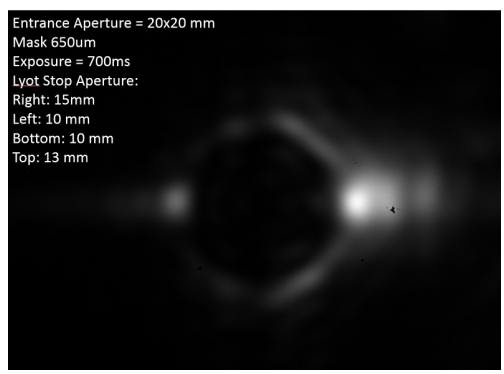

Figure 6: Image acquired with the LHC beam halo monitor in the frame of quantifying the diffraction leakage.

This parasitic light spot, which was never observed during the lab tests, might therefore be explained by the source of the LHC synchrotron light. Indeed, the in-vacuum mirror will reflect the light produced by the dipole magnet from its edge up to 3.3m inside [7].

ISBN 978-3-95450-177-9

The edge of the in-vacuum mirror might therefore diffract some of this light and act as a secondary light source.
A way to block this parasitic light before the image plane would be to place another motorized rectangular aperture at the plane where the in-vacuum mirror is imaged by the field lens (i.e after 1m), so doing hiding the edge of the mirror from the subsequent optics.
To test this hypothesis, one can make a comparison of this parasitic light spot at injection and top energy. At injection, the light emitted by the undulator covers all the in-vacuum mirror. Since the shape of the source is not the same as at top energy, it is to be expected that the shape of the parasitic spot will be different. If this is not the case, it would suggest that this light spot has another origin, such as internal reflections. This test is yet to be carried out.
Fig. 7 shows the power of synchrotron light on the extraction mirror at injection and top energy.

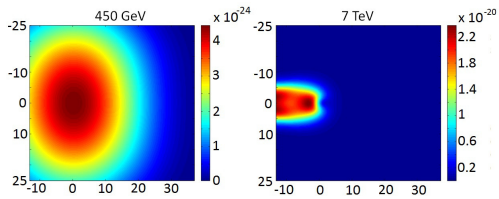

Figure 7: Simulation of the LHC SR power (in units of W · mm^{-2} per proton) at the extraction mirror at injection (left) and top energy (right).

CONCLUSION AND PERSPECTIVES

Successful tests of the LHC beam halo monitor were conducted on a test stand and allowed the optical and mechanical design of the system to be validated.
The system was able to distinguish the halo from the core for a test lamp with a contrast of 10^7, well above the 10^4 contrast expected for this prototype with beam, for which the main limitation is expected to come from diffraction. [1]
Tests of the real system performed with the LHC proton beam at 6.5TeV, showed a parasitic spot with an intensity of 10^{-4} with respect to the beam core, above the level of the halo expected to be observed.
A potential cause of this parasitic light is the diffraction of the synchrotron light on the edge of the in-vacuum mirror, which then effectively acts as a secondary light source. A way to avoid the propagation of this light to the image plane would be to add a second adjustable Lyot stop at the image plane of the mirror created by the field lens. Tests are foreseen to be carried out at injection energy, in order to verify this hypothesis, which would then allow mitigation measures to be put in place for further testing of the coronagraph for beam halo measurements in late 2016.

REFERENCES

[1] T. Mitsuhashi, "Design of coronagraph for the observation of the beam halo at LHC", in *Proc.IBIC'15*, Melbourne, Australia, September 2015, paper TUCLA03.

[2] T. Mitsuhashi, "Beam halo observation by coronagraph", in *Proc. DIPAC'05*, Lyon, France, June 2005, paper ITMM03.

[3] T. Mitsuhashi, "Design and construction of coronagraph for observation of beam halo", in *Proc.EPAC'04*, Lucerne, Switzerland, July 2004, paper THPLT070.

[4] T. Mitsuhashi, "Observation of beam halo with coronagraph", presented at the 7th European Workshop on Beam Diagnostics and Instrumentation for Particle Accelerators. (DIPAC'05), Lyon, France, Jun. 2005. http://epaper.kek.jp/d05/TALKS/ITMM03_TALK.PDF

[5] T. Mitsuhashi, "Design of Coronagraph for the observation of beam halo at LHC", presented at the 4th International Beam Instrumentation Conference. (IBIC'15), https://accelconf.web.cern.ch/AccelConf/IBIC2015/talks/tucla03_talk.pdf

[6] E. Bravin, "Coronagraph implementation, choice of beam", presented at the Simulations and Measurements of Long Range Beam-Beam Effects in the LHC Event Lyon, France, Dec. 2015. https://indico.cern.ch/event/456856/contributions/1968803/attachments/1196062/1738201/BSRT_BBLR.pdf

[7] G. Trad, "Development and Optimisation of the SPS and LHC beam diagnostics based on Synchrotron Radiation monitors", LPSC, Grenoble, France, Rep. NNT : 2015GRENY005, May. 2015. http://inspirehep.net/record/1375119/

ISBN 978-3-95450-177-9

SINGLE SHOT TRANSVERSAL PROFILE MONITORING OF ULTRA LOW CHARGE RELATIVISTIC ELECTRON BUNCHES AT REGAE

H. Delsim Hashemi*, DESY, Hamburg, Germany

Abstract

Relativistic electron microscopes are increasingly under consideration in dream experiments of observing atomic scale motions as they occur. Compared to ordinary electron microscopes that are with energies limited to few tens of keV, relativistic electrons reduce the space-charge effects strongly. This enables packing more electrons in shorter bunches and thereby capturing atomic scale ultra-fast dynamics even in a single shot. A typical relativistic-electron-microscope, based on an RF-gun, can provide experiments with couple of thousands to millions of electrons bunched in a few μm length and a transversal dimension of a fraction of a mm. After scattering from a sample diffracted electrons are distributed over transversal dimensions typically two orders of magnitude larger. For transversal diagnostics before scattering a cost effective solution is implemented while for Diffraction Pattern (DP) detection the goal is imaging the entire pattern with single-electron imaging sensitivity and good signal to noise in single shot and keeping well depth as high as possible.

INTRODUCTION

Beam quality demands for relativistic electron microscopy are extraordinary. To study e.g. proteins a coherence length of 30 nm is required which translates into a transverse emittance of 5 nm at a spot size of 0.4 mm. In order to study chemical reactions or phase transitions in pump-probe experiments short bunch lengths down to 10 fs and a temporal stability of the same order are required. These are challenging parameters for an electron source, which can only be reached at a low bunch charge of about 100 fC [1]. REGAE (Relativistic Electron Gun for Atomic Exploration) has been commissioned at DESY with the goal to produce electron bunches as required for electron diffraction [2]. REGAE employs a photocathode S-band RF gun that operates at high accelerating fields providing means to suppress space charge induced emittance growth. Space-charge forces that limit the density of electrons too, scale inversely with the energy of electrons squared. This explains the advantage of relativistic electrons. The draw back for scintillator base transversal diagnostics is the reduction of energy loss in a typical energy of 5 MeV. This fundamental problem makes it challenging to image relativistic-electrons. Radiation damage is another draw back with relativistic-electrons.

* hossein.delsim-hashemi@desy.de

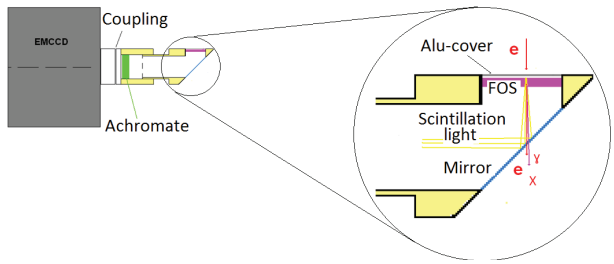

Figure 1: Schematic layout of DP-detector. Electron beam hits the 150 μm thick CsI scintillator of FOS in normal angle and generates the scintillation light that gets coupled efficiently to the fiber optics. The image that is formed at the exit of fiber plate is reflected by a mirror towards the camera. This mirror is transparent for x-rays and energetic electrons and reflects the scintillation light to the coupling optics of the camera.

INDIRECT DIAGNOSTICS USING SCINTILLATORS

Due to high radiation damage in the energy range of 3 to 5 MeV direct electron detection is not an option. Here scintillators can be used to make a copy of electron-beam transversal profile. Geometrically there are two ways to use a scintillator to detect the transversal distribution of electrons; transmissive and reflective. In transmissive option usually scintillator is perpendicular to the electron beam and the light generated in forward direction can be collected by a downstream mirror. This mirror can be a metal coated thin silicon wafer. Such mirror can be transparent for electrons and x-rays and reflect visible scintillation light to be coupled to a camera, see Fig. 1.

In reflective geometry, scintillator is holded with 45° to the electron-beam axis and backward scintillation light is lens coupled toward a camera. This is mainly used for diagnostics at injector part of REGAE [3].

Detection System Parameters

For an electron-imaging system, N_e, the total number of electrons generated in one pixel can be expressed as a function of the performance characteristics of the various detection-system parameters. For a lens coupled CCD it can be written as:

$$N_e = n_e \eta \, g \, QE \tag{1}$$

where n_e is the number of electrons per unit area (e.g. the area on the scintillator that is imaged to a pixel of the CCD),

ISBN 978-3-95450-177-9

η is the number of visible photons generated in scintillator per electron, g is the optical coupling efficiency and QE is the quantum efficiency of CCD. It is clear that a scintillator with higher light-yield, a more efficient geometrical coupling and higher CCD quantum efficiency are beneficial. Scintillator light-yield and quantum-efficiency of CCD are both function of wavelength thus, matching should be taken into consideration as much as possible. Using a back illuminated cooled chip Electron Multiplying Charge Coupled Device (EMCCD; e. g. Andor iXon3-DU-888-EC-BV [4]) can provide a $QE \approx 0.9$ for an emission which has its peaks around green light. The optimization of the other two factors namely η and g is coupled to the resolution of the detector system and mechanical design constraints. The number of generated photons per passage of electron can be increased with thicker scintillator but thicker scintillator ruins out the resolution. State of the art x-ray detector Fiber Optics Scintillator (FOS [5]), can be used to generate considerably high number of visible photons, in forward direction, that can be coupled to fibers resulting in a good detection-efficiency and resolution. The angular spread of the light at the output of FOS is not Lambertian and features a sharp peak in the forward direction. This results in an improved optical coupling efficiency to the CCD.

Geometrical Coupling Efficiency

Define $F(\theta)$ as:

$$F(\theta) = \int_0^{\theta} f(\theta')sin(2\theta')d\theta' \tag{2}$$

where $f(\theta)$ is the normalized angular distribution of the radiance of the scintillator and θ is the meridian angle, g can be written as:

$$g = T\,\frac{F(\theta_{max})}{F(\pi/2)} \tag{3}$$

with T being bulk transmission of the optical setup [6–8]. Applying this formalism to FOS and an ordinary Lambertian scintillator one can see that with FOS coupling efficiency is considerably higher.

In order to optimize collecting optics knowledge of spatial distribution of scintillator emission is required. In general simulation tools can be used to deal with radiance problem provided enough optical data of the scintillator. A direct measurement of radiance would result in a way to cross check simulations and develop an understanding of different processes in scintillation. When a complicated situation like FOS is under study experimental result are necessary due to the complication that arise in simulation with the coupling of the emission to the fibers. Furthermore the aluminum coating that works as the shielding of the stray light and reflector for backward scintillation light makes the situation with FOS even more complicated to simulate.

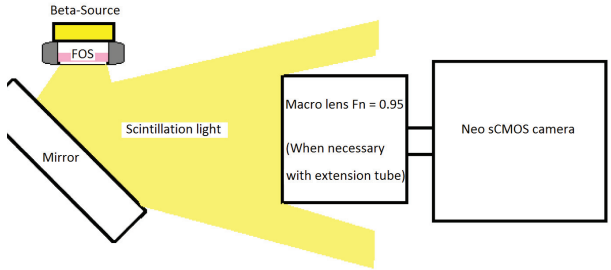

Figure 2: Layout of the setup to measure the radiance of FOS.

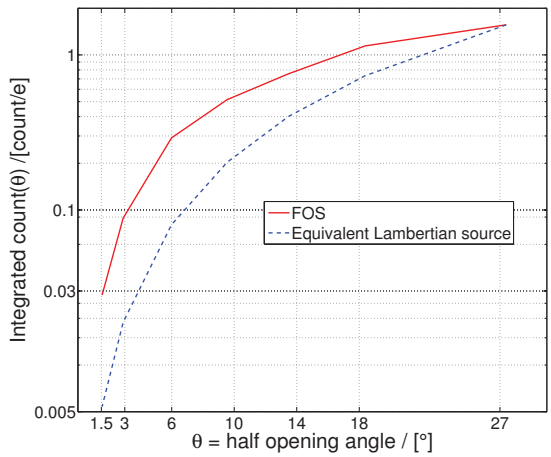

Figure 3: β-source is used to produce scintillation light and counts that scale with the collected light as a function of distance to the FOS are shown. For comparison a Lambertian source radiance is also shown that adjusted to emit the same amount of light into largest cone covered in the closest distance to the FOS.

For the measurement a setup that is illustrated in Fig. 2 is used. Background is reduced considerably using a light tight black closure that houses the entire setup. In the analysis the still remaining background as well as read-out offset and contribution of bad-pixels are removed by using signal minus background shots. At different distances from source a sharp focus is first achieved and then background (T seconds exposure without source, typical T = 100 seconds) is recorded. Then source is placed in and signal shots are recorded exposing again T seconds. As camera Neo sCMOS [9] cooled to −35° is used. Integrated counts over the ROI (background removed) is proportional to the collected light and as a function of distance is shown in Fig. 3 for FOS. For comparison the radiance of a properly adjusted Lambertian source is also plotted. It is well known that the total intensity emitted into half opening angle θ in forward direction for a Lambertian source is given by the integral:

$$f(\theta) = \pi f(0) \int_0^{\theta} sin(2\theta')d\theta' \tag{4}$$

ISBN 978-3-95450-177-9

Where θ varies between 0 and $\pi/2$. In order to make a sensible comparison instead of full hemisphere, integration can be limited to the maximum angle that was covered by FOS setup in the closest distance to β-source (largest opening angle of 27°). Then it is set equal to the integrated counts for the FOS and extracting the resulted constant, $f(0)$, for maximum luminance in normal direction the functionality of Lambertian source is derived. Given the realistic situation in accelerator diagnostics setup in terms of vacuum window aperture size etc. FOS collection is close to an order of magnitude higher than a Lambertian scintillator. In many studies simplified forms of Eq.3 and Eq. 2 for Lambertian or point source are used [8]. The real g can be only deduced from integration of radiance, like what is derived here experimentally and shown in Fig. 3, in Eq. 3. As it is clear from Fig. 3 FOS output in backplane is neither like a point source nor Lambertian.

DETECTIVE QUANTUM EFFICIENCY (DQE)

Assuming that n_e in Eq. 3 follows Poisson's statistics the intrinsic signal to noise ratio reads as $\sqrt{n_e}$. This means that the input signal introduces an upper limit to detection efficiency. DQE can be defined as [10]

$$DQE = \frac{(S/N)^2_{out}}{(S/N)^2_{in}} \tag{5}$$

One can describe DQE as a generalization of camera quantum efficiency to include the statistical behavior of electron to photon conversion in scintillator and photon to electron in camera chip as well as statistical behaviour of amplification process in camera electronics. Even for an ideal camera with QE = 1, DQE can be smaler than one, because the conversion to scintillation photons introduces a statistical noise among all other contributions. The DQE can be considered as the fraction of incident events that are registered by the detection system. As higher DQE is as shorter exposure of events is needed to get the same quality image and information. Detector setups composed of scintillator, coupling optics, intensifier or electron multiplier and camera can be compared by measuring DQE. For such comparisons with same n_e measuring either DQE or $(S/N)_{out}$ is the same. DQE can be used to compare detection systems that are prepared to work at different n_e level. Furthermore effects like coupling optic differences from a setup to another results in changes in total number of photons coupled to the camera chip that can be unfolded when DQE is used.

In order to measure DQE one needs a source that is as stable as possible. This is why a β-source is chosen with activation in the range of 2.4 MBq. Here the two detectors that are operational at REGAE will be considered. One is based on an EMCCD [4] lens coupled to FOS (called in the following D1) and the second one is a Neo sCMOS lens-coupled to a Photek large area image-intensifier [11] that gets its input again lens-coupled from FOS (called in the following D2). For both detectors the number of electrons is controlled by exposure time of FOS to the β-source. For D1 two case with EM-gain of 50 and 300 are examined. EM-gain of 300 is maximum ordinary gain where EMCCD shows the highest sensitivity to the extreme low light intensities and EM-gain of 50 is a moderate value. With D2 one case with the same number of electrons per pixel as of D1 experiments and another one with lower electrons per pixel are acquired which the latter fits the best to the maximum gain applied to the intensifier. For any of these four measurements a background, a background subtracted signal (call it reference) and finally a series of 50 shots of signal are measured. From reference shot one can obtain σ of the spot assuming a Gaussian profile. Then the total counts in the reference can be extracted that corresponds to the total particle number exposed to the FOS (integrating over 3σ). Selecting a central spot of one-σ size one can read the counts in reference image and background. As the next step the integral count in the one-σ long central region is taken for all signal shots and the corresponding background count is subtracted from them. Mean value of these one-σ long signal minus background and their standard deviation can be used to deduce the $(S/N)^2_{out}$. From the total integrated count and total integrated count over the ROI and activation of the $\beta - source$ and the applied exposure time one can get $(S/N)^2_{in}$ (assuming Poisson statistics). In Table 1 the results are summarized. D1 is in operation since 2012 and has provided means to record diffration patterns from experiments with low intensities reaching to the aim of single electron per pixel detection in single shot. One typical result is shown in Fig. 4 (that will be discussed later). D2 is a new detector that can provide experiments with much better detectability as is shown in Table 1.The possibility of higher number of full resolution (5.5 MPixels) frames per second reaching to 38 with highest bit depth of 16 bits is demonstrated in commissioning. With highest gain of intensifier at D2 it is possible to image patterns that have single electron feature detected with good signal to noise ratio and a well depth up to 140 electrons per pixel. Well depth can be increased when sensitivity level is compromised. Another advantage of D2 in comparison to D1 is the short gating time that can be achieved. It is possible to gate down to 50 ns the Photek intensifier then there will be an improvement compared to D1 why an EMCCD needs several ms exposure to capture a shot thus suffering from contribution of dark-charge as will be explained later.

Table 1: DQE for REGAE Detectors

Detector	EM-gain	$\langle e/pixel \rangle$	DQE
D1	50	2.4	0.17
D1	300	2.4	0.15
D2	-	1	0.72
D2	-	2.25	0.6

ISBN 978-3-95450-177-9

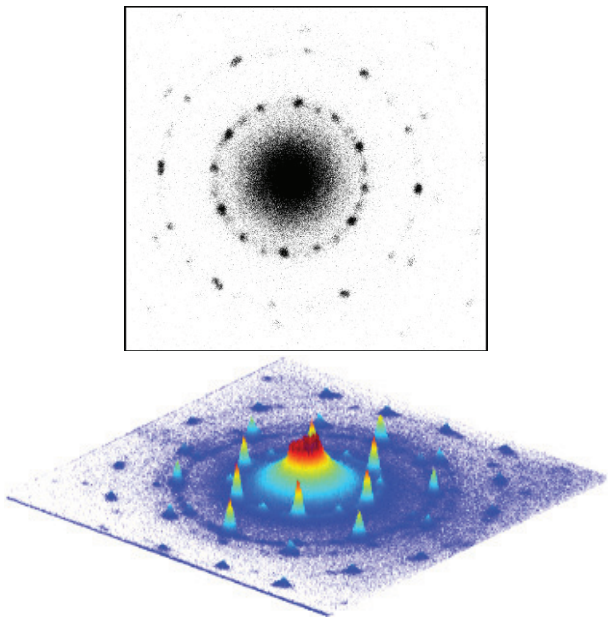

Figure 4: Top: 6 fC total charge is diffracted by a sample and resulted diffraction pattern is recorded in single shot. Bottom: Averaged over 200 shots like in the top.

DIFFRACTION PATTERN DETECTION

D1 employs the transmissive scintillator geometry, see Fig.1. The core of the converter layout is composed of an FOS. This FOS is oriented perpendicular to the electron beam thus the Scheimpflug effect is corrected. A thin silicon-wafer coated with aluminum couple scintillation light to the collecting optics. This mirror acts as the reflector for the visible scintillation light and is transparent to the energetic-photons (namely X- or γ-rays) or relativistic electrons. The Si-wafer is $100\mu m$ thick therefore practically no relativistic electron gets reflected backwards. The entire setup is in UHV of the accelerator and at the same time fully light tight such that no background photon enters to the detector setup (see Fig. 1). Lens coupling is done by a relay optics composed of two achromates (50 mm diameter) that image, with required de-magnification of ≈ 0.8, the output of FOS to the camera chip. The entire FOS and coupling mirror are designed such that they can be moved into/out-of the beamline. D2 is installed downstream D1 and is a fixed installation.

Experimental Results

In one of many diffraction experiments conducted at REGAE, electron bunches of a total charge 6 fC were used to get single shot diffraction images as Fig. 4-top using D1 detector. In each shot about 35 fC dark-charge contributes to the background. Dark-charge distribution varies from shot to shot. If one corrects for the shot to shot transversal jitter a superposition of many shots can improve the contrast of diffraction pattern against dark charge. After corrections are applied what contributes in the readout count, apart from diffraction orders, are the EMCCD read-out off-set and hot spots of dark-charge. By subtracting this off-set one can derive a calibration taking the advantage of in operation precise charge measurement diagnostics at REGAE [12]. Off-set of the image can be esstimated using areas of the image that are far from any diffracted orders and hot dark current spots. The background and off-set free integral count in all diffraction orders area and total charge can be used to deduce the absolute calibration that also will result in an estimation of dark charge. In Fig. 4-bottom, 200 shots are aligned and averaged. Using this image one can get percentage of the total charge that diffracts into individual different diffraction orders. As it is clear from image, detectability varies as a function of number of electrons that are diffracted into orders. For single shot at the top of Fig. 4 the number of electrons per pixel (with area $13 \times 13 \mu m^2$) is fraction of electron (see Table 2).

Table 2: Electron Distribution in Different Orders

Order. no.	Intensity %	no. of electrons	no. of pixels	$\langle e/pixel \rangle$
0	92	33000	57256	0.58
1	5.1	1850	8010	0.23
2	2.84	1025	9125	0.11

ACKNOWLEDGMENTS

This work is supported by many groups at DESY, HASYLAB and CFEL and individuals including D. Gitaric, S. Bajt and M. Spiwek.

REFERENCES

[1] M. Hada et al., Opticsinfobase online publication JT2A.47, ICUSD2012.

[2] S. Manz et al., Faraday Discussions, Volume 177, 2015.

[3] Sh. Bayesteh et al., proceedings IBIC 2013, MOPF06.

[4] http://www.andor.com/scientific-cameras/ixon-emccd-camera-series

[5] http://www.hamamatsu.com/jp/en/J6677.html

[6] W. Swindell, Med. Phys. 18, 1152-1153 (1991).

[7] Tong Yu and John M. Boone, Med. Phys. 24(4), April 1997.

[8] Hong Liu et al., Med. Phys. 21(7) July 1994.

[9] http://www.andor.com/scientific-cameras/neo-and-zyla-scmos-cameras/neo-55-scmos

[10] Mark W. Tate et al., Rev. Sci. Instrum. 68(1), January 1997.

[11] http://www.photek.com/pdf/datasheets/detectors

[12] D. Lipka et al., proceedings IBIC 2013, WEPF25.

ISBN 978-3-95450-177-9

A SCINTILLATING FIBRE BEAM PROFILE MONITOR FOR THE EXPERIMENTAL AREAS OF THE SPS AT CERN

I. Ortega Ruiz*, J. Spanggaard, G. Tranquille, CERN, Geneva, Switzerland
A. Bay, G. J. Haefeli, Ecole Polytechnique Fédérale de Lausanne (EPFL), Lausanne, Switzerland

Abstract

The CERN Super Proton Synchrotron (SPS) delivers a wide spectrum of particle beams (hadrons, leptons and heavy ions) that can vary greatly in momentum and intensity. The profile and position of these beams are measured using particle detectors. However, the current systems show several problems that limit the quality of such monitoring. We have researched a new monitor made of scintillating fibres read-out with Silicon Photomultipliers (SiPM), which has the potential to perform better in terms of material budget, range of intensities measured and available detector size. In addition, it also has particle counting capabilities, extending its use to spectrometry or Time-Of-Flight measurements. Its radiation hardness is good to guarantee years of functioning. We have successfully tested a first prototype of this detector with different particle beams at CERN, giving accurate profile measurements over a wide range of energies and intensities. It only showed problems during operation with lead ion beams, believed to come from crosstalk between the fibres. Investigations are ongoing on alternative photodetectors, the electronics readout and solutions to the fibre crosstalk.

INTRODUCTION

In the experimental areas of the SPS, protons are extracted during 4.8 seconds and collided with primary, secondary and sometimes tertiary targets, in order to produce beams of particles that can be selected and sent to the experimental users. These beams can be composed of hadrons (protons, kaons, pions, antiprotons...), leptons (electrons, positrons, muons...) and lead ions. Their momenta can vary greatly, from 1 to 400 GeV/Z/c, and their intensities from 10^3 to 10^8 particles per second. The profile and position of these beams are typically measured using Delay Wire Chambers (DWC), Multi Wire Proportional Chambers (MWPC) or Scintillator Finger Scanners (FISC). Replacement detectors for the wire chambers are actively being sought as they are ageing and the expertise to produce them is gradually being lost.

In addition, two new beam lines dedicated to neutrino R&D will be commissioned in 2017, in collaboration with Fermilab and other institutes. The monitors for these lines will form a spectrometer for particle momentum measurement and therefore need to count single particles, while covering an area of $200 \times 200\,\mathrm{mm}^2$.

* inaki.ortega@cern.ch

SCINTILLATING FIBRES

Scintillating plastic fibres (SciFi) have emerged as one of the best active materials for the monitors of the experimental areas. They are extensively used for charged-particle tracking in high energy physics, for example in the LHCb and ATLAS ALFA experiments at CERN [1, 2].

The scintillating fibres have a core made of polystyrene cladded with one or two layers of lower refractive index material. This gradient of refractive index allows a fraction of the light created inside the fibre to be trapped by total internal reflection. The polystyrene fibre core usually employs a two level doping system: a primary scintillator emitting in the UV and a wavelength shifter to capture the short reach UV photons and re-emit them in the visible wavelength region. This shift in wavelength also enhances the match in terms of quantum efficiency for common photodetectors. The processes of energy absorption, scintillation and wavelength shifting are mediated by very fast quantum processes that yield a photon time distribution with rise time and decay time of 1-3 ns [3]. Light production typically reaches up to 8000 photons per MeV of energy deposited, although the trapping efficiency of square fibres varies between 4.2% and 7.3% [4, 5]. Depending on the amount of dopants, the light emitting properties of the fibres can be changed and their radiation hardness can be improved.

Radiation Hardness

A very important characteristic of a beam monitor is its radiation hardness. The detector should be able to operate continuously and reliably for years with beams of intensities of 10^8 particles/second or 10^6 Pb ions/s. The radiation damage is mainly manifested as a shorter attenuation length of the fibre resulting in less light collected by the photodetectors. Data from literature shows that short fibres of less than 40 cm can withstand doses of up to 10 kGy before showing significant damage [6].

Simulations of the SciFi monitor carried out with Geant4 [7] show that for a single beam extraction of 10^8 particles, an absorbed dose of 100 mGy can be expected per fibre. Such short fibres should therefore withstand up to 10^5 of such beam extractions, guaranteeing several years of operation before having to be replaced.

Material Budget

It is important for a beam monitor to perturb the measured beam as little as possible. A charged particle traversing a medium of thickness x is deflected due to Coulomb scattering from nuclei, characterized by the radiation length X_0 and the nuclear interaction length λ [8]. Comparing the

ISBN 978-3-95450-177-9

x/X_0 of different monitors it is possible to establish their relative propensity for scattering. Table 1 shows a study of the most common monitors. A SciFi detector made of two planes (horizontal and vertical) of 0.5 mm square fibres has a material budget slightly below the current monitors.

Table 1: Comparison of x/X_0 for Different Monitors

Detector	x/X_0 (%)
MWPC	0.34
DWC	0.25
SciFi 1 mm	0.47
SciFi 0.5 mm	0.24

FIRST PROTOTYPE

A first detector was built with only one plane for simplicity. It is composed of 64 Saint-Gobain BCF-12 scintillating fibres of 1 mm thickness and square shape. The length of the fibres is 35 cm and they are packed together along one row, leaving no space between them. As the electronics readout chip used in this detector only has 32 channels, it was decided to read-out only every other fibre. This gives a spatial resolution of 2 mm within an active area of 64 × 64 mm^2. The SiPM are directly coupled to one end of the fibres [Fig. 1], while a mirror is glued on the other end to increase the light collected.

The scintillating fibre detector can be operated in vacuum, avoiding additional vacuum windows and so further decreasing the total material budget.

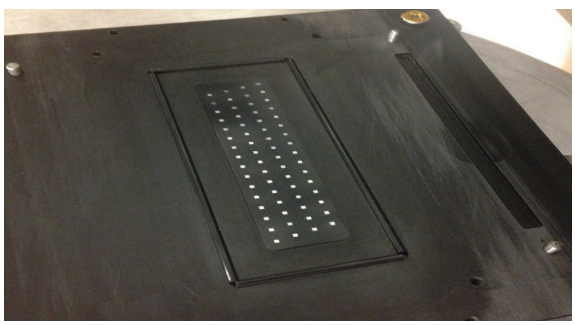

Figure 1: Fibre connector showing the part where the SiPM are coupled.

Photodetectors

The photodetectors chosen to read the light from the scintillating fibres were Silicon Photomultipliers (SiPM), specifically the Multi-Pixel Photon Counter (MPPC) model S13360-1350 from Hamamatsu [9] (although other brands (SensL and KETEK) were also tested in the laboratory). These silicon devices show a very good photo-detection efficiency of 40% in the relevant light-emitting wavelength range (435 – 450 nm). They have high gain (≈ 10^6) and provide fast pulses with sub-nanosecond rise time and 50-100 ns fall time. Other advantages are their compact size, their insensitivity to magnetic fields and their low operating voltage (< 100 V). Their most important drawbacks are the high dark count rate (typically ≈ 100 kHz/mm^2) and their temperature dependence, which can cause changes in the gain.

An alternative to read out multiple scintillating fibres efficiently are Multi-Anode Photomultipliers (MAPMT). We have tested the Hamamatsu H7546 [10], which has 64 channels over an active area of 18.1 mm × 18.1 mm. It shows a good quantum efficiency (≈ 35%), large gain (≈ 10^6), fast rise and fall times of 1-2 ns and 2-3 ns respectively and a lower dark count rate than the SiPM (≈ 100 Hz). However, the MAPMT has problems with gain uniformity and crosstalk between channels. For the first prototype we favoured the SiPM as they were considered to be a new technology with a big margin for improvement and potentially lower future production costs.

Readout Electronics

The analogue pulses from the SiPMs were processed by the CITIROC ASIC [Fig. 2], developed by OMEGA Microelectronics [11]. This chip allows amplification, discrimination and integration of 32 SiPM signals simultaneously. Another interesting feature is a fine-tuning of the SiPM voltages, allowing gain equalization, as each individual SiPM requires a slightly different operating voltage in order to achieve a homogenous detector response. The CITIROC has a trigger line composed of a fast shaper (≈ 15 ns) and a discriminator, which produces a logical signal whenever the incoming pulse exceeds a pre-set threshold. The logical pulses were sent to VME Scalers, where the profile was reconstructed, with every channel corresponding to one of the fibres read out from the detector [Fig. 3].

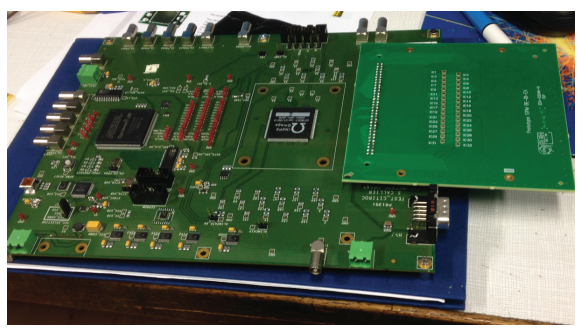

Figure 2: The CITIROC board with the SiPM PCB pluged onto it.

BEAM TESTS AT CERN

The prototype was tested in the H8 beam line of the SPS North Experimental Area at CERN [Fig. 4]. It was installed close to two other profile monitors: a DWC placed upstream and a FISC downstream. This allowed direct comparison be-

ISBN 978-3-95450-177-9

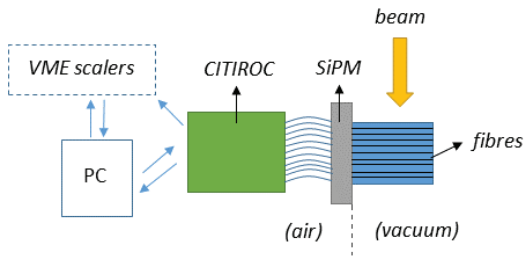

Figure 3: Schematic of the detector showing its main parts.

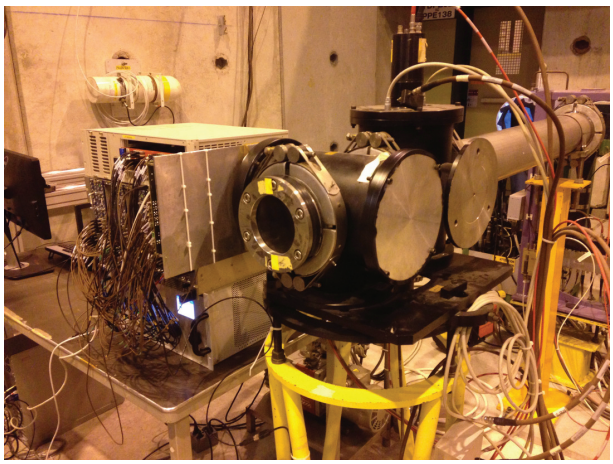

Figure 4: The SciFi monitor installed in H8: the vacuum tank in the centre houses the fibres, while the SiPM and the electronics stay on the outside (left of the figure).

tween them. A scintillator counter placed upstream provided accurate intensity measurements.

We monitored hadrons and leptons with momenta between 20 GeV/c and 180 GeV/c and intensities from 10^3 to 10^6 particles/s. The profiles have been analysed with Root [12] to fit a Gaussian curve and find the $r.m.s.$. In the following figures [5, 6 and 7] we show some of the profiles seen by the SciFi, the DWC and the FISC of beams of protons mixed with pions of momenta 180 GeV/c and different intensities. An analysis of these profiles is shown in Table 2.

The SciFi monitor worked satisfactorily in all situations, whilst the DWC had troubles with the high intensities, showing distorted profiles or artificial tails; the FISC on the other hand was unable to work at intensities lower than 10^4 particles/s. The intensity measured by the fibres was also seen to agree well with the intensity from the scintillation counter.

Lead Ion Run

Once per year, the SPS cycle changes to lead ions, Pb(82, 208), providing beams of these heavy particles directly to the experimental areas. Lead ions deposit four orders of magnitude more energy than MIPs, which means that the light produced and collected also grows by four orders of magnitude. It was therefore necessary to lower the operating voltage of the SiPM to decrease the photon detection efficiency and avoid saturation.

As shown in Table 3, for lead ions the profiles from the SciFi were seen to be wider than those from the DWC, in particular for high intensity beams. We believe that the origin of these wider profiles in the SciFi are due to crosstalk between the fibres. This crosstalk is caused by primary UV photons created during the scintillation that can escape the fibre and travel to neighbouring fibres, where they excite the wavelength shifting dopants. Because of the larger energy deposition from Pb-ions, a much larger number of these crosstalk photons are created, explaining the wider profiles. This could be avoided in the future by treating the fibre cladding with a UV absorber or reflector.

CONCLUSIONS AND PROSPECTS

A scintillating fibre monitor has been successfully tested in the H8 beam line at CERN where it has shown that it can replace the existing beam monitors over a wide range of intensities, presenting less material for the beam and giving more accurate profiles.

A second prototype using MAPMT instead of SiPM for light detection has now also been built to allow both technologies to be compared before deciding on the final design. It was planned to be tested in the beamlines in the summer of 2016, but technical problems have pushed the tests to October of the same year. In addition, two new versions of the detector have been built to investigate solutions to the crosstalk: one detector has the fibres untreated, whilst the fibres of the other are coated with an ultra-thin aluminium layer following the example of ATLAS ALFA [2]. New front-end electronic boards will also be tested, replacing the VME Scalers to allow tagging events with both spatial and time information. This will enable the possibility of reconstructing both the transverse and longitudinal profiles of the beam.

It is foreseen that the CERN neutrino platform will use this fibre monitor as a spectrometer, with the possibility of using it as a Time-Of-Flight (TOF) system also being investigated. The use of a specialized ASIC, such as the STiC [13], would theoretically allow TOF measurements with sub nanosecond time resolution.

REFERENCES

[1] LHCb Collaboration, "LHCb tracker upgrade technical design report", CERN, Geneva, Switzerland, Rep. No. CERN-LHCC-2014-001, 2014.

[2] ATLAS Collaboration, "ATLAS forward detectors for measurement of elastic scattering and luminosity", CERN, Geneva, Switzerland, Rep. No. ATLAS-TDR-18, CERN-LHCC-2008-004, 2008.

[3] T.O. White, "Scintillating fibres", *Nucl. Instr. Meth. Phys. Res. Sect. A*, vol. 273, p. 820-825, 1988.

[4] *Plastic scintillating fibres*, Product catalogue, Kuraray Co., Ltd.; `http://Kuraraypsf.jp/`

ISBN 978-3-95450-177-9

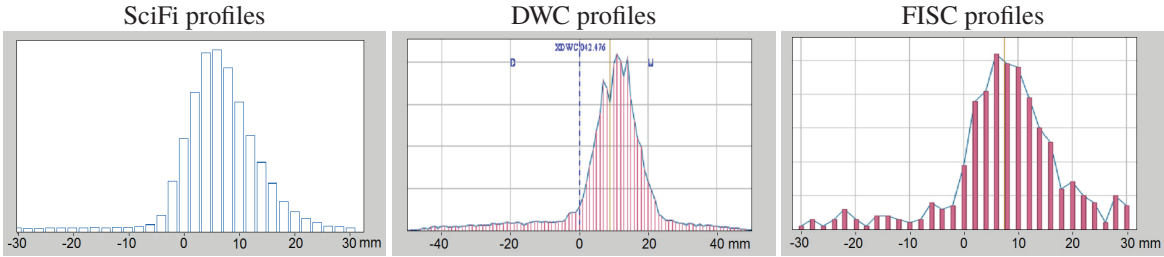

Figure 5: Profiles of a 180 GeV/c proton/pion beam of $I = 3.4 \times 10^4$ particles/s

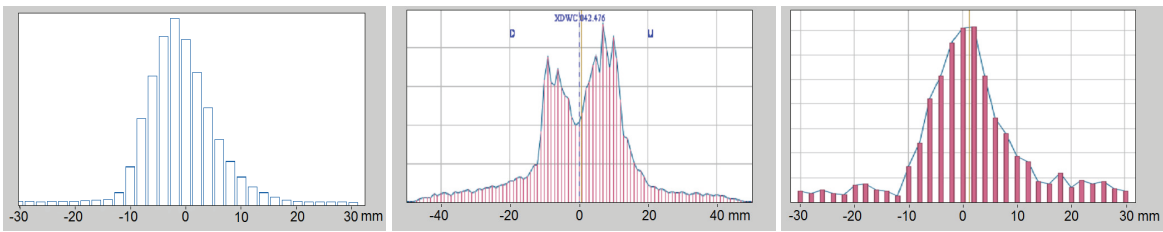

Figure 6: Profiles of a 180 GeV/c proton/pion beam of $I = 8.2 \times 10^4$ particles/s

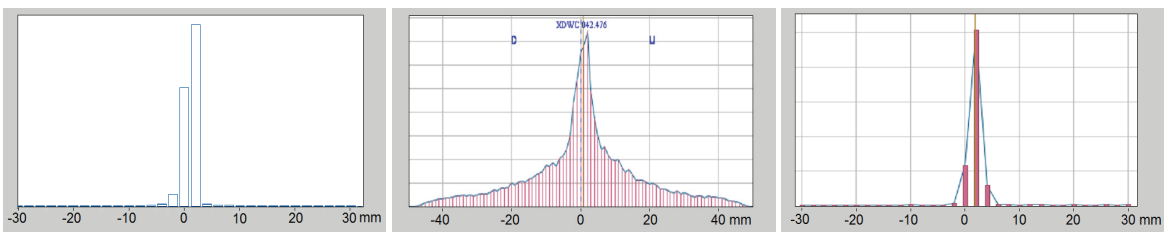

Figure 7: Profiles of a 180 GeV/c proton/pion beam of $I = 6.5 \times 10^5$ particles/s

Table 2: Comparison of the *r m s* .of the Previous Figures Shown (5, 6 and 7)

Intensity(particles/s)	σ(mm) **SciFi**	σ(mm) **DWC**	σ(mm) **FISC**
3.4×10^4	5.6	5.8	6.6
8.2×10^4	5.4	11.2	6.2
6.5×10^5	0.9	4.0	1.1

Table 3: Comparison of the *r m s* .of Different Pb(82,208) Beam Profiles

Intensity(particles/s)	σ(mm) **SciFi**	σ(mm) **DWC**
3.7×10^2	5.5	4.2
2.4×10^4	7.7	7.0
1.0×10^6	9.6	5.1

[5] *Scintillating optical fibers*, Product catalogue, Saint-Gobain Crystals; `www.crystals.saint-gobain.com`

[6] D. Acosta *et al.*, "Effects of radiation damage on scintillating fibre calorimetry", *Nucl, Instr. Meth. Phys. Res. Sect. B*, vol. 62, p. 116-132, 1991.

[7] S. Agostinelli *et al.*, "GEANT4-a simulation toolkit", *Nucl. Instr. Meth. Phys. Res. Sect. A*, vol. 506, p. 250-303, 2003.

[8] K. A. Olive *et al.* (Particle Data Group), "The review of particle physics", Chapter: Passage of particles through matter (rev.), *Chin. Phys. C*, vol. 38, 090001, 2015.

[9] *MPPC (multi-pixel photon counter) S13360-1350*, Datasheet, Hamamatsu Photonics K.K.; `www.hamamatsu.com`

[10] *Multianode photomultiplier tube assembly H7546*, Datasheet, Hamamatsu Photonics K.K.; `www.hamamatsu.com`

[11] J. Fleury *et al.*, "Petiroc and Citiroc: front-end ASICs for SiPM read-out and ToF applications", *J. Instrum.*, vol. 9, 2014.

[12] R. Brun and F. Rademakers, "ROOT-an object oriented data analysis framework", *Nucl. Instr. Meth. Phys. Res. Sect. A*, vol. 389, p. 81-86, 1997.

[13] T. Harion *et al.*, "STiC-a mixed mode silicon photomultiplier readout ASIC for time-of-flight applications", *J. Instrum.*, vol. 9, 2014.

ISBN 978-3-95450-177-9

DESIGN AND APPLICATION OF THE WIRE SCANNER FOR CADS PROTON BEAMS*

L. D. Yu†, J.S.Cao, H.P. Geng, C. Meng, Y.F. Sui,
Key Laboratory of Particle Acceleration Physics & Technology,
Institute of High Energy Physics, Chinese Academy of Sciences, Beijing 100049, China

Abstract

CADS Injector-I accelerator is a 10-mA 10-MeV CW proton linac, which uses a 3.2-MeV normal conducting 4-Vane RFQ and superconducting single-spoke cavities for accelerating. Seven wire scanners are designed and used to measure the beam profile of CADS Injector-I. In this paper, principal of operation, instrumentation and programming of these wire scanners are discussed. Some results of beam profile and emittance measurement with these wire scanners are also presented.

INTRODUCTION

The ADS project in China (CADS) is a strategic plan to solve the nuclear waste problem and the resource problem for nuclear power plants in China. One of the two front end injectors—injector-I of CADS has been designed and constructed by the Institute of High Energy of Physics(IHEP) [1]. Beam diagnostic and monitoring instruments play an important role during the machine commissioning and operation. One of those instruments is wire scanner which is employed to verify the focusing lattice, verify the functionality of the steering magnets, provide data for quad scan style emittance measurements, and helped to verify beam position diagnostics. A total of 7 wire scanners have been indigenously developed. At several critical points of the injector I linac such a set of wire scanner will be installed. In this paper principal of operation, instrumentation and programming of C-ADS wire scanners are discussed. The measured results are also presented.

WIRE SCANNER

Instrumentation

A drawing of the CADS wire scanner is shown in Fig. 1. A 100μm diameter gold plated tungsten wire is stretched simultaneously to X, Y and U directions which is 45 degree tilted from the X direction. The wires are oriented such that when the scanner insertion axis is inclined 45 degree above the beam plane, the three wires are oriented horizontally, vertically and in the 45-degree direction. In this way a single axis of motion allows the beam to be scanned in three axes. The three wires are offset from each other so that no more than one wire at a time is within the beam centre. Figure 2 shows the picture of the wire mover stage and the vacuum chamber.

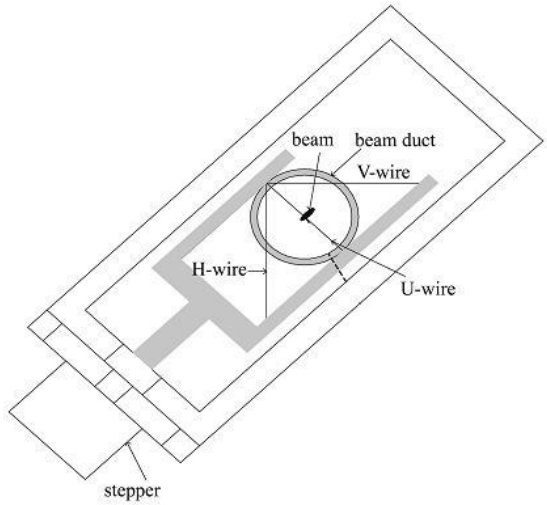

Figure 1: Schematic drawing of the wire scanner.

Figure 2: Overview system of wire scanner.

Control System

The wire scanner in CADS is controlled through PXI control system [2]. National Instrument (NI) PXI-8115 microcontroller is used for this application. The step motor is

* Work supported by China ADS Project (XDA03020000)
† yuld@ihep.ac.cn

ISBN 978-3-95450-177-9

selected to provide a 2.1 N·m torque, which is required to overcome the vacuum force and move the wire card into and out of the beam. A photometer is also needed to measure the position of the wire card and is installed on the body of the system. The current generated by the wire scanner is amplified by the current amplifier and led to a NI-PXI6251 A/D converter. A schematic diagram of the wire scanner is shown in Fig. 3.

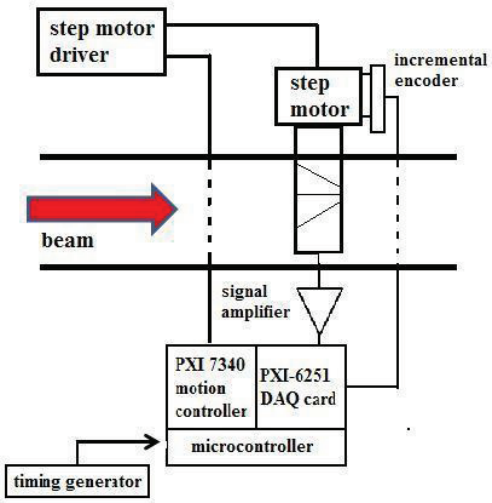

Figure 3: A schematic diagram of wire scanner.

Software Description

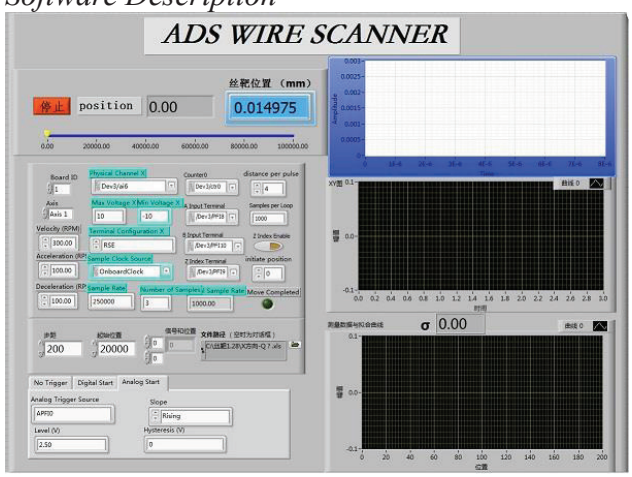

Figure 4: Graphic interface of the LabView based application for wire scanner.

To allow a complete beam scan to be done automatically, a special Labview based application was developed. Figure 4 shows a snapshot of the control screen used to set the measurement parameters and to display the data acquired by the wire scanner.

The user can specify, from the graphic screen, the initial and the final position and the displacement between subsequent measurements. The motor places the wire at the initial position and then moves it uniformly according to the chosen step. While moving, the signal and position are recorded and the acquisition is repeated until the wire comes to the final position. The scanning speed is around 30sec for one profile.

MEASURED RESULTS

MEBT-1 Layout

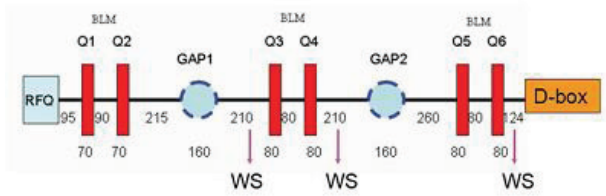

Figure 5: The layout of MEBT-1 for CADS injector-I.

We have carried out many beam profile and emittance measurements using the installed wire scanners. Here, we will show the emittance measurement of the Medium Energy Beam Transport (MEBT) Line-1.

The MEBT Line-1 of injector-I plays an important role in transporting and matching the beam from the RFQ exit to the entrance of the super-conducting Spoke-012 cavities. To quantify the beam quality and validate the design for the cryo-modules, the beam transverse emittance have been measured using a wire scanner and the quad-scan method recently [3]. The layout of MEBT-1 is shown in Fig. 5. MEBT-1 line is composed of three doublets (Q1 to Q6) and two bunchers (GAP1 and GAP2). Three wire scanners have been installed to measure the transverse beam sizes. In our measurements, we use the second wire scanner to measure the beam sizes.

Method

We consider two methods to calculate the beam sizes. First is the Gaussian with offset method. In this method, we use the function shown in Eq. 1 to fit the wire scanner data, and obtain the beam sizes.

$$I = \mathrm{B} + \mathrm{A} * \exp\frac{-(\chi-\chi_0)}{2\rho_x^2} \quad (1)$$

In Eq. 1, I is the wire scanner intensity, B is the background offset, A is the maximum intensity of the Gaussian function, x_0 is the center of the Gaussian function, normally can be set to the position where the signal has a maximum intensity, and σ_x is the fitted beam size.

The second method is direct calculation method. We use the wire scanner data to direct calculate the root mean square beam size. The formula is shown in Eq. 2.

$$\sigma_x = \sqrt{< x^2 >} = \sqrt{\frac{\sum I_i (x_i - x_0)^2}{\sum I_i}} \quad (2)$$

In Eq. 2, I_i is the signal intensity at position x_i.

We use typical narrow-pointed and wide-plump wire scanner signals as an example to show the difference of the two fitting methods. Figure 6 shows the different fitting results for both types of wire scanner signals. For the wide-plump signal, the two results are roughly the same. For the narrow-pointed signal, the formula calculation result is almost two times larger than Gaussian fitting results. We note that in the Gaussian fitting curves, the top of the signal is not well fitted. And because of the long tail of the signal, the formula calculated beam size is much larger.

ISBN 978-3-95450-177-9

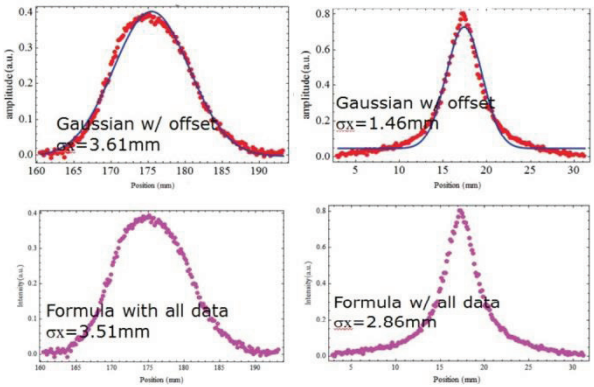

Figure 6: Fitting results for wide-plump and narrow-pointed signal with two different fitting methods.

Emittance Results

Table 1: Fitting Results of Beam Emittances at Horizontal and Vertical Planes with Two Different Fitting Methods. The unit of $\beta_{x,y}$ is m/rad, and $\varepsilon_{x,y}$ is mm mrad.

	Gaussian	Formula
α_x	-1.22	-1.07
β_x	0.113	0.10
ε_x	0.168	0.192
α_y	2.87	1.83
β_y	0.3	0.176
ε_y	0.13	0.279

The emittance difference between Gaussian fitting and formula calculation methods is ~ 20% in horizontal and ~ 115% in vertical. The difference in emittance at horizontal plane is relatively small compared to the vertical plane. This is because the wire scanner signals at vertical plane are mostly narrow-pointed distribution which have a big difference in beam sizes when using different fitting methods as described in the previous section.

From the RFQ design results, the MEBT-1 input beam parameters should be $\alpha_x = -1.31$, $\beta_x = 0.12$ m/rad, $\varepsilon_x = 0.20$ mm· mrad, $\alpha_y = 1.46$, $\beta_y = 0.13$ m/rad, $\varepsilon_y = 0.20$ mm·mrad. From Table 1, we can see that the fitting result with the formula calculation method agrees the best with the RFQ simulation results. The disagreement of the Gaussian fitting results might come from the fitting methods of beam sizes, which may not be proper when the beam phase space is severely tilted or much deviated from Gaussian distribution.

SUMMARY

Seven wire scanners have been built for high current proton beams in the C-ADS injector I. The software was developed based on LABVIEW. The beam size and emittance measurement have been carried out with these wire scanners. Two different methods for analysing the beam sizes with the wire scanner data have been discussed. We also discuss the fitted beam emittance. The results show that the emittance calculated with the beam sizes fitted by the formula is in good agreement with the RFQ simulation result.

REFERENCES

[1] H. Chen *et. al.*, "ADS Accelerator Program in China", IHEP-FNAL Workshop on Proton Accelerator, Beijing, February 15-16, 2011.

[2] L. Yu *et. al.*, "Design and Application of Double-slit Emittance for CADS Proton Beams", MOPMB034, Proceedings of IPAC2016, Busan, Korea, 2016

[3] H. Geng *et. al.*, "Emittance Measurement with Wire Scanners at C-ADS Injector I", MOPOY027, Proceedings of IPAC2016, Busan, Korea, 2016

ISBN 978-3-95450-177-9

SCINTILLATION AND OTR SCREEN CHARACTERIZATION WITH A 440 GeV/c PROTON BEAM IN AIR AT THE CERN HIRADMAT FACILITY

S. Burger†, B. Biskup[1], S.Mazzoni, M.Turner[2], CERN, Geneva, Switzerland
[1]also at Czech Technical University, Prague, Czech Republic
[2]also at Graz University of Technology Theoretical Physics Institute, Vienna, Austria

Abstract

Beam observation systems, based on charged particles passing through a light emitting screen, are widely used and often crucial for the operation of particle accelerators as well as experimental beamlines. The AWAKE [1] experiment, currently under construction at CERN, requires a detailed understanding of screen sensitivity and the associated accuracy of the beam size measurement. We present the measurement of relative light yield and screen resolution of seven different materials (Chromox, YAG, Alumina, Titanium, Aluminium, Aluminium and Silver coated Silicon). The Chromox and YAG samples were additionally measured with different thicknesses. The measurements were performed at the CERN's HiRadMat [2] test facility with 440 GeV/c protons, a beam similar to the one foreseen for AWAKE. The experiment was performed in an air environment.

INTRODUCTION

The accelerators at CERN use more than 250 beam instruments based on scintillation and/or Optical Transition Radiation (OTR) screens. Even though the emission of scintillation and OTR light is very well understood, comparative measurements of commonly used screen types are hard to find.

We tested 13 typical screen materials (see Table 1 and Fig. 1) in the HiRadMat [2] test facility. We used a 440 GeV/c proton bunch from the CERN SPS populated with 10^{11} protons with a radial proton beam size of $\sigma = 2$ mm.

EXPERIMENTAL SETUP

Layout

Figure 2 shows a 3D model of the experimental setup. A linear stage with a stepper motor is used to select screens. The screens are positioned at 45 degrees with respect to the incoming beam. A mirror reflects the light emitted by the screens to a CCD camera (WATEC 902H3) equipped with a 25 mm focal length camera lens. This optical line gives calibration values of ~100µm/pixel in both the horizontal and vertical planes.

Two rotatable optical filter wheels are placed in front of the camera lens to, if necessary, reduce the light transmission from 100% down to 0.00001% in 14 steps.

A second linear translation stage is available to move an aluminium foil of 100µm thickness in front of the screen to prevent any light created upstream from reaching the camera. Additionally, we surrounded the setup with a blackened metal box that has two openings for the entrance and exit of the beam. The presence of a beam dump located approximately 10 meters downstream our setup resulted in an elevated background noise on the camera image due to backscattering.

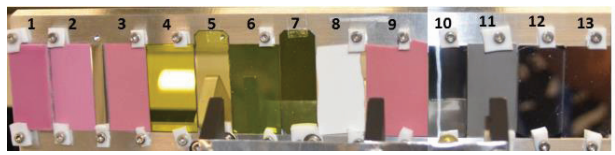

Figure 1: Image of the screen material samples mounted on the screen holder.

Table 1: Material Samples Shown in Figure 1

Screen Nr.	Material	Thickness [mm]	Supplier
1	Chromox (Al_2O_3:CrO_2)	3.0	*CeraQUest*
2	Chromox (Al_2O_3:CrO_2)	1.0	*CeraQuest*
3	Chromox (Al_2O_3:CrO_2)	0.5	*CERN stock*
4	YAG (YAG:Ce)	0.5	*Crytur*
5	YAG (YAG:Ce)	0.1	*Crytur*
6	YAG back-coated (YAG:Ce + Al)	0.5	*Crytur*
7	YAG back-coated (YAG:Ce + Al)	0.1	*Crytur*
8	Alumina (99% purity)	1.0	*GoodFellow*
9	Chromox-old type (Al_2O_3:CrO_2)	1.0	*CERN stock*
10	Aluminium	1.0	*CERN stock*
11	Titanium	0.1	*GoodFellow*
12	Aluminium coated Silicon	0.25	*MicroFabSolutions*
13	Silver coated Silicon	0.3	*Sil'Tronix*

Control and Acquisition

The measurement setup is controlled via VME based modules. The control of the filter wheels, light for calibration and the image acquisition are made through the standard CERN beam observation electronics [3].

We used an analogue camera that is not synchronized with the proton beam. The camera triggers every 20ms and integrates over a 20ms period. The acquisition is performed by capturing the image in the acquisition board on ever vertical sync. from the video signal (i.e. each 20ms).

† stephane.burger@cern.ch

ISBN 978-3-95450-177-9

A timing signal linked to the extraction of the beam from the SPS triggers the image to be stored as a beam measurement.

Since there is no synchronisation between the camera and the extraction timing of the CERN SPS, there is an uncertainty of up to 20ms between when the proton beam arrives and when the frame from the camera is captured. This does not affect the light yield of OTR screens as the light emission is instantaneous during the passage of the proton bunch. As the proton bunch length is only a few ns, much shorter than the camera exposure time, we can safely assume that all light is captured in a single frame. Capturing scintillation light is, however, different. The light emitted follows an exponentially decaying profile with a decay constant that depends on the screen material and can reach up to tens of milliseconds. As such, depending on when the proton beam hits the screen with respect to the camera trigger, a different fraction of the emitted light is integrated in a single camera frame. In order to cope with this effect, we rejected all measurements that had a significantly lower light yield than the maximum measured for each screen, keeping approximately 70% of the recorded images. Using a camera synchronised to the extraction timing of the CERN SPS beam would solve this problem.

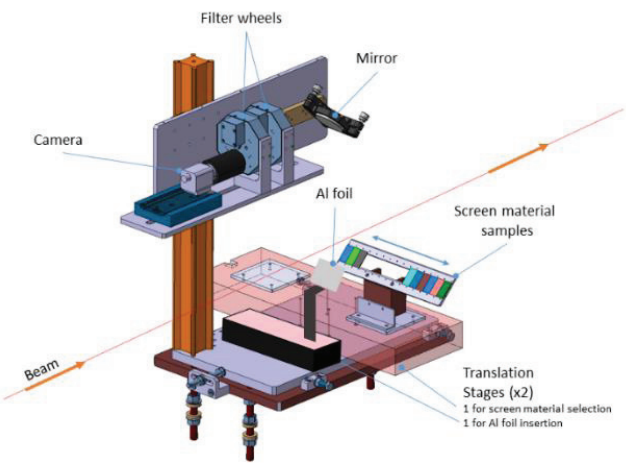

Figure 2: Experimental setup of the screen test.

THEORETICAL ASPECT

Light Emission in Air

When a charged particle beam propagates in air instead of the usual high vacuum of accelerator beam pipes, several parasitic light emitting processes can contribute to the signal measured by the camera:

1) Forward OTR photons are generated by the interaction of the protons with the vacuum pipe exit window. However, in our case the contribution from this can be considered as negligible, as the vacuum window is 1.94m upstream of the measurement.
2) Cherenkov and luminescence photons are generated all along the 1.94 m path in air from the vacuum exit window up to the measurement station.

These two processes are considered as parasitic light that add, by reflection on the screen, to the scintillating or OTR light generated by the screen itself. The higher the reflectivity of the screen, the more parasitic light contributes. We tried to supress this effect by inserting an opaque foil 43 mm in front of the light emitting screen (see Fig. 3). However, such a foil is a source of (forward) OTR for the measurement screen that has to be accounted for. When measuring OTR screens, the forward OTR produced by the foil interferes with the backwards OTR produced by the screen under test. The total light yield and angular distribution depends critically on the energy of the beam, the radiation wavelength and the distance between the two radiators [4, 5]. In the present case, the so-called formation length defined as $l_f = \gamma^2\lambda/2\pi$ is 1.75 cm at a central wavelength of 500 nm, so that the total light yield emitted by the two screens is approximately twice that of a single screen.

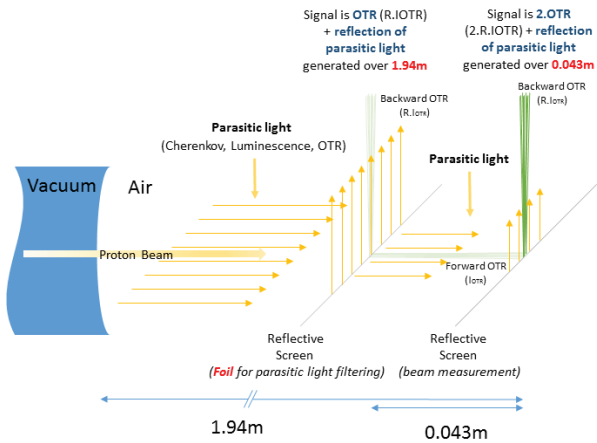

Figure 3: Layout of the different light emission processes included in the screen measurements. The foil inserted before the beam screen blocks the parasitic light generated upstream in the air but itself generates forward OTR that reached the measurement screen.

The expected scintillation light yield is not straightforward to calculate, and so was only measured.

Cherenkov

Protons in air produce Cherenkov photons with an angular distribution of θ [6]:

$$\theta(E) = \cos^{-1}\left(\frac{1}{\beta(E).ng(P)}\right) \quad (1)$$

where βis the beam relative velocity and *ng* is the index of refraction of air.

The number of generated photons N_{ch} was calculated as:

$$N_{ch} = 2\alpha.\pi.L.\left(\frac{1}{\lambda a} - \frac{1}{\lambda b}\right).\sin\left(\theta(E)\right)^2 \quad (2)$$

where α is the fine structure constant, *L* is the length of the air channel where the light is generated and λ_a-λ_b is the spectral bandwidth.

ISBN 978-3-95450-177-9

Luminescence

The number of photons N_{sc} created by luminescence in air (in 4π) was estimated as [7]:

$$N_{sc}(L,\alpha) = \frac{\rho.Na}{M}.\left(\frac{Pe}{Pi}\right).\sigma_{sc}.L \quad (3)$$

where ρ is the air density, Na is the Avogadro constant, M the molar mass of air, Pe/Pi is the ratio of the air pressure to the atmospheric pressure, σ_{SC} is the scintillation cross section and L is the length of the air channel where the light is generated.

OTR

The OTR light process on the measurement screen generates photons following the expression [6]:

$$N_{OTR}(E) = 2.R.\frac{2\alpha}{\pi}.\ln\left(\frac{\lambda b}{\lambda a}\right).\left(\ln\left(2\gamma(E)\right) - \frac{1}{2}\right) \quad (4)$$

where R is the screen reflectivity and γ is the Lorentz factor.

As results of Eqs.(1, 2, 3 and 4), the calculated light yields for all processes are presented in Table 2, taking into account the acceptance of the optical system.

Table 2: Expected Light Yields from OTR Screens and Expected Contributions from Parasitic Light for no Blocking Foil and with Blocking Foil Inserted

	Without Foil	**With Foil**
Path length of protons in air	1.94 [m]	0.043 [m]
Number of photons	N	N_f
N_{OTR} (protons on screen)	2.98E-2	2.98E-2
N_{Ch} (protons in air)	4.266	1.132
N_{Lu} (protons in air)	6.60E-2	1.23E-04
Total	$N_{OTR}+N_{Ch}+N_{Lu}$	$2xN_{OTR}+Nf_{Ch}+Nf_{Lu}$
Ntotal	4.36E+00	1.19E+00
N/Nf	3.66E+00	

For both cases (without and with foil), the Cherenkov light contributes with 2 orders of magnitude more photons than OTR or Luminescence.

This means that for highly reflective OTR screens (Ag coated Si, Al coated Si), the main contribution of parasitic light to our measurement comes from photons produced by Cherenkov radiation. Inserting the blocking foil reduces this contribution by a factor of four.

The contribution of parasitic signal in the case of a scintillating screen cannot be easily calculated, as the light yield of the screen is a priori not known. However, due to the higher photon yield of scintillation and the lower optical reflectivity of the surfaces, we expect it to be less important than in the OTR case.

MEASUREMENTS AND RESULTS

Systematic Measurements

Some 10 to 25 measurements per screen were obtained, with the majority taken with the light blocking foil inserted. The optical filters were carefully chosen to avoid image saturation. Figure 4 shows a typical measurement with (right) and without (left) the blocking foil. The parasitic light suppression by the foil is clearly visible.

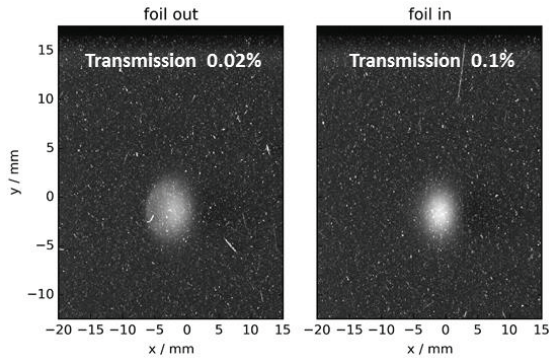

Figure 4: Example of raw images of the proton beam in air on a Silver coated Si OTR screen without (left) and with (right) blocking foil in place. The change of intensity as well as beam size is clearly visible.

Analysis Process

After subtracting the background, the pixels are integrated over the vertical axis, resulting in an integrated horizontal profile. We normalized the image with respect to the beam intensity and choice of filter. The data shown in Figs. 5 and 6 represent the mean (marker) and standard deviation (error bar) of each pixel column. Finally, a Gaussian fit is performed, which gives the relative yield and measured beam sigma.

Results

Figures 4 and 5 show that the main differences between blocking foil in and out are the lower light yield and reduced sigma of the Gaussian fit. Additionally the centre of the Gaussian shifts for the silver coated silicon and alumina screens. We explain this difference in yield and sigma by the contribution of the parasitic light, which is considerably reduced with the blocking foil in as mentioned in the previous section. In the case of Silver coated Silicon (top plot of Fig. 5), the light yield with blocking foil inserted is 6.6 times less than without the foil. In the case of scintillator screens (middle and bottom plots), this difference is lower than expected. The shift of the centre of the Gaussian is not yet understood, but we suspect this to be due to a change in the reflectivity and/or the diffusivity of the material combined with errors in the alignment of the optical line.

ISBN 978-3-95450-177-9

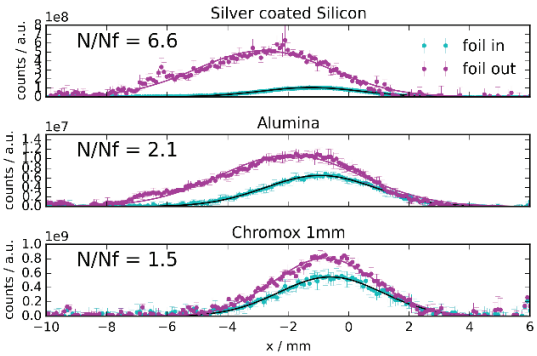

Figure 5: Results of the beam profile measurement showing the response of the silver coated silicon, Alumina and Chromox screens with and without blocking foil.

Figure 6 shows the measurement of all screens with the light blocking foil inserted. Based on this data, Tables 3 and 4 give the relative yield and relative sigma obtained from the Gaussian fit for all screen materials.

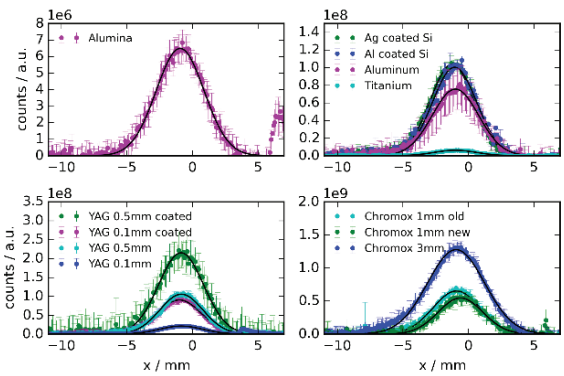

Figure 6: Results of beam profile measurements showing the response of all screens listed in table 1 with a foil blocking the parasitic light installed 43mm upstream.

Table 3: Light Yield Measured on each Screen with a Foil Positioned 43mm Upstream to Block Part of the Parasitic Light. The Values are Referenced to a 1mm Thick Chromox Screen as it is Commonly Used in Many of the CERN Beam Observation Systems

	Type	Yield [%]	Error [%]
Al_2O_3:CrO_2 3mm	Scint.	232.73	2.34
Chromox 1mm (old type)	Scint.	118.18	3.08
Al_2O_3:CrO_2 1mm	Scint.	100	3.64
YAG:Ce 0.5mm + Al back Coated	Scint.	40.00	4.55
YAG:Ce 0.5mm	Scint.	19.27	4.72
Si + Ag coated	OTR	18.91	3.85
Si + Al coated	OTR	18.18	4.00
YAG:Ce 0.1mm + Al back Coated	Scint.	15.45	35.25
Aluminium 1mm	OTR	14.55	25.00
YAG:Ce 0.1mm	Scint.	3.87	3.29
Alumina (99%) 1mm	Scint.	1.20	7.58
Titanium 0.1mm	OTR	1.13	9.68

As expected, the 3 mm thick Chromox screen gives both the highest yield and the largest beam size due to its thickness. Due to their high reflectivity the OTR screens (except for titanium) have a yield only a few times lower than scintillating material, which for comparison is 3 orders of magnitude difference in vacuum, due to the contribution of reflected parasitic Cherenkov light generated upstream. The best resolution was obtained by the Titanium screen, probably due to its diffusive aspect and low reflectivity. Titanium additionally has the lowest light yield.

Table 4: Sigma measured on each screen with a foil positioned at 43mm upstream to block part of the parasitic light. The values are referenced to the Titanium screen as it gives the smallest sigma value of 1.61mm

	Type	Sigma diff. with ref. Ti screen [%]	Error [%]
Titanium 0.1mm	OTR	0	2
YAG:Ce 0.5mm	Scint.	+1.86	6
YAG:Ce 0.1mm	Scint.	+2.48	5
Si + Ag coated	OTR	+2.48	4
Si + Al coated	OTR	+4.35	4
YAG:Ce 0.5mm + Al back Coated	Scint	+5.59	10
Chromox 1mm	Scint	+5.59	10
Aluminium 1mm	OTR	+8.07	7
Chromox 1mm (old type)	Scint	+11.18	6
YAG:Ce 0.1mm + Al back Coated	Scint.	+11.80	50
Alumina (99%)	Scint.	+12.42	7
Chromox 3mm	Scint	+34.78	7

CONCLUSION

The light emission from a proton beam of 440 Gev/c in air was measured for three scintillators (Alumina, Chromox and YAG) of different thicknesses and four OTR emitting screens (Ag coated Si, Al coated Si, Ti and Al). A light blocking foil was inserted to reduce the contribution of parasitic light created upstream of the target material. Nevertheless, the majority of the photons observed due to Cherenkov light generated as the relativistic proton beam passes through the air in front of the screen. The conclusion is therefore that no precise OTR vs scintillator light yield and subsequent resolution studies can be performed with this data. Future studies under vacuum are thus foreseen to better asses these questions. However, these set of measurements represent an extremely useful reference for setting up a beam imaging system in air.

ACKNOWLEDGEMENT

The authors want to thank E. Bravin and T. Lefevre for all fruitful discussions that helped in the understanding of this screen study. Also, the contribution of J. J. Gras on the data logging was very much appreciated. The research leading to these results has received funding from the European Commission under the FP7 Research Infrastructures project EUCARD-2, grant agreement no. 312453”””

ISBN 978-3-95450-177-9

REFERENCES

[1] E. Gschwendtner *et al.*, "AWAKE, The Advanced Proton Driven Plasma Wakefield Acceleration Experiment at CERN", NIMA DOI: 10.1016/j.nima.2016.02.026.

[2] I. Efthymiopoulos *et al.*, "HiRadMat: A new irradiation facility for material testing at CERN", Proceedings of IPAC 2011, San Sebastian, Spain.

[3] S. Burger and E. Bravin, "A new Control System for the CERN TV Beams Observation", CERN-AB-Note-2008-041-BI.

[4] Wartski *et al.*, "Interference phenomenon in optical transition radiation and its application to particle beam diagnostics and multiplescattering measurements", J. Appl. Phys. 46, 3644 (1975).

[5] M. Bergamaschi *et al.*, "Optical Transition Radiation interference in the near and far-field regions", manuscript in preparation.

[6] Jackson J. D. "Classical Electrodynamics", Wiley 1999.

[7] Bosser *et al.*, "N2 and Xe Gas Scintillation Cross-Section, Spectrum, and Lifetime Measurements from 50 MeV to 26 GeV at the CERN PS and Booster", Nucl. Instrum. Methods Phys. Res., A 492 (2002) 74-90.

ISBN 978-3-95450-177-9

SCINTILLATING SCREENS INVESTIGATIONS WITH PROTON BEAMS AT 30 keV AND 3 MeV

C. Simon*, F. Harrault, F. Senee, O. Tuske, CEA-Saclay/DRF/Irfu, Gif sur Yvette, France
E. Bordas, F. Leprêtre, Y. Serruys, CEA-Saclay/DEN, Gif sur Yvette, France
P. Ausset, INPO, Orsay, France
J. Fils, GSI, Darmstadt Germany

Abstract

Luminescent screens hit by accelerated charged particle beams are commonly used as beam diagnostics to produce a visible emitted light, which can be sensed by a camera. In order to investigate the characteristics of the luminescence response of several scintillators, the beam shape and the observation of the transverse position, experiments were done with different low intensity proton beams produced by two different test benches.

This study is motivated by the need to identify scintillator materials for the development of a 4-dimensional emittancemeter which will allow the characterization of the beams, in particular the emittance measurement (size, angular divergence).

This paper describes the experimental setups and our investigations of the optical properties of various scintillating materials at two different proton beam energies respectively about 30 keV and 3 MeV. The light produced by these screens is characterized by yield, flux of the emitted light versus the beam intensity, time response, and long life-time and they are compared.

INTRODUCTION

The characterization of the beams, in particular the emittance measurement (size, angular divergence) is a key point, both in the understanding of physical phenomena involved, such as space charge compensation, interaction with the residual gas, interaction with solid interfaces, or the dynamics of plasma ion sources, as in the validation of accelerators design.

As part of collaboration with the IPNO, a 4 Dimensions Emittancemeter (EMIT4D) [1] is under development. It will provide, in a single measurement, the beam distribution in the transverse 4-dimensional phase space (X, X', Y, Y'), characterizing the beam with a high accuracy.

The principle of this instrument is simple. A screen drilled with 2D series of holes of very small diameter (called pepper-pot) intercepts the beam. It samples a grid of transverse beam positions. The particles passing through the holes will strike further a scintillator screen that emits light radiation. Physical properties of the original beam are reconstructed through the analysis of this radiation, collected by a dedicated video system (like a digital camera).

As part of this project, some measurements were done with several scintillators at two different proton beam energies respectively about 30 keV and 3 MeV in order to study the properties of each scintillator and determine which one could be used with beam intensity from 0.1 µA to 5 µA and energy from few 10 keV up to few MeV.

* claire.simon@cea.fr

SCINTILLATORS

The scintillators selection is based on the materials available and on use as diagnostics in proton beam production. Scintillation screens under study, like crystals, powder screens, and ceramics, are presented in Table 1. The "powder" scintillators have been provided by the CEA DAM except the BaF_2 provided by GSI. The thickness of the powder layer is also specified. Crystal scintillators YAG:Ce were bought at Crytur [2], BGO and Prelude 420 at St Gobain [3].

Table 1: List of Scintillators Under Study

Name Composition	Density g/cm^3	Light yield (photons/keV)	Thickness (mm)
P22 Y_2O_2S:Eu		45	0.008
P46 Y_3AlO_{12}:Ce^{3+}	4.5	6	0.008
P31 ZnS:Cu	4.09	130	0.01
BaF_2	4.88	10	
BGO	7.13	8-10	0.25
YAG:Ce	4.5	16.7	0.25 & 1
Prelude420 $Lu_{1.8}Y_2Si0_5$:Ce	7.1	32	0.25
Al_2O_3:Cr	3.63	0.367	5

EXPERIENCE SETUPS

The measurements were done on two experimental setups at two different proton beam energies respectively about 30 keV and 3 MeV. The width of the beam spots was about 1 mm and the beam current was not higher than 5 µA in both cases.

Low Energy Proton-Beam Production

The proton beam is produced by the ALISES 2 ion source developed at the CEA Saclay [4]. This ion source prototype delivers a pulsed beam of protons up to 34 mA at 40 keV of extraction energy. The extracted beam is transported to the diagnostic chamber, through the BETSI beam line [5] like shown Fig. 1.

ISBN 978-3-95450-177-9

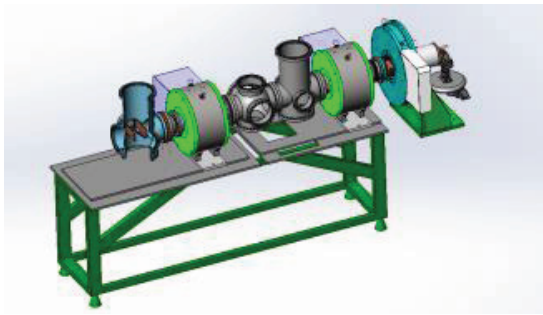

Figure 1: BETSI beam line with ALISES 2 ion source. The studied screens are installed at the end of the line (on the left) in the diagnostic chamber.

In the diagnostic chamber, a water-cooled cone shaped hole with an exit aperture of 1.1 mm was installed in front of the scintillator screen to reduce the beam intensity around 0.2 µA. The scintillators are maintained on a linear translator in order to move the beam impact point on the surface. To measure the beam intensity at the screen position, a collector for ion beam current measurements was installed behind the scintillators. To reduce the secondary electron production that would increase the measured current value, the collector is equipped with a permanent magnet. The scintillator is positioned with a 50° angle to record the emitted light at the interaction point with a camera. The camera used is an Allied Vision GUPPY, connected in FireWire, synchronized with the ion source pulse and set to collect light during the machine pulse length. The camera is located outside the chamber at about 400 mm from the interaction point. Great care has been taken to be sure that the camera pixels do not get saturated while the emitted light is collected. The camera is controlled and recorded under LabView environment. The setup is presented in Fig. 2.

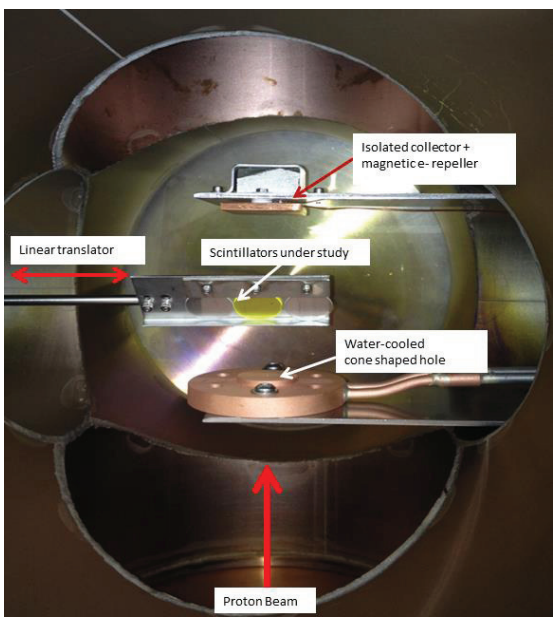

Figure 2: The diagnostic chamber, at BETSI, with the scintillators fixed onto a linear translator. In front of the scintillator, a hole reduces the beam intensity. Behind, a collector is installed for ion beam current measurements. This picture is taken at the viewport of the camera.

3 MeV Energy Proton-Beam Production

The proton beam at 3 MeV is produced by a 3 MV Pelletron accelerator, Épiméthée, equipped with an ECR multi-charged ion source. This accelerator, installed at CEA Saclay, is one of the accelerators of JANNUS facility [6]. On this machine, the current density can vary from 25 nA /cm² to few µA /cm² in a not-pulsed mode. To do the measurements with this 3 MeV energy proton beam, a setup similar to that of BETSI was installed at the accelerator Épiméthée. A mechanical translator with the screen samples was mounted on a CF100 flange. To reduce the beam diameter, a diaphragm of about 2 mm was used and the current intensity was adjusted around 0.1 µA. Several Faraday cups can be inserted to measure the beam intensity. The camera was installed on the chamber.

RESULTS

For each measurement presented in this report, the visible emitted light was obtained by integrating the light output in a region-of-interest chosen to be the central brightest region of the irradiated beam spot.

Light Emitted Intensities by Scintillators Under Study

Figure 3 presents the scintillation response of different scintillators as a function of number of irradiating protons. The beam energy is the same for all studies, about 35 keV. Beam current and pulse duration are different but, to allow the comparison of scintillation yield and degradation, each measurement was converted in number of protons. The powder scintillators P22, P31 and P46 produced the highest visible emitted light. Concerning the BaF_2 scintillator, we have to increase the camera aperture about 128 times to detect its visible emitted light. Indeed, its wavelength of maximal emission is in UV spectrum while the used camera detects only the light emitted in the visible spectrum.

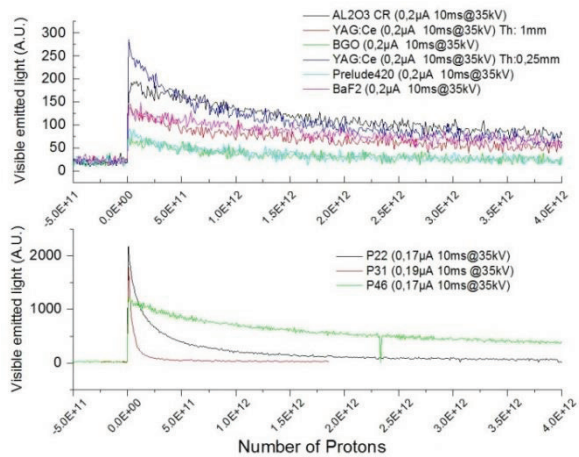

Figure 3: Visible emitted light from studied scintillator screens as a function of protons particles number at beam energy of 35 keV.

ISBN 978-3-95450-177-9

Figure 3 shows a fast degradation of scintillation for powder scintillators P22 and P31. The scintillators which have the lowest degradation are the scintillators P46, YAG:Ce and Al_2O_3:Cr.

The composition of the powder scintillator P46 is close to a YAG:Ce scintillator. Figure 4 shows a comparison between the YAG:Ce materials with different thickness. It seems that the light is higher with a smaller thickness.

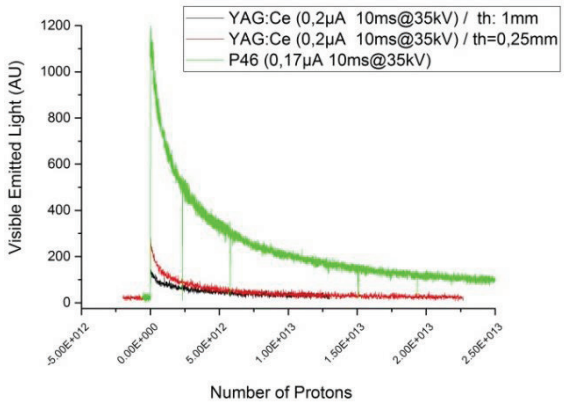

Figure 4: Visible emitted light from YAG:Ce and P46 scintillators as a function of protons particles number at beam energy of 35 keV.

Influence of the Pulse Length

The time collection of the camera has been increased in order to collect the light emitted during the pulse time of 20 ms. In Fig. 5, the visible emitted light was normalized to show that the scintillation yield degradation of this intensity follows the same decay with two different pulse lengths (10 ms and 20 ms). We also noted that the emitted light intensity is twice as high as for the 20 ms pulse length.

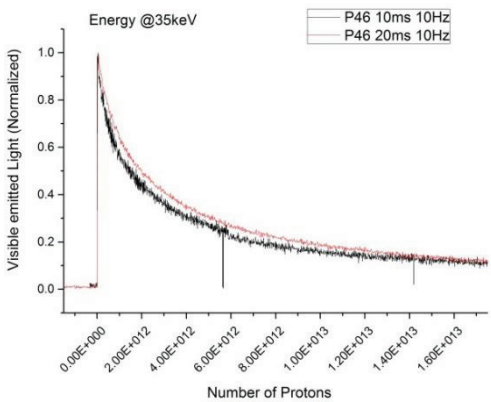

Figure 5: Normalized light output of scintillator P46 vs number of particles with different pulse lengths

Influence of the Pulse Repetition Rate

To check if the thermal heat up due to particle implantation plays a crucial part on the scintillation yield degradation, two measurements at two different repetition rates, 4 and 10 Hz, with the same beam intensity, were done. Results are presented in Fig. 6. In spite of a difference of power deposition, estimated from 0.24 to 0.6 mW, no influence of the repetition rate on the light output amplitude and scintillation yield degradation can be observed.

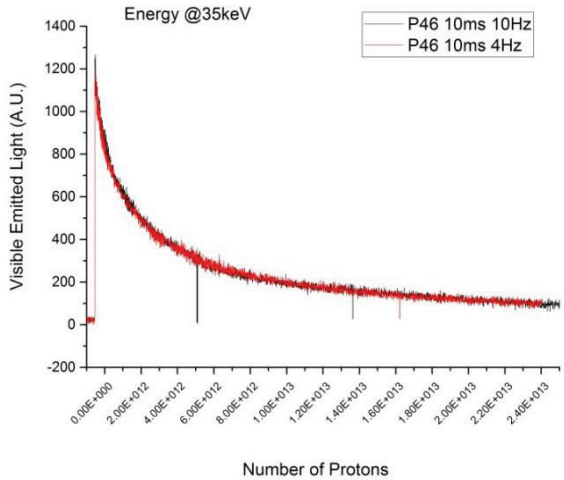

Figure 6: Light yield of scintillator P46 vs number of particles with different repetition rate.

Influence of Energy

To check the influence of energy on the scintillation yield degradation, several measurements were done at different energies from 35 keV to 3 MeV. Figure 3 shows that the materials YAG:Ce, P46 and Al_2O_3 have the slowest light output degradation. Those scintillators were, therefore, chosen to be studied at energy of 3 MeV.

First measurements showed that the Al_2O_3 had an important remanence and caused major breakdowns. This scintillator has been set aside.

In Fig. 7, the visible emitted light was normalized to compare the behaviour of scintillator P46 at two different energies, 35 keV and 3 MeV. The light output is much less degraded at 3 MeV. This observation was also reported in some studies on other scintillators [7].

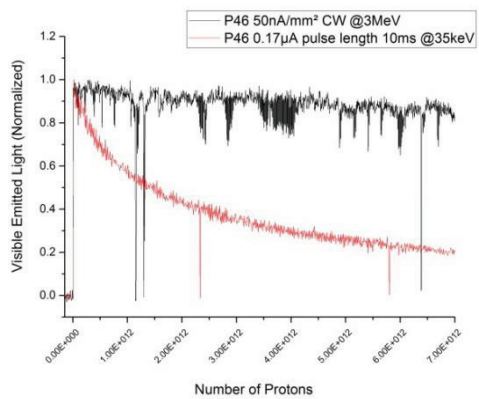

Figure 7: Light yield of P46 scintillator as a function of number of protons irradiated at beam energies of 35 keV and 3 MeV

In Fig. 8, a test was carried out with the YAG:Ce at 3 MeV and with beam density of 100 nA/mm². To understand if the degradation is irreversible, the irradiation was stopped for several minutes. The amplitude of light output

ISBN 978-3-95450-177-9

resumes at the same amplitude. Degradation is therefore irreversible. When the bombarding of protons number is high, even at 3 MeV we observe a notable degradation.

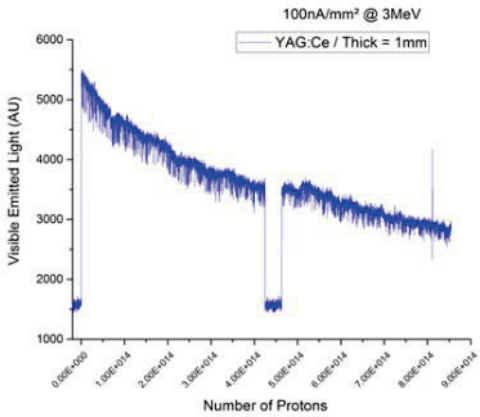

Figure 8: Visible Emitted light from YAG:Ce as a function of protons particles number irradiated by protons at beam energy of 3 MeV with a beam interruption done during the measurement.

DISCUSSION

A theoretical calculation to determine the beam penetration in scintillator P46 can be done. The stopping power for protons is given by [8], with the density of P46, beam penetration at 35 keV can be calculated around 21 nm and at 3 MeV around 24 µm. At low energy, the power is concentrated on a very small volume, which could explain the degradation.

The luminescence of a scintillator is due to the presence of defects and impurities producing local energy levels in the region called "forbidden band" between the conduction and valence bands. The incoming low energy particle have three kinds of interaction on the material: activators in which the photo-emission accompanies the transition of an electron of the material to the ground state, defects in which the energy is only dissipated by thermal effect and excitons in which electrons may return to the valence band or to the conduction band without emission of photon. The photoemission results in an interaction between the transition process of an electron from the conduction band to the valence band and thermal dissipation processes. Birks [9] states that the exponential decay of the luminescence production efficiency observed vs the bombardment time by low energy incident ions is due to the absorption of photons by damaged sites.

CONCLUSION

Several scintillators were investigated under proton radiation with variable beam conditions. At low energy, the visible emitted light for all scintillators shows degradation. This degradation depends on the number of protons. Even at 3 MeV, this degradation is present with an important number of protons. More investigations can be done to find a material with a limited degradation but for the moment, the P46 material seems to be the most suitable scintillator for our EMIT4D. This scintillator has the slowest light output degradation as compared to the other materials and a high light yield.

ACKNOWLEDGEMENT

We thank our colleagues from CEA Saclay in particular N. Pichoff, J. Schwindling, D. Uriot for their support, their advices and their help during the development of those studies. We also tank GSI for the supply of BaF_2 scintillator and the CEA/DAM for the supply of powder scintillators.

REFERENCES

[1] A. Dumancic *et al*., "EMIT4D," *Journées Accélérateurs 2015*, Roscoff, Paris, France. https://www.researchgate.net/publication/306056164_4D_emittancemeter?channel=doi&linkId=57ac8ae908ae0932c9748f5a&showFulltext=true
[2] http://www.crytur.com/.
[3] http://www.crystals.saint-gobain.com/.
[4] O. Delferrière *et al.*, "Advanced Light Ion Source Exctraction System for a New Electron Cyclotron Resonnance Ion Source Geometry at Saclay," *Rev. Sci. Instrum.*," 83. doi:10.1063/1.3660820
[5] O. Tuske *et al*., "BETSI, a new test bench for ion sources optimization at CEA SACLAY," *Rev. Sci. Intstrum.*, Feb2088, Vol. 79, Issue 2, p02B710.
[6] http://jannus.in2p3.fr/spip.php
[7] L.Y. Lin *et al*., "Study of Scintillation Stability in KBr, YAG:Ce, CaF2:Eu and CSI:Tl Irratiated by Various-Energy Protons," *IBIC2014*, Monterrey, CA, USA
[8] http://physics.nist.gov/cgi-bin/Star/ap_table.pl
[9] J.B. Birks. "Theory and Practice of Scintillation counting," *Pergamon press New York* (1964), USA.

ISBN 978-3-95450-177-9

A NEW BEAM LOSS MONITOR CONCEPT BASED ON FAST NEUTRON DETECTION AND VERY LOW PHOTON SENSITIVITY

J. Marroncle*, A. Delbart, D. Desforge, C. Lahonde-Hamdoun, P. Legou, T. Papaevangelou, L. Segui, G. Tsiledakis, CEA Saclay, DRF/DSM/IRFU, Gif sur Yvette, France

Abstract

Superconductive accelerators may emit X-rays and Gammas mainly due to high electric fields applied on the superconductive cavity surfaces. Indeed, electron emissions will generate photons when electrons impinge on some material. Their energies depend on electron energies, which can be strongly increased by the cavity radio frequency power when it is phase-correlated with the electrons.

Such photons present a real problem for Beam Loss Monitor (BLM) systems since no discrimination can be made between cavity contributions and beam loss contributions. Therefore, a new BLM is proposed which is based on gaseous Micromegas detectors, highly sensitive to fast neutrons, not to thermal ones and mostly insensitive to X-rays and Gammas. This detector uses Polyethylene for neutron moderation and the detection is achieved using a ^{10}B or $^{10}B_4C$ converter film with a micromegas gaseous amplification. Simulations show that detection efficiencies > 8 % are achievable for neutrons with energies between 1 eV and 10 MeV.

INTRODUCTION

This paper deals with the design of a new Beam Loss Monitor based on Micromegas detectors devoted to fast neutron detection.

We will present, firstly, the motivation to develop this new BLM followed by a brief Micromegas working principle description. Then, simulation results will be presented to confirm that all the specifications are fulfilled, which mainly are fast neutron detection with a good efficiency, but very low sensitivity to thermal neutrons as well as to X-rays and γ's. Time response has been investigated to finally propose the addition of a faster monitor for safety purposes. The R&D program will be briefly discussed before to conclude.

WHY NEW BEAM LOSS MONITORS?

The idea to develop a new kind of BLM was triggered by the construction of new powerful accelerators as ESS for instance. Beam line part of them uses superconductive technology, where their accelerating cavity surfaces are submitted to very huge electric fields. These later release electrons from time to time which are accelerated under the RF electric fields covering an energy spectrum up to few MeV. When these electrons impinge on material, they may generate important photon fluxes with energy range from X-Rays to γ's. These phenomena concern also the RFQ, but at lower energy. Such photons, emitted at the lowest beam energy, contribute particularly as background to the external BLM, since the beam loss signal comes only from neutral particles (neutrons and photons) which are the only ones able to escape from the beam pipes or structures. Therefore, photon-sensitive BLMs may deliver signals which are not correlated to beam losses, but to cavity behaviours. As we can't discriminate between photons coming from beam losses or cavities, we propose a BLM blind to photon contributions. Note that it is less dramatic for higher beam energy where lost particles may have higher energy, producing numerous hadronic by-products which can be efficiently detected by usual BLM like ion chambers.

Another important criterion for BLM is the ability to locate the beam losses. It may be achieved with neutrons, but only with fast neutrons. Indeed, neutrons may be thermalized in the accelerator, particularly on the concrete wall. They will be detected after few rebounds, far from their emission locations.

To summarize, the requirements for BLM used on superconductive accelerator, especially for those working at low beam energy, are the following:

- Fast neutron detection, insensitive to thermalized ones
- Blind to X-rays and gammas.

We propose to design such a BLM, called neutron BLM (nBLM), based on Micromegas detectors [1].

MICROMEGAS WORKING PRINCIPLE

Micromegas detectors were invented at CEA Saclay in 1995 [2] and have been submitted, since their births, to a lot of improvements, modifications to fulfil new specifications and detection schemes. Micromegas is a Micro-Pattern Gaseous Detector (MPGD) as sketched on Fig. 1.

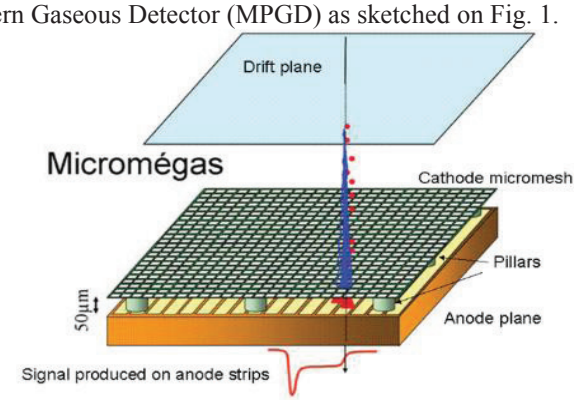

Figure 1: Micromegas scheme.

* Jacques.marroncle@cea.fr

ISBN 978-3-95450-177-9

It can be seen as a parallel plate gas detector inside which a fine mesh is strengthened dividing the detector into 2 parts:

- The drift region (thickness about 1 to 10 mm),
- The amplification region (30 to 150 µm)

The different electrodes are typically polarized around −1000 V for the drift plane, -500 V for the micromesh while the stripped anode (read-out) is grounded. Therefore an incident particle entering through the drift plate ionizes the gas molecules, releasing primary electrons which drift toward the micromesh. Then, these electrons gain energy under the huge electric field influence encountered in the amplification region, allowing to generate secondary ionization processes. Finally, they induce fast electric signals on strips processed by the read-out electronics.

To improve the response uniformity of such a detector, the micromesh is maintained parallel to the drift plate and the anode by several pillars.

Various Micromegas versions were developed and few are able to sustain counting rates as hugged as 10^8 particles/cm^2/s, while active area may cover large surfaces like for the New Small Wheel project for the LHC upgrade [3]. Nowadays, they can even take cylindrical shapes [4], spatial and time resolutions can achieve values lower than 50µm and 30 ps respectively [5]. Thanks to new technologies, bulk Micromegas with resistive electrodes have reduced drastically spark rates, hence the dead time of the monitor, which is a very relevant parameter for BLMs commonly associated to the accelerator safety.

SIMULATIONS FOR NEUTRON BLM OPTIMIZATION

The aim of these simulations is to optimize several parameters to design a first nBLM prototype. The requirements are a highest detection efficiency for fast neutrons but low for thermal and, moreover, a high blindness to photons.

Simulations were done using firstly FLUKA [6-9] and later on GEANT 4 [10]. It was checked that results obtained from both codes are similar.

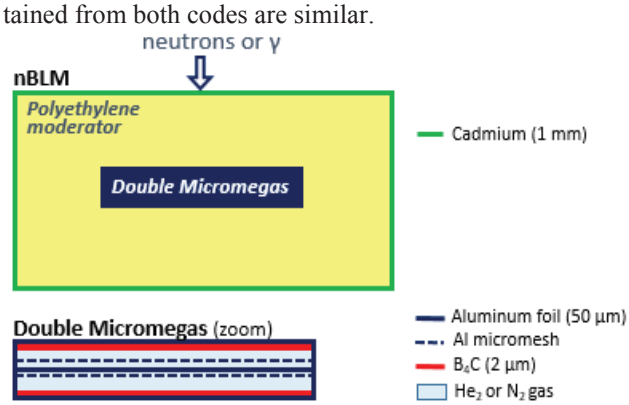

Figure 2: nBLM structure with a zoom on the double Micromegas. Overall size of such a monitor is about 22×22×10 cm^3.

nBLM Rejection and Efficiency

To fulfil the requirements, we have considered a detector made of the following materials (Fig. 2):

- An external envelop for enclosing the entire detector, made with cadmium to absorb thermal neutrons.
- Polyethylene moderator: the width can be changed for adjusting the neutron energy threshold.
- Double Micromegas are used with two B_4C thin converter films mounted inside the detectors for neutron detection [11]. Helium gas or other gas like N_2 (≈ 1.1 bar) can be flushed but helium is preferable to decrease the gamma response contribution.

To simulate neutron responses, a double exponential energy spectrum ranging from 0.1 eV up to 100 MeV was considered (Fig.3-bottom). Neutrons are then withdrawing few cm upstream and transversely to the nBLM, with an angular divergence of 10 mrad as depicted on Fig. 3-top.

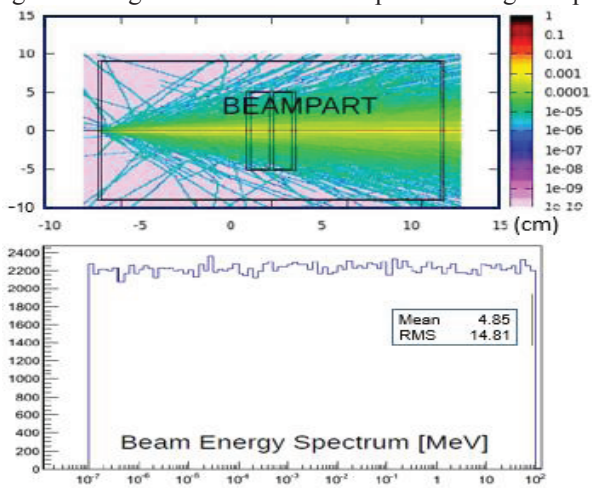

Figure 3: Neutron impacting on nBLM (2 cm moderator thickness) as seen by FLUKA (top) and the flat neutron double exponential energy spectrum (bottom).

Neutron Efficiency The polyethylene moderator thickness was simulated to optimize the nBLM efficiency by withdrawing 1 million of incident neutrons. On Fig. 4-left the results for 2, 4 and 6 cm are represented. We may note that the neutron energy threshold can be tune by varying the moderator thickness, but the efficiency behaviour changes drastically. On the right the neutron spectrum for an energy threshold at 10 keV, which exhibits an overall 3.8% detection efficiency, is displayed. If the incident neutron energy range is reduced to 1 eV up to 1 MeV, the efficiency increases above 5% for 4 cm moderator thickness.

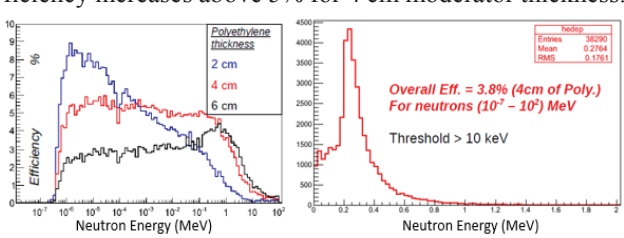

Figure 4: Neutron efficiency for 2, 4 and 6 cm moderator thickness (left) and the detected neutron spectrum for 4 cm thickness of polyethylene (right).

ISBN 978-3-95450-177-9

Thermal Neutron Response Neutrons with energy ranging from 10 meV to 1 eV were simulated. Processes like neutron capture by cadmium $^{113}Cd(n,\gamma)Cd^{114}$ with a released γ were investigated too.

Another γ background is provided by the interaction of thermalized neutrons with ^{10}B which produces Li and α particles and a γ (480 keV) for 94% of this reaction. The nBLM response for such a γ was simulated and the result is presented in Fig. 5. As shown, a simple energy threshold at 20 keV is enough to remove almost this contribution.

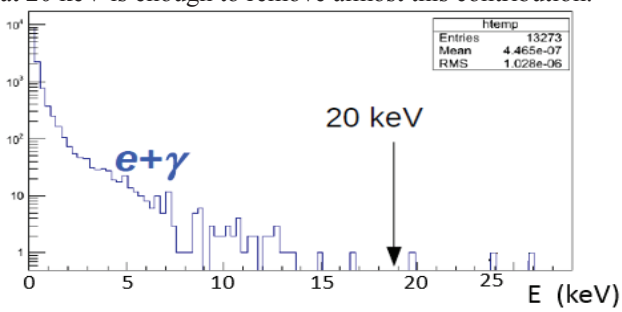

Figure 5: e^- and γ by-products of $n+^{10}B$ reaction.

The total thermal neutron contribution can be seen on Fig. 6. The efficiency is 0.007% for a detection threshold set at 10 keV and nBLM becomes blind if it is increased down to 30 keV. Helium gas is used for this study.

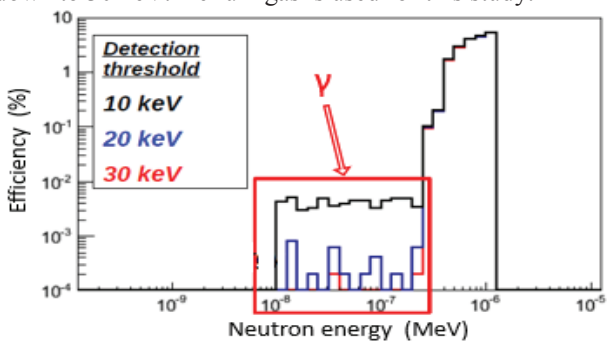

Figure 6: Thermal neutron efficiency for 4 cm moderator thickness. γ decays from Cd and 10B are highlighted in red.

Photon Response Simulation was done with a double exponential flat photon energy spectrum ranging from 10 keV to 100 MeV (Fig. 7). Using helium gas and 4 cm of polyethylene moderator, nBLM efficiency is below 0.006% for detection threshold of 10 keV and almost blind for 30 keV.

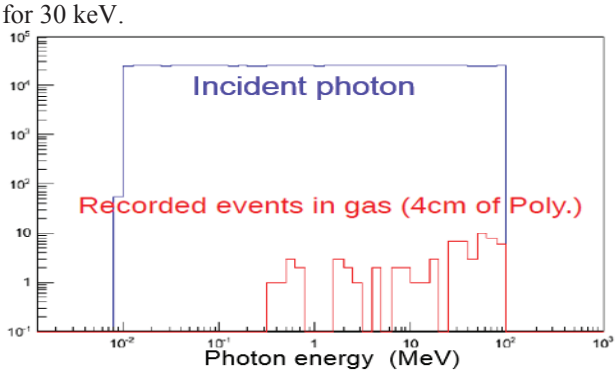

Figure 7: Incident photons (blue) and detected ones (red) for an nBLM integrating 4 cm moderator and He gas.

Under 10 keV, X-rays are absorbed in cadmium and aluminium. The transparency of photons is obviously understood since Micromegas used small amount of material, mainly gas and a thin micromesh resulting in a really short radiation length.

As a preliminary conclusion, it seems that a nBLM with a double Micromegas working with helium gas and surrounded by 4 cm of polyethylene moderator fulfils the specifications. With such a nBLM we have also simulated its angular response to neutrons. Neutron beam is launched on the centre of the entrance window perpendicularly to it (θ=0°). Such beam with angles θ=30° and θ=60° for a double Micromegas with 4 B_4C layers (for increasing the recording efficiency) were investigated as shown on Fig. 8.

Due to the thermalization of neutrons inside the moderator, the angle effect is quite weak. Such a behaviour allows to expect also an efficiency for nBLM greater than the active surface of the double Micromegas itself.

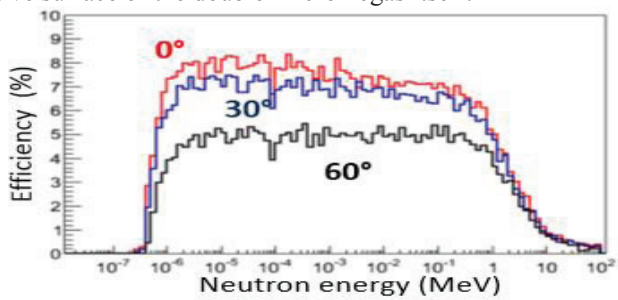

Figure 8: nBLM angular response to neutrons.

Experimental and Simulation Data Comparison Experimental data are obtained by a Micromegas detector with one B_4C plate, placed on top of a polyethylene cylinder that surrounds a ^{252}Cf neutron source, as shown in Fig. 9 (left plot). This spectrum is well reproduced by simulations based on FLUKA MC (Fig. 8 - right plot).

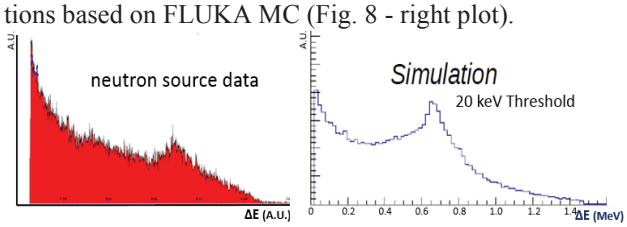

Figure 9: 252Cf data and simulation obtain by a Micromegas detector and sets of moderators.

Timing

BLM are very often linked to machine safety operations, thus in order to avoid irreversible damages they need to deliver quite fast signal which should then be processed by MPS for instance.

Time study was done with 1 MeV neutron beam transversely colliding to a nBLM located at 1 m downstream with an angular divergence of 10 mrad. On Fig. 10 the duration time Δt to get part of the events or "event ratio" is represented. For instance, all events are detected above Δt=300 µs, while only 17% of them below 10 µs.

ISBN 978-3-95450-177-9

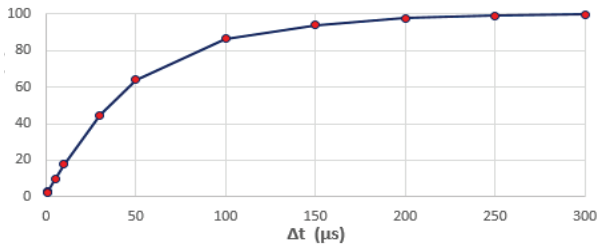

Figure 10: nBLM time response.

Due mainly to moderation time, this nBLM is quite slow, which can be a handicap for safety for which time responses of the order of the μs are required. At the low energy part of the accelerator where neutron emission is already weak, accentuated by a drop of 80% (at 10 μs), it may become difficult or impossible to alarm the safety system quickly. Therefore, we propose to add a fast neutron detector in front of the previous one.

This detector must be fast (≪1 μs) to warn efficiently in case of problem, in other words when lot of particles will be emitted!

Fast Neutron Detector

A new Micromegas will be used with helium or neon gas and 2 mm polypropylene convertor to generate recoil protons followed by a 5 mm drift region. A thin aluminium layer (50 nm) between the convertor and the Micromegas will insure the neutron energy threshold adjustment (E_n>0.5 MeV). The relevant parameter is the time response which can be seen on Fig. 11, where time responses have been simulated for neutrons [0.1 to 100 MeV] versus their incident energy (left) and the deposited one (right). In the whole energy range, time is far below 8 ns. Time is calculated from the neutron emission point to its detection which is achieved as soon as its energy deposited is greater than the threshold (10 keV).

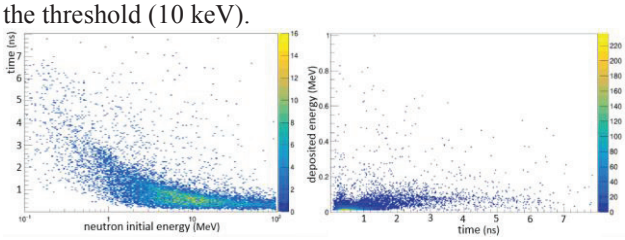

Figure 11: Time response for the fast Micromegas versus incident and deposited neutron energies.

A check of photons contamination has been done and is shown in Fig. 12. A simple cut around 20 keV is enough to remove almost all photons.

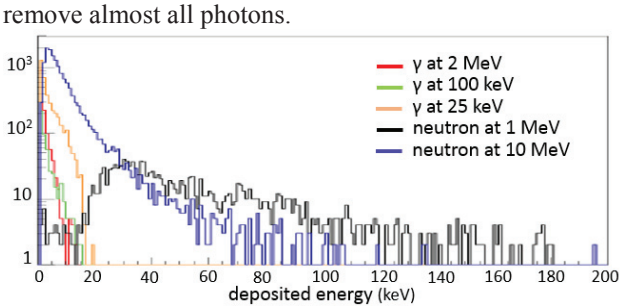

Figure 12: Fast Micromegas neutron and γ responses.

The neutron efficiency for such a detector is about 3 10^{-4} and 8 10^{-4} for neutron energy of 1 and 10 MeV respectively at 10 keV detection threshold. A low efficiency is compliant with an emergency in which a huge neutron flux should be emitted. Investigation with neon gas was also done and are promising too.

For beam loss system, the final monitor will be made with a fast nBLM set in front of a "slow" one depicted previously.

R&D Program for nBLM

A R&D program for nBLM is already in progress. After a first simulation stage, nBLM prototypes will be manufactured and their neutron and γ responses will be measured.

As shown, neutron signals are quite big allowing to count them individually; a fast low noise front-end electronics based on counting rates has to be design.

They are many aspects which may be investigated to optimize the nBLM like the hardness of the detector, the gas working system in sealed mode [12].

CONCLUSION

This paper deals with the design of BLM based on Micromegas to detect fast neutrons with a really low photon efficiency. It may be dedicated to the low energy part of the high beam intensity for the forecoming new facilities.

First simulations showing the feasibility of such a detector were reported in this article. Prototypes will then be designed in order to measure their neutrons and photons responses and to investigate their radiation hardness.

The first part of ESS beam line, the MEBT and the DTL (3.6 to 90 MeV), should be equipped with such nBLMs. The possibility to install them in Saraf is under study.

ACKNOWLEDGEMENT

Authors want to thanks I. Dolenc Kittelmann and T. Shea from ESS, for fruitful discussion and collaboration about BLM.

REFERENCES

[1] M. Houry *et al.*, NIM, A 557 (2006), 648-656.

[2] Y. Giomataris, P. Rebourgeard, J.P. Robert and G. Charpak, "Micromegas: A high-granularity position sensitive gaseous detector for high particle-flux environments", *Nuc. Instrum. Meth.,* A 376 (1996) 29.

[3] J. Galán et al., *Jour. Of Instrumentation*, Vol. 8, April 2013.

[4] B. Radics et al., *Rev. of Scient. Instrum.*, 86, 083304 (2015).

[5] T. Papaevangelou et al., "Fast Timing for High-Rate Environments for Micromegas", in Proc. MPGD 2015, Trieste, Italy, October 2015.

[6] (a) A. Fasso et al., FLUKA: A Multi-Particle Transport Code, CERN-2005-10, 2005. INFN/TC_05/11, SLAC-R-773.
(b) A. Ferrari et al., FLUKA: A Multi-Particle Trans-Port Code, (Program version 2011).

ISBN 978-3-95450-177-9

[7] G. Battistoni et al., The FLUKA code: Description and Benchmarking, in Proc. AIP Conf. Proc. 03, vol. 896, 2007, pp.31. http://dx.doi.org/10.1063/1.2720459.

[8] V. Vlachoudis, *Flair for FLUKA*, version 0.7, September 2008.

[9] V. Vlachoudis, FLAIR: A powerful but User Friendly Graphical Interface for FLUKA, International Conference on Mathematics, Computational Methods & Reactor Physics (M&C 2009) Saratoga Springs, New York, May 3–7, 2009.

[10] GEANT Collaboration, S. Agostinelli et al., GEANT4-a simulation toolkit, NIM A 509 (2003) 250.

[11] C. Höglund et al., *Journal of Applied Physics*, 111, 104908 (2012).

[12] M. Frotin et al., "Sealed operation, and circulation and purification of gas in the HARPO TPC", arXiv:1512.03248, (2015).

ISBN 978-3-95450-177-9

BEAM LOSS AND ABORT DIAGNOSTICS DURING SuperKEKB PHASE-I OPERATION

H. Ikeda*, J. W. Flanagan, H. Fukuma, T. Furuya and T. Tobiyama, KEK, High Energy Accelerator Research Organization, Ibaraki 305-0801, Japan

Abstract

Beam commissioning of SuperKEKB Phase-I started in Feb., 2016. In order to protect the hardware components of the accelerator against the Ampere class beams, the controlled beam abort system was installed Because of the higher beam intensity and shorter beam lifetime of SuperKEKB than that of KEKB, a beam abort monitor system was prepared aiming to monitor the machine operation and to diagnose the hardware components. The system collected the data of all aborts, totalling more than 1000 in this operation period, and we diagnosed not only the hardware performance but the tuning software by analysing the relations between beam current, loss monitor signals and RF cavity voltages. This paper will give the outline of the monitoring system, and will present typical examples of signal and diagnoses.

Table 1: Machine Parameters of SuperKEKB

Parameter	LER	HER	DR	unit
Energy	4.0	7.0	1.1	GeV
No. of bunches	2500		4	
Circumference	3016		135.5	m
Max. stored current	3.6	2.6	0.07	A
Emittance (h)	3.2	4.6	42.5	nm
Emittance (v)	8.64	12.9	3150	pm
Bunch length	6.0	5.0	6.53	mm
βx/βy at IP	32/0.27	25/0.30		mm
Luminosity	$8x10^{35}$			$cm^{-2}s^{-1}$
RF frequency	509			MHz

INTRODUCTION

SuperKEKB [1] is an electron-positron collider with a design luminosity of $8x10^{35}$ $cm^{-2}s^{-1}$. The beam size at the interaction point (IP) will be squeezed to the nm level and the beam currents will be 2.6 A and 3.6 A for electrons and positrons, respectively, to achieve the design luminosity. The machine parameters of SuperKEKB are listed in Table 1.

High current beams may cause damage to sensitive detector and accelerator components. In KEKB, we had several problems and needed to improve the system each time. For example, an IP chamber was melted by strong synchrotron radiation, some collimators were damaged by high intensity beam, and imperfect beam dumps due to the wrong abort timing were observed. The collimators were upgraded and the abort system was improved using fast loss monitor and beam phase signal etc. It is important to check all accelerator systems before installation of the detector for higher current operation. We operated the accelerator without the Belle detector for five months in Phase-I.

* hitomi.ikeda@kek.jp

ABORT AND ABORT MONITOR SYSTEM

In order to protect the hardware components of the detector and the accelerator against the high beam currents, we installed the controlled abort system. The abort monitor system was prepared also for diagnosing and optimizing the abort system.

Abort Kicker and Trigger System

The beam abort kicker is composed of a tapered vertical magnet, a horizontal magnet, a Lambertson DC septum magnet, and additional pulsed quadrupole magnets for LER and a sextupole magnet for HER to increase the beam cross-section to avoid damaging the extraction widow [2]. The dump duration corresponds to one revolution time, i.e. 10 μsec. The beam is distributed in every two RF buckets with an empty bucket space of 200 ns which covers build-up time of the abort kicker magnet. It is also required to synchronize the kicker timing with this abort gap for the protection of hardware. This abort trigger system collects four types of abort trigger requests [3].

1. Direct trigger from hardware components such as RF, vacuum, magnet and monitor.
2. Trigger from loss monitor.
3. Trigger from synchrotron oscillation phase.
4. Manual abort which is requested for machine stop and various studies.

The abort request signals from each hardware component are converted to optical signals and collected to VME modules in 12 local control rooms (LCR). The request signals from LCRs, software abort request signals, and manual abort request signals are collected in the central control room (CCR) and sent to the abort kicker within 20 μsec.

Abort Monitor System

Our monitoring system consists of four data loggers. The SuperKEKB ring circumference is 3 km with 12 LCRs as shown in Fig. 1. Loss monitor signals are collected at 4 LCRs, RF signals are collected at 6 LCRs and the data loggers are located in 4 LCRs. Collected signals include beam current measured by a DCCT, beam loss signals from PIN photo-diodes (PINs) and ion chambers (ICs), signals from the RF cavities, i.e. cavity voltages and output power of klystrons, the beam phase signal showing the deviation from the synchronous phase, the injection trigger timing and the abort request signal.

ISBN 978-3-95450-177-9

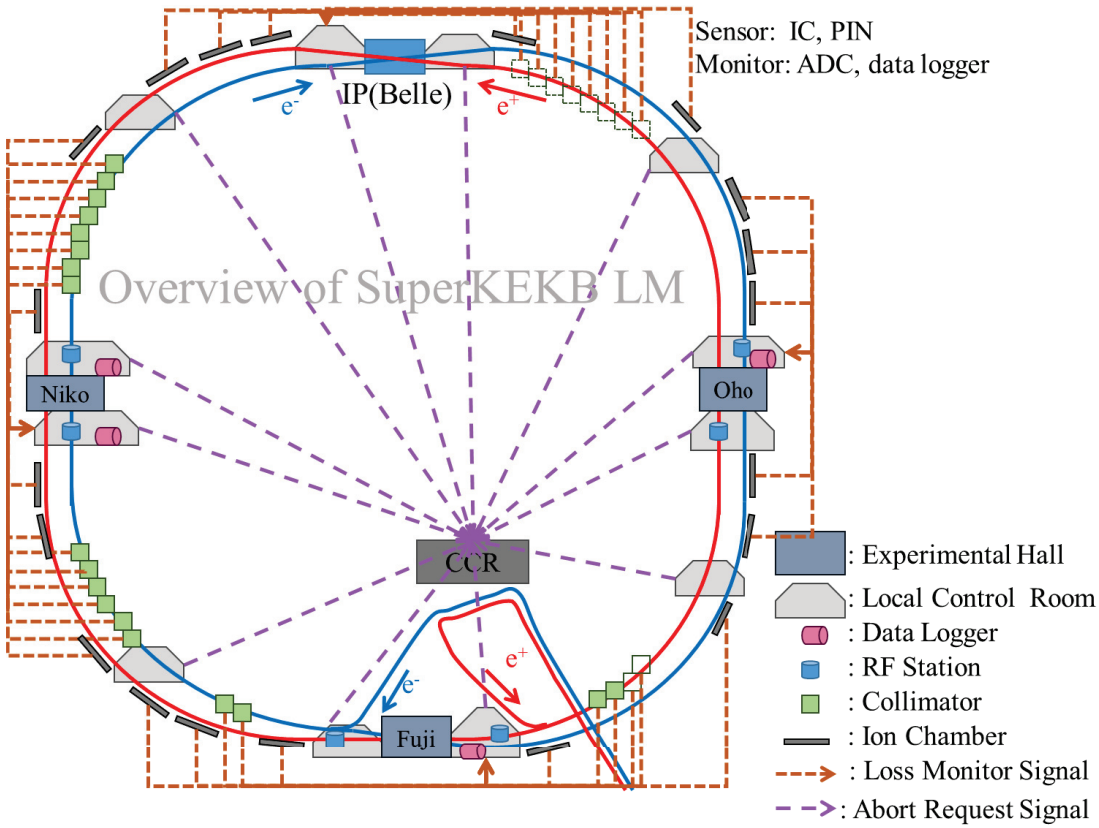

Figure 1: Overview of beam loss monitor and abort monitor system at SuperKEKB phase I.

The logging time is from 300 ms to 600 ms for every abort with a sampling time of 1 μs to 5 s, which depends on the type of logging apparatus. The recorded data is sent to the CCR via the KEKB control network and monitored by the operators.

DATA ANALYSIS

The beam commissioning started in Feb. 2016. Both injection and abort system tuning were done at the beginning of commissioning. The total number of events collected by four data loggers after March was more than 5000. The number of beam aborts was about 1500 and about 95% of the aborts were recorded. The other 5% were missed due to too-short intervals of successive manual aborts in the kicker timing studies. The manual abort data was the reference of each signal response time as shown in Fig. 2. The beam current is measured by DCCT and the signal has a delay of 45 μs which depends on the distance from DCCT to LCR, and has a decay slope of 90 μs. This is the normal behaviour of the DCCT signal when the beam is normally aborted at the correct timing. If the decay time and the slope differ from this example, we consider the abort abnormal. We analysed all abort data to find the causes. The results will be described for three types of abort triggers separately: the hardware trigger, the loss monitor trigger and the beam phase trigger.

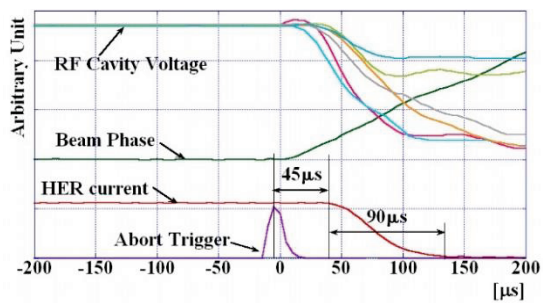

Figure 2: Manual abort.

Hardware Abort

Each hardware component has its own interlock signal for abort request. Since abort request signals of the magnet and vacuum systems are relatively slow, the beam condition worsens before the abort kicker is fired. As a result, the beam is aborted by the beam loss monitor trigger or the beam phase abort trigger. The RF system has many interlock signals to avoid hardware damage and beam instability. Figure 3 describes an example what happened when an abort was requested by an RF component. In this case, we found one RF cavity voltage (Vc) was down at 3 ms before the abort trigger. As a result of analysis, we understood that at first a piezo frequency tuner was broken, resulting in the cavity frequency becoming detuned. As a result, the Vc of the cavity was reduced to 80 % of the desired voltage, which was the abort trigger level set to protect the cavity.

ISBN 978-3-95450-177-9

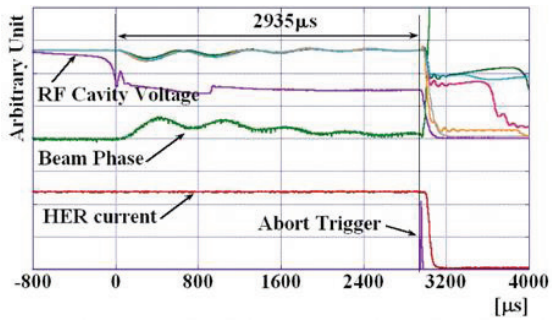

Figure 3: RF hardware abort.

Loss Monitor Abort

A loss monitor system of ion chambers and PIN photodiodes was prepared to protect the accelerator hardware against unexpected sudden beam losses. Most PINs were fixed on the collimators of each ring, and identified the ring in which the beam loss occurred. On the other hand, ICs were installed in the whole tunnel and covered a wide range in space, but could not distinguish the ring [4]. Some examples of the abort caused by beam loss will be shown.

Two-Ring Abort Figure 4 is an example where both rings abort, but not at the same time. HER beam loss is observed 2.5ms before the HER abort trigger signal, while the LER abort is requested before that. We found the LER abort trigger came from the RF fast arc sensor, and understood that the noise of HER beam loss was detected by the LER RF sensors since the beam was lost at the LER RF section. After that, the HER beam was aborted by LM PIN request. Therefore, we adjusted the LM interlock level to avoid such a fake LER abort.

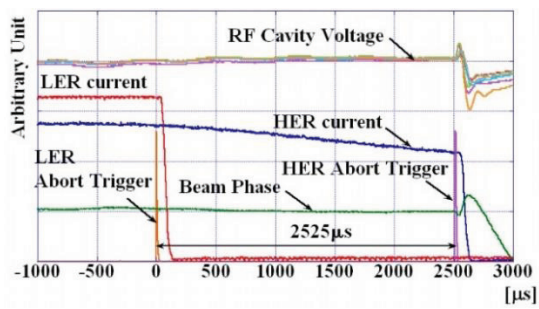

Figure 4: Loss monitor abort caused by HER beam loss.

Injection Timing Problem We found that some LM aborts happened at the end or start of injection. In order to check the relation between injection timing and abort timing, each timing signal was sent to the abort monitor logger. Injection timings are sent to injection kickers installed upstream and downstream of an injection point, and a septum magnet installed near the injection point, respectively. The upstream injection kicker was found not to receive the final injection trigger as shown in Fig. 5. As a result, the stored beam was kicked only by the downstream kicker, and the beam was lost at that time. This problem was caused by injection trigger system software, and was fixed after understanding the reason.

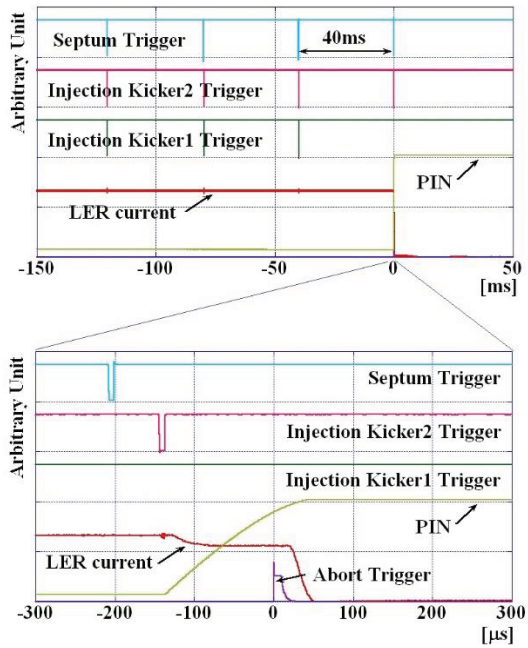

Figure 5: Beam loss that synchronized for injection timing.

Vacuum Problem As beam currents increased, loss monitor aborts with beam phase oscillation increased. Figure 6 describes that the beam phase starts to oscillate and the beam loss occurs with PIN signal. We investigated the reason and found vacuum pressure spikes taking place somewhere in this type of beam loss. It was supposed that the vacuum spike was caused by dust trapping, leading to beam oscillation. Finally the beam was lost at a narrow aperture of the ring. Even if vacuum bursts happened anywhere, the position of the beam loss did not change. The PINs which requested the abort were located downstream of the injection point in this case. The PINs located on collimators were able to make abort requests after we adjusted collimators to protect the beam pipes elsewhere. This type abort is expected to be reduced after further vacuum scrubbing.

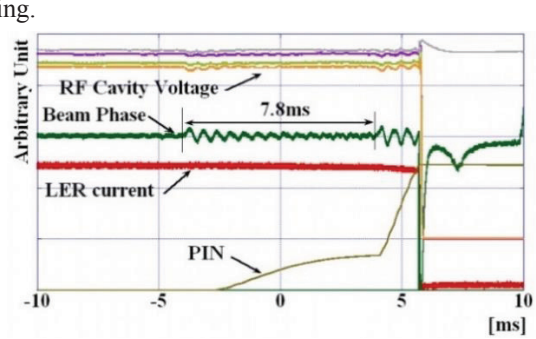

Figure 6: Loss monitor abort with beam phase oscillation.

Beam Phase Abort

Because of the strong interaction between accelerated beam and RF cavities, the cavities tripped whenever high current beam was lost. On the other hand, when one of the cavities tripped, the coherent synchrotron motion of the beam occurred and caused beam loss. The synchronous

ISBN 978-3-95450-177-9

phase between the beam oscillation and the reference RF phase were monitored, and the beam phase (BP) abort trigger was introduced when the phase difference reached a threshold level. If the LM does not detect beam loss, the BP starts oscillation due to the change of the RF voltage, and results in a BP abort.

RF Quench When a BP abort was requested as shown in Fig.7, at first we checked whether RF signals were normal or not. Vc of an RF cavity jumped up during a quench, and the klystron power increased gradually over 75 ms. Finally, the power reached to the interlock level, and turned off. As a result, the BP rose up then reached the threshold level. This BP abort request is fast enough to protect the RF cavity.

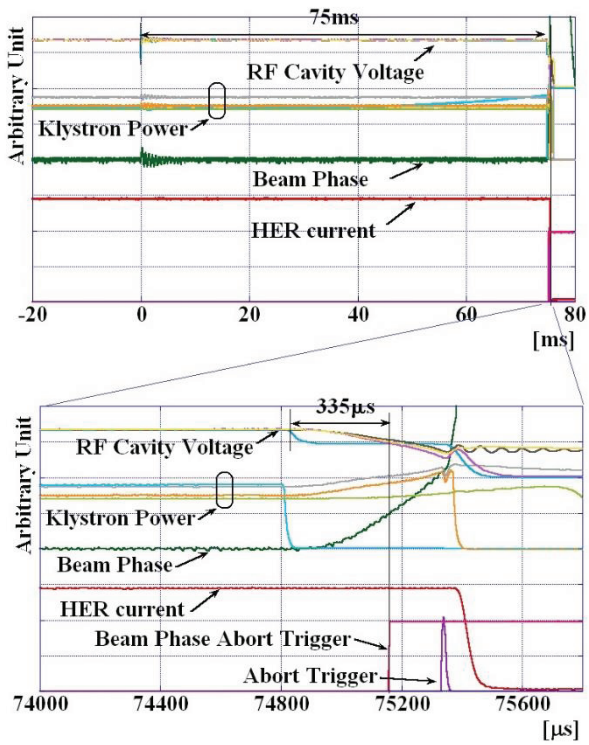

Figure 7: Beam phase abort caused by RF down.

Earthquake Figure 8 describes another type of BP abort. The abnormal behaviour of a cavity was found at 2.5 ms before the BP abort request, and the Vc dropped 0.5 ms afterwards. The BP signal starts to rise in response to the RF drop, and the PINs signals jumped up at the same time as the abort. It means something caused the vibration of hardware components including RF cavities. At that time, we sensed an earthquake and concluded the earthquake is the source of the abort.

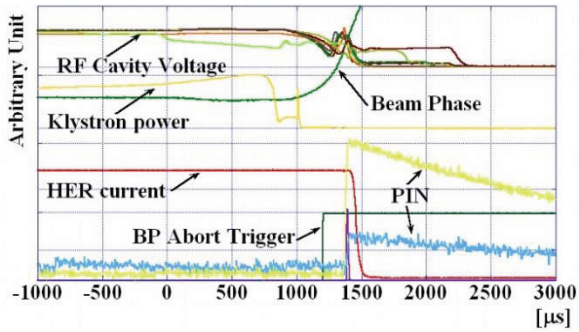

Figure 8: BP abort caused by earthquake.

CONCLUSION

We diagnosed more than 1500 aborts during Phase I operation up to 1 A, and classified them by the abort causes. Figure 9 shows the monthly statistics. Many manual aborts were required to find the optimum kicker timing for the various kicker magnet voltage and optics. Other studies for beam instability measurement, beam size measurement, detector background measurement, and others also required manual aborts. The rather large number of RF aborts in May and June was due to problems with a frequency tuner and insufficient HOM dumping. Aborts caused by beam loss accompanied by vacuum spikes occurred at higher current operation. The beams were correctly dumped by the abort system after optimizing the abort trigger timing. The abort system of the LER will be improved by adding a pulsed quadrupole magnet to increase the beam size at the extraction window before Phase II commissioning.

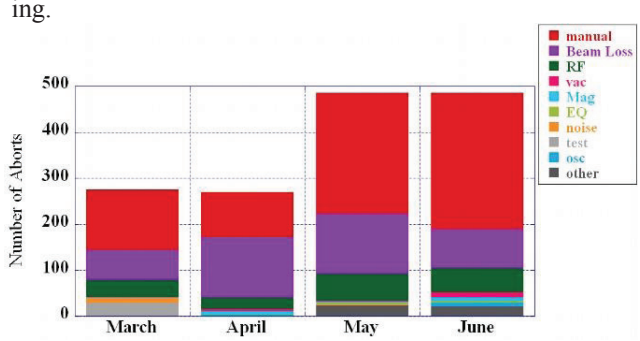

Figure 9: Abort statistics.

REFERENCES

[1] Y. Ohnishi *et al.*, "Accelerator Design at SuperKEKB", *Prog. Theor. Exp. Phys.*, 2013, 03A011.

[2] T. Mimashi *et al.*, "SuperKEKB Beam Abort System", *IPAC2014*, Dresden, Germany, MOPRO023.

[3] S. Sasaki *et al.*, "Upgrade of Abort Trigger System for SuperKEKB", *ICALEPCS2015*, Melbourne, Australia, MOPGF141.

[4] H. Ikeda *et al.*, "Beam Loss Monitor at SuperKEKB", *IBIC2014*, Monterey, CA, USA, TIPD22.

ISBN 978-3-95450-177-9

SYNCHRONOUS LASER-MICROWAVE NETWORK FOR ATTOSECOND-RESOLUTION PHOTON SCIENCE

K. Şafak†, F. X. Kärtner[1], A. Kalaydzhyan, O.D. Mücke, W. Wang, M. Xin[1]
CFEL - DESY, Hamburg, Germany
M. Y. Peng, MIT, Cambridge, Massachusetts, USA
[1]also at MIT, Cambridge, Massachusetts, USA

Abstract

Next-generation photon-science facilities such as X-ray free-electron lasers and intense-laser beamline centers are emerging worldwide with the goal of generating sub-fs X-ray pulses with unprecedented brightness to capture ultrafast chemical and physical phenomena with sub-atomic spatiotemporal resolution. A major obstacle preventing this long-standing scientific dream to come true is a high precision timing distribution system synchronizing various microwave and optical sub-sources across multi-km distances. Here, we present, for the first time, a synchronous laser-microwave network providing a timing precision in the attosecond regime. By developing new ultrafast timing detectors and carefully balancing optical fiber nonlinearities, we achieve timing stabilization of a 4.7-km fiber link network with 580-attosecond precision over 52 h. Furthermore, we realize a complete laser-microwave network incorporating two mode-locked lasers and one microwave source with total 950-attosecond jitter integrated from 1 μs to 18 h.

INTRODUCTION

Drift-free and long-distance transfer of time and frequency standards provides high-temporal resolution for ambitious large-scale, scientific explorations. To name a few: sensitive imaging of low temperature black bodies using multi telescope arrays [1]; gravitational deflection measurements of radio waves using very-long-baseline interferometry [2]; synchrotron light sources [3], gravitational-wave detection using large laser interferometers [4], and next-generation photon science facilities such as X-ray free-electron lasers (XFELs) [5] and laser-based attoscience centers [6]. Among these, XFELs and attoscience centers demand the most challenging synchronization requirements with sub-femtosecond precision to generate ultrashort X-ray pulses for the benefit of creating super microscopes with subatomic spatiotemporal resolution [7]. To achieve this, it is necessary to develop an attosecond-precision timing distribution system (TDS) to synchronize various microwave and optical sub-sources across the km-scale facilities to deliver the timing stability required for seeded FEL operation and attosecond pump-probe measurements.

So far, there has been no TDS meeting this strict requirement. Although research in attosecond X-ray pulse generation has progressed rapidly in the past few years [8], sub-atomic-level measurements cannot be performed due to the lack of a high-precision timing control. Hence, low temporal precision provided by the current synchronization systems remains to be a major obstacle from realizing attosecond hard-X-ray photon-science facilities.

There are two general synchronization schemes reported so far. The first scheme uses microwave signal distribution via amplitude modulation of a continuous-wave laser and employs electronic phase-locking techniques to synchronize various microwave and pulsed laser sources [9]. However, this technique cannot deliver better than ~100-fs RMS jitter across the facility [10] due to low phase discrimination with microwave mixers and high noise floor at photodetection. The second scheme [11], which is further developed in this paper, uses ultralow-noise pulses generated by a mode-locked laser as its timing signal to synchronize optical and microwave sources using balanced optical cross correlators (BOCs) [12,13] and balanced optical-microwave phase detectors (BOMPDs) [14,15], respectively. While this pulsed scheme has breached the 10-fs precision level [15-18], realization of sub-femtosecond precision requires further development of the timing detectors (i.e., BOCs and BOMPDs) and deep physical understanding of optical pulses shaping in fiber transmission.

This paper starts with the recent developments achieved in timing detection schemes, and then demonstrates the synchronous laser-microwave network delivering attosecond precision.

TIMING DETECTORS

The primary elements to realize a high precision TDS are the timing detectors as they dictate the smallest timing errors to be detected by the system.

Polarization-noise-suppression in SH-BOCs

Second-harmonic BOC (SH-BOC) (see Figure 1(a)) operating with 1550-nm input pulses is the most widely used timing detector in our system employed to stabilize the transmission delays of our fiber based timing links.

In this SH-BOC scheme, a polarization beam splitter (PBS) spatially combines two orthogonally polarized pulse trains at 1550-nm central wavelength. The input pulses travel in a double-pass configuration inside a periodically poled potassium titanyl phosphate (PPKTP) crystal. The end facet of the crystal has a dichroic coating (DC), which is highly reflective for 1550 nm and anti-reflective for 775 nm wavelength. In this way, the SH pulse generated during the forward pass of the fundamen-

† kemal.shafak@desy.de

ISBN 978-3-95450-177-9

tal harmonics is separated. The dichroic beam splitter (DBS) on the reverse pass is highly reflective for 775 nm at 45° incident and splits the other second-harmonic pulse from the fundamentals. Finally, a balanced photo detector (BPD) converts the timing error between the input pulses into a voltage signal by detecting the power difference in the generated SH light.

Ideal SH generation for BOC is achieved when the polarization states of the input pulses are perfectly orthogonal to each other. Since all optical components have finite polarization extinction ratios in reality, some portion of the optical power is always projected along the undesired polarization axes of the SH-BOC (see Figure 1(b)). These undesired pulses cause a background noise and make it impossible to lock the system at the zero crossing, i.e., zero AM-to-PM conversion point of the SH-BOC. We are able to remove this noise from our detection using a highly birefringent crystal before the SH-BOC as shown in Figure 1(c). The large birefringence temporally separates the undesired polarization components of the input pulses (i.e., E_{1y} and E_{2x}) so that only the desired ones (i.e., E_{1x} and E_{2y}) can generate SH light. When employed in a TDS, the polarization-noise-suppressed BOC (PNS-BOC) will yield higher signal-to-noise ratio (SNR) and improve the long-term timing stability by removing the background intensity fluctuations of the undesired polarization components.

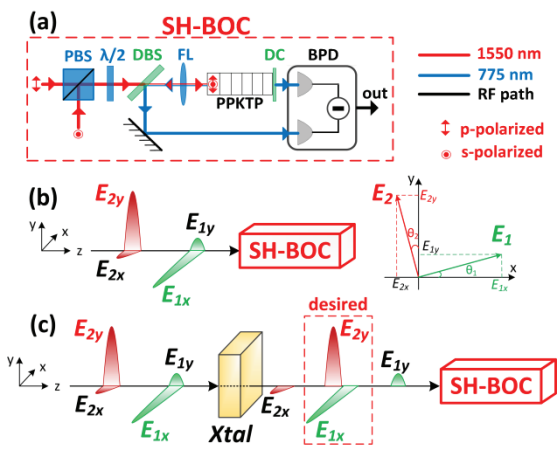

Figure 1: (a) Schematic of type-II second-harmonic BOC for input pulses at 1550 nm. (b) E_1 and E_2 have finite polarization extinction ratios projecting E_{1y} and E_{2x} as noise sources on the opposite principle axes of the type-II crystal. (c) A highly birefringent crystal (Xtal) can avoid this situation by temporally separating the undesired polarization components.

Free-space Coupled BOMPDs

Since XFELs employ many optical and microwave sources in a synchronous operation to generate their radiation, a TDS must also utilize an efficient optical-to-microwave timing detector. To avoid the disadvantages of direct photodetection (e.g., high detection noise floor and excess AM-to-PM conversion) we employ BOMPDs in our TDS, which is an optoelectronic phase-locking technique converting the phase error between an optical pulse train and a microwave into an intensity modulation of the optical signal [14]. Previous designs of the BOMPD have achieved promising local synchronization results with ~1-fs precision in short time scales (below 1 s) [15]. Nonetheless, they suffer from long-term timing drifts and locking-volatilities due to their vulnerability against environmental changes.

To improve the long-term stability, we have developed free-space coupled BOMPD (FSC-BOMPD) as shown in Figure 2. Key improvements in this BOMPD architecture are as follows. First, free-space optical components are used for the optical beam distribution to the bias, reference and signal paths. Total fiber length of the SGI is spliced to be as short as possible. Compared with the fiber-coupled approach [14,15], free-space optics effectively reduces the long-term drifts caused by the environment. Second, high-frequency operation (13 GHz) at the bias path ensures unidirectional phase modulation in the phase modulator. Since the counter-clockwise pulses do not accumulate phase in the modulator anymore, the SGI becomes repetition rate independent and is more robust against unequal path lengths and environmental fluctuations. Third, down-mixing of the detected SGI output is performed at the lowest frequency possible to maximize SNR at photodetection and to minimize thermally induced phase changes in the reference path. Fourth, free-space delay stages are employed to adjust the relative time delay between the BOMPD paths, which allow precise phase tuning without backlash, microwave reflection and excess loss when compared to electronic phase shifters. Lastly, an AM-PM suppression ratio of -50 dB is achieved by carefully optimizing AM- and PM-sensitive components in the reference and bias paths.

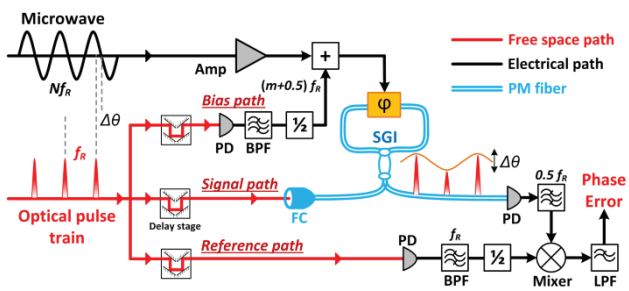

Figure 2: Schematic of free-space-coupled BOMPD. Δθ: phase error; PD: photodetector; BPF: bandpass filter; ½: frequency divider; +: diplexer; Amp: electronic amplifier; LPF: lowpass filter; φ: phase modulator; SGI: Sagnac-interferometer; FC: fiber collimator.

LASER-MICROWAVE NETWORK

Experimental Setup

Timing precision of an operational TDS is determined by the relative instability between the remote slave optical and microwave oscillators that are synchronized to the master laser by a timing network consisting of many fiber links.

ISBN 978-3-95450-177-9

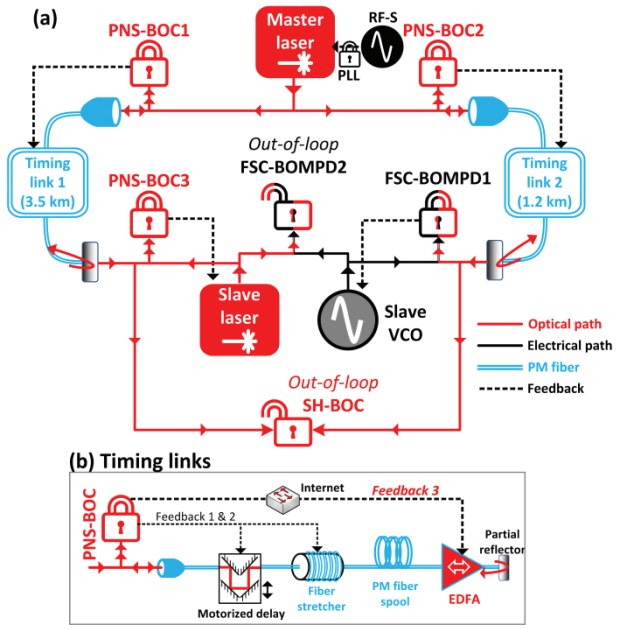

Figure 3: (a) Experimental setup for the laser-microwave network stabilized by PNS-BOCs and FSC-BOMPDs. (b) Components of the timing links and the applied feedback controls. All timing detectors are symbolized with "lock symbols" shown under their abbreviations. Closed lock refers to an in-loop detector; whereas open lock corresponds to a free-running out-of-loop detector. RF-S: RF synthesizer; PLL: phase-locked loop; PM: polarization maintaining; EDFA: erbium doped fiber amplifier.

We demonstrate such a laser-microwave network experimentally as depicted in Figure 3 incorporating two mode-locked lasers and one microwave source. Our master laser is a mode-locked laser operating at 1554-nm central wavelength with 216.67-MHz repetition rate locked to a RF reference. The output of the master laser is split into two independent timing links with a total length of 4.7 km. Each link consists of a polarization-maintaining (PM) dispersion-compensated fiber spool (1.2 km and 3.5 km long), a PM fiber stretcher, a motorized delay stage and a bi-directional fiber amplifier (EDFA). A partially reflecting mirror at the end of each link reflects 10% of the optical power back to the link input. The reflected pulses are then combined with fresh pulses from the master laser in PNS-BOCs, which measure the propagation delay fluctuations in the links and generate error voltages. Then the fiber stretchers and the motorized delays are activated to compensate for fast jitter and long-term drift, respectively. Our theoretical analysis shows that even in the absence of environmental noise, residual link dispersion and nonlinearities add considerable excess jitter through link transmission and feedback loop [19]. Therefore, residual second- and third-order dispersion of the links are carefully compensated with additional dispersion-compensating fiber to suppress the link-induced Gordon-Haus jitter and to minimize the output pulse durations for high SNR in the BOCs. The link power is adjusted to minimize the nonlinearity-induced jitter as well as to maximize the SNR for BOC locking. Link power fluctuations can also induce temporal shifts in the pulse center-of-gravity through a composite effect of link residual dispersion and nonlinearity [19]. Therefore, we employ a third feedback control on the pump current of the EDFAs to stabilize the link power fluctuations (Feedback 3 in Figure 3(b).

The link outputs are used to synchronize a remote laser (e.g., serving as a pump-probe laser at the FEL end station) and a voltage-controlled oscillator (VCO) (e.g., serving as a microwave reference of the FEL Linacs) simultaneously. A third PNS-BOC is built to synchronize the slave laser to timing link 1 output, whereas the slave VCO is locked to timing link 2 output with a FSC-BOMPD. Finally, timing stability of the link network is measured with an out-of-loop SH-BOC (i.e., by combining the link outputs before remote synchronization), whereas the performance of the complete laser-microwave network is evaluated with an out-of-loop FSC-BOMPD.

Experimental Results

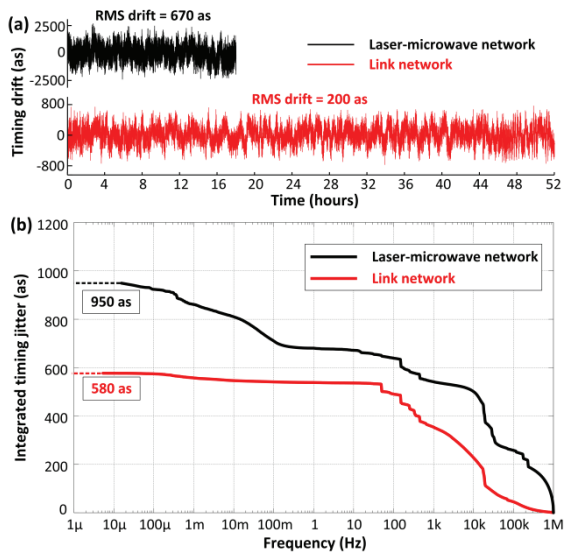

Figure 4: Out-of-loop timing measurement results. (a) Timing drift below 1 Hz and (b) integrated timing jitter.

Stabilization of the timing link network is operated continuously for 52 h and the red curve in Figure 4(a) shows the measured residual timing drift between the two link outputs. The improvements in the timing detection and feedback scheme result in an unprecedented timing error of only 200 as RMS measured by the out-of-loop SH-BOC below 1-Hz offset frequency. The total integrated timing jitter of the link network from 6 μHz to 1 MHz is only 580 as (Figure 4(b), red curve), corresponding to a relative timing instability of 3.1×10^{-21}. The majority of the timing jitter stems from the offset frequencies larger than 1 kHz (i.e., ~500 as for [1 kHz - 1 MHz]) whereas the noise sources within the locking bandwidth of the link stabilization are effectively suppressed (i.e., only ~290 as for [7 μHz - 1 kHz]).

After characterizing the link network performance, we activate the remote synchronization of the slave laser and

ISBN 978-3-95450-177-9

VCO and observe the out-of-loop timing results with the free-running FSC-BOMPD2. The synchronous laser-microwave network shows an unprecedented long-term precision of 670 as RMS over 18 h (Figure 4(a), black curve). Compared with previous mode-locked laser based timing transfer results [20], this setup includes ten-times longer fiber links and an additional remote microwave synchronization system, yet it still achieves more than an order-of-magnitude improvement. The relative timing stability between the two remotely synchronized devices within the full frequency range from 15 μHz to 1 MHz is only 950 as RMS (Figure 4(b), black curve). Excess noise below 100 mHz, is limited by the length fluctuations of the conventional coaxial cables in all RF paths of the FSC-BOMPDs, which can be improved in future work by reducing the electronics into an integrated board or using special phase-stable cables with lower thermal-expansion ratios.

CONCLUSION

The system discussed here represents the first demonstration of a large-scale attosecond-precision laser-microwave network that has the potential of enabling attosecond-precision hard-X-ray photon-science facilities. In turn, this may drive new scientific efforts toward the making of atomic and molecular movies at the attosecond timescale, thereby opening up many new research areas in biology, chemistry, fundamental physics and material science. Besides, this technique will also accelerate developments in many other fields requiring high spatio-temporal resolution such as ultrastable clocks, gravitational wave detection and coherent optical antenna arrays.

REFERENCES

[1] A. Wootten and A. R. Thompson, "The Atacama Large Millimeter/Submillimeter Array", *Proceedings of the IEEE*, vol. 97, no. 8, pp. 1463-1471, 2009.

[2] H. Schuha and D. Behrend, "VLBI: A fascinating technique for geodesy and astrometry", *Journal of Geodynamics*, vol. 61, pp. 68-80, 2012.

[3] D. H. Bilderback, P. Elleaume and E. Weckert, "Review of third and next generation synchrotron light sources", *J. Phys. B: At. Mol. Opt. Phys.*, vol. 38 pp. S773–S797, 2005.

[4] B. P. Abbott *et al.*, "LIGO: The Laser Interferometer Gravitational-Wave Observatory," *Rep. Prog. Phys*, vol. 72, no. 076901, pp. 1-25, 2009.

[5] P. Emma *et al.*, "First lasing and operation of an angstrom-wavelength free-electron laser", *Nat. Photonics*, vol. 4, pp. 641-647, 2010.

[6] G. Mourou and T. Tajima, "The Extreme Light Infrastructure: Optics' Next Horizon", *Optics & Photonics News*, vol. 22, pp. 47-51, 2011.

[7] J. Ulrich, A. Rudenko, and R. Moshammer, "Free-electron lasers: new avenues in molecular physics and photochemistry", *Annu. Rev. Phys. Chem.*, vol. 63, pp. 635–660 (2012).

[8] E. Prat and S. Reiche, "Simple Method to Generate Terawatt-Attosecond X-Ray Free-Electron-Laser Pulses", *Phys. Rev. Lett.*, vol. 114, pp 244801, 2015.

[9] R. Wilcox, J. M. Byrd, L. Doolittle, G. Huang, and J. W. Staples, "Stable transmission of radio frequency signals on fiber links using interferometric delay sensing", *Opt. Lett.*, vol. 34, no. 20, pp. 3050-3052, 2009.

[10] M. Glownia *et al.*, "Time-resolved pump-probe experiments at the LCLS", *Opt. Express*, vol. 18, pp. 17620–17630, 2010.

[11] J. Kim, J. A. Cox, J. Chen, and F. X. Kärtner, "Drift-free femtosecond timing synchronization of remote optical and microwave sources", *Nature Photon.*, vol. 2, pp. 733-736, 2008.

[12] T. R. Schibli *et al.*, "Attosecond active synchronization of passively mode-locked lasers by balanced cross correlation", *Opt. Lett.*, vol. 28, pp. 947-949, 2003.

[13] P. T. Callahan, K. Safak, P. Battle, T. Roberts, and F. X. Kärtner, "Fiber-coupled balanced optical cross-correlator using PPKTP waveguides", *Opt. Express,* vol. 22, pp. 9749-9758, 2014.

[14] J. Kim, F.X. Kärtner, and F. Ludwig, "Balanced optical-microwave phase detectors for optoelectronic phase-locked loops", *Opt. Lett.,* vol. 31, no. 24, pp. 3659-3661, 2006

[15] M. Y. Peng, A. Kalaydzhyan, and F. X. Kärtner, "Balanced optical-microwave phase detector for sub-femtosecond optical-RF synchronization", *Opt. Express*, vol. 22, pp. 27102-27111, 2014.

[16] M.Y. Peng *et al.*, "Long-term stable, sub-femtosecond timing distribution via a 1.2-km polarization-maintaining fiber link: approaching 10− 21 link stability", *Opt. Express,* vol. 21, no. 17, pp. 19982-19989, 2013.

[17] K. Şafak, M. Xin, P. T. Callahan, M. Y. Peng, and F. X. Kärtner, "All fiber-coupled, long-term stable timing distribution for free-electron lasers with few-femtosecond jitter", *Struct. Dyn.,* vol. 2, pp. 041715, 2015.

[18] M. Xin, K. Şafak, M. Y. Peng, P. T. Callahan, and F. X. Kärtner, "One-femtosecond, long-term stable remote laser synchronization over a 3.5-km fiber link," *Opt. Express* 22, 14904–14912, 2014.

[19] M. Xin *et al.*, "Attosecond precision multi-km laser-microwave network", *Light Sci. Appl.,* vol. 6, pp. e16187, 2017.

[20] K. Jung *et al.*, "Frequency comb-based microwave transfer over fiber with 7×10^{-19} instability using fiber-loop optical-microwave phase detectors", *Opt. Lett.,* vol. 39, no. 6, pp. 1577-1580, 2014.

ISBN 978-3-95450-177-9

ELECTRO-OPTICAL METHODS FOR MULTIPURPOSE DIAGNOSTICS

R. Pompili*, M.P. Anania, M. Bellaveglia, F. Bisesto, E. Chiadroni, A. Curcio, D. Di Giovenale
G. Di Pirro, M. Ferrario, Laboratori Nazionali di Frascati, 00044 Frascati, Italy
A. Cianchi, University of Rome Tor Vergata, 00133 Rome, Italy
A. Zigler, Racah Institute of Physics, Hebrew University, 91904 Jerusalem, Israel

Abstract

Electro-Optical Sampling (EOS) based temporal diagnostics allows to precisely measure the temporal profile of electron bunches with resolution of few tens of fs in a non-destructive and single-shot way. At SPARC_LAB we adopted the EOS in very different experimental fields. We measured for the first time the longitudinal profile of a train of multiple bunches at THz repetition rate, as the ones required for resonant Plasma Wakefield Acceleration (PWFA). By means of the EOS we demostrated a new hybrid compression scheme that is able to provide ultra-short bunches (< 90 fs) with ultra-low (< 20 fs) timing-jitter relative to the EOS laser system. Recently we also developed an EOS system in order to provide temporal and energy measurements in a very noisy and harsh environment: the electrons ejected by the interaction of a high-intensity (hundreds TW class) ultra-short(35 fs) laser pulses with solid targets by means of the so-called Target Normal Sheath Acceleration (TNSA) method.

INTRODUCTION

The research activity of the SPARC_LAB test-facility [1] (LNF-INFN, Frascati) is currently focused on advanced acceleration techniques for electrons, protons and heavier ions. The demand to accelerate particles to higher and higher energies is currently limited by the effective efficiency in the acceleration process that requires the development of large facilities. By increasing the accelerating gradient, the compactness can be improved and costs reduced.

For the acceleration of electrons, the technique that guarantees gradients of the order of GV/m relies on plasma acceleration [2, 3]. In this case a *driver* pulse, consisting in an electron bunch (Plasma Wakefield Acceleration, PWFA) or a laser pulse (Laser Wakefield Acceleration, LWFA), excites a wakefield in a plasma. Such wakefield is then used in order to accelerate electron coming directly from plasma (so-called self-injection schemes [4–6]) or a subsequent *witness* bunch, externally injected by a linac [7, 8]. Both in the particle and laser driven schemes, ultra-short bunches are required in order to produce larger wakefields and avoid an excessive growth of emittance and energy spread. In the latter one, in particular, a very demanding task is represented by the synchronization between the laser and the witness bunch, that requires relative timing-jitters of the order of few femtoseconds [7].

In the field of protons and ions acceleration, energies in multi-MeV range have been obtained in the past decade by means of the so-called Target Normal Sheath Acceleration (TNSA) method [9–11], in which an high-intensity short-pulse laser interacts with solid targets. The typical timescale for particle emission is on the sub-picosecond level but so far no direct and time-resolved measurement was able to determine the exact mechanism of the acceleration process and cross-check the developed theoretical models [12].

From the previous considerations it follows that precise time-resolved measurements with sub-picosecond resolution are of great interest for different aspects of particle acceleration. In the following we report about the use of electro-optic methods in such fields, showing that it represents a valuable tool for a deeper understanding of the physical processes involved.

TEMPORAL MEASUREMENT FOR TRAINS OF ELECTRON BUNCHES

The Electro-Optical Sampling (EOS [13]) is a temporal diagnostics that allows to measure the bunch longitudinal charge distribution by means of nonlinear crystals like ZnTe and GaP. Being a single-shot and non-intercepting device able to provide temporal resolution of the order of few tens of fs [14, 15], it is widely used in accelerator facilities [16–19]. Its working principle relies on the electro-optic (or Pockels) effect induced in such crystals by the Coulomb field generated by a relativistic bunch. The crystal becomes birefringent, i.e. characterized by two refractive indices $n_{1,2}$ along its principal optical axes. If at the same time a linearly polarized laser crosses the crystal, the crystal birefringence makes its polarization elliptical, i.e. the two orthogonal components of the laser electric field cumulate a relative phase delay given by

$$\Gamma(t) = \frac{\omega_L d}{c}(n_1 - n_2) \propto E_b(t)\,, \qquad (1)$$

where ω_L is the laser central frequency and d is the crystal thickness. From eq. 1 it follows that the bunch temporal profile $E_b(t)$ is imprinted on the phase delay $\Gamma(t)$.

At SPARC-LAB facility we used Ti:Sa IR laser (λ = 800 nm, 70 fs rms pulse duration) in order to measure the longitudinal profile of a 110 MeV comb-like electron beam [20] consisting in two consecutive bunches of 80 pC delayed by 800 fs. The laser is directly derived from the photo-cathode laser system, resulting in a natural synchronization with the electron beam. The bunch longitudinal profile is retrieved by means of the spatially encoding technique [18], in which the laser crosses the nonlinear crystal with an angle of 30°.

Fig. 1(a) shows an electro-optic signal measured by using a 100 μm-thick GaP crystal. By projecting the signal along

* riccardo.pompili@lnf.infn.it

ISBN 978-3-95450-177-9

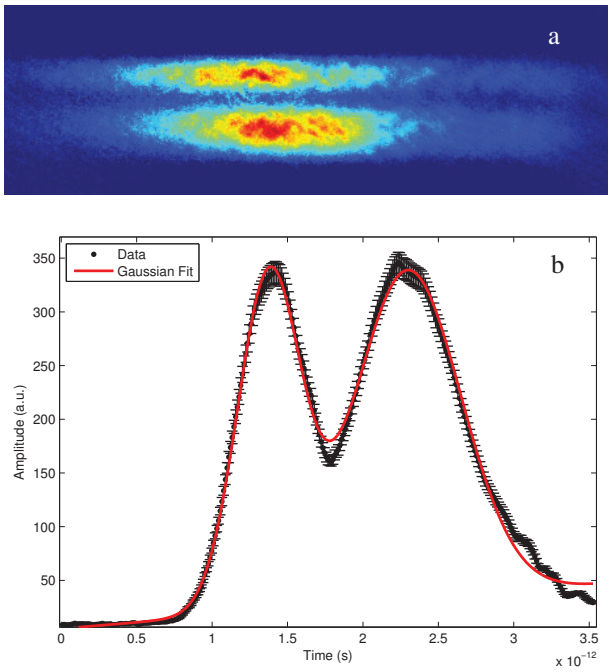

Figure 1: (a) Electro-optic signal of a comb-like bunch obtained with a 100 μm-thick GaP crystal. (b) Corresponding temporal profile obtained by projecting the signal in (a).

the vertical axis, the time profile of fig. 1(b) is obtained. A Gaussian fit has been calculated on such profile, resulting in bunch durations of 160 fs and 200 fs (rms), in agreement with results obtained with a RF-Deflector device [21]. This represents the first measurement done with the EOS diagnostics of an electron beam consisting in multiple bunches.

TIME-OF-ARRIVAL MONITOR

As anticipated, one of the most stringent requirements regarding the external injection of a linac-accelerated witness bunch in a laser-driven plasma accelerator concerns the ultra-low timing-jitter between the ultra-short bunch and the laser pulse. For instance, with plasma densities of $n_e \approx 10^{17}$ cm^{-3} (corresponding to 30 GV/m peak accelerating field) the timing-jitter must be below 30 fs, i.e. much smaller than the plasma oscillation period. Recently we demonstrated a new hybrid compression scheme able to simultaneously compress the bunch duration and reduce its arrival timing-jitter (ATJ) relative to the photo-cathode (PC) laser [22]. Our results prove that bunches with duration below 90 fs (rms) and relative ATJ lower than 20 fs (rms) can be obtained by combining RF-based compression by velocity-bunching (VB) with magnetic compression (MC) in a non-isochronous dogleg line. The proposed method could be of great interest for all experiments foreseeing a fs-level synchronization between an electron beam and a laser pulse, as seeded-FEL [23] and x/γ-rays production by Thomson scattering [24, 25].

The underlying principle for the simultaneous bunch compression and relative ATJ reduction relies on the differences in dynamics between particles in the same bunch and bunches in different shots. By means of the hybrid scheme we used VB in order to shorten the duration of the low energy (5.3 MeV) beam exiting from the gun. In these conditions space-charge forces strongly affect the beam LPS. On the contrary, the time-of-flight and mean energy are not perturbed. Starting from the gun, the bunch time of arrival is mainly linked to the release time from the cathode but after VB compression its timing is strongly linked to the RF field phase-jitter. It follows that at the end of the linac the bunch is no more linked to the PC laser timing. The measured jitter is in this case $\sigma_t \approx 60$ fs. At this point, the correlation between the PC laser and the time-of-flight is restored by the dogleg. The different dynamics between the bunch inner structure and its longitudinal centroid allows us to reduce the ATJ relative to the PC laser in the dogleg while preserving its duration. Fig. 2 shows the bunch time-of-arrival measured with an EOS system installed at the end of the dogleg line. Since the employed probe laser is directly split from the PC laser system, the histogram represents the relative timing-jitter between the bunch and PC laser. By collecting 330 consecutive shots, the resulting ATJ is $\sigma_t \approx 19$ fs, about three times smaller than the one obtained at linac exit. The bunch duration downstream the dogleg is about 86 fs. Measurements on the bunch duration, conducted both at the end of the linac and the dogleg, show that it is possible to take control of the longitudinal beam dynamics while reducing down to about 19 fs(rms) the relative ATJ between the electron bunch and the external PC laser system.

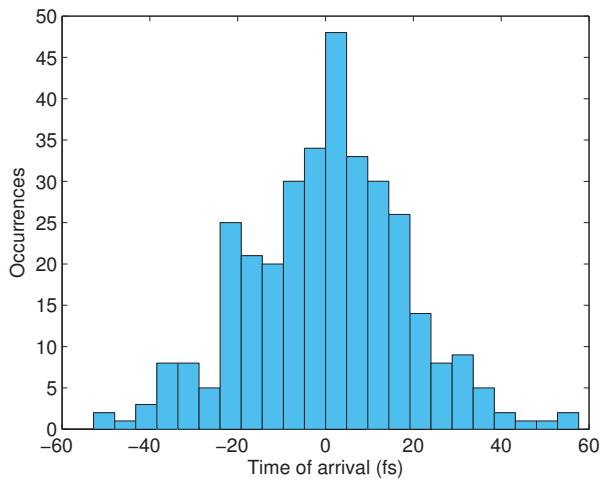

Figure 2: Collected time of arrival for 330 consecutive shots measured by the EOS. The resulting ATJ is $\sigma_t \approx 19$ fs.

TEMPORAL EVOLUTION OF THE ACCELERATING FIELD IN TNSA PROCESS

The interaction of a high-intensity short-pulse laser with thin solid targets [26, 27] generates jets of electrons that are emitted by the target and positively charge it, leading to

ISBN 978-3-95450-177-9

the formation of the electrostatic potential that in turn governs the ion acceleration [9–11] in the TNSA process [28]. The typical timescale of such phenomena is on the sub-picosecond level. So far only indirect evidences of the escaping electron component have been recorded but a detailed and time-resolved study of the release mechanism has not been carried out yet. We employed the Electro-Optical Sampling diagnostics also in this field with the goal to measure the energy and temporal evolution of the ejected electrons.

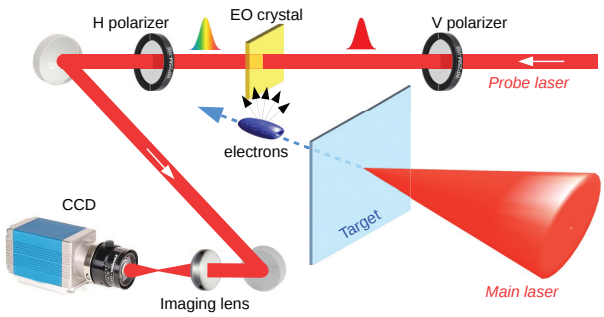

Figure 3: Setup of the experiment. The FLAME laser is focused on a metallic target that ejects electrons. The EOS diagnostics, based on a ZnTe crystal located 1 mm downstream the target, measures the temporal profile of the emitted electrons by means of an ultra-short probe laser.

The experiment was carried out with the FLAME laser at SPARC_LAB. It consists a 130 TW Ti:Sapphire laser system delivering 35 fs (FWHM), up to 4 J pulses at 800 nm central wavelength and 10 Hz repetition rate. The laser beam was focused $f/10$ off-axis parabolic mirror with focal length $f = 1$ m. The setup of the experiment is shown in Fig. 3. Once the electron cloud is emitted by the target, its temporal charge profile is spatially imprinted along the transverse profile of the probe laser, temporally synchronized with the electrons in correspondence of the ZnTe crystal.

A typical electro-optic signal is shown in fig. 4(a). The geometry of our EOS setup (the bunch is moving below the crystal and normally to it while the probe laser propagates laterally from right to left) determines the curved shape of the retrieved signals. The snapshots show that the escaping energetic electrons present a secondary broadened temporal structure, as reported in fig. 4(b). The first emitted bunch has approximately 1.2 nC charge and it is followed by a second broadened structure carrying a larger amount of particles (about 3 nC). The delay between the two structures is about 1.5 ps. This result represents the first measurement with sub-picosecond resolution ever done of the fast electron component released in laser-matter interactions.

CONCLUSIONS

Electro-Optical sampling represents a valuable tool allowing to measure the temporal profile of particle beams with high temporal resolution. The results presented here show that it can be adapted to very different experimental conditions. Its non-destructive feature is a key requirement

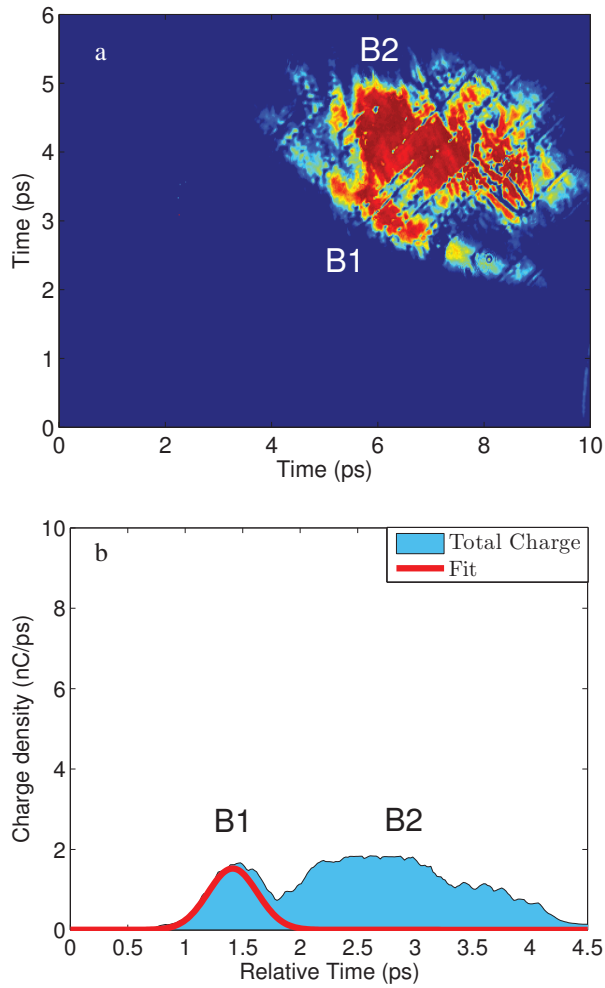

Figure 4: (a) Signature of the escaping electrons from target. The emitted charges are, respectively, 1.2 nC (B1) and 3 nC (B2). The gaussian envelopes represent the extrapolated charge profiles of each bunch. (b) Corresponding longitudinal charge profiles.

for a temporal diagnostics that has to be used to monitor, for instance, the injection of electron beams (consisting in multiple bunches) in a beam-driven plasma accelerator. Being single-shot, it allows to measure the time of arrival of electron beams with respect to the employed laser in order to estimate the overall timing-jitter. Finally, it can provide time-resolved measurements in laser-driven experiments as, for instance, the interaction of high intensity laser with solid targets, in order to fully understand the physical process of TNSA.

ACKNOWLEDGEMENT

This work has been partially supported by the EU Commission in the 7th Framework Program, Grant Agreement 312453-EuCARD-2 and the Italian Research Minister in the framework of FIRB - Fondo per gli Investimenti della Ricerca di Base, Project n. RBFR12NK5K. The work of one of us (A.Z.) was partially supported by BSF foundation.

ISBN 978-3-95450-177-9

REFERENCES

[1] M Ferrario, et al. SPARC_LAB present and future. *Nuclear Instruments and Methods in Physics Research Section B: Beam Interactions with Materials and Atoms*, 309:183–188, 2013.

[2] I. Blumenfeld, et al. Energy doubling of 42GeV electrons in a metre-scale plasma wakefield accelerator. *Nature*, 445:741–744, February 2007.

[3] M Litos, et al. High-efficiency acceleration of an electron beam in a plasma wakefield accelerator. *Nature*, 515(7525):92–95, 2014.

[4] A. J. Gonsalves, et al. Tunable laser plasma accelerator based on longitudinal density tailoring. *Nature Physics*, 7:862–866, November 2011.

[5] W. P. Leemans, et al. GeV electron beams from a centimetre-scale accelerator. *Nature Physics*, 2:696–699, October 2006.

[6] J. Faure, et al. Controlled injection and acceleration of electrons in plasma wakefields by colliding laser pulses. *Nature*, 444:737–739, December 2006.

[7] Andrea R Rossi, et al. The external-injection experiment at the sparc_lab facility. *Nuclear Instruments and Methods in Physics Research Section A: Accelerators, Spectrometers, Detectors and Associated Equipment*, 740:60–66, 2014.

[8] R Assmann, et al. Sinbad-a proposal for a dedicated accelerator research facility at desy. *Proceedings of IPAC2014, Dresden, Germany, TUPME047*, 2014.

[9] EL Clark, et al. Energetic heavy-ion and proton generation from ultraintense laser-plasma interactions with solids. *Physical Review Letters*, 85(8):1654, 2000.

[10] RA Snavely, et al. Intense high-energy proton beams from petawatt-laser irradiation of solids. *Physical Review Letters*, 85(14):2945, 2000.

[11] AJ Mackinnon, et al. Enhancement of proton acceleration by hot-electron recirculation in thin foils irradiated by ultraintense laser pulses. *Physical review letters*, 88(21):215006, 2002.

[12] J-L Dubois, et al. Target charging in short-pulse-laser–plasma experiments. *Physical Review E*, 89(1):013102, 2014.

[13] I Wilke, et al. Single-shot electron-beam bunch length measurements. *Physical review letters*, 88(12):124801, 2002.

[14] B Steffen, et al. Electro-optic time profile monitors for femtosecond electron bunches at the soft x-ray free-electron laser flash. *Physical Review Special Topics-Accelerators and Beams*, 12(3):032802, 2009.

[15] MH Helle, et al. Extending electro-optic detection to ultrashort electron beams. *Physical Review Special Topics-Accelerators and Beams*, 15(5):052801, 2012.

[16] Steven P Jamison, et al. High-temporal-resolution, single-shot characterization of terahertz pulses. *Optics letters*, 28(18):1710–1712, 2003.

[17] G Berden, et al. Electro-optic technique with improved time resolution for real-time, nondestructive, single-shot measurements of femtosecond electron bunch profiles. *Physical review letters*, 93(11):114802, 2004.

[18] Adrian L Cavalieri, et al. Clocking femtosecond x rays. *Physical review letters*, 94(11):114801, 2005.

[19] R Pompili, et al. First single-shot and non-intercepting longitudinal bunch diagnostics for comb-like beam by means of electro-optic sampling. *Nuclear Instruments and Methods in Physics Research Section A: Accelerators, Spectrometers, Detectors and Associated Equipment*, 740:216–221, 2014.

[20] M. Ferrario, et al. Laser comb with velocity bunching: Preliminary results at SPARC. *Nuclear Instruments and Methods in Physics Research A*, 637:43, May 2011.

[21] David Alesini, et al. Rf deflector design and measurements for the longitudinal and transverse phase space characterization at sparc. *Nuclear Instruments and Methods in Physics Research Section A: Accelerators, Spectrometers, Detectors and Associated Equipment*, 568(2):488–502, 2006.

[22] R Pompili, et al. Femtosecond timing-jitter between photocathode laser and ultra-short electron bunches by means of hybrid compression. *New Journal of Physics*, 18(8):083033, 2016.

[23] A Petralia, et al. Two-color radiation generated in a seeded free-electron laser with two electron beams. *Physical review letters*, 115(1):014801, 2015.

[24] C Vaccarezza, et al. The sparc_lab thomson source. *Nuclear Instruments and Methods in Physics Research Section A: Accelerators, Spectrometers, Detectors and Associated Equipment*, 2016.

[25] A Bacci, et al. Electron linac design to drive bright compton back-scattering gamma-ray sources. *Journal of Applied Physics*, 113(19):194508–194508, 2013.

[26] Bruce A Remington, et al. Modeling astrophysical phenomena in the laboratory with intense lasers. *Science*, 284(5419):1488–1493, 1999.

[27] Teresa Bartal, et al. Focusing of short-pulse high-intensity laser-accelerated proton beams. *Nature Physics*, 8(2):139–142, 2012.

[28] SC Wilks, et al. Energetic proton generation in ultra-intense laser–solid interactions. *Physics of Plasmas (1994-present)*, 8(2):542–549, 2001.

ISBN 978-3-95450-177-9

NOVEL ACCELERATOR PHYSICS MEASUREMENTS ENABLED BY NSLS-II RF BPM RECEIVERS*

Boris Podobedov#, Weixing Cheng, Yoshiteru Hidaka, Brookhaven National Laboratory, Upton, NY 11973, USA
Dmitry Teytelman, Dimtel Inc., San Jose, CA 95124, USA

Abstract

NSLS-II light source has state-of-the-art RF BPM receivers that were designed and built in-house incorporating the latest technology available in the RF, digital, and software domains. The recently added capability to resolve the orbits of multiple bunches within a turn as well as further improvement in transverse positional resolution for single- and few-bunch fills [1] allowed us to perform a number of novel beam dynamics measurements. These include measuring small impedances of vacuum chamber components, and of extremely small (~1e-5) current-dependent tune shifts, as well as obtaining an amplitude-dependent tune shift curve from a single kicker pulse.

In this paper we briefly review the unique capabilities of NSLS-II BPMs and present examples of beam physics measurements that greatly benefit from them.

INTRODUCTION

NSLS-II is a recently constructed 3 GeV synchrotron light source at the Brookhaven National Laboratory presently in routine operations for a growing user community. By design, the vertical beam size at NSLS-II could be as low as 3 microns RMS, so a very significant effort went into ensuring that orbit stability is guaranteed to be a small fraction of that. To that extent state-of-the-art RF BPM receivers were designed and built in-house [2-8]. Among many challenging BPM specifications the key ones are related to the resolution and long term stability. The BPMs were commissioned some time ago and all of the design specifications have been confirmed with beam. Reaching turn-by-turn (TbT) resolution of 1 μm and 200 nm for 10 kHz sampled orbit was reported in [4], for measurements with long bunch trains (NSLS-II user operations typically run with ~1000 bunches filling consecutive 500 MHz RF buckets; harmonic number is 1320).

However, with the standard BPM signal processing the resolution for single bunch fills is a lot lower, i.e. ~10 μm TbT at 0.5 mA [4]. Also, standard processing does not resolve the positions of individual bunches within a turn. Since better single-bunch resolution as well as the ability to measure TbT positions of at least a few bunches stored in the ring is strongly desired for some sensitive beam dynamics experiments we have recently addressed both of these issues by special BPM signal processing [1].

Briefly, intra-turn capability was achieved by separately processing fractions of BPM button ADC samples acquired on every turn, with each fraction timed to the bunch of interest. This also provided some resolution improvement for single- and few-bunch fills. Additionally resolution was improved by including multiple revolution harmonics in the TbT position calculation. With this new BPM signal processing we can resolve up to 8 bunches stored in the ring, essentially limited by the bandwidth of the BPM front-end filter that stretches the FWHM duration of a single bunch pulse to ~20 ADC samples out of the total of 310 acquired every turn. The resolution improvement for single bunch fills was about one order of magnitude, down to ~1 μm TbT at 0.5 mA.

BEAM PHYSICS MEASUREMENTS

The ability to resolve multiple bunches within a turn combined with improved BPM resolution allowed us to carry out a number of novel beam physics measurements. Here we concentrate on the measurements of small relative tune shifts and the related ones for transverse coupling impedances. More are described in the accompanying IBIC'16 talk and in [1].

Small Relative Tune Shifts

The standard way of measuring betatron tunes is by exciting the beam with a pinger magnet. At NSLS-II this measurement is usually done with a short, low current bunch train, typically 1-2 mA in 100 consecutive buckets. TbT positions are recorded on 180 regular RF BPMs around the ring. The data from each BPM is processed individually to obtain 180 tune values. Their average gives the final measured tune while their RMS spread provides the measurement error. If a large number of turns is processed, we typically find that, for each individual measurement, the final tune value could be resolved to better than 1e-6.

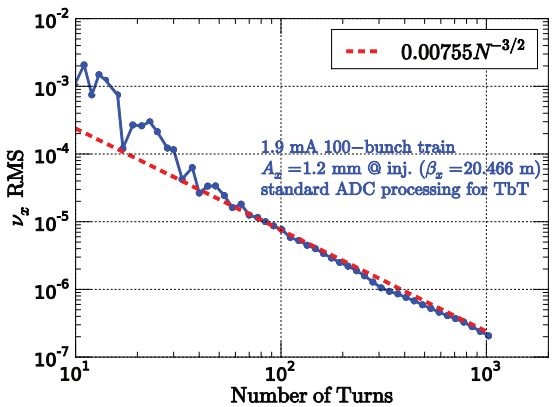

Figure 1: RMS of horizontal tune vs. number of turns.

* Work supported by DOE contract DE-AC02-98CH10886.
# boris@bnl.gov

ISBN 978-3-95450-177-9

Figure 1 presents a measurement, taken after a single horizontal ping with the total of 1000 TbT positions recorded. For each BPM the tune was found by the interpolated FFT method with DFT fine-tuning, and by processing only the first $N \leq 1000$ turns. RMS of these 180 tunes vs. N, plotted in Fig. 1, converges well to the expected [10, 11] asymptotic scaling $\sim N^{-3/2}$.

For the number of turns approaching one thousand the tune measurement error is ~2e-7 (RMS). Thus, over short timescales (1000 turns is 2.64 ms), the tune is very stable and could be measured with very good accuracy.

Unfortunately conventional beam physics measurements that require varying the bunch charge, or other parameters, cannot directly benefit from this, because over longer timescales, required for any parameter variation, the tunes are much less stable. For instance, repeated pinger measurements, performed at 20 second intervals, result in shot-to-shot tune jitter at the level of few times 1e-4 or more. Similar levels of tune stability are confirmed with the bunch-by-bunch feedback system that uses entirely different hardware and algorithms for tune measurement [9].

Our new method, however, allows one to overcome the limitations coming from the tune jitter. Recording and processing TbT positions of two (or more) simultaneously stored bunches of different charge, we can keep taking advantage of very good tune stability over short timescale.

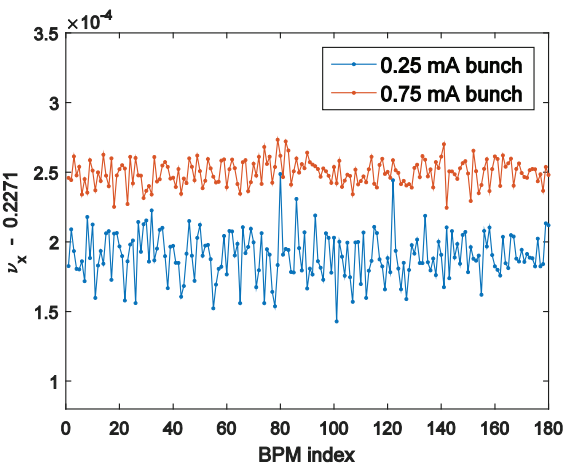

Figure 2: Horizontal tunes of two stored bunches.

This is illustrated in Fig. 2, showing the result of horizontal tune measurement with two bunches, of unequal charge, stored in the ring diametrically opposite to each other. The pinger magnet timing was adjusted to provide equal kick to both bunches. 100k-sample ADC data buffers (i.e. ~320 turns), triggered on a ping, were recorded for 180 regular BPMs. The 100-sample-long boxcar windows, centered on the bunches, were applied before the TbT positions for each bunch were calculated using 25 revolution harmonics (maximum number within the bandwidth of the so-called "pilot tone filter" [7], ON at the time). Performing a statistical analysis for 180 BPMs we obtained ν_x = 0.22729 ±1.71e-05 (0.25 mA bunch) and ν_x = 0.22735 ± 9.06e-06 (0.75 mA bunch), with ± numbers indicating one standard deviation.

The resulting tune difference was $\Delta\nu_x$=(6.0 ± 1.9)*1e-5, proving that even for as few as N=300 turns we can comfortably resolve the tunes of two bunches to the level much lower than the few times 1e-4 typical tune stability.

Even without increasing single bunch currents this relative tune resolution could be improved further by 1) increasing the number of turns; 2) using a short low current train such as one used for Fig. 1 as a "low charge per bunch reference" as opposed to using a single bunch; and 3) further increasing the number of revolution harmonics used for TbT position calculations up to ~50 to match the front-end filter bandwidth (possible when "pilot tone filter" is off). Scaling from currently available data we believe that tune resolution of ~1e-6 RMS should be reachable.

Furthermore, since the relative measurement is performed, this resolution should be preserved over a much longer timescale than that of the individual measurement. This is because the most likely sources of the short term tune drift (quadrupole PS noise, RF frequency noise plus non-zero chromaticity, etc.) are affecting the reference and the high current bunches by the same amount. Thus precise repeated measurements, while varying the bunch charge or other parameters should be possible.

Impedance from Relative Tune Shifts

The ability to measure relative tunes of unequal charge bunches with good precision is immediately applicable to the measurement accuracy of transverse coupling impedances, $Z_{x,y}(\omega)$, or kick factors, related to the impedances by $k_{x,y} \propto \int Im[Z_{x,y}(\omega)]|\tilde{\rho}(\omega)|^2\, d\omega$, where $\tilde{\rho}(\omega)$ is the Fourier transform of the longitudinal beam density. The kick factors determine current-dependent tune shifts,

$$\delta\nu_{x,y}(Q) = -k_{x,y} Q \frac{<\beta_{x,y}>}{4\pi\, E/e}, \qquad (1)$$

due to an impedance-carrying vacuum chamber component with the average beta functions $<\beta_{x,y}>$, where Q and E are the bunch charge and energy. Denoting the low-current reference bunch and the high-current bunch by corresponding subscripts we get for the kick factor,

$$k_{x,y} = \frac{4\pi\,(\nu_{x,y\_ref} - \nu_{x,y\_hi})E/e}{(Q_{hi} - Q_{ref})<\beta_{x,y}>}. \qquad (2)$$

For example, if, for the charge difference of 1 nC we are able to resolve the tune difference of 1e-6, then, at 3 GeV and taking a 4 m beta function, we could measure kick factors as low as 10 V/pC/m. In the vertical plane such a kick factor would be equal to that due to the resistive wall of an Al vacuum chamber pipe with 12 mm vertical aperture that is only one meter long! (we assumed elliptical cross-section with large horizontal-to-vertical aspect ratio and a 5 mm RMS Gaussian bunch typical for NSLS-II). Clearly, the ability to resolve impedance components as small as this would be highly desirable.

Of course, machine tunes are global quantities, so generally one cannot attribute the tune shifts in (2) to a par-

ISBN 978-3-95450-177-9

ticular impedance component. However, for the components with controllable geometry (in-vacuum undulators, scrapers, etc.) the impedance they present to the beam can be changed, and therefore easily isolated. For fixed impedance components, similarly to [13], this isolation could be achieved with local bumps.

We illustrate this method with the measurement of one of the NSLS-II vertical scrapers, which essentially consists of two 1 cm thick and 3 cm wide vertically movable rectangular blades made of Cu. The measurement was done with a 100 consecutive bucket train of 1.4 mA total current plus a 0.3 mA camshaft bunch stored in an RF bucket ½ the ring circumference away from the train. Both were kicked to the same amplitude with a vertical pinger, while ~900 turns worth of ADC data for 180 BPMs were recorded, and then processed, with ADC windows, to get the tunes. Several measurements like this were taken as the top scraper blade was moved closer to the beam. In Fig. 3 one can see a significant increase in the relative tune shift as the scraper impedance becomes more and more dominant. From (2) the total tune shift in Fig. 3 of ~3e-4 corresponds to the kick factor of ~600 V/pC/m (β_y at the scraper location is 26 m). As expected the kick factor is quite high, and detailed comparison with the impedance models is in progress. Note, however, that the error-bars in Fig. 3 are on the order of 3e-6, giving us confidence that much smaller kick factors are measurable with this method.

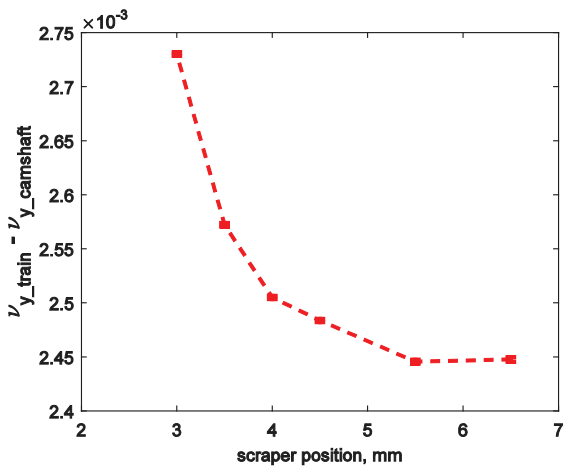

Figure 3: Relative tune shifts due to vertical scraper.

We now present preliminary results for a much more challenging ring component, specifically an (out-of-vacuum) undulator chamber in a low-β (cell 21) ID straight of NSLS-II. This chamber is 4.8 m long Al pipe with 60x11.5 mm^2 elliptical cross-section. Gradual tapered transitions to a larger cross-section as well as some other components are located on both sides of this chamber, but the resistive wall impedance is expected to dominate. Unlike the scraper, the chamber impedance is fixed, so impedance localization was done with local bumps. Specifically, we applied vertical bumps that created parallel displacement in the 21ID straight and virtually no orbit perturbation elsewhere. We used the same fill pattern as the one for the scraper measurement above. The tune difference was measured, in order, for -4 mm bump, without the bump, and then with 4 mm bump (see Fig. 4).

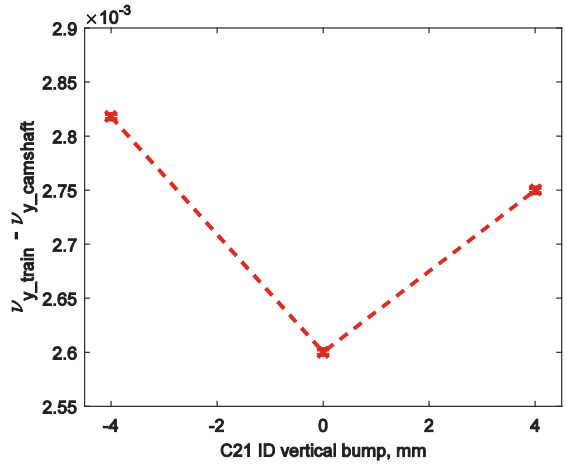

Figure 4: Relative tune shifts with local bumps in C21 ID.

Some asymmetry in the tune shifts is evident. We attribute most of it to some charge loss in the camshaft bunch during the measurement as well as to the bump imperfection. Still, averaging the tune shifts from the positive and negative bumps we can estimate the kick factor for a 4 mm vertically displaced beam from (2). To get the kick factor for the beam centered through chamber we use the well-known resistive wall expressions from [13] and get ~210 V/pC/m ($< \beta_y >$ is 2.84 m). This is significantly higher than the 56 V/pC/m resistive wall kick factor one calculates for this chamber assuming pure Al and a separately measured bunch length of 16.2 ps at 0.3 mA. Note however, that the actual chamber is NEG coated with nominal layer thickness of 1 μm, which could explain some if not most of this discrepancy. Further investigation is ongoing.

Other Methods of Impedance Measurement

So far we focused on impedance measurements with kicked beams that rely on precise measurements of relative tune shifts. While we believe this method holds a lot of potential, we emphasize that many other methods would benefit from simultaneous measurements of unequal charge bunches because this reduces the effects of machine drifts. For instance, the resolution of the local bump method for measurements of the effective impedance from closed orbits of low and high charge bunches [12] is limited by closed orbit drifts. If, however, the orbits of high and low charge bunches are measured simultaneously, the resolution could be significantly improved. While so far we have not explored this due to size limitations for ADC data buffers available for off-line analysis, we will use this technique as an independent cross-check when closed orbits of multiple bunches are implemented in FPGA and are available through EPICS.

ISBN 978-3-95450-177-9

Measurements of Tune Shift with Amplitude

Another technique that became available with new BPM capabilities is a single-shot measurement of amplitude-dependent tune shift curve. This time bunches of equal charge need to be kicked to different amplitudes, which is accomplished by placing them at the different amplitude locations along the kicker waveform. Furthermore, this measurement does not require resolving the tunes of individual bunches but only the tunes of groups of bunches kicked to the same amplitude. This is why bunch separation is unnecessary, so the measurement is presently performed with a long bunch train overlapping with the rising portion of the kicker pulse. This single shot technique allows one to overcome tune jitter limitations, and it favourably compares to the multi-shot, conventional method. This is further illustrated in the accompanying talk and in [1].

SUMMARY AND FUTURE WORK

Single-bunch resolution of NSLS-II BPMs was recently improved by an order of magnitude to about one micron TbT at ~1 nC/bunch. This improvement was achieved through special processing of ADC signals which additionally provides the new capability of resolving TbT signals from several bunches stored in the ring. Having this capability on all NSLS-II RF BPMs is extremely valuable for sensitive collective effect or single particle dynamics measurements. It allows us to simultaneously measure bunches with different charges (or kick amplitudes) thus eliminating harmful effects of machine drifts.

We presented some novel accelerator physics measurements enabled by these new BPM capabilities. These include a new technique of probing the ring impedance by measuring relative tune shifts between the bunches of unequal charge. This technique is very accurate because it takes advantage of extremely good tune stability over very short timescales thus allowing to resolve relative tunes to the level of 1e-5 or better. Another novel technique is a single-shot measurement of amplitude-dependent tune shifts. More studies are in progress. We presently believe that many of them could greatly benefit from including additional diagnostics available through the bunch-by-bunch feedback system.

ADC signal processing that resolves the orbits of multiple bunches within a turn has been so far done off-line. It is presently being implemented in FPGA, so that improved positional resolution and multi-bunch capability will be available in real time through EPICS and the present limitation on data buffer length of 3.2 k-turns of TbT data (1 million ADC samples) will no longer apply. This will allow us, for example, to analyze the individual closed orbits of multiple stored bunches vastly expanding our toolkit for studying beam dynamics at NSLS-II.

Finally, we would like to acknowledge the enormous help we received from many of our NSLS-II colleagues but especially from Kiman Ha, Joe Mead, Om Singh and Kurt Vetter (presently at ORNL).

REFERENCES

[1] B. Podobedov *et al.*, "Single Micron Single-Bunch Turn-by-Turn BPM Resolution Achieved at NSLS-II," IPAC'2016, pp. 2095-2098.
[2] K. Vetter *et al.*, "NSLS-II RF Beam Position Monitor", PAC'2011, pp. 495-497.
[3] K. Vetter *et al.*, "NSLS-II RF Beam Position Monitor Update", BIW'2012, pp. 238-241.
[4] W. Cheng *et al.*, "Characterization of NSLS2 Storage Ring Beam Orbit Stability", IBIC'2015, pp. 625-629.
[5] W. Cheng, B. Bacha, O. Singh, "NSLS2 Beam Position Monitor Calibration", BIW'2012, pp. 77-79.
[6] W. Cheng *et al.*, "Performance of NSLS2 Button BPMs", IBIC'2013, pp. 678-681.
[7] O. Singh *et al.*, "NSLS-II BPM and Fast Orbit Feedback System", IBIC'2013, pp. 316-322.
[8] J. Mead *et al.*, "NSLS-II RF Beam Position Monitor Commissioning Update", IBIC'2014, pp. 500-504.
[9] W. Cheng *et al.*, "Commissioning of Bunch-by-Bunch Feedback System for NSLS2 Storage Ring", IBIC'2014, pp. 707-711.
[10] R. Bartolini *et al.*, "Precise Measurements of the Betatron Tune", Part. Accel. 55, 1 (1996).
[11] N. Biancacci and A. Thomás, "Using AC Dipoles to Localize Sources of Beam Coupling Impedance", Phys. Rev. Accel. Beams 19, 054001 (2016).
[12] V. Kiselev, V. Smaluk, "A Method for Measurement of Transverse Impedance Distribution along Storage Ring", DIPAC 1999, pp. 202-204.
[13] A. Piwinski, "Wake Fields and Ohmic Losses in Flat Vacuum Chambers", DESY HERA 92-04 (1992).

ISBN 978-3-95450-177-9

MEASUREMENTS OF LONGITUDINAL COUPLED BUNCH INSTABILITIES AND STATUS OF NEW FEEDBACK SYSTEM

G. Rehm*, M.G. Abbott, A.F.D. Morgan, Diamond Light Source, Oxfordshire, UK

Abstract

We have modified the vertical bunch-by-bunch feedback at Diamond Light Source to also provide a longitudinal kick on a separate input. Using our existing drive/damp system and a modulator/amplifier to the required 1.5 GHz we are thus able to characterise the damping rates of all coupled bunch instabilities, while not able to provide feedback. At the same time, we have started the development of a completely new longitudinal feedback system based on commercially available components, providing 500 MS/s, 14 bit conversion in and 16 bit out, powerful Virtex 7 field programmable gate array for digital signal processing and 2 GB of on board buffer for recording data. We report on the status of the development and our plans to bring the new system into use.

INTRODUCTION

At Diamond we have been working on *transverse* Bunch-by-Bunch Feedbacks (BBFB) for nearly a decade [1–4], and have concluded an major upgrade of the Digital Signal Processing (DSP) in firmware and software in 2014 [5–7] providing unique capabilities. So naturally, when asked to provide a *longitudinal* BBFB system to deal with potential Coupled Bunch Instabilities (CBI) introduced by Higher Order Modes (HOM) of a pair of normal conducting Radio Frequency (RF) cavities which will be installed at Diamond in summer 2017, we preferred to build one ourselves rather than opt for a commercial solution. However, our existing system is built around the *Libera Bunch-by-Bunch Processor* (LBBB) [8,9] which is unfortunately no longer available due to obsolescence of its components. Even if we had spares available in house, it did not appear prudent to build a new system based on 10 year old obsolete electronics, so we searched for an alternative.

After several discussions with potential suppliers we found the best option for us is to put together a system using modular commercially available Printed Circuit Board (PCB) components. We found this to be the better solution compared to having a dedicated PCB designed, as it avoids hardware development and the associated costs, and offers a path to a potential multitude of applications by re-using modular parts of the whole system.

At the same time, we thought what tests we could do before we would install the longitudinal kicker cavity, with its own lengthy development and manufacturing [10, 11]. We concluded that we could use a spare LBBB to provide drive signals and analysis of longitudinal CBI, which we would excite using the parasitic *longitudinal* coupling impedance of a pair of vertical kicker striplines driven in common mode (as opposed for the vertical kick which is achieved by driving the pair in differential mode).

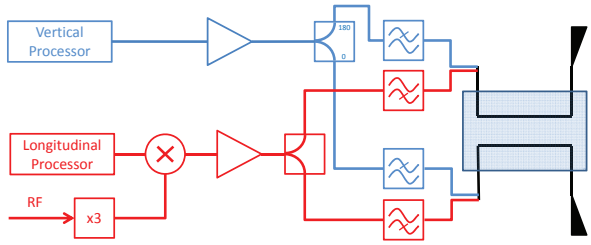

Figure 1: Block diagram of the connections of vertical and longitudinal BBFB to the vertical kicker stripline.

Consequently, the first part of the paper will concern the measurement setup and results for longitudinal CBI made so far using the vertical striplines, while the second part will summarise the status of our development of a new feedback processor.

LONGITUDINAL CBI MEASUREMENT

In search of providing longitudinal kicks with a bandwidth of 250 MHz without the dedicated longitudinal kicker installed, we found that the vertical striplines used as part of the transverse BBFB do provide a coupling as well. This coupling impedance scales with $\sin(\omega l/c)$ where l is length of the striplines (280 mm in our case) [12]. From this we select to excite the 250 MHz bandwidth below $3f_{RF} \approx 1.5$ GHz, which provides a strongly varying though always non-zero impedance.

The block diagram in Fig. 1 illustrates how we manage to continue to provide vertical BBFB while at the same time exciting longitudinal oscillations. The output for the vertical is amplified (at baseband 0-250 MHz) then fed through a 180° splitter to differentially drive the striplines. On the other side, the output for the longitudinal is up-converted to 1.5 GHz, then amplified and fed through a 0° power splitter to the striplines. Both signals are combined using a pair of diplexers with a cross over frequency of 1 GHz, thus allowing concurrent action in both planes.

We then apply a method of 'drive-damp' experiments described in more detail elsewhere [13] using a spare LBBB, with the only difference that on the longitudinal system we are driving at frequencies $\omega = (pM + \mu)\omega_0 + \omega_S$ with $p = 3$ (third RF harmonic), $M = 936$ our harmonic number, $\mu = 0, 1, \ldots, 935$ the scanned modes, ω_0 our revolution frequency and $\omega_S \approx 2\pi \cdot 2$ kHz our synchrotron frequency.

Part of the analysis of CBI is already done in the FPGA as part of our DSP code implemented in the LBBB [6]. We are measuring the complex amplitude of the driven mode

* guenther.rehm@diamond.ac.uk

ISBN 978-3-95450-177-9

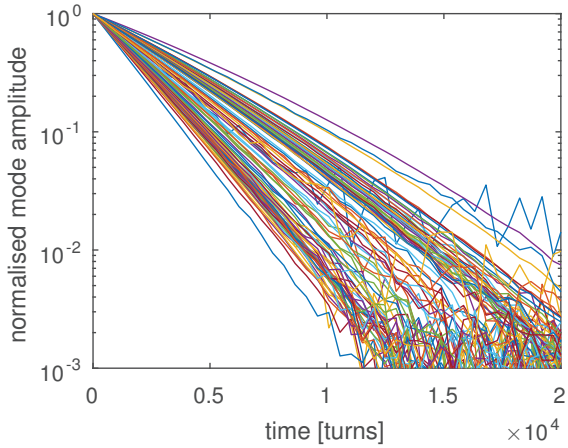

Figure 2: Normalised magnitude during damping of longitudinal CBI after excitation. Only every tenth mode of the total of 936 is shown for clarity.

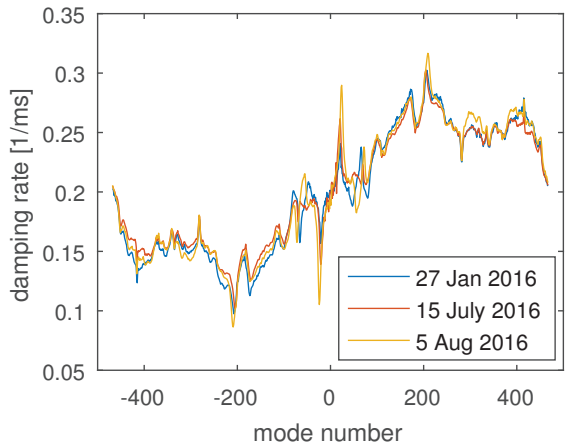

Figure 3: Damping rates of all longitudinal CBI.

by multiplying the input bunch position stream with $\sin(\omega)$ and $\cos(\omega)$ and averaging the result over two synchrotron periods (480 turns). We then only record this complex amplitude for 10 points during the drive time (4800 turns) and 50 points (24000 turns) during the damping (when excitation is switched off and natural damping is observed). The FPGA then immediately advances to the excitation of the next mode, scanning through 18.5 modes every second and completing a whole set of 936 grow damp experiments in 52 s.

The advantage of this upstream FPGA processing is a massive reduction of the data that needs to be transferred out: in 52 s the ADC has produced $52\,\text{s} \cdot 500\,\text{MHz} \cdot 2\,\text{B} \approx 48.4\,\text{GB}$ of data, while our on-board analysis reduces this to a mere $60 \cdot 936 \cdot 4\,\text{B} \approx 219\,\text{kB}$.

Measurement Results

In order to improve further on the signal to noise ratio, we repeat the whole 936 mode grow-damp experiment 100 times and compute the average complex amplitudes of that. The magnitude of a subset of mode amplitudes during damping is shown in Fig. 2. By fitting the natural logarithm of the mode amplitudes with straight lines, we directly retrieve the damping rates.

These damping rates have been measured three times during operation with 300 mA stored beam and are shown in Fig. 3. The average damping rate of $0.2\,\text{ms}^{-1}$ is synchrotron damping, while the deviations are caused by the aliased impedance of the whole machine. The overall pattern is nicely symmetric around mode 0 as is predicted by theory. The most critical point is then mode -209 which has the lowest damping rate, so this mode would go unstable first if beam current was increased to 550 mA or earlier if damping was reduced for instance by powering off one or both of the two super conducting wigglers.

The sharp resonance at mode -10 is also interesting as it has changed over the course of these three measurements. Potentially, this could be related to a HOM of our RF cavities moving slightly during this time. We plan further investigations of this for instance with one cavity parked.

NEW FEEDBACK PROCESSOR

The demands on a feedback processor are quite clearly defined: its interfaces are analogue signals in and out which range from DC to half bunching frequency, typically pre-processed by a low level RF front-end and post-processed by a modulator including potential frequency translation. Analogue to Digital (ADC) and Digital to Analogue Converters (DAC) sampling at precisely the bunching frequency will connect to a Field Programmable Gate Array (FPGA) in which DSP routines are used to provide the actual feedback and additional functionality. Latency through the whole system needs to be fully deterministic down to the few 10 ps level, and group delay needs to be flat to the same level over the whole range of operation from DC to half bunching frequency.

Hardware

We found an FPGA Mezzanine Card suitable for this specification in the *FMC-500* [14], which offers two channels of ADC at up to 500 MS/s, 14 bit and two channels of DAC at up to 1230 MS/s, 16 bit. A flexible on board Phase Locked Loop (PLL) chip allows for synchronisation of the conversions with an externally delivered RF clock. A framework for FPGA support is available, however as this is designed for Innovative Integration FPGA boards only we found little use of it. So we resorted to writing Serial Peripheral Interface (SPI) and drivers to set up the integrated circuits and routed the data channels to the FPGA.

This FMC module needs to be connected to a carrier with an FPGA, and to this end we selected the *AMC525* [15], which features a Virtex 7 690T, 2 GB of on board Double Data Rate 3 (DDR3) memory, 2 High Pin Count (HPC) FMC slots, Peripheral Component Interconnect Express (PCIe) and Gigabit Ethernet connections on the rear connector and an on board Freescale QorIQ PPC2040 processor

ISBN 978-3-95450-177-9

Figure 4: Photo of the assembly of FMC-500 (top right) and FMC-DIO-5Ch-TTL-A (bottom right) on the AMC525. Dimensions are 180 mm by 150 mm.

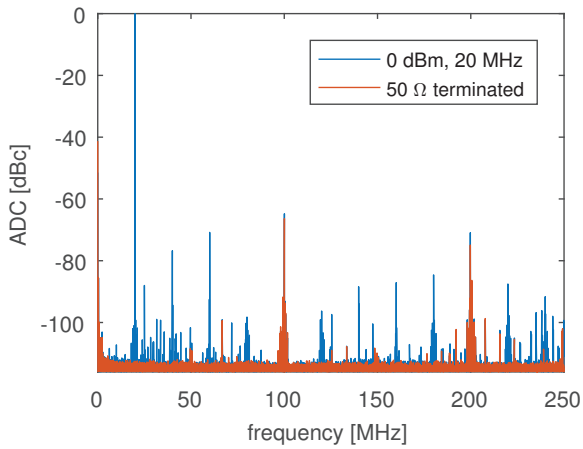

Figure 5: Spectrum with and without a 0 dBm 20 MHz tone (filtered by a crystal to remove harmonics from the generator). Fast Fourier Transform of 2^{25} points.

for FPGA firmware uploads from a 32 GB flash memory. The processing capabilities of this FPGA are by far superior to the LBBB, for instance it offers 3600 DSP blocks where the Virtex 2 provided only 136.

In the other FMC slot on the *AMC525* we place a *FMC-DIO-5Ch-TTL-A* Open Hardware Module [16], which we use for additional trigger signals. Again, the FPGA interface to this had to be developed by us, but integration turned out to be straight forward.

Finally, the stack of two FMC modules on the carrier (as shown in Fig. 4) is used inside a *VT814* Micro-TCA crate which also houses a Intel processor card *AMC720* [15] which runs our standard install of Redhat Enterprise Linux on which we will implement an EPICS driver. For this selection we were motivated by alignment with other use cases to select a rather larger crate with redundant power supplies.

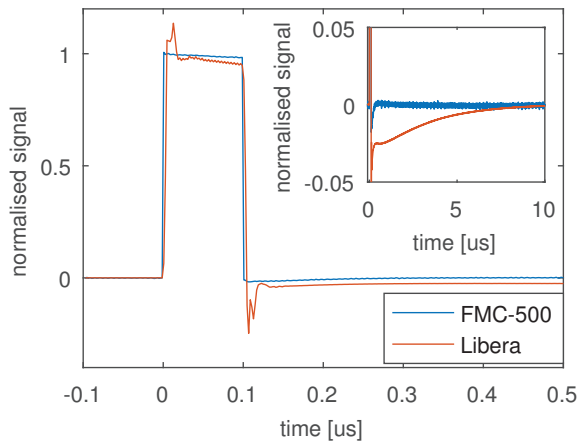

Figure 6: Normalised time response to a 100 ns pulse. Main graph shows pulse detail, while inset shows longer term settling.

Programming

We have implemented the following on the FPGA so far: a Peripheral Component Interconnect Express (PCIe) interface to the Central Processing Unit (CPU), two DDR3 memory controllers, an 256 bit wide Advanced eXtensible Interface bus to transport data between these and the ADC, DAC and our DSP application as well as register interface and SPI to configure ADC, DAC and PLL on the FMC-500. We also implemented a low-voltage differential signaling parallel interface for the ADC and DAC data flows with associated clocks.

PCIe and SPI are supported on the CPU with Linux drivers and utilities also developed in house. We have convinced ourselves that reading the memory on the *AMC525* works reliably and at swift speeds of 2 GB/s. Copying this into CPU memory slows the process to 1 GB/s, while subsequent reading and converting to double length floating point numbers in Matlab® is managed at 290 MB/s, which is still more than 100 times faster than the comparable procedure on the LBBB.

For producing a good sample clock from the externally supplied bunching frequency f_{RF} we have two options: Either we feed it straight through the PLL circuit, or we configure the PLL circuit to lock its voltage controlled oscillator at $5 f_{RF}$ to the external input and then output 1/5 of that frequency as sample clock. We have evaluated both options, and the straight through option delivers better phase noise at small offset frequencies of 1-10 kHz, which is particularly important for longitudinal feedbacks which look for synchrotron oscillation sidebands just a few kHz away from harmonics of the revolution frequency.

Finally, we have begun operating the ADC to the DDR3 and subsequently reading out the memory into Matlab® (running on the *AMC720*). This way we have managed to provide evidence of the excellent dynamic range (see Fig. 5). It shows that the 3rd harmonic at -70 dBc is the

ISBN 978-3-95450-177-9

highest harmonic (and that might still come from the generator despite the crystal filter used), while there are signals visible around 100 MHz and 200 MHz even without input signal originating from the reference clock (fundamental and higher harmonics aliased back). We are investigating if this unused device can be switched off or removed.

The impulse response of this DC coupled ADC compared to the AC coupled LBBB (see Fig. 6) is also excellent. While the splitting of the input into four 125 MS/s samplers on the LBBB lead to some few ns long spikes and the AC coupling lead to drooping of the flat high and low signals, both these effects are absent on the *FMC-500*.

CONCLUSIONS

We presented measurements of longitudinal CBI in the current state of the Diamond storage ring before installation of normal conducting RF cavities. We plan to continue using this system for comparative measurement beyond the installation of the dedicated longitudinal kicker cavity in March 2017 and up to the installation of the normal conducting RF cavities in Summer 2017.

At the same time we will continue to finish the implementation of the new BBFB by adding our DSP code and EPICS driver. The complete system will provide a capable system not only for our longitudinal BBFB, but can also be used without modification for the transverse. We hope that by selecting commercially available modular components there will be interest in this system also at other accelerators.

REFERENCES

[1] A.F.D. Morgan, G. Rehm, I. Uzun, *First Tests of the Transverse Multibunch Feedback at Diamond*, DIPAC 2007.

[2] A.F.D. Morgan, G. Rehm, I. Uzun, *Performance and Features of the Diamond TMBF System*, EPAC 2008.

[3] I. Uzun, M.G. Abbott, M.T. Heron, A.F.D. Morgan, G. Rehm, *Operational Status of the Transverse Multibunch Feedback System at Diamond*, ICALEPCS 2011.

[4] G. Rehm, M.G. Abbott, A.F.D. Morgan, J. Rowland, I. Uzun, *Measurement of Lattice Parameters Without Visible Disturbance to User Beam at Diamond Light Source*, BIW 2010.

[5] M.G. Abbott, G. Rehm, I. Uzun, *Capability Upgrade of the Diamond Transverse Multibunch Feedback*, IBIC 2013.

[6] M.G. Abbott, G. Rehm, A.F.D. Morgan, *New Features and Measurements using the Upgraded Transverse Multibunch Feedback at Diamond*, IBIC 2014.

[7] M.G. Abbott, G. Rehm, I. Uzun, *Architecture of Transverse Multi-Bunch Feedback Processor at Diamond*, ICALEPCS 2015.

[8] Instrumentation Technologies, *Libera Bunch-by-Bunch*, `http://www.i-tech.si`

[9] E. Plouviez, P. Arnoux, F. Epaud, J. Jacob, J.M. Koch, N. Michel, G.A. Naylor, J.-L. Revol, V. Serriere, D. Vial, *Broadband Bunch by Bunch Feedback for the ESRF using a Single High Resolution and Fast Sampling FPGA DSP*, EPAC 2006.

[10] A.F.D. Morgan, G. Rehm, *Initial Work on the Design of a Longitudinal Bunch-by-Bunch Feedback Kicker at Diamond*, IBIC 2015.

[11] A.F.D. Morgan, G. Rehm, *Design for the Diamond Longitudinal Bunch-by-Bunch Feedback Cavity*, IBIC 2016.

[12] K. Ng, *Impedances of stripline beam-positron monitors*, Particle Accelerators, 1988, 23 (2), pp 93-102.

[13] R. Bartolini, R.T. Fielder, G. Rehm, and V.V. Smaluk, *Analysis of Multi-bunch Instabilities at the Diamond Storage Ring*, IPAC 2016.

[14] Innovative Integration, *FMC-500, FMC Module with 2x 500 MSPS 14-bit A/D, 2x 1230 MSPS 16-bit DACs with PLL and Timing Controls*, `http://www.innovative-dsp.com/products.php?product=FMC-500`

[15] Vadatech, `http://www.vadatech.com/`

[16] CERN Open Hardware Repository, *FMC DIO 5ch TTL A*, `http://www.ohwr.org/projects/fmc-dio-5chttla`

ISBN 978-3-95450-177-9

BEAM BASED CALIBRATION OF A ROGOWSKI COIL USED AS A HORIZONTAL AND VERTICAL BEAM POSITION MONITOR

F. Trinkel*, F. Hinder, D. Shergelashvili, IKP, Forschungszentrum Jülich, 52425 Jülich, Germany,
RWTH Aachen, 52062 Aachen, Germany
H. Soltner, ZEA-1, Forschungszentrum Jülich, 52425 Jülich, Germany
for the JEDI collaboration†

Abstract

Electric Dipole Moments (EDMs) violate parity and time reversal symmetries. Assuming the CPT-theorem, this is equivalent to CP violation, which is needed to explain the matter-over-antimatter dominance in the universe. The goal of the JEDI collaboration (Jülich Electric Dipole moment Investigations) is to measure the EDM of charged hadrons (p and d). Such measurements can be performed in storage rings by observing a polarization build-up, which is proportional to the EDM. Due to the smallness of this effect many systematic effects leading to a fake build-up have to be studied. A first step on the way towards this EDM measurements is the investigation of systematic errors at the storage ring COSY (COoler SYnchrotron) at Forschungszentrum Jülich. One part of these studies is the control of the beam orbit with high precision. Therefore a concept of Beam Position Monitors (BPMs) based on pick-up coils is used. The main advantage of the coil design compared to electric-pick-up BPMs is the stronger response to the bunched-beam frequency and the compactness of the coil itself. A single Rogowski BPM measures the beam position in horizontal and vertical direction. Results of such a BPM in an accelerator environment are presented.

INTRODUCTION

The goal of the JEDI collaboration is to measure the EDMs of charged particles (p and d) at the storage ring COSY [1, 2]. To create an EDM signal an RF Wien filter introduces a vertical polarisation build-up of the stored polarized particles. This signal is proportional to the particles' EDM [3, 4]. To handle systematic effects, it is important to control the orbit with high precision. These systematic effects can contribute to an unwanted polarization build-up, which may erroneously be interpreted as an EDM signal [5]. The existing orbit control system at COSY will be improved to fulfil these requirements [6]. Furthermore, an investigation started with the goal to develop a prototype of a SQUID-based BPM [7]. For this SQUID-based BPM Rogowski coils are used as magnetic pick-ups [8]. This SQUID-based BPM development is divided into different steps. A first step is the test of a Rogowski coil, which is used as a BPM. The Rogowski coil consists of a torus, which is divided into four segments. Each segment is wound with a thin copper wire to measure the voltage, induced by the bunched beam. With this configuration it is possible to measure the beam position in the horizontal and the vertical plane. An advantage of the Rogowski coil BPM is its thickness of only 1 cm compared to the length of the existing BPMs with an extent of about 13 cm for one plane. This allows for installations in places with tight spatial constrains.

DESIGN OF ROGOWSKI PICK-UP COIL AND COSY INSTALLATION

The idea to measure the beam position with a segmented Rogowski coil is based on the measurement of the magnetic field induced by the particle flux. The geometry can be characterised by two radii. The radius R defines the distance from the centre of the tube to the centre of the torus and the radius a is the radius of the torus itself. In the presented setup the radius R is 40 mm and the radius a = 5 mm. The sketch of the different segments of the Rogowski coil BPM is shown in figure 1. Each segment is wound with a thin copper wire, which has the diameter of 150 μm. The number of windings for each segment is about 350. The depicted coordinate system is used in the following mathematical derivation. The segments are labelled with the numbers 1 to 4. The torus consist of vespel, which is vacuum-proofed.

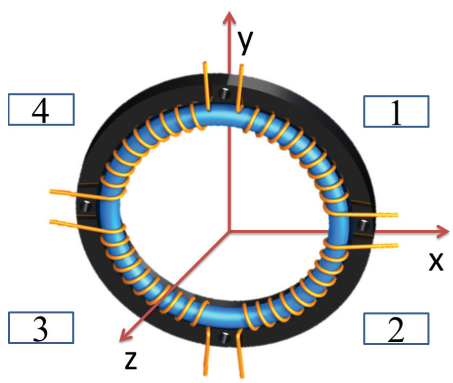

Figure 1: Sketch of a Rogowski coil BPM arrangement, which measures the horizontal and vertical beam position.

Two Rogowski coil BPMs with a distance of 13.3 cm to each other were installed in COSY storage ring to measure beam positions in the horizontal and in the vertical plane. The front Rogowski coil is installed on a fixed frame to use it as a reference BPM to suppress systematic effects like cycle to cycle orbit changes. The rear Rogowski coil is placed on a piezo table. The travel range is from −20 mm to 20 mm in horizontal and vertical plane. The resolution of the piezo

* f.trinkel@fz-juelich.de
† http://collaborations.fz-juelich.de/ikp/jedi/index.shtml

ISBN 978-3-95450-177-9

tables is 1 μm. With this setup it is possible to move the Rogowski coil BPM to certain positions and to perform a calibration of this BPM in an accelerator. The whole setup is shown in figure 2.

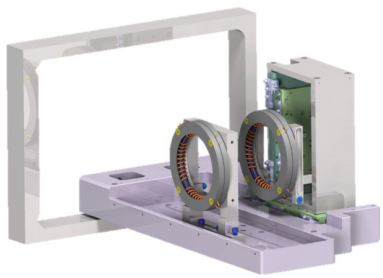

Figure 2: Schematics of the measurement setup, which was installed in the accelerator COSY. Front Rogowski coil BPM is mounted to a fixed frame. The rear one is mounted on a piezo table, which can be moved in horizontal and vertical direction.

Position Determination

In [9] the theoretical description of the magnetic field generated by a particle beam and the induced voltage for a horizontal or vertical Rogowski coil BPM is derived. The formula to calculate the horizontal (x) and the vertical (y) beam position with a Rogowski coil BPM divided into four segments is given by the following equations:

$$x = \frac{\pi\sqrt{R^2-a^2}}{2}\,\frac{(U_1+U_2)-(U_3+U_4)}{U_1+U_2+U_3+U_4},$$
$$y = \underbrace{\frac{\pi\sqrt{R^2-a^2}}{2}}_{m}\,\frac{(U_1+U_4)-(U_2+U_3)}{U_1+U_2+U_3+U_4}. \qquad (1)$$

The sensitivity m is given by $\frac{\pi\sqrt{R^2-a^2}}{2}$ and depends only on the torus parameters R and a. The induced voltage in the corresponding segment is denoted by U_i (compare figure 1).

MEASUREMENTS AT COSY

Accelerator Setup

The measurement is performed with a bunched deuteron beam (about 10^9 particles) with a momentum of 970 MeV/c and a revolution frequency of 750 kHz. The measurement time of one cycle amounts to 220 s. As preparation for the measurement, the piezo table is moved to a certain position, before the beam is injected. Subsequently the induced voltages are measured with the two Rogowski coil BPMs after each applied trigger signal. In total 38 trigger signals are used for the data acquisition in one cycle.

Readout Scheme for one Rogowski coil BPM

Each pick-up segment of the BPM is connected to a pre-amplifier with a high input impedance (0.5 MΩ) with an amplification of 13.5 dB. The pre-amplified signals are fed into two synchronized lock-in amplifiers[1]. The four voltages are measured and recorded with the data acquisition, when a trigger signal is sent. The reference frequency of the lock-in amplifier is the beam revolution frequency, defined by the bunching cavity. Figure 3 shows a schematic drawing of the wiring. The COSY RF signal is converted into a TTL pulse and sent to the lock-in amplifier. The chosen 3 dB filter width of the lock-in amplifier is 15.7 Hz. This filter leads to an effective averaging time of 10.2 ms (≈8000 turns). The sampling rate of the device is set to 225 Sa/s.

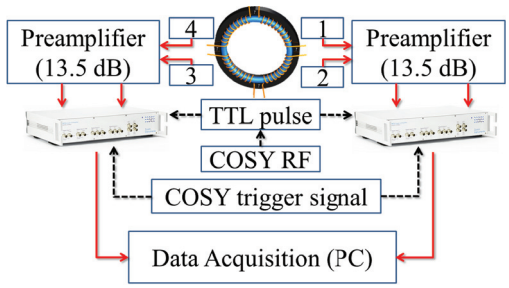

Figure 3: Readout scheme for the signals of one Rogowski coil BPM.

ROGOWSKI COIL CALIBRATION METHOD

The goal of the Rogowski coil BPM calibration is to compare the piezo table resolution with the resolution of the Rogowski coil BPM itself. A calibration of the Rogowski coil BPM increases the accuracy of beam position determination. The main idea of the calibration algorithm is taken from [10]. At first a grid measurement is performed with the help of the installed piezo tables. Before the particle beam is injected, the Rogowski coil BPM 1, placed on the piezo table, is moved to one defined position. Then the beam is injected and the voltages of Rogowski coil BPM 1 and Rogowski coil BPM 2 are measured after each trigger signal. This procedure is repeated at several positions as shown in the 2D graph of figure 4 (left). A sketch of the applied piezo table positions is shown in figure 4 on the left side. With this measurement grid the beam position resolution of the Rogowski coil BPM 1 is determined. But the measured beam positions are not coincide with the applied table positions. Therefore, a Rogowski coil BPM calibration is performed to reduce systematic effects like offsets or a rotation of the torus. The Rogowski coil BPM is calibrated with respect to the electrical centre of the system. The right sketch in figure 4 illustrates the coordinate system of the piezo table (x_T, y_T) and the coordinate system of the Rogowski coil BPM (x'', y''), which is rotated by the angle φ to the electrical centre (x', y'). The calibration algorithm minimizes the χ^2:

$$\chi^2 = \chi^2_x + \chi^2_y. \qquad (2)$$

The χ^2 is split into a horizontal and vertical components. These components are defined in equation 3. The χ^2_x con-

[1] HF2LI from Zürich Instruments (http://www.zhinst.com/)

ISBN 978-3-95450-177-9

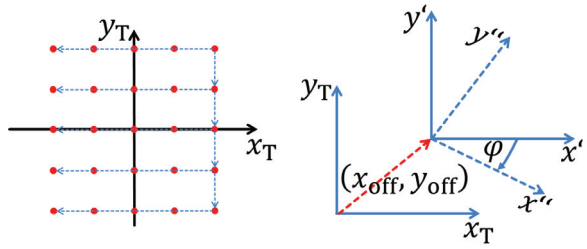

Figure 4: Left: coordinate system of the piezo table system. The dots show schematically the applied grid positions. Right: sketch of the coordinate system of the piezo table (x_T, y_T) and the coordinate system (x'', y'') of the Rogowski coil BPM, which is rotated with respect to the electrical centre by the angle φ. x_{off} and y_{off} define the offset to the electrical centre (x', y').

siders the square of the horizontal beam position correction defined by the terms $x'\cos(\varphi) - y'\sin(\varphi)$ minus the table position x_T and the offset to the electrical centre x_{off}. The numerator is weighted by the square of the errors on the horizontal and vertical beam position with respect to the rotation angle φ and fluctuation of the beam itself $\sigma_{x,\,fluc}$ and $\sigma_{y,\,fluc}$.

$$\chi^2_x = \frac{(x'\cos(\varphi) - y'\sin(\varphi) - x_T - x_{off})^2}{(\sigma_x\cos(\varphi))^2 + (\sigma_y\sin(\varphi))^2 + (\sigma_{x,\,fluc})^2}$$
$$\chi^2_y = \frac{(y'\cos(\varphi) + x'\sin(\varphi) - y_T - y_{off})^2}{(\sigma_y\cos(\varphi))^2 + (\sigma_x\sin(\varphi))^2 + (\sigma_{y,\,fluc})^2} \quad (3)$$

The vertical component is calculated analogously. The orbit fluctuates by 23 μm in horizontal plane and 32 μm in vertical plane for each cycle and represents the orbit stability of the accelerator COSY. This variation is measured with the Rogowski coil BPM 2 on the fixed frame.

With equation 4 the horizontal and vertical beam position is determined. The factors g_2, g_3 and g_4 are calibration factors and weight the measured voltage with respect to induced voltage U_1. In this way different numbers of windings for each segment and different pre-amplification are taken into account. The factors m_x and m_y correct possible manufacturing errors of the torus radii.

$$x' = m_x \cdot m \cdot \frac{U_1 + g_2U_2 - g_3U_3 - g_4U_4}{U_1 + g_2U_2 + g_3U_3 + g_4U_4},$$
$$y' = m_y \cdot m \cdot \frac{U_1 + g_4U_4 - g_2U_2 - g_3U_3}{U_1 + g_2U_2 + g_3U_3 + g_4U_4}. \quad (4)$$

After minimization and calculation of the calibration factors (g_2, g_3, g_4, x_{off}, y_{off}, φ, m_x, m_y) the horizontal and vertical beam position is determined with equation 5.

$$x_{cor} = x'\cos(\varphi) - y'\sin(\varphi) - x_{off}$$
$$y_{cor} = y'\cos(\varphi) + x'\sin(\varphi) - y_{off} \quad (5)$$

All measured voltages from each trigger signal with the corresponding piezo table position are used as input data for the minimization.

Data Analysis

The beam position in horizontal and vertical directions are calculated with and without the calibration factors for each trigger signal. One measurement consists of 38 trigger signals for one applied table position. A linear fit is applied to the 200 s cycle to calculate the mean position over the cycle. An example of this procedure is shown in figure 5 for one horizontal displacement, where the calibration factors are applied.

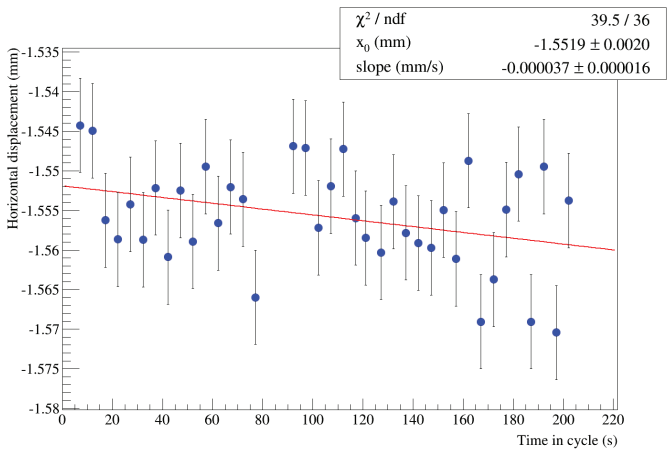

Figure 5: Corrected horizontal beam position. A linear fit is applied to determine the mean position of the cycle. The slope reflects possible drifts of the beam position during the cycle.

The mean position is given by the parameter x_0. The slope reflects possible drifts of the beam position during the cycle. Each position has a position accuracy of around 5 μm. In figure 6 the mean horizontal (x_0) against the mean vertical beam position (y_0) without calibration factors is shown. The Rogowski coil BPM detects the beam in horizontal and vertical direction with respect to the applied piezo table positions, but the data points suggest a rotation to the electrical centre. There is also an offset to the applied piezo table positions.

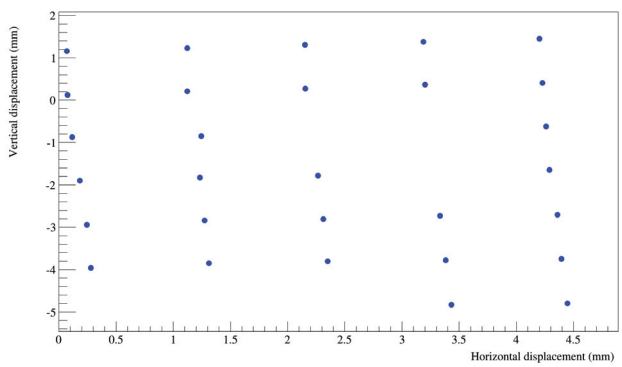

Figure 6: Measured beam position without calibration factors.

After minimization the calculated calibration factors are applied to the measured data. Table 1 presents the deter-

ISBN 978-3-95450-177-9

mined and applied calibration factors and the corresponding χ^2.

Table 1: Calibration Factors After Applying the Minimization Algorithm

Calibration factor	value	error
x_{off} (mm)	+3.5166	± 0.0004
y_{off} (mm)	-8.8333	± 0.0006
g_2 (%)	96.437	± 0.041
g_3 (%)	102.128	± 0.002
g_4 (%)	109.261	± 0.046
φ (mrad)	-47.08	± 0.21
m_x (%)	96.765	± 0.025
m_y (%)	97.192	± 0.027
χ^2	1.48	

Figure 7 represents the measured data points after using the calibration factors. In addition the applied piezo table positions are shown. The corrected points are marked with blue dots and the table positions with boxes. The result shows that the calibration method works and there is a good agreement between adjusted table positions and corrected beam positions. The error on the beam position in horizontal direction is around 24 μm and for vertical direction 33 μm. It includes the fluctuation of the beam after each injections ($\sigma_{i,fluc}$) and the accuracy of beam position determination ($\sigma_{i_0,}$).

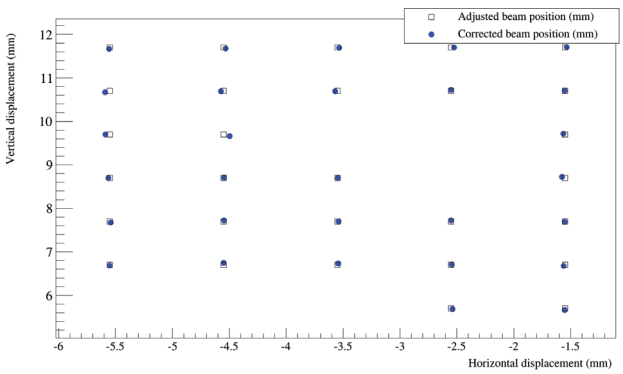

Figure 7: Corrected beam position with respect to the applied piezo table positions.

SUMMARY

A new concept of a magnetostatic BPM, which detects the beam position in horizontal and vertical beam position, is presented. A beam based calibration method is explained and applied. The results demonstrate the possibility to measure with one Rogowski coil BPM the horizontal and vertical beam position. With the help of the introduced calibration method it is possible to correct the measured beam position to the applied table positions and also to improve the accuracy of the beam displacement measurement.

Outlook toward Future Developments

In future work, two calibrated Rogowski coil BPMs will be installed in the vicinity of a new RF Wien Filter at COSY. This enables an alignment of the particle beam with respect to the centre of the Wien Filter. This configuration allows for studies of systematic effects relevant for EDM measurements. For a next beam time a calibrated Rogowski coil BPM will be installed to see the performance of a pre-calibrated system and to improve the accuracy of the position determination. Also a next step on the way to the SQUID-BPM will be the reduction of the coil temperature to decrease the noise level of the induced voltages.

ACKNOWLEDGMENT

The authors acknowledge the COSY operation group for their helpful support during the installation of the Rogowski coil in COSY as well as during the measurements.

REFERENCES

[1] R. Maier, "Cooler synchrotron COSY — Performance and perspectives", *Nuclear Instruments and Methods in Physics Research Section A: Accelerators, Spectrometers, Detectors and Associated Equipment 390*, pp. 1–8 (1997) http://dx.doi.org/10.1016/S0168-9002(97)00324-0

[2] C. Weidemann, F. Rathmann, H. Stein, *et al*., "Toward polarized antiprotons: Machine development for spin-filtering experiments", *Physical Review Special Topics - Accelerators and Beams 18*, 020101 (2015) http://dx.doi.org/10.1103/PhysRevSTAB.18.020101

[3] F. Rathmann, A. Saleev, N.N. Nikolaev, "The search for electric dipole moments of light ions in storage rings", *Journal of Physics: Conference Series 447*, 012011 (2013) http://dx.doi.org/10.1088/1742-6596/447/1/012011

[4] W. M. Morse, Y. F. Orlov, Y. K. Semertzidis, "rf Wien filter in an electric dipole moment storage ring: The 'partially frozen spin' effect", *Physical Review Special Topics - Accelerators and Beams 16*, 114001 (2013) http://dx.doi.org/10.1103/PhysRevSTAB.16.114001

[5] M. Rosenthal, A. Lehrach, "Spin Tracking Simulations Towards Electric Dipole Moment Measurements at COSY", *in Proceedings 6th International Particle Accelerator Conference*, IPAC'15, Richmond, VA, USA (2015). http://jacow.org/IPAC2015/papers/thpf032.pdf

[6] C. Böhme, M. Bai, F. Hinder, *et al*., "Studies for a BPM Upgrade at COSY", TUPB017, IBIC'15, Melbourne, Australia (2015).

[7] H. Ströher, "Search for electric dipole moments using storage rings", *Horizon 2020 proposal, Excellent Science Call: ERC-2015-AdG, Type of action: ERC-ADG Proposal number: 694340* http://collaborations.fz-juelich.de/ikp/jedi/public_files/proposals/Proposal-SEP-210276270.pdf

[8] W. Rogowski, W. Steinhaus, "Die Messung der magnetischen Spannung", *Archiv für Elektrotechnik 1*, pp. 141–150 (1912) http://dx.doi.org/10.1007/BF01656479

ISBN 978-3-95450-177-9

[9] F. Hinder, H. Soltner, F. Trinkel, *et al*., "Development of New Beam Position Monitors at COSY", *in IBIC 2015 International Beam Instrumentation Conference Proceeding*, TUPB015, IBIC'15, Melbourne, Australia (2015) http://ibic.synchrotron.org.au/papers/tupb015.pdf

[10] M. Tejima, "BEAM BASED CALIBRATION FOR BEAM POSITION MONITORS ", *in IBIC 2015 International Beam Instrumentation Conference Proceeding*, TUPB015, IBIC'15, Melbourne, Australia (2015) http://ibic.synchrotron.org.au/papers/tubla01.pdf

ISBN 978-3-95450-177-9

A NOVEL ELECTRON-BPM FRONT END WITH SUB-MICRON RESOLUTION BASED ON PILOT-TONE COMPENSATION: TEST RESULTS WITH BEAM

G. Brajnik*, S. Carrato, University of Trieste, 34127 Trieste, Italy
S. Bassanese, G. Cautero, R. De Monte, Elettra-Sincrotrone Trieste, 34149 Trieste, Italy

Abstract

In this paper we present a novel and original four-channel front end developed for a beam position monitor (BPM) system. In this work, we demonstrate for the first time the continuous calibration of the system by using a pilot tone for both beam current dependency and thermal drift compensation, completely eliminating the need for thermoregulation. By using this approach, we were also able to investigate several odd and well-known behaviours of BPM systems; the influence of important issues, like the non-linearity of ADCs and the gain compression of amplifiers, which do affect the reliability of the measurement, have been fully understood. To achieve these results, we developed a new radio-frequency front end that combines the four pick-up signals originated by the beam with a stable and programmable tone, generated within the readout system. The signals from a button BPM of Elettra storage ring have been acquired with a 16-bit, 160 MS/s digitizer controlled by a CPU that evaluates the acquired data and applies the correction factor of the pilot tone. A final resolution equal to 1 µm, for a vacuum chamber with an average radius of 19 mm, has been measured with a long-term stability better than 1 µm.

INTRODUCTION

Accuracy in BPM systems is strongly influenced by the following factors: beam current dependency (to achieve the proper dynamic range, the gains of the preamplifiers have to be adjusted), thermal drifts of electronics (filters, amplifiers, ADCs) and variations of the frequency response of the cables due to changes in temperature or humidity. All of these issues are responsible for inter-channel gain differences, which modify the calculated position.

Typically, every factor has its own compensation method: e.g. gain calibration look-up tables, thermal controlled racks, low-loss cables. The proposed strategy aims to correct all the factors simultaneously: a fixed sinusoidal tone (used as the same reference for all the channels) is added to the original signal coming from the beam (called carrier). A similar technique is already known [1–3], but for the first time experimental results have shown the improvement in resolution due to this method. In order to achieve an effective correction, the pilot tone frequency has to fall near the carrier one, without, however, interfering with the latter. The position of the tone is crucial: only the gaps between the beam harmonics (spaced by the inverse of revolution period) are suitable frequencies [4].

* gabriele.brajnik@elettra.eu

PROPOSED COMPENSATION

Let $a(t)$ be the input signal coming from the beam, $p(t)$ the pilot tone and $h_A(t)$ the response of channel A. The output of the chain, after the coupler, the filter and the amplifier is a convolution: $s_A(t) = h_A(t) * [a(t) + p(t)]$. Moving to the frequency domain and using the Fourier transforms in calligraphy upper case, the output can be written as $\mathcal{S}_A(f) = \mathcal{H}_A(f) \cdot [\mathcal{A}(f) + \mathcal{P}(f)] = \mathcal{A}_M(f) + \mathcal{A}_P(f)$, where $\mathcal{A}_M(f) = \mathcal{H}_A(f) \cdot \mathcal{A}(f)$ and $\mathcal{A}_P(f) = \mathcal{H}_A(f) \cdot \mathcal{P}(f)$. The complete evaluation of $\mathcal{H}_A(f)$, if $\mathcal{P}(f)$ is used, is not required if we suppose that f_P (the pilot frequency) and f_C (the carrier frequency) are close to each other, allowing us to write $\mathcal{H}_A(f_P) \approx \mathcal{H}_A(f_C)$. In this case, it can be written:

$$\mathcal{A}(f_C) = \frac{\mathcal{A}_M(f_C)}{\mathcal{H}_A(f_C)} = \frac{\mathcal{A}_M(f_C)}{\mathcal{A}_P(f_P)} \cdot \mathcal{P}(f_P) \qquad (1)$$

Extracting the amplitudes from $\mathcal{A}(f_C)$ for each channel and substituting them in the typical difference-over-sum (DoS) equation [5, 6] render it possible to calculate compensated spatial coordinates corrected for variations or mismatches of the preamplifiers:

$$X = L \cdot \frac{(A_M/A_P + D_M/D_P) - (B_M/B_P + C_M/C_P)}{A_M/A_P + B_M/B_P + C_M/C_P + D_M/D_P}; \qquad (2)$$

$$Y = L \cdot \frac{(A_M/A_P + B_M/B_P) - (C_M/C_P + D_M/D_P)}{A_M/A_P + B_M/B_P + C_M/C_P + D_M/D_P}. \qquad (3)$$

where A_M, B_M, C_M, D_M are the amplitudes of the measured carrier and A_P, B_P, C_P, D_P are the amplitudes of the pilot tone.

Obviously, to obtain a continuous and effective correction, care must be taken in treating the analog signals, as well as choosing appropriate computing power to digitally demodulate both carrier and pilot.

ANALOG RF FRONT END

Figure 1 shows the block diagram of the system: a low-phase-noise PLL generates the pilot tone (whose frequency and amplitude are programmable), which is split into four paths by a high-reverse-isolation splitter that guarantees more than 52 dB of separation between the outputs. A coupler sums the tone with the signal from the pick-ups, adding further 25 dB of isolation to prevent inter-channel crosstalk from the path of the pilot tone. At this point, all the signals pass through a bandpass filter, centered at 500 MHz

ISBN 978-3-95450-177-9

with a bandwidth of 15 MHz, and two variable-gain stages, composed of low-noise, high-linearity amplifiers (G=22 dB, F=0.5 dB, OIP3=+37 dBm, P1dB=+22 dBm) and digitally controlled attenuators (7 bits, up to 31.75 dB of attenuation, steps of 0.25 dB).

In order to achieve the expected results, the splitter must be temperature-insensitive, as well as the four couplers. Indeed, this architecture allows us to compensate the part of the system after the couplers, i. e. filters, attenuators, amplifiers. It has to be noted that being the front end a separate unit, it can be placed as near as possible to the pick-ups (tunnel area), with two main advantages: better signal-to-noise ratio and the possibility to compensate the cables (which are usually long).

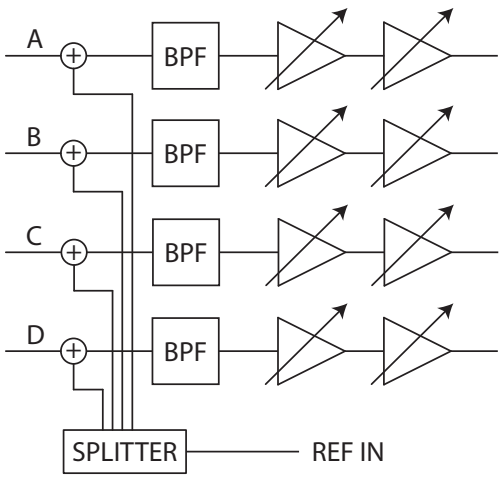

Figure 1: Block diagram of the RF front end.

MEASUREMENT SETUP

The RF front end has been placed in Elettra tunnel area and connected to a button BPM of the storage ring (the average radius of the chamber is about 19 mm). Four cables of about 20 meters deliver the amplified signals to an in-house assembled digitizer (16 bit, 160 MS/s) located in the service area, that undersamples the 499.654 MHz carrier and the 504.6 MHz pilot tone respectively at 19.654 MHz and 24.6 MHz. The raw data stream from the ADCs is collected by an FPGA and transmitted via an Ethernet link without any processing. The position is calculated offline, so that the FFT of each channel provides the amplitude of the carrier and the pilot.

A clock conditioner with two cascaded PLLs ensures the correct synchronization of the system with the storage-ring clock (1.156 MHz) and generates both a low-jitter sampling clock (measured to be around 100 fs), a fundamental condition for undersampling applications, and a reference clock for the pilot-tone synthesizer.

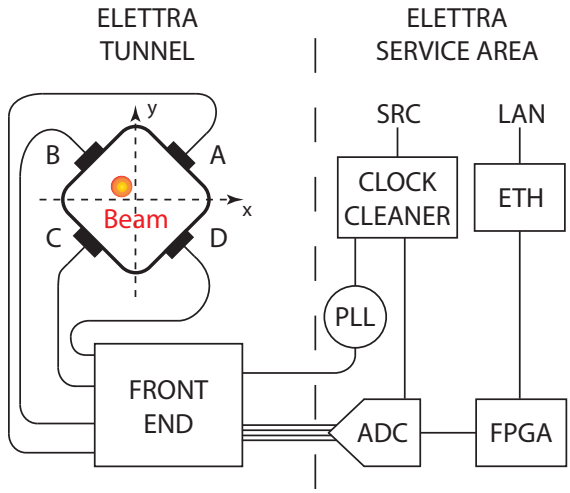

Figure 2: Block diagram of the setup.

INVESTIGATED ISSUES

With this setup (Figure 2), numerous sets of data have been acquired to understand several issues that affect the reliability of the measurement.

Temperature Dependence

Thanks to four sensors placed on every ADC and one in the front-end box, a strong dependence between temperature and the amplitude of the signals (and so the position) has been found.

Simulating a centered and stable beam with a splitter that divides a real signal from a storage ring button BPM, it can be shown that identical thermal drifts affect the carrier and the pilot (figure 3); the compensation greatly improves the standard deviation of the position, from 1.26 µm to 0.54 µm in a 24-hours time window, allowing us to separate it into two contributions: the part due to temperature variation and the actual resolution of the measurement.

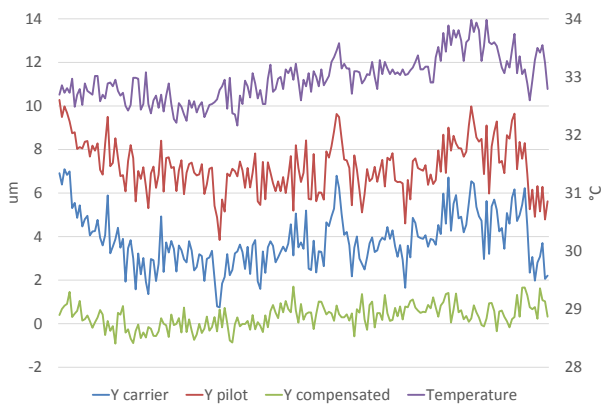

Figure 3: Changes in temperature and positions in a 24-hours time window.

ISBN 978-3-95450-177-9

Gain Compression

According to their datasheet, the low-noise amplifiers have a high 1dB compression point, but the high sensitivity of the position algorithm shows compression effects of 0.1dB at a lower input level. A technique to prevent it is to bias the amplifiers at an appropriate point; anyway, supposing the carrier saturates the amplifier, the pilot level decreases in a very similar way, so the loss can be recovered using the compensation.

Non-linearity of ADCs

It is well known that the transfer characteristic of ADCs suffers from non-linearity errors: the critical factor in our case is the integral non-linearity (INL). In order to evaluate these phenomena, we use the pilot tone as a fixed and stable beam. So, changing its global amplitude (but not among the channels), should keep the position almost in the same point thanks to the normalization made by the DoS.

Indeed, moving on the characteristic curve of the ADCs (input voltage vs. output code), discontinuities appear in the amplitudes digitized by the ADCs and obviously in the position. These discrepancies are about 110 µV in amplitude, which correspond to the INL of the used ADCs, nominally 4-5 LSB.

Again, given that the signal coming from the beam is added to the pilot tone, the latter can be used to coerce the working range of the ADCs. If a small signal is coming from the beam, a higher pilot allows us to shift it in a more suitable zone of the transfer characteristic.

RESULTS WITH BEAM

The following results have been collected with Elettra storage ring running in normal operation, 2.0 GeV and 310 mA. The BPM pick-ups used are close to an insertion device and between two bellows. The bellows assure the mechanical decoupling from the rest of the machine vacuum chamber. The beam orbit is kept stable at the center position by the global feedback. The input signal coming from the beam is −6 dBm, carrier and pilot amplitudes mesasured at the ADCs input are both 0 dBm, for a total amplitude of +6 dBm, that corresponds at the 80% of the ADCs working range.

The intrinsic resolution of the system has been measured in about 150 nm, using the pilot as a stable reference, an FFT of 2.4 MS and a chamber radius of 19 mm, .

First of all, we want to evaluate the influence of the pilot on the calculated position without compensation: no changes have been seen switching on and off the tone.

Subsequently, a single bunch has been injected to obtain a hybrid filling pattern. Also in this case the bunch does not affect in a significant way the position. Figure 4 shows the front-end output with a single bunch in the gap between two trains of bunches: the filter impulse response can be clearly seen.

Deliberate beam movements have been performed, with steps of 1 µm and 10 µm: the positions calculated by the system have been reported in Table 1, where the compensation shows an improvement of 2.5 µm.

Nevertheless, compensation is also useful for long-term stability. Figure 5 illustrates beam position in a 24-hours time window with and without correction: the standard deviation is reduced by a factor of two, from 1.36 µm to 0.76 µm, always considering an average chamber radius of 19 mm.

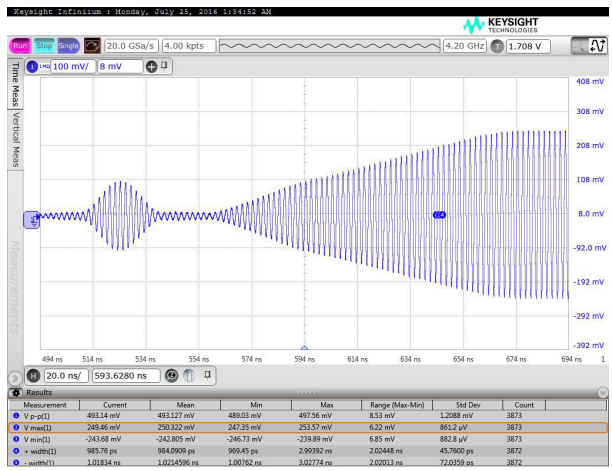

Figure 4: Front end output with a hybrid filling pattern: single bunch in the gap.

Table 1: Vertical Beam Movements

Actual movements	Measured position Uncompensated	Compensated
+1 µm	+0.5 µm	+1.0 µm
−1 µm	−2.5 µm	−1.1 µm
+10 µm	+8.4 µm	+9.2 µm
−10 µm	−12.6 µm	−10.1 µm

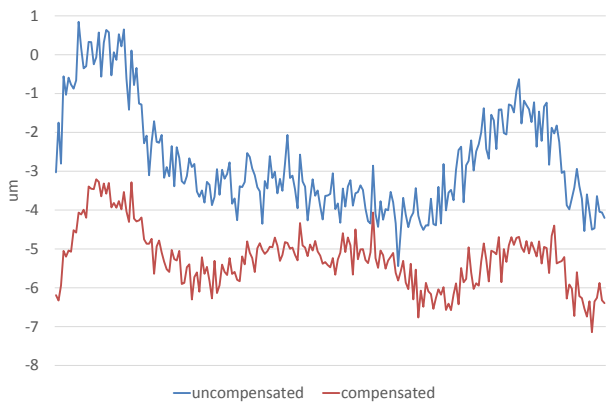

Figure 5: Beam Y-position in a 24-hours time window.

CONCLUSION

In this paper, a novel RF front end for electron beam position monitors capable of sub-micron resolution and continuous calibration has been presented. Several tests confirm the

ISBN 978-3-95450-177-9

effectiveness of the compensation by using a pilot tone coupled with the signal coming from the beam: this approach can correct inter-channel gain mismatches and thermal drifts, without using thermal regulators. Moreover, the experience with this system helped us to better understand a number of issues that affect data acquisition in the BPM field.

Further developments are under way, in both hardware and software: an FPGA Mezzanine Card (FMC) with four 16-bit, 210 MS/s ADCs is ready to be tested and linked with an FPGA. Improvements will be made on the front end, by handling the automatic gain control (AGC) of the preamplifiers, by adding an amplification stage to recover cable losses and by considering a pilot-frequency hopping scheme to increase the compensation efficiency.

The position calculation and compensation will be implemented in the FPGA: two digital receivers will demodulate the signals, extracting the amplitudes of the carrier and of the pilot at the same time after decimation and additional filtering. At this point, just before the calculation of the position with the traditional difference-over-sum equation, the system will be able to apply or not the compensation, allowing the users to evaluate its effectiveness.

REFERENCES

[1] M. Dehler, *et al.*, "New digital BPM System for the Swiss Light Source", *Proceedings of DIPAC 1999*, pp. 168-170.

[2] R. Baron, F. Cardoso, J. Neto, S. Marques and J. Denard, "Development of the RF Front-End Electronics for the Sirius BPM System", *Proceedings of IBIC 2013*, p. 670.

[3] J. Mead, *et al.*, "NSLS-II RF Beam Position Monitor Commissioning Update", *Proceedings of IBIC 2014*, pp. 500-504.

[4] G. Brajnik, S. Carrato, S. Bassanese, G. Cautero and R. De Monte, "Pilot tone as a key to improving the spatial resolution of eBPMs", *AIP Conference Proceedings*, vol. 1741, p. 020013 (2016).

[5] R. E. Shafer, "Beam position monitoring", *AIP Conference Proceedings*, vol. 212, pp. 26-58 (1989).

[6] P. Forck, P. Kowina and D. Liakin, "Beam position monitors", *CERN accelerator school on beam diagnostics*, pp. 187-228 (2008).

ISBN 978-3-95450-177-9

ACCURATE BUNCH RESOLVED BPM SYSTEM

F. Falkenstern, F. Hoffmann, J. Kuszynski, M. Ries
Helmholtz-Zentrum Berlin, Germany

Abstract

Operation of storage rings with multiple beams stored on different closed orbits as well as beam dynamics studies for complex fill patterns require accurate and stable measurement of the beam position for each individual bunch [1].
Analog BPM systems are usually optimized for measuring the closed orbit averaged over all buckets and many turns. Therefore no information about the position of individual bunches is supplied. The new bunch resolved BPM electronics, currently under development at HZB, is based on the analysis of RF-signals delivered by a set of four stripline / pick-up electrodes. These signals in combination with a low jitter master clock and commercially available DAQ cards allow to measure the bunch-resolved beam position with a resolution of a few micrometer.
Experiments performed at BESSY II and MLS demonstrate the performance of the setup and will be discussed.

INTRODUCTION

HZB operates two electron storage ring based light sources named BESSY II and MLS [2]. BESSY II is operated at an electron energy of 1.7 GeV with a maximum current of 300 mA distributed to 400 buckets. Whereas MLS is operated at 629 Mev with a current of up to 200 mA stored in 80 buckets. The main RF cavities of both rings operate at a frequency of about 500 MHz providing a bucket spacing of approximately 2 ns.
Different fill patterns and optics modes (i.e. low alpha) allow our users to work with optimal synchrotron light conditions at the beamlines. This flexibility of beam conditions leads to high requirements in the field of beam diagnostics.
For measurement of the average orbit the analog BPM system is used. The major advantage of this system is a high position resolution of about 1 micrometer for currents between 1 mA und 300 mA. Due to averaging, no external timing is required. The disadvantages is that there are no information about the position for each individually bunches and turns. In future upgrades of both storage rings this information may become necessary, therefore an alternative approach has to be explored.

DIAGNOSTICS REQUIREMENTS

What are the main challengers of bunch-resolved BPM diagnostic systems for the storage ring?

A) Capture the position of each individual bunch with an accuracy in the µm range.
B) Measurement results of the bunch position don't depend on temperature drifts.
C) The measurement data has to be linear with the orbit changes.
D) Large dynamic range of bunch currents from 10 µA to 10 mA.
E) The synchronous phase shift over the full fill pattern and small changes of beam phase with respect to the master clock should have no influence.
F) Cross talk between neighboring bunches due to ringing or reflections on the scale of 2 ns should be minimized.
G) Measurement results of the bunch position don't depend on orbit bumps (large displacements).

The following solution was found meeting all requirements.

A) A 14-Bit ADC with an analog BW of more than 500 MHz was chosen. The principle of under sampling allows to achieve a very good amplitude resolution. This technique is already being used in our fill pattern monitor "BunchView" [3].
B) The BPM signal will be multiplexed. So each of 4 signal channel has the same path of filter, amplifier and ADC. In other words only one active detector for all channels is used. This schematic has very good results in relation to thermal drift and aging of electronic parts.
C) A data acquisition card with a very linear 14 Bit ADC for a wide dynamic range of analog amplitudes is applied.
D) Linearity of the DAQ hardware will allow to apply normalization.
E) The approach of a sampling scope with 100 GHz is used for finding the maximum of the amplitude of the bunch signals.
F) A low pass filter (LPF) of about 750 MHz is applied to minimize the cross-talk to following bunches.
G) In the case of driving the orbit bumps it is important to have a good electrical separation between channels of the RF switch. The bad isolation between channels will be affected the X by change Y and vice versa.

The main component of the DAQ system is provided by using standard commercial equipment. A major advantage is the use of LabVIEW for controlling and

ISBN 978-3-95450-177-9

FPGA programming with straight forward implementation in the existing control system.

It shall be explicitly stated, that the presented approach is of bunch-by-bunch not turn-by-turn nature, i.e. averaging will be performed over multiple turns.

GENERAL SETUP

The basic layout of the system is shown in Fig. 1.

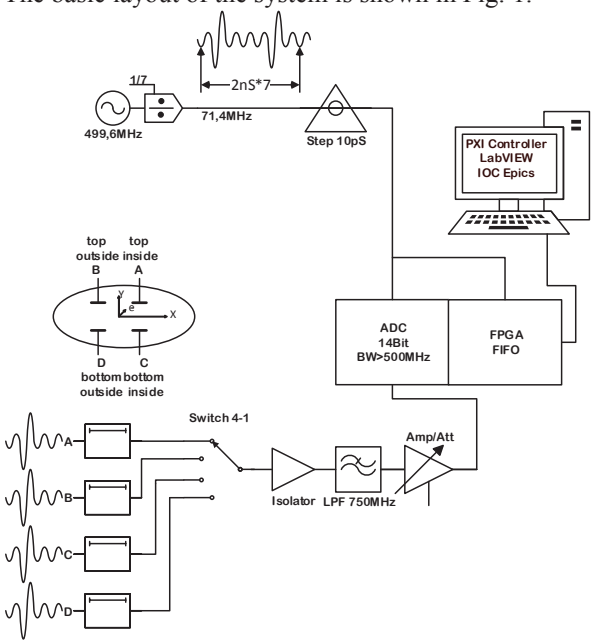

Figure 1: Block diagram of the bunch-resolved BPM system.

The signal induced from circulating electron bunches to striplines or button pickups will be adapted and connected to inputs of a RF multiplexer. It is important to connect the BPM pulse source and the input of switch connectors with high performance RF cable and with the minimum connect adapters to avoid the RF interference and thermal drifts between channels. In the case of RF reflections, the four to each other matched signals minimized the X, Y errors of the BPM measurement.

$X= [(A+C)-(B+D)]/(A+B+C+D)$

$Y= [(A+B)-(C+D)]/(A+B+C+D)$

The output of switch is connected to an isolator, it is a combination of attenuator and amplifier with a high directivity, defined as a difference between isolation and forward gains. So if there are impedance changes of filters or amplifiers or ADC do not influence the ideal out impedance of 50 Ohm of the RF multiplexer. Each of four BPM signal A, B, C, D has the same path of the RF detector. In the case of thermic drifts, no linearity of the detector (LPF, Amp, ADC) there are the same error for each channel.

The applied LPF has two functions. The first is the classical task of RF noise rejection. On the other hand, a special response pattern is generated with respect to the 2 ns bunch spacing. Therefore, the influence of a bunch signal to the next following bunch signal is minimized [3].

Different filters are applied for stripline and pickup detectors considering the different signal response.

The amplifier / attenuator matches the analog RF signal to the dynamic range of the ADC. For operation with high single bunch (SB) currents of up to 15 mA the signal has to be attenuated. Whereas small bunch currents, e.g. low alpha operation, require to amplify the signal.

The detected RF signal will be digitalized with the 14 Bit ADC and stored in the FPGA memory. In the first development stage we can average over 20 samples at BESSY II (400 buckets) or 100 samples at MLS (80 buckets) for each bunch while switching the RF multiplexer with 1 kHz.

The next steps will be to find a better agreement between the number of average and the switch frequency of the BPM system.

The master clock will be divided by factor of 7 and shifted with the digital delay to achieve a maximum amplitude, i.e. S/N ration. Therefore, the bunch-resolved BPM system samples every 7th bunch full fill pattern over 7 turns. The reduced sampling rate of 500 MHz/7 enables increasing the signal to noise performance of ADC and simplified the FPGA programming because of more relaxed timing demands.

In the case of phase drift of machine or phase bunch transients in the fill pattern it is possible to adjust the digital delay for the master clock. So a 5 bit of digital output of FPGA for control delay with 10ps steps is used. The available range of 320 ps (32x10 ps) is large enough to find the peak amplitude of the bunch's signal, as the synchronous phase transient at BESSY II is usually smaller than 200 ps. In addition, information about the bunch-resolved synchronous phase is extracted – see Fig. 2.

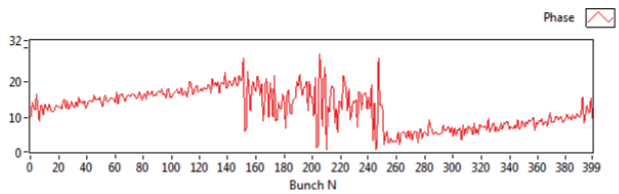

Figure 2: Longitudinal phase in units of 10 ps for a multi bunch fill induced by the gap at BESSY.

However, the additional sampling increases the computed time for the BPM data. The system is implemented in a NI PXIe chassis that includes an FPGA card with ADC, Switch card and a PXI Controller.

EXPERIMENTAL RESULTS

The first prototype of the system has been tested at both machines. The MLS features 80 buckets and is usually operated with a homogeneous fill pattern without gap.

ISBN 978-3-95450-177-9

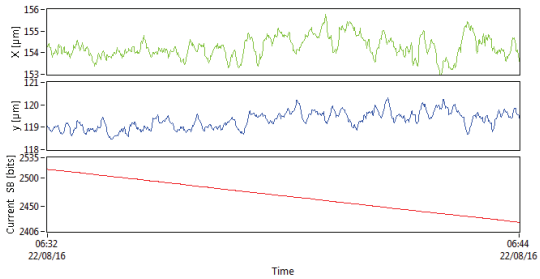

Figure 3: Position of one single bunch at MLS storage ring in decay mode.

For equally populated bunches a spatial resolution of better than 3 µm was achieved as shown in Fig. 3. Displacements of about 10 mm can be generated.

At BESSY II there is a complex fill pattern (bunch train of different intensity) with a gap and five strong SBs, as shown in the upper part of Fig. 4. The positions error is bigger, because of cross talk of strong SB signals to following bunch signals in the storage ring. This is the worst case for the BPM System. However, a spatial resolution of better than 100 µm for all fill bunches in the storage ring at BESSY is achieved – see Fig. 4 lower part.

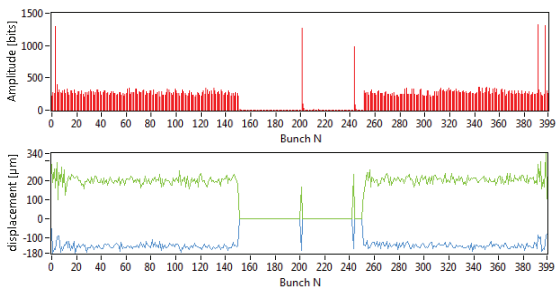

Figure 4: Fillpattern (over) and positions (under) of all filling bunches at BESSY II storage ring.

The first suprising result for orbit separation was achieved during low alpha operation of BESSY II. A significant displacement was observed for one individual bunch, which as intentionally excited for pseudo single bunch applications (PPRE-bunch) [4]. The data acquired by the system is shown in Fig. 5, while the excited bunch is depicted in red with a measured displacement of about 200 µm with respect to the reference orbit.

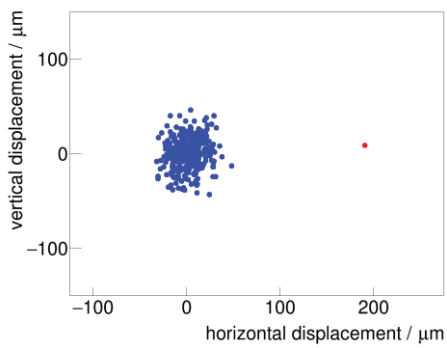

Figure 5: Spatial separation of individual bunches (PPRE bunch is marked in red]) in low alpha mode at BESSY II.

This phenomenon was later verified with other diagnostics and is in agreement with the expectations from beam dynamics.

A second experiment was performed during operation with resonance island buckets at both rings [5,6]. In order to estimate the coordinates of the transverse resonance island buckets only small change of the LabVIEW program is needed. For example of 3 horizontal islands it will be used the samples from 7*3 turns for estimate the coordinates X and Y for each islands. As if we have a 3 times "bigger" ring.

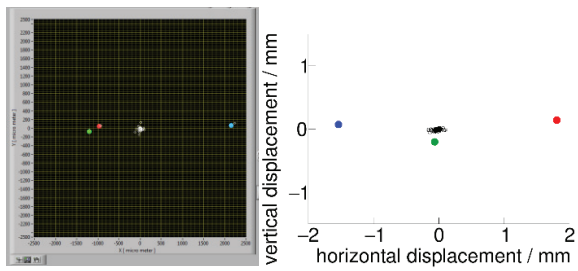

Figure 6: Orbit separation with 3 islands mode at BESSY II (left) and MLS (right). Both machines were operated with a homogenous fill pattern in the core beam, where one bunch was transferred to a single island [5]. The displacement of the stable, closed orbit of the island bucket was measured for the first turn (red), the second turn (green) and the third turn (blue).

Figure 6 shows the measured beam position during island bucket operation. A homogeneous fill pattern was used, where one bunch was repopulated to a single island bucket [5].

SUMMARY AND OUTLOOK

The availability to measure of BPM data of each bunch in the storage ring allows a better understanding of beam physics in the storage ring and can be used for multi beam operation in the future. The using of commercial card from NI with ADCs + FPGAs meets all technical requirements of the BPM electronics. The combination of the 4 good equalized analog BPM signals from pickups in the vacuum chamber and RF switch with high isolations give the opportunity create very good and stable analog RF signal for the BPM detector. In the card with 2 or 4 ADC it is possible to integrate of 2 or 4 BPM system with the same extern sample clocks. It reduces the costs for one BPM station and enables other interesting physical measurements.

REFERENCES

[1] A. Jankowiak *et al.* editors, "BESSY VSR – Technical Design Study", Helmholtz-Zentrum Berlin, 2015.

[2] J. Feikes *et al.*, "Metrology Light Source: The first electron storage ring optimzed for generating coherent THz radiation", 2009.

ISBN 978-3-95450-177-9

[3] F.Falkenstern, *et al.*, "BunchVIEW", *DIPAC'09*, Basel, Switzerland, 2009.

[4] K.Holldack, *et al.*, "Single Bunch X-Ray Pulses On Demand From A Multi-Bunch Synchrotron Radiation Source", Nature Communications, 2014.

[5] M. Ries *et al.*, "Transverse Resonance Island Buckets at the MLS and BESSY", *IPAC2015*, Richmond, VA, USA.

[6] P. Goslawski *et al.,* "Resonance Island Experiments at BESSY II for User Applications", *IPAC2016,* Busan, Korea.

ISBN 978-3-95450-177-9

CERN PS BOOSTER TRANSVERSE DAMPER: 10 kHZ - 200 MHZ RADIATION TOLERANT AMPLIFIER FOR CAPACITIVE PU SIGNAL CONDITIONING

A. Meoli*, A. Blas, R. Louwerse, CERN, Geneva, Switzerland

Abstract

After connection to the LINAC4, the beam intensity in the PS Booster is expected to double and thus, an upgrade of the head electronics of the transverse feedback BPM is necessary. In order to cover the beam spectrum for an effective transverse damping, the pickup (PU) signal should have a large bandwidth on both the low and high frequency sides. Furthermore, in order to extend the natural low frequency cut-off from 6 MHz (50 Ω load) down to the required 10 kHz, with no modification of the existing PUs, a high impedance signal treatment is required. The electronic parts should withstand the radiation dose received during at least a year of service. This constraint implies the installation of the amplifier at a remote location. A solution was found inspired by the technique of oscilloscopes' high impedance probes that mitigates the effect of transmission line mismatch using a lossy coaxial cable with an appropriate passive circuitry. A new large bandwidth, radiation tolerant amplifier has been designed. The system requirements, the analysis, the measurements with the present PUs, the design of the amplifier and the experimental results are described in this contribution.

INTRODUCTION

New pick-up (PU) head amplifiers are needed in the CERN PSB (Proton Synchrotron Booster) for the specific needs of the transverse feedback (TFB) system. This latter feedback was installed in order to damp transverse instability of the beam and it is fully operational with the present beam as injected from the LINAC2 (linear accelerator).

As shown in the Table 1, in 2018 a higher beam intensity (factor 2.5 increase) is expected from the new LINAC4. This will mean a higher voltage on the beam position pick-up installed in the ring and a potential saturation or destruction of the head amplifiers presently installed.

The beam spectrum, as sensed by the beam PUs, is populated at the harmonics of the revolution frequency and at so-called betatron side bands (amplitude modulation) around the revolution lines. The transverse betatron motion is inherently due to the architecture of a synchrotron where the beam experiences a certain number of transverse oscillations at each turn (revolution). This number of oscillations is called the tune and it is a non-integer value (Q.q) with a fractional part q. The side-bands observed in the transverse error signal, calculated as the difference of signals from two opposite pick-up up electrodes of a given H or V plane, are located $q{\cdot}f_{\mathrm{rev}}$ apart from each of the revolution harmonics. f_{rev} is the beam revolution frequency. With minimum values of $q = 0.1$ and $f_{\mathrm{rev}} = 1$ MHz, the lowest frequency betatron band is located at 100 kHz.

In order to have a good damping rate at 100 kHz, the phase error at this frequency should be minimal; this is why a low-frequency −3 dB cut-off pole is requested at 10 kHz. On the higher end of the spectrum, the limit is mainly technological. The head amplifier is required to have the widest possible bandwidth considering the potential high frequency instabilities. Nevertheless, our present limited knowledge of the machine impedance does not allow for precise specifications in that direction, so we are aiming at amplifiers having a bandwidth equivalent to what the PU itself can supply.

Table 1: CERN PSB Machine Parameters with LINAC4

Proton kinetic energy, E_{k}	160 MeV → 2 GeV
Velocity factor, β	0.533 → 0.948
Revolution frequency, f_{rev}	1 MHz → 1.8 MHz
Maximum protons per bunch, N_{p}	$2.5 \cdot 10^{13}$ ppb
Minimum bunch length, 4σ	≈150 ns

PICK-UP

The pick-up is using 4 conductive plates engraved on the inner surface of a ceramic tube inside which the beam will flow. This ceramic tube is enshrined inside a cylindrical stainless steel tube. The capacitance between each plate of the PU and its grounded support is measured to be around 630 pF. Under the presence of beam, the PU plate can be represented as a current generator [1] feeding the electrode capacitance in parallel with the monitoring circuit load.

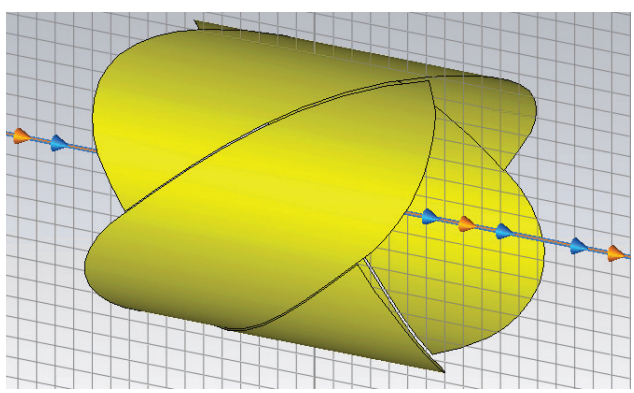

Figure 1: CST PU Model.

* alessandro.meoli@cern.ch

ISBN 978-3-95450-177-9

PU Bandwidth Estimation

The lowest cut-off (high-pass) frequency of the pickup, depends on its load impedance. On the high frequency side, the bandwidth is more difficult to predict. The bandwidth depends on the detailed dimensions and impedances of the setup together with the beam velocity (β).

A practical way to measure the PU response is to use the so-called stretched wire technique that reproduces a TEM field [2] representing, with enough precision, an ultra-relativistic beam ($\beta \approx 1$). A conductive wire is placed inside the pick-up along the supposed beam trajectory, and is fed by a swept sine-wave from a Vector Network Analyzer (VNA) as shown in Figure 2. The induced signal is taken from the PU electrode to the 50 Ω measurement port of the VNA.

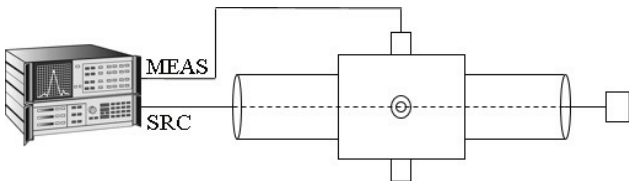

Figure 2: Test bench set-up.

In this measurement one gets the amplitude and phase response of the PU. Both parameters are important, but the phase is most critical as the PU is embedded in a feedback loop where a total 90° phase shift corresponds to a lack of damping and 180° to an unstable behaviour. From the phase response with respect to frequency, the pure delay contribution can be cancelled in order to focus on the non-linear phase error that should be within ±45°.

The PU has also been simulated with a numeric solver (CST studio [3]) using a simplified model. As shown in Figure 3, the PU gain is flat and identical on both the measurement and simulation up to 220 MHz and the measured non-linear phase is within the ±45° boundaries up to 320 MHz when $\beta = 1$.

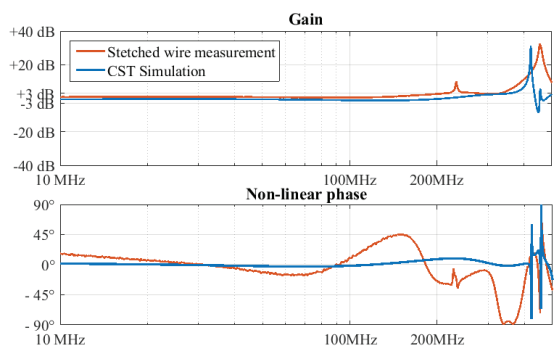

Figure 3: PU frequency response.

PU Signal Amplitude Estimation

Taking into account a high impedance loading in order to limit the natural differentiating behaviour of the PU, one can assume within the obtained bandwidth that a centred beam will induce a voltage [4]:

$$V_{\mathrm{PU}}(t) = \frac{1}{\beta c C} \cdot \frac{A}{2\pi r} \cdot I_{\mathrm{beam}}(t) \qquad (1)$$

Where V_{PU} is the voltage on the PU electrode, β is the velocity beam factor, c is the speed of light, C is the electrode capacitance, r is the beam pipe radius, A is the PU electrode surface and I_{beam} is the beam current.

Table 2: Signal Amplitude Estimations

Beam parameters	Radial offset	V_{PU}
4σ=150 ns,	0 mm	≈25 V_{pp}
$N_p = 2.5 \cdot 10^{13}$ ppb	10 mm	≈30 V_{pp}
	80 mm	≈80 V_{pp}

The PU sensitivity (defined as the variation of the difference signal of two opposite electrodes, due to a beam transverse displacement) has been measured using the stretched wire technique and has been found to be ≈0.2 dB/mm. This value has been used in Figure 4 to estimate the voltage on one PU electrode depending on the beam position expressed in polar coordinates. The radius is the distance from the centre trajectory and the angle is expressed with respect to the considered electrode azimuth.

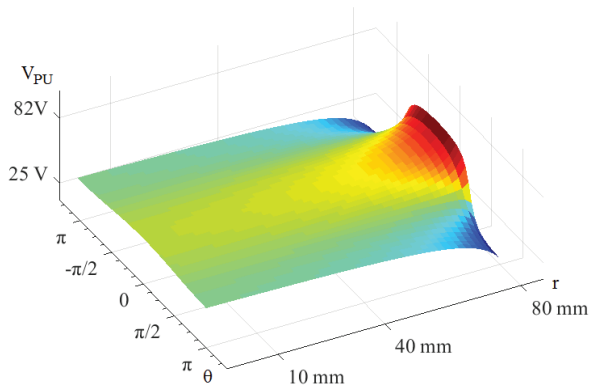

Figure 4: PU's electrode signal amplitude estimation.

As shown in the Figure 5, up to a 20 mm beam position offset the PU response was measured to be linear.

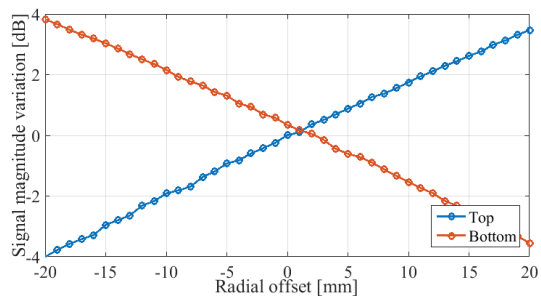

Figure 5: PU Sensitivity.

ISBN 978-3-95450-177-9

RADIATION CONSTRAINTS

The signal from the head amplifier is essential for the TFB system. As such it is an essential part as no high intensity beams (above $4 \cdot 10^{12}$ charges per bunch) can be accelerated without it. In order to extend the electronics lifetime, it was chosen to place it at a reasonable distance from the beam pipe as it is the main source of harmful radiation. The dose decreases exponentially with the distance. At the selected amplifier's location, the radiation dose has been measured with the present accelerated beam. The measured values, together with those estimated for a doubling of the intensity, are reported in table 3.

Table 3: Average Dose Measured and Estimated

Beam intensity	Average dose
$1 \cdot 10^{13}$ ppb	≈3.5 Gy/year
$2.5 \cdot 10^{13}$ ppb	≈ 8 Gy/year

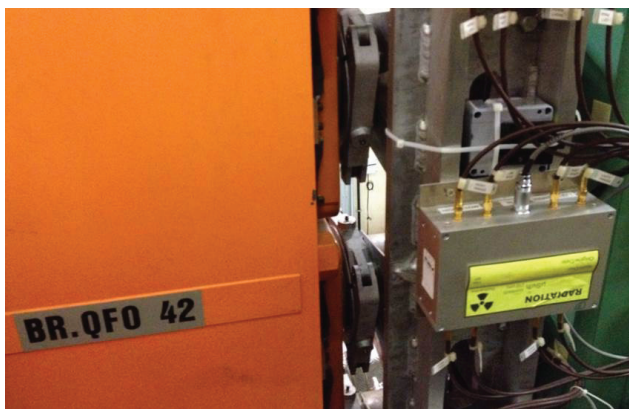

Figure 6: Dosimeter and electronics location.

HEAD ELECTRONICS

As the Head amplifier ends up being distant from the PU connector, a transmission line needs to connect both parts. A one-meter line was found to be sufficient in terms of length. To match the load impedance requirements from the PU perspective, the line must present a high impedance at low frequencies. A lossless coaxial cable terminated with a high unmatched impedance would cause standing waves. To keep a good signal integrity it was chosen to benefit from the design used in oscilloscope probes. This approach is also used in the CERN SPS [5]. This technique is using a lossy coaxial line and a passive network on both ends [6] that allow covering a very large bandwidth with a high perceived impedance.

The high impedance is beneficial in terms of bandwidth, however it may cause a problem when electrons from secondary emissions hit the electrodes, causing an offset signal. As this offset value will depend on the impedance value, a shunt resistive potentiometer will be added to possibly lower the input impedance of the probe as empirically needed.

Table 4: Lossy Cable Characteristics

Resistance, R	210 Ω/m
Inductance, L	0.6 μH/m
Capacitance, C	33 pF/m

Figure 7 depicts the details of the passive networks on both ends of the lossy transmission line.

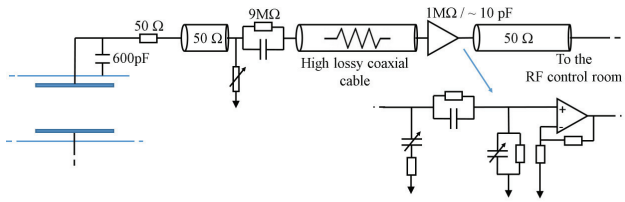

Figure 7: Head amplifier topology.

The designed amplifier setup reaches all the project requirements as can be observed in Figure 8. The frequency response is flat (±3 dB) up to 200 MHz and the non-linear phase error is smaller than ±6°.

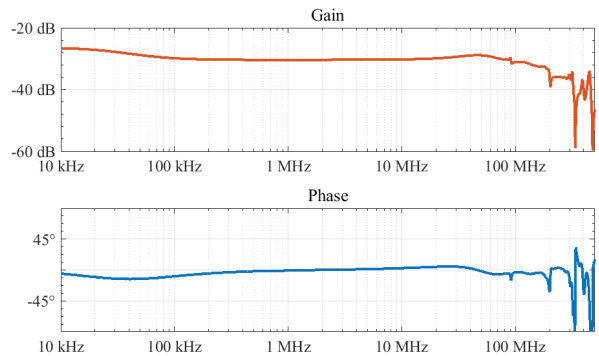

Figure 8: Head amplifier setup frequency response.

In order to increase the tolerance to radiation, the number of active components has been reduced and passive components without PTFE or PVC have been selected. Active components widely known and tested have been used and for the unknown ones a validation test has been planned. In a radioactive environment, single event upsets can be encountered that result in a higher current demand from active components and may cause a thermal damage. In order to avoid such a destruction, current limiting components (polymeric positive temperature coefficient devices) have been installed in different critical paths. These components act as auto-resettable fuses.

To avoid premature replacing and to change the boards at the correct timing, a dosimeter on board is under implementation.

The final validation at the component level is planned for the end of September 2016 and the installation in the machine for the long shut-down 2 (LS2) in 2018.

ISBN 978-3-95450-177-9

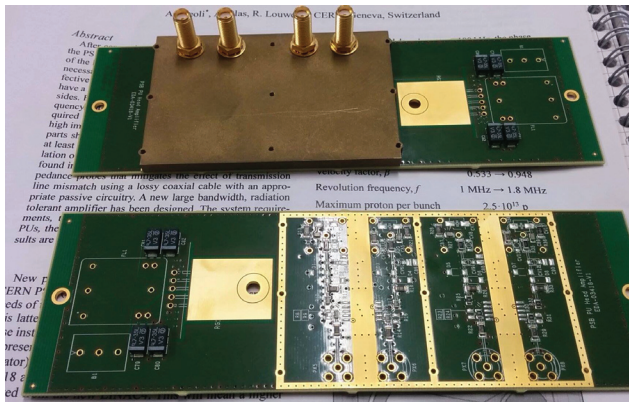

Figure 9: Prototypes boards.

CONCLUSION

A head amplifier setup has been designed to measure the beam position in the CERN PSB even when loaded with the maximum beam intensity expected after the PSB connection to LINAC 4. Its bandwidth extends from 10 kHz to 200 MHz thanks, at the low frequency end, to a passive probe setup as used in commercial oscilloscopes, and on the high frequency side, to high frequency commercial operational amplifiers.

The distance from PU to amplifier allowed by the high impedance probe allows for the reduction of radiation doses. Selected radiation hardening components should further extend the circuit lifetime.

ACKNOWLEDGEMENT

The authors wish to acknowledge W. Hofle, H. Damerau, L. Soby and J. Belleman for helpful discussions and constructive comments, F.G. Guillot-Vignot for the assistance and the numerous tips concerning the stretched wire measurements, S. Danzeca for the radiation level measurements and components tests, P. Vulliez and TS-DEM for the PCB design and manufacturing.

REFERENCES

[1] R. E. Shafer, “Beam Position Monitoring”, in *Proc. AIP Conference*, Upton, NY, USA, Oct 1989, paper 212, 26.

[2] A. Argan, L. Palumbo, M.R. Masullo, V.G. Vaccaro, “On the Sands and Rees Measurement Method of the Longitudinal Coupling Impedance”, in *Proc. Particle Accelerator Conference*, New York, USA, 1999, Volume 3, 1599.

[3] CST Studio, `http://www.cst.com`

[4] P. Forck, P. Kowina and D. Liakin, “Beam Position Monitors” in *CAS, CERN Accelerator School*, Dourdan, France, 2008, pp. 187.

[5] W. Hofle, R. Louwerse, private communication, Jan. 2016.

[6] J. Weber, *Oscilloscope Probe Circuits*. Beaverton, OR, USA: Tektronix, 1969.

ISBN 978-3-95450-177-9

SIMULATION OF BUNCH LENGTH AND VELOCITY DEPENDENCE OF BUTTON BPMS FOR LINACS USING CST PARTICLE STUDIO®

M. Almalki* KACST, Riyadh, Saudi Arabia
P. Forck, T. Sieber, R. Singh, GSI, Darmstadt, Germany

Abstract

At non-relativistic velocities at a proton LINAC, the electromagnetic field generated by the beam has a significant longitudinal component, and thus the time evolution of the signal coupled to the BPM electrodes depends on bunch length and beam velocity. Extensive simulations with the electromagnetic simulation tool CST Studio® were executed to investigate the dependence of the induced BPM signal on different bunch lengths and velocities. Related to the application, the simulations are executed for the button BPM arrangement as foreseen for the FAIR Proton LINAC. These investigations provide the required inputs for the BPM system and its related technical layout such as analogue bandwidth and signal processing electronics. For the BPM electronics, it is important to estimate the contribution of the harmonic used for the data processing. Additionally, the analogue bandwidth of the BPM system is determined from studying the output signal of the button BPM as a function of bunch length at different beam velocities. This contribution presents the results of the simulations and comments on general findings relevant for a BPM layout and the operation of a hadron LINAC.

INTRODUCTION

The electromagnetic fields generated by a beam and thus the time evolution of the signal coupled out by a pickup depend on beam velocity. In the limit of relativistic velocities, the generated beam fields are pure transverse electric and magnetic known as Transverse Electric and Magnetic (TEM) mode. A TEM mode has an electric and magnetic field vector perpendicular to the propagation direction. Thus, the electric field is longitudinally concentrated above and below the beam [1]. For moderate beam velocities $\beta > 0.9$ the resulting field can be also approximated to first order by TEM field distribution and the image current mirrors the same time behavior as the beam is traveling. At low beam velocities $\beta < 0.5$, the electromagnetic field is no longer a TEM wave [2]. In this regime the power coupled out by the pickup is much lower than the power carried by the beam due to the reduction in the coupling of high-frequency Fourier components.

On the other hand, it is important to keep in mind that the accurate determination of the bunch length is not trivial. The reason is the presence of the advanced Coulomb-field of the moving bunches, in particular for low $\beta < 0.5$ range [3]. The geometric length of the bunch Δz along the $z-$axis depends on the particle velocity β which can be calculated from [3]

$$\Delta z = \beta c \Delta t_b \tag{1}$$

where $\Delta t_b = 2\sigma_b$. The reason is that the derivative of a Gaussian Function has the maximum and the minimum exactly at $\pm\sigma$.

CST STUDIO® SIMULATIONS

The simulations have been carried out using the CST Particle Studio Wakefield solver [4] to study bunch length and velocity dependence of button BPMs for LINACs. The Wakefield solver is the most appropriate for studying the BPM response and the simulations are driven by a bunch of charged particles in the time domain. A 3D model of a BPM of four button pickups has been created in the CST Particle Studio® as shown in Figs. 1.

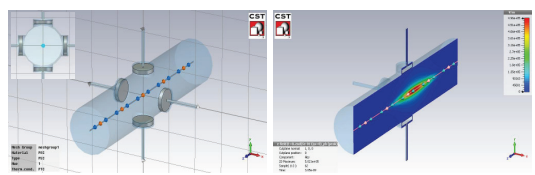

Figure 1: Left: A 3D model of the pick-up monitor as simulated in CST Particle Studio®. Right: The absolute value of the electric field of a bunch of $\sigma = 100$ ps long and $\beta = 0.37$

The wakefield has been simulated up to a 150 *mm* length along the beam coordinate. The excitation source is defined by a Gaussian-shaped longitudinal charge distribution with beam bunch charge of 1 nC in the z direction. The pickup response, expressed as the output signal in time and frequency domains, is obtained for each simulation run reflecting the pickup's interaction with the beam. The output voltages convergence versus mesh size has been investigated prior to utilizing the results. The convergence has been examined at three beam velocity $\beta = 0.08$, 0.27 and 0.37 with a bunch length chosen to be 150 ps. Figs. 2 demonstrates the results of the Wakefield solver at different mesh settings. The results show a solid convergence of the output signals and frequency spectrums in the interesting frequency range for $\beta = 0.08$, 0.27 and 0.37. A visible difference is only observed in the frequency spectrum for $\beta = 0.08$ with the mesh setting of 150000.

SIMULATIONS AND RESULTS

The CST simulations have been carried out to investigate the bunch length characteristics for the interesting dynamic range in proton LINAC which assumed to be between 50 to

* mmmalki@kacst.edu.sa

ISBN 978-3-95450-177-9

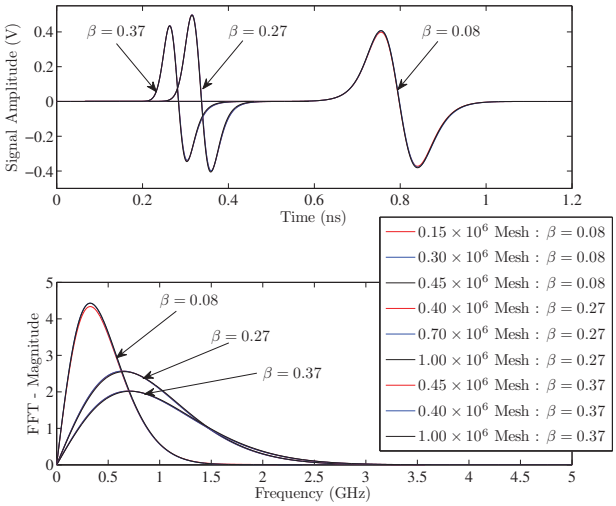

Figure 2: BPM output voltage from a single port in time (up) and frequency (down) domains versus mesh size. The beam parameter are β = 0.08, 0.27 and 0.37, σ = 150 ps, 1 nC bunch charge.

700 ps [5,6] . The length of the signal produced by the pickup Δt_s is compared with bunch length $\Delta t_b = 2\sigma_b$ at different beam velocities β = 0.08, 0.27 and 0.37, correspond to E = 3 MeV, 30 MeV and 70 MeV, respectively. A centered beam is used in the simulations and the bunch length is varied. A button pickup of 14 mm diameter was used and beam pipe is chosen to be 30 mm. The span of simulated bunch length starts from σ_b = 30 up to 960 ps. The first set of results are shown in Figs. 3, 4 and 5 illustrating the pickup signals in the time domain (left) and the corresponding Fourier transformation in the frequency domain (right) as a function of the bunch length σ_b.

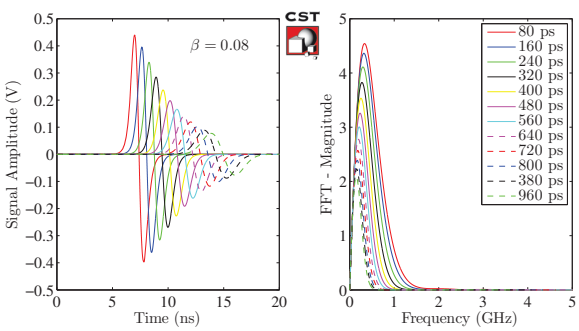

Figure 3: The legend shows the bunch length σ_b and the plotted signals represent output voltage from a single port in time (left) and frequency (right) domains for β = 0.08.

One can observe the response of the pickup signal σ_s to the change in bunch length. For low β beam the amplitude of the output signal is lower and the signal is longer. The reason is that the electric field components are less perpendicular to the beam direction as for higher values of β as discussed in [2] for a moving charge. Fig. 6 shows the change in

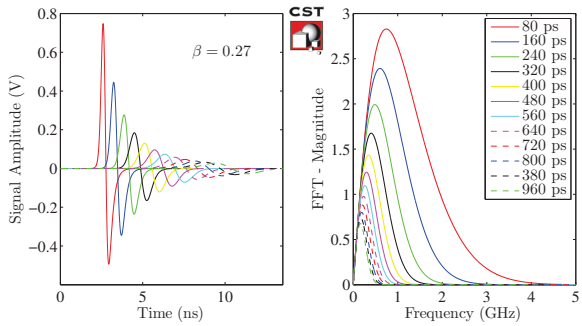

Figure 4: The legend shows the bunch length σ_b and the plotted signals represent output voltage from a single port in time (left) and frequency (right) domains for β = 0.27.

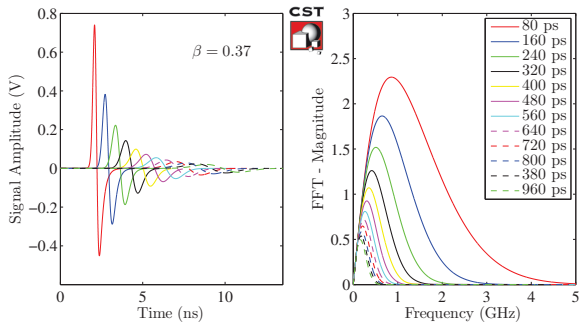

Figure 5: The legend shows the bunch length σ_b and the plotted signals represent output voltage from a single port in time (left) and frequency (right) domains for β = 0.37.

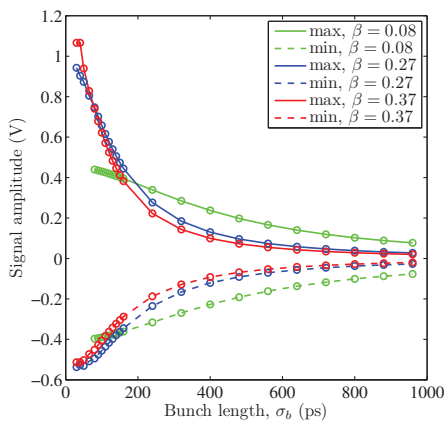

Figure 6: The change in the maximum and the minimum values of the pickup signal versus bunch length σ_b.

the signal maximum and the signal minimum values for different β values as a function of bunch length σ_b, which summarizes the output signal behaviour in Figs. 3, 4 and 5. One can notice that the maximum of the pickup signals decreases as a function of the bunch length as expected from some theoretical models [1]. For short bunches (σ_b < 300 ps) and higher beam velocities (β = 0.27 and 0.37) the maximum and minimum (in the negative side) values of the pickup signal decrease much faster than for the low

ISBN 978-3-95450-177-9

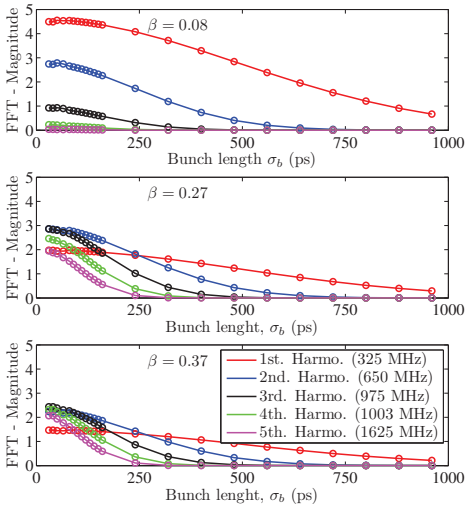

Figure 7: The Fourier components of the pickup signals at five harmonics of the bunching frequency versus bunch length.

β value (β = 0.08). For longer bunches (σ_b > 600 ps) the proportional decrease in the maximum and minimum values is still valid but the change is not significant. The signal amplitudes expressed in the Fourier components as a function of bunch length is depicted in Fig. 7 for five harmonics. The first observation is that for a short bunch lengths of σ_b < 200 ps the pickup signal contains a high amplitude value of higher harmonics of the beam-bunching frequency in comparison to the longer bunches. For β = 0.08, it is noticeable that the first harmonic is always dominant. The major contribution in the spectrum comes from the first two harmonics while the contribution is very weak for higher harmonics, especially for bunches longer than σ_b > 150 ps. As the beam becomes faster and the bunch is short σ_b < 200 ps the frequency spectrum is shifted so that the contribution of the 1st harmonics is smaller than the followings harmonics (2nd, 3rd and 4th harmonics). Based on Fig. 7, the 1st and the 2nd harmonics are present always in the spectrums with sufficient strength and both can be used for the data signal processing. However, the signal information should be obtained from the 2nd harmonic harmonic in order to suppress the rf-leakage contribution from the nearby CH-cavity to the BPM intertank.

A depictive aspect in this investigation is shown in Fig. 8. The bunch length Δt_b is characterized by relating bunch length with the time difference between the maximum and the minimum values of the pickup signal Δt_s. It shows a linear proportional relationship between the pickup signal and bunch length. This proportionality goes to a certain limit depending on β value. Below that limit there is no more change in the output signal length Δt_s so that the pickup signal remains constant as the bunch length further decreases. Knowing these limits and the proportionality range for each β value are useful for estimating bunch length from the output signal shape. For example, for β = 0.27 the pickup signal of length σ_s = 526 ps leads to a bunch length of σ_b = 480 ps. The linear limit was calculated for each β case by applying a linear fit on the curve from σ_b = 560 ps for both β = 0.27 and 0.37 and σ_b = 720 for β = 0.08. The slope of the curves a_1 are 0.89, 95 and 0.96 for β = 0,08, 0.27 and 0.37, respectively.

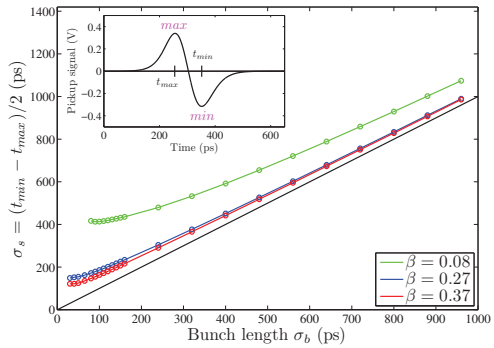

Figure 8: The relationship between the bunch length σ_b and the length of the pickup signal σ_s extracted from the time difference between the minimum and the maximum values of the pickup signal.

CONCLUSION

The CST simulations were executed to investigate the dependence of the induced BPM signal on different bunch lengths and beam velocities. These investigations provide useful inputs for the BPM system and its related technical layout. For the technical layout of the electronics, the signal amplitudes expressed in the Fourier components showed that the 2nd harmonic used for the signal processing is present always in the spectrums with sufficient strength. The bunch length shows a linear proportional relationship with the output pickup signal. This proportionality goes down to a certain limit depending on β value. These limits and the proportionality constants for each β value are useful for estimating bunch length from the output signal shape and to design the processing analogue electronics for the BPM system.

REFERENCES

[1] E. Shafer, "Beam Position Monitor Sensitivity for Low-β Beams", Beam Instrumentation Workshop, vol. 319, no. 1, pp. 303-308. AIP Publishing, 1994.

[2] P. Forck, P. Kowina, D. Liakin. Beam Position Monitors?. CERN accelerator school on beam diagnostics (2008). CERN Yellow Report CERN-2009-005, pp.187- 228, 2009.

[3] P. Strehl. Beam Instrumentation and Diagnostics, "Particle Acceleration and Detection", Springer, Berlin, 2006.

[4] Computer Simulation Technologies AG, `https://www.cst.com/`

[5] R. Brodhage. "Particle distribution with space charge using LORASAR code", private communication, 2013.

[6] M. Almalki, "Beam position monitor system for pro- ton LINAC for FAIR", PhD thesis, IAP University of Frankfurt, 2015.

ISBN 978-3-95450-177-9

DEVELOPMENT STATUS OF A STABLE BPM SYSTEM FOR THE SPring-8 UPGRADE

H. Maesaka†, RIKEN SPring-8 Center, Kouto, Sayo, Hyogo, 679-5148, Japan
H. Dewa, T. Fujita, M. Masaki, S. Takano[1],
Japan Synchrotron Radiation Research Institute, Kouto, Sayo, Hyogo, 679-5198, Japan
[1]also at RIKEN SPring-8 Center, Kouto, Sayo, Hyogo, 679-5148, Japan

Abstract

We are developing a stable and precise BPM system for the low-emittance upgrade of SPring-8. Key requirements for the BPM system are: 1) long-term stability of the radiated photon beam direction well within the intrinsic photon divergence, 2) single-pass resolution better than 100 μm for a 100 pC single-bunch for first-turn steering in the beam commissioning, and 3) BPM center accuracy better than 100 μm rms with respect to an adjacent quadrupole to achieve the design performance of the upgraded storage ring. Based on these requirements, a button-type BPM head and a readout electronics are being developed. Some prototypes of the BPM head were manufactured and the machining accuracy was confirmed to be sufficient. For the readout electronics, a MTCA.4-based system and an upgrade of a commercial BPM electronics are under study. Since radiation damage to the signal cable of the present BPM system was found to be a cause of humidity-dependent drift of BPM offset, measures against the radiation damage are considered for the new BPM cable. The preparation of a beam test of the new BPM system is in progress to confirm the overall performance.

INTRODUCTION

A low-emittance upgrade of SPring-8 was recently proposed in order to provide much more brilliant x-rays to experimental users [1]. The natural emittance of an electron beam after the upgrade is estimated to be 140 pm rad without any radiation damping by insertion devices (IDs), while the emittance of the present SPring-8 storage ring is 2.4 nm rad. The emittance can be further reduced to 100 pm rad by operating IDs thanks to radiation damping. This low emittance value is realized by using 5-bend achromat lattice and by reducing the beam energy from 8 GeV to 6 GeV. As a result, the brilliance of x-ray radiation is expected to be more than one orders of magnitude higher than the present SPring-8.

Since the horizontal beam size becomes smaller, the stability of the beam position should also be improved. The beam size at the center of an ID is approximately 25×5 μm^2 rms. Therefore, the beam position stability is required to be 1 μm level. Although the vertical beam size is comparable to the present SPring-8, the present BPM system has some drift problems of more than 10 μm [2]. Thus, we plan to replace the present BPM system with new one, which goes for the stability of 1 μm level.

Since the upgraded SPring-8 can provide brilliant x-rays with a small source size, small divergence and a high coherent flux, the stability of the photon beam axis is the most important. The upgraded SPring-8, for example, enables a direct nano-focusing scheme wherein primary x-ray radiation from an undulator can be directly focused to a nanometer spot without any secondary virtual sources by using downstream apertures [3]. In this beamline, the stability of the photon beam axis is critical and it should be well within the intrinsic photon divergence. The required stabilities are sub-μm and sub-μrad for the photon beam position and direction, respectively. Consequently, a stable electron BPM and a photon BPM are necessary [4].

In addition to the stability issue, the BPM system is indispensable to the beam commissioning of the upgraded SPring-8. For the first-turn beam steering, single-pass BPM measurements with high accuracy and high resolution (100 μm rms) are demanded, since the dynamic aperture becomes significantly narrower (< 10 mm) than the present storage ring [1]. After the success of beam storage, the beam orbit is adjusted to the center of each multi-pole magnets in order to achieve the design performance of the upgraded SPring-8. Thus, a BPM system with high single-pass resolution (100 μm rms) and high position accuracy (10 μm rms) is necessary.

In this article, we describe an outline of the BPM system for the SPring-8 upgrade, such as the development status of a BPM head and a readout electronics, and the improvement of the BPM stability. The design of the BPM head is detailed in Ref. [5].

BPM SYSTEM FOR THE SPring-8 UPGRADE

BPM System Overview

The SPring-8 storage ring consists of 48 unit cells and each cell is equipped with 7 BPMs after the upgrade. In total, 336 BPMs will be utilized for the machine operation. The BPM electrode was selected to be a button type [5]. The readout electronics for each BPM is designed to have measurement functions of both closed-orbit distortions (COD) and single-pass (SP) trajectories with sufficient precision and accuracy.

Required Performance

As mentioned in the introduction, the BPM system for the SPring-8 upgrade should have sufficient stability, high-resolution and high-accuracy. Main specifications of the BPM system are summarized in Table 1.

† maesaka@spring8.or.jp

ISBN 978-3-95450-177-9

Table 1: Main Specifications of the BPM System

COD measurement resolution	0.1 μm rms (100 mA, 1 kHz bandwidth)
COD measurement stability	5 μm maximum (1 month)
COD measurement accuracy after beam-based alignment	10 μm rms
SP measurement resolution	100 μm rms (100 pC single-bunch)
SP measurement accuracy with respect to an adjacent Q-magnet	100 μm rms (±200 μm maximum)

The most stringent requirement for a COD measurement is sub-μm position stability and resolution coming from a direct nano-focusing beamline. Therefore, the resolution is set to 0.1 μm rms at 1 kHz bandwidth. Although the stability of 5 μm maximum is not sufficient for a direct nano-focusing beamline, it is still challenging and is enough for most of the conventional beamlines. Nevertheless, we plan to pursue the improvement of the photon beam stability by developing a photon BPM.

The displacement of the electron beam from the field center of a multipole magnet should be 10 μm level to achieve the design performance [1]. This requirement comes from the alignment tolerance of multipole magnets (a few 10 μm). Therefore, the offset of the BPM center from an adjacent quadrupole magnet should be measured by a beam-based alignment (BBA) with 10 μm accuracy.

In the early stage of the beam commissioning, a SP trajectory measurement is necessary to guide an injected electron beam throughout the storage ring. The SP resolution is required to be less than 100 μm rms for an injected single bunch of 100 pC charge [1]. Furthermore, the displacement of a BPM electric center with the field center of an adjacent quadrupole magnet is demanded to be within 100 μm rms and ±200 μm maximum [1], in order to reduce any unwanted kick from multipole magnets.

BPM Head

Figure 1 shows a schematic drawing of the BPM head and the button electrode. The beam duct has 20 mm-wide flat-tops and the vertical aperture is 16 mm. Two button electrodes are attached on each flat-top with a horizontal span of 12 mm. The button diameter is 7 mm, which is large enough to obtain required signal intensity for the SP resolution [5]. In order to reduce the error on the electric center position, the machining accuracy is set to a few 10 μm for both the electrode and its lodging hole in the BPM head. The displacement error on the electric center with respect to the reference plane is estimated to be less than 50 μm.

The material of the button electrode and the central pin was selected to be molybdenum, since the material should be non-magnetic to avoid any field interference with adjacent magnets and highly conductive to minimize trapped-mode heating by ohmic losses. The beam duct is made of stainless steel, which is the same material with the other vacuum chambers. The heat input from the 100 mA stored beam was estimated to be 1.1 W maximum [5], which is small enough to suppress the mechanical distortion within a few μm. The BPM connector was selected to be a reverse-polarity SMA jack, because the spring strength of the inner socket of a normal female SMA connector might be lost after a thermal process for brazing the ceramic and the metals of the button electrode.

The BPM head is supported from the same girder as magnets and vacuum chambers. In this case, the relative position between the BPM head and an adjacent quadrupole magnet is not changed after a realignment of the girder. The displacement between the reference planes of a BPM head and a quadrupole magnet is measured by a laser tracker survey within 50 μm rms accuracy. The total error on the BPM electric center position is approximately 70 μm rms by taking a quadratic sum of the machining error and the survey error. There remains a margin in the BPM alignment error and it is reserved for the calibration error of the readout electronics etc.

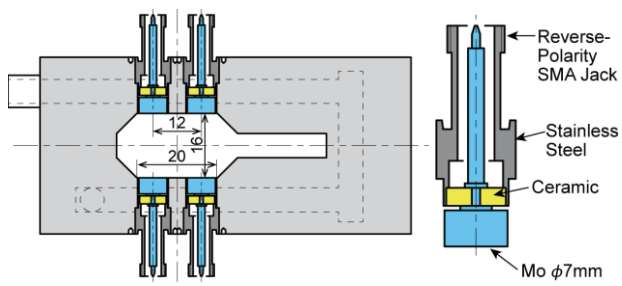

Figure 1: Schematic drawings of the cross-sections of the BPM head (left) and the button electrode (right).

BPM Electronics

We are considering two candidates for the BPM electronics, our original design and the new generation of Libera Brilliance+ [6]. They are developed in parallel and the final decision will be made before the mass-production.

The original design is based on the new digital low-level RF (LLRF) system [7], which utilizes the MTCA.4 standard [8]. A schematic diagram of the BPM electronics is illustrated in Fig. 2. Single-ended signals from 2 BPMs (8 channels in total) are fed into a rear transition module (RTM). The signals are conditioned by band-pass filters, step attenuators and amplifiers, and converted to balanced differential signals. These signals are transferred to an advanced mezzanine card (AMC) and recorded by fast analog-to-digital converters. Since a direct under sampling scheme (~300 MSPS) of a 508 MHz acceleration signal is chosen for the RF detection method of the LLRF system, the same scheme is used for the BPM system. The noise figure of the electronics was estimated to be approximately 14 dB including the power loss of the signal cable (~2 dB). We are considering to use calibration tone, having a slightly shifted frequency from a BPM signal, for the gain calibration of the electronics.

ISBN 978-3-95450-177-9

For Libera Brilliance+, the specification of the position resolution for both SP and COD looks sufficient for our requirement. Therefore, we are considering further improvements of measurement stability. Since the control system of the SPring-8 is MADOCA [9], the control software should be modified to support the MADOCA system.

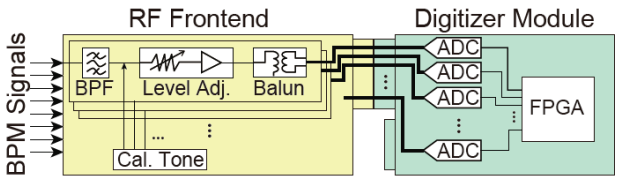

Figure 2: Schematic diagram of the MTCA.4-based BPM electronics. The left half is the RF front end RTM and the right is the digitizer AMC.

DEVELOPMENT STATUS OF THE BPM SYSTEM

BPM Electrode

The design of the BPM electrode has been almost completed [5] and we produced prototype electrodes (Fig. 3). All the total of 24 electrodes manufactured passed a heat cycle test from the room temperature to the baking temperature of 150 ˚C without any vacuum leaks. RF properties and electrical insulation were confirmed to be sufficient. The machining accuracy was also evaluated to be 10 µm level for a precise part and the mechanical strength was checked by a destruction test. Although this first prototype was successfully produced, a copper washer is used at the brazing part. Since copper might be corroded by active gasses generated by radiation, we are trying to produce second prototype without any corrodible metals.

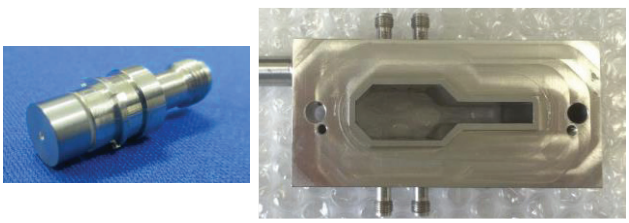

Figure 3: Photographs of a prototype BPM electrode (left) and a prototype BPM block (right).

BPM Block

A prototype of the BPM block was also produced by using prototype electrodes, as shown in Fig. 3 (right). The beam duct was made from stainless steel block bored by wire electric discharging. Since the stainless steel vacuum chamber connected to the BPM has 100 µm-thick copper plating in order to reduce resistive wall impedance, we tried a copper coat of the BPM block. However, it was difficult to manage the accuracy of the inner dimensions of the beam duct with 10 µm level. Since the resistive wall impedance of the BPM block is sufficiently small thanks to its compactness, we chose not to plate copper in the BPM block.

The electrodes were attached to the block by electron beam welding. After the welding, the inner surface of the electrode was slightly pulled out by several 10 µm due to the shrinkage of the welded part. Therefore, the height of the electrode was adjusted at the machining stage by taking the shrinkage into account. As a result, the height of the button surface was controlled within 50 µm.

BPM Electronics

For the BPM electronics based on MTCA.4, we are developing a common AMC digitizer with the digital LLRF system [7], which has 10 AD converters with a 300 MSPS sampling rate and a 16-bit resolution. A general purpose SoC (System-on-Chip) FPGA AMC for fast orbit feedback control is also developed. The digitizer and FPGA AMCs will be delivered in March 2017. The RF frontend RTM is under design and it will be produced in 2017. The other modules such as a CPU module and a MCH (MicroTCA Carrier Hub), are already available.

For Libera, we have been evaluating the performance of the current version of Libera Brilliance+ and we started discussions on the expected improvement of the new generation. An existing BPM head of the present SPring-8 was read out by a Libera Brilliance+ in order to evaluate the position resolution. Although the sensitivity of the present BPM head is different from the new BPM, the result can be scaled to the upgraded SPring-8 by a calculated sensitivity. The SP resolution was obtained to be 50 µm rms for a 100 pC bunch in case of the upgraded SPring-8. This result corresponds to the noise figure of 14 dB including the cable loss, which is comparable to that of the MTCA.4-based design. The COD resolution was less than 0.1 µm rms for 10 kHz throughput data. Thus, both SP and COD resolutions were confirmed to be sufficient.

Signal Cable

Investigations of the drift problem in the present BPM system revealed that one of the most significant causes was radiation damage to signal cables, which gave rise to a humidity-dependent drift [2], as shown in the upper half of Fig. 4. In this figure, we define balance error to evaluate a BPM drift. The beam position can be calculated from 3 electrodes out of 4, and 4 beam position values are obtained from 4 combinations of 3 electrodes. The balance error is defined as the maximum difference among the 4 values.

Chemical analyses of damaged cables revealed that the radiation-damaged insulator of the coaxial cable tends to absorb vapor in the air and the characteristic impedance of the cable becomes sensitive to ambient humidity. Therefore, we replaced the damaged cables and the humidity-dependent drift disappeared, as shown in the lower half of Fig. 4. Thus, we are surveying radiation-resistant coaxial cables and considering radiation shields for the new BPM system.

Beam-based Alignment

In order to precisely obtain the offset of the BPM electric center from the field center of an adjacent quadrupole mag-

ISBN 978-3-95450-177-9

net, we are testing a beam-based alignment (BBA) technique.

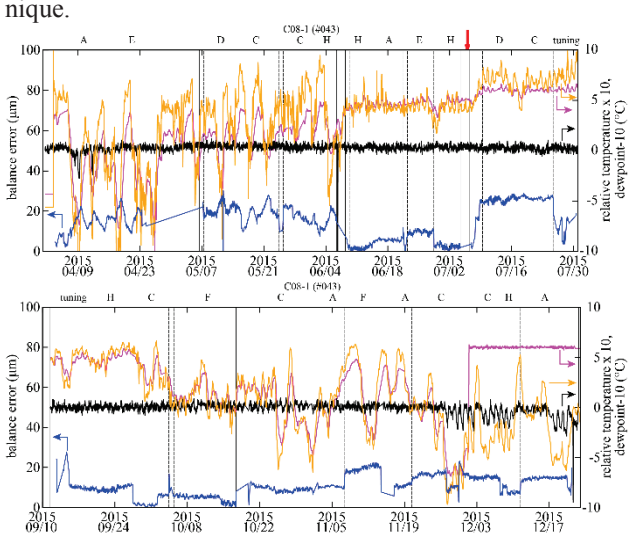

Figure 4: Trend graphs of the balance error of a current BPM (blue lines). The upper figure shows the data before the cable replacement and the lower one is those with new cables. The dew point of the accelerator tunnel (electronics area) is plotted by a magenta (orange) lines. The relative electronics temperature (x10) is shown by black lines.

Figure 5 shows results from a BBA test experiment. The beam position was shifted by generating a local bump orbit and the field strength of an adjacent quadrupole magnet was changed by 1%. Each plot shows a variance of beam position differences for all the BPMs as a function of the height of the bump orbit. The parabolic function was fitted to each data set (solid line). The bottom of the fitted function is the quadrupole magnet center. The reproducibility of the result was 10 μm rms. In the next step, we will confirm the measurement accuracy and optimize the measurement procedure for quick machine tuning.

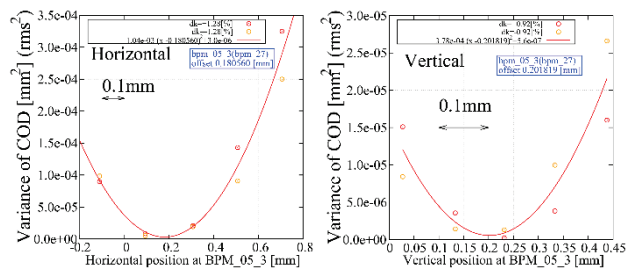

Figure 5: Beam-based alignment data from one of the BPMs. Left and right plots show horizontal and vertical directions, respectively.

Beam Test

We are preparing a beam test setup of the new BPM system in the present SPring-8 and start data taking in this fall. A BPM head with prototype electrodes for the beam test was produced and installed in this summer shutdown. Cables and readout electronics for the upgraded SPring-8 are also evaluated in this test. We will confirm the basic performance of the BPM head, such as signal intensity, waveform and temperature rise, and estimate the long-term stability of the whole BPM system.

SUMMARY

For the low-emittance upgrade of SPring-8, a stable and precise BPM system is necessary. Requirements for the BPM are 5 μm long-term stability and 0.1 μm resolution for COD and high single-pass resolution and accuracy of 100 μm rms. We designed a precise BPM electrode and block to reduce the error on the electric center of the BPM head within 50 μm. Some prototypes of the BPM head were produced and the machining accuracy was confirmed to be sufficient. For the readout electronics, the development of a MTCA.4-based system and the evaluation of Libera Brilliance+ are in progress. Since radiation damage to signal cables was found to be a cause of a humidity-dependent drift, a radiation-hard cable and a radiation shield are under study. A beam-based alignment technique has been tested for the precise orbit tuning with 10 μm rms accuracy with respect to the field center of a quadrupole magnet. We continue the development and perform some beam experiments to complete the BPM system for the SPring-8 upgrade.

ACKNOWLEDGMENT

The authors acknowledge Hiroshi Sumitomo from SPring-8 Service Co., Ltd. for his great efforts in the development of the BBA tool and the data analysis.

REFERENCES

[1] SPring-8-II Conceptual Design Report, Nov. 2014, http://rsc.riken.jp/pdf/SPring-8-II.pdf

[2] T. Fujita, *et al.*, "Long-term Stability of the Beam Position Monitors at SPring-8", in *Proc. IBIC'15*, Melbourne, Australia, Sep. 2015, paper TUPB020, pp. 359-363.

[3] C. T. Schroer and G. H. Falkenberg, "Hard X-ray nanofocusing at low-emittance synchrotron radiation sources", *Journal of Synchrotron Radiation*, vol. 21, Pt. 5, pp. 996-1005, 2014.

[4] H. Maesaka, "Comparison of Beam Diagnostics for 3rd and 4th Generation Ring-based Light Sources", in *Proc. IPAC'15*, Richmond, VA, USA, May 2015, paper THYC1, pp. 3657-3661.

[5] M. Masaki, *et al.*, "Design Optimization of Button-type BPM Electrode for the SPring-8 Upgrade", *presented at IBIC'16*, Barcelona, Spain, Sep. 2016, paper TUPG18, this conference.

[6] Instrumentation Technologies, http://www.i-tech.si

[7] H. Ego, *et al.*, "RF System of the SPring-8 Upgrade Project", *presented at IPAC'16*, Busan, Korea, May 2016, paper MOPMW009, pp. 414-416.

[8] PICMG MicroTCA open standard, https://www.picmg.org/openstandards/microtca/.

[9] R. Tanaka, *et al.*, "Control System of the SPring-8 Storage Ring", *presented at ICALEPCS'95*, Chicago, USA, Oct. 1995, paper W2B-c, p. 201.

ISBN 978-3-95450-177-9

COMMISIONING OF BEAM POSITION AND PHASE MONITORS FOR LIPAc *

I. Podadera †, A. Guirao, D. Jiménez, L. M. Martinez, J. Molla,
A. Soleto, R. Varela, CIEMAT, Madrid, Spain

Abstract

The LIPAc accelerator is a 9 MeV, 125 mA CW deuteron accelerator [1] which aims to validate the technology that will be used in the future IFMIF accelerator. Several types of Beam Position Monitors –BPM's- are placed in each section of the accelerator to ensure a good beam transport and minimize beam losses. LIPAc is presently under installation and commissioning of the second acceleration stage at 5 MeV [2]. In this stage two types of BPM's are used: four striplines to control the position at the Medium Energy Beam Transport line (MEBT), and three striplines to precisely measure the mean beam energy at the Diagnostics Plate. The seven pickups have been installed and assembled in the beamlines after characterization in a wire test bench, and are presently being commissioned in the facility. In addition, the in-house acquisition system has been fully developed at CIEMAT. In this contribution, the results of the beam position monitors characterization, the tests carried out during the assembly and the status of the electronics system are reported.

PICKUP MANUFACTURING

MBPM

Four striplines are installed along the MEBT (Fig. 1) to track the beam from the RFQ to the MEBT. The BPM's chambers are installed in the middle of the combined magnets (quadrupole and two steerers) as seen in Fig 1. This makes the design, installation and assembly quite challenging, due to the very tight space available. In addition, all the materials should be non-magnetic to avoid any perturbance in the quality of the magnetic field.Three vacuum chambers were manufactured: two containing one BPM each, and a longer one containing two BPM's located in consecutive magnets. Compact welded bellows are inserted, shielded inside to protect them to the spray particles of a high CW current hadron accelerator, and welded to rotating flanges. Due to the compact design the fabrication (realized by Vacuum Projects in Spain) was quite complicated. The feedthroughs were very prone to crack due to overheating during TIG welding, although the feedthrough manufacturer supported this technique. After many attempts and empirical studies, laser welding had to be used for the first welding whereas the welding of other pieces in the chamber was kept by TIG. Once each BPM body was fabricated, it was welded to the rest of the vacuum chamber. This was also a challenging process, especially in the last chamber with two BPM's, since the tolerances were quite small. During all the manufacturing process, the machined pieces were metrology controlled, taking especial care to the BPM assembly and the coordinates of the fiducial points with respect to the reference frame. Finally, the chambers underwent an ultrasonic cleaning and a vacuum leak test to verify the tightness for a proper operation in LIPAC.

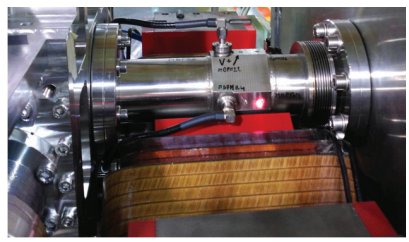

Figure 1: Picture of MBP02 mounted in the MEBT between the poles of the second MEBT magnet.

DBPM

The three units of the Diagnostics Plate BPM (DBPM) have been manufactured and tested (Fig. 2), based in the design presented in [3]. All the units have been manufactured in the CIEMAT workshops. As in the case for the MBPM, metrology was watched along all the procedures. Prior to and after the final welding assembly the unit was measured usign a 3D coordinate machine. Once the assembly was finished several acceptance tests were done. The first one was the test of the vacuum leak of the device. A leak below 10^{-12} mbar·l/s was detected, which is far beyond the requirements for the LIPAc.

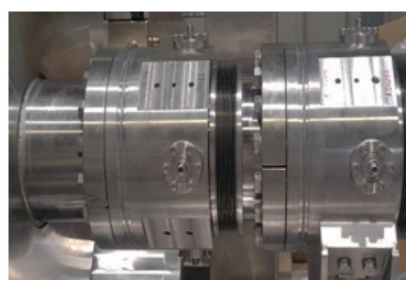

Figure 2: Picture of two of the DBPM's mounted in the Diagnostics Plate.

RF CHARACTERIZATION

A series of electromagnetic tests were performed to validate each pickup prior to the installation in the beamline. The two main tests that are done to characterize the pickup are: the coupling between the channels in the frequency range of

* Work partially supported by the Spanish Ministry of Economy and Competitiveness under project AIC-A-2011-0654 and FIS2013-40860-R
† ivan.podadera@ciemat.es

ISBN 978-3-95450-177-9

interest, and the time domain reflectometry response of each electrode. Both are compared with the simulation and the other pickups. Figures 3, 4, 5 and 6 show respectively the comparison between the measured coupling values between adjacent and opposite electrodes of the DBPM's and the simulated ones. At the regions of interest, around 175 MHz and 350 MHz, the discrepancy between the measured and simulated values is less than 2 dB. It should be noticed than the dispersion is lower for DBPM's, where the coupling is higher.

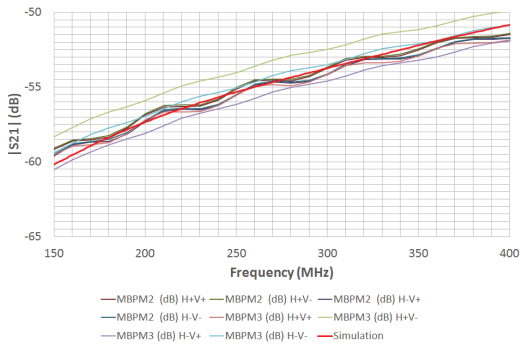

Figure 3: Comparison of the measured adjacent electrode coupling of the MBPM's with the simulation.

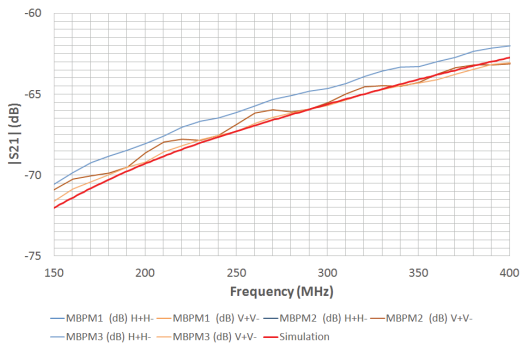

Figure 4: Comparison of the measured opposite electrode coupling of the MBPM's with the simulation.

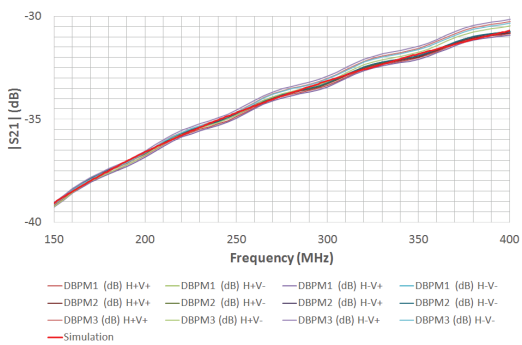

Figure 5: Comparison of the measured adjacent electrode coupling of the DBPM's with the simulation.

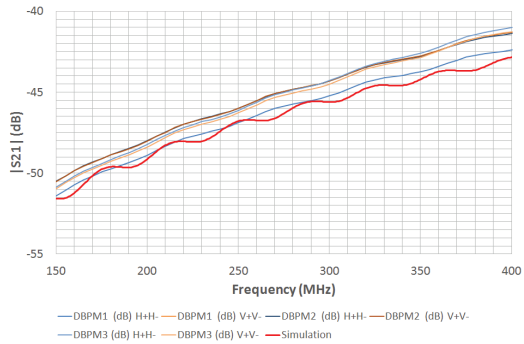

Figure 6: Comparison of the measured opposite electrode coupling of the DBPM's with the simulation.

Wire Test Bench

Prior to installation in the beamline, a mapping of the signals of each pickup was performed in the wire test bench constructed at CIEMAT laboratory (Fig. 7) [4]. The sensitivity, linearity and offset of the electrical signal with respect to the mechanical one are the main parameters to be analyzed. As discussed in previous works, for low-beta beams the parameters obtained in the test bench cannot be directly used in the accelerator. BPM sensitivity is energy and frequency dependent. To obtain the parameters to be used in the accelerator the mapping obtained in the test bench should be fit with the analytical function. Then, once the right values of beam radius b and electrode angle ϕ are obtained, it is possible to use them to get the sensitivity value at the right energy and frequency. For LIPAC BPM's, the interest is to get the inversed sensitivity at 5 and 9 MeV for 175 and 350 MHz. The inversed sensitivity can be defined in different ways. In this work,the inversed sensitivity k_x is defined as:

$$k_x = \frac{\Delta_x}{\Sigma} \tag{1}$$

where $\Delta_x = I_R - I_L$ and $\Sigma = I_R + I_L$, and I_R and I_L are the currents induced in the right and left electrode respectively.

Table 1: Summary of the MBPM and DBPM Wire Measurements.

	Wire meas.		Analytical
BPM Id.	k_x (mm)	k_y (mm)	k_1 (mm)
MBP01	13.54	13.46	12.58
MBP02	13.66	13.81	12.58
MBP03	14.57	13.7	12.58
MBP04	13.64	13.7	12.58
DBP01	31.9	30.4	26.19

Table 1 summarizes the sensitivity results obtained in the test bench for the MBPM's and the DBP01. For each BPM a preliminary fitting to the analytical equation has been done taking into account the mean result of the series of each monitor type. The fitting is done using the analytical

ISBN 978-3-95450-177-9

solution for low-beta beams [5, 6]. With this approach, a half aperture value of 26.1 mm for the MBPM's and 58 mm for the DBPM's. The values obtained are bigger than the nominal half apertures of the pickups, 24 mm and 50 mm for MBPM and DBPM respectively. However, as anticipated in [6], it corresponds to the mean value of the aperture of the stripline.

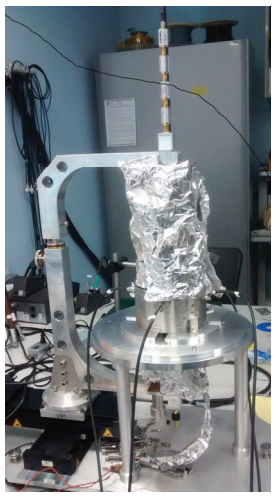

Figure 7: Picture of a DBPM's being characterized.

The inversed sensitivities at 175 and 350 MHz calculated analytically from the fitting are 11.4 and 8.14 mm for the MBPM's, and 20.7 and 12.3 mm for DBPM's. There is a small discrepancy (less than 10 % between those values and the obtained in the simulations. Further data analysis is required to investigate the source of those discrepancies.

ACQUISITION ELECTRONICS

The acquisition system (Fig. 8) has been designed and manufactured for all the LIPAC BPM's as explained in detail in [7], yet based on commercial digitizers. The system uses an analog front-end to house the system calibration switches and an intermediate frequency stage, plus ancillary boards such as timing and clock distribution, on CompactPCI. As such, all parameters for controlling the system are available for windows & Linux OS via Ethernet, and given the low event rate output of the BPM system the integration in the Central Control System is via an ASYN driver. Currently the timing boards are rather simple, consisting on a fan-out buffer with pulse generation and counting capabilities for statistics and monitoring, because the timing outputs for the BPM system from LIPAc consist only of the Trigger and Gate synchronization pulses [8]. The digitizer remains the VHS-ADC from Nutaq (formerly Lyrtech) for the first series of the prototype mainly because historical reasons. The front-end analog board is manufactured and it is in the test phase of the boards. The system is expected to be shipped to LIPAC in the following months.

CONCLUSIONS AND OUTLOOK

The beam position monitors required for the following commissioning stage of the LIPAc prototype accelerator have been successfully designed, manufactured, characterized and integrated by CIEMAT. Further data processing of the mapping of each pickup will be performed to minimize the positioning error of the beam in the accelerator. In parallel, the electronics is being commissioned to be ready before the start of the next beam commissioning phase of LIPAC next year.

Figure 8: Picture of the acquisition electronics test bench.

ACKNOWLEDGEMENTS

We would like to thank all the companies (Vacuum Projects, Tecnovac) involved during the manufacturing of the pickups and the acquisition electronics for their support during the project.

REFERENCES

[1] P. Cara *et al.*, "The Linear IFMIF Prototype Accelerator (LIPAc) design development under the European-Japanese collaboration", Proc. of IPAC 2016, Busan, Korea.

[2] J. Knaster *et al.*, "The installation and Start of Commissioning of the 1.1 MW Deuteron Prototype Linac for IFMIF", Proc. of IPAC 2014, Shanghai, China.

[3] I. Podadera *et al.*, "Design Status of Beam Position Monitors for the IFMIF-EVEDA Accelerator ", MOPD06, Proc. of DIPAC 2009, Basel, Switzerland, 2009.

[4] I. Podadera *et al.*, "Status of the Beam Position Monitors for LIPAc ", MOPC019, Proc. of IBIC 2013, Oxford, UK, 2013.

[5] J.H. Cupérus, "Monitoring of particle beams at high frequencies", Nucl. Instrum. Meth., 145 (2), pp. 219-231, 1977.

[6] R.E. Shafer, "Beam position monitoring", AIP Conf. Proc., 249, p. 601, 1990.

[7] A. Guirao *et al.*, "Update on the Development of the New Electronic Instrumentation for the LIPAc/IFMIF Beam Position Monitors", Proc. of International Particle Accelerator Conference IPAC 2015, MOPTY043, pp. 1025-1028, Richmond, USA, 2015.

[8] H. Takahashi *et al.*, " Present status of MPS and TS for IFMIF/EVEDA accelerator", Proc. of International Particle Accelerator Conference IPAC 2010, WEPEB006, Kyoto, Japan, 2010.

ISBN 978-3-95450-177-9

DESIGN OF THE TRANSVERSE FEEDBACK KICKER FOR ThomX

M. El Ajjouri, N. Hubert, A. Loulergue, R. Sreedharan, Synchrotron SOLEIL,
Gif sur Yvette, France
D. Douillet, A.R. Gamelin, D. Le Guidec, LAL, Orsay, France

Abstract

ThomX is a Compton back-scattering source project in the range of the hard X rays to be installed in 2017. The machine is composed of an injector Linac and a storage ring where an electron bunch collides with a laser pulse accumulated in a FabryPerot resonator. The final goal is to provide an X-rays average flux of 1013 ph/s. To keep up with this flux, it is required to install a transverse feedback system to suppress instabilities generated by injection position jitter sources, resistive wall impedance or collective effects. This paper describes the design and simulation studies of the stripline kicker that will be used for the transverse feedback system.

Introduction

ThomX [1] is a demonstrator for a Compton back-scattering source in the hard X-ray range to be installed in Orsay, France, in 2017 [2]. A single electron bunch will be accelerated every 20 ms by a 50 MeV LINAC and stored in a 16 m circumference storage ring to interact with a high energy laser (fig. 1).

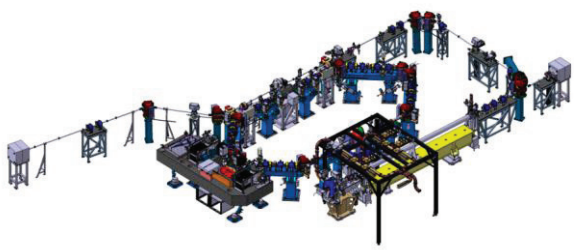

Figure 1: Layout of the ThomX facility.

By operating at low energy (50 MeV) the natural damping effect of the synchrotron radiation is weak and the beam stability becomes a crucial matter. The computed instability growth time and the corresponding kicker strength requirement for the different types of instabilities are listed in table 1. The results indicate that for Thom-X, the most critical effect comes from the injection orbit jitter inducing emittance growth at a growth rate of ~5 μs once the bunch stored in the ring.

Table 1: Instabilities Estimate for ThomX Ring

source	Growing time	Kicker strength $\Delta x'$
Beam pipe Geometries	160μs	> 10nrad
Resistive Wall	600μs	> 2 nrad
Ions	< 100 μs	> 20nrad
Injection Jitter	5 μs	2 μrad

ThomX Transverse Feedback

To cope with these instabilities, it was decided to use a digital transverse feedback system, composed of a wide-band detector button beam position monitor (BPM) a RF front-end, a FPGA based processor, a power amplifier and a stripline kicker (fig. 2). The system is capable of detecting a coherent transverse motion and applying a counter kick to damp it, bunch by bunch and turn by turn, with one (or even 2) bunches.

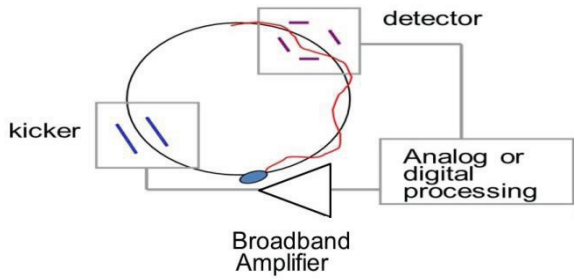

Figure 2: Digital feedback system.

Stripline Kicker Impedance Matching

The stripline kicker has 4 electrodes connected to electrical feedthrough at both ends. The electrodes are 300 mm long that corresponds to λ/2 of RF frequency (500 MHz). To maximize the transmission power, we must adapt the electrode impedance with the external transmission impedance lines (amplifier and cables are 50 ohm).

The formula to calculate the characteristic impedance Z for the different modes is the following [3, 4]:

$$Z = \frac{V^2}{2 * E * c} \qquad (1)$$

where c is the speed of light, V is the electric potential between stripline electrode and vacuum pipe, and E is the electric field. We use the Poisson electromagnetics 2D software [5] (fig. 3) to calculate the electric field for different dipole, quadrupole and sum mode (table 2).

Table 2: The Potential Applied to each Electrode to Calculate Electric Field

Field mode	E1	E2	E3	E4
Sum	+V	+V	+V	+V
V Dipole	+V	-V	-V	+V
H Dipole	+V	+V	-V	-V
Quadrupole	+V	-V	+V	-V

ISBN 978-3-95450-177-9

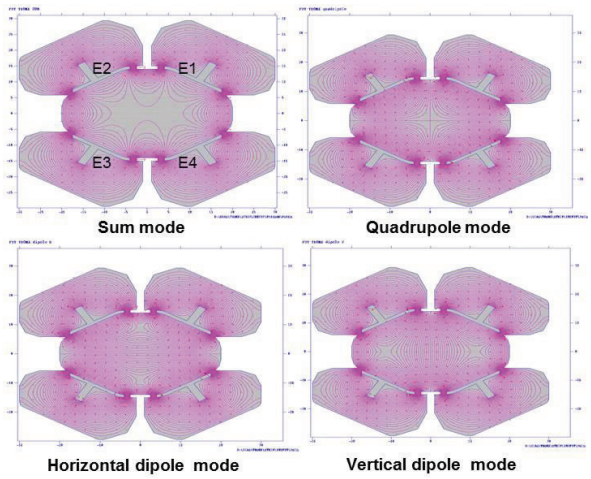

Figure 3: Electric field result in the stripline kicker.

The Impedance of different modes are in (table 3).

Table 3: Characteristic Impedance of Different Modes

	Sum	V Dipole	H Dipole	Quadrupole
Z	54,86Ω	50,07Ω	48,86Ω	47,39Ω

The impedance Zch is calculate with following formula

$$Zch=\sqrt{Zsum * Zquadrupole}=\sqrt{ZVdipole * ZHdipole} \quad (2)$$

Stripline shape has been optimized to have *Zch* is equal to 51Ω in one case (sum and quadrupole) and 49.5 in the other (dipole).

Shunt Impedance

The shunt impedance Z_{sh} is given by the following formula [6]

$$Z_{sh}= 2 * Z_{ch}\left(\frac{g\perp * c}{2\pi f * R}\right)^2 sin^2\left(\frac{2\pi f * L}{c}\right) \quad (3)$$

where *Zch* is the characteristic impedance, *L* the stripline length, R is the inner radius *c* is the speed of light and *f* frequency. With 2D electrostatic model we determine the transverse geometry factor

$$g\perp = |E_{(x=0;y=0)}| * R \quad (4)$$

where E is the electric field obtained applying unit potential on two diagonal electrodes and R is inner electrodes radius. The transverse geometry factor is about 0.65 for ThomX stripline.

The shunt impedance Zsh is representative of the stripline efficiency. Higher is the shunt impedance, the better the efficiency of the kicker. At 250MHz, the shunt impedance is 6.8kΩ (fig. 4).

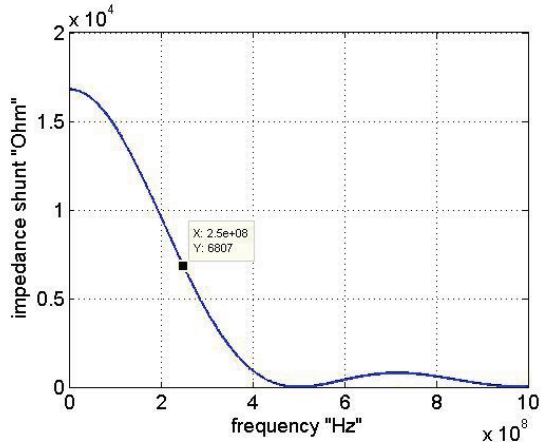

Figure 4: Stripline shunt impedance versus frequency.

3D model Design and Simulation

Starting from Poisson 2D model, the 3D model was built (fig. 5) with Ansys HFSS [7].

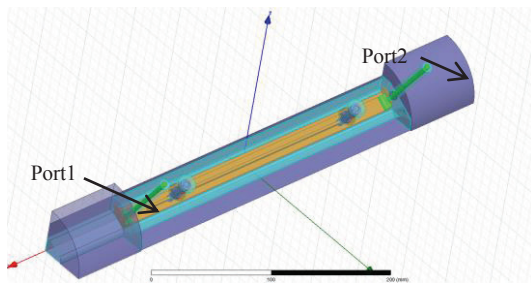

Figure 5: 3D stripline model.

ANSYS HFSS Frequency Domain Solver is used to minimize and calculate scattering parameters. The stripline kicker has a geometrical symmetry. To reduce the memory usage and the computation time, we simulate a quarter of the structure.

The S11 reflection coefficient represents how much power is reflected from the port (fig. 6).

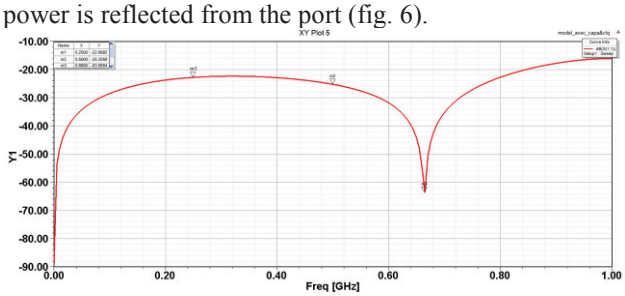

Figure 6: S11 parameter is below -22 dBm on the range of interest DC-250 MHz.

The S21 transmission coefficient represents how much power is transmitted from the Port1 to Port2 (fig. 7)

ISBN 978-3-95450-177-9

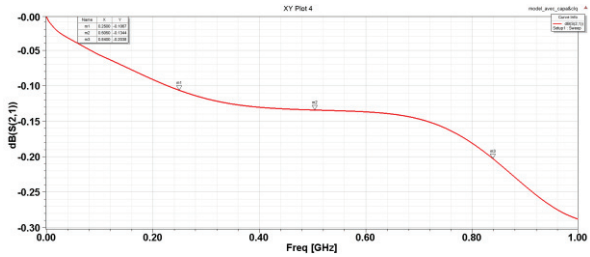

Figure 7: S21 parameter.

The feedback system must have a bandwidth from DC to 250 MHz. We must optimize reflection and transmission parameters on this range. The S11 value should be minimized to avoid power reflection at the input port, to avoid any damage on the amplifier driver. In our case the S11 has a value lower than -20 dB over the entire bandwidth of interest. The simulation takes into account an ideal vacuum feedthrough and coper foil used for electrodes expansion during the baking operation.

Wake Impedance Simulation

To achieve ThomX expected performances and determine the possible sources of beam instability, the simulation of the total machine impedance are being done [8]. The kicker is potentially an important source of impedance mismatch for the storage ring, so we need to estimate its impact and try to find how minimizing it.

Longitudinal impedance has been optimized adding (as it had been done for SOLEIL striplines [9]) 0.5 mm capacitive gaps at each side of the electrodes (fig. 8&9). This capacitive gap, combined with the inductance of the feedthroughs and metal foil, and 50 ohms impedance of electrodes, creates a low pass filter. The cutoff frequency of this filter depends on the height of the capacitive section.

Wakefield simulations are performed with the wakefield solver of CST Particle Studio [10].

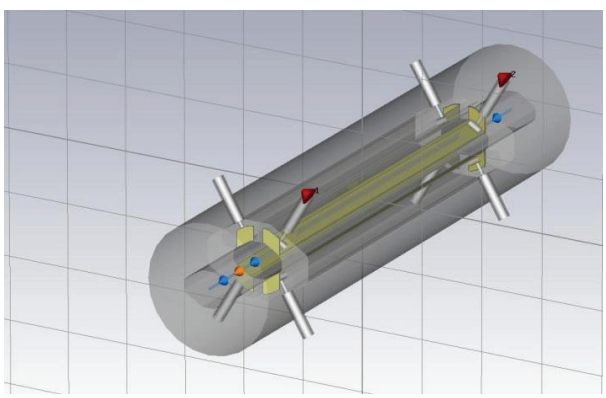

Figure 8: The CST model.

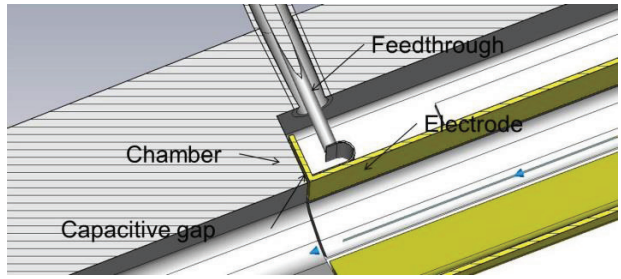

Figure 9: Capacitive gap between electrode and chamber body.

To assess the impact of the capacitive gap, the real part of the longitudinal impedance is extracted. Without this capacity, stripline impedance simulation shows peaks in the 3 to 4 GHz range (fig. 10). Those peaks are attenuated by introducing a capacity gap of 5 mm height, and completely damped with a capacity of 10 mm height. But in this case we observe significant peaks in high frequency 13.5 GHz.

Complementary simulations are being done to select the best capacitive gap according to the beam characteristics.

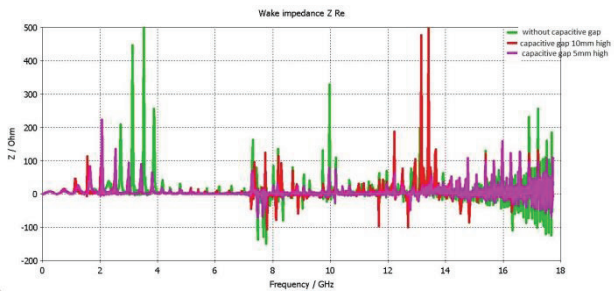

Figure 10: Real part of longitudinal impedance: green without capacity, magenta for a 5 mm height capacity and red for a 10 mm height capacity.

Mechanical Design

Electrodes and stripline body are made of AISI 316 LN stainless steel. The four electrodes are 300 mm long, 1mm thick with one rib in the middle on the external side to avoid any distortion. They are positioned at 30° to the horizontal with respect to the beam axis. Their shape reproduces the ThomX vacuum chamber inside geometry (fig.11) to minimize variation of chamber cross section seen by the beam and thus the stripline impedance.

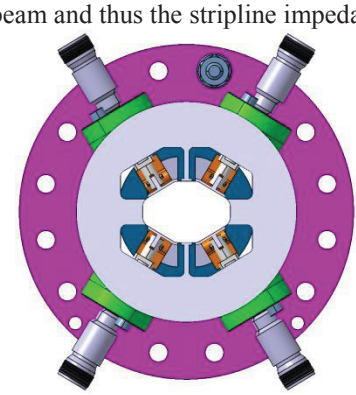

Figure 11: stripline cross-section.

The electrodes are fixed and mechanically aligned through ceramic rods for electric isolation. They are electrically connected to UHV feedthrough at both ends

ISBN 978-3-95450-177-9

through flexible copper sheets to avoid any damage during baking process (fig.12).

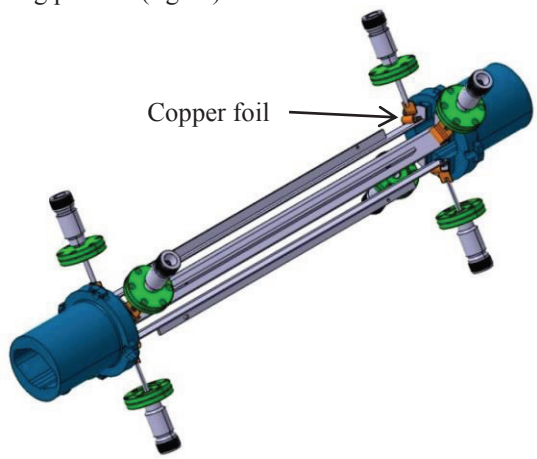

Figure 12: Electrical connections at both ends of the electrodes are made through a flexible copper sheet to avoid damage during baking process.

Feedthroughs are mounted on flanges, and all parts are screwed together, so that the stripline can be fully dismounted for future needs (fig.13).

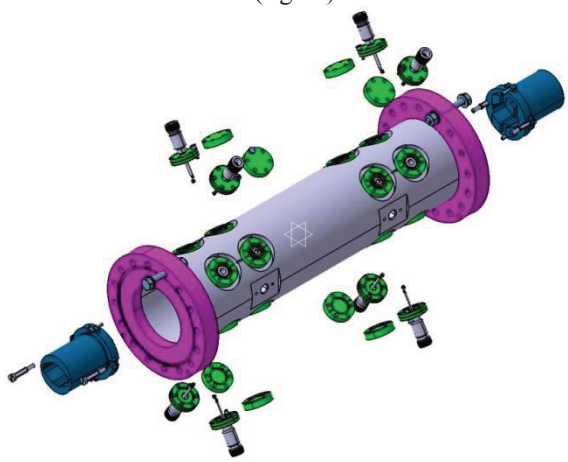

Figure 13: General view of the stripline.

CONCLUSION

The stripline design is in its final phase. Production should start in the next months, so that the stripline will be ready for ThomX installation in spring 2017. Before installation, electromagnetic measurements on a wire test bench [8] will be performed to compare theoretical and experimental results.

REFERENCES

[1] A. Variola, J. Haissinski, A. Loulergue, F.Zomer, "ThomX technical design report", LAL RT 14-21 SOLEIL/SOURA- 3629, 2014.

[2] I. Chaikovska *et al.*, "Status of the Preparation to the Commissioning of ThomX Storage Ring", Proceedings of IPAC2016, Busan, Korea.

[3] U. Iriso, T.F. Günzel and F. Perez, "Design of the stripline and kickers for ALBA", Proceedings of DIPAC2009, Basel, Switzerland.

[4] W.B. Li, B.G. Sun, Z.R. Zhou *et al.*, "Design and Simulation of the Transverse Feedback Kicker for HLS II", Proceedings of IPAC2011, San Sebastián, Spain.

[5] Poisson Superfish, `http://laacg.lanl.gov/laacg/services/download_sf.phtml#ps0`

[6] D. Olsson, "Design of Stripline Kicker for Tune Measurements in the MAX IV 3 GeV Ring", Electromagnetics Research Symposium Proceedings, Stockholm, Sweden, Aug. 12-15, 2013.

[7] ANSYS, `http://www.ansys.com/Products/Electronics/ANSYS-HFSS`

[8] A. Gamelin *et al.*, "Impedance simulation and Measurements for ThomX ring", Proceedings of IPAC2016, Busan, Korea.

[9] C. Mariette, *et al.*, "Excitation stripline for Soleil Fast transverse feedback", Proceedings of DIPAC2007, Venice, Italy.

[10] Computer Simulation Technology, `https://www.cst.com/`

ISBN 978-3-95450-177-9

NOVEL ELECTROSTATIC BEAM POSITION MONITORS WITH ENHANCED SENSITIVITY

M. Ben Abdillah†, Institut de Physique Nucléaire, Orsay, France

Abstract

Beam Position Monitors (BPM) measure the beam transverse position, the beam phase with respect to the radiofrequency voltage, and give an indication on beam transverse shape. Electrostatic BPMs are composed of four electrodes that transduce the associated electromagnetic field to the beam into electrical signal allowing the calculation of the beam parameters mentioned above. During commissioning and/or experiences phases that needs very low beam current; the precision of the BPM measurements is reduced due to the low sensitivity of electrostatic BPM to beam current. This paper addresses the design, the realization and the testing of a new set of electrostatic BPMs with large electrodes. It emphasizes the strong points of these BPMs in comparison with BPMs present in SPIRAL2 facility.

INTRODUCTION

The idea of developing a BPM with enhanced sensitivity arose at the qualification of SPIRAL2 BPM that shows weak received signals by the BPM electrodes at low beam currents (less than 150µA). Novel electrostatic BPM were designed taking into account mechanical constraints (space, stability) while offering better current sensitivity.

BEAM POSITION MONITORS

A BPM has four electrodes that couple to the beam through the image charge produced by the beam [1]. The BPM electrode is considered as capacitor C that is charged by the beam and discharged through a 50Ω resistor connected to ground. As for SPIRAL2 BPM [2], the electrode receives a multi-tone signal due to the beam bunched with an accelerating frequency 88.0525MHz. Only 1st and 2nd harmonic tones are taken into account in this study. A generic example of electrostatic BPM is sketched in Figure 1.

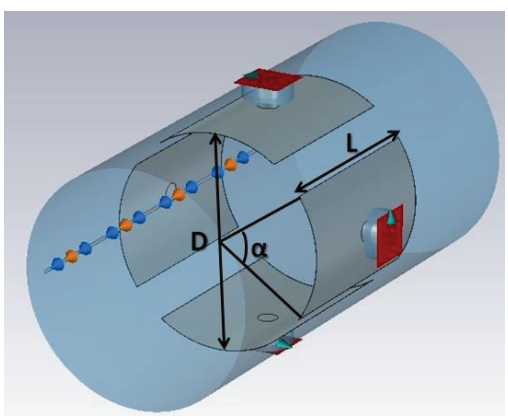

Figure 1 : Generic example of electrostatic BPM.

BPM diameter D, angular length α and length L have direct effects on BPM current and position sensitivities.

For instance, the formula for position sensitivity K_p for Gaussian beams at β=1 is:

$$K_p(dB/mm) = \frac{320}{\ln(10)}\frac{\sin(\alpha/2)}{D\cdot\alpha}$$
$$\alpha \text{ in radians and } D \text{ in mm}$$

Table 1 shows the type of proportional relation between these parameters, this guided the design of SPIRAL2 BPM and the new BPM.

Table 1: Proportional Relation Between BPM Sensitivities and Design Parameters

Parameter	Current sensitivity	Position Sensitivity
D	$1/D^2$	1/D
α	α	sin(α/2)/α
L	sin(πL.f/v)	No effect
C	1/C	No effect

v is the beam speed and f is the accelerating frequency.

As for SPIRAL2 BPM, the design of the new BPM took into account the fact that the BPM will be inserted in the vacuum pipe inside the quadrupoles which will be buried at their turn in the quadrupole magnet. Therefore, BPM diameter D was set to 40mm. the electrode angular length α was set to 63deg as it's a tradeoff between current sensitivity and position sensitivity. Change in BPM diameter should bring 1.5dB enhancement in BPM current sensitivity; it also raises BPM position sensitivity.

Main focus is pointed on the levels of the received signal tones at the first harmonic (176.105MHz) and the second harmonic (352.21MHz). Only BPM length L is modified in order to maximize sensitivity to beam current at the first and the second harmonic while maintaining sensitivity to beam position at these tones.

BPM ELECTRICAL SIMULATIONS

BPM simulations were run under Mathcad using the method described by Shafer [1]. BPM length L was swept over 180mm range and special focus was put over the level of signal received by BPM electrodes for centered low β (β= 0.08) beams.

Simulations, run with MathCad, show an enhanced output level at the first and second harmonic for L=65mm than the 39mm set for SPIRAL2 BPM (see Figure 2).

†abdillah@ipno.in2p3.fr

ISBN 978-3-95450-177-9

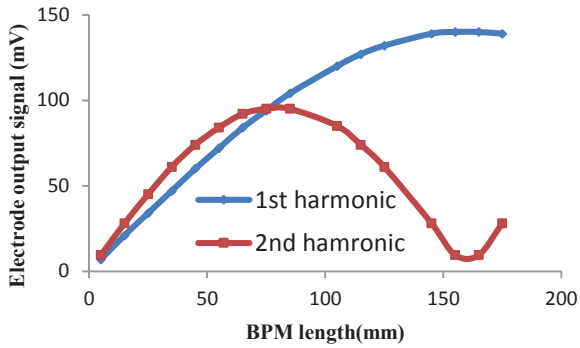

Figure 2: BPM simulations (beam current=5mA, centered beam, β=0.08).

BPM MECHANICAL DESIGN

Increasing BPM length to 65mm raises interrogations about mechanical realization: the electrode stability and cylindrical shape should be maintained with a good precision. The design adopted for SPIRAL2 BPM electrodes is based on a single contact between the electrode button and the electrodes, this design risked to show less stable and reproducible BPM with longer electrodes. Discussions with SOLCERA Advanced Materials lead to the inclusion of small anti-gazing ceramic plots on the corners of the electrode in order to offer a better stability and reproduction of the BPM. This solution should also reduce the difference between electrodes capacitances. The ceramic plots are 6mm large, 2mm deep and long.

The new solution is sketched in Figure 3.

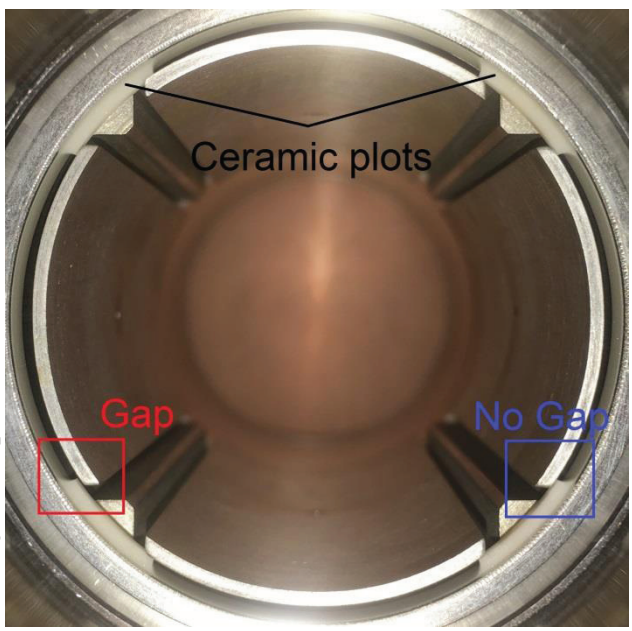

Figure 3: BPM with anti-gazing ceramic plots.

NEW BPM REALIZATION

As for SPIRAL2 BPMs, reverse polarity female SMA connectors are integrated. Few feed-throughs were made for the BPM realization; this led to a hard pairing of feed-throughs. Strong effort was put on pairing face to face electrodes as they directly influence the BPM electrical centre. Electrodes capacitances (see Table 2) and TDR response (see Figure) are depicted below.

Table 2: BPM Button and Electrode Capacitances

Position	Electrode	Button
Up (U)	13.66	1.31
Down (D)	13.61	1.36
Left (L)	13.96	1.34
Right (R)	13.62	1.37
U/D Difference	0.05	0.05
L/R Difference	0.34	0.03

The U/D difference is the same for buttons and electrodes whether it is worse for L/R difference.

Further investigations of the BPM realization shows a gap in the Left electrode between the ceramic barrettes and the plate (see red and blue boxes in Figure 3). This explains the raise in the left electrode capacitance.

For comparison, over the twenty SPIRAL2 BPMs, the U/D and L/R differences vary from 0.04pF to 0.4pF.

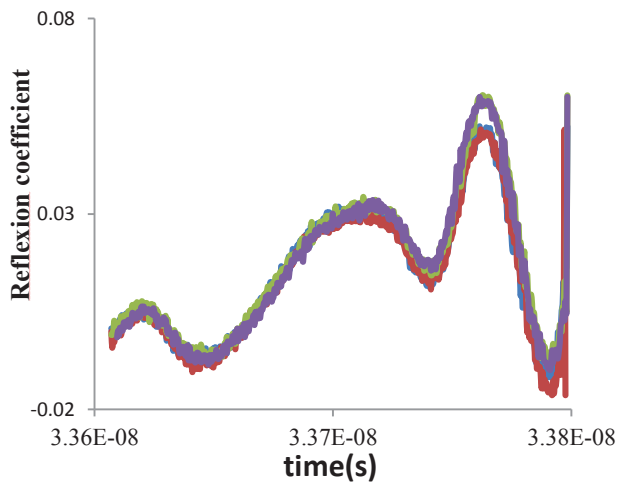

Figure: New BPM electrodes TDR responses.

Face to face electrodes have identical TDR response while there is a small difference between the four electrodes responses

NEW BPM CHARACTERIZATION

Current Sensitivity Measurement

The test setup, shown in Figure 4, is used. A cylindrical copper wire is inserted in the centre of the BPM. The calibrated VNA port1 sends a sinusoidal CW signal at 176.105MHz along the copper wire inside the BPM, the VNA port2 is connected to one of the four BPM electrodes while the others electrodes and the copper wire termination are loaded with 50Ω charge.

ISBN 978-3-95450-177-9

50Ω matching measurements show S11 and S22 levels way below -25dB.

S21 magnitude is measured for both New BPM and SPIRAL2 BPM and results shows 8 dB enhancement.

Table 3: S21 Magnitude Measurement Results

BPM	S21(dB)			
New	U	D	L	R
	-25.52	-25.48	-25.55	-25.5
SPIRAL2	U	D	L	R
	-33.5	-33.42	-33.56	-33.45

The symbols U, L, R and D refer to the upper, lower, left and right electrodes of the BPM (Shown in Table 3).

The measurement results are in a good agreement with simulations. The 2dB shortage is partially due to higher electrode capacitance for the new BPM.

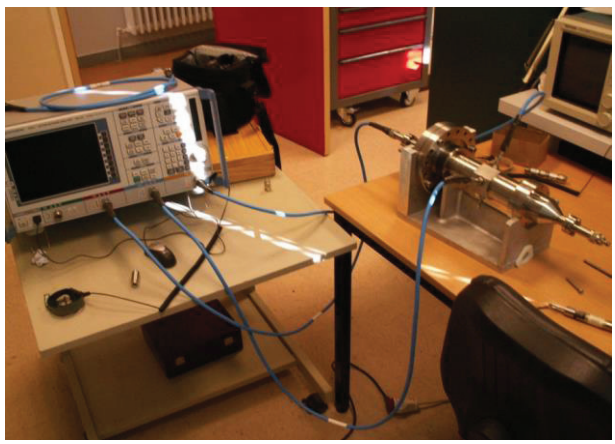

Figure 4: BPM current sensitivity measurement setup.

Position Sensitivity Measurement

The test setup used for SPIRAL2 BPMs [3] is repeated for the new BPM: the BPM electrical centre (relative to its mechanical centre) and position sensitivity are measured at 176.105MHz and compared to estimated values.

Results are depicted in Table 4, higher values of face to face differences between electrodes capacitance results in a further electrical centre coordinates for the New BPM. New BPM position sensitivity is in a good agreement with estimations.

Table 4: BPMs Electrical Centre and Position Sensitivity

BPM	New	
Electrical Centre	X	Y
	18µm	174µm
Sensitivity	Estimated	Measured
	1.68dB/mm	1.62dB/mm

For comparison, over the twenty SPIRAL2 BPMs, the electrical centres vary from 10µm to 300µm.

CONCLUSION

Novel electrostatic BPM design (optimized electrode length) offers a maximized current sensitivity while maintaining the position sensitivity intact. The mechanical arrangement is offering a stable and easily reproducible BPMs. The design and realization could be easily adapted to BPMs operating on other accelerator.

Although mechanical realization is not optimal, measurements show a strong gain in BPM current sensitivity.

The next step is to eliminate gaps between electrode corners and anti-gazing ceramics, re-characterize the BPM and ultimately test it with beam either on IPHI [4] or SPIRAL2 facilities.

ACKNOWLEDGEMENTS

I would like to address special thanks to J.Lesrel (IPN) and J.L.Billaud (SOLCERA) for their constant support along this project.

REFERENCES

[1] R.E. Shafer, “Beam Position Monitoring”, in *AIP Conf. Proc.* 249, 601 (1992)

[2] P. Ausset and M. Ben abdillah, “Operation if the Beam Position Monitor for the SPIRAL2 LINAC on the test bench of the RFQ”, in *Proc. 5th Int. Beam Instrumentation Conf. (IBIC’16)*, Barcelona, Spain, September 2016, WEPG11.

[3] M. Ben abdillah and P. Ausset, “Development of Beam Position Monitors for the SPIRAL2 LINAC”, in *Proc. 1st Int. Beam Instrumentation Conf. (IBIC’12)*, Tsukuba, Japan, October 2012, paper TUPA18, pp. 374-377.

[4] P. Ausset, “First results from the IPHI beam instrumentation”, in *Proc. 5th Int. Beam Instrumentation Conf. (IBIC’16)*, Barcelona, Spain, September 2016, TUPG34.

ISBN 978-3-95450-177-9

LCLS-1 CAVITY BPM ALGORITHM FOR UNLOCKED DIGITIZER CLOCK

T. Straumann, S. R. Smith, SLAC, Menlo Park, USA

Abstract

Cavity BPMs commonly use the fundamental TM010 mode (excited either in the x/y cavity itself or in a separate "reference" cavity) which is insensitive to beam position as a reference signal, not only for amplitude normalization but also as a phase/time reference to facilitate synchronous detection of the signal derived from the position-sensitive TM110 mode. When taking these signals into the digital domain the reference and position signals need to be acquired by a synchronous clock. However, unless this clock is also locked to the accelerating RF absolute, timing information is lost which affects the relative phase between reference and position signals (assuming they are not carefully tuned to the same frequency).

This contribution presents a method for estimating the necessary time of arrival information based on the sampled reference signal which is used to make the signal detection insensitive to the phase of the digitizer clock. Running an unlocked digitizer clock allows for considerable simplification of infrastructure (cabling, PLLs) and thus decreases cost and eases maintenance.

INTRODUCTION

Cavity Beam-Position Monitors (BPMs) inherently offer a very high resolution [1, 2]. A beam of charged particles passes a cylindrical cavity and excites the electro-magnetical eigenmodes of the device. The coupling of the beam to some of these modes, in particular the "dipole-mode" TM110 is very sensitive to the transversal beam position. The structures to extract the signals from the cavity are carefully designed to be sensitive to TM110 only and reject other modes [3].

TM110 is also excited by a centered but oblique beam trajectory and "slanted" bunches [1] but the resulting signal is in phase-quadrature to the position signal.

The fundamental TM010 mode of a second, "reference", cavity which is largely insensitive to the beam-position is also measured so that the position-sensitive signal can be normalized to the beam charge and phase.

Figure 1 shows the typical hardware employed to acquire the cavity-BPM signals. Three RF signals (e.g, X-band), originating at the X- and Y-ports of the main cavity as well as the output of the reference cavity are fed into a analogue receiver and subsequently digitized. The receiver uses multiple mixing stages and/or an image-rejecting configuration.

In order to maintain the highest possible resolution of the system and to reject (or, depending on the application: detect) the effects of an oblique trajectory (or bunch) a phase-synchronous detection algorithm is commonly used [1, 2, 4] with the reference cavity establishing the necessary time or phase reference.

Obviously, the three channels must use a common LO as well as a common ADC clock in order to maintain phase-synchronicity among the channels.

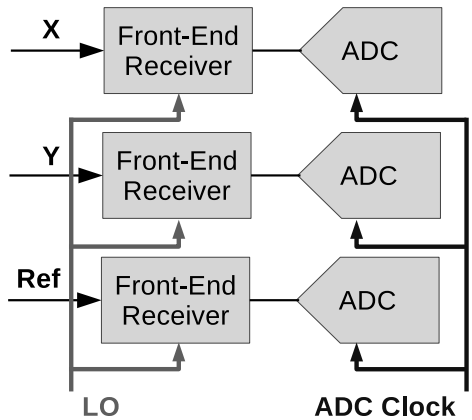

Figure 1: Cavity BPM receiver hardware block diagram.

A synchronous detection algorithm amounts to the estimation of the amplitude of a "known" signal (shape) in the presence of noise [5]. A generic, linear and time-discrete detector for a signal $s(t)$ which is assumed to be time- and band-limited (i.e., it can reasonably approximated by a suitable periodic continuation) can be described by Eq. (1):

$$\hat{A} = \frac{1}{N} \Sigma_{n=0}^{N-1} s(nT_s - t_o) f(nT_s) \qquad (1)$$

i.e., the signal is *correlated* with a (normalized[1]) "test"-function $f(t)$.

In addition to the test-function we also must know or estimate the "starting" time t_o of the signal which is also called "Time of Arrival" or TOA.

The subject of this paper is a method for TOA estimation which is suitable for cavity BPMs with a free-running ADC clock. The ADC is usually triggered by the timing system but the TOA depends on the phase of the ADC clock and is unknown to at least $\pm\frac{1}{2}$ sampling period.

REVIEW OF COMMON METHODS FOR TOA ESTIMATION

In the context of cavity BPMs it is important to consider that one of the advantages of a synchonous detector is its superior SNR when the signal amplitude is small, which is the case when the beam passes close to the electrical center of the main cavity.

[1] so that $\frac{1}{N} \Sigma_{n=0}^{N-1} f^2(nT_s) = 1$.

ISBN 978-3-95450-177-9

This observation suggests that the signal of the *reference* cavity which is always available with a good SNR is the preferable target for TOA estimation – provided that it can be assumed that the relative timing between reference and positional signal remains constant *all the way* down to the ADCs.

Several methods have and can be used:

- Tune the cavities to the same frequency (e.g. [4], [6], [7]). By using a complex exponential for the test function in Eq. (1), t_o will cancel out.
- Phase-lock the ADC clock to the beam and thus maintain a fixed timing (probably – the publications are not always very explicit – used by several authors; e.g., [8]).
- Observe an auxiliary signal (e.g., crystal-detector, [1]) and use for TOA estimation.
- Use an algorithm to estimate TOA from the reference signal.

The last approach has the advantage that neither careful tuning nor an expensive clock distribution infrastructure is required. Since it can use the phase information contained in the reference signal we can also expect this method to yield a better estimate than a crystal-detector.

ALGORITHM FOR TOA ESTIMATION

We shall now proceed to present the algorithm used at LCLS. In order to simplify the mathematical notation we will use a continuous-time representation but assume that all signals are time- and band-limited (see above) so that carrying the results into the discrete-time domain is straightforward.

TOA Definition

Consider a causal signal $s(t)$ and a "suitable", normalized test-function $f(t)$ so that the correlation integral:

$$R(\hat{\tau}) = \int_0^\infty s(t+\hat{\tau})\, f(t)\, \mathrm{d}t \tag{2}$$

exists. We then define the *time of arrival*, τ_A, *with respect to the test-function* $f(t)$, as the value of $\hat{\tau}$ which maximises the above correlation, Eq. (2).

If $f(t)$ is chosen to be proportional to the signal shape then $R(\hat{\tau})$ is proportional to the signal autocorrelation and has a single maximum at $\hat{\tau} = 0$ (because the signal is assumed to be time-limited it cannot be periodic). In some respects (e.g., maximization of SNR in white noise) such a choice is indeed optimal [5] but any $f(t)$ for which Eq. (2) has a maximum is suitable.

Spectral Representation

The Fourier-transform of Eq. (2) is

$$R(\hat{\tau}) = \frac{1}{2\pi} \int_{-\infty}^{+\infty} S(\omega) F^*(\omega) \mathrm{e}^{-j\omega\hat{\tau}}\, \mathrm{d}\omega \tag{3}$$

where the asterisk denotes the complex conjugate of $F(\omega)$, the Fourier-transform of $f(t)$.

At this point we must pay some attention to the fact that the reference-signal of a cavity BPM does not only have an unknown TOA with respect to the digitizer clock – any (unlocked) LO(s) in the system also introduce an unknown *phase shift*. Such a phase shift can be described in the frequency-domain

$$\phi(\omega) = +j\,\mathrm{sign}(\omega)\phi$$

Adding an estimated phase shift $\hat{\phi}$ to Eq. (3) and making use of the hermititian symmetry yields

$$R(\hat{\tau}, \hat{\phi}) = \frac{1}{\pi} \int_0^{+\infty} |S(\omega)F(\omega)| \cos(\Psi(\omega) - \underline{\hat{\phi}} - \omega\hat{\tau})\, \mathrm{d}\omega \tag{4}$$

where Ψ is the phase between S and F^*. The estimated phase $\hat{\phi}$ must be zero for $\omega = 0$ and is constant elsewhere (due to the sign function vanishing at $\omega = 0$). We use the symbol $\underline{\hat{\phi}}$ to emphasize the special behavior of $\hat{\phi}(0)$. This is important to remember when moving to a discrete-time representation.

TOA and Phase Estimation

We can now proceed to search for the time $\hat{\tau}$ and phase $\hat{\phi}$ which maximise Eq. (4). We omit the explicit dependence of S, F and Ψ on ω, the integration boundaries, introduce $A = |SF|$, take the partial derivatives to $\hat{\phi}$ and $\hat{\tau}$, respectively, and set equal to zero:

$$\frac{\partial R(\hat{\tau}, \hat{\phi})}{\partial \hat{\phi}} = 0 = -\frac{1}{\pi} \int A \sin(\Psi - \underline{\hat{\phi}} - \omega\hat{\tau})\, \mathrm{d}\omega \tag{5}$$

$$\frac{\partial R(\hat{\tau}, \hat{\phi})}{\partial \hat{\tau}} = 0 = -\frac{1}{\pi} \int A \sin(\Psi - \underline{\hat{\phi}} - \omega\hat{\tau})\, \omega\, \mathrm{d}\omega \tag{6}$$

Our next assumption is that close to the optimum, the phase error

$$\Delta(\omega) = \Psi(\omega) - \underline{\hat{\phi}} - \omega\hat{\tau} \tag{7}$$

is very small so that we can approximate $\sin(x) \approx x$. It is very important to note that we do *not have to assume that the estimated phase nor the estimated TOA be small!* We just assume that the linear phase $\hat{\phi} - \omega\hat{\tau}$ "tracks" the phase Ψ of the correlation well.

If, e.g., we use the signal shape itself for the test function $f(t)$ then Ψ becomes a linear function of the LO phase and the unknown TOA, and Eq. (7) simplifies to

$$\Delta(\omega) = \Psi(\omega) - \underline{\hat{\phi}} - \omega\hat{\tau} = \underline{\phi^{LO}} + \omega\,\tau_A - \underline{\hat{\phi}} - \omega\hat{\tau}$$

i.e., when the estimated $\hat{\phi}$ and $\hat{\tau}$ match the 'true' values then Δ vanishes everywhere.

The linearized system of equations can be stated

$$\begin{array}{lllll} \hat{\phi} & \int A\,\mathrm{d}\omega & + \hat{\tau} & \int A\,\omega\,\mathrm{d}\omega & = \int A\,\Psi\,\mathrm{d}\omega \\ \hat{\phi} & \int A\omega\,\mathrm{d}\omega & + \hat{\tau} & \int A\,\omega^2\,\mathrm{d}\omega & = \int A\,\Psi\omega\,\mathrm{d}\omega \end{array} \tag{8}$$

and trivially solved for $\hat{\phi}$ and $\hat{\tau}$. Again: when moving into the discrete-time domain then we must be careful with the DC term and remember that $\mathrm{sign}(\omega) = 0$.

ISBN 978-3-95450-177-9

However, the estimator is even useful if the phase Ψ of the correlation SF^* deviates from a linear phase. Because phase- and time-shift are linear operations and the estimator is also linear this means that a *differential* estimation between two "shots" of a signal with each one having a random phase- and time-delay is still possible (see Appendix).

RESULTS

The proposed algorithm has been implemented in the BPM processing software at SLAC. An AltiVec™ [9] co-processor is employed to FFT the raw signals and to compute the various sums in Eq. (8). The phase and TOA of the positional signals are corrected in the frequency-domain and then correlated with a filter response (still in frequency domain). This operation is equivalent with a digital downconversion as it is used by several authors [1], [4] and yields the desired complex amplitude from which position and trajectory angle can be extracted. The details are, however, beyond the scope of this paper.

Figure 2 shows the digitized signal of a LCLS reference cavity for two beam pulses. The effect of the unlocked ADC can easily be seen.

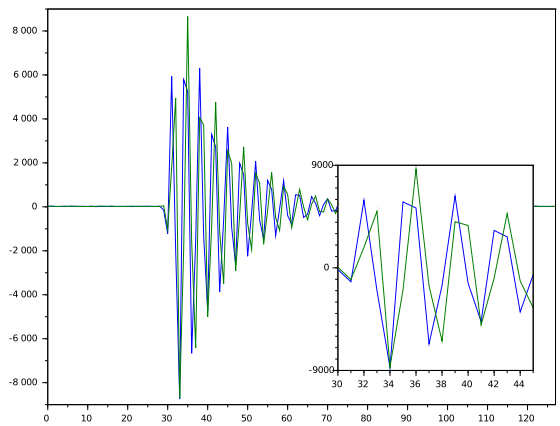

Figure 2: Reference signal of two beam pulses with unlocked ADC and LO. The sub-plot zooms to samples #30 – 45.

As an example, we used a test function $f(t)$ which has the frequency-response of an ideal band-pass and covers a bandwidth of 20 frequency bins (see Fig. 3). The time-domain response is depicted in Fig. 4.

The result of applying the phase- and TOA estimation to the original waveforms is presented in Fig. 5. In addition, the waveforms were normalized to the beam-charge – something that would not be done in case of a position calculation but was performed here to show how the two waveforms match up after correcting for TOA.

A time-shift by a (not necessarily integer-) multiple of the sampling interval can trivially be performed in the frequency-domain.

CONCLUSION

A method for TOA estimation has been presented which can be used by the signal-processing of a cavity BPM system

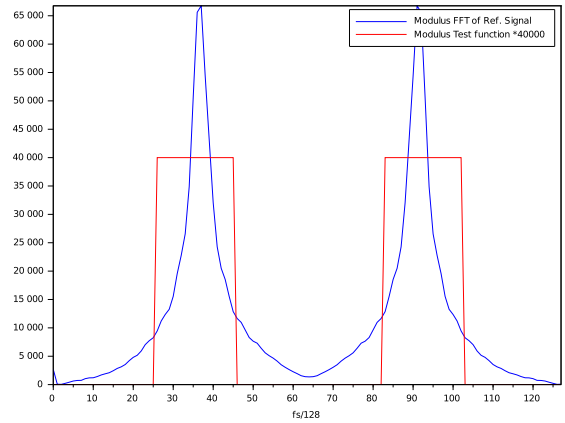

Figure 3: FFT (modulus) of the beam pulses and response of the test function (multiplied by 40000 to make it visible).

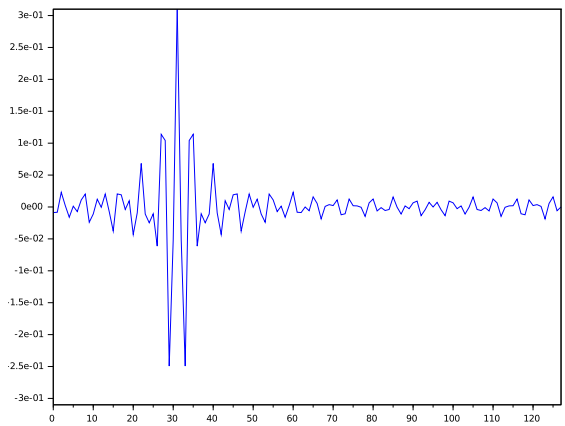

Figure 4: Time-domain response of the example test function.

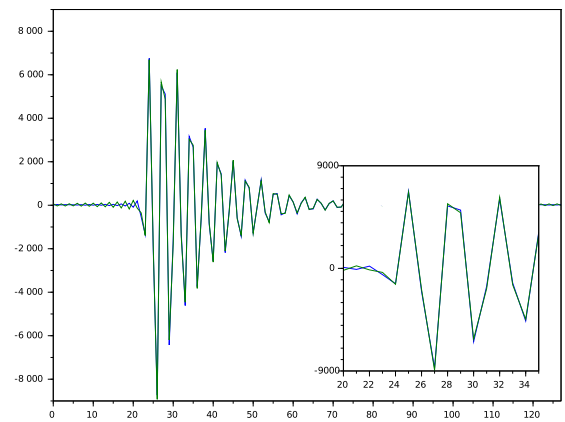

Figure 5: Reference signal of two beam pulses after applying the correction for $\hat{\tau}$ and $\hat{\phi}$.

in order to correct for the effect of an unlocked digitizer clock even if the reference- and position cavities are not tuned to exactly the same frequency.

Relaxing the tuning requirements and obsoleting the need for a clock- distribution infrastructure results in considerable savings.

ISBN 978-3-95450-177-9

ACKNOWLEDGEMENT

Work supported by U.S. Department of Energy Contract No. DE-AC02-76SF00515.

APPENDIX

We can abbreviate Eq. (8) using matrix notation

$$M\ \hat{x} = y$$

with $\hat{x}$ a column-vector containing the estimated values, M the matrix which depends only on the amplitude function $A(\omega)$ and y which involves integrals of the phase but is linear in the phase

$$y(\Psi + \gamma) = y(\Psi) + y(\gamma)$$

In particular, computing $y(\phi)$ with ϕ = const (arbitrary phase shift) and $y(\omega\tau)$ (arbitrary time shift) we note that the coefficients of y become identical with the coefficients of M and thus

$$M\ \hat{x} = y(\Psi) + M\ x$$

with the vector x containing ϕ, τ. Therefore, a non-vanishing $y(\Psi)$ merely introduces a phase and time-offset and the difference in estimation between two "shots" with unknown x_1 and x_2 reduces to

$$\begin{aligned} M\ \hat{x}_2 - M\ \hat{x}_1 &= y_2 - y_1 = y(\Psi) - y(\Psi) + M\ x_2 - M\ x_1 \\ M\ (\hat{x}_2 - \hat{x}_1) &= M\ (x_2 - x_1) \end{aligned}$$

which shows that the estimator yields the "exact" result (in absence of measurement errors, noise etc.) for phase- and time-*differences*.

REFERENCES

[1] S. Walston *et al.*, "Performance of a High Resolution Cavity Beam Position Monitor System," in *Nucl. Instrum. Meth.*, A578 1-22, Jun. 2007.

[2] D. Lipka, "Cavity BPM Designs, Related Electronics and Measured Performances," in *Proc. DIPAC'09*, Basel, Switzerland, 2009.

[3] Z. Li, R. Johnson, S. R. Smith, T. Naito, and J. Rifkin, "Cavity BPM with Dipole-Mode Selective Coupler," SLAC, Menlo Park, USA, SLAC-PUB-11913.

[4] Y.I. Kim *et al.*, "Cavity Beam Position Monitor System for the Accelerator Test Facility 2," *Phys. Rev. ST Accel. Beams*, Vol. 15, Iss. 4, April 2012.

[5] A.D. Whalen, "Detection of Signals in Noise," Academic Press, New York and London, 1971.

[6] H. Hayano *et al.*, "Development of a High-Resolution Cavity Beam-Position Monitor," *Phys. Rev. ST Accel. Beams*, Vol. 11, Iss. 6, June 2008.

[7] H. Maesaka *et al.*, "Performance of the RF Cavity BPM at XFEL/SPRING-8 'SACLA'," in *Proc. FEL'11*, Shanghai, China, 2011.

[8] B. Keil *et al.*, "Status of the SwissFEL BPM System," in *Proc. IBIC'15*, Melbourne, Australia, 2015.

[9] AltiVec, `https:en.wikipedia.org/wiki/AltiVec`

ISBN 978-3-95450-177-9

DESIGN FOR THE DIAMOND LONGITUDINAL BUNCH-BY-BUNCH FEEDBACK CAVITY

A. F. D. Morgan, G. Rehm
Diamond Light Source, Oxfordshire, UK

ABSTRACT

In 2017 it is planned to install some additional normal conducting cavities into the Diamond storage ring. In order to deal with the potential higher order modes in these, we are designing a longitudinal bunch-by-bunch feedback system. This paper will focus on the design of the overloaded cavity kicker, adapted to the Diamond beam pipe cross section. The design has evolved in order to reduce the strong 3^{rd} harmonic resonance seen on the introduction of the racetrack beam pipe. Through a combination of geometry optimisation and the addition of integrated taper transitions this harmonic has been greatly reduced while also minimising sharp resonances below 15 GHz. The major features will be described, as well as the expected performance parameters.

DESIGN

The design comprises a pillbox cavity, with additional coaxial ports coupled via ridged waveguides. In a development on our previous work, the design frequency was moved to 1.875 GHz from the lower 1.625 GHz. This was in order to move more of the higher order modes (HOMs) above the cutoff frequency of the beam pipe and to space out the remaining lines. 2.125 GHz was also considered, but found to generate additional lower frequency HOMs in the structure.

Theoretically, the ridged waveguide structure and the waveguide to coaxial transition both act as high pass filters, and care must be taken to make sure that the overall cutoff frequency is low enough such that all of the higher order modes can be coupled out of the cavity. In practice they behaved more like band pass filters, so the aim was to extend the pass band to as high a frequency as possible.

The coupling structures were originally modelled separately, in order to iterate the model faster. Figure 1 shows a representation of the modelled geometry. The best result was then incorporated into the full model. Figure 2 shows the transmission through the waveguide and coaxial structures. The pass band extended from 1.8 GHz to 8 GHz. Although not ideal it was decided that it was good enough to be incorporated into the full model.

Although useful starting points can be obtained by modelling elements separately, the optimisation must be done on the full model so as to take into account of the interactions between elements. As an example, even with the waveguide and coaxial coupler optimised, there were still unwanted resonances in the wake impedance of the full model. With the original cavity, pipe and couplers, tuning the geometry in various ways could not achieve overall suppression of the

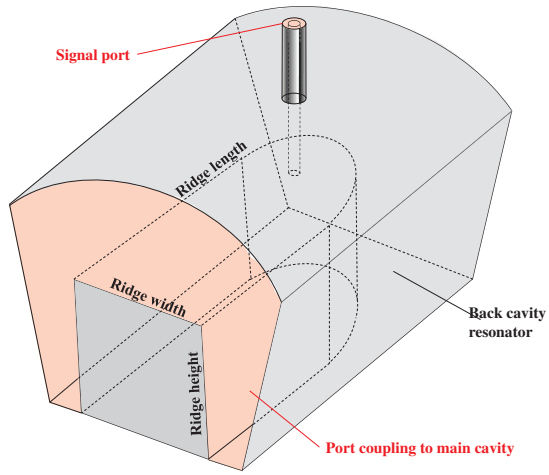

Figure 1: Sketch of the coupler geometry.

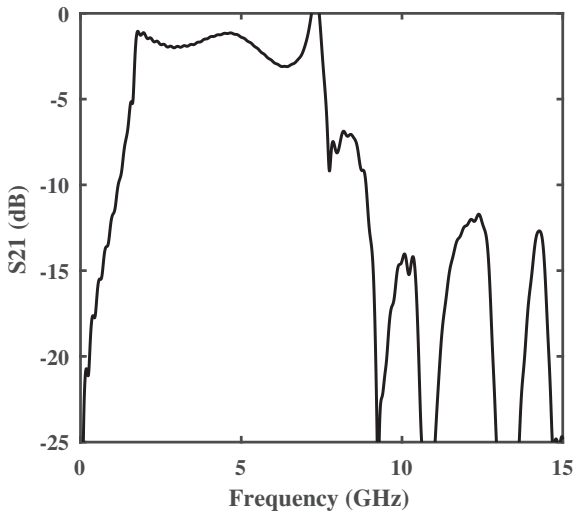

Figure 2: The transmission through the coupling structures as initially added to the full model.

HOM resonances. If one set of resonances was suppressed then another was enhanced.

Only when tapers were added to the model was the overall suppression of these unwanted features realised. After some investigation it was found that tapers moving from the Diamond standard racetrack profile on outer ends of the structure, to a circular profile at the central cavity performed best. Tapers were resisted originally as they are known to

ISBN 978-3-95450-177-9

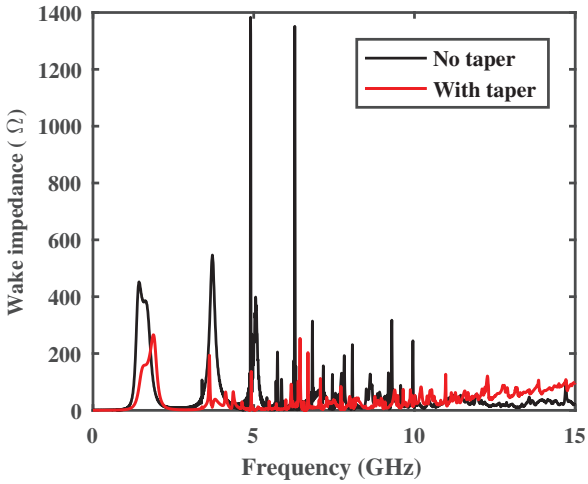

Figure 3: Adding the tapers gave sufficient overall HOM suppression.

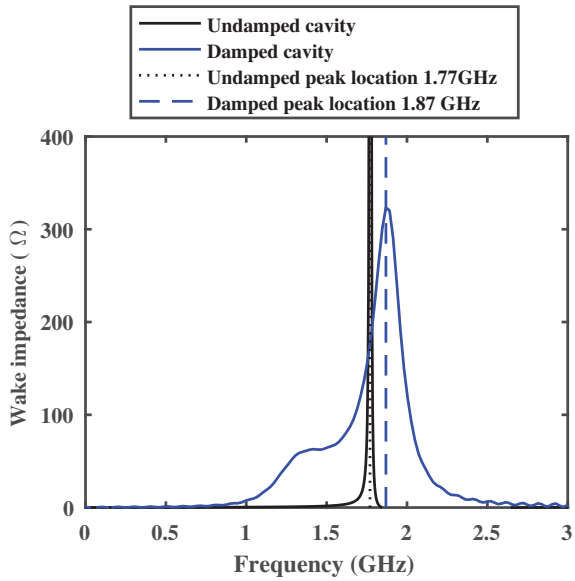

Figure 4: The addition of damping structure moves the resonance frequency from 1.77 GHz to the target of 1.87 GHz.

add additional harmonics lines [1], however with careful tuning of the taper angle the damping effects on the original unwanted harmonics was stronger than the unwanted harmonics introduced by the taper. Fortunately as the tapers were integrated directly into the design, longer, lower angle tapers were able to be used. Figure 3 shows an example of the HOM suppression achieved by adding the tapers.

One detrimental effect of adding the tapers was that the floor of the wake impedance began to rise above a particular frequency. In the case of Fig. 3 this can be seen starting at around 9 GHz. By keeping the tapers shallow the start of this rise was pushed up to around 15 GHz which was deemed acceptable as there is very little beam power at and above those frequencies.

The main cavity radius is defined by the target resonance desired. The cavity radius of the full design is different from that of a simple pillbox cavity due to the waveguides and transitions connecting the main cavity to the ports (see Fig. 4). This again highlighted the need to model the full structure early in the design process.

The curved ends of the coupling waveguide ridge remained curved, similar to the LNLS design [2], for the same reasons of improving the coupling between the ridged waveguide and the coaxial line. However it was found that changing the base of the ridged waveguide and back cavity resonator to be flat rather than following the radial curve had the effect of broadening the bandwidth, and suppressing some of the spikes introduced by adding the taper.

The exact amplitudes of the HOM resonances are somewhat dependent on the level of meshing used and the details of the feedthrough structure and ceramic behaviour. However, investigations showed that in terms of the meshing, finer meshing tended to reduce the amplitudes.

The feedthroughs are specified to be 50 Ω parts. The ceramic is AlO_3, but for the loss calculation, the tangent δ was unknown for this particular ceramic. In this case, the tangent δ of the most similar ceramic was used.

Once the design changes were implemented, another round of optimisation was done so that performance could be maximised. Once a final design was decided upon, a series of sensitivity scans were performed on the geometric parameters in order to identify those most sensitive to changes. As expected, the gap above the ridge in the coupling waveguide proved the most sensitive, changing the peak wake impedance in the operation band by 25 Ω per 100 μm. Increasing the peak impedance in this way had the cost of reducing the bandwidth, so the mechanical tolerance was reduced in order to achieve the balance between the two operating requirements found in the design process. The nose stub (see Fig. 6) also needed additional consideration as it moved the peak frequency. Less sensitive but still needing care was the ridge depth and length as deviations of 800 μm had the potential to enhance particular HOMs (see Fig. 1).

In order to close the loop in the design process, the mechanical drawings were exported as STL files and imported into both GdfidL [3] and CST [4] modelling software. This was then compared with the results from the final design written in native GdfidL input code. The agreement was very good giving us confidence that the mechanical drawings accurately represent our requirements (see Fig. 5).

PERFORMANCE

An overview of the final design is shown in Fig. 6. It will be constructed of three sections. The upstream and down stream sections contain the coupling structures and the tapers, and are shown in fig. 7. These slot into a middle

ISBN 978-3-95450-177-9

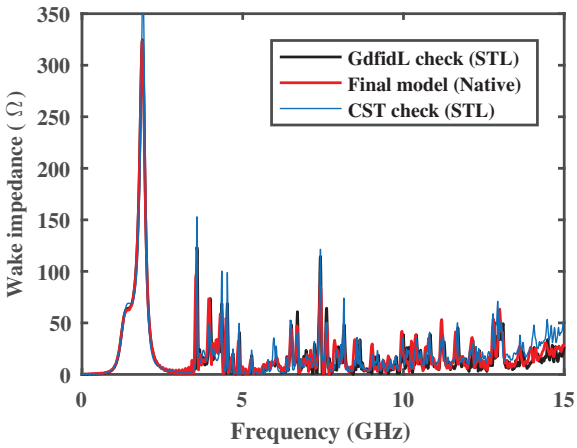

Figure 5: The comparison of the final EM model and the resulting mechanical drawings.

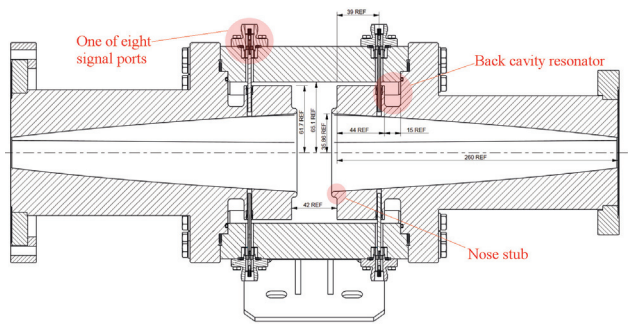

Figure 6: Slice view of the final cavity design.

section to form the main cavity. RF fingers are used to maintain good isolation between adjacent couplers.

The minimum wake impedance within the operational band is 137 Ω, as shown in fig. 8, which implies a minimum shunt impedance of 274 Ω [5]. The peak wake impedance is 306 Ω giving a peak shunt impedance of 612 Ω.

From our analysis of the energy loss in the structure [6], we know that most of the energy lost from the beam is emitted

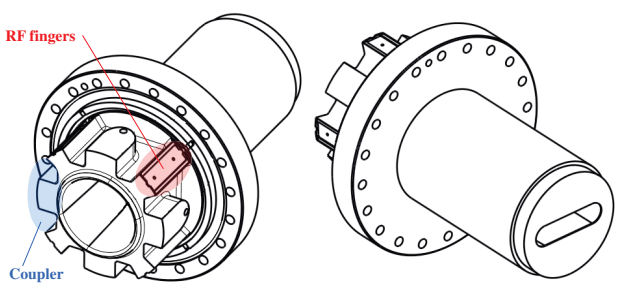

Figure 7: 3D representations of the upstream and downstream section. With a 90 degree angle for ease of viewing.

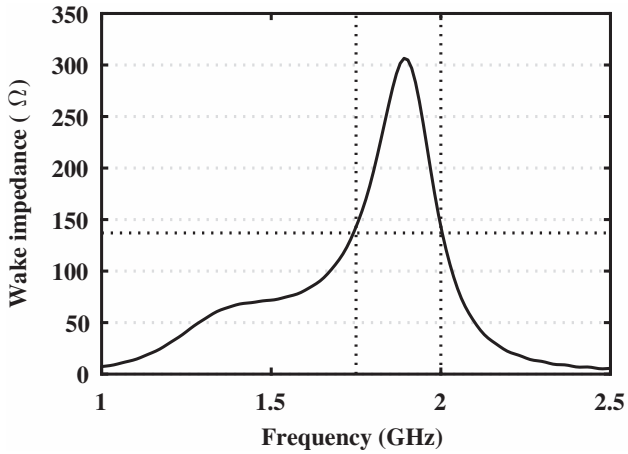

Figure 8: The wake impedance around the operating frequency. The dashed vertical lines show the operating region while the dashed horizontal lines show the minimum wake impedance.

Table 1: The Vast Majority of the Power is Extracted by the Signal Ports

Component	Power loss (%)
Beam ports	15
Signal ports	77
Cavity surface	7.7
Coaxial pin	0.3
Feedthrough ceramic	~0

out of the signal ports. Of the 8% lost into the cavity, the vast majority is lost across the internal surface. Very little is lost in the coaxial pins and feedthrough ceramic (see Table. 1). This has implications for the analog chain as there is potentially substantial power sent to the amplifier from the cavity. The plan is to use circulators to redirect this beam induced power safely into a high power load.

Because the bunch spectrum changes with operational conditions, and machining tolerancing can move the resonance frequencies by small amounts, we used a basic $P = I^2R$ relationship to estimate a worst case scenario of power coupled from the beam. The wake impedance was separated into sections each containing a single RF harmonic (500 MHz, 1 GHz, 1.5 GHz etc.). The maximum wake impedance for each section was found and combined with the expected current in that frequency range, based on a gaussian roll off which mimics the frequency behaviour of the beam. Table 2 summarises the results of this approach.

Table 2: Worst Case Beam Induced Power Estimates

	Frequency ranges (GHz)		
Operating current	0-1.75	1.75 - 2.25	2.25 - 15.25
300 mA	17 W	25 W	35 W
500 mA	47 W	71 W	98 W

ISBN 978-3-95450-177-9

Table 3: More Realistic Case Beam Induced Power Estimates

Operating current	Frequency ranges (GHz) 0-1.75	1.75 - 2.25	2.25 - 15.25
300 mA	8 W	12 W	10 W
500 mA	22 W	32 W	28 W

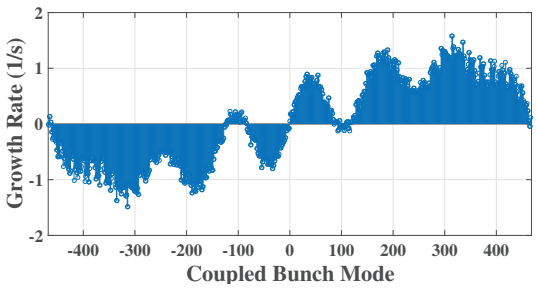

Figure 9: The growth rate of the coupled bunch modes.

For a 500 mA beam this basic approach gave 71 W coupled out in the operational band, and 98 W at frequencies above that, up to 15 GHz. For our usual operating current of 300 mA, these numbers reduce to 25 W in the operational band and 35 W for the HOMs. As this represents all modes in each section coupling as much as the worst mode in that section, this is an unrealistically pessimistic scenario. However, this upper bound means that we are comfortable that the analog chain, which is specified to cope with 200 W of power, will be suitably robust. In reality we expect the power load to be lower away from the operating band, as one is unlikely to hit all the strong resonances simultaneously. By running the same type of analysis but this time using the mean value of wake impedance for each section, the contribution from the general background is more clearly seen (see Table 3).

The impact of installing the cavity was investigated using a modified version of calculations in MatLab [7] obtained from LNLS, based on the Wang formalism [8]. This predicts the expected growth rate of coupled bunch modes caused by the cavity. For this design the maximum instability growth rate was 1.5/s implying a growth time of 370000 turns for current operating conditions. The effects of increasing the stored current from 300 mA to 500 mA was also investigated, but the maximum growth rate only increases to a still small value of 4/s. Figure 9 show the typical result under normal conditions.

The transverse wakes were also checked, as shown in figure 10, and found to be a benign 20 Ω/mm, which is of the same order as many other existing components.

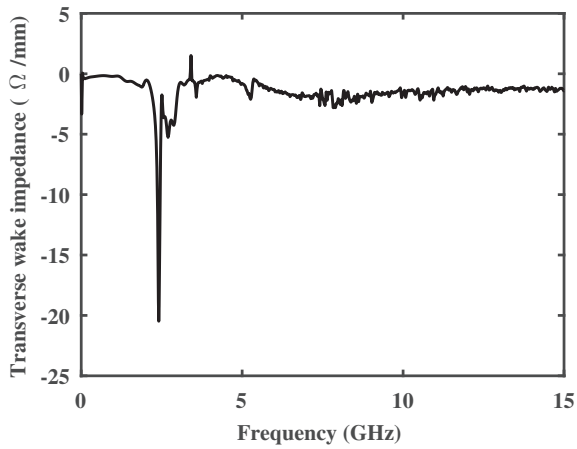

Figure 10: The transverse wake of the cavity.

CONCLUSION

A longitudinal feedback cavity has been designed for use in the Diamond storage ring. The design is highly damped in order to achieve the required bandwidth. It also has integral tapers in order to counteract the detrimental effect of the size and shape of the Diamond beam pipe through the cavity. Checks have been done on the expected impact on the ring after installation and they are expected to be minimal.

The authors would like to thank Richard Fielder for doing the comparison modelling in CST.

REFERENCES

[1] A. F. D. Morgan, G. Rehm, *Initial work on the design of a longitudinal bunch-by-bunch feedback kicker at diamond*, IBIC 2015.

[2] L. Sanfelici et.al., *Design and impedance optimisation of the LNLS-UVX longitudinal kicker cavity*, IBIC 2013.

[3] http://www.gdfidl.de

[4] http://www.cst.com

[5] D. A. Goldberg and G. R. Lambertson., *Dynamic devices: A primer on pickups and kickers*, AIP Conf. Proc. 1992 Vol.249 p 537.

[6] A. F. D. Morgan, G. Rehm, *Considerations and improved workflow for simulation of dissipated power from wake losses*, IBIC 2015.

[7] http://www.mathworks.com

[8] M. Wang, *Longitudinal symmetric coupled bunch modes*, BNL-51302.

ISBN 978-3-95450-177-9

A NEW STRIPLINE KICKER FOR PF-AR TRANSVERSE FEEDBACK DAMPER

R. Takai*, T. Honda, T. Nogami, T. Obina, Y. Tanimoto, M. Tobiyama
KEK Accelerator Laboratory and SOKENDAI, 1-1 Oho, Tsukuba, Ibaraki 305-0801, Japan

Abstract

A feedback damper equipped with a long stripline kicker was used to damp transverse beam oscillation at the Photon Factory Advanced Ring (PF-AR), which is a 6.5-GeV synchrotron radiation source of KEK. Recently, the stripline kicker was renewed to one having shorter electrodes and a smaller loss factor because its insulating support was broken by the beam-induced thermal stress and caused frequent electric discharges inducing dust trapping phenomena. In this paper, we present details of the new stripline kicker, from design to installation, as well as demonstrate results of beam oscillation damping obtained with the new kicker.

INTRODUCTION

The Photon Factory Advanced Ring (PF-AR), which is a 6.5-GeV electron storage ring of KEK, is known as a unique synchrotron radiation source dedicated to single-bunch operations to provide high-intensity pulsed X-rays. It is operated in decay mode in which the stored beam current is added twice daily up to 60 mA. The principal parameters of the PF-AR are listed in Table 1.

Table 1: Principal Parameters of the PF-AR

Operation Energy	6.5 GeV
Injection Energy	2.85 GeV
Stored Current	60 mA
RF Frequency	508.57 MHz
Circumference	377.26 m
Harmonic Number	640
Number of Bunches	1
Revolution Frequency	795 kHz
Tunes (x/y/s)	10.17/10.23/0.05
Damping Time (x/y/s)	2.5/2.5/1.2 ms
Natural Emittance	294 nm rad
Natural Bunch Length	18.6 mm (62 ps)

A long stripline feedback kicker comprising four stainless steel pipes with length of about 1.4 m was installed in the west straight section of the ring to damp the transverse oscillations of injected and stored beams. In order to reduce their self-weight deflection, an insulating support made of machinable ceramics "Photoveel [1]" was attached at the midpoint of each electrode. Since user operation commenced in the autumn of 2012, we frequently observed sudden increases in the vacuum pressure accompanied by beam loss around these insulating supports. Inspection of the kicker enabled us to find the damaged insulating supports. We considered this damage to have been caused by thermal stress due to energy loss of the stored single bunch. These supports were previously suspected to cause frequent electric discharges, thereby inducing dust trapping phenomena [2]. Photos of the original kicker electrodes and their insulating support parts taken during the inspection are shown in Fig. 1. Although the time domain reflectometry (TDR) response was acceptable, we found that the head of the bolt supporting the kicker electrode via the Photoveel part discolored to become black due to electric discharges and the Photoveel part itself was partially melted and broken. We continued the user operation by reducing the maximum stored current from 60 mA to 55 mA so as not to exceed the threshold of electric discharges because it was difficult to repair the damaged insulating supports in a short time. A new stripline kicker was designed and fabricated in parallel with this restricted user operation, and finally installed in the summer of 2015.

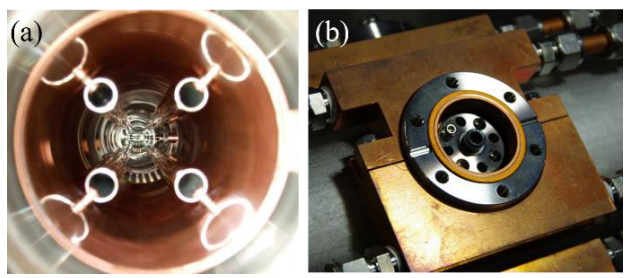

Figure 1: Photos of (a) the original kicker electrodes and (b) their insulating support parts.

In this paper, we describe the details of our new stripline kicker, from design to installation, and show the results of beam oscillation damping with the new kicker.

DESIGN OF STRIPLINE KICKER

Shunt Impedance

To quantitatively evaluate the stripline kicker performance, we need to calculate the transverse shunt impedance defined as follows [3]:

$$R_\perp = \frac{{V_\perp}^2}{2P}, \tag{1}$$

where P is the rms input power to the kicker electrode, and $V_\perp$ is the transverse deflecting voltage generating between the electrodes. This deflecting voltage for a vertical kick is calculated using the following expression:

$$V_\perp = \left| \int_0^L \left[E_y(z) + cB_x(z) \right] dz \right|, \tag{2}$$

* ryota.takai@kek.jp

ISBN 978-3-95450-177-9

where the beam propagates in the z-direction, c is the speed of light, L is the length of the kicker electrode, and $E_y(z)$ and $B_x(z)$ are the vertical electric and horizontal magnetic fields, respectively. Note that we took no account of the beam transient effect because the deflecting fields experienced by the propagating beam in the kicker are almost constant in our case. The deflecting fields for arbitrary kicker structures were numerically calculated by the HFSS simulation code [4]. The validity of the numerical calculation was verified in advance assuming a simple stripline kicker whose shunt impedance can be calculated analytically.

Design Policies

At first, the original kicker was modeled and its transverse shunt impedance was calculated by the above numerical method to define our design policies. As shown in Fig. 1, the original kicker is composed of four stainless steel pipes rotated by 45° from the orthogonal symmetric position. The outer diameter and length of the each electrode are 18 mm and 1360 mm, respectively. These are mounted in a 101.3-mm-inner-diameter beam duct so that the center of the each electrode is positioned 36 mm apart from the center of the duct. The characteristic impedance of each electrode is approximately 54 Ω. Supposing a case when we use it as a vertical kicker and input a high-frequency power of 1 W at 20 MHz[1] from the four downstream ports with the dipole mode, then the transverse shunt impedance was calculated to be 193 kΩ by Eqs. (1) and (2). Since we were able to sufficiently suppress the beam oscillation with the original kicker, we set the following equation as a necessary condition to be satisfied by the new kicker:

$$R_\perp > 190\ \mathrm{k\Omega}\ @\ 20\ \mathrm{MHz}\,. \qquad (3)$$

We need not be overly concerned about the electrode length, namely the kicker bandwidth, because the PF-AR is dedicated to single-bunch operation.

Besides, it is important to minimize the energy lost when the beam passes through the kicker structure (a loss factor) to suppress the heat generation of the kicker electrode, which may cause machine troubles. In the numerical simulation with GdfidL [5], the loss factor of the original kicker was estimated to be 250 mV/pC for an electron beam with a bunch length of 8.3 mm (28 ps). When converted into the power loss for the beam current of 60 mA, it becomes 1.1 kW. Since this power loss increases to 1.5 kW when there is an insulating support at the midpoint of each electrode, we can see that about 400 W of power had been lost around the support. In addition to condition (3), the new kicker is also required to satisfy the following condition:

$$P_{\mathrm{loss}} < 1.1\ \mathrm{kW}\ @\ 60\ \mathrm{mA}\,. \qquad (4)$$

[1] This frequency almost corresponds to the upper limit of the bandwidth of our final power amplifiers.

Basic Structure

Based on these design policies, three basic structures were considered for the new kicker: Types A, B, and C. Cross-sectional shapes at the input/output port position of the three structures are shown in Fig. 2. In Type A, the original pipe electrodes are replaced with concaved electrodes shaped like a cylinder divided into four sections in the longitudinal direction. The inner diameter of the circular beam duct was set to 90 mm according to the inner horizontal width of racetrack-shaped ducts connected to both ends of the kicker. The electrode thickness is 2 mm and the electrode width was chosen such that the opening angle relative to the duct axis becomes 60°. The distance from the duct axis to the electrode surface was determined to be 33.9 mm by using HFSS such that the characteristic impedance of each electrode becomes 50 Ω. The shunt impedance calculation showed that 1380-mm-long electrodes are required to satisfy condition (3) in this structure ($R_\perp = 198$ kΩ @ 20 MHz). The loss factor for the beam of the same bunch length as the original kicker simulation was estimated to be 134 mV/pC, corresponding to a power loss of 600 W. That is, the power loss is reduced by half, but electrodes of the same length are required to generate the same deflecting voltage compared to the original kicker.

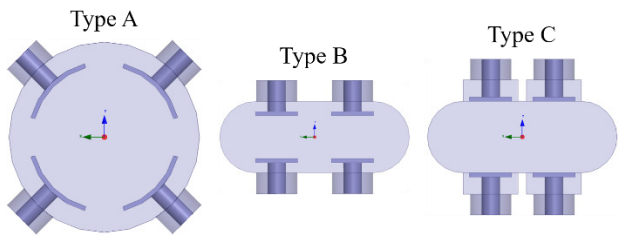

Figure 2: Basic structures considered for the new stripline kicker.

As mentioned above, the normal beam duct of the PF-AR is racetrack-shaped with inner horizontal and vertical widths of 90 mm and 34 mm, respectively. In Type B, the planar electrodes are built directly in the normal duct. In such a structure, there is no need to install additional shape-conversion ducts that cause the power loss. Since the internal space is restricted, two sets of parallel planar electrodes, with thickness of 2 mm and width of 20 mm, are arranged in the horizontal direction. The closest horizontal and vertical distances between the electrodes are set to 16 mm and 20.4 mm, respectively. In this structure, the transverse shunt impedance in the horizontal direction is different from that in the vertical direction because of the asymmetric pattern of the electrodes. Considering that the vertical shunt impedance is smaller than the horizontal one, 900-mm-long electrodes are sufficient to clear condition (3) ($R_{\perp v} = 229$ kΩ @ 20 MHz). The loss factor was estimated to be 164 mV/pC, corresponding to a power loss of 740 W. Although the vertical aperture of this structure is narrow, it has good deflecting efficiency and a smaller power loss than the original kicker.

Type C has a structure in which the same planar electrodes as Type B are contained in recess grooves provided

ISBN 978-3-95450-177-9

in the top and bottom faces of the normal duct. The closest horizontal distance between the electrodes was narrowed to 10 mm because of 3-mm gaps provided between the groove and the electrode. Since the electrodes are arranged to be flush with the inner duct surface, the closest vertical distance between the electrodes is 34 mm. The groove depth was set to be 10.2 mm such that the characteristic impedance of each electrode becomes 50 Ω. The electrode length required to comply with condition (3) was calculated to be 1200 mm ($R_{\perp v} =$ 199 kΩ @ 20 MHz). The loss factor was estimated to be 104 mV/pC, corresponding to a power loss of 470 W. As planned, the power loss significantly decreased, but the electrode cannot be shortened that much to attain the required length. Furthermore, in case such a cavity-like structure is provided, we have to devise a structure to avoid trapping a part of the higher-order modes of the beam wakefield in the structure; for example, smoothing the step difference sections at both ends of each groove to suppress the beam wakefield.

We evaluated the basic structure of the new kicker from the above three candidates and decided to adopt Type B, which has the shortest electrodes and requires no shape-conversion ducts. However, in order to avoid the characteristic impedance mismatch due to the self-weight deflection without insulating supports that cause additional power losses, the 900-mm-long electrodes should be divided into two 450-mm-long electrodes arranged in the longitudinal direction.

Minor Improvement

When actually fabricating the Type-B structure, we added a minor improvement. To improve the mechanical strength of each electrode, the width was extended outward by 5 mm, and each extending section was bent inward with an angle of 45°. The characteristic impedance of each electrode was readjusted to be 50 Ω by narrowing the vertical distance between the electrodes to 17.6 mm (the closest vertical distance is 10.5 mm). According to this improvement, almost the same shunt impedance as before the improvement could be obtained even by the 860-mm-long electrodes ($R_{\perp v} = 247$ kΩ @ 20 MHz)[2]. The loss factor slightly increased to 200 mV/pC, corresponding to a power loss of 900 W, but it remains smaller than that of the original kicker. Although the total power loss may increase if the long electrodes are divided in half along the longitudinal direction, it is not expected to become a serious problem because there are no lossy structures such as insulating supports. Figure 3 shows the longitudinal beam coupling impedance for the improved kicker evaluated by the GdfidL simulation. Relatively large peaks around 4 GHz are considered not to be trapped locally because the cut-off frequency of the normal duct is 1.8 GHz.

[2] As for the horizontal direction, the shunt impedance was calculated to be 485 kΩ, which is sufficient to satisfy condition (3).

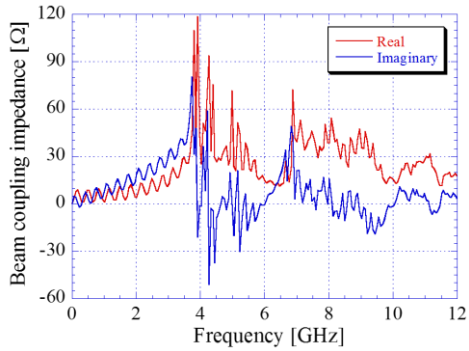

Figure 3: Real and imaginary parts of the longitudinal beam coupling impedance for the improved kicker. The simulated beam bunch length is 8.3 mm (28 ps).

FABRICATION AND INSTALLATION

Two of the same kicker ducts were fabricated corresponding to the divided electrodes. The electrode length of each kicker duct was extended to 460 mm so that the ceramics seals of feedthroughs located at both ends of each electrode cannot be directly seen from the beam. The beam coupling impedance will not be affected by this change. A schematic drawing of one of the two kicker ducts and a photo of the internal electrodes are shown in Fig. 4. The kicker duct and electrodes were produced from a stainless steel. The inner surface of the duct, and the surface of the electrodes were coated with copper to reduce the beam-induced wall heating. Furthermore, a special feedthrough with a bending structure on the inner conductor was used as one of the two feedthroughs supporting each electrode to absorb the longitudinal thermal elongation [6]. Physical interference between the adjacent feedthrough flanges (EIA-7/8) was prevented by changing the inner conductor length. The characteristic impedance of each electrode was measured by TDR and adjusted to be in the range of 50±2 Ω by using 0.2-mm-thick shim rings.

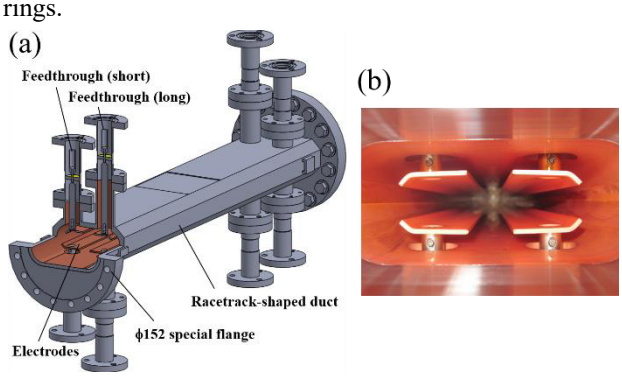

Figure 4: (a) Schematic drawing of the new stripline kicker duct and (b) photo of the inner electrodes.

The two kicker ducts were arranged in series and installed in the southwest straight section of the ring. For the time being, we use them as a long kicker by connecting the adjacent ports with each other by short coaxial cables. They can also be used as two broadband kickers in future. Figure 5 shows a photo of the installed kicker

ISBN 978-3-95450-177-9

ducts and a block diagram of the PF-AR feedback damper system including the new kicker. The beam signal is picked up by dedicated striplines and inputted to the analog detection circuit named "Bunch Oscillation Detector (BOD) [7]" via a low pass filter, programmable attenuator, and gating module. The horizontal and vertical oscillation components detected by the BOD are combined with each other after phase control and pulse modulation, after which they are sent to the final broadband amplifiers (R&K, A20-200-R). The amplified feedback signals are fed to the new kicker from the four downstream ports and kick back the oscillating beam. The output signals from the four upstream ports are attenuated by 20-dB dummy loads and sent to the local control room for monitoring. Each port of the kicker and each dummy load are cooled by airflow and their temperatures are constantly monitored by operators.

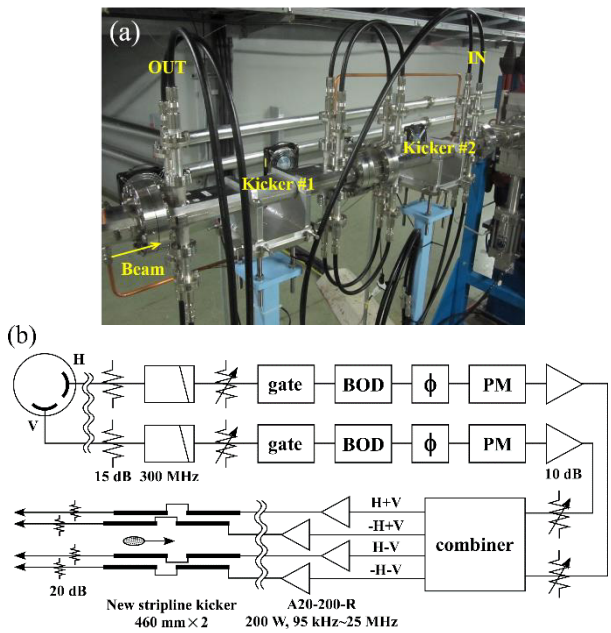

Figure 5: (a) Photo of the installed kicker ducts and (b) block diagram of the PF-AR feedback damper system. PM in the block diagram stands for pulse modulator.

We demonstrated that the new kicker functions correctly by performing a damping test of the beam oscillation excited by the tune measurement system. At the PF-AR, betatron tunes are measured by superposing the tracking generator output of a spectrum analyzer (Advantest, U3741) for monitoring the BOD output on the feedback kicker input. We excited betatron oscillations by using this system and checked whether the amplitudes of the tune spectra were changed, depending on the opening/closing of the feedback loop. The results for the horizontal and vertical directions are shown in Fig. 6. These spectra were obtained by averaging over 10 independent measurements with a stored beam current of 42 mA. On closing the feedback loop, we can see that the spectral amplitudes decrease by approximately 11 dB and 5 dB for the horizontal and vertical directions, respectively. In addition, we have also confirmed that spectral peaks due to beam instabilities, which appear only in the horizontal direction spontaneously, disappear when the feedback loop is closed. These results demonstrate that the new kicker works correctly as a part of the feedback damper system.

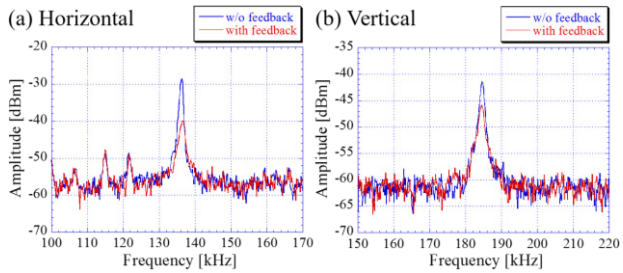

Figure 6: Tune spectra for the (a) horizontal and (b) vertical directions excited by the tune measurement system. The origins of a few peaks on the lower-frequency side of the horizontal tune are unknown.

SUMMARY AND FUTURE PLANS

The stripline kicker for the PF-AR feedback damper system was renewed. The new kicker can realize a higher shunt impedance and a smaller power loss with shorter electrodes compared to those achieved with the original kicker. The new kicker was installed in the southwest straight section of the ring in the summer of 2015, and exhibits good damping performance for beam oscillation. Abnormal signs such as sudden increases in the vacuum pressure and rapid heat generations of the kicker components have not been observed since the installation.

A new beam transport line for the PF-AR (AR-BT) enabling the 6.5-GeV full-energy injection is under construction since July 2016. Beam commissioning using the new AR-BT will start in January 2017. The dedicated striplines to detect beam oscillation at the front end of the damping system will be replaced with an existing button BPM not used for COD correction during commissioning. The feasibility of this replacement has already been confirmed with the actual stored beam. In the near future, we plan to renew the aging analog circuits including the BOD as well.

REFERENCES

[1] http://www.ft-ceramics.co.jp/eng/products/machinable/Mica/

[2] Y. Tanimoto, T. Honda, and S. Sakanaka, "Experimental demonstration and visual observation of dust trapping in an electron storage ring", *Phys. Rev. ST Accel. Beams*, vol. 12, p. 110702, 2009.

[3] D. A. Goldberg and G. R. Lambertson, "Dynamic Devices: A Primer on Pickups and Kickers", *AIP Conf. Proc.*, vol. 249, p. 537, 1992.

[4] http://www.ansys.com/Products/Electronics/ANSYS-HFSS

[5] http://www.gdfidl.de/

[6] M. Arinaga *et al.*, "Progress in KEKB beam instrumentation systems", *Prog. Theor. Exp. Phys.*, vol. 2013, p. 03A007, 2013.

[7] P. L. Pellegrin, "T.A.R. Bunch Oscillation Detector", TRISTAN Design Note, TN-82-011, 1982.

ISBN 978-3-95450-177-9

INTRA-TRAIN POSITION AND ANGLE STABILISATION AT ATF BASED ON SUB-MICRON RESOLUTION STRIPLINE BEAM POSITION MONITORS

N. Blaskovic Kraljevic, T. Bromwich, P. N. Burrows, G. B. Christian, C. Perry, R. Ramjiawan,
John Adams Institute, Oxford, UK,
D. R. Bett, CERN, Geneva, Switzerland

Abstract

A low-latency, sub-micron resolution stripline beam position monitoring (BPM) system has been developed and tested with beam at the KEK Accelerator Test Facility (ATF2), where it has been used to drive a beam stabilisation system. The fast analogue front-end signal processor is based on a single-stage radio-frequency down-mixer, with a measured latency of 16 ns and a demonstrated single-pass beam position resolution of below 300 nm using a beam with a bunch charge of approximately 1 nC. The BPM position data are digitised on a digital feedback board which is used to drive a pair of kickers local to the BPMs and nominally orthogonal in phase in closed-loop feedback mode, thus achieving both beam position and angle stabilisation. We report the reduction in jitter as measured at a witness stripline BPM located 30 metres downstream of the feedback system and its propagation to the ATF interaction point.

INTRODUCTION

The designs for the International Linear Collider (ILC) [1] and the Compact Linear Collider (CLIC) [2] require beams stable at the nanometre level at the interaction point (IP). In support of this, one of the goals of the Accelerator Test Facility (ATF2) at KEK, Japan, is to achieve position stability at the IP of approximately 2 nm. To this end, the Feedback On Nanosecond Timescales (FONT) project [3] operates a position and angle feedback system in the ATF2 extraction line [4]. In order to achieve the required level of position stability at the IP, the FONT feedback system needs to stabilise the beam to 1 μm at the entrance to the final focus system; this requires a BPM processing scheme capable of delivering position signals accurate to the sub-micron level on a timescale of the order of 10 ns.

The FONT beam position monitoring system makes use of three 12 cm stripline BPMs (P1, P2 and P3), which are located in the diagnostics section of the ATF2 extraction line and are placed on individual x, y movers (Fig. 1), and a witness stripline BPM (MFB1FF) located ~30 m downstream (Fig. 2). The BPMs are connected to specially developed analogue processing electronics [6] in order to deliver appropriate position signals to a digital hardware module [7] that digitises the signals and returns the sampled data to a computer where they are logged. The BPM system has achieved a demonstrated resolution of ~300 nm at a charge of $\sim 0.5 \times 10^{10}$ electrons/bunch [6].

BPM PROCESSOR DESIGN

A schematic of the processor module is shown in Fig. 3 and a photograph of a partially disassembled module is shown in Fig. 6. The operation is as follows: the top (V_T) and bottom (V_B) stripline BPM signals are subtracted using a 180° hybrid to form a difference (Δ) signal and are added using a resistive coupler to form a sum signal. The resulting signals are then band-pass filtered and down-mixed with a 714 MHz local oscillator (LO) signal phase-locked to the beam before being low-pass filtered

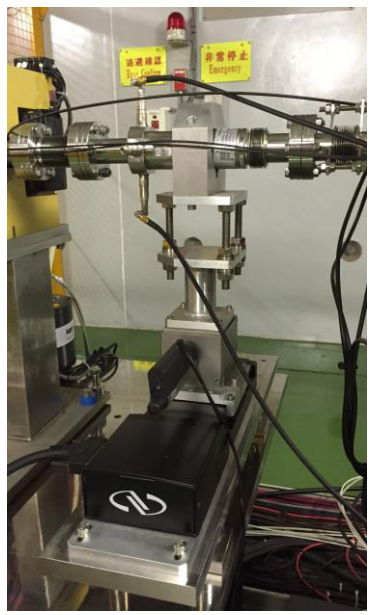

Figure 1: Photograph of the stripline BPM P3 and its mover.

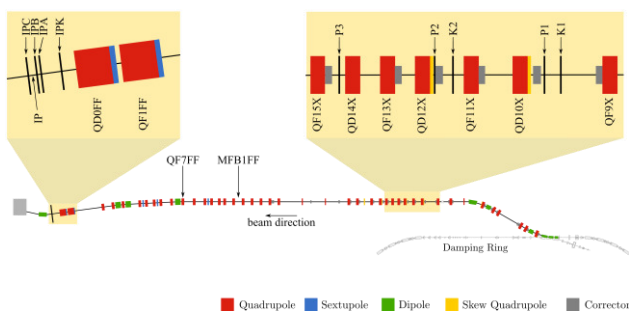

Figure 2: Layout [5] of the ATF2 extraction and final focus beamline with the FONT regions shown in detail.

ISBN 978-3-95450-177-9

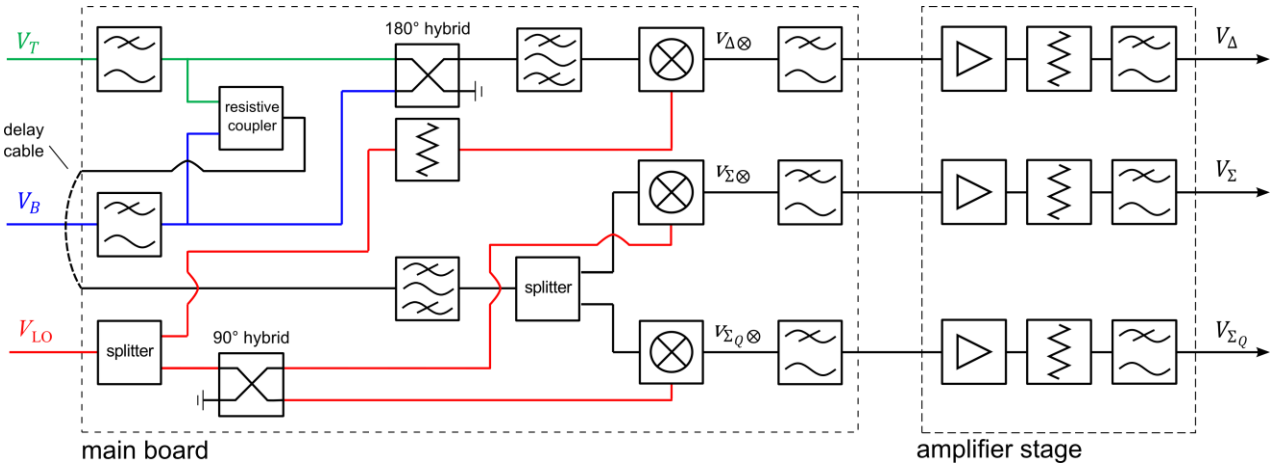

Figure 3: Schematic diagram illustrating the structure of the BPM analogue processor.

and amplified using 16 dB low-noise amplifiers. The hybrid, filters, and mixer were selected to have latencies of the order of a few nanoseconds in order to minimise the overall processor latency.

The phasing of the LO with respect to the beam signal is maintained using an adjustable phase shifter on the LO input to the processor (Fig. 4). In the sum channel, a 90° hybrid is used to downmix the raw sum signal with two orthogonal phases of the LO, producing an in-phase sum signal (Σ) and quadrature-phase sum signal (Σ_Q). The phase of the difference channel is accurately matched to that of the in-phase sum signal via a custom loopback cable in the sum channel. Hence the optimal phasing of both the Δ and Σ signals is achieved by minimising the Σ_Q signal.

The latency of the processor, that is the time interval between the arrival of the stripline signals at the inputs and the peak of the signals at the outputs, has been measured by using a test bench to provide realistic beam proxy input signals and observing on an oscilloscope the arrival time of the processed output signal. Subtracting from this the time of arrival at the oscilloscope of the input when the processor is bypassed, the processor latency before the amplifier stage was found to be 10.4 ± 0.1 ns, and 15.6 ± 0.1 ns including the amplifier stage (Fig. 5).

The three output signals (Δ, Σ, Σ_Q) from the BPM processor are digitized using analogue-to-digital converters (ADCs) on the FONT5 digital board, capable of converting at up to 400 MHz with 14-bit resolution. Low-noise amplifiers, with a gain of 16 dB, built into the processor modules are used to boost the input levels to just above the digitiser noise floor, and hence maximise the dynamic range of the measurement system. The ADCs, and sampling logic of the FONT5 board's Field Programmable Gate Array (FPGA), are clocked in a system-synchronous mode at 357 MHz, this being a convenient frequency derived from the machine RF. The ADC clock may be delayed in increments of 70 ps to allow sampling at the exact time the bunch arrives. There are nine ADCs in total and so a single board is able to fully record the data from three BPMs.

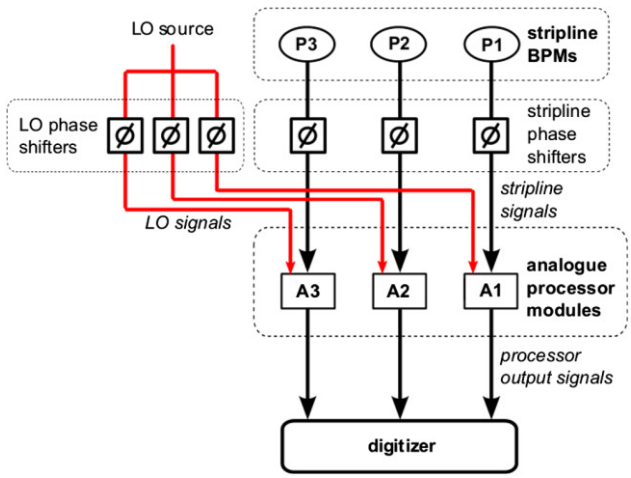

Figure 4: Schematic of the BPM system. For each BPM, a phase shifter is used on one of the stripline signals to adjust the relative path lengths of the two input signals at the BPM processor, and another phase shifter is used to adjust the phase of the LO signal at each processor.

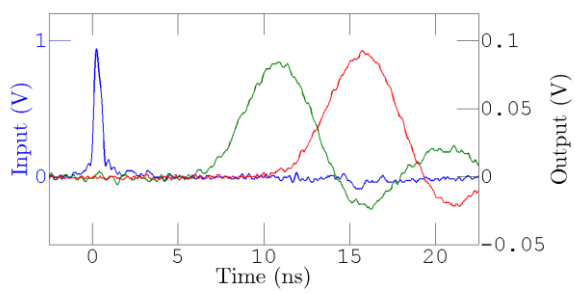

Figure 5: Input beam proxy V_T signal (blue, left-hand scale) and processor output V_Δ signal before the amplifier stage (green, right-hand scale, with factor 5 multiplication), and after the amplifier stage (red, right-hand scale), vs time.

ISBN 978-3-95450-177-9

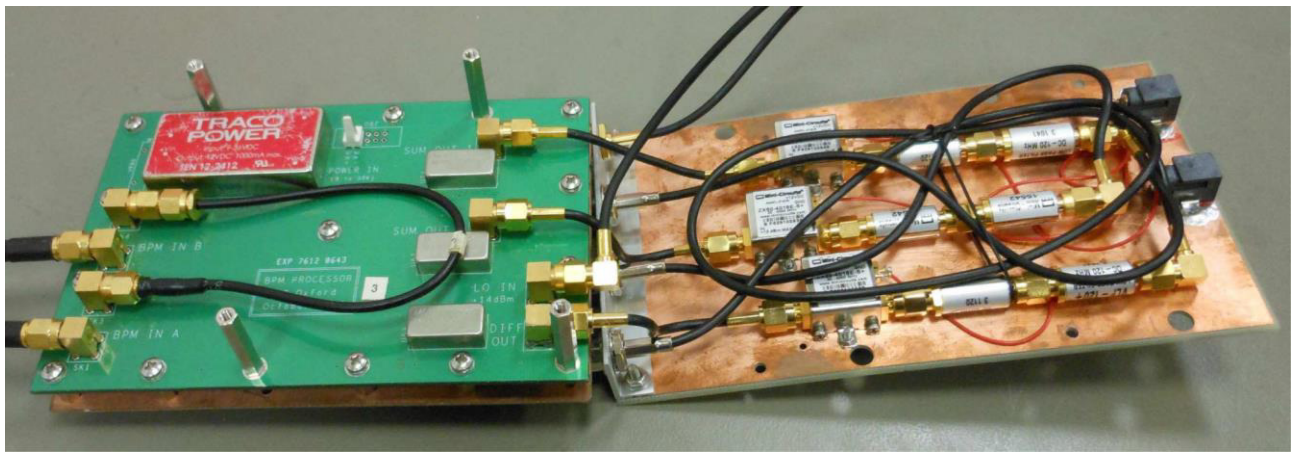

Figure 6: Photograph of the BPM analogue processor. The unit is partially disassembled for viewing purposes.

FEEDBACK RESULTS

Two stripline BPMs (P2 and P3) have been used to drive a pair of kickers (K1 and K2) local to the BPMs (Fig. 7) and nominally orthogonal in betatron phase, to form a two-phase closed-loop feedback system to stabilise the position and angle of the beam at the entrance to the final focus [8].

For these demonstrations, a beam consisting of two bunches separated by 182 ns was used. The feedback tests therefore involve measuring the vertical position of bunch one and correcting the vertical position of bunch two. The system was typically operated in an 'interleaved' mode, whereby the feedback correction was toggled on and off on alternate machine pulses; the feedback 'off' pulses thereby provide a continual 'pedestal' measure of the uncorrected beam position. The feedback correction of the beam was witnessed at MFB1FF.

Figure 8 shows the result of the feedback operation as measured at P2, P3 and MFB1FF. The position jitter is reduced from 1.6 µm to 610 nm at P2, and from 1.8 µm to 520 nm at P3. This factor of ~3 reduction in jitter is successfully preserved out to MFB1FF, with the beam jitter being stabilised from 30 µm to below 10 µm.

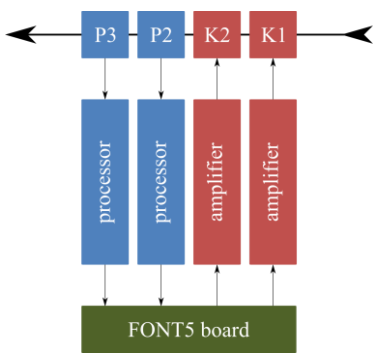

Figure 7: Block diagram of the feedback system.

Figure 10 shows the measured feedback performance at P2, P3 and MFB1FF as a function of bunch charge. Also shown is the expected jitter [9] that can be attained on operating the feedback (σ_{Y_2}) given the feedback off values for the position jitter of the two bunches (σ_{y_1}, σ_{y_2}) and the bunch-to-bunch position correlation ($\rho_{y_1 y_2}$):

$$\sigma_{Y_2}^2 = \sigma_{y_1}^2 + \sigma_{y_2}^2 - 2\sigma_{y_1}\sigma_{y_2}\rho_{y_1 y_2}. \quad (1)$$

The results show that the feedback successfully reduces the position jitter to the expected level given the measured incoming beam conditions.

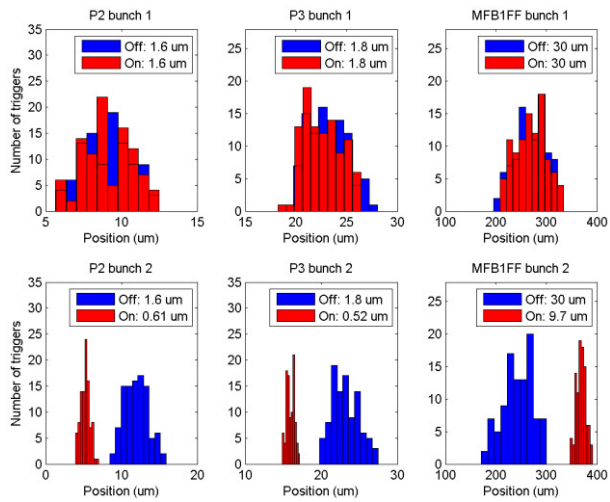

Figure 8: Distribution of the vertical position of bunches 1 and 2 in P2, P3 and MFB1FF with (red) and without (blue) application of the feedback correction. Values of the position jitter are quoted for each BPM.

ISBN 978-3-95450-177-9

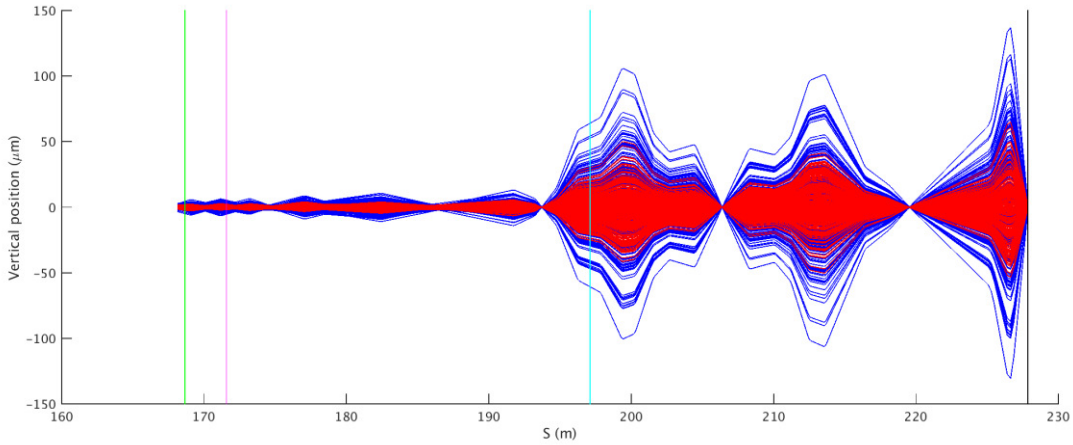

Figure 9: Vertical bunch position versus longitudinal distance S in the lattice, for an ensemble of triggers, propagated from measured positions at P2 and P3 for data with (red) and without (blue) application of the feedback correction. The vertical lines indicate the location of P2 (green), P3 (magenta), MFB1FF (cyan) and the IP (black).

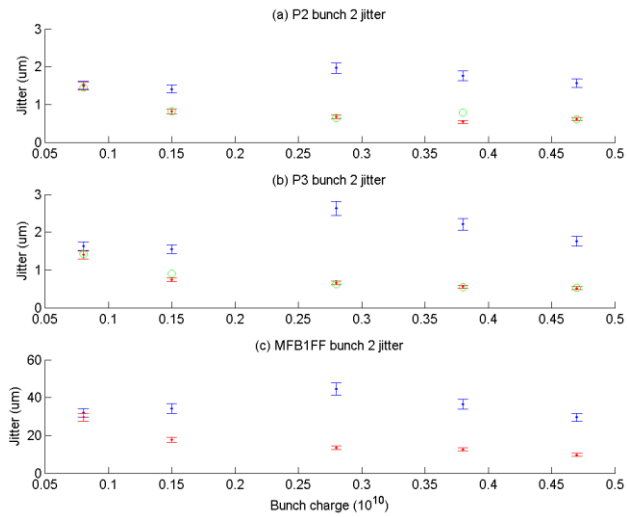

Figure 10: Bunch 2 position jitter measured in (a) P2, (b) P3 and (c) MFB1FF for a range of bunch charges with (red) and without (blue) application of the feedback correction. Expected jitter with feedback is shown in green.

The results at P2 and P3 have been propagated using vertical position and angle (y, y') transfer matrices through the ATF2 line to the IP. Figure 9 shows the result of propagating the measured vertical positions at P2 and P3 to the IP, illustrating the reduction in position jitter throughout the lattice on operating the feedback system.

CONCLUSIONS

Beam position and angle stabilisation has been demonstrated using a coupled-loop system consisting of two stripline BPMs and the two kickers in the ATF2 extraction line. Vertical beam stabilisation has been achieved at the 600 nm level locally at the feedback BPMs, and the propagation of the correction has been demonstrated in simulation and confirmed using a witness stripline BPM located approximately half way along the ATF2 line.

REFERENCES

[1] C. Adolphsen et al., The ILC technical design report, volume 3: Accelerator, JAI-2013-001, 2013.

[2] M. Aicheler et al., CLIC conceptual design report, CERN-2012-007, 2012.

[3] www-pnp.physics.ox.ac.uk/~font

[4] B. I. Grishanov et al., ATF2 proposal, vol. 2, KEK Report 2005-9, 2005.

[5] G. R. White et al., Phys. Rev. Lett., vol. 112, p. 034802, 2014.

[6] R. J. Apsimon et al., Phys. Rev. ST Accel. Beams, vol. 18, p. 032803, 2015.

[7] B. Constance, DPhil thesis, Oxford University, 2011.

[8] R. J. Apsimon et al., Physics Procedia, vol. 37, p. 2063, 2012.

[9] N. Blaskovic Kraljevic, DPhil thesis, Oxford University, 2015.

ISBN 978-3-95450-177-9

PERFORMANCE OF NANOMETRE-LEVEL RESOLUTION CAVITY BEAM POSITION MONITORS AND THEIR APPLICATION IN AN INTRA-TRAIN BEAM POSITION FEEDBACK SYSTEM

N. Blaskovic Kraljevic, T. Bromwich, P. N. Burrows, G. B. Christian, C. Perry, R. Ramjiawan,
John Adams Institute, Oxford, UK
D. R. Bett, CERN, Geneva, Switzerland
T. Tauchi, N. Terunuma, KEK, Tsukuba, Ibaraki, Japan
S. Jang, Dept. of Accelerator Science, Korea University, Sejong, South Korea
P. Bambade, LAL, Orsay, France

Abstract

A system of three low-Q cavity beam position monitors (BPMs), installed in the interaction point (IP) region of the Accelerator Test Facility (ATF2) at KEK, has been designed and optimised for nanometre-level beam position resolution. The BPMs have been used to provide an input to a low-latency, intra-train beam position feedback system consisting of a digital feedback board and a custom stripline kicker with power amplifier. The feedback system has been deployed in single-pass, multi-bunch mode with the aim of demonstrating intra-train beam stabilisation on electron bunches of charge ~1 nC separated in time by c. 220 ns. The BPMs have a demonstrated resolution of below 50 nm on using the raw measured vertical positions at the three BPMs, and has been used to stabilise the beam to below the 75 nm level. Further studies have shown that the BPM resolution can be improved to around 10 nm on making use of quadrature-phase signals and the results of the latest beam tests will be presented.

INTRODUCTION

A number of fast beam-based feedback systems are required at future single-pass beamlines such as the International Linear Collider (ILC) [1]. For example, at the interaction point (IP) a system operating on nanosecond timescales within each bunch train is required to compensate for residual vibration-induced jitter on the final-focus magnets by steering the electron and positron beams into collision. The deflection of the outgoing beam is measured by a beam position monitor (BPM) and a correcting kick applied to the incoming other beam (Fig. 1). In addition, a pulse-to-pulse feedback system is envisaged for optimising the luminosity on timescales corresponding to 5 Hz.

The Feedback on Nanosecond Timescales (FONT) project has developed ILC prototype systems, incorporating digital feedback processors based on Field Programmable Gate Arrays (FPGAs), to provide feedback correction systems for sub-micron-level beam stabilisation at the KEK Accelerator Test Facility (ATF2) [2]. Demonstration of an upstream closed-loop feedback system that meets the ILC jitter correction and latency requirements is described in [3], together with results demonstrating the propagation of this correction along the ATF2 line. The ultimate aim is to attempt beam stabilisation at the nanometre-level at the ATF2 IP.

In order to achieve the required BPM resolution, three low-Q cavity BPMs have been developed, installed and optimised in the ATF2 IP region. We report here the BPM resolution measured with the ATF2 beam and the results achieved using one of these cavity BPMs to drive local feedback correction at the IP.

EXPERIMENTAL SET-UP

An overview of the ATF2 extraction and final focus beamlines, showing the positions of the system components in the IP region, is given in Fig. 2. The IP region contains the three C-band cavity BPMs IPA, IPB and IPC, operated on an x, y mover system [5], with IPB being used in the single-loop IP feedback system described below. The cavity BPM design quality factors are shown in Table 1. The IP feedback correction is applied using a stripline kicker (IPK). The final focus magnets (QF1FF, QD0FF) can be used to steer the beam by introducing a position offset or to move the x and y beam waists longitudinally along the beamline. The offset of the QF7FF magnet can be used to change the pitch of the beam trajectory through the IP region.

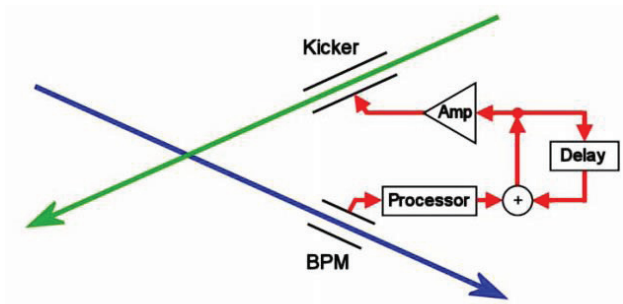

Figure 1: Schematic of IP intra-train feedback system with a crossing angle.

Table 1: Cavity BPM Design Quality Factors [6]

Quality factor	y dipole mode
Loaded quality factor, Q_L	579
Internal quality factor, Q_0	3996
External quality factor, Q_{ext}	677

ISBN 978-3-95450-177-9

A schematic of the IP feedback system is given in Fig. 3. Determining the position of the beam at IPB requires both the dipole mode signal of IPB and the monopole mode signal of a reference cavity (Ref). The cavities were designed such that the y-port frequency of both signals is 6.426 GHz [6]. The signals are down-mixed to baseband using a two-stage down-mixer [7], as follows. The first stage down-mixer (M1) takes the 6.426 GHz reference and IPB signals and mixes each with an external, common 5.712 GHz local oscillator (LO) to produce down-mixed signals at 714 MHz. The second stage down-mixer (M2) mixes the IPB 714 MHz signal using the reference 714 MHz as LO, giving two baseband signals: I (IPB and reference mixed in phase) and Q (IPB and reference mixed in quadrature). The I and Q signals are subsequently digitised in the FONT5 digital board (Fig. 4) and normalised by the beam bunch charge; the charge is deduced from the amplitude of the reference cavity signal using a diode detector. The charge-normalised I and Q signals are calibrated against known beam position offsets (by moving the BPM mover), allowing the IPB vertical beam position to be known in terms of a linear combination of charge-normalised I and Q.

BPM RESOLUTION RESULTS

The resolution of the system of three BPMs was measured as follows. Firstly, each BPM was calibrated, allowing the position of the beam to be calculated using:

$$y = \frac{I'}{qk} = \frac{I\cos\theta_{IQ} + Q\sin\theta_{IQ}}{qk} \quad (1)$$

where q is the charge measurement, and k and θ_{IQ} are constants obtained from the calibration. Note that this particular linear combination of the orthogonal I and Q terms is referred to as I'. A linear combination orthogonal to I' exists, and is referred to as Q':

$$I' = I\cos\theta_{IQ} + Q\sin\theta_{IQ}; \quad (2)$$
$$Q' = -I\sin\theta_{IQ} + Q\cos\theta_{IQ}. \quad (3)$$

Secondly, a 300-pulse data set was taken. The beam position measured at the first two BPMs is used to predict the beam position at the third using one of two methods. In the geometric method, the position at IPC is predicted using:

$$y_{\mathrm{IPC}} = a_1 y_{\mathrm{IPA}} + a_2 y_{\mathrm{IPB}}. \quad (4)$$

where a_1 and a_2 are obtained from the beam propagation transfer matrices. In the fitting method, linear regression is performed to find the fit coefficients c_1, c_2,.... in an equation of the type:

$$I'_{\mathrm{IPC}} = c_1 I'_{\mathrm{IPA}} + c_2 I'_{\mathrm{IPB}} + c_3. \quad (5)$$

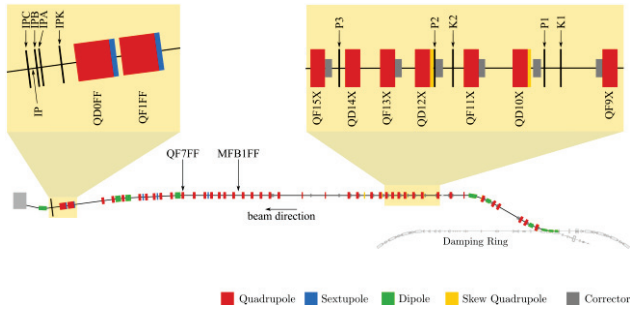

Figure 2: Layout [4] of the ATF2 extraction and final focus beamline with the FONT regions shown in detail.

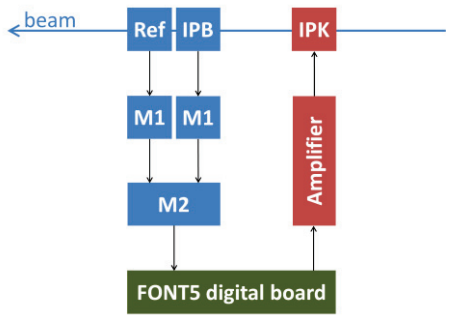

Figure 3: Schematic of IP feedback system showing the cavity BPM (IPB), reference cavity (Ref), first and second down-mixer stages (M1 and M2), FONT5 digital board, amplifier and kicker (IPK).

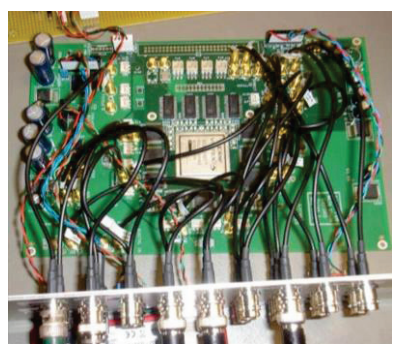

Figure 4: FONT5 digital feedback board.

Having obtained the fit coefficients, Eq. (5) is used to calculate the predicted I' values at IPC, which can then be converted to predicted positions using Eq. (1). Additional fit parameters (such as Q' or q) can be added to Eq. (5). The residual of the measured and predicted positions at the third BPM is calculated, and the standard deviation δ of the residuals is computed. The resolution is then calculated by scaling δ by a geometric factor [7]:

ISBN 978-3-95450-177-9

$$\text{Resolution} = \frac{\delta}{\sqrt{1+a_1^2+a_2^2}}. \quad (6)$$

The results in Table 2 show that a base resolution of around 50 nm can be achieved using the geometric method. Transitioning to fitting brings the resolution down by a factor 3, and including the Q' term to the fit brings the resolution down further to the order of 10 nm.

Table 2: Resolution of the Triplet Cavity BPM System Using Geometric and Fitting Methods. Statistical Errors are Shown

Method	Resolution (nm)
Geometric	49.5 ± 2.0
Fitting I' & constant	16.4 ± 0.7
Fitting I', Q' & constant	14.1 ± 0.6
Fitting I', Q', q & constant	13.4 ± 0.6

FEEDBACK RESULTS

We summarise here the results of beam tests of the FONT5 feedback system. Further results are reported in [8, 9].

The accelerator was set up to provide two bunches per pulse of beam extracted from the damping ring, with a bunch separation of 215.6 ns. This separation was found typically to provide a high degree of measured vertical bunch position correlation between the two bunches. The feedback tests therefore involve measuring the vertical position of bunch one and correcting the vertical position of bunch two. The system was typically operated in an 'interleaved' mode, whereby the feedback correction was toggled on and off on alternate machine pulses; the feedback 'off' pulses thereby provide a continual 'pedestal' measure of the uncorrected beam position. For the purpose of recording data with BPM IPB the longitudinal location of the beam waist in the IP region was adjusted by varying the strengths of the two final focus magnets QF1FF and QD0FF. For the results reported here the beam waist was typically set near the position of IPB.

The IP feedback system latency was measured and found to be 212 ns [10]. The performance of the feedback system was measured using IPB; Fig. 5 shows the vertical position of both bunches with feedback off and on. The IP feedback reduced the vertical beam jitter from an r.m.s. deviation of 420 nm to 74 nm (Table 3). Fig. 6 shows the bunch 2 position versus bunch 1 position for this data set. The feedback removes the correlated component between the bunches, reducing the bunch-to-bunch position correlation from 98.2 % to approximately zero (Table 3).

Table 3: Position Jitter of Bunch 1 (σ_{y_1}) and 2 (σ_{y_2}) and Bunch-to-bunch Position Correlation ($\rho_{y_1 y_2}$) with and without Application of the IP Feedback Correction

Feedback	σ_{y_1} (nm)	σ_{y_2} (nm)	$\rho_{y_1 y_2}$ (%)
Off	412 ± 29	420 ± 30	$+98.2^{+0.3}_{-0.4}$
On	389 ± 28	74 ± 5	-13 ± 10

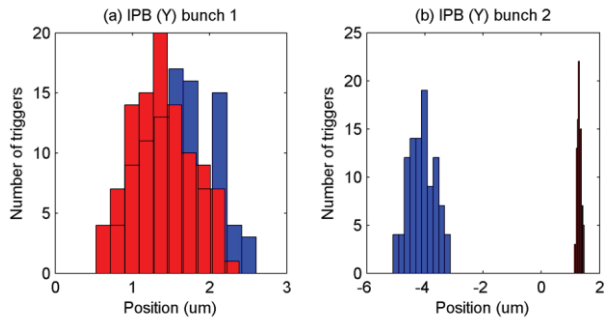

Figure 5: Distribution of the vertical position of (a) bunch 1 and (b) bunch 2 in IPB with (red) and without (blue) application of the IP feedback correction.

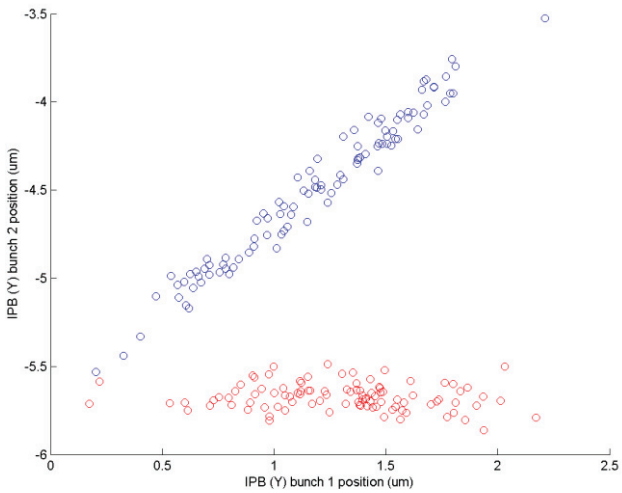

Figure 6: Vertical position for bunch 2 versus bunch 1 in IPB with (red) and without (blue) application of the IP feedback correction.

ISBN 978-3-95450-177-9

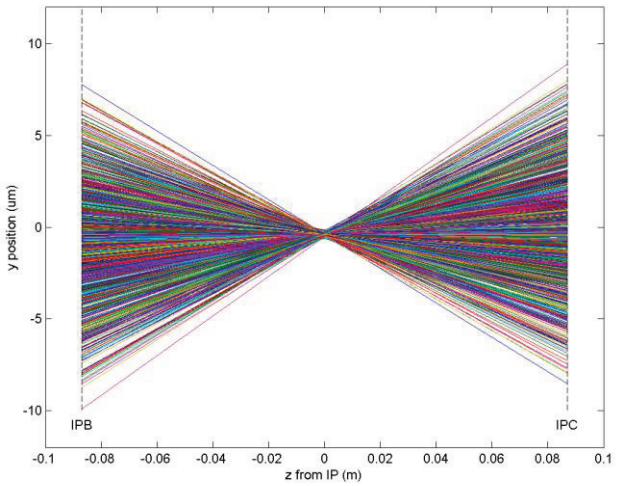

Figure 7: Vertical bunch position y, obtained for each trigger by linearly interpolating the measured beam positions at IPB and IPC, versus longitudinal distance z from the IP.

The jitter that can be attained with feedback on (σ_{Y_2}) can be calculated from the feedback off values for the jitter of the two bunches (σ_{y_1}, σ_{y_2}) and their correlation ($\rho_{y_1y_2}$):

$$\sigma_{Y_2}^2 = \sigma_{y_1}^2 + \sigma_{y_2}^2 - 2\sigma_{y_1}\sigma_{y_2}\rho_{y_1y_2} \geq 2\sigma_r^2 \qquad (7)$$

where σ_r is the BPM resolution [11]. The above equation yields an expected jitter with feedback on of $\sigma_{Y_2} = 79.4$ nm, which agrees with the measured value of 74 ± 5 nm. Furthermore, Eq. (7) sets an upper limit to the resolution of $\sigma_r \lesssim 50$ nm, which agrees with the resolution measurements presented above.

OUTLOOK

Future plans consist in using two IP BPMs in order to stabilise the beam at a location between them. Preliminary measurements have been taken simultaneously at BPMs IPB and IPC, located equidistantly either side of the IP. Given the absence of magnetic fields in the IP region, the beam trajectories can be calculated by linearly interpolating the positions measured at the two BPMs as shown in Fig. 7. The results show that, under typical operating conditions, the position jitter is ~3 µm at IPB and IPC. The beam waist can be clearly reconstructed at a location 0.3 mm downstream of the nominal IP with an interpolated position jitter of 82 nm.

In addition to the benefit of stabilising the beam at a location other than the BPM itself, the use of two BPMs to perform the measurement has the potential of improving the position resolution available to the feedback system. In the configuration where IPB and IPC are used to stabilise the beam at the IP, the vertical position at the IP would be taken as the average of the vertical positions measured at IPB and IPC. Thus, the error on this mean position would be $\sigma_r/\sqrt{2}$ where σ_r is the resolution of either BPM [11]. The challenge in this mode of operation results from the requirement of a large BPM dynamic range of over 10 µm whilst preserving the BPM resolution.

CONCLUSIONS

Three low-Q cavity BPMs have been developed, installed and optimised in the ATF2 IP region. A BPM resolution of below 50 nm has been achieved on using the raw measured vertical positions with the expected beam propagation. Fitting the beam transport, and making use of the BPM quadrature-phase signal Q', brings the resolution down to around 10 nm.

Beam stabilisation using one of these cavity BPMs has been demonstrated successfully. Vertical beam position stabilisation to below the 75 nm level has been achieved using a local IP feedback system. The system has a demonstrated latency of 212 ns. Work is ongoing to improve the resolution of the cavity BPMs and to work towards operating a feedback system using the inputs from two IP BPMs.

REFERENCES

[1] C. Adolphsen *et al.*, The ILC technical design report, volume 3: Accelerator, JAI-2013-001, 2013.

[2] B. I. Grishanov *et al.*, ATF2 proposal, vol. 2, KEK Report 2005-9, 2005.

[3] N. Blaskovic Kraljevic *et al.*, Proceedings of IBIC2016, Barcelona, Spain, TUPG15.

[4] G. R. White *et al.*, Phys. Rev. Lett., vol. 112, p. 034802, 2014.

[5] O. R. Blanco *et al.*, Proceedings of IPAC2015, Newport News, VA, USA, MOPHA003.

[6] S. Jang *et al.*, Proceedings of IPAC2016, Busan, Korea, THOAA02.

[7] Y. Inoue *et al.*, Phys. Rev. ST Accel. Beams, vol. 11, p. 062801, 2008.

[8] N. Blaskovic Kraljevic *et al.*, Proceedings of IPAC2014, Dresden, Germany, THOAA02.

[9] N. Blaskovic Kraljevic *et al.*, Proceedings of IPAC2015, Newport News, VA, USA, MOPTY083.

[10] M. R. Davis, DPhil thesis, Oxford University, 2014.

[11] N. Blaskovic Kraljevic, DPhil thesis, Oxford University, 2015.

ISBN 978-3-95450-177-9

DESIGN AND BEAM TEST RESULTS OF THE REENTRANT CAVITY BPM FOR THE EUROPEAN XFEL

C. Simon*, M. Baudrier, M. Luong, L. Maurice, O. Napoly,
CEA-Saclay/DRF/Irfu, Gif sur Yvette, France
N. Baboi, D. Lipka, D. Noelle, G. Petrosyan DESY, Hamburg, Germany
R. Baldinger, B.Keil, G. Marinkovic, M. Roggli, PSI, Villigen, Switzerland

Abstract

The European X-ray Free Electron Laser (E-XFEL) will use reentrant beam position monitors (BPMs) in about one quarter of the superconducting cryomodules. This BPM is composed of a radiofrequency (RF) reentrant cavity with 4 antennas and an RF signal processing electronics. Hybrid couplers, near the cryomodules, generate the analog sum and difference of the raw pickup signals coming from two pairs of opposite RF feedthroughs. The resulting sum (proportional to bunch charge) and difference signals (proportional to the product of position and charge) are then filtered, down-converted by an RF front-end (RFFE), digitized, and digitally processed on an FPGA board.

The task of CEA/Saclay was to cover the design, fabrication and beam tests and deliver these reentrant cavity BPMs for the E-XFEL linac in collaboration with DESY and PSI.

This paper gives an overview of the reentrant BPM system with focus on the last version of the RF front end electronics, signal processing, and overall system performance.

Measurement results achieved with prototypes installed at the DESY FLASH2 linac and in the E-XFEL injector are presented.

INTRODUCTION

The European XFEL [1] is an X-ray free electron laser user facility installed in Hamburg, Germany. The beginning of commissioning is planned by the end of 2016. This accelerator has a superconducting 17.5 GeV main linac based on the TTF technology and its parameters are summarized in Table 1.

Table 1: E-XFEL Accelerator Parameters

Parameter	Value
Typical beam sizes (RMS)	20 – 200 µm
Nominal bunch charge	0.02 – 1 nC
Bunch spacing	≥ 222 ns
Macro-pulse length	600 µs
Number of bunches within macro-pulse	1 – 2700
Nominal macro-pulse repetition rate	10 Hz

Each module includes a string of eight 1.3 GHz RF cavities, followed by a BPM connected to a superconducting quadrupole. Two types of cold BPMs are installed along the machine: cold reentrant BPMs and button BPMs which are not discussed here [2].

The cold reentrant BPM has a beam pipe aperture of 78 mm. It has to measure position and charge, to allow bunch to bunch measurements with a resolution better than 50 µm, a charge between 20 pC and 1 nC and an operating dynamic range of ± 10 mm.

To measure the behaviour of reentrant BPM with the electronics final version in its environment (Modular BPM Unit), beam measurements were done on a reentrant cavity BPM installed in a warm part at FLASH2 [3] and on the first cold reentrant BPM installed in the 3.9 GHz cryomodule during the commissioning of the E-XFEL injector [4].

REENTRANT BPM SYSTEM

This type of BPM is composed of a radio-frequency reentrant cavity [5], which has to operate in a clean and cryogenic environment, and an analog front end electronic (RFFE) which provides the signals to a digital back end, connected to the control system.

Passing through the cavity, the beam excites electromagnetic fields (resonant modes), which are coupled by four feedthroughs to the outside. The voltage differences (Δ) from two opposite antennas correspond to the voltage of the dipole field in the X and Y axis and the sums (Σ) correspond to the voltage of the monopole field. The Δ and Σ signals are obtained from passive 4-ports 180° hybrid couplers. Each coupler is connected to a pair of opposite antennas and transmits the signals to the radio-frequency Front end electronics via some cables.

Figure 1: Reentrant RFFE board.

The reentrant Radio-Frequency Front End board (Fig.1) uses a single stage down-conversion to process the Δ/Σ signals. It is based on a Printed Circuit Board (PCB) with surface mount components and uses the VME64x form factor as required by the generic E-XFEL digitizer and

* claire.simon@cea.fr

ISBN 978-3-95450-177-9

crate electronics called Modular BPM Unit (MBU) developed by PSI. The electronics of the E-XFEL BPM system follows a modular design approach [6]. This crate, contains a generic digital back-end (GPAC) with two ADC mezzanine boards, and either two reentrant BPM RFFEs or one reentrant cavity BPM RFFE and up to two button BPM RFFEs together, as well as power supplies, fans, a rear IO module with digital and multi-gigabit fiber optic IOs for timing and control system interfaces (Fig: 2).

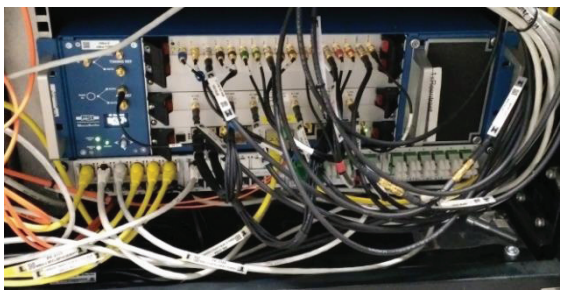

Figure 2: MBU crate installed at the E-XFEL injector with one reentrant RFFE (top), one button RFFE and the generic digital back-end with two ADC mezzanine boards.

RF/Analog Electronics

The RFFE analog electronics design, presented in Fig. 3, has three channels to perform single-stage down-conversion of X/Y positions and reference (charge). Monopole and dipole mode frequencies of the pickup are respectively 1255 MHz and 1724 MHz [7].

On the Δ channels, a band pass filter centered around 1725 MHz, was designed to reject the monopole mode frequency and high order modes. Its bandwidth of 102 MHz also provides a noise reduction. Band pass filters, followed by a variable gain section, allow the analog gain adjustment to the beam charge. It combines two selectable paths: one with a direct path and one with a 31.5 dB range step programmable variable attenuator and low noise amplifier (LNA). A diode is added to protect the variable attenuator and LNA in case of excessive beam offsets. To protect mixers from possible high output power, RF limiters are used.

The very low external quality factor (Q = 24) [7] and the amplitude level of the monopole mode allows the electronics to filter around the dipole mode frequency and still to obtain a sufficiently large signal level. The Σ channel has only one gain range and uses the same variable attenuator and LNA. A diode for the LNA protection is added in case of the wrong switching of attenuator.

The signals are, then, translated to a lower IF signal by an in-phase/quadrature-phase (I/Q) down-conversion on each channel using a local oscillator (LO) signal. The I/Q down-conversion is composed of mixers used for systems with high dynamic range, and 90 ° hybrid couplers chosen for their low phase and amplitude imbalances. The LO signal operates around the dipole mode frequency and is locked to the reference signal 216.666 MHz from the machine. To generate this signal, a phase-locked loop (PLL) is combined to a divider using an intermediate frequency 9.028 MHz. A programmable phase shifter allows keeping a constant phase on the Σ signal thanks to a digital feedback implemented on a FPGA on the GPAC. With a 216.666 MHz on-board oscillator integrated to the electronics, the LO signal can also operate without external reference clock in a free-running mode. To communicate with the digital board and pilot PLL, phase shifter, variable attenuators, I2C bus is used.

The output I/Q IF signals are then amplified by differential amplifiers. They deliver to ADCs, a pulse signal of full width around 15 ns for the charge signal reading and around 25 ns for the beam position signal reading with a shape close to a Gaussian shape.

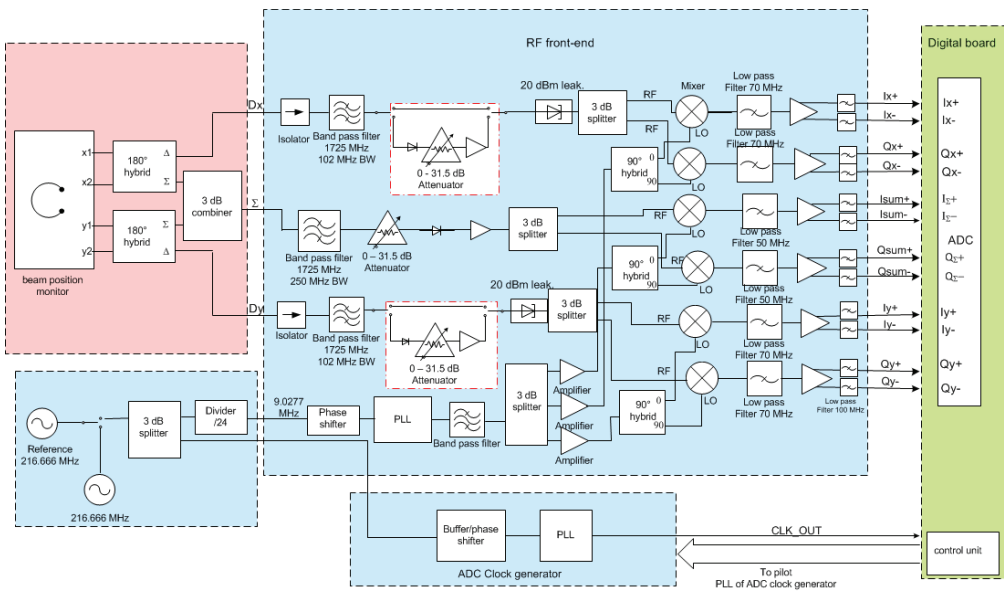

Figure 3: Block diagram of the cold reentrant BPM.

ISBN 978-3-95450-177-9

This I/Q down-conversion of Δ and Σ channels allow the digital back-end to determine the sign of the beam position just by comparing the phases of the signals, independently of beam arrival time jitter and external reference clock phase. A serial EEPROM to identify each BPM, a hot swap control to safely insert and remove modules without switching off MBU power are, also, inserted on this RFFE board.

The ADC clock, generated at 162.5 MHz and integrated on the PCB, is also locked to the reference signal and uses a programmable phase shifter and PLL. The sampling and the interface to the control-system are carried with 16 bits ADCs digital electronics operating at 160 Msps, designed and programmed by PSI.

The timing of signals from Δ channels is adjusted by the adding of some delays (cables) to get their top to the same time of the Σ channel maximum.

Digital Signal Processing

A signal processing algorithm [8] is used to determine the beam positions (X and Y) and charge from the signals read by ADCs. This algorithm was implemented in the FPGA board. The ADC phase is automatically tuned for a peak detection of RFFE output signals. Then, a cartesian-to-polar conversion is performed to determine the amplitude and phase of each channel. To compensate some imperfections due to non-ideal analog components, a pre-calibration is performed for I/Q imbalance, attenuation and phase settings of the digital step attenuators and final correction gain factors. Scaling coefficients are also implemented to give the right value.

BEAM MEASUREMENTS

In 2015-2016, beam tests were done with a reentrant BPM installed in a warm section at FLASH2 (Fig. 4) and another BPM installed in the 3.9 GHz cryomodule at the E-XFEL injector (Fig. 5).

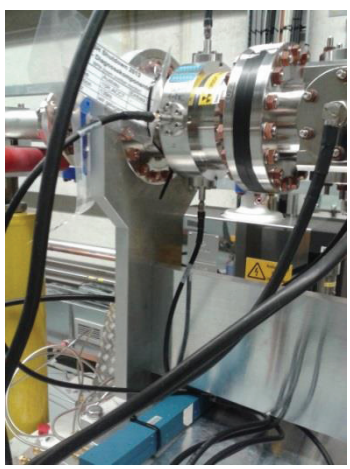

Figure 4: Reentrant BPM (centre) installed on the linac FLASH2 with 180° hybrid couplers.

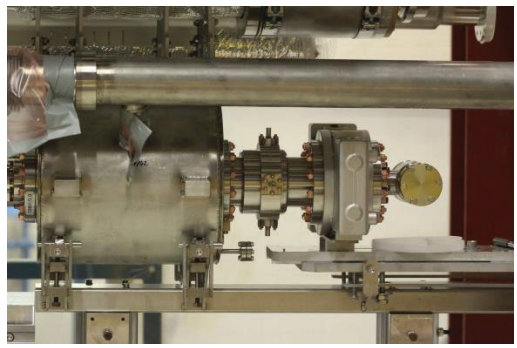

Figure 5: Cold Reentrant BPM with its quadrupole installed at the 3.9 GHz cryomodule.

For an optimal operation on the accelerator, the reentrant BPMs are fully integrated into the DOOCs E-XFEL accelerator control system (a parallel EPICS system from PSI is also implemented to allow laboratory tests and precalibration).

The absolute calibration of the BPM charge reading is carried out by comparing the charge read by a nearby toroid to the charge read by the BPM studied. Figure 6 shows a good correlation between charge reading of the cold reentrant BPM and the reading of the nearby toroid.

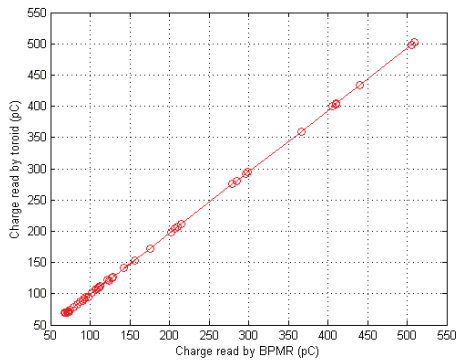

Figure 6: Charge read by toroid vs charge read by the cold reentrant BPM at the E-XFEL injector

To calibrate the position reading, the relative beam displacement (Δx) at the BPM location is calculated by using a transfer matrix (R_{12}) between steerers and BPM (made of drifts) for different values of drive current in the steerers: $\Delta x = R_{12}.\Delta x_0$ (where Δx_0 is the beam angle at steerer position). The steerers are used to deflect the beam, and the magnets between the steerers and the BPM are switched off to reduce errors and simplify calculation. An average of 100 points for each steerer setting is used and a calibration coefficient is computed from a linear fit of the predicted position to the measured position. After adjustment of coefficients, Fig. 7 shows a good linearity in a dynamic range ± 13 mm in horizontal and vertical planes for a charge of 0.4 nC. An offset on Δx and Δy channels was added in the acquisition software to read a zero in this condition.

ISBN 978-3-95450-177-9

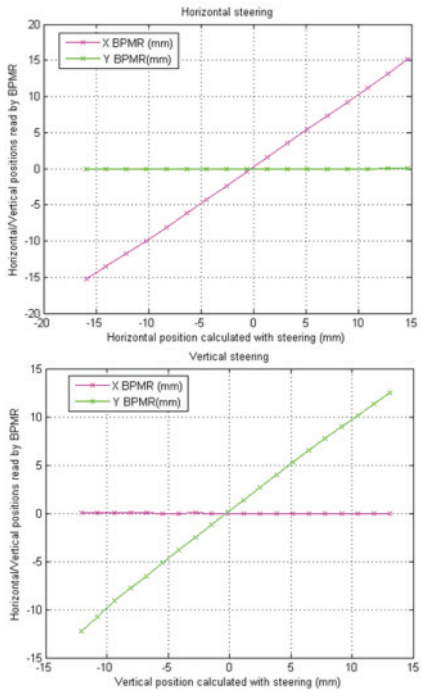

Figure 7: Calibration results from horizontal (top) and vertical (down) steerings with a charge around 0.4 nC at FLASH2.

Figure 8 illustrates the beam position as a function of charge. Here changing the charge by ± 5 %, the beam position does not change within < 100 µm.

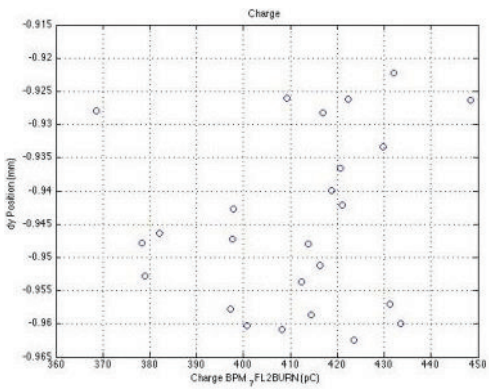

Figure 8: Position read by reentrant BPM installed at FLASH2 vs charge read by the reentrant BPM.

Resolution

Some resolution measurements were done with reentrant BPMs installed on the FLASH2 linac and E-XFEL injector. Two different configurations can be used: one with no amplifier (direct path) used for high charges and one with one amplifier used for the low charges. To cancel the beam jitter, the reentrant BPM resolution is measured by correlating the reading of the reentrant BPM in one plane against the readings of all other BPMs in the same plane [9]. Table 2 presents the resolution measurements. These resolution measurements were done, for the "direct path", with a dynamic range of ± 10 mm at 1 nC.

Table 2: Reentrant BPM Resolution Measurements

Beam charge (pC)	Machine	Configuration	Resolution (µm)
450	FLASH2	"Direct path"	~5
100	FLASH2	"Direct path"	~7
30	FLASH2	"Amplifier"	~10
500	E-XFEL	"Direct path"	~5
100	E-XFEL	"Amplifier"	~4
50	E-XFEL	"Direct path"	~30
50	E-XFEL	"Amplifier"	~8

CONCLUSION

Beam tests done at the FLASH2 linac and at the E-XFEL injector showed that the specifications like linearity, dynamic range and resolution for the E-XFEL cold reentrant BPM are fulfilled. These measurements, also, allow qualifying a calibration procedure to minimize the difference between the predicted and measured values.

ACKNOWLEDGEMENT

We thank our colleagues from CEA Saclay, DESY and M. Stadler from PSI for their contribution, their support, and their advice during the development of this project. We also acknowledge the operators and support teams for their help during the measurements done on the FLASH2 linac and the E-XFEL Injector.

REFERENCES

[1] R. Brinkmann, "The European XFEL Project", Proc. *FEL2006,* Berlin, Germany, 2006.

[2] D. Treyer *et al.*, "Design and beam test results of button BPMs for the European XFEL", *IBIC2013*, Oxford, UK, 2013.

[3] N. Baboi, D.Noelle, "Commissioning of the FLASH2 Electron Beam Diagnostics in respect to its use at the European XFEL" *IBIC2014*, Monterrey, CA, USA, 2014.

[4] F. Brinker, "Commissioning of the European XFEL injector", *IPAC2016*, Busan, Korean, 2016.

[5] C. Simon *et al.*, "Fabrication Process for the European XFEL re-entrant cavity BPM", *IBIC 2014*, Monterrey,CA, USA, 2014.

[6] B. Keil *et al.*, "A Generic BPM Electronics Platform for European XFEL, SwissFEL and SLS", *IBIC14,* Monterrey, CA, USA, 2014.

[7] C. Simon, *et al.*, "Performance of a reentrant cavity beam position monitor", Physical review special topics – accelerators and beams 11, 082802 (2008).

[8] B. Keil *et al.*, "Beam-based calibration and performance optimization of cavity BPMs for swissFEL, E-XFEL and FLASH2", Proceedings. *IBIC2014,* Monterrey, CA, USA, 2014.

[9] N. Baboi *et al.*, in Proceedings of the *12th Beam Instrumentation Workshop (BIW2006),* Batavia, IL, 2006, *AIP Conf.* Proc. No. 868 (AIP, Batavia, IL, 2006), http://dx.doi.org/10.1063/1.2401409

ISBN 978-3-95450-177-9

DESIGN OPTIMIZATION OF BUTTON-TYPE BPM ELECTRODE FOR THE SPring-8 UPGRADE*

M. Masaki†,1, H. Dewa[1], T. Fujita[1], H. Maesaka[2], S. Takano[1,2]
[1] Japan Synchrotron Radiation Research Institute, Kouto, Sayo, Hyogo, 679-5198, Japan
[2] RIKEN SPring-8 Center, Kouto, Sayo, Hyogo, 679-5148, Japan

Abstract

The design of a button-type BPM electrode for the SPring-8 upgrade has been optimized from the perspectives of 1) mechanical structure, 2) rf characteristics, and 3) thermal issue. We have adopted the electrode structure without a sleeve enclosing a button to maximize the button diameter. To minimize the beam impedance and the trapped mode heating of the electrode, the rf structure has been optimized by 3D electro-magnetic simulations. The reduction of the heating suppresses thermal deformation of the electrode and the BPM block, and improves thermal stability of the BPM system. The mechanical tolerance of the electrode was defined to fit the error budget for the total BPM offset error of 100 μm rms.

INTRODUCTION

The BPM system of the storage ring for the SPring-8 upgrade [1, 2] has been designed to satisfy the requirements of long-term stability, resolution and accuracy. The specifications of the BPM system are summarized in ref. [3]. For the stability, a drift of the BPM offset less than 5 μm in a month is required. In a beam commissioning phase, a resolution of single-pass (SP) trajectory measurements better than 100 μm rms is necessary for an injected single bunch beam of 100 pC charge. The demanded accuracy for the SP measurement is within 100 μm rms and ±200 μm maximum. We have optimized the design of a button-type electrode for the new BPM system to meet the requirements. The points of the design optimization are 1) the maximization of signal intensity to satisfy the required resolution, 2) the specifications of necessary mechanical tolerances to fit the error budget for the total BPM offset, and 3) the minimization of heating to reduce thermal drift of the BPM offset. This paper focuses on the design of the button-type BPM electrode. The development status of the whole BPM system is described in a separate paper [3].

MECHANICAL DESIGN

Button Diameter

The vacuum chambers for the new ring have narrow apertures [4] due to small bore diameters of the strong quadrupole and sextupole magnets [5]. A cross-section of the BPM head is shown in Fig.1. The vertical aperture of the beam pipe is 16 mm. The button electrodes are mounted with the horizontal span of 12 mm on 20 mm-wide flat tops of the upper and lower sides. For satisfying the required signal intensity, it is necessary to maximize the button diameter in the narrow mounting space. Hence, we have adopted the electrode structure without a sleeve enclosing the button. No sleeve structure is also beneficial to eliminate the impedance and the trapped modes associated with an annular slot around the sleeve in a housing hole for the electrode. Figure 2 shows a schematic drawing of the designed button electrode. The maximized button diameter is 7 mm.

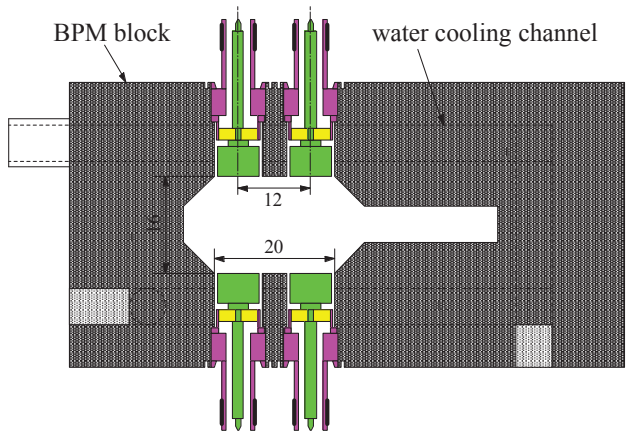

Figure 1: Cross section of the BPM head.

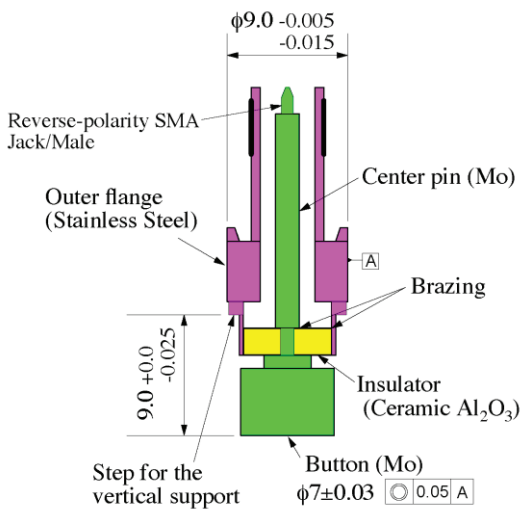

Figure 2: The designed BPM button electrode.

* Work supported by RIKEN SPring-8 Center
† masaki@spring8.or.jp

ISBN 978-3-95450-177-9

Materials

The BPM head will be made of non-magnetic materials to avoid magnetic interference with adjacent quadrupole and sextupole magnetic fields. We selected stainless steel (316L) as a material of the water-cooled BPM block welded to the vacuum chamber made of the same stainless steel. The material of the outer flange of the electrode welded to the block is also stainless steel (316L). To suppress the heating of the button and center pin of the electrode thermally connected to the block only through the insulator of alumina ceramic, as their material, we have selected molybdenum (Mo) with high electric and thermal conductivities which are nearly ten-times larger than that of stainless steel or titanium. Molybdenum also suits for high-accuracy machining.

Mechanical Tolerance

To satisfy the error budget defined for the BPM offset of 100 μm rms, we have specified machining tolerances of the button electrode (Fig. 2) and its mounting hole of the BPM block. The tolerances of the button diameter and the vertical mounting position in the BPM block are specified as ±30 μm and 50 μm as an offset back into the hole, respectively. To ensure the horizontal position accuracy of the button, we have specified the concentricity of 50 μm between the button and the outer flange of the electrode which fits in the housing hole of the BPM block.

RF AND THERMAL SIMULATIONS

The results of simulation studies for the design optimization are summarized in this section. The RF characteristics (beam signals, beam coupling impedances and trapped modes) were calculated using CST STUDIO SUITE [6] and the thermal issues were analysed using ANSYS [7].

Ohmic Loss Minimization

Trapped resonance modes excited in a coaxial structure of the BPM electrode lead to heating and beam coupling impedance. The dominant resonance modes contributing to loss factor κ_{loss} coming from the beam impedance are excited in a gap between the button and the housing hole as shown in the next section (Fig. 5). Therefore, the geometric dimensions relevant to the strength of the main trapped mode resonances are the size of the gap and the button thickness. Narrowing the gap simply reduces the resonance strengths, though, it requires tighter machining tolerance to avoid electric short between the button and the housing hole. We selected the same gap of 0.5 mm as the BPM button of the present SPring-8, since we have experienced no troubles with the electric short or discharge. The button thickness was optimized to minimize the ohmic loss. The total ohmic loss P_{loss} of a BPM head including loss in four electrodes and wall loss is expressed by,

$$P_{loss} = \kappa_{loss}(\sigma_t)\frac{Q_b^2}{T_b} - 4P_{sig}\ , \qquad (1)$$

where Q_b, T_b and P_{sig} are bunch charge, bunch spacing and output signal power per button electrode, respectively.

The loss factor κ_{loss} in frequency domain is defined by

$$\kappa_{loss}(\sigma_t) = \frac{1}{2\pi}\int_0^\infty h(\omega;\sigma_t)d\omega. \qquad (2)$$

The function $h(\omega, \sigma_t)$ is the longitudinal impedance of a BPM head weighted with a power spectrum of a bunched beam,

$$h(\omega;\sigma_t) = 2Re[Z_\parallel(\omega)]e^{-\omega^2\sigma_t^2}. \qquad (3)$$

Here, $Z_{//}$ and σ_t are longitudinal impedance and bunch length (rms), respectively. Figure 3 shows the total ohmic loss as a function of the button thickness for a temporary bunch fill pattern of 0.25 mA/bunch*406 which gave the maximum heat load among the equally spaced bunch fill patterns for a total stored current of 100 mA. In the calculation, bunch lengthening due to potential well distortion was taken into account by a preliminary beam impedance model for the whole of the new ring. Here, the bunch length σ_t is evaluated to be 14 ps for the bunch current of 0.25 mA. We selected a button thicknesses of 5 mm giving the minimum ohmic loss in the calculation.

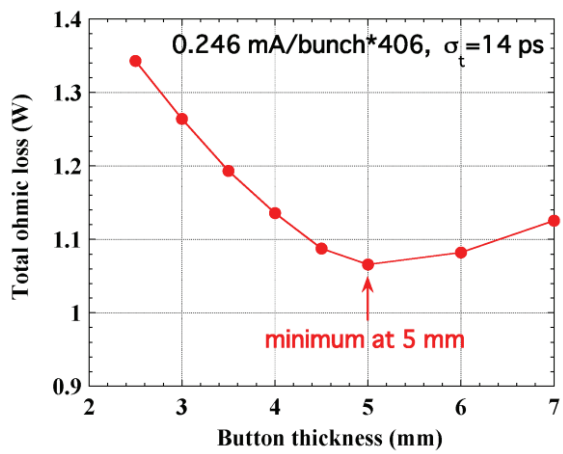

Figure 3: The total ohmic loss of a BPM head as a function of the button thickness calculated for a temporary bunch fill pattern of 0.25 mA/bunch*406 with a total stored current of 100 mA (see text).

Trapped Modes Analysis

The frequency spectrum of the trapped resonance modes is given by $h(\omega, \sigma_t)$ of Eq. (3). Figure 4 shows the function $h(\omega, \sigma_t)$ calculated for the BPM head with the optimized electrodes. The diameter and height of the button are ϕ7 mm and 5 mm, respectively. The bunch length of 14 ps (rms) is assumed.

ISBN 978-3-95450-177-9

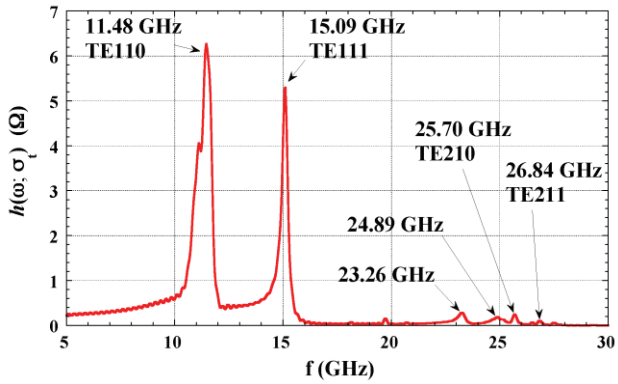

Figure 4: Calculated frequency spectrum of the trapped resonance modes (see text).

Two resonance peaks at the frequencies of 11.48 and 15.09 GHz stand for the main trapped modes. Some weak resonance modes are also excited in the frequency range from 20 to 30 GHz. We computed the electro-magnetic fields distributions of each mode at the resonance peak frequencies. Figure 5 shows the distributions of magnetic fields, which can cause heating of the BPM electrode and the block. The trapped modes classified as TE-modes by the computed field distributions are excited in the gaps of 0.5 mm between the buttons and the housing holes for the electrodes. The weak resonance modes at 23.26 and 24.89 GHz are also excited in the ceramic around the center pin.

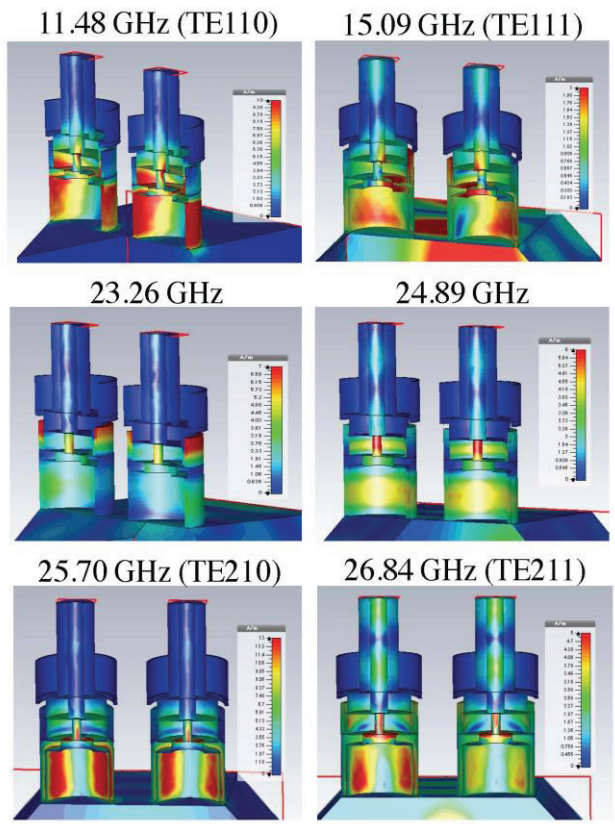

Figure 5: Computed magnetic field distributions of the trapped modes at the resonance frequencies in Fig. 4.

Heating of the BPM Electrode and the Block

It is important to evaluate the trapped mode heating of the BPM electrode and its housing hole, and the wall current heating of the BPM block. Thermal deformations of the button and the block could cause a drift of the BPM offset, which deteriorates the long-term stability of the BPM system. The BPM block is water-cooled to remove the heat dissipated in the electrodes and their housing holes, and the heat by wall current loss. To evaluate the heat input to each part of the electrode (the button, center pin) and the inside of the housing hole, we calculated the contribution to the loss factor of each trapped mode by integrating the resonance peak corresponding to each mode shown in Fig. 4. Here, the contribution of the wall current loss is subtracted from the integrals. The heat input to each part is given by the sum of the integrated ohmic losses of the relevant trapped modes. Figure 6 shows the evaluated heat input to the molybdenum button side, center pin, inside of the housing hole of the stainless steel BPM block, and the flat-tops of the beam pipe inside the block. The temporary bunch fill pattern of 0.25 mA/bunch*406 with the bunch length of 14 ps is assumed. The total heat input evaluated for the whole of the BPM head is 1.1 W. We have computed the temperature distribution of the BPM head with the heat input condition shown in Fig. 6. The temperature of the cooling water for the BPM block is set at 30 ˚C, and its flow velocity in the cooling channel with 6 mm diameter is 0.6 m/s. The heat transfer coefficient from the block to the cooling water is calculated to be 4300 W/m^2/K for turbulent flow condition. The natural heat dissipation to the surrounding air of 27 ˚C is also taken into account with the heat transfer coefficient of 5 W/m^2/K. The heat generated at the molybdenum button and center pin is transferred to the water-cooled block through the alumina ceramic with thermal conductivity of 18 W/m/K which is close to that of stainless steel. The computed temperature distribution is shown in Fig. 7. The maximum temperature obtained in the calculation is 31 ˚C on the button surface.

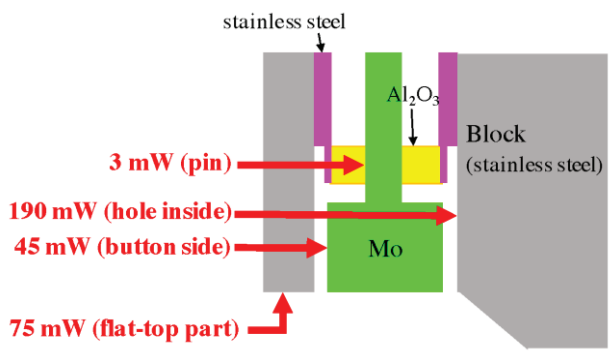

Figure 6: The heat input model for thermal simulation of the BPM electrode and the BPM block (see text).

ISBN 978-3-95450-177-9

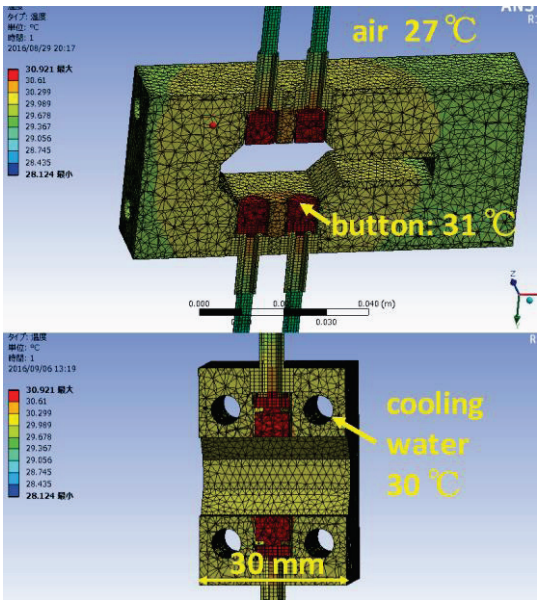

Figure 7: Computed temperature distribution of the BPM head. Maximum temperature is 31 ˚C on the button of the electrode.

Signal Intensity

In the vicinity of the center of a BPM, a beam position (x_b, y_b) is calculated by

$$(x_b, y_b) = \left(k_x \frac{V_1 - V_2 - V_3 + V_4}{V_1 + V_2 + V_3 + V_4}, k_y \frac{V_1 + V_2 - V_3 - V_4}{V_1 + V_2 + V_3 + V_4}\right), \quad (4)$$

where V_1, V_2, V_3, V_4 are the signal intensities from the four button electrodes. For the designed BPM electrode (Fig. 2) and BPM block (Fig. 1), the horizontal and vertical sensitivity coefficients (k_x, k_y) are calculated to be (6.8 mm, 7.7 mm). The beam signal voltage V for satisfying the demanded position resolution σ_{resol} is given by

$$V > \frac{k_{x,y}}{2\sigma_{resol}} \sigma_V, \quad (5)$$

where σ_V is the signal voltage fluctuation due to thermal and electric noises. The thermal noise power at an input to a signal processor circuit is estimated to be -101 dBm for the bandwidth of 10 MHz at the room temperature of 300 K. When the noise figure of a processor is assumed to be 14 dB including cable loss for the original designed circuit [3] as one of the candidates of BPM electronics for the SPring-8 upgrade, the equivalent input noise power is -87 dBm, that is corresponding to the signal voltage fluctuation σ_V of 10 μV. From Eq. (5) with the vertical sensitivity coefficient k_y of 7.7 mm, we can calculate the signal voltage of 0.38 mV or power of -55 dBm required for the resolution σ_{resol} of 100 μm. For the SP measurement of a single bunch beam of 100 pC charge, the signal power spectrum with 10 MHz bandwidth calculated for the designed ϕ7*5 mm button electrode is shown in Fig. 8. The signal intensity at the detection frequency of the processor circuit, same as the RF frequency of 508.76 MHz, is -53 dBm larger than the requirement.

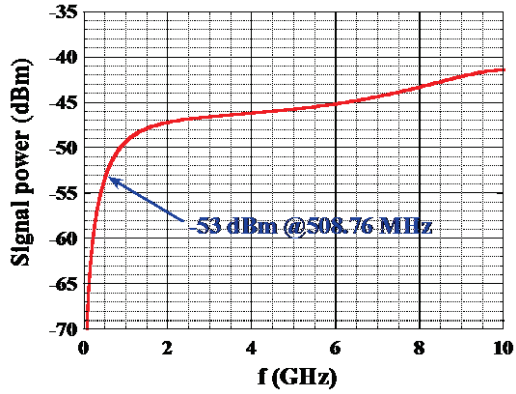

Figure 8: Calculated power spectrum of the BPM output signal in 10 MHz bandwidth for a 100 pC single bunch.

SUMMARY

We have designed and developed the button-type BPM electrodes for the SPring-8 upgrade. The mechanical structure and the tolerances, and the materials are optimized to maximize the signal intensity, to satisfy the allowable BPM offset error, and to minimize the trapped mode heating of the electrode. Manufacturing of the prototypes of the designed electrode is in progress. We have a plan for a beam test of the prototypes at the present SPring-8 storage ring. The performance of the designed BPM electrode (the signal intensity, the signal waveform, and the heating by electron beam) will be verified.

ACKNOWLEDGEMENT

Authors would like to thank B. K. Scheidt for useful comments and discussions on the materials for the button electrode.

REFERENCES

[1] SPring-8-II Conceptual Design Report, Nov. 2014, http://rsc.riken.jp/pdf/SPring-8-II.pdf

[2] H. Tanaka, *et al.*, "SPring-8 Upgrade Project", in Proceedings of IPAC2016, Busan, Korea, May 2016, WEPOW019, pp. 2867-2870.

[3] H. Maesaka, *et al.*, "Development Status of a Stable BPMSystem for the SPring-8 Upgrade", presented at IBIC2016, Barcelona, Spain, Sep. 2016, TUPG06, this conference.

[4] M. Oishi, *et al.*, "Design and R&D for the SPring-8 Upgrade Storage Ring Vacuum System", in Proceedings of IPAC2016, Busan, Korea, May 2016, THPMY001, pp.3651-3653.

[5] T. Watanabe, *et al.*, "Magnet Development for SPring-8 Upgrade", in Proceedings of IPAC2016, Busan, Korea, May 2016, TUOCB03, pp.1093-1095.

[6] CST STUDIO SUITE, http://www.cst.com/

[7] ANSYS, http://www.ansys.com/

ISBN 978-3-95450-177-9

THE CMS BEAM HALO MONITOR AT THE LHC: IMPLEMENTATION AND FIRST MEASUREMENTS

N. Tosi*[1], INFN Bologna, Italy
on behalf of the CMS Collaboration
[1]also at DIFA, Università di Bologna, Italy

Abstract

A Cherenkov based detector system has been installed at the Large Hadron Collider (LHC), in order to measure the Machine Induced Background (MIB) for the Compact Muon Solenoid (CMS) experiment. The system is composed of forty identical detector units formed by a cylindrical Quartz radiator directly coupled to a Photomultiplier. These units are installed at a radius of 1.8 m and a distance of 20.6 m from the CMS interaction point. The fast and direction-sensitive signal allows to measure incoming MIB particles while suppressing the much more abundant collision products and albedo particles, which reach the detector at a different time and from a different direction. The system readout electronics is based on the QIE10 ASIC and a μTCA based back-end, and it allows a continuous online measurement of the background rate separately per each bunch. The detector has been installed in 2015 and is now fully commissioned. Measurements demonstrating the capability of detecting anomalous beam conditions will be presented.

INTRODUCTION

The increase in beam energy and luminosity in the LHC Run II, started in 2015, also meant an increase in Machine Induced Background (MIB) for the experiments. The Beam Radiation Instrumentation and Luminosity (BRIL) project designed, built and currently operates detectors that measure Luminosity and MIB in several regions of the CMS experiment [1]. Among the MIB detectors are instruments designed for protection of the sensitive inner silicon detectors of CMS from severe beam loss events and others that detect when the MIB reaches levels that would interfere with data taking efficiency. The Beam Halo Monitor (BHM) [2] is the outermost such detector, and it is sensitive to beam gas interactions happening upstream of CMS as well as beam halo interactions with the upstream collimators.

THE DETECTOR

Concept

The BHM has to be able to detect and correctly identify MIB particles in the context of a particle flux dominated by products of high energy *pp* collisions. Detection and identification are based on techniques that exploit differences between MIB and other particles, combined into a single instrument:

- The MIB flux is dominated by muons, due to absorption and decay of other particle types, while a significant fraction of the *pp*-collision products is composed of neutral particles.
- The MIB originated from the incoming beam and the *pp*-collision products travel in opposite direction.
- At several locations along the beampipe, the MIB and the majority of *pp*-collision products arrive with maximal time separation between each other (exactly half of the bunch spacing, 12.5 ns).

A Cherenkov based detector can make use of all these characteristics, thanks to Cherenkov radiation being emitted promptly and in a known direction with respect to the particle trajectory.

Detector Hardware

Each BHM detector unit is composed of a synthetic quartz cylinder, 100 mm long and 52 mm in diameter, acting as Cherenkov radiator, directly coupled to a fast, UV-sensitive photomultiplier tube (PMT). Particles travelling from the quartz towards the PMT (from right to left in Fig. 1) emit Cherenkov Light that reaches the photocathode. Particles travelling in the opposite direction also emit light, but this is instead absorbed by a layer of black paint applied to the free face of the quartz. These elements are enclosed in a three layer shielding to protect the PMT from the residual field of the CMS solenoid and to absorb the large flux of low energy particles present in the cavern.

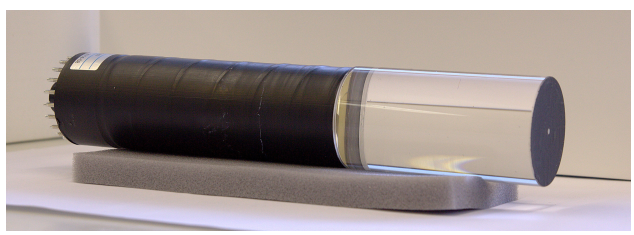

Figure 1: The active elements of the BHM detector unit: a 52 mm diameter quartz cylinder attached to an Hamamatsu R2059 photomultiplier.

The complete detector has twenty units on each end of CMS, mounted around the rotating shielding as shown in Fig. 2. They are located at a radius of 1.8 m and a distance of 20.6 m from the CMS interaction point and pointed towards the incoming beam. The large signal produced by the Hamamatsu R2059 PMT is brought to the readout electronics located in the service cavern via high bandwidth triaxial

* nicolo.tosi@cern.ch

ISBN 978-3-95450-177-9

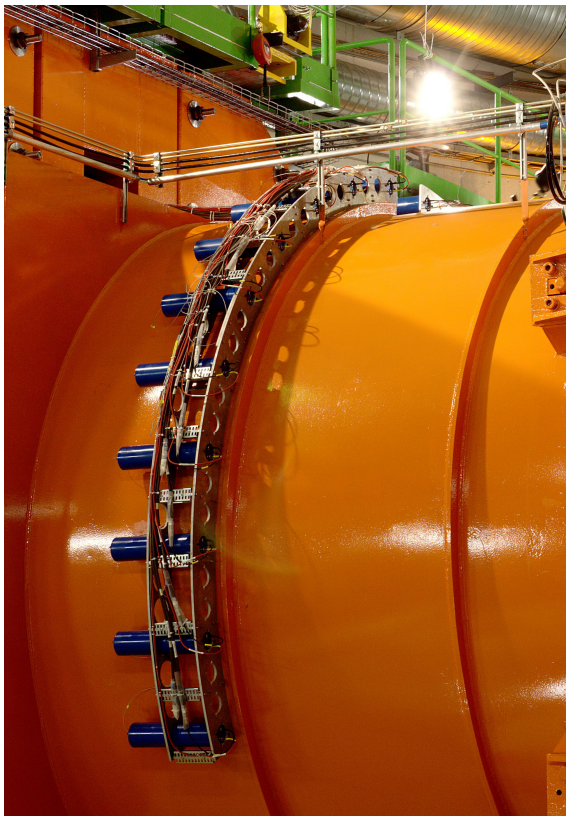

Figure 2: The BHM mounted on the rotating shielding around the beampipe in CMS.

cables, over a length of about 80 m. The PMT power supply and an LED pulse generator for monitoring are also located in the service cavern and connected to each unit with long cables and optical fibers, respectively.

Readout

The readout electronics uses components developed for the Phase 1 upgrade of the CMS Hadron Forward Calorimeter (HF) [3]. This is composed of a front-end equipped with the QIE10 charge integrating ADC and TDC, as well as a μTCA based back-end.

The readout electronics collects hit count information separately per each bunch crossing (BX), with a further subdivision into four equal time slices in each BX. These counts are integrated over a period of 2^{14} LHC orbits, equivalent to about 1.4 s, and are readout with no deadtime over a network connection. Amplitude spectra and single event waveforms can also be acquired for offline analysis and monitoring purposes.

PERFORMANCE IN 2015 AND 2016

The BHM detector was installed in the CMS cavern in early 2015, and its readout electronics and data acquisition software were completed in the fall of the same year. A temporary, VME-based system provided the initial data readout.

Initial Tests

Early during the commissioning of BHM, the LHC operators performed several experiments with the settings of the CMS tertiary collimator (TCTs) aperture. One such experiment was recorded and the MIB rates are shown in Fig. 3. This first measurement demonstrated the basic functionality of BHM.

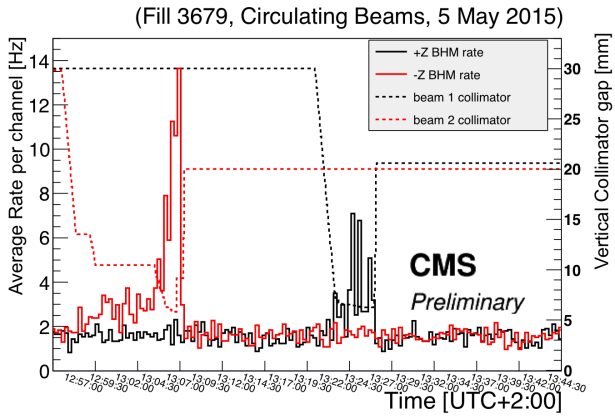

Figure 3: The BHM rates readout by VME scalers during collimators' setting: The dashed lines show the collimator gap for Beam 1 (black) and Beam 2 (red) TCT vertical collimators. The solid lines show the respective BHM average rate per channel for Beam 1 sensitive detectors (black) and Beam 2 sensitive detectors (red).

Normal Operating Conditions

The discrimination of MIB is based on both a minimum amplitude threshold and a requirement on timing. One BX is subdivided into four time slices; the MIB is contained within one such slice, while collision products are distributed over all slices, due to large variations in their time of flight. An example of this distribution for a typical LHC fill is shown in Fig. 4.

Due to the distance of BHM from the interaction point, there is a significant difference in the proportion of collision products to MIB within a train of bunches. For a train of N colliding bunches, the BHM will measure 6 BX which contain only MIB hits, $N - 6$ which contain hits from both MIB and pp-collisions and a further 6 with only collision hits, as shown on the right side of Fig. 5. Software corrections, calculated using these last 6 bunches in a train, are applied to the MIB time slice counts in the middle of the train to subtract the contamination from collision products. Two rates, averaged over all channels on each end and normalized for beam intensity, are calculated and published every *LumiSection* (≈23 s).

Angular Distribution The shape of the LHC tunnel and beamline elements dictates the angular distribution of MIB around the beamline. A simulation of the flux, shown in Fig. 6, predicted a low flux of particles below the beamline (which was therefore not instrumented), due to absorbtion by

ISBN 978-3-95450-177-9

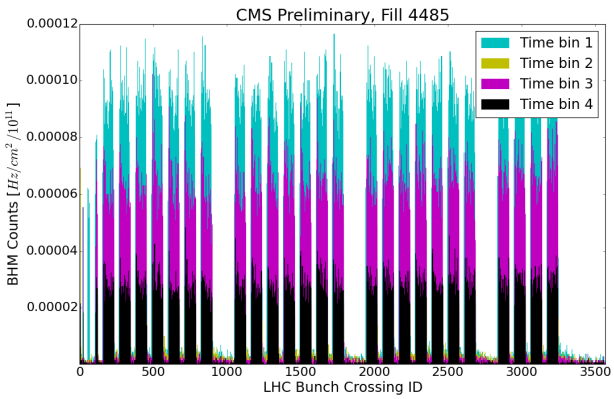

Figure 4: Bunch crossing occupancy histogram for one channel of BHM. MIB is expected to arrive at a time corresponding to bin 1 (cyan). This plot shows a fill with good beam conditions: all bunch trains produce a small and uniform MIB contribution.

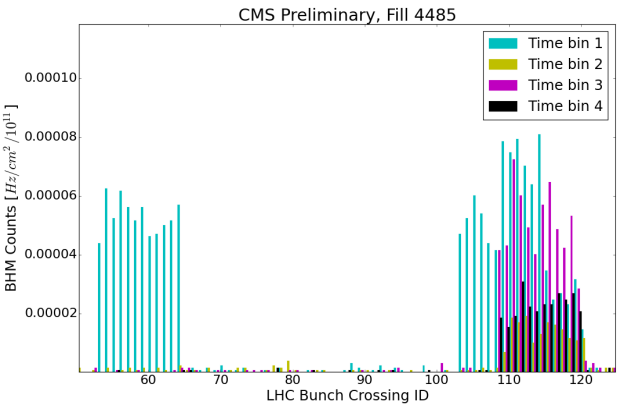

Figure 5: Detail of bunch crossing occupancy histogram for one channel of BHM. MIB is expected to arrive at a time corresponding to bin 1 (cyan). The peaks on the left side are purely MIB, produced by twelve non colliding bunches. The peaks on the right side include contributions from collision products of twelve bunches as well as MIB.

the tunnel floor, as well as an increased flux on the horizontal plane, in correspondence of the collimator jaws. Measurements, shown in Fig. 7 show a general agreement with the prediction.

Collimator Scans

As part of the LHC Machine Development 310, several pilot bunches were excited provoking beam losses, while several collimators, including the TCTs adjacent to CMS, were adjusted across a wide range of apertures. As BHM is, by construction, especially sensitive to particles produced in interactions with the TCTs, a set of measurements (shown in Fig. 8) was taken in order to correlate the BHM measurement with the TCT aperture. An approximate exponential dependence on collimator aperture is observed, consistent with expectations.

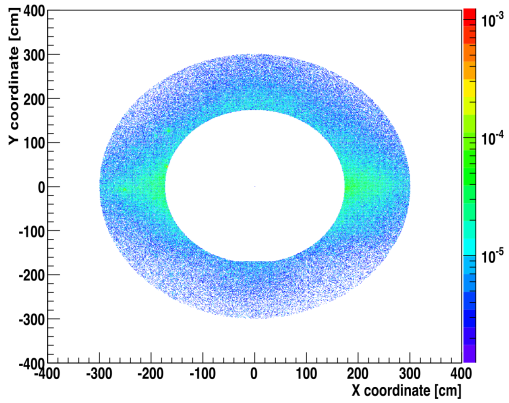

Figure 6: Simulation of the flux distribution in the XY plane of the MIB flux at the detector location (z = 20.6 m), from [2].

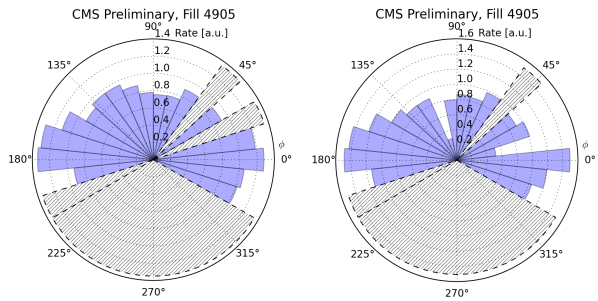

Figure 7: Angular distribution, around the beam pipe, of Machine Induced Background rate for Beam 1 (left) and Beam 2 (right). Each slice corresponds to one BHM channel. The rates are normalized to the average rate. The hatched areas are not instrumented or not available.

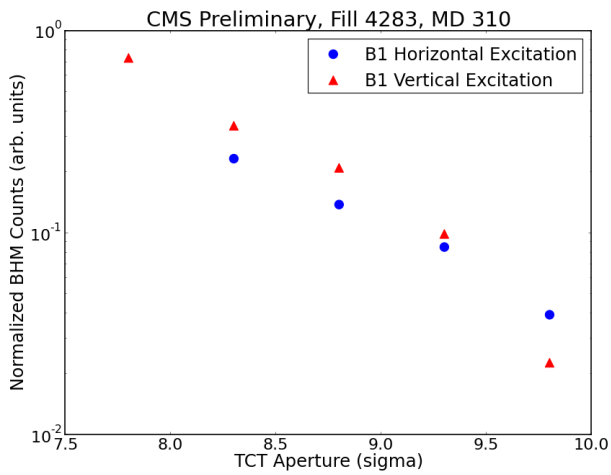

Figure 8: BHM count rates of all Beam 1 channels during Machine Development 310. An aperture scan of the tertiary collimators (TCTs) was performed while pilot bunches were excited. The ratio of the BHM count rate to the total beam loss, as measured by the Point 7 Beam Loss Monitor, is shown as a function of the TCT aperture.

ISBN 978-3-95450-177-9

Beam Gas Test

A series of tests was conducted between May and June 2016 to determine the effect of beam gas interaction in the LHC experiments. In the first such test, during LHC fill 4905, a vacuum getter cartridge was heated, releasing trapped atoms into the beam, in the vicinity of the TCTs, at about 150 m from the CMS interaction point. Vacuum pressure, measured by several gauges, increased by five orders of magnitude with respect to normal operating conditions, and the MIB rate measured by BHM followed closely the evolution of the pressure over time, as can be seen in Fig. 9 and Fig. 10.

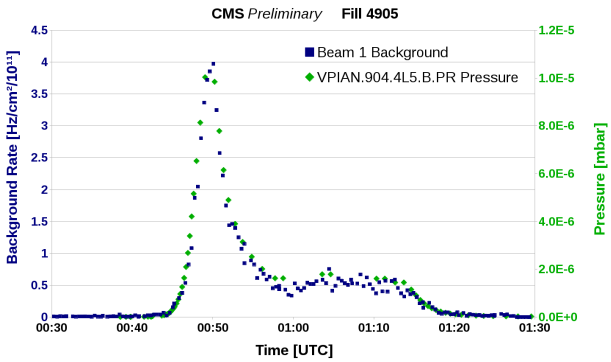

Figure 9: Time variation of MIB rates measured by BHM shown together with beampipe vacuum pressure, measured by the VPIAN.904.4L5 pressure sensor, for Beam 1.

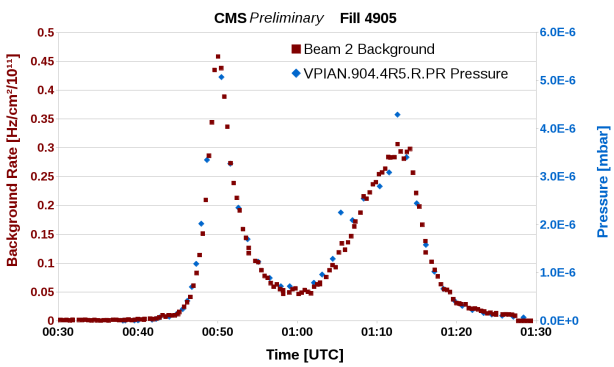

Figure 10: Time variation of MIB rates measured by BHM shown together with beampipe vacuum pressure, measured by the VPIAN.904.4R5 pressure sensor, for Beam 2.

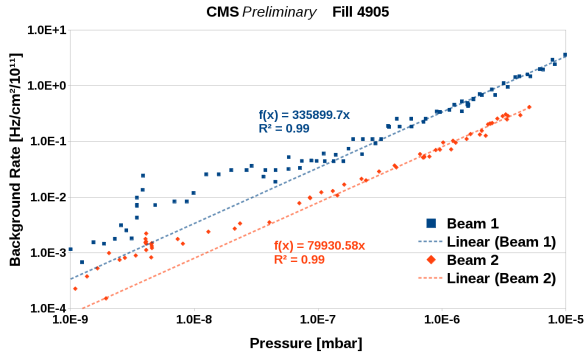

Figure 11: MIB rates versus beampipe Vacuum pressures, measured by the VPIAN.904 pressure sensor, for Beam 1 and Beam 2.

A linear correlation exists between measured pressure and MIB rate above a certain pressure, as shown in Fig. 11. Below $\approx 10^{-7}$ mbar, additional contributions to MIB, such as the baseline halo background and occasional noise hits, spoil the linear dependence. Additional analyses are in progress to quantify the effect of the increasing MIB rate on the CMS data taking efficiency.

CONCLUSIONS

The Beam Halo Monitor was installed in CMS at the beginning of 2015 to measure Machine Induced Background. It has met all its design requirements, and it is sensitive to increase of MIB beyond the normal operating conditions.

The detector is expected to remain operational and sensitive to beam background even with the upgrade to High Luminosity LHC.

REFERENCES

[1] A. Dabrowski *et al.*, "Upgrade of the CMS Instrumentation for luminosity and machine induced background measurements", *Nucl.Part.Phys.Proc.*, vol. 273-275, p. 1147, 2016.

[2] S. Orfanelli *et al.*, "A novel Beam Halo Monitor for the CMS experiment at the LHC" *J.Inst.* 10 no.11, P11011, 2015.

[3] J. Mans *et al.*. "CMS Technical Design Report for the Phase 1 Upgrade of the Hadron Calorimeter" CERN, Geneva, Switzerland, CERN-LHCC-2012-015/CMS-TDR-010, 2012.

ISBN 978-3-95450-177-9

BEAM-LOSS MONITORING SIGNALS OF INTERLOCKED EVENTS AT THE J-PARC LINAC

N. Hayashi*, Y. Kato, A. Miura, JAEA/J-PARC, Tokai, Ibaraki, Japan
K. Futatsukawa, T. Miyao, KEK/J-PARC, Tokai, Ibaraki, Japan

Abstract

It is important to understand why the beam loss occurs during user operation. It is understandable that the beam loss results from RF cavities failure. However, it would be still useful to study the beam loss detailed mechanism and to know which beam loss monitor (BLM) experiences the highest loss or is most sensitive. This may lead a reduction in the number of interlocked events and a more stable accelerator operation. The J-PARC Linac BLM has a simple data recorder that comprises multiple oscilloscopes. Although its functionality is limited, it can record events when an interlock is triggered. Of particular interest here are the events associated with only the BLM Machine Protection System (MPS). These may reveal hidden problems with the accelerator.

INTRODUCTION

The Japan Proton Accelerator Research Complex (J-PARC) is a high-intensity proton accelerator facility with three experimental hall, Materials and Life Science Experimental Facility (MLF), Hadron Experimental Facility (HD) and Neutrino Experimental Facility (NU). The accelerator parts are a 400-MeV linac, a 3-GeV Rapid-Cycling Synchrotron (RCS) and the Main Ring (MR), which is operated with 30 GeV. The designed beam power and intensity of the RCS at repetition rate of 25 Hz are 1 MW and 8.3×10^{13} protons per pulse (ppp), respectively. On a one-shot basis, this goal was achieved in early 2015 [1]. That same year, there were two MLF target failures at 500 kW. Since then, the nominal operational beam power and intensity of the RCS have been limited to 200 kW and 1.8×10^{13} ppp, respectively, for the MLF. The MR is operated with cycles of 2.48 and 5.52 s for the NU and HD, respectively. While most of the RCS beam is supplied to the MLF, four consecutive batches of two bunches each are injected from the RCS to the MR within either of these cycles. Operational MR beam powers of over 425 kW and 42 kW are achieved for the NU and HD.

The designed linac beam current and macro-pulse length are 50 mA and 500 μs, respectively. However, the peak current of the linac has been kept to 40 mA so far in 2016. The linac bunch structure has also been changed at the request of users. The typical bunch structure for the MLF is 300 μs macro-pulses in the linac and one bunch in the RCS. For the HD, the macro-pulse length is the same as that for the MLF, but the intensity is typically 1.2×10^{13} ppp. For the NU, the macro-pulse is the designed 500 μs length and a typical RCS intensity is 5×10^{13} ppp.

* naoki.hayashi@j-parc.jp

It is important to understand the over-all accelerator behavior, performance and characteristics, particularly in relation to the beam loss. The Machine Protection System (MPS) is usually triggered when a machine or instrument mal-functions or a beam loss monitor (BLM) hits its predefined threshold. The consequence in either case is that the beam is automatically stopped by the MPS.

It is certainly the case that failure of a RF cavity can cause a beam loss. Hence, it is useful to study the detailed correlation between RF cavity failures and the beam-loss pattern. This requires event data from many recorders with time identification. Sometime, a BLM will trigger the MPS without any sign of machine failure. This could be because of beam instability, accidental beam loss, or some other sources. Understanding beam losses and the entire machine characteristics further would help to reduce the number of MPS events and improve accelerator operation.

LINAC AND BEAM MONITORS

The linac comprises various sub-systems. Its front end is an RF-driven H^- ion source [2] and a 3-MeV RFQ [3]. Three drift-tube-linac (DTL) and 16 separated drift-tube-linac (SDTL) cavities then follow, and the H^- beam reaches 190 MeV at this point. After that, 21 annular-ring coupled structure (ACS) cavities that were added in 2013 accelerate the beam up to 400 MeV [4]. The linac-to-3 GeV RCS beam transport line (L3BT) has a length of 190.5 m[1] and includes a 90 degree arc section in between two straight sections. The final ACS cavity, is showing in Fig. 1, along with debunchers 1 and 2, and 0-degree and 30-degree beam dumps. There are two more beam dumps (100-degree and 90-degree) downstream of the second straight section. These four beam dumps are used during beam tuning. The arc section contains six bending magnets from the marked BM01 to BM06 in Fig. 1.

A proportional chamber type BLM (BLMP) is adapted as the main BLM [5]. Its pre-amplifier is placed either in the sub-tunnel (B1F) or in the machine tunnel (B2F). The signal unit is in the klystron gallery (1F). Its high voltage (HV) is set to 2 kV. The maximum raw output is < 5 V. There are many BLMs distributed all over the linac. In particularly, after 7^{th} SDTL, each SDTL and ACS cavity has its own BLMP. In total, 79 BLMPs are connected to the MPS. The number of BLMP is 31 and 5 in the L3BT and in the beam dump area, respectively. $BLMP14$, $BLPM18$, and $BLMP21$ are located between the debuncher cavity 1

[1] It comprises four subsections. Straight section before arc is 33.0 m, Arc section is 44.9 m, Straight section after arc is 59.1 m, and Injection section (to the RCS) is 53.5 m.

ISBN 978-3-95450-177-9

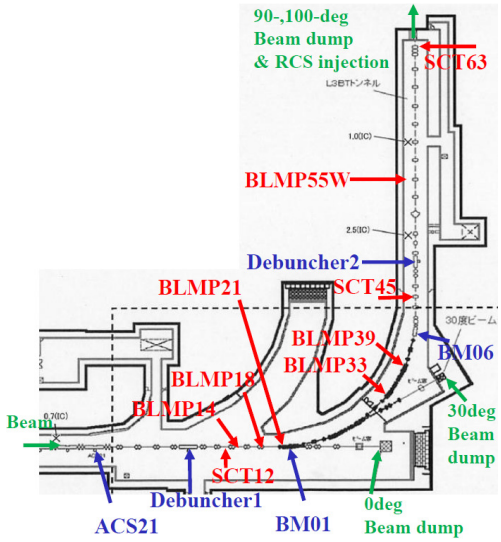

Figure 1: Downstream section of the linac after the final RF cavity ACS21. Locations of SCT and BLMP are indicated.

and the beginning of the arc-section. *SCT*12 (Slow Current Transformer, monitors the beam current) is also located at the right after the debuncher 1. *BLMP*33 is in front of BM04 and *BLMP*39 is in front of BM05. *SCT*45 and *BLMP*55*W* are in the second straight section. In contrast to the RCS or MR BLMP, the linac BLMP MPS is triggered by the raw waveform and not by a signal integral. Although the integrated value might be more stable, the response time would be longer. The MPS for the linac is designed to stop the beam within 5 μs. The MPS thresholds can be changed using EPICS, most are set to 1.3 or 1.6 V. Inside the MPS unit, a comparator and two PLCs judge whether the raw BLMP signal is too wide. Presently, the threshold width is set to 340 ns. Description about the MPS and a MPS unit can be found in references [6, 7].

WAVEFORM ARCHIVING SYSTEM

The raw BLM waveform archiving system comprises multiple oscilloscopes[2]. There are more than 50 oscilloscopes for the entire linac. At present, 12 of these actively archive the data when the MPS is triggered. The sampling rate is 100 Msample/s (10 ns/step), the record length is 100 ksample, and the sampling time is 1 ms. The scope parameters are monitored and can be modified through EPICS. During a communication between the EPICS IOC and the oscilloscopes, the system is locked, no trigger is accepted and the data are not archived for about a second. This interrupt occurs every several seconds and this dead time is a problem of this system.

The MPS stops the beam within several μs. However, the associated beam trigger from the timing system has an inherent delay. Several triggers are fired even after the MPS event, usually leading to some empty BLM data being recorded. That is why the archive system records 20 consecutive waveforms. The archive system records not only the BLM signals but also some SCT and fast current transformer (FCT, monitors the beam phase) waveforms.

[2] Yokogawa, DL1640.

INTERLOCKED EVENT

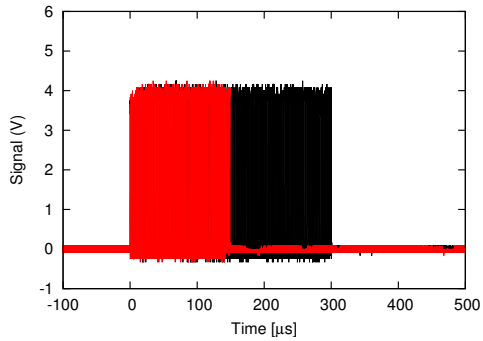

Figure 2: The linac beam current pattern recorded by SCT12. The vertical axis is the beam current; 1 V corresponds to 10 mA. Black is the normal case, and red is a pattern of an MPS event that interrupts beam.

In this section, we present SCT and BLMP waveform examples associated with an MPS trigger. In several cases, an accompanying MPS of the RCS BLMP is observed. As the RCS injection, a painting scheme is adopted for an injection period, which is now 300 μs macro-pulse (see the black line in Fig. 2). If the linac MPS stops the beam sooner than expected (e.g., the red line in Fig. 2), the beam already injected in the RCS becomes unstable, leading to further beam loss and a BLMP MPS signal.

BLMP MPS Associated with RF Failure

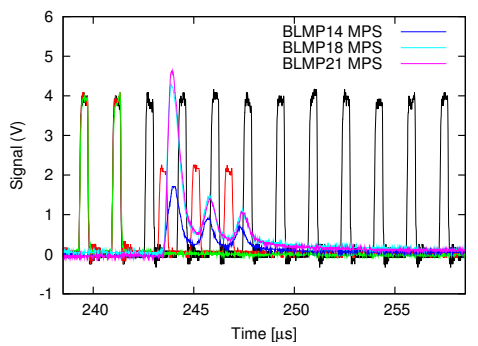

Figure 3: Snapshot of an interlocked event. MPS was triggered by SDTL04. Black and red are same as Fig. 2. Green is *SCT*45, blue, sky-blue and cyan are BLMP signals. The beam was stopped after 247 μs, but the the interlock occurred around 243 μs.

These events are relatively simple, and hence, it is reasonable to observe beam loss. The beam cannot be properly accelerated because of RF failure. Since we know which RF cavity is causing the problem, we can use these events as references. An obvious feature is the delay of the intermediate

ISBN 978-3-95450-177-9

pulse. To match it to the RCS RF bucket, the linac beam is immediately chopped after the RFQ exit. This pulse is referred as the intermediate pulse. If one RF cavity fails, the acceleration chain breaks down at that point. Since no acceleration afterwards, the intermediate pulse is observed as delayed pulse at the SCT.

Figures 3 is a typical example of delayed pulse. By comparing black and red lines, the delay is about 700 ns. Beam loss is associated with the three peaks that correspond to the following intermediate pulse. The amount of beam loss should be constant, but *BLMP*21 signal peak decreases from one pulse to the next, probably because of BLMP signal saturation. The same BLMP pattern is also detected on *BLMP*14 and *BLMP*18. It takes 5 μs before the beam is stopped. Similar examples for SDTL11 and ACS01 are

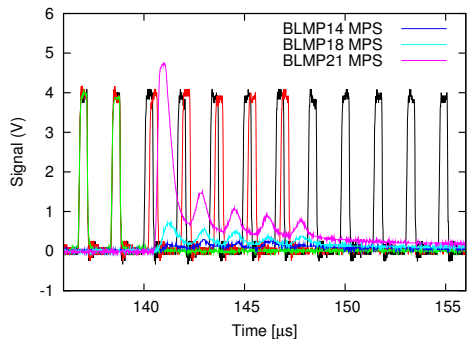

Figure 4: Same as Fig. 3 but for SDTL11 MPS.

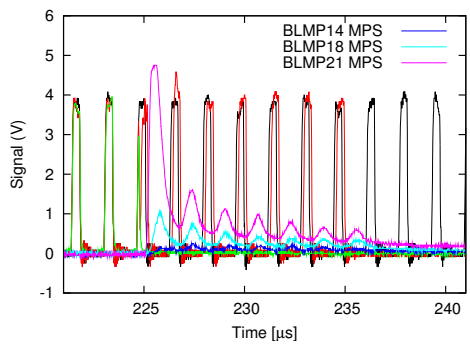

Figure 5: Same as Fig. 3 but for ACS01 MPS.

shown in Figs. 4 and 5. There are five BLMP signal peaks for the SDTL and seven for the ACS section. It takes 5 to 7 μs to stop the beam at the SDTL and 10 μs at the ACS.

Two more examples are shown in Fig. 6 and 7, this time for ACS15 and ACS21 MPS, respectively. In the case of ACS15, *BLMP*21 shows a similar pattern to that seen in the upstream cavity. However, in the case of ACS21, there is no significant loss at *BLMP*21, and intermediate pulse after the 90-degree arc section is observed on *SCT*45. The estimated energy up to ACS20 is about 390 MeV. However, sending lower energy beam through the arc section with some loss on *PBLM*55*W* is possible.

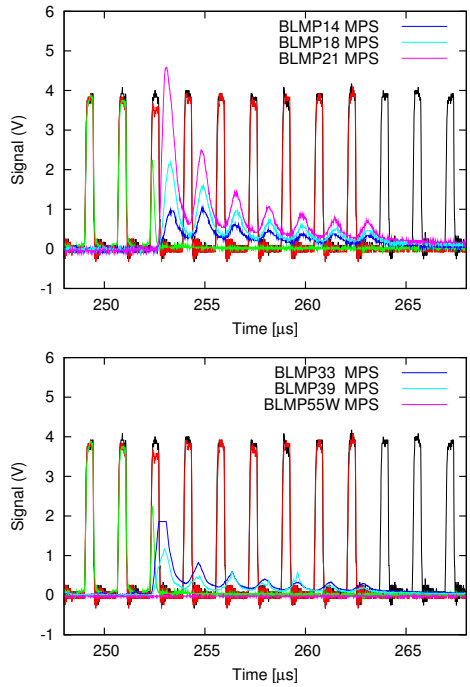

Figure 6: Same as Fig. 3 but for ACS15 MPS. Because *SCT*45 is located after the 90-degree arc, the beam did not reach at *SCT*45 after the interlock occurred. The BLMP groups before the arc and in the middle of it show a large beam loss. A part of *BLMP*33 signal peak was overshot.

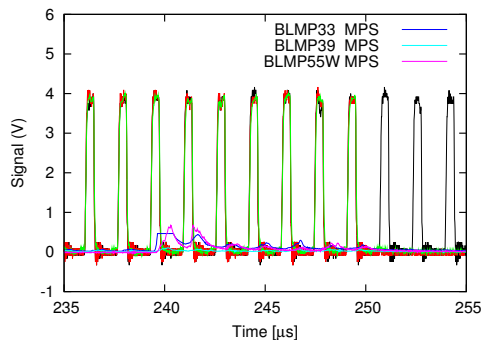

Figure 7: Same as Fig. 3 but for ACS21 MPS. The beam was stopped at 250 μs, but the moment of interlocked is estimated to have occurred just before 245 μs. A part of *BLMP*33 signal peak was overshot.

BLMP MPS only (part 1)

Although rare, multiple BLMP MPS signals can be triggered without any other machine failure. An example of such an event is shown in Fig. 8. This pattern can be compared with the previous cases in relation to the delay of the intermediate pulse and the number of BLMP signal peaks. We believe that some ACS cavity causes problems without generating an MPS signal.

There were noticeable number of multiple BLMP MPS events at the end of last February and at the beginning of last March. This type of event has not been recently detected.

ISBN 978-3-95450-177-9

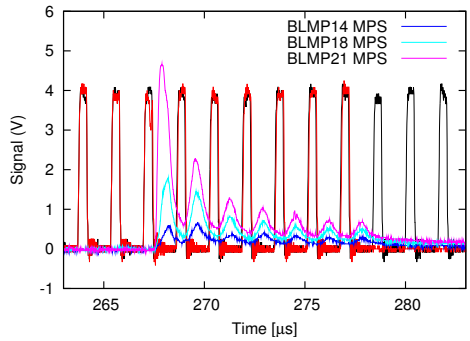

Figure 8: Same as Fig. 3 but due to multiple BLMP MPS.

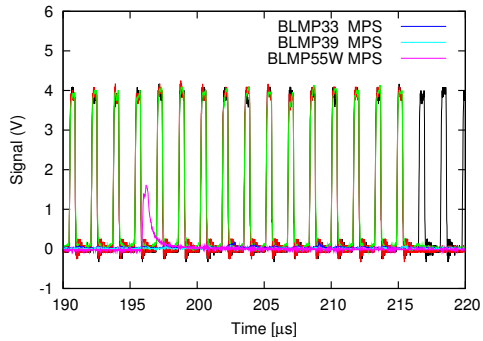

Figure 10: Same as Fig. 3 but for a single BLMP55W MPS. It takes longer than that of *BLMP*21 to stop the beam.

All archived events show a delay in the intermediate pulse from the head of the macro-pulse. This might be related to a problem with the timing-module (e.g., a missing trigger).

BLMP MPS only (part 2)

This is an important issue that needs to be solved to ensure stable accelerator operation. For most of the linac BLMP MPS, only single BLMP triggers the MPS. Although we searched for a coincidence signal, no such event was found. The *BLMP*21 signal peak was similar to that in the RF MPS case, but it was only a single peak and not a continuous loss. The BLMP signal width might be slightly thinner than that in the RF MPS case. These examples are shown in Figs. 9 and 10. It takes approximately 10 μs because of *BLMP*21 and 20 μs because of *BLMP*55*W*. In either case, the intermediate pulse pattern from *SCT*45 does not show any beam loss. At worst, there are over 20 events per day, whereas on others there can be fewer than five per day.

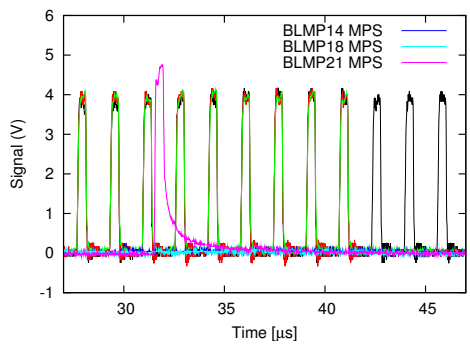

Figure 9: Same as Fig. 3 but for a single BLMP21 MPS. The difference here from RF MPS event, is that there is no continuous loss and no coincidence with *BLMP*14 or *BLMP*18.

DISCUSSION

The majority of single BLMP MPS events do not necessarily interrupt the beam. Rather, they cause relatively small beam losses that are not continuous. However, the justification for this is not straightforward. The overall frequency of this kind of MPS event seems to fluctuate, which is presumably related to a particular beam condition. It would be better to identify the true source, but this has not proved possible so far. High sensitivity is good for detecting small beam-loss signals. However, the signal of a large loss is relatively small because of saturation. The BLMP MPS threshold cannot be an integrated signal. As an ad-hoc solution, it might be an idea to reduce the HV setting and/or change the MPS threshold or signal-width criteria.

Because of timing-module problems, once the chopper that creates the intermediate pulse structure did not properly work. It did not cause the beam loss in the linac, but a heavy beam loss occurred in the RCS. A bad bunch structure can be confirmed by using this archive system.

CONCLUSION

We have presented BLMP waveform data with interlocked events. The failure of an RF-cavity MPS is associated with BLMP MPS events. The delay of chopped pulses depends on the location of the failed RF cavity. Although rare, events occur that suggest that some RF cavities must be failing without leaving an identifying signature. This can be estimated by comparing reference RF MPS events. There are many single BLMP MPS events, and action should be taken to reduce them. The archive system itself should be made more intelligent to reduce the dead time.

REFERENCES

[1] M. Kinsho, Proceedings. of IPAC2016, Busan, Korea, May 8 - 13, 2016, 999-1003 (2016).

[2] A. Ueno, et al., NIBS 2012, Jyväskylä, Finland, September 3-7, 2012. AIP Conf. Proc. **1515**, 331 (2013).

[3] Y. Kondo, et al., Proceedings of LINAC2014, Geneva, Switzerland, August 31 - September 5, 2014, 267-269 (2014).

[4] H. Ao, et al., Proceedings of IPAC2013, Shanghai, China, May 12-17, p.3845-3847(2013).

[5] S. Lee, et al., Proceedings of EPAC2004, Lucerne, Switzerland, p.2667-2669 (2004).

[6] H. Sakaki, et al., Proceedings of APAC2004, Gyeongju, Korea, p.622-624 (2004).

[7] H. Yoshikawa, et al., Proceedings of ICALEPCS07, Knoxville, Tennessee, USA, p.62-64 (2007).

ISBN 978-3-95450-177-9

TIMING WINDOW AND OPTIMIZATION FOR POSITION RESOLUTION AND ENERGY CALIBRATION OF SCINTILLATION DETECTOR

J. Zhu, M.H. Fang, J. Wang, Z.Y. Wei§
Nanjing University of Aeronautics and Astronautics, Nanjing 210016, P. R. China

Abstract

We studied fast plastic scintillation detector array. The array consists of four cuboid bars of EJ200， each bar with PMT readout at both ends. The geometry of the detector, energy deposition in the scintillator， signal generation and energy response have been simulated based on Monte Carlo. The detection efficiency and the real events selection have been obtained while the background noise has been reduced by using two-end readout timing window coincidence. We developed an off-line analysis code, which is suitable for massive data from the digitizer. We set different coincidence timing windows, and did the off-line data processing respectively. It can be shown that the detection efficiency increases as the width of the timing window increases, and when the width of timing window is more than 10 ns, the detection efficiency will slowly grow until it reaches saturation. Therefore, the best timing window parameter τ as 16 ns is obtained for the on-line coincidence measurement. When exposure to ^{137}Cs γ -ray irradiation, a 12 cm position resolution can be achieved while reaching the timing resolution of 0.9 ns. The pulse integration of signals of the detector is in proportion to the energy of incident particles. Furthermore, the geometrical mean of the dual-ended signals, which is almost independent of the hit position, could be used as the particle energy. Therefore, this geometrical mean as the energy of incident particle is calibrated via the Compton edges of ^{60}Co source, ^{137}Cs source and the natural ^{40}K, ^{208}Tl, and the reliability of the calibration results has been improved. Besides, the energy response is linear.

INTRODUCTION

When an incident particle interacts in a scintillator, it can cause ionization and excitation of the atoms and molecules of the scintillator. The energy of the incident particle is deposited in the scintillator [1]. The decay of excited atoms and molecules back to their ground states results in a emission of photons with two decay components: the fast one with decay time less than a nanosecond， and the slow one has decay time of hundreds of nanoseconds. The photons are collected on photocathode of the photomultiplier tube (PMT), and then these photons are converted to photoelectrons and amplified. The output signals of the scintillation detector depend on both the energy and the hit position of the incident particle. Besides, false signals come from the dark current and noise also. When the dual-ended readout is taken, we need methods to get hit position and energy of the particles, and also need to select the real events [2]. In this paper, we got real events from incident particles with the background noise reduced by using two-end readout timing window coincidence.

EJ-200 plastic scintillation detector array and its data acquisition system have been set up for radiation measurement in our laboratory. The scintillation detector array consists of four EJ-200 plastic scintillators which have dual-ended PMTs. The EJ-200 plastic scintillator combines two main benefits of long optical attenuation length and fast timing. On the basis of coincidence measurement, we picked out the real events from the timing window of signals, and optimized the timing resolution, position resolution and energy response of the detector.

SCINTILLATION DETECTION AND DATA ACQUISITION SYSTEM

The plastic scintillator used in this work was provided by the ELJEN Enterprises, USA. The scintillator (denoted by the ELJEN number EJ-200) had dimensions: 5 cm × 5 cm × 125 cm. The decay time of the scintillator is at the level of ns, and the rise time is less than 1 ns. The EJ-200 plastic scintillator was coupled to an ET Enterprises 9813B PMT. A VME bus system was used in our laboratory, and a schematic diagram of the detection system is shown in Fig. 1.

The DT5751 is a 4 channels 10 bit 1 GS/s Desktop Waveform Digitizer with 1 Vpp input dynamic range on single ended MCX coaxial connectors. The DT5751 Waveform Digitizer, which is taken in on-line coincidence measurement, has replaced some complex modules in the traditional coincidence circuits.

The V6533 is a 6 channels High Voltage Power Supply in 1 unit wide VME 6U module.

The online Digital Pulse Processing for Pulse Shape Discrimination firmware (DPP-PSD) was used in this study. Under the frame of DPP-PSD, we got the on-line waveforms and the energy histograms. Besides, the lists for the on-line data were obtained from the digitizer, and were further processed by ROOT, an off-line data-analysis software.

§ email address: wzy_msc@nuaa.edu.cn

ISBN 978-3-95450-177-9

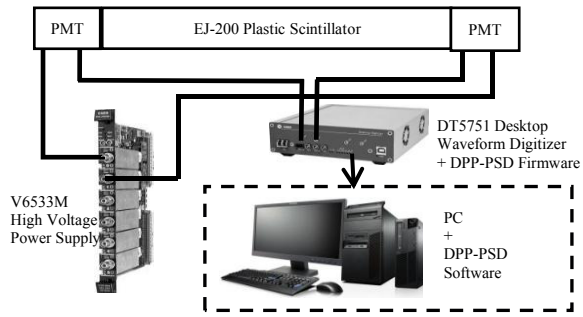

Figure 1: Schematic diagram of the experimental setup.

SIMULATION AND ITS RESULTS

The core idea of the coincidence measurement is to pick out the real event according to the timing window of signals. The key technical parameter of the coincidence circuits is the coincidence timing window τ. See in Fig. 2, if x, the distance between the hit position and the left side of the scintillator, corresponds to time t_1, and L-x, the distance between the hit position and the right side of the scintillator, corresponds to time t_2, then, the timing window of signals can be represented by $\tau = |t_1 - t_2|$. If the incident particles hit in the middle of the detector, $|t_1 - t_2| = 0$; If the incident particles hit in either end of the detector, $|t_1 - t_2|$ is up to the maximum value of the timing window. The true events take place in the span of $|t_1 - t_2|$. When the time interval between two pulses is less than τ, it outputs the coincidence pulse; otherwise it rejects. The timing window parameter can be used both in on-line analysis and off-line analysis.

The detector has been simulated based on Monte Carlo, including its geometry and particle interactions in the scintillator.

In Fig. 2, x, the distance between the hit position and the left side of the scintillator, is shown, and Δt, the time difference between the signals at both ends of the detector, is shown in Fig. 3, then, the $\Delta t - x$ curve is simulated in Fig. 4.

In Fig. 4, the time difference of signals at both ends of the scintillator is linear to the distance x, and $\Delta t - x$ is linear up to 9 ns. Considering the transit-time jitter of the PMT, which is determined as 1.17 ns, then, the maximum time difference in case of a true event is estimated to be 11 ns.

We developed an off-line analysis code, which is suitable for massive data from the digitizer, in order to find a reasonable timing resolution window for on-line experiment. The detection efficiency $\varepsilon_c(t)$ can be expressed as the ratio between the number of the coincidence particles(denoted by N_c) and the number of the particles produced by the radiation source during detection (denoted by N), which as shown in Eq. (1):

$$\varepsilon_c(t) = \frac{N_c}{N} \times 100\% \quad . \qquad (1)$$

The simulations based on the ^{137}Cs γ-ray source were done. The experiment time is 1000 s. Set different coincidence timing windows, and do the off-line data processing respectively. Detection efficiency versus coincidence timing window is given in Fig. 5. The black dots in the figure stand for experiment data and the curve is a fitted curve obtained by the off-line programs based on ROOT. It can be observed that detection efficiency is changing over the value of the coincidence timing window, and the width of timing window is more than 10 ns, the detection efficiency will slowly grow until it reaches about 20%. Therefore, this paper sets the best timing window parameter τ as 16 ns for the on-line coincidence measurement.

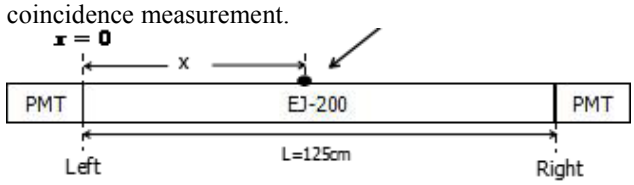

Figure 2: Schematic diagram of the distance between the hit position and the left side of the scintillator.

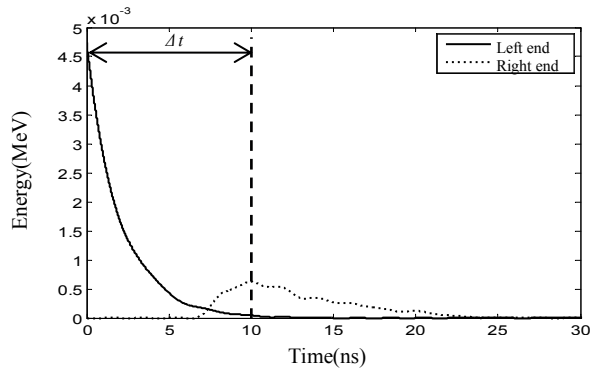

Figure 3: Schematic diagram of the time difference between the signals at both ends of the detector (x=0).

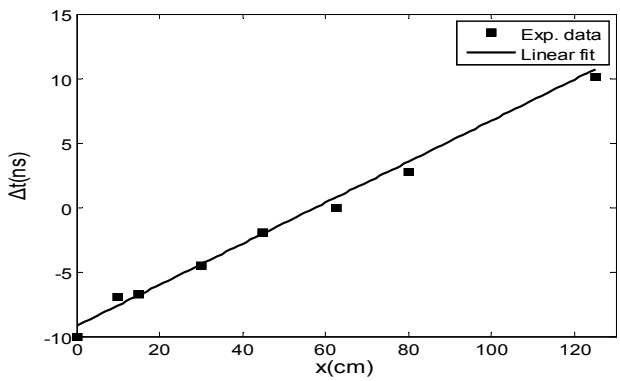

Figure 4: Δt (ns) , time difference of signals at both ends of the detector vs. x (cm), the distance between the hit position and the left side of the scintillator.

POSITION RESOLUTION AND ENERGY RESPONSE

This paper finds the best coincidence timing window parameter as 16 ns for the on-line coincidence measurement, see Fig. 5.

ISBN 978-3-95450-177-9

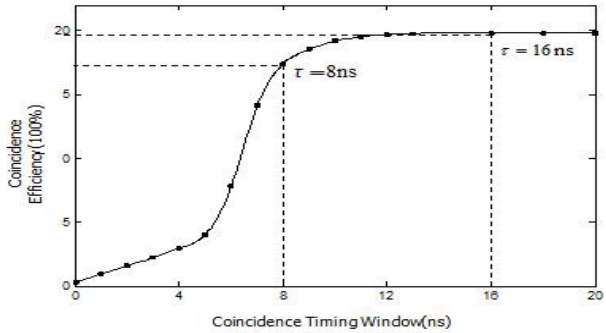

Figure 5: Detection efficiency vs. the coincidence timing window for the scintillation detector.

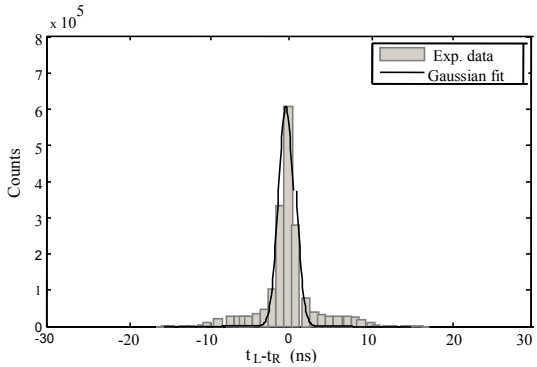

(a) in the middle

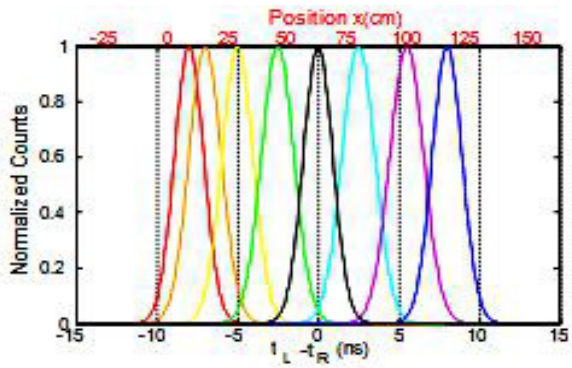

(b) on different positions

Figure 6: Time difference of signals generated from real events at both ends of the scintillator through Gaussian fitting with the ^{137}Cs source (a) in the middle of the scintillator and (b) on different positions.

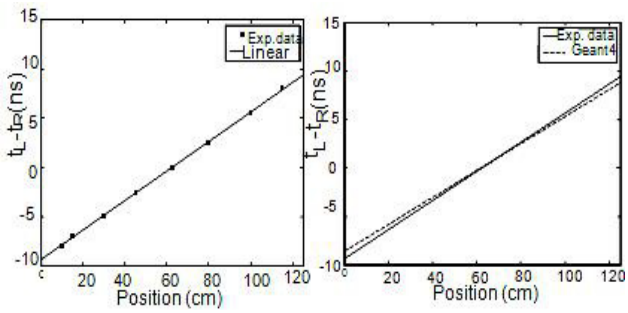

Figure 7: Time difference versus the position of the radiation source : experiment results (left) and simulation results by Geant4 code (right).

Since the two PMTs at both end of the plastic scintillation detector studied in this work are nearly the same, the timing resolution of the detector, σ_t , can be defined as Eq. (2):

$$\sigma_t^2 = \sigma_1^2 + \sigma_2^2 . \quad (2)$$

Where σ_1 and σ_2 represent the timing resolution at each end of the detector, respectively. Besides, if the scintillator used in this work has the intrinsic timing resolution (denoted by σ_s) and substituting the transit-time spread of the PMT, σ_{PMT} , for its timing resolution [3], and then σ_t , the timing resolution of the scintillation detector in this work can be represented by Eq. (3):

$$\sigma_t^2 = \sigma_s^2 + 2\sigma_{PMT}^2 . \quad (3)$$

The effective transmission speed of the signals in the scintillator is represented by c_{eff} [4]. Furthermore, it has been concluded that the integral charge of the signals at both ends, $\ln(Q_L/Q_R)$, is linearly associated with x. Therefore, the position resolution σ_x is shown as Eq. (4):

$$\sigma_x = \sigma_t \times c_{eff} . \quad (4)$$

By exposing the scintillation detector to the ^{137}Cs γ -ray source, a timing resolution of 0.9 ns is reached (when the best coincidence timing window $\tau = 16$ ns), see Fig. 6. Time difference of signals, which is generated from real events at both ends of the scintillator, and the position of the radiation source is near to a linear relationship (see Fig. 7), which fits the simulation results by Geant4. In Fig. 7, the slope of the fit line is 0.15, and the position resolution of the detector reaches 12 cm. The pulse integration of signals of the detector is in proportion to the energy of incident particles [5]. Furthermore, the geometrical mean of the dual-ended signals, which is almost independent of the hit position, could be used as the particle energy (see Eq. (5)):

$$Q_{GM} = \sqrt{Q_L Q_R} . \quad (5)$$

Where Q_{GM} represents the the geometrical mean of the dual-ended signals, and Q_L (or Q_R) represents the integral charge of the signals at the left (or right) end of the detector .

Therefore, this geometrical mean as the energy of incident particle is calibrated via the Compton edges of ^{60}Co source, ^{137}Cs source and the natural ^{40}K, ^{208}Tl, and the reliability of the calibration results has been improved. The gamma ray energy, E_γ, Compton edges, E_0, the ADC number of the photopeak, ch_p, the standard deviation of the photopeak, σ, the ADC number of the Compton edges,

ISBN 978-3-95450-177-9

ch_c, are listed in Table 1. The energy calibration of the detector see Fig. 8. It is shown that the energy response is linear within the lower energy range.

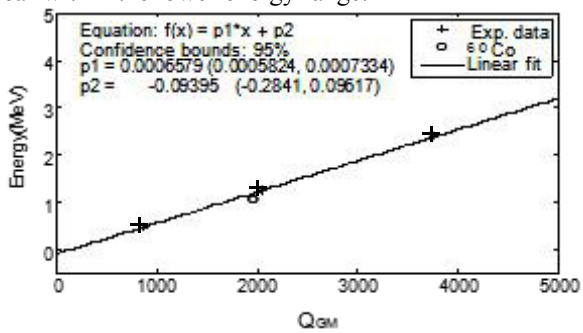

Figure 8: The energy calibration of the detector : crosses are experimental data and the curve represents the best-fitting.

Table 1: The Compton Edges of Different Radioactive Sources

γ	$E_{\gamma(MeV)}$	$E_{0(MeV)}$	ch_p	σ	ch_c
^{60}Co	1.173 1.333	1.0408	1603	312	1968
^{137}Cs	0.662	0.4777	679	154	860
^{40}K	1.461	1.2435	1710	289	2048
^{208}Tl	2.614	2.3812	3148	520	3756

CONCLUSION

The real event selection, timing resolution, position resolution and energy response of the EJ-200 plastic scintillation detector have been analyzed using timing window coincidence measurement. The detector was simulated based on Monte Carlo, including its geometry, energy deposition in the scintillator, photon collection and signal generation. The decay time of the pulse of scintillator is at the level of ns, and the rise time is less than 1 ns. Theoretical derivation and simulation results showed that Δt , time difference of signals at both ends of the detector, was linear with x, distance between the hit position and the left side of the scintillator, and Δt -x curve was linear up to 9 ns. Besides, time and position response have been measured by exposing to a ^{137}Cs γ -ray source. The best coincidence timing window parameter is 16 ns, and the position resolution is up to 12 cm. Since the pulse integration of signals of the detector is in proportion to the energy of incident particles, the geometrical mean of the dual-ended signals, which is almost independent of the hit position, could be used as the particle energy to calibrate the energy response of the detector via the Compton edges of ^{60}Co source, ^{137}Cs source and the natural ^{40}K, ^{208}Tl. The reliability of the calibration results has been improved. It was shown that the energy response of the detector was linear within the experimental energy range.

REFERENCES

[1] A. V. Kuznetsov *et al.*, "Position-sensitive neutron detector", *Nuclear Instruments and Methods in Physics Research A*, vol. 477, pp. 372–377, 2002.

[2] Wu, Zhihua *et al.*, *The research methods of nuclear physics,* Beijing: Atomic Energy Press, 1997.

[3] Liu,Yang *et al.*, "Measurement of TTS of Fine-Mesh PMT with Cherenkov Light", *Journal of University of Science and Technology of China*, vol. 35, no. 5, pp. 608-612, 2005.

[4] L. Lüdemann, K. Knoche *et al.*, "A Large-area Position-sensitive Detector for Fast Neutrons", *Nuclear Instruments and Methods in Physics Research A*, vol. 334, pp. 495-503, 1993.

[5] L. Karsch, A. Bohm *et al.*, "Design and Test of A Large-area Scintillation Detector for Fast Neutrons" , *Nuclear Instruments and Methods in Physics Research A*, vol. 460, pp. 362-367, 2001.

ISBN 978-3-95450-177-9

USE OF CR-39 PLASTIC DOSIMETERS FOR BEAM ION HALO MEASUREMENTS

I. Eliyahu, A. Cohen, E. Daniely, B. Kaizer, A. Kreisel, A. Perry, A. Shor and L. Weissman†,
Soreq Nuclear Research Center, Yavne 81800, Israel,
O. Girshevitz, BINA, Bar-Ilan University, Ramat-Gan 52900, Israel

Abstract

The first testing of CR-39 solid-state nuclear track dosimeters for beam halo measurement were performed at the SARAF phase I accelerator with ~ 2 MeV proton beams. Beam pulses of 90 nA peak intensity of the shortest possible duration (15 ns) available at SARAF were used for direct irradiation of standard CR-39 personal dosimetry tags. The lowest intensity and duration were used to minimize the beam core saturation on CR-39 tags. Other irradiations were done with beam pulses of 200 ns and 1 mA peak intensity. Specially prepared large area CR-39 plates with central hole for the beam core transport were used in the latter tests.

Weak beam structures were clearly observed in both types of irradiation. The tests showed feasibility of low energy beam halo measurements down to resolution level of a single proton. Different CR-39 etching conditions were studied. The advantages and drawback of the method are discussed.

INTRODUCTION

Beam halo phenomenon and growth of beam emittance are important issues for high-intensity linear accelerators as it directly translated to beam loss and accelerator activation. Special research programs were dedicated to the study of the beam halo formation [1] and appreciable progress was achieved [2]. Nevertheless, beam halo remains difficult to predict, measure and control. Even the definition of halo is a subject of some controversy [3,4]. From theoretical aspect the beam-dynamic predictions of weak beam tails are not always reliable due to complexity of the non-linear and time dependent effects leading to halo formation. From experimental point side the main difficulty is measurement of spatial distribution of weak beam tails at the presence of the many order of magnitude more intense beam core. Development of a simple and reliable tools and methods for beam halo diagnostics is highly desirable.

The first phase of the Soreq Applied Research Facility (SARAF) is operational since 2010 while the second phase is under design and planned to be commissioned starting at 2020. At phase I SARAF linac delivers CW and pulsed proton and deuteron beams at intensity up to 2 mA and at energy up to 4 MeV and 5.5 MeV for protons and deuterons respectively. At full specification SARAF will deliver 5 mA CW proton and deuteron beams at 40 MeV. The facility should satisfy hands-on maintenance requirement which in the case of intense beam require very low beam loss along the accelerator and the beam lines. In this respect understanding and control of the beam halo is a subject of great importance. The exact origin of the beam halo is not known but at least a significant contribution comes from the linac injector [5]. Hence, study of beam halo at the medium energy section is essential for halo tracking over the entire accelerator.

Importance of halo measurements was realized at the early stage of the SARAF project when significant efforts were spent in preparation for the beam halo measurements program [6]. Later on, however, this program was not vigorously pursued due to numerous challenges of the phase I accelerator commissioning and large number of physics experiments requested by the users. At the present, the SARAF team plans on launching only a limited halo research program, with limited beam time.

CR-39, allyl diglycol carbonate, is a plastic polymer commonly used for eyeglass lenses production. This material is also used since the 1970-s for nuclear track detection of cosmic rays, charge particles and fast neutrons [7]. The Soreq dosimetry department uses CR-39 radiation tags for personal radiation monitoring over the course of a few decades. For this halo investigation, we took advantage of significant experience accumulated at our research center with CR-39 and tested possibility of using of these detectors as simple means of beam halo diagnostics.

TESTS OF CR-39

Several issues should be taken in account when considering using CR-39 material for diagnostics of intense beams. Track detectors have very high sensitivity and thereby capability to detect each individual particle of the beam. On the other hand, the track detectors have a very low level of saturation. Thus, the beam fluence has to be reduced by many orders of magnitudes without changing the peak intensity to ensure successful use of the detectors. A fast beam chopping is an optimal technique for drastically reducing beam current while maintaining the beam profile of the intense beam. In the case of mA beam intensity even a single beam bunch may result in CR-39 saturation in the beam core. The possible way to overcome this problem is to use CR-detectors with a central hole for the beam core transport. Thus, only image of the beam periphery will be taken.

Additional question which should be considered is the conditions of CR-39 development after exposure. The

† weissman@soreq.gov.il

ISBN 978-3-95450-177-9

tracks produced by particles are revealed using chemical etching in potassium hydroxide (KOH) solution at constant temperature and different etching time. The number of the tracks and diameter of the tracks depends on these conditions [8]. The developing conditions have to be optimized on in order to obtain the image with best sensitivity to the region of interest.

As a first step we performed direct irradiation of standard personal CR-39 detectors. This irradiation coincided with the first test of a new fast chopper. The concept of the chopper includes fast sweep of the beam over a collimator in the low-energy sections [9] before entrance into the RFQ. In these tests the shortest pulses of 15 ns (~ 3 bunches) were obtained, more recent work with the fast chopper achieved single bunch per pulse of 0.3 ns, which will be helpful in future measurements.

Typical intensity of SARAF phase I beam, 1-1.5 mA, is very intense for direct irradiation even with such short pulses. The beam intensity was reduced by more than four orders of magnitudes using an aperture and strong beam defocus using the solenoid magnets in the low-energy beam transport (LEBT) line. A 2.5 MeV 70 nA CW beam was measured by a Faraday cup behind the irradiation point. A quartz viewer was used for the tuning beam in the irradiation plane

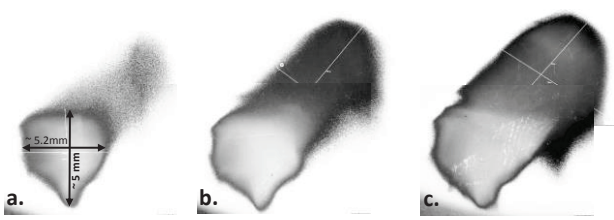

Figure 1: Images of on CR-39 tags taken with 1 (a), 1000 (b) and 100000 (c) fast chopper pulses

After beam tuning a CR-39 personal tag (30×42 mm^2) was introduced at the irradiation position and was irradiated by a few pulses produced by the fast chopper. To obtained broader range of CR-39 response we performed a series of irradiations of a few tags with 1, 10, 100, 1000, 10000 and 100000 fast chopper pulses. At each irradiation only one CR-39 was in the irradiation chamber to avoid background signal from beam scattering.

After irradiation the CR-39s were developed in KOH solution (400 gr KOH per a litter) at temperature of 80 ^{o}C for five hours. The developed CR-39s were examined by a microscope. Images of the tags irradiated by 10, 100 and 100000 fast chopper pulses are shown in Fig. 1. The zoom of the microscope did not allow for utilizing the whole area of interest, so each image is "stitched" from two pictures. Each image exhibits an intense core and weak tail. Even for a single pulse, the beam core is saturated. This contradicts our estimation of the fluence expected from a signal fast chopper pulse (~10^4 protons). It is possible that that the problem was in performance of the fast chopper for non-conventional LEBT beam optics used in this test. With increase of the fluence the saturation region expands but the main features of the image are consistent. Individual pits are clearly observed in the weak tail region (Fig. 2). Typical pit diameter is 6-7 μm. The individual pits can be readily counted using MATLAB software.

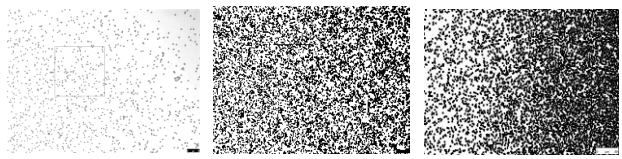

Fig. 2. Examples of magnified tail regions.

Furthermore digitization of images allows one to perform analysis of the pits distributions. An example of digitize image is shown in Fig. 3. The density of pits distribution was converted to a grey-scale intensity distribution using the ROOT software package [10]. Two dimensional distributions can be analysed and one dimensional projection can be taken using the ROOT package (Fig. 3). The grayscale intensity can be calibrated by direct integration of the pits density in the original image.

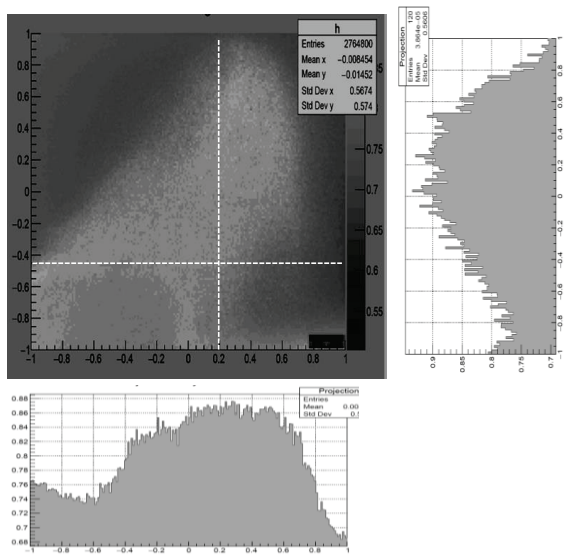

Fig. 3. Digitized image of an irradiated CR-39 with horizontal and vertical projections of the grey scale intensity.

Special efforts were taken to establish the optimum etching time. Several CR-39 tags were irradiated by 80 nA 2.5MeV protons using a single fast chopper pulse. Each of the irradiated detectors was developed at the same conditions (concentration of KOH solution and temperature) for periods of 1, 2 and 3 hours. After each developing period the tags were examined using the microscope and images were taken. Images of an irradiated CR-39 detector taken after 1, 2 and 3 hours development are shown in Fig. 4. It is evident from the figure that developing time of an hour results only in weak appearance of the core and no sign of the tail. Individual pits in the

ISBN 978-3-95450-177-9

weak tail start to appear after two hours of development and three hours corresponds to good image of the tail. Five hours etching time seemed to result in overdeveloping of pits (not shown here). The shape of the core is different comparing to Fig. 1. This is due to the different settings of the quadruple lenses upstream from the irradiation station. The orientation of the tail in the two irradiations is not affected by different quads settings. It appears that 2 hours is the minimum time required for developing CR-39 at these conditions.

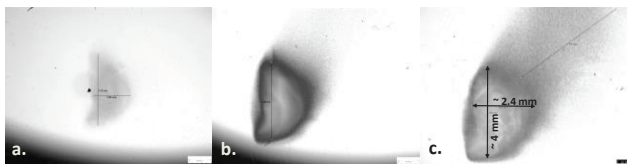

Fig. 4. Images of a single pulse with the fast chopper taken after developing the CR-39 during 1 hour (a), 2 hours (b), 3 hours (c). The area of integration is indicated.

It is clear that CR-39 detectors are not suitable for direct irradiation at high intensity linacs even for the shortest available beam pulses and greatly reduced beam intensity. The beam core has to be measured with other diagnostic tools. In the next series of test we have prepared a number of CR-39 detectors with a large hole in the middle in the area of the beam core. Large sheet of approximately 1 mm thick of allyl diglycol carbonate polymer were acquired [11]. A few of 40×40 mm^2 plates with a central hole of 14 mm diameter were cut from the sheet using a laser CNC cutter.

Protons beams of 2.2 MeV were used in this irradiation. In this test the nominal LEBT optics was used and the typical beam intensity of 1 mA was obtained at the exit of the accelerator. After tuning of the beam a CR-39 target was mounted and irradiated. In this experiment we used the SARAF slow chopper installed in the low-energy section [9]. A single 200 ns pulse, the shortest duration provided by the slow chopper, was applied on the CR-39 target.

An example of images, obtained by 2 hours developing, is shown in Fig. 5 A weak beam structure on periphery of the hole is clearly observed. The details of the observed weak tails are shown in the inserts.

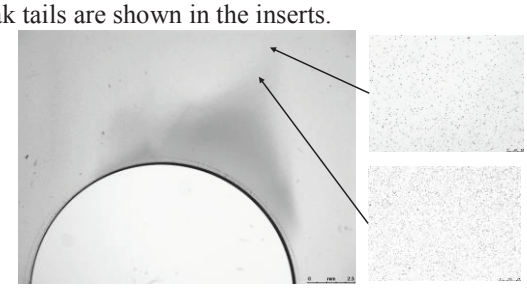

Fig. 5. Example of image taken with collimated CR-39 plate. An 1 mA 200 ns pulse has passed through the hole.

CONCLUSION AND FUTURE PLANS

First tests with irradiation of CR-39 detectors demonstrated feasibility of their use for high-quality quantitative measurements of the weakest beam tails structures. These measurements have to be combined with measurements of the beam core which have to be performed with conventional diagnostics tools. The advantages of CR-39 for beam halo measurements are low cost, simplicity and quantity of information obtained in a single exposure. The disadvantages are rather cumbersome off-line processing and low saturation threshold which lead to failure in a case of fluence miscalculation. Some additional efforts are needed for finding the optimum etching conditions for each specific beam species and energy.

As the next step we are planning detailed measurement of the beam distribution at the exit of the SARAF RFQ, which will be modernized in 2017. The core of distribution will be measured with a set of standard x-, y-profilers while the beam periphery will be studied with a set of CR-39 plates with holes of different diameters. This study will be essential for choosing the working range of the medium energy transport (MEBT) line beam scrappers and for overall commissioning of the SARAF phase II linac.

We would like to acknowledge Dr. D. Berkovits and Dr. I. Eisen for their comments to this report.

REFERENCES

[1] T.P. Wangler *et al*., *Nucl. Instr. And Meth*. A 519, 425. (2004).
[2] Theory and Design of Charged Particle Beam, M. Reiser, *Wiley-VCH* 2008, chapter 7 and references therein.
[3] P.A.P. Nghiem *et al*, HB2012, Benjin China (2012).
[4] A.S. Fisher, *IBIC15*, THBLA01, Melbourne, Australia (2015)
[5] A. Alexandrov and A. Shishlo, HB2016, THMY5Y01, Malmo, Sweden (2016).
[6] I. Mardor *et al*., *LINAC06*, TUP010, Knoxville, USA (2006)
[7] R.M. Cassou and E.V. Beton, Nucl. Track Detection, Vol. 2, p. 173-179, Pergamon Press 1978.
[8] M.J. Rosenberg *et al*., *Rev. Sci. Instr.* 85, 043302 (2014).
[9] A. Shor *et al*., JINST 7 C06003 (2012).
[10] http://www.root.cern.ch
[11] http:// www.homalite.com

ISBN 978-3-95450-177-9

ONLINE TOTAL IONISATION DOSIMETER (TID) MONITORING USING SEMICONDUCTOR BASED RADIATION SENSORS IN THE ISIS PROTON SYNCHROTRON

D. M. Harryman*, A. Pertica, Rutherford Appleton Laboratory, Oxfordshire, UK

Abstract

During routine operation, the radiation levels in the ISIS proton synchrotron become high enough to permanently affect systems and electronics. This can potentially cause critical components to fail unexpectedly or denature over time, causing disruption for users of the ISIS facility or a loss of accuracy on a number of systems. To study the long term effects of ionising radiation on ISIS systems and electronics, the total dose received by such components must be recorded. A semiconductor based online Total Ionisation Dosimeter (TID) was developed to do this, using pin diodes and Radiation sensing Field Effect Transistors (RadFETs) to measure the total ionisation dose. Measurements are made by feeding the TIDs with a constant current, with the threshold voltage on each device increasing in relation to the amount of radiation that it has received. This paper will look at preliminary offline results using off the shelf Field Effect Transistors (FETs) and diodes, before discussing the development of the RadFET online monitor and the results it has gathered thus far. Finally the paper will look at future applications and studies that this type of monitor will enable.

INTRODUCTION

ISIS is a pulsed spallation neutron and muon source facility, consisting of a H^- linear accelerator (Linac) and a proton synchrotron. The Linac accelerates H^- ions up to an output energy of 70 MeV, these ions then have their electrons removed with a stripping foil on injection into the synchrotron. The protons (H^+ ions) are then accelerated up to 800 MeV before being extracted and directed to one of two target stations. ISIS runs in user cycles, during these cycles the accelerator runs for 24 hours a day for 6-8 weeks, this is when scientists use the neutrons and muons created by the facility to study materials in the target station beam lines. Maintenance operations are carried out during shutdown periods between these cycles, it is best to change components and systems during these shutdown periods, to avoid disrupting the users of the facility.

When the accelerator is being operated, some areas like the synchrotron, become off limits due to the amount of radiation produced. While radiation exposure to personnel has always been monitored at ISIS, historically it has not been done for systems and components. To try and predict when components or systems may fail due to radiation damage, an online TID monitor has been developed, using off the shelf FETs, pin diodes, and application specific RadFETs. The developed TID monitor allows for a number of studies to take place, such as component characterisation, however this paper will primarily focus on the development of the monitor.

Semiconductors are permanently affected by ionising radiation [1]. As high energy particles travel through the gate of a FET, the radiation induced charges get trapped in the gate and create electron hole pairs (see Fig. 1) [1, 2]. Metal Oxide Semiconductor Field Effect Transistors (MOSFETs) have been shown to be more susceptible to radiation effects than the more generic FETs, due to this, they will be the type of FETs used in these experiments.

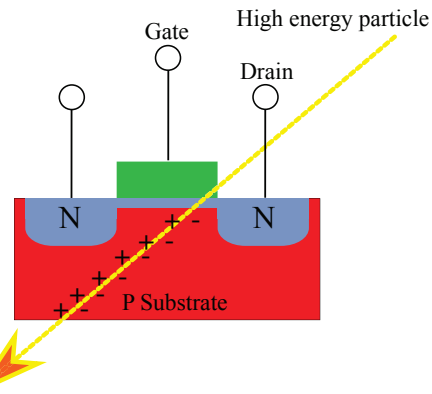

Figure 1: High energy particles creating electron hole pairs and trapping charges in the gate of a Field Effect Transistor (FET) as they travel through.

When biasing a FET or diode that's been irradiated with a constant current the voltage measured back will be proportional to how much radiation the component has been subjected to [2]. This allows for these components to be used as dosimeters. Organisations like the Tyndall Institute have made specific FETs, called RadFETs for just this type of application [3].

The RadFETs used in this experiment were the Tyndall TY1004 [3]. The thicker metal oxide gates of RadFETs have a larger exposed surface area. They are thus by design more susceptible to radiation damage. The TY1004 RadFETs have an 400 nm oxide gate, whereas typical off the shelf FETs will only have an oxide gate of a few nm. FETs with a thinner metal oxide gate will result in components that are less sensitive to radiation damage, but can measure a larger dose capacity. The voltages produced from the TY1004 RadFETs are factory calibrated against precise dose measurements and can be converted using a supplied transfer function Eq. (1) [3].

* daniel.harryman@stfc.ac.uk

ISBN 978-3-95450-177-9

$$Dose = (a\Delta V)^{\frac{1}{b}} \text{ Rads} \quad (1)$$

where:

$$a = 0.06594$$
$$b = 0.41169$$

PRELIMINARY EXPERIMENTS

Offline Setup

To test that standard FET based devices would record dose measurements like RadFETs, preliminary tests were carried out using off the shelf IRF9530 FETs and BPW34 pin diodes [4, 5]. BPW34 diodes have been used in similar applications before and will measure the non ionising energy loss [6], whereas the FETs will measure the total ionisation dose [2]. To take the voltages, the FETs were placed in a reader circuit configuration (see Fig. 2) and driven with a 8.6 µA current. A similar circuit was used to test the diodes where they were driven by a 1 mA current instead.

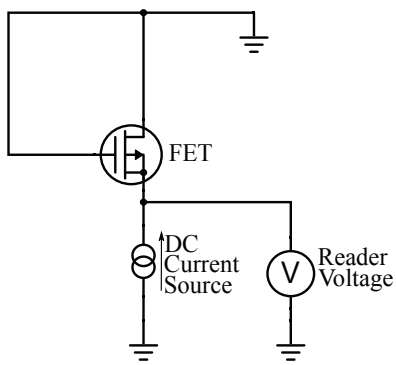

Figure 2: FET Reader circuit configuration.

Irradiating the Components

To test and irradiate the diodes and FETs, they were placed in aluminium die cast boxes with three of each component to a box (see Fig. 3) to increase the sample size.

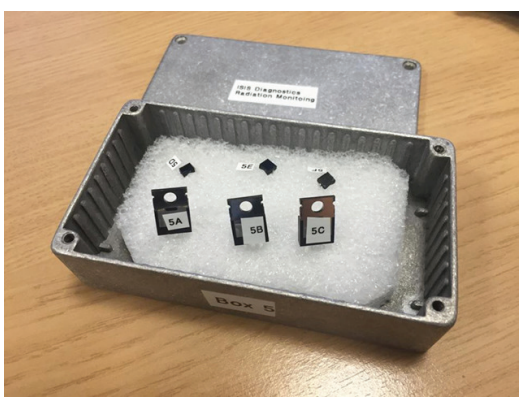

Figure 3: BPW34 Pin diodes and IRF9530 FETs in die cast box.

Four of these boxes were placed at different locations around the synchrotron, while another box was kept in an office as the control. The box locations were chosen so that the radiation levels measured in each one would be varied, with the higher doses expected near the injection beam dump, and the beam collimators.

Preliminary Results

The boxes were exposed for one user run, and voltage measurements were taken at three points: before installing the boxes, during the mid cycle off day, and at the end of the user cycle. The results show (see Fig. 4) that after an entire user cycle the reader voltage from the FETs located near the injection beam dump and collimators had increased by approximately 0.8 V and 0.1 V respectively. When testing the FETs in the straights, and the control, the results show that they stayed very close to their initial values.

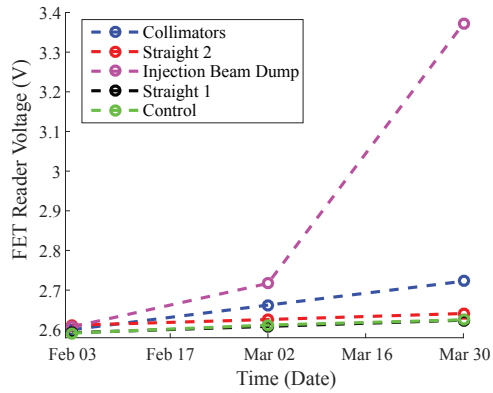

Figure 4: Reader voltage vs time for IRF9530 FETs placed in different locations.

The BPW34 diode results (see Fig. 5) were similar to the FETs, with the diodes located by the injection beam dump and collimators increasing by approximately 0.9 V and 0.2 V respectively. Much like the FETs the diodes located in the straights and control box also stayed relatively close to their initial values.

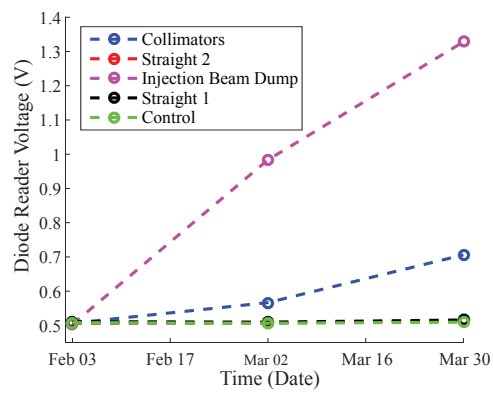

Figure 5: Reader voltage vs time for BPW34 diodes placed in different locations.

ISBN 978-3-95450-177-9

It was expected that the box placed by the collimators would have deteriorated more than the one by the injection beam dump, as there are more beam losses by the collimators. As the collimators are highly radioactive, access from personnel is restricted. This meant the box could not be placed directly by the collimators, but instead about 2 m away on top of the closest dipole magnet. This explains why the results from the injection beam dump are higher than the results from the beam collimators.

The two boxes placed on the straights are both about 3 m away from the beam pipe in areas with low beam losses, and thus the negligible change in voltage was expected. Overall the results from this user cycle demonstrated that the change in voltage measured from the FETs and diodes was positively correlated to the expected dose they had been exposed to.

MEASUREMENT SYSTEM

Based on the preliminary offline results obtained with the off the shelf components, an online monitor that can be sampled on demand was built using RadFETs along with BPW34 pin diodes. When the RadFETs and diodes are being irradiated they should have all terminals connected to ground, this is to prevent polarising the components and making them more sensitive to radiation. A custom circuit (see Fig. 6) and PCB was developed to supply and switch the constant current, as well as buffer the signals measured from the components.

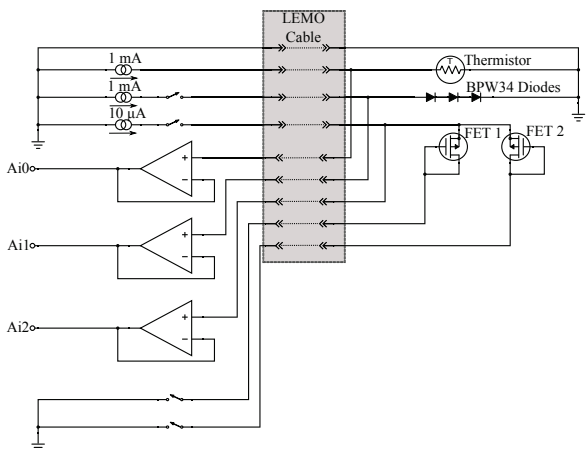

Figure 6: TID power switching and signal conditioning circuit.

The main controller used for the switching, data acquisition and analysis was a National Instruments cRIO [7]. The cRIO, the PCB, and associated power supplies were assembled inside in a custom Schroff chassis (see Fig. 7), and then installed in an area at the centre of the proton synchrotron, behind concrete shielding to protect from radiation damage.

For this experiment, a cable was fed from the inner synchrotron to a sensor board which housed three BPW34 pin diodes in series, a TY1004 RadFET, and a thermistor. The thermistor was used to gather temperature data, as readings from the diodes and RadFETs may be temperature dependant. The cRIO sampled each sensor once every 10 seconds and recorded an average measurement every 30 minutes. For the online measurements, the pin diodes were driven with 1 mA current and the RadFETs 10 µA current. The cRIO's analogue input module was used to acquire the data from the sensors, it's DIO module was to switch the sensor supply to and from ground. At the time of writing this paper, the cRIO has been measuring from one sensor board that has been placed by the injection beam dump. This location was chosen as it yielded the highest increase in voltage in the preliminary results.

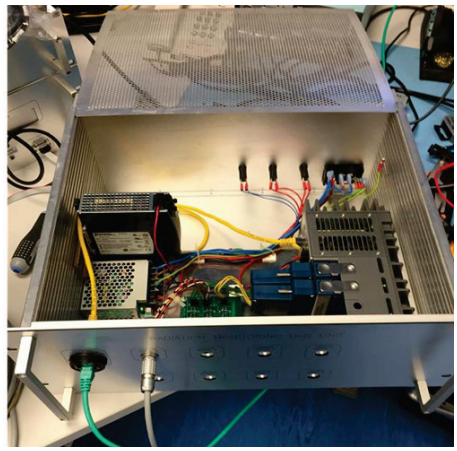

Figure 7: National Instruments cRIO measurement system in custom Schroff chassis.

RESULTS

The results displayed (see Fig. 8) were taken between the 3rd of April until and the 20th of August. Over this time the accelerator went through two user cycles. The first user cycle was a typical cycle delivering proton pulses to both ISIS target stations with a repetition rate of 50 Hz. Due to maintenance and upgrades carried out on the first target station, for the second user cycle only the second target station was receiving proton pulses from the synchrotron at a repetition rate of 10 Hz. This drops the average synchrotron current from approximately 200 µA to 40 µA.

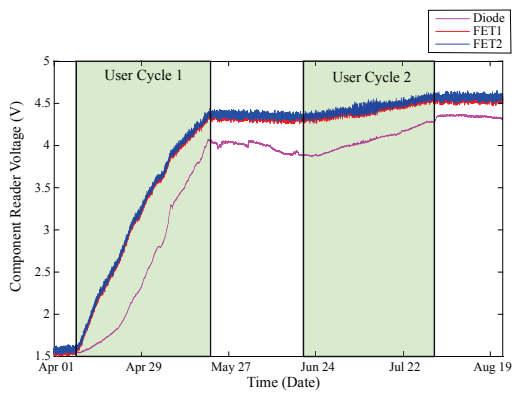

Figure 8: Component reader voltage vs time graph.

ISBN 978-3-95450-177-9

The voltages from the components start to rise at the beginning of the first user run, before levelling off during the shut down period. The diodes showed some annealing during this time as the measured voltage drops off slightly, the RadFETs also show some annealing, though it is not as much as the diodes.

By processing the FET voltage readings through the function given by Eq. (1), a dose over time graph can be obtained (see Fig. 9). The graph is split, divided by the two user runs and accelerator shut downs. The increase in ionising dose for the first user run was about 8800 rads, whereas for the second user run it was approximately 1600 rads. Given the drop in synchrotron current and repetition rate for the second run this is to be expected, and it shows that the measured dose scales with accelerator intensity.

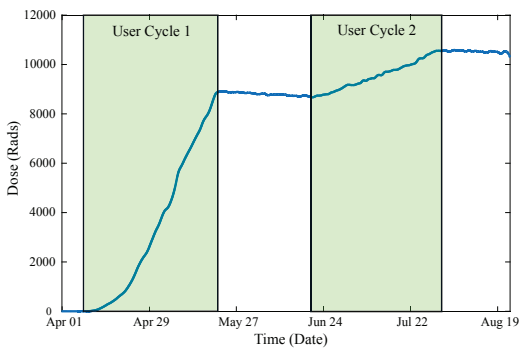

Figure 9: Dose vs Time Graph.

SUMMARY

Completed Work

Preliminary offline measurements have been carried out to test how off the shelf MOSFETs and pin diodes may react to ionising radiation. The theory that the more radiological dose a FET or diode has absorbed, the higher the threshold or reader voltage, has been reinforced with these experiments. Data gathered from these tests has been useful in building an online TID monitor that can be used for new studies, such as component characterisation.

The online TID monitor has successfully logged and recorded the total ionisation dose in a single location. The results gathered from the sensors track with not only the running schedule of the accelerator, but also the intensity of the run. During the shut down, there was annealing observed in both the BPW34 pin diodes, and the TY1004 RadFETs. As well as TID measurements, temperature data has been logged using a simple thermistor. During the user cycles the air conditioning is on, leaving the temperature flat during the runs but variable during shutdown periods.

Future Monitor Development

The TID monitor has been completed and is now functional, while this allows for more studies to take place, there is still some work that can be done to improve the monitor itself. Currently there is only one sensor board connected to the TID monitor, in the future more sensor boards can be added to monitor multiple locations at once.

It is believed that the readings from the RadFETs and the pin diodes are temperature dependant. As the synchrotron air conditioning has been active during the user cycles, it is believed this has not effected the readings a great deal. More analysis should be done on the temperature data acquired, as there may be a need in the future, to monitor radiation dose in non temperature controlled environments.

Future Studies

The monitor now allows for TID measurements of different components, systems, materials, and locations. By measuring the dose failure point of any of these parts, through long term testing, or accelerated testing, predictions can be made of when these parts need to be replaced or upgraded. Should these predictions be correct, these parts can be replaced during a shutdown period and not unexpectedly during an ISIS user cycle. This will result in less disruption to users, and an overall improvement in ISIS reliability.

REFERENCES

[1] A. M. Chugg, “Ionising radiation effects: a vital issue for semiconductor electronics”, *Engineering Science and Education Journal*, vol. 3, pp. 123-130, Jun. 1994.

[2] S. Danzeca, G. Spiezia, L. Dusseau, “Total Ionizing Dose measurements for electronics: A comparison of RadFET and Floating Gate dosimeter”, Presentation [Online], Dec. 2014. Available: https://indico.cern.ch/event/355137/contributions/1765221/attachments/704650/967340/Students_Coffee_2014_-_Total_Ionizing_Dose_measurements_for_electronics.pdf

[3] Tyndall Works, "400 nm RADFET in 8L Side Braze Ceramic Package", TY1004 datasheet, 2015.

[4] Vishay Semiconductor, "Silicon PIN Photodiode", BPW34 datasheet, Aug. 2011. [Revised Jun. 2016].

[5] Fairchild Semiconductor, "12A, 100V, 0.300 Ohm, P-Channel Power MOSFETs" IRF9530 datasheet, Jan. 2002.

[6] J. Hartert, J. Bronner, V. Cindro, A Gorisek, I. Mandie, and M. Mikuz, "The ATLAS radiation dose measurement system and its extension to SLHC experiments," in Proc. Topical Workshop Electronics for Particle Physics, Naxos, Greece, Sep. 15-19, 2008 [Online], Available: https://cds.cern.ch/record/1158640/files/p269.pdf

[7] National Instruments. (2016, Sep, 05) *The CompactRIO Platform* [Online]. http://www.ni.com/compactrio

ISBN 978-3-95450-177-9

COSY BPM ELECTRONICS UPGRADE

C. Böhme, A. J. Halama, V. Kamerdzhiev,
Forschungszentrum Jülich, Germany

Abstract

The Cooler Synchrotron COSY delivers proton and deuteron beams to the users since the early 90s. The experiments are carried out using the circulating beam as well as the beams extracted from the ring and delivered by three beamlines. The original BPM system still operational in the ring does not fulfill the requirements for new experiments. It utilizes cylindrical and shoe-box type diagonally cut capacitive pick-ups. The most signal processing is done the analog way. Additionally to its age and the increasing failure rate, the analog processing introduces large drifts in e.g. the offset, which regularly require a significant effort for manual calibration. Even then the drifts render it impossible to match the requirements of the planned JEDI experiment, which is an orbit with a maximum of 100 μm RMS deviation. Therefore an upgrade of the readout electronics was decided. The decision process is described, the implications listed and the current status is reported.

INTRODUCTION

The COoler SYnchrotron (COSY) of the Forschungszentrum Jülich is a 184 m long racetrack-shaped synchrotron and storage ring for protons and deuterons from 300 MeV/c (protons) or 600 MeV/c (deuterons) up to 3.7 GeV/c. Built in are devices for stochastic as well as electron cooling. The stored ions can be polarized or unpolarized. Commissioned in 1993, the electronic parts of the BPM system are not only outdated, but start failing while spare parts for repair are hard to acquire. In addition, for the planned EDM [1] precursor experiment a higher beam position measurement accuracy is needed than can be reached with the used components. Therefore different upgrade scenarios for the BPM system were investigated.

CURRENT STATUS

COSY is equipped with 29 shoebox-style BPMs. During commissioning 27 BPMs of two types were installed, a cylindrical type with 150 mm diameter and a rectangular type 150 mm · 60 mm [2]. The selection was made to fit into the beam pipe, which is round in the straight sections and rectangular in the arcs in order to fit into the dipole magnets. Recently 2 BPMs were added with special geometries to fit within the beam pipe of the 2 MeV electron cooler [3]. These two use their own electronics for readout, which is different from the others.

All other BPMs are read out by the same type of electronics [4], whose concept is shown in Figure 1. The readout electronic for each BPM, except for the pre-amplifiers, is housed in one VXI crate, consisting of 2 analog modules, 2 digital modules, one CPU, and one timing receiver. The

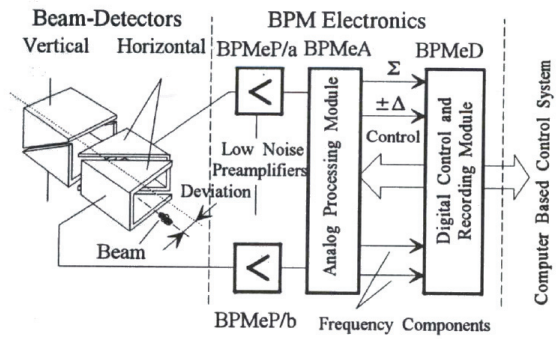

Figure 1: Current Beam Position Monitor electronics assembly [4].

pre-amplifiers are directly connected to the N-type vacuum feedthrough of the pick-ups. This pre-amplifier has a fixed gain of 13.5 dB with an input impedance of 500 $k\Omega$ and a bandwidth of 100 MHz (-3 dB). The gains and offsets of two pre-amplifiers have to be exactly matched for one plane of one BPM in order to avoid incorrect measurements. The preamplified signals are fed into an analog module, where sum and delta signals are produced using a hybrid. These signals are then treated separately and can be further amplified in 6 dB steps from 0 dB to 66 dB. Both the sum and the delta branches have two signal paths. A narrowband path features 3 possible filter settings with bandwidths of 10 kHz, 100 kHz, or 300 kHz and an additional amplifier that can be set from 0 dB to 18 dB in 6 dB steps. The broadband path with 10 MHz bandwidth can be used for turn-by-turn measurements while the narrowband signals are used for closed orbit measurements. The analog outputs are unipolar, the sign of the narrowband delta signal is detected separately and the information is transmitted by a separate TTL signal line. After the analog signal processing the signals are digitized in a digital module. This is done using 20 MHz 8 bit ADCs. For the narrowband signal the sampling frequency is lowered to 1 MHz or 100 kHz, depending on the selected analog bandwidth. For the sum signal only 7 of the 8 bits of the ADC are used, the 8th bit is used to indicate the polarity of the delta signal. The digital module generally has the capability to buffer 4096 data points, while few modules can store up to 64k data points that can be used for turn-by-turn measurements. The CPU in the VXI crate calculates out of the narrowband signal the beam position using a scaling factor for the specific BPM geometry. It is also possible to transfer the raw broadband data to the control system display and export it, for e.g. computation of the turn-by-turn position.

ISBN 978-3-95450-177-9

LIMITATIONS OF THE CURRENT HARDWARE

First, the position measurement is highly dependent on the pre-amplifiers used for the two pick-up electrodes of one plain having identical characteristics, even better than usual production variations of electronic components. Therefore, at the time of construction, extensive tests have been performed to figure out component pairs with identical characteristics. Recent tests of selected pairs showed that the matching of the pairs is still good, even after years of operation. In addition, until now no defects were found for this part, so that there is no pressing need to replace the preamplifiers.

The analog modules have several issues [5]. They are failing at an increased rate, although until now most modules could be repaired. The modules require an extensive calibration procedures performed regularly, otherwise parameter drifts decrease the measurement accuracy . Therefore using an in situ calibration signal seems to be more promising than the calibration procedure by adjusting potentiometers on the testbench.

The digital modules seem to be the most outdated with only 8 bit sampling resolution, from which for the sum signal uses only 7 bits. The modules don't show a high failure rate so that the low resolution and the limited storage for turn-by-turn measurements are basically the main drivers of an upgrade.

As described above, the position calculation is done by the embedded CPUs. If introducing a calibration signal into the signal chain, the calibration data gathered has to be used for calculating the position. Here the hardware limitations, especially the low memory of the CPU modules, come into account, which does not allow the storage of larger lookup tables of correction values.

REQUIREMENTS

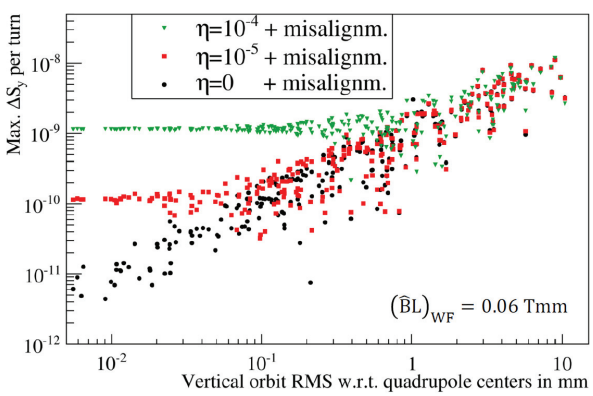

Figure 2: Calculated spin buildup per turn for different presumed EDM values. Depending on the real EDM value the beam has to be aligned in respect to the quadrupole magnets with a certain accuracy. This leads to the accuracy required from the BPMs. [6].

Shown in Figure 2 is the required beam positioning accuracy of the EDM experiment for different presumed EDM values [6]. This accuracy reflects the possibility to align the beam with respect to the quadrupole magnets. In order to do this, the BPM accuracy is of course only one part, other elements of the accelerator like the steering magnets are as well involved. As assumption a orbit with a maximum of 100 μm RMS deviation is the goal of the upgrade. The mechanical design of the COSY BPM does not support an accurate positioning of the pickups themselves e.g. by use of fiducial marks. A beam based alignment could reduce the BPM positioning uncertainty significantly and has to be considered.

UPGRADE BOUNDARIES

Several upgrade scenarios have been discussed. In all scenarios some common constraints have to be considered:

- The BPM pick-ups will remain unchanged, although they are not equipped with position markers, so their absolute position is only known within some error margin.
- Up to now no test signal for calibration purposes is used. In every upgrade scenario the introduction of test signals is mandatory.

Calibration Signal

Up to now the BPM system doesn't have a calibration signal path. Independent of the selected upgrade scenario it appears crucial to inject a calibration signal in front of the pre-amplifier. The generation of the calibration signal and the distribution is still under discussion. A solution may only need one test signal that will be switched through the channels or being splitted by passive elements, in order to make sure the test signal will be identical for all channels.

To feed the test signal into the signal path, passive couplers or active switches are under consideration. With the advantage of the passive coupler, that it is less likely to fail, and the disadvantage, that during beam operation a calibration will not be possible. These facts have to be considered.

Another design choice under discussion is the central generation of a calibration signal vs. the local one. While a central signal generation can be performed with one high precision instrument, the distribution introduces signal variations from BPM to BPM. A local generation would have to be performed by a cheaper generator but will probably have a lower precision.

Readout Electronics Upgrade

Like other recently planned BPM systems [7, 8] the goal is to digitize the signals as early as possible in the signal chain.

Several hardware options have been considered:

- Instrumentation Technology Libera Hadron

ISBN 978-3-95450-177-9

- System based on Spectrum M4I.4421-X8 high speed digitizer
- DESY / XFEL / ESS solution based electronics based on the μTCA4 standard
- National Instruments solution similar to SNS upgrade [9]

The Libera hadron platform was chosen for the BPM readout within the FAIR project [10]. Due to the fact that the Research Center Jülich is responsible for the design and construction of the HESR, the same hardware was chosen as a potential candidate for the COSY BPM upgrade as well. This approach insures an efficient use of resources. The new Libera B is based on μTCA and is a modular system. Each chassis can host the electronics to read out 4 BPMs. The maximum sampling frequency is 250 MHz with 16 bit resolution. Most of the software provided by the manufacturer was build to FAIR specifications, with some extensions for other use-cases.

A system based on a Spectrum M4I.4421-X8 high speed digitizer was evaluated. The digitizer features four 16-bit 250 MHz ADCs. The card features a switchable input range from ±0.2 V to ± 10 V. This feature would probably lead to the fact that the pre-amplification could remain untouched with the existing 13.5 dB fixed gain amplifiers, except of course the introduction of a calibration signal. The digitizer is in form of an 8 lane PCIe card. The processing of the signals would in this case, unlike all other solutions, not be done in a FPGA but in the processor of the hosting PC.

Although not being identical, latest developments from DESY including XFEL and the ESS, based on the μTCA4 standard, could be a prototype for a COSY solution. At least for the ESS case most of the designated hardware is commercially available, e.g. Struck fast digitizer cards.

Another possibility investigated was the solution proposed for a BPM readout electronic upgrade at SNS [9]. There National Instruments ADCs and FPGA modules are used for the processing of the signals. This decision was taken because with the NI hardware the FPGA used for processing can be programmed using the NI graphical programming framework LabView.

Decision After a recommendation of a review committee late 2015 the decision was made to prefer the Instrumentation Technology Libera Hadron system for an upgrade. This decision was made because of the timeline of the EDM precurser experiment and that the LIBERA brings a tested software collection for signal processing, while all other solutions would have implicated the own development of software for readout and position calculation. Furthermore, the efficient use of resources, by only using one system in both projects of the IKP, COSY and HESR, emphasized that decision.

This decision came along with two other results. First, as the input range of the LIBERA can not be switched, a switchable amplifier has to replace or to be added to the fixed-gain pre-amplifiers now used. The second decision made was to use the EPICS protocol for further extensions or replacements of accelerator parts, with the goal to completely switch to an EPICS based control system in the long term. Although still in the evaluation, it is highly probable that the Control System Studio (CSS) framework will be used along with EPICS.

FIRST MEASUREMENTS WITH LIBERA HADRON

In order to start integration of the LIBERA Hadron one system was already bought and is under test. The shown results are the result of tests with the hardware to evaluate the complete signal chain.

Pre-Amplifiers

As described already, the input of the LIBERA system is with a fixed input range. Therefor the necessity of switchable amplifiers is seen, in order to utilize the input range as complete as possible. For testing purposes 4 FEMTO DHPVA-100 switchable amplifiers were ordered including a custom modification to an input impedance of 500 kΩ. The gain is switchable in 10 dB steps between 10dB and 60 dB. Figure 3 shows a measurement of a COSY beam taken at

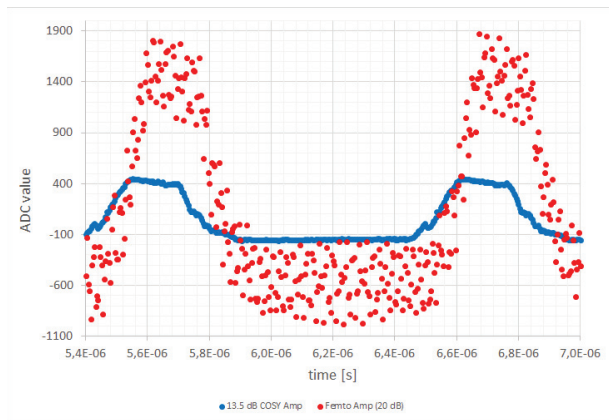

Figure 3: Measured signal using the LIBERA Hadron ADCs for beam in COSY. While using the traditional COSY fixed gain amplifiers the noise is much lower compared to switchable amplifiers bought for testing purposes and modified from the producer to an input impedance of 500 kΩ.

the same time at two neighboring BPMs. One was equipped with the traditional 13.5 dB fixed gain amplifier while the other used the switchable FEMTO amps, in this case set to a gain of 20 dB. Calculating the RMS value between two bunches, the traditional COSY amp has a value of 150 while the FEMTO has a vale of 600, both in ADC raw values. Because of this behavior the selection process for a new amplifier is still ongoing. A possible alternative to replace the traditional amps completely might also be to keep them in place and add a second stage amplifier with a switchable gain.

ISBN 978-3-95450-177-9

Beam Noise Measurements

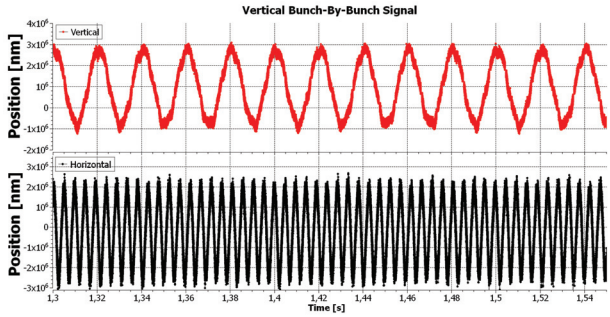

Figure 4: Measured bunch-by-bunch position of the COSY beam. The measurement shows a beam oscillation of 50 Hz in the vertical plain and one with 200 Hz in the horizontal plain. The calibration of the measurement system to the calculated position of the beam has not been verified yet, therefor the absolute position of the beam might be scaled by a unknown factor.

While running test measurements to familiarize ourselves with the LIBERA Hadron functions, a noise in the beam position could be observed. With the traditional BPM system only narrowband measurements slower than 1 Hz are possible or the observation of the broadband ADC raw data. From this data a bunch-by-bunch position would have to be calculated manually, with the amount of stored data point, being up to 4096 at 20 MHz, only very few bunches can be stored. In the recorded data the beam shows an oscillation in the vertical plain of 50 Hz and in the horizontal plain with 200 Hz. The calibration of the LIBERA system towards the geometrical properties of the BPM has up to now not been cross-checked, therefor a constant factor might have to be applied to the beam position data shown in Figure 4. This behavior requires further examination.

CONCLUSIONS

Although the old electronics is still performing within the specifications it was designed for, the much tighter specifications for the EDM precursor experiment require an upgrade of the BPM electronics. The LIBERA Hadron system was recommended for the upgrade by an expert committee. In the meantime several options for the pre-amplifier system are investigated to match the input range of the LIBERA system to the BPM signals with different beam properties. Within the design a calibration signal is envisaged as well, which is not available up to now. In addition the decision was made to use the EPICS standard as future base for the control system. Some test measurements were showing new aspects of the beam behavior not seen with the old system and its standard GUI. These behavior has to be examined further.

REFERENCES

[1] A. Lehrach on behalf of the JEDI Collaboration, "Beam and Spin Dynamics for Storage Ring Based EDM Search," *IPAC2015*, Richmond, VA, USA, WEAB2.

[2] R. Maier *et. al.*, "Non-Beam Disturbing Diagnostics at COSY-Jülich," *EPAC'90*, Nice, France, June 1990, p. 800.

[3] V. B. Reva *et. al.*, "Cosy 2 MeV Cooler: Design, Diagnostic and Commissioning," *IPAC2014*, Dresden, Germany, MOPRI075.

[4] J. Biri *et. al.*, "Beam Position Monitor Electronics at the Cooler Synchrotron COSY Jülich," Eight Conference on Real-Time Computer Applications in Nuclear Physics, Vancover, June 1993.

[5] F. Hinder *et. al.*, "Beam Position Monitors @ COSY," JEDI Collaboartion Internal Note, 13/2015, June 16, 2015.

[6] M. Rosenthal *et. al.*, "Spin Tracking Simulations Towards Electric Dipole Moment Measurements at COSY," *IPAC2015*, Richmond, VA, USA, THPF032.

[7] H. Hassanzadegan *et. al.*, "System Overview and Current Status of the ESS Beam Position Monitors," *IPAC2014*, Dresden, Germany, THPME166.

[8] K. Lang *et. al.*, "Performance Tests of Digital Signal Processing for GSI Synchrotron BPMs," *PCaPAC08*, Ljubljana, Slovenia, TUP002.

[9] A.V. Aleksandrov "SNS Beam Diagnostics: Ten Years After Commissioning," *IBIC2015*, Melbourne, Australia, MOBLA02.

[10] M. Znidarcic et. al., "Hadron BPM For The FAIR Project," *IPAC2015*, Richmond, VA, USA, MOPTY040.

ISBN 978-3-95450-177-9

BEAM DIAGNOSTICS FOR MEDICAL ACCELERATORS*

C.P. Welsch#, Cockcroft Institute and The University of Liverpool, UK
on behalf of the OMA Consortium

Abstract

The Optimization of Medical Accelerators (OMA) is the aim of a new European Training Network that has received 4 ME of funding within the Horizon 2020 Programme of the European Union. OMA joins universities, research centers and clinical facilities with industry partners to address the challenges in treatment facility design and optimization, numerical simulations for the development of advanced treatment schemes, and beam imaging and treatment monitoring. This paper presents an overview of the network's research into beam diagnostics and imaging. This includes investigations into applying detector technologies originally developed for high energy physics experiments (such as VELO, Medipix) for medical applications; integration of prompt gamma cameras in the clinical workflow; identification of optimum detector configurations and materials for high resolution spectrometers for proton therapy and radiography; ultra-low charge beam current monitors and diagnostics for cell studies using proton beams. It also summarizes the network-wide training program consisting of Schools, Topical Workshops and Conferences that will be open to the wider medical and accelerator communities.

INTRODUCTION

In 1946 R.R. Wilson introduced the idea of using heavy charged particles in cancer therapy. In his seminal paper [1] he pointed out the distinct difference in depth dose profile between photons and heavy charged particles: While photons deposit their energy along the beam path in an exponentially decreasing manner, heavy charged particles like protons and ions show little interaction when they first enter the target and deposit the dominant portion of their energy only close to the end of their range. This leads to an inverse dose profile, exhibiting a well-defined peak of energy deposition (the Bragg Peak). The depth of the Bragg Peak in the target can be selected precisely by choosing the initial energy of the particles. This allows for a significant reduction of dose delivered outside the primary target volume and leads to substantial sparing of normal tissue and nearby organs at risk. The field of particle therapy has steadily developed over the last 6 decades, first in physics laboratories, and starting in the late 90's in dedicated clinical installations. By March 2013 about 110,000 people had received treatment with particle beams, the vast majority having been treated with protons and around 15,000 patients with heavier ions (helium, carbon, neon, and argon). The latter are considered superior in specific applications since they not only display an increase in physical dose in the Bragg peak, but also an enhanced relative biological efficiency (RBE) as compared to protons and photons. This could make ions the preferred choice for treating radio-resistant tumors and tumors very close to critical organs. Proton- and ion therapy is now spreading rapidly to the clinical realm. There are currently 43 particle therapy facilities in operation around the world and many more are in the proposal and design stage. The most advanced work has been performed in Japan and Germany, where a strong effort has been mounted to study the clinical use of carbon ions. Research in Europe, particularly at GSI, Germany and PSI, Switzerland must be considered outstanding. Initial work concentrated predominantly on cancers in the head and neck region using the excellent precision of carbon ions to treat these cancers very successfully [2]. Also, intensive research on the biological effectiveness of carbon ions in clinical situations was carried out and experiments, as well as Monte Carlo based models including biological effectiveness in the treatment planning process were realized [3]. This work has directly led to the establishing of the Heavy Ion Treatment center HIT in Heidelberg, Germany [4]. HIT started patient treatment in November 2009 and continues basic research on carbon ion therapy in parallel to patient treatments. Several other centers offering carbon ion and proton therapy are under construction or in different stages of development across Europe, e.g. five proton therapy centers are being built in the UK, one more has been commissioned in Marburg, Germany and the Medaustron facility has also started patient treatment recently. The OMA network presently consists of 14 beneficiary partners (three from industry, six universities, three research centers and 2 clinical facilities), as well as of 17 associated and adjunct partners, 8 of which are from industry.

RESEARCH

Continuing research into the optimization of medical accelerators is urgently required to assure the best possible cancer care for patients and this is one of the central aims of OMA [5]. The network's main scientific and technological objectives are split into three closely interlinked work packages (WPs):

- Development of novel beam imaging and diagnostics systems;
- Studies into treatment optimization including innovative schemes for beam delivery and enhanced biological and physical models in Monte Carlo codes;

*This project has received funding from the European Union's Horizon 2020 research and innovation programme under the Marie Skłodowska-Curie grant agreement No 675265.
#c.p.welsch@liverpool.ac.uk

ISBN 978-3-95450-177-9

- R&D into clinical facility design and optimization to ensure optimum patient treatment along with maximum efficiency.

The following paragraphs outline the research program targeting advanced beam diagnostics for medical accelerators.

Online Beam Monitoring

Compared to conventional radiotherapy, proton therapy is still a developing technology. While the accelerator systems required to provide a 200-400 MeV proton beams are a mature technology, numerous challenges, both clinical and technical, must be overcome before proton therapy has as sound a clinical footing as e.g. X-ray radiotherapy [6]. Amongst these challenges, effective imaging is of critical importance. All projects in this WP target the development of beyond state-of-the-art diagnostics that will provide more detailed and complete information about the beam. Individual projects provide mutually complementary information and will be exploited in parallel to achieve full beam characterization. Results from all projects in this WP will be taken into account for the treatment optimizations carried out in WP3 and benefit the facility and beam line design studies in WP4.

The Vertex Locator (VELO) which was developed for the LHCb experiment at CERN [7], is an example of a silicon micro-strip detector positioned around the experiments interaction region. By the use of two types of strip geometries the radial and azimuthal coordinates of traversing particles are measured. VELO provides precise measurements of track coordinates which are used to reconstruct the primary collision vertex as well as displaced secondary vertices that are characteristic of B-meson decays. It is hence a promising technology for non-invasive real time beam monitoring applications. A Fellow based at the University of Liverpool/Cockcroft Institute will use the VELO detector to design, build up and test a stand-alone monitor for online beam monitoring in medical accelerators and link it to an overall diagnostics concept with other Fellows working on facility design and optimization. The Fellow will improve and enhance a stand-alone version of the VELO detector as shown in Fig. 1 [8].

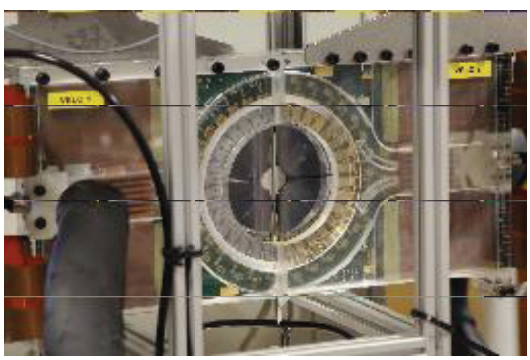

Figure 1: Photograph of the VELO detector that will be used as online beam monitor for quality assurance.

This will include optimizing a local positioning, control, ventilation (with dry air) and cooling system. Extensive measurements will then be carried out to establish a halo-dose correlation data base for different machine settings. This data will then be used for benchmarking Monte Carlo simulations against real data and contribute to enhanced treatment models in WP3.

High-speed Radiation Detection Platform

Another promising detector technology that was originally developed for high energy physics applications and has already found widespread medical applications is the Medipix family of detectors [9]. These are solid state hybrid X-ray pixel detectors working in photon counting mode and suitable for a wide range of applications including X-ray and particle beam imaging. A Fellow based at Amsterdam Scientific Instruments will develop a new type of high-speed hybrid pixelated detector based on the Medipix readout chip and target readout speeds of more than 1 kHz; roughly one order of magnitude faster than the current frame rates of up to 120 Hz. Comprehensive information about the beam requires its measurement before it enters the patient and after it has left them. In state-of-the-art ion beam delivery schemes the tumor volume is 'painted' spot by spot with a so-called 'pencil beam' scanned by magnets. Ion therapy offers extremely high precision in beam delivery and hence demands very high accuracy to ensure that the maximum penetration depth coincides with the tumor. Typically 10% of the ions undergo nuclear collisions with nuclei of the patient tissue along their paths, resulting in the instantaneous emission of prompt gamma rays. These are emitted along the ion trajectories, escape the patient and hence give an opportunity to produce an image of the beam inside the patient. As part of this project a dedicated software for a PC-based readout system will be designed with high speed data processing and analysis. The Fellow will also study the interaction of particles with matter and charge collection in different sensors, realize MC simulations of various detector geometries and combine these with a verification of the detector efficiency for different particle species. This has enormous potential for integration at various locations in the main accelerator and treatment beam lines and efficient integration will be considered with the other Fellows in this WP and work carried out by those studying facility optimization.

Imaging Solutions for a Prompt Gamma Camera

An early career researcher at IBA will develop software tools to perform and test the various new treatment workflows made possible by a 'prompt gamma camera'. To complement information about the beam, it would be highly desirable to monitor its intensity in a parasitical way that does not affect the beam during measurement [10]. Currently, ionization chambers are the most commonly used detector type for beam intensity

ISBN 978-3-95450-177-9

measurement. However, they use thin foils which are passed by the beam and decrease the beam's quality by scattering. This Fellow will work on the development of dedicated software tools that are necessary to perform and test the various new treatment workflows made possible by the camera, using the iMagX platform developed by IBA [11]. Measured data will be compared with the delivered spots by means of irradiation logs without synchronization with the scanning controller, feedback on the penetration depth provided by the camera will be combined with feedback on the entrance point of the beam by optical means. Expected profiles will be simulated in multiple error scenarios with CERN and benchmarked against real data from measurements done across the OMA network.

RF-based Measurement of Ultra Low Charges

To complement information about the beam, it would be highly desirable to monitor its intensity in a parasitical way that does not affect the beam during measurement. Currently, ionization chambers are the most commonly used detector type for beam intensity measurement. However, they use thin foils which are passed by the beam and decrease the beam's quality by scattering. To mitigate this problem ESR4 will develop a sensitive RF-based current monitor for fully non-interceptive beam current measurement and connect this to ESR1 studies. To mitigate this problem a Fellow at PSI will develop a sensitive RF-based current monitor for fully non-interceptive beam current measurement and connect this to studies at Liverpool University. The work will target the measurement of beam currents as low as 0.3 nA. The design will be based on previous developments at the host [13], but will also take into account developments at other institutes through secondments. A prototype will be used for scans at PROSCAN and fully characterized during the 2nd year in the project.

Calorimeter for Proton Therapy and Radiography

An alternative is to use protons for imaging: an energy is chosen such that the protons do not stop within the body of the patient but pass through to be detected. Using the same proton beam for both imaging and treatment ensures the patient does not have to be moved between imaging and treatment: in addition, the anatomical information acquired from the imaging does not have to be adjusted from a different imaging modality. A conceptual proton Computed Tomography (pCT) system consists of a series of tracking layers upstream and downstream of the patient, with some method of measuring the final energy of the diagnostic protons. Individual proton energy measurements at the 1% level are therefore essential for a proton imaging system.

In addition, an accurate calorimeter would also provide valuable quality assurance measurements of the treatment protons. In order to ensure that treatment is carried out safely, a range of quality assurance (QA) procedures are carried out each day before treatment starts. The majority of this time is spent verifying the Bragg Peak and depth dose curve of several proton beam energies. These energy QA measurements take significant time to set up and adjust for different energies.

A project at UCL seeks to adapt existing calorimetry technology for the precise measurement of proton energy in a clinical setting, see Fig. 2. This technology was developed by the UCL High Energy Physics group for the SuperNEMO experiment [14]. Preliminary calculations indicated that such a SuperNEMO detector could achieve an energy resolution in the region of 1% for clinical proton energies. Early experimental measurements using the 60 MeV clinical proton beam at the Clatterbridge Centre for Oncology demonstrated that the detector performance is as anticipated.

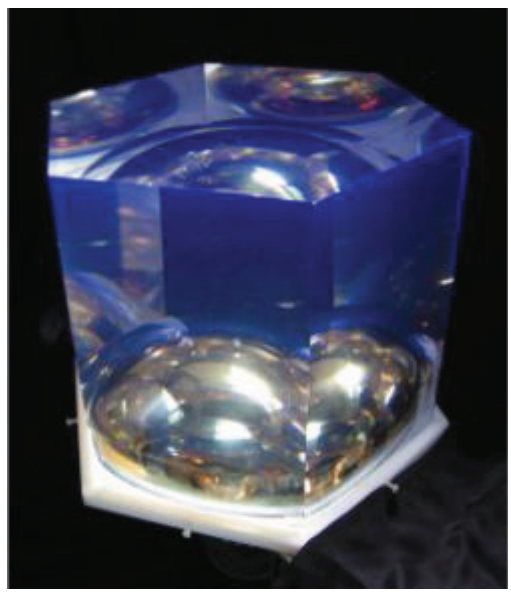

Figure 2: Photograph of detector for calorimeter applications at UCL, UK.

Existing Geant4 simulations will be adapted to optimize detector configuration for proton therapy. The PVT scintillator is already well characterized, reducing the initial effort required. Further measurements will be made with the Clatterbridge proton beam to fully characterize the performance of the detector. This will form the basis of the calorimetry stage for a proton CT system. In addition, this detector will also be used as the basis for a fast energy QA system. This would allow several energies to be measured across the full energy range available at the nozzle in only a few minutes, significantly reducing the time taken to carry out the daily QA.

Radiobiological Effectiveness of Protons

A Fellow at the University of Seville/CNA, Spain will investigate into the overall optimization of beam diagnostics for determination of all essential beam parameters. They will study the radiobiological effects of protons using the CNA facilities. Its 3 MV tandem accelerator and the cyclotron (delivering 18 MeV protons) will provide protons with energy ranges of interest for

ISBN 978-3-95450-177-9

radiobiological studies, irradiating cell samples. Beam diagnostics and dose measurements prior to, during and after irradiation are key to a full understanding: radiochromic film at the position of the cell samples, transmission ionization chambers for dosimetry; and CR-39 nuclear track plates for proton fluence measurements will be used and results analysed with GSI. Silicon detectors will be used at the position of the cell samples to determine proton energies with AMS. Finally the "low-dose hyper-radiosensitivity (LDHRS)" phenomenon [11] will be studied with protons to understand the dependence of LDHRS on the type of radiation and linear energy transfer (LET). This will provide a framework for cell studies and important information for a critical performance assessment of all diagnostics R&D in this WP.

TRAINING EVENTS

Training within OMA consists of research-led training at the respective host, in combination with local lectures, as well as participation in a network-wide training program that is also open to external participants. This training concept is based on the successful ideas developed within the DITANET, oPAC and LA3NET projects [12-14]. 3 week-long international Schools, open to all OMA Fellows and up to 50 external participants on Monte Carlo Simulations, Medical Accelerators and Particle Therapy will be organized. All Schools will be announced via the project home page [5]. To further promote knowledge exchange and ensure that all Fellows are exposed at highest possible level to the techniques and methodologies developed in the other WPs, three 2-day Topical Workshops covering two scientific WPs at a time will be organized. These will cover 'Facility Design Optimization for Patient Treatment', 'Diagnostics for Beam and Patient Monitoring', and 'Accelerator Design & Diagnostics'. In the last year of the project a 3-day international conference will be organized, with a focus on the novel techniques and technologies developed within the network.

SUMMARY

An overview of the R&D program in beam diagnostics within the recently approved OMA project was given. The network is a very large European training network and the first that has even been evaluated with a 100% mark. OMA will train 15 early stage researchers over the next four years and most Fellows will start their projects on 1 October 2016. The consortium consists of universities, research centers, clinical centers, and industry partners and will also organize a large number of training events. This includes Schools, Topical Workshops, an international conference and various outreach events which will all be open also for participants from outside of the project.

REFERENCES

[1] R. Wilson, *Radiology* 47 (1946) 498-491.
[2] D. Schulz-Ertner, *et al.*, Int. J. Rad. Onc. Biol. Phys., 58, (2004), pp. 631–640 and G. Kraft, Progr. in Particle and Nuclear Physics 46 (2001).
[3] M. Krämer, *et al.*, *Phys. Med. Biol.* 45 3299 (2000) and T. Elsässer, et al, *Int. J Rad. Onc. Biol. Phys.* 78 (2010), p. 1177–1183.
[4] S.E. Combs, *et al.*, *Radiotherapy and Oncology* 95 (2010), p. 41-44.
[5] Optimization of Medical Accelerators Project, http://www.oma-project.eu
[6] J.S. Löffler and M. Durante, *Nature Reviews Clinical Oncology* 10, 411 24 (2013).
[7] The LHCb Collaboration, CERN-LHCC/200029, CERN (2002).
[8] T. Cybulski, *et al.*, "Design and first operation of a silicon-based non-invasive beam monitor", *Proc. of IPAC2014*, Dresden, Germany, paper THPME185.
[9] K.-F. Pfeiffer, *et al., Nucl. Instr. and Meth. A* 509 (2003), p. 340; X. Llopart, M. Campbell, *Nucl. Instr. Meth. A* 509 (2003), p. 157.
[10] J Smeets *et al.*, *Phys. Med. Biol.* 57 (2012) p. 3371–405.
[11] U. Schneider and E. Pedroni, *Medical Physics* 22, 353 (1995).
[12] DITANET, http://www.liv.ac.uk/ditanet
[13] OPAC, http://www.opac-project.eu
[14] LA^{3}NET, http://www.la3net.eu

ISBN 978-3-95450-177-9

ACCELERATOR OPTIMIZATION THROUGH BEAM DIAGNOSTICS

C.P. Welsch#, Cockcroft Institute and The University of Liverpool, UK
on behalf of the oPAC Consortium

Abstract

A comprehensive set of beam diagnostics is key to the successful operation and optimization of essentially any accelerator. The oPAC project received 6 M€ of funding within the EU's 7th Framework Programme. This has allowed to successfully train 23 Fellows since 2011. The network joins more than 40 institutions from all around the world, including research centers, universities and private companies. One of the project's largest work packages covers research in beam diagnostics. This includes advanced instrumentation for synchrotron light sources and medical accelerators, enhanced beam loss monitoring technologies, ultra-low emittance beam size diagnostics, diagnostics for high intensity beams, as well as the development of electronics for beam position monitors. This paper presents an overview of the research outcomes from the diagnostics work package and the demonstrated performance of each monitor. It also shows how collaborative research helps achieving beyond state-of-the-art solutions and acts as an ideal basis for researcher training. Finally, an overview of the scientific events the network has been organizing for the wider accelerator community is given.

INTRODUCTION

The optimization of the performance of particle accelerators was the goal of the Marie Curie Initial Training Network (ITN) oPAC [1]. The project received 6 M€ of funding from the European Union within the 7th Framework Programme, making it the largest-ever ITN. It successfully trained 23 Fellows across 4 scientific work packages (WPs) and allowed them to develop expert knowledge in a number of different fields, such as engineering, physics, electronics, IT and material sciences. Training through network-wide events including schools and topical workshop, participation in international conferences, and secondments for specific skill-building has allowed them to carry out cutting edge research whilst providing them with a broad set of skills that is expected to be an excellent basis for their future careers.

RESEARCH

The results from the oPAC Fellows' research have resulted in more than 100 contributions to international conferences and workshops. More than 30 papers have already been published in peer-reviewed journals and several more are currently in preparation as results from research projects are being analyzed and Fellows are finalizing their doctoral theses. The following sections present the results from three selected research projects that all formed part of the beam diagnostics work package.

The developments in this WP received additional support by a dedicated hands-on training day in beam instrumentation hosted by Bergoz in June 2013. This familiarized all Fellows in the first year of their project with the particular challenges in carrying out measurements of the detailed characteristics of charged particle beams and allowed them to discuss progress in all sub projects. Of particular importance for instrumentation development is that no single monitor has yet been developed that is able to monitor all properties of a beam, i.e. several different technologies usually need to be combined to get a full understanding of the beam inside its vacuum chamber. Most oPAC projects initially targeted the development of a single detector (prototype) for a specialized purpose. Information from this monitor was then combined with other detectors and linked to the accelerator control and data acquisition system to obtain a full understanding about the beam.

Beam Size Measurements at ALBA using Interferometry

Synchrotron radiation interferometry is now a reliable method to measure the horizontal and vertical beam size at the ALBA storage ring in Barcelona, Spain. The technique, developed by T. Mitsuhashi, allows determining the beam size by measuring the visibility of the interferogram, obtained by making the visible part of the synchrotron radiation interfere using a double slit interferometer. Due to the layout of the ALBA diagnostic beam line Xanadu interferometry measurements were not completely straight forward. Fellow Laura Torino introduced several enhancements to the existing set-up to overcome existing limitations, in particular: The light selected by a photon shutter cuts the light horizontally whilst the first extraction mirror selects only the upper lobe of the produced radiation. This generates a final footprint that is dominated by Fraunhofer diffraction. The use of a double slit system allows the selection of several different fringes of the footprint. Fringes generated by Fraunhofer diffraction don't have necessarily the same phase. This might provoke a loss of contrast affecting the visibility measurements. To reduce this effect the slits were substituted by pinholes to select a more compact region of the footprint and consequently, a reduced number of fringes. Furthermore, the 7 mirrors guiding the light up to the Xanadu optical table are "in-air". The air turbulence in the tunnel or in the beam line can provoke vibrations of the optical elements that are converted in a rigid displacement of the centroid of the interferogram image on the CCD sensor.

*This project has received funding from the European Union's Seventh Framework Programme for research, technological development and demonstration under grant agreement no 289485.
#c.p.welsch@liverpool.ac.uk

ISBN 978-3-95450-177-9

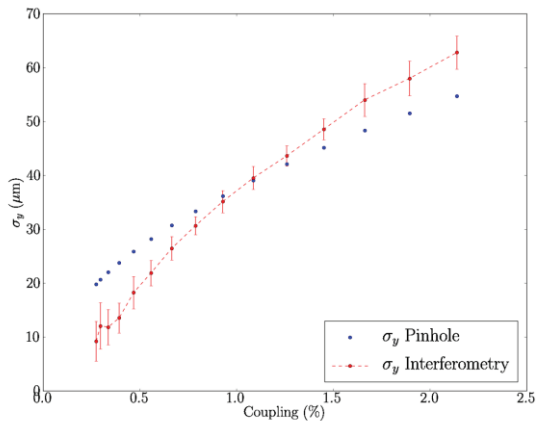

Figure 1: Vertical beam size measurements σ_y from the pinhole (blue) and the interferometer (red).

The incoherent sum of artificially displaced images also produces a loss of contrast in the visibility measurements. Reducing the CCD exposure time is an intuitive and efficient way to solve this problem, but also causes a reduction in intensity of the image which leads to an impossibility in the visibility measure, due to the reduced dynamic range of the CCD camera. To overcome this problem a matching algorithm was developed to superimpose low exposure time images (0.1 ms) and improve the contrast and the dynamic range of the interferogram. The reliability of these measurements, both for horizontal and vertical beam size, was verified in several ways. It was possible to study depth of field effects on the horizontal beam size by performing measurements for different distances between the pinholes. In addition, the effectiveness of vertical beam size measurements was verified by performing so-called coupling scans: By changing the emittance coupling using skew magnets the vertical beam size also varies. The results obtained with the interferometer follows the ones obtained with the x-ray pinhole. The x-rays used for pinhole measurements, and the visible light for the interferometry come from two consecutive bending magnets at slightly different locations. For this reason the measurements do not exactly coincide, but the trend is nicely confirmed, as shown in Fig. 1. Further details are given in [2].

Position Detection for Ultra-Low Intensity Heavy-Ion Beams

The Collector Ring (CR) at the Facility for Antiproton and Ion Research (FAIR) will mainly be used for collecting and pre-cooling high-intensity radioactive ion beams and antiprotons. It can also be used for isochronous mass spectrometry for neutron-rich or neutron-deficient exotic nuclei when it is tuned to a special ion-optical setting. The ultra-low intensity of these beams then imposes stringent sensitivity requirement on beam detection techniques. An RF cavity as a Schottky noise detector has proven to be an extremely sensitive beam diagnostic device with its ability to detect even single ions [3]. As an upgrade of the existing Schottky resonator installed in the Experimental Storage Ring (ESR) a position-resolving cavity has been proposed for the CR. This cavity, together with the intensity-sensitive one, will be able to distinguish the revolution orbits of stored ions for nuclear mass measurements. The measured positions will be used as a key input for subsequent analyses to correct for the anisochronism effect in the measurement and help improve the accuracy and precision of the evaluated atomic masses [4]. In contrast to a conventional cavity-based BPM the present design offsets the beam pipe to a side of the cavity and utilizes the resonant monopole mode [5]. Consequently, the shunt impedance, which is a measure of the coupling strength between the cavity and the beam exhibits an inclined trend over the aperture around a fairly high mean value. Having normalized the signal to a reference from the intensity cavity the position can be deduced by means of magnitude discrimination. In order to enhance the intensity sensitivity and position resolution of the cavity much effort has been devoted to the optimization of the cavity geometry so as to attain adequate mean value and slope of the shunt impedance. oPAC Fellow Xiangcheng Chen, based at GSI, carried out analytic and numerical studies into the design. First, the electric field inside the cavity was solved for a rectangular box and elliptic cylinder. The optimum dimensions were then selected in accordance with the experimental requirements. Second, an electromagnetic field solver was used to investigate changes in resonant frequency and shunt impedance taking into account realistic values for beam pipe and plunger. In order to verify the design two scaled prototypes have been manufactured and tested by Chen on a purpose-built benchtop. The electric fields inside the prototypes were measured by perturbation with a ceramic bead. The latter was held by a cotton thread while the cavity was moved by a motorized displacement unit. The resonant frequency was obtained from transmission measurements using a vector network analyzer. A dedicated Java application coordinates the movement-measurement cycle. In order to account for any temperature drift a reference measurement was taken before each perturbation measurement. The entire profiling process takes 5 hours and is fully automated. As an example the measured shunt impedance of the rectangular prototype is shown in Fig. 2. It is in very good agreement with the associated simulation studies.

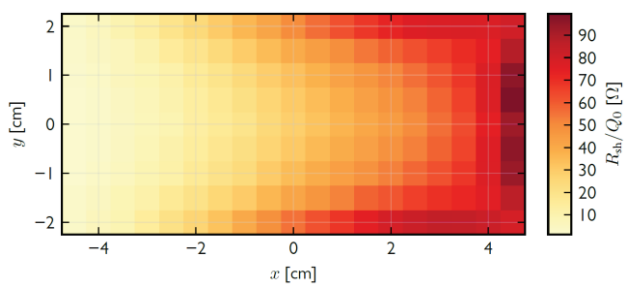

Figure 2: Measured shunt impedance of the rectangular Schottky monitor prototype.

ISBN 978-3-95450-177-9

Cryogenic Current Comparator for Low Energy Antiproton Beams

A Cryogenic Current Comparator (CCC) monitor optimized for the AD and ELENA rings at CERN has been developed by M. Fernandes, based at CERN, and first measurements with beam have been carried out, see Fig. 3 [6]. These are the first CCC beam current measurements performed in a synchrotron using both, coasting and short-bunched beams.

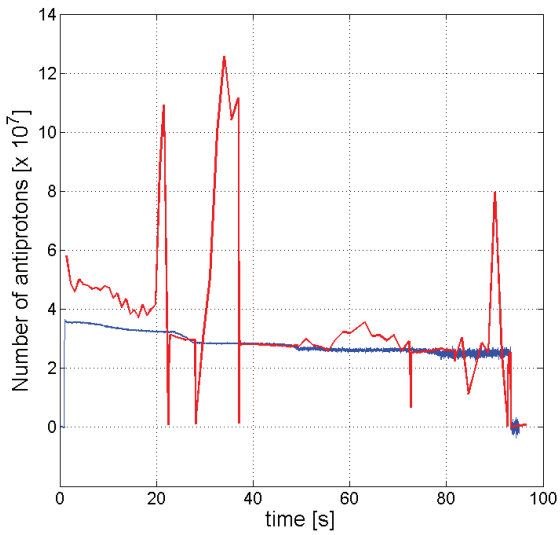

Figure 3: Comparison between measurement with Schottky noise based monitor (in red) and CCC (blue).

The CCC is currently the only device able to measure non-perturbatively very low-beam intensities. A particular improvement is the possibility of absolute calibration of the experiments receiving the particle beam using data from the CCC, as well as cross-calibration of other intensity monitors for which no simple calibration method is available. A current intensity resolution of 30 nA was successfully demonstrated after low-pass filtering with a cut-off frequency at 10 Hz. The system was able to cope with a beam current signal slew-rate exceeding 8 kA/s maintaining the SQUID/FLL stability. A new cryostat mechanical design provided for an excellent decoupling of mechanical perturbations, enabling the CCC monitor to attain this performance even when the connected cryocooler unit was operating.

TRAINING EVENTS

Training within oPAC was provided to all Fellows locally by the host institute, primarily through cutting edge research, specialized lectures and seminars, as well as network-wide training offered by the whole consortium. In addition, oPAC has organized a series of Topical Workshops and Schools for its Fellows which were also open to the wider accelerator community.

International Schools

At the start of their training all oPAC Fellows participated in either the established CERN Accelerator School or the Joint Universities Accelerator School. This provided them a sound training basis as they took on their projects within the Network. Both Schools included lectures and tutorials covering accelerator physics, relativity and electro-magnetism, particle optics, longitudinal and transverse beam dynamics, synchrotron radiation, linear accelerators, cyclotrons and general accelerator design. An oPAC School on Accelerator Optimization was then organized by the consortium between 7th-11th July 2014 at Royal Holloway University of London, UK. It covered advanced techniques for the optimization of particle accelerator performance - in particular the combination of different fundamental techniques to push the limits of accelerators ever further.

All Fellows initially met for a dedicated researcher skills School in Liverpool, UK in June 2013. During the week-long School they were provided with subject-specific training in addition to generic topics, including project management, scientific writing, problem solving techniques and building bridges between academia and industry. The Fellows were asked to present a short summary of their projects as part of presentation skills training and also to develop a detailed project plan of their oPAC projects. Towards the end of their projects all Fellows followed a 4-day advanced researcher skills workshop which brought them again to Liverpool. The transition to permanent employment from postgraduate research is a challenging prospect in an ever more competitive job market. The workshop provided dedicated and practical support to help the Fellows in their future careers. External and internal trainers provided an extremely broad training throughout the week. This included support in career planning by providing practical and specific advice on CV writing and interview skills, writing competitive grant applications and science communication and networking. The university's business gateway team and Dr. Marco Palumbo, IPS Fellow in the physics department, contributed dedicated sessions on intellectual property rights, commercialization and entrepreneurship that were very positively received by the course participants.

Topical Workshops

oPAC also organized a whole series of Topical Workshops. This included expert training days on 'Simulation Tools' (CST, Germany) and 'Beam Diagnostics' (Bergoz, France), a 2-day Topical Workshop on the Grand Challenges in Accelerator Optimization at CERN, Switzerland on June 27th/28th 2013 [7], a workshop on Beam Diagnostics hosted by CIVIDEC [8] and one on Libera Technology at Instrumentation Technologies. Most recently, a workshop on Computer-Aided Optimization of Accelerators (CAoPAC) was held at the GSI Centre for Heavy Ion Research in Darmstadt, Germany from 10 – 13 March 2015 [9]. This was a special event for the network

ISBN 978-3-95450-177-9

as it was organized by the Fellows of the network, providing them with the opportunity to take charge of a whole event from scratch, with a limited time-frame, limited resources, and the challenge of offering an interesting event to attract a good number of participants. In 2016, the Fellows were invited to a careers workshop held in June in Krakow, Poland. A Topical Workshop on Beam Loss Monitors, organized immediately after this IBIC conference, was the final event to date [10].

Accelerator Symposium and Conference on Accelerator Optimization

An international Symposium on Lasers and Accelerators for Science & Society took place on the 26th of June in the Liverpool Arena Convention Centre. The event was a sell out with delegates comprising 100 researchers from across Europe and 150 local A-level students and teachers. The aim was to inspire youngsters about science and the application of lasers and accelerators in particular. It is now possible to share the enthusiasm of the accelerator experts through online presentations [11]. Finally, the network has organized a 3-day international conference on accelerator optimization in Seville, Spain [12].

SUMMARY

oPAC has successfully trained 23 early stage researchers between 2012 and 2015. The network has also organized a large number of international schools and topical workshops that have benefited the world-wide accelerator community. On the basis of the extremely positive feedback that was received from the community, the consortium has recently organized a Fellow reunion and careers workshop, as well as a Topical Workshop on Beam Loss Monitors [13] that follows after this IBIC conference. Additional future events will be considered based on the demand and input from the wider beam instrumentation community.

REFERENCES

[1] http://www.opac-project.eu
[2] L. Torino *et al.,* "Limitations and Solutions of Beam Size Measurements via Interferometry at ALBA", *Proc. IBIC2015*, Melbourne, Australia.
[3] F. Nolden, *et al.*, "A fast and sensitive resonant Schottky pick-up for heavy ion storage rings". *Nucl. Instrum. Meth. A* 659, 2011, 69.
[4] X. Chen, *et al.*, "Accuracy Improvement in the Isochronous Mass Measurement Using a Cavity Doublet." *Hyperfine Interact.*, 2015.
[5] M.S. Sanjari, *et al.*, "Conceptual Design of Elliptical Cavities for Intensity and Position Sensitive Beam Measurements in Storage Rings." *Phys. Scr.*, (2015).
[6] M.F. Fernandes, *et al.*, "Cryogenic Current Comparator for Storage Rings and Accelerators", *Proc. IBIC2015*, Melbourne, Australia.
[7] http://indico.cern.ch/event/243336
[8] http://indico.cern.ch/event/293158
[9] http://indico.cern.ch/event/333414
[10] http://indico.cern.ch/event/527597
[11] http://indico.cern.ch/event/368273
[12] http://indico.cern.ch/event/380975
[13] http://indico.cern.ch/event/527597

ISBN 978-3-95450-177-9

THE FRASCATI LINAC BEAM-TEST FACILITY (BTF) PERFORMANCE AND UPGRADES*

B. Buonomo, C. Di Giulio, L. G. Foggetta†, INFN – Laboratori Nazionali di Frascati, Via Enrico Fermi 40, I-00044 Frascati (Rome), Italy.
P. Valente, INFN – Sezione di Roma, P.le Aldo Moro 2, I-00185 Rome, Italy.

Abstract

In the last 11 years the Beam Test Facility (BTF) of the Frascati DAFNE accelerator has gained an important role in the development of particle detectors development. Electron and positron beams can be extracted to a dedicated transfer line, where a target plus a dipole and collimator system can attenuate and momentum-select secondary particles.

The BTF can thus provide a wide range of beam parameters: energy (from about 50 to 750/540 MeV for electrons/positrons), charge (up to 10^{10} particles/bunch) and pulse length (1.5-40 ns), with a maximum repetition rate of 50 Hz.

Beam spot and divergence can be adjusted, down to sub-mm and 2 mrad. Photons can be produced on a target, and energy-tagged inside a dipole by Silicon micro-strip detectors. A shielded Tungsten target is used for neutron production: about $8 \cdot 10^{-7}$/primary, 1 MeV neutrons are produced.

In addition to these activities, a dedicated particle physics experiment (PADME) has been recently approved for running at the BTF, with an intermediate intensity positron beam.

In order to cope with the increasing beam requests, an upgrade program of the facility has been proposed, along three main lines: consolidation of the DAFNE LINAC, in order to guarantee stable operation in the longer term; upgrade of the maximum beam energy to 1 GeV; doubling of the existing beam-line and experimental hall.

BTF LINE DESCRIPTION AND PRESENT PERFORMANCE

The Beam-Test Facility (BTF) of the INFN Frascati Laboratories is an extraction and transport line, optimized for the production of electrons and positrons in a wide range of intensity, energy, beam spot dimensions and divergence, starting from the primary beam of the DAFNE LINAC. Each of the 50 pulses/s accelerated by the LINAC can be either driven to a small ring for emittance damping (and from there injected into the DAFNE collider rings), or to the BTF line, by means of pulsed dipoles.

A variable depth target (from 1.7 to 2.3 X_0) spreads the momentum distribution of the incoming beam, then secondary electrons (or positrons) are momentum selected by means of a 45° dipole and collimators (in the horizontal plane). The beam intensity is thus greatly reduced, depending on the chosen secondary beam energy central value (from about 50 MeV up to almost the primary beam energy) and spread (typically better than 1%, depending on the collimators settings) [1].

The beam is then transported to the experimental hall and focussed by means of two quadrupole FODO doublets. The layout of the beam selection and transport line is shown in Fig. 1, together with the shielded experimental area.

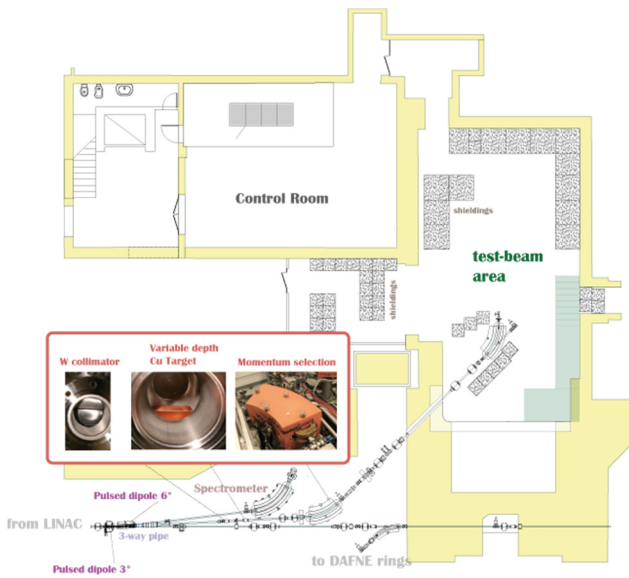

Figure 1: Layout of the BTF line and area, in the inset pictures of (from the left): Tungsten collimators pair, Copper beam-attenuating target, energy-selecting dipole magnet.

Availability and Flexibility

The facility can operate essentially in two different modes: "parasitic", when the DAFNE collider is operating and only LINAC bunches not injected into the rings are available; "dedicated", when the collider is not operating and all LINAC bunches are available for the beam-test. Considering the frequency of electron and positron injections for DAFNE and the number of available bunches, an average of 20 pulses/s is delivered for BTF operation.

The facility has been steadily operating since 2004, with an average of more than 200 beam-days/year, and 25 user groups/year. Beam time is generally allotted in one week shifts (Monday to Monday, 24/7 operation). A small fraction of the shifts have been dedicated to:

- production of tagged photons, by means of a dedicated active Bremsstrahlung target and energy-tagging system, made up of Silicon micro-strip detectors [2];
- electro-production of neutrons on a Tungsten target, shielded by an optimized assembly of polyethylene and Lead [3].

ISBN 978-3-95450-177-9

Table 1: BTF Beam Main Parameters Achieved in the Different Operation Modes

Parameter	"Parasitic" mode		Dedicated mode	
	With target	Without target	With target	Without target
Electrons or positrons	selectable at BTF	depending on DAFNE injection	selectable at BTF	selectable at LINAC
Energy (MeV)	30-500	510	30-700	250-750 (e-) 250-550 (e+)
Energy spread	1% at 500 MeV	0.5%	1% at 500 MeV	0.5-1%
Intensity	1-10^5	10^7-1.5×10^{10}	1-10^5	10^3-3×10^{10}
Pulse length	10 ns		1.5-40 ns	
Repetition rate	10-49 particles/s (depending on DAFNE injection)		1-49 particles/s	

By using the horizontal and vertical collimators, the beam intensity can be tuned from several thousands down to "single" electrons per pulse, i.e. producing a Poisson distribution with a given average multiplicity, that is the preferred operations mode for the characterization and calibration of particle detectors [4].

The main parameters achieved in the two different operation modes, with and without attenuating the beam with the BTF target, are reported in Table 1.

DAQ, Diagnostics, and Services

We have implemented a number of diagnostics detectors, both for intensity and beam spot monitoring, in the full range of intensities (from the full LINAC beam down to single particle). A wide range of services are available in the experimental hall (shown in Fig. 3), such as gas, vacuum, networking, low and high voltage supplies, trigger and timing, etc. [5].

Data from the Silicon micro-strip [6], FitPIX [7] and GEM TPC detectors [8] are made available to the users thanks to a new software framework based on MEMCACHED [9].

FitPIX is a Silicon, 55 μm pitch, 256×256 pixels detector (14×14 mm^2 active area). A typical beam spot imaged at the reference energy of 450 MeV is shown in Fig. 2: a transverse size of the order of $\sigma_{x,y}$=0.4 mm has been achieved after optics and collimators optimization, mainly limited by the multiple scattering on the thin (500 microns) Beryllium window at the exit of the vacuum beam-pipe. However a beam spot of σ=5 mm was still achieved for an optimized 30 MeV electron beam.

The angular divergence is of the order of few mrad, strongly depending on the focussing and on the beam energy, and again the effect of the exit window is not negligible.

Further details on the high resolution transverse diagnostics can be found in these proceedings [10].

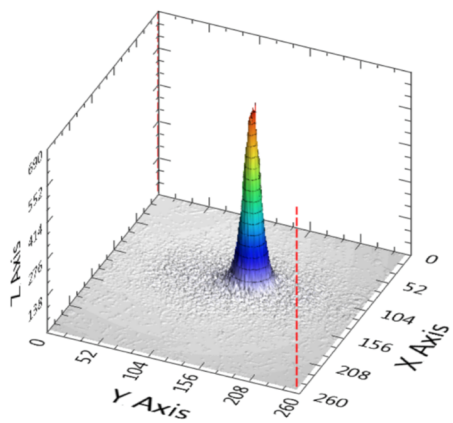

Figure 2: Typical 450 MeV electron beam imaged with the FitPIX detector (1 pixel=55 μm).

Figure 3: View of the BTF experimental hall showing the last part of the beam transport line, from the left: vacuum valve, quadrupole doublet (yellow), 45° beam switching magnet (orange), lead/polyethylene shielding box for neutron production target.

ISBN 978-3-95450-177-9

BTF UPGRADES

The increasing number of requests for beam has motivated a wide program of consolidation and improvement of the facility [11], along three main directions: consolidation of the LINAC infrastructure, in order to guarantee a stable operation in the longer term; upgrade of the LINAC energy, in order to increase the facility capability (especially for the almost unique extracted positron beam); doubling of the BTF beam-lines, in order to increase the access capability, coping with the significant increase of users.

LINAC Consolidation

The Frascati LINAC is a 60 m long, S-band (2856 MHz), travelling wave, constant gradient linear accelerator modelled on the SLAC design. The 16 accelerating sections are fed by four RF power stations composed by line modulators powering 45 MWp klystrons with SLED compression.

The most critical parts of the LINAC sub-systems, are the modulators, and in particular their control and safety interlocks. Even though maintenance activities in the last years concerned mainly the RF stations, still a number of critical components are the original parts installed more than 20 years ago [12]. In order to carry on a complete refurbishing of the modulators a test RF station has to be built for the qualification and test of the new systems.

Energy Upgrade

In the present configuration a 15 m drift space is present between the end of the LINAC and the switch-yard driving the beam towards the DAFNE rings or the BTF line. This gives the opportunity of adding at least four SLAC-type accelerating sections, made up of 86 disk-loaded cells for a length of 3.05 m.

A fifth RF station, identical to the existing ones, with a 45 MWp klystron and a SLED pulse compressor, feeding the four new sections would allow increasing the final energy of at least 260 MeV, allowing to reach about 1 GeV for electrons and 800 MeV for positrons. The upgraded RF distribution layout is shown in Fig. 4.

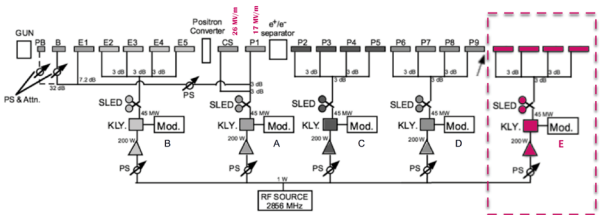

Figure 4: Proposed layout of the RF distribution for the upgraded LINAC.

A higher accelerating field (of at least 50%) can be achieved doubling the number of new RF stations, allowing to reach an energy gain of 90 MeV in the additional four accelerating sections.

Beam-line Doubling and Extended Pulse

Recently the PADME experiment for the search of new fundamental forces, in particular of a vector (dark photon) or axial-like mediator, has been approved, aiming at a sensitivity of $\varepsilon=10^{-3}$ for the coupling, in a mass range up to 24 MeV/c^2, using the annihilation of about 10^{13}, 550 MeV positrons on a thin target [13-15].

In order to host for a few years a long-term installation with the size and complexity of a full-fledged high-energy physics experiment, without severely limiting the use of the beam-test, a second beam-line has to be realized.

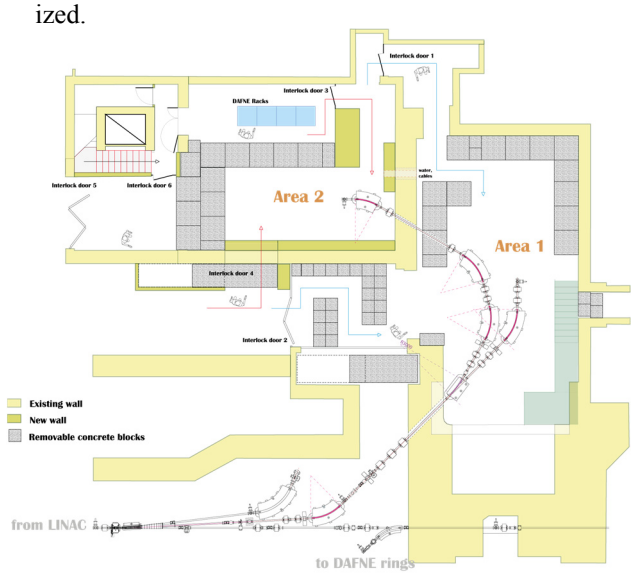

Figure 5: The new BTF lines and the modified layout of the building for hosting two separated experimental areas.

The idea for the new layout is schematically shown in Fig. 5: a beam-splitting dipole, wrapped around a double-exit pipe, can drive beam pulses from the upstream BTF beam-line alternatively to the two new lines. In case, the dipole can be connected to a pulsed power supply for a fast switch between the two lines.

The first line drives the beam in the existing experimental hall (“Area 1” in the picture), also profiting of the existing concrete block-house, while the second will transport the beam, with three additional dipoles, in the area presently used as BTF control room (“Area 2”), with minor civil engineering work.

A complete optimization of the new lines optics has been performed, in order to define the new beam elements requirements, both using G4-beamline and MAD-X [16], as shown in Fig. 6-7.

ISBN 978-3-95450-177-9

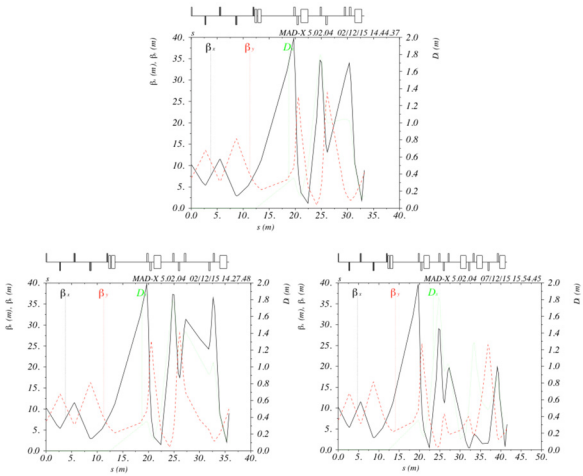

Figure 6: MAD-X results for the β function and dispersion of the present BTF (top) and for the new lines "1" and "2" (bottom left and right respectively).

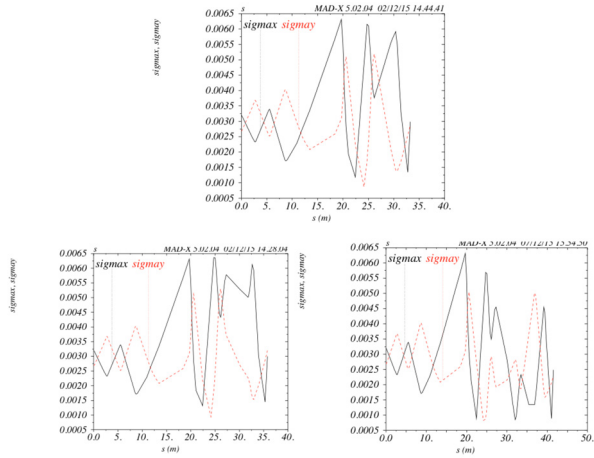

Figure 7: MAD-X results for the envelope (σ_x and σ_y) of the present BTF (top), and for the new lines "1" and "2" (bottom left and right respectively).

The PADME experiment sensitivity is essentially limited by the pile-up probability in the calorimeter [17], thus imposing a limit on the number of positrons in the beam. It would be then useful to further extend the range of the LINAC beam pulse length beyond the 40 ns presently achieved.

In order to do that, an upgrade program for the LINAC thermo-ionic gun is under way, aiming at extending the beam pulse up to a few hundreds of ns, while keeping the energy spread under control.

CONCLUSIONS

The continuous improvement of the performances and services of the BTF facility has produced an increased number of beam requests, mainly from the detector development community.

Recently PADME, a fixed-target experiment, aiming at exploring light dark matter models with the BTF positron beam, has been approved, thus posing further requirements both in terms of beam parameters and enlargement of the infrastructure. This has been one of the main drives of the BTF upgrade program.

ACKNOWLEDGEMENT

This work is supported by the H2020 project AIDA-2020, GA no. 654168.

REFERENCES

[1] G. Mazzitelli, A. Ghigo, F. Sannibale, P. Valente and G. Vignola, *Nucl. Instrum. Meth. A* 515 (2003) 524-542.
[2] S. Hasan et al., *Proc. of 9th ICATPP*, C05-10-17 (2005) 217-222.
[3] M. Prata et al., *Eur. Phys. J. Plus* 129 (2014) 255.
[4] B. Buonomo, G. Mazzitelli and P. Valente, *IEEE Trans. Nucl. Sci.* 52 (2005) 824-829.
[5] B. Buonomo, L. G. Foggetta and P. Valente, *Proc. of IPAC 2015*, C15-05-03 (2015) MOPHA049.
[6] B. Buonomo et al., *Proc. of DIPAC 2005*, C05-06-05.5 (2005) 166-168.
[7] L. G. Foggetta, B. Buonomo and P. Valente, *Proc. of IPAC 2015*, C15-05-03 (2015) MOPHA048.
[8] F. Murtas et al., *Nucl. Instrum. Meth. A* 617 (2010) 237-241.
[9] B. Buonomo, C. Di Giulio, L. G. Foggetta and P. Valente, "The Frascati LINAC Beam-Test Facility (BTF) Performance and Upgrades",*Proc. of IBIC 2016* (these proceedings) WEPG73.
[10] B. Buonomo, C. Di Giulio, L. G. Foggetta and P. Valente, "Frascati Beam-Test Facility (BTF) High Resolution Beam Spot Diagnostics", *Proc. of IBIC 2016* (these proceedings) MOPG65.
[11] P. Valente et al., "Linear Accelerator Test Facility at LNF. Conceptual Design Report", arXiv:1603.05651 [physics.acc-ph] (2016); INFN-16-04-LNF.
[12] B. Buonomo and L. G. Foggetta, *Proc. of IPAC 2015*, C15-05-03 (2015) TUPWA057.
[13] M. Raggi and V. Kozhuharov, *Adv. High Energy Phys.* 2014 (2014) 959802.
[14] M. Raggi, V. Kozhuharov and P. Valente, *EPJ Web Conf.* 96, 01025 (2015).
[15] J. Alexander et al., "Dark Sectors 2016 Workshop: Community Report", arXiv:1608.08632 [hep-ph] (2016). [16] B. Buonomo, C. Di Giulio, L. G. Foggetta and P. Valente, "Studies of the doubling of the Frascati Beam-Test Facility (BTF) line", AIDA-2020-NOTE-2016-002, CERN, 2016.
[17] V. Kozhuharov, M. Raggi, P. Valente et al., The PADME experiment technical document, *in preparation*.

ISBN 978-3-95450-177-9

TESTING THE UNTESTABLE: A REALISTIC VISION OF FEARLESSLY TESTING (ALMOST) EVERY SINGLE ACCELERATOR COMPONENT WITHOUT BEAM AND CONTINUOUS DEPLOYMENT THEREOF

A. Calia, K. Fuchsberger, M. Hostettler, CERN, Geneva, Switzerland

Abstract

Whenever a bug in some piece of software or hardware stops beam operation, loss of time is rarely negligible and the cost (either in lost luminosity or real financial one) might be significant. Optimization of the accelerator availability is a strong motivation to avoid such kind of issues. Still, even at large accelerator labs like CERN, release cycles of many accelerator components are managed in a "deploy and pray" manner. In this paper we will give a short general overview on testing strategies used commonly in software development projects and illustrate their application on accelerator components, both hardware and software. Finally, several examples of CERN systems will be shown on which these techniques were or will be applied (LHC Beam-Based Feedbacks and LHC Luminosity Server) and describe why it is worth doing so.

INTRODUCTION

An accelerator is a complex system, consisting of many interlinked components, which are typically organized in a control system of different layers from top-level applications to actual hardware.

Fig. 1 shows a vertical slice of a typical accelerator control system stack: On top there is the application layer, consisting of a set of physics-aware applications used by operators, which accesses the hardware through a middle layer. Below, the hardware layer is responsible of actually driving the hardware interacting with the beam.

An accelerator component is typically on one of these layers, and accessing or being accessed by one or more neighbouring components from the other layers. E.g. a top-level software component can access different hardware components through the middle layer, while a hardware component is often accessed by different top-level applications.

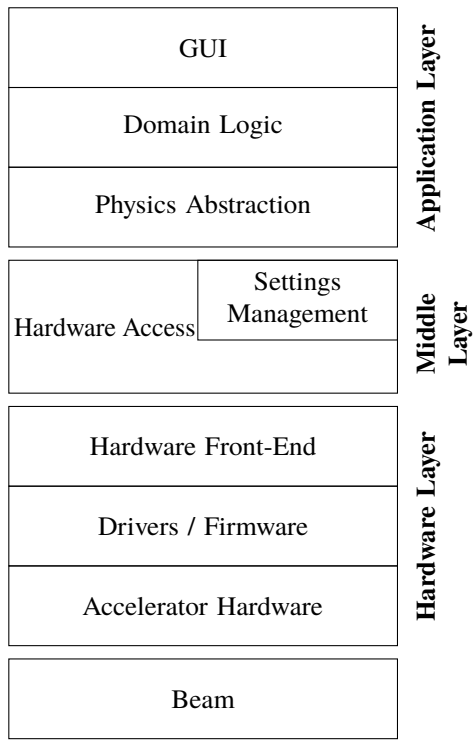

Figure 1: Vertical slice of a typical control system.

EXECUTION MODE

For testability of individual components or any subset of the whole control system, it is required to reduce the coupling between neighbouring components. To facilitate decoupling, we propose different "execution modes" for an accelerator component, which can make it independent of the input and output of other components for testing and development purposes.

Simulation

In a simulation mode, the component's inputs are based on a model. This model is dynamic and can be affected by the execution of a component. The purpose of a simulated model is to test the component in a dynamic environment that can be close to the reality (production).

Ideally, it is possible to create various simulation models to effectively test the component under different circumstances. For a web service, a particularly interesting test is to verify the behaviour when network communications are very unstable and randomly slow. In the case of a hardware component, a challenging model can produce random noise in the inputs signals of the hardware cards.

Scenario

A scenario is composed by a set of fixed values that are the inputs of a component. Given the scenario's input, it is possible to assert the component's output to spot errors.

Scenarios can be created from particular situations that the component must be able to handle. These situations can be artificially made, based on the component's design, or can be derived from experience. The latter case is especially true in a high-availability system. In these kind of systems it is precious to not introduce regressions during updates.

ISBN 978-3-95450-177-9

Production

In production mode, the component is executed without any restriction and it is not aware of the ongoing test. In this context, all the components in production mode must be able to fully access hardware and low-level systems.

For security reasons, the only part that can differ from the real operational mode is the environment. If the component (or components) to test are software, the environment is allowed to be a sand-box in which a failure is not propagated to the real operational environment. For a hardware component, a testing facility that replicates the real environment is highly advised.

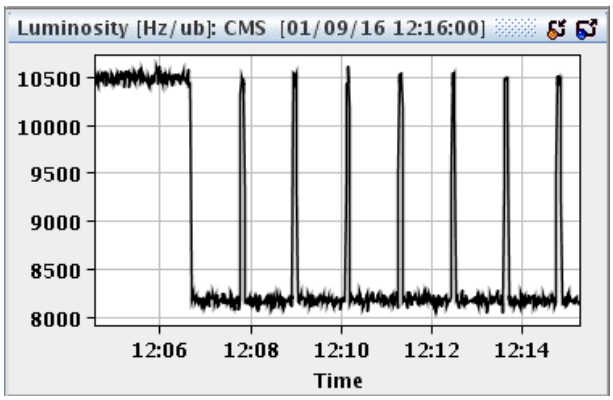

Figure 2: LHC Luminosity Server in full simulation mode, showing a luminosity plot while running a scan pattern used for luminosity calibration. Since the server runs in simulation mode, no accelerator controls are accessed and the response (beam displacements and resulting luminosity) is simulated.

TESTING STRATEGIES

Unit Tests

Unit Tests test each subcomponent, e.g. a class in a software project or a part of a hardware device, individually against a predefined set of scenarios and expected results.

Ideally unit tests should be implemented in an automated fashion on every layer of the system to quickly spot and pinpoint most breaking changes during development. No communication between components are involved in such tests.

Single-Component Integration Tests

Single-Component Integration Tests shall ensure proper linking and communication between the individual subcomponents, i.e. that the full component behaves correctly in a particular scenario. While the subcomponents of the component being tested should be linked as they are in production, all communication to other components should be mocked.

Such tests can either run automatically against a predefined set of scenarios and expected responses, or manually with the component in simulation mode.

Integration Tests with Other Components

Once a component is found to be working, proper communication to neighbouring components needs to be tested. To allow this, two or more components are linked together, while all components not involved in the tests should be mocked up.

Such a test could e.g. ensure that a control application can communicate to the hardware access layer, without actually driving hardware. On the other hand, it could also allow testing a hardware, it's drivers and front-end layer without beam, and without the upper layers of the control system.

During the testing, the scope of tests can gradually be extended by involving more components, up to the final commissioning with beam.

Sanity Checks in Operation

To ensure reliable operation over an extended period of time without degradation, operational hardware can run through a set of unit or single-component integration type tests in every machine cycle. E.g. at the LHC, the Beam Loss Monitors (BLM) execute a set of "sanity checks" when preparing the machine for injection. [1]

ERROR HANDLING AND LOGGING

Once an accelerator component has been deployed, commissioned and put in operation, it is crucial to detect problems and report them to the operators. The worst case is a component silently failing without any notice or explanation.

In case of a software component, this requires that possible errors and exceptions are properly handled, logged and possibly displayed to the user. If the error is recoverable from but could possibly affect further operations, a warning should be issued to the user. If the software component can't recover from a particular error, it must fail in a well-defined way, providing any available information on what problem occurred to the user.

However, care must be taken not to raise false warnings, as this leads to the warnings being ignored by the users. For later offline analysis by the developers, a verbose debug log and telemetry data can be collected through a central logging and tracing service.

CONTINUOUS INTEGRATION

Continuous Integration (CI) refers to the ability of continuously build and integrate software. This means run tests with the latest version of each dependency to have finer integration. With this approach it is possible to immediately spot errors and regressions since the changes between each test run are small, possibly just a commit.

The CI process is often delegated to a CI server (Fig. 3) that is also able to deploy a SNAPSHOT (development) version of the software.

The deployment to production is a critical step since the software may be used in operations, for example during Physics Collisions in the LHC. Therefore, a Continuous

ISBN 978-3-95450-177-9

Deployment (CD) approach cannot be done in a automatic way.

Nevertheless, the CI server can build and test the new version of the software and set it ready for deployment. Then, whenever the machine operator decides it is safe to deploy, the CI server perform the deployment. This step should be fully automatized and during the process all the running instances of the software should be automatically restarted and the links to run them updated.

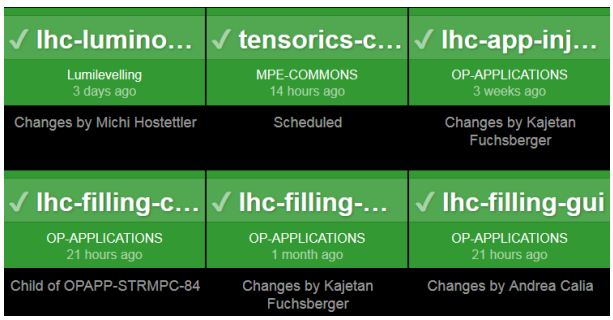

Figure 3: CI server dashboard. It is used to keep track of regressions introduced by commits on key projects. Each time a project is updates, the corresponding and dependant tests are run.

EXAMPLES

LHC Luminosity Server

The LHC Luminosity Server is used to control the beams at the LHC collision points. In routine operation, it is mostly used to perform automatic scans, displacing the beams slightly against each other, to find the optimal head-on collision point. For absolute calibration of the luminosity monitors of the LHC experiments using the Van-der-Meer method [2], it can also run arbitrary scan patterns as requested by the experiments.

The Luminosity Server features a built-in simulation mode, which allows to develop and test scan strategies and patterns without accessing the middle layer at all. Hence every developer can fearlessly start their own instance of the server locally for testing and development, without interfering with other developers or even beam operation.

For integration tests with other components, the Luminosity Server also provides partial simulation (Fig. 4), communicating with some neighbouring components while simulating others. This is e.g. used to test the communication with an LHC experiment regardless of and without affecting any LHC beam operation in parallel, which saved several hours of beam time in 2016 during the preparation of the luminosity calibration sessions.

LHC Beam-Based Feedbacks

A system which could be tested only with beam for a long time, is the LHC beam based feedback system. It processes input from about 2000 devices (orbit, tune), calculates corrections at a rate of 12.5 Hz and sends out corrections to about 500 correction magnets.

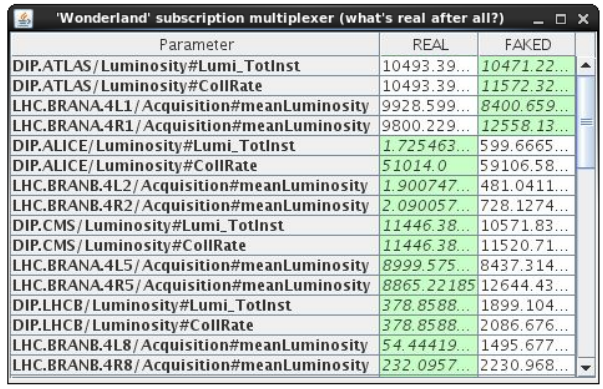

Parameter	REAL	FAKED
DIP.ATLAS/Luminosity#Lumi_TotInst	10493.39...	10471.22...
DIP.ATLAS/Luminosity#CollRate	10493.39...	11572.32...
LHC.BRANA.4L1/Acquisition#meanLuminosity	9928.599...	8400.659...
LHC.BRANA.4R1/Acquisition#meanLuminosity	9800.229...	12558.13...
DIP.ALICE/Luminosity#Lumi_TotInst	1.725463...	599.6665...
DIP.ALICE/Luminosity#CollRate	51014.0	59106.58...
LHC.BRANB.4L2/Acquisition#meanLuminosity	1.900747...	481.0411...
LHC.BRANB.4R2/Acquisition#meanLuminosity	2.090057...	728.1274...
DIP.CMS/Luminosity#Lumi_TotInst	11446.38...	10571.83...
DIP.CMS/Luminosity#CollRate	11446.38...	11520.71...
LHC.BRANA.4L5/Acquisition#meanLuminosity	8999.575...	8437.314...
LHC.BRANA.4R5/Acquisition#meanLuminosity	8865.22185	12644.43...
DIP.LHCB/Luminosity#Lumi_TotInst	378.8588...	1899.104...
DIP.LHCB/Luminosity#CollRate	378.8588...	2086.676...
LHC.BRANB.4L8/Acquisition#meanLuminosity	54.44419...	1495.677...
LHC.BRANB.4R8/Acquisition#meanLuminosity	232.0957...	2230.968...

Figure 4: LHC Luminosity Server in partial simulation mode. Here, e.g. the luminosities provided by the LHC experiments can either be picked up, or replaced by simulated values. The GUI provides a real-time view of both the real value and the output of the simulator, and the data source can be changed at any time.

For a very long time it was considered too complicated to write a testing framework for this system. Finally, when in 2015 an attempt was started anyhow, it proved to be less complicated than expected. This is a very good example which shows that with clever slicing of a system and starting with simple tests, practically any system can be tested. Part of the "fear" before starting to create the testing system was based on the assumption that a full simulation framework would have to be created, which would have to be as fast as the feedback system. This of course would have been very difficult and a lot of effort.

Instead going for the full simulation approach, the team started out creating the simplest possible tests (using ***scenarios***) and moving on to complicated ones. First challenges here were to get the system running in a testing environment. Already this required restructuring proved to make the components more decoupled. Since the feedback system uses UDP packets to get input values and send corrections, this was the obvious point to inject test data. By going small steps, the team learned on the way how the system worked and finally found ways to probe the system with well defined scenarios (e.g. orbit outliers, constant orbits ...) without ever closing the (simulation) loop.

In the meantime, there exist about 50 well defined tests run on a ***CI server***, which form a basic safety net. They are all formulated in a concise DSL (Domain Specific Language), to keep them short and clear [3]. Work still has to continue in the future to evolve the framework together with new features of the feedback system. ***Unit tests*** were not existent for the original system. However, for new features which are added, such unit test are developed and will soon also run within continuous integration.

ISBN 978-3-95450-177-9

A similar approach is planned to be taken for other beam instrumentation systems in the near future (Beam Loss Monitors, Wirescanners).

More examples

In the above sections we picked only some examples from projects from recent history to demonstrate the basic concepts. However, there are many other projects which follow already similar approaches. Some more worth mentioning are:

- To measure the chromaticity of the LHC, a simple application was developed in 2015 [4]. This application modulates the RF frequency measures, the tune and deducts the chromaticity values from harmonic fits to both, tune signals and RF signal. Next to standard unit tests, this project uses a similar approach than the Luminosity Server: When in ***development mode***, it has a (very simple) model running which calculates tune from the modulation and thus provides self-consistent input signals for the application.
- A special system to survey power converter currents and trigger interlocks in case of anomalies was developed for the LHC [5]. Also this system has a dedicated ***development mode*** to allow to work without any hardware access.
- YASP (Yet Another Steering Program), the standard tool for orbit steering in all CERN accelerators, also provides a ***simulation*** mode for development and debugging.

While all these examples make heavy use of their simulation modes, an integrated simulation mode across several systems is currently not implemented anywhere in the current accelerator control system at CERN. However, to achieve more ***integration tests with other components***, such a mode would be highly desirable and future efforts will have to go in that direction.

CONCLUSIONS

Testing distributed systems, like accelerator systems, is hard but not impossible. While common practices in the software domain in general, it is still less common in our environment, especially the closer it gets to hardware (where it also is more difficult). In the previous sections we categorized the different level of tests and gave examples how they can be and how they are currently applied on different projects. In order to enable fearless development and testing of accelerator components, we consider the following approaches as important (most important first, most complex last):

1. Any kind of ***development mode*** is practically a must. This allows to develop, debug and test the component (software, hardware) in isolation and removes the risk to accidentally access e.g. a real device during development. This already enables (at least manual) ***single component integration tests***.

2. For proper operation it is crucial to have proper ***error reporting*** on all layers (Faults, Exceptions). Warnings should only be issued in case the user is able to act on them.

3. To enable post-mortem diagnosis, centrally stored and easily searchable ***tracing information*** is indispensable.

4. For any software component, ***unit tests*** are usually a standard approach. Next to providing a first safety net against regressions, they also enforce a cleaner code structure, if applied from the beginning.

5. If possible, ***automated testing*** is preferable compared to a manual approach. If tests are automated, then the step to ***continuous integration*** is a small one and is highly recommended.

6. For hardware components, periodic ***sanity checks*** during operation can ensure the proper functioning of devices and help spotting degradation early.

7. It can get relatively complex to implement ***integration tests with other components***. However, they pay off at some stage, because the only alternative for an accelerator is to stop operation and test the components interactions in production.

REFERENCES

[1] J. Emery et al., "First experiences with the LHC BLM sanity checks", Topical Workshop on Electronics for Particle Physics 2010, Aachen, Germany.

[2] S. Van Der Meer, ISR-PO/68-31, KEK68-64

[3] S. Jackson et al., "Testing Framework for the LHC Beam-Based Feedback System", this conference.

[4] K. Fuchsberger, G.H. Hemelsoet, "LHC Online Chromaticity Measurement - Experience After One Year of Operation", this conference.

[5] K. Fuchsberger et al., "LHC Orbit Correction Reproducibility and Related Machine Protection", Proc. IPAC 2012, New Orleans, Louisiana, USA.

ISBN 978-3-95450-177-9

THE ALIGNMENT OF CONVERGENT BEMLINES AT A NEW TRIPLE ION BEAM FACILITY

O. F. Toader, T. Kubley, F.U. Naab, E. Uberseder, Michigan Ion Beam Laboratory, University of Michigan, Ann Arbor, Michigan, USA

Abstract

The Michigan Ion Beam Laboratory (MIBL) at the University of Michigan in Ann Arbor Michigan, USA, has recently upgraded its capabilities from a two accelerator to a three accelerator operation mode. The laboratory, equipped with a 3 MV Tandem, a 400 kV Ion Implanter and a 1.7 MV Tandem, has also increased the number of available beamlines from three to seven with two more in the planning stages. Multiple simultaneous ion beam experiments are already in progress and scientists conduct state of the art experiments involving light and heavy ions. The MIBL staff had to overcome multiple challenges during the physical alignment process of the accelerators, beamlines and experimental end-stages. Not only the position of the accelerators changed, but the target chambers were moved into a different room behind a one meter thick concrete wall. At the same time, a beamline from each accelerator had to converge and connect to a single chamber at a precise angle. This paper focuses on the alignment process of all the equipment involved in triple ion beam experiments and especially on the procedures to align the ion beams on a target.

INTRODUCTION

Ion beam irradiation experiments, if properly conducted, can simulate the radiation damage that occurs in materials inside a nuclear reactor. While radiation effects induced by neutrons can be successfully emulated by protons and heavy ions irradiations in much shorter times, researchers tried to find a way to also simulate the presence of transmutation products in reactors. Building on the successes of other facilities (TIARA-Japan and JANNUS-France), the Michigan Ion Beam Laboratory (Fig. 1.a,b,c) as part of the Department of Nuclear Engineering and Radiological Sciences at the University of Michigan, is now in the position to deliver dual and triple ion beam irradiations experiments.

THE PARTICLE ACCELERATORS

The laboratory is equipped with three accelerators: a 3 MV Tandem, a 1.7 MV Tandem and a 400 kV Implanter. The 3 MV Tandem (model 9SDH-2) high current Pelletron accelerator (Fig. 2a) was built by National Electrostatics Corporation (NEC). The 1.7 MV accelerator (Fig. 2b) is a solid-state, gas insulated, high frequency Tandetron built by General Ionex (now HVEE) that operates in the 0.3 MV to 1.7 MV range delivering very stable DC beams. The 400 kV implanter (Fig. 2c) is an air-insulated device also built by NEC that can deliver ion beams from any element in the periodic table, with beam fluences of 1 mA or more for some gas ions, on an area with a diameter in excess of 6 inches (15 cm). The implantation stage can be cooled to LN temperatures or heated up to 800 ^{0}C.

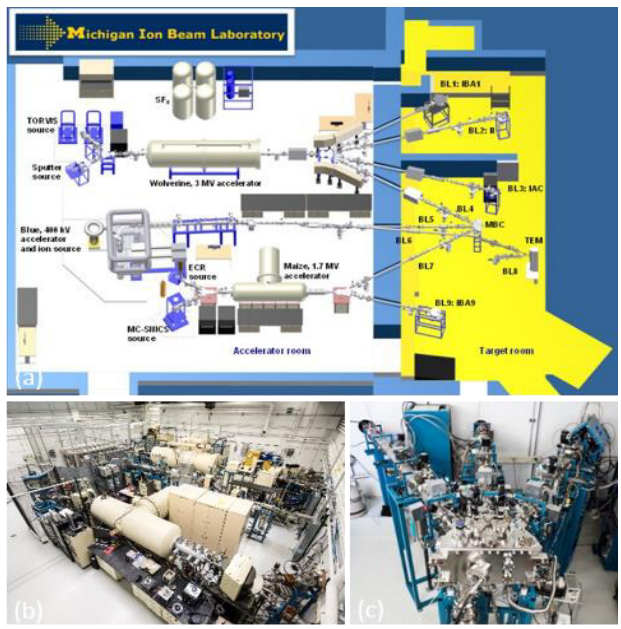

Figure 1: (a) AutoCAD drawing of the lab in the new configuration, (b) Overhead view of the lab (c) View of the multiple ion beam chamber designed to simultaneously accommodate up to three ion beams on a target.

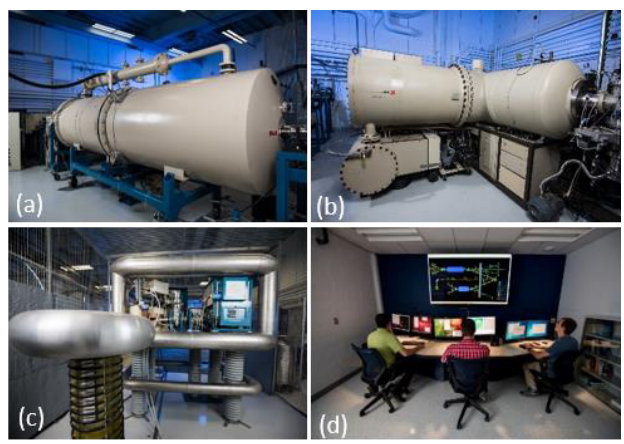

Figure 2: MIBL particle accelerators: (a) 3 MV Tandem – Wolverine (W), (b) 1.7 MV Tandetron – Maize (M), (c) 400 kV ion implanter – Blue (B) and (d) view of the Control Room (CR) of the three accelerators that now operate in remote control mode.

ISBN 978-3-95450-177-9

THE ION SOURCES

The accelerators are equipped with many different types of ion sources. Sources for light ions: TORVIS (NEC), ECR (Pantechnik) and Alphatross (NEC) that are used for the production of protons, alpha particles and deuterium in Fig. 3d, 3b and 3f respectively. The sources for heavy ions are of sputter type: PS120 (Peabody Scientific) and MC SNICS (NEC) in Fig 3a and 3c respectively. These sources work with Cs as a sputtering element. The only positive ion source in MIBL is Danfyzik 921 shown in Fig 3d. installed in the Implanter. This source can operate in gas mode, liquid mode and sputter mode. The sputtering is induced with an Ar beam.

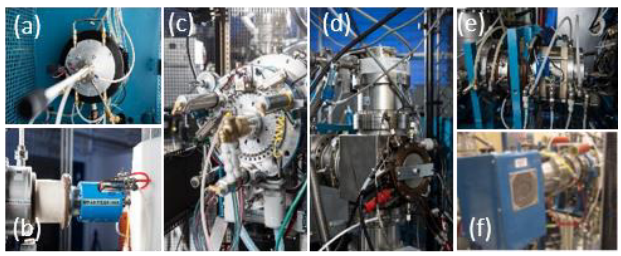

Figure 3: The ion sources: (a) PS 120 (b) ECR (c) SNICS (d) Torvis (e) 921 and (f) Alphatross.

THE BEAMLINES

The laboratory has two experimental rooms and seven active beamlines with two extra beamlines in planning stages (Fig 1a). The North Target Room (NTR) hosts BL1 used for surface analysis experiments (NRA, RBS, ERD and PIXE) and BL2 used in protons and heavy ions irradiation experiments. The South Target Room (STR) hosts BL3 through BL9. BL3 is used in experiments involving simultaneous protons and high temperature, high pressure corrosion experiments. Beamlines 4 (from Wolverine), 5 (from Blue) and 7 (from Maize) are part of a group that can deliver dual and triple ion beams irradiation experiments. The first part of BL5, terminated with a chamber in THE Accelerator Room, is the ion implantation beamline. Future BL6 and BL8 (in planning stages) will interface with a Transmission Electron Microscope (300 kV FEI) for in-situ observation of radiation damage experiments.

THE ALIGNMENT

The alignment (of sources, low energy beamlines, accelerators and high energy beamlines) was a difficult process that presented the lab staff with multiple challenges: (1) three accelerators, nine beamlines, of which three beamlines with one common target, four single ion beamlines and two beamlines still in planning stages; (2) two different center lines, with two accelerators at 56 inches (~1.42m) high and one at 68 inches (~1.72 m) from ground; (3) two different rooms with 12 inch (~30 cm) height difference (target room lower); (4) four feet (~1.2 m) thick wall between rooms, with no direct line of sight or overhead crane to move heavy components. The first step in the alignment process, consisted of mechanically aligning the ion sources, the accelerator and beamlines with a transit scope and overlapping crosshairs. Once the beamlines were under vacuum, a special target or end-station (Fig 4a) was used. A beam fluorescent, ceramic piece was mounted on the surface allowing the visualization of both a laser beam and an ion beam (beam focused in Fig 4b and rastered in Fig 4c). The green laser beam was focused through a quartz port and travelled along the center of each beamline (Fig 4d). Finally, the profile from a BPM (Fig 4e) was used to confirm the shape and size of the ion beam. In order to guarantee that the ion beam hits the desired spot on the experimental stage, the laser beam must perfectly align with the ion beam on the target. During actual experiments the target may not be fluorescent to the ion beam and then the laser spot is used to confirm the location of the beam.

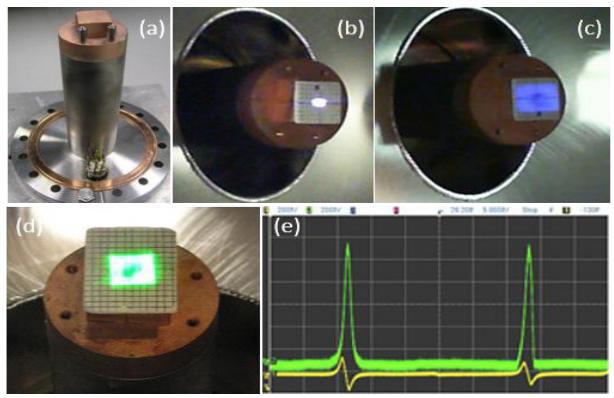

Figure 4: (a) stage, (b) focused beam on the stage, (c) rastered beam on stage, (d) laser light overlap on the ion beam and (e) BPM profile of the focused beam.

The alignment procedure, repeated for each single ion beamline and for the three converging beamlines, consisted in the following steps: (a) centering the focused beam and the focused laser spot on the ceramic piece (separately and overlapped) and (b) rastering the beam and opening the beam apertures to different sizes to confirm that the rastered beam and the defocused laser beam spots coincide. Examples are shown in Figure 5.

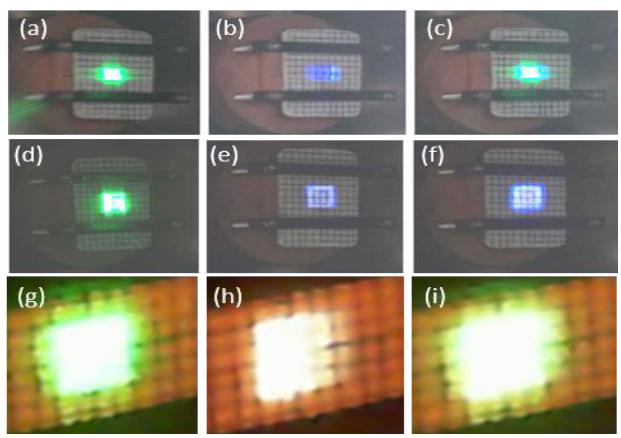

Figure 5: laser beam, ion beam and overlapped laser and ion beams: BL4: (a, b and c), BL7: (d, e and f) and BL2: (g, h and i).

ISBN 978-3-95450-177-9

SUMMARY

Finalizing the new setup at MIBL with 7 beamlines, required extensive work for the alignment of ion sources, low energy beamlines, accelerators and experimental beamlines. During the immediate future (4-8 months) the installation and commissioning of BL6 and BL8 will begin to allow the interface to the FEI TEM to be designed and built. It is expected that the process will take between 2-3 months and the ordering of new equipment is ongoing today. MIBL is now in the position to successfully deliver well aligned ion beams to multiple targets as well as simultaneous ion beams to one target.

ISBN 978-3-95450-177-9

BLIP SCANNING SYSTEM POWER SUPPLY CONTROL*

Z. Altinbas†, R. Lambiase, C. Theisen, Brookhaven National Laboratory, Upton, NY, USA

Abstract

In the Brookhaven LINAC Isotope Producer (BLIP) facility, a fixed target is bombarded by proton beam to produce isotopes for medical research and cancer treatment. This bombardment process causes spot heating on the target and reduces its lifetime. To mitigate this problem, an upgrade to the beamline has been made by spreading the beam on the target in a circular pattern, which allows the target to heat more uniformly. The beam is steered in a circular pattern by a magnet with orthogonal (X and Y) windings. Each of these two windings is independently powered as part of a resonant circuit driven by a power amplifier. This paper describes the hardware platform used as well as the software implementation of the resonant circuit design and its feedback loop.

OVERVIEW

The BLIP facility is faced with a high demand for isotopes. To increase the production, the target needs to be bombarded with higher current beam. Focused beam with increased beam current causes heat damage on the target. To prevent this, the heat has to be distributed within the target. This can only be achieved if the target is scanned by the beam in a moving pattern. A set of ferrite core windings was designed to generate a dynamic magnetic field that steers the beam in a circular pattern. Increasing the current into the magnet results in a wider circle. The magnet's two windings are physically perpendicular to each other and are independently powered by two power amplifiers. To minimize the power required to energize these windings, a resonant circuit was designed. Without the resonant circuit, an amplifier with a much higher apparent power would be needed to power each winding. As inherent with resonant circuits, the energy is transferred between the inductor (the winding) and the matching capacitors. The power amplifiers are needed to supply only the initial energy to charge the capacitors at start-up, as well as to make up for the losses in the system. A small portion of these losses is due to the magnet leads. The windings are placed around the beam pipe in the tunnel, about 18 feet in front of the target. Due to high radiation in the tunnel, the resonating capacitors are located in a remote control room. The connections between the resonant capacitors and the windings are made via Kapton insulated litz wires. Kapton was chosen because of its high tolerance to radiation; and litz wire was chosen to mitigate the AC skin effect. The long leads contribute to the resistive losses in the resonant circuit.

The windings and the components of the resonant circuits are required to run at a frequency of 4.9 kHz. This frequency was chosen to spread the beam on the target for specific number of turns (circles) per beam pulse. The pulse width of the beam that is sent to the BLIP facility is 450 μs. At approximately 5 kHz, the beam scribes two and a quarter turns on the target. The scanning system was designed to run continuously as opposed to a pulsed ringing circuit. This is advantageous in two ways. First, running continuously allows for continuous monitoring of proper operation of the equipment. In a ringing circuit, a misfire will not be known until after the beam has been sent to the target. Second, the beam distribution is precisely controlled in the continuous system by a lookup table. In a pulsed system, the only control would be the starting current.

To keep the power amplifier running with minimum power, the load – the inductor and the capacitors (LC) – needs to be matched to the impedance of the power amplifier. This is achieved by adding a transformer in parallel with the capacitors. The turn ratio of the transformer is determined by the ratio of the resistive losses of the resonant circuit to the power amplifier impedance. Since the impedance of the resonant circuit is higher than the power amplifier impedance, the transformer steps up the voltage. Having a matched impedance system ensures the amplifier supplies the minimum power required to run the system.

HARDWARE

As mentioned in the above section, all the components of the resonant circuit except the windings are located in a remote room. Interface chassis were built to house these components. Each winding has two interface chassis. The first chassis provides access to the litz wire leads and includes the resonant capacitors, while the second chassis contains the impedance matching transformer and connection point to the power amplifier. Each chassis also includes a dedicated current transformer and a dedicated voltage sensor to measure the magnet current and voltage, and the power amplifier current and voltage, respectively. These measurements are acquired by the power supply control system to regulate the feedback loops. A pair of interface chassis is shown in Figure 1.

National Instruments' PXIe hardware platform was chosen as the power amplifier controller. Each power amplifier is controlled by its own function generator module which has the capability to generate 20 MHz sine waves with 14-bit resolution (NI PXI-5402). These modules are configured to generate two separate sine waves. These outputs have adjustable amplitude and have a nominal 90° phase shift, as an input to each power amplifier. To read the current and voltage measurements, an oscilloscope/digitizer module is utilized. The PXIe-5105 is an 8-

* Work supported by Brookhaven Science Associates, LLC under Contract No. DE-AC02-98CH10886 with the U.S. Dept. of Energy.
† ALTINBAS@BNL.GOV

ISBN 978-3-95450-177-9

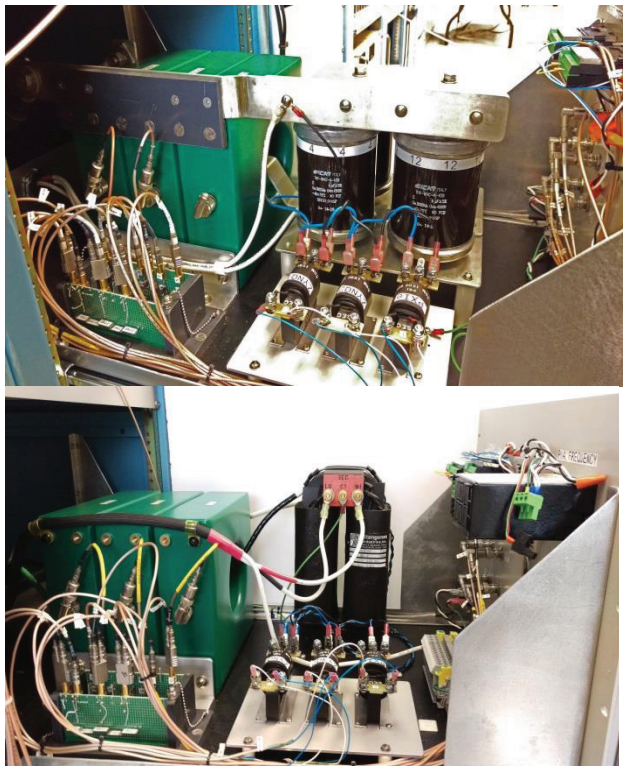

Figure 1: Two interface chassis: One with the resonant capacitors (top) and one with the matching transformer (bottom). The current and voltage transformers are shown in both.

channel, 12-bit analog to digital converter board with a 60 MHz real-time sampling rate. In addition, there are digital I/O boards used for interlock outputs and synchronization with beam pulse. For synchronization and fast interlock I/O, a PXIe-6341 providing 24 TTL I/O lines is used. For slow interlock outputs, such as relay switches, a PXI-6515providing 32 isolated channels at +/- 30 VDC is utilized. The controller, where all real-time computation is done, is a 2.3 GHz Intel Core i7 processor running a LabVIEW Real-Time Operating System (NI PXIe-8135). The program that is running on the processor and communicating with all the I/O modules is written in LabVIEW. LabVIEW is a graphical programming language from National Instruments and it stands for LABoratory Virtual Instrument Engineering Workbench. The PXIe chassis with all the modules is shown in Figure 2.

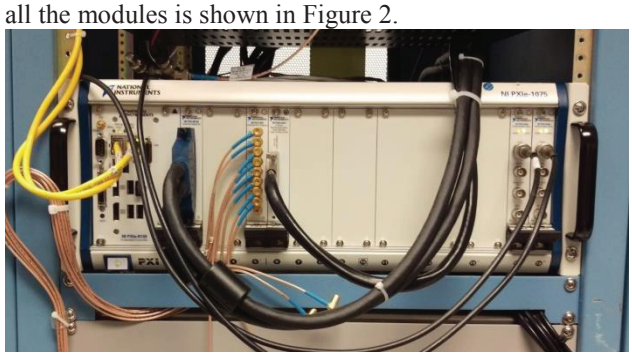

Figure 2: The National Instruments PXIe platform with 18-slot chassis and I/O modules.

SOFTWARE

To maintain the efficient transfer of the voltage between the windings and the capacitors, the system has to run as close as possible to its resonant frequency. The accuracy of the circular beam pattern on the target also needs to be maintained. The circular shape of the magnetic field is obtained by keeping the two sine waves of each amplifier 90° out of phase. On the other hand, the phase shift between the current and voltage of the same amplifier has to remain zero. The amplitude of both sine waves is also required to be tightly controlled in order to maintain a constant diameter for the circle being scanned onto the target. Both the frequency and the current can drift due to heat. Heat can also cause changes in inductance and/or capacitance. Therefore, feedback loops are necessary to maintain a stable system. A power supply control circuit was designed as seen in Figure 3. This design was implemented in software using LabVIEW.

As mentioned in the Hardware section, each system has its own readbacks via a current and a voltage transformer. Power amplifier current and voltage, as well as the magnet current and voltage measurements, are brought back to the 8 channels of PXIe system's digitizer board, 4 for each winding/power amplifier combination. These measurements are used to derive frequency, amplitude and phase information. The computation necessary for the feedback loops is done on this information.

As seen in the schematic in Figure 3, there are four main feedback loops: Two amplitude feedback loops, one frequency feedback loop, and one phase feedback loop. Each winding has its own amplitude feedback loop, but there is only one frequency feedback loop for both systems because the amplifiers are locked together in a master-slave configuration. The amplitude feedback loops are software implemented PI loops with gains. The frequency feedback loop also utilizes a PI loop, and it operates on the phase sum of the power amplifier sine waves. Phase data of the voltage and current measurements for each amplifier is extracted and summed with the other amplifiers phase data. The frequency of the sine waves is adjusted with this phase sum to keep the systems frequency locked and on resonance.

Subsequently, the amplitudes of the each sine wave are adjusted with the result of the amplitude feedback loops. These loops sum the difference between a given setpoint and the magnet current readback and integrate this difference. The results of these computations, which are in amperes, are then converted to voltage values that are appropriate for the power amplifier input.

Lastly, the phase feedback loop maintains the phase shift between the two sine waves (power amplifier outputs). This 90° phase shift determines the magnetic field pattern and subsequently, the path in which the beam is deposited on the target. Each power amplifier has its own independent function generator board in the PXIe system. Even though these boards are initialized as phase locked to each other in the software implementation, they each have their own on-board oscillator as clocks and as the

ISBN 978-3-95450-177-9

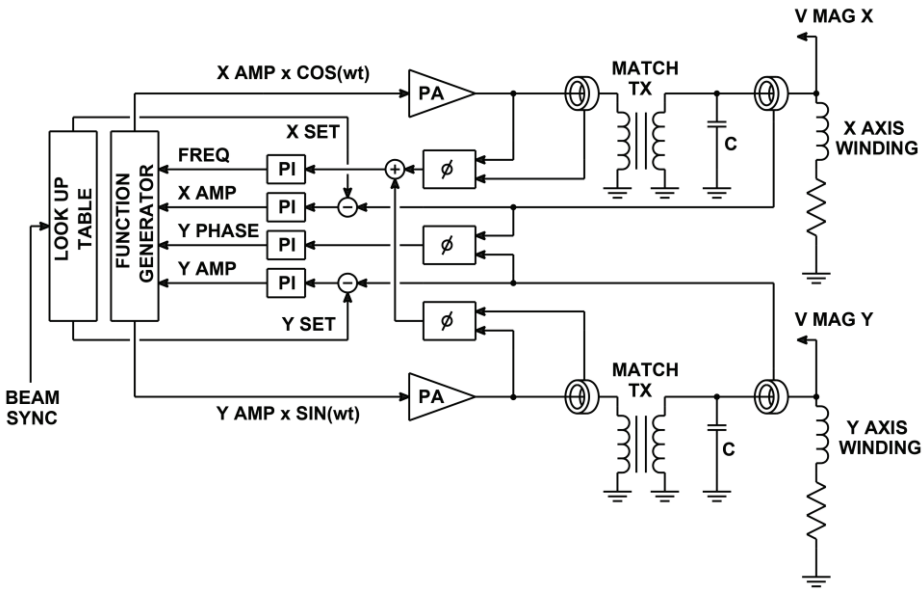

Figure 3: Schematic of the power amplifier control that is implemented by software.

frequency and amplitude of the sine waves get adjusted, the phase deviates slightly over time. The phase feedback loop corrects for this deviation to ensure the two sine waves stay 90° out of phase at all times.

Amplitude feedback is the most critical parameter and uses most of the computational resources. The amplitude feedback loop currently operates at a nominal 2 ms rate. Originally the goal was a 1 ms update rate, but hardware constraints within the PXIe could not accommodate that speed. Frequency and phase adjustments are not so time critical, and are made approximately every half second.

Coarse amplitude changes, or setpoints, (not to be confused with the feedback adjustments) can be made during operations in order to change the diameter of the circle being scanned onto the target. Concentric circles of specific diameters can be achieved with the use of a programmable setpoint table. This table is represented as the "Look Up Table" in Figure 3. However, these coarse changes should not be made while beam is present.

A beam pulse is received at the BLIP facility at a 6.67 Hz rate. This is roughly a period of 150 ms. However, the beam pulse width is only 450 µs. Since it is not desirable to make large changes to the magnetic field while beam is present, a timing signal is used by the PXIe system to provide the necessary synchronization. Settling time must be taken into account. An externally generated TTL pulse signals the arrival of the beam pulse. A software delay is added to this pulse to assure clearance from the beam and also allows for settling times before resuming feedback corrections to the windings which control the diameter of the circular pattern.

The 2 ms rate at which the amplitude adjustments are applied, is determined by the bandwidth required by the closed loop system. This bandwidth determines how fast the amplitude setpoints can be applied, and operate at that amplitude stably. The settling time of the power amplifier and the resonant circuit in between the amplitude changes is essential to keep the system stable. If the amplitude feedback loop adjustment is done too fast, the system can go unstable; and if it's done too slowly then the system won't be ready at the expected amplitude by the time the beam pulse arrives.

All aforementioned computations and feedback loops are done in one main while loop that iterates nominally every 2 ms. In addition to these calculations, the impedance of the windings are computed in this loop. The impedance value allows us to detect a short circuit in the winding. The main loop also determines under what conditions the power amplifiers should be shut down to prevent damage. In the case of an overcurrent – winding current exceeds the maximum value that could be handled by the entire magnet structure –, the resonant frequency and the impedance both going outside the allowed margins, the PXIe system interlocks the power amplifiers and beam is inhibited immediately. These statuses, along with some computational results, are sent back to a higher level custom accelerator interface via TCP/IP. The computational results include, but are not limited to, magnet current and voltage, power amplifier current and voltage, calculated impedance of the magnet, the interlock status, etc. These are reported to the user once per second. One issue was encountered during the data delivery process. When this reporting mechanism is enabled, the main loop unexpectedly can come to a brief halt, as often as 2 or 3 times a day. This obviously affects the feedback loops, making them go unstable due to large errors once the loop resumes. The cause of this is not fully understood and is currently being investigated in concert with National Instruments.

CONCLUSION

The resonant circuit and the PXIe system completed its first operational year [1]. The fundamental purpose of this beam scanning equipment was to increase the production of medical isotopes. Despite the minor control incon-

ISBN 978-3-95450-177-9

venience caused by disabling data reporting, this fundamental purpose has been successfully accomplished. The BLIP scanning system reliably boosts the production up to the limit of the beam production.

REFERENCES

[1] R. J. Michnoff et al., "The Brook haven Linac Isotope Production (BLIP) Facility Raster Scanning System First Year Operation with Beam", presented at IBIC'16, Barcelona, Spain, Sep. 2016, paper MOPG28, this conference.

ISBN 978-3-95450-177-9

BEAM DIAGNOSTICS AT SIAM PHOTON SOURCE

P. Klysubun†, S. Klinkhieo, S. Kongtawong, S. Krainara, T. Pulampong, P. Sudmuang, N. Suradet,
SLRI, Nakhon Ratchasima, Thailand

Abstract

In recent years the beam diagnostics and instrumentation of Siam Photon Source (SPS), Thailand synchrotron radiation facility, have been significantly improved for both the booster synchrotron and the 1.2 GeV storage ring. Additional diagnostics have been designed, fabricated, and installed, and the existing systems have been upgraded. This paper describes the current status of the beam diagnostics at SPS, as well as their respective performances. These systems include beam position monitors (BPMs), a diagnostics beamline, beam loss monitors (BLMs), real-time tune measurement setups, and others. Apart from the instrument hardware, the acquisition electronics along with the processing software have been improved as well. The details of these upgrades are reported herewith.

INTRODUCTION AND OVERVIEW

Siam Photon Source [1,2] is the Thailand 1.2 GeV synchrotron light source operated by Synchrotron Light Research Institute (SLRI). The facility is located in the province of Nakhon Ratchasima, approximately 250 km northeast of Bangkok. The accelerator complex comprises of a thermionic electron gun, a 40 MeV linac (LINAC), a low energy beam transport line (LBT) transferring 40 MeV electrons to a 1.2 GeV booster synchrotron (SYN), followed by a high energy beam transport line (HBT) transporting the electron beam to a 1.2 GeV storage ring (STR). The maximum stored beam current has been 150 mA, but soon will be increased after the installation of a new 300 kV RF cavity and a 80 kW solid-state RF amplifier, replacing the old 120 kV cavity and 30 kW amplifier, just completed in August this year. Delivered user beamtime ranges from 4,000 – 4,500 hours per year. Currently there are 10 photon beamlines utilizing the generated synchrotron radiation from infrared to x-ray spectral regions. To ensure stable and reliable operation, as well as to aid machine physicists in maximizing the machine performances, several types of beam diagnostics are placed along the electron beam paths to measure and monitor the characteristics of the electron beam.

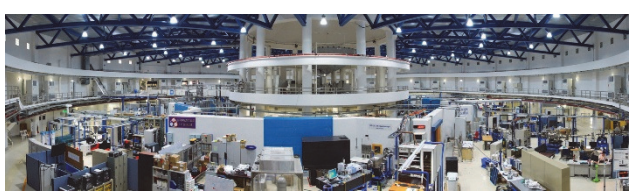

Figure 1: SPS experimental hall.

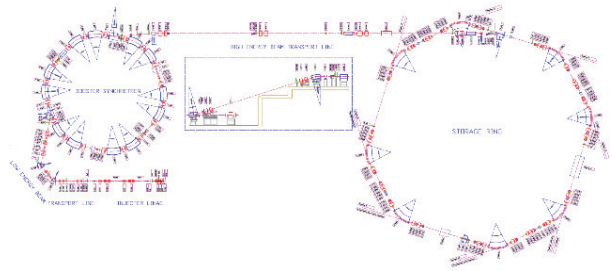

Figure 2: SPS machine layout.

LINAC AND LBT DIAGNOSTICS

Current Monitors (CMs)

Three wall current monitors (WCMs) placed along the beam path are used to measure the beam current in the linac section. The first CM (CM1) is located between the first and the second pre-bunchers (PB1 and PB2). The second and third CMs (CM2, CM3) are located at the entrance and the exit of the linac, respectively. A Pearson Electronics Model 3100 pulse current transformer (LCT) is located at the end of the LBT just before the beam entering the injection septum.

Screen Monitors (SMs)

The LBT is equipped with 3 SMs to monitor the transverse beam profile as well as the beam position. CCD cameras capture the beam images and send them to the control room. A unified control system controls the screens, the CCD cameras, as well as the lighting.

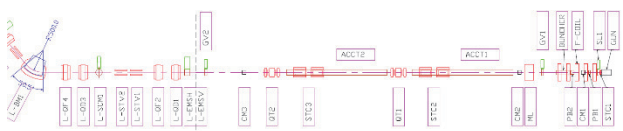

Figure 3: Linac and part of the LBT.

BOOSTER SYNCHROTRON AND HBT DIAGNOSTICS

Direct Current Current Transformer (DCCT)

The booster synchrotron is equipped with a DCCT capable of measuring 0 – 100 mA (± 0.2 mA) beam current. The output voltage is displayed directly on an oscilloscope in the control room.

† pklysubun@slri.or.th

ISBN 978-3-95450-177-9

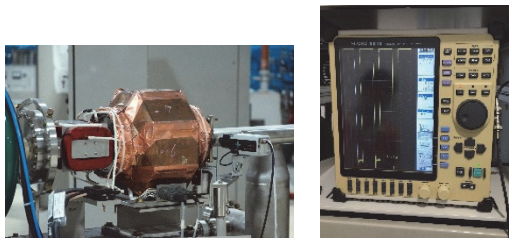

Figure 4: Booster DCCT (left) and oscilloscope displaying beam current in the control room (right).

Stripline Kicker

The stripline kicker is used to excite the beam for betatron tune measurement. [3] White noise generated with a function generator is sent to the stripline kicker. The resulting turn-by-turn signal is picked up by a button-type BPM connected to a Libera SPARK module. The collected signal is then analyzed with a MatLAB computer code. At first when we did not possess a necessary equipment for amplifying the white noise signal synchronously with the increasing beam energy, tune measurement at higher beam energy was found to be rather difficult. In 2016 we replaced the old Agilent 33250A function generator with a new Keysight 33500B 2-channel function generator. The white noise signal from one channel is combined with the ramping pattern from the other and sent to the stripline kicker. The whole measurement during energy ramping has to be performed piecewise (in 9.4 msec duration) with the help of a delay unit due to the limit of the Libera SPARK buffer size. The obtained set of data can be easily stitched together in software.

Fast kicker can also be used in place of the stripline kicker. This tune measurement setup has proved to be extremely useful for controlling machine parameters to maintain constant tunes during energy ramping and optimization of the operating point.

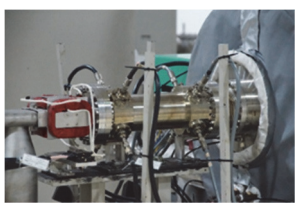

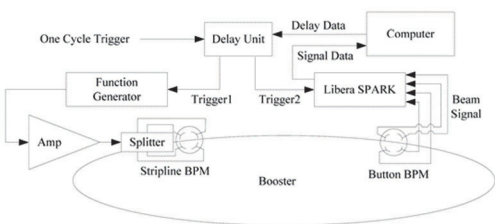

Figure 5: (Top) Stripline kicker. (Bottom) Schematic of the tune measurement setup. [3]

Screen Monitors (SMs)

The booster synchrotron and the HBT are equipped with 4 and 5 SMs, respectively. The control system is the same one described in the previous section.

Current Monitors (CMs)

Two WCMs are positioned in the HBT to monitor the beam current delivered to the storage ring. One integrated current transformer (ICT) from Bergoz Instrumentation (Bergoz Turbo-ICT FEFA) was recently added at the beginning of the HBT.

STORAGE RING DIAGNOSTICS

Beam Position Monitors (BPMs)

Originally there were 5 button-type BPMs in each of the 4 superperiods of the storage ring. Four additional BPMs were later added upstream and downstream of the 2.2 T Multipole Wiggler (MPW) and the 6.5 T Superconducting Wavelength Shifter (SWLS), resulting in the total of 24 BPMs overall. The button pick-up has N-type connector, and the button signals are collected and processed by Bergoz MX-BPM-118.00MHz electronic modules. Due to noisy signals all the BPM cables were replaced in 2011 with higher quality cables with better EM shielding and lower loss rate (HUBER&SHUNER SUCOFEED cables). [4] Instead of using the beam position data from the Bergoz electronics, we opt to calculate the transverse beam position from the electrode signals with 16-bit Allen-Bradley Programmable Logic Controllers (PLCs). The beam position from the PLCs are then moving averaged with a LabVIEW code. The sampling interval is 100 msec. [4] The averaged transverse position data can be accessed by MatLAB via Open Process Control (OPC) Toolbox.

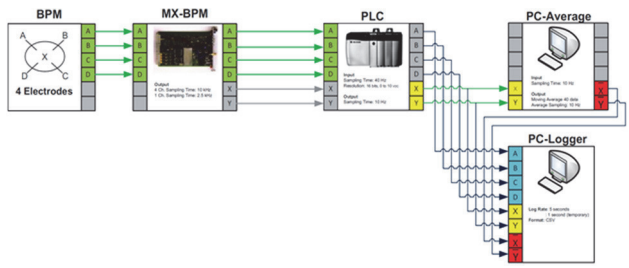

Figure 6: SPS storage ring BPM system. [5]

Diagnostics Beamline

The SPS diagnostics beamline [6] measures the transverse beam profile as well as monitors positional stability of the beam by utilizing optical synchrotron radiation (SR) from a bending magnet. The setup comprises of direct optical imaging and SR interferometer. The first beam splitter splits half of the light to the direct imaging system, which has an apochromatic lens focusing the beam to a CCD camera. The distance from the source point to the lens is 8.5 m. The rest of the beam is transmitted to the horizontal and vertical interferometers to measure the transverse beam profile in each plane. Both the beam image and the interference patterns are fitted using LabVIEW programming codes to determine the transverse beam profile. The schematic of the setup is shown in Fig. 7.

ISBN 978-3-95450-177-9

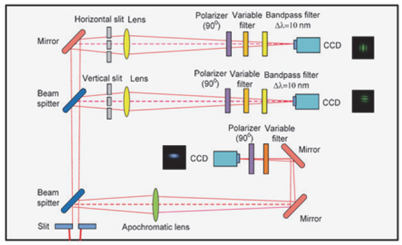

Figure 7: Schematic layout of the transverse beam profile monitor. [6]

Beam Loss Monitors (BLMs)

The SPS storage ring BLM system has received a major overhaul in 2014 in order to enhance its performance. [7] The system consists of 50 Bergoz PIN-diode type BLMs spread around the ring. Each of the BLM unit contains 2 PIN diodes operating in coincidence mode, and is powered by a regulated low noise power supply. Placement of these BLMs is not fixed since they were designed to be easily movable to accommodate investigation of beam loss. Mostly they are placed in the areas with large betatron and dispersion functions. RF shielded cables (HUBER&SHUNER RG-223/U) carry the beam loss signal to a National Instruments PXIe-6612 counter modules based on PXI Express platform. There are a total of 8 counter modules which are installed in an NI PXIe-1078 PXI Express chassis with a NI PXIe-8820 2.2 GHz Celeron dual-core controller processor and 2 GB, 1333 MHz memory. The PXI platform was chosen because of its performance, ruggedness, cost effectiveness, and expandability. The loss rate is calculated and displayed with the use of a LabVIEW code.

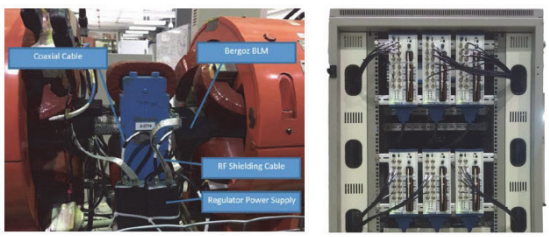

Figure 8: BLM unit (left) and PXIe counter modules (right). [7]

Direct Current Current Transformer (DCCT)

The storage ring is equipped with a DCCT capable of measuring 0 – 600 mA (± 0.1 mA) stored beam current. The output voltage is read by an Agilent 34401A digital multimeter (DMM). The integration time of the DMM is set to 10 NPLCs (Number of Power Line Cycles), which corresponds to 0.2 s. The readout is then sent to the PLC.

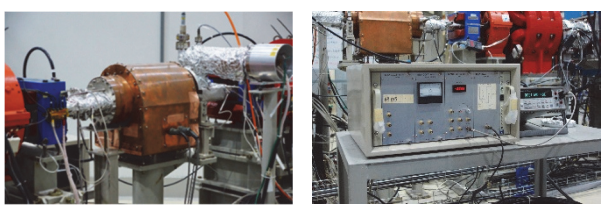

Figure 9: Storage ring DCCT.

Stripline Kicker

The stripline kicker is used for real-time tune measurement. The schematic of the setup is depicted in Figure 10. FM signal is generated by a Rohde & Schwarz SMC100A signal generator and sent to one of the striplines to excite the beam. The beam response is pick-up by two other striplines in diagonal position. The two signals are then combined with 180° phase difference. The sum signal is then sent to a Tektronix RSA5103A real-time spectrum analyzer.

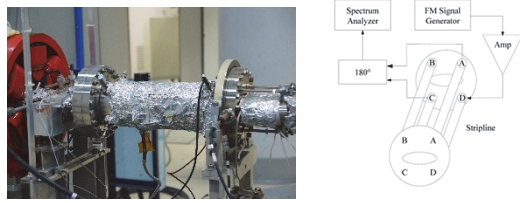

Figure 10: Stripline kicker (right) and real-time tune measurement setup (left) for the SPS storage ring. [3]

ACKNOWLEDGEMENT

The authors would like to express their gratitude to Guenther Rehm of Diamond Light Source and June-Rong Chen of Taiwan Photon Source for their technical assistance and support.

REFERENCES

[1] P. Klysubun *et al.*, "Operation and improvement of the Siam Photon Source", *Nucl. Instrum. Meth. A*, vol. 582, p. 18, 2007.

[2] P. Klysubun *et al.*, "Operation and recent development at the Siam Photon Source", in *Proc. APAC'07*, Indore, India, Jan. 2007, paper THC3MA01, pp. 607-609.

[3] S. Kongtawong *et al.*, "Improvement of tune measurement system at Siam Photon Source", in *Proc. IBIC'15*, Melbourne, Australia, Sep. 2015, paper MOPB056, pp. 184-186.

[4] S. Klinkhieo *et al.*, "Improvement of the Siam Photon Source storage ring BPM system", in *Proc. IBIC'12*, Tsukuba, Japan, Oct. 2012, paper MOPA21, pp. 101-103.

[5] N. Suradet *et al.*, "Improvement of hardware and software setup for the acquisition and processing of Siam Photon Source BPM signal", in *Proc. IBIC'12*, Tsukuba, Japan, Oct. 2012, paper MOPA34, pp. 1-3.

[6] P. Sudmuang *et al.*, "Beam size measurement at Siam Photon Source storage ring", in *Proc. IPAC'12*, New Orleans, LA, USA, May 2012, paper MOPPR054, pp. 906-908.

[7] N. Suradet *et al.*, "Improvement of the Siam Photon Source beam loss monitor system", in *Proc. IBIC'15*, Melbourne, Australia, Sep. 2015, paper MOPB058, pp. 190-192.

ISBN 978-3-95450-177-9

FIRST RESULTS FROM THE IPHI BEAM INSTRUMENTATION

P. Ausset†, M. B. Abdillah, S. Berthelot, C. Joly, J. Lesrel, J.F. Yaniche, IPN 91406 Orsay, France
D. Bogard, B.Pottin, D.Uriot, CEA-Saclay, 91191Gif sur Yvette Cedex

Abstract

I.P.H.I. is a High Intensity Proton Injector (CNRS/IN2P3; CEA/Irfu and CERN collaboration) located at Saclay and now on operation. An ECR source produces a 100 keV, 100 mA C.W. proton beams which will be accelerated at 3 MeV by a 4 vanes R.F.Q. operating at 352.2 MHz. Finally, a High Energy Beam Transport Line (HEBT) delivers the beam to a beam stopper. The HEBT is equipped with appropriate beam diagnostics to carry beam current, centroid beam transverse position, transverse beam profiles, beam energy and energy spread measurements for the commissioning of IPHI. These beam diagnostics operate under both pulsed and CW operation. However transverse beam profile measurements are acquired under low duty factor pulsed beam operation using a slow wire scanner. The beam instrumentation of the HEBT is reviewed and the first measurements at 3 MeV are described.

INTRODUCTION

Since the front end is the most critical part of a High Power Proton Accelerator (HPPA), it was decided to realize a high power proton injector named IPHI under a CNRS/IN2P3, CEA/Irfu and CERN collaboration. IPHI has been designed to be a possible front end for a HPPA devoted to fundamental and applied research: radioactive beams production, neutron sources and transmutation. The aim of IPHI was also to validate the technical choices, to demonstrate operational reliability and to measure the beam parameters of the accelerated beam by the RFQ. IPHI was also designed in the frame of the SPL (Superconducting Proton Linac) study at CERN as a 3 MeV test stand to become the low energy part of the linear accelerator "Linac4" [1]. IPHI consists of an E.C.R. proton source named SILHI (100 mA, 95 keV) followed by a Low Energy Beam Transfer Line (LEBT). A Radio Frequency Quadrupole (length: 6m), operating at 352.2 MHz performs the acceleration of the proton beam up to 3 MeV. Finally the straight section of the High Energy Beam Transfer line (HEBT) may transfer the total power (300 kW) of the beam to a beam stopper (BS) [2]. The deflected section of the HEBT may transfer only a small fraction of the total beam power (few tens of W) for energy dispersion measurement. IPHI is planned to work under C.W. operation but during tests and commissioning periods pulsed mode operation has to be considered to lower the mean power of the beam in order to prevent the accelerator structure and the interceptive beam diagnostics from excessive heating or even from destruction.

BEAM DIAGNOSTICS

General Considerations

The source ECR source SILHI 100 kV, installed on a high voltage (100 kV) platform produces the required high intensity (100 mA) proton beams either under C.W. or pulsed mode operation according to the selected temporal structure of the radiofrequency signal feeding her magnetron. The LEBT contains the necessary magnetic elements to transport to the RFQ and to centre on the axis of the beam pipe the beam: two solenoids for the focusing of the beam and two pairs (horizontal and vertical) steerers for the beam alignment. An iris controls the beam intensity. The LEBT contains also beam diagnostics for beam current measurements and visualization of the transverse beam profile at the entrance of the cone located on the RFQ.

The general layout of the HEBT is shown in Fig.1. The straight section (dipole "off") is equipped with beam diagnostics in order to:

- Help to the safe transport of the proton beam to a beam stopper able to withstand the full power of the beam: 300 kW under the C.W. mode operation.
- Provide a sufficient characterization of the beam accelerated by the RFQ during the commissioning period and the daily operation: beam current, position, energy, energy dispersion, transverse profile
- Operate under pulsed mode (pulsed mode operation of the ECR source) for machine commissioning or experimental operation and the nominal C.W. mode.
- Test and evaluate non-intrusive techniques for measuring transverse beam profiles of high average power beams. These techniques will have to be brought to operation due to the large quantity of beam energy deposited in any possible intrusive sensor leading to its destruction or to a high activation induced level.

The deflected section (dipole "on") is primarily devoted to energy spread measurements under pulsed mode beam operation (low average beam power operation). For this purpose, an object slit will be located in the straight section before the dipole and an image slit followed by a Faraday cup at the end of the deflected section. The list of the beam diagnostics types in IPHI is given in Table 1.

†ausset@ipno.in2p3.fr

ISBN 978-3-95450-177-9

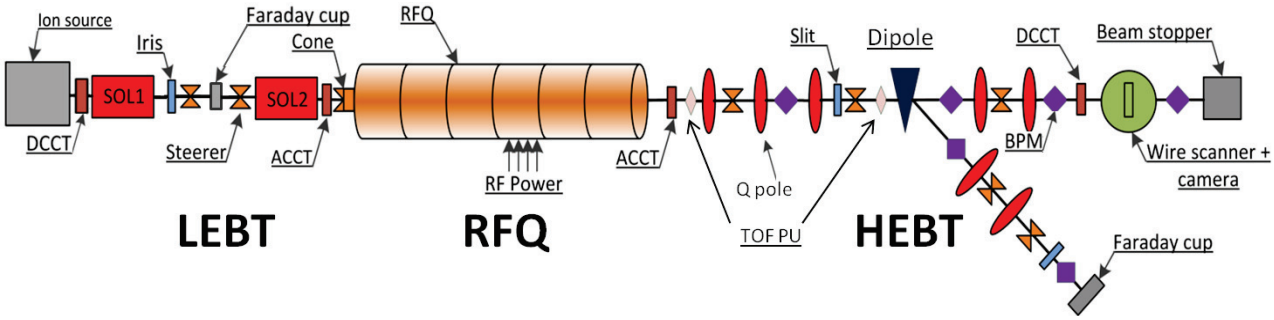

Figure 1: General layout of IPHI.

Table1: List of the Beam Diagnostics Type in IPHI

Measurement	Diagnostic	Location
Current	DCCT – ACCT	LEBT- HEBT
	Faraday cup	LEBT - HEBT
Position	PU - BPM	HEBT
	Lumines-cence	LEBT
Profile	Wire scanner	HEBT
Energy	PU – TOF	HEBT
Energy dispersion	Spectrometry	HEBT

BEAM CURRENT MEASUREMENT

Destructive current measurement in the LEBT is achieved by means of a water cooled Faraday cup located in the LEBT upstream the second solenoid which may acts also as a beam stopper. This Faraday cup and its associated electronics exhibit a sensitivity of 1V/20 mA and the bandwidth (0-50 kHz) allows the observation of the beam pulse under pulsed mode operation.

For non-destructive current measurements, beam current transformers are used throughout IPHI to monitor both average and peak currents. DC beam current transformers are used in the LEBT as well as in the HEBT under CW and very low pulsed duty factor operation. These DC current transformers are MPCT from Bergoz Company. The sensitivity is 1V/20 mA. Two identical ACCT are used, one in the LEBT and one in the HEBT for beam pulse observation and beam current measurement under pulsed mode operation. These ACCT are home-made and built with a VITROVAC 6025F core (outer diameter: 230 mm, inner diameter 130mm, height: 25 mm). Their main characteristics are: Sensitivity: 1V/20 mA; bandwidth: 4 Hz - 6 MHz; resolution: 10 µA. The two ACCT and the two DCCT are housed in a very efficient magnetic shielding.

An example of signal acquisition by the Beam current transformers is given in Fig. 2.

The signals of the Faraday cup of the LEBT, ACCT and DCCT are sent to the acquisition system (LabVIEW) for signal processing: average current, number of charges during the beam pulse or selected integration duration and next to the Command and Control system to calculate the RFQ beam transmission efficiency.

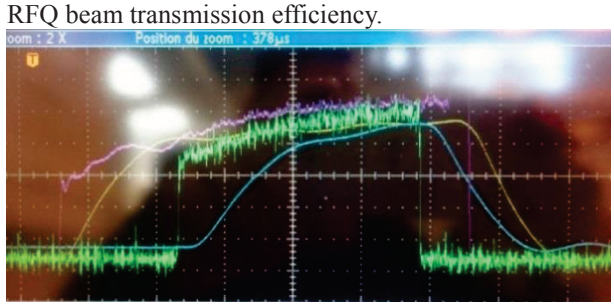

Figure 2: Measurements of the beam current in IPHI. Purple and yellow traces: signals of the ACCT and DCCT upstream the RFQ. Green and blue traces: same measurements with the other couple of ACCT and DCCT downstream the RFQ.

BEAM POSITION MEASUREMENT

Six Beam Position Monitors (BPM) are needed to transport safely the beam: 5 designed for a 33 mm chamber radius (3 in the straight section, 2 in the deflected one) and the last one (before the beam stopper) for a 75 mm radius. Electrostatic Pick Up type has been chosen to measure the transverse beam centroid position (Fig. 3). The core, feed-through and assemblies have been built by the French company PMB. The space between electrode and core is 2 mm with a tolerance of ± 0.05 mm. The four standard Metaceram 50 Ω feedthroughs are terminated by SMA connectors. During the brazing process the four electrodes have been positioned by using a template to insure the axial symmetry of the four electrodes [3].

Electrical Signal Amplitude:

The amplitude of the signal at the terminals of a load connected to the electrode depends on the charge linear distribution seen by this electrode.

- Due to the space force charge and to the energy spread, simulations show (TRACEWIN code) that the linear charge density decreases as the beam propagates to the beam stopper (rms width: σ_z)
- Due to the low value of β (~ 0,08), the image charge distribution is spread longitudinally along the beam pipe wall (radius a) according to:

$$\sigma_{Wall} rms = \frac{a}{\gamma\sqrt{2}} \quad \text{With } \gamma = (1-\beta^2)^{\frac{-1}{2}}$$

ISBN 978-3-95450-177-9

- The current I (t) flowing into the electrode can be expressed versus linear charge distribution λ(z) or current beam and has been computed (see Table 2). Bench test measurement agrees with the calculated sensitivity: 8.5 mV per mA beam.
- Electrodes signals are processed by a Log-Ratio Beam Position Monitor electronics module from Bergoz Company. The expected beam intensity dynamic range measurable is 40 µA – 100 mA.

Figure 3: View of an IPHI BPM.

Errors Signal Analysis:

- Electrical and mechanical centre misalignment leads to an offset measurement of 150 µm for the bloc prototype (Mechanical calibration system accuracy: ~ 40 µm on our test bench)
- The voltage button is obtained by the product of i_{button} by the impedance Zc of the cable seen by the electrode for low frequencies and by $\frac{Z_c}{1+Z_c C_b \omega}$ for high frequencies where C_b is the total capacitance of the electrode versus ground: 9.4 pF. The capacitance dispersion value between the four electrodes is less than ± 0.1pF.
- Discrepancy between the characteristic impedance Zc of the cables leads to offset measurements: 400 µm offset deviation has been measured for 1% dispersion of Zc
- Impedance mismatches between Zc and the input impedance of the Log Ratio module increase the Voltage Standing Wave Ratio and induce error measurements.
- The position sensitivity of ~ 17 µm/mV measured for the BPM associated with its electronics on our laboratory BPM test bench, decreases as the input voltage decreases under input amplitude signal of - 60 dBm. After measurements, -80dbm (corresponding to a ~ 60 µA beam intensity on the first electrode) at the input of the electronic module is the lower limit. (Fig. 4) For current well above 10 µA, the non-linearities are still acceptable in order to centre the beam with a precision of 100 µm by successive iterations.
- The test bench measurement are only valid for β = 1. For the lower value of β = 0.08 corresponding to our beam, the positions measured for a beam travelling in a cylindrical chamber of radius a and at a frequency f must be multiplied by (1+G), according to [4], where G is:

$$G = 0.139.\left(\frac{2.\pi.f.a}{\beta.\gamma.c}\right)^2 - 0.0145\left(\frac{2.\pi.f.a}{\beta.\gamma.c}\right)^3$$

Table 2: Calculated Signal Amplitude for Each B.P.M (straight beam transfer line)

BPM	$\sqrt{\sigma_{wall}^2 + \sigma_{im}^2}$	I_{pp} @ 352 MHz seen by electrode	$V_{electrode}$ (mV pp) (50Ω)
1st	25 mm	17 mA	130
2nd	30 mm	8.8 mA	64
3rd	30mm	7.8 mA	58
4th	57 mm	~0.1 mA	~0.1 mV

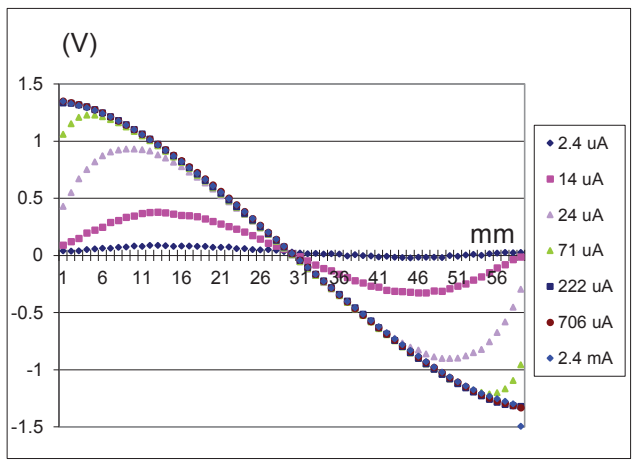

Figure 4: Variation of the output signal of the LR-BPM module with the displacement of the central rod and for different currents in the rod. These measurements have been obtained on our laboratory BPM test bench.

The first measurements were carried on IPHI under a beam intensity of 60 mA on the first BPM. However these measured were smeared by a fraction of the RF signal at 352 MHz propagating in the vacuum chamber. This problem remains to be solved.

BEAM PROFILE MEASUREMENTS

The transverse charge distributions and the transverse emittance of the beam at the exit of the RFQ will be measured and drawn from the transverse profiles measurements according to beam dynamics colleagues' statement. For this purpose a wire scanner (WS), traditionally used for transverse profiles measurements, has been built. It is located in the straight section of the HEBT after the dipole [5].

ISBN 978-3-95450-177-9

- A 30 µm diameter SiC fibber has been selected to be moved through the beam. This fibber cannot withstand the CW operation. The resolution of the "heat equation" leads to limit the beam pulse duration to 300 µs, repetition rate to 1s (100 mA, 3 MeV)
- The two carbon fibbers, (horizontal and vertical measurements) are mounted in a "V" design on an alumina frame moving at 45 ° to the axis of the beam line. Two biasing wires surround the signal wires.
- The maximum size of the beam to be sensed is 10 cm; the total displacement of the frame is 33 cm and is moved by a stepper motor. (Minimum value of the step: 1 µm)

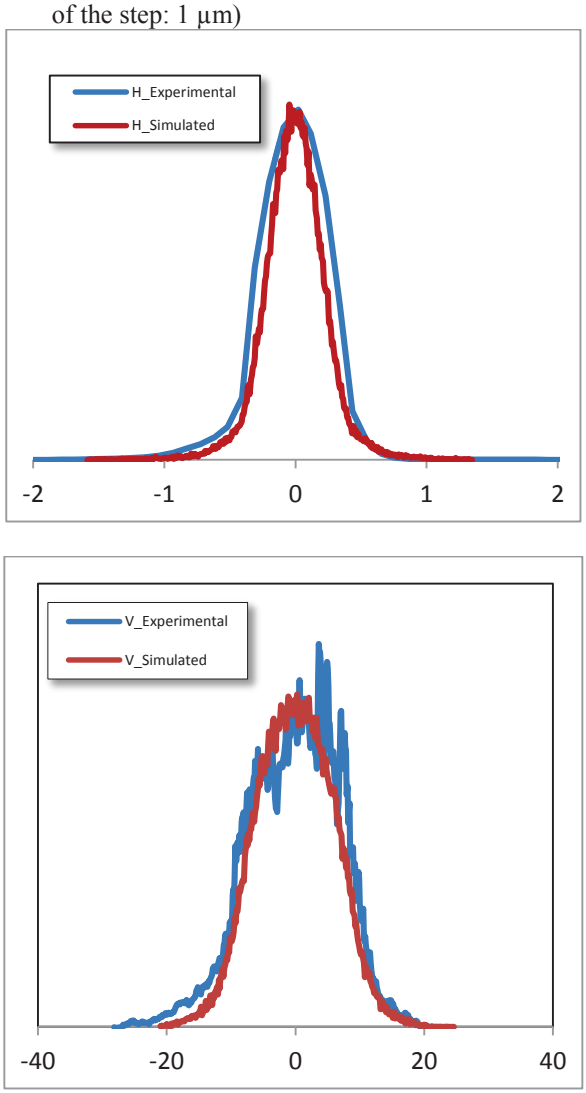

Figure 5: Measurements of the horizontal (up) and vertical (down) transverse beam profiles (mm) with the WS (blue traces) of the accelerated beam (proton 3MeV, 60 mA, pulse duration: 400µs, repetition: 1s). Red traces are simulated beam profiles.

- The transconductance of the amplifier associated with each signal wire has a 1V/ mA gain conversion; 1.5 nA rms noise in a 0-76 kHz bandwidth.

BEAM ENERGY MEASUREMENT

The kinetic energy of the protons is established by the RFQ through which they have passed. As β =0,08, time of flight technique has been called for IPHI to measure the time a particular bunch takes to travel between two electrostatic electrodes P.U. are separated by a distance of 1,3855m ± 0.1 mm. The accuracy on the time measurement must be at least 20 ps to reach a relative accuracy of 10^{-3} on the energy measurement. Pick Up probes have been built (inner diameter: 66 mm; length: 10 mm; Capacitance: 26 pF). Their signals are sent to a phase meter. One degree accuracy is expected. A third P.U. electrode (8 cm from the first one) has been added in order to discriminate uncertainty on energy measurement if needed.

The energy of the accelerated beam was checked by applying the current to the coil of the dipole to produce the nominal magnetic field necessary to send the beam in the deflected section of the HEBT.

ACQUISITION AND SUPERVISION

Four PXI chassis (PCI extended for instrumentation) implemented with LabVIEW software, acquire diagnostics signals and receive their commands from the supervision system EPICS by an Ethernet connection.

CONCLUSION

Beam diagnostics for IPHI will allow the characterisation of the beam accelerated by the RFQ. The beam current, beam transverse profiles and beam position diagnostics are now under operation. The beam energy measurement by the TOF technique remains to be put on operation. However a fraction of the RF signal induces a strong perturbation of the diagnostics signals. This problem has to be cured.

ACKNOWLEDGEMENTS

It is a pleasure to acknowledge the constant support of the IPHI and SILHI CEA teams, in particular the help of Raphaël Gobin. We want also to thank warmly our colleagues of the "Electronics Group" and of the "mechanical study group" of the Accelerator Division of IPNO for their constant assistance during the IPHI project.

REFERENCES

[1] C. Rossi *et al.*, "The SPL Front end: a 3 Mev H- Test Stand at CERN". *LINAC2004*, August 2004, Lübeck.
[2] B. Pottin *et al.*, "Status Report on the French High Intensity Proton Injector at Saclay (IPHI)". *LINAC2012*, September 2012, Tel-Aviv.
[3] M.C. Solal, "Design, Test, and Calibration of an Electrostatic The SPL Front end: a 3 Mev Beam Position Monitor" *Phys. Rev. STAB* 13, 032801(2010).
[4] Robert E. Shafer, *AIP Conf. Proc.* 319. 1994.
[5] P. Ausset *et al.*, "Optical Transverse Beam Profile Measurements for High Power Proton Beam". *EPAC2002*, June 2002, Paris.

ISBN 978-3-95450-177-9

LEReC INSTRUMENTATION DESIGN & CONSTRUCTION *

T. Miller†, M. Blaskiewicz, A. Drees, A. Fedotov, W. Fischer, J. Fite, D. M. Gassner R. Hulsart, D. Kayran, J. Kewisch, C. Liu, K. Mernick, R. Michnoff, M. Minty, C. Montag, P. Oddo, M. Paniccia, I. Pinayev, S. Seletskiy K. Smith, Z. Sorrell, P. Thieberger, J. Tuozzolo, D. Weiss, A. Zaltsman,
BNL, Upton, NY 11973, USA

Abstract

The Relativisitc Heavy Ion Collider (RHIC) at BNL will collide ions with low center-of-mass energies of 7.7 – 20 GeV/nucleon, much lower than 100 GeV per nucleon. The primary motivation is to explore the existence of the critical point on the QCD phase diagram. An electron accelerator is being constructed to provide Low Energy RHIC electron Cooling (LEReC) [1] to cool both the blue & yellow RHIC ion beams by co-propagating a 10 – 50 mA electron beam of 1.6 – 2.6 MeV. This cooling facility will include a 400 keV DC gun, SRF booster cavity and a beam transport with multiple phase adjusting RF cavities to bring the electron beam to one ring to allow electron-ion co-propagation for ~20 m, then through a 180° U-turn electron transport so that the same electron beam can cool the other counter-rotating ion beam, and finally to a beam dump. The injector commissioning is planned to start in early 2017 and full LEReC commissioning planned to start in early 2018. The instrumentation systems that will be described include current transformers, BPMs, profile monitors, multi-slit and single slit scanning emittance stations, time-of-flight and magnetic energy measurements, and beam halo and loss monitors.

INTRODUCTION

Full operation of LEReC is planned for 2019-20 with cooling of the RHIC ion beams using bunched electron beams of 1.6 – 2.6 MeV [1, 2]. With delivery of a 750 keV DC gun from Cornell University [3] (planned for operation at 400 keV) in October of this year, the injection section is being installed to support commissioning of the gun, followed by installation of the rest of the machine in the summer of 2017. The electron beam has a nested pulse structure [4], where 80 ps bunches at 704 MHz are grouped in macrobunches and positioned to overlap with the 9.1 MHz RHIC ion beam. The macro bunch size varies 30 – 24 bunches and its maximum charge varies 130 – 200 pC (incl. 30% margin) depending on the range of ion bunch length. The machine layout is shown in Fig. 1.

ELECTRON BEAM INSTRUMENTATION

The parameters measured in each section of the machine layout are quantified in Table 1. Details of each instrument type are elaborated on below.

Gun Instrumentation

In support of HV conditioning of the DC gun, a 24-bit ADC board measuring the voltage across a 350 Ω shunt resistor in series with the HVPS and the cathode and sits at the cathode potential in the SF_6 tank. It is powered via a "power over fiber" link [5]. Cathode current is reported during HV conditioning where the current is kept below 100 µA. The gun has a floating anode biased positive to < 1kV to provide ion collection between the gun and booster. A Keithley 6514 electrometer will monitor the anode current.

Table 1: Parameters Measured in Each Machine Section

Tt-Total; **Inj**-Injection; **Tr**-Transport; **Mg**-Merger; **Dia**-Diagnostic; **Cl**-Cooling; **Ex**-Extraction

Tt	Measure	Inj	Tr	Mg	Dia	Cl	Ex
13	Profile	3	1	1	1	6	1
4	Charge	2			1		1
7	Current	4			1		2
41	Position	8	9	2	2	17	3
1	Halo	1					
3	Emittance	1				2	
2	Δp/p			1		1	
1	Energy					1	
1	Long. Φ Sp				1		
15	Beam Loss	4	3	1		5	2

Profile Monitors

Beam profile monitors (PM) employ YAG:Ce crystals and optics for 50-µm resolution. All 13 PMs have low impedance vacuum chambers [6]. YAG:Ce crystals are 100 µm thick with 100 nm Al coatings. All but one PM have 45° polished Cu or SS mirrors that can withstand a single full-power macrobunch @ 1Hz. The PM in the diagnostic section will have a mirrorless design to withstand 250 µs long trains. Tilted lens optics will correct for depth-of-field limitations associated with its 45° YAG crystal. All PM's are pneumatically driven and use GigE digital cameras.

The Prosilica GT1600 camera with iris control is being investigated for use with P-Iris type lenses for remote control of iris settings to help cope with wide macrobunch intensities during commissioning. All PM's have LED illumination and optical features next to and in the same plane as the YAG crystal to assist in focusing of the optics. A 450 nm laser is included to test the response and focus of the YAG crystal by simulated beam scintillation. Two of the PM's in the cooling section are hybrid devices [6] with a horizontal-plane BPM integrated into the chamber.

* Work supported by BSA under DOE contract DE-AC02-98CH10886
† tmiller@bnl.gov

ISBN 978-3-95450-177-9

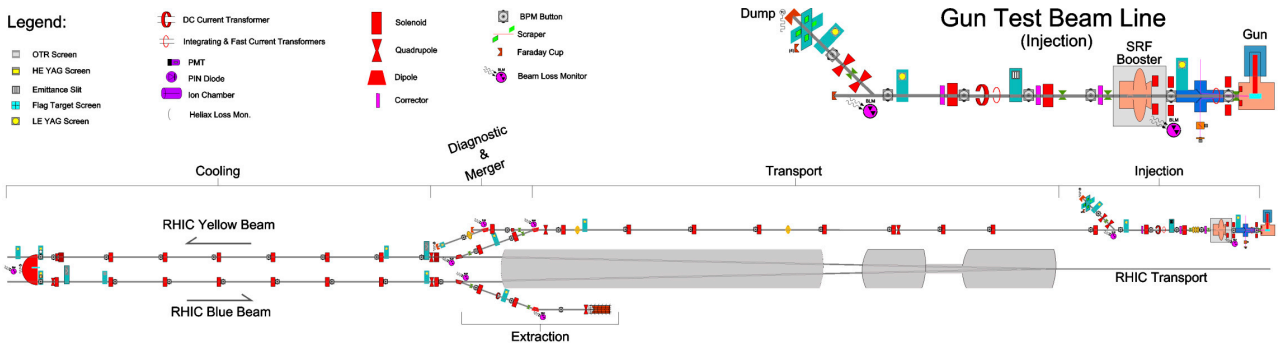

Figure 1: Layout of LEReC electron accelerator showing the five sections. An enlarged view of the injection section as it will be set up during the Gun Test is shown on the right.

Charge and Current

Beam charge is measured by one in-flange integrating current transformer (ICT), Bergoz model ICT-CF6-60.4, in the injection section, and by the three Faraday cups in the electrically isolated beam dumps, in the injection section spur, diagnostic section and extraction section. Beam current is measured by four Fast Current transformers (FCT), Bergoz model FCT-CF6.75"-96.0-UHV-ARB, one at the beginning of the injection line and one upstream of each beam dump. The FCTs are tuned to a narrow band at 704 MHz with a Q = 5 and a 5V/A ratio. Signals from the above mentioned devices are all digitized by FMC164 daughter cards with 16-bit 250 MS/s ADCs supported by a Zynq-7000 FPGA on a ZC706 board by Xilinx.

The first FCT in the injection section is used by the MPS to trip if the beam current exceeds the limit of the current specified by the auto-detected machine mode, based on beam destination [7]. The subsequent three FCTs, upstream of each beam dump (Injection, Diagnostic, and Extraction) are used by the MPS to trip on beam loss by differential current measurements along trajectories toward each beam dump.

Additionally, two DC current transformers (DCCT), Bergoz model NPCT-S-115, will differentially measure low level losses, between the Injection and extraction sections, to detect small losses causing slow heating of the beam line. Under development, recent tests suggest resolutions of 1 – 5 μA with 63 kHz sampling and 1 second averaging.

Due to the low rigidity of the 1.6 MeV electron beam, all ceramic surfaces will be shielded to avoid charge build-up that can deflect the beam. A cylindrical shield attached at one end was made for both the ICT and DCCTs. The FCTs are being ordered with Bergoz's ARB option that hides the ceramic behind a 3-mm gap between opposing flange faces extending beneath the ceramic from both sides.

Beam Position Monitor

Button-style BPMs (41 in total) are 4-button dual plane types, except for the two horizontal BPMs in the Hybrid PM's [6]. The strictest requirement for position monitoring is a 50-μm relative accuracy between the electron and ion beams in the cooling section where the angle between them of < 100 μrad is necessary for effective cooling.

Dual electronics modules share each cooling section BPM – one with a 700-MHz band-pass filter for electrons and one with a 39-MHz low-pass filter for ions. Custom VME-based V301 electronics modules [8] are being installed, for 2×17 cooling section BPMs, and 8 elsewhere.

The 39-MHz modules will measure both electrons and ions. In order to have an identical response to both the electron macro bunches (with a 704 MHz internal structure) and the ion bunches, the 9-MHz structure of both beams will be isolated with digital filters. Avoiding interference of the two beams' signals, the electron train will be measured in the ion beam abort gap and the ion beam measured one bunch per turn. The selected ion bunch will be sequenced through all buckets, with the corresponding electron bunch suppressed. With this sequenced electron bunch suppression, reduced cooling of each ion bunch will only be about 0.9% instead 100% for one bunch.

The V301 modules are being equipped with position alarms with 12-μs response times to trip the MPS. This will be one of the two primary lines of defense that the MPS [7] relies upon to turn off the electron beam.

Relative phase between modules will also be measured to determine beam energy during the 400 keV low energy test of the DC gun by resolving the time of flight between selected BPMs.

Libera Brilliance Single Pass electronics, repurposed from the ERL [9], will be used at 16 locations outside of the cooling sections. The 17 BPMs in the cooling section use 64 conical-style 28-mm buttons in 5-inch chambers, made by MPF [10]. The rest of the transport employs a mixture of 40 new 15-mm buttons made by MPF and 56 x 9-mm buttons (repurposed from the ERL).

Beam Halo Monitor

In order to measure the beam halo, a four-quadrant halo monitor will be installed at the end of the diagnostic spur in the injection section. Repurposed from the ERL, each of the four stepper-controlled 5mm-thick copper blades will be mounted to provide a minimum aperture of 40 mm. Each blade is 30 mm wide and can travel from 20 mm to 43 mm from beam center. The blades are isolated and connected to integrating amplifiers and are digitized with the same electronics as are used for the faraday cups.

ISBN 978-3-95450-177-9

Emittance

Emittance measurements are planned in three locations to ensure normalized emittance < 2.5 μm. In the injection section, a dual multi-slit mask, 2.0 m upstream of a PM is pneumatically driven. Based on the expected beam size, divergence and energy, a 10-slit array was made with slits 150 μm wide, separated by 1.35 mm covering an area 12 x 15 mm. Two such arrays are placed orthogonally on one tungsten mask 1.50 mm thick for horizontal and vertical emittance measurements.

The mask design can accommodate measurements of three beam energies, 400 keV, 1.6 MeV, and 2.6 MeV. Simulations of emittance measurements with beam phase space distribution from Parmela calculations were performed to optimize the slit geometry and drift length from multi-slit to the profile monitor for the three energies. Measurement errors for the three energies of 0.15%, 23.5%, and 24.3% respectively were predicted [11, 12].

In the cooling section, two emittance slit scanners [6] being installed next year, have large 2-mm thick tungsten masks with orthogonal 150-μm wide slits that are stepper-driven at 45° for H+V measurements in one scan. Downstream PMs will take images at a 1 Hz rate while the masks scan at 0.5 mm/sec over a 30 mm spot to include all particles in the beam.

Energy Spread

The electron beam must have an energy spread of $\Delta p/p < 5\times10^{-4}$ for effective cooling of the ion beam. Thus $\Delta p/p$ is measured in two locations. The beam is temporarily focused to a minimum on a PM during the measurement. The first measurement is made at the mid point of the merger section. By comparing the beam sizes (σ_x, σ_y) on the screen, the difference $\Delta\sigma$ gives the dispersion due to the energy spread. The second measurement is made across the 180° dipole in the cooling section where three PM's are used [6]. The first PM will insert a slit 150 μm wide in a 1.5 mm thick tungsten mask to define the horizontal size (σ_x). A second PM down stream of the dipole will, with the dipole off, measure σ_{x1} at a distance (d_1). A third PM, at an equivalent distance (d_1) but along the path through the dipole, will measure σ_{x2} of the beam after the dipole. The resolution will be < 5% $\Delta p/p$.

Energy

Absolute energy of the electron beam is measured in two ways. A time-of-flight energy measurement at 400 keV will be made by the V301 BPM modules [8], during gun commissioning. The 180° dipole is used as a magnetic energy spectrometer [6] for beam energies of 1.6 – 2.6 MeV in conjunction with up and downstream BPMs. Accounting for various possible errors in measurements and in the magnet field, we expect to measure beam energy with an accuracy of 2.6×10^{-3} [13].

The magnetic field of the 180° dipole will be continuously monitored by an NMR probe, built by Caylar [14], installed in the gap. It will measure the average field (195 gauss for 1.6 MeV beam) at a 1-Hz rate. The probe is optimized for low field measurements of 180 – 325 gauss with an accuracy of 50 milligauss and a noise floor of < 20 milligauss. Needing only slow correction, the feedback from the NMR probe will simply modify the magnet power supply set-point via software in the control system.

Longitudinal Phase Space

For low $\Delta p/p$, short bunches of 80 ps are produced in the gun to mitigate the effect of the RF curvature in the LINAC and then chirped, stretched, linearized and de-chirped by the four cavities [15]. The energy chirp introduced in the 704-MHz SRF booster cavity stretches the bunch to mitigate effects of the high space charge. The chirp is then linearized by the 2.1-GHz warm cavity just downstream of the booster and then de-chirped by the 704-MHz warm cavity at the end of the transport section. Moreover, a 9-MHz warm cavity in the middle of the transport section compensates for periodic transient beam loading across the macro bunch. In order to achieve minimum beam energy-spread, each cavity must be tuned in amplitude and phase, in addition to the laser phase and DC gun voltage, resulting in 10 parameters to optimize. This necessitates the "Longitudinal Phase Monitor" (LPM) in the diagnostic section while tuning to optimizing the longitudinal phase space.

The LPM is comprised of a 704-MHz transverse mode deflecting cavity [16] located just after a 20° dipole and upstream of the mirrorless PM. The $\Delta p/p$ of the macrobunch is displayed on the PM as the dipole expresses the $\Delta p/p$ as horizontal $\Delta\sigma_x$ and the deflecting cavity tilts the beam to express the beam's longitudinal axis onto the vertical axis. This gives an image of $\Delta p/p$ vs time (or length – z).

With a horizontal beam size σ_x = 250 μm and a dispersion of 1 m at the PM, a $\Delta p/p$ of 5×10^{-4} results in an increased σ_x = 560 μm. We require a $\Delta p/p$ resolution of 1×10^{-4} (1/5 of nominal) to properly tune the V and Φ of the RF cavities. This translates to a required resolution of the PM of 100 μm (met by the 50-μm design resolution.)

In order to measure RF field stability in the presence of beam loading transients, the profile must be taken after the cavities have stabilized. Thus this PM must withstand a macrobunch train length up to 250 μs [17]. As the Prosilica GT GigE digital camera has a 20ns trigger jitter [18], it will be gated to capture only the last 10 μs [19]. Once the RF system is properly tuned, its response to a single macro bunch will be equivalent to that of a long train. Thus, the PMs in the cooling section are designed to withstand single macro bunches at 1 Hz.

Beam Loss Monitor

The machine has several vulnerable spots where a normal incident beam can breach the vacuum chamber in as little as 30 μs. This requires a comparable reaction of the MPS [7] with fast trip indicators. Thus, in addition to the beam position alarms, an array of fast beam loss detectors will be installed. This will consist of 16 PMT-based sensors, 8 RHIC style ion chamber sensors, and 8 PIN diode sensors all repurposed from the ERL [9]. The PMT sensors are based on a design used for the 12 GeV up-

ISBN 978-3-95450-177-9

grade to CEBAF [20] at JLAB. The ion chambers are spares produced for the BLM system [21] in RHIC. The PIN diode detectors are model BLM "Beam Loss Monitors", from Bergoz Instrumentation. These detectors will constitute eight groups of all three types distributed to each bending magnet and around the SRF booster. The remaining eight PMTs will be distributed along the transport and in the cooling section.

The PMT sensors were used in CEBAF at energies above 5 MeV. To increase their sensitivity to the 1.6 MeV beams in LEReC, scintillating fibers, 2 – 12 m long, will be coupled to the PMTs. The fibers are BCF-60 radiation hardened 1 mm diameter fibers by Saint Gobain [22]. The total length of fibers will cover the entire length of the LEReC machine.

The signals from the PMTs will be processed by VME based 8-channel FPGA electronics cards [23] purchased from JLAB. With a 1-μs fast shutdown output to the MPS, this PMT BLM card also has a log amplifier to provide 5 decades of dynamic response to aid in the commissioning of the machine with low beam power.

COOLING INSTRUMENTATION

Energy Matching

For successful e-beam cooling of the RHIC beam, the energies of the two beams must be matched with 10^{-4} accuracy. To start, the absolute e-beam energy must be set to an accuracy of better than 10^{-2} [13]. While the energy of the ion beam can be known to $<1\times10^{-4}$, the electron energy will be initially set to 5% by the RF voltage and then to 0.3% by the magnetic spectrometer. Yet finer e-beam energy will be attained by observing the recombination monitors where the rate will be maximized with further alignment and scanning of the RF phase. The final e-beam energy will be set by observing the Schottky spectrum while further adjusting the position and RF phase.

Recombination Monitor

As an indicator of proper alignment of the electron and ion beams for cooling, PIN diodes attached to rate counters will be installed in one of the cold arcs of RHIC to detect radiation from lost Au^{78+} ions from recombination. Energy matching of the electron and ion beams of at least 2% is required. Recombination will indicate an energy match of up to 0.1%. Recombined ions are lost in a local dispersion bump created in a special RHIC orbit with a deviation of 7σ in one of the arcs [24]. Recombination rates of better than 4 MHz are expected, less the attenuation due to the vacuum chamber and obscuring objects in the tunnel. A successful test was done during the RHIC 2016 run showing that lost ions can be detected outside the cryostat.

Schottky Monitor

Analyzing the Schottky spectrum from the RHIC wall current monitor (WCM), the evidence of cooling can be seen as was done at FermiLab in their recycler [2, 25]. The Schottky spectrum will be used as a probe to find the precise electron beam energy. The RHIC has a momentum acceptance aperture of $\Delta p/p = \pm4\times10^{-3}$. The RHIC beam will be debunched after injection to fill the aperture. Adding the copropagating electron beam will concentrate the ion beam energy at the electron beam energy, forming a peak in the Schottky spectrum from the WCM that will be off-center by $\Delta f/f = \eta\, \Delta p/p$. The electron energy will be iteratively adjusted accordingly by the RF voltage until the energies are matched to 1×10^{-4}. With the proper RF voltage setting found by this iterative process, the debunched ion beam will be dumped and a properly bunched ion beam reinjected so that the energies of the two beams will match and the peak will form in the Schottky spectrum on-center, indicating cooling of the ion beam.

STATUS AND CONCLUSION

The commissioning of the DC gun and test beam line are planned to run in parallel with the 2017 RHIC run. The gun will be delivered to BNL high voltage conditioning will be completed this fall. The entire gun test beam line will be installed and ready for pre-beam tests before the start of the upcoming RHIC run.

During the 2017 RHIC shutdown next summer, construction of the transport, merger and the diagnostic sections will be completed as well as the addition of the 180° dipole and instrumentation in the cooling section. Full operation of LEReC is planned for the 2019 RHIC run.

ACKNOWLEDGEMENTS

The authors would like to acknowledge the contributions of B. Dunham, J. Dobbins, K. Smolenski and other members of the Wilson Lab at Cornell University, as well as members of the Accelerator Components & Instrumentation Group, especially A. Curcio, L. DeSanto, D. Lehn, and A. Weston, as well as members of the design room, especially K. Hamdi, J. Halinski, V. De Monte, and G. Whitbeck.

REFERENCES

[1] A. Fedotov *et al.*, "Bunched Beam Electron Cooler for Low-Energy RHIC Operation", in *Proc. NA-PAC'13,* Pasadena, CA, USA, Sept. 2013, paper TUOAA1.

[2] A. Fedotov, "Towards Demonstration of Electron Cooling with Bunched Electron Beam", Technical Note C-A/AP/#445, BNL, Upton, NY, USA.

[3] N. Nishimori, et al, "Review of Experimental Results from High Brightness DC Guns: Highlights in FEK Applications," in *Proc. FEL'15,* Daejeon, Korea, Aug. 2015, paper MOD01.

[4] D. M. Gassner, *et al.*, "Instrumentation for the Proposed Low Energy RHIC Electron Cooling Project", in *Proc. IBIC'13*, Oxford, UK, Sept. 2013, paper TUPF24.

ISBN 978-3-95450-177-9

[5] "Power Over Fiber Kit," Lumentum Operations, LLC, California, USA https://www.lumentum.com/en/products/power-over-fiber-kit
[6] T. Miller, *et al.*,"Multifunction Instrument Designs with Low Impedance Structures for Profile Energy, and Emittance Measurements for LEReC at BNL", in *Proc. IBIC'15,* Melbourne, Australia, Sept. 2015, paper TUPB007.
[7] S. Seletskiy, *et al.*,"Conceptual Design of LEReC Fast Machine Protection System", presented at the *IBIC'16,* Barcelona, Spain, Sept. 2016 , paper WEPG19, this conference.
[8] Z. Sorrell, P. Cerniglia, R. Hulsart, R. Michnoff, "Beam Position Monitors for LEReC," presented at the *IBIC'16,* Barcelona, Spain, Sept. 2016, paper MOPG08, this conference.
[9] D. M. Gassner, *et al.*,"BNL Energy Recovery LINAC Instrumentation", in *Proc. ERL'11*, Tsukuba, Japan.
[10] MPF Products Inc, South Carolina, USA, http://mpfpi.com
[11] P. Piot, *et al.*, "A Multislit Transverse-Emittance Diagnostic for Space-Charge-Dominated Electron Beams," in Proc. *PAC-97,* Vancouver, Canada, May 1997, paper 5P064, pp 2204 – 2206.
[12] C. Liu, *et al.*, "Multi-slit based emittance measurement study for BNL ERL "in *Proc. IPAC'13,* Shanghai, China, May 12-17, 2013, paper MOPWA083.
[13] S. Seletskiy,"How to Measure Energy of the LEReC Electron Beam with Magnetic Spectrometer", Technical Note, BNL, Upton, NY, USA, BNL-112095-2016-IR.
[14] CAYLAR, France, http://www.caylar.net
[15] S. Belomenstnykh, *et al.*,"SRF and RF Systems for LEReC LINAC", in *Proc. IPAC'15,* Richmod, VA, USA, May 2015, paper WEPWI050.
[16] R. Akre, *et al.*, "A Transverse RF Deflecting Structure for Bunch Length and Phase Space Diagnostics", in *Proc. PAC'01*, Chicago, IL, USA, June 2001, pp 2353 - 2355.
[17] S. Seletskey, P. Thieberger and T. Miller, "Study of YAG Exposure Time for LEReC RF Diagnostic Beamline" presented at the *IBIC'16,* Barcelona, Spain, Sept. 2016, paper MOPG69, this conference.
[18] T. Naito and T. Mitsuhashi,"YAG:Ce Screen Monitor Using a Gated CCD Camera", in *Proc. IBIC'14,* Monterey, CA, USA, Sept. 2014, paper TUPD08.
[19] Allied Vision Technologies,"Prosilica GT Technical Manual", V2.8.1, May 11, 2016, p. 37 https://www.alliedvision.com
[20] J. Perry, *et al.*,"The CEBAF Beam Loss Sensors", in *Proc. PAC'93*, Washington DC, May 1993, pp 2184 - 2186.
[21] R. L Witkover, R. J. Michnoff and J. M. Geller, "RHIC Beam Loss Monitor System Initial Operation", in *Proc. PAC'99*, New York, NY, 1999, pp. 2247 – 2249.
[22] Saint Gobain, France, http://www.crystals.saint-gobain.com/Scintillating_Fiber.aspx
[23] J. Yan and K. Mahoney,"New Beam Loss Monitor for 12 GeV Upgrade", in *Proc. ICALEPCS'09*, Kobe, Japan, Oct. 2009, paper WEP092.
[24] F. Carlier, "Radiative Recomtination Detection to Monitor Electron Cooling Conditions During Low Energy RHIC Operations", in *Proc. IPAC'16,* Busan, Korea, May, 2016, pp. 1239 – 1242, paper TUMR007.
[25] V. Balbekov and S. Nagaitsev,"Longitudinal Schottky Spectra of Bunched Beams", in *Proc. EPAC'04,* Lucerne, Switzerland, pp. 791 – 793, paper MOPLT109.

ISBN 978-3-95450-177-9

A PPS COMPLIANT INJECTED CHARGE MONITOR AT NSLS-II*

A. Caracappa†, C. Danneil, R. Fliller, D. Padrazo, O. Singh, BNL, Upton, USA

Abstract

The Accumulated Charge Monitor Interlock (ACMI), a PPS compliant system, was developed to ensure the Accelerator Safety Envelop (ASE) limits for charge generation in the NSLS-II Injector are never violated. The ACMI measures the amount of charge in each injection cycle using an Integrating Current Transformer (ICT). For logistical reasons, adding a redundant ICT was impractical so in order to achieve the high reliability required for PPS this system is designed to perform self-tests by injecting calibrated charge pulses into a test coil on the ICT and analyzing the returning charge signal. The injector trigger rate is 1.97Hz and self-tests are performed 250 msec after every trigger pulse. Despite the lack of a redundant charge measurement the ACMI achieved the high reliability rating required for PPS with a mean time between failure (MTBF) rate greater than 10^6 hours. The ACMI was commissioned in 2014 and has operated to date without any major problems. In 2015 a second ACMI system was commissioned to monitor charge in another region of the injector system.

INTRODUCTION

The ASE sets limits on the maximum charge allowed in a single injection shot and the maximum accumulated charge allowed in a one-hour window. The ASE also sets a limit on the one-minute accumulated charge during Top-Off operations at the NSLS-II facility. The ACMI was developed as part of the NSLS-II PPS to ensure that these ASE limits are never violated. The ACMI uses a single ICT to make the charge measurement. It was not practical to install a second ICT which would have allowed redundant charge measurements to be made. Complicating matters further, the ICT (Bergoz ICT-CF6"-60.4-40-70-20:1) is not a safety-rated device and the ACMI must assume that it can fail at any time. Without a redundant measurement the ACMI would have to use a different strategy to ensure that the single charge measurement is accurate. The ICT came equipped with a test coil which is used by the ACMI to perform self-tests between each injector trigger. For each self-test the ACMI launches a calibrated charge pulse to the ICT test coil and analyzes the returning charge signal in the same manner as the actual beam. Any deviation between the expected and measured charge values for the self-tests generates a fault. The LINAC trigger signal is not generated by a PPS compliant system and the ACMI must assume that the trigger signal could fail at any time. The ACMI carefully monitors the trigger timing applying strict limits on the trigger rate. The ACMI also monitors the ICT at all times ensuring that charge is only detected within a proper time window derived from the trigger timing. The ACMI was required to undergo independent reliability analyses and rigorous internal reviews to ensure the system is PPS compliant.

ACMI SYSTEM

Figure 1 shows the block diagram for the ACMI. The system is built around a safety-rated PLC (Fig. 2: Allen-Bradley 1768-43S). Two PCBs were designed for this system, the Timing Generator and the Analog Processor. An HMI panel allows diagnostic information to be displayed on the ACMI cabinet. The PLC also sends diagnostic information to an EPICS IOC for remote monitoring and data archiving. A few analog and critical timing signals are sent to a VME digitizer for further monitoring. Any fault detected by the ACMI disables the LINAC gun. The only user inputs into the ACMI are PPS compliant reset signals to clear any latched faults.

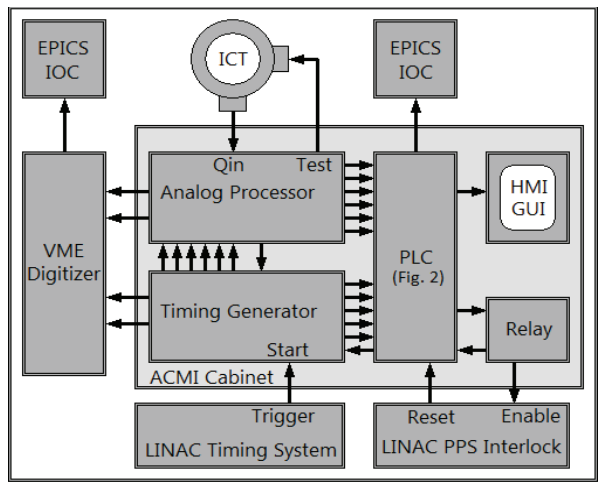

Figure 1: ACMI block diagram.

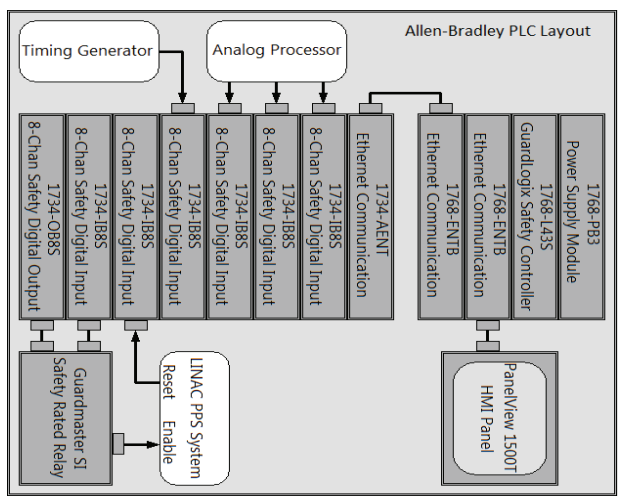

Figure 2: PLC layout.

* Work supported by DOE
† caracapp@bnl.gov

ISBN 978-3-95450-177-9

Timing Generator

A block diagram for the Timing Generator is shown in Fig. 3. The system is designed around an Altera Complex Programmable Logic Device (CPLD) (EPM3128A) which is clocked by a 100 MHz oscillator. The CPLD is programmed using Quartus-II software and an algorithm was developed to generate all the critical timing signals required to process the charge signals for the beam and for the self-tests. A trigger signal from the LINAC timing system initiates the timing sequence. Figure 4 shows the basic timing signals generated to process the beam charge signals on the Analog Processor. Processing of the beam charge is completed in under 100 usec. 250 msec after the LINAC trigger the Timing Generator initiates a self-test by creating a Test pulse that is reshaped on the Analog Processor and driven into the ICT test coil. The timing sequence shown in Fig. 4 is repeated for the charge signal generated by the self-test. Processing of the self-test is completed before the arrival of the next trigger signal.

The trigger signal is not PPS compliant and therefore must be monitored carefully. The Timing Generator measures the time delay between each trigger pulse and will generate a fault if the 1.97Hz trigger frequency appears to change by more than +/-2%. If the Analog Processor detects a charge signal above a threshold setting then a charge-above-threshold signal (QAT) is sent to the Timing Generator. The Timing Generator issues a fault if the QAT signal falls outside the proper integration window (SampA in Fig. 3) indicating that charge was detected at a time it was not expected.

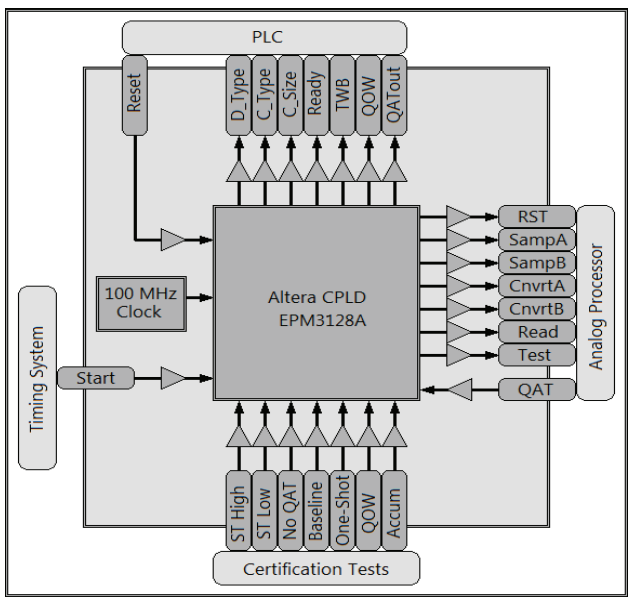

Figure 3: Timing generator block diagram.

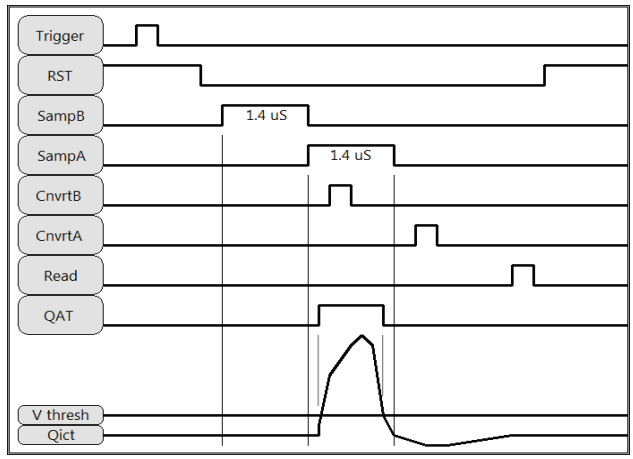

Figure 4: Basic timing diagram.

A series of inputs into the Timing Generator are provided which allow operators to generate various fault conditions on demand. This is useful during annual ACMI re-certifications where detection of every fault mode is tested and verified.

Analog Processor

A block diagram of the Analog Processor is shown in Fig. 5.

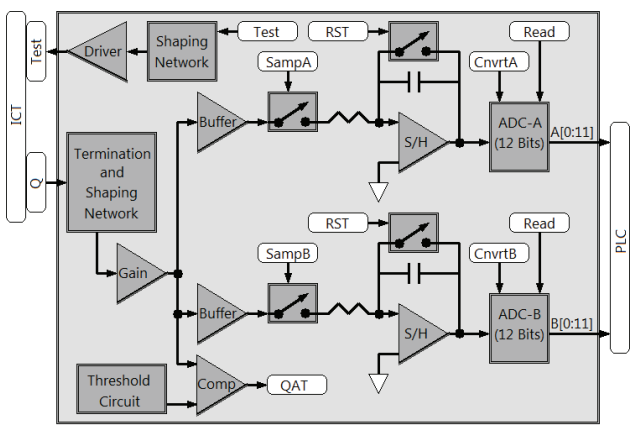

Figure 5: Analog processor diagram.

The charge signal from the ICT passes through a termination and shaping circuit in order to increase its size and width before integration. This signal is passed to two identical sample-and-hold (S/H) amplifiers. Critical timing signals (shown in Fig. 4) are used to perform the integration of the amplified charge signal and the baseline signal which immediately precedes the charge signal. Once integration is complete the value is held on the S/H amplifiers until they are digitized on two ADCs using other timing signals. When digitization is complete the data is sent to the PLC for further processing.

Another copy of the amplified charge signal is also sent to a comparator where it is compared to a threshold voltage. The threshold voltage is set as low as possible to detect very small charge signals but high enough so that it

ISBN 978-3-95450-177-9

is above local noise sources. At NSLS-II this threshold is set low enough to detect injected shots as small as 0.15nC. The comparator output generates the QAT signal that is used in the Timing Generator to determine if the detected charge falls within the proper time window.

For each self-test, a Test pulse from the Timing Generator is reshaped on the Analog Processor and driven into the ICT test coil. The Timing Generator produces all the critical timing signals so that the returning charge signal for the self-test can be processed on the Analog Processor in the same manner as the actual beam.

Reliability Studies

Since the Timing Generator and the Analog Processor were new designs they were required to have an independent reliability analysis. A fault-tree analysis and a thermal stress analysis were performed on each design[1]. The fault-tree analysis uses reliability data for each component on the PBC to determine the probability of failure for every critical signal path in the design. The thermal stress analysis determines the probability of failure based on the heat load calculated for each component. In both cases the MTBF rate was determined to be well above the required 10^6 hours. These designs were also extensively reviewed by engineering and safety experts at NSLS-II who approved their use in the NSLS-II PPS.

PLC Processing

The PLC processes the beam data by first subtracting the baseline measurement from the charge measurement to obtain the charge reading. There are two FIFO stacks in the PLC where charge is accumulated. The larger stack contains all charge readings for the past hour (about 7092 entries) and the sum of all these readings is compared to the one hour ASE limit. The smaller stack contains all charge readings over the past minute. The smaller stack accumulates readings only during Top-Off operations at NSLS-II and the charge sum is compared to the one minute ASE limit. While processing each beam event the PLC monitors for all fault conditions listed in Table 1:

Table 1: Beam Generated Faults

Fault Condition	Limit
Charge Reading HIGH	>16.0nC
Charge Reading LOW	<-0.2nC
Baseline Measurement HIGH	>0.2nC
Baseline Measurement LOW	<-0.2nC
LINAC Trigger Rate HIGH	>2.1Hz
LINAC Trigger Rate LOW	<1.9Hz
1-Hour Accumulation Rate HIGH	>82.9uC/Hr
1-Min Accumulation Rate HIGH	>30.0nC/Min

The self-test are processed in the PLC in much the same way as the beam however the self-test readings are not accumulated. The timing for the beam is set up so that on the Analog Processor ADC-A digitizes the charge signal and ADC-B digitizes the baseline. The charge reading for the beam is obtained by performing an (A-B) subtraction. Half of all self-tests use this (A-B) timing scheme and the other half use a (B-A) timing scheme where the roles of the two ADCs are reversed. The two timing schemes are used to verify that both digitization paths through the Analog Processor are working correctly. Self-tests also occur in two sizes, 17nC and 0.5nC which span the range of injected shots typically produced at NSLS-II. Since both sizes for self-tests are above the 0.15nC charge threshold every self-test must generate a QAT signal. The two timing schemes and the two sizes result in four different self-tests. One self-test is performed after each LINAC trigger and all four self-test will be performed for every four LINAC triggers. The Timing Generator tells the PLC which self-test is being performed. While processing self-tests the PLC monitors for all fault conditions listed in Table 2:

Table 2: Self-Test Generated Faults

Fault Condition*	Limit
17nC Self-Test HIGH	>17.5nC
17nC Self-Test LOW	<16.5nC
17nC Self-Test Baseline HIGH	>0.2nC
17nC Self-Test Baseline LOW	<-0.2nC
0.5nC Self-Test HIGH	>0.53nC
0.5nC Self-Test LOW	<0.47nC
0.5C Self-Test Baseline HIGH	>0.2nC
0.5nC Self-Test Baseline LOW	>-0.2nC
17nC Self-Test with no QAT	N/A
0.5nC Self-Test with no QAT	N/A

*For both (A-B) and (B-A) timing schemes

The PLC also monitors itself and will issue a fault if any of its internal watchdog timers are violated or if communication to any of its IO modules is interrupted.

Noise Considerations

Whenever a charge signal is above the 0.15nC threshold a QAT pulse is generated. The Timing Generator determines if the QAT pulse lies within the integration window for the beam or self-test. If the QAT pulse is outside the integration window then a charge-outside-window (QOW) fault is issued. QOW events cannot be accumulated and might result in an ASE limit violation so it is vital that they are all detected. Noise sources present a challenge if they cross the 0.15nC threshold. If a large noise spike generates a QAT signal it will almost certainly lie outside the integration window and the ACMI will declare a QOW fault. These events form the majority of nuisance trips generated by the ACMI and are usually due to operations of nearby klystrons or pulsed magnet systems. Transients from these systems get picked up along the coaxial cables run between the ICT and the ACMI. Charge signals generated by the ICT propagate along the cables as a balance current signal while transient noise propagate as an unbalanced signal. Passing the coaxial cable through ferrite beads will attenuate any unbalance signal while leaving the balanced signals unaffected. With properly

ISBN 978-3-95450-177-9

chosen ferrite beads it was possible to reduce the size of the transient signals by more than 30dB. Careful routing of these cables away from noise sources and the use of grounded conduits further reduced the size of the transient noise. By the time the ACMI was commissioned the rate of nuisance trips was reduced to acceptable levels.

It was also important to use high-quality linear power supplies with the ACMI and to have a carefully planned grounding scheme eliminating ground loops. Many different isolation techniques (optoisolators, pulse transformers, etc) were employed in the ACMI especially on the Analog Processor where the high precision measurement is made. Applying all these techniques, the ACMI achieved a level of accuracy equal to a Bergoz NPCT module with a full-scale accuracy of 0.1%.

ACMI Calibration, Certification and Operation

As part of the NSLS-II PPS the ACMI must undergo an annual calibration and certification procedure [2,3]. The first part of the calibration procedure determines the signal ratio between the test input and the charge output of the ICT. These measurements are made with calibrated bench equipment and not the ACMI. The ratio measurement is performed primarily to determine if the ICT properties are changing due to aging effects. The second part of the calibration procedure involves sending charge pulses of varying sizes between 0.5 and 19nC to the test coil of the ICT and comparing the ACMI reading to the reading obtained using the bench equipment. The calibration constants for the ACMI are determined from this data.

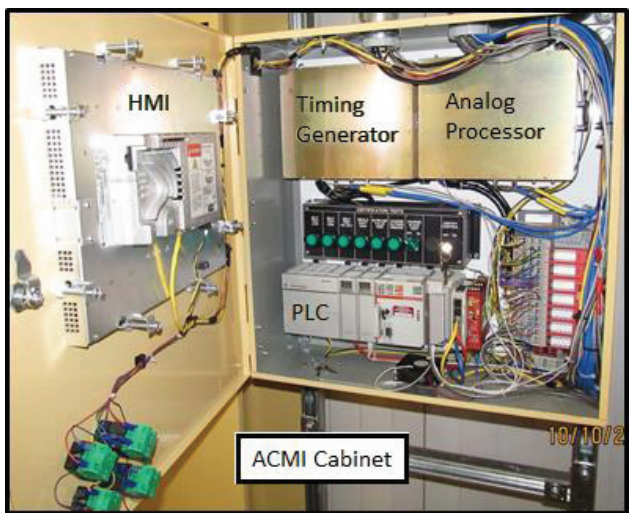

Figure 6: ACMI cabinet.

The certification procedure requires a demonstration that every fault mode described earlier be correctly detected and processed by the ACMI. It is not permitted to use actual beam for these fault tests. The Timing Generator is used to generate many of the fault conditions. Within the ACMI cabinet (Fig. 6) a panel is provided to generate most of the system faults (Fig. 7). Pressing any of these buttons will cause the Timing Generator to produce test pulses that mimic the conditions for that fault. The test pulses are sent to the ICT test coil and the returning charge signal is processed by the ACMI in the normal manner. The ACMI must detect the indicated fault to pass that test. There are also procedures to generate any fault not covered by this panel.

Once the calibration and certification procedures are complete the ACMI can be put into operations for up to one year. While in operations the ACMI is constantly monitored for any condition that might affect its performance. Diagnostic information for the ACMI is presented at the ACMI cabinet on an HMI monitor and remotely using an EPICS based GUI. All ACMI readings for both the actual beam as well as the self-tests are archived. Archived data is analyzed off-line to determine if there are any disturbing trends.

Figure 7: Certification test panel.

Conclusion

Charge monitoring systems for injector systems have been around a long time but are generally not safety-rated systems. The need to integrate these systems into the PPS has become an important issue for any modern facility. Meeting the requirement for PPS can be very difficult and the ACMI faced many problems:

- No redundant measurement
- Incorporation of non-safety-rated devices
- Incorporation of newly designed devices
- High noise levels from external systems
- Exhaustive review process

The ACMI overcame all these obstacles and in 2014 this system was fully integrated into the NSLS-II PPS. In 2015 a second ACMI system was commissioned to monitor charge in a different part of the injection system.

REFERENCES

[1] ACMI MTFB 8.8.2014, http://www.bnl.gov
[2] ICT and ACMI Calibration, PS-C-ASD-PRC-178, http://www.bnl.gov
[3] ACMI Interlock PPS Test, PS-C-ASD-PRC-168, http://www.bnl.gov

ISBN 978-3-95450-177-9

A PPS COMPLIANT STORED BEAM CURRENT MONITOR AT NSLS-II*

A. Caracappa†, C. Danneil, A.J. Della Penna, R. Fliller, D. Padrazo, O. Singh, BNL, Upton, USA

Abstract

A requirement for top-off operations at the NSLS-II facility is at least 50mA stored ring current. The Stored Beam Current Monitor (SBCM) is part of the NSLS-II Top Off Safety System (TOSS) that determines the storage ring current based on Pick-Up Electrode (PUE) readings. The SBCM downconverts the 500 MHz component of the PUE signal to 2 MHz. The 2 MHz signal is rectified, averaged down to a bandwidth of 500 Hz, and compared to a threshold voltage equivalent to 55mA of stored beam. A redundant SBCM system was also constructed and these two systems must agree that the stored beam is above the threshold to enable top-off operations. The SBCM is also required to remain accurate over wide range of possible fill patterns up to a total current of 500 mA. Under normal conditions for top-off operations the SBCM measurement accuracy is about 1%. The SBCM was commissioned in 2015 as part of the Top-Off Safety System (TOSS) which is responsible for ensuring safe top-off operations at NSLS-II.

INTRODUCTION

The NSLS-II facility operates primarily in top-off mode where charge is injected into the storage ring at about one minute intervals while beamline safety shutters are open in order to maintain a relatively constant stored current. The TOSS is a multi-levelled interlock designed to ensure that top-off operations at NSLS-II are executed safely. One requirement of the TOSS is that there be at least 50mA of stored beam in the ring. The detection of stored beam indicates that critical ring systems, such as RF and magnet power supplies, are working correctly. The SBCM is a sub-system of the TOSS that performs the stored current measurement. The use of DCCTs or high-speed digitizers in the SBCM design was ruled out because these devices are not safety-rated and their inclusion in a safety rated system would have been difficult to develop.

In order to facilitate meeting the requirements for TOSS the SBCM is designed as a fully analog processor. The SBCM processes PUE signals generated by the beam in order to determine the stored current. The RF cavity frequency of 500 MHz organizes the ring into 1320 RF buckets with the beam typically occupying 80% of these buckets during top-off operations. The gap formed by the empty buckets modulates the 500 MHz PUE signals at the ring rotation frequency of 378.78 KHz (Fig. 1).

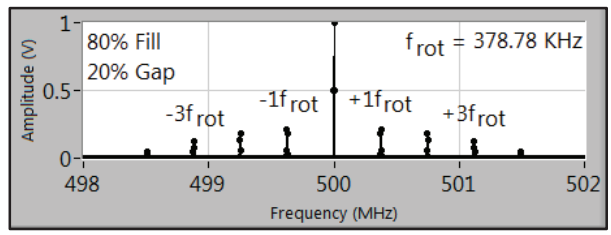

Figure 1: Modulated PUE Signal.

At the frequency range shown in Figure 1 parasitic elements in the analog circuit would make the current measurement difficult to perform. If the PUE signal is mixed with a 498 MHz local oscillator the pattern shown in Figure 1 is regenerated at 2 MHz and at 998 MHz. A 20 MHz low-pass filter blocks the signals centered on 998 MHz. The current information encoded on the PUE signal is preserved on the downcoverted 2 MHz signal. The modulation of the PUE signal is also downconverted as shown in Figure 2.

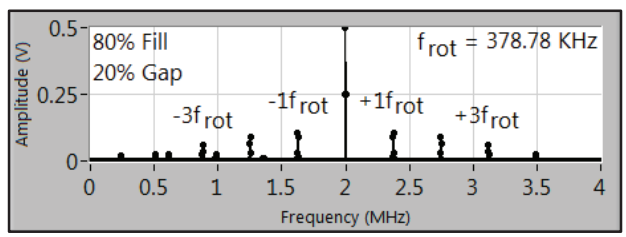

Figure 2: Downconverted PUE Signal.

The downconverted PUE time-domain signal is shown on the left side of Figure 3. The plot shows about 2 ring revolutions of data. The right side of Figure 3 shows the absolute value of the downconverted signal.

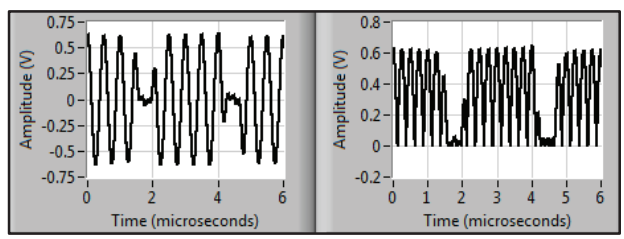

Figure 3: SBCM Time-Domain Signals.

The absolute value is averaged over about 750 ring revolutions to obtain the SBCM reading. For a given fill pattern the relationship between the SBCM reading and the stored current is highly linear with nonlinearities below 1%. Different fill patterns will have slightly different proportionality constants. The fill pattern dependence will be discussed in depth later.

SBCM SYSTEM

Figure 4 shows the block diagram for the SBCM. A 5:1 combiner module located on the girder with the PUEs performs the passive sum of the PUE signals and allows a

* Work supported by DOE
† caracapp@bnl.gov

ISBN 978-3-95450-177-9

test signal to be added into the sum for SBCM certification tests. Outside the storage ring a cabinet houses all SBCM components for both the primary and redundant systems. Two PCBs were developed for the SBCM, a mixer circuit and a rectifier circuit. In order to establish a safety rating both of these circuit designs were submitted for independent fault tree and thermal stress analyses. Both circuits received mean time between failure ratings above the required 10^6 hours [1]. The output of the rectifier circuit controls a safety relay which indicates that the minimum required current is stored.

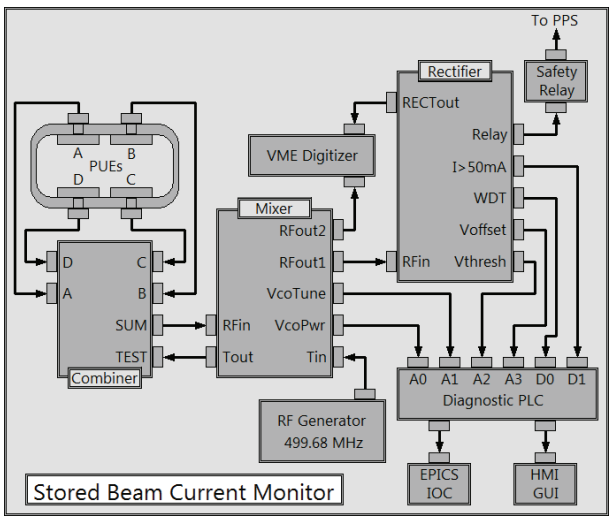

Figure 4: SBCM Block Diagram.

The performance of the SBCM is monitored using a PLC which reads a number of diagnostic signals from the mixer and rectifier circuits. The PLC displays system information locally on the SBCM cabinet using a GUI on an HMI panel. The PLC also sends system information to an EPICS IOC for remote monitoring. A VME digitizer is used to monitor the 2 MHz downcoverted signal. The diagnostic monitoring is not part of the safety function of this system and is not designed to that level.

During SBCM certification tests an RF Generator is connected to the mixer circuit to provide a "fake" beam signal to the combiner module. The RF Generator is calibrated so that any value of simulated stored current can be created on demand.

Combiner Module

The combiner module consists of two passive combiner components (Figure 5). A 500 MHz RF signal can be applied at the test input to provide "fake" beam for various tests otherwise that input is terminated. The RFout signal is the sum of all the input signals.

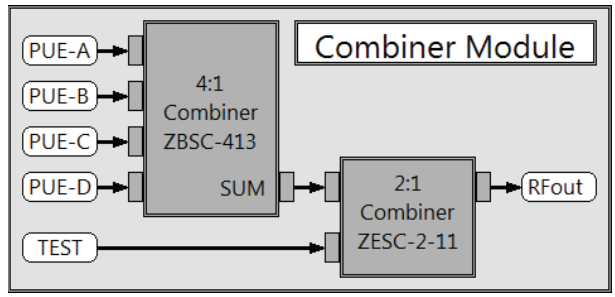

Figure 5: RF Combiner Module.

Mixer Module

The block diagram for the mixer module is shown in Figure 6. The sum signal from the combiner module is sent to the mixer input (RFin). A bandpass filter passes the 500 MHz component of the input which is then mixed with a local oscillator. The oscillator is adjusted to 498 MHz and passed through a directional coupler. The through port of the coupler goes to the mixer and the coupled port goes to a RMS power detector to monitor the local oscillator power. Only the 2 MHz component of the mixer output is passed by the 20 MHz lowpass filter. That signal is split and sent to amplifiers to drive the two RF outputs. One RF output is sent to the rectifier module for further processing and the other output is sent to a VME digitizer to monitor the 2 MHz signal.

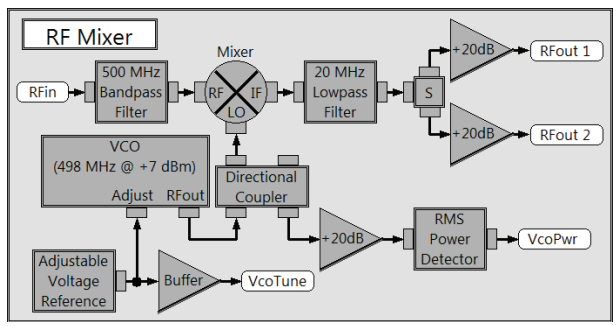

Figure 6: RF Mixer Module.

Rectifier Module

The block diagram for the rectifier module is shown in Figure 7. The mixer output is sent to RFin and the absolute value is formed using the circuit shown in Figure 8. The rectified signal is averaged using a 500 Hz lowpass filter. A voltage reference is adjusted to provide a threshold level equivalent to 55mA of stored ring current. A comparator is used to determine if the averaged rectified signal is above the threshold. Hysteresis is applied to the threshold voltage to keep the transitions of the comparator output clean.

ISBN 978-3-95450-177-9

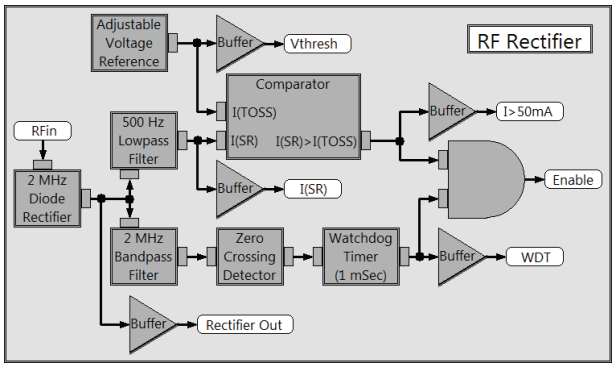

Figure 7: Rectifier Module.

The absolute value circuit (Fig. 8) works well for RF inputs below 5 MHz. Above 5 MHz the effects of parasitic capacitance cannot be ignored. The offset voltage acts as a zero adjustment. The circuit is set up with a gain of 10.

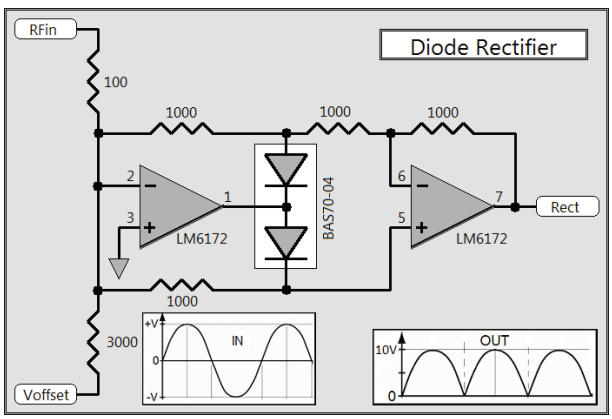

Figure 8: Diode Rectifier Schematic.

A second copy of the rectified signal is passed through a 4 MHz bandpass filter to remove the DC offset. A zero-crossing detector and a watchdog timer determine if transient signals are present. This is done to ensure that the output of the circuit in Fig.8 has the proper time structure. If the threshold comparison and the watchdog timer are satisfied then an enable signal closes a safety relay that ties directly into the TOSS.

BUNCH PATTERN DEPENDENCY

Top-off operations normally use an 80% fill pattern however other fill patterns are permitted. The TOSS specification demands that the SBCM disable top-off operations whenever the stored current is below 50mA for any fill pattern between 20% and 100%. Since the vast majority of top-off operations use an 80% fill pattern the SBCM is calibrated to that pattern. The threshold setting for the SBCM is chosen so that the measurement error for other fill patterns does not result in a violation of the TOSS specification. Figure 9 shows the changes in the modulation sidebands around the downconverted PUE signal for an 80% and 20% fill pattern with the same total current. Note that a 100% fill pattern would have no modulation sidebands.

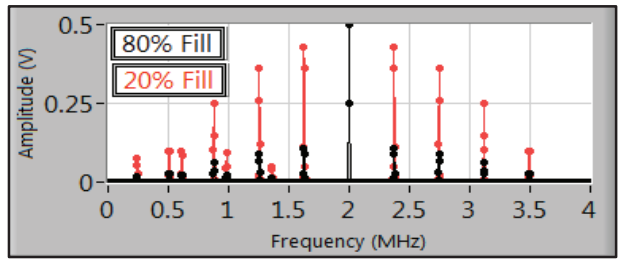

Figure 9: Sideband Dependency on Fill Pattern.

The modulation sidebands will contribute differently to the average of the diode rectifier signal for different fill patterns. For a given fill pattern the relationship between the stored current and the SBCM reading is linear however different fill patterns have different slope terms as shown in Figure 10.

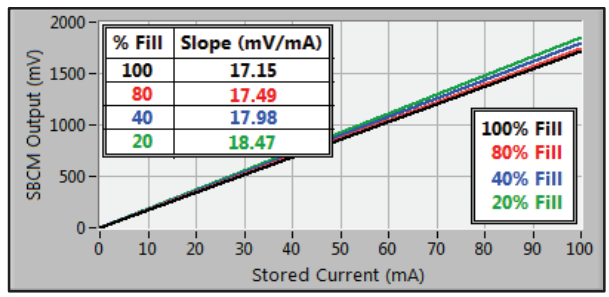

Figure 10: Slope Dependency on Fill Pattern.

In Fig. 11 the data in Fig. 10 is expanded around the threshold level for the SBCM:

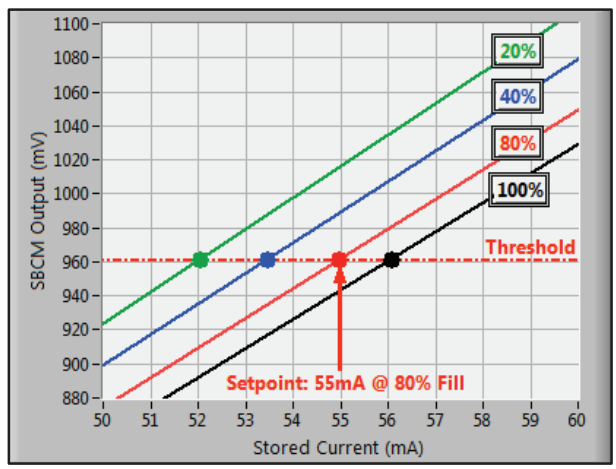

Figure 11: Determining Threshold for SBCM.

The SBCM threshold is set to the SBCM output for 55mA of stored current with an 80% fill pattern. This setting ensures that the TOSS specification for the SBCM is never violated for any fill pattern between 20% and 100%. Figure 12 shows the percent error generated by the fill pattern for the SBCM output as compared to the SBCM output of an 80% fill pattern.

ISBN 978-3-95450-177-9

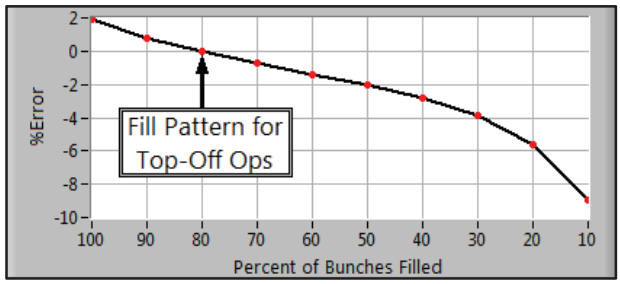

Figure 12: SBCM Error versus Fill Pattern.

The SBCM is calibrated against a DCCT current reading using an 80% fill pattern. While operating with this fill pattern the SBCM is as accurate as the DCCT. In fact the SBCM was used to diagnose a previously undetected fill pattern dependency of the DCCT itself.

The discussion of fill pattern dependency has been thus far limited to the case where there is one bunch train of charge and one gap. The case where a fill pattern has more than one gap was also studied carefully. For example, measurements were made for an 80% fill pattern with 1 gap, 2 gaps, 4 gaps and so on (see Fig. 13). The multiple gaps tend to push some of the modulation sidebands out of the passband for the RF mixer circuit and will therefore bring the SBCM measurement closer to the measurement with a 100% fill pattern. The gap number dependency for the SBCM was determined to be less than 1% for one to four gaps and any fill pattern between 20% and 100%.

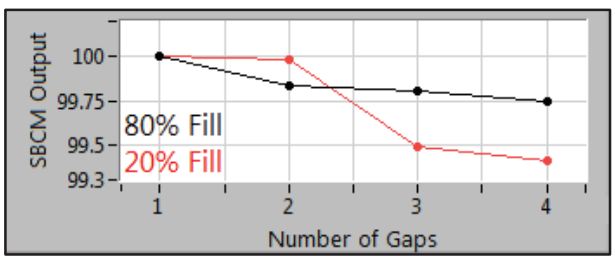

Figure 13: Gap Number Dependency for SBCM.

The SBCM dependency on beam position relative to the PUEs is not significant for typical beam motions which may be present during operations. The dependency on the storage ring RF frequency or the local oscillator frequency is also not significant for the deviations in these frequencies typically seen during operations.

SBCM OPERATIONS

The SBCM was commissioned in 2015 as part of the TOSS for the NSLS-II PPS. Procedure for calibration and certification of this system were developed and are performed semi-annually [2, 3]. The SBCM is calibrated by comparing the SBCM output to a DCCT current reading for a 20%, 40%, and 80% fill pattern with stored currents between 0 and 200mA. This data is analyzed off-line and the analysis is used to make an administrative decision on the threshold settings for both SBCM systems. Once the threshold setting have been entered into the SBCM hardware a final test with beam is performed to verify the threshold setting is correct for the 20%, 40% and 80% fill patterns. Certification of the SBCM is performed with "fake" beam which is slowly ramped across the threshold setting while the status of the TOSS interlock is monitored.

The two SBCM systems have been in operations for over a year with few problems. Adjustments were made to the hysteresis circuits in the Rectifier Module to further debounce the comparator output and reduce chatter in the safety-rated relays during the very slow transitions across the threshold setting. Although not part of the TOSS a third SBCM was commissioned as a test bed for future development of the SBCM project.

CONCLUSION

Safely executing top-off operations are vital to fulfilling the mission of the NSLS-II facility. It can be very difficult to meet all the requirements for a safety rated system when a complex measurement must be made. The SBCM distills the current measurement down to a small number of reliable analog components while maintaining the accuracy and stability required for this safety system. Although the SBCM displays a fill pattern dependency it was found to be within the measurement tolerance over the require range of 20% to 100% fill patterns. For the 80% fill pattern predominantly used during top-off operations the SBCM is still one of the most accurate stored current measurements at the NSLS-II facility and the only current measurement which is PPS compliant.

REFERENCES

[1] SBCM MTFB Reports, *LT-EL-SR-BI-TSS-0103*, http://www.bnl.gov

[2] TOSS SBCM Calibration, *PS-C-ASD-PRC-190*, http://www.bnl.gov

[3] TOSS Certification and Test Procedure, *PS-C-ASD-PRC-196*, http://www.bnl.gov

ISBN 978-3-95450-177-9

THE CHERENKOV DETECTOR FOR PROTON FLUX MEASUREMENT (CpFM) IN THE UA9 EXPERIMENT

S. Montesano*, W. Scandale[1], CERN, 1211 Geneva 23, Switzerland
F. M. Addesa, G. Cavoto, F. Iacoangeli, INFN Sezione di Roma, Rome, Italy
L. Burmistrov, S. Dubos, V. Puill, A. Stocchi, LAL, Orsay, France
[1] also at LAL, Orsay, France

Abstract

The UA9 experiment at the CERN SPS investigates the possibility to use bent crystals to steer particles in high energy accelerators. In this framework the CpFM have been developed to measure the beam particle flux in different experimental situations. Thin movable fused-silica bars installed in the SPS primary vacuum and intercepting the incoming particles are used to radiate Cherenkov light. The light signal is collected outside the beam pipe through a quartz optical window by radiation hard PMTs. The PMT signal is readout by the WaveCatcher acquisition board, which provides count rate as well as waveform information over a configurable time window. A bundle of optical fibers can be used to transport the light signal far from the beam pipe, allowing to reduce the radiation dose to the PMT. A first version of the CpFM has been successfully commissioned during the data taking runs of the UA9 Experiment in 2015, while a second version has been installed in the TT20 extraction line of the SPS in 2016. In this contribution the design choices will be presented and the final version of the detector will be described in detail.

INTRODUCTION

Since 2009, the UA9 Experiment investigates the possibility to use bent silicon crystals to steer beams of charged particles, and in particular to improve the performance of a multi-stage collimation system [1]. The main installation of the experiment is in the Long Straight Section 5 (LSS5) of the CERN SPS and includes three goniometers to operate five different crystals, one dedicated movable absorber, several scrapers, detectors and beam loss monitors (BLM) to probe the effect of the crystal on the beam halo [2]. A schematic representation of the layout of the experiment is reported in Fig. 1.

The main process that is investigated is the so-called "planar channeling": particles impinging on a crystals with a direction close to the one of the lattice planes are forced to move between the planes by the atomic potential, with high efficiency; if the crystal is bent, the trapped particles follow the bending and are deflected. When an optimized crystal intercepts the beam halo to act like a collimator, about 80% of the particles are channeled, coherently deflected and dumped on the absorber (see Fig. 1), effectively reducing the beam losses in the sensitive areas of the accelerator [3–8].

* simone.montesano@cern.ch

ISBN 978-3-95450-177-9

Requirements for the Detector

In order to fully characterise this system, the flux of the particles diffusing to the crystal should be characterized, as well as the "deflected beam" due to the particles extracted towards the absorber by the crystal. Initial estimations are performed using the variation of the primary beam intensity measured by the Beam Current Transformer (BCT) and intercepting the extracted beam with a Medipix detector enclosed in a Roman Pot [3, 9].

The existing instrumentation allowed to perform several measurements, however, the optimal detector for these measurements would be:

- installed directly in the beam pipe vacuum, to avoid the interaction of the protons with the Roman Pot window;
- able to measure the number of protons extracted from a single SPS bunch (during UA9 operations the bunch length is 3 ns and the minimal bunch distance is 25 ns);
- able to resolve the signal generated by a single proton up to few tens of protons (the estimated extraction rate is of the order of 10^7 p/s with a revolution time of 23 µs - i.e. few protons extracted per machine turn);
- radiation-hard in order to reliably operate in the accelerator tunnel;
- movable in the direction transversal to the beam, to allow measurements at different apertures of the collimation system and to avoid interfering with the beam during standard machine operations.

THE CHERENKOV DETECTOR FOR PROTON FLUX MEASUREMENT

In order to comply with the requirements listed above, the concept of the CpFM was conceived. A sketch of the detector is reported in Fig. 2, with its main elements: a radiator that intercept particles inside the beam pipe and create the Cherenkov light, a bellow to allow moving the radiator, an interface transmitting the light outside the beam pipe, a photomultiplier (PMT) to collect the light and electronics to readout the PMT signal. Several investigations and measurements [10] performed in the last few years have allowed to carefully select all the components of the chain.

The Cherenkov Radiator

When choosing the technology of the sensor, different options were considered: silicon and gas detectors posed important issues with respect to operation in the beam pipe vacuum, while scintillator materials were considered not

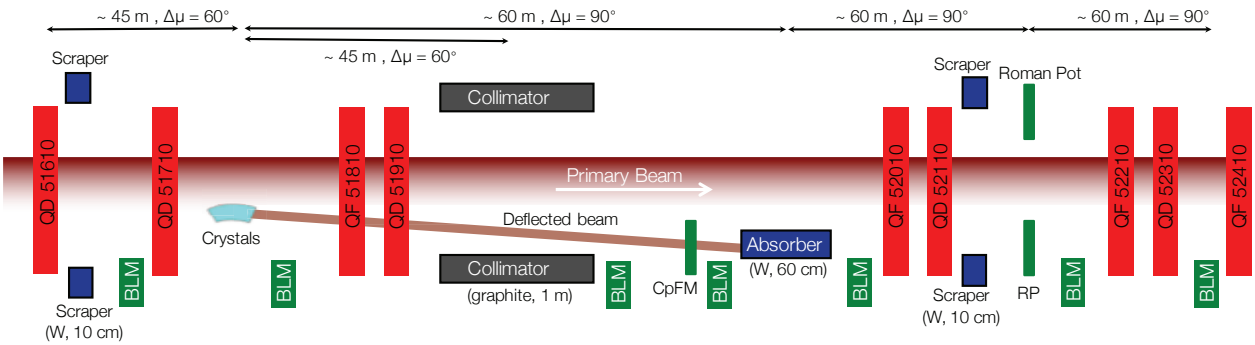

Figure 1: Schematic layout of the UA9 Experiment in the SPS LSS5. The quadrupoles defining the phase advance among different elements are represented by red boxes.

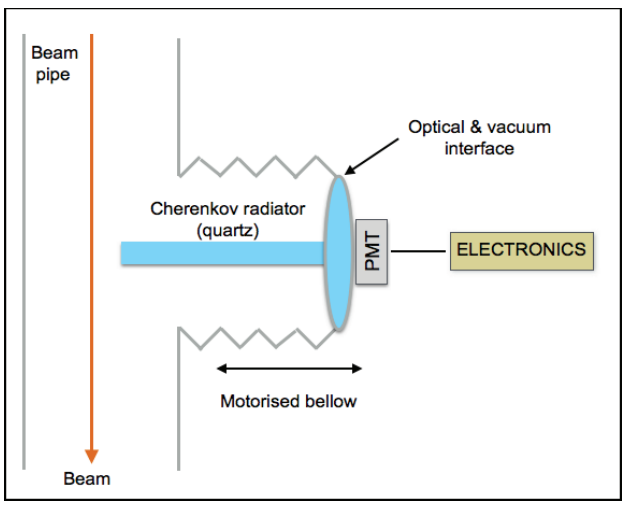

Figure 2: Conceptual sketch of the CpFM.

enough resistant to radiation. Finally it was decided to use a Fused Silica radiator to produce Cherenkov light.

Fused Silica is a synthetically made quartz which has been studied during the R&D for several detectors. The requirement to move the sensor completely out of the beam pipe during normal machine operations set a minimum length for the radiator, which should also transport the generated light through internal reflection from the tip intercepting the beam to the other end of the bar, interfaced with the external of the beam pipe. An extensive simulation campaign has been performed comparing different shapes for the radiator (L-shape, J-shape and I-shape bars were compared, as well as bars with round or rectangular sections) and defining the required polishing (100 nm RMS) and flatness (100 nm). While the best light yield is obtained for L-shaped bars, it turned out difficult to obtain L-bars with the required polishing. Therefore the produced detectors were equipped with I-bars with rectangular section and 5 mm length in the beam direction.

Cherenkov photons are generated with an angle $\theta_c = 47°$ with respect to the direction of the incoming particles, which can be assumed to be parallel to the beam pipe. After multiple reflection inside the radiator, photons reach the end of the bar where they are collected (see Fig. 3). In order to maximise the photons collected, the collection surface should be perpendicular to the direction of the photons. Measurements where performed interfacing a bundle of optical fibres to the end of the radiator and confirmed that the signal is collected with good efficiency only when the bar has an angle of ~47° with respect to incoming particles. Since the integration of an inclined bar requires a large aperture in the tank hosting the detector, it was chosen to cut the end of the bar with an end surface inclined by 47° and to keep the radiator perpendicular to the beam direction.

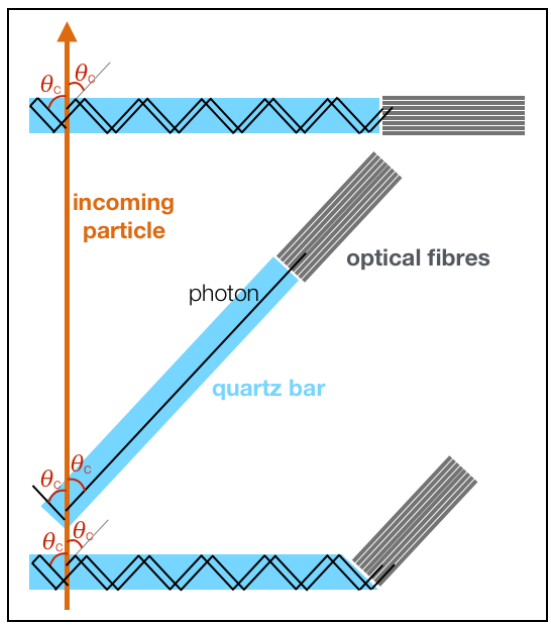

Figure 3: Effect of the Cherenkov angle on the collection of the signal at the end of the radiator.

The Optical and Vacuum Interface

The light generated in the radiator must be transmitted outside the beam pipe and collected by a PMT. In order to limit the number of interfaces traversed by the light it was attempted to feed the quartz bar through a vacuum flange and braze the ensemble to ensure vacuum tightness. The

ISBN 978-3-95450-177-9

issue did not have an easy solution, therefore it was chosen to use a commercial quartz viewport to ensure the interface for vacuum and light. Measurements allowed to estimate a reduction of the signal by a factor maximum 2 when using a glass slab as interface. In order to match the 47° inclination of the end surface of the radiator, a special flange had to be designed (see Fig. 4).

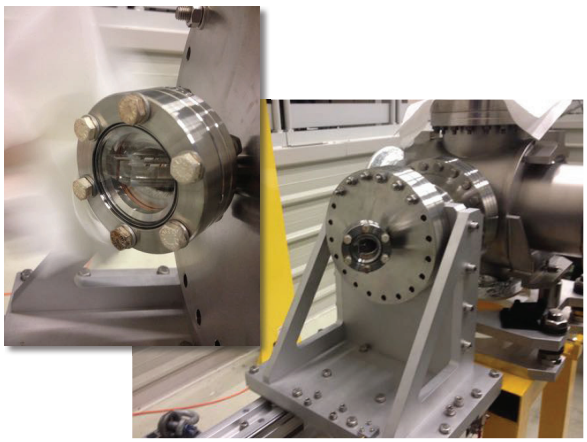

Figure 4: The tilted optical window of the CpFM.

The Photomultiplier

In order to choose a PMT for the CpFM, few radiation-hard devices were considered. Extensive tests were performed for two of them (HAMAMATSU R762 and R7378A, see Table 1 for the main characteristics) that showed good timing properties and sensitivity for the needed wavelengths. In the end the R7378A was chosen for its higher quantum efficiency and, given the good linearity and the low expected proton flux during UA9 data taking, it was decided to use a standard voltage divider to power it.

Table 1: Main Characteristics of the PMTs Under Test

	R762	**R7378A**
Window material	Synthetic Silica	Synthetic Silica
Photocathode diameter (mm)	15	22
Photocathode material	Bialkali	Bialkali
Typical gain	10^6	2×10^6
Typical dark current (nA)	1	1
Maximum sensitivity (nm)	420	420
Typical radiant sensitivity (mA/W)	85	85
Rising Time (ns)	2.5	1.5

THE CpFM FOR UA9 IN SPS

The first CpFM device was designed and built for installation in SPS at the beginning of 2015. It was chosen to use a general purpose tank with large flanges and to design a motorization system that could adapt to it (see Fig. 5, left).

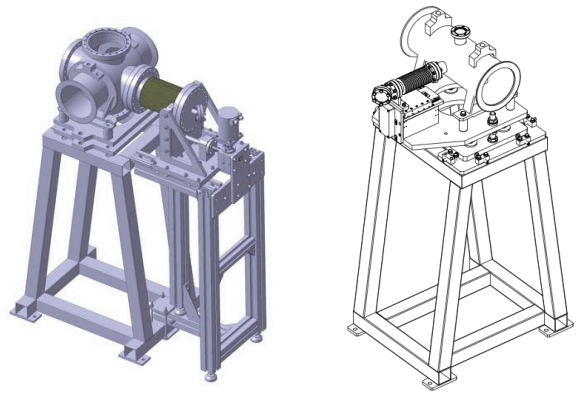

Figure 5: 3D model of the tank hosting the CpFM in the LSS5 of SPS (on the left) and in TT20 (on the right).

Two quartz radiators are used in this detector (see Fig. 6, left) to allow an estimation of the background. At the beam position, one of the bar is 5 mm closer to the beam and is meant to intercept the flux of protons to be measured. The other bar, being retracted from the beam to be measured, should provide a measurement of the background. The bars are supported by a clamping system: one side of the clamp is attached to the flange, while the other is provided by a short aluminum plate kept in position by a screw. Both sides touch the quartz bar only with two 0.5 mm-thick shoulders perpendicular to the long direction of the bars, to minimize the interface between metal and quartz and reduce the loss of light. The distance between the bars is defined by a 0.2 mm-thick aluminum plate clamped between them.

It was decided to reduce the radiation dose to the PMTs, moving them at the floor level, far from the beam pipe. The light signal is therefore transported by an optical fibre bundle composed of 2 channels of 100 fibres each. Fibres are radiation resistant and made of Fused Silica, in order to be transparent to the wavelengths of interest. The bundle is shielded from light by a flexible, stainless steel pipe.

The electronics chosen to readout the detector is the WaveCatcher [11]. This board is able to sample the analog signal of the detector over a configurable time interval (from 320 ns up to 2.4 µs) and to perform simple measurements on the signal. In addition, it counts the number of times that the signal in each channel crosses a user defined threshold. The usual trigger for the UA9 Experiment is used to read out the board (i.e. the SPS revolution signal downscaled by a factor 1000, and synchronised with the passage of the filled bunch in LSS5). Since the WaveCatcher is not radiation resistant, low attenuation cables are used to bring the signal of the PMTs to a shielded area in the SPS tunnel, where the WaveCatcher is installed. The board is then connected to a

ISBN 978-3-95450-177-9

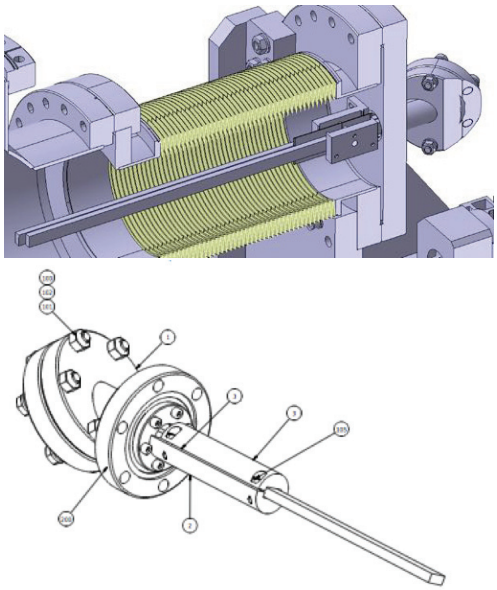

Figure 6: Bar holder and tilted optical window of the CpFM in the LSS5 of SPS (on top) and in TT20 (on the bottom).

standard PC outside the accelerator through USB protocol over an optical link.

The CpFM detector has undergone a detailed commissioning during the data taking runs of the UA9 Experiment and is routinely used for measurements during 2016.

THE CpFM FOR TT20

A second version of the CpFM was built to study the proton flux extracted from the SPS towards the North Area facility and was installed in the TT20 extraction line during 2016. The beam is substantially different with respect to the LSS5 situation, since a constant spill of the order of 10^{13} p over 4 s is expected. For this reason the electronics used for acquisition must to be changed and few different decisions have been taken, such as installing long low attenuation cables that bring the PMT signal directly outside the accelerator.

The tank hosting the detector has been redesigned from scratch, which allowed to build a more compact device, easier to install and to align in the beam line (see Fig. 5). The size of the bellow and of the flanges has been reduced and the optical fibre bundle has been removed, connecting the PMT directly to the optical window.

Assuming that the background will be negligible with respect to the beam to be measured, the design is based on a single quartz bar. The clamping system that holds the bar is therefore simplified, the plates have been changed to two hollow half-cylinders to reduce the risk to damage the bar during installation and transport (see Fig. 6, right). The contact points between quartz and metal are still provided by thin shoulders, but the distance between them has been increased.

The detector is entering the commissioning phase, the first signals have been acquired and are being analysed.

CONCLUSION

A new concept of Cherenkov detector has been designed to perform proton flux measurements in the framework of the UA9 Experiment. The detector is compatible with the vacuum and radiation hardness requirements for CERN accelerators.

During the development of the detector few interesting technological issues were raised but not solved: their solution would allow to build a detector with improved performance. A detailed paper describing all the simulation effort, the measurements and the beam tests that led to the final design is in preparation.

A first version of the device has been installed in the LSS5 of the SPS, has been commissioned and is routinely used by the UA9 Collaboration. A second version of the detector with few changes in the design has been installed in the TT20 extraction line and is entering the commissioning phase.

AKNOWLEDGMENTS

The authors would like to thank the other members of the UA9 Collaboration, the CERN EN/STI, BE/OP, BE/RF, TE/VSC groups for the support during the design, the construction and the tests of the detector.

REFERENCES

[1] The UA9 Experiment, `http://ua9.web.cern.ch`

[2] S. Montesano and W. Scandale, "Apparatus And Experimental Procedures To Test Crystal Collimation", in *Proc. IPAC'12*, New Orleans, Louisiana, USA, paper THEPPB011, pp. 3254–3256.

[3] W. Scandale *et al. Physics Letters B*, vol. 692, no. 2, pp. 78–82, Jul. 2010.

[4] W. Scandale *et al. Physics Letters B*, vol. 703, no. 5, pp. 547–515, Jun. 2011.

[5] W. Scandale *et al. Physics Letters B*, vol. 714, no. 2–5, pp. 231–236, Jul. 2013.

[6] W. Scandale *et al. Physics Letters B*, vol. 726, no. 1–3, pp. 182–186, Aug. 2013.

[7] W. Scandale *et al. Physics Letters B*, vol. 748, pp. 451–454, Jul. 2015.

[8] W. Scandale *et al. Physics Letters B*, vol. 758, pp. 129–133, May 2016.

[9] E. Laface *et al.*, "Crystal Collimation Efficiency Measured With the Medipix Detector in SPS UA9 Experiment", in *Proc. IPAC'10*, Kyoto, Japan, paper THPEC084, pp. 4252–4254.

[10] L. Butrmistrov *et al.*, *NIM A*, vol. 787, pp. 173–175, Dec. 2014.

[11] D.Breton *et al*, "The WaveCatcher family of SCA-based 12-bit 3.2-GS/s fast digitizers", in *proceedings of IEEE Real Time 2014*, Nara, Japan.

ISBN 978-3-95450-177-9

DEVELOPMENT OF HIGH RESOLUTION BEAM CURRENT MEASUREMENT SYSTEM FOR COSY-JÜLICH

Yu. Valdau[1*], L. Eltcov, Rheinische Friedrich-Wilhelms-Universität Bonn, Helmholtz-Institut für Strahlen- und Kernphysik, Nussallee 14-16, D-53115, Bonn, Germany
S. Trusov[2], S. Mikirtytchiants, Forschungszentrum Jülich, Institute für Kernphysik, D-52425, Jülich, Germany,
P. Wüstner, Forschungszentrum Jülich, Zentralinstitut für Engineering, Elektronik und Analytik (ZEA), Systeme der Elektronik (ZEA-2), D-52425, Jülich, German
[1] also at Forschungszentrum Jülich, Institute für Kernphysik, D-52425, Jülich, Germany,
[2] also at Skobeltsyn Institute of Nuclear Physics, Lomonosov Moscow State University, RU-119991 Moscow, Russia

Abstract

An experiment to test Time Reversal Invariance at COSY (TRIC) requires a precise beam life-time determination. For this, a high resolution bunched beam current measurement system based on the Fast Current Transformer and Lock-In Amplifier has been build. The first tests of the system, read out by a new DAQ, have been done at COSY and at a test stand in the laboratory where bunched beam current was simulated using a conductive wire. A relative resolution of 1.9×10^{-4} for the signal in the wire, equivalent to 1 mA of bunched beam current in COSY, has been obtained in the laboratory. This resolution is sufficient for the realization of the TRIC experiment.

MOTIVATION

A test of Time Reversal Invariance (TRIC experiment) is under preparation at COSY-Jülich [1]. The experiment is planned as a null transmission experiment in the storage ring using a T-violation sensitive observable $A_{Y,XZ}$ available in double-polarised *pd* scattering. A polarised proton beam, together with a tensor polarised deuterium gas target located in one of the straight sections of COSY, will be used for the TRIC experiment. The $A_{Y,XZ}$ observable will be determined from the difference of beam life-times measured for two independent beam-target spin polarisation states. This is the reason why the TRIC experiment puts very stringent requirements on the precision of beam life-time determination and hence resolution in the beam current measurement. The minimal resolution of 10^{-4} integrated over one second in the beam current measurement will allow us to reach the goal of the project after one month of measurement and to improve the present upper limit on the T-violation by an order of magnitude.

COSY BEAM PARAMETERS

Unfortunately, it is not possible to reach resolution better than 10^{-3} in the coasted beam current measurement using a conventional DC Beam Current Transformers (BCT) [2]. But a much higher sensitivity and resolution can be obtained for the averaged bunched beam current measurement using inductive or capacitive pick-ups [3]. Since COSY can provide both bunched and unbunched beams at the energy of the TRIC experiment (see parameters of the COSY beam in Tab. 1) it was decided to construct a new high resolution beam current measurement system for COSY using an inductive sensor, sensitive to the bunched beam, together with modern readout electronics.

Table 1: COSY Beam Parameters During the TRIC Experiment

Beam Parameter	Expected value
Beam momentum	521 MeV/c
Revolution Frequency	793345 Hz
Bunch length	200 ns
Bunch shape	Gaussian
Number of protons in ring	$\sim 10^{10}$
Averaged current	1 mA

Since TRIC is a precision experiment, which crucially depends on the precision of the beam current measurement, it was decided to build a test stand in the laboratory to have possibility to study parameters of the sensors and the readout chain with conductive wire independently from the availability of the COSY beam.

FAST CURRENT TRANSFORMER

Two Fast Current Transformers (FCT) with similar parameters have been ordered from the Bergoz Instrumentation company for the TRIC experiment at COSY [4]. Sensors are made in on-flange UHV compatible configuration with a calibration winding. This kind of configuration simplifies sensor installation and requires less than 10 cm of space in the ring. The FCT installed in one of the straight section of the COSY ring is presented in Fig. 1. The device has a conductive break inside and is ready to use after the installation. Since beam intensity in COSY is relatively small, the device installed in the ring is equipped with a custom build low noise preamplifier to work with readout electronics located outside of the accelerator tunnel. Calibration winding

*y.valdau@fz-juelich.de

ISBN 978-3-95450-177-9

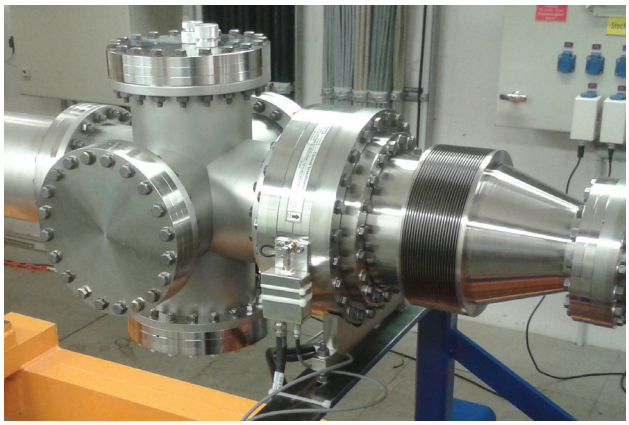

Figure 1: The Fast Current Transformer from Bergoz Instrumentation installed at COSY. The FCT in the ring is equipped with a custom build preamplifier and a current source for calibration. The main parts of the readout and calibration module are installed outside the tunnel.

is connected to the custom build precision current source which allows one to calibrate the FCT using a dedicated calibration module in parallel to the normal COSY operation. Analog parts of readout electronics and the calibration module described in Ref. [5].

TEST STAND IN THE LABORATORY

The test stand (see Ref. [6]) for the beam current measurement devices has been build to study the performance of equipment for the precision experiments planned at COSY. In the test stand, presented in Fig. 2, a beam current of COSY is simulated using a precisely positioned conductive wire and an arbitrary wave form generator. The test stand consists of a wire positioning system, COSY beam position monitor (BPM) and sets of tubes used to support and accommodate devices under study. Modular construction enables fast implementation of new devices in the laboratory and cross checking with devices at COSY. Main parameters of the wire positioning system of the laboratory test stand are summarized in Tab. 2.

Table 2: Parameters of the Test Stand for the Beam Current Sensitive Devices

Parameters of test stand	Value
Wire diameter	50 μm
Movement range	±8 cm
Movement step	10 μm
Positioning uncertainty horizontal	100 μm
Positioning uncertainty vertical	92 μm

The signal in the wire is generated by a custom-built current source which is driven by an arbitrary wave form generator [7]. The signal is terminated by an active load system on the other side of the wire. The load system enables monitoring of the signal generated in the wire and of the amount of reflections and noise.

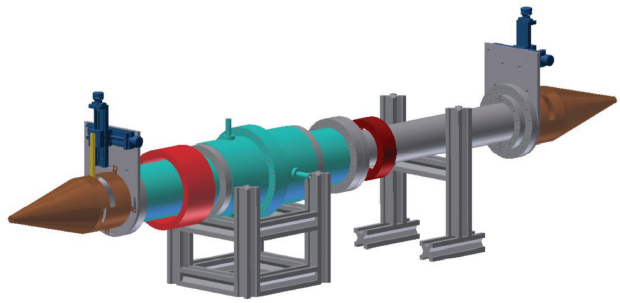

Figure 2: The test station for the beam current measurement devices. Different beam current sensors can be implemented in to the test stand. The wire inside the tube is moved using XY tables (blue) mounted on both sides of the system. The wire tension system is covered inside the tapers (copper colored).

MEASUREMENTS AT COSY

The scheme of the FCT measurement system prepared for COSY is presented in Fig. 3. The preamplifier and current source are connected to the FCT installed in the COSY tunnel. An amplified signal is transferred over a coaxial cable to the measurement setup inside the COSY hall. The signal is split between the Lock-In Amplifier [8] (LIA), readout over the Ethernet, and main amplifier which distribute it to other users. COSY RF system is used as a reference frequency for LIA. The hardware trigger signal for all the systems in the readout is prepared using a dedicated trigger module which accepts all the important for the experiment signals from COSY and other parts of experimental apparatus. This module, as well as all the other devices, is read out and controlled by an common Data Acquisition (DAQ) software over Ethernet. The calibration module provides a high precision rectangular voltage signal to the current source connected to a calibration winding of the FCT.

The first measurements done at COSY confirmed the extremely good sensitivity of the FCT from the Bergoz Instrumentation. At first, the bunched beam intensity in the ring was calibrated using a standard COSY BCT and later was reduced by readjusting the injection beam line. Beam current in the range from 2×10^9 down to 4×10^4 protons in the ring has been detected by the FCT.

MEASUREMENTS IN THE LABORATORY

To perform a detailed studies of the FCT parameters in the laboratory the second readout system, presented in Fig. 4, analogous to the one used at COSY, has been build. The signal from the FCT is readout using the same set of devices as at COSY and readout over Ethernet using the same DAQ. The signal in the conductive wire of the test stand is generated using a sender device and an Arbitrary Waveform Generator which is controlled by the DAQ. The signal in the

ISBN 978-3-95450-177-9

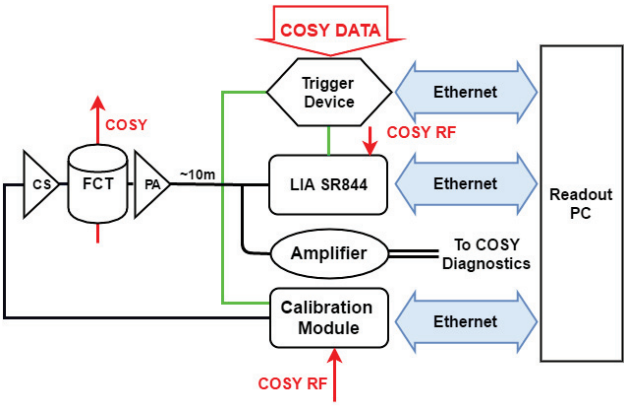

Figure 3: The Fast Current Transformer readout scheme at COSY. The pre-amplifier (PA) and the current source (CA) are connected to the FCT installed at COSY, while all the other systems are installed outside of the tunnel. The trigger and calibration modules as well as the Lock-In Amplifier are readout via Ethernet using a common DAQ which runs on a readout PC.

wire is monitored using a receiver device on the other side of the test stand using a readout scheme identical to that of the FCT. In the laboratory, the trigger module, controlled over the network, generates all the necessary hardware trigger signals for our readout system.

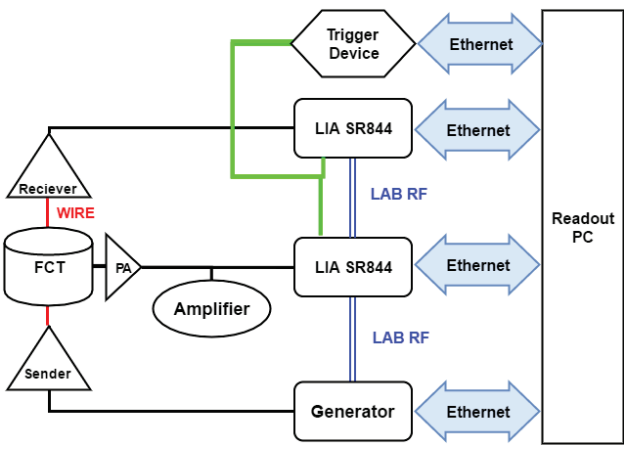

Figure 4: The Fast Current Transformer readout scheme in the laboratory. Similar to the readout scheme presented in Fig. 3 all the devices controlled by a common DAQ discussed in a next section but instead of COSY beam, an electrical signal in a conductive wire is generated by an arbitrary wave form generator.

DATA ACQUISITION SYSTEM

The data acquisition system was developed to perform series of measurements initiated either by a trigger device or a software process (see Fig. 5). Most of the code is written in C++11 under the Linux operations system. The system is oriented on the usage of commercially available devices with TCP/IP or RS-232 serial interfaces with LAN-Serial

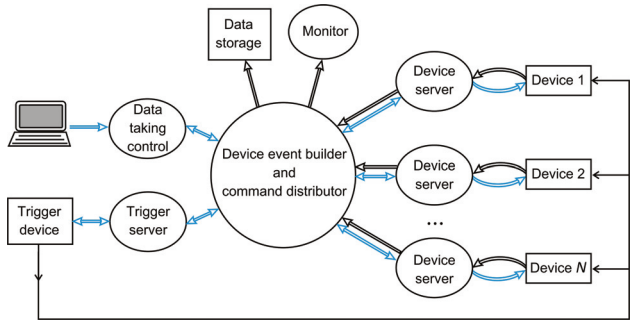

Figure 5: Layout of the DAQ prepared for the high resolution beam current measurement system. All the physical devices (rectangles), including custom build trigger model, are communicating with software (ovals) running on a readout and control PCs over the 1Gb Ethernet. All the readout devices get hardware trigger signals from the trigger device via dedicated coaxial lines.

adapters. It allows one to make the software more uniform and escape the limitations on length of the serial bus.

An interactive `dt_commander` control process gets ASCII text commands on standard input and sends them to an event builder and command distributor (`dev_evb` process) as XDR strings. One can write a simple process which writes commands required to perform long series of measurement to standard output. For example, initialize devices, start measurements, sleep for a measurement time, pause data taking, change parameters, resume data taking, and so on. The output of this process is piped to `dt_commander` to provide exactly the same execution as for interactive input.

A dedicated trigger device obtains input TTL signals from an external source (accelerator synchronization module or multichannel generator), handles them by FPGA and provides output hardware signals: BOS (begin of series), BOM (begin of measurement), EOM (end of measurement) and EOS (end of series). The device (as well as software trigger simulator) can also send corresponding XDR strings to LAN and obtain commands on the same socket. The use of hardware signals allows one to provide better synchronization between devices than using string commands distributed by TCP/IP.

A trigger server process (`trg_server`) controls the trigger device and provides communication with an event builder and command distributor. It allows to get data-taking control commands and correspondingly changes the state of the trigger device. The event builder and command distributor (`dev_evb`) process sends trigger and data taking commands to device servers, obtains data from them and build an event corresponding to one measurement (in BOM – EOM time interval), writes (if requested) a data file and sends data to TCP/IP socket for on-line monitoring or including them in a data stream of a global DAQ.

Device server code (`dev_server`) is an interface process between the `dev_evb` process and the hardware device. It translates input commands into series of device specific commands for execution, loads them in the device and re-

ISBN 978-3-95450-177-9

ceives answers. The main function of `dev_server` does not depend on the device type. The device specifics are implemented in a child class which inherits from the base interface class providing abstract methods to execute common data-taking and trigger commands, and read out data. Hence, no changes to `trg_server` are needed to add a new device into the readout. All used devices allowed one to perform measurements in parallel with data read- out, and make a few measurements per one trigger signal. This allows one not to overload the host computer by device services.

In the laboratory, all processes are running on the Intel(R) Core(TM) i3-3220 CPU@3.30GHz computer with 4 cores under the disk-less Debian Wheezy operation system. As an option, each `dev_server` may be used directly as part of a global DAQ, but a dead time larger than BOM – EOM time interval makes simultaneous work with fast systems like VME or CAMAC problematic. The output data provided by `dev_evb` could be included in a common data stream asynchronously with dead time depending on data transfer time only.

For the analysis and presentation of the experimental data, stored with new DAQ, a simple analysis software has been written using the ROOT package from CERN.

RESULTS

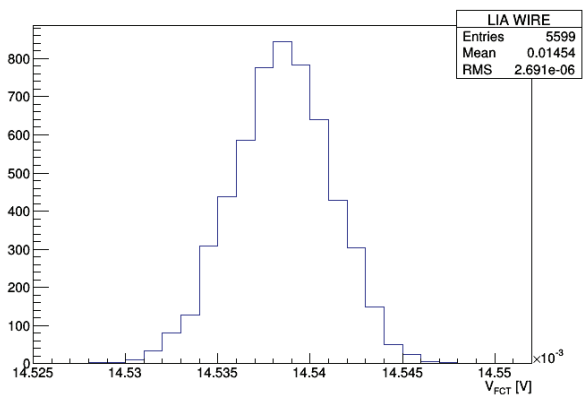

Figure 6: Current in the wire measured using the FCT in the laboratory. An electrical current which simulates 1 mA beam current of COSY has been measured by an FCT in the test stand using the measurement scheme presented in Fig. 4. The voltage signal generated by FCT was measured for 1.5 h using a LIA.

The relative resolution of 1.9×10^{-4} for the bunched beam current of 1 mA has been obtained in the laboratory (see Fig. 6). Parameters of the LIA used in the readout allows an order of magnitude better resolution but our measurements in the laboratory are limited by external factors like general system stability and temperature variations (2×10^{-3} per grad. Celsius), which need further understanding.

CONCLUSION

A system for the high resolution beam current measurement, based on the Fast Current Transformer from the Bergoz Instrumentation, has been built and installed at COSY and in the laboratory. The FCT sensitivity to the COSY bunched beam current across almost five orders of magnitude has been demonstrated. The relative resolution of 1.9×10^{-4} has been reached in the laboratory for the current of 1 mA in a conductive wire. To improve system resolution and better understand possible systematic effects of the FCT on a TRIC result further tests in the laboratory and at COSY are planned.

REFERENCES

[1] Yu. Valdau, B. Lorentz, and D. Eversheim, COSY Proposal #215.

[2] P. Fock, "Lecture Notes on Beam Instrumentation and Diagnostics", Joint University Accelerator School, January – March 2011.

[3] M. K. Covo, Rev. of Sci. Instr. 85 (2014) 125106; C. Courtois *et al.*, *Nucl. Instrum. Meth.*, A 768 (2014) 112.

[4] Bergoz Instrumentation, Fast Current Transformer, User's Manual, Rev. 3.1, (2015), devices 3272 and 3273 FCT-CF10"-147.6-40-UHV-5.0-CAW.

[5] L. Eltcov, Magister Thesis (in Russian), "Design and implementation of the bunched beam current measurement system for COSY", Peter the Great SPbSTU, Russia, 2016.

[6] S. Kirfel, Master Thesis, "Design and implementation of a test station for beam current measurement devices", FH Aachen, Germany, 2014.

[7] Agilent Technologies, User manual, "Agilent 33500 Series Waveform Generator", USA, 2012.

[8] Stanford Research Systems, User's Manual, "Model SR844 RF Lock-In Amplifier", revision 2.7, USA, 2007.

ISBN 978-3-95450-177-9

DESIGN OF A VERY COMPACT 130 MeV MØLLER POLARIMETER FOR THE S-DALINAC*

T. Bahlo†, J. Enders, T. Kürzeder, N. Pietralla, J. Wissmann
Institut für Kernphysik, TU Darmstadt, Darmstadt, Germany

Abstract

At the **S**uperconducting **Da**rmstadt **Lin**ear **Ac**celerator S-DALINAC [1] it is possible to accelerate electron beams to a maximum energy of up to 130 MeV with a beam current of up to 20 μA. In the **S**-DALINAC **P**olarized **In**jector SPIN [2] polarized electrons with a polarization of up to 86% can be produced. The polarization can be measured with two already mounted Mott polarimeters in the injector beam line, where the electrons can have energies of up to 10 MeV. To allow a polarization measurement behind the main accelerator a Møller polarimeter suitable for energies between 50 MeV and 130 MeV is currently being developed. The rather low and variable beam energies and the resulting big and also variable scattering angle distribution combined with very strict spatial boundary conditions at the designated mounting area necessitate a very compact set-up for the polarimeter.

S-DALINAC

The S-DALINAC is a recirculating linear electron accelerator capable of producing cw electron beams with a maximum energy of 130 MeV and beam currents of up to 20 μA. Its floor plan is shown in Fig. 1. In order to provide electrons with polarizations of over 80%, inside the spin-polarized injector a special GaAs cathodes is illuminated with a laser beam to produce polarized electrons via the photo effect. These electrons are preaccelerated to an energy of 100 keV by a static electric field. To manipulate the spatial spin orientation, the electrons pass a wien filter and solenoid allowing the operator to align the spin orientation to the preferences of the experiment or polarimetry setups. In front of the s.c. injector beam line there is a low energy Mott-Polarimeter usable with electron energies between 100 keV and 250 keV for an incident measurement of the absolute polarization. Additionally there is a Mott-Polarimeter optimized for energies up to 10 MeV behind the s.c. injector and a mountable Compton-Transmission-Polarimeter at the first experimental area. After passing the s.c. main accelerator, it is at this time not possible to measure the polarization until now. Therefore a Møller-Polarimeter for electron energies between 50 MeV and 130 MeV is currently being developed and will be installed at the marked position shown in Fig. 1.

MØLLER POLARIMETRY

For electron energies of more than 10 MeV Mott polarimetry is not applicable any more. To measure the polarization Møller polarimeters are commonly used for high energy electron beams. Although the Møller scattering crossection is not directly dependent of the participants' spin, one can exploit Pauli's principle that suppresses scattering events with the same orientation of the two involved electrons' spins. It can be shown that this suppression is maximal for a center-of-momentum frame scattering angle of 90° resulting in a maximal analyzing power of the polarimeter if this angle is used. Of course the laboratory frame scattering angle strongly depends on the incident energy of the electrons, what has to be taken into account when positioning the detectors. In Møller Polarimeters the electron beam of unknown absolute polarization scatter on a longitudinally polarized ferromagnetic target. In a first measurement the target material is polarized parallel to the beams polarization and the detected events produced by symmetrical scattered electrons is accumulated. In a second measurement either the target polarization, or the beam polarization is flipped to produce antiparallel spin orientations. The amount of detected events is expected to increase since no Pauli suppression is expected to occur. By comparing the amount of events of both measurements, it is possible to calculate the beams polarization. Generally one finds two different types of Møller polarimeters: One-arm polarimeters only detect and count one of the two scattered electrons making it necessary to strongly collimate the scattered beam. Background radiation represents a big problem for this type of polarimeter making it necessary to shield the detectors very well. Two-armed polarimeters on the other hand detect and count both scattered electrons coincidentally, strongly reducing the random background from the primary beam and activated material in close distance. This allows greater angle acceptances and therefore higher counting rates. The Møller Polarimeter that is currently being designed for the S-DALINAC will be such a two-armed type using coincidence counters.

POLARIMETER FLOORPLAN

As depicted in Fig. 2 the Møller Polarimeter will be placed right next to the high energy scraper system of the S-DALINAC leaving an area of about two by three meters for scattering, beam separation, detection and dumping. It is not possible to separate the Møller electrons horizontally due to the scraper system blocking the left hand side of the polarimeter. Therefore the Møller electrons have to be separated vertically and additionally be steered further to the right. Since both, target chamber and beam dump, produce a lot of background radiation the detectors have to be positioned carefully to minimize underground events.

* Work supported by the DFG under grant No. SFB 634
† tbahlo@ikp.tu-darmstadt.de

ISBN 978-3-95450-177-9

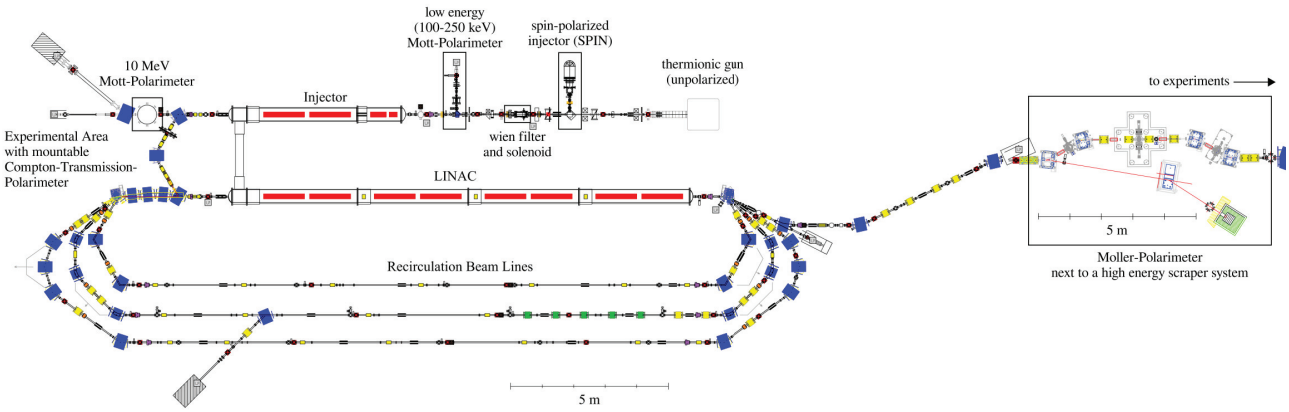

Figure 1: floorplan of the S-DALINAC with highlighted polarimetry setups.

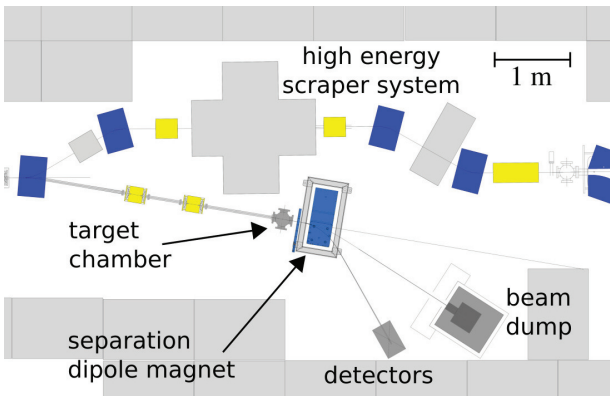

Figure 2: floorplan of the Moeller Polarimeter.

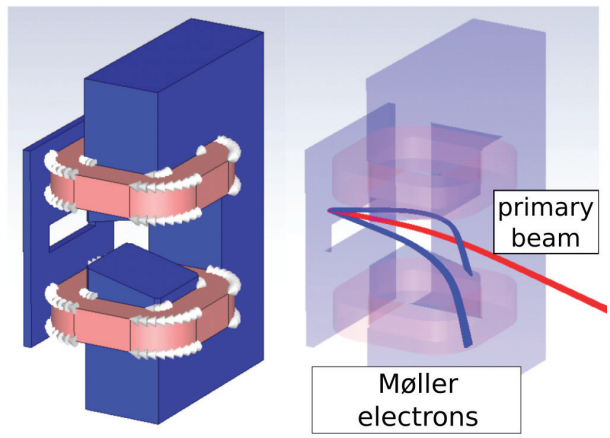

Figure 3:
left: yoke of the separation dipole magnet with its mirror plates (blue) and excitation coils (light red).
right: trajectories of a 50 MeV primary beam and Møller scattered electrons for a COM scattering angle of (90 ± 5) degree.

BEAM SEPARATION

Due to strict geometrical boundary conditions the separation of the Møller scattered electrons from the primary beam and the focusing of the scattered electrons have to be accomplished within two meters of the beamline. Additionally the low incident energy and therefore big scattering angles and the big energy acceptance this polarimeter has to provide necessitates a combined function separation dipole magnet with a wide gap as shown in Fig. 3. The divergence angle of the gap is 13°, allowing the deflection and focusing of all relevant Møller scattered electrons within the energy range of 50 MeV (6° to 10°) to 130 MeV (4° to 6°). By adjusting the transverse entrance position of the incident beam it was possible to reduce the vertical divergence angle of the scattered electrons to nearly zero creating two nearly horizontal Møller electron beams. This allows an arbitrary placement of the detectors in longitudinal direction without introducing additional geometric challenges.

TARGET CHAMBER

To exploit Møller scattering to measure the polarization of the electron beam the target polarization has to be well known. Furthermore this polarizable target has to be sufficiently thin to avoid multi-scattering. Therefore one has the options to use a ferromagnetic foil that is polarized perpendicular to the foils face or one that is polarized in-plane. Since the perpendicular polarization would require a magnetic excitation that could only be provided by s.c. coils, in this setup the in-plane polarization is preferred. To be able to still hit a target that is aligned to the beam direction, a target angle of 20° has to be introduced. In order to avoid systematical errors caused by the target tilt, the target frame provides two target foils with a 20° and a −20° tilt angle. Additionally the target frame provides a BeO-target that can be observed by a camera to adjust the beam position. The Møller target material is a soft-magnetic alloy called *Vacoflux50* which consists of 50% Iron and 50% Cobalt and saturates at a magnetic excitation of approximately 40 A/cm. Outside the target chamber a pair of Helmholtz coils provides excitation parallel to the incident beam direction. The target frame and the corresponding vacuum chambers are shown in Fig. 4 (side view) and Fig. 5 (top view).

ISBN 978-3-95450-177-9

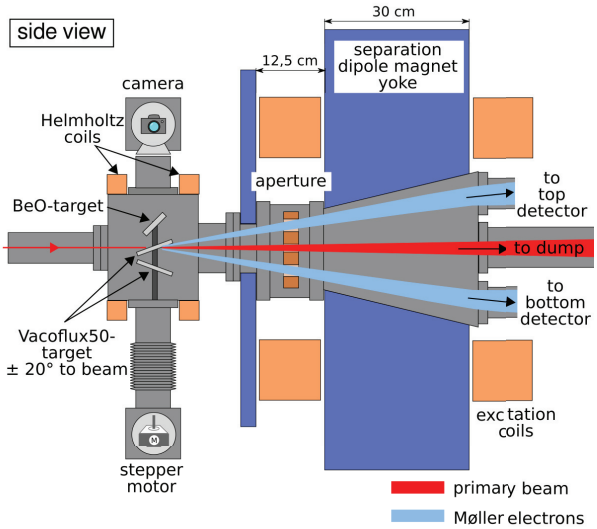

Figure 4: side view of the Møller target chamber and the yoke chamber demonstrating the beam separation.

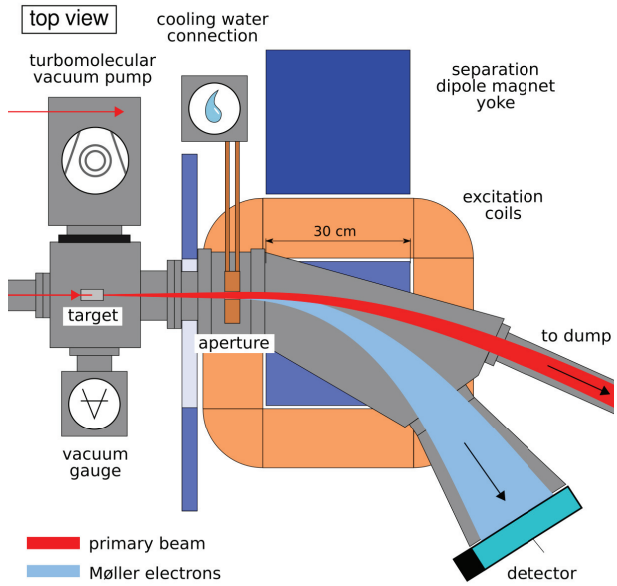

Figure 5: top view of the Møller target chamber and the yoke chamber demonstrating the beam separation.

Aperture

In order to reduce background events generated by scattered electrons hitting the inner walls of the yoke chamber due to their random energies the installation of a special aperture as shown in Fig. 4 and Fig. 5 is currently being studied. The aperture consist of a copper block with a hole for the primary electrons that still have approximately their incident energy and are dumped in the Faraday cup behind the separation dipole as shown in Fig. 2. Two additional slits on the top and bottom of the aperture filter the symmetrical scattered Møller electrons in the vertical direction within a precisely defined acceptance in respect to the scattering angle and the azimuthal angle. This aperture geometry of course has to be adjusted to the particular beam energy being used for the experiment due to the corresponding Møller scattering angle. At this time it is still unclear if the introduction of a aperture increases the analyzing power of the polarimeter by increasing the counting rate asymmetry, due to reduced background or if the background from the surrounding will make it neccessary to maximize the absolute counting rate by removing the aperture and therefore maximizing the angle acceptance of the polarimeter. Detailed simulations are currently being evaluated.

DETECTOR

With this polarimeter setup the dispersion of the separation dipole filters all incoming scattered electrons with respect to their energy. Therefore the used detector does not need to provide information about the detected energy rendering its task to be a pure counter. Furthermore it should be fast to measure with high counting rates to accumulate good statistics in a shorter period of time. Furthermore only electrons should be detected, since only the scattered electrons provide information about the polarization. All these criteria lead to a detector system consisting of a cherenkov counter which is both fast and insensitive to gamma radiation. In this setup, several stripes of quartz glass are used in combination with photo diodes. The top and bottom detector count coincidentally detected electrons and accumulate the absolute amount of detected electrons.

CONCLUSION AND OUTLOOK

To introduce a possibility to measure the electron beam polarization after the passage of the main accelerator of the S-DALINAC a new Møller polarimeter has been designed. The targets consists of two Vacoflux50 foil targets tilted by ±20° and are polarized in-plane by a pair of Helmholtz coils. This two-arm polarimeter setup separates the Møller scattered electrons vertically and counts them using several cherenkov detectors in a coincidence circuit. The benefits of a specialized collimator is still being investigated. A complete three dimensional model of the polarimeter has already been created using CAD software and is currently being used for detailed particle tracking simulations.

REFERENCES

[1] A. Richter, EPAC '96, Sitges (1996) 110.

[2] J. Enders, AIP Conf. Proc. 1563, 223 (2013).

ISBN 978-3-95450-177-9

THE NEXT GENERATION OF CRYOGENIC CURRENT COMPARATORS FOR BEAM MONITORING*

V. Tympel†, J. Golm[1], R. Neubert, P. Seidel, Institute for Solid State Physics, Jena, Germany
M. Schmelz, R. Stolz, The Leibniz Institute of Photonic Technology IPHT, Jena, Germany
V. Zakosarenko, Supracon AG, Jena, Germany
F. Kurian, M. Schwickert, T. Sieber, T. Stöhlker[1,2], GSI Helmholtz Center for Heavy Ion Research, Darmstadt, Germany
[1]also at Helmholtz Institute, Jena, Germany
[2]also at Institute for Optics and Quantum Electronics, Jena, Germany

Abstract

A new ***C**ryogenic **C**urrent **C**omparator* with *e**X**tended **D**imensions (CCC-XD)*, compared to earlier versions built for GSI, is currently under development for a non-destructive, highly-sensitive monitoring of nA-intensities of beams for larger beamline diameters planned for the new FAIR accelerator facility at GSI. The CCC consists of a:

1) flux concentrator,
2) superconducting shield against external magnetic field and a
3) superconducting toroidal coil of niobium which is read out by a
4) Superconducting Quantum Interference Device (SQUID).

The new flux concentrator (1) comprises a specially designed highly-permeable core made of nano-crystalline material, in order to assure low-noise operation with high system bandwidth of up to 200 kHz. The superconducting shielding of niobium (2) is extended in its geometric dimensions compared to the predecessor CCC and thus will suppress (better -200 dB) disturbing magnetic fields of the beamline environment more effectively. For the *CCD-XD* readout, new SQUID sensors (4) with sub-µm Josephson junctions are used which enable the lowest possible noise-limited current resolution in combination with a good suppression of external disturbances.

The *CCC-XD* system, together with a new dedicated cryostat, will be ready for testing in the CRYRING at GSI in spring 2017. For the application of a CCC in the antiproton storage ring at CERN a pulse shape correction has been developed and tested in parallel. Results from electrical measurements of two components (1 and 4) of the new *CCC-XD* setup will be presented in this work.

INTRODUCTION

Cryogenic Current Comparator (CCC) is a non-destructive, highly-sensitive charged particle beam measurement system using the magnetic field of the moving charged particles, well described in [1, 2]. Figure 1 shows the general principle with the main parts flux concentrator and flux compensator. Using superconducting components for the coils, the transformer and the Superconducting Quantum Interference Device (SQUID) for the magnetic field measurement it is possible to measure DC currents. That means that it is possible to measure a constant particle flow too. CCCs are in use at GSI [3] and CERN [4]. Figure 2 shows the schematic of a CCC system with the main components: flux concentrator, shielding, pick-up coil and matching transformer, SQUID and cooling.

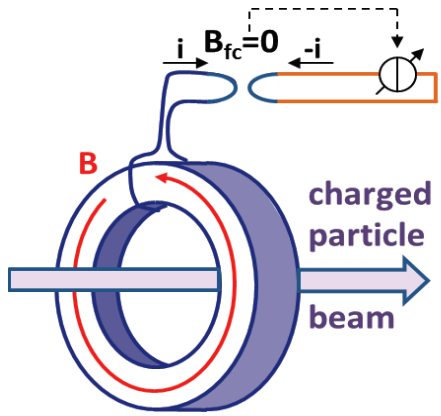

Figure 1: The general principle of a CCC with a flux concentrator and a closed loop current measurement system with compensation current as measurement value.

New Challenges

The CCC application at FAIR leads to two basic challenges: a bakeable ultra high vacuum (UHV) beam tube and a larger beam tube diameter of 150 mm. The required new cryostat is described in [5]. The larger diameter also leads to an extended core diameter of the flux concentrator. Therefore, the new CCC with *eXtended Dimensions* is called *CCC-XD*.

Other challenges of the *CCC-XD* are the desired higher system bandwidth of up to 200 kHz, a higher sensitivity und a better noise immunity. The flux concentrator with its soft magnetic core and the SQUID as magnetic field sensor are the important components to improve the performance of the *CCC-DX* system in this area. Investigation in the field of soft magnetic core materials and the development of a new SQUID design, as described in this work, will ensure the achievement of the forecast targets.

* Work supported by BMBF, project number 05P15SJRBA
† volker.tympel@uni-jena.de

ISBN 978-3-95450-177-9

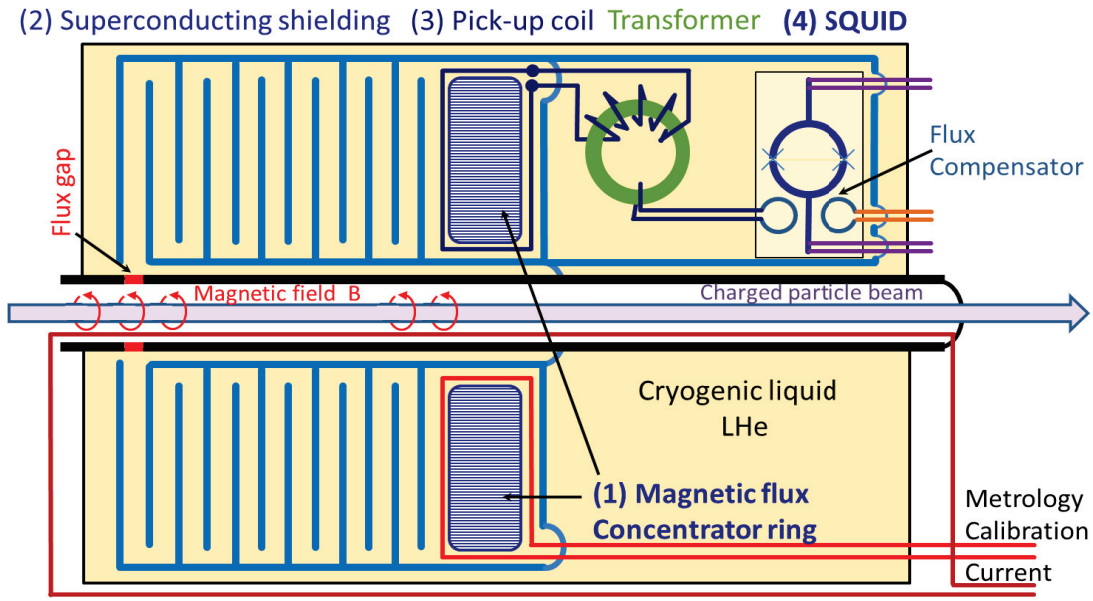

Figure 2: Schematic of a CCC with the main components.

ADVANCED FLUX CONCENTRATOR

The larger beamline diameter of the new FAIR accelerator facility leads to an inner diameter of 274 mm for the flux concentrator (see Fig. 3). A special three-piece core package was composed by wrapped ribbons of nanocrystalline Soft Magnetics (see Fig. 4). The ribbon thickness itself is very small – only about 15 µm. The material is produced by a specific thermo-magnetic, gas and heat treatment process of amorphous Fe-alloy (NANOPERM® $Fe_{73.5}$ Cu_1 Nb_3 $Si_{15.5}$ B_7) ribbons which defines the magnetic parameters and the temperature dependencies [6, 7]. More than 1000 layers are necessary to create a single core for the *CCC-DC* flux concentrator.

For the core package characterisation a high precision LS-RS-measurement setup based on an Agilent E4980A LCR-meter, LabVIEW and C++ programs and a wide-neck cryostat was developed.

Figure 3: Real core package GSI328plus with an outer diameter of 330 mm and a depth of 100 mm.

Two scroll pumps SCROLLVAC SC 15 D allow the extension of the temperature range from room temperature down to below 2 K. Due to thermo-magnetic annealing process a variation of the electrical parameter is possible. The accurately investigations of nanocrystalline Soft Magnetics at low temperatures with smaller cores began in Jena at 2010 [8]. The aim is to create a core material with a high permeability to get a high inductance as well as low magnetic losses to get a low core noise, accompanying with a large bandwidth and at a low temperature. The measured electrical parameters are the series inductance L_s and the series resistance R_s. The materials now can be described by a complex permeability $\mu = \mu' - i{\cdot}\mu''$. The real μ' is proportional to L_s and the imaginary part μ'' is proportional to R_s / f with f as the measured frequency. The complex permeability μ is in fact a function $\mu(f, T)$ with the frequency f and the temperature T.

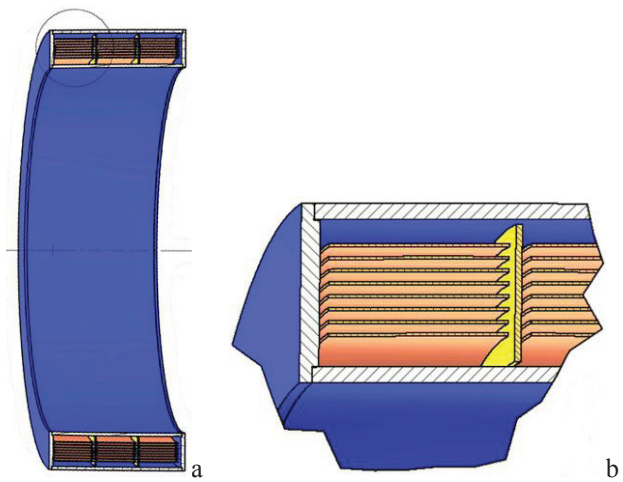

Figures 4: a: Virtual cut through the core package; b: Enlarged cut through a NANOPERM® ribbon core (only schematic: real ribbon thickness ≈ 15 µm).

ISBN 978-3-95450-177-9

The recipe of the thermo-magnetic annealing process is very important for the function $\mu(f, T)$. Figure 5 shows the inductance L_s of a single turn coil (in electrical engineering called A_L-value) as a function of the temperature for different core materials. All cores were created from NANOPERM® with different annealing recipes by the company MAGNETEC. As shown in Fig. 5 it is necessary to measure $\mu(f, T)$ for each ordered core batch, but there is also a variation in the same core batch as shown in Fig. 6.

Figure 7 (real part μ') and Fig. 8 (imaginary part μ'') show the final measurement results of a GSI328plus core package at 4.2 K. We can see the excellent performance of the measurement system with low 3-sigma errors. The selected GSI328plus No. 1 has at 4.2 K a high and nearly constant μ'-value up to 20 kHz. We can achieve 20 % of the maximum inductance at 200 kHz and still 10 % at 500 kHz. The maximum imaginary part μ'' is in the frequency area of 65 kHz, helpful to get low magnetic losses and low noise.

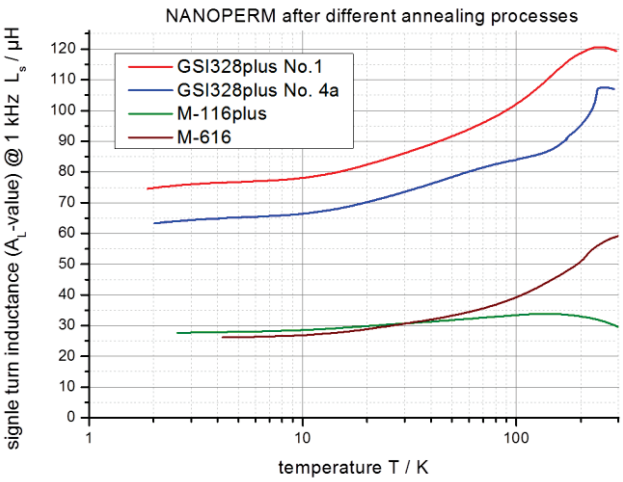

Figure 5: Different recipes of the thermo-magnetic annealing process lead to changed characteristics. GSI328plus No.1 and No. 4a are from different batches.

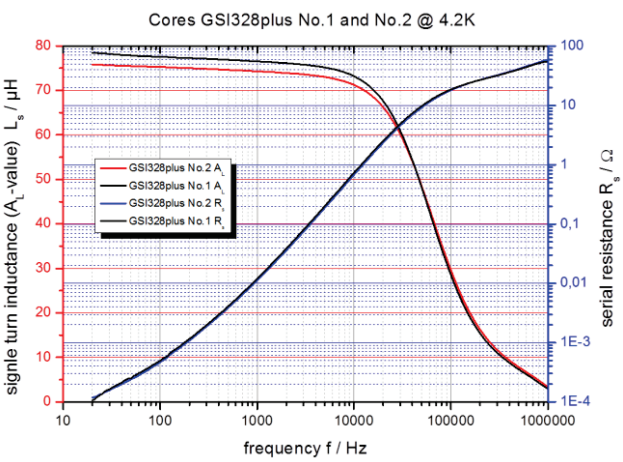

Figure 6: Two core packages of GSI328plus from the same core batch with different A_L-values.

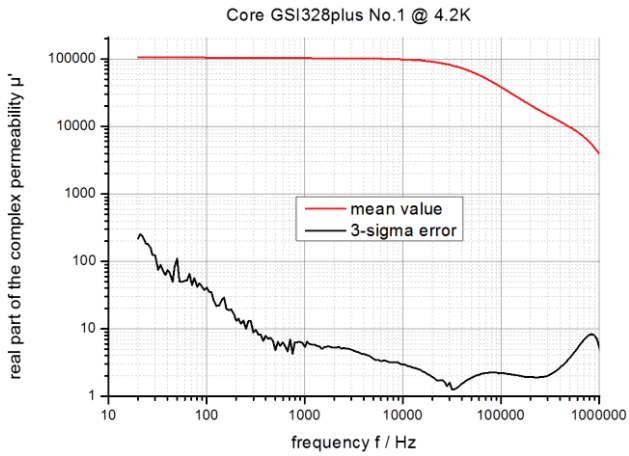

Figure 7: Precision measurement of the real part μ'.

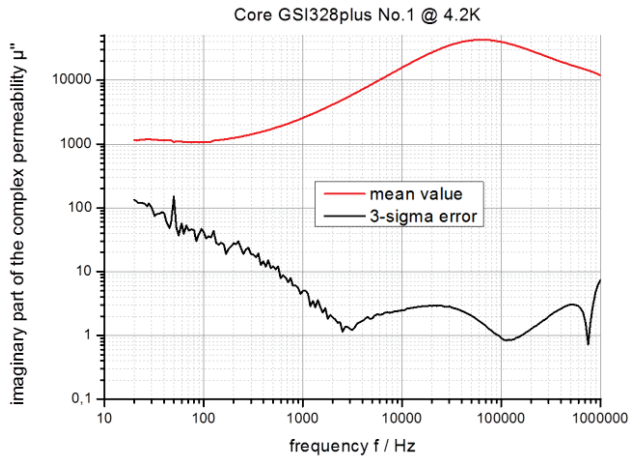

Figure 8: Precision measurement of the imaginary μ''.

THE NEW SUB-µM SQUID

The SQUID performance is essential for the whole system. Calculations strongly suggest that smaller Josephson junctions could lead to a better SQUID performance.

Estimations

Figure 9 shows the electrical schema with the input current I_A, matching transformer L_A / L_T, coupler coil L_K, SQUID inductance L_{SQ} and the change of SQUID flux $\Delta\Phi_{SQ}$. Equation (1) is used to calculate the relation between $\Delta\Phi_{SQ}$ and I_A as a function of the inductances including an additional parasitic inductance L_{par}:

$$\frac{\Delta\Phi_{SQ}}{I_A} = \frac{\sqrt{L_A \cdot L_T \cdot L_K \cdot L_{SQ}}}{L_T \cdot L_K \cdot L_{par}} \quad (1)$$

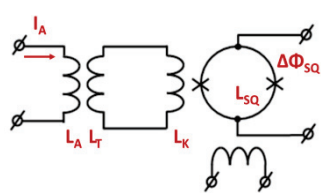

Figure 9: Electrical schematic of the CCC.

ISBN 978-3-95450-177-9

Table 1 shows a comparison between standard and sub-µm SQUIDs with its parameters and calculations by $L_A \approx 100$ µH. The calculation leads to a five times better noise performance for the sub-µm SQUID. Figure 10 is a SEM image of a first realisation of the new design.

Table 1: SQUID Specifications

SQUID	Standard CSBlue	Sub-µm CE1K
L_{SQ} [nH]	0.30	0.18
L_K [µH]	0.32	2.7
$\Delta\Phi_{SQ}/I_A$ [µA/Φ_0]	0.21	0.10
Φ_n [µΦ_0/√Hz]	≈ 5	≈ 2
Noise performance [pA/√Hz]	1.0	0.2

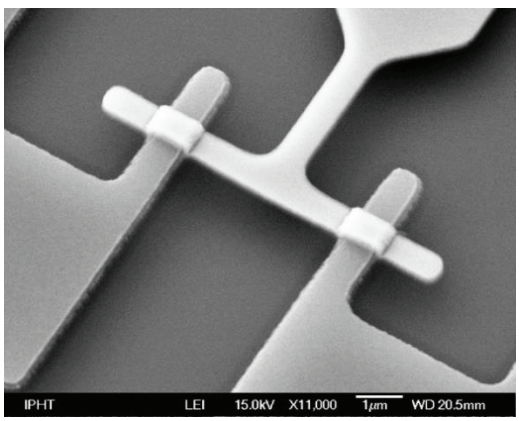

Figure 10: SEM image of sub-µm sized Josephson junctions of the new IPHT CE1K SQUID with critical dimensions below one micron.

Noise Measurement

First noise measurements without flux concentrator are shown in Fig. 11. The white flux noise between 100 Hz and 20 kHz is 1.3 µΦ_0/√Hz with a ratio $\Delta\Phi_{SQ}/I_A$ of 0.12 µA/Φ_0 the noise performance is 0.16 pA/√Hz.

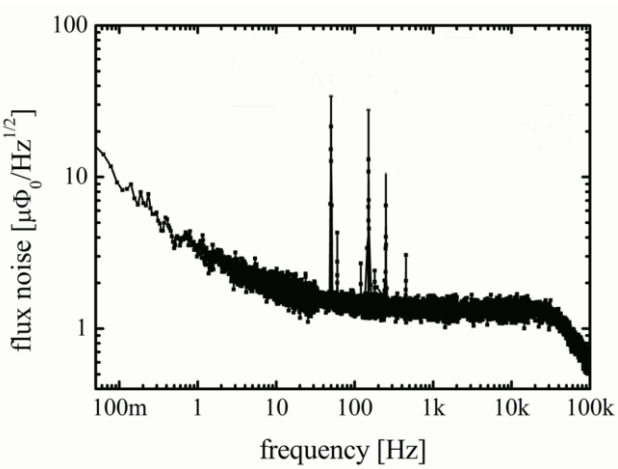

Figure 11: Measurement of the CE1K flux noise with a noise performance of 0.16 pA/√Hz.

CONCLUSION

The CCCs in operation already have demonstrated their potential at beam lines at GSI and CERN. The newly developed core materials will allow higher signal frequencies and lower noise. The use of new sub-µm-SQUID will enable a decreased noise and higher system bandwidth. Within the current research project the magnetic and acoustic disturbing signals shall be reduced to improve the CCC operations in critical environment. Alternative shielding constructions and their magnetic field suppression will be evaluated. In the meantime the *CCC-XD* for CRYRING is still under construction, the related cryostat - considering AD CCC measuring results - is in preparation.

ACKNOWLEDGEMENT

This project is supported by the BMBF, project number 05P15SJRBA.

REFERENCES

[1] W. Vodel et al., "SQUID-Based Cryogenic Current Comperators", in *Applied Superconductivity, Handbook on Devices and Applications, Volume 2*, P. Seidel, Ed. Weinheim, Germany: Wiley-VCH, 2015, pp 1096-1110.

[2] F. Kurian, "Cryogenic Current Comparators for precise Ion Beam Current Measurements", Ph.D. thesis, Phys. Dept., University of Frankfurt, Germany, 2015.

[3] M. Schwickert et al.," Beam Current Monitors for FAIR", in *Proc. 5th Int. Particle Accelerator Conf. (IPAC'14),* Dresden, Germany, June 2014, paper THPME103, pp. 3483-3485.

[4] M. Fernandes et al., "A Cryogenic Current Comparator for the Low Energy Antiproton Facilities at CERN", in *Proc. Int. Beam Instrumentation Conf. (IBIC'15)*, Melbourne, Australia, Sep. 2015, paper MOPB043, pp. 143-147.

[5] T. Sieber et al., "An Optimization Studies for an advanced Cryogenic Current Comparator (CCC) system for FAIR interesting talk", presented at IBIC'16, Barcelona, Spain, Sep. 2016, paper WEPG40, this conference.

[6] *Magnetec*, "Softmagnetic High-Tech material NANOPERM"; http: //www.magnetec.de/fileadmin/pdf/pb_np.pdf

[7] G. Herzer, "Modern soft magnets: Amorphous and nanocrystalline materials", *Acta Materialia*, vol. 61(3), pp. 718-734, Feb. 2013.

[8] R. Geithner, "Untersuchung der Tieftemperatureigenschaften magnetischer Materialien für den Einsatz im Kryostromkomparator ", Ph.D. thesis, Phys. Dept., University of Jena, Germany, 2013.

ISBN 978-3-95450-177-9

DIAGNOSES AND CONTROLS OF SINGLE e-PULSE EXTRACTION AT THE LCLS-I FOR THE ESTB PROGRAM*

J.C. Sheppard †, T. Beukers, W.S. Colocho, F.J. Decker, A.A. Lutman, B.D. McKee, T.J. Smith, M.K. Sullivan, SLAC National Accelerator Laboratory, Menlo Park, CA

Abstract

A pulsed magnet is used to kick single electron bunches into the SLAC A-line from the 120 Hz LCLS-1 bunch train. These single bunches are transported to the End Station Test Beam facility. It is mandated that extraction from the LCLS beam does not disturb the non-kicked pulses. An 8.7 mrad kick is required to extract a bunch; without compensation the following bunch experiences a 3 μm kick; with compensation this kick is reduced to less than 0.1 μm which is well within the jitter level of about 0.2 μm. Electron and photon diagnostics were used to identify problems arising from eddy currents, beam feedback errors, and inadequate monitoring and control protocol. This paper discusses the efforts to diagnose, remedy, and control the pulse snatching.

INTRODUCTION

A set of pulsed magnets are used to horizontally extract single electron bunches at 5 Hz into the SLAC A-line from the 120 Hz LCLS-1 [1] bunch train. These single bunches are transported to the End Station Test Beam facility as either primary beam or secondaries created in a Cu target [2]. An 8.7 mrad kick is required to extract primary beam. Anomalous magnetic fields produced by eddy currents deflect subsequent LCLS-1 pulses. Without compensation, the first bunch following extraction (so-called n+1) experiences a 3 μm normalized kick. This disturbance is exacerbated by improper set up of the undulator launch feedback system which in turn drives the full bunch train away from the nominal kicker off trajectory. With proper setup of the feedbacks the disturbance is limited to the first (n+1) and second (n+2) bunches after extraction. An air core, pulsed post kicker is used to compensate the unwanted deflections. With compensation, the 3 μm normalized kick is reduced to less than 0.1 μm which is well within the undulator launch jitter level of about 0.2 μm.

This paper discusses the actions taken to eliminate the disturbance to the non-extracted LCLS-1 bunches.

PULSED KICKERS

A set of three pulsed magnets are to kick single LCLS-1 bunches into the SLAC A-Line. The first set of magnets are run with a single pulsed current supply [3] and the third pulsed magnet is powered by a second power supply (a fourth pulsed magnet is being prepared for installation in spring of 2017 and will be powered in series with the existing third magnet). At maximum current, the three magnets are sufficient for extraction of beams with energies up to 16.5 GeV. The pulser also generates a controllable reverse current pulse 1 ms after the primary pulse. This back swing pulse is used in the cancellation of eddy currents.

Each magnet consists of a pair of 1-m long, air core coils. Initially the coils were supported in an aluminum frame and mounted on an Al baseplate. The baseplate was supported in the accelerator housing on a steel girder. After the problems of the eddy currents were identified, 80/20 T-slot™ Al frame members [4] and Al baseplate were replaced with G10 pieces to break up eddy current flow paths and to remove the baseplate "mirror." The effect was to reduce the eddy current fields that affected subsequent bunches by a factor of about 10 from about 10 μm to about 1 μm. Figures 1 a,b,c show the pulsed current waveform; the original magnet with Al frame and baseplate; and the G10 modified magnet.

Figure 1a: Pulse kicker current waveform.

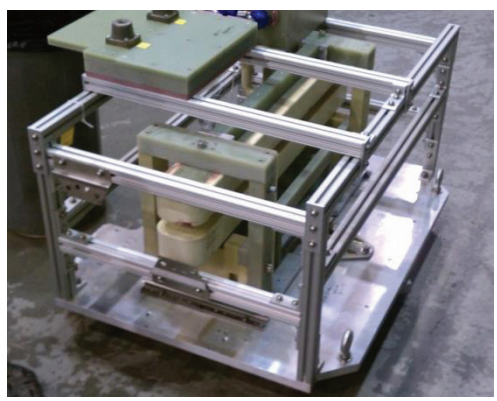

Figure 1b: Original Al frame and baseplate kicker magnet.

* Work supported by DoE Contract DE-AC02-76SF00515, 10/01/2012-09/30/2017

† email address: jcs@slac.stanford,edu

ISBN 978-3-95450-177-9

Figure 1c: G10 modified kicker magnet.

BEAM POSITION MONITOR DIAGNOSTICS AND FEEDBACK ISSUES

33 RF cavity beam position monitors (bpms) [5] are installed in the undulator. These bpms have a resolution of about ±1 microns rms. Six bpms located near the entrance to the undulator are used measure the launch error with respect to a reference orbit. The square root of normalized Courant-Snyder launch invariant is calculated from bpm trajectories. The LCLS beam has a typical normalized, launch jitter of ~300 nm rms.

The same 6 bpms are used in a different processor to determine the launch error and feedback on the launch using corrector magnets. The feedback system for the launch error consists of four 30-Hz loops running independently of each other but using the same sensors and actuators. A missing pulse results in a bpm reporting a zero offset. The feedbacks incorporate the zero into the data stream and adjust the correctors accordingly. This problem is fixed by telling the feedback to ignore the missing pulses. Similarly extraction of pulse n resulted in a deflection of the n+1 pulse. Due to the offset of the n+1 pulse, in steady state the launch feedbacks generate a negative going response to the n+5 pulse with an amplitude, A, of

$$A = \frac{G}{1-(1-G)^6} \approx \frac{1}{6-15G} \qquad (1)$$

wherein G is the gain of the feedback loop (G=0.05 for the LTU 30Hz transverse loops). The response is proportional to the residual n+1 kick from extraction of the nth pulse, $R=A\Delta_{n+1}$. Because the loops run at 30Hz, every 4th pulse is displaced (n+5, n+9, n+13, n+17, and n+21) [6]. This effect is turned off by masking out the n+1 pulse from the feedback.

POST KICKER

An air core pulsed magnet was designed and installed to compensate to the residual kick at the n+1 pulse. The magnet is an X-Y set of nested PEP-I corrector coils (24 turns, 20.3 cm long, 15.2 cm wide, 12.7 cm separation 2.1e-4 kGm/A) A unipolar power supply is used since the direction of the residual kick does not vary. This scheme was initially installed as a test and found to work well and was subsequently extended to being pulsed on the n+1 and n+2 pulses. Figures 2 a,b show the beam displacement without and with correction. This data was collecting using the Beam Synchronous Acquisition utility [7] with records data from 1149 monitors for up to 2800 sequential beam pulses. The 2800 beam pulses are averaged in 24 bins corresponding to 5 Hz pulse extraction from a beam rate of 120 Hz. Figures 3 a,b show the corrector current waveform and the installed corrector pair.

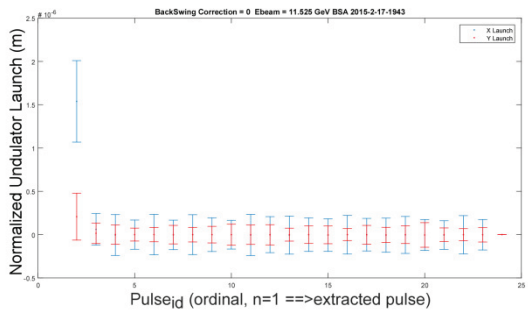

Figure 2a: Normalized undulator launch without post kicker correction.

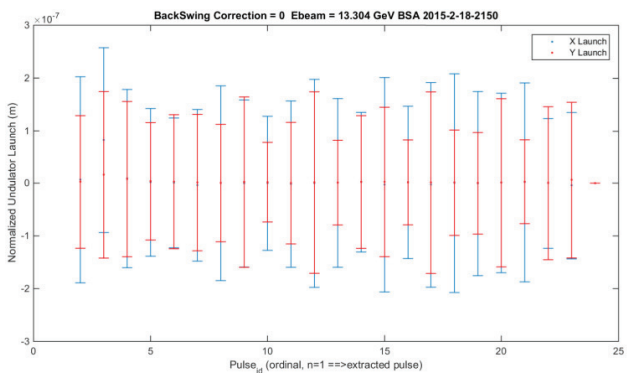

Figure 2b: Normalized undulator launch with post kicker correction.

In figures 2a and 2b, the horizontal axis is the ordinal Pulse$_{id}$ wherein n=1 is the extracted pulse; the vertical axis is the normalized undulator launch.

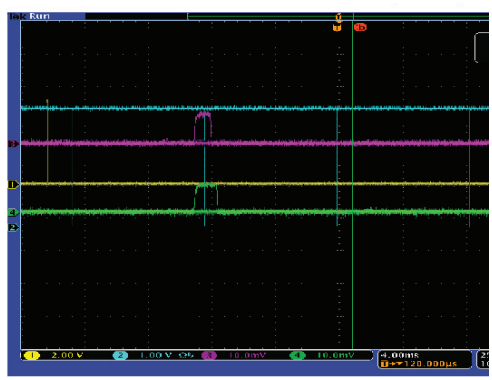

Figure 3a: Post kicker current waveform; note toroid calibration = 100A/V.

ISBN 978-3-95450-177-9

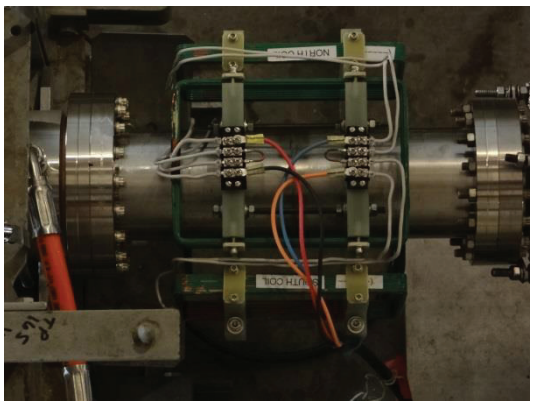

Figure 3b: Post kicker corrector coils installed in the SLAC BSY.

END STATION A (ESA) EXTRACTION CONTROL

An online, live time launch monitor system was developed to ensure that the kicker compensation was properly set up and did not drift off. Called Tuning Diagnostics, this program calculated the launch into the undulator on a pulse-by-pulse basis. To protect against flyers, each new orbit was added with a damping factor to a running average of the previously measured orbit. This averaging effectively reduces the bandwidth of the measured launches. Alarm and abort set points on the measured launch error are used to (1) warn an Operator that the launch error exceeds a warning threshold and (2) shuts off pulse extraction if the launch error exceeds the acceptable tolerance. Shut off requires Operator intervention to manual restart pulse extraction after having diagnosed and remedied the offend cause of the launch error. Figure 4 a,b shows the Control System displays used to set up, monitor, and control A-Line extraction. An extensive Operations procedure has been developed. This procedure is used by the control room staff to set up and maintain beam delivery to ESTB

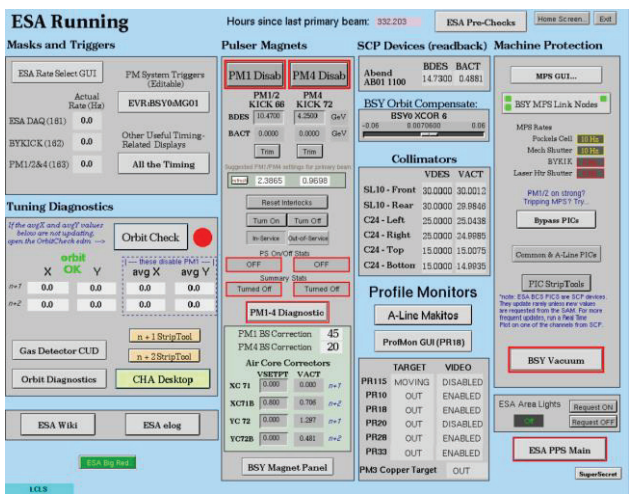

Figure 4a: Control system operator interface for A-Line extraction.

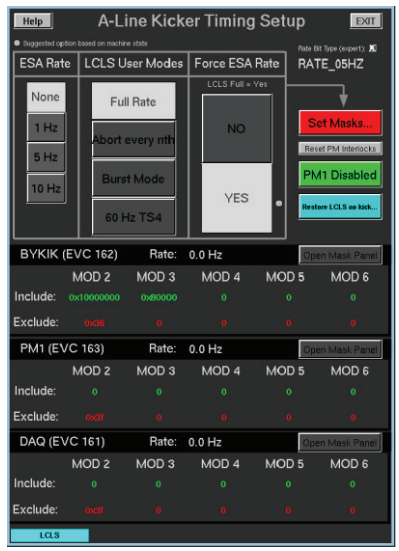

Figure 4b: Time system interface panel.

PHOTON DIAGNOSTICS

Prior to the initial fixes to the kicker magnets, feedback process, and improved operations procedures, the presence of 5 Hz pulse extraction could be seen on the intensity profile of the LCLS xray pulse intensity. This was directly observed on the gas detector displays. After the initial fixes but with still a measurable ~1 μm n+1 orbit disturbance, the gas detectors were essentially blind to the finite albeit small orbit distortions and most users could run compatibly with A-Line extraction. However some users were sensitive to the small pointing errors even though there were no total intensity fluctuations. With the addition of the post kicker systems, there were effectively no orbit distortions. To resume Operations, tests were made in each hutch for each mode of operation to ensure that properly set up pulse extraction did not measurably disturb the quality of the xray beam delivered to the samples. These measurements were made using direct images of the xrays on screens located at the sample positions [8]. The images were acquired at 120 Hz and analyzed. Figures 5a,b,c show the xray spot profiles measured at XCS YAG2 The xray energy was 7.87 keV at a corresponding electron energy of 13.3 GeV. The data has been binned into the 24 event periods. At present, A-Line extraction is compatible with nearly all modes of LCLS-1 operations.

ISBN 978-3-95450-177-9

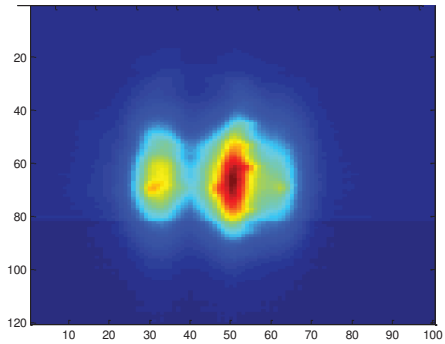

Figure 5a: 7.87 keV xray spot on XCS YAG2.

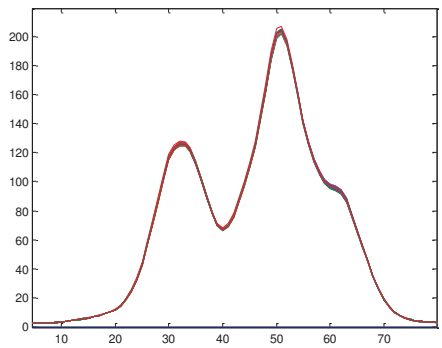

Figure 5b: Horizontal projection of XCS YAG2.

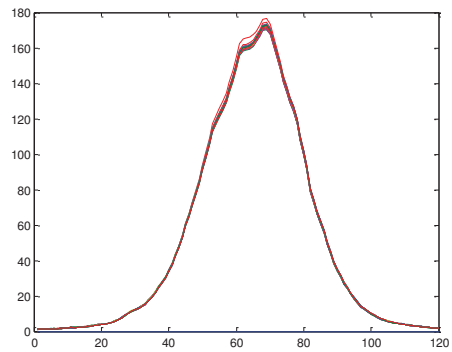

Figure 5c: Vertical projection of XCS YAG2.

The double lobe of the xray spot is a consequence of the imperfections of the surface of the xray imaging mirrors. The effect of perturbing the 120 Hz pulse train is seen in Figures 5a and b as a single trace out of the 23overlayed projection that is slightly different from the others. This perturbation is not observable on the electron diagnostics or on the xray intensity monitors.

SUMMARY

Initial A-Line extraction has found to be disruptive to the quality of xray beams delivered to the LCLS users. The problems arose for eddy current effects, electron feedback errors, a lack of diagnostic methods, and inadequate operations procedures. These issues have been fixed through modifications to the primary kicker magnets, the addition of a low strength post kicker corrector pair, the development of real time electron launch diagnostics, controls to limit errant operation, and the development of operations procedures. A-Line extraction to the ESTB runs concurrent with LCLS-1 users.

ACKNOWLEDGEMENTS

The authors acknowledge the contributions of J.L. Nelson, J.L. Turner, L. Piccoli, K.L Luchini, J.W. Krzaszczak, and J. Koglin to the understanding and fixing of the problems.

REFERENCES

[1] P. Emma *et al.*, "First lasing and operation of an ångstrom-wavelengthfree-electron laser," Nature Photonics 4 (2010) 641.
[2] C. Hast, *et al.*," ESTB: A new beam test facility at SLAC," SLAC_ PUB - 14602, September, 2011.
[3] V.V. Nesterov and A.R. Donaldson," High current high accuracy IGBT pulse generator," http://accelconf.web.cern.ch/AccelConf/p95/ARTICLES/WAA/WAA11.PDF 1996.
[4] 80/20 Inc., www.8020.net
[5] R. Lill, *et al.*, Design and performance of the LCLS cavity BPM system," SLAC_PUB-13067 , June, 2007.
[6] J.C. Sheppard and T.J. Smith, "Feedback and pulse extraction in the LTU," unpublished SLAC memo, January, 2015
[7] P. Krejcik,*et al.* ,"Timing and synchronization at the LCLS," SLAC-PUB-12593, June, 2007
[8] http://www.lightsources.org/facility/lcls

ISBN 978-3-95450-177-9

THE CERN BEAM INSTRUMENTATION GROUP OFFLINE ANALYSIS FRAMEWORK

B.Kolad, J-J Gras, S. Jackson, S. Bart Pedersen, CERN, Geneva Switzerland.

Abstract

Beam instrumentation (BI) systems at CERN require periodic verifications of both their state and condition. An instrument's condition can be diagnosed by looking for outliers in the logged data which can indicate the malfunction of a device. Presently, experts have no generic solution to observe and analyse an instrument's condition and as a result, many ad-hoc Python scripts have been developed to extract historical data from CERN's logging service. Clearly, ad-hoc developments are not desirable for medium/long term maintenance reasons and therefore a generic solution has been developed. In this paper we present the Offline Analysis Framework (OAF), used for automatic report generation based on data from the central logging service. OAF is a Java / Python based tool which allows generic analysis of any instrument's data extracted from the database. In addition to the generic analysis, advanced analysis can also be performed by providing custom Python code. This paper will explain the steps of the analysis, its scope and present the kind of reports that are generated and how instrumentation experts can benefit from them. It will subsequently demonstrate how this approach simplifies debugging, allows code re-use and optimises database and CPU resource usage.

INTRODUCTION

Both scientific and business domains have witnessed exponential growth of available data. Processing and analysing huge amounts of data is a major problem and has become it's own scientific field leading to the creation of many commercial and open source tools over the years. The need for similar tools in the Beam Instrumentation group at CERN has already been identified in the past [1]. The BI group decided to make their own tool because of the group's very specific constraints (the database can only be accessed via a dedicated java API, and users often need tailor made reports). LHC systems produce large quantities of data which can be used for checking the health of various beam instrumentation systems. OAF aims to simplify and unify the work-flow of the data analysis and problem detection.

After the evaluation of technologies on which we could base our analysis solution, Java, C++ and Python emerged as the primary candidates. These three programming languages have a long history at CERN and are widely used inside the organisation. We finally choose Python, as it offers a rich choice of scientific libraries for numerical and statistical analysis (for example we make heavy use of the Python Panda and Matplot libraries). Furthermore, prototyping in an interpreted language is also much faster than in languages requiring compilation. Python is also beginner friendly and can be used by users with limited programming experience – an important feature for our needs if OAF is to offer a *custom analysis* feature which allows broader analysis via dedicated code supplied by instrument experts.

STATUS BEFORE OAF

Data logged by the LHC is stored in a so-called logging database [2] and is accessible via a web-based user interface (Timber) which accesses data via a Java API, but provides limited analysis capabilities. This data is regularly extracted and analysed off-line by experts, to elicit useful information about an instruments performance. In the absence of a standard means to do this, instrument specialist inevitably started developing various independent tools. Each of these tools had to support the same set of operations:

- Data extraction
- Statistical analysis
- Production of a report document

The absence of any framework to guide the developers of analysis tools, lead to many problems including:

- Code duplication
- Sub-optimal means of data extraction (by performing an out of process system call, which in turn ran a generic Java command line tool)
- The data extracted by the Java command tool was subsequently dumped into a text file and then parsed into various python data structures
- Some scripts were moved to newer Python / library versions while others remained on out-dated versions
- Very often authors of scripts stayed at CERN for a limited period of time leaving the maintenance burden on newly arrived colleagues.

Dealing with this script *zoo* became a complex software engineering task in itself, and it was soon obvious that the common functionality of these various scripts had to be handled differently so that the maintenance of the infrastructure of the resulting framework should not concern the instrument experts.

DATA SOURCE

The Logging Service stores data coming from pre-defined signals into an Oracle database, and provides a Java API accompanied by a generic GUI (Timber) which can be used to extract and visualise logged data.

ISBN 978-3-95450-177-9

Forcing data retrieval only via this API allows for a better monitoring of database loads and avoids requests for the amount of data that could potentially take down the entire database. Data can be extracted by creating dedicated queries, or by the use of a so-called snapshot (a stored query identified by a unique name). Rather than using the aforementioned Java command tool, OAF retrieves data by directly calling the Java API using JPype[3] with the desired snapshot name. JPype allows the use of Java libraries directly in Python programs which is very convenient and avoids storing variables in temporary files as was done in the past. A dedicated Python module converts Java objects into python dictionaries for easy analysis by the framework.

FRAMEWORK ARCHITECTURE

One of the most basic software design principles in modern software engineering is the separation of tasks. A computer program should be divided into distinct components that, are responsible for single well defined tasks. In previous ad-hoc scripts this principle was violated and quite often a single module performed many distinct tasks (extracting data, analysis, producing the report, etc.). One of OAF's design goals was modularity which implicitly embraces the separation of tasks principle. Adopting this principle, simplifies the maintenance and development process. If for example the underlying Java API ever changes, only one module has to be updated, and the rest of the framework is shielded from this change. It also allowed different members of the OAF team to work independently on different modules after agreeing on common interfaces. The resulting OAF framework consists of following parts:

- DB connection module which is responsible for accessing and converting data to an agreed python data structure.
- Excel files which define the configuration of the analysis. Configuration is achieved by the modification of several spreadsheets. This allows the configuration of many features of the framework including a list of participants to be notified when a report has been generated, the declaration of new variables based on extracted ones, the criteria for alarms, the choice of plots, etc. It is important to note that this part is fully generic so that instrumentation experts do not have to provide any code in order to configure this part of the analysis.
- Report Generator GUI. OAF is a command line tool with parameters such as the date of the analysis, snapshot name etc. provided as command line arguments. The Report Generator is a GUI which simplifies the request for a new report, with for example, dates chosen from a calendar widget.
- A module with generic analysis code. The common part of all analysis is performed in this module with its configuration retrieved from the Excel spreadsheet.
- Optional modules with custom code. In the case where more sophisticated analysis is required, OAF provides a place holder for dedicated code to be provided by the instrumentation expert.
- Web application which allows browsing existing reports in an easy and user friendly way.

ANALYSIS FLOW

Automation is an important aspect of the OAF framework. A typical analysis can be divided into separate phases, which are well defined and roughly correspond to the functionality of the modules described previously (Fig. 1).

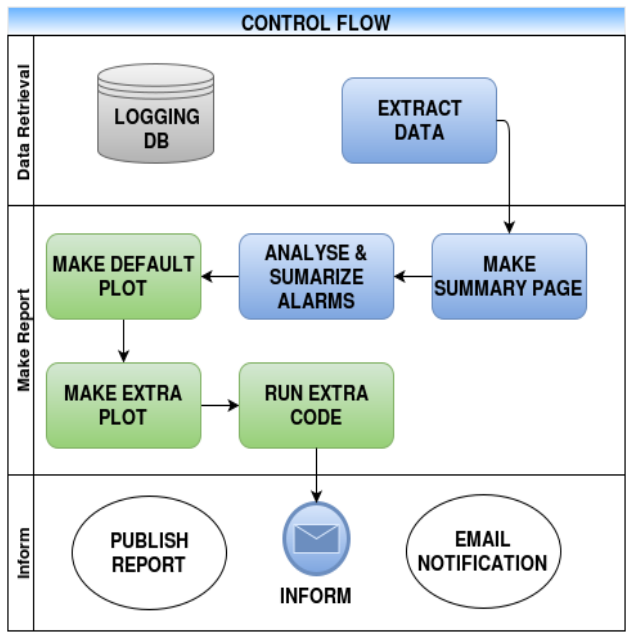

Figure 1: Analysis control flow. Blue: mandatory steps. Green optional steps.

Analysis is fully automated and can be invoked on a daily basis by a time-based scheduler (Linux CRON).

OAF provides generic core functionality to perform each of the following steps during an analysis:

- Extract Data: retrieve data from the database and perform data conversions
- Make summary page: describe the scope of the report, along with devices and variables used
- Analyse alarms: provide statistics on extracted data and perform checks with user-configured constraints
- Make default plots (Optional): produce results and reports of available data and alarms
- Make extra plots (Optional): produce more complex plots such as FFTs etc
- Run Expert Code (Optional): runs third party code submitted by the expert
- Inform: Depending on provided configuration E.g. sends emails with the report, stores report for further analysis

ISBN 978-3-95450-177-9

STRUCTURE OF THE REPORT FILE

The first page of the report provides information about devices and variables covered by the analysis and specified time window, with a summary of any alarm raised. The rest of the report is made up of plots and tables as defined by the configuration provided in the Excel spreadsheet. For each device retrieved, plots of the extracted data along with any related alarms are generated.

For example, the BLM-LHC-temp report diagnoses the condition of an LHC beam loss monitor acquisition card. In this case the temperature of the card is the parameter we want to monitor. Figure 2 shows this measured temperature for 16 different cards for a given VME crate. Each point on the graph contains statistics such as average, minimum and maximum values along with the standard deviation for a daily measurement. The green band indicates the range of allowed temperature values. In figure 2 we can immediately identify six outliers indicating a failure of temperature measurement for cards 5 to 7 and cards 13 to 15.

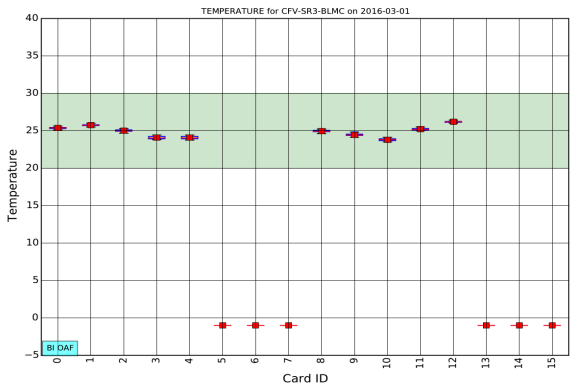

Figure 2: Example of an OAF plot.

There are numerous alarms, various plot types, and several facilities to perform variable conversions which relieves the user from writing such code. OAF can raise alarm in the following instances:

- DISCRETE: alarm raised if values do not belong to the given list of values.
- MEASURE: alarm raised if values do not remain within given range.
- STATUS_BIT: alarm raised if the state of status bit register does not correspond to the nominal state of each bit
- SWITCH: alarm is raised each time a value is changed.

Sets of available plots includes:

- HISTOGRAM
- FFT
- STATISTICS (mean, deviations)
- and many others..

Quite often we need to transform the extracted data in order to carry out further analysis. The most common conversion types have been identified and are made available to the user. Generated this way variables can be plotted in the generic plots, as well as being used for the alarm checking. More than twenty types of conversions are available including statistics calculations, FFTs, etc.

EXAMPLE USE CASE

The daily BCT_SPS_safety reports, provide offline monitoring of the 2 DC current transformers used in the SPS North Area for personal safety matters. The report contains a check which compares the recordings of these 2 DCCTs during the last 24 hours. All differences are reported as a potential error of one DCCT. As an example we can see in Fig. 3 that a spurious signal appeared on BCT_897 (blue trace) around 00:45 on the 7th of August 2016. This automatic analysis is particularly useful to track this kind of rare event.

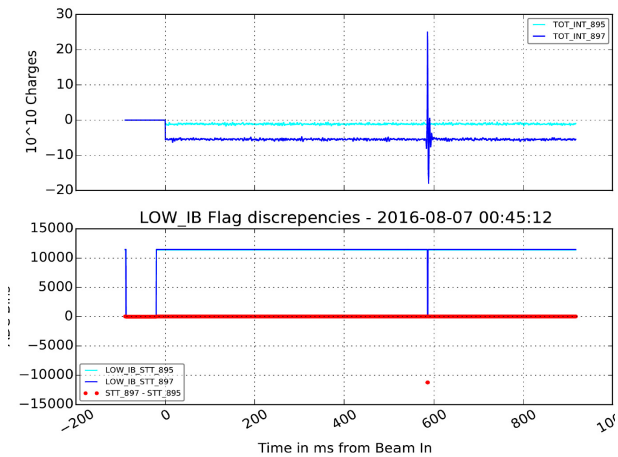

Figure 3: Top Plot : Signal proportional to DC beam current during an SPS Cycle (one trace for each DCCT). Bottom plot : Shows the evolution of the 2 status flags during the cycle (high level = OK for extraction, low level = NOT OK for extraction) and in red, the difference of the two flags.

RESULTS

OAF analysis tasks are executed every night by an automatic CRON task. After the analysis is performed, interested recipients receive an email with a short summary of the findings (how many alarms ware raised etc.) and a link to the report. Adding a configuration of new analysis is done via an Excel configuration file, which is a much more robust and easier than the previous approach (creating dedicated python script). We can easily extend OAF to support more types of alarms or plots just by updating the generic part of the framework without breaking backward compatibility with existing analysis tasks. Making such changes previously required separate modification of each python script.

Presently, some forty reports are produced every day, covering beam position measurement, loss

ISBN 978-3-95450-177-9

measurement, current measurement and profile measurement in all of CERN's accelerator complex (LHC, SPS, PS, PS BOOSTER...). Two thirds of these reports only rely on the generic code and features. Some reports use expert code included into the framework to add some specific analysis and plots. Finally, a recurrent "OAF outcomes" topic has been added to our regular internal technical board meetings where we present interesting observations to all BI experts as well as explaining any new features of the framework.

ACKNOWLEDGEMENT

We thank P. Odier, CERN, for providing information on BCT_SPS_safety report usage.

REFERENCES

[1] S. Jackson, "A framework for off-line verification of beam instrumentation system at CERN", in *Proc. 14th Int. Conf. on Accelerator and Large Experimental Physics Control Systems (ICALEPCS'13)*, San Francisco, USA, Oct. 2013, paper MOPPC139, pp. 435-438

[2] C. Roderick et al., "The LHC Logging Service: Handling Terabytes of On-line Data", in *Proc. 12th Int. Conf. on Accelerator and Large Experimental Physics Control Systems (ICALEPCS2009)*, Kobe, Japan, Oct. 2009, paper WEP005, pp. 414-416.

[3] `http://jpype.sourceforge.net/`

ISBN 978-3-95450-177-9

IMPROVEMENTS TO THE LHC SCHOTTKY MONITORS

M. Wendt*, M. Betz, O.R. Jones, T. Lefevre, T. Levens, CERN, Geneva, Switzerland

Abstract

The LHC *Schottky* monitors have the potential to measure and monitor some important beam parameters, e.g. tune, momentum spread, chromaticity and emittance, in a non-invasive way. We present recent upgrade and improvement efforts of the transverse LHC *Schottky* systems operating at 4.81 GHz. This includes optimization of the slotted waveguide pickups and a re-design of the RF front-end electronics to detect the weak, incoherent *Schottky* signals in presence of large, coherent beam harmonics.

INTRODUCTION

The theory of bunched beam transverse *Schottky* signals reveals the measurement of machine parameters, such as tune, chromaticity, emittance, etc. based on the observation of coherent and incoherent motion of the bunched particles [1]. The associated dipole moment of each particle, following betatron and synchrotron motion, can be expressed as *Fourier* series, showing upper (usb) and lower (lsb) betatron sidebands around each revolution harmonic h, which further splits into synchrotron satellites.

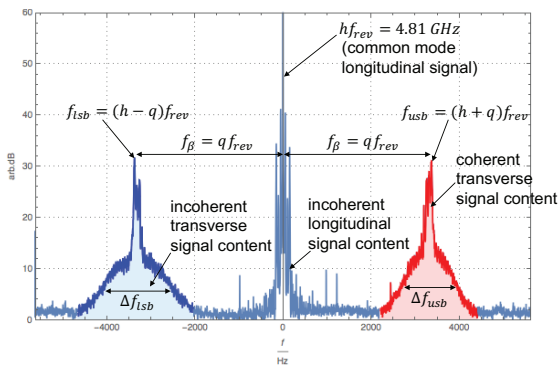

Figure 1: Typical LHC *Schottky* spectrum.

The *Fourier* representation hints to perform the observation of these tiny particle fluctuations in the frequency domain. Figure 1 shows a downconverted *Schottky* spectrum (h = 427746, f_{rev} = 11.245 kHz) for a bunch of $n \approx 10^{11}$ protons (charge state z = 1) in the LHC at injection energy. In practice, even with a very well centered beam, the longitudinal common mode revolution harmonics are always present, and usually dominant. In this low-resolution measurement the synchrotron sideband modulation is "smeared' out" to the usb and lsb incoherent *Schottky* signal "humps". Clearly visible on top of these incoherent signal humps are the coherent betatron sidebands, whose intensity is dependent on the longitudinal bunch shape and amplitude of any residual coherent oscillations. These allows the measurement of the fractional betatron tune $q = f_\beta / f_{\mathrm{rev}}$.

* manfred.wendt@cern.ch

The chromaticity $\acute{Q}$ is derived from the different widths Δf_{usb}, Δf_{lsb} of the respective usb and lsb *Schottky* humps.

$$\acute{Q} = \eta\left(h\frac{\Delta f_{\mathrm{lsb}} - \Delta f_{\mathrm{usb}}}{\Delta f_{\mathrm{lsb}} + \Delta f_{\mathrm{usb}}} + q\right) \approx \eta h \frac{\Delta f_{\mathrm{lsb}} - \Delta f_{\mathrm{usb}}}{\Delta f_{\mathrm{lsb}} + \Delta f_{\mathrm{usb}}} \qquad (1)$$

with η being the phase slip factor, which is 3.183e-4 for the LHC, The approximation is true for $h \gg \eta$ and $\Delta f_{\mathrm{lsb}} - \Delta f_{\mathrm{usb}} \neq 0$. At 4.81 GHz $h \approx 4.28e5$, so that $\eta h \approx 136$, implying that a 1% difference in width represents 1 unit of chromaticity. The momentum spread $\Delta p/p$ is proportional to the average width of the sidebands

$$\frac{\Delta p}{p} \propto \frac{\Delta f_{\mathrm{lsb}} + \Delta f_{\mathrm{usb}}}{2 f_{\mathrm{rev}} h \eta}, \qquad (2)$$

and the emittance can be estimated from the total signal power contained in a given sideband hump, with $A_{\mathrm{usb}}\Delta f_{\mathrm{usb}} \equiv A_{\mathrm{lsb}}\Delta f_{\mathrm{lsb}}$. This, however, requires independent calibration.

THE LHC SCHOTTKY MONITOR SYSTEM

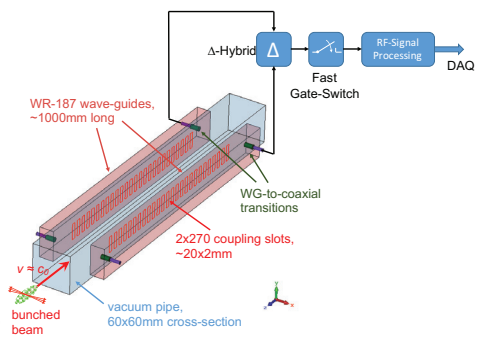

Figure 2: Simplified overview of the LHC *Schottky* monitor system (beam pickup not to scale).

The LHC *Schottky* monitoring system (Fig. 2) was designed and built in frame of the US LARP collaboration with Fermilab [2, 3]. An operation frequency of 4.8 GHz was selected as the best compromise between avoiding overlapping *Schottky* sidebands at very high frequency, and being within the single bunch coherent spectrum at low frequency. A symmetric arrangement of slotted waveguide couplers is used to provide a broadband *Schottky* beam pickup, followed by an RF front-end with narrowband, triple-stage down-conversion and a 24-bit audio digitizer based DAQ system. While the 200 MHz bandwidth of the beam pickup offers single bunch time resolution, selected by a fast gate switch, the following low-noise receiver has a final bandwidth of ~15 kHz, slightly larger than the 11 kHz LHC revolution frequency. The LHC is equipped with four such *Schottky* monitoring systems, a horizontal and a vertical unit for each beam.

ISBN 978-3-95450-177-9

During LHC Run 1 the LHC *Schottky* monitors performed very well with lead ion beams (PB^{82+}), due to the fact the the total *Schottky* signal power density in the sidebands scales with z^2. Unfortunately with protons the incoherent *Schottky* signal levels were often too close to the noise floor to extract useful beam parameters. The amplifiers in the RF front-end also suffered from saturation effects due to high level, out-of-band common mode signals. Despite common mode suppression of more than 40 dB through the use of a Δ-hybrid, the intensity of the residual coherent harmonics were much higher than expected, linked to the non-Gaussian particle distribution of the bunch. An instantaneous dynamic range between incoherent *Schottky* signals and common mode revolution harmonics over 100 dB is therefore required, which is a major challenge for the RF signal processing.

SCHOTTKY BEAM PICKUP

The slotted rectangular cross-section waveguides of the *Schottky* beam pickup couples to the TEM field of the beam through their fundamental TE_{01} mode . The dimensions of the array of 270 rectangular slots was optimized through a semi-analytical approach [4], to obtain a tight coupling to the beam, while ensuring the phase velocity of the TE_{01} Δ-mode $v_p \approx c_0$. Both ends of each waveguide are equipped with a "mode-launcher", which is a waveguide(WG)-to-coaxial transition [5], the downstream pair act as signal ports, while the upstream pair is used to feed a test tone signal for calibration and maintenance purposes.

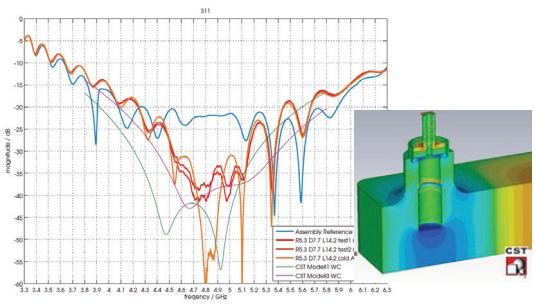

Figure 3: Return-loss of the optimized waveguide-to-coaxial mode launcher.

Beam measurements and a detailed RF verification of the four *Schottky* pickups revealed a higher than anticipated return-losses (10 dB) from the WG-coaxial mode launchers, initiating a redesign. All four *Schottky* monitors received a complete overhaul during the long LHC shutdown of 2014. This included incorporating a new WG-coaxial mode launcher, as well as a variety of other mechanical and RF improvements. Figure 3 shows the $|S_{11}|$ return-loss results of the improved mode launcher, comparing simulations and measurements under different test conditions [6]. Due to the tolerances of the coaxial feedhroughs, each WG-coaxial launcher had to be fine tuned by some bending and rotating of the coaxial pin to achieve the maximum performance.

The transfer response (Fig. 4) between beam and downstream output ports indicates an operation frequency sweet

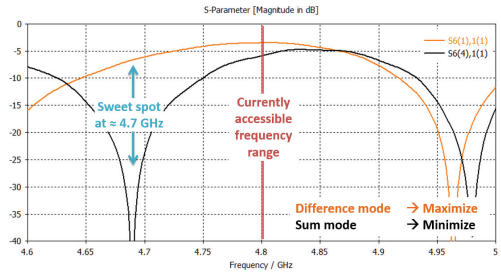

Figure 4: Simulation of the *Schottky* pickup transfer response.

spot near 4.7 GHz for better suppression of the common mode (sum) signal. This was, however, not confirmed through beam measurements. While the redesigned WG-coaxial launcher improved the RF properties of the *Schottky* pickup, an $|S_{31}|$ isolation measurement after installation between the output ports discovered substantial remaining reflection effects, probably caused by the rather low waveguide cutoff frequency of the beam ports (f_{TE01} = 2.5 GHz). Figure 5 shows ~20 dB isolation with well terminated beam ports under laboratory measurement conditions (green and blue traces), but strong coupling >10 dB after installation (red trace), which is explained by reflections due to discontinuities in the beam pipe.

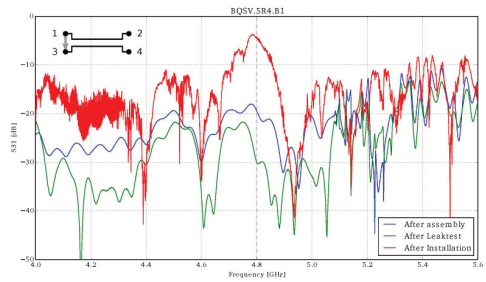

Figure 5: Remaining isolation between the output ports before and after installation of the *Schottky* beam pickup.

RF SIGNAL PROCESSING

Figure 6 gives an overview of the RF hardware for the processing of the *Schottky* signals. It consists out of an RF front-end for bunch gating and signal conditioning at 4.81 GHz, which is located in the LHC accelerator tunnel. This is followed by a RF back-end triple-stage downconverter located in the LHC alcove along with the DAQ electronics.

The RF front-end is mounted directly on the *Schottky* beam pickup to keep the signal cables short for minimum insertion losses. A so-called "compensation path" consists out of a remote controlled attenuator and phase shifter, and is used to equalize the two output signals of the *Schottky* beam pickup to minimize the common mode signal contribution at the output of the Δ-hybrid. This compensation path was kept unchanged, however, most other parts of the RF front-end were substantially modified to better accommodate the dynamic range requirements and single bunch gating capabilities.

ISBN 978-3-95450-177-9

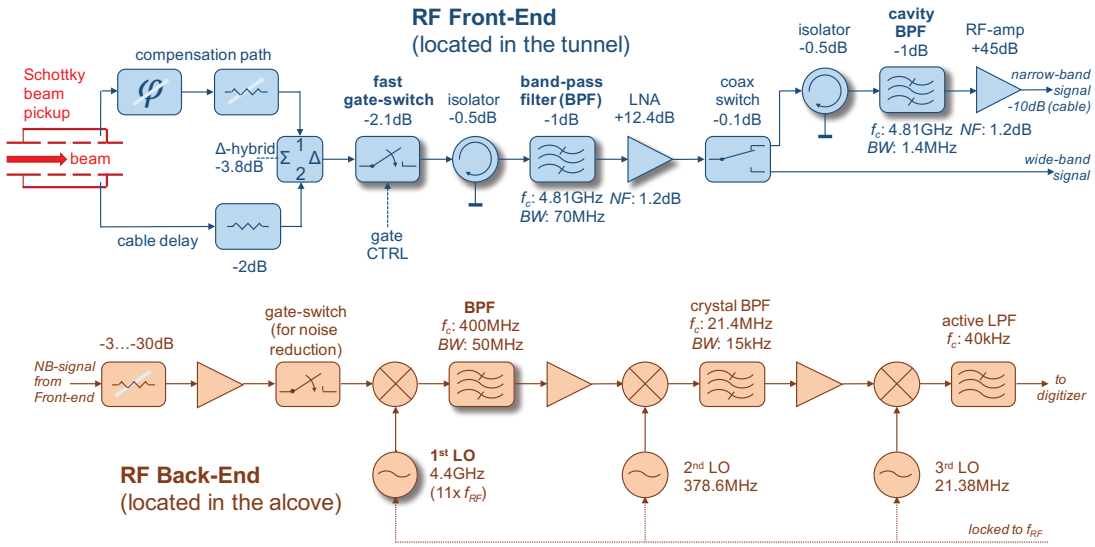

Figure 6: Simplified block schematics of the RF *Schottky* signal processing.

The RF back-end received only minor modifications, e.g. the low-pass filter of the 1st 400 MHz IF stage was replaced by a band-pass filter for image rejection purposes, and the original 4.4 GHz fixed frequency 1st LO can now also be varied. Beam studies at different operating frequencies in the range 4.5-4.9 GHz, supported by a YIG band-pass filter in the RF front-end, did not discovered a more favorable operating frequency than 4.8 GHz. A gate-switch is used for noise-reduction, with the switching time matched to the ∼1 μs decay time of the cavity filter in the RF front-end.

RF Front-End Modifications

As Fig. 6 shows, the RF front-end is split into a low-gain (12 dB) wide-band (70 MHz) section before the coaxial switch, followed by a high-gain (45 dB) narrow-band (1.4 MHz) section. The wide-band signal can be temporarily switched to a signal analyzer to minimize the common-mode signal by tuning the compensation path.

The main noise contribution originates from the signal attenuation, defined by the insertion loss of ∼10 dB between beam pickup electrode and input of the low-noise amplifier (LNA), plus the LNA noise figure of $NF \approx 1.2$ dB.

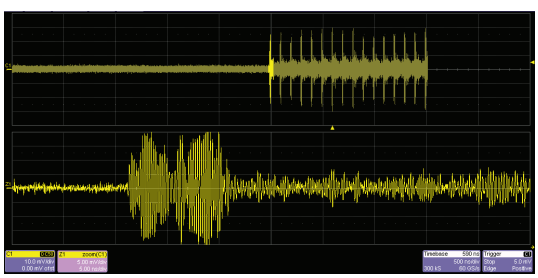

Figure 7: Bunched beam *Schottky* signals (time domain).

Fast Gate-Switch Following the Δ-hybrid, a DC-28 GHz SPDT gate-switch with ∼1 ns switching times is used to select one or more bunches from the LHC beam. VNA-based measurements around 4.8 GHz show an insertion loss of 2 dB, a return loss of ∼14 dB, and isolation >50 dB. The switch can handle rather high signals up to +20 dBm (0.1 dB compression), which is important to avoid saturation effects due to the high common mode signal contents it has to handle.

Figure 7 shows the time domain response of the *Schottky* system at the Δ-hybrid output using a fast oscilloscope (20 GHz BW, 60 GSPS). The upper trace shows a section of a LHC bunch train with 100 ns spacing, the lower trace zooms the waveform response of the first bunch. A single bunch response time of ∼10 ns is observed, followed by some unwanted reflection effects, as expected from the VNA measurements shown in Fig. 5. A dedicated switch driver (gate CTRL) was developed for fine control of the switching times of the gate pulse, synchronized with the accelerator RF, to precisely extract the *Schottky* bunch signal from a given bunch.

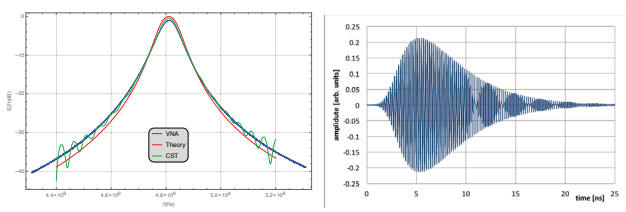

(a) Frequency domain (b) Time Domain

Figure 8: Characteristics of the *Bessel* interdigital band-pass.

4.8 GHz Interdigital Band-pass Filter Different types of low insertion loss band-pass filters were tested, including a YIG-filter with a remote controlled adjustable resonance frequency. A band-pass filter of moderate bandwidth (10-15%) is required as a pre-selector, and helps to "clip" high common mode signal levels which otherwise tend to saturate the low-noise amplifier (LNA).

ISBN 978-3-95450-177-9

A self-built 2-stage *Bessel* band-pass filter, based on interdigital airline resonators [7] was found to be a good compromise in terms of insertion loss, selectivity, and impulse response. Figure 8 (a) compares the measured and simulated $|S_{21}(f)|$ transfer function, while Fig. 8 (b) shows the corresponding measured time-domain response $s_{21}(t)$. With a total decay time of $5\tau \approx 25$ ns, this design gives some flexibility to locate this filter either before or after the fast gate-switch.

4.8 GHz Cavity Band-pass Filter After gating, there is no need for a ns-scale time resolution, hence narrow-band filtering was applied to minimize integrated spectral power. A modified pill-box cavity was used as a single stage bandpass filter with a bandwidth of < 0.03 %.

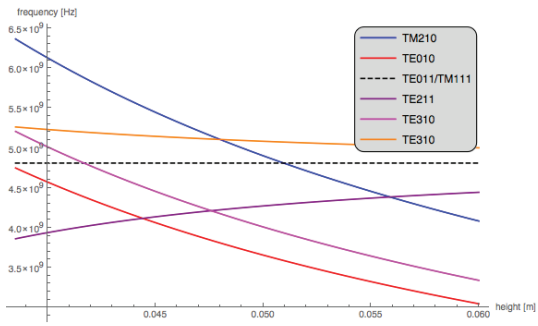

Figure 9: Mode-chart of an ideal "pill-box" resonator.

A mode chart for an ideal cylindrical resonator (Fig. 9) allows its height h to be optimized for maximum separation of the eigenmodes ($h \approx 50$ mm, $r = 46.5$ mm for $f_{\mathrm{TE011}} \approx 4.8$ GHz). Modifications on both end caps help to detune the degenerated TM_{111}-mode [8], and provide a simple solution to fine-tune f_{TE011}. With brass as the cavity body material a quality factor $Q_0 \approx 9300$ is obtained, while tuning the coupling loops to a minimum insertion loss of ~2.2 dB gives $Q_L \approx 3700$, corresponding to a total signal decay time of ~1 μs. Silver-plating would approximately double Q_0, as well as the decay time, but the cavity then becomes more sensitive to variations of the ambient temperature in the accelerator tunnel.

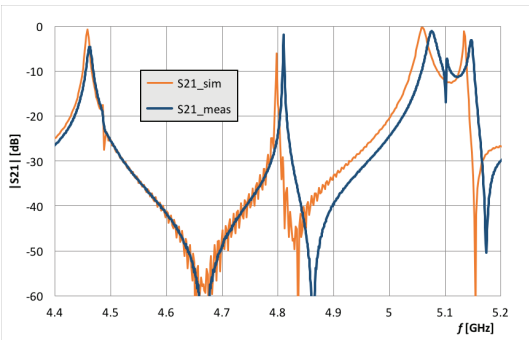

Figure 10: $|S_{21}(f)|$ transfer function of the cavity band-pass.

FIRST RESULTS AND OUTLOOK

An example of first results with beam for a refurbished *Schottky* monitor is presented in Fig. 1, and have been discussed recently in more detail in [9]. A new peak detection algorithm allows the extraction of the coherent tune with a resolution $<10^{-4}$ while different fitting algorithms are currently under study for chromaticity calculation. The improved *Schottky* diagnostics are also helping during machine development periods for specific studies such as measuring the beam-beam tune shift, effects of wakefields on the tune, synchrotron tune shifts vs. RF manipulations, etc.

For bunched proton beams the high common mode coherent revolution harmonics and the reflection effects remain a challenge, and still present some limitations for a simple, turn-key operation of the *Schottky* systems.

REFERENCES

[1] S. Turner, "Proceedings of the CAS", CERN, Geneva, Switzerland, CERN-95-06, Nov. 1995, Vol. II, pp.749-782.

[2] R. Pasquinelli, LARP-doc-482-v3, 2008, http://larpdocs.fnal.gov/LARP-public/DocDB/ShowDocument?docid=482

[3] F. Caspers., et.al., "The 4.8 GHz Schottky Pickup System", in *Proc. of Particle Accelerator Conf. (PAC'07)*, Albuquerque, NM, USA, June 2007, paper FRPMN068, pp. 4174–4176.

[4] D. McGinnis, "Slotted Wavguide Slow-Wave Stochastic Cooling Arrays", in *Proc. of Particle Accelerator Conf. (PAC'99)*, New York, NY, USA, March/April 1999, paper TUP100, pp. 1713–1715.

[5] D. Sun, "Design of LHC Schottky Pickup", Fermilab internal document, RF Technote, April 2006.

[6] M. Ehret, "Untersuchung eines breitbandigen Koaxial-Hohlleiteruübergangs für einen Schottky-Strahldiagnosedetektor", Ms.Sc. thesis in German language, University of Applied Sciences Offenburg, Germany, December 2013.

[7] G. Matthaei, L. Young, E.M.T. Jones, "Microwave Filters, Impedance-Matching Networks, and Coupling Structures", McGraw-Hill, 1964, pp. 616–626.

[8] B. Yassini, et.al., "A Ka-Band Fully Tunable Cavity Filter", IEEE Trans. on Microwave Theory and Techniques, Vol. 60, No. 12, Dec. 2012, pp. 4002–4012.

[9] M. Betz., et.al., "Upgrade of the LHC Schottky Monitor, Operational Experience and First Results", in *Proc. of Particle Accelerator Conf. (IPAC'16)*, Busan, Korea, May 2016, paper MOPMB060, pp. 226–228.

ISBN 978-3-95450-177-9

REVIEW OF CHROMATICITY MEASUREMENT APPROACHES USING HEAD-TAIL PHASE SHIFT METHOD AT RHIC *

V.H. Ranjbar, A. Marusic, M. Minty, Brookhaven National Lab, Upton NY 11973, USA

Abstract

We review tests of the head-tail phase shift method using various approaches at BNL's RHIC. Both the standard and some more exotic approaches to measure the phase differential between the head and tail of a bunched beam has been attempted at RHIC. The standard kick beam and measured phase evolution of the head and tail of a given bunch has been tried at RHIC. Additionally a more exotic approach to measure the head versus tail phase difference has been tried. In this approach we used a BBQ pickup and kicker with the input stripline signal to the BBQ mixed with a nano second pulse timed to the head and tail of the bunch. In this way we hoped to force the BBQ to sample the head or tail of the bunch depending on the pulse timing. We report on the results and challenges which each approach presented.

HEAD-TAIL PHASE SHIFT METHOD

The head-tail phase shift approach relies on the measurement of the phase difference that develops between betatron oscillations at fixed longitudinal positions relative to the center of the RF bucket. The maximum phase shift is proportional to the chromaticity and given by the following formula:

$$Q' = \frac{-\eta \Delta\Phi}{2\omega_0 \Delta\tau} \quad (1)$$

Here Q' is the chromaticity, η the momentum compactions factor, $\Delta\Phi$ the betatron phase difference between two points $\Delta\tau$ difference away from each other in the RF bucket in time.

Single Kick Based Method

The approach was first worked out at the SPS by R. Jones [1] with theoretical analysis by Fartoukh [2]. A single kicked method was used with the sampling occurring at 1/2 synchrotron period from the time of the applied kick. This was because phase difference was maximal at this point since the phase difference would oscillate with $(cos(\omega_s t) - 1)$, where ω_s is the synchrotron frequency.

Although the approach was fist tested in the SPS, it was never used for actual operations. This was due to the fact that the non-linearities of the fields in the SPS caused very rapid decoherence of the kicked oscillations thus making it very difficult to obtain a good signal at 1/2 synchrotron period after the kick (about several hundred turns). Also this approach was destructive to the beam causing emittance blow up and thus only could be possibly used during machine tune up.

Later the approach was also tested at the Tevatron [3]. In this case there was more success due to the fact that the Tevatron at injection had a much longer coherence time. Thus it was actually used for tune up during operations for a while. Then when octupoles were used to help control the head-tail instability, this created decoherence times similar to that in the SPS.

TESTS AT RHIC

Concurrently with the work at the Tevatron tests were also performed at RHIC, however there is little in the way of published documentation for this work. Later we conducted several tests at RHIC, which we now present here.

During the FY14 APEX studies, we used the Artus kicker to excite the beam and acquired turn-by-turn data in the vertical and horizontal planes. This was done using a Tektronics scope attached to the yellow meter long stripline located at A0 house.

The data acquisition was done in a similar manner as was performed in the Tevatron system. The difference signal was sampled as a poxy for the average relative beam position. The reflection of the signal which creates a doublet signal was separated by splitting, delaying and re-summing. The final signal was digitized by the scope sampling turn-by-turn.

We performed 18 measurements at 100 GeV using the Au beam, while scanning through different chromaticity settings. In Fig. (1, 2) the turn by turn difference signal is shown for the horizontal and vertical planes as well as the FFT for the signal.

When compared to the signals we used to get in the Tevatron (see Fig. 3) it is immediately obvious that the decoherence is much faster and the signal to noise worse. We barely could acquire a signal through one decoherence period (1/2 synchrotron period).

Simulation

One major difference in the RHIC accelerator from the SPS's and Tevatron is the nature of the RF system. RHIC runs with at least two RF harmonics for the longitudinal motion stability at higher intensities. We were concerned that the additional RF component might alter the betatron phase dependence on chromaticity. So to understand this better we simulated this using M. Blaskiewicz RF modeling code (BTFTranf). We compared the case with two versus a single RF component (see Fig. (4,5)) and found that while there was some distortion in the phase oscillations, generally the phase difference scaled with chromaticity and longitudinal $\Delta\tau$ magnitude and it was possible to extract correct chromaticity values despite this.

Analysis

As can be seen in Fig. (1) and (2) by about 6-800 turns when the synchrotron period is at 1/2, the signal was rather

* Work supported by the URA., Inc., under contract DE-AC02-76CH03000 with the U.S. Dept. of Energy.

ISBN 978-3-95450-177-9

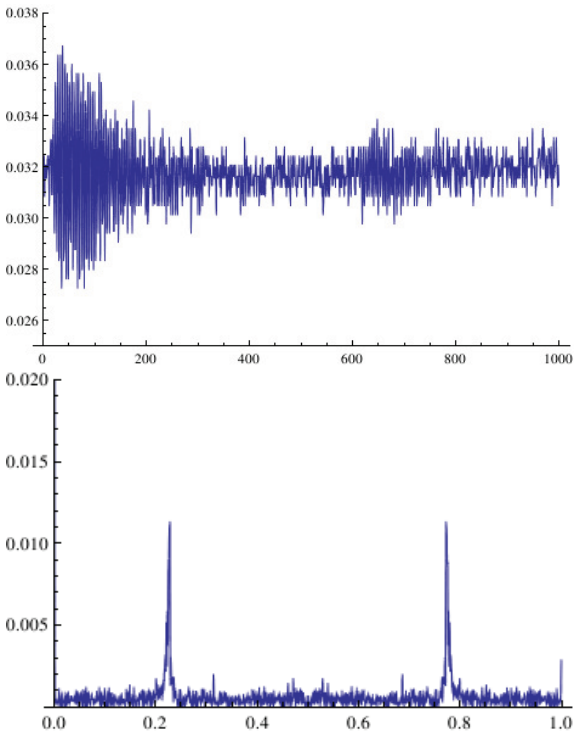

Figure 1: Vertical turn-by-turn difference signal (top) and FFT (bottom)

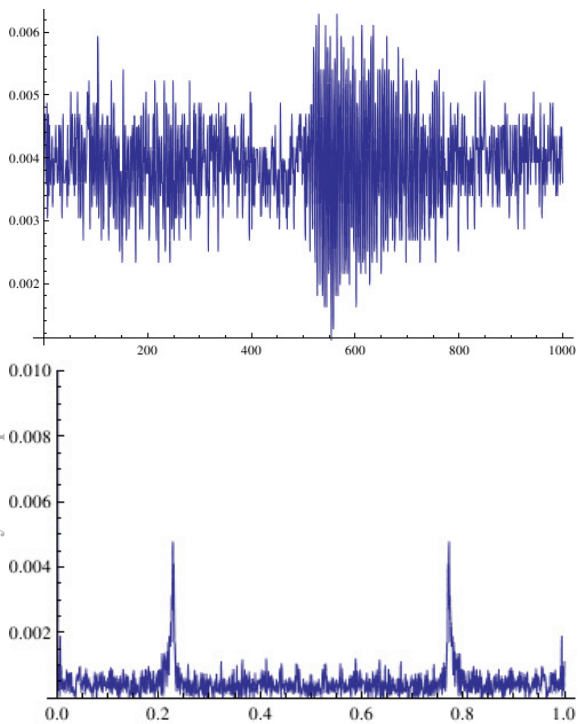

Figure 2: Horizontal turn-by-turn difference signal (top) and FFT (bottom)

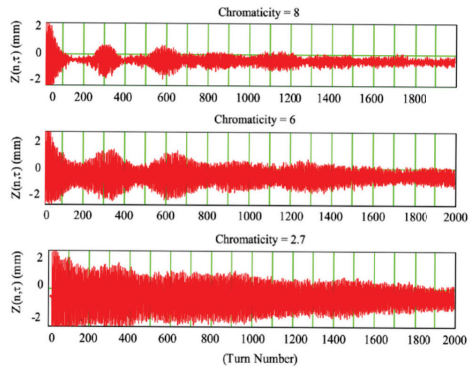

Figure 3: Horizontal turn-by-turn in Tevatron at injection

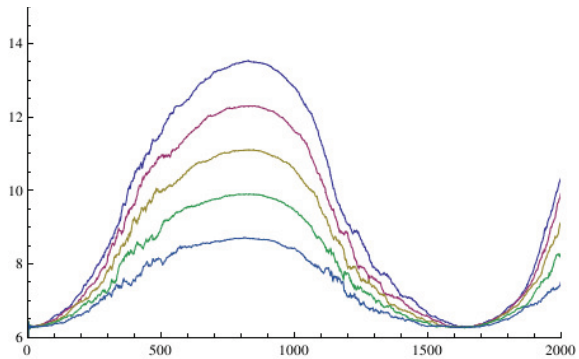

Figure 4: Simulation of head-tail phase shift with a single RF frequency. The Phase shift between different head-tail bunch slices plotted against turn number (x axis)

weak. For the Horizontal also the data was also cut off so we didn't get enough samples into the optimal time period. The result was that our phase plots were very noisy and not clean like what was observed in the old Tevatron data or in our simulations(see Fig. (6)). To improve this we took 24 $\Delta\tau$ samples in steps of 2 nsecs, marching towards the bunch center. For each $\Delta\tau$ turn-by-turn evolution we took from turn 600 to 800 divided the phase by $1/(1-cos(Q_s 2\pi n_{turn}))$ to

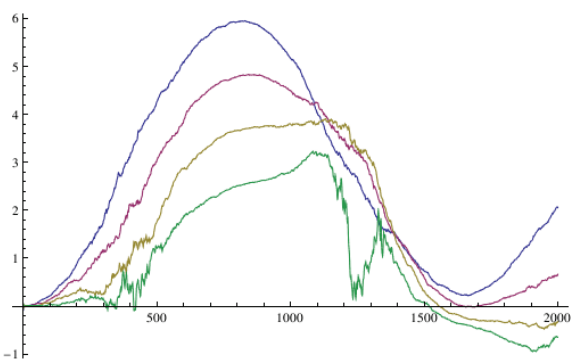

Figure 5: Simulation of head-tail phase shift with two RF frequencies. The Phase shift between different head-tail bunch slices plotted against turn number (x axis)

ISBN 978-3-95450-177-9

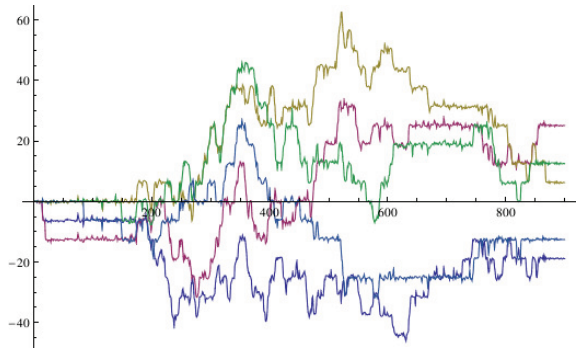

Figure 6: The Phase shift between different head-tail bunch slices plotted against turn number (x axis) as actually measured at RHIC

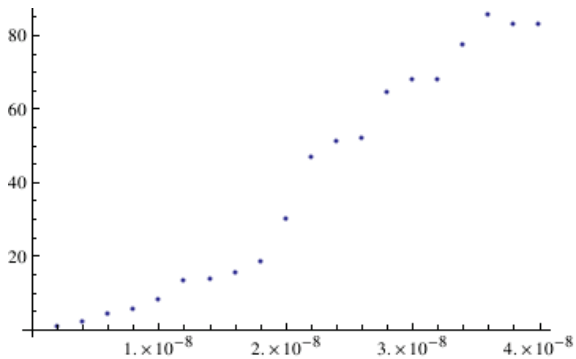

Figure 7: Plot of average Head-Tail phase difference for various $\Delta\tau$. From the slope one should be able to deduce chromaticity.

remove the component dependent on the synchrotron oscillations and averaged them. This seems to have helped for the data from the vertical plane. As you can see in Fig. (7) there is a clear slope between Δtau and phase difference. Using the fit from this slope we then estimated the chromaticity which is shown plotted against vertical chromaticity settings in Fig. (8). Here the fitted slope of the chromaticity settings and those provided by the head-tail phase shift method is 1.6. Without a direct measurement via the standard δ RF approach it's difficult to determine weather the deviation from a slope of 1 is due to a mis-calibration of the magnet settings or a fault of the method (though given the range of the chromaticity settings its probably the later).

CONTINUOUS KICK METHOD

Due to signal to noise issues and the fast decoherence time in machines with large non-linearities, the use of a continuously driven system have been explored. At first it was not obvious if a head-tail phase would develop in this case. However analytical, numerical and experimental tests at the Tevatron [4] demonstrated that indeed a phase shift does develop in these systems.

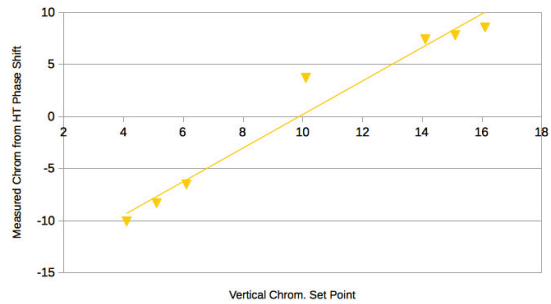

Figure 8: Head-Tail measurement of Chromaticity in vertical plane versus Chromaticity set points for RHIC at 100 GeV.

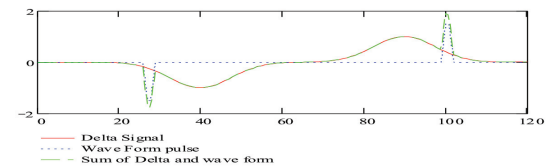

Figure 9: A schematic of how an external pulse could be mixed with the raw signal from a stripline to force the bbq to sample a fixed location in the bunch.

BBQ Signal Sampling

It is difficult to continuously drive a system with a signal to noise large enough for a standard digitizers, with out blowing up the emittance. Thus a detection method using the Based Band Tune system (BBQ) system was considered at the SPS and at the Tevatron. This is because the BBQ can detect betatron motion with a very weak driving kick which leave the emittance perserved. The concept was to flip the polarity on one of the diodes in the BBQ so that both the postive and negative peak of the doublet would be sampled in a button BMP.

However tests at the Tevatron demonstrated that the sampled location relative to the RF bucket would jitter and was function of orbit, bunch length and other factors. Thus this set up could not deliver reliable and consistent chromaticity measurements.

Pulse Mixing Tests

To control the sampled position of the BBQ in the bunch, we proposed summing a controlled square pulse of <= 0.5 nsecs to force the BBQ to select only the local peak and thus betatron oscillations at the location of the pulse. In this case we can separate the pulse from the reflected pulse by appropriate summing and delays as was done in the standard setup at the Tevatron. Using the positive pulse for head sampling and the negative for tail. A schematic of the pulse summing method is shown in Fig. (9).

Tests at RHIC in 2012-2014 showed that when the pulse was summed, this generated a large amount of noise in the signal which appeared to swamp any observed effect. Later a more gaussian like pulse was tried but it too generated a large noise effect in the BBQ electronics.

ISBN 978-3-95450-177-9

CONCLUSION

There was some success in extracting phase shifts which correlated with chromaticity using the standard kick method in RHIC. However this approach suffers from two issues: First requires a destructive measurement with a decoherence which depends strongly on the very parameter which is trying to be measured. Second, due to the fast decoherence acquiring a good signal is difficult and requires some bit of data processing. A better approach might be to use the RHIC spin flipper system to non-destructively excite the beam. Or more could be done to understand the limitations on the BBQ electronics in the case of the summed pulse method.

REFERENCES

[1] D. Cocq, O. R. Jones, H. Schmickler, "The Measurement of Chromaticity Via a Head-Tail Phase Shift", 8th Beam Instrumentation Workshop (BIW'98) , Stanford, CA, USA, May 1998.

[2] S.Fartoukh and R. Jones, "Determination of Chromaticity by the Measurement of Head-Tail Phase Shifts: simulations, results from the SPS and a robustness study for the LHC", LHC Project Report 602 2002.

[3] V. Ranjbar, "Chromaticity Head-Tail Application for the Tevatron," FERMILAB-FN-0753.

[4] C. Y. Tan and V. H. Ranjbar, Phys. Rev. ST Accel. Beams **11**, 032802 (2008). doi:10.1103/PhysRevSTAB.11.032802

ISBN 978-3-95450-177-9

STATUS OF BEAM CURRENT TRANSFORMER DEVELOPMENTS FOR FAIR

M. Schwickert, F. Kurian[1], H. Reeg, T. Sieber, GSI Helmholtzzentrum für Schwerionenforschung, Darmstadt, Germany
[1]also at Helmholtz-Institute Jena, Germany
R. Neubert, P. Seidel, Friedrich-Schiller University Jena, Germany
K. Hofmann, Technical University Darmstadt, Darmstadt, Germany
E. Soliman, German University in Cairo, Cairo, Egypt

Abstract

In view of the upcoming FAIR project (Facility for Antiproton and Ion Research) several long-term development projects had been initiated with regard to diagnostic devices for beam current measurement. The main accelerator of FAIR will be the fast ramped superconducting synchrotron SIS100. Design parameters of SIS100 are acceleration of 2×10^{13} protons/cycle to 29 GeV for the production of antiprotons, as well as acceleration and slow extraction of p to U ions at 10^9 ions/s in the energy range of 0.4-2.7 GeV/u and extraction times of up to 10 s. For high-intensity operation non-intercepting devices are mandatory, thus the developments presented in this contribution focus on purpose-built beam current transformers. First prototype measurements of a dc current transformer based on a Tunnelling Magneto Resistance sensor are presented, as well as recent achievements with a SQUID-based Cryogenic Current Comparator.

FAIR ACCELERATOR FACILITY

Presently, the technical layout of the FAIR accelerator complex is being finalized and civil construction of the accelerator tunnel will start soon. FAIR consists of the fast-ramped superconducting synchrotron SIS100, the high-energy beam transport system (HEBT) interconnecting the synchrotrons with the pBar-Target for production of anti-protons, the super-fragment separator (SFRS) for the production of rare isotopes, the collector ring (CR) for stochastic pre-cooling of rare isotopes and anti-protons, and the high-energy storage ring (HESR) for internal target experiments [1]. Existing GSI accelerators serve as injectors for the FAIR machines. Primary goal of the novel facility is the production of heavy ion beams with unprecedented intensities close to the space charge limit of the synchrotron. The workhorse of FAIR will be SIS100, designed to produce up to 5×10^{11} U^{28+} ions/s with energies of 400-2700 MeV/u. Particles will be extracted either in single bunches of e.g. 30 ns as required for the production of anti-protons, or as slowly extracted beam with extraction times of several seconds for the radioactive ion beam program of FAIR.

For effective usage of the accelerator chain a multiplexed machine operation is foreseen which will allow to provide beams to up to four different physics experiments inside one machine super-cycle. Especially the planned high-intensity operation calls for a reliable online transmission control system. Beam current transformers will be the main source of intensity signals along the accelerator chain. Each section of the FAIR complex has special requirements and, ideally, beam current transformers are purpose-built instruments for each use case.

REQUIREMENTS FOR BEAM CURRENT MEASUREMENT

The accelerator control system of FAIR will require the measurement data of beam current transformers for various applications. Besides regular transmission monitoring, operating and archiving systems will monitor the beam currents during injection, accelerating ramp and during fast and slow extraction to calculate extraction efficiencies online. This is done e.g. to prevent recurring beam losses leading to unnecessary activation of machine components. Additionally, the planned machine protection system requests the generation of a 'beam-presence flag' and a 'setup-beam flag' from the current transformer signals. The setup-beam flag identifies beam settings that are used for preliminary test runs and accelerator commissioning, typically performed at low beam intensities. A signal threshold is monitored for beam current monitors along the related accelerator chain to verify the conditions for the setup-beam flag. The beam-presence flag on the other hand identifies machine settings that have previously been validated for high-current operation of the machine. In this state the online transmission control based on transformer signals is set to very small tolerance bands to protect the accelerator chain from potential beam-induced damages.

Since many years commercial solutions for beam current transformers are available on the market. However, for special use cases, demanding e.g. for very high dynamic range of beam intensities, or the measurement with ultra-high sensitivity in the nanoampere range, purpose-built transformers are required.

TUNNELING MAGNETO RESISTANCE DC CURRENT TRANSFORMER

The goal of the research project for a novel DC current transformer (DCCT) was to create an instrument that allows for precise online measurement of accelerated and stored beams with a large dynamic range of beam intensi-

ISBN 978-3-95450-177-9

ties (µA to 150 A) and bunch frequencies up to 5 MHz. Due to its design the present GSI-built DCCT shows faulty signals at beam currents of >70 mA with bunch frequencies around 1.2 MHz, which will be standard operating parameters for SIS100. The novel DCCT is based on the clamp-on amperemeter design, consisting of a split toroid, which facilitates dismounting, e.g. for vacuum bake-out. The toroid is made from amorphous VITROVAC 6025F and acts as a flux concentrator. In the present design a beam current of 1 A leads to an induction of 80 µT in both gaps of the toroid, cf. Fig. 1. Two magnetic sensors are placed inside the toroid gaps and give a direct measure of the magnetic field inside the toroid. A number of different B-field sensor types were studied for the usage inside the novel DCCT.

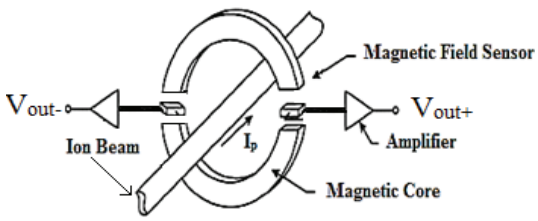

Figure 1: Schematic layout of the novel DCCT.

The DCCT development consists of three major steps. Firstly, different types of commercially available magneto-resistance (MR) sensors were tested and an amplifier PCB was developed for the most appropriate sensors. In a subsequent step the MR sensor signal was used as input for a zero flux feedback loop.

MR Sensor Study and Noise Analysis

For the detection of low magnetic fields two main types of MR sensors are available: Giant Magneto-Resistance (GMR) and Tunnel Magneto-Resistance (TMR) sensors. The functional structure is identical for all MR sensors and the field measurement is based on the change of the electrical resistivity of a thin film structure in the presence of an external magnetic film. In the standard layout four thin film resistors form a Wheatstone bridge. Whereas the GMR has two shielded resistors in the bridge causing unipolar output, the TMR has a bipolar output. For the application inside a novel DCCT the bipolar output is desirable because it facilitates to upgrade the device with a 'zero-flux' feedback loop.

For a theoretical noise analysis the performance of MR sensors was evaluated using the detectivity D as optimization parameter: $D := \sqrt{S_V}/R_{BV}$, where S_V is the output noise power spectral density [V/√Hz] and R_{BV} is the sensitivity of the magnetic field sensor [V/T]. The total output noise power spectral density S_V is given by the summation of all uncorrelated noise contributions, i.e. thermal shot noise, flicker noise, thermal magnetic noise and magnetic flicker noise. Separate PCBs were produced for each MR sensor and noise spectra were measured inside a magnetic shield. Best results were obtained with an MMLP57FD TMR-sensor [2] with a measured detectivity of D=15.6 nT/√Hz, thus the novel DC current transformer was named tunnelling magneto resistance DCT (TDCT).

Stretched Wire Tests

Three different PCBs were selected for a test setup consisting of a stretched wire carrying a DC current placed in the center of the split toroid. The sensors were mounted inside the 10 mm air gaps of the split toroid and the whole setup was covered with a mu-metal box to attenuate external magnetic fields. Figure 2 depicts the measurement results for the selected MMLP57FD sensor leading to a minimum detectable DC current of 62 µA [3].

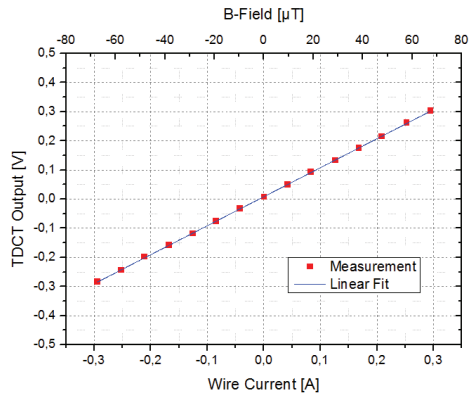

Figure 2: Stretched wire measurement with TMR-sensor MMLP57FD, note the good linear response.

Closed-Loop TDCT

In order to further increase the current sensitivity of the TDCT a feedback-loop was implemented. The principle of this 'zero-flux' instrument is to convert the amplified sensor voltage to a proportional current and to feed it to a coil wound around the toroid. The feedback current produces a magnetic field opposite to the field generated by the ion beam. As a result, the total magnetic field inside the air gap becomes zero. Therefore, the bipolar nature of the TMR sensor is preferred in order to set a proper working point and to counteract the magnetic flux in both polarities. For the closed-loop system two TMR sensors are placed inside the two air gaps of the split toroid. Purpose-built PCBs were manufactured to amplify the TMR voltage signal by a factor of 10. Using commercially available operational transconductance amplifiers (OTA) the amplified voltage is transformed to a proportional current, thus generating a sufficiently high feedback current. In addition n windings are wound around the toroid to further increase the magnetic field. First tests with the closed-loop system yielded promising results and are presently ongoing.

CRYOGENIC CURRENT COMPARATOR

Even though the FAIR facility is designed to provide ion beams with highest beam intensities, during slow extraction with long extraction times of up to 10 s the mean beam current drops to the nanoampere range. Thus special instruments are required to allow online beam

ISBN 978-3-95450-177-9

monitoring of beam currents well below the detection threshold of standard DC current transformers [4]. Recently, the long-term development project of a Cryogenic Current Comparator (CCC) at GSI yielded very promising results with a sensitivity of 120 pA/√Hz, i.e. three orders of magnitude lower than the sensitivity of a standard fluxgate DCCT. The detection principle of the CCC is based on the precise measurement of the beam's azimuthal magnetic field. In the CCC setup shown in Fig. 3 the ion beam passes a toroidal sensor assembly that consists of a high-permeability magnetic alloy toroid acting as a flux concentrator. This toroid is enclosed in a superconducting pick-up coil connected to a high-precision DC-SQUID with readout electronics. Both, the pick-up coil and the toroid are encapsulated inside a meander-shaped magnetic shield to effectively attenuate any disturbing external magnetic field. The whole CCC sensor has to be embedded inside a lHe-cryostat because the DC-SQUID, as well as the magnetic shield require operation at 4.2 K [5].

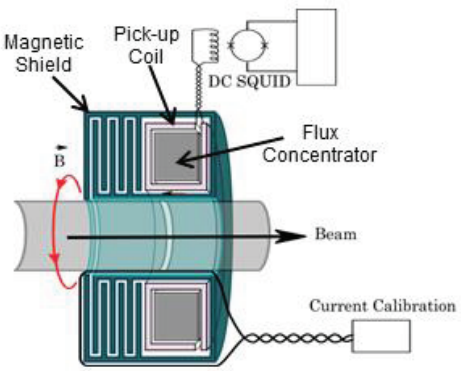

Figure 3: Schematic view of the CCC sensor assembly.

The aim of the CCC development was to further improve the current sensitivity and frequency behaviour of the CCC setup. Since the CCC current resolution is limited by the overall system noise, the electromagnetic noise contribution of each sensor part had been studied. To increase the attenuation of any disturbing non-azimuthal field component the superconducting magnetic shield was geometrically optimized using FEM simulations [6]. In addition, the magnetic permeability of various toroid materials was studied at lHe temperature, and finally nano-crystalline Nanoperm material was selected due to its high permeability and constant frequency response [7]. Also the noise figure of the DC-SQUID sensor was significantly improved by replacing the formerly used but meanwhile outdated UJ-111 SQUID with a commercial DC-SQUID and readout unit. Thus, all constituents of the CCC sensor setup underwent significant upgrades, however, beam tests with the existing CCC prototype setup revealed additional sources of distortions that had not been investigated so far. During beam tests with a 600 MeV/u Ni^{26+}-beam spurious flux jumps of the SQUID signal were observed, that deteriorate the intensity measurement. An example is depicted in Fig. 4. The blue curve shows the long-term CCC signal for three successive spills, where the baseline shift for the first two spills is clearly visible. The inserts show the spill signals with higher time resolution. Obviously, the red intensity signal was strongly disturbed by a flux jump, caused by strong high frequency noise exceeding the slew rate of the SQUID flux-locked loop electronics. Because of the periodic nature of the SQUID V-ϕ characteristic, a flux jump causes a sudden baseline offset in the intensity plot, corresponding to integer multiples of ϕ_0 (ϕ_0=h/2•e, elementary flux quantum). For the given setup the beam current corresponding to 1 ϕ_0 is 69.53 nA.

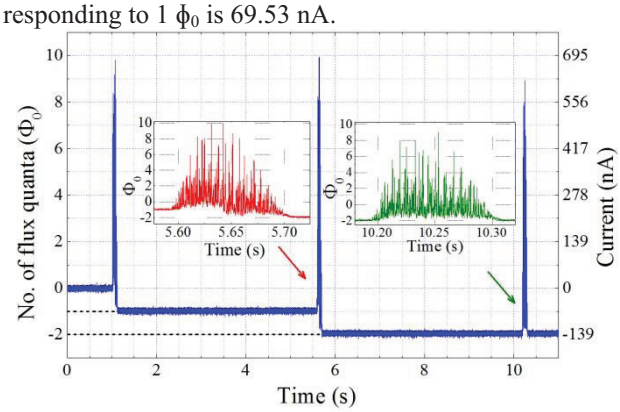

Figure 4: Flux jump of the SQUID signal observed during slow extraction of 5×10^9 Ni^{26+} with 125 ms extraction time, i.e. an average current of 60 nA (see text).

Another challenge for stable long-term CCC operation is the extreme sensitivity of its superconducting elements to temperature fluctuations. During beam tests with the CCC prototype small pressure variations in the liquid helium surface and the resulting temperature fluctuations were found to cause long-term drifts as well as short term fluctuations in the CCC baseline. Detailed investigations of these effects are presently ongoing [8].

CONCLUSION

Online beam current measurements for the upcoming FAIR facility make special demands for purpose-built beam current monitors. The development of a TDCCT yields promising results and the system will be upgraded to a zero-flux instrument. Investigations on the CCC performance and several optimization steps gave important input for the advanced CCC system, which is presently under construction for FAIR.

REFERENCES

[1] http://www.fair-center.eu

[2] http://www.dowaytech.com/en/.

[3] E. Soliman, K. Hofmann, H. Reeg, M. Schwickert, Proc. IEEE Sensors Applications Symposium 2016, pp 1-5.

[4] http://www.bergoz.com/index.php?option=com_content&view=article&id=35&Itemid=472

[5] A. Peters, *et al.*, Proc. BIW 1998, p.163 (1998).

[6] H. de Gersem, *et al.*, Proceedings of EPNC 2016, pp 95-96.

[7] R. Geithner, *et al.*, Cryogenics 54, p. 16 (2013).

[8] T. Sieber, *et al.*, WEPG40, these proceedings.

ISBN 978-3-95450-177-9

MICRO PATTERN IONIZATION CHAMBER WITH ADAPTIVE AMPLIFIERS AS DOSE DELIVERY MONITOR FOR THERAPEUTIC PROTON LINAC

E. Cisbani*, A. Carloni, S. Colilli, G. De Angelis, S. Frullani, F. Ghio,
F. Giuliani, M. Gricia, M. Lucentini, C. Notaro, F. Santavenere,
A. Spurio, G. Vacca, Istituto Superiore di Sanità, 00161 Rome, Italy
E. Basile, Azienda Ospedaliera Papardo, 98158 Messina, Italy
A. Ampollini, P. Nenzi†, L. Picardi, C. Ronsivalle,
M. Vadrucci, ENEA C.R. Frascati, 00044 Frascati (Rome), Italy
D. M. Castelluccio, ENEA (FSN-SICNUC-PSSN), 40129 Bologna, Italy
C. Placido, Sapienza University of Rome, 00185 Rome, Italy
[1]also at Istituto Superiore di Sanità, 00161 Rome, Italy

Abstract

A dedicated dose delivery monitor is under development for the TOP-IMPLART proton accelerator, the first LINAC for cancer therapy. It is expected to measure the beam intensity profile to precisely monitor the fully active 3+1D (x/y/z and intensity) dose delivery of each short pulse (few µs, 0.1-10 µA pulse current at ~ 100 Hz) of the therapeutic proton beam (up to 230 MeV). The monitor system consists of planar gas chambers operating in ionization regime with cathode plane made of micro pattern pads alternately connected by orthogonal strips. The dedicated readout electronics features trans-impedance amplifier that dynamically adapts its integrating feedback capacitance to the incoming amount of charge, then opportunistically changing its gain. The measured absolute sensitivity is about 100 fC (better than 0.03 relative sensitivity), the dynamic range up to 10000 (2 gain settings) with time response at the level of few ns, and virtually no dead time. Small scale chamber prototype (0.875 mm pitch pads) and readout electronics have been tested and characterized under both electron (5 MeV) and proton (up to 27 MeV) beams.

INTRODUCTION

According to the World Health Organization, cancers are the leading causes of morbidity and mortality; the annual cases are expected to rise by about 70% in the next 2 decades [1]. The clinical issue is exacerbated by the relevant costs of the cancer care (compare to euro 126 billion/years in European Union in 2009 [2]). Several approaches have been developed for cancer control and cure: surgery, chemotherapy, immunotherapy, radiotherapy, hormonal therapy, ultrasound therapy. Hadrontherapy, which mainly uses accelerated protons or ions, is rapidly expanding in cancers treatment, especially for the control of tumours in the proximity of vital organs or close to radiosensitive healthy organs. In fact hadrontherapy is an intrinsically highly accurate technique, due to the peculiar hadron property to release the largest amount of dose at the end of its path in the tissue while the lateral spread is small and the entrance integral dose is relatively low. Moreover the penetration in the body depends on the initial energy of the hadron. This accuracy results in effective irradiation of the tumour, thereby reducing the dose to the surrounding healthy tissues and thus leading to lower morbidity. However hadrontherapy construction and operation costs are large compared to the other therapies and this represents a serious drawback for its diffusion.

The innovative TOP-IMPLART project [3] moves in the direction of highest therapeutic impact and at the same time costs reduction by the exploitation, for the first time in cancer therapy, of a dedicated LINAC proton accelerator. Key features offered by the LINAC are the pulse current modulation (fully intensity modulated therapy), high repetition rate (better organ motion compensation), negligible power loss from synchrotron radiation (easier radioprotection), simpler injection and extraction than in circular accelerators, modular construction.

The highest conformation of the dose delivery achievable by the TOP-IMPLART requires an accurate monitoring of the beam parameters on a pulse by pulse basis; the dose delivery shall provide real-time measurements of the beam intensity profile, beam centroid position and its direction in order to guarantee that the prescribed dose is optimally delivered. The peculiar characteristics of the TOP-IMPLART LINAC[1] reflect on the following main requirements for the dose delivery monitor: good spatial resolution ~ 0.1 mm, large input dynamic range ≥ 10^4, good sensitivity ~ 100 fC, rapid response < 1 ms.

DOSE DELIVERY DETECTOR AND MULTI GAIN READOUT ELECTRONICS

The dose delivery monitor will be based on a set of 2 independent transmission ionization chambers with segmented readout planes (~ 30 × 30 cm^2 active transverse area). Design of the chamber cathode exploits recent developments in

* evaristo.cisbani@iss.it, contact person
† paolo.nenzi@enea.it, presenter at the conference

[1] Beam specifications: cross section ~ 1 mm, peak current 0.1–10 µA, average current 10 nA, pulse width 1–5 µs, pulse frequency 1–100 Hz.

ISBN 978-3-95450-177-9

Micro Pattern Gaseous Detectors (MPGD) with copper pads connected by strips on both side of a thin (50 µm kapton foil) to guarantee simultaneous x and y readout; the chambers will operate in ionization region (high voltage around 200-400 V) to collect the whole ionized charge and at the same time minimize saturation effects and prevent discharge phenomena. The gap between anode and cathode will be filled by air (or mixture of inert gases) whose environmental parameters are continuously monitored (to correct for its density, mainly).

A small scale ~ 7×7 cm^2 prototype has been developed to test the main design solutions and eventually improve them. A peculiar cathode plane consisting of x and y strips (pitch of 0.875 mm with a pad-like pattern (Fig. 1) has been adopted to maximize the field uniformity (according to Garfield based analysis [4]), to reduce the overall chamber thickness (water equivalent thickness of 0.16 mm) and to obtain both coordinates on a single chamber.

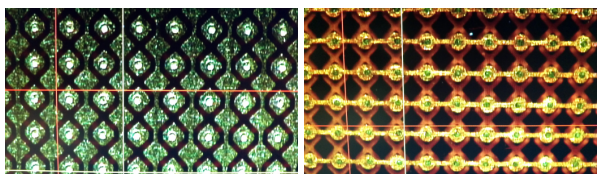

Figure 1: Detail of the layout of the cathode plane with the pad pattern; left: side exposed to the charge collection, right: external side with strips connected to the pads of the other side by filled vias.

64 out of 80 available channels on each axis are readout by a dedicated electronics able to offer high sensitivity and wide dynamic range to match the variation of the single proton pulse current during the planned treatment. The electronics basically consist of two main blocks: the input stage where each channel has a trans-impedance amplifier and a multi gain amplification logic; the output stage with a multiplexing logic that route the collected charges of the different channels into a single ADC input as well as the status information of each channel gain.

The multi gain amplification mechanism (Fig. 2) is the main peculiar aspect of the readout: as soon as the voltage on the feedback capacitor C_1 of the trans-impedance amplifier is larger than a precise voltage reference, an analog switch (driven by a latch) inserts an additional capacitor C_2, typically with $C_2 > C_1$ in parallel to the initial capacitor C_1 thus reducing the gain of the trans-impedance amplifier and therefore increasing the dynamic gain of the system. The information of the analog switch status is recorded together with the total charge on the feedback capacitor(s) related to V_{OUT}. This mechanism can be extended to several gain states; the prototype electronics consists of two gains only. A multiplexed sample and hold scheme is used, in the prototype, to read all the channels information on a single ADC.

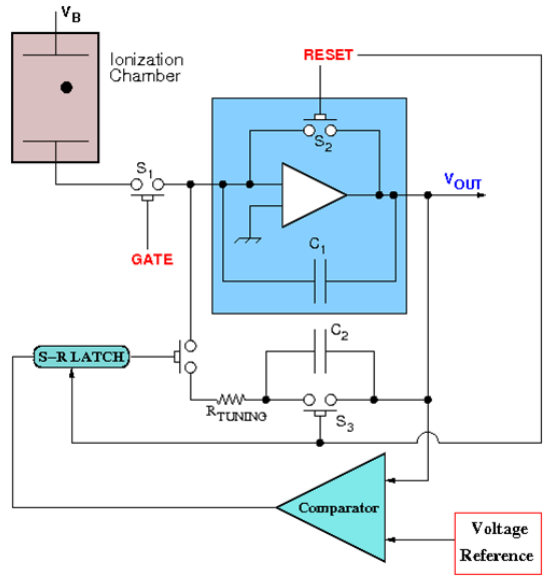

Figure 2: Schematic representation of the adaptive multi gain amplification logic.

The open box of the chamber prototype system is presented in Fig. 3, where the electronics cards are clearly visible.

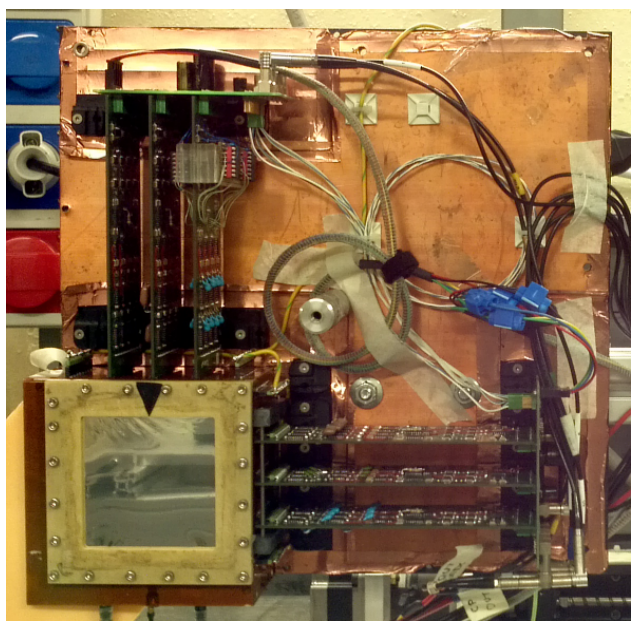

Figure 3: The small chamber prototype (bottom left) and the acquisition electronics, normally shielded by a plastic box with an internal copper layer all around, as visible behind the boards.

GAIN CHANGE CALIBRATION PROCEDURE

Each gain state has its own pedestal value which needs to be measured to correctly estimate the collected charge and then the beam intensity. While the pedestal of the first state

ISBN 978-3-95450-177-9

is directly measured by the conventional procedure (acquisition without beam), the current electronics prototype does not include a direct mechanism to force a gain change and therefore the conventional procedure cannot be used. On the other hand a somehow electronics independent evaluation of the pedestals of the other states can be useful for a better characterization and debugging. For these reasons, a relatively simple method has been developed: assuming each channel i of the electronics at the end of a pulse e can be in one of two gain states g_i^1 and g_i^2, with $g_i^1 > g_i^2$; the collected charge $Q_i(e)$ on the strip i for a given beam pulse e is

$$Q_i(e) \propto g_i(e) \left[D_i(e, g_i) - D_i^p(g_i) \right] \quad (1)$$

where $D_i(e, g_i)$ is the ADC value of the electronic channel connected to the strip (depend on pulse e state of the channel) and $D_i^p(g_i(e))$ is the pedestal of that channel, which depends on the state of the electronics.

At the transition between the two states, the collected charge must be a continuous curve. The continuity condition can be expressed by:

$$\max_{e \in g(e)=g^1} Q(e) = \min_{e \in g(e)=g^2} Q(e) \quad (2)$$

where the strip index i has been dropped for clarity.

In fact the raw ADC values corresponding to the charge $Q(e)$ as presented in Fig. 4 does show an evident discontinuity due to the fact that the pedestals are not subtracted.

Substituting Eq. (1) in the previous Eq. (2), one gets:

$$g^1 \left[D_{max}(e, g^1) - D^p(g^1) \right] = g^2 \left[D_{min}(e, g^2) - D^p(g^2) \right]$$

which can be used to estimated the pedestal $D^p(g^2)$ of state g^2 when the corresponding pedestal of state g^1 is known (by conventional pedestal estimation, as mentioned above), and then fulfill the continuity condition.

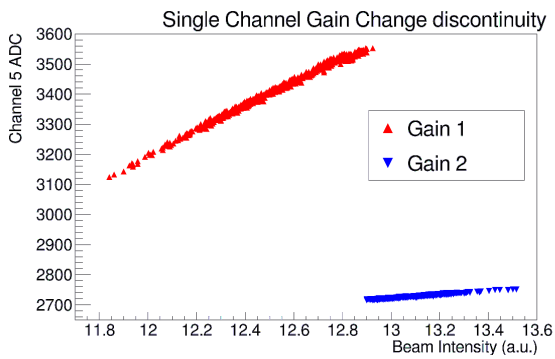

Figure 4: Collected charge (as ADC raw values) on a channel that undergoes gain changes due to the beam intensity pulse-to-pulse variations. Each point represents a pulse. The gap between the two lines of points at the discontinuity (x 12.9) is related to the pedestal of the two gain states as discussed in the text. The slopes of the lines are proportional to the feedback capacitances (referring to Fig. 2: $C_1 = 10$ pF and $C_2 = 100$ pF).

PRELIMINARY RESULTS WITH THE TOP-IMPLART PROTON BEAM

The dose delivery prototype has been preliminary tested under a 5 MeV pulsed electron beam and recently installed at the end of the TOP-IMPLART beam line which is currently able to deliver a rather stable 27 MeV beam as described in [5].

The electron accelerator had a significant level of electromagnetic induced noise; measurements in this conditions have been valuable to optimize, in particular, the signal-to-noise response of the dose delivery prototype, improving shielding and cabling complexity.

The TOP-IMPLART LINAC offers a much more electromagnetic friendly environment and the good performance of the dose delivery has immediately emerged as shown in one of the first acquisition of the beam x and y intensity profiles as function of the beam pulses, reported in Fig. 5, where the dose delivery record clean beam oscillations over pulses.

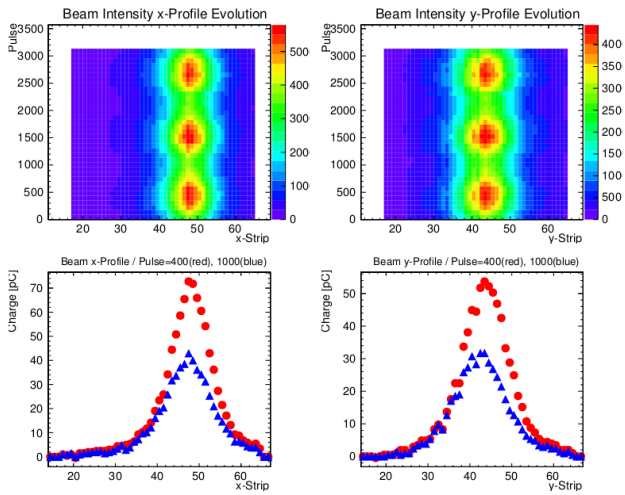

Figure 5: Example of beam transverse profile as recorded by the dose delivery prototype chamber. Top: x and y profiles versus beam pulses; bottom: x and y profiles corresponding to the highest and lowest intensity pulses. Beam frequency of 10 Hz. The beam oscillations of $\sim$ 2 min period were caused by small uncompensated temperature fluctuations in the cavities.

The single channel response equalization has been obtained comparing the beam profiles acquired at approximately 1 m from the beam pipe exit window (reference run) to the corresponding Gaussian fits (left plots of Fig. 6); the correction factors are estimated for each strip as the ratio of the fit predicted charge and the measured one (few known bad channels have been masked). These correction factors are applied to all subsequent measurements and an example of the good quality of the equalization is reported on the right plots of Fig. 6, which have been obtained in different high voltage and position respect to the reference run.

The dose delivery is currently under a preliminary dosimetric calibration by comparing its response to the response

ISBN 978-3-95450-177-9

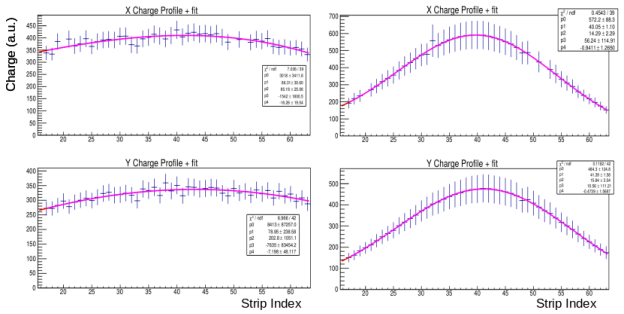

Figure 6: Equalization of the channel responses; left: profiles of the reference run used for the equalization (high voltage is 400 V); right: equalized channel responses (high voltage is 300 V, different position relative to the beam pipe exit window); the error bars represent the statistical errors and are mainly due to the beam fluctuation. The curves on top of the data are Gaussian fits. Three known faulty channels are masked in the x axis profiles.)

of small irradiated Gafchromic films and Alanine dosimeter pills. The chamber and the small dosimeters experience a different irradiation fields and their correlation need a careful evaluation. In this direction the two 1-dimensional profiles of the beam measured by the chamber have been transformed in a 2-dimensional beam intensity cross section assuming that the two x and y accumulated profiles does correspond to the respective differential profile on the single strips of the orthogonal axis; that is:

$$Q_{ij} = \frac{Q_i Q_j}{\sum_i Q_i + \sum_j Q_j}$$

where Q_i and Q_j are the charge collected on strips i and j of x and y axes respectively while Q_{ij} is the estimate charge on pixel i, j represented by the corresponding intersection of the two strips. On the other hand, the collected (or estimated) charges can be converted into local delivered dose by means of linear calibration factors, provided by the dosimetric measurements[2].

Figure 7 reports an example of the dose profiles and the reconstructed dose cross section, where the dose factors have been estimated by simple analytic considerations[3]; the obtained dose values are used as a preliminary orientation during the ongoing tests.

CONCLUSIONS

The modular design of a LINAC accelerator offers the rather unique opportunity of a concurrent exploitation of the beam during its realization, and therefore an expected

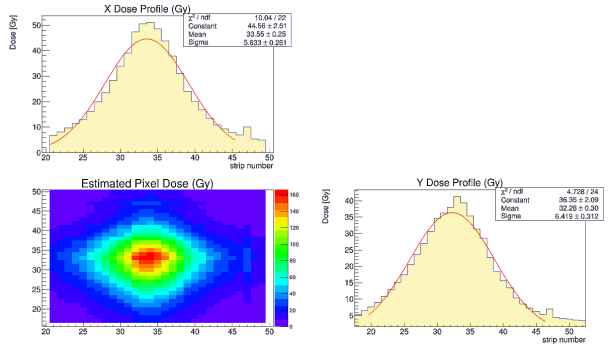

Figure 7: Beam 1-dimensional measured profiles and derived (under specific assumptions of the shape of the beam) 2-dimensional intensity cross section. The red curves are Gaussian fits of the beam profiles.

simpler commissioning and tuning of the beam itself and the components of the final therapeutic system.

The prototype of the dose delivery monitor for the TOP-IMPLART, the first LINAC accelerator dedicated to proton therapy, is under test, characterization and calibration using the currently available 27 MeV proton beam.

The preliminary results, few of them reported above, show a good response of the system, though deeper tests are underway to fully characterize key features such as the adaptive multi gain electronics as well as the saturation limit of the chamber. Possibility of an adaptive mechanism for the bias voltage of the chamber, in analogy to the multi gain electronics, is under evaluation to extend the intrinsic dynamics of the ionization regime.

ACKNOWLEDGEMENT

Large part of the latest achievements of the presented work has been funded by a research contract from the Italian Regione Lazio.

REFERENCES

[1] WHO Fact sheet n. 297, http://www.who.int/mediacentre/factsheets/fs297/en/

[2] R. Luengo-Fernandez *et al.*, "Economic burden of cancer across the European Union: a population-based cost analysis", *The Lancet Oncology*, vol. 14, no. 12, p. 1165, Nov. 2013.

[3] C. Ronsivalle *et al.*, "The TOP-IMPLART Project", *Eur. Phys. J. Plus*, vol. 126, no. 68, p. 1, Jul. 2011.

[4] D.M. Castelluccio, "A novel realtime beam monitoring system in proton therapy treatments", Medical Physics Specialization thesis, Technology and Health Department, Italian National Institute of Health, Rome, Italy, 2010.

[5] P. Nenzi *et al.*, "Commissioning Results of the TOP-IMPLART 27 MeV Proton Linear Accelerator", presented at IBIC2016, Barcelona, Spain, paper WEPG29, this conference.

[2] It is worth mention that in clinical operations the data of the calibrated dose delivery system are compared to those evaluated and provided by the treatment planning system.

[3] The dose factor for generic sensitive element k is approximately given, in the ionization regime with full charge collection, by $d_k/Q_k = w_E/(\rho_{air} v_k)$, where w_E is the effective single pair ionization energy, ρ_{air} the density of the air at the measurement conditions, v_k, probably the trickiest parameter, is the active volume contributing to the charge in k.

ISBN 978-3-95450-177-9

BUNCH ARRIVAL-TIME MONITORING FOR LASER PARTICLE ACCELERATORS AND THOMSON SCATTERING X-RAY SOURCES

J. Krämer, J.P.Couperus, A. Irman, A. Köhler, M. Kuntzsch, U. Lehnert, P. Michel, U. Schramm, O.Zarini
Helmholtz-Zentrum Dresden-Rossendorf, Dresden, Germany

Abstract

The ELBE center of high power radiation sources at Helmholtz-Zentrum Dresden-Rossendorf combines a superconducting CW linear accelerator with Terawatt- and Petawatt- level laser sources. Figure 1 shows a layout of the facility and an overview of the secondary sources. Key experiments rely on precise timing and synchronization between the different radiation pulses. An online single shot monitoring system has been set up in order to measure the timing between the high-power Ti:Sa laser DRACO and electron bunches generated by the conventional SRF accelerator. This turnkey monitoring system is suitable for timing control of Thomson scattering x-ray sources and external injection of electron bunches into a laser wakefield accelerator.

INTRODUCTION

ELBE Accelerator and High-Power Lasers

The ELBE accelerator produces electron bunches up to an energy of 40 MeV in continuous wave (CW) operation [1]. The nominal repetition rate is 13 MHz while various pulse patterns can be generated by the two injectors. The first injector is a thermionic DC-gun operating at 235 kV followed by two normal conducting buncher cavities. It provides electron pulses with a charge of up to 100 pC. The second injector is a superconducting photo gun (SRF-Gun) that will provide electron bunches with a charge of up to 1 nC [2]. The main accelerator consists of two cryo modules, each equipped with two 9-cell TESLA-type cavities [3].

Adjacent to the conventional accelerator, two high power lasers have been set up, enable new experiments with high electric fields and ultra-fast time scales. The chirped pulse amplification Ti:sapphire system DRACO (Dresden laser acceleration source) produces laser pulses up to 6 J at a repetition rate of 10 Hz or 45 J at 1 Hz [4].

A fully diode-pumped laser system - PEnELOPE (Petawatt, Energy-Efficient Laser for Optical Plasma Experiments) is being constructed in the same area. A five stage amplifier system relying on Yb:CaF2 as gain medium is designed for pulse energies of 150 J and a pulse duration of <150 fs at a repetition rate of 1 Hz [5].

Main fields of research are the development of novel compact and brilliant sources of energetic particle beams and potential applications, e.g., in the field of radiation oncology [6].

Thomson X-ray Source

The combination of high power lasers and the ELBE accelerator offers the opportunity to explore the physics of high-intensity laser-electron interaction. One application is the operation of a picosecond narrow-bandwidth Laser-Thomson-backscattering X-ray source. Here both beams are interacting in a dedicated target chamber. The generated narrowband X-rays are highly collimated and can be reliably adjusted from 12 keV to 20 keV by tuning the electron energy (24–30 MeV) [7].

In order to provide a constant photon flux the spatial as well as the temporal overlap between both pulses have to be ensured. Both beams are transpoerted up to 100 meters so that temperature drifts and mechanical vibrations affect the pointing and arrival-time stability at target position.

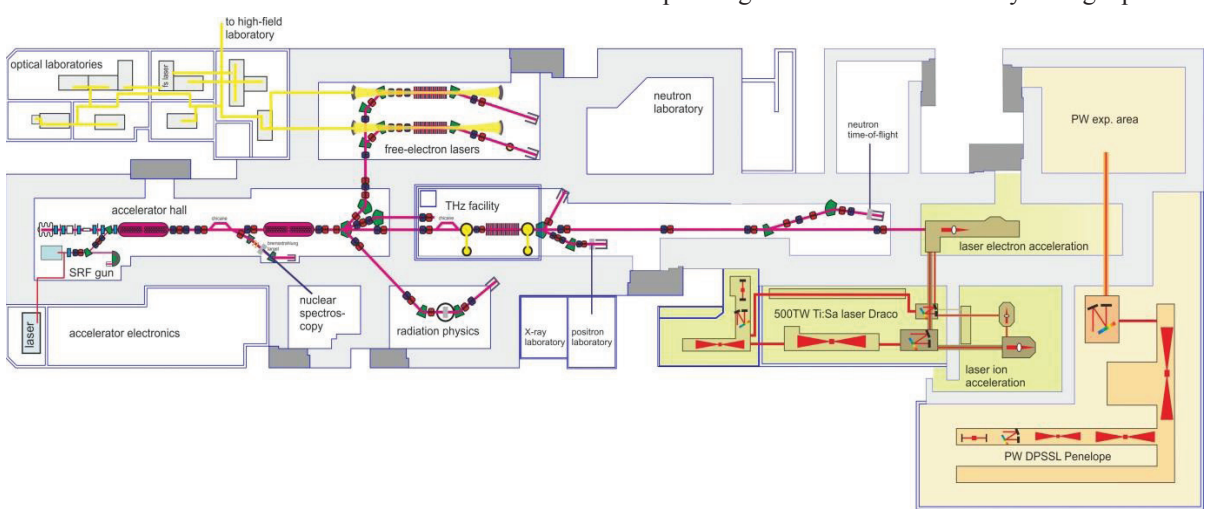

Figure 1: Layout of the ELBE - Center for high power radiation sources.

ISBN 978-3-95450-177-9

ARRIVAL-TIME MONITOR

Measurement Setup

The implemented bunch arrival-time monitor (BAM) directly measures the temporal relation between the laser pulse and the electron bunch next to the target for every single shot. Accordingly, no further external timing reference is needed. A broadband RF pickup acquires a probe of the particle bunch's electric field and modulates a fraction of the high power laser pulse in a fast electro-optical modulator (EOM). The amplitude modulation gives a direct measure for the timing between both beams. Figure 2 schematically shows the interaction point of both beams and the implemented BAM diagnostic.

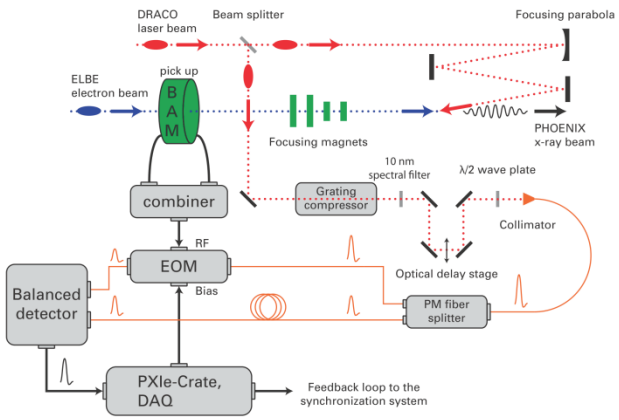

Figure 2: Thomson scattering X-ray source with implemented arrival-time online diagnostic.

The reference signal from the electron bunch is generated by a FLASH-type button pickup, developed by DESY [8]. It has an RF bandwidth of 12 GHz and was used before for the ELBE-BAM system operating at 1550 nm.

A beam splitter takes out a fraction of the main DRACO laser pulse serving as the optical reference signal. It is sent through a grating compressor to compensate for the chromatic dispersion in the following optical fiber. A spectral filter can be applied to adapt for the spectral bandwidth of the EOM. Limiting the optical bandwidth improves the extinction ratio of the used EOM (Photline NIR-MX800-LN-20) which gives a higher dynamic range and better resolution of the setup [9]. The EOM has a RF bandwidth of about 25 GHz.

An optical delay line allows adjusting the optical path length of the laser reference signal in order to match to working point of the BAM to the temporal overlap of the laser and electron beam of the Thomson source. Furthermore, calibrating the BAM is possible during operation without affecting the X-ray production.

After coupling the laser into an optical fiber, the laser signal is divided in a reference path and a measurement path using a polarization maintaining (PM) fiber splitter. The coupling ratio is chosen that the insertion loss of the EOM is compensated and both signals have the same amplitude on the detector at the working point.

The reference signal is used to normalize intensity fluctuations of the high power laser, which would appear as an arrival-time shift.

It has been found that a static splitting ratio gives not enough flexibility to adjust the power levels on the detector. The next iteration of the BAM will use a free space power divider based on a polarizing beam cube (PBC) and half lambda wave plates.

The balanced detector amplifies the amplitude difference between reference and measurement signal with a selected gain. The used model provides also the single detector responses so that signal conditioning can be done in the digital domain in order to minimize the noise floor of the measurement.

For the digital data processing a National Instruments PXIe-Crate is used. It is equipped with a fast ADC operating at 250 MHz to acquire the detector signals and a FPGA to calculate the relative arrival-time and to generate time stamps for each individual pair of pulses.

In the future the timing signal can be used for a slow feedback on the synchronization system between laser and electron accelerator. By adjusting the phase of the laser oscillator with an electronic phase shifter the arrival-time on the target position can be kept constant.

FIRST RESULTS

The setup has recently been commissioned and characterized during a Thomson beam time. Therefor a calibration measurement has been performed, meaning a temporal shift of the laser pulse with respect to the electron pulses. Figure 3 shows the calibration curve after optimization and the used working point. The rising edge has been linearized by fitting an appropriate function response function to the inverse of the response function. The system gives a resolution of 167 fs RMS at a bunch charge of 47 pC. The dynamic range allows linear measurements within 27 ps before it comes to over-modulation in the EOM which gives ambiguous measurement results.

The resolution is mainly limited by high losses of the RF cabling (3.5 meters) due to spatial restriction and the imbalance of signal path and reference path.

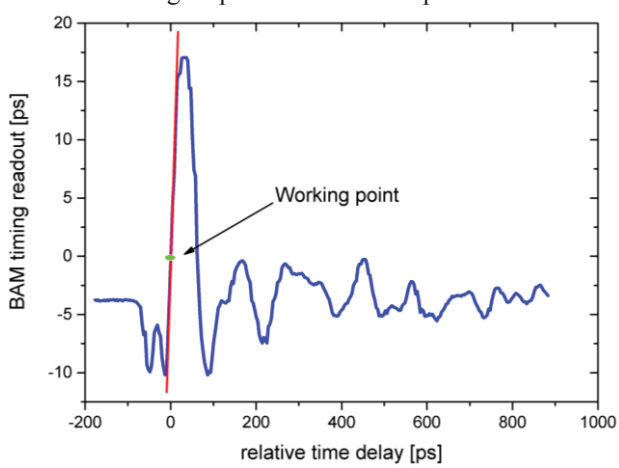

Figure 3: Calibration plot of the BAM setup.

ISBN 978-3-95450-177-9

The BAM has been used to monitor the arrival-time during the operation of the X-ray source. Figure 4 shows the relative arrival-time jitter of 3000 consecutive shots at 10 Hz repetition rate. A drift of 15 ps peak-to-peak between both sources could be observed while the fast jitter is on the order of 2 ps peak-to-peak.

This corresponds to measurements that have been taken earlier with BAMs installed at the ELBE beamline [10].

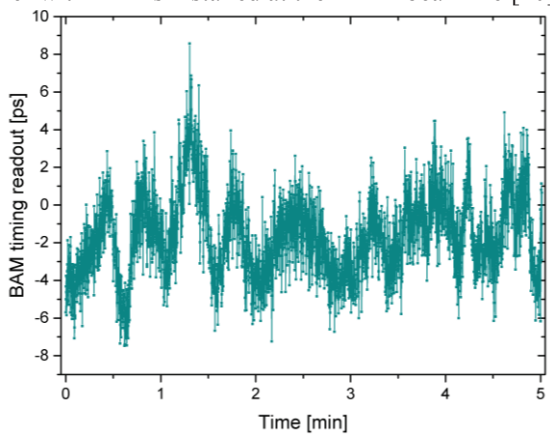

Figure 4: Measured arrival-time jitter between laser pulses and electron bunches on a time scale of 5 minutes.

CONCLUSION

An online timing diagnostic has been set up which enables non-invasive and single shot timing measurements with high accuracy. In the first commissioning run, a resolution of 167 fs RMS at a bunch charge of 47 pC was demonstrated.

The system has been used to monitor the arrival-time between high power laser pulses and relativistic electron bunches. A fluctuation of more than 15 ps could be observed on a five minute time scale.

OUTLOOK

The diagnostic system can be used for systematic jitter studies in order to improve the machine stability. The recovered signal can furthermore be used for a slow feedback to stabilize the arrival-time on target.

The resolution of the online monitor can be improved by using an RF-pickup providing a signal with higher spectral content. At ELBE two EuXFEL-type pickups are in use offering a spectral bandwidth of up to 40 GHz [11]. This pickup is foreseen as a future upgrade of the described setup.

As a next step the PM fiber splitter will be replaced by a free-space power divider based on a polarizing beam cube. By adjusting the preceding lambda half wave plate the power level can be perfectly balanced on the photo diodes.

REFERENCES

[1] F. Gabriel, P. Gippner, E. Grosse, D. Janssen, P. Michel, H. Prade, a. Schamlott, W.Seidel, a. Wolf, R. Wünsch, "The Rossendorf radiation source ELBE and its FEL projects", Nuclear Instruments and Methods in Physics Research Section B:Beam Interactions with Materials and Atoms 161–163 (2000) 1143–1147A.

[2] Arnold, M. Freitag, P. Murcek, *et al.*, "Commissioning and First RF Results of the Second 3.5 Cell SRF Gun for ELBE", 27th Linear Accelerator Conference (LINAC14), Geneva, Switzerland, 2014.

[3] B. Aune *et al.*, "Superconducting TESLA cavities", Phys. Rev. ST Accel. Beams 3, 092001.

[4] K. Zeil, S.D. Kraft, S. Bock, M. Bussmann, T.E. Cowan, T. Kluge, J. Metzkes, T. Richter, R. Sauerbrey, U. Schramm, "The scaling of proton energies in ultrashort pulse laser plasma acceleration", New Journal of Physics 12 (4) (2010) 045015.

[5] M. Siebold, F. Röser, M. Löser, D. Albach, U. Schramm, PEnELOPE - a high peak-power diode-pumped laser system for laser-plasma experiments, Proc. SPIE 8708, 870805 (2013).

[6] K. Zeil, M. Baumann, E. Beyreuther, T. Burris-Mog, T.E. Cowan, W. Enghardt, L. Karsch, S.D. Kraft, L. Laschinsky, J. Metzkes, D. Naumburger, M. Oppelt, C. Richter, R. Sauerbrey, M. Schuerer, U. Schramm, J. Pawelke, "Dose controlled irradiation of cancer cells with laser accelerated proton pulses", *Appl. Phys. B 110*, 437 (2013)

[7] A. Jochmann, A. Irman, M. Bussmann, J. P. Couperus, T. E. Cowan, A. D. Debus, M. Kuntzsch, K. W. D. Ledingham, U. Lehnert, R. Sauerbrey, H. P. Schlenvoigt, D. Seipt, Th. Stöhlker, D. B. Thorn, S. Trotsenko, A. Wagner, and U. Schramm, "High Resolution Energy-Angle Correlation Measurement of Hard X Rays from Laser-Thomson Backscattering", *Phys. Rev. Lett. 111*, 114803, http:\\dx.doi.org/10.111.4803

[8] F. Löhl, V. Arsov, M. Felber, K. Hacker, W. Jalmuzna, B. Lorbeer, F. Ludwig, K.-H. Matthiesen, H. Schlarb, B. Schmidt, P. Schmüser, S. Schulz, J. Szewinski, A. Winter, J. Zemella, "Electron Bunch Timing with Femtosecond Precision in a Superconducting Free-Electron Laser". In: Physical Review Letters 104 (2010), S. 4.

[9] iXblue, http://www.photonics.ixblue.com/

[10] M. Kuntzsch, U. Lehnert, R. Schurig, *et al.*, "CW Beam Stability Analysis in Time and Frequency Domain", 3rd International Beam Instrumentation Conference (IBIC 2014), Monterey, USA, 2014.

[11] A. Angelovski, M. Kuntzsch, M. K. Czwalinna, *et al.*, "Evaluation of the cone-shaped pickup performance for low charge sub-10~fs arrival-time measurements at free electron laser facilities". In: *Physical Review Special Topics - Accelerators and Beams* 18 (2015), S. 012801.

ISBN 978-3-95450-177-9

NOVEL APPROACH TO THE ELIMINATION OF BACKGROUND RADIATION IN A SINGLE-SHOT LONGITUDINAL BEAM PROFILE MONITOR

H. Harrison,*G. Doucas, A. J. Lancaster, I. V. Konoplev, H. Zhang,
The John Adams Institute, Department of Physics,
University of Oxford, Oxford OX1 3RH, United Kingdom
A. Aryshev, M. Shevelev, N.Terunuma, J. Urakawa,
KEK: High Energy Accelerator Research Organization, 1-1 Oho, Tsukuba, Ibaraki 305-0801, Japan

Abstract

It is proposed to use the polarization of coherent Smith-Purcell radiation (cSPr) to distinguish between the cSPr signal and background radiation in a single-shot longitudinal bunch profile monitor. A preliminary measurement of the polarization has been carried out using a 1 mm periodic metallic grating installed at the 8 MeV electron accelerator LUCX, KEK (Japan). The measured degree of polarization at $\theta = 90°$ (300 GHz) is 72.6 ± 3.7%. To make a thorough test of the theoretical model, measurements of the degree of polarization must be taken at more emission angles - equivalent to more frequencies.

INTRODUCTION

Developments in particle accelerators place increasing demand on beam diagnostic tools. At facilities operating with sub-ps bunch lengths or experiencing large bunch-to-bunch variation, a non-destructive single-shot longitudinal bunch profile monitor is essential. cSPr has been suggested as a technique for non-destructive longitudinal bunch diagnostics, using spectral analysis of the radiation to determine the bunch profile [1]. This has been successfully demonstrated for a "multi-shot" system [2], now a "single-shot" monitor is being designed. The new monitor will be able to extract all the information needed from each bunch to reconstruct its longitudinal profile. The proof-of-principle "multi-shot" experiments carried out at FACET, SLAC (USA) faced the challenge of extracting the cSPr signal from a high background environment, a problem that needs to be taken into account for any future monitor. It is proposed to use the polarization of cSPr to separate the signal from the background radiation - which is likely to be unpolarized [2] - according to the relation shown in Eq. 1:

$$G_{\parallel} = gG_{\perp} = g\left(\frac{I_{\parallel} - bI_{\perp}}{a - b}\right) \tag{1}$$

where the cSPr signal G_i is expressed in terms of the measured signal I_i and the ratios of the two orientations of radiation $a = \frac{G_{\parallel}}{G_{\perp}}$ and $b = \frac{B_{\parallel}}{B_{\perp}}$.

Previous studies have shown that cSPr is polarized [2–4], however, there has not yet been an extensive study of this property or a conclusive comparison with any theoretical model. Before this idea can be incorporated into the design of the single-shot cSPr monitor it is necessary to perform accurate measurements of the polarization of cSPr and demonstrate that it is possible to predict its degree of polarization via simulation. This paper will demonstrate a good preliminary agreement between the experiment and theory.

* hannah.harrison@physics.ox.ac.uk

THEORY AND SIMULATION

Smith-Purcell radiation is emitted when a charged particle travels above a periodic grating. The particle induces a surface current on the grating surface which emits radiation at the discontinuities of the grating. The radiation is spatially distributed according to the following dispersion relation:

$$\lambda = \frac{l}{n}\left(\frac{1}{\beta} - \cos\theta\right) \tag{2}$$

where λ is the measured wavelength at observation angle θ, $\beta = \frac{v}{c}$ is the normalized electron velocity, l is the grating periodicity and n is the order of emission of radiation.

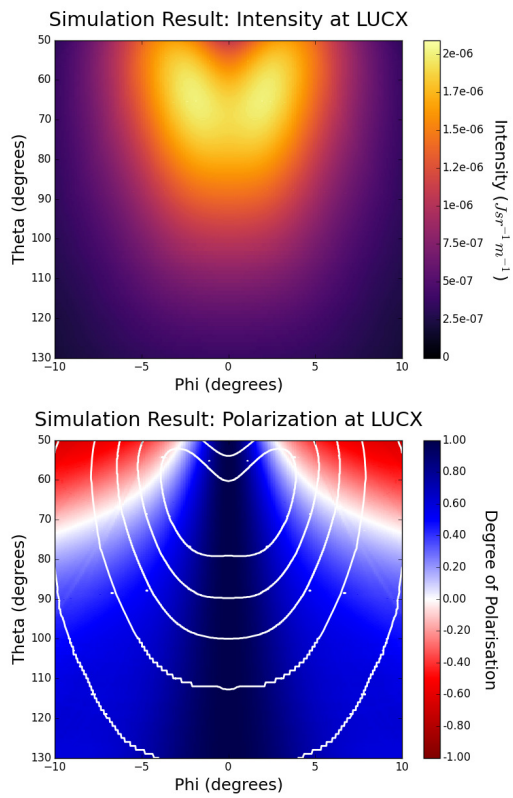

Figure 1: Simulation of intensity (top) and degree of polarization (bottom, contours show intensity), of cSPr generated by the interaction of a 1 mm period grating and an 8 MeV beam. θ and ϕ are the angles along and around the beam.

ISBN 978-3-95450-177-9

The theory of Smith-Purcell radiation has been written about and can be found in a number of papers [5, 6]. The theoretical model used here is the Surface Current Model (SCM), details of which can be found in [7]. SCM combines the effects of the grating geometry and the bunch form. Semi-analytic code developed using SCM predicts the energy emitted at specific positions relative to the grating and the degree of polarization at various observation points.

In Fig. 1 the SCM predicts that cSPr emitted at $\theta = 90°, \phi = 0°$ will be 100% polarized with electric field perpendicular to the grating grooves. Any experimental measurement will have to take into account the non-zero acceptance angles $\delta\theta$ and $\delta\phi$ at the detector. For a detector with aperture of 100mm^2 at a distance of 220mm from the grating, the predicted degree of polarization is $\approx 97\%$. These predictions are for a 1 mm period grating using typical beam parameters for the LUCX facility. It is our aim to test this aspect of the theory through comparison with experimental data.

EXPERIMENTAL LAYOUT

The experiment was carried out at LUCX, KEK [8], with the beam parameters shown in Table 1.

Table 1: LUCX, Beam Parameters

Parameter	Expected values
Beam energy, typ	8 MeV
Intensity/bunch, max	50 pC
Bunch length	150 fs to 10 ps
Repetition rate, max	12.5 bunch trains/s
Normalized emittance, $\epsilon_x \times \epsilon_y$	$4.7 \times 6.5\,\pi$mm mrad

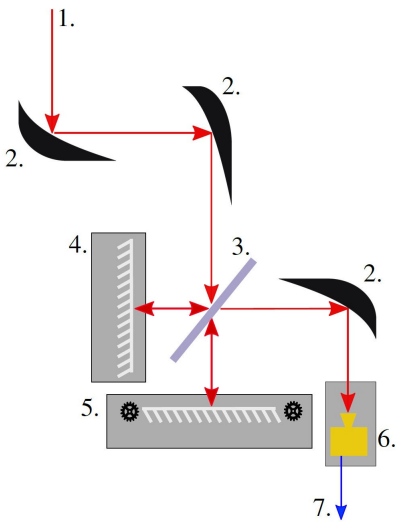

Figure 2: Diagram of Experimental Setup. 1. Radiation from THz Chamber, 2. Parabolic Mirror, 3. Beam Splitter, 4. Plane Mirror, 5. Plane Mirror on Motorised Stand, 6. Detector Mounted on Stand, 7. Signal to ADC or Oscilloscope.

The LUCX facility includes a vacuum chamber for THz radiation studies [9]. A 1 mm periodic sawtooth grating was placed inside this vacuum chamber, with the periodic structure arranged parallel to the beam and the grooves perpendicular to the direction of travel of the beam. According to Eq. 2 the wavelength of first order ($n = 1$) cSPr emitted at 90° from this grating should be 1 mm (300 GHz).

An interferometer was used to measure the frequency spectrum of the cSPr [10]. The layout of the interferometer and optical components interacting with the radiation upon its exit from the chamber are shown in Fig. 2. A Zero Bias Diode with a detection range from 325 GHz to 500 GHz [11] and a cut-off frequency of 268 GHz [12], was used to measure the cSPr emitted. The detector is polarization sensitive, only accepting radiation polarized in one direction. In order to measure the degree of polarization the detector was rotated to different angles, this was achieved by attaching it to a rotating stand. A wire polarizer was also attached to this stand, in front of the detector. By maintaining a constant angle between the polarizer and the detector the polarization dependency of the detector is eliminated from the results, this setup is shown in Fig. 3.

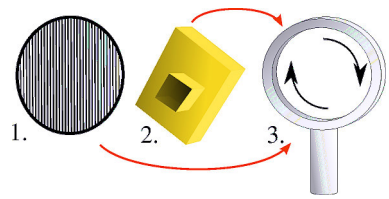

Figure 3: Diagram of Experimental Setup. 1. Wire Polarizer, 2. Detector, 3. Rotating Stand. Red arrows indicate that both the detector and the polarizer are bolted to the rotating stand.

RESULTS

The experimental results are split into two parts. First, determining that cSPr has been generated and is detectable by the system outlined, and second, measuring the degree of polarization. The degree of polarization of cSPr p_g is calculated as shown in Eq. (3) where G_i is the cSPr signal and $\parallel$ and $\perp$ represent the two possible orientations - parallel to and perpendicular the grating grooves.

$$p_g = \frac{G_\parallel - G_\perp}{G_\parallel + G_\perp} \tag{3}$$

Detecting cSPr

The grating was positioned close to the electron beam and the interferometer (Fig. 2) was used to generate a frequency spectrum for the radiation emitted at 90° to the grating. This is shown in Fig. 4 and shows a sharp peak around 300 GHz as expected.

This is compared to the frequency spectrum generated by coherent transition radiation (CTR) using the same experimental setup. CTR is broadband and so only limited by the detector response. This is shown in Fig. 4 and demonstrates that the cSPr signal is narrowband and not limited by detector response.

ISBN 978-3-95450-177-9

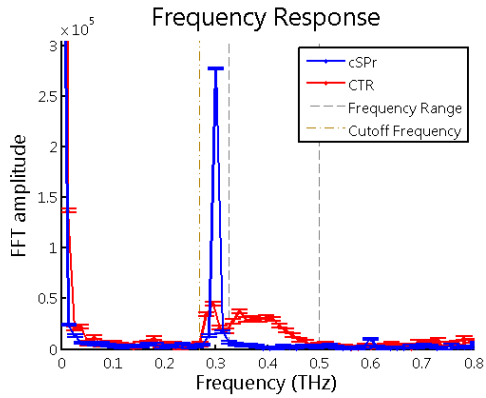

Figure 4: Frequency spectrum of cSPr compared with broadband CTR with the same detector and experimental set-up.

Measuring Degree of Polarisation

In order to calculate the polarization of the cSPr signal the detector and polarizer were attached to a rotating stand as illustrated in Fig. 3, replacing the detector in Fig. 2. The stand was rotated almost 360° and measurements were taken at 2° intervals. When the wire polarizer is parallel and perpendicular to the grating grooves minima and maxima are expected respectively.

According to Malus's Law (Eq. 4) the intensity of polarized radiation is proportional to a squared sinusoid of the rotation angle [13]. The raw data shown in Fig. 5 and has several features of interest which make it inappropriate for fitting with this type of curve. The minima and maxima are not equally spaced (the maxima are found at 80° and 280°) nor are the values of the signal measured at them consistent.

$$I = I_0 \cos\theta^2 \tag{4}$$

It is suspected that the detector was not correctly centered on the rotating stand and moved relative to the focus of the radiation during its rotation. The detector misalignment has been included in the fitting routine for Fig. 5. The model used to create the fit shown in Fig. 5 is given in Eq. 5:

$$y = (a + b\sin(c + d\theta)^2) \times (e + \sin(f + g\theta)^2) \tag{5}$$

where y is the signal, θ is the angle of rotation and a, b, c, d, e, f and g are the coefficients to be estimated. The fit can be split into two parts: the sinusoidal modulation due to the polarization of the incoming radiation Eq. 6 (as described by Malus's law) and the deviation of the detector from the focus of the radiation Eq. 7.

$$y_1 = a + b\sin(c + d\theta)^2 \tag{6}$$

$$y_2 = e + \sin(f + g\theta)^2 \tag{7}$$

The detector misalignment y_2 is plotted in Fig. 6. The raw data is normalized against this to correct for the misalignment of the detector and the rescaled data is fitted with Eq. 6, shown in Fig. 7.

This plot clearly shows two minima and two maxima which are spaced 180° apart respectively and are consistent

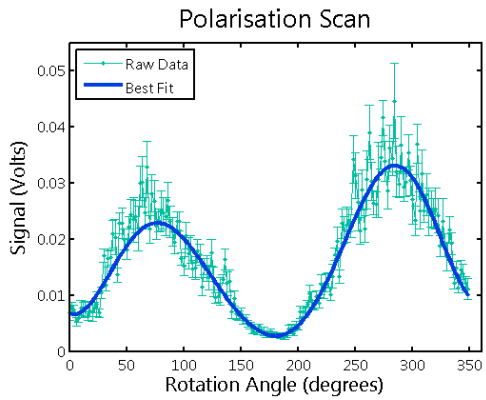

Figure 5: Measured raw data for a 360° rotation of the detector and polarizer (Fig.3). The model used for the fit is Eq. 5 and the goodness of fit parameter is $R^2 = 0.936$.

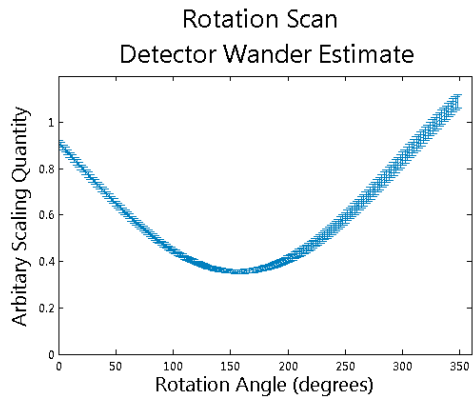

Figure 6: The estimated variation in the signal due to the movement of the detector around the focus of the radiation.

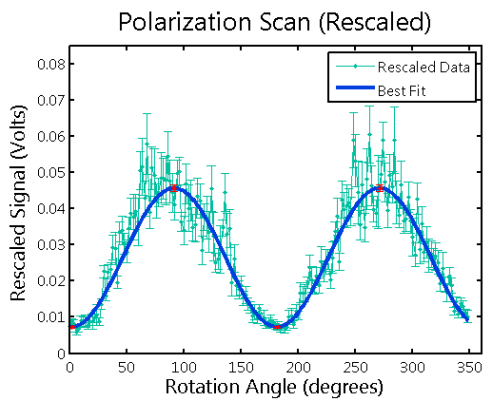

Figure 7: The rescaled data for a 360° rotation of the detector and polarizer (Fig. 3). The mode used for the fit is Eq. 6. The goodness of fit parameter is $R^2 = 0.917$.

in value. Substituting the the values of the maxima and minima of this fit into Eq. 3 as $G_{\parallel}$ and $G_{\perp}$ respectively, a value of the degree of polarization at 90° to a 1 mm period grating can be calculated: $72.6 \pm 3.7\%$. This does not consider background radiation (shown previously to be undetectable [4]) so it is likely to be an underestimate of the actual value.

ISBN 978-3-95450-177-9

CONCLUSION AND DISCUSSION

The value for the degree of polarization calculated for cSPr at 300 GHz demonstrates that the radiation is polarized with the electric field perpendicular to the grating grooves.Given the unknown noise floor of the data during the experiment, this is likely to be an underestimate of the actual value Fig.1. However, to test the theoretical predictions thoroughly measurements of the degree of polarization at several frequencies (varying θ) and orientations (varying ϕ) will be required. More work is needed to prove that our theoretical model can make accurate predictions about the behavior of the polarization of cSPr, the results so far suggest it would be possible to use the degree of polarization of cSPr to separate it from unpolarized background radiation.

ACKNOWLEDGMENTS

This work was supported by the: UK Science and Technology Facilities Council (STFC UK) through grant ST/M003590/1, the Leverhulme Trust through the International Network Grant (IN–2015–012), the Photon and Quantum Basic Research Coordinated Development Program from the Ministry of Education, Culture, Sports, Science and Technology, Japan and JSPS KAKENHI: 23226020 and 24654076. H. Harrison would like to thank STFC UK (ST/M50371X/1) and John Adams Institute of Accelerator Science (University of Oxford) for supporting their DPhil project. Thanks to Peter Huggard (STFC, RAL) and Byron Alderman (STFC, RAL) for helpful discussion about infra-red detectors. For more information on the design of the longitudinal bunch profile monitor please refer to IBIC MOPG62.

REFERENCES

[1] J. H. Brownell and G. Doucas, "Role of the grating profile in Smith-Purcell radiation at high energies," *Phys. Rev. ST Accel. Beams*, vol. 8, pp. 1–11, 2005.

[2] H. L. Andrews *et al.*, "Reconstruction of the time profile of 20.35 GeV, subpicosecond long electron bunches by means of coherent Smith-Purcell radiation" *Phys. Rev. ST Accel. Beams*, vol. 17, pp. 1–13, 2014.

[3] Y. Shibata *et al.*, "Coherent Smith-Purcell radiation in the millimeter-wave region," *Phys. Rev. E*, vol. 57, no. 1, pp. 1061 – 1074, 1998.

[4] H. Harrison *et al.*, "First Steps Towards a Single-Shot Longitudinal Profile Monitor," *Proc. 7th International Particle Accelerator Conf. (IPAC '16)*, Busan, Korea, May. 2016, pp. 340– 343.

[5] D. V. Karlovets and a. P. Potylitsyn, "Comparison of Smith-Purcell radiation models and criteria for their verification," *Phys. Rev. ST Accel. Beams*, vol. 9, pp. 1–12, 2006.

[6] A. S. Kesar, "Smith-Purcell radiation from a charge moving above a grating of finite length and width," *Phys. Rev. ST Accel. Beams*, vol. 13, pp. 1–8, 2010.

[7] J. Brownell, J. Walsh, and G. Doucas, "Spontaneous Smith-Purcell radiation described through induced surface currents," *Phys. Rev. E*, vol. 57, no. 1, pp. 1075–1080, 1998.

[8] M. Fukuda *et al.*, "Upgrade of the accelerator for the laser undulator compact X-ray source (LUCX)," *Nucl. Instrum. Meth. Phys. Res. A*, vol. 637, no. 1 (Suppl.), pp. S67–S71, 2011.

[9] A. Aryshev *et al.*, "Development of Advanced THz Generation Schemes at KEK LUCX Facility," *Proc. 10th Annual Meeting of Particle Accelerator Society of Japan (PASJ'13)*, Nagoya, Japan, Aug. 2013, pp. 873–876.

[10] M. Shevelev *et al.*, "Coherent radiation spectrum measurements at KEK LUCX facility," *Nucl. Instrum. Meth. Phys. Res. A*, vol. 771, pp. 126–133, 2015.

[11] Virginia Diodes, "Zero Bias Detectors - VDI Model: WR2.2ZBD," `http://vadiodes.com/index.php/en/products/detectors?id=122/`.

[12] Virginia Diodes, "Virginia Diodes Inc. Waveguide Band Designations," `http://vadiodes.com/VDI/pdf/waveguidechart200908.pdf`. Last modified 29/06/2010.

[13] H. A. Radi and J. O. Rasmussen, "Interference, Diffraction and Polarization of Light," in Principles of Physics For Scientists and Engineers, Heidelberg, Germany: Springer-Verlag, 2013, pp. 603–634.

ISBN 978-3-95450-177-9

DESIGN OF A TIME-RESOLVED ELECTRON DIAGNOSTICS USING THz FIELDS EXCITED IN A SPLIT RING RESONATOR AT FLUTE

M. Yan*, E. Bründermann, S. Funkner, A.-S. Müller, M. J. Nasse, G. Niehues,
R. Ruprecht, M. Schedler, T. Schmelzer, M. Schuh, M. Schwarz, B. Smit,
Karlsruhe Institute of Technology, Karlsruhe, Germany
M. Dehler, N. Hiller, R. Ischebeck, V. Schlott, Paul Scherrer Institute, Villigen, Switzerland
T. Feurer, M. Hayati, Universität Bern, Bern, Switzerland

Abstract

Time-resolved electron diagnostics with ultra-high temporal resolution is increasingly required by the state-of-the-art accelerators. Strong terahertz (THz) fields, excited in a split ring resonator (SRR), have been recently proposed to streak electron bunches for their temporal characterisation. Thanks to the high amplitude and frequency of the THz field, temporal resolution down to the sub-femtosecond range can be expected. We are planning a proof-of-principle experiment of the SRR time-resolved diagnostics at the accelerator test-facility FLUTE (Ferninfrarot Linac und Test Experiment) at the Karlsruhe Institute of Technology. The design of the experimental chamber has been finished and integrated into the design layout of the FLUTE accelerator. Beam dynamics simulations have been conducted to investigate and optimise the performance of the SRR diagnostics. In this paper, we present the design layout of the experimental setup and discuss the simulation results for the optimised parameters of the accelerator and the SRR structure.

INTRODUCTION

Temporal characterization of electron bunches is an important diagnostic tool for the control and optimisation of accelerators.The generation of ultra-short electron bunches in the femtosecond regime demands for time-resolved diagnostics with appropriate resolution. RF transverse deflecting structures have been demonstrated to be capable of providing few-femtosecond temporal resolution [1]. Recently, a new time-resolved diagnostics using THz fields excited in a split ring resonator (SRR) has been proposed [2, 3]. Thanks to the short pulse duration, high resonant frequency and high field enhancement of the THz pulses [4], such SRR diagnostics could allow for femtosecond resolution with single shot capability. Moreover, the small size of the SRR structures in the sub-millimeter range makes them more flexible in the integration into the accelerator, and combining several of them provides potentials for even better resolutions.

Analog to systems using RF deflecting structures, the SRR setup maps the temporal coordinate onto a transverse coordinate. As illustrated in Fig. 1, a driving laser system generates intense single cycle THz pulses though optical rectification. The THz pulses are absorbed in the split ring resonator structure and excite electric field enhancement for the resonant frequency inside the gap. The electron bunches, which are generated by the same driving laser system through the photoelectric effects on a cathode, interact with the high amplitude THz field in the gap and are deflected in the transverse direction. The longitudinal density distribution of the electron bunch is translated into a transverse density distribution, which can be measured using a transverse beam imaging screen.

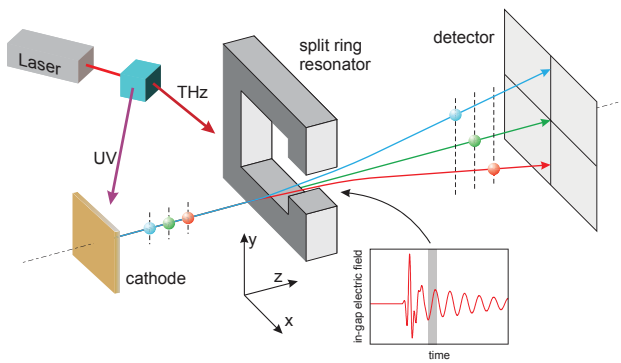

Figure 1: Principle of the SRR diagnostics [2].

In the following, the physical formulation of the streaking effect is shortly introduced for a SRR deflecting in the vertical direction. For an electron at a location z relative to the reference particle, the accumulated transverse momentum obtained from the THz field is

$$p_y = \frac{e}{c} \cdot V_0 \sin(kz + \Psi_0), \tag{1}$$

where V_0 is the integrated deflecting field through the gap, k the wavenumber of the THz field, Ψ_0 the phase of the THz field. For operation around the zero-crossing phase with $\Psi_0 = 0$, the vertical momentum can be approximated by

$$p_y = \frac{e}{c} \cdot V_0 kz, \tag{2}$$

which is in linear dependence on the longitudinal position z of the electrons inside the bunch. After a beam transport section to a downstream imaging screen, this vertical deflection is further translated into a vertical offset of

$$y = Sz, \quad S = \sqrt{\beta_{y,\mathrm{SRR}}\beta_{y,\mathrm{screen}}} \cdot \sin(\Delta\mu_y)\frac{eV_0k}{\gamma E_0}, \tag{3}$$

where the streak parameter S describes the strength of the streaking effect, $\beta_{y,\mathrm{SRR}}$ and $\beta_{y,\mathrm{screen}}$ are the beta-functions at the locations of the SRR and the screen, respectively, $\Delta\mu_y$

* minjie.yan@kit.edu

ISBN 978-3-95450-177-9

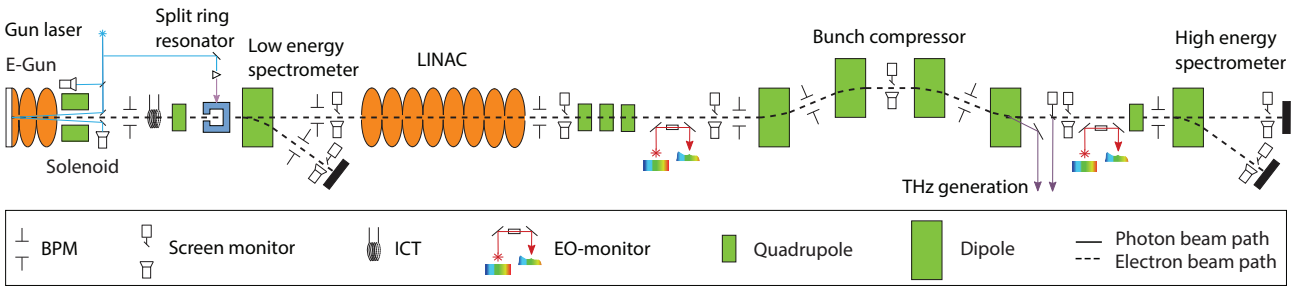

Figure 2: Schematic layout of FLUTE including various diagnostics elements. The proof-of-principle experiment for the SRR diagnostics is located upstream of the low energy spectrometer. Not to scale.

the vertical phase advance from the SRR to the screen, γ the Lorentz-factor, E_0 the rest energy of electrons.

The achievable longitudinal resolution at the screen is given by the unstreaked beam size at the screen (assuming the unstreaked beam size can be resolved by the imaging system) divided by the streak parameter and reads as

$$R_z = \frac{\sqrt{\epsilon_N/\gamma}\cdot\gamma E_0}{\sqrt{\beta_{y,\mathrm{SRR}}}\cdot\sin(\Delta\mu_y)eV_0k}, \quad (4)$$

with ϵ_N being the normalized emittance of the electron bunch. Since the small gap size is the main limiting factor for the allowed transverse beam size $\sigma_{y,\mathrm{SRR}}$ of the electron bunch, and thus the beta-function $\beta_{y,\mathrm{SRR}}$, Eq. 4 can be formulated using the relation $\sigma_{y,\mathrm{SRR}} = \sqrt{\beta_{y,\mathrm{SRR}}\cdot\epsilon_N/\gamma}$ to

$$R_z = \frac{\epsilon_N E_0}{\sigma_{y,\mathrm{SRR}}\cdot\sin(\Delta\mu_y)eV_0k}. \quad (5)$$

It can be derived from this equation that a better resolution requires three aspects: smaller normalized emittance, which is a measure of the quality of the electron bunch to be measured; larger aperture at the SRR, stronger integrated deflecting field, and higher resonant frequency, all of which are defined by the design of the SRR structures; phase advance of 90 degrees from the SRR to the measurement location, which can be optimised in the accelerator optics designs.

In the following, the design of the proof-of-principle experiment for the SRR diagnostics, which is a collaboration among PSI (Villigen, Switzerland), KIT (Karlsruhe, Germany) and University of Bern (Bern, Switzerland), will be presented and the simulation results will be discussed.

EXPERIMENTAL SETUP

The accelerator test-facility FLUTE is currently under construction at KIT in collaboration with PSI and DESY. Its aims range from investigation of space charge and coherent radiation induced effects, bunch compression studies, systematic comparison of simulation code with measurement results, to studies with intense THz radiation [5]. Furthermore, it will serve as a test bench for advanced diagnostics and instrumentation.

The schematic layout of FLUTE is shown in Fig. 2. The total length of the accelerator is ~15 m. In the RF photocathode gun, electrons are generated and accelerated to an energy of ~7 MeV. A solenoid focuses the electron bunch before it being accelerated by the main *S*-band linac accelerating structure to the energy of ~41 MeV. After a matching section with a quadrupole triplet, the electron bunch is longitudinally compressed in a magnetic bunch compressor.

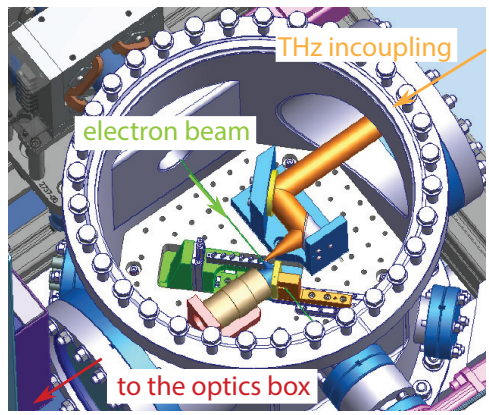

Figure 3: Technical drawing of the vacuum chamber.

The proof-of-principle experiment for the SRR diagnostics will be conducted at the low-energy section at FLUTE, as indicated in Fig. 2. The laser from the driving laser system with the fundamental wavelength of 800 nm and a pulse duration of 35 fs will be converted through third harmonic generation to a wavelength of 266 nm. The UV light will be further temporally stretched to a pulse duration of ~ps to reduce space charge effects in the generated electron bunch. The accelerated electron bunch will be deflected in the vertical direction by the SRR, and propagates towards a screen station in the straight section, where the vertically lengthened beam can be imaged. The vertically streaked electron bunch can be transported through a horizontal dipole onto the screen station in the dispersive section as well, where the energy distribution of the bunch can be measured in the horizontal plane in addition.

The intense THz radiation for exciting the SRR structures will be generated using the same driving laser system as used for the UV light required for the photo cathode. The short laser pulse of 35 fs with the fundamental wavelength of 800 nm will be directly propagated through a Lithium Niobate ($LiNbO_3$) inorganic crystal and produces THz pulses based on optical rectification techniques.

ISBN 978-3-95450-177-9

The THz pulses will be incoupled into a vacuum chamber housing the SRR structures. Figure 3 shows the technical drawing of the chamber interior. Two in-vacuum parabolic mirrors are available for focusing the THz radiation. An array of SRR structures with various geometries is mounted on a movable stage. A scintillator screen with the in-vacuum objective and the optics box will provide high-resolution transverse electron beam diagnostics [6].

SIMULATION RESULTS

Uncompressed electron bunches directly from the gun will be used for the proof-of-principle experiment. One of the main challenges is to transversely focus the electron bunch to propagate it through the small size of the SRR gap. Beam dynamics simulations using ASTRA [7] have been performed to optimise the gun and solenoid parameters with considerations of the space charge effect. The 3-dimensional electric and magnetic field distributions inside the gap, which have been simulated using the CST MWS program [8], have been integrated into the ASTRA simulation for a full characterization of the SRR streaking effect. The particle distributions are tracked to the locations of the two screens and pixelated into transverse images with a resolution of 10 μm/pixel.

The parameters of the SRR and the optimised accelerator settings are summarized in Table 1. The simulation is performed with 10^5 macro particles. Figure 4 shows the rms transverse beam sizes from the cathode to the entrance of the SRR. The vertical beam size has been chosen to be small to fit into the gap aperture, and at the same time as large as possible for a better longitudinal resolution (cf. Eq. 4).

Table 1: Simulation Parameters

Accelerator settings	
Laser rms pulse length	2 ps
Laser rms transverse size	5 μm
Bunch charge	50 fC
Gun gradient	120 MV/m
Gun phase	0 degree
Solenoid magnetic field	0.24 T
Bunch energy	7 MeV
Normalized rms transverse emittance	2.7 nm
SRR parameters	
Gap size in x	20 μm
Gap size in y	20 μm
Gap width in z	10 μm
Resonant frequency	300 GHz
Peak electric field	500 MV/m
Integrated field	10 kV

The simulated transverse particle distribution and the transverse electric field distribution at the entrance of the SRR is shown in Fig. 5, with indications of the SRR geometry in the gap region. The rms beam sizes are 4 μm in both the horizontal and vertical plane. The vertical deflecting field is homogeneous in the gap region. With increasing distances from the gap centre, the horizontal field component increases, which puts constraints on the horizontal beam sizes to avoid beam shape distortion.

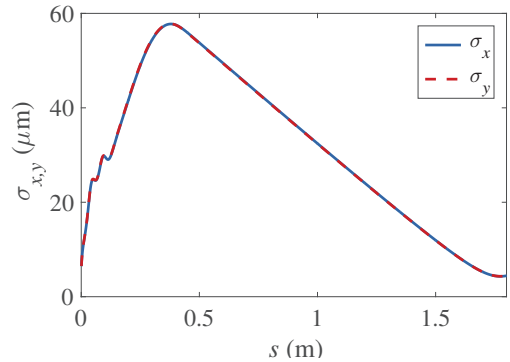

Figure 4: Transverse rms beam sizes from the cathode to the entrance of the SRR structure.

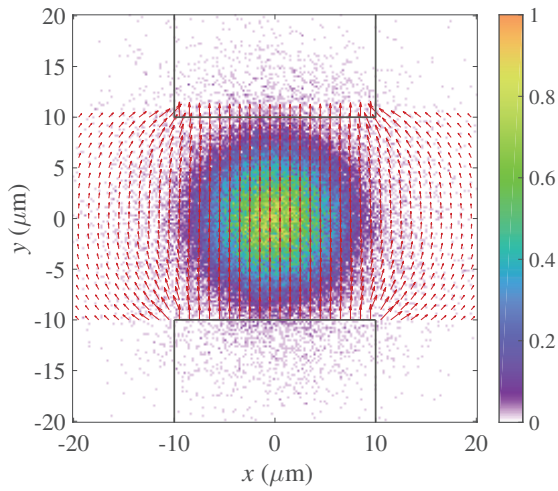

Figure 5: Transverse particle density distribution (color coded) from ASTRA simulation and transverse electric field distribution (red arrows) from CST simulation at the entrance of the SRR gap. The geometry of the gap is indicated by the black lines.

Figure 6 compares the simulated particle distribution at the exit of the SRR with the THz deflecting field switched on (left column) to that without the deflecting field (right column). Since the electron bunch with a rms bunch length of ~2 ps is comparable to the wavelength of ~3 ps of the resonant THz field, the deflecting field imposes several modulation periods on the vertical momentum (see Fig. 6 top left). It should be noted that those electrons located outside the gap region do not see the main deflecting field and therefore do not experience vertical momentum transfer. The bunch centre, which has the highest energy as a result of the on-crest operation of the gun, interacts at the zero-crossing phase with the deflecting field. The correlation between the vertical momentum and the energy is plotted in Fig. 6 bottom row.

ISBN 978-3-95450-177-9

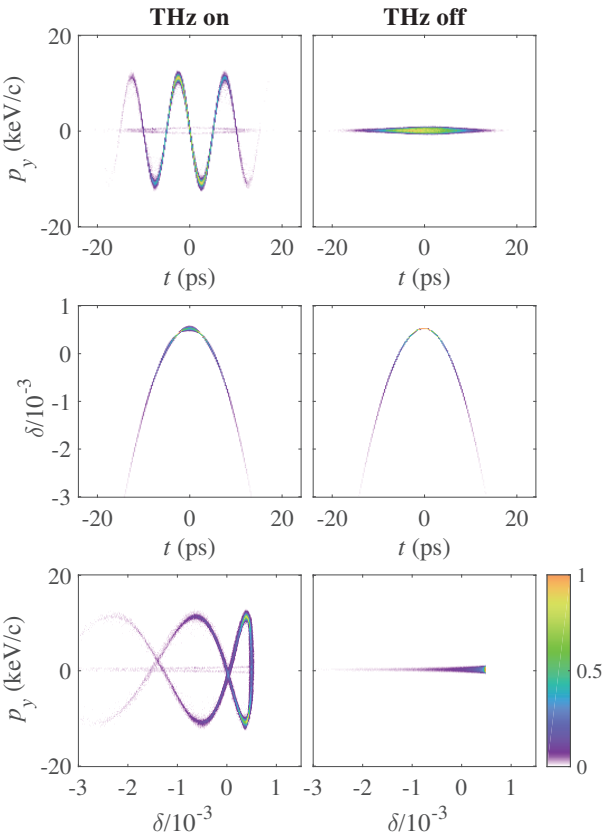

Figure 6: Particle distribution at the exit of the SRR structure at the exit of the SRR structure with the THz deflecting field switched on (left column) and off (right column). The color code corresponds to the particle density.

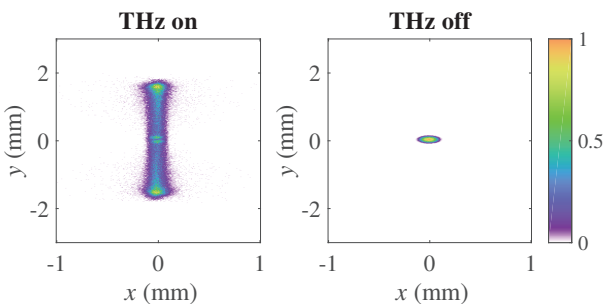

Figure 7: Simulated image of the electron bunch on the screen in the straight section. The color code corresponds to the image intensity.

In order to maximize the streaking effect (cf. Eq. 3), the accelerator optics has been designed to ensure a vertical phase advance of ~90 degrees from the location of the SRR to the location of the screens. The pixelated transverse image of the simulated distribution on the screen in the straight section is shown in Fig. 7. The increase of the vertical rms beam size from 0.05 mm to 1.11 mm, with the THz field switched off and on, respectively, is a clear indication for the streaking performance.

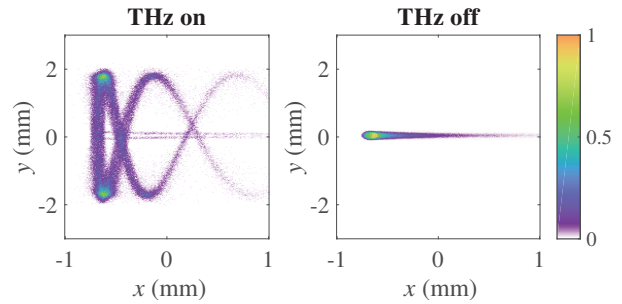

Figure 8: Simulated image of the electron bunch on the screen in the dispersive section. The color code corresponds to the image intensity.

More details can be seen in the simulated image on the screen in the dispersive section (see Fig. 8). While the horizontal axis scales linearly with the energy deviation δ, the vertical axis is a linear transformation from the vertical momentum p_y. The correlation between p_y and δ is very well represented in the transverse image on the dispersive screen, and is in good agreement with that expected from Fig. 6 bottom left. The broadening of the horizontal beam size in the energy slices is caused by the initial horizontal slice beam sizes that limit the energy resolution.

According to Eq. 5, the longitudinal resolution for this proof-of-principle setup at FLUTE is estimated to be $R_t = R_z/c = 18$ fs (using parameters from Table. 1). It should be noted that the assumed peak field gradient of 500 MV/m is based on a prudent estimate of the field enhancement in the gap. Peak gradient in excess of 1 GV/m for a resonant frequency of 1 THz could be expected, making temporal resolution in the few-femtosecond range possible.

SUMMARY AND OUTLOOK

A proof-of-principle experiment has been planned at the test facility FLUTE. The design of the experimental setup has been finished and the experimental chamber is now being built. Integration into the accelerator is expected in 2017. Beam dynamics simulations with considerations of the full THz field distribution have shown the feasibility of the SRR diagnostics. The streaking effect of the THz field should be easily detectable.

REFERENCES

[1] C. Behrens *et al.*, Nature Communications **84**, 3762 (2014).

[2] J. Fabianska *et al.*, Scientific Reports **4**, 5645 (2014).

[3] M. Dehler *et al.*, in *Proc. IBIC'15*, MOPB048 (2015).

[4] S. Bagiante *et al.*, Scientific Reports **5**, 8051 (2014).

[5] M. J. Nasse *et al.*, Rev. of Sci. Instrum. **84**, 022705 (2013).

[6] R. Ischebeck *et al.*, Phys. Rev. ST Accel. Beams **18**, 082802 (2015).

[7] K. Flöttmann, "ASTRA: A Space Charge Tracking Algorithm", `http://www.desy.de/~mpyflo`

[8] CST Microwave Studio, `http://www.cst.de`

ISBN 978-3-95450-177-9

5 MeV BEAM DIAGNOSTICS AT THE MAINZ ENERGY-RECOVERING SUPERCONDUCTING ACCELERATOR MESA

S. Heidrich *, K. Aulenbacher, Institute of Nuclear Physics, Mainz, Germany

Abstract

Within the next few years, a new energy-recovering superconducting electron accelerator will be built at the Institute of Nuclear Physics in Mainz. For injection into the main accelerator the beam parameters need to be known. This requires a high resolution longitudinal beam diagnostic system at the 5 MeV-injection arc. The system employs two 90° vertical deflection dipoles, which aims to achieve an energy resolution of 240 eV and a phase resolution of 46 µm.

As a second challenge, the transverse emittance measurements will take place at full beam current. This demands an extremely heat resistant diagnostic system, realised by a method similar to flying wire.

MAINZ ENERGY-RECOVERING SUPERCONDUCTING ACCELERATOR

The **M**ainz **E**nergy-recovering **S**uperconducting **A**ccelerator **MESA** will run in two different beam modes. The energy recovering mode allows beam currents up to 1 mA at a maximum beam energy of 105 MeV, while the external beam mode achieves an energy of 155 MeV but limits the maximum current to 150 µA. The part of the beam diagnostics discussed in this article will be installed downstream of the normal-conducting pre-accelerator at 5 MeV. Here, the beam will have a normalized transverse emittance of about 1 µm, an energy spread in the order of 2 keV and a bunch length of about 240 µm. For the second stage of MESA, 10 mA beam current is envisaged. The preinjector **MAMBO** (**Mi**lliampere **Bo**oster) is already designed for this average current. [1]

LONGITUDINAL BEAM DIAGNOSTICS

The design of the longitudinal beam diagnostic combines a magnetic energy spectrometer with a dipole cavity for bunch length measurements. A set-up sketch of the system is displayed in Figure 1. First, the beam is guided through a 90° deflection dipole which causes a transverse spread depending on the energy distribution of the beam. By then collimating the dispersed beam through a 100 µm-gap, an energy window of ±240 eV is cut out. As displayed in Figure 2, the beam shows a large phase dispersion caused by the R_{51} element of the dipole transformation matrix at this point. This phase smearing compromises the subsequent bunch length measurement and needs to be compensated with an additional quadrupole directly behind the collimator and a second 90° dipole. By that, the energy measurement system becomes achromatic and the phase smearing vanishes.

Then, the energy collimated beam is guided to the phase measurement system which consists of a focusing quadrupole, a 500 W 1.3 GHz dipole cavity, a defocusing quadrupole and a tungsten wire which cuts out a 60 µm long part of the bunch. The radiation caused by the interaction between the beam and the wire is proportional to the integrated current of the selected phase space and is measured with a scintillation detector. To scan the whole longitudinal phase space, the phase of the dipole cavity is shifted and the beam is steered over the energy collimator. To compensate the influence of the steerer on the R_{51} matrix element, a second steerer has to be employed downstream of the energy collimator.

The measured phase space can be displayed in real time with a repetition rate of 10 Hz.

Contrary to the transverse diagnostics it is not possible to operate at full beam current. Instead, a pulsed or single bunch mode needs to be implemented.

It has to be mentioned that the energy spectrometer deflects the beam vertically while the injection arc has a horizontal set up. However, it may be assumed that the longitudinal phase space does not depend on the observation direction.

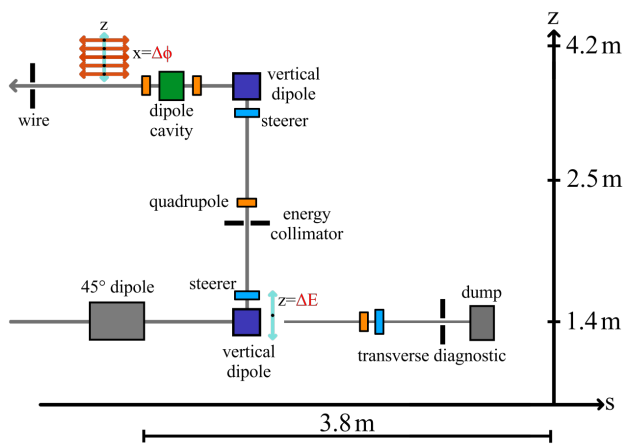

Figure 1: The longitudinal beam diagnostic consists of a vertically deflecting 90° energy spectrometer with subsequent chromatic correction and a dipole cavity which is used to measure the extension of the beamlets.

* s.heidrich@uni-mainz.de

ISBN 978-3-95450-177-9

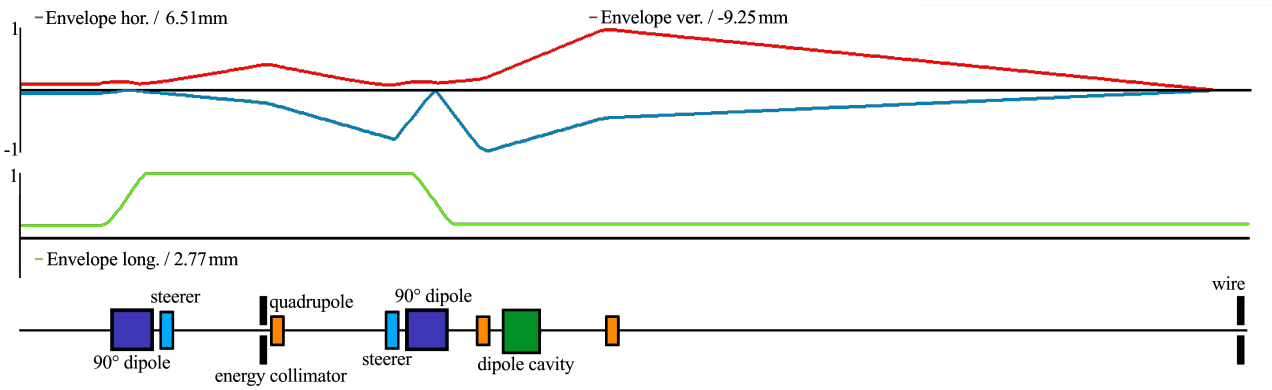

Figure 2: The transverse and longitudinal beam envelopes are displayed for the longitudinal diagnostic system. Phase smearing increases the size of the longitudinal envelope from 0.6 mm to 2.77 mm downstream of the first 90° dipole. Using a second identical dipole allows to correct this behaviour, so that the energy spectrometry does not influence the following phase measurement. Before entering the dipole cavity, both transverse envelopes rise to several millimeters, which calls for examination of nonlinear contributions in the cavity and the quadrupoles.

The resolution r_ϕ of the phase measurement system is given by

$$r_\phi = \pm \frac{c}{\omega_{\mathrm{rf}}} \times \arcsin\left(\frac{\sigma_{\mathrm{x}}}{R_{12}\tan(\alpha_0)}\right) \quad (1)$$

with [2]

$$\alpha_0 = 1.46 \times 10^{-3}\ \mathrm{mrad}\sqrt{Q_0 P_{\mathrm{rf}}}. \quad (2)$$

Here, c is the speed of light, ω_{rf} is the circular frequency of the cavity, σ_{x} equals the size of the focused beam spot, R_{12} describes the corresponding element of the beam transformation matrix behind the cavity, α_0 is the angular amplitude of the cavity kick, Q_0 is the quality of the cavity (typically around 10000) and P_{rf} stands for the available RF Power.

For the MESA set-up, the RF power available for diagnostics is limited to 500 W. An increase would involve high costs and tough requirements for the cooling system of the cavity.

Since the phase measurement lies 2.4 m above the pre-accelerator, the achievable drift length can be set to 6 m without interfering with any other components. To further increase the phase resolution, two quadrupoles are implemented adjacent to the cavity. They are able to focus the beam on the detector wire while magnifying the kick of the cavity by a factor of 1.77. This is done by setting R_{12} to 12.36 m.

In this first order calculation, the achievable beam size is $\sigma_{\mathrm{x}} = 50\,\mu\mathrm{m}$ and the circular frequency is $\omega_{\mathrm{hf}} = 2\pi \times 1.3\,\mathrm{GHz}$. Inserting those values into equation (1) gives a resolution of $r_\phi = \pm 45.6\,\mu\mathrm{m}$.

TRANSVERSE BEAM DIAGNOSTICS

To scan the transverse beam profile, the beam is steered over a fixed tungsten wire with 10 µm radius. The resulting radiation is proportional to the integrated beam current and can easily be measured by a scintillation detector behind the wire. In combination with an additional quadrupole, the profile measurements can then be utilized to determine the emittance of the beam [3].

To ensure that the diagnostic wire does not melt during irradiation, it is necessary to evaluate the deposited heat load for a maximum current of 1 mA. Therefore, the set-up was simulated with *FLUKA* [4] [5] for a strongly focused beam with a radius of 10 µm. The resulting power deposition reaches a maximum of about 4.6 GW mm^{-3} A^{-1}. Under the assumption that the cooling only takes place by black body radiation, the temperature of the wire can be calculated by solving equation (3). Here, P is the deposited power density, Q defines the specific heat capacity of tungsten, R is the wire radius, ρ stands for the material density, T equals the temperature, ϵ is the emissivity and k_B is the Boltzmann constant.

$$\dot{T} = \frac{P}{Q\rho} - \frac{2\epsilon k_{\mathrm{B}}}{Q\rho R}(T^4 - T_0^4) \quad (3)$$

The melting point of the wire would then be reached within 1 µs. Consequently, the beam is steered over the wire for just one 1 kHz cycle by a fast ferrite magnet and is then allowed to cool down for a few seconds before running the next measurement.

It is expected that the dumping of the beam directly downstream of the diagnostic wire will lead to a large amount of background radiation. To evaluate the signal to noise ratio r_{sn}, the shielded set-up was simulated with *FLUKA* for two cases. Case a: The diagnostic wire is exposed to the beam; Case b: The wire is excluded. Since the signal to noise ratio will be reduced when the beam size is increased, a large beam size of $\sigma_x = 1$ mm was simulated for a tungsten wire with the radius $R = 10\,\mu\mathrm{m}$. The simulation results are displayed

ISBN 978-3-95450-177-9

in Figure 3. For case a, the amount of deposited energy in the detector per incoming electron is $E_a = 3579(10)$ eV, for case b it is $E_b = 44(8)$ eV. This leads to a signal to noise ratio of

$$r_{sn} = \frac{E_a - E_b}{E_b} = 80.3 \pm 10. \quad (4)$$

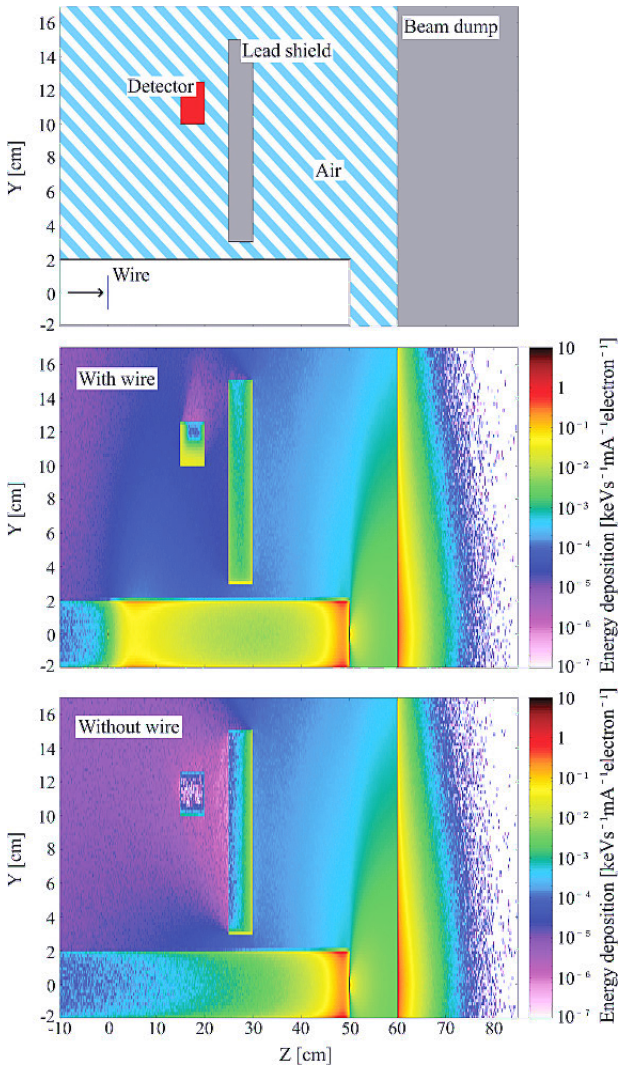

Figure 3: The influence of the background radiation was evaluated by simulating the detector set-up with and without the diagnostic wire. The results show that the energy deposition in the detector drops by two magnitudes when the diagnostic wire is excluded.

Without further post-processing, the measurements of the beam size are limited in their precision by the diameter of the wire.

In the following, a procedure is described that aims to compensate the wire size and consists of three steps:

Step 1 The produced radiation strongly depends on the radial distance of an impacting electron to the axis of the wire. Thus, the signal response to different impact points needs to be evaluated. Intuitively it could be assumed that the signal intensity would only depend on the path-length of the electron through the target, which is given by the thickness of the wire at the respective position. However, this assumption does not match the simulation results of several point-like impact areas on a tungsten wire with the radius $R = 15\,\mu$m, which are displayed in Figure 4. Most likely, this discrepancy is caused by multi scattering processes and needs to be further investigated. In a first approach, the data was fitted with a high order polynomial function $w(x) = a - kx^{10}$, which in the following will be used as the weighting function of the wire.

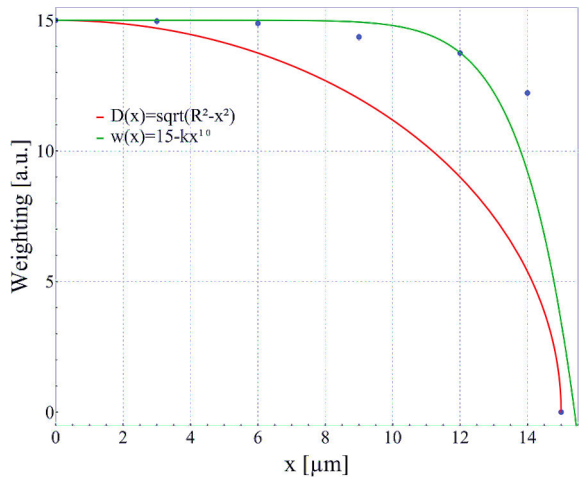

Figure 4: The dependency of the wire signal on the position of point-like impact areas was simulated to evaluate the weighting function. The results show that the height of the signal is not proportional to the thickness $D(x)$ of the wire at the position of the impact point. For further calculations, a high order polynomial fit was used.

Step 2 With the weighting function, a measurement of the beam profile can be simulated.

Equation (5) gives the wire signal intensity depending on the position of the wire axis in relation to the center of the beam ($x = x_0 = 0$).

$$I_{\mathrm{meas}}(x_0) = \int_0^{\Delta t} \tau(t)\,\mathrm{d}t \int_{x_0-R+x(t)}^{x_0+R+x(t)} J(x) \times w(x)\,\mathrm{d}x\,. \quad (5)$$

Here, Δt is the time resolution of the detector, R defines the radius of the wire and $\tau(t)$ equals the temporal weighting function of the detector, which is assumed to be constant. $J(x)$ is the density distribution of the beam profile and assumed to be gaussian. If the beam profile is not gaussian, $J(x)$ needs to be replaced accordingly.

To simulate a measurement, the beam size of interest and a list of wire positions is initially set and then processed

ISBN 978-3-95450-177-9

with equation (5). Figure 5 shows the simulation results for a beam size of $\sigma_x = 10\,\mu m$ at 31 equidistant wire positions and a wire radius of $R = 15\,\mu m$. In this case, the measurement would overestimate the true beam size by 27.5 %.

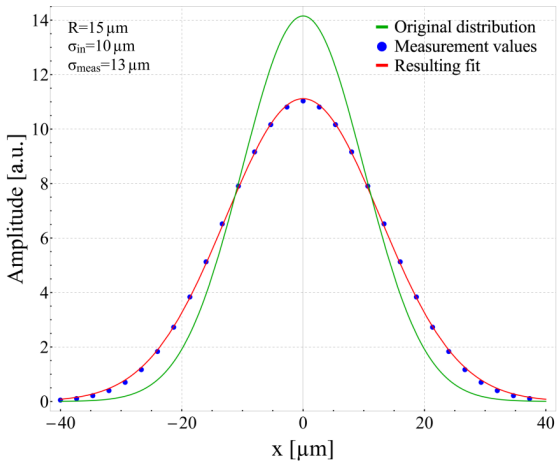

Figure 5: By using the calculated weighting function, a single wire measurement can be simulated. The ratio of the resulting "measured" beam size σ_{meas} to the initial "true" beam size σ_{in} then gives the correction factor of the measurement.

Step 3 The results of a real measurement can be processed by repeating step 2 for every beam size of interest. Figure 6 shows the correction factors of 20 simulations from $\sigma_x = 10\,\mu m$ to $\sigma_x = 50\,\mu m$. By employing the resulting correction curve on the list of measured beam sizes, the influence of the wire thickness can be compensated.

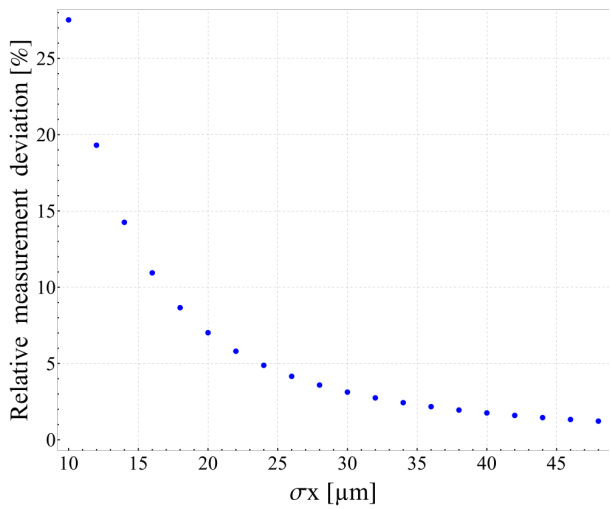

Figure 6: The correction factors depend on the material and the diameter of the diagnostic wire as well as on the beam size. The displayed values are the results for a tungsten wire with a radius of 15 µm. In this case, the measurement of the beam profile results in an overestimation of up to 27.5 % for a minimum beam size of 10 µm.

OUTLOOK

Except the 90° dipole magnets all discussed systems are in a preliminary design status and will be built within the next two years.

There are concerns about the influence of the second order transformation matrix elements on the longitudinal diagnostics. They may lead to additional phase smearing, which needs to be further investigated.

For full current beam profile measurements, an appropriate beam dump needs to be designed to withstand a maximum beam power of 50 kW.

The compensation procedure of the wire size for transverse beam profile measurements assumes a gaussian beam profile, which especially for high current densities may not be true. Additionally any roughness or bending of the wire is neglected. These issues needs to be further investigated with an experimental set up under real conditions.

CONCLUSION

The working principles of a longitudinal and transverse beam diagnostic system for MESA at 5 MeV were discussed. It was shown that the longitudinal diagnostics could provide an energy resolution of 240 eV and a phase resolution of 46 µm.

The described transverse system could be used to perform full current beam profile measurements. A procedure to calculate correction factors for the influence of the diameter of the diagnostic wire may lead to an optimization of the achievable resolution.

ACKNOWLEDGEMENTS

The work at the injection arc and the beam diagnostics of MESA is supported by the **DFG** (**D**eutsche **F**orschungs**g**emeinschaft) through the excellence cluster **PRISMA** (**Pr**ecision Physics, Fundamental **I**nteractions and **S**tructure of **Ma**tter).

REFERENCES

[1] R.Heine, K. Aulenbacher, "MESA - Sketch of an Energy Recovering Linac for Nuclear Physics Experiments at Mainz", Proceedings of IPAC2012, New Orleans, Louisiana, USA (2012).

[2] K.W. Nilles, "Master thesis: Die Apparatur zur schnellen Diagnostik des longitudinalen Phasenraumes am Injektorlinac des Mainzer Mikrotrons", MAMI, Mainz, Germany (1989).

[3] H. Wiedemann "Particle Accelerator Physics Third Edition", Springer (2007), doi:10.1007/s12541-016-0037-5

[4] A. Ferrari, P.R. Sala, A. Fasso', and J. Ranft "FLUKA: a multi-particle transport code", CERN-2005-10 (2005), INFN/ TC_ 05/ 11, SLAC-R-773.

[5] T.T. Böhlen, F. Cerutti, M.P.W. Chin, A. Fassò, A. Ferrari, P.G. Ortega, A. Mairani, P.R. Sala, G. Smirnov, V. Vlachoudis "The FLUKA Code: Developments and Challenges for High Energy and Medical Applications", Nuclear Data Sheets 120, 211-214 (2014).

ISBN 978-3-95450-177-9

MEASUREMENT OF FEMTOSECOND ELECTRON BEAM BASED ON FREQUENCY AND TIME DOMAIN SCHEMES

K. Kan[#1], M. Gohdo, T. Kondoh, I. Nozawa, J. Yang , Y. Yoshida[#2]
The Institute of Scientific and Industrial Research (ISIR), Osaka University, Osaka 567-0047, Japan

Abstract

Ultrashort electron beams are essential for light sources and time-resolved measurements. Electron beams can emit terahertz (THz) pulses using coherent transition radiation (CTR). Michelson interferometer is one of candidates for analyzing the pulse width of an electron beam based on frequency-domain analysis. Recently, electron beam measurement using a photoconductive antenna (PCA) based on time-domain analysis has been investigated. The PCA with enhanced radial polarization characteristics enabled time-domain analysis for electron beam because of radially polarized THz pulse of CTR. In this presentation, measurement of femtosecond electron beam with 35 MeV energy and < 1 nC from a photocathode based linac will be reported. Frequency- and time- domain analysis of THz pulse of CTR by combining the interferometer and PCA will be carried out.

INTRODUCTION

Short electron bunches with durations of picoseconds to femtoseconds are useful for generation of light in terahertz (THz) range [1]. Such electron beams are used in time-resolved studies of ultrafast phenomena and reactions, including ultrafast electron diffraction (UED) [2] and pulse radiolysis [3-5]. Electro-optic sampling [6], which is one of detection techniques of THz light pulse, is used in diagnostics of electron bunches. In EO samplings for electron bunch length measurement, the birefringence of EO crystals is induced by the beam electric field, and laser polarization corresponding to the longitudinal electron beam profile is detected [7,8]. EO monitors based on the temporal decoding have revealed the Coulomb field of a root mean square (rms) width of 60 fs from femtosecond electron bunches [8]. Interferometers [9] have been also used for the detection of single mode or multimode THz pulses generated by electron bunches and slow-wave structures [10,11]. Smith-Purcell radiation, which uses metallic gratings, has also been analyzed by interferometers [12,13]. Coherent transition radiation (CTR), which is generated by electron bunches crossing a boundary between different media, has been measured by interferometers and grating-type spectrometers [14-16]. Photoconductive antennas (PCAs), which are composed of semi-insulating semiconductor with electrodes, are widely used for both generation and detection of THz pulses in THz time-domain spectroscopy [17-20]. PCAs could be good candidates for analyzing temporal electric field profiles of electron bunches due to the correlation between electric-field-induced current output and THz electric field strength [20]. THz pulses of CTR are radially polarized [21] due to the diverging electric fields from the beam center. Therefore, a PCA with radial polarization characteristics is considered to be useful for the measurement of THz pulse from an electron bunch. Recently, Winnerl *et al.* reported fabrication of a large-aperture PCA, and the radially polarized field pattern of focused THz pulses was measured [22]. Generation of high-power THz pulses from a PCA using a high-voltage source has been studied for acceleration of electron beam [23]. Polarization components of radially polarized THz pulses from a PCA with interdigitated electrodes were also investigated using a wire grid polarizer [24]. Time-domain measurement of CTR using the PCA as a detector has been also conducted. The scheme is based on measurement of radially polarized THz pulses of CTR with a large-aperture PCA [24], which has radial polarization components. The combination of an interferometer and PCA will enable frequency and time-domain analysis of THz pulse of CTR.

In this paper, measurement of CTR from a femtosecond electron beam was conducted based on frequency and time-domain schemes. The energy and charge of the electron beam were 35 MeV and <1 nC at a repetition rate of 10 Hz, respectively. Frequency spectra of CTR were measured by a Michelson interferometer. On the other hand, time profiles of CTR were measured by a PCA driven by a femtosecond laser.

EXPERIMENTAL ARRANGEMENT

Femtosecond electron bunches were generated by a photocathode-based linac, which consists of a 1.6-cell S-band radio frequency (RF) gun with a copper cathode, a 2-m-long traveling-wave linac, and an arc-type magnetic bunch compressor. The photocathode of RF gun was excited by UV pulses (262 nm) of a picosecond laser with an energy of <180 μJ/pulse and a pulse width of 5 ps FWHM at 10 Hz. The electron bunches generated in the gun were accelerated in the linac using a 35-MW klystron at a repetition rate of 10 Hz. In the linac, the electron bunches were accelerated to 35 MeV at a linac phase of 100° which is suitable for the bunch compression [16]. The accelerated electron bunches were compressed to femtosecond by the magnetic bunch compressor, which was composed of bending magnets, quadrupole magnets, and sextupole magnets. THz pulses of CTR were generated by the compressed electron bunches and measured.

Schematic diagram and picture of measurement system for CTR using the interferometer and PCA [24] were shown in Fig. 1. CTR was generated on the interface of a mirror (M1) as shown in Fig. 1 (a). The beam energy and bunch charge were 35 MeV and 740 pC/pulse, respectively. Collimated THz pulses of CTR were separated by a beam

#1: koichi81@sanken.osaka-u.ac.jp
#2: yoshida@sanken.osaka-u.ac.jp

ISBN 978-3-95450-177-9

splitter (BS1). One THz pulse was introduced to the interferometer. In the interferometer, the THz pulse was separated by a beam splitter (BS2) again. Superposed THz pulses were detected by a liquid-helium-cooled silicon bolometer. Interferogram, which was the bolometer output as a function of a moving mirror (Delay1), was obtained for the frequency-domain measurement. The other THz pulse was introduced to the PCA. The PCA made from semi-insulating GaAs was irradiated by femtosecond laser pulses from electrode/photomask side. The energy of laser pulses was set to 300 μJ/pulse (800 nm, <130 fs FWHM, Tsunami with Spitfire, Spectra-Physics). The time delay of the laser pulses was adjusted by a delay line (Delay2). Output of electric-field-induced current due to CTR was changed by photo-induced charge carriers on the PCA only when the laser pulse was irradiated on the PCA. Therefore, electric field profile of CTR was obtained as a dependence of the current from the PCA on the time delay for the time-domain measurement. A current transformer (CT) was set in the upstream for the both measurement systems to evaluate bunch charge. The signal from the PCA through pads on the GaAs was measured by an oscilloscope through a 50 Ω terminator and an amplifier (5307, NF, gain 100). In the bolometer, a filter of crystal quartz with garnet powder was used for the detection of THz pulse with frequencies of <3 THz. The signal from the bolometer was measured by another oscilloscope. The two signals were obtained with the both schemes at the same time although the sweeping ranges were different. The both beam splitters were made of high-resistivity silicon with a thickness of 0.38 mm. Some components were set in a vacuum chamber as shown in Fig. 1 (b).

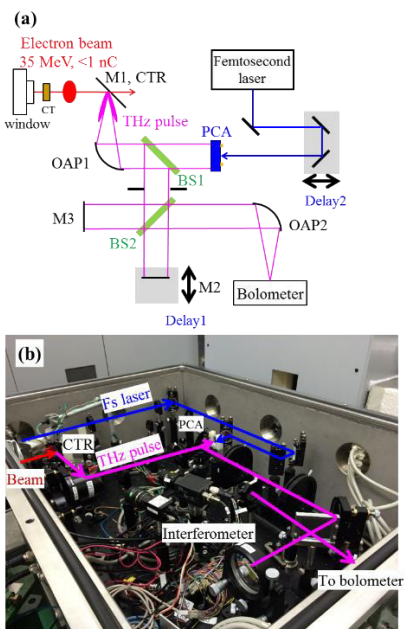

Figure 1: (a) Schematic diagram of measurement system for CTR. CT: a current transformer; M: a plane mirror; OAP: an off-axis parabolic mirror; BS: a beam splitter; I: an iris with an aperture of 9 mm in diameter. (b) Picture of the optical system set in a vacuum chamber.

RESULTS AND DISCUSSIONS

The results of frequency and time-domain measurement of CTR are shown in Fig. 2. Time-domain data from the interferometer and PCA were shown in Fig. 2 (a). The time delays of the interferometer and PCA corresponded to the position of Delay 1 and Delay 2, respectively, in Fig. 1 (a). Each data was calculated by the average of 10 sweeps. Fitting lines of filtered model [15,16] and Gaussian distribution were shown for the data of interferometer and PCA, respectively, based on an assumption of Gaussian electron bunch distribution. Calculated bunch lengths were obtained as 94 and 430 fs in rms for the cases of interferometer and PCA, respectively. The discrepancy of the bunch lengths would be due to the difference of detectable bunch length of each method, which corresponds to each bandwidth. Detectable fast signal in the PCA would depend on laser pulse width of the femtosecond laser, response time of PCA, timing jitter between the laser and electron bunch, and spectral absorption of semi-insulating GaAs although the qualitative analysis is difficult at this point. Figure 2 (b) shows frequency spectra calculated by the Fourier transform using the data in Fig. 2 (a). The detectable ranges of the interferometer and PCA in this study would be estimated as <2 and <1 THz roughly, respectively, according to the decrease in the spectral components. Previously, a similar PCA [24] was used for the generation of THz pulses at frequencies of <1 THz. The detectable range of the PCA would be reasonable with compared the experimental results in the generation of THz pulses from a PCA. There seemed to be some instabilities in the case of the PCA, however the frequency and time-domain measurements were conducted by the interferometer and the PCA. The optimization of the termination resister for the PCA would be required for the stabilization of data because of a current measurement. In the future, driving the PCA with a shorter laser pulse [19] would be also carried out for improving the PCA detector system based on broadband detection.

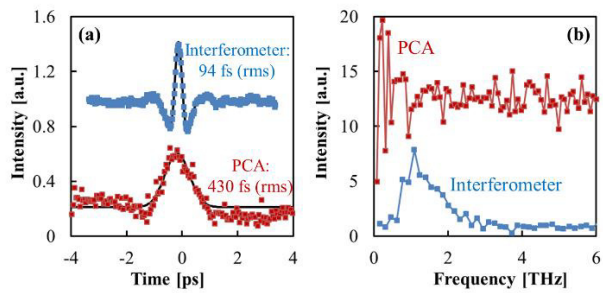

Figure 2: Results of (a) time and (b) frequency-domain measurement of CTR obtained by the interferometer and PCA. (a) Fitting lines of filtered model and Gaussian distribution were shown for the data of interferometer and PCA, respectively. Factors and offset were adjusted for comparison. (b) Only factors were adjusted for comparison.

ISBN 978-3-95450-177-9

CONCLUSION

Measurement of CTR from a femtosecond electron beam was conducted based on frequency and time-domain schemes. The system was composed of a Michelson interferometer and PCA. Calculated bunch lengths were obtained as 94 and 430 fs in rms for the cases of interferometer and PCA, respectively. The detectable ranges of the interferometer and PCA were estimated as <2 and <1 THz, respectively. Instabilities in the case of the PCA were observed, however the frequency and time -domain measurements were conducted by the interferometer and PCA.

ACKNOWLEDGEMENT

This work was supported by KAKENHI (JP25870404, JP26249146, and JP15H05565) and a Grant for Basic Science Research Projects was received from The Sumitomo Foundation.

REFERENCES

[1] A. F. G. van der Meer, Nucl. Instrum. Meth. A 528, 8 (2004).
[2] P. Musumeci et al., Ultramicroscopy 108, 1450 (2008).
[3] T. Kondoh et al., Radiat. Phys. Chem. 84, 30 (2013).
[4] J. Yang et al., Nucl. Instrum. Meth. A 629, 6 (2011).
[5] K. Kan et al., Rev. Sci. Instrum. 83, 073302 (2012).
[6] M. Nagai et al., *Opt. Express* 20, 6509 (2012).
[7] I. Wilke et al., *Phys. Rev. Lett.* 88, 124801 (2002).
[8] G. Berden et al., *Phys. Rev. Lett.* 99, 164801 (2007).
[9] B. I. Greene et al., *Appl. Phys. Lett.* 59, 893 (1991).
[10] A. M. Cook et al., *Phys. Rev. Lett.* 103, 095003 (2009).
[11] K. Kan et al., *Appl. Phys. Lett.* 99, 231503 (2011).
[12] H. L. Andrews et al., *Phys. Rev. ST Accel. Beams* 12, 080703 (2009).
[13] K. Kan et al., *Electron. Comm. Jpn.* 99, 22-31 (2016).
[14] T. Takahashi et al., *Phys. Rev. E* 50, 4041 (1994).
[15] A. Murokh et al., *Nucl. Instrum. Meth. A* 410, 452 (1998).
[16] I. Nozawa et al., *Phys. Rev. ST Accel. Beams* 17, 072803 (2014).
[17] D. H. Auston, *Appl. Phys. Lett.* 26, 101 (1975).
[18] M. Tani et al., *Jpn. J. Appl. Phys.* 36, L1175 (1997).
[19] S. Kono et al., *Appl. Phys. Lett.* 79, 898 (2001).
[20] M. Tani et al., *Semicond. Sci. Technol.* 20, S151 (2005).
[21] D. Daranciang et al., *Appl. Phys. Lett.* 99, 141117 (2011).
[22] S. Winnerl et al., *Opt. Express* 17, 1571 (2009).
[23] M. J. Cliffe et al., *Appl. Phys. Lett.* 105, 191112 (2014).
[24] K. Kan et al., *Appl. Phys. Lett.* 102, 221118 (2013).

ISBN 978-3-95450-177-9

BUNCH EXTENSION MONITOR FOR LINAC OF SPIRAL2 PROJECT

R. Revenko†, J.-L. Vignet,
GANIL, Caen, France

Abstract

A semi-interceptive monitor for bunch shape measurement has been developed for the LINAC of SPIRAL2. A Bunch Extension Monitor (BEM) is based on the registration of X-rays emitted by the interaction of the beam ions with a thin tungsten wire. The time difference between detected X-rays and accelerating RF gives information about distribution of beam particles along the time axis. These monitors will be installed inside diagnostic boxes on the first five warm sections of the LINAC. The monitor consists of two parts: X-ray detector and mechanical system for positioning the tungsten wire into the beam. Emitted X-rays are registered by microchannel plates with fast readout. Signal processing is performed with constant fraction discriminators and TAC coupled with MCA. Results of bunch shape measurements obtained during commissioning of RFQ for SPIRAL2 are presented.

INTRODUCTION

Semi-interceptive beam diagnostics for measurements of longitudinal bunch profile have been designed for LINAC of SPIRAL2 [1, 2]. It will be used for measurement and control of bunch extension during LINAC tuning and optimization of beam parameters. The operation principle of BEM is based on the registration of X-rays emitted by interaction of ions of the accelerator beam with a thin tungsten wire. The monitor performs precise measurements for X-rays arrival time that gives information about average distribution of ions along the time axis. The LINAC of SPIRAL2 is operated at 88 MHz that corresponds to period 11.36 ns between bunches and its extension of phase typically σ_φ rms = 7°–8° (or σ_t rms = 220–260 ps). Main beam parameters for LINAC specified in Table 1. Five BEMs will be installed at the beginning of the LINAC inside the first five warm sections.

Table 1: Parameters of LINAC Beam

Parameter	Value
Frequency	88.0525 MHz
Period	11.36 ns
Energy at LINAC entrance	0.75 MeV/A
Maximum intensity (deuterons)	5 mA
Maximum power (deuterons)	7,5 kW
Minimum σ_φ rms	7°
Minimum σ_t rms	220 ps

The BEM will operate with high-intensity beams up to 5 mA and must provide reliable measurements with temporal resolution not worse than 1° of phase at 88 MHz of accelerated frequency. Some restrictions are imposed to the BEM design. A lack of space inside of the diagnostic box imposes to have a compact system. Also materials used for the BEM should not contaminate the superconducting cavities of cryomodule. These requirements were taken into account during the BEM design.

Different working principles of longitudinal bunch measurements were compared. Registration of SEs emitted from the wire would have required an accelerating potential of few kV. That leads to steering effect for the beam ions and requires an additional electrostatic compensation system. Using of backscattered ions does not provide required temporal resolution due to energy spread and a considerable difference of ions drift times depending on the point of interaction on the wire. Registration of X-rays is more suitable to avoid the use of accelerating potential and to minimize time spread for different drift paths. A disadvantage of this method is a longer time of acquisition related to low efficiency for X-rays registration. In our case it varies between 0.5 and 3 minutes.

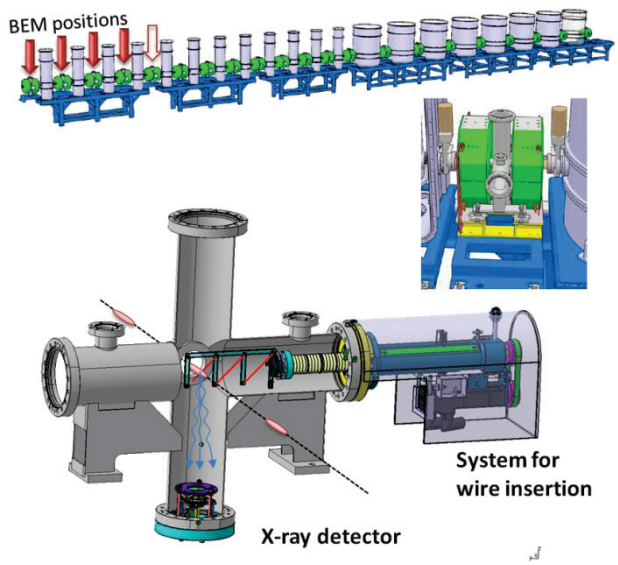

Figure 1: BEM installed at diagnostic box and its positions on LINAC warm sections.

HARDWARE

The BEM is mounted inside of warm section and occupies two flanges of diagnostic box (Fig. 1). It consists of an X-ray detector and a mechanical system for positioning the wire inside the beam.

The mechanical system of wire insertion is able to perform positioning of the wires with accuracy better than few tens of microns. A wire holder has three identical positions with wires and allows replacing one wire with another in case of damage (Fig. 2, right). Integrity of the wire can be verified using measurements of collected beam current. The wire holder is electrically isolated from the other mechanical parts of actuator and connected to I/V converter

ISBN 978-3-95450-177-9

with ADC. It allows measuring current from the wire with accuracy of 7.6 nA (least significant bit). These measurements permit to obtain a distribution of the beam current on the transverse plane and to optimize the wire position in the maximum of the beam density. Preliminary simulations with TRACEWIN have found the optimal configuration for wire placement with minimal influence on the beam emittance. Placing of five BEM in series requires placing of wires in a sequential alternating orientation (Hor-Ver-Ver-Hor-Ver). However, orientations of all wires were tilted by additional 45° since the top flange of diagnostic box is occupied with a turbo molecular pump.

Tungsten wire with 150 microns diameter was chosen for X-ray production. Thermal loading and mechanical durability of this wire were studied for SEM grid profiler for used at LINAC and a limitation factor of duty cycle for maximum beam current was found. For proton beam with $I_{macropulse}$ = 1mA, it is 10 ms at a maximum repetition rate of 10 Hz. It was empirically found that if the duty cycle is bigger than 10 ms, it induces unproportional increasing of X-rays emission. It totally destroys information about temporal structure of the beam and can be explained as a process of X-rays emission due to thermal heating of the wire.

The X-ray detector of BEM (Fig. 2, left) is based on microchannel plates coupled with fast readout anode. Two MCPs HAMAMATSU F1551-01 with channel of 12 microns diameter are assembled in chevron configuration. Entrance of the MCP is covered by a copper collimator of 10 mm thick with 4 mm diameter hole. The distance between beam axis and surface of the first MCP is 255 mm and gives solid angle for registration of 2×10^{-4} str. A gap of 3 mm between the first and the second microchannel plates was implemented to increase the amplitude of output signal. It was necessary to transmit this signal through a cable of 55 meters length to put the electronics outside the LINAC cave.

Aluminum foil of 22 microns thick polarized at +50 V is placed before detector. This foil serves to stop charged particles such as electrons or ions from backscattering of the beam and ionization of residual gas. At the same time, it stays practically transparent to X-rays with energies >10 keV with the coefficient of transmission more than 86%. Aluminum foil protects the detector from saturation and decreases its loading by three orders of magnitude due to differences in efficiency of registration for X-rays and ions.

Signal processing is performed with constant fraction discriminator and time-to-amplitude converter coupled with multichannel analyzer. The resolution of electronics was measured and estimated better than 15 ps [3].

Figure 2: Photos of X-ray detector (left) and mechanical system for wire insertion (right) of BEM.

TEMPORAL RESOLUTION

Preliminary estimation of temporal resolution for detector with two BEMs and β+ - decay source of ^{22}Na have been done. The source of ^{22}Na has a decay schema with emission of positron and 1.27 MeV gamma simultaneously. Emitted positrons have average energy about 150 keV. Positrons at energies below a few eV are able to interact with electrons by annihilation into two photons with energies of 511 keV emitted in opposite directions. A copper foil of 300 microns thickness was used for thermalisation of positrons. The coefficient of transmission for positrons in this foil is 4.5×10^{-6} thus practically all positrons escaped from the source are stopped in the foil. A source of ^{22}Na with copper foil in a sandwich arrangement was placed between two X-ray detectors of BEM. Detectors were included in coincidence schema and distribution of coincidence times between them was measured.

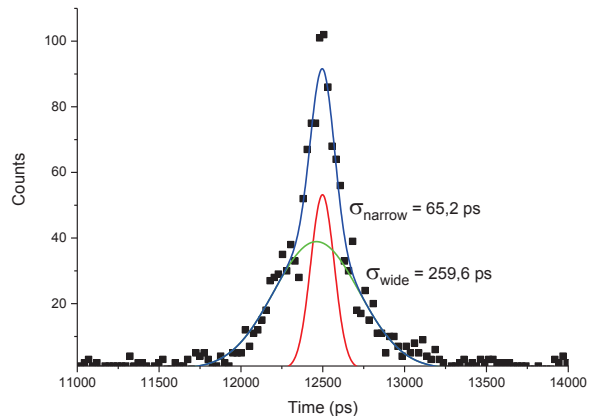

Figure 3: Coincidence spectrum obtained with source ^{22}Na.

Measured coincidence spectrum is depicted on Fig. 3. This spectrum is the convolution of several coincidence spectra with different values of width. Spectrum with the narrowest distribution is related to registration of two photons with energies 511 keV as they are emitted simultaneously. Spectrum with wider distribution is corresponded to coincidence of one photon of 511 keV with gamma of 1.275 MeV. The time delay for the positron to thermalize depends on the properties of matter (concentration of electrons) and is used in the technique of PALS (Positron Annihilation Lifetime Spectroscopy). In this case the time coincidence spectrum has broader distribution and is the convolution of several spectra with exponential decays. To analyze the obtained spectrum we have used simplified approach. Coincidence spectrum was fitted as superposition of two Gaussians with different widths. Width of the narrowest Gaussian divided by √2 has been used for estimation of temporal resolution for BEM. Thus the preliminary evaluation of temporal resolution for bunch shape measurements can be estimated as σ = 47 ps or 1.5° of phase resolution at 88 MHz acceleration frequency. It should be noticed that optimization of electronics was not possible due to a low coincidence count rate. Measured value of temporal resolution is an upper bound and therefore obtained value could be improved.

ISBN 978-3-95450-177-9

MEASUREMENTS

Series of tests for BEM with beams of protons and helium ions have been done during the commissioning phase of for 88 MHz RFQ of the LINAC. During this period an intermediate test bench (BTI) was installed at the place of medium energy line just after the first rebuncher (Fig. 4). This test bench is used for characterization of beam diagnostics of SPIRAL2. Variations of rf-amplitude and phase of rebuncher produce a strong effect on a longitudinal bunch shape and were used for characterization of longitudinal profile measurements. The BEM was installed at one position with Fast Faraday Cup (FFC) on a beam axis. That allows making direct comparisons of the results BEM and FFC [4].

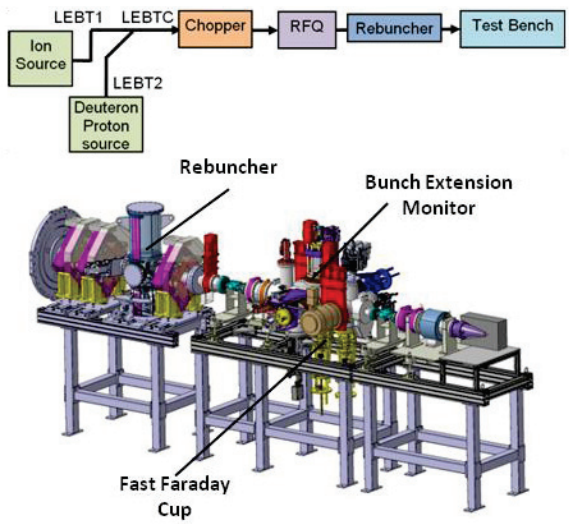

Figure 4: Diagram of injector (top) and general view of intermediate test bench (bottom).

Count rate at the detector without wire insertion into the beam was measured before performing bunch extension measurement. Background count rate was estimated less than 0.1 counts per second. Typically operating count rate for BEM is few tens counts per second that gives ratio noise to signal better than 1%. Measurement of background count rate of BEM placed at vicinity of operated cryomodule has been performed previously [3]. Results of this measurement are shown a lack of background produced by superconducting cavity in the range of applied acceleration field up to 8 MV/m (nominal value for acceleration field is 6.5 MV/m).

Comparison of measurements BEM and FFC have been done for phase variation of rebuncher with beam of protons and obtained results are in a good agreement (Fig. 5, top). Widths of bunches were measured in the range from 240 to 1400 ps (Fig. 5, bottom). FCC has a restriction for a minimal measured width σ rms= 320–330 ps due to limitation of bandwidth.

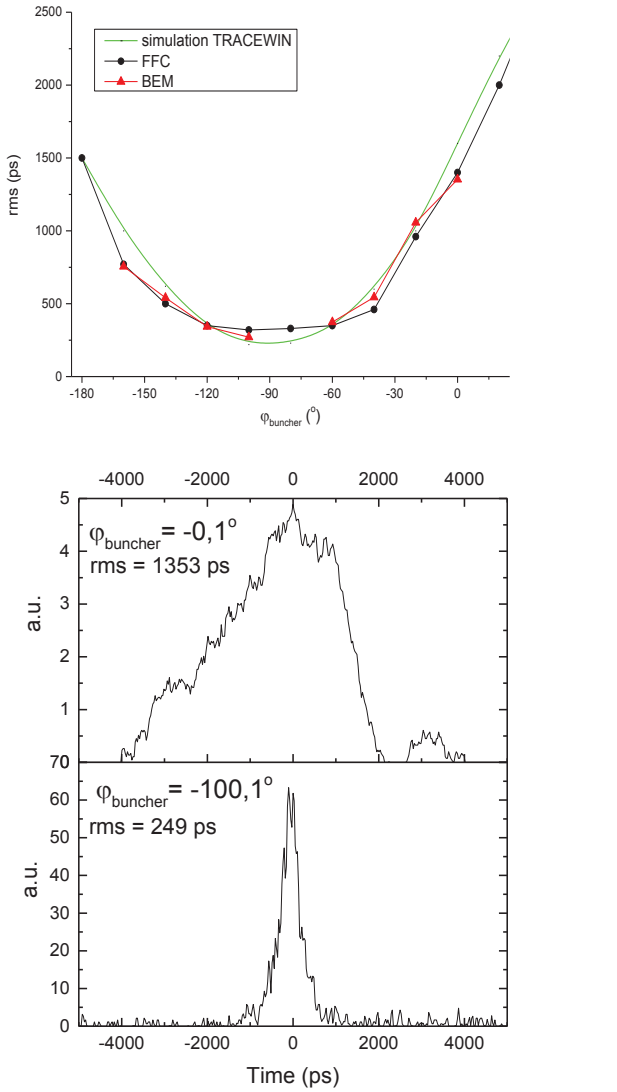

Figure 5: Width of bunch as function of buncher phase for proton beam $I_{macropulse}$ = 5mA (top) and measured longitudinal bunch profiles (bottom).

Series of measurements with beam of ions $^4He^{2+}$ and variation of rf-amplitude applied to the buncher cavity have been done (Fig. 6). Measurements with BEM show modification of bunch profile at different values of voltage of rebuncher. At the low voltage of rebuncher the second peak at the left side from principal ones corresponds to the ions that have velocities less than main part of ions inside a bunch. Increasing of voltage at rebuncher accelerates these ions to the energies of the main part and at high values of voltage it results to over-acceleration and formation of a bump on the right side bunch profile.

ISBN 978-3-95450-177-9

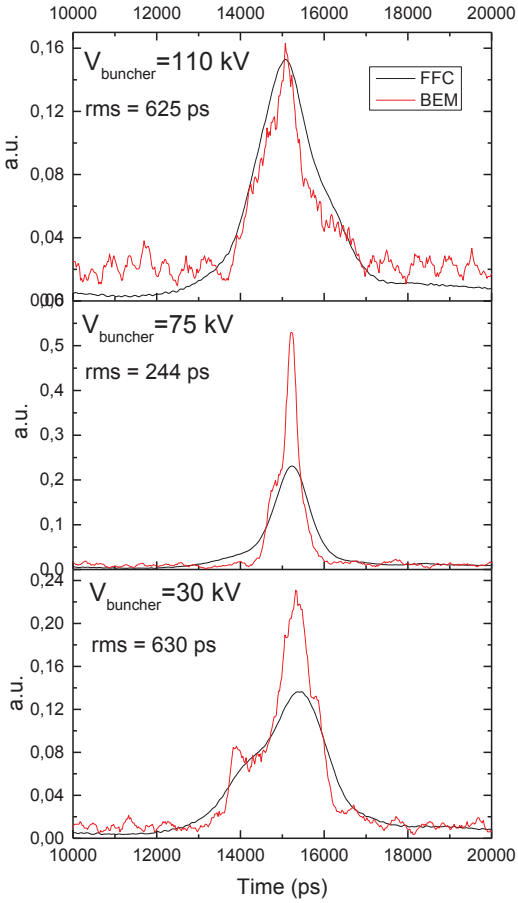

Figure 6: Bunch shapes measured with BEM and FFC at different values of applied $V_{buncher}$. Parameters: $^4He^{2+}$, $I_{macropulse}$ = 0.6 mA, $\phi_{buncher}$ = -67.9°, duty cycle = 1 ms/100 ms.

Some differences between shapes of longitudinal profile measured with FFC and BEM probably can be explained due to fact that only small beam fraction 3-4% in transversal plane interacts with a wire while FFC collects all ions of the beam in transversal plane. Additional investigation with measurements of bunch shape profile at different transversal positions of the wire will be performed.

Measurements of bunch profile have been performed with variation of $I_{macropulse}$ from 1 mA to 0.1 mA with helium beam (Fig. 7). Other parameters as rf-amplitude and phase of buncher stayed constant during these measurements. Measured longitudinal bunch profiles have shape variations from quasi-gaussian at maximal intensity to the shape with more fine structure with several satellite peaks at lower values of intensity. That can be explained as decreasing of influence of space charge forces inside the bunch. Coulomb repulsion forces of the space charge produce smoothing of fine structure. As it can be observed from Fig. 7, measured profile for intensity 0.2mA has structure with two principal peaks. More narrow peak has FWHM = 129 ps (σ = 55 ps) that is also confirms to previous estimation of temporal resolution for the BEM.

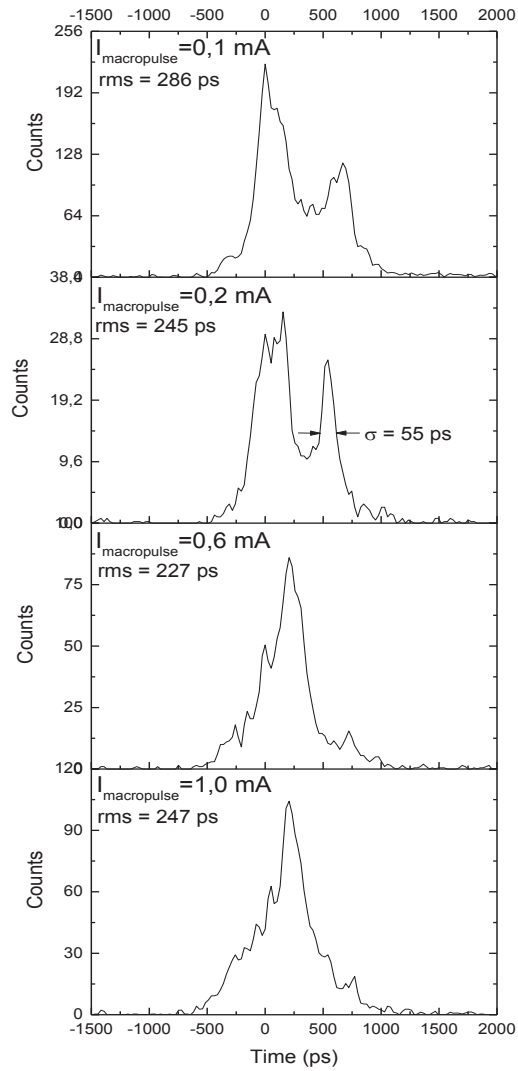

Figure 7: Longitudinal bunch profiles measured for different values of $I_{macropulse}$. Parameters: $^4He^{2+}$, $V_{buncher}$ =75 kV, $\phi_{buncher}$ = -67.9°, duty cycle varies from 1 ms/100ms to 10 ms/100 ms.

CONCLUSIONS

A novel device for bunch shape measurements have been developed and successfully tested with beam conditions of LINAC for SPIRAL2. Results of measurements were compared with measurements of FFC and were shown complete reliability in a range from 240 to 1400 ps of rms. Estimation of time resolution have been performed for this detector and confirmed with measurements. It was shown that it is not worse than 47 ps or 1.5° of phase at 88 MHz acceleration frequency and sufficient for bunch shape measurements. Further improved with optimization of some parameters of electronics could be done in a future. Some additional measurements with different positions of wire in the beam transversal plane will be performed.

ISBN 978-3-95450-177-9

REFERENCES

[1] R. Revenko *et al.*, "Bunch Extension Monitor for LINAC of SPIRAL2 facility", IBIC13, Oxford, UK, (2013), WEPC20, http://jacow.org/

[2] J.-L. Vignet *et al.*, "A Bunch Extension Monitor for the SPIRAL2 LINAC", IBIC2014, Monterey, California, USA (2013), MOPD26, http://jacow.org/

[3] R. Revenko *et al.*, "Spiral2 Bunch Extension Monitor", LINAC 2014, Geneva, Switzerland (2014), THIOC01, http://jacow.org/

[4] C. Jamet *et al.*, "Energy and Longitudinal Bunch Measurements at the SPIRAL2 RFQ exit", IBIC2016, Barcelona, Spain (2016), WEPG42, http://jacow.org/

ISBN 978-3-95450-177-9

STABLE TRANSMISSION OF RF SIGNALS AND TIMING EVENTS WITH ACCURACY AT FEMTOSECONDS

M. Liu*, X. L. Dai, C. X. Yin, SINAP, Shanghai, China

Abstract

We present a new design of femtosecond timing system. In the system, the RF signal and timing events are transmitted synchronously in one single optic-fibre with very high accuracy. Based on the theory of Michelson interferometer, the phase drift is detected with accuracy at femtoseconds. And phase compensation is accomplished at the transmitter with two approaches afterwards. Moreover, the traditional event timing system is integrated into the new system to further reduce the jitter of timing triggers. The system could be applied in synchrotron light sources, free electron lasers and colliders, where distribution of highly stable timing information is required. The physics design and the preliminary results are demonstrated in the paper.

INTRODUCTION

Timing information with high precision is required to synchronize devices and equipments in large accelerator facilities. The SINAP timing system, as one of the traditional event timing systems, distributes triggers and clocks with jitter at picoseconds. [1] The delay and width step of the timing signals is in different levels from picoseconds to nanoseconds. [2] The SINAP timing system is successfully applied in Pohang Light Source II [3][4], Shanghai Synchrotron Radiation Facility, Beijing Electron-Positron Collider II, SuperKEKB [5], Chinese Spallation Neutron Source, Brazil Sirius Light Source, Shanghai Advanced Proton Therapy Facility [6] and so on.

However, the traditional event timing system can't meet the requirement of new experiment methodology like pump-probe technology in the third generation light sources. Moreover, the synchronization of electron gun, lasers and experiment equipment in the fourth generation light sources, free electron lasers, demands higher accuracy. A level of 10-100 femtoseconds should be achieved for the accuracy of the triggers and clocks.

Laser modules but not electronic ones are mainly utilized to form the new highly stable timing system. One technical route makes use of mode locked laser as the reference base, and detects the variation of the transmission delay by the technique of balanced cross-correlation, and compensates the delay with optical feedback methods. [7] The other technical route makes use of continuous wave laser as the reference base, and detects the variation of the transmission delay by the theory of Michelson interference, and compensates the delay with electronic feedback method. [8]

We designed the system, which is based on the theory of the Michelson interference. The RF signal is modulated in continuous wave laser carrier. The phase drift of laser carrier is detected by sensing the phase of the beat frequency signal, which increases the measuring precision remarkably. The phase drift is compensated by optical approaches. The system aims to stabilize the phase of transmitted RF signal to 0.01°. The traditional event timing system is integrated to transmit event stream in the same fibre, from which the timing triggers benefit to decrease the original jitter.

SYSTEM DESIGN

The detection and compensation of the phase drift is accomplished at the transmitter side. Therefore, the transmitter is much more complex than the receiver. Such design improves the scalability and reduces the cost for large systems.

The transmitter of the system is divided into the optical part and the electronic part. A collection of available commercial modules is utilized to form the optical part, which is primarily the Michelson interferometer. The core modules are the continuous wave laser, the analog modulator, the acousto-optic frequency shifter and the optical delay modules. The RF signal is modulated in continuous wave laser carrier. The photodiode receives the beat frequency signal by heterodyne interference. An optical delay line and a fibre stretcher compensate the drift along the fibre.

The phase drift caused by ambient temperature change is sensed in the electronic part, and then the optical path variation is calculated and is used to control optical delay modules. A wavelength division multiplexer multiplexes the event stream and modulated RF signal onto one single fibre.

The receiver of the system is less complex. It reflects the optical wave as one arm of the Michelson interferometer, recovers the RF signal and event codes.

The structure of the system is illustrated in Fig. 1.

*liuming@sinap.ac.cn

ISBN 978-3-95450-177-9

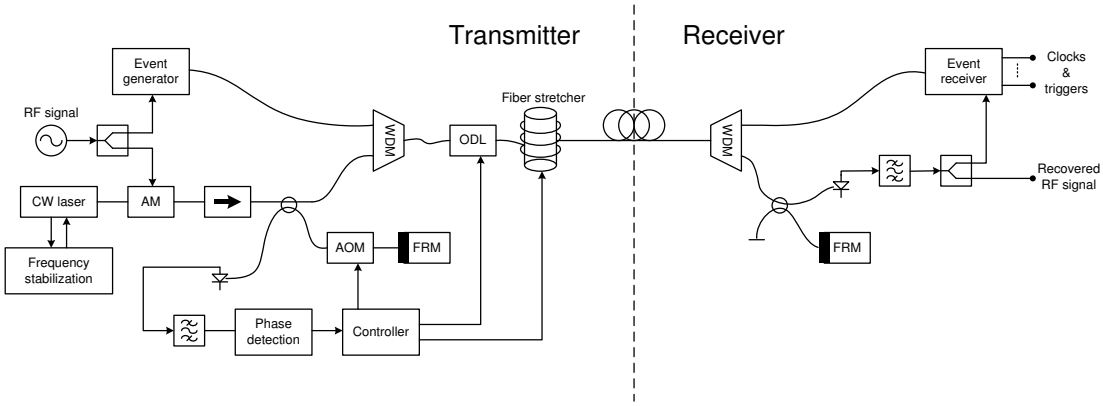

Figure.1: The structure of the system.

Signal Modulation and Transmission

It is assumed that the fibre laser generates ideal monochromatic light. The RF signal modulates the optical wave. The modulated signal

$$E_{AM}(t) = \left[1 + b\cos\omega_{rf}t\right]\cos\omega_{op}t, \quad (1)$$

where ω_{rf} is the angular frequency of the RF signal, ω_{op} is the angular frequency of the optical wave, and b is the modulation index. The RF waveform determines the envelope of the optical carrier. The photodiode at the receiver side recovers the RF signal.

When the change of the ambient temperature occurs, the refractive index variation of the fibre contributes most to the phase drift of the recovered RF signal. It is proximately 30 picosecond/℃/km.

Phase Drift Detection and Correction

The system makes use of the theory of Michelson interference to detect the phase drift. One arm of the interferometer is the modulated laser signal passing through the acousto-optic frequency shifter twice and reflected at the transmitter. The other arm of the interferometer is the modulated laser signal reflected from the receiver to the transmitter. The photodiode at the transmitter receives the beat frequency signal. After neglecting the small quantity of the phase and filtering the DC and high-frequency components, the output of the photodiode

$$I_d = \cos\left(2\omega_{fs}t + \frac{2\omega_{op}l}{c}n\right), \quad (2)$$

where ω_{fs} is the angular frequency of the acousto-optic frequency shifter, l is the length of the fibre from the transmitter to the receiver, and n is the refractive index of the fibre.

According to Equation (2), the phase of the laser carrier at the receiver is converted one-to-one to the phase of acousto-optic frequency. Since the frequency of the acousto-optic frequency shifter is 10^{-6} lower than the laser carrier, the method of the heterodyne interference improves the measuring precision effectively.

The electronic part at the transmitter acquires the phase drift and sends the controlled quantities to the motorized variable optical delay line and the optic fibre stretcher to correct the phase drift of the fibre coarsely and finely respectively.

Transmission of Event Stream and RF Clock in One Fibre

The traditional timing system is integrated to the system so as to transmit low-precision and high-precision signals to different types of equipments in the large accelerator facility.

The RF signal is modulated in the laser carrier of 1560nm, while the event stream is modulated in the laser carrier of 1310nm. The WDM at the transmitter makes it possible to deliver the two signals in one fibre. And then the WDM at the receiver conducts the demultiplex and separates the two signals. Therefore, in one fibre optic network, both of event stream and stabilized RF signal can be distributed.

At the receiver of the system, the phase-compensated RF signal can be used to align the recovered event codes. The temperature drift effect of the fibre to the triggers and the clocks is eliminated. However, the contribution of electronics noise to the jitter still exists.

PRELIMINARY TEST

We made use of Tektronix TDS694C oscilloscope and Agilent E4440A spectrum analyzer to measure the recovered RF signal and the beat frequency signal of the optical prototype of the system qualitatively. The test bench is illustrated in Fig. 2.

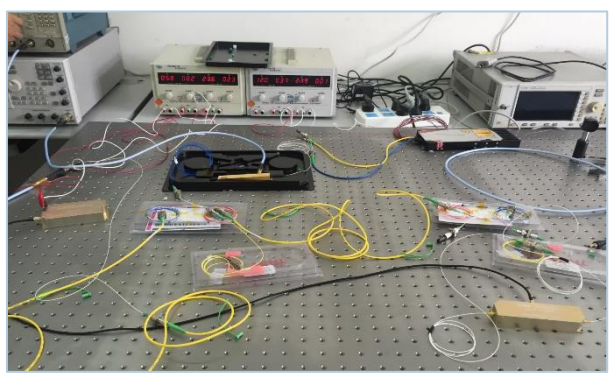

Figure 2: The prototype of the optical system.

ISBN 978-3-95450-177-9

The wavelength of the continuous wave laser is 1560nm. The frequency of the RF signal is 2856MHz. The frequency of the acousto-optic frequency shifter is 50MHz, so the frequency of the beat wave is 100MHz.

The frequency spectrum of the recovered RF signal at the receiver is illustrated in Fig. 3. A band-pass filter will be necessary to stop the DC component and the higher harmonics.

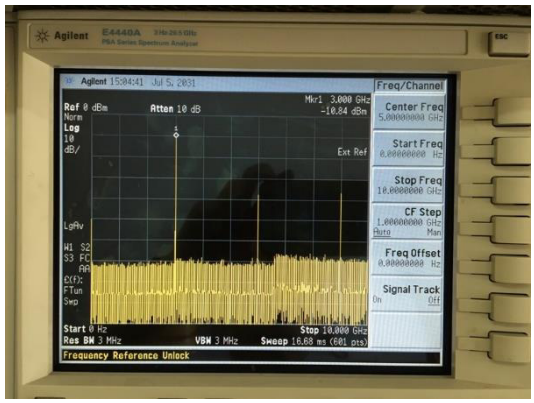

Figure 3: The frequency spectrum of the recovered RF signal.

The waveform of the beat frequency signal at the transmitter is illustrated in Fig. 4, and the frequency spectrum of it is illustrated in Fig. 5. It is observed that the frequency of the RF signal mixed in the beat frequency signal, and the frequency spectrum confirmed it. A band-pass filter will also be necessary to stop DC and higher frequency components.

Figure 4: The waveform of the beat frequency signal.

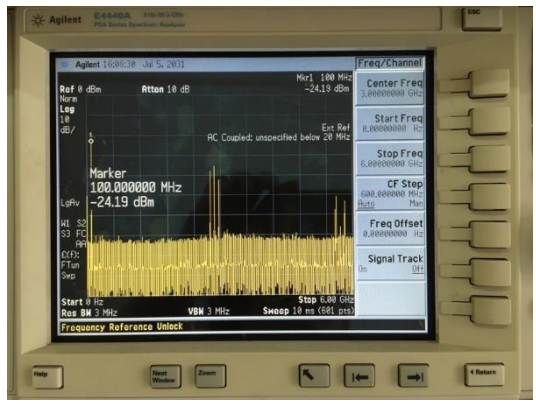

Figure 5: The frequency spectrum of the beat frequency signal.

CONCLUSION

The physics design of the system and the preliminary results of the optical prototype are described in the paper. The initial qualitative test confirmed the physics design.

The temperature change causes frequency shift of the laser. The effect also affects the phase of the recovered RF signal. We will adopt a frequency feedback device made up of a saturated absorption line to stabilize the frequency of the laser.

The ambient temperature also affects the optical components such as the acousto-optic frequency shifter and the photodiode. We will utilize a temperature control box to make the core components perform stable.

The electronic part of the system is still in the phase of hardware design. The feedback loop of phase control will be realized until the electronic part is added into the system.

ACKNOWLEDGMENT

The project was supported by the National Natural Science Foundation of China (No.11305246) and the Youth Innovation Promotion Association CAS (No. 2016238).

REFERENCES

[1] M. Liu, “Research of a New Timing System”, Doctoral Dissertation, 2010.
[2] M. Liu, C. X. Yin, L. Y. Zhao *et al.*, Proc. of IPAC’13 (2013) 2992-2994.
[3] S. J. Park, S. S. Park, W. H. Hwang *et al.*, Proc. of LINAC’10 (2010) 698-702.
[4] S. Shin, S. Kwon, D-T. Kim *et al.*, Proc. of IPAC’12 (2012) 1089-1091.
[5] H. Kaji, K. Furukawa, M. Iwasaki *et al.*, Proc. of ICALEPCS’15 (2015) 629-632.
[6] B. Q. Zhao, L. Y. Zhao, M. Liu *et al.*, Proc. of IPAC’16 (2016) 4231-4233.
[7] J. Kim, J. Chen, Z. Zhang *et al.*, Long-term femtosecond timing link stabilization using a single-crystal balanced cross correlator. Optics Letters 32 (2007) 1044-1046.
[8] R. Wilcox, J. M. Byrd, L. Doolittle *et al.*, Proc. of IPAC’10 (2013) 1399-1401.

ISBN 978-3-95450-177-9

X-RAY SMITH-PURCELL RADIATION FOR NON-INVASIVE SUBMICRON DIAGNOSTICS OF ELECTRON BEAMS HAVING TeV ENERGY*

A.A. Tishchenko†, D.Yu. Sergeeva, National Research Nuclear University MEPhI, Moscow, Russia

Abstract

We present the general theory of X-ray Smith-Purcell radiation from ultrarelativistic beams proceeding from our earlier results. The theory covers also the case of oblique incidence of the beam to the target, which leads to the conical effect in spatial distribution of Smith-Purcell radiation and allows one to count the divergence of the beam; also, the analytical description of the incoherent form-factor of the beam is given.

INTRODUCTION

Non-invasive diagnostics is one of the topical problems for the facilities like DESY, SLAC and the future ones like CLIC, ILC, etc. All modern diagnostics schemes are based on optical radiation which restricts limitation on the beam length and diagnostic resolution due to the diffraction (Rayleigh) limit. We suggest X-ray Smith-Purcell radiation as an instrument operating with smaller wavelengths and hence much more suiting for non-invasive submicron beam diagnostics.

Diffraction radiation (DR) arises when a charged particle moves near a target. The Coulomb field of the particle polarized the target material and the polarization currents arise, which leads to the radiation generation. Smith-Purcell radiation (SPR) is a special case of DR occurring when the target is a periodic structure.

Both these types of radiation are usually called the polarization radiation because the source of the radiation in these schemes is the target material rather than the charged particles itself [1].

As it follows from the definitions given above, when both DR and SPR are generated, there is no direct interaction between the particle and the target. It means that DR and SPR can be a base for noninvasive diagnostics. And, generally speaking, the information obtained can be both about the beam and about the target [2, 3].

We construct the theory of Smith-Purcell radiation at frequencies

$$\omega >> \omega_p, \qquad (1)$$

where ω_p is the plasma frequency, which usually has values about $20-30\,eV$. In this frequency region the response of dielectric or metal to the external field is similar, because behavior of the conductivity electrons and electrons bounded in atoms coincides in the electromagnetic field acting at frequencies higher than the atomic ones. Consequently, the properties of target material are defined by the function $\varepsilon(\omega)$, which has the form:

$$\varepsilon(\omega) = 1 - \omega_p^2/\omega^2 . \qquad (2)$$

DR in the high-frequency limit $\omega >> \omega_p$, was investigated in the papers [4] for non-relativistic particles, and in [5] for gratings, i.e. X-ray SPR. Non-relativistic particles, however, emits DR only for impact-parameters of the order of the wavelength, which is not the case for X-ray domain. The analytics in the paper of M.J. Moran [5], on the other hand, was based on the theoretical description given in [6] by M.L. Ter-Mikhaelyan, who developed the theory an infinitely thin perfectly conducting target. This makes these results inapplicable for frequencies larger than optical ones. After that, the basis of the X-ray DR theory was given in [7] and for X-ray SPR in [8] for single-particle radiation.

PROPERTIES OF RADIATION

Let us consider the generation of SPR from the beam consisting of N_e electrons. The target is a grating of N elements (slabs, strips, grooves, etc) with the period d. The slab sizes in x, y, z directions are a, infinite, half-infinite, correspondingly, see Fig. 1. The beam is supposed to move at a constant distance h from the target surface. The particle velocity is $\mathbf{v} = v(\cos\alpha, \sin\alpha, 0)$.

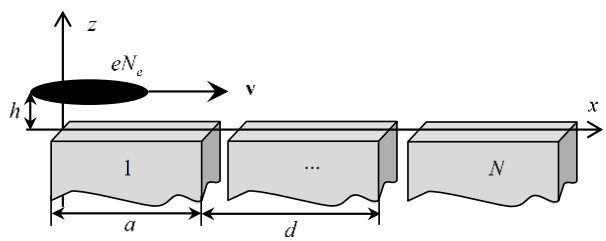

Figure 1: Generation of the Smith-Purcell radiation from a beam of electrons.

The main characteristic of the radiation we will operate with is the spectral-angular distribution of the radiation, which can be written in form

*This work was supported by the Leverhulme Trust International Network, grant IN-2015-012, grant RSF 16-12-10277 and by the Competitiveness Programme of National Research Nuclear University "MEPhI".

†Tishchenko@mephi.ru

ISBN 978-3-95450-177-9

$$\frac{d^2W(\mathbf{n},\omega)}{d\Omega d\omega}=\frac{d^2W_1(\mathbf{n},\omega)}{d\Omega d\omega}4\sin^2\left(\frac{a\varphi}{2}\right)\frac{\sin^2(dN\varphi/2)}{\sin^2(d\varphi/2)}F, \quad (3)$$

where $d^2W_1/d\omega d\Omega$ is the distribution of radiation energy from a single particle, F is the form-factor of the bunch,

$$\varphi=\frac{\omega}{c}\frac{1}{\beta_x}\left(1-n_x\beta_x-n_y\beta_y\right), \quad (4)$$

$\boldsymbol{\beta}=\mathbf{v}/c$; n_x and n_y are the components of the wave vector of radiation in vacuum $\mathbf{k}=\mathbf{n}\,\omega/c$.

Testing of the ratio of sines in Eq. (3) for maxima it is easy to obtain the Smith-Purcell dispersion relation:

$$\frac{d}{\lambda}\frac{1}{\beta_x}\left(1-n_x\beta_x-n_y\beta_y\right)=m, \quad m=1,2.... \quad (5)$$

The form-factor has the form [9]

$$F=N_eF_{inc}+N_e\left(N_e-1\right)F_{coh}, \quad (6)$$

where its parts, i.e. incoherent form-factor F_{inc} and coherent one F_{coh}, contain information about such beam parameters as sizes, form, energy, emittance.

The chosen coordinate system and the angles of radiation are shown in Fig. 2. The unit wave-vector $\mathbf{n}$ is defined as:

$$\begin{aligned} n_x&=\sin\theta\cos\phi,\\ n_y&=\cos\theta,\\ n_z&=\sin\theta\sin\phi. \end{aligned} \quad (7)$$

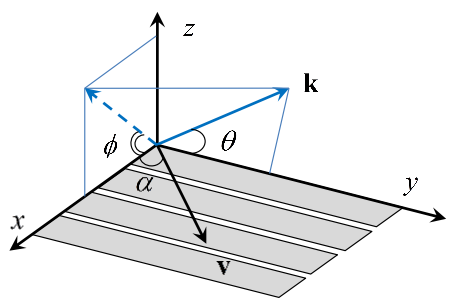

Figure 2: Chosen coordinate system and the angles of radiation.

The distribution of X-ray Smith-Purcell radiation energy from a single particle has the form [8]:

$$\frac{d^2W_1(\mathbf{n},\omega)}{d\Omega d\omega}=\frac{e^2}{c}\left(\frac{\varepsilon(\omega)-1}{4\pi\beta_x\varphi}\right)^2e^{-2\rho h}\frac{\omega^4}{c^4}P, \quad (8)$$

where e is the charge of an electron,

$$P=\frac{\left\|\left[\mathbf{n}',\left[\mathbf{n}',\mathbf{A}\rho^{-1}-i\mathbf{e}_z\right]\right]\right\|^2}{\left|\rho-i(\omega/c)\sqrt{\varepsilon(\omega)-1+n_z^2}\right|^2}, \quad (9)$$

$$\varphi=\frac{\omega}{c}\frac{1}{\beta_x}\left(1-n_x\beta_x-n_y\beta_y\right), \quad (10)$$

$$\rho=\frac{\omega}{c\beta\gamma}\sqrt{1+\gamma^2\beta_x^{-2}\left(n_y\beta^2-\beta_y\right)^2}, \quad (11)$$

$$\mathbf{A}=\frac{\omega}{\beta_xc}\left(1-n_y\beta_y-\beta_x^2,n_y\beta_x-\beta_x\beta_y,0\right), \quad (12)$$

and $\mathbf{n}'=\varepsilon^{-1/2}(\omega)\left(n_x,n_y,\sqrt{\varepsilon(\omega)-1+n_z^2}\right)$ is the unit wave-vector of the radiation in the media.

The radiation is maximal when the argument of exponent in Eq. (8) is minimal, i.e. when ρ is minimal:

$$n_y=\frac{\beta_y}{\beta^2}, \quad (13)$$

It means that the radiation is distributed over a conical surface with the main axis along y direction, see Fig. 3. The analytical description for SPR was given in [8], and the similar effect can also be seen in diffraction radiation [10].

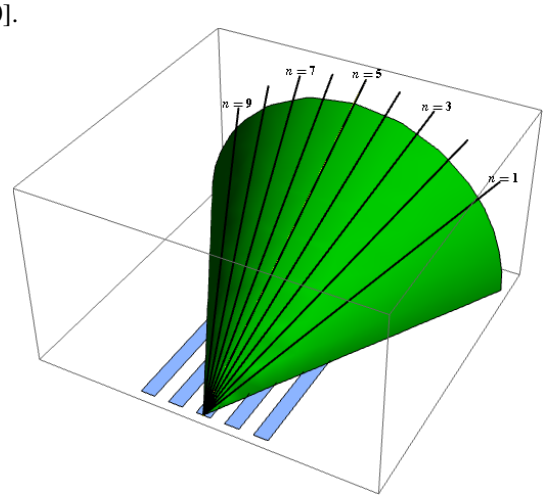

Figure 3: Conical distribution of Smith-Purcell radiation. The black lines correspond to the Smith-Purcell peaks.

The coherent and incoherent form-factors for uniform distribution and for Gaussian distribution for $\alpha=0$ were obtained and explored theoretically in [2, 3, 11]

For the beam moving at oblique angle α to the periodicity direction the form-factors can be calculated as:

ISBN 978-3-95450-177-9

$$F_{inc} = \int_V d^3 r \left| e^{-i\mathbf{rQ}} \right|^2 f(\mathbf{r}),$$
$$F_{coh} = \left| \int_V d^3 r e^{-i\mathbf{rQ}} f(\mathbf{r}) \right|^2, \quad (14)$$

where the integrals are taken over the bunch volume V, the distribution function of the particles in the bunch $f(\mathbf{r})$ is the written in the system where the bunch is at rest,

$$\mathbf{Q} = \left(q_x \cos\alpha + q_y \sin\alpha, -q_x \sin\alpha + q_y \cos\alpha, q_z \right), \quad (15)$$

$$\mathbf{q} = \left(\frac{\omega - k_y v_y}{v_x}, k_y, -i\rho \right). \quad (16)$$

For the cylindrical bunch of the length l and the radius r_0 with the uniform distribution of the particles, moving at the angle α to the target periodicity, one can find:

$$F_{inc} = 2\frac{I_1(2\rho r_0)}{2\rho r_0},$$
$$F_{coh} = 4\frac{\sin^2(\omega l/2v)}{(\omega l/2v)^2}\frac{I_1^2(r_0\omega/c\beta\gamma)}{(r_0\omega/c\beta\gamma)^2}. \quad (17)$$

As one can see from Eq. (17), the coherent form-factor does not depend on the observation angle and the angle between the beam velocity and the direction of periodicity. In the incoherent form-factor this dependence exits (in ρ), but it is rather weak, and in the maxima defined by Eq. (13) it disappears.

The distribution of the Smith-Purcell peaks generated by a cylindrical bunch is shown in Fig. 4. The graph was plotted taking into account Eq. (13).

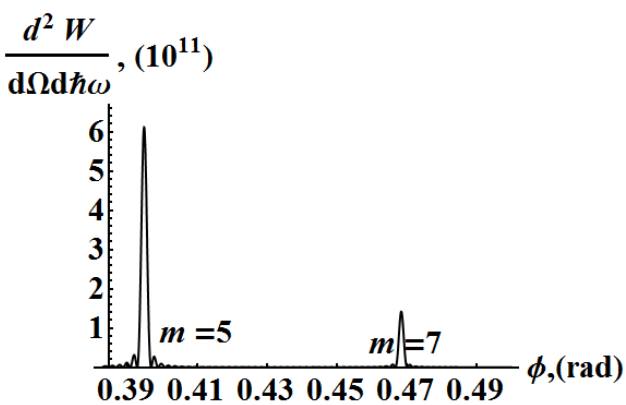

Figure 4: The distribution of X-Ray SPR over the conical surface at $\theta = \arccos(\beta^{-1}\sin\alpha)$. Here $\gamma = 2\cdot 10^6$ (electron energy $E = 1TeV$), $\hbar\omega_p = 26.1eV$ (beryllium), $d = 0.9\,\mu m$, $a = 0.45\,\mu m$, $\lambda = 12\,nm$, $h = 60\,\mu m$, $\alpha = 30^0$, $N = 20$, $N_e = 10^{10}$, $r_0 = 30\,\mu m$, $l = 60\,\mu m$.

If we suppose that the particles in the bunch moves at different angles to the general direction of the bunch, then Eq. (17) will contain the factor describing the velocity distribution, or even information about the divergence of the beam [12].

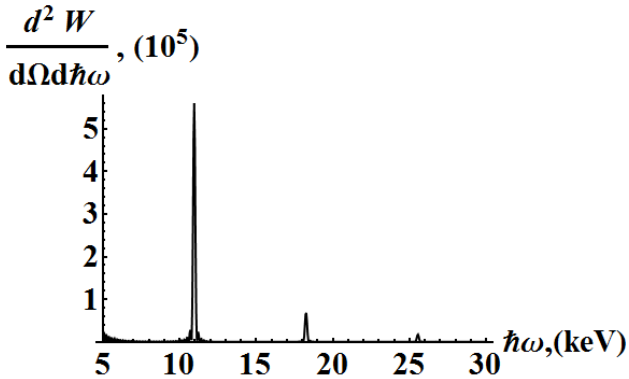

Figure 5: The distribution of X-Ray SPR over the conical surface at $\theta = \arccos(\beta^{-1}\sin\alpha)$, $\phi = 5^0$. Here $\gamma = 2\cdot 10^6$ (electron energy $E = 1TeV$), $\hbar\omega_p = 26.1eV$ (beryllium), $d = 0.1\,\mu m$, $a = 0.05\,\mu m$, $h = 1\,\mu m$, $\alpha = 30^0$, $N = 20$, $N_e = 10^{10}$, $r_0 = 1\,\mu m$, $l = 60\,\mu m$.

The Fig. 5 shows the distribution of the radiation intensity over radiated photons energies, and one can see the clear peaks of SPR, suitable for diagnostics.

CONCLUSION

Thus, X-ray SPR is emitted at the frequencies up to

$$\omega = \frac{\gamma c}{2h}, \quad (18)$$

which for the electron energies of the order of 1 TeV can reach the photon energies up to some 30-40 of KeV. Manufacturing the gratings with a period from some hundreds to tens of nanometres, we can obtain the SPR peaks under the angles from 3-4 to some tens of degrees, which is suitable for the experimental diagnostics schemes. The expression for spectral-angular distribution, generalizing the one obtained in [8], contains the information about both the target and beam parameters, including the length of the beam, which opens new possibility of submicron non-invasive diagnostics for the future electron colliders like CLIC, ILC, etc. In contrast with the optical range based diagnostics schemes, X-ray range makes it possible the non-invasive diagnostics with submicron and even nanometres accuracy.

ISBN 978-3-95450-177-9

REFERENCES

[1] A.P. Potylitsyn, M.I. Ryazanov, M.N. Strikhanov and A.A. Tishchenko, *Diffraction Radiation from Relativistic Particles*, Berlin, Germany: Springer-Verlag, 2011.

[2] D.Yu. Sergeeva, M.N. Strikhanov and A.A. Tishchenko, "UV and X-ray diffraction radiation for submicron noninvasive diagnostics", in *Proc. of 4th Int. particle Accelerator Conf. (IPAC'13),* Shanghai, China, May 2013, paper MOPME062, pp. 616-619.

[3] A.A. Tishchenko, D.Yu. Sergeeva and M.N. Strikhanov, "Properties of polarization radiation from charged particles beam", *Vacuum*, vol. 129, p. 157, 2016.

[4] J.C. McDaniel, D.B. Chang, J.E. Drummond, W.W. Salisbury, "Smith-Purcell Radiation in the High Conductivity and Plasma Frequency Limits", *Applied Optics,* vol. 28, pp. 4924-4929, 1989.

[5] M.J. Moran, "X-ray generation by the Smith-Purcell effect", *Phys. Rev. Lett.,* vol. 69, p. 2523, 1992.

[6] M.L. Ter-Mikhaelyan, *High-Energy Electromagnetic Processes in Condensed Media,* , New York: Wiley, 1972. (p. 382)

[7] A.A. Tishchenko, A.P. Potylitsyn, M.N. Strikhanov, "Diffraction radiation from an ultrarelativistic charge in the plasma frequency limit", *Phys. Rev. E*, vol. 70, p. 066501, 2004.

[8] D.Yu. Sergeeva, A.A. Tishchenko and M.N. Strikhanov, "Conical diffraction effect in optical and x-ray Smith-Purcell radiation", *Phys. Rev. ST-AB*, vol. 18, 052801, 2015.

[9] D.Yu. Sergeeva, A.A. Tishchenko and M.N. Strikhanov, "UV and X-ray diffraction and transition radiation from charged particles", *Nucl. Instrum. and Methods B,* vol. 309, p. 189–193, 2013.

[10] D.Yu. Sergeeva, A.A. Tishchenko and M.N. Strikhanov, "Conical effect in diffraction radiation", *Nucl. Instr. and Methods B,* vol. 355, pp. 155–159, 2015.

[11] D.Yu. Sergeeva and A.A. Tishchenko, "X-Ray Smith-Purcell radiation from a beam skimming a grating surface", in *Proc of 36th Int. Free-Electron Laser Conf. (FEL'14),* Basel, Switzerland, Aug. 2015, paper TUP013, pp. 378-383.

[12] D.Yu. Sergeeva, A.A. Tishchenko and M.N. Strikhanov, "Influence of beam divergence on form-factor in X-ray diffraction radiation", *Nucl. Instr. and Methods B,* vol. 355, pp. 175–179, 2015.

ISBN 978-3-95450-177-9

BUNCH LENGTH MEASUREMENT BASED ON INTERFEROMETRIC TECHNIQUE BY OBSERVING COHERENT TRANSITION RADIATION

I. Nozawa†, M. Gohdo, K. Kan, T. Kondoh, J. Yang, Y. Yoshida
The Institute of Scientific and Industrial Research, Osaka University, Osaka, Japan

Abstract

Generation and diagnosis of ultra-short electron bunches are one of the main topics of accelerator physics and applications in related scientific fields. In this study, ultra-short electron bunches with bunch lengths of femtoseconds and bunch charges of picocoulombs were generated from a laser photocathode RF gun linac and an achromatic arc-type bunch compressor. Observing coherent transition radiation (CTR) emitted from the electron bunches using a Michelson interferometer, the interferograms of CTR were measured experimentally. The bunch lengths were diagnosed by performing a model-based analysis of the interferograms of CTR.

INTRODUCTION

Generation of ultra-short electron bunches with femtosecond bunch lengths has been progressed with the development of accelerator technologies such as photocathode RF (Radio Frequency) guns, bunch compression techniques and plasma acceleration techniques. The femtosecond electron bunches are essential for physical application in accelerator science such as free-electron lasers[1], laser-Compton scattering x-ray sources[2] and terahertz-light sources based on coherent radiation[3]. In addition to the application mentioned above, it takes an important role in time-resolved measurement like pulse radiolysis in radiation chemistry. The pulse radiolysis is one of the most powerful tools in radiation chemistry to investigate ionizing radiation-induced phenomena. As for this measurement, the ultra-short electron bunch is used as a pump source to ionize the chemical sample, and the kinetics of the radiation-induced phenomena is measured as transient absorption using an ultra-short laser pulse stroboscopically, so the time resolution of the system is mainly determined by the electron bunch lengths. So far, much effort has been paid to improve the time resolution, and the best time resolution of 240 fs was attained using 100-fs electron bunches generated from a laser photocathode RF gun linac and a magnetic bunch compressor at Osaka University in 2011[4].

On the other hand, longitudinal diagnosis of the ultra-short electron bunches is also one of the key topics in accelerator physics and its related fields. The main reason to activate this study is that there is no established bunch length measurement technique for <100-fs electron bunches. Hitherto, many bunch length measurement techniques have been proposed and experimentally demonstrated to diagnose the <100-fs electron bunches. For example, bunch length measurements using coherent radiation (CR)[5,6], electro-optic (EO) crystals[7] and deflecting cavities have been proceeded to diagnose the temporal bunch length of femtosecond electron bunches.

In this study, bunch length measurement based on interferometric technique was demonstrated by monitoring coherent transition radiation (CTR). Details will be described below, but the bunch lengths were estimated by analyzing an autocorrelation of CTR measured using a Michelson interferometer.

EXPERIMENTAL SETUP

Photocathode RF Gun Linac

Figure 1 shows the schematic of the linac system at Osaka University. The linac system has three beam lines, and achromatic-arc beam line was used to generate the ultra-short electron bunches. The linac system is mainly composed of three sections: a photocathode RF gun with a copper cathode, an S-band acceleration cavity and an achromatic arc-type magnetic bunch compressor. The photocathode is driven by a 266-nm femtosecond UV pulse of the third harmonic of a Ti:sapphire femtosecond laser with a regenerative amplifier (Tsunami with Spitfire, Spectra Physics). The electron bunch is accelerated at 4 MeV at the exit of the gun and the solenoid mounted at the exit of the gun is used for emittance compensation. The electron bunch is accelerated by the RF electric field inside the 2-m long S-band traveling wave cavity. The beam energy of the electron bunch at the exit of the linac is 35 MeV, and the electron bunch is energy-correlated inside the cavity for bunch compression using the achromatic arc-type magnetic bunch compressor. The bunch compressor is composed of two bending magnets, four quadrupole magnets and two sextupole magnets. The sextupole magnets in the compressor served to compensate for the second-order effect due to the fringing fields of the magnets, which will cause bunch length growth because of the nonlinear transformation of the energy-phase correlation.

Bunch Length Measurement System

Figure 2 shows the schematic diagram of the bunch length measurement system based on a Michelson interferometer. In this scheme, the CTR was emitted from the electron bunches at a boundary between a vacuum and an aluminium mirror (M1). The mirror (M1), scintillators (ZnS) and an infrared light source (IRS, IRS-001C, IR System) for calibration of the measurement system were mounted on the rotational stage, so the transverse beam shape could be checked during the measurement. The CTR was collimated to parallel light by an off-axis parabolic mirror (OAP1) since it could be considered to be a point source of electromagnetic (EM) waves in infrared region. After that,

†nozawa81@sanken.osaka-u.ac.jp

ISBN 978-3-95450-177-9

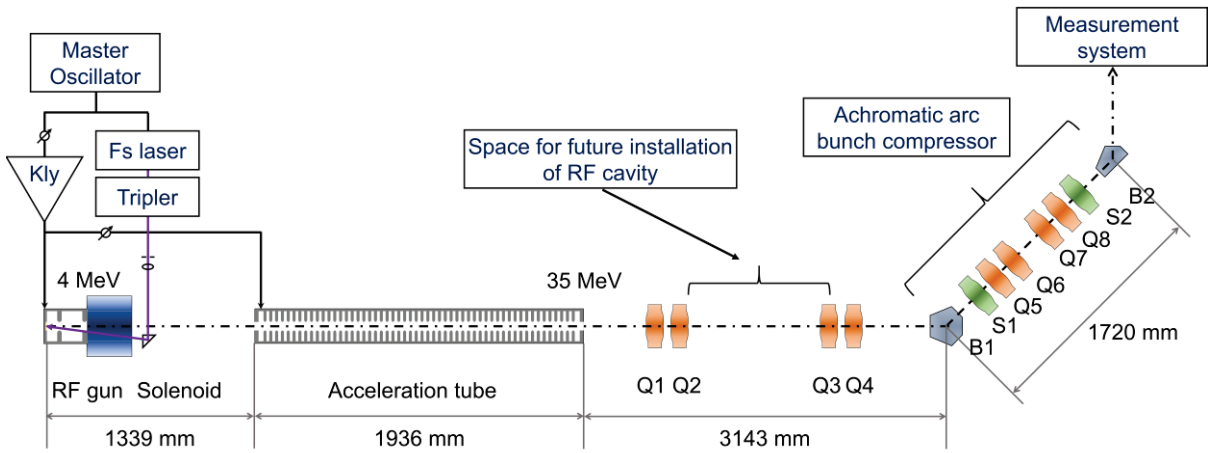

Figure 1: Schematic diagram of a laser photocathode RF electron gun linac and a magnetic bunch compressor. Q: quadrupole magnet; B: bending magnet; S: sextupole magnet.

the EM waves were guided to the Michelson interferometer. The CTR was collimated and then split in two by a beam splitter (BS1) made of a 375-um thick high-resistivity silicon (HRSi) wafer. One of the EM waves was reflected by a fixed mirror (M4), while the other was reflected by a position-tunable mirror (M5) on a delay stage. Finally, the two EM waves were converged, and the autocorrelated EM wave was fed to the detectors. The autocorrelated signal as a function of the position of M5 is called as an interferogram. Two infrared light detectors were used simultaneously for the detection of the interferograms. One is a liquid-helium-cooled silicon bolometer (general purpose 4.2-K system, Infrared Laboratories) and the other is a liquid-nitrogen-cooled MCT photoconductive detector (P2748, Hamamatsu photonics). The interferogram contains information about frequency spectrum of CTR, and the spectrum has a relation with a longitudinal charge distribution of the electron bunch. Thus, information of the bunch length of the electron bunch can be obtained by analyzing the interferogram. All optical elements except for infrared detectors were placed in a vacuum. The bunch length measurement system was optimized and calibrated by using the IRS. The surface of IRS was coated with a black-body spray. The filament of the IRS was set to 1173 K and was considered to emit blackbody radiation according to Planck's law.

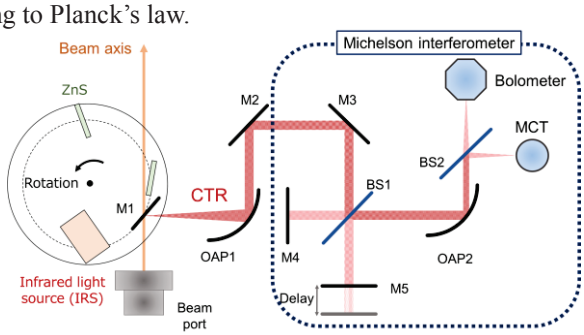

Figure 2: Schematic diagram of the Michelson interferometer. M: aluminium mirror, OAP: off-axis parabolic mirror, BS: beam splitter, MCT: Mercury cadmium telluride detector.

RESULT AND DISCUSSION

Observation of Coherent Transition Radiation

In general, the intensity of CR is known to be proportional to the bunch charge of the electron bunch. Thus, dependence of CTR on the bunch charge was checked experimentally in order to confirm whether the measured radiation was CTR or not. Figure 3 shows the result of the dependence of CTR on the bunch charge. The horizontal and vertical axes denote the bunch charge and the integral of the signal detected using the bolometer. The bunch charge was measured by a current transformer at the exit of the bunch compressor. The solid line denotes the quadratic function fitted to the experimental data by means of the least-squares method. As a result, the experimental data were agreed well with analytical model, and it means that the radiation measured in this experiment was CR.

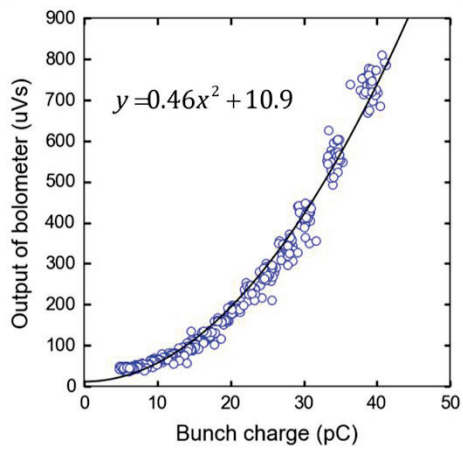

Figure 3: Dependence of intensity of CTR on bunch charge and fitting curve of quadratic function.

Bunch Length Measurement of Ultra-Short Electron Bunches

The bunch length measurement was carried out using measurement system as shown in Fig. 2. Femtosecond electron bunches were generated at the condition that the

ISBN 978-3-95450-177-9

bunch charge was 6.6 pC and the accelerating phase was set to 110°. Figure 4 shows the interferogram of CTR detected using the MCT detector. The number of the average was 5 times. The rms bunch length was estimated to be 7.4 fs by least squares fittings of the interferogram by the sensitivity model as described in reference[5]. Using this analytical model, the whole interferogram including the oscillation lying down beside the centerburst could be well expressed. This oscillation was caused by deficiency of the low frequency components.

Figure 5 shows the frequency spectrum of CTR, which was calculated by performing the Fourier transform of the interferogram of CTR. The solid line denote the fitting curve based on sensitivity model in the frequency domain[5]. The red dashed lines denote the curve calculated based on sensitivity models (1 fs) and the blue dashed line denote the sensitivity model (20 fs). Using sensitivity model, the frequency spectrum of CTR obtained experimentally was also expressed well in the frequency domain.

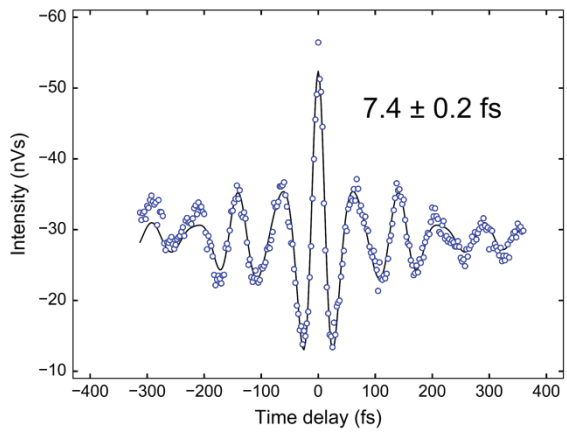

Figure 4: Interferogram of CTR and fitting curve based on sensitivity model.

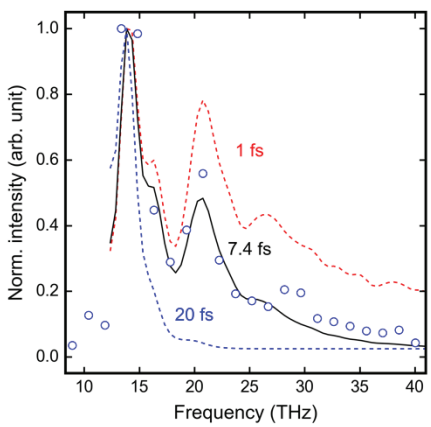

Figure 5: Frequency spectrum of CTR. The solid line denote the fitting curve based on sensitivity model. The red and blue dashed lines denote curves calculated based on sensitivity models.

CONCLUSION

The ultra-short electron bunches were generated using the linac system at Osaka University. The <10-fs electron bunch was successfully measured by monitoring coherent transition radiation with the Michelson interferometer. Experimental data of the interferogram and frequency spectrum were agreed well with the analytical model both in the time and frequency domain.

ACKNOWLEDGEMENT

We thank the staff of the research laboratory for quantum beam science at the Institute of Scientific and Industrial Research, Osaka University. This work was supported by KAKENHI (26249146) and JSPS Research Fellowships for Young Scientists (15J02667).

REFERENCES

[1] T. Shintake *et al.*, *Phys. Rev. ST Accel. Beams* 12, 070701 (2009).

[2] J. Yang *et al.*, *Nucl. Instrum. Methods Phys. Res.*, Sect. A 428, 556 (1999).

[3] M. Schreck *et al.*, *Phys. Rev. ST Accel. Beams* 18, 100101 (2009).

[4] J. Yang *et al.*, *Nucl. Instrum. Methods Phys. Res.*, Sect. A 629, 6 (2011).

[5] I. Nozawa *et al.*, *Phys. Rev. ST Accel. Beams* 17, 072803 (2014).

[6] A. Murokh *et al.*, *Nucl. Instrum. Meth. A* 410, 452 (1998).

[7] I. Wilke *et al.*, *Phys. Rev. Lett.* 88, 124801 (2002).

ISBN 978-3-95450-177-9

OTR MEASUREMENTS WITH SUB-MeV ELECTRONS*

V. A.Verzilov†, P. E. Dirksen, TRIUMF, Vancouver, Canada

Abstract

It is a quite common belief that beam imaging using Optical Transition Radiation (OTR), produced by sub-MeV electron beams, is impossible or at least requires special highly sensitive instrumentations. The TRIUMF electron linac, presently undergoing a commissioning stage, is capable of delivering up to 10 mA of CW electron beams. Simulations showed that such a powerful beam generates substantial amount of OTR light even at electron energies available at the output of the thermionic electron source. The experiment was then setup to test the prediction. This paper reports OTR measurements for the range of electron energies 100 - 300 keV performed with an ordinary CCD camera.

INTRODUCTION

In spite of the fact that Optical Transition Radiation has become a standard diagnostics tool in beam imaging techniques, grey areas still exist where its application requires additional studies. In particular, OTR imaging of sub-MeV electron beams is often considered impossible or at least unpractical due to low light intensity that quickly goes down with the beam energy. However, OTR techniques still remain attractive even at low energies; since they do not suffer from saturation effects inherent to scintillating materials, OTR targets do not charge up and can typically sustain much higher beam powers. Several studies were dedicated to the subject over the last few decades. Successful observation of beam images from 1 MeV electron beam with a CCD camera was reported in Ref. [1]. A decade later OTR imaging was applied to an 80keV electron beam [2]. This time a weak light dictated the use of an intensified camera. With the help of an intensifier, OTR images were obtained even for 10 keV electrons [3].

Higher beam intensities available with long pulse or CW superconducting accelerators make low energy OTR imaging nearly as routine as at multi-MeV beam energies. At the TRIUMF electron accelerator, an ordinary CCD camera was adequate to observe beams with the energy of 100 - 300 keV (β in the range of 0.2 - 0.6).

GEOMETRY OPTIMIZATION

Planning of low energy OTR measurements requires careful optimization of the experimental geometry in order to maximize the light intensity. It is very well known that for highly relativistic ($\gamma \gg 1$) particles, OTR light from a metallic mirror is highly collimated around a direction which makes an angle with the normal to the mirror surface that is equal and opposite to an angle of the particle incidence, measured with respect to the same normal. When $\gamma \sim 1$ the properties are quite different: the radiation is emitted in a broad range of angles. For the case of an ideally conducting perfect mirror, the OTR energy emitted in the backward direction per unit solid angle and unit frequency interval in the plane formed by the particle momentum and normal to the surface can be found to have a simple form (see Ref. [4] and references therein):

$$W_\omega = \frac{e^2}{\pi^2 c}\beta^2 \cos^2\psi \left(\frac{\sin\theta - \beta\ \sin\psi}{(1-\beta\cos(\theta+\psi))(1+\beta\cos(\theta-\psi))}\right)^2 \quad (1)$$

In this equation ψ is the angle between the beam and the surface normal and θ is angle between the normal and radiation direction. If, as it is typically the case, radiation is observed at right angle to the beam, then $\theta = \pi/2 - \psi$ and Eq. (1) is reduced to

$$W_\omega{}^{90^\circ}(\psi) = \frac{e^2}{4\pi^2 c}\beta^2 \left(1 + \frac{\cos 2\psi}{1-\beta\sin 2\psi}\right)^2 \quad (2)$$

In Figure 1 the quantity $W_\omega{}^{90}$ is plotted as function of the angle ψ for two beam energies of 100 keV and 300 keV.

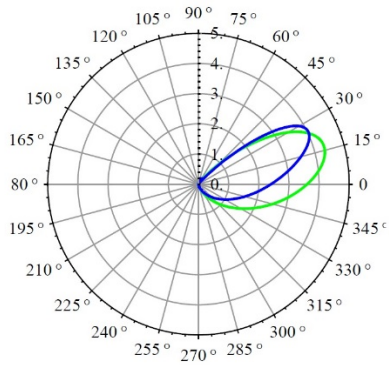

Figure 1: OTR intensity emitted at 90° to the beam direction as function of the angle $\boldsymbol{\psi}$ for beam energies 100 keV (green) and 300 keV (blue). Data plotted by the green line were multiplied by a factor of 3.

From Eq. (2) one can find that the radiation intensity reaches its maximum value

$$W_\omega{}^{90^\circ}(\psi_{max}) = \frac{e^2}{4\pi^2 c}\beta^2(1+\gamma)^2 \quad (3)$$

for an angle ψ_{max} entirely determined by the velocity of beam particles:

$$\psi_{max} = \frac{1}{2}\arcsin\beta \quad (4)$$

From Eq. (4) it follows that $\psi_{max} \to \pi/4$ when $\beta \to 1$ as one would naturally expect for a highly relativistic beam. However, for the energies of interest the intensity is rather low for $\psi = \pi/4$. Instead, Eq. (4) tells us that, optimally,

*Finding is received from National Research Council of Canada
†verzilov@triumf.ca

ISBN 978-3-95450-177-9

the OTR target normal should make the following angles to the beam direction: 25.5° and 16.6° for 300 keV and 100 keV, respectively.

In our experimental setup the angle ψ was fixed to 25° and, therefore, the target tilt was optimized for measurements at 300 keV. The OTR intensity as function of the angle θ expected for such a geometry from Eq. (1) is plotted for both energies of interest in Fig. 2. The plot suggests that the 90° angle between the camera and the beam is still not optimal. Lower beam energies favour larger observation angles. However, small loss in the intensity is well compensated by practical benefits and lower beam image distortion.

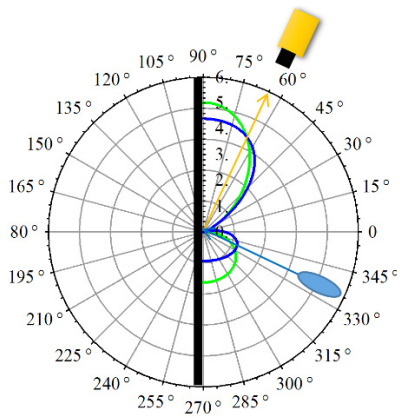

Figure 2: OTR intensity from a target tilted by an angle $\boldsymbol{\psi = 25°}$ as function of the observation angle $\boldsymbol{\theta}$ for beam energies 100 keV (green) and 300 keV (blue). Data plotted by the green line were multiplied by a factor of 3. Vertical black line indicates orientation of the OTR target.

EXPERIMENTAL SETUP

The experiment was performed using the electron source of the TRIUMF superconducting linear accelerator which is presently undergoing a commissioning phase.

The accelerator is designed to generate high power electron beams with an energy up to 50 MeV and will be primarily used to produce radioactive ion beams via photofission for the ARIEL (Advanced Rare IsotopE Laboratory) facility [5].

The electron source allows CW and pulsed beam operation up to an average current of 10 mA. The main components of the source are a gridded dispenser cathode in a SF_6 filled vessel, and an in-air high voltage power supply. Unique features of the gun are its cathode/anode geometry to reduce field emission, and transmission of RF modulation via a dielectric (ceramic) waveguide through the SF6. The beam can be modulated by applying a superposition of DC and RF voltages to the grid. In order to match the beam to the accelerator structure, the electron source provides electron bunches with a charge up to 15.4 pC at a repetition frequency of 650 MHz, a subharmonic of the linac operating frequency of 1300 MHz. Additionally, the duty factor of operation can be changed between 0.1% -100 % by superimposing a macro-pulse structure at Hz to kHz frequency.

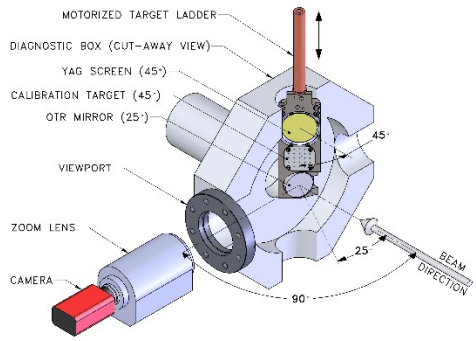

Figure 3: The experimental setup for OTR low energy imaging.

According to beam dynamic simulations the minimum energy required for the direct injection of the beam into a 9-cell SC accelerator is 250 keV. The energy of the source is varied by High Voltage applied to the anode of the gun up to a maximum value of 300 kV.

The OTR measurements were performed using a profile monitor located ~2 m downstream of the electron source. The OTR target was mounted on a motorized actuator with its normal oriented at 25° with respect to the beam direction. The target was a commercial 9.5 mm thick aluminium mirror with a diameter of 38 mm. In addition, a YAG scintillator and a camera calibration target were mounted at 45° on the same frame. The YAG screen was a 0.52 μm thick layer of P46 phosphor powder deposited on an aluminium substrate with a diameter of 50 mm. The camera, model GigE Manta G-032, was mounted at 90° with respect to the beam. It was equipped with a Computar motorized zoom lens, model H10Z1218. The camera features an adjustable gain and minimum exposure time of 26 μsec.

RESULTS

The chosen geometry of the measurements helped to mitigate the problem of the blackbody light emitted from the thermionic source. In fact the blackbody radiation was reflected by the mirror away from the camera. Still some light scattered from the target frame could be observed. It turned out that optimal regime for the measurements was operating the source with millisecond-range long pulses repeated at 50 Hz with a peak beam current around 100 μA. The beam current was kept low to minimize damage to the OTR mirror, a concern that eventually turned out to be unjustified. No signs of damage on the mirror surface were observed upon completion of the experiment.

Beam images were measured at two beam energies of 300 keV and 100 keV with both OTR and YAG screens to compare the results obtained by different techniques. The camera gain and beam pulse length were adjusted to accommodate the difference in the light intensity from two screens and to avoid saturation effects. To observe the OTR with a minimum amount of beam the camera gain was set in the range 30-36, while for the YAG phosphor it

ISBN 978-3-95450-177-9

was at the minimum value of 0. It was found that to obtain a usable beam image, at least 150 nC of beam charge was required at 300 keV and about 400 nC for 100 keV beam. Processing of OTR images required measuring and subtracting the background. For YAG screen images the background level was negligible. Raw OTR images after the background subtraction are shown in Fig. 4a and Fig. 6a.

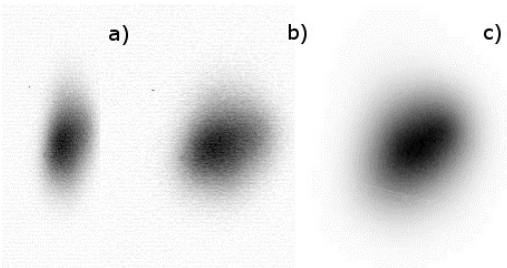

Figure 4: Raw OTR image (a), OTR image transformed to the beam coordinate space (b), YAG image (c). Beam energy is 300 keV.

Due to the target tilt by the angle ψ, coordinates in the image space relate to the beam space coordinates as

$$\begin{pmatrix} x_b \\ y_b \end{pmatrix} = \begin{pmatrix} 1/\tan\psi & 0 \\ 0 & 1 \end{pmatrix} \begin{pmatrix} x_i \\ y_i \end{pmatrix} \quad (5)$$

OTR images transformed according to Eq. (5) are shown in Fig. 4b and Fig. 6b. For YAG screen $\psi = 45°$ and image coordinates are the same as beam coordinates. No image transformation is required in this case. YAG screen beam images are present in Fig. 4c and Fig. 6c.

Both OTR and YAG images look very much alike including a tilt of the beam elliptical shape. For quantitative comparison of beam sizes, horizontal and vertical profiles were obtained from the images and are shown in Fig. 5 and Fig. 7 for the beam energies of 300 keV and 100 keV, respectively.

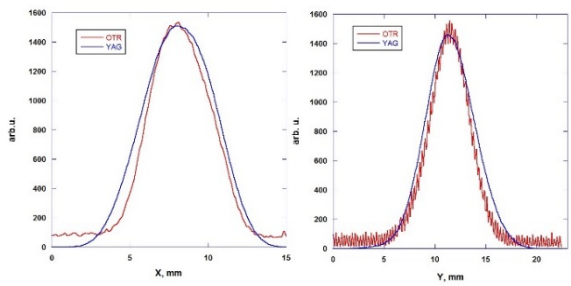

Figure 5: Horizontal and vertical beam profiles obtained from OTR and YAG images. Beam energy is 300 keV.

It can be seen that the OTR vertical profiles look much noisier. We believe that this is a feature of the camera (or a CCD sensor) manifesting itself in a slightly different amount of signal in odd and even lines of the image. The effect is only observable at high camera gains and gradually fades out as the gain is reduced.

Vertical and horizontal beam sizes were then calculated by applying the Gaussian fit to the beam profiles. For

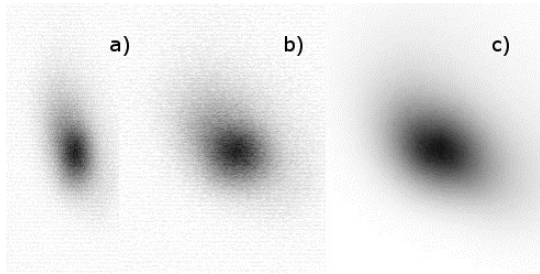

Figure 6: Raw OTR image (a), OTR image transformed to the beam coordinate space (b), YAG image (c). Beam energy is 100 keV.

OTR, both horizontal and vertical 1-σ beam sizes were the same amounting to 2.7 mm and 3 mm for 300 keV and 100 keV cases, respectively. For the YAG, all beam sizes were about 3.4 mm for both beam energies.

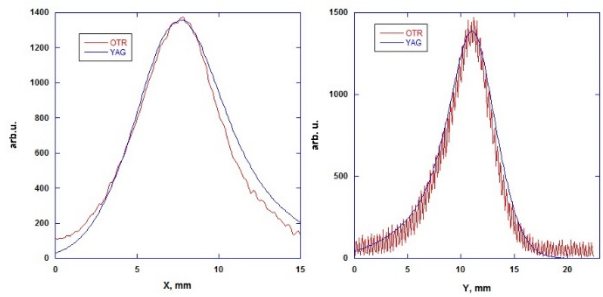

Figure 7: Horizontal and vertical beam profiles obtained from OTR and YAG images. Beam energy is 100 keV.

Taking into account that OTR and YAG measurements were performed with substantially different beam pulse lengths we conclude that the agreement between the two techniques is acceptably good. This result suggests that OTR can confidently complement the YAG beam imaging at the source energies of the TRIUMF electron linac with an obvious benefit of tolerating much higher beam powers than phosphor screens.

REFERENCES

[1] M. Castellano *et al.*, "Analysis of optical transition radiation emitted by a 1 MeV electron beam and its possible use as diagnostics tool", *Nucl. Instr. Meth.*, A357, p.231, 1995.

[2] C. Ball, E. Bravin, E. Chevallay, T. Lefevre, G. Suberlucq, "OTR from non-relativistic electrons", in *Proc. DIPAC'03*, Mainz, Germany, May 2003, paper PM04, p. 95.

[3] R. B. Fiorito, B. L. Beaudoin, S. J. Casey, D. W. Feldman, P. G. O'Shea, B. Quinn, A. G. Shkvarunets, "OTR measurements of the 10 keV electron beam at the University of Maryland electron ring (UMER)", in *Proc. PAC'07*, Albuquerque, USA, June 2007, paper FRPMS033, p.4006.

[4] G. M. Garibian, "Transition radiation for a charged particle at oblique incidence", Sov. Phys. JETP, vol.11, No 6, p.1306, 1960.

[5] R. E. Laxdal *et al.*, "Status of superconducting electron linac driver for rare ion beam production at TRIUMF", in *Proc. LINAC'14*, Geneva, Switzerland, September 2014, paper MOIOC01, p.31.

ISBN 978-3-95450-177-9

HIGH-ENERGY X-RAY PINHOLE CAMERA FOR HIGH-RESOLUTION ELECTRON BEAM SIZE MEASUREMENTS*

B. Yang, S.H. Lee, J. Morgan and H. Shang,
Advanced Photon Source, Argonne National Laboratory, Argonne, IL 60439 USA

Abstract

The Advanced Photon Source (APS) is developing a multi-bend achromat (MBA) lattice based storage ring as the next major upgrade, featuring a 50 – 80-fold reduction in emittance. Combining the reduction of beta functions, the electron beam sizes at bend magnet sources may be reduced to reach 5 – 10 μm for 10% vertical coupling. The x-ray pinhole camera currently used for beam size monitoring will not be adequate for the new task. By increasing the operating photon energy to 120 – 200 keV, the pinhole camera's resolution is expected to reach below 4 μm. The peak height of the pinhole image will be used to monitor relative changes of the beam sizes and enable the feedback control of the emittance. We present the simulation and the design of a beam size monitor for the APS storage ring.

INTRODUCTION

A new generation of storage-ring based synchrotron radiation sources using multi-bend achromat (MBA) lattices are being planned, designed, constructed, and commissioned worldwide [1,2]. These rings are expected to operate with total emittance two-orders of magnitude lower than many of the third-generation synchrotron radiation sources. Table 1 lists the expected beam sizes at the bend magnet sources after the APS Upgrade (APS-U) at 66 pm total emittance. Due to small beta functions inherent to the MBA lattices, the electron beam sizes in these rings are in the micrometre range, with the potential of reaching sub-micrometre level for vertical couplings under 1%. Robust and accurate diagnostics for these minute beam sizes are important for the operations of these new sources.

In this work, we will discuss the plans and design of the beam size monitor (BSM) for the APS-U MBA storage ring. We will cover the simulated performance of the high-energy x-ray pinhole camera, conceptual design, and alternative techniques to be implemented in parallel.

Table 1: Expected e-beam Sizes for APS-U Storage Ring

Plane	Horizontal		Vertical	
Beta function	1.8 m		3.9 m	
Vertical coupling	Full	10%	Full	10%
Beam size (μm)	7.8	10.4	11.3	5.0

COMPUTER SIMULATION

Pinhole images can be modelled using the well-known Fresnel diffraction algorithm. At wavelength λ, the photon intensity at the image plane can be expressed as, $I_0(x') = |A(x')|^2$ where the photon wave amplitude is

$$A(x') = \frac{A_0'}{1+i}\left\{F\left[\sqrt{\frac{2}{\lambda f}}\left(f\varphi+\frac{d}{2}\right)\right]-F\left[\sqrt{\frac{2}{\lambda f}}\left(f\varphi-\frac{d}{2}\right)\right]\right\}. \quad (1)$$

The length parameter f is given by $1/f=1/S+1/S'$, where S is the distance from the source to the pinhole, S' is the distance from the pinhole to the image plane. Furthermore, $\varphi = x'/S'$, d is the total width of the pinhole slit, A_0' is an amplitude constant, and the complex Fresnel integral is defined as

$$F(x) = C(x) + iS(x) = \int_0^x e^{i\pi t^2/2}dt. \quad (2)$$

If we map the image coordinates x' back to the source plane coordinates x using the optical magnification of the beamline, $x = x'/M = x'S/S'$, the intensity at the mapped source can be obtained simply by using $\varphi = x/S$ and a different amplitude constant in Eq. (1). Finally, for finite source sizes, the calculated intensity distribution needs to be convolved with the source distribution. The program *sddsfresnel* implements these algorithms and can be used to calculate the one-dimensional Fresnel profile for a given geometry and a source profile.

For the planned APS bend magnet beamline with S = 8.5 m, S' = 11.5 m, numerical calculation shows that the resolution of the pinhole camera is near optimal for slits width of 10 μm for photon energy of 120 keV. Figure 1 shows the normalized diffraction profiles from such a pinhole with source sizes ranging from 0 to 20 μm. We can see that the profiles can be clearly resolved down to 5 μm, but not below 3 μm. Since photons with energy of 100 – 500 keV are often referred to as soft gamma rays, this work is really about soft gamma ray pinhole camera techniques.

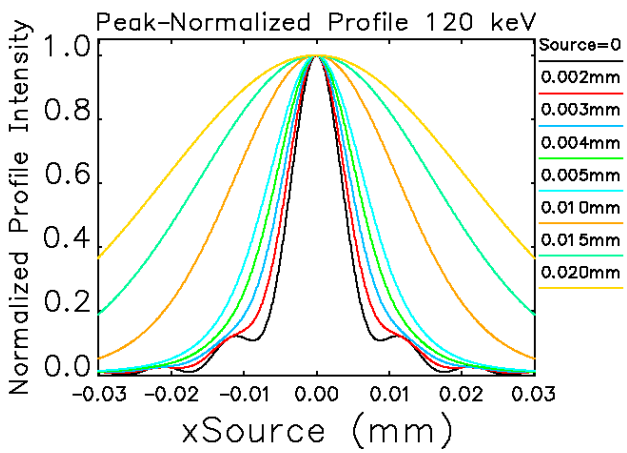

Figure 1: Fresnel diffraction profile using monochromatic 120 keV photons for zero source size; and convolution with Gaussian source with rms width of 2 – 20 μm. All profiles are normalized at the peak for easy comparison.

* Work supported by U.S. Department of Energy, Office of Science, under Contract No. DE-AC02-06CH11357.

ISBN 978-3-95450-177-9

BEAMLINE DESIGN

Source

The APS-U beam size monitor will use one or more bend magnet (BM) sources where a three-pole wiggler (3PW) may be installed. The peak field of an APS-U 3PW is 1.17 T. At ±0.5 mrad from optical axis, the effective field is approximately 1.0 T. Figure 2 shows the x-ray flux through a 10-μm square pinhole at 8.5 m from the sources. The 3PW is highly desirable since it generates 10 – 200 times more photons in 100 – 200 keV region than the APS-U BM sources with 0.55 – 0.61 T field.

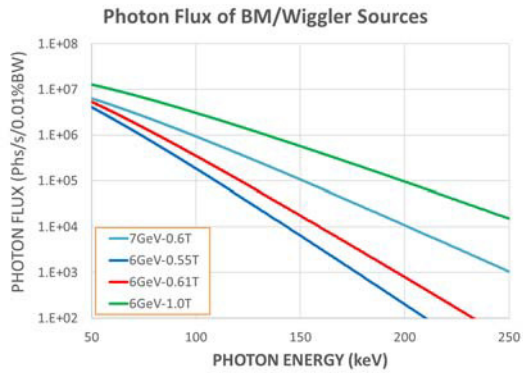

Figure 2: Spectral photon flux through a 10 μm square pinhole at 8.5 m from an APS-U bend magnet/wiggler source with 6-GeV/200 mA electron beam. Pinhole flux of current APS source (7GeV/100mA) is shown for comparison.

Pinhole Slits

Since the x-ray beam at 8.5 m from the source is wider than the 10-μm pinhole width, it is estimated that in order to reduce the background of profile measurements to under 1% of the peak counts, the blade transmission needs to be less than 0.1%. Figure 3 plots the transmission efficiency of 3 – 6 mm tantalum and tungsten blades. We can see that The useable photon energy is 155 – 165 keV for 3-mm Ta and W blades, and 210 keV for 5-mm W or 6-mm Ta blades.

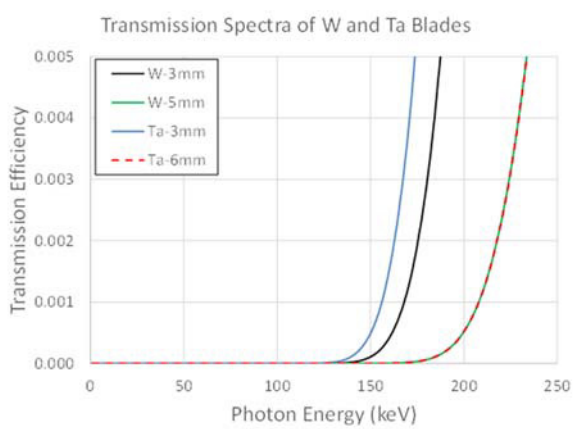

Figure 3: Transmission spectrum of tungsten (3 mm and 5 mm) and tantalum (3 mm and 6 mm) blades.

Detectors

At 4:3 magnification, the entire diffraction profile has a FWHM around 20 μm and requires spatial resolution of the detector to be 2 μm RMS or better. This spec is difficult for commonly used scintillation screens in x-ray pinhole cameras: to obtain required spatial resolution, the screen thickness should be 10's of μm or less, which results in very low efficiency for high-energy photons. We propose to use 5-μm slits to define the spatial resolution, after which a monochromator and an efficient detector can be used. Simulation shows that the slit will not broaden the image peak significantly. However, it does make it difficult to measure horizontal and vertical profiles in a same setup. We will build two beamlines side-by-side for measuring horizontal and vertical beam sizes separately.

To select the desired photon energy, we propose to use single crystal monochromators. Table 2 lists the properties of selected crystals and Figure 4 shows proposed optics design. We note that a larger deflection angle (2θ) makes it easier for the beam dump to block the white x-ray beam entirely from reaching the detector and to reduce the background counts. While many semiconductor and scintillator detectors have high efficiency for gamma ray photons below 200 keV, the highly concentrated dose in a small region of 10 – 20 microns in radius may destroy the detectors quickly and degrade its efficiency locally. Gaseous ion chambers will be used to avoid these localized radiation damages.

Table 2: Property of a Few Selected Crystals

Crystal	Si(111)	Ge(111)	Ge(220)
Bandwidth $\Delta E/E$ (10^{-4})	1.31	3.41	1.57
2θ at 120 keV	1.89°	1.81°	2.96°
2θ at 200 keV	1.13°	1.09°	1.78 °

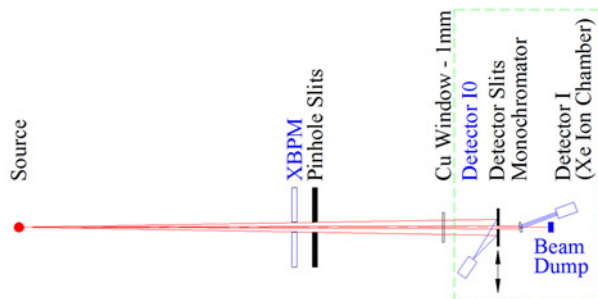

Figure 4: Soft-gamma-ray pinhole camera detector using a crystal monochromator.

Table 3 summaries the key design parameters of the APS-U soft gamma ray pinhole camera. We will keep the optical transport in vacuum until the detector slits. This approach has two advantages: (1) The narrow slits will be kept in vacuum and will not be oxidized or contaminated in air. (2) Broadening of the beam image due to scattering from the window will be minimized due to the short distance between the window and the detector.

ISBN 978-3-95450-177-9

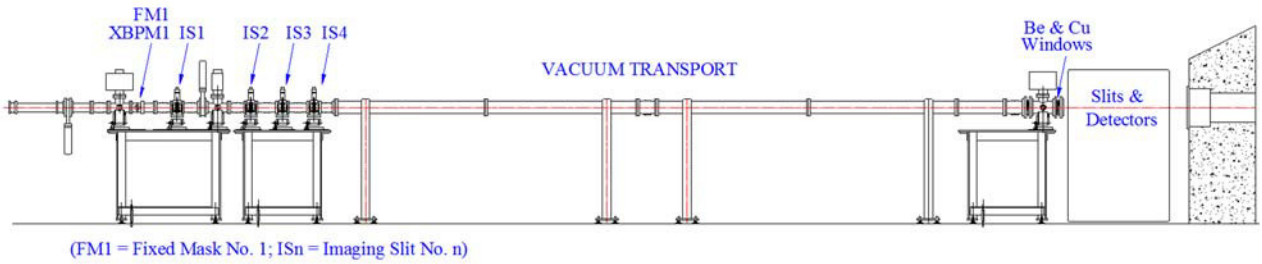

Figure 5: Beamline layout.

Table 3: APS-U Beam Size Monitor Design Parameters

Photon energy	**120 keV**	**200 keV**
Source distance	8.5 m	
Detector distance	11.5 m	
Imaging slit width	10×500μm	8×500 μm
Detector slit width	5×100 μm	4×100 μm
Absorption of 20 cm Xe	13%	4%
Source size range	> 5 μm	> 4 μm

Beamline Layout

Figure 5 shows the beam size monitor beamline which will be contained entirely in the accelerator tunnel in one of the unused bend magnet front ends. The beamline is divided into four functional branch lines by the first fixed mask. Table 4 lists these branch lines: The first branch line (BL1) uses the upstream bend magnet source to measure the e-beam angle and position so the orbit feedback control system can keep the beam centred on the optics and detectors of the BSM. The second and the third beamlines (BL2 and BL3) uses the 3PW source to measure the horizontal and vertical e-beam sizes. The fourth branch line (BL4) uses the downstream BM source and x-ray diffraction from selected apertures for photon energy in 6 – 12 keV range.

Table 4: APS-U Beam Size Monitor Branch Lines

Branch line	**Measurements functions**
1. XBPM	Beam angle and source position
2. Horizontal	Horizontal γ-pinhole camera
3. Vertical	Vertical γ-pinhole camera
4. X-ray diffraction	Fresnel diffraction pattern

In this beamline, the first fixed mask (FM1) is the only component with power load over 100 W. Its water-cooled absorber and the two flanges will be machined from a solid piece of CuCrZr similar to those tested recently in NSLS II [3]. Figure 6 shows the thermal analysis of this mask. For normal operations with the current APS bend magnet source in the test beamline, the maximum temperature is 61˚C and the maximum von Mises stress is 100 MPa. At the worst missteering, the temperature increases to 64˚ C and the stress to 152 MPa. In both cases, the mask operates well within the safe operating region of the material. The analysis for FM1 with 3PW source is in progress, which is expected to result in minor adjustments in the mask design.

MODE OF OPERATION

Absolute Beam Size Measurements

The basic operation mode of the beamline is absolute beam size measurements, i.e., horizontal and vertical beam profile measurements. In this mode, the detector slits are scanned horizontally in BL2 and vertically in BL3. Figure 7 shows the simulated beam profiles from these measurements, where the effects of the detector slits width are taken into account. Other than subtle differences near the first minimum for small beam sizes (< 4 μm), these profiles look almost identical with those in Figure 1.

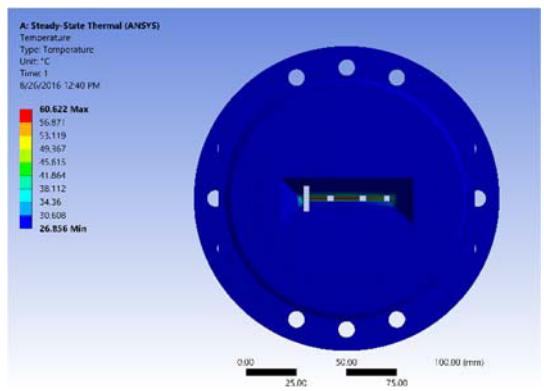

Figure 6: Thermal analysis of the first fixed mask which divides the APS BM beam into four branch beamlines.

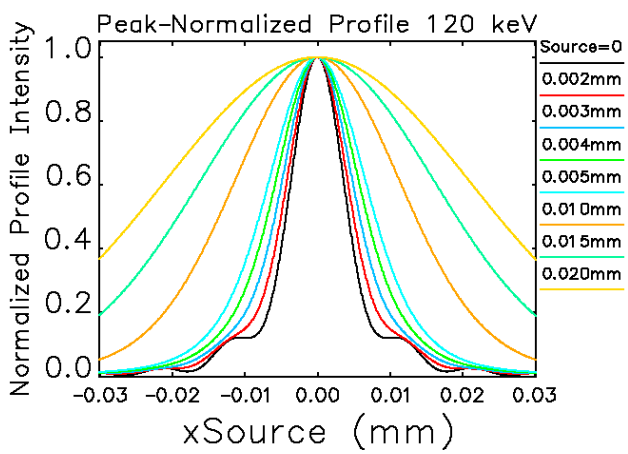

Figure 7: Calculated photon beam intensity profiles using monochromatic 120 keV x-rays for source size of 0 – 20 μm. The imaging and detector slits are 10 μm and 5 μm wide, respectively.

ISBN 978-3-95450-177-9

Relative Beam Size Measurements

To stabilize beam size / emittance during user operations or experimentally minimize vertical couplings, it is desirable to have faster data stream reflecting beam size changes in real time for feedback controls. If we place the detector slits at the diffraction peaks in BL2 and BL3, the intensity ratio of the two detector signals for each line (*I*, *I0*) is directly correlated with e-beam sizes. Figure 8 shows the ratio *I0/I* as a function of the beam size for detector slits of 2 – 12 μm. We can make several observations from the plot:

- The intensity ratios are sensitive to the source size change. For example, for ±10% size change near 10 μm, the intensity ratio changes ±7.7%. On the other hand, it is not very sensitive to the detector slit width until the beam size is below 5 μm.
- For any given slit width, the intensity ratio is reasonably sensitive to beam size changes down to 2-μm level.
- The beam size range of 2 – 25 μm covers the planned user operations with ample margins. If the curve in Figure 8 is properly calibrated at two beam sizes between 10 μm to 25 μm, the intensity ratio can even be used as an absolute beam size data with usable accuracy.
- If the detector slit is not at the peak due to beam motion (see Figure 7), the signal drop from *I*-detector can be misconstrued as an increase in beam size. To avoid this problem: (A) a good XBPM system at BL1 is important for keeping the two pinholes aligned with the source; and (B) a wider detector slit is usually more favourable since it is less sensitive to the beam motion.

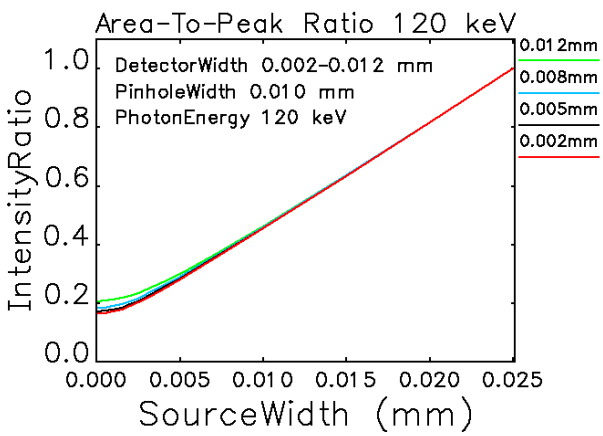

Figure 8: The normalized intensity ratio *R=I0/I* for three different pinhole aperture sizes at 120 keV photon energy.

ALTERNATIVE TECHNIQUE

While the soft gamma ray pinhole cameras have sufficient resolution for measuring nominal beam sizes in user operations, future machine development may produce beam sizes below 4 μm and require diagnostics with better resolution. From Figure 7, we see that for small beam sizes in 1 – 4 μm range, the diffraction profile is most sensitive to source size change in the skirt region, around the first and second minima. We can take advantage of this feature and push the working range of the soft gamma ray pinhole to 1-μm level, provided we can maintain a good signal-to-noise ratio for the pinhole camera.

An alternative approach is to build an x-ray diffraction line in BL4, and install an optical aperture at ~ 9 m location and measure the monochromatic diffraction image at the 20 m mark. Using a square optical aperture, the diffraction pattern will be sensitive to the beam sizes down to several micrometres at 8 keV x-ray energy [4]. Using a pair of Young's double slits as the optical aperture will offer even higher beam size sensitivity. Figure 9 shows diffraction patterns at 8 keV from a mask with two 10-μm slits separated by 80 μm. The pattern is very sensitive to source size change between 1 – 5 μm region.

CONCLUSION

Fresnel diffraction calculation shows that a soft gamma ray pinhole camera (120 – 200 keV) using an imaging slit and a detector slit will be able to resolve electron beam sizes down to 3 – 4 μm level in one-dimensional profile measurements. When the two slits are both centered on the optical axis, the transmitted gamma ray flux provides a fast, but less accurate measurement on beam sizes down to 2-μm level. The conceptual design of the APS-U beam size monitor is based on these simulations and is expected to fulfil the requirements of the APS Upgrade. An additional branch line will be allocated for x-ray diffraction measurements, as an assurance for meeting resolution specifications and also as an option for future upgrade.

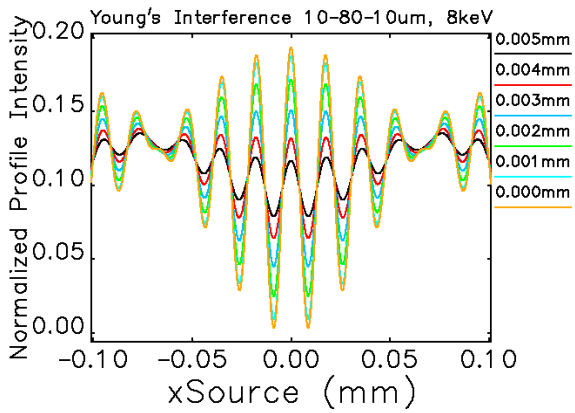

Figure 9: 8-keV x-ray diffraction pattern from Young's double slits of 80μm spacing with source and image distances of 9 m and 11 m respectively.

REFERENCES

[1] R. Hettel, "DLSR design and plans: an international overview", *J. Synchrotron Rad.* 21, pp. 843-855 (2014).

[2] M. Borland, V. Sajaev, Y. Sun, A. Xiao, "Hybrid Seven-Bend-Achromat Lattice for the Advanced Photon Source Upgrade" *IPAC 2015,* pp. 1776 – 1779 (2015).

[3] S. Sharma, "A Novel Design of High Power Masks and Slits," *MEDSI 2014*, Melbourne, Australia.

[4] M. Masaki, Y. Shimosaki, S. Takano, M. Takao, "Novel Emittance Diagnostics for Diffraction Limited Light Sources Based on X-ray Fresnel Diffractometry," *IBIC 2014,* pp. 274-278.

ISBN 978-3-95450-177-9

RECENT RESULTS FROM NEW STATION FOR OPTICAL OBSERVATION OF ELECTRON BEAM PARAMETERS AT KCSR STORAGE RING

O. Meshkov†,[1], V. Borin, V. Dorokhov, A. Khilchenko, A. Kotelnikov, A. Kvashnin, L. Schegolev, A. N. Zhuravlev, E. I. Zinin, P. V. Zubarev, BINP SB RAS, Novosibirsk, 630090, Russia
V. Korchuganov, G. Kovachev, D. G. Odintsov, A. Stirin, Yu. Tarasov, A. Valentinov, A. Zabelin, NRC Kurchatov Institute, Moscow, 123182, Russia
[1]also at NSU, Novosibirsk, 630090, Russia

Abstract

The new station for optical observation of electron beam parameters at electron storage ring SIBERIA-2 is dedicated for measurement of transverse and longitudinal sizes of electron bunches with the use of synchrotron radiation (SR) visible spectrum in one-bunch and multi-bunch modes and for the study of individual electron bunches behavior in time in the conditions of changing accelerator parameters. The paper briefly describes the main components of the diagnostics and experimental results obtained with them.

OPTICAL OBSERVATION STATION

SR Beam Line

Fig. 1 represents the model of SR beam line and optical table. The beam line has two collimators forming round shape of a SR beam and supressing a stray light.

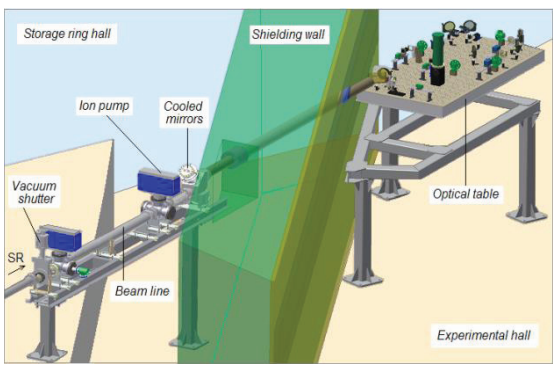

Figure 1: Model of SR beam line with the diagnostics devices placed on the optical table.

First collimator (cooled) is installed at SR beam line entrance. The second collimator (non-cooled) is installed after the quartz vacuum window. The inlet part of vacuum SR beam line (is not shown in Fig. 1) comprises SR absorber and ion pump. The optical part of SR spectrum is separated from the SR fan with two mirrors. The first optically polished cooled copper mirror is installed inside the vacuum unit at the distance about 6 m from source point. The mirror is coated with gold. The second Al – coated mirror reflecting the optical radiation is manufactured from the glass.

†O.I.Meshkov@inp.nsk.su

Both mirrors can be mechanically adjusted for precise alignment of the light beam. Lead beam stopper is installed inside the part of beam line passing through the shielding wall for to absorb scattered X-rays. The complete length of the beam line from source point to the main lens of diagnostics placed at the optical table is about 10 m. The computed values of synchrotron radiation from bending magnet at λ = 500 nm are presented in Table 1.

Table 1: Computed Parameters of Synchrotron Radiation from Bending Magnet at λ = 500 nm

Divergence, $\sigma_{SR} = (3\lambda/4\pi R)^{1/}$	$1.8 \cdot 10^{-3}$ rad
Diffraction limit, $\sigma_D \approx (\lambda^2 R/12\pi^2)^{1/3}$	≈0.011 мм
Minimal radial size, $\sigma_R \approx R(\sigma_{SR})^2/2$	≈0.03 мм

Layout of the Optical Diagnostics

The measurement part of the optical diagnostics [1] consists of six independent devices with different functions located on the optical table outside the storage ring shielding wall. We use the STANDA optical table.

Transverse beam sizes precise measurement system is based on the double-slit interferometer serves to measure bunch vertical size with a resolution about several μm.

Bunch longitudinal sizes measurement system is based on the optical dissector tube with electrical focusing and deflection is also used for the diagnostics of longitudinal multi-bunch instability caused by electron bunches interaction with high modes of cavity electromagnetic field. The marker is used for determining and controlling the temporal scale of the dissector. Dissector tube temporal resolution is 40 ps FWHM [2]. The light reflects to dissector from the Edmund Optics 6'' pellicle beamsplitter

TV camera is used for observation of the electron beam cross-section image on the video monitor in main control room.

The CCD camera is based on high resolution Allied Vision Technology 1280×960 pixels EG1290 CCD camera with a 100 Mbit Ethernet interface. The result of computer processing of signal from CCD-matrix is a visual two-dimension image of electron beam cross-section, x - and y - curves of electron density distribution within beam, FWHM of Gaussian curve on both coordinates and position of center of electron beam [4].

ISBN 978-3-95450-177-9

Turn-by-turn beam transverse cross-section measurement systems records at 16 points y - and x - distribution of electron density within a chosen bunch, determines betatron and synchrotron tunes (defined by way of Fourier analysis of bunch dipole oscillations triggered by kick) as well as investigates y - or x - dynamics of a bunch shape. The diagnostics provides a one-turn distribution during tens of thousands turns of beam and is based on Silicon Sensor 16- elements avalanche photodiode array AA-16-0.13-9 SOJ22GL.

EXPERIMENTAL RESULTS

Transversal Beam Dimensions

We tested the double-slit interferometer s varying separation of slits D within 15 – 30 mm with step of 5 mm (Fig. 2) during routine run of SIBERIA-2. The visibility of interference patterns is correlated well with theoretical calculations.

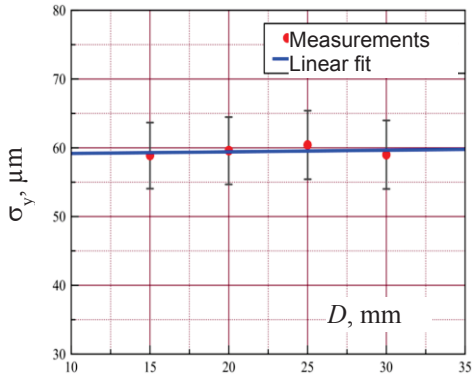

Figure 2: Vertical beam size determined with a different slit separation D.

Another method of measurements of transversal dimensions of a beam is provided by projection optics and CCD camera (Fig. 1). Calibration of spatial scale of CCD camera was done with controllable shift of the position of the beam.

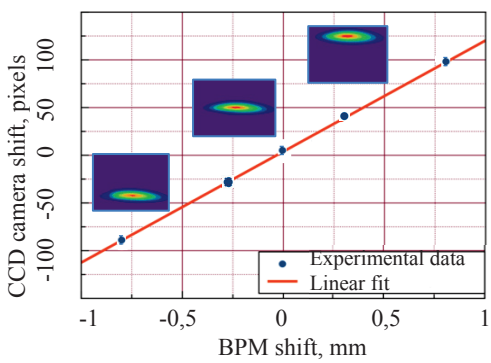

Figure 3: Shift of the beam image at the CCD camera vs BPM data.

The beam was vertically shifted by the magnet corrector and beam position was measured by Beam Position Monitors (BPM). The center of mass of beam image at CCD matrix was computed as well. The data of BPM had a good coincidence with values computed from numerical model of the accelerator. (Fig. 3). The spatial scale of one pixel of CCD matrix was determined as 9±0.2 μm. Taking into account the instrumental function, the measured horizontal beam size σ_x = 480 μm is in a good agreement with the expected value.

Measurement of Longitudinal Beam Size with Dissector and Streak Camera

The dissector LI-602 [2-4] is a traditional component of the optical diagnostics of the accelerators of Budker Institute of Nuclear Physics. It is a very reliable and sensitive device which can be applied for permanent control of longitudinal beam profile

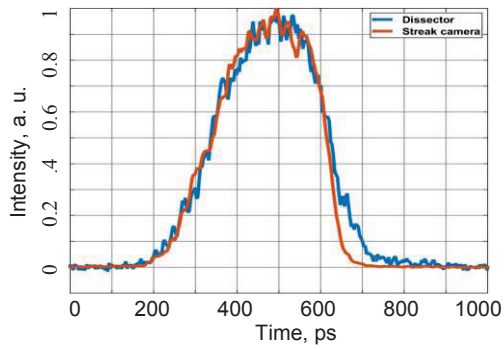

Figure 4: Comparison of the beam profiles acquired by the dissector and streak camera, $I_b \approx 12$ mA.

The disadvantage of the LI-602 is a relatively low temporal resolution τ, about 40 ps FWHM. Recently the new version of the dissector with τ ≈ 3 ps was developed [5,6].

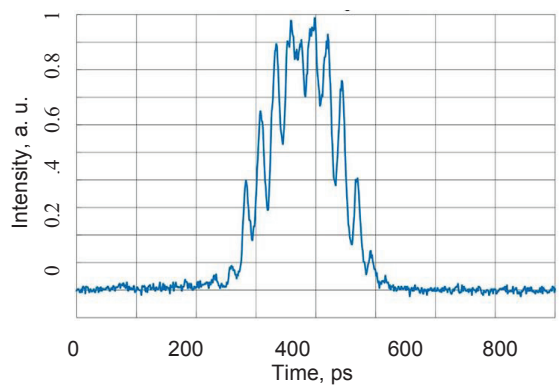

Figure 5: Distortions of the signal of the dissector caused by synchrotron oscillations, $I_b \approx 2$ mA.

The instrumental function of the dissector can be easily measured with a permanent light source [4], but a true temporal resolution of the device depends on the stability of the jitter of RF sweep voltage of the dissector relative to arrival time of electron beam to the observation point. The feature of the dissector is a high sensitivity to the phase oscillations of the beam (Fig.5). We have compared the measurements of the beam length by the dissector and by streak camera PS-1/S1 [7], Fig. 4, 6. Streak camera was temporary supplemented to the optical diagnostics.

ISBN 978-3-95450-177-9

The experiments were done at single bunch mode of operation of SIBERIA-2 and at the energy of injection E = 446 MeV. The lengthening of the beam due to microwave instability is clearly seen (Fig. 6).

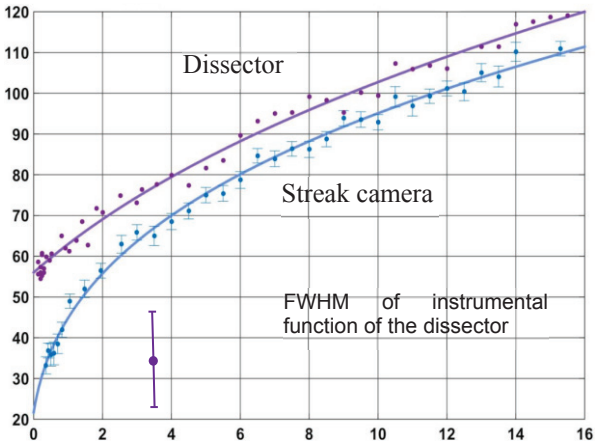

Figure 6: Beam length vs beam current measured by optical dissector and streak camera at $E = 446$ MeV.

The wideband impedance $Z_{\parallel}/n \approx 2{,}9\pm0.5$ Ohm of vacuum chamber of SIBERIA-2 was computed from the results obtained with streak camera [8-10]:

$$\sigma_z^3 = \frac{R^3 \alpha \left| Z_{\parallel}/n \right|_{BB}}{\sqrt{2\pi} E Q_s^2} I_b$$

R – an average radius of the orbit, α - compaction factor, Q_s – synchrotron frequency, n – harmonic number of the revolution frequency.

The data of dissector are systematically exceeded the data of streak camera at the value about 10 ps. This discrepancy increases at the beam current less than 2 mA due to synchrotron oscillations which are distorted an operation of the dissector (Fig. 5). Synchrotron oscillations appear at this value of the beam current at the energy of injection because of decrease of a feedback between the beam and accelerating RF cavity. On the other hand a Fourier transform of the dissector signal enables us to determine a synchrotron frequency (Fig. 7).

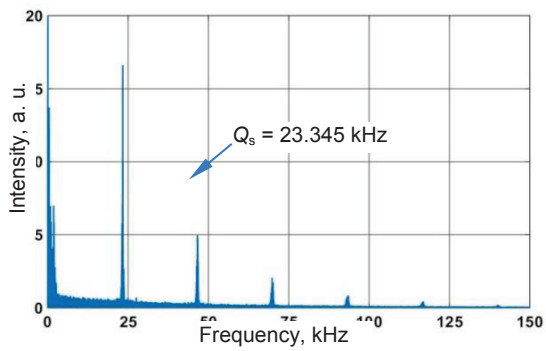

Figure 7: Synchrotron frequency obtained by Fourier transform of the dissector signal

Measurement of Transversal Beam Profile with Linear APD Array

Turn-by-turn beam transverse cross-section measurement systems [11] serves the purpose of measuring y- and x- distribution of electron density within a chosen bunch, betatron and synchrotron tunes (defined by way of Fourier analysis of bunch dipole oscillations triggered by kick) as well as investigating y- or x- dynamics of beam shape in a chosen separatrix. The diagnostics should provide a one-turn distribution during hundreds of thousands turns of a beam. The systems use a linear photo-detector based on 16 - element avalanche photodiode array. The device includes AA16-0.13-9 SOJ22GL photodetector unit and signal recorder. The photodetector unit is built on a photodiode strip consisting of 16 integrated avalanche photodiodes. Dimensions of the single sensitive element are 648×208 μm and a pitch between two elements is 320 μm.

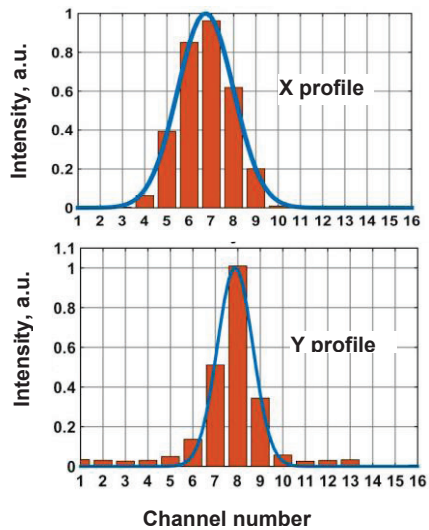

Figure 8: The vertical and radial beam profiles of a single bunch acquired with APD at a single beam turn.

Figure 8 represents the x, y beam profiles of a single bunch acquired with the APD.

CONCLUSION

The station of beam optical diagnostics is commissioned at SIBERIA-2 storage ring. The diagnostics is able to measure all the beam dimensions and meet the requirements of accelerator physics experiments and experiments with the use of SR related to the knowledge of parameters of separate electron bunches.

ACKNOWLEDGMENTS

The measurements of longitudinal beam profile were implemented due to financial support of the Russian Science Foundation (Projects N 14-29-00295).

ISBN 978-3-95450-177-9

REFERENCES

[1] E. Fomin *et al.*, "New Station for Optical Observation of Electron Beam Parameters at the Electron Storage Ring SIBERIA-2", paper TUPG027, Proceedings of BIW2012, Newport News, p. 189, 2012.

[2] E. I. Zinin *et al., At. Energ.,* 20, 320 (1966).

[3] E. I. Zinin *et al., Nucl. Instrum. Methods*, 208, 439 (1983).

[4] V.Smaluk, "Particle beam diagnostics for accelerators - Instruments and methods", Saarbrucken: VDM Publishing, 2009, 276 p. ill.

[5] E.I. Zinin and O.I. Meshkov, "Optical dissector for longitudinal beam profile measurement", JINST, 2015 1748-0221 10 P10024 doi:10.1088/1748-0221/10/10/P10024.

[6] E.I. Zinin, O.V. Anchugov, V.L. Dorokhov *et al.*, "Direct temporal-resolution calibration of new-generation dissector", *JINST*, 2016 1748-0221 11 T03001 doi:10.1088/1748-0221/11/03/T03001.

[7] V. P. Degtyareva, Yu. V. Kulikov, M. A. Monastyrsky *et al.*, in *Proc. SPIE,* 491, 239 (1984).

[8] Chao A.W., Tigner M., "Handbook of Accelerator Physics and Engineering", Singapore: World Scientific, 1999.

[9] Chao A. Physics of Collective Beam Instabilities. New York: Wiley, 1993.

[10] Clarke J.A., "Bunch Lengthening Thresholds on the Daresbury SRS", Proceedings of PAC1995. Dallas, USA, 1995.

[11] V.L.Dorokhov *et al.*, "The New Optical Device for Turn to Turn Beam Profile Measurement", Proceedings of IBIC2016, Barcelona, Spain, paper WEBL04, this conference.

ISBN 978-3-95450-177-9

STUDY OF THE RADIATION DAMAGE ON A SCINTILLATING FIBERS BASED BEAM PROFILE MONITOR

E. Rojatti*, G. Calvi, L. Lanzavecchia, A. Parravicini, C. Viviani, CNAO, Pavia, Italy

Abstract

The Scintillating Fibers Harp (SFH) monitors are the beam profile detectors used in the High Energy Beam Transfer (HEBT) lines of the CNAO (Centro Nazionale Adroterapia Oncologica, Italy) machine. The use of scintillating fibers coupled with a high-resolution CCD camera makes the detector of simple architecture and with high performances; on the other hand, fibers radiation damage shall be faced after some years of operation. The damage appears in multiple ways, as efficiency loss in light production, delayed light emission, attenuation length reduction. The work presents measurements and analysis performed to understand the phenomenon, in such a way to deal with it as best as possible. The connection between dose rate, integral dose and damage level is investigated as well as the possible recovery after a period of no irradiation. The influence of the damage effects on profiles reconstruction and beam parameters calculation is studied. Data elaboration is modified in such a way to compensate radiation damage effects and protract the SFH lifetime, before the major intervention of fibers replacement. Methods and results are discussed.

THE SCINTILLATING FIBERS HARP MONITORS

The Scintillating Fibers Harp (SFH) monitors [1] are beam profile detectors installed along the High Energy Beam Transfer (HEBT) lines of the CNAO (Centro Nazionale di Adroterapia Oncologica) accelerator. Their active area is made up of two orthogonal harps of scintillating fibers (for the horizontal and the vertical beam profiles reconstruction) which are guided up to the chip of a CCD camera and mapped for the signal read out. The CCD output signal per fiber (12 bits digital signal) is proportional to the number of particles crossing the fiber, to their energy and depends on the camera configuration parameters. A different correction factor (called "calibration factor") is applied to each fiber at profiles reconstruction in order to equalize the different fibers response, which can vary due to fibers geometry, composition and coupling with camera chip.

The CNAO beam extraction takes 1 to 10 seconds, and thus several beam profile acquisitions, with a good compromise between acquisition rate[1] and integration time, are needed to monitor the beam longitudinal profile during the extraction time and to correctly measure beam parameters (barycenter and width). Fig.1 shows the 3D reconstruction, on the horizontal plane, of one extracted spill.

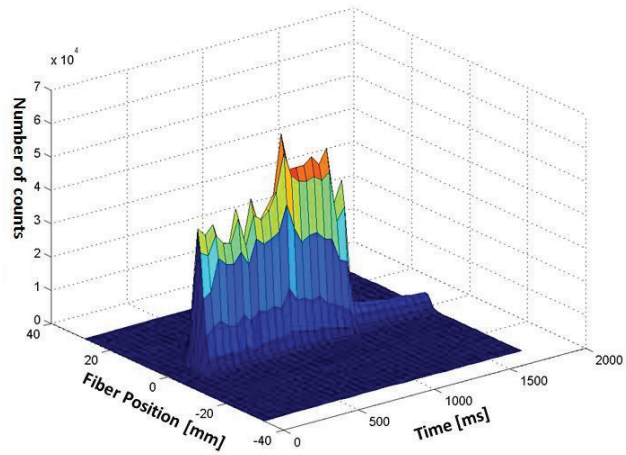

Figure 1: Example of one extracted spill longitudinal profile, reconstructed on the horizontal plane from one SFH measurement.

RADIATION DAMAGE ON SCINTILLATING FIBERS

Several studies concerning the radiation damage on scintillating fibers have been published [2]. The topic is very complex and far from being fully understood. In case of the SFH detectors, the radiation damage appears both as reduction of light production and as reduction of fibers transparency, mainly involving the central region of the SFH sensitive area which is mostly hit by the beam. The first effect emerges clearly taking one image of the beam profile after having enlarged the beam on purpose (Fig.2): the enlarged-beam profile shows a depression indicating a reduced light production efficiency for the most irradiated fibers.

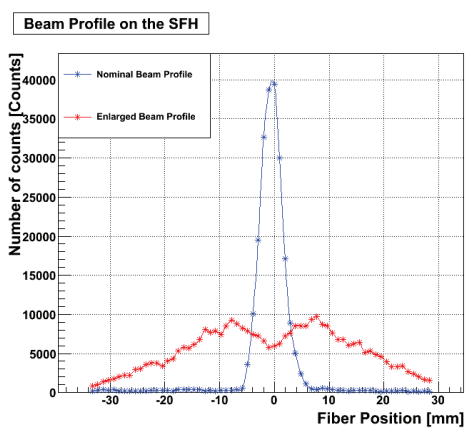

Figure 2: Nominal (blue line) and enlarged (red line) beam profiles on one SFH.

* elisa.rojatti@cnao.it

[1] The maximum camera acquisition rate is 50 Hz.

ISBN 978-3-95450-177-9

Both the effects are visible in Fig.3, which represents a 2D reconstruction (for simplicity called "intensity map" from this point on) of the detector response on the horizontal plane (vertically displaced fibers) to the same beam (with fixed parameters) moved up to different positions of the detector sensitive area by means of two scanning magnets[2]. More precisely a Proton beam with 8E+08 particles per spill, 10 mm FWHM and 60 MeV kinetic energy is displaced in 121 different positions uniformly spaced in both the dimensions. The integral signal per spill is computed and plotted in function of the spill barycenter position. The radiation damage appears, on the intensity map, as a depression located at about the center of the horizontal plane (X ≃ 0 mm) in correspondence of the vertical plane positive region (Y > 0 mm). The depression depth increases as the Y-coordinate increases and the deeper point, located at X ≃ 0 mm and Y ≃ 18 mm, corresponds to an efficiency loss of about 40% with respect to the peripheral fibers. This effect results mainly from fibers loss of transparency. Indeed, due to the detector geometry, the light produced on the positive region of the vertical plane has to cross the more damaged area (corresponding to the region which is mainly intercepted by the beam, around the active area center) before being read out by the camera. As a consequence, the detector response loss is observed, although the vertical plane positive region is not directly damaged by radiation.

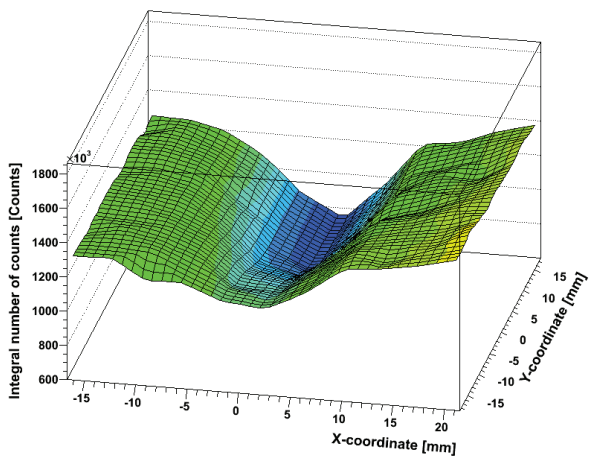

Figure 3: SFH response on the the horizontal plane to a Proton beam with 8E+08 particles per spill, 10 mm FWHM and 60 MeV fixed kinetic energy, moved up to 121 different positions on the detector active area.

Damage Dependence on the Amount of Dose

Measurements illustrated in this section have been aimed at investigating the fibers radiation damage level dependence on the amount of received dose. For this purpose two consecutive intensity maps were performed, then the active area was irradiated with a total dose of about 115 Gy, and after the irradiation two intensity maps more were performed: the first one immediately after the irradiation and the second one after 24 hours of no irradiation, in order to investigate the capability of scintillating fibers recovery. The irradiation was performed by means of 360 consecutive spills made up of 8E+08 Protons per spill, 10 mm FWHM, 60 MeV kinetic energy and beam barycenter fixed on the detector active area center. Fig.4 shows the integral number of counts per spill read out by the camera on one plane during the irradiation.

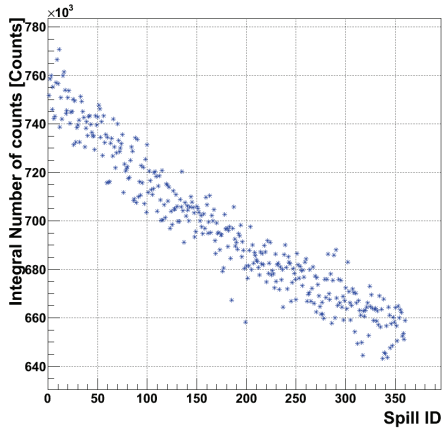

Figure 4: SFH response during the irradiation of the detector active area with 360 consecutive spills with 8E+08 Protons per spill, 10 mm FWHM, 60 MeV energy and fixed barycenter on the detector active area center (115 Gy of total dose delivered).

As one can observe the detector response decreases during the irradiation: the total number of counts is reduced of about 15% after the total amount of dose received (115 Gy). Fig.5 shows data extracted from the intensity maps performed before and after the detector irradiation. In particular it illustrates the detector response on the horizontal plane at fixed coordinate (Y = 0) on the vertical plane.

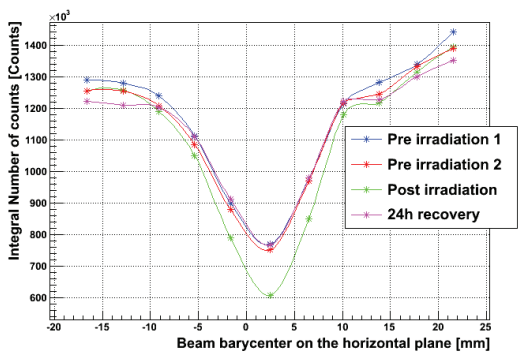

Figure 5: Detector response to 11 consecutive spills with equal features (8E+08 Protons per spill, 10 mm FWHM, 60 MeV kinetic energy) on the horizontal plane at fixed coordinate (Y=0) on the vertical plane, before and after an intense irradiation on the central region.

[2] The scanning magnets, at the end of each HEBT line, are commonly used for the "active scanning" method to "paint" each tumor slice area with the pencil beam.

ISBN 978-3-95450-177-9

The efficiency depression on the horizontal plane is visible both before and after the irradiation, as a permanent and irreversible damage. At the same time, as a consequence of the irradiation, the depression becomes deeper, but this additional efficiency reduction is restored after only 24 hours of no irradiation.
From these preliminary measurements a few conclusions can be drawn:

- The efficiency loss can affect measurements if one SFH is used continuously over a long time. The only procedure at CNAO which implies this kind of use of the SFH detectors is called "steering", and consists in irradiating the SFH active area center with 160 consecutive spills of increasing energies. The increase of beam energy implies a lower energy release in the scintillating fibers and thus a minor damage with respect to the damage level resulting from the irradiation with 160 consecutive spills of fixed energy as reported in Fig.4. For this reason the efficiency loss during the "steering" procedure can be considered negligible for a good profiles reconstruction and beam parameters computation;

- Thanks to the scintillating fibers recovery only the irreversible damage has to be taken into account for data processing and eventually corrected.

DATA CORRECTION

The best solution to face up to SFH scintillating fibers radiation damage would be fibers replacement on all the affected detectors after an arbitrary period depending on the amount of received dose. However this solution implies a major intervention in terms of time and cost, which one would like to postpone as far as possible. Alternatively a data correction software procedure has been implemented to compensate the radiation damage only by analyzing and manipulating the acquired data.
This procedure consists in processing a correction factors map on each detector plane. In order to extract the correction factors one SFH is placed at the isocenter[3] and one intensity map per plane is performed. The beam profiles acquired with different barycenter values on both planes are normalized with respect to the beam intensity. An appropriate fit is applied on each normalized beam profile. By fixing the beam position on one plane, the correction factors per each profile on the opposite plane are obtained, fiber by fiber, as the ratio between the fitting curve and the raw beam profile (not normalized). Although only a few discrete beam barycenter positions can be investigated ecause of obvious machine limitations, the correction factors per fiber on one plane for all the possible beam barycenter positions on the opposite plane can be extracted by means of mathematical extrapolation. The 2D correction factor map thus obtained for each plane is applied to the raw data after a rough beam barycenter estimation. Fig.6 shows the SFH output signal map obtained from the one in Fig.3 after the correction factors application to the acquired data. As one can observe the corrected SFH response to the beam is quite uniform throughout the whole active area.

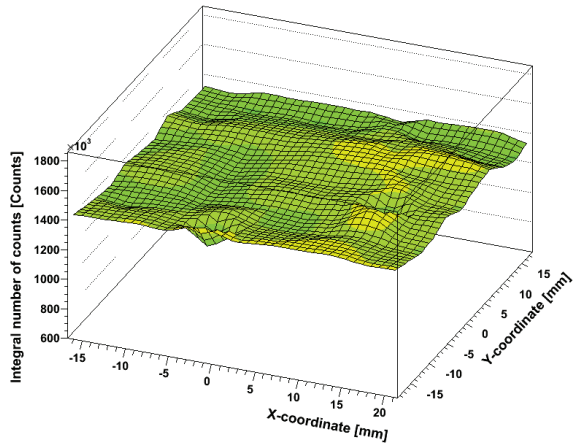

Figure 6: SFH output signal map extracted after correction factors application to the acquired data.

The procedure here above illustrated, although rigorous and reliable, is quite demanding and time consuming from an operational point of view. Indeed it requires to dismantle one SFH from the beam line and to place it at the isocenter. A more empirical procedure has been implemented to quickly and easily correct the effect of the radiation damage on the SFH detectors installed on the beam lines. It consists in scanning the beam in 4 or 5 positions on the horizontal (vertical) plane, keeping the vertical (horizontal) position around the center. The scanning is performed with the nominal or the enlarged beam in such a way to be able to identify the depression position on the beam profile (as illustrated in Fig.2) per each beam position. The response of the central damaged fibers can be corrected by multiplying the fiber output signal for an appropriate factor. This procedure allows to extract only one set of correction factors for the horizontal (vertical) plane which may compensate adequately the radiation damage only in case the beam is quite centered on the detector, that is usually true. This method, although far less rigorous than the one previously described, represents a quick and feasible solution to face the fibers damage, as shown in Fig.7.

Beam Parameters Computation Before and After Data Correction

The main use of the SFH detectors is the beam barycenter determination from reconstructed beam profiles. Fig.8 shows the beam barycenter values computed on both the planes before and after data correction by means of the 2D correction factors map. Values are compared with those acquired by the Dose Delivery (DD) which is a ionization detector installed at the end of each extraction line, in charge of checking the beam position during patients treatment.

[3] The isocenter is the point in which the target to be irradiated shall be positioned. The exact number of delivered particles may be know at the isocenter.

ISBN 978-3-95450-177-9

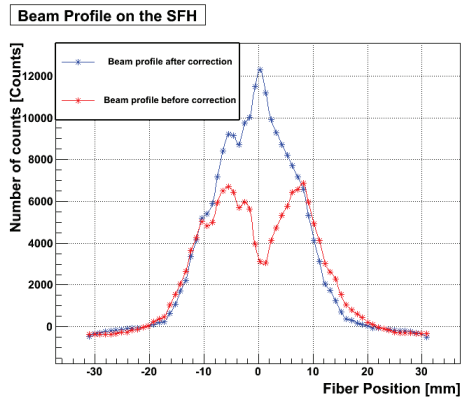

Figure 7: Beam profiles acquired before and after data correction by means of the empirical method.

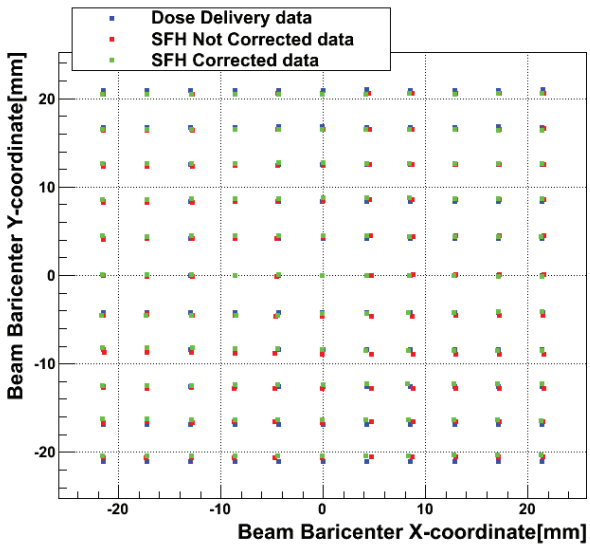

Figure 8: Beam barycenter values on the horizontal and vertical plane extracted from data before and after the correction factors application to the 2D intensity map. Comparison with reference values acquired by the Dose Delivery.

Fig.9 illustrates the difference (for simplicity called "Delta"), on the horizontal plane, between the beam barycenter values coming from the DD acquisition and, respectively, the not corrected and corrected values extracted from the SFH acquisition. Only the two outer fixed positions on the vertical plane (Y = -20 mm and Y = 20 mm) are taken into account here to compute the differences. Data points connected by the solid line are computed before SFH data correction, while those connected by the dashed line are computed after data correction. The systematic error introduced by the radiation damage, calculated as the standard deviation of the sample made up by the Delta values, is ~0.15 mm in case of not corrected data and ~0.07 mm after data correction. This result demonstrates the increase of the measurement accuracy after data correction as a consequence of the goodness of the algorithm used.

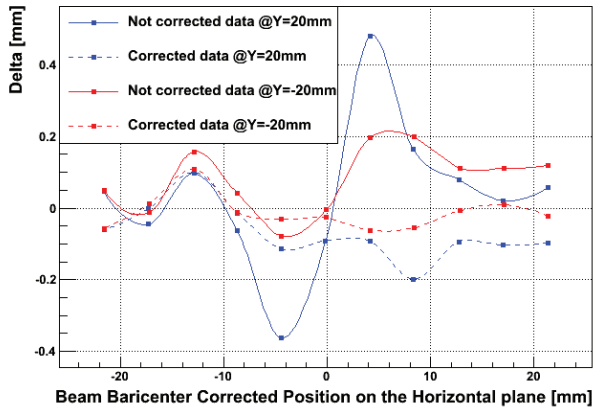

Figure 9: Differences (Delta [mm]) on the horizontal plane between barycenter values coming from the DD acquisition and values coming from one SFH acquisition before (solid line) and after (dashed line) data correction, for the two outer positions on the vertical plane (Y= -20 mm and Y = 20 mm).

CONCLUSION

Several studies on the radiation effects on the SFH scintillating fibers have been performed at CNAO. The main goal has been to find a method to manage the radiation damage effects on the scintillating fibers before the major intervention of fibers replacing. A robust procedure has been implemented: it is based on the determination of a map of correction factors per each plane of one detector. Each factor is computed taking into account the beam position on the active area and is used for off-line data correction. Consecutive tests on profiles reconstruction have demonstrated that thanks to the correction, applied on raw data, the beam barycenter can be measured with a major accuracy than the one obtained without data correction. Although reliable and efficient, this procedure presents a few operational difficulties. Consequently a less robust, but quicker and easier method to compute correction factor, has been implemented. It can be applied on all the SFH detectors. The goal of radiation damage handling and managing has been reached in both cases.

ACKNOWLEDGEMENT

We would like to thank Sir M. Haguenauer and Sir J. Bosser for their technical support during the years of operation of the SFH detectors and for their suggestions in facing up to the radiation damage phenomenon.

REFERENCES

[1] E. Rojatti et al., "Scintillating fibers used as profile monitors for the CNAO HEBT lines", in Proc. of IPAC, Richmond, Virginia, USA (2015).

[2] H.A.Klose et al., "On the measurement of degradation and recovery of scintillating plastic fibers", NIMB, Volume 135, Issues 1-4, (1998).

ISBN 978-3-95450-177-9

TEST OF THE IMAGING PROPERTIES OF INORGANIC SCINTILLATION SCREENS USING FAST AND SLOW EXTRACTED ION BEAMS*

A. Lieberwirth[1,2,3], W. Ensinger[2], P. Forck[1,3,#], O. Kester [1,3], S. Lederer[1,2], T. Sieber[1], B. Walasek-Höhne[1], GSI Helmholtz-Zentrum für Schwerionenforschung, Darmstadt, Germany
also at [2] Technical University Darmstadt, Institute for Material Science, Germany
also at [3] University Frankfurt, Institute of Applied Physics, Germany

Abstract

Inorganic scintillation screens (phosphor P43 and P46, single crystal YAG:Ce, ceramic Alumina and Chromium-doped Alumina), as used for transverse profile determination, were investigated concerning light output, profile reproduction and spectral emission. The screens were irradiated with ion pulses extracted from the synchrotron SIS18 at 300 MeV/u and intensities from about 10^6 to 10^{10} particles per pulse using either 1 µs fast extraction or ≈ 300 ms slow extraction. The light output coincides for both extraction modes. For all materials the optical emission spectrum is independent on the ion species and beam intensities. Radiation hardness tests were performed with up to 10^{12} accumulated Nickel: The phosphor P46 and single crystal YAG:Ce show no significant decrease of light output, while for P43 and Chromox a decrease by 5 to 15 % was measured.

OVERVIEW OF INVESTIGATIONS

Intersecting scintillation screens determine two dimensional beam images and are frequently used for transverse profile measurements in beam transfer lines [1]. The following properties have been investigated:

- emission characteristics for different ion species (p, N, Ni, Xe, U) with a kinetic energy of 300 MeV/u
- dynamic range and linearity between the incident particle intensities and the light output within a range of 10^6 to 10^{10} particles per pulse (ppp)
- spectral emission for various ions and intensities
- radiation hardness i.e. possible variation of the emission characteristics as a function of fluence.

As scintillators we investigated phosphor screens P43 and P46 consisting of crystalline powder with a typical gain size of 10 µm, two different single crystal YAG:Ce and ceramics disks made of pure Alumina A999 (99.99 % purity) and Chromium-doped Alumina (Cr with 0.04 % weight), the properties are compiled in Table 1. All screens were irradiated in air.

The ion beams were extracted from the synchrotron SIS18 at GSI with intensities varying from $6{\cdot}10^6$ ppp up to $2{\cdot}10^{10}$ ppp. The pulse duration was 300–400 ms for slow and 1 µs for fast, single turn extraction at a general requested kinetic energy of 300 MeV/u. One standard deviation of the beam profile was typically σ ≈ 3 mm.

A resonant transformer was used to measure the current of the fast extracted beam with an accuracy of 15% [2]. For intensity measurements in slow extraction mode a detector was used, that consists of an Ionization Chamber (6.5 mm 80 % Ar +20 % CO_2 gas mixture, separated by two 100 µm stainless steel walls from the vacuum, measurement accuracy: 15%) and a SEM (three 100 µm Al plates, measurement accuracy: 15%) [3]. Additionally, the beam passed a 50 µm thick stainless steel foil to air 72 cm before the target ladder. Thus the beam was stripped and the kinetic energies at the target surface were calculated numerically by the code LISE [4] as summarized in Table 2.

Table 1: Investigated Scintillation Screens, ∅ 5 to 8 cm

Name	Material	Thick.	Supplier
#1 P43	Gd_2O_2S:Tb	50 µm	ProxiVision
#2 P46	$Y_3Al_5O_{12}$:Ce	50 µm	ProxiVision
#3 P46	$Y_3Al_5O_{12}$:Ce	20 µm	Crytur
#4 YAG:Ce	$Y_3Al_5O_{12}$:Ce	250 µm	Crytur
#5 YAG:Ce	$Y_3Al_5O_{12}$:Ce	1 mm	SaintGobian
#6 Alumina	Al_2O_3	800 µm	BCE
#7 Chromox	Al_2O_3:Cr	800 µm	BCE

Table 2: The Beam Kinetic Energy *E* in Front of the Target

Projectile	Slow extr. *E* [MeV/u]	Fast extr. *E* [MeV/u]
Proton $^1_1$H	299.2	299.8
Nitrogen $^{14}_7$N	297	299
Nickel $^{58}_{28}$Ni	298	297
Xenon $^{124}_{54}$Xe	281	295
Uranium $^{238}_{92}$U	272	292

OPTICAL SETUP AND ANALYSIS

The scintillation screens on the target ladder were mounted with 45° orientation with respect to the beam plane with an optical setup mounted perpendicular to the target surface as shown in Fig. 1. It consists of two types of cameras (blue in Fig. 1):

Camera #1: AVT Marlin or Stingray, 1/2" CCD chip, 8 bit resolution, monochrome, mounted with a distance of 50 cm with respect to the targets slightly below the optic axis and recorded the two dimensional response of the scintillation screen. The camera was equipped with a Pentax C1614ER lens of 16 mm focal length and remote-

* Funded by German Ministry of Science BMBF under contract number 05P12RDRBJ and Frankfurt Institute of Advanced Science FIAS
# corresponding author: p.forck@gsi.de

ISBN 978-3-95450-177-9

ly controlled iris. The spectral transmittance ranges from 360 to 1000 nm [5]. To further increase the dynamic range of the measurements a neutral-density-filter (Hoya ND03, 5% transmission) could be mounted additionally. The recorded images served for investigations in light output L and the beam profiles.

Camera #2: PCO 1600, 12.2 mm x 9.0 mm CCD sensor size, 14 bit resolution, monochrome, mounted on a Horiba CP140-202 spectrometer with an average dispersion of 50 nm/mm [6] and a wavelength range from 230 to 800 nm. A Pentax C2514-M lens of 25 mm focal length [5] with a wavelength range from 360 to 1000 nm was used. It was focused on an adjustable slit, mounted in horizontal orientation on the input of the spectrometer. To increase the light input the slit was opened until a wavelength resolution of 8.5 nm FWHM was reached. The distance to the target was about 70 cm.

Images were recorded simultaneously from both cameras during irradiation. Background images were recorded shortly before incoming pulses and subtracted from the beam images. The spectra obtained by camera #2 were folded with the transmission efficiency of the optical system.

In the following the term light output L refers to the light recorded by camera #1. The term light yield Y describes the light output normalized to the energy loss ΔE per single ion in the scintillation material and to the delivered particles per pulse as $Y = L/(\Delta E \cdot ppp)$; ΔE is calculated using the LISE code [4] .

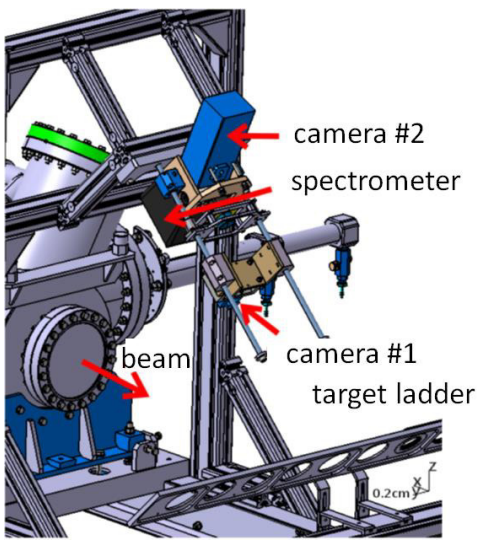

Figure 1: Scheme of the experimental setup. The distance between the air window and the target ladder is 72 cm.

LIGHT OUTPUT AND YIELD

As an example for the light output L the comparison for all investigated scintillation screens under irradiation of fast extracted Uranium beam is depicted in Fig. 2. The errors bars are between 5% and 20% concerning L, as originated by the signal-to-noise-ratio in the recorded images and 15% error concerning the number of irradiated particles per pulse. In the investigated ranges of $3 \cdot 10^6$ till $2 \cdot 10^8$ ppp all investigated materials respond linear to the number of irradiated particles per pulse i.e. no saturation effect was observed. From the investigated phosphor screens the highest light output is observed from the P43 material. Only YAG:Ce (Saint Gobain) showed an even higher light output. It is supposed that the screen thickness of 1 mm and the resulting large energy deposition is responsible for this observation. The lowest light output is observed from pure Aluminum Oxide. Chrome-doping induces here a factor of ≈ 5 more light. Investigations in slow extraction mode show similar results. Comparable data with other ion beam parameter were reported earlier [7-11].

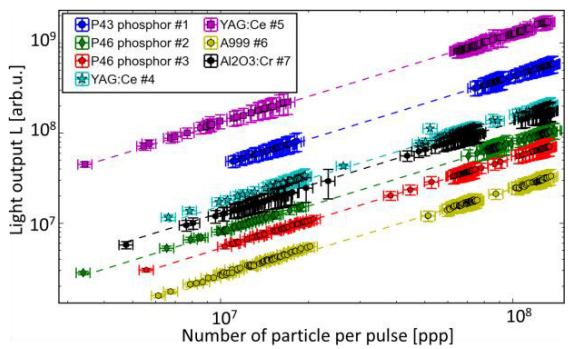

Figure 2: Light output L of all investigated targets under irradiation with a fast extracted Uranium beam as function of irradiating particles per pulse.

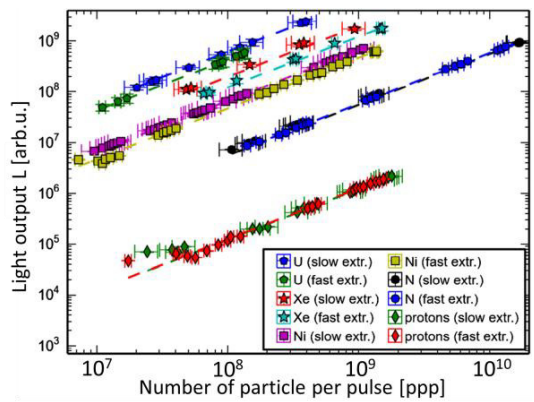

Figure 3: Light output L of the P43 phosphor screen induced by various projectiles as function of the number of irradiating particles per pulse for slow and fast extraction.

Figure 3 shows the light output of the material P43 phosphor for fast and slow extraction for several ions. For better visibility only each 15th data point is plotted with errors between 5% and 25% concerning L and 15% concerning the number of irradiated particles per pulse in both extraction modes. All ions were accelerated to the same energy per nucleon; the actual beam energies are summarized in Table 2. As can be seen, protons induce the lowest light output and for increasing atomic number of the projectile the slope increases up to the light output induced by Uranium ions.

ISBN 978-3-95450-177-9

To summarize those findings, the relative light yield was calculated and normalized to the yield from Nitrogen for each scintillation screen individually. Figure 4 depicts the results for the investigated ions as a function of the stopping power *dE/dx* in the scintillation material. For all materials the light yield decreases for heavier projectiles, however the ratio of light yields for protons to Uranium differs for all screen materials by a factor less than 5. This coincides with previous finding [11]. Within the error bars, the behavior is independent on the beam delivery time (1 µs or 300 ms), i.e. there is no time dependent saturation effect for the given beam intensities.

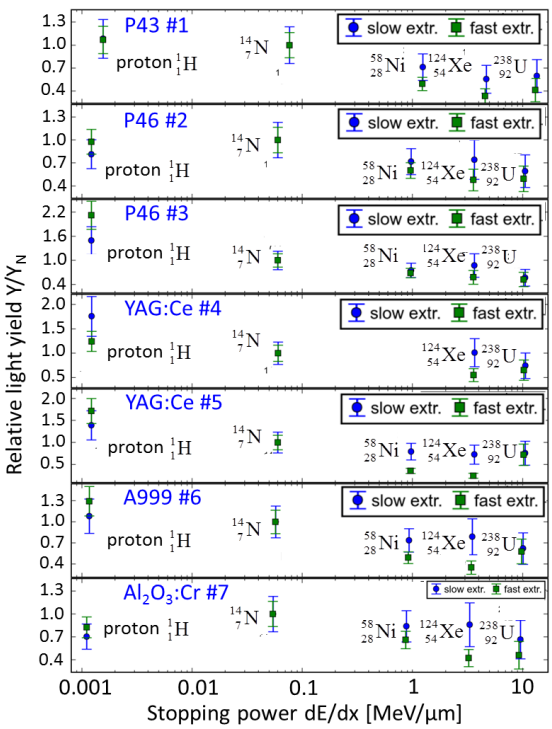

Figure 4: Relative light yield *Y* of all scintillators in dependence of the stopping power *dE/dx* of the investigated projectiles for slow and fast extraction mode.

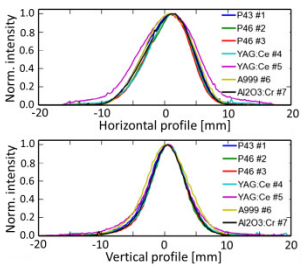

Figure 5: Horizontal and vertical beam profiles obtained from the scintillation screens under irradiation with a fast extracted Xenon beam at 10^9 ppp.

PROFILE REPRODUCTION

From the recorded images the beam profiles were calculated by projection in horizontal and vertical direction. Figure 5 shows a comparison of beam profiles from the investigated scintillators during irradiation with fast extracted Xenon beam. The phosphor and ceramic screens as well as single crystal YAG:Ce #4 show the same projections, i.e. the beam properties are well reproduced. In case of the single crystal YAG:Ce #5 the beam appears broader in horizontal direction only, which is most likely assigned to the 1 mm thickness of the target and the increased scattering in the screen.

RADIATION HARDNESS TEST

Investigations concerning possible degradation of the scintillation efficiency for Nickel ions very performed. Figure 6 depicts the irradiation by about 1100 pulses of Nickel ions with typically $2{\cdot}10^9$ ppp. The irradiation was stopped for 15 min and then continued by 100–150 pulses to check for any permanent modification of the materials.

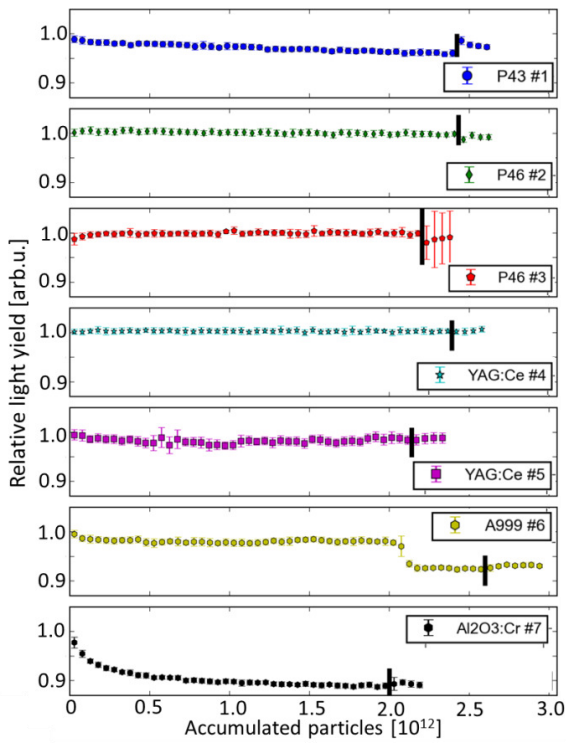

Figure 6: Light yield as a function of accumulated Nickel ions of ≈1100 pulses with $2{\cdot}10^9$ ppp. For better visibility the data points of 20 pulses are binned. The black bar indicates a break of irradiation of 15 min.

The data points in Fig. 6 were binned to a beam intensity of $\approx 5{\cdot}10^{10}$ (20 points), statistical deviations of the single pulses are used as error bars. A decrease of less than 5% is observed for P43 phosphor after a deposit of $2{\cdot}10^{12}$ ions. P43 starts from the initial value of light yield after the 15 min break, but the yield decreases with a considerable slope. Single crystal YAG:Ce and the corresponding phosphor P46 were found to be stable. A larger decrease was found for Al_2O_3:Cr with 10% loss of light yield.

Figure 7 shows the corresponding beam widths as characterized by the second statistical moment σ_{hor} and $\sigma_{vert.}$ Sudden steps of the beam size during irradiation of Alumina and during the breaks are caused by beam instabilities. During the permanent irradiation six screens show

ISBN 978-3-95450-177-9

constant beam sizes, only YAG:Ce #5 shows a systematic image degeneration. The recorded beam size is unchanged after the irradiation break for the three targets, P43 #1, P46 #2 and YAG:Ce #4.

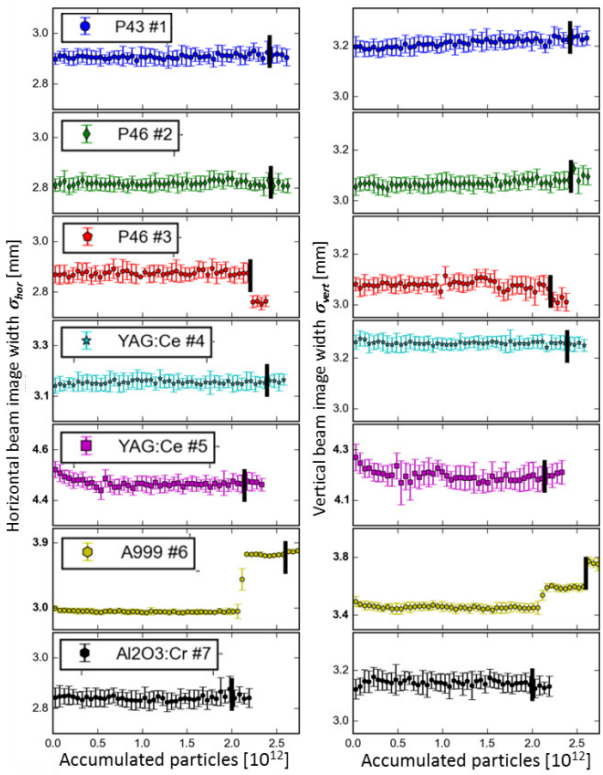

Figure 7: Horizontal and vertical standard deviation of the profiles with the same parameters as in Fig. 6.

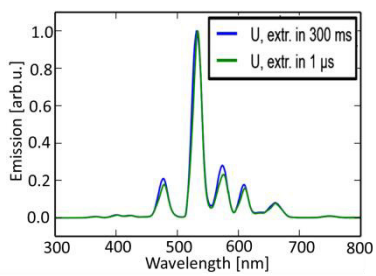

Figure 8: Emission spectra of P43 for Uranium of 10^9 ppp for fast and slow extraction mode.

EMSSION SPECTRA

An example of the emission spectrum of P43 under Uranium irradiation is shown in Fig. 8 averaged over the 10^8 till 10^9 ppp irradiation campaign. The spectra for both extraction modes show the same characteristics, which was also the case for all other ion species. Moreover, the spectrum is comparable to the one obtained by electron or x-ray irradiation [12], which was unexpected due to the significantly higher energy deposition from a single ion compared to an electron or photon. In general, for all screen materials, projectiles and extraction modes no modification of the emission spectra was recorded during the radiation hardness tests [7].

CONCLUSION

Detailed tests of several inorganic scintillation screens were performed for 300 MeV/u ions. For the same beam conditions but different screens the light output varies by about a factor of 100. For low and medium intensities no saturation of the light output were recorded providing a large dynamic range for profile determination. Within the experimental uncertainties, similar light output levels were achieved independent on the extraction time, which was chosen quite differently to be 1 µs and some 100 ms, respectively. Correspondingly, no saturation was observed even for heavy ions with large energy deposition and a beam delivery comparable to the luminescence lifetime of some materials. The ratio of the light yield, i.e. the amount of photons per single particle energy loss, decreases from protons to Uranium by a factor of two to five for the various materials. The radiation hardness test proves the stability in particular for single crystal YAG:Ce #4 and the corresponding phosphors P46 #2 and #3. The beam profiles are well reproduced by these materials. Chromox suffers from a decrease of light yield as a function of fluence, but the beam profile is still well reproduced. The optical emission spectra depend neither on the irradiating ion (despite large differences in energy deposition) nor on the extraction time and is comparable to the one obtained from electron or x-ray irradiation. The emission spectra remain unchanged even after deposition of some 10^{12} ions. Further results are published elsewhere [7-11].

Among the investigated materials YAG:Ce #4 and P46 will be a good choice for the installation at the High Energy Beam Transport lines at FAIR usable for low and medium intensities.

REFERENCES

[1] B. Walasek-Höhne, G. Kube, in *Proc. DIPAC 2011*, Hamburg, Germany, p. 533 (2011).
[2] H. Reeg, N. Schneider, in *Proc. DIPAC 2001*, Grenoble, France, p.120 (2001).
[3] P. Forck, T. Hoffmann, A. Peters, in *Proc. DIPAC 1997*, Frascati, Italy, p. 165 (1997).
[4] O.B. Tarasov, D. Bazin etal., LISE++, http://lise.nscl.msu.edu/lise.html
[5] Pentax C1614ER HR and C2514-M Specification
[6] HORIBA, www.horiba.com
[7] A. Lieberwirth *et al.*, Nucl. Instrum. Meth. B **365**, 533 (2015).
[8] P. Forck *et al.*, in *Proc. IPAC 2014*, Dresden, Germany, p. 3480 (2014).
[9] A. Lieberwirth *et al.*, in *Proc. IBIC 2013*, Oxfors, UK, p. 553 (2013).
[10] K. Renuka *et al.*, in *Proc. BIW 2012*, Newport News, USA, p. 183 (2012).
[11] K. Renuka *et al.*, IEEE Trans. Nucl. Sc. **59**, p. 2301, dx.doi.org/10.1109/TNS.2012.2197417 (2012).
[12] E. Gorokhova *et al.*, IEEE Trans. Nucl. Sci. **52**, 3129 dx.doi.org/10.1109/TNS.2005.862827 (2005).

ISBN 978-3-95450-177-9

IONIZATION PROFILE MONITOR SIMULATIONS - STATUS AND FUTURE PLANS

M. Sapinski*, P. Forck, T. Giacomini, R. Singh, S. Udrea, D. M. Vilsmeier, GSI, Darmstadt, Germany
B. Dehning, J. Storey, CERN, Geneva, Switzerland
F. Belloni, J. Marroncle, CEA/IRFU, Gif-sur-Yvette, France
C. Thomas, ESS, Lund, Sweden
R. M. Thurman-Keup, FNAL, Illinois, U.S.A.
K. Satou, J-PARC, Tokai, Japan
C. C. Wilcox, R. E. Williamson, STFC/RAL/ISIS, Oxford, United Kingdom

Abstract

Nonuniformities of the extraction fields, the velocity distribution of electrons from ionization processes and strong bunch fields are just a few of the effects affecting Ionization Profile Monitor measurements and operation. Careful analysis of these phenomena require specialized simulation programs. A handful of such codes have been written independently by various researchers over the recent years, showing an important demand for this type of study. In this paper we describe the available codes and discuss various approaches to Ionization Profile Monitor simulations. We propose benchmark conditions to compare these codes among each other and we collect data from various devices to benchmark codes against the measurements. Finally we present a community effort with a goal to discuss the codes, exchange simulation results and to develop and maintain a new, common codebase.

INTRODUCTION

The Ionization Profile Monitors were first buildt in the 1960s as simple devices to measure transverse profiles of particle beams without affecting them. The basic idea of the device is that the distribution of electrons or ions from the rest gas ionization mirrors the original beam distribution, however the effects of guiding field nonuniformities, beam space charge or initial velocities due to the ionization process can affect the measurement. A number of numerical simulations have been written dealing with those aspects. Because of their specificity - for instance tracking of low energy electrons or ions, beam charge distributions - the established codes, like Geant4 [1] or CST Studio [2], are usually not applicable to IPM simulations.

In this paper first we present the most important stages of an IPM simulation. These logical stages can be used to modularize the simulation code. In the second part we present simulation codes known to us. These codes were discussed during the Ionization Profile Monitor simulation kickoff workshop [3]. They show a variety of approaches to IPM simulations. Finally we discuss the collaborative tools prepared in order to compare various codes, benchmark them against measurements and share the results. More information can be found on the collaboration's TWiki pages [4].

It should be stressed that other beam devices, for instance Beam Fluorescence Monitors or even electron lenses, can be simulated using similar techniques.

SIMULATION COMPONENTS

The simulation can be divided into the following stages, which cover various physics phenomena and can be used to modularize the simulation code:

- **Ionization** - The purpose of this component is to generate the initial momenta of the particles to be tracked. The most promising approach is to use - if available - a realistic double differential cross section (DDCS) for obtaining the energies and scattering angles of ionization products. The ionization process depends on the beam particle type, beam energy and the residual gas species, therefore an appropriate cross section model for each beam configuration can be chosen.

- **Guiding fields** - The purpose of this component is to provide the externally applied electric and magnetic fields in the volume where the particles must be tracked. Usually either uniform fields are used or a field map is imported from an EM-solver. In most applications the field nonuniformities are just sources of errors, but in some cases fields are deeply nonuniform and their precise knowledge is fundamental in order to reconstruct the real beam profile.

- **Beam fields** - This module provides the electromagnetic fields generated by the beam. For highly relativistic beams the electric field is mainly transverse to the beam and its longitudinal component can be neglected. In such case a '2D' approach in which the longitudinal shape of the beam is modelled by a simple shifting of the bunch charge distribution with time is often used. Other approaches include solving Poisson's equation analytically or using EM solvers. This allows for the creation of a three-dimensional field map. The magnetic field of the beam is usually neglected because its impact on slowly-moving ionization products is much smaller than the electric field.

* m.sapinski@gsi.de

ISBN 978-3-95450-177-9

- **Particle tracking** - The purpose of this module is to update the positions and velocities of the tracked particles at each time step of the trajectory before they reach the detector. The motion depends on the initial velocities and on the electric and magnetic fields of the IPM chamber and the beam. Most codes consider only non-relativistic motion of particles. Various approaches exist such as analytic solutions of the equations of motion for special cases or numerical solutions using a Runge-Kutta-method.

Other components, whose effect is of minor importance for typical IPM, but which can be critical for other applications, are:

- **Gas dynamics** - Simulation of rest gas thermal motion or motion due to gas injection (for instance cold gas jet) or gas burnout - all these effects lead to a non-uniform gas density in vacuum;
- **Wakefields** - Simulation of transient electric and magnetic fields due to mirror charges on beamline components;
- **Synchrotron radiation** - For relativistic beams gas ionization can be caused by synchrotron radiation generating additional profiles;
- **Multiple beams** - In cases when multiple beams are present in the vacuum chamber (eg. electron lens) their impact on the measurement should be estimated.

KNOWN SIMULATION CODES

In Table 1, existing codes are summarized including their approach to the main simulation components. Most of the codes are not public. A short description of each code is provided below.

GSI Code

The GSI code, developed around 2002, is used for a quick estimation of the influence of the electromagnetic field of ion bunches on the transverse profile measurements with IPM. The bunches have the shape of a prolate spheroid, with the spherical case treated separately. The charge density distribution within bunches may be chosen to be homogeneous or parabolic $\rho(r, z) \propto 1 - [(r/b)^2 + (z/a)^2]$. These assumptions allow for computation of the electrostatic field of the bunches using analytic formulas [5]. The field in the laboratory frame is computed through the Lorentz transformation. The guiding fields are uniform and can be separately activated. Both electrons and ions may be tracked. These particles are randomly generated within the volume of the bunches and have a spatial distribution in accordance with the bunch charge density. No interaction is considered between them, thus each one is tracked independently according to the classical laws of motion until it reaches the detector plane or a user defined time limit gets exceeded, in which case the particle is discarded. While ions are generated at rest, for electrons a simple double-differential cross-section (DDCS) model can be applied to generate their velocities.

PyECLOUD-BGI

This code is an adaption of the PyECLOUD package used to study the electron cloud built-up [6]. It has been created in 2012 to address the issue of beam space-charge influence on profile measurements for LHC monitors [7]. It assumes an ultra-relativistic beam and uses an analytic formula to compute the transverse electric field of a two-dimensional elliptical Gaussian charge distribution [8]. For a circular beam Gauss' law is used to compute the electric field. The simulation incorporates electric and magnetic guiding fields which are assumed to be uniform and perfectly aligned. The initial velocities of electrons are computed according to the DDCS [9]. The tracking of electrons is performed according to an analytic formula that is obtained by solving the equations of motion of a charged particle in a constant transverse electromagnetic field. The code is public [4].

FNAL Code

The IPM simulation code at FNAL was originally developed to track low energy electrons in an electron beam profiler for the proton beams. The code was adapted to solve for electron trajectories in the IPMs. Of particular interest was the behavior of the ionization products in the new, gated IPMs [10]. The simulation is written in MATLAB, utilizing its parallelization capabilities, and implements a numerical solver for the relativistic equations of motion of the electrons or ions. The solver is a second order ODE solver with the added feature that the momentum is scaled to preserve its magnitude when applying the solver to the magnetic portion of the guiding fields. The guiding fields are typically calculated via interpolation of externally pre-calculated 3D field maps. For the FNAL IPM, a 2D electric and a 3D magnetic field maps are used. In the case of the fields of the beam, only a single bunch fields are evaluated however, with the proper time shifts in the solver, one can effectively simulate a train of bunches. Since the bunch fields are evaluated externally, the bunch shape is not limited to any particular functional form. Typically a Gaussian shape is used and there is a separate MATLAB function to produce the fields for that shape. The initial momenta of the ionization electrons are chosen from a $1/E^2$ distribution [11]. The initial momenta of the ions are taken from the thermal energy distribution of an ideal gas. The simulation is not very user friendly with many separate functions or scripts that must be called to setup it up correctly.

ISIS Code

The ISIS IPM simulation begins with beam data being recorded from the machine, providing both an input for the simulation and also a benchmark to compare the results against. The 2D beam profile is measured with SEM grids located close to the IPM, and this is used alongside intensity measurements to define the beam within the simulation. Alternatively, purely theoretical beam distributions can be

ISBN 978-3-95450-177-9

Table 1: The Current Simulation Codes. See Text for the Details.

Name/Lab	Language	Ionization	Guiding field	Beam shape	Beam field	Tracking
GSI code	C++	simple DDCS	uniform E,B	parabolic 3D	3D analytic relativ.	numeric R-K 4th order
PyECLOUD-BGI /CERN	python	realistic DDCS	uniform E,B	Gauss 3D	2D analytic relativ. only	analytic
FNAL	MATLAB	simple SDCS	3D map E,B	arbitrary	3D numeric relativ. (E and B)	num. MATLAB rel. eq. of motion
ISIS	C++	at rest	CST map E only	arbitrary (CST)	2D numeric (CST) non-relativ.	numeric Euler 2nd order
IFMIF	C++	at rest	Lorenz-3E map E only	General. Gauss	numeric (Lorenz-3E) non-relativ.	
ESS	MATLAB	at rest	uniform E,B	Gauss 3D	3D numeric (MATLAB) relativ.	numeric MATLAB R-K
IPMSim3D /J-PARC	python	realistic DDCS	2D/3Dmap E, B	Gauss 3D	2D numeric (SOR) relativ. only	numeric R-K 4th order

defined. The beam's field is calculated using CST EM Studio [2], in which the beam is modelled as concentric elliptic cylinder charge distributions with the same aspect ratio as the measured beam. The charge levels are chosen to represent an elliptic distribution within the beam and are calculated to match the measured beam intensity. This beam is placed inside a 3D model of the IPM that also includes the guiding field. The internal fields of the monitor are then calculated and exported for use in a C++ ion tracking code. To approximate a time dependent space charge, a second electric field is calculated with the beam removed from the model. The tracking code itself generates a uniform distribution of ions within the beam's volume, and tracks the motion of these through the electric fields calculated in CST. The equations of motion are solved using a 2nd order Euler method. For the extracted beamline IPM the electric field is swapped for the guiding field after 200 ns to model the beam leaving the monitor. When modelling synchrotron IPMs, an electrostatic approximation of the average charge within the monitor is used. During post-processing an elliptic weighting is applied to each ion based on its initial position to compensate for the initially uniform ion distribution. A further weighting is applied based on the longitudinal angle of incidence at which each ion reaches the detectors, to account for the variation in detection efficiency. This weighting was measured using an in-house vacuum tank test at ISIS [12].

IFMIF Code

The IFMIF code was created to design the IFMIF/LIPAc monitor and to investigate space-charge correction algorithm [13]. The beam transverse profile $\overrightarrow{P}$ is described by a Generalized Gaussian Distribution (GGD). In this case the space-charge impacts only on the 2nd (σ) and the 4th (kurtosis) moments of the distribution. The distortion of the profile is described in matrix formalism: $\overrightarrow{P}_{\text{meas}} = \text{M} \times \overrightarrow{P}_{\text{real}}$. A set of M-matrices for various beam parameters is prepared using the tracking procedures written in C++. Guiding (only E) and beam fields are calculated using Lorenz-3E [14]. The correction procedure uses the σ and kurtosis of the measured profile, beam intensity, beam energy and the value of the guiding field to select the proper M-matrix. The procedure is iterative.

ESS Code

The ESS code was developed initially in MATLAB, for the purpose of investigation of the space charge effect on the performance the IPM in the ESS Cold Linac sections. The code solves the classical equations of motion for arbitrary charged particles exposed to electromagnetic fields. The equations of motion are solved using the standard MATLAB's ODE solver, based on non-linear Runge-Kutta method. The fields are composed of uniform and static guiding fields and dynamic fields given by a 3D Gaussian distribution of moving moving charges. The field generated by the bunch is calculated at the position of the particles and given time by the ODE solver. It is generated in the bunch rest-frame and then transformed to the lab-frame using Lorentz transformation. Bunches periodically cross the IPM interaction volume, and this is taken into account in case of particles with large mass which can "see" several bunches before leaving the beam. The initial spatial distribution of tracked particles is randomly generated following the bunch 2D transverse distribution, and linearly along the longitudinal axis. The detector is modelled by means of an event function used by the ODE solver. It calculates the time at which the particles cross the detector surface and returns their positions and speeds as an additional output to the time – phase space output of the ODE solver. The limitation of the code is extremely high electric field, which would drive the particles to relativistic motion already in the interaction region. Finally, in order to improve the code performance, MATLAB's multi-processing or rewriting the code in a C++ are considered.

ISBN 978-3-95450-177-9

J-PARC Code - IPMsim3D

The IPMsim3D code assists IPM design works. It simulates charged particle trajectory in 3D, traveling in guiding fields and beam fields of circulating bunched beams. The electric and magnetic fields maps are calculated by using external code POISSON/Superfish [15] in case of 2D and CST Studio [2] in case of 3D. Uniform fields can also be selected. The charge density of beam is defined as 3D Gaussian distribution and the beam is assumed to be relativistic. At first, 2D grids are set internally and unit charge is distributed on each grid according to the transverse charge density. Then iterative calculations determine the self-consistent potential and the electric field on each grid. The longitudinal charge distribution is used to normalize the line density. This method, called succesive over-relaxation (SOR), will be adapted to a more general density distribution.

A charge particle equation of motion is solved based on the 4^{th} order Runge-Kutta method. The initial position of the tracked particle is generated according to the transverse and longitudinal charge density. The initial momentum is calculated from analytic DDCS, the same as in PyECLOUD-BGI. The semi-empirical single differential ionization cross sections for some gas species are also used, where the electron emission angle is assumed to be perpendicular to the beam axis. The tracking is stopped when the particle crosses the detector surface. This code is public [4] and it was used to design IPM for CERN PS [16].

COMMON TOOLS

In order to facilitate the comparison of various codes against each other and against measurements a specialized data format, based on the W3C XML standard, was developed. During development the focus was not only on introducing a common data format but also on creating a convenient way of storing metadata about measurements. A file contains a number of beam profiles and/or images together with important information about the type of the beam and the configuration of the device - IPM for example - such as extraction voltage and magnetic field. Specification of the proposed format is available [4].

A Python GUI has been developed for visualization and processing the XML data [4]. A set of benchmark beams have been proposed. A comparison of one such beam (CERN PS case) using two codes is shown in Fig. 1.

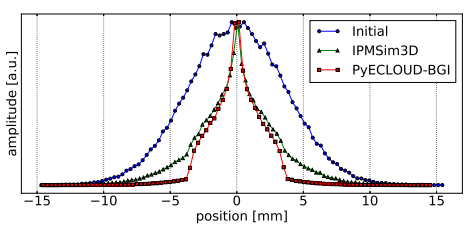

Figure 1: Comparison of profiles obtained with two simulation codes for PS benchmark beam (electron detection).

CONCLUSIONS AND PLANS

A collaboration effort to simulate effects related to beam interaction with rest gas and measurement of the beam profile using the ionization process have been launched. The goals are to exchange information between researchers working in different laboratories and share experience in the design and understanding of these devices.

Currently a few of the described codes are still under independent development, however a common effort to develop a universal, modular multi-purpose approach is also ongoing.

REFERENCES

[1] IEEE Trans. Nucl. Sci. 53 No. 1 (2006) 270-278.

[2] CST - Computer Simulation Technology, `http://www.cst.com/`.

[3] IPM simulation kickoff workshop, CERN, March 2016, `https://indico.cern.ch/event/491615/`.

[4] IPMSim, `https://twiki.cern.ch/twiki/bin/view/IPMSim/`.

[5] P. Strehl, "The Electromagnetic Fields of Bunches" in "Beam Instrumentation and Diagnostics", pp. 341-375, Springer, 2006 (ISBN 978-3-540-26404-0).

[6] G. Iadarola et al.,"Electron Cloud Simulations with PyECLOUD", Proc. of ICAP2012, WESAI4.

[7] D. Vilsmeier, "Profile distortion by beam space charge in Ionization Profile Monitors", CERN-THESIS-2015-035.

[8] M. Bassetti et al., "Closed expression for the electrical field of a two-dimensional gaussian charge", CERN-ISR-TH/80-06, 1980.

[9] A.Voitkiv et al., "Hydrogen and helium ionization by relativistic projectiles in collisions with small momentum transfer", J.Phys.B: At.Mol.Opt.Phys.32 (3923-3937), 1999.

[10] J.R. Zagel et al., "Third Generation Residual Gas Ionization Profile Monitors at Fermilab", in Proc. of IBIC2014, TUPD04.

[11] F. Sauli, "Principles of Operation of Multiwire Proportional and Drift Chambers", CERN 77-09, 1977.

[12] C. C. Wilcox, "An Investigation into the Behaviour of Residual Gas Ionization Profile Monitors in the ISIS extracted Beamline", these proceedings.

[13] J. Egberts, "IFMIF-LIPAc Beam Diagnostics: Profiling and Loss Monitoring Systems", thesis, Univ. Paris Sud, 2012.

[14] INTEGRATED Engineering Software, `https://www.integratedsoft.com/`.

[15] J.H. Billen, et al., "POISSON/SUPERFISH on PC Compatibles", Proc. of Linear Accelerator Conf. TH4-60, 778, 1992.

[16] J.W. Storey et al.,"Development of an IPM Based on a Pixel Detector for CERN Proton Synchrotron", Proc. of IBIC2015, TUPB059.

ISBN 978-3-95450-177-9

CALIBRATION OF X-RAY MONITOR DURING THE PHASE I OF SuperKEKB COMMISSIONING

Emy Mulyani*, SOKENDAI, 1-1 Oho Tsukuba Ibaraki 305-0801, Japan
J.W Flanagan[1], KEK, 1-1 Oho Tsukuba Ibaraki 305-0801, Japan
[1] also at SOKENDAI, 1-1 Oho Tsukuba Ibaraki 305-0801, Japan

Abstract

X-ray monitors (XRM) have been installed in each SuperKEKB ring, the Low Energy Ring (LER) and High Energy Ring (HER), primarily for vertical beam size measurement. Both rings have been commissioned in Phase I of SuperKEKB operation (February-June 2016), and several XRM calibration studies have been carried out. The geometrical scale factors seems to be well understood for both LER and HER. The emittance knob ratio method yielded results consistent with expectations based on the machine model optics (vertical emittance ϵ_y is ≈8 pm) for the LER. For the HER, the vertical emittance ϵ_y is ≈41 pm, which is 4× greater than the optics model expectation. Analysis of beam size and lifetime measurements suggests unexpectedly large point response functions, particularly in the HER.

INTRODUCTION

The SuperKEKB accelerator is designed to collide e^-e^+ at a design luminosity of 8×10^{35} cm^{-2} s^{-1}(40× larger than that of KEKB)[1]. Measuring and controlling parameters of the accelerator beams is essential to achieve maximum performance from the accelerator; e.g., it is necessary to keep the single-beam vertical size small in order to obtain high luminosity. The XRMs have been installed in both SuperKEKB rings for vertical beam size measurement. Several XRM calibration studies have been carried out during the Phase I of SuperKEKB commissioning.

XRM APPARATUS

Two XRMs have been installed at SuperKEKB: one for electrons (HER) and one for positrons (LER). Each apparatus consists of three primary components: beamline, optical elements and detection system.

Beamline

Table 1: Beamline Parameters

Parameter	LER	HER	Unit
Energy	4	7	GeV
Source to optics (L)	9.259	10.261	m
Optics to detector (L′)	31.789	32.689	m
Air gap (f)	10	10	cm
Thickness of Be filter (T)	0.5	16	mm
Thickness of Be window (T′)	0.2	0.2	mm

* mulyani@post.kek.jp

Each of the SuperKEKB rings has four straight sections and four arc-bends. The X-ray sources are the last arc-bends located immediately upstream of the straight sections in Fuji (LER) and Oho (HER). The beamlines are about 40 m long from the source points to the detectors. A list of the parameters for the beamlines are shown in Table 1. The optical elements (pinhole and coded apertures) are located in optics boxes ≈9–10 m from the source points, for geometrical magnification factors of ≈3× for both lines. Beryllium filters are placed between source points and optic boxes to reduce the incident power levels for both lines. A 0.2 mm thick Be window is also placed at the end of each beamline to separate vacuum (beamline) and air (detector box).

Optical Elements

Three optical elements have been designed and installed in each ring: a single slit, a multi-slit coded aperture (17 slits) and a Uniformly Redundant Array (URA) coded aperture (12 slits) as shown in Fig. 1 [2]. These optical elements consist of 18–20 μm thick gold masking material on 600 μm thick diamond substrates.

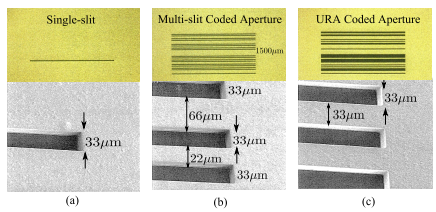

Figure 1: Three types of optical elements at 70× magnification and 1000× Scanning Electron Microscope (SEM): (a)Single-slit, (b) Multi-slit coded aperture and (c) URA coded aperture.

Detection System

For phase I of SuperKEKB commissioning, a cerium-doped yttrium-aluminum-garnet (YAG:Ce) scintillator is combined with a CCD camera for the x-ray imaging system as shown in Fig. 2. The resolution of this optical systems will be discussed in systematic resolution section.

GEOMETRICAL SCALE FACTORS

The geometrical scale factors based on beam-based measurement (see Fig. 3) are measured by moving either the beam or optical elements (single slit and coded apertures), observing how the peak features move, then calculating the ratio of geometric magnification M and scintillator camera

ISBN 978-3-95450-177-9

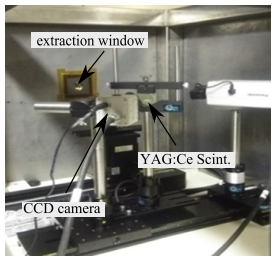

Figure 2: Detection system for phase I of SuperKEKB commissioning. Inside the detector box is a Be extraction window and a 141 μm thick YAG:Ce scintillator combined with CCD camera.

scale m (μm/pixel). When the beam is moved, the ratio M/m is determined by fitting Eq. 1:

$$P_1 = \Big(-\frac{M}{m}\big(1 - \frac{ds_1}{ds}\big)\Big) y_1 - \frac{M}{m}\frac{ds_1}{ds} y_2 + \alpha \qquad (1)$$

where P_1 is the position (in pixels) of a peak feature from x-rays that passed through a slit onto the scintillator, ds_1 is distance from source point to upstream BPM, ds is distance between upstream/downstream BPM and y_1, y_2 are y values (in μm) of the upstream and downstream BPMs, respectively. The parameter α represents the offset between beam and detector coordinate systems. When the mask is moved, the ratio $(M+1)/m$ is determined by fitting Eq. 2.

$$P_1 = \frac{M+1}{m} y_{mask} + \alpha \qquad (2)$$

where y_{mask} is the position of the mask in μm. Geometric magnification factors agree well between tape measurements and beam-based measurements at both lines, within 0.9–4.6 %, as shown in Table 2, where estimated systematic errors are shown for tape measurements, and statistical errors shown for beam-based measurements.

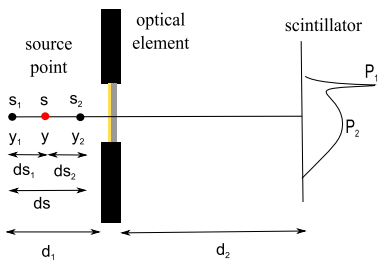

Figure 3: A schematic for the geometrical scale factors check, consisting of a source point with two BPMs at upstream and downstream, optical elements and peak feature images at scintillator detector. P_1 is the peak feature from an x-ray that passed through a slit onto the scintillator, and P_2 is the peak feature from x-rays that punched through the Au mask.

EMITTANCE CONTROL KNOB

The emittance control knob ratio method measures the overall scaling factor between the reported beam size measurements and the true beam size [3]. The variation of the vertical beam size by changing the bump height can be represented as:

$$(\sigma_y^{meas})^2 = (c\sigma_{y_0})^2 + (cA)^2(h - h_0)^2 \qquad (3)$$

with correlation between beam size σ_y, emittance ϵ_y and beta function β as:

$$\sigma_y = \sqrt{\epsilon_y \beta} \qquad (4)$$

where σ_{y_0} and σ_y^{meas} are the true vertical beam size and the beam size measured by the XRM. The parameters h and h_0 are the bump height and its offset, c is the calibration (scaling) factor and A is a linear coefficient where $A^2 = \Delta\epsilon_y \times \beta_y$, and $\Delta\epsilon_y$ is the expected change in emittance for a unit change in bump height. The values of $\Delta\epsilon_y$ and β_y given by the optics model are shown in Table. 3. The results of this method for both lines are shown in Figs. 4, 5 and Table 4, with a minimum beam size for the LER of 19 μm, and for the HER of 29 μm. By using Eq. 4 and the parameters in Table. 3, we can determine the vertical emittance for both rings: ϵ_y ≈11 pm (≈118 pm) for LER (HER). The value for the LER is close to the design value (≈ 10 pm), but is much higher than design for the HER. To investigate this discrepancy, a study of smearing factors (point spread functions) was made using beam lifetime data, in the next sub-section.

Table 2: Geometrical Scale Factors Check

Parameters		
LER (Tape Measurement)		
M/m	(pixels/mm)	66.2 ± 0.2(0.3 %)
(M+1)/m	(pixels/mm)	85.5 ± 0.2(0.2 %)
LER (Beam-Based Measurement)		
M/m	(pixels/mm)	69.5 ± 0.5(0.7 %)
(M+1)/m	(pixels/mm)	86.0 ± 0.6(0.65 %)
HER (Tape Measurement)		
M/m	(pixels/mm)	60.9 ± 0.2(0.3 %)
(M+1)/m	(pixels/mm)	80.0 ± 0.2(0.2 %)
HER (Beam-Based Measurement)		
M/m	(pixels/mm)	59.2 ± 0.5(0.9 %)
(M+1)/m	(pixels/mm)	79.3 ± 0.1(0.13 %)

Table 3: Beam Parameter

Parameter	LER	HER
$\Delta\epsilon_y$	70.0946 pm	43.0096 pm
β_y	67.1721 m	7.636 47 m

Lifetime Studies

The beam lifetime was also recorded during the emittance control knob studies. A bunch of charged particles (electrons/positrons) in a ring decay due to a variety of mechanisms: quantum lifetime (emission of synchrotron radiation), Coulomb scattering (elastic scattering on residual gas

ISBN 978-3-95450-177-9

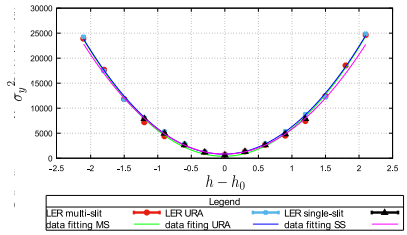

Figure 4: The LER emittance control knob data for all optical elements at 200 mA of beam current, with data points fitted by the function shown in Eq. 3.

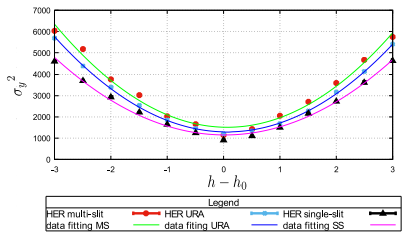

Figure 5: The HER emittance control knob data for all optical elements at 190–195 mA of beam current, with data points fitted by the function shown in Eq. 3.

atoms), Bremsstrahlung (photon emission induced by residual gas atoms) and the Touschek effect (electron-electron scattering). None of these mechanisms is related to the beam size except for the Touschek effect. The Touschek lifetime is related to the beam size as shown in Eq. 5 [4].

$$\frac{1}{\tau} = \frac{1}{\tau_{tk}} + \frac{1}{\tau_{qu}} + \frac{1}{\tau_{cs}} + \frac{1}{\tau_{bs}},$$
$$\frac{1}{\tau} = \frac{r_c^2 c Q}{8\pi e \sigma_y \sigma_x \sigma_z} \frac{\lambda^3}{\gamma^2} D(\epsilon) + C \qquad (5)$$

where τ is the total lifetime, τ_{tk} is the Touschek lifetime, $D(\epsilon)$ is the Touschek lifetime function (approximately constant for small ϵ), τ_{qu}, τ_{cs} and τ_{bs} are the quantum, coulomb and bremsstrahlung scattering lifetimes, respectively (written as a constant parameter C in Eq. 5). In this analysis, we only change the σ_y and the other parameters are constant, giving the simplified equation shown in Eq. 6.

Table 4: Emittance Control Knob Calibration

Mask	σ_{y0}(μm)	Cal. factor (c)
	LER	
single-slit	28.3 ± 1.1(3.9 %)	1.03 ± 0.01(1.0 %)
multi-slit	19.1 ± 4.3(22.4 %)	1.07 ± 0.01(0.9 %)
URA	27.4 ± 2.8(10.2 %)	1.06 ± 0.01(0.9 %)
	HER	
single-slit	30.9 ± 1.1 (3.6 %)	1.09 ± 0.02(1.8 %)
multi-slit	31.1 ± 1.5(4.9 %)	1.25 ± 0.03(2.4 %)
URA	29.9 ± 0.5(1.6 %)	1.20 ± 0.01(0.8 %)

$$\frac{1}{\tau} = \alpha \frac{1}{\sigma_y} + C \qquad (6)$$

By fitting $\frac{1}{\tau}$ vs $\frac{1}{\sigma_y}$ data via Eq. 6 (see Fig. 6), we obtained negative values for C, representing non-Touschek lifetime sources. The non-positive value of C indicates that the lifetime is heavily dominated by the Touschek lifetime, and further suggests the presence of a positive asymptote in the beam size.

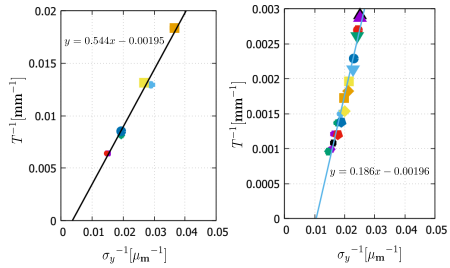

Figure 6: Relation between lifetime and beam size for multi-slit mask at LER (left) and HER (right) fitted by Eq. 6.

If a beam of initial size σ_{y_0} is convolved with a Gaussian smearing function of size σ_s to make a measured beam size σ_y^{meas}, then the measured beam size can be represented by adding the real beam size and the smearing size in quadrature as shown in Eq. 7.

$$\sigma_y^{meas} = \sqrt{(\sigma_{y_0})^2 + (\sigma_s)^2}$$
$$\sigma_{y_0} = \sqrt{(\sigma_y^{meas})^2 - (\sigma_s)^2} \qquad (7)$$

If we consider just the Toushek effect then the correlation between τ and σ_y^{meas} becomes:

$$\tau = \alpha \sigma_{y_0} = \alpha \sqrt{(\sigma_y^{meas})^2 - (\sigma_s)^2} \qquad (8)$$

Fitting the τ vs σ_y^{meas} data via Eq. 8 with α and σ_s as free parameters gives results like those shown (for multi-slit masks) in Fig. 7. By using Eq. 4 and the parameters in Table. 3, we can calculate the true minimum beam size σ_{y0} from the smallest measured beam size σ_y^{meas}, and corresponding vertical emittance ϵ_{y_0}. The average values over measurements made with all three optical elements, for σ_s, σ_{y0} and ϵ_{y_0} are shown in Table 5. From this table, we see that the smearing function for the HER is much larger than that for the LER. Also, even after accounting for this smearing function, the HER emittance is about 4 times larger than the design value.

SYSTEMATIC RESOLUTION

Based on the above discussion, there are smearing factors for both rings that need to be understood. Regarding the detector, there are some parameters that will affect the spatial resolution: defect of focus, diffraction effect and spherical

ISBN 978-3-95450-177-9

Table 5: The averages of smearing factor, minimum beam size and vertical emittance measured with all 3 optical elements

Parameter	LER	HER
σ_s	12.1 ± 2.1 μm	32.8 ± 0.4 μm
σ_{y_0}	23.5 ± 0.3 μm	17.8 ± 0.8 μm
ϵ_y	≈8 pm	≈41 pm

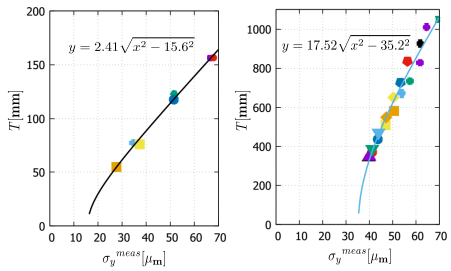

Figure 7: Relation between lifetime and beam size for multi-slit mask at LER (left) and HER (right) fitted by Eq. 8.

aberration [5]. If R_f is the spatial resolution, dz is the depth of the scintillator (141 μm), NA is the numerical aperture of the camera (0.03132), M is the magnification of the XRM (3.2) and λ is the wavelength of visible light from scintillator (550 nm), the relations between them are given as Eqs. 9-11.

$$R_f = \frac{dzNA}{M}, \text{defect of focus} \quad (9)$$

$$R_f = \frac{\lambda}{MNA}, \text{diffraction effect} \quad (10)$$

$$R_f = \frac{dz(NA)^2}{M}, \text{spherical aberration} \quad (11)$$

The effects contribute ≈ 5 μm of smearing as expressed at the source point. Besides those three effects, the resolution of detector can also be limited by the spatial distribution of the deposited energy imparted from ionizing radiation. This distribution is affected by scattered x-rays or secondary electrons that may deposit energy far away from the primary photon interaction site. EGS5 code[6] was used to calculate the absorbed dose of an x-ray pencil beam passing through the Be filter, optical elements, Be window and onto the flat surface of the 141 μm thick YAG scintillator, to determine the effect of scattering anywhere in the beam line or detector on the point spread function of the imaging system.

The geometry of the XRM beamlines used in the EGS5 simulation is shown in Fig. 8 and Table 1. The EGS5 calculation result seen in Fig. 9 shows that the scattered background falls off by an order of magnitude within 1 μm. Altogether, contributions from sources in Eqs. 9-11 and scattering effects (EGS5 simulation) only for sources of point spread in the XRM of ≈6 μm as expressed at the source point. This is insufficient to account for the observed smearing according to the lifetime studies. Other possible sources of smearing or resolution loss might be beam tilt or motion, camera misfocus or some source of scattering not simulated

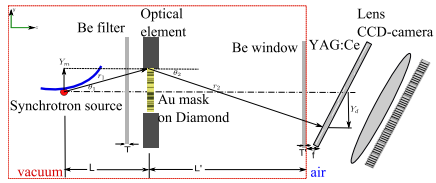

Figure 8: Schematic of XRM Beam Line. The beam passes through the Be filter, optical elements and Be window, and is then deposited in the 141 μm thick YAG scintillator.

by EGS5, such as impurities or inhomogeneities in the Be filters.

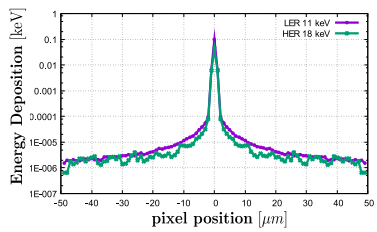

Figure 9: Deposited energy in YAG:Ce. The scattering range is <1 μm with a background/peak ratio of ≈ 10^{-4}.

CONCLUSION

We have presented some calibration studies during the Phase I of SuperKEKB commissioning. The geometrical magnification factors seem to be well understood for both LER and HER. The overall performance is reasonable for the LER, and yielded results consistent with expectations based on the optics estimation with ≈8 pm of vertical emittance (ϵ_y). For the HER, the vertical emittance ϵ_y is ≈41 pm which is 4× higher than the optics estimation. In addition, some smearing is observed, not all of which is fully accounted for yet. For our future plan, we plan to study possible sources of smearing either at the x-ray source point or in the beamline.

REFERENCES

[1] "SuperKEKB Design Report", https://kds.kek.jp/indico/event/15914/

[2] E.Mulyani, and J.W.Flanagan, *"Design of Coded Aperture Optical Elements for SuperKEKB X-ray Beam Size Monitors"*, in Proc. of IBIC2015, Melbourne, Sept 2015, TUPB025, pp. 377-380.

[3] N.Iida at al., *"Synchrotron Radiation Interferometer Calibration Check by Use of a Size Control Bump in KEKB"*, in Proc. of PAC07, Albuquerque, New Mexico, TUPAN042, pp. 1978-1480.

[4] H. Wiedemann, Particle Accelerator Physics I. Springer-Verlag Berlin Heidelberg, 2rd ed., 1999.

[5] A. Koch et al.,J. Opt. Soc. Am. A., Vol. 15, No. 7 pp. 1940-1951, July 1998.

[6] *The EGS5 Code System*, http://rcwww.kek.jp/research/egsegs5_manualslac730-130308.pdf

ISBN 978-3-95450-177-9

PREPARATORY WORK FOR A FLUORESCENCE BASED PROFILE MONITOR FOR AN ELECTRON LENS

S. Udrea†, P. Forck, GSI Helmholtzzentrum für Schwerionenforschung, Darmstadt, Germany
E. Barrios Diaz, O. R. Jones, P. Magagnin, G. Schneider, R. Veness, CERN, Geneva, Switzerland
V. Tzoganis, C. Welsch, H. Zhang, Cockcroft Institute, Warrington, United Kingdom

Abstract

A hollow electron lens system is presently under development as part of the collimation upgrade for the high luminosity upgrade of LHC. Moreover, at GSI an electron lens system also is proposed for space charge compensation in the SIS-18 synchrotron to decrease the tune spread and allow for the high intensities at the future FAIR facility. For effective operation, a very precise alignment is necessary between the ion beam and the low energy electron beam. For the e-lens at CERN a beam diagnostics setup based on an intersecting gas sheet and the observation of beam induced fluorescence (BIF) is under development within a collaboration between CERN, Cockcroft Institute and GSI. In this paper we give an account of recent preparatory work with the aim to find the optimum way of distinguishing between the signals due to the low energy electron beam and the relativistic proton beam.

BIF SETUP FOR TRANSVERSE DIAGNOSTICS

Electron lenses (e-lens) [1] have been proposed and used to mitigate several issues related to beam dynamics in high current synchrotrons. The e-lens system at CERN will be comparable to those used at FNAL and BNL. The main difference will be the use of a hollow electron beam.

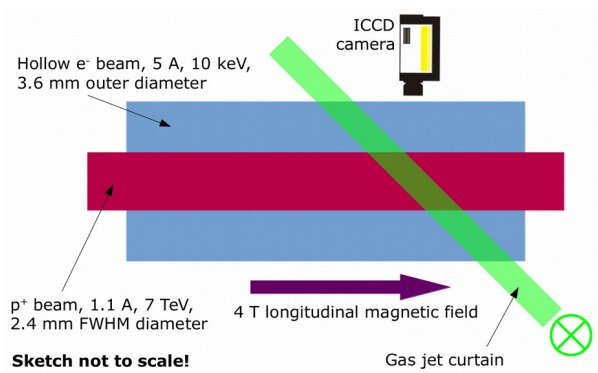

Figure 1: A schematic of the e-lens system planned at CERN for the collimation of the HL-LHC proton beam and the associated transverse beam diagnostics.

The parameters of the CERN e-lens are summarized in Fig. 1: the up to 1.1 A, 7 TeV, 2.4 mm FWHM diameter proton beam of the HL-LHC will be embedded in an up to 5 A, 10 keV hollow electron beam with an outer diameter of about 3.6 mm and an inner one of 2.4 mm. The interaction between the two beams takes place within an approximately 4 T longitudinal magnetic field, which stabilizes the electron beam. The proposed beam induced fluorescence (BIF) setup is composed of a perpendicular supersonic gas jet curtain [2] inclined such as to allow for the observation of the fluorescence radiation resulting from the interaction of the electron and proton beams with the gas molecules. To obtain an image of the transverse profiles of the beams a camera system with suitable optics is intended, which consists of an image intensifier made of micro channel plates (MCP) in chevron configuration and a CCD camera with appropriate optics.

RELEVANT FLUORESCENCE PROCESSES

From detection perspective the most appropriate gas to be employed in the supersonic gas jet curtain is nitrogen [3]. The main reasons are its high fluorescence efficiency and, based on present knowledge, it may allow distinguishing between the electron and the proton beam.

At wavelengths in the range 300–700 nm most of the fluorescence of N_2 molecules and N_2^+ molecular ions excited and ionized by protons or electrons results from two processes:

$$N_2 + p/e^- \rightarrow (N_2^+)^* + e^- + p/e^- \rightarrow N_2^+ + \gamma + e^- + p/e^- \quad (1)$$

$$N_2 + e^- \rightarrow (N_2)^* + e^- \rightarrow N_2 + \gamma + e^- \quad (2)$$

The first one is based on the electronic transition $B^2\Sigma_u^+ \rightarrow X^2\Sigma_g^+$ of the molecular ion with wavelengths around 391 nm (depending upon involved vibrational and rotational states) while the second process drives the electronic transition $C^3\Pi_u \rightarrow B^3\Pi_g$ of the neutral molecule with wavelengths around 337 nm. Moreover, the second process cannot be initiated directly by protons because it implies a spin flip mechanism. Thus one expects different photon intensities in the two spectral regions within the areas excited by the proton and ion beams, respectively.

CROSS–SECTIONS AND INTEGRATION TIMES

Proton Excitation

Data for fluorescence from N_2 at relativistic proton energies is provided in [4]. There it is shown that the change of the emission cross-sections with energy closely follows the proton's energy loss as described by a Bethe-Bloch-like expression. From this data one can extrapolate the cross-section at 7 TeV proton energy by the following expression:

$$\sigma_p = A_1 \cdot [(1+e^{-x}) \cdot (x + B_1) - 1] \quad (3)$$

with $A_1 = 1.789 \cdot 10^{-21}$ cm^2, $B_1 = 10.3$, $x = 2 \cdot \ln(p \cdot c / E_0)$, $E_0 = 0.938$ GeV – rest energy of the proton – and $p \cdot c$ the proton's momentum. At LHC maximum energy $p \cdot c \approx 7$ TeV resulting in $\sigma_p \approx 3.4 \cdot 10^{-20}$ cm^2, with a 70 % correction made for the main transition of the N_2 ion.

† email address s.udrea@gsi.de

ISBN 978-3-95450-177-9

Electron Excitation

Data about fluorescence cross-sections due to excitation/ionization through electrons can be obtained from [5]. In the case of radiation emitted by N_2 around 337 nm the cross-section drops for electron energies above a few tens of eV according to:

$$\sigma^{e}_{337} = A_2 \cdot E^{-2} \tag{4}$$

with $A_2 = 1.48 \cdot 10^{-15}$ cm^2·eV^2. Thus for 10 keV electrons one would expect $\sigma^{e}_{337} \approx 1.48 \cdot 10^{-23}$ cm^2.
The cross-section for light emission due to N_2^+ behaves at electron energies above 100 eV according to the Bethe–Oppenheimer approximation [6]:

$$\sigma^{e}_{391} = A_3 \cdot E^{-1} \cdot \ln(B_3 \cdot E) \tag{5}$$

with $A_3 = 1.66 \cdot 10^{-15}$ cm^2·eV and $B_3 = 2.4 \cdot 10^{-2}$ eV^{-1}. Hence at 10 keV one obtains $\sigma^{e}_{391} \approx 9.1 \cdot 10^{-19}$ cm^2.

Integration Times

We will take the following parameters into consideration for the estimation of the integration times needed to obtain a proper image of the interaction region between the charged particle beams and the gas jet curtain: a gas number density $n = 2.5 \cdot 10^{10}$ cm^{-3}, a curtain thickness $d = 0.5$ mm, $T = 0.65$ transmittance of the optical system including windows, a transmittance $T_f = 0.3$ of an optical filter within its transmission band, an acceptance solid angle $\Omega = 4\pi \cdot 10^{-5}$ sr, an efficiency η_{pc} of the MCP's photocathode of 20% and a detection efficiency η_{MCP} of the MCP of 50%. Since the integration time scales inverse proportionally with the (average) charged particle current, we will consider $I = 1$ A. Thus the average number of photons detected within a time Δt is given by:

$$N_\gamma = \sigma \cdot \frac{I \cdot \Delta t}{e} \cdot n \cdot d \cdot \frac{\Omega}{4\pi} \cdot T \cdot T_f \cdot \eta_{pc} \cdot \eta_{MCP} \tag{6}$$

With the assumed numerical values $N_\gamma \approx 1.5 \cdot 10^{21} \cdot \sigma \cdot \Delta t$, with $[\sigma] = \text{cm}^2$ and $[\Delta t] = \text{s}$. In case of proton excitation this results in an average time of 20 ms/photon, while for excitation through electrons this is 0.7 ms/photon. The average integration time corresponding to the emission due to the neutral molecule turns out to be prohibitively large: 45.5 s/photon.
BIF based beam diagnostics performed at GSI showed that a few hundred of photons are usually enough for obtaining well defined profiles. Thus one would expect that an integration time of up to about 10 s is needed to obtain an adequate signal from the proton beam, while a few hundred of milliseconds would be sufficient for detecting the electron beam.

Secondary Electrons

The analysis above considered just the primary beams. However, due to the strong longitudinal magnetic field low energy secondary electrons produced through ionization of the gas curtain and background gas molecules will be forced to gyrate around the magnetic field lines while also suffering a **E×B** drift on circular average trajectories around the beam axis. For the sake of simplicity we will neglect here the **E×B** drift.

Most of the secondary electrons produced by ionization due to relativistic protons have their momenta oriented almost perpendicular to the one of the projectile [7]. The energies of these electrons may exceed 100 eV, nonetheless most of them have energies below this value. As an example we consider a 30 eV electron in a homogeneous magnetic field and assume that just 0.1% of its energy is due to the longitudinal movement. This results in a time needed to pass through the gas curtain of about 5 ns during which the electron would actually travel over approximately 16 mm, due to its gyration movement. For the cross-section we consider the average between σ^{e}_{337} and σ^{e}_{391} at 30 eV, since according to [5] they are of the same order of magnitude. Hence its value is $\bar{\sigma}^{e} \approx 3.8 \cdot 10^{-18}$ cm^2.
Under these conditions secondary electrons have the potential to generate much more photons than the primary protons. Yet, to estimate the number of photons that would originate from these electrons, one has to evaluate the amount of secondary electrons passing the gas curtain per unit time. To this end the background gas has to be taken into consideration. The mean free path of secondary electrons at a pressure of about 10^{-8} mbar is of the order of 10 km along the magnetic field lines if one considers for instance the ionization cross-section of about 10^{-16} cm^2. Therefore they can reach the curtain, even if generated far away from it.
In a steady state situation, by neglecting any other contributions besides ionizations produced within the homogeneous field region, the electron flux through the ends of this region would amount the number of electrons generated inside it per unit time. For estimation purposes we consider just 1 m length and an ionization cross-section of about 10^{-18} cm^2 due to the protons [4]. Taking into account that approximately 50% of the electrons have their momenta towards the gas curtain the secondary electron current has a value of about $1.25 \cdot 10^{-8}$ A, far too low to allow for a significant contribution from these electrons, even with the increased cross-section and path travelled within the gas curtain.
The situation is similar in the case of fluorescence at 391 nm and secondary electrons generated by the main electron beam. However, the cross-section for the generation of radiation at 337 nm by electrons at few tens of eV is five orders of magnitude higher than the one of the primary electrons. In addition, by using the Bethe–Oppenheimer approximation for extrapolating the data in [5] the ionization cross-section for 10 keV electrons estimates to 10^{-17} cm^2, one order of magnitude higher than for 7 TeV protons. Finally, from the double differential cross section data published in [8] for 2 keV electrons, one may expect that secondary electrons are predominantly generated in forward direction. Thus, with proper placement of the gas curtain and an accumulation length larger than 1 m, the amount of radiation generated by secondary electrons may become of the same order of magnitude as the one due to the primary ones. If one succeeds to also increase Ω by a factor of 10 the specific integration time at 337 nm would drop to about 2.3 s/photon, for a primary current of 1 A. Besides, the integration time can be further reduced, if a higher

ISBN 978-3-95450-177-9

background gas pressure can be allowed and a reduction of the primary electron beam energy may be afforded.
Hence, one may conclude that making use of fluorescence arising from neutral nitrogen has to rely on secondary, low energy electrons.

THE OPTICAL SYSTEM

The optical system has to fulfil certain conditions, resulting from the experimental demands. It should have a large acceptance solid angle and high transmittance. When positioned at an angle with respect to the gas curtain, it should allow for a depth of field (DOF) of at least 5 mm, which would also ensure proper imaging if the beams are slightly displaced from the ideal position. Because of the small transversal sizes of the proton and electron beams and the relatively low resolution of the MCP detector of about 20 lp/mm, it should provide a magnification close to ±1. Finally, the field of view should have a diameter not below 15 mm.
Within the paraxial approximation, and considering a relatively small DOF the maximum diameter Φ_{max} of a spot at the detector corresponding to a point source in the image plane is related to the magnification β, the acceptance solid angle Ω and the DOF as follows:

$$\Phi_{max} = \frac{DOF}{\sqrt{\pi}} \cdot \sqrt{\Omega} \cdot |\beta| \qquad (7)$$

Thus one cannot increase acceptance and/or magnification without reducing the DOF, if the blur of the image is to be kept below a certain level.
Presently three types of systems which can be realized from off the shelf parts are under consideration:

- a single corrected triplet optimized for $\beta = -1$ and having a focal length of 200 mm
- three corrected triplets each optimized for $\beta = -1$ and having a focal length of 120 mm
- three corrected triplets, the first with a focal length of 100 mm and the other two both with a focal length of 50 mm

The first two systems have the advantage of a large acceptance solid angle of about $4\pi \cdot 10^{-4}$ sr at $\beta = \pm 1$ but are unflexible. The third system has a higher flexibility, but a lower acceptance of about $8\pi \cdot 10^{-5}$ sr and a magnification of 0.85. More detailed computations are ongoing to assess the residual geometric and chromatic aberrations and allow for a final decision.

PARTICLE DYNAMICS

As shown earlier in this article, most of the radiation is emitted by N_2^+. The corresponding excited states have a life time of about 60 ns [4]. During this time the ions move under the influence of the strong longitudinal magnetic field and the electric fields of the proton and electron beams. To study the movement of the ions under the given conditions a software got implemented based on the numerical tools provided by the numpy and scipy libraries [9].
The DC annular electron beam has a transversal profile which is flat between the inner radius and the outer one. The beam is considered to have only transversal components of the electric field. Its own magnetic field is also neglected.

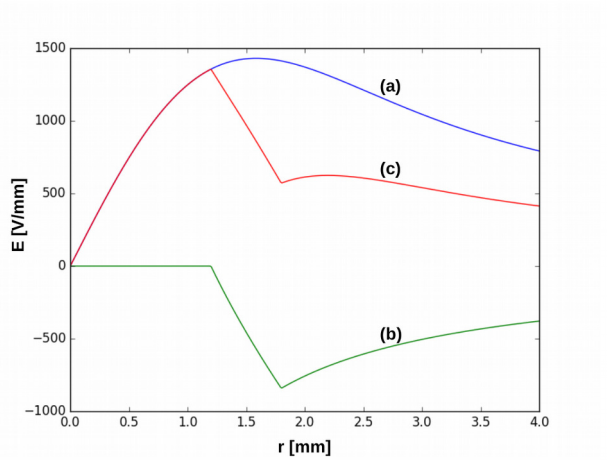

Figure 2: The transverse electric fields: (a) proton bunch at highest charge density, a total of $2.2 \cdot 10^{11}$ protons and 2.4 mm FWHM, (b) electron beam with a current of 5 A and 10 keV electrons, $\Phi_{in} = 2.4$, $\Phi_{out} = 3.6$ mm (c) superposition of the two fields.

The LHC beam is modelled as a train of bunches with a frequency of 40 MHz. Each bunch has a parabolic longitudinal profile with a total duration of 1 ns and a Gaussian transversal profile. Because of the very high proton energy, just the transversal component of the electric field is taken into consideration, while the beam's magnetic field is neglected, since it is much smaller than the external 4 T solenoid field. Fig. 2 shows the transverse electric fields and their superposition.

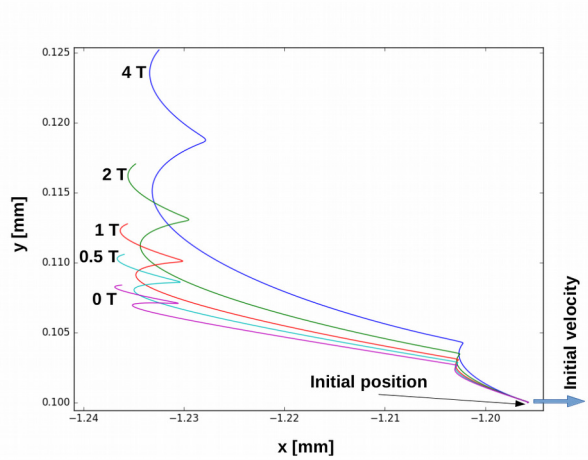

Figure 3: N_2^+ trajectories for different solenoid field strengths. The axis of the two beams is out of this image, at (0, 0). The tracking lasts for 60 ns and one can observe the effect due to proton bunches passing by. Beam parameters as for Fig. 2.

The influence of the solenoid magnetic field on the movement of an N_2^+ ion produced at the inner radius of the annular electron beam is illustrated in Fig. 3. The tracking time is 60 ns. The ion has an initial velocity of 1 km/s, close to typical values for gas jet curtains [10]. This velocity changes very quickly due to the high field intensities. The magnetic field induces a drift which makes the ion move further from the initial position than

ISBN 978-3-95450-177-9

in its absence. The maximum displacement is of a few tens of micrometers.

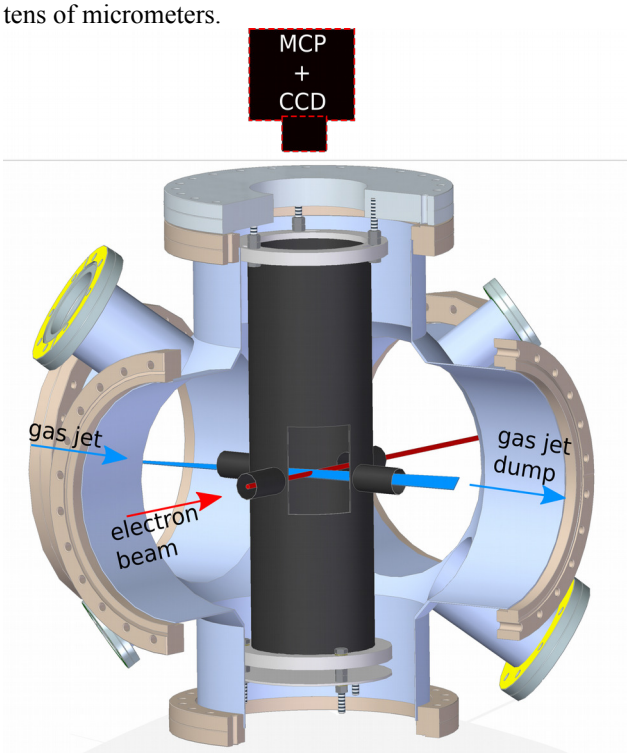

Figure 4: Schematic of the experimental setup at the Cockroft Institute. The blackened insertion chamber has five lateral openings, two pairs for the gas jet curtain and the electron beam respectively and one for introducing a scintillator.

EXPERIMENTAL TEST SETUP

An experimental test setup has been realized at the Cockroft Institute for first experiments to verify the predictions with respect to the photon yield and also investigate the possibility of using neon instead of nitrogen. The setup consists of a gas jet system [2, 10] capable to produce a curtain with a width of several millimetres, a sub-millimetre thickness and a particle density of about 10^{10} cm^{-3}, an electron gun delivering up to 10 µA and a maximum energy of 5 keV, an ICCD camera and a filter wheel with interference filters with a bandwidth of 10 nm and central wavelengths at 337, 391, 431 and 471 nm. Moreover a dedicated, blackened insertion chamber has been designed, constructed and installed in the main experimental chamber to reduce stray light. A schematic of the setup is shown in Fig. 4.
Commissioning of the setup showed that the main issue are the very long integration times needed due to the low electron beam current. This makes the proper relative alignment of the electron beam with respect to the gas jet very tedious. Measurements are planned for the fall 2016 after completion of the setup's adjustment.

CONCLUSIONS

Production rates and corresponding integration times for photons emitted by N_2 and N_2^+ at 337 and 391 nm respectively have been assessed based on available cross-section data and extrapolation formulas. It has been shown that most of the fluorescence signal is due to N_2^+ and that the primary electron beam at 10 keV leads to a much weaker emission from N_2. Hence the contribution of excitations by secondary, low energy electrons has been investigated, with the result that they may considerably increase the fluorescence signal at 337 nm.
Numerical tracking of N_2^+ ions in the relevant electric and magnetic fields showed that during the life time of the excited level and under the assumed initial conditions they do not move by more than about 40 µm from the position at which they got ionized. This distance is much smaller than the beam sizes involved and should only weakly affect the profile measurement.
An experimental test setup has been commissioned at the Cockroft Institute and is available for first experiments to check the theoretical predictions with respect to photon production rates.

ACKNOWLEDGEMENT

The authors would like to acknowledge fruitful discussions with D. Vilsmeier and M. Sapinski.

REFERENCES

[1] V. Shiltsev, V. Danilov, D. Finley, and A. Seryus, "Considerations on compensation of beam-beam effects in the Tevatron with electron beams", *Phys. Rev. ST Accel. Beams*, vol. 2, p. 071001, Jul. 1999.

[2] V. Tzoganis and C. P. Welsch, "A non-invasive beam profile monitor for charged particle beams", *Appl. Phys. Lett.*, vol. 104, p. 204104, May 2014.

[3] F. Becker, "Non-destructive Profile Measurement of intense Ion Beams", Ph.D. thesis, Phys. Dept., Technische Universität Darmstadt, Germany, 2009.

[4] M. A. Plum, E. Bravin, J. Bosser, and R. Maccaferri, "N_2 and Xe gas scintillation cross-section, spectrum, and lifetime measurements from 50 MeV to 25 GeV at the CERN PS and Booster", *Nucl. Instr. Meth. A*, vol. 492, pp. 74-90, 2002.

[5] Y. Itikawa, "Cross Sections for Electron Collisions with Nitrogen Molecules", *J. Phys. Chem. Ref. Data*, vol. 35, pp. 31-53, 2006.

[6] W. L. Borst and E. C. Zipf, "Cross Section for Electron-Impact Excitation of the (0,0) First Negative Band of N_2^+ from Threshold to 3 keV", *Phys. Rev. A*, vol. 1, pp. 834-840, Mar. 1970.

[7] A. B. Voitkiv, N. Gruen, and W. Scheid, "Hydrogen and helium ionization by relativistic projectiles in collisions with small momentum transfer", *J. Phys. B: At. Mol. Opt. Phys.*, vol. 32, pp. 3923-3937, 1999.

[8] R. R. Goruganthu, W. G. Wilson, and R. A. Bonham, "Secondary-electron-production cross sections for electron-impact ionization of molecular nitrogen", *Phys. Rev. A*, vol. 35, pp. 540-558, Jan. 1987.

[9] S. van der Walt, S. C. Colbert, and G. Varoquaux, "The NumPy Array: A Structure for Efficient Numerical Computation", *Comp. in Sci. & Eng.*, vol. 13, pp. 22-30, 2011.

[10] H. Zhang, V. Tzoganis, A. Jeff, A. Alexandrova, and C. P. Welsch, "Characterizing Supersonic Gas Jet-Based Beam Profile Monitors", in *Proc. IPAC'16*, Busan, Korea, May 2016, paper MOPMR046, pp. 357-360.

ISBN 978-3-95450-177-9

SPOT SIZE MEASUREMENTS IN THE ELI-NP COMPTON GAMMA SOURCE

F. Cioeta†, E. Chiadroni, A. Cianchi, G. Di Pirro, G. Franzini, L.Palumbo, V.Shpakov,
A. Stella, A.Variola, LNF-INFN, Frascati, Italy,
M. Marongiu, A. Mostacci, Sapienza University, Rome, Italy

Abstract

A high brightness electron Linac is being built in the Compton Gamma Source at the ELI Nuclear Physics facility in Romania. To achieve the design luminosity, a train of 32 bunches with a nominal charge of 250 pC and 16 ns spacing , will collide with the laser beam in the interaction point. Electron beam spot size is measured with an OTR (optical transition radiation) profile monitors. In order to measure the beam properties, the optical radiation detecting system must have the necessary accuracy and resolution. This paper deals with the studies of different optic configurations to achieve the magnification, resolution and accuracy desired considering design and technological constraints; we will compare several configurations of the optical detection line to justify the one chosen for the implementation in the Linac.

INTRODUCTION

The goal of this paper is the characterization of different lenses in terms of resolution and magnification for the optical diagnostics for the ELI-NP-GBS LINAC.

The optical diagnostics systems in ELI-NP-GBS will provide an interceptive method to measure beam spot size and beam position in different positions along the LINAC. In a typical monitor setup, the beam is imaged via OTR using standard lens optics, and the recorded intensity profile is a measure of the particle beam spot [1]. In conjunction with other accelerator components, it will also possible to perform various measurements on the beam, namely: its energy and energy spread (with a dipole or corrector magnet), bunch length (with a RF deflector) and the Twiss parameters (with quadrupoles).

The expected beam rms size along the Linac, provided by preliminary beam dynamics simulation, will vary in the 30μm - 1000μm range (as reported in Fig.1).

An evaluation has been done in order to find the best lenses setups and to find a compromise between resolution, magnification and costs for each position.

The optical acquisition system is constituted by a camera Basler scout A640-70 gm with a macro lens (see Fig.2). It has been seen, during the experimental tests, the macro lens is most suitable in order to obtain the requirements of high resolution and magnification. A movable slide is used to move the system between 60 cm and 130 cm of distance from target. These values represent the maximum and minimum distance between the camera sensor and the OTR.

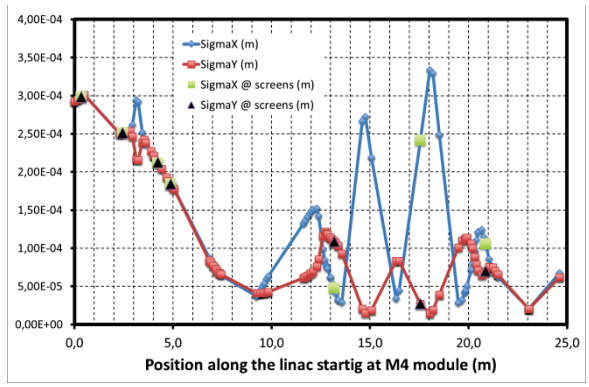

Figure 1: Spot size of the beam in the low energy line after S-band photoinjector.

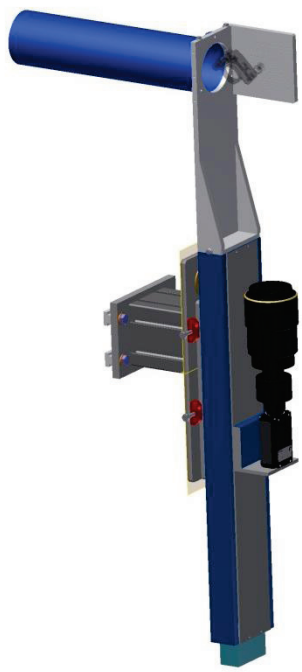

Figure 2: The ELI-GBS optic setup with a camera "Basler Scout A640 70 gm" and a macro lens mounted in a movable slide.

OPTICS CONFIGURATION

For each ELI-GBS diagnostics station the camera system can be regulated at a distance between 60 and 130 cm from the OTR. The reasons of these values are linked at mechanical and geometric constraints because the beam line is placed at 1.5 meters from the floor (see Fig.3).

† fara.cioeta@lnf.infn.it

ISBN 978-3-95450-177-9

Therefore, in order to avoid the possible damage of the optics devices due to the radiation emitted by the beam, each system must to be positioned at minimum 60 cm from the target and the maximum reachable distance to obtain the required magnification values is 130 cm from the target.

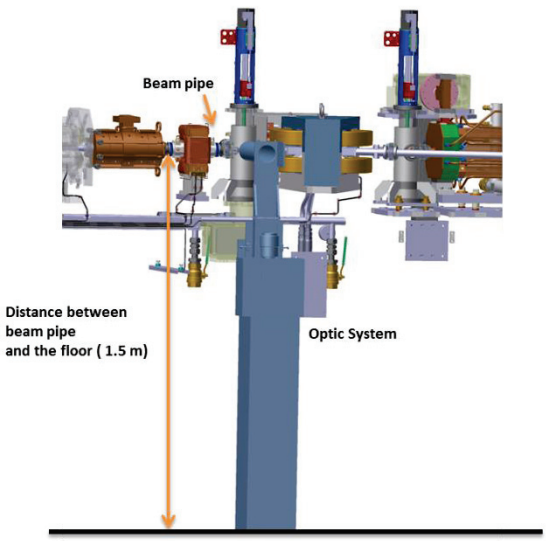

Figure 3: 3D model an optic system along the LINAC.

The maximum magnification (1:1) was tested and compared to the one indicated in the datasheet in order to validate the measure procedure.

The magnification and the resolution of the images at the minimum and the maximum distances (60 and 130 cm) for various lens setup have been measured. In order to do so, we used a “Thorlabs" Calibration target based on the “USAF 1951" target (see Fig. 4).

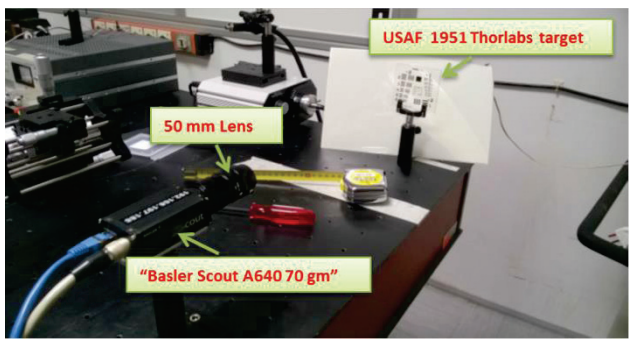

Figure 4: Test-bench with a 50mm microscope lens mounted on a Basler camera.

MAIN PARAMETERS

Resolution

The “USAF 1951” target allows to test the resolution of the optic setup. It consists of reference line patterns with well-defined thicknesses and spacings to be placed in the same plane as the object being imaged. By identifying the largest set of non-distinguishable lines, one determines the resolving power of a given system.

A pixel profiling procedure has been implemented by using a simple image software ("Pixel Profile"). We estimate the contrast value by evaluating the rate between the difference in intensity values of the pixels corresponding to the black lines and the one corresponding to the white spaces, and their sum; we consider the lines resolved if the contrast value is above 0.1. In the example of figures 5, the line series that respect the specification is the element 1 of the group 5: therefore, we have $x = 32$ and a resolution of $31\ \mu m$.

An equivalent method is instead based on the evaluation of the edge profile of a black rectangle in the calibration target: we can apply the Fourier transform to the lines spread function, which is the derivative of the edge profile [2]. The result is the so called Modulation Transfer Function (MTF) which is equivalent to the contrast function: therefore, if we take its abscissa when the MTF is equal to 0.1, we have the number of line pairs per millimeter; of course the resolution will be the inverse.

Moreover, the use of better camera with half of the resolution ($3.75\ \mu m px^{-1}$ instead of $7.4\ \mu m px^{-1}$) does not increase too much the overall resolution.

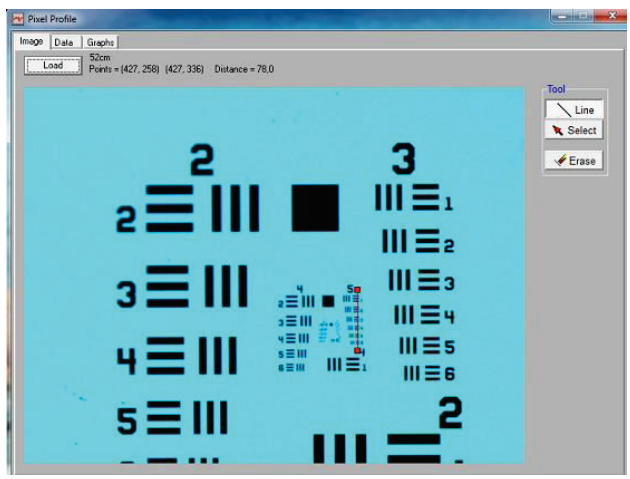

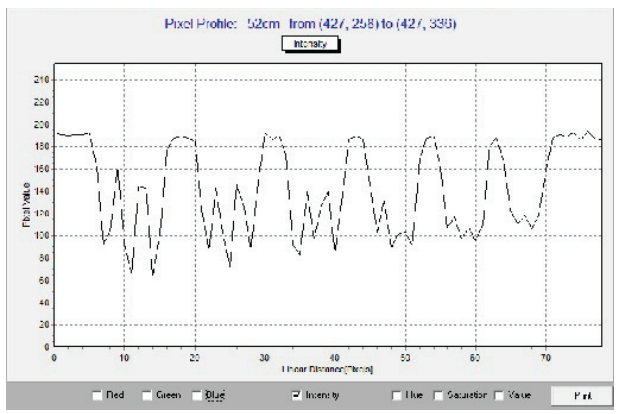

Figure 5: Screen-shots of “Pixel Profile" (“Image" (U) and “Graph" (D) screens): drawing a line on the image

ISBN 978-3-95450-177-9

produce the intensity graph and a table of all the pixels values.

Magnification

The USAF target is composed by group of lines of known size: if we define a parameter x given by $x = 2^{Group+(Element-1)/6}$ that represents the number of line pairs per millimeters, the resolution in millimeters can be calculated as is $1/x$; and the sizes of each line which are $L = \frac{2.5}{x}$ for the length, and $W = 1/2x$ for the width [3]. Making a line profiling from the images that we acquire (see Fig. 5), we can measure the size in pixels of the line (N) and, knowing the pixel size of the camera sensor (7.4x7.4 µm), the size of the line in the image plane. Therefore, the magnification is $M = \frac{L}{7.4N}$.

In ELI-NP GBS being the size of the beam variable the range of magnification required goes from 1: 1 to 1: 5.
The "USAF 1951" calibration target is useful for the study of the magnification as a function of the distance between the target and the sensor, and the focal length.

OPTICS MEASUREMENTS

Several lens with different focal lengths have been tested and for each commercial lens, at the same distance, the resolution and magnification have been calculated. Table 1 shows the kind of objectives tested and the two main parameters with relative field of view. The field of view is simply what the lens together with the camera can see from left to right and from top to bottom (see Fig.6).

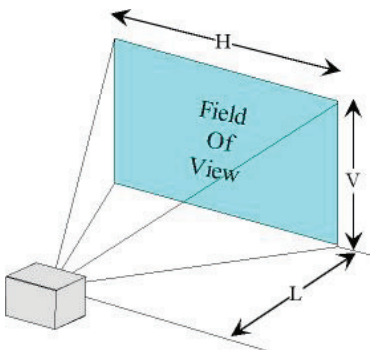

Figure 6: H is horizontal field of view from left to right and V is the vertical field of view from bottom to top.

This parameter depends on two factors: the focal length of the lens and the physical size of the camera sensor. Since it depends on sensor size it's not a fixed characteristic of a lens and it can only be defined if the size of the sensor that will be used is known. Therefore, once we know the magnification, we can evaluate the achievable field of view multiplying the resolution of the camera sensor (*659 px x 494 px*) with the magnification and the pixel size (*7.4 µm per px*). This parameter is very important in order to know how much of the screen target we can see and, therefore, to be sure to see the whole beam. Hence, if the beam is large, we need a high value of magnification in order to see a big portion of the screen target; however, if the field of view is too low, there might be the chance that we cannot see an off center beam. This is not the case of our machine, since the expected misalignment is well below the case of a beam outside the area seen by the camera, even in the case of the lower field of view achievable which is *5 mm x 4 mm*.

During the measurements, several optics configuration have been tested in order to evaluate a good magnification and resolution: camera with lens or camera with lens and tele-converter. The tele-converter allows us to obtain a macro lens comparable to a telephoto lens with the advantage in terms of cost, magnification and high resolutions. Thus using the tele-converter, we achieve the covered area is four times increased , the focal length is double but there is only one disadvantage in terms of aperture namely the fall of light is equal to two diaphragms. However, in our case this disadvantage is not a problem because the decrease of the luminosity is more evident for greater focal length. As we can see in the table 1 the best results are obtained with a *180 mm* lens with tele-converter (2x) that gave us the magnification of 1; also the *180 mm* lens with tele-converter (1.4x) gave us good results since it allows us to obtain the 1:5.

Table 1: Comparison Between Different Lens at 60 mm and 130 mm of Distance from the Target

Lens [mm]	Distance [cm]	Resolution [µm]	M	Field of View [mm]
50	60	223	8.33	40x30
105	60	88	4	21x16
	130	198	12	59x44
105 + tele-conv.2x	60	39	1.9	9x7
	130	111	5.5	27x20
180	60	44	2	10x7
	130	125	6	31x23
180+tele-conv. 2x	**60**	**31**	**1**	**5x4**
	130	**70**	**3**	**15x11**
180 + tele-conv.1.4x	60	321	1.3	6x5
	130	111	5	24x18

We also have tested a lens with variable focal length between *75 mm* and *200 mm* in order to estimate the chance to change the focus in function of the beam dimension along the LINAC supposing a greater versatility of the lens in several situations. We have supposed that a variable focus would have allowed to use the same objective along the LINAC but we saw with the test bench that the results, in terms of magnification and resolution, did not meet our expectations. Certainly is possible to achieve even better results with a *300 mm* lens: however, the *300 mm* lens cannot be used due to the limited dimension of the diagnostic station.

ISBN 978-3-95450-177-9

CONCLUSION

In general, the relation between the magnification and the distance is quasi-linear and the slope decreases with the focal length as it can be seen in Fig. 7. Therefore, the best solution in our case is shown by the black line. In this case we do not have the large possibility to change the magnification but, in function of the requirements of this accelerator, this lens is a valid device to study the characteristics of the beam.

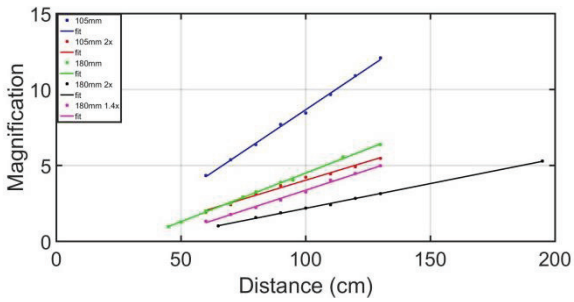

Figure 7: Magnitude as a function of the distance between camera sensor and the target for different lenses: it's clear that for bigger focal length we have a lower slope.

A camera system configuration has been selected considering the ratio between magnification, resolution (see red line Fig. 8) and the costs, consisting of a Basler Scout A640-70 gm camera equipped with *105 mm* lens while *180 mm* lens with tele-converter 2x will be used in the diagnostic stations collocated in the more critical points along the LINAC (see Tab. 2).

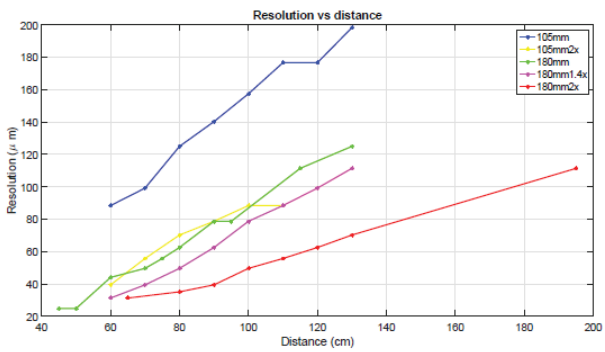

Figure 8: Resolution as a function of the distance between camera sensor and the target for different lenses.

Table 2: Optical System Proposed for ELI-NP-GBS in Order to Measure the Spot Size of the Beam

Station	Beam Size (um)		Solution proposed n.1
	X	Y	
LELDIASCN002 (energy measurements)	1000	1000	Camera Lens 105 mm+ tele-converter 2x
LELDIASCN003	500	500	Camera Lens 105 mm+ tele-converter 2x
LELDIASCN004	400	400	Camera Lens 105 mm+ tele-converter 2x
LELDIASCN005	280	280	Camera Lens 105 mm+ tele-converter 2x
LELDIASCN006	250	250	Camera Lens 105 mm+ tele-converter 2x
LELDIASCN007 (energy measurements)	180	180	Camera Lens 180 mm+tele-converter 2x
LELDIASCN008 (quad scan, long. measurements)	220	220	Camera Lens 180 mm+tele-converter 2x
LELDIASCN09	100	100	Camera Lens 105 mm+ tele-converter 2x
LETDIASCN01 (beam size under 0.1mm)	80	80	Camera Lens 180 mm+tele-converter 2x
LETDIASCN02 (beam size under 0.1mm)	27	27	Camera Lens 180 mm+tele-converter 2x
LEDDIASCN01 (beam size under 0.1mm)	65	65	Camera Lens 180 mm+tele-converter 2x
LEDDIASCN02	100	100	Camera Lens 105 mm+ tele-converter 2x

REFERENCES

[1] M. Marongiu *et al, "Design issues for the optical transition radiation screens for the ELI-NP Compton Gamma source"*, Nuclear Instruments and Methods in Physics Research (2016) 1–4.

[2] A. Variola, "*Utilisation du rayonnement optique pour l'etude des caracteristiques spatiotemporelles d'un faisceau d'electrons. Application a TTF*", Ph.D. dissertation, Universite de Paris-Sud, France, 1998.

[3] Thorlabs App Note: "*Resolution Test Targets*", https://www.thorlabs.com/newgrouppage9.cfm?objectgroup_id=4338

ISBN 978-3-95450-177-9

THERMAL SIMULATIONS FOR OPTICAL TRANSITION RADIATION SCREEN FOR ELI-NP COMPTON GAMMA SOURCE

F. Cioeta†, D. Alesini, A. Falone, V. Lollo, L. Pellegrino, A.Variola
LNF-INFN, Frascati, Italy,
M. Ciambrella, M. Marongiu, A. Mostacci, L. Palumbo, Sapienza University, Rome, Italy
V. Pettinacci, INFN-Roma, Rome, Italy

Abstract

The ELI-NP GBS (Extreme Light Infrastructure-Nuclear Physics Gamma Beam Source) is a high brightness electron LINAC that is being built in Romania. The goal for this facility is to provide high luminosity gamma beam through Compton Backscattering. A train of 32 bunches at 100Hz with a nominal charge of 250pC is accelerated up to 740 MeV. Two interaction points with an IR Laser beam produces the gamma beam at different energies. In order to measure the electron beam spot size and the beam properties along the train, the OTR screens must sustain the thermal and mechanical stress due to the energy deposited by the bunches. This paper is an ANSYS study of the issues due to the high quantity of energy transferred to the OTR screen. They will be shown different analysis, steady-state and thermal transient analysis, where the input loads will be the internal heat generation equivalent to the average power, deposited by the ELI-GBS beam in 512 ns, that is the train duration. Each analyses will be followed by the structural analysis to investigate the performance of the OTR material.

INTRODUCTION

The essential part of the Linac in the ELI-GBS is the beam diagnostics and instrumentation because allows to measure and to observe the spot size of the beam along the machine. In order to measure the beam profile the Aluminum or Silicon Optical Transition Radiation screen are used. The radiation is emitted when a charged particle beam crosses the boundary condition between two media with different optical properties and different dielectric constant. This radiation hits the screen for several cycles during the experiments; thus we want to study, with the finite element analysis (Ansys Code), the OTR material behaviour under thermal stress for 512 ns, train duration. After the thermal analysis the scope is to study the performance of the material through structural analysis in order to investigate the deformation and the equivalent stress for each pulse (of 32 bunches).

It will be demonstrate that the analysis is in agreement with the theoretical study where was evaluated the conduction cooling after the heating of a ELI-GBS beam train. In fact the screen cannot completely cool down in the time between two subsequent pulses; therefore, for each bunch there is an increase of temperature of 0.3° C for Al and 0.4° C for Si. As shown in Fig. 1, it can be seen that after 10 ms from the first pulse, the temperature is 295. 3K for the aluminum and 295. 4K for the silicon. However after few cycles, an equilibrium is reached and the cumulative temperature effect is negligible.[1]

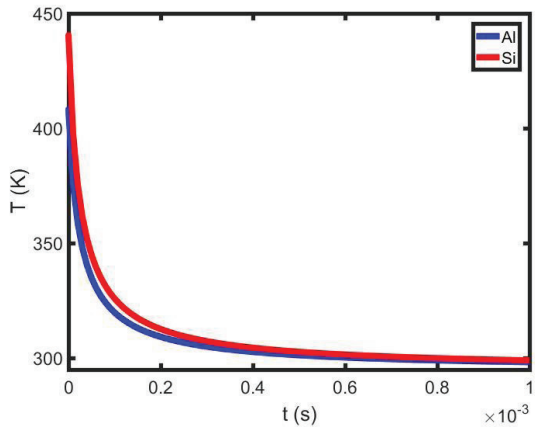

Figure 1: Temporal evolution of the conduction cooling after the heating of a ELI-GBS bunch train (σx =47.5 μm, σy =109 μm). The values refer to the center of the impact area of the beam to the target (x = 0, y = 0).

ANSYS ANALYSIS

The first step in creating geometry is to build a 3D solid model of the item we are analysing and define the material properties. The target has been modelled with 20x20x1 mm Aluminum plate and the worst case of the dimensions of the area hit by the beam are listed in Tab.1.

Table 1: Instantaneous Temperature Increase for an Impulse Train of 32 Bunches with a Charge of 250 pC Each. It Has Also Been Emphasized the Worst Case Scenario for the ELI-GBS

σ_x (σ_y)[μm]	ΔT^+ Al [K]	ΔT^+ Si [K]
298(298)	6	8
251(252)	9	12
211(213)	12	16
184(184)	17	21
47.5(109)	**109**	**141**
241(27.4)	85	110
106(70)	76	99

After the 3D model generation, the OTR has been meshed using hexagonal elements, with size decreasing from the border to the centre. This mapping is crucial to finely impose the energy releasing, concentrating elements only in the target volume that the beam hits. This model is suitable to carry out both steady-state and transient thermal analyses. The cooling mechanism considered is the only

† fara.cioeta@lnf.infn.it

ISBN 978-3-95450-177-9

conduction from the heated area to the screen flange; the temperature of the flange is independent from the temperature of the heated area and equal to the machine working temperature that corresponds to the room temperature in our case, 22°C: indeed, the site is located in an oversized conditioned environment to remove heat to an extent greater than that emitted by the accelerator. [2].

Assuming an electron beam with a Gaussian spatial distribution we did a steady state analysis because it represents, with a good approximation, the maximum value of temperature increase reaching the equilibrium after a certain amount of thermal stress cycles. Instead, with the thermal transient, it is possible to evaluate the temperature evolution for each pulse along the transient.

STEADY-STATE

Two steady-state thermal analyses, for two different materials Aluminum and Silicon, have been performed in order to determine temperature distributions caused by thermal loads not varying over time. Through the results of steady state is possible to perform a static structural analysis considering the physics properties of the material listed in the table below.

Table 2: Physics and Structural Properties of Aluminum and Silicon OTR [3]

Physics Properties	Symbol	Al	Si
Specific heat (J*kg-1*k^{-1})	c_p	900	700
Density) kg*m^{-3})	ϱ	2700	2330
Melting Temperature (K)	T_{melt}	933	1687
Emissivity	ε	0.18	0.67
Thermal Conductivity(W*m^{-1}*K^{-1})	k	205.5	143.5
Thermal Diffusivity (m^2*s^{-1})	α	8.5x10^{-5}	8.8x10^{-5}
Tensile Strength (MPa)	σ_{ten}	110	225
Coefficient Thermal liner expansion (K^{-1})	α	23.9x10^{-6}	2.5x10^{-6}
Young Moduls (GPa)	E_y	70	150

Aluminum Gaussian Distribution

The aluminum OTR profiles have as boundary condition the room temperature 22°C and a Gaussian distribution of the power released on the OTR screen as body load. The power is implemented trough a dedicated command APDL in Ansys, associating the correct Gaussian load to all the target nodes, including those belonging to the elliptic beam section.

The temperature increase calculated is about 14 °C respect to the initial temperature, (see Fig. 2). This result is due to at the thermal inertial of the material and its physics property.

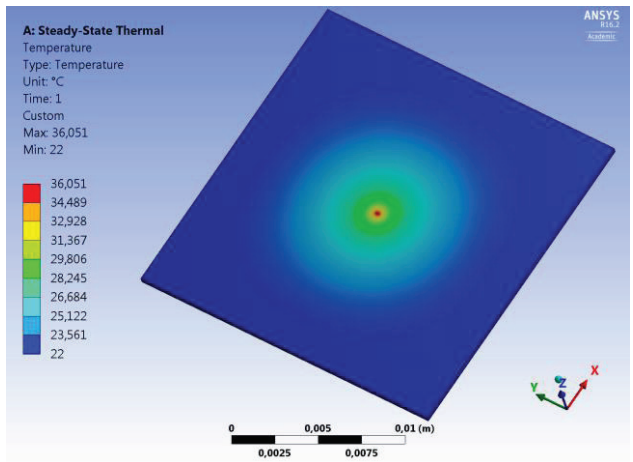

Figure 2: Temperature results at regime considering an Gaussian internal heat generation distribution in a little area 1mm thick and 47.5 µm,109 µm large. This dimension are the one expected during operation at the ELI-GBS in the worst case (Al bulk screen).

Structural Analysis

Using thermal results, output of the previous calculation, a coupled structural analysis has been carried out to evaluate the mechanical behavior of the OTR screen, in terms of deformation, equivalent stress (von Mises) and structural error. As expected the OTR shows a symmetric behavior and the total displacement is about 0.18 µm, with a maximum load of 13.8 MPa (see Fig.3).

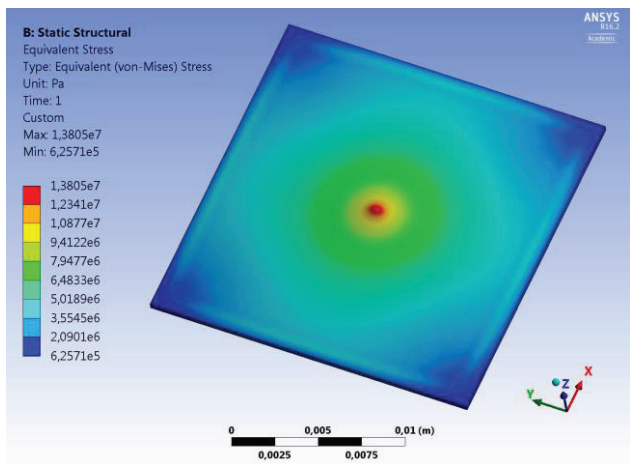

Figure 3: Von Mises equivalent Stress calculated for the Steady-State Aluminum structural analysis

The structural error confirmed the bias strategy used to define target meshing; the regions where the result can be affected by a computational error (due to for example at the size or shape of the mesh), are on the border and in any case by negligible values (see Fig.4).

ISBN 978-3-95450-177-9

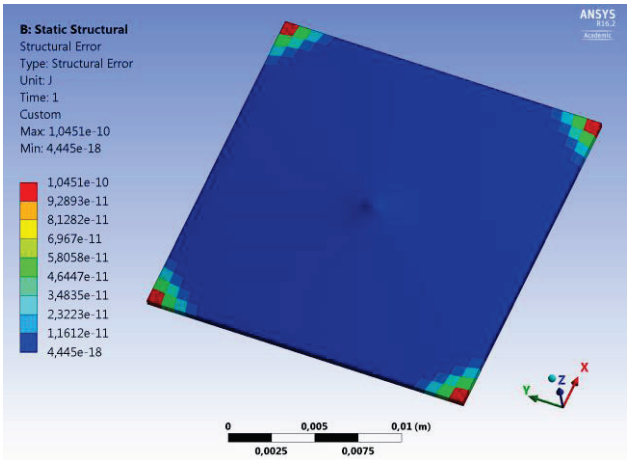

Figure 4: Thermal error for a structural static analysis considering an Gaussian internal heat generation distribution.

Silicon Gaussian Distribution

For the Silicon OTR, the same steady state analysis has been conducted, with the same boundary condition and the Gaussian power distribution. In this case the temperature increase calculated, respect to initial value (22° C) is 14.6°C. Hence, the two materials have a comparable thermal behaviour considering the similar final temperature. As expected, in terms of deformations, the silicon is more rigid than Aluminum (higher Young modulus): the deformation calculated is 0.020 μm with a correspondent equivalent stress by 3.25 MPa.

TRANSIENT ANALYSIS

In the ELI-NP-GBS the variation of temperature distribution over time is necessary to evaluate the temperature increase for each pulse and, then, to estimate the maximum stress reached by the target during each cycle.

Aluminum (Gaussian Distribution): Transient-Thermal

Given the same boundary conditions of the steady state, for this analysis the load is a Gaussian distribution power implemented through a dedicated script imposing an heat generation equivalent to the energy released on the OTR in 512 ns, by the first pulse of the hitting electron beam. The real time-stepping has been simulated, inside an overall analysis period by 10 ms, duration of each macro pulse (beam repetition rate is 100 Hz).

The maximum temperature achieved, after 512 ns, is 129,15 °C and the final temperature after the cooling is 22.5 °C, as depicted in Fig. 5. It's evident that OTR screen cannot completely cool down in the time between two subsequent pulses, and temperature increases by 0.5°C after first. With the previous steady-state analysis, imposing the average power, it has been verified that temperature increase reaches the equilibrium.

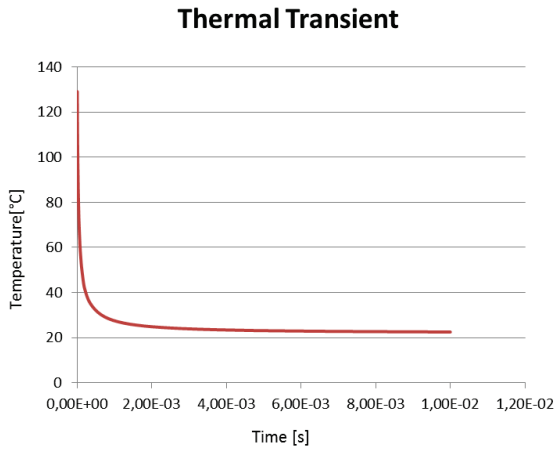

Figure 5: Thermal Transient behavior of Aluminum OTR in ELI-GBS. The temperature curve tends to constant value after 10 ms before the second impulse.

Aluminum (Gaussian Distribution): Transient-Structural

For the first beam pulse simulated, the maximum displacement calculated is about 10 nm, in function of a maximum equivalent stress by 1.4 MPa (see Fig. 6).

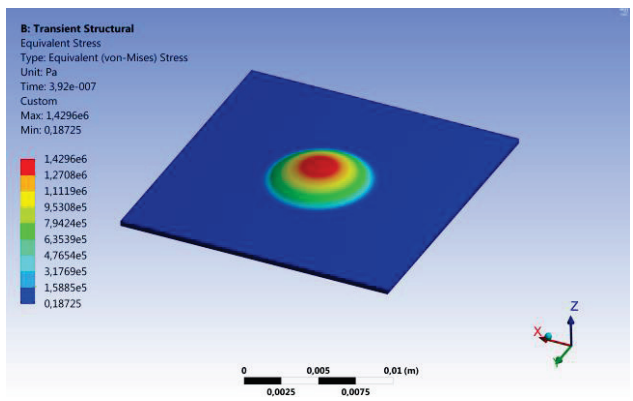

Figure 6: Stress equivalent evolution of Aluminum for one bunch train after 512 ns in the ELI-NP-GBS worst case.

Silicon (Gaussian Distribution): Transient-Thermal

In this case when the beam hits the target, the temperature increases until 159°C and also in this analysis the OTR cool down until 22.4°C. We expected this result because in agreement with the theoretical study.

Silicon (Gaussian Distribution): Transient-Structural

Also in this simulation, for the first beam pulse, the maximum displacement calculated is about 1.07 nm, in function of a maximum equivalent stress by 0.45 MPa (see Fig. 7).

ISBN 978-3-95450-177-9

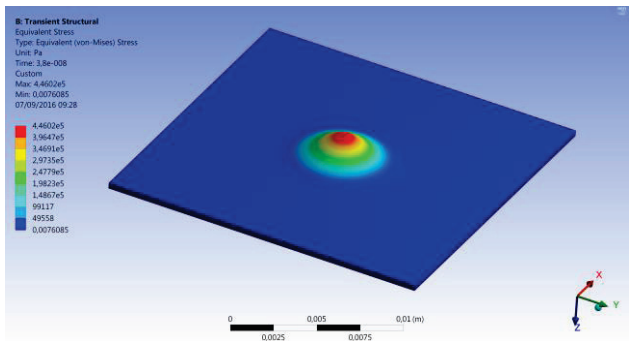

Figure 7: Von Mises equivalent Stress calculated for the transient Structural analysis (made by Silicon, for one bunch train after 512 ns in the ELI-NP-GBS worst case).

CONCLUSION

This paper compares thermal an mechanical results for Silicon and Aluminum OTR screens, performing both steady-state and transient analyses to simulate the energy releasing effects of the ELI-NP-GBS electron beam in the target interaction. The Silicon is the material chosen for the OTR, transient analysis shows a better thermo-mechanical behavior for a single cycle (see Table 3).

Table 3: Maximum Values of Deformation and Equivalent Stress (Von Mises) for the Both Materials Analysed

Material	Maximum Deformation [nm]	Maximum Von Mises [MPa]
Aluminum	10	1.4
Silicon	**1.07**	**0.45**

The next step of the FEM study will be an optimization of the time-stepping imposed in the transient, in order to reduce the necessary computational time and memory to simulate a number of cycles up to the equilibrium. The consequent resulting stress will be used to evaluate the fatigue life of the OTR. Then the final step will be the implementation of all brackets and mechanical support components of the OTR, evaluating the whole system dissipation. The expected result of the last analysis is to confirm that the additional mechanical sup-ports and brackets do not induce further thermal dissipation and hence they do not degrade the thermal-mechanical features of the whole OTR system.

REFERENCES

[1] M. Marongiu *et al,* "Design issues for the optical transition radiation screens for the ELI-NP Compton Gamma source", *Nuclear Instruments and Methods in Physics Research* pp. 1–4 (2016).

[2] V. Balandin and N. Golubeva, "Survival and thermal heating of materials for the OTR screens at the TTF2", 2001, unpublished.

[3] Material parameters taken by: http://www.matweb.com/

ISBN 978-3-95450-177-9

PERFORMANCE STUDIES OF INDUSTRIAL CCD CAMERAS BASED ON SIGNAL–TO–NOISE AND PHOTON TRANSFER MEASUREMENTS

G. Kube, DESY, Hamburg, Germany

Abstract

Area scan sensors are widely used for beam profile measurements in particle beam diagnostics. They provide the full two–dimensional information about the beam distribution, allowing in principle to investigate shot–to–shot profile fluctuations at moderate repetition rates. In order to study the performance and to characterize these cameras, photon transfer is a widely applied popular and valuable testing methodology. In this report, studies based on signal–to–noise and photon transfer measurements are presented for CCD cameras which are in use for beam profile diagnostics at different DESY accelerators.

INTRODUCTION

Area scan CCD or CMOS sensors are widely used in beam diagnostics because they provide the full two–dimensional information about the transverse particle beam distribution. For this purpose the information about the particle beam charge distribution is converted in an optical intensity distribution which is recorded by the area scan detector. This light distribution can either be generated in an interaction of the particle beam with material, resulting in atomic excitations which are followed by radiative relaxations (e.g. in scintillating screen or beam induced fluorescence monitors [1, 2]). Alternatively, light extracted from the electromagnetic fields accompanying an ultra–relativistic particle beam can be utilized as it is the case e.g. for synchrotron, transition or diffraction radiation based monitors [3].

For high resolution beam profile measurements, care has to be taken that any resolution broadening introduced by the basic underlying physical process and/or the optical system has to be small. In addition, the conversion process from the charged particle distribution in digital numbers in the data acquisition system has to be linear to avoid any misinterpretation of measured beam sizes and shapes. The linearity may be distorted either by the generation of the photon intensity distribution (e.g. by saturation effects in scintillators or microbunching instabilities in high–brightness electron beams [4]), or in the conversion from a photon distribution into a set of digital numbers in the camera.

The objective of the present study is to focus on the last aspect and to characterize the quality of area scan cameras which are in use for beam profile diagnostics. While there is no principal difference in the characterization between CCD and CMOS sensors, in the following only industrial CCD cameras are considered which are in use at different DESY accelerators. The sensor characterization is based on the Photon Transfer (PT) method which is a valuable methodology employed for solid state imager and camera system investigations. In the next section the PT basic principle is introduced and it is demonstrated how sensor parameters can be derived from Signal-to-Noise Ratio (SNR) measurements. Afterwards, the laboratory setup together with CCD performance measurements is presented.

PRINCIPLE OF CHARACTERIZATION

PT is widely used for image sensor testing because it is a straightforward method to determine numerous sensor parameters by analyzing only two measured quantities, average signal and rms noise. Detailed information about PT can be found in textbooks (e.g. Ref. [5]), and the European Machine Vision Association even derived the EMVA Standard 1288 according to this method [6]. Following this standard a brief introduction in the underlying mathematical model is given in this section. According to Ref. [6] this model is valid if (i) the amount of photons collected by a pixel depends on the radiative energy density, (ii) noise sources are stationary and white, (iii) only the total quantum efficiency is wavelength dependent, (iv) only the dark current depends on temperature, and (v) the sensor is linear, i.e. the digital signal y increases linear with the number of photons received. It is interesting to point out that the latter condition imposes a lower limit on the applicable wavelength region because the quantum yield in silicon is larger than one for photon wavelengths smaller than 400 nm [7].

As illustrated in Fig.1(a), the digital image sensor converts photons impinging on the pixel area in a series of steps into a

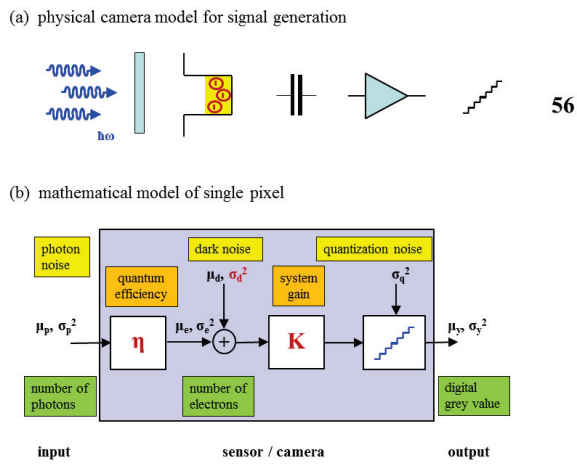

Figure 1: (a) Physical camera model: a number of photons hitting a sensor pixel creates a number of electrons via the photoelectric effect. The resulting charge is converted by a capacitor to a voltage, then amplified and digitized. As result a digital grey value is generated. (b) Mathematical model of a single pixel.

ISBN 978-3-95450-177-9

digital number. The number of incoming photons n_p follows a Poisson distribution, due to their statistical fluctuations it is suitable to characterize the process by the mean number of incoming photons μ_p with corresponding variance $\sigma_p^2 = \mu_p$. A fraction of the incoming photons is absorbed and generates photo electrons in the CCD pixel with μ_e the mean number of accumulated charges. A Poisson random process (photon emission with mean μ_p) that is thinned by binomial selection with success probability (quantum efficiency) η is again following a Poisson distribution with mean $\mu_e = \eta\mu_p$ and variance $\sigma_e^2 = \mu_e$, which can be rewritten as $\sigma_e = \sqrt{\eta}\sigma_p$.

In the camera electronics, the accumulated charge is converted into a voltage, amplified and finally transformed to a digital number y, assuming each of these processes to be linear. In the mathematical model shown in Fig.1(b) the individual processes are summarized in a single quantity, the overall system gain K with units Digital Number (DN) per electrons. With μ_d the mean dark electrons, the mean digital signal or grey value μ_y can be written as

$$\mu_y = K(\mu_e + \mu_d) = K\eta\mu_p + \mu_{y,dark} \ . \qquad (1)$$

Here $\mu_{y,dark}$ indicates the mean dark signal $K\mu_d$.

A similar consideration can be performed for the temporal noise which is characterized by its corresponding variance σ_i^2, where i stands for an arbitrary noise source. The variance of the fluctuations of the accumulated charges σ_e^2 is often referred as shot noise, all other noise sources depend on the specific sensor and camera electronic layout and their variances add up in a linear way due to the linear signal model. Treating the whole camera as a black box as it is indicated in Fig.1(b), it is sufficient to consider only two additional noise sources [6]: the ones related to sensor read out and amplifier circuits, described by a signal independent normal distributed source with variance σ_d^2, and the final analog-to-digital conversion which is distributed uniformly between the quantization intervals and has a variance $\sigma_q^2 = 1/12\,\mathrm{DN}^2$. According to the laws of error propagation, the total variance σ_y^2 of the digital signal y is given by

$$\sigma_y^2 = K^2(\sigma_d^2 + \sigma_e^2) + \sigma_q^2 \ , \qquad (2)$$

which can be rewritten as

$$\sigma_y^2 = K(\mu_y - \mu_{y,dark}) + \sigma_{y,dark}^2 \qquad (3)$$

using Eq. (1) and $\sigma_{y,dark} = K\sigma_y$. Furthermore it is assumed that the contribution of the quantization noise is negligible compared to the dark noise.

Eqn. (1) and (3) are fundamental for the sensor characterization because they represent linear relations for experimentally accessible parameters. According to Eq. (1), a measurement of the mean grey value as function of the mean number of incoming photons delivers ($K\eta$) as slope and $\mu_{y,dark}$ as offset. A measurement of the variance of the grey values as function of the background corrected mean grey value results in K as slope and $\sigma_{y,dark}^2$ as offset according to Eq. (3). As consequence, a number of relevant sensor parameters is accessible from these measurements.

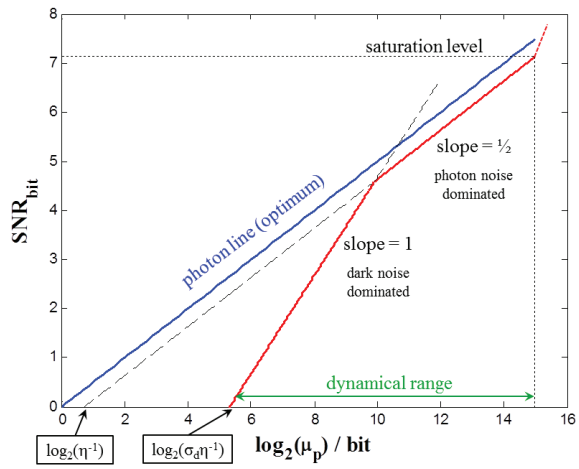

Figure 2: SNR as function of the incoming number of photons for an ideal (blue) and a real (red) sensor. More details see text.

Signal-to-Noise Ratio The quality of a detector signal is usually expressed by the Signal–to–Noise Ratio (SNR), defined by $\mathrm{SNR} = (\mu_y - \mu_{y,\mathrm{dark}})/\sigma_y$. Using Eqn. (1), (3) and taking the base 2 logarithm $\log_2(\mathrm{SNR}) = \mathrm{SNR_{bit}}$, SNR can be rewritten as

$$\mathrm{SNR_{bit}} = \log_2(\eta) + \log_2(\mu_\mathrm{p}) - \tfrac{1}{2}\log_2(\eta\mu_\mathrm{p} + \sigma_\mathrm{d}^2) \ . \qquad (4)$$

It is interesting to consider the case of an ideal sensor with quantum efficiency $\eta = 1$ and no noise, i.e. $\sigma_d = 0$. In this situation $\mathrm{SNR_{bit}} = 1/2\log_2(\mu_\mathrm{p})$ or $\mathrm{SNR} = \sqrt{\mu_p}$, i.e. SNR represents the pure photon shot noise. It is obvious that a real sensor cannot be better than an ideal sensor. As consequence, in the SNR diagram in Fig.(2) the curve of a real sensor is always below the photon line. Moreover, two limiting cases can be considered:

shot noise dominated: $\eta\mu_p \gg \sigma_d^2$. For high photon intensities the SNR relation Eq. (4) can simply be written as

$$\mathrm{SNR_{bit}} = \tfrac{1}{2}\log_2(\mu_\mathrm{p}) + \tfrac{1}{2}\log_2(\eta) \ . \qquad (5)$$

As shown in Fig.(2), in this region the SNR yields a straight line with slope $\frac{1}{2}$ which crosses the x–axis in the point $\log_2(\eta)$, i.e. the minimum detectable number of photons (SNR = 1:1) amounts to η^{-1}, assuming the sensor would have a pure shot noise characteristics.

dark noise dominated: $\eta\mu_p \ll \sigma_d^2$. Unfortunately a real sensor is also affected by the dark noise. For very low photon intensities the SNR relation is transformed into

$$\mathrm{SNR_{bit}} = \log_2(\mu_\mathrm{p}) + \log_2(\eta\sigma_\mathrm{d}^{-1}) \ . \qquad (6)$$

If the dark noise dominates the SNR yields a straight line with slope 1, crossing the x–axis in the point $\log_2(\eta\sigma_d^{-1})$. As consequence, the minimum detectable signal (SNR = 1:1) of the real sensor amounts to $\sigma_d\eta^{-1}$.

If the photon intensity is further increased, saturation occurs at a saturation irradiation $\mu_{p,sat}$ which corresponds to

ISBN 978-3-95450-177-9

a saturation capacity $\mu_{e,sat} = \eta\mu_{p,sat}$. For a k-bit digital camera, the digital values will then be clipped to the maximum digital grey value $2^k - 1$. According to Ref. [6] the saturation capacity must not be confused with the full–well capacity, it is normally lower because the signal is clipped to the maximum digital value before the physical pixel saturation is reached. As consequence of the signal clipping, the variance σ_y^2 decreases and SNR_{bit} steeply increases. From the minimum detectable signal and the saturation irradiation the dynamical range of the sensor can be deduced as indicated in Fig.(2).

Therefore, also the analysis of the SNR diagram gives access to a number of important sensor parameters. In the next section, the laboratory setup for the camera characterization together with the measurement procedure will shortly be described.

SETUP AND MEASUREMENT

The camera is mounted together with a flat field illumination onto an optical bench in the laboratory, the distance between both is about 720 mm. The camera is operated without objective lens, no obstacles like diffusors or apertures are placed in the light path such that the homogeneity of the illumination is determined directly by the light source itself. During operation, the whole setup is covered with a light shielding in order to avoid stray light contributions.

As light source a flatfield LED illumination (CCS TH-100/100) with peak wavelength $\lambda_p = 470$ nm is used which has a rather good surface homogeneity with variations in the order of about 5% in the central part. However, in order to resolve individual noise contributions as the sensor fixed patter noise, a homogeneity of better than 1% would be required [5]. The light source irradiance was calibrated with a cw powermeter (Ophir Nova II with PD300-UV detector head), and with knowledge of the CCD exposure time t_{exp} and the pixel area the irradiance can be converted in a number of incoming photons μ_p.

For the measurement of a PT resp. an SNR sequence μ_p has to be varied. This was realized by operating the light source with fixed irradiance and changing t_{exp}. Advantage of this method is that the light source is kept in thermal balance, disadvantage is that for each exposure time a background image for the determination of $\mu_{y,dark}$ has additionally to be taken, because the number of thermally induced electrons contributing to the dark signal linearly depends on t_{exp} [6]. CCD readout was performed based on the TINE AVINE video system [8, 9].

In order to have sufficient statistical significance in the measurements, for each t_{exp} a series of 10 images was recorded and the determination of mean μ_y and total variance σ_y^2 of the digital signal was performed in a selected ROI of 50×50 pixel.

ANALYSIS

The measurements were performed for three camera types which are in operation at DESY: (i) Basler Aviator avA1600-50gm in used at the PETRA III accelerator, (ii) JAI BM-141GE in use at PETRA III, REGAE and PITZ, and (iii) Sony XCG-H280E in use at REGAE. In the following, data are shown only for camera (i). For the remaining cameras, only the derived parameters will be quoted.

Fig.3 shows PT measurements derived for the Basler Aviator avA1600-50gm. Fitting the responsitivity curve (a) in a range between minimum intensity and 70% of saturation capacity with a straight line following the recommendation in Ref. [6] results in a slope 0.0802 which corresponds to $K\eta$ according to Eq. (1). Repeating the procedure for the PT curve (b) results in a slope $K = 0.1793$ DN/e$^-$ and an offset of $\sigma^2_{y,dark} = 5.093$ DN^2 according to Eq. (3).

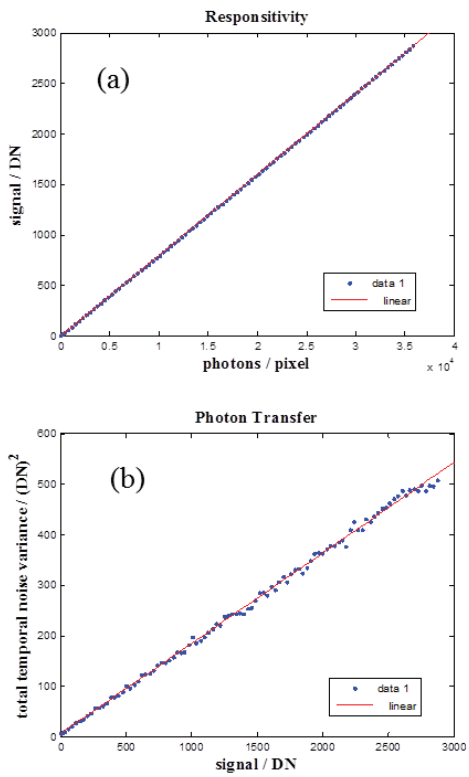

Figure 3: PT curves for the Basler Aviator avA1600-50gm. (a) Responsitivity curve according to Eq. (1). (b) PT curve according to Eq. (3). Both curves were fitted with a straight line in a region between minimum intensity and 70% of saturation capacity [6].

In Table 1 the parameters are summarized after combination (column 2) and compared to the the EMVA data sheet (column 4) [10]. Instead of using the overall system gain K the reciprocal parameter is often quoted as indicated in the table. Furthermore, the noise is expressed in units of e$^-$ instead of DN which can simply be converted by multiplication with K^{-1}. As one can see from this comparison, the measurement is in satisfactory agreement with the data sheet parameters. Nevertheless there is a larger discrepancy in K^{-1}. The measurement was repeated with different cameras of this type and this discrepancy could be reproduced in each

ISBN 978-3-95450-177-9

Table 1: Quantum efficiency η, inverse system gain K^{-1}, and temporal dark noise σ_d, as derived from the PT diagrams (column 2), the SNR analysis (column 3) and taken from the data sheet (column 4). The error in η is estimated to be in the order of 5%, in K^{-1} in the order of 7% and of σ_d in the order of 2%.

item	PT	SNR	data sheet
η	45%	40%	40%
K^{-1}	5.6 e$^-$/DN	-	4.8 e$^-$/DN
σ_d	12.6 e$^-$	12.2 e$^-$	11 e$^-$

measurement. Therefore there is a suspicious that the gain in the data sheet is not quoted correctly.

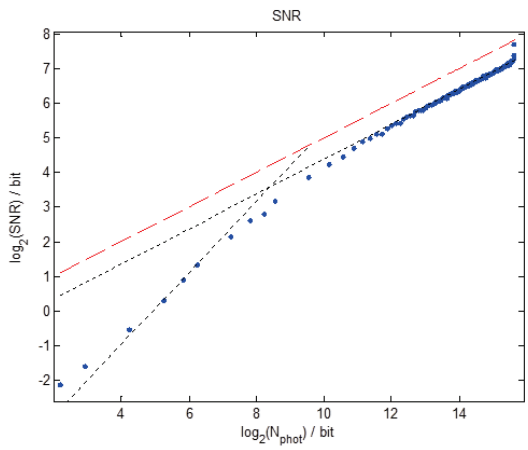

Figure 4: SNR diagram. The photon line is indicated by the red dashed line, the slope 1 and slope $\frac{1}{2}$ interpolations by the black dashed lines.

Fig.4 shows she same data set plotted as SNR diagram. From the intersection points of the slope 1 and slope $\frac{1}{2}$ interpolations, the quantum efficiency and the temporal dark noise σ_d can be deduced. Both parameters which are shown in column 3 of Tab.1 are in good agreement with the PT measurements and the data sheet.

In addition, from the steep increase in the SNR diagram at about 15.52 bit the saturation irradiance can be derived to $\mu_{p,sat} = 2^{15.52} = 46988$ which corresponds to a saturation capacity of $\mu_{e,sat} = 18800e^{-1}$. This value is in excellent agreement with the one from the data sheet [10]. Furthermore, with knowledge of the saturation irradiance and the minimum detectable signal $\mu_{p,min} = \sigma_d/\eta = 30.6$, the dynamical range can be deduced according to $DR = \mu_{p,max}/\mu_{p,min} = 1535$, corresponding to $DR = 10.6$ bit and compared to 10.7 bit as quoted in the data sheet.

SUMMARY

In this report, a method to derive camera sensor parameters independently of manufacturer data sheets is presented which is based on the analysis of PT and SNR diagrams according to Refs. [5, 6]. It is very helpful because not every manufacturer will provide all relevant sensor parameters which are accessible via these measurements. By application of this method it is possible to compare the camera performance based on a standard set of parameters.

It was shown that the measured parameters of a Basler Aviator avA1600-50gm are in good agreement with the ones from the camera data sheet. The analysis was repeated not only for one but for more cameras of this model type, showing a very good agreement. Moreover, different camera types were under investigation and the results are summarized in Table 2. The Sony XCG-H280E for example shows a very high quantum efficiency and dark noise for high sensitivity applications, but also a rather low saturation capacity with acceptable dynamical range. The JAI BM-141GE at the other hand has also a very high η, but with higher noise and better $\mu_{e,sat}$. Depending on the dedicated application, with the knowledge of the relevant sensor parameters a purposeful camera selection can therefore be performed.

Table 2: Parameter Comparison for Different CCDs

item	Basler	JAI	Sony
η	42.5%	60%	58%
K^{-1}	5.6 e$^-$/DN	4.1 e$^-$/DN	2.0 e$^-$/DN
σ_d	12.4 e$^-$	15.3 e$^-$	8.8 e$^-$
$\mu_{e,sat}$	18800 e$^-$	16080 e$^-$	6540 e$^-$
DR	10.6 bit	9.3 bit	9.6 bit

ACKNOWLEDGMENT

The author thanks S. Weisse (DESY Zeuthen) for providing the TINE AVINE video server, and H. Delsim–Hashemi (DESY) for making available the access to the JAI and Sony cameras.

REFERENCES

[1] B. Walasek–Höhne and G. Kube, Proc. DIPAC'11, Hamburg, Germany, May 2011, WEOB01, p.553 (2011).
[2] P. Forck, Proc. IPAC'10, Kyoto, Japan, May 2010, TUZMH01, p.1261 (2010).
[3] G. Kube, Proc. IBIC'14, Monterey (CA), USA, September 2014, TUIZB1, p.263 (2014).
[4] S. Wesch and B. Schmidt, Proc. DIPAC'11, Hamburg, Germany, May 2011, WEOA01, p.539 (2011).
[5] J.R. Janesick, *Photon Transfer*, (SPIE Press, Bellingham, Washington USA 2007).
[6] EMVA Standard 1288, Release 3.1, Release Candidate (2012): `www.emva.org`
[7] F.J. Wilkinson *et al.*, J. Appl. Phys. **54** (1983) 1172.
[8] S. Weisse *et al.*, Proc. ICALEPCS'09, Kobe, Japan, October 2009, MOD003, p.34 (2009).
[9] S. Weisse *et al.*, Proc. ICALEPCS'11, Grenoble, France, October 2011, MOPMS033, p.405 (2011).
[10] Basler AG – Industrial Camera Manufacturer, `www.baslerweb.com`

ISBN 978-3-95450-177-9

EXPERIMENTAL RESULTS OF A COMPACT LASERWIRE SYSTEM FOR NON-INVASIVE H⁻ BEAM PROFILE MEASUREMENTS AT CERN'S LINAC4

S. M. Gibson*, G. E. Boorman, A. Bosco, Royal Holloway, University of London, UK
T. Hofmann[1], U. Raich, F. Roncarolo, CERN, Geneva, Switzerland
[1] also at Royal Holloway, University of London, UK

Abstract

A non-invasive laserwire system is being developed for quasi-continuous monitoring of the transverse profile and emittance of the final 160 MeV beam at CERN's LINAC4. As part of these developments, a compact laser-based profile monitor was recently tested during LINAC4 commissioning at beam energies of 50 MeV, 80 MeV and 107 MeV. A laser with a tunable pulse width (1-300 ns) and ~200 W peak power in a surface hutch delivers light via a 75 m LMA transport fibre to the accelerator. Automated scanning optics deliver a free space < 150 micron width laserwire to the interaction chamber, where a transverse slice of the hydrogen ion beam is neutralised via photo-detachment. The liberated electrons are deflected by a low field dipole and captured by a sCVD diamond detector, that can be scanned in synchronisation with the laserwire position. The laserwire profile of the LINAC4 beam has been measured at all commissioning energies and is found in very good agreement with interpolated profiles from conventional SEM-grid and wire scanner measurements, positioned up and downstream of the laserwire setup. Improvements based on these prototype tests for the design of the final system are presented.

MOTIVATION

Non-invasive Beam Diagnostics at LINAC4

Conventional beam diagnostics such as SEM-grids and wire scanners inherently obstruct a significant fraction of the particle beam during measurements. To enable quasi-continuous monitoring of CERN's new LINAC4 160 MeV H⁻ accelerator, a laserwire system is being developed that probes the particle beam properties via photo-detachment interactions as the H⁻ ions traverse a narrow beam of light. As only 10^8 of the 10^{14} H⁻ ions in each LINAC4 pulse are typically neutralised by this laserwire, the technique is essentially non-invasive.

The ultimate aim of these developments is to install a permanent dual-laserwire system for use at LINAC4 top energy of 160 MeV, to measure the transverse emittance and beam profile. In our previous studies, a prototype laserwire emittance scanner was successfully demonstrated at the 3 MeV and 12 MeV commissioning phases of LINAC4 [1–3]. By scanning the vertical position of the laserwire with respect to the beam, the transverse emittance was reconstructed from the spatial distribution of neutralised H^0 atoms recorded by a downstream segmented diamond detector. The main H⁻ beam was deflected by a dipole magnet, which for those measurements formed part of the diagnostics test bench at LINAC4.

The main dipole was not present for LINAC4 commissioning at 50 MeV through to 107 MeV beam energies, instead, the opportunity was taken to develop a new setup to measure the transverse beam profile, based on the electrons liberated by the photo-detachment process.

Beam Profile Monitor Design

The design of the beam profile monitor was presented previously [4] and is shown here for completeness in Figure 1. The laser beam delivery optics from the prototype were adapted and reused to direct light into a new, compact interaction chamber, in which the laserwire is orthogonal to the incoming H⁻ beam. A transverse slice of the H⁻ beam is neutralised as the H⁻ beam passes through the laserwire focus, liberating low energy (27 keV for 50 MeV H⁻) electrons that are readily deflected through 90° by a 0.9 mTm integrated field of a weak dipole magnet. The main H⁻ beam remains almost undeflected by the weak dipole. The electrons are collected by a fast 4 mm × 4 mm, sCVD diamond detector, that can be moved vertically in synchronisation with the laserwire position, allowing the beam profile to be reconstructed.

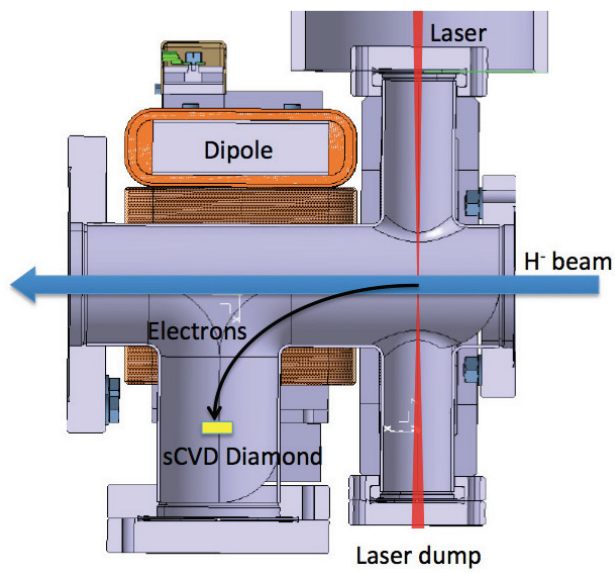

Figure 1: Conceptual design of the H⁻ beam profile monitor [4].

* stephen.gibson@rhul.ac.uk

ISBN 978-3-95450-177-9

EXPERIMENTAL SETUP

Laser and Fibre Transport

A V-GEN (VPFL-ISP-1-40-50) $\lambda = 1064$ nm fibre-laser with pulse widths tunable between 1–300 ns is housed in a dedicated hutch in the surface level klystron gallery above LINAC4. Due to the low (kW) peak power and favourably large linewidth $\lambda_L > 1$ nm, the light can be transported 75 m to the tunnel in a Large Mode Area optical fibre, without significant perturbation in the pulse shape from non-linear Stimulated Brillouin Scattering inside the fibre, as proven in earlier studies [4].

Diagnostic Test Bench

The temporary diagnostics test bench illustrated in Figure 2 was positioned at the end of the DTL cavities and later after the first PIMS cavity, to characterise the beam at energies of 50 MeV and up to 107 MeV respectively.

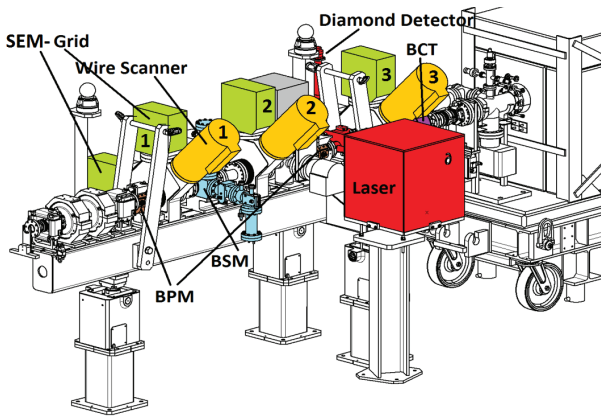

Figure 2: Diagnostics test bench used for LINAC4 commissioning of 50 MeV, 80 MeV and 107 MeV H^- beam [5].

The setup includes wire scanners and SEM-grids for transverse profile and emittance measurements; two beam positions monitors to determine the mean transverse position and beam energy from time of flight measurements between both BPMs. The beam current was measured with the BCT and the longitudinal bunch profile was assessed with the bunch shape monitor (BSM). The laser beam delivery optics box is shown in red, which focuses light into the vacuum chamber of the laser beam profile monitor, pictured in Figure 3.

Focusing Optics, Photodiode and Energy Meter

An internal view of the focusing optics in the beam delivery system is shown in Figure 4 revealing the single sided AR-coated beam sampler, S, that diverts a 4% reflection to the photodiode for normalisation of pulse-to-pulse fluctuations. The fine vertical position of the focusing optics assembly is remotely-controlled to scan the laserwire position. In the lowest position, light is diverted to a moveable camera for in-situ laser beam characterisation. A 50 mm × 50 mm active area pyroelectric energy meter is attached on the far side of the IP in Figure 3 and doubles as the laser dump. This integrates the absolute energy of the train of amplified laser pulses that intercept each LINAC4 macropulse.

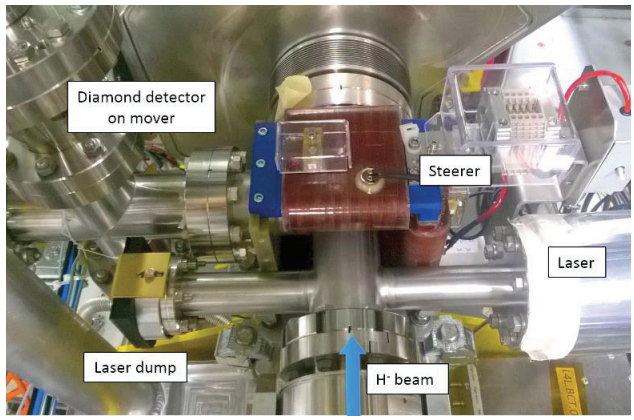

Figure 3: Vacuum-chamber for laser interaction and steerer magnet to deflect electrons towards the diamond detector [4].

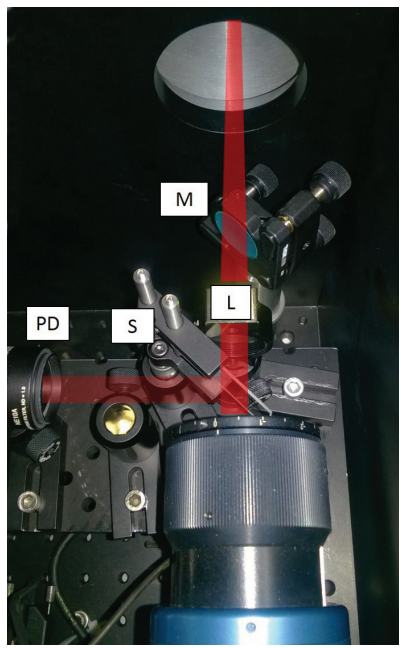

Figure 4: Controllable optics overlaid by the expanded laser beam that is focused by a 500 m lens (L) towards the IP with the H^- beam. An AR-coated beam sampler (S) diverts a 4% reflection to the photodiode.

SYSTEM CHARACTERISATION

Laserwire Spatial and Temporal Properties

The narrow beam of light is generated by fibre-coupled collimation and focusing optics in the beam delivery system. This also incorporates mirrors to divert the laserwire to a camera that can be translated over a range surrounding the equivalent focus of the interaction point (IP). Therefore the spatial characteristics of the laserwire can be measured in-situ using techniques described previously [2, 3]. The result shown in Figure 5 for the 50 MeV setup indicates an improved performance of the laserwire focus, compared to the previous 3/12 MeV measurement campaigns. Due to the lower M^2, the Rayleigh range is longer in both planes and

ISBN 978-3-95450-177-9

the waist is slightly thinner. The small optical astigmatism does not influence the measurement, which is in the vertical plane only.

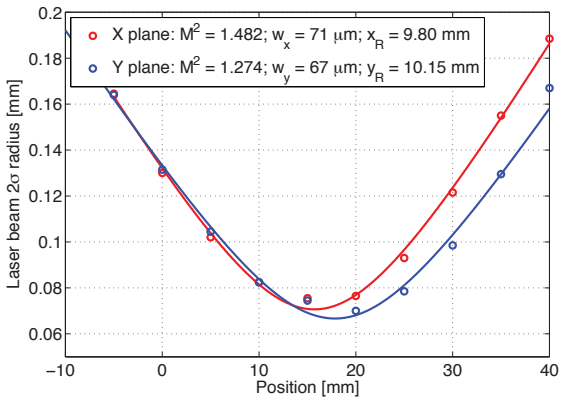

Figure 5: Spatial characteristics of the laser beam at the interaction point with H^-.

Pulse-to-pulse fluctuations in the laser power can be a significant source of error. Pulses from the V-GEN laser were measured to have a 3% RMS peak power stability after propagation through the 75 m fibre. To mitigate this error, the diamond detector signal is normalised per pulse by the photodiode signal recorded just before the IP.

Diamond Detector Response

Electrons liberated by each laser pulse are recorded by the single-crystal chemical vapour deposition (sCVD) diamond detector [4]. Initial laboratory tests with an α-source verified that the diamond sensor, with a 500 V bias applied and scaled by a 40 dB amplifier gain, gave close to the expected 6.7 pC charge for 100% CCE.

The response of the diamond detector was assessed by a scan of the laser pulse energy. The integrated charge of the diamond signal per laser pulse is plotted versus the integrated photodiode signal, for a range of pulse energies in Figure 6. The diamond detector response is found to linearly follow the photodiode signal, with a small offset thought to be due to a background of stray protons, H^0 or H^- directly impacting the diamond sensor in the 50 MeV setup.

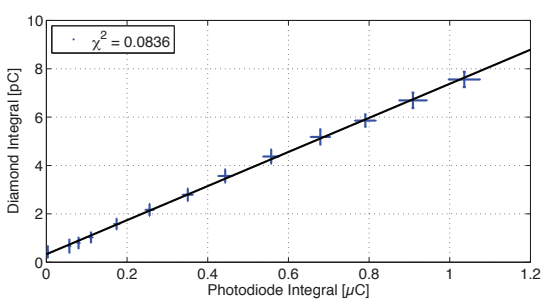

Figure 6: Integral of pulse signals recorded with the diamond detector versus the photodiode before the IP with the 50 MeV H^- beam.

Beamlet Measurements

Each transverse slice of H^- beam neutralised by the laserwire liberates a thin beamlet of electrons, that is magnetically steered towards the diamond sensor. The field was adjusted to compensate for the different electron momenta at each H^- beam energy, and ensure the beamlet strikes the target 4 mm × 4 mm sensor, which is placed in the focal plane of the dipole, optimised by tracking simulations [4]. The photodetachment cross-section, σ_{PD}, also varies with beam energy due to the relativistic Doppler-effect: σ_{PD} = 3.86, 3.94 and 3.98 $.10^{-17}$ cm^2 for E_{kin} 50, 80 and 107 MeV respectively.

The beamlet size was determined at 80 MeV by keeping the laserwire stationary and performing a two dimensional scan of the vertical (Y) position of the diamond detector, and the horizontal beamlet position (Z) by varying the magnetic field. The recorded diamond signal is shown in Figure 7. In Figure 8 the beamlet size is obtained by a projection along the Y-axis as $\sigma_Y = 0.45 \pm 0.1$ mm, and a similar analysis gives $\sigma_Z = 0.4 \pm 0.1$ mm. While the results match the horizontal beamlet size expected from tracking simulations, the beamlet is broader than the expected $\sigma_Y = 0.1$ mm in the vertical plane, which is attributed to stray fields in X and Z that deflect electrons slightly in the Y-plane. Crucially, the result shows that the beamlet is small enough to be captured entirely by the active surface of the diamond detector.

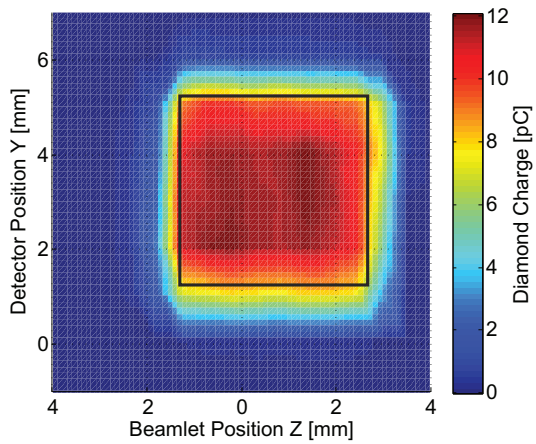

Figure 7: Integrated charge recorded during a two-dimensional scan of the diamond detector and inferred horizontal position of the beamlet. The black frame indicates the 4 mm × 4 mm surface of the diamond sensor.

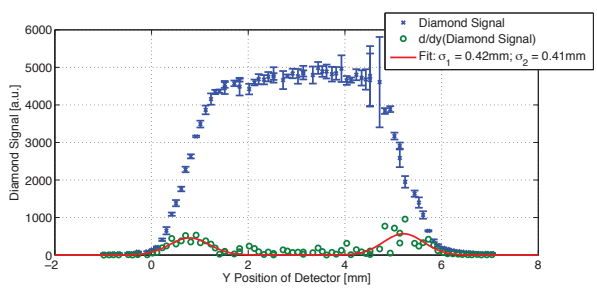

Figure 8: A fine scan of vertical detector position. The vertical beamlet size is extracted from the signal derivative.

ISBN 978-3-95450-177-9

BEAM PROFILE MEASUREMENTS

The vertical size of the H⁻ beam was measured by laserwire and diamond detector scans at the three beam energies of 50, 80 and 107 MeV, corresponding to Figures 9, 10 and 11. For all results, the diamond charge at each 2D position of the laserwire and diamond detector was determined by averaging the diamond pulse signals over the laser pulse train corresponding to at least one LINAC4 macropulse. At each laserwire position the maximum charge value in the range of diamond detector positions is obtained to plot the beam profile.

The laserwire profile is compared with those from SEM-grids and wire scanners positioned close to the laserwire. Accounting for H⁻ beam drift, the σ_Y recorded with the laserwire is found to lie extremely close to the interpolated value between SEM-grid measurements, as in the upper plot of Figure 9. In the lower plot of Figure 9 and in Figures 10 and 11, the SEM-grid and wire scanner results have been scaled to the position of the laserwire and show good agreement. Any discrepancies between the laserwire and linear interpolation of the SEM / WS profiles were monitored for multiple measurements and at different beam energies and found to be consistently below an error on the beam σ of $< \pm 2\%$. This is at a level similar to the difference between SEM / WS devices placed at the same measurement plane, indicating the laserwire has a similar performance.

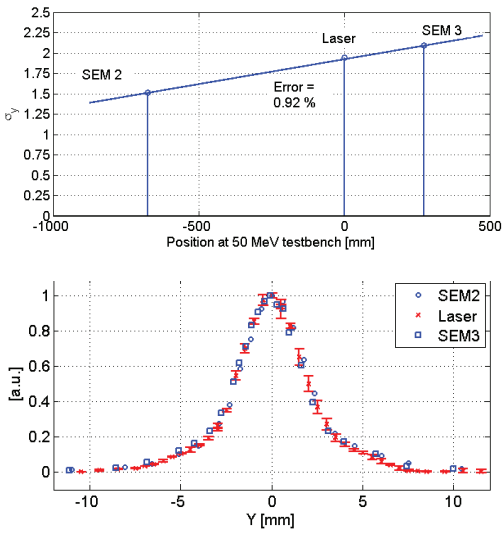

Figure 9: The vertical size of the 50 MeV H⁻ beam was measured using SEM grids and the laserwire. The laserwire profile is overlaid with profiles from the SEM grids scaled to the laserwire position.

SUMMARY AND OUTLOOK

A compact, non-invasive laserwire to measure H⁻ beam profiles based on detection of photo-detached electrons has been demonstrated at LINAC4 commissioning energies of 50, 80 and 107 MeV. The electron beamlet size was small enough to be entirely captured by the diamond sensor, which responds linearly with laser pulse energy. The beam profiles

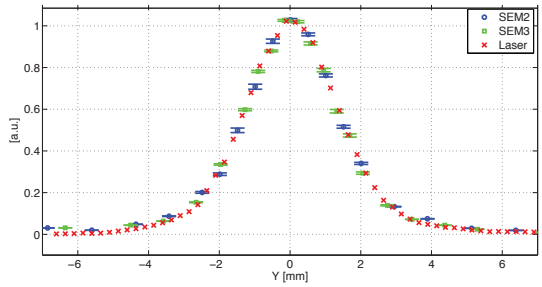

Figure 10: Comparison of SEM-grid σ-scaled profiles with the laserwire profile for the 80 MeV H⁻ beam.

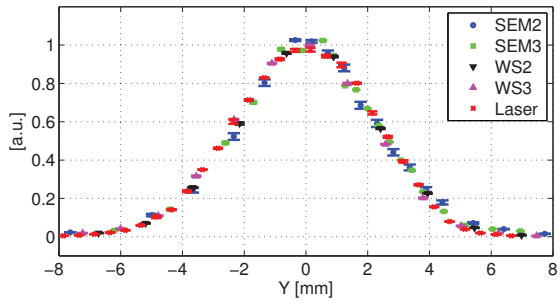

Figure 11: Overlay of 107 MeV H⁻ beam σ-scaled profiles recorded with different devices.

are in good agreement, $< \pm 2\%$, with nearby SEM-grids and wire scanners. Based on these and our earlier results, a permanent laserwire at 160 MeV will be installed to measure the transverse emittance in both planes, and will include beam profile monitors that measure the photo-detached electrons.

ACKNOWLEDGEMENT

Work supported by EU Marie Curie Network grant GA-ITN-2011-289191 and UK STFC grant ST/N001753/1. We thank A. Vorozhtsov and J. Bauche for providing the steerer magnet and field map, and thank the LINAC4 commissioning team for the opportunity to test our novel instrument.

REFERENCES

[1] T. Hofmann et al, "Experimental results of the laserwire emittance scanner for LINAC4 at CERN", *Nucl. Instr. and Meth. in Phys. Res.*, section A 830, p526–531 (2016).

[2] T. Hofmann et al, "Demonstration of a laserwire emittance scanner for hydrogen ion beams at CERN", *Phys. Rev. ST Accel. Beams*, 18 122801, p1–11 (2015).

[3] S.M. Gibson et al, "A fibre coupled, low power laserwire emittance scanner at CERN LINAC4", THPME190, Proc. of IPAC 2014, Dresden, Germany.

[4] T. Hofmann et al, "Design of a laser based profile-meter for LINAC4 commissioning at 50 MeV and 100 MeV", TUPB055, Proc. of IBIC 2015, Melbourne, Australia.

[5] U. Raich et al, "Beam instrumentation performance during commissioning of CERN's LINAC4 to 50 MeV and 100 MeV", MOPMR026, Proc. of IPAC2016, Busan, South Korea.

ISBN 978-3-95450-177-9

LANSCE ISOTOPE PRODUCTION FACILITY EMITTANCE MEASUREMENT SYSTEM*

J. Sedillo, D. Baros, J. O'Hara, L. Rybarcyk, R. Valicenti, H. Watkins,
LANL, Los Alamos, NM 87545, USA

Abstract

A new beam diagnostic system for emittance measurement is under development for the Isotope Production Facility (IPF) beamline located at the Los Alamos Neutron Science Center (LANSCE). This system consists of two axes; each composed of a harp and slit actuation system for measuring the emittance of 41, 72, and 100-MeV proton beam energies. System design details and project status will be discussed with installation and commissioning of this system scheduled to conclude by February 2017.

INTRODUCTION

In July 2015, research and development efforts were authorized for the creation of additional beam diagnostic systems at LANSCE's Isotope Production Facility. Among these systems was the inclusion of a new beam emittance and transverse profile monitoring diagnostic located in the IPF beamline. Design efforts have culminated in a dual-axis system comprised of four NI compactRIO embedded controllers capable of driving four actuators (2 orthogonal slits and two orthogonal harps) while simultaneously acquiring beam waveform data from 154 harp wires. After deployment in February of 2017, the system will measure the emittance and transverse profiles of proton beams with nominal energies of 41, 72, and 100 MeV [1].

SYSTEM LOCATION AND OVERVIEW

The IPF beamline diverges from the LANSCE main beamline at the transition region after the 100 MeV drift tube linac (DTL) acceleration stage. From there, the IPF proton beam passes through a drift space before impinging on the IPF target. Beam properties at the emittance device are: nominal energy of either 41, 72, or 100 MeV; 4Hz macropulse repetition rate; 150μsec pulse width; and 0.1 to 21mA peak beam current.

Figure 1 shows the IPF beamline where the emittance actuators will be located. Two orthogonally mounted slit actuators will reside 7.5 meters upstream of the two orthogonal harp actuators. The IPF target is located approximately 2.7 meters downstream of the harps.

This emittance diagnostic is one of several systems under development for enhancing the beam measurement capabilities of the IPF from which improvements in isotope production reliability, diversity, and yield are expected [1].

*Work supported under the auspices of the United States Department of Energy, Office of Science.

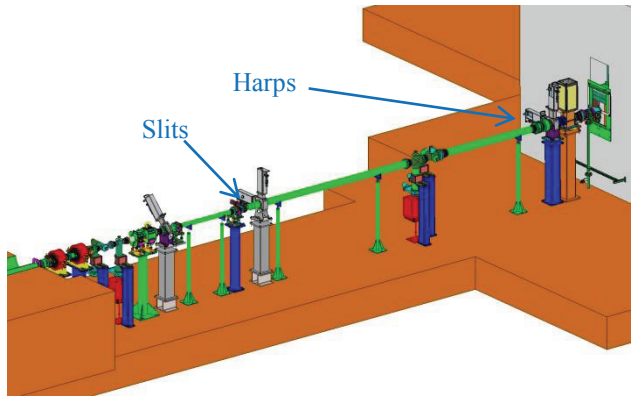

Figure 1: IPF beamline model. Beam direction is left to right.

SLIT DESIGN

Beam emittance measurement begins with the slit. The IPF slits have been designed with a 0.508-mm slit aperture size and a 14-mm slit thickness. The slit size allows for a relatively higher resolution emittance scan relative to the beam spot size of 48-mm (2-RMS) while minimizing slit-induced scattering. The slit thickness of 14-mm (copper substrate) was specified to fully absorb the intercepted beam. An additional provision for slit biasing has been included via an SHV connection. A computer rendering of the slit design is shown below in Fig. 2.

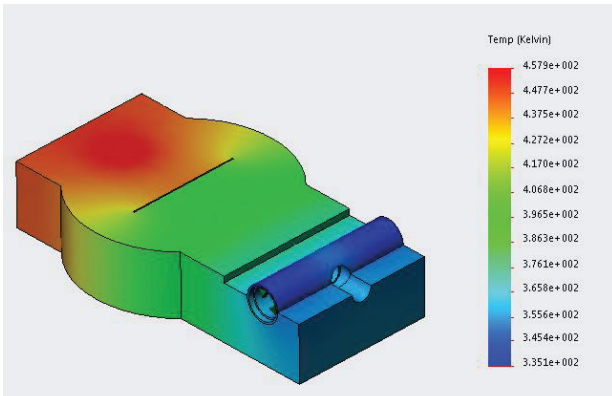

Figure 2: IPF slit model with thermal analysis.

HARP SENSOR DESIGN

The beam characteristics of interest are sensed by the harps. The IPF harps have been designed with 77-lines of transverse beam resolution spanning a 77-mm plane with 1-mm spacing. This configuration places approximately 49 wires within the beam's spot-size envelope of 48-mm. Sensors are composed of 0.079-mm-thick Silicon-carbide

ISBN 978-3-95450-177-9

fibers spanning a circuit board upon which they are retained. A hook, spring, and collet configuration maintains sensor tension and placement on the circuit board while also maximizing sensor density. Signals induced in the sensors travel along the harp circuit board's traces, through two high-density connectors, along kapton-insulated cables, to two mil-spec vacuum feedthroughs prior to interfacing with the harp's facility cabling. A computer rendering of the harp sensor is shown in Fig. 3.

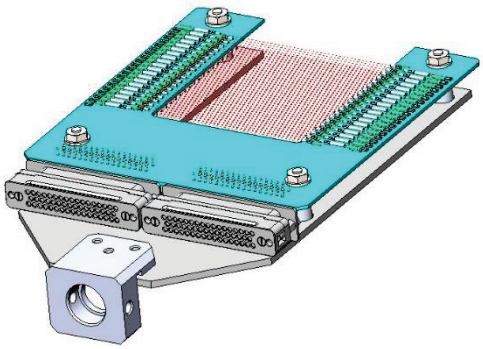

Figure 3: IPF harp fork design model (single-axis).

ACTUATOR DESIGN

Slit and harp actuators were developed on a common actuator platform. This actuator has a stepper motor, brake, and resolver assembly coupled to a linear stage via a synchronous drive gearbelt transmission. Slits and harps are suspended in the beam cavities with a cylindrical support arm coupled to the actuator's linear stage. The support arm is sheathed within a flexible stainless-steel bellows for vacuum isolation from atmosphere. Movement of the support arm via the actuation mechanism allows the sensor to scan the beam in a multitude of positions along a single axis. Computer renderings of the harp and slit are shown in Fig. 4 and Fig. 5, respectively.

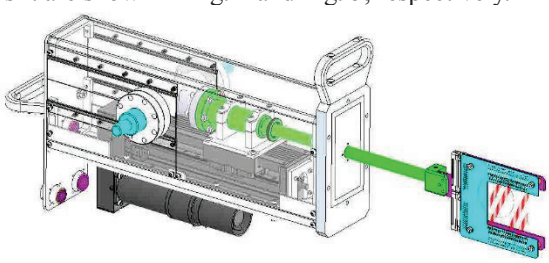

Figure 4: Harp actuator model.

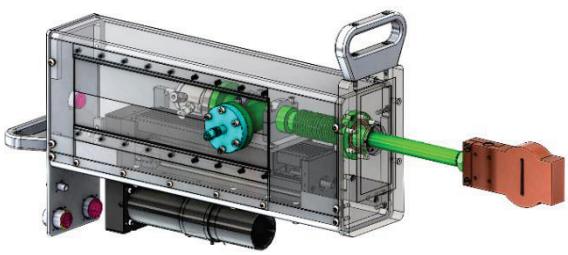

Figure 5: Slit actuator model.

CONTROLLER HARDWARE

Each axis of the emittance-measurement system will be operated by two cRIO-9038 embedded controllers in a master-slave relationship. The first of these is the master controller which will be configured to acquire the 154-channels of harp sensor waveform data, serve as the primary EPICS IOC (Experimental Physics and Industrial Control System Input-Output Controller) for client interfacing, and sensor positional calculator for the slave controller. The slave controller will function as an actuator motion control system by controlling the positioning of the emittance system's slit and harp heads. The hardware diagram of the master controller is shown at the top of Fig. 6 with the slave controller shown below the master.

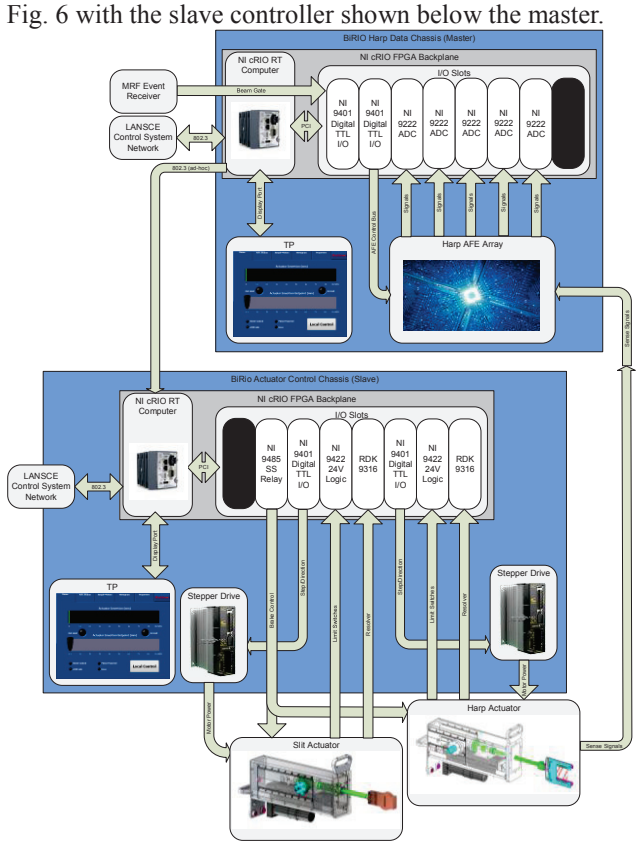

Figure 6: Emittance control system hardware diagram.

The master controller will derive acquisition capabilities deployed recently for the legacy LANSCE emittance systems [2]. These capabilities include: simultaneous, 100 kS/sec, waveform acquisition across all 154 channels; variable pre and post-trigger sampling; and real-time data availability. Furthermore, the master controller will also house newly-developed high-density analog conditioning cards capable of measuring currents from 270 uA down to 3 uA, feature variable gain control, wire bias isolation, and auto-zeroing [1].

The slave controller will derive motion control capabilities developed previously for the LANSCE-RM (Risk Mitigation) project [3]. Locating the motion control functionality for both the slit and the harp within a single controller will provide for the fastest motion control synchronization required of an emittance measurement.

ISBN 978-3-95450-177-9

The synergistic relationship of the controllers allows for high-density sensor waveform acquisition with associated motion control, enabling such data acquisition methods as single-axis emittance measurements, single-axis harp measurements, and, when used in coordination with the controllers of the orthogonal axis; a two-axis, harp-based, transverse profile measurement. Furthermore, the importance of these measurements is compounded by the beam-rastering capabilities of the IPF beamline.

CONCLUSION

Development efforts dedicated to the IPF emittance measurement system's progress are beginning to yield tangible control system hardware and sensor actuation mechanisms. Near-term efforts will focus on the system's software development followed by testing, calibration, and integration with an expected completion by February 2017.

REFERENCES

[1] H. Watkins, *et al.*, "Upgrades to the LANSCE Isotope Production Facilities Beam Diagnostics," IBIC2016, Barcelona, Spain, paper WEPG31.
[2] D. Baros, *et al.*, "Bridging the Gap; Updating LANSCE Digitizers," IBIC2016, Barcelona, Spain, paper WEPG74.
[3] J. Sedillo, *et al.*, "First Test Results of the New LANSCE Wire Scanner," paper MOP236, PAC'11.

ISBN 978-3-95450-177-9

DESIGN AND IMPLEMENTATION OF NON-INVASIVE PROFILE MONITORS FOR THE ESS LEBT

C.A. Thomas*, T. Gahl, T. Grandsaert, H. Kocevar,
H. Lee, A. Serrano, T. Shea, European Spallation Source ERIC, Lund, Sweden

Abstract

We present in this paper the design and implementation of the Non-invasive Profile Monitors for the ESS LEBT. Non-invasive Profile Monitors at ESS measure the transverse profile of the high power proton beam. As such the NPM for the LEBT is not different from NPM designed for other sections of the ESS linac, however, it received the requirement to measure the position of the beam accurately with respect to the centre of the vacuum chamber, representing the reference orbit. This particular requirement led to implement a specific design to provide absolute position measurement to the system. In the following we will first describe the design and the associated functionalities, and then we will present the performance measurements of this built system, fully integrated into the control system. Finally we will discuss the performance in comparison to the initial requirements.

INTRODUCTION

For the commissioning and operation of the ESS source and LEBT, beam transverse profile and r.m.s size are required for the characterisation of the beam lattice along the LEBT and at the entrance of the RFQ. In addition beam position and angle at the entrance of the RFQ is also required. For the measurement of the beam transverse profile and size, Non-invasive Profile Monitors (NPM) have been designed. An NPM for ESS consists of two 1D profile measurements, based on the interaction's by-product of the vacuum chamber residual gas with the accelerated protons. For the LEBT NPM, the beam profile is measured by means of two imaging systems, using the induced gas fluorescence to perform an image of the beam [1]. In the LEBT, no conventional beam position monitor (BPM) is installed, i.e. based on the RF technology. However, the information on the position can be provided by the measurement of the centroid on the beam distribution profile. But to provide this measurement in the ESS general coordinate system, additional knowledge to the usual NPM imaging system has to be provided. In the following, we will present the design and the performance of the NPM for the LEBT, matching the requirement of the beam size and beam position. The requirements for the profile, the beam size and the beam position are summarized in the table 1

NPM DESIGN FOR THE LEBT

The NPM for the LEBT is based on imaging the proton induced fluorescence. It is composed of an optical system and a camera. The design of the system has been optimised to satisfy several criteria, based on point spread function, depth of field, capture efficiency, and field of view, sensitivity and signal to noise ratio across the range of current from 1 mA to 70 mA. All these performance criteria together with the geometry of the vacuum chamber define the optical system the sensitivity and the size of the camera sensor. To start with, the viewport size is defined as a requirement to be large enough so that it offers a minimum numerical aperture of NA = 0.22. This condition is matched by design with a viewport on a CF DN-100 flange, with 105 mm aperture, and with the distance to the centre of the vacuum chamber, 230 mm. The main objective for the requirement on the numerical aperture of the viewport of the NPM is to provide a potential capture of 1% of the total solid angle of the emitted photons, 4π. In the design of the optical system, the object numerical aperture may match the one offered by the viewport. However, this might not always be possible to achieve due to additional constraint.

Table 1: Requirements for the Beam Profile, Size and Position

Profile Error (%)	**r.m.s Size** (%)	**Beam Error**	**Position Error** (mm)
1	10		0.1

In the following we will expose how the optical system has been selected to match as close as possible the expected performance.

In addition to the optical performance for imaging, the system is expected to deliver information on the centre of the beam with respect to the centre of the vacuum chamber, i.e. in the ESS general coordinate system. This can be achieve on the condition that the position of the sensor with respect to the focal plan image is known with the required accuracy. We will present how this can be achieve with the required precision.

System Optimisation for the Imaging Performance

The system schematic is show in the Fig. 1. The source is composed of point sources distributed with the proton beam transverse distribution and linearly along the beam path, and which are emitting uniformly over 4π solid angle. The photon flux emitted by the source per unit length of interaction along the beam path, the gas fluorescence excited by the protons, can be estimated by:

$$N_{ph} = \sigma_f \frac{P_g}{\bar{R}T} N_a \quad (1)$$

* cyrille.thomas@esss.se

ISBN 978-3-95450-177-9

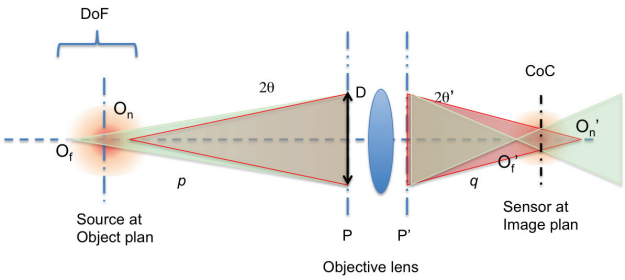

Figure 1: Imaging system schematic for the beam induced fluorescence. The point sources O_n and O_f are imaged in $O_{n'}$ and O_f' respectively; their cones of light project on the camera sensor such that their extreme rays coincide with the CoC; the distance between O_f and O_n represents the DoF. The objective lens aperture, D, defines how much power it can transmit through; the distances p and q from object and source, to object and source principal plans respectively, define the magnification for the conjugate points.

where σ_f is the cross-section for the fluorescence, P_g is the pressure of the gas, $\bar{R}$ is the gas constant, T the temperature of the gas, and N_a the Avogadro constant. The typical cross-section for the hydrogen gas excited by protons [2], at 75 keV over the transition 1s to 3p, is $\sigma_{f:1s-3p} \approx 0.14 \times 10^{-16}\text{cm}^2$. This excitation transition induces fluorescence of the hydrogen at the Balmer α ray at $\lambda \approx 656.2$ nm. In the LEBT the gas pressure is expected to be $P_g = 10^{-5}$ mbar at room temperature T=295 K. So the total number of photons expected from the source is $N_{ph} \approx 2.45 \times 10^{10}$ cm^{-1}.

The image of the proton beam is performed by the objective lens, from which the principle characteristics are: the physical aperture, D, which combined the focal length, f, gives the effective numerical aperture (NA, eq. **??**), and in addition with the distance to the object gives the effective numerical aperture (NA_o Eq. 6); the Depth of Field, (DoF, Eq. 8), depends on the circle of confusion (CoC and on NA.

The expressions used for the selection of the objective lens are the following [3]:

$$m = \frac{q}{p} = \frac{s_{\text{CCD}}}{s_{\text{object}}} \tag{2}$$

$$f = \frac{p\,m}{m+1} \tag{3}$$

$$N = \frac{f}{D} \tag{4}$$

$$\text{NA} = n\sin(\theta) = n\sin\left(\arctan\left(\frac{D}{2f}\right)\right) \approx \frac{D}{2f} \tag{5}$$

$$\text{NA}_o = \frac{\text{D}}{\text{2f}}\frac{m}{m+1} \tag{6}$$

$$R = 1.22\frac{\lambda}{\text{NA}_o} \tag{7}$$

$$\text{DoF} = \frac{2N\text{CoC}\,(m+1)}{m^2 - \left(\frac{N\text{CoC}}{f}\right)^2} \tag{8}$$

m is the lateral magnification of the objective lens[1], which can be calculated with either the distances object - principal plane object and image - principal plane image, p and q respectively, or with the size of the field of view and the size of the camera sensor; NA_o is the numerical aperture object; R is the diffraction limited of the Airy radius, image of a point source; λ is the photons source wavelength through the lens; $N = f/D$ is the f-number of the objective lens.

The source is composed of distributed point sources emitting over $4\,\pi$ solid angle, the fraction of the power of light reaching the sensor is given by:

$$T_l = \sin\left(\frac{\theta}{2}\right)^2 \approx \frac{\text{NA}_o^2}{4} \tag{9}$$

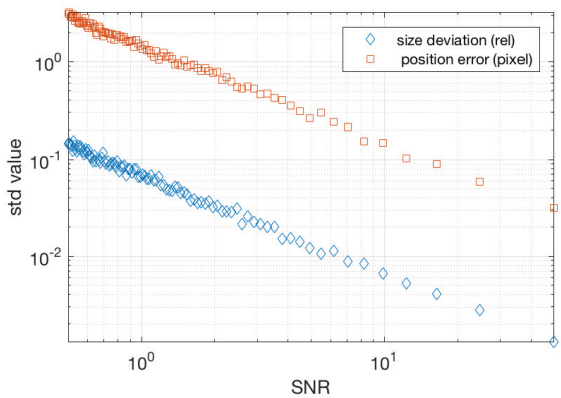

Figure 2: Deviation from the r.m.s value and centre of mass: the results come from a fit of a Gaussian with added noise.

In order to match the requirements shown in table 1, the optical system should deliver the following performance:

the profile measurement error depends on the signal to noise ratio (SNR) which can be evaluated as[2]

$$\text{SNR} = \frac{\eta\,\mu_p}{\sqrt{\eta\,\mu_p + \sigma_d^2 + \sigma_q^2/K}} \tag{10}$$

where η is the quantum efficiency , μ_p the photon flux per pixel, σ_d the r.m.s dark noise, σ_q the r.m.s digital noise, and K the overall sensor gain.

For an ideal sensor, where $\eta\,\mu_p \gg \sigma_d^2 + \sigma_q^2/K$, SNR = $\sqrt{\eta\,\mu_p}$.

Assuming the beam to be Gaussian, and analyses by a standard non-linear fit algorithm, one can evaluate the deviation of the measurement of the profile as function of SNR. Figure 2 presents the results of such an analysis. The figure shows the standard deviation of series of fit of a Gaussian with added noise. The result shows the deviation from the r.m.s size is less than 10% and the position measured with the centre of mass of the Gaussian is less than a pixel both for SNR $>$ 1. This implies that the requirement on the

[1] the magnification is chosen here to be absolute: $m = |m|$

[2] Eq. 10 is based on EMVA Standard 1288, Standard for Characterization of Image Sensors and Cameras

ISBN 978-3-95450-177-9

profile error is likely to be matched with an optical system performance presenting a large T_l.

In addition, the accuracy of the width measurement is also influenced by R and CoC, which are diffraction and geometrical quantities accounting for the size of a point source on the sensor. This size is called the point spread function, σ_{PSF}. Assuming a Gaussian distribution of the point spread function, the measured size can be expressed as:

$$\sigma_m = \sqrt{\sigma_{b,m} + \sigma_{PSF}} \tag{11}$$

where $\sigma_{b,m}$ is the image beam size.

Using Eq. 11, one can express the minimum relative size for which the requirement on the beam size precision, Δ, is satisfied when

$$\left(\frac{\sigma_{PSF}}{\sigma_{b,m}}\right) < \sqrt{2\Delta} \tag{12}$$

The last the requirement on the position is discussed is the next sub-section. With Eq. 12 and 10, one can use the equations from 2 to 9 to select the optical system for the LEBT NPM.

Table 2 shows the results from applying the formulae for the selection of the lens, based on the vacuum chamber geometry, and several standard camera sensor sizes. We have started to select sensor sizes to define the magnification which satisfies a FOV equal to $7 \times \sigma_b$, taking the largest expected beam size, to ensure the wings of the beam distribution to be imaged. This guaranties the least uncertainty on the fit. Once m is defined, one can set the focal length, using the known distance of the lens to the beam. Then one can select the aperture of the lens and then define NA_o, R and T_l. Finally with selection of the acceptable circle of confusion, DoF is defined. So with all this, we need to select a lens which provides the largest T_l together with the largest DoF, and the smallest R. The calculation shown in Tab. 2 shows that a typical 4/3" sensor associated with a with $f = 50$ mm objective lens opening at $N = 1.4$ would be suitable for the NPM in the LEBT. It would allow to have $T_l \approx 10^{-3}$, and thus from Eq. 1, the total number of photon on the sensor is $N_{sensor} = N_{ph}\,(h_{CCD}/m)\,T_l \approx 135 \times 10^6$. In turn, if we assume almost 100% of the intensity is distributed over 6σ, the average number of photons per pixel is $\mu_p = N_{sensor}\,\Delta_{px}/(6m\sigma_{b,m})$, with Δ_{px} the pixel size. So from Eq. 10 one can deduce SNR $= \sqrt{N_{sensor}\,\Delta_{px}/(6m\sigma_{b,m})}\,\sqrt{\eta}$. A typical camera with a 4/3" sensor is $17 \times 13\,\text{mm}^2$ and $\Delta_{px} = 5\,\mu$m. For a beam size $\sigma_b = 10$ mm, $m = 0.24$, SNR $= 216\,\sqrt{\eta}$, implying that the profile requirement is satisfied for most camera quantum efficiency. In addition, with $\sigma_{PSF} <$ CoC $= 0.1$ mm, the requirement on the size accuracy is also satisfied for any r.m.s beam size larger than 1 mm.

System Design for BPM Performance

The beam position requirement implies that the NPM has to return a position of the beam within and error less 0.1 mm and with respect to the centre of the vacuum chamber in the ESS general coordinate system. In order to achieve this, one has to position the optical axis of each of the imaging systems of the NPM in the ESS general coordinate system, and then, the absolute position of the image sensor has to be known with respect to the focal plan. This is achieved firstly by the use of an commercial objective lens which has a focusing mechanism and infinity focus position marked, and then by adding an encoded motor to control the focus of the lens. With this mechanical assembly, the position of the sensor with respect to the focal plan is always known within a high accuracy provided by the encoder resolution. As a result the position of the object plan is also known with the same precision, by means of the lens equation.

Table 2: Lens performance and characteristics for given values of the sensor size, with the object at $p = 250$ mm from the lens, $N = 1.4$, CoC $= 0.1$ mm, $\lambda = 0.5$ µm, and with FoV $= 70$ mm

Sensor size (mm)	m	f (mm)	DOF (mm)	NA_o ($\times 10^{-2}$)	R (µm)	T_l ($\times 10^{-4}$)
7	0.1	22.7	31.2	3.21	19	2.6
9	0.13	28.5	19.3	4.0	15	4.1
13	0,19	39.2	9.7	5.5	11	7.7
15	0.21	44.1	7.5	6.2	9.8	9.7
17	0.24	48.9	6.0	6.9	8.8	12
22	0.31	59.8	3.8	8.5	7.2	18
24	0.34	63.8	3.2	9	6.8	20
36	0.51	84.9	1.6	12	5.1	36

$$XY = ff' \tag{13}$$

with $X = p - f$ and $Y = q - f$ are the distances from object and image to the focal plans object and image respectivley, and f and f' are the focal lengths object and image respectively. Figure 3 shows the object position from the front flange of the lens, as function of the image sensor position. On the right axis, the accuracy required on the knowledge of the position of the sensor for $\Delta p = 0.1$ mm.

SYSTEM UNIT PROTOTYPE

The design of the NPM is made of two identical units, composed of a camera and motorised lens controlling the focus, assembled in a mechanical assembly, design to hold the unit in position, and permit its alignment in the coordinate system. The motor for the lens has en encoder reporting the position of the C-mount camera sensor with respect to the focal plane. The motor is integrated in the EPICS control system, and it is driven by a GeoBrick[3] for the prototype. The motor controller will migrate to the ESS standard motor con-

[3] http://deltatau.co.uk/geo-brick-lv/

ISBN 978-3-95450-177-9

troller based on EtherCAT Technology[4]. Both controllers are integrated into EPICS control. The lens selected is a 50 mm fixed focal length, F# 1.4, commercially available. The camera is GiGE-vision, allied vision camera GT 3300, selected for the sensor size to match magnification and field of view, and existing EPICS control. The motors are standard 2-phase stepper motors, and together with the encoder and the appropriated linear mechanics provide the required step motion to be less than 2μm.

ALIGNMENT AND CALIBRATION

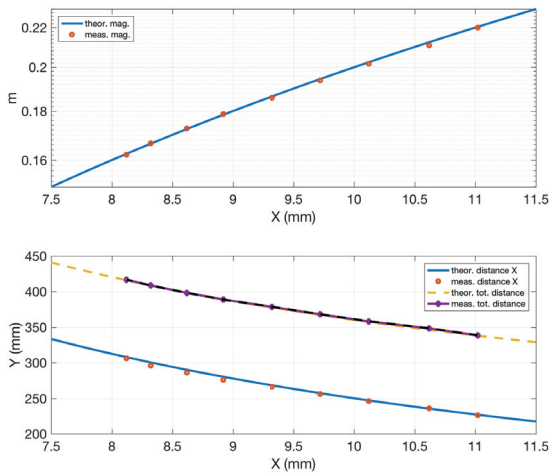

Figure 3: Optical system calibration of the magnification (top graph), and prediction of the distance of the object to the focal plane, and to the image position (bottom graph). The continuous and dash lines are extracted from lens equations, knowing the mechanical offset of 5 mm introduced to image the beam at the nominal 230 mm from the viewport flange.

The alignment of the NPM is done in several steps. Firstly, the optical axis is measured, with the support of the Alignment and Survey team. The measurement consists in putting a fiducialised target in the center of the camera image at two points distances at least from the camera. These points are measured in the ESS coordinate system with the Alignment instrument[5]. Then the fiducials on the NPM unit assembly are used to measure the position of the camera. These points are used to align the camera so that the optical axis intercepts orthogonally the beam axis. With this procedure the points along the optical axis are projected within one pixels or less on the center of the camera sensor. Then the angular error on the camera alignment is expected to be less than 700μrad for two points measured at 250 mm and 350 mm from the lens.

[4] www.beckhoff.com/EtherCAT

[5] LEICA ABSOLUTE TRACKER AT960-LR

The resulting beam position error measured at the centre of the image for a nominal beam distance at 250 mm from the lens is less than 20μm. Measurement performed after alignment of the unit shows a deviation from the reference axis of the order of 100μm across the 90 mm measured focusing range of the camera.

The calibration of the unit brings knowledge on the magnification, the distance of the object to the image, as function of the known distance camera sensor to focal plane. The image sensor is located at the standard C-mount distance from the flange of the lens, which is located with high accuracy (< 5μm) with the Alignment tool. The magnification is provided by measurement on a calibrated target, which is moved along the optical axis. The encoder position which has been calibrated so that it reports the distance image to focal plane, is recorded for each of the calibration target. The results of the calculation of the magnification and the corresponding total distance is shown in Fig. 3. The agreement with the theoretical prediction is better than 1%.

The resolution of the unit is measured by means of a sharp edged target. Detail of the measurement and calculation is not shown, however, the measured point spread function presents an r.m.s width of the order of 10μm. The sensitivity of the unit remains to be measured.

CONCLUDING REMARKS

We have designed and built a prototype of the first of the NPM for the ESS linac. This profile monitor to be installed in the LEBT section of the ESS linac, has received the additional requirement to be a beam position monitor. The prototype has been tested successfully. The camera resolution, the field of view all match the requirements. The requirement on the beam position is also matched. The alignment procedure has proven that the centre of the image can be within 100μm from the accelerator beam axis defined in the ESS general coordinate system.

ACKNOWLEDGMENTS

We would like to thank the Alignment and Survey team at ESS which has been supporting us in the design and for the qualification of the alignment procedure.

REFERENCES

[1] P Forck and A Bank. Residual Gas Fluorescence for Profile Measurements at the GSI UNILAC. In *EPAC*, 2002.

[2] E. Fitchard, A.L. Ford, and J.F. Reading. Hydrogene-atom excitation and ionization by proton impact in the 50- to 200-keV energy region. *Physical Review A*, 16, 1977.

[3] L. Larmore. *Introduction to photographic principles*. Dover Publications, 1965.

ISBN 978-3-95450-177-9

SPACE CHARGE STUDIES FOR THE IONISATION PROFILE MONITORS FOR THE ESS COLD LINAC

C.A. Thomas*, European Spallation Source ERIC, Lund, Sweden
F. Belloni, J. Marroncle, CEA, Saclay, France

Abstract

In this paper, we present the results from a numerical code developed to study the effect of space charge on the performance of Ionisation Profile Monitors. The code has been developed from the analytical expression of the electromagnetic field generated by a 3D bunch of charged particles moving along one axis. This transient field is evaluated to calculate the momentum gained by a test moving particle, but not necessary co-moving with the bunch, and included in a non-linear ordinary differential equation solver (Runge-Kutta) to track the 3D motion of the test particle. The model of the IPM is complete when an additional constant electric field is included to project the test particle onto a screen. The results from this code, modelling the IPM to be developed for the ESS Cold Linac, are presented here, and the impact of the space charge on the measurement of the beam profile is discussed.

INTRODUCTION

One of the challenges brought by high power beam such as provided by the ESS linac is that they can damage or simply destroy any material they interact with. For the measurement of transverse beam profile in two orthogonal axis, established method such as Wire-Scanners can not be applied as the wire breaks under a too long interaction with the beam. At ESS to palliate this, Non-invasive Profile Monitors (NPMs) will be in use for all beam with a pulse longer than 50µs and with a 62.5 mA peak current. NPM as called for ESS are based on the interaction between the residual gas chamber and the proton beam, which gives rise to ionisation and to fluorescence of the gas particles. In the superconducting cavities section of the Linac, NPMs use the ionisation byproduct of the interaction. An NPM at ESS is then composed of two orthogonal instruments called Ionisation Profile Monitors, IPM. This instrument is composed of a High-Voltage cage, which project on choice the ions or electrons produced by the proton beam, onto a screen where the beam profile is detected and read-out. One of the issues with this instrument is that its performance depends on the linearity of the projection. The projectiles being charged particles, they will be also interacting with the electromagnetic field generated by the proton bunches. Therefore, high charged bunches are likely to give an addition transverse to the projectiles, giving an error to the read position of the projected projectile. In this paper, we present a numerical code based on a model of the IPM. With this code we investigate the effect of the space charge on the profiles, showing the range of application of the IPM to the ESS beam.

* cyrille.thomas@esss.se

MODEL OF THE IPM AND NUMERICAL MATLAB IMPLEMENTATION

The simple numerical model to investigate the influence of the bunched proton beam of ESS on the IPM performance is described by Eq. 1

$$m\frac{d}{dt}\vec{v} = \vec{F} \tag{1}$$

and with m the mass of the particle, $\vec{v}$ its speed in 3D, and $\vec{F}$ the 3D force felt by the particle.

In the case of the force to be generated by a bunch of charged particles moving at the relative speed in one direction that we choose to be given by the unit vector **z**, one can write the force $\vec{F}$ as:

$$\vec{F} = q\left(\vec{E} + \vec{v}\times\vec{B}\right) = q\begin{cases}\left(1-\beta_b\frac{v_z}{c}\right)E_x\\ \left(1-\beta_b\frac{v_z}{c}\right)E_y\\ E_z+\beta_b\left(E_x\frac{v_x}{c}+E_y\frac{v_y}{c}\right)\end{cases} \tag{2}$$

where q is the charge of the particle, and $\vec{v} = v_x\hat{\mathbf{x}} + v_y\hat{\mathbf{y}} + v_z\hat{\mathbf{z}}$, the speed of the particle in 3D; $\beta_b = v_b/c$ the relativistic speed of the bunch, and c the speed of light; $\hat{\mathbf{i}}$ represents the unit vector in the lab frame.

The field generated by the relativistic bunch moving along z axis is given by [1]:

$$\vec{E} = \begin{pmatrix}E_x\\E_y\\E_z\end{pmatrix} = \begin{pmatrix}\gamma_b\bar{E}_x\\\gamma_b\bar{E}_y\\\bar{E}_z\end{pmatrix} \tag{3}$$

with $\gamma_b = \frac{1}{\sqrt{1-\beta_b^2}}$ the Lorentz factor related to the bunch relativistic speed. $\vec{\bar{E}} = \bar{E}_x\mathbf{x}+\bar{E}_y\mathbf{y}+\bar{E}_z\mathbf{z}$ is the field generated by the bunch in the rest frame coordinate of the bunch, with its origin in the center of the bunch and with unit vectors **i** colinear to $\hat{\mathbf{i}}$, and in which the coordinates transform as:

$$\bar{x} = x \quad \bar{y} = y \quad \bar{z} = \gamma_b(z-\beta_b ct) \tag{4}$$

and the dimensions of the 3D Gaussian bunch we consider here is:

$$\bar{\sigma_x} = \sigma_x \quad \bar{\sigma_y} = \sigma_y \quad \bar{\sigma_z} = \gamma_b\sigma_z \tag{5}$$

The expression of the 3D field generated by the 3D Gaussian bunch is given by:

ISBN 978-3-95450-177-9

$$\vec{E} = \frac{Q_b}{4\pi\epsilon_0}\frac{1}{\sqrt{\pi}}\begin{pmatrix} \int_0^\infty dq \frac{2\bar{x}}{q_x^{3/2}} \frac{1}{\sqrt{q_y q_z}} e^{-\frac{\bar{x}^2}{2q_x}-\frac{\bar{y}^2}{2q_y}-\frac{\bar{z}^2}{2q_z}} \\ \int_0^\infty dq \frac{2\bar{y}}{q_y^{3/2}} \frac{1}{\sqrt{q_x q_z}} e^{-\frac{\bar{x}^2}{2q_x}-\frac{\bar{y}^2}{2q_y}-\frac{\bar{z}^2}{2q_z}} \\ \int_0^\infty dq \frac{2\bar{z}}{q_z^{3/2}} \frac{1}{\sqrt{q_x q_y}} e^{-\frac{\bar{x}^2}{2q_x}-\frac{\bar{y}^2}{2q_y}-\frac{\bar{z}^2}{2q_z}} \end{pmatrix} \quad (6)$$

with

$q_x = q + \bar{\sigma_x}^2$, $q_y = q + \bar{\sigma_y}^2$, $q_z = q + \bar{\sigma_z}^2$

The function evaluated the field as given by Eq. 6 is implemented in Matlab and is used to solve the motion equation of particles of charge q and mass m, distributed initially with the transverse bunch distribution and linearly along the axis motion, moving under the force F given by the field of the 3D Gaussian bunch and an external field applied in the **y** direction. This code is implemented in Matlab, and uses the non-linear Runge-Kutta solver for the Ordinary Differential Equation (ODE) described by 1.

Benchmarking

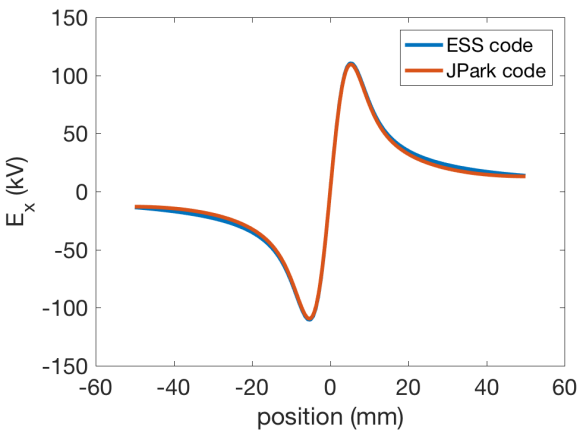

Figure 1: Benchmark of the bunch electric field.

The numerical code is validated by means of benchmarking against analytic solutions and other numerical code, and finally experimental measurements. The first check was performed on the expression of the bunch electric field. The field for a Gaussian bunch has been generated by CST[1], within a collaboration working on modeling IPMs [2]. A comparison with the Gaussian bunch generated by CST and the expression 3 for the case of the PS at CERN is shown in the Figure 1. All aspects of the field have been check, including numerical artifacts. The bunch characteristics for the benchmark against other codes are chosen to be the PS bunch at 26 GHz: r.m.s transverse size, $\sigma_{x,y} = 3.4\,\text{mm} \times 1.4\,\text{mm}$, bunch length, $\sigma_z = 750\,\text{ps}$ ($\sigma_z \approx 224.8\,\text{mm}$); number of protons, 1.33×10^{11}. The model for the calculation of the field is based in both numerical code on a 3D Gaussian distribution, however, the one difference is in our case the bunch extends to infinity, and in the benchmarking code, the field extension is calculated by means of the Dirichlet bounding condition, which is at x = ±50mm in this case. This can probably explain the difference that can be observed on the figure, and which is of the order of 10%. The agreement in the centre of the bunch, and where the intensity is maximum is better than 3%. Therefore, our model applies well to beam propagating in large beam pipe diameter, which is the case for the ESS Linac.

Once the implementation of the Eq. 6 is validated, we also check for the correct implementation of Eq. 1. In our model, the bunch moves at given speed, and periodically repeats, disappearing and re-appearing at each end of the bunch trajectory along the axis $\hat{\mathbf{z}}$ at the distance $D = T_0/2 \times \beta_b c$. The position of the bunch is located depending on the time, which is set by the ODE solver.

RESULTS FOR THE ESS BEAM

Table 1: Characteristics of the ESS Proton Beam in the Cold Linac Sections

Beam property	**Min.**	**Max.**
Transverse r.m.s size (mm)	0.5	10
Longitudinal Bunch r.m.s size (mm)	0.5	1.3
Energy (MeV)	90	2000
Protons per Bunch	10^8	10^9
RF frequency (MHz)	352.54	
Pulse length (ms)	2.86	

In order to investigate the impact of the space charge on the performance of the IPM under design for the ESS Cold Linac sections, simulation using the code describe above have been done using the ESS beam parameters, and for two kind of particles, electrons and H^+. The beam parameters used for the simulations are shown in the Tab. 1. The external field of the IPM cage is set to be constant everywhere and only an Electric field is applied. In the design of some other IPM, an additional magnetic field co-linear to the electric field is applied [3,4]. This is not the case for the ESS design, mainly due by the lack of space available at the location of the IPMs. The intensity of the electric field is varied between 50 kV/m and 1000 kV/m. The longitudinal bunch length does not vary significantly for the nominal lattice, and assuming all the cavities perfectly tuned. However, we also varied the bunch length between 0.5 mm and 10 mm, in order to probe the impact of the bunch length on the transverse profile IPM measurement.

Proton Beam Space Charge on Electrons

Figures 2 and 3 present part of our first results selected to illustrates some of the main features of the interaction between the cold plasma and the proton beam. We have selected here initial condition with a round beam of r.m.s

[1] Courtesy of K. Satou - J-Parc, CST: https://www.cst.com.

ISBN 978-3-95450-177-9

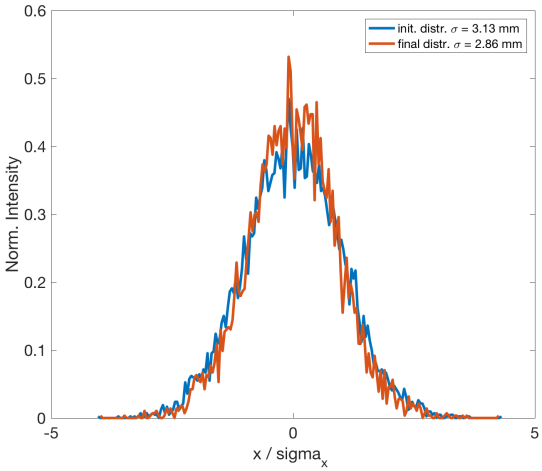

Figure 2: Distribution of electrons on the screen and at initially Gaussian distributed with a r.m.s $\sigma_{x,y} = 3.2$ mm

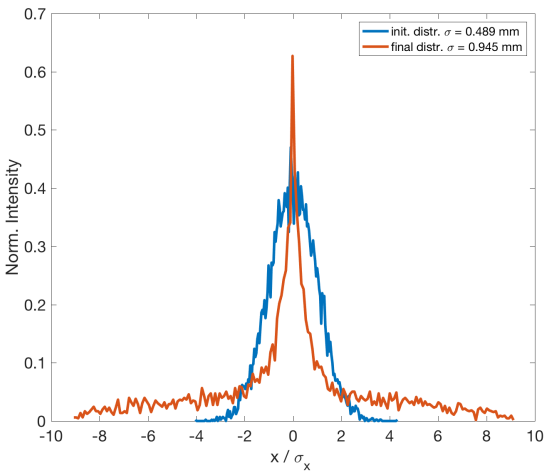

Figure 3: Distribution of electrons on the screen and at initially Gaussian distributed with a r.m.s $\sigma_{x,y} = 0.5$ mm

Gaussian size $\sigma_{x,y} = 0.5$ mm, and $\sigma_{x,y} = 3.2$ mm respectively. The rest of the initial parameters are given in the Tab. 1. The initial Gaussian distributions for each of these simulation is also shown for comparison with the profile measured in the IPM. We also normalised the distribution so that its integral is equal to 1. The space charge effect on opposite charged particles from the charge of the beam, and projected by the IPM HV cage is somehow a focusing effect. The particles are attracted towards the center of the beam while been projected towards the screen. For large r.m.s beam values, typically larger than $\sigma_{x,y} = 3$ mm, and for the large enough field strength, here it is 300 kV/m, the projection seems to be converging to a point rather far from the screen, see Fig. 4. The trajectories do not cross each others, so the final distribution at the screen is smaller, but by only a few percent, as seen in the Fig. 2.

For smaller beam sizes than 3 mm and very small beam as illustrated in Fig. 3, the space charge effect is strong. The

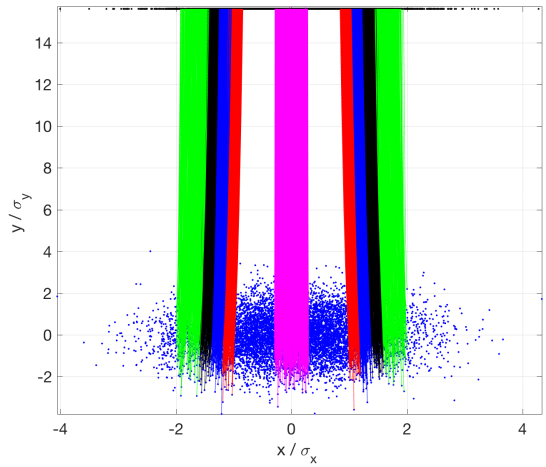

Figure 4: Distribution of electrons on the screen and at initially Gaussian distributed with a r.m.s $\sigma_{x,y} = 3.2$ mm. The colors of the trajectories represent particles for which their initial position is within a slice of the beam, in the center, $|x| < 0.2\sigma_x$ (magenta), in the strongest field positions, $\sigma < |x| < 1.2\sigma$ (red), $1.2\sigma < |x| < 1.4\sigma$ (blue), $1.4\sigma < |x| < 1.6\sigma$ (black), $1.6\sigma < |x| < 2\sigma$ (green).

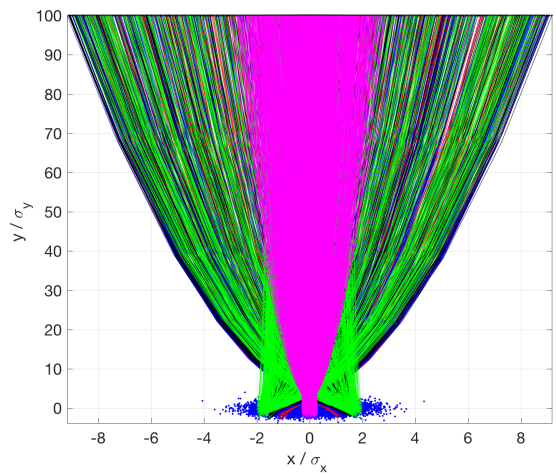

Figure 5: Distribution of electrons on the screen and at initially Gaussian distributed with a r.m.s $\sigma_{x,y} = 0.5$ mm. The sliced colored trajectories are the same as in Fig. 4.

distribution at screen is no longer Gaussian. The trajectories as shown in Fig 5, with the same color code for the slices as in Fig. 5, converge and the initial positions have been projected symmetrical to the centre of the beam. So the distribution at screen although not Gaussian remains symmetric. The final r.m.s size is twice as the initial one.

Proton Beam Space Charge on H^+

Similar space charge effects can be observed on the ions. we focus here on the H^+ species, produced from the ionisation of H_2 molecules, main species in the vacuum chambers residual gas. We have been performing the same simulations

ISBN 978-3-95450-177-9

as for the electrons, with the same or within the same range initial beam sizes conditions. The trajectories are repulsed, as expected from the same charged particle as the charge of the beam combined with the HV cage electric field. The resulting r.m.s size distribution is shown in the Fig. 6. The sizes are normalised to the initial beam size, and plotted as function of the initial beam sizes, and for several HV field strength[2]. The values remain under 10% of the initial values for high field strength and for beam larger than 2-3 mm. For smaller beam size, the high field strengths selected for the simulation are not strong enough and the space charge effect is driving the motion of the ions.

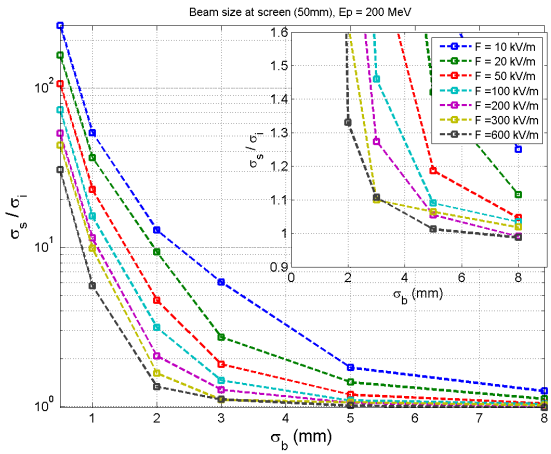

Figure 6: Size of the H^+ distribtion for which the mean value along the E-field axis equals the screen one. The screen position is at 50 mm from the centre of the beam axis. The protons energy is 200 MeV. The profile are retrieved from the projections of the particles projection on the virtual screen, at a time when the centre of mass of the particles is at the screen

DISCUSSION AND CONCLUDING REMARKS

For both particles type, electrons and protons, the proton beam with the ESS characteristics seems to have the same effects: for beam sizes larger than 3 mm, the effect is to distort slightly the distribution. The effect leads to a calculated r.m.s size within 10% of the initial beam size conditions. For smaller beam sizes, the effect is stronger, and the distortion is more pronounced until it is not Gaussian anymore. The question remains whether the distorted distribution can be used to retrieved the initial beam size. An initiative to do so has been started [5]. It is now continued within this development of IPMs for the ESS beam. The trajectories may be characteristic enough to enable the retrieval of the initial beam sizes. There are several approaches we intend to investigate. One is to generate a large look-up table, comparing the resulting distributions. A similar approach has been done for the evaluation of the beam size measured by means of coded apertures [6]. Another approach would be to used a specific transformation, which would lead to a deconvolution method. Both approach will be studied, with the objective to enable the retrieval of the beam size as measured by the IPM is the range of the r.m.s beam sizes from 0.5/mm up to 10 mm and beyond.

[2] The ending conditions between the electron and proton simulation are different: with electrons, the distribution is calculated for particles positions at the screen provided by the implementation of the 'events' function for the Matlab ODE solver; for the proton simulations, we had an earlier 'events' function implemented, and the distribution comes from the projection of the particles positions at the time the proton cloud center of mass as reached the screen

REFERENCES

[1] R Wanzenberg. Nonlinear Motion of a Point Charge in the 3D Space Charge Field of a Gaussian Bunch. Technical Report May, DESY, 2010.

[2] Mariusz Sapinski et al. Ionization profile monitor simulations - status and future plans. In *IBIC*, 2016, this conference: TUPG71.

[3] R. Connolly, P. Cameron, W. Ryan, T.J. Shea, R. Sikora, and N. Tsoupas. A prototype ionization profile monitor for rhic. In *PAC*, pages 2152–2154, 1997.

[4] K. Satou, N. Hayashi, S. Lee, and T. Toyama. a Prototype of Residual Gas Ionization Profile Monitor for J-Parc RCS. In *EPAC*, pages 1163–1165, 2006.

[5] Jan Egberts. *IFMIF-LIPAc Beam Diagnostics: Profiling and Loss Monitoring Systems put*. PhD thesis, Paris Sud, 2012.

[6] J.P. Alexander, A. Chatterjee, C. Conolly, E. Edwards, M.P. Ehrlichman, E. Fontes, B.K. Heltsley, W. Hopkins, A. Lyndaker, D.P. Peterson, N.T. Rider, D.L. Rubin, J. Savino, R. Seeley, J. Shanks, and J.W. Flanagan. Vertical beam size measurement in the cesr-ta storage ring using x-rays from synchrotron radiation. *Nuclear Instruments and Methods in Physics Research Section A: Accelerators, Spectrometers, Detectors and Associated Equipment*, 748:96 – 125, 2014.

ISBN 978-3-95450-177-9

PRELIMINARY MEASUREMENT ON POTENTIAL LUMINESCENT COATING MATERIAL FOR THE ESS TARGET IMAGING SYSTEMS

C.A. Thomas*, M. Hartl, Y. Lee, T. Shea, European Spallation Source ERIC, Lund, Sweden
E. Adli, H. Gjersdal, M.R. Jaekel, O. Rohne, University of Oslo, Olso, Norway
S. Joshi, University West, Trollhättan, Sweden

Abstract

We present in this paper the preliminary measurements performed on luminescent materials to be investigated and eventually coated on the ESS target wheel, the Proton Beam Window separating the end of the ESS Linac and the entrance of the ESS target area, and the ESS Dump. Among all the properties of the luminescent material required for the target imaging systems, luminescence yield and luminescent lifetime are essential for two reasons. The first one is trivial, since this material is the source for the imaging system and sets its potential performance. The lifetime is not generally of importance, unless the object is moving, or time dependence measurements are to be done. In our case, the target wheel is moving, and measurement of the beam density current may have to be performed at the 10μs scale. Thus luminescence lifetime of the coating material should be known and measured. In this paper, we present the luminescence measurements of the photo-luminescent lifetime of several materials currently under studies to be used eventually for the first beam on target.

INTRODUCTION

One of the challenges presented by high power proton beams for neutron spallation is the level of control required to prevent any damage on material of the target that must not be illuminated by the beam, or on the target itself not to be damaged. This level of control can be partly achieved by means of imaging the beam power density distribution deposited on the surface of the target. For such a system to be deployed at ESS, a luminescent material has to be identified and qualified. The qualification of such a material goes through reviews and tests of the candidate material properties, such as its luminescence yield, decay time, temperature sensitiveness, but also the thermo-mechanical resistance of the coated material to the beam impact and to high radiation dose, and to its luminescence properties under extremely high fluence, and finally, the qualified control of the industrial coated process. In this paper we address one of these aspect which is the measurement of the luminescence decay time. There are several ways to measure this decay time. Two possible ways are the time domain response, provided by a direct measurement of the luminescent pulse excited by a short proton bunch, and frequency domain response, from the measurement of the amplitude and phase luminescence excited by a frequency modulated source. The first method uses short bunches, and for instance short proton bunches delivered by facility like HiRadMat can be used for such a measurement. The second method is developed on a test bench for luminescent materials which can be photo-excited. The main objective of this test bench is to get time decay without the need of an accelerator of short bunched proton beams, and without time access restrictions. The method developed by Lakowicz *et al.* [1], consists in measuring the amplitude and phase response of the luminescent material under intensity modulated source and as function of the modulation frequency. The method is complementary to the time-domain lifetime measurement. It can provide a fine measurement of multi-exponential intensity decays but also non-exponential decays resulting from resonance energy transfer, time-dependent relaxation or collisional quenching. In the following, we firstly describe the experimental setup for the test bench for the frequency-domain luminescent lifetime measurement. Then we will present results from frequency-domain lifetime measurements on the chromium alumina coated for the SNS target imaging system. We will then discuss the method and the results obtained with it and within the perspective of using a similar luminescent coating material for the ESS target imaging system. Finally, we conclude on the performance and usage of the frequency-domain lifetime bench towards the selection process of the luminescent coated material for the ESS target imaging system.

EXPERIMENTAL SETUP

Frequency-Domain Lifetime Bench Setup

Our frequency domain lifetime measurement setup is shown in the Fig. 1. It consists of a modulated UV source (Thorlabs UV source DC3100-365), and two optical path, one towards the reference detector (Thorlabs PDA10), and the other towards the photo-luminescent sample. The luminescent light from the sample is detected by means of another fibre coupling assembly, which incorporates a filter for the source wavelength, and a second detector ((Thorlabs PDA10 or PDA36, depending on the bandwidth and sensitivity required). The signals from the two detectors together with the source modulation reference signal are sent to an oscilloscope, where the data is acquired. A detail description of the setup, the method and the analysis is explain in [1] and in [2].

Model for the Frequency-Domain Lifetime Measurement

As described in [2], the lifetime decay can be measured by fitting the amplitude and phase response of the lumines-

* cyrille.thomas@esss.se

ISBN 978-3-95450-177-9

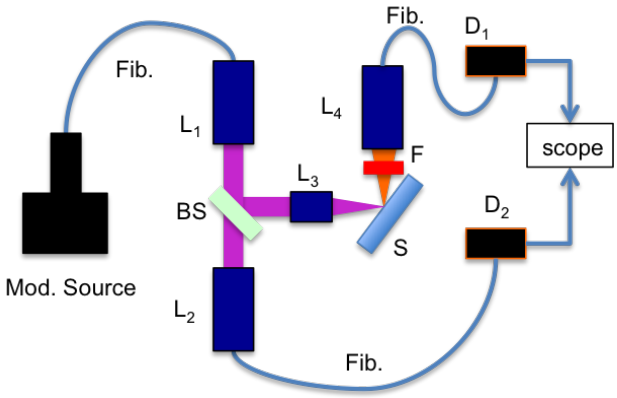

Figure 1: Frequency Domain lifetime measurement setup. The Modulated source is coupled to a fiber bundle (Fib.), and then collimated. The UV light is separated into two branch by a 90:10 beam spliter (BS), one coupling the 10% of the UV light intensity to another fiber connected to a selected detector for its sensitivity and bandwidth, and the other to focus the 90% UV onto the sample (S). The luminescent light is collected by a fiber coupling lens assembly that includes a filter F, which blocks the UV light. The fiber is connected to the second detector also selected according to bandwidth and sensitivity at the emitted luminescent wavelength. All signals are acquired in an oscilloscope using the electrical signal from the source as a reference trigger.

cence to the modulated excitation. The signal intensity decay modulation and phase can be predicted for any decay law by means of the following sine and cosine transforms of the intensity decay $I(t)$:

$$N_\omega = \frac{\int_0^\infty I(t)\sin(\omega t)}{I(t)} \quad (1)$$

$$D_\omega = \frac{\int_0^\infty I(t)\cos(\omega t)}{I(t)} \quad (2)$$

with ω the radial modulation frequency. For a signal composed of exponential decays, Eq. 1 and 2 can be written as:

$$N_\omega = \frac{\sum_i \frac{\alpha_i \omega \tau_i^2}{1+\omega^2\tau_i^2}}{\sum_i \alpha_i \tau_i} \quad (3)$$

$$D_\omega = \frac{\sum_i \frac{\alpha_i \tau_i}{1+\omega^2\tau_i^2}}{\sum_i \alpha_i \tau_i} \quad (4)$$

then the calculated phase and modulation amplitude of the signal response is given by:

$$\phi_{c\omega} = \arctan\left(\frac{N_\omega}{D_\omega}\right) \quad (5)$$

$$m_{c\omega} = \left(N_\omega^2 + D_\omega^2\right)^{1/2} \quad (6)$$

We have been implementing this model in Matlab, and built a fit function based on Marquadt Levenberg non-linear fitting algorithm. The validity of the model, i.e. the probability that the number of time decay values and their associated weights chosen for the fit is appreciated by means of a χ^2 calculation:

$$\chi^2 = \frac{1}{\nu}\sum \frac{|m - m_{c\omega}|^2}{\delta m^2} + \frac{|\phi - \phi_{c\omega}|^2}{\delta\phi^2} \quad (7)$$

with ν the number of free parameters, typically the number of measurement points less the number of fit parameters; δm and $\delta\phi$ are the experiment error bars on the measurement of the amplitude and phase response; m and ϕ the amplitude and phase response.

The validity of the model is given by a tabulation depending on ν. The result of the χ^2 has to be less than the values predicted using the Normal probability density distribution. In the other case, the result implies that random noise could also be responsible for the obtained measurement result[1].

RESULTS WITH THE FREQUENCY DOMAIN LIFETIME METHOD

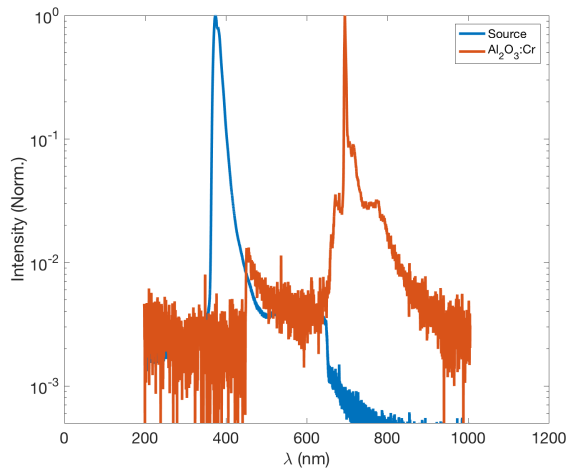

Figure 2: Spectra of the source at 365nm and the chromium alumina photo-excitation response, exhibiting the so-called R lines at around 693 nm and 695 nm

The first measurements we performed on the test bench is to acquire the spectrum of the source, and the photo-excitation spectrum, with and without the bandpass filter applied to suppress most of the light from the source. Figure 2 present these spectra. The spectrometre resolution is 0.7 nm r.m.s. So it doesn't resolve the R lines and the other lines that can be seen in the sides of the main peak. These lines will contribute all to the fluorescence lifetime. The frequency domain method is able in principle to retrieve the lifetime and weight of all these lines. However, in this case, the model should be extended to the spectral dimension.

[1] More detail and explanation can be found in the Encyclopedia of Mathematics online https://www.encyclopediaofmath.org/

ISBN 978-3-95450-177-9

Then Eq. 3 and 4 contain also a wavelength dependency. We will not derive this, since our model integrates over all wavelengths from 450 nm to 1100 nm. Based on values from the literature [3] and also values extracted from measurements in the time domain performed at SNS [4, 5], the apparent lifetime of the chromium alumina is of the order of 1 ms. Taking this into account, we expect the decay of the modulation to happen in the range from DC to 10 kHz. Therefore we selected the range of frequencies for the measurement of our sample to be from 50 Hz to 10 kHz. The results of the measurement is presented in the Fig. 3. The top graph shows the amplitude modulation for a sine modulation of the source as function of the modulation frequency. The bottom graph is the phase of the signal less the phase of the source signal, with respect to the reference signal as picked up from the second branch of the setup (Fig. 1). In the graph, the results from the most probable fit, associated with the acceptable χ^2 test result and small residual from the fit is also shown. The trial of model started with a single time decay, and then we increased the number of parameters of the fit, and calculated for each of the results the corresponding χ^2 parameter. The results are shown in the table 1. The values of the decays found are mostly in the sub-ms and ms range. The χ^2 values are shown in the table, together with the residual of the fit. The minimum for these two quantities are for 5 and 3 decay times for the χ^2 and for the residual respectively. The smallest residual indicates the best fit, and the smallest χ^2 the largest deviation from the null-hypothesis, i.e. the most probable fit. In practice, increasing the number of fit parameters should result in a significant decrease of the χ^2 test, until it converges and start growing again, until it disqualifies the hypothesis of the initial free independent number of time decays. So from the last two lines of the Tab. 1, the most probable result is then between 3 and 4 independent time decays.

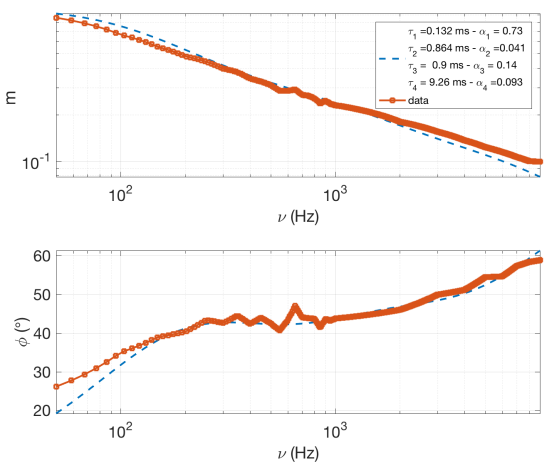

Figure 3: Luminescence frequency response for the Chromium Alumina coated on the SNS target.

Table 1: Results of the non-linear fit using models with 1,2, ...etc. , n_τ time decays. The decay time values τ_i are given in ms. The associated weights α_i are rounded and $\sum_i \alpha_i = 1$. The last two lines show the values of the χ^2 test (Eq. 7) and the residual values of the fit returned from the fitting function; Measurement on the data lead to $\delta m = 0.055$ and $\delta\phi = 0.2$. The total number of sample points is 49, thus $\nu = 49 - n_\tau$,.

#	1	2	3	4	5	6
τ_1	0.7	0.18	0.10	0.13	0.14	0.18
α_1	1	0.84	0.66	0.73	0.75	0.84
τ_2	-	5.97	0.65	0.86	1.11	3.26
α_2	-	0.16	0.23	0.04	0.10	0.035
τ_3	-	-	8.94	0.90	1.03	3.49
α_3	-	-	0.1	0.14	0.05	0.039
τ_4	-	-	-	9.26	6.73	3.98
α_4	-	-	-	0.09	0.04	0.036
τ_5	-	-	-	-	12.47	11.59
α_5	-	-	-	-	0.04	0.01
τ_6	-	-	-	-	-	14.1
α_6	-	-	-	-	-	0.037
χ^2	306.2	4.3	1.14	1.17	1.13	1.81
Res.	99.2	2.44	0.27	0.36	0.485	2.00

Time Decay and ESS Target Imaging

One of the Imaging system under design for the ESS will be delivering an image of each of the pulses sent to the Target Wheel (TW), with the requirements to determine the footprint of the proton power density distribution to be within the nominal area, the average power density to be uniform within 20% of the nominal average power density. The calculation to be performed on the image are relatively simple on a still image. However, the TW is moving at ≈ 7.8 mm/ms. With the luminescent lifetime decays measured, the image of a beamlet footprint will continue to emit over many ms, extended the beam footprint in the TW motion by many mm. This might render impossible the task to evaluate 99% of the power density footprint to be within ±4 accuracy from the nominal position of the beam on target. For still targets, like for instance the Tuning Dump and the Proton Beam Window (PBW), beamlet images, measurement of the power density footprint position will be possible. More advanced diagnostics though, at a fraction of the 2.86 ms pulse, might not be possible with this luminescent material.

CONCLUDING REMARKS

A bench test for the measurement of the lifetime decay of the luminescent material to be coated on the ESS target and Dump have been deployed. The setup is operational and luminescent material in-use at SNS as been measured as a potential candidate material for ESS Target Imaging Systems. Further improvement of the setup might follow.

ISBN 978-3-95450-177-9

For instance the selection of the detectors to allow a larger bandwidth extending in the MHz range will be necessary for the measurement of faster decays of new materials yet to be tested. Also the detection with an oscilloscope might be improved by using dedicated acquisition electronics. This should improve signal to noise and phase noise, although in this measurement, the noise figure mostly come from the detectors itself.

The bench is part of a series of qualification tests derived in order to down-select pre-selected luminescent materials for their proton luminescent yield, their yield at 200 degrees, their lifetime under high radiation dose, and high displacement per atom, their narrow-band spectrum and for their luminescence lifetime decay. The sample material measured has been passing most of these selection criteria, but doesn't satisfy entirely the last criteria. However, this material constitute so far the best known luminescent material for high power target beams. The search for a similar material, and the studies to understand its qualifying properties for the usage in high power target beams continues in order to provide the required luminescent material for the ESS.

REFERENCES

[1] Joseph R. Lakowicz, Gabor Laczko, and Ignacy Gryczynski. "2-GHz frequency-domain fluorometer", *Review of Scientific Instruments*, 57(10):2499–2506, 1986.

[2] Joseph R. Lakowicz. *Principles of fluorescence spectroscopy*. Springer, New York, 2006.

[3] T. M. Hensen, M. J. a. de Dood, and A. Polman. "Luminescence quantum efficiency and local optical density of states in thin film ruby made by ion implantation", *Journal of Applied Physics*, 88(9):5142, 2000.

[4] T. J. McManamy, T. Shea, W. Blokland, K.C. Goetz, C. Maxey, G.Bancke, and S. Sampath. "Spallation neutron source target imaging system operation", In *AccApp11*, April 2011.

[5] Willem Blokland, T. McManamy, and T. Shea. "SNS Target Imaging System Software and Analysis", In BIW, pages 93–97, 2010.

ISBN 978-3-95450-177-9

LONGITUDINAL DIAGNOSTICS METHODS AND LIMITS FOR HADRON LINACS

A. Shishlo†, A. Aleksandrov, ORNL, Oak Ridge, TN 37831, USA

Abstract

A summary of the longitudinal diagnostics for linacs is presented based on the Spallation Neutron Source (SNS) linac example. It includes acceptance phase scans, Bunch Shape Monitors (BSM), and a method based on the analysis of the stripline Beam Position Monitors' (BPM) signals. The last method can deliver the longitudinal Twiss parameters of the beam. The accuracy, applicability, and limitations of this method are presented and discussed.

INTRODUCTION

The SNS linac accelerates H^- ions up to 1 GeV. It has two parts: a normal temperature linac and a SCL which is the world's first of the kind high power hadron superconducting linac. The SCL accelerates negative hydrogen ions from 186 MeV to 1 GeV with 81 six-cell niobium elliptical superconducting RF cavities [1]. The SNS power ramp up started in 2006, and in 2009 SNS reached 1 MW level. During this time, an unexpected beam loss in an SCL was encountered. This beam loss was reduced to the acceptable level by empirically lowering the field gradients of the SCL quadrupoles without understanding the loss mechanism. That led to efforts by the accelerator physics group to understand and to control the beam sizes in all three dimensions in the SNS superconducting linac. Later the mechanism of the unexpected beam loss was identified as the Intra Beam Stripping (IBSt) process [2,3]. This explained our success in the loss reduction, but future improvements depend on our ability to measure and control the linac bunch sizes along the SCL including the bunch length. To measure this parameter the new method of non-invasive longitudinal diagnostics was developed [4].

In the present paper we are going to describe the new approach, its accuracy, conditions of applicability in hadron linacs, and its limitations. In the beginning, we will give the overview of traditional longitudinal diagnostics in the SNS linac. Then we will discuss the possibility and conditions of using the Beam Position Monitor's (BPMs') signal for the bunch length measurements. After that, we will describe the scheme of the new method where we combine a short RF cavity, a drift space, and the BPM to measure the longitudinal Twiss. We are going to present formulas for estimating parameters of the cavity and a drift length necessary for successful application of the method. At the end we will discuss the results of application of this method to the SNS linac.

SNS BUNCH LENGTH DIAGNOSTICS

At SNS the direct measurements of the bunch length in the linac and transport lines are performed by the Bunch Shape Monitors (BSM) [5]. The SNS linac has 4 BSMs in the warm section right before the SCL part. These BSMs were used to check the bunch shape at the entrance of SCL. The measurements showed that we have a longitudinally unmatched beam in this section, and the longitudinal emittance at the SCL entrance is substantially higher than the design value. The last BSM was also used to benchmark a new BPM-based method [4]. Unfortunately, the BSMs as beam intercepting devices are not used in the superconducting linac because of a possibility of a cavities' surface contamination.

Another method for the bunch length measurement is the widely used acceptance phase scan. This method was used at SNS for the Drift Tube Linac cavities in the warm linac and for SCL [6]. The classical variant of the acceptance scan uses a Faraday cup with energy degrader to measure the transmission of the beam through a long accelerator cavity as a function of the cavity phase. In the case of the SNS superconducting linac the combination of the beam current monitors and beam loss monitors was used [6]. For the SCL this method is very time consuming, creates a lot of beam loss in the SCL during the scan, and it has errors that cannot be evaluated.

The new suggested method uses the BPMs to measure the longitudinal bunch length. The next section will discuss the conditions for reliable measurements of this parameter.

BUNCH LENGTH AND BPM SIGNALS

The analysis of the spectral density of the sum signal of all four BPM's quadrants was performed a long time ago [7]. The Fourier amplitude of the surface charge density on a beam pipe is defined by geometry, relativistic parameters of the beam, and a Fourier amplitude of the longitudinal density of the bunch [7]

$$u_\omega \propto \frac{A_\omega}{I_0\left(\frac{R\cdot\omega}{\gamma\cdot\beta\cdot c}\right)} \quad (1)$$

where ω is BPM's frequency, R is the beam pipe radius, c is the velocity of light, A_ω is the Fourier amplitude of the longitudinal density of the bunch, I_0 is the modified Bessel function, and γ, β are relativistic parameters.

The modified Bessel function in the formula (1) describes the attenuation of the signal for higher frequencies because of the pure geometry. We can get the detailed longitudinal shape of the bunch only in the ultra-relativistic case, when $\gamma \to \infty$, and the useful frequencies will be limited only by the external circuit. In the

† shishlo@ornl.gov

ISBN 978-3-95450-177-9

realistic cases of hadron accelerators ($\beta < 1$) our frequency response will be limited. Let's estimate the region of the bunch length for which the BPM's signal with a particular frequency can be used for measurements.

Let's assume that the bunch has a Gaussian longitudinal charge density distribution

$$\lambda(z) = q \cdot N \cdot \frac{1}{\sqrt{2\pi\sigma_z^2}} \cdot \exp\left(-\frac{z^2}{2 \cdot \sigma_z^2}\right) \qquad (2)$$

where $\lambda(z)$ is the longitudinal charge density along the longitudinal coordinate z, q and N are the charge and the number of particles in the bunch, and σ_z is the RMS length of the bunch in meters. The amplitude of the Fourier harmonic of (2) for a particular frequency ω is

$$A_\omega(\sigma_\varphi) = A_{\max} \cdot \exp\left(-\frac{\sigma_\varphi^2}{2}\right) \qquad (3)$$

where $A_{\max}$ is maximal value of the amplitude, and σ_φ is the RMS length of the bunch in radians.

After inversion, formula (3) will give us the bunch length as function of the BPM's amplitude signal if we assume the constant relativistic parameters in the equation (1)

$$\sigma_\varphi = \sqrt{2 \cdot \ln\left(\frac{A_{\max}}{A_\omega}\right)} \qquad (4)$$

To find the acceptable range of BPM amplitudes for the bunch length measurements we have to estimate the relative error of σ_φ from the formula (4)

$$\frac{\delta\sigma_\varphi}{\sigma_\varphi} = \frac{1}{2 \cdot x \cdot \ln(x)} \cdot \frac{\delta A_\varphi}{A_{\max}} \; ; \; x = \frac{A_\varphi}{A_{\max}} \qquad (5)$$

The relative error of the bunch length measurements as a function of BPM amplitude is shown on Fig. 1 for the case when $\delta A_\omega / A_{\max} = 1\%$.

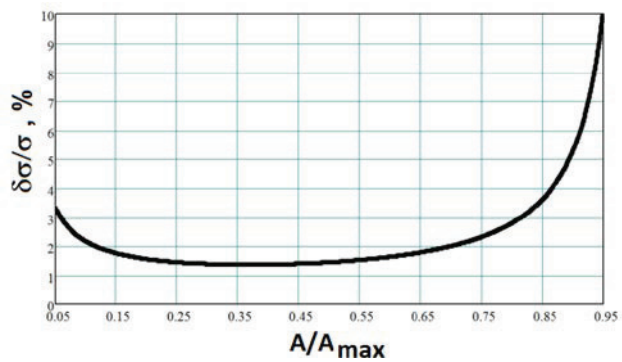

Figure 1: The relative error of bunch length measurements by using the formula (4). The BPM amplitude error is assumed 1%.

The Fig 1 shows that acceptable range of the BPM's amplitudes is between 10 and 90 % of the maximal value of the amplitude. If the BPM's amplitude is too big or too small we cannot extract the bunch length with a good accuracy. The Fig. 2 shows a corresponding range of the RMS bunch lengths by using equation (3). We can see that the measurable RMS bunch lengths are between 30 and 120 degrees.

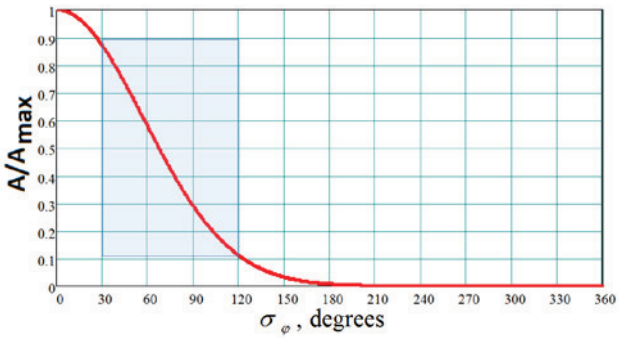

Figure 2: The range of measurable bunch lengths for the BPM's amplitude in 10%-90% range of the maximal value.

Typical bunches in the linac are much shorter (only several degrees) because of the necessity to provide effective acceleration and to avoid the big nonlinearities and beam loss. It means that BPM cannot be used as a device for the RMS bunch length measurements in linacs under normal circumstances. Nevertheless, if we allow beam debunching when the RMS bunch length will reach the region shown in Fig. 2, we can use BPMs to measure this length. In [4] it was suggested to use a combination of three elements (a short RF cavity, a drift space and a BPM) to measure not only the RMS bunch length, but also the longitudinal Twiss at the entrance of the RF cavity. In the following sections we will discuss the necessary parameters of this system.

PHYSICAL VARIABLES DESCRIPTION

In our analysis we will describe the bunch as an ensemble of particles with particular phases φ and energy deviations dE relative to the synchronous particle. The bunch as a whole is characterized by the second order correlations over the ensemble of particles

$$\left\langle \varphi^2 \right\rangle = \sigma_\varphi^2 \; ; \; \left\langle dE^2 \right\rangle = \Delta E^2 \qquad (6)$$

$$\left\langle \varphi \cdot dE \right\rangle = K_{corr} \cdot \sigma_\varphi \cdot \Delta E \qquad (7)$$

The first two (in formula (6)) are squares of the RMS longitudinal size and the energy spread respectively, and the last one (in formula (7)) is a phase-energy correlation. The different types of correlations are shown in Fig. 3.

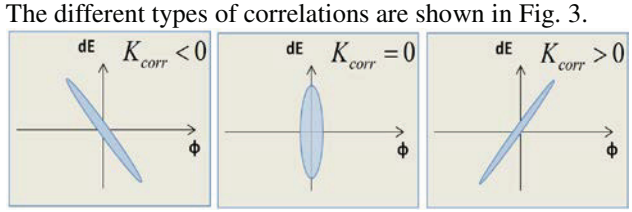

Figure 3: The longitudinal phase space for different types of phase-energy correlations.

ISBN 978-3-95450-177-9

The second order statistical correlations are related to the more recognizable Twiss parameters (emittance, alpha, and beta)

$$\varepsilon_{rms} = \sqrt{\langle \varphi^2 \rangle \cdot \langle dE^2 \rangle - \langle \varphi \cdot dE \rangle^2} \quad (8)$$

$$\alpha_{Twiss} = -\frac{\langle \varphi \cdot dE \rangle}{\varepsilon_{rms}} \quad ; \quad \beta_{Twiss} = \frac{\langle \varphi^2 \rangle}{\varepsilon_{rms}} \quad (9)$$

These parameters are often used as input of beam envelope tracking accelerator models. The correct model and the initial Twiss parameters allow predicting the RMS sizes for the whole linac and performing the beam matching procedure to reduce halo growth and beam loss.

RF CAVITY+DRIFT+BPM LATTICE

Our goal is to find the initial longitudinal Twiss parameters by using a system that consists of an RF cavity, a drift space which is long enough to allow for the necessary beam debunching, and the BPM for the bunch length measurements. In the beginning, we will perform our analysis for the case with negligible space charge effects. The final (at the BPM's position) and initial (at the RF cavity's entrance) longitudinal coordinates of the particles are related through the transport matrix for the RF cavity and the drift

$$\begin{pmatrix} \varphi_{BPM} \\ dE_{BPM} \end{pmatrix} = M_{drift} \cdot M_{RF} \cdot \begin{pmatrix} \varphi_0 \\ dE_0 \end{pmatrix} \quad (10)$$

where the drift and the short (few accelerating gaps) RF cavity transport matrices are

$$M_{Drift} = \begin{pmatrix} 1 & \frac{L}{\bar{\lambda}_{RF}} \cdot \frac{1}{m\gamma^3\beta^3} \\ 0 & 1 \end{pmatrix}; \quad \bar{\lambda}_{RF} = \frac{\beta \cdot c}{\omega_{RF}} \quad (11)$$

$$M_{RF} = \begin{pmatrix} 1 & 0 \\ -qV_0 \cdot \sin(\phi_{RF}) & 1 \end{pmatrix} \quad (12)$$

where L is the length of the drift, m is the mass of the particle, and $\omega_{RF}, qV_0, \phi_{RF}$ are the RF frequency, the maximal energy gain provided by the RF cavity, and the synchronous particle phase.

After substituting (11, 12) into (10) we get the expression for final phase of the arbitrary particle in the bunch

$$\varphi_{BPM} = m_{1,1} \cdot \varphi_0 + m_{1,2} \cdot dE_0 \quad (13)$$

where the transport matrix components are

$$m_{1,1} = 1 - \frac{L}{\bar{\lambda}_{RF}} \frac{qV_0 \sin(\phi_{RF})}{m\gamma^3\beta^3} \quad (14)$$

$$m_{1,2} = \frac{L}{\bar{\lambda}_{RF}} \frac{1}{m\gamma^3\beta^3} \quad (15)$$

After we calculate the square of both sides of the equation (13) and average over the ensemble, we get the final RMS longitudinal size at the BPM position

$$\sigma_{BPM}^2(\phi_{RF}) = \left(1 - \frac{L}{\bar{\lambda}_{RF}} \frac{qV_0 \sin(\phi_{RF})}{m\gamma^3\beta^3}\right)^2 \sigma_0^2 + 2\left(1 - \frac{L}{\bar{\lambda}_{RF}} \frac{qV_0 \sin(\phi_{RF})}{m\gamma^3\beta^3}\right)\left(\frac{L}{\bar{\lambda}_{RF}} \frac{K_{corr}\sigma_0 \Delta E}{m\gamma^3\beta^3}\right) + \left(\frac{L}{\bar{\lambda}_{RF}} \frac{\Delta E}{m\gamma^3\beta^3}\right)^2 \quad (16)$$

The final RMS bunch length according to the formula (16) will have three components. The first and last ones are defined by the initial size and the energy spread correspondingly, and the middle component is the phase-energy correlation contribution. Let's consider these components one by one.

DRIFT LENGTH

In the beginning, we assume zero energy spread in the bunch. In this case the final longitudinal size will be defined by the RF cavity parameters and the initial size. To get the substantial size growth $\sigma_{BPM} >> \sigma_0$ we have to provide the length of the drift no less than

$$L \geq \bar{\lambda}_{RF} \cdot \frac{m\gamma^3\beta^3}{qV_0} \cdot \frac{\sigma_{BPM}}{\sigma_0} \quad (17)$$

In this formula we assume the maximal defocusing effect from the cavity when ϕ_{RF} = -90^0 for the particles with positive charge. Let's estimate the drift length for beginning of the SNS superconducting linac. The SCL RF cavities have the following parameters $\bar{\lambda}_{RF}$ = 0.06 m, qV_0 = 10 MeV, β = 0.55. The typical initial bunch length is about 3^0, and at the BPM position we want to have at least 60^0. For these parameters the minimal drift length is 32 meters. We can easily create the drift like this by switching off all downstream RF cavities.

Formula (17) shows the fast growth of the necessary drift length with the energy of the beam. For the SNS case, L should be more than 200 meters when the beam reaches energy 400 MeV at the end of the medium beta part of the superconducting linac. This dependency is one of the serious limitations of the method. Some of the possible ways to mitigate this condition will be simultaneous scans of several cavities.

ENERGY SPREAD

If we assume that there is no phase-energy correlation in formula (16), there will be only two contributions: one from the initial bunch length and another from the energy spread. Comparing them we can have two extreme cases

$$qV_0 \cdot \sigma_0 << \Delta E \text{ or } qV_0 \cdot \sigma_0 >> \Delta E \quad (18)$$

where the bunch length σ_0 is in radians.

In the first case of equation (18) we will be able to extract from the BPM's data only the bunch length, and for

ISBN 978-3-95450-177-9

the second case it will be only the energy spread. Both these cases are unfortunate for us, because our goal is to get the full set of the longitudinal Twiss parameters (8, 9). It will be possible if our values approximately satisfy the following condition

$$qV_0 \cdot \sigma_0 \approx \Delta E \quad (19)$$

In this case we will get from our data both the initial bunch length and the initial energy spread. In Fig. 4 it is shown the dependency of the bunch length at two positions of the BPMs for the same parameters as for formula (17) in the previous section and the initial RMS energy spread 235 keV. We can clearly see the base value defined by the energy spread and a variable part approximately proportional to the $\sin^2$ function for both distances. To plot these graphs we used formula (16). The shift of 90^0 was chosen to emphasize a resemblance of the simulation to the real data which will be shown later. The bunch length in Fig. 4 is calculated for BPM's frequency 402.5 MHz which is a half of the RF cavity frequency that was used in the estimation after equation (17).

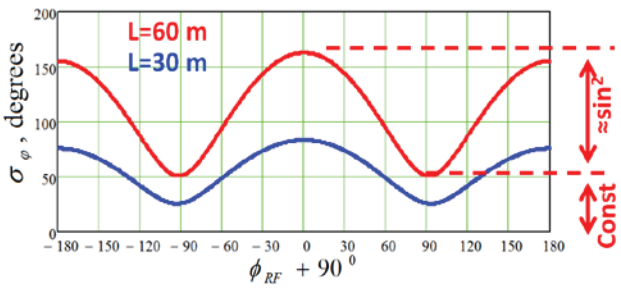

Figure 4: RMS longitudinal sizes of the bunch at two distances as function of the synchronous phase of the first SCL cavity.

In Fig. 5 it is shown the BPMs' amplitudes for the bunch lengths from Fig. 4. In Fig. 5 we can see that the distance 30 meters as a BPM position can be used for bunch length measurements only for particular cavity phases, because the BPM amplitude signal should be in the 10% - 90% range of the maximal amplitude. The distance 60 meters is good for all phases. The doubling of the necessary drift length relative to the estimation in the previous section is explained by the reduced BPM's frequency used at the SNS SCL. This selection of the BPM's frequency was necessary to reduce the noise level in the BPM electronics from cavities' RF.

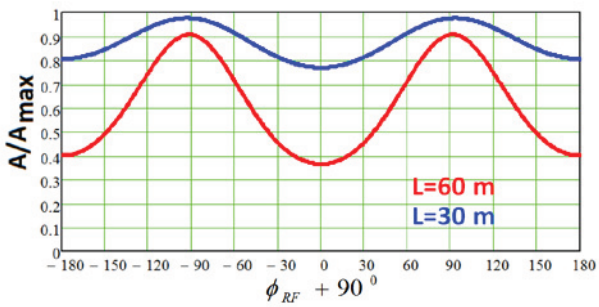

Figure 5: Amplitudes of BPMs at two distances as function of the synchronous phase of the first SCL cavity.

PHASE-ENERGY CORRELATION

In the presence of a phase-energy correlation in the ensemble of particles in the bunch the curves shown in Fig. 5 will be deformed. To plot these curves we have to use the formula (16) with a non-zero correlation coefficient K_{corr}. Fig. 6 shows the deformation of the curves for positive and negative correlation coefficients relative to the case of no-correlations shown in Fig. 5. It also means that we can extract the information about the correlation from measurements to complete the longitudinal Twiss parameters that we want to find.

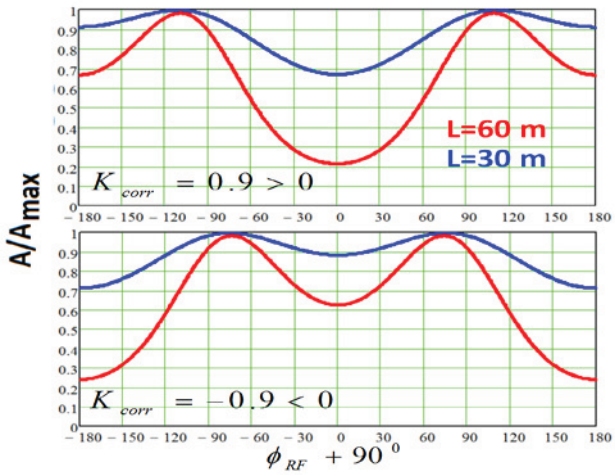

Figure 6: Amplitudes of BPMs at two distances for two cases of the phase-energy correlation

TWISS PARAMETERS CALCULATION

Formula (16) could be rewritten in a new form

$$\sigma^2_{BPM}(\phi_{RF}) = F(\phi_{RF})\sigma_0^2 + B(\phi_{RF})\langle \varphi dE \rangle + C\Delta E^2$$

On the left side of this equation we have the value that we will measure with BPMs, and on the right side we have three unknown values: the squared RMS bunch length, the correlation, and the squared energy spread. It means that we need measurements for at least three cavity phases. In this case we will have a linear system of three equations and three unknowns. In reality we can have more equations and represent them in the following form

$$\begin{bmatrix} \sigma^2_{BPM}(\phi^{(1)}_{RF}) \\ \dots \\ \sigma^2_{BPM}(\phi^{(N)}_{RF}) \end{bmatrix} = \begin{bmatrix} F(\phi^{(1)}_{RF}) & B(\phi^{(1)}_{RF}) & C \\ \dots & \dots & \dots \\ F(\phi^{(N)}_{RF}) & B(\phi^{(N)}_{RF}) & C \end{bmatrix} \begin{bmatrix} \sigma_0^2 \\ \langle \varphi dE \rangle \\ \Delta E^2 \end{bmatrix}$$

When the number of measurement points N is more than 3, we can solve this system by using the Least Square Method. The algorithm including the parameters error estimation for our particular task is described in [4]. After we extract the unknown second order correlations, the longitudinal Twiss parameters can be calculated from formulas (8, 9).

SPACE-CHARGE EFFECTS

All formulas in the previous sections can be used directly if we do not have substantial space charge effects.

ISBN 978-3-95450-177-9

If these effects are present we can use these formulas to estimate the parameters of the system. The final analysis should be done by using the transport matrices (11, 12) generated by the one of the envelope computer simulation codes like Trace3D. In this case the solution process will include application iteration or general fitting algorithms.

APPLICATION FOR SNS SCL

The suggested method was applied for the SNS superconducting linac. We performed the phase scan of the first cavity in the SCL with all other cavities switched off. The signals from all downstream BPMs were recorded and analysed by using the transport matrix generated by a code similar to Trace3D. The total number of BPMs was 14. With the phase scan from -180^0 to $+180^0$ and the phase step 5^0 we had 1008 equations in the system from the previous section of this paper. The accuracy of the longitudinal Twiss parameters was 1-3%. A picture of the BPM amplitudes during the phase scan of the first SCL cavity is shown in Fig. 7. We can see a clear resemblance to the picture in Fig. 6. An important point in these measurements and analysis was the calibration of the BPMs' amplitudes. We performed this calibration by using the production setup for the SCL linac, so we can be sure that we have a very short bunch in the whole SCL. The observed BPMs' amplitudes at the production were considered A_{max} values. We also took into account the Bessel function with the correct energies along SCL when we translated these amplitudes from production energies to the phase scan conditions.

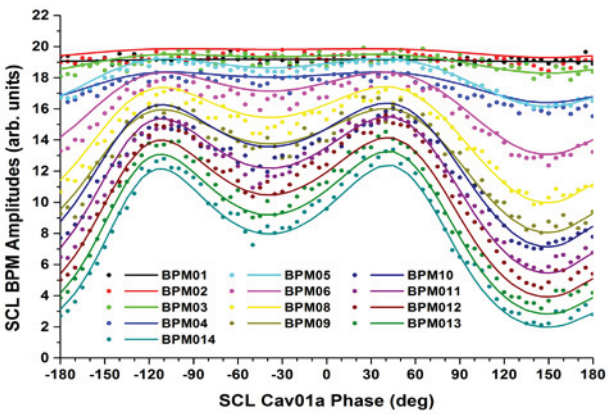

Figure 7: The BPM amplitudes during the first SCL cavity phase scan. Points are measurements; lines are from the envelope model.

As we mentioned above, we can use every cavity in the SCL as a measuring device if we have enough drift space before the BPM for beam to debunch. Fig. 8 shows the bunch length along the first half of SCL. The line on Fig. 8 is a result of simulation with initial Twiss from the analysis of the first cavity data. The Fig. 8 shows a good agreement between measurements and the model.

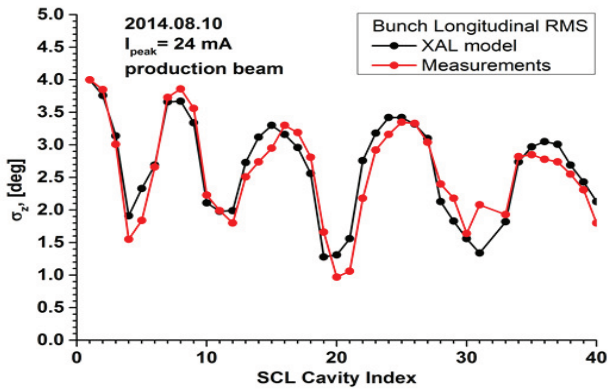

Figure 8: The RMS bunch length along the SCL. Measurements were performed by using the method described here.

CONCLUSION

The accuracy, applicability, and limitations of the original method (RF+drift+BPM) of the longitudinal Twiss parameters measurement was analysed. The successful application of this method to the SNS superconducting linac has been demonstrated.

ACKNOWLEDGMENT

This manuscript has been authored by UT-Battelle, LLC, under Contract No. DE-AC0500OR22725 with the U.S. Department of Energy. This research was supported by the DOE Office of Science, Basic Energy Science, and Scientific User Facilities. The United States Government retains and the publisher, by accepting the article for publication, acknowledges that the United States Government retains a non-exclusive, paid-up, irrevocable, world-wide license to publish or reproduce the published form of this manuscript, or allow others to do so, for the United States Government purposes. The Department of Energy will provide public access to these results of federally sponsored research in accordance with the DOE Public Access Plan (http://energy.gov/downloads/doe-public-access-plan).

REFERENCES

[1] S. Henderson et al., NIM A, Vol. 763 (2014), pp 610-673.

[2] V. Lebedev et al., "Intrabeam Stripping in H-Linacs," Proceedings of the LINAC2010 Conference, Tsukuba, Japan, September 12-17, 2012, pp. 929-931.

[3] A. Shishlo et al., *Phys. Rev. Lett.* 108, 114801 (2012).

[4] A. Shishlo, A. Aleksandrov, *Phys. ST Accel. and Beams* 16, 062801 (2013).

[5] A. V. Feschenko, "Methods and Instrumentation for Bunch Shape Measurements", *Proc. Part. Acc. Conf. PAC 2001*, Chicago, p. 517 (2001).

[6] Y. Zhang et al., *Phys. Rev. ST Accel. and Beams* 11, 104001 (2008).

[7] J.H. Cupérus, "Monitoring of particle beams at high frequencies" , *Nuc. Inst. Methods*, V 145, Issue 2, 1977, pp. 219–231.

ISBN 978-3-95450-177-9

THE WALL CURRENT TRANSFORMER – A NEW SENSOR FOR PRECISE BUNCH-BY-BUNCH INTENSITY MEASUREMENTS IN THE LHC

M. Krupa*,[1], M. Gasior
CERN, Geneva, Switzerland
[1] also at Lodz University of Technology, Lodz, Poland

Abstract

The Wall Current Transformer (WCT) is a new bunch-by-bunch intensity monitor developed by the CERN Beam Instrumentation Group to overcome the performance issues of commercial Fast Beam Current Transformers (FBCT) observed during Run 1 of the LHC. In the WCT the large magnetic cores commonly used in FBCTs are replaced with small RF transformers distributed around the beam pipe. Rather than directly measuring the beam current, the WCT measures the image current induced by the beam on the walls of the vacuum chamber. The image current is forced to flow through a number of screws which form the single-turn primary windings of the RF transformers. The signals of the secondary windings are combined and the resulting pulse is filtered, amplified and sent to the acquisition system. This paper presents the principle of operation of the WCT and its performance based on laboratory and beam measurements.

INTRODUCTION

During the LHC Run 1 (2008-2013) two commercial Fast Beam Current Transformers (FBCT) were installed on each LHC Ring: one used operationally and one spare used mostly for development. The bunch-by-bunch intensity measurements obtained with the FBCTs were observed to be sensitive to both the beam position at the transformer location and the bunch length [1]. This undesirable sensitivity was proven to be linked to the FBCT itself and significantly perturbed the bunch-by-bunch intensity measurements.

As an attempt to improve the situation, two new sensors were designed during the LHC Long Shutdown 1 (2013-2014) and subsequently installed for Run 2 (2015 onwards). The Integrating Current Transformer (ICT) [2], developed in collaboration with Bergoz Instrumentation, was installed on LHC Ring 1 while a Wall Current Transformer (WCT), developed by the CERN Beam Instrumentation Group, was installed on LHC Ring 2. In 2015 the two new monitors replaced the development FBCTs while the two operational FBCTs, upon which multiple intensity data users relied, were left in place to compare the three different technologies. This comparison showed that the best results were obtained with the WCT, leading to the operational systems being replaced with WCTs for the 2016 run.

The WCT design is derived from the Inductive Pick-Up (IPU) developed in 2003 at CERN for the CTF3 Drive Beam Linac [3]. Instruments applying similar ideas had also been developed in the past [4, 5]. Whilst the IPU was designed for beam position measurements, the WCT was carefully optimised for precise LHC bunch current measurements.

PRINCIPLE OF OPERATION

A simplified cross section of the WCT is shown in Fig. 1. The WCT uses small RF transformers instead of the large magnetic cores typically found in FBCTs. The transformers are mounted on internal Printed Circuit Boards (PCB) and uniformly surround the vacuum chamber. The image current is forced to flow through conducting screws connecting both sides of a dielectric insert brazed to the vacuum chamber. The screws go through the centre of each transformer to form single-turn primary windings. The secondary windings of the transformers are soldered to the PCBs and loaded with resistors of a few ohms, converting the secondary current into voltage. The signals of all RF transformers are passively combined into a single WCT output providing a signal proportional to the instantaneous beam current.

In parallel to the screws, both sides of the dielectric insert are connected by an RF bypass to provide a well-controlled image current path at frequencies above a few GHz, beyond the useful WCT bandwidth. The bypass consists of resistors and capacitors soldered to a flexible PCB that is mounted directly on the vacuum chamber.

The WCT is enclosed in a metal housing. The space between the housing and the conductive screws is filled with ferrite cores which increase the inductance of the housing as seen by the image current. This forces the low-frequency

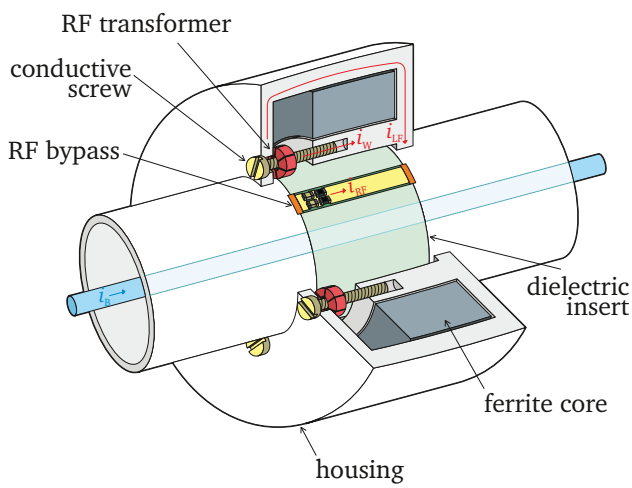

Figure 1: Cross section of the WCT.

* michal.krupa@cern.ch

ISBN 978-3-95450-177-9

currents to flow through the conductive screws and improves the low frequency cut-off of the sensor by more than two orders of magnitude.

The LHC WCT was designed to be installed over the existing FBCT dielectric insert brazed to the LHC vacuum chamber. The parts establishing the low-impedance path for the image current, including the conductive screws, are made of gold-plated copper. All the other parts are made of aluminium. The WCT can be installed, removed and modified with no impact on the accelerator vacuum. All mechanical parts are split in half and can be successively assembled around the vacuum chamber. This feature made it possible to replace the two operational FBCTs with new WCTs within a day during the 2015/2016 winter shutdown.

As the LHC WCT is designed for precise absolute bunch current measurement it can be calibrated with long current pulses. Each RF transformer features an additional single-turn calibration winding connected through a series resistor to the common WCT calibration input via a passive distribution network. The individual branches of the network are designed to be decoupled from the beam signal by increasing their high-frequency impedance with lossy inductive components. This significantly reduces the level of the signal induced on the calibration winding by the passing beam which would otherwise compromise the quality of the WCT output signal.

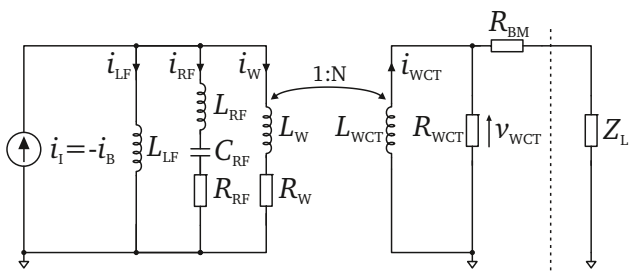

Figure 2: Electrical model of the WCT.

As shown in Fig. 2, upon arriving at the edge of the dielectric insert, the image current I_I (equal in value to the beam current I_B but with the opposite sign) can follow one of the three paths. These paths are designed to have appropriate impedances to conduct the desired frequency components of the image current. The very-low-frequency current flows through the ferrite-loaded housing L_{LF}. The high-frequency current passes through the RF bypass ($L_{RF} + C_{RF} + R_{RF}$) which is designed to have very low impedance at high-frequencies. The intermediate-frequency current flows through the conductive screws ($L_W + R_W$) and couples to the secondary winding of the RF transformers L_{WCT}.

Typically the LHC bunches are spaced by $T_b = 25$ ns. To ensure direct bunch-by-bunch measurements, with no signal leakage from one bunch to the other, the high frequency cut-off of the WCT must be greater than $1/T_b = 40$ MHz. In practice it should be much larger to leave margin for the limited bandwidth of the acquisition chain.

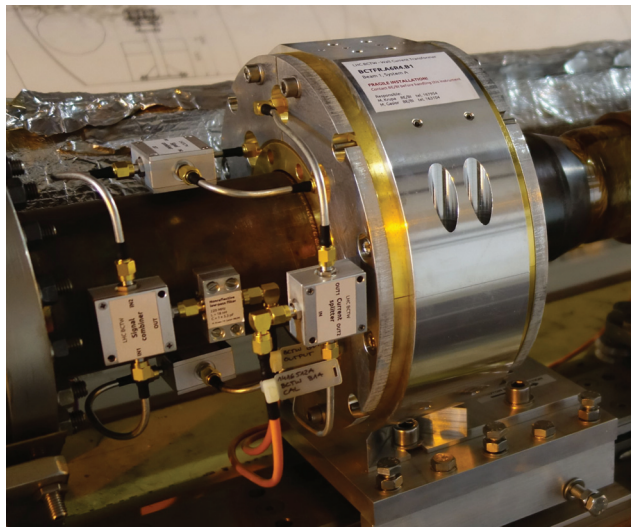

Figure 3: The WCT installed in 2016 as the operational LHC Ring 1 bunch-by-bunch intensity monitor.

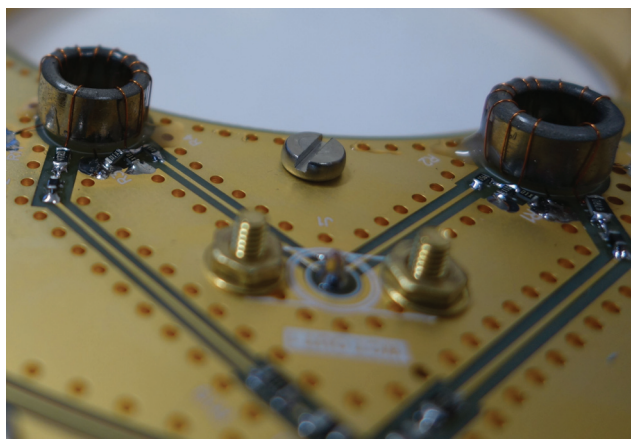

Figure 4: Two of the eight internal WCT RF transformers.

Being a transformer-based instrument, the WCT has no DC response. However, the low cut-off frequency of the WCT must be low enough that the baseline of the output signal does not drift significantly over the baseline sampling period. Currently, in the LHC, this is performed once per revolution $T_r \approx 89\,\mu$s. Therefore, the low cut-off frequency of the WCT has to be much lower than $1/T_r \approx 11$ kHz.

The LHC WCT was therefore designed in such a way to ensure that the image current components in the range from a few hundred Hz up to over 100 MHz would flow through the conductive screws ($L_W + R_W$).

A picture of the WCT installed in March 2016 is shown in Fig. 3 with two of its eight internal RF transformers shown in Fig. 4.

The output signal of the LHC WCT is filtered at 400 MHz directly at the output of the combiner network with a non-reflective low-pass filter built and optimised for this application. The filter lowers the peak amplitude of the output signal and stretches it to adapt it to the acquisition system. The output pulse length can be easily modified by replacing the external filter. The LHC WCT is also equipped with a front-end amplifier located approximately 1 m away from

ISBN 978-3-95450-177-9

the monitor. The output signal of the amplifier is sent over some 25 m of a good quality coaxial cable to a distribution amplifier installed in the acquisition rack. Each channel of the distribution amplifier has an independently controlled gain and a bandwidth adjusted to the proceeding acquisition systems. The distribution amplifier additionally compensates the low cut-off frequency of the WCT extending the monitor's bandwidth down to 100 Hz.

LABORATORY MEASUREMENTS

The frequency response of the FBCT, ICT and WCT measured in the laboratory is shown in Fig. 5. The measurements were performed with the sensors installed on a spare LHC vacuum chamber containing a brazed dielectric insert. The chamber was used to build a 50 Ω matched coaxial setup allowing high frequency measurements to be carried out. Due to the size of the chamber, measurements at frequencies above 2 GHz were very challenging.

The FBCT and WCT were measured in two configurations: with their full bandwidth and in the actual configuration used in the LHC. The FBCT was connected to an 80 MHz filter as used during LHC Run 1 to reduce its beam position sensitivity. The LHC WCT output is filtered at 400 MHz to stretch the output pulses and limit their peak amplitude.

As seen in the measurements, the bandwidth of the FBCT extends up to 1 GHz with ±1 dB fluctuations starting at 40 MHz and a strong 18 dB notch at 450 MHz. The bandwidth of the WCT extends over 2 GHz with ±1 dB fluctuations starting at 400 MHz. The ICT bandwidth is significantly lower, having a high frequency cut-off at 100 MHz. The low cut-off frequency of all sensors is in the order of a few hundred Hz.

The longitudinal impedance of the FBCT and WCT was measured with the same coaxial setup by comparing the transmission through the setup with the sensors installed and with the sensors replaced by a shunt bypass [6].

As shown in Fig. 6 the longitudinal impedance of the WCT is much lower than that of the FBCT. For high frequencies the mechanical housing of the FBCT can be excited by the beam and can resonate. The housing of the WCT is filled with ferrite cores which are lossy at high frequencies and therefore prevent any resonant modes.

BEAM MEASUREMENTS

Beam position sensitivity of the FBCTs, ICT and WCT was determined during a dedicated beam study session in 2015 [8]. At the location of the instruments, vertical, horizontal and diagonal beam position scans were performed. Due to limitations of the LHC optics it was not possible to introduce offsets of equal amplitudes in both planes for all monitors. The beam was displaced by 1.5 mm to 3 mm. The results obtained are shown in Fig. 7 and summarised in Table 1. Both FBCTs suffered from a significant sensitivity to beam displacement, up to 8.2×10^{-3} mm^{-1} depending on the offset plane. The ICT showed a slight sensitivity to horizontal beam offsets, in the order of 0.2×10^{-3} mm^{-1} while

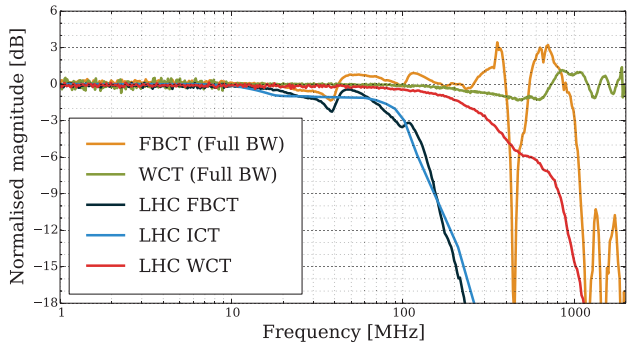

Figure 5: Laboratory measurements of the frequency response of the FBCT, ICT and WCT.

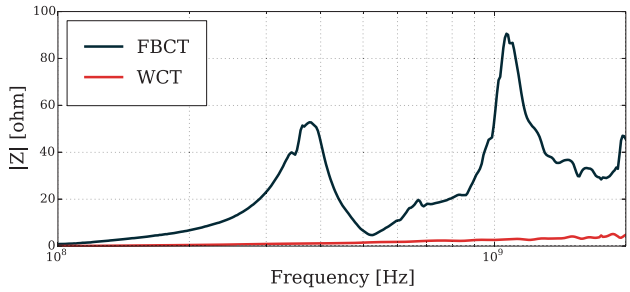

Figure 6: Laboratory measurements of the longitudinal impedance of the FBCT and WCT.

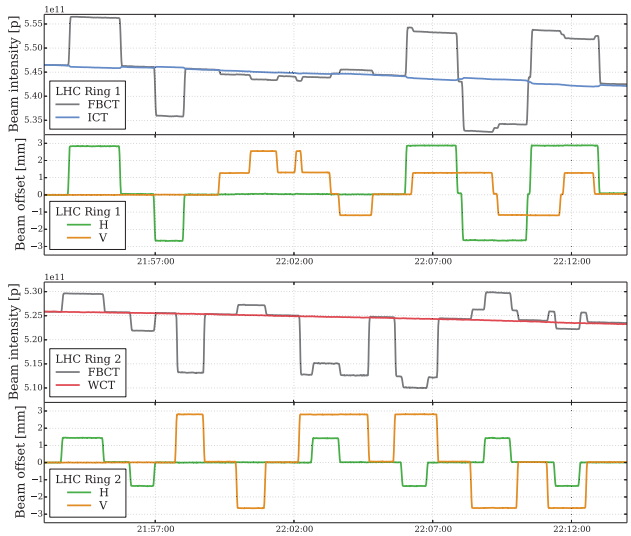

Figure 7: Beam position sensitivity of the FBCT, ICT and WCT. The intensity plots show the last 5% of the total beam intensity.

no position sensitivity could be observed for the WCT within the measurement resolution of 0.05×10^{-3} mm^{-1}.

The time response of the three instruments to a single nominal bunch is shown in Fig. 8. The main pulse is 9 ns long for the ICT and 12 ns long for the FBCT when filtered at 80 MHz. In both cases the pulses are followed by tails extending to 40 ns and 50 ns, respectively. The response of the WCT is a single pulse stretched by the filters of the amplification chain to around 22 ns as required by the current acquisition system. The full-bandwidth WCT response is about 2 ns long followed by a 1 ns reflection. It should be

ISBN 978-3-95450-177-9

Table 1: Beam position sensitivity of the LHC Ring 1 (R1) and Ring 2 (R2) FBCTs, ICT and WCT. The unit is [10^{-3} mm^{-1}], i.e. 1 in the table translates to 0.1 % change of the intensity reading for a 1 mm beam position change.

Axis	FBCT R1	FBCT R2	ICT	WCT
Horizontal	6.5	5.1	0.2	< 0.05
Vertical	1.4	8.2	0.1	< 0.05

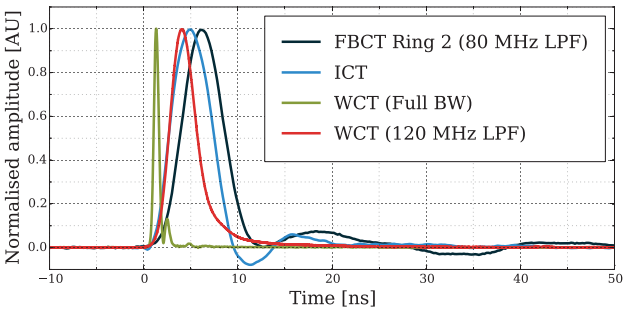

Figure 8: The response of the FBCT, ICT and WCT to a single nominal LHC bunch.

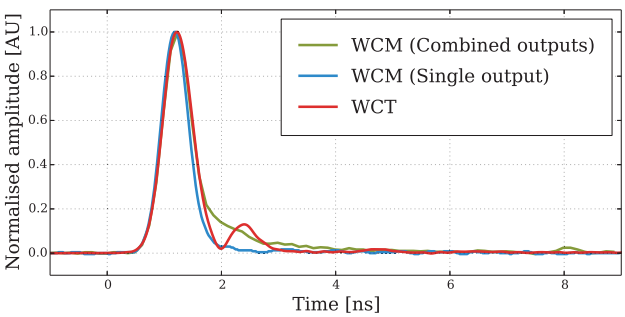

Figure 9: The response of the WCM and WCT to a single nominal LHC bunch.

noted that in case of the LHC any signal leakage outside of the 25 ns window is measured as belonging to the following bunch and compromises the measurement.

The full-bandwidth response of the WCT with beam was also compared to that of a "traditional" LHC Wall Current Monitor (WCM) [7]. The WCT and WCM output signals were acquired with a 3 GHz-bandwidth oscilloscope.

The results of measurements performed on a nominal LHC bunch with a 1 ns 4σ bunch length are shown in Fig. 9. The WCM response can be improved by using a single output and avoiding mismatches introduced through combination of all 8 of its outputs. The WCT pulse is seen to match the single output WCM response but suffers from a 15 % reflection coming 1 ns after the main signal, suspected to be caused by the internal WCT PCB signal combiners. An improvement to this would therefore be required if the WCT were also to be used for longitudinal diagnostics.

CONCLUSIONS

The LHC Wall Current Transformer is based on a relatively unknown technology which is well-suited for bunch-by-bunch intensity measurements. Due to its relatively simple mechanical design it can be installed, removed and modified with no impact on the accelerator vacuum. The WCT developed for the LHC has 400 MHz bandwidth, is optimised for the precise measurement of nanosecond bunches spaced by 25 ns and can be calibrated with long current pulses.

After a year of testing and commissioning of the new instruments, it was concluded in 2015 that the WCT was the most suitable sensor to measure bunch intensity in the LHC. During the 2015/2016 winter technical stop the two operational FBCTs were therefore replaced by WCTs. As of 2016, the WCT became the operational bunch-by-bunch intensity monitor in the LHC. Installation of the WCTs has led to a significant improvement in LHC bunch-by-bunch intensity measurements. It is the only sensor to show no measurable sensitivity to the beam position and no signal leakage outside the 25 ns window. In addition, longitudinal bunch measurements with a full-bandwidth WCT give very similar results to that of the operational LHC Wall Current Monitor.

ACKNOWLEDGEMENTS

The authors would like to thank their colleagues from the CERN Beam Instrumentation Group, especially: S. Bart Pedersen, D. Belohrad, J.J. Gras and J. Kral for their work on the acquisition systems as well as T. Lefevre and L. Soby for their support during the development of the Wall Current Transformer.

REFERENCES

[1] P. Odier, D. Belohrad, J.-J. Gras and M. Ludwig, "Operational Experience and Improvements of the LHC Beam Current Transformers", in Proc. DIPAC 2011, Hamburg, Germany, paper TUPD69, pp. 467-469, 2011

[2] L. Soby *et al.*, "A New Integrating Current Transformer for the LHC", in Proc. IBIC 2014, Monterey, CA, USA, paper WEPF06, pp. 540–543, 2014.

[3] M. Gasior, "An Inductive Pick-Up for Beam Position and Current Measurements", in Proc. DIPAC 2003, Darmstadt, Germany, paper CT01, pp. 53-55, 2003.

[4] K. Satoh, "New Wall Current Beam Position Monitor", in Proc. PAC 1979, San Francisco, CA, USA, pp. 3364-3366, 1979.

[5] V.P. Cherepanov, "Image Current Monitor for Bunched Beam Parameters Measurements", in Proc. DIPAC 1995, Travemuende, Germany, pp. 142-144, 1995.

[6] F. Caspers, "Impedance Determination from Bench Measurements", CERN Note CERN-PS-2000-004 (RF), Geneva, Switzerland, 2000

[7] T. Bohl, J.F. Malo "The APWL Wideband Wall Current Monitor", CERN Note CERN-BE-2009-006, Geneva, Switzerland 2009

[8] M. Krupa, D. Belohrad, M. Gasior, T. Lefevre and L. Soby, "Summary of LHC MD 398: Verification of the dependence of the BCTF measurements on beam position and bunch length' CERN ATS Note CERN-ACC-Note-2015-0031 MD, Geneva, Switzerland, 2015

ISBN 978-3-95450-177-9

DIAGNOSTIC DATA ACQUISITION STRATEGIES AT FRIB *

S. Cogan†, S. Lidia, R. C. Webber, Facility for Rare Isotope Beams, East Lansing, MI, USA

Abstract

Strategies for data acquisition and processing will be discussed in the context of the Facility for Rare Isotope Beams (FRIB). Design decisions include selecting and designing electronics hardware, data acquisition cards, firmware design, and how to integrate with EPICS control system. With over 300 diagnostic devices and 16 unique types of devices, timing for synchronous data acquisition is important. Strategies to accelerate development as well as reduce maintenance requirements will be discussed, including using common hardware and firmware whenever possible, and defining a common data reporting structure for use by most devices. MicroTCA.4 platform is used to integrate data acquisition cards, distribute timing information, and machine protection signals.

FRIB MACHINE REQUIREMENTS

The Facility for Rare Isotope Beams (FRIB) is a new scientific user facility for low energy nuclear science. Under construction on campus and operated by Michigan State University, FRIB will provide intense beams of rare isotopes [1].

FRIB will deliver the highest intensity beams of rare isotopes available anywhere. The superconducting linear accelerator (linac) will accelerate ion species from ^{18}Ar up to ^{238}U with energies of no less than 200 MeV/u and provide beam power up to 400 kW. Although designed to support full-scale CW operation, low current and pulsed modes will also be utilized, so diagnostics must support a large dynamic range, from 1 nA to 1 mA of beam current. Figure 1 shows a schematic overview of the accelerator.

Machine Protection and Availability

In order to achieve high reliability and high availability, permanent accelerator component damage should be prevented, beam loss and residual activations should be minimized, and beam downtime minimized. This leads to an array of diagnostic devices which monitor a variety of beam loss mechanisms. A machine protection system (MPS) has been designed to detect and respond quickly (< 35 μsec) to beam loss events and terminate the beam [3]. This is achieved by monitoring not-OK (NOK) signals from a multitude of MPS nodes which digitize diagnostic data and make local NOK decision in less than 15 μsec. The remaining 20 μsec of the time budget is used to communicate the NOK signal to the MPS Master and to terminate beam production and transport. Table 1 is simplified picture of the acute (fast) and chronic (slow) losses which we must detect. Table 2 shows an overview of diagnostic devices utilized not only for machine protection (MPS), but also for tuning, commissioning, and general diagnostic information [2]. *Italicized devices* * will provide input to MPS.

Table 1: Acute and Chronic Beam Loss Detection

Beam Loss	Diagnostic Response Time
100% (2 J)	15 usec
10% (0.2 J)	150 usec
Slow (0.1 W/m)	seconds

Table 2: FRIB Diagnostic Devices

Device	Total #
Beam Position Monitor *	149
Beam Current Monitor (ACCT) *	12
BLM - Halo Monitor Ring *	66
BLM - Ion Chamber *	47
BLM - Neutron Detector *	24
BLM – Fast Thermometry System *	240
Profile Monitor (Lg., Sm. Flapper)	41
Bunch Shape Monitor	1
Allison Emittance Scanner (2 axis)	2
Pepper pot emittance meter	1
Wire Slit Emittance Scanner (2 axis)	1
Faraday Cup	7
Fast Faraday Cup	2
Viewer Plate	5
Selecting Slits System - 300 W	5
Collimating Apertures - 100 W	2
Intensity Reducing Screen System	2

Implications for Data Acquisition

To achieve MPS requirements (not all of which are discussed here, see [3]), diagnostic devices should have a response time of 5 μsec (analog bandwidth DC to 35 kHz), digitized sample rates of at least 1 MS/sec and support a large dynamic range, from < 1 nA to 1mA, depending on the device. To respond to beam loss events in less than 15 μsec, MPS decisions are made in real-time locally by the data acquisition electronics. Field programmable gate arrays (FPGAs) are utilized to provide real-time signal processing and MPS decision, with close integration to digitizing hardware, often combined in a single electronics board. Additionally, FPGAs allow custom firmware to incorporate accurate timestamp from a global timing system (GTS) and provide ability for improved signal processing, including digital filters, background noise subtraction, advanced threshold triggering, etc.

* This material is based upon work supported by the U.S. Department of Energy Office of Science under Cooperative Agreement DE-SC0000661, the State of Michigan and Michigan State University.

† cogan@frib.msu.edu

ISBN 978-3-95450-177-9

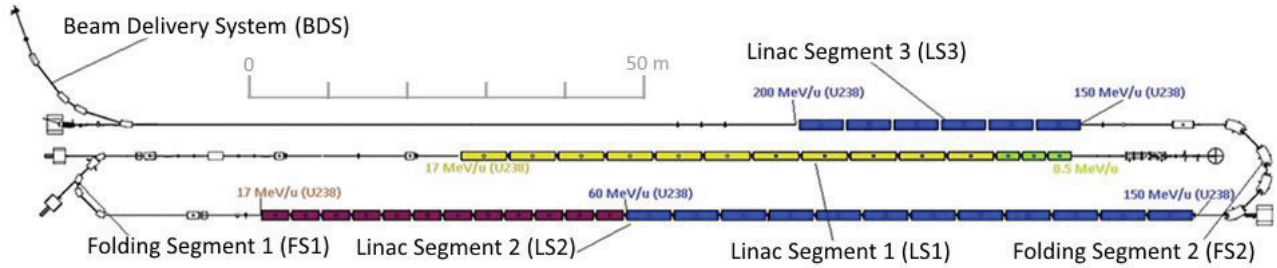

Figure 1: Schematic of FRIB accelerator, three linac segments and two folding segments.

Beam Modes and Structure

Figure 2 illustrates various beam modes at FRIB. The primary beam mode will deliver near continuous (CW) beam, however, a 50 usec beam gap is introduced at ~100 Hz to reset beam current transformer readings and facilitate sampling of signal backgrounds. This leads to actual duty factor of 99.5%. Pulsed modes are used to achieve relatively low duty factor for beam commissioning and tuning. Beam power ramp-up modes exist to slowly heat the isotope production target and avoid damage to due to thermal shock. The duty factor ramps from 0% to 99.5%, with up to 250 beam on / off pulses during each 10 msec cycle. The beam structure for each 10 msec cycle is broadcast to the data acquisition hardware by the global timing system (GTS), which indicates beam events such as start-of-cycle (every 10 msec), beam on / off, and global timestamp events. The 50 µsec beam gap for diagnostics appears at the beginning of every 10 ms beam cycle, so the processing of background signal continues regardless of beam mode (pulsed, CW, or ramp-up). Modulation of the CW beam current is performed with an electrostatic chopper in the Front End, upstream of Linac Segment 1.

Global Timing System

The global timing system (GTS) distributes event codes across the system to keep all receivers aware of the state of the beam (on or off), start-of-cycle events (with or without beam), global timestamp (POSIX time), and custom diagnostics codes for synchronized trigger acquisitions. GTS event codes are distributed by fiber optic throughout the machine, providing up to 1 event code every 80.5MHz, which is locked with the fundamental RF cavity frequency. Each data acquisition (DAQ) device connected with MPS needs access to this information to keep local data timestamps in sync with global clock, and to respond appropriately to various beam modes.

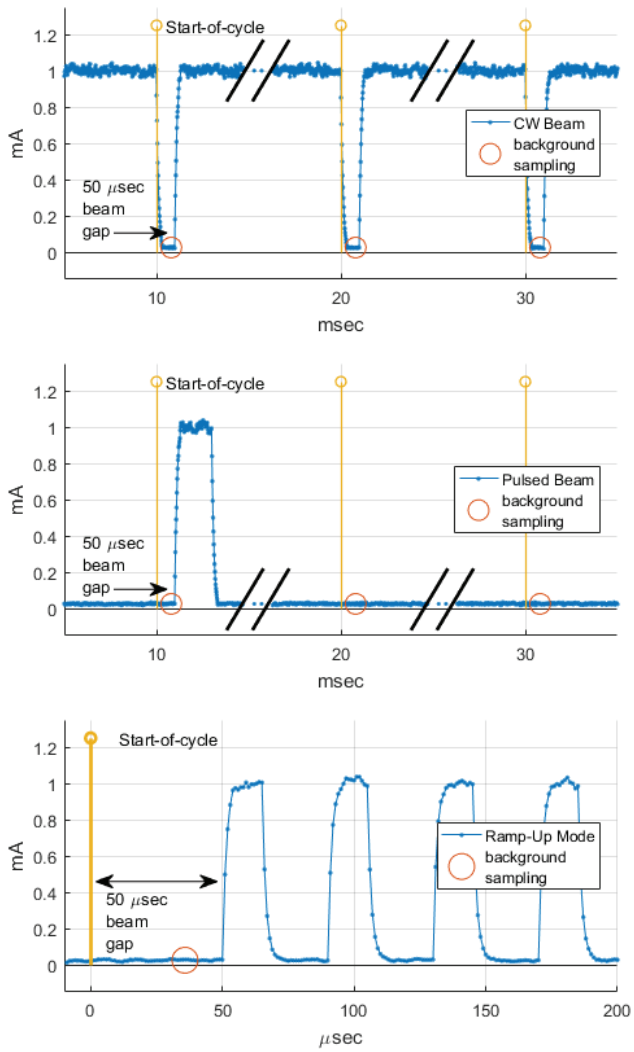

Figure 2: Illustration examples of beam modes and timing, (a) continuous CW mode, (b) pulsed beam mode, and (c) ramp-up beam mode.

DATA ACQUISITION HARDWARE

At FRIB there are hundreds of diagnostic devices requiring connections to both MPS and GTS systems, in addition to network connections to the control systems network, EPICS. A potentially large number of fiber optic (GTS), Ethernet (EPICS), and trigger signal (MPS) cables need to be managed.

In addition to these connectivity requirements, the variety of diagnostics devices have different requirements and operating modes. Some are continuously monitoring, while others are intermittent-use. Some have MPS requirements, others do not. Diagnostic devices have varied response times and dynamic range requirements.

It is an option to design a unique data acquisition (DAQ) system for each device, with connections and components optimized for each device. However, a large number of unique DAQ systems can ultimately be quite burdensome to develop and maintain.

ISBN 978-3-95450-177-9

Simplification: Leverage Commonality

Leveraging hardware commonality has been a design goal for the FRIB diagnostics DAQ systems. It should be clear that utilizing a small number of DAQ systems results in fewer systems to learn, develop, and maintain. In the short term, the full diagnostic scope can be developed more rapidly. Much of the firmware and software interfaces can be shared, for faster development and passing new feature updates to multiple devices. In some cases, we also adapted electronics designed in-house or open source for our diagnostic applications, with minor changes. Some of the efforts to simplify hardware, firmware, and software will be discussed in detail.

MicroTCA Chassis-Based Platform

A chassis-based hardware platform has significant advantages for FRIB diagnostics. While individual "pizza box" systems were considered for some systems, a chassis platform with multiple payload slots demonstrated several advantages. Advantages include common power supply management, thermal management, easy to add/replace boards, and common data busses between cards in the chassis for shared signals, reducing need for external cables.

While many card carrier platforms exist, it was desired to avoid those which were proprietary, which tend to be expensive and sometimes difficult to integrate with custom hardware. VME and MicroTCA.4 [4] [5] were two relatively open standards which were considered, both of which see significant usage at physics research installations. A thorough comparison of these technologies is beyond the scope of this paper, but MicroTCA.4 was chosen as the primary platform for our fast-sampling diagnostics with connection to MPS. MicroTCA's use of modern high-speed serial busses such as PCIe (Gen3) and Ethernet (GbE) provide fast access to data, allowing us to consolidate numerous EPICS drivers (IOC) into a single CPU module, one per chassis. VME and CompactPCI primarily support slower legacy parallel busses. MicroTCA also includes some valuable features such as remote power module management, thermal management and monitoring, and support for rear-transition-modules (RTM) which provide additional input/output interface.

MicroTCA is a more complicated standard than some alternatives, and we experienced significant compatibility issues early on, most of which have been addressed. With most issues resolved, we have managed to build some robust and reliable test systems. MicroTCA allows us to leverage several commercial off-the-shelf (COTS) modules, such as the chassis, power module, processor card (CPU), and MicroTCA Carrier Hub (MCH). For MicroTCA DAQ cards, many COTS and customized COTS options exist.

MicroTCA Backplane Signals

MicroTCA has allowed us to significantly simplify the cabling to various control systems. The AMC backplane provides power to each card, as well as data busses between cards, such as PCIe, Ethernet, and general use M-LVDS I/O ports. While each chassis can contain up to 12 payload DAQ cards, for diagnostics we use two slots to consolidate key interfaces to the larger control system, using the AMC backplane for intra-chassis distribution, illustrated in Fig. 3.

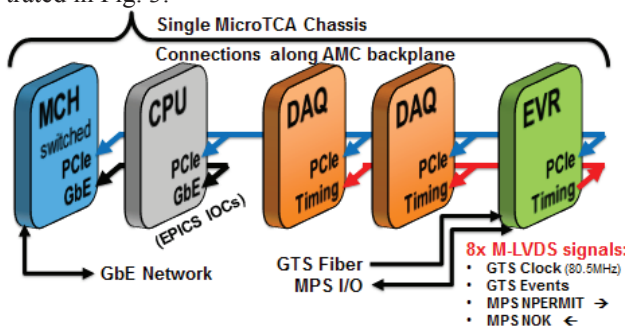

Figure 3: MicroTCA data bus distribution.

The first slot is a processor card (CPU) which is the single interface to the EPICS control system network, with multiple IOC drivers running on Debian Linux OS. MicroTCA backplane provides switched PCIe connection to each DAQ card, and measurement and configuration data is passed simply between CPU and DAQ cards by PCIe register reads and writes. An Ethernet protocol stack is not necessary in the FPGA, and is completely handled by Linux running on the CPU module.

The second slot is for our event receiver (EVR). This is a custom FPGA-based board which receives and decodes events from the GTS fiber bitstream and handles the interface to the MPS system, utilizing custom trigger in/out signals. The GTS and MPS signals utilize bidirectional M-LVDS signals on the AMC backplane, part of the MicroTCA standard generally utilized for passing triggers and interlocks (ports 17-20). The GTS and MPS signals are distributed in parallel to all other cards in the chassis, while the EVR card monitors and consolidates the MPS not-OK (NOK) signals from each card.

The end result is a MicroTCA chassis with up to 10 DAQ cards, one fiber optic interface to GTS, one interface to MPS, and one Ethernet drop, capable of monitoring up to 80 or more channels / devices.

Data Acquisition (DAQ) Hardware

We utilize FGPAs and custom signal processing algorithms to meet our real-time MPS requirements, but developing custom firmware for FPGAs is often challenging and time-intensive. We would like to share hardware and firmware between as many diagnostic devices as we can.

Since leveraging common hardware for different devices can often lead to common/shared firmware development which can lead to common software drivers and software modules, it is clear that hardware choices have a ripple effect that can significantly impact the scope of work for software and application developers downstream.

DAQ hardware that meets the strictest requirement can often be utilized for devices with an easier requirement. In that case, the DAQ hardware may be over-specified and more expensive than a lower cost alternative, but the benefits for shared development and sourcing may outweigh the potential upfront material costs. For example, a DAQ

ISBN 978-3-95450-177-9

card with a time response of 5 μsec can serve a device with a longer time response. A sample rate of 1 MS/sec may not be required for every device, but it is straightforward to integrate and decimate to lower sample rates.

FRIB device requirements were collected and analyzed, and plans were made to consolidate these to a small number of DAQ boards. Firmware was also designed to offer runtime configurability for certain aspects related to MPS function and response time, and hardware was chosen which supports runtime configurable dynamic range switching. Attention to such details early on allowed us to consolidate hardware in three main categories, served by three different MicroTCA cards.

Full Current Measurement Our beam current monitor (BCM) uses AC-coupled transformers (ACCT) and external trans-impedance amplifier to deliver fast response (>300 kHz analog bandwidth), over 1 mA range, and a unique differential current monitoring scheme for MPS. For this task we selected the [6] Struck SIS8300-L2 10-channel digitizer and FPGA board combined with [7] SIS8900 RTM analog conditioning board.

Low Current Measurement Beam loss monitors such as halo monitor rings, ion chambers, and neutron detectors will generate currents in a lower range, usually less than 100 uA. MPS algorithms involve a configurable integration window combined with configurable threshold limit. Various intermittent-use devices will utilize this same hardware, even though MPS function is not required, including faraday cups and scanning wire profile monitors. We worked with CAENels to provide a customized version of their AMC-PICO-8 MicroTCA board [8], an 8-channel fast sampling picoammeter. Our custom version includes two runtime-selectable dynamic ranges (16 uA and 130 uA) and faster response (DC to 35 kHz) compared to COTS version. CAENels also provided support for integration of custom firmware developed by FRIB for MPS functionality and GTS integration.

Fast Voltage Measurement We have planned many (149) beam position monitors (BPM), each with 4 buttons to digitize at high speed. We will process the 2nd harmonic (161 MHz) of the 80.5 MHz bunching frequency. A system designed specifically for BPMs is required. After investigating several BPM DAQ systems, we chose to leverage the same MicroTCA digital board which was used for our EVR card. This is a general purpose digital FPGA board, developed by FRIB for use in multiple applications including machine protection system master and slave nodes, and low-level RF controls hardware. This FRIB digital board may be used either inside or outside a MicroTCA chassis. It made sense to leverage the hardware and firmware expertise already developed in-house to achieve a low cost per-channel, and get a jump start on development. A new RTM board was designed for the BPM application, providing analog signal conditioning and digitization, and designed to interface with the FRIB digital board. The fully in-house development gives us complete control over hardware and firmware design for this critical system.

FIRMWARE SIMPLIFICATION

The three FPGA boards thankfully all utilize common FPGA design tools, as all FPGAs are Xilinx. HDL code is developed modularly when possible to make possible sharing of modules between designs.

To simplify and accelerate development of signal processing algorithms for FPGAs, we have been utilizing the Xilinx Vivado High-Level Synthesis (HLS) tool [9]. It is one of several tools which allows the developer to code C or C++ functions which are synthesized to portable HDL, such as Verilog or VHDL, which can be imported to a larger FPGA project.

A detailed discussion of HLS is beyond the scope of this document, however the attraction of such a tool should be clear: C or C++ offers familiarity and ease of programming in a popular high-level language. Development of signal processing algorithms can be coded effectively in C, and HLS handles the conversion to efficient HDL code, automatically incorporating math IP cores, FPGA resource sharing, pipelining, and timing constraints. As should be expected, there is a learning curve to get started, and this tool does not replace the need for HDL expertise, but such tools can be very powerful to accelerate development of FPGA-based solutions which would otherwise be quite complex in HDL alone. Vivado HLS seems particularly well suited for math-intensive signal processing tasks, accelerating development time and resulting in efficient FPGA resource usage.

SOFTWARE AND DATA REPORTING

As mentioned previously, multiple diagnostic devices which share the same firmware benefit from shared software at the driver level. In an effort to standardize software development further, a common beam data reporting scheme was created, which will apply to all MicroTCA based diagnostics.

A common beam data reporting scheme capitalizes on the fact that no matter what beam mode we are in (CW, pulsed, ramp-up), there is always the 10 msec beam cycle period. This provides a natural time window over which to integrate or average the measurement, and to report simple statistics. Most of our diagnostic devices measure current, so the FPGA firmware will calculate the total integrated current over the 10 msec beam cycle, track min and max values during that period, and report how much time the beam was expected to be on. The software IOC driver will acquire these measurement records at 100 Hz (see Table 3 and Fig. 4), continuously providing 100 Hz sampled data waveforms and also providing further averaging/decimation as desired. For example, a 1 Hz average current value is reported and calculated by averaging 100 of the last 100 Hz average current samples, beginning at the start-of-second GTS event, which is synchronous across all devices.

ISBN 978-3-95450-177-9

Table 3: 100 Hz Beam Measurement Record

Beam Measurements @ 100 Hz
Total Charge (integrated current)
Beam ON Time
Average Beam Current (over 10 msec)
Typical Beam Current (during ON time)
Min / Max Current
Timestamp (start-of-cycle)

Calculated offset value may also be included, where the offset is calculated during the 50 µsec diagnostic beam gap, using the previous gap or multiple gap averaging.

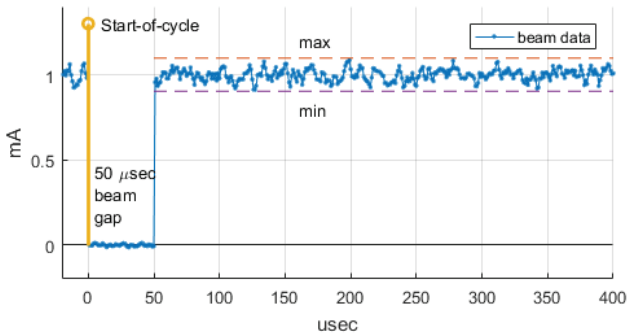

Figure 4: Illustration of beam cycle structure.

The beam position monitor reports different kind of data: X, Y position, magnitude (intensity), and phase. However, BPM will still utilize the 100 Hz period to average and decimate reporting.

All devices will also support triggered acquisitions of N samples, decimated by factor of M, where N and M are configurable and decimation is implemented in IOC software.

All devices also store and continuously update a history of raw data, sampled at 1 MS/sec, for 1 second per channel. This is implemented by local DDR memory on the FPGA board, operated as a ring buffer. This fulfils an MPS requirement that each device reports 1 second of history data preceding an MPS "trip" event when the machine protection system shuts down the beam. An MPS trip will freeze all ring buffers shortly after beam shut down, and the contents of the ring buffers may be examined. Data is timestamped in a synchronous way across the entire machine, made possible by the GTS. Figure 5 illustrates what a portion of the ring buffer might look like after an MPS trip event.

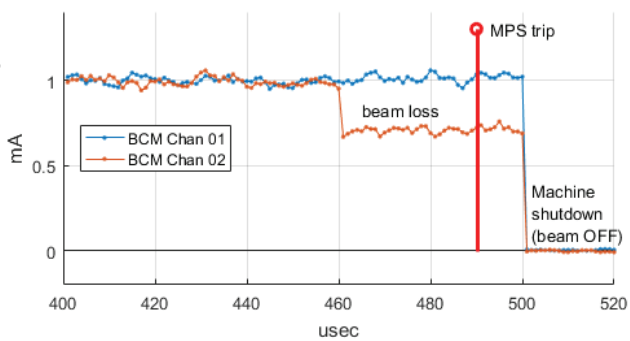

Figure 5: Differential BCM data leading up to MPS trip.

The 1 second MPS ring buffer requires 4 MB per channel, perhaps 8 GB or more for the entire array of diagnostics. It should be noted that to reduce network traffic, the ring buffer memory local to each DAQ card may be masked or ignored, such that only certain devices of interest are read back.

This common diagnostics data reporting structure is easily utilized by high-level software / application developers, and enables straightforward plotting data from multiple different devices on a common time scale.

CONCLUSION

An effort to reduce the number of independent hardware/firmware/software development efforts where possible has enabled a small diagnostics electronics team at FRIB to make fast progress.

A high degree of commonality was achieved for diagnostic DAQ hardware. Three MicroTCA DAQ cards cover about 75% of devices. This led to shared firmware and software development at low-level. Common beam data reporting standards will simplify high-level software development.

Additional factors for efficient development included leveraging existing in-house hardware development efforts (FRIB digital board), good support by industry partners for custom firmware development, and HLS tools to provide accelerated HDL algorithm development using C language.

Proper functioning beam diagnostics are a critical component of the machine tuning and commissioning. We are on our way to delivering high quality beam diagnostics for upcoming front-end commissioning.

REFERENCES

[1] J. Wei, et al., "FRIB accelerator status and challenges", LINAC'12, Tel Aviv, August 2012, p. 417, http://www.JACoW.org

[2] S. Lidia, et al., "Overview of beam diagnostic systems for FRIB", Proceedings of IBIC 2015, Melbourne, Australia, http://www.JACoW.org

[3] S. Lidia, et al., "FRIB machine protection system design and validation studies", Proceedings of IBIC 2015, Melbourne, Australia, http://www.JACoW.org

[4] PICMG MicroTCA Overview, https://www.picmg.org/openstandards/microtca/

[5] MTCA.4 at a glance, http://tesla.desy.de/doocs/MTCA/MTCA.4.html

[6] Struck Innovative SIS8300 µTCA for Physics Digitizer, http://www.struck.de/sis8300.html

[7] Struck Innovative SIS8900 µTCA for Physics RTM for SIS8300 Digitizer, http://www.struck.de/sis8900.html

[8] CAENels AMC-PICO-8, 8-channel Bipolar 20-bit Picoammeter, http://www.ca enels.com/products/amc -pico -8/

[9] Vivado High-Level Synthesis, http://www.xilinx.com/products/design-tools/vivado/integration/esl -design.html

ISBN 978-3-95450-177-9

BEAM DIAGNOSTICS CHALLENGES FOR BEAM DYNAMICS STUDIES

O. R. Jones, CERN, Geneva, Switzerland

Abstract

This seminar reviews the performance and limitations of present beam instrumentation systems in relation to beam dynamics studies, and gives an overview of the main requirements from the accelerator physics community for new or improved measurements that need an R&D effort on beam diagnostics.

INTRODUCTION

Beam dynamics studies are an essential element in the smooth running of all accelerators. Such efforts are important for the commissioning of a machine, modifying initial design parameters to increase performance, and to understand the issues and challenges that arise during accelerator exploitation [1].

Routine measurements during standard operation, such as adjustment of the orbit and optimisation of the tune, coupling and chromaticity are not addressed in this seminar, although some of the diagnostic devices used for such measurements will be covered. The emphasis is instead on specific measurements during machine set-up, such as the measurement and correction of the machine optics in both synchrotrons and linacs or transport lines. Also discussed are more advanced measurements for the understanding of impedance and space charge effects, detecting instabilities, and the identification of sources driving the diffusion of particles to high oscillation amplitudes.

MEASURING THE MACHINE OPTICS FUNCTIONS IN SYNCHROTRONS

The measurement and correction of optics parameters has been an area of intensive study since the advent of strong focusing synchrotron accelerators, where perturbations from field imperfections and misalignments became a concern. Traditionally, colliders have led the development of methods for optics control based on turn-by-turn centroid position data, while lepton storage rings have focused on closed-orbit-response techniques [2]. Both of these methods rely heavily on the use of the beam position system of the accelerator, and are now often driving its requirements.

Turn-by-turn Techniques

In 1983 a major achievement took place in the CERN-ISR, where the Beam Position Monitors (BPMs) were used successively around the collider to measure the relative amplitude and phase advance of the β-function by observing the amplitude and phase of induced betatron oscillations [3]. This was the first time that machine optics had successfully been reconstructed from individual BPM data, at that time using a BPM system that was entirely based on analogue technology.

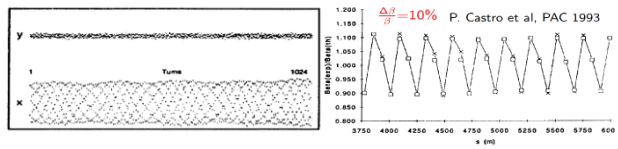

Figure 1: LEP β-beating example. Left: turn-by-turn BPM data. Right: Δβ/β for a section of the machine.

The first optics measurements using digital, turn-by-turn BPM data were performed at CERN-LEP (Fig. 1) [4]. The β-function at each BPM location was extracted from the phase advance between 3 BPMs, assuming a good knowledge of the focusing elements in between (Eq. 1).

$$\beta^{BPM1}_{measured} = \beta^{BPM1}_{model}\left(\frac{\{cot\varphi_{12} - cot\varphi_{13}\}_{measured}}{\{cot\varphi_{12} - cot\varphi_{13}\}_{model}}\right) \quad (1)$$

This method, known as "β from phase", was also used in CESR (Cornell, USA) in 2000 to minimize the β-beating, the difference between the measured β and the design β (Δβ/β), with an rms of only 2% [5]. This is still one of the best optics correction achieved in a lepton collider.

One of the limitation of this method is its reliance on good quality BPM data. Identifying BPMs giving poor readings or BPMs with excessive noise was therefore very important. A major step forward in achieving a more robust analysis was taken at SLAC in 1999, where singular value decomposition (SVD) techniques were used to isolate faulty BPMs and identify noise components affecting the oscillation data [6].

The 3 BPM method developed at LEP has recently been extended for the LHC to take into account any number of BPMs [7], resulting in a much better overall resolution in the measurement of the β-functions.

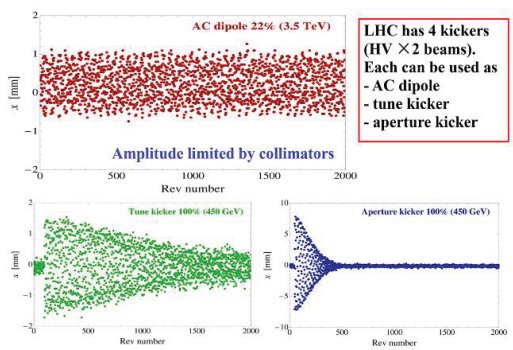

Figure 2: Examples of excitation for optics measurements in the LHC. Top: AC-dipole excitation. Bottom: Examples of single kicks at injection energy.

In order to initiate a sufficient large centroid motion to be visible on a turn-by-turn basis with the BPM system, the beams typically need to be kicked to relatively high

ISBN 978-3-95450-177-9

amplitude using a fast magnetic or electro-magnetic kicker. The disadvantage of this technique is that the oscillations are often quickly damped, which lead to significant emittance blow-up in hadron machines. The former is a big drawback for optics measurement as the amount of useful BPM data available is then highly limited. An alternative excitation technique uses an "AC Dipole" excitation, originally developed at RHIC (BNL, USA) for crossing polarisation resonances [8]. Here, a forced oscillation is put onto the beam near the betatron tune, but still outside the tune spread. If performed adiabatically, this leads to a steady, high amplitude oscillation without emittance blow-up, which is excellent for turn-by-turn optics measurements (Fig. 2).

Closed-Orbit-Response Techniques

Measurement of optics functions in synchrotron light sources is dominated by the use of closed orbit response techniques. This involves exciting individual dipole corrector magnets, measuring the orbit and using analysis routines such as LOCO (Linear Optics from Closed Orbits [9]) to extract the lattice optics functions. Using such techniques SOLEIL (France) and DIAMOND (UK) have been able to measure and correct the β-beating to an rms value of less than 0.4%.

Closed orbit response measurements typically take longer that turn-by-turn measurements, as each of the hundreds of corrector magnets in the ring needs to be excited individually and the corresponding orbit measured. Nevertheless, recent advances in automating these techniques now allow such a measurement to be carried out in under a minute in some synchrotron light sources. This is unfortunately not scaleable to the LHC, where the slow response of the thousand or so superconducting corrector magnets would imply very long measurement times.

With recently improved BPM electronics now providing high resolution turn-by-turn data, turn-by-turn optics measurement techniques are starting to compete with orbit response measurements. A campaign is currently ongoing at several 3rd generation light sources to compare the two methods. Nevertheless, the turn-by-turn techniques do not yet have the sensitivity to measure β-beating at below the 1% level.

Beam Instrumentation Challenges for Improved Optics Measurements in Synchrotrons

There are three main challenges to improving our understanding of the machine optics functions using turn-by-turn techniques.

Firstly, the excitation needs to be reduced in order to limit emittance growth in hadron machines and avoid non-linearities due to strong sextupoles in next generation synchrotron light sources making use of multi-bend achromats. This implies improving the turn-by-turn resolution of the BPM systems, in order to obtain the same signal to noise performance for smaller excitation levels. It should be noted that the BPM resolution in itself is not currently limiting the measurement of the β-function, as the excitation is adapted accordingly.

Secondly, optics measurements would benefit from a much better BPM linearity in the range of the excitation and in the overall calibration from BPM to BPM. Light sources are currently at the 1-2% level, the LHC at the 3-4% level. Improving this to below the 1%level would allow the use of the oscillation amplitude as well as the phase for β-function reconstruction.

Thirdly, all machines would benefit from a better BPM design to lower the coupling impedance these BPMs present to the beam. This is a serious issue for synchrotron light sources where the machines becomes more sensitive to collective effects as lower beam emittances are achieved, with the BPMs accounting for a significant fraction of the total impedance budget. In addition, the short range, high frequency wakes induced by the BPMs can result in beam induced heating. Many studies are already underway to address this issue (see e.g. [10]).

OPTICS MEASUREMENT & OPTIMISATION IN LINACS AND TRANPORT LINES

Optics Measurement in Linacs and Transport Lines

In single pass structures such as linacs and transport lines, it is important to match the beam line optics to the incoming beam. Two procedures are frequently used: multi-wire (or multi-screen) emittance measurements and quadrupole scans. Both methods are based on wire scanners or screen monitors measuring the transverse beam size. The beam size (x) at a location s can be expressed in terms of the optical α and β functions and the emittance at an upstream location s_0 as

$$\langle x^2(s)\rangle = R_{11}^2\beta(s_0)\epsilon - 2R_{12}R_{11}\alpha(s_0)\epsilon + R_{12}^2\gamma(s_0)\epsilon \qquad (2)$$

with R being the transfer matrix between s_0 and s. In a quadrupole scan, the transfer matrix elements R11 and R12 are varied, by changing the strength of a quadrupole between s_0 and s. Beam-size measurements for at least 3 different quadrupole settings are required in order to solve for the three independent unknown parameters: ε, $\beta(s_0)$ and $\alpha(s_0)$. The fourth parameter, $\gamma(s_0)$ is not free, but determined by $\gamma = (1+\alpha^2)/\beta$. A multi-wire (or multi-screen) emittance measurement is very similar. Here, the quadrupole gradients stay constant, but the R matrices between s_0 and the various beam size measurement devices are different. Again, at least 3 measurements are required. This procedure also provides an absolute measure of the emittance

If a beam is injected into a ring or linac with a mismatch, the beam will filament until its distribution approaches a shape that is matched to the optics of the ring or linac lattice. This filamentation causes the beam emittance to increase. Knowledge of α and β allow quadrupole magnet settings to be adjusted so as to match the optical

ISBN 978-3-95450-177-9

functions to the injected beam and minimize any emittance increase.

Figure 3 shows an example of how this technique can be further improved through the use of tomographical techniques to fully reconstruct the initial phase space density distribution of the beam. Things get more complicated when space charge effects are present, as the measured profiles can no longer be tracked back to the initial profile using linear transformations. Instead, the measurements act as input to simulation codes which attempt to reconstruct the initial distribution based on the optical functions and the measured final profiles, taking into account these space charge effects [11].

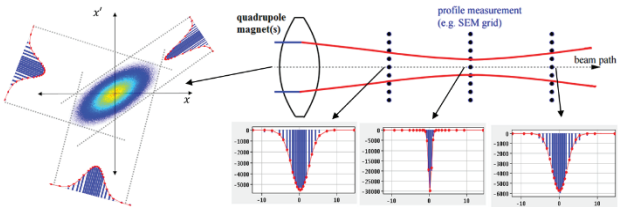

Figure 3: Using tomography to reconstruct the initial phase space distribution in a linac or transport line.

Optimisation of Linacs

For next generation linear colliders the challenge lies in aligning all the thousands of components in the accelerator sufficiently well to limit emittance growth, in particular the BPMs and quadrupoles. Chromatic dilution, the emittance increase due to misaligned quadrupoles, scales with the square root of the number of quadrupoles (and associated BPMs). This means that with the sheer number of quadrupoles in these machines, typically several thousand, even alignment at the 10μm level can lead to significant increase in the emittance.

Beam-based alignment techniques, in particular dispersion free steering, are therefore foreseen to reduce this alignment error to the tens of nm level [12]. This relies on the fact that a beam travelling through the centre of a quadrupole will follow the same path regardless of its energy, while an-off momentum beam travelling with an offset through a quadrupole will undergo a deflection depending on its energy. By measuring and correcting the trajectories of beams of different energy it is therefore possible to thread the beam through the centre of all quadrupoles, limiting the overall emittance increase. This was recently demonstrated at the FACET facility at SLAC [13].

An efficient way of performing dispersion free steering is to introduce an energy chirp on the bunch train passing through the linac. If the BPM system has enough temporal resolution it is then possible to obtain trajectory information for different energies during the passage of a single bunch train.

Beam Instrumentation Challenges for Optics Measurements in Linacs and Transport Lines

The main challenge for optics measurements in linacs is to provide on-line emittance measurements. While slit and grid techniques and 3 wire-grids or screens can be used for setting-up with low intensity beams, non-invasive techniques are required for emittance measurements on high intensity, high power machines. For H^- linacs, laser based systems have successfully been developed to fulfil this role, with the Spallation Neutron Source (SNS) at Oak Ridge National Laboratory (USA) using this method on their production beams [14] and Linac4 at CERN having tested a similar system during its commissioning phases [15]. The principle is similar to slit and grid emittance measurements, but where the slit is replace by a thin laser beam that strips one electron from the H^- ions to produce a slice of neutral H^0 atoms. The remaining H^- ions in the main beam are deflected using a dipole magnet, leaving the neutral H^0 atoms to drift to a detector. The resulting profile gives the angular distribution of the particles in the original slice. By scanning the laser through the beam in both horizontal and vertical planes a full 4D reconstruction of the emittance can be obtained.

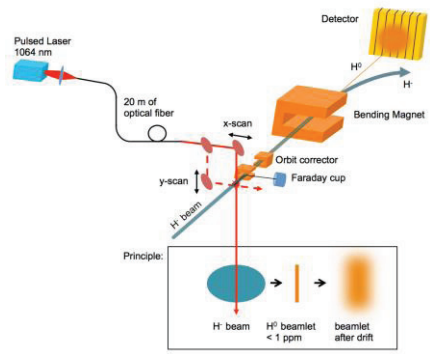

Figure 4: The laser emittance meter at CERN's Linac4.

While this technique provides a non-invasive method for emittance determination in H^- linacs, a viable system for proton linacs still needs to be developed. Ionisation profile monitors have been studied as a possibility, but suffer from space charge effects with high intensity beams, while luminescence monitors are limited by the low light yield for the operational vacuum pressures used in such accelerators.

For next generation linear colliders the challenge lies in providing high resolution BPMs with good temporal resolution for single shot dispersion free steering measurements. CLIC, for example, will have over 4000 BPMs specified to have a position resolution of 50nm, combined with 50ns temporal resolution. To quantify the success of such systems in limiting emittance growth, single shot beam size measurements of sub-micron sized beams will also be required, another of the challenges facing the beam instrumentalists developing systems for such machines.

BEAM DYNAMICS STUDIES USING BETATRON TUNE SPECTRA

Betatron tune measurements are useful for a variety of accelerator physics applications. The tune shift with quadrupole strength gives the local beta function, the tune shift with RF modulation the chromaticity, the tune shift with

ISBN 978-3-95450-177-9

beam current the transverse impedance and the tune shift with amplitude the strength of non-linear fields. Comprehending these tune spectra is also important for the optimisation of beam lifetime, limiting emittance growth, and reducing beam losses through the understanding of instabilities, space charge effects, beam-beam interactions etc.

A normal tune spectrum consists of several components. As the measurement is usually taken using a single BPM in the ring, the main components are revolution lines generated by the periodicity of the circulating beam. These are usually either filtered out by the front-end electronics or simply not displayed in the spectrum reported in the control room. The tune from coherent betatron motion in the plane of excitation is displayed in fractional tune units, from 0 to 0.5 (or 0.5 to 1) of the revolution frequency. If coupling is present a second peak at the tune frequency corresponding to the other plane will also be visible. An example of the beam response to single kick excitation and the corresponding frequency spectrum is shown in Fig. 5.

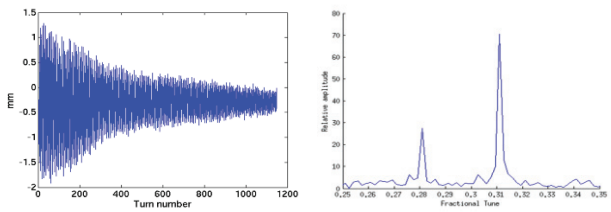

Figure 5: BPM response to a beam exited with a kick (left). Frequency spectrum in the presence of coupling (right).

In the presence of synchrotron motion the interplay between longitudinal motion and transverse betatron motion of an ensemble of particles leads to an amplitude modulation of the centroid of the particle bunch, as measured by a BPM, which depends on chromaticity. This manifests itself as sidebands that appear on either side of the main tune peak in the spectrum (Fig. 6). The distance of these sidebands from the tune can be modified by impedance and space charge effects (Fig. 7) and hence provides important information for optimising machine performance [16].

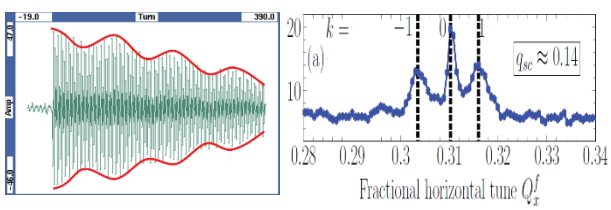

Figure 6: Amplitude modulation of the BPM response in the presence of synchrotron motion and chromaticity (left). Frequency spectrum (right).

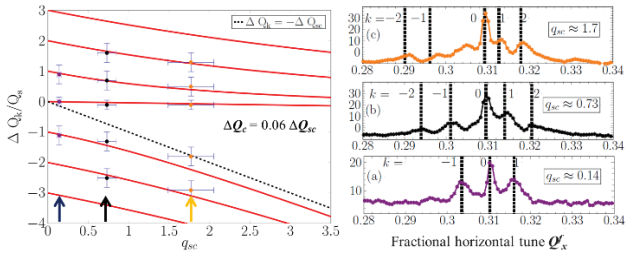

Figure 7: Simulated and measured synchrotron sideband separation for various space charge regimes at the GSI SIS18 (left). Corresponding tune spectra (right).

Tune spectra are also one of the main tools to study transverse instabilities caused by impedance, space charge, electron cloud, beam-beam, etc. Understanding the origin of such instabilities is important to find an appropriate cure which usually involves an interplay between the machine chromaticity, higher order magnetic fields and active transverse damping. Here, the challenge for instrumentation lies in detecting the instability at an early enough stage and then capturing its evolution in as much detail as possible.

The initial detection typically relies on highly sensitive transverse diagnostics, such as the recently developed Base Band Tune (BBQ) system installed at several hadron accelerators worldwide [17]. This permits a signal to be generated at the onset of an instability which subsequently triggers other systems capable of bunch-by-bunch or even intra-bunch measurements for categorising the instability.

Much work is currently ongoing to provide instrumentation for intra-bunch diagnostics on sub-nanosecond bunches [18], where the direct sampling techniques used to date are limited by the dynamic range of high frequency digitizers, the quality of broadband difference hybrids, the relatively short acquisition lengths possible and the large data volumes generated.

The future detectors for such systems will be required to have a wide bandwidth response from MHz to over 10 GHz, in order to resolve the complicated intra-bunch motion that can arise with such instabilities. One technique that is currently being investigated for such measurements involves replacing a standard electro-magnetic pick-up with an electro-optical pick-up (Fig. 8 and [19]). With such an approach the electro-magnetic field of the bunch is used to rotate the polarisation state of a laser traversing a birefringent crystal placed close to the beam. By comparing the variation of the resulting polarisation as a function of time from two crystals on opposite sides of the beam, the position variation along the bunch can be reconstructed. The advantage of such a technique is that bandwidth limiting coaxial cables are replaced by optical fibres, greatly enhancing the overall bandwidth of the system.

ISBN 978-3-95450-177-9

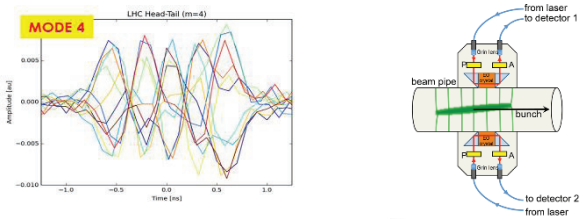

Figure 8: A mode 4 head-tail instability captured on a single bunch in the LHC using direct sampling (left). Schematic representation of an electro-optical BPM (right).

UNDERSTANDING THE BEAM HALO

For high energy or high power accelerators too much beam in the halo can lead to damage of accelerator components, either due to instantaneous beam loss or through long term irradiation. Beam halo control is therefore essential and is best achieved by tuning the machine to avoid populating the tails of the bunch distribution. The beam diagnostic challenges here lie in developing non-invasive techniques with a high enough dynamic range to resolve a beam halo a factor 10^{-5} lower in intensity than that in the beam core.

Synchrotron light sources, FELs and high energy hadron accelerators, such as the LHC, can all use synchrotron light to provide a non-invasive, transverse image of the beam distribution. To be able to measure the beam halo, however, requires an imaging system that eliminates the diffraction fringes created by the intense light from the beam core as is passes through the aperture of the first optical element. These fringes can have an intensity as high as 10^{-2} of the peak intensity and would mask any halo at the 10^{-5} level. To reduce this effect a coronagraph, developed by Lyot in 1936 for solar astronomy, can be used. Such a technique has already been demonstrated at the KEK Photon Factory to achieve a $6x10^{-7}$ ratio for background to peak intensity [20], and is now being actively studied as a possibility for halo diagnostics for the High Luminosity LHC upgrade.

SUMMARY

Beam dynamics studies are extremely important to push the performance of existing machines, to understand beam stability issues that arise during operation and to study new accelerator physics possibilities for future accelerators. This can only be achieved through partnership with beam instrumentalists striving to enhance the beam diagnostics available for such studies. This results in a better understanding of our machines and pushes the accelerator physicist to develop enhanced correction algorithms and simulation tools.

The main beam instrumentation challenges for the future include the design of high resolution, extremely linear, turn-by-turn BPM systems; non-invasive beam size measurements; high bandwidth detectors for intra-bunch transverse diagnostics; high bandwidth readout systems with on-the-fly data processing and reduction; high dynamic range beam halo diagnostics.

Much of this seminar is based on an excellent workshop "Beam Dynamics meets Diagnostics" held in 2015 as part of the EuCARD2 programme [21].

ACKNOWLEDGEMENT

I would like to acknowledge the input of A. Aleksandrov, V. Dimov, P. Forck, T. Levens, L. Nadolski, R. Tomas Garcia and M. Wendt during the preparation of this seminar and for allowing me to reproduce material from detailed presentations given on many of the subjects dicussed.

REFERENCES

[1] F. Zimmerman, “Measurement and Correction of Accelerator Optics”, SLAC, Stanford, USA, Rep. SLAC-PUB-7844, 1998.

[2] R. Tomás, “Review of Linear Optics Measurements and Corrections in Accelerators”, *in Proc. IPAC16*, Busan, Korea, May 2016, paper MOYCA01, pp. 20-26.

[3] J. Borer *et al.*, “Measurements of betatron phase advance and beta functions in the ISR”, CERN, Geneva, Switzerland, Rep. CERN/LEP/ISR/83-12, 1983.

[4] P. Castro, “Luminosity and beta function measurement at the electron-positron collider ring LEP”, CERN, Geneva, Switzerland, Rep. CERN-SL-96-070-BI, 1996.

[5] D. Sagan *et al.*, “Betatron phase and coupling measurements at the Cornell Electron/Positron Storage Ring”, *Phys. Rev. ST Accel. Beams*, vol. 3, p. 092801, 2000.

[6] J. Irwin *et al*., “Model-Independent beam dynamics analysis”, *Phys. Rev. Lett.,* vol. 82, issue 8, p. 1684, Feb. 1999.

[7] A. Langner and R. Tomás, “Optics measurement algorithms and error analysis for the proton energy frontier”, *Phys. Rev. ST Accel. Beams*, vol. 18, p. 031002, 2015.

[8] M. Bai *et al.*, “RHIC vertical ac dipole commissioning”, in *Proc. EPAC’02*, pp. 1115–1117.

[9] J. Safranek, “Experimental determination of storage ring optics using orbit response measurements”, *Nucl. Instrum. Meth. in Physics Research*, vol. A388, issues 1-2, pp. 27-36, Mar. 1997.

[10] H. O. C. Duarte *et al.*, “Design and impedance optimization of the SIRIUS BPM button”, *in Proc. IBIC13,* Oxford, UK, Sept. 2013, paper TUPC07, pp. 365-368.

[11] V. Dimov *et al.*, “Emittance reconstruction techniques in presence of space charge applied during the linac4 beam commissioning”, *in Proc. HB2016,* Malmö, Sweden, July 2016, paper WEPM1Y01.

[12] D. Schulte, “Different options for dispersion free steering in the CLIC main linac”, *in Proc. PAC05*, Knoxville, Tennessee, 2013, pp. 1251-1253.

[13] A. Latina et al., “Experimental demonstration of a global dispersion-free steering correction at the new linac test facility at SLAC”, *Phys. Rev. ST Accel. Beams*, vol. 17, p. 042803, 2014.

[14] Y. Liu *et al.*, “Laser wire based transverse emittance measurement of H^- beam at spallation neutron source”, *in Proc. IPAC2015*, Richmond, USA, May 2015, paper MOPHA041, pp. 879-881.

ISBN 978-3-95450-177-9

[15] T. Hofmann *et al.*, "Experimental results of the laserwire emittance scanner for LINAC4 at CERN", *Nucl. Instrum. Meth. A830,* 2016, pp. 526-531.

[16] R. Singh et al., "Measurements and interpretation of the betatron tune spectra of high intensity bunched beam at SIS-18", *in Proc. HB2012,* Beijing, China, Sept. 2012, paper TUO1C05, pp. 310-314.

[17] M. Gasior, "Faraday cup award: high sensitivity tune measurement using direct diode detection", *in Proc. BIW12*, Newport News, USA, April 2012, paper MOAP02, pp. 1-8.

[18] T. Levens *et al.*, "Recent developments for instability monitoring at the LHC", *in Proc. IBIC2016*, Barcelona, Spain, Sept. 2016, paper THAL02.

[19] S. Gibson et al., "High frequency electro-optic beam position monitors for intra-bunch diagnostics at the LHC", *in Proc. IBIC15*, Melbourne, Australia, Sept. 2015, paper WEDLA02, pp. 606-610.

[20] T. Mitsuhashi, "Beam halo observation by coronagraph", *in Proc. DIPAC2005*, Lyon, France, June 2005, paper ITMM03, pp.7-11.

[21] Workshop on "Beam Dynamics meets Diagnostics", Florence, Italy, Nov. 2015. https://indico.gsi.de/conferenceDisplay.py?confId=3509

ISBN 978-3-95450-177-9

BEAM SIZE MEASUREMENTS USING INTERFEROMETRY AT LHC

G. Trad*, E. Bravin, A. Goldblatt, S. Mazzoni, F. Roncarolo, CERN, Geneva, Switzerland
T. Mitsuhashi, KEK, Ibaraki, Japan

Abstract

During the long LHC shutdown 2013-2014, both the LHC and its injector chain underwent significant upgrades. The most important changes concerned increasing the maximum LHC beam energy from 4 TeV to 6.5 TeV and reducing the transverse emittance of the beam from the LHC injectors. These upgrades pose challenges to the measurement of the transverse beam size via Synchrotron Radiation (SR) imaging, as the radiation parameters approach the diffraction limit. Optical SR interferometry, widely used in synchrotron light facilities, was considered as an alternative method to measure the 150 µm rms beam size at top energy as it allows measurements below the diffraction limit. A system based on this technique was therefore implemented in the LHC, for the first time on a proton machine. This paper describes the design of the LHC interferometer and its two SR sources (a superconducting undulator at low energy and a bending dipole at high energy), along with the expected performance in terms of beam size measurement as compared to the imaging system. The world's first proton beam interferograms measured at the LHC will be shown and plans to make this an operational monitor will be presented.

INTRODUCTION

Measuring the transverse emittance of the beam is fundamental in every accelerator. This is particularly true for colliders, since the precise determination of the beam emittance is essential to maximize and control the luminosity. In the LHC, where it is not a directly accessible quantity, the emittance is inferred from the measurement of the transverse beam sizes and the knowledge of the accelerator optics. The LHC Beam Synchrotron Radiation Telescope (BSRT) is the only instrument offering non-invasive, continuous beam size monitoring via direct imaging of the emitted visible Synchrotron Radiation (SR). After the CERN long shutdown in 2013-2014, the maximum LHC beam energy was increased from 4 TeV to 6.5 TeV and the transverse emittance of the injected beam was reduced following upgrades in the injector chain upgrades. This makes the measurement of the transverse beam size via SR imaging a real challenge, as the radiation parameters approach the diffraction limit. Since the optical SR interferometer, widely used in synchrotron light facilities, allows beam size measurements below the diffraction limit, a system based on this technique was therefore implemented in the LHC, for the first time in a proton machine. In this paper, the design of the LHC interferometer is presented and its final version, installed in June 2016, is described. The characterization of its components and the commissioning process with beam will also be discussed. Additionally the LHC beam size measurement via the world's first measured proton beam interferograms will be shown and plans to make the interferometer an operational monitor will be presented.

* georges.trad@cern.ch

LHC SR SOURCE

The LHC is equipped with two SR monitors (one per beam) used to characterise the transverse and longitudinal beam distributions. The SR source is a combination of a dedicated undulator and a beam separation dipole (D3). The visible SR emission point shifts gradually with the energy ramp from the undulator (at injection energy, 450 GeV) to the D3 which dominates from 1.2 TeV onwards [1]. The D3 is a 9.45 m long superconducting dipole and at 7 TeV, its maximum field is 3.9T giving a bending angle of 1.58 mrad and a radius of curvature of ~6 Km. The undulator was designed to enhance the visible SR component from injection energy up to ~1.2 TeV, until the contribution of visible SR from D3 becomes detectable. The undulator is installed 937 mm upstream of D3 and shares the same cryostat. It is made of two 28 cm periods with a peak field of 5 T, thus resulting in the undulator parameter "K" 0.0712.
The emitted SR is intercepted by an extraction mirror installed in the beam vacuum and sent through a vacuum window to the BSRT. Figure 1 shows the SR intensity distribution on the extraction mirror, as simulated for injection and top energy.

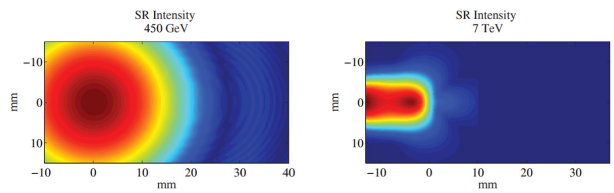

Figure 1: Simulated SR Intensity on the extraction mirror of the LHC at injection (left) and Flat Top (right).

SR IMAGING LIMITATION

The visible SR imaging system is based on two focusing stages, offering the possibility of switching between two different sets of lenses. One optimized for 400-600 nm operation at injection and the other for Near Ultra-Violet (NUV, 250 nm) imaging at high energy [2]. It is worth mentioning that the NUV operation was found beneficial in terms of resolution at high energy where the beam size is as small as 170 µm. In fact in LHC Run II, the BSRT resulted reliably operational for bunch-by-bunch measurements and crucial

ISBN 978-3-95450-177-9

for several studies (beam-beam, instabilities and Electron Cloud studies). Crosschecks with independent emittance measurements, such as the luminosity scans, confirmed the accuracy of the BSRT beam size measurement to the level of 5%.

However, due the intrinsic limitation of the imaging system, originating from the error ϵ on the determination of the optical resolution σ_{LSF} that impacts the emittance ε_{Beam} determination [3], soon with the decreasing beam sizes, the SR imaging technique will be unsuitable for measurements.

INTERFEROMETRY

Direct imaging for beam size measurement is ultimately diffraction limited and very sensitive to the cross-calibration techniques. Interferometry is the best alternative to measure the small beam size with visible SR. It consists of determining the size of a spatially incoherent (or partially coherent) source by probing the spatial distribution of the degree of coherence after propagation, with a theoretically achievable resolution of a few microns. A rigorous derivation of the principle can be found in [4]. In the following only a brief summary of the technique is given.

Principle

The LHC interferometer is a wavefront-division-type two-beam SR interferometer using polarized, quasi-monochromatic light. The spatial coherence of the SR is probed by measuring the first order degree of mutual spatial coherence Γ.

The double slit samples the incoming wavefront to obtain the one-dimensional interference pattern along the vertical or horizontal axis. The intensity of the interference pattern measured on the detector plane is given by:

$$I(x) = I_0\left[sinc\left(\frac{2\pi a}{\lambda_0 R}x\right)\right]^2 \cdot \left\{1 + |\Gamma| \, cos\left(\frac{2\pi D}{\lambda_0 R}x + \phi\right)\right\} \quad (1)$$

with a the half of the single slit width, D the separation between the two slits, λ_0 the wavelength of observation, I_0 the sum of the incoherent intensities from both slits, ϕ an arbitrary phase and R the distance from the lens to the detector plane.

The visibility of the interferogram fringes, using the intensities I_{max} at the peak of the interference fringe and I_{min} at its valley, is defined as:

$$V = \frac{I_{max} - I_{min}}{I_{max} + I_{min}} = \frac{2\sqrt{I_1 \cdot I_2}}{I_1 + I_2}|\Gamma| \quad (2)$$

where I_1 and I_2 is the light passing through the first and the second slit respectively. The beam size is derived based on the Van Cittert-Zernike theorem [4], where the degree of coherence Γ is the Fourier transform of the intensity distribution of the source. The beam size can be obtained from the interferograms in the following two ways.

1-Fixed slit separation mode

This mode relies on the hypothesis of Gaussian beams. By acquiring and fitting the interference pattern to obtain the spatial coherence modulus $|\Gamma|$, the beam size σ_x is obtained using:

$$\sigma_x = \frac{\lambda_0 R_0}{\pi D}\sqrt{\frac{1}{2} ln \frac{1}{|\Gamma|}} \quad (3)$$

with R_0 being the distance from the source to the double slits (for the LHC, 29.3 m at 450 GeV and 26.5 m at high energies).

2-Slit separation scanning mode

The intensity pattern is recorded for varying slit separation D and the beam shape $f(x)$ is obtained by applying an inverse Fourier transform of the resulting curve $\Gamma(D)$. Assuming Gaussian distributions:

$$\sigma_x = \frac{\lambda_0 R_0}{2\pi\sigma_v} \quad (4)$$

with σ_V being the RMS width of $|\Gamma|$ (D).

LHC INTERFEROMETER

After testing the prototype during the 2015 LHC run the final setup of the interferometer was installed in June 2016. It features a new slit assembly that allows the measurement of the horizontal and the vertical beam sizes with the possibility to change the slit width, separation, height and center remotely. The system can also be operated as a 2D interferometer by inserting at the same time the horizontal and vertical slits. The 2015 polarizer (seen to introduce additional focusing with strong astigmatism) was replaced with a high quality precision linear polarizer constructed by laminating a polymer polarizing film between two high-precision glass substrates (flatness better than $\lambda/6$). This was installed immediately at the entrance of the gated intensified sCMOS camera used to acquire the images. The overall magnification of the system was adapted to accommodate the full interferogram on the central region of the sensor.

COMMISSIONING AT 6.5TEV

The interferometer commissioning started in August 2016. A set of tests was carried out to check the functioning of all the 23 motorized component of the interferometer. The aim of these studies was to validate the light alignment, the focus, the magnification, the polarization and the slit configuration. To rule out the additional effects of the incoherent depth of field of the dipole SR, estimated to be dominant when measuring the horizontal beam size [5], this section will describe only a set of vertical beam size measurement via interferometry and how they compare to the imaging system.

Wavefront Distortion

One of the main concerns when designing an interferometer is the preservation of the SR wavefront from the extraction point up to the slits, since any distortion affects the beam size measurement. The quality of the in-vacuum

ISBN 978-3-95450-177-9

extraction mirror represents a major concern since it is exposed to heating by both SR and electro-magnetic coupling with the beam. Additionally, in order to reach the desired reflectivity over the whole visible SR spectrum, the coating process involves the deposition of multiple dielectric layers deposition. The resulting flatness is in the order of $\lambda/4$ peak to valley over the total mirror surface at ~600 nm. The extraction mirror deformations leads to an effective double slit separation. It depends on the mirror tilt, the distance from the source to the extraction mirror and on the distance from the mirror to the double slits. By design the latter was kept as small as possible such that the effects are minimized to <~ 2% for all possible slit separations for typical mirror deformations. The mirror was as well checked using the installed “Hartmann Mask" line [6], that confirmed that no deterioration of its surface flatness is caused by the full intensity circulating beam [7].

Double Slit Height Dependence

When designing an interferometer, the slit height is normally chosen to cover the whole angular distribution of the SR radiation. However, when the SR is intense enough, restricting the slit height is beneficial for two reasons. Firstly, sampling small areas of the SR wavefront (i.e. using a smaller surface of the extraction mirror and successive optics) minimizes the waveform distortion and aberration effects. In addition, coupling effects between the horizontal and vertical beam size measurements that could become important when the two planes are very different [4] are minimized.
For LHC interferometer commissioning the SR intensity was enough even when reducing the slit height to 500 µm. Despite the fact that no dependence of the measured beam size was observed for various slit heights all the following measurements, unless otherwise stated, use a slit height of 500 µm.

Wavelength Dependence

The interferometer is equipped with two bandpass filters with a central wavelength of 400 and 560 nm, and width ±10 nm. Although the lenses are optimized for 500 nm operation no big aberrations are expected for either wavelengths. Figure 2 shows the interferograms recorded for various slit separations with the fringe visibilities extracted for each separation using the 560 nm filter. Under the assumption of Gaussian beams, the fit of $V(D)$ gives a beam size of 375 µm. A similar measurement with the 400 nm bandpass filter resulted in a beam size of 369 µm. The two measurements are fully compatible and indicate that the measurements are practically immune to aberrations and tiny shifts in focus. This is confirmed by a set of simulations that estimate the error introduced by chromatic aberrations originating from the finite width of the bandpass filter to be < 1% for σ_{Beam} >200 µm [3].

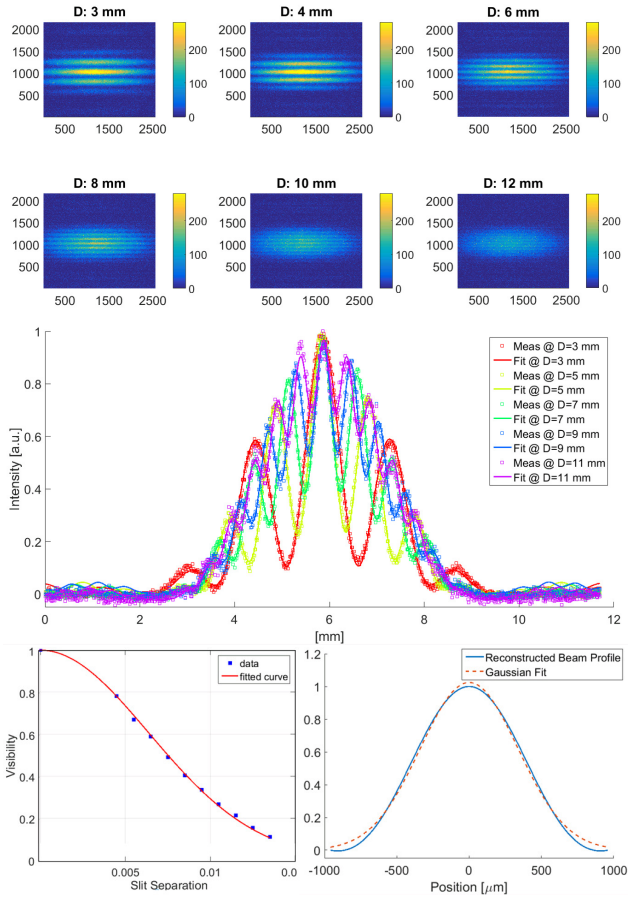

Figure 2: Interferogram recorded for various slit separation using the 560 nm filter. The projections are fitted using Eq. 1 and the inferred visibility is plotted against the slit separation and fitted with a Gaussian curve to extract the beam size by applying an inverse fourier to $|\Gamma(D)|$.

Frame Exposure Dependence

Beam oscillations and vibrations or air turbulence on the optical bench provoke a smearing of the interferogram visibility and a displacement of its centroid. The camera exposure was increased gradually from 200 µs to 200 ms in the interferograms presented in Fig. 3. Since the LHC revolution frequency is ~89 µs, this corresponds to integrating over 2 turns up to ~ 2000 turns. The measured beam size, 366 (MEAN) ±5.6μm (RMS), had very little dependence on the exposure time.

Intensifier Gain Dependence

The effect of image intensifier saturation on the recorded interferogram can be seen in Fig. 4 which shows the patterns recorded as the voltage applied to the image intensifier is changed from 0 to 2000 mV, and histograms of the pixel values. As long as the gain is kept lower than 900 mV the brighter pixels remain at values <= 1000 with the corresponding change of visibility resulting in an error on the beam size of <= 4%

ISBN 978-3-95450-177-9

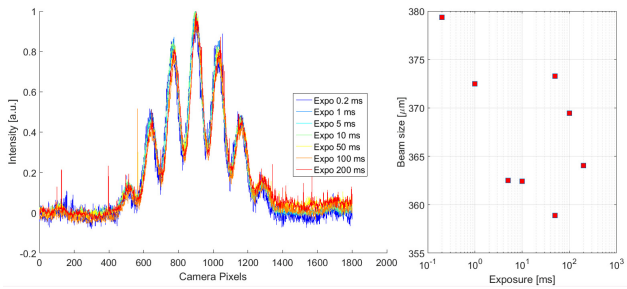

Figure 3: Left: interferograms at λ=560 nm and D=6 mm for various camera exposure times ranging from 200 µs to 200 ms. Right: beam size extracted for each exposure.

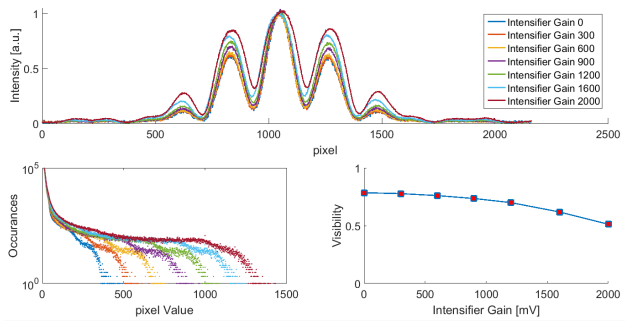

Figure 4: Upper plot, interferograms at λ=560 nm, D=3 mm recorded with various intensifier gains. Bottom left: histogram of pixel intensities. Bottom right: visibility curve as function of the intensifier gain.

Polarization Dependence

The horizontal and vertical polarizations of the SR lead to interference fringes shifted by π rad in phase [4]. When measuring both polarizations this results in a loss of the visibility (see Fig. 5) and an overestimation of the beam size. Since the polarizer is mounted on a motorized, rotating stage, a scan of the angle was carried out to identify the nominal position of the polarizer for selecting exclusively the H polarization (which is more intense than V).

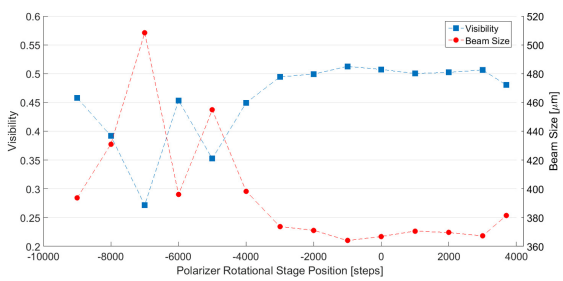

Figure 5: Visibility and the corresponding beam size for several positions of the polarizer rotational stage.

Double Slit Center Effect

If the double slit setup is not aligned with respect to the vertical fan opening of the SR, an intrinsic imbalance of the slit illumination is introduced. This contributes to an overestimation of the beam size even after applying the correction of Eq. 2. Such an effect can be interpreted as a consequence of the incoherent depth of field and the SR cone opening dependence on offsets in the bending plane [8]. Figure 6 clearly shows this effect when the center of the double slits was shifted by ±8 mm from the nominal position. The error on the beam size measurements can be as high as 20 % when the slits are far from the medium plane, but remains within 5% when misaligned by ±2 mm.

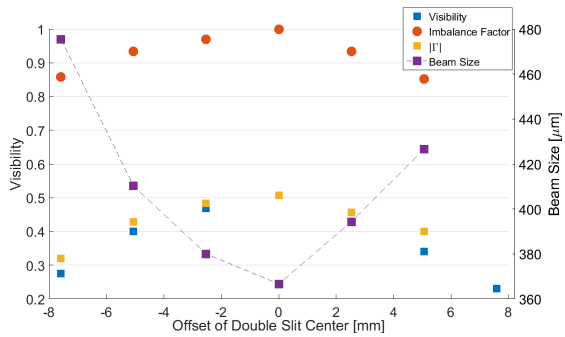

Figure 6: Intensity imbalance factor, fringes visibility before and after correction and the corresponding inferred beam size shown for various positions of the double slit center.

Detector Linearity

The interferogram visibility is strongly affected by the linearity of the detector (camera+intensifier), something which was tested in the laboratory. A broadband fiber lamp with very stable flux is used as a light source. A set of accurately calibrated neutral-density filters with optical density <= 0.1% error in the 400 nm to 650 nm range [9] was used to vary the light input on the intensifier while images were recorded. The results are shown in Fig. 7. After subtracting the background image (with no light input) the detector shows a good uniformity (< 1% variation) and a good linearity with the maximum deviation from the linear fit < 5% (except for very low lighting conditions).

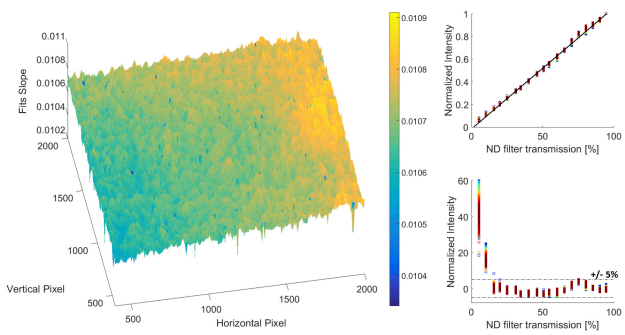

Figure 7: Detector uniformity and linearity as measured in the laboratory.

Benchmarking with the Imaging System

The beam size measured with interferometry was compared to the beam size measured via imaging in the BSRT.

ISBN 978-3-95450-177-9

The BSRT is operated in gated mode measuring bunch by bunch size, from which an average beam size is calculated. The beam size from imaging was always found smaller than the beam size from the interferometer by a factor of ~ 1.4. The relative bunch by bunch size measured via interferometry (Fig. 8) was however found to be compatible with that observed through imaging.

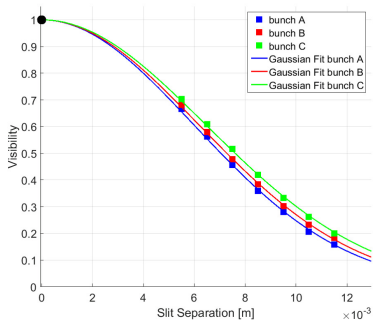

Figure 8: Visibility curve as function of slit separation for three different bunches with different sizes.

COMMISSIONING AT INJECTION ENERGY

Contrarily to Flat Top energy, the SR intensity emitted by the undulator at injection is low (3 orders of magnitude less). Since the beam size to be measured is also bigger (~1 mm), the visibility curve as function of the slit separation decays very rapidly and only small D values can be used. In order to obtain a useful interferogram to resolve the beam size, for a separation D in the order of 2.5 mm the suitable slit width should be around 0.5 mm. Unfortunately for slit widths <1 mm even with the smallest achievable optical magnification the pattern is as big as the detector area and no reliable fits could be obtained since the background is hardly recognizable. Therefore for the measurements at 450 GeV the width is set to 1 mm. Figure 9, shows horizontal and vertical beam size measurement, for two different bunches with the minimum slit separation possible (2.4 mm and 2.6 mm for the horizontal and vertical planes respectively). The extracted beam sizes are summarized in Table 1. The results are found very much compatible with the imaging values and discrepancies are ~ 5%.

Table 1: Horizontal and vertical beam size measurement at Injection for 2 different bunches via imaging and interferometry.

		bunch 1		bunch 62	
	σ [mm]	H	V	H	V
450 GeV	Imaging	1.22	1.6	1.15	1.4
	Interferometer	1.20	1.53	1.14	1.34

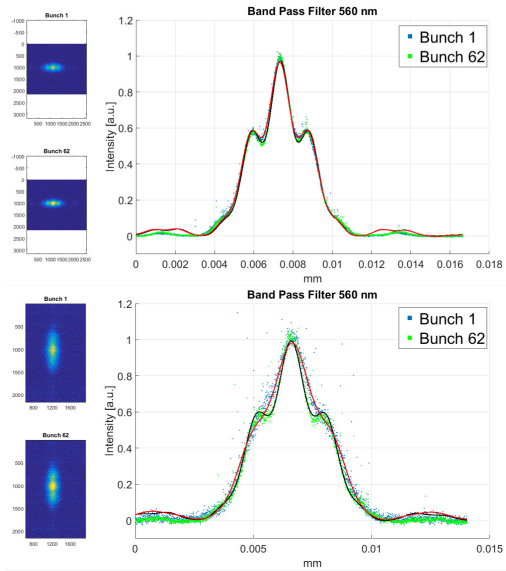

Figure 9: Top Plot:Interferogram with D=2.4 mm, a=1.5 mm for horizontal size measurement with 200 ms exposure at λ=560 nm. Bottom Plot:Interferogram with D=2.6 mm, a=1 mm for vertical size measurement with 200 ms exposure at λ=560 nm.

2D INTERFEROMETER

The interferometry setup also allows the simultaneous measurement of the horizontal and vertical beam size. Two dimensional interferograms are obtained by arranging the motors to obtain four small slits distributed along the corners of a rectangle whose sides D_H and D_V represent the slit separation for the horizontal and vertical planes respectively. The results of a set of measurements in this configuration, for different slit separations, as well as a comparison to separate 1D scans are shown in Fig. 10. The excellent agreement

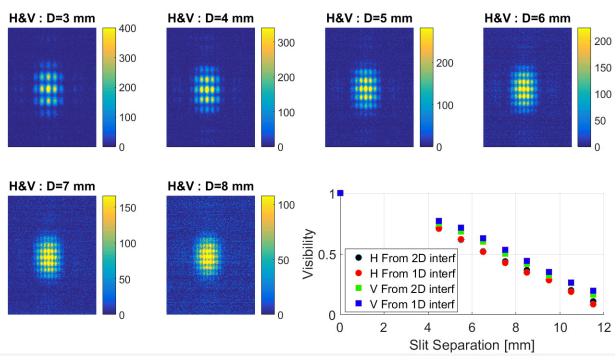

Figure 10: Interferograms recorded while scanning simultaneously the slit separation in the H and V plane. The visibilities from this 2D scan are compared to the ones obtained using separately the two assemblies.

obtained (< 5% discrepancy on beam size), shows that the coupling between the two planes is negligible and proves the feasibility of a 2D interferometer setup.

ISBN 978-3-95450-177-9

CONCLUSIONS

This paper covered the main aspects of the LHC interferometer design, implementation and commissioning. A comprehensive set of measurements were performed to compare the interferometer results to the standard imaging system at both the injection energy and 6.5 TeV. While good agreement was observed at injection energy, a scaling factor of about 1.3 is yet to be understood between the two systems at top energy. Nevertheless interferometry was able to provide coherent relative bunch size measurements at 6.5 TeV. The feasibility of 2S interferometric measurements has also been demonstrated.

REFERENCES

[1] A.Fisher,"Expected Performance of the LHC Synchrotron-Light Telescope (BSRT) and Abort-Gap Monitor (BSRA)" PAC, SLAC-PUB-14098,2010.

[2] Goldblatt A, Bravin E, Roncarolo F, Trad G. "Design and Performance of the Upgraded LHC Synchrotron Light Monitor." Proc. of IBIC. 2013 Sep 1.

[3] G. Trad, "Development and Optimisation of the SPS and LHC beam diagnostics based on Synchrotron Radiation monitors," Ph.D. thesis, Beams. Dept.,CERN, 2015.

[4] T. Mitsuhashi, "Beam Profile and Size Measurement by SR Interferometers", in Beam Measurement: Proceedings of the Joint US-CERN-Japan-Russia School on Particle Accelerators.

[5] Trad G, Bravin E, Goldblatt A, Mazzoni S, Roncarolo F. "A novel approach to synchrotron radiation simulation". Proc. of IPAC, 2014.

[6] Mitsuhashi, Toshiyuki, and Mikio Tadano, "Measurement of Wavefront Distortion Caused By Thermal Deformation Of Sr Extraction Mirror Based on Hartmann Screen Test And Its Application For Calibration Of SR Interferomterter." PAC, 2001.

[7] Trad, Georges, et al. "Performance of the upgraded synchrotron radiation diagnostics at the LHC." 7th International Particle Accelerator Conference (IPAC'16), Busan, Korea, May 8-13, 2016. JACOW, Geneva, Switzerland, 2016.

[8] T. Mitsuhashi, private communication, August 2016.

[9] T. Mitsuhashi, "Measurement of small transverse beam size using interferometry" Proc. of DIPAC 2001 – ESRF, Grenoble, France

ISBN 978-3-95450-177-9

BEAM SHAPE RECONSTRUCTION USING SYNCHROTRON RADIATION INTERFEROMETRY

L. Torino, U. Iriso, ALBA-CELLS, Cerdanyola del Vallès, Spain

Abstract

Synchrotron Radiation Interferometry (SRI) through a double-aperture system is a well known technique to measure the transverse beam size using visible light. In many machines the beam is tilted in the transverse plane, but the SRI technique only allows to directly measure the size of the projection of the beam shape along the axis connecting the two apertures. A method to fully reconstruct the beam in the transverse plane using SRI has been developed and successfully tested at the ALBA synchrotron light source. This report shows the full beam reconstruction technique and presents the results at different couplings. We also discuss how this technique could improve the measurement of very small beam sizes, improving the resolution of standard SRI.

INTRODUCTION

Transverse beam size measurements are used to monitor the beam quality in accelerators. In synchrotron light sources, a direct image of the beam transverse plane can be provided by x-ray pinholes [1], while direct imaging using the visible part of the synchrotron radiation cannot be performed due to diffraction limitations.

Another widely used method to measure the transverse beam size is the Synchrotron Radiation Interferometry (SRI), which is based on the analysis of the spatial coherence of the synchrotron light and has been used in accelerators since the late 90s [2].

As opposed to the imaging techniques like the x-ray pinhole camera, the standard SRI technique using a double-aperture system only provides the projected beam size (in the aperture axis direction), and therefore information about possible beam tilt is lost.

A method to reconstruct the full transverse beam profile using a rotating double-aperture system, which allows to properly measure the beam size and relative beam tilt angle has been developed. The technique can also be used to perform ultra-low vertical beam size measurements, crucial for the newest machines.

SYNCHROTRON RADIATION INTERFEROMETRY AT ALBA

The SRI setup is located in the ALBA diagnostic beamline Xanadu [3]. The radiation is produced by a bending magnet, the visible part is extracted and imaged by a Young-like interferometry.

The interferometry system is composed by two pinholes, a lens to focus the interference fringes, a telescopic ocular to magnify the interferogram, a narrow band color filter and a polarizer to select the wavelength and polarization of the light. The final results are captured by a CCD. A sketch of the measurement setup is presented in Fig. 1.

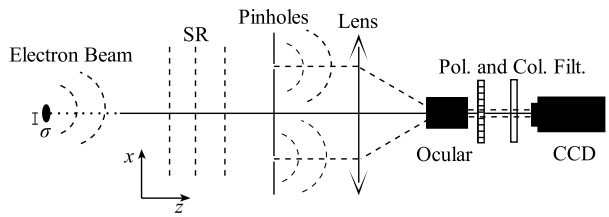

Figure 1: Sketch of the SRI experimental setup: The synchrotron radiation (SR) produced by the beam passes through the double-pinhole system and is imaged through a lens and an objective ocular to the CCD. The radiation polarization and the wavelength are selected through a polarizer (Pol.) and a color filter (Col. Filt.).

The formula describing the interferogram intensity along the direction parallel to the axis passing through the pinholes (x) is:

$$I(x) = I_0 \left\{ \frac{\mathrm{J}_1\left(\frac{2\pi a x}{\lambda f}\right)}{\left(\frac{2\pi a x}{\lambda f}\right)} \right\}^2 \times \left\{ 1 + V \cos\left(\frac{2\pi D x}{\lambda f}\right) \right\}, \quad (1)$$

where I_0 is the light intensity, a is the pinholes radius, λ is the radiation wavelength, f is the focal length of the imaging system, D is the distance between the pinholes and V is the visibility. The visibility is the contrast of the interferogram fringes: $V = \frac{I_{Max} - I_{Min}}{I_{Max} + I_{Min}}$, where I_{Max} and I_{Min} are respectively the maximum and the minimum of the interferogram fringe at the center.

Equation 1 is used to fit a slice of the measured interferogram, letting the visibility as free parameter. Assuming that the beam has a Gaussian distribution along the direction of the pinholes axis, the beam size is obtained as:

$$\sigma = \frac{\lambda L}{\pi D} \sqrt{\frac{1}{2} \log\left(\frac{1}{V}\right)}, \quad (2)$$

where L is the distance between the source point and the pinholes. The larger is the visibility the smaller is the beam size. Examples of interferograms used to measure the beam size projections are presented in Fig. 2.

FULL BEAM RECONSTRUCTION

Since the SRI only measures the projection of the beam on the double aperture axis, we proceed to measure the projection along different axis by rotating the pinholes system. Figure 2 presents interferograms obtained for pinholes rotated at 0°, 45°, 90° and 135°, and the corresponding fit.

ISBN 978-3-95450-177-9

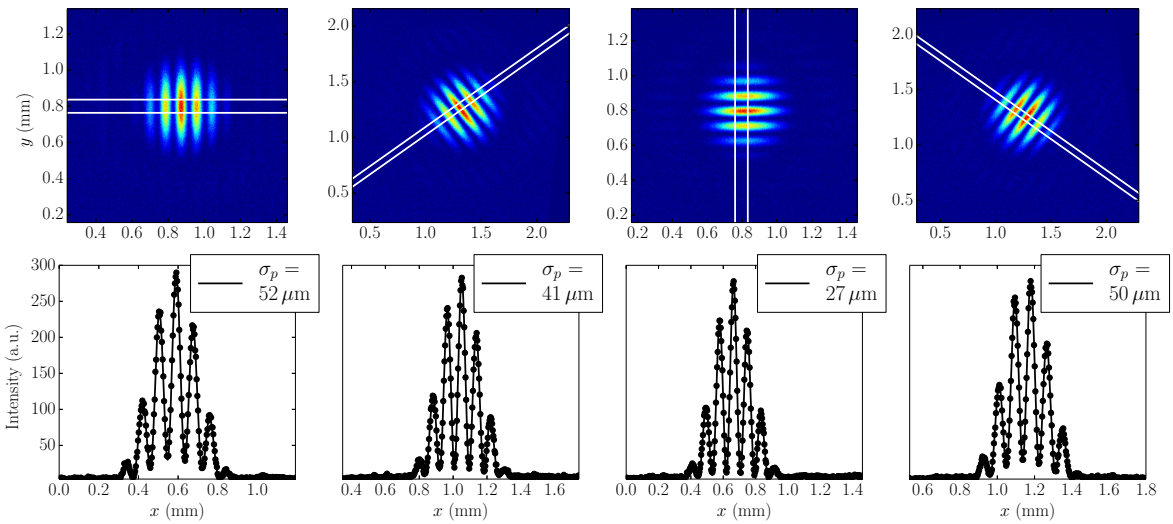

Figure 2: Interferograms and fits for the pinholes axis rotated of 0°, 45°, 90° and 135°.

Each measurement provides a pair of parallel lines tangent to the beam transverse section in two points. Merging the pairs of lines the full beam shape is reconstructed. The precision of the reconstruction is limited by the number of projection measured.

A full beam reconstruction was performed taking data every 5° in the range [0°, 200°], the result is presented in Fig. 3. The reconstruction clearly shows a tilted elliptic beam.

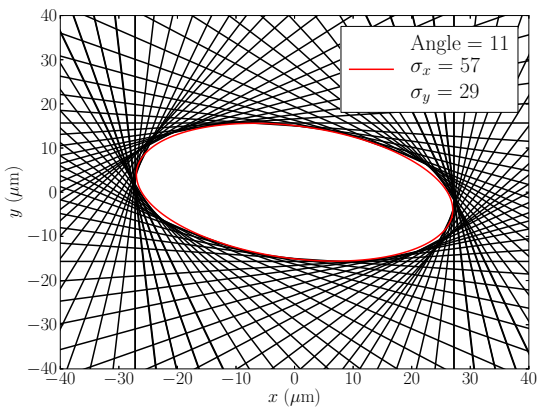

Figure 3: Beam reconstruction calculating the tangent lines from the projections.

Elliptic Beam

Assuming an elliptic beam, an analytical expression can be inferred to express the projected beam size σ_p with respect to the double-pinhole rotation angle θ. A detailed explanation is presented in [4], next we show some guide-lines about how to obtain the $\sigma_p(\theta)$ expression.

The equation of an ellipse is written as a function of the polar angle θ as:

$$\begin{aligned} x(\theta) &= \sigma_u \cos(\theta) \\ y(\theta) &= \sigma_v \sin(\theta) \end{aligned} \tag{3}$$

where σ_u and σ_v are the ellipse's horizontal and vertical semi-axis and correspond to the effective beam sizes or the ellipse eigenvalues.

The measured projection at each angle σ_p is given by [4]:

$$\sigma_p(\theta) = \sqrt{x^2(\theta) + y^2(\theta)}. \tag{4}$$

If the ellipse is tilted the maximum and the minimum projections will not be on axis ($\theta = 0$ and $\theta = \frac{\pi}{2}$), and a phase Φ must be added:

$$\theta \to \theta + \Phi. \tag{5}$$

The phase Φ provides the tilt of the ellipse.

The final equation describing the projection as a function of θ is finally given by substituting Eq. 3 and 5 in Eq. 4:

$$\sigma_p(\theta) = \sqrt{\sigma_u^2 \cos^2(\theta + \Phi) + \sigma_v^2 \sin^2(\theta + \Phi)}. \tag{6}$$

We can use Eq. 6 to fit the measurements shown in Fig. 3, with σ_u, σ_v and Φ as free parameters. The result is shown in the top plot of Fig. 4. Having three parameters and using a Least Squares fit method, the minimum number of measurements needed to reconstruct the ellipse is four.

From the same set of data, the four projections for θ equal to 0°, 45°, 90° and 135° were extracted. Data and the fit using Eq. 6 are presented in the middle plot of Fig. 4. In both cases the results for the beam sizes and the tilt are:

$$\sigma_u = 54\mu\text{m}, \qquad \sigma_v = 29\mu\text{m}, \qquad \Phi = 11°, \tag{7}$$

which are compatible with the values expected for this parameters at the Xanadu source point.

ISBN 978-3-95450-177-9

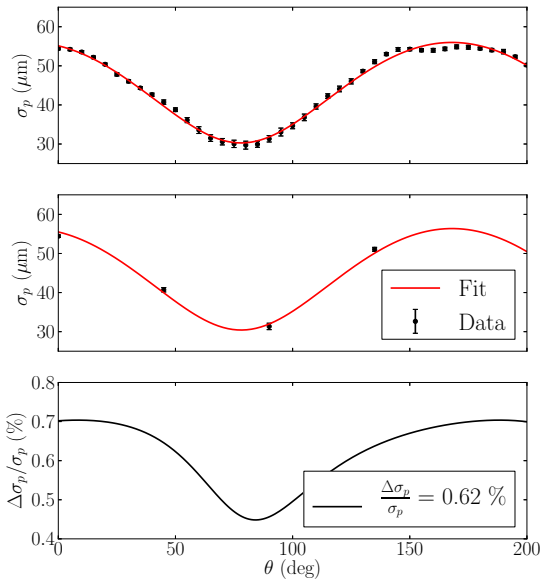

Figure 4: Beam projection as a function of the pinhole rotation angle θ. In the first plot all the 40 measurements, while in the second the projections at 0°, 45°, 90° and 135° are presented. The third plot (black line) is the difference between the fits obtained with 40 and 4 points as a percentage of the 40 points curve.

Finally, in the bottom plot of Fig. 4 the difference between the two fit curves as a percentage of the first is presented. The maximum deviation is less than 1 µm. This value is smaller with respect to the statistical error associated with standard SRI beam size measurements ($\simeq$1 µm), thus the beam shape reconstruction using only 4 point is reliable.

Coupling Scan

In order to proof the reconstruction technique consistency, measurements were performed at five different values of the machine coupling. In this way the tilt, the horizontal, and the vertical beam sizes changes. A LOCO [5] was launched at each coupling in order to compare the results obtained by the measurements with the theoretical values.

LOCO provides the beam ellipse eigenvalues and the tilt at the source point. The same values were measured using the 4 points SRI reconstruction. The reconstructed ellipses are presented in Fig. 5. Figure 6 presents the comparison between the SRI reconstruction and LOCO. Results for the beam sizes are consistent at least for the first four values of the coupling. The measured value of tilt has some discrepancy always lower than 5° but still within the error bar. Considering that the pinholes were tilted without any precision check on the starting alignment with respect to the rotation stage, the result is considered consistent.

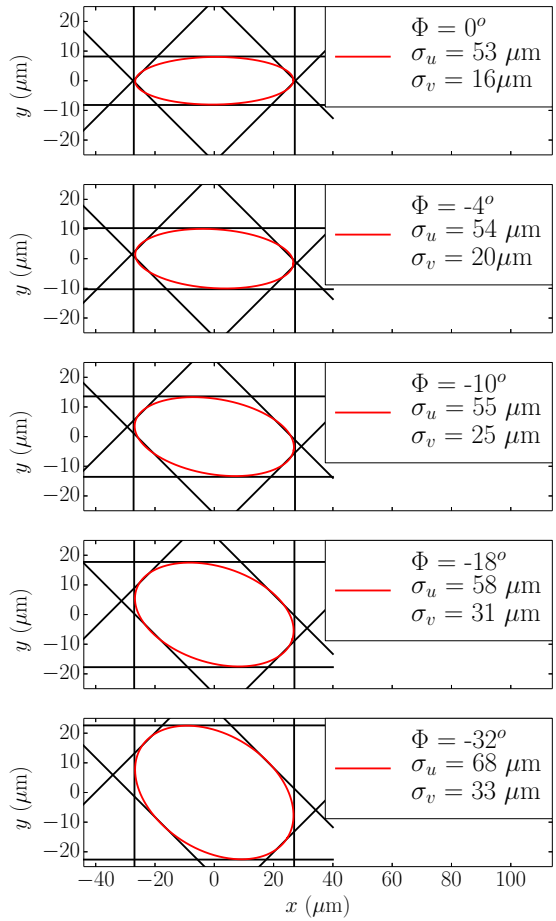

Figure 5: Reconstruction of the beam at different couplings. Black lines are calculated from real data while the red ellipse is drown from the result of the fit.

ULTRA-SMALL BEAM SIZE MEASUREMENT

In future light sources the vertical beam size will be so small that could not be measurable even with SRI technique. A possibility to obtain the smallest vertical beam size is to use Eq. 6 using SRI reconstruction, and infer the beam ellipse eigenvalues. Simulations have been performed using SRW [6] to study the feasibility of the method. An elliptic beam with zero tilt ($\Phi = 0°$, $\sigma_u = \sigma_x$, and $\sigma_v = \sigma_y$) and an horizontal beam size of 55 µm has been generated. The vertical beam size has been changed from 2 to 10 µm. To perform the beam reconstruction, projections measurements have been simulated sampling the rotation angle every 15°. The vertical projection (corresponding to 90°) has not been considered.

The projections as function of the angles have been finally fitted using Eq. 6 to obtain the beam ellipse parame-

ISBN 978-3-95450-177-9

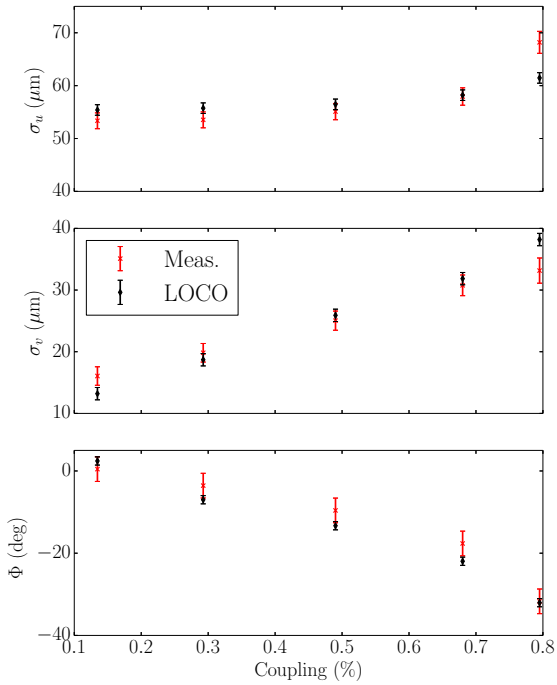

Figure 6: Comparison between the SRI reconstruction and the results from LOCO for the horizontal and vertical beam size and the beam tilt at the Xanadu location.

ters. As an example, Figure 7 presents the results obtained by simulated a non-tilted beam with horizontal and vertical beam sizes respectively of 55 µm and 5 µm. Results are compatible with the expected values.

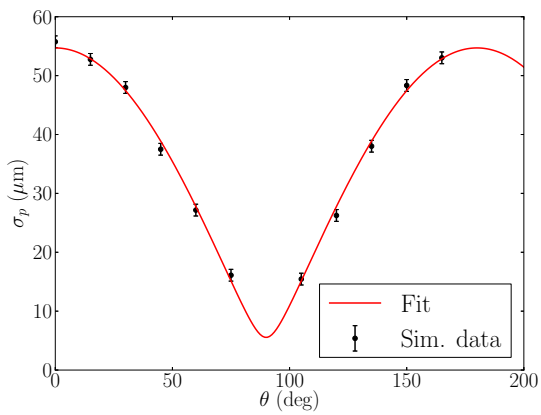

Figure 7: SRW simulated 5 µm vertical beam size reconstruction using the rotated SRI technique. Black dots are data, the error bar is fixed to 1 µm, black dashed line is the theoretical curve expected, red line is the result of the fit using Eq. 6.

Results for the different vertical beam sizes, at a fixed horizontal beam size of 55 µm and at 0° tilt angle, are listed in Table 1.

Table 1: Results of simulations of small vertical size reconstruction.

σ_y Theo. (µm)	σ_y Rec. (µm)
2	2.2
5	5.4
7	6.9
10	9.7

CONCLUSION

In this report a method to perform a full reconstruction of the transverse beam shape using the SRI technique has been proposed.

The ALBA beam shape has been reconstructed measuring its projection along several axis by rotating the double pinhole system.

It has been proved that a simplification of the technique can be applied for elliptic beam. In this case, only four projections are needed to reconstruct the full beam transverse shape. To verify the results, measurements have been performed at different couplings.

Finally a new method to indirectly measure ultra-small beam sizes has been proposed based on the same technique. SRW simulations has been performed in order to confirm the validity of the method.

ACKNOWLEDGMENTS

This work owes a lot to T. Mitsuhashi (KeK), fort the valuable help in developing the SRI in its first stage. We want to acknowledge the ALBA accelerator division, and special thanks to all the ALBA staff for the efforts to maintain and improve the facility.

REFERENCES

[1] G. Kube, "Review of synchrotron radiation based diagnostics for transverse profile measurements" DIPAC 2007, Venice (Italy), MOO1A03 (2007)

[2] T. Mitsuhashi, "SR Monitor – Special topics", BIW 2012, Newport (USA), TUAP02 (2012)

[3] L. Torino et al, "Limitations and Solutions of Beam Size Measurements via Synchrotron Radiation Interferometry at ALBA", IBIC 2015, Melbourne (Australia), TUPB049 (2015)

[4] L. Torino et al, "Full Transverse Beam Reconstruction using Synchrotron Radiation Interferometry" Submitted to PRST-AB

[5] G. Benedetti et al. "LOCO in the ALBA Storage Ring" IPAC 2011, San Sebastian (Spain), C110904 (2011)

[6] O. Chubar et al, "Accurate and Efficien Computation of Synchrotron Radiation in the Near Field Region", EPAC 1998, Stockholm (Sweden), C980622 (1998)

ISBN 978-3-95450-177-9

THE NEW OPTICAL DEVICE FOR TURN TO TURN BEAM PROFILE MEASUREMENT

V. Dorokhov* , A. Khilchenko, A. Kotelnikov, A. Kvashnin, O. Meshkov[1], P. Zubarev
BINP SB RAS, Novosibirsk, 630090, Russia
also at [1]NSU, Novosibirsk, 630090, Russia
V. Korchuganov, A. Stirin, A. Valentinov, NRC Kurchatov Institute, Moscow, 123182, Russia

Abstract

The electron beam quality determines the main synchrotron radiation characteristics therefore beam diagnostics is of great importance for synchrotron radiation source performance. The real-time processing of the electron beam parameters is a necessary procedure to optimize the key characteristics of the source using feedback loops.

The frequency of electron beam cycling in the synchrotron storage ring is about 1 MHz. In multi-bunch mode electrons are grouped into a series of bunches. The bunch repetition frequency depends on the total number of bunches and usually reaches hundreds of MHz. The actual problem is to study the separate bunch dimensions' behavior under multi-bunch beam instabilities.

To solve this problem a turn-to-turn electron beam profile monitor is developed for siberia-2 synchrotron light source. The linear avalanche photodiodes array is applied to imaging. The apparatus is able to record a transversal profile of selected bunches and analyze the dynamics of beam during 106 turns. The recent experimental results obtained with the diagnostics are described.

INTRODUCTION

We have developed the same device several years ago and successfully used it at VEPP-4M electron-positron collider [1-4]. The Fast Profile Meter (FPM) based on the Multi-Anode Photomultiplier Tube is a part of the VEPP-4M optical diagnostic system. We have successfully applied the FPM for determination of synchro-betatron resonances, phase oscillation monitoring, measurement of the beam spread and study of collective effects.

The device includes a MAPMT, a 12-byte ADC, a controller module, an internal memory of 4Mb and 100 Mb ethernet interface. It can record 2^{17} profiles of a beam at 16 points. Discontinuity of the records can vary within $1 \div 2^8$ turns of a beam. Revolution time of a beam in the VEPP-4M is 1220 ns and the recording time can last between 0.16 s to 20 s. As a result, the device can analyze the frequency oscillation of a beam in the range of 10 Hz — 1MHz. Fig. 1 represents a single beam profile fitted with Gaussian function.

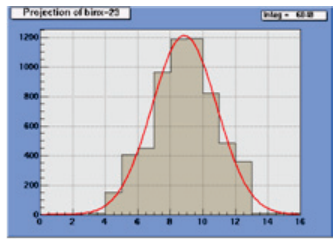

Figure 1: Example of the single beam profile fitted by the Gauss function.

The optical arrangement (Fig. 2) allows us to change the beam image magnification on the cathode of MAPMT from 6× to 20×, which is determined by the experimental demands. The set of remote controlled grey filters, included into optical diagnostics, allows selecting a suitable level of the light intensity with the dynamic range about 10^3.

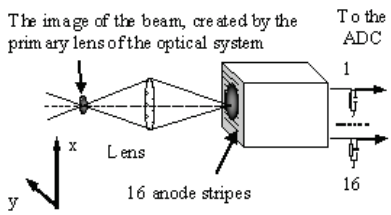

Figure 2: Optical layout of the diagnostics. The lens sets up a beam image on the photocathode of the MAPMT. The radial profile measurement is shown.

Fig. 3 presents the beam size and position behavior in the case of beam-beam instability, restored from FPM data.

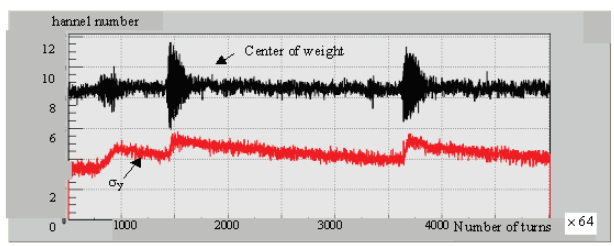

Figure 3: Beam dipole oscillations (black plot) and σy behavior (red plot) during the beams convergence at the interaction point. Duration of the single turn is 1220 ns. The channel constant is 0.12 mm.

The currents of the electron and positron beams were restricted by beam-beam effects (Ie = 3 mA, Ip = 3.4 mA), and the positron beam was the "strong" one. Both the di-

*dorohov_vl@mail.ru

ISBN 978-3-95450-177-9

pole oscillations and the beam size increase during the evolution of instability. Every "flash" of oscillations is accompanied by beam losses.

Nevertheless, the FPM based on MAPMT had some disadvantages. At first, the photomultiplier is designed to operate in photon count mode and has a low value of an average anode current. We guess that it was a reason of statistical noise of measurements of beam position and beam transversal dimensions (Fig. 3). So, the fluctuations of Gaussian curve half-width were about ten percent at stable condition of a beam. At second, the approach applied for acquirement of anode signals [2] can't be used for multi-bunched beam. Besides it, we have recognized that "slow" beam instabilities with duration about period of synchrotron frequency can be accompanied by betatron oscillations and it is desirable to record both transversal beam profiles synchronously during hundreds of thousands of beam revolutions. We have designed a new version of FPM taking into account the operating experience of MAPMT.

FPM BASED ON LINEAR AVALANCHE PHOTODIODE ARRAY

Two new FPM became a part of new optical diagnostics of synchrotron radiation storage ring SIBERIA-2 at Kurchatov Institute [5]. Parameters of 2.5 GeV electron beam of SIBERIA-2 storage ring at the azimuth of station disposition are given in Table 1.

Table 1: Electron beam parameters at SIBERIA-2

Revolution frequency, MHz	2.4152
Bunch repetition rate, MHz	2.415 – 181.14
Bunch sizes, mm: σy, σx, σs	0.059, 0.45, 20
Bunch duration (FWHM), ns	0.16

Beam of the accelerator consists 75 bunches. Turn-by-turn beam transverse cross-section measurement systems serves the purpose of measuring y- and x- distribution of electron density within a chosen bunch, betatron and synchrotron tunes (defined by way of Fourier analysis of bunch dipole oscillations triggered by kick) as well as investigating y- or x- dynamics of beam shape in a chosen separatrix. The diagnostics should provide a one-turn distribution during hundreds of thousands turns of a beam. The systems use a linear photo-detector based on 16 - element avalanche photodiode array (APDA). The device includes AA16-0.13-9 SOJ22GL photodetector unit and signal recorder. The photodetector unit is built on a photodiode strip consisting of 16 integrated avalanche photodiodes. Dimensions of the single sensitive element are 648×208 μm and a pitch between two elements is 320 μm (Fig. 4).

The optical scheme similar presented in Fig.2 creates an image of a beam on APDA. It takes the radiation intensity distribution on the electron beam profile.

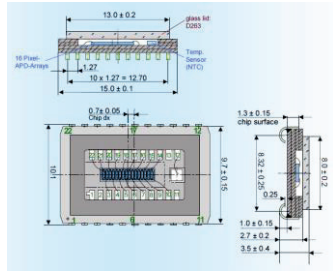

Figure 4: Package of AA16-0.13-9 APD linear array.

Electric pulses from the photodiodes are fed to inputs of analog integrators. The integrator operates continuously without reset between two adjacent pulses. Varying continuously the integrator output level consistently takes the value of every input pulse integral (Figure 5, 6).

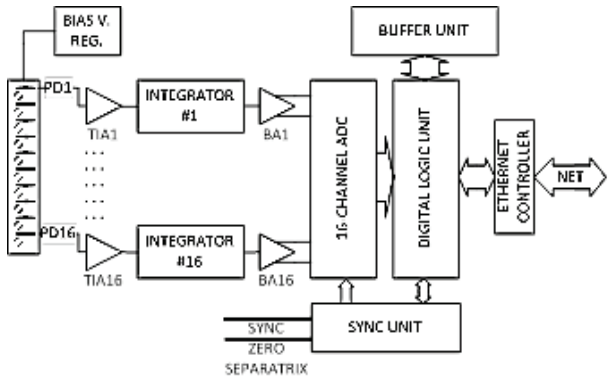

Figure 5: Functional diagram of the device.

This technique improves the integrator performance. The integrator is designed for input pulse repetition rate of 200 MHz. The 16-channel signal recorder fixes the integrals values, performs their 12-bit analog-to-digital conversion and buffering in the internal 3 Gb memory.

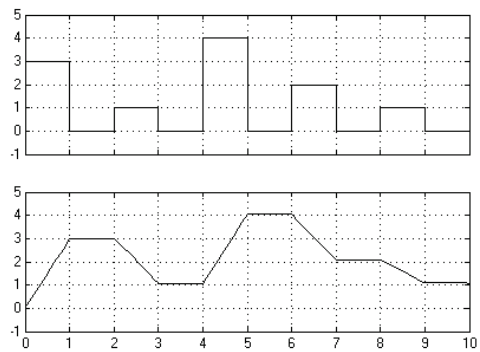

Figure 6: The integrator model in Simulink. Input signal (the 1st diagram) and output signal (the 2nd diagram).

The accumulated data is transferred via Ethernet 100BASE-T. The recorder also contains a synchronization unit consisting of a clock synthesizer with a phase-locked loop (PLL) and digital delay elements to adjust the clock phase of analog-to-digital converter (ADC). This unit synchronizes the recorder with a frequency of bunches and provides timing of the registration process to the zero separatrix. The device parameters are listed in the Table 2.

ISBN 978-3-95450-177-9

Table 2: Device parameters

Frame resolution, pixels	1x16
Frame rate, Mfps	50
Time resolution, ns	5
Dynamic range, bit	12
Memory, frames	15625000
Data transfer speed, Mbps	100
Spectral range, nm	450…1050
Pixel size, um	320
Max quantum efficient, %	85
Max avalan. multiplication	100
Max power consumption, W	25
Supply voltage, V	220
Module size, mm	100x100x400

Multi-channel registration of each bunch is possible but requires technically complex solution (16-channel ADC with 200 MHz sampling rate). The compromise solution is to record every 5th bunch with the ability to select a specific sequence of bunches (16-channel 50 MHz ADC with serial outputs is used). Any sequence can be chosen by configuring the synchronization unit via device GUI (Fig. 5).

EXPERIMENTAL RESULTS

The new version of FPM measures a complete charge of the signal corresponding to the separated bunch of a beam. The signal recorded into the internal memory during one turn of a beam of SIBERA-2 storage ring is presented in Fig. 7. It is a signal of one of 16 channels of APDA.

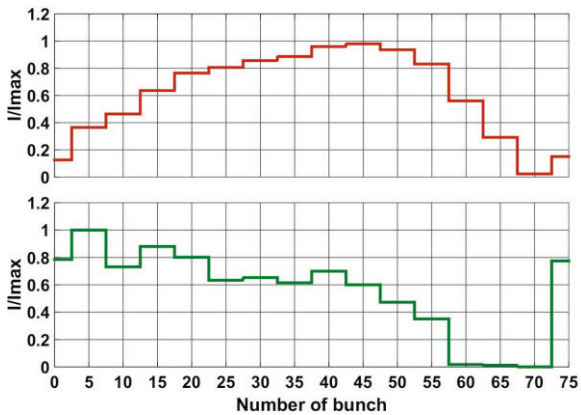

Figure 7: The integrated signal from the channel of APDA recorded by ADC.

The beam had about 70 bunches with a gap between 57th and 72nd separatrix. The signal of each 5th bunch was recorded. The upper curve represents a change in value of the signal at the exit of the integrator. The "steps" on the curve appears after the signal of corresponding bunch arrives. The lower curve represents the restored distribution of intensity of bunches. The value of the signal at the upper curve between 57 and 72 separatrix decrease due to feedback discharging the integrator.

Figure 8 represents the x, y beam profiles of a single bunch acquired with the APDA.

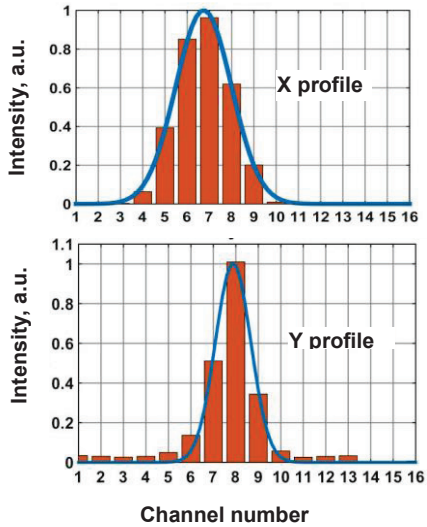

Figure 8: The vertical and radial beam profiles of a single bunch acquired with APDA at a single beam turn.

The spatial resolution of both versions of FPM is practically the same and depends on the magnification of the projection optics. But the average accuracy of the new version of the device is better significantly.

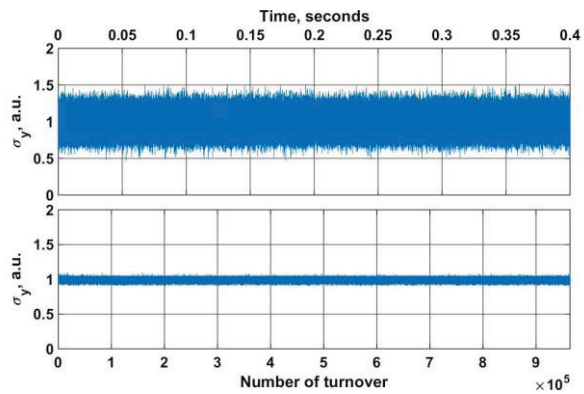

Figure 9: Comparison of an accuracy of the old (upper plot) and the new (lower plot) versions of FPM.

Figure 9 represents the ratio $\sigma_y^i / \langle \sigma_y \rangle$ for old and new FPM at the stable condition of the beam, where σ_y is a vertical beam size and i is a turn number. The number of SR photons per bunch acquired by the devices was the same. The decrease of the statistical noise of new FPM is connected with a high quantum efficiency of APDA as well.

The vertical profiles of the bunches recorded at one turn of the SIBERIA-2 beam are presented in Fig. 10.

ISBN 978-3-95450-177-9

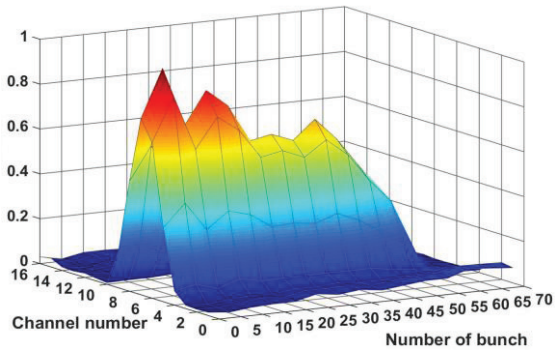

Figure 10: Vertical profiles of the bunches recorded at one beam turn.

The beam tunes can be measured with the new FPM as well. Figure 11 represents the measurements of the vertical betatron tune with frequency synthesizer. The synthesizer excites the vertical oscillations of the beam and frequency sweeps linearly in a time. The spectrum of beam oscillations computed from Fourier transform of coordinate of beam image acquired by FPM. It is seen that spectrum of beam respond contains two frequencies: frequency of excitation and vertical betatron tune. The amplitude of betatron oscillations is peaked at the moment of resonance, at about 0.35 seconds. This value of the frequency is determined as a vertical tune by software driving the synthesizer. The data of optical diagnostics are the same, but it provides also a behavior of vertical tune during a time. The temporal spectrum of betatron frequency contains an obvious 50-Hz harmonic which can be caused by noise of a power supply of quadrupole lenses.

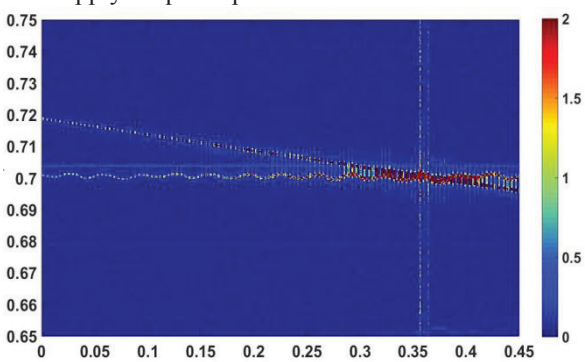

Figure 11: Measurement of the vertical betatron tune with FPM.

DISCUSSION

We have a restricted experimental experience with a new version of FPM yet, but believe that it has a better parameters and more experimental opportunities in comparing with the predecessor. The device was designed for the storage ring with RF frequency of 181 MHz. The temporal resolution of APDA restricts the possibility to apply it for accelerators operating at 500 MHz. The spatial resolution of the optical diagnostics is restricted by the diffraction limit, but this problem can be solved with X-ray optics, say, a beryllium lens. The phosphors with a response time about 3 ns can be manufactured now [6]. It allows acquiring the beam image created by beryllium lens with a proper temporal resolution. The FPM can be applied for routine runs of cyclic accelerators, but is more useful for experiments in the accelerator physics.

CONCLUSION

The Fast Profile Meter based on avalanche photodiode array is successfully tested at SIBERIA-2 storage ring. The device described must continuously implement 15625000 measurements of the vertical or horizontal electron beam profile at 16 points with a time resolution of 5 ns at 50 MHz rate. It will make possible to monitor single bunches of the beam and study multi-bunch beam instabilities.

REFERENCES

[1] O. I. Meshkov et al. The upgraded optical diagnostics of the VEPP-4M collider. Proceedings of EPAC 2004, Lucerne, Switzerland, pp. 2739-2741.

[2] Bogomyagkov A.V., Gurko V.F., Zhuravlev A.N., et al. New fast beam profile monitor for electron-positron colliders. *Review of Scientific Instruments*, v. 78 Issue: 4, Article Number: 043305.

[3] Kiselev V.A., Muchnoi N.Y., Meshkov O.I., et al. Beam energy spread measurement at the VEPP-4M electron-positron collider, *JINST*, v. 2, June 2007.

[4] S. Glukhov, V. Kiselev, E. Levichev et. al. Study of beam dynamics during crossing of resonance in the VEPP-4M storage ring. *Beam Dynamics Newsletter*, No. 48, April 2009.

[5] O. Meshkov, V. Borin, V. Dorokhov et al, Recent results from new station for optical observation of electron beam parameters at KCSR storage ring, TUPG67, this conference.

[6] Hamamatsu fast decay phosphor J13550-09D.

ISBN 978-3-95450-177-9

LONGITUDINAL PHASE SPACE DIAGNOSTICS FOR ULTRASHORT BUNCHES WITH A PLASMA DEFLECTOR

I. Dornmair* [2], K. Floettmann [3], A. R. Maier [3], B. Marchetti [1], C. B. Schroeder [1]
[1]Center for Free-Electron Laser Science & Department of Physics, University of Hamburg, Germany
also at [2]Lawrence Berkeley National Laboratory, Berkeley, California, USA
also at [3]DESY, Hamburg, Germany

Abstract

The plasma-based deflector is a new method to diagnose the longitudinal phase space of ultrashort electron bunches. It harnesses the strong transverse fields of laser-driven plasma wakefields to streak an electron bunch that is injected off-axis with respect to the driver laser. Owed to the short plasma wavelength and the high field amplitude present in a plasma wakefield, a temporal resolution around or below one femtosecond can be achieved with a plasma length of a few millimeters. Limitations arise from beam loading, synchronization and higher order correlations of the transverse fields. Amongst the possible applications are experiments aiming at external injection into laser-driven wakefields, or the diagnostics of laser-plasma accelerated beams.

INTRODUCTION

Laser Plasma Accelerators (LPA) can provide high accelerating gradients in the order of 10 to 100 GV/m, and the acceleration of electron bunches to several GeV has been shown over few centimeter distances [1, 2]. The technology is therefore a promising candidate especially for drivers of next generation light sources. However, the beam quality is still a major challenge for the field, especially in terms of energy spread, emittance and divergence after the plasma.

In a laser plasma accelerator, a high power laser pulse is focused into a plasma target. Typical laser parameters here are a few Joules pulse energy, several tens of femtoseconds pulse length and a focal spot size around 15 μm. In the plasma, the laser pulse trails a wakefield. The ponderomotive force of the laser pulse causes a charge separation leading to large electric fields both in the longitudinal and in the transverse directions. The characteristic length scale is the plasma period with around 10 to 100 μm length for typical parameter ranges. Short electron bunches can be injected into the wakefield internally, i.e. from the plasma background, or externally from a conventional accelerator [3, 4], which has not been demonstrated so far. The usually large energy spread of plasma accelerated beams can be connected to the finite electron bunch length in combination with the short plasma period. For both injection strategies it is therefore vital to gain access to the longitudinal phase space of the injected bunch, in order to optimize the beam quality.

The bunch length of LPA beams has been measured to around 1.4 to 1.8 fs rms with coherent transition radiation [5] or to 2.5 fs rms employing Faraday rotation of a probe laser [6]. The resolution of a longitudinal phase space diagnostic consequently needs to be around or below one femtosecond, a feat that so far has only been achieved with X-band TDS cavities [7]. The use of those cavities in LPA is extremely challenging, not only due to their large size and cost, but also due to the lack of synchronization of the RF to the LPA driver laser. We therefore proposed [8] to employ the strong fields and short periods in plasma wakefields to streak the electron bunch.

PLASMA BASED DEFLECTOR

In the linear regime, i.e. for a normalized peak vector potential of the driver laser $a_0^2 = (eA/m_e c^2)^2 \ll 1$, the electric fields in the wake exhibit a longitudinally sinusoidal structure [9]. The transverse shape of the longitudinal field follows the laser intensity profile, while the shape of the transverse fields follows the derivative of the laser intensity profile in the respective transverse coordinate. An electron bunch that is injected at a transverse offset with respect to the driver laser and at a phase where the transverse fields have a zero-crossing will then experience streaking fields. For a Gaussian driver laser, the optimum transverse offset is one standard deviation of the laser intensity profile, since there the transverse fields are maximal. An illustration of the setup can be seen in figure 1.

The temporal resolution of the setup can be calculated in a similar manner as for conventional TDS cavities, and is given by

$$\Delta\xi/c \geq \frac{\epsilon_{ny} m_e c}{\sigma_y e k_p V}. \quad (1)$$

Here, ξ is the internal bunch coordinate, ϵ_{ny} is the normalized transverse emittance, σ_y is the rms electron beam size inside the plasma, $k_p = (ne^2/m_e\epsilon_0 c^2)^{1/2}$ is the plasma wavenumber at a density n, and V the effective voltage given by the integral of the peak transverse fields over the plasma length.

The resolution of a plasma-based deflector profits from the short plasma period and consequently large wavenumber, as well as from the strong fields present in the wakefield. Also, a low emittance of LPA beams has been measured with 0.1 - 0.2 mm mrad [10, 11]. On the other hand, a resolution reduction can be expected from the electron beam size σ_y, as it needs to be significantly smaller than the laser spot size, and will consequently be around 10 μm even for large laser spot sizes.

* irene.dornmair@desy.de

ISBN 978-3-95450-177-9

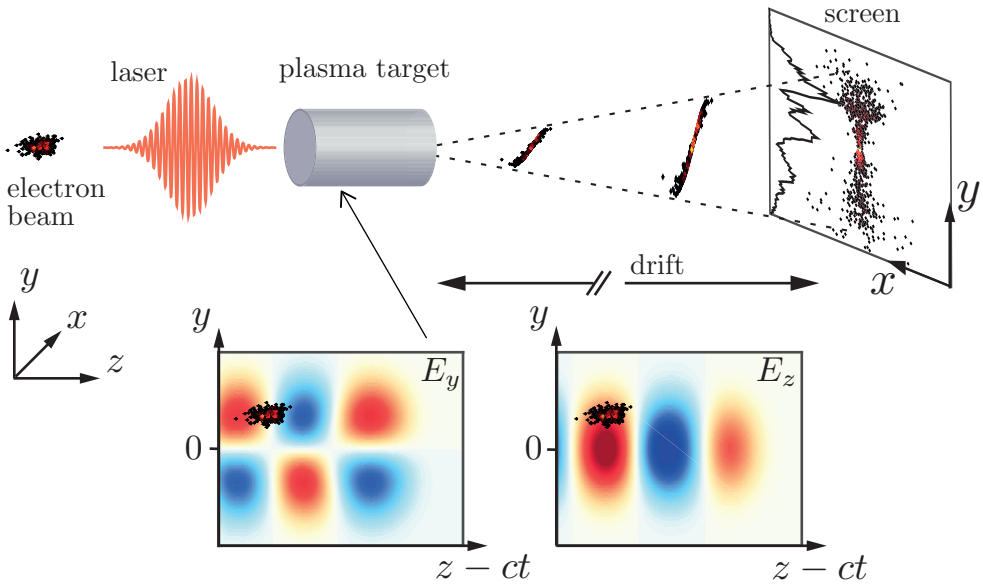

Figure 1: Sketch of the plasma deflector setup. A high power laser pulse drives a linear plasma wakefield, and the probed electron bunch is injected off-axis with respect to the driver laser propagation axis. The wakefield for a Gaussian driver laser is given below in arb. u. The optimum bunch position in the wake is at the transverse maximum and the longitudinal zero-crossing of E_y. In a drift or beam optics after the plasma, the transverse momentum change is transfered into a change of position, carrying the time information.

LIMITING EFFECTS

Several effects can limit the resolution and applicability of the plasma-based deflector. Due the finite electron beam size compared to the wakefield width, which is determined by the laser spot size, the electron bunch will sample over part of the curvature of the transverse fields. Particles at the side of the bunch will experience a smaller streaking slope than those in the center. The loss of resolution depends on the position within the bunch, assuming its center is at the longitudinal zero-crossing of E_y, and can be calculated to

$$\Delta\xi \geq \sqrt{\frac{5}{2}}\left(\frac{\sigma_y}{\sigma_r}\right)^2 |\xi|, \tag{2}$$

with the rms width of the Gaussian laser intensity denoted as σ_r. To reduce the influence of this effect, the laser spot size needs to be chosen much larger than the electron beam size.

Another limitation arises from beam loading, i.e. the electron bunch driving its own wakefield in the plasma. This will modify the streaking fields, and sets a limit on the maximum beam charge. This effect is especially pronounced at the tail of the bunch, where the beam-driven wake is already built up, while at the head of the bunch the influence of beam loading is small. If this is a dominant effect, a transversally larger driver laser allows to increase the electron beam size and reduce the bunch density, thereby suppressing beam loading without pronouncing the resolution reduction from higher order correlations of the streaking field.

The arrival time of the probed electron bunch needs to be synchronized to the driver laser. An electron bunch injected internally in LPA will be intrinsically synchronized to the driver laser of this stage. Applying the plasma deflector to such a beam allows to use part of the same laser system for both stages, thereby keeping the intrinsic synchronization. The plasma deflector is therefore well suited for beams from previous LPA stages. In the case of electron beams from conventional accelerators, the plasma deflector might best be suited for experiments aiming at external injection. There, a sophisticated synchronization system between the RF and driver laser is required anyway for the timing of the external injection experiment, in addition to a high-power laser system and a plasma target. The plasma deflector then would not require any additional equipment.

The tolerable arrival time jitter is given by the plasma period, which is typically in the range of 100 fs. A synchronization to the 10 fs level then needs to be achieved. However, this constraint can be relaxed by decreasing the plasma density, which leads to an increase of the plasma period like $\lambda_p \propto n^{-1/2}$.

CONCLUSION

Due to their short bunch length, laser plasma accelerated beams call for novel diagnostics concepts. One option to gain access to the longitudinal phase space is the plasma deflector, which, owing to the short plasma period and high fields, can achieve a theoretical temporal resolution below one femtosecond. In order to achieve a high resolution, detrimental effects like the transverse field curvature or beam loading have to be minimized.

ISBN 978-3-95450-177-9

ACKNOWLEDGEMENT

We gratefully acknowledge funding through BMBF Grant No. 05K13GU5, and the computing time provided on the supercomputers JUROPA and JURECA under project HHH20 and on the PHYSnet cluster of the University of Hamburg. Work at LBNL was supported by the Director, Office of Science, Office of High Energy Physics, of the U.S. Department of Energy under Contract No. DE-AC02-05CH11231

REFERENCES

[1] X. Wang *et al.*, "Quasi-monoenergetic laser-plasma acceleration of electrons to 2 GeV", *Nat. Commun.* 4, 1988, 2013.

[2] W. Leemans *et al.*, "Multi-GeV Electron Beams from Capillary-Discharge-Guided Subpetawatt Laser Pulses in the Self-Trapping Regime", *Phys. Rev. Lett.* 113, 245002, 2014.

[3] B. Zeitler *et al.*, "Merging conventional and laser wakefield accelerators", *SPIE Optics + Optoelectronics* 8779, 877904, 2013.

[4] A. R. Rossi *et al.*, "The External-Injection experiment at the SPARC_LAB facility", *NIM A* 740, 60, 2014.

[5] O. Lundh *et al.*, "Few femtosecond, few kiloampere electron bunch produced by a laser–plasma accelerator", *Nat. Phys.* 7, 219, 2011.

[6] A. Buck *et al.*, "Real-time observation of laser-driven electron acceleration", *Nat. Phys.* 7, 543, 2011.

[7] A. Buck *et al.*, "Few-femtosecond time-resolved measurements of X-ray free-electron lasers", *Nat. Commun.* 5, 3762, 2014.

[8] I. Dornmair *et al.*, "Plasma-driven ultrashort bunch diagnostics", *Phys. Rev. Accel. Beams* 19, 062801, 2016.

[9] E. Esarey *et al.*, "Physics of laser-driven plasma-based electron accelerators", *Rev. Mod. Phys.* 81, 1229, 2009.

[10] E. Esarey *et al.*, "Ultralow emittance electron beams from a laser-wakefield accelerator", *Phys. Rev. ST Accel. Beams* 81, 1229, 2012.

[11] G. R. Plateau *et al.*, "Low-Emittance Electron Bunches from a Laser-Plasma Accelerator Measured using Single-Shot X-Ray Spectroscopy", *Phys. Rev. Lett.* 109, 064802, 2012.

ISBN 978-3-95450-177-9

ACCURATE MEASUREMENT OF THE MLS ELECTRON STORAGE RING PARAMETERS

R. Klein, G. Brandt, T. Reichel, R. Thornagel,
Physikalisch-Technische Bundesanstalt (PTB), Berlin, Germany
J. Feikes, M. Ries, I. Seiler,
Helmholtz-Zentrum Berlin für Materialien und Energie (HZB), Berlin, Germany

Abstract

The Physikalisch-Technische Bundesanstalt (PTB, the German national metrology institute) uses the Metrology Light Source (MLS) as a primary radiation source standard. This requires the accurate measurement of all storage ring parameters needed for the calculation of the spectral radiant intensity of the synchrotron radiation. Therefore, instrumentation has been installed in the MLS for the measurement of, e.g., the electron beam energy, the electron beam current or the electron beam size that outperforms that usually installed in electron storage rings used as a common synchrotron radiation source.

INTRODUCTION

The PTB, the German metrology institute, utilizes the electron storage ring Metrology Light Source (MLS) [1] in Berlin - Adlershof for the realization of the radiometric units in the near infrared, visible, ultraviolet and vacuum ultraviolet spectral range. For this purpose the MLS can be operated as a primary source standard, i.e. the spectral radiant intensity of the synchrotron radiation (SR) is calculated by means of the Schwinger equation [2]. The primary source can then be used for the calibration of other radiation sources or of wavelength- or energy dispersive instruments [3]. The input parameters for the calculation of the spectral radiant intensity are the electron beam energy, electron beam current, the effective vertical size of the electron beam and the magnetic induction at the source point of the SR. For calibration applications, e.g. the spectral radiant power transmitted through a flux-defining aperture also is of interest. For this, also the geometrical parameters of the experiment have to be measured which are the distance to the source point and the vertical observation angle with respect to the orbital plane. These parameters have to be measured accurately since there measurement uncertainty determines the uncertainty of the calculated spectral radiant intensity. PTB operates equipment for the measurement of the storage ring parameters over a wide range. Especially the electron beam energy and electron beam current can be varied over a wide range (see below) to create tailor-made conditions for various calibration tasks. Table 1 summarizes typical storage ring parameters and the related uncertainties in their determination. The influence of the uncertainty of the measured parameter in the calculation of the spectral power depends on the wavelength. For the uncertainties listed in Table 1 the spectral radiant power can be calculated with a relative uncertainty well below 0.1 % for wavelength longer than 10 nm. In this spectral range the MLS is used for UV and VUV radiometry. The relative uncertainty gradually rises to almost 1 % for a wavelength of 1 nm as can be seen in Fig. 1. In this shorter wavelength range it might sometimes be better to use the neighboring BESSY II electron storage ring, that is operated by PTB in special user shifts as a primary source standard, mainly for the X-ray spectral range [4].

Table 1: Typical Operation Parameters of the MLS as a Primary Source Standard and Related Uncertainty in the Measurement of these Parameters.

Parameter	**Typical value**	**Typical (rel.) uncertainty**
electron energy W	628.5 MeV	$2 \cdot 10^{-4}$
magnetic induction B	1.38 T	$1 \cdot 10^{-4}$
electron beam current I (example)	20 mA	$2 \cdot 10^{-4}$
eff. vert. source size Σ_y	1.5 mm	10 %
vert. observation angle ψ	0 µrad	5 µrad
distance d	20 m	5 mm

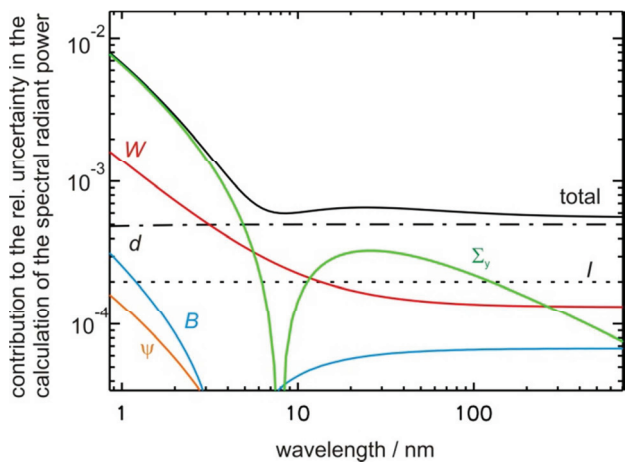

Figure 1: Contribution of the parameters' uncertainties to the calculation of the spectral power. The symbols marking the various lines are explained in Tab. 1, first column; the uncertainty in the parameters is listed in the third column of this table.

ISBN 978-3-95450-177-9

MEASUREMENT OF THE STORAGE RING PARAMETERS

In the following the measurement technique for the storage ring parameters are briefly described, for further details and the description of the measurement of the geometrical parameters please refer to ref. [5].

Electron Beam Energy

The electron energy is used from 105 MeV, the injection energy, up to 630 MeV, the normal operation energy. Performance of the storage ring in terms of beam lifetime and stability is optimized for the range from 150 MeV up to 630 MeV.

Within this large range, the electron energy is measured by the technique of Compton backscattering of laser photons (CBS) [6]. Therefore, a CO_2 laser beam is aligned anti-parallel to the electron beam in the straight section of the undulator and the scattered photons are recorded with an energy-dispersive high purity Germanium detector (HPGe). From the cut-off of the backscattered photon spectrum (see Fig. 2), the electron energy can be calculated. Due to the rather small electron beam energy the technique of resonant spin depolarization (RSD), e.g. also applied by PTB at the BESSY II electron storage ring [7], cannot be applied at the MLS since polarization built-up would take more than 30 hours.

For a validation of the CBS technique and the identification of possible systematic errors, the laser was switched from its normal operation at a CO_2 wavelength (around 10.6 µm) to a CO wavelength (around 5.4 µm). The then measured electron beam energies were 627.78(8) MeV and 627.79(19) MeV, respectively and show a very good agreement (the values in parenthesis show the standard uncertainties). For 150 MeV operation of the MLS the measured energies were 150.38(27) MeV and 149.80(22) MeV, respectively and also agree within the expanded uncertainties.

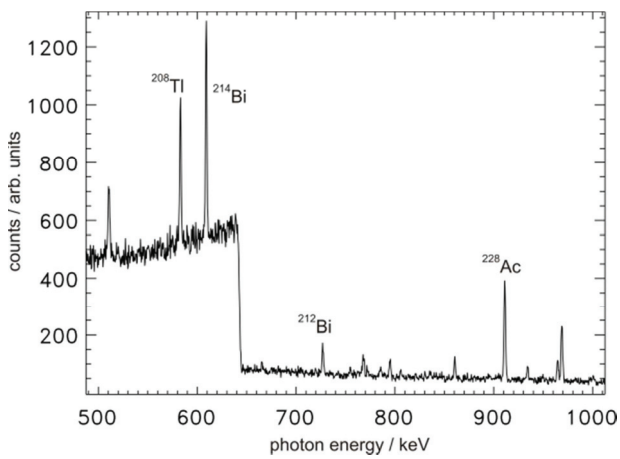

Figure 2: Typical spectrum of back-scattered photons recorded with an HPGe detector, here at 600 MeV electron beam energy. Lines from suitable radio-nuclides used for the energy calibration of the HPGe detector are also shown.

The CBS set-up is also used for general storage ring diagnostics and research. As example Fig. 3 shows the shift of the cut-off of the backscattered photons while the rf frequency is changed by a certain amount. From the related change of the electron beam energy, e.g., the momentum compaction factors can be determined for different operation modes of the MLS [8].

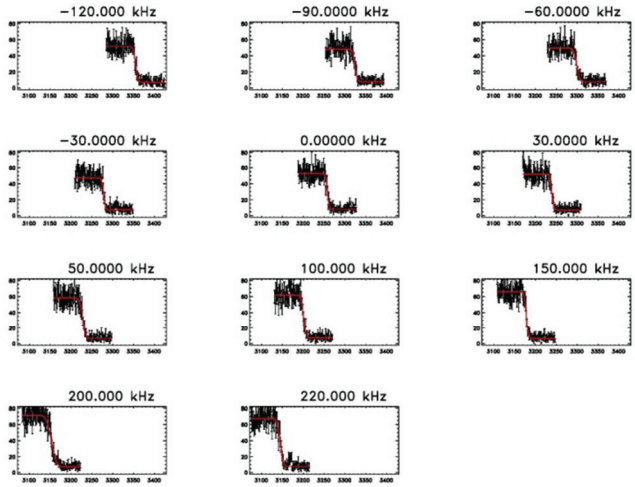

Figure 3: Example for a measurement for general storage ring diagnostics: the radio frequency was shifted and the shift in electron energy was observed by Compton backscattering (x-axis: HPGe detector channel, y-axis: counts).

Magnetic Induction

The synchrotron radiation source point of the beamline using the calculable radiation is located in middle of magnet. A specially designed bending magnet vacuum chamber allows a nuclear magnetic resonance probe to be brought to the source point of the radiation after a beam dump has been performed. The source point lies in a region of the bending magnet with very low field gradients which has been checked by a field mapping of the bending magnet before installation. The relative uncertainty for the determination of the magnetic induction at the radiation source point is dominated by the residual magnetization of the stainless steel tube housing the NMR probe and positioning in accuracy which are estimated to contribute to less than 10^{-4} to the relative uncertainty.

Electron Beam Current

The MLS is operated with electron beam currents between 1 pA (one stored electron) and the maximum allowed beam current of about 200 mA, thus e.g. enabling PTB to match the photon flux to the sensitivity of the devices to be calibrated over a dynamic range of more than 11 decades. Currents in the upper range, i.e. above several mA, are measured with two DC parametric current transformers. Electron currents in the lower range, i.e. below 1 nA, are determined by counting the number

ISBN 978-3-95450-177-9

of stored electrons. For this, the electrons are gradually removed out of the storage ring by a mechanical scraper, which is moved closely to the electron beam, while measuring the step-like drop of the synchrotron radiation intensity by cooled photodiodes. These photodiodes have a 10 mm by 10 mm area and are placed at a distance of about 2.5 m to the source point and are illuminated by the SR. Since they are placed in vacuum, they accept all wavelengths of the synchrotron radiation spectrum.

Electron beam currents in the middle range, i.e. from about 1 nA up to several mA, are determined by three sets of windowless linear Si photodiodes with different filters, that are illuminated by synchrotron radiation. The calibration factors of these photodiodes, which relate the photo current to the electron beam current, are determined by comparison with the electron beam current measured at the upper and lower end of the range as described above [9].

The equipment for the electron counting in the lower range was recently improved [9] so that counting even at currents around 1 nA (1000 electrons) is possible at an electron beam energy of 630 MeV. For a special calibration task, i.e. calibration of single photon detectors, the MLS had to be operated at a reduced electron beam energy of 540 MeV in order to reach a wavelength at around 1.5 µm with the existing U125 undulator. But at 540 MeV, one electron only creates about 35 % of the photodiode signal as compared to the 630 MeV operation. Nevertheless, counting of around 500 electrons could be successfully performed as can be seen in Fig. 4.

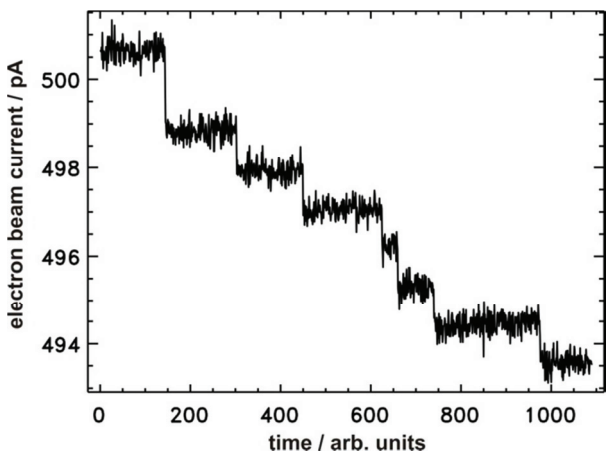

Figure 4: Electron beam current measurement by electron counting for an electron energy of 540 MeV.

Effective Vertical Source Size

Important for most calibration tasks is the so-called effective vertical source size Σ_y, i.e. the influence of the vertical electron beam σ_y size and beam divergence $\sigma_{y'}$ at the distance d to the source point at which the calibration is performed:

$$\Sigma_y = \left(\sigma_y^2 + d^2\,\sigma_{y'}^2\right)^{1/2}$$

The vertical photon distribution of the synchrotron radiation has to be convoluted with this effective vertical source size. The effective vertical source size can be directly and accurately measured with a Bragg polarimeter [10]. This device measures the vertical distribution of the synchrotron radiation at a photon energy of 1103 eV (Bragg condition for reflection by means of a Beryll crystal) only for the polarization component perpendicular to the orbital plane (by means of the Brewster condition). The measured distribution which shows a distinct drop at the orbital plane is then compared to the theoretical distribution by adjusting the vertical beam size appropriately in order to best fit the measured data.

General Beam Size Diagnostics

For a general diagnostics of the storage ring, e.g. for the investigation of effects influencing the beam size, beam stability diagnostics or the investigation of instability driven by trapped ions, a fast and reliable system for direct observation of the beam size is needed. By knowledge of the optical functions of the storage ring the vertical beam size could be calculated from the measured effective beam size [5], but measurements with the Bragg polarimeter are too complicated for everyday's use. Therefore, two optical imaging systems have been installed at the MLS. One of these is imaging the spot in a ring position with equivalent optical functions as the source point of the beamline using the calculable radiation. This imaging system is furthermore optimized to image the beam if only one electron is stored [11].

For the validation of the beam size measured with this optical imaging system, the beam size was simultaneously measured with a X-ray camera like system. The X-ray camera like system was based on the Bragg polarimeter mentioned above. Additionally, slits with 100 µm in width were introduced into the optical path. E.g. a horizontally orientated slit was used for the measurement of the vertical beam size and a vertically slit for the measurement of the horizontal beam size. The Bragg polarimeter was always operated in such an orientation that the polarization component that is parallel to the orbital plane was observed. The measurements were performed for various operation modes of the MLS, leading to different beam sizes. The result is shown in Fig. 5. The black symbols mark the beam sizes measured for the vertical beam dimension, the red ones that for the horizontal beam dimension. Both values pretty much agree if a resolution limit of approx. 120 µm is assumed for the optical systems. The resolution limit at that time was a bit higher as estimated from diffraction or depth of source effects, but is more than sufficient for typical beam size values at the MLS. The resolution limit has been improved meanwhile to below 80 µm by improved alignment.

ISBN 978-3-95450-177-9

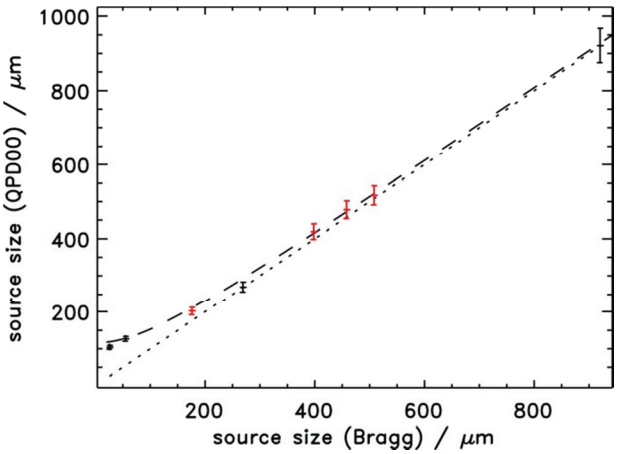

Figure 5: Measured beam sizes in the vertical (black) and horizontal (red) directions for various settings of the MLS. On the x-axis the values measured by the X-ray camera like operation of the Bragg polarimeter, on the y-axis the corresponding values measured with the first optical imaging system are drawn. The dotted line marks the diagonal, i.e. if exactly the same values with both devices would have been measured, the dashed line if a resolution limit of 120 µm for the optical system is assumed.

A similar result for the resolution limit at that time was obtained if the measured values for both systems are observed simultaneously while the beam size is altered by excitation, as is shown, e.g., for the vertical direction in Fig. 6. For larger values the measured beam sizes follow a straight line (dashed red), the slope of which exactly agrees with the square root of the ratio of the ß - functions at the source point positions

$$slope = \sqrt{\beta_y(s_{QPD00}) \Big/ \beta_y(s_{QPD01})}$$

imaged by the two devices (measurement: 0.923(1), theory: 0.92). For vertical beam sizes approaching the resolution limit, a deviation from this behaviour is observed. This also indicated to a similar resolution limit at that time.

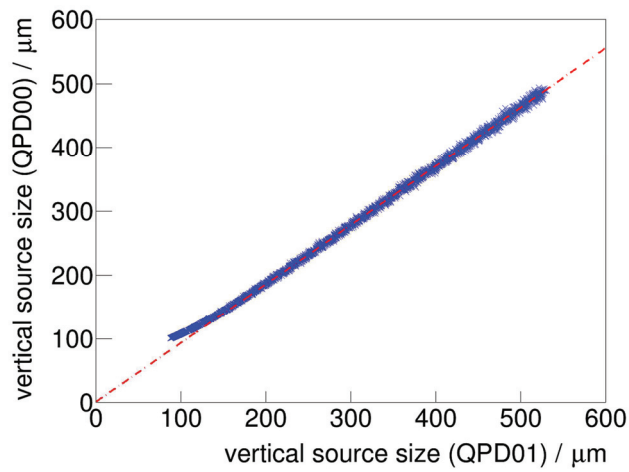

Figure 6: Measured vertical beam size by the two optical imaging systems.

SUMMARY

The PTB is operating the MLS as a primary source standard in the spectral range from the near infrared to the vacuum ultraviolet spectral region. This is possible because all parameters needed to calculate the spectral radiant intensity based on the Schwinger equation are measured with low uncertainty, yielding a relative uncertainty in the spectral radiant power below 0.1% in the spectral region the MLS is optimized for.

REFERENCES

[1] J. Feikes *et al.*, Proceedings of EPAC 2008, Genoa, Italy, pp. 2010.
[2] J. Schwinger, Phys. Rev. 75, (1949) 1912.
[3] B. Beckhoff *et al.*, Phys. Status Solidi B 246 (2009), 1415.
[4] R. Thornagel, R. Klein and G. Ulm, Metrologia 38, (2001) 385.
[5] R. Klein *et al.*, Phys. Rev. ST Accel. Beams 11, 110701-1 (2008).
[6] R. Klein *et al.*, Nucl. Instr. and Meth. A 384, (1997) 293.
[7] R. Klein *et al.*, Nucl. Instr. and Meth. A 486, (2002) 545.
[8] M. Ries, doctoral thesis, Humboldt University, Berlin, 2013.
[9] R. Klein *et al.*, Proceedings of IBIC 2013, Oxford, UK, pp. 903.
[10] R. Klein *et al.*, Proceedings of IPAC 2011, San Sebastian, Spain, pp. 1165.
[11] C. Koschitzki *et al.*, Proceedings of IPAC 2010, Kyoto, Japan, pp. 894.

ISBN 978-3-95450-177-9

MEASUREMENT OF THE BEAM RESPONSE TO QUADRUPOLE KICK BY USING STRIPLINE PICKUP MONITOR AT J-PARC MAIN RING

Y. Nakanishi, A. Ichikawa, A. Minamino, K. G. Nakamura, T. Nakaya, Kyoto University, Japan
T. Koseki, H. Kuboki, M. Okada, T.Toyama, KEK, Japan

Abstract

In high intensity proton synchrotrons, linear and nonlinear betatron resonances cause beam loss. When the betatron tune spreads over a resonance line, the betatron oscillation amplitude will get larger, causing large beam loss. Our study aims for a direct measurement of the betatron tune spread by using a quadrupole kicker and a four-electrode monitor. The monochromatic RF signal is transfered to the kicker and we induce an oscillation by kicking the beam. The amplitude of the quadrupole oscillation will depend on the number of particles having a certain tune. In the beam test at J-PARC MR, the dipole kicker was used as a quadrupole kicker by exciting the two facing electrodes in-phase. We measured the response to the kick at several frequencies. We observed that the amplitude of the quadrpole oscillation depends on the kicker frequency and the number of particles per bunch. This demonstrates that the quadrupole oscillation can be induced by a kicker and the possibility of measuring the number of particular tune particles from the response. We will present the result of the beam test and our prospect and the comparison between the experimental result and a numerical calculation.

INTRODUCTION

J-PARC, Japan Proton Accelerator Research Complex, has a high intensity accelerator. J-PARC accelerator consists of three parts, LINAC (Linear accelerator), RCS (3 GeV Synchrotron) and Main Ring (30 GeV Synchrotron).

It is important to consider the beam loss upon increasing the beam power [1,2]. The beam loss is caused by the coherent motion and the incoherent motion of the beam. The incoherent motion is mainly induced by space charge, and this effect make the incoherent tune spread. In J-PARC, tune spread has estimated by not a direct measurement but a simulation. If tune spread can be measured, we can know a betatron bare tune which makes tune spread smaller than under current operation.

We aim for measuring tune spread caused by the space charge effect in this measurement. The response by a normal quadrupole kicker was measured in J-PARC MR.

When the beam run under an unideal operation, for instance the injection mismatch and the error field effect, the beam circulates involving the small quadrupole oscillation. After the injection, the beam width gradually increases until it becomes stable. Kickers, which use monochromatic RF signal and make the normal quadrupole force, kick the beam and induce the quadrupole oscillation.

THE METHOD OF MEASUREMENT

This measurement was carried out on J-PARC MR. Table 1 shows the parameter of the used beam.

Table 1: Beam Parameter

Horizontal tune	22.40
Vertical tune	20.75
Revolution frequency	185743.5Hz

Table 2: Kicker Setting Parameter

Maximum power	3kW×2
RF frequency	222854 Hz, 215854 Hz, 208854 Hz, 201854 Hz, 194854 Hz, 247615 Hz
Kicker angle	102μrad / m / turn

Table 3: Beam Intensity

	The number of protons per bunch
(I)	$0.99(\pm0.01)\times10^{13}$
(II)	$1.28(\pm0.01)\times10^{13}$
(III)	$1.39\ (\pm0.02)\times10^{13}$

Two power amplifier are connected to kickers. The maximum power is 3 kW for each amplifier. Three kickers are arranged in series. The kicker consists of two electrodes in the vacuum pipe. We use it as a dipole kicker in the usual operation, but in this measurement, as a quadrupole kicker by exciting the two facing electrodes in-phase [3]. The beam passes through the kicker, particles having a certain tune oscillate larger. The relationship between a resonance tune of particles and the kicker RF frequency is given by Eq. (1), (2). [4]

$$2\nu_x = n_x \pm f_{RF}/f_{rev} \quad (1)$$

$$2\nu_y = n_y \pm f_{RF}/f_{rev} \quad (2)$$

$\nu_{x,y}$ is betatron tune in x and y direction, $n_{x,y}$ is an integer, f_{RF} is the kicker RF frequency, and f_{rev} is revolution frequency in MR.

The response is measured by four-electrode monitor [5]. Table 2 shows the parameters of kicker operation. Maximum power is sum of three kicker power. Two means the number of electrodes in each kicker. The angle gradient per turn is 102 μrad/m in this quadrupole kicker. The beam was kicked after 1s from the beam injection. This is because the beam is affected by the injection mismatch and the beam largely oscillates just after the injection. Figure 1 shows the

ISBN 978-3-95450-177-9

schematic view of kicker setup. The signal from a signal generator, AFG3252 Textronix, was separated by power splitter, Mini-circuits ZFSC-2-6+. The signal was amplified by R&K A101 K101- 6565R RF Power Amplifier. Data was taken in 0.2s by an oscilloscope, LECROY-HDO6104-MS. The measurement starts before 0.04s from the beginning of kicker operation. Sampling rate was 2.5×10^8Hz, and ADC bit was 12bit. 8329-300 w/Blower made by Bird Electronic Corporation was used for an attenuator.

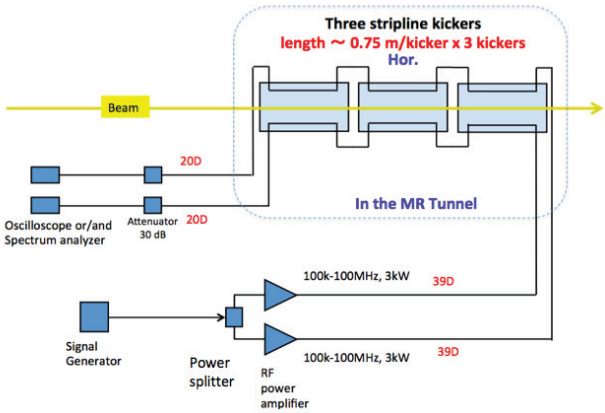

Figure 1: Schematic view of kicker setup.

Data was taken three times in each parameter setting. The value in Table 3 is the number of particle in starting to measure the data. The beam loss was existed, and particles vanished by $0.02 \times 10^{13} protons$ in the condition (I), $0.05 \times 10^{13} protons$ in (II), $0.08 \times 10^{13} protons$ in (III). This change realized by changing the thinning ratio [6]. This measurement was carried out on six RF frequencies indicated in Table 2. The parameter was corresponded to the blue line in Figure 2. The RF frequency of quadrupole kicker can be transferred to tune by Eq. (1) and (2). Tune spread is represented by the black area in Figure 2 [7]. The tune spread is calculated by Space Charge Tracking Program. The condition is shown in Table 4. The six frequencies were chosen not to cross over the RF kicker resonance line in both x and y direction.

Other Measurements

We measured on the two conditions:

(a) Beam was not injected, and kicker RF turns on.

(b) Beam was present in the ring, and kicker RF turns off.

The measurement in the (a) condition is for checking whether there is an unpredicted path through which the kicker RF signal propagates to electrodes.

Table 4: Beam Parameter in the Simulation

Power	200kW
The number of particles	1.33×10^{13} protons per bunch
Emittance in x direction	$16\ \pi\ mmmrad\ (2\sigma)$
Emittance in y direction	$24\ \pi\ mmmrad\ (2\sigma)$
Bunching factor	0.2
Betatron bare tune	(22.4, 20.75)

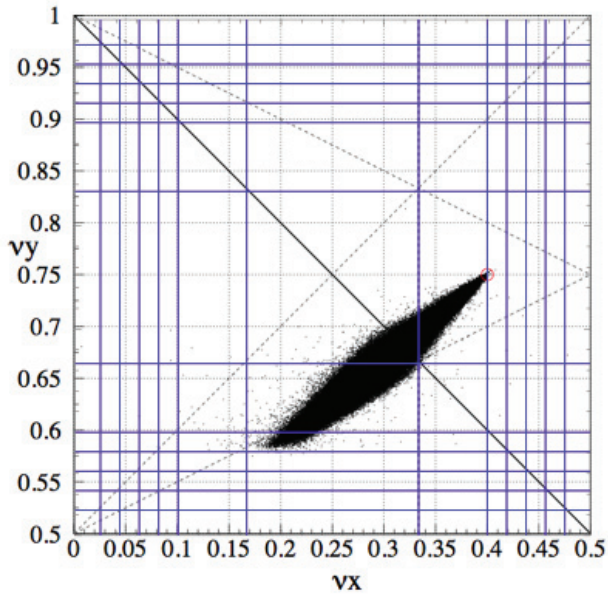

Figure 2: Tune spread diagram and the kicker RF resonance line. Horizontal axis is tune in x direction, and vertical is in x direction.

THE SIGNAL PROCESSING

One set of the data includes four channels, 371476 pulses per pulse included in the data from the oscilloscope. First, the data is divided into a bunch. The period is 5.384μs for a turn. Each data has 37147 turns. Second, the data was changed by Fourier transform. The time window is 5.384μs, the period for sampling is 4ns. We got the Fourier spectrum and the peak is existed and $V_i (i = 1,2,3,4)$ is defined by the height of the peak. Normal quadrupole moment is calculated by Eq. (3) [8]. V_1, V_2, V_3 and V_4 correspond the signals of right, left, up, down.

$$Q = (V_1 + V_3 - V_2 - V_4)/(V_1 + V_3 + V_2 + V_4). \quad (3)$$

The sensitivity factor is $K_Q = 237.4[1/m^2]$ in this monitor, where $Q = K_Q \times (< x^2 > - < y^2 >)$.

Q was transformed with Fourier transform. Time window is 0.1599[s].

ISBN 978-3-95450-177-9

RESULT

Figure 3 shows the frequency spectrum of turn by turn Q when the kicker RF frequency is 247615Hz. The horizontal axis is frequency[Hz] and the vertical axis is the Fourier power.

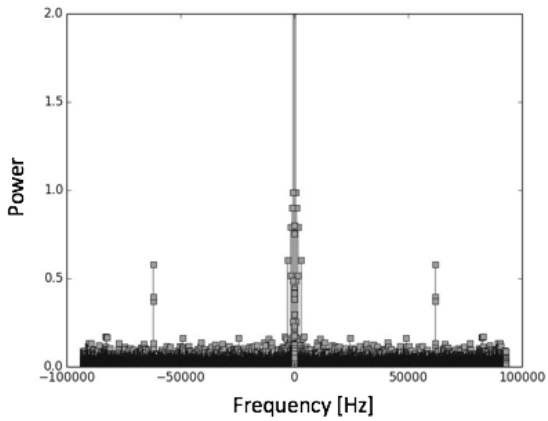

Figure 3: Frequency spectrum of the turn by turn quadrupole moment (29715turn).

In another measurement (a), Q has no mean. The Fourier transformed signal had no peak around the kicker RF frequency. We can conclude that the signal transferred from a kicker to electrodes is small enough not to consider the contribution.

The result of the measurement (b) is shown in Figure 4. From (b) measurement, the signal didn't have a peak around the RF frequency. This can conclude that the peak was induced by kicker RF. Furthermore, it turns out that the quadrupole oscillation occurred by injection mismatch is undetectable.

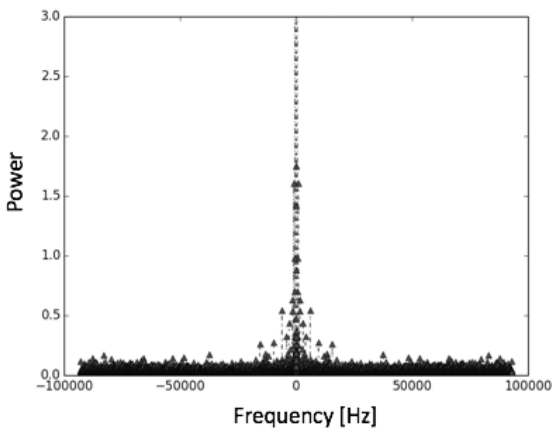

Figure 4: Frequency spectrum of the turn by turn quadrupole moment in measurement (b).

DISCUSSION

The frequency of Fourier peak almost corresponds to the predicted one calculated by Eq. (4).

$$f_{pre} = f_{kicker} - f_{rev} \quad (4)$$

f_{pre} is the predicted frequency of peak in the frequency spectrum. f_{kicker} is the frequency of the kicker RF. f_{rev} is revolution frequency of the beam in the ring.

The predicted frequency calculated by Eq. (4) is 61879.5Hz in the case that the kicker RF frequency is 247615Hz. On the other hand, the frequency in the three measurement is all 61886.8Hz. The measured frequency is larger than predicted value by 7~9Hz. This gap comes from some or one possible reasons, which can be considered unstable kicker RF, unstable revolution frequency, the band width of Fourier transformation ~6.25Hz, the effect of beam optics.

The peak height is defined as q_{peak}. This Fourier power at the frequency spectrum peak corresponds to the amplitude of quadrupole oscillation.

Figure 5 shows the relation of q_{peak} and the frequency of kicker RF in (II).

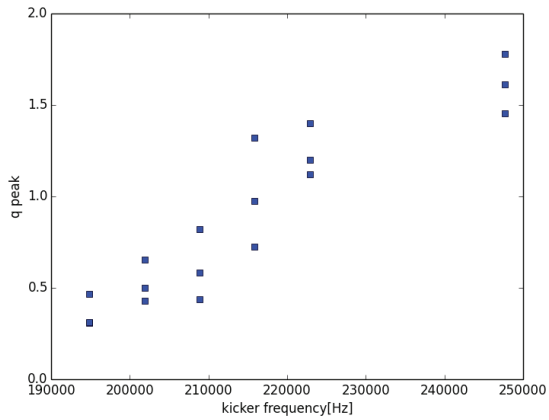

Figure 5: The intensity of quadrupole resonance.

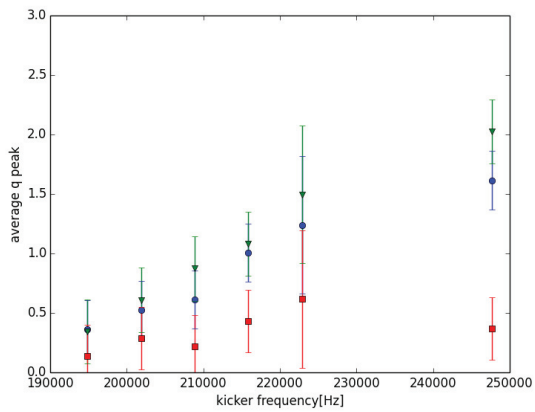

Figure 6: The intensity of quadrupole resonance.

The peak has a large width when the kicker RF frequency is 247615Hz and the number of particles is (II) and (III). A possible reason is that vertical resonance line on tune diagram is covered with the tune spread. So q_{peak} is

ISBN 978-3-95450-177-9

defined as sum of the heights on four points around the peak.

Figure 6 shows the average of three q_{peak} which measured on the same condition. The red square is average q_{peak} in (I). The blue is in (II), and the green is in (III). In Figure 7, the vertical axis is changed to tune by Eq. (5).

$$(f_{RF}/f_{rev} - 1) \cdot 0.5 + 20.5 = \nu_y \qquad (5)$$

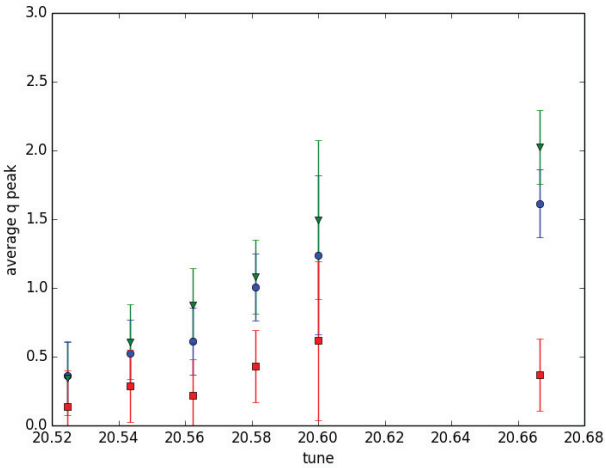

Figure 7: The intensity of quadrupole resonance. The horizontal axis is kicker RF tune. Bare tune is 20.75.

The longitudinal axis represents the intensity of quadrupole oscillation and it depends on the number of particles per bunch and the kicker RF frequency. If the particle which has a certain betatron tune only (or mostly only) can be resonant with kicker RF being satisfied with Eq. (1) and (2), the spectrum in Figure 7 represents the spectrum of tune spread. This result doesn't clearly indicate the change of spectrum due to the change of beam intensity [9]. One reason is that the RF frequency was changed by 7kHz, but this is too rough to get the change of spectrum. Another reason can be that the beam intensity in (II) and (III) could not have a large difference. However, the difference between the spectrum in (II) and (I) can be found and this may be caused by the transition of tune spread.

The Beam Intensity

In Figure 8, beam intensity on two conditions was plotted. Orange line is the average number of particle in three measurements in kicker RF on ($f_{kick} = 247615$ [Hz]). Blue line is in kicker RF off. The difference of the number of particles between RF on and off is 2.65×10^{10} at the end of measurement. The beam intensity during measurement is not different between the two conditions. This means that the beam loss is not clearly caused by the resonance induced by the quadrupole kicker. Figure 8: The number of particles during the measurement.

CONCLUSION

The quadrupole oscillation induced by the RF quadrupole kicker was measured. The resonance arose from the

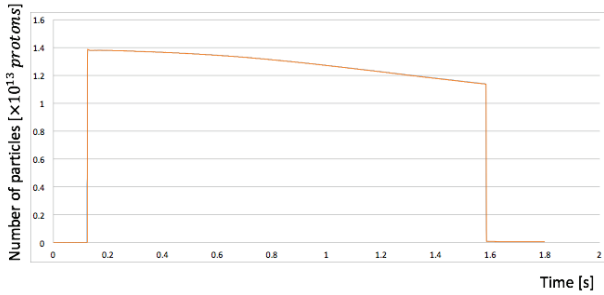

kicker was observed. The amplitude of the resonance oscillation, q_{peak}, depends on the kicker RF frequency. The q_{peak} spectrum depended on the number of particles per bunch.

The additional measurement is planned. The simulation with frozen space charge by transfer matrix approach is now calculated. Vlasov eq. and Maxwell eq. including the external quadrupole RF kick will be also meaningful for our consideration.

APPENDIX

An author (YN) acknowledges the support of MEXT and JSPS in Japan with the Grant-in-Aid for Scientific Research on Innovative Areas 25105002 titled ``Unification and Development of the Neutrino Science Frontier''.

REFERENCES

[1] S. Igarashi, in *Proc. PASJ 2016*, MOOLP04 (2016).
[2] T. Koseki *et al.*, "Beam commissioning and operation of the J-PARC main ring synchrotron", *Prog. Theor. Exp. Phys.* (2012) 02B004.
[3] T.Toyama and M.Okada, "The Kick Angle Calibration of the Exciter in the J-PARC MR", presented at IBIC'16, Barcelona, Spain, September 2016, paper TUP077, this conference.
[4] L.Smith, "Effect of gradient errors in the presence of space-charge forces", *Pros. Int. Conf. on High-Energy Accelerators*, Dubna, 1963, p.897.
[5] K.Nakamura, "The development of J-PARC MR Intra-bunch Feedback System for getting higher intensity neutrino beam on T2K experiment", Kyoto Univ., 2015, Master thesis, in Japanese.
[6] J-PARC, http://j-parc.jp/public/Acc/ja/bunch_linac2rcs.html
[7] S. Igarashi, The Accelerator Technical Advisory Committee (ATAC) for the J-PARC Project, March 6 – 8, 2014.
[8] T.Miura *et al.*, "The measurement of transverse quadrupole mode in KEK-PS Main Ring", *The 14th Symposium on Accelerator Science and Technology*, Tsukuba, Japan, Nov. 2003.
[9] R.Bar, "Measurement of space-charge-induced frequency shifts of quadrupolar beam oscillations in the SIS", *Nuclear Instruments and Methods in Physics Research*, A 415, 1998, pp.460-463.

ISBN 978-3-95450-177-9

NUMERICAL COMPARATIVE STUDY OF BPM DESIGNS FOR THE HESR AT FAIR

A. J. Halama, C. Böhme, V. Kamerdzhiev, F. Klehr, S. Srinivasan
Forschungszentrum Jülich, Germany

Abstract

The Institute of Nuclear Physics 4(IKP-4) of the Research Center Jülich (FZJ) is in charge of building and commissioning the High Energy Storage Ring (HESR) within the international Facility for Antiproton and Ion Research (FAIR) at Darmstadt. Simulations and numerical calculations were performed to characterize the beam position pickup design that is currently envisaged for the HESR, i.e. a diagonally cut cylindrical pickup. The behavior of the electrical equivalent circuit has been investigated with emphasis on capacitive cross coupling. Based on our findings, performance increasing changes to the design were introduced. A prototype of the BPM pickup was constructed and tested on a dedicated test bench. Preliminary results are presented. Another proposed design was characterized and put into comparison, as higher signal levels and higher position sensitivity are expected. That is a symmetrical straight four-strip geometry. Additionally an extensive study was conducted to quantify the effect of manufacturing tolerances. Driven by curiosity an eight-strip pickup design was considered, which would allow for beam size measurements, utilizing the non-linearity.

CAPACITIVE PICKUPS

Capacitive pickups are widely used in particle accelerators as intensity and position monitors. Being non-destructive devices these pickups are of great interest especially in ring accelerators and those where beam may not be lost. Capacitive pickups such as the cylindrical diagonally cut electrodes facilitate the image current, which is influenced by the beam with close resemblance to a perfect current source, as it is mostly modelled in the equivalent circuit. Its pulse shape is given by the time derivative of the longitudinal beam recorded at the pickup location. As a design choice for the HESR the voltage of an electrode shall reflect the longitudinal time structure proportionally. For this case the main frequency contribution of the signal must lie above the cut-off frequency of the RC couple. This is achieved by the high input impedance of the attached preamplifier. The voltage of a centered beam is [1]:

$$U_{img}(t) = \frac{1}{\beta c C_{el}} \frac{A}{2\pi b} I_{beam}(t) \tag{1}$$

With β:=normalized velocity, c:= speed of light, A:= electrode inner surface area and b:= BPM radius. If at least two opposing electrodes are used, a linear response of the voltage versus the beam position can be seen in the centre region of nonlinear BPM such as strip types or buttons. Whereas the cylindrical diagonally cut BPM offers a linear response in the entire region. The linear response can be generalized as the normalized difference signal. Thus the difference over sum ratio is used to describe the linear behaviour [1][2]. For x and similarly y, with S being the sensitivity:

$$x = \frac{1}{S_x}\frac{U_r - U_l}{U_r + U_l} - x_{off} = \frac{1}{S_x}\frac{\Delta_x}{\Sigma_x} - x_{off} \tag{2}$$

To account also for higher order behaviour, ether a lookup table or use a two-dimensional polynomial can be used. For x and similarly y:

$$x = \sum_{i=1}^{N}\sum_{j=1}^{N} K_{x,ij}\left(\frac{\Delta_x}{\Sigma_x}\right)^i \left(\frac{\Delta_y}{\Sigma_y}\right)^j \tag{3}$$

Simulation Boundary Conditions and Formalism

An equivalent circuit has been used to model the voltage response driven by a current source. The circuit evaluation for these studies was carried out using LTspice IV.

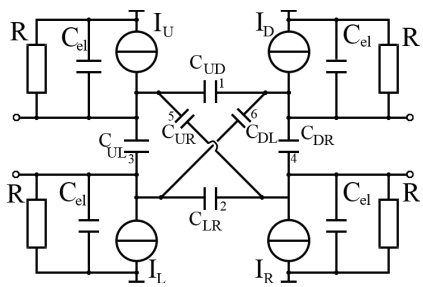

Figure 1: Equivalent circuit of a capacitive four electrode pickup.

For the case of 4 electrodes there are 10 capacitances, i.e. four capacitances against ground, which correspond to C_{el} in Eq. (1). The remaining ones are interconnecting all electrodes, all as illustrated in Fig. 1. The capacitances for the presented results have been determined using COMSOL Multiphysics 5.0 AC/DC analysis, as it allows for static electric field simulations with fixed and floating potentials. The dependence on the beam position is introduced as a geometrical scaling factor, Γ, which would be $\Delta\phi/2\pi$, for a centred beam. It increases for a beam that approaches the electrode. $\Delta\phi$ is the average angular coverage. The scaling factor can be determined for any geometry.

$$\Gamma(\phi_1, \phi_2, r, \theta) = \frac{\int_{\phi_1}^{\phi_2} \frac{l_{BPM}(\phi)}{(\vec{r}_{BPM}(\phi) - \vec{r}_{Beam}(\theta))^2}\,\mathrm{d}\phi}{\int_0^{2\pi} \frac{l_{BPM}(\phi)}{(\vec{r}_{BPM}(\phi) - \vec{r}_{Beam}(\theta))^2}\,\mathrm{d}\phi} \tag{4}$$

With θ and $\vec{r}_{Beam}$ pointing at the beam. Eq. (4) has been derived empirically with the intention to reflect the position dependent influence, driven by the electrical field of the

ISBN 978-3-95450-177-9

beam. The integrals can be solved for example for strip type BPMs with a continuous length and a given angular coverage, so $\phi_{1,2} = \mp\frac{\phi_0}{2}$ [2].

$$\Gamma(r,\theta) = \frac{\phi_0}{2\pi}\left(1 + \frac{4}{\phi_0}\sum_{n=1}^{\infty}\frac{1}{n}\left(\frac{r}{b}\right)^n cos(n\theta)sin\left(\frac{n\phi_0}{2}\right)\right) \quad (5)$$

The resulting scaling factor Γ can only be used to describe pencil beams and radially symmetrical beams. For elliptical beams a Gaussian distribution can be applied. Using this toolset, response maps of the electrode voltages, difference over sum ratios and sensitivity distributions can be obtained to characterize BPM types and geometries.

Diagonally Cut BPM

The chosen design for HESR BPMs at the current stage is the cylindrical diagonally cut BPM [3], as it offers high reliability due to its linear response. It is shown in Fig. 2

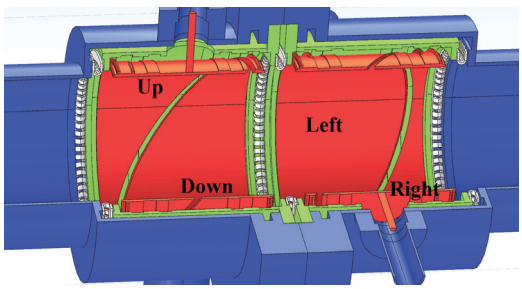

Figure 2: Cut view on diagonally cut BPM model, red: electrodes, green: grounded housing, blue: beam pipe.

Using COMSOL, a simplified model of the BPM with housing cylinder and surrounding beam pipe has been modeled in accordance with the CAD model. With simulated capacitances plugged into Eq. (1), the expected output voltage was calculated and compared to thermal noise levels. The beam conditions were taken as: 10^8 $\bar{p}$, T_{kin} = 3 GeV and l_{bunch} = 150 m. The initial design has been modified to reduce C_{el} and enhance thereby the signal strength. These changes were: shortening screws to the mechanically necessary length, widening the feedthrough hole in the housing cylinder, chamfering edges, removing mechanically unnecessary pieces, increasing the cut from 2 mm to 3 mm and increasing the distance of the electrode to the housing cylinder. According to simulation results, these changes lowered the capacitance against ground by approximately 25 %. Regarding the capacitances, the latest simulation results are shown in table 1. Subscripted numbers indicate the location in Fig. 1.

Given these results and the dimensions of the BPM, the voltage for a centred beam at each electrode with estimated capacitances of the feedthrough and preamplifier is 275 μV for the upper and right electrode, and 280 μV for the bottom and left electrode. The sensitivity in the centre region is 1.36 %/mm in both planes. The capacitances against ground are different for electrodes located closer to the centre, which causes an measured position offset. The cross electrode

Table 1: Simulated Capacitances, Diagonally Cut BPM

Port A	Port B	$Capacitance_{AB}$ [pF]
Up or Right	GND	17.44
Down or Left	GND	16.73
Up_1/ $Left_2$	$Down_1$/ $Right_2$	5.84
Up_3/ $Down_4$	$Left_3$/ $Right_4$	0.104
$Down_5$	$Left_5$	0.658
Up_6	$Right_6$	0.021

capacitances are distributed asymmetrically. This introduces a slight tilt of the linear response plane, causing crosstalk and a slightly position dependent sensitivity. The last two effects can only be seen with high resolution, as for example the simulation allows. Under measurement conditions these are mostly negligible. The displacement of the electrical centre is 0.68 mm in x and 0.59 mm in y. These are expectancy values for a flawless BPM.

Comparison of Measurement and Model

A stretched wire test bench has been constructed in the IKP-4 for characterization tests of BPMs. Two pairs of linear drive stages translate a wire as beam analogue, through which a specfic pulse is sent. Optical micrometres assure precise matching of the wire with desired positions. A fast 16bit ADC PCIe-card reads preamplified voltages from the electrodes. Data processing is done via a LabVIEW software. With help of the test bench one was able to confirm signal level expectations for the BPM and measure its sensitivity. The test bench measurement yields a sensitivity of (1.318 ± 0.003) %/mm in one plane and (1.330 ± 0.003) %/mm in the second plane. The electrical centre was measured at the position 0.21 mm vs. 0.94 mm. These results comply well with the expectations. The systematic difference in sensitivity and offset can be explained by manufacturing tolerances. An additional insight will be obtained soon as precise capacitive measurements of the pickup are planned.

Strip Type BPM

The capacitive strip type BPM has been investigated for comparison with expectations of higher signal levels, higher centre sensitivity, symmetric crosstalk conditions, and a small offset from the absolute mechanical centre positon. The capacitances are shown in tab. 2. A model image is shown in Fig. 3

Table 2: Simulated Capacitances, Strip Type BPM

Port A	Port B	$Capacitance_{AB}$ [pF]
Any electrode	GND	17.06
Any electrode	Port A+180°	0.449
Any electrode	Port A±90°	2.211

As one can see, the capacitances for the same geometrical relations are equal. Due to this fact, the unwanted

ISBN 978-3-95450-177-9

features of the diagonally cut design are being circumvented. Space limitations for this geometry are different, therefore it could be longer than the diagonally cut BPM. For a length of 270 mm and an angular coverage of 70°, the electrode voltage for a centred beam is 390 μV. The expected sensitivity is 3.59 %/mm.

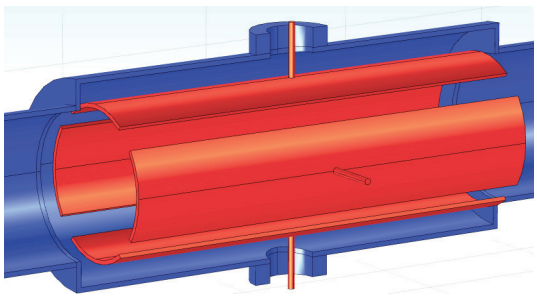

Figure 3: Model image of simplified strip type BPM, red; electrodes, blue; beam pipe.

Misalignment Analysis

To show that the strip type design is robust towards mechanical misalignments an extensive study has been conducted. About 150 models were created with angular and translational misalignments in different error magnitudes. Each electrode has been randomly pitched (1.5°), yawed (1.5°), rolled (4°) and shifted (2 mm) along three axis with the denoted maximum values in parentheses for the maximum error case. RMS deviations between ideal positions and misaligned BPM positions have been calculated. The RMS deviation scaled according to the error magnitude. If individual lookup tables are used, it could be shown, that the misalignments cause less of a disturbing effect than the non-linearity itself. RMS deviations were small at the centre. The analysis showed that any compensation method for the non-linearity would be able to correct for misaligned errors, too. The used misalignments were exaggerated chosen far beyond reasonable manufacturing tolerences. Fig. 4 shows linear projections of an intact and a misaligned BPM, using the linear approximation (Eq. (2)) and centre sensitivity value.

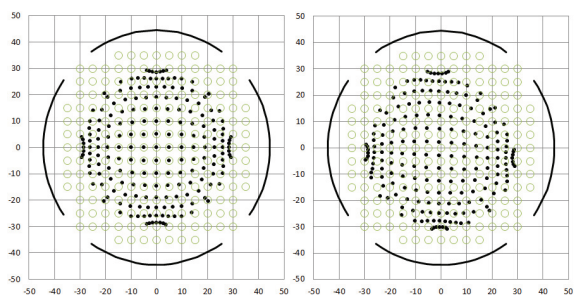

Figure 4: Projection plot of ideal and misaligned strip type BPM.

Disadvantages

Although the strip type BPM outperforms the diagonally cut BPM as expected with a higher signal strength and higher sensitivity, the major disadvantage of the strip type BPM is the non-linear response. So one has to invest into more sophisticated calculation schemes as in Eq. (3). Due to the non-linearity, the measured beam position is dependent on the beam size. An approximate position can still be retrieved with an error. Despite the cross plane capacitance influence the sensitivity map of the diagonally cut BPM is reasonably flat and can be used for beam position determination. Minor adjustments to the coefficients, like adding an (position dependent) offset and a crosstalk term, makes the design still yielding. This BPM shows only little dependency towards beam size and makes it thereby a more versatile device and easy to use.

CONCEPT OF BEAM SIZE MEASUREMENT

The size dependency was studies exclusively with transverse Gaussian distributions. Looking at strip type BPMs, it can be shown that Eq. (5) holds only true for pencil beams and beams of equal horizontal and vertical size (i.e. σ_x=σ_y). This is why beam position monitors with linear responses are more preferred to show no or only a little size dependency. The dependency of non-linear pickups can be used to determine the beam size in return with an expanded model and design. For this purpose a simple model of a BPM with eight electrodes has been developed, where only two electrodes are shifted outwards, one in x (2) and the other in y (0) direction.

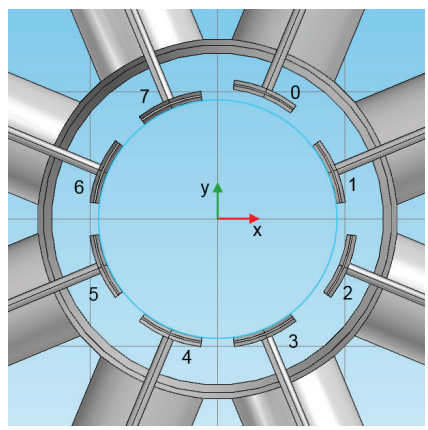

Figure 5: Cross-sectional view on eight strip BPM.

As there are eight electrodes, a specific configuration can be chosen, as which some electrodes act as ‘Up’ electrode, some as ‘Down’ etc. If the coefficient matrix is known, the beam position from the signals on all electrodes can be calculated. As implied before the read position is faulty, if the coefficient matrix has been determined for a pencil beam. To introduce a size relation, each coefficient can be a

ISBN 978-3-95450-177-9

function of beam size in x and y.

$$x = \sum_{i=0}^{N}\sum_{j=0}^{N}\left(\sum_{l=0}^{M}\sum_{m=0}^{M} G_{x,ij\,ml}\,\sigma_x^l\sigma_y^m\right)\left(\frac{\Delta_x}{\Sigma_x}\right)^i\left(\frac{\Delta_y}{\Sigma_y}\right)^j \quad (6)$$

A number of unique configurations have been found that would yield stable and reliable coefficient matrices. Each configuration can be rotated by 45° (i.e. shifting each index by one), mirrored and flipped. This way, up to 16 versions of a single configuration are obtained. Labelling each electrode from 0 to 7 some of these configurations are shown in table 3, enumeration is shown in Fig. 5:

Table 3: Examples for Some Configurations

Up	Down	Left	Right
6,7,0,1	2,3,4,5	4,5,6,7	0,1,2,3
0,7	5,6	0,7	1,2
0,6,7	4,5,6	0,6,7	1,2,3
0,6,7	2,3,4	5,6	1,2

For a given beam that passes through the BPM with a sufficient ellipticity, the beam position can be calculated with an estimated initial beam size (σ_x=σ_y= 0 for simplicity). Taking Eq. (6), each configuration will yield a differing result from the actual beam position, where those do not necessarily coincide. The standard deviation of the estimated beam position is in such a case relatively high. As one approaches the actual beam size the standard deviation decreases and shows its minimum at that spot. If this procedure is continued for an entire sweep through all σ_x and σ_y combinations, one can see that certain combinations of sizes induce the exact same voltage distribution on the electrodes. This can be seen as a valley of minimum standard deviations in a plot over all beam sizes. This is shown in Fig. 6.

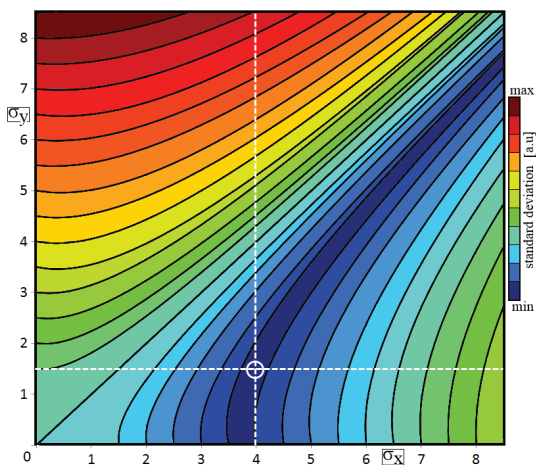

Figure 6: 2D plot of position standard deviation vs. beam size. For beam with dimension σ_x = 4 mm, σ_y = 1.5 mm.

This implies that certain beam sizes are indistinguishable from one another. These isolines can be characterized e.g. for beams with $\sigma_x > \sigma_y$ as in Eq. (7). With c being the axis intersect, a and b as fitting coefficients. If two such beam size monitors are used at locations with zero dispersion, the spot of common emittance, and therefore the actual beam size can be found. The beam size monitors should be located, such that one detects a bigger width in x (Eq. (7)) and the other in y (Eq. (8)).

$$\sigma_{x_1} = \frac{a_1\sigma_{y_1}^2 + b_1\sigma_{y_1} + c_1^2}{\sigma_{y_1} + c_1} = \tilde{f}_1(\sigma_{y_1}) \quad (7)$$

$$\sigma_{y_2} = \frac{a_2\sigma_{x_2}^2 + b_2\sigma_{x_2} + c_2^2}{\sigma_{x_2} + c_2} = \tilde{f}_2(\sigma_{x_2}) \quad (8)$$

$$\sigma_{x,y}(s) = \sqrt{\epsilon_{x,y}\beta_{x,y}(s)} \quad (9)$$

$$\sigma_{y_1} = \tilde{f}_1\left(\sqrt{\frac{\beta_{x_2}}{\beta_{x_1}}}\tilde{f}_2(\sigma_{y_1})\right)\sqrt{\frac{\beta_{y_1}}{\beta_{y_2}}} \quad (10)$$

With Eq. (10), the beam size can be found, if the equality condition is fulfilled. This is equivalent to finding the axis intersect, $d(\sigma_y) = 0$ in Eq. (11).

$$d(\sigma_{y_1}) = \tilde{f}_1\left(\sqrt{\frac{\beta_{x_2}}{\beta_{x_1}}}\tilde{f}_2(\sigma_{y_1})\right)\sqrt{\frac{\beta_{y_1}}{\beta_{y_2}}} - \sigma_{y_1} \quad (11)$$

$$d(\sigma_{y_1}) \approx -\sigma_{y_1} + e \quad (12)$$

$$e = d(0) = \frac{a_2\frac{\beta_{x_2}}{\beta_{x_1}}c_1^2 + b_2\sqrt{\frac{\beta_{x_2}}{\beta_{x_1}}}c_1 + c_2^2}{c_2 + \sqrt{\frac{\beta_{x_2}}{\beta_{x_1}}}c_1}\sqrt{\frac{\beta_{y_1}}{\beta_{y_2}}} \quad (13)$$

For roughly $\sigma_{x_1} > 3\sigma_{y_1}$ and $\sigma_{y_2} > 3\sigma_{x_2}$, $d(\sigma_{y_1})$ can be approximated as in Eq. (12). The slope in the linear approximation of $d(\sigma_{y_1})$ is about −1, so the beam size at location one is equal to e. From the isoline relations (Eq. (7, 8)) and the emittance relation (Eq. (9)), σ_{x_1}, σ_{y_2}, and σ_{x_2}, as well as ϵ_x and ϵ_y can be calculated.

CONCLUSIONS

The shown analytical studies present a reliable method for the characterization of BPM geometries. A theoretical method for a beam size measurement for elliptical beams and for known size ratios has been presented. The next step will be to construct and test the device.

ACKNOWLEDGEMENT

Thanks to B. Breitkreutz, B. Lorentz, B. Nauschütt, P. Niedermayer, H. Soltner, H. Stockhorst and R. Stassen.

REFERENCES

[1] P. Fork et al., “Beam Position Monitors”, CERN Accelerator School 2009, GSI, Germany.

[2] R. E. Shafer, “Beam Position Monitoring”, AIP Conference Proceedings 1989, Los Alamos National Laboratory.

[3] C. Böhme, “Beam Position Monitors for the HESR”, Annual Report 2014, Forschungszentrum Jülich, Germany.

ISBN 978-3-95450-177-9

COMMISSIONING OF THE BUNCH-BY-BUNCH TRANSVERSE FEEDBACK SYSTEM FOR THE TPS STORAGE RING

Y. S. Cheng†, K. H. Hu, K. T. Hsu, C. H. Huang, C. Y. Liao
NSRRC, Hsinchu 30076, Taiwan

Abstract

Taiwan Photon Source (TPS) finished its Phase II commissioning in December of 2015 after installation of two superconducting RF cavities and ten sets of insertion devices in mid-2015. The storage ring achieved to store beam current up to 520 mA. Intensive insertion devices commissioning were performed in the second quarter of 2016 and delivered beam for beam-line commissioning and performed pilot experiments. One horizontal stripline kicker and two vertical stripline kickers were installed in May 2015. Bunch-by-bunch feedback system were commissioning in the last quarter of 2015 and the second quarter of 2016. Commercial available feedback processors and power amplifiers were selected for the feedback system integration. Beam property and performance of the feedback system were measured. Problems and follow-up measures are also addressed. Results will be summarized in this report.

INTRODUCTION

The TPS is a 3 GeV synchrotron light source which was performed Phase I commissioning without insertion devices (ID) and with two 5-cell Petra cavities in the last quarter of 2004 and the first quarter of 2015 up to 100 mA stored beam [1]. Phase–II commissioning was done in the last quarter of 2015 with 10 sets of IDs and two KEKB-type superconducting RF modules and reached 520 mA stored beam maximum. Transverse coupled-bunch instability, caused by the resistive wall impedance and fast ion will deteriorate beam quality. Bunch-by-bunch feedback will suppress various transverse instabilities to ensure TPS achieve its design goals. Vertical bunch by bunch feedback loop was commissioning [2] in the first quarter of 2015 with prototype vertical kicker to test functionality includes feedback, bunch cleaning, single bunch transfer function, tune measurement. Power amplifier from AR and R&K were tested. One horizontal kicker and two vertical kickers were installed in the shutdown period of the second and the third quarter of 2015. Commissioning of both planes with insertion devices operation was started in the last quarter of 2015 and the second quarter of 2016.

Threshold current for the longitudinal instability appeared at ~80 mA when using with two 5-cell Petra cavities without insertion devices. Longitudinal instability disappeared up to 500 mA stored beam current during phase-II commissioning equip with two KEK-B type superconducting cavities with 10 sets of insertion devices in the last quarter of 2015. Transverse instabilities are dominated by wall resistivity and ion in TPS storage ring.

† cheng.ys@nsrrc.org.tw

STATUS OF THE FEEDBACK SYSTEM

Two vertical kickers and one horizontal kicker were installed during mid-2015 shutdown. Concept of these kickers is derives from the design of PSI/SLS [3] and adapt to fit vacuum duct of TPS at ID straight. Length of the electrode is 300 mm. Shunt impedance at low frequency is about 40 kΩ and 25 kΩ for vertical and horizontal kicker respectively, Perspective drawing and installation at the storage ring are shown in Fig. 1. To save space to accommodate more insertion devices, all kickers install at upstream of in-vacuum undulator (IU22) at three 7 m long straight. Three kickers are distributed at three short straight. This prevents the option to install all feedback electronics at the same site. Three in-vacuum insertion devices were install at these kickers respectively.

The horizontal kicker was installed at upstream of SR03 (upstream straight of lattice cell #3), and two vertical kickers were installed at upstream cell SR11 and SR12. Feedback electronics for horizontal and vertical planes where installed at different areas in which shared RF front-end is impossible. The kicker electrodes are not well match to 50 Ohm. Measured impedance is around 75~95 Ohm between the feedthrough structure and electrode respect to the vacuum chamber. This leads to large broadband beam power picked up which prevent power amplifier work properly, high power low pass filter with cut off frequency 350 MHz were installed at each power amplifier output to block high frequency beam power to enter power amplifier output.

Horizontal kicker x 1 set Vertical kicker x 2 sets

Figure 1: Transverse kickers install at upstream of three 7 m short straight which in-vacuum undulators located.

Feedback electronics of bunch-by-bunch equip feedback functionality, such as housing keep, filter design, timing adjustment, etc. It supports bunch oscillation data capture for analysis to deduce rich beam information, tune measurement, bunch clearing, beam excitation, etc. Features of the planned system include the latest high dynamic range ADC/DAC (12 bits), high performance FPGA, flexible signal processing chains, flexible filter design, bunch feedback, tune measurement, bunch

ISBN 978-3-95450-177-9

cleaning, various beam excitation scheme, flexible connectivity, and seamless integration with the control system. An on-line control interface to operate feedback system and off-line analysis tools should be included.

The iGp12 feedback processor from Dimtel [4] were selected with EPICS embedded. This simplify the system integration efforts a lot. A functional block diagram of the bunch-by-bunch feedback system current delivery for TPS are shown as Fig. 2 for horizontal plane and Fig. 3 for vertical planes.

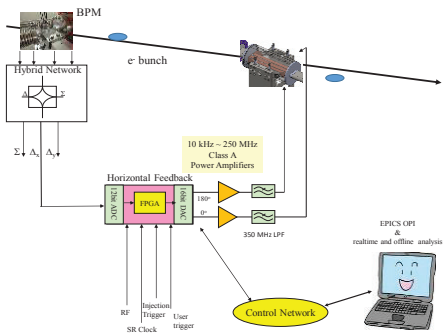

Figure 2: Configuration of the horizontal bunch-by-bunch feedback loop.

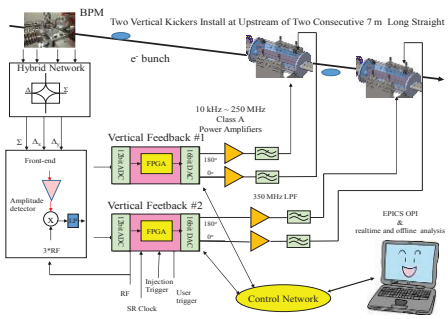

Figure 3: Configuration of the vertical bunch-by-bunch feedback loops.

COMMISSIONING OF HIGH STORED BEAM CURRENT

Commissioning of the prototype vertical feedback loop was performed in January 2015 to check functionalities of the system up to 100 mA stored beam [2]. Commissioning both horizontal and vertical feedback loops were performed in the last quarter of 2015 and the second quarter of 2016 after SRF cavities and 10 sets of insertion devices installed. Feedback functionalities have been tested for the stored beam current more than 500 mA. However, current version of stripline kickers especially horizontal plane suffered from higher outgassing due to over temperature issues happened when operate at high current (450~520 mA) for a short duration at this moment. New kickers are in design and implementation, these kickers are scheduled installed to replace current kickers in 2017.

Horizontal Plane

Grow/damp experimental and analysis [5] for horizontal plane was performed. Figure 4 shows that the experimental performed at stored beam current 300 mA. Growth rate is around of 0.2~0.3 $ms^{-1}$of the strongest modes, while damping rate is about 3 ms^{-1}. Similar measurement is performed at 400 mA also as shown in Fig. 5. Growth rate is around of 0.5 ms^{-1}, while damping rate is 10 ms^{-1}. Sufficient damping for high stored beam current will not cause any problem. However, damping rate can be varied by adjust feedback gain. Horizontal instability are contributed by resistive wall and ion related instability. Strength is weak compare to vertical plane.

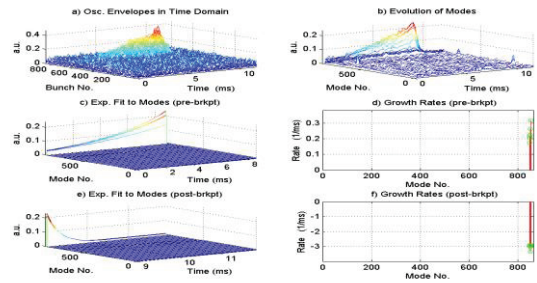

Figure 4. Grow/damp experiment of horizontal plane at beam current 300 mA with five in-vacuum IDs close gap. Resistive wall and ion induced instabilities are dominated. Feedback gain is set at minimum. Increase damping rate is easily by increase gain of the feedback loop.

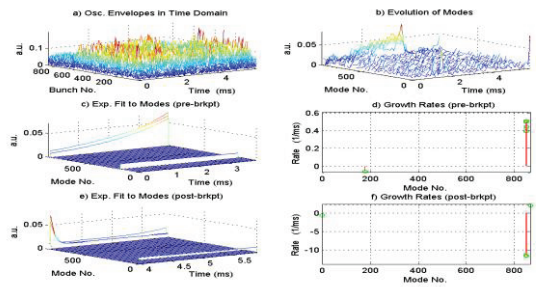

Figure 5: Horizontal modal spectrum at 400 mA with all IDs open gap.

Vertical Plane

Grow/damp experimental for vertical plane was performed at several stored beam current. Figure 6 shows that the experimental perform at stored beam current 93 mA without insertion devices. Growth rate is in the order of 0.2 ms^{-1}, while damping rate is the order of 10 ms^{-1}. Feedback loop gain is set at minimum.

Figure 7 shows that the experimental perform at stored beam current 300 mA with 5 insertion device closed its gaps out of 10 installed insertion devices. Growth rate is in the order of 0.5 ms^{-1}, while damping rate is the order of 40 ms^{-1}. Strength of vertical plane is large than horizontal plane. Figure 8 shows that the experimental perform at stored beam current 360 mA with all insertion device open gaps; growth/damping rate are 1 ms^{-1}/40 ms^{-1} respectively. For beam current 400 mA with all insertion device open gaps; growth/damping time are 1 ms^{-1}/40 ms^{-1} respectively as shown in Fig. 9. The growth rate will be increase three time to about 3 ms^{-1} when number of insertion devices increase to more than 20 sets and all insertion devices close

ISBN 978-3-95450-177-9

gap in future, Growth rate of vertical instability is large than horizontal plane due to small vertical aperture and small gap insertion devices.

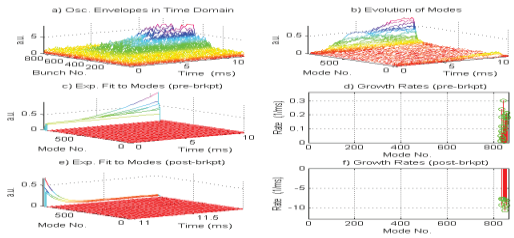

Figure 6: Grow/damp experiment of vertical plane at beam current 93 mA.

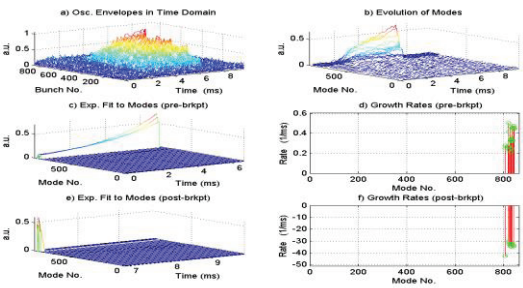

Figure 7: Grow/damp experiment of vertical plane at beam current 300 mA with five in-vacuum IDs close gap.

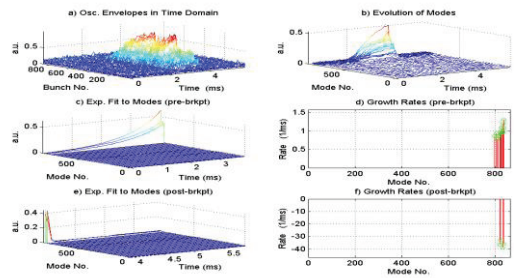

Figure 8: Grow/damp experiment of vertical plane at beam current 360 mA.

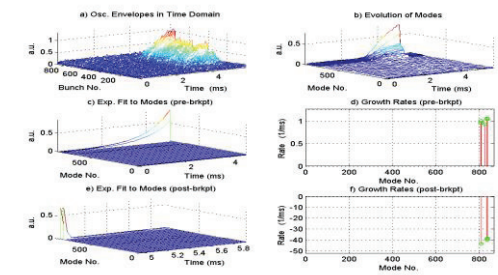

Figure 9: Grow/damp experiment of vertical plane at beam current 400 mA.

Longitudinal Plane

Longitudinal motion at Phase I commissioning before April 4, 2015 with two 5-cell Petra cavity are strong. In late March 2015, the beam can be stored up to 100 mA before April shutdown. Typical behaviour in longitudinal plan is shown in Fig. 10. Strong in-phase synchrotron motion and a strong mode 800 for all stored bunch was observed. The mode 800 might be caused by the TM_{021} high order mode of 5-cell Petra cavity [6].

Phase II commissioning started from September 2015 after install two superconducting RF cavities and 10 sets of insertion devices. To compatible with beamline optic and machine safety, 300 mA was chosen for beam line commissioning and pilot experiments maximum at this moment. Higher stored beam current were tested during some specific window to check weakness of the TPS. Modal spectra is shown in Figure 11 for 400 mA stored beam. No unstable longitudinal mode observed. Figure 11 shows the streak camera observation for 480 mA longitudinal stable beam.

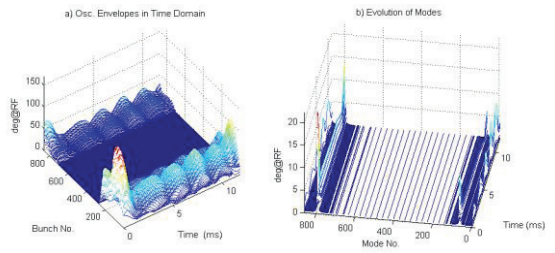

(a) Two 5-cell Petra RF cavities at 93 mA.

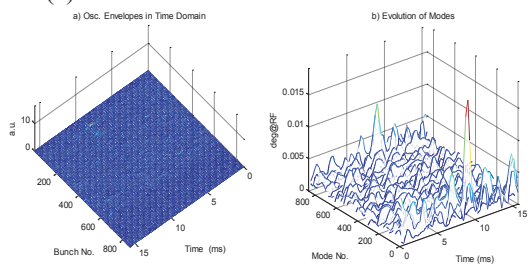

(b) Two KEKB type superconducting RF cavities at 400 mA.

Figure 10: Evolution of longitudinal oscillation envelope and modes for TPS working with Petra cavities and SRF cavities before April 2015 and after August 2015.

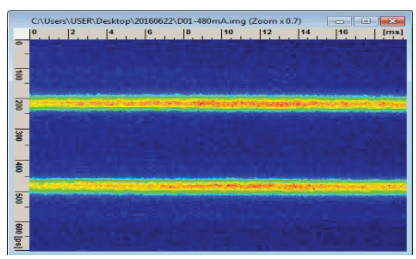

Figure 11: Longitudinal stable beam observed at 480 mA on June 22, 2016.

PROBLEMS AND SOLUTIONS

Current version of transverse kickers operate at higher store beam current (450 ~ 520 mA) has higher gassing especially of the horizontal kicker. TPS have been several chance test stored 500 mA to test tolerance of hardware and RF system, the first one is in December 12, 2015 maximum stored beam current reach more than 520 mA. However, the reading of nearby ion gauge of transverse kickers increase two order of magnitude for the horizontal kicker and one order of magnitude in vertical kicker. The burst of the vacuum pressure cause stored beam current sudden loss about 50 mA stored beam current as shown in Fig. 12. Outgassing rate abrupt increase when stored beam current

ISBN 978-3-95450-177-9

higher than 450 mA. Vacuum pressure double compare with 30 mA at these area for 400 mA continue operation (12 hours) without big problem happened as shown in Fig. 13. Oxidation of the N-type feed-through centre pin due to overheat at downstream of outside electrode and inner electrode are observed, they might due to heat transfer from electrode to the centre pin and/or bad RF connect of the of feedthrough and the cable connector.

Revise horizontal kicker design to reduce the pick-up beam power and to improve RF contact of the feedthrough centre pin; 7/8" EIA feedthrough with water cooling [7] will adopt to increase safety margin for new kickers. Implement new horizontal kicker and install are the short term goal which are necessary for 500 mA stored beam current operation in future. Vertical kickers are slightly better but still have outgassing phenomenon. New vertical kickers will implement and install later after the horizontal kicker problem solved.

Horizontal feedback channel adopt direct RF sampling without RF front-end. Signal quality of the horizontal plane is bad due to small signal level which need further improvement. Implement a RF front-end is the current efforts.

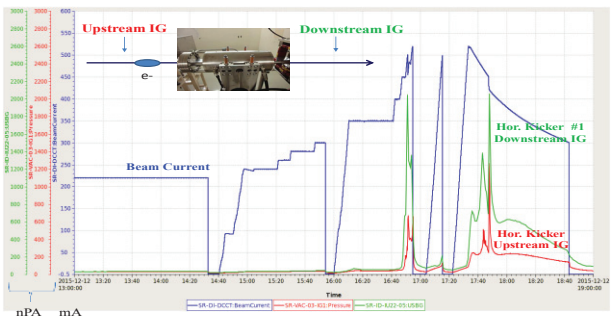

Figure 12: Vacuum burst happened when stored beam current over certain threshold (450 mA~ 520 mA) for a short duration on December 12, 2015. Ion gauge near downstream of horizontal stripline kicker detect a huge pressure spike which caused sudden reduce of beam current.

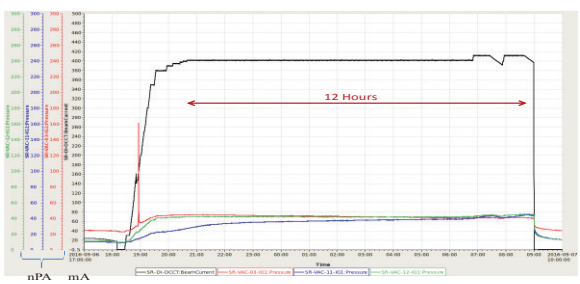

Figure 13: Vacuum pressure increase two times compare to 30 mA observed by the downstream ion gauge of horizontal kicker and vertical kicker #1 for 12 hours 400 mA operation from 21:00, September 6 to 09:00, September 7.

SUMMARY

Commissioning of the bunch-by-bunch system was performed in the last quarter of 2015 and the second quarter of 2016 during Phase II commissioning of the TPS accompany with commissioning of the phase I seven beamlines. Functionalities of the feedback were tested for stored beam current up to 520 mA with all insertion devices open gap and 300 mA for five installed ID closed gap. Hugh outgassing was happened near the horizontal kicker site when stored beam current in the range of 450 mA to 520 mA, new horizontal stripline kickers will be installed at early 2017. The system are ready for various study soon. Due to machine time, there is no chance to do systematic study up to now, such as measure growth/damping rate as function of beam current and feedback parameters, fast ion effect should be done as soon as possible. Resistive wall induced instability are dominated accompany with ion caused instability based upon analysis of the measured data. Lots of information accumulated during commissioning, it will useful for future optimization.

ACKNOWLEDGEMENT

Help from the operation team, beam dynamics peoples, vacuum group are highly appreciated. Their helps are indispensable for various tests. Thanks efforts of the task force to design and to implement revised version of kickers, high current operation will not possible without new kickers. Many technical discussions with Dmitry of Dimtel are fruitful.

REFERENCES

[1] C. C. Kuo, *et al.*, "Commissioning Results of Taiwan Photon Source", *IPAC2015*, Richmond, VA, USA, TUXC3, pp 1314-1318.

[2] Y. S. Cheng, *et al.*, "Preliminary Commissioning of the Bunch-by-Bunch Transverse Feedback System for the TPS Storage Ring", *Proceedings of IBIC 2015*, Edinburgh, Scotland, THPCH062, pp 2928-2930.

[3] D. Michal, *et al.*, "Current Status of the ELETTRA/ SLS Transverse Multi Bunch Feedback", Proceedings of *EPAC 2000*, Vienna, Austria. WEP4A15, pp 1894-1896.

[4] Dimtel, Inc., San Jose, USA; http://www.dimtel.com.

[5] S. Prabhakar, "New Diagnostics and Cures for Coupled Bunch Instabilities". PhD Thesis, Stanford University, 2000. SLAC-R-554.

[6] A. Roth, "Breitbandige Feedback-Systeme zur Dämpfung kohärenter Strahlinstabilitäten am Stretcherring ELSA", Doktorarbeiten, Physikalisches Institut der Universität Bonn, Oktober 2013.

[7] Makoto Tobiyama, "BPM Electrode and High Power Feedtrhough – Special Topics in Wideband Feedthrough, *Proceedings of IBIC 2012*, Tsukuba, Japan, TUTA02, pp 297-301.

ISBN 978-3-95450-177-9

HOM CHARACTERIZATION FOR BEAM DIAGNOSTICS AT THE EUROPEAN XFEL INJECTOR*

N. Baboi#, T. Hellert[1], L. Shi[2], T. Wamsat,
DESY, Hamburg, Germany
[1]also at The University of Hamburg, Hamburg, Germany
R.M. Jones[2], N. Joshi[2]
Cockcroft Institute, Daresbury, UK
[2]also at The University of Manchester, Manchester, UK

Abstract

Higher Order Modes (HOM) excited by bunched electron beams in accelerating cavities carry information about the beam position and phase. This principle is used at the FLASH facility, at DESY, for beam position monitoring in 1.3 and 3.9 GHz cavities. Dipole modes, which depend on the beam offset, are used. Similar monitors are now under design for the European XFEL. In addition to beam position, the beam phase with respect to the accelerating RF will be monitored using monopole modes from the first higher order monopole band. The HOM signals are available from two couplers installed on each cavity. Their monitoring will allow the on-line tracking of the phase stability over time, and we anticipate that it will improve the stability of the facility. As part of the monitor designing, the HOM spectra in the cavities of the 1.3 and 3.9 GHz cryo-modules installed in the European XFEL injector have been measured. This paper will present their dependence on the beam position. The variation in the modal distribution from cavity to cavity will be discussed. Based on the results, initial phase measurements based on a fast oscilloscope have been made.

INTRODUCTION

Higher Order Modes (HOM) [1] are excited by electron bunches passing the superconducting accelerating cavities of the European X-ray Free Electron Laser (E-XFEL) in the north of Germany [2]. While HOMs can harm the beam, they can also be used for beam monitoring, since their properties depend on the beam properties, such as offset, charge and arrival time.

It is planned to build specialised monitors for the E-XFEL, on one hand for beam alignment and transverse position monitoring [3], and, on the other, for direct, on-line tracking of the beam phase with respect to the accelerating RF [3,4]. These monitors are currently under design [5,6], based on the experience at the Free Electron Laser in Hamburg (FLASH) [7]. There, monitors are installed at so-called TESLA accelerating cavities [3], as well as at 3rd harmonic cavities [8,9], working at 1.3 and respectively 3.9 GHz. The advantages of such monitoring are information on the beam at locations where there is no standard diagnostics, the relatively low cost, the possibility to align the beam in the cavities and reduce harmful HOMs. Also one can obtain information on the cavity alignment inside the cryo-module. The phase measurement will be the first direct, on-line measurement in superconducting cavities.

In the *European XFEL*, energetic electron pulses will produce extremely intense X-ray flashes in the undulator sections. The electrons are accelerated by ca. 100 superconducting cryo-modules, each containing eight cavities. Some of the main parameters of the electron beam are shown in Table 1.

Table 1: Main Parameters of the E-XFEL Electron Beam

Electron beam parameter	
Max. energy [GeV]	17.5
Bunch charge [nC]	0.02 - 1
Max. bunch frequency [MHz]	4.5
Max. bunch number / pulse	2700
Pulse repetition frequency [Hz]	10
Max. pulse length [μm]	600

While the commissioning of the complete accelerator is planned to start by the end of 2016, the first E-XFEL injector started operation in December 2015 [10]. This contains a 1.3 GHz and a 3.9 GHz cryo-module [11]. The latter shapes the bunch energy profile in order to increase the peak current.

A picture of a *TESLA and* a *3rd harmonic cavity* is shown in Fig. 1. The 1.3 GHz TESLA Nb cavity has 9 cells and is ca. 1 m long. RF power is input through the power coupler, while the HOM power generated by the beam is extracted through 2 special couplers mounted in the beam pipes at either end. The 3.9 GHz cavity is basically scaled down by a factor 3 from the TESLA cavity, except mainly the beam pipes which are larger. These enable the propagation of the HOMs through the entire eight-cavity module so that the HOM power is extracted more efficiently. Eight cavities are mounted in either type of module with the power coupler downstream. In this paper we name the cavities by their position within the module, e.g. C4 is the 4th cavity. H1 will denote the HOM coupler close to the input coupler (downstream for 1.3 GHz modules), and H2 at the other cavity end.

The *HOM-based beam position monitoring* idea relies on the fact that the dipole mode strength depends linearly on the beam position and charge. In the TESLA cavities, a dipole mode at ca. 1.7 GHz, with a high R/Q, giving the

* The work is part of EuCARD-2, partly funded by the European Commission, GA 312453
# nicoleta.baboi@desy.de

ISBN 978-3-95450-177-9

HOM-beam interaction strength [12], was chosen. No clearly identifiable, well separated mode is present in the 3.9 GHz cavities therefore a band of modes around 5.46 GHz was chosen [9]. This band contains modes propagating within the whole cryo-module, therefore in order to get also cavity-related information, modes in the 5th dipole band, around 9.06 GHz will also be monitored, since they are trapped within each cavity.

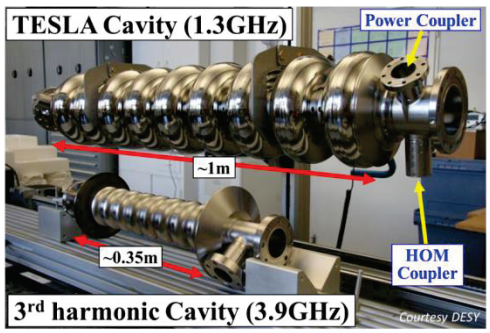

Figure 1: Picture of a TESLA and a 3rd harmonic cavity.

Monopole modes do not depend on the beam offset making a better candidate for beam phase monitoring with respect to the accelerating RF. Modes around 2.4 GHz were chosen for this purpose. No phase diagnostics is planned so far in the harmonic cavities.

In preparation of the HOM-based diagnostics, several measurements and studies were made on both types of cavities for the E XFEL, as summarized in this paper. The following section presents the HOM spectra measured in individual 1.3 GHz cavities during cold RF tests, as well as in individual 3.9 GHz cavities and chains of cavities. In the 3rd section, the beam spectra measured in the TESLA module in the E-XFEL injector are discussed. The subsequent section shows the first beam phase measurements made in the same cavities.

HOM SPECTRA

After production, each superconducting cavity for the E-XFEL went through a series of tests, including transmission measurements between the two HOM couplers during cold tests [13]. Since HOM monitors are planned to be installed at the cavities of the first five 1.3 GHz accelerating modules, their spectra were analysed and are presented in the following subsection. Extensive measurements were made also in the 3.9 GHz cryo-module and are presented later in this section.

Transmission Spectra of 1.3 GHz Cavities

Figure 2 shows the quality factors Q of the modes in the first 3 HOM bands of the cavities in the first five E-XFEL cryo-modules. The data was taken from the cavity database [14]. The modes with high R/Q [12] around 1.7, 1.87 and 2.45 GHz have Qs below 10^5, as required by the multi-bunch beam dynamics.

The frequency spread can be seen in detail for the dipole mode around 1.7 GHz in Fig. 3, together with the neighbouring modes. For several cavities, most in the first cryo-module, the mode is shifted towards higher frequency. These are all from one of the two producing companies, and are not expected to be a challenge for the linac operation. Also for the HOM-based position monitoring the frequency shift does not pose a problem, since the modes are still within the bandwidth of the electronics of 20 MHz, marked by the 2 red lines. The frequency is up-shifted in these cavities also for the modes around 2.4 GHz, also without a problem for the electronics [6].

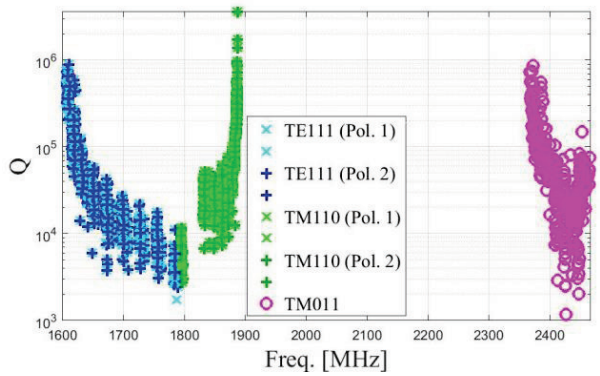

Figure 2: Quality factors of the first 2 dipole bands (TE111 and TM110-like) and of the first monopole HOM band (TM011-like) versus mode frequency. Each dipole mode has 2 polarizations.

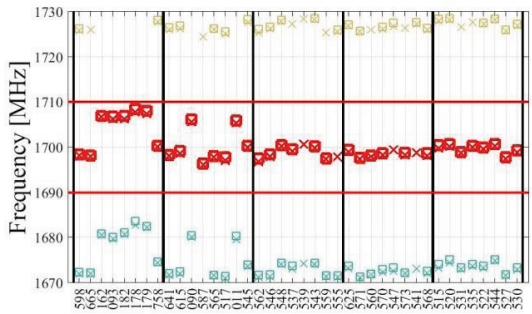

Figure 3: Frequency of the 1.7 GHz dipole mode (red marks), to be used for beam position monitoring, for the cavities in the first 5 TESLA modules. The neighbouring modes are also plotted. The black vertical lines, delimit each cryo-module. The red lines mark the bandwidth of the electronics.

Transmission Spectra of 3.9 GHz Cavities

The spectra of the individual 3.9 GHz cavities were measured before assembly at room temperature [15,16]. A very similar spectrum was found for the 1st and 2nd dipole bands. The 5th dipole band, on the other hand, is very sensitive to slight geometrical variations, which is reflected by the very different spectra observed for the different cavities.

After assembly and cool down, the spectra were measured again for each cavity in the module as well as for the whole chain of 8 cavities. Fig. 4 show the transmission spectra S21 of the first 2 dipole bands measured across C1, across the first 4 cavities (C1-C4), and through the entire chain (C1-C8). One observes that most of the modes

ISBN 978-3-95450-177-9

propagate through the entire chain. The qualitative behaviour expected from simulations was confirmed by the measurements [17].

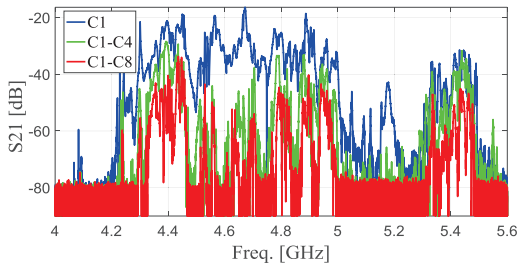

Figure 4: S21 measured across the first cavity, across the first 4 cavities and across the whole cavity chain of the 3.9 GHz module in the E-XFEL injector.

BEAM SPECTRA IN 1.3 GHZ CAVITIES

During the commissioning of the E-XFEL injector, we measured the spectra around the frequencies of interest for all eight cavities of the 1.3 GHz module. Fig. 5 shows the spectrum around 1.7 GHz measured from C2H2 and C6H2 with a Tektronix Real-Time Spectrum Analyser (RSA6114A). One notices the double peaks, indicating the two polarisations of each dipole mode. The mode frequency is quite different for the two cavities, and one notices the different separation of the peaks for the two cavities.

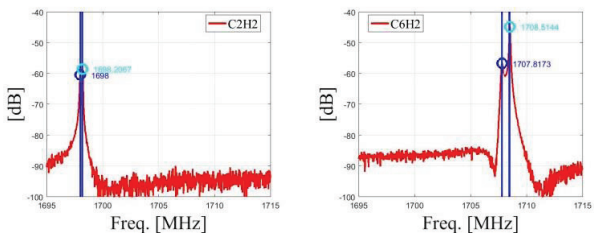

Figure 5: Beam spectrum of dipole mode to be used for beam position monitoring, for C2H2 (a) and C6H2 (b). Each curve is the average of 5 spectra. The blue vertical lines are the mode frequencies from [14].

In order to study the mode behaviour, the transverse beam position was varied with two magnetic steerers, one horizontal and one vertical. Two beam position monitors (BPM) [18], one upstream and one downstream of the module were used to inferr the beam position in the middle of each cavity. The RF as well as all magnets between the two BPMs were switched off.

The dependence on the beam position of the amplitude of each of the two polarisations for C6H2 is shown in Fig. 6. The left plot corresponds to the left peak in Fig. 5b, while the right plot is for the 2nd polarization. One notices that the lower polarization responds mostly to vertical beam movement, and vice versa. There is however a slight rotation of the two polarisations. This rotation differs from cavity to cavity. For us this means that we cannot use for diagnostics one single mode, like in a standard cavity beam position monitor, but we have to employ a complex data analysis procedure [3,9].

From the analysis of such transverse scans one can deduce the relative transverse cavity alignment inside of the cryo-module [3]. This requires, especially at such low energies, 4D scans filling the transverse space (x,x′,y,y′). Such scans are planned after the prototype electronics is available for beam tests. Note that for a more accurate analysis of the two polarizations a Lorentzian fit has to be made.

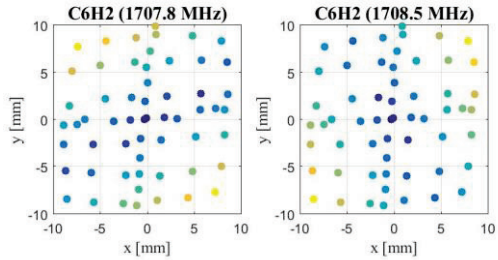

Figure 6: HOM signal amplitude from C6H2 as a function of the beam position in the middle of C6. The two plots correspond to the two polarizations in Fig. 5b.

Figure 7 shows the beam spectrum from C6H2 around 2.4 GHz. The vertical lines indicate where HOMs peaks are expected [14]. Several peaks can be seen in addition. None of the peaks vary with the beam position. It was found that the additional peaks come from the nearby cavities, i.e. their monopole modes propagate through the beam pipe to the HOM coupler of the neighbouring cavity. This is not expected to be an issue for the HOM-based phase monitoring.

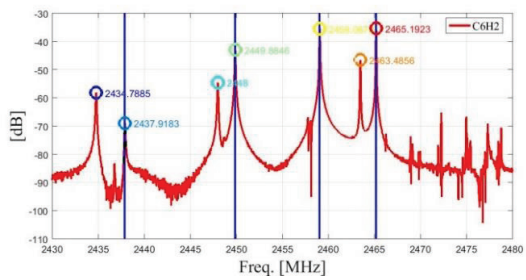

Figure 7: Monopole mode spectrum of C6H2. The blue vertical lines are the mode frequencies from [14].

HOM-BASED PHASE MEASUREMENTS

Although the HOM couplers have been designed to reject the accelerating mode, there is still a significant amount of RF power leaking through. This enables us to measure at the same time, through the same cable, both beam excited modes around 2.4 GHz, and the accelerating mode at 1.3 GHz, and determine the RF phase with respect to the beam arrival time [3].

Such measurements were made at the E-XFEL by splitting the signal from one coupler, filtering around 1.3 and around 2.4 GHz respectively, then recombining the two signals and monitoring the signal with a Tektronix scope TDS6604B with 20GS/s and 6 GHz bandwidth. Similar measurements have been made at FLASH [4]. Fig. 8 shows the phase obtained from both HOM couplers of one cavity. Initially the phase was calibrated to show

ISBN 978-3-95450-177-9

0 deg (the first 25 measurements). Then the RF phase was changed by 5 degrees in each direction. The setup could monitor this change. By comparing the measurement from each coupler, a phase resolution of 0.12 deg rms is obtained in this case.

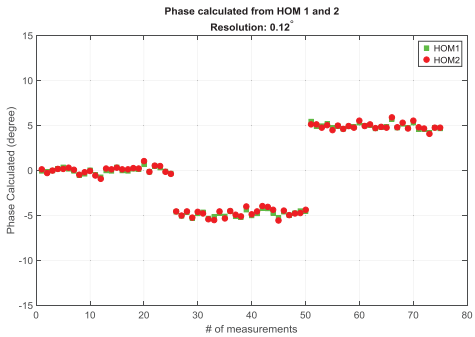

Figure 8: RF phase with respect to the beam calculated from signals from both HOM couplers, HOM1 (green) and HOM2 (red), of one cavity.

SUMMARY

In preparation for the HOM-based diagnostics now under design for the E-XFEL, we analysed the HOM spectra in the first five 1.3 GHz modules and the 3.9 GHz module. The selected modes are within the bandwidth of the electronics. For the monopole modes one could also observe peaks from the neighbouring cavities, which do not constitute a problem for the phase monitoring.

The dependence of the dipole spectra on the beam position was analysed. There is a variation from cavity to cavity in the polarization rotation, which makes a complex signal processing necessary.

Further measurements are planned after the start of beam operation of the entire E-XFEL linac, and when the prototype electronics is available for beam tests.

ACKNOWLEDGEMENT

We thank the E XFEL shift crew for the help during the beam measurements. Special thanks are addressed to Alexey Sulimov for the fruitful discussions.

REFERENCES

[1] R.M. Jones, “Wakefield suppression in high gradient linacs for lepton linear colliders”, *Phys. Rev. ST Accel. Beams*, vol. 12, p. 104801, 2009.

[2] M. Altarelli *et al.* (eds.), “The European X-Ray Free-Electron Laser. Technical Design Report”, DESY, Hamburg, Germany, Rep. DESY 2006-097, 2007.

[3] S. Molloy *et al.*, "High Precision Superconducting Cavity Diagnostics with Higher Order Mode Measurements," *Phys. Rev. ST-Accel. Beams.*, vol. 9, p. 112802, 2006.

[4] L. Shi *et al.*, “Measurement of Beam Phase at FLASH using HOMs in Accelerating Cavities”, ”, in *Proc. 7th Int. Conf. on Particle Accelerators (IPAC2016)*, Busan, Korea, 2016, paper MOPOR039, pp. 686-688.

[5] T. Wamsat *et al.,* “First Tests of a Micro-TCA-Based Downconverter Electronic for 5GHz Higher Order Modes in Third Harmonic Accelerating Cavities at the XFEL”, in *Proc. 3rd Int. Beam Instrumentation Conference (IBIC2014)*, Monterey, CA, USA, 2014, paper TUPF12, pp. 337-341.

[6] S. Bou-Habib *et al.*, “New Design of High Order Modes Electronics in MTCA.4 Standard for FLASH and the European XFEL”, in *Proc. 2nd Int. Beam Instrumentation Conference (IBIC2013)*, Oxford, UK, 2013, paper TUPC31, pp. 443-446.

[7] M. Vogt *et al.*, “The Superconducting Soft X-ray Free-Electron Laser User Facility FLASH”, in *Proc. 7th Int. Conf. on Particle Accelerators (IPAC2016)*, Busan, Korea, 2016, MOPOW010, pp. 729-731.

[8] N. Baboi *et al.*, “Commissioning of the Electronics for HOM-based Beam Diagnostics at the 3.9 GHz Accelerating Module at FLASH”, in *Proc. 3rd Int. Beam Instrumentation Conference (IBIC2014)*, Monterey, CA, USA, 2014, paper TUPF06, pp. 311-314.

[9] P. Zhang, *Beam Diagnostics in Superconducting Accelerating Cavities*, Springer Theses, Springer International Publishing, 2013.

[10] F. Brinker, “Commissioning of the European XFEL Injector”, in *Proc. 7th Int. Conf. on Particle Accelerators (IPAC2016),* Busan, Korea, 2016, paper TUOCA03, pp. 1044-1047.

[11] P. Pierini *et al.*, “Preparation of the 3.9 GHz System for the European XFEL Injector Commissioning”, in *Proc. 17th Int. Conf. on RF Superconductivity (SRF2015)*, Whistler, BC, Canada, 2015, paper TUPB018, pp. 584-588.

[12] R. Wanzenberg, “Monopole, Dipole and Quadrupole Passband of the TESLA 9-cell Cavity”, DESY, Hamburg, Germany, TESLA 2001-33, 2001.

[13] A. Sulimov *et al.*, “”, in *Proc. 17th Int. Conf. on RF Superconductivity (SRF2015)*, Whistler, BC, Canada, 2015, paper THPB068, pp. 1277-1278.

[14] P.D. Gall *et al.*, “XFEL Database User Interface”, in *Proc. 17th Int. Conf. on RF Superconductivity (SRF2015),* Whistler, BC, Canada, 2015, paper THPB039, pp. 1168-1170.

[15] N. Han *et al.*, "Higher Order Mode Measurements and Analysis in 1.3 GHz and 3.9 GHz Superconducting Cavities at FLASH and the European-XFEL," DESY Summer Student Report, DESY, Hamburg, Germany, 2015.

[16] L. Shi *et al.*, “Measurements and Characterization of Higher Order Modes for the 3.9 GHz Cavities at the European-XFEL”, DESY, Hamburg, Germany, report in preparation, 2016.

[17] T. Flisgen, private communication, 2016.

[18] D. Lipka *et al.*, “First Experience with the Standard Diagnostics at the European XFEL Injector”, presented at *5th Int. Beam Instrumentation Conference (IBIC2016)*, Barcelona, Spain, 2016, paper MOBL02, this conference.

ISBN 978-3-95450-177-9

DESIGN OF STRIPLINE BEAM POSITION MONITORS FOR THE ESS MEBT

S. Varnasseri, I. Bustinduy, A. Ortega, I. Rueda, A. Zugazaga, ESS Bilbao, Bilbao, Spain
R.A. Baron, H. Hassanzadegan, A. Jansson, T. Shea, ESS- ERIC, Lund, Sweden

Abstract

There will be overall 8 Beam Position Monitors (BPM) installed in the ESS MEBT. Seven of them will be used for the measurement of beam position, phase and intensity. One BPM will be used for the fast timing characterization of the chopped beam. The design is based on shortened stripline to accommodate the signal level for low velocity proton beam within MEBT. Due to mechanical space limits, all the BPMs are embedded inside quadrupoles; which requires special care on the magnetic properties of the materials within BPM sets and in particular the feedthroughs. The prototype electromagnetic and mechanical design is finished and its manufacturing is underway. This paper gives an overview of the electromagnetic and mechanical design and related analysis including position signal sensitivity of the BPMs.

INTRODUCTION

ESS MEBT (Medium Energy Beam Transport) with energy of 3.62 MeV is part of the European Espallation Source (ESS) to be operational at Lund, Sweden early 2020 [1]. It requires various beam diagnostics instruments including the position, phase and intensity measurement devices. As part of the beam diagnostics instruments necessary for future commissioning and normal operation of accelerator, we have designed and manufactured a prototype of stripline beam position monitor (BPM). The proton beam has a repetition frequency of 14 Hz of pulses of 2.8 ms and nominal amplitude of 62.5 mA. The BPM pick ups are of stripline type which are housed inside quadrupole magnets (Figure 1). The main reason is due to lack of longitudinal mechanical space within compact MEBT to install all the BPMs. The BPM sensitivity to displacement, voltage signal level, frequency response and mechanical restrictions are the main factors in the design of stripline. Table 1 shows the main beam parameter related to BPM design analysis.

Table 1: BPM Related Beam Parameters

Parameter	Value	Unit
Beam energy	3.62	MeV
Beam current (avg.)	62.5	mA
Particles/bunch	1.1e9	
Readout frequency	704	MHz
RF frequency	352	MHz
Bunch length	60-180	ps
Pulse length (max.)	2.8	ms

In principle the second RF harmonic of 704.42 MHz of the electrode signal is used for BPM signal processing readout system. The BPM sensitivity with the nominal MEBT beam requires to be larger than 0.8 dB/mm and the voltage amplitude reaching to electronics has to be compatible with margin to input level of electronics. The design of stripline monitors is based on transmission line with 50 Ω characteristics impedance. Furthermore the bunch length is not fixed during the passage within MEBT, so the voltage amplitude on electrodes slightly varies depending on the physical location of BPMs. In the following sections, the electromagnetic design, characteristics and mechanical realization of the first prototype is described.

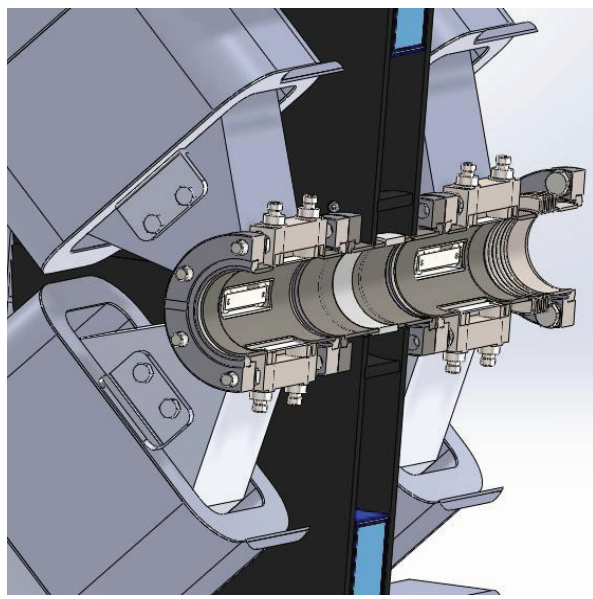

Figure 1: A CAD image of two BPM blocks embedded within two adjacent quadrupole magnets.

The overall BPM accuracy shall be smaller than +/-200 µm. This includes electronics errors, BPM sensor tolerances, errors of BPM welding on the beam pipe and alignment errors. Furthermore the BPM stripline shall be fabricated so that error contribution due to mechanical tolerances and electrodes imperfections does not exceed +/- 100 µm of the overall BPM accuracy. These values implied by other elements and overall tolerances within MEBT section.

ELECTROMAGNETIC ANALYSIS

The bunches passing through the BPMs distributed within MEBT section vary in length at different locations. This will change the bunch charge frequency spectrum and therefore the BPMs will generate slightly different signal amplitudes at different physical locations. This is true also for the signal timing shape which goes out of the BPM striplines due to different frequency components.

ISBN 978-3-95450-177-9

Fig. 2 shows the bunch charge frequency spectrum variation with the bunch length. At frequency of 704 MHz, there is around 24% increase in charge contribution of bunches with 60 ps in comparison with the 180 ps.

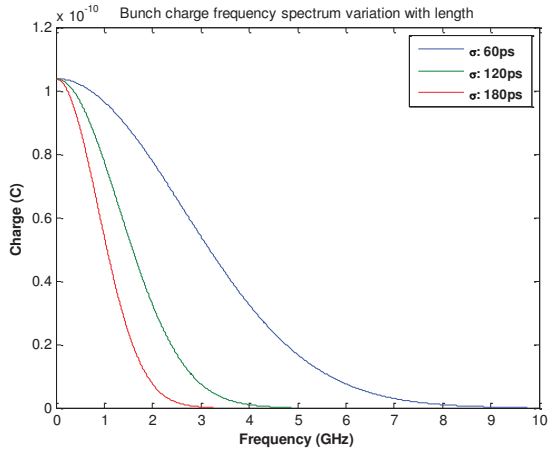

Figure 2: Bunch charge frequency spectrum variation.

Since the BPMs are installed inside the quadrupoles of MEBT, several options have been investigated and finally the stripline solution with shortened length of strip electrodes has been chosen. All the 8 BPM blocks are identical, however due to mechanical integration reasons, six of the blocks include also a 25 mm bellow. The BPM model is cylindrical with one pair of strips in each plane (parallel and perpendicular to gravity) with 45^0 transverse angle between adjacent strips. The 2D and 3D analysis at low velocity beam (ß=0.088) were carried for the whole block of BPM. Figure 3 shows a snapshot of the block for 704 MHz components. In order to foresee the electrode output signal characteristics, the electrode response at various possible bunch lengths and at the low energy of MEBT was analysed. The signal feedthroughs are non-magnetic weldable SMA type with outer diameter of 9.54 mm and pin diameter of 2.4 mm. For the brazing of ceramic to stainless steel body of connectors no magnetic material is used. The reason was to eliminate any magnetic noise disturbance from BPM on the magnetic field harmonics of quadrupole magnets. The quadrupole yoke gap is 15 mm, which provide 1 mm free space for mechanical alignment purposes of the BPM block. In the design of BPM stripline, the dimension of the SMA feedthrough was integrated in the model, and the whole model has been analysed as signal port device. Simulations show high dependence of the characteristics impedance of the BPM to the material, spacer dimensions and gap between the electrode and the body wall. So the alumina AL_2O_3 as spacer was chosen in order to secure the gap distance within required tolerances. Other materials like Macor was found not to provide higher performance than alumina; in addition has lower thermal conductivity of 1.46 W/m^{0}C in comparison to the alumina 96% with thermal conductivity of 24.7 W/m^{0}C. The gap between electrode and the body is 5±0.01 mm. The characteristic impedance reference is 50 Ω and the high resolution bandwidth (20dB) is 1.2 GHz. The length of the strips in combination with the strip thickness has been optimized in order to produce high signal amplitude at 704 MHz.

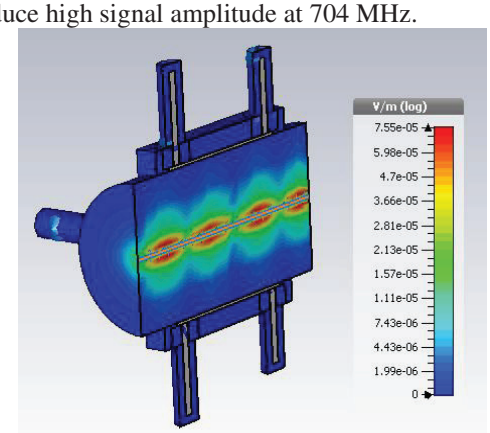

Figure 3: Snapshot of analysis for processing frequency of 704 MHz, 50 Ω and short terminations.

Both ends of strips are e-beam welded to feedthrough pins. Upstream port is connected via the coaxial cable to the electronics front end, while the downstream port is terminated with a 50 Ω termination. It is possible to terminate the downstream port to a short, when it is required for some dedicated measurements.

Signal Port Responses and Coupling

In order to match the stripline output impedance to the electronics input impedance of 50 Ω, the high frequency analysis of the BPM block was part of the design process. Furthermore, the high frequency coupling between adjacent and in-front electrodes are extracted from the S parameters. In the Figure 4, the transmission and reflection parameters and coupling of one electrode in relation to the adjacent electrode (S13) and in-front electrode (S15) is plotted. The plot shows at the frequency of interest 704 MHz, the coupling of adjacent electrodes is -50 dB and in-front electrodes coupling is -60 dB. Also the electrode reflection response around the interested frequency is expected to be better than -35 dB.

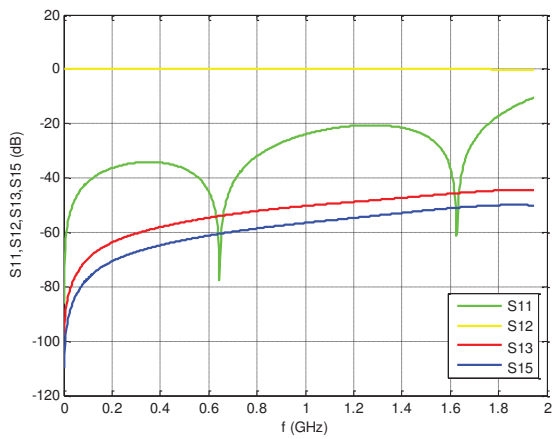

Figure 4: S-parameters of the Stripline electrode.

Beam Transfer Impedance

The beam transfer impedance is defined by equation 1.

$$Z_t(f) = \frac{V_{pu}(f)}{I_b(f)} \quad (1)$$

ISBN 978-3-95450-177-9

In which Z_t , V_{pu} , I_b are the transfer impedance, pick-up induced voltage and beam current respectively.

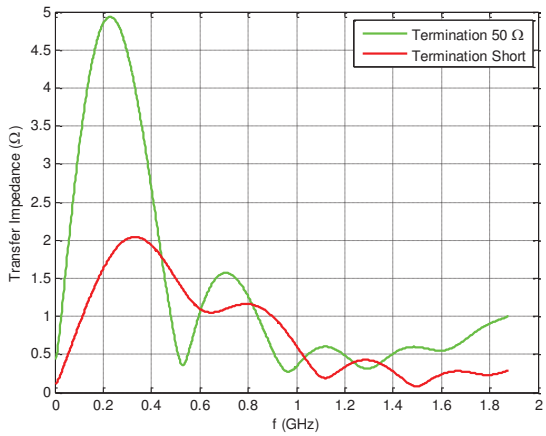

Figure 5: Transfer impedance for 50 Ω (green) and short termination (red) vs. frequency component of bunch.

Figure 5 shows the transfer impedance of one electrode vs. the frequency component of charge bunches. The design of BPM is optimized in order to have the peak output power for the interest frequency component of 704 MHz. The graph shows a transfer impedance of 1.6 Ω at the frequency of 704 MHz with a terminated port at strips downstream.

Single Bunch and Multi Bunch Time Domain Response

The nominal number of particle per bunch of 1.1e9 protons is considered for the 3D simulation in order to evaluate the voltage amplitude on the output port of the stripline. The multi bunch analysis was performed to evaluate the power available at the 2nd harmonic of the MEBT stripline signal. These analysis provided information for the BPM electronics design, and also an estimation of the undesirable high frequency modes excited by the beam. RF cables attenuation as function of frequency is considered in the analysis by taking into account the skin effect losses. Table 2 shows the total peak voltage of the stripline electrode output for low energy beam and various bunch lengths.

Table 2: Stripline Voltage Amplitude Variation with Bunch Length at 3.62 MeV

Bunch Length(σ)	Voltage (pk)
180 ps	295 mV
150 ps	302 mV
120 ps	308 mV
105 ps	320 mV
60 ps	340 mV

Note that these values are corresponding to the peak values. The electromagnetic simulation voltage results for single bunch were repeated at RF bunching frequency of 352 MHz to provide the RF power available at the interest harmonic. The result is shown in Figure 6, in which the simulations were performed for the rms bunch length of σ=180 ps.

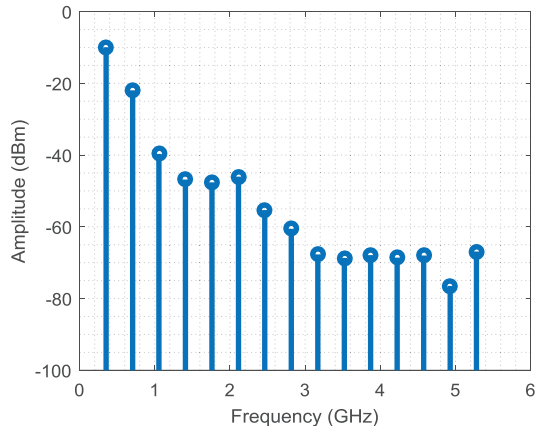

Figure 6: Multi bunch expected signal at the stripline for rms bunch length of 180 ps.

Linearity and Displacement Sensitivity

Simulation has been carried out for various scenarios of off-centre beam. The beam displacement (mm) with quanta of 1 mm up to 9 mm shows a linear variation of the strip voltage up to 3 mm with a sensitivity of 45 mV/mm as total voltage (including all frequency components). From 3 mm to 9 mm the total voltage amplitude (mV) starts to change from linear to slight quadratic fitting of $6.7x^2 + 29x + 295$. Δ/Σ interpretation gives a sensitivity of 0.13 [mm^{-1}] in both horizontal and vertical planes for the processing electronics.

MECHANICAL PROTOTYPE

A mechanical prototype is under fabrication at ESS-Bilbao. Several issues are investigated during the production, including the magnetic properties of materials after welding process, rf parameters of the ports, mechanical tolerances, vacuum leakage, e-beam welding process of the pieces, fabrication alignment, temperature stability and other related electrical measurements. The feedthrough, strips and body material is stainless steel and all the welding is based on e-beam. The tolerances vary between 5 µm of the ceramic spacer to 20 µm of the body outer diameter. The tight tolerances help to minimize possible errors from the fabrication part on the overall performance of the BPM blocks. Due to tight mechanical integration of MEBT components, the rotatable CF flanges on both sides of the block has been foreseen, which eases the screwing of the BPM blocks to upstream and downstream components.

REFERENCES

[1] https://europeanspallationsource.se
[2] R. Shafer, Beam Position Monitoring, AIP Conf. Proc. 212, (1990) p. 26-58

ISBN 978-3-95450-177-9

ORBIT FEEDFORWARD AND FEEDBACK APPLICATIONS IN THE TAIWAN LIGHT SOURCE

C.H. Kuo, P.C. Chiu, K.T. Hsu, K. H. Hu
NSRRC, Hsinchu 30076, Taiwan

Abstract

Taiwan Light Source (TLS) is a 1.5 GeV third-generation light source with circumference 120 meters. TLS is operated at 360 mA top-up injection mode. The storage ring is 6-fold symmetry with 6-meter straight sections for injection, RF cavity, and insertion devices. There are three undulators were installed in three straight sections to delivery VUV and soft X-ray for users. Beside there undulators, a conventional wiggler (W200 installed at straight sections to provide hard X-ray to serve user. Working parameters of hard X-ray sources are fixed without cause problem on operation. However, undulators should be changing its working parameters during user experiments performed. These undulators during its gap/phase changing will create orbit perturbation due to its field errors. Orbit feedback is main tool to keep orbit without change. However, some correctors setting of the orbit feedback system are easy to saturation due to large perturbation come from U90. To keep functionality of the orbit feedback system working in good condition, combines with orbit feedback and feed-forward is proposed and reported in this conference.

INTRODUCTION

The current orbit feedback system was deployed in ten years ago. There are various correctors are installed in the storage of TLS. The corrector open loop gain is from 30 Hz to 100 Hz with vacuum chamber. Therefore, the orbit feedback system cannot be operated at full bandwidth. These correctors are shared with same power-supply for close orbit correction and feedback. The main setting range of corrector is for close orbit request. There is one fifth setting range of full scale for orbit feedback. That is easy to saturate for corrector. The main orbit perturbation source is from insertion device by the operation experience during the past twenty years. To accommodate fast operation of various insertion devices and provide better orbit stability, the BPM electronics and corrector power supplies are replaced step by step. Figure 1 shows the beam position reading during the phase change of EPU5.6 undulator with and without orbit feedback response at the R1BPM0 and R1BPM8 which are equipped with Libera Brillance [1,2]. Orbit perturbation due to EPU5.6 is suppressed by feedback system while high speed operation of the insertion devices is still restrained by low closed loop bandwidth of the orbit feedback system. The feed-forward orbit control for insertion is also applied with orbit feedback system to reduce corrector strength of orbit feedback and keep from saturation.

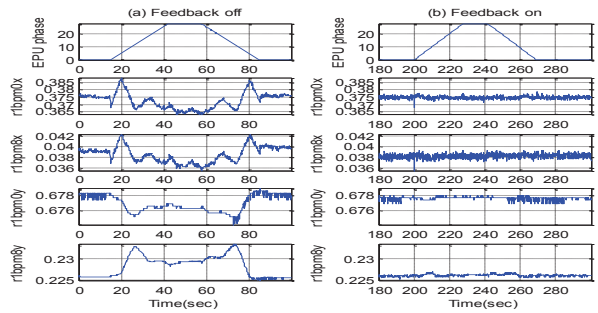

Figure 1: Effectiveness of the orbit feedback loop versus phase change of the EPU5.6 undulator. (a) without feedback; (b) with feedback.

To satisfy stringent orbit stability requirement of the TLS, low noise corrector power supply, and reliable orbit feedback system for long-term operation are necessary.

FEEDBACK SYSTEM

BPM Electronics

Libera Brilliance's integration had risen from 2007. The migration is gradually deployed not to interfere with the routine operation. To reduce GbE jitter and achieve better performance, numbers of Libera Brilliances are grouped together to produce a packed GbE UDP packet to reduce the number of IP packets. All Libera Brilliance will be grouped together [3].

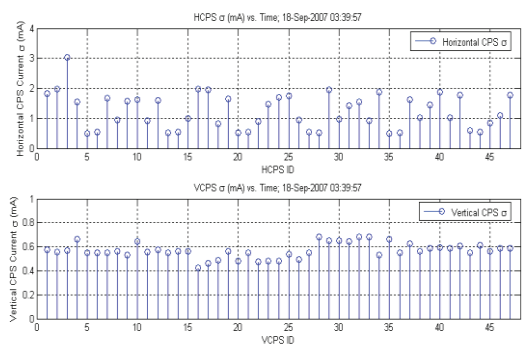

Figure 2: Power supply performance of the old power supply and the MCOR 30 power supply.

The corrector power supply is already replaced by MCOR 30. Standard deviation of the vertical power supplies (vertical corrector) and horizontal power supplies (horizontal corrector) in 100 sec readings are shown in Fig. 2. The power supply current readings of the vertical corrector power supply have the around 0.5 mA standard deviation since it is limited by the 16 bit ADC module.

ISBN 978-3-95450-177-9

Power supplies performance can be better than 16 bits. Each MCOR crate can be equipped 8 MCOR 30 power supply modules to save space. System bandwidth is determined by a whole of power supply, corrector and the vacuum chamber from 30 Hz to 100 Hz with difference plane.

The fast BPM data delivery of the orbit feedback system is by reflective memory that is employed to shares fast orbit data without consuming extra CPU resource. The orbit data will be acquired by several VME G4 PowerPC CPU modules equipped with two GbE ports. The orbit data will be shared by the reflective memory mounted to the 5 VME nodes for beam position acquisition, feedback engine and the diagnostics node. After the migration completed, higher sampling rate (5 KHz or 10 kHz will be determined according the computing power of existed CPU module) is planned rather than the current 1 kHz sampling rate [4, 5, 6].

Noticeable jitter will introduce if 10 kHz rate UPD packages transmitted by many Liberas and processed by a G4 PowerPC CPU module running LynxOS. This may degrade performance of feedback system and even lead to instability. The Libera group which packs numbers of Liberas payload data into a single UDP packet to reduce the GbE traffic is therefore concluded and its operation is being in implementation phase. It is planned that each PowerPC CPU will receive an UDP package from a group of Libera Brilliance to eliminate the problem of processing jitter.

Since there are no dedicated fast correctors at TLS, setting of the DC closed orbit control and the fast correction signal will sum in an analogue way. It will be implemented by an in-house made interface card mounted to the leftmost slot of MCOR crate which adds the setting command and feedback correction setting to the power modules. Since the switching power supplies will replace all of the current linear power supplies, we expect the integration will be accomplished in the meanwhile. New corrector power supply combined with magnet and vacuum provide an about 100 Hz and 30 Hz open loop bandwidth in vertical and horizontal plane respectively. Closed loop bandwidth can achieve 100 Hz in vertical plane without problem. To achieve more than 60 Hz or higher bandwidth in horizontal plane, a compensator is in study.

Capture fast orbit data for 10 seconds are valuable to the orbit performance monitoring, system modelling and post mortem analysis for some unexpected events. A diagnostics node will be setup for this purpose. The captured data will be analysis in Matlab environment. Hardware and software trigger mechanism with pre-post transient recorder will support. Combined with post mortem buffer for turn-by-turn data inside the Libera Brilliance and data captured by this diagnostic node might be very useful for clarifying various reasons of beam trip, this is essential to improve system reliability.

BPM Data Access and Grouping

There are several data format flows are provided by the Libera Brillance with EPICS interface including of 10 Hz rate data for DC closed orbit correction, turn-by-turn data with software/hardware trigger and on demand access for accelerator physics study, streaming 10 kHz fast data for orbit feedback application. The fast data is also very useful for beam diagnostic.

FEEDFORWARD SYSTEM

There is only slow corrector in the TLS. The corrector power supply for both orbit feedback and close obit control in the range of ±10 Amp corresponding to +/- 30 μrad and 600 μrad maximum kick angle respectively. These power supplies will be controlled by analogue interface directly. The most corrector strength is for close orbit control request. There is ±2 Amp that is reserved for orbit feedback. The maximum orbit perturbations are from insertion devices in the routine operation. The U9 gap moving with orbit perturbation is shown in the Figure 3, 4. There are few hundreds micro meter orbit difference when U9 gap is from open to minimum gap.

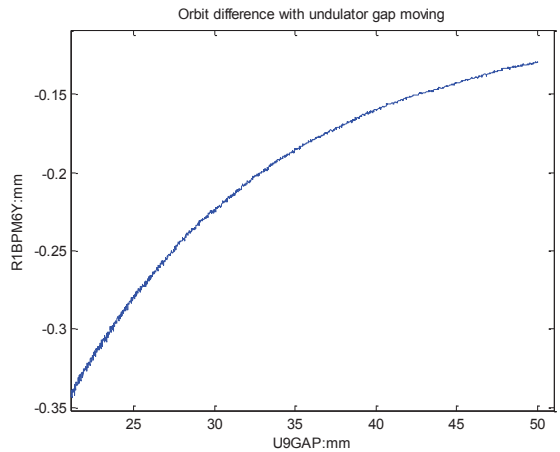

Figure 3: U9 gap moving without orbit feedback. There is 200um orbit perturbation in the R1BPM6Y.

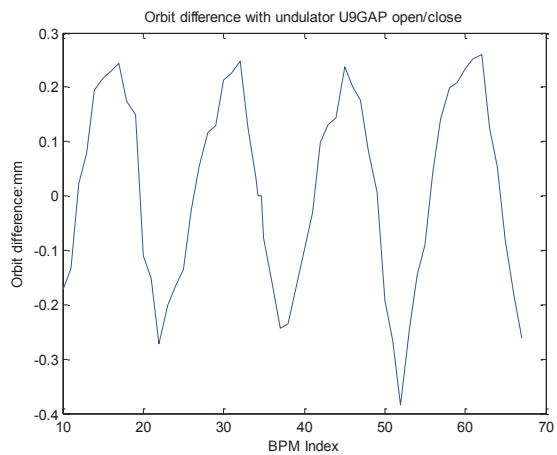

Figure 4: Full orbit difference between U9 gap open and close without orbit feedback and feed forward control.

ISBN 978-3-95450-177-9

These insertion device operations will take saturation of corrector. Feed forward control with gap difference is by the neighbourhood correctors of insertion devices that will be effective to reduce this status. Fig. 5 shows corrector reading difference that orbit feedback is only turned on, or orbit feedback and feed forward of both are turned on when insertion device gap is moving.

The corrector strength is transferred to other correctors successfully from close loop correctors of orbit feedback. The feedback and feedforward is operated together that will lock orbit and keep from saturation. The operation performance is shown in the Fig.6. There is 5 um orbit difference with feedback and feed forward in this best sensible location.

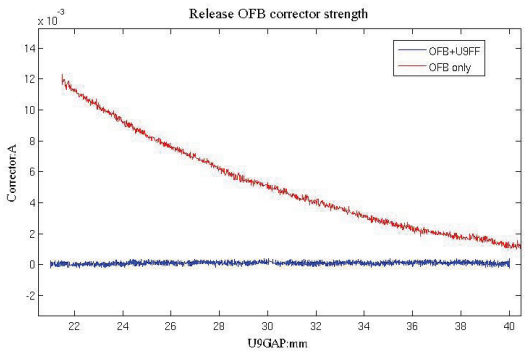

Figure 5: Corrector power-supply reading when U9 gap control with feed forward or feedback system.

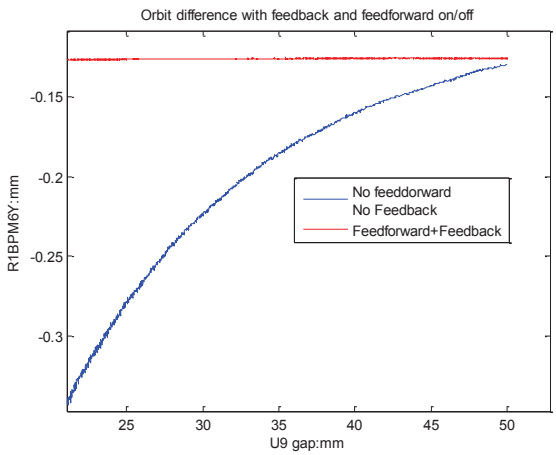

Figure 6: U9 gap control and orbit perturbation with feedback and feedforward on/off. Blue line is no feedback, no feed forward. Red line is feedback and feed forward on.

The feed-forward control has advantage those are simpler in their layout, hence are economical and stable too due to their simplicity. Since these are having a simple layout so are easier to construct. But they are very inaccurate in terms of result output and hence they are unreliable too. Due to the absence of a feedback mechanism, they are unable to remove the disturbances occurring from external sources. It is sensed to lattice variety of storage ring. Fast feed forward table update and easy operation are necessary before the route operation.

The feed forward table build up is shown in the Fig. 7. It takes to 3 minutes roughly from open gap to minimal gap. There are some measurement noises. Polynomial fitting is applied to remove these errors.

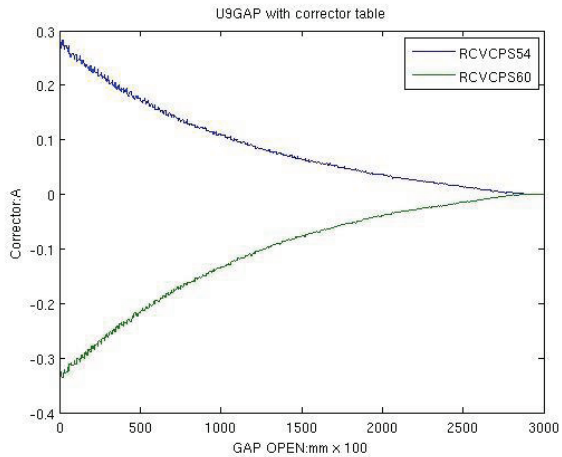

Figure 7: Fast feedforward table establish from minimal gap.

SUMMARY

BPM system and corrector power supply control system both have been integrated and operated in the orbit feedback system. In the most part of orbit perturbation, orbit feedback can process it, but corrector strength isn't enough. Orbit feedback and feed forward both are integrated and code were developed to keep from corrector saturation. Preliminary testing with real beam is ongoing. Graphic user interface will be developed for routine operation in the future.

REFERENCES

[1] http://www.i-tech.si
[2] P. Leban, et al., "First Measurements of a New Beam Position Processor on Real Beam at Taiwan Light Source", Proceedings of the *PAC 2011*, New York, U.S., 2011.
[3] A. Bardorfer, et al., "LIBERA GROUPING: Reducing the Data Encapsulation Overhead", Proceedings of the *EPAC08*, TUPC003
[4] C. H. Kuo, et al., "Fast Orbit Feedback System Upgrade with New Digital BPM and Power Supply in the TLS", *DIPAC'07*
[5] C. Steier, et al., "Operational Experience Integrating Slow and Fast Orbit Feedbacks at the ALS", Proceedings of *EPAC 2004*, Lucerne, Switzerland.
[6] N. Hubert, et al., "Commissioning of Soleil Fast Orbit Feedback System", Proceedings of *EPAC08*, Genoa, Italy.

ISBN 978-3-95450-177-9

A HETEROGENEOUS FPGA/GPU ARCHITECTURE FOR REAL-TIME DATA ANALYSIS AND FAST FEEDBACK SYSTEMS

M. Vogelgesang*, L.E. Ardila Perez, M. Caselle, S. Chilingaryan, A. Kopmann, L. Rota, M. Weber
Karlsruhe Institute of Technology, Karlsruhe, Germany

Abstract

We propose a versatile and modular approach for a real-time data acquisition and evaluation system for monitoring and feedback control in beam diagnostic and photon science experiments. Our hybrid architecture is based on an FPGA readout card and GPUs for data processing. To increase throughput, lower latencies and reduce overall system strain, the FPGA is able to write data directly into the GPU's memory. After real-time data analysis the GPU writes back results back to the FPGA for feedback systems or to the CPU host system for subsequent processing. The communication and scheduling processing units are handled transparently by our processing framework which users can customize and extend. Although the system is designed for real-time capability purposes, the modular approach also allows standalone usage for high-speed off-line analysis. We evaluated the performance of our solution measuring both processing times of data analysis algorithms used with beam instrumentation detectors as well as transfer times between FPGA and GPU. The latter suggests system throughputs of up to 6 GB/s with latencies down to the microsecond range, thus making it suitable for fast feedback systems.

INTRODUCTION

The repetition rates of modern linear accelerators such as European XFEL and TELBE [1, 2] cause increasing challenges for the development of detectors and beam diagnostics tools. With the recent developments of fast analog to digital readout systems, beam diagnostics has therefore become a big data problem. Although FPGAs emerged as ideal devices to perform on-line data analysis on large amounts of data, the implementation of particular data analysis algorithms still requires specific in-depth knowledge of the hardware and is, compared to software solutions, associated with significantly higher development costs despite efforts of FPGA vendors. At the same time, the data transmission link between the detector and the computational units or external storage is typically the bottleneck that limits the amount of data that can be processed in a given time frame.

Processing the acquired data off-line is a potential solution for most applications, however as soon as on-line monitoring or a feedback control loop is an essential part of the application, stable *real-time* data analysis with guaranteed low latencies is required. In case of on-line monitoring, data must be transferred to the processing machine as fast as possible with low variance in time. Conventional systems either based on a local temporary storage or network interconnects are not suitable due to insufficient transfer times.

* matthias.vogelgesang@kit.edu

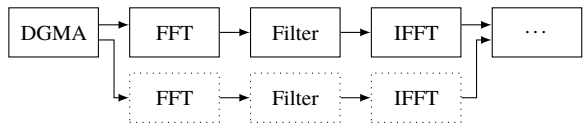

Figure 1: Overview of multi-GPU data stream processing: after inserting the data into a buffer within the DGMA filter, the data processing steps consisting of filtering in the frequency domain can be executed on separate GPUs for higher throughput.

In this paper, we will present a hardware/software architecture that bridges fast data acquisition using FPGAs and fast data processing with GPUs. Using direct memory accesses, we can decrease latency as well as increase throughput by utilizing the entire connection bandwidth. This data acquisition infrastructure is accessible from within our data processing framework which – in this particular use case – is used to analyse digitized spectrometer data in a heterogeneous compute environment. It automatically distributes data among multi-core CPUs and GPUs and uses multi-level parallelism to achieve a higher processing throughput than conventional single-threaded computing. The processing pipeline is flexible and can be re-arranged as well as extended by the user to accommodate for different applications. By adopting the proposed solution, the development time of a particular experimental setup can be reduced significantly.

ARCHITECTURE

FPGA-based Data Acquisition Platform

Our core data acquisition platform is based on our custom "Hi-Flex" FPGA board, that uses a Xilinx Virtex 7 device and is connected to the host computer through a PCI-Express (PCIe) 3.0 8-lane connection. The board has integrated DDR3 memory of 4 GB and an internal maximum throughput of 120 Gbit s^{-1}. Two industry standard FMC connectors (fully populated) are used to interface different mezzanine boards, which host the frontend electronics of different application-specific detectors such as 2D pixel detectors [3] or 1D linear array detectors [4]. The FPGA has an in-house developed Direct Memory Access (DMA) engine for PCIe 2.0 / 3.0 compatible with Xilinx FPGA families 6 and 7 supporting DMA data transfers between main system memory and GPU memory. The DMA engine is described in more detail in [5].

Data Processing Framework

The basis for processing the input data in real-time is our heterogeneous data processing framework, initially devel-

ISBN 978-3-95450-177-9

oped for X-ray image processing tasks [6]. As shown in Figure 1 the core concept is a graph defined by the user who specifies the flow of data through a set of nodes that process input data to produce some result. The tasks within these nodes is scheduled by the run-time system and executed on processing units such as CPU threads and GPU kernels. By duplicating chains of tasks intelligently as denoted by the dotted nodes, the system can make use of multiple levels of parallelism including pipelining, multi-threading, fine-grained data parallelism within a GPU as well use of multiple GPUs per machine. To process data on the GPUs, specific GPU kernel code is written and executed using the vendor-independent OpenCL standard [7].

The framework has a variety of options to access it in order to accommodate for different user requirements. The most straightforward way consists of chaining and parameterizing the plugins on the command line. For example, to read data from the FPGA, compute a one-dimensional FFT on the multi-dimensional data and write the result into an HDF5 file, the user merely has to run

```
ufo-launch
  direct-gma width=256 height=4096 ! \
  fft dimensions=1 ! \
  write filename=output.hdf5:/dataset
```

on the command line. As one can see, the user can entirely concentrate on devising the correct processing chain for his end result and does not have to worry about execution on the target platform. Besides using the framework in this immediate mode, it can also be linked to from any C or C++ program as well as being called from most third-party scripting languages such as Python via a meta-bindings. Since each task is a plugin following a simple interface, users can extend the framework by implementing new functionality as new plugins.

Low Latency Data Transfers

In order to obtain the maximum throughput of the FPGA's and GPU's PCIe connection as well as to process data on the GPUs in real-time, we have to avoid any intermediate data copies between system and GPU memory. Using AMD's DirectGMA extension for OpenCL we can tightly integrate DMA-based data transfers and transmit data directly into the GPU without storing the acquired data temporarily in system memory.

In order to initiate a data transfer on the FPGA, the physical bus addresses of the GPU memory regions to be written have to be set in special FPGA registers. For CPU writes these addresses are provided by our FPGA kernel driver. With GPUs these memory addresses are retrieved by passing the allocated OpenCL buffer to the AMD-specific `clEnqueueMakeResidentAMD()` call. Unlike general GPU buffers, FPGA-accessible GPU buffers are limited in size, for example on an AMD W9100 the maximum buffer size is about 90 MB. Therefore, we use a double buffering approach that swaps multiple temporary buffers in order to keep the DMA engine running. While filling one half of the restricted buffer, the content of the other half is transferred using `clEnqueueCopyBuffer()` to a non-DMA buffer which has the size of the final buffer. When both DMA transfer and internal copy finish, the roles of the buffers reverse, i.e. the first buffer is copied and the second is filled. Once the large buffer is filled completely, it is swapped for processing by the GPU. Using this strategy, we can overlap both DMA transfers as well as data processing. This mechanism is working because data is copied much faster within a GPU (about 320 GB/s on a W9100) than between FPGA and GPU (8 GB theoretical throughput for PCIe 3.0 x8). Besides transfers from FPGA to GPU, the GPU can also write back to FPGA registers and memory regions that were made accessible to compute kernels. This requires passing known physical FPGA bus addresses to the `clEnqueueMakeResidentAMD()` call. This creates a virtual proxy buffer that can be used by the GPU kernel to write seemingly *into* the FPGA address space. This facility is necessary for trigger applications that have to avoid passing the trigger information first to the CPU.

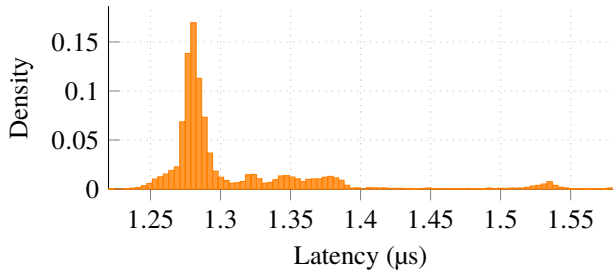

Figure 2: Round-trip latency distribution of data going from FPGA to GPU and back again.

RESULTS AND USE CASES

In this section we will investigate the behaviour of our proposed system both on a lower level comparing data throughput and latency as well as on a higher level measuring data processing times.

Performance

Figure 2 shows the latency distribution measured for data transfered from FPGA to GPU and back to the FPGA again. An FPGA-side timer is started as soon as a write happens. Meanwhile, a GPU kernel is launched that polls for that data to arrive. Once the kernel thread registers a change, it triggers a response causing write back to the FPGA. As we can see, the mean latency of data transfers of about 1.31 µs with a jitter of 0.06 µs suggests applicability of our system for most monitoring and feedback applications.

In Figure 3, the system throughput is plotted for a increasingly larger datasets. Each transfer is measured with three different data block sizes that were transmitted at once. The throughput includes the data transfer as well as all as any overheads induced by startups and the run-time system. With this in mind, we can see a throughput that is near full utiliza-

ISBN 978-3-95450-177-9

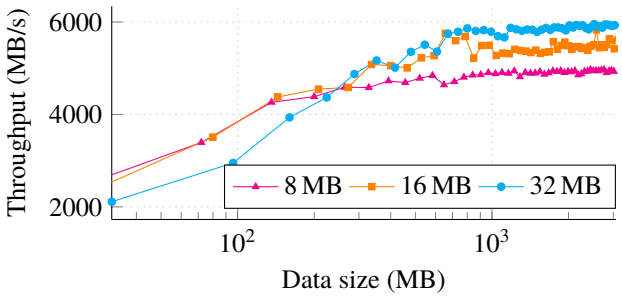

Figure 3: System throughput from FPGA to GPU for different data block sizes and including all overheads.

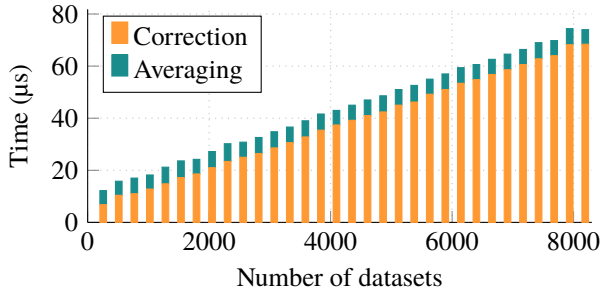

Figure 4: Kernel execution times for processing averaging and background correction on an AMD S1970.

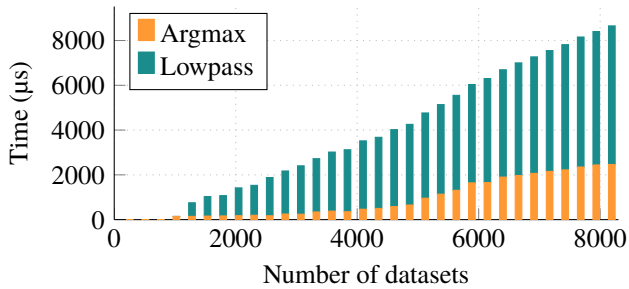

Figure 5: Kernel execution times for specific analysis.

tion of the PCIe bus for larger data sizes and is sufficient for even the highest demanding photon science experiments.

KALYPSO Data Analysis

As a typical application example for a beam diagnostic solution, we have chosen KALYPSO, a linear array detector developed to allow real-time monitoring of longitudinal bunch profiles measured with Electro Optical Spectral Decoding setups. The detector setup and characteristics is described in detail in [8]. The main idea of this detector setup consists of the reconstruction of the bunch profile from the measured spectrum of a laser pulse. In order to measure the bunch profile, three different measurements have to be acquired: the background signal, the unmodulated signal with the laser pulse used as a reference and the modulated signal where the laser pulse contains the information of the bunch profile. The discretized spectrum of the laser pulse is acquired and digitized on a dedicated card that is connected to the "Hi-Flex" FPGA board.

The most fundamental work required for subsequent data analysis is the interpretation of the raw ADC channel data transferred from the FPGA board and *correction* for background noise. The first step consists of *averaging* the stream of background and unmodulated data sets d_b and d_u over time, i.e. $\hat{d}_{\{b,u\}}[i] = \frac{1}{n}\sum d_{\{b,u\}}[i][j]$ for the i-th channel of the j-th out of n pre-recorded datasets. This data is used to remove static background and dark noise from the currently recorded datasets d_m, i.e.

$$\hat{d}_m[i][j] = \frac{d_m[i][j] - \hat{d}_b[i \bmod 256]}{\hat{d}_u[i \bmod 256]}.$$

Each time raw data is accessed, the transmitted value has to be masked with `0x3fff` in order to retrieve the 14 bit ADC values from a 16 bit data packet. Because of data dependencies, we map one GPU thread to one ADC channel to parallelize the averaging which results in 256 threads running in parallel. The data correction itself is free of any data dependencies, thus one GPU thread computes the corrected value for one input.

Figure 4 shows the execution time for averaging and correction. Averaging is constant, with a mean execution time of 5.975 µs, because the same background and unmodulated data is used for each run, the time for correction scales linearly and is approximately $t(n) = (0.00777n + 5.105)$ µs.

To smoothen the high variance of the input data a low pass filter based on moving averages has been implemented. Similar to the regular averaging filter, the kernel for *moving averages* maps one GPU thread to one particular ADC channel, computing the moving averages with a default order of 3 for all datasets. In certain applications such as measurement of the arrival time, it is necessary to find out which of the channels a has the largest value at the moment, i.e. one wants to determine $a_i = \text{argmax}_j d[i][j]$. This is a simple search across all datasets which also requires mapping of one GPU thread to one channel. Figure 5 compares the execution time for these two kernels: unlike the previous pre-processing tasks these steps take several milliseconds to compute thus are only useful in a monitoring environment.

Besides these fundamental tasks, we can also make use of the existing *transpose* filter to re-interpret the dataset columns as rows and do subsequent computations in time domain. Moreover, we can use the existing *fft* and a newly written *powerspectrum* filter to compute the frequency components of the signal. Whereas the power spectrum computation can be parallelized in the same way as the background correction kernel with similar performance characteristic, the FFT is a more complex filter requiring appropriate padding and more time.

CONCLUSION

In this paper, we introduced a comprehensive data acquisition and processing system with low latencies and high throughput properties as its main characteristics. The core

ISBN 978-3-95450-177-9

components of the system are tight coupling between data acquisition and processing that is driven by the acquiring FPGA rather than the host CPU. Unlike conventional data paths, writing from FPGA to the GPU directly allows lower latencies and higher total throughput and enables real-time monitoring, control and feedback systems. To realize real-time monitoring we also off-load critical pre-processing to the GPU with average execution times in the µs range.

The entire setup was used to measure and analyse data with the KALYPSO detector setup and has proven to be a viable alternative to conventional off-line data analysis given insight into the data while acquiring it. In the future, we will investigate how the analysis can be visualized in a user-friendly way and how the result can be incorporated in the entire feedback loop.

ACKNOWLEDGEMENT

This work was partially funded by the German Federal Ministry of Education and Research (BMBF) as UFO-2 under the grant 05K10VKE. The authors would also like to thank Patrik Schönfeldt and Miriam Brosi for the data and helpful discussions.

REFERENCES

[1] B. Green, S. Kovalev, J. Hauser, M. Kuntzsch, H. Schneider, S. Winnerl, W. Seidel, S. Zvyagin, U. Lehnert, M. Helm *et al.*, "Telbe-the super-radiant thz facility at elbe," *Verhandlungen der Deutschen Physikalischen Gesellschaft*, 2013.

[2] M. Altarelli, R. Brinkmann, M. Chergui, W. Decking, B. Dobson, S. Düsterer, G. Grübel, W. Graeff, H. Graafsma, J. Hajdu *et al.*, "The european x-ray free-electron laser," *Technical Design Report, DESY*, vol. 97, pp. 1–26, 2006.

[3] M. Caselle, S. Chilingaryan, A. Herth, A. Kopmann, U. Stevanovic, M. Vogelgesang, M. Balzer, and M. Weber, "Ultrafast streaming camera platform for scientific applications," *IEEE Transactions on Nuclear Science*, vol. 60, no. 5, pp. 3669–3677, 10 2013.

[4] L. Rota, M. Vogelgesang, L. A. Perez, M. Caselle, S. Chilingaryan, T. Dritschler, N. Zilio, A. Kopmann, M. Balzer, and M. Weber, "A high-throughput readout architecture based on pci-express gen3 and directgma technology," *Journal of Instrumentation*, vol. 11, no. 02, 2016.

[5] L. Rota, M. Caselle, S. Chilingaryan, A. Kopmann, and M. Weber, "A high-throughput pcie dma architecture for gigabyte data transmission," *IEEE Transactions on Nuclear Science*, vol. 62, no. 3, pp. 972–976, 6 2015.

[6] M. Vogelgesang, S. Chilingaryan, T. dos Santos Rolo, and A. Kopmann, "Ufo: A scalable gpu-based image processing framework for on-line monitoring," in *High Performance Computing and Communication 2012 IEEE 9th Int. Conf. on Embedded Software and Systems (HPCC-ICESS), 2012 IEEE 14th Int. Conf. on*, 6 2012, pp. 824–829.

[7] A. Munshi, B. Gaster, T. Mattson, J. Fung, and D. Ginsburg, *OpenCL programming guide*. Addison-Wesley Professional, 2011.

[8] L. Rota, M. Caselle, N. Hiller, A. Müller, and M. Weber, "An ultrafast linear array detector for single-shot electro-optical bunch profile measurements," in *Proceedings of the 3rd Int. Beam Instrumentation Conf.*, 9 2014.

ISBN 978-3-95450-177-9

FAST ORBIT FEEDBACK WITH LINUX PREEMPT_RT

Yaw-Ren Eugene Tan, Australian Synchrotron, Clayton, Australia
Daniel de Oliveira Tavares, LNLS, Campinas, Brazil
David J. Peake, The University of Melbourne, Melbourne, Australia

Abstract

The fast orbit feedback (FOFB) system in development at the Australian Synchrotron (AS) [1] aims to improve the stability of the electron beam by reducing the impact of insertion devices and targeting orbit perturbations at the line frequency (50 Hz, 100 Hz and 300 Hz). The system is designed to have a unity gain at a frequency greater than 300 Hz with a simple PI controller with harmonic suppressors in parallel (as was done at Elettra). With most of the system in place (position aggregation, power supplies and corrector coils) we decided to implement a PC based feedback system to test what has been installed as well as the effectiveness of the proposed control algorithms while the firmware for the FPGA based feedback processor is being developed. This paper will report on effectiveness of a feedback system built with CentOS and the PREEMPT patch running on an Intel CPU.

INTRODUCTION

The ultimate goal of the feedback system is to ensure that the transverse RMS beam motion up to 100 Hz is kept to less than 9.0 µm horizontally and 1.6 µm vertically.

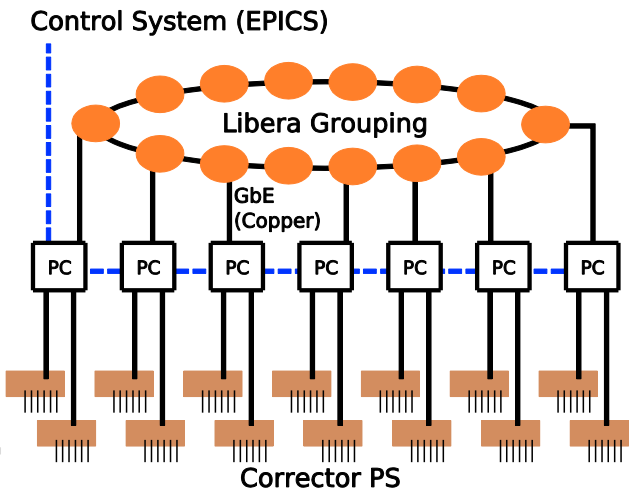

Figure 1: Distributed PCs processing the Fast Acquisition Data from the EBPMs and calculating the correction for the power supplies. No direct synchronisation between PCs. Control of the feedback system is through EPICS process variables running on a virtual server.

Figure 1 shows the distributed configuration of the seven PCs used to control the 14 power supplies around the storage ring. Each of the seven PCs receive real-time Fast Acquisition (FA) position data from the Libera Electron beam position processors (EBPMs), calculate and transmit the correction to the magnet power supplies through a 10 MBaud serial link. The synchronisation of the corrections between the PCs depends on the ability of the application to process the data in a repeatable time period and the synchronicity of the FA data transmitted by the EBPMs.

LINUX PREEMPT_RT PATCH

To achieve a repeatable processing period, with a tolerance of 10s of µs, a "realtime" operating system is required. There are many potential candidates, such as RTEMS and VxWorks, however in the interest of minimising the development time, a decision was made to attempt it with our nominal production operating system at the AS (CentOS) with a PREEMPT_RT patched kernel.

The PCs use a PCI-x serial card by Axxon to communicate with the power supplies (the Linux serial driver had to be patched to get the card to operate at the maximum rate). The test the "realtime" nature of the operating system and applications, a test program was written to transmit data packets at a rate of 5 kHz (using *clock_nanosleep* to set the period) and the period of the transmitted serial data measured on an oscilloscope. The program was tested with CentOS 5 (kernel 2.6.29.6-rt24; Intel Core2 Q8400 2.66 GHz) and CentOS 7 (kernel 3.10.75-rt80; Intel Celeron G1840 2.80 GHz).

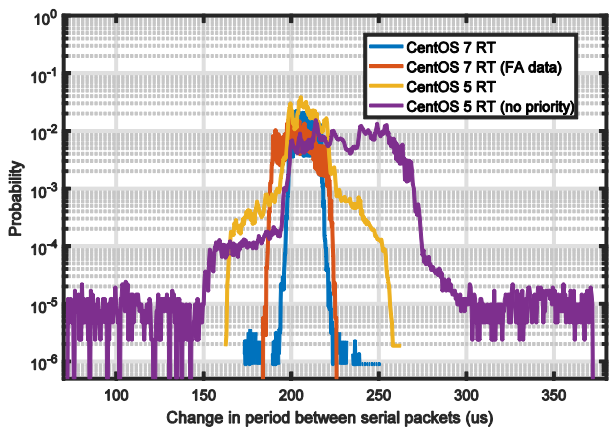

Figure 2: The newer kernel performs better and by setting a high scheduling priority the peak to peak jitter can be reduced to <100us. In the best case the peak to peak jitter is < 80 us with greater than 99.995% occurring within a 30 us window. If the serial output is triggered by the incoming FA data the jitter is subsequently worse due to jitter on the processing of the incoming data. (The sample size varies from 350k to 1300k).

The results of the measurements shown in Figure 2 indicate that upgrading from CentOS 5 to CentOS 7 reduces the jitter by almost half. In the best case more than

ISBN 978-3-95450-177-9

99.995% of the measured period was within a 30 µs window. Without the patch, such a tight timing control is not possible.

The periodicity of the incoming FA data packets was also tested by measuring the period between packets using *clock_gettime*. The purpose is to test the response of the network interface (it is known that the EPBMs transmit the packets with timing jitters less than µs). Using the on-board Realtek (RTL8111/8168/8411) gigabit network interface the measured periods were between 1 µs to 400 µs, which is unacceptable. Changing to an Intel (82574L) gigabit network interface, the measured periods were between 70 µs and 130 µs with an average of 99.4 us.

Figure 2 (second trace) also shows the jitter in the period when the incoming packets is used as a trigger to transmit the serial data with a width of ~50 µs. With a potential processing latency of 80 µs (discussed later in this report), the system is unable to run the feedback loop at 10 kHz and can only run at 5 kHz.

SYNCHRONICITY BETWEEN PCS

The synchronisation of the PCs is vital and depends on the EPBMs synchronously transmitting the FA data. The serial output from two PCs was monitored and the difference in the transmission time was measured. The results in Figure 3 show a static offset of 13 µs with a spread of 2 µs showing that the data packets are well synchronised with fixed offsets relative to each other. The static offsets are sufficiently small that it will not degrade the efficiency of the system however it is sufficiently small to not (at 1 kHz an offset of 30 µs corresponds to a phase shift of 11 degrees).

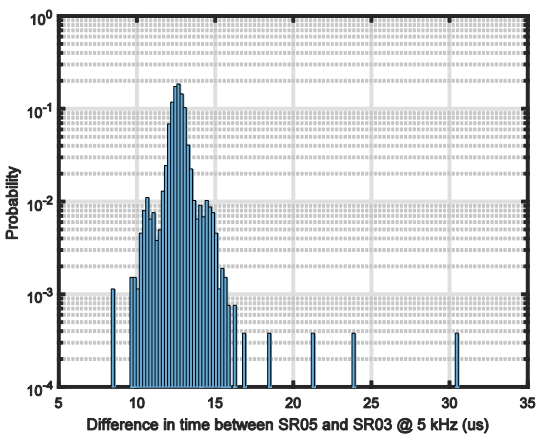

Figure 3: An offset of 13 us between two PCs is observed with a FWHM spread of 2 us (dataset of 2700).

CONTROL ALGORITHM

The feedback system uses a combination of a PI controller and harmonic suppressors at 50 Hz, 100 Hz and 300 Hz with a bandwidth of 0.2 Hz, 0.4 and 1.2 Hz, respectively. This method follows the system successfully implemented at Elettra [2]. The coefficients for the biquad peak filters were pre-calculated using Matlab for 50 Hz, 100 Hz and 300 Hz (for a sample rate of 5029 S/s). Phase delays were not tested, however with an estimated system latency of around 200 µs the phase error at 300 Hz should be less than 22 degrees.

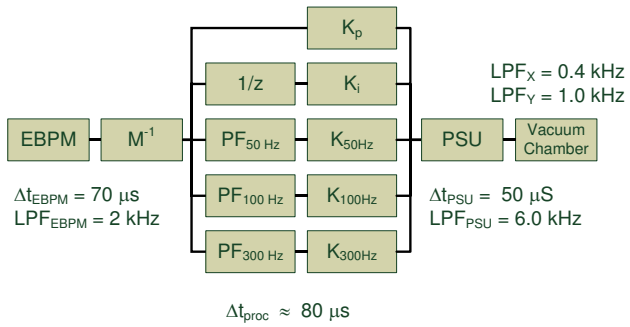

Figure 4: Block diagram showing the EBPMs, inverted BPM-corrector response matrix (M^{-1}), corrector magnet power supply (PSU) and the vacuum chamber. The feedback system uses a PI controller (K_p, K_i) as well as harmonic suppressors (using peak filters, PF) with the corresponding gain control (K_{freq}). The latencies (Δt) and frequency response (LPF) for the EBPM, PSU and vacuum chamber have been measured [1] while Δt_{proc}, is an estimate based on simulations shown later in this report.

RESULTS

After a few false starts we were soon running with the full system. The integrated horizontal and vertical RMS beam motion averaged across all insertion devices is show in Figure 5. The results with the feedback system are compared against to two operational modes related to the RF system. The AS Storage Ring is to operate with four warm RF cavities generating a total potential of 3 MV. For operational reasons a decision was made to run with three RF cavities and to drop the voltage to 2 MV. While rotating through the different triplet of cavities, the beam stability was observed to improve significantly when one particular cavity was not operational. This single cavity contributed significantly to the 50 Hz perturbations. Since then this cavity has been left on standby and work to isolate the cause of the perturbation to the beam has so far been unsuccessful.

Figure 6 shows the efficiency of the harmonic suppression on the line frequency perturbations, between -15 dB and -30 dB reduction in noise.

Matlab Models

The elements in the feedback system as shown in Figure 4 can be modelled in Matlab however a missing part is the processing latency of the PCs. In Figure 7 the measured results are compared against a model and the total system latency of the model changed to get the best fit at the higher frequencies. The best fit gave a total system latency of 200 µs. Removing all other known fixed delays in system (see Figure 4), the processing delay can be inferred to be around 80 µs.

ISBN 978-3-95450-177-9

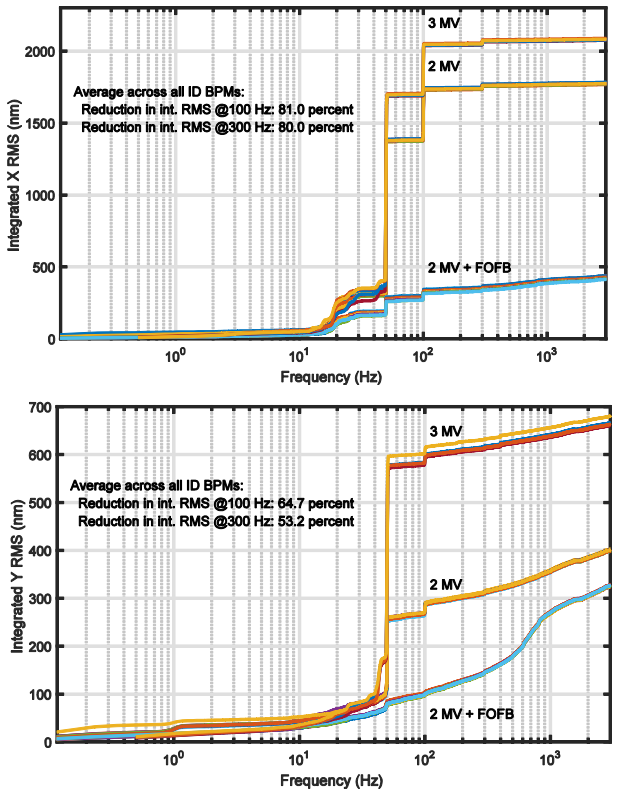

Figure 5: Integrated horizontal (top plot) and vertical (bottom plot) RMS averaged across all insertion device BPMs. There are 4 data sets shown here for three different conditions: 4 cavity operation (3 MV), 3 cavity operation (2 MV), with FOFB.

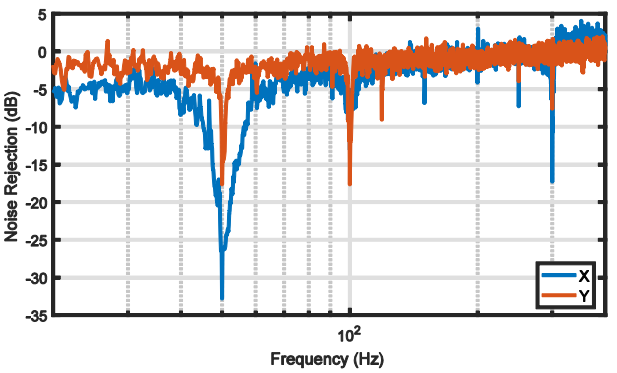

Figure 6: Efficiency of the harmonic suppressors showing between -15 dB and -30 dB reduction in noise. The harmonic suppression at 300 Hz for Y was disabled.

During the design phase, the initial estimates for the zero gain frequency crossing was 300 Hz (horizontally) and 370 Hz (vertically). With the PC based FOFB system the zero gain frequency crossing was measured to be as much as 325 Hz (horizontally) and 400 Hz (vertically) and with the FPGA implementation, this is expected to increase to above 400 Hz in both planes.

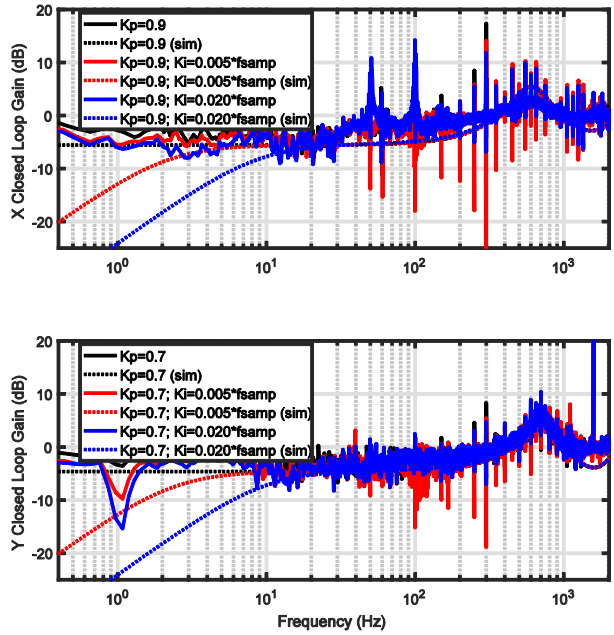

Figure 7: Ratio of the spectrum with and without feedback enabled with different integral coefficients, K_i. The measured results are compared to simulated bode plots calculated in Matlab assuming the properties shown in Figure 4 and a total system latency of 200 µs.

Insertion Device Perturbations

One of the goals of the fast feedback system is to ensure that perturbations from scanning insertion devices are minimised. In Figure 8 gap and phase scans on an APPLE II undulator are started under three conditions: with fast feedback (FOFB), with slow feedback (SOFB; 1 Hz) and no feedback.

The results with FOFB showed that it is possible to maintain orbit distortions to less than one µm even with large perturbations. The frequency analysis of the orbit perturbation during gap and phase scans showed that the perturbations had frequency components up to 10 Hz. Therefore with appropriate values for K_i it was possible to damp the perturbation by an order of magnitude (20 dB). The integral component also successfully damps a 1 Hz vertical perturbation as seen in Figure 7 and Figure 8 (as fuzziness to the vertical position with no FOFB).

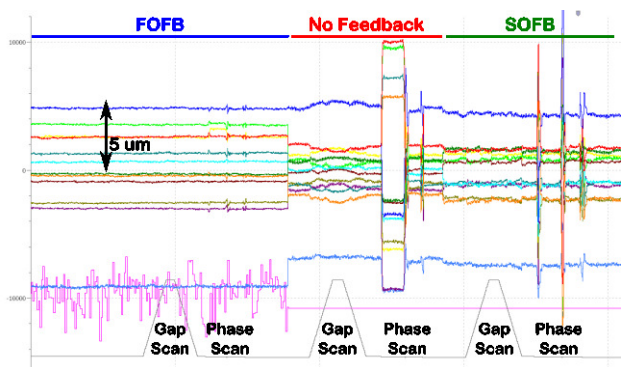

Figure 8: The APPLE II is the most disruptive of Insertion Devices (IDs). The gap and phase was scanned with

ISBN 978-3-95450-177-9

fast feedback (FOFB), slow feedback (SOFB; 1 Hz) and no feedback. Large vertical perturbation during the phase scan seen without feedback was caused by a fault in the feedforward table. FOFB can maintain vertical orbit perturbations below 1 µm.

Slow and Fast Correctors

The storage ring now has a set of slow Horizontal and Vertical Corrector Magnets (42 HCM and 56 VCM) and a set of Horizontal and Vertical Fast Corrector magnets (42 HFC and 42 VFC).

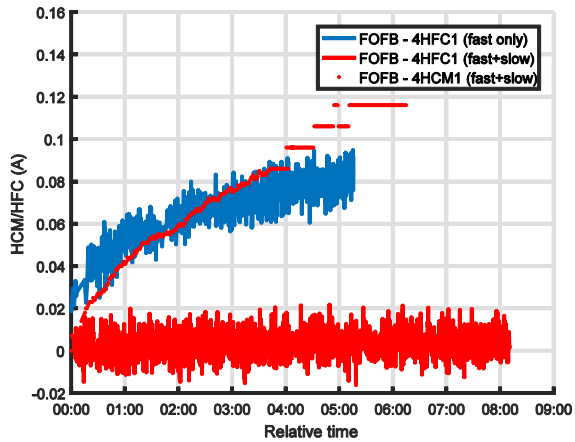

Figure 9: With only the fast correctors, the DC component starts to drift. By understanding the relationship between the slow and fast correctors, the "DC" component can be offloaded from the fast correctors to the slow correctors, thereby maintaining a "DC" value close to zero for the fast correctors.

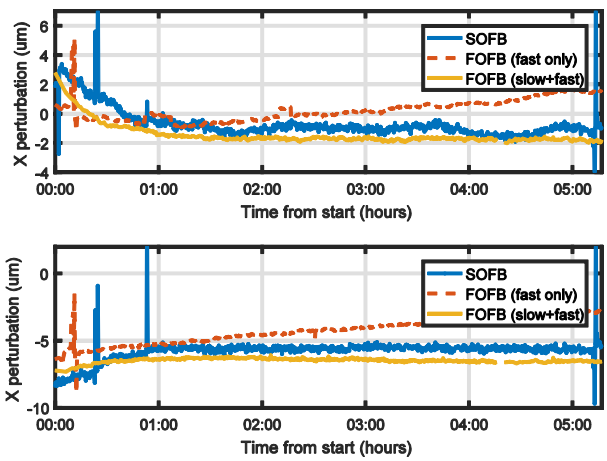

Figure 10: Example of two horizontal orbit positions when operating with feedback. With SOFB there is an initial period after injection where the storage ring is warming up, resulting in a drift of a few µm. With FOFB and just the fast correctors, there are additional drifts associated, to a more extensive shut down period and therefore longer warm up time and the feedback does not compensate for the slow drifts. With FOFB utilising both fast and slow magnets, the slow drift is eliminated and the position over the 5 hour period is more stable. The initial drift seen all three cases is likely caused by movements in the vacuum chamber as the ring warms up after a maintenance period.

The first 5 hour test of the FOFB system kept the slow magnets static. As expected the DC component of the fast corrector magnets drifted. This is a concern because the full range of the fast corrector power supplies is only ±1 A. It is therefore important to ensure that the DC component does not eventually saturate the power supply. In the second 8 hour test, the method for managing slow and fast correctors developed at Soleil was successfully implemented [3] to utilise both sets of magnets (RF corrections are excluded for now). Figure 9 shows that with this implementation, the DC drift is no longer present. Figure 10 shows that utilising the fast and slow correctors ensures better long term stability of the feedback system.

CONCLUSION

A PC based FOFB system has been developed over a short period of time with standard PC components to operate at a cycle rate of 5 kHz. The PI controller successfully damped frequencies below 30 Hz while the harmonic suppressors reduced the line frequency perturbations by as much as 30 dB. The zero gain cross over frequency was better than expected, measured at 325 Hz (horizontally) and 400 Hz (vertically).

Developing this system and running it has shown what the FOFB system is capable of doing (commissioning in Jan 2017), how it works and highlighting deficiencies in the original design. The refinements and diagnostics developed for this project has led to additions to the design of the system that would otherwise have not been discovered until commissioning. Implementing the FOFB in this manner is straight forward with minimal initial hardware costs. However there are open questions regarding the reliability and maintenance over its 10 year life span. Otherwise it is a very useful platform for prototyping control algorithms and diagnostics.

ACKNOWLEDGEMENT

I would like to acknowledge the assistance from Andrew Starritt for his help on EPICS, Ron Bosworth with sourcing and assembling the PCs and to the Operators at the AS that helped with run the system and collect data.

REFERENCE

[1] Y.-R. E. Tan, et. al, "Fast Orbit Feedback System at the Australian Synchrotron", in *Proc. IBIC'15*, Melbourne, Australia, TUB002, pp 293-297.

[2] M. Lonza, d. Bulfone, V. Forchi, G. Gaio, "Commissioning of the Elettra Fast Orbit Feedback System", in *Proc. PAC07*, Albuquerque, USA, MOPAN024, pp 203-205.

[3] N. Hubert, L. Cassinari, J-D. Denard, A. Nadji, L. Nadolski, "Global Orbit Feedback Systems Down to DC using Fast and Slow Correctors", in *Proc. DIPAC09*, Basel, Switzerland, MPPC01, pp. 27-31

ISBN 978-3-95450-177-9

DEVELOPMENT OF A PROTOTYPE ELECTRO-OPTIC BEAM POSITION MONITOR AT THE CERN SPS

A. Arteche*, A. Bosco, S. M. Gibson, Royal Holloway, University of London, Egham, UK
N. Chritin, D. Draskovic, T. Lefèvre, T. Levens, CERN, Geneva, Switzerland

Abstract

A novel electro-optic beam position monitor capable of rapidly (< 50 ps) monitoring transverse intra-bunch perturbations is under development for the HL-LHC project. The EO-BPM relies on the fast optical response of two pairs of electro-optic crystals, whose birefringence is modified by the passing electric field of a 1 ns proton bunch. Analytic models of the electric field are compared with electromagnetic simulations. A preliminary opto-mechanical design of the EO-BPM was manufactured and installed at the CERN SPS in 2016. The prototype is equipped with two pairs of 5 mm cubic $LiNbO_3$ crystals, mounted in the horizontal and vertical planes. A polarized CW 780 nm laser in the counting room transmits light via 160 m of PM fibre to the SPS, where delivery optics directs light through a pair of crystals in the accelerator vacuum. The input polarization state to the crystal can be remotely controlled. The modulated light after the crystal is analyzed, fibre-coupled and recorded by a fast photodetector in the counting room. Following the recent installation, we present the detailed setup and report the latest status on commissioning the device in-situ at the CERN SPS.

MOTIVATION AND CONCEPT

An electro-optic beam position monitor (EO-BPM) is being developed for high frequency, intra-bunch measurements at the High-Luminosity Large Hadron Collider [1]. The main aim of the new instrument is to determine the mean transverse displacement along each $4\sigma = 1$ ns proton bunch, with a time resolution of < 50 ps. Existing head-tail monitors based on stripline BPMs are capable of measuring intra-bunch instabilities, with a bandwidth of 3–4 GHz that is limited by the pick-ups, cables and acquisition system [2]. In contrast, an EO-BPM is essentially a conventional button-BPM in which the pick-ups have been replaced with electro-optic crystals, to target bandwidths of 10–12 GHz or more, due to the fast optical response of the crystal in the transient electric field of the bunch.

The electro-optic response is measured using polarized light from a continuous wave, 780 nm laser source, housed away from the accelerator in the low radiation, accessible environment of a counting room. The light is conveyed in 160 m PM delivery fibre to collimation and polarization optics at each pick-up, and transmitted through the crystal, parallel to the particle beam direction. The light that emerges after the crystal typically has a different polarization state, due to the natural birefringence of the crystal. When the particle bunch passes, the electric field penetrates the crystal and via the Pockels effect, induces a change in the birefringence of the crystal, thus rapidly modifying the polarization state of the emerging light. An analyzer is placed after the crystal and the subsequent intensity of light is coupled into a return SM fibre and recorded by a fast photodetector. By taking the difference signal between pick-ups on the opposite sides of the beam pipe, the transverse displacement along the bunch can be deduced. In an alternative interferometric layout, coherent light is exploited to optically suppress the common mode signal, such that the detector directly measures the difference signal between the two pick-ups [1].

As a proof of these concepts, a prototype EO-BPM has been developed and was recently installed for tests in the CERN SPS. The following sections report on the detailed opto-mechanical design of the electro-optic pick-ups that were installed, including electromagnetic simulations of the geometry to assess the electric field strength penetrating the crystal. The installed layout in the CERN SPS is reviewed, including the fibre coupled, remotely controlled polarization optics. Finally, experimental validation of the sensitivity of the crystal to electric fields equivalent to those expected from the simulation is presented.

ELECTRO-OPTIC PICK-UP DESIGN AND SIMULATION

Prototype Opto-Mechanical Design

The conceptual design of the EO-BPM has compact, fibre-coupled optics directly mounted to the eo pick-up. For the CERN SPS prototype, however, a more flexible approach was decided, to enable reconfiguration and investigation of the polarization states. Therefore the fibre-coupled collimation and polarization optics were mounted on a small external breadboard adjacent to the pick-up, with light coupled into and out of the pick-up by a free space laser beam. The opto-mechanical design of the pick-up [3] is illustrated in Figure 1, showing the superposed path of the laser beam.

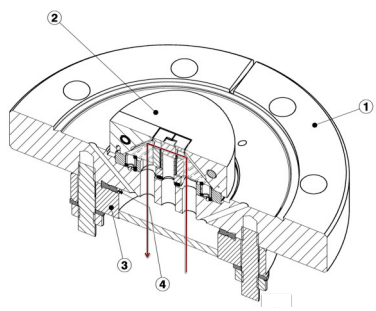

Figure 1: Laser beam trace inside the eo pick-up: 1. Flange. 2. Button. 3. Viewing port. 4. Copper gasket.

* alberto.arteche.2014@live.rhul.ac.uk

ISBN 978-3-95450-177-9

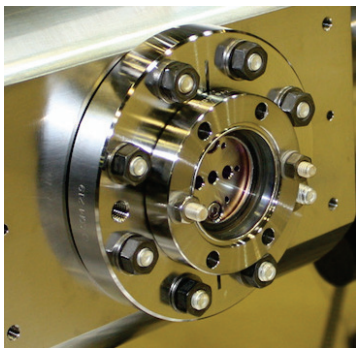

Figure 2: External view of pick-up in BPM body.

Figure 3: Pick-up components: ceramic holders, prisms and crystal.

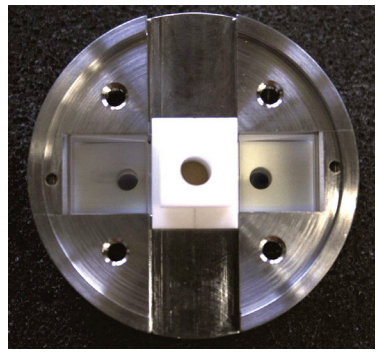

Figure 4: Top view shows reflected path through crystal.

Four such pick-ups have been installed in the CERN SPS and each consists of three components connected by copper gaskets: a button, an external flange and a viewing port, as in Figures 2–4. The incident laser beam is reflected using two right-angled prisms, surrounding a MgO_2:$LiNbO_3$ 5 mm cubic crystal, that is held within a ceramic support of mica. The incoming beam is linearly polarized and the passing proton bunch Coulomb field interacts over the crystal resulting in a polarisation modulation in the output laser beam. An anti-reflection coated viewport provides the interface between the vacuum and the free space beam optics.

Analytic Model

The pick-up signal is based on the linear electro-optic Pockels effect, which modifies the refractive indices of the crystal traversed by the polarized laser beam, in proportion to the induced electric field penetrating the crystal. An analytic model was developed as a function of the bunch and crystal parameters to study the pickup performance and design.

The Coulomb field time profile at a radius, r_0, from the proton beam axis is given by the convolution of a single particle electric field, E_p, and the charge density function, $\rho(t)$, of the bunch:

$$E_\mathrm{bunch}(r_0,t) = E_\mathrm{p}(r_0,t) * \rho(t). \tag{1}$$

The charge density is typically defined as a Gaussian distribution, $\rho(t) = N_\mathrm{p} e^{-t^2/2\sigma^2}/\sqrt{2\pi}$, where N_p is the number of protons in the bunch, centred on $t = 0$. When dealing with relativistic proton bunches ($v/c \to 1$), the particle electric field, E_p, depends upon the proton charge, e_0, the relativistic γ, and the crystal dielectric constant, ϵ, as follows [4]:

$$E_\mathrm{p}(r_0,t) = \frac{\gamma e_0}{4\pi\epsilon} \cdot \frac{r_0}{(r_0^2 + \gamma^2 v^2 t^2)^{3/2}}. \tag{2}$$

When the Coulomb field is propagating in free space, $\epsilon = \epsilon_0$. At the point where the Coulomb field reaches the crystal face, the propagation gives rise to a discontinuity at the interface position between vacuum and the dielectric crystal sample. The impact on the penetration is given by applying the new dielectric constant over equation 2, considering $\epsilon = \epsilon_0\epsilon_z$. For $LiNbO_3$, in the SPS bunch power spectrum scenario, it can be assumed $\epsilon_z = 28$ [5].

Applying the Fourier transform properties over equation 2, the time profile can be obtained as an inverse Fourier transform of the profile in the frequency ω domain:

$$E_\mathrm{bunch}(r_0,t) = \frac{N_\mathrm{p} e_0}{2\sqrt{2}\pi^{3/2}\gamma v^2 \epsilon} \cdot \mathrm{FT}^{-1}\left\{ e^{-\frac{1}{4}\sigma^2\omega^2} \omega K_1\left[\frac{r_0 \cdot \omega}{v\gamma}\right]\right\}, \tag{3}$$

where K_1 is the modified Bessel function of the second type. The maximum electric field value E_max that takes place at $t = 0$, corresponds with $\omega = 0$ in the domain profile. Expanding equation 3 around the maximum, results in $K_1[r_0\omega/\gamma\beta] \simeq \gamma\beta/r_0\omega$. By substitution, an expression for the maximum Coulomb field is obtained:

$$E_\mathrm{bunch}(r_0, t=0) = E_\mathrm{max} = k \cdot \frac{N_p}{\beta\sigma} \cdot \frac{1}{r_0} \tag{4}$$

with $\beta = v/c$, thereby:

$$k = \frac{e_0}{2\sqrt{2}\pi^{3/2} c \epsilon_0}. \tag{5}$$

Considering $\beta \simeq 1$ for SPS proton bunches, the maximum electric field at a given position r_0 depends strictly upon the charge and the bunch length through σ. Equation 4 accurately predicts the maximum strength of the Coulomb field as it propagates in vacuum up to the beam pipe radius. Applying equation 4 at the interface would generate a step given by a factor $1/\epsilon_z$ when propagating through the dielectric medium.

Electromagnetic Simulation

A powerful numeric electromagnetic simulation has been carried out in CST studio to clarify the interaction of the propagating particle bunch electric field at the crystal interface and how the field propagates inside the dielectric. This study is vital to estimate the expected extent of the electro-optic modulation, since the effect is linearly dependent on the penetrating electric field strength.

Figure 5 illustrates the simplified layout of the simulated button; components that were considered irrelevant were removed to optimise the simulation. The simulated pieces

ISBN 978-3-95450-177-9

were the button with a simplified shape, the crystal and the mica holder. The crystal cube had no electrical contacts and the side facing the proton bunch is non-metalized. The geometry shown in Figure 5 was simulated by applying the parameters in Table 1 that are relevant for the CERN SPS.

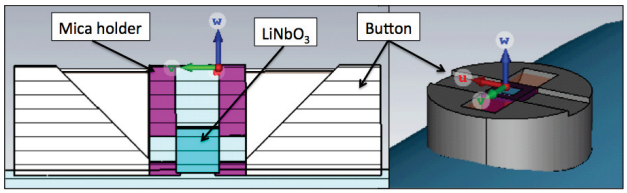

Figure 5: Transversal section and general view of the electro-optic button pickup in the CST visual interface.

Table 1: SPS Bunch and $LiNbO_3$ Sample Parameters

Bunch intensity	1.15×10^{11}	protons per bunch
Bunch length = 4σ	1	ns
SPS beam energy	450	GeV
Pipe radius	66.5	mm
Crystal dimension	cubic 5x5x5	mm

Two cases were simulated: the crystal was first removed to explore the penetration of the E-field into the cavity that is, in the second case, occupied by the $LiNbO_3$ crystal. The eo crystal is an anisotropic material that is characterised by three dielectric constants [5], with ϵ_z parallel to the radial dimension and $\epsilon_x = \epsilon_y$. Figure 6 shows how the maximum electric field varies with the radial position for both the numeric CST simulation and the analytic prediction of Equation 4. The beam pipe radius for the SPS prototype is 66.5 mm, and the vertical dashed lines depict the radial positions of two faces of the 5 mm cubic crystal.

The upper plot of Figure 6 shows the radial E-field penetration through the metallic slot of the pick-up and into the empty cavity for the case when the crystal is removed. The observed decay of the electric field in the cavity is explained by the impedance of the slot aperture. With the crystal in place, the electric field drops rapidly in the analytic prediction due to the $1/\epsilon_z = 1/28$, factor of the dielectric constant and remains below 1 kV/m. The numerical simulation, as detailed in Table 2, also converges to the analytic model inside the crystal, though the first few points are considered an unphysical result of the numerical approach at the discontinuity of the interface.. The laser beam passes through the crystal centre, corresponding to a radial position $r_0 = 68.8$ mm. Thus the electric field strength responsible for the electro-optic modulation is estimated to be ~0.7 kV/m, which implies a per mil signal / background detection.

Table 2: Electric-Field Results Inside the Crystal.

Radial position [mm]	67.5	68	69	70
Electric field [kV/m]	0.936	0.853	0.664	0.442

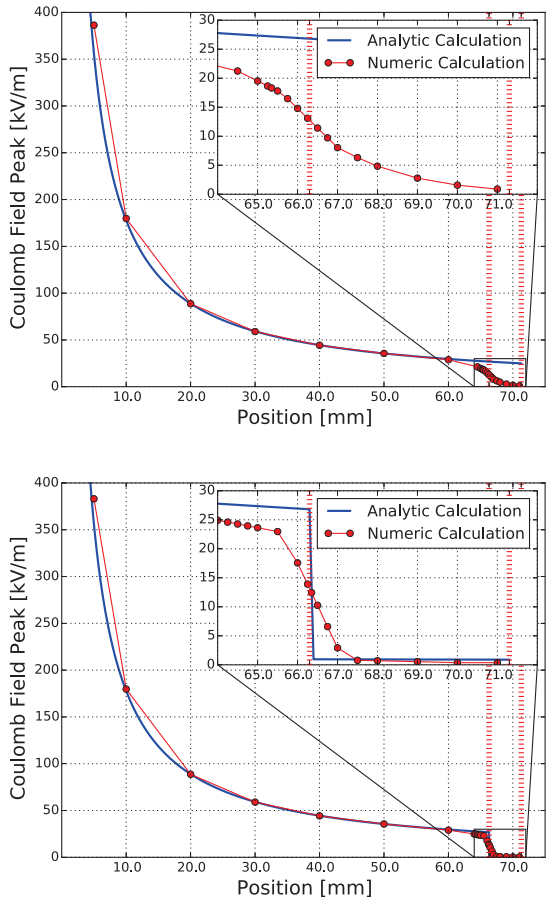

Figure 6: Coulomb field radial penetration into: the vacant pick-up cavity (top); and with the crystal in place (bottom).

PROTOTYPE EO-BPM AT THE CERN SPS

In 2016 a prototype EO-BPM was installed at the CERN SPS adjacent to the existing HT monitor [1]. The prototype includes four pick-ups with an identical mechanical design as presented in Figures 1–4. The opposing pair of

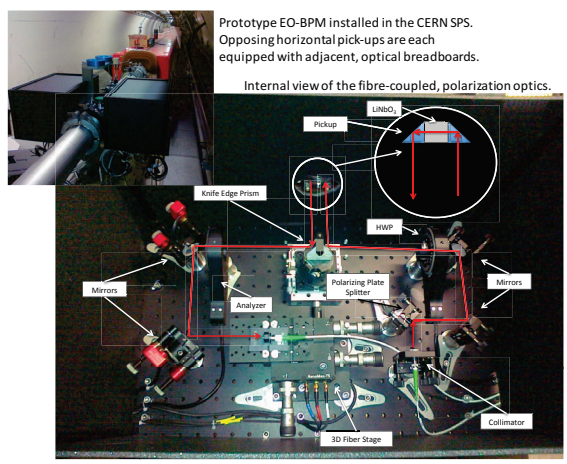

Figure 7: Fibre-coupled collimation optics control and analyze the polarization before and after the eo pick-up.

ISBN 978-3-95450-177-9

3% doped MgO_2 $LiNbO_3$ crystals in the vertical plane were metallic-coated on the sides facing the beam, whereas the pair in the horizontal plane were uncoated on the sides facing the beam, to check THz radiation penetration into the crystal. The horizontal pick-ups was initially equipped with two breadboards, each containing fibre-coupled, radiation tolerant, remote-controlled polarization state and analyzer optics as shown in Figure 7, for flexible, online reconfiguration and investigations of the polarization state. 160 m of PM fibre conveys light from a 780 nm laser to the collimator shown. A knife edge prism diverts light into and out of the EO pick-up. The modified polarization state is analyzed, fibre coupled, and monitored by a distant fast photodetector.

CRYSTAL RESPONSE MEASUREMENTS

Optical bench tests were performed to validate the detection method when approaching realistic conditions. Figure 8 shows the setup that recreates the pick-up configuration, with automated polarization control optics surrounding the eo-crystal, in a HV safety case. A pulse voltage was ap-

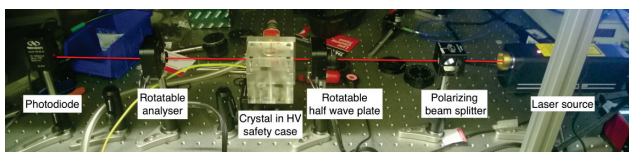

Figure 8: Crystal characterisation setup.

plied across the crystal while linearly polarized light was normally incident on the face of the crystal, with a 45° axial orientation. Even for a pulse of 10 V applied across a 5 mm MgO_2:$LiNbO_3$ crystal, a signal is detectable by a photodiode after the crossed analyzer, as in Figure 9. Azimuthal

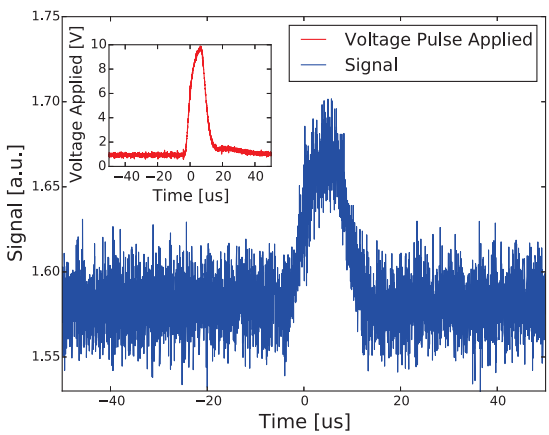

Figure 9: Optical response to an applied low voltage pulse.

scans of the analyzer enable the polarization state due to the natural birefringence of the crystal to be evaluated, as in Figure 10. By inserting a Soleil-Babinet compensator after the crystal, and before the analyzer, the polarization state can be readjusted to optimise the signal. By this method and a model of the polarization state, it was confirmed that

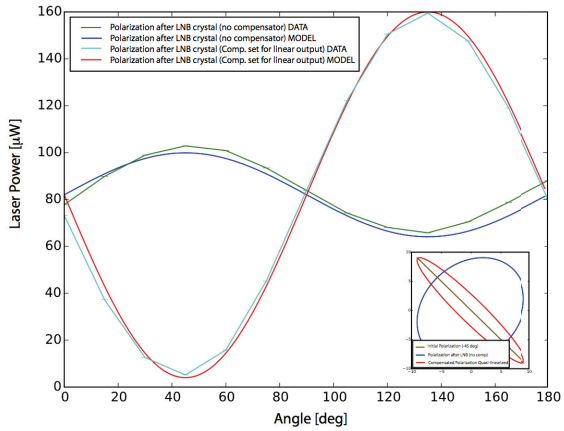

Figure 10: Natural and linearised polarization states.

the maximum signal is obtained by setting the polarization state after the crystal to be circular. For the CERN SPS EO-BPM, a narrow linewidth (<200 kHz), tunable laser will be installed, that enables the natural birefringence effect to be modified by fine adjustment of the wavelength, to optimise the working point of the instrument.

SUMMARY AND OUTLOOK

A prototype EO-BPM was recently installed in the CERN SPS, with remote controlled, fibre-coupled polarization and analyzer optics. The strength of the electric field penetrating the crystal has been evaluated by electromagnetic simulations. Optical measurements of the crystal response confirm applied voltage pulses of the expected field strength are detectable. Methods to adjust the working point of the instrument have been developed and a narrow linewidth, tunable laser will be installed soon for initial beam tests.

ACKNOWLEDGEMENTS

We thank the CERN vacuum group and SPS team for their support. Work funded by UK STFC grant ST/N001583/1, JAI at Royal Holloway University of London and CERN.

REFERENCES

[1] S. M. Gibson et al., "High frequency electro-optic beam position monitors for intra-bunch diagnostics at the LHC", WEDLA02, Proc. of IBIC 2015, Melbourne, Australia.

[2] T. Levens et al., "Recent developments for instability monitoring at the LHC", THAL02, Proc. of IBIC 2016, Barcelona, Spain.

[3] P. Y. Darmedru, *"Conception mécanique d´un instrument de mesure de position d´un faisceau de particules"*, CERN EN report, Groupe 2A04, 2015.

[4] J. D. Jackson "Classical Electrodynamics", John Wiley and sons, Inc., 3rd edition, 1999.

[5] R. S. Weis and T. K. Gaylord, *Appl. Phys.* A 37, p191-203 (1985).

ISBN 978-3-95450-177-9

PHASE AND ENERGY STABILIZATION SYSTEM AT THE S-DALINAC

T. Bahlo*, C. Burandt, L. Jürgensen, T. Kürzeder, N. Pietralla, J. Wissmann
Institut für Kernphysik, TU Darmstadt, Darmstadt, Germany
F. Hug, JGU Mainz, Germany

Abstract

The **S**uperconducting **Da**rmstadt **Lin**ear **Ac**celerator S-DALINAC is a recirculating electron accelerator with a design energy of 130 MeV operating in cw. Before entering the 30 MeV main accelerator the low energetic electron beam passes both a normal-conducting injector beamline preparing the beam's 3 GHz time structure as well as a superconducting 10 MeV injector beamline for preacceleration. Since the superconducting injector accelerates on-crest while the main accelerator accelerates off-crest the beam phase is crucial for the efficiency of the acceleration process and the minimization of the energy spread. Due to thermal drifts of the normal- conducting injector cavities this injection phase varies by about 0.2 degree over a timescale of an hour. In order to compensate for these drifts, a high level phase controller has been implemented. Additionally a low energy scraper system has been installed between the injector and main linac in order to lock both the phase and the energy spread at the linac entrance.

MOTIVATION

The S-DALINAC (see Fig. 1) is a recirculating electron accelerator providing electron beams with energies up to 130 MeV in cw operation. It provides beam currents between several nA and 60 μA for nuclear structure and astrophysical experiments since 1987 [1]. The electron beam can be produced by two alternatively usable sources. The thermionic electron gun produces an unpolarized beam while the **S**-DALINAC **P**olarized **In**jector [2] creates polarized electron beams by illuminating a GaAs cathode with a laser beam. After beam preparation in the n.c. injector beamline including chopper and prebuncher cavities the electron bunches enter the s.c. 10 MeV injector. There the electrons are preaccelerated on-crest by niobium cavities working at a resonance frequency of 3 GHz. Leaving the s.c. injector the electron beam can either be used for nuclear resonance fluorescence experiments at the **D**armstadt **H**igh **I**ntensity **P**hoton **S**etup DHIPS [3] or it can be guided to the main accelerator by a 180°-arc. The main accelerator can be used up to four times using the three recirculations in order to reach the design energy of 130 MeV. It has been shown that the energy spread can be reduced significally from 120 keV to 30 keV by using a non-isochronous recirculating mode [4]. Theoretically this mode reproduces the same energy spread as before the first injection to the main linac. This depends heavily on the correct injection phase since a mismatch of 2° can increase the relative energy spread from $8 \cdot 10^{-5}$ to $3 \cdot 10^{-4}$. Experience shows that the beam phase behind the s.c. injector drifts and oscillates on a timescale of several hours. An example measurement of these dynamics without compensation can be seen in Fig. 2. The reason for these phase shifts still is not fully understood. One possible explanation are instabilities of the high voltage supply of the source, that already have been observed. Another possibility is a thermal drift of the n.c. beam preparation cavities. To compensate for these drifts a high-level phase controller has been developed. This controller now locks the exit phase of the s.c. injector. To decrease the energy spread even further an additional low energy scraper system has been installed. This system can eliminate the beam halo and it can prevent any energetically mismatched electrons leaving the s.c. injector. Furthermore it can reduce the energy spread of the beam arbitrarily but reduces the intensity simultaneously.

* tbahlo@ikp.tu-darmstadt.de

PHASE CONTROLLER

To adjust the phase behind the s.c. injector it has to be changed before entering it. The following three devices have a significant influence on the exit phase, that has been measured by a rf monitor.

Chopper The Chopper forces the continuous electron beam of the electron gun on a cone-shaped trajectory that wanders over an aperture converting the continuous beam into a bunched one. This obviously defines the reference phase for every adjacent rf device.

Prebuncher The buncher cavity introduces a velocity gradient within every electron bunch by decelerating the early electrons and accelerating the late ones while leaving the reference particle's velocity unchanged. This focuses the bunch longitudinally after a defined distance. By shifting the buncher's phase an overall acceleration or deceleration can be introduced that changes the travel time to the injector entrance and therefore the entrance phase.

s.c. 2-cell cavity The 2-cell cavity is used to preaccelerate the low-energy electrons for the not sufficiently β-graded cavities of the injector. Although it is operated on-crest, it can be used similary to the buncher to adjust the exit phase using time-of-flight effects.

The results shown in Fig. 3 motivate the use of the buncher for beam phase adjustments since it is the most efficient and linear device that has been tested.

Implementation

Hardware The low-level control system of the rf cavities is implemented on an in-house developed board [5]

ISBN 978-3-95450-177-9

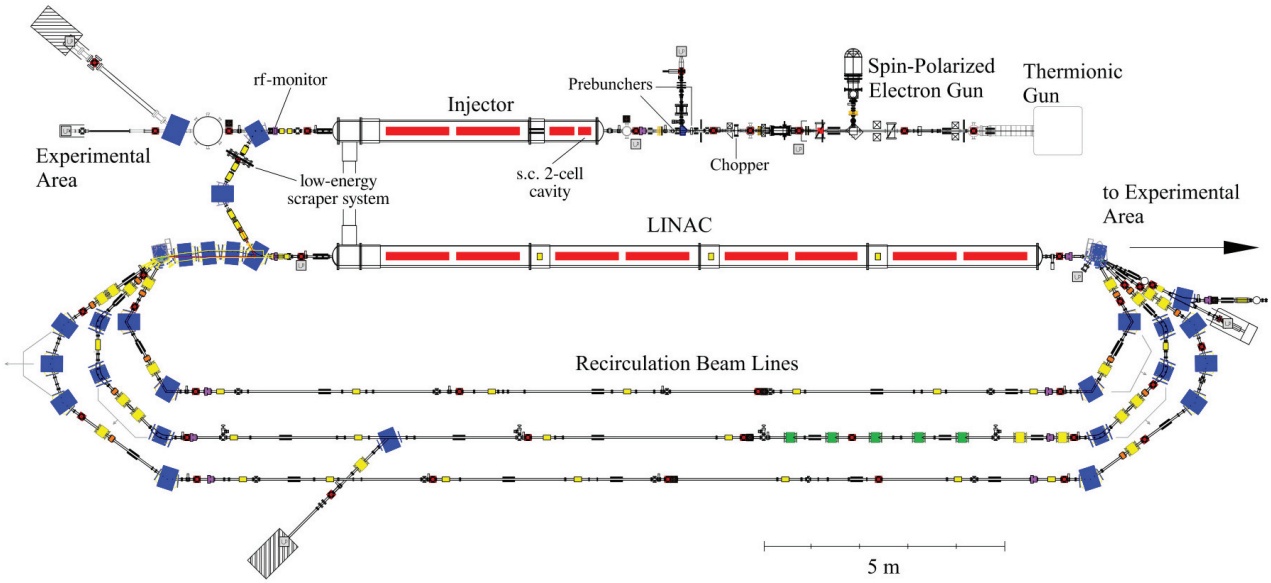

Figure 1: floorplan of the S-DALINAC showing the n.c. cavities and the low energy scraper system

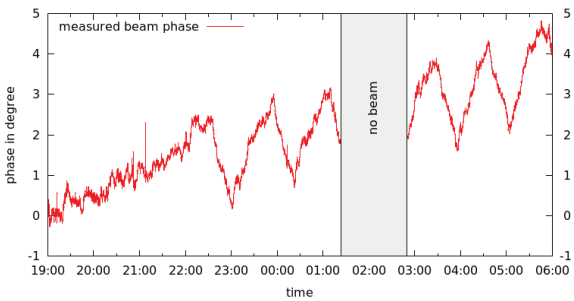

Figure 2: Measured beam phase behind the s.c. injector with visible phase drifts and oscillations

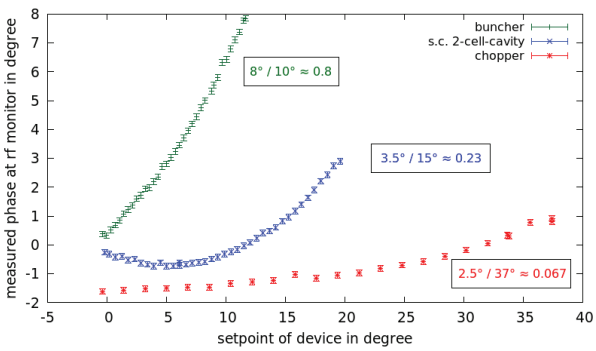

Figure 3: Measurement of the influence on the beam phase behind the s.c. injector

using a Xilinx Spartan-6 FPGA module. The probe signal of the cavity is mixed down to the base band and fed to the controller board, where it is analyzed digitally. The FPGA-Module uses integral and proportional control algorithms to adjust the amplitude and phase. The adjusted signal is converted to the 3 GHz band and fed to the cavities as a new input signal. Additionally the board provides slower process data with a sample rate of up to ten samples per second over CAN-bus.

Software The process data provided by the low level control board is read and managed by a PC acting as a EPICS-Input-Output-Controller (IOC) [6], that converts the data to a human readable format. The new developed phase control algorithm is implemented as software control-loop on this IOC.

Algorithm The injector phase controller reads the phase of rf monitor behind the s.c. injector and compares it with a desired exit phase. The difference to the desired phase is fed to the actual control loop that consists of a parallel proportional and integral controller as shown in Fig. 4. Most of the phase compensation is achieved by the proportional controller with its proportional gain of 0.1 while the weak integral controller with its time constant over over 1 s only compensates for the remaining offset that the proportional controller leaves systematically.

First Results of the Phase Controller

Measured result from first tests of the phase controller are shown in Fig. 5. The control algorithm has been activated and monitored over several hours. Comparing Fig. 5 with with Fig. 2, it is clearly visible that the whole dynamic of the measured phase is shifted to the phase setpoint of the controlled buncher phase leaving the measured phase constant. To quantify the improvement, the measured phase behind the injector has been monitored over 2.5 hours. With the control algorithm being deactivated the standard deviation has been 0.15° and decreased to 0.02° with activated controller.

ISBN 978-3-95450-177-9

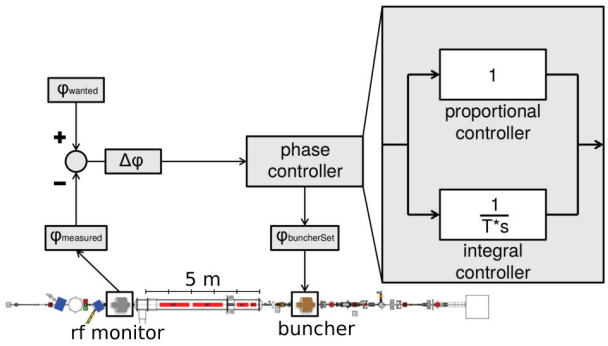

Figure 4: Schematic view of the injector phase controller algorithm

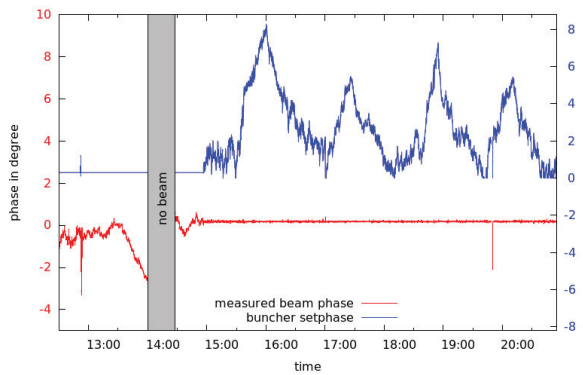

Figure 5: Comparison of the measured beam phase behind the s.c. injector and the controlled setphase of the n.c. pre-buncher

LOW ENERGY SCRAPER SYSTEM

Electron scraper systems stop parts of the electron beam by using blocks made out of materials with a high stopping power. This principle can be used to remove any halo and to define the energy spread, if the scraper blocks are placed at a position where the beam is expanded by dispersion.

Material

Materials the can be used as scraper brackets need to be suitable for high vacuum conditions, need to have a high stopping power for electrons, and need to provide a high heat conductivity. The stopping power determines the minimal thickness of the brackets to definitely stop the electrons. A good heat conductivity guarantees a good heat distribution and an efficient heat transfer to the cooling water, since the low energy scraper brackets of the S-DALINAC need to withstand a beam power of up to 200 W. Additionally it would be desirable to use a material that can be machined by the in-house workshop. Therefore copper was picked because it is best in both, thermal conductivity and electron stopping power.

Bracket Geometry

To optimize the geometry of the scraper brackets several simulations have been done using GEANT4 [7]. Figure 6 shows a schematic of the used geometry. Using a realistic beam profile the chamfer angle α and length L have been optimized. The chamfer angle turned out to be very important for a smooth temperature distribution and showed a optimum at 3°. The length of the parallel section L can increase the energy spread if chosen too long while introducing temperature hotspots if chosen too short. An optimum has been found at L = 20 mm The necessary cooling power

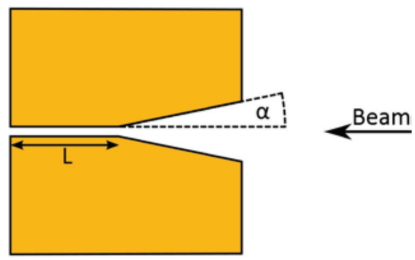

Figure 6: Schematic of the scraper brackets geometry

has been derived using CST MPHYSICS STUDIO 2013 [8]. With a worst-case scenario and a suitable water cooling the maximum temperature was simulated to 338 K what seems reasonable.

Beam Dynamics

To create a energy defining scraper system, a position had to be chosen where the beam is expanded by dispersion. Inside the 180°-arc between injector and main linac it was possible to shift some quadrupoles and to gain some space for a system with an overall length of up to 200 mm. The beam dynamics were changed in such way that the arc stays achromatic and isochronous. The new beam dynamics calculation done using XBEAM [9] is shown in Fig. 7. At the scraper's position the dispersion is a constant in the horizontal component and is set up with a value of 4 mm/%.

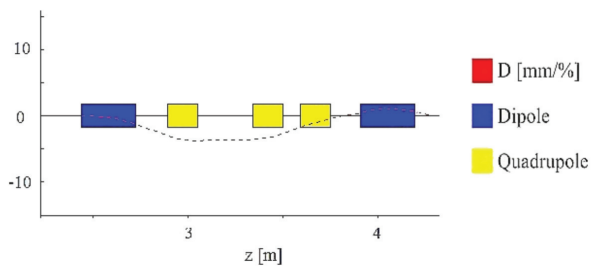

Figure 7: XBEAM simulation of the beam line showing a constant dispersion at the scraper's position

Construction

Due to the limited space in beam direction, the scraper chamber containing the scraper brackets as well as a light emitting BeO-target behind the brackets had to be design very short. The BeO-target is used to check the beam position, size and shape and has to be movable. Additionally

ISBN 978-3-95450-177-9

the brackets have to be mounted electrically isolated to be able to measure the individual charge deposition. This is foreseen to be used as an additional diagnostic parameter. A sectional view of the final design is shown in Fig. 8. The

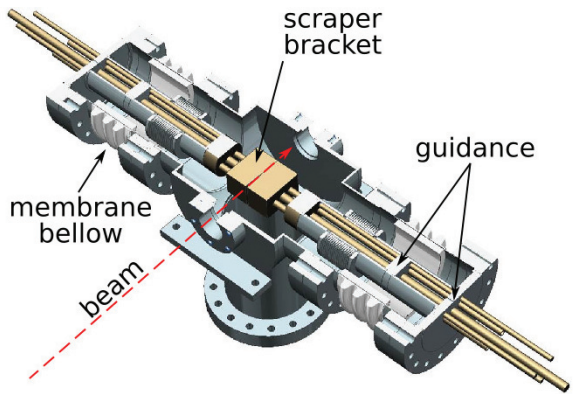

Figure 8: 3D-CAD model showing the sectional view of the scraper system

scraper brackets are guided using three brass bars and two cooling water pipes made out of copper. The membrane bellows allow a stroke of 30 mm. The precise motion of the brackets is done using a self-developed articulated jack with a stepper motor at the end of each side which can be seen in Fig. 9. The smallest step size is calculated to be less than 0.1 mm.

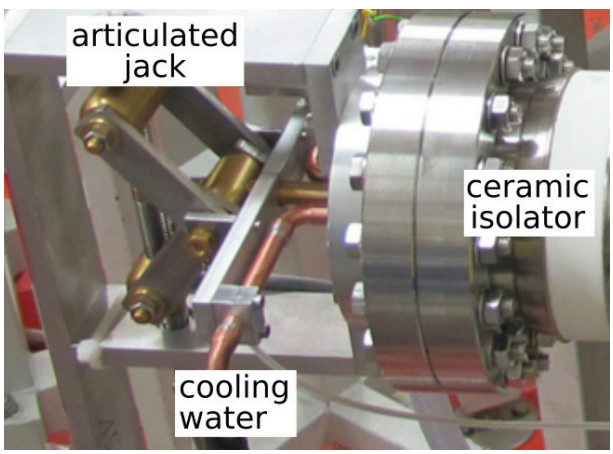

Figure 9: Articulated jack driven by a step motor for exact positioning

Commissioning

A first test of the scraper system has been done with a 140 nA electron beam at an energy of 5.8 MeV behind the s.c. injector. The beam has passed the following main linac only once to avoid an increase of the energy spread due to the recirculation. At a final energy of 24.6 MeV the energy spread and beam current have been measured using a spectrometer with a thin Au-foil target of 1.0 mg/cm². The result are shown in Fig. 10. It can easily be seen, that the energy spread could be reduced from 15 keV to less than 10 keV.

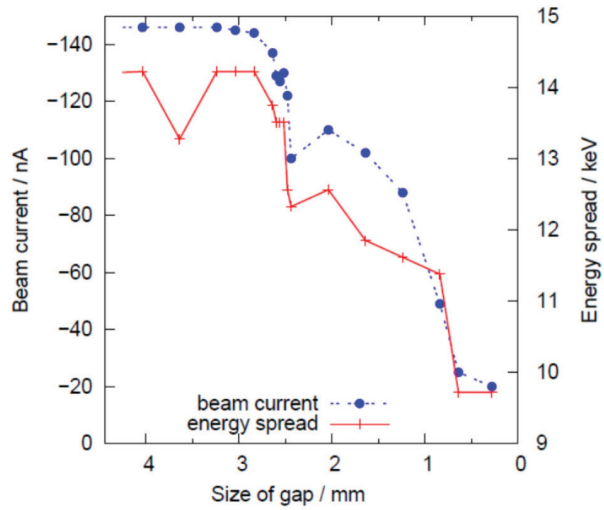

Figure 10: First commissioning by measuring the change of energy spread using scattering at a thin Au-foil (1.0 mg/cm²). The beam energy has been 24.6 MeV in single-pass mode.

As expected one can also see the decrease of the beam current since the energy spread is decreased using a destructive method by stopping parts of the beam. The fluctiations of the curve can be explained by the energy and phase variations that have already been described in the phase controller section. During this scraper measurement the injector phase controller was not yet implemented.

CONCLUSION AND OUTLOOK

Both the injector phase controller as well as the low energy scraper system have been tested individually and showed a very satisfying performance. The phase controller reduced the phase variations by a factor of 7.5 in respect to a 2.5 hour standard deviation, while the scraper system successfully showed the intended decrease of the energy spread. The influence of the phase controller on the actual energy spread at the experiment still has to be investigated and both system need to be tested synchronously to see the overall effect on the beam stability. This will be done during upcoming beamtimes.

REFERENCES

[1] A. Richter, EPAC '96, Sitges (1996) 110.

[2] J. Enders, AIP Conf. Proc. 1563, 223 (2013).

[3] K. Sonnabend *et al.*, Nucl. instr. & Meth. A 640, (2011), 6-12.

[4] F. Hug *et al.*, LINAC'12, Tel Aviv, 531 (2012).

[5] M. Konrad, Phys. Rev. ST Accel. Beams 15, 052802 (2012).

[6] EPICS, `http://www.aps.anl.gov/epics/`

[7] S. Agostinelli *et al.*, Nucl. Instr. & Meth. A 506 (2003), 250-303.

[8] CST AG: CST MICROWAVE STUDIO 2013.

[9] T. Winkler, In-house developed code (1993).

ISBN 978-3-95450-177-9

OPERATION OF THE BEAM POSITION MONITOR FOR THE SPIRAL 2 LINAC ON THE TEST BENCH OF THE RFQ

P. Ausset†, M.B. Abdillah, F. Fournier, IPN, Orsay, France
S.K. Bharade, G. Joshi, P.D. Motiwala, BARC, Mumbai, India
R. Ferdinand, D. Touchard, GANIL, Caen, France

Abstract

SPIRAL2 project is based on a multi-beam superconducting LINAC designed to accelerate 5 mA deuteron beams up to 40 MeV, proton beams up to 33 MeV and 1 mA light and heavy ions (Q/A = 1/3) up to 14.5 MeV/A. The accurate tuning of the LINAC is essential for the operation of SPIRAL2 and requires measurement of the beam transverse position, the phase of the beam with respect to the radiofrequency voltage, the ellipticity of the beam and the beam energy with the help of Beam Position Monitor (BPM) system. The commissioning of the RFQ gave us the opportunity to install a BPM sensor, associated with its electronics, mounted on a test bench. The test bench is a D-plate fully equipped with a complete set of beam diagnostic equipment in order to characterize as completely as possible the beam delivered by the RFQ and to gain experience with the behavior of these diagnostics under beam operation. This paper addresses the first measurements carried with the BPM on the D-plate: intensity, phase, transverse position and ellipticity under 750 KeV proton beam operation

GENERAL DESCRIPTION OF SPIRAL2

SPIRAL2 facility is being installed in Caen, France. It includes a multi-beam driver accelerator (5mA/40Mev deuterons, 5mA/14.5MeV/A heavy ions). The injector is constituted by an ECR ion source (Q/A= 1/3), an ECR deuteron/proton source, a low energy beam transfer line (LEBT) followed by a room temperature RFQ which accelerates beam up to an energy of 0,75MeV/u. A medium energy transfer line (MEBT) transfers the beam to the superconducting Linac.

The Linac is composed of 19 cryomodules: 12 contain one β = 0.07 cavity and 7 contain two β = 0.12 cavities. All cavities in the cryomodules operate at F = 88.0525MHz.

The superconducting Linac is designed to accelerate deuterons, protons, heavy ions Q/A= 1/3 and Q/A = 1/6 for a future injector. (Table 1)

Table 1: SPIRAL 2 Main Beam Parameters

Particle	Current Max (mA)	Energy (MeV/u)
Proton	5	2 - 33
Deuteron	5	2 - 20
Q/A = 1/3	1	2 - 14.5
Q/A= 1/6	1	2 - 8

†ausset@ipno.in2p3.fr

SPIRAL2 nominal mode of operation is planned to be C.W. mode. The considerations on commissioning and tuning periods of the LINAC lead to consider also pulsed mode operation in order to minimize the mean power of the beam. The shortest duration of a macro-pulse will be 100 µs. The repetition rate may be as low as 1Hz and as high as 1 kHz. The intermediate configurations have to be taken in account in order to reach the C.W. operation. The step to increase or decrease either the macro pulse duration or the repetition rate will be 1µs.

SPIRAL2 BEAM POSITION MONITORS

General Description

A doublet of magnetic quadrupoles is placed between the cryomodules for the horizontal and vertical transverse focusing of the beam. Beam Position Monitors (BPM), of the electrostatic type, is inserted in the vacuum pipe located inside the quadrupoles of the LINAC.

Each BPM sensor contains four probes on which beam image currents induce bunched-beam electrical signals. The electronics board associated with each BPM sensor processes the electrical signals and enables the measurement of beam transverse position, phase, energy and transverse beam ellipticity$\sigma_x^2 - \sigma_y^2$, where σ_x and σ_y are the standard deviations of the transverse size of the beam.

BPM Acquisition Modes

The BPMs data and measures are acquired under CW or pulsed mode operation in three modes: Normal, post mortem and electrode signal reconstruction.

A synchronizing signal “SF” is distributed simultaneously to the SPIRAL2 diagnostics, including the BPM to indicate that the beam is present during its high level.

Normal mode: the electronics module acquires the data on the SF rising edge after a delay and during a given integration time. The integration time must be less than the time where the SF signal is high. Both the delay and the integration times are selected by the operator.

Data: beam centroid transverse position and beam ellipticity, electrode received signal amplitude and vector sum in phase and magnitude of the four electrodes are transferred to the VME local memory on the fall of “SF” signal. EPICS driver reads the data every 200ms from the local VME memory.

BPM Specifications

The main specifications for the BPM system are summarized in Table 2.

ISBN 978-3-95450-177-9

Table 2: Main SPIRAL2 BPM Specifications

Parameter	Measurement resolution	Measurement range
Position	± 50µm	± 10 mm
	± 150µm	± 20 mm
Phase	± 0.5deg	±180 deg
Ellipticity	± 20%	
Beam current		0.15 – 5 mA

BPM Sensor Mechanical Design

Capacitive sensors have been selected (Electrodes aperture diameter: 48 mm, length in the direction of the beam: 39 mm, subtended lobe-angle: 62°) (Figure 1).

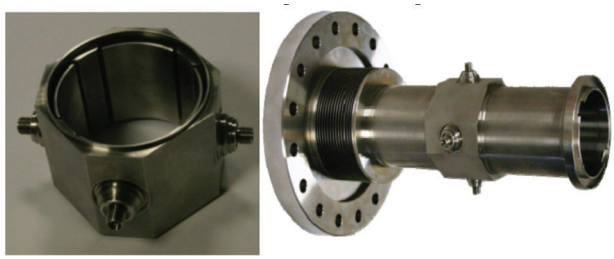

Figure 1: Left: SPIRAL2 BPM central block with the capacitive electrodes. Right: BPM with its flanges.

A dedicated test bench based on a coaxial transmission line has been designed and built in order to characterize each BPM: electrical center coordinates, position and ellipticity sensitivities at β=1[1].

BPM Sensor Readout Electronics Module

Each BPM sensor feeds an electronic module through eighty meter long coaxial cables. The 20 BPM electronics modules are located in three VME 64x crates. Each module contains an analog and a digital board. The design of the analog module of the card is based on the scheme of auto-gain equalization using offset tone having frequency slightly offset from the RF reference [2]. The electronic module is able to work either at 88.0525 MHz or at 176.1050 MHz to deliver the required information.

The Accelerator Control Division of Bhabha Atomic Research Centre realized the BPM Electronics modules.

Two prototypes of the BPM readout electronics module were qualified in IPN leading to several upgrades in order to meet specifications. The prototypes results are in a good agreement with results obtained with the measurement setup used to characterize the BPMs. [3].

BPM TESTS ON THE SPIRAL2 INTERMEDIATE TEST BENCH (ITB)

General Description of the ITB

An "Intermediate Tests Bench" (ITB) has been assembled as part of the injector commissioning plan [4]. The ITB is positioned after the focusing quadrupole following the first re-buncher of the M.E.B.T. Two other focusing quadrupoles are placed between the re-buncher, and the RFQ. A beam stopper able to withstand nearly the full power of the beam terminates the ITB which includes 18 beam diagnostics identical to the SPIRAL2 driver ones. The aim of the ITB is to fully characterize the properties of the beam accelerated by the RFQ and also to study the behaviour of these diagnostics. All kinds of measurements may be carried: beam intensity, transverse beam position, profiles and emittance, phase and longitudinal emittance with a beam energy equal to 750KeV/A.

Control command operation gathers the measurements performed by all these diagnostics almost on real time (every 200ms). Figure 3 shows the ITB.

BPM Current Dynamic Range

The first tests of the BPM and its associated electronics was to check the beam current dynamic range over which the BPM electronics are working properly. The beam current is given by the Faraday cup (CF) of the ITB on one side and by the magnitude of the four vector sum of the four electrodes given by the BPM electronics at F = 88.0525 MHz and 2.F on the other side. Horizontal and vertical slits located in the LEBT vary the beam intensity.

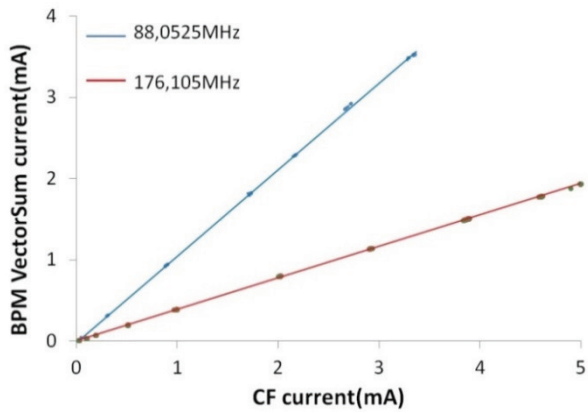

Figure 2: BPM beam current dynamic range.

Measurements were performed on fall January 2016. They showed an upper limitation of the measurement range (CF current = 3.5mA) at F due to the saturation of the front end of the BPM electronics (see Figure 2) where as it is fully operational at 2.F. This saturation is assigned to a difference in signal magnitude obtained during the beam operation compared to that obtained by the beam dynamics simulation.

Further tests were performed on this issue on June 2016 where 10dB attenuations were added at the analogue inputs of the readout electronics analogue inputs, this leaded to the following dynamic range: 75 µA - 5.5 mA at F and 60 µA – 5.5 mA at 2.F.

ISBN 978-3-95450-177-9

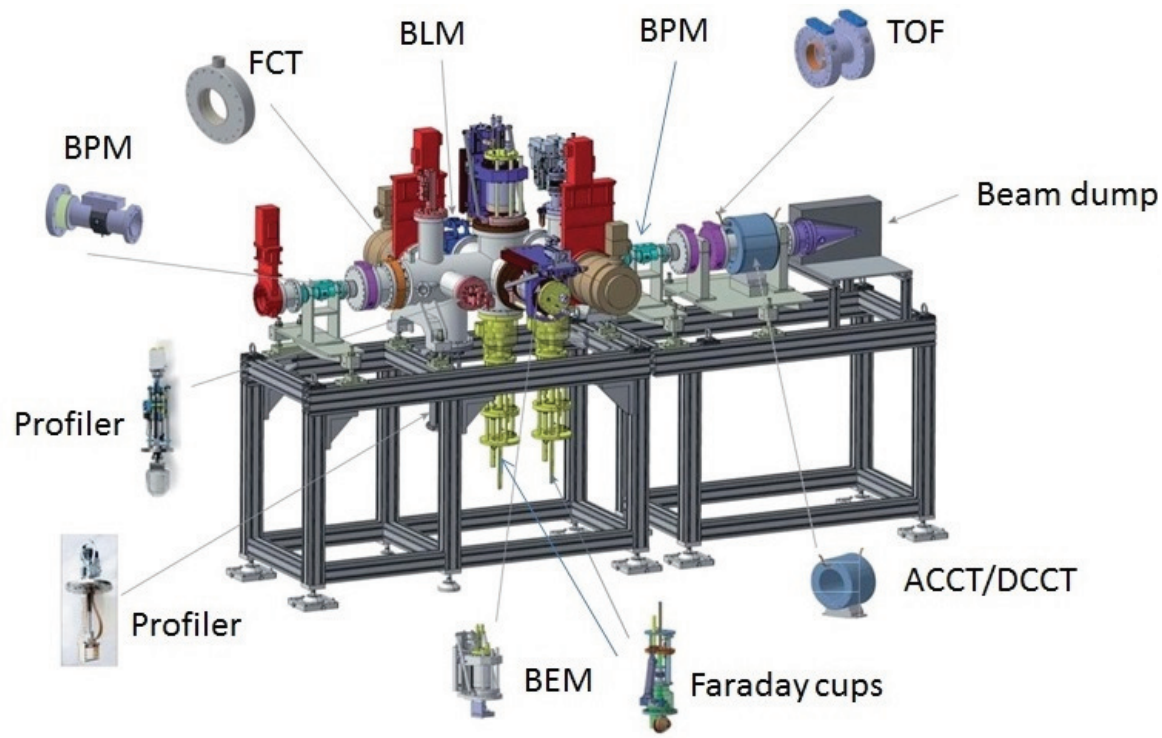

Figure 3: View of the Intermediate Test Bunch equipped with a full set of beam diagnostics.

BPM Phase Measurement

The phase relative to the accelerating RF signal has been measured simultaneously by the BPM and by one of the three electrostatic P.U. electrodes of the time of flight (TOF) energy measurement system mounted on the ITB. The BPM is measuring the phase at F and 2.F whereas the TOF is only measuring it at F. The RFQ phase was swept over 360° with a 10° step over different beam currents. The results of the BPM and TOF measurements were gathered in order to show the mean value of the measured phase and the range over which the phase is fluctuating.

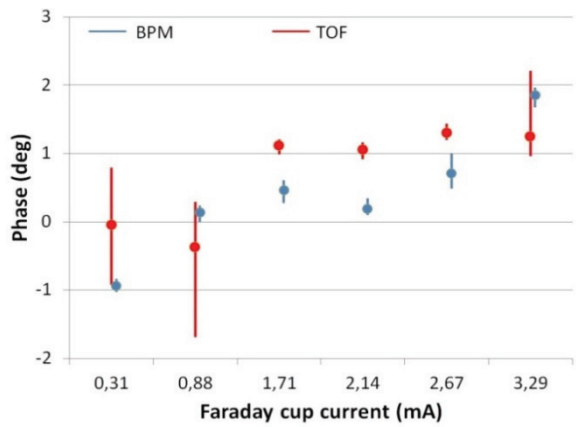

Figure 4: Beam phase measurement with BPM and a PU –TOF electrode at 88.0525MHz.

The results (Fig. 4) show a proper behaviour and a good agreement with the electrode of the TOF system over the measured beam current dynamic range: the fluctuation is within 1° for medium and high current where as it is less precise for the TOF at low beam currents.

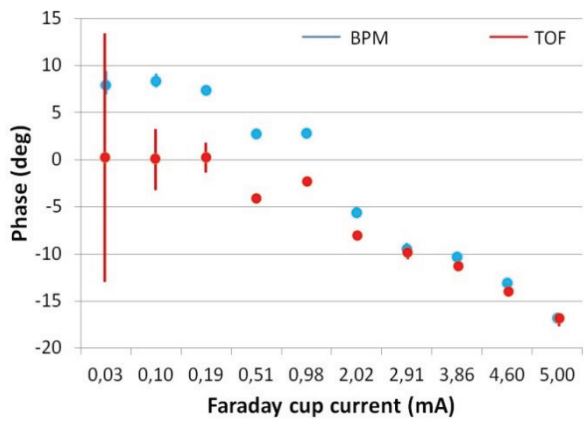

Figure 5: Beam phase measurement by a BPM at 176.105MHz and a TOF PU electrode at 88.0525MHz.

BPM phase measurements were also simultaneously performed at 2.F. with the TOF electrode (same manner as previously) however the beam conditions were different. TOF measurements at F were performed. The results are sketched in fig. 5. The same comments reported at F apply for 2.F.

Beam Position Measurements

The beam position measurements were simultaneously performed by the BPM and the secondary emission monitor (SEM) profiler (pulsed mode operation) located after a drift space downstream in the ITB. The results obtained with the BPM measurements at F and 2.F have been com-

ISBN 978-3-95450-177-9

pared to the profiler measurements (frequency independent). The BPM position sensitivity was set to 25.7 mm for all the measurements. The beam position was changed by varying the current of a steerer DC13 located in the quadrupole Q13 located just before the BPM. It was swept over the range [-5A; 4A] with a 1.5A step. An example is given in Figure 6

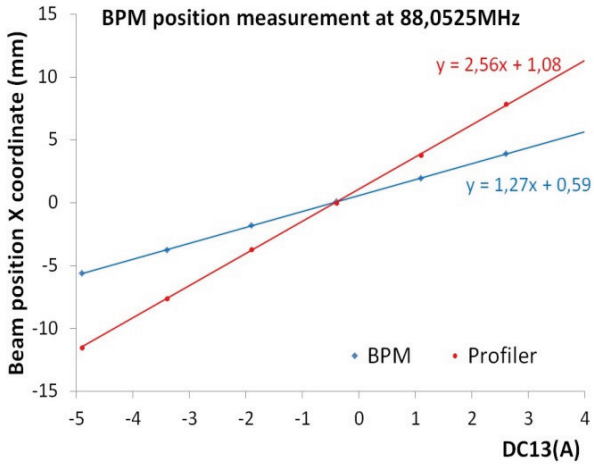

Figure 6 : Beam position measurement at 88.0525MHz.

The expected linear response of the BPM is confirmed. The results are gathered in the table 3 for F and 2.F. The BPM position sensitivity remains roughly constant over the current dynamic range. Considering the low value of the velocity (β ~ 0.04) of the beam accelerated by the RFQ, we took in account Shafer study [5] which states that the beam position sensitivity at a frequency f for a beam travelling in a cylindrical chamber of radius r should be multiplied by (1+G) where G is:

$$G = 0.139.\left(\frac{2.\pi.f.r}{\beta.\gamma.c}\right)^2 - 0.0145\left(\frac{2.\pi.f.r}{\beta.\gamma.c}\right)^3$$

With the help of the measured positions of the SEM profiler, we were able to calculate easily the expected position on the BPM. Therefore we applied the adequate correction to the sensitivities at 88.0525MHz and 176.105MHz drawn from our measurements on our laboratory test bench (S= 25.7 mm at β ~ 1). It came out in good agreement with the estimations of Shafer.

Table 3: Beam Position Sensitivity

Beam Current	Measured Sensitivity		Theoretical Sensitivity	
	F	*2*F*	*F*	*2*F*
4mA	21.9mm	16.7mm	22.3mm	15.9mm
1.5mA	21.6mm	16.3mm	22.3mm	15.9mm
0.25mA	21.6mm	16mm	22.3mm	15.9mm

BPM Ellipticity Measurement

The quantity $\sigma_x^2 - \sigma_y^2$ is delivered by the BPM electronics and as well drawn from the SEM profiler measurements. The BPM ellipticity sensitivity was set to 354 mm² for all measurements. The beam 2D shape was modified by changing the current in the quadrupole Q13 located before the BPM (beam current equal to 1.2mA). The current of Q13 was swept over a range [2.5A - 30A] with a 2.5A step leading to significant changes of the ellipticity.

The linear behaviour of the BPM ellipticity towards Q13 current is confirmed by the measurements (fig. 7). The same behaviour is confirmed by the BPM measurements at 176.105MHz. Further investigations should be run to explain the discrepancies between beam dynamics simulations and measurements.

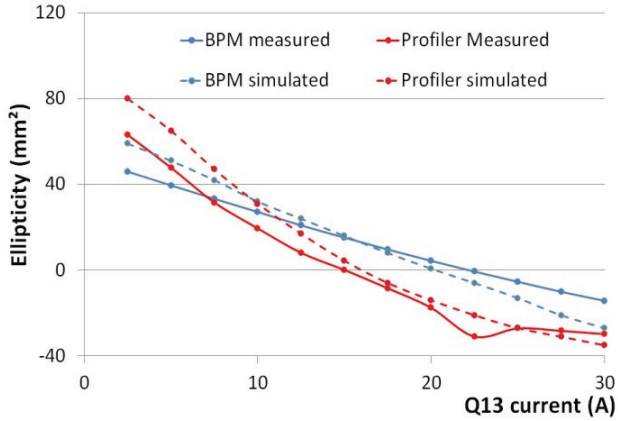

Figure 7: Beam ellipticity measurement at 88.0525MHz.

CONCLUSION

The BPM sensors realized with its associated electronics for the Linac of SPIRAL 2 have been put on operation on the ITB of SPIRAL2. We will be able to measure the transverse position of the beam and the phase of the beam with respect to the RF signal. However further investigations have to be made concerning the ellipticity measurement. A second BPM sensor with its electronics module will be mounted very soon on the ITB in order to check the energy measurement by means of the BPM.

ACKNOWLEDGMENTS

It is a pleasure to acknowledge the constant support of the SPIRAL 2 team during these experiments.

REFERENCES

[1] M. Ben Abdillah and P.Ausset, "Development of Beam Position Monitors for the SPIRAL2 LINAC", in *Proc. 1st Int. Beam Instrumentation Conf. (IBIC'12)*, Tsukuba, Japan, October 2012, paper TUPA18, pp. 374-377.

[2] G. Joshi *et al.*, "An offset tone based gain stabilization technique for mixed-signal RF measurement systems", *Nucl. Instr. Meth.*, vol. A 795, 2015, pp. 399-408.

[3] P. Ausset and M. Ben Abdillah, "Development of the Beam Position Monitors system for the LINAC of SPIRAL2", in *Proc. 2nd Int. Beam Instrumentation Conf. (IBIC'13)*, Oxford, UK, September 2013, paper WEPC15, pp. 702-705.

[4] P. Ausset *et al*, "SPIRAL2 injector diagnostics", in *Proc. DIPAC 09*, Basel, Switzerland, pp. 110-112.

[5] R.E. Shafer, "Beam Position Monitor Sensitivity for Low-β Beams", in *Proc. 17th Linac Conf. (LINAC'94)*, Tsukuba, Japan, August 1994, paper THPA84, pp. 905-907.

ISBN 978-3-95450-177-9

A VERSATILE BPM SIGNAL PROCESSING SYSTEM BASED ON THE XILINX ZYNQ SOC*

R. Hulsart†, P. Cerniglia, N.M. Day, R. Michnoff, Z. Sorrell,
Brookhaven National Laboratory, Upton, Long Island, New York, USA

Abstract

A new BPM electronics module (V301) has been developed at BNL that uses the latest System on a Chip (SoC) technologies to provide a system with better performance and lower cost per module than before. The future of RHIC ion runs will include new RF conditions as well as a wider dynamic range in intensity. Plans for the use of electron beams, both in ion cooling applications and a future electron-ion collider, have also driven this architecture toward a highly configurable approach [1]. The RF input section has been designed such that jumpers can be changed to allow a single board to provide ion or electron optimized analog filtering. These channels are sampled with four 14-bit 400MSPS A/D converters. The SoC's ARM processor allows a Linux OS to run directly on the module along with a controls system software interface. The FPGA is used to process samples from the ADCs and perform position calculations. A suite of peripherals including dual Ethernet ports, µSD storage, and an interface to the RHIC timing system are also included. A second revision board which includes ultra-low jitter ADC clock synthesis and distribution and improved power supplies is currently being commissioned.

SYSTEM ARCHITECTURE

A VME form factor was chosen for the initial design of this BPM system (Fig. 1), which leverages off of the existing VME infrastructure found throughout RHIC and its injector facilities. A VME bus interface was not included in the design, only power and serial timing links are distributed on the VME backplane. The V301 name designates it as a third-generation VME design.

ANALOG INPUT SECTION

Analog Filters

Much of the versatility available on this BPM platform is due to the options for the RF filtering section (Fig. 2). Three separate signal paths are available on the PCB which can be selected by altering soldered jumpers. For most ion beam measurements (RHIC), the pulse length which is received from the pickup electrodes is sufficient to be oversampled by the 400MSPS A/D converters, and so only a low-pass filter (nominally 39MHz) is used to remove unwanted high-frequency components. Filters with different cut-off frequencies can also be substituted,

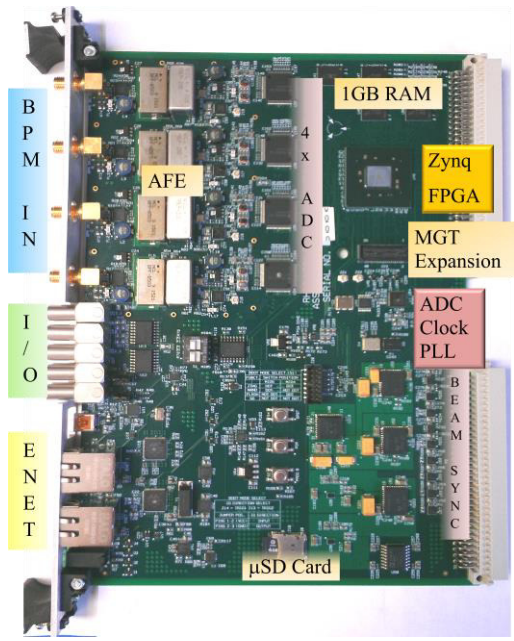

Figure 1: BPM Electronics

such as a 200MHz low pass which has been used for the BLIP raster BPM. The second and third signal paths are used to connect band pass filters of different package styles, used for measuring very narrow electron beam pulses. When used for low-repetition rate or single-bunch e-beam measurements the ringing response of a 503MHz filter is used to extend the sampling period. Narrowband processing at other frequencies is also possible by choosing similar band pass filters in the same package style. A smaller footprint SAW type band pass filter centered at 707MHz is the third option which will find use in the LEReC project which uses a 704MHz bunch frequency.

Low pass filters (nominally 800MHz) are also included at the board input and around each gain stage, to remove any high-frequency noise and/or aliased frequencies.

Gain and Attenuation

Each RF input channel has a set of two gain stages, nominally +20dB each. An Analog Devices RF amplifier (ADL5536) is used, which has a good response over the frequency range, and only uses a single +5V supply. Before each of the gain stages, a 7-bit programmable digital step attenuator allows adjustments in 1/4dB increments, from 0-31.75dB of attenuation. In addition, each gain stage can be bypassed by moving soldered jumpers. This is important for applications (such as RHIC stripline BPMs) where large input signals are present and high gain is not necessary.

*Work supported by Brookhaven Science Associates, LLC under Contract No. DE-AC02-98CH10886 with the U.S. Department of Energy
† rhulsart@bnl.gov

ISBN 978-3-95450-177-9

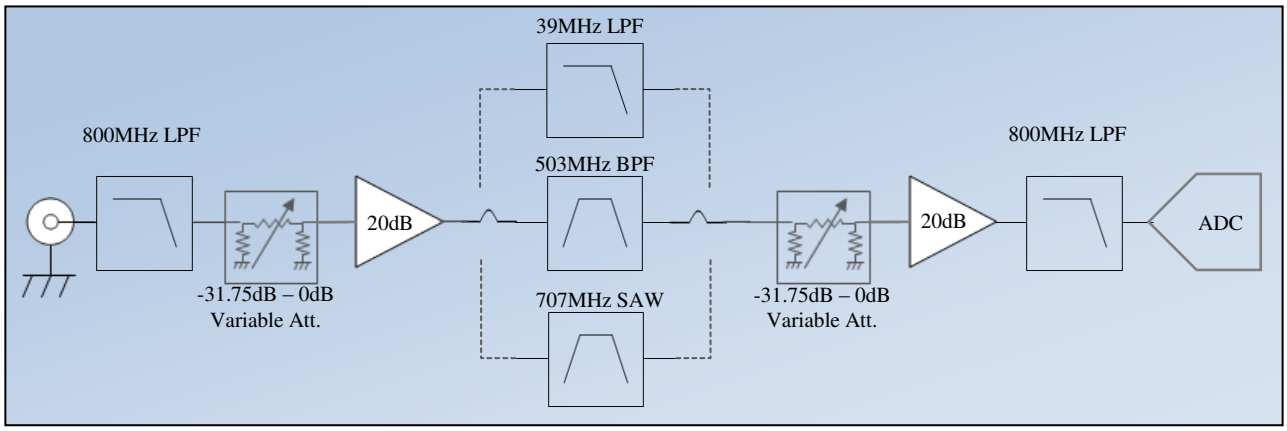

Figure 2: Analog Signal Processing Chain.

ANALOG TO DIGITAL CONVERSION

ADC's

Each analog channel is sampled by the Texas Instruments ADS5474 converter, which has a 14-bit width and can be clocked at sample rates up to 400MHz. The analog input of this device requires a differential signal, so RF transformers are used to couple to the single ended input. The internal 2.2V reference of the ADC is used in a bipolar configuration, where +/-1.1V of input voltage corresponds to a (signed) full scale digital output. These digital outputs consist of 14 sets of differential pair data lines terminated into 100 ohms, using the LVDS signalling standard. Careful consideration to impedance control and trace length matching was performed on over 128 traces on the printed circuit board in order to achieve reliable data transfers at the rated 400MSPS x 14bits (equivalent to 5.6Gbit/s).

ADC Clock Synthesis

The major addition to this design during its second hardware revision was an external PLL clock synthesis IC, used as a clock source for the ADCs. The Analog Devices AD9517-4 was chosen for its range of features including digitally controlled fine phase shifting ability and low additive jitter. A local oscillator or external input clock can be used as a reference for the PLL to lock to. The internal VCO has a frequency range of 1450-1800MHz, allowing a variety of ADC clock rates to be synthesized. The serial link carrier received over the VME P2 connector includes a RF synchronous 28MHz clock (for RHIC applications) which when used as a PLL reference allows the ADC's to be phase locked with the machine RF. Configuration of the PLL/Synthesizer can be accomplished though software (SPI bus) and changed as needed to suit many different accelerator BPM requirements.

DIGITAL PROCESSING SYSTEM

System Architecture

The Zynq System on a Chip (SoC) device is a hybrid between an ARM dual-core microprocessor and a Field Programmable Gate Array (FPGA). So far in this application all of the sampling and position calculations have been implemented as logic in the FPGA, and the processor is used to run a Linux derived operating system which allows communication with higher level accelerator controls systems, including some local data processing running as C++ code. A bank of 1GB DDR3 RAM serves as the main system memory, and a µSD card slot provides for non-volatile storage. Two Ethernet ports are included, one is connected directly to the ARM processor peripheral bus and is managed by the Linux OS as a standard Ethernet interface, which is used for communication with the rest of the accelerator controls network. The other Ethernet link is connected to FPGA logic, and can be used for custom high-speed data distribution for fast feedback systems.

Sample Processing

Up until this point in development, very little narrowband processing has been used in practice. Instead a high speed multiply-accumulator block controlled by a state machine loads a set of n-samples from the A/D inputs and performs a sum of squares. A small set of pipeline registers allows a software threshold to be set in order to start accumulating samples, or an external trigger signal can be used. When a sample counter expires the sums for each channel are passed to a calculation block. This operation can be sustained at up to the full 400MSPS sample rate, allowing steaming calculations to be performed with only a few sample gap necessary from time to time, in order to reset the accumulators.

Position Calculation

The two accumulated sums of squares for a pair of channels, which usually corresponds to the horizontal or vertical plane of measurement (although this system can also be configured for a diagonally mounted BPM), are used to find the position of the beam by obtaining the normalized ratio of the difference over the sum. After converting to floating-point representation, the square root of each sum is taken, and then the difference and sum terms are used to form the ratio, which is 0 near the center and approaches unity near the extents of measurement. Both a linear and cubic scaling coefficient is applied to

ISBN 978-3-95450-177-9

the ratio, which is determined by the particular BPM geometry. The entire calculation takes ~300ns to complete. In order to provide the ability to perform bunch-by-bunch, turn-by-turn streaming measurements for a RHIC bunch spacing of 106.5ns, this block is pipelined. Since its longest path (square-root) is ~60ns, it can calculate position for each separate RHIC bunch.

Data Delivery

Another finite state machine manages the accumulation of arrays of bunch samples, which are then delivered as a set (or turn) depending on the application. Dedicated blocks of memory are used to store 1K or deeper sets of averaged turn-by-turn data. Another block uses a running average method to effectively low-pass the position data for slower data delivery. A memory mapped interface is used to transfer data to the software running on the ARM processor, at either a fast 1KHz or slow 1Hz depending on the data type. C++ software routines then package this data and deliver it via the ADO software interface used throughout the CAD complex at BNL. Additional signal processing algorithms such as FFTs have been added to the processing code as well. Another set of memory mapped registers allow settings and diagnostics of lower level logic functions on the FPGA from the software side.

One of the great advantages of using a SoC architecture is in this regard. New interfaces can be added or modified between the programmable logic and the microprocessor with relative ease, without modification of the hardware. This has allowed for continuous improvement of the BPM processing algorithms and opened the possibility for applications to other accelerators for which it was not originally designed.

Boot Process

Envisioning a future large-scale BPM deployment for an accelerator such as RHIC with hundreds of BPMs, a remote boot capability was designed into the system. Each V301 module looks to the root folder on its µSD card for a boot loader, which contains the kernel image of the Linux operating system. A non-volatile ram disk image of the file system is uncompressed into RAM and serves as the root file system. After the Ethernet network is established, a remote file system share (NFS) is used to load individual scripts based on the hostname of the BPM, which is the only specific information stored on the card. The FPGA bit file which contains its logic configuration is also loaded at runtime over a network share. This allows a single file stored on a controls server to be deployed to many BPM systems simultaneously. In addition, hardware replacement in the field is performed by simply swapping the µSD card from the failed module to a new one, and plugging it back in.

Ancillary Peripherals

A block of ten connectors can be found on the front panel of the V301. Two of these connections use high-speed buffers to connect to the FPGA, and are used as external trigger inputs (or outputs if desired). In addition there are a set of four isolated digital outputs, and another four digital inputs, using magnetically isolated buffers. These can be used for interlock applications, for example, where a position excursion beyond a set limit can generate an interlock output to a machine protection system. Inputs can also be used for responding to MPS faults, such as logging and delivering a post-mortem BPM data set.

A high speed data connector was also added during the second revision, which breaks out the remaining three high speed (MGT) serial links included as part of the FPGA. This connector can be used to communicate via a fiber optic link at gigabit speeds, or possibly interface with other A/D converters, DAC's, etc. A test cable to connect two BPM modules together has been used to effectively double the number of channels to eight, for future BPM applications such as CBETA where more than four buttons are required for a single BPM (rectangular beam pipes).

VERSATILE APPLICATIONS

RHIC BPM System

The existing BPM system at RHIC consists of over 700 individual measurement planes each connected to a two channel integrated electronics module, most of which have been in service since the late 1990's. Despite its excellent performance to date many of the components are obsolete and repairs are becoming more difficult. Much of the motivation for this new BPM design has been toward replacing the existing electronics with a low cost but equal or better performing next generation system. A great deal of use has been made with real RHIC beam in order to develop earlier prototypes of this system. The 39MHz low pass filter that was chosen has been shown to work well with the various RF frequencies that RHIC uses.

To date a few of these BPM electronics modules have been installed alongside existing hardware, so the results can be compared. Responding and delivering data when requested via the beam sync serial link has been another area of development. This will allow data from these modules to be synchronized with other BPM data, making its use in higher level orbit feedback and management systems possible.

One area in RHIC that could benefit from bunch by bunch position measurements is at the abort kicker and beam dump BPM. It is installed between the two, allowing measurements of the trajectory of each bunch as it is kicked into the dump. Due to fluctuations in the magnet voltage waveform the particles do not all receive the same kick, and follow slightly different paths. Data taken using a prototype of this hardware can be shown (Fig. 3) to closely match the expected positions (similar shape to the magnet voltage waveform).

RHIC DX BPMs

At each of the six intersection regions of RHIC, there are a pair of BPMs that are located in the common beam

ISBN 978-3-95450-177-9

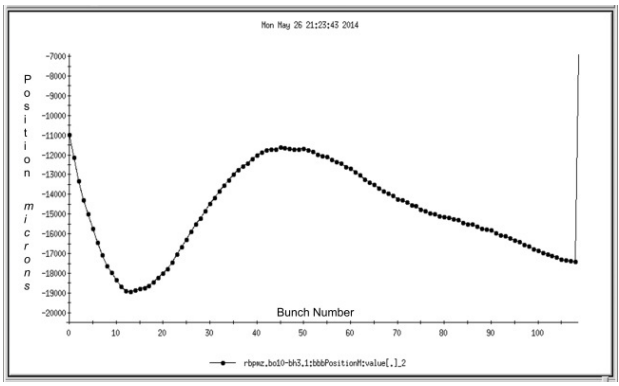

Figure 3: RHIC dump BPM bunch by bunch position.

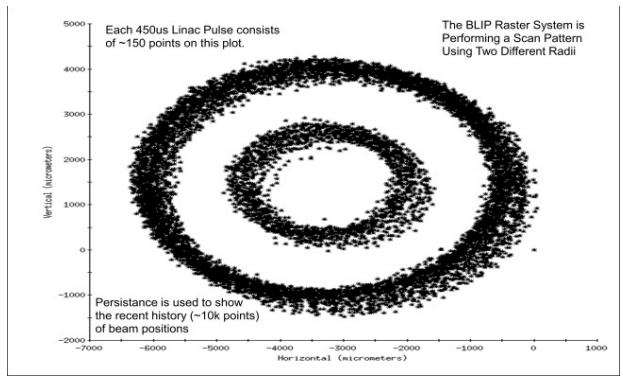

Figure 4: BLIP raster BPM x-y position.

pipe on either side of the collision point, which see both of the ion beams. Their longitudinal separation is such that when the two rings are 'cogged' into collisions, the bunches at the DX BPMs are separated by approximately 50ns, half of the nominal 9MHz spacing with a single beam. Since the existing electronics can only process a single sample per turn (~100kHz), each DX BPM signal is split to two modules, each timed separately in order to capture the blue or yellow ring bunch. Calibration of both of these modules becomes critical when measuring the difference between the two ion beam positions within the same BPM pickup assembly.

With much higher sample rates, a single V301 module can be used to sample both beams. Using the same analog hardware channels eliminates the dependence on calibration when computing a position difference. A higher cut-off frequency low pass filter (200MHz) is used instead of the 39MHz, as it was found that there was interference between adjacent bunches (beams) when the lower frequency filter was used. A successful test run of the electronics at the 2 o'clock RHIC intersection region was completed this past year, and there are plans to install the additional modules to complete all of the DX BPM locations during the current shutdown period.

BLIP Raster Upgrade BPM System

A dual plane BPM was installed in the BLIP beam line at the BNL Linac as a part of the BLIP Raster Upgrade Project [2]. The V301 was also chosen to process signals from the two split-can type pickups installed in the new beam line. One unique requirement was the ability to measure the beam motion while being scanned at a 5kHz rate in a circle. Each Linac pulse of ~450μs duration produces about 2.25 rotations in a circular pattern.

The same firmware used to measure bunch by bunch positions at RHIC is used to slice up the very long Linac pulse into smaller ~100 sample chunks by lowering the sample rate to 25MHz. Each pseudo-bunch is therefore spaced a few microseconds apart, and has a separate position calculated for it, which are put together into an array. When correlated against a similar array taken with the other plane's positions, a circle emerges.

This display (Fig. 4) is used with a persistence mode showing the past few thousand pulses and has proven very useful in monitoring the rastering patterns at BLIP.

Future upgrades at the BNL Linac will also include installations of V301s, using existing BPM pickups.

Electron Beam Measurements

The Brookhaven Accelerator Test Facility (ATF) has been used on numerous occasions to prototype and test this new BPM hardware using electron beams as a signal source. Different pickups (buttons and striplines) have been installed in the beam line and connected to these electronics. The ATF can produce single bunch electron pulses at a 1Hz repetition rate. All tests so far have used a 503MHz band pass filter as the main analog processing component. This filter 'rings' and provides a series of 15-20 samples to compare with those of the other channel and compute position. Measurement noise levels are close to what is expected without heavy time-averaging and raster scans have been used to measure the linearity of a few BPM assemblies.

A future upgrade to RHIC, the LEReC project, will be installing a number of new BPM pickups [3], both in a RHIC warm-bore section and a new electron transport beam line. Many of these BPMs will be connected to V301 modules, which has configuration options for both electron and ion signals. In the cooling section of LEReC, relative phase and position measurements will be used to overlap the ion and electron beams to produce the cooling effect. Much work is ongoing to develop the firmware and software to support these capabilities.

REFERENCES

[1] R. Michnoff, *et al.*, "Preliminary Design of a Real-Time Hardware Architecture for eRHIC" *ICALEPCS 2015,* Melbourne, Australia (2015), paper THHB2O01.

[2] R. Michnoff, *et al.*, "The Brookhaven LINAC Isotope Production Facility (BLIP) Raster Scanning System First Year Operation with Beam" *IBIC 2016,* Barcelona, Spain (2016), paper MOPG28.

[3] Z. Sorrell, *et al.*, "Beam Position Monitors for LEReC," presented at the *IBIC 2016,* Barcelona, Spain (2016), paper MOPG08.

ISBN 978-3-95450-177-9

A FPGA BASED COMMON PLATFORM FOR LCLS2 BEAM DIAGNOSTICS AND CONTROLS*

J. Frisch, R. Claus, M. D'Ewart, G. Haller, R. Herbst, B. Hong, U. Legat, L. Ma, J. Olsen, B. Reese, L. Ruckman, L. Sapozhnikov, S. Smith, T. Straumann, D. Van Winkle, J. Vasquez, M. Weaver, E. Williams, C. Xu, A. Young.
SLAC National Accelerator Laboratory, Menlo Park CA USA

Abstract

The LCLS2 is a CW superconducting linac driven X-ray free electron laser under construction at SLAC. The high beam rate of up to 1MHz, and ability to deliver electrons to multiple undulators and beam dumps, results in a beam diagnostics and control system that requires real time data processing in programmable logic. The Advanced Instrumentation for Research Division in the SLAC Technical Innovation Directorate has developed a common hardware and firmware platform for beam instrumentation based on the ATCA shelf format. The FPGAs are located on ATCA carrier cards, front ends and ADC /DAC are on AMC cards that are connected to the carriers by high speed serial JESD links. External communication is through the ATCA backplane, with interlocks and low frequency components on the ATCA rear transition module (RTM). This platform is used for a variety of high speed diagnostics including stripline and cavity beam positon monitors (BPMs).

KEY FEATURES

A new instrumentation / control platform has been developed for LCLS2 in order to provide the following features that were not all available with existing platforms:

- Ethernet communication within a c to simplify hotswapping and control of distributed systems.
- Timing data stream distributed to all application cards to allow beam parameter dependent processing.
- Analog front ends integrated with ADCs / DACs, but separate from digital systems to allow digital and analog engineers to work independently and to provide independent upgrade paths
- Large application card area with vertical space for RF shielding to simplify the design of high performance RF systems
- High system density with efficient use of rack space for analog connections.
- Widely-used telecom hardware.

HARDWARE OVERVIEW

The "Common Platform" is based on the Advanced Telecommunications Computing Architecture [1] (ATCA) that is widely used in industry. The SLAC common platform is based on the following components (figure 1, 2):

- ATCA Shelf: This is the "crate" that holds the electronics cards, power supplies, etc.
- Backplane: Provides high speed data connections from all cards to slots 1 and 2.
- Management: Provides IPMI for shelf components (commercial)
- Network Switch: This is an ATCA carrier card that is located in slot 1 with access to Ethernet to each carrier card, and which provides a 10Gb, or 40Gb uplink. (typically commercial, custom also available)
- Carrier Card: This card contains a FPGA and has serial connections to the backplane Ethernet, and to the RTM and dual AMC cards. The carrier card also contains DC-DC power supplies from the -48V to a variety of voltages used by the AMC cards.
- AMC card: These contain the analog front ends, ADCs and DACs, and timing chips
- RTM card: These are connected directly to the FPGA on the carrier card and are used for miscellaneous I/O and network connections.

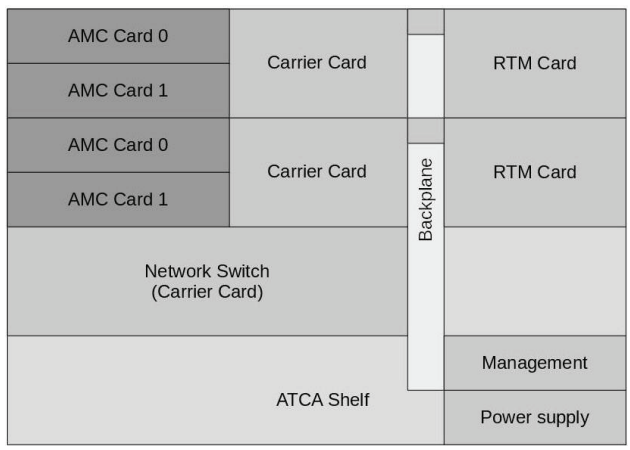

Figure 1: Common platform components.

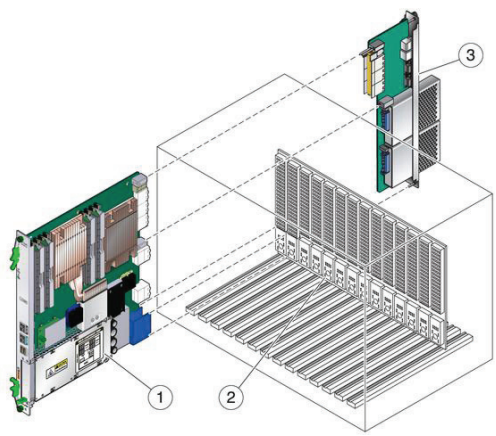

Figure 2: ATCA shelf and cards.

*Work supported by US Department of Energy, Office of Science under contract DE-AC02-76SF00515

ISBN 978-3-95450-177-9

HARDWARE DESIGN

The high average throughput required for LCLS2 instrumentation necessitates the use of programmable logic for processing data. The digital and analog portions of the design are separated, with. the FPGA, memory and network interfaces on the carrier card.

Each carrier card supports two, double-width, full-height AMC daughter cards. The AMC slots are backwards compatible to support standard ATCA cards, but include extra DC power supplies on otherwise unused pins. (These supplies are controlled through IPMI and only activated with compatible AMC cards).

The use of full height AMC cards provides extra vertical room for RF shielding for noise sensitive systems and extra front panel connector space.

The choice of ADCs / DACS is generally tied to the required analog bandwidth and dynamic range requirements, so they are included on the AMC cards. Most AMC card ADC / DACs use JESD204b [2] serial interfaces, however parallel digital is also supported.

The system is designed to minimize network cables. The ATCA backplane carries primary data communication, management, machine protection data, and a timing data stream to each carrier. In a typical configuration only analog signal cables are required to the application cards.

The RTMs provide extra connector space for special purpose networks, and general purpose low speed analog and digital. If only a single carrier card is required in one location, the networks can be directed to the associated RTM card, eliminating the need for a network switch in the shelf. This allows operation in a NAD-like configuration.

The ATCA standard provides a number of useful functions:

- Hot swap for carrier cards and RTMs. This allows the use of multiple functions in a shelf without interfering with maintenance.
- System management and monitoring.
- High speed (10Gb) networking with future upgrade paths.
- Temperature rating 50°C
- A variety of shelf sizes from 1 slot to 14 slots, with vertical and horizontal orientations.
- Ethernet backplane communication which simplifies dividing systems between multiple shelves.

BACKPLANE / NETWORKS

The Common Platform uses a standard dual-star configuration of an ATCA backplane. This provides the following networks (figure 3)

- 10Gb Ethernet (4 lanes) from slot 1 in a "star" to all other cards. This is the ATCA "fabric" network. It is used for general high speed data transmission to the Ethernet switch located in slot 1.
- One lane from slot 2 in a "star" to all other cards. This is used for the serial timing data stream. This is part of the 2nd ATCA "fabric" network.
- One lane from slot 2 in a "start" to all other cards. This is used for Machine Protection System data. This if part of the 2nd ATCA fabric network.
- IPMI to all slots for configuration / monitoring.

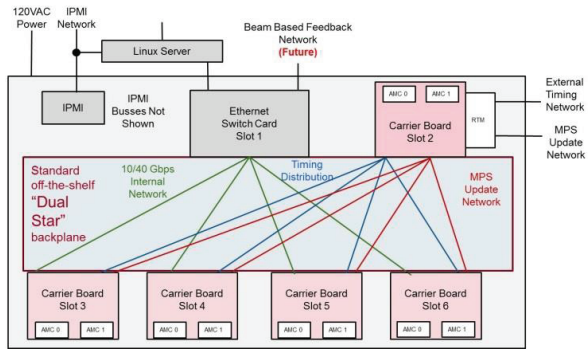

Figure 3: Common platform networks.

CARRIER CARD DESIGN

The SLAC-designed carrier card is based on a Xilinx *Kintex Ultrascale* XCKU040 or XCKU060 FPGA, the latest generation of chips available when the design was frozen. The FPGA is interfaced to 8GB of DDR3 memory, and to the networks described in the previous section (figure 4).

Each AMC daughter card uses dual 172-pin connectors (ATCA B+ AMC) rated to 12.5Gbit. The XCK040 FPGA provides 7 bi-directional serial lanes (typically configured as JESD204b) to the carrier card, the XCK060 (same package) provides 10 lanes. This provides a total data rate from ADCs of 87.5Gb/s or 125Gb/s. With typical 8b/10b encoding that supports 4.3Gs/s of 16 bit ADCs with the smaller FPGA and 6.25Gs/s with the larger. Simultaneous use of full data rate on ADCs and DACs is supported.

The carrier card includes DC-DC converters from the shelf -48V to its internal supplies and supplies to the AMC cards. For most designs this eliminates the need for DC-DC converters on the noise sensitive AMC cards.

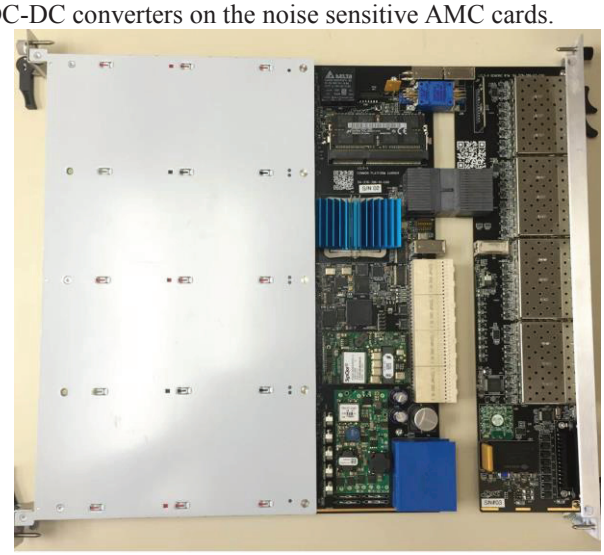

Figure 4: Carrier Card, FPGA is under blue heat sink. Network RTM card is attached on the right.

ISBN 978-3-95450-177-9

AMC CARDS

The AMC cards are 148.5mm X 180.6mm, with approximately 20 mm of clearance above the boards for components and shielding. AMC cards include analog electronics and ADC / DACs. A number of AMC cards are under development for LCLS and LCLS2.

General Purpose ADC / DAC Card

This card is intended for applications requiring high performance ADCs / DACs. This includes:

- IF digitizers for cavity BPMs,
- Toroid readouts
- Bunch length monitor readout based on Coherent Synchrotron Radiation (CSR)
- Radiation monitors (fibers, ion chambers etc.)

The card contains four channels of 16 bit, 370Ms/s ADCs. One of the digitizers is used to measure an internally generated trigger to correct for the clock vs trigger timing in the algorithm.

The card also contains 2 channels of 16 bit, 370Ms/s DAC for signal generation, and general purpose digital and fiber outputs.

The general purpose cards are complete, and being used for development of LCLS2 beam instrumentation.

Stripline BPM

This card contains bandpass filters (typically 60MHz bandwidth around 300MHz), Variable gain amplifier chains, and calibration circuits,

It uses the same 16 bit 370Ms/s digitizers as the general purpose card, but operating in the second Nyquist band. Prototype BPM cards are currently being tested.

LCLS1 LLRF System

The LCLS 1 room temperature LLRF system is being upgraded to modern hardware. A pair of AMC cards and an RTM on one carrier card provides RF control, read back and fast interlocks for a standard LCLS1 RF station. [3].

The system provides ten channels of LLRF input with downmixers, and LO generation. The digitizer clocks and LO used FPGA based PLLs to allow locking to the accelerator reference RF and timing system. The firmware allows locked or unlocked operation [4].

Changing a few components (filters and RF splitters) allows the card to operate from 400MHz to 3GHz.

Prototypes have been tested with a measured phase noise at 2856MHz of < 0.005ºRMS in a 1MHz bandwidth.

In addition to use on the LCLS LINAC, this system is being used for the SPEAR Booster upgrade, and is planned for use on the SPEAR ring RF upgrade in the future. A 1300MHz version for superconducting RF systems has also been tested with good performance.

TIMING SYSTEM

A new timing system has been developed for the LCLS2. It consists of a 3.7Gb/s data stream which uses 8b/10b encoding to provide 16 bit words at the 185.7 MHz reference clock frequency, corresponding to the 1300MHz accelerator frequency / 7, the same as the injector RF gun frequency.

The timing data is transmitted in 3200 bit frames, at a frame rate of 928kHz, corresponding to the maximum beam rate in the LCLS2. The bits in each frame contain information about that beam pulse, including pulse ID, destination, requested charge, and markers for 60Hz power line synchronization. The frame also contains a bit "pattern" that specifies when each triggered device should operate.

The timing data stream is distributed by an external fiber network to a carrier card in slot 2 of each ATCA shelf. From that carrier card, the data stream is transmitted on the ATCA fabric (1 lane) to all carrier cards. The data is transmitted approximately 100us in advance of the beam, allowing time for transmission delays in the 4km long accelerator system and for processing / triggering in advance of beam pulses.

The FPGA on each carrier card contains firmware to decode the data stream. This serves multiple functions:

- Tag data with a pulse ID for non-realtime applications.
- Modify processing algorithms based on beam destination or parameters.
- Provide external hardware triggers
- Provide internal triggers in firmware or hardware for signal processing.
- Provide a distributed check that the beam is being directed to the correct destination.

The Common Platform hardware and firmware can also decode the data stream from MRF timing systems [5], allowing its use in LCLS1 applications. The frequencies of LCLS1 and LCLS2 are harmonically related and in the future the LCLS2 timing system will be able to perform all functions required for both systems.

FIRMWARE

The Common Platform firmware is written in a modular fashion to allow signal processing / application development to be done independently of platform / communication firmware (figure 5). Most application development is done in Mathworks Simulink with Xilinx System Generator [6].

ISBN 978-3-95450-177-9

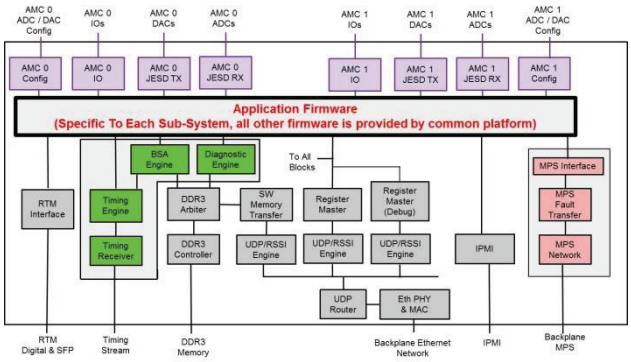

Figure 5: Firmware block diagram.

MACHINE PROTECTION

The LCLS2 fast machine protection system makes use of the Common Platform hardware and firmware. Each instrumentation card (BPM, etc.) compresses its data, associates it with a pulse ID from the timing system, then transmits the data on the backplane to a card in slot 2, using the MPS network, which is not shared with any other traffic. From there the data is sent on a private network to the mitigation nodes which run the MPS algorithm and either reduce beam rate or shut off the beam.

Since each card has the timing data, and that data includes the beam destination, all BPMs can locally check for beam present in the wrong line, or lack of beam when it should be present. This provides an independent check that the various system kickers are responding correctly to the timing patter request.

The slot 2 MPS card is a standard SLAC carrier card running a simplified set of firmware which transmits the MPS data.

OTHER APPLICATIONS

The Common Platform system is generally useful for applications requiring high throughput real time data processing in a compact high reliability form factor.

An example application is the RF system for a Transition Edge Sensor using a microwave multiplexer. This sensor is intended for a variety of applications including high energy resolution X-ray imaging and cosmic microwave background measurements [6].

The sensor array is operated at ~100mK temperatures, which each pixel coupled with a SQUID to a resonant circuit in the 4-8GHz frequency range. Measurements are made by tracking changes in the resonance frequencies of the sensor. The electronics must generate a comb of RF tones to drive the sensor, each tone being tuned to track the pixel resonance.

The common platform implementation of this uses a pair of AMC cards on a carrier to provide 4GHz bandwidth of signal generation and measurement in a 4-8GHz frequency range. Each AMC contains 2, dual channel 3Gs/s digitizers with internal DDC, and 2 dual channel 3Gs/s DACs with DDS, along with band selection multiplexers, and local oscillators. The FPGA will generate tones to track up to 4000 resonances.

Electronics / RF design of this system is nearing completion, with first hardware expected in late 2016.

REFERENCES

[1] https://www.picmg.org/openstandards/advancedtca/
[2] http://www.eetimes.com/document.asp?doc_id=1279796
[3] Van Winkle et al. “The SLAC LINAC LLRF Controls Upgrade”, WEPG16, IBIC 2016, Barcelona.
[4] http://www.mrf.fi/index.php/timing-system
[5] https://www.xilinx.com/products/design-tools/vivado/integration/sysgen.html
[6] de Lange, G. J, *Low Temp Phys* (2014) 176: 408.

ISBN 978-3-95450-177-9

THE SLAC LINAC LLRF CONTROLS UPGRADE*

D. Van Winkle†, M. D'Ewart, J. Frisch, B Hong, U. Legat, J. Olsen, P. Seward, J. Vasquez, SLAC National Accelerator Laboratory, Menlo Park, USA

Abstract

The low level RF control for the SLAC LINAC [1] is being upgraded to provide improved performance and maintainability. RF control is through a high performance FPGA based DDS/DDC system built on the SLAC ATCA common platform. The klystron and modulator interlocks are being upgraded, and the interlocks are being moved into a combination of PLC logic and a fast trip system. A new solid state sub-booster amplifier will eliminate the need for the 1960s vintage high RF phase shifters and attenuators.

OVERVIEW

The legacy RF system at SLAC has been in operation for over 50 years. Despite working extremely well for many years, many parts of the system are showing signs of wear including effects as esoteric as copper erosion in some water cooled chassis. A rough block diagram of the legacy RF system is shown below in Fig. 1.

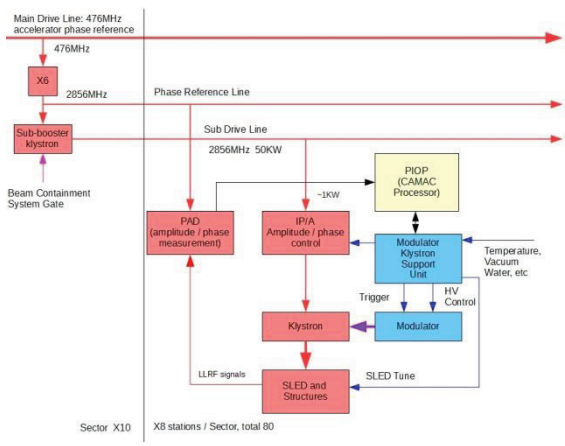

Figure 1: Legacy RF system.

To mitigate these effects and to provide for upgradeability well into the future, the US Department of Energy is investing in upgrading the system using modern FPGA based technology. When upgrading a system such as this, many conflicting requirements must be met at once. During the design process, many platforms were evaluated for applicability and maintainability. We evaluated: VME, PXI, mTCA for physics, ATCA, and conventional chassis. At the same time this evaluation was going on for LLRF upgrades at SLAC, the diagnostics, machine protection and other groups were evaluating their own common platform solution and had decided on ATCA as their platform of choice. Because of that decision and our own evaluations, it was decided that the system will be designed into the ATCA platform. A high level block diagram of the new LLRF system is shown in Fig. 2.

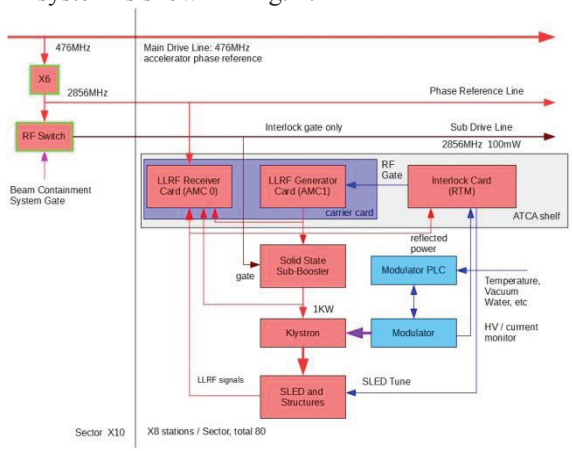

Figure 2: Upgraded RF system.

DETAILS OF NEW SYSTEM

The system is being designed into a new platform based upon the telecommunications system ATCA [2]. The system incorporates two advanced mezzanine cards (AMC cards) which plug into a carrier card that contains the FPGA for all signal processing functions. The overall common platform system allows for enough flexibility that the design can be used for other diagnostic and machine protection functions simply by designing other AMC cards with the specific functionality required for those systems. Further details of the common platform system are covered at another paper in this conference [3].

Specifications and Backwards Compatibility

The LLRF system has to completely replace the old system which was based upon CAMAC controls and other custom chassis within the larger LINAC system. In addition, the system will not be able to be upgraded as a whole at one time; the design incorporates a method for upgrading as little as one station at a time. To that end, there are several requirements on the new system for it to fit into the existing infrastructure of beam containment (BCS), timing systems and other legacy systems:

- The new system must maintain compatibility with the existing BCS system without compromising the beam containment functions as currently implemented.
- The new system must replace the legacy Modulator Klystron Support Unit (MKSU) that serves to protect the high power pulsed klystrons and modulators.
- The new system must use solid state sub-boosters for each Klystron, rather than the legacy sector (8 klystron) sub-booster klystron.

* Work supported by US Department of Energy, Office of Science under contract DE-AC02-76SF00515
† dandvan@slac.stanford.edu

ISBN 978-3-95450-177-9

In addition, this new system has to meet or exceed the old electrical specifications of the legacy system. The important specifications are shown in table 1.

Table 1: System Specifications

SPEC	VALUE
Noise (phase)	< 0.01 degrees 1 MHz BW
Noise (amplitude)	< 0.01% 1 MHz BW
Drift (phase)	0.1 degrees
Drift (amplitude)	0.1% (1min) (2 degrees C)
RF Channel Bandwidth	>10 MHz
RF Channel Resolution	16 bit resolution
Non-linearity	0.1 degrees for 6 dB change
Modulator Voltage Readback	14 bits resolution

One final requirement was that the system be capable of handling all current and future RF frequencies used at SLAC (LCLS I - 2856 MHz, LCLS II – 1300 MHz, SSRL Booster – 358.54 MHz, SSRL Ring – 476 MHz).

Detailed Hardware Description

In order to provide enough channels for all potential uses, we determined that 10 channels of RF down-conversion, 1 Channel of RF up-conversion and 2 Channels of Baseband signal detection were necessary. It was further determined that the interlock functions previously handled by the MKSU would be split between a new ATCA rear transition module (RTM) and the klystron modulator control PLC. A more detailed block diagram of the final implementation is shown in Fig. 3.

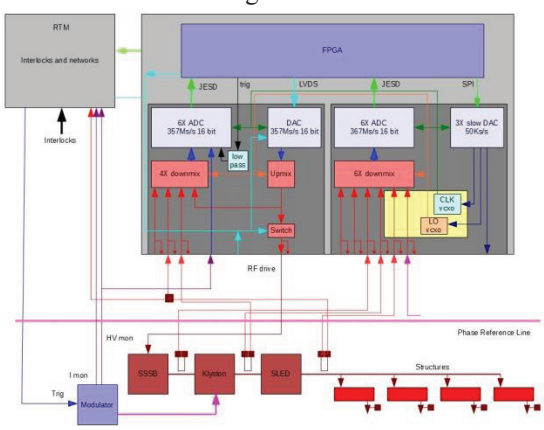

Figure 3: Detailed block diagram.

To enable handling of the multiple clocks and LO's necessary to down-convert all SLAC frequencies it was decided that a daughter card piggy-backed on one of the AMC cards would be used to provide clock and LO signals to both AMC cards. A new pulsed solid-state sub-booster amplifier will be designed to drive each of the 8 klystrons per sector.

AMC Cards The two AMC cards will use the same basic architecture throughout. Each card will contain 3 ADC chips running at approximately 350 Msamp/sec (depending on input frequency). Each chip contains 2 ADCs for a total of 6 ADC channels per board. Because there simply was not enough pins to run parallel bit ADCs we chose to use the relatively new standard of JESD204B serial lanes.

We further broke the design down into what we called a precision card and an up-converter card. The Precision card will be used for comparing critical feedback signals to a reference signal from a phase reference line as shown in Fig 2. This is similar to what the LLRF team designing the LCLS-II system is doing, however we are doing it for differing reasons. Our main reason for splitting the cards in this manner is to get the maximum dynamic range achievable without interference from the signal generation card. Any other precision signals should be input to this card as well. The up-converter card will be used to create the corrected (or feedback) signal that will be fed to the structures (or cavity) depending on application.

The precision card contains six identical RF down-converters with a block diagram as shown in Fig. 4.

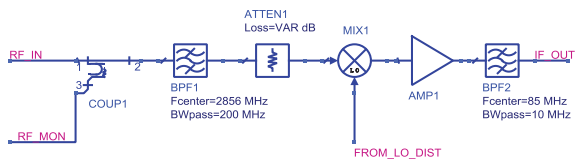

Figure 4: RF Down-converter block diagram.

The up-converter card contains 4 down-converters identical to the ones used on the precision card as well as two buffered baseband signals. One of the baseband signals will be used to monitor the klystron modulator voltage and the other is used internally for timing synchronization of the RF pulse amplitude. The up-converter card also contains a 16 Bit parallel DAC. We had to use a parallel DAC instead of a JESD204B DAC because during initial testing we found excessive latency with the original DAC we had planned on using. The DAC outputs an IF at approximately 85 MHz (depending on application) and uses the same LO as the down-converters to up-convert to 2856 MHz.

Solid State Sub-Booster (SSSB) The purpose of the SSSB is to provide enough input power to drive the linac klystrons to their rated output power with minimal phase noise degradation and reliable long term performance. The SSSB is required to produce up to 1kW pulses 5 us in duration at up to a 240 Hz rate (standard operation is 120 Hz). We are planning to use a hybrid approach of buying GaN-HEMT amplifier modules (bricks) from an outside vendor and installing them into a custom chassis that will be contained in the same rack as the rest of the LLRF system. Interlock RTM The interlock rear transition module's, (RTM) main function is to protect the klystron from various conditions that could result in destruction of the klystron. Previously this was all handled by the MKSU with only a trigger going from the MKSU to the klystron modulator. The new interlock RTM will handle the fast interlocks while the slow interlocks (water, vacuum, Magnet,

ISBN 978-3-95450-177-9

temperature etc.) will be handled in the modulator itself. Fig. 5 shows a block diagram of the interlock scheme.

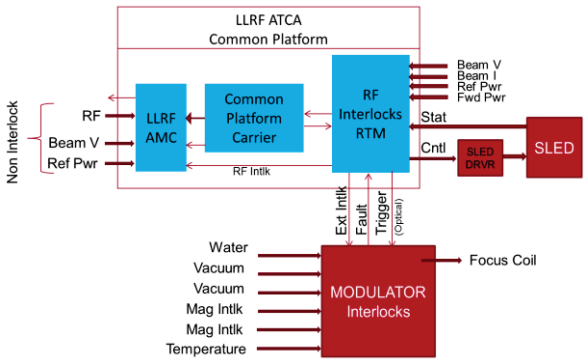

Figure 5: Interlock scheme.

Detailed Firmware Description

The firmware for the LLRF scheme for the SLAC LINAC is a very complex design with many facets (Timing, amplitude and phase adjustments). Over the many years of SLAC operation, many feedbacks have been added on top of the original system to allow for much more stable operation than the original SLAC linac and as a result, the new system must fit seamlessly into those feedbacks with no adverse effects.

All of the main controllability of the system relies on individual klystron phase and amplitude control. To achieve this, a fiducial riding on top of the 476 MHz was used to time the pulse with the arrival of the beam. In that way there was a guarantee that the trigger would be timed in phase with the RF signal being amplified and distributed to the structures of the main linac. With the addition of LCLS-I to SLAC, a new even system was added [4] which essentially split the timing into two differing systems; One being the fiducial system and one being the event system. The event system is used to time a myriad of other systems around the machine (BPM's cameras etc) One goal of this new system is to combine the timing into one system only with a fiber going to each station with the timing information and as a result complicates the firmware implementation.

To achieve pulse to pulse timing stability of less than 100ps on the envelope of the RF, we need a way to detect the trigger at much less than the roughly 2.7ns time allowed by our system clock. To achieve sub-clock sample timing, a novel interpolation scheme was created by running the trigger through a low pass filter, sending to an ADC and then using DSP interpolation to detect the zero crossing with sub time sample resolution. This new timing information is then used to create an interpolated baseband signal which is multiplied (digitally) onto a digitally controlled oscillator which is phase locked to the incoming phase reference IF. A block diagram of the overall firmware scheme is shown in Fig. 6.

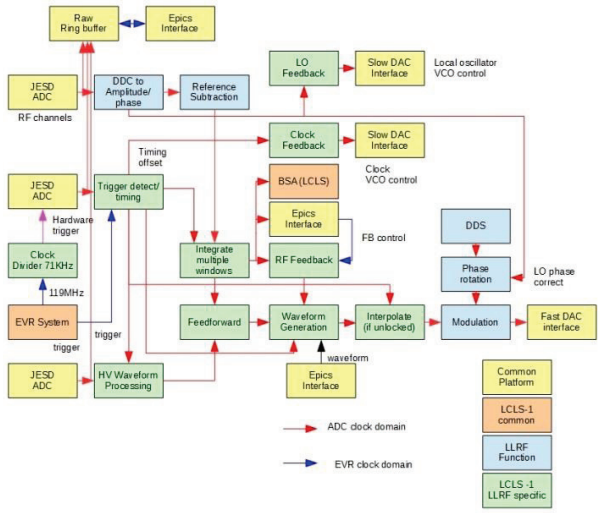

Figure 6: Detailed firmware block diagram.

PROTOTYPE RESULTS

Prototype cards for the LCLS-I LLRF system have been built and initial firmware has been developed to allow for data taking and offline data processing. We present some of the results here.

Phase Accuracy To measure phase accuracy, a common signal is sent into two channels of down-conversion, sampled at an IF/Sample ratio of 5/21 (for near IQ sampling [5]. The near IQ down conversion is filtered by a simple 21 average filter and then digitally down converted to baseband. The LO is locked to the IF of the incoming 2856 MHz signal and the clock is locked using one ADC channel which is sampling an external 119/7 MHz signal (derived from the 2856 Mhz. The locking and measurement scheme is shown below in Fig. 7.

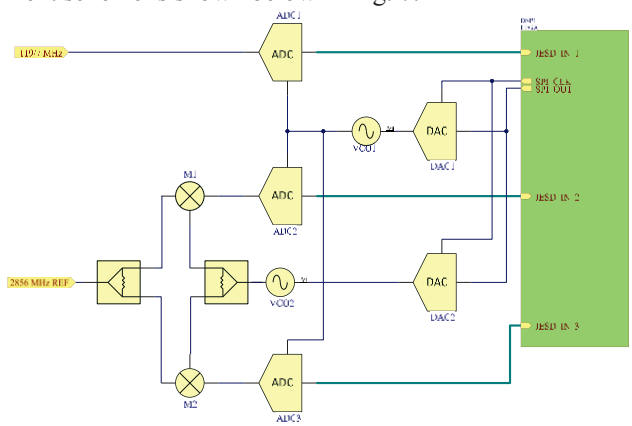

Figure 7: Phase measurement and locking scheme.

To calculate the base phase error, the two IQ signals from ADC2 and ADC3 are converted to phase and amplitude using a cordic algorithm in matlab. The phase signals are then further filtered with a 1MHz lowpass butterworth filter to approximate the final processing band bandwidth. An FFT of the single side band (SSB) results are shown below in Fig. 8. The LO and Clock used in our system while fairly low noise should not be considered phase noise. By using the phase subtraction technique we get

ISBN 978-3-95450-177-9

several orders of magnitude improvement by the subtraction of common noise. In fact, the LO and Clock can be run open loop with reduced performance. Further processing this data shows an RMS phase error of 0.0052 degrees integrated from 100 Hz to 1 MHz this was measured at an intermediate fan speed.

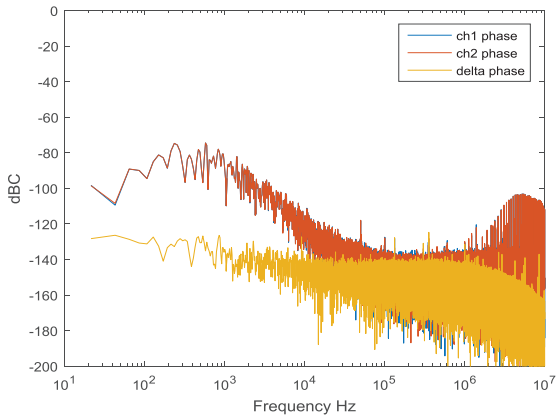

Figure 8: SSB difference phase noise plot.

Amplitude Accuracy Using the amplitude data from the algorithm mentioned in the phase accuracy section, we calculate at ch1 and ch2 amplitude errors at 0.0093 and .0096% respectively.

Output Phase Noise The output phase noise of the system must also meet very stringent requirements. To verify the performance we generated an output signal at 2856 MHz using prototype firmware. The SSB output phase noise as measured by an Agilent E5052B phase noise analyser is shown below in Fig. 9.

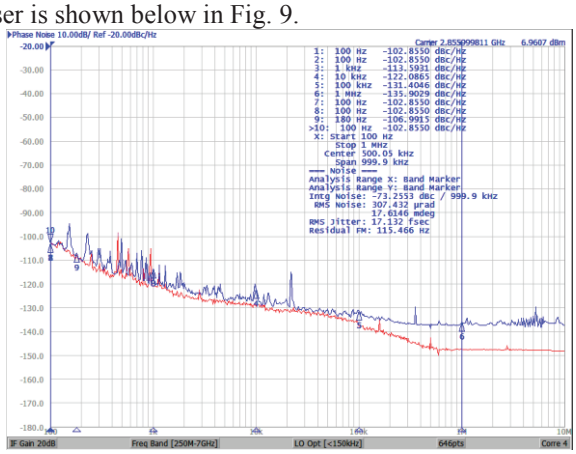

Figure 9: 2856 MHz output phase noise.

The red line in Fig. 9 is the input reference noise. The blue line is the output phase noise which tracks the input phase noise quite well up to around 100 kHz at which point it becomes dominated by the noise floor of the output circuitry. This needs further investigation. The integrated rms noise from 100 Hz to 1 MHz is 0.0176 degrees.

Other Performance Tests One particular test meriting investigation is potential phase degradation under full ATCA fan speed. We ran the system at full fan speed and did, in fact, see a degradation of the phase noise. However, as can be seen in Fig. 10, the full integrated phase noise is still below the 0.01 degree phase specification. To further mitigate this problem, we are planning on testing some dampening material on the oscillator daughter card as we expect that vibration on that card may be contributing to this added phase noise.

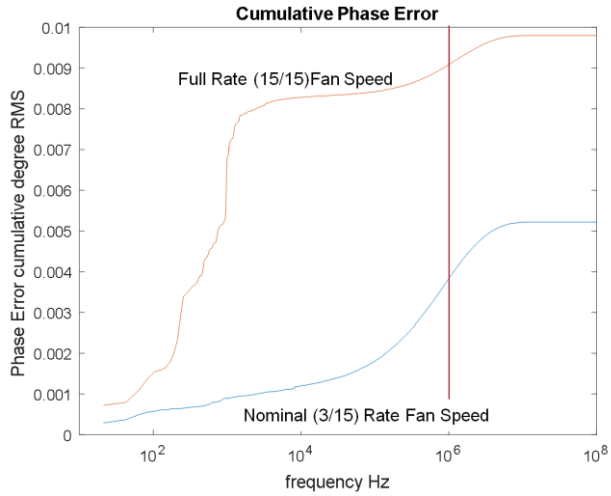

Figure 10: Phase error at full fan speed.

CONCLUSIONS

We have designed and tested prototype hardware for the LINAC upgrade project at SLAC. Testing to date shows that the system as currently built nearly meets all specifications. The layout designs of the two AMC cards are in the process of being modified as of the writing of this paper. The new boards are expected to be tested on beam later this calendar year to show full proof of concept prior to moving into production mode and installation into all 80 RF stations contained within the LCLS-I LINAC.

REFERENCES

[1] A New Control System for the SLAC Accelerator Klystrons for SLC, *IEEE Transactions on Nuclear Science*, Vol. NS-30, No. 4, August 1983.

[2] PICMG, `http://www.picmg.org`

[3] Josef Frisch, Richard Claus, John Mitchell D'Ewart, Gunther Haller, Ryan Herbst, Bo Hong, Uroš Legat, Lili Ma, Jeff Olsen, Benjamin Reese, Larry Ruckman, Leonid Sapozhnikov, Stephen Smith, Till Straumann, Daniel Van Winkle, Jesus Alejandro Vasquez, Matthew Weaver, Ernest Williams, Chengcheng Xu, Andrew Young, "A FPGA Based Common Platform for LCLS2 Beam Diagnostics and Controls," presented at the 2016 International Beam Instrumentation Conf. (IBIC '16), Barcelona, Spain, Sept. 2016, paper WEPG15, this conference.

[4] J. Dusatko, S. Allison, M. Browne, P. Krejcik, "The LCLS Timing Event System," Proceedings of BIW10, Santa Fe, New Mexico, USA, April 2012, paper TUPSM083.

[5] L. Doolittle, H. Ma, M. Champion, "Digital Low-Level RF Control Using Non-IQ Sampling", Proceedings of LINAC 2006, Knoxville, TN, US

ISBN 978-3-95450-177-9

BATCH APPLICATIONS OF DIGITAL BPM PROCESSORS FROM THE SINAP *

L.W. Lai, F.Z. Chen, J. Chen, Z.C. Chen, Y.B. Leng#, Y.B. Yan, W.M. Zhou
SSRF, SINAP, Shanghai, China

Abstract

During the past several years a digital BPM (DBPM) processor has been developed at the SINAP. After continuous development and optimization, the processor has been finalized and has come to batch application on the signal processing of cavity BPMs and stripline BPMs at the Dalian Coherent Light Source (DCLS) and the Shanghai Soft X-ray FEL (SXFEL). Tests have been done to evaluate the performances, such as the noise level, the SNR and the cross talk. The system resolution of the cavity and stripline BPMs can achieve 1um and 10um respectively. The test results on the Shanghai Deep-Ultra-Violet (SDUV) and the DCLS will be introduced.

INTRODUCTION

A prototype of the DBPM has been developed successfully at the SINAP during the past few years [1~5]. Some tests and applications have been carried out at the Shanghai Synchrotron Radiation Facility (SSRF)[6]. Since 2015, two FEL facilities, DCLS and SXFEL, have been under constructions. Dozens of stripline BPMs and cavity BPMs are planted along the LINAC accelerators and the undulators. To handle the BPM data acquisitions and the position calculations, a new in-house BPM processor has been designed.

The main system structure of the previous DBPM has been kept for the new design, and some optimizations and modifications are implemented aiming at the application on FEL. Figure 1 is an overview of the system structure. It consists of 4 input RF signal conditioning blocks, 4 analogue to digital converters (ADC), a digital signal processing module, and a CPU running control system.

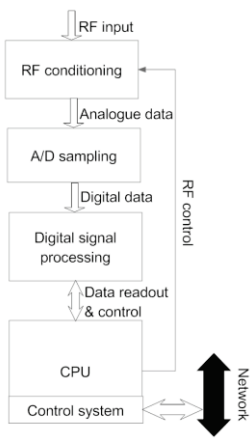

Figure 1: DBPM processor architecture.

*Work supported by National Natural Science Foundation (No. 11305253, 11575282)
#lengyongbin@sinap.ac.cn

HARDWARE DESIGN

The processor includs four input channels, and it mainly consists of three boards: a carrier board implementing the RF conditioning and digitizer with ADCs, a mother board holds FPGA and other peripheral components and interfaces, and an ARM board conducting system control (as shown in Figure 2).

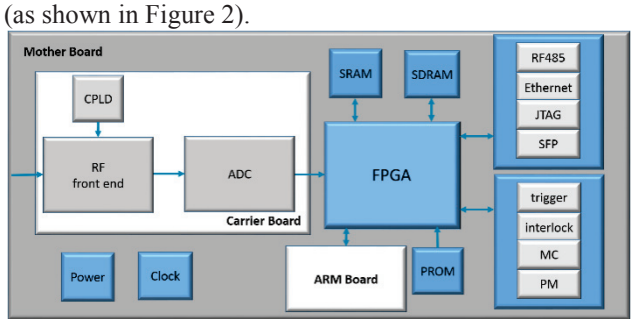

Figure 2: Hardware diagram.

RF Carrier Board

There are four input channels on RF carrier board. Each channel has two functions: the RF conditioning and the ADC digitizer. Figure 3 is the signal conditioning flow of one channel. The brief descriptions are:

- Two surface acoustic wave (SAW, TFS500A) bandpass filters, whose centre frequencies are 500MHz and their 3dB bandwidths are 12MHz.
- Three low pass filters (LFCN-575) located at different processing sections.
- Three fixed amplifiers and one 31dB digital step attenuator with 31dB dynamic range, which is controlled by a CPLD on the board.

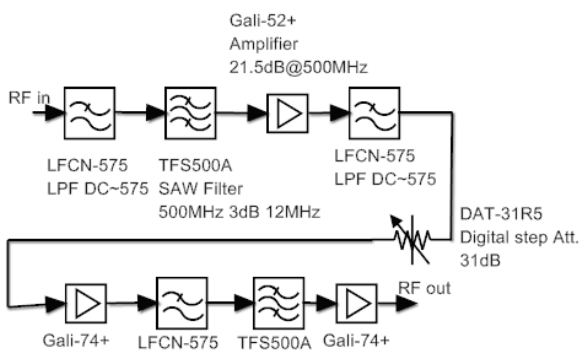

Figure 3: RF conditioning flow.

After conditioning, the RF signal is digitized by a 16bits ADC at the rate is 117.2799MHz. Clock source can be selected to be internal or external.

ISBN 978-3-95450-177-9

Mother Board

The main components on the mother board are: a Xilinx FPGA chip XCV5SX50T, a couple of DDR2 SDRAMs, a power supply, an RF board connector, an ARM connector, an Ethernet port, a UART port, and an external I/O. The FPGA and the ARM communicate through the 1x PCIE bus, The RF board is controlled by the FPGA through the SPI bus, as shown in Figure 4.

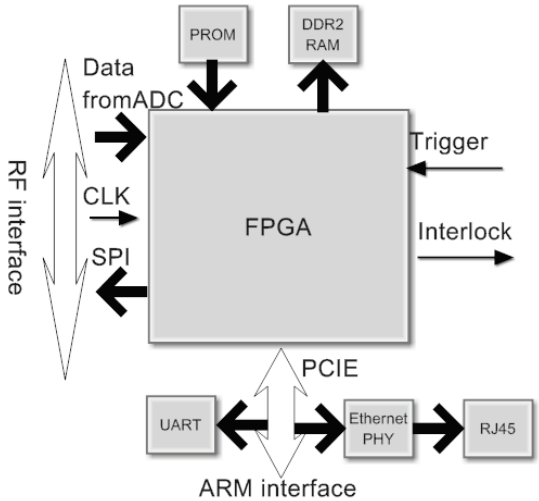

Figure 4: Mother board hardware block diagram.

ARM Board

An IMX6Q is chosen to act as a system controller. The IMX6Q is set to boot from an SD card, therefor it is convenient for batch production.

Figure 5 is the hardware pictures.

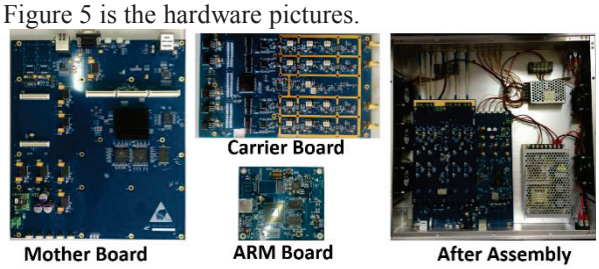

Figure 5: Hardware pictures.

FIRMWARE AND SOFTWARE DESIGN

System interfaces and signal processing functions are implemented on the FPGA. As illustrated in Figure 6, the firmware design on the FPGA includes an SPI interface with an RF board, a PCIE interface with an ARM board, 4 ADC data inputs, clocks, RAM interfaces, and an innovative self-trigger module. The self-trigger module detects the pulse arrive time and generates trigger signals when the beam passes the BPM pickups. After the trigger, a 4×2048 points FIFO in the FPGA will capture four channels of 1024 points data before and after the trigger separately. Once the FIFO is full, the FPGA will send out a sign to the ARM and restart a new cycle after the data is read out. This design enables the system work without external trigger input and improves the adaptability. Figure 7 is the function illustration of this module.

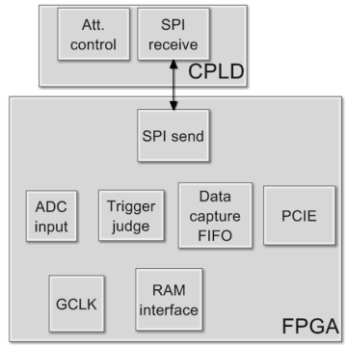

Figure 6: Firmware structure.

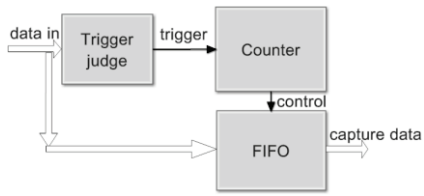

Figure 7: Self-trigger module.

The IMX6Q on ARM board runs ARM Linux OS and EPICS control system. Raw data read from FPGA is processed on IMX6Q because of low beam rate at 50Hz. Figure 8 is the EDM configure panel. Both Hilbert and FFT algorithms are implemented for user selection to calculate the amplitude and the phase on each channel. And different position calculations are supplied according to different BPM types. At the same time, the processor can be set to work with external or internal trigger.

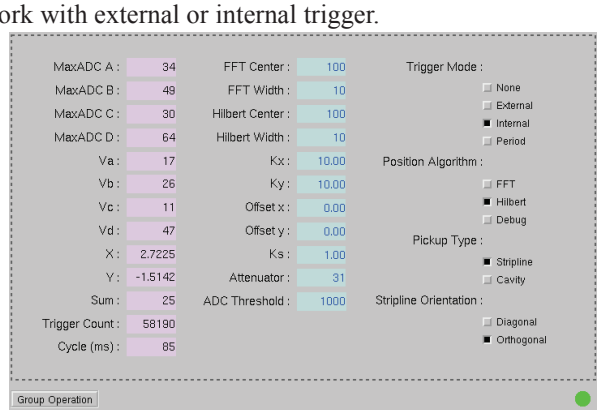

Figure 8: Configure panel.

AUTOMATIC TEST PLATFORM AND PERFORMANCE EVALUATION

Dozens of processors are used at the DCLS and the SXFEL. Manual lab test of this large amount of instruments is tedious and time consuming. An automatic test platform described in Figure 9 has been designed to improve the test efficiency. A PC running Matlab and EPICS controls the RF output signal source and the DBPM attenuator settings through TCP/IP protocol.

ISBN 978-3-95450-177-9

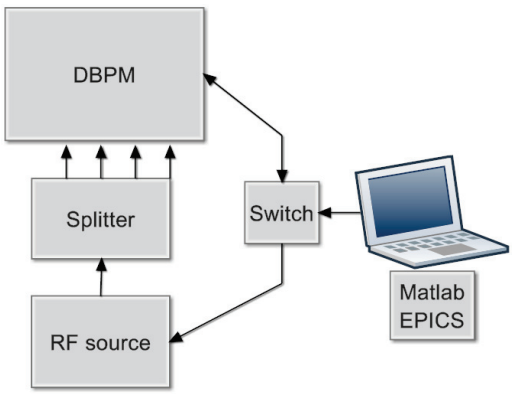

Figure 9: Automatic test platform.

Figure 10 shows the test results of one processor. Figures (a) and (b) show that the noise level and the crosstalk keep almost the same low level when the attenuator is set to be 16~31dB. Figure (c) shows the good linearity between the setting and the output of the gain. Figure (d) indicates that the SNR can be better than 76dB, which means that the effective bits is greater than 12bits.

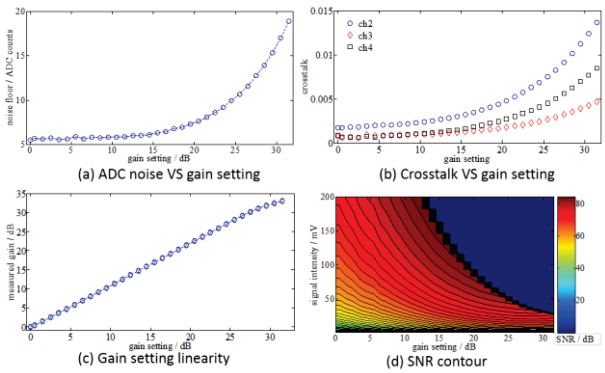

Figure 10: Performance test results.

TESTS AT THE SDUV

The SDUV is an FEL test facility in SINAP. Three adjacent cavity BPMs are installed on the LINAC accelerator to evaluate the performance of the cavity BPM system.

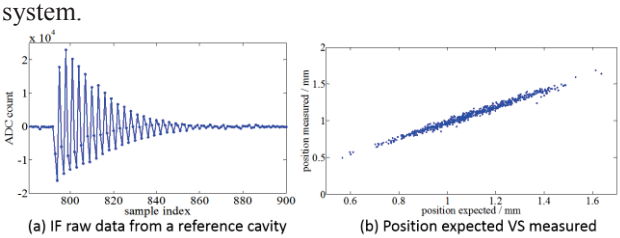

Figure 11: Test results on SDUV.

Test results show that DBPM can capture the cavity BPM intermediate frequency (IF) signal correctly, and the resolution can be better than 1 μm, which reaches the performance requirement of the cavity BPM system.

APPLICATION AT THE DCLS

There are 8 stripline BPMs and 10 cavity BPMs at the DCLS. All DBPMs are installed in this July. Figures 12 and 13 are the pictures of the batch production and application of the DBPM at the DCLS. Because the accelerator is still under commissioning, precise BPM system performance evaluations will be carried out in the future.

Figure 12: Batch production and application on DCLS.

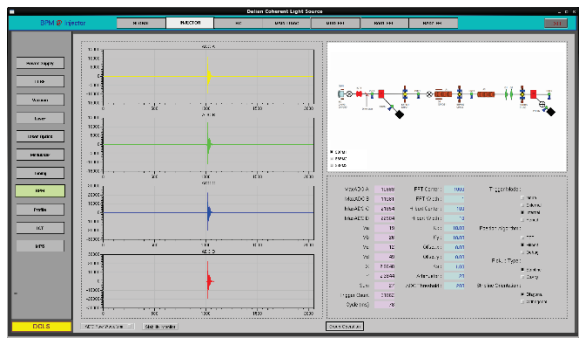

Figure 13: DCLS BPM panel.

CONCLUSIONS

A new DBPM processor has been designed for both stripline and cavity BPM. The effective bits can be greater than 12 when the input signal level and attenuation value are fitted. SDUV tests show that the DBPM works correctly. DBPMs have been applied on DCLS, system performance evaluations will be carried out in the future.

REFERENCES

[1] Lai Longwei, Leng Yongbin, et al., "DBPM signal processing with field programmable gate arrays", Nuclear Science and Techniques, 2011.

[2] Longwei Lai, Yongbin Leng, et al., "The Study and Implementation of Signal Processing Algorithm for Digital Beam Position Monitor", PAC2011, New York, U.S.A, 2011.

[3] Xing Yi, Yongbin Leng, Longwei Lai, et al., "A Calibration Method for the Rf Front-end Asymmetry of the DBPM Processor", DIPAC'11.

[4] Xing Yi, Yongbin Leng, Longwei Lai, etc. "RF front-end for digital beam position monitor signal processor", NST, 2011.

[5] Y.B. Leng, G.Q. Huang, L.W. Lai, Y.B. Yan, X. Yi, "Online Evaluation of New DBPM Processors at SINAP", ICALEPCS 2011.

[6] L.W. Lai, et al., "An Intelligent Trigger Abnormal Beam Operation Monitoring Processor at the SSRF", IPAC2015, Richmond, U.S.A, 2015.

ISBN 978-3-95450-177-9

CAVITY BPM SYSTEM FOR DCLS*

Jian Chen, Jie Chen, Longwei Lai, Yongbin Leng†, Yingbin Yan, Luyang Yu, Renxian Yuan,
SSRF, SINAP, Shanghai, China

Abstract

Dalian Coherent Light Source (DCLS) is a new FEL facility under construction in China. Cavity beam position monitor (CBPM) is employed to measure the transverse position with a micron level resolution requirement in the undulator section. The design of cavity, RF front end and data acquisition (DAQ) system will be introduced in this paper. The preliminary measurement result with beam at Shanghai Deep ultraviolet (SDUV) FEL facility will be addressed as well.

INTRODUCTION

In order to meet the growing demands of the biological, chemical and material science research, an increasing number of FEL user facilities have been constructed and being proposed in the world. Dalian Coherent Light Source is a extreme ultraviolet (EUV) coherent light source based on ultra-fast lasers and electron accelerator techniques, it will be the first FEL user facility operating exclusively in the EUV wavelength region based on the principle of high-gain harmonic generation (HGHG) scheme and the aim is to generate the FEL radiation with wavelength range from 50 to 150 nanometer [1].

The DCLS facility is located in the northeast of China and under commission now. The entire facility consists of the following parts:

1. A photo-injector will produce electron pluses of 500 pC with normalized emittance below 1 mm • mrad.
2. The linear accelerator will accelerate the electrons to 300 Mev which consists of 6 S-band accelerator structures and a movable chicane for electron bunch compression.
3. The undulator complex where the seed laser induces an energy modulation for the electron beam in the modulator and then converted into a density modulation in the dispersion chicane, a selected higher harmonic is then amplified in the radiator to generate the FEL radiation with wavelength of 50 ~ 150 nm.
4. The photo beam line and diagnostic line.

For the electron beam in the undulator section, the demanded position resolution is less than 1 um@0.5nC because the electron beam and the generated photo beam must be overlapped in the undulator section for sufficient FEL interaction between them. In SXFEL and DCLS, a C-band cavity BPM worked at 4.70 GHz for both position cavity and reference cavity is employed in order to achieve this requirement. In total, 10 CBPMs were utilized in the undulator sections of the DCLS. The schematic layout is shown in Fig. 1.

*Work supported by National Natural Science Foundation of China (No.11575282 No.11305253)
†lengyongbing@sinap.ac.cn

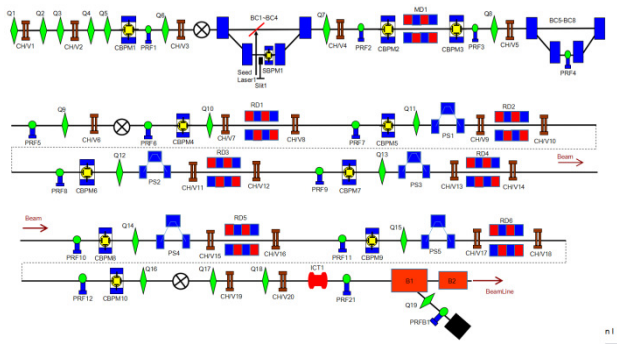

Figure 1: Schematic layout of CBPMs in the undulator section.

The CBPM system of DCLS is comprised of cavity pickup, a dedicated RF front end and DAQ system. Fig. 2 show the diagram of the system. More details and relevant results are described in the following section.

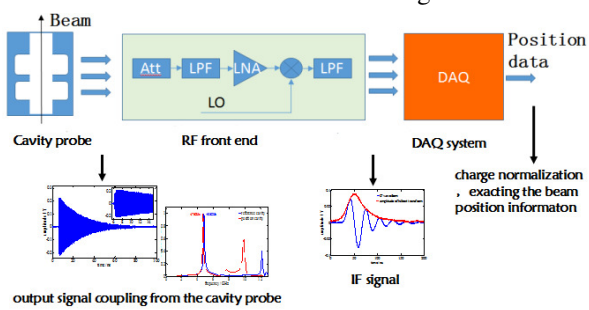

Figure 2：Diagram of the CBPM system.

DESIGN AND FABRICATE OF THE CAVITY PICKUP

A low Q factor cavity BPM was designed and tested in the last year [2,3], although it has the strengths of high efficient coupling structure and better SNR but the performance was limited by the DAQ system due to the short duration time about 2~5 ns. Considering the single-bunch working mechanism both in SXFEL and DCLS, we redesigned a high Q factor CBPM to matching with the electronics for getting a better performance. Table 1 illustrate the high Q factor CBPM design parameters.

Table 1: Design Parameters of the CBPM

Parameter	TM110	TM010
Frequency	4.70 GHz	4.70 GHz
Q	~ 8000	~ 8000
Number of ports	4(X:2, Y:2)	2

Comparing to the low Q cavity we designed before, the material changes from stainless steel of 304 to oxygen-

ISBN 978-3-95450-177-9

free copper so as to raise the Q value. The distance of the two cavities also increased from 35 mm to 45 mm in order to reduce the possibility of signal coupling between position cavity and reference cavity. The three-dimension structure of the cavity is shown in Fig. 3.

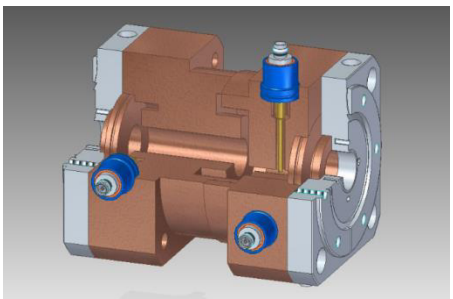

Figure 3: Three-dimension structure of the high Q CBPM.

In terms of fabricating, three sets of cavity prototype was processed and tested by Agilent N5230A PNA-L network analyzer. Analyzing the resonant frequency and correspondent Q factor by measuring the S21 parameter of the symmetric output port. Fig. 4 illustrate the S21 parameter of the one of the prototype measured by network analyzer.

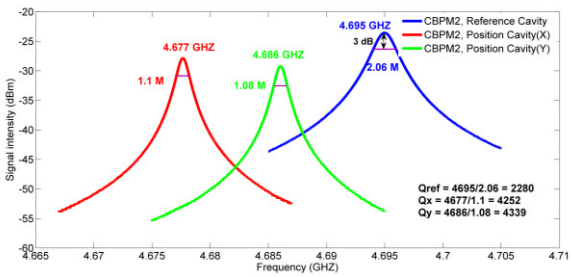

Figure 4: S21 parameter of the CBPM2 measured by network analyzer.

Combing with the designed parameters and processing technology, the specification of the cavity processing are determined and listed in Table 2.

Table 2: Specification of the Cavity Processing

	Working frequency	Q factor
Reference cavity	4693±3 MHz	2230±10%
Position cavity (X)	4680±3 MHz	4250±10%
Position cavity (Y)	4688±3 MHz	4250±10%

RF FRONT END

Design of the Front End

The RF signal coupled from the cavity will be converted to IF signal by the dedicate RF front end and then processed, the simplified block diagram is illustrated in Fig. 5.

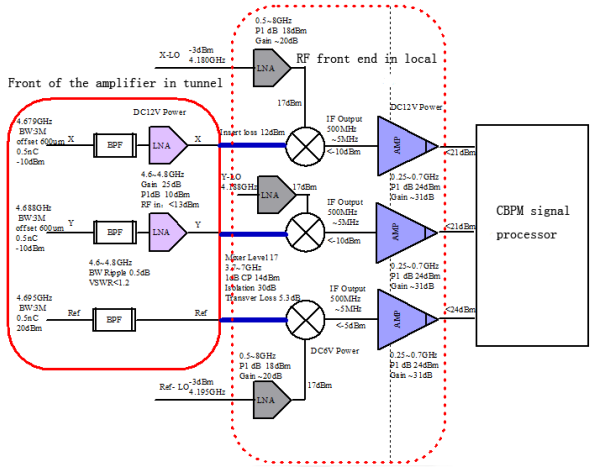

Figure 5: Block diagram of the RF front end.

The RF front end adopts two-stage amplifier structure, a cavity BPF filter with center frequency of 4.7 GHz and a LNA with gain of 25 dB make up the front of the amplifier which located in the accelerator tunnel, as close as possible to the pick-up to minimize the RF signal losses from the connected cables. The amplified RF signal then transfer to the RF front end in local station, down-convert to IF signal about 500 MHz by the mixer with the Lo signal which phase is locked to a machine reference signal that has a stable phase relative to the electron bunch. The IF amplifier accomplishes the last gain adjusting to fulfill the input requirement of ADCs.

Test of the Front End

The RF front end including the front of the amplifier was tested in laboratory, Fig. 6 is the diagram of the test. A signal generator simulate the output of the cavity (attenuation of 12dB from cables located in tunnel also included) and another simulate the machine frequency of 2856 MHz which can generate Lo signal and sampling clock by Lo signal generator.

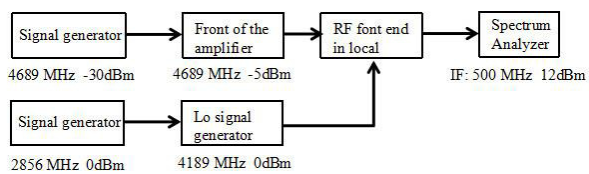

Figure 6: Diagram of the RF front end test in laboratory.

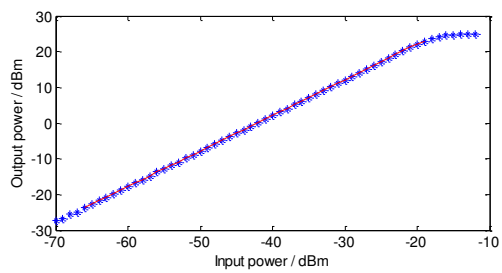

Figure 7: Gain line test of the RF front end.

The gain line test of the whole RF front end also have been done as shown in Fig .7. Because the attenuation of the cable between the two parts of the RF front end is put into the simulated cavity output signal in tested and com-

ISBN 978-3-95450-177-9

bine with the output saturation of the front of the amplifier, the input power should be less than -7 dBm which can easily achieve for cavity coupling signal.

DAQ SYSTEM

The IF signals from RF front end need to be digitized and processed by processor. Our group start the research on the digital BPM (DBPM) processor a few years ago [4], base on the requirements of the cavity BPM signals process we optimized the performance and then used in the CBPM system. Fig. 8 show the simplified diagram of the DBPM processor. The requirement of the cavity BPM processor is that the resolution of the ADC better than 12 bit and the sampling rate lager than 100 MHz, real time signal processing can be done in the FPGA and the data achieves the long-distance communication and remote control by EPICS channel access.

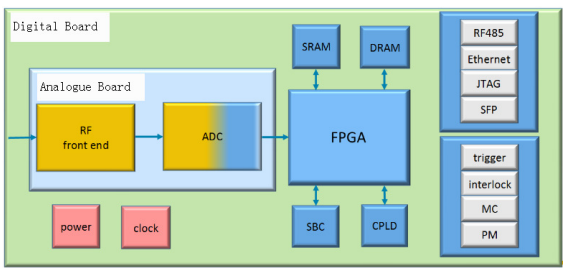

Figure 8: Simplified diagram of the DBPM processor.

The performance evaluation of the DBPM prototype also has been done in laboratory, the power of 0 to 200 mV input by using a signal generator to simulate the IF signal. Fig. 9 illustrate the gain line test result of the DBPM prototype by change the gain of the IF amplifier. And the mapping of the signal intensity and the gain setting also can be seen in Fig. 10.

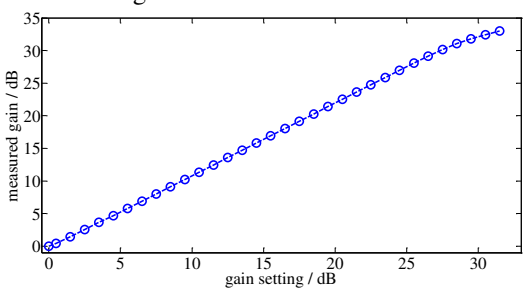

Figure 9: Gain line test result of the DBPM prototype.

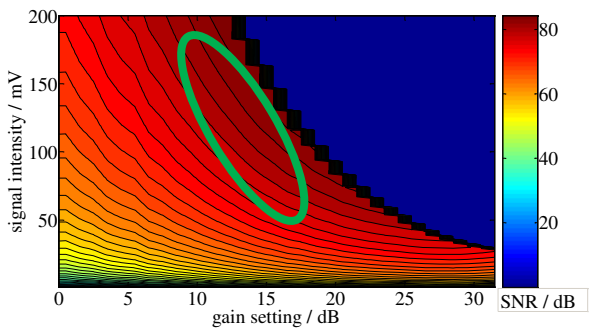

Figure 10: SNR mapping of the signal intensity and the gain setting of the DBPM prototype.

From the test results mentioned above, the DBPM prototype has a better linear gain response and the SNR is better than 75 dB when the intensity of the IF signal lager than 25 mVpp, which can meet the requirement of the cavity BPM processor.

The batch processing and test of the DBPM for DCLS has been accomplished now. Fig. 11 show the photograph of the DBPM processor.

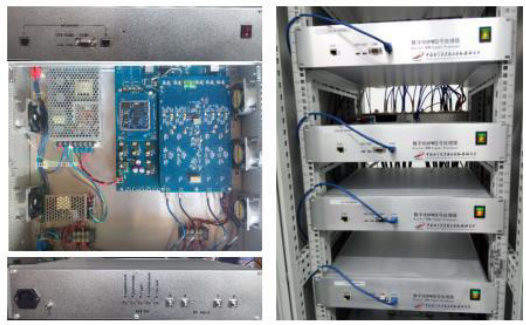

Figure 11: Photograph of the DBPM processor.

BEAM TEST AT SDUV

The cavity BPM system had also been tested with beam at SDUV facility to verify the physical design of the cavity and the performance of the whole system.

Cavity Evaluation

A broadband oscilloscope is used to test the working frequency and the Q factor of the cavity pick-up with beam and comparing with the results of the cold test, not only can evaluate the performance of the cavity but also can determine the acceptance standard of the batch processing. Fig. 12 and 13 show the RF signals and correspond frequency spectrum of the one of the CBPM.

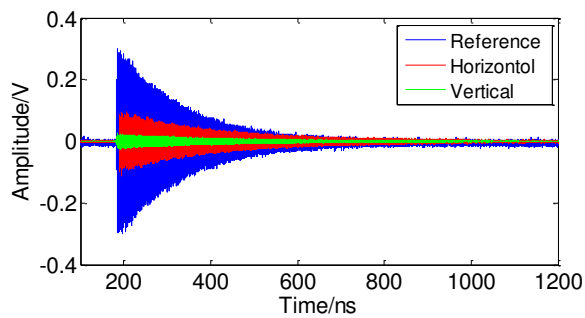

Figure 12: RF signals of the CBPM.

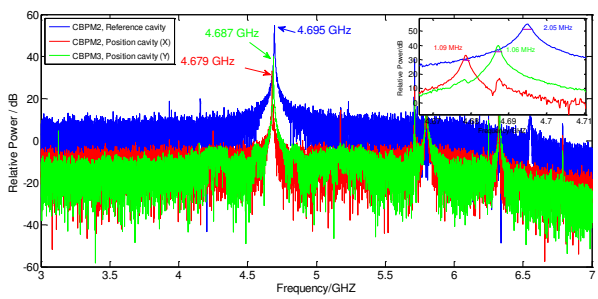

Figure 13: Frequency spectrum of the CBPM.

ISBN 978-3-95450-177-9

The results show that the waveform and frequency spectrum of the RF signals are consistent with the expectations. Furthermore, the results with beam are agree with the cold test very well. Therefore, the measurement results of S21 parameter can be the acceptance standard for cavity batch process to meet the requirement of the project.

Noise Assessment of the CBPM System

For the sake of finding the influence of the environment background noise to the resolution of the CBPM system, we did the experiment of using DBPM to collect the environment noise data when beam on and off respectively. The level of the noise are shown in Fig. 14.

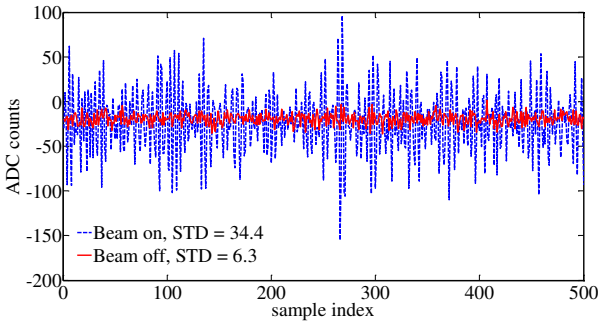

Figure 14: The level of the noise when beam on and off.

From the results we can see that the amplitude of the interference signals with beam on is lager than the condition of beam off about 6 times, which will become the one of the biggest restriction to promote the resolution of the CBPM system. In addition, one of the port of the RF front end was split by power divider and then sampled by the two channels of the DBPM to evaluate the path of the noise coupling. Fig. 15 illustrate the linear dependence of the noise picked up by different channels which indicate that the noise coupling to the system in the part of the RF front end.

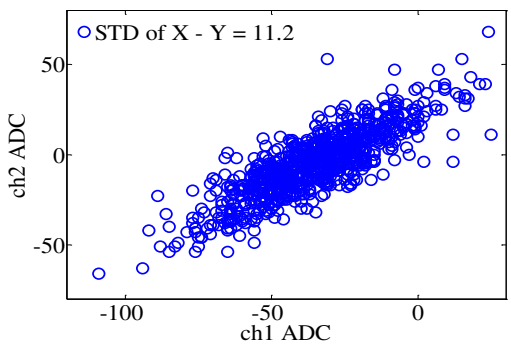

Figure 15: The linear dependence of the noise picked up by different channels.

From the assessment of the CBPM system, the suppression of the environment background noise is one of the most important roles for the CBPM system. So the electromagnetic shielding, grounded of the electronics and the test of the background noise should be considered in the scene of installation.

CONCLUSION

The cavity BPM system of DCLS is comprised of a cavity pick up, dedicated RF front end and DAQ system and the design and preliminary test with beam has been completed. The experiment results show that the performance of the CBPM system accord with the expectation and the batch processing is in progress.

The performance evaluation of the whole cavity BPM system show that:

1. Test results with beam in cavity pick-up evaluation are consistent with the cold test with S21 parameter, which can be the acceptance standard of the batch processing to meet the requirement of the project.
2. The output signal amplitude of the RF front end should be optimized within 100~200 mV to get the best SNR.
3. The electromagnetic shielding, grounded of the electronics and the test of the background noise should be considered in the scene of installation.

DCLS is under the commission stage, more experiment and further evaluation of the cavity BPM system will be made in the near future. And we are looking forward more better results after optimize the condition of beam.

REFERENCES

[1] Weiqing Zhang *et al.*, "The Perspective and Application of Extreme-UV FEL at Dalian", *FEL'13*, New York, NY, USA, Aug 2013, Slides THOCNO01.

[2] H. Maesaka *et al.*, "Sub-micron resolution rf cavity beam position monitor system at the SACLA XFEL facility", Nuclear Instruments and Methods in Physics Research A 696 (2012) 66-74.

[3] J. Chen *et al.*, "Beam experiment of low Q CBPM prototype for SXFEL", in *Proc. IPAC'16,* Busan, Korea, May 2016, paper MONP049, pp. 202-204.

[4] Yi Xing, "Research of signal conditioning and high speed data acquisition techniques for particle accelerator beam diagnostics", Ph.D. thesis, Phys. University of Chinese academy of sciences, Beijing, China, 2012.

ISBN 978-3-95450-177-9

CONCEPTUAL DESIGN OF LEReC FAST MACHINE PROTECTION SYSTEM*

S. Seletskiy†, Z. Altinbas, M. Costanzo, A. Fedotov, D. M. Gassner, L. Hammons, J. Hock, P. Inacker, J. Jamilkowski, D. Kayran, K. Mernick, T. Miller, M. Minty, M. Paniccia, I. Pinayev, K. Smith, P. Thieberger, J. Tuozzolo, W. Xu, Z. Zhao
BNL, Upton, USA

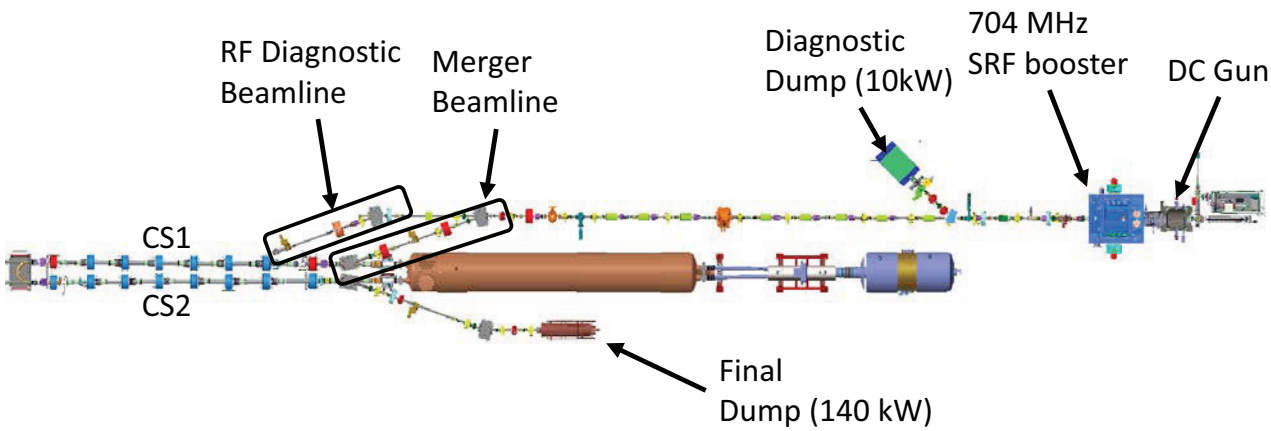

Figure 1: LEReC layout.

Abstract

The low energy RHIC Electron Cooling (LEReC) accelerator will be running with electron beams of up to 110 kW power with CW operation at 704 MHz. Although electron energies are relatively low (< 2.6 MeV), at several locations along the LEReC beamline, where the electron beam has small (about 250 um) RMS radius design size, it can potentially hit the vacuum chamber with a large incident angle. The accelerator must be protected against such a catastrophic scenario by a dedicated machine protection system (MPS). Such an MPS shall be capable of interrupting the beam within a few tens of microseconds. In this paper we describe the current conceptual design of the LEReC MPS.

LEREC LAYOUT AND PARAMETERS

The LEReC accelerator [1] consists of the 400 keV DC photo-gun followed by the 1.6-2.4 MeV SRF Booster, the transport line, the merger that brings the beam to the two cooling sections (CS1 and CS2) and the cooling sections followed by the 140 kW dump. The LEReC also includes two dedicated diagnostic beamlines: the low-power beamline capable of accepting 10 kW beam and the RF diagnostic beamline.

The LEReC layout is schematically shown in Fig. 1.

We are planning to start the gun commissioning in the winter of 2017 with the short beamline that does not include the SRF Booster and ends at 10 kW beam dump.

The LEReC beam train consists of 9 MHz macro-bunches. Each macro-bunch consists of N_b=30 bunches repeated with 704 MHz frequency. The length of each bunch at the cathode is 80 ps. The charge per bunch (Q_b) can be as high as 200 pC.

We will have the ability to work with macro-bunch trains of various length (Δt), various number of macro-bunches per train (N_{mb}), and various time delay (T) between the trains.

Also, as an alternative to our nominal operational mode with continuous train of 9 MHz macro-bunches, we will have the capability to run a continuous wave (CW) of 704 MHz bunches.

Table 1: LEReC Beam Modes

Beam modes	Goals
Low Current Mode (**LCM**) Q_b=30-130 pC; N_b = 30; N_{mb} = 1; T = 1 s	Optics commissioning: beam trajectory, beam envelope, rough RF setting, emittance measurement
RF Studies Mode (**RFSM**) Q_b=130 pC; N_b = 10,15,20,25,30; $\Delta t \leq$ 250 us; T = 1 s - 10 s	RF fine-tuning. Study beam longitudinal dynamics.
Transitional Mode 1 (**TM1**) Q_b=130 pC; N_b = 30; $\Delta t \leq$ 1000 ms; T = 1 s	Gradual transition from LCM to HCM with nominal Q_b.
Transitional Mode 2 (**TM2**) Q_b=30 - 130 pC; N_b = 30;	Alternative to TM1
High Current Mode (**HCM**) Q_b=130 pC;	Get to the design parameters
CW mode (**CWM**) Q_b=50 pC; 704 MHz CW	Alternative to HCM

* Work supported by Brookhaven Science Associates, LLC under Contract No. DE-AC02-98CH10886 with the U.S. Dept. of Energy.
† seletskiy@bnl.gov

ISBN 978-3-95450-177-9

The LEReC beam modes and their use are summarized in Table 1.

In the coming gun test we are going to utilize the LCM, TM2, HCM and CWM. TM2, HCM and CWM will be used with a reduced beam charge suitable for the 10 kW dump.

The RFSM and TM1 will be required for the complete LEReC commissioning planned for 2018 and will require laser R&D.

MPS REACTION TIME

In this paper we discuss the fast part of the LEReC MPS, which is designed to protect the machine from the damage caused by the loss of electron beam.

The RMS transverse beam size throughout the accelerator is larger than 1 mm with the exception of three locations in the merger line. In the two merger bends and in the middle of the merger line the beam is focused to 250 um RMS radius.

The design electron beam energy is 1.6 MeV, 2.0 MeV and 2.6 MeV, while our initial gun test will be performed with just 400 keV. The RF system can support electrons of up to 3 MeV energy.

The vacuum chamber in each of our bending magnets is of Y shape. Hence, the missteered beam can hit the vacuum chamber crotch at a normal incident angle.

The beam missteering with magnets is a slow process that does not define the MPS reaction time. On the other hand, the beam missteering due to the jump in the RF phase can happen in a few microseconds. Yet, a significant jump in energy will change beam focusing and, most importantly, the beam energy simply cannot get high enough for the beam to hit the "crotch" in the bending magnet vacuum chamber at 90° angle. Therefore, the worst case scenario of ultra-focused beam hitting a vacuum chamber at a normal incident angle cannot be realized.

It follows from the geometry of the chamber that the beam with 250 um RMS radius (R) can be deposited on the vacuum chamber at the maximum grazing angle (α) of 35 mrad.

We estimate the temperature increase of the stainless steel vacuum chamber of width (w) in time t as:

$$\Delta T = \frac{Pt \sin\alpha}{C_s w \rho 2\pi R^2} \qquad (1)$$

Where C_s and ρ are respectively the specific heat capacity and density of stainless steel, and P is the beam power.

The stainless steel temperature to yield is 170 °C. Applying (1) to the failure happening for the worst parameters taken for the beam with R=250 um we obtain the time to yield of 37 us. If we apply (1) to the (highly improbable) case of the beam with R=1 mm deposited on the vacuum chamber at a normal incident angle we obtain the time to yield of 21 us.

Thus, building a substantial safety margin into our system we require the MPS reaction time to be 20 us.

The estimates performed with (1) were double-checked and confirmed by ANSYS simulations.

LOW CURRENT MODE

It is essential for successful machine commissioning that in the LCM the MPS allows any beam steering as well as complete loss of the beam.

In the LCM the beam can be deposited on the vacuum chamber, the YAG profile monitor equipped with the copper mirror inclined at 45° with respect to the beam direction, the emittance slit, the vacuum valve or the beam scraper.

To estimate the thermal effect of the beam loss in the LCM we apply (1) to the case of the beam with the timing pattern specified for the LCM (Table 1) and with R=0.25 mm deposited on a stainless steel surface with a normal incident angle and to the case of the beam with R=1 mm deposited on the copper surface at 45° angle. The results of such calculations are presented in Fig. 2.

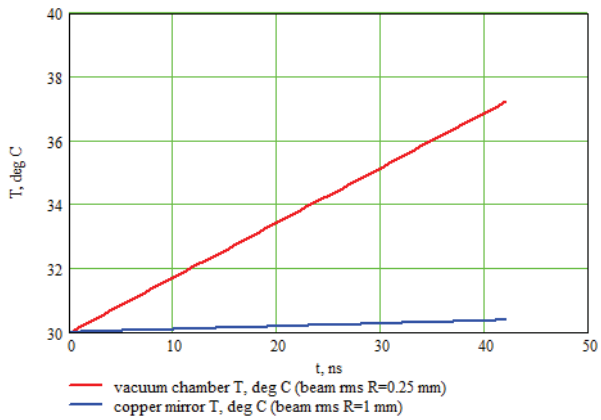

Figure 2: Red trace shows the effect of 42 ns long macro-bunch with R=0.25 mm and Q_b=130 pC hitting the stainless steel surface at a normal incident angle. The blue trace shows the thermal effect on the copper mirror intercepting 42 ns long macro-bunch with R=1 mm and Q_b=130 pC at 45° angle.

It is obvious that the effect of complete beam loss in the LCM is well within the range of elastic deformation of both stainless steel and copper. We do not expect any fatigue failure from such a small thermo-mechanical stress.

We conclude that the LCM is ultimately a safe operation mode that does not require any control of beam trajectory or beam losses.

POSSIBLE FAILURE SCENARIOS

We consider the following possible machine failures:

1. Beam lost inside the gun.
2. There is a possible laser failure that will result in the train of electron bunches having the same average beam power but carrying a charge per bunch which differs from the design one. These wrong-charge bunches will be not focused properly and will get lost at the entrance of the SRF Booster.

ISBN 978-3-95450-177-9

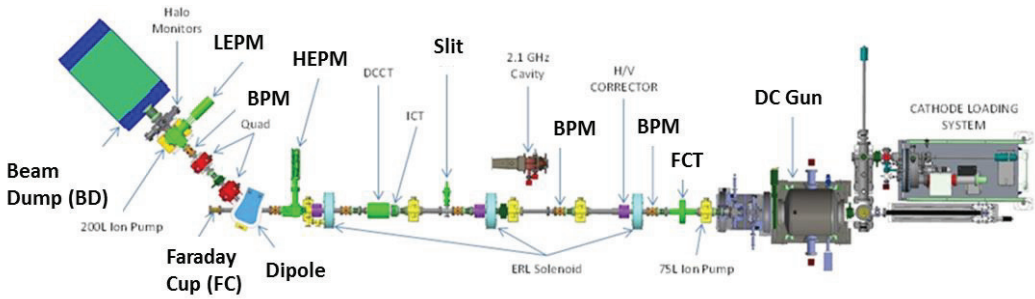

Figure 3: Layout of LEReC gun test.

3. Beam having a wrong power is lost on the insertion device, dump or vacuum chamber.

We shall exclude the possibility of beam losses inside the gun. To do so we will initially use administrative controls, which will require an operator to start commissioning with minimally observable charge and current to establish good beam trajectory out of the gun prior to increasing beam charge. After the beam trajectory out of the gun is established, the MPS will be monitoring the settings of the anode corrector current and of the laser input mirrors position.

After detailed studies of the possible beam losses in the SRF Booster due to the laser failure described above we concluded that the planned Booster quench protection is adequate enough to guarantee that no damage is done to the SRF system. Therefore the MPS will rely on the quench detection signal to shut down the accelerator in a timely fashion.

Finally, we plan both proactive and reactive responses from the MPS to protect accelerator against the failure described in item 3.

The scheme of proactive protection involves automatic detection of the present beam power and of the surface, which the beam is supposed to hit. It also includes continuously monitoring the readings of a number of beam position monitors (BPMs) and tripping the accelerator in case the beam trajectory goes outside of the allowed range.

The reactive part of machine protection will rely on detecting the beam losses exceeding allowed threshold. We plan to install a number of beam loss monitors (BLMs) in the strategic locations and also to detect losses from the differential readings of the fast current transformers (FCTs) located downstream of the gun and upstream of each of the beam dumps [2].

Thus, the MPS will rely on BPM, FCT and BLM readings. We expect the FCT and BLM reaction times to be within a few microseconds range. The BPM readings are updated every 12 us.

MPS LOGIC

The MPS determines the surface, which the beam is supposed to hit, from the settings of the dipoles and from what insertion devices are inserted into the beamline. These inputs to the MPS are called qualifiers.

Depending on the qualifiers MPS determines what beam power is allowed for the present machine settings.

The actual beam power is calculated from the current readings of the FCT and from the assumed beam energy.

Next, the MPS compares the measured beam power to the allowed one and if the measured power exceeds the allowed limit then the MPS trips the machine. Another cause for the MPS to trip the machine above certain power limit is the BPM readings outside of the allowed range.

Finally, the MPS always monitors the BLM readings and in case the losses are above the predefined limit the MPS trips the accelerator.

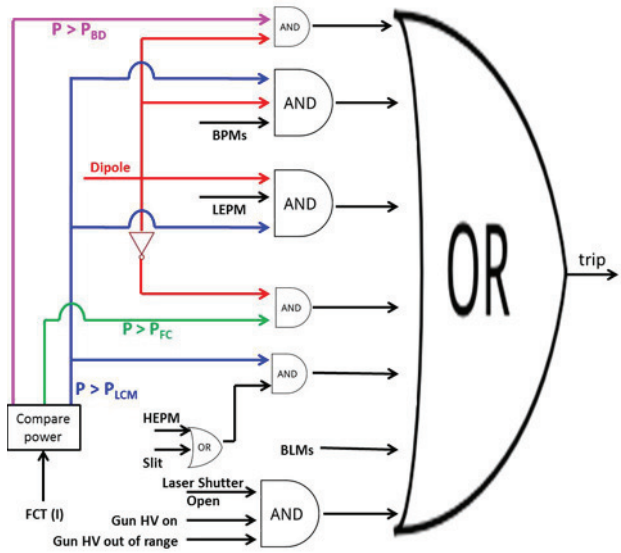

	0	1
Dipole	Off	On
BPMs	In range	Not in range
LEPM	Out	In
HEPM	Out	In
Slit	Out	In
BLMs	Losses are below limit	Losses are above limit

Figure 4: MPS Logic for the LEReC gun test.

To clarify the described concepts we will consider the MPS logic for the simple beamline that will be commissioned during LEReC gun test (Fig. 3).

The logic of the MPS for the gun test is schematically shown in Fig. 4.

ISBN 978-3-95450-177-9

The LEReC gun test beamline consists of the DC gun and the transport line to the beam dump (BD) which includes a single dipole magnet. If the dipole is turned on then the beam is transferred to the BD, if the dipole is turned off then the beam is transported to the Faraday cup (FC). Both the BD and the FC have the beam power levels (P_{BD} and P_{FC}) that they can accept.

The energy of the beam in the gun test is defined by the gun only and is expected to be 400 keV. Therefore, beam power is completely defined by the current as read by the FCT.

The insertion devices in the gun test beam line include the emittance measurement slit and the high energy profile monitor (HEPM) installed upstream of the dipole as well as the low energy profile monitor installed downstream of the dipole (LEPM). The insertion devices can accept the LCM beam. If the beam power exceeds the power of the low current mode beam (P_{LCM}) then the MPS trips the machine.

The MPS monitors beam trajectory in the BPMs upstream and downstream of the dipole for beam power $P>P_{LCM}$.

Finally, we have two additional operation modes, the "isolation mode" and "laser alignment mode".

In the isolation mode the laser shutter is closed so that the gun and the laser conditioning can be performed independently. The qualifier for this mode is the status of the laser shutter.

In the laser alignment mode the gun high voltage (HV) is turned off, so that the laser can be aligned on the cathode. The status of the gun HV is the qualifier for this mode.

MPS TO LASER INTERFACE

The MPS trips the accelerator by shutting down the laser beam to the photocathode.

The sequence of the laser devices used to shape the pulse trains in the time domain is schematically shown in Fig. 5.

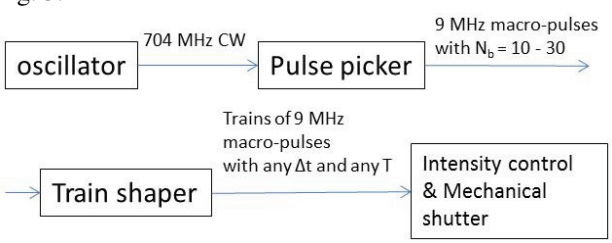

Figure 5: Laser pulse shaping scheme.

The CW train of laser pulses coming out of the oscillator is chopped into the 9 MHz macro-pulses by the pulse picker - an electro-optic modulator (EOM) with a fast (~1 ns) rise/fall time. Since the pulse picker has to be fine-tuned for the high extinction ratio it must be physically by-passed to switch to the CWM. Hence, it cannot be used by the MPS.

The train shaper is a Pockels cell (PC) followed by a half-wave plate (HWP). Depending on the HWP angle the PC either passes the laser pulses through or blocks the laser when the voltage is applied. The first polarization is used to create the trains of macro-bunches of particular length with some repetition rate. The second polarization is used in CWM.

The PC can withstand the high voltage only for 5% of its switching period. Therefore, in the CWM it can be used by the MPS only in combination with the fast mechanical shutter. That is, when a trip condition is detected the MPS will apply a voltage to the PC for 50 ms, which is enough time to close the shutter (shutter closing time is a few milliseconds).

The Intensity Controller consists of the EOM for intensity stabilization and the HWP for intensity limitation. The EOM is used to cut a few percent of laser intensity to smooth the intensity variation. The remotely controlled HWP is used to set the required laser intensity.

The EOM can be used to shut down the laser since its "0 Voltage" state corresponds to zero laser output. The alignment of the EOM can get as bad as 2 % after it was exercised several times. Thus we expect that about 2 % of the nominal laser intensity will be reaching the cathode until the mechanical laser shutter is completely closed.

We plan to use both the PC and the intensity control EOM together with the mechanical shutter to block the laser beam to the photocathode.

CONCLUSION

We discussed the conceptual design of the fast Machine Protection System for the Low Energy RHIC Electron Cooling accelerator.

The MPS is designed to protect the insertion devices, the vacuum chamber and the beam dumps from excessive deposit of the electron beam.

The MPS will detect any possible fault condition and will shut down the electron beam within 20 us by inhibiting the laser beam to the photocathode.

REFERENCES

[1] A. Fedotov, "Bunched beam electron cooling for Low Energy RHIC operation", in ICFA Beam Dynamics letter No. 65, p. 22 (December 2014).

[2] T. Miller et al., "LEReC instrumentation design & construction", presented at the IBIC'16, Barcelona, Spain, Sept. 2016, paper TUPG35.

ISBN 978-3-95450-177-9

AN OPTICAL FIBRE BLM SYSTEM AT THE AUSTRALIAN SYNCHROTRON LIGHT SOURCE

M. Kastriotou*[1, 2], E.B. Holzer, E. Nebot del Busto [1, 2], CERN, Geneva, Switzerland
[1] also at University of Liverpool, Liverpool, UK
[2] also at Cockcroft Institute, Warrington, UK
C.P. Welsch, Cockcroft Institute, Warrington; University of Liverpool, UK
M. Boland, SLSA, Clayton, Australia; University of Melbourne, Australia

Abstract

Increasing demands on high energy accelerators are triggering R&D into improved beam loss monitors with a high sensitivity and dynamic range and the potential to efficiently protect the machine over its entire length. Optical fibre beam loss monitors (OBLMs) are based on the detection of Cherenkov radiation from high energy charged particles. Bearing the advantage of covering more than 100 m of an accelerator with only one detector and being insensitive to X-rays, OBLMs are ideal for electron machines.

The Australian Synchrotron comprises an 100 MeV 15 m long linac, an 130 m circumference booster synchrotron and a 3 GeV, 216 m circumference electron storage ring. The entire facility was successfully covered with four OBLMs. This contribution summarises a variety of measurements performed with OBLMs at the Australian Synchrotron, including beam loss measurements during the full booster and measurements of steady-state losses in the storage ring. Different photosensors, namely Silicon Photo Multipliers (SiPM) and fast Photo Multiplier Tubes (PMTs) have been used and their respective performance limits are discussed.

INTRODUCTION

Optical fibre beam loss monitors comprise an optical fibre coupled to a photosensor. Their operation principle is the detection by the photosensor, of Cherenkov photons [1], which are generated in the fibre by high energy charged particles produced through a beam loss. With the advantages of covering long distances while being sensitive to electrons and insensitive to X-rays, these monitors can be favorable for the machine protection of light sources.

The position reconstruction of OBLMs for electron storage rings has been discussed in past studies [2]. In the present paper the potential of covering the complete machine and the performance of OBLMS during normal operation of a light source is examined at the Australian Synchrotron Light Source.

EXPERIMENTAL SETUP

The Australian Synchrotron

In the Australian Synchrotron [3], electrons are generated in a 500 MHz thermionic gun and enter a 15 m linac, which accelerates them to 100 MeV. The electrons are then injected into a 130 m booster ring that further accelerates them up to 3 GeV. During the last few tens of milliseconds of the 600 milliseconds ramping cycle, the closed orbit is altered via a slow bumping technique. This allows the beam to be centered at the extraction point within the field of the fast magnet that kicks the beam into the Beam To Storage ring (BTS) transfer line. At the end of the BTS, another kicker magnet injects the beam into Sector 1 of a 216 m circular storage ring that consists of 14 sectors with a double bend achromat lattice. Sector 11 contains the beam scrapers used to concentrate the beam losses at this location and so protect the multiple insertion devices located elsewhere in the ring.

During standard operation, the storage ring holds a beam current of 200 mA, injected in trains of 75 bunches and a current of approximately 0.5 mA. Nominally, the beam fills 300 out of the 320 available 500 MHz buckets. Beam lifetimes as good as 200 hours can be reached. When operating in single bunch mode, the bunch charge can be varied in the range of 10^{+5} – 10^{+9} electrons [4].

Installation

The entire accelerator complex of the Australian Synchrotron Light Source was covered for the observation of beam losses with a set of only four optical fibres. Each fibre consists of a 200 µm pure silica core, 245 µm cladding and a 345 µm acrylate coating. A dark nylon jacket provides protection against ambient light and mechanical breakage.

The schematic of the installed cables and their respective photon sensors is shown in Fig. 1. Two fibres were installed symmetrically on the inner and outer side of the linac, each covering half of the booster ring. One of these also covered a large fraction of the BTS transfer line as well as the booster extraction point. Only one optical end of each of these fibres is extracted to the roof of the facility, at Sector 2. The other two fibres cover half of the storage ring, each with photosensors installed in both ends [2].

Photosensors

Two types of photosensors have been examined in the present study: A Hamamatsu fast photomultiplier tube (H10721-10) and a Silicon Photomultiplier (Multi Pixel Photon Counter S12572-015C) [5]. The latter is coupled to a transimpedance amplifier (comprised of a Texas Instruments THS3061 operational amplifier [6] and a feedback resistor)

* maria.kastriotou@cern.ch

ISBN 978-3-95450-177-9

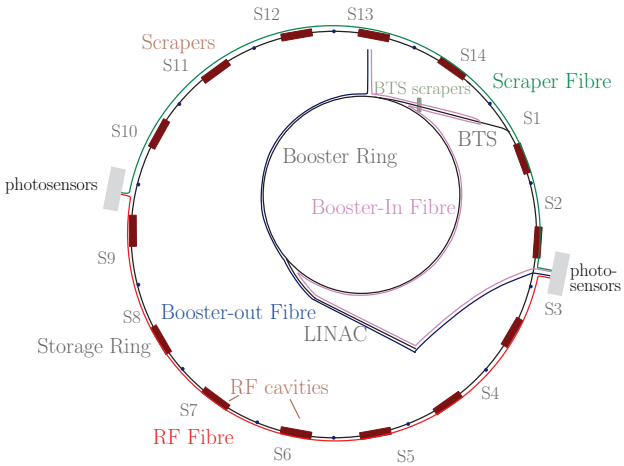

Figure 1: A sketch of the four optical fibre BLMs installed at the Australian Synchrotron Light Source. The Scraper fibre (green) and the RF fibre (red) cover the Storage Ring, the Booster-In fibre (magenta) covers the linac and half the booster ring, while the Booster-out fibre (blue) covers the linac, half of the booster ring and the BTS line.

enclosed in a custom made RF shielded module with low pass filters in the bias input to reduce noise as described in [7]. The back-end electronics for the acquisition of the signals are described in detail in [2].

STEADY-STATE LOSSES

Method

Two beam losses scenarios were studied during the injection of electrons into the storage ring. In the first case injection losses were studied by injecting single bunches into the storage ring, with beam already circulating and the beam scrapers entirely open. In the second case, nominal 75 bunch trains were injected into a previously empty storage ring, with the beam scrapers positioned to leave an 11 mm gap.

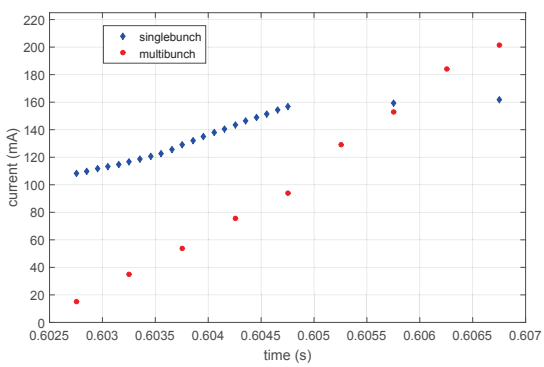

Figure 2: Circulating beam in the storage ring after each set of 50 shots in the single bunch and 25 shots in the multi bunch case, with respect to the trigger timing.

Table 1: Experimental Cases Studied

bunches	Scrapers	sample interval	time window
1	open	1 ns	56 000 ns
75	nominal	10 ns	500 000 ns

The data presented here were collected at Sector 2, from the downstream of the scraper fibre using the fast-PMT and the upstream of the RF fibre via the SiPM (channel A and B respectively). As the data acquisition depth was limited to 56 µs (single bunch case) and 500 µs (multi bunch case), to look at losses at later times the trigger time was delayed. For each trigger timing, 50 shots with 56000 samples and 1 GHz sampling rate were taken in the case of single bunch injections, whereas in the multi bunch case 25 shots with 50000 samples and 0.1 GHz sampling rate were acquired. The characteristics of the two different measurements are summarised in Table 1. Fig. 2 shows the beam current after each number of datasets acquired per trigger timing, as measured by the beam current monitor of the storage ring for the two cases.

Since steady-state losses are expected to be on the order of a few electrons per turn, an estimation of the OBLM background for such a measurement is essential. Without beam in the machine 30 background datasets were acquired and the mean value of the signals obtained is presented in Fig. 3. To ensure that the signals detected in the steady-state case were real beam losses, a value greater than the maximum of the background signals was considered as a cutoff value, with $V_{cut} = 0.0006$ V for channel A and $V_{cut} = 0.0137$ V for channel B. These background signals are attributed mainly to the photosensors, and the difference between them comes from their different noise levels. In the case of the SiPM, an offset is also introduced by the transimpedance amplifier front end electronics.

The detected charge (charge that the photosensor generates) for the PMT was calculated from all samples whose

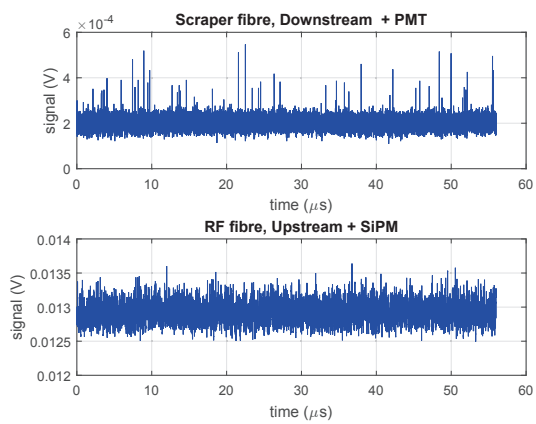

Figure 3: Background of the fibres covering the storage ring.

ISBN 978-3-95450-177-9

value was higher than the selected cutoff, as:

$$C_{PMT} = \frac{\sum (V - V_{off})_{(V>V_{cut})} \times t}{R}, \quad (1)$$

where $R = 50\,\Omega$ the measurement load and t is the sample interval. The signal offset V_{off} has been estimated as the mean value of the background signal. For the SiPM with the transimpedance amplifier readout, the respective value for the generated charge has been calculated as:

$$C_{SiPM} = \frac{2 \times \sum (V - V_{off})_{(V>V_{cut})} \times t}{R_F}, \quad (2)$$

where $R_F = 0.5\,\mathrm{k}\Omega$ is the feedback resistor.

Due to the different time windows and in order to compare the two cases, the detected current was estimated as $I_{sb} = C_{sb}/56000\,(\mathrm{A})$ and $I_{mb} = C_{mb}/500000\,(\mathrm{A})$ for the single bunch and the multi bunch case respectively.

Results

A comparison of the two measurements is summarised in Fig. 4. Each point corresponds to the mean value of the signal for the number of datasets acquired per trigger timing. In Fig. 4a, the signals of the Scraper fibre downstream end, coupled to the PMT, are presented. In both cases the exponential loss decay, which is characteristic of the beam injection process, can be observed. During this time the losses measured for the multi bunch (scrapers in) case are up to two orders of magnitude higher than the ones of the single bunch case (scrapers out), which is attributed both to the larger beam charge and the presence of scrapers. When reaching the steady-state the signals of the multi bunch are slightly higher, again probably due to the higher charge and beam cleaning at the scrapers. Figure 4b, shows the signals of the RF fibre upstream end connected to the SiPM. In this case, losses at injection are not observable. However, the single bunch case shows losses constantly higher than in the multi bunch case, when the beam has been cleaned before, which indicates the detection of steady-state losses by the OBLMs.

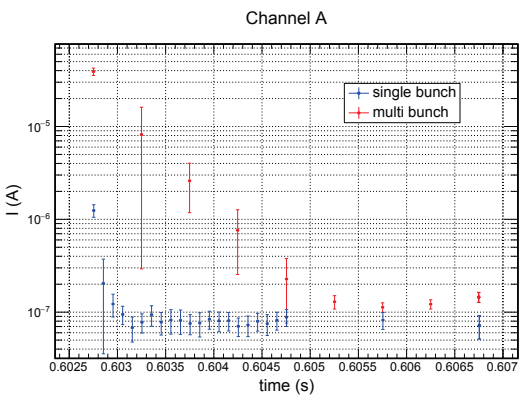

(a)

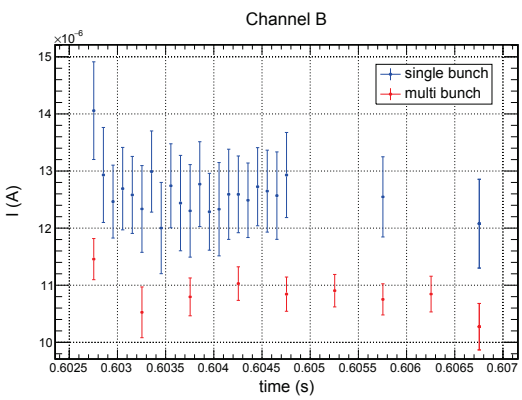

(b)

Figure 4: Comparison of the detected current in the single bunch and the multi bunch case. (a) For Channel A, with a fast PMT coupled to the downstream of the Scraper fibre. (b) For Channel B, with an SiPM coupled to the upstream of the RF fibre.

BEAM LOSSES DURING THE BOOSTER CYCLE

Method

The beam losses during the complete booster cycle of the Australian Synchrotron, from the beam injection to the extraction through the BTS to the Storage Ring, have been measured with the installed OBLMs.

For this study the Booster-In fibre was connected to the fast-PMT and the Booster-Out fibre to the SiPM. The fiber background, i.e. the signal measurement in absence of circulating beam, estimated as an average of 30 shots is presented in Fig. 5. The booster background signals are very similar to the ones observed for the storage ring (Fig. 3), which points to the noise coming mainly from the photosensors themselves. A value of $V_{cut} = 0.000\,36\,\mathrm{V}$ was considered as an offset for the Booster-In fibre and the PMT, and of $V_{cut} = 0.0134\,\mathrm{V}$ for the Booster-Out fibre and the SiPM. As above, different times of the booster cycle are explored by delaying the trigger time. For each point 50 shots were

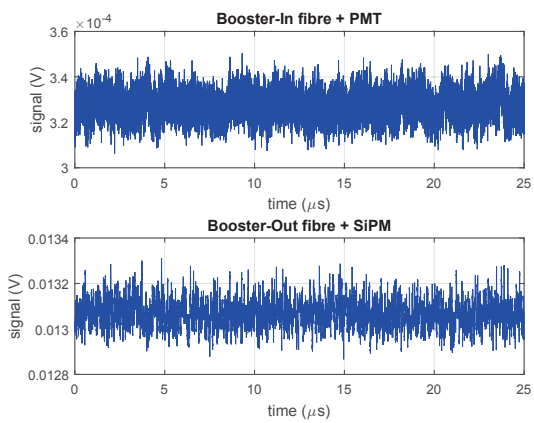

Figure 5: Background of the two fibres covering the Linac, Booster and BTS line.

ISBN 978-3-95450-177-9

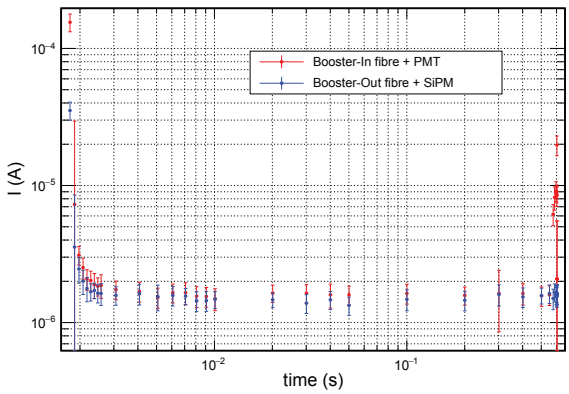

Figure 6: Beam losses during the booster cycle as detected by the Booster-In fibre coupled to a fast-PMT, and the Booster-Out fibre coupled to an SiPM. Due to the different gain of the photosensors, the two signals can only be compared qualitatively and not quantitatively.

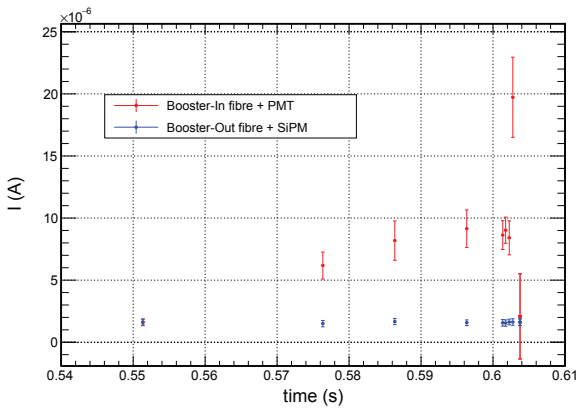

Figure 7: Losses during the last milliseconds of the booster cycle before extraction to the storage ring (zoom of Fig. 6).

acquired, with 1 GHz sampling rate and 25000 samples. The charge collected by the photon sensors was estimated via Eq. (1) and (2) for the PMT and SiPM respectively. For consistency with the previous results, the detected current was calculated as $I = C/25000$ (A).

Results

Figure 6 shows the signals detected by the two booster fibres throughout the full cycle. The injection into the booster is rather noticeable with detected charges that reach up to 100 µA. In the following milliseconds, an exponential decay characteristic of the injection process is observed. After the first 4 ms the losses reach a plateau compatible with zero signal. However, the signals observed on the plateau are consistently higher than the range of dark current expected for the two photon sensors, namely: 1 nA for the fast PMT and 100 nA for the SiPM.

The beam extraction to the storage ring is illustrated in higher detail on Fig. 7. A gradual increase of the losses in the case of the Booster-In fibre can be observed, which is attributed to losses developed in the BTS line, a location covered only by this fibre. The losses increase further as the beam is injected to the storage ring and after the injection decrease to the value of the plateau. In the Booster-Out fibre the extraction losses cannot be observed. This is due to the fact that this particular fibre does not cover the BTS line region.

CONCLUSION

Optical fibre BLMs have been installed and tested for their performance at the Australian Synchrotron Light Source facility. It has been demonstrated that OBLMs are capable of detecting losses during beam injection to the storage ring, and that they have the capability of detecting steady-state losses. Two photosensors, a fast-PMT and an SiPM, were examined showing similar behaviour. The main difference between the two detectors is their noise levels, and the higher noise of the SiPM may render the detection of very low signals more challenging.

ACKNOWLEDGMENT

The authors of this paper would like to thank the operators of the Australian Synchrotron Light Source for their invaluable help on the execution of the experiments.
This work has been partly funded by the Royal Society via the International Exchange Scheme project PPR10353.

REFERENCES

[1] Jelley, J. V., "Čerenkov Radiation and its Applications", 1958, Pergamon Press, London

[2] E. Nebot del Busto et al., "Position resolution of optical fibre-based beam loss monitors using long electron pulses", IBIC'15, Melbourne, September 2015, WEBLA03

[3] J. Boldeman et al., "The physics design of the Australian Synchrotron Storage Ring", Nucl. Instr. and Meth., A 521, 2004

[4] E. Nebot del Busto et al., "Measurement of Beam Losses at the Australian Synchrotron", IBIC'14, Monterey, September 2014, WECZB3

[5] Hamamatsu Photonics K.K., http://www.hamamatsu.com/

[6] Texas Instruments Inc., http://www.ti.com/

[7] M. Kastriotou et al., "A Versatile Beam Loss Monitoring System for CLIC", IPAC'16, Busan, May 2016, MOPMR024

ISBN 978-3-95450-177-9

RELATION BETWEEN SIGNALS OF THE BEAM LOSS MONITORS AND RESIDUAL RADIATION IN THE J-PARC RCS

M. Yoshimoto#, H. Harada, M. Kinsho, K. Yamamoto
J-PARC, JAEA, Tokai, Ibaraki, 319-1195, Japan

Abstract

To achieve routine high power MW-class beam operation requires that the machine activations are within a permissible level. Thus, our focus has been to reduce and manage beam losses. Following the issues with the ring collimator in April 2016, the GM counter now measures the residual dose along the ring. These detailed dose distributions can now provide more details of the beam loss. Here, a new BLM is proposed that detects the spot area beam loss to determine the relation between the residual dose distribution and the beam loss signals. The new BLM will allow for a detailed map of the beam losses.

INTRODUCTION

The 3-GeV Rapid Cycling Synchrotron (RCS) of the Japan Proton Accelerator Research Complex (J-PARC) accelerates protons from 400 MeV to 3 GeV kinetic energy at 25 Hz repetition rate. The average beam current is 0.333 mA and the design beam power is 1 MW [1]. In addition, the RCS has two functions as a proton driver for neutron/muon production at the Material and Life science experimental Facility (MLF) and as a booster of the Main Ring synchrotron (MR) for the Hadron experimental facility (HD) and Neutrino experimental facility (NU). In order to maintain such routine high power MW-class beam operation, the machine activations must be kept within a permissible level. Therefore, we adopt a ring collimator system to remove the beam halo and localize the beam loss at the collimator area [2]. Fig. 1 shows the schematic view of the RCS ring and the ring collimator system. The RCS ring collimator system consists of a primary collimator, also referred to as "scatter", which scatters the halo particles, and five secondary collimators, so-called "absorbers", which absorb those scattered particles.

During April, 2016, the ring collimator system experienced serious trouble. A collimator control system failure occurred followed by a vacuum leak at the secondary collimator no. 5 (Col-Abs. no. 5). In order to restart the user beam operation, the Col-Abs. no. 5 was replaced with spare ducts, which did not have radiation shielding. In addition, as a precaution, every other collimator from this system must be stopped. As a result, it is difficult to maintain localization of the beam loss in the RCS after the restart of the beam operation. Therefore, a series of particle tracking experiments were carried out to examine how the particles were lost under various collimator arrangements. The change in the beam loss profile and variations in the radiation dose were estimated in advance. After solving the problem with the collimator, we tried tuning the beam to minimize the beam loss without adjusting the collimator. Subsequently, the user beam operations are restarted [3]. In addition, we measured the residual dose along the ring every short maintenance period to investigate the influence of the collimator trouble.

In this paper, we report measurement results of the residual dose distribution along the ring. The relation between the residual dose distribution and the beam loss signals indicates new knowledge of the RCS beam loss sources and mechanism. In addition, we introduce a new beam loss monitor (new BLM), which detects the spot area beam loss to evaluate the residual radiation of the ring.

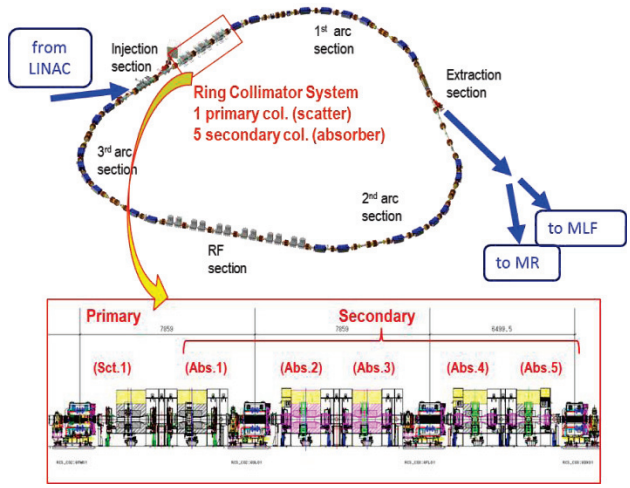

Figure 1: Schematic view of the Japan Proton Accelerator Research Complex (J-PARC) rapid cycling synchrotron (RCS) and the ring collimator system.

RESIDUAL DOSE MEASUREMENT

The beam loss profiles along the ring were predicted to change drastically due to the replacement of the Col-Abs. no. 5 with the spare ducts. Thus, detailed distributions of the residual dose along the ring were measured using a Geiger–Müller counter and compared with the distribution of the beam loss signals obtained by proportional counter-type beam loss monitors (P-BLMs). Fig. 2 shows the comparison between the beam loss signals and the residual dose distributions on four sides of the duct along the ring. The P-BLMs are installed along the ring and beam lines, and they are mainly used in the interlock system for machine protection [4]. The P-BLM signals are integrated and archived at every beam-shot. The RCS has a threefold symmetric lattice that partitions

yoshimoto.masahiro@jaea.go.jp

ISBN 978-3-95450-177-9

into 27 FODO cells (three cells in each straight section and six cells in each arc section). Next, a few P-BLMs are placed in every cell with typical locations under the steering magnets as shown in Fig. 2. Therefore, it is difficult to obtain the definitive loss profile because the P-BLM is aimed at detecting significant beam loss at every cell. On the other hand, we measure the residual dose upstream and downstream of all bending magnets (BMs) and quadrupole magnets (QMs) in contact with inner, outer, upper, and lower sides of the each vacuum duct. In comparison with the P-BLM signals, the residual dose measurement results can indicate the detailed beam loss profiles in the ring and clearly distinguish the four side beam loss distributions. In particular, the inner side distribution exhibits a characteristic pattern. These results are stored in references to evaluate the influence of replacing the Col-Abs. no. 5 with the spare ducts. After the beam was tuned to minimize beam losses obtained by the P-BLMs, the user beam operation were restarted. Residual dose measurements were then carried out during every short maintenance period. The RCS operation status for every residual dose measurement is summarized in Table 1. A transition of the beam loss distribution during beam operation and transition of the residual dose distribution after the beam stop are shown in Fig. 3.

Table 1: Rapid cycling synchrotron (RCS) operation status for every residual dose measurement

	4/11	4/14	4/20	4/27
Operation period	Before restart	Half-day operation	One-week operation	Two-week operation
User (power)	MLF (205kW)	MLF (205kW) MR/NU (360kW)	MLF (205kW) MR/NU (385kW)	MLF (207kW) MR/NU (386kW)
Beam stop	4/4 7:00	4/14 7:45	4/20 9:00	4/27 9:00
Measurement	13:15–20:31	14:18–17:13	13:38–16:13	15:35–18:27
Elapsed time	174.3h–181.5h	6.5h–9.5h	4.5h–8.0h	6.5h–10h
Worker dose		0.05 mSv/h 0.01 mSv/h	0.09 mSv/h 0.02 mSv/h	0.13 mSv/h 0.03 mSv/h

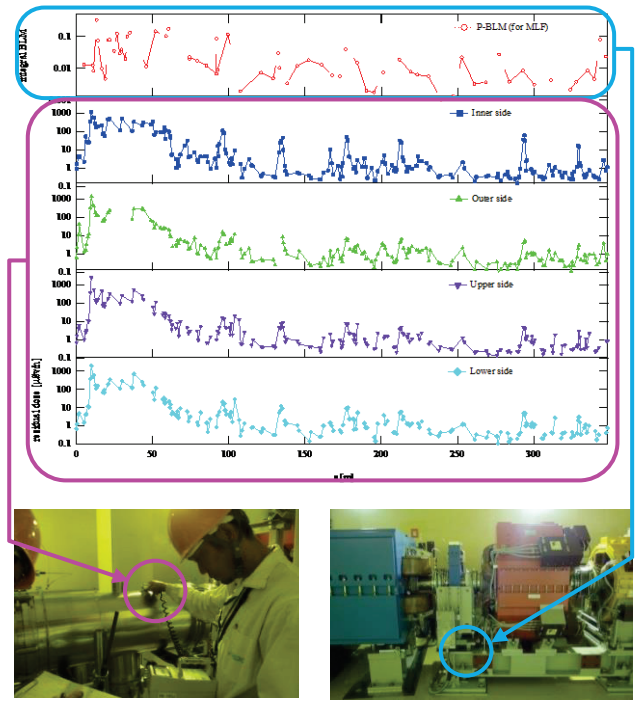

Figure 2: Comparison between the beam loss signals and the residual dose distributions along the four sides of the duct along the ring.

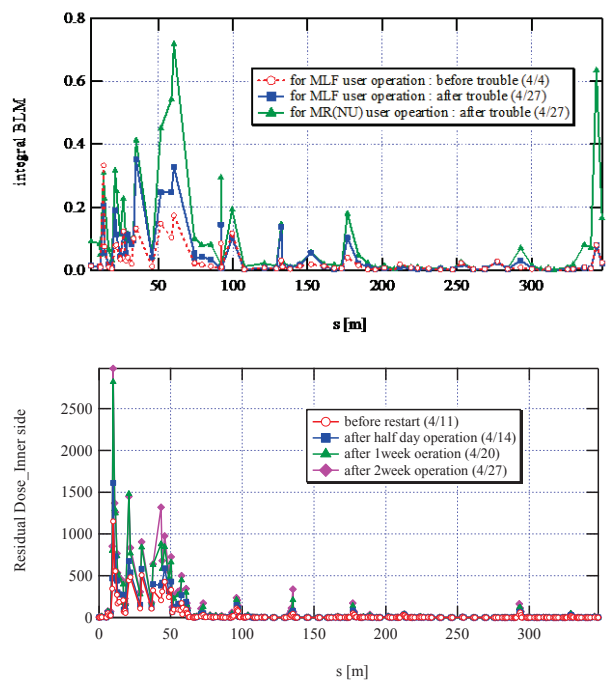

Figure 3: Influence of the spare ducts replacement of Col-Abs. no. 5. Upper plots show the comparison of the beam loss distributions before and after removing the Col. Abs. no. 5. Lower plots show the transition of the residual dose distributions after restarting the beam operation.

ISBN 978-3-95450-177-9

After restart of the user beam operation, the RCS was operated in two different modes according to the beam destinations. Thus, two beam loss profiles, not only for MLF user operation, but also MR/NU user operation, are measured independently. During MLF user operation, the beam losses increased by a factor of two. In addition, twice the amounts of beam loss for MLF are measured for MR/NU. The cause of the increase in beam loss is that an RCS beam power equivalent to 556 kW is needed to achieve the MR beam power of 360 kW. In either case, beam losses were expected during RCS operation. The reference residual dose was measured after a lapse of one week from the beam stop. Recovering from the collimator trouble required some time because the radioactivity level of the Col-Abs. no. 5 was significantly high. On the other hand, residual dose measurement in every short maintenance period was carried out after about 6 h from the beam stop. Therefore, the lower plots in Fig. 3 refer to the compounding residual dose. From the plots, the MR/NU beam losses have very little influence on the residual dose compared to those for MLF since approximately 10% of the beam extracted from the RCS is transported to the MR and the remaining 90% is transported to the MLF.

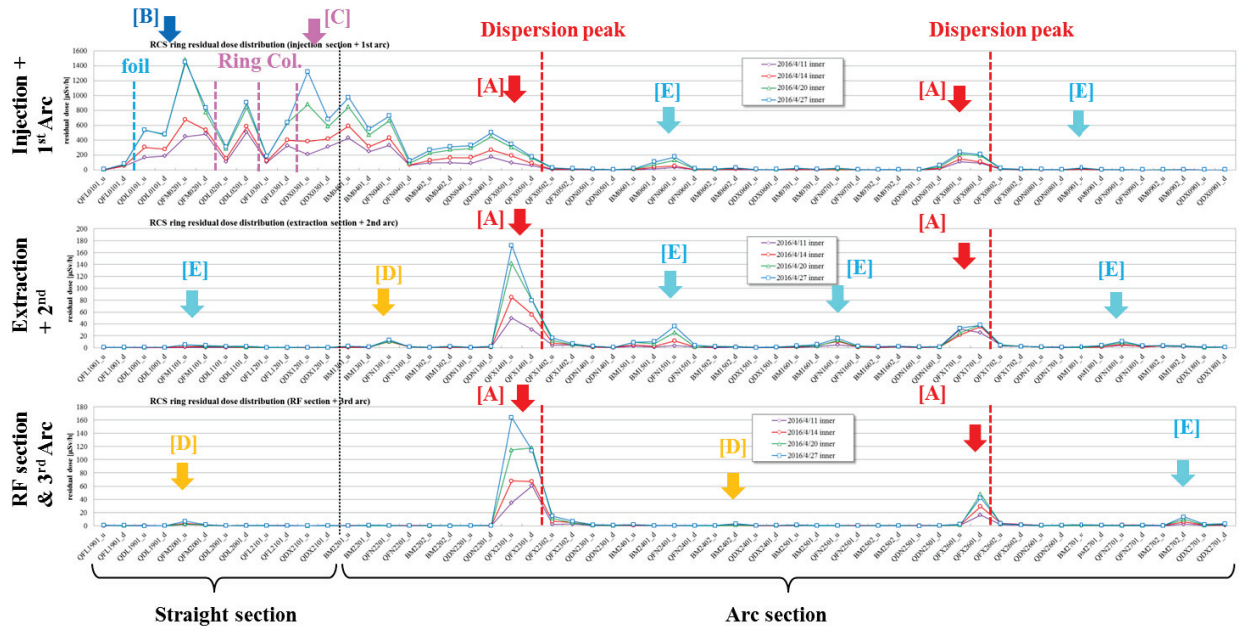

Figure 4: Transition of the measured residual dose distribution for the further study of the sources or the mechanism of the beam losses in the RCS ring.

In order to analyse the configuration of the beam loss profile, the transition of the measured residual dose is plotted as shown in Fig. 4. These distributions are divided into the three sections as related to the threefold symmetric lattice of the RCS. In addition, the horizontal axis changes from the position (s [m]) to the magnet ID. An auxiliary black straight line shows a boundary line between the straight section and the arc section, and red dotted lines show the dispersion peak positions. From the plots, there are some conspicuous beam loss structures and they can be classified into the five categories: [A], [B], [C], [D], and [E]. The beam losses categorized as [A] appear slightly above the dispersion peaks. These "dispersion peak beam losses" are caused by particle scattering and energy loss. The beam losses denoted as [B] appear at the injection area. These "injection beam losses" are caused by interactions with the stripper foil. In detail, there are two areas with high doses of radiation, and they are caused by different particles as follows: one appears above the ring collimator, caused by large angle scattering particles at the foils. To reduce this residual dose level, an additional collimator was installed, which is referred to as an "H0 collimator," at the H0 dump septum magnet [5]. However, the H0 collimator control system is adopts the same system as the ring collimators. Thus, adjustments between the beam and the H0 collimator cannot be done, and the beam losses increase after restarting the user beam operation. Since the collimator system upgrade was designed and tested, the beam losses can be minimized by adjusting the collimators after the summer-long maintenance period. The other appears around the stripper foil and it is caused by secondary particles due to nuclear reactions at the foil [6]. This radio-activation is an intrinsically serious problem for the RCS, which adopts the charge exchange multi-turn beam injection scheme with the stripper foil [7]. To reduce this radioactivity, we decreased the foil hitting rate by expanding the transverse painting area [8]. The beam losses denoted as [C] appear below the ring collimators. These "ring collimator beam losses" are caused by secondary particles generated in the ring collimators. The spare ducts exclude radiation shields, and subsequently secondary particles are leaked and radio-activated below the vacuum chambers. The spare

ISBN 978-3-95450-177-9

ducts are replaced with the straight vacuum duct with the radiation shielding. As a result, it is expected to reduce the "ring collimator beam losses" following the summer period. New Col-Abs no. 5 has been manufactured and is planned to be installed in the ring during the summer of 2017. The [D] beam losses appear at a few areas around the ring. These beam losses are small and the residual dose level is almost unchanged after restart. The cause is a long-lived nuclide that had been generated by the beam loss a long time ago, namely these beam losses have not occurred in these areas until now. The beam losses denoted as [E] also appear at a few areas around the ring, and these residual dose levels are not so high. However, they increase during user beam operation. From the beam tracking simulation, it is highly possible that the beam core particles are scattered by the secondary collimators and not the primary collimator, and then lost at unexpected aperture limits. Thus, these "absorber scattering beam losses" are not so high and cannot be detected by the beam loss monitor. However, they should be characterized as an important indicator of finer ring collimator adjustment.

SPOT AREAR BEAM LOSSES DETECTION WITH THE NEW-BLM

Transitions of the residual dose measured on the inner side and outer side along the spare ducts were measured as shown in Fig. 5. These beam losses are caused by the secondary particles generated by the ring collimators, and also denoted as [C]. However, there is a large residual dose imbalance between the inner and outer sides of the spare ducts. The reason for the dose imbalance is that the scatter or absorbers of the ring collimators lose their overall balance. Indeed, residual doses on the inner and outer copper block in the Col-Abs. no. 5 are 10 mSv/h and 40 mSv/h, respectively. On the other hand, the residual doses on the inner and outer copper block in the Col-Abs. no. 4 are 125 mSv/h and 10 mSv/h, respectively. Using the P-BLM, which detects significant beam loss at every cell, obtaining a finer symmetric adjustment of the scatters and absorbers horizontally and vertically is quite difficult. Therefore, to understand the horizontal and vertical balance of the beam loss, a new BLM that can detect the spot area beam loss is required. To meet these criteria, the scintillator is made smaller and fits on the duct directly. Accordingly, it can enhance the sensitivity to the beam loss generated at the contact area, and limit impact of the ones at a position relatively separated from the scintillator. The left photograph in Fig. 6 shows the new BLM. It is constructed with a small plastic scintillator (EJ-212, 20 mm × 20 mm × 50 mm) and a high-sensitivity photomultiplier tube (PMT: Hamamatsu H11934-100-10). After the connection, aluminum foil, used as a reflector, and shielding tape are wrapped on the scintillator. To investigate the scintillator's performance, two new BLMs were installed on the inner and outer sides of the Ti reducer duct, which is a component of the spare ducts as shown in Fig. 6. Each PMT applies a negative high voltage of −0.5 kV, and both outputs are connected directly to an oscilloscope via correctly terminated 50 Ohm. Typical measured raw signals are shown in Fig. 7. From the comparison results, a large imbalance of the beam losses is clearly detected. In addition, the inner and outer integrated values from the waveforms are 51 mVms and 125 mVms, respectively. On the other hand, the residual doses at the same place are 0.913 mSv/h and 2.23 mSv/h. The ratio of the integrated BLM signal is 51:125 and the ratio of the residual dose is 0.913:2.23. Both ratios are equal to the ratio 1:2.4, namely both experimental results are consistent.

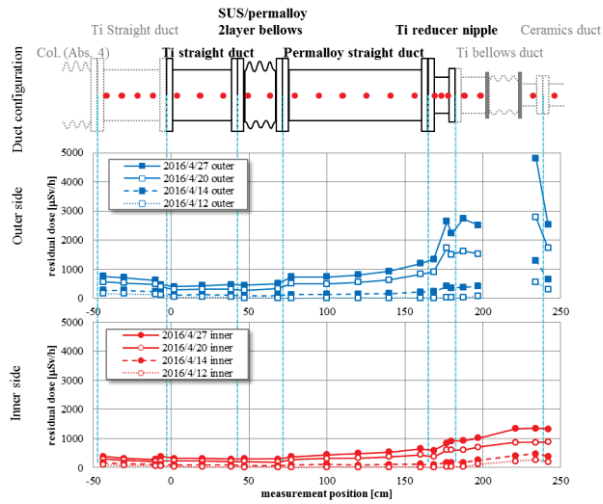

Figure 5: Comparison of the measured residual dose distributions between on the inner and outer sides along the spare ducts.

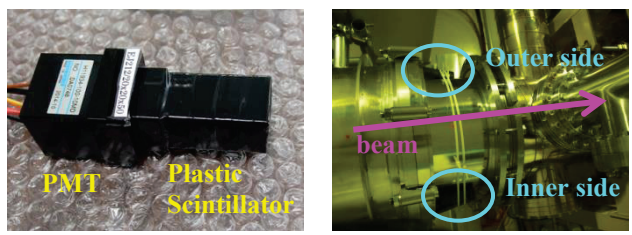

Figure 6: Photos of the new beam loss monitor (BLM) to detect the sport area beam losses (left), and installation of the two new BLMs on the inner and outer sides of the spare ducts (right).

After the beam stop during this summer shut down period, the radioactivity in the vacuum duct was measured using the new BLMs. The high PMT voltage increased up to the highest rated voltage of −0.9 kV to detect the gamma rays emitted from the vacuum duct. Two-second waveform data was acquired by means of the oscilloscope after changing the terminated resistor to 1 M Ohm and averaging offline. Radioactive decay curves obtained from the new BLM are plotted in Fig. 8. In addition, the residual dose measured by the GM counter at the near position is plotted in Fig. 8 to compare with the new BLM measurement results. From the comparison, relations between radioactivity and beam loss can be established.

ISBN 978-3-95450-177-9

Thus, we can evaluate the residual dose exactly by using the new BLM without the risk of exposure to the workers.

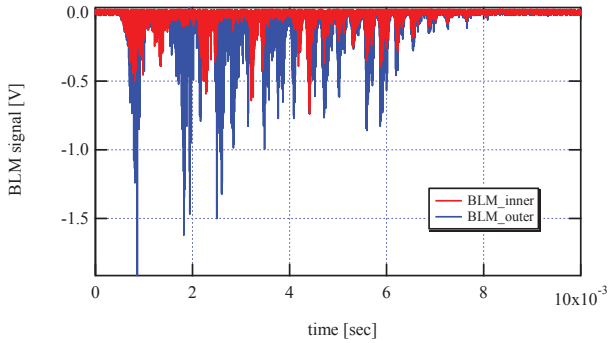

Figure 7: Typical measurement result of the new BPMs.

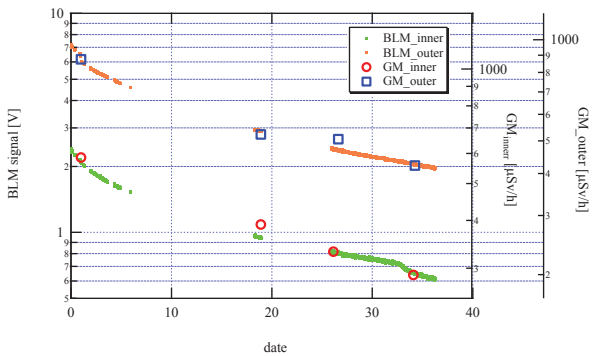

Figure 8: Decay curves of the radioactivity in the vacuum ducts obtained by the new BLM and residual dose at the near point measured by the GM counter.

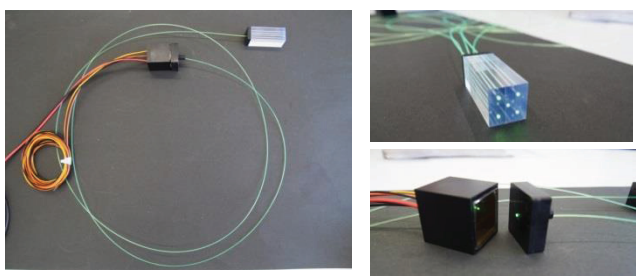

Figure 9: Assembly work of the upgraded new BLM. The photomultiplier tube (PMT) can be separated from the spot area of the beam losses to be connected with the plastic scintillator by the optical fibers.

If the detailed distribution of the residual dose is obtained by the new BLMs, many new BLMs should be set along the ring. In this case, they may be set near the magnet or inside the collimator shielding, and the magnetic field or the high level radiation should induce an operation error of the PMT. Thus, the new BLM will be upgraded to reduce some of the detrimental effects to the PMT. Therefore, the PMT is separated from the plastic scintillator and connected to it by optical fibers, as shown in Fig. 9. After the assembling work, offline analysis must be used to evaluate optical transmission line transition loss and waveform distortion. When the upgrade-BLM is installed in the ring, an optical fiber connector, which is constructed with the PMT and optical fibers, is aligned along the upgrade-BLM. Background noise signals generated in the optical fibers themselves can be corrected by subtracting the connector signal from the upgrade-BLM signal.

SUMMARY

Following the ring collimator damages that occurred in April, 2016, the residual does along the ring has been measured using a GM counter. The detailed residual dose distributions exhibit some conspicuous beam loss structures, and the classification of the beam loss structures provide us with further information of the beam loss. In particular, finding the absorber scattering beam losses is a milestone for finer ring collimator adjustment.

In order to establish the relation between the residual dose distribution and the beam loss signals, we developed and tested a new BLM, which can detect the spot area beam loss. In addition, we proposed an upgrade to the new BLM so that it can be used near the magnet and inside the collimator shielding. It is expected that a detailed map of beam losses can be obtained using the new BLM.

REFERENCES

[1] High-intensity Proton Accelerator Project Team, JAERI Report No. JAERI-Tech 2003-044 and KEK Report No. 2002-13.

[2] K. Yamamoto, “Efficiency simulations for the beam collimation system of the Japan Proton Accelerator Research Complex rapid-cycling synchrotron”, PRST-AB 11, 123501 (2008).

[3] K. Yamamoto *et al.*, “A malfunction of the beam collimator system in j-parc 3 gev rapid cycling synchrotoron”, in Proc. of PASJ2013, MOP007 (in Japanese).

[4] K. Yamamoto, “Signal response of the beam loss monitor as a function of the lost beam energy”, Proc. of IBIC2015, Melbourne, Australia (2015), MOPB021.

[5] S. Kato *et al.*, “Localization of the large-angle foil-scattering beam loss caused by the multiturn charge-exchange injection”, PRST-AB 16, 071003 (2013)

[6] M. Yoshimoto *et al.*, “Maintenance of radio-activated stripper foils in the 3 GeV RCS of J-PARC”, JRNC, 3, 305 (2015), PP 865-873.

[7] E. Yamakawa *et al.*, “Measurements and PHITS Monte Carlo Estimations of Residual Activities Induced by the 181 MeV Proton Beam in the Injection Area at J-PARC RCS Ring”, JPS Conf. Proc. 8, 012017 (2015).

ISBN 978-3-95450-177-9

EVALUATING BEAM-LOSS DETECTORS FOR LCLS-2*

Alan S. Fisher#, Clive Field, Ludovic Nicolas, SLAC, Menlo Park, California 94025, USA

Abstract

The LCLS x-ray FEL occupies the third km of the 3-km SLAC linac, which accelerates electrons in copper cavities pulsed at 120 Hz. For LCLS-2, the first km of linac will be replaced with superconducting cavities driven by continuous RF at 1300 MHz. The normal-conducting photocathode gun will also use continuous RF, at 186 MHz. The laser pulse rate will be variable up to 1 MHz. With a maximum beam power of 250 kW initially, and eventually 1.2 MW, the control of beam loss is critical for machine and personnel safety, especially since losses can continue indefinitely in linacs, and dark current emitted in the gun or cavities can be lost at any time. SLAC protection systems now depend on ionization chambers, both local devices at expected loss sites and long gas-dielectric coaxial cables for distributed coverage. However, their ion collection time is over 1 ms, far slower than the beam repetition rate. We present simulations showing that with persistent losses, the space charge of accumulated ions can null the electric field inside the detector, blinding it to an increase in loss. We also report on tests comparing these detectors to faster alternatives.

INTRODUCTION

LCLS and LCLS-2

The Linac Coherent Light Source (LCLS) is an x-ray free-electron laser (FEL) that began operation in 2009 [1]. It occupies the third kilometer of SLAC's 3-km copper room-temperature linac. Both the linac and the photocathode radio-frequency (RF) gun are pulsed at 120 Hz with 2856 MHz. The first km of the linac was removed in the past year to make way for LCLS-2, which will use continuous 1300-MHz RF in superconducting cavities, with a normal-conducting photocathode RF gun at 186 MHz and a bunch rate of up to 1 MHz. Operation will begin (before upgrades) at an electron energy of 4 GeV and a beam power of 250 kW, increasing to 1.2 MW. Table 1 compares the parameters of both machines.

Beam Loss and Safety Systems

Beam-loss instrumentation follows a tiered structure. During normal operation, diagnostics monitor and locate sources of loss, and aid in tuning. The machine protection system (MPS) blocks the beam or halts it if losses exceed a threshold, or for other causes (insertion of an obstacle such as a valve, an excessive temperature). Beam containment (BCS) stops the accelerator if a loss of beam current or radiation from beam loss would indicate possible harm to people or to devices like protection collimators. Safety-systems detectors are deployed in twos for redundancy.

Table 1: Parameters of the LCLS Normal-Conducting Linac and the LCLS-2 Superconducting Linac

Parameter	LCLS	LCLS-2
Electron energy	15 GeV	4 (later 8) GeV
Bunch charge	20 to 250 pC	20 to 250 pC
Beam power	450 W	**0.25 (later 1.2) MW**
Gun frequency	2856 MHz	185.7 MHz
Linac frequency	2856 MHz	1300 MHz
RF pulse rate	120 Hz	Continuous
e^- bunch rate	120 Hz	92.9 (later 929) kHz
Photon energy	0.2 to 5 keV	1 to 15 (later 25) keV

The detectors discussed here are evaluated primarily for BCS, but their signals will be split outside the tunnel for independent processing for BCS, MPS, and diagnostics.

The highest level of protection, the personnel protection system (PPS), interlocks access to the machine and shuts it off if radiation is found in occupied areas. PPS instrumentation will not be further considered here.

Unlike LCLS, which has 8 ms (a 120-Hz period) to shut off, LCLS-2 has continuous RF. Losses must be detected in as little as 100 μs, after which the beam must be shut off within 100 μs (see Table 2). Losses can arise from high-power photocurrent, or from dark current due to field emission in the gun or linac modules. Dark current can be emitted at any time and can travel through several cryomodules in either direction depending on the RF phase at emission.

IONIZATION DETECTORS

BCS at SLAC has long relied on two types of ionization detector. We describe these here and discuss whether ion collection is sufficiently fast for LCLS-2.

Protection Ion Chamber (PIC)

A PIC is a point loss detector, placed within 0.5 m of a site such as a collimator needing protection against damage. Figure 1 shows the design, a stainless-steel cylinder containing a stack of 32 plates biased alternately at ground or (typically) −300 V. At this voltage, collection of electrons takes 2 μs, but ions require 1 ms.

Both the PICS and the LIONs discussed next are generally filled to 125 to 150 kPa with a mixture of 95% Ar and 5% CO_2. However, the LCSL-2 model and the experiment (both discussed below) use 100% Ar.

*SLAC is supported by the U.S. Department of Energy, Office of Science, under contract DE-AC02-76SF00515
#afisher@slac.stanford.edu

ISBN 978-3-95450-177-9

Table 2: BCS Requirements for Point and Line Radiation Detectors

Device	Trip Level	Response Time
Point detector: Protects stoppers and collimators	Detect loss of 25 J in 100 ms, then shut off within 100 µs. Sample at ≥ 40 kHz	250 kW for 100 µs 25 kW for 1 ms 2.5 kW for 10 ms ≤250 W is safe
Long detector: Measure inside shielding wall for protection outside	Linac: 10 krad/hr over 10 m Beam Transfer Hall: 3–20 rad/hr (adjustable) over 5 m (lower due to less shielding)	600 ms

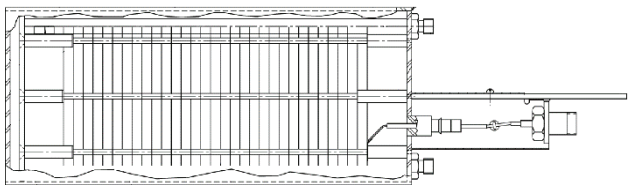

Figure 1: Cutaway view of a PIC. The housing is a stainless-steel cylinder with a 114-mm outer diameter and a 270-mm length. The 32 plates each have an area of 56.5 cm^2 and are 6.35 mm apart. The plates are alternately grounded or connected to a bias voltage.

Long Ionization Chamber (LION)

A SLAC LION (Figure 2) is a gas-dielectric Heliax coaxial cable (made with continuous helically-wound copper strips) that detects losses along (typically) 30 to 50 m of the tunnel. A +250-V bias on the center conductor drives charge radially, with a collection time of 6 µs for electrons but 6 ms for ions. The charge moves in both directions along the cable. One end leads to a high-voltage supply, an integrator and a digitizer. The other end has a high-impedance termination drawing a small DC current, which indicates that the system is functioning.

1-D Model of an Ionization Chamber

The possible loss of significant beam power and an ion collection time far longer than the interval between pulses both suggest that ion space charge may accumulate inside a chamber. An experimental and numerical study of ionization chambers for protons in the NuMI experiment at Fermilab [2] found that ion screening can completely null the field in part of the chamber, creating a "dead zone." This motivated the development of a one-dimensional model of charge flow in the SLAC chambers.

The model assumes a uniform ionization rate $I(t)$ per unit volume generated by beam loss and a recombination rate per unit volume $\beta n_i n_e$ proportional to the product of electron and ion densities. The PIC behavior is computed for the x coordinate between a pair of plates. The signal current is then scaled by 31 to account for all plates. The LION model computes the radial behavior in a uniformly ionized 1-cm length of cable.

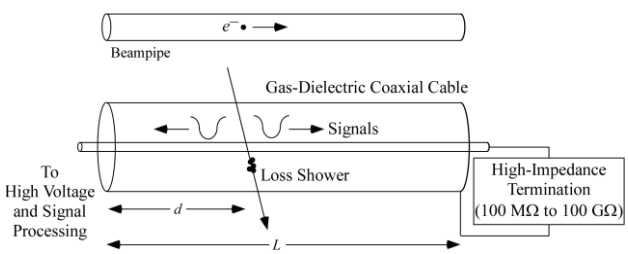

Figure 2: Sketch of LION. The normal inner- and outer-conductor diameters are18.1 and 46.5 mm respectively.

Both detectors are filled with 100 kPa of Ar, a common gas for ionization chambers, to avoid both the complexity of molecular fragmentation and also the creation of negative ions, which move as slowly as positive ions and would further contribute to the accumulation of space charge.

At this pressure, the mean free path is much smaller than the chamber size, and so particle drift is modeled by a mobility $\mu_{i,e}$ (with a velocity $\mathbf{v}$ proportional to the electric field $\mathbf{E}$), although the electron mobility has a weak dependence on E. The particle flux $\mathbf{J}_{i,e}$ also includes a diffusive component. $\mathbf{E}$ is given self-consistently by Gauss's Law. The governing equations are:

$$\begin{aligned} \mathbf{J}_{i,e} &= \pm\mu_{i,e} n_{i,e}\mathbf{E} - D_{i,e}\nabla n_{i,e} \\ \frac{\partial n_{i,e}}{\partial t} &= -\nabla\cdot\mathbf{J}_{i,e} + I - \beta n_i n_e \\ \varepsilon_0 \nabla\cdot\mathbf{E} &= e(n_i - n_e) \end{aligned} \quad (1)$$

Electrodes are charge sinks but not sources: electrons or ions can flow in but not out. The surface charge Q on each electrode is determined self-consistently through Gauss's Law and by the requirement that the bias supply provides enough charge to maintain a constant voltage:

$$\begin{aligned} Q &= \varepsilon\int_S \mathbf{E}\cdot d\mathbf{S} \\ V_0 &= -\int_a^b \mathbf{E}\cdot d\mathbf{u} \end{aligned} \quad (2)$$

We measure instead the charge Q_{ext} flowing through the external circuit from the bias supply. A change ΔQ is the sum of Q_{ext} and the charge of collected electrons or ions:

$$\Delta Q = Q_{\text{ext}} \pm e\int_S \mathbf{J}_{i,e}\cdot d\mathbf{S} \quad (3)$$

Radiation Field

A FLUKA model [3] relates the power lost on a beam stop to the radiation dose rate in the vicinity. From Figure 3, the dose rate at a radial distance of 50 cm is about 50 rad/(W·hr) over a longitudinal span of 50 cm.

Table 2 sets limits for long detectors of 3 to 20 rad/hr in the beam-transfer hall (between the linac and undulators) and 10 krad/hr in the linac. The corresponding power is 60 to 400 mW (36 to 240 mJ in the specified 600 ms), and

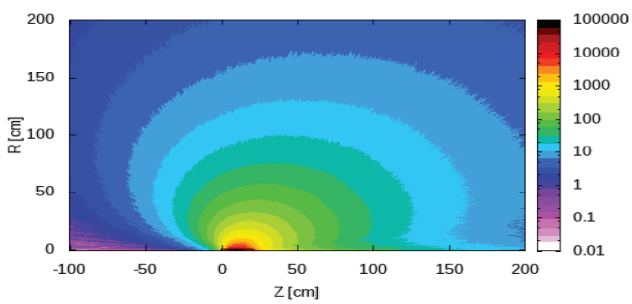

Figure 3: Model of the radiation field showing a loss near a beam stop. The color scale is in rad/(W·hr).

ISBN 978-3-95450-177-9

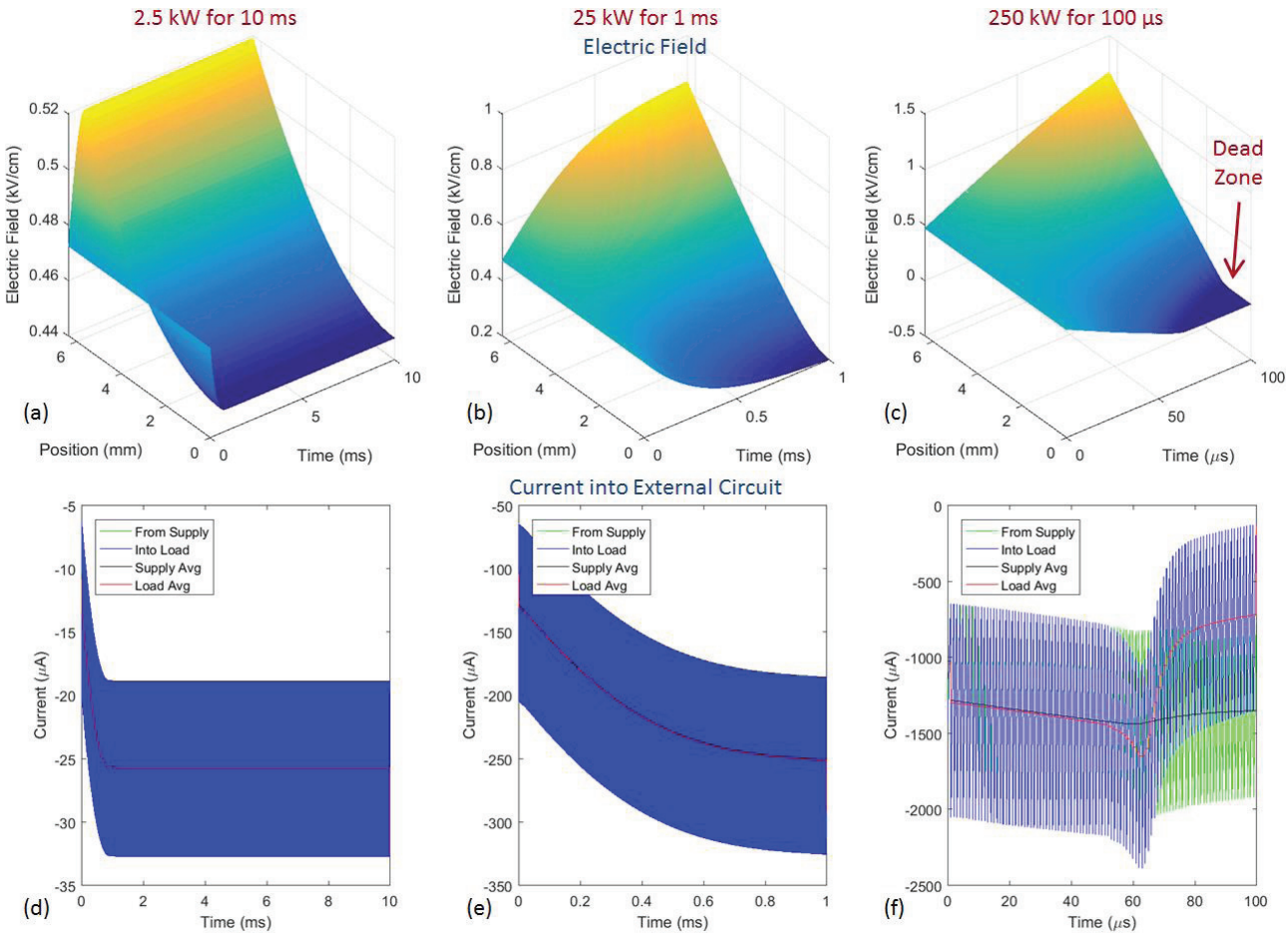

Figure 4: PIC model for three cases from Table 2. The electric field (a-c) progresses toward dead-zone formation as losses increase. In (c) the field near the positive electrode reaches zero after 60 µs. The external current equilibrates in 1 ms (d,e), but has a sudden reduction as the dead zone forms (f). The 1-MHz cycle of electron response is visible at the 100-µs time scale of (f) but becomes a broad blue band (covering an identical green band) in (d) and (e).

200 W (120 J in 600 ms) respectively. These powers are below the limits for point detectors, since the two types serve different purposes. The long detectors may trip first if placed near point losses.

Model Results: PIC

Figure 4 shows the evolution of the electric field (a–c) and the external current (d–f) in a PIC biased at −300 V, for three cases from Table 2. Losses with power levels of 2.5, 25 and 250 kW begin at t = 0, repeating at 1 MHz and reaching the 25-J trip threshold in 10, 1 and 0.1 ms respectively. When losses are low (a,d), the electric field between the plates is barely perturbed, but the current to the load takes 1 ms to equilibrate due to the slow ion drift. In the 250-kW case (c,f), field lines from the negative plate terminate on ion space charge before reaching the positive plate, completely screening the field there within 60 µs. Electron and ion transport halts in this dead zone (except for diffusion), and the density grows quickly with the periodic losses. The signal current becomes erratic.

Model Results: LION

In Figure 5 a LION biased at the standard +250 V exhibits similar behavior, exacerbated by the longer electrode separation and somewhat lower voltage. A negative bias would be worse: the field's 1/r dependence makes it weaker at the outer electrode and so easier to screen.

Because the trip levels of Table 2 for long detectors (≤200 W) are much lower than those for point detectors and below the moderate loss of Figure 5(a), a dead zone does not develop. But if the LION is exposed to a large point loss not protected by a point detector, then it can develop a dead zone.

ALTERNATIVE DETECTORS

The slow ion response compared to the bunch separation and the required trip time, along with the formation of a field-free dead zone for a loss of the full beam power (even before the upgrade to 1.2 MW), led us to consider alternatives not based on gas ionization.

For point losses we are evaluating diamond detectors [4]. Losses generate electron-hole pairs in a 1-cm^2 slice of

ISBN 978-3-95450-177-9

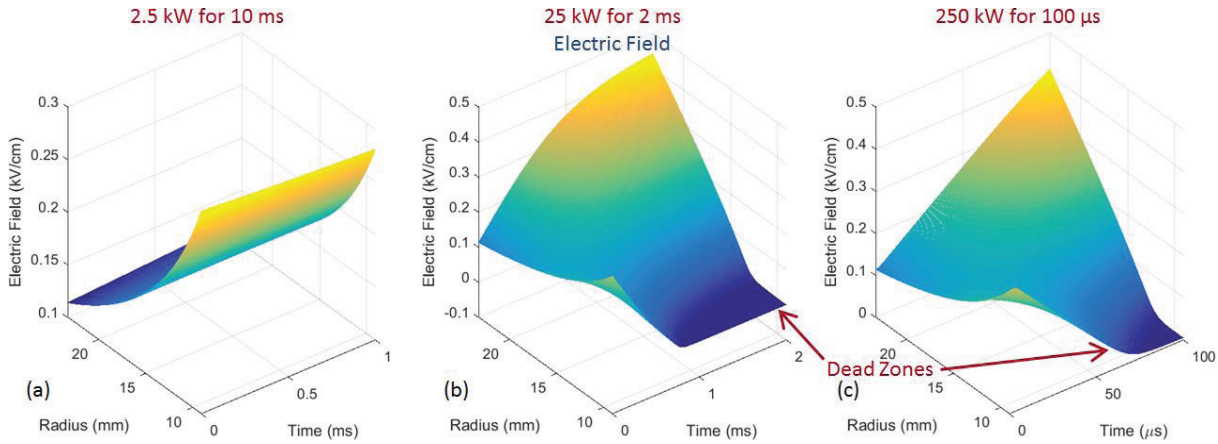

Figure 5: LION model for the cases of Figure 4. Due to the longer drift distance, the dead zone appears for a lower loss.

synthetic polycrystalline diamond. The high mobility in a thin (500 µm) crystal gives 5-ns pulses.

For long detectors we are considering Cherenkov emission in radiation-hard optical fibers. A multimode fiber with a 600-µm core [5] was tested for radiation hardness up to 1.25 Grad for use in the LHC at CERN, in particular in the CMS end cap [6–8]. These would be installed in one-sector (100 m) lengths. A photomultiplier (PMT) or silicon photomultiplier (SiPM) would detect the light at one end; at the other, an LED outside the tunnel would periodically pulse to monitor transmission.

EXPERIMENTAL TEST

An experimental test compared a PIC and a short LION to two types of diamond (standard and high-radiation) and to an optical fiber run along the LION (Figure 6). A 180-pC, 5.115-GeV electron beam hit tungsten plates at 5 Hz. The diamonds and fiber were faster and less noisy than the PIC and LION. We next will test 100 m of fiber and diamonds in a linac sector to gain operational experience.

REFERENCES

[1] P. Emma *et al.*, "First lasing and operation of an ångstrom-wavelength free-electron laser," Nature Photonics **4** (2010) 641.

[2] R.M. Zwaska *et al.*, "Beam Tests of Ionization Chambers for the NuMI Neutrino Beam," IEEE Trans Nucl. Sci. **50** (2003) 1129.

[3] M. Santana Leitner, "Fluence to dose conversion E-curves for silicon and polyethylene. A FLUKA user-routine to convert fluence into energy deposition in small radiation sensitive accelerator components," SLAC Radiation Physics Note RP-14-20, example 3, doses near a stopper.

[4] https://cividec.at/

[5] FBP600660710, Polymicro division of Molex.

[6] I. Dumanoglu *et al.*, "Radiation-hardness studies of high OH^- content quartz fibres irradiated with 500 MeV electrons," Nucl. Instrum. Methods A **490** (2002) 444.

[7] K. Cankoçak *et al.*, "Radiation-hardness measurements of high OH^- content quartz fibres irradiated with 24 GeV protons up to 1.25 Grad," Nucl. Instrum. Methods A **585** (2008) 20.

[8] F. Duru *et al.*, "CMS Hadronic EndCap Calorimeter Upgrade Studies for SLHC 'Čerenkov Light Collection From Quartz Plates'," IEEE Trans Nucl. Sci. **55** (2008) 73.

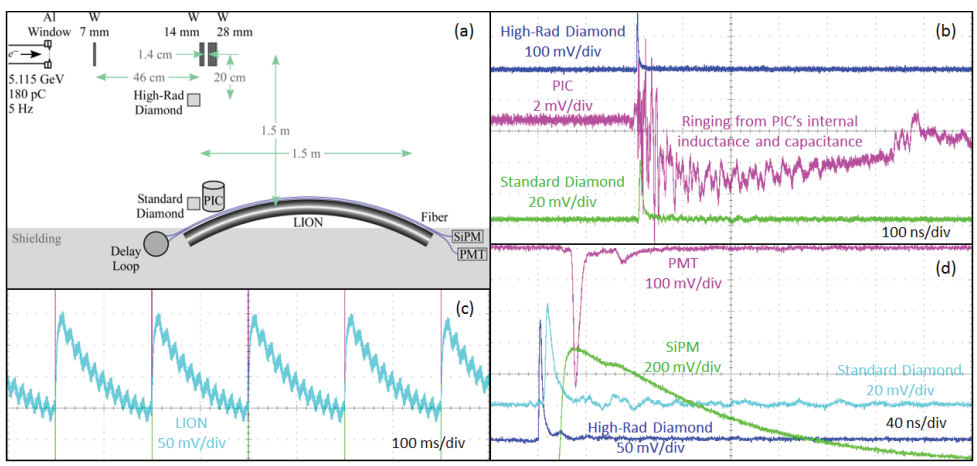

Figure 6: (a) Experimental layout. Signals from (b) PIC and diamonds; (c) LION, with a very slow time scale and large 60-Hz noise; (d) PMT and SiPM. (The SiPM pulse is long because a transimpedance amplifier is needed.)

ISBN 978-3-95450-177-9

BEAM DIAGNOSTICS FOR CHARGE AND POSITION MEASUREMENTS IN ELI-NP GBS

G. Franzini†, F. Cioeta, O. Coiro, D. Pellegrini, M. Serio,
A. Stella, A. Variola, INFN-LNF, Frascati (Rome), Italy
A.Mostacci, S. Tocci, University of Rome "La Sapienza", Rome, Italy

Abstract

The advanced source of Gamma-ray photons to be built in Bucharest (Romania), as part of the ELI-NP European Research Infrastructure, will generate photons by Compton back-scattering in the collision between a multi-bunch electron beam and a high intensity recirculated laser pulse. An S-Band photoinjector and the following C-band Linac at a maximum energy of 720MeV, under construction by an European consortium (EurogammaS) led by INFN, will operate at 100Hz repetition rate with trains of 32 electron bunches, separated by 16ns and a 250pC nominal charge. The different BPMs and current transformers used to measure transverse beam position and charge along the LINAC are described. Design criteria, production status and bench test results of the charge and position pickups are reported in the paper, together with the related data acquisition systems.

INTRODUCTION

The ELI-NP GBS (Extreme Light Infrastructure-Nuclear Physics Gamma Beam Source) is a high intensity and monochromatic gamma source under construction at IFIN-HH in Magurele (Romania). The photons will be generated by Compton back-scattering at the interaction between a high quality electron beam and a high power recirculated laser. Two interaction regions are foreseen: one with electrons accelerated up to 280 MeV (low Energy LINAC), the other with electrons up to 720 MeV (high Energy LINAC). The LINAC will deliver a high phase space density electron beam, whose main parameters are listed in Table 1 and depicted in Figure 1 [1].

Table 1: Main Characteristics of the GBS Electron Beam

Parameter	Value
Maximum Energy	720 MeV
Macro Pulse rep. rate	100 Hz
Number of bunches per Macro Pulse	up to 32
Bunch Spacing	16.1 ns
Bunch Length (σ_t)	0.91 ps
Bunch Charge	25 pC – 250 pC

Various diagnostics devices have been foreseen to be installed in the LINAC, in order to measure the properties of both the macropulses and the single bunches. Both intercepting and non-intercepting type of measurements will be implemented. The devices used for the intercepting type of measurements are Optical Transition Radiation (OTR) screens. A total of 23 stations will be installed along the LINAC: 12 on the Low Energy LINAC, 11 on the High Energy LINAC. They will be used to measure the Beam Position (Centroid) and the Spot Size of the beam. They will also be used to measure the beam energy and its spread, the bunch length and the Twiss parameters, in conjunction with a dipole, an RF deflector and quadrupoles respectively.

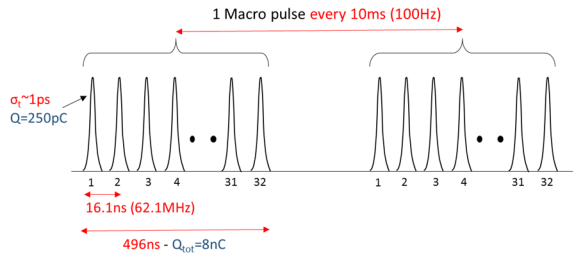

Figure 1: GBS Electron Beam representation.

The devices used for non-intercepting measurements are Beam Charge Monitors (BCM) and Beam Position Monitors (BPM).

The former ones are based on the Integrating Current Transformers (ICT) [2], which will be installed in 4 different positions (3 in the low energy LINAC, 1 in the high Energy LINAC).

Concerning the Beam Position Monitors, two different types will be installed: Stripline Beam Position monitors are the most common. 29 of them will be installed, specifically 13 in the Low Energy LINAC, 16 in the High Energy LINAC. Moreover, near the interaction points (both at low energy and high energy), a total of 4 Cavity Beam Position Monitors will be installed (see Fig.2).

BEAM CHARGE MONITORS

Beam charge monitors (BCM) will be installed in four positions: the first one will be located right before the first S-band accelerating structure; the second one will be located at the end of all the accelerating structures of the Low Energy LINAC, before the so-called “dogleg”; the third and the fourth will be installed before the low energy and the high energy interaction points. These four locations will allow studying the losses of charge of the beam at the key-points of the LINAC.

BCMs will have the capability to measure the charge of every single bunch, within the macro pulse. The ICT [2] (see Fig.3) could be seen as a band-pass filter and the passage of the beam bunches could be considered as the input signal.

ISBN 978-3-95450-177-9

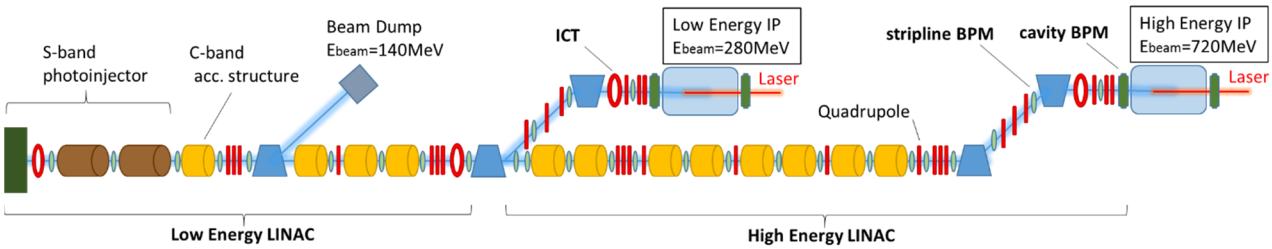

Figure 2: Simplified layout of ELI GBS. Both dump lines after the interaction points and some accelerator components are not depicted (i.e. corrector magnets).

The low and high cutoff frequency are in the order of few kHz and hundreds of MHz respectively (see Table 2).

Table 2: Main Parameters of the ICTs for GBS. In parenthesis the measured values in laboratory.

Parameter	ICT Type I	ICT Type II
Sensitivity in a 50Ω load	5 Vs/C *(4.96 Vs/C)*	10 Vs/C
Beam charge to output charge ratio in 50Ω load	~10:1	~5:1
Output pulse duration (6σ)	5 ns *(5.6 ns)*	5 ns
Output signal droop	3.59 %/μs *(3.57%/ μs)*	N/A
f_{low} / f_{high}	5.3kHz/191MHz *(4.5kHz/180MHz)*	9.7kHz / 112MHz

The frequency content associated to the beam bunch is significantly higher (hundreds of GHz) than the high cutoff frequency. As a result, rise and fall time are both slowed down and a bunch of ~1ps will induce an output signal with a duration significantly higher. Nevertheless, even if the original shape of the signal is lost, the charge of the output signal is proportional to the charge of the bunch. Therefore, by integrating the ICT output and calculating the charge associated to it, it is possible to measure the beam charge (see Eq. (1)).

$$Q_{bunch} = \frac{1}{S} * \int_0^{16ns} V_{out}(t)dt \qquad (1)$$

In Equation (1), $V_{out}(t)$ is the output voltage read by a measuring device (with R_{in}=50Ω); S is the sensitivity of the ICT in Vs/C (taking account of the reading device resistance of 50Ω); 16ns is the time interval between bunches and represents the maximum time allowed to integrate the output signal associated to a single bunch.

The ICT output signal generated by a single beam bunch has a nominal duration of 5ns, which not exceeds the interval between bunches (16ns), to allow bunch by bunch measurements.

The signal is digitized with ADC model M9210A from Agilent, whose main parameters are shown in Table 3.

We plan to use four ADC in single channel mode, in order to achieve the maximum sampling rate. The M9210A will be installed in two Input Output Controllers (IOC). The latter is a cPCI crate embedded system, LINUX based, with a dedicated control software written in EPICS. The acquisition of a full train of bunches will be synchronized with the timing signal (100Hz), handled by the IOC. The software will then record the samples from the ADC up to 512ns, dividing them in 32 windows of 16ns each and will calculate the charge for each window, by applying a calibration factor and offset compensation chosen by the user.

The nominal values of the ICTs main parameters are shown in Table 2. The main difference between type I and II is a factor of two on the sensitivity of the device. Moreover, the Type-I is resistant to temperature up to 150°C, to allow baking procedures. The Type-2 ICT has also a calibration coil integrated into it. This could be used for testing and for calibrating the device on a regular basis, by sending to it an electrical signal with a waveform generator.

Table 3: Main parameters of the ADC (Agilent M9210A) for the BCM

Parameter	ADC – M9210A
Resolution	10 bit
Sampling rate (single ch.)	4 GS/s
Analog Bandwidth	1.4 GHz
Input Range	50mV_{p-p} / 5V_{p-p} (programmable)

ICT Characterization

Since there will be limited possibilities to set up an electronic laboratory in site, our goal is to prevent any possible problem on diagnostic devices, in order to not slow down the commissioning activities. Thus, we performed a full characterization of the Type-I ICT already acquired, with a test bench set up at the INFN-LNF. Furthermore, the test bench components are portable and could also be used on site during the commissioning phase, as a diagnostic tool for the ICTs.

The test bench includes a waveform generator / pulse generator (the models used are Stanford DG535 and Picosecond mod.1000) which send signals to an "input" loop built in laboratory, coupled to the ICT (see Fig.3). The latter is made of a copper strip connected in series to five resistors in parallel, with a total resistance of ~50Ω. The design of the input spire allows to reduce its inductance, so as to minimize unwanted reflections [3].

ISBN 978-3-95450-177-9

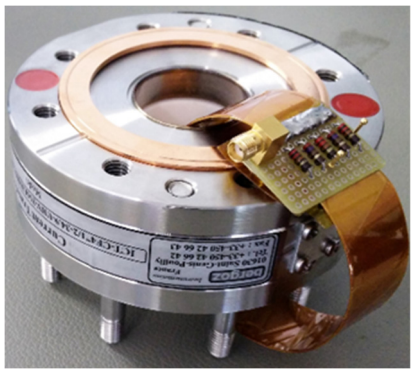

Figure 3: ICT Type-1 with the "input" loop coupled to it used to send electrical signals.

In order to acquire and digitize output signals we used a Picoscope 6404D with a LabVIEW VI. This ADC has a resolution of 8 bit, a maximum sampling rate of 5 GS/s, an analog BW of 500MS/s and an input range of 50mV$_{p-p}$ / 5V$_{p-p}$.

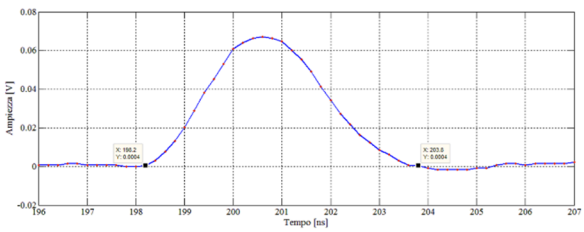

Figure 4: ICT Type-I output signal for an input pulse of 1ns, with an amplitude of 3.2V and a charge of 35pC.

We measured all the most important parameters of the ICT Type-1: they are roughly equal to the nominal ones (see Table 2). As such, no further analysis is necessary for our purposes.

We also investigated the effect of cables (connecting the ICT output to the reading electronics) of different lengths. We sent a sequence of pulses with a time interval of 16ns to the ICT and we measured the output signals for different cable lengths (type RG223): 1.5m, 50m, 100m. As it is possible to see in Figure 5, with this type of cable, a length of 50m could be considered the limit, in order to not have relevant overlap errors between bunches. In the case of GBS, the maximum cable path length could slightly exceed this limit. For this reason, we selected the FSJ1-50A 1/4" coaxial cable, which have lower attenuation effects than the RG-223.

We also studied the possible error in charge measurements introduced by the sampling frequency of the ADC. In order to do so, a pulse of fixed properties has been sent to the input loop and the integral of the output pulse (duration ~5.6ns) has been measured for different sampling rates.

As shown in Fig.6, the value of the integral of the output reach a specific value for sampling rates higher than 625MS/s. For lower values, the sampling rate introduces a systematic error in the measurements: in the case of the measurement proposed here, lower rates lead to higher value of the integral.

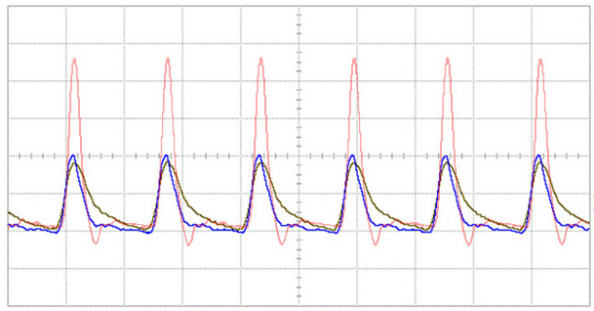

Figure 5: Output signals for different lengths of RG223 cable (red: 1.5m, blue: 50m, gold: 100m). Time scale: 10ns/div. Red and blue plots: 2mV/div. Gold plot: 1mV/div.

Nevertheless, this error is dependent on the synchronization of the signal and the ADC samples. As such, the error could also lead to lower values of the integral. The relative standard deviation calculated at 1250MS/s is ~1.4% and is maintained roughly equal up to 5000MS/s. This brings to the conclusion that the M9210A digitizer have a high enough sampling rate, even by using both channels (2000MS/s), opening to the possibility to use the dual channel option for future upgrades or as spares.

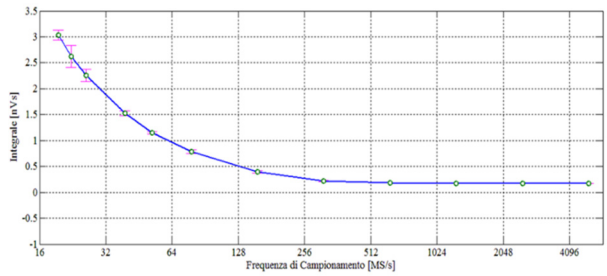

Figure 6: Value of the integral of the ICT output puls with a fixed input, for different sampling rates.

BEAM POSITION MONITORS

Stripline BPM

A total of 29 installed BPMs will be installed. They are the main devices used for ELI GBS to measure the average position of the macro pulse along the LINAC. Their design is the same for all of them (Fig.7), except for the one installed on the dump line after the low energy interaction point.

The pickup selected for use is generally referred to as stripline and is composed of four stainless steel electrodes of length l=140mm and width w=7.7mm, mounted with a π/2 rotational symmetry at a distance d=2mm from the vacuum chamber, to form a transmission line of characteristic impedance Zo=50Ω with the beam pipe. Their angular width is ~26 degrees and the acceptance is Ø34mm.

Time domain reflectometry measurements have been performed to select the final strip width to get the best impedance matching.

The amplitude of the frequency response presents a sinusoidal shape with maxima at odd multiples of c/4l (~535MHz), selected to be as close as possible to the operating frequency of the detection electronics and to present

ISBN 978-3-95450-177-9

non zero response at the LINAC frequency of 2856 MHz allowing measurements of any satellite bunch.

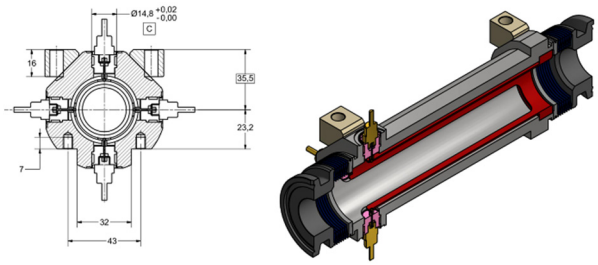

Figure 7:Main BPM model for ELI GBS.

In the Dump line BPM, the beam width and its possible position misalignment require a large BPM acceptance. Thus we have designed this BPM for an acceptance of Ø100mm and with a frequency response similar to the other BPMs. This assures that the output signals will have the same frequency content of the other BPMs, allowing to use the same acquisition system, based on LIBERA Single pass E system by Instrumentation Technologies. The latter is specifically designed as a BPM signal processing system and each of them will contain four modules. Each module will handle the signals coming from one BPM. Thus, a total of 8 LIBERA Single Pass E systems will be used in ELI GBS. By providing calibration factors, the latter gives the possibility to directly calculate the position of the beam, by means of polynomial equations.

The calibration factors, used in the polynomial equations, will be extrapolated from the measurements and calibration performed at ALBA laboratories [4] for each BPM and will be implemented directly in the LIBERA Single Pass E acquisition systems.

We also plan to calculate the charge of each macropulses by using the output signals of the BPM, in order to increase the number of the charge measurements (although only for the whole macro pulse) all along the LINAC.

Cavity BPM

In order to have higher precision beam position measurements (<1μm) and the possibility to measure it bunch by bunch, a total of four Cavity BPM are foreseen. They will be installed immediately before and after the two interaction points with the laser, where the precision on the beam position is more compelling. The cavity pick-up is the PSI BPM16 model, consisting of one cavity for charge measurements (used as a reference) and two position cavities with low quality factor (Q=42.4) [5].

The low Q allows to measure the charge and the position of the beam bunch by bunch. In fact, the output signals associated to the passage of a single bunch will decay faster (about 9ns) than the time interval between bunches (16ns).

The readout electronics will be specifically designed for the cavity BPM of ELI GBS by Instrumentation Technologies. Its development is in progress and the measurements done with a prototype developed during the first project phase confirmed the feasibility of the development and the performance of the RF front-end [6].

CONCLUSION

An overview of the devices involved in non-intercepting beam position and charge measurements of ELI GBS has been presented in this paper.

Since there will be limited possibilities to set up an electronic laboratory in site, our goal is to characterize all the devices and prevent any possible problem before the commissioning activities will start. Thus, we have set up a test bench at LNF to characterize ICTs. From our measurements, they will be capable to measure the charge bunch by bunch, within the project requirements.

Stripline BPMs, used for the macro pulse position and charge measurements, are at the final stage of testing and calibration at ALBA laboratories. We will then calculate and implement the calibration factors within the acquisition system.

Cavity BPMs, used for precise bunch by bunch position and charge measurements near the interaction points, have been acquired and the acquisition system is currently under development.

ACKNOWLEDGEMENT

We acknowledge the contribution of U.Frasacco, E.Gaspari, C.Mencarelli at LNF-INFN for the accurate technical support.

REFERENCES

[1] L. Serafini *et al.*, “Technical report eurogammas proposal for the ELI-NP Gamma Beam System.”, arXiv:1407.3669, 2014.

[2] Bergoz Instrumentation, “Integrating Current Transformer User’s Manual Rev 3.0”, http://www.bergoz.com/.

[3] S. Tocci, “Progetto e realizzazione di un banco per la caratterizzazione di un toroide impiegato nella misura di carica trasportata da un fascio di elettroni in un acceleratore lineare”, Master thesis, Facoltà di Ingegneria, Università “La Sapienza” (Roma), 2016.

[4] A.A. Nosych *et al.*, “Measurements and calibration of the stripline BPM for the ELI-NP facility with the stretched wire method” *Proceedings of IBIC2015*, Melbourne, Australia.

[5] F. Marcellini *et al.*, “Design of cavity BPM pickups for Swissfel”, *Proceedings of IBIC2012*, Tsukuba, Japan.

[6] M. Cargnelutti *et al.*, “Design and simulation of the cavity BPM readout electronics for the ELI-NP Gamma Beam System”, *Proceedings of IPAC2016*, Busan, Korea.

ISBN 978-3-95450-177-9

COMMISSIONING RESULTS OF THE TOP-IMPLART 27 MeV PROTON LINEAR ACCELERATOR*

P. Nenzi†, A. Ampollini, G. Bazzano, L. Picardi, M. Piccinini, C. Ronsivalle, V. Surrenti, E. Trinca, M. Vadrucci, ENEA C.R. Frascati, Frascati, Italy

Abstract

The results of a 27MeV proton LINAC commissioning are presented. The LINAC, operating at the ENEA Frascati Research Center, consists of a 425MHz injector followed by a 3GHz booster. The injector is a commercial LINAC, the PL7 model produced by ACCSYS-HITACHI, composed by a duoplasmatron proton source with einzel lens, a 3MeV RFQ (Radio-Frequency Quadrupole) and a 7MeV DTL (Dritf-Tube LINAC). Wide injection current range (0-1.5mA) is obtained varying extraction and lens potentials. The booster LINAC consists of sequence of 3 SCDTL (Side-Coupled DTL) modules whose output energies are 11.6MeV, 18MeV and 27MeV, respectively. Each of the 3 modules requires less than 2MW peak power. All modules are powered by a single 10MW peak-power klystron. The output beam has been characterized at 10Hz PRF (Pulse Repetition Frequency) using fast AC transformers, Faraday cup and ionization chamber for current (and, by integration, charge) monitoring, whereas energy has been measured using a novel detector based on LiF (Lithium-Fluoride) crystals. Systematic measurements have been performed to investigate the sensitivity of output beam to machine operating parameters (SCDTL temperatures, stability of injector and RF power) highlighting the existing correlations. The LINAC is part of a 150MeV protontherapy accelerator under development in the framework of the TOP-IMPLART Project.

INTRODUCTION

TOP-IMPLART (Terapia Oncologica con Protoni – Intensity Modulated Proton Linear Accelerator for Radio Therapy) is a Regione Lazio (local government) founded project [1] for the development of a compact-size proton LINAC for cancer treatment with the main characteristics shown in table 1.

Table 1: TOP-IMPLART Accelerator Characteristics

Parameter	Value
Depth in tissue (max)	15 g/cm^2
Proton energy (max)	150 MeV
Dynamic energy variability	90-150 MeV
Dose rate	1-10 Gy/min

The TOP-IMPLART LINAC, is a 150MeV pulsed accelerator, under development at the ENEA Frascati Research Center, where it is currently under assembling and testing, inside a dedicated 30 meter concrete bunker.

* Work supported by Regione Lazio, agreement TOP-IMPLART Project
† paolo.nenzi@enea.it

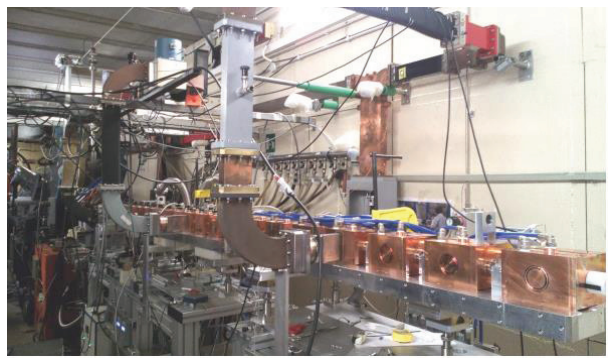

Figure 1: Actual layout of the TOP-IMPLART LINAC.

TOP-IMPLART is composed by two main sections: a commercial 7 MeV injector, produced by AccSys-Hitachi company, operating at 425 MHz, followed by a high-frequency booster operating at 2997.92 MHz designed by ENEA. The two frequencies have no harmonic relation and, thus, no RF synchronization between the sections has been adopted.

The injector is composed by a duoplasmatron ion source followed by an RFQ and a DTL. The booster is composed by SCDTLs [2,3] up to 65 MeV and CCLs up to 150 MeV. Actually only three, of the four SCDTLs (see Fig. 1) in the medium energy section are operational, reaching an output energy of 27MeV, with the fourth SCDTL expected to be installed by the end of the year, to reach 35MeV. The principal design parameters of the medium energy section are summarized in Table 2. The four SCDTLs are powered by a single TH2090 klystron tube (15MW peak-power, 15kW average) installed into a PFN (Pulse Forming Network) modulator developed in around 1990. Klystron and modulator have been adapted to the requirements of the TOP-IMPLART project and integrated into the accelerator.

The pulse length is 15μs-80μs for the injector and, 1μs-4μs for the booster. The PRF can be varied between 1 and 100Hz. In its present layout, closed loop feedback is fully operational in the duoplasmatron source (current control) and in the RFQ (frequency, phase and amplitude feedback), and only partially in the DTL (only frequency and phase feedback). The booster section operates in open-loop.

Table 2: Medium Energy Section Characteristics

SCDTL #	1	2	3	4
# tanks	9	7	7	5
Cells/tanks	4	5	6	6
Bore Hole diameter (mm)	4	4	5	5
Total Length (m)	1.12	1.1	1.4	1.1
Output Energy (MeV)	11.6	18	27	35

ISBN 978-3-95450-177-9

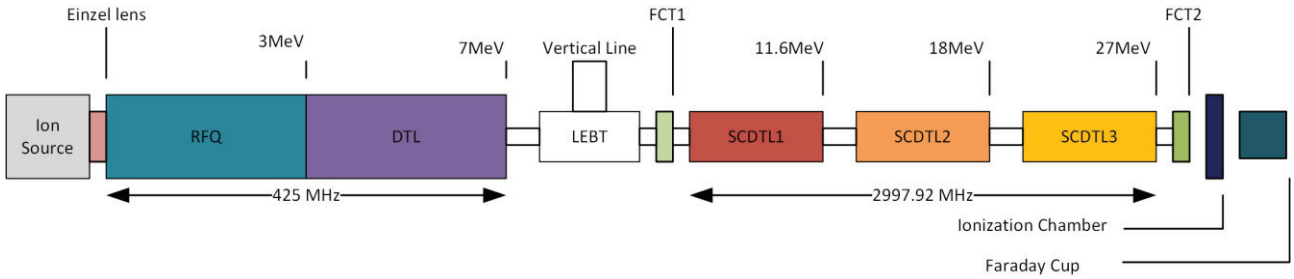

Figure 2: Schematic layout of the part of the TOP-IMPLART LINAC actually in operation.

Beam Diagnostics Instrumentation

TOP-IMPLART application requires precise control of output beam, current (and charge), energy, and position, those parameters are subject to measurement during all the construction of the accelerator.

The principal diagnostic implemented in the booster section consists of two AC current transformers ("FCT1" and "FCT2" in Fig.2) to measure the input and output current, respectively. The output transformer operates at atmospheric pressure (outside the vacuum pipe) and can be moved as long as the accelerator construction progresses. The current transformers have been produced by Bergoz Instrumentation according to the specification provided by ENEA. Table 3 summarizes their main characteristics (mechanical and electrical). The short axial length of the transformer has been one of the specification allowing for integration in the space between SCDTL sections, without significantly altering the spacing in the FODO lattice.

The transformers have been provided with calibrated amplifiers to obtain an overall gain of 1000V/A over a 1MΩ load, with a negligible droop for μs-duration pulses.

Output current and charge are also measured by a Faraday cup and a ionization chamber, the latter designed by ISS (Istituto Superiore di Sanità, Roma), operating at a bias voltage of 200V. Electrodes are realized with aluminated mylar (12μm mylar, 4μm aluminum). Electrodes spacing is 2mm. This redundancy is necessary as the low current level in the booster section (10-40μA) is almost at the bottom of the sensitivity of the current transformer.

A new multielectrode chamber is under development [4].

Table 3: ACCT Main Characteristics

Parameter	Value
Mechanical	
Outer Diameter	95 mm
Inner Diameter	10 mm
Bore Hole	6 mm
Axial Length	20 mm
Electrical	
Bandwidth (3dB)	>1 MHz
Gain (1MΩ load)	10V/10mA
Droop	<0.45%/ms
Output noise (mean)	<500μV
Output noise (stdev)	<2mV

Beam energy is measured by analyzing the Bragg peak position in a lithium fluoride (LiF) crystal. Commercially available 10x10 mm^2, 1 mm thick polished crystals have been positioned with the polished faces parallel to the beam propagation direction. The protons lose energy interacting with the crystal and creating color centers whose density is proportional to the dose [5]. As such centers emit visible photoluminescence after irradiation in the blue spectral range, by a fluorescence microscope equipped with a sCMOS camera the visible image of the irradiated LiF crystal is acquired: the photoluminescence intensity is proportional to the energy lost by protons in the crystal and the beam energy is obtained by measuring the distance between the crystal border and the intensity peak. The energy reference values are obtained by SRIM/TRIM simulations. Beam position and dimension are obtained from image analysis of the spot generated by the beam on a fluorescent target. The spot image is acquired by a monochromatic digital camera Basler model acA640-120gm equipped with an F2/35mm lens, each pulse, synchronously with the pulse trigger and digitized.

COMMISSIONING RESULTS

Commissioning of the 27MeV beam has been carried on observations spanning from 5 to 20 minutes after a warm-up time of 2 hours.

Injector Stability

The current provided by the injector is controlled varying the voltage on an einzel lens placed after the ion source. Figure 3 shows the current, measured on FCT1, at different lens voltages, keeping the extraction voltage constant at 28.4kV.

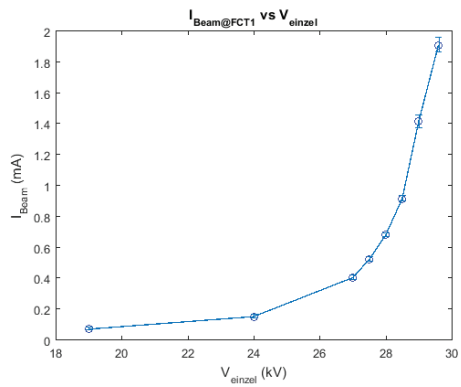

Figure 3: Injector beam current at different einzel potentials. Error bars represent 3 standard deviations.

ISBN 978-3-95450-177-9

Data analysis reveals that the variation of the injector current is below 3% (3σ) for einzel voltages down to 27kV.

An increase of variability is observed at lower voltages (and beam current) that is, most probably, due to the noise level in the system. The stability of the injector current is determined by the stability of the current generated by the ion source and of the fields in the RFQ and DTL.

In order to identify the sources of variability, the above mentioned parameters have been analyzed.

The proton current, generated by the ion source, is measured by the injector electronics and presented as a voltage signal proportional to the current. This signal has a mean of μ=2.01V and a standard deviation of σ=0.01V (corresponding to 1.5% at 3σ), roughly half of that of beam current. The remaining part of the variability is due to the variability of the RFQ and DTL fields.

Figure 4 shows the results of the spectral analysis of the measurements for a lens voltage of 29.6kV: The injector current periodogram (top panel) shows peaks in two regions. The first region extends from 0Hz to 0.7Hz and the second from 2.1Hz to 2.2Hz. The center and bottom panels clearly show that the spectral components in the first region are due to the arc current (the ion source), whereas the one in the second region to the DTL field. No significative spectral components have been identified for the RFQ. The peaks present in DTL field can be attributed to the missing amplitude feedback loop.

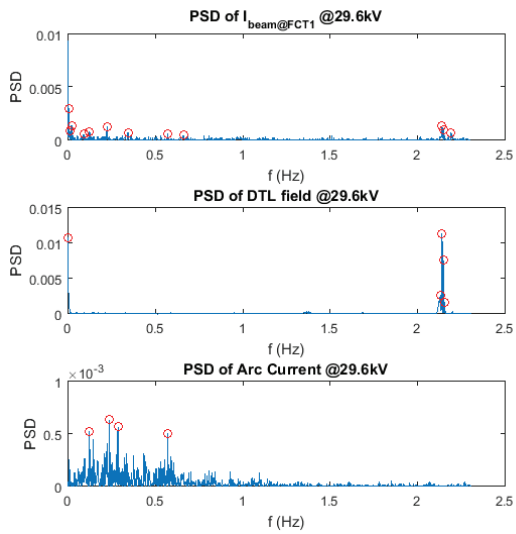

Figure 4: Power Spectral Density of the injector current (top panel), DTL field signal (center panel) and, arc current (bottom panel).

RF Power Stability

Figure 5 shows the RF distribution network of the medium energy section of the 3GHz booster. Full description of the RF generation and distribution network of the TOP-IMPLART LINAC is presented in [6]. The variable power dividers PD1 and PD2 sets the correct RF level for the SCDTL structures and the phase relations are established by the phase shifters PS1 and PS2.

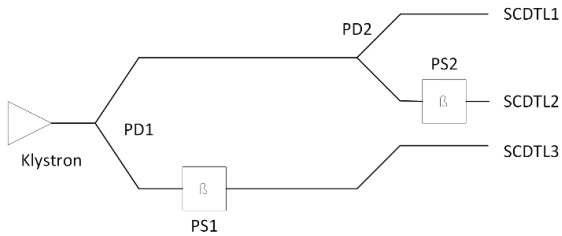

Figure 5: Schematic representation of the RF drive system for the medium energy section, in the present layout.

The peak power at the input of PD1 and electromagnetic field envelope for the three SCDTLs have been measured (Fig. 6): the power at PD1 input is 6.3MW (5% stability) with a temporal evolution shown in the top left panel.

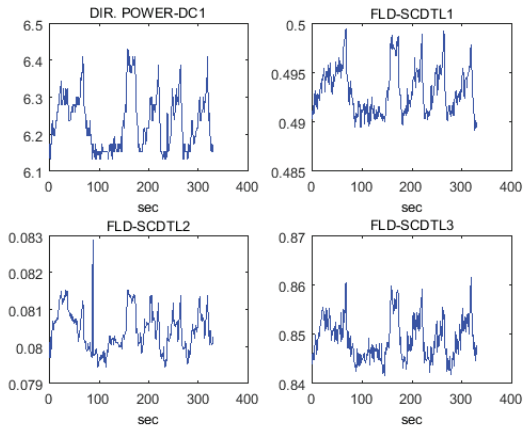

Figure 6: RF power (MW) at the input of PD1 (top left) and electromagnetic fields envelope (V) in the three SCDTLs.

SCDTL field are measured by a loop pickup placed in the accelerating tanks connected to a detector diode. The values in Fig. 6 are the voltage developed on the diodes at 50Ω load. The stability of the fields is better than 2.7%.

Beam Energy

Beam energy, as measured using the LiF crystal, is shown in Fig. 7.

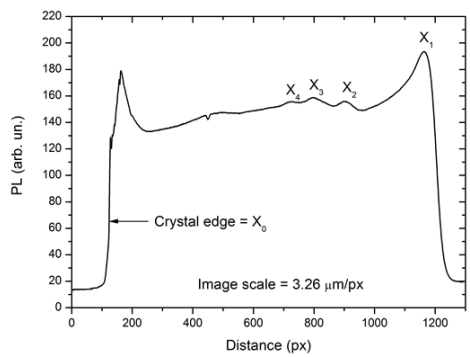

Figure 7: Photoluminescence intensity profile in LiF.

The intensity profile shows four peaks at different positions in the crystal. X1 is the Bragg's peak corresponding to an energy of 27MeV (energy has been computed with SRIM). Table 4 reports all peaks energies.

ISBN 978-3-95450-177-9

Table 4: Beam Energy Peaks in LiF

Peak #	Distance (µm)	Energy (MeV)
X_1	3390±4	27
X_2	2356±4	23.1
X_3	2194±4	21.2
X_4	1956±4	20.0

Spot Size and Centroid Stability

The output beam is elliptical, with the horizontal axis larger than the vertical one. This is consistent with the quadrupole arrangement in SCDTL3, as the last quadrupole focuses on the vertical axis. Spot size and position of the centroid has been evaluated for three different einzel lens voltages: 29.6kV, 27.5kV and 20kV. Spot size does not change in all three measurements. The horizontal and vertical axes measure (average value ±1 standard deviation) σ_x=1.56±0.0092 mm and σ_y=1.17±0.0054 mm.

Spot centroid position shows a slight dependence with the einzel lens voltage that is lower than 150µm in the x direction and 60 µm in the y direction. The temporal analysis of beam position reveals a correlation between x and y centroid position oscillation as it is shown Fig. 8 for an einzel lens voltage of 27.5kV. This correlation is the consequence of the rotation of one or more quadrupoles in the accelerator.

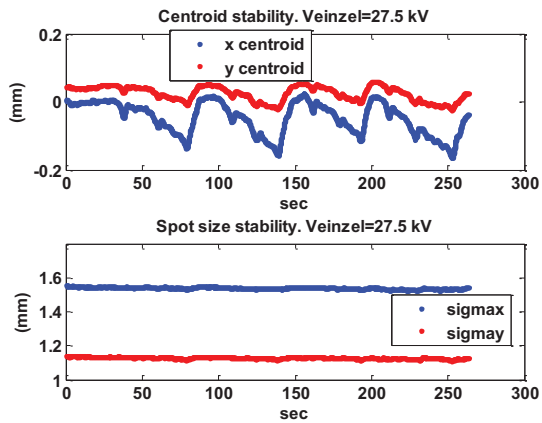

Figure 8: Centroid position and stability vs time for einzel lens voltage of 27.5kV.

Output Beam

The current and charge of the 27MeV beam has been measured. Current measurements have been performed using both the Faraday Cup and FCT2, placed after a 500µ thick aluminium spacer inserted to stop secondary electron emission from the beam pipe. Figure 9 shows that both measurements agree on the pulse current value of 40µA (the Faraday cup develop 2mV on a 50Ω load). The lower bandwidth of the FCT2 is evident from the comparison of signal rise times, nevertheless is sufficient to reach the final amplitude level for the 3.2µs TOP-IMPLART pulse width.

The ionization chamber has been used to measure the output pulse charge. Figure 10 shows the measured charge for different values of the einzel lens voltage.

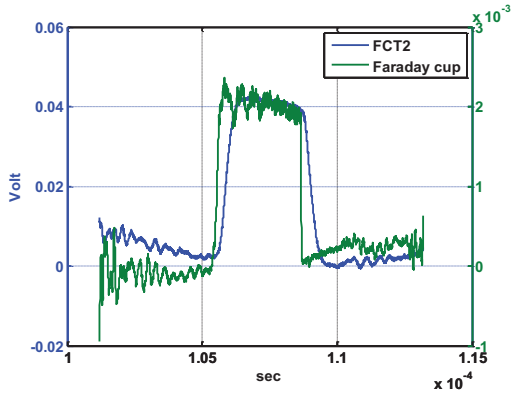

Figure 9: 27MeV current pulse measured by FCT2 and the Faraday Cup (terminated on 50Ω impedance).

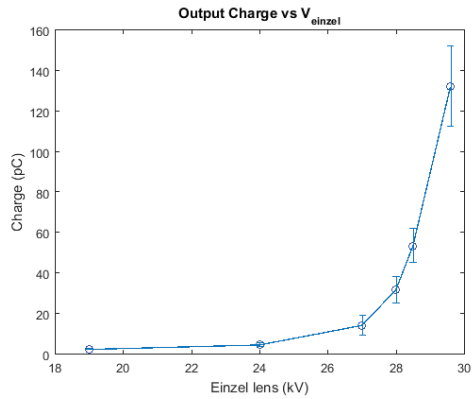

Figure 10: 27MeV beam pulse charge versus einzel lens voltage (Error bars represent 3 standard deviations).

CONCLUSION

The commissioning results for the 27MeV beam of the TOP-IMPLART accelerator have been presented. The accelerator is undergoing a major upgrade consisting in the completion of the medium-energy section, the replacement of the old klystron and modulator with a TH2157A 10 MW peak power klystron and the K1 solid state modulator produced by SCANDINOVA. Feedback loop for the new system will be installed and tested to improve the stability.

REFERENCES

[1] C. Ronsivalle *et al.*, "The TOP-IMPLART project", Eur. Phys. J. Plus 2011. 126

[2] C. Ronsivalle *et al.*, "First acceleration of a proton beam in a Side Coupled Drift tube Linac", Europhysics Letters 2015. 111:5.

[3] P. Nenzi *et al.*, in *Proc. IPAC'15*, pp. 2245-2248.

[4] E. Cisbani et al., "Beam Micro Pattern Ionization Chamber with Adaptive Amplifiers as Dose Delivery Monitor for the Therapeutic Proton LINAC", presented at IBIC'16, Barcelona, Spain, Sep. 2016, paper TUPG51, this conference.

[5] M. Piccinini *et al.*, "Photoluminescence of radiation-induced color centers in lithium fluoride thin films for advanced diagnostics of proton beams", Appl. Phys. Lett. 106 (2015) 261108-1-4.

[6] V. Surrenti *et al.*, in *Proc. IPAC'15*, pp. 897-900

ISBN 978-3-95450-177-9

UPGRADES TO THE LANSCE ISOTOPE PRODUCTION FACILITIES BEAM DIAGNOSTICS *

H. Watkins, D. Baros, D. Martinez, L. Rybarcyk, J. Sedillo, R. Valicenti,
Los Alamos National Laboratory, 87545, USA

Abstract

The Los Alamos Neutron Science Center (LANSCE) is currently upgrading the beam diagnostics capability for the Isotope Production Facility (IPF) as part of an Accelerator Improvement Project (AIP). Improvements to measurements of: beam profile, beam energy, beam current and collimator charge are under development. Upgrades include high density harps, emittance slits, wire-scanners, multi-segment adjustable collimator, data acquisition electronics and motion control electronics. These devices will be installed and commissioned for the 2017 run cycle. Details of the hardware design and system development are presented.

INTRODUCTION

IPF Purpose

The purpose of the Isotope Production Facility (IPF) is to produce isotopes, not commercially available, for research, development and treatment in the United States. They currently produce Strontium-82 isotopes for cardiac imaging as well as a variety of other isotopes used for medical treatment and study. The isotopes produced at IPF impact approximately 30,000 patients per month [1]. The facility uses beams at 41, 72 and 100MeV for isotope production.

IPF Upgrades

The IPF facility is planning an upgrade as part of its scheduled beam window replacement in 2017. This upgrade is focused on increasing yield of the facility, reducing programmatic risk and improving beam diagnostics. The improved diagnostics capability will ensure that the beam profile, intensity and incident energy are well understood in an effort to improve target survival at increased beam currents [2].

PROFILE MEASUREMENTS

Three upgrades to beam profile measurements will be completed as part of the IPF upgrade. The existing harp will be replaced with a higher resolution device. An emittance measurement and wire scanner measurement will be added upstream of the harp. These measurements will be placed at three separate locations along the IPF drift length to characterize the beam. The harp will serve a dual purpose as both a profile measurement and a collector for emittance.

Actuators

The IPF beam line transitions from a 4” diameter beam pipe to a 6” diameter beam pipe after the raster magnets and prior to the target. The challenge for actuators in these locations is the large stroke length required to scan wires and harps. This sets a requirement for actuators to achieve a 20 cm stroke and 1 mm scan resolution. Figure 1 shows three new designs created to meet the profile measurement requirements that all used a common off the shelf (COTS) slide table and actuation stage.

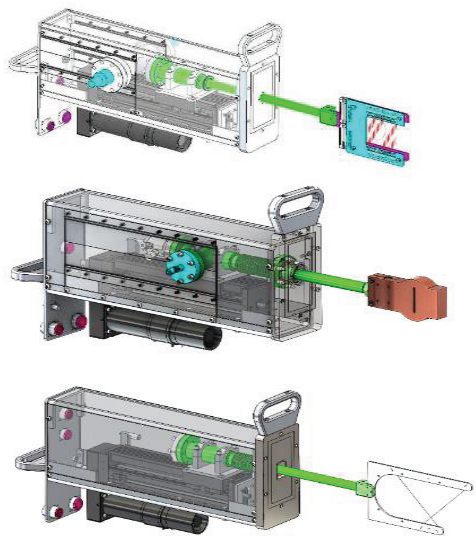

Figure 1: Three Types of Actuators

High Density Harp

Another challenge of the IPF upgrade was the high density harp. The requirements were to design a device with a 7.6cm profile width and 1mm wire resolution. The harp head assembly needs 77 wires in both the horizontal and vertical planes.

The harp head design achieved this high density requirement by using a dual sided printed circuit board (PCB) that spaced wires 2 mm apart on each side. Figure 2 shows how the hook and spring were used to tension a silicon carbide (SiC) wire across the PCB.

*Work supported by the U.S. Department of Energy, Contract No. DE-AC52-06NA25396 LA-UR-16-26712

ISBN 978-3-95450-177-9

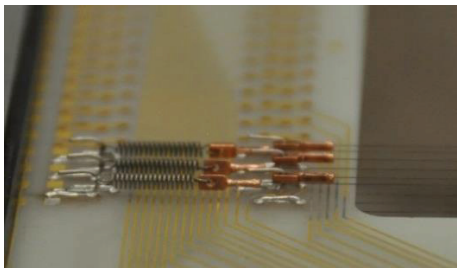

Figure 2: Hook, spring and crimp attached to G10 harp frame.

The signal connections route to an edge connector that transitions the signal to radiation tolerant wiring before exiting through the vacuum feedthrough shown in figure 3.

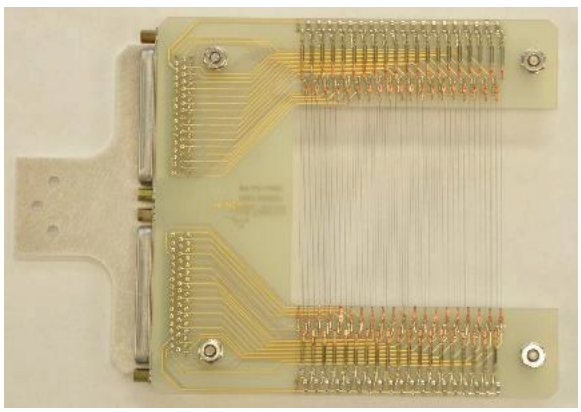

Figure 3: Harp head assembly

Analog Signal Conditioning

The analog conditioning module is used to measure the secondary emission current of the wires. The requirements for the analog circuitry were to measure currents from 270uA down to 3uA during beam tuning along with a 50VDC bias being applied to the wire.

Figure 4 shows the resulting circuit with an AC coupled input with a 2 kOhm load. The signal across the load is then gained up and conditioned by a pair of instrumentation amplifiers cascaded to provide programmable gain from 1-10000. A discrete filter is used to produce a 150kHz corner frequency to limit the bandwidth of the analog front end. An auto zero circuit is used to keep the AC coupled circuit from drifting by integrating the noise when beam is off. A final buffer amplifier is used to output the signal to the data acquisition electronics.

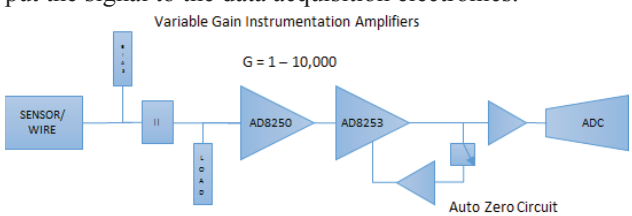

Figure 4: Analog Conditioning Circuit

The analog conditioning circuit is placed on a 3U cPCI card with 16-channels and remote gain control. The channel count matches that of the data acquisition system.

Data Acquisition System

The data acquisition (DAQ) system requirements are to sample and analyze the data at 100KSPS so that profiles can be analyzed across the beam pulse of 150μsecs. A buffer in the DAQ provides both pre-trigger and post-trigger samples. Integration and current calculations are done on board the FPGA hardware and results are then sent across the EPICS control network to the measurement client. The DAQ system also provides analog conditioning control and timing acquisition to coordinate the measurement.

The DAQ controller is based on the National Instruments (NI) 9038 cRIO that includes a real time Intel Atom processor as well as a Xilinx FPGA. The analog to digital converter is a 16-bit 100 KSPS synchronous sample module with 16-channels. The controller is mounted in a 4U chassis that also includes an 8-slot cPCI backplane that interfaces with the sensors.

Figure 5: DAQ Chassis

The chassis in figure 5 is produced by a 3rd party vendor, Bira Systems Inc, who assembles all the specified components and provides a final system that is tested and verified.

Wire Scanner

The final profile measurement is a wire scanner that uses a horizontal and vertical wire on a single fork. A requirement that the wire not be crossed when intercepting beam creates a stroke requirement of 19.4cm to scan both wires through the beam.

The electronics design for actuator and data acquisition are based on a previous wire scanner for LANSCE that uses an NI cRIO platform for the controller. [3]

BEAM ENERGY

Beam energy calculations are important to the IPF facility to determine the isotope production yield for a specific target. The requirement for beam energy is to measure energy at 41, 72, and 100MeV with 50 keV resolution. This measurement will use existing strip line beam position monitors in the IPF line. The measurement will be a phase- based measurement which uses the fundamental

ISBN 978-3-95450-177-9

acceleration frequency of 201.25MHz to determine the time of flight of particles at three separate locations along the beam line.

Long drift lengths have a benefit of providing improved energy resolution as shown in figure 6. The drawback to the long length is ambiguity between different energies since knowledge of the integer cycles between BPMs must be known for a particular energy set point. Having three different drift lengths provides a course and fine resolution measurement where the course measurement can provide evidence of cycle mis-calculations and the long drift lengths provide fine resolution as shown in figure 7.

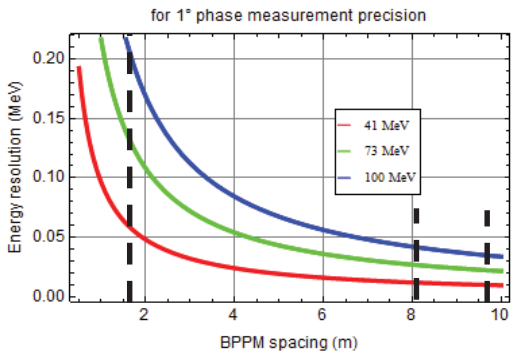

Figure 6: ToF Energy Resolution vs Spacing

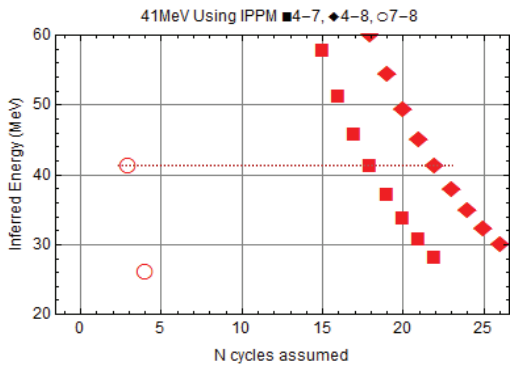

Figure 7: Energy vs Cycles

Time of Flight Electronics

The electronics for the time of flight measurement consists of an analog signal conditioning unit that takes in four electrodes from the BPM and band pass filters the 201.25 MHz fundamental frequency. A 240 MSPS digitizer then samples the four electrodes plus a reference frequency channel to make phase measurements using an I/Q demodulator technique embedded in a Stratix IV FPGA. All the hardware is COTS except for the analog card. Figure 8 shows hardware contained in a hybrid VPX/cPCI chassis.

Figure 8: Beam Energy Chassis

BEAM CURRENT

Beam monitors exist in the IPF beam line however their sensitivity is limited to average beam currents of 2-5 µA minimum. Experimental isotope production sometimes requires average beam currents of 100 nA be delivered to IPF. The lower limit boundary of the current measurements is set by the electronics used for measuring the peak current from the toroid current monitors.

A high sensitivity current module is being evaluated as an alternative to the system that is in place today. The high sensitivity module would not cover the entire range of measurements but would become active when peak currents dropped below 1mA.

Challenges

The challenge with the high sensitivity current monitor is interferers. There are two main interference frequencies that are picked up by the current monitor. The two frequencies of concern are 5 kHz and 72 kHz. The source of the 5 kHz interferer is understood. The IPF beam is rastered around the target by two steering magnets. These magnets are set to raster the beam at a 5 kHz frequency which is also picked up by the current monitor. The 72 kHz interferer is of unknown origin. Additional testing is planned to pin point the source of this interference and efforts will be made to mitigate its impact on the current monitors.

COLLIMATOR

The last diagnostic to be upgraded at IPF is the active and adjustable collimator. The existing collimator is not adjustable and beam current on the segments is not measured. The new design will provide an adjustable aperture from 1.4 to 2.3 inches with a 500 Watt limit per segment. Beam impinging on the collimator will be measured as well as temperature monitoring of the segments.

ISBN 978-3-95450-177-9

Segments

The collimator will have eight graphite segments designed to completely stop beam. Four segments will be fixed and four will be adjustable. The charge on each segment will be monitored by remote electronics along with biasing of each segment. Figure 9 shows the range of aperture size the collimator will provide.

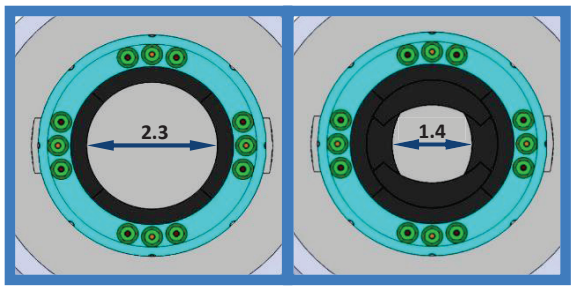

Figure 9: Collimator Aperture Sizes [4]

Temperature

IPF has had issues in the past with the collimator being damaged thermally. Therefore, this design will include a temperature sensor on each segment. Temperature information will be logged to gain knowledge of the thermal levels encountered during beam delivery to the IPF target.

Actuation

The collimator will be actuated by pull straps mounted upstream of the segments. A flexure is used to translate the strap displacement to collimator aperture adjustment. A slide table and motor assembly similar to the profile monitors will be used along with a chassis controller that will include DAQ and motion control.

CONCLUSION

Commissioning of these diagnostics is scheduled in Q2 2017 during the maintenance outage at LANSCE. The design and procurement stages of the project have been completed. Current work is assembling and testing of the various components needed to complete each diagnostic.

REFERENCES

[1] E.R. Birnbaum, "LANL Accelerator Improvement Project Mission Need and Operational Impacts", Presentation, LANL.

[2] E.R. Birnbaum, K. D John, J. L. Erickson, M. Pieck, "LANL AIP Proposal: IPF Beam Transport Upgrade Project", Proposal, LA-UR-14-26690, LANL document.

[3] J. Sedillo, *et al.*, "First Test Results of the new LANSCE Wire Scanner", PAC'11 New York, NY, USA, March 2011, MOP236.

[4] E. Swensen, "Active Collimator Mechanical Design", Presentation, LANL.

ISBN 978-3-95450-177-9

FIRST HEATING WITH THE EUROPEAN XFEL LASER HEATER*

M. Hamberg†, Uppsala University, Uppsala, Sweden,
F. Brinker, M.Scholz, DESY, Hamburg, Germany

Abstract

The EU-XFEL laser heater is installed and commissioning phase is ongoing. In this paper I discuss the steps undertaken and report the first heating of electron beams observed in the injector section.

INTRODUCTION

The European XFEL is a 3.4 km long free-electron laser (FEL) which will deliver radiation in the wavelength regime of 0.05 to 4.7 nm. To avoid problems with longitudinal micro bunching instabilities a laser heater is implemented. The interaction region is located in a chicane and consists of a 0.7 m permanent magnet undulator in which IR-laser pulses are overlapping electron bunches during the passage and induces a phase space modulation. When the electron bunches leave the chicane section via two bending magnets the modulation is smeared out and leave a net "heating effect". This in turn increases the overall stability and therefore the overall brightness level of the FEL. The principle has previously been proven [1-2].

The EU-XFEL Laser Heater is a Swedish in kind contribution and has earlier been described in detail [3-5]. In this paper I report the commissioning steps undertaken and the first recorded heating outputs observed in the injector section and finish with a conclusion and outlook.

USER INTERFACE

Most of the Laser Heater features are controlled through the DESY Distributed Object Oriented Control System (DOOCS) control system via the JAVA DOOCS DATA DISPLAY (JDDD) interface [6-7]. The interface displays the laser heater in a schematic way. Each optical station such as the laser laboratory on level 5 in the injector building, optical stations 0 and 1 (OS0 & OS1 close before and after the interaction region on level 7 respectively) can easily be operated separately.

PRECONDITIONING

Given the default electron energy of 130 MeV, a laser wavelength (λ_L) of 1030 nm and the wiggler period (λ_w) of 7.4 cm the undulator gap had to be 42.43 mm to fulfill the known resonance condition :

$$B_w = \frac{2\pi \cdot m_e \cdot c}{q_e \cdot \lambda_w} \cdot \sqrt{2\left(\frac{\lambda_L}{\lambda_w} \cdot 2 \cdot \gamma^2 - 1\right)}$$

The laser pulse was set to 22 ps flattop FWHM for IR (which corresponds to 22 ps for the UV cathode laser as well), laser pulse energy was limited to ~4μJ per pulse at interaction region since the foreseen heater amplifier was not yet installed. Due to preliminary conditions waiting for the amplifier the laser spot size in the interaction region was tuned to σ≈0.6 mm as opposed to the e-beam σ≈0.3 mm.

TRANSVERSE OVERLAP & SETTING THE STAGE

To accomplish heating of the electron bunches overlap of the laser beam has to be assured. The transverse overlap is obtained by reading out the positions on Cromox screens directly before and after the interaction region of the undulator where both, the electron and the laser beams can be observed. The laser beam position is adjusted with the two orthogonal linear stages making up the periscope on OS0. Due to the design the overlap can be adjusted in the X- and Y-direction independently by one translation stage each. An example of illustrated laser spot and, electron beam and laser simultaneously can be seen in Fig. 1.

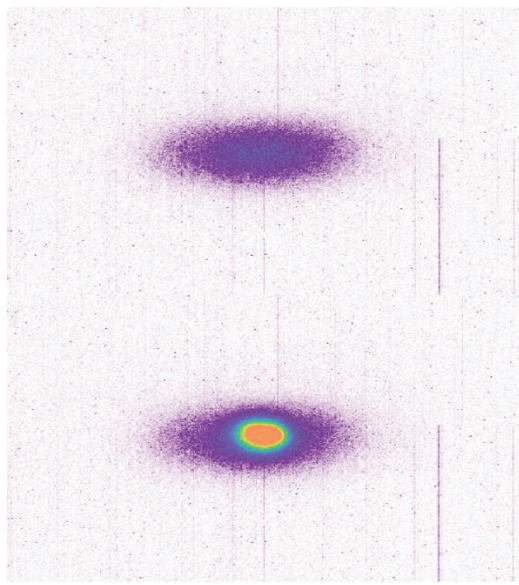

Figure 1: Cromox screen directly before undulator with top only laser, bottom, e-beam and laser illustrating transverse overlap.

TEMPORAL OVERLAP & HEATING

The temporal overlap was first controlled via a rough delay line adjusted by hand and adjusted after read out from a photo diode at the inlet of OS1 after the undulator. A 4 GHz oscilloscope was used to display the signal from the laser and undulator synchrotron light respectively.

Once the course overlap was found a fine delay line based on a retroreflector mounted on a 210 mm motorized linear stage with ~μm resolution was ready for use. Due

* Work supported by Swedish Research council, Sweden, and DESY, Hamburg, Germany
† mathias.hamberg@physics.uu.se

ISBN 978-3-95450-177-9

to the travel back and forth the double length is passed which corresponds to an adjustment possibility of up to 1.4 ns which is sufficient for the purpose. The electron bunch and laser pulse length was in the first test set to 22 ps and a reasonable step size for the fine delay line was selected to be ~7 ps corresponding to 200 divisions of the full pathway.

As readout of the heating we choose to illustrate the electron bunch width standard deviation at the dispersive section before the dump of the injector with a screen station. The electron optic was optimized for this measurement in order to get a low beta function and a high dispersion at the place of the screen. The first scan resulted in the spectrum shown in Fig. 2. The extra energy from the heating should result in a net broadening effect which also was discovered at the preset 0 position. Each pixel corresponds to ~1.4 keV energy spread. The observed increase of the energy spread from 14 keV to 18 keV is in agreement with the low laser power at that time.

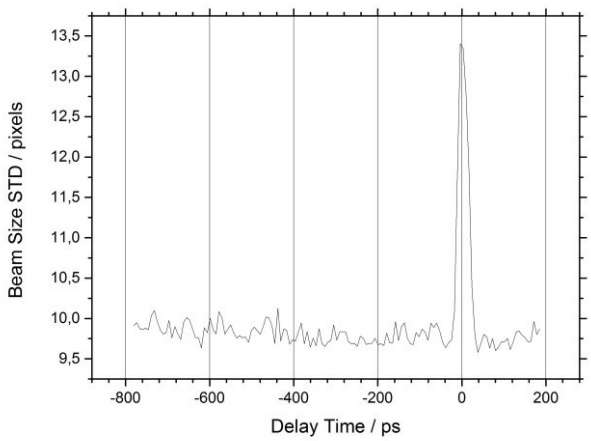

Figure 2: Fine delay line scan illustrating the first sign of heating of the electron bunches by displaying bunch width standard deviation at the dispersive section vs delay line position given in ps.

Subsequently the laser stacker was removed to more than double the peak power. The duration time was still 22 ps FWHM for the IR but instead ~10-12 ps FWHM for the UV pulses going to the electron gun. No strong change in heating effect was observed however.

Investigations while turning on the transverse deflecting structure (TDS) and observing the trace in the dispersive section. This is illustrated in Fig. 3 when the laser is blocked and unblocked respectively. It is clear that the trace is becoming fuzzier during laser overlap i.e. is heated.

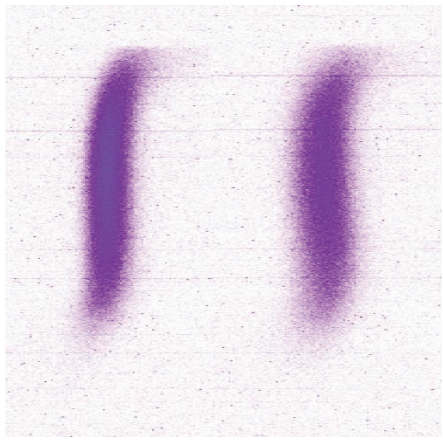

Figure 3: OTR screen in dispersive section after the laser heater and TDS switched on with left, only laser blocked, right, laser unblocked clearly showing a fuzzier trace.

UNDULATOR GAP SCAN

As mentioned the initial undulator setting was chosen to match the 130 MeV e-beam energy and the undulator gap set to 42.4 mm. Gap scans were undertaken showing results displayed in Fig. 4. Where the main resonance is clearly visible.

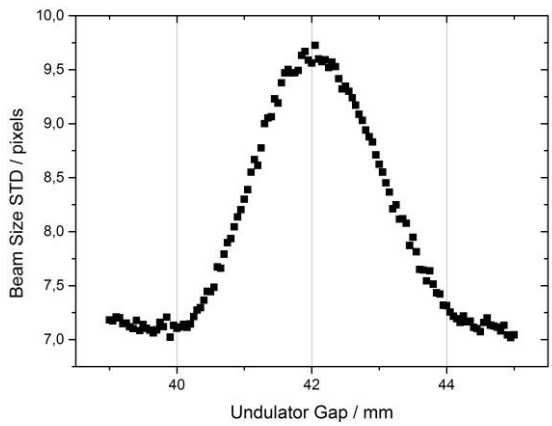

Figure 4: Undulator gap scan versus heating of the electron bunches by displaying bunch width standard deviation in pixels.

The gap scans where repeated at different energies. The gaps where the resonances were found a shown in Fig. 5 together with the theoretical values. The observed offset of about 0.3% in energy is well within the precision of the energy measurement.

ISBN 978-3-95450-177-9

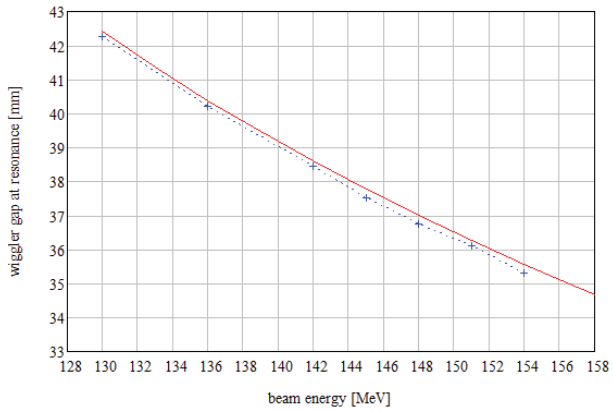

Figure 5: Measured and theoretical undulator / wiggler gap vs. beam energy.

ATTENUATOR SCAN

Also the limited laser energy of ~4 µJ inside of the interaction region was scanned for optimization using a λ/2 plate in a stepper motor driven rotation stage and with a subsequent polarization dependent beam splitter cube. The limited energy does not indicate any obvious resonance as can be seen in Fig. 6.

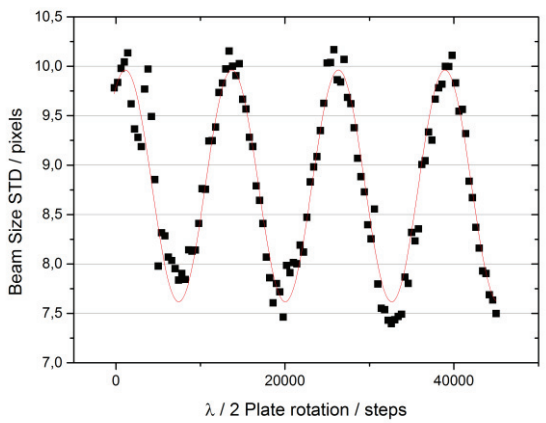

Figure 6: Laser energy scan by rotating λ/2 plate before polarization dependant beam splitter cube.

CONCLUSION AND OUTLOOK

It is clear that the EU-XFEL laser heater is demonstrating heating.

Currently the commissioning is ongoing with implementation of a laser amplifier able to produce energies over 200 µJ per pulse [8]. This also implies undertaking minor adaptations due to the change of length and optimization of the incoming laser beam for the laser heater to run under the specified beam conditions. Additional foreseen adaptations include a simplified laser width adjusting routine. For the 4D laser routing and stabilization system mentioned as the worlds most advanced, an automatized attenuation system is implemented to optimize the power levels on the position sensitive detectors in the system. It is also foreseen to if needed use the 4D system as a fast scale delay line to adopt for temporal drifts on picosecond scale. Such drifts could be monitored by a cross correlator possibly based on two photon-absorption. Additionally, the mirrors inside of the UHV section are chosen to be of metal to avoid beam disturbance. They should be recoated with an amorphous gold coating completely without grain structure or crystallinity to increase the laser damage threshold further.

Next commissioning step will be to redo the laser-electron beam interaction measurements in the injector section with the higher energies from the amplifier and optimized specs. This will also be compared in detail with theoretical calculations.

Finally, a full commissioning investigating the impact on the EU-XFEL SASE will be undertaken and is foreseen in 2017.

ACKNOWLEDGEMENT

I thank DESY and Swedish research council under Project number DNR-828-2008-1093 for financial support. In addition, I thank TEM Messtechnik, FMB Berlin and all involved DESY groups for excellent support.

REFERENCES

[1] Z. Huang *et al., Phys. Rev. ST Accel. Beams* 13 (2013) 020703

[2] S. Spampanati *et. al, Phys. Rev. ST Accel. Beams* 17 (2014) 120705.

[3] M.Hamberg and V. Ziemann, TUPSO25, Proceedings of *FEL2013*, New York, NY, USA.

[4] M.Hamberg and V. Ziemann, THPRO024, Proceedings of *IPAC2014*, Dresden, Germany.

[5] M.Hamberg and V. Ziemann, Proceedings of *FEL2015*, Daejeon, South Korea, paper TUP038.

[6] http://doocs.desy.de

[7] E. Sombrowski *et al.*, Proceedings of *ICALEPCS* 2007, Oak Ridge, USA, paper MOPB05.

[8] F. Moglia *et al.*, EuroPhoton 2016, Vienna, Austria.

ISBN 978-3-95450-177-9

THE MEASUREMENT AND CONTROLLING SYSTEM OF BEAM CURRENT FOR WEAK CURRENT ACCELERATOR

Junhui Yue, Lingda Yu, Yuguang Xie, Yulan Li, Zhongjian Ma, IHEP, CAS, Institute of High Energy Physics, Chinese Academy of Sciences, Beijing 100049, China

Abstract

For some detectors' calibration, a very weak electron current provided by accelerator is necessary. In order to control the beam current to the detector, 8 movable slits in which the position resolution of the stoppers is better than 5μm are installed along the accelerator. For the weak current measurement, 9 movable current monitors based on scintillator are installed along the beam line. These monitors can measure the very weak current, even to several electrons. The monitors can be pulled away the beam axis when the electron beam goes to the downstream.

INTRODUCTION

In order to calibration some detectors, a small linac is designed and installed in the campus of IHEP. This accelerator consists of a weak current electron gun, a RF chopper, a 1.0m-long accelerator tube and a 3.0m-long accelerator tune, 8 movable slits, 9 current monitors, and other systems. It can provide 0.1~5MeV beam and 5~50MeV beam. These two kinds of beams are sent to the same target chamber by the bending magnets. The schematic diagram of weak current is shown in Fig. 1.

For the charge of pulse is above 1nC, ordinary monitor is enough. In pC region, a charge sensitive and low noise detector has been development. In fC region, thermo luminescence dosimeters (TLD) and two dimensional radiation dosimeters would be candidates [1]. For aC region, that means there are only several electrons in the pulse, plastic scintillator is used to detector the electron, the detailed description is in this paper.

THE SELECT OF MATERIAL AND THICKNESS OF STOPPER

In order to step by step decrease the beam intensity, 8 movable slits are installed along the accelerator. Slit 1 is horizontal and Slit 2 is vertical, they can decrease the beam intensity to 1/20 with the help of solenoid because of the space change. Slit 3 and Slit 4 have the same effect. Slit 5 also decrease the beam intensity with the RF chopper because of time change. Other horizontal slits cooperate with the bending magnet to decrease the beam intensity. In order to effectively block the electrons, the material of stopper is carefully selected and the thickness is needed to calculate. Lead target, aluminium target and tungsten target are calculated by FLUKA program. Tungsten target is effect to block the electron and avoiding other effects. The result is showed in Fig. 2. For the 50MeV electrons，90 percent energy are deposited in tungsten target, the thickness is not more than 2.25cm, so all the stoppers, 2.25cm thickness tungsten is used. Other target needs thicker material, it is not easy to design and manufacture.

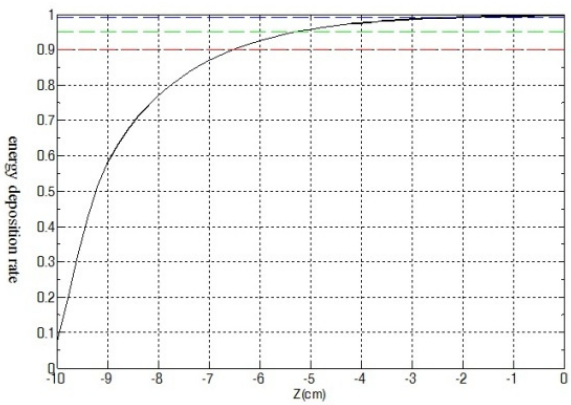

Figure 2: The energy deposition of 50MeV electron in tungsten target.

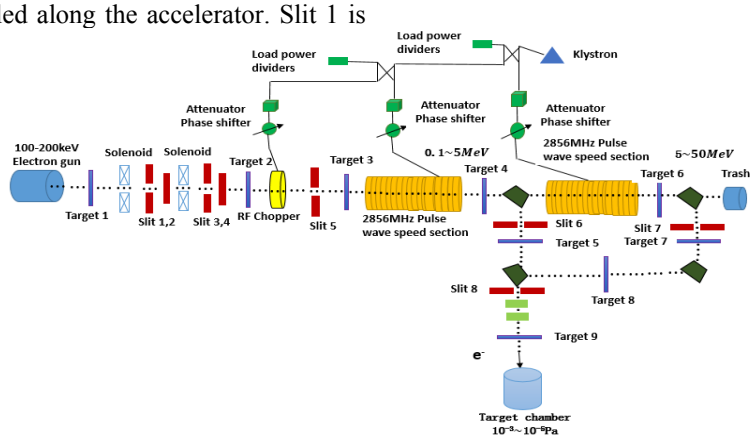

Figure 1: The Schematic diagram of weak current accelerator.

ISBN 978-3-95450-177-9

CURRENT MEASUREMENT SYSTEM BASED ON PLASTIC SCINTILLATOR

The current of electron gun is μA level. The beam current is lower in other place of accelerator, so convention methods cannot be used to measure the beam current. In pC region, a beam monitor using a charge sensitive amplifier and a two dimensional monitor using a scintillator and a CCD camera are developed at Osaka Prefecture University [1].

In this paper, plastic scintillator is used to measure ultra-low beam intensity. Plastic scintillator has such advantages as quickly response, high energy resolution, and high photon yield. Plastic scintillator coupled with PMT by light guide. The electron goes through the scintillator and produces light, small PMT whose peak response is 400~430nm is used to match the wavelength of the light produced by scintillator. Pulse produced by PMT to be sent to the pre-amplifier and the amplifier, and then is digitized by ADC. Because light intensity is linear with beam intensity, so using the calibration coefficient, beam current can be derivate. The schematic diagram of weak current measurement is shown in Fig. 3.

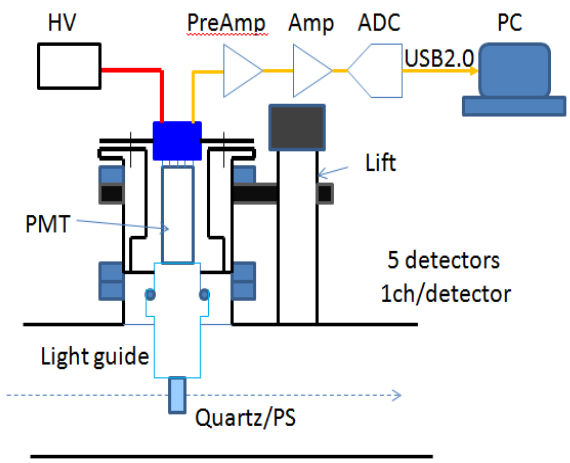

Figure 3: The schematic diagram of weak current measurement.

SLIT AND CURENT MONITOR MOVING SYSTEM

Every slit has two stoppers, every stopper need to be moved by motor, in order to precisely control the beam intensity, the moving step of stopper is 5μm. The repeat location accuracy of scintillator will be 20μm. Motion Controller NI PXI-7334 is used to control the motor. Signal Acquiring card NI PXI-6602 to read the data of grating-rule to insure the accuracy position. 1μm position resolution Sino grating ruler KA-500 is to be used. Fig. 4 and Fig. 5 are shown testing of slits and movable monitors in the lab.

Figure 4: The slits were tested in the Lab.

Figure 5: The current monitors were tested in the Lab.

CALIBRATION RESULT

Before the scintillators are used to measure the beam intensity, calibration needs to be done by radioactive source. Here β source ^{207}Bi is used to calibration the monitor. Fig. 6 shows the output waveform from the electronics, the pulse produce by PMT is negative.

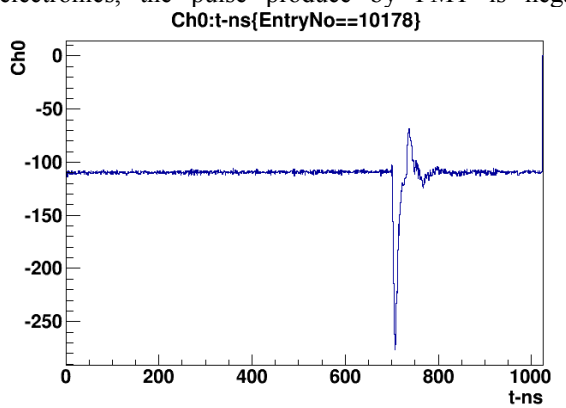

Figure 6: The pulse output from electronics.

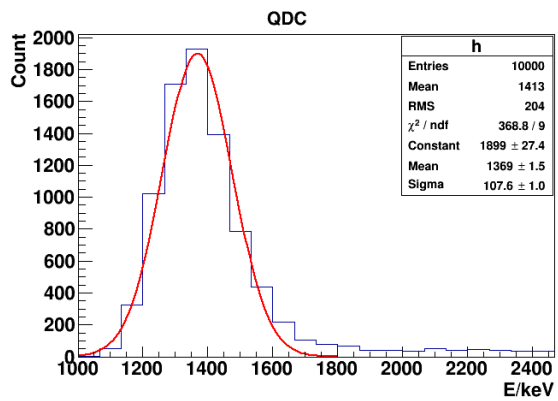

Figure 7: Calibration result of plastic scintillator by ^{207}Bi.

ISBN 978-3-95450-177-9

The statistical result is shown in Fig. 7, 1369keV in the Figure 7 correspond to the 976keV (we know the energy of beta beam of ^{207}Bi is 976keV), so there is a coefficient of 976/1369.

PRELIMINARY MEASURE RESULTS

The pulse waveforms produced by monitor 1- 4 are shown in the Fig. 8. The clear beam current signal can be acquired by the oscilloscope. In the first phase, the task is let the beam goes through the entire accelerator and arrive to the target chamber to check the design and other instruments. In the next phase, decreasing the beam intensity along the accelerator and need to know how many electrons pass through the monitor are important.

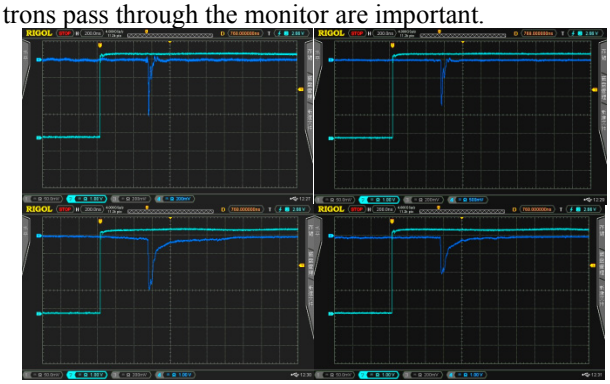

Figure 8: Pulse waveform produced by Monitor 1-4.

CONCLUSION

In this paper, the beam current measurement and controlling system and some preliminary results have been shown. 8 movable slits are used to control the current, 9 monitor based on plastic scintillator are used to measure ultra-lower beam intensity. The preliminary result shows the current monitor can response to ultra-low intensity beam pulse, but some further study is need to be done.

REFERENCE

[1] S.Okuda, Y.Tanaka, R.Taniguchi, T.Kojima, “Low Intensity Electron Beam Monitoring and Beam Application at OPU”, in *Proceedings of Linac 2006*, Knoxville, Tenessee, USA, August 2006, paper TUP018, pp.286-288.

ISBN 978-3-95450-177-9

HEAVY ION BEAM FLUX AND IN-SITU ENERGY MEASUREMENTS AT HIGH LET*

S. Mitrofanov†, I.Kalagin,V. Skuratov, Y. Teterev
FLNR JINR, Dubna, Moscow Region, Russia
V. Anashin, United Rocket and Space Corporation, Moscow, Russia

Abstract

The Russian Space Agency with the TL ISDE involvement has been utilizing ion beams from oxygen up to bismuth delivered from cyclotrons of the FLNR JINR accelerator complex for the SEE testing during last seven years. The detailed overview of the diagnostic set-up features used for low intensity ion beam parameters evaluation and control during the corresponding experiments is presented. Special attention is paid to measurements of ion flux and energy at high LET levels and evaluation of ion beam uniformity over large (200x200 mm) irradiating areas. The online non-invasive (in-situ) time of flight technique designed for low intensity ion beam energy measurements based on scintillation detectors is considered in details. The system has been successfully commissioned and is used routinely in the SEE testing experiments.

INTRODUCTION

Onboard equipment of spacecraft is exposed to ionizing radiation from the Earth's natural radiation field, as well as galactic and solar cosmic rays during its operation. There are two types of effects in microelectronic circuits caused by radiation: 1—those related to accumulated dose; and 2—those caused by a singular hit of a swift heavy ion (single event effect, SEE). Despite its relatively minor contribution (~1%) of the total amount of charged particles, it is heavy ions that cause the most damage to microelectronics hard ware components due to the high level of specific ionization loss. Hence, to reproduce the effects of the heavy ion component of cosmic radiation for the prediction of electronic device radiation hardness usage of low intensity (up 10^6 ions cm^{-2} s^{-1}) heavy ion beams with linear energy transfer (LET—the measure of energy losses per path length in the material) levels in silicon, specific for the ion energy range of 50–200MeV/nucleon, is supposed. Taking into account that actual integrated circuits in metal and plastic packages, as well as ready to use electronic boards need to be tested, ion beams with energies in the range of 3–50 MeV/nucleon are used in model experiments. This entire means that the accepted method of SEE testing requires measurements of ion flux in the range from 1 to 10^5 ions (cm^{-2}*s^{-1}), ion fluence up to 10^7 ions/cm^2, beam uniformity at the device under test (DUT) and energy of ions. The SEE testing facility is established [1] at the U400M and U400 cyclotrons at the accelerator complex of the Flerov Laboratory of Nuclear Reactions (FLNR) of the Joint Institute for Nuclear Research (JINR) [2]. Ion beam parameters used for SEE testing, like ion type and energy, the LET and ion flux range, are listed in Table 1.

Table 1: Ion Beam Parameters Used for the Low Energy SEE Testing

Accelerated ion	Extracted ion	Energy, MeV	LET, MeV/(mg/cm^2)	Ion flux, cm^{-2}s^{-1}
$^{16}O^{2+}$	$^{16}O^{8+}$	56±3	4.5	$1 \div 10^5$
$^{22}Ne^{3+}$	$^{22}Ne^{10+}$	65±3	7	$1 \div 10^5$
$^{40}Ar^{5+}$	$^{40}Ar^{16+}$	122±7	16	$1 \div 10^5$
$^{56}Fe^{7+}$	$^{56}Fe^{23+}$	213±3	28	$1 \div 10^5$
$^{84}Kr^{12+}$	$^{84}Kr^{32+}$	240±10	41	$1 \div 10^5$
$^{136}Xe^{18+}$	$^{136}Xe^{46+}$	305±12	67	$1 \div 10^5$
$^{209}Bi^{22+}$	$^{209}Bi^{58+}$	490±10 (820±20)	95 (100)	$1 \div 10^5$

Since becoming operational in 2010, the low energy beam (3÷6 MeV/nucleon) facility has been available to users. The facility for the SEE testing at high energy (15÷64 MeV/nucleon) was successfully commissioned in January'14. The third line is based on U400 (commissioned in December'14) and after modernization of this cyclotron in 2018 there will be the possibility to make the SEE testing with the fluent energy variation for every ion.

BEAM FLUX CONTROL

The wide range of beam control systems are used during irradiation. To catch the beam movable probes inside the U400M are used. Diagnostic elements such as the luminophor and the Faraday cup are used during rough beam adjusting at high intensity. For the fine beam tuning and beam profile control, double side Si strip detector (Fig.1) and arrays of scintillators detectors are installed.

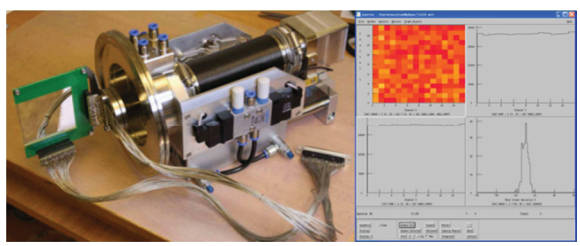

Figure 1: Double-side Si strip detector. Dual axes (X-Y) orthogonal beam detection Kr beam profile as example.

*This work was sponsored by the Russian Federal Space Agency by special agreement between Institute of Space Device Engineering and Joint Institute for Nuclear Research.
†mitrofanov@nrmail.jinr.ru

ISBN 978-3-95450-177-9

The last one provides on-line control of beam flux. The beam uniformity and flux are determined using an array of five active particle detectors. Two kind of active detectors utilized in the diagnostic system routinely - proportional counters and scintillation detectors. The four detectors are placed in corners (for the ion beam halo control of DUT irradiating area and the fifth in its center (Fig.2). The choice for this type of counters was done due to their operation simplicity.

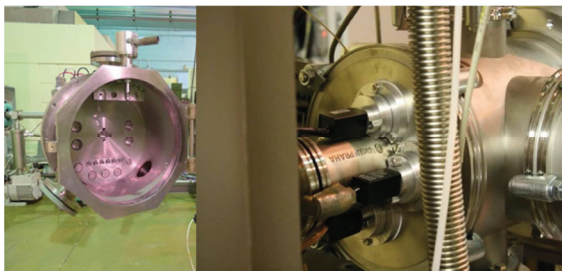

Figure 2: Arrays of scintillators detectors.

To increase the reliability of ion fluence measurements, total number of ions which hit the target is controlled additionally by using polycarbonate or polyethylene terephthalate track detectors placed in close vicinity of any testing device in all irradiation sessions (Fig.3).

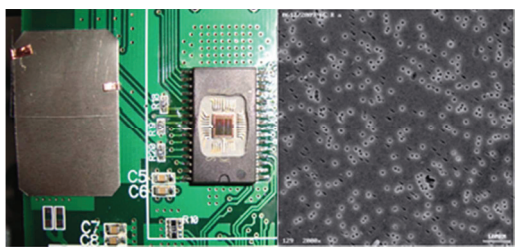

Figure 3: Polymer track detector and the DUT. SEM micrograph of polymer track detector.

The efficiency of swift heavy ion registration by such detectors is close to 100%. Besides of ex situ monitoring of accumulated ion fluence, polymer track detectors are used also for precise determination (with accuracy no worse than 5%) of the beam uniformity over the irradiating area after change from one ion to another (Fig.4.).

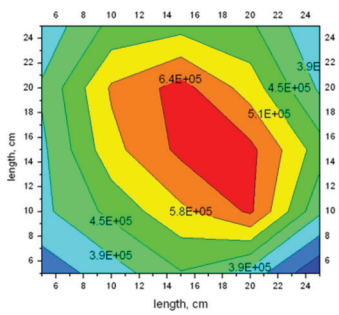

Figure 4: Ar beam distribution over the irradiating area.

As a future development of the low intensity ion beam monitoring, it's suggested to use the SiC based detectors. Therefore, the special attention in research should be payed to study the response of such detectors at high 60-100 MeV/(mg/cm2) LET levels.

METHOD AND INSTRUMENTATION FOR ENERGY MEASUREMENT

Testing is carried out according to the procedure based on international standards, such as those given in [3]. The standards apply to ions with energies <10 MeV/nucleon. These standards have the following requirements to the ion beam. Set of ions with different LET values in the material of tested devices should be used in the tests. There should be no impurities of other atoms in the irradiating ion beams. In this case it is impossible to clean out the ion beam of impurities, a minor presence of impurities is allowed, and their content must be known. It is required by the standards that the LET be known with an accuracy no worse than ±10%. Based on this, the energy of the ions must be measured with the same accuracy. It also should be able to verify matching with the specified type of ion, the absence or the presence of impurities and their contents. It is recommended in [3] to use surface barrier semiconductor detectors for measuring the energy of ions. From our point of view this method is not convenient as it requires constant calibration of the detector. Since the ion types in one irradiation session can vary in a broad range, from oxygen to bismuth, for example, one takes into account a well-known difficulty, namely a strong signal dependence on the LET level, while using the surface barrier semiconductor detectors. The time of flight method is free of this disadvantage. It is often used in experimental high energy particle physics (more than tens of MeV per nucleon). In this method one and the same charged particle is consistently recorded by two fast detectors installed along the beam at a known distance flight base. One of the principal conditions of this method is that the energy loss in the particle detector that is mounted in the beginning of the flight base must be so small that the speed change can be neglected. It is difficult to implement this condition for heavy ion energy within the range of interest because of the short path of the ions in matter. The most often used non-invasive method in this energy range is to determine the time of flight by recording signals induced by the same ion beam micro bunch from two pickup probes spaced along the beam line [4–6]. Micro bunches are a natural time structure of ion beams accelerated in the circular accelerator. The occurrence of micro bunches is caused by a certain acceptance phase band in the acceleration process using a high frequency electric field. The signals from the pickup probes can be registered with a fast dual beam oscilloscope. The image obtained with the oscilloscope during measurement of energy of krypton ions $^{84}Kr^{27+}$ is shown below on Fig. 6.

ISBN 978-3-95450-177-9

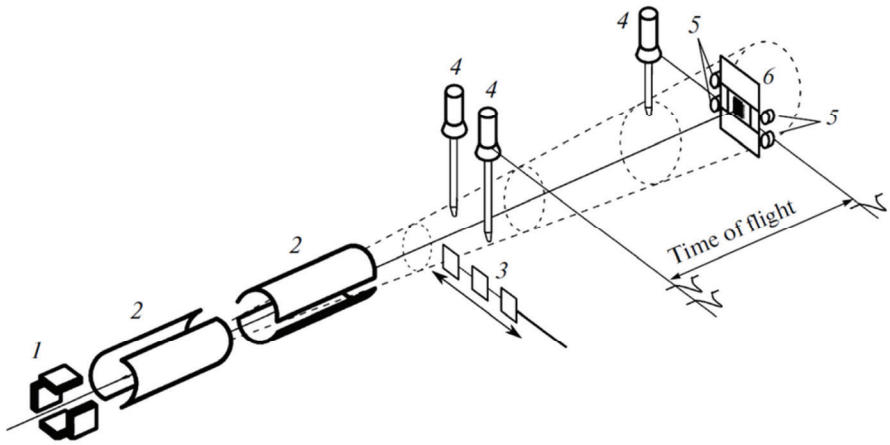

Figure 5: Scheme of the ion beam transport line and experimental set up for low energy SEE testing at the U400M cyclotron: 1—Beam positioning magnet; 2—X–Y magnetic scanning system; 3—set of degrading foils; 4—scintillation detectors; 5—proportional counters; and 6—device under test. See explanations in text.

There are certain complications in the application of this method for the described task. One of them is that due to the fact that the minimum beam current necessary for the correct method to work is 0.3 mkA. Beam currents used for SEE testing are smaller by several orders. Moreover, existing accelerators cannot achieve this value of current for all types of ions used for testing.

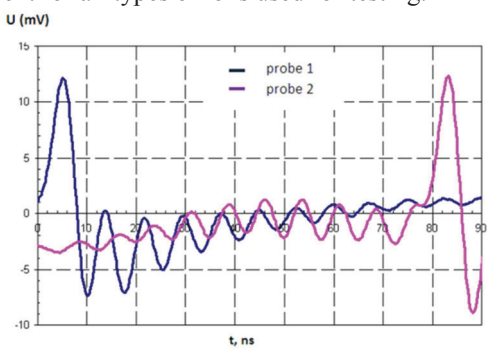

Figure 6: TOF signals generated by 3 MeV/amu Kr ions. Distance between pick-up probes – 1.9 m. Ion beam current – 0.3 μA

We realized the online noninvasive time of flight technique in a substance similar to the pickup probes method, with the difference of using here scintillation detectors instead. Detectors with a substantially smaller size compared with the scanning beam cross section were used. They were mounted on the periphery of the scanning ion beam in such a way that they don't overshadow each other and the DUT as shown at Fig.6. The signals from the detectors were sent to a two channel time to digital converter (TDC). Signal from one of the front detectors was used as the "start" event and signals from two other detectors were used as "stop" events. The TDC was connected to a computer outside the experimental hall via Ethernet connection. As an example, the result of the measurements performed on the beam line is given. Argon ions were extracted from the cyclotron with energy of 7.5MeV/nucleon. The specified energy range for SEE testing typically is 3–6 MeV/nucleon. A degrader with a set of tantalum foils of different thickness is used to choose appropriate ion energy. The measured flight times and the corresponding energy values of argon ions are listed in Table 2.

Table 2: Comparison of the Measured and Calculated (SRIM) Ar Ion Energy

Ta degrader thickness, μm	Measured time of flight, ns	Ion energy, MeV/nucleon	
		measured	calculated
0	42 ± 0.5	7.53 ± 0.16	7.53±0.16
5	46 ± 0.5	6.28 ± 0.14	6.28 ± 0.17
9	50 ± 0.5	5.32 ± 0.10	5.21 ± 0.18
12.5	56 ± 0.5	4.24 ± 0.08	4.28 ± 0.19
15	61.5 ± 0.5	3.51 ± 0.06	3.47 ± 0.20

Measurements were carried out on the ion beam both extracted from the accelerator and after passage of tantalum degraders with thickness of 5, 9, 12.5, and 15 μm. Calculated with SRIM software [7], values of energy are also listed. Beam energy after extraction was taken as the initial value in the calculations. Errors in the results of the calculations correspond to error of the initial value.

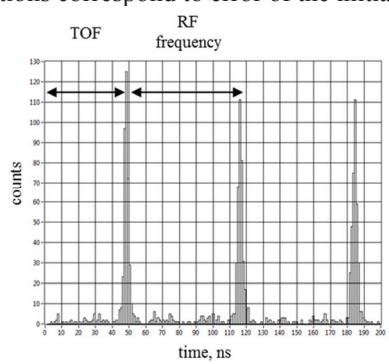

Figure 7: Ar experimental spectrum.

ISBN 978-3-95450-177-9

Comparison of measurements and calculations showed that the measurement error is no worse than ±3% and it is caused both by statistical and by systematic errors of the time of flight measurement. The measurement duration is about 1–2 min.for our method. The usual TOF spectrum measured for Ar-40 ions (initial energy - 301 MeV) at the U400M cyclotron shown at Fig.7. Total ion energy (after 5 mkm of Ta) 250 MeV is determined by time between zero and first bunch maximum. Time between maxima of bunches corresponds to cyclotron RF frequency. The method fully meets the requirements for SEE testing. If it is required to improve accuracy to use this method for other experiments, one can increase length of the flight base. Use of degrading foils additionally allows one to determine the content of impurities in the ion beam. A clean from impurities ion beam corresponds to one peak on the recorded spectrum. An ion beam with impurities results in split peaks on the spectrum after passing the degrader (Fig.8).

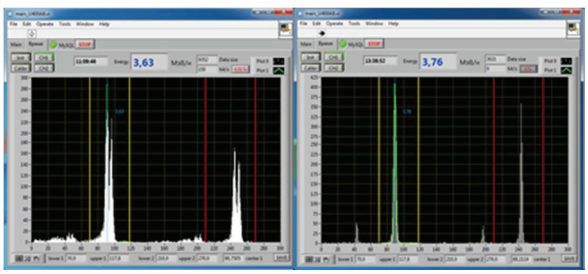

Figure 8: Intensity ratio of the peaks occurred after splitting corresponds to the proportion of impurities. One can determine LET of the impurity by the offset of the peak on the spectrum.

REFERENCES

[1] V.A. Skuratov, V.S. Anashin, A.M. Chlenov *et al.*, *Proc 12th Eur. Conf. on Digital Object Identifier: Radiation and Its Effects on Components and Systems (RADECS)*, 2012, vol. 59, p. 756.

[2] Joint Institute for Nuclear Research, http://fls2.jinr.ru/flnr/u400m.html

[3] *Test Procedures for the Measurement of Single_Event Effects in Semiconductor Devices from Heavy Ion Irradiation. EIA/JEDEC STANDARD, EIA/JESD57*, Electronic Industries Association, 1996, http://www.jedec.org/sites/default/files/docs/jesd57.pdf

[4] B. Wolf, *Handbook of Ion Sources*, Boca Raton, FL: CRC, 1995.

[5] M. Kisielinski, J. Woitkowska, "The proton beam energy measurement by a time-of-flight method", *Nukleonika*, 2007, vol. 52, no. 1, p. 3.

[6] G.G. Gulbekian, B.N. Gikal, I.V. Kalagin *et al.*, "A System for Beam Diagnostics in the External Beam Transportation Lines of the DC-72 Cyclotron", *Proc. DIPAC'03*, Mainz, 2003, p. 155.

[7] SRIM Software, http://www.srim.org/

ISBN 978-3-95450-177-9

DESIGN OF AN ELECTRON CLOUD DETECTOR IN A QUADRUPOLE MAGNET AT CesrTA*

J. P. Sikora†, S.T. Barrett, M. G. Billing, J. A. Crittenden, K. A. Jones, Y. Li, T. O'Connell
CLASSE, Cornell University, Ithaca, NY 14853, USA

Abstract

We have designed a detector that measures the electron cloud density in a quadrupole magnet using two independent techniques. Stripline electrodes collect electrons which pass through holes in the beam-pipe wall. The array of small holes shields the striplines from the beam-induced electromagnetic pulse. Three striplines cover a roughly 0.45 radian azimuth near one of the pole tips. The beam-pipe chamber has also been designed so that microwave measurements of the electron cloud density can be performed. Beam-position-monitor-style buttons have been included for excitation and reception of microwaves and the chamber has been designed so that the resonant microwaves are confined to be within the 56 cm length of the quadrupole. This paper provides some details of the design including CST Microwave Studio® time domain simulation of the stripline detectors and eigenmode simulation of the TE_{11} modes in the resonant chamber. The detector is installed in the Cornell Electron Storage Ring and is part of the test accelerator program for the study of electron cloud build-up using electron and positron beams from 2 to 5 GeV.

INTRODUCTION

At the Cornell Electron Storage Ring (CESR) we have been comparing electron cloud (EC) measurements with the results of simulations both with and without external magnetic fields for several years as part of the test accelerator (CesrTA) program [1, 2]. One measurement technique uses an electrode to sample the electron current that impacts the beam-pipe wall [3]. The simulation of EC buildup in a quadrupole shows that for a 20-bunch train of 5.3 GeV positrons, there is a non-linear increase in EC density with bunch populations greater than 1.0×10^{11} [4]. At low bunch populations, the impact of the electrons on the beam-pipe wall is centered on the poles of the quadrupole since the low energy cloud electrons generally follow the magnetic field lines. At bunch populations above 1.0×10^{11}, there is a splitting of the area of electron impact about the pole face. This splitting is large enough that our previous detector, centered on the pole face and 6 mm wide, was not wide enough to include the peak electron currents [4]. As a result, while the data shows a non-linear increase in electron current, it is not as large as predicted by the simulation.

In order to confirm the simulation results we designed and constructed a new detector (Fig. 1) with three 6-mm-wide segments, so that it would cover a wider azimuth about the pole face. Since a new vacuum chamber was to be constructed for the detector, the chamber was also designed to support measurements of EC density made using resonant microwaves [5], an independent measurement technique.

The detector is positioned inside a new quadrupole magnet (Fig. 2) that is placed near an existing quadrupole of the same polarity. Since they are powered independently, the field of the detector quadrupole can varied from zero to about 3.6 T/m with beam in the storage ring by applying a compensating reduction in the strength of the nearby quadrupole. The new quadrupole has an aperture of 150 mm dia., leaving a radial space of about 25 mm for the new detector, between the outer diameter of the beam-pipe and the pole face.

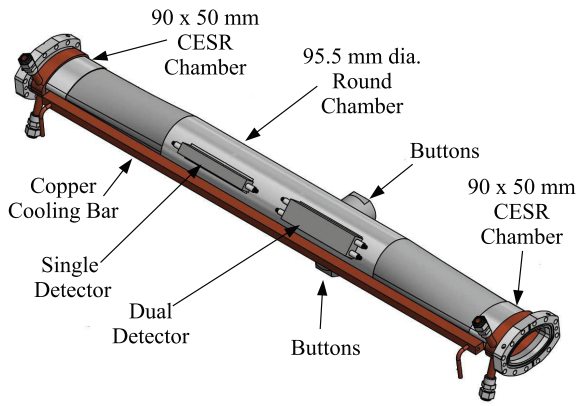

Figure 1: The detector chamber with electron detectors and the button electrodes used for microwave measurements.

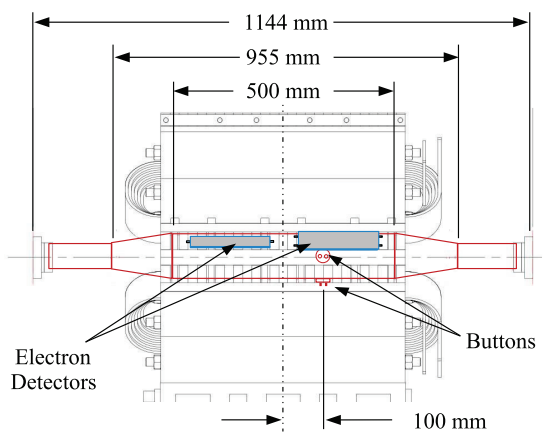

Figure 2: Detector chamber within the quadrupole magnet.

* This work is supported by the US National Science Foundation PHY-0734867, PHY-1002467 and the US Department of Energy DE-FC02-08ER41538, DE-SC0006505.

† jps13@cornell.edu

ISBN 978-3-95450-177-9

STRIPLINE DETECTOR

The overall design of the stripline detector includes an array of 0.79-mm-diameter holes in the beam-pipe wall that attenuate the beam-induced signal and allow cloud electrons to pass through. The electrons are collected by a 10 mm wide electrode biased at +50 V. The signal from the electrode is routed to amplifiers and an oscilloscope for data collection.

Comments on an Earlier Detector

Our earlier design for a stripline detector in a quadrupole was based on a flex circuit of 0.125-mm-thick Kapton with a copper collector on one side and a ground plane on the other. This detector was used in our initial observations of trapping of electrons in a quadrupole [6]. The design choice came from the limited radial space for the insertion of the detector between the beam-pipe wall and the pole face of the quadrupole as well as a history of using flex circuits of this type for detectors that measure DC currents from the electron cloud [7]. With 10 mm wide copper on Kapton, the 100-mm-long stripline collector has an impedance of a little more than 2 ohms. This requires a tapered matching section for connection to the 50-ohm vacuum feedthrough, cable, etc. Limited longitudinal space for this taper results in a poor impedance match at lower frequencies. So while we obtained a usable signal from this detector, post-process filtering was required and there was room for improvement.

Design of the Present Detector

For the present detector, we took advantage of the 25 mm radial detector space provided by the larger aperture quadrupole and designed a stripline collector with a 50 ohm impedance. CST Microwave Studio® was used to determine that the dimensions shown in Fig. 3 result in 50 ohms. All conductive parts are made of 304 stainless steel with no dielectric except for ceramic supports at the connections to the vacuum feedthroughs. The feedthroughs are manufactured by Solid Sealing Technology, Inc., part number FA25858.

There are three striplines in the design, a single stripline centered on the pole face and a pair of striplines azimuthally positioned to either side of center. The pair of striplines are in the same vacuum enclosure, separated by a conductive wall. The single and double striplines are in different longitudinal positions along the same pole. Simulations indicate that the longitudinal variation in the EC density within the quadrupole field should be small, so the three detectors are in a similar electron cloud buildup environment.

Arrays of 300 holes, 0.79 mm in diameter, are fabricated in 2.7 mm thick stainless plates using Die-sink electrical discharge machining (EDM) as shown in Fig. 4. These plates are then tack-welded into slots made in the beam-pipe so that the plate surfaces are flush with the wall. The holes for the central detector are normal to the plate surface since the magnetic field (and low energy electron trajectories) will be normal to the pole face. For the two outer detectors, the holes are angled at 0.158 radian so that they will be roughly aligned with the magnetic field at their position off the center of the pole face.

During detector assembly, stainless tees are tack-welded to the feedthrough inner conductors and the stripline plate is attached with screws shown in Fig. 5. The screws are tack-welded in place once the stripline has been tested, before the final welding of the detector assembly onto the beam-pipe.

The detectors were tested during the assembly, using a time delay reflectometer, which showed that the stripline impedance was close to 50 ohms and the feedthroughs were closer to 60 ohms. Unfortunately, after the final weld of the detector boxes onto the beam-pipe, one of the dual detector striplines was found to be shorted at one end. So we will have the central detector and only one of the offset detectors for the upcoming measurements.

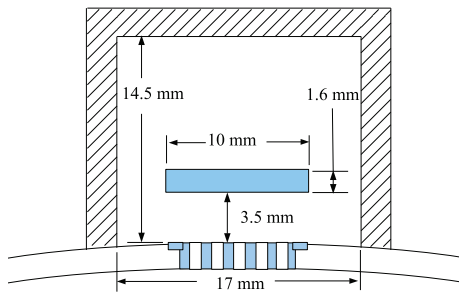

Figure 3: An array of small holes allows electrons to enter the detector vacuum space and be collected on the stripline.

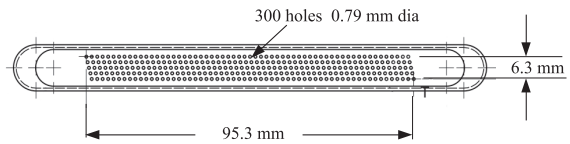

Figure 4: Holes are made in stainless steel plates which are then spot welded into slots in the beam-pipe wall.

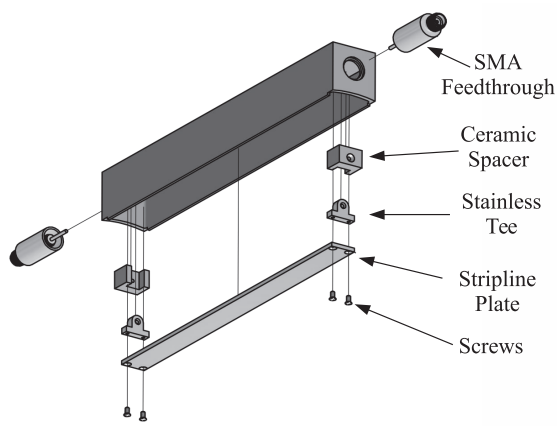

Figure 5: Exploded view of the single stripline detector.

ISBN 978-3-95450-177-9

MICROWAVE DETECTOR

Beam-pipe with changes in cross-section will have a resonant response to microwaves. For rectangular beam-pipe, the lowest frequency waveguide mode is TE_{01}; for round beam-pipe, it is the TE_{11} mode. If the changes in cross-section produce significant reflections, resonances similar to those of a waveguide shorted at both ends will be seen. The resonances will be characterized by the number of half wavelengths m in the resonant field along the length of the waveguide.

The presence of an electron cloud will shift the resonant frequency of the beam-pipe by an amount that is proportional to the EC density. This effect is used for density measurement [5]. Generally, beam-pipe resonances are not intentional, but the new chamber presented the opportunity to make design choices with microwave measurements in mind. In the overall design, the length of the round section of beam-pipe needs to be long enough to accommodate the stripline detectors, but short enough to confine the resonant fields to be within the quadrupole's magnetic field.

The standard cross section of CESR beam-pipe is roughly elliptical with vertical side-walls. The horizontal dimension is 90.5 mm and the vertical dimension about 50 mm. The measured cutoff frequency of the TE_{01} mode of this beam-pipe is 1.8956 GHz [8]. The beam-pipe for the stripline detectors is round and tapers both horizontally and vertically down to the standard CESR cross-section – a geometry that provides resonant modes in the beam-pipe.

CST Microwave Studio® was used to find the eigenmodes of the chamber when the inner diameter of the round beam-pipe was 95.5 mm – larger than either the horizontal or vertical dimension of the standard CESR beam-pipe. With this geometry, the fields of the first four TE_{11} modes – two horizontal, two vertical – are primarily within the quadrupole field region as shown in Fig. 6, with resonant frequencies below the cutoff frequency of the CESR beam-pipe.

When the diameter was made 88.9 mm, slightly smaller than the horizontal dimension of the CESR beam-pipe, the simulation shows that the modes with vertical E-field are not confined, but propagated out into the CESR pipe. This is because the frequencies of these vertical modes are above the 1.8956 GHz cutoff frequency of the CESR beam-pipe. The lowest modes with horizontal E-field are confined, but their frequencies are higher than the lowest vertical modes. There is the potential for some of the vertical and horizontal mode frequencies to overlap, depending on the details of the CESR beam-pipe beyond the chamber. So in the design, the larger 95.5 mm inner diameter is used.

In order to excite the beam-pipe with microwaves, beam-position-monitor-style buttons are used in pairs– one button to couple microwaves in and the other to couple microwaves out of the beam-pipe. Two pairs of buttons are included – one pair on the bottom of the beam-pipe, the other on the side. This allows the excitation and detection of both horizontal and vertical TE_{11} modes in the round beam-pipe. The buttons are offset longitudinally by 100 mm to allow coupling to both the $m = 1$ and $m = 2$ resonances.

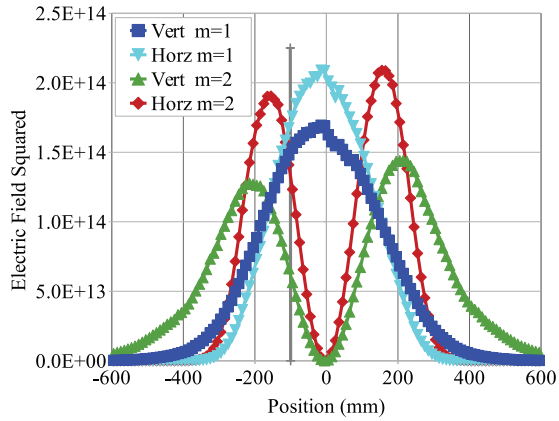

Figure 6: The results of a Microwave Studio® simulation show that the resonant microwave fields of the lowest four modes are contained within the 560-mm-long quadrupole magnet. Zero is the longitudinal center of the quadrupole.

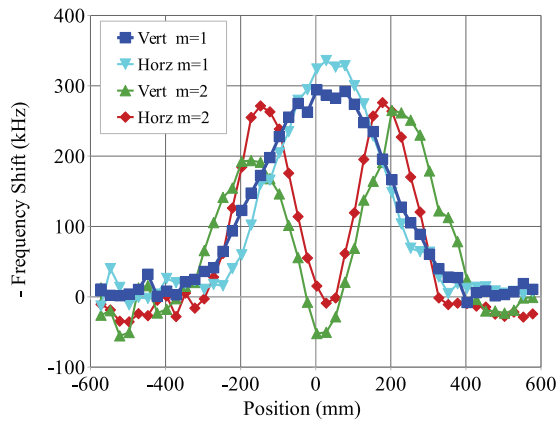

Figure 7: Beadpull measurements of the first two horizontal and first two vertical modes of the completed chamber.

After the chamber was fabricated, we wanted to confirm the nature of the resonances that had been predicted by simulation. We recorded the shift in resonant frequency produced by a 0.3 cm^3 dielectric bead as it was pulled through the assembled chamber. The frequency shift is proportional to the square of the resonant electric field at the location of the bead [9, 10]. Our measurement is somewhat crude in that it uses the peak response of a spectrum analyzer instead of a phase locked loop circuit. But the beadpull results in Fig. 7 are sufficient to confirm the simulation results of Fig. 6, i.e. that the first four modes are mostly confined to be within the 560 mm length of the magnet.

MAGNET CONSTRUCTION

The quadrupole that surrounds the detector is a duplicate of a magnet made in 2004, which required the machining of existing laminations and adding spacers to produce a larger

ISBN 978-3-95450-177-9

aperture [11]. The machining was performed on the laminations of four quadrants which had been previously stacked. The coils are formed using 1/4 inch square copper tubing with a round 1/8 inch diameter water channel. There are 72 turns on each pole comprised of an assembly of 6 coils of 12 turns each. For cooling, the six coils are grouped as 3 pairs, with a water flow of about 0.12 gallons/minute through each coil pair at 60 psi. Several of these coils had been built in 2004 and were taken out of storage and tested. To obtain a gradient of 3.6 T/m, a current of about 110 amps will be provided by a remotely variable standard CESR magnet power supply.

SUMMARY

We have designed and built an electron cloud detector intended for use in a quadrupole magnet. Two independent measurement techniques will be used in the same chamber – sampling the flux of electrons onto the wall of the beampipe and measuring the cloud-induced shift in the resonant frequency of the chamber. The chamber and magnet are to be installed in CESR in September 2016.

REFERENCES

[1] M.G. Billing *et al.*, "The Conversion of CESR to Operate as the Test Accelerator, CesrTA. Part 3: electron cloud diagnostics ," *Journal of Instrumentation* **11** P04025 (2016), doi:10.1088/1748-0221/11/04/P04025.

[2] J. P. Sikora *et al.*, "Cross-Calibration of Three Electron Cloud Density Detectors at CESRTA," in Proc. of IBIC'14, Monterey, California, USA, Sept. 2014, THCXB1, pp. 722-26, (2014).

[3] J.A. Crittenden *et al.*,"Shielded Button Electrodes for Time-Resolved Measurements of Electron Cloud Buildup," *Nucl. Instrum. Methods Phys. Res.*, **A749**, pp. 42-46, (2014), http://dx.doi.org/10.1016/j.nima.2014.02.047, Preprint, arXiv:1311.7103 [physics.acc-ph].

[4] J.A. Crittenden *et al.*, "Progress in Detector Design and Installation for Measurements of Electron Cloud Trapping in Quadrupole Magnetic Fields at CesrTA," in Proc. of IPAC'16, Busan, Korea, May 2016, WEPMW004, p. 2420, (2016).

[5] J.P. Sikora *et al.*,"Electron Cloud Density Measurements in Accelerator Beam-Pipe Using Resonant Microwave Excitation," *Nucl. Instrum. Methods Phys. Res.*, **A754**, pp. 28-35 (2014), http://dx.doi.org/10.1016/j.nima.2014.03.063, Preprint, arXiv:1311.5633 [physics.acc-ph].

[6] M. G. Billing *et al.*,"Measurement of Electron Trapping in the Cornell Electron Storage Ring," *Phys. Rev. ST Accel. Beams* **18**, 041001 (Apr. 2015).

[7] J. R. Calvey *et al.*, "Comparison of Electron Cloud Mitigating Coatings Using Retarding Field Analyzers," *Nucl. Instrum. Methods Phys. Res.*, **A760**, pp. 86-97 (2014), http://dx.doi.org/10.1016/j.nima.2014.05.051, Preprint, arXiv:1402.1904 [physics.acc-ph].

[8] J.P. Sikora *et al.*, "Microwave Modeling for Electron Cloud Density Measurements at CESRTA," in Proc. of IPAC'15, Richmond, Virginia, USA, May 2015, MOPWI031, pp. 1227-29, (2015).

[9] L.C. Maier and J.C. Slater, "Field Strength Measurements in Resonant Cavities," J. Appl. Phys. **2**3, 68 (1952); doi: 10.1063/1.1701980.

[10] R. G. Carter, "Accuracy of Microwave Cavity Perturbation Measurements," *Microwave Theory and Techniques, IEEE Transactions on*, vol.**49**, no.5, pp.918-923, May 2001.

[11] M.A. Palmer *et al.*, "Design, Fabrication and Characterization of a Large-aperture Quadrupole Magnet for CESR-c," in Proc. of PAC'05, Knoxville, Tennessee, USA, May 2005, MPPT080, p.4063, (2005).

ISBN 978-3-95450-177-9

NONDESTRUCTIVE HIGH-ACCURACY CHARGE MEASUREMENT OF THE PULSES OF A 27 MeV ELECTRON BEAM FROM A LINEAR ACCELERATOR

A. Schüller*, J. Illemann, R.-P. Kapsch, C. Makowski, F. Renner
Physikalisch-Technische Bundesanstalt (PTB), Braunschweig, Germany

Abstract

This work presents instruments and measurement procedures which enable the non-intercepting absolute measurement of the charge of single beam pulses (macro-pulses) from a 0.5 to 50 MeV electron linear accelerator (LINAC) with high accuracy, i.e. with a measurement uncertainty < 0.1 %.[1] We demonstrate the readout and calibration of a Bergoz integrating current transformer (ICT) for a 27 MeV beam. The signal from the ICT is calibrated against a custom-made Faraday cup (FC) with a high degree of collection efficiency (> 99 %) for electron beams in the energy range of 6 to 50 MeV.

INTRODUCTION

The National Metrology Institute of Germany, the Physikalisch-Technische Bundesanstalt (PTB), operates a custom-designed electron LINAC for fundamental research in dosimetry for radiation therapy (see Fig. 1). The LINAC works on the same principle as medical LINACs applied for cancer treatment. A pulsed electron beam is shot at a metal target for the generation of bremsstrahlung with therapeutically relevant dose rates. In contrast to medical LINACs, all beam parameters can be continuously adjusted and measured with a high degree of accuracy. In this way, it is possible to study radiation effects as a function of their fundamental physical quantities. One crucial quantity is the charge per beam pulse which is directly proportional to the dose of the generated photon radiation. Due to the discontinuous operating principle of a LINAC the charge of the pulses fluctuates somewhat (typical for PTB's research LINAC: 3 %). For the non-intercepting absolute measurement of the charge of the beam pulses, a beam intensity monitoring system based on an ICT, commercially available from Bergoz Instrumentation [1], is used. The signal from this monitoring system is calibrated against the charge measurement by means of a temporarily installed FC in combination with an electrometer, calibrated traceably to PTB's primary standards. The collection efficiency of the FC is determined by a cancellation measurement.

SETUP

The ICT (transformer winding: 50:1) is mounted directly as a vacuum component in the beamline ("G" in Fig. 1). A bare wire called a "Q-loop" is mounted within the ICT aperture by means of two additional flanges with an electrical feedthrough on both sides of the ICT as shown in Fig. 2. Via the Q-loop, the FC current can be conducted through the ICT for the determination of the collection efficiency of the FC.

The FC is temporarily installed behind the ICT (at "H" in Fig. 1). It shares the same vacuum as the beam. A photo of the FC glued into a vacuum adapter is shown in Fig. 3. The design of the FC is optimized with regard to high collection efficiency for electron beams with energies of 6 to 50 MeV. Its structure is shown in Fig. 4. The FC is composed of a sequence of 1.5 cm C, 2 cm Al, 2 cm Cu, and 4.2 cm WCu-alloy (80 % W).

The measurement of the charge collected by the FC is carried out by a precise electrometer (Keithley 616). In order to avoid saturation effects during a pulse, a 33 nF capacitor is installed at its input. The electrometer is thus suitable for pulse resolved charge measurements.

The ICT output voltage is recorded by means of a waveform digitizer (WD) also referred to as a transient recorder (Spectrum M3i.4142). Due to the high radiation exposure in the vicinity of the beamline, the WD is placed outside the radiation protection bunker. In order to improve the signal-to-noise ratio at the end of the required 40 m coaxial cable, a voltage amplifier (FEMTO HVA-200M-40-B) is used as a preamplifier at the output of the ICT. The preamplifier is enclosed by a pile of lead bricks. The wiring of the setup is shown in the block diagram in Fig. 5.

SIGNAL ACQUISITION

Faraday Cup

Every charge pulse from the FC fed into the electrometer input causes a voltage step at its analog output. The output voltage U_{out} is measured by a high-accuracy digital multimeter (Agilent 3458A). It is controlled by a LabVIEW program (see Fig. 5). At every LINAC trigger event, the device records 200 data points with an interval of 200 μs (6 ms pre-trigger, 34 ms post-trigger). The voltage difference ΔU_{out} between before and after the charge pulse is determined. If U_{out} exceeds -100 V, then the electrometer is discharged by closing the remote "zero" contact. The electrometer is calibrated by a reference charge Q_{ref} generated by means of custom-made air capacitors with traceably calibrated capacitance C_{air} and a reference voltage U_{ref}. The charge Q_{ref} collected by the electrometer at a change in the reference voltage by ΔU_{ref} amounts to

* andreas.schueller@ptb.de

[1] All uncertainties quoted in this article are expanded uncertainties based on a coverage factor $k = 2$ (two standard deviations), providing a coverage probability of about 95 %.

ISBN 978-3-95450-177-9

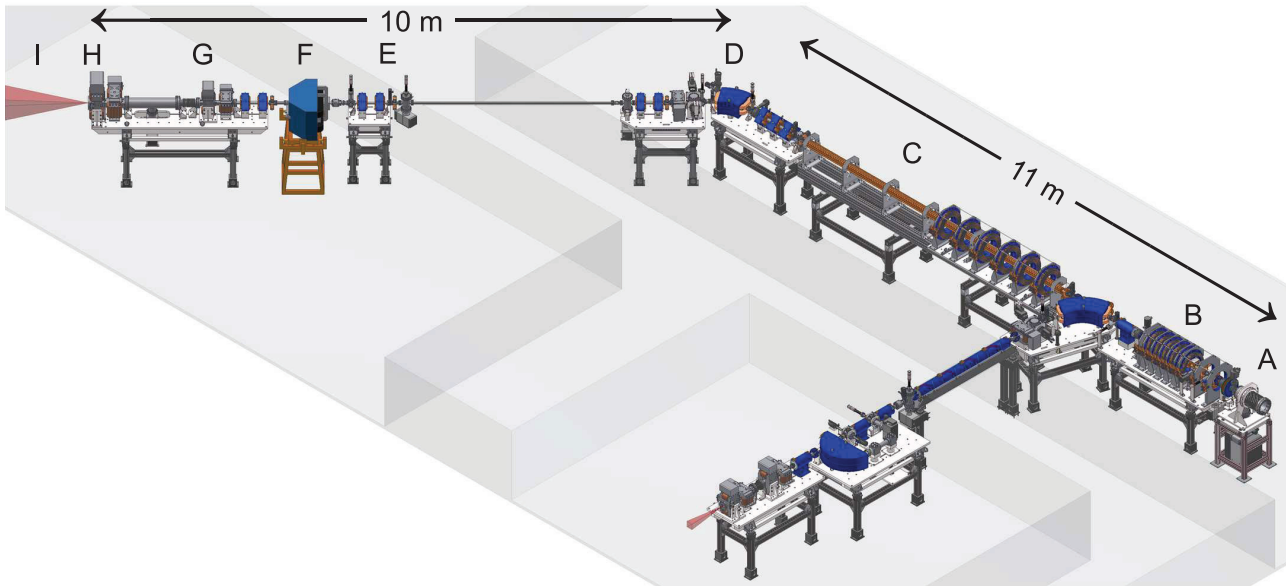

Figure 1: Drawing of PTB's electron LINAC for fundamental research in dosimetry for radiation therapy. A: electron gun. B: low-energy section (0.5 to 10 MeV). C: high-energy section (6 to 50 MeV). D: dipole magnet for energy separation and beam dump. E: collimator. F: magnetic spectrometer. G: ICT. H: Faraday cup or metal target. I: photon radiation. Gray areas: walls of the radiation protection bunker.

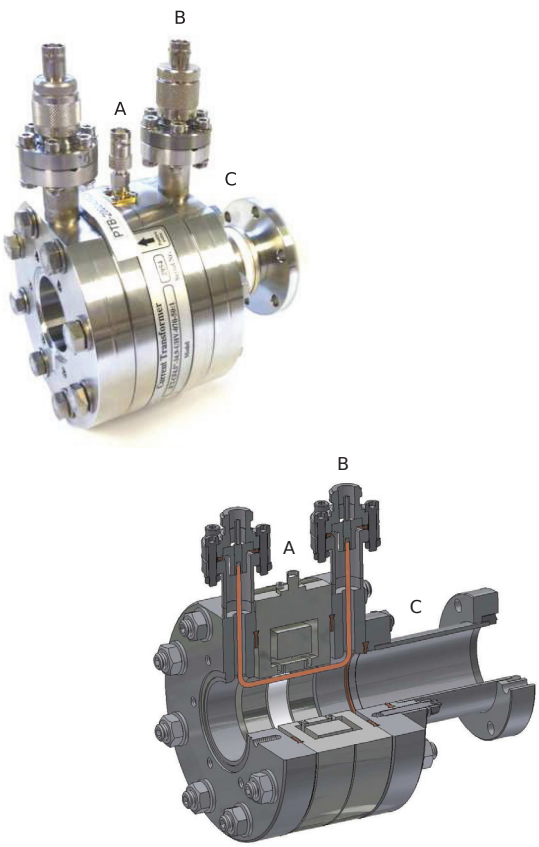

Figure 2: Photo (top) and sectional drawing (bottom) of the ICT (A) with an in situ wire (Q-loop) through the ICT screwed on electrical feedthroughs at additional flanges (B) and a vacuum ceramic break (C).

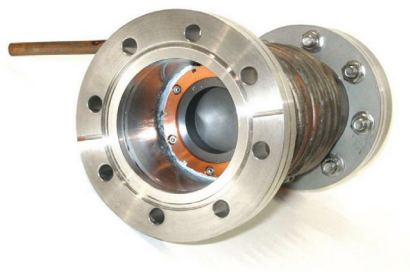

Figure 3: Photo of the Faraday cup glued into a vacuum adapter with a water cooling coil welded on the outside wall.

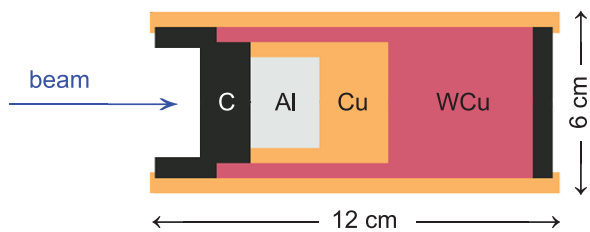

Figure 4: Drawing of the structure of the Faraday cup.

$Q_{\mathrm{ref}} = C_{\mathrm{air}} \cdot \Delta U_{\mathrm{ref}}$. From the corresponding electrometer response ΔU_{out}, the calibration coefficient is determined to be $N_{\mathrm{E}} = Q_{\mathrm{ref}}/\Delta U_{\mathrm{out}}$. The relative uncertainty of the calibration coefficient is $u(N_{\mathrm{E}})/N_{\mathrm{E}} = 0.007$ %. The charge from the FC is $S_{\mathrm{FC}} = N_{\mathrm{E}} \cdot \Delta U_{\mathrm{out}}$. The statistical uncertainty contribution due to random noise at the readout of the electrometer amounts to $u_{\mathrm{stat}}(S_{\mathrm{FC}}) = 0.008$ nC (0.013 % of the pulse charge to be measured). The relative uncertainty of the mea-

ISBN 978-3-95450-177-9

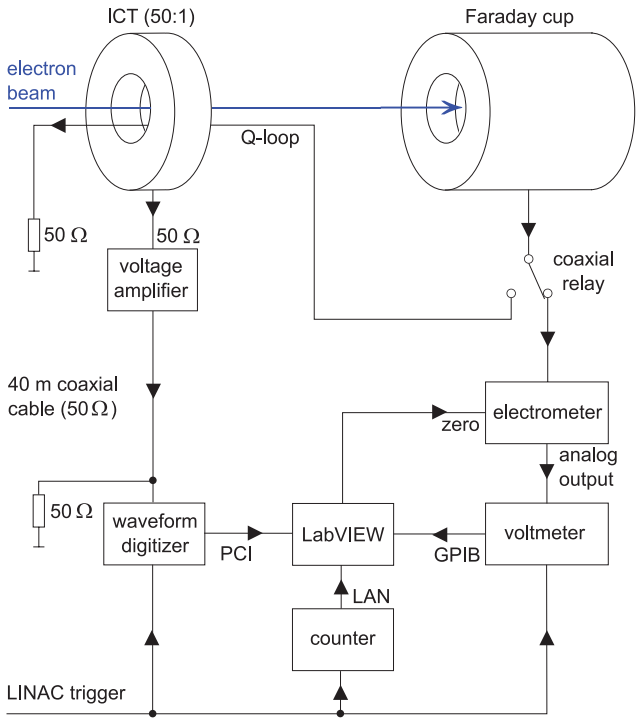

Figure 5: Block diagram of the setup.

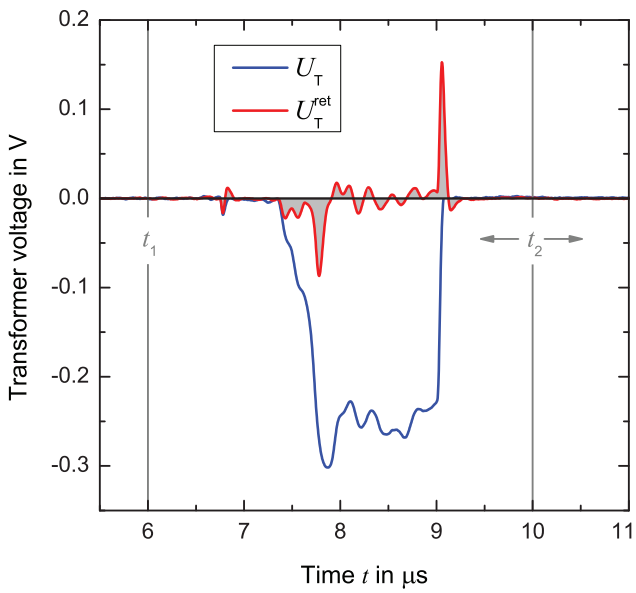

Figure 6: Blue curve: time resolved transformer voltage $U_T(t)$ for a typical LINAC beam pulse (27 MeV, −60 nC). Red curve: transformer voltage at return of the FC current through the ICT via the Q-loop $U_T^{ret}(t)$. Pulse integration limits: $t_1 = 6$ µs and $t_2 \geq 9.3$ µs.

surement of a single charge pulse from the FC amounts to $u(S_{FC})/S_{FC} = 0.033$ %.

Current Transformer

The blue curve in Fig. 6 shows the transformer voltage $U_T(t)$ from the preamplifier connected to the ICT for a typical LINAC beam pulse (27 MeV, −60 nC) as a function of time with respect to the LINAC trigger, as recorded by the WD. The offset is already subtracted in $U_T(t)$. The voltage-time integral of the ICT output pulse is proportional to the charge of the beam pulse. The transformer signal in terms of a charge is given by

$$S_T = \frac{n_T}{n_G R_T} \int_{t_1}^{t_2} U_T(t)\mathrm{d}t \qquad (1)$$

where $n_T = 50$ is the number of turns of the transformer winding, $R_T = 25\ \Omega$ is the nominal load impedance of the transformer[2], and $n_G = 10$ is the nominal gain of the preamplifier (20 dB). The integration limits $t_1 = 6$ µs and $t_2 \geq 9.3$ µs contain the pulse edges. S_T depends on t_2 due to the signal droop of the transformer, i.e. a transformer voltage $U_T(t) > 0$ after the negative peak of the pulse. The peak ends at $t \approx 9.1$ µs, therefore $t_2 = 9.3$ µs is a reasonable choice.

If the grounding of the ICT is connected to the grounding of the beamline, then synchronous noise from the running LINAC picked up on the transmission cable results in a significant zero signal and thus an offset b_1 in S_T with large fluctuations (about 1 % of the charge to be measured). In order to realize a floating connection with respect to the beamline grounding, the ICT is mounted in a galvanically isolated manner between two vacuum ceramic breaks ("C" in Fig. 2). For the isolated ICT (at $t_2 = 9.3$ µs), the offset due to the synchronous noise is $b_1 < 0.005$ nC (< 0.01 % of the charge to be measured) and is thus negligible.

The uncertainty contribution due to random noise from the WD and the preamplifier increases linearly with t_2. For $t_2 = 9.3$ µs, it amounts to about 0.03 nC. Thus, the statistical contribution to the relative uncertainty of the measurement of the charge of a single beam pulse of about −60 nC is $u_{stat}(S_T)/S_T = 0.05$ %.

FARADAY CUP COLLECTION EFFICIENCY

The collection efficiency of the FC is determined by a cancellation measurement as proposed by Pruitt [2]. It is based on a comparison of the beam current, measured by means of the ICT, with the FC current, measured by the same ICT. For this purpose, the FC current is returned through the ICT via the Q-loop. The effects of the electron beam current and the counteracting FC current on the ICT are canceled out if both are equal. Otherwise, the FC collection efficiency can be determined from the residual transformer voltage. The red curve in Fig. 6 shows the residual transformer voltage U_T^{ret} at the return of the FC current through the ICT. Since the FC current transits the ICT with a certain delay with respect to the electron beam pulse, negative or positive spikes appear where the beam pulse shape

[2] 50 Ω embedded in the ICT and 50 Ω termination at the input of the preamplifier are connected in parallel.

ISBN 978-3-95450-177-9

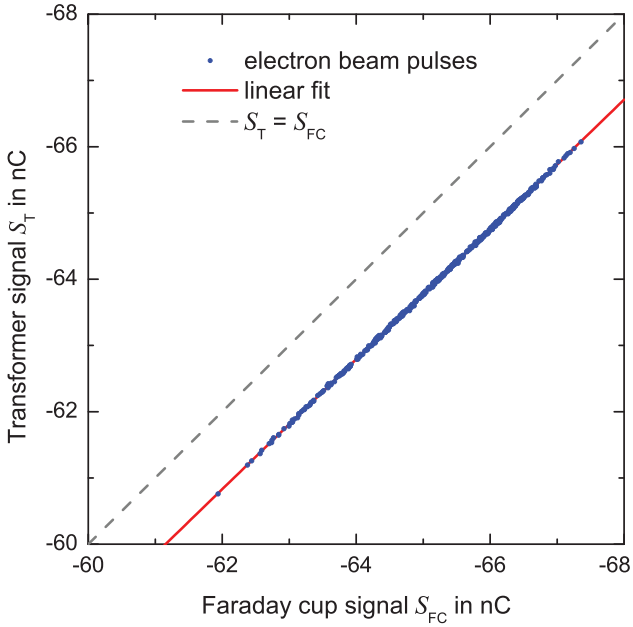

Figure 7: Transformer signal S_T of 500 sequent single beam pulses as a function of the simultaneously collected corresponding charge S_{FC} from the FC.

features falling or rising edges, respectively. From the residual transformer signal S_T^{ret} (replacing U_T by U_T^{ret} in Eq. (1)), the loss L of the FC is determined as $L = \langle S_T^{ret} \rangle / \langle S_T \rangle$. S_T^{ret} and S_T are alternately measured by means of a coaxial relay, which switches randomly between feeding the FC current in the electrometer or in the Q-loop (see Fig. 5).

A signal droop after the pulse is not resolved in $U_T^{ret}(t)$. Thus, S_T^{ret} is independent of t_2 (for $t_2 > 15\ \mu$s).[3] S_T depends on t_2 but since S_T^{ret} is small, the collection efficiency $\eta = 1 - L$ changes only marginally with t_2. Effects due to the signal droop on η are thus negligible (<0.01 %).

Since the Q-loop wire is placed at the inner edge of the ICT aperture (see Fig. 2), effects due to a spatial inhomogeneity, i.e. due to the different positions of the beam and the Q-loop, are investigated. The Q-loop is gradually shifted to the center of the ICT aperture and along the inner edge, while a charge pulse from a pulse generator is sent through the ICT aperture via the Q-loop. Effects due to a spatial inhomogeneity are negligible (<0.01 %).

The collection efficiency of the FC for 27 MeV electrons determined by the cancellation measurement is $\eta = 0.9921$. The relative uncertainty is $u(\eta)/\eta = 0.052$ %. The pulse charge is $Q_P = S_{FC}/\eta$.

CALIBRATION

The transformer signal S_T may deviate from the beam pulse charge, among other things, due to the voltage loss at the 40 m coaxial cable between the ICT and the WD, due to the signal droop of the ICT, or due to the gain error of the preamplifier or the WD. Therefore, S_T is calibrated against the corresponding absolute measured charge from the FC. The transformer signal S_T and the FC signal S_{FC} of each beam pulse are acquired and evaluated simultaneously. In order to ensure a clear assignment of $S_T(i)$ to $S_{FC}(i)$, the current pulse number i is verified in real-time by means of a stand-alone counter (see Fig. 5).

The blue dots in Fig. 7 represent the transformer signals S_T of about 500 sequent single LINAC beam pulses as a function of the simultaneously collected FC charges S_{FC}. The red line results from a linear fit $S_T = m_1 \cdot S_{FC} + b_1$. From the standard deviation of the residua from the linear fit, the statistical contribution to the relative uncertainty is determined to be $u_{stat}(S_T)/S_T = 0.05$ %.[4] The calibration factor $N_T = 1/m_1$ is obtained from the slope m_1. The dashed line in Fig. 7 indicates the equality $S_T = S_{FC}$ and visualizes the deviation to be corrected. The deviation is mainly caused by the voltage loss at the 40 m coaxial cable.

In order to determine the pulse charge Q_P, the transformer signal calibrated to the FC signal has to be corrected by the FC collection efficiency η. The charge of a single beam pulse measured nondestructively by means of the beam intensity monitoring system is given by

$$Q_P = N_T \cdot (S_T - b_1)/\eta. \quad (2)$$

The relative uncertainty of the nondestructive measurement of a single LINAC beam pulse of about −60 nC amounts to $u(Q_P)/Q_P = 0.082$ %.

CONCLUSION

The charge of each single electron beam pulse from PTB's research LINAC can be measured nondestructively (non-intercepting) with a relative measurement uncertainty < 0.1 % by means of a beam intensity monitoring system based on an ICT. The system is traceably calibrated to PTB's primary standards. The calibration factor N_T is valid for the actual setup (in particular including the 40 m coaxial cable) and the chosen integration interval (t_2 in eq. (1)). The offset due to synchronous noise b_1 is small if the ICT is isolated from the beamline grounding and it can be neglected in most cases.

A full description of the beam intensity monitoring system and its characterization is the subject of a longer article submitted for publication [3].

REFERENCES

[1] Bergoz Instrumentation, `http://www.bergoz.com`

[2] J. Pruitt, "Electron beam current monitoring system", *Nucl. Instr. Meth.*, vol. 92, pp. 285–297, 1971.

[3] A. Schüller *et al.*, "High-accuracy nondestructive charge measurement of the pulses of a 27 MeV electron beam from a linear accelerator", submitted for publication.

[3] $U_T^{ret} = 0$ not until $t > 15\ \mu$s since a small part of the signal is delayed due to pulse-shape deformations caused by cable reflections.

[4] The noise at the readout of the FC is about four times less than the noise at the readout of the ICT and thus contributes only marginally to the combined statistical uncertainty.

ISBN 978-3-95450-177-9

MEASUREMENT UNCERTAINTY ASSESSMENTS OF THE SPIRAL2 ACCT/DCCT

S. Leloir#, T. André, C. Jamet, G. Ledu, S. Loret, C. Potier de Courcy,
GANIL, Caen, France

Abstract

Four instrumentation chains with AC and DC Current Transformers (ACCT-DCCT) will equip the lines of SPIRAL2 facility to measure the beam intensity and line transmissions. These measures are essential to tune and supervise the beam, to assure the thermal protection of the accelerator and to control that the intensities and transmissions are below the authorized limits. As such, the uncertainties of measurement chains must be taken into account in the threshold values.

The electronic has been designed with high requirements of quality and dependability by following different steps; from prototyping, the qualification through an Analysis of Failure Modes and Effects Analysis (FMEA) [1] until final fabrication.

This paper presents the measurement uncertainty assessments of the ACCT/DCCT chains.

INTRODUCTION

The SPIRAL2 facility at GANIL in France is planned to accelerate deuteron, proton and heavy-ion beams with a RFQ and a superconducting linear accelerator. Table 1 recalls the main beam characteristics.

Table 1: Beam Specifications

Beam	P	D+	Ions (1/3)
Max. Intensity	5 mA	5mA	1 mA
Max. Energy	33 MeV	20 MeV/A	14.5 MeV/A
Max. Power	165 kW	200 kW	43.5 kW

A DCCT bloc is set up at the entrance of the Radio Frequency Quadrupole (RFQ) and three ACCT/DCCT blocs (Fig. 1) will be installed at the Linac entrance, the Linac exit and the Beam Dump entrance (Fig. 2). [2]

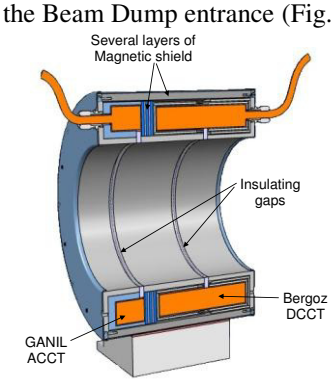

Figure 1: ACCT-DCCT bloc section.

sebastien.leloir@ganil.fr

These non-destructive beam intensity diagnostics are required to:

- ✓ Control and monitor the beam intensity
- ✓ Control and monitor the transmissions (intensity differences between two blocs),
- ✓ Control the intensity quantity sent to the Beam Dump Linac over 24 hours.

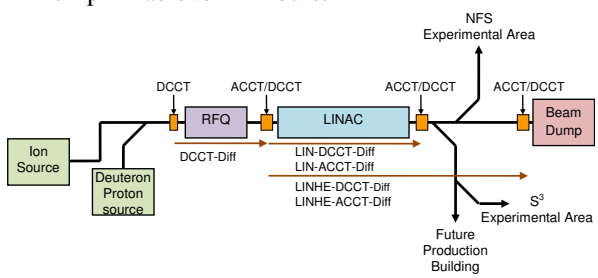

Figure 2: Beam Intensities and transmissions.

MEASURING CHAIN DESCRIPTION

DCCT Measuring Chain

The figure 3 shows a schematic overview of the DCCT chain. The transformer and the first electronic are commercial devices (Bergoz ref: NPCT-175-C030-HR).

In order to decrease the offset fluctuation, the DCCT is maintained at a temperature of 40°C±1°C.

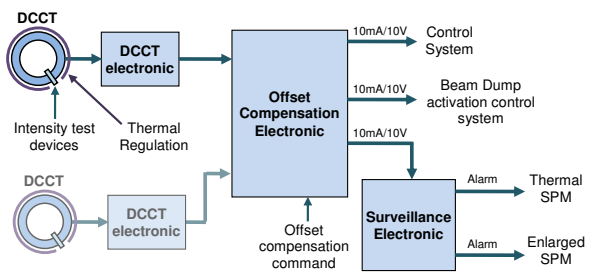

Figure 3: DCCT chain.

The electronic card "offset compensation":

- ✓ sets the zero point, with a manual command before each start of new beam tuning
- ✓ generates the transmission signal (difference of two intensity signals)
- ✓ distributes the intensity and transmission signals at different systems

The surveillance cards carry out moving averages of their input signal. These averages are compared to thresholds and the cards generates alarms in case of overtake. The alarms (a cut-off request) are sending to the Machine Protection Systems (Thermal and Enlarged MPS) [3].

ISBN 978-3-95450-177-9

ACCT Measuring Chain

The transformer and its electronics were developed by the Ganil's Electronic Group (Fig.4). The transformer is a nanocrystalline torus with winding turns ratio of 300:1.

The pre amplifier is a courant to tension convertor. It is placed as close as possible to the transformer for minimize the noise but outside the linac room to be protected of the radioactive effects.

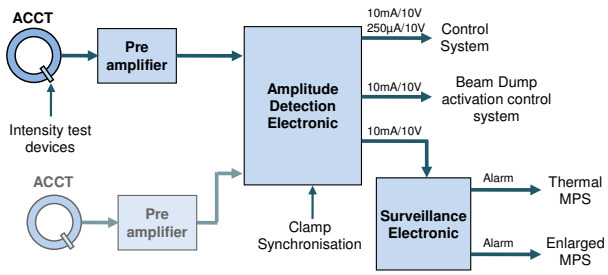

Figure 4: ACCT chain.

The amplitude detection electronics have a main function; regenerate the DC signal non-transmitted by the ACCT. This function is realized by an electronic clamping clocked on the "clamp synchronisation" signal. The slow chopper modulates the intensity and periodically "cut" the beam. The "clamp synchronisation" signal indicates when the beam is "off", at the middle of the beam absence.

Like the compensation offset electronic, the amplitude detection card generates beam intensity and transmission signals and distributes them at the different systems.

The surveillance of thresholds is the same as DCCT chain.

UNCERTAINTY EVALUATIONS

Study and Design Stage

The first uncertainty evaluations on the prototype electronics have guided the development of ACCT/DCCT chains [4]. The main influences were the subject of specific studies. Four of them are listed in the table 2.

Table 2: Example of Optimization Studies

Influence parameters	Results
Room temperature on DCCT sensor	Implementation of system to stabilize the transformers temperature.
External Electromagnetic Field	Three shielding layers protect the sensors. Definition of PCB EMC design rules for the electronic cards
Disturbances between AC and DC sensors.	A vertical shield plate is installed between the sensors to minimize the effect of DCCT magnetic modulator on the ACCT.
ACCT Low Drop	Choice of the nanocrystalline torus with winding of 300 turns. Implementation in preamplifier a function to decrease the resistance value of ACCT winding. Clamp function trigged in the middle of the time off.

The sums of uncertainties determine the measurement limits of both chains. These limits of the prototypes were accepted and validated in the design review meeting.

Validation and Qualification Stage

Now, the ACCT-DCCT chains are manufactured in the definitive version. Their validation and their qualification require new uncertainty evaluations more accurate and final. These evaluations were realized at first from measures in laboratory and will be completed by measures on site without and with beam.

These assessments are used to identify the dynamics of measures, to qualify the systems and to define compliance checking templates for the periodic tests.

Also, the goal is to take into account the total uncertainties in the threshold values. The applied thresholds are equal to the desired threshold minus the uncertainties. This ensures that the intensities and the transmissions don't exceed the operating ranges authorized.

For evaluate the total uncertainties, all the influence parameters should be identified and quantified [4].

Several test benches were set up to characterize these parameters. For example, the figure 5 presents the test bench used to evaluate the gain and linearity influences.

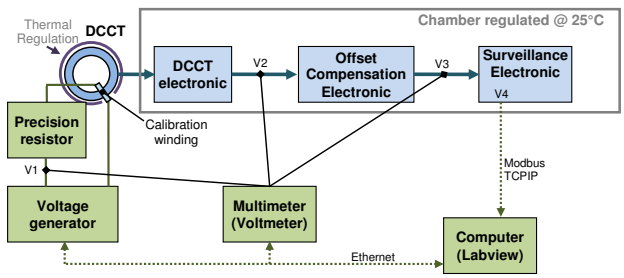

Figure 5: Gain & linearity test bench.

The electronic cards is stabilized in a chamber at 25°C and the sensor maintained at 40°C, to suppress the temperature influence. The calibration winding of 1 turn, resistor and voltage generator simulate the beam intensity.

A multichannel multimeter measures the output voltages of the generator. Only, the multichannel voltmeter must be calibrated. Furthermore, the measurement uncertainty associated with voltmeter and precision resistor is lower than the generator.

A Labview program drives the voltage generator and the voltmeter to automate measurements.

The measurements were performed on a complete chain. However, the uncertainties are evaluated on each following parts:

- ✓ sensor & electronic card of DCCT
- ✓ offset compensation electronic card
- ✓ surveillance electronic card

A requirement is to avoid redefining the total uncertainty values, when an electronic card is replaced for

ISBN 978-3-95450-177-9

maintenance reasons. That means the uncertainties of each parts should take into account the maximum parameters of all the cards. So, typical gain, gain dispersion and highest non-linearity were determined for each part.

Uncertainty Results

The table 3 and 4 list the main uncertainties. All the values were calculated from laboratory measurements.

Table 3: Main Uncertainties of Average Intensities

Sources of uncertainty	ACCT	DCCT
Gain & Linearity	0.04%	0.45%
Sensor Temperature	-	13µA(1)
Electronic Temperature	-	23µA(2)
Noise(3)	10nA	2µA
Clamp	2.5µA	-
Initialization Offset with surveillance cards	50nA	5µA
Gain & Linearity of surveillance cards	0.35%	0.35%

(1) DCCT range 20mA -Thermal regulation at 40°C ±0.5°C
(2) Ambient temperature range: 18° - 31°C
(3) Noise measured in laboratory

Table 4: Main Uncertainties of Average Transmissions

Sources of uncertainty	ACCT	DCCT
Gain & Linearity on the intensity	0.035%	0.12%
Gain & Linearity on the loss	0.04%	0.45%
Sensors Temperature	-	26µA
Electronic Temperature	-	9µA(1)
Noise	15nA	3µA
Clamp	4µA	-
Initialization Offset with surveillance cards	75nA	7µA
Gain & Linearity of surveillance cards	0.35%	0.35%

(1) Temperature difference of electronics: 5°C max.

For DCCT chain, the temperature and the noise (external magnetic fields) are the two predominant sources of uncertainty.

For ACCT chain, it's the "clamping" function. The frequency of 1Hz is very restrictive because the signal can't be average in a short time. To decrease "clamping" uncertainty, a solution is to multiply the frequency by 100 to reduce it by a 10 factor.

The table 5 and 6 presents the total uncertainty values for few values the intensities and transmissions.

Table 5: Examples of Intensity Uncertainty

Beam Intensity	Uncertainty	
	I ACCT	I DCCT
5mA	±23µA	±82µA
1mA	±7µA	±51µA
50µA	±3µA	±43µA

Table 6: Examples of Transmission Uncertainty

Beam Intensity	Transmission Loss	Uncertainty	
		ΔI ACCT	ΔI DCCT
5mA	250 µA	±7µA	±52µA
1mA	250 µA	±7µA	±48µA
50µA	50 µA	±5µA	±45µA

ACCT uncertainties are lower than those of DCCT. More particularly, the ratio for intensities of few 100µA is about 10.

CONCLUSIONS

The overall chain ACCT-DCCT is manufactured validated and will be installed on the accelerator before the end of the year 2016. The characterization and the qualification should continue on site without and with beam. For example, the influence of the extern magnetic fields should be quantified with SPIRAL2 in operating. The qualification will finish by tests with the other interfaced systems. Mainly, the response times between beam overrun and its cut off must be verified.

REFERENCES

[1] C. Jamet *et al.*, "Failure Mode and Effects Analysis of the beam intensity control for the Spiral2 accelerator", IBIC2014, Monterey, California, USA.
[2] C. Jamet *et al.*, "Beam Intensity and Energy Control for the SPIRAL2 Facility", LINAC2012, Tel-Aviv, Israel.
[3] M-H. Moscatello *et al.*, "Machine Protection System for the SPIRAL2 Facility", IPAC2012, New Orleans, Louisiana, USA.
[4] S. Leloir *et al.*, Measurement and control of the beam intensity for the SPIRAL2 Accelerator, IBIC 2013, Oxford, England.

ISBN 978-3-95450-177-9

OPTIMIZATION STUDIES FOR AN ADVANCED CRYOGENIC CURRENT COMPARATOR (CCC) SYSTEM FOR FAIR*

T. Sieber[1†], J. Golm[2,3], P. Kowina[1], F. Kurian[2,3], R. Neubert[4], M. Schwickert[1], T. Stöhlker[1, 2, 3], V. Tympel[4]

[1]GSI Helmholtz Center for Heavy Ion Research, Darmstadt, Germany
[2]Institute for Optics and Quantum Electronics, Friedrich-Schiller-University Jena, Germany
[3]Helmholtz-Institute Jena, Germany
[4]Institute for Solid State Physics, Friedrich-Schiller-University Jena, Germany

Abstract

After successful tests with the GSI-CCC prototype, measuring beam intensities down to 2 nA at a bandwidth of 2 kHz, a new advanced Cryogenic Current Comparator system with extended geometry (CCC-XD) is under development. This system will be installed in the upcoming Cryring facility for further optimization, beam diagnostics and as an additional instrument for physics experiments. After the test phase in Cryring it is foreseen to build four additional CCC units for FAIR, where they will be installed in the HEBT lines and in the Collector Ring (CR). A universal cryostat has been designed to cope with the various boundary conditions at FAIR and at the same time to allow for uncomplicated access to the inner components. To realize this compact cryostat, the size of the superconducting magnetic shielding has to be minimized as well, without affecting its field attenuation properties. Hence detailed FEM simulations were performed to optimize the attenuation factor by variation of geometrical parameters of the shield. The beam tests results with the GSI-CCC prototype, and the developments for FAIR, as well as the results of simulation for magnetic shield optimization are presented.

INTRODUCTION

For the FAIR [1] project at GSI various new developments in the field of beam diagnostics are necessary to cover the enhanced spectrum of beam parameters. The slow extracted beams from the SIS100 synchrotron can – due to the long extraction times – have intensities which are far below the sensitivity range of regular beam transformers. For that reason it is planned to install ultrasensitive Cryogenic Current Comparators (CCC), based on superconducting SQUID technology at five locations at FAIR. With this device current measurements in the nA range have been achieved with high bandwidth (10 kHz) at GSI [2].

The CCC consists basically of a superconducting niobium torus, which represents shielding and pick-up at the same time, and a SQUID system with related electronics. The geometry and attenuation properties of the Nb torus were optimized by extensive simulation calculations. In parallel a new cryostat, enclosing the pickup and sensor unit has been developed, which fulfils the requirements at FAIR.

In addition, the analysis of spills from the FAIR synchrotrons requires a high bandwidth in combination with an excellent long term stability of the system. Since a temperature dependent baseline drift was observed during the measurements with the GSI prototype [3, 4] (as well as with the CERN/AD CCC [5]), the temperature dependence of offset and bandwidth are currently investigated in detail. Figure 1 shows the planned distribution of CCCs at FAIR.

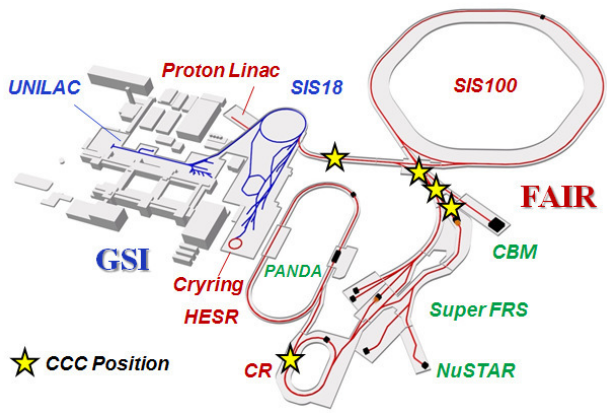

Figure 1: CCC locations at FAIR.

INTENSITY MEASUREMENTS WITH THE GSI PROTOTYPE CCC

The CCC measures the absolute beam current by detecting the beam magnetic field with a SQUID sensor, which is shielded from external fields by a pickup/shielding combination [6]. In practice the CCC voltage output is calibrated to a known current, applied through a current loop. The calibration loop is wound around the magnetic shield producing an azimuthal magnetic field which is detected by the SQUID analogue to the beam current measurement. Following that scheme, the prototype CCC measured a test current down to 4 nA with a signal to noise ratio of 6dB. The noise limited current sensitivity of the CCC installed in the beam line was calculated to 0.2 nA/√(Hz) at 1 Hz and to 2 pA/√(Hz) at 100 Hz.

* work supported by the BMBF under contract No. 05P15SJRBA
† T.Sieber@gsi.de

ISBN 978-3-95450-177-9

To compare the current measured by CCC with a standard technique, a Secondary Electron Monitor (SEM), installed about 1 m downstream the CCC, measured the same beam signals. During this campaign the CCC was able to measure the beam current down to 5 nA with a signal to noise ratio of 5 dB [7]. Figure 2 shows the spill structure of a slowly extracted Ni^{26+} ion beam at 600MeV extracted over 120 ms measured by both devices. It shows excellent correspondence with good time resolution.

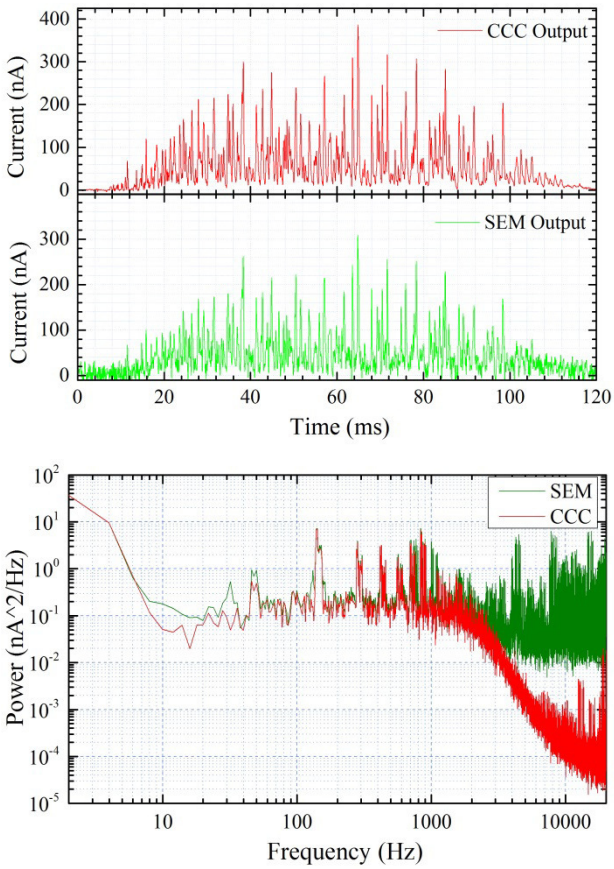

Figure 2: Upper: Comparison of the beam current signal measured by CCC and SEM. Lower: Corresponding FFT spectrum with normalized intensities and averaged over 9 spills.

From earlier investigations [8] it is known that the time structure of the extracted beam from SIS18 contains ripples caused by the magnet power converters. The FFT spectrum in figure 2 confirms that these ripples are 50 Hz and its odd harmonics as predicted. It also confirms that the CCC is the appropriate tool to study this phenomenon, since the cut-off at around 3 kHz is not visible in the SEM FFT spectrum due to background noise.

TEMPERATURE AND PRESSURE DEPENDENCE OF THE SYSTEM

The He exhaust line of the CCC bath cryostat is connected to a helium recycling system. Any fluctuations in the pressure at the exhaust of liquid helium boil-off result in temperature fluctuations inside the liquid helium cryostat. To study the influence of these fluctuations, simultaneous measurement of temperature, pressure and CCC output signal were analyzed. In case of the helium boil-off connected to the recovery line, 2.5 Hz and 5 Hz oscillations were found, which is further confirmed by the pressure sensor output. Figure 3 shows the FFT spectra of the output signals of both measurements. Here the temperature inside the liquid helium cryostat was increased by increasing the pressure (basically closing and opening the exhaust line). In parallel to the pressure measurement, a silicon diode temperature sensor installed close to the SQUID measured its working temperature.

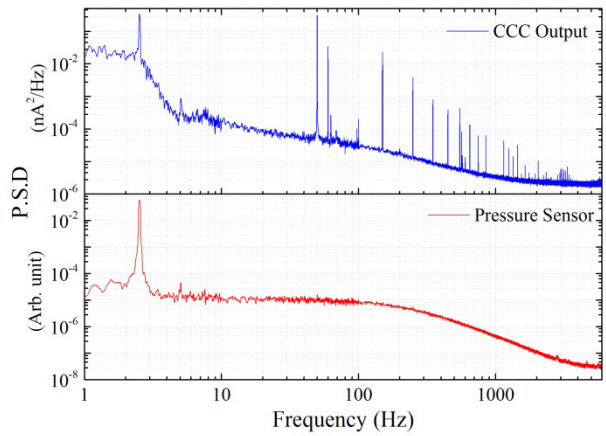

Figure 3: FFT of the output signals of CCC and pressure sensor showing the influence of pressure variation.

Figure 4 shows the CCC signal following the pressure variation up to 13 mbar, which is equivalent to a temperature variation of 32 mK. The corresponding relative current increase at the CCC output is equivalent to 650 nA.

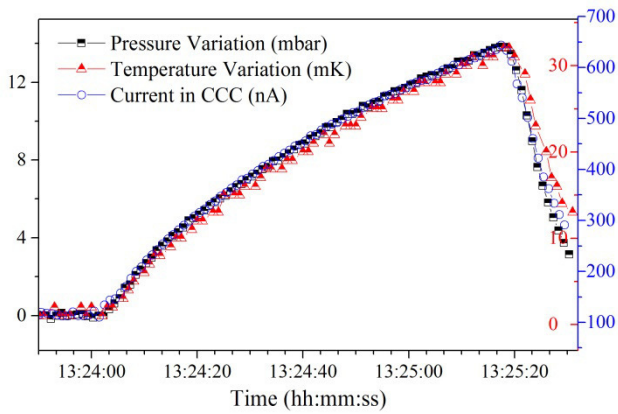

Figure 4: Time development of CCC output at variation of pressure and temperature.

Although the baseline drift does principally not affect the current resolution, it leads to the requirement of more frequent re-calibration. Therefore the measurements underline the importance of minimum thermal load as well as regulated pressure (backpressure controller) at the exhaust. Drifts during normal operation are typically more than a factor 100 smaller than shown in Fig. 4.

ISBN 978-3-95450-177-9

OPTIMIZATION OF THE MAGNETIC SHIELD GEOMETRY

Given by the extremely low azimuthal magnetic field strength of the beam current, non-azimuthal magnetic stray fields need to be suppressed to highest possible degree. This is realized using a superconducting magnetic shield folded into a meander shaped cavity around the pickup coil. As the geometrical parameters such as the inner and outer diameters and number of meanders define the field attenuation, detailed simulations were performed using the FEM simulation package COMSOL multiphysics™ to determine the influence of these parameters on the field attenuation.

Field attenuation of an external transverse magnetic field was simulated for shields with different dimensions. Major conclusions from the simulations were: 1) the gap width (g, as shown in the Figure 1a) between the superconducting meander plates does not influence the attenuation factor; 2) field attenuation reduces as the diameter of the shield is increased as required by the larger beam tube diameter at FAIR as shown in Figure 1b. To retain the attenuation of ~ -120 dB of GSI prototype shielding (inner/outer diameter: 75/125 mm) the number of meanders had to be increased from 8 to 12 meanders in the FAIR shielding (inner/outer diameter: 125/175 mm).

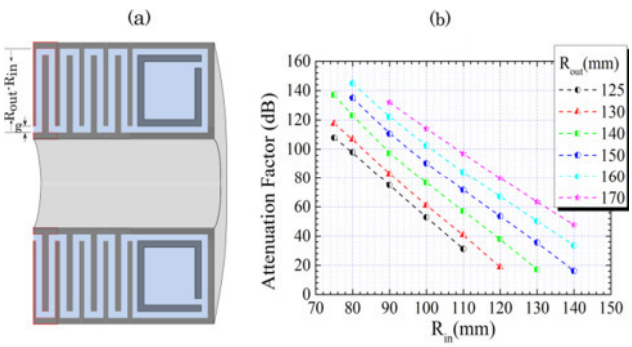

Figure 5: (a) Cross-sectional view of the magnetic shield geometry model. (b) Attenuation factor plotted for various inner and outer diameters of the magnetic shield.

THE CCC CRYOSTAT FOR FAIR

The cryostat for FAIR has to fulfill two basic requirements. 1) It has to accommodate a warm UHV beam tube 2) the beam tube must have a diameter of 150 mm. Additionally the cryostat has to provide excellent vibration damping and a good access to the CCC components without disassembling the whole structure. A design which has been worked out to match these requirements is shown in Figure 5. The isolation vacuum chamber consists of a rectangular stainless steel frame covered with O-ring sealed aluminum windows, which allow direct access to the inner components. The lower half of the front- and backside is made from steel and has a DN 250-CF contour for mounting of a big connection flange. On this flange the UHV beam tube is fixed from both sides. The beam tube itself is equipped with a ceramic gap and bellows to suppress mirror currents and vibrations. The stainless steel/aluminum tank houses a thermal shield (copper) covered by MLI, which is at the bottom of the tank connected to a refrigerator. The refrigerator shall provide the cooling down to <50 K to the shield. It is fixed with suspension wires (which also carry the thermal shield) to the top and bottom plates. The basic idea of this design is that shield and container can be lifted upwards from the vacuum tank if the UHV beam tube is removed to the side and suspensions at the bottom are released.

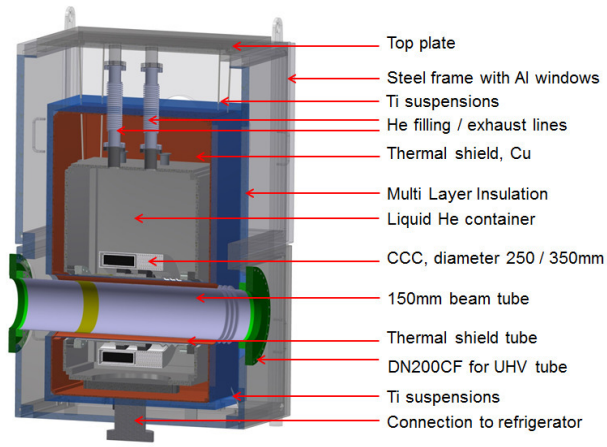

Figure 6: Schematic view of the FAIR CCC cryostat.

SUMMARY AND OUTLOOK

During beam experiments at GSI the outstanding performance of the CCC for current measurements in the nA range could be demonstrated. It was also shown that the CCC is an appropriate tool for calibration of other diagnostics devices (SEM) and for the investigation of the spill structure from a synchrotron. Concerning the temperature/pressure behaviour of the system, a strong baseline drift underlines the requirement of minimum thermal load and backpressure control.

Based on the experience with the GSI prototype, the CCC system is currently adapted to the requirements at FAIR. A magnetic shielding with enhanced dimensions has been designed by electromagnetic simulations. At the same time an advanced cryostat was developed, combining the operational requirements for FAIR with a test device for further CCC development. The FAIR CCC will be installed in Cryring@ESR in spring 2017 for test operation and ring commissioning. In this stage helium will be filled manually, tests with a He re-liquefier will take place in a second stage.

REFERENCES

[1] O. Kester, “Status of the FAIR Facility”, *IPAC 2013,* p. 1085 (2013).

[2] M. Schwickert *et al.*,”Beam Curent Monitors for FAIR”, *IPAC’14,* Proceedings, Dresden, Germany paper THPME103.

[3] A. Peters *et al.*, ”A Cryogenic Current Comparator for the absolute Measurement of nA Beams”, *AIP Conf. Proc. 451* pp.163-180 (1998).

ISBN 978-3-95450-177-9

[4] F. Kurian *et al.*,"Measurements with the Upgraded Cryogenic Current Comparator", Proc. *IBIC'13,* Oxford, UK, paper TUPF30.
[5] M. Fernandes *et al.,* "A Cryogenic Current Comparator for the Low Energy Antiproton Facilities at CERN", Proc. *IBIC'15.* Melbourne, Australia, paper MOPB043.
[6] R. Geithner *et al.*, " Cryogenic Current Comparators for Storage Rings and Accelerators", Proc. *IBIC'15.* Melbourne, Australia, paper MOPB013.
[7] F. Kurian, "Cryogenic Current Comparators for precise Ion Beam Current Measurements", PhD thesis, University of Frankfurt, Germany, 2015
[8] P. Forck *et al.*, "Measurement and Improvements of the Time Structure of a Slowly Extracted Beam from a Synchrotron", Proc. *EPAC'00,* Vienna, Austria, paper MOP4B03.

ISBN 978-3-95450-177-9

MEASUREMENT OF COUPLING IMPEDANCES USING A GOUBAU LINE

F. Stulle*, J. Bergoz, Bergoz Instrumentation, Saint-Genis-Pouilly, France
H. W. Glock, Helmholtz-Zentrum für Materialien und Energie GmbH, Berlin, Germany

Abstract

Longitudinal coupling impedances can be deduced from S-Parameter measurements performed on a Goubau Line. The Goubau Line, also known as single wire line, is a variant of the coaxial wire method. Both setups use a wire for mimicking the particle beam. Coaxial tapers at the wire ends adapt the wave impedance to the 50 Ω impedance of coaxial cables, sources and receivers. But for guiding the electromagnetic wave, the Goubau Line relies on the realistic boundary conditions imposed by an insulated wire instead of using a coaxial shield. Equations for the deduction of longitudinal coupling impedances are reviewed and applied to Goubau Line measurements. Goubau Line measurements and CST Studio simulations are compared, showing good agreement.

INTRODUCTION

The coaxial wire method is a well-established technique for the deduction of coupling impedances [1-3]. The wire is mimicking the particle beam. A coaxial shield is used to guide the electromagnetic fields. Coaxial tapers on both ends adapt the wave impedance to the 50 Ω impedance of coaxial cables, sources and receivers. Using a vector network analyzer, S-parameters of the setup with and without device under test (DUT) are obtained. These measurements are sufficient to mathematically deduce coupling impedances of the DUT with high accuracy.

The Goubau Line [4] is a variant of the coaxial wire method. The important difference is that for guiding the electromagnetic wave it relies on the realistic boundary conditions of an insulated wire, instead of using a coaxial shield. That a single wire in open space can act as a waveguide had already been shown in the early days of electrodynamics [5-7].

Such a setup allows for more flexibility because it does not need to be adapted to the DUT geometry. Additionally, the DUT can be easily placed off-axis. On the other hand, it cannot be considered lossless, which is a usual assumption when analyzing S-parameters obtained by the coaxial wire method. Consequently, the standard equations, which are used to analyze data taken with the coaxial wire method, should be carefully examined before applying them to Goubau Line measurements.

We review the calculation of the longitudinal coupling impedance from S-parameter measurements. Assumptions and simplifications are discussed in view of their applicability to Goubau Line measurements. Afterwards, longitudinal coupling impedances are compared which were obtained from Goubau Line measurements and by CST Studio wakefield simulations [8].

*stulle@bergoz.com

The DUT was a pair of vacuum flanges intended to house a current transformer (Fig. 1). However, no current transformer was installed inside.

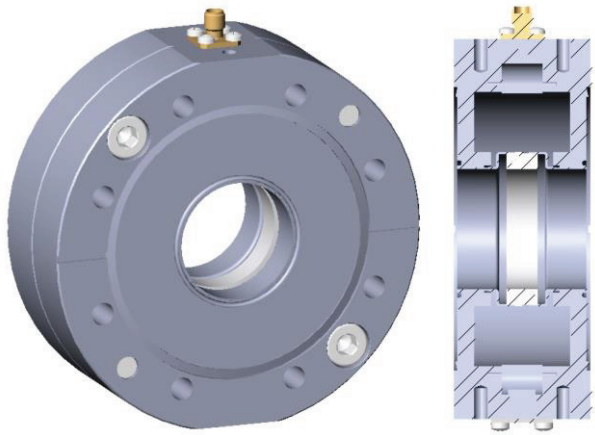

Figure 1: Drawing of the tested vacuum flanges.

Of interest is the coupling impedance induced by the ceramic gap and the surrounding cavity, which can be considered a single lumped impedance. For the particle beam, the metal parts left and right of the gap are like pieces of the vacuum chamber.

Note that such a DUT was chosen to demonstrate Goubau Line measurements and to facilitate simulations. The results are not representative for the real beam instrumentation installed in an accelerator.

CALCULATION OF LONGITUDINAL COUPLING IMPEDANCES

Coupling impedances are the frequency-domain equivalent to the time-domain wake potentials. One can be obtained from the other by (inverse) Fourier transform.

The impact of these coupling impedances on a highly relativistic particle beam is like that of a complex impedance on a current flowing in an electronic circuit. Consequently, they can be analyzed by using scattering parameters (S-parameters) (Fig. 2).

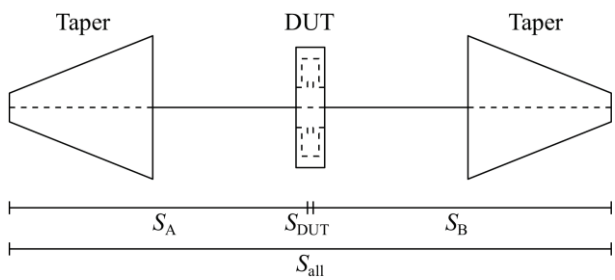

Figure 2: Definition of scattering matrices. The setup is in general asymmetric, i.e. S_A and S_B differ.

ISBN 978-3-95450-177-9

A single, lumped impedance Z_{DUT} leads to a reflection coefficient

$$S_{11,\mathrm{DUT}} = \frac{Z_{\mathrm{DUT}}}{Z_{\mathrm{DUT}} + 2\,Z_0}.$$

Z_0 is the wave impedance of the measurement setup at the position of the DUT. The DUT can be considered symmetric:

$$S_{22,\mathrm{DUT}} = S_{11,\mathrm{DUT}}$$
$$S_{12,\mathrm{DUT}} = S_{21,\mathrm{DUT}}.$$

And the relation $S_{21,\mathrm{DUT}} = 1 - S_{11,\mathrm{DUT}}$ applies, which is valid for any two-port network consisting of an arbitrary series impedance.

Consequently, the scattering matrix of the DUT can be written as:

$$S_{\mathrm{DUT}} = \begin{pmatrix} S_{11,\mathrm{DUT}} & 1 - S_{11,\mathrm{DUT}} \\ 1 - S_{11,\mathrm{DUT}} & S_{11,\mathrm{DUT}} \end{pmatrix}.$$

The part of the measurement setup left of the DUT is described by the scattering matrix

$$S_{\mathrm{A}} = \begin{pmatrix} S_{11,\mathrm{A}} & S_{12,\mathrm{A}} \\ S_{21,\mathrm{A}} & S_{22,\mathrm{A}} \end{pmatrix}.$$

The part of the measurement setup right of the DUT is described by the scattering matrix

$$S_{\mathrm{B}} = \begin{pmatrix} S_{11,\mathrm{B}} & S_{12,\mathrm{B}} \\ S_{21,\mathrm{B}} & S_{22,\mathrm{B}} \end{pmatrix}.$$

In general, S_{A} and S_{B} will differ. Both will be reciprocal, i.e. $S_{12,\mathrm{A}} = S_{21,\mathrm{A}}$ and $S_{12,\mathrm{B}} = S_{21,\mathrm{B}}$.

By transforming the scattering matrices (S-parameters) to scattering transfer matrices (T-parameters) and matrix multiplication, the scattering transfer matrix of the overall setup can be calculated:

$$T_{\mathrm{all}} = T_{\mathrm{A}}\,T_{\mathrm{DUT}}\,T_{\mathrm{B}}.$$

S_{all} is then obtained from T_{all} by back-transformation.

To deduce Z_{DUT} two sets of measurements need to be performed. One reference, S_{ref}, without the DUT. And another, S_{all}, with the DUT. Either the measured transmission coefficients S_{21} or the reflection coefficients S_{11} can be used:

$$Z_{\mathrm{DUT,T}} = 2\,Z_0\,\frac{(S_{21,\mathrm{all}} - S_{21,\mathrm{ref}})(S_{22,\mathrm{A}}\,S_{11,\mathrm{B}} - 1)}{S_{21,\mathrm{all}}\,(1 - S_{22,\mathrm{A}})(1 - S_{11,\mathrm{B}})} \quad (1)$$

and

$$Z_{\mathrm{DUT,R}} = 2\,Z_0\,\frac{S_{22,\mathrm{A}}\,S_{11,\mathrm{B}} - 1}{1 - S_{11,\mathrm{B}}} \times \left(1 - S_{22,\mathrm{A}} + \frac{S_{21,\mathrm{A}}^2\,(1 - S_{11,\mathrm{B}})}{(S_{11,\mathrm{all}} - S_{11,\mathrm{ref}})(S_{22,\mathrm{A}}\,S_{11,\mathrm{B}} - 1)}\right)^{-1} \quad (2)$$

Eqns. 1 and 2 share the dependence on the reflection coefficients $S_{22,\mathrm{A}}$ and $S_{11,\mathrm{B}}$. But eqn. 2 additionally depends on the transmission coefficient $S_{21,\mathrm{A}}$; meaning that more information is required to obtain correct results.

In general, $S_{22,\mathrm{A}}$, $S_{11,\mathrm{B}}$ and $S_{21,\mathrm{A}}$ need to be estimated from system knowledge. Overall accuracy of Z_{DUT} will depend on the quality of this estimation.

For well-matched coaxial wire setups, $S_{22,\mathrm{A}}$ and $S_{11,\mathrm{B}}$ can be neglected, $S_{21,\mathrm{A}}$ can be considered a lossless delay and the measured value of $S_{11,\mathrm{ref}}$ will result zero. In such a case, eqns. 1 and 2 simplify to the well-known equations by Hahn and Pedersen [3].

A first-order Taylor expansion of eqns. 1 and 2 yields for small $S_{22,\mathrm{A}}$ and $S_{11,\mathrm{B}}$:

$$Z_{\mathrm{DUT,T}} \approx 2\,Z_0\,\frac{(S_{21,\mathrm{ref}} - S_{21,\mathrm{all}})(S_{22,\mathrm{A}} + S_{11,\mathrm{B}} + 1)}{S_{21,\mathrm{all}}}$$

and

$$Z_{\mathrm{DUT,R}} \approx 2\,Z_0\,\frac{S_{22,\mathrm{A}} + S_{11,\mathrm{B}} + 1}{\frac{S_{21,\mathrm{A}}^2}{S_{11,\mathrm{all}} - S_{11,\mathrm{ref}}}(S_{22,\mathrm{A}} - S_{11,\mathrm{B}} + 1) - 1}.$$

GOUBAU LINE MEASUREMENTS

Since a Goubau Line has open boundary conditions, some signal power is always lost due to radiation. Additionally, reflections occur at the transitions from the cones to the wire and at the transitions to the DUT. Hence, establishing exact knowledge of $S_{22,\mathrm{A}}$, $S_{11,\mathrm{B}}$ and $S_{21,\mathrm{A}}$ is difficult, hindering an accurate determination of Z_{DUT}.

These S-parameters can be approximated when exploiting system knowledge. The Goubau Line cones follow a known shape. The corresponding impedance profile can be calculated. The characteristic wave impedance along the wire can be obtained from analytical equations given in [4]. The position of the DUT can be measured and its aperture diameter is in any case a known value.

By combining all values, the wave impedance at any point along the Goubau Line can be approximated. Thus S-parameters can be estimated allowing the application of eqns. 1 and 2 without further simplifications. Nevertheless, it should be noted that different approximations are possible leading to similar but not the same results.

Such an approach is not only applicable for Goubau Line measurements, but also for measurements performed on similar setups, including the coaxial wire setup using an outer shield. To limit the influence of errors on the S-parameter approximation, it will always be beneficial if reflection coefficients remain small and transmission parameters remain large. Both is fulfilled for the Goubau Line set up at Bergoz Instrumentation over a wide range of frequencies; even if the DUT is placed off-axis.

The Goubau Line used for the measurements consisted of a single cone and a 0.5 mm diameter enamel coated copper wire. Behind the DUT, the RF wave was absorbed by RF absorbers (Fig. 3). Since such a setup does not allow transmission measurements, all Goubau Line results are derived from reflection measurements.

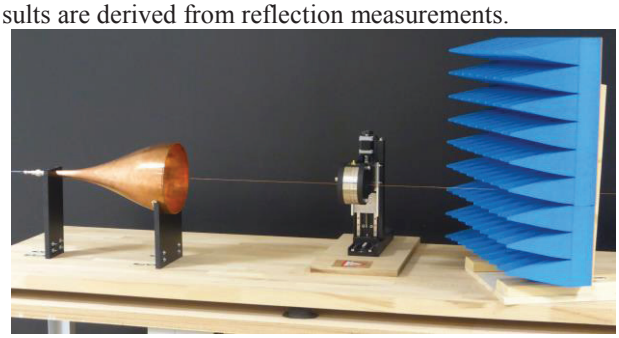

Figure 3: Goubau Line used for reflection measurements. The DUT is supported by micro-movers, allowing accurate positioning.

ISBN 978-3-95450-177-9

WAKEFIELD SIMULATIONS

Wakefield and impedance simulations were performed using CST Studio [8]. Applying the CST ParticleStudio wakefield solver these simulations resemble the passage of a charged particle bunch in the time domain using an explicit algorithm. This is done by discretizing the empty space, the dielectric components and the metallic boundaries on a hexagonal grid, where the integral representations of Maxwell's equations are transferred to a discrete matrix-vector equation.

The fields are excited by imposing a charge and current distribution equivalent to that of a Gaussian-shaped bunch traversing the structure on the beam axis. The wake potential is registered and by Fourier transformation converted into an impedance spectrum. The temporal evolution is done in small time steps, for every time step the field values and their time derivatives are updated.

Since this numerical model does not contain any kind of a central wire it is best suited for comparison to Goubau Line measurements.

The actual simulations used a hexagonal grid of 42.53 million mesh points. The length of the Gaussian excitation was 5 mm (1σ). The wake was computed for a length of 20 m.

SIMULATION AND MEASUREMENT RESULTS

The DUT was a pair of empty current transformer flanges with a total length of 40 mm and 34.9 mm aperture diameter (Fig. 1). They included a ceramic gap made of Alumina. For the Goubau Line measurements, the DUT was placed 1 cm off-axis with respect to the wire. For the wakefield simulations, the excitation was placed 1 cm off-axis with respect to the DUT axis.

The wakefield simulations were performed using three different values for the relative permittivity ε_r of the Alumina gap; $\varepsilon_r = 9.9$, 10.7 and 12.0. This parameter has some influence on the frequency of the resonances. A lower ε_r results higher resonance frequencies, a higher ε_r results lower resonance frequencies (Fig. 4).

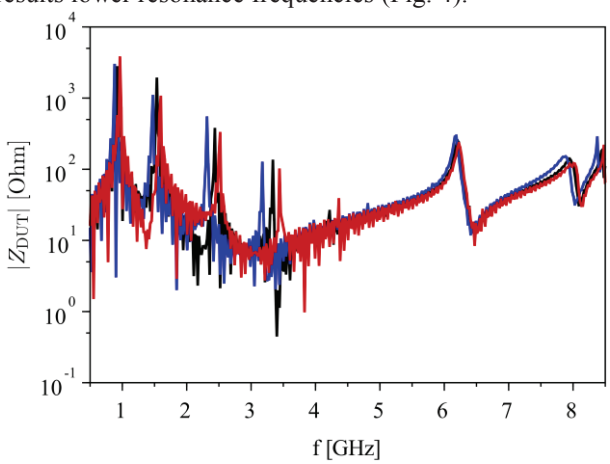

Figure 4: Simulated Z_{DUT} using $\varepsilon_r = 9.9$ (red), $\varepsilon_r = 10.7$ (black) and $\varepsilon_r = 12.0$ (blue).

For comparison to the Goubau Line measurements $\varepsilon_r = 10.7$ was chosen since this value matched measured resonance frequencies very well. It lies within the range of $\varepsilon_r \approx 9 - 12$ found in literature. The real ε_r of the Alumina gap is not known.

The reference measurement $S_{11,ref}$ was done with the ceramic gap shorted by copper tape. $S_{11,all}$ was measured after removing this tape. Care was taken that the DUT position remained unchanged. Differences in position would add a strong background to the calculated coupling impedances, deforming resonances or even hiding weaker ones. Figure 5 shows the measured magnitudes of $S_{11,ref}$ and $S_{11,all}$.

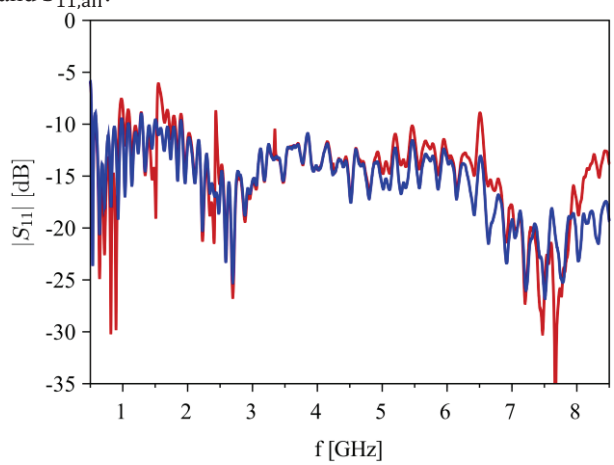

Figure 5: Measured reflection coefficients $S_{11,ref}$ (blue) and $S_{11,all}$ (red).

While some differences are visible, which hint to an influence of the DUT, these are not striking. Only after analysis using eqn. 2 their real importance becomes visible. Figure 6 compares Z_{DUT} obtained from above measurements to CST Studio simulations.

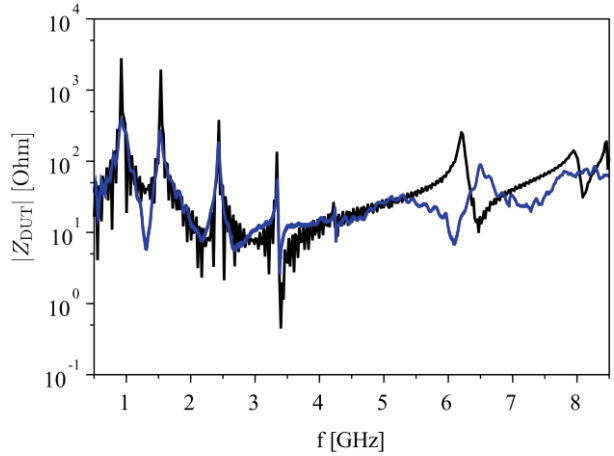

Figure 6: Z_{DUT} obtained by measurement (blue) and by simulation for $\varepsilon_r = 10.7$ (black).

Up to about 5 GHz, simulated and measured Z_{DUT} agree very well. Both contain the same resonances, which are all located at the same frequencies and generally have similar amplitudes. Though the measured resonances are usually weaker.

ISBN 978-3-95450-177-9

One resonance around 6.3 GHz shows up in the simulations and measurement with inverted amplitude, which is not understood.

Above 7.5 GHz the simulations contain resonances which in the measurements lead to a smoothly increased Z_{DUT} only.

Despite the observed differences and the fact that in the simulations ε_{r} had been tuned to match measured resonance frequencies, the similarities are significant. This emphasizes that simulation and measurement results are valid. Both allow not only to identify resonance frequencies, but also to examine resonance strength.

On-Axis DUT

A measurement has also been performed with a centered DUT (Fig. 7). Comparing it to the previous off-axis results (Fig. 6) reveals the importance of the DUT position. Consequently, this comparison reveals the importance of performing measurements or simulations at different DUT positions.

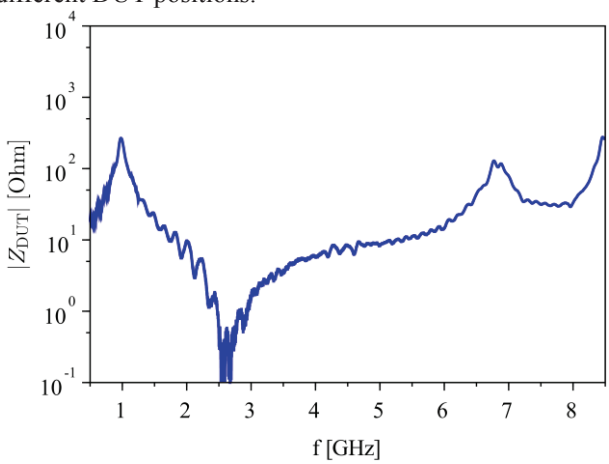

Figure 7: Measured coupling impedance for a centered DUT.

Only the lowest frequency resonance close to 1 GHz remains at similar strength. Up to 6.5 GHz the spectrum does not show any sign of other resonances.

CONCLUSION

The longitudinal coupling impedance of a pair of current transformer flanges has been deduced from Goubau Line measurements and CST Studio simulations. Up to about 5 GHz both approaches resulted the same resonance frequencies and similar resonance amplitudes. At higher frequencies differences could be identified which remain to be understood.

Since the relative permittivity of the Alumina gap was not known, this value had to be scanned in the CST Studio simulations. A value of $\varepsilon_{\mathrm{r}} = 10.7$ resulted in best agreement to the measurements.

The results show that Goubau Line measurements can be used to identify resonances in vacuum components. Despite the fact that knowledge about Goubau Line characteristics remains limited, accuracy is sufficient to distinguish different resonance strengths and to resolve even weak resonances. Furthermore, the Goubau Line working principle, namely its open boundaries, allows for easy off-axis measurements.

Flexibility regarding the DUT geometry and position is the major advantage of a Goubau Line over conventional coaxial wire setups.

Further studies are planned to understand the observed discrepancies. Transmission measurements will be performed using a second cone instead of the RF absorbers. Other devices will be tested.

REFERENCES

[1] A. Faltens et al., “An analog method for measuring the longitudinal coupling impedance of a relativistic particle beam with its environment”, Proc. of 8th HEACC, Geneva, Switzerland, August 1971

[2] M. Sands, J. Rees, “A bench measurement of the energy loss of a stored beam to a cavity”, SLAC Report PEP-95, August 1974

[3] H. Hahn, F. Pedersen, “On coaxial wire measurements of the longitudinal coupling impedance”, BNL report 50870, April 1978

[4] G. Goubau, “Surface Waves and their Application to Transmission Lines”, J. Appl. Phys. 21, 1950

[5] A. Sommerfeld, “Ueber die Fortpflanzung electrodynamischer Wellen längs eines Drahtes”, Ann. Phys. 303, 1899

[6] D. Hondros, “Über elektromagnetische Drahtwellen”, Ann. Phys. 335, 1909

[7] F. Harms, “Elektromagnetische Wellen an einem Draht mit isolierender zylindrischer Hülle”, Ann. Phys. 328, 1907

[8] CST Studio 2015, Computer Simulation Technology AG, Darmstadt, Germany, http://www.cst.com

ISBN 978-3-95450-177-9

ENERGY AND LONGITUDINAL BUNCH MEASUREMENTS AT THE SPIRAL2 RFQ EXIT

C. Jamet #, W. Le Coz, G. Ledu, S. Loret, C. Potier de Courcy
GANIL, Caen, France

Abstract

A new step of the SPIRAL2 commissioning started in December 2015 with the acceleration of a first proton beam at the RFQ exit. A test bench, with all the different diagnostics which will be used on the SPIRAL2 accelerator, was installed directly after the first rebuncher of the MEBT line in order to qualify beams but also to test and make reliable the diagnostic monitors.

In 2016, different ion beams are qualified by the diagnostic test bench. This paper describes the results of the energy measurements done by a Time of Flight monitor and the longitudinal measurements using a fast faraday cup.

INTRODUCTION

The SPIRAL2 driver is designed to accelerate and deliver proton beams, deuteron and ion beams with q/A=1/3 to NFS (Neutron for Science) and S3 (Super Separator Spectrometer) experimental rooms. Table 1 shows the main beam characteristics.

Table 1: Beam Specifications

Beam	P	D+	Ions (1/3)
Max. Intensity	5 mA	5mA	1 mA
Max. Energy	33 MeV	20 MeV/A	14.5 MeV/A
Max. Power	165 kW	200 kW	43.5 kW

Currently, an Intermediate Test Bench is installed in the MEBT line. The commissioning is in progress in the accelerator part composed by 2 sources (a proton/deuteron source and an ion source with a q/A=1/3), the LEBT lines, a chopper, a RFQ, a rebuncher as shown in the figure 1.

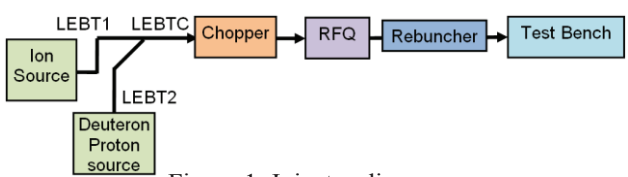

Figure 1: Injector diagram.

A first proton beam was accelerated through the RFQ in December 2015. In the first semester of 2016, the commissioning was done with proton and helium beams in pulse and CW mode, up to the nominal beam intensities. In parallel, the installation of the accelerator process continues.

INTERMEDIATE TEST BENCH

The "Intermediate Test Bench" or "Diagnostic Plate" was built to test all the different diagnostics which will be used on the SPIRAL2 Accelerator.

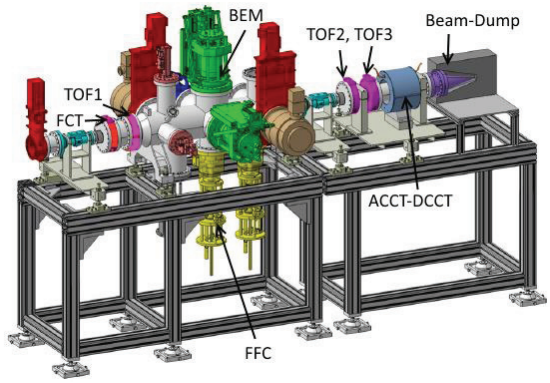

Figure 2: View of the intermediate test bench.

The Test Bench is installed after 3 quadrupoles and the first-rebuncher of the MEBT in order to validate the RFQ, the diagnostics by measuring the following beam characteristics (Figure 2):

- Intensity with ACCT, DCCT transformers and Faraday Cup (FC)
- Transverse Profiles with Multiwires beam profile monitors (SEM) and Ionization Gas monitor
- Transverse emittance with an Allison Scanner Emittancemeter (H an V)
- Phases and Energy with the Time of Flight (TOF) monitor
- Longitudinal profile with a Fast Faraday Cup (FFC) and a Beam Extension Monitor (BEM)
- Beam Position, Phase and Ellipticity with 2 Beam Position Monitors (BPM)

BEAM ENERGY PRINCIPLE

The beam energy is measured by using 3 electrodes pick-up (TOF1, TOF2 and TOF3). The energy is calculated, with a Time of flight method [1].

A dedicated electronic measures, using an I/Q demodulation method, the In-phase component I(t) and the Quadrature component Q(t) of the first harmonic [2].
An EPICS Interface, connected to the TOF electronic device by a Modbus-TCP communication, calculates the phases and the amplitudes from these components [3]. From the difference phases, the energy is determined.

BEAM ENERGY MEASUREMENTS

Beam and TOF Features

The beam features were the following (table 2):

- Proton Intensity: from few 10µA to 5mA
- Helium $^{4}He^{2+}$ Intensity: few 10 µA to 1 mA
- Slow Chopper duty cycle: From 1/10000 to 1/1
- Chopper Frequency: 1Hz to 5 Hz

ISBN 978-3-95450-177-9

Table 2: TOF Features

Features	Values
Frequency (MHz)	88.0525
Period (ns)	11.36
Energy E (MeV/A)	0.73
Velocity β=v/c	0.04
Length between 2 bunches Lacc (cm)	13.6
Length between TOF1-TOF2 (m)	1.616
Length between TOF2-TOF (cm)	13
Bunch number between TOF1-TOF3	12
Electrode diameter (mm)	80

Electronic Initialization

Before measuring the energy, the electronic device can be initialized to increase the accuracy. Without signals, an offset subtraction allows to decrease the offset level of the 3 modules from -70 dBm to -110 dBm. The cable lengths between the electrodes and the system were adjusted very precisely. However, a test signal can be sent on the 3 electrodes with the same delay, a phase compensation between pick-ups allows to correct few tenths of degree. The type of accelerated particles is automatically retrieved from the data base of the control system.

Proton Energy Measurements

The beam energy is firstly measured with the RFQ "on" and the rebuncher "off" with different beam intensities.
VRFQ = 50 kV, I crest = 3.9 mA

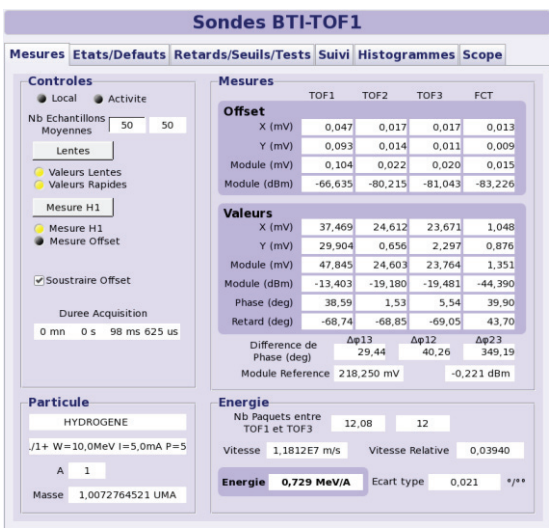

Figure 3: TOF values with rebuncher "off".

The table "Valeurs" in the page "mesures" of the graphical Interface (figure 3) indicates the X and Y signal components of the 3 electrodes, the FCT (Fast Current Transformer) and the modules and phases.

The bunch number, the energy E13 and this standard deviation are displayed in the "Energie" frame.
Separately, in order to verify the value, the energy is also calculated between each electrode on an excel spreadsheet. The 3 values are very similar around 729.32 MeV.

Helium Energy Measurements

VRFQ = 80 kV, I crest = 1.1 mA,
The 3 energy values are shown in table 3.

Table 3: Energy Measurements

Energy (keV)	Rebuncher off	Rebuncher on V = 75 kV, φ = -67,9°
E 12 (TOF1-TOF2)	727.95	727.28
E 13 (TOF1-TOF3)	727.96	727.28
E 23 (TOF2-TOF3)	728.07	727.30

The rebuncher is started at 75kV and its phase is tuned at -67.9° to find the same TOF phases with the rebuncher off. The rebuncher phase is after shifted on 360° (fig. 4).

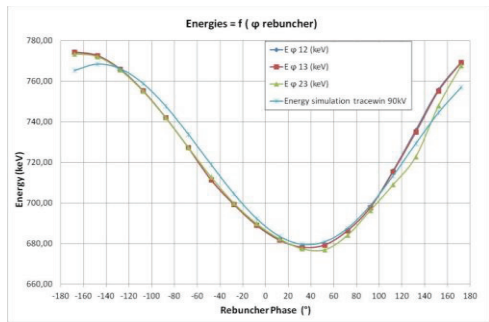

Figure 4: Energy in function of the rebuncher phase.

Histograms and Standard Deviations

The "histogrammes" sheet shows histograms, standard-deviations of the phase and the energy values.

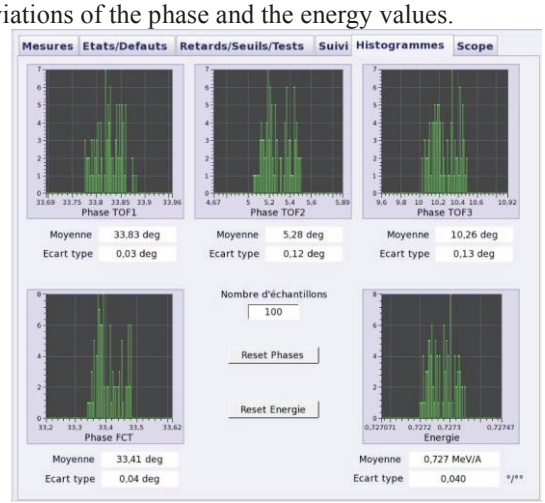

Figure 5: Phases and energy histograms.

The standard deviations give information of the ratio signal/noise. The histogram shapes indicate the nature of noises or disturbances.

A Gaussian histogram, with a low standard deviation like in the figure 5 means a good degree of precision (better than 10^{-4} in energy).

Optimization and Improvements

When the rebuncher is started and when its phase is shifted, the beam is accelerated or decelerated in function of the phase. The bunch numbers change.

$$\varphi 12 = N12 * 360 + (\varphi TOF1 - \varphi TOF2)$$
$$\varphi 13 = N13 * 360 + (\varphi TOF1 - \varphi TOF3)$$

ISBN 978-3-95450-177-9

$$N12 = integer\left(\frac{L12}{Lacc}\right) = Int\left(\frac{L12}{L23} * \frac{360}{\varphi 23}\right)$$
$$N13 = integer\left(\frac{L13}{Lacc}\right) = Int\left(\frac{L13}{L23} * \frac{360}{\varphi 23}\right)$$

L xy: Length between TOFx/TOFy
10 < N12 <11 and 11<N13<12

N12 and (φTOF1-φTOF2), N13 and (φTOF1-φTOF3), don't change exactly at the same moment due to the measurement errors. So when the bunch number changes, φ12 and φ13 can have a jump of 360°.

To resolve this problem, the solution consists to choose E12 or E13 in function of N12 and N13. The bunch number that is farthest from the value change is chosen.

LONGITUDINAL BUNCH MEASUREMENTS

A Fast Faraday Cup (FFC) will be positioned at the end of the MEBT to visualize, characterize the bunch lengths and will be used to tune the 3 rebunchers of the MEBT.

Diagnostic Description

The FFC is a coaxial Faraday Cup with a water-cooled on the outer conductor. The inner conductor (central part) is cooled by conduction via tree ceramic rods. A polarized grid, in front of the coaxial core, is used to shield the cup against the bunch advanced field and to suppress the secondary electrons effects (see fig. 6).

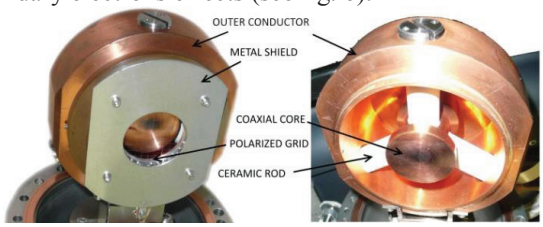

Figure 6: FFC Pictures

The diameter of the central part is 45 mm.
Thermal calculations give the following limits:
The central part limitation: 400 W in continuous beam, 10ms/200ms with a pulse power of 7.5 kW (Pmax)
The grid limitation: 1ms/200ms with a pulse of 7.5 kW.

FFC Bandwidth

The FFC bandwidth is measured with a Vector Network Analyzer, Agilent 8753 ES by reflection (fig 7.).

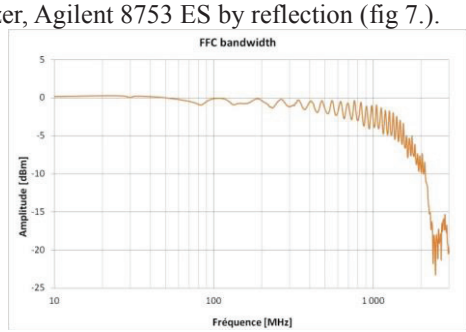

Figure 7: FFC frequency spectrum

The FFC bandwidth at -10 dBm is 2 GHz.

Acquisition System

An oscilloscope Agilent DSO9404A with 4 analog channels and bandwidths of 4GHz digitalizes the pulse FFC signal. This oscilloscope was chosen also for its EPICS drivers. A 4 dB attenuator is connected just right after the vacuum feedtrough. The oscilloscope is located at a distance of about 50m in a process room. A high-voltage power supply polarizes the grid in the range of +/-1500v.

The oscilloscope acquisition is armed on the "Beam synchronization" signal and trigged on the "RF reference" (fig.8). "Beam synchronization" indicates the beam presence depending of the beam modulation done by the chopper, RFQ or sources.

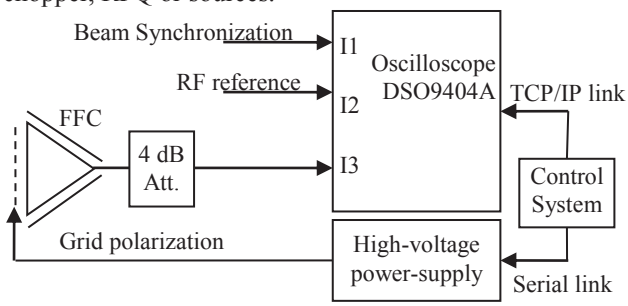

Figure 8: System Scheme

Proton Bunch Measurements

VRFQ = 50 kV, Vrebuncher = 45 kV, I beam = 4 mA

The phase of the rebuncher is tuned to be in the "rebunch mode". The time standard deviation of the beam bunch is calculated with the following formulas.

$$t_p = \frac{\sum_{i=0}^{n} V_{ffc}(t_i) * t_i}{\sum_{i=0}^{n} V_{ffc}(t_i)} \qquad \sigma_t^2 = \frac{\sum_{i=0}^{n} V_{ffc}(t_i) * (t_i - t_m)^2}{\sum_{i=0}^{n} V_{ffc}(t_i)}$$

tp: pulse time position
σt: standard deviation in time
FWHM = 800 ps.

The calculated value from the pulse (fig.9) gives σt = 328 ps while the tracewin simulated value is 220 ps.

The spectral density is determined from the pulse signal by a matlab program.

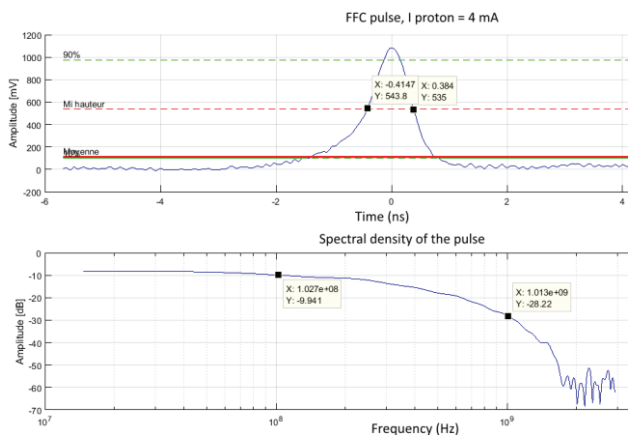

Figure 9: Spectral density of the proton pulse.

ISBN 978-3-95450-177-9

The attenuation between the 100 MHz level and the 1GHz level is equal to 18.3 dB.

Helium Bunch Measurements

VRFQ = 80 kV, I beam = 1.1 mA

The rebuncher phase is tuned and the FFC pulses are acquired for different rebuncher voltages (fig. 10).

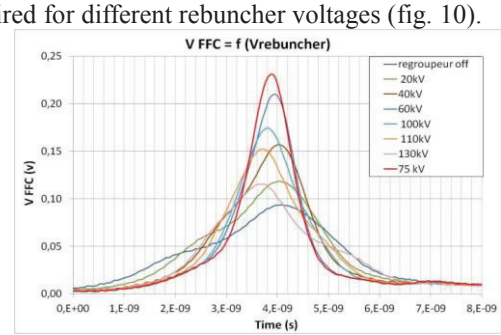

Figure 10: FFC pulse in function of the rebuncher voltage.

The bunch length is optimized at 75 kV and the pulse time values at this voltage are:

FWHM: 1,05 ns

σt calculated from the pulse = 443 ps

σt simulated with tracewin = 280 ps

BEM and FFC comparison

A Bunch Extension Monitor (BEM) is installed at the same location than the FFC. The BEM principle consists to insert a wire inside the beam and collect the X-rays on a microchannel plate. An integrating electronic device allows to reconstruct the bunch shape [4].

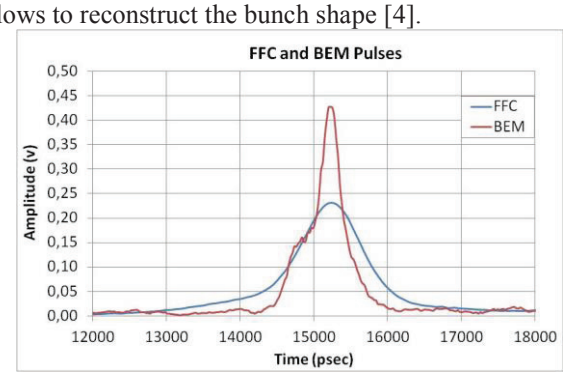

Figure 11: FFC and BEM pulses.

The BEM amplitude is normalised to have the same pulse area than the FFC one. The FFC pulse shape is larger than the BEM pulse (fig. 11).

At 75kV, the rebuncher phase is rotated over 360°, the pulse width is shown in function of this phase (fig. 13).

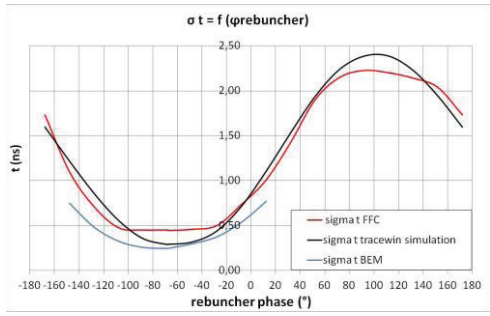

Figure 13: σt_{FFC} in function of the rebuncher phase

The FFC curve shows a time resolution limitation. The minimum σt value is equal to 440 ps. In comparison, the BEM length goes down to 244 ps with a tracewin simulated σt = 280 ps. Following these measurements, the pulse enlargement due to the FFC limited bandwidth and cable distortion is estimated between 120 to 160 ps.

FFC Grid Polarization Influence

The voltage applied to the grid modifies the shape of the FFC pulse. A negative voltage repels the electrons of the secondary emission on the cup, in contrary to a positive voltage which collects these electrons (fig.14).

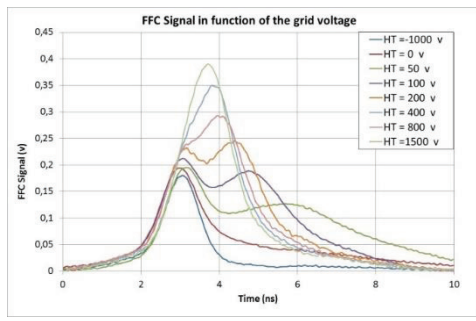

Figure 14: FFC signal in function of the grid voltage.

A low positive voltage generates a slow exit of the electrons. The second pic, produced by the secondary electrons, appears with a time delay from 1 to 3 ns. To minimize the width, the grid voltage is tuned at -1000 v.

CONCLUSION

The SPIRAL2 RFQ injector commissioning is started since the beginning of 2016 with proton and helium beams. It will soon continue with heavier ion beams.

As shown, the results of the energy and bunch length monitors are encouraging. Their functioning responds to the needs and will allow the characterization of the various injector beams.

TOF monitor studies will be done to compare signal amplitude with simulations, to measure the ratio signal/noise in function of the beam intensity and to compare the measurements with the calculated accuracy.

A signal processing of the Fast Faraday Cup should minimize the signal enlargement caused by the limited bandwidth of the Faraday cup.

ISBN 978-3-95450-177-9

REFERENCES

[1] W. Le Coz *et al.*, "Measurement and Control of THE Beam Energy for the SPIRAL2 Accelerator", IBIC13, Oxford, England
[2] C. Jamet *et al.*, "Phase and amplitude measurement for the SPIRAL2 Accelerator", DIPAC09, Basel, Switzerland.
[3] W. Le Coz *et al.*, "Progress on the beam Energy Monitor for the SPIRAL2 Accelerator", IBIC2014, Monterey, California.
[4] R. Revenko *et al.*, "Bunch Extension Monitor for LINAC of SPIRAL2 Project", IBIC 2016, Barcelona, Spain.

ISBN 978-3-95450-177-9

A PROCEDURE FOR THE CHARACTERIZATION OF CORRECTOR MAGNETS

S. Gayadeen *, M. Furseman, G. Rehm, Diamond Light Source, Chilton, U.K.

Abstract

At Diamond Light source, the main assumption for the Fast Orbit Feedback (FOFB) controller design is that the corrector magnets all have the same dynamic response. In this paper, a procedure to measure the frequency responses of the corrector magnets on the Diamond Storage Ring is presented and the magnet responses are measured and compared in order to assess whether this assumption is valid. The measurements are made by exciting a single corrector magnet with a sinusoidal input and measuring the resulting sinusoidal movement on the electron beam using electron Beam Position Monitors (eBPMs). The input excitation is varied from 10 Hz to 5 kHz using a 10 mA sine wave. The amplitude ratio and the phase difference between the input excitation and the beam position excitation are determined for each input frequency and the procedure is repeated for several magnets. Variations in both gain and phase across magnets are discussed in this paper and the effect of such variations on the performance of the FOFB controller performance is determined.

INTRODUCTION

The Fast Orbit Feedback (FOFB) Controller at Diamond performs global orbit correction to 172 horizontal and vertical correctors respectively using the position from 171 horizontal and 171 vertical electron Beam Position Monitors (eBPMs). The main assumption of the FOFB design is that all corrector magnets in the Storage Ring have the same dynamic effect on beam position. This assumption allows the FOFB controller to be decoupled into a static part (implemented as the inverse of the Response Matrix) and a dynamic part (implemented as IIR filters on the outputs of the inverse Response Matrix). If the dynamics of the corrector magnets are dissimilar, then the decoupled control approach may no longer be valid and significant differences in dynamics may limit the ability of the FOFB controller to attenuate disturbances.

Two straights in the Diamond Storage Ring (I13 and I09) were modified with vertical mini-beta and horizontally focusing optics [1], resulting in the need for two extra correctors in each modified straight in both planes. The additional correctors are different in design to the standard correctors used around the rest of the Storage Ring. Moreover the mini-beta correctors are fitted around a different vacuum chamber cross section. A method to measure the dynamic response of the Storage Ring correctors was developed so that the dynamics of the mini-beta correctors can be compared to the standard corrector magnets and the impact on the FOFB performance can be determined. The procedure to obtain the required measurements for such characterisation and the analysis of the measurements are presented in this paper.

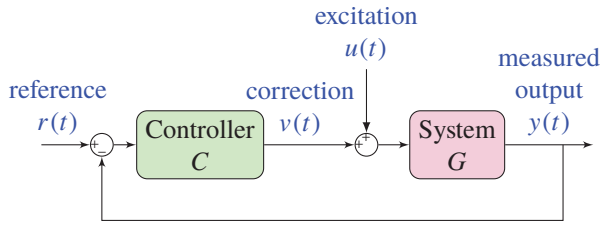

Figure 1: System representation.

FREQUENCY RESPONSE OF A SYSTEM

A general representation of the system to be characterised is shown in Fig. 1 where the system to be characterised is represented by G (referred to as the open loop system) which includes dynamics contributed by the magnet power supplies, the magnet itself and the vacuum vessel. Also included in G are external disturbances acting on the electron beam. The FOFB controller is represented by C, which takes the difference of the beam position at all eBPMs, $y(t)$ and the golden orbit, $r(t)$ as an input. An external excitation, $u(t)$ can be added to the calculated output $v(t)$, which then becomes the correction applied to the corrector magnets.

A common way of modelling the system G, is to find the frequency response, or response to a sinusoid. An input signal $u(t)$ that is a harmonic signal with angular frequency ω, can be expressed as

$$u(t) = u_0 \sin(\omega t) \tag{1}$$

If the system is properly damped, then after some time the transient behaviour of the system will damp and the output $y(t)$ is also harmonic with the same frequency and its amplitude and phase with respect $u(t)$ are determined by the complex value of $G(j\omega)$ i.e. the complex number that is obtained when $s = j\omega$ is substituted in the expression of the transfer function $G(s)$ [2]. Specifically, the gain $|G(j\omega)|$ equals the ratio of the amplitudes of the output and input signals and the phase angle $\angle G(j\omega)$ is equal to the phase shift. The gain and phase shift are shown as functions of the angular frequency in a Bode plot. The information in such a plot is used as a model of the linear, time-invariant system $G(s)$ and can be used to compute the output of the system for a given input.

To measure the frequency response, the system is excited at a user defined set of M excitation frequencies $\{\omega_i\}_{i=1,\ldots,M}$ and associated amplitudes $\{u_{0_i}\}_{i=1,\ldots,M}$. When the system is excited, information is only obtained at the chosen excitation frequencies, so that the frequency grid should normally

* sandira.gayadeen@diamond.ac.uk

ISBN 978-3-95450-177-9

be chosen where required dynamic behaviour is expected. Additionally, the variance of the estimated model decreases with increasing number of excitation frequencies. The amplitude of the excitation is set to obtain optimal signal to noise performance. However, the amplitude should be chosen such that any amplitude or rate limiters in the system are not activated, as such nonlinearities would affect the measured response.

To characterise the open loop response, the FOFB controller is turned off (i.e. $v(t) = 0$ in Fig. 1) and the excitation signal, $u(t)$ is turned on, so that the output signal is a direct measurement of the system dynamics which can be written in terms of transfer functions described by s i.e.

$$Y(s) = G(s)U(s) \tag{2}$$

By substituting $s = j\omega$, the magnitude of the system $G(j\omega)$ is expressed as the ratio of the amplitudes of the excitation and the output signals and the phase of the system $G(j\omega)$ is expressed as the difference between the phases of the output signal and the excitation signal i.e.

$$\begin{aligned} |G(j\omega)| &= \frac{|Y(j\omega)|}{|U(j\omega)|} \\ \angle G(j\omega) &= \angle Y(j\omega) - \angle U(j\omega) \end{aligned} \tag{3}$$

When the FOFB controller is switched on and the excitation is active, the output signal, $y(t)$ includes the effect of the FOFB controller dynamics as well as the system dynamics and is given by

$$\begin{aligned} Y(s) &= G(s)(U(s) + V(s)) \\ Y(s) &= \frac{G(s)}{1 + G(s)C(s)} \end{aligned} \tag{4}$$

The sensitivity function [2] is defined as transfer function between the disturbances acting on the beam and the beam position which is described by

$$S(s) = \frac{1}{1 + G(s)C(s)} \tag{5}$$

The magnitude of the sensitivity function at a particular frequency indicates the level of attenuation the closed loop achieves. From (2) and (4), by dividing the measured frequency response when the FOFB controller is on by the response with the FOFB turned off, the sensitivity function can be determined.

MEASUREMENT PROCEDURE

The FOFB system calculates the orbit correction on distributed VxWorks PowerPC processors at s sample rate $f_s = 10072$ Hz. The processors can be programmed via EPICS to provide individual excitation signals for each corrector which is added to the calculated output from the FOFB controller, or DC set-point when open loop. Almost arbitrary excitation frequencies are possible as the controller advances the sine wave excitation by a programmed phase advance each tick. The resulting orbit data is collected by the eBPMs and is also archived at f_s [4], which is later read back to provide data for the analysis.

The algorithm for measurement of the frequency response of a corrector is described in the following steps:

1. The required corrector is excited with a sinusoidal signal of amplitude u_0 and frequency $f = \frac{\omega}{2\pi}$ Hz at time t_{start}, ending at time $t_{\text{end}} = t_{\text{start}} + N/f$ where N is the number of cycles of the excitation and is chosen by the user.

2. Beam position data from all enabled BPMs is collected from time t_{start} to t_{end}. To ensure synchronization of the input and output signals, a large window of data is taken and then sliced to the exact duration of the excitation using a global timestamp.

3. The output sinusoid from each BPM can be expressed as
$$\begin{aligned} y(t) &= y_0 \sin(\omega t + \phi) \\ &= I \sin(\omega t) + Q \cos(\omega t) \end{aligned} \tag{6}$$
The IQ data is extracted by multiplying the output by $\sin(\omega t)$ and $\cos(\omega t)$ respectively and filtering the high frequency component by taking the mean over N.

The above process is repeated to generate measurements for any required excitation frequency (up to Nyquist ($f_s/2$). Therefore for each excitation frequency, a complex number is obtained which has an amplitude (normalised by the input amplitude) equal to the gain of the system and a phase corresponding to the phase of the system i.e.

$$\begin{aligned} y &= \sqrt{I^2 + Q^2} \\ \phi &= \arctan \frac{Q}{I} \end{aligned} \tag{7}$$

where the gain of the system k is give by $k = y_0/u_0$.

CHARACTERISATION PROCEDURE

Fig. 2a and Fig. 2b show the measured frequency response observed by a single eBPM between 10 Hz to 3 kHz for the two mini-beta corrector magnets in straight I13 and a standard corrector magnet. The mini-beta correctors for both straights were found to have the same response, therefore only the responses of those in straight I13 are presented in this paper. Typically, an excitation amplitude of 10 mA was used however, the second corrector in each straight required a larger excitation amplitude (40 mA) which was determined by preliminary excitation tests. The magnitude of the responses shown in Fig. 2a and Fig. 2b are normalised to unity gain for comparison of the dynamic behaviour. It should be noted that the measured gain (in mm/A) is equivalent to the response matrix element for the corresponding corrector magnet and eBPM.

The procedure for identifying a transfer function model that is appropriate of the design of the FOFB controller is described in the following steps:

ISBN 978-3-95450-177-9

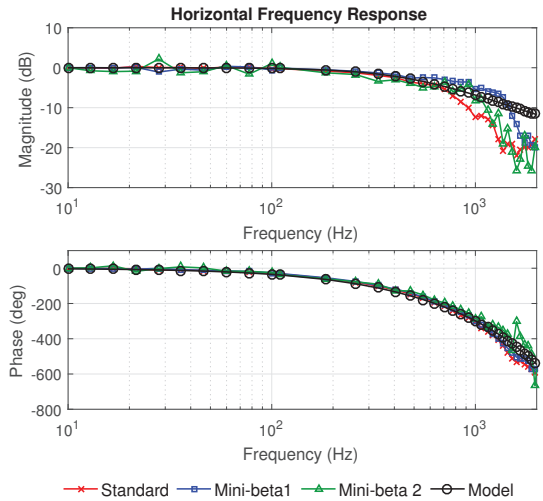

(a) Horizontal frequency response measurements.

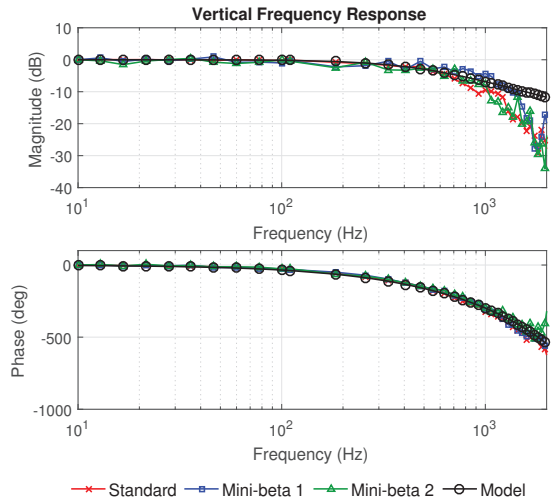

(b) Vertical frequency response measurements.

Figure 2: Frequency response measurements for a standard corrector (red '×') and mini-beta correctors (blue '□' and green '△') compared to the modelled frequency response (black '○') for horizontal and vertical planes. The model is a first order model with bandwidth of 500 Hz and delay of 600 μs.

1. The approximate order of the model is determined. The high frequency roll-off is determined by the order of the model i.e. for a first order model, the high frequency roll-off is −20 dB/decade. The measured responses exhibit an approximate first order response which takes the form

$$g(s) = k\frac{a}{s+a} \tag{8}$$

where k is the steady state gain. The user should decide whether a first order model is accurate enough or that a higher order model is required for the purpose of the model.

2. The open loop bandwidth is determined. The bandwidth, a of the open loop system is defined as the frequency (in rad.s^{-1}) at which the magnitude of the frequency response drops by 3 dB. Table 1 shows the measured bandwidths for the different corrector magnets.

3. The open loop delay is determined. The measured phase responses of the corrector magnets are greater than that expected for a first order system, indicating that there is a delay element in the transfer function. The delay can be extracted from the phase information of the frequency response and fitted by a linear regression. The model with a delay term included is written as

$$g(s) = k\frac{a}{s+a}e^{-s\tau_d} \tag{9}$$

where τ_d is the delay in the system. To determine the delay, τ_d the measured phase of the system dynamics $\angle G(j\omega)$ is expressed as a first order system plus a delay, taking the form

$$\begin{aligned}\angle G(j\omega) &= \angle\left(\frac{a}{j\omega+a}e^{-j\omega\tau_d}\right)\\ \angle G(j\omega) &= \angle\left(\frac{a}{j\omega+a}\right)+\angle\left(e^{-j\omega\tau_d}\right)\end{aligned} \tag{10}$$

By using the relationship in (10) the delay element can be extracted and expressed as

$$-\tau_d\omega = \angle G(j\omega) - \angle\left(\frac{a}{j\omega+a}\right) \tag{11}$$

Fig. 3 shows the measured delays for each magnet for horizontal and vertical planes.

Table 1: Measured Bandwidth for a Standard Corrector and the Mini-beta Correctors for Vertical and Horizontal Planes

Magnet	Horizontal	Vertical
Standard	500 Hz	500 Hz
Mini-beta 1	700 Hz	700 Hz
Mini-beta 2	500 Hz	500 Hz

The measured responses show that the first mini-beta corrector has a bandwidth of 700 Hz and the second, a bandwidth of 500 Hz which matches the bandwidth of the standard corrector magnet. The measurements for the second mini-beta corrector are noisier than that taken for the standard corrector and first mini-beta corrector. This indicates that the excitation amplitude was too small for satisfactory signal to noise performance, however using larger amplitudes for the excitation activated a rate limiter which limited the bandwidth of the open loop measurement. A delay of 600 μs was determined to be the best fit for all magnets.

ISBN 978-3-95450-177-9

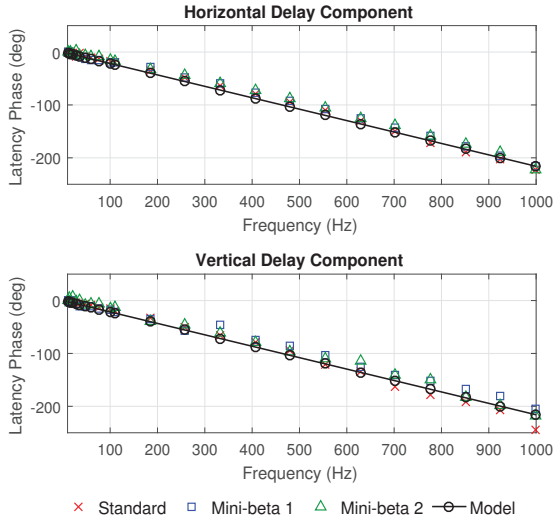

Figure 3: Phase introduced by the system latency in horizontal and vertical planes for a standard corrector (red '×') and mini-beta correctors (blue '□' and green '△') compared with a linear fit (black '○') of a 600 μs delay.

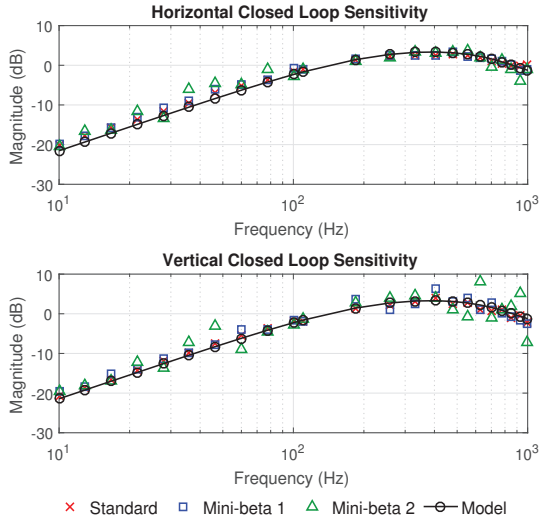

Figure 4: Measured sensitivity in horizontal and vertical planes for a standard corrector (red '×') and mini-beta correctors (blue '□' and green '△') compared to the theoretical response (black '○').

The derived models are also included in Fig. 2a and Fig. 2b. The model captures the dynamic behaviour of the system up to the bandwidth and fits the phase roll-off well. The model with the structure given in (9) using the bandwidth of the standard corrector magnet for each plane was discretized [3] and used for the FOFB design. Therefore it is important to assess the impact of the dynamic differences between the magnets on the performance of the FOFB controller.

The sensitivity function given in (5) is used to determine how well the corrector performs in terms of disturbance rejection and is shown in Fig. 4 for each corrector magnet in the horizontal and vertical planes. Also included in Fig. 4 is the theoretical sensitivity for the standard corrector which predicts that at 10 Hz, the closed loop provides around 20 dB attenuation of disturbances but at the cost of amplifying disturbances above 150 Hz by a maximum of 3 dB at 400 Hz. The sensitivity of the standard and mini-beta correctors provide similar levels of attenuation at most frequencies. The data shows that there is no significant difference in sensitivity measurements at low frequencies, which is expected because the frequency response of the corrector magnets do not differ below 500 Hz in each plane.

CONCLUSIONS

The advantage of the frequency response approach to modelling the open loop response is that it can be measured directly and gives the frequency response immediately. Furthermore, the user experiment parameters such as the relevant dynamic frequencies, the duration of each excitation, the sample frequency and the type of input signal can be easily modified by the user. Also, as the input and output signals are only analysed at specific frequencies, the amount of data is reduced significantly from the number of time domain samples to the number of considered frequencies. Finally, frequency domain identification can deal equivalently with time continuous models as with time discrete models, which are useful for the design of the FOFB controller. The main advantage of the procedure outlined in this paper is the ease with which the experimental data can be used for design purposes. No significant processing is required to obtain a Bode plot which can then be used to derive a simple model of the open loop to inform the design of an appropriate compensator.

REFERENCES

[1] B. Singh, R. Fielder, I.P.S Martin, G. Rehm and R. Bartolini,"Implementation of Double Mini-Beta Optics at the Diamond Light Source," IPAC'11, San Sebastián, July 2011, p. 2103.

[2] G.F. Franklin, D.J. Powell and A. Emami-Naeini, *Feedback Control of Dynamic Systems*. Upper Saddle River, NJ, USA: Prentice Hall PTR, 2001.

[3] M.G. Abbott, G. Rehm and I.S. Uzun, "A New Fast Data Logger and Viewer at Diamond: The FA Archiver," ICALEPCS'11, Grenoble, October 2011, p. 1247.

[4] S. Gayadeen, S.R. Duncan and M.T. Heron, "Fast Orbit Feedback Control in Mode Space," ICALEPCS'13, San Francisco, October 2013, p. 1082.

ISBN 978-3-95450-177-9

LONGITUDINAL PHASE SPACE MEASUREMENT AT THE ELI-NP COMPTON GAMMA SOURCE

L. Sabato[1*], University of Sannio, Dept. of Engineering, Corso G. Garibaldi, 107, Benevento, Italy
P. Arpaia, A. Liccardo, Federico II University of Naples,
Dept. of Electrical Engineering and Information Technology, Via Claudio 21, Naples, Italy
D. Alesini, G. Franzini, C. Vaccarezza, A. Variola, Istituto Nazionale di Fisica Nucleare - Laboratori Nazionali di Frascati (INFN-LNF), via Enrico Fermi, 40, Frascati, Italy
A. Giribono, A. Mostacci, L. Palumbo, Sapienza University of Rome,
Dept. Scienze di Base e Applicate per l'Ingegneria (SBAI), Via Antonio Scarpa, 14, Rome, Italy
[1]also at Istituto Nazionale di Fisica Nucleare (INFN) Naples, via Cintia, Naples, Italy

Abstract

Virtual bunch length measurement can be carried out by means of ELEGANT code for tracking the bunch particles from RF deflector to the screen. The technique relies on the correlation between the bunch longitudinal coordinate and transverse coordinates induced through a RF deflector. Therefore, the bunch length measurement can be carried out measuring the vertical spot size at the screen, placed after the RF deflector. The deflecting voltage amplitude affects the resolution. Adding a dispersive element, e.g. a magnetic dipole between RF deflector and the screen, the full longitudinal phase space can be measured. In this paper, we discuss some issues relevant for the electron linac of the Compton source at the Extreme Light Infrastructure - Nuclear Physics (ELI-NP).

INTRODUCTION

The Gamma Beam Source (GBS) at ELI-NP is going to be an advanced Source of up to 20 MeV Gamma Rays based on Compton back-scattering, i.e. collision of an intense high power laser beam and a high brightness electron beam with maximum kinetic energy of about 720 MeV. This infrastructure is going to be built in Magurele, near Bucharest (Romania) [1, 2]. The GBS electron linac can run at maximum repetition rate of 100 Hz. Therefore, at room temperature the specifications on the requested spectral density can be reached only by multiple bunch collisions. The final optimization foresees trains of 32 electron bunches separated by 16 ns, time needed to recirculate the laser pulse in order to allow the same laser pulse to collide with all the electron bunches in the RF pulse, distributed along a 0.5 μs RF pulse [1].

The properties of the single bunch and the whole train of bunches have to be measured in order to achieve high brightness in high repetition rate machine [3, 4]. In particular, bunch length measurement can be done using a Radio Frequency Deflector (RFD) and a screen in an electron linac. This disruptive measurement technique is well-known and widespread used in high brightness Linacs around the world, e.g. at the SLAC free electron laser [5, 6] or at SPARC-LAB linac [7].

In this paper, the effect of a non-negligible energy chirp on bunch length virtual measurements is treated. Moreover, the energy chirp affects energy spread measurements. The simulations are carried by means of ELEctron Generation ANd Tracking (ELEGANT) code [8]. In section **MEASUREMENT TECHNIQUE**, the basic idea, the working principle and the procedure of the bunch length measurement technique using a RFD are explained. In section **SIMULATION RESULTS**, the RFD and bunch parameters of GBS linac case are reported and the bunch length virtual measurements are discussed.

MEASUREMENT TECHNIQUE

Basic Idea

Different types of measurements can be done with a RFD. Bunch length measurements can be done using only a RFD and a screen. Adding a dispersive element, e.g. a magnetic dipole between RF deflector and the screen, the full longitudinal phase space can be measured. The basic idea of these measurements is based on the property of the RFD transverse voltage to introduce a correlation between the longitudinal and vertical coordinates of the bunch at the screen position. Therefore, the bunch length measurement can be carried out measuring the vertical spot size at the screen, placed after the RF deflector [7, 9].

Working Principle

When the particles pass through the RFD, they feel a deflecting voltage when they pass through the RFD. The effect on every particle is a change in vertical divergence [10]. Considering the bunch length much smaller than RF wavelength (i.e. $kz_0 \ll 1$), we can assume the RFD voltage is [6, 11]:

$$V(z_0) \approx V_t \left[kz_0 cos(\varphi) + sin(\varphi) \right]. \quad (1)$$

where z_0 is the position of the particles along the beam axis with the origin in the RFD, $k = 2\pi/\lambda_{RF}$, λ_{RF}, V_t, and φ are the deflecting voltage wavelength, amplitude, and phase, respectively.

Therefore, RFD gives a vertical divergence change [6]:

$$\Delta y_0'(z_0) = C_{rfd} \left[kz_0 cos(\varphi) + sin(\varphi) \right], \quad (2)$$

* luca.sabato@unisannio.it

ISBN 978-3-95450-177-9

where $C_{rfd} = qV_t/(pc)$, q is the electron charge, p is the particle momentum, and c is the speed of light. Assuming $\langle z_0 \rangle = \langle y_0 \rangle = 0$ m and $\langle y_0' \rangle = 0$ rad, the vertical bunch centroid at screen is [6]:

$$C_{y_s} = LC_{rfd} sin(\varphi). \quad (3)$$

Assuming also $\langle y_0' z_0 \rangle = 0$ m, $\langle y_0 z_0 \rangle = 0$ m^2, and a negligible energy chirp, the rms vertical spot size at screen is [6]:

$$\sigma_{y_s}^2 = \sigma_{y_s,off}^2 + K_{cal}^2 \sigma_{t_0}^2, \quad (4)$$

where $\sigma_{y_s,off}$ is the rms vertical spot size at the screen with RFD off [12], σ_{t_0} is the rms bunch length (in seconds), and K_{cal} is a calibration factor:

$$K_{cal} = \omega_{RF} LC_{rfd} cos(\varphi), \quad (5)$$

where ω_{RF} is the deflecting voltage angular frequency. The calibration factor is a coefficient that relates the vertical coordinate at the screen with the bunch longitudinal time coordinate. Comparing (3) and (5), an important relation can be noticed:

$$K_{cal} = \omega_{RF} p, \quad (6)$$

where p is the slope of the plot vertical bunch centroid versus RFD phase. Equation (6) means that the coefficient K_{cal} can be directly calculated measuring the bunch centroid position at screen for different values of the RFD phase, i.e. it is possible to self-calibrate the measurements [13].

Measurement Procedure

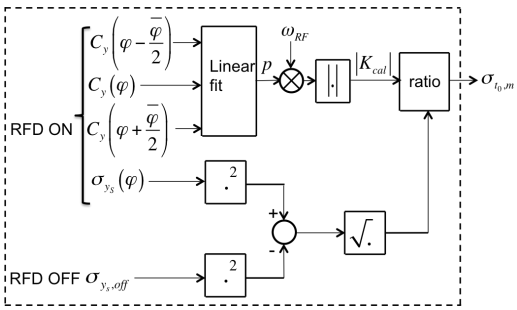

Figure 1: Bunch length measurement procedure.

The bunch length measurement procedure is divided in four steps (Fig. 1) [12, 14]:

- first step: carry out the measurement of the rms vertical spot size at the screen with RFD off;
- second step: make measurements of vertical bunch centroid for different values of RFD phase with RFD on and then calculate the calibration factor by means of a linear fit (6);
- third step: make the measurement of the rms vertical spot size at the screen with RFD on;
- fourth step: carry out the bunch length measurement from (4):

$$\sigma_{t_0,m} = \frac{\sqrt{\sigma_{y_s}^2 - \sigma_{y_s,off}^2}}{|K_{cal}|}. \quad (7)$$

SIMULATION RESULTS

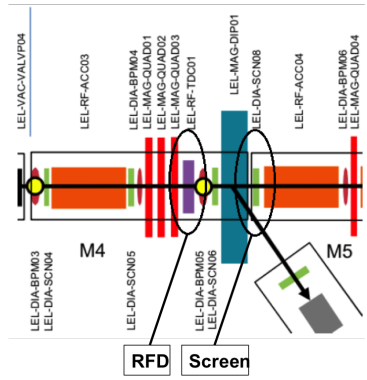

Figure 2: Zoom of GBS linac layout between the first and the second C-band accelerating section [1].

A nominal beam represented by 50000 particles has been tracked by means of ELEGANT code from LEL-RF-TDC01 RFD to LEL-DIA-SCN08 screen (Fig. 2), placed between the first and second C-band accelerating section of GBS electron linac [1]. The GBS electron linac bunch at RFD and RFD parameters are reported in Tables 1 and 2, respectively. The correlations between particle longitudinal position and vertical position $\langle y_0 z_0 \rangle$ and divergence $\langle y_0' z_0 \rangle$ at LEL-RF-TDC01 RFD are negligible, on the contrary the energy chirp is non-negligible (see Fig. 3).

Table 1: GBS Electron Linac Bunch Parameters (E Is the Bunch Energy)

σ_{y_0} [mm]	$\sigma_{y_0'}$ [μrad]	$\langle y_0 y_0' \rangle$ [m·rad]	σ_{t_0} [ps]	E [MeV]
0.3464	57.57	$-1.986 \cdot 10^{-8}$	0.9117	118

Table 2: GBS Electron Linac Bunch Parameters at Screen

V_t [MV]	f_{RF} [GHz]	L [m]
1	2.856	1.1380

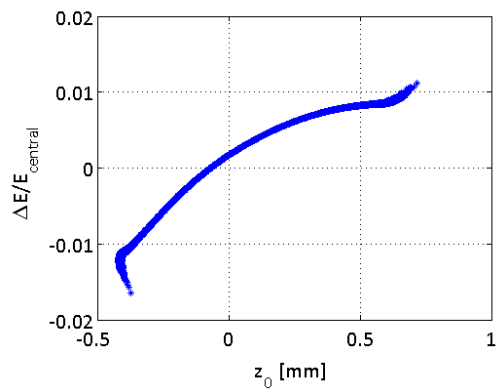

Figure 3: Longitudinal trace space of the Bunch before RFD.

ISBN 978-3-95450-177-9

In Fig. 3, the longitudinal trace space of the bunch before RFD is reported and a correlation between the particle energy expressed in terms of $\Delta E/E_{central}$ and the particle longitudinal coordinate z_0 can be noticed. The energy chirp doesn't affect the vertical bunch centroid at screen after the RFD, and so the calibration factor (see Figs. 4 and 5). On the contrary, the energy chirp affects the vertical spot size at screen (see Fig. 6) and so the bunch length virtual measurement (see Fig. 7).

Vertical Bunch Centroid at Screen and Calibration Factor

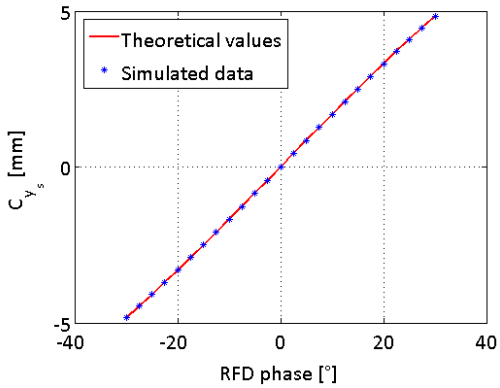

Figure 4: Theoretical predictions eq. (3) (in red line) and simulated data (in blue stars) of the vertical bunch centroid at screen versus RFD phase.

Figure 4 shows a good agreement between theoretical predictions eq. (3) and simulated data of the vertical bunch centroid at screen versus RFD phase. For every RFD phase, the calibration factor can be calculated by means of a linear fit of five different vertical bunch centroid measurements varying the RFD phase in a range of 3° eq. (6). Figure 5 shows a good agreement between theoretical eq. (5) and calculated from vertical centroid calibration factor eq. (6) versus RFD phase.

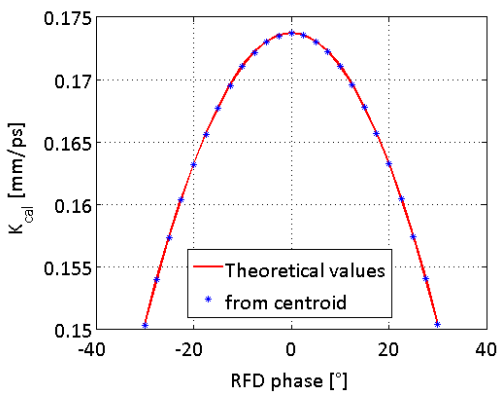

Figure 5: Theoretical eq. (5), in red line, and calculated from vertical centroid eq. (6) calibration factor versus RFD phase.

Vertical Spot Size at Screen

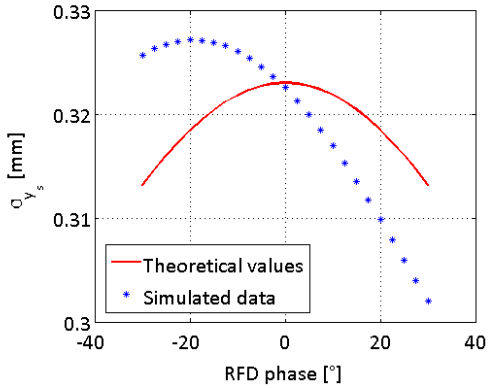

Figure 6: Theoretical predictions eq. (6) (in red line) and simulated data (in blue stars) of the vertical spot size at screen versus RFD phase.

Figure 6 shows a discrepancy between theoretical predictions eq. (6) and simulated data of the vertical spot size at screen versus RFD phase. This discrepancy is due to the energy chirp of the bunch at the entrance of RFD (see Fig. 3). For RFD phase offset of some degrees, corresponding to a vertical centroid offset of about 1 mm (see Fig. 4), the vertical spot size at screen relative error due to energy chirp can be of the order of 1% and this affects the bunch length virtual measurements.

Effects of Energy Chirp on Bunch Length Virtual Measurements at GBS Electron Linac

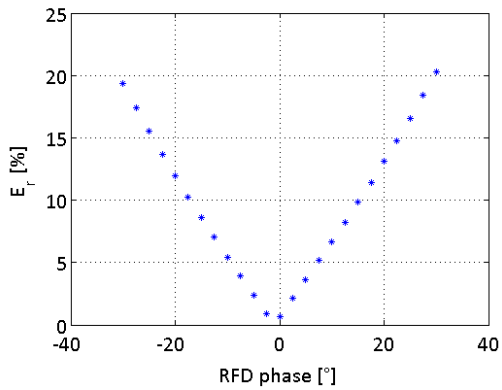

Figure 7: Bunch length virtual measurement relative error versus RFD phase.

The bunch length virtual measurement relative error can be defined:

$$E_r = \frac{|\sigma_{t_0} - \sigma_{t_0,m}|}{\sigma_{t_0}}, \tag{8}$$

where σ_{t_0} is the rms bunch length at RFD (see Table 1) and σ_{t_0} is the rms bunch length virtual measurement given by eq. (7). In Fig. 7, the bunch length virtual measurement relative error versus RFD phase is plotted. In the case of

ISBN 978-3-95450-177-9

GBS electron linac, for RFD phase offset of some degrees, the bunch length virtual measurement relative error due to energy chirp can be of the order of 5%. It can be noticed that the bunch length relative error is minimum when the RFD phase offset is null.

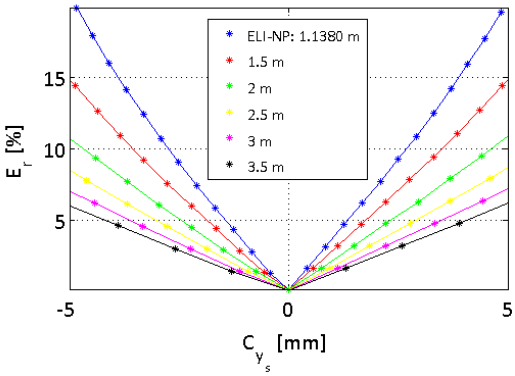

Figure 8: Bunch length virtual measurement relative error versus RFD phase varying the distance between RFD and screen (blue: ELI-NP case 1.1380 m, red: 1.5 m, green: 2.0 m, yellow: 2.5 m, magenta: 3.0 m, black: 3.5 m).

The bunch length virtual measurement relative error versus RFD phase varies with the distance between RFD and screen (see Fig. 8). In Fig. 8, L varies between almost 1.14 m (GBS linac case) and 3.5 m (SPARC-LAB linac case). For a fixed vertical centroid offset, the bunch length virtual measurement relative error due to energy chirp is greater when the distance between RFD and screen is smaller. For a vertical centroid offset of about 1 mm and L=3.5 m, the bunch length virtual measurement relative decreases to about 1%.

CONCLUSIONS

In this paper, the importance of the energy chirp for bunch length measurament is treated. The contribution of the energy chirp in bunch length measurement increases when the RFD offset increases. Therefore, in the case of a bunch with a non-negligible energy chirp, the vertical centroid offset plays a fundamental role in the bunch length measurement relative error. In particular, the bunch length virtual measurement relative errors varying RFD phase in the case of GBS electron linac are presented in this paper. The relative errors are due to the non-negligible energy chirp of the bunch at RFD. In particular, the energy chirp doesn't affect the vertical bunch centroid at screen after the RFD, and so the calibration factor. On the contrary, the energy chirp affects the vertical spot size at the screen and so the virtual bunch length measurement. When the RFD phase offset is null, the bunch length relative error is minimum.

In the case of GBS electron linac, for RFD phase offset of some degrees, the bunch length virtual measurement relative error due to energy chirp can be of the order of 5%. For a fixed vertical centroid offset, the bunch length virtual measurement relative error due to energy chirp is greater when the distance between RFD and screen is smaller. For a vertical centroid offset of about 1 mm and L=3.5 m (SPARC-LAB linac case), the bunch length virtual measurement relative decreases to about 1%.

ACKNOWLEDGEMENT

The authors would like to thank M. Borland for useful suggestions and discussion.

REFERENCES

[1] L. Serafini, et al., "Technical design report eurogammas proposal for the eli-np gamma beam system," *arXiv preprint arXiv:1407.3669*, 2014.

[2] "The white book of eli nuclear physics bucharest-magurele, romania," *avaible on-line at http://www.eli-np.ro/documents/ELI-NP-WhiteBook.pdf*.

[3] A. Mostacci, et al., "Chromatic effects in quadrupole scan emittance measurements," *Physical Review Special Topics - Accelerators and Beams*, vol. 15, no. 8, 2012.

[4] A. Cianchi, et al., "Six-dimensional measurements of trains of high brightness electron bunches," *Physical Review Special Topics - Accelerators and Beams*, vol. 18, no. 8, 2015.

[5] G. Loew and O. H. Altenmueller, "Design and applications of rf separator structures at slac," in *5th Int. Conf. on High-Energy Accelerators, Frascati*, 1965, pp. 438–442.

[6] P. Emma, J. Frisch, and P. Krejcik, "A transverse rf deflecting structure for bunch length and phase space diagnostics," *LCLS Technical Note*, vol. 12, 2000.

[7] D. Alesini, et al., "Rf deflector design and measurements for the longitudinal and transverse phase space characterization at sparc," *Nuclear Instruments and Methods in Physics Research Section A: Accelerators, Spectrometers, Detectors and Associated Equipment*, vol. 568, no. 2, pp. 488–502, 2006.

[8] M. Borland, "Elegant: A flexible sdds-compliant code for accelerator simulation," Argonne National Lab., IL (US), Tech. Rep., 2000.

[9] D. Alesini and C. Vaccarezza, "Longitudinal and transverse phase space characterization," SPARCRF-03/003, INFN/LNF, Frascati, Tech. Rep., 2003.

[10] H. Wiedemann *et al.*, *Particle accelerator physics*. Springer, 2007, vol. 314.

[11] R. Akre, L. Bentson, P. Emma, and P. Krejcik, "Bunch length measurements using a transverse rf deflecting structure in the slac linac," in *Proc. EPAC'02, Paris, France, June*, 2002.

[12] L. Sabato, et al., "Metrological characterization of the bunch length system measurement of the eli - np electron linac," in *Proc. 14th IMEKO TC10, Milan, Italy, June 2016*, pp. 203–208.

[13] D. Alesini, et al., "Sliced beam parameter measurements," in *Proc. DIPAC09, Basel, Switzerland, May 2009, paper TUOA01*, pp. 146–150.

[14] L. Sabato, et al., "Metrological characterization of the bunch length measurement by means of a rf deflector at the eli-np compton gamma source," in *Proc. IPAC'16, Busan, Korea, May 2016, paper MOPMB018*, pp. 122–125.

ISBN 978-3-95450-177-9

PRESENT STATUS OF THE LASER CHARGE EXCHANGE TEST USING THE 3-MeV LINAC IN J-PARC

H. Takei†, E. Chishiro, K. Hirano, Y. Kondo, S.I. Meigo, A. Miura, T. Morishita, H. Oguri, K. Tsutsumi, J-PARC Center, Japan Atomic Energy Agency, Tokai, Ibaraki, JAPAN

Abstract

The Accelerator-driven System (ADS) is one of the candidates for transmuting long-lived nuclides, such as minor actinide (MA), produced by nuclear reactors. For efficient transmutation of the MA, a precise prediction of neutronics of ADS is required. In order to obtain the neutronics data for the ADS, the Japan Proton Accelerator Research Complex (J-PARC) has a plan to build the Transmutation Physics Experimental Facility (TEF-P), in which a 400-MeV negative proton (H^-) beam will be delivered from the J-PARC linac. Since the TEF-P requires a stable proton beam with a power of less than 10 W, a stable and meticulous beam extraction method is required to extract a small amount of the proton beam from the high power beam using 250 kW. To fulfil this requirement, the Laser Charge Exchange (LCE) method has been developed. The LCE strips the electron of the H^- beam and neutral protons will separate at the bending magnet in the proton beam transport. To demonstrate the charge exchange of the H^-, a preliminary LCE experiment was conducted using a linac with energy of 3 MeV in J-PARC. As a result of the experiment, a charge-exchanged H^+ beam with a power of about 5 W equivalent was obtained under the J-PARC linac beam condition, and this value almost satisfied the power requirement of the proton beam for the TEF-P.

INTRODUCTION

The Accelerator-driven System (ADS) is one of candidates for transmuting long-lived nuclides such as minor actinide (MA) produced by nuclear reactors [1]. For the efficient transmutation of MA, precise prediction of the neutronic performance of ADS is required. In order to obtain the neutronics data for the ADS, the Japan Proton Accelerator Research Complex (J-PARC) has a plan to build the Transmutation Physics Experimental Facility (TEF-P) [2]. The critical assembly installed in the TEF-P, which is a small and low power reactor, operates below 500 W to prevent excessive radio-activation. To perform the experiments at the TEF-P with such reactor power, with an effective neutron multiplication factor (k_{eff}) of around 0.97, the incident proton beam power must be less than 10 W. Because the J-PARC accelerators focus on much higher beam power, a low power proton beam extraction device of high reliability is indispensable.

The development of a laser charge exchange (LCE) technique for extraction of the low power proton beam from the high power proton beam is now underway. The LCE technique was originally developed to measure the proton beam profile [3]. To apply the LCE technique to the beam separation device for the TEF-P, it is important to evaluate the efficiency of conversion to the low power proton beam and the long-term power stability of the low power proton beam in order to keep the thermal power of the assembly constant. Thus, a preliminary LCE experiment to measure the power of the low power proton beam was conducted using a linac with energy of 3 MeV in J-PARC. In this paper, the preliminary results of the LCE experiment are presented.

LASER CHARGE EXCHANGE

Figure 1 illustrates the concept of the LCE device for the TEF-P [4]. When a laser beam is injected into a negative proton (H^-) beam with energy of 400 MeV from the J-PARC linac, the charge of the H^- beam crossed with the laser beam becomes neutral (H^0). Since the outer electron of the H^- is very weakly bound to the atom, it can easily be stripped by a laser light in the wavelength range of 800~1100 nm as shown in Fig.2 [5]. These H^0 protons do not sense the magnetic field of a bending magnet, and are completely separated from the remaining H^- beam at the exit of the bending magnet. However, it is well-known that pre-neutralized H^0 particles are produced by collision with the remaining gas in accelerator tubes and are transported with the main proton beam. When we apply the LCE technique to the H^- beam with the pre-neutralized protons, it becomes impossible to predict the total power of the extracted beam.

To eliminate the pre-neutralized protons, we were trying to perform laser injection and beam bending simultaneously in one magnet. When the laser is injected in the magnetic field of the bending magnet, the pre-neutralized proton goes straight along the beam inlet direction and can be separated from the clean low power proton beam at the exit of the bending magnet. The charge-exchanged H^0 beam reaches the stripping foil. After passing the stripping foil, the H^0 beam is converted to a positive proton (H^+) beam and then delivered to the TEF-P target. A material with a low melting temperature will be used as the stripping foil to avoid high power beam injection to the TEF-P target. Hereafter, the low power H^+ beam extracted from the high power H^- beam by using this LCE strategy is referred to as "the stripped H^+ beam."

Figure 2 shows the photoneutralization cross-section of H^- ions as a function of photon wavelength in the centre-of-mass frame. We chose a fundamental wavelength of 1064 nm from the commercial Nd:YAG laser because this wavelength is near the peak of the photoneutralization cross-section of H^- ions. Even taking the Lorentz contraction effect into consideration, the photoneutralization cross-section for the H^- beam with energy of 400 MeV using the fundamental wavelength of Nd:YAG laser is

† takei.hayanori@jaea.go.jp

ISBN 978-3-95450-177-9

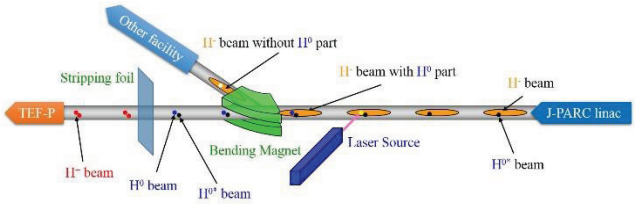

Figure 1: Conceptual diagram of the LCE device for TEF-P. The neutralized proton due to interaction by the laser light is written as "H^{0}", and the pre-neutralized proton due to interaction by the remaining gas in accelerator tubes is written as "H^{0*}".

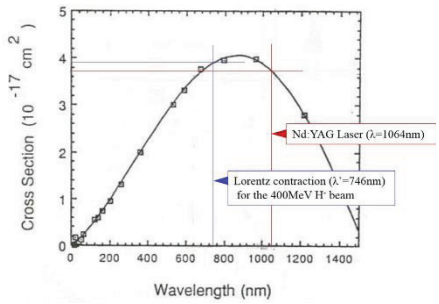

Figure 2: Cross section for H^- photoneutralization as a function of photon wavelength in the centre-of-mass frame. The blue line shows the Lorentz contraction for the H^- beam with 400 MeV.

Table 1: Specifications of the H^- beam for the J-PARC linac and the 3-MeV linac

	J-PARC linac	3-MeV linac
Energy (MeV)	400	3
Maximum beam current (A)	5.0×10^{-2}	3.0×10^{-2}
Macropulse length (s)	5.0×10^{-4}	2.0×10^{-4}
Repetition rate (Hz)	25	25
Maximum beam power (W)	2.5×10^{5}	4.5×10^{2}
RF Frequency (MHz)	324	324
Beam power for a micro-bunch (W)	1.57	6.95×10^{-3}

almost the same as that for the stationary H^- ions using 1064 nm laser light. On the other hand, the Lorentz contraction effect of the collision with the 3-MeV H^- beam and the 1064 nm laser light is insignificant. It is possible to experimentally estimate the conversion efficiency of the LCE for the TEF-P from the results of the LCE experiment with the 3-MeV linac.

Table 1 describes the specifications of the H^- beam for the J-PARC linac and the 3-MeV linac. Here, the 3-MeV linac has two operational modes. Specifications for one of these two modes, *i.e.* the LCE experiment mode, are represented in this table. Based on theoretical considerations [4], the outer electrons of the H^- ions can be stripped with an efficiency of almost 100% by using a commercial Nd:YAG laser having a pulse power of a few joules. Therefore, it is expected that a stripped H^+ beam with a power of 1.57 W can be obtained from a microbunch of the H^- beam delivered from the J-PARC linac.

LCE EXPERIMENT

Experimental Devices

At J-PARC, a linac with energy of 3 MeV has been constructed for the development of accelerator components such as beam scrapers, bunch shape monitors, laser profile monitors, and so on. This linac consists of an H^- ion source, a low energy beam transport, a radio frequency quadrupole (RFQ) linac, a medium energy beam transport, and beam dumps. For further details about these devices, see ref. [6]. Hereafter, the linac with energy of 3 MeV is referred to as "the RFQ linac."

As shown in Figs. 3 and 4, the proton beam line consists of three quadrupole magnets which have a steering

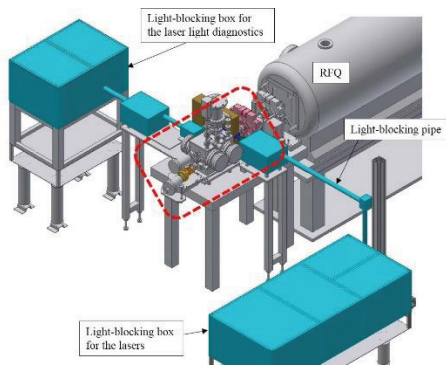

Figure 3: Layout of the RFQ linac with the laser system. The laser system are painted with light blue. Enlargement portion surrounded by the red dotted rectangle is shown in Fig.4.

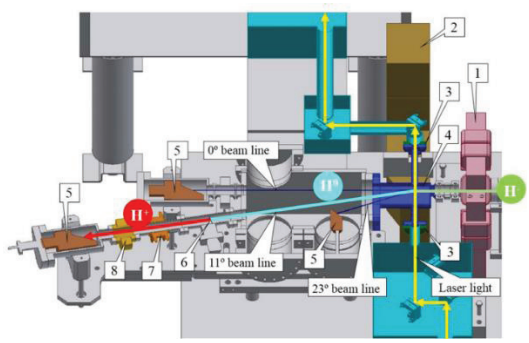

Figure 4:Schematic View of the LCE devices (1- quadrupole magnet, 2- bending magnet, 3- quartz viewing port, 4- vacuum chamber, 5- beam dump, 6- stripping foil, 7- BPM, 8- SCT).

Table 2: Specifications of the Nd:YAG laser and the He-Ne laser

	Nd:YAG laser	He-Ne laser
Operation mode	Pulsed	Continuous Wave
Wavelength (m)	1.064×10^{-6}	6.328×10^{-7}
Pulse width (s)	$(5\sim9)\times10^{-9}$	——
Pulse energy (J)	1.6	——
Pulse repetition rate (Hz)	25	——
Power (W)	40	2.0×10^{-2}

ISBN 978-3-95450-177-9

function, a bending magnet, a beam position monitor (BPM), beam current monitors, and beam dumps. The LCE devices were installed at the end of the proton beam line. That is, the titanium vacuum chamber was located between two magnetic poles of the bending magnet, in which the H^- beam collided with the Nd:YAG laser light at a near right angle. Two quartz viewing ports were fitted to the vacuum chamber. The commercial high power Q-switched Nd:YAG laser was located on an anti-vibration table. Table 2 describes the specifications of the Nd:YAG laser. The laser light was reflected by ten plane mirrors and transmitted through one quartz viewing port from the laser main body to the collision point. This optical path length was 4.25 m. After the collision with the H^- beam, the laser light was propagated to the termination point in the light-blocking box used for the laser light diagnostics. During the propagation, which was 3.16 m in length, there were five reflections by the plane mirror and one transmission through the quartz viewing port.

In this light-blocking box, three types of diagnostics for the Nd:YAG laser light were located. The first was a laser power meter (Gentec-EO, UP55N-50S-VR) to measure and absorb the laser light, the second was a photon beam profiler (Gentec, Beamage 4M) to measure the profile and the position of the laser light, and the third was a biplanar phototube (Hamamatsu Photonics K.K., R12290U-51) to measure the time structure of the laser light.

To keep the H^+ beam power constant over longer periods, it was important to keep the position of the Nd:YAG laser light at the collision point constant. However, it was difficult to adjust the position of the invisible laser pulse of the Nd:YAG laser. Therefore, the visible laser light from the commercial He-Ne laser was used as a guide beam. The specifications of the He-Ne laser are also described in Table 2.

The trajectory of the H^- beam from the RFQ was bent by the bending magnet with a deflection angle of 23º, and transported to the beam dump provided in the most downstream part of the 23º beam line. As the Nd:YAG laser light was injected in the centre of the magnetic pole of the bending magnet, the H^0 beam was transported to the beam line with the deflection angle of 11.5º and introduced to the stripping foil. Hereafter, this beam line is referred to as "the 11º beam line." The H^0 beam was converted to the H^+ beam by passing the stripping foil (cobalt-base alloy foil, Haver). From the upstream to the downstream of the 11º beam line, a BPM, a slow current transformer (SCT), and a Faraday cup (FC) serving as a beam dump were positioned.

Experimental Method

At the end of June 2016, a preliminary LCE experiment to measure the power of the stripped H^+ beam was conducted using the H^- beam derived from the RFQ linac.

First, the position of the H^- beam was measured by the BPM without exciting the bending magnet, and the trajectory of the H^- beam was adjusted by using steering magnets so that the H^- beam was passed through the centre position of the BPM. Beam width and emittance of the H^- beam were obtained with the beam emittance monitor placed 0.3 m downstream of the quadrupole magnet by using Q scan technique. As a result of the measurement, the root-mean-square (RMS) width in the vertical direction (σ_v) at the collision point was estimated as about 2.8 mm.

After exciting the bending magnet, the H^- beam was transported to the 23º beam dump and collided with the Nd:YAG laser light. Then, the deflection angle of the H^- beam was decided by fine-tuning the magnetic field strength of the bending magnet so that the stripped H^+ beam was passed through the centre position of the BPM located in the 11º beam line. By using beam current monitors such as SCT and FC, the current amount of the stripped H^+ beam was measured.

Figure 5 shows the photon profile for the Nd:YAG laser observed by the photon beam profilers. From this figure, it can be seen that the RMS-radius of the Nd:YAG laser light was 3 mm at the exit of the laser main body and 4.7 mm at the termination point. The RMS-radius of the Nd:YAG laser light could be estimated as 3.9 mm at the collision point with the H^- beam if the spread of the Nd:YAG laser light was assumed to be increased in proportion to the optical path length. Therefore, from the viewpoint of the vertical direction for the H^- beam, the narrow H^- beam collided with the wide Nd:YAG laser light.

In addition, the Nd:YAG laser power was set to half of the rated output power (20 W, 0.8 J/pulse) to protect the quartz viewing port. The power of the Nd:YAG laser light gradually decreased until it reached the termination point due to the reflection by 15 plane mirrors and the transmission through two quartz viewing ports, and the laser power at the termination point was 14.7 W. Consequently, the total transmittance was estimated as 74%.

Figure 6 shows the time structure of the Nd:YAG laser light as a function of the laser power. Here, the values shown in the upper right corner of this figure are the laser powers at the termination point. The time profile of the

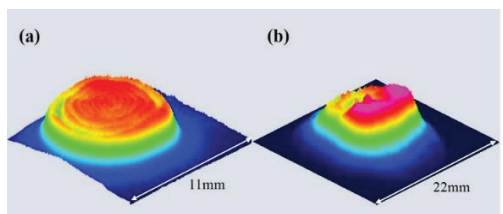

Figure 5: Three-dimensional photon profile for the Nd:YAG laser at (a) the exit of the laser main body and (b) the termination point.

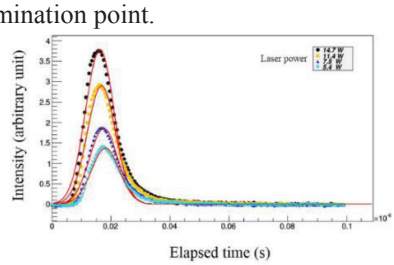

Figure 6: Time structure of the Nd:YAG laser light as a function of the laser power at the termination point.

ISBN 978-3-95450-177-9

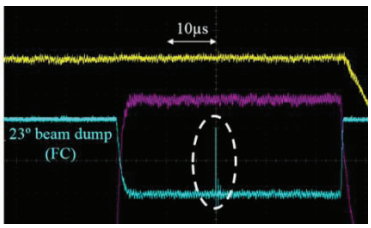

Figure 7: Current waveform of the H^- beam observed at the 23° beam dump.

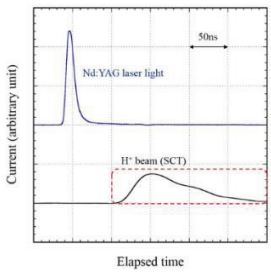

Figure 8: Waveform of the Nd:YAG laser pulse and the H^+ beam observed at the SCT of the 11° beam line.

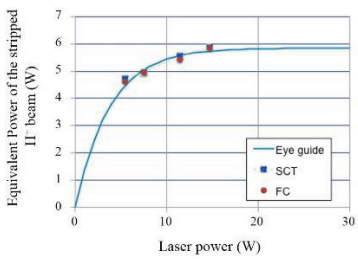

Figure 9: H^+ beam power as a function of the Nd:YAG laser power at the termination point.

Nd:YAG laser light with a power of 14.7 W had the pulse width of 4.8 ns (1σ), and the time profile was independent of the laser power. From the time profile of the laser, it was obvious that a pulse of the Nd:YAG laser light collided with the 4.98 microbunches of the H^- beam. Therefore, a stripped H^+ beam with a power of 7.5 W equivalent could be obtained under the assumption that the conversion efficiency for the horizontal direction of the H^- beam was 100%.

Preliminary Results

The light-blue broken line in Fig. 7 represents the current waveform of the H^- beam observed at the 23° beam dump. This light-blue current waveform represents a single macropulse, and the rapid rise and fall part surrounded by the white dotted circle is due to the lack of the H^- beam caused by the LCE. This lack was observed from the first shot of the Nd:YAG laser light after beginning the LCE experiment, and then we confirmed the collision between the H^- beam and the Nd:YAG laser light. Figure 8 shows the pulse waveform of the Nd:YAG laser light observed at the biplanar phototube and the H^+ beam observed at the SCT of the 11° beam line. From the figure, it can be seen that the pulse waveform of the H^+ beam was obtained after the laser light, and the power of the H^+ beam was 0.026 W from the time integral of the H^+ beam current inside the dotted-red rectangle. If the laser light from this Nd:YAG laser system collided with the H^- beam delivered from the J-PARC linac, a stripped H^+ beam with a power of about 5 W would be obtained from the following equation.

$$0.026(\mathrm{W}) \times \frac{400\ (\mathrm{MeV})}{3\ (\mathrm{MeV})} \times \frac{50(\mathrm{mA})}{30(\mathrm{mA})} = 5.7(\mathrm{W}) \qquad (1)$$

This value almost satisfied the power requirement (less than 10 W) of the proton beam for the TEF-P.

Figure 9 shows the equivalent power of the stripped H^+ beam under the J-PARC linac beam condition as a function of the Nd:YAG laser power. Here, the powers of the stripped H^+ beam were obtained using the SCT and FC. We confirmed that the equivalent powers of the stripped H^+ beam measured by using the SCT and FC were in good agreement, and the stripped H^+ beam with a power of about 5W equivalent was expected even if the laser power of the present Nd:YAG laser system was set to the lower value of 5W.

CONCLUSION

For the extraction of the low power H^+ beam (less than 10 W) from the high power H^- beam (400 MeV, 250 kW) by the LCE technique, a preliminary LCE experiment to measure the power of the stripped H^+ beam was conducted using the H^- beam with energy of 3 MeV from the RFQ linac in J-PARC. As a result of this experiment, the stripped H^+ beam with a power of about 5 W equivalent was obtained under the J-PARC linac beam condition, and this value almost satisfied the power requirement (less than 10 W) of the proton beam for the TEF-P.

In this experiment, we focused on the power of the stripped H^+ beam. We will conduct a further experiment to confirm the beam quality of the laser and the H^-, as well as the long-term power stability of the stripped H^+ beam.

REFERENCES

[1] K. Tsujimoto *et al.*, "Feasibility of Lead-Bismuth-Cooled Accelerator-Driven System for Minor-Actinide Transmutation", *Nucl. Tech.*, vol. 161, pp. 315-328, 2008.

[2] H. Oigawa *et al.*, "Conceptual Design of Transmutation Experimental Facility", in *Proc. Global2001*, Paris, France (CD-ROM, 2001).

[3] Y. Liu et al., "Laser wire beam profile monitor in the spallation neutron source (SNS) superconducting linac", *Nucl. Instr. Meth.*, vol. A612, pp. 241-253, 2010.

[4] S. Meigo *et al.*, "A Feasibility Study of H^- Beam Extraction Technique Using YAG Laser", JAERI, Tokai, Ibaraki, JAPAN, Rep. JAERI-Tech 2002-095, Dec. 2002, (in Japanese).

[5] John T. Broad and William P. Reinhardt, "One- and two-electron photoejection from H^- : A multichannel J-matrix calculation", *Phys. Rev.*, vol. A14, pp. 2159-2173, 1976.

[6] K. Hirano *et al.*, "Development of beam scrapers using a 3-MeV linac at J-PARC", in *Proc. 13th Annual Meeting of Particle Accelerator Society of Japan*, Chiba, Aug. 2016, paper MOP005, (in Japanese).

ISBN 978-3-95450-177-9

KALYPSO: A Mfps LINEAR ARRAY DETECTOR FOR VISIBLE TO NIR RADIATION

L. Rota*, M. Balzer, M. Caselle, M. Weber, IPE-KIT, Karlsruhe, Germany
G. Niehues, P. Schönfeldt, M. J. Nasse, A.S. Mueller, LAS-KIT, Karlsruhe, Germany
N. Hiller, A. Mozzanica, PSI, Villigen, Switzerland
C. Gerth, B. Steffen, DESY, Hamburg, Germany
D. R. Makowski, A. Mielczarek, TUL-DMCS, Lodz, Poland

Abstract

The acquisition rate of commercially available line array detectors is a bottleneck for beam diagnostics at high-repetition rate machines like synchrotron lightsources or FELs with a quasi-continuous or macro-pulse operation. In order to remove this bottleneck we have developed KALYPSO, an ultra-fast linear array detector operating at a frame-rate of up to 2.7 Mfps. The KALYPSO detector mounts InGaAs or Si linear array sensors to measure radiation in the near-infrared or visible spectrum. The FPGA-based read-out card can be connected to an external data acquisition system through a high-performance PCI-Express 3.0 data-link, allowing continuous data taking and real-time data analysis. The detector is fully synchronized with the timing system of the accelerator and other diagnostic instruments. The detector is currently installed at several accelerators: ANKA, the European XFEL and TELBE. We present the detector and the results obtained with Electro-Optical Spectral Decoding (EOSD) setups.

INTRODUCTION

Electro-Optical Spectral Decoding (EOSD) is a well-established technique to measure the longitudinal bunch profile in a non-destructive way [1, 2] and with sub-picosecond spatial resolution [3]. A detailed description of EOSD can be found in [4]. In a typical EOSD setup, a chirped laser pulse is modulated inside an Electro-Optical crystal by the Coulomb field of the electron bunch. In this way the information on the temporal profile of the bunch is contained in the spectrum of the laser pulse. A spectrometer with a linear array detector is commonly used to measure the spectrum and reconstruct the bunch profile. While, in principle, this diagnostic technique allows single-shot measurements over many bunches, the bottleneck of current experimental setups lies in the linear array detector used in the spectrometer.

In particular, the acquisition rate of the detector has to match the bunch repetition rate of the accelerator machine (*e.g.:* 4.5 MHz at the European XFEL, 2.7 MHz during single-bunch operation at ANKA) to obtain single-shot resolution on a turn-by-turn basis. Moreover, the data acquisition system (DAQ) must be able to sustain high data-rates to allow the analysis of the beam dynamics over long time scales (*i.e.*:, a large number of samples). To the best of our knowledge, the line rates of commercial linear detectors reach only a few hundreds of kHz [5, 6].

An alternative approach, based on the method of photonic time-stretch, has been recently implemented by Roussel *et al.* [7] to lift the aforementioned limitation on the acquisition rate. This method enables an unprecedented acquisition rate in EOSD experiments (up to 62.5 MHz, an order of magnitude higher than what can be currently accomplished with linear array detectors) by using an oscilloscope to sample the signal of a fast photodiode. However, because of the finite memory depth of oscilloscopes, only a limited amount of samples can be acquired in a given time frame. This method is therefore not suitable for long observation times or experiments where real-time data analysis and fast-feedback are required.

In order to overcome such limitations, we have developed KALYPSO (KArlsruhe Linear arraY detector for MHz-rePetition rate SpectrOscopy), a novel linear array detector operating at line-rate of up to $2.7 \cdot 10^6$ fps (frames per second). In this contribution, we describe the architecture of the system and its application as beam diagnostic tool in the near-field EOSD setup of ANKA.

DETECTOR ARCHITECTURE

KALYPSO consists of a detector board and an FPGA-based readout card. The detector board mounts the sensor, the front-end amplifier and the Analog-to-Digital Converter (ADC). The sensor is a Si or an InGaAs linear array, with

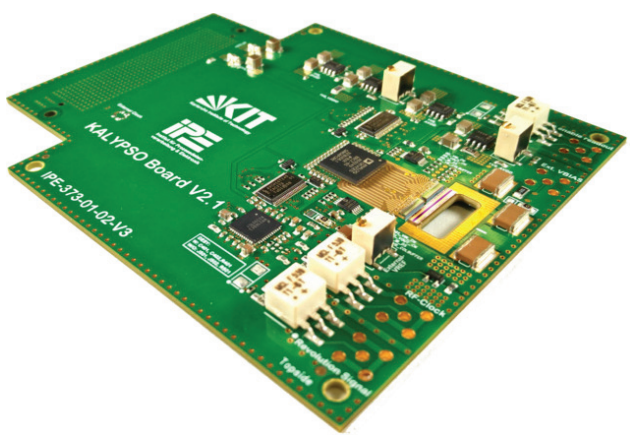

Figure 1: Picture of the KALYPSO detector board with InGaAs sensor.

* Author's contact: lorenzo.rota@kit.edu

ISBN 978-3-95450-177-9

256 pixels and a pitch of 50 µm, to detect radiation in the visible and near-infrared spectrum up to wavelengths of 1.7 µm. The sensor is connected to the readout ASIC with high-density gold ball-to-wedge wire-bonds. With respect to the architecture described in [8], a dedicated version of the GOTTHARD chip [9] with an improved output stage has been selected as front-end amplifier. The novel GOTTHARD 1.6 chip, designed at PSI, consists of a charge-sensitive pre-amplifier, a channel buffer and an output buffer. Each output is connected to 16 channels through an analog multiplexer, which has been tested at a switching frequency of 62.5 MHz, therefore limiting the maximum framerate of the system to 2.7 MHz. The analog outputs are digitized by a commercial ADC with 14 bits resolution and a maximum sampling rate of 65 MSPS (AD9249 from Analog Devices). The latency of the detector board when operating at the maximum line-rate is less then 300 ns[1], and it is mainly introduced by the internal pipeline of the ADC. Additional components are also installed on the board to synchronize the detector with the accelerator's timing system and other detectors. The detector card is connected to the back-end card through an FMC connector. A picture of the first prototype mounting an InGaAs sensor is shown in Figure 1.

The readout card used at ANKA is based on a Xilinx Virtex7 FPGA and controls the detector's operation. The data-acquisition (DAQ) system is based on a custom PCI-Express 3.0 Direct Memory Access engine with a maximum throughput of 6.4 GB/s [10], therefore allowing streaming operation at the maximum repetition rate of the detector. Real-time data analysis can be performed inside the FPGA or on a custom processing framework based on Graphical Processing Units (GPUs). While the former solution offers real-time data elaboration without the need of additional hardware, the latter allows for more flexibility in the data evaluation [11], in addition to the possibility to store the raw data and perform off-line data analysis. Thanks to the industry standard connector, the detector card can be easily integrated with different DAQ system, as is the case with the European XFEL: the integration of KALYPSO in a µTCA readout and timing is currently ongoing at DESY.

MEASUREMENTS WITH EOSD SETUP AT ANKA

We performed characterization measurements with the first prototype board mounting an InGaAs sensor at the near-field EOSD setup of ANKA (for which a detailed description can be found in [12])[2].

A Yb-doped laser operating at wavelength of 1050 nm has been used as source. The average power of each laser pulse hitting the detector is 6 pJ. With this incident power, the highest gain mode of the GOTTHARD chip (15 mV/fC) and integration time of 32 ns were choosen to achieve a Signal-to-Noise Ratio (SNR) of around 30. An external reverse bias of 1 V was applied to the sensor. We measured a leakage current of 20 µA, therefore its noise contribution can be considered negligible. These settings were used for all the measurements here reported.

In order to measure the bunch profile, three different measurements have been done: the background signal (recorded when no light is hitting the detector), the un-modulated signal (recorded with the laser pulse, but without the modulation of the electron bunch) and the modulated signal.

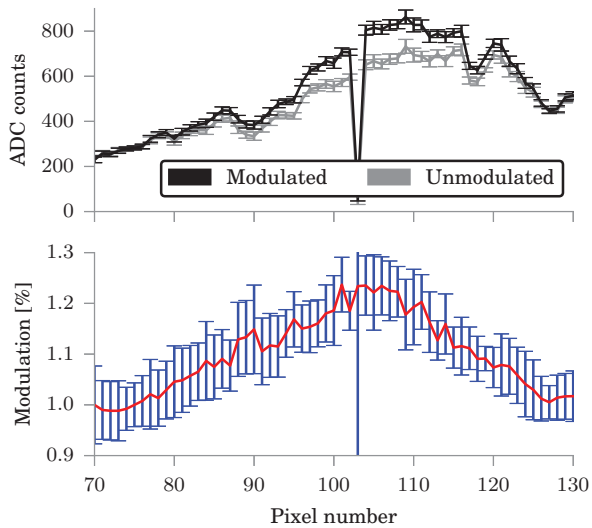

Figure 2: Top: modulated and un-modulated (averaged) signals recorded with KALYPSO. Bottom: relative modulation of the laser pulse (single-shot). In both plots the error bars show the standard deviation.

The background and the un-modulated signal are acquired before the acquisition of the modulated signal, and the average over a large number of samples (> 10^5 samples) is taken as reference. The background is subtracted from both the un-modulated and the modulated signal before calculating the relative modulation, as shown in Figure 2. Because the average modulation of the laser pulse is around 10%, the requirements on the noise detector become particularly challenging: if the modulation has to be measured with a SNR of 10, the SNR of the modulated signal has to be higher than 100. However, even with an incident light power for each laser pulse as low as 6 pJ, the formation of substructures on the bunch profile has been observed successfully, as shown in Figure 3.

CONCLUSION AND FUTURE WORK

We have developed a linear array detector with a frame-rate of 2.7 Mfps. The detector has been developed to upgrade the acquisition rate of existing EOSD setups currently installed at ANKA, the European XFEL and ELBE.

The first prototype of the KALYPSO detector, based on an InGaAs sensor and the new GOTTHARD 1.6 chip, has

[1] The latency is here defined as the time interval between the arrival of the laser pulse and the acquisition of the corresponding digitized value inside the back-end card.

[2] Pixels number 105 and 135 exhibits a higher noise because of a defective wire-bonding.

ISBN 978-3-95450-177-9

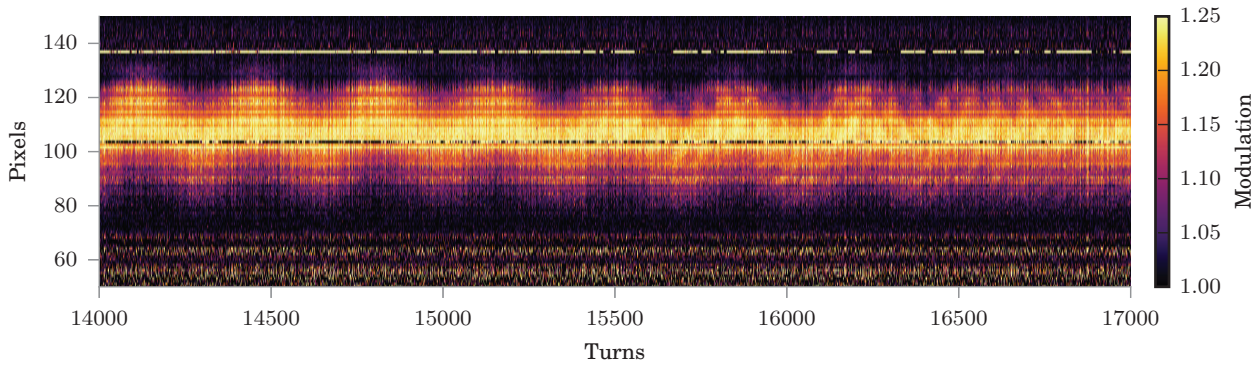

Figure 3: Raw measurement data of the longitudinal bunch profile recorded with KALYPSO over multiple turns. The acquisition rate of KALYPSO was set to 2.7 Mfps, so that each vertical line corresponds to a single-shot and turn-by-turn measurement of the bunch profile. The synchrotron oscillation of the electron bunch is visible on the left side. On the right side, the build-up of substructures on the bunch profile (the so-called microbunching effect) can be observed. The full dataset consists of $5 \cdot 10^5$ turns.

been successfully tested as a beam diagnostic tool in the EOSD setup at ANKA. With an incident light power as low as 6 pJ, the detector achieves a SNR of around 30, which is sufficient to detect the formation of substructures on the bunch profile. When coupled with a high-throughput DAQ system, it enables single-shot and turn-by-turn measurement of the beam longitudinal profile over a large number of turns ($> 10^7$ turns) at the bunch revolution frequency of 2.7 MHz. Moreover, because of the low-latency introduced by the detector board, KALYPSO can be used as diagnostic tool in fast-feedback systems.

Additional measurements are currently ongoing at ANKA and at the European XFEL in order to fully characterize the performance of the system with both InGaAs and Si sensors. In particular, the noise contribution of each component of the system (electronics, laser instabilities, jitter in the timing synchronization) will be studied. In the meantime, maintenance of EOSD setup (in particular, the in-vacuum laser path) is also being carried out at ANKA. With an estimated increase in the incident laser power by a factor of 10, we expect a significant improvement in terms of SNR and a better resolution

Finally, a novel front-end ASIC is being developed at KIT in collaboration with PSI, in order to further improve the frame-rate and the noise performance of the system. A prototype chip, designed in CMOS 0.11 µm technology with a target frame-rate of 5 Mfps has been submitted to the foundry and will be characterized in the next months.

ACKNOWLEDGEMENT

The authors would like to thank Simon Kudella and Pia Steck for their precious help with the wire-bonding process. This work is partially funded by the BMBF contract number: 05K16VKA.

REFERENCES

[1] V. Arsov *et al.*, "Electro-optic spectral decoding for single-shot characterisation of the coherent transition radiation pulses at FLASH," in *Proceedings of FEL 2007*, 2007, p. WEPPH047.

[2] A. Borysenko *et al.*, "Electron Bunch Shape Measurements Using Electro-optical Spectral Decoding," *Physics Procedia*, vol. 77, pp. 3–8, 2015.

[3] B. Steffen *et al.*, "Electro-optic time profile monitors for femtosecond electron bunches at the soft x-ray free-electron laser FLASH," *Physical Review Special Topics - Accelerators and Beams*, vol. 12, no. 3, p. 032802, 2009.

[4] I. Wilke *et al.*, "Single-Shot Electron-Beam Bunch Length Measurements," *Physical Review Letters*, vol. 88, no. 12, p. 124801, Mar. 2002.

[5] Teledyne DALSA Inc. (2016) Piranha4 line camera. [Online]. Available: http://www.teledynedalsa.com/imaging/products/cameras/line-scan/piranha4/P4-CM-04K10D/

[6] A. Anchlia *et al.*, "A 400 KHz line rate 2048 pixel modular SWIR linear array for earth observation applications," R. Meynart, S. P. Neeck, and H. Shimoda, Eds., Oct. 2015, p. 96390T.

[7] E. Roussel *et al.*, "Electro-Optical Measurements of the Longitudinal Bunch Profile in the Near-Field on a Turn-by-Turn Basis at the Anka Storage Ring," in *Proceedings of International Beam Instrumentation Conference, IBIC*, 2015, p. MOPB006.

[8] L. Rota *et al.*, "An ultrafast linear array detector for single-shot electro-optical bunch profile measurements," in *Proceedings of International Beam Instrumentation Conference, IBIC*, 2014, p. TUPOD010.

[9] A. Mozzanica *et al.*, "The GOTTHARD charge integrating readout detector: design and characterization," *Journal of Instrumentation*, vol. 7, no. 01, p. C01019, 2012.

[10] L. Rota *et al.*, "A high-throughput readout architecture based on pci-express gen3 and directgma technology," *Journal of Instrumentation*, vol. 11, no. 02, 2016.

ISBN 978-3-95450-177-9

[11] M. Vogelgesang *et al.*, "A heterogeneous FPGA/GPU architecture for real-time data analysis and fast feedback systems," in *these proceedings*, p. WEPG07.

[12] N. Hiller *et al.*, "Single-shot electro-optical diagnostics at the ANKA storage ring," in *Proceedings of International Beam Instrumentation Conference, IBIC*, 2014.

ISBN 978-3-95450-177-9

PROGRESS ON THE PITZ TDS

H. Huck*, P. Boonpornprasert, L. Jachmann, W. Koehler, M. Krasilnikov, A. Oppelt,
F. Stephan, DESY, Zeuthen, Germany
L. Kravchuk, V. Paramonov, A. Zavadtsev, INR of the RAS, Moscow, Russia
C. Saisa-ard, Chiang Mai University, Chiang Mai, Thailand

Abstract

A transverse deflecting system (TDS) is under commissioning at the Photo Injector Test Facility at DESY, Zeuthen site (PITZ). The structure was designed and manufactured by the Institute for Nuclear Research (INR RAS, Moscow, Russia) as prototype for the TDS in the injector part of the European XFEL. Last year the deflection voltage was limited for safety reasons, but after thorough investigations of the waveguide system we are now able to operate the cavity close to design specifications. The PITZ TDS streaks the electron beam vertically, allowing measurements of the longitudinal bunch profile, and, in combination with a subsequent horizontal bending magnet, also of the longitudinal phase space and slice energy spread. Furthermore, several quadrupole magnets and screen stations can be employed for horizontal slice emittance measurements using the TDS. This paper describes the progress in commissioning of the hardware, measurement techniques and simulations, and outlines the prospects of reliable slice emittance measurements at 20 MeV/c, where space charge forces complicate the determination of transfer matrices.

INTRODUCTION

X-ray Free Electron Lasers (XFELs) pose stringent requirements on the quality of their driving electron beams, especially in terms of peak current and emittance. Higher peak currents and lower emittances yield higher radiation power and reduce the total undulator length necessary to reach FEL saturation. In particular, the small normalized transverse core slice emittance (i.e. the emittance or "focusability" of the central, high-current parts of the electron bunches), is a major figure of merit. Measurements of the longitudinal charge profile to determine the peak current as well as slice emittance measurements can be performed using a transverse deflecting RF cavity or multi-cell structure (TDS).

Transverse fields inside the structure deflect electrons depending on their arrival time with respect to the RF phase. Near the zero-crossing phase the beam is sheared, linearly mapping the longitudinal charge profile to a transverse, e.g. vertical axis on an observation screen downstream. The horizontal axis can then be utilized for other longitudinally resolved measurements: In combination with a horizontally dispersive bending magnet, live images of the full longitudinal phase space can be observed on the screen, while the quadrupole-scan emittance measurement technique allows for slice emittance measurements [1, 2].

* holger.huck@desy.de

In the simple case of a pure drift space (length L) between TDS and screen, a longitudinal slice of the bunch (relative position z) hits the screen at vertical position [3]

$$y = S \cdot z = \frac{eV_0 k}{pc} \cdot L \cdot z, \tag{1}$$

where p denotes the electron momentum, c the speed of light, and the shear parameter S depends on the deflecting voltage V_0 and wave number k. In the general case, the longitudinal resolution can be expressed as [3, 4]

$$\sigma_z \gtrsim \frac{2}{eV_0 k} \frac{m_0 c^2}{\sin(\Delta\psi)} \sqrt{\frac{\gamma\epsilon_n}{\beta_{\mathrm{TDS}}}} \tag{2}$$

with the beta function β_{TDS} in the TDS, normalized emittance ϵ_n, relativistic factor γ and betatron phase advance $\Delta\psi$ between TDS and screen.

PITZ LAYOUT

At the Photo Injector Test Facility at DESY, Zeuthen site (PITZ), electron guns for the European XFEL and the Free-electron laser FLASH are being tested and optimized. Projected emittance requirements for the nominal European XFEL run parameters have been met [5], recently for the start-up phase as well [6]. In order to measure and optimize also the slice emittance (and other parameters), a TDS is installed in the high energy section of the PITZ beamline, between the first emittance measurement station and the phase space tomography module (Fig. 1). The TDS, designed [7] and manufactured by the Institute for Nuclear Research of the Russian Academy of Sciences as a prototype of the TDS in the injector section of the European XFEL [8, 9], is under commissioning since 2015 [10]. The cell dimensions were selected to have the same cells for all three structures in the European XFEL TDS and are realized in its prototype for PITZ [11]. Table 1 summarizes the most important parameters of the cavity.

Table 1: Design Parameters of the PITZ TDS

Deflecting voltage	1.7 MV
Input power	2.11 MW
RF Frequency	2997.2 MHz
Pulse length	3 µs
Structure Length	0.533 m
Number of cells	14+2
Phase advance per cell	$2\pi/3$
Quality factor at 20 °C	11780

ISBN 978-3-95450-177-9

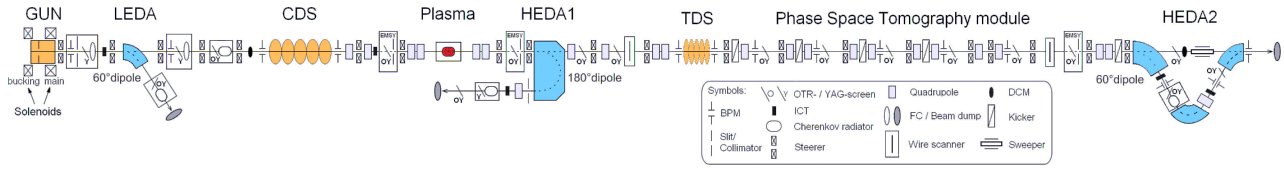

Figure 1: Current layout of the PITZ beamline (PITZ 3.0). Electron bunches which are streaked vertically by the TDS can be monitored on several YAG and OTR screens in the tomography module. Alternatively, their full longitudinal phase space can be analyzed in the high energy dispersive arm HEDA2, 7.3 m downstream the TDS. During the measurements presented in this paper, the plasma cell was replaced by an empty beam tube.

COMMISSIONING STATUS

Initially, the deflecting structure was only conditioned up to intermediate power levels of about 0.5 MW, limited by high reflected power readings near the klystron [10]. Following a thorough recalibration of cables and directional couplers, it was concluded that no urgent changes to the waveguide system are necessary. Afterwards conditioning the structure to higher power levels went smoothly, with only minor vacuum activity. Present RF power readings from the directional couplers at the klystron exit and at the structure entrance are shown in Fig. 2 (top). The blue circles in the bottom plot are estimations of the power in the structure based on the actual deflection of a 23-MeV electron beam. Since this method only works well with a pure drift space between TDS and screen, for higher deflection voltages the streaked beam was clipped by apertures and the screen frame, resulting in strong systematic errors not covered by the error bars.

The maximum obtained power in the structure so far is 1.9 MW, coming close to the nominal design value of 2.1 MW. The limiting factor is still the reflection at the klystron coupler, which has been measured to be almost 80 dBm at 1.9 MW power in the structure. This value is considered safe for the klystron, but stable operation is only guaranteed by the manufacturer up to 74 dBm.

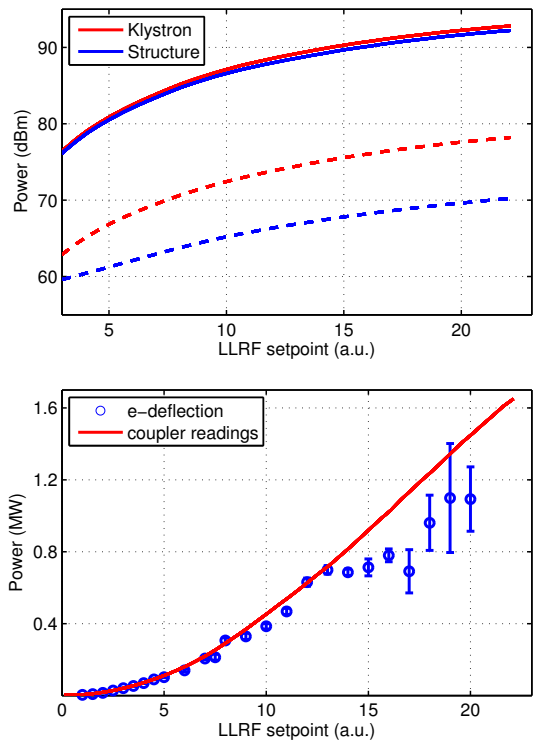

Figure 2: Forward (solid lines) and reflected (dashed lines) power readings from the directional couplers at the klystron and structure (top), and comparison with measured electron beam deflection (bottom).

TDS CALIBRATION

The shear parameter S of the TDS is determined experimentally for every bunch length measurement, since not only the power in the structure, but also the beam energy, focusing and even steering of the beam can change its value. The screen position of the beam centroid is recorded under variation of the RF phase in the TDS. A linear fit of this phase scan yields the zero-crossing phase and S. A dedicated Matlab tool handles this calibration procedure and data acquisition simultaneously, as a typical scan with 5-10 images times 5-10 phase steps yields enough statistics for the bunch length, which is calculated for each image separately. In order to properly take into account bunches which are already tilted (i.e. having a transverse-longitudinal correlation) before entering the TDS, the phase scan is repeated on the other slope of the RF (i.e. at inverted voltage). The real bunch length l can then be calculated by a quadratic fit [12], equivalent to $l^2 = (l_+^2 + l_-^2)/2 - l_0^2$, where $l_{+/-}$ denotes the streaked bunch length on both slopes and l_0 the focused, unstreaked beam size (scaled in the same way), which is always measured before the two phase scans.

BUNCH LENGTH MEASUREMENTS

Preliminary TDS measurements [10] suggested a slight overestimation of the bunch length in simulations. To investigate these discrepancies, more detailed measurements for a set of different laser spot sizes and bunch charges have been performed, accompanied by ASTRA [13] simulations. Photocathode laser pulses with a Gaussian temporal profile of 11 to 12 ps length (FWHM) were used, the gun was operated at a gradient of 53 MV/m at the cathode, and the final beam momentum after the booster was 21.5 MeV/c. For the simu-

ISBN 978-3-95450-177-9

lations, the measured transverse laser profiles were taken as input, using a more realistic though still radially symmetric "core plus halo" model [6]. A subset (three different laser spot sizes) is presented in Fig. 3.

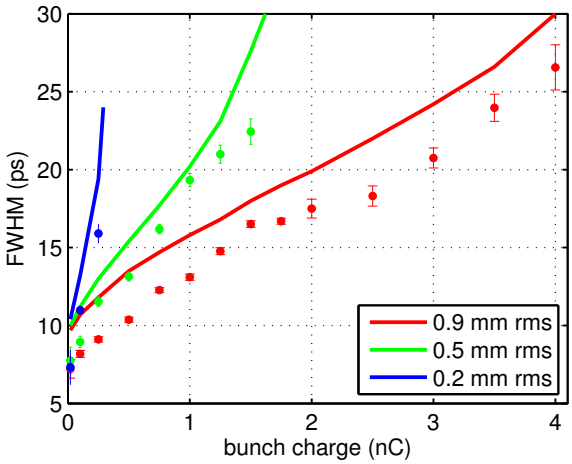

Figure 3: Bunch length (FWHM) vs. bunch charge, measured (dots) and simulated (lines), for different rms laser spot sizes (0.2, 0.5 and 0.9 mm) on the cathode.

The overall, qualitative trend is the same in measurements and simulations. As expected, the bunch length primarily depends on laser intensity, quickly growing with growing space charge density at the cathode. When approaching the space charge limit (i.e. maximum extractable charge), the bunch length reaches values of 20-30 ps. However, the measured bunch length is consistently shorter than the simulated one, by several ps. This discrepancy is neither explainable by statistical errors (error bars) nor by phase jitters. Possible explanations are systematic measurements errors (see below), deficiencies of the emission model, or shorter laser pulses, since their actual length and shape could not be measured last year. While many discrepancies vanish under the assumption of 9-ps pulses (Fig. 4), values close to the space charge limit still do not agree or are even worse as in the case of 0.375 mm spot size.

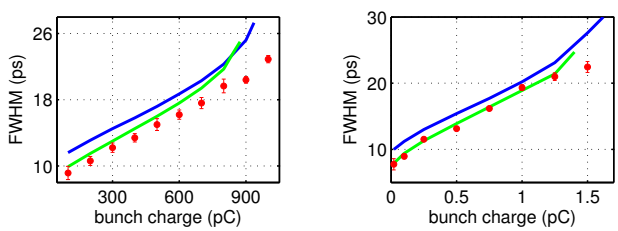

Figure 4: Bunch length (FWHM) vs. bunch charge for rms laser spot sizes of 0.375 mm (left) and 0.5 mm (right). Dots are TDS measurements, blue and green lines ASTRA simulations assuming Gaussian laser pulses of 11.5 and 9 ps, respectively.

During the measurements, strong inhomogeneities (burned spot and vertical gradient) in the sensitivity of the YAG screen were observed, which are believed to be the major systematic error source.

The shot-to-shot standard deviation of the measured bunch lengths as well as the linearity error of the calibration curve were approx. 4 % for the measurements presented here. In future, this error might be reduced by RF feedback, better fitting routines, and more homogenous screens. Furthermore, normalization of the raw images by a screen sensitivity map is under consideration.

The temporal resolution is given by the FWHM spot size of the unstreaked beam. It varied between 0.5 and 1.0 ps, but should go down with higher deflecting voltage and better focusing to ≈ 0.1 ps for pure profile measurements, and 0.3 ps for slice emittance as well as for full longitudinal phase space measurements [4].

SLICE EMITTANCE

Motivation

At PITZ, the projected emittance is usually measured using the slit-scan method, shortly after the CDS booster (Fig. 1) at a beam energy of 20-24 MeV. The main solenoid as only focusing element (beside RF fields) is used to fine-tune the alignment of slices in order to minimize the projected emittance at the measurement station. Recent measurements and simulations have shown that, for the case of long (11 ps FWHM) Gaussian cathode laser pulses, the projected emittance cannot be reduced by increasing the gun gradient from 53 to 60 MV/m, although the slice emittance should go down. Furthermore, projected and slice emittance are not generally minimized by the same solenoid current. This is illustrated in Fig. 5, which shows the evolution of beam size and emittance along the PITZ beamline, simulated in ASTRA for a bunch charge of 100 pC and a laser spot size of 0.2 mm (rms) on the cathode. Here, the projected emittance and core slice emittance are minimum when focusing roughly to the end and the start of the booster, respectively.

Measurement Technique

First tests of scanning the gradient of a single quadrupole right before the TDS and using linear matrix optics to determine the slice emittance showed that this simple approach is not feasible for PITZ. The obtained emittance values were much higher than in simulations, and the statistical errors, obtained by error propagation from the confidence levels of the fit parameters, were of the order of 100 percent. There are several reasons for that. Firstly, space charge forces at low energies of ≈ 20 MeV significantly influence the transverse focusing and thus the transport matrices. Secondly, single-quad scan implies strong changes of the beam size and the intensity on the observation screen, yielding to systematic errors due to limited dynamic range, noise handling and slice mixing, and to strong statistical errors when the horizontal beam size approaches the resolution of the optical system (mostly the pixel size).

ISBN 978-3-95450-177-9

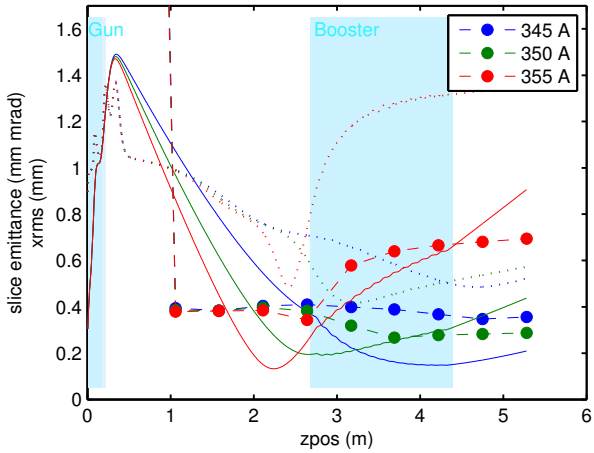

Figure 5: Evolution of the projected emittance (dotted lines), core slice emittance (dashed lines/circles) and beam size (solid lines) along the PITZ beamline. The colors refer to three different solenoid currents.

In order to overcome these issues and obtain reliable slice emittance measurements at PITZ, the following approach will be tested in the upcoming measurement weeks.

In a first step, the projected emittance is experimentally minimized by tuning the solenoid strength. Using the slit-scan technique, not only the projected emittance but also the Twiss parameters are determined, which can be used as input for space charge matching simulations. Thus a set of N quadrupole settings suitable for a multi-quad scan [2] can be obtained. The main idea here is to keep the beam size σ_i on the observation screen roughly constant (but not to small, see above), while scanning the (horizontal) betatron phase. For each longitudinal slice, the emittance is finally derived from the beam moments $\langle x_0^2\rangle$, $\langle x_0'^2\rangle$, $\langle x_0 x_0'\rangle$ at the reference point (i.e. the starting point of the matching simulations), which can be obtained by solving

$$\sigma_i^2 = {R_{11}^i}^2\langle x_0^2\rangle + {R_{12}^i}^2\langle x_0'^2\rangle + 2R_{11}^i R_{12}^i\langle x_0 x_0'\rangle, \qquad (3)$$

with the measurement index (i.e. quadrupole setting) $i = 1..N$ and transport matrices R derived from simulations. In a last step, the solenoid strength can be fine-tuned (re-matching required) to minimize the slice emittance.

CONCLUSION AND OUTLOOK

The PITZ TDS, a prototype for the injector TDS of the European XFEL, is now operated near design specifications, and used for measuring the bunch length and longitudinal phase space. There is a strong request in slice emittance measurements using the PITZ TDS, and a measurement procedure that should overcome the difficulties of space charge forces at 20 MeV is under development. In the near future, the TDS will also be employed for analyzing the self-modulation of electron bunches inside a plasma cell, as well as for slice energy spread measurements, which might enhance the understanding of the microbunching instability.

REFERENCES

[1] M. Röhrs et al.,"Time-resolved electron beam phase space tomography at a soft x-ray free-electron laser", Phys. Rev. ST Accel. Beams 12, 050704 (2009).

[2] E. Prat et al., "Emittance measurements and minimization at the SwissFEL Injector Test Facility", Phys. Rev. ST Accel. Beams 17, 104401 (2014).

[3] P. Emma et al., "A Transverse RF deflecting structure for bunch length and phase space diagnostics", LCLS-TN-00-12 (2000).

[4] D. Malyutin, "Time resolved transverse and longitudinal phase space measurements at the high brightness photo injector PITZ", PhD thesis, University of Hamburg, Hamburg (2014).

[5] M. Krasilnikov et al., "Experimentally minimized beam emittance from an L-band photoinjector", Phys. Rev. ST Accel. Beams 15, 100701 (2012).

[6] G. Vashchenko et al., "Emittance Measurements of the Electron Beam at PITZ for the Commissioning Phase of the European XFEL", Proc. FEL'15, pp. 285-288, Deajeon, Korea (2015).

[7] L. Kravchuk et al., "Layout of the PITZ transverse deflecting system for longitudinal phase space and slice emittance measurements", LINAC2010, TUP011 (2010).

[8] M. Altarelli et al. (Editors), "The European X-Ray Free-Electron Laser Technical design report" (DESY XFEL Project Group et al., 2007).

[9] W. Decking and T. Limberg, "European XFEL Post-TDR Description", XFEL.EU TN-2013-004-01 (2013).

[10] H. Huck et al., "First Results of Commissioning of the PITZ Transverse Deflecting Structure", Proc. FEL'15, pp. 110-114, Deajeon, Korea (2015).

[11] A. Anisimov et al., "Input Couplers for the Dipole Mode Periodic Structures", RuPac 2010, 328 (2010).

[12] R. Akre et al., SLAC-PUB-9241, May 2002 (EPAC 02)

[13] "A Space-charge TRacking Algorithm, ASTRA", `http://www.desy.de/~mpyflo`

ISBN 978-3-95450-177-9

A THz DRIVEN TRANSVERSE DEFLECTOR FOR FEMTOSECOND LONGITUDINAL PROFILE DIAGNOSTICS

S.P. Jamison†, E.W. Snedden, D.A. Walsh
Accelerator Science and Technology Centre,
STFC Daresbury Laboratory, Warrington WA4 4AD, United Kingdom
M.J. Cliffe, D.M. Graham, D.S. Lake
School of Physics and Astronomy & Photon Science Institute
The University of Manchester, Manchester M13 9PL, United Kingdom

Abstract

Progress towards a THz-driven transverse deflecting longitudinal profile diagnostic is presented. The deflector is driven with sub-picosecond quasi-single cycle THz fields generated by non-linear optical rectification. To utilize the large deflection field strength of the source for longitudinal diagnostics it is necessary to maintain the single-cycle field profile of the THz pulse throughout the interaction with the relativistic beam. Our scheme allows for the octave spanning bandwidth of the single-cycle pulses to propagate without dispersion at subluminal velocities matched to co-propagating relativistic electrons, by passing the pulse distortion and group-carrier walk-off limitations of dielectric loaded waveguide structure. The phase velocity is readily tuneable, both above and below the speed of light in a vacuum, and single-cycle propagation of deflecting fields at velocities down to 0.77c have been demonstrated.

INTRODUCTION

Measurement of coherent diffraction or transition radiation (CDR and CTR), together with methods of phase retrieval promise the ability to characterise bunch longitudinal charge density profile at the few-femtosecond level, although issues of ambiguity in phase retrieval remain. A range of electro-optic techniques have been demonstrated that provide unambiguous temporal profile, but they have yet to achieve capability in the few femtosecond regime. Transverse defecting structures are currently the only diagnostic devices that are capable of unambiguous femtosecond resolution longitudinal profile, and in addition they are capable of characterising electron-bunch 'slice' parameters which are inaccessible to the CDR/CTR and electro-optic techniques. Transverse deflecting structures however come with significant demands on location and space within an electron transport system, along with large RF infrastructure costs. Here we describe progress towards developing a THz driven transverse deflection diagnostic that offers significantly smaller footprint and flexibility in location, reduced infrastructure costs, and potential for sub-femtosecond temporal resolution.

In a transverse deflecting structure the measurement of temporal properties is driven by a time varying transverse kick and drift space and electron beam optics converting the temporally dependant kick into a transverse displacement. The achievable time resolution of the transverse streak is underpinned by the longitudinal gradient of the deflection force, $\frac{\partial F_\perp}{\partial z} \sim \omega \int dz\, E_\perp^{peak}\,(z - tc\beta_s)$, where $c\beta_s$is the phase velocity of the deflection field and the synchronised particle beam, and ω the frequency of the deflection field. For deflection fields at THz frequencies, with a 2-orders of magnitude increase in the longitudinal gradient compared to an RF driven structure with the same peak deflection fields, high time-resolution can be obtained with either significantly reduced peak field strengths, or reduction in physical interaction space (or a combination of both). Laser generated single-cycle sources are well established within the ultrafast laser and THz spectroscopy communities, and sources with 10-100MV/m field strengths in single-cycle sub-picosecond pulses have been widely demonstrated in conventional THz non-linear materials [1,2], while sources of GV/m field strengths have been demonstrated in more exotic organic materials [3]. While much of the historic development of THz sources has been driven by demand in materials science, within the accelerator community there has been significant interest in generating high-field sources for atto-second photon diagnostics. For such an application the electric field of a THz pulse provides a time dependent acceleration of soft-xray liberated photoelectrons, and from analysis of the photo-electron energy spectra the arrival time and temporal duration of the xray pulse can be inferred.

The application of THz pulses for particle acceleration has been previously proposed by several groups [4,5,6], and more recently acceleration of low energy electron beams has been demonstrated [7,8]. Deflection of relativistic beams with THz pulses has been considered recently by Fabianiska et al. [9], where it was proposed to use split ring resonators to enhance the field strength and provide a significant deflection force within the gap of the resonator. To further enhance the time resolution or provide deflection on higher energy beams it is natural to consider an extended interaction length, which introduces the necessity to match the THz carrier-wave velocity with the electron bunch velocity. Waveguide or resonant structures offer a route to slow the phase velocity to less than the velocity of light in vacuum for a 'phase-matched' interaction, but such an approach inherently comes with unavoidable dispersion and distortion of the single-cycle pulse. The dispersion gives rise to a decaying field

† email address: steven.jamison@stfc.ac.uk

ISBN 978-3-95450-177-9

strength with propagation distance, and group velocity walk-off between the THz envelope and the electron bunch. Here we demonstrate a concept that produces sub-picoseond single cycle pulses with deflecting electric and magnetic fields that propagate at velocities less than the vacuum speed of light without distortion or dispersion. The ability to match the velocity of the single-cycle deflecting fields with a particle beam makes the concept scalable to higher integrated deflection impulse through scaling of the interaction length.

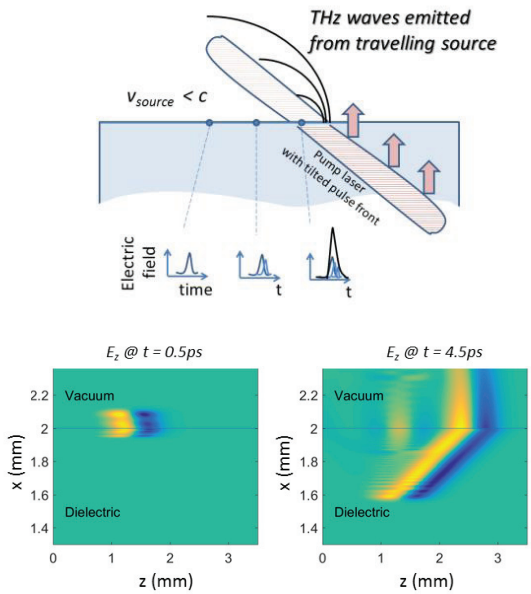

Figure 1: (Top) Conceptual schematic for the generation of a subluminal single-cycle THz pulse near the surface of a non-linear medium. The laser is propagating in a normal-incidence direction with respect to the material surface, with an effective travelling source produced by the local arrival time-delay of the tilted pulse front. The optical carrier wave-fronts are themselves travelling normal to the surface and cannot be used directly for the electron-beam interaction. (Bottom) FDTD calculation of the THz field generated by a bipolar THz source near a dielectric surface, with source velocity β_s=0.995.

THz TRAVELLING WAVE DEFLECTOR

Our scheme uses optical rectification to generate single-cycle THz pulses with transverse magnetic and electric fields co-propagating with an electron beam. To overcome the challenges of maintaining a sub-luminal velocity matching with the electron beam, and to eliminate the dispersion of the single cycle pulse, we transfer the task of propagation from the THz regime to the optical regime with a propagating travelling-wave pump laser for the THz generation; the interaction between the THz and electron beam is through 'locally' produce single-cycle electric and magnetic fields. For optical rectification sources, the temporal profile or carrier-wave of the THz pulse at the generation location follows the time derivate of the optical pulse envelope. To achieve a sub-luminal carrier wave we exploit this group-to-phase conversion together with optical pulse front tilts giving a controllable arrival-time delay at different generation locations with the non-linear generation material, as shown schematically in Figure 1. While a travelling source can also be produced simply with an optical beam incident at an oblique angle to the non-linear material, for a planar medium such an arrangement is restricted to effective velocities greater than the vacuum speed of light by the laws of refraction. The excitation of the THz sources through tilted optical pulse fronts allows coupling of the optical energy into the non-linear material at sub-luminal velocities.

The out-coupling of the THz fields from inside the source material to the vacuum region is subject to conditions of boundary continuity and refraction, and for conventional many-cycle electromagnetic waves the transition from super-luminal to sub-luminal source propagation is equivalent to meeting conditions for the critical-angle of total internal reflection and post-boundary evanescent wave propagation [10]. For the single cycle pulses generated by optical rectification the classification of the post-boundary fields as non-propagating and exponentially decaying in amplitude is no longer appropriate. To provide a detailed and quantitative picture of the single-cycle propagation from a sub-luminal source, finite difference time domain (FDTD) simulations have been undertaken.

An example calculation of emission from (and into) the surface under sub-luminal conditions is presented in Fig 1. For the calculation a travelling bipolar THz source matching that expected for optical rectification of an ultrashort laser pulse is imposed within the dielectric material. The source is given an effective velocity $c\beta_s$ which can be chosen to match the velocity of the electron bunch. In line with the optical rectification generation process there is no magnetic field source and the electric field of the source term is polarized purely in the z-direction, which also corresponds to our chosen source propagation direction. As apparent in the results of Fig. 1, after an initial stage of propagation where the field is established in the region above the source plane, a stable pulse is obtained, travelling with a wavefront normal to the surface and with a velocity set by the effective source velocity.

In Fig. 2 we present the results of a simulated interaction of a 10 MV/m travelling wave deflector with a 200 MeV electron beam. The bunch transverse distribution is for a 0.3 mm.mrad normalised emittance, typical of a RF injector. The transverse beam size at injection is Δx_{rms} = 30 μm. The particle phase space evolution was obtained through numerical solution of the relativistic equation of motion. A fourth-order Runge-Kutta algorithm was embedded within the FDTD field evaluation algorithm, with particle velocities and positions updated at each time step of the FDTD code. The position and momentum of 5000 electrons were tracked as they propagated through the

ISBN 978-3-95450-177-9

field structure. As shown in Fig. 2, after 10mm interaction a significant transverse kick is achieved, and even with a pure drift space following the interaction a time resolution of <10 fs is predicted. A higher time resolution could be obtained through optimisation of electron beam transport or through longer interaction length.

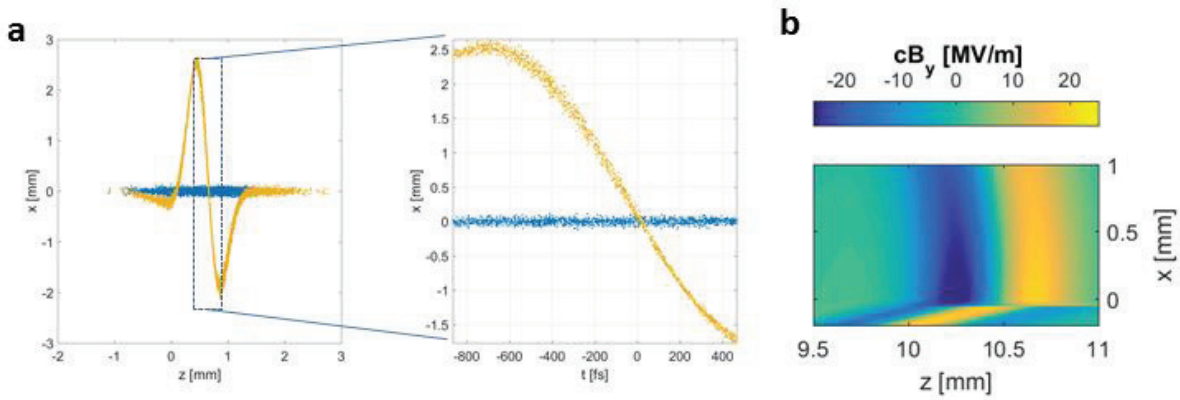

Figure 2: (a) simulated deflection imposed on a 200 MeV, ε = 0.3 mm.mrad beam with a 1 cm interaction region and a 1 metre drift. Blue: without THz pulse. Orange: with a 10 MV/m THz source driving the interaction. (b) FDTD simulations of the magnetic field produced in the vacuum region by a travelling wave THz source.

EXPERIMENTAL DEMONSTRATION

We have experimentally demonstrated a sub-luminal travelling-wave THz source meeting the criteria described above. The non-linear medium for the optical rectification THz generation was a 10mm x 10mm ZnTe single crystal, and a separate ZnTe crystal was used for electro-optic detection of the THz near the emitter surface. The probe laser for the electro-optic detection was scanned across the source, enabling a spatial and temporal mapping of the THz fields as they propagate across the surface. The experimental arrangement is shown schematically in Fig. 3a. The pulse front tilt on the optical pump beam was obtained by a diffraction grating, and the tilt was able to be tuned to give effective source velocities above and below the speed of light in vacuum. The electro-optic detection used a retro-reflection geometry, with the probe incident normally onto the generation surface and retro-reflected by the dielectric-air boundary in the detection ZnTe crystal. After interaction of the probe with the THz, the probe polarisation was analysed through a standard 'balanced detection' arrangement.

The spatial-temporal mapping of the THz evolution shown in Fig3b is for a pulse travelling at v=1.02c; As will be reported elsewhere [11], we have experimentally characterised single-cycle pulses traveling with velocities from 0.77c to 1.75c. The ZnTe non-linear media used in the demonstration reported here is not amenable to generation of very high field strengths. An alternative material, LiNbO3, is widely used material for generating >10MV/m THz pulses. While the significant disparities in optical and THz refractive indices in this material lead to it acting as a 'chenkov' non-collinear THz source, we have also devised an arrangement and demonstrated single-cycle travelling source in LiNbO3 [11].

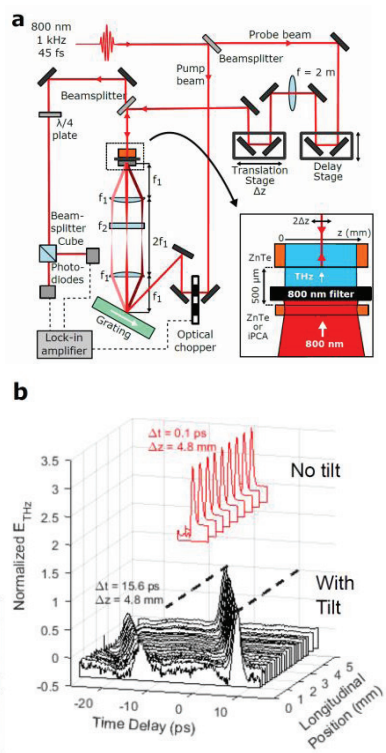

Fig. 3. (a) Schematic of the experimental system for measuring the THz travelling wave emitted from a ZnTe optical rectification source optically excited with a tilted pulse-front, and (b) plots showing the spatio-temporal mapping of the THz pulse measured 500μm above the ZnTe surface.

ISBN 978-3-95450-177-9

ACKNOWLEDGEMENT

This work was supported by the United Kingdom Science and Technology Facilities Council [Grant No. T/G008248/1]; the Engineering and Physical Sciences Research Council [Grant No. EP/J002518/1]; and the Accelerator Science and Technology Centre through Contract No. PR110140.

REFERENCES

[1] H. Hiror, A. Doi, F. Blanchard, K. Tanaka, "Single-cycle terahertz pulses with amplitudes exceeding 1MV/cm generated by optical rectification in $LiNbO_3$", Appl. Phys. Lett. 98, 091106 (2011).

[2] J.A. Fülöp, L. Pālfalvi, M.C. Hoffmann, J. Hebling, "Towards generation of mJ-level ultrashort THz pulses by optical rectification", Opt. Express 19, 15090 (2011).

[3] C. Vicario, B.P. Monoszlai, C.P Hauri, "GV/m Single-Cycle Terahertz Fields from a Laser-Driven Large-Size Partitioned Organic Crystal", Phys. Rev. Lett. 112, 213901 (2014).

[4] S.P. Jamison *et al.*, "Phase Space manipulation with laser-generated Terahertz pulses", Proceeding of 35th free electron Laser conference, Nara, Japan. p512 (2012).

[5] L.J. Wong, A. Fallahi, F.X. Kärtner, "Compact electron acceleration and bunch compression in THz waveguides", Opt. Express 21 9792 (2013).

[6] L. Pālfalvi, J. Fülöp, G. Toth, J. Hebling, "Evanescent-wave proton postaccelerator driven by intense THz pulse", Phys. Rev. Spec. Top. Accel. Beams. 17, 031301 (2014).

[7] W.R. Huang *et al.*, "Toward a terahertz-driven electron gun", Scientific Reports 5, 14899 (2015).

[8] E.A. Nanni *et al.*, "Terahertz-driven linear electron acceleration", Nat. Commun. 6, 8486 (2015).

[9] J. Fabianska, G. Kassier, T. Feurer, "Split ring resonator based THz-driven electron streak camera featuring femtosecond resolution", Scientific Reports. 4, 5645 (2013).

[10] W.L. Mochan, V.L. Brudny, Comment on "Noncausal time response in frustrated total internal reflection?", Phys. Rev Lett. 87, 119101 (2001).

[11] D.A. Walsh, D.S. Lake, E.W. Snedden *et al.*, "Demonstration of sub-luminal propagation of single-cycle terahertz pulses for particle acceleration", arXiv 1609.02573 (2016).

ISBN 978-3-95450-177-9

A HIGH RESOLUTION SINGLE-SHOT LONGITUDINAL PROFILE DIAGNOSTIC USING ELECTRO-OPTIC TRANSPOSITION*

D.A. Walsh†, S.P. Jamison[1], E.W. Snedden, ASTeC, STFC Daresbury Lab, Daresbury, UK
[1]also at The Photon Science Institute, University of Manchester, Manchester, UK
T. Lefevre, CERN, Geneva, Switzerland

Abstract

Electro-Optic Transposition (EOT) is the basis for an improved longitudinal bunch profile diagnostic we are developing in ASTeC as part of the CLIC UK research program. The scheme consists of transposing the Coulomb field profile of an electron bunch into the intensity envelope of an optical pulse via the mixing processes that occur between a CW laser probe and Coulomb field in an electro-optic material. This transposed optical pulse can then be amplified and characterised using robust laser techniques – in this case chirped pulse optical parametric amplification and frequency resolved optical gating, allowing the Coulomb field to be recovered. EOT is an improvement over existing techniques in terms of the achievable resolution which is limited by the EO material response itself, reduced complexity of the laser system required since nanosecond rather than femtosecond lasers are used, and insensitivity of the system to bunch-laser arrival time jitter due to using a nanosecond long probe. We present results showing the retrieval of a THz pulse (Coulomb field stand-in) which confirms the principle behind the EOT system.

INTRODUCTION

The use of electro-optic (EO) techniques for the measurement of longitudinal bunch profiles has for many years held the potential to provide high temporal resolution, non-destructive measurements, and single shot aquisition. The core principle behind all EO techniques is that for suitably relativistic energies the Coulomb field of each electron flattens out, becoming more disc like, resulting in the overall Coulomb field of the bunch becoming an accurate representation of the charge distribution. When this Coulomb field propagates through an EO material the most common, but not always appropriate, approximation is that the refractive index is then modulated through the Pockels effect. A laser pulse is then used to probe this E-field induced change using techniques borrowed or developed from the fields of generation and detection of ultrashort THz pulses, which have very similar properties.

A number of schemes have been developed but there are often trade-offs in system performance or practicality. Spectral decoding [1] whilst simple to implement has a practically limited resolution of a few hundred fs, has a limited (few ps) sampling window, and requires a potentially complex ultrashort pulse laser. However, demonstrations using fibre lasers have been made alleviating this last drawback. Spatial encoding [2] and temporal encoding [3, 4] have higher temporal resolutions, but also have finite sampling windows, and due to the necessary cascaded nonlinear processes require high pulse energy regeneratively amplified laser systems which are very complex and sensitive. There are also methods that improve upon the resolution of Spectral Decoding via the implementation of standard optical pulse diagnostics such as Temporal E-field Cross-correlation (TEX) [5]. This is based on Spectral Interferometry and inherits both the associated resolution enhancement (tens of fs is possible), but also the significant alignment sensitivity associated with interferometric measurements. It has also been suggested that FROG methods could be used to analyse the spectral decoding signals for enhanced resolution (PG-FROG, BMX-FROG [6, 7]), but again this has a limited sampling window along with the requirement of high energy ultrashort pulse lasers to drive the required cascaded nonlinear optical processes.

EOT [8-10] is significantly different to the previously mentioned techniques in that the probe laser field is not necessarily derived from an ultrashort laser pulse. Instead of a compressed or chirped femtosecond pulse, the Coulomb field is probed with a single frequency laser. By applying a more fundamental description of the EO effect as one of nonlinear frequency mixing it can readily be shown, and has been demonstrated [11], that this maps the spectrum of the Coulomb field onto optical sidebands of the probe laser. As nonlinear optical mixing preserves the relative phase information of the spectral components of the Coulomb field this process also transfers information of its temporal profile into the electric field of the new optical waves, as

$$E^{out}(t) \propto \left(\frac{d}{dt}E^{in}(t)\right) \cdot E_{eff}^{bunch}(t), \qquad (1)$$

where $E^{out}(t)$ is the newly generated EOT pulse, $E^{in}(t)$ is the input probe, and $E_{eff}^{bunch}(t)$ is the Coulomb field temporal profile accounting for spectral variations in the material response. What this indicates is that the amplitude of the Coulomb field is now mapped into the *envelope* of the new optical wave, with sign changes effectively becoming π phase jumps in the optical carrier wave.

This process now allows the use of Frequency Resolved Optical Gating (FROG) [12] – a standard and robust optical pulse diagnostic – to recover the Coulomb field profile from this new wave. Traditional FROG methods cannot be applied directly to the THz frequency range to recover the field directly as this would necessarily require recov-

* Funded by CERN contract KE1866/DG/CLIC and carried out at STFC Daresbury Laboratory
† david.walsh@stfc.ac.uk

ISBN 978-3-95450-177-9

ering the absolute phase information (i.e. the carrier envelope phase), whilst FROG methods only reveal relative spectral phase. This difficulty has been overcome by the recent development of "ReD-FROG" [13], but this technique still requires the use of an ultrashort laser probe pulse for cross-correlation as nonlinear materials suitable for a self-referenced FROG scheme do not exist at THz frequencies.

In the EOT diagnostic schema this new optical pulse is characterised using a variation of FROG known as GRENOUILLE [13]. A GRENOUILLE measurement is essentially a single-shot spectrally resolved autocorrelation from which a spectrogram is obtained. This is followed by the application of robust and experimentally proven algorithms to recover the temporal profile / spectral amplitude & phase. The self-referencing nature of autocorrelation is central to this diagnostic as it obviates the need for an ultrashort pulse probe, and the combination of this method with the now potentially several nanoseconds long probe pulse makes the EOT diagnostic highly tolerant to electron bunch timing jitter. GRENOUILLE is the most sensitive self-referenced FROG, but it still requires higher pulse energies than is expected from the EOT process with practical laser pulse energies and Coulomb field strengths. Because of this a temporal profile preserving broad bandwidth optical amplifier based on non-collinear optical parametric amplification, which is pumped by the same nanosecond laser from which the probe is derived, is integrated into our design. The >60 THz bandwidth design of this amplifier, with a gain capable of exceeding 1000x, has been reported elsewhere [8, 9].

EO methods are still not commonly implemented accelerator diagnostics, which may be due to the complexity and reliability of the amplified ultrashort pulse laser systems needed for high resolution systems. As all the optical pulses needed for the EOT diagnostic are on the nanosecond scale, they can all be derived from a Q-switched laser. This type of laser is commercially available as 'turn-key' systems having industrial levels of reliability.

PROOF OF PRINCIPLE

As part of system development and design it was necessary to verify the transposition principle central to the EOT diagnostic. As access to a suitable accelerator was not available a laser laboratory based experiment was devised around a laser driven large area photoconductive antenna (PCA) THz source, which operated as a stand in for the Coulomb field. The <3 THz bandwidth of this source was insufficient for testing the temporal resolution of the system, which in our design is limited by the material response itself (sub ~50 fs rms if GaP is used), however, the moderate THz field strength of >100 kV/m and consistent pulse parameters allowed a multi-shot autocorrelation based FROG measurement to be performed.

A schematic of the experimental system is shown in Fig. 1. The primary laser system was a 1.5 mJ, 50 fs, 500 Hz amplified Ti:Sapphire laser, which was split into 2 beams: 90% of the energy was used to pump the 75 mm diameter PCA, and the remaining 10% was used to generate the probe pulses. To accomplish this it was propagated through a scanning delay line and a 4-f spectral filter. The filter is convenient device that allows the spectral content of the ultrashort pulse to be filtered, without introducing dispersion, by adjusting the width of a slit aperture placed at its centre. In this way access to either a scanning 50 fs probe for THz Time Domain Spectroscopy (THz-TDS), or a narrow linewidth (~45 GHz) 10ps long probe, was accessible, for first measuring a true reference temporal profile and then performing the EOT evaluation respectively. The PCA bias voltage was triggered at half the rep rate of the laser (250 Hz) to facilitate lock-in detection. The THz and optical beams were then combined coaxially on an ITO coated glass substrate, after which they propagated to the EO crystal (4 mm ZnTe) where the nonlinear mixing took place. In order to make the THz-TDS reference measurement the following quarter wave plate was used to circularise the transmitted waves prior to entering a balanced detection scheme. The outputs of the balanced diodes were fed into a lock-in amplifier (SRS530) that triggered with the same 250 Hz as the PCA.

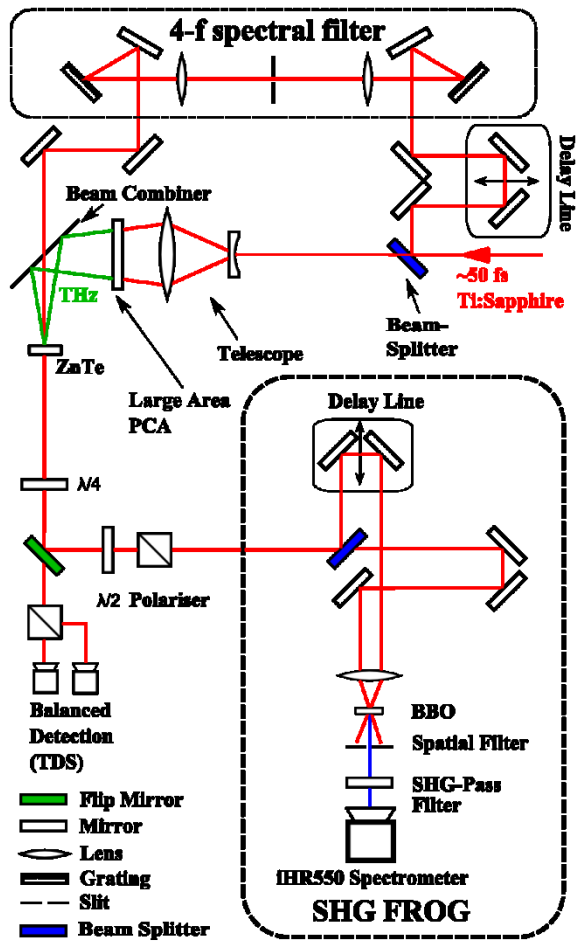

Figure 1: Schematic of the EOT verification system.

Once the reference trace was recorded (blue line, Fig. 3b), the quarter wave plate was set to cancel residual birefringence in the ZnTe so that a maximum extinction of the "THz-off" narrow-linewidth probe could be

ISBN 978-3-95450-177-9

achieved on the following Glan-Laser polariser. This separated the newly generated EOT pulse from the remaining, much higher energy, single frequency probe. The EOT pulse was then coupled into a home-made scanning autocorrelation FROG based on second harmonic generation in a 0.3 mm thick BBO crystal, an iHR550 imaging spectrometer, and a DiCAM Pro intensified camera.

The EOT pulse energy was measured to be just 0.5 nJ, leading to the need for 7680 single shot spectra to be averaged at each of the 128 time delays (62.5 fs steps) of the FROG spectrogram to reduce the noise to usable levels. Recording of the full spectrogram took several hours. This spectrogram was then analysed using commercially available and verified FROG deconvolution software, including pre-processing to remove excess noise and background signal. The processed spectrogram is shown Fig. 2 alongside the FROG recovered version.

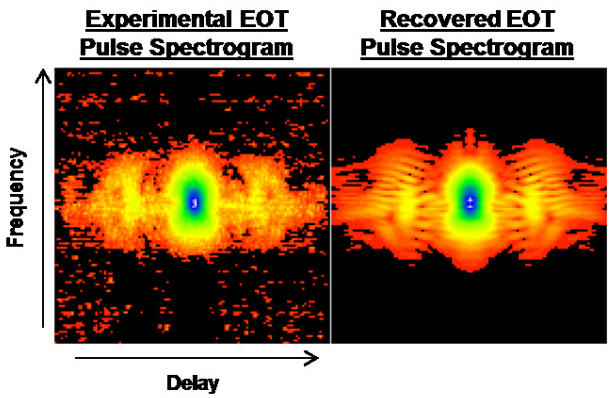

Figure 2: Filtered experimental and FROG recovered spectrograms shown in false colour to enhance visibility. The similarity in the traces can be seen.

The good agreement between the experimental and recovered spectrograms is clear, and is a good indicator that the FROG deconvolution was successful, despite the remaining noise. The FROG error was 0.007 – which is typical for a 128x128 spectrogram.

The temporal profiles are compared in Fig. 3. The FROG code returns intensity and phase, and THz-TDS returns the E-field, but it is straight forward to calculate the equivalent profiles as has been done here. There is a good match in the traces, including the electric field sign change at ~0.5 ps. However, in this particular measurement a well-known phase ambiguity of $\pm n\pi$ for well-separated pulses in SHG FROG necessitated the manual addition of π phase for the oscillations at ~2 ps in order for the profiles to match. It is envisaged that an improved signal-to-noise ratio, along with measuring a Coulomb field which should be monopolar, will mitigate this.

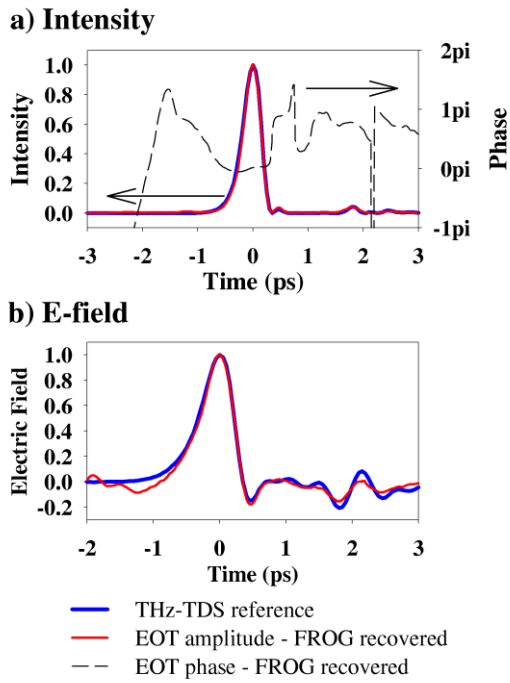

Figure 3: A comparison of the temporal profiles of the THz pulse measured via THz-TDS and EOT / FROG.

SUMMARY

We have demonstrated that the EOT process faithfully maps the THz temporal electric field profile into the temporal envelope of an optical pulse, which was then recovered using an autocorrelation based FROG technique. This verifies the core principles behind the proposed EOT electron bunch diagnostic, allowing us to proceed with developing this jitter insensitive diagnostic whose resolution is now only limited to the EO material response. The practical issue of having sufficient pulse energy will be addressed by implementing a non-collinear optical parametric amplifier in the EOT pulse path before the GRENOUILLE measurement is made. The main components of this EOT system are now tested, and a complete system is in the final stages of construction. It is anticipated that a complete end to end test (on a laser based THz pulse), using commercial nanosecond lasers (a Continuum Surelite and Sirah Cobra), will be performed soon.

REFERENCES

[1] F. G. Sun, Z. Jiang, and X.-C. Zhang, "Analysis of terahertz pulse measurement with a chirped probe beam", *Applied Physics Letters,* vol. 73, pp. 2233-2235, 1998.

[2] J. Shan, A. S. Weling, E. Knoesel, L. Bartels, M. Bonn, A. Nahata, *et al.*, "Single-shot measurement of terahertz electromagnetic pulses by use of electro-optic sampling", *Optics Letters,* vol. 25, pp. 426-428, 2000.

[3] S. P. Jamison, J. L. Shen, A. M. MacLeod, W. A. Gillespie, and D. A. Jaroszynski, "High-temporal-resolution, single-shot characterization of terahertz pulses"," *Optics Letters,* vol. 28, pp. 1710-1712, 2003.

ISBN 978-3-95450-177-9

[4] G. Berden, S. P. Jamison, A. M. MacLeod, W. A. Gillespie, B. Redlich, and A. F. G. van der Meer, "Electro-optic technique with improved time resolution for real-time, nondestructive, single-shot measurements of femtosecond electron bunch profiles", *Physical Review Letters,* vol. 93, p. 114802, 2004.

[5] N. H. Matlis, G. R. Plateau, J. van Tilborg, and W. P. Leemans, "Single-shot spatiotemporal measurements of ultrashort THz waveforms using temporal electric-field cross correlation", *Journal of the Optical Society of America B,* vol. 28, pp. 23-27, 2011.

[6] P. R. Bolton, J. E. Clendenin, D. H. Dowell, P. Krejcik, and J. Rifkin, "Electro-optic sampling of single electron beam bunches of ultrashort duration", *Nuclear Instruments and Methods in Physics Research Section A: Accelerators, Spectrometers, Detectors and Associated Equipment,* vol. 507, pp. 220-223, 7/11/ 2003.

[7] M. H. Helle, D. F. Gordon, D. Kaganovich, and A. Ting, "Extending electro-optic detection to ultrashort electron beams", *Physical Review Special Topics - Accelerators and Beams,* vol. 15, p. 052801, 2012.

[8] S. P. Jamison, D. A. Walsh, and W. A. Gillespie, "A femtosecond resolution electro-optic diagnostic using a nanosecond laser", presented at the IBIC2013, Oxford, UK, 2013.

[9] D. A. Walsh, W. A. Gillespie, and S. P. Jamison, "A femtosecond resolution electro-optic diagnostic using a nanosecond laser", presented at the FEL2013, New York, USA, 2013.

[10] D. A. Walsh, E. W. Snedden, and S. P. Jamison, "The time resolved measurement of ultrashort terahertz-band electric fields without an ultrashort probe", *Applied Physics Letters,* vol. 106, p. 181109, 2015.

[11] S. P. Jamison, G. Berden, P. J. Phillips, W. A. Gillespie, and A. M. MacLeod, "Upconversion of a relativistic Coulomb field terahertz pulse to the near infrared", *Applied Physics Letters,* vol. 96, p. 231114, 2010.

[12] R. Trebino, *FROG*: Springer US, 2000.

[13] E. W. Snedden, D. A. Walsh, and S. P. Jamison, "Revealing carrier-envelope phase through frequency mixing and interference in frequency resolved optical gating", *Optics Express* vol. 23, pp. 8507-8518, 2015/04/06 2015.

ISBN 978-3-95450-177-9

NON-INVASIVE BUNCH LENGTH DIAGNOSTICS OF SUB-PICOSECOND BEAMS*

S.V. Kuzikov†,1,2, A.A Vikharev, Institute of Applied Physics, Russian Academy of Sciences, Nizhny Novgorod, Russia
S. Antipov, Euclid Techlabs LLC, Bolingbrook, IL, USA
also at [1]Euclid Techlabs LLC, Bolingbrook, IL, USA
also at [2]Lobachevsky University of Nizhny Novgorod, Nizhny Novgorod, Russia

Abstract

We propose a non-invasive bunch length measurement system based on RF pickup interferometry. A device performs interferometry between two broadband wake signals generated by a single short particle bunch. The mentioned wakes are excited by two sequent small gaps in beam channel. A field pattern formed by interference of the mentioned two coherent wake signals is registered by means of detecror's arrays placed at outer side of beam channel. The detectors are assumed to be low cost integrating detectors (pyro-detectors or bolometers) so that integration time is assumed to be much bigger than bunch length. Because rf signals come from gaps to any detector with different time delays which depends on particular detector coordinate, the array allows to substitute measurements in time by measurements in space. Simulations with a 1 ps beam and a set of two 200 micron wide vacuum breaks separated by 0.5 mm were done using CST Particle Studio. These simulations show good accuracy. One can recover the detailed temporal structure of the measured pulse using a new developed synthesis procedure.

RF PICK-UP INTERFEROMETRY FOR BUNCH LENGTH MEASUREMENTS

We propose to design a device that will effectively perform interferometry between two broadband wake signals generated by the beam. At high repetition rates, interferometer scans at accelerators can be performed quickly. In a matter of seconds, the data can be averaged to improve the signal to noise ratio and allow the use of inexpensive pyro-detectors as opposed to bolometers. As a result one get spatial autocorrelation function for single shot measurement.

Measurements of ~10 ps Bunch Length

In the case of relatively long beams (10 ps) we propose to utilize power diodes with coaxial RF pickups arranged in pairs. A beam pickup intercepts a small fraction of the image current flowing along the beam pipe (Fig. 1). Two signals are combined with a time delay in a coaxial combiner.

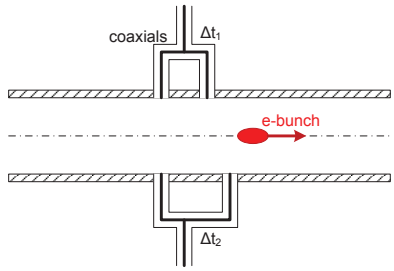

Figure 1: 10 ps resolution non-invasive bunch length measurement setup based on coaxial pairs placed along the z-direction.

Depending on the time delay between the RF pickups, the combined power varies as a function of time.The figure 2 shows the results of a simulation that involves a 10 ps beam passing by two RF pickup probes combined with variable delays. By using several pairs with different delays an autocorrelation function can be produced (Fig. 3).

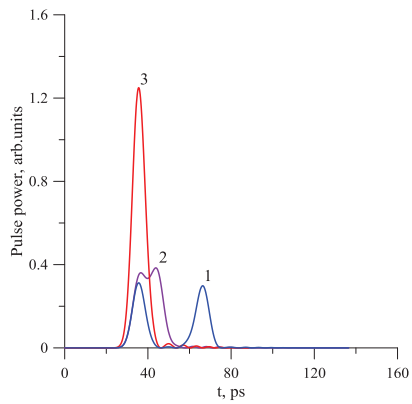

Figure 2: Power time dependence for various time delays.

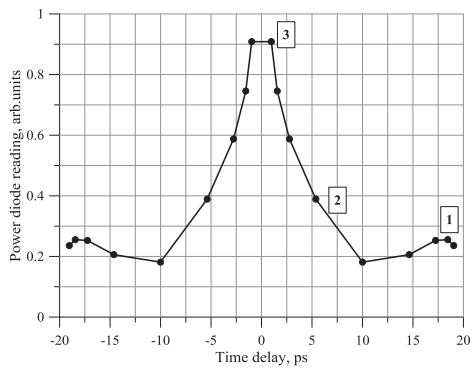

Figure 3: Pyro-detector's output for various time delay pairs.

*This work was supported by the Russian Scientific Foundation (project #16-19-10448).
†email address: sergeykuzikov@gmail.com

ISBN 978-3-95450-177-9

Measurements of Sub-picosecond Bunches

For this case the bunch length detection setup is depicted in Fig 4. As the beam passes the small gap its field radiates from the gap and travels towards the array of detectors. Due to the microstrip configuration there is no cut off for the excited mode so that signals of >1 THz spectrum width can be accurately measured. Depending on detector location the pulses from the first and second break will arrive with some relative time delay. Spatial interference scaled by $1/r$ in intensity will again correspond to an autocorrelation function. A commercial mm-wave - THz camera can be used as detector array [1].

The simulation with a 1 ps beam and a set of two 200 micron wide vacuum breaks separated by 0.5 mm was done using CST particle studio. The Fig. 5 shows the signal evolution with time. As the beam propagates a strong signal is generated at each break. These signals proceed to interfere and we measure them with an array of integrating pyro-detectors, bolometer arrays or a THz camera (red circles indicated on Fig. 5).

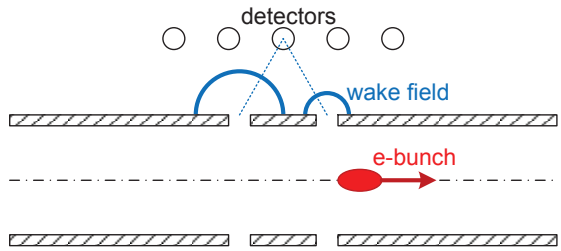

Figure 4: 1 ps non-invasive bunch length measurement setup.

The Fig. 6 shows autocorrelation function measured with probes placed parallel to the beam trajectory at the edge of the outer shell. Taking the measurements from this array of 11 detectors placed 2.5 mm away from the vacuum break wall, we obtained an autocorrelation function. Again we see that autocorrelation function characteristic width corresponds to the bunch length. In the simulation we used x-ray FEL parameters: 1 kA peak current beam (σ_z = 1 ps) produced 1 kW peak power. With ~1 kHz repetition rate the duty cycle is low – 1e-6 leading to 1 μW average power. This is well within the sensitivity level of pyro-detectors [1]. A cryo-cooled bolometer is even more sensitive.

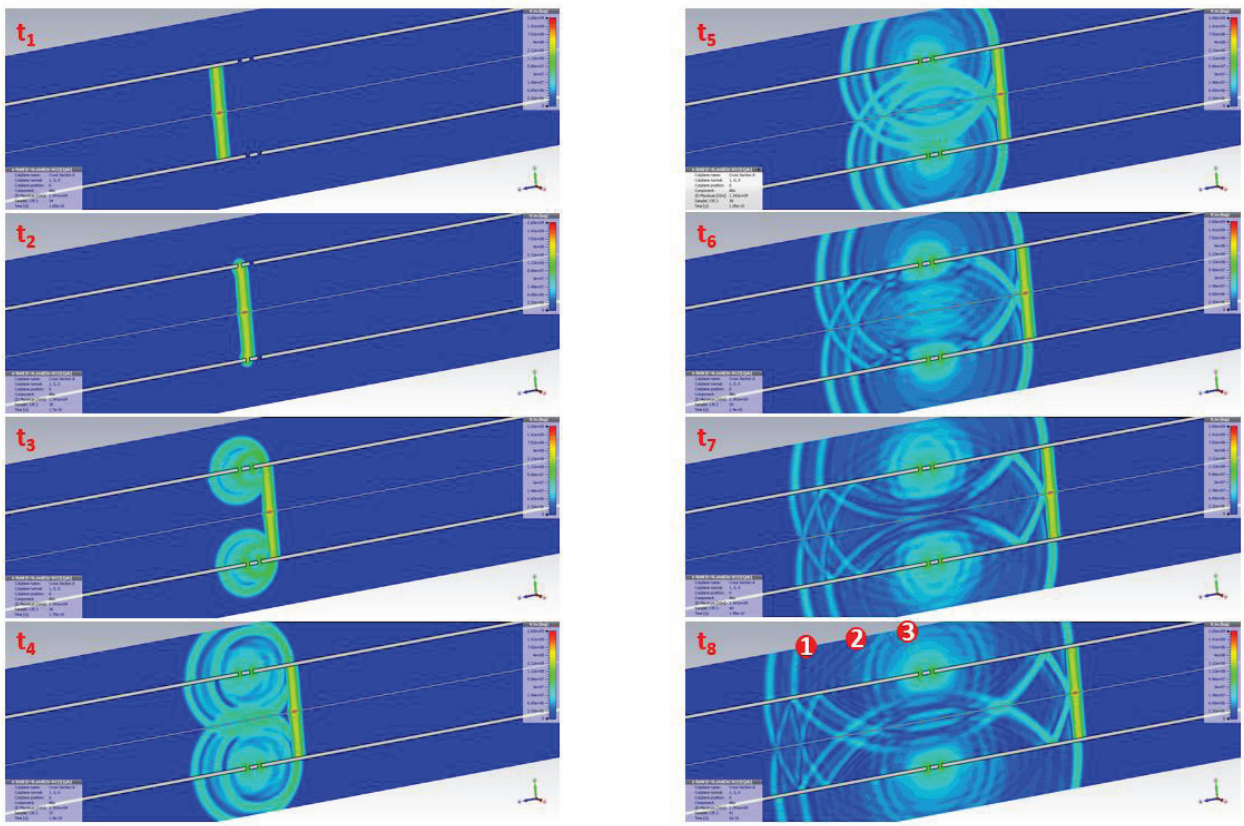

Figure 5: CST simulation of a 1 ps beam passing by two 200 micron vacuum breaks separated by 0.5 mm. Consequent shots at times t1, t2, … t8 are presented. There is an interference between excited pulses which can be measured with a detector array. The detector array location is shown on t8 with red circles.

ISBN 978-3-95450-177-9

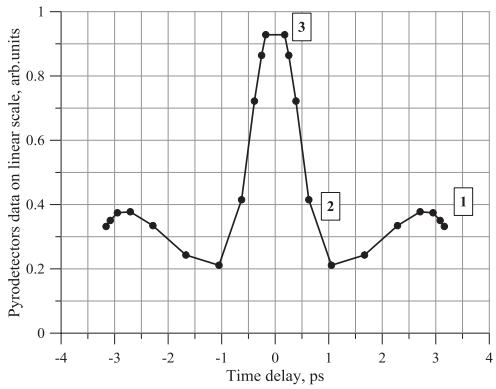

Figure 6: Pyro-detector's output for various time delay pairs, i.e. autocorrelation function.

SYNTHESIS PROCEDURE TO RECOVER PULSE SHAPE

A pyro-detector integrates (over time) the intensity of a sum of two identical pulses separated by a time delay τ, - $E(t)$ and $E(t+\tau)$:

$$\int_{-\infty}^{+\infty} |E(t)+E(t-\tau)|^2 dt = 2W + 2C(\tau), \quad (1)$$

W is the energy in the pulse and $C(\tau)$ is the autocorrelation function. This is measured in the experiment for various values of τ either by moving the mirror in an interferometer [2] or by combining signals in separate RF pickup pairs with various delays τ, as proposed here or by measuring at different positions for spatial correlation as proposed and implemented for CTR interferometry [3].

Note that Fourier transform of the autocorrelation function equals to the square of the absolute value of the Fourier transform, $F(\omega)$, of the original signal:

$$\int_{-\infty}^{+\infty} C(\tau)\cdot\exp(i\omega\tau)d\tau = \left|\int_{-\infty}^{+\infty} E(t)\cdot\exp(i\omega t)dt\right|^2 = |F(\omega)|^2 \quad (2)$$

The Eqs. (1) and (2) allow to describe the problem of pulse shape recovery. One knows the absolute value of Fourier transform, one also knows that function describing pulse shape $u(t)$ is the real function, the phase of $u(t)$ is flat (or it is flat with finite number of jumps on π in general case). Using this information one needs to find the unknown phase of spectrum and pulse shape $u(t)$ as well. As a rule there is also an additional information that $u(t)$ is defined at some time interval T, $u(t)$ equals to zero everywhere out of the mentioned interval.

In order to solve this incorrect mathematical problem an iteration procedure can be implemented. One chooses an initial approach for the unknown function $u_0(t)$ (for example, a rectangular shape can be used), then the Fourier transform $F_0(\omega)$ has to be calculated. The absolute value of the obtained $F_0(\omega)$ does not generally coincide with the square root of Fourier's transform for the measured autocorrelation function. That is why, for the next iteration one can hide the obtained $|F_0(\omega)|$, but to keep the obtained phase. So a new Fourier function is to be:

$$F_1(\omega) = |F(\omega)|\cdot\exp(j\arg[F_0(\omega)]). \quad (3)$$

Knowing a new approach of Fourier transform, one calculates a new approach $u_1(t)$. For a next step, one produces $u_2(t)$, saving the absolute value of $u_1(t)$ within time interval T and inserting the flat phase. The flat phase corresponds to the particular case, when frequency dispersion is negligibly small so that pulse shape does not degrade at distance to measuring detectors. In a general case the phase, as it was mentioned, can include as big jumps as π. In this case the obtained phase should be processed using a filter which has in output 0 or π in dependence on to that value $\arg[u_n(t)]$ is closer.

According to the described procedure one can calculate $F_n(t)$ and $u_n(t)$ respectively. From iteration to iteration these functions approach to the given $|F(\omega)|$ and to the true $u(t)$ correspondingly.

The proposed procedure belongs to methods studied in the papers [4-7]. In particular, a similar procedure was used for recovering of amplitude and phase distributions of quasi-optical wavebeams [6]. In these papers it was noted that multiple solutions can arise. The procedure is not necessary going to a true distribution. The only statement is that from iteration to iteration the mutual content of a function at current iteration and true function does not reduce. A quality of the procedure depends on many factors. Nevertheless, in most cases the procedure provides good accuracy better that 1%.

CONCLUSION

The carried out simulations show that picosecond as well as sub-picosecond bunch lengths can non-destructively be measured for a single shot using interferometry between two broad-band signals produced by bunch itself. An iterative synthesis procedure allows also recovering a particular longitudinal bunch shape.

REFERENCES

[1] TeraSense, http://terasense.com/products/sub-thz-imaging-cameras/
[2] A. Murokh *et al.*, Nucl. Instr. and Meth. A 410, 452 (1998).
[3] G. Andonian *et al.*, "A Real-time Bunch Length Terahertz Interferometer", Proceedings of EPAC08, Genoa, Italy, TUPC073.
[4] F. Bakkali Taheri *et al.*, "Electron bunch profile reconstruction based on phase-constrained iterative algorithm", PHYSICAL REVIEW ACCELERATORS AND BEAMS 19, 032801 (2016).
[5] S.V. Kuzikov, "Paraxial Approach to Description of Wave Propagation in Irregular Oversized Waveguides", International Journal of Infrared and Millimeter Waves, Vol. 18, No.5, 1997, pp. 1001-1014.
[6] A.V. Chirkov *et al.*, "Mode content analysis from intensity measurements in a few cross-sections of oversized waveguides", International Journal of Infrared and Millimeter Waves, Vol. 18, No. 6, 1997, pp. 1323-1334.

ISBN 978-3-95450-177-9

A TRANSVERSE DEFLECTING STRUCTURE FOR THE PLASMA WAKEFIELD ACCELERATOR EXPERIMENT, FLASHForward

R. D'Arcy*, V. Libov, J. Osterhoff
DESY, Hamburg, Germany

Abstract

The FLASHForward project at DESY is an innovative plasma-wakefield acceleration experiment, aiming to accelerate electron beams to GeV energies over a few centimetres of ionised gas. These accelerated beams must be of sufficient quality to demonstrate free-electron laser gain; achievable only through rigorous analysis of both the drive- and accelerated-beam's longitudinal phase space. The pulse duration of these accelerated beams is typically in the few femtosecond range, and thus difficult to resolve with traditional diagnostic methods. In order to longitudinally resolve these very short bunch-lengths, it is necessary to utilise the properties of a transverse RF deflector, which maps longitudinal onto transverse co-ordinates. It is proposed that this type of device – commonly known as a Transverse Deflecting Structure (TDS) due to its 'streaking' in the transverse plane – will be introduced to the FLASHForward beam line in order to perform these single-shot longitudinal phase space measurements. The initial investigations into the realisation of this diagnostic tool are outlined.

INTRODUCTION

The FLASHForward facility [1] at DESY aims to accelerate electron beams to GeV energies over a few centimetres of ionised gas through the principle of Plasma Wakefield Acceleration (PWFA). The FLASHForward beam line utilises sections of the FLASH Linac [2] to extract compressed electron bunches for injection into plasma. Longitudinal diagnosis of both the drive beam entering – as well as the witness beam exiting – the plasma are necessary to the understanding of PWFA physics processes. The resulting accelerated witness bunches, with bunch lengths limited by the plasma wavelength, exit the plasma with a priori unknown bunch parameters. Expected bunch parameter ranges for both driver and witness bunches on FLASHForward can be seen in Table 1, demonstrating the diverse nature of these beams. It is therefore essential to diagnose these beams in full 6D phase space.

The longitudinal and transverse diagnostics provided by a Transverse Deflecting Structure (TDS) system would reveal key information about these drive beams, allowing for the maximising of energy gain in the plasma through bunch shaping. The capability to diagnose witness beams would also yield invaluable insight into the results of acceleration, providing a tool to differentiate between the nuances of distinct injection schemes (thus confirming the validity of particle-in-cell codes), as well as an additional resource in optimising the system for FEL gain. No prior PWFA facility has benefitted from the functionality of an X-band TDS to diagnose both drive and witness bunches. This paper will concern itself with the design, implementation, and simulations of such a system.

PROPOSED TDS SYSTEM

Due to the proximity of the FLASHForward and FLASH2 beam lines, it is proposed that an X-band RF system is shared in order to mitigate costs. The proposed experimental plan can be seen in Fig. 1. In this setup, a low-level RF source would supply power to a klystron and modulator unit. These components would sit outside the experimental hall in the adjacent corridor. A high-power acceptance mechanical X-band RF switch would then direct 100% of the RF power to either the FLASHForward or FLASH2 waveguides and X-band TCAV sections. Once this system has been commissioned, a pulse compression unit will be installed to increase the peak power supplied to the cavities.

The voltage kick experienced by a beam travelling through a deflecting cavity is defined by

$$V[MV] = R[MV/m\sqrt{MW}]\; l[m]\; \sqrt{P[MW]} \quad , \qquad (1)$$

where R and l are the shunt impedance and length of the cavity, respectively, and P is the power supplied to the cavity. Although designs for the cavity and RF source have yet to be finalised, initial figures of $R \sim 6\ MV/m\sqrt{MW}$, $l \sim 1.0\ m$, and $P \sim 25\ MW$ are expected. For this reason, a voltage kick of 30 MV will be assumed in all further calculations unless otherwise stated.

BEAMLINE DESIGN

It is common practice to employ a TDS system for both longitudinal phase space and transverse slice emittance measurements. In order to successfully measure these param-

Table 1: Driver and Witness Bunch Parameters Expected at FLASHForward

Parameter	Driver	Witness
E [GeV]	0.5–1.2	1.2–2.5
$\Delta E/E$ (uncorrellated) [%]	<0.1	1
$\varepsilon_{n,(x,y)}$ [μm]	2–5	0.1–1
$\beta_{x,y}$ (in plasma) [mm]	20	1
σ_t [fs]	50–500	1–100
Q [pC]	20–1000	1–500

* richard.darcy@desy.de

ISBN 978-3-95450-177-9

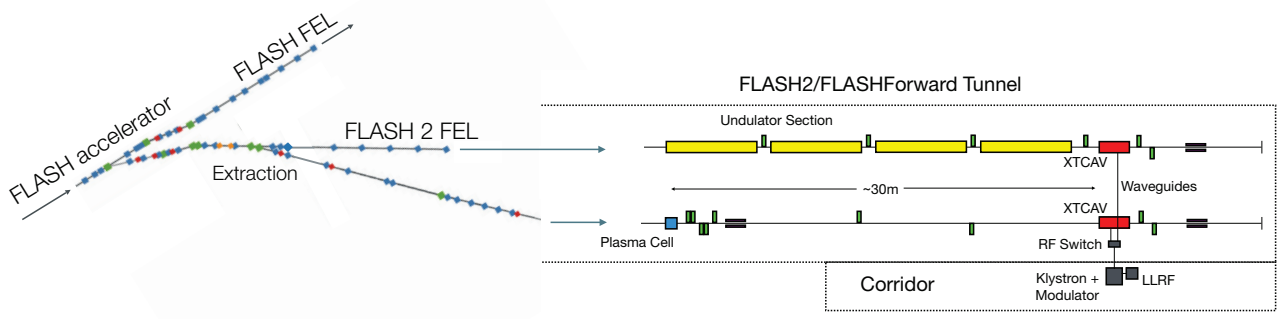

Figure 1: A schematic of the FLASH beam line, demonstrating extraction into FLASH2, with subsequent extracting into FLASHForward. A sketch of the proposed experimental hall layout is also shown, with the placement of the shared RF source and respective deflecting cavities illustrated.

eters, a beam line design is required to meet certain constraints.

For the case of the longitudinal phase space measurement, these constraints are predominantly defined by the desire to maximise the streak of the TDS,

$$S = \sqrt{\beta_y(s)\beta_y(s_0)}|\sin\mu_y(s_0,s)|\frac{eVk}{E} \quad , \qquad (2)$$

where $\beta_y(s)$ and $\beta_y(s_0)$ are the vertical beta functions at the imaging screen and TDS, respectively, $\mu_y(s,s_0)$ is the vertical phase advance between the TDS and the screen, E is the beam energy, V is the cavity voltage, and k is the RF wave-number. The longitudinal resolution is thus defined as

$$R_z = \frac{\sigma_y}{S} = \sqrt{\frac{\varepsilon_y(s)}{\beta_y(s_0)}}\frac{1}{|\sin\mu_y|}\frac{E}{eVk} \quad . \qquad (3)$$

From an optics standpoint, a maximal streak requires a phase advance of $n\pi/2$ (where n is an odd integer) and large beta function in the streaking plane at the TDS (chosen as y in the case of FLASHForward). The energy resolution is defined as

$$R_\delta = \frac{\sigma_x}{|D_x|} = \sqrt{\varepsilon_x}\frac{\sqrt{\beta_x}}{|D_x|} \quad , \qquad (4)$$

where D_x is the dispersion introduced by the dipole downstream of the TDS. Again, in order to maximise the energy resolution, it is necessary to maximise dispersion, either with a large dipole field or a large distance between the dipole and imaging screen.

For the case of the slice emittance measurement, the constraints combine those of a typical quad scan – i.e. a progression in phase advance between the reference point, just upstream of the first scanning quadrupole (see Fig. 2 for placement) and measurement location, $\mu_x(s_{\mathrm{ref}},s)$, ideally covering a range of $[0,\,\pi]$ – and, again, maximising the streak from the TDS.

A summary of all the beam line constraints required for optimisation in the case of FLASHForward are outlined in Table 2.

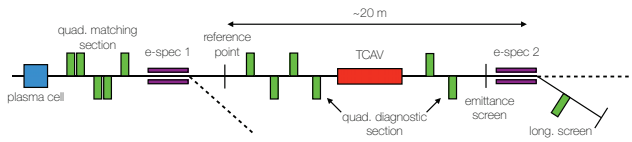

Figure 2: A sketch of the post-plasma cell beam line optics configuration defined by the constraints outlined in Tab. 2.

This particular level of control over optics cannot be achieved by a single quadrupole, but instead requires a number of quadrupoles at least equal to the number of optimisation constraints [3]. The beam line downstream of the reference point therefore requires a minimum of five quadrupoles. In this case, due to hardware availability, an additional six quadrupoles are added between the reference point and the emittance screen (four upstream of the TDS and two downstream), with a final quadrupole in the dispersive section for added experimental flexibility. A sketch of this optics configuration can be seen in Fig. 2. The variables used for optimisation are thus the strengths of the quads and the drifts between them.

Table 2: A Summary of the Optimisation Constraints Required for Slice Emittance and Longitudinal Phase Space Measurements at FLASHForward

Parameter	Constraint	Location
	in both cases	
β_y	< 10 m	screen
β_x	> 10 m	screen
μ_y	$\pi/2$	TDS to screen
β_y	> 100 m (maximised)	TDS
	slice emittance	
μ_x	$[0,\,\pi]$	ref. point to screen
	long. phase space	
D_x	> 0.5 m	screen

ISBN 978-3-95450-177-9

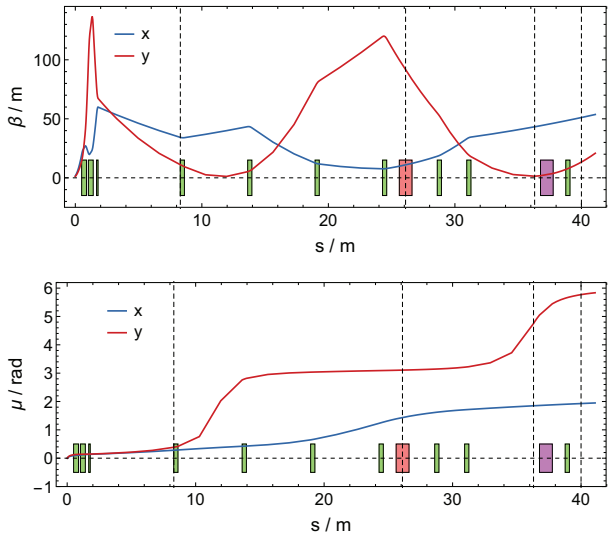

Figure 3: The beta function and phase advance in both transverse planes for the matched slice emittance midpoint case. The location of the quadrupoles (green), TDS (red), and dipole (purple) are indicated on the plot. The vertical dashed lines represent (from left to right) the reference point, centre of the TDS, emittance screen, and dispersive screen.

LINEAR OPTICS AND MATCHING

The beam line depicted in Fig. 2 was substantiated in `elegant` [4] in order to match the optics to the constraints outlined in Tab. 2.

Matching for the case of slice emittance was chosen as the first step in optimisation due to the complexity of optics required to fit the full $[0, \pi]$ phase advance range in x. The midpoint case of $\mu_x(s_{\text{ref}}, s) = \mu_y(s_0, s) = \pi/2$ was used as a starting point, with a progression in μ_x around this point. The beta functions and phase advances for the matched midpoint case can be seen in Fig. 3. The values of these constraints after optimisation for this midpoint case – $\beta_y(s_0) = 99.9\ m$, $\beta_y(s) = 1.4\ m$, $\beta_x(s) = 43.2\ m$, $\mu_y(s_0, s) = 1.6\ rad$, and $\mu_x(s_{ref}, s) = 1.6\ rad$ – are all within the tolerances of the optimisation routine.

The location of, and distances between, the quads were then fixed by this midpoint solution, leaving the quad strengths as the only optimisation variables. A successful demonstration of this matching over $0<\mu_x<\pi$ can be seen in Fig. 4.

The beam line fixed by the slice emittance optimisation was then used to match for the longitudinal phase space constraints. The result of this matching, in the form of the beta functions and phase advances in both transverse planes, can be seen in Fig. 5. The values of these constraints after optimisation – $\beta_y(s_0) = 99.9\ m$, $\beta_y(s) = 2.7\ m$, $\beta_x(s) = 60.0\ m$, $\mu_y(s_0, s) = 1.6\ rad$, and $D_x = 0.87\ m$ – once again indicate successful matching.

By inputting the values from the longitudinal phase space matching to Eqs. 3 & 4, the longitudinal and energy resolutions for this case are 1.37 fs and 2×10^{-4} (respectively) for a typical FLASHForward drive beam with $E = 1\ GeV$ and $\varepsilon_{n,(x,y)} = 2\ \mu m$, and a deflecting cavity with $V = 30\ MV$ and $f = 11.99\ GHz$ ($k = 0.026\ m^{-1}$).

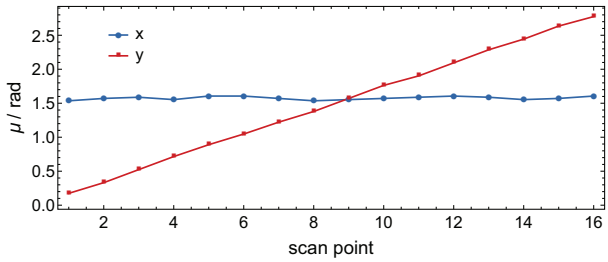

Figure 4: The evolution of μ_x over an almost full range of $[0, \pi]$, with μ_y fixed at $\pi/2$ in each case. The x-axis simply represents the optimisation scan point number.

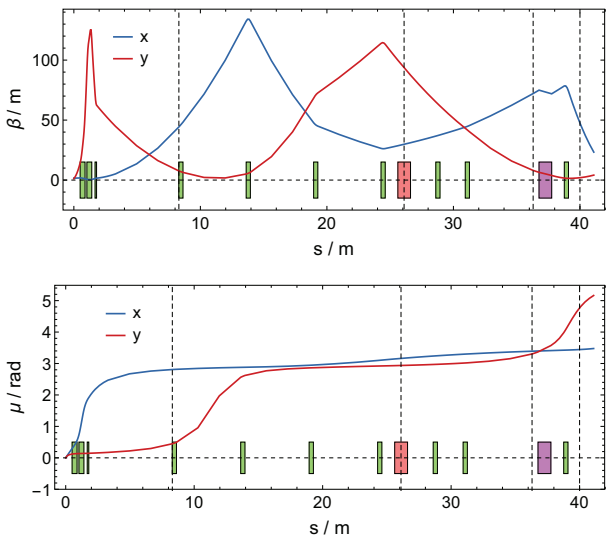

Figure 5: The beta function and phase advance in both transverse planes for the matched longitudinal phase space case. As in Fig. 3, the optics elements and screens are illustrated on each plot.

PARTICLE TRACKING

After matching with linear optics a distribution from a full 3D simulation of FLASH was used for particle tracking [5]. The longitudinal phase space at the exit of the plasma cell for this distribution can be seen in Fig. 6. The distribution has an irregular shape due to collective effects (e.g. coherent synchrotron radiation in the bunch compressors, space charge, etc.) experienced in the upstream Linac. Such beams with potentially harmful centroid offsets may be seen at FLASHForward, highlighting the necessity for phase space analysis. For this reason, the example distribution in Fig. 6 will be used for further analysis.

The distribution in Fig. 6 is propagated through the entirety of the beam line shown in Fig. 2. This bunch will experience a transverse kick from the TDS (mapping the longitudinal plane z onto the transverse plane y) and a bending

ISBN 978-3-95450-177-9

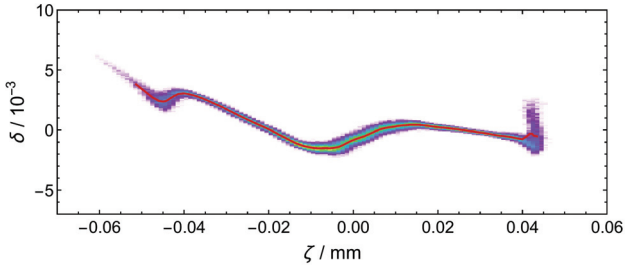

Figure 6: The longitudinal phase space of the input distribution, used for particle tracking in the FLASHForward `elegant` beam line. The y- and x-axis represent the relative energy spread and centre of mass frame of the bunch, respectively.

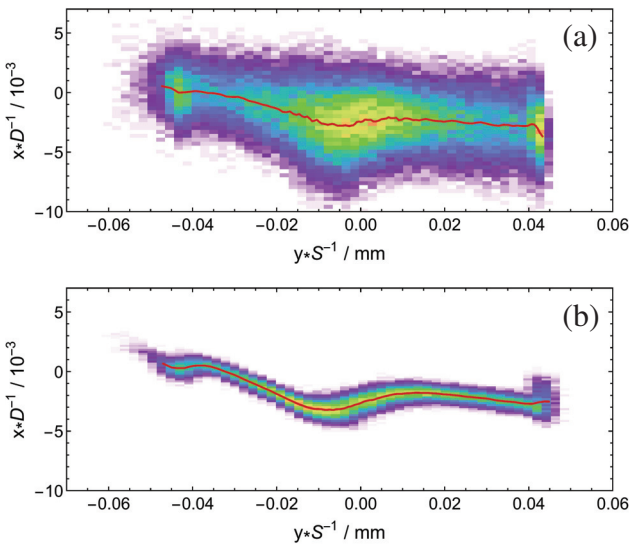

Figure 7: The reconstructed longitudinal phase space at the dispersive screen for a streaking voltage of a) 30 MV, and b) 6 MV.

force from the dipole (equating the longitudinal plane δ with the transverse plane x). This allows the longitudinal phase space distribution entering the TDS to be reconstructed from the transverse plane at the dispersive screen. This reconstruction is shown in Fig. 7 for two streaking voltages, with the axes normalised by the TDS streak and dipole-induced dispersion for x and y respectively.

According to the Panofsky-Wenzel theorem [6], off-axis particles travelling through an RF deflecting cavity experience longitudinal electric fields. This leads to the energy smearing seen in both cases, with the larger streak resulting in a larger energy smear. This smearing can be reduced through a reduction in the streak (most easily realised by decreasing the cavity voltage), however this comes at the cost of longitudinal resolution.

It is the compromise between R_z and R_δ which is of the utmost importance when attempting single-shot measurements with a TDS. The results shown here indicate that it may be difficult to find a single-shot working point for this particular drive beam scenario whilst maximising resolution in both planes.

However, the energy spread induced by a TDS is defined as,

$$\sigma_\delta = \frac{eVk}{E}\,\sigma_y \quad , \tag{5}$$

so a reduction in the emittance of the beam would reduce the induced energy spread. As can be seen in Tab. 1, the witness beams expected at FLASHForward should have much smaller emittances than those of the drive beam, leading to a reduction in energy spread.

Additionally, it has been demonstrated that the analytical energy spread induced by a TDS correlates extremely well with experimental results [7]. If these experimental results can be recreated on FLASHForward then the factors limiting high resolution longitudinal phase space measurements may be observed and quantified, aiding in offline corrective methods.

CONCLUSIONS AND OUTLOOK

A post-plasma beam line, with the inclusion of a TDS system for transverse and longitudinal diagnostics, has been designed for FLASHForward. All necessary constraints for this design have been met via substantiation and matching of the beam line in `elegant`. Both linear optics and particle tracking demonstrate successful TDS operation. The simulation package has indicated a need for compromise between the energy and longitudinal resolution when operating with typical FLASHForward drive beams. However, offline corrective methods through experimental commissioning of the system have been shown to mitigate these limitations in other systems.

The results of this study will be furthered to cover the entire parameter phase space expected for both FLASHForward drive and witness bunches – the results of which will aid in finalising the design of the TDS system. Once the system is built and installed on FLASHForward, a comparison with experimental data will be made.

ACKNOWLEDGEMENTS

Thanks go to Stephan Wesch for his help and support with the `sdds2math` plotting packages. The authors would also like to thank the Helmholtz ARD program VH-VI-503 for their funding and support.

REFERENCES

[1] B. Foster *et al.*, NIM A 806 (2014) 175.

[2] K. Tiedtke, *et al.*, *New Journal of Physics* 11 (2009) 023029.

[3] E. Prat, *et al.*, *Phy. Rev. ST Accel. Beams* 17 (2014) 104401.

[4] M. Borland, Advanced Photon Source LS-287 (2000).

[5] G. Feng, private communications.

[6] W. K. H. Panofsky, W. Wenzel, *Rev. Sci. Instr.* 27:967 (1956).

[7] C. Behrens, C. Gerth, *Proc. of DIPAC11*, Hamburg, Germany (2011) TUPD31.

ISBN 978-3-95450-177-9

LASER ARRIVAL TIME MEASUREMENT AND CORRECTION FOR THE SwissFEL LASERS

M. Csatari Divall†, C. P. Hauri, S. Hunziker, A. Romann, A. Trisorio, Paul Scherrer Institut, 5232 Villigen PSI, Switzerland

Abstract

SwissFEL will ultimately produce sub-fs X-ray pulses. Both the photo-injector laser and the pump lasers used for the experimental end stations therefore have tight requirements for relative arrival time to the machine and the X-rays. The gun laser oscillator delivers excellent absolute (including reference jitter) jitter performance at ~25 fs integrated from 10 Hz-10MHz. The Yb:CaF_2 regenerative amplifier, with an over 1 km total propagation path, calls for active control of the laser arrival time. This is achieved by balanced cross-correlation against the oscillator pulses and a translation stage before amplification. The experimental laser, based on Ti:sapphire laser technology will use a spectrally resolved cross-correlator to determine relative jitter between the optical reference and the laser, with fs resolution. To be able to perform fs resolution pump-probe measurements the laser has to be timed with the X-rays with <10 fs accuracy. These systems will be integrated into the machine timing and complemented by electron bunch and X-ray timing tools. Here we present the overall concept and the first results obtained on the existing laser systems.

INTRODUCTION

Excellent timing jitter can be achieved in modern mode-locked solid state lasers [1]. They are standardly used as master oscillator to act as the heart of large accelerator complexes, as timing signals can be distributed in stabilized fiber links over many km's [2]. However to reach required energy to drive photo-injectors, as well as for experiments in FEL's, further amplification is needed. To reach mJ levels of energy in each pulse at up to kHz repetition rates, regenerative and multi-pass amplifiers are used. These include many roundtrips and propagation both in material as well as in air and make the output pulse arrival dependent on environmental factors, such as temperature, humidity, pressure, vibrations and air-flow [3]. To reach required specification, active stabilization of the laser arrival time is necessary. In the following section we describe the laser systems to be used at SwissFEL as well as the required timing stability and present a general concept for laser timing stabilization.

Laser Systems at SwissFEL

Table 1 summarizes the laser parameters and timing requirements for both laser systems. The experimental laser system [4] is based on chirped-pulse amplification in Ti:Sa from Coherent. The system is seeded by Vitara Oscillator and pulses are amplified in Legend Elite Duo HE+ amplifier, with a custom made post amplifier stage and Revolution pump lasers. With this layout it provides a compressed output energy > 20 mJ, centred at 800 nm and at 100 Hz repetition rate.

Table 1: Laser Specifications and Timing Requirements

Parameter	Experiment Laser	Gun Laser	Units
Wavelength	800	260	nm
Meas. resolution	10 (1)	25	Fs
Overall rms jitter	150	40	Fs
Pulse length	0.03	4-10	ps
Rise and fall-time	10	700	fs
Pulse Energy	10	2	mJ
Reference wavelength	1560		nm
Pulse length	180		fs
Pulse energy	0.2		nJ

The gun laser is a hybrid fiber front-end Yb:CaF_2 CPA system, operating at 1041 nm [5]. The oscillator from OneFive[1] at 71.4 MHz delivers broadband pulses and seeds the regenerative amplifier (Amplitude Systeme[2]), which is operating at up to 100 Hz repetition rate. The pulses reach 2.5mJ energy before compression. The system has a UV output, a short probe diagnostic output and an IR beam for the laser heater, all with their individual compressors.

The reference laser is also delivered by OneFive, operating at 1560 nm, delivering 180 fs pulses in stabilized and dispersion compensated fiber links, with 0.2 nJ energy in each pulse. The repetition rate of the master oscillator is at 142.8 MHz, which is twice of the seed oscillators, used for the laser systems. It is expected that the added timing jitter of the links is below 10 fs rms, with a drift of less than 10 fs peak to peak over 24h [6].

Timing Overview

Figure 1 shows the general concept for obtaining timing overlap between the laser output and the master reference link. In both cases the pulse train from the link is compared on a fast ADC with the output pulses from the laser and coarse overlap is obtained via free-space delay stages.

† marta.divall@psi.ch

[1] http://www.onefive.com/

[2] http://www.amplitude-systemes.com/amplifiers-s-pulse.html

ISBN 978-3-95450-177-9

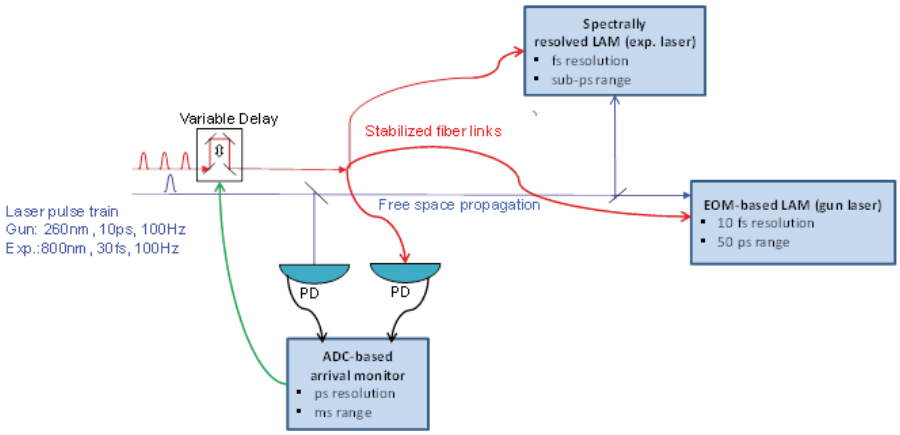

Figure 1: General concept for laser arrival time measurement (LAM) and control.

Eventually this can become part of the stabilized link, where a phase-shift can be set while maintaining the same stability from the reference. For the experimental laser a spectrally resolved cross-correlator will be used, which has shown to achieve fs resolution [7]. For the gun laser it is important to compensate for the drift up to the entrance of the gun and therefore timing measurements must take place in the UV. Here, a technology well established for Beam Arrival Monitors (BAM) will be used [8], based on ultra-broadband electro-optical modulators driven by fast photo-diode signals generated by the UV pulse. From this system 10 fs resolution is expected.

GUN LASER TIMING

Figure 2 shows the general layout of the laser system with the laser arrival related hardware. Near the oscillator there is a LAM development area aiming to stabilize the output of the regenerative amplifier, as well as space for optical locking of the oscillator against the optical reference, which is planned for 2017. The pulse is compressed after the chirped pulse regenerative amplifier and converted to UV. After pulse shaping both in space at time, detailed in [5] the laser is propagated to the tunnel output port. Here, part of the beam is taken for development of the UV LAM and for temporal characterization of the UV pulses. The beam is then sent into the tunnel, where the final LAM will be installed to generate timing error signals against the optical reference, using part of the beam entering the gun. The error signal will be fed back to the translation stage before the regenerative amplifier to compensate for slow drifts.

Oscillator

The oscillator delivers three outputs. The main, 2nJ free-space output seeds the amplifier. The output of the pulse-picker is also available with quasi 71.4 MHz to be used for LAM development. The additional fiber outputs at ~0.18nJ are used for synchronization and to generate clock-signals. The laser is locked to the master RF distribution system (42nd harmonic of the laser), showing an excellent 23.8 fs integrated absolute jitter 10Hz-1MHz, which is well within the specification for the gun operation. More details on the oscillator performance can be found in [9].

Amplifier

The cw diode pumped regenerative amplifier provides the required IR energy in a single stage with high beam quality. However the amplifier build-up time mounts to several microseconds, corresponding to over 1 km total propagation path. To ensure good passive stabilization all the components are packaged in a single, thermally stabilized box. This ensures also high mechanical stability of the system preventing sensitivity to environmental changes and vibration.

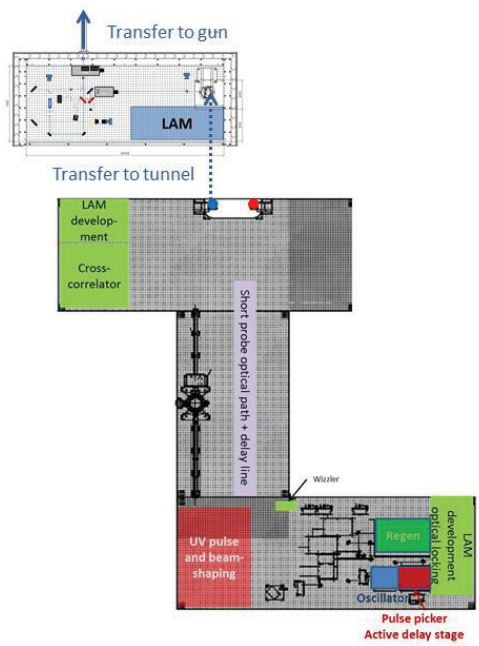

Figure 2: Layout of the gun laser system, with the position of the laser arrival monitors

Timing jitter characterization was performed by the company (Amplitude Systeme) on a similar laser system, running at 10 kHz. With active stabilization, using

ISBN 978-3-95450-177-9

Smaract delay stages[3], a 5 fs additive jitter was achieved (0.1 Hz-10 kHz) over an hour [10].

Amplifier box Before the delivery of the laser system, extensive tests were carried out on the amplifier box to estimate timing drifts due to environmental changes as well as vibration. For this an interferometer (Renishaw XL-80[4]) was used. The optics were placed were the cavity mirror positions were planned, with the interferometer outside the box (Fig. 3.). The total path-length for the HeNe beam was 169 cm, corresponding to 11.27 ns delay in double path. The final system laser system has 2 µs build-up time with an allowable 40fs total drift shot to shot. Our aim was therefore to show that the drifts and shot-to shot variations stay below 68nm/roundtrip. Temperature sensors were installed to monitor the environment and the box.

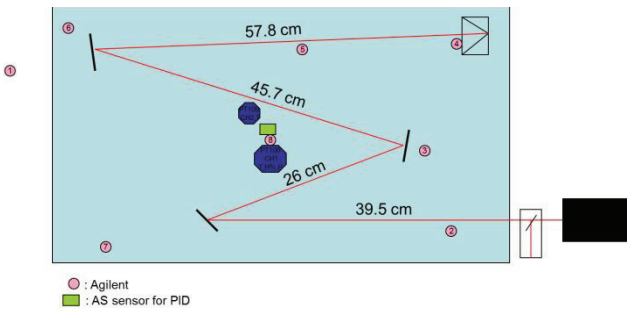

Figure 3: Experimental setup to measure performance of the laser box, using interferometry

The measurement shown on Fig. 4 was performed at 10 Hz with the temperature recorded every 2 seconds. The temperature changes of the box matches well the outside temperature and the optical path-length drift show clear correlation to these changes.

Drift, corresponding to the total build-up time of the amplifier, would be 16 ps/°C. The laboratory temperature is stabilized to 0.1°C, which would give a drift ~1.6 ps. It is clear, that active stabilization is necessary. Tests will be done in the future to stabilize the box temperature independently to 0.01°C. For this, resistors are installed and equally distributed underneath the amplifier box and are connected to a PID loop driving a heating unit.

Further measurements were performed to analyse the sensitivity of the box to vibrations and to determine characteristic frequencies. These measurements are shown on Fig. 5. The box and the table were tapped by a rubber hammer a few times to see how vibration propagates into the box. The measurement results were compared to the vibrations picked up by the table to identify characteristic frequencies of the box. Peaks were found at 360 Hz and 490Hz. This is important, as the laser will run at 100 Hz and therefore these vibrational modes will appear as shot to shot noise no possible to compensate for. High quality optical table and proper fixing of the box will ensure the damping of these modes. Short term measurements have shown 40 fs/min equivalent drift, which is easy to compensate for. Shot to shot jitter at 50 kHz sampling rate gave 0.19 fs equivalent jitter, which is excellent and shows that with active stabilization the system can deliver the specified jitter and drift.

Extensive measurements and correction are planned in the final position of the amplifier, using a balanced optical cross-correlator and comparing the output pulses of the amplifier with the seed oscillator.

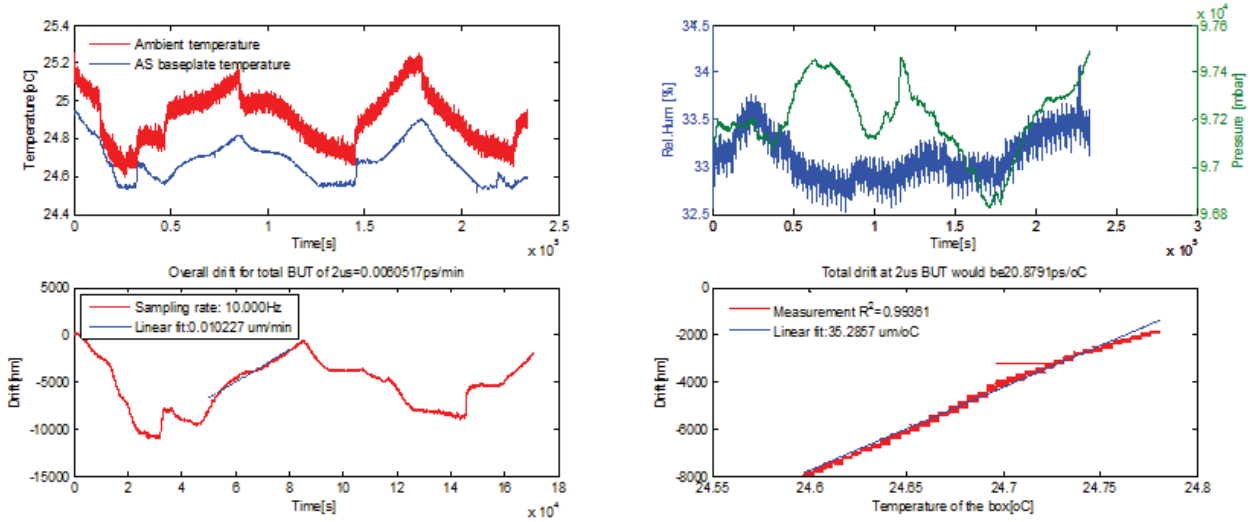

Figure 4: Interferometric drift measurements performed on the amplifier box showing correlation between ambient and box temperature (top left), as well as drift of the optical path with the temperature change (bottom left) and correlation plot (bottom right). Other environmental changes were also recorded during the measurement (top left).

[3] http://www.smaract.com/products/linear-positioners/slc-series
[4] http://resources.renishaw.com/en/details/manual-laserxl-english--61500

ISBN 978-3-95450-177-9

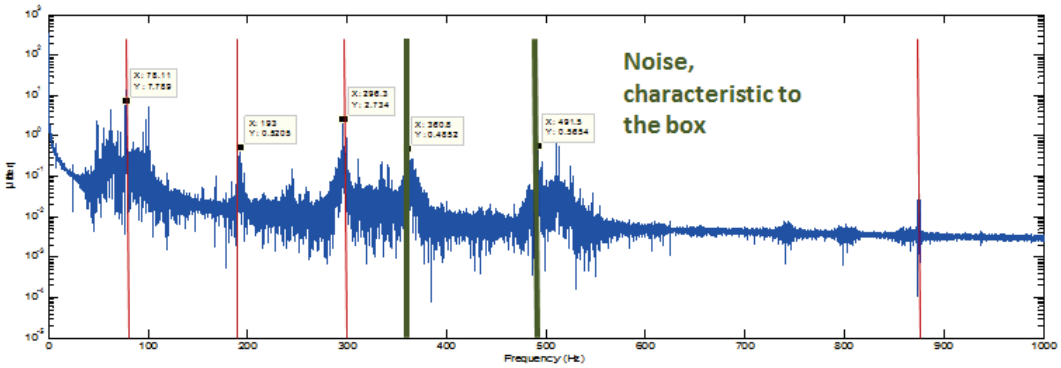

Figure 5: Vibrational noise of the laser box.

EXPERIMENTAL LASER TIMING

The laser oscillator in the final configuration will be optically locked to the master reference of the machine, delivered in the stabilized fiber links. Expected performance is similar to that one of the gun laser. The amplification and transport to the experimental station will give a total path length in the order of 100 m. As the laser room is on the top floor, while the experiment is below, the air-conditioning systems are decoupled and the propagation path will change significantly with the environment. It has been shown for the former Ti:Saph based gun laser system, that drifts in the order of few 100 fs is expected from such beamlines [7].

Figure 6 shows the experimental station ESA [11], where the laser is delivered. The compression and the conversion to other wavelengths from the fundamental of the Ti:Sa system (~795 nm) takes place here. Optical link is delivered for the LAM, which performs the correction after compression and before conversion, using spectrally resolved cross correlation. This setup has a demonstrated resolution of <0.3 fs and is described in detail in [7]. With this technique, the output from a comparable Ti:Sa amplifier system was stabilized to 2.36 fs rms.

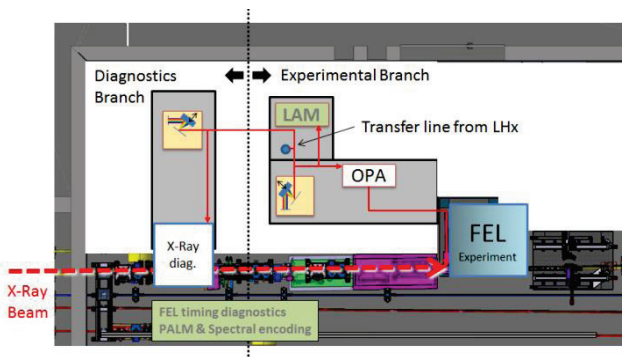

Figure 6: Layout of the timing diagnostics in ESA.

CONCLUSION

High precision timing diagnostics and correction system is well on its way for both gun and experimental lasers at SwissFEL. Further tests are planned for the final location of the lasers, using the developed tools. 10 fs measurement resolution and 40fs shot to shot jitter is expected for the gun laser, while sub-fs resolution has been demonstrated and correction to the few fs level is expected for the experimental laser.

REFERENCES

1. S. Zhang *et al.*, "Phase noise comparison of short pulse laser systems", *in Proc. FEL'06*, Berlin, Germany, Aug 2016, paper TUPPH061, pp. 466-469.
2. K. Predehl *et al.*, "920-Kilometer Optical Fiber Link for Frequency Metrology at the 19th Decimal Place", *Science* vol. 336, pp. 441-444, 2012.
3. M. Csatari Divall et al., "Timing Jitter Studies of the SwissFEL Test Injector Drive Laser", *Nucl. Instr. Meth. PRSA*, vol. 735, pp. 471-479, 2014.
4. C. Erny and C. P. Hauri, "The SwissFEL Experimental Laser Facility", *J. Synch. Rad.*, vol.23, pp. 1143-1150, 2016.
5. A. Trisorio, M.C. Divall, C.P. Hauri, C. Vicario, A. Courjeaud, "New Concept for the SwissFEL Gun Laser", *in Proc. FEL'13*, Nov. 2013, New York, NY, USA, paper TUPSO88, pp. 442-446.
6. S. Hunziker, *et al.*, "Reference Distribution and Synchronization Systems for SwissFEL: Concept and First Results," in *Proc. IBIC'14*, Monterey, Ca., USA, Sept 2014, paper MOCZB2, pp. 29-33.
7. M. Csatari Divall, P. Mutter, E. J. Divall and C. P. Hauri. "Femtosecond Resolution Timing Jitter Correction on a TW Scale Ti:sapphire Laser System for FEL Pump-probe Experiments", *Optics Express*, vol. 23, p. 29929, 2015.
8. V. Arsov *et al.*,"Commissioning and Results from the Bunch Arrival-time Monitor Downstream the Bunch Compressor at the SwissFEL Injector Test Facility", in *Proc. FEL'14*, Basel, Switzerland, Sept 2014, paper THP085, pp. 433-936.
9. A. Trisorio *et al.,* "Ultra-high Performance Low-noise Ytterbium Doped Fiber Optical Oscillator for Free Electron Laser Applications", submitted for publication.
10. A. Casanova, Q. D'Acremont, G. Santarelli, S.Dilhaire, A. Courjaud, "Ultrafast Amplifier Additive Timing Jitter Characterization and Control", *Opt Lett.,* vol. 41, pp. 898-900, March 2016.
11. Christopher J. Milne (ed.) "Experimental Station A: Conceptual Design Report", http://www.psi.ch/swissfel/CurrentSwissFELPublicationsEN/ESA_CDR_v4_with_coverpage_%282%29-VM16.pdf

ISBN 978-3-95450-177-9

UNAMBIGUOUS ELECTROMAGNETIC PULSE RETRIEVAL THROUGH FREQUENCY MIXING INTERFERENCE IN FREQUENCY RESOLVED OPTICAL GATING

E.W. Snedden*, D.A. Walsh and S.P. Jamison[1],
Accelerator Science and Technology Centre, STFC Daresbury National Laboratory,
Warrington, WA4 4AD, United Kingdom
[1]also at Photon Science Institute, The University of Manchester,
Manchester, M13 9PL, United Kingdom

Abstract

We demonstrate a method for full and unambiguous temporal characterization of few-cycle electromagnetic pulses, including retrieval of the carrier envelope phase (CEP), in which the interference between non-linear frequency mixing components is spectrally resolved using Frequency Resolved Optical Gating (FROG). We term this process Real-Domain FROG (ReD-FROG) and demonstrate its capabilities through the complete measurement of the temporal profile of a single-cycle THz pulse. When applied at THz frequencies ReD-FROG overcomes the bandwidth limitations relating probe and test pulses in Electro-Optic (EO) sampling. The approach can however be extended generally to any frequency range and we provide a conceptual demonstration of the CEP retrieval of few-cycle optical field.

INTRODUCTION

Few-cycle electromagnetic pulses offer a means to both control and probe physical processes active on femtosecond timescales. State-of-the-art accelerator facilities incorporate or produce such pulses at multiple levels of operation, including: the output of 4th generation light sources, such as the CLARA free electron laser test facility [1]; the production of coherent transition radiation from a relativistic electron bunch [2]; and the intrinsic coulomb field of a relativistic electron bunch. In the latter two examples the radiation is directly related to the longitudinal properties of the bunch and thus can be utilized for diagnostic purposes [3] . The characterization of such ultrashort radiation is therefore often a crucial element of accelerator operation [4].

All information relating to the temporal properties of an ultrashort field can be derived from knowledge of the pulse spectrum and spectral phase: $\tilde{E}(\omega) = \tilde{A}(\omega)e^{i\tilde{\phi}}(\omega)$. The spectral phase can be mathematically described by the series expansion:

$$\tilde{\phi}(\omega) = \phi^{CE} + \tilde{\phi}^{(1)}(\omega) + \frac{1}{2}\tilde{\phi}^{(2)}(\omega) + \ldots \qquad (1)$$

The zero-order term of Eq. (1) (ϕ^{CE}) is referred to as the carrier envelope phase (CEP). For pulses in which the electric field envelope consists of many cycles this term can be identified as a time-shift of the carrier within the envelope. In few or single-cycle pulses however the distinction between the carrier and envelope components is no longer appropriate and the CEP plays a fundamental role in determining the temporal profile.

While many methods are available to measure relative changes in CEP (for example, f-2f interferometery [5]), schemes to measure the absolute value of CEP are more specific, being limited by constraints in frequency and often involve complex experimental arrangements [6]. Obtaining the full temporal field profile typically requires a separate system dedicated to the measurement of the pulse envelope and higher-order spectral phase components. Towards this latter case Frequency Resolved Optical Gating (FROG) has found common application due to its robustness and ease of experimental implementation [7]. In all forms FROG incorporates the measurement of an intensity spectrogram which is derived from a non-linear interaction between multiple pulses. As a measurement of intensity however it has been widely held that FROG techniques are incapable of determining the CEP.

In beam diagnostic applications, Electro-Optic (EO) sampling has found extensive use as a means of characterizing the complete temporal profile – including the CEP – of few and single-cycle THz pulses produced by relativistic electron sources [3]. EO sampling requires that the THz field is interrogated by a δ-like optical probe field and thus is subject to bandwidth limitations relating the probe and test fields. EO sampling has been utilized in recent work [8,9] to characterize the CEP of far-infrared pulses; as ϕ^{CE} presents as a spectral invariant, knowledge of the CEP at THz frequencies within the pulse (as can be obtained through EO sampling) is sufficient for reconstruction of the complete temporal profile following a separate FROG measurement.

In this work we demonstrate that unambiguous retrieval of an ultrashort pulse including the CEP can proceed directly from a single FROG measurement in which the interference between harmonic components is resolved. We develop a theoretical framework for this method termed Real-Domain FROG (ReD-FROG) [10], describing how it conceptually relates to EO sampling. A proof-of-principle experiment is presented in which the CEP of a single-cycle THz pulse is accurately retrieved. We finally demonstrate the conceptual application of self-referenced ReD-FROG to the recovery of an octave-spanning optical field.

* edward.snedden@stfc.ac.uk

ISBN 978-3-95450-177-9

THEORY

We derive the framework of ReD-FROG for a second-order interaction mediated by the non-linear susceptibility $\chi^{(2)}$; the following approach can however be extended to higher-order non-linear interactions. The non-linear output of a second-order interaction combining fields $\tilde{E}_1(\omega)$ and $\tilde{E}_2(\omega)$ is given by:

$$I(\omega;\tau) = \left| R(\omega) \int_{-\infty}^{\infty} \mathrm{d}\Omega \tilde{E}_1(\omega-\Omega)\tilde{E}_2(\Omega)\exp(i\Omega\tau) \right|^2 \quad (2)$$

where we measure intensity I introduce τ as the parameter expressing the relative time delay between pulses. To simplify the following discussion we neglect the frequency response of the non-linear interaction (expressed by $R(\omega)$ in Eq. (2)). To make the effect of CEP on the non-linear output, we explicitly separate the zero-order spectral phase term in the expression for electric field:

$$\tilde{E}_{\mathrm{total}}(\omega) = \begin{cases} \tilde{E}(\omega)\exp(i\phi^{CE}) & ;\ \omega > 0 \\ \tilde{E}^*(|\omega|)\exp(-i\phi^{CE}) & ;\ \omega < 0 \end{cases} \quad (3)$$

We impose that the electric field is a strictly real quantity and thus $\tilde{\phi}(\omega)$ must take a Heaviside-step functional form; this is key to realising a measurement of CEP. Inserting Eq. (3) into Eq. (2) yields:

$$\begin{aligned} I(\omega;\tau) \quad = \quad & |SFG(\omega;\tau)|^2 + |DFG_+(\omega;\tau)|^2 + |DFG_-(\omega;\tau)|^2 \\ & +2\Re\left\{ SFG(\omega;\tau)DFG_+^*(\omega;\tau)\ \mathrm{e}^{i2\phi_2^{CE}} \right\} \\ & +2\Re\left\{ SFG(\omega;\tau)DFG_-^*(\omega;\tau)\ \mathrm{e}^{i2\phi_1^{CE}} \right\} \\ & +2\Re\left\{ DFG_+(\omega;\tau)DFG_-^*(\omega;\tau)\ \mathrm{e}^{i2\phi_1^{CE}-i2\phi_2^{CE}} \right\} \quad (4) \end{aligned}$$

where

$$\begin{aligned} SFG(\omega;\tau) &\equiv \int_0^{\omega} \mathrm{d}\Omega\, \tilde{E}_1(\omega-\Omega)\tilde{E}_2(\Omega;\tau), \\ DFG_-(\omega;\tau) &\equiv \int_{\omega}^{\infty} \mathrm{d}\Omega\, \tilde{E}_1^*(\Omega-\omega)\tilde{E}_2(\Omega;\tau) \\ DFG_+(\omega;\tau) &\equiv \int_0^{+\infty} \mathrm{d}\Omega\, \tilde{E}_1(\omega+\Omega)\tilde{E}_2^*(\Omega;\tau). \quad (5) \end{aligned}$$

Both sum-frequency (SFG) and difference-frequency (DFG) terms appear without frequency constrictions. Lines 2-4 of Eq. (4) demonstrate that measured intensity is dependent on the value of ϕ^{CE} if there is spectral overlap between SFG and DFG components. For this overlap to occur the bandwidth of the test pulse (defined Δ) is comparable to the lowest frequency components (ω_L), obeying $\Delta \geq 2\omega_L$. If we re-write Eq. (4) allowing for the harmonic field components to overlap with the fundamental fields $\tilde{E}_1(\omega)$ and $\tilde{E}_2(\omega)$, this bandwidth constraint is alleviated to $\Delta \geq \omega_L$.

The effect of pulse bandwidth on the observation of CEP in a second-order non-linear interaction obeying Eq. (2) is shown in Fig. 1, in which the input fields are at optical and THz frequencies respectively. The THz field is taken with the spectral profile $\omega^2 e^{-\omega^2}$ consistent with ~100 fs single-cycle radiation peaking at 6 THz; the optical pulse is assumed as a transform-limited Gaussian field with varying bandwidth. The absolute phase of the THz field is varied across columns ($\frac{\pi}{6}$, $\frac{\pi}{3}$ and $\frac{\pi}{2}$ from left to right). The effect of CEP variation is increasingly measurable as the spectral overlap between SFG and DFG components increases with optical bandwidth.

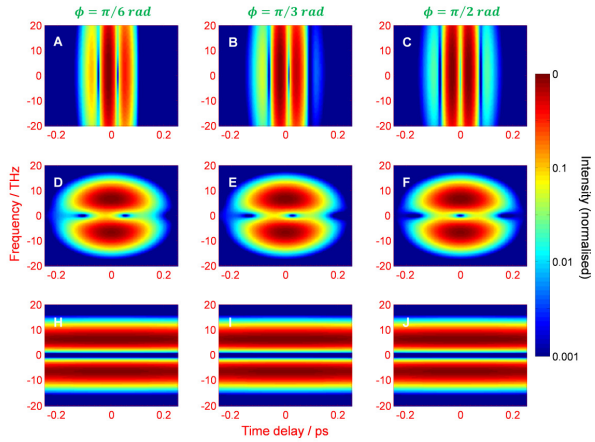

Figure 1: Influence of ϕ^{CE} on intensity spectrograms resolving the non-linear interaction of transform-limited optical and THz pulses, in which the CEP of THz (~100 fs, 6 THz) is varied across columns and the optical pulse duration varied across rows: rows A-C) optical pulse duration 10 fs, D-F) 100 fs and H-J) 1000 fs. Spectrograms are plotted with logarithmic intensity scale and are centered at the optical carrier frequency (375 THz).

The top row is representative of the bandwidth limit $\Delta\omega_{opt} \gg \omega_{THz}$, which is equivalent to the EO sampling limit in which the optical pulse being much shorter than the THz field. In this case any information relating to the optical field is lost and the intensity spectrogram is solely determined by the temporal field profile of the THz field. Retrieval of the THz field proceeds merely by integrating along the frequency axis; use of the FROG algorithm is not required. The middle row is representative of the case $\Delta\omega_{opt} \equiv \omega_{THz}$. Retrieval of *both* the optical and THz fields is possible through use of a suitable FROG algorithm (we demonstrate such a retrieval in Fig. 2 below), with information relating to the CEP encoded at the optical carrier frequency. The bottom row is representative of EO transposition, in which $\Delta\omega_{opt} \ll \omega_{THz}$ and the THz spectrum is transposed to optical frequencies. While it is clear from Fig. 1 that the THz field including CEP information cannot be directly obtained through analysis of this intensity spectrogram, we have demonstrated elsewhere that a separate self-referenced FROG measurement of the transposed field can be used to obtain the THz field [11]. Figure 1 demonstrates that the case of EO sampling can be viewed as specific case of ReD-FROG; equivalently ReD-FROG can be considered to extend THz detection beyond the bandwidth limitations of sampling.

ISBN 978-3-95450-177-9

EXPERIMENT

As a proof-of-concept of ReD-FROG, we present the results of an experiment in which a single-cycle THz pulse produced from a large-area semi-insulating GaAs photoconductive antenna is combined with an optical pulse (~500 fs) in [$\bar{1}$10] oriented ZnTe crystal [10]. The optical probe was stretched from an initial duration of 45 fs using a grating-based zero-dispersion 4-f filter. The frequency-mixing signal (Eq. (2)) was isolated from the fundamental input using a polarizer and analyzed using a spectrometer (Jobin-Yvon iHR550) with CCD detector (PCO DiCamPRO). The relative delay between the optical and THz beams was varied using a linear translation stage.

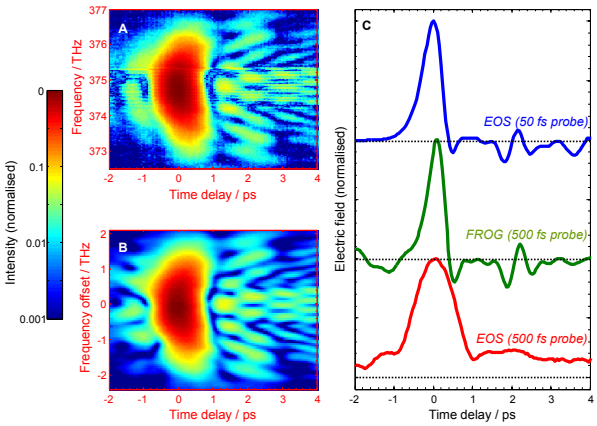

Figure 2: A) Measured and B) retrieved spectrograms resolving the interaction between ~500 fs optical probe (1 THz bandwidth) with ~1000 fs single-cycle THz pulse. C) Comparison of retrieved THz field (middle) with same field obtained with EO sampling with 45 fs (top) and ~500 fs optical probe.

The measured spectrogram is shown in Fig. 2A; this can be compared against the ReD-FROG retrieved spectrogram in Fig. 2B. Interference fringes between the SFG and DFG components can be clearly resolved at ~375 THz. A modified version of the PGCPA FROG algorithm was used to obtain the time-domain THz and optical fields from the spectrogram, in which both fields were constrained to be real in the time domain by ensuring the equivalent Hermitian property in the frequency domain. The retrieved spectrogram had a FROG error of 0.01 (512×512 grid size). The ReD-FROG retrieved time-domain field is compared against the same field inferred by EO sampling (obtained under balanced-detection conditions using the compressed 45 fs optical probe) in Fig. 2C; excellent agreement is observed. For comparison, the field obtained from EO sampling using the stretched 500 fs probe is also shown in Fig. 2C; this combination of fields does not satisfy the bandwidth criterion for EO sampling and the THz field duration is subsequently overestimated.

EXTENSION TO OPTICAL FREQUENCIES

The framework of ReD-FROG outlined above can be applied at any frequency range, assuming the bandwidth criterion $\Delta \sim \omega_L$ is met. It can therefore be applied at infra-red and optical frequencies without significant alteration; the development of octave-spanning single-shot spectrometers will greatly aid experimental implementation [2]. A conceptual demonstration of ReD-FROG at optical frequencies is given in Fig. 3A and C for the self-referenced measurement of a transform-limited Gaussian pulse (375 THz, 75 THz bandwidth) for two values of ϕ^{CE}. The pulse is combined with itself through second-order non-linear mixing and the interference between SFG and DFG components with the fundamental field resolved. The effect of CEP can be resolved in the spectrogram in interference features centered at 200 and 525 THz. The retrieved fields using the ReD-FROG algorithm incorporating the real-field constraint are shown in Fig. 3B and D, with the absolute value of CEP obtained accurately.

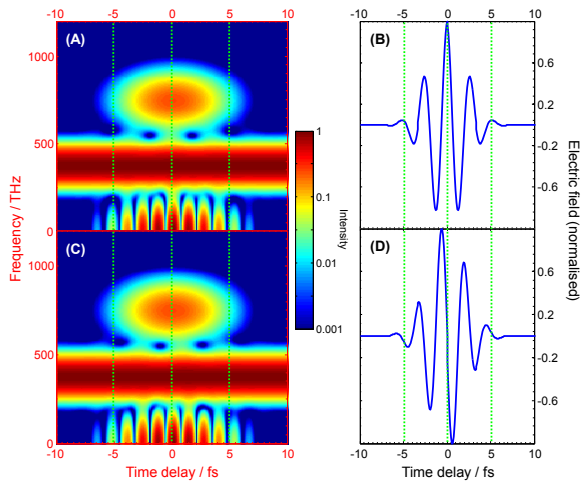

Figure 3: Spectrograms for a self-referenced measurement of a Gaussian transform-limited optical pulse (375 THz, 75 THz bandwidth), A) $\phi^{CE} = 0$ and C) $\phi^{CE} = \frac{\pi}{2}$ rad. B), D): electric field profiles recovered by ReD-FROG from spectrograms A) and C) respectively.

CONCLUSIONS

We have developed the method of ReD-FROG, in which the full temporal profile of an electromagnetic pulse including the CEP can be retrieved from a spectrogram in a single measurement. Information relating to the CEP is resolved in the interference between harmonic components obtained from non-linear frequency mixing; by introducing a real-field constraint into the FROG algorithm we unambiguously recover the temporal profile. A proof-of-concept experiment in which the temporal profile of a single-cycle THz

ISBN 978-3-95450-177-9

pulse is detailed and demonstrates the potential of ReD-FROG to overcome bandwidth limitations inherent to EO sampling. This method opens up new possibilities in the characterization of ultrashort electromagnetic radiation and demonstrates that, contrary to long-held expectations, that FROG is capable of direct absolute phase measurement.

REFERENCES

[1] J.A. Clarke *et al.*, "CLARA conceptual design report", *J. Instrum.*, vol. 9, p. T05001, 2014.

[2] S. Wesch *et al.*, "A multi-channel THz and infrared spectrometer for femtosecond electron bunch diagnostics by single-shot spectroscopy of coherent radiation", *Nucl. Instrum. Methods Phys. Res. Sect. A*, vol. 665, p. 40, 2011.

[3] G. Berden *et al.*, "Benchmarking of Electro-Optic Monitors for Femtosecond Electron Bunches", *Phys. Rev. Lett.*, vol. 99, p. 164801, 2007.

[4] J. van Tilborg *et al.*, "Temporal Characterization of Femtosecond Laser-Plasma-Accelerated ELectron Bunches Using Terahertz Radiation", *Phys. Rev. Lett.*, vol. 99, p. 164801, 2007.

[5] D.J. Jones *et al.*, "Carrier-envelope phase control of femtosecond mode-locked lasers and direct optical frequency synthesis", *Science*, vol. 288, p. 635, 2000.

[6] G.G.. Paulus *et al.*, "Measurement of the phase of few-cycle laser pulses", *Phys. Rev. Lett.*, vol. 91, p. 253004, 2003.

[7] R. Trebino *et al.*, "Simple devices for measuring complex ultrashort pulses", *Laser Photon. Rev.*, vol. 3, p. 314, 2009.

[8] Y. Nomura, H. Shirai, and T. Fuji, "Frequency resolved optical gating capable of carrier-envelope phase determination", *Nat. Commun.*, vol. 4, p. 3820, 2013.

[9] H. Shirai, Y. Nomura, and T. Fuji, "Real-time waveform characterization by using frequency-resolved optical gating capable of carrier-envelope phase determination", *IEEE Photon. J.*, vol. 6, p. 3300212, 2014.

[10] E.W. Snedden, D.A. Walsh, and S.P. Jamison, "Revealing carrier-envelope phase through frequency mixing and interference in frequency resolved optical gating", *Opt. Express*, vol. 23, p. 8507, 2015.

[11] D.A. Walsh, E.W. Snedden, and S.P. Jamison, "The time resolved measurement of ultrashort terahertz-band electric fields without an ultrashort probe", *Appl. Phys. Lett.*, vol. 106, p. 181109, 2015.

ISBN 978-3-95450-177-9

BUNCH SHAPE MEASUREMENTS AT THE NATIONAL SUPERCONDUCTING CYCLOTRON LABORATORY ReAccelerator (ReA3)*

R. Shane†, S. M. Lidia, Z. Liu, S. Nash, A. C. C. Villari, O. Yair
Facility for Rare Isotope Beams, East Lansing, USA

Abstract

The longitudinal bunch shape of a reaccelerated heavy-ion beam at the National Superconducting Cyclotron Laboratory's (NSCL) ReA3 beamline was measured using an Ostrumov-type bunch-shape monitor. The phase of the last accelerating cavity was varied to change the bunch length, while the energy was kept constant by adjusting the amplitude of the voltage on the cavity. Two peaks were observed in the longitudinal projection of the bunch shape distribution. The widths of the two peaks did not vary much when the cavity phase was changed, while the peak separation decreased to the point that the two peaks became unresolvable as the bunching was increased. The relative amplitudes of the two peaks was very sensitive to tuning parameters. This, coupled with a lack of information about the transverse profile of the bunch, complicated the analysis and made a simple width assignment difficult. Measurements were also made with an MCP timing grid for comparison. The general shape and trend of the two data sets were similar; however, the widths measured by the timing grid were about 30-50% smaller.

INTRODUCTION

We have utilized a borrowed bunch shape monitor (BSM) [1] to perform measurements at the ReAccelerator (ReA3) facility at the National Superconducting Cyclotron Laboratory (NSCL) [2,3]. For this measurement, a beam of ^{42}Ar was stopped in a gas stopper and subsequently reaccelerated by ReA3. The beam had a pulse structure at 5 Hz with a duty factor of 20%, and an average current of about 6-30 epA.

The ReA3 accelerator uses prototypes of the RF cavities for the Facility for Rare Isotope Beams (FRIB). Bunch-shape measurement is required at the charge-stripping area of the FRIB accelerator. The experience and understanding gained in this set of measurements will help to reduce future development cost of the bunch-shape monitoring system for FRIB.

A schematic showing the principle of operation for the BSM is shown in Fig. 1. Secondary electrons are emitted when beam ions strike a tungsten wire. The wire is held at a large negative potential (up to -10 kV), which causes the electrons to accelerate away. A collimating slit selects a narrow beamlet of electrons. These collimated electrons pass between RF deflection plates which provide transverse modulation of the electrons. The deflector is synced to the accelerator frequency (ω = 80.5 MHz).

* This material is based upon work supported by the U.S. Department of Energy Office of Science under Cooperative Agreement DE-SC0000661, the State of Michigan and Michigan State University.
† email address: shane@frib.msu.edu

The electrons, now spread transversely, impinge on an MCP, and a camera is used to view the electron distribution on the phosphor screen. Varying the phase offset (φ_0) between the deflector and accelerator shifts the spatial distribution on screen.

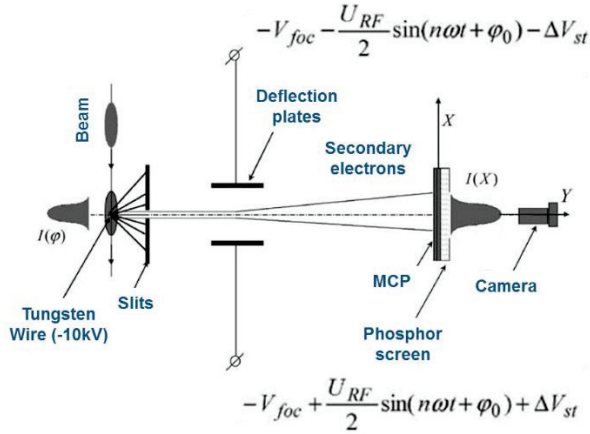

Figure 1: Schematic of bunch-shape measurement technique, adapted from Ref. [1].

DATA

The raw greyscale images from the camera are averaged over 127 captures, and then a threshold is applied on the intensity to produce black and white images as shown in Fig. 2 (top). These are projected onto the horizontal axis to produce a one-dimensional waveform of the longitudinal bunch shape, as shown in Fig. 2 (bottom). Three waveforms were recorded at each RF deflection phase, with a variance of about 10% of the peak intensity. A running average reduces this to about 3%.

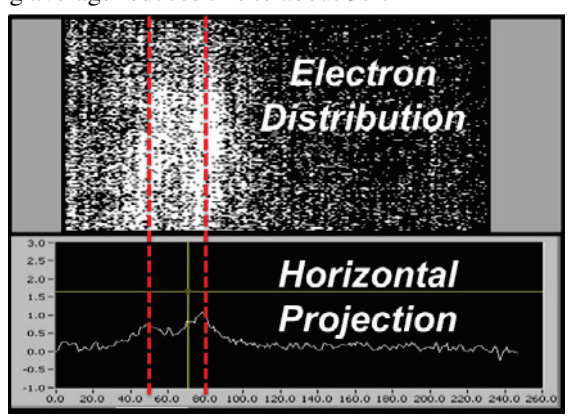

Figure 2: (top) Raw camera image showing the electron distribution intensity. (bottom) Projection of the distribution onto the horizontal axis.

ISBN 978-3-95450-177-9

ANALYSIS

Background Subtraction

For each measurement, the RF deflector has a fixed phase offset relative to the beam. As the deflector phase is varied, the position of the electron distribution on the screen changes. To extract the background, we first adjusted the phase so the peak (corresponding to beam bunch) was on the far left (to get the background for right side). Then we changed the phase until the peak was on the far right (to get background for the left side). These two measurements are shown in Fig. 3, along with the extracted background.

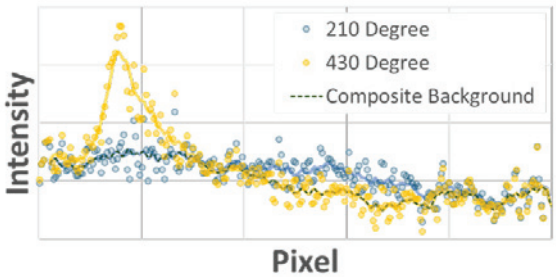

Figure 3: Background from two measurements.

Calibration

The calibration of the camera image "pixels" to equivalent "degrees" of phase in the beam bunch can be obtained by plotting the position of the bunch in the image against the deflector phase. An example of this is shown in Fig. 4. This relationship is actually sinusoidal, as shown in the top of Fig. 4, but we get better phase resolution (more pixels per degree), as well as almost linear calibration, if we stick to phases near the inflection point of the sine wave, shown with the blue box in Fig. 4. Using the position of either peak in the distribution gave similar calibration, as can be seen in the bottom of Fig. 4.

Experimental Complications

One issue we faced was the low duty factor of the pulsed beam, coupled with the lack of trigger for the camera and data acquisition. Practically, this meant that half or more of the acquired images were taken between pulses, greatly decreasing our signal to background ratio.

Another complication is illustrated in Fig. 5. During some of the measurements, the beam current dropped significantly. Retuning of the beam was required in order to continue taking measurements. Although the cavity phases were not adjusted, the beam shape changed, as can be seen in Fig. 5. There is one, taller peak in the distribution before the retuning, with perhaps a small shoulder. After retuning, the peak is smaller, and the small shoulder is approximately equal amplitude.

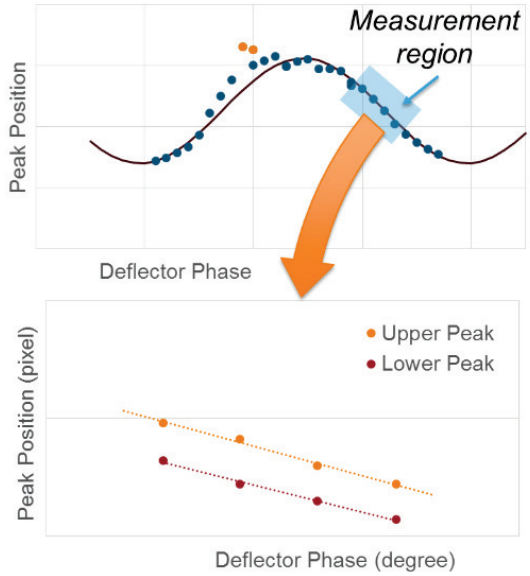

Figure 4: Calibration of the pixel-phase relationship.

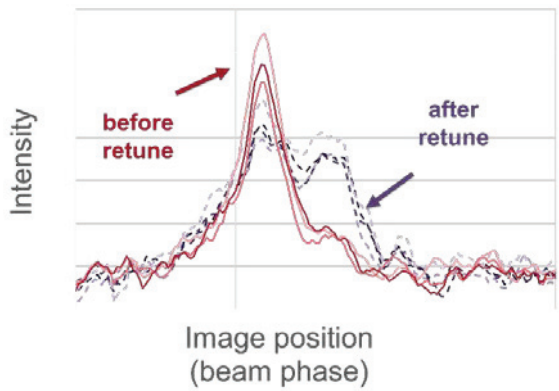

Figure 5: Bunch changes after tuning higher current.

RESULTS

Bunch Shape

The bunch shape measured for three bunching conditions are shown in Fig. 6. These bunching conditions are achieved by setting the last ReA3 cavity phase to -15, -30, and +15 degrees. The standard operating condition is at -15 degrees, while the bunching is increased for -30 degrees, and there is debunching at +15.

There are two peaks in the measured bunch shape distribution. A double Gaussian fit was used to approximate the bunch shape, and the systematics of the fit parameters were analyzed. The width of each peak did not vary much when the cavity phase was changed, but the peak separation decreased and peaks became unresolvable with increased bunching.

For comparison, measurements were also taken with an MCP grid timing system. These are shown in Fig. 6 as well.

ISBN 978-3-95450-177-9

Bunch Width

The complex bunch shape means that typical width measures (e.g. FWHM) do not give robust values that reflect the overall size of the bunch. In addition, the sensitivity of the two peak amplitudes to tuning (Fig. 5) meant that it would be easy to underestimate the bunch width, if one peak amplitude was very small. Therefore, the width near the base of the bunch shape was used. These values are shown in Table 1 for both the BSM and the timing grid.

The systematics under different bunching conditions are as expected – there is more bunching, and thus a narrower width, when the ReA Cavity phase was changed from -15 to -30 degrees.

Table 1: Extracted Bunch Widths from BSM and Timing Grid (TG) for Three ReA Cavity Phases

ReA Cavity Phase:	**-15 deg**	**-30 deg**	**+15 deg**
BSM width	92°	84°	69°
TG width	70°	52°	50°

Comparison to Timing Grid Measurement

As mentioned above, measurements were also made with an MCP timing grid for comparison. The general shape and trend of the two data sets were similar, as seen in Fig. 6. There are two, well-separated peaks in the bunch at -15 degree cavity phase, while at -30 degrees, there is only one (or perhaps two closely overlapping peaks). The width at +15 degrees should be larger than that at -15 degrees, but for both measurement systems, the width was narrower at +15 degrees. Our guess is that this could be due to different tuning conditions during the measurements at the two phases.

Although the general shape and trend of the measurements were similar, the widths measured by the timing grid were about 30-50% smaller than those measured by the BSM. Again, this may be due to differences in tuning during the two sets of measurements.

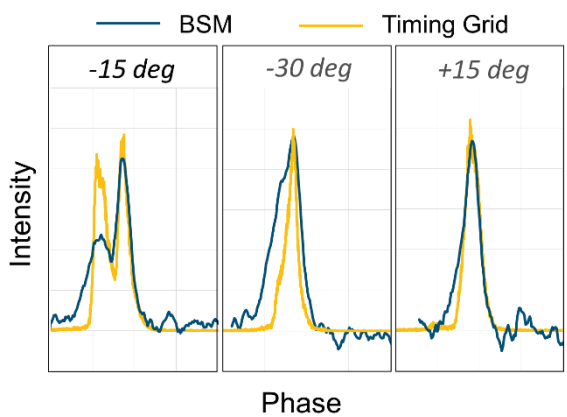

Figure 6: Bunch shapes measured by BSM and timing grid under three different bunching conditions (ReA cavity phases -15, -30, and +15 degrees).

CONCLUSION

Discussion

We successfully measured bunch shape at the NSCL ReAccelerator. The beam was $^{42}Ar^{17+}$ pulsed at 5 Hz with a duty factor of 20%, and an average current of 6-30 epA. The shape and length of the beam bunch was changed by varying the phase of the last ReA RF cavity.

There was a significant effect on the bunch shape from uncontrolled tuning parameters, for example when tuning to increase the beam current. This made simple width assignment impossible, and made it difficult to compare between measurements.

Differences between the BSM and timing grid are about 30-50%. It is likely that this is partly related to differences in the tuning during the measurements, and possibly also non-linearity of the calibration.

Improvements

One very troublesome issue was the poorly understood effect of uncontrolled tuning parameters. In order to minimize this effect, we plan to take BSM and timing grid data sets under consistent beam conditions. In addition, we would like to take data at more ReA cavity phases (bunching conditions) to understand the systematic trends more clearly.

There are several areas for improvement possible in this bunch shape measurement. We can reduce the background by syncing the acquisition to the beam-pulse frequency, or triggering the camera image capture with the pulsed beam.

Additionally, taking more data for each measurement will result in a lower uncertainty and higher resolution. However, the acquisition system limits the number of image captures that are averaged into a single waveform. It also requires one to save snapshots manually. Switching to a continuous or automatic acquisition will streamline the data taking, and avoid both these problems.

ACKNOWLEDGMENT

We greatly appreciate the ReA3 operations staff for their help and support in carrying out these measurements.

REFERENCES

[1] N.E Vinogradov, et al., “A detector of bunch time structure for cw heavy-ion beams,” Nucl. Instr. Meth. A, vol. 526, pp. 206 – 214, Jul. 2004.

[2] O. K. Kester, et al., “ReA3 - the Rare Isotope Re-accelerator at MSU”, Proc. LINAC2010, p. 26 – 30.

[3] W. Wittmer, et al., “Results from the Linac Comissioning of the Rare Isotope ReAccelerator – ReA”, Proc. PAC2013, pp. 360 – 362.

ISBN 978-3-95450-177-9

SYNCHRONIZATION OF ps ELECTRON BUNCHES AND fs LASER PULSES USING A PLASMONICS-ENHANCED LARGE-AREA PHOTOCONDUCTIVE DETECTOR

E. J. Curry*, M. Jarrahi, P. Musumeci, N. T. Yardimci†, UCLA, Los Angeles, CA 90095, USA
B. T. Jacobson, RadiaBeam Technologies, Santa Monica, CA 90405, USA

Abstract

Temporal synchronization between short relativistic electron bunches and laser pulses at the ps and sub-ps level is required for accelerator applications like inverse Compton scattering based light sources. Photoconductive antennas with THz and sub-THz bandwidth which are gated by fs lasers provide this level of timing resolution. This paper describes the operating principals of the diagnostic along with bench-top experimental results with recently developed plasmonics-enhanced large-area devices. A vacuum chamber with robust electronic noise reduction has been designed for upcoming beam-based experiments.

INTRODUCTION

Modern high-brightness photo-injectors have evolved to produce bunched beams of relativistic electrons with ps and sub-ps duration, while commercial laser technology has reduced pulse lengths of high-power IR sources to 100 fs and below. These two advances have led to a merging of these disciplines into a new scientific field where each core technology must operate at peak performance and be synchronized in time with a resolution better than the pulse lengths involved, such as in inverse Compton scattering, where the electron bunch and laser pulse must arrive simultaneously and collide at the interaction point.

SYNCHRONIZATION MEASUREMENT METHODS

A traditional way for synchronizing electron beam and laser pulses is by using signals from button or stripline beam position monitor for electrons timing [1] while monitoring laser pulses with a biased photodiode. To acquire sub-ps resolution, optical and cable delays must be characterized and the analog signals must be sampled by a high-bandwidth oscilloscope.

Instead of directly measuring beam or laser signal, several techniques have been developed for bunch length measurements and synchronization known as electro-optic sampling (EOS) methods, where the bunch profile is encoded in a signal [2]. Each scheme exploits the changes in optical properties, e.g. birefringence, of some material due to the presence of the passing electric field of the beam. Our EOS setup uses a Wollaston prism configured for doubly-balanced diode detection.

Another method for beam and laser synchronization uses a photoconductive antenna (PCA) which behaves like an optically gated THz sensor. The gate is provided by a fs laser pulse which allows charge flow in a photoconductive substrate for the duration of the illuminating pulse. THz fields generated by the ps or sub-ps electron bunches can be extracted via a transition radiation foil, or measured directly by placing the PCA detector in close proximity to the electron beam. Bunch length measurements have been made [3] using transition radiation and specially designed radially polarized PCA detectors [4]. However, we pursue directly measuring the Coulomb field of the electron bunches by placing the detector inside of the beam vacuum chamber [5].

EXPERIENCE WITH COMMERCIALLY AVAILABLE PCA SENSORS

Last year we made attempts to adapt a commercially available PCA sensor for beam measurements at the UCLA Pegasus beamline [6]. The sensor had a 5 μm gap in the dipole antenna structure. A large laser spot illuminating a movable pin-hole was used to limit the probe beam size and position the spot in the dipole gap. Bench test of the device mounted in this manner [5] showed this detector should be sensitive to the peak THz field amplitudes excited in close proximity to the Pegasus beam.

However, these beam measurements were unsuccessful. Three issues have been identified that contributed to the failed measurement attempt: maintaining laser alignment one the pinhole assembly was pumped down, the presence of large electronic noise backgrounds, and the overall device sensitivity to THz fields. Over the past year, we have addressed each of these issues, as described in the remainder of this contribution.

DESCRIPTION OF PLASMONICS-ENHACED LARGE-AREA PHOTOCONDUCTIVE DETECTORS

Incorporation of plasmonic contact electrodes into PCAs has been proven to be an efficient concept to increase the sensitivity and responsivity of the conventional photoconductive detectors [7]. In this project, a novel large-area plasmonic photoconductive device based on a 2-D plasmonic nano-antenna array is used. By using a large-area design, the optical beam doesn't have to be focused tightly anymore. Therefore, the device can accommodate higher optical pump power levels without any thermal breakdown and offers much easier optical alignment. Moreover, the nano-antennas are designed to have low RC parasitic loading; hence, the detector offers a

*ejcurry99@gmail.com
†yardimci@ucla.edu (photoconductive detector design)

ISBN 978-3-95450-177-9

broad detection bandwidth [8]. The plasmonic nano-antennas are designed to increase the interaction between the optical beam and the THz pulse. Therefore, high responsivities can be achieved with this detector.

The schematic design of the plasmonic-enhanced detector is shown in Fig. 1. It is 0.5 mm x 0.5 mm in area and fabricated on top of a low-temperature-grown GaAs substrate. The geometry of the plasmonic nano-antennas is designed to excite the surface-plasmon waves at 800 nm wavelength. Therefore, extraordinary optical absorption is achieved at this wavelength, providing a much shorter average path length for the photo-generated carriers. The gap between nano-antenna tips is chosen to optimize the optical transmission and the induced electric fields at THz frequencies. Thus, when a THz pulse is incident on the detector a strong electric field is induced between nano-antenna tips. Since the average path length of photo-generated carriers is short and the THz fields induced within the device active area is strong, the majority of the photo-generated carriers can be drifted to the contact electrodes in less than a picosecond. Hence, very high responsivities can be achieved.

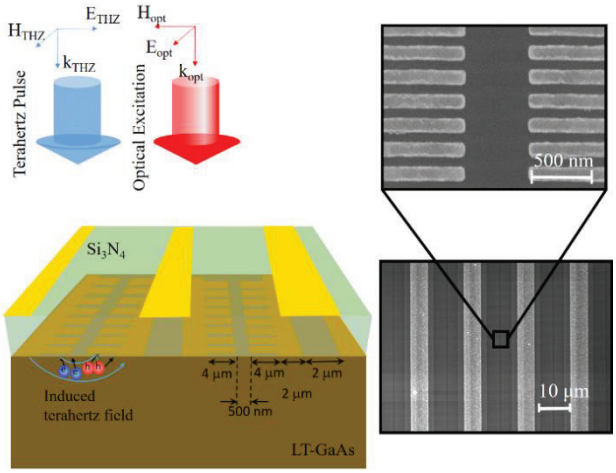

Figure 1: Schematic diagram of the presented large-area plasmonic photoconductive detector (left). SEM images of the 2D plasmonic nano-antenna array (right).

Moreover, the length of the dipole antennas is chosen to be much smaller (4 µm) than the THz wavelength to provide broadband radiation detection. Experimentally, we could observe signal up to 6 THz using a broad-band source.

The 2D nano-antenna arrays are connected to interdigitated lines. A Si_3N_4 anti-reflection (AR) coating is used to further enhance the optical transmission. Strips of metal are applied on top of the AR coating to block the laser light directly above every second gap between the interdigitated lines. This eliminates charge flowing in the opposite direction which interferes destructively with the current generated by the plasmonic nano-antennas. SEM images of the plasmonic nano-antenna array are shown in Fig. 1 (right).

CHARACTERIZATION OF THREE PLASMONICS-ENHANCED PHOTO-CONDUCTIVE DEVICES

We present measurements of THz detection using three PCA structure types. The primary PCA used in this experiment is described above and has been optimized for THz detection. Another PCA chip design, optimized for THz emission rather than detection, was available in two sizes of active area. A photo of all three mounted is shown in Fig. 2. We include these additional measurements for comparison with the PCA optimized for THz detection performance and to provide insight into the potential scaling of the PCA performance with area of the active region.

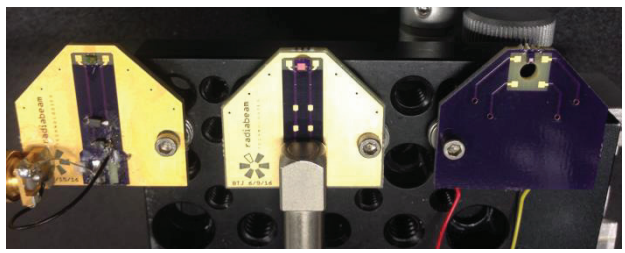

Figure 2: Photograph of the three PCA designs used for the measurements presented here. At left is the PCA optimized for THz detection, in the middle is the large area PCA optimized for THz emission, and at right is the small area PCA optimized for THz emission.

The THz pulse was produced via pulse-front-tilted optical rectification of 800 nm IR pulses in stoichiometric lithium niobate (sLN) and focused using a pair of off-axis parabolic mirrors (OAP), as shown in Fig. 3. To characterize the THz source, we performed EOS measurements of the near-single cycle pulse using a balanced detection scheme with a 0.5 mm thick ZnTe crystal.

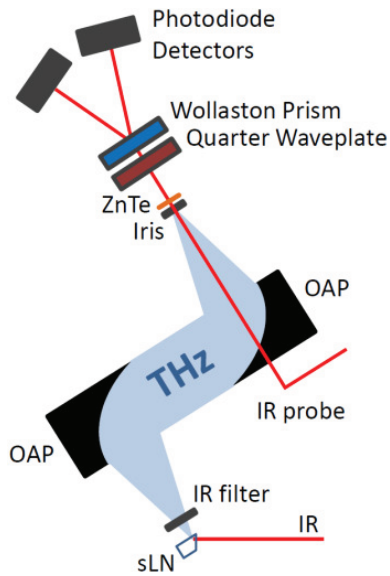

Figure 3: Diagram of THz generation and balanced detection set-up for EOS. The ZnTe crystal is replaced by a PCA for antenna measurements.

ISBN 978-3-95450-177-9

For each measurement, an iris was used for coarse alignment of the board relative to the THz focus, followed by fine adjustment with a 3-D translation stage to locate the peak field. The incident IR probe power was adjusted to maximize the signal. A transimpedance amplifier with a gain of 10^3 and bandwidth of 500 kHz converts the detector current to a voltage, which is terminated by 50 Ohms, and captured by a sampling oscilloscope. The peak value of this waveform is averaged for several pulses at each position in the delay scan.

In Fig. 4 (top), we show the EOS measurement of the near single-cycle THz pulse, followed in Fig. 4 (bottom) by the measurement using the PCA optimized for THz detection. The time delay between the initial, positive peak and second, negative peak was 0.33 ps for the EOS measurement and 0.53 ps for the PCA measurement. The PCA measurement provided a significantly better signal to noise ratio than the EOS technique. Using the standard deviation of the background signal, measured when the THz pulse was not temporally overlapped with the IR probe, we found a peak signal to noise ratio of 7.4×10^3 for the EOS measurement and 31.4×10^3 for the PCA measurement.

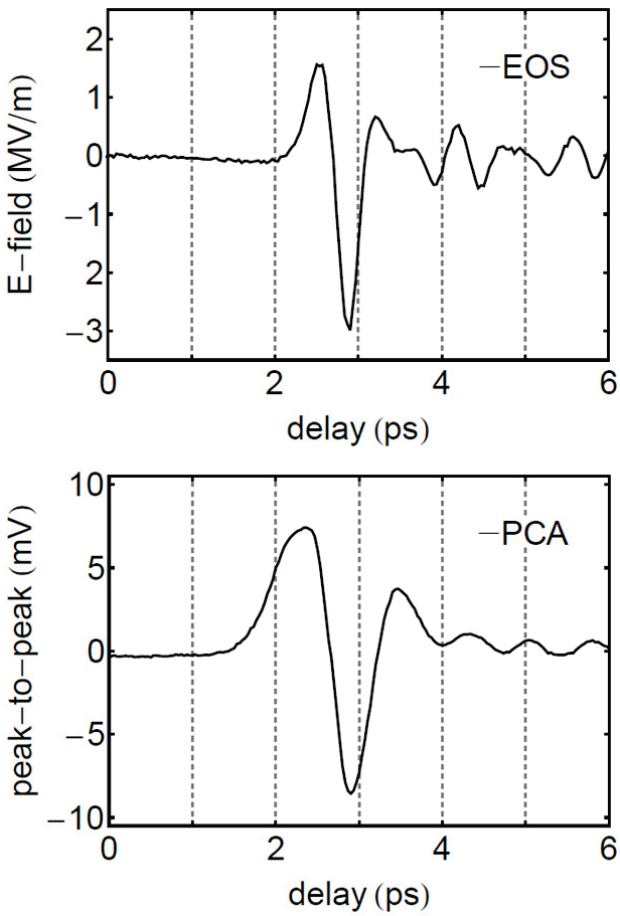

Figure 4: Measurements of the THz pulse using (top) EOS in a ZnTe crystal and (bottom) a PCA optimized for THz detection.

Accurately measuring the small signal currents generated by these devices has proven to be challenging in the accelerator noise environment, hence we seek to find detectors which produce the largest current outputs for a given THz and laser probe intensity. Two other plasmonic-enhanced devices were available and evaluated for accelerator/laser synchronizing applications. Despite the fact that these devices have a design optimized for THz emission, we compare the effect of increasing the active area by measuring the signal from a small and a large area devise.

The active area of the smaller photoconductive device is 0.5 mm × 0.5 mm. The second device is a larger version, 4 times in size, with an active area of 1 mm × 1 mm. These two devices were designed to operate with high-bias voltage, a property required for use as a high-power THz emitter, as described in [8]. The delay scan is shown in Fig. 5. The large peak signal provided by the 1 mm^2 PCA, in this case nearly a factor of two greater than the smaller area device, may be key to overcoming the noise background during a beam test. However, the signal to noise ratio *decreased* by 30 %, from 3.5×10^3 for the small area device to 2.5×10^3 in the case of the larger active area. In each case, this signal to noise ratio is roughly a factor of 10 worse than we measured using the chip optimized for detection.

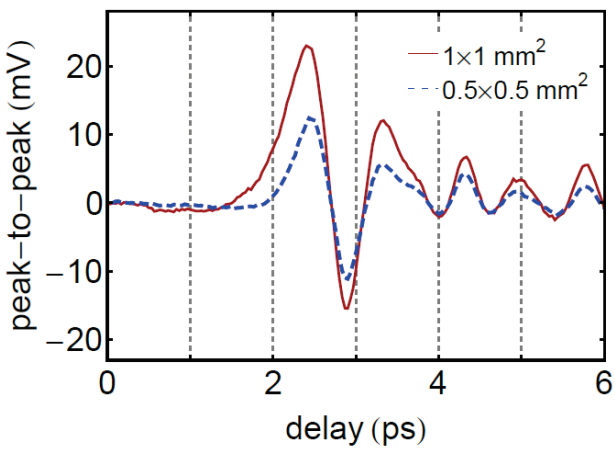

Figure 5: Measurements of the THz pulse using two PCA's, optimized for THz emission, with large (solid red) and small (dashed blue) area.

To summarize these measurements, we have found that each devise examined reproduces the near-single cycle THz waveform with features in close agreement with the reconstruction from the EOS method. The devise optimized for detection exhibits the highest signal to noise ratio. Using two devices optimized for THz emission, we find that the sensitivity increases with the active area, but at the cost of lower signal to noise over the first device.

ROBUST NOISE REDUCTION

Electronic background noise in the accelerator lab environment presents significant challenges for measuring the small current output of photoconductive detector. Ambient RF from the accelerator drive system and transient ground currents induced by the high voltage pulses delivered to the klystron are the two main noise sources com-

ISBN 978-3-95450-177-9

peting with the detector output. Therefore, steps have been taken to isolate the signal.

The detector chip is mounted on a two-layered printed circuit board (PCB) with epoxy and electrically connected by wire bonds to signal trace covered by solder mask. Bare gold cladding covering the top and bottom layers of the PCB provide ground isolation around the chip and traces, as well as preventing the accumulation of charge from any scraped beam halo.

Shielding within and outside of the beam vacuum chamber is achieved using triaxial cables. The two inner conductors carry the detector current while the outermost conductor is tied to ground. Signal leaves the PCB through a 50-Ohm triaxial connector (Fig. 6). An in-vacuum triaxial cable connects the PCB to a triaxial feedthrough. An air-side triaxial cable transports the signal to the amplifier.

Figure 6: CAD rendering of the THz detector PCB mounted on a retractable mechanical feedthrough to bring the chip near the electron beam (blue arrow). The probe laser (red arrow) enters the vacuum chamber through a viewport (not shown). With the tee suppressed (right), the triaxial signal coupling can be seen.

The THz detector is mounted on a movable actuator for positioning the sensor directly below the beam. The longitudinal component of the relativistic electron beam's Coulomb field is transformed into the radial component forming the so-called "pancake" distribution, producing a time-varying electric field radially polarized with THz bandwidth in the lab frame. The antenna array in the sensor couples to linearly polarized THz. Therefore, to sample the correct polarization over the active area, the sensor is to be positioned just below the beam with the thin edge aligned to the beam vector. In this case, the THz is vertically polarized at the chip. The system will mount to a cross on the PEGASUS beamline at UCLA with a viewport for coupling the laser into the vacuum chamber, where it strikes the large-area detector.

The laser probe must be linearly polarized with its field oscillating in the horizontal direction, 90 degrees with respect to the THz field. The spatial alignment of the beam spot on the detector is not critical, as opposed to PCA devices with conventional antennas where a ~10 μm spot must be placed within a ~10 μm gap in the single antenna structure. The large area of the device greatly reduces the complications in alignment of using the plasmonics-enhanced THz detector for in-vacuum applications.

CONCLUSION

We have considered beam and laser synchronization using plasmonics-enhanced large-area photoconductive detectors. Our experiences have shown that the transient RF and high-voltage noise background present in accelerator enclosure environments requires both highly shielded cables and feedthroughs for signal isolation as well as higher sensitivity PCA devices. Three newly fabricated designs have been PCB mounted and characterized using a bench-top pulsed THz source. The combination of enhanced sensitivity and noise reduction will be evaluated in upcoming beam test to measure the Coulomb THz field from the PEGASUS beam at UCLA this year.

REFERENCES

[1] A. Angelovski *et al.*, "Evaluation of the cone-shaped pickup performance for low charge sub-10 fs arrival-time measurements at free electron laser facilities," *Phys. Rev. ST Accel. Beams,* vol 18, p. 012801, Jan. 2015.

[2] M. Brunken *et al.,* "Electro-optic sampling at the TESLA test accelerator: experimental setup and first results," TESLA Report 2003-11, 2003.

[3] K. Kan *et al.*, "Measurement of temporal electric field of electron bunch using photoconductive antenna", in *Proc. IPAC'16*, Richmond, VA, USA, May 2015, pp. 1623-1625.

[4] K. Kan *et al.*, "Radially polarized terahertz waves from a photoconductive antenna with microstructures," *Appl. Phys. Lett.,* vol 102, p. 221118, June 2013.

[5] E.J. Curry, B.T. Jacobson, A.Y. Murokh, and P. Musumeci, "Sub-picosecond shot-to-shot electron beam and laser timing using a photoconductive THz antenna", in *Proc. IBIC'15*, Melbourne, Australia, September 2015, pp. 243-245.

[6] D. Cesar *et al.,* "Demonstration of single-shot picosecond time-resolved MeV electron imaging using a compact permanent magnet quadrupole based lens," *Phys. Rev. Lett.,* vol 117, p. 024801, July 2016.

[7] W. Berry, N. Wang, M. R. Hashemi, M. Unlu, and M. Jarrahi, "Significant performance enhancement in photoconductive terahertz optoelectronics by incorporating plasmonic contact electrodes," *Nat. Comm.,* vol 4, 1622, Mar 2013.

[8] N. T. Yardimci, S. H. Yang, C. W. Berry, and M. Jarrahi, "High-power terahertz generation using large-area plasmonic photoconductive emitters," *IEEE Trans. THz Sci. Technol*., vol 5, pp. 223-229, Mar 2015.

ISBN 978-3-95450-177-9

SINGLE-SHOT THz SPECTROSCOPY FOR THE CHARACTERIZATION OF SINGLE-BUNCH BURSTING CSR

J. Raasch†, M. Arndt, K. Ilin, A. Kuzmin, A. Schmid, M. Siegel, S. Wuensch, Institute of Micro- and Nanoelectronic Systems, Karlsruhe Institute of Technology (KIT), Karlsruhe, Germany
A.-S. Mueller, J. L. Steinmann,
Laboratory for Applications of Synchrotron Radiation, KIT, Karlsruhe, Germany
G. Cinque, M. D. Frogley, Diamond Light Source, Didcot, United Kingdom
J. Hänisch, B. Holzapfel, Institute for Technical Physics, KIT, Karlsruhe, Germany

Abstract

An integrated array of narrow-band high-T_c $YBa_2Cu_3O_{7-x}$ (YBCO) detectors embedded in broad-band readout was developed for the future use at synchrotron light sources as a single-shot terahertz (THz) spectrometer. The detection system consists of up to four thin-film YBCO nanobridges fed by planar double-slit antennas covering the frequency range from 140 GHz up to 1 THz. We present first results obtained at the ANKA storage ring and at Diamond Light Source during operation of two and four frequency-selective YBCO detectors, respectively.

INTRODUCTION

Brilliant Coherent Synchrotron Radiation (CSR) from short, relativistic electron bunches opens a broad range of applications, amongst them terahertz (THz) imaging and spectroscopy. One prominent way to generate CSR is the use of dedicated low-alpha optics in an electron storage ring [1]. Herein, the bunch length is reduced to sub-mm dimensions leading to the coherent emission at wavelengths longer than the overall bunch length, thus in the THz frequency range. The low-alpha mode, however, entails electron beam instabilities, the so-called micro-bunching, once the beam current exceeds a certain threshold [2]. This leads to a variation in the temporal and spectral shape of the emitted THz radiation pulses. The micro-bunching is characterized by the occurrence of bursts of THz radiation at wavelengths shorter than the overall bunch length. These instabilities restrain the possible range of usage of CSR. Moreover, the micro-bunching instabilities limit the possible bunch compression and thus the level of emitted THz radiation power. Optimization of the emitted CSR requires a deeper understanding of the micro-bunching mechanisms. To this end, single-shot and turn-by-turn resolution of the THz signal is needed.

The short pulse lengths during low-alpha operation (ps/sub-ps) combined with high revolution frequencies (above 100 kHz) prevents the use of most room-temperature and liquid helium cooled semiconductor THz detectors. Response times of commercial pyroelectric sensors and semiconducting bolometers are limited at around tens of milliseconds and several hundred nanoseconds, respectively [3]. As compared to that, the characteristic times during the measurements at ANKA are 15 – 20 ps full width at half maximum (FWHM) for the pulse lengths and 2 ns between two consecutive pulses, corresponding to 500 MHz repetition rate [4]. At Diamond Light Source the characteristic pulse length was about 8 ps FWHM, the repetition frequency is the same as at ANKA [5]. Superconducting detectors offer both a high sensitivity and fast response times. First bunch-by-bunch resolution of CSR pulses was demonstrated by the use of superconducting NbN hot-electron bolometers with response times of 165 ps FWHM by Semenov et al. [6]. However, the resolution of the single pulse's temporal shape is not viable with those detectors.

Highest temporal resolution in direct detection is offered by detectors based on the high-T_c material $YBa_2Cu_3O_{7-x}$ (YBCO). Response times as fast as 16 ps FWHM have been demonstrated [7]. Here the limiting factor was identified to be the readout electronics rather than intrinsic response times of YBCO that lie in the range of 1 – 2 ps only [8]. Moreover YBCO THz detectors offer zero bias detection combined with the unique feature of electrical field sensitivity, both of them being based on the intrinsic detection mechanism for direct THz irradiation [9, 10].

At ANKA the overall bunch length of individual CSR pulses could be observed using the YBCO detection system [7]. The substructure on the bunch that arises during bursting can however not be resolved with state-of-the-art electronics. Therefore single-shot THz spectroscopy is a promising new candidate to gain further insight into the bunch profile. For that, single-shot spectral resolution needs to be combined with the ability to resolve individual bunches in a multi-bunch environment. By transforming the information from the single-shot spectra to the time domain, even shorter bunch lengths and substructures can be observed.

Due to its fast intrinsic relaxation processes YBCO was selected as detector material and embedded into narrow-band antennas combined with broad-band readout, as described in the next section. The second part of this report focuses on first tests of planar double-slot antennas under pulsed irradiation that have been conducted at the ANKA storage ring. The narrow-band operation of an array consisting of four detectors has been demonstrated

This work was supported by the German Federal Ministry of Education and Research (Grant 05K13VK4), by the Helmholtz International Research School for Teratronics and the Karlsruhe School of Elementary Particle and Astroparticle Physics: Science and Technology.
† juliane.raasch@kit.edu

ISBN 978-3-95450-177-9

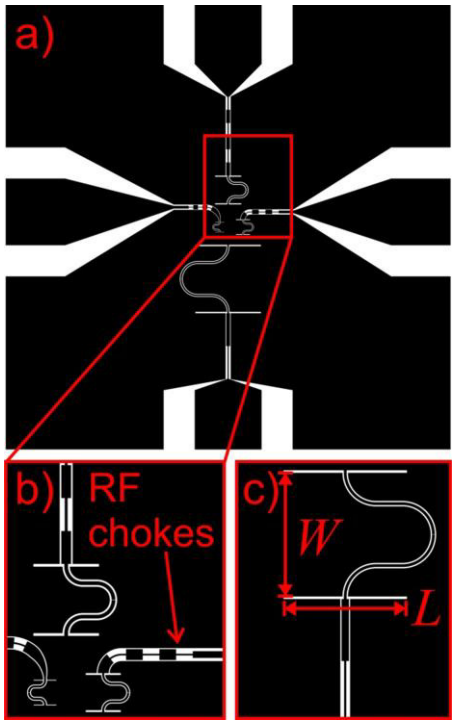

Figure 1: (a) Four-detector array with close-up view of the RF chokes (b) and the high impedance antenna design (c). The gold metallization is depicted in black and white areas correspond to the bare sapphire substrate.

recently at the MIRIAM beamline B22 at Diamond Light Source.

YBCO DETECTION SYSTEM

Antenna Design

The frequency-selective coupling of radiation to the YBCO detecting element is realized with planar double-slot antennas which were designed for center frequencies of 140 GHz, 350 GHz, 650 GHz and 1.02 THz. Figure 1a shows the array design of the 3 mm × 3 mm detector chip. Simulations of the antennas were performed with CST Microwave Studio [11]. Recently a good coupling efficiency and narrow-band behaviour were demonstrated for double-slot antennas combined with a YBCO detecting element [12].

To cope with the demand for excellent matching between the antenna and the YBCO detector impedance, the antenna layout has been adapted for higher impedances as can be seen in Fig. 1c. Therefore, the slot length L was set to $\lambda/2$ to achieve high slot impedance. The coplanar waveguide between slot and detector also has a length of $\lambda/2$ to retain the impedance at the position of the detecting element. The curving of the waveguide with the off-centred detecting element ensures an optimum distance W between the two slots. An additional benefit of the long waveguide is the improved narrow-band behaviour of the antenna. Antenna impedances as high as 300 Ω to 350 Ω are provided by this design. For a detector impedance

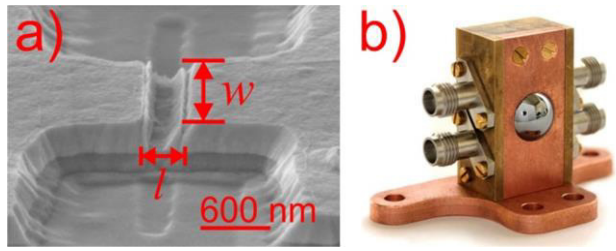

Figure 2: (a) SEM image of readily processed YBCO detecting element with typical lateral dimensions of $l = 180$ nm and $w = 1500$ nm. The 200 nm thick gold metallization layer can be distinguished from the underlying ceramic layers (CeO_2, PBCO and YBCO). (b) 4-channel detector block with silicon lens.

with a real part of 350 Ω the simulations predict antenna bandwidths of approximately 7% for all four antennas.

Isolation between the detector and the readout path at the antenna frequency is obtained through RF-chokes, see Fig. 1b. The distance between the individual antennas of the array was chosen to minimize detector crosstalk while maintaining a high directivity. Further information on the array design process can be found in [12].

Detector Fabrication

For the YBCO detectors double-side polished R-plane sapphire was used as substrate. This ensures the transmission of THz radiation with low dielectric losses ($\varepsilon_r = 10.06$, $\tan\delta = 8.4 \cdot 10^{-6}$ at 77 K), [13]. High-quality YBCO thin films are grown by pulsed laser deposition (PLD). The deposition of 8 nm CeO_2 and 25 nm $PrBa_2Cu_3O_{7-x}$ (PBCO) buffer layers allow for the epitaxial growth of a 25 nm thick YBCO film [14, 15]. The superconducting thin film is sandwiched between the buffer layers and a 25 nm PBCO capping layer acting as protection during patterning. A gold film is deposited atop the multilayer structure to benefit from the lower surface resistance of gold as compared to YBCO at frequencies above 150 GHz [16]. *In-situ* deposition of a 20 nm thin gold film ensures good contact resistances between gold and YBCO. Further 180 nm of gold were deposited *ex-situ* using DC magnetron sputtering. As compared to PLD grown gold films, the sputtered gold films exhibit significantly improved film-thickness homogeneity and guarantee reproducible etching due to the smaller grains.

Patterning of the YBCO detectors was carried out in two steps. At first, the length l of the detecting element was defined by removing the gold in the area of the actual detecting element. The patterning of the resist mask was done by electron-beam lithography (EBL), and gold etching was realized as a combination of argon-ion milling and wet-chemical etching. Herein the ion milling allows for anisotropic etching of the first 180 nm of the slit while the wet-etching solution removes the remaining 20 nm without altering the oxygen content of the underlying ceramic layers. The slit area of the gold removal can be seen as small cavities adjacent on both sides of the detecting element in Fig. 2a. The second step defines the width

ISBN 978-3-95450-177-9

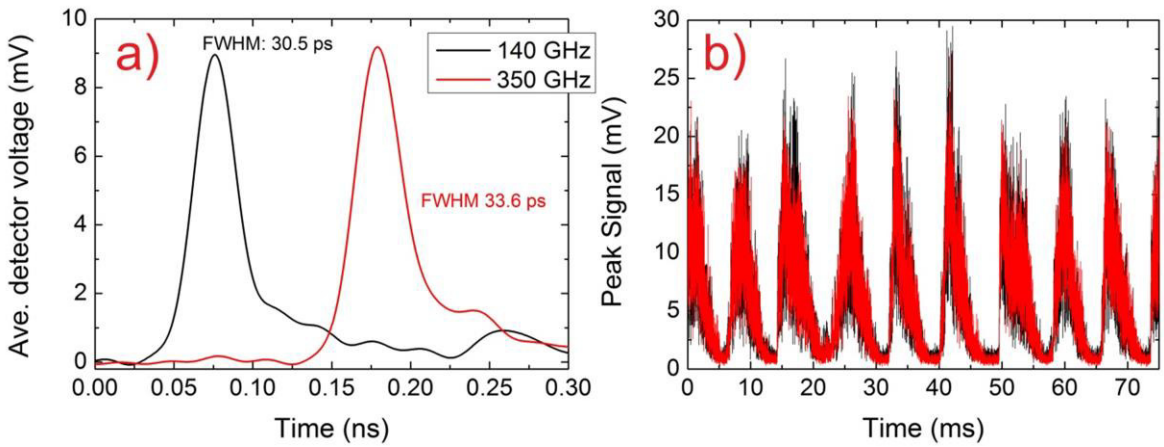

Figure 3: (a) Single-shot detector responses of the 140 GHz and 350 GHz detector. (b) Bursting at 140 GHz and 350 GHz as observed at the IR2 beamline at ANKA.

of the detecting element and the planar narrow-band antennas as well as the coplanar design of the detector chip. To this end, consecutive EBL and argon-ion milling are carried out. Further details on the fabrication process can be found in [17].

The patterning process described above enables the fabrication of superconducting structures with critical temperatures as high as $T_c \approx 84$ K. Intrinsic responsivities to pulsed excitations of up to 1.0 V/pJ have been demonstrated at the ANKA synchrotron [18].

Cryostat Design

Direct readout of the YBCO detector array is done through broad-band connection lines. For that, the sapphire chip is glued to the flat side of a high-resistivity silicon lens, which along with the narrow-band antennas is acting as a hybrid antenna [19]. The back-side illuminated detector is mounted in a four-channel detector block (Fig. 2b) made of copper to ensure good thermal coupling to the cold plate of the liquid nitrogen cryostat used to provide the operation temperature of 77 K. Four V-compatible coaxial readout lines for frequencies up to 65 GHz connect the detector block to four room-temperature broad-band SHF BT65 bias tees. The RF ports of the bias tees are fed to a real-time oscilloscope to read out the signal coming from the detectors, while the DC ports are used for the biasing of the individual YBCO detectors. To this end, the system is equipped with four individual precision current sources.

TWO-CHANNEL MEASUREMENTS AT ANKA

A prototype detection system with two narrow-band detectors operating simultaneously at 140 GHz and 350 GHz was tested at the IR2 beamline of the ANKA storage ring during low-alpha operation at 1.3 GeV. The filling pattern consisted of a single bunch.

The detectors were operated at 80 K bath temperature and biased at their working point of optimal sensitivity. An Agilent DSA-X 93204A real-time oscilloscope with 32 GHz bandwidth was used to read out both detectors simultaneously. No amplifier was employed.

The detector signals recorded during a single CSR pulse are depicted in Fig. 3a. The difference in peak time can be accounted to variations in the length of the readout paths. Both detectors exhibit response times of approximately 30 ps (FWHM) [20]. Here, the limiting factor is the readout bandwidth rather than the detector speed. A simultaneous recording of the bursting at both frequencies can be seen in Fig. 3b.

FOUR-CHANNEL SIMULTANEOUS DETECTION AT DIAMOND

The 4-channel detector array has been examined at the MIRIAM beamline at Diamond Light Source. The synchrotron was operated in low-alpha mode at an energy of 3 GeV and a bunch length of 3.5 ps rms [21]. The beam current amounted to 10 mA and was kept constant by top-up every hour, thus ensuring stable conditions above the bursting threshold. The filling pattern was designed as a hybrid filling consisting of a multi-bunch train of 200 bunches and a single bunch at a distance of 368 buckets. The current in every single bunch corresponded to 50 µA.

A cut-off of about 50% in the frequency range between 300 – 500 GHz has been observed at the experimental endstation posing additional requirements to the YBCO detector sensitivity [22]. Figure 4 shows the single-shot peak signal of all four detectors during two different bursts recorded on a bunch-by-bunch basis. As can be seen, the detector sensitivity is sufficient to detect the bursting CSR in the frequency range of 140 GHz up to 1 THz. In Fig. 4a the low frequencies start to appear first when the bunch compresses whereas the higher frequencies start to burst later. However, in Fig. 4b a different kind of burst can be seen. The burst is less intense but longer in duration. Moreover, initially all four frequencies appear simultaneously (approximately at 39.15 ms) but the higher frequencies decline first.

ISBN 978-3-95450-177-9

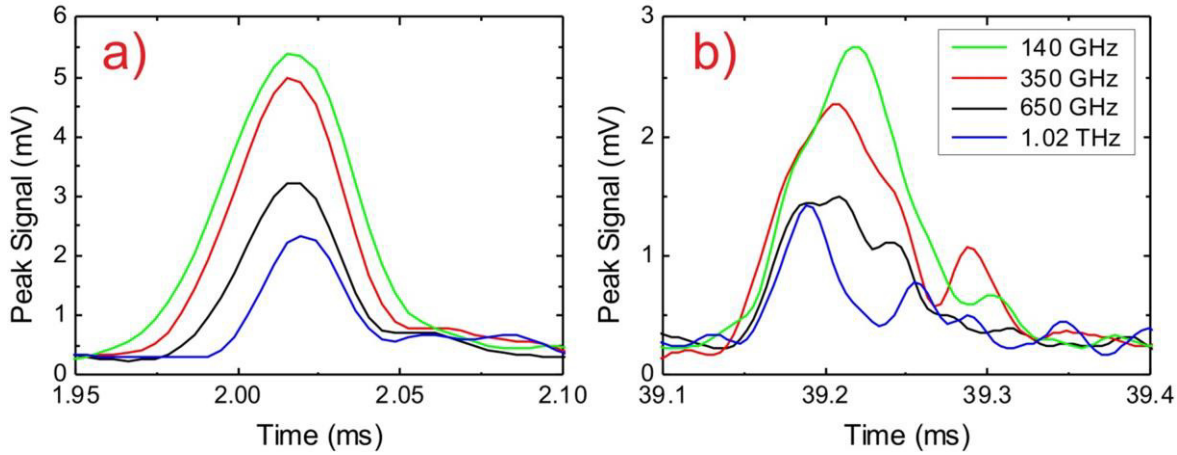

Figure 4: Bursting CSR at Diamond Light Source. Two different burst patterns and their frequency dependence are depicted in (a) and (b).

The frequency-dependent behaviour of the individual detectors was investigated by Fourier-Transform Infrared interferometry and via THz bandpass filters. Both measurement methods show good agreement and for the specific case of the 650 GHz antenna a center frequency between 650 and 700 GHz is observed. The detailed discussion of these results can be found in [23].

CONCLUSION

We have developed a THz detection system that enables the single-shot bunch-by-bunch monitoring of CSR at four distinct frequencies. To this end, a fabrication process aiming for ultimate detector sensitivity has been implemented and custom-made narrow-band antennas have been designed to match the high detector impedance. At two and four frequencies, respectively, the bursting behaviour has been observed at the ANKA storage ring and Diamond Light Source revealing frequency-dependent behaviour of the bursts. From those measurements, the need for single-shot spectroscopic resolution of bursting CSR becomes apparent.

Future development of the single-shot THz spectroscopy system includes calibration to be able to use the existing four-channel setup for characterizing bursting CSR. Extending the range of use to higher frequencies and the evolution of the system to larger pixel numbers will make it available also for the application at linear accelerators. This demands the introduction of new readout concepts as the herein presented direct readout with real-time oscilloscopes is limited to four channels and lacks memory depth. One approach to overcome this limitation has been presented by Caselle et al. in the form of the KAPTURE readout electronics [24].

ACKNOWLEDGEMENT

The authors would like to thank the beamline scientists and technical staff at the infrared beamlines at ANKA for the continuous support. Moreover, we thank Diamond Light Source for access to and extensive assistance at the MIRIAM beamline, B22 (SM 12495), that contributed to the results presented here, as well as for support from the EU.

REFERENCES

[1] M. Abo-Bakr *et al.*, *Phys. Rev. Lett.* 90, p. 094801, 2003.

[2] G. Stupakov and S.Heites, *Phys. Rev. ST Accel. Beams* 5, p. 054402, 2002.

[3] `http://www.terahertz.co.uk`

[4] N. Hiller *et al.*, in *Proc. IPAC'13*, MOPME014, p. 500.

[5] W. Shields *et al.*, *Jour. of Phys.: Conf. Ser.* 357, p. 012037, 2012.

[6] A. D. Semenov *et al.*, in *Proc. IRMMW-THz 2009*, p. 1.

[7] P.Thoma *et al.*, *Appl. Phys. Lett.* 101, p. 142601, 2012.

[8] M. Lindgren *et al.*, *Appl. Phys. Lett.* 74, p. 853, 1999.

[9] D.Y. Vodolazov and F. M. Peeters, *Phys. Rev. B* 76, p. 014521, 2007.

[10] J. Raasch *et al.*, *IEEE Trans. Appl. Supercond.* 25, p. 2300106, 2015.

[11] `https://www.cst.com`

[12] A. Schmid *et al.*, *IEEE Trans. Appl. Supercond* 26, p. 1, 2016.

[13] T. Konaka *et al.*, *Jour. of Supercond.* 4, p. 283, 1991.

[14] X. D. Wu *et al.*, *Appl. Phys. Lett.* 58, p. 2165, 1991.

[15] J. Gao *et al.*, *J. Appl. Phys.* 71, p. 2333, 1992.

[16] W. Rauch *et al.*, *Jour. Appl. Phys.* 73, p. 1866, 1993.

[17] P. Thoma et al., *IEEE Trans. Appl. Supercond.* 23, p. 2400206, 2013.

[18] J.Raasch et al., in *Proc. IPAC'14*, THPME125, p. 3533.

[19] A. D. Semenov *et al.*, *IEEE Trans. Microw. Theory Tech.*, 55, p. 239, 2007.

[20] A. Schmid *et al.*, in *Proc. IPAC'16* MOPMB016, p. 115.

[21] G. Cinque *et al.*, *Rend. Fis. Acc.Lincei* 22, p.S33, 2011.

[22] G. Cinque, private communication, Aug. 2016.

[23] A. Schmid *et al.*, submitted for publication.

[24] M. Caselle *et al.*, in *Proc. IPAC'14,* THPME113, p. 3497.

ISBN 978-3-95450-177-9

SINGLE-SHOT THz SPECTROMETER FOR BUNCH LENGTH MEASUREMENTS*

S.V. Kutsaev, A. Murokh, M. Ruelas, H. To
RadiaBeam Systems, LLC, Santa Monica, CA, 90403, USA
V. Goncharik
Logicware Inc, New York, NY, 11235, USA

Abstract

We present a new diagnostic instrument designed to measure bunch length in RF particle accelerators. Typically, scanning-type Michelson or Martin-Puplett interferometers are used to measure the coherent radiation from a short bunch to deduce the bunch length. However, this requires averaging over several shots, revealing only the average bunch length. We propose to measure the emitted coherent spectrum of a short bunch emission that contains the same spectral information as the bunch shape using single-shot spectrometry. In this paper, we present design considerations and first experimental results obtained at FACET for this instrument that allows shot-to-shot measurement of the spectrum emitted by a short electron bunch.

INTRODUCTION

Electron bunch length monitors are an important diagnostic tool for current and upcoming accelerators. The short bunch lengths of single-pass linacs have traditionally made use of RF transverse deflecting cavities [1,2,3] or interferometric methods [4,5]. RF deflecting cavities streak the electron bunch onto a screen and is a destructive measurement limited by available RF power. Interferometric methods exploit the fact that the emitted coherent spectrum of a bunch contains the spatial information of the bunch structure. This technique is attractive in that it is potentially non-destructive when paired with coherent synchrotron radiation or diffraction radiation. However, scanning-type Michelson or Martin-Puplett interferometers are incapable of shot-to-shot measurements.

A single-shot, non-destructive, high-repetition-rate bunch length monitor is a greatly desired diagnostic. A cascaded multi-stage grating spectrometer has the potential to fill this gap in diagnostic techniques [6].

SINGLE-SHOT SPECTROMETER

Since a single-shot spectrometer allows for reliable detection and measurement of RF pulse shortening, it can be used for identification of occurrences of RF breakdown (RFBD). The first prototype of our THz spectrometer was designed for RFBD detection in 120 GHz high-gradient accelerating sections developed at the SLAC National Accelerator Laboratory [7]. Operations with short pulses required narrow bandwidth (2GHz) and high frequency resolution (100 MHz).

This version of the spectrometer was designed, prototyped and built by RadiaBeam Systems, LLC [8]. It was tested at SLAC and the proof-of-principle operation was demonstrated. It was revealed that the alignment and optics systems must be enhanced, as well as more robust electronics added.

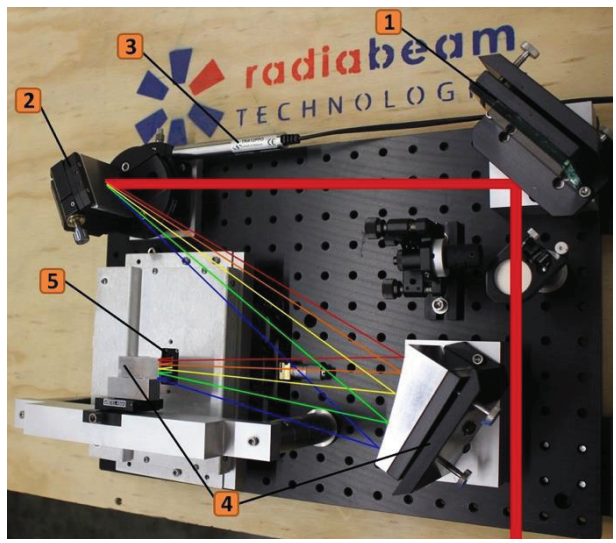

Figure 1: Physical layout of final spectrometer design, shown with dimensions and optical path

The design of the THz single-shot spectrometer is an adaptation of the DESY broadband multi-channel spectrometer [9], and consists of several core elements shown in Figure 1:

1) Reflecting mirror to deflect the signal to the grating,
2) Diffraction grating to spatially separate the signal by frequencies,
3) Motorized mounting to rotate the grating,
4) Aluminum 2D parabolic mirrors to focus the signal on the linear detector array,
5) Electronic board with pyroelectric detector to acquire the THz radiation signal

DESIGN UPGRADE

Unlike the spectrometer for RFBD detection, for which a narrow-band, high-resolution spectroscopy is required, the bandwidth of the spectrometer for bunch length measurements must be much larger than the RFBD design. This upgrade can be accomplished with two simultaneous techniques: adding additional stages with

* This work was supported by the U.S. Department of Energy, Office of High Energy Physics, under contract DE-SC0013684

ISBN 978-3-95450-177-9

cascading central frequencies and increasing the bandwidth of each stage.

The broadband version of the spectrometer requires several major changes. First, the grating will be redesigned to provide larger angular spread and thus better resolution of the frequency components. In this case, we will be able to use discrete pyro-detectors that have significantly better speed and sensitivity. Figure 2 shows the upgraded design of the single-shot spectrometer that will be used for bunch length measurements.

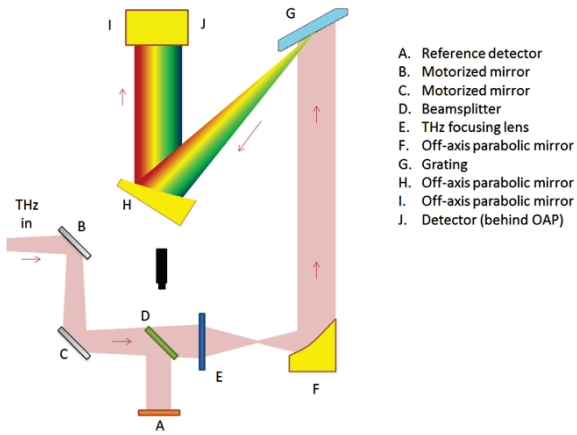

Figure 2: Preliminary broadband spectrometer design for beam length measurements. The linear polarizer is not shown.

The improved spectrometer design includes the following features:

- Collimating system: Polymethylpentene (TPX) THz lens and an off-axis parabola
- Alignment system: one laser beam arrives from both ends of grating
- External alignment system: 2 mirrors
- New detector board with discrete detector
- Linear polarizer to increase extinction ratio

The broad-band spectrometer is currently in the final modelling stage but will not be built until spring 2017. The improved broadband design will be tested using a THz source at the Advanced Photon Source Injector Test Stand [10].

ELECTRONICS SYSTEM

The spectrometer design was made possible by the availability of a custom-made linear array of 32 small pyro-detectors from the RadiaBeam Real-Time Interferometer [11]. Each pyro-detector is only 0.5 mm in width and 1 mm in height. The total span of the array is 32 mm. To spread across the array, the diffracted beam, which has a narrow angular spread, requires only about 55 cm of optical path length. This optical path length is an important parameter for the spectrometer design since the shorter length allows for a more compact spectrometer, and also reduces the total THz power loss due to reflection and atmospheric absorption.

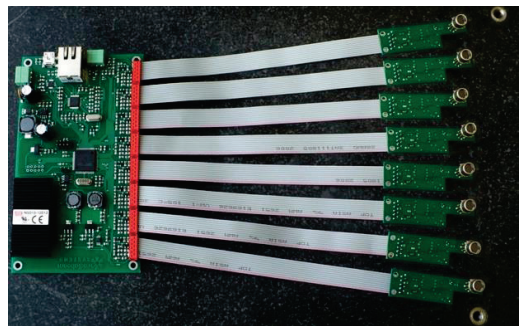

Figure 3: Prototype multichannel data acquisition system.

Since the existing detector board cannot be used for broadband spectroscopy, a new robust discrete-detectors-based electronics board that will be used in future commercial versions of the spectrometer was developed (see Figure 3). Though it was designed for QS5-IL Hybrid Pyroelectric detectors from Gentec Electro-Optics, it can be readily adapted to other discrete pyros. This sensor possesses sufficient sensitivity as a THz radiation spectrometer and fast thermal response. In this configuration, the pyroelectric detector element is combined with a low noise operational amplifier. QS-IL detectors are designed to maximize voltage output at low frequencies and therefore include load and feedback resistors in the 100 GΩ to 300 GΩ range. They are also formed into 8-pin TO packages that allow the addition of an “external resistor” to lower the output and increase the bandwidth.

After the input action, the signal voltage from the output of QS5-IL pyroelectric sensor is stored by the peak detector and then digitized by a 16-bit ADC. The peak detector can operate at frequencies much higher than those for which there are ADCs. Using the peak detector with a programmable threshold avoids the omission of an observable signal. The threshold level can be set above the noise level. The 12-bit ADC is used for viewing QS5-IL detector output signals and simplifying the tuning of the THz-spectrometer. The sensor boards are connected to the control board via flat ribbon cables up to one meter in length.

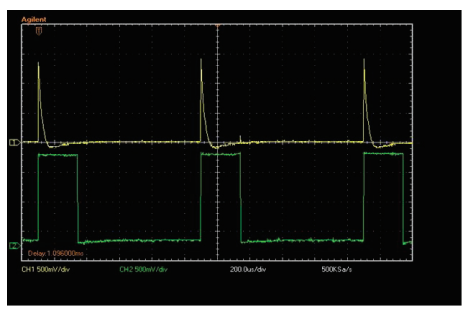

Figure 4: Response of peak detector (yellow) to a series of xenon lamp pulses (green) – right.

The developed system was tested by radiating the detectors with a series of Xenon lamp pulses. Figure 4 demonstrates the response of a peak detector to this radiation, which is clear and demonstrates the operational principle of the electronics.

ISBN 978-3-95450-177-9

MULTISTAGE SPECTROMETER

The wideband spectrometer will be limited in frequency span to about a GHz, which is insufficient for bunch length measurements. To further extend the frequency range of the spectrometer, several stages can be cascaded. Such a technique has been used at DESY [12] with success. In this technique, the THz pulse is sent to the first stage grating and the zeroth-order reflection (containing longer wavelengths) is forwarded to the next level. Successive spectrometer stages use a grating with a central frequency shifted to successively longer wavelengths. This cascaded spectrometer scheme is shown in Figure 5. Only the available pulse energy limits the total device bandwidth.

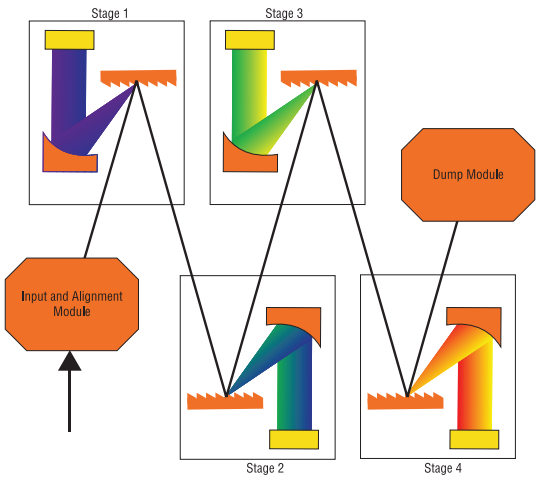

Figure 5: A cascaded spectrometer is shown with four stages, an input module, and an exit module. Additional stages can be added to expand the range of wavelengths covered or to allow smaller wavelength steps.

The spectrometer will make use of a remotely actuated alignment and collimation mechanism for ease of use in changing conditions. The collimating mechanism will use an adjustable beam expander to adjust the convergence of the incoming beam. The additional alignment mechanism, while not strictly required, was prompted by the difficulty in aligning the system during prototype testing; systems installed in a radiation-free environment could easily omit this module.

SUMMARY

We built and field-tested the first prototype of single-shot high-resolution, wide-bandwidth THz spectrometer. This device, with modifications discussed, allows shot-to-shot measurements of bunch lengths by increasing the total bandwidth. The bandwidth is widened by adding additional stages with cascading central frequencies and widened individual bandwidths. A turnkey single-shot bunch length monitor has applications in various high-brightness and high-current accelerators and the spectrometer is being extended to fulfil this need. A possible realization of the commercial product is shown in Figure 6.

Figure 6: Rendering of the commercial envisioned device.

ACKNOWLEGMENTS

We thank efforts of SLAC FACET team that enabled field test of the spectrometer, and particularly, Valery Dolgashev, Massimo Dal Forno, and Christine Clarke.

REFERENCES

[1] P. Krejcik *et al.*, "Commissioning of the New LCLS X-Band Transverse Deflecting Cavity with Femtosecond Resolution," *Proc. of IBIC 2013*, Oxford, 2013.
[2] D. Alesini *et al.*, *Nucl. Instrum. & Meth. A* 568, pp 488-502, 2006.
[3] J. H. Lee *et al.*, "Slice emittance measurement using rf deflecting cavity at PAL-XFEL ITF," *Proc. Free-Electron Laser Conf.*, Basel, 2014.
[4] P. Evtushenko, "Bunch Length Measurements at JLAB FEL," *Proc. of FEL 2006*, Berlin, Germany, 2006.
[5] J.H. Ko *et al.*, "Electron Bunch Length Measurement using coherent Radiation Source of fs-THz Accelerator at Pohang Accelerator Laboratory," *Proc. of IPAC'16*, Busan, Korea, 2016.
[6] C. Behrens *et al.*, "Constraints on photon pulse duration from longitudinal electron beam diagnostics at a soft x-ray free-electron laser," *Phys. Rev. Accel. Beams* 15, 030707, 2012.
[7] M. Dal Forno *et al.*, *Phys. Rev. Accel. Beams* 19, 011301, 2016.
[8] S.V. Kutsaev *et al.*, "Single-shot THz Spectrometer for Measurement of RF Breakdown in mm-wave Accelerators," *Proc. of IPAC'16*, Busan, Korea, 2016
[9] S.Wescha *et al.*, *Nucl. Inst. and Meth. A*, v. 665, 2011, p. 40–47.
[10] A.V. Smirnov *et al.*, *PRST-AB 18*, 090703 (2015)
[11] J. Thangaraj *et al.*, *Rev. Sci. Instrum.* 83, 043302 (2012).
[12]. S. Wesch et al., *Nucl. Instr. & Meth. A,* 665, pp 40-47, 2011.

ISBN 978-3-95450-177-9

THERMAL SIMULATIONS OF WIRE PROFILE MONITORS IN ISIS EXTRACTED PROTON BEAMLINE 1

D. W. Posthuma de Boer*, A. Pertica, ISIS, STFC, Rutherford Appleton Laboratory, Oxfordshire, OX11 0QX, UK

Abstract

Wire scanners and secondary emission (SEM) grids are used for measurements of transverse beam profile at the ISIS neutron and muon source. Silicon carbide-coated carbon fibre wires are used in profile monitors throughout the ISIS accelerator. One such SEM grid is currently installed close to the target in Extracted Proton Beamline 2 (EPB2) and is intercepted by the 800 MeV proton beam at a repetition rate of 10 Hz. Future profile measurements will require another of these monitors to be installed close to the target in EPB1; intercepted with a repetition rate of 40 Hz.

Wires intercepting the ion beam are heated due to the deposition of beam-energy. Thermal simulations for the higher repetition rate were performed using ANSYS and a numerical code. The numerical code was then expanded to include various beam, wire and material properties. Assumptions for temperature dependent material emissivities and heat capacities were included in the simulation. Estimated temperatures due to the energy deposited by protons, and approximate values of deposited energy from the expected neutron flux are presented. The effects on wire-temperature of various beam and wire parameters are also discussed.

INTRODUCTION

Intercepting wires are used at accelerator facilities around the world to measure transverse and longitudinal beam properties. Beam particles either knock electrons from the wire or deposit some charge, inducing a current which is proportional to the flux of the beam. By measuring the relative current at multiple transverse positions, a beam profile can be obtained [1].

The ISIS facility at the Rutherford Appleton Laboratory is a spallation neutron and muon source delivering an average of 0.2 MW of proton beam power to two target stations (TS1 & TS2). During acceleration and extraction wire-based monitors are used to measure the transverse beam profile. At ISIS the intercepting wires are silicon-carbide (SiC) coated carbon fibres with a diameter of 142 µm.

A wire grid is currently installed in EPB2 close to the TS2 target, with the wires intercepting the beam at a rate of 10 Hz. Future profile measurements will require a second grid to be installed in EPB1 close to the TS1 target. These wires will intercept the 800 MeV proton pulses at a repetition rate of 40 Hz. Thermal simulations are required to verify that wires in EPB1 will be able to withstand temperatures resulting from this higher repetition rate.

* david.posthuma-de-boer@stfc.ac.uk

THEORY

Charged Particles in Matter

Energetic charged particles passing through a medium interact electromagnetically with atomic electrons, depositing energy by ionising constituent atoms. For a singly charged particle with a velocity $v = \beta c$, energy E and relativistic factor γ, passing through a material with atomic number Z and number density n, the energy deposited into the material per unit particle path length x; the stopping power $S(E)$, follows the Bethe-Bloch equation

$$S(E) = -\frac{\mathrm{d}E}{\mathrm{d}x} \approx \frac{4\pi\hbar^2\alpha^2 nZ}{m_e\beta^2}\left[\ln\left(\frac{2v^2\gamma^2 m_e}{I_e}\right) - \beta^2\right], \quad (1)$$

where α is the fine structure constant, I_e is the effective ionisation potential, m_e is the electron mass, c is the speed of light and $\hbar$ is the Dirac constant [2]. An example of this for 800 MeV protons travelling in a tungsten medium is shown in Fig. 1. As the protons travel through the medium they lose kinetic energy to atomic electrons, increasing the value of $S(E)$ [2]. A sharp increase in the stopping power; known as the Bragg peak, is seen towards the end of the range.

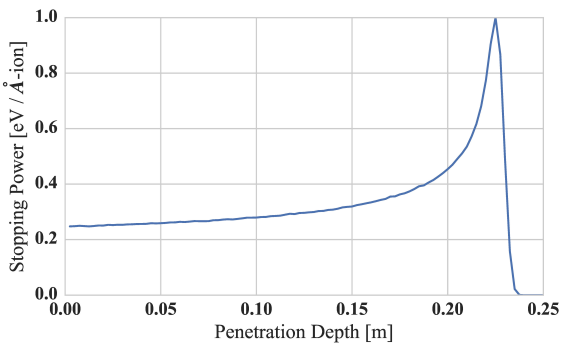

Figure 1: Results of a SRIM simulation showing the stopping power for 800 MeV protons in tungsten [3].

Thermal Effects

From the definition of the constant-volume heat capacity it can be found that the change in temperature, ΔT, of an object is given by:

$$\Delta T = \int \frac{1}{M c_v}\,\mathrm{d}U, \quad (2)$$

where U is the internal energy of an object, M is the energy-absorbing-mass and c_v is the constant-volume specific heat capacity of the material. Equation (2) shows that when energy is deposited into an object there is an associated increase in temperature [4].

ISBN 978-3-95450-177-9

Heat loss takes place by means of thermal conduction, convection and radiation. As profile monitor wires are thin and will be heated in vacuum, only radiation will be considered; the loss of energy by emission of photons. The total radiated power is given by the Stefan-Boltzmann law:

$$\dot{Q} = \epsilon\sigma A(T_1^4 - T_2^4), \quad (3)$$

where Q is the heat energy, T_1 is the temperature of the radiating object, T_2 is the ambient temperature, ϵ is the material emissivity, A is the materials surface area and σ is the Stefan-Boltzmann constant [4].

SIMULATION

Simulating the heating of wires as they intercept the proton beam will require that a calculation be made for the energy deposited per proton. This is given by integrating $S(E)$ over the proton's path through the wire. As a worst-case approximation all protons will be assumed to traverse the full wire diameter, d as indicated in Fig. 2; the largest direct path. Since the wire thickness is on the order of 100 µm and the range of 800 MeV protons in tungsten is approximately 20 cm; as shown in Fig. 1, the stopping power will be assumed to be constant. The energy deposited per proton was thus given by $E_{\text{ion}} = S(E) \cdot d$. Stopping powers were obtained from *PSTAR Tables* [5] and *SRIM* [3].

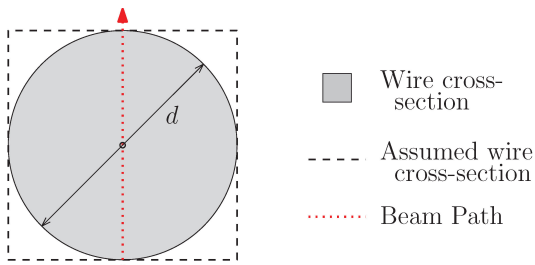

Figure 2: Assumed wire cross section in relation to physical dimensions; the assumed proton trajectory is also shown.

The assumed beam parameters are listed in Table 1. A frequency of 50 rather than 40 Hz will be used to calculate for the worst-case. Heating due to energy deposited by the beam will be calculated using Eq. (2). Cooling towards an ambient temperature of 300 K will be calculated using Eq. (3). Simulations were performed with ANSYS® 15.0 and a custom numerical code written in python.

Table 1: Assumed Beam Parameters at the End of EPB1

Parameter	Value
Beam σ	2.5 cm
Protons per bunch	1.5×10^{13}
Bunch length	100 ns
Bunch spacing	250 ns
Bunches per pulse	2
Pulse frequency	50 Hz
Beam energy	800 MeV

Material Properties

Equations (1), (2) and (3) show that the energy deposited into an object, the associated temperature increase as well as the radiated power each depend on the object's material properties. These properties are temperature dependent, and can vary due to manufacturing and finishing processes [6]. Material properties are often considered to be constant in such simulations [7], however in order to test the impact of temperature dependence, assumptions will be made for temperature dependent heat capacities and emissivities. The assumed emissivities for carbon fibres, SiC fibres and tungsten wires are shown in Fig. 3.

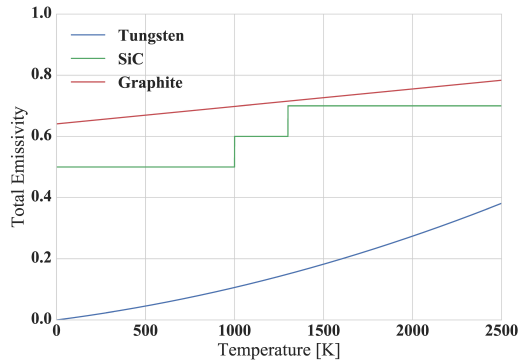

Figure 3: Assumed emissivities for simulated wire materials.

RESULTS

Comparison of Simulation Tools

Simulations of 30 µm diameter tungsten wires in a 181 MeV proton beam were initially run to compare predictions with previously published results, and to benchmark the two simulation techniques. Temperatures predicted by ANSYS® and the numerical code are shown in Fig. 4, where the temperature independent results appear to agree with those previously published; oscillating between around 3000 and 3500 K [8]. The simulations were then run with temperature dependent material properties. The two simulation methods were consistent, predicting maximum temperatures of approximately 1000 K lower than the temperature independent results (see Fig. 4).

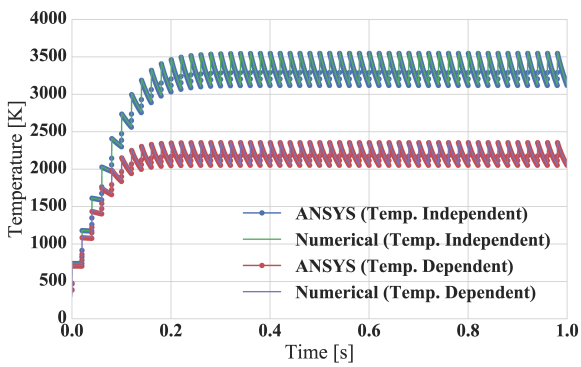

Figure 4: ANSYS® and numerical simulation results with constant and temperature dependent material properties.

ISBN 978-3-95450-177-9

ISIS Beam Parameter Results

Numerical simulations were then run for the beam parameters shown in Table 1. One wire or beam property was varied for each simulation; each giving a result resembling Fig. 4. The maximum predicted wire temperature was then recorded and plotted against the variable parameter.

Tungsten wires were predicted to have the highest temperature for a given wire radius as shown in Fig. 5. Carbon fibres had the lowest predicted temperature due to their relatively low stopping power, and the comparatively high emissivity. No wires were predicted to exceed melting or sublimation temperatures [9, 10].

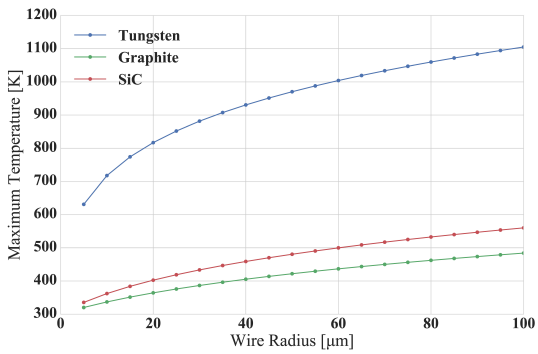

Figure 5: Variation of maximum temperature with intercepting wire radius; simulated with a numerical code.

Figure 6 shows the variation of maximum temperature with beam energy. The predicted variation in temperature over this energy range was 40, 20 and 25 K for tungsten, graphite and SiC respectively. Again no wires were predicted to exceed melting or sublimation temperatures.

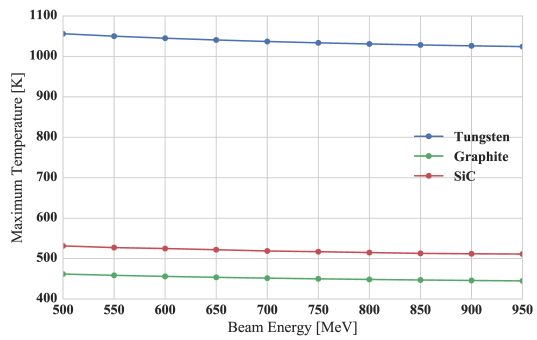

Figure 6: Variation of maximum temperature with incident proton beam energy; simulated with a numerical code.

Neutron Flux Considerations

Due to the close proximity of the simulated wires to the TS1 target, neutrons originating from the target were also expected to deposit energy. The heating associated with this energy was also considered. A constant neutron production rate of 2×10^{16} s^{-1} was assumed, distributed symmetrically over the surface of a sphere. The separation of the wires from the target was assumed to be 1 m, and the interception rate was found from the rectangular wire cross-section. It was also assumed that 3×10^{10} cm^{-2} neutrons provided a dose of 1 Gy [11]. This increased the simulated maximum temperature by less than 1% for all materials with the beam parameters shown in Table 1.

CONCLUSION

Simulations of wire heating using ANSYS® and a numerical code were run with temperature independent material properties and found to agree with previously published results. The simulations were then modified to include approximate temperature dependent properties. This resulted in a reduction in predicted maximum temperature of approximately 1000 K. It should be noted that the assumptions made for material properties do not necessarily describe real wire materials and would ideally be measured experimentally.

Numerical simulations were then run for a near-target wire grid monitor with tungsten wires, carbon fibres and SiC coated carbon fibres. Maximum temperatures for different wire & beam properties were recorded with none of the simulated wires reaching melting or sublimation temperatures, even with a neutron flux contribution.

While heating due to secondary neutrons was considered, other secondary particles were neglected. A more complete analysis would additionally include the energy deposited by photons and other secondary particles from the target.

REFERENCES

[1] P. Strehl, *Beam Instrumentation and Diagnostics*. Springer Berlin Heidelberg, 2006.

[2] M. Thomson, *Modern Particle Physics*, Cambridge University Press, 2013, pp. 10–14.

[3] J. F. Ziegler *et al.*, "SRIM – The stopping and range of ions in matter (2010)", *Nucl. Instr. Meth. B*, vol. 268, Jun. 2010.

[4] L. M. Jiji, *Heat Conduction*. Springer Berlin Heidelberg, 2009, pp. 11, 354.

[5] Stopping-Power and Range Tables for Electrons, Protons, and Helium Ions, `http://physics.nist.gov/PhysRefData/Star/Text/contents.html`

[6] D. Alfano *et al.*, "Emissivity and catalycity measurements on SiC-coated carbon fibre reinforced silicon carbide composite", *Journal of the European Ceramic Society*, vol. 29, pp. 2045-2051, Jan 2009.

[7] T. Yang *et al.*, "Thermal analysis for wire scanners in the CSNS Linac", *Nucl. Instr. Meth. A*, vol. 760, pp. 10-18, Oct. 2014.

[8] H. Akikawa *et al.*, "Wire Profile Monitors in J-PARC Linac", in *Proc. LINAC'06*, Knoxville, Tennessee, USA, Aug. 2006, paper TUP021, pp. 293–295.

[9] D. R. Lide, 4-122 and 12-94, in *Handbook of Chemistry and Physics*, 79th Ed. CRC Press, 1998.

[10] H. O. Pierson, *Handbook of Refractory Carbides and Nitrides*, William Andrew, 1996.

[11] J. Gibson and E. Piesch, *"Neutron Monitoring for Radiological Protection"*, IAEA, Vienna, 1985.

ISBN 978-3-95450-177-9

THEORY OF X-RAY TRANSITION RADIATION FROM GRAPHENE FOR TRANSITION RADIATION DETECTORS*

A.A. Tishchenko†, A.S. Romaniouk, D.Yu. Sergeeva, M.N. Strikhanov, National Research Nuclear University MEPhI, Moscow, Russia

Abstract

We present the theory of transition radiation for monolayers in X-ray domain from the first principles and consider the pros and cons of using graphene-monolayer in transition radiation detectors.

INTRODUCTION

Transition Radiation Detectors (TRD) are used in many modern experiments like ATLAS and ALICE in CERN, FENIX in BNL, AMS-02 experiment in space, etc. Usually they are used to separate particles with gamma factor less than 500 and more than 1500. However, to increase separation threshold TRD technique requires significant improvement.

Cut-off frequency of the transition radiation (TR) spectrum is proportional to the Lorenz-factor γ, which extends the spectrum to the X-ray domain, see Fig. 1. The cut-off frequency is defined as:

$$\omega_c = \gamma\omega_p. \tag{1}$$

This frequency is proportional to the plasma frequency ω_p of the material which depends on the electron density and the effective mass of electron m_e :

$$\omega_p^2 = 4\pi NZe^2/m_e, \tag{2}$$

with e being the electron charge, NZ being the number of electrons in the unit volume of the target.

In paper [1] it was suggested to use TR radiators based on graphene-monolayer. The idea is based on the fact that some fraction of conductivity electrons in graphene has zero (or very little) mass and, hence, as plasma frequency is inversely proportional to the mass of electron it could shift the TR spectrum to the region of higher frequencies with respect to the ordinary materials. Indeed, it is seen from Eq. (2) that if the effective electron mass goes to zero, then both the plasma frequency and the cut-off frequency from Eq. (1) go to infinity:

$$m_e \to 0, \quad \Rightarrow \quad \gamma\omega_p \to \infty. \tag{3}$$

*This work was supported by the grant RFBR 14-22-03053 (ofi-m) and, partially, by the Competitiveness Program of National Research Nuclear University MEPhI.

†tishchenko@mephi.ru

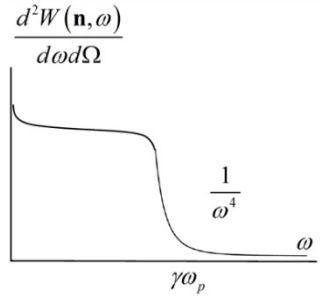

Figure 1: Cut-off of the transition radiation spectrum at high frequencies.

Calculation of the characteristics of the radiation from any monolayer can not be a limiting case of zero-thickness film from the theory for the film of arbitrary thikness, because the latter uses normally boundary conditions, which is not the case for monolayer.

Below we present the theory of transition radiation for monolayers in X-ray domain from the first principles [2, 3] and consider the pros and cons of using graphene-monolayer in TRDs.

MICROSCOPIC THEORY OF RADIATION FROM A MONOLAYER

Let us consider the generation of TR by a single charged particle, for example, by an electron. The target is a monolayer consisting of N atoms or molecules or any small particles with the size less than the wavelength.

Microscopic Maxwell's equations for such a system have the form:

$$\begin{cases} rot\mathbf{H}^{mic}(\mathbf{r},\omega) = \dfrac{4\pi}{c}\mathbf{j}'(\mathbf{r},\omega) - \dfrac{i\omega}{c}\mathbf{E}^{mic}(\mathbf{r},\omega), \\ rot\mathbf{E}^{mic}(\mathbf{r},\omega) = \dfrac{i\omega}{c}\mathbf{H}^{mic}(\mathbf{r},\omega), \\ div\mathbf{H}^{mic}(\mathbf{r},\omega) = 0, \\ div\mathbf{E}^{mic}(\mathbf{r},\omega) = 4\pi\left(\rho^0(\mathbf{r},\omega) + \rho^{mic}(\mathbf{r},\omega)\right), \end{cases} \tag{4}$$

where

$$\mathbf{j}'(\mathbf{r},\omega) = \mathbf{j}^0(\mathbf{r},\omega) + \mathbf{j}^{mic}(\mathbf{r},\omega). \tag{5}$$

The exact solution of the system Eq. (4) is :

ISBN 978-3-95450-177-9

$$\mathbf{E}^{mic}(\mathbf{r},\omega)=\mathbf{E}^{0}(\mathbf{r},\omega)+$$
$$+\frac{4\pi i}{\omega}\int d^3q e^{i\mathbf{qr}}\frac{k^2\mathbf{j}^{mic}(\mathbf{q},\omega)-\mathbf{q}\left(\mathbf{q},\mathbf{j}^{mic}(\mathbf{q},\omega)\right)}{q^2-k^2}, \quad (6)$$

which can be represented as:

$$E_i^{mic}(\mathbf{r},\omega)=E_i^{0}(\mathbf{r},\omega)+\hat{A}_{ij}E_j^{mic}(\mathbf{r},\omega), \quad (7)$$

where $\hat{A}_{ij}$ is the operator. As the first approximation the field acting upon the particles at the points $\mathbf{r}=\mathbf{R}_a$ can be exchanged by some average field that we call the local field, i.e.

$$E_j^{mic}(\mathbf{r},\omega)\big|_{\mathbf{r}=\mathbf{R}_a}\approx E_j^{loc}(\mathbf{r},\omega). \quad (8)$$

Therefore, from Eq. (7) it follows that

$$E_i^{mic}(\mathbf{r},\omega)=E_i^{0}(\mathbf{r},\omega)+\hat{A}_{ij}E_j^{loc}(\mathbf{r},\omega). \quad (9)$$

The main problem is to express the $E_j^{loc}(\mathbf{q},\omega)$ through the field of the external sources, i.e. the field of moving electrons $\mathbf{E}^{0}(\mathbf{r},\omega)$.

To do this it is necessary to average the field in two different ways.

First, let us average it over the positions of all N particles the monolayer:

$$E_i(\mathbf{R}_a,\omega)=\left\langle E_i^{mic}(\mathbf{R}_a,\omega)\right\rangle=$$
$$=\int d^3R_b\,g(\mathbf{R}_b)E_i^{mic}(\mathbf{R}_a-\mathbf{R}_b,\omega), \quad (10)$$

where $\langle\ldots\rangle$ stands for the averaging. The result can be written in the general form:

$$E_i=E_i^{0}+\hat{B}_{ij}E_j^{loc}. \quad (11)$$

Second, let us average it over the positions of all the particles relatively the given one:

$$E_i^{loc}(\mathbf{R}_a,\omega)=\int\prod_{s=1}^{N-1}d^3R_{an_s}w\left(\mathbf{R}_{an_s}\right)E_i^{mic}(\mathbf{R}_a;\mathbf{R}_n,\omega), \quad (12)$$

where $\mathbf{R}_n=\left(\mathbf{R}_{n_1},\ldots,\mathbf{R}_{n_{N-1}}\right)$. The result of the averaging can be written as:

$$E_i^{loc}=E_i^{0}+\hat{C}_{ij}E_j^{loc}. \quad (13)$$

The macroscopic field in any point can be obtained from Eq. (11) as

$$E_i(\mathbf{r},\omega)=E_i^{0}(\mathbf{r},\omega)+\frac{\alpha(\omega)}{2\pi^2}\times$$
$$\times\left\langle\sum_b\int d^3p\frac{p^2u_{is}(\mathbf{p})}{p^2-k^2}E_s^{loc}(\mathbf{R}_b,\omega)\exp\left[i\mathbf{p}(\mathbf{r}-\mathbf{R}_b)\right]\right\rangle, \quad (14)$$

where

$$u_{is}(\mathbf{p})=\delta_{is}-p_ip_s/p^2,\quad k=\omega/c. \quad (15)$$

To find the field of radiation in the wave zone, we use the well-known asymptotic formula:

$$\int d^3p\frac{f(\mathbf{p})}{p^2-k^2-i0}\exp[i\mathbf{pr}]=2\pi^2\frac{\exp[ikr]}{r}f\left(k\frac{\mathbf{r}}{r}\right), \quad (16)$$

which is correct at $kr\gg1$. As the result, the radiation field can be obtained in form:

$$E_i^{r}(\mathbf{r},\omega)=\alpha(\omega)k^2\times$$
$$\times\left\langle\sum_b\frac{\exp\left[ik|\mathbf{r}-\mathbf{R}_b|\right]}{|\mathbf{r}-\mathbf{R}_b|}u_{is}\left(\frac{\mathbf{r}-\mathbf{R}_b}{|\mathbf{r}-\mathbf{R}_b|}\right)E_s^{loc}(\mathbf{R}_b,\omega)\right\rangle. \quad (17)$$

For $r\gg R_b$ Eq. (17) takes the form:

$$E_i^{r}(\mathbf{r},\omega)=\frac{\exp[ikr]}{r}\alpha(\omega)k^2u_{is}(\mathbf{n})\times$$
$$\times\left\langle\sum_b E_s^{loc}(\mathbf{R}_b,\omega)\exp[-i\mathbf{kR}_b]\right\rangle, \quad (18)$$

where $\mathbf{k}=\mathbf{n}\omega/c$, $\mathbf{n}=\mathbf{r}/r$.

The distribution of the radiation energy per unit solid angle and per unit frequency, emitted by all particles in the layer, can be written as

$$\frac{d^2W(\mathbf{n},\omega)}{d\Omega d\omega}=cr^2\left|\mathbf{E}(\mathbf{r},\omega)\right|^2. \quad (19)$$

Let us average Eq. (18) over all positions of the particles in the layer $z=0$ and supposing that the particles of the monolayer are distributed uniformly in that plane :

$$\left\langle\sum_b\mathbf{n}\times\mathbf{E}^{loc}(\mathbf{R}_b,\omega)\exp\{-i\mathbf{kR}_b\}\right\rangle=$$
$$=n_1\iint dX_bdY_b\mathbf{n}\times\mathbf{E}^{loc}(\mathbf{R}_b,\omega)\exp\{-i\mathbf{kR}_b\}=$$
$$=n_1(2\pi)^2\mathbf{n}\times\mathbf{E}^{loc}(k_x,k_y,Z_b=0,\omega). \quad (20)$$

Substituting Eq. (20) into Eq. (19) we can obtain:

ISBN 978-3-95450-177-9

$$\frac{d^2W(\mathbf{n},\omega)}{d\Omega d\omega} = (2\pi)^4 \frac{\omega^4}{c^3} n_1^2 |\alpha(\omega)|^2 \times \times \left|\mathbf{n}\times\mathbf{E}^{loc}(\mathbf{K}, Z_b = 0, \omega)\right|^2, \quad (21)$$

where $\mathbf{K} = (k_x, k_y)$. The relation between the local field and the Coulomb field of the moving electrons for the case of monolayer was obtained in [2, 3]:

$$E_i^{loc}(\mathbf{q}, z, \omega) = = \left\{ \frac{\delta_{ij} - e_i e_j}{1 - \pi n_1 a \alpha(\omega)} + \frac{e_i e_j}{1 + 2\pi n_1 a \alpha(\omega)} \right\} E_j^0(\mathbf{q}, z, \omega). \quad (22)$$

As the result we obtain the spactral-angular distribution of radation from a monolayer in form

$$\frac{d^2W_m(\mathbf{n},\omega)}{d\Omega d\omega} = \frac{4e^2\omega^4 n_1^2}{c^3 v_z^2 \left[K^2 - \frac{\omega^2}{c^2} + \frac{(\omega - \mathbf{Kv})^2}{v_z^2}\right]^2} \times \times \left| \frac{\mathbf{n}\times\left((\mathbf{v} - v_z\mathbf{e})\frac{\omega}{c^2} - \mathbf{K}\right)}{\alpha^{-1}(\omega) - \pi a n_1} + \frac{\mathbf{n}\times\mathbf{e}\left(\frac{\omega v_z}{c^2} - \frac{\omega - \mathbf{Kv}}{v_z}\right)}{\alpha^{-1}(\omega) + 2\pi a n_1} \right|^2. \quad (23)$$

Here a is the parameter characterizing the structur of the monolayer [3].

In case $\theta \ll 1$ for the normal incidence neglecting corrections of the order of γ^{-2} we get more simple expression:

$$\frac{d^2W_m(\mathbf{n},\omega)}{d\Omega d\omega} = \frac{4e^2 n_1^2 (\omega^2/c^3)}{\left|\alpha^{-1}(\omega) - \pi a n_1\right|^2} \frac{\theta^2}{\left(\theta^2 + \gamma^{-2} + \frac{\omega_{p\,eff}^2}{\omega^2}\right)^2}. \quad (24)$$

Here the effective frequency

$$\omega_{p\,eff} = \begin{cases} 0, & vacuum \\ \omega_p, & matter \end{cases} \quad (25)$$

describes the case when the radiation from a monolayer is formed inside the matter being characterized by some ω_p.

As we work at rather high frequencies, the polarization of the particles the monolayer consists of takes the form

$$\alpha(\omega) = Z\frac{e^2}{m\omega^2}, \quad (26)$$

where Z is the number of electrons in the particle.

Therefore, for X-ray TR from a separate monolayer covering the substrate we obtain from Eq. (24) the final expression:

$$\frac{d^2W_m(\mathbf{n},\omega)}{d\Omega d\omega} = \frac{4e^2 n_1^2 (\omega^2/c^3)}{\left|\frac{m\omega^2}{Ze^2} - \pi a n_1\right|^2} \frac{\theta^2}{\left(\theta^2 + \gamma^{-2} + \frac{\omega_{p\,eff}^2}{\omega^2}\right)^2}. \quad (27)$$

To figure out what the result looks like, let us compare Eq. (27) with the standard one for X-ray TR

$$\frac{d^2W_{film}(\mathbf{n},\omega)}{d\Omega d\omega} = \frac{e^2}{c}\frac{2}{\pi^2}\left(\frac{\omega_{p\,eff}}{\omega}\right)^4 \times \times \frac{\theta^2 \sin^2\left[\frac{l\omega}{4c}\left(\theta^2 + \gamma^{-2} + \frac{\omega_{p\,eff}^2}{\omega^2}\right)\right]}{\left(\theta^2 + \gamma^{-2} + \frac{\omega_{p\,eff}^2}{\omega^2}\right)^2 \left(\theta^2 + \gamma^{-2}\right)^2}. \quad (28)$$

Indeed, the value

$$\left(\frac{l\omega}{4c}\right)^2 \left(\theta^2 + \gamma^{-2} + \frac{\omega_{p\,eff}^2}{\omega^2}\right)^2 = \left(\frac{l}{L_f}\right)^2, \quad (29)$$

where

$$L_f = \frac{4c}{\omega}\frac{1}{\theta^2 + \gamma^{-2} + \omega_{p\,eff}^2/\omega^2} \quad (30)$$

is the formation length for radiation in the substance. In the simplest case $\theta = 0$, $\omega = \gamma\omega_p$ one gets $L_f = \gamma^2\lambda/\pi$, which for thin films used in TRD usually exceeds considerably the film thickness l.

The ratio is then can be written as

$$\frac{d^2W_{film}(\mathbf{n},\omega)}{d^2W_m(\mathbf{n},\omega)} = \frac{(\omega_{p\,eff}/\omega)^4 \left|\frac{m\omega^2}{Z\pi e^2 n_1} - a\right|^2}{2(\omega^2/c^2)(\theta^2 + \gamma^{-2})^2} \left(\frac{l}{L_f}\right)^2. \quad (31)$$

Here we consider two cases. The first one is

$$\frac{m\omega^2}{\pi e^2 n_1} < a. \quad (32)$$

This implies rather low frequencies, which is not the case for TR detectors. The second case is

$$\frac{m\omega^2}{\pi e^2 n_1} > a, \quad (33)$$

ISBN 978-3-95450-177-9

for which we have

$$\frac{d^2W_{film}(\mathbf{n},\omega)}{d^2W_m(\mathbf{n},\omega)} = \frac{c^2}{\omega^2}\frac{2n^2}{Z^2n_1^2\gamma^{-4}}\left(\frac{l}{L_f}\right)^2 = \frac{1}{2}\left(\frac{ln}{Zn_1}\right)^2. \quad (34)$$

Taking $n/n_1 = 10^3\,\mu m^{-1}$, $l = 0{,}6\mu m$, $Z = 6$ we obtain

$$d^2W_m(\mathbf{n},\omega) = \left(2\times10^{-4}\right)d^2W_{film}(\mathbf{n},\omega). \quad (35)$$

which is very small, but in principle can be measured.

CONCLUSION

Thus, we show that at high frequencies the monolayer radiate less intensively, than a thin film. Numerical estimations show, however, that in principle the contribution of monolayers could be measured comparing with that for macroscopically thick film.

The second interesting thing is that the conditions of formation of the radiation field are different for the cases when the graphene monolayer is towards the film or downwards, and this should lead to the asymmetry in case of the stacks of films relatively the direction of the flight of the electrons.

Along with that there is no any extension of the spectrum of X-ray TR, as it can be expected from general consideration, just because the condition of zero-mass for the conductivity electrons in graphene does not work at high frequencies. For all these reasons we can say, that graphene, instead of its interesting physical properties, is not of practical interest for transition radiation based detectors.

REFERENCES

[1] M.L. Cherry, “Measuring the Lorentz factors of energetic particles with transition radiation”, *Nucl. Instr. and Methods A,* vol. 706, p. 39, 2013.

[2] M.I. Ryazanov, A.A. Tishchenko, “Emission of a fast charged particle passing through a monomolecular film”, *Laser Physics*, vol. 12, p. 1442, 2002.

[3] M.I. Ryazanov, A.A. Tishchenko, “Clausius-Mossotti-Type relation for planar monolayers”, *JETP*, vol. 103, p. 539, 2006.

ISBN 978-3-95450-177-9

INCOHERENT AND COHERENT POLARIZATION RADIATION AS INSTRUMENT OF THE TRANSVERSAL BEAM SIZE DIAGNOSTICS*

D.Yu. Sergeeva†, M.N. Strikhanov, A.A. Tishchenko, National Research Nuclear University MEPhI, Moscow, Russia

Abstract

Polarization radiation, which includes diffraction radiation (DR), transition radiation (TR), Smith-Purcell radiation, and others, can be a good instrument for beam diagnostics. All information about the beam size is contained in the so-called form-factor of the beam. The form-factor represents the sum of two parts corresponding to the coherent and incoherent radiation. Contrary to the general opinion the incoherent part does not always equal unity. In this report we give theoretical description of the incoherent and coherent parts of the form-factor both for Gaussian and uniform distribution of the ultrarelativistic particles in the bunch. The theory constructed describes also the case of beam skimming the target, which leads to mixing of DR and TR. We show that the incoherent part depends on the transversal size of the beam, and dependence differs for different distributions. The role of the incoherent part of the form-factor of the bunch for different parameters is discussed.

INTRODUCTION

Diffraction radiation (DR), Smith-Purcell radiation (SPR), transition radiation (TR) have the similar nature: they arise due to the dynamic polarization of the target material by the Coulomb field of a charged particle. So, they can be called polarization radiation. The theory of polarization radiation from a single particle are well developed, except for X-ray polarization radiation.[1]

X-ray radiation makes the sub-micron beam diagnostics possible, because for such short waves the Rayleigh limitation is not a problem.

The spectral-angular distribution of the energy of radiation from a beam can be obtained as the distribution of energy for radiation from a single particle $d^2W_1/d\omega d\Omega$ multiplied by form-factor F [2]:

$$\frac{d^2W(\mathbf{n},\omega)}{d\Omega d\omega} = \frac{d^2W_1(\mathbf{n},\omega)}{d\Omega d\omega} F. \qquad (1)$$

The form-factor has two terms, corresponding to the coherent and incoherent radiation:[2-6]

$$F = NF_{inc} + N(N-1)F_{coh}, \qquad (2)$$

with N being the number of the particles in the bunch.

*This work was supported by the Leverhulme Trust International Network, grant IN-2015-012, and by the Competitiveness Program of National Research Nuclear University "MEPhI".

†DYSergeyeva@mephi.ru

Usually the incoherent form-factor is supposed to be equal to unity, like it occurs for synchrotron radiation or transition radiation from an infinite media of an infinite slab. For polarization radiation from the target edge (DR, SPR, TR from a finite slab) the incoherent form-factor does not equal unity:

$$F_{inc} \neq 1. \qquad (3)$$

This fact was explained in detail in the paper [2].

One of the main features of the spectral-angular distribution of the polarization radiation is its dependence on the impact-parameter, i.e. the shortest distance between the moving charge and the target surface; see the parameter h in Fig. 1. This dependence is:

$$\frac{d^2W_1(\mathbf{n},\omega)}{d\Omega d\omega} \propto \exp(-2\rho h), \qquad (4)$$

where ρ is some function which will be defined below. From Eq. (4) it is clear that the far the particle from the target surface is, the less intensive the radiation is:

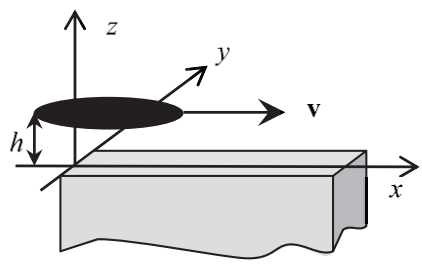

Figure 1: Generation of the radiation by moving the bunch near the target.

FORM-FACTOR

The way to obtain the formula for the coherent and incoherent form-factor was described in [7] for the Diffraction radiation and Smith-Purcell radiation:

$$F_{inc} = \int_V d^3r \left|e^{-i\mathbf{rq}}\right|^2 f(\mathbf{r}),$$
$$F_{coh} = \left|\int_V d^3r e^{-i\mathbf{rq}} f(\mathbf{r})\right|^2, \qquad (5)$$

where the integral is over the bunch volume V, $f(\mathbf{r})$ is the function of distribution of the particles in the bunch written in the system where the bunch is at rest.

ISBN 978-3-95450-177-9

For the polarization radiation (diffraction radiation, Smith-Purcell radiation) the vector $\mathbf{q}$ has the form [7]:

$$\mathbf{q}=\left(\frac{\omega}{c\beta},k_y,-i\frac{\omega}{\gamma\beta c}\sqrt{1+\gamma^2\beta^2n_y^2}\right), \quad (6)$$

where $\beta=v/c$, v is the particle velocity, c is the speed of light, γ is the Lorentz factor, $\mathbf{k}=\mathbf{n}\,\omega/c$ is the wave-vector of the radiation. The coordinate system is shown in Fig. 1.

If the distribution in the bunch does not depend on the relative position of the particles, then the transversal and longitudinal parts of the form-factor can be written as the separate terms:

$$\begin{aligned}F_{inc}&=F_{inc}\left(r_0\right),\\ F_{coh}&=F_{tr}\left(r_0\right)F_l\left(l\right),\end{aligned} \quad (7)$$

where r_0 is the transversal bunch size, l is the length of the bunch.

For example, for the cylindrical bunch of the length l and the radius r_0 with the uniform distribution of the particles it is easy to find [2]:

$$\begin{aligned}F_{inc}&=2\frac{I_1\left(2\rho r_0\right)}{2\rho r_0},\\ F_{coh}&=4\frac{\sin^2\left(\omega l/2v\right)}{\left(\omega l/2v\right)^2}\frac{I_1^2\left(r_0\omega/c\beta\gamma\right)}{\left(r_0\omega/c\beta\gamma\right)^2},\end{aligned} \quad (8)$$

where $\rho=\frac{\omega}{\gamma\beta c}\sqrt{1+\gamma^2\beta^2n_y^2}$, and $I_1\left(x\right)$ is the modified Bessel function of the first order.

For the Gaussian distribution:

$$f\left(\mathbf{r}\right)=\frac{1}{\sigma_x\sigma_y\sigma_z}\frac{1}{\left(\sqrt{\pi}\right)^3}\exp\left[-\frac{x^2}{\sigma_x^2}-\frac{y^2}{\sigma_y^2}-\frac{z^2}{\sigma_z^2}\right] \quad (9)$$

the calculations are more difficult and the result can be seen in the paper [8]. In a brief form these formulae can be written as:

$$\begin{aligned}F_{inc}&=\frac{1}{2}\exp\left[\rho^2\sigma_z^2\right]\left(1-\Phi\left[\rho\sigma_z-\frac{h}{\sigma_z}\right]\right),\\ F_{coh}&=\frac{1}{2}\exp\left[\frac{\rho^2\sigma_z^2}{4}\right]\left(1-\Phi\left[\frac{\rho\sigma_z}{2}-\frac{h}{\sigma_z}\right]\right)e^{-\frac{\omega^2\sigma_x^2}{4c^2\beta^2}-\frac{k_y^2\sigma_y^2}{4}},\end{aligned} \quad (10)$$

where $\Phi\left(x\right)=\frac{2}{\sqrt{\pi}}\int_0^x e^{-t^2}dt$ is the Laplace function. It may seem that these exponents increase indefinitely with $\omega\to\infty$, which is contained in ρ. However, it is known that for $x\to\infty$ the asymptotic form of Laplace function is

$$\Phi\left(x\to\infty\right)\approx 1-\frac{e^{-x^2}}{x\sqrt{\pi}}. \quad (11)$$

Thus, F_{coh} and F_{inc} decrease with growing of frequency from Eqs. (8) and (10) it is seen that the transversal size of the beam can be detected from both the coherent and incoherent radiation.

ANALYSIS OF THE FORM-FACTORS

Below we will consider both the incoherent and coherent form-factors taking into account the exponent in Eq.(4), because it is the term which can strongly influence the radiation intensity and properties, while all other terms, contained in the distribution of energy of radiation from a single particle $d^2W_1/d\omega d\Omega$, do not.

For the analysis let us define the polar angle θ and the azimuthal angle φ of the radiation as:

$$\begin{aligned}n_x&=\cos\theta\cos\varphi,\\ n_y&=\cos\theta\sin\varphi,\\ n_z&=\sin\theta.\end{aligned} \quad (12)$$

Comparison of Eq. (8) and (10) shows that coherent form-factor of the bunch with the Gaussian distribution depend on the angles of radiation observation, while the coherent form-factor factor of the bunch with the uniform distribution dos not depend on.

In Figs. 2 and 3 the form-factors multiplied by the exponent from Eq. (4) both for the uniform distribution (black curves) and for the Gaussian distribution (red dashed curves) are shown in dependence on the wavelength of radiation.

The dependence of the form-factors on the transversal size of the bunch $r_0=\sigma_z=\sigma_y$ is shown in Fig. 4. Here the black curve corresponds to the uniform distribution, and the red dashed curve corresponds to the Gaussian distribution.

It should be noted that the constructed theory is valid in X-ray frequency domain, i.e. at frequencies

$$\omega >> \omega_p \quad (13)$$

where the responses of the dielectric and metal to the external field are the same. Here ω_p is the plasma frequency. That is why the behavior of the curves at long wavelength can be incorrect.

ISBN 978-3-95450-177-9

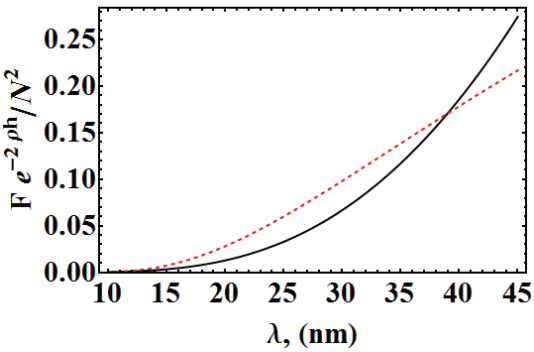

Figure 2: Form-factors normalized to N^2 for coherent radiation for the uniform distribution (black curves) and for the Gaussian distribution (red dashed curves) of the particles in the bunch. Here $\gamma = 10^4$, $h = 50\ \mu m$, $\theta = \gamma^{-1}$, $\phi = 0$, $\sigma_y = \sigma_z = 40\ \mu m$, $r_0 = \sigma_z$, $l = 2\sigma_x$, $\sigma_x = 5\ nm$.

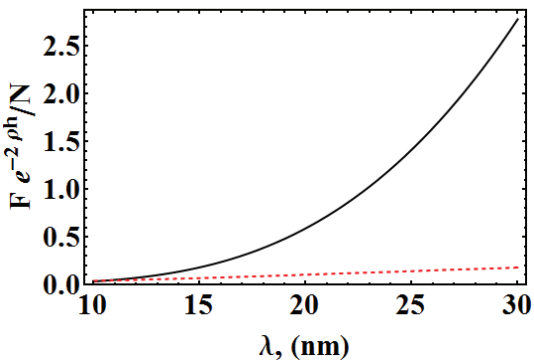

Figure 3: Form-factors normalized to N for incoherent radiation for the uniform distribution (black curves) and for the Gaussian distribution (red dashed curves) of the particles in the bunch. All the parameters are the same as in Fig. 2, but $\sigma_x = 80\ \mu m$.

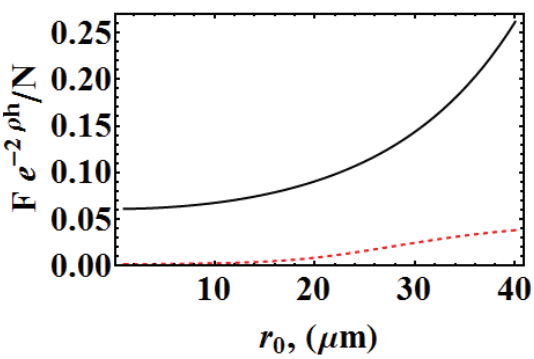

Figure 4: Form-factors normalized to M for the uniform distribution (black curves) and for the Gaussian distribution (red dashed curves) of the particles in the bunch. All the parameters are the same as in Fig. 2, but $\lambda = 10\ nm$.

CONCLUSION

Thus, the theory developed describes the diffraction radiation of electron ultra-relativistic beams in X-ray frequency domain. Speaking of Diffraction radiation we mean, of course, also Smith-Purcell radiation, which can be considered as DR in case the target is a periodical grating.

Using short wavelength radiation, one can define the beam size with a good accuracy, which is enough even for submicron beam diagnostics. The obtained analytical expressions give us the intensity of radiation as a function of its size, i.e., measuring the intensity one can retrieve the information about the bunch.

What is interesting is that the dependence on the bunch size is contained not only in the coherent radiation, but also in the incoherent radiation, which opens new horizons in the beam diagnostics technique.

REFERENCES

[1] A.P. Potylitsyn, M.I. Ryazanov, M.N. Strikhanov and A.A. Tishchenko, "*Diffraction Radiation from Relativistic Particles"*, Berlin, Germany: Springer-Verlag, 2011.

[2] D.Yu. Sergeeva, A.A. Tishchenko and M.N. Strikhanov, "UV and X-ray diffraction and transition radiation from charged particles", *Nucl. Instrum. and Methods B,* vol. 309, p. 189–193, 2013.

[3] H.L. Andrews *et al*., "Longitudinal profile monitors using Coherent Smith-Purcell radiation", *Nucl. Instr. and Methods A,* vol. 740, p. 212, 2014.

[4] J.H. Brownell, J. Walsh and G. Doucas, "Spontaneous Smith-Purcell radiation described through induced surface currents", *Phys. Rev. E,* vol. 57, p. 1075, 1998.

[5] G. Doucas *et al*., "Determination of Longitudinal Bunch Shape by means of Coherent Smith-Purcell Radiation", *Phys. Rev. ST AB,* vol. 5, p. 072802, 2002.

[6] D.Yu. Sergeeva, M.N. Strikhanov and A.A. Tishchenko, "UV and X-ray Diffraction Radiation for Submicron Noninvasive Diagnostics", in *Proc. of 4th Int. particle Accelerator Conf. (IPAC'13),* Shanghai, China, May 2013, paper MOPME062, pp. 616-619.

[7] D.Yu. Sergeeva, A.P. Potylitsyn, A.A. Tishchenko and M.N. Strikhanov, "Smith-Purcell Radiation from Microbunched Beams", in *Proc of 37th Int. Free-Electron Laser Conf. (FEL'15),* Daejeon, Korea, Aug. 2015, paper WEP087, pp. 752-756.

[8] D.Yu. Sergeeva and A.A. Tishchenko, "X-Ray Smith-Purcell Radiation from a Beam Skimming a Grating Surface", in *Proc of 36th Int. Free-Electron Laser Conf. (FEL'14),* Basel, Switzerland, Aug. 2015, paper TUP013, pp. 378-383.

ISBN 978-3-95450-177-9

PERFORMANCE EVALUATION OF MOLYBDENUM BLADES IN AN X-RAY PINHOLE CAMERA

L.M. Bobb, A.F.D. Morgan, G. Rehm, Diamond Light Source, Oxfordshire, U.K.

Abstract

At Diamond Light Source transverse profile measurements of the 3 GeV electron beam are provided by x-ray pinhole cameras. From these beam size measurements and given knowledge of the lattice parameters the emittance, coupling and energy spread are calculated. Traditionally, tungsten blades are used to form the pinhole aperture due to the opacity of tungsten to x-rays in the keV spectral range. The physical properties of tungsten also make it difficult to work. To achieve the 25 μm × 25 μm aperture size required for high resolution measurements it is necessary to mount these tungsten blades in an assembly whereby the pinhole aperture size is defined by precisely machined shims. Here we propose to replace the tungsten blade and shim arrangement with machined molybdenum blades and evaluate the performance of the resulting imaging system.

INTRODUCTION

In order to provide high brilliance x-rays for user experiments, third generation synchrotron radiation facilities must operate with low vertical emittance beams. The emittance of the electron beam is derived from measurements of the transverse beam profile [1, 2] and may be controlled via a feedback system [3]. This necessitates the need for high resolution, robust and online beam size monitoring.

There are various non-invasive techniques to measure the transverse beam profile using synchrotron radiation in the visible to x-ray spectral range [4–7]. In this paper we focus on the use of x-ray pinhole cameras.

Currently there are two pinhole cameras in the vertical emittance feedback system which are referred to as "pinhole 1" and "2" respectively. The layout of these pinhole cameras is shown in Fig. 1. Two different bending magnet locations provide synchrotron radiation to each of the pinhole cameras. The synchrotron radiation is passed from the storage ring vacuum to air through a 1 mm thick aluminium window. Due to the spectral transmission of aluminium the transmitted beam is filtered. The beam is filtered further by its transmission through air from the window to the pinhole and from the pinhole to the PreLude 420 scintillator screen. The source has a spectrum from approximately 15 keV to above 60 keV [1]. To prevent oxide growth the pinhole assemblies are kept under nitrogen.

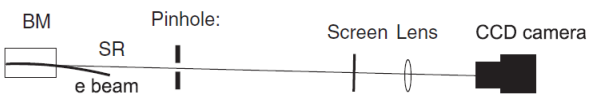

Figure 1: Schematic of the pinhole camera system [1].

The pinhole assembly arrangement of pinhole systems 1 and 2 are identical. The pinhole apertures are formed by stacking two orthogonal sets of (25 mm(h) × 1 mm(v) × 5 mm(d)) tungsten blades separated by precisely machined shims. The thickness of the shims between the tungsten blades sets the aperture size e.g. to form a 25 μm aperture a pair of 25 μm thick shims are positioned between the ends of a pair of tungsten blades.

The spatial resolution of an imaging system may be described by the point spread function (PSF). The PSF is assumed to be constant on relatively long timescales for a given imaging system and is approximated by a Gaussian distribution of standard deviation σ_{PSF}. For a pinhole camera imaging system the overall PSF may be represented as

$$\sigma^2_{PSF} = \sigma^2_{pinhole} + \sigma^2_{camera} \quad (1)$$

with

$$\sigma^2_{pinhole} = \sigma^2_{diffraction} + \sigma^2_{aperture} \quad (2)$$

and

$$\sigma^2_{camera} = \sigma^2_{screen} + \sigma^2_{lens} + \sigma^2_{CCD} \quad (3)$$

where the subscripts denote the sources of the PSF contributions. The PSF contribution associated with imaging the scintillator screen denoted σ_{camera} may be measured using a knife-edge. The PSF contribution from the pinhole denoted $\sigma_{pinhole}$ may be calculated given the aperture size is known [1].

Due to the tungsten and shim arrangement, although the thickness of the shim is known, the absolute effective aperture size available to pass beam is not well defined. The

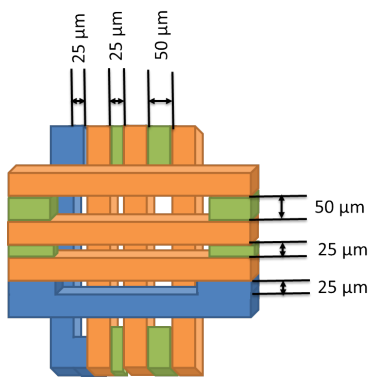

Figure 2: A schematic of the downstream view of the pinhole 3 assembly showing the arrangement of the machined molybdenum blades (blue), tungsten blades (orange) and shims (green).

ISBN 978-3-95450-177-9

effective aperture size depends on the shim thickness, the shim positioning, the amount of burring from cutting the shims to fit in the pinhole assembly, the pressure applied to the tungsten stack once mounted in the holder and the orientation angle of the pinhole assembly relative to the synchrotron radiation beam.

A third pinhole system referred to as "pinhole 3" has been installed for research and development to improve the design and operation of the x-ray pinhole cameras used for vertical emittance feedback. Pinhole 3 is nominally identical to the pinhole 2 imaging system.

To reduce the number of degrees of freedom of the pinhole assembly, the tungsten and shim arrangement could be replaced by machined molybdenum blades. In this case the aperture size is defined by the machined depth in the molybdenum blade. The pinhole assembly under test in the pinhole 3 system features 25 μm × 25 μm apertures formed using molydenum blades and tungsten blades with shims as shown in Fig. 2. This arrangement allows a direct comparison to be made between the two aperture designs.

COMPARISON OF PINHOLE ANGLE SCANS

The pinhole assembly is mounted on translation and rotation mechanisms to allow for remote alignment with the synchrotron radiation beam. Horizontal and vertical angle scans were performed for the 25 μm × 25 μm molybdenum and tungsten apertures of pinhole system 3.

During each scan, a 2D Gaussian was fitted to each image and the horizontal and vertical beamsizes $\sigma_{x,y}$, peak intensity and fit error were recorded. These parameters were then normalised relative to their maximum or minimum value and plotted as a function of rotation angle. In Figures 3 and 4 the horizontal and vertical angle scans are shown respectively for the molybdenum (dashed lines) and tungsten (solid lines) apertures.

In both the horizontal and vertical scans, from a rotation angle of −0.175 deg the peak intensity is expected to increase linearly reaching a maximum at 0 deg and be symmetric about the 0 deg position. Due to the length of the pinhole assembly along the beam path, it is appropriate to consider the pinhole aperture as a three dimensional tunnel rather than a two dimensional screen. Therefore it is expected that the maximum peak intensity should be recorded when the pinhole assembly is aligned in parallel with the incident beam.

In Figures 3 and 4 the peak intensity of the tungsten aperture shows the expected behaviour whereas the molybdenum aperture exhibits a non-linear distribution with strong asymmetry. Referring to the bottom left aperture of Fig. 2, the observed asymmetry may be explained by the blade arrangement of the pinhole assembly. Within each stack, the molybdenum aperture has a molybdenum blade on one side and a tungsten blade on the other. The non-linear dependence of the measured peak intensity must be related to the transmission of x-rays in molybdenum and could indicate

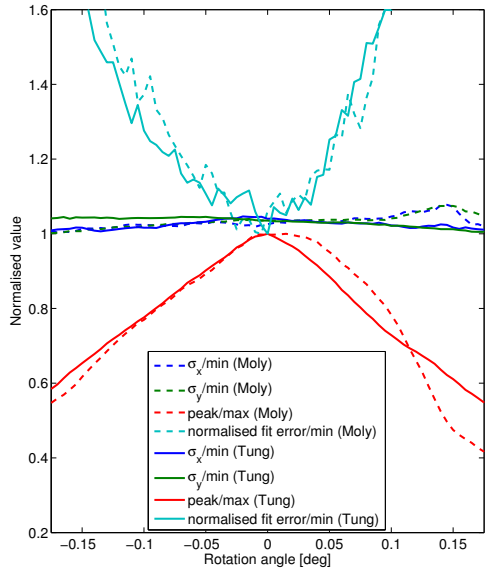

Figure 3: Horizontal rotation scans on pinhole camera 3 of the molybdenum aperture (dashed lines) and tungsten aperture (sold lines).

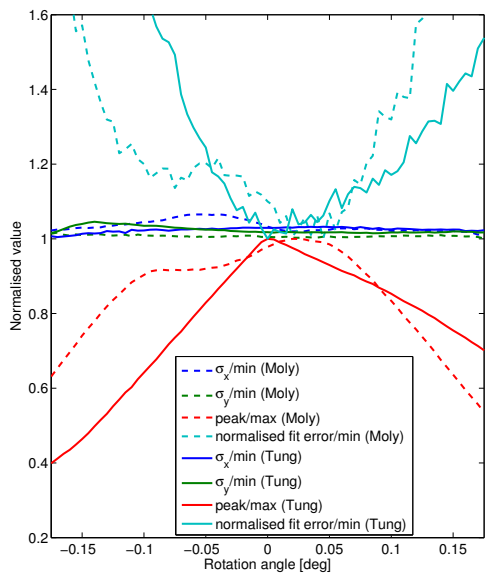

Figure 4: Vertical rotation scans on pinhole camera 3 of the molybdenum aperture (dashed lines) and tungsten aperture (sold lines).

oxide or nitride growth on the molybdenum blades. This behaviour is more strongly shown in the vertical scan than the horizontal scan.

The measured transverse beam sizes and fit errors as a function of rotation angle in the horizontal and vertical directions are not seen to strongly differ between the molybdenum and tungsten apertures.

ISBN 978-3-95450-177-9

PSF MEASUREMENT USING THE TOUSCHEK LIFETIME

Coulomb scattering of charged particles in a stored beam causes an exchange of energies between the transverse and longitudinal motion. The Touschek effect is the transformation of a small transverse momentum into a large longitudinal momentum due to scattering. In this single scattering event, both of the particles are lost since one particle has too much energy and the other has too little [8].

The loss of particles due to the Touschek effect may considerably reduce the beam lifetime in storage rings. The Touschek lifetime T_ℓ for the ultrarelativistic case is defined as

$$\frac{1}{T_\ell} \approx \left\langle \frac{cr_p^2 N_p}{2\sqrt{\pi}\gamma^2\sigma_s\sqrt{\sigma_x^2\sigma_y^2 - \sigma_p^4 D_x^2 D_y^2 \delta_m^2}} \right\rangle, \quad (4)$$

where r_p is the classical particle radius, c is the speed of light, N_p is the number of particles in the bunch, γ is the Lorentz factor, σ_s is the bunch length, $\sigma_{x,y}$ are the horizontal and vertical beam sizes, σ_p is the relative momentum spread, $D_{x,y}$ are the horizontal and vertical dispersions and δ_m is relative momentum spread. The brackets denote the average over the whole circumference of the storage ring [8].

In the case of a plane orbit and without coupling of the horizontal dispersion [8, 9], the vertical dispersion D_y is zero and Eq. (4) reduces to

$$\frac{1}{T_\ell} \approx \left\langle \frac{cr_p^2 N_p}{2\sqrt{\pi}\gamma^2\sigma_s\sigma_x\sigma_y\delta_m^2} \right\rangle. \quad (5)$$

Assuming all other parameters remain constant, the Touschek lifetime size is directly proportional to the vertical beam size. To ensure the simplification to the plane orbit case is appropriate, the term in the root of the denominator $\sigma_x^2\sigma_y^2 - \sigma_p^4 D_x^2 D_y^2$ was compared when D_y is zero and when D_y is set to the real value of 4.54×10^{-3} m. Values have been taken from measurements on pinhole camera 2: σ_x is 43.3 μm, σ_y is 15.8 μm, σ_p is 1.1×10^{-3}, D_x is 2.23×10^{-2} m and D_y is 4.54×10^{-3} m. It is found that with the plane orbit approximation this denomination term is increased by 3.3% which is within the measurement error.

The images acquired from the pinhole camera are fitted with a 2D Gaussian distribution. Considering the vertical beam size only, it is known that the measured beam size will be larger than the true beam size due to the PSF. Therefore the measured beam size σ_M is given by

$$\sigma_M = \sqrt{\sigma_y^2 + \sigma_{PSF}^2}. \quad (6)$$

From Eq. (6) it is seen that when $\sigma_y \gg \sigma_{PSF}$ such that the PSF is negligible then the measured beam size is equal to the true beam size i.e. $\sigma_M = \sigma_y$. The effect of the PSF contribution to the measurement increases as the true beam size is reduced. In order to obtain the true beam size σ_y from the measurement, the PSF spread value σ_{PSF} must be known.

With the 400 bunch and 200 mA beam current the measured beam lifetime τ is Touschek dominated such that $\tau \approx T_\ell$. In the Touschek dominated regime the measured beam lifetime is used as a proxy measurement for the true beam size as

$$\sigma_y = k\tau, \quad (7)$$

where k is a scaling factor. Substituting Eq. (7) into Eq. (6) the measured beam size is

$$\sigma_M = \sqrt{(k\tau)^2 + \sigma_{PSF}^2}. \quad (8)$$

The 2D Gaussian fitter outputs the beam size σ_y by removing the PSF contribution from the measured beam size using Eq. (6). In order to obtain the measured beam size σ_M from the fitter, the PSF value σ_{PSF} is set to zero.

With the Touschek dominated beam and starting from a large vertical beam size, using the skew quads the vertical beam size was gradually reduced. For each skew squad setting the beam lifetime τ, current and measured beam size σ_M were recorded.

In Fig. 5 the measured beam size versus beam conditioning number is shown for pinholes 1, 2 and the molybdenum aperture of pinhole system 3. The beam conditioning number is the product of beam lifetime and current. At large beam sizes a linear regime is observed in Fig. 5. This is expected since the PSF is negligible in comparison to be the beam size such that $\sigma_M = k\tau$. As the beam size becomes comparable to the PSF, at approximately 1250 mAh in Fig. 5, the data is no longer linear and the PSF cannot be ignored.

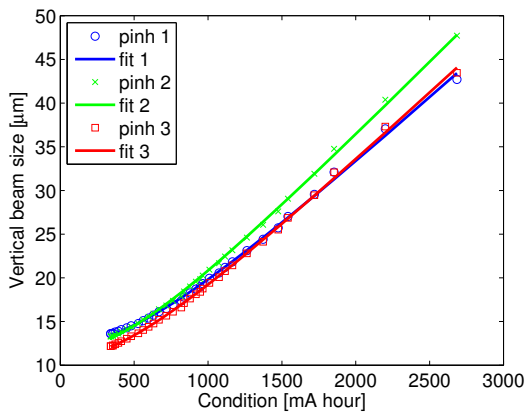

Figure 5: A plot of the measured vertical beam size against beam conditioning number for pinhole systems 1, 2 (measurement 1) and the molybdenum aperture of pinhole system 3.

Each dataset has been fitted using the method of least squares with Eq. (8) to obtain the scaling parameter k and PSF σ_{PSF} for each pinhole imaging system. The fit results are shown in Table 1. The scaling factor is expected to be constant given the assumption of Eq. (7). The average scaling factor from Table 1 is $(1.57 \pm 0.09) \times 10^{-2}$ μm mA^{-1} h^{-1}.

ISBN 978-3-95450-177-9

Table 1: Fit Results of the Scaling Factor and PSF from Figures 5 and 6

Pinhole camera	Measurement 1		Measurement 2	
	k [μm mA^{-1} h^{-1}]	σ_{PSF} [μm]	k [μm mA^{-1} h^{-1}]	σ_{PSF} [μm]
1	0.0155	12.36	0.0143	12.33
2	0.0173	11.67	0.0160	11.70
	Molybdenum		**Tungsten**	
3	k [μm mA^{-1} h^{-1}]	σ_{PSF} [μm]	k [μm mA^{-1} h^{-1}]	σ_{PSF} [μm]
	0.0159	10.82	0.0152	16.28

In Fig. 6 the measured beam size versus beam conditioning number is shown for pinholes 1, 2 and the tungsten aperture of pinhole system 3. The fit results are shown in Table 1. Comparing the PSF values from Table 1 of pinhole cameras 1 and 2, there is a difference of 0.03 μm between the repeated measurements showing a good level of repeatability. The mean PSF values for pinhole cameras 1 and 2 are 12.35 μm and 11.68 μm respectively. The repeated PSF measurement for pinholes 1 and 2 should be consistent since no changes were made to these imaging systems.

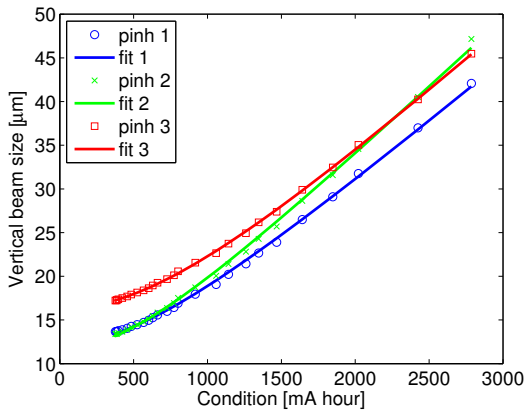

Figure 6: A plot of the measured vertical beam size against beam conditioning number for pinhole systems 1, 2 (measurement 2) and the tungsten aperture of pinhole system 3.

The PSF measurements from the molybdenum and tungsten apertures of the pinhole 3 system show a difference of 5.46 μm. From visual inspection the tungsten aperture is approximately double the size of the molybdenum aperture. The PSF measurement on pinhole 3 is larger than that of pinhole system 2. Since these systems are nominally the same it is likely that the tungsten aperture on pinhole 3 is also larger than that on pinhole 2.

Given that the pinhole systems 2 and 3 are nominally identical, the PSF value of the tungsten aperture on pinhole 2 may be compared with the molybdenum aperture on pinhole 3. In Table 1, the molybdenum aperture has a PSF value which is 0.85 μm smaller than the tungsten aperture indicating that the aperture size using the simpler molybdenum setup is closer to the specification value of 25 μm.

CONCLUSION

Angle scans of the pinhole assembly relative to the incident synchrotron radiation beam have been performed to study the opacity of molybdenum to keV x-rays. Results show that although the peak intensity as a function of angle for the molybdenum aperture is somewhat non-linear in comparison to tungsten, this has a negligible affect on the beam size measurement.

PSF measurements of each pinhole imaging system were acquired using the Touschek lifetime with a good level of repeatability. By replacing the tungsten and shim assembly with machined molybdenum blades, the numerous of degrees of freedom which affect the aperture size in the pinhole system were removed such that the PSF was reduced.

REFERENCES

[1] C. Thomas et al., "X-ray pinhole camera resolution and emittance measurement", Phys. Rev. ST Accel. Beams 13, 022805, (2010).

[2] A. Andersson et al., "Determination of a small vertical electron beam profile and emittance at the Swiss Light Source", Nucl. Instrum. Meth. A591, (2008), 437–446.

[3] I.P.S. Martin et al., "Operating the Diamond Storage Ring with Reduced Vertical Emittance", Proc. of IPAC2013, Shanghai, China, MOPEA071.

[4] J. Breunlin et al., "Methods for measuring sub-pm rad vertical emittance at the Swiss Light Source", Nucl. Instrum. Meth. A803, (2015), 55–64.

[5] P. Elleaume et al., "Measuring Beam Sizes and Ultra-Small Electron Emittances Using an X-ray Pinhole Camera", J. Synchrotron Rad., (1995). 2, 209-214.

[6] T. Mitsuhashi, "Measurement of small transverse Beam Size Using Interferometry", Proc. of DIPAC 2001, ESRF, Grenoble, France, IT06.

[7] K. Iida et al., "Measurement of an electron-beam size with a beam profile monitor using Fresnel zone plates", Nucl. Instrum. Meth. A506, (2003), 41–49.

[8] A. Piwinski, "The Touschek effect in strong focusing storage rings", DESY 98-179, 1998, `http://arxiv.org/abs/physics/9903034`.

[9] R. Dowd et al., "Achievement of ultralow emittance coupling in the Australian Synchrotron storage ring", Phys. Rev. ST Accel. Beams 14, 012804 (2011).

ISBN 978-3-95450-177-9

BEAM INDUCED FLUORESCENCE MONITOR R&D FOR THE J-PARC NEUTRINO BEAMLINE

M. Friend*, High Energy Accelerator Research Organization (KEK), Tsukuba, Japan
C. Bronner, M. Hartz, Kavli IPMU (WPI), University of Tokyo, Tokyo, Japan

Abstract

Proton beam monitoring is essential for the J-PARC neutrino beamline, where neutrinos are produced by the collision of 30 GeV protons with a long carbon target. Along with continued upgrades to the J-PARC beam power, from the current 420 kW to 1.3+ MW, there is also a requirement for monitor upgrades. A Beam Induced Fluorescence monitor is under development, which would continuously and non-destructively measure the proton beam profile spill-by-spill by measuring fluorescence light from proton interactions with gas injected into the beamline. Monitor design is constrained by the J-PARC neutrino beamline configuration, where a major challenge will be getting sufficient signal to precisely reconstruct the proton beam profile. R&D for a pulsed gas injection system is under way, where injected gas uniformity and vacuum pump lifetime are main concerns. Design of a light detection system is also under way, where light transport away from the high radiation environment near the proton beamline, as well as fast detection down to very low light levels, are essential.

J-PARC PROTON BEAM OVERVIEW

The J-PARC proton beam is accelerated to 30 GeV by a 400 MeV Linac, a 3 GeV Rapid Cycling Synchrotron, and a 30 GeV Main Ring (MR) synchrotron. Protons are then extracted using a fast-extraction scheme into the neutrino beamline, which consists of a series of normal- and superconducting magnets used to bend the proton beam towards the neutrino production target for generation of a neutrino beam pointing towards the Super-Kamiokande detector for the T2K Long-Baseline Neutrino Oscillation Experiment [1]. Beam monitoring is essential for both protecting beamline equipment from possible mis-steered beam, as part of a machine interlock system, and as input into the T2K analysis.

Table 1: J-PARC Proton Beam Specifications

	Protons/Bunch	Spill Rate
Current (2016)	2.75×10^{13}	2.48 s
Upgraded (2018~)	$2.75 \rightarrow 4.00 \times 10^{13}$	1.30→1.16 s

The J-PARC 30 GeV proton beam has an 8-bunch beam structure with 80 ns (3σ) bunch width and 581 ns bucket length. J-PARC currently runs at 420 kW with the plan to upgrade to 750+ kW by 2018 and 1.3+ MW by 2026. This will be achieved by increasing the beam spill repetition rate from the current 1 spill per 2.48 s, to 1.3 s and finally 1.16 s, along with increasing the number of protons per bunch from 2.75×10^{13} to 4×10^{13} as shown in Table 1. With this increased beam power comes increased necessity for minimally destructive beam monitoring, as each of the currently-in-use beam profile monitors cause 0.005% beam loss (where all but the most down-stream beam profile monitor is remotely inserted into the beam orbit only during beam tuning).

* mfriend@post.kek.jp

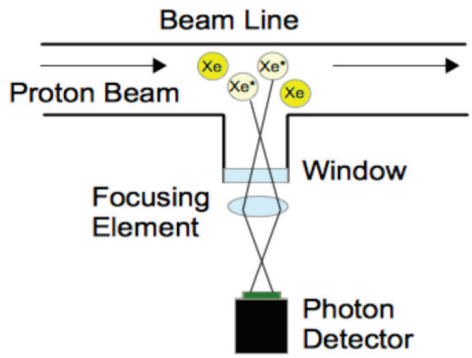

Figure 1: Schematic diagram of BIF monitor.

The proton beam spot size varies along the neutrino line from ~2–8 mm (1σ) and is ~4.2 mm at the neutrino production target. Current non-destructive beam position monitors continuously measure the beam position with a precision of 450 μm, while destructive monitors measure the beam width with a precision of 200 μm during beam orbit tuning. Any new monitoring system should exceed this beam position precision and match this beam width precision if possible.

Development of a new non-destructive Beam Induced Fluorescence (BIF) monitor [2] for the J-PARC neutrino beamline is underway. In a BIF monitor, the beam profile is measured when the passing beam ionizes some of the gas particles in the beamline. The particles then fluoresce when returning to the ground state, and the transverse profile of this fluorescence light will match the transverse profile of the proton beam. A simple BIF monitor schematic is shown in Fig. 1.

NON-DESTRUCTIVE MONITOR REQUIREMENTS

The BIF monitor must be designed taking into account the specific requirements of the J-PARC neutrino beamline as given below.

ISBN 978-3-95450-177-9

Space-Charge Effects

Beam space-charge effects are a major contributor to the choice of developing a non-destructive Beam Induced Fluorescence Monitor, rather than the alternative Ionization Profile Monitor (IPM) [3]. As shown in Fig. 2, the transverse field from the charge of the proton beam itself can reach as high as 4×10^6 V/m for a 2 mm width bunch containing 1.5×10^{13} protons. Acceleration of ions or electrons in this field would distort the measured beam profile, where a highly impractical magnet of >1 T would be required to counteract this effect in an IPM.

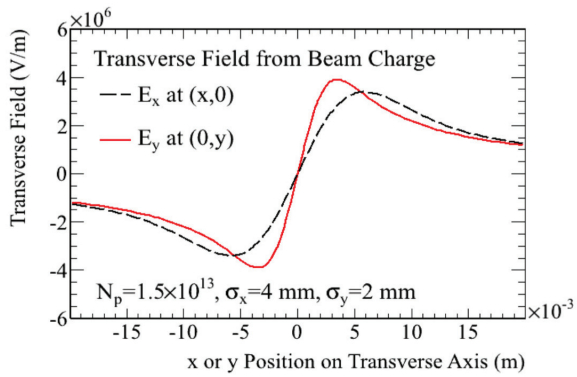

Figure 2: Transverse field induced by proton beam space-charge.

Space charge effects can also cause distortion of the BIF profile if particles ionized by the beam passage move in the beam field before fluorescing. In this case, choosing a gas with a short fluorescence lifetime or a large mass can help to mitigate this distortion. Another option is to use fast photosensors with ns-timescale readout or gated timing such that only early fluorescence light is measured.

Gas Choice

Because the residual gas level in the J-PARC neutrino beamline is around 1×10^{-6} Pa, which would yield ~1 detected photon after the passage of 2×10^{14} protons with reasonable acceptance and efficiency assumptions, injected gas must be used for this monitor.

Table 2: Relative measured fluorescence parameters of N_2 and Xe gas from Ref. [4].

	λ (nm)	Lifetime (ns)	keV/photon Lost	Cross Section (Relative)
N_2	68	380-470	3.6	Xe x 3.3
Xe	6, 51	380-640	46	Xe x 1

Detailed fluorescence data exists for N_2 and Xe [4], as shown in Table 2, so these gas choices have been considered so far. N_2 produces about 10 times more light than Xe, due to its higher cross section and lower energy loss per visible photon generated, but has a slower fluorescence lifetime and is lighter than Xe, making it more susceptible to profile distortion due to drift in the high space-charge field, as shown in Fig. 3. However, making a fast timing cut reduces both this drift, as shown in Fig. 4, and the amount of light collected from N_2, effectively equalizing the performance of the two gasses.

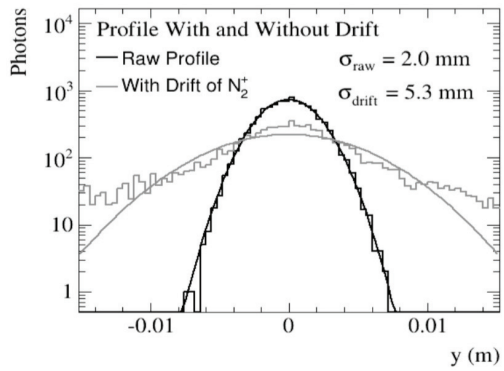

Figure 3: True beam profile and measured beam profile after drift in the beam induced space-charge field.

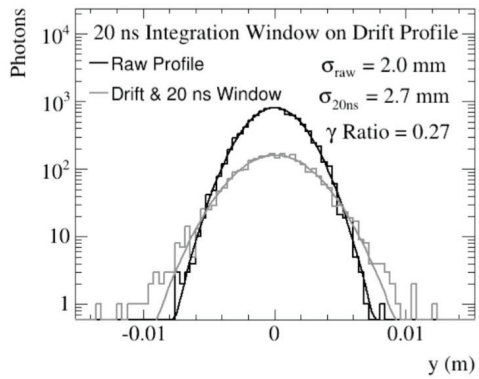

Figure 4: True beam profile and measured beam profile after drift in the beam induced space-charge field after a timing cut.

Pump lifetime and performance should also be considered – standard beamline ion pumps work well with N_2; however new pumps (ie. turbo-molecular pumps coupled to scroll pumps with collected outflow) would probably be needed for injecting Xe gas. N_2 is therefore now being considered more practical, but other gasses are also under consideration.

MONITOR COMPONENTS

The main components of the BIF monitor are the gas injection, light transport and focusing, and light detection systems, as described below.

Gas Injection

Pulsed gas injection, with one pulse coming directly before each beam spill, is planned in order to limit the total amount of gas injected into the beamline. Pulse valves can be pulsed with <160 ms pulse times and at high repetition rate

ISBN 978-3-95450-177-9

for continuous duty. This device is therefore being studied as an option for a pulsed gas source.

The configuration of the gas injection and vacuum pumps is also being studied, where pulsed gas injected and then allowed to diffuse into the beamline may be more cost effective and simple to use than a "gas sheet" configuration. However, vacuum pump lifetime must be considered, and excess particles impinging on any one pump could cause degradation to that one pump or overall degradation of the vacuum in the J-PARC neutrino beamline.

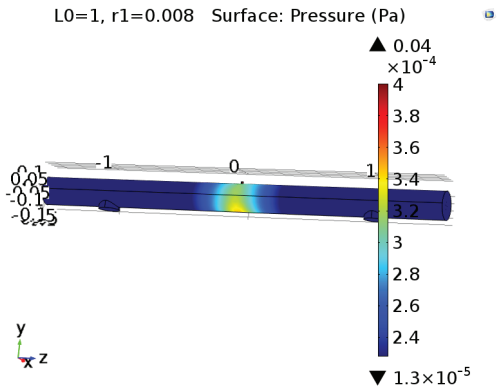

Figure 5: Pressure on the walls in a vacuum vessel simulated assuming steady-state gas injection by COMSOL Multiphysics®.

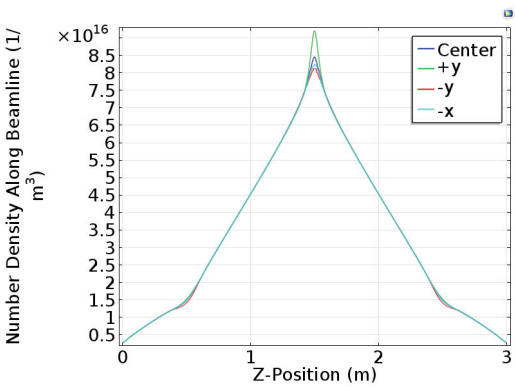

Figure 6: Number density of particles within a vacuum vessel simulated assuming steady-state gas injection by COMSOL Multiphysics®.

COMSOL Multiphysics® software is being used to model the system and understand gas uniformity and the number of incident particles on pumps in the beamline. As shown in Figs. 5 and 6, simulations show that gas uniformity improves away from the gas injection and pumping points.

Interlock in the case of a gas leak or injection valve malfunction is also essential in order to protect beamline equipment (and particularly super-conducting magnets in the beamline). Therefore an interlock system consisting of fast closing valves and gas pressure monitoring is also under consideration.

Light Transport and Focusing

Light transport away from the high-radiation area near the beamline is essential, as discussed below. A pair of plano-convex lenses with a long focal length and large diameter will be used to focus the light onto a detection element 1–2 m from the beampipe. Lenses rather than mirrors will be used, since it was determined using a Geant4 simulation that transported profile distortion is lower when lenses are used; lenses may also be more radiation hard. Large diameter lenses help to reduce losses or distortions of the light near the edges of the profile.

Light Detection

Light detection in a high radiation environment is particularly challenging, as ionizing particles impinging on detection components can cause noise and damage instrumentation. Two light detection options are currently under study with different advantages and disadvantages.

Optical Fibers and MPPC Option Multi-Pixel Photon Counters (MPPCs) are a potential inexpensive option for light detection. However, it is well known (and has been confirmed by the authors) that MPPCs are not robust to radiation and can quickly degrade in a high radiation environment. Therefore, using optical fibers to transport light away from the beamline, as shown as shown in Fig. 7, is one light detection option.

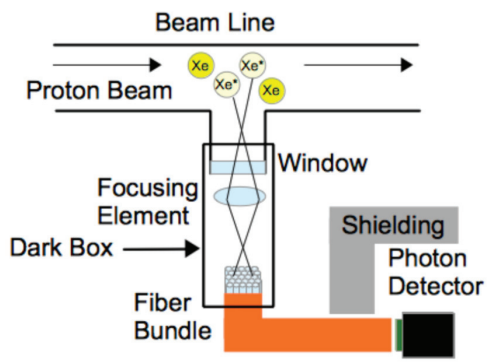

Figure 7: Light detection with optical fibers transporting light 10s of meters from the beamline to shielded MPPCs.

The authors have done various tests of both optical fibers and MPPCs in the high-radiation environment near the J-PARC beamline, and have found substantial noise induced in both components by the proton beam passage even ~1 meter away from the beamline, as shown in Fig. 8 in optical fibers. It was found that shielding, particularly by the concrete walls of a sub-tunnel, could be used to reduce this noise, but careful consideration of the configuration of possible shielding and optical fibers is important.

One advantage of this configuration is the ability to do ns-timescale readout by a Flash Analog-to-Digital Converter (FADC). Readout of the MPPCs by FADC would allow for cutting out slow-timescale fluorescence light or even observing the distortion of the beam profile due to motion

ISBN 978-3-95450-177-9

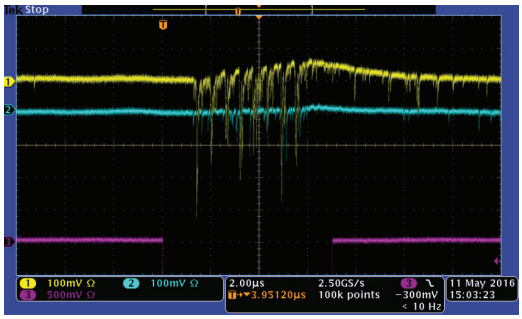

Figure 8: Noise test of silica-core optical fibers near the beamline, where the yellow curve corresponds to an unshielded fiber and the blue curve corresponds to a shielded one. Observed 8-peak noise structure corresponds to the 8-bunch J-PARC beam structure.

of ionized gas particles in the beam space-charge field as a function of time.

MCP and CID Option Light detection by a radiation-hard Charge Injection Device (CID) camera (where the camera controller is placed in a lower-radiation environment) is an option that has proven to work well even in high-radiation environments.

However, BIF light levels are too low and fast readout is impossible using a camera, such that coupling to a gatable image intensifier would be essential. Investigation of image intensification and gating by a Microchannel Plate (MCP) gatable image intensifier is under study, where an MCP could allow for gating times of <10s of ns and light amplification by a factor of $>10^4$. In this case, radiation hardness of the MCP is also essential, and substantial shielding or special design of a radiation-hard MCP may be necessary.

Preliminary images of a test pattern from an MCP and camera are shown in Figs. 9 and 10.

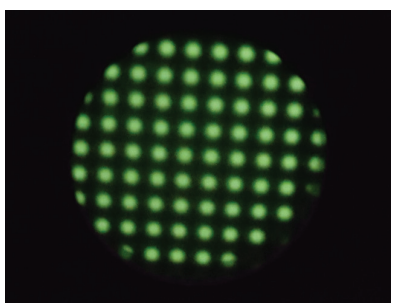

Figure 9: Light pattern imaged by MCP.

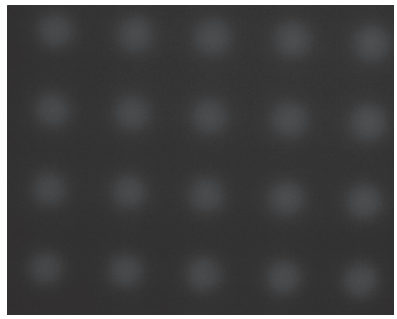

Figure 10: Light pattern from MCP imaged by camera.

CONCLUSION

Development of a BIF monitor for the J-PARC neutrino beamline is underway, including the design of a pulsed gas injection system, light transport system, and two light detection options. Installation of a working prototype monitor in the J-PARC neutrino beamline is planned in 2018.

ACKNOWLEDGMENT

The authors would like to thank the members of the neutrino beam group at J-PARC for their valuable help and support. This work was supported by the Japanese MEXT KAKENHI grant system.

REFERENCES

[1] K. Abe *et al.*, "The T2K Experiment", *Nucl. Instr. and Meth. A* vol. 659, no. 106, 2011

[2] F. Becker *et al.*, "Beam induced fluorescence (BIF) monitor for transverse profile determination of 5 to 750 MeV/u heavy ion beams", in *Proc. DIPAC'07*, Venice, Italy, paper MOO3A02, pp 33-35, etc.

[3] R. Connoly *et al.*, "Beam profile measurements and transverse phase-space reconstruction on the relativistic heavy-ion collider" *Nucl. Instr. and Meth. A* vol. 443, p. 215–222, 2000, etc.

[4] M.A. Plum *et al.*, "N_2 and Xe gas scintillation cross-section, spectrum, and lifetime measurements from 50 MeV to 25 GeV at the CERN PS and Booster", *Nucl. Instr. and Meth. A* vol. 492, no. 74, p. 74–90, 2002

ISBN 978-3-95450-177-9

NON-INVASIVE BEAM PROFILE MEASUREMENT FOR HIGH INTENSITY ELECTRON BEAMS

T. Weilbach, M. Bruker, Helmholtz-Institut Mainz, Germany,
K. Aulenbacher, KPH Mainz, Helmholtz-Institut Mainz, Germany

Abstract

Beam profile measurements of high intensity electron beams below 10 MeV, e.g. in energy recovery linacs or magnetized high energy electron coolers, have to fulfill special demands. Commonly used diagnostic tools like synchrotron radiation and scintillation screens are ineffective or not able to withstand the beam power without being damaged. Non-invasive methods with comparable resolution are needed.

Hence, a beam profile measurement system based on beam-induced fluorescence (**BIF**) was built. This quite simple system images the light generated by the interaction of the beam with the residual gas onto a PMT. A more elaborated system, the Thomson Laser Scanner (**TLS**) — the non-relativistic version of the Laser Wire Scanner — is proposed as a method for non-invasive measurement of all phase space components, especially in the injector and merger parts of an ERL. Since this measurement suffers from low count rates, special attention has to be given to the background.

Beam profile measurements with the BIF system will be presented as well as a comparison with YAG screen measurements. The recent status of the TLS system will be presented.

INTRODUCTION

High-intensity electron beams are getting more and more popular. Because of their high beam power, the use of conventional destructive diagnostic tools is limited. Energy recovery linacs (ERL) can make use of the emitted synchrotron radiation for profile measurements, but this is only possible after the main linac. In the injector and merger section, they need non-intercepting beam diagnostic devices which can withstand the beam power of several 100 kW. The planned electron cooling devices easily reach several MW of beam power. Because of energy recuperation in the collector, they allow only a very small beam loss, which is not compatible with normal destructive diagnostics.

There are already several non-destructive beam diagnostic methods established, which are used in different accelerators, such as a scintillation profile monitor [1] at COSY or the laser wire scanner at the synchrotron source PETRA III [2]. These methods can be adapted for the profile measurement of high-intensity electron beams with energies in the MeV range.

EXPERIMENTAL SETUP

All measurements are done at the polarized test source (PKAT) [3] shown in Fig. 1 at the Mainzer Mikrotron (MAMI). In this source, a NEA-GaAs [4] photo cathode is used to generate an electron beam with an energy of 100 keV.

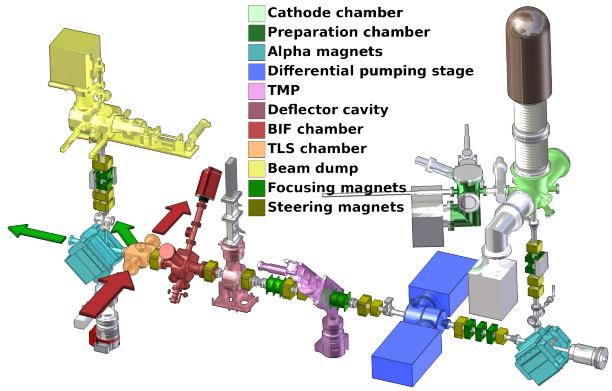

Figure 1: The polarized test source PKAT. The first differential pumping stage (blue) separates the source vacuum (green) from the beam line vacuum. A second differential pumping stage (purple) separates the BIF (red) and the TLS chamber (orange) from the rest of the beam line. The Faraday cup (yellow) monitors the beam current throughout the measurements.

The NEA-GaAs cathode requires a pressure much lower than 10^{-10} mmbar for stable operation. Therefore, a first differential pumping stage separates the source vacuum from the beam line vacuum (blue). A second differential pumping stage, consisting of two turbo molecular pumps (purple), surrounds the BIF and TLS chambers. This allows local pressure bumps of up to 10^{-5} mbar while maintaining the UHV condition at the cathode.

The beam transport system consists of dipole (alpha and steering magnets) and quadrupole magnets as well as two solenoid doublets. Several conventional (luminescent and scintillating) screens and the Faraday cup at the end of the beam line allow for a setup of the electron beam and also for comparison measurements with the new non-invasive diagnostic methods.

The PKAT can operate in several modes which differ in the time structure of the electron beam. For the BIF measurements, we use the dc mode, in which a blue laser diode generates either a dc beam or a pulsed beam with a repetition rate of several Hz with a length of a few 100 µs. In that mode, the source is limited to 500 µA.

For the TLS measurements, a larger current is needed. Since the power supply can only provide 3 mA of dc current, a pulsed system with a pulse length of about 20 ns and a rep. rate of 150 kHz was built. Thus the PKAT can create an electron beam with a peak current of 30 mA while the average current is approximately 90 µA. The red arrows in Fig. 1 show the incident laser while the green arrows show

ISBN 978-3-95450-177-9

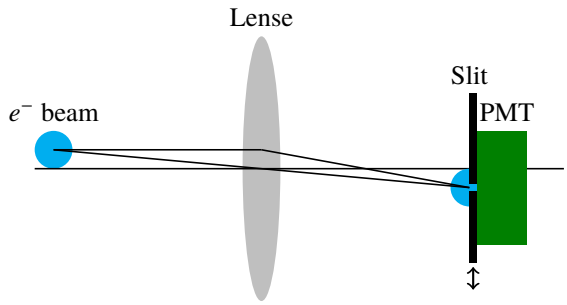

Figure 2: Schematic view of the beam induced fluorescence profile measurement done with a PMT and a slit. The light created by the energy loss of the electron beam is imaged with a lens onto a PMT. A moving slit in front of the PMT provides the spatial resolution needed for profile measurements.

Table 1: Typical BIF Profile Measurement Conditions

Beam energy	100 keV
Beam current	100 µA
Residual gas pressure	$\approx 10^{-5}$ mbar
PMT voltage	1000 V
Slit width	0.2 mm

the two possible detector positions for the measurement of the scattered photons.

BEAM-INDUCED FLUORESCENCE

For protons and ions, beam profile measurement based on beam-induced fluorescence is a common technique [5]. The idea is to image the fluorescing residual gas on a photo detector with a spatial resolution. Instead of a detector with a spatial resolution, a photomultiplier tube (PMT) with a slit in front of it can be used. The slit cuts out a small slice of the electron beam image at the PMT as indicated in Fig. 2. By moving the slit up and down and measuring the photon intensity, a beam profile can be measured.

The intensity of the photons is proportional to the pressure and the beam current. As stated above, the current is limited so the only possibility to enhance the signal is to raise the residual gas pressure. A gas dosing valve is used to insert N_2 gas in the vacuum system. Nitrogen converts 3.6 keV of average energy loss into one visible photon [6]. The energy loss of the electron beam can be calculated with a modified form of the Bethe-Bloch formula. Another advantage of N_2 is that it can be pumped out of the vacuum system very easily. Therefore, residual gas pressures of 10^{-5} mbar can be generated in the BIF chamber without destroying other parts of the apparatus. Table 1 shows the typical conditions during a measurement.

Figure 3 shows typical experimental results. The PMT is used in the counting mode with a discriminator and a rate meter. The rate is measured with respect to the slit position. In this measurement, the beam current was 75 µA and the focus of the beam was changed with the solenoid in front

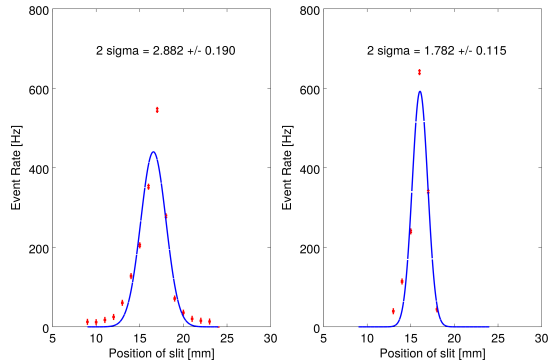

Figure 3: BIF measurement with statistical errors with different focusing strengths of the solenoid in front of the BIF chamber. The measurement is shown in red and the Gaussian fit in blue. Left: Solenoid current 50 mA, right: Solenoid current 500 mA.

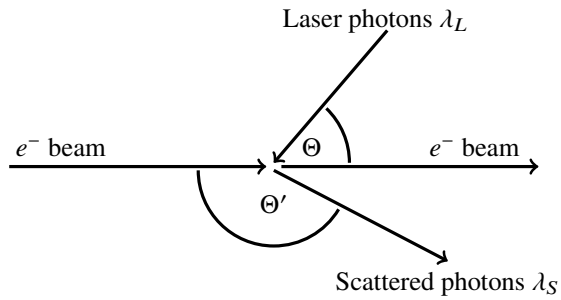

Figure 4: Thomson scattering scheme. The angle between electron beam and incident laser beam is Θ while Θ' is the angle between the electron beam and the scattered photons.

of the BIF chamber. The width of the beam changes due to the changing focusing strength of the solenoids. A Gaussian function (blue) is fitted to the measured values including statistical errors (red) to extract the beam width.

THOMSON SCATTERING

Thomson scattering describes elastic scattering of a photon on a free electron. It is the low-energy limit of the Compton scattering process. Fig. 4 shows a schematic view of Thomson scattering.

A photon λ_L hits the electron beam with an angle Θ and is scattered with the scattering angle Θ'. The scattered photon λ_S gains energy due to the Doppler shift. The wavelength of the scattered photon as a function of the angle between incident photon and electron and the angle between scattered photon and electron can be evaluated with

$$\lambda_S = \lambda_L \frac{(1 + \beta \cos \Theta')}{(1 + \beta \cos \Theta)} \quad (1)$$

where β is the electron velocity in units of the speed of light. The number of scattered photons can be calculated with the following equation:

ISBN 978-3-95450-177-9

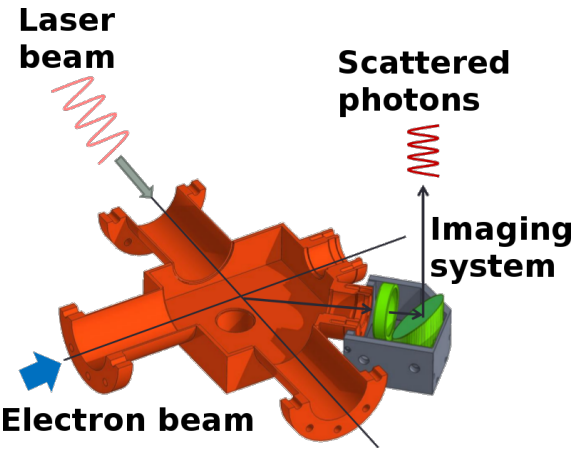

Figure 5: Half section of the TLS chamber (orange) and the detector system. The angle between laser and electron beam is $\Theta = 90°$ whereas $\Theta' = 135°$ is the angle between electron beam and scattered photons. The imaging system (green) consists of a lens and a parabolic mirror.

$$R = \frac{1}{2} r_e^2 \left(1 + \cos^2 \Theta'\right) N_L n_e P \epsilon \Delta\Omega l \frac{(1 + \beta \cos(\Theta))}{(1 + \beta \cos(\Theta'))\gamma} \quad (2)$$

with r_e = classical electron radius, N_L = number of incident photons per Joule, n_e = electron density, P = laser power, ϵ = detector system efficiency, $\Delta\Omega$ = detector solid angle, l = interaction length, $\frac{(1+\beta\cos(\Theta))}{(1+\beta\cos(\Theta'))\gamma}$ = factor resulting from Lorentz transformation.

For our experiment, we are using the following angles: $\Theta = 90°$ and $\Theta' = 135°$. With an electron energy of 100 keV, a current of 25 mA, $P = 130$ W, $\epsilon = 0.17$, $\Delta\Omega = 0.01$, $l = 3$ mm (beam diameter) the expected rate is about 5 Hz.

The rate of the scattered photons is proportional to the integrated electron density along the path of the laser through the electron beam (calculations were made for a homogeneously charged electron beam while the laser passes the center). By moving the laser beam through the electron beam vertically, a profile measurement can be done. Due to the low cross section, which is mostly dominated by the classical electron radius squared, the required laser power is very high. This was the reason why the pioneer experiment done in 1987/88 suffered from very low count rates [7]. Figure 5 shows a half section of the CAD-model of the TLS chamber. The paths of the electron beam, the incident Laser beam, and the scattered photons are indicated. Due to the limited space, the detector cannot be placed in the scattering plane. Therefore, an imaging system consisting of a lens and a parabolic mirror images the interaction region onto the PMT passing two bandpass filters that reduce the background created by the laser.

Since we are using a pulsed electron beam and a pulsed laser system, the synchronization of both has to be guaranteed.

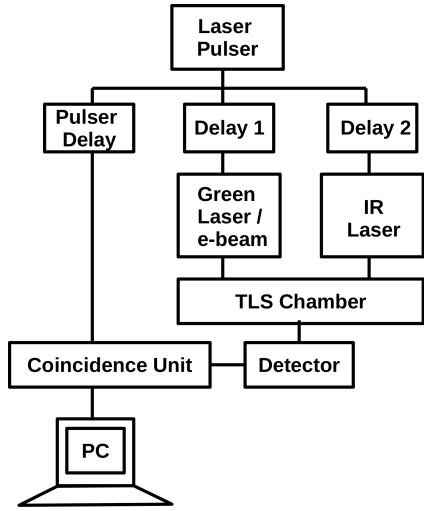

Figure 6: Schematic diagram of the synchronization system. The pulser delay as well as delay 1 and delay 2 can be changed individually to achieve a synchronous arrival of the electron beam, which is generated by the green laser, and the IR laser beam at the interaction point.

Synchronization

To ensure a simultaneous arrival of the laser and the electron beam, an elaborated synchronization scheme has been built. This is shown in Fig. 6. The common time base is the laser pulser which triggers all following elements. The pulser delay is used for the coincidence unit while delay 1 and delay 2 compensate for the time of flight of the electron beam. Thus with the right delays, a synchronization of the electron beam and the laser can be guaranteed as shown in Fig. 7.

The most important laser properties are given in Tab. 2. The high power of the IR laser can be used for the synchronization of the apparatus. While the photons pass the vacuum window, a few of them get scattered and have their wavelengths shifted to the transmission band of the bandpass filters so they are detectable with the PMT. For the TLS measurement, the photon background caused by this is a problem but the signal can be used for the adjustment of the delay lines (Fig. 7, red points). To obtain a correct timing of the electron beam signal, we caused a beam loss in the TLS chamber in front of the detector. This also creates photons with different wavelengths so some of them are able to reach the detector (Fig. 7, black points). In contrast to the IR signal, the signal generated by the beam loss can be reduced or even made to disappear for a good optics setup of the beam line.

Background Reduction

Different background sources have been identified, such as ambient light from the lab that enters through vacuum windows, or even pressure sensors which are installed in the PKAT [8]. One can get rid of most of these sources by a sufficient shielding of the detector system or switching

ISBN 978-3-95450-177-9

Table 2: TLS Laser System Properties

IR laser power	130 W
IR wavelength	1030 nm
IR pulse length	16 ns
Green laser power	11 W
Green wavelength	515 nm
Green pulse length	19 ns
Rep. rate	150 kHz

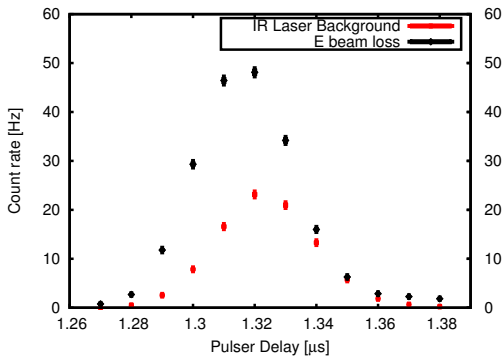

Figure 7: Measurement of the background signal caused by the IR laser and the measurement of the beam loss of the electron beam in the TLS chamber. The delay lines are adjusted so that both signals overlap each other to ensure a simultaneous arrival of both beams.

them off like the pressure sensor. Furthermore, if these sources generate light in a dc manner, the background is suppressed due to the duty cycle of the pulsed laser system and the coincidence unit by a factor of about 350. The biggest problem is the beam-correlated background, which is not suppressed. The two most important sources for that are electron beam loss and the IR laser itself. First measurements have shown that the electron beam loss can be held on a level of a few Hz with a proper adjustment of the beam optics [9]. The IR background however is more complicated to reduce and is higher than the electron beam loss. Figure 8 shows the results of several measurements. The first measurement (red) shows the initial conditions. The background was well above 200 Hz, making TLS profile measurement very time consuming if not impossible. A first improvement was the insertion of two blackened pipes in the vacuum chamber. This reduced the background by the IR laser by a factor of 3 to 4 (black). Unfortunately, after the fourth measured point the laser broke down, so no further measurements were possible. Therefore, we designed a new TLS chamber where the vacuum window has no direct line of sight to the detector system. In addition, two apertures were introduced into the chamber to reduce the solid angle of the photons scattered by the windows. Finally, the whole chamber was blackened on the inside to absorb stray light. The third curve (blue) shows the huge impact on the background which was achieved. The background is below 10 Hz nearly at every mirror position, so that TLS profile measurements are now possible. The vertical movement of the laser is generated by a system of

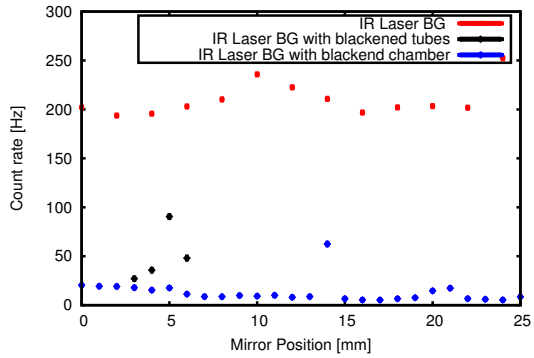

Figure 8: Different IR background levels for different experimental setups. The IR background in the initial chamber (red), with additional blackened tubes (black) and with the new blackened and improved chamber (blue). The vertical movement of the laser is generated by a system of moving mirrors, i.e. the mirror position represents the laser position during the scanning process. The hot spot at 14 mm is reproducible, very narrow (less than 1 mm), and seems to be an impurity of the vacuum window.

moving mirrors, i.e. the mirror position represents the laser position during the scanning process.

OUTLOOK

For comparison measurements a YAG screen is also installed in the BIF chamber and measurements with BIF and YAG are planned for the near future. Since the Background for the TLS measurement seems to be under control the final profile measurement will be carried out soon.

REFERENCES

[1] C. Boehme et al., "Gas Scintillation Beam Profile Monitor at COSY Jülich", TUPSM005, Proceedings of BIW 2010, Santa Fe, New Mexico USA.

[2] M.T. Price et al., "Beam Profile Measurements with the 2-D Laser-Wire Scanner at PETRA", FRPMN094, Proceedings of PAC 2007, Albuquerque, New Mexico USA.

[3] P. Hartmann: "Aufbau einer gepulsten Quelle polarisierter Elektronen", Dissertation 1997, JGU Mainz, Germany

[4] D.T. Pierce et al., Appl. Phys. Lett. 26 (1975) 670.

[5] F. Becker, "Beam Induced Fluorescence Monitors", WEODO1, Proceedings of DIPAC 2011, Hamburg, Germany.

[6] M.A. Plum et al., Nucl. Instr. Meth. A 492 (2002), p. 74.

[7] C. Habfast et al., "Measurement of Laser Light Thomson-Scattered from a Cooling Electron Beam", Appl. Phys. B 44, 87-92 (1987).

[8] T. Weilbach et al.: Optical Electron Beam Diagnostics for Relativistic Electron Cooling Devices, Proceedings of COOL 11, Alushta, Ukraine, 2011.

[9] K. Aulenbacher et al.: Exploring New Techniques for Operation and Diagnostics of Relativistic Electron Coolers, Proceedings of COOL 15, Newport News, Virginia, USA, 2015.

ISBN 978-3-95450-177-9

AN INVESTIGATION INTO THE BEHAVIOUR OF RESIDUAL GAS IONISATION PROFILE MONITORS IN THE ISIS EXTRACTED BEAMLINE

C. C. Wilcox†, B. Jones, A. Pertica, R. E. Williamson, STFC, Rutherford Appleton Laboratory, UK

Abstract

Non-destructive beam profile measurements at the ISIS neutron source are performed using Multi-Channel Profile Monitors (MCPMs). These use residual gas ionisation within the beam pipe, with the ions being guided to an array of 40 Channeltron electron multipliers by a high voltage drift field.

Non-uniform transverse electric fields within these monitors are caused by the drift field and the beam's space charge. Longitudinally, a saddle point located between the drift field plate and the opposing compensating field plate introduces extra complexity into the ion motion. To allow for detailed studies of this behaviour, an MCPM has been placed in Extracted Proton Beamline 1 (EPB1) where the beam is well defined. Simulations of the profiles obtained by this monitor are performed using machine measurements, CST EM Studio and a simple C++ particle tracking code.

This paper describes the process used to simulate MCPM profiles along with a comparison of simulated and measured results. Trajectories of detected ions from their creation to the Channeltrons are discussed, together with a study of Channeltron detection characteristics carried out in the ISIS diagnostics laboratory vacuum tank.

INTRODUCTION

ISIS is a spallation neutron and muon source based at the Rutherford Appleton Laboratory in the UK. The facility consists of a 70 MeV H^- linear accelerator, an 800 MeV proton synchrotron and two EPBs, which transport the accelerated protons to two target stations (TS1 & TS2). The synchrotron operates at a repetition rate of 50 Hz, with four out of every five proton pulses being delivered to TS1 at a rate of 40 Hz and the remaining pulses being delivered to TS2 at a rate of 10 Hz.

Non-destructive profile measurements at ISIS are performed with residual gas ionisation monitors. These utilise the interaction between the proton beam and molecules of the residual gas within the monitor's volume, which creates electron-ion pairs. A drift field, typically of 15 kV, is applied across the monitor to guide the created ions towards an array of detectors. As the level of ionisation at any point within the monitor is directly proportional to the beam intensity at that location [1], a 1D beam profile can be constructed by comparing the quantities of ions arriving at each detector in the array.

Over the past decade, the ISIS design of ionisation profile monitor has undergone multiple stages of evolution to improve both the acquisition speed and accuracy of the measured profiles [2]. The monitors consist of two high voltage electrodes, placed on opposing sides of the monitor to ensure there is no overall influence on the beam trajectory, as shown in Fig. 1. The primary electrode applies a drift field which drives residual gas ions towards a 240 mm wide array of 40 Channeltron electron multipliers. This part of the monitor is referred to as the MCPM, and uses the 4800 series Channeltrons manufactured by Photonis [3], arranged with a regular spacing of 6 mm between each Channeltron centre. The compensating electrode drives ions towards a single, larger 4700 series Channeltron which is connected to a linear motor. This single channel monitor (SCPM) is scanned across the beam aperture and used to calibrate the gains of each of the MCPM Channeltrons, as described in [2].

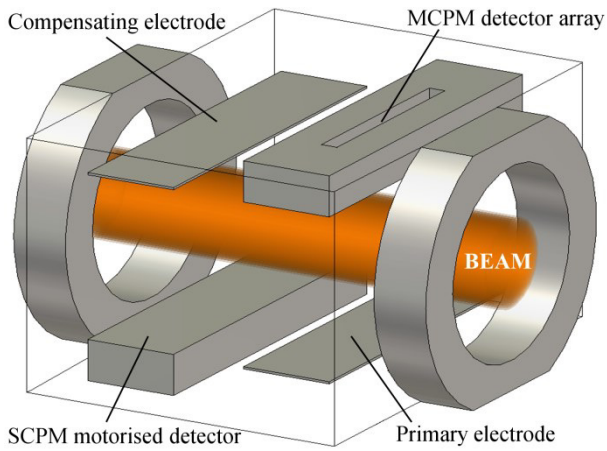

Figure 1: The layout of an ISIS profile monitor.

MEASUREMENT ERRORS

In order to understand high intensity loss mechanisms in the synchrotron and to establish good beam models, it is essential that accurate profile measurements can be taken both quickly and non-destructively.

Accurate measurements depend on the created residual gas ions travelling directly towards the detectors without undergoing any additional transverse motion. For example, in a horizontal profile monitor the ideal ion trajectory is a direct vertical path between the creation and detection points, resulting in an accurate horizontal measurement. However, both the shape of the drift field generated by the electrodes and the effect of the beam's space charge field cause additional transverse ion motion, introducing a broadening effect into the profile measurement (Fig. 2). Furthermore, a saddle point in the electric field exists in the centre of the monitor, created by the interaction between the primary and compensating electrodes.

A profile correction scheme has been developed from previous studies [4] to account for the effects of the drift field and space charge on measurements. Previous investigations have yielded good results when this correction is applied to the monitors located in the synchrotron [5, 6].

† christopher.wilcox@stfc.ac.uk

ISBN 978-3-95450-177-9

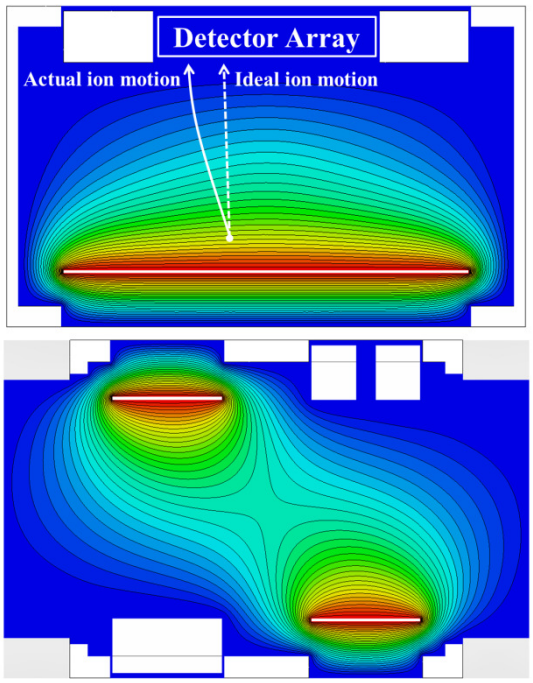

Figure 2: Non-uniform electrostatic potential distributions within the MCPM: transverse (top) and longitudinal (bottom), showing the central saddle point.

To perform a thorough benchmarking of the synchrotron profile monitors and the correction scheme, a monitor was relocated to EPB1, where the beam is well defined due to a large number of diagnostics. The monitor was placed in close proximity to a pair of secondary emission grid profile monitors (known as 'harp' monitors) as shown in Fig. 3. These allow accurate but destructive profile measurements to be taken, something not possible in the synchrotron, providing a reliable and direct comparison for the corrected MCPM measurements.

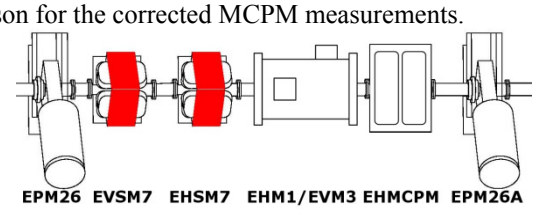

Figure 3: Schematic of the EPB1 layout surrounding the MCPM. EPM26 and EPM26A are harp monitors and EHM1/EVM3 is a dual plane position monitor.

Initial results showed that, unlike the monitors placed in the synchrotron, the EPB1 MCPM measured broader profiles than expected, with corrected profiles remaining wider than those measured by the nearby harp monitors. As a result, to better understand the internal behaviour of the monitor a detailed simulation process has been developed to calculate both the ion trajectories within the MCPM and the associated beam profile measurement.

SIMULATION MODEL

To calculate the monitor's internal electric fields, a 3D model of the monitor geometry is used, created with the finite element modelling software CST EM Studio [7]. The beam's space charge field is modelled using twenty-five concentric elliptic charge distributions of increasing radii, placed within the monitor to represent the beam (as shown in Fig. 1). The total charge within the monitor is calculated from the beam intensity and is arranged to represent an elliptic distribution within the beam. The drift field voltage is applied to the electrodes as an electrostatic potential. During routine operation this is set to 15 kV but can be varied between 0 – 30 kV. The software then calculates a 3D matrix of electric field values within the monitor, which is exported with a resolution of 2 mm in each plane. To approximate a time dependent space charge in the ion tracking phase, a second electric field is calculated with the beam removed from the model.

Calculation of the ion trajectories within the monitor is carried out using a custom written C++ ion tracking code. A uniform distribution of stationary ions is generated within the beam's volume and these are then tracked through the electric fields calculated by CST. The kinematic equations of motion are used to calculate the change in each ion's position and velocity in time steps of 1 ns. As there is no magnetic field within the monitor, the acceleration of each ion within a time step is calculated from the Lorentz force applied by the local electric field as shown in Eq. (1). The equations of motion are solved with a second order Euler method, which is considered to be sufficiently accurate given the small time step size.

$$F_{\text{LORENTZ}} = q\left(\vec{E} + \vec{v} \times \vec{B}\right), \quad \vec{B} \equiv 0$$
$$\therefore\ F_x = qE_x = ma_x \qquad (1)$$

To account for the space charge effect disappearing once the beam leaves the monitor, the electric field values used by the tracker are swapped for the beam-independent field after 200 ns of motion have been simulated. While in reality there are two separate 100 ns bunches travelling through EPB1, these are approximated to a single, longer bunch in the simulation for simplicity. It should be noted that this time dependence is only applied in simulations of the EPB1 profile monitor. Models of synchrotron profile monitors instead use an electrostatic approximation of the average charge within the monitor during operation.

Due to the size of the monitor the 2 mm resolution of the electric field matrices is considered adequate and no interpolation is performed on the values. The simulation runs until every ion has either reached the detectors or moved outside of the tracking region. If an ion travels into a Channeltron, its final time step is calculated precisely (i.e. to less than 1 ns) and the final step of motion is recalculated, giving the precise location at which it is detected.

An IDL [8] code is used to post process the ion trajectories and generate the simulated profile measurement. The positions at which the ions reach the Channeltron detector array are split into 6 mm bins, each corresponding to a Channeltron location, and a histogram is plotted to represent the MCPM profile measurement. An elliptic weighting is applied to each ion based on its initial position, to compensate for the use of a uniform initial distribution in the tracking code. A further weighting can be applied to model the detection efficiency of the Channeltrons, as discussed in the detector characterisation section.

ISBN 978-3-95450-177-9

BENCHMARKING MEASUREMENTS

To verify the simulation model, profile measurements were recorded in EPB1 at multiple beam intensities from both the MCPM and the adjacent harp monitors. When combined with the measured intensities, these harp measurements ensured that the beam passing through the MCPM was well defined, with known positions and 95% widths in both planes. This beam definition was subsequently used as an input throughout the simulation procedure, meaning the results could be directly compared with the profiles measured by the MCPM.

Once agreement between simulation and measurement had been observed, the behaviour and dominant sources of error in the monitor were studied in more detail, as described below.

SIMULATION RESULTS

The simulation produces results that match closely with associated machine measurements, particularly when a low intensity beam is used. Figure 4a) demonstrates this, showing a close agreement between simulation and measurements taken at 10% of standard operating intensity. Variation between the 95% widths of the simulated and measured profiles is less than 1.5 mm, a satisfactory result when considering that the monitor itself has a resolution of 6 mm.

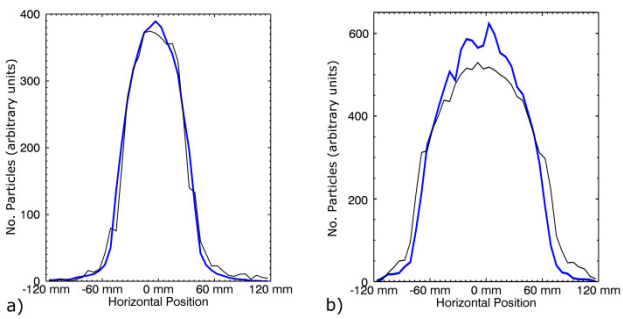

Figure 4: Comparisons of simulated (blue) and measured (black) MCPM profiles in EPB1, taken at a) low intensity operation and b) standard operating intensity.

Simulations at higher intensities show greater variation when compared with measurements (Fig. 4b). While the overall shape of the profile remains a good match, the 95% widths differ by 15 mm at standard operating intensity, with the levels of profile broadening observed in the EPB not being reproduced by the simulation.

This result is in line with the previously mentioned benchmarking measurements of the profile correction scheme, which found increased levels of broadening in the EPB1 monitor compared with profiles measured in the synchrotron. As simulated profiles agree with measurements across all intensities in the synchrotron, studies are currently underway to identify the source of this behaviour in the EPB.

Ion Trajectories

The complexity of the ion motion within the monitor can be seen in Figs. 5 and 6, which show the trajectories of ions that reach the Channeltrons and therefore form the profile measurement. The effect of the saddle point can be seen, causing extra ions from the monitor's centre to reach the detectors, many via indirect paths. Approximately 20% of the detected ions are created in this saddle point region, causing further broadening of the profile in addition to the drift field and space charge effects.

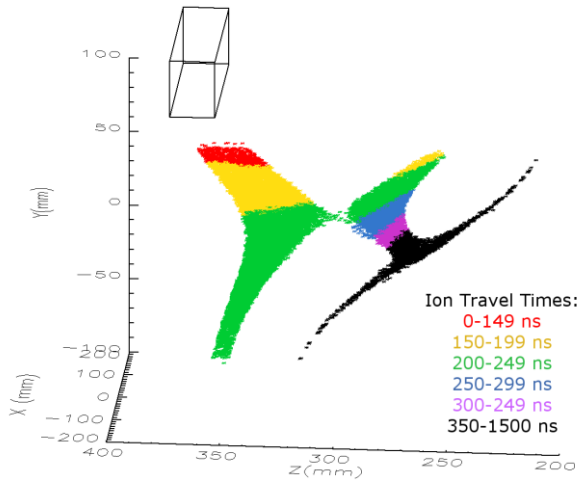

Figure 5: Initial positions of ions that travel into the detector array. The different colours denote the time of flight from creation to detection. The position of the MCPM detector array is shown as a black box.

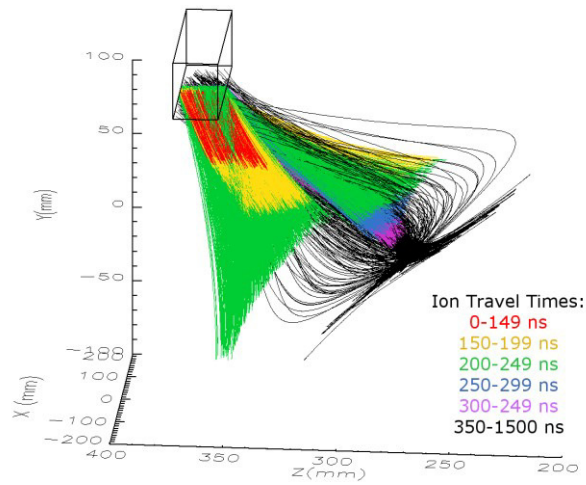

Figure 6: Trajectories of ions that reach the detectors, shown in the longitudinal plane.

Due to the irregular trajectories taken by many of the ions travelling towards the detectors from the saddle point, their angles of incidence upon entering the Channeltrons are significantly higher than those of other detected ions. Figure 7 shows that this angle can be used to separate the detected ions into two distinct groups, a result which has important implications. Firstly, as many of the ions arriving at sharper angles have taken indirect trajectories, they are undesirable in the profile measurement as they contribute to the artificial broadening. Consequently any future modification to the MCPM housing that can prevent these ions reaching the detector would improve the overall performance of the monitor. Secondly, the scale of variation in angles means that the Channel-

ISBN 978-3-95450-177-9

tron detection efficiency at different angles must be characterised and included in the simulation.

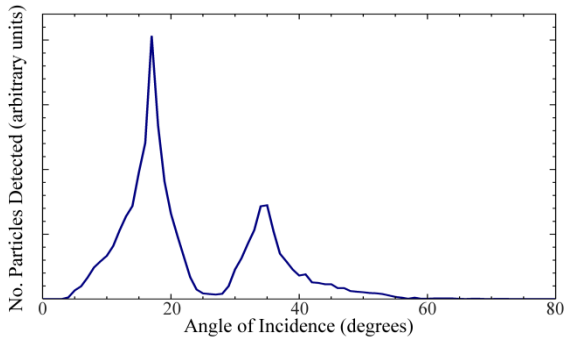

Figure 7: Longitudinal angles of incidence at which ions enter the detector.

DETECTOR CHARACTERISATION

Detailed data on the angular acceptances of the Channeltrons used in the monitor is not available from Photonis. As a result, a miniature test assembly was built containing a single 4700 series Channeltron and an array of four 4800 series Channeltrons, with both sets of detectors placed inside housings of identical geometries to those used in the full monitor. The test assembly was then fixed to a rotatable plate within a vacuum tank and an ion gun was used to test the response of the Channeltrons at different angles. The majority of the residual gas within EPB1 is water vapour, meaning the dominant residual gas ion species are of hydrogen and oxygen. The IDL code was used to calculate the kinetic energies of these species as they reach the detectors, with the majority arriving at energies of 4-4.5 keV. To match these conditions as closely as possible the vacuum tank ion gun was set up to produce 4 keV helium ions.

The assembly was rotated to vary the incident angle of the ion beam and the Channeltron current measurements were used to calculate their detection efficiencies. The results presented in Fig. 8 show the significant efficiency variations observed in both types of Channeltron within the range of angles seen in the simulation results. Furthermore the different models of Channeltron exhibited very different behaviours, a result that was unexpected.

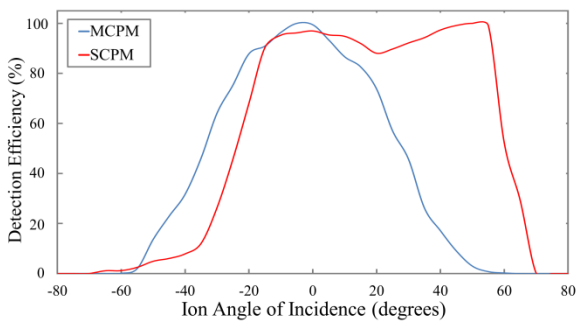

Figure 8: Variation in Channeltron detection efficiency with ion angle of incidence. The MCPM contains 4800 series Channeltrons while the SCPM uses a 4700 series.

The results from the MCPM Channeltrons were used to generate an extra weighting for the simulated profile measurement during the post processing stage. This will be applied during future studies, with saddle point ions generating roughly half the current of those created directly below the detector array. The levels of variation observed and the asymmetrical results obtained from the SCPM Channeltron highlight the importance of considering the performance of the detectors in detail as part of the simulation process.

CONCLUSIONS AND FUTURE WORK

Simulations of the ISIS MCPMs have been carried out and compared against well-defined benchmarking measurements performed in EPB1. Close agreement between simulated and measured profiles has been achieved at low beam intensities, allowing for more detailed modelling of ion behaviour and error mechanisms within the monitor. The properties of the Channeltrons have been measured as a function of incident angle and the results will be used to enhance the accuracy of future simulations.

Modifications for future iterations of the profile monitors will be tested using the Channeltron test assembly. Adjustments to the detector housing with the aim of preventing detection of ions arriving at angles of incidence larger than 25 degrees will be targeted, to remove the effect of the ions created near the monitor's saddle point.

Future studies are planned to provide alternative data for benchmarking the simulation and studying the monitor's behaviour. A fast acting amplifier will be used to measure the time structure of ions arriving at the Channeltrons. Measurements will also be taken with the compensating field deactivated, removing the saddle point from the monitor and reducing the time spread of detected ions.

The simulation's time dependent electric field approximation will be improved to accurately model the proton bunch structure within EPB1, which contains two 100 ns bunches with a separation of 225 ns. The smaller timescales involved suggest this simulation component will have a larger effect on results than at present.

REFERENCES

[1] P. Strehl, *Beam Instrumentation and Diagnostics*, Springer, 2006.
[2] S. A. Whitehead, P. G. Barnes, G. M. Cross, S. J. Payne and A. Pertica, "Multi-Channeltron based profile monitor at the ISIS proton synchrotron", in *Proc. BIW10*, Santa Fe, pp. 106-110.
[3] Photonis, https://www.photonis.com
[4] R. E. Williamson, B. G. Pine, S. J. Payne and C. M. Warsop, "Analysis of measurement errors in residual gas ionisation profile monitors in a high intensity proton beam", in *Proc. EPAC08*, Genoa, pp. 1317-1319.
[5] C. M. Warsop *et al.*, "Studies of loss mechanisms associated with the half integer limit on the ISIS ring", in *Proc. HB2014*, East Lansing, pp. 123-127.
[6] B. Jones, D. J. Adams and C. M. Warsop, "Injection optimisation on the ISIS synchrotron", in *Proc. EPAC08*, Genoa, pp. 3587-3589.
[7] CST, http://www.cst.com
[8] IDL, http://www.harrisgeospatial.com

ISBN 978-3-95450-177-9

PROFILE MEASUREMENT BY THE IONIZATION PROFILE MONITOR WITH 0.2T MAGNET SYSTEM IN J-PARC MR

Kenichirou Satou†, Hironori Kuboki, Takeshi Toyama, J-PARC/KEK, Tokai, Japan

Abstract

A non-destructive Ionization Profile Monitor (IPM) is widely used to measure transverse profile. At J-PARC Main Ring (MR), three IPM systems have been used not only to measure emittances but also to correct injection miss matchings. To measure beam profiles at the injection energy of 3GeV, the high external E field of +50kV/130mm at the maximum is used to guide ionized positive ions to a position sensitive detector; transverse kick force originating from space charge E field of circulating beam is a main error source which deteriorates profile.

The strong B field is also used to compensate the kick force. To measure bunched beam at the flat top energy of 30GeV in the fast extraction mode in good resolution, the strong B field of about 0.2T is needed. One set of magnet system, which consists of a C-type and two H-type magnets, were developed and installed in one IPM system. The IPM chamber was inserted between the 2 poles of the C-type magnet. To make the line integral of B field along the beam axis zero, the H-type magnets have the opposite field polarity to that of the C-type magnet and were installed on both sides of the C-type magnet. Details of the magnet system and its first trials will be presented.

INTRODUCTION

The residual-gas ionization profile monitor (IPM) is one of the most ideal diagnostic tools to measure a transverse profile non-destructively. The most promising way to obtain a clear profile is to measure positive ions using a strong dipole E field (Eext), because this system does not being affected with electron contaminations from electron clouds, a discharge problem on HV feeder. The Eext should be much larger than the strong beam space charge E field (Esc). However, due to the technical limitation of HV being able to apply to an insulator between electrodes, profile distortion will be set in case of high density beams of J-PARC, SNS, LHC, and so on. To reconstruct the original profile from an obtained profile, the numerical calculation methods were developed [1-3], however, before calculation, original profile shape should be assumed.

Another method is to use a uniform magnetic guiding field (Bg), which is parallel to Eext, to collect detached electrons. The Bg converts Esc kick force to gyro-motion along Bg and so called E×B drift along beam axis, where the initial momentum of a detached electron and also a velocity gain from Esc determines radius of the gyro-motion. And this radius determines profile measurement accuracy. However the electron contamination problems are left to be settled. Due to this contamination issue, it is hard to measure the beam tail profile.

Our choice is to use the both methods [4, 5]. We have developed a magnet system for one IPM system (Horizontal type IPM) out of three, and started operation from this June. The Fig. 1 shows photo of horizontal IPM system with new developed magnet system. After describing the details of the magnet, the first measurement results are reported.

Figure 1: Photo of horizontal IPM system installed at address 76 of J-PARC MR.

MAGNET REQUIREMENTS AND PERFORMANCES

The magnet system consists of one C-type main magnet and two H-type correction magnets. The correction magnets are used to cancel the B field integral along the beam axis (BL product) so as not to kick the beam; magnet polarity is opposite

To check the Bg intensity required to measure profiles within 1% accuracy, the profile simulation code IPMsim3D [6, 7] was used. The profile distortions for different Bg settings were checked for a designed maximum beam pulse at the flat top energy of 30GeV. In these calculations, the Gaussian shape was assumed for initial transverse and longitudinal profiles. The expected beam parameters are listed as follows, where 1σ beam emittance for x, and y were set as, 4.4πmm·mrad, and 7.0πmm·mrad, respectively.

- Beam energy:30GeV
- Beam intensity: 4E13 particles per bunch (ppb)
- Transverse beam size: σ_x=2.7mm, σ_y=4.4mm
- Longitudinal beam size: σ_t=10ns

At the IPM centre, the beta function for x and y is β_x=13.1m, β_y=21.6m, respectively, and dispersion function is 0. The initial momentum of an electron was calculated based on the double differential ionization cross section of ref [8]. And Eext was set as -

† kenichirou.satou@j-parc.jp

ISBN 978-3-95450-177-9

30kV/130mm. The obtained profiles in case of Bg=0.05T and 0.2T are shown in Fig. 2. The profiles were fitted with the Gaussian function.

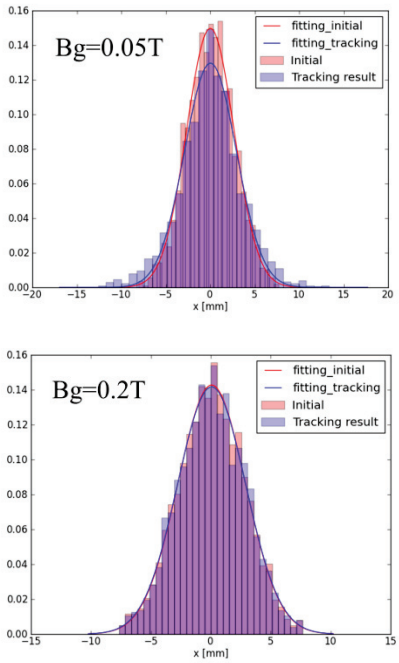

Figure 2: The profiles before (red) and after (blue) the particle tracking calculations. The solid lines are the Gaussian function fitting results.

The ratios of the beam widths obtained from profiles after tracking calculation to the initial ones are shown in Fig. 3. As can be seen from the figure, The Bg>0.2T is needed to measure profile within 1% accuracy.

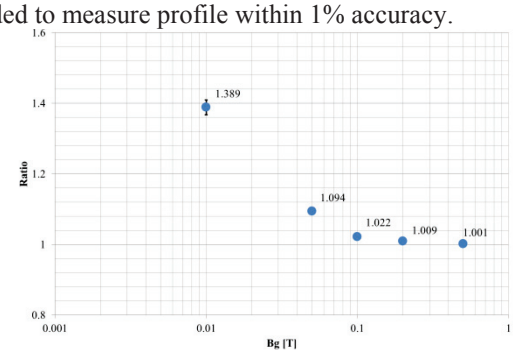

Figure 3: The ratio of calculated beam size to the initial one.

The error field of Bg, the z component Bg_z, makes profile distortion because of the presence of horizontal kick force, Esc_y × Bg_z. The 1% Bg_z/Bg_y makes position shift by at the most 200um and this value can be negligibly small when compared to the horizontal beam size of 2.7mm. The estimated beam size change is only 0.3%.

The design specifications are as follows,

- C-type
  - Pole gap[mm]: 220
  - Maximum Bg[T]: 0.25
  - Effective area[mm]:x=-45~45, y=-40~40, z=-20~20
  - Error fields: Bg_x/Bg_y, Bg_z/Bg_y<1%
  - Flatness of Bg_y: <5%
  - Cooling: Water
- H-type
  - Pole gap[mm]: 150
  - Maximum Bg[T]: 0.13
  - Effective area[mm]:x=-45~45, y=-40~40, z=-20~20
  - Error fields: Bg_x/Bg_y, Bg_z/Bg_y<1%
  - Flatness of Bg_y: <5%
  - Cooling: Air

Figure 4: The C-type magnet pole shape.

The pole shape was determined so as to meet the requirements of error fields and flatness through iterative simulations using the code OPERA-3D [9]. The Fig. 4 shows C-type magnet pole shape. Results of field measurements along the beam axis at a test bench are shown in Fig. 5 and Fig. 6. The error fields were at the most 0.4% and flatness was 1% as shown in Fig. 5, however a part of the errors were caused by the miss-alignment of the magnets. The output field linearity to the input current was checked and shown in Fig. 6. As can be seen from the figure, although the maximum field reaches to 0.29T at 60A in case of C-type magnet, it shows nonlinearity above 0.2T at 40A. As for the H-type magnet, the maximum field was 0.16T at 35A and it shows good linearity for whole range.

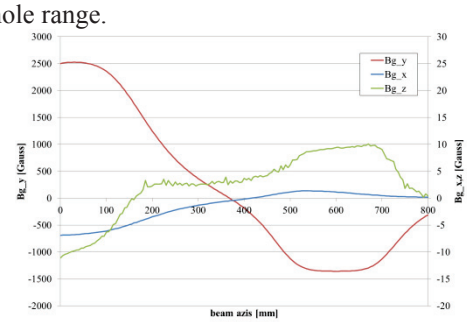

Figure 5: The magnetic fields along beam axis, from the C-type magnet centre to the H-type magnet.

ISBN 978-3-95450-177-9

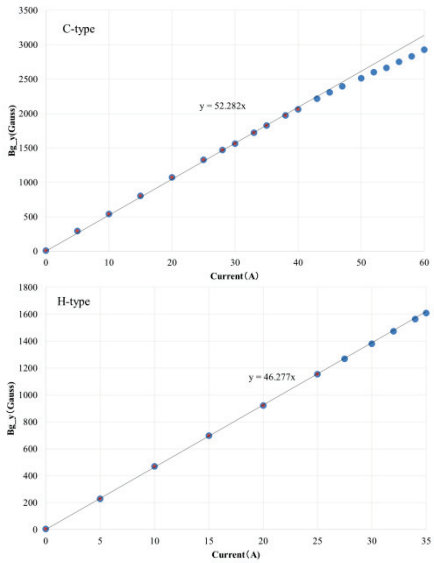

Figure 6: Output fields linearity to the input current.

INTENSITY BALANCE TUNING OF THE MAGNET SYSTEM

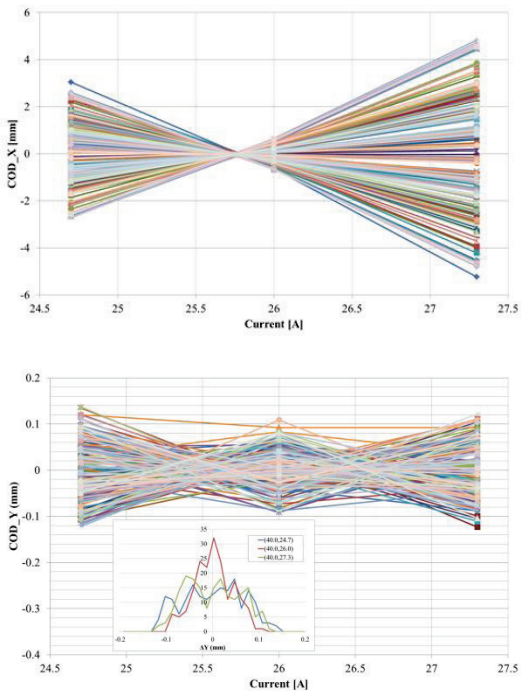

Figure 7: The COD changes for x (COD_x) and y (COD_y) measured with 186 BPMs. The horizontal axis means H-type magnet's current settings which is common for both H-type magnets, where the current setting for C-type magnet was 40A. The histograms of COD_y at different current settings are also shown.

The magnetic field intensity balance between C type and H-type magnets was checked. The residual BL product makes dipole kick and the dipole kick makes the Closed Orbit Distortion (COD). The ratio of the field intensities of the C-type and the H-type magnet, that is the input current setting, should be tuned so as not to show clear COD changes, for example, larger than the typical position resolution of the Beam Position Monitor (BPM) system of about 100μm. We have checked position changes measured by using 186 BPMs after the current settings of (40.0, 24.7), (40.0, 26.0), (40.0, 27.3), where the first element means current setting of C-type magnet and the second element means that of both two H-type magnets in unit of ampere.

The CODs measured at all BPMs are shown in Fig. 7. The cross points showing COD_x = 0mm suggest that the current setting of (40.0, 25.7) is appeared to be the balanced setting. We have also checked the vertical CODs and these does not shows clear position deviations, however the histograms of the (40.0, 26.0) setting shows somewhat smaller width than that of the others. Since the magnet alignment criterion was less than 1mrad, so we expect that the alignment error of the H-type magnet induces small vertical kick and thus CODs, which are less than 100μm.

PROFILE MEASUREMENTS

The first trial of profile measurements were made with the Bg=0.2T and the different HV settings of 4.0kV, 10.0kV, 20.0kV, and 30.0kV. The 2 stage type MCP with 32ch multi-strip anodes has been used as a signal multiplication and charge pick-up device. The width of each strip is 2.5mm. Turn-by-turn beam profiles measured from the beam injection are shown in Fig. 8, where the beam energy and intensity was 3GeV and 5E12 ppb, respectively, and only 1 bunch beam was injected. The beam conditions for the cases 10.0kV and 30.0kV were different from the others; the dipole oscillation was remained due to insufficient injection tunings. Note that the outermost two signals out of 32chs in total, the signals at 38.75mm and -38.75mm, do not work at present due to a failure of front end signal amplifiers.

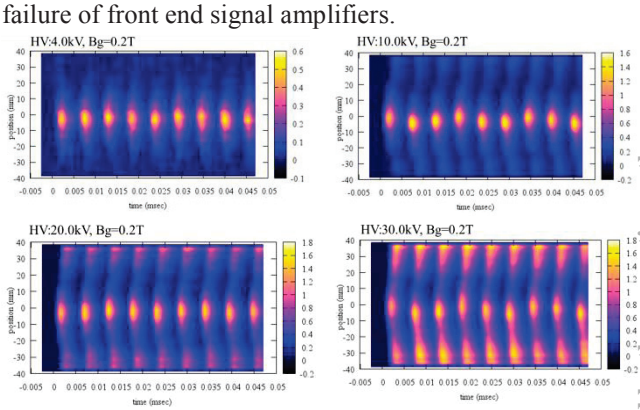

Figure 8: The contour maps of beam profiles with Bg=0.2T and different HV settings, 4.0kV, 10kV, 20kV, and 30kV.

As can be seen in the figure, the electron contaminations appeared on both sides of the MCP detector was increasing with increasing the HV. The ratio of signal intensity of contaminations to real beam signals, which is the ratio of averaged voltage at x=-36.2mm to averaged voltage at the centre, is shown in Fig. 9.

ISBN 978-3-95450-177-9

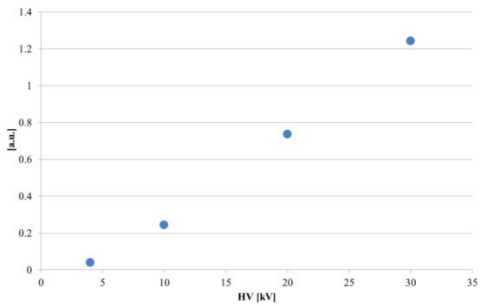

Figure 9: The ratio of electron contaminations to the real beam signals.

DISCUSSIONS

The electron contamination has different and unique profile as shown in Fig. 8 and also different time structure as shown in Fig. 10. The output signal from the anode at x=-36.2mm whose main contribution is likely coming from the electron contamination is compared with the signal from the anode at centre whose main contribution is likely coming from a real beam signal. The beam signal in case of positive ion collection mode without Bg is also shown.

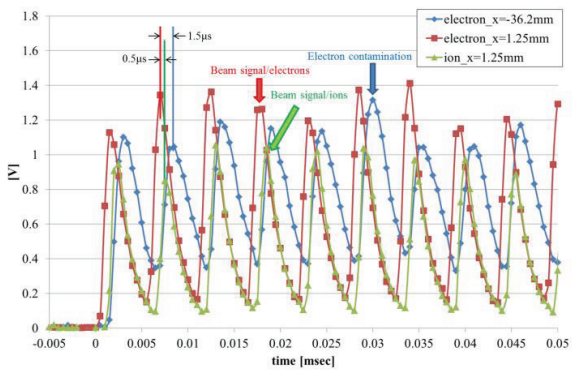

Figure 10: Signals from charge pick-up anodes at -36.2mm and 1.25mm in case of electron collection mode with Bg=0.2T (HV=20kV), and also signal from centre anode in case of ion collection mode without Bg (HV=30kV).

The time difference between a real beam signal of electrons and ions is about 500ns. This time difference is the result of the time of flight (TOF) to the MCP detector, a few ns in case of electrons and a few hundred ns for ions. The electron contamination shows somewhat broad structure and likely arrived on the detector surface at about 1.5μs after beam passage.

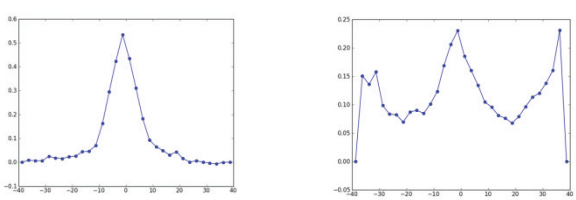

Figure 11: The profiles at 1μs and 5.5μs after beam injection in case of HV=10.0kV setting.

The source of the electron contamination is now unknown and under investigation though, by selecting the timing and minimizing the HV as small as possible, a clear beam profile can be obtained. The Fig. 11 shows profiles at 1μs and 5.5μs after beam injection. However this method cannot be applicable to the full bunch (8 bunches) injection scheme because of the time structure of a bunch train.

There are two candidates for the contamination sources. One is a secondary electrons induced by the ion collisions. At the same time of electron collection with Bg, the same number of ions will accelerate opposite direction and finally collide with electrodes faced MCP detector surface. The noble ion trap method was developed to suppress the ion collisions completely and applied for the new IPM system of CERN-PS [10]. However a signal from this electron would have same time structure of ion collection mode because the TOF of electrons from the surface is negligibly small compared with the TOF of ions to the collision point.

The other candidate is electrons generated outside the effective area of the IPM where uniform fields of Eext and Bg are applied. The tracking simulations were made only for electrons generated near the centre of IPM chamber. The ionization process, electron cloud generation, and discharge problem between electrodes would be sources of the electron generation. To study the electron contamination issue, the IPMsim3D code will be modified so as to calculate electron trajectory traveling through the fringe fields of Eext and Bg together with Esc.

REFERENCES

[1] Jan. Egberts."IFMIF-LIPAc Beam Diagnostics. Profilingand Loss Monitoring Systems", PhD thesis, Paris-Sud University, 2012.

[2] W. S. Graves. "Measurement of Transverse Emittance in the Fermilab Booster", PhD thesis, University of Wisconsin - Madison, 1994.

[3] J. Amundson *et al.*, "Calibration of the Fermilab Booster Ionization Profile Monitor", *Phys. Rev. STAB*, 6:102801, 2003.

[4] K. Satou *et al.*, "IPM system for J-PARC RCS and MR", *Proceedings of HB2010*, WEO1C05.

[5] K. Satou *et al.*, "Beam Diagnostic System of the Main Ring Synchrotron of J-PARC", *Proceedings of HB2008*, WGF11.

[6] IPMSim3D Simulation Code, https://twiki.cern.ch/twiki/pub/IPMSim/Availble_Codes/ipmsim3d.tar.gz

[7] M. Sapinski *et al.*, "Ionization Profile Monitor Simulations –Status and Future Plans", *IBIC2016, Barcelona, Spain*, TUPG71.

[8] A.Voitkiv, N.Gruen,W.Scheid, "Hydrogen and Heliumionization by Relativistic Projectiles in Collisions with Small Momentum Transfer", *J.Phys.B: At.Mol.Opt.Phys*.32 (3923-3937), 1999.

[9] Finite Element Analysis Programs Including TOSCA, Elektra, SCALA, CARMEN, SOPRANO and TEMPO, http://operafea.com/

[10] J. W. Stony *et al.*, "Development of an Ionization Profile Monitor Based on a Pixel Detector for the CERN Proton Synchrotron", *Proceedings of IBIC2015*, TUPB059.

ISBN 978-3-95450-177-9

3D DENSITY SCANS OF A SUPERSONIC GAS JET FOR BEAM PROFILE MONITOR

H. Zhang#, V. Tzoganis, K. Widmann, C. Welsch
Cockcroft Institute and The University of Liverpool, Warrington, WA44AD, UK

Abstract

Recently, we have developed a novel beam profile monitor based on a supersonic gas jet. It can be applied to some extreme situation while other methods are not applicable such as for the high intensity and energy beams with destructive power and for the short life beam which requires minimum interference. The resolution of this monitor depends on the jet thickness and homogeneity, and thus we developed a movable gauge to investigate the gas jet distribution in a 3D manner. In this paper, we will present the measurement of the distribution of the gas jet and discuss the future improvement for the jet design.

INTRODUCTION

Beam profile monitors are essential diagnostics for particle accelerators. With undergoing constructions of proposed high intensity and high power machine like ESS or HL-LHC, the conventional invasive diagnostics are not well suited because of the destructive beam power. Previously, IPM and BIF were used in similar situations based on the ionization or excitation of residual gas by the projectile beams [1]. The usage of the residual gas makes the diagnostic non-invasive but the signal level is low requiring long integration. Recently, a supersonic gas jet based monitor [2-4] was developed at the Cockcroft Institute .Using the gas jet with a high directional speed and high density, the probability of ionization or excitation of the gas molecules will increase dramatically. Therefore, the integration time will be much reduced, even to a level where shot to shot measurement will be possible.

Previously, we reported the results of such monitor to measure a two-dimensional profile of a 5 keV, 7uA electron beam. [4]. Preliminary results have shown that the jet properties could affect the monitor performance. However, the jet homogeneity and density distribution is still unknown.

In this paper, we will present a subsystem dedicated to measure the gas jet profile in 3D and results about the jet density and homogeneity will be discussed in details.

GAS JET SETUP AND MEASUREMENT

The details of the setup are shown in figure 1 and were described previously [4-6]. The supersonics gas jet is generated by injecting high pressure gas (1-10 bar) from gas tank pass through a small nozzle with diameter 30 μm into a low pressure region (10^{-4} mbar). With further collimations, the gas jet can travel mono-directionally and be shaped into a screen-like curtain for diagnostic purpose. The differential pumping sections were designed to remove collimated gas molecular and maintain an ultra-high vacuum environment in the interaction chamber. Dumping sections are used for dumping the jet.

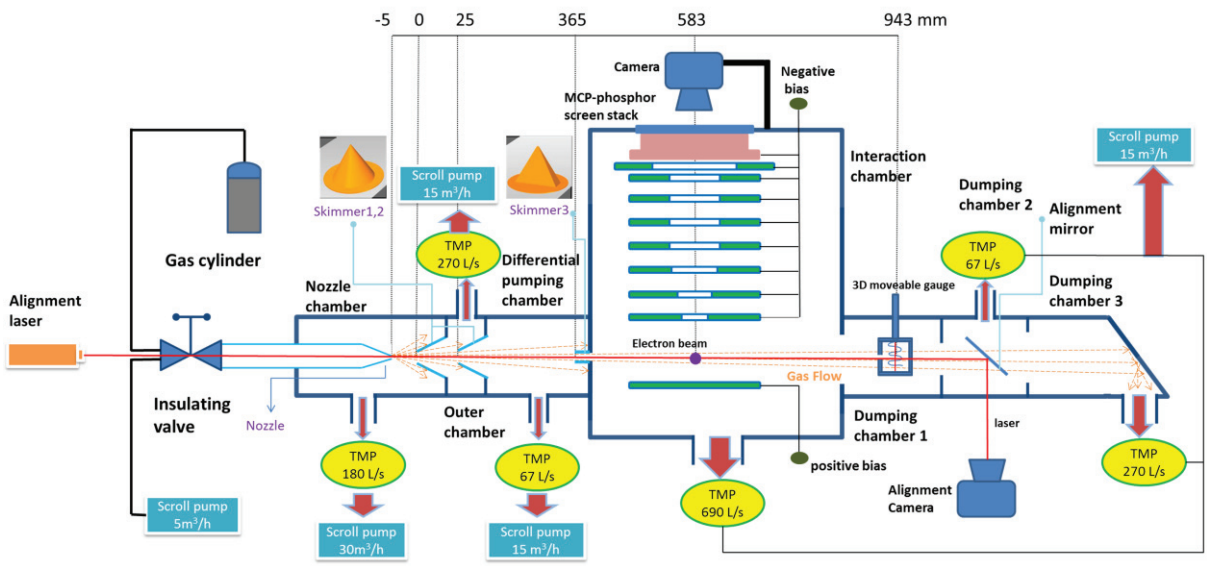

Figure 1: Schematic drawing of the complete setup.

#hao.zhang@cockcroft.ac.uk

ISBN 978-3-95450-177-9

The beam image of a 5 keV and 10 μA electron beam was detected by collecting the ions using external electric field and MCP-phosphor screen stack, where the ions are generated by the interaction of the E-beam and the gas jet and represent the distribution of the projectile E-beam. One representative measurement is shown in figure 2.

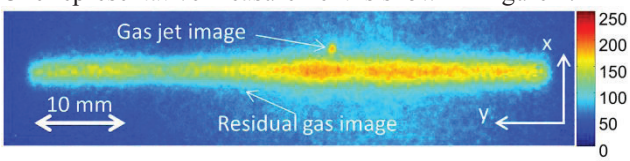

Figure 2: Images of the electron beam from both gas jet and residual gas.

3D MOVEABLE GAUGE SYSTEM

To measure the density distribution of the supersonic gas jet, a compression gauge solution [7] is adapted here. Based on that principle, we have installed a 3D moveable ion gauge assembly [8]. The assembly includes a CF Full Nipple DN40CF as shown in figure 3 with the bottom side closed by a fixed flange and the other side attached to a Granville Phillips Series 274 Nude Gauges. This component is then connected with a VACGEN Miniax XYZ manipulator powered by three stepper-motors to allow a 3-dimentional movement with a resolution of 5 μm. On the tube of the nipple 40 mm above the bottom, there is a 10 mm (length) * 0.5 mm (width) slit which is the only opening to accept the gas flow.

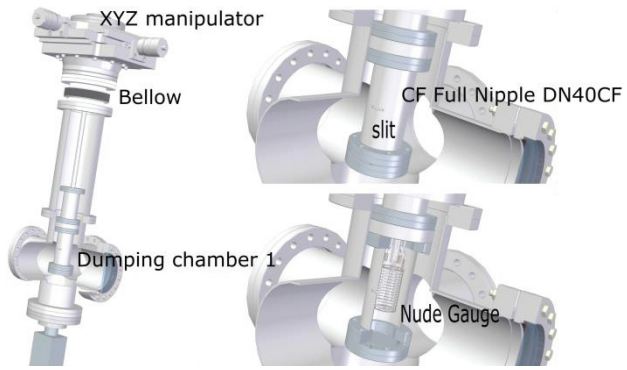

Figure 3: Mechanic drawing of the movable gauge system.

The gauge is powered by a VG IGC26 ion gauge controller and its signal is amplified by a pico-ampere meter and then recorded by oscilloscope. After the jet is fired, part of the jet enters the tube, the gas molecules accumulate inside and the density is measured by the gauge. If we assume that the gas diffusion is a much faster process that when gas molecular enters the tube, it will distribute equally immediately, the net gross rate of gas molecular inside the tube will be proportional to the gradient of the signal strength. Note that the baseline signal represents the stagnation density of the gas molecules inside the tube. Since the ion gauge itself is a heat source, and the heat inside the tube is not easy to be dissipated, continuous operation of the gauge will cause the baseline signal to increase and possibly overflow the pico-ampere meter. To prevent that, special care were taken regarding the timing of the whole system by using the emission inhibit function of the gauge controller. The full timing table is shown in Figure 4. Note when the gauge inhibit is low the ion gauge is switched on and initially there will be a sudden rise of signal for the gauge reading due to the initialization. Therefore, there is a long delay between the gauge switched on and the pulse valve open to allow the gauge signal to return to the normal baseline.

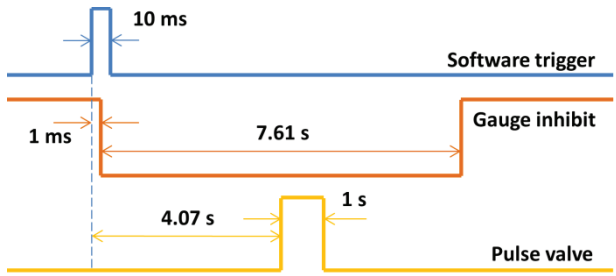

Figure 4: Timing diagram.

Typical measurements are shown in figure 5, where two processes can be identified. A quicker rise of the signal closely following the pulse valve trigger indicates the jet entering the tube while the slow rise indicates the density gradient flow from the background gas.

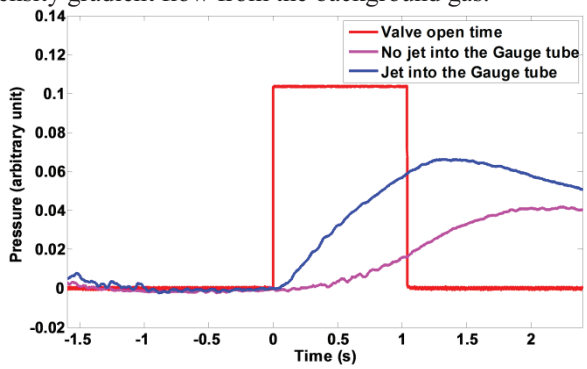

Figure 5: Pressure measured at the movable ionisation gauge.

With the software trigger generated by a control PC, the whole 3D scanning can be easily automated as the flow chart shown in figure 6.

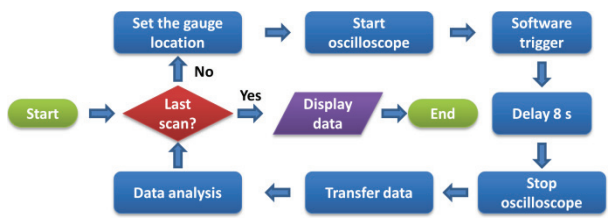

Figure 6: Data collection and analysis flow chart.

As shown in Figure 5, during the pulse valve gate time, the gradient of the gauge signal represent the number of gas molecular change. We choose the linear growth part of the signal, e.g. from 0.24 s to 0.56 s after the pulse

ISBN 978-3-95450-177-9

valve open, which will be better to reflect the change due to the gas jet. Then we fit the data to find the gradient which will represent the number density change inside the tube. We did four transverse 2D scans with different longitudinal position from -1.5 mm to 0 mm of the jet with a transverse range of 12.5 mm * 20 mm with a step size of 0.5 mm. The data is shown in Figure 7. For all cases, the horizontal size is about 10.0 mm and the vertical size is about 5.5 mm. The difference among them is quite small and it could be due to the fact that we don't have enough transverse resolution or the growth of the jet size is small to be detected in a 1.5 mm range.

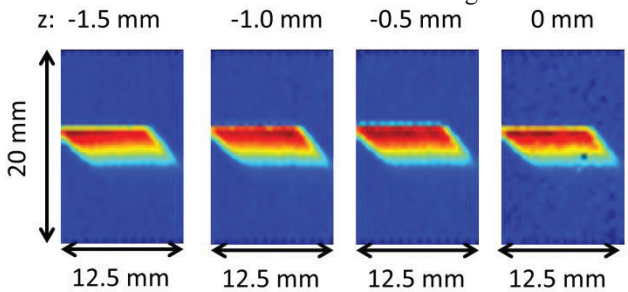

Figure 7: Normalized number density change recorded by a moveable gauge with a rectangular slit.

In the horizontal axis, since the length of the slit is much larger than the jet waist, the number density change will be a constant in the middle of the slit and only drops when the jet is intercepted by the edge of the slit. Thus, the distribution measured here will be dominated by the slit length no matter how small the step size is. However, if we differentiate the value of the number density change around the edges in its horizontal axis, we can obtain the normalized density distribution along the horizontal axis. The smaller the step size is the finer distribution we get after differentiation. Vertically, because the slit width is much smaller than the jet length and comparable to the step size, we can use the measured distribution in the vertical axis as the jet density distribution directly.

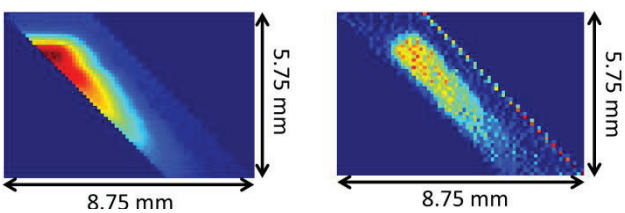

Figure 8: Edge scan and the associated jet density distribution.

Based on this, we did a finer scan with a step size of 0.125 mm only around the left edge of the previous scan as shown in the left image of Figure 8. By differentiating the result in horizontal axis, we get a normalized jet density distribution image as shown in the right side of Figure 8. The size of the jet is measured as 5.44 mm * 1.55 mm in full width, and the tilted angle is 42.9 degree. With originally 4.0 mm * 0.4 mm, the length of the jet increased 1.36 times and the width of the jet increased 3.88 times which indicate the growth is non-isotropic.

From the measurement of the normalized jet distribution, we can estimate the jet size in the interaction location assuming a linear expansion in each direction, which is 4.66 mm * 0.92 mm. Then the jet thickness contribution to the uncertainty of the measurement σ_{jet} will be [4]

$$\sigma_{\text{jet}} = \frac{w_{\text{jet}}}{2\sqrt{3}\cos(\theta)}$$

where w_{jet} is the width of the jet 0.92 mm and θ is the Jet angle 42.9 degree, which gives σ_{jet} as 0.36 mm. Previous analysis reported a lower value of σ_{jet} because we assumed the jet would keep its aspect ratio.

CONCLUSIONS

In this paper, we describe a system to measure the 3D density distribution of a supersonic jet used as a beam profile monitor. Details are presented about the mechanical setup and relevant components, timing system and measurement procedure as well as the measurement results. Current measurements about the transverse profile of the jet further corrects the model we use to estimate the uncertainty from the jet width when measure y size of the projectile beam. Further work can be done to calibrate this system to get the absolute value of the 3D jet density under different operation condition such as stagnation gas pressure from the gas tank, different skimmer sizes and locations and different gas species. Comparison with simulation data is undergoing which will allow us to optimize the monitor system to produce better jet suitable for measuring the projectile beam profile more efficiently and accurately.

ACKNOWLEDGMENT

This work is supported by the Helmholtz Association under contract VH-NG-328, the European Union's Seventh Framework Programme for research, technological development and demonstration under grant agreement no 215080 and the STFC Cockcroft core grant No. ST/G008248/1.

REFERENCES

[1] P. Forck, *Proceedings of IPAC2010*, Kyoto, Japan, pp. TUZMH01, 2010.
[2] V. Tzoganis and C. P. Welsch, *Appl. Phys. Lett.*, vol. 104, no. 20, 2014.
[3] H. Zhang, *et al.*, *Proceedings of IPAC2016*, Busan, Korea, pp. MOPMR046, 2016.
[4] H. Zhang, *et al.*, submitted to *PRAB*.
[5] V. Tzoganis, *et al.*, *Vacuum*, vol. 109, pp. 417–424, 2014.
[6] M. Putignano, PhD thesis, University of Liverpool, 2012.
[7] Y. Hashimoto, *Proceedings of IBIC2013*, Oxford, UK, pp. WEPF17, 2013.
[8] H. Zhang, *et al.*, *Proceedings of IBIC2015*, Melbourne, Australia, pp. TUPB075, 2015.

ISBN 978-3-95450-177-9

A HARDWARE AND SOFTWARE OVERVIEW ON THE NEW BTF TRANSVERSE PROFILE MONITOR

B.Buonomo, C. Di Giulio, L.G. Foggetta†, INFN – Laboratori Nazionali di Frascati, Frascati, Italy
P.Valente, INFN – Sezione di Roma, Rome, Italy

Abstract

In the last 11 years, the Beam-Test Facility (BTF) of the DAFNE accelerator complex, in the Frascati laboratory, has gained an important role in the EU infrastructures devoted to the development of particle detectors. The facility can provide electrons and positrons, tuning at runtime different beam parameters: energy (from about 50 MeV up to 750 MeV for e- and 540 MeV for e+), intensity (from single particle up to 1010/bunch) and pulse length (in the range 1.5–40 ns). The bunch delivery rate is up to 49 Hz (depending on the operations of the DAFNE collider) and the beam spot and divergence can be adjusted, down to sub-mm sizes and 2 mrad (downstream of the vacuum beam-pipe exit window), matching the user needs. In this paper we describe the new implementation of the secondary BTF beam transverse monitor systems based on ADVACAM FitPIX® Kit detectors, operating in bus synchronization mode externally timed to the BTF beam. Our software layout includes a data producer, a live-data display consumer, and a MEMCACHED caching server. This configuration offers to BTF users a fast and easy approach to the transverse diagnostics data using TCP/IP calls to MEMCACHED, with a user-friendly software integration of virtually any DAQ system. The possibility of sharing mixed data structures (user-generated and BTF diagnostics) allows to completely avoid the complexity of hardware synchronization of different DAQ systems.

THE DAΦNE BEAM TEST FACILITY (BTF)

The BTF (Beam Test Facility) is part of the DAΦNE accelerator complex: it is composed of a transfer line driven by a pulsed magnet allowing the diversion of electrons or positrons, usually injected into to the DAΦNE damping ring, from the high intensity LINAC towards a fully equipped experimental hall. The facility can provide runtime tuneable electrons and positrons beams in a defined range of different parameters. The beam energy can be selected from about 50 MeV up to 750 MeV, for electrons, and 540 MeV for positrons. In dedicated mode (DAΦNE off), the beam pulse length can also be adjusted in 0.5 steps from 1.5 to 40 ns. The delivery rate is depending on the DAΦNE injection frequency (25 or 50 Hz) with a duty cycle also changing according to the DAΦNE injection status, up to 49 bunches/s. Two major modes of operations are possible, depending on the user needs: high and low intensity. In the high intensity mode the LINAC beam is directly steered in the BTF hall with a fixed energy (i.e. the LINAC one, fixed to 510 MeV during the collider operations) and with reduced capability in multiplicity selection (typically from 1010 down to 104 particles/bunch). In the low intensity mode a step Copper target, allowing the selection of three different radiation lengths (1.7, 2 or 2.3 X0), is inserted in the first portion of the BTF line for intercepting the beam: this produces a secondary beam with a continuous full-span energy (from LINAC energy down to 50 MeV) and multiplicity (down to single particle/bunch), according to the setting of a 43° selecting dipole and of two sets of horizontal and vertical collimators. The typical momentum band is well below 1% down to 50 MeV. A pulsed dipole magnet at the end of the LINAC allows alternating the beam between the DAΦNE damping ring and the test beam area, thus keeping a pretty high BTF duty cycle, assuring an average of at least 20 bunches/s during the injection in DAΦNE, when BTF operates in the low intensity regime.

BTF PIXEL DETECTOR LAYOUT

A general overview of the BTF detectors and a description of the related software can be found here [1, 2].

Detector beam-testing generally require a fast transverse beam imaging during runtime, with some pre-analysis capability and, as in the BTF case, with a stable, reproducible and well-known response in the full range of energy, multiplicity and transverse dimensions of the particle beam. In addition, taking into account the BTF heavy work-cycle (beam is generally allocated in one-week slots for a minimum of 25 up to 40 weeks/years, including BTF-dedicated shifts), the equipment has to be reliable, robust, and with an easy maintenance, in order to guarantee full readiness and high-availability for the users purposes. For the same reasons, the related low-level software has to comply with these demanding requirements: not only very high reliability, but also easy and efficient integration in the vast variety of user acquisition software codes. Concerning the high level software, we decided to have the possibility of a fully featured runtime data display using LabVIEW®.

ADVACAM Silicon Pixel Detector

In [1], we described the setup based on a MEDIPIX-like silicon pixel detector with ADVACAM FitPIX® Kit electronics, at first made routinely available to the users via the basic version of the provided software, PIXET®, implemented in the BTF timing and virtual machine sub-systems. This solution well accomplished data acquisition and data-logging tasks (customizable thanks to the possibility of python scripting), but we decided to move to a completely custom low level C-code to better match our facility

†luca.foggetta@lnf.infn.it

ISBN 978-3-95450-177-9

and user requirements of a run-time data retrieval and handling of the pixel data (sharing with heterogeneous acquisition and storage systems, data display, basic analysis and beam parameters extraction, etc.), capable of sustaining the full BTF repetition rate of 50 Hz.

FitPIX is a Medipix/Timepix detector interface with readout speed of up to 90 frames per second for single detector layer, in particular our Timepix sensors have a square pixel of 55 µm side arranged in a 256×256 pixels matrix (side length about 15 mm) for a square sensitive area of about 2 cm² and 300 µm of thickness.

Multiple FitPIX devices can be used essentially for two purposes: forming a particle tracker or as multilayer imager. The integration of a multiple sensors can be done essentially with two methods: the first by attaching up to four Timepix detector layers (single gap of 3.6mm, maximum overall longitudinal length about 20mm); the second possibility, allowing an arbitrary gap between each sensor plane, is to connect more FitPIX devices in daisy chain, with an external bus for the synchronization and master/slave trigger signals. In both cases the electronics communicates with a computer via the USB 2.0 interface for configuration, control and data retrieval [3].

BTF FITPIX Detector Usage

In order to have a completely arbitrary access to live data at the maximum frame-rate within the BTF duty cycle, we have implemented software architecture with a typical producer-consumer layout, implementing data caching on MEMCACHED(MC) server, to allow more than one different consumers at the same time (see below). This has been possible exploiting all the available programming solutions: starting with the python scripting capability of the provided software kit, down to low-level programming, which required some interaction with ADVACAM for a full exploitation of the Linux libraries. We have a fully working version of the software for the single FitPIX, the multidetector-single FitPIX, and more FitPIX devices in daisy chain. As a by-product, the same software architecture allowed us to have a similar implementation for a GEMPIX tracker [4], a four sensors detector with a software configuration similar to the four stacked layers in a single FitPIX.

We initially started with profiling a single FitPIX in different proprietary software configurations (bundle PIXETPRO software with Python scripting capabilities) with external (50Hz) trigger, and single frame acquisition vs. multiple frame acquisition with acquisition repetitions. As long as the fired pixel multiplicity is less than 10 (e.g. in a cosmic run, or in the single-particle BTF beam regime, defined as low data regime), the amount of data stays well below one MTU. In the following Tab. 1 we summarize the PIXETPRO software timing profile with a BTF external trigger at 50Hz: timing responses are reported for both Windows7 (PIXET WIN) running on a dual core, 3GHz, 8GB RAM PC with MC calls. In the PIXETPRO software, we explored the possibility to export data via Python scripting in the Windows environment (PIXET WIN Py) using the python-memcached package. In our test conditions, we were able to cope with the continuous frame rate only in multiple frame mode readout, but without actually sending the data on MC (again, via Python scripting).

In those tests, we have also measured a minimum baseline ~26ms delay before getting the first frame in each new acquisition due to DAC setup, thus degrading a little the maximum achievable rate in multi-frame acquisition during repetitions, as clearly visible in the values for single vs multiple frame acquisitions in Tab. 1. Due to the not negligible impact of this delay and in order to accomplish full rate data retrieval we had then to develop custom software with runtime extraction of each frame in multi-frame acquisition.

Table 1: Time Profiling PIXET Software with Python Scripting on MC

CODE (OS)	MC	Trigger	Trigger Type	Frame time [s]	N frames	N Rep	Acq. Rate [Hz]
PIXET(WIN) Py	Y	50 Hz	HW_Start	1.00E-05	1000	10	23.26
PIXET(WIN) Py	Y	50 Hz	HW_Start	1.00E-05	1	1000	24.61
PIXET(WIN) Py	N	50 Hz	HW_Start	1.00E-05	1000	10	48.48
PIXET(WIN) Py	N	50 Hz	HW_Start	1.00E-05	1	1000	24.90

PRODUCER SOFTWARE LAYOUT

We achieved the best performance of our code by using C/C++ compiled code in an Ubuntu 14.04LTS environment, using the multiple frame acquisition, and by interfacing to a modified API library, in strong collaboration with the ADVACAM software engineers. For a single FitPIX, a multiple frame acquisition is managed by a single thread handling the FitPIX USB interrupt. After each triggered frame a (intra-thread) function diverts the frame data on the library internal memory, calling also a call-back function. This process is automatic in multiple frame acquisition, so we limit to 1000 frames for each repetition in order to keep the memory usage below 2GB per FitPIX. The call-back function is programmable by the user code and it is used for managing the frame data in the user space. Our choice was to get directly the frame data at each interrupt: as measured in Table 3, this dump time to the user memory (USB_N, where N is the FitPIX device) used by the call-back function is normally distributed with an average value of 60µs, so we are perfectly in time for each frame interrupt (data are for double FitPIX configuration, slightly better values are obtained for single FitPIX). In order to measure

ISBN 978-3-95450-177-9

the performance the custom software, for each of the FitPIX configurations, can also perform the following tasks:

- Set the MC pushing attributes for each FitPIX
- Detect the configuration and setup the active FitPIX, especially in defining the type of triggering and synchronization for more FitPIX (if any)
- Create one multiple frame acquisition thread for each active FitPIX. Each thread is sensitive to an internal interrupt for each new available frame, releasing a fast call-back function in order to download frame data
- The call-back function extracts each frame in the multi-frame acquisition, and picks up a nanosecond timer value for the frame interrupt
- Acquire frame data and header, prepares and compress the data payload
- Export processed data on Memcached server

The software starts by command line, where some parameters overwrite the configuration file, to maintain the possibility of simple batch procedure.

Table 2: Time Profiling BTF Compiled Code

Trigger	Trigger FitPIX	Frame time [s]	N frames	Rep	MC	Sparse file	Acq. Rate [Hz]
50 Hz	HW_Start	1.00E-05	1000	10	N	N	**49.97**
50 Hz	HW_Start	1.00E-05	1	1000	N	N	**25.03**
50 Hz	HW_Start	1.00E-05	1000	10	Y	N	**31.00**
50 Hz	HW_Start	1.00E-05	1	1000	Y	N	**24.92**
50 Hz	HW_Start	1.00E-05	1000	10	Y	Y	**49.98**
50 Hz	HW_Start	1.00E-05	1	1000	Y	Y	**25.21**
Auto	PXC_TRG_NO	1.00E-05	1000	10	Y	Y	**41.80**
Auto	PXC_TRG_NO	1.00E-05	1	1000	Y	Y	**26.40**
Auto	PXC_TRG_NO	1.00E-05	1000	10	Y	Y	**78.64**
Auto	PXC_TRG_NO	1.00E-05	1	1000	Y	Y	**38.60**

Processed Data Structure

We have optimized the data structure in order to deliver the minimum necessary information for each frame in the different use-cases. We have then implemented three possible data structures:

- array = send all the matrix data (65536 pixel value data, indirect pixel indexing),
- sparse mode 2dim array = a variable size bi-dimensional array [2,N]. Each slice is the couple of pixel data: pixel number and pixel value
- ultra sparse mode array = each array element stores the over threshold pixel number

All of these cases are headed by the following values:

- Case and FitPIX configuration identifier;
- Time tag (resolution 0.1 ms);
- number of fired pixel;
- frame number;

The data types are in dependence of the used FitPIX configuration: for single layer FitPIX (as imaging detector) all of the values are unsigned short int, with the header expressed in 6 array elements. For multiple-layers FitPIX we use unsigned int, especially for low data regime, with five header elements (still six for compatibility, one being spare). The FitPIX configuration file and data are tagged with the serial identifier of the chip, unique id for a multiple FitPIX configuration.

MEMCACHED

MEMCACHED(MC) [5] is an Ethernet based in-memory key-value store for arbitrary data (strings, objects). In the BTF network environment, it is installed in native version on a virtual machine, running Linux (2.6.18-308.11.1.el5xen quad-cored), with 2GB RAM.

The producer software pushes the processed FitPIX data in these key-value couples on the MC server, where the key name has the FitPIX detector unique identifier, protecting so the source. The producer and the consumer C/C++ codes use standard MC calls provided by the POSIX, thread-safe libmemcached [6] library. For the consumer software, written in LabVIEW, we use our custom MC API's. This choice has been driven by the high reliability obtained in a heavy data load environments of the DAΦNE Control System, BTF [1, 2] and the very good performance obtained within the !CHAOS project [7, 8], where this configuration has been tested via multiple, concurrent producer and consumer calls.

Overall Timing Result Discussion

We profiled the call-back from its interrupt-starting to the data pushing on MC (Table 3 and 4), for a double FitPIX configuration both for the two data regime. Normally, we stay within 1ms for low data one, as we need. Table 2 is a summary for the overall acquisition rate of our software, where the MC column tells if we are pushing (or Not) to MEMCACHED and the sparse file column tells if we

ISBN 978-3-95450-177-9

push the full matrix (sparse file equal to N) or we perform shrinking below one MTU per frame. Again is clear the bottleneck of the MC pushing in full matrix regime, however still within or close to the BTF Ethernet band-width. Another important achievement has been the excellent stability of the producer, running without any problem for months, while providing data to different (BTF or users) consumers.

Table 3: Two Detector, Low Data, Timing Profile

Low	USB_0	USB_1	MC_0	MC_1
Mean[s]	5.9E-05	5.9E-05	8.62E-04	8.9E-04
Std[s]	1.7E-05	1.7E-05	1.79E-04	1.5E-04

Table 4: Two Detector, Full Matrix, Timing Profile

Full	USB_0	USB_1	MC_0	MC_1
Mean[s]	5.8E-05	6.0E-05	2.23E-02	2.33E-02
Std[s]	1.6E-05	1.5E-05	2.09E-03	1.37E-03

OVERVIEW ON CONSUMER SOFTWARE

LabVIEW and C/Root Example Code

We have developed a LabVIEW runtime display of FitPIX data and extracted beam parameters display (such as 3-d transverse image, beam centroid and Gaussian fit data), working both as shot by shot (instantaneous) and in cumulative mode.

In addition, we have developed a combined C/Root code, released freely on [9], that fetches MC keys and integrates ROOT library to save ROOT trees, both in single and in multiple FitPIX configurations. This software makes a wide use of the information encapsulated in the data header, also allowing data integrity checking, e.g. by comparing the frame number vs. frame time. This is a simple comparison but very useful when acquiring multiple FitPIX devices: after getting the MC Key, it gives the chance to discard aged, non-synchronous data. This code is provided as an example code for FitPIX integration in users DAQ software.

Table 5: Two Detector, Low Data Regime, Consumer Timing

Frame	Max Delay [s]	framerate [Hz]	Rejected
100000	0.010	49.98	0
100000	0.005	49.95	1
100000	0.002	49.95	6
100000	0.001	49.63	486

Data Synchronization with Users DAQ

Thanks to the usage of the MC functions, the integration in any user code is now just a matter of few plain C code include and calls. Allowing the BTF users such an easy integration in any, heterogeneous DAQ software, already during the first phases of the beam-time, was indeed one of the major objectives of this work.

From the point of view of consumer (C code) data fetching, Table 5, we show that the consumer software rejection function senses a single event jitter delay of 5ms (the minimum time-tag difference between two synchronized FitPIX MC keys) after 100000 calls, mainly due to producer thread time jitter. This guarantees a complete software data alignment within the user DAQ cycle, even for the data coming for two FitPIX devices in the BTF typical tracking setup (shown in Fig. 1). Users can easily implement this integration after having set NTP synchronization on their PC, before performing one of these actions: fetching the MC keys in a separate database for a delayed offline data-matching; implementing our example code in their own DAQ cycle, when providing a trigger signal to the FitPIXs; or, if the DAQ cycle is fast enough, even without any hardware synchronization, just matching the time of the two data streams (DAQ and FitPIX).

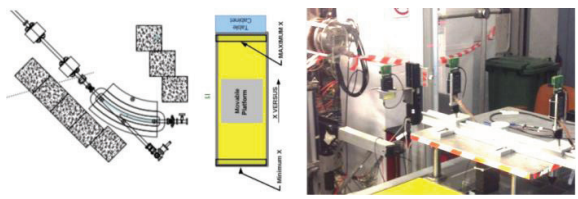

Figure 1: Three FitPIX layout in BTF.

ACKNOWLEDGEMENT

This work is supported by the Horizon 2020 project AIDA-2020, GA no. 654168.

We would like to thank Daniel Tureček and Pavel Soukup, ADVACAM, for the fruitful experience sharing in low-level libraries and hardware development. We are grateful also, among our users, especially to Francesco Renga and Giovanni Tassielli: their requirements are constantly pushing our facility for improvement.

REFERENCES

[1] L.G. Foggetta, B. Buonomo, and P. Valente, "Evolution of Diagnostics and Services of the DAÎ¦NE Beam Test Facility", in *Proc. 6th International Particle Accelerator Conference*, Richmond, VA, USA, 2015, paper MOPHA049, pp. 904-906.

[2] P. Valente et al, "Frascati Beam-Test Facility (BTF) High Resolution Beam Spot Diagnostics", in *International Beam Instrumentation Conference (IBIC16),* Barcelona, Spain, 2016, paper MOPG65, this conference.

[3] V. Kraus et al, "FITPix — fast interface for Timepix pixel detectors", Journal of Instrumentation, Volume 6, January 2011.

[4] F.Murtas et al, "Applications of triple GEM detectors beyond particle and nuclear physics", Journal of Instrumentation, Volume 9, January 2014.

[5] https://memcached.org/

[6] http://libmemcached.org/

[7] http://chaos.infn.it/

[8] A. Stecchi et al., "!CHAOS Status and Evolution", in *Proc. 6th International Particle Accelerator Conference*, Richmond, VA, USA, 2015, paper MOPHA046, pp. 894-896

[9] https://svn.lnf.infn.it/filedetails.php?repname=btf_science&path=%2Ftrunk%2FMC_btf%2FMC_read_tracker%2FreadMC_tracker_Example.cc

ISBN 978-3-95450-177-9

BRIDGING THE GAP; UPDATING LANSCE DIGITIZERS*

D. Baros, J. Sedillo, H. Watkins, Los Alamos National Laboratory, 87545, USA

Abstract

The Los Alamos Neutron Science Center (LANSCE) is currently upgrading equipment that is used to digitize transverse beam profile measurements. Emittance measurements were originally digitized using legacy equipment, known as RICE (Remote Indication and Control Equipment). This required 38 RICE modules distributed along the half-mile long accelerator simultaneously recording 4 channels each to populate the 76 data points needed to create a single emittance profile. The system now uses a National Instruments cRIO controller to digitize the entire profile in a single chassis. Details of the hardware selection and performance of the system for different timing structures are presented.

INTRODUCTION

LANSCE is a National Research Facility which contains a half-mile-long linear accelerator. (LINAC). The LANSCE LINAC creates proton beams with energies up to 800 million electron volts and is capable of accelerating protons to 84% the speed of light. LANSCE achieved full energy on June 9, 1972 and continues to run to this day with much of its late 1960's – early 1970's technology intact.

An example of this late 1960's technology is the data acquisition and control system for the LANSCE LINAC better known as RICE (Remote Indication and Control Equipment).

RICE

RICE was custom built as part of the first large-scale effort to use computers to control an accelerator. Designed in the late 1960's, before CAMAC and VME standards, it was created to provide control and data readout (industrial I/O) for most devices in the LANSCE LINAC. Its architecture was designed to directly map onto the architecture of the LINAC and thus is tightly coupled to the LINAC hardware.

An average RICE module contains 30 analog inputs, 50 digital inputs, 8 analog commands and 30 digital command channels. There are 66 RICE modules distributed along the LANSCE LINAC.

The layout of the LANSCE LINAC is illustrated in Figure 1 (individual RICE modules are represented by circled numbers). The 66 RICE Modules are connected to one uVAX computer in a star topology configuration.

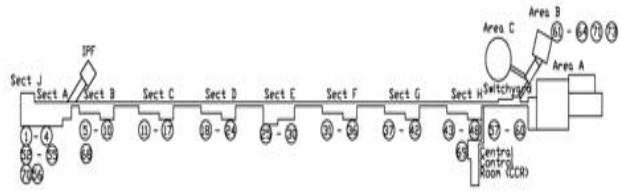

Figure 1: LANCE LINAC.

A RICE module consists of three separate components: the RICE chassis, the RICE Input/Output (I/O) chassis and the Analog Data System (ADS) chassis. The RICE chassis is a serial to parallel and parallel to serial word encoder/decoder. The RICE I/O chassis is used to interface the RICE system with the accelerator inputs/outputs and can address up to 128 binary channels. The ADS chassis is a 128 channel differential A/D converter used for analog readback of accelerator devices [1].

EMMITTANCE (RICE)

Beam emittance at LANSCE was originally obtained by utilizing 4 analog data point channels on 38 separate RICE modules. These RICE modules simultaneously record the data to produce the 76 data points needed for a single emittance profile. The data points (12-bits) were generated by inserting a 20 mil copper slit and a 76 wire collector with 1 mm pitch into the beam line and simultaneously recording data on each of the wires as it passes through the beam.

The EMRP (EMittance Replay Program) software program plots the emittance data with amplitude as a function of position and collector wire index. The data in the plot is correlated by the same time offset from the beginning of the beam pulse. In order to observe beam behaviour in different points of time along the beam pulse, the hardware triggering offsets need to be changed and scans retaken. This process can take upwards of 8 hours to collect longitudinal measurements across the pulse.

Currently LANSCE utilizes six Emittance systems:

- IBEM – H- Injector
- TAEM – H+ Transport
- TBEM – H- Transport
- TDEM – Low Energy Beam Transport
- TREM – Transition Region Transport
- IDEM – Ion Source Test Stand.

Each system represents a specific beam species in a critical location along the accelerator. These systems are primarily used for beam tuning to detect the position of the beam in the accelerator and to characterize beam quality. An example of a TAEM02 Horizontal emittance scan is shown in Figure 2.

*Work supported by the U.S. Department of Energy, Contract No. DE-AC52-06NA25396 LA UR 16 26713

ISBN 978-3-95450-177-9

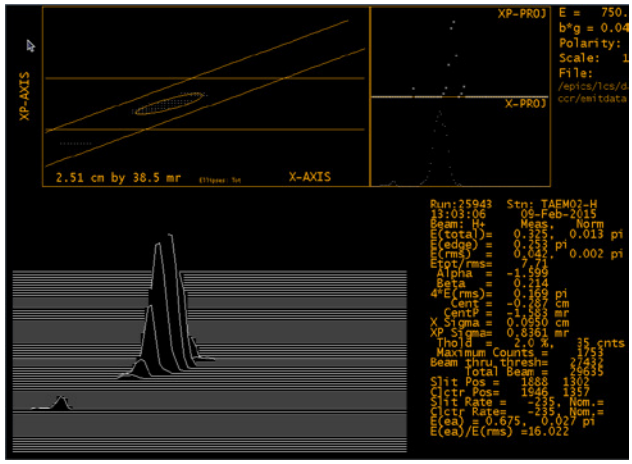

Figure 2: TAEM02 - H Emittance Scan (RICE).

Although this process has been working successfully for decades, the RICE system has become difficult to maintain due to dwindling spares and obsolete replacement parts. The RICE system is currently being phased out and replaced with National Instruments (NI) Compact RIO (cRIO) Programmable Automated Controller (PACS) system (16 bit).

EMMITTANCE (CRIO)

The cRIO system is a reconfigurable control and data acquisition system. It is a high performance system that is very reliable with individual modules Mean Time Before Failure (MTBF) ranging from 37,141 hours. to 2,172,740 hours [2]. It is a commercial modular system that utilizes a variety of hot swappable I/O modules that can be used for a variety of applications.

Requirements

The upgrade task was to create an emittance scan that displayed the same characteristics as the old system to ensure that scans could be used to compare with older documentation. This also presented an opportunity for LANSCE to enhance of the legacy emittance system. The two areas that were improved:

1. The disadvantage of the data acquisition system being distributed over the length of the facility rather than being centralized at the device.
2. The disadvantage that a scan plot is limited to a single time offset from the beginning of the beam pulse.

Chassis Configuration

The NI cRIO system was selected to accomplish these tasks. The cRIO system consisted of the following components:

- NI cRIO-9024 – Real time controller with 800MHz, 512 MB DRAM and 4 GB Storage
- NI cRIO-9118 – 8-slot, Virtex-5 LX110 CompactRIO Reconfigurable Chassis.
- NI cRIO-9401 – 10MHz, 5V TTL logic module.
- NI cRIO-9220 - 16-channel, 100kHz, +/-10V Analog-to-digital conversion modules (x5).

Figure 3: Emittance cRIO Chassis.

Results

The new cRIO system was installed during the 2015 run cycle as a proof of concept for one emittance station. Figure 4 shows a TAEM02 Horizontal emittance scan taken with the new cRIO emittance chassis, confirming the measurement could perform as a direct RICE replacement.

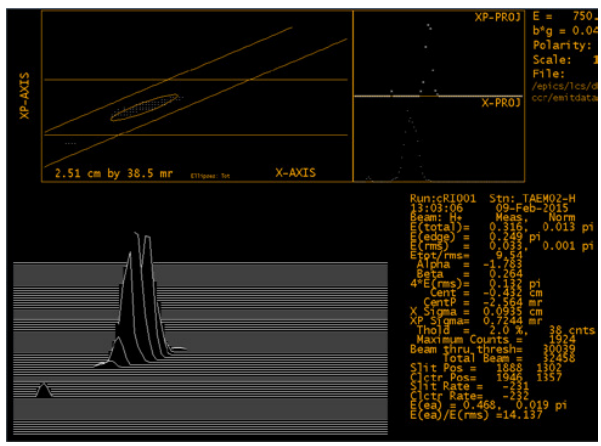

Figure 4: TAEM02 – H Emittance Scan (cRIO).

CONCLUSION

These results demonstrated that the new system was functionally equivalent to the old system, so the cRIO system was installed and has been operating successfully during the 2016 run cycle. The improvements to the emittance system due to the new cRIO systems are:

1. The cRIO system is now located in the two locations were the emittance hardware is located.
2. Data is now recorded at 700 time slices 10usec apart instead of a single time slice which provides more emittance data in a shorter amount of time.
3. The new system allows emittance data to be observed in time. The data can be observed as an animated emittance plot.

Overall the cRIO emittance system is a vast improvement over the RICE system, it is a bridge between the old and the new until a completely new emittance system can be developed.

ISBN 978-3-95450-177-9

REFERENCES

[1] D. Baros, "Upgrading the Data Acquisition and Control System of the LANSCE LINAC", *PAC 2011*, New York, USA, Paper MOP256.

[2] National Instruments CompactRIO , Data Acquisition Platform, http://www.ui.com/compactrio

ISBN 978-3-95450-177-9

THE BEAM PROFILE MONITORING SYSTEM FOR THE CERN IRRAD PROTON FACILITY*

F. Ravotti†, B. Gkotse[1], M. Glaser, E. Matli, G. Pezzullo, CERN, 1211 Geneva 23, Switzerland
K.K. Gan, H. Kagan, S. Smith, J. D. Warner, Ohio State University, Columbus, OH 43210, USA
[1]also at Université Européenne de Bretagne, Brest, France

Abstract

To perform proton irradiation experiments, CERN built during LS1 a new irradiation facility in the East Area at the Proton Synchrotron accelerator. At this facility, named IRRAD, a high-intensity 24 GeV/c proton beam is used. During beam steering and irradiation, the intensity and the transverse profile of the proton beam are monitored online with custom-made Beam Profile Monitor (BPM) devices. In this work, we present the design and the architecture of the IRRAD BPM system, some results on its performance with the proton beam, as well as its planned upgrades.

INTRODUCTION

In High Energy Physics (HEP) experiments such the one at the CERN Large Hadron Collider (LHC), devices are frequently required to withstand a certain radiation level. As a result, detector materials, equipment and electronic systems must be irradiated to assess their level of radiation tolerance. To perform these irradiations, CERN built a new irradiation facility on the T8 beam-line of the East Area at the Proton Synchrotron (PS) accelerator. At this facility, named IRRAD, a Gaussian 24 GeV/c proton beam of variable size ranging from ~5×5 mm^2 to ~20×20 mm^2 is used to irradiate experimental devices [1].

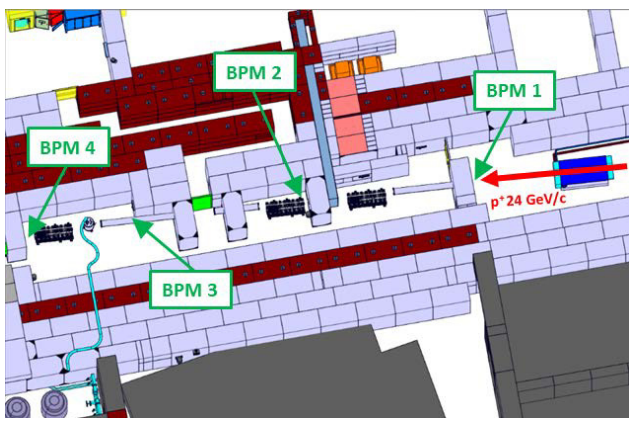

Figure 1: Position of the four BPM devices along the IRRAD facility at CERN.

The proton beam on T8 is delivered in spills with a maximum intensity of 5×10^{11} proton per spill and about 400 ms duration. Several spills per PS accelerator super cycle (CPS) are delivered to IRRAD resulting in a variable beam intensity, depending on the number of users simultaneously served by the whole CERN accelerator complex. As a figure of merit, three spills per CPS of 30 basic periods are delivered to IRRAD, resulting in an average flux $>8\times10^{13}$ p/cm^2/h over one centimetre squared surface. During irradiations, it is thus necessary to monitor in real-time the intensity and the transverse profile of the proton beam.

The IRRAD BPM uses a 39-channels pixel detector to monitor the beam position. The pixel detector, that must withstand high-cumulated radiation levels, is constructed using thin foil copper pads positioned on a flex circuit. When protons pass through the copper pads, they induce a measurable current. To measure this current and thus determine the proton beam intensity, a new data acquisition system was designed as well as a new database and on-line display system. In its final configuration, the IRRAD facility exploits four BPM detectors located along the path of the irradiation beam as shown in Fig. 1.

The new BPM data acquisition system uses low noise integrators. The voltages from each integrator are scaled and limited before connection to a 16-bit ADC. Furthermore, an Arduino Yún collects the data from the ADC and controls its transmission over the Ethernet port to a server for further processing and storage. Finally, the live beam position and intensity data are available to the IRRAD users, as well as to the operators at the CERN Control Centre (CCC), via a dedicated web-based display.

Two BPM data acquisition systems were assembled in 2014 and were used to read out two BPM detectors during the commissioning of the new facility. Four additional BPM data acquisition systems were later installed at the beginning of the irradiation run 2015 and, since then, are operational.

In this work, we detail the design and the architecture of the IRRAD BPM system, as well as its performance and foreseen upgrades.

OPERATION PRINCIPLE AND CHOICE OF THE DETECTOR MATERIAL

The need for an on-line method to determine the position and the profile of the high-intensity proton beam of IRRAD motivated the feasibility study of an instrument based on the proton-induced Secondary Electron Emission (SEE) from thin metal foils [2]. Secondary emission of electrons from the surface of a plate occurs when a charged particle beam crosses it. The liberated charge comes mainly from delta rays escaping from the plate, with a small contribution due to the secondaries produced in the interactions of the beam particles with the plate. The total collected charge is proportional to the intensity of the impinging beam. For

* Work supported by the European Union's Horizon 2020 Research and Innovation programme under Grant Agreement no. 654168 as well as from the European Commission project AIDA.
† e-mail address: Federico.Ravotti@cern.ch

ISBN 978-3-95450-177-9

IRRAD, the foils are required to withstand high-radiation levels (10^{17}-10^{18} p/year are cumulated on a few square cm area) and be made of a low cost and relatively short radioactivity lifetime material. Moreover they have to be, on the one hand, thin to avoid the proton scattering but on the other hand, thick enough to allow easy handling. Finally, the material has to show a SEE yield strong enough to avoid the usage of an external bias and thus maintain the operation principle as simple as possible. Aluminium (Al) and Copper (Cu) foils have been chosen as a good compromise to satisfy these requirements. More information about the preliminary measurements leading to this choice are given in Ref. [3].

HARDWARE & SYSTEM ARCHITECURE

Detectors

The main BPM detector element for the measurement of the proton beam profile consists in 39 separate pixels (Cu pads of 4×4 mm^2 spaced by 0.5 mm one to the other) covering a total area of 36 mm × 27 mm on the beam transversal plane. These pixels are built on a six layers Kapton/Cu flex circuit as shown in Fig. 2. The Cu pads in the various internal layers are connected through vias, while a top and a bottom Cu layer act as shields. The Cu thickness is of 1.75 µm/layer, while the Kapton one is of 120 µm/layer for a total overall thickness of ~700 µm. Fig. 3 shows one of the four BPM detector installed in its final position inside the IRRAD facility.

In addition to the main BPMs, Single-pad BPM detectors were also built for the alignment of the remote controlled tables used in IRRAD [4]. These consist in one single Cu pixel with a variable active area of 5×5 mm^2, 7×7 mm^2 or 10×10 mm^2. One of these BPM single-pad detectors is shown on the top of Fig. 2. The single-pad devices provide a binary signal indicating whether the samples loaded on a given irradiation system are being irradiated or outside the proton beam spot.

Figure 2: BPM pixel detector for beam profile with 39-pads (bottom) and single-pad (top).

The BPM pixel detectors are directly connected to the data acquisition (DAQ) system by a shielded, high-speed 40-channel, 50Ω/40AVG micro-coaxial cable from Samtec [5]. The cables linking the four IRRAD BPM detectors to the DAQ systems, located outside the irradiation area, are 20 m to 35 m long.

Data Acquisition System (DAQ)

The BPM DAQ unit shown in Fig. 4 has been designed to measure detector signals in the 10pA-to-500pA range with an adjustable dynamic range. This uses commercial off the shelf, low-noise switched integrators (Burr Brown ACF2101) to amplify the detector signals. A TI ADS1115 analog-to-digital converter (16 bit, 2-3 bits noise) subsequently measures the charge integrated over the 400ms proton spills. A commercially available Arduino Yún microcontroller board, based on the ATmega32u4, finally handles the whole DAQ process, including the timing synchronization and the background noise acquisition.

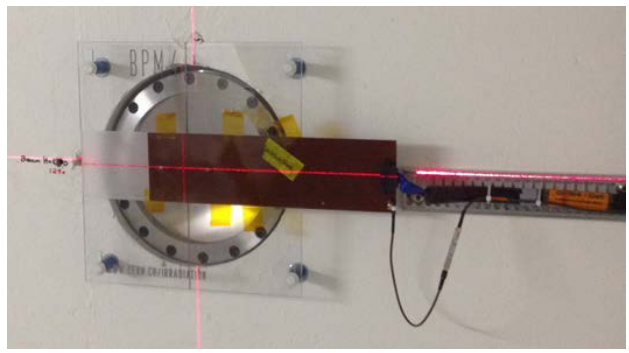

Figure 3: BPM pixel detector installed in the IRRAD.

Fifty channels can be read out in parallel by the DAQ (analog inputs): 40 channels from the main BPM pixel detector (through the Samtec cable) and other 10 auxiliary channels (LEMO connectors on the front panel visible in Fig. 3) to read out, for instance, the single-pad detectors. The DAQ unit has also three outputs. An *Analog Output* port provides the inverted output of the integrators and it is used to show the output of a selected integrator channel during operation. The *Reset Output* and the *Gate Output* are, instead, used to check in real time (with an oscilloscope) the synchronization of the timing parameters of the BPM with the signals provided by the PS accelerator [6].

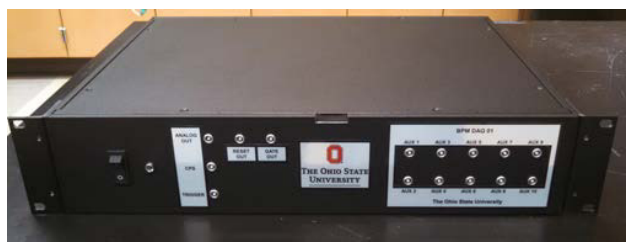

Figure 4: IRRAD BPM Data Acquisition System.

Moreover, the DAQ unit is equipped with the following digital (input) ports:

- *Trigger* (configurable NIM/TTL): this signal, directly connected to the Arduino, it is used to inform that a proton spill will occur upon its reception (beam trigger);
- *CPS* (configurable NIM/TTL): this signal can be used to inform the Arduino that, after this input signal is

ISBN 978-3-95450-177-9

received, a new super cycle of the PS accelerator (CPS) begins;

as well as with two communication ports:

- *USB 2.0* (located on the rear panel): this port is used to provide external storage media to the Arduino as well as to update the DAQ software;
- *Ethernet* (located on the rear panel): this port is used by the Arduino to access the CERN network over a wired connection.

The rest of the system architecture includes a local HP Server running a dedicated software used to collect, through Ethernet, the data from the DAQ units and to send them to a centralized ORACLE database where the spill-by-spill beam positions are archived for later analysis.

BPM Data Display

The beam profile information from the IRRAD facility is displayed in real-time on a dedicated series of CERN web pages*. These are used by the IRRAD facility operation team and users to check beam quality and the alignment of the irradiation systems, as well as by the PS accelerator operation team at CCC to setup and steer the irradiation beam over the T8 beam-line.

Figure 5: "main" BPM web display.

Figure 5 shows one of the user interface pages of the web-application developed to retrieve and display the beam profile information from the ORACLE database. This application performs a first level data correction (e.g. background compensation) and the analysis of the displayed data. The "main" BPM page shows, for every BPM device, the intensity over each of the 39-pads (bottom left corner) and computes the basic information about the horizontal (x) and vertical (y) Gaussian beam profiles such as the centroid (x_0,y_0), the sigma ($\sigma_{x,y}$), and the Full Width at Half Maximum (FWHM). Moreover, this page also provides information about the longitudinal beam profile, by displaying the integrated beam-induced charge over time (bottom right corner).

The "BPM all" page shown in Fig. 6 provides instead in a combined view the footprint of the proton beam recorder simultaneously in the four locations along the IRRAD beamline. This allows, on one hand to fully control the beam trajectory over the ~30 m long IRRAD facility, as well as to optimize the irradiation of materials and samples by choosing, case by case, the appropriate beam spot for a given irradiation experiment. Finally, by integrating the current measured with the 39-pads, or by a subset of them, it is possible to monitor during operation the total proton intensity delivered to IRRAD or the proton flux impinging on small-size samples during irradiation (bottom of Fig 6).

Figure 6: "BPM all" web display.

SYSTEM PERFORMANCE

In order to use the BPM data as an operational tool to monitor the beam conditions, it is essential that the response of the BPM detector follows linearly the variation of the beam intensity. Although the material being irradiated and crossed by the beam may affect the amplitude of the BPM signal, the BPM1 device, installed upstream IRRAD (see Fig. 1), can be used and calibrated for this purpose.

The plot in Fig. 7 shows the variation of the total current integrated by BPM1 as a function of the proton spill intensity. The reference beam intensity of each proton spill was measured using a Secondary Emission Chamber (SEC) provided by the CERN Beam Instrumentation Group [7]. The agreement of the two data series is better than +/- 7%.

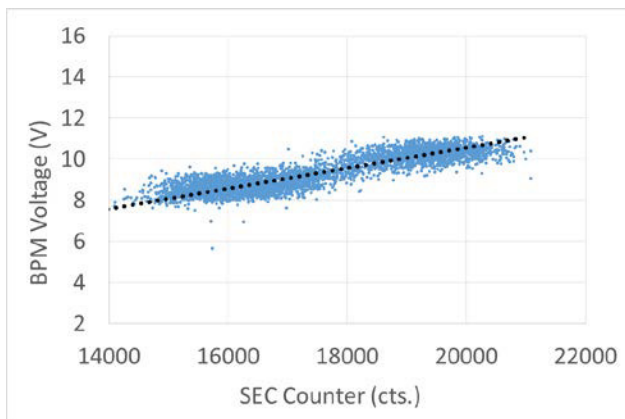

Figure 7: response of BPM1 (total current, V) compared with a SEC device (counts).

* www.cern.ch/opwt/irrad

ISBN 978-3-95450-177-9

OUTLOOK

The successful exploitation of the four main 39-pad pixelated BPM devices, installed along the IRRAD beam-line, motivated the upgrade (within the EU-funded project AIDA-2020 [8]) of the initial BPM system. The upgrade consists of new, pixelated BPM detectors with different spatial resolution and/or various total area coverage. In particular, some of these new BPM devices, called "mini-BPMs" with 9-pads and covering a smaller area of 22×22 mm^2, will replace some of the single-pad BPMs already in use. A couple of mini BPMs installed at the front and at the back of the IRRAD remote-controlled tables will improve the precision and speed-up their alignment procedure.

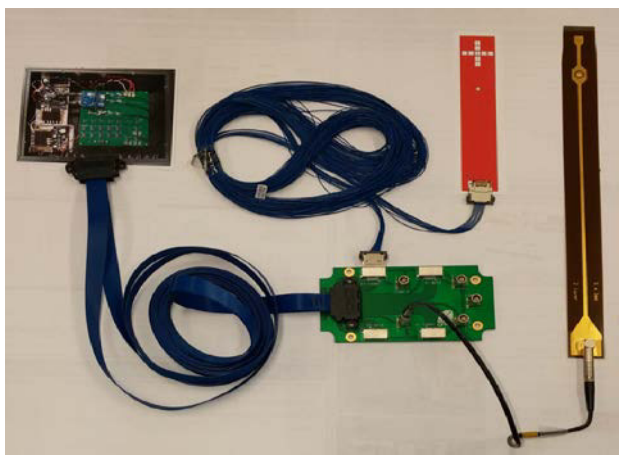

Figure 8: the mini-BPM system. Four mini-BPM devices can be connected to one DAQ unit via a channels-concentrator PCB (bottom of the picture).

For this upgrade, new DAQ units were produced while the first prototypes of mini-BPM devices were manufactured. Since the new mini-BPM uses only 9-channels per device, a channels-concentrator PCB has been developed in order to merge the signals from four mini-BPM detectors into a unique 40-channel cable such as the existent architecture, based on 50-channel readout unit, can be efficiently exploited. The four spare channels can be still used to connect single-pad BPM devices. The new connectivity for the mini-BPM devices is shown in Fig 8.

Figure 9 shows the profiles obtained with the first prototypes of mini-BPMs and visualized with a custom-made application running on a PC in the IRRAD counting room.

Another improvement ongoing for the BPM system concerns the reconstruction and analysis of the beam profile envelope. The current online algorithm computing the centroid and the sigma of the Gaussian beam (see previous section and Fig. 5), treats the experimental points as discrete variables assuming an ideal beam trajectory. Although these values are good enough for beam operation, they are often not precise enough for physics data analysis. For this reason, a new algorithm based on *Python* libraries is being developed for the on-line reconstruction of the 3D beam envelope.

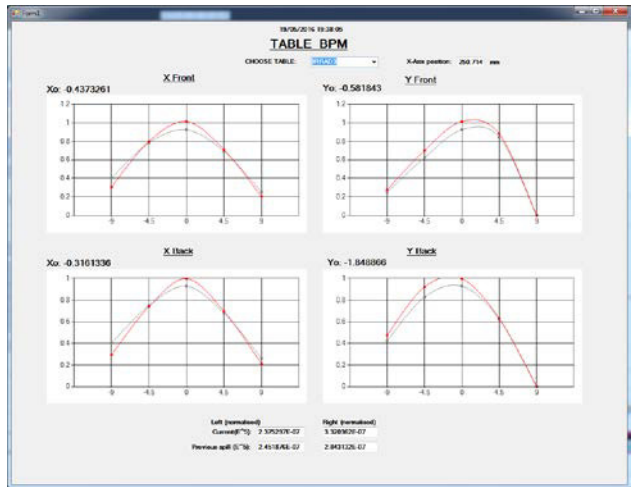

Figure 9: profiles obtained with mini-BPM mounted on an irradiation table.

First validation tests for this new algorithm, performed on the 2016 beam data, showed a precision down to ~2% in the determination of $\sigma_{x,y}$ and down to ~4% for the centroid, w.r.t. the best fit of the BPM data obtained from the least square method.

ACKNOWLEDGEMENT

The authors would like to thank Tony Smith (Liverpool University), Nicola Pacifico and Christophe Sigaud (CERN EP) for their assistance in the development of the BPM system, as well as for their contribution in the construction of the initial prototypes.

REFERENCES

[1] F. Ravotti, *et al.*, "IRRAD: The New 24 GeV/c Proton Irradiation Facility at CERN" in *Proc. of Twelfth International Topical Meeting on Nuclear Applications of Accelerators (AccApp'15)*, Washington, DC, Nov. 10-13, 2015.

[2] K. Bernier, *et al.*, "Calibration of secondary emission monitors of absolute proton beam intensity in the CERN SPS north area", CERN, Geneva, Switzerland, Yellow Report 97-07, 1997.

[3] F. Ravotti, M. Glaser, M. Moll, "Dosimetry Assessments in the Irradiation Facilities at the CERN-PS Accelerator", *IEEE Trans. Nucl. Sci.,* 53(4), pp. 2016-2022, 2006.

[4] M. Glaser, M. Moll and F. Ravotti, "Movable Irradiation Tables Operational", CERN, Geneva, Switzerland, AIDA Milestone Report MS31, 2013.

[5] Samtec web-page, `https://www.samtec.com/`

[6] J. Warner, *et al.,* "New Beam Profile Monitoring System for the Proton Irradiation Facility at the CERN PS East Area", in *Proc. of DPF2015*, Ann Arbor, MI, Aug. 4-8, 2015, unpublished.

[7] F. Ravotti, M. Glaser, M. Moll, "Upgrade scenarios for irradiation lines: Upgrade of the Proton Irradiation Facility in the CERN PS East Area", CERN, Geneva, Switzerland, AIDA Deliverable Report D8.4, 2014.

[8] AIDA-2020 project, `http://www.cern.ch/aida2020`

ISBN 978-3-95450-177-9

STATUS OF THE TWO-DIMENSIONAL SYNCHROTRON RADIATION INTERFEROMETER AT PETRA III*

A.I. Novokshonov, A.P. Potylitsyn,Tomsk Polytechnic University (TPU), Tomsk, Russia
G. Kube, M. Pelzer, G. Priebe, Deutsches Elektronen-Synchrotron (DESY), Hamburg, Germany

Abstract

Synchrotron radiation based emittance diagnostics at modern 3^{rd} generation light sources is mainly based on beam profile imaging in the X-ray region in order to overcome the resolution limit imposed by diffraction. A possibility to circumvent this limitation is to probe the spatial coherence with a double-slit interferometer in the optical spectral region. The light source PETRA III at DESY is using this type of interferometer since several years in order to resolve vertical emittances of about 10 pm.rad. The device is set up behind a 30 m long optical beamline, connecting the accelerator tunnel and the optical hutch. In order to increase the measurement stability, a much shorter optical beamline with reduced number of optical elements was recently commissioned. At the end of the beamline, a two-dimensional interferometer was installed which allows to deduce transverse emittances in both planes simultaneously. This contribution summarizes the status of beamline and interferometer commissioning.

PRINCIPLE

The principle of the interferometric method is based on the investigation of the spatial coherence of SR. In order to quantify the coherence properties usually the first order degree of mutual spatial coherence $\gamma(D)$ is used (c.f. for example Ref. [1]) with D the distance between two wavefront dividing slits, see Fig. 1. The interferometer itself is a wave-front–division-type two-beam interferometer which uses polarized quasi monochromatic radiation. The intensity of the interference pattern (interferogram) measured in the detector plane directly depends on γ [2]:

$$I(y_0) = I_0 \left[\mathrm{sinc}(\frac{2\pi a}{\lambda R} y_0)\right]^2 \left[1 + |\gamma| \cos(\frac{2\pi D}{\lambda_0 R} + \varphi)\right] \quad (1)$$

with a the half of the single slit height and D, R as indicated in Fig. 1, λ_0 the wavelength of observation and I_0 the sum of the incoherent intensities from both slits. If the condition of Fraunhofer diffraction (i.e. far–field limit) holds, the van Cittert–Zernicke theorem [3] relates the degree of coherence γ with the normalized source distribution $f(y)$:

$$\gamma(\nu) = \int \mathrm{d}y f(y) \exp(-i2\pi\nu y) \,, \quad (2)$$

where $\nu = \frac{D}{\lambda_0 R_0}$ denotes the spatial frequency. The beam size information is encoded in the interferogram such that as smaller the beam size, as deeper the modulation depth of the interference pattern. In the case of an ideal point source, the intensity in the minima of the pattern would amount to $I_{min} = 0$, resulting in a visibility of $V = \frac{I_{max} - I_{min}}{I_{max} + I_{min}} = |\gamma| = 1$. The visibility of an extended source will always have a visibility $V < 1$.

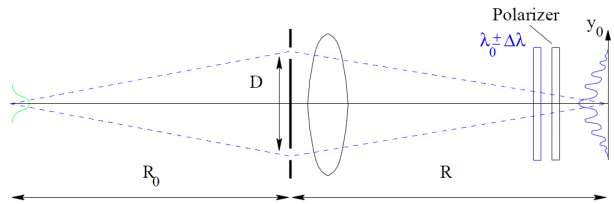

Figure 1: Principle setup for interferometric beam size measurements.

If the beam shape $f(y)$ is known to be normal distributed with width σ_y, the integral in Eq. (2) can be solved analytically which results in an equation by which the beam size can directly be determined:

$$\sigma_y = \frac{\lambda_0 R_0}{\pi D} \sqrt{\frac{1}{2} \ln \frac{1}{\gamma(D)}} \,, \quad (3)$$

while $\gamma(D)$ has to be fitted from the recorded interferogram. A comprehensive overview and more details about the development of SR interferometers can be found in Ref. [4].

EXISTING SETUP

Since 2011 an interferometric measurement is in use at the 3^{rd} generation light source PETRA III at DESY, Hamburg (Germany) in order to resolve the small vertical emittance of $\varepsilon_y = 10$ pm rad. The setup is installed behind an about 30 m long optical beamline which is described in Ref. [5]. However, this setup suffers from many problems:

(i) Due to the long distance between source point and slits the setup is very sensitive on temperature drifts, a correlation between measured emittance values and ambient temperature is visible. (ii) The beamline is equipped with several optical elements (3 lenses and 6 mirrors), each of them introducing additional uncertainties. (iii) The interferometric setup occupies the place of the streak camera, i.e. simultaneous measurements of vertical and longitudinal beam sizes are not possible. (iv) The present interferometric setup allows to measure only vertical beam sizes, a simultaneous horizontal interferometric measurement would be preferable.

In order to overcome these problems, a new optical beamline with extended interferometric setup was installed in

* This work was partly supported by the Russian Federation Ministry of Science and Education within the program "Nauka" Grant # 3.709.2014/K.

ISBN 978-3-95450-177-9

PETRA III and recently put into operation. This new setup and first commissioning results will be presented in the subsequent sections.

NEW INTERFEROMETRIC BEAMLINE

Fig. 2 shows a sketch of the new optical diagnostics beamline together with the interferometer setup. The light extraction point SOL 19 for bending magnet synchrotron radiation (SR) is located about 70 m away from the injection point in the PETRA storage ring. The distance from the SR source point inside the dipole magnet to the extraction mirror is the same than in the old beamline, also the dipole magnet and the extraction chamber are of the same type than in the previous setup and therefore described in Ref. [5].

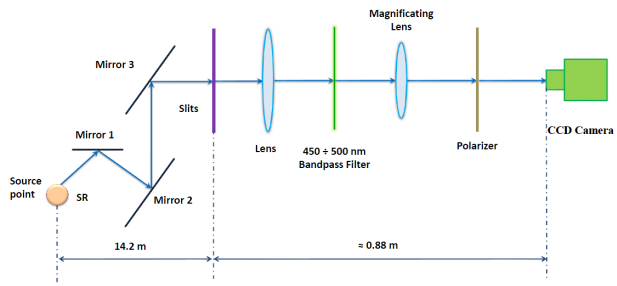

Figure 2: Sketch of the new optical diagnostics beamline together with the interferometer. Mirror 1 is an integrated part of the extraction chamber and deflects the light horizontally to the inner part of the PETRA ring. Mirror 2 and 3 are located in air: mirror 2 deflects the light in vertical direction out of the tunnel to the measuring hut which is sitting on top of the tunnel roof, mirror 3 deflects the light back to the horizontal direction in the direction of the interferometer setup which is mounted onto an optical table.

The light is guided out of the tunnel by mirror 2 and then adjusted to the interferometer by mirror 3. The interferometer consists of the slit system, a lens (Borg 50 ED, f' = 500 mm) with nominal focal length of 510 mm, a bandpass filter (FWHM = 10 nm), a magnification lens to widen the interference pattern, a Glan–Thomson polarizer to select the σ–polarization (Karl Lambrecht Corporation, MGT25S20), and a CCD camera (JAI BM-141GE) to record the interferograms. CCD readout was performed based on the TINE AVINE video system [6, 7].

During the beamline and interferometer commissioning, several bandpass filters in the range from 450 nm to 500 nm were under investigation. Finally it was decided to operate the monitor with a central wavelength of 450 nm because of the better resolution and still sufficient intensity.

As can be seen from Fig. 2, in the new setup the number of mirrors is reduced by a factor of two and no more lenses are required. Moreover, the distance between source point and slits amounts to 14.2 m and therefore is more than two times shorter than in the previous setup. With the reduced number of optical elements and the shorter overall beamline length, the situation should be considerably improved having in mind the list of problems (points (i) and (ii)) from the previous section. In addition, with the new beamline the previous one will be ready to bring back the streak camera into operation, such allowing simultaneous measurements of transverse and longitudinal beam sizes and eliminating point (iii) from the list of problems.

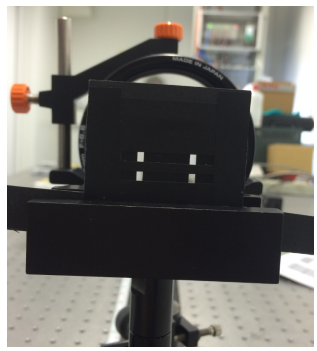

Figure 3: Slit system of the two–dimensional interferometer.

In order to extend the setup for emittance diagnostics in both transverse planes (problem (iv)), it is possible to set up two one–dimensional interferometers by splitting the wave front as it was done in Ref. [8]. However, this would increase the complexity of the setup and introduce an additional optical element in the light path which might distort the wavefront. Therefore it was decided to set up a two–dimensional interferometer as it was done before at SPring–8 in Japan [9].

A photo of the slit system in use is shown in Fig. 3. The horizontal distance between the slits amounts to 7 mm, the vertical one to 16 mm. The slit widths is 1 mm. Mirror 2 rotates the interferogram by 90^o, therefore the slits are rotated by the same angle as can be seen from the photo.

In order to operate and control the interferometer from the accelerator control room a Matlab© client application shown in Fig.4 was developed which allows the communication with the TINE Video server and performs online data analysis. The analysis is performed based on two one–dimensional fits using two data sets for the horizontal and vertical plane which are extracted from a small region around the central part of the recorded interferogram.

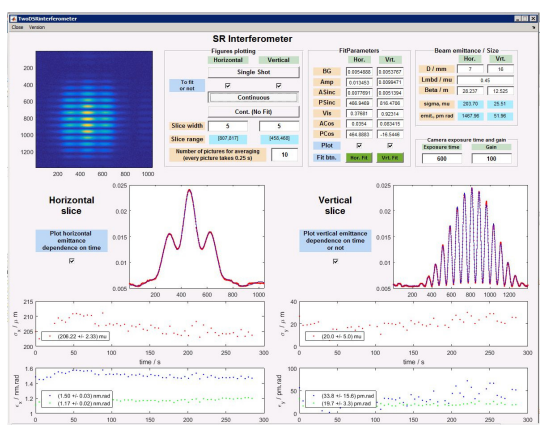

Figure 4: Matlab interface for control and online–analysis.

ISBN 978-3-95450-177-9

OPERATIONAL EXPERIENCE

After the beamline commissioning first beam sizes were obtained. Measured sizes are listed in Tab.1 together with the design values. The error in the horizontal beam size is in the order of 1% and in the vertical one in the order of 10%.

Table 1: Comparison of Beam Sizes

parameter	vertical	horizontal
beam size (measured)	20 μm	180 μm
beam size (design)	12 μm	184 μm

As can be seen the horizontal measurement is in good agreement with the design value, but for the vertical one the difference is about a factor of two. It is assumed that this difference is caused by vibrations which directly can be observed. For illustration Fig.5 shows three consecutive shots, recorded with a small CCD exposure time t_{exp}. As can be seen the position of the interferograms is changing from shot to shot such that an interferogram taken with longer t_{exp} for intensity accumulation would be smeared out, resulting in an increase in the extracted beam sizes. In the horizontal plane this influence is considerably less pronounced because of the larger beam size, but in the vertical plane it clearly affects the measurement.

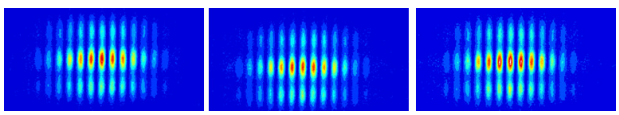

Figure 5: Three consecutive interferograms, recorded with a small CCD exposure time.

In order to support this assumption, vertical emittance measurements were carried out as function of the CCD exposure time which are shown in Fig. 6. It is obvious from this figure that the extracted emittances are considerably smaller for smaller t_{exp}, thus corroborating the vibrational influence. Considering the strong increase in the vertical beam size in the region of $t_{exp} = 300 - 400\ \mu s$, the excitation frequency seems to be in the order of a few kHz.

In order to overcome this limitation a straightforward solution would be to operate the CCD only with small exposure

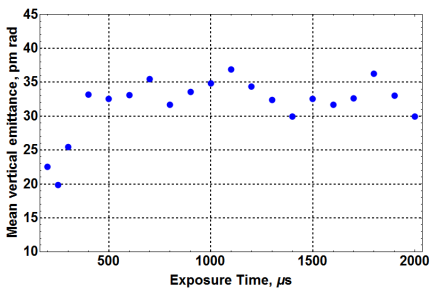

Figure 6: Vertical emittance measurement as function of the CCD exposure time.

times. However, in this case the intensity of the recorded images is rather low and it turned out that the fit for the vertical beam size determination is rather unstable. This effect is illustrated in Fig. 7 where emittance values even higher than 100 pm rad were sometimes generated.

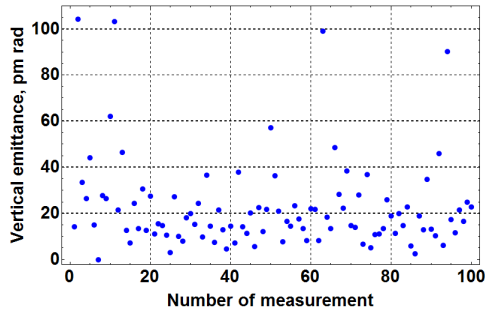

Figure 7: Series of 100 consecutive vertical emittance measurements for $t_{exp} = 200\mu s$.

To avoid the vibrational influence and get comparable results it was decided to use an algorithm which was successfully implemented before at the interferometric beamline of the ALBA light source in Spain [10]. According to this method several interferograms are recorded with small CCD exposure time and finally summed up to have sufficient intensity for a reliable fit operation. However, before summing up each interferogram is shifted in position relative to each other such that the position of the central maximum in all images will be the same.

The result of this technique is shown in Fig. 8 where corrected and uncorrected interferograms are plotted for both planes. From this comparison it is obvious that the correction will improve the beam size determination. In addition, Fig.9 shows two interferograms taken under different conditions: the left one is a superposition of 5 corrected interferograms with 150 μs exposure time, the right one is a single interferogram with 750 μs exposure time. In fact both interferograms have the same total exposure time, but the interference pattern in the corrected on is much sharper compared to the uncorrected.

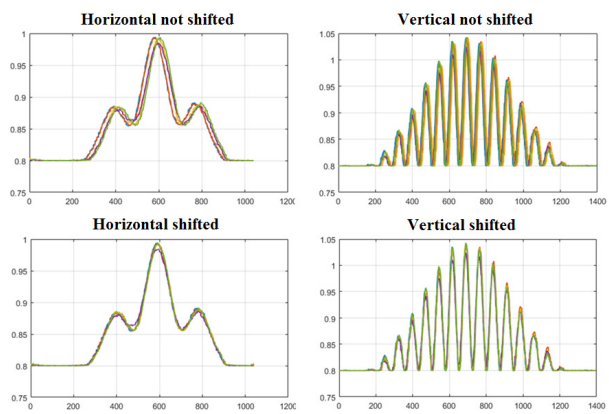

Figure 8: Comparison of position corrected and uncorrected interference patterns for both planes.

ISBN 978-3-95450-177-9

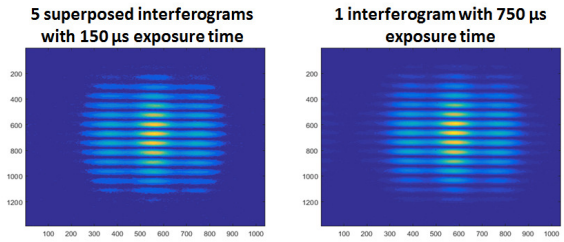

Figure 9: Comparison of corrected and uncorrected interferograms for the same total CCD exposure time.

In Fig.10 100 vertical consecutive emittance measurements are plotted, using the correction algorithm with 20 superposed interferograms at a CCD exposure time of 200 μs. Compared to the results shown in Fig.7 which were taken for the same t_{exp} but based on a single interferogram, it is obvious that the correction stabilizes the fitting algorithm due to the higher statistical significance resulting from the higher intensity. With the help of this correction presently

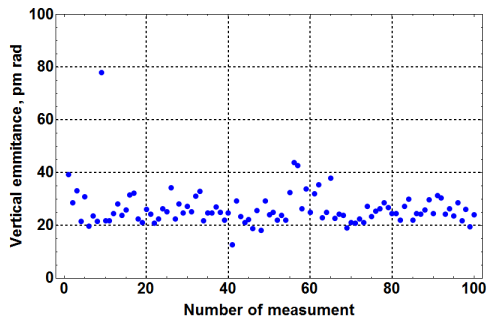

Figure 10: 100 consecutive vertical emittance measurements using the correction algorithm with 20 superposed interferograms at a CCD exposure time of 200 μs.

vertical beam sizes down to 15.5μm can be resolved which are close to the design value of 12μm according to Tab.1.

However, drawback of the correction is the increase in time which is required in order to generate a beam size information: for a single interferogram it takes about 0.25 s to extract beam parameters, if the correction is based on several interferograms this time has to be multiplied by their number in first order.

SUMMARY AND OUTLOOK

In this report the commissioning of a new optical beamline for a two–dimensional interferometric setup at the light source PETRA III is presented together with first operational experiences. It is shown that the new setup avoids the inherent disadvantages of the old one and provides online emittance diagnostics in both transverse planes.

The new setup is limited in the vertical plane by image stability issues caused by vibrations. A correction algorithm is presented by which it is possible to reduce this influence and to extract beam sizes close to the design values.

The origin of these vibrations is still an open question. The beam stability in the vicinity of the radiation source point was investigated based on turn–by–turn measurements with the BPM system, resulting in a (rms) beam stability of about 1 μm in the vertical plane and 1.7 μm in the horizontal one, thus being to small to explain the observations. Presently different causes are under investigation.

Apart from this problem the new setup is already in use for online emittance diagnostics in the accelerator control room, both for daily emittance control and for dedicated machine studies. As an example, Fig.11 shows a screen shot of the monitor panel where a sudden emittance increase caused by ion instabilities is observed.

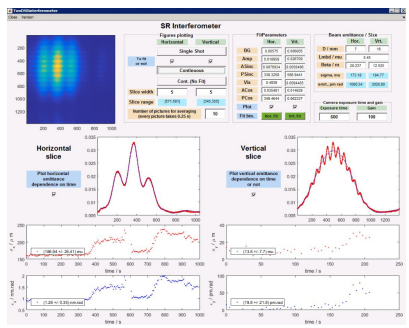

Figure 11: Monitor screen shot showing emittance increase due to ion instabilities.

ACKNOWLEDGEMENTS

The authors thank A. Affeldt, A. Delfs, S. Warratz and R. Zahn (DESY) for substantial help and support during the design and installation of the new beamline.

REFERENCES

[1] M. Born and E. Wolf, Principles of Optics, Pergamon Press Ltd., New York, 1980.

[2] T. Mitsuhashi, Proc. of the Joint US–CERN–Japan–Russia School on Particle Accelerators, Montreux, 11-20 May 1998, (World Scientific), pp. 399-427.

[3] P.H. Van Cittert, Physica **1**, 201 (1934).
F. Zernike, Physica **5**, 785 (1938).

[4] T. Mitsuhashi, Proc. BIW'04, Knoxville (Tennessee), USA, May 2014, AIP Conf. Proc. **319**, 3 (2004).

[5] H.C. Schröder *et al.*, Proc. DIPAC'11, Hamburg, Germany, May 2011, MOPD30, p.113 (2011).

[6] S. Weisse *et al.*, Proc. ICALEPCS'09, Kobe, Japan, October 2009, MOD003, p.34 (2009).

[7] S. Weisse *et al.*, Proc. ICALEPCS'11, Grenoble, France, October 2011, MOPMS033, p.405 (2011).

[8] H.Hanyo *et al.*, Proc. of PAC'99, New York, USA, March 1999, p.2143 (1999).

[9] M. Masaki and S. Takano, Proc. DIPAC'01, Grenoble, France, May 2001, PS17, p.142 (2001).
M. Masaki and S. Takano, J. Synchrotron Rad. **10** (2003), 295.

[10] L. Torino and U. Iriso, Proc. IBIC'15, Melbourne, Australia, September 2015, TUPB049, p.428 (2015).

ISBN 978-3-95450-177-9

SUB-fs RESOLUTION WITH THE ENHANCED OPERATION OF THE X-BAND TRANSVERSE DEFLECTING CAVITY USING AN RF PULSE COMPRESSION SLED CAVITY*

P. Krejcik#, G.B. Bowden, S. Condamoor, Y. Ding, V.A. Dolgashev, J.P. Eichner, M.A. Franzi, A.A. Haase, J.R. Lewandowski, T. Maxwell, S.G. Tantawi, J.W. Wang, L. Xiao, C. Xu,
SLAC, Menlo Park, CA 94025, USA

Abstract

The successful operation of the x-band transverse deflecting cavity (XTCAV) installed downstream of the LCLS undulator has been further enhanced by the recent addition of an RF pulse compression "SLED" cavity that doubles the temporal resolving power of this powerful diagnostic system for measurement of the longitudinal profile of both the electron bunch and the x-ray FEL pulse. RF pulse compression has allowed us to use the existing SLAC X-band klystron with nominal output power of 50 MW and extend the RF pulse length by a factor 4 to give us 4 times the peak power after compression. A new, innovative SLED cavity was designed and built at SLAC to operate efficiently at X-band. The elegant design uses a small spherical cavity combined with a polarizing mode coupler hybrid. We report on the installation, commissioning and beam measurements demonstrating the sub-femtosecond resolution of the XTCAV system.

INTRODUCTION

The X-band RF deflecting structure, commonly referred to as the XTCAV, installed at the SLAC National Accelerator Laboratory Linac Coherent Light Source, LCLS, has been in operation for two years now, serving as a diagnostic for both the electron beam and the x-ray photons[1]. The features setting this device apart from other RF deflecting cavities are the x-band operation together with the placement of the device at the end of the FEL undulator in the electron beam dump line. Operation at X-band has resulted in about a factor 8 greater kick strength than the S-band devices installed in the linac. This allows us to measure and resolve the femtosecond long bunches that we are able to produce in the LCLS. By installing the device downstream of the undulator and viewing the streaked beam on a screen in a region with vertical dispersion we are able to both observe the longitudinal phase space of the electron bunches and witness the time-dependant energy loss within the bunch due to the FEL process. The location of the deflecting structure and observation screen relative to the undulator is shown schematically in Fig. 1. Since these components are downstream of the undulator their operation is non-invasive to normal operation for photon users. There is one caveat to this statement which we will mention when the RF jitter performance is discussed.

* This work was supported by Department of Energy Contract No. DE-AC0276SF00515
#pkr@slac.stanford.edu

The XTCAV system has allowed a multitude of diagnostics to be performed that characterize the temporal profile of both the electron and photon beams [2]. The temporal profile of the photon beam is reconstructed from the energy loss temporal profile of the electrons, and is recorded on a shot by shot basis by the photon users to correlate with their experiment data. The XTCAV has also enabled exotic setups to be implemented at the LCLS such as twin bunch operation, two-color experiments and slotted spoiler foil operation [3].The XTCAV system is invaluable in this set up since one can observe which slices of the bunch are lasing and at what relative energy.

To make this versatile system even better we have sought to boost the temporal resolution of the measurements by doubling the transverse kick strength of the XTCAV which in turn requires increasing the input RF power by a factor 4.

SLED PRINCIPLE

SLED is an acronym used at SLAC that originally meant *SLAC Linac Energy Doubler*, where RF pulse compression was used to double the accelerating gradient of the SLAC linac by adding RF storage cavities to the output of the klystron. The S-band output power of the klystron could be compressed a factor 4 with two high-Q cavities connected by a hybrid coupler. SLED has since become a generic name for any RF pulse compression cavity scheme. Although a two cylindrical cavity SLED scheme with hybrid coupler could be designed for X-band operation it was considered too complex and costly to implement at this shorter wavelength.

Instead, a new and elegant SLED cavity design was recently conceived, built and tested at SLAC [4] based on a single, compact spherical cavity with a polarizing, mode converting coupler.

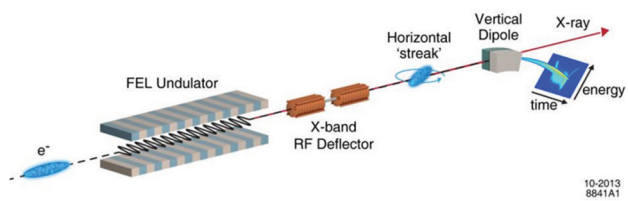

Figure 1: Layout of the X-band RF deflecting structure at the exit of the LCLS undulator where the beam is streaked horizontally and the electrons are bent vertically onto a spectrometer screen.

ISBN 978-3-95450-177-9

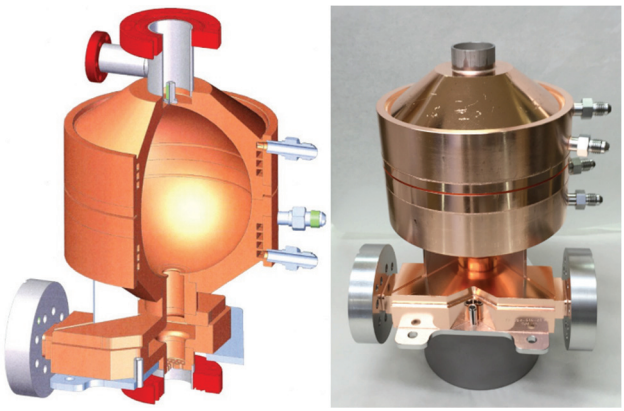

Figure 2: Cut-away view of the X-band SLED cavity together with a photo of the brazed cavity and coupler assembly.

The spherical SLED cavity, shown in Fig. 2, is fabricated from brazed copper and has an internal diameter of less than 12 cm. The quality factor for a perfect sphere depends only on the sphere diameter, a, and the skin depth, δ, and is $Q_0 = \frac{a}{\delta}$, giving Q_0=94,000 for δ=0.61 μm at 11.424 GHz.

The input TE01 mode converts to both TE01 and TE02 modes in a widened rectangular waveguide region, and their magnetic field components will couple to two perpendicular polarized TE11 modes in the circular wave guide. The geometry is adjusted so the phases of the two polarized modes are in quadrature. If the circular waveguide feeds a spherical cavity as shown in Fig. 3, two corresponding polarized spherical modes will act in similar fashion to the two modes from the two cylinders in a traditional S-band SLED system.

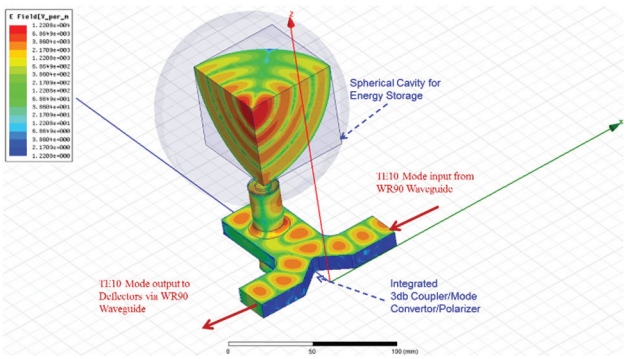

Figure 3: The incoming TE01 waveguide mode converts to two TE11 modes in the circular guide which couples to the two circularly polarized spherical modes in the cavity.

SLED INSTALLATION AT THE XTCAV

The SLED cavity is mounted at the output of the X-band klystron located in the support building above the beam line tunnel. The chosen location is a compromise between accessibility for cooling and instrumentation versus subjecting the long waveguide run to the deflecting structure to the high peak power from the SLED output.

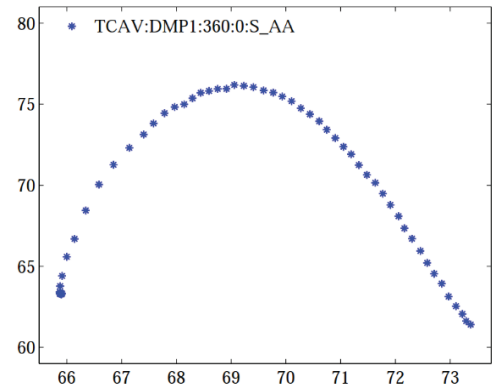

Figure 4: Temperature sensitivity of the SLED cavity is shown when the output power [MW] is plotted versus temperature [deg. F].

The waveguide and waveguide windows had previously seen 50 MW output power from the klystron so we spent several weeks gradually raising the peak power to the new level of around 200 MW in order to RF condition the cavity, waveguide and windows.

The SLED cavity is cooled from a separate chiller system so that its temperature may be set independently to either tune or detune the system. When tuned, the SLED cavity is kept at 69°±0.5°F, as shown in Fig. 4. If it is desired to run the system in non-SLED mode the temperature of the cavity is raised by a nominal 20°F to detune it. In non-SLED operation a klystron pulse of up to 50 MW peak power and 200 ns duration is applied to the deflecting structure, whose fill time is 100 ns. The chosen method of using the temperature to detune the cavity avoids the use of expensive and complex mechanical tuners for the job.

When the system is operated in SLED mode the RF pulse is lengthened to 1 μs and the output phase is flipped 180°in the last 200 ns of the pulse. The fast phase change is implemented by programming the I&Q modulator used in the programmable Phase and Amplitude Controller (PAC) in the low level RF system.

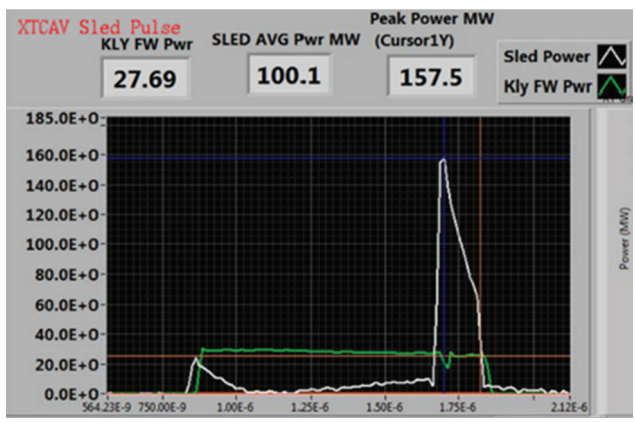

Figure 5: SLED RF output pulse from the SLED cavity (white) peaks rapidly when the phase is reversed and gives 4 times the average power in the last 200 ns compared to the 1 us pulse from the klystron (green).

ISBN 978-3-95450-177-9

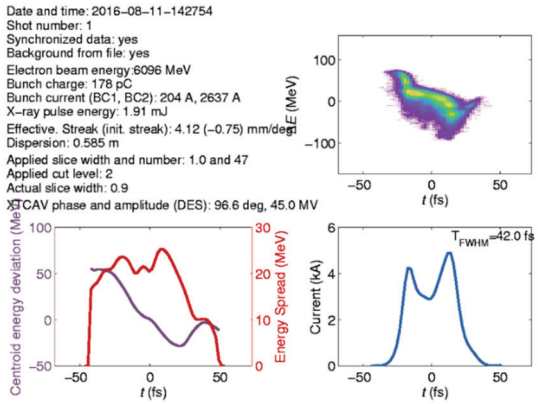

Figure 6: Streaked image (top right), longitudinal charge profile (bottom right) and reconstructed photon profile (bottom left) during non-SLED operation.

The power from the output side of the SLED cavity coupler remains quite low at the beginning of the klystron RF pulse, as shown in Fig. 5. However, when the phase flip occurs in the klystron RF, the output from the SLED cavity rapidly increases producing the characteristic narrow SLED pulse seen in Fig. 5.

The output pulse length from the X-band klystron is increased by a factor 5 in order to operate in SLED mode and this brings with it a new set of challenges. The average output power of the klystron is 5 times higher and this has an impact on the expected peak power performance and expected lifetime of the tube. The X-band klystrons are only manufactured in small quantities at SLAC and limited experience is available in regard to long term performance.

The longer klystron pulse also requires a longer output pulse from the modulator requiring a change in the pulse forming network. The modulator was initially unable to handle the increase in average power which required us to replace the AC power line transformer with a higher rated unit.

BEAM MEASUREMENT

Successful measurement with the XTCAV system requires that the RF be timed to the beam arrival to within 8.4 ns (1 timing clock cycle) and that the RF phase be set to the zero phase crossing within 0.1°X-band. This is done empirically by first observing the steering of the beam by the XTCAV at about 10% of the nominal RF power.

The calibration of the strength of the kick is done by scanning the RF phase about the zero crossing by ±1°X-band, or less, and observing the centroid displacement at the profile monitor screen. The deflection is measured directly in screen pixels and does not rely on an exact knowledge of the screen magnification in pixels per mm. Since LCLS operates over a large range of energies from 4 to 14 GeV the relative deflection strength will vary by a factor up to 3.5.

A software package is used at SLAC (TREX) to perform the XTCAV calibration and record and analyse the streaked image. The longitudinal profile for the electron beam and the photon beam is reconstructed, as shown in Fig. 6 for the nominal non-SLED operating amplitude of 45 MV, and in Fig. 7 for the new SLED operating amplitude of 85 MV. The effective streak is observed to increase from 4.12 mm/°X-band to 8.45 mm/°X-band

The temporal resolution is both a function of the energy-dependant effective streak and the un-streaked beam size. The performance is summarized in Table 1. However, it should be noted that the best resolution of 0.5 fs for the lowest energy electron beam is very difficult to sustain because of RF phase jitter which causes results in deflections large enough to trip beam loss monitors.

Table 1: Comparison of Operating Parameters for Non-SLED and SLED Modes

		Non-SLED	SLED
Klystron power	MW	50	40
Klystron pulse length	μs	0.2	1
XTCAV kick amplitude	MV	45	85
Effective streak at 6 GeV	mm per °X-band	4.12	8.45
Temporal resolution HXR (10kV)	fs	4	2
Temporal resolution SXR (1kV)	fs	1	0.5

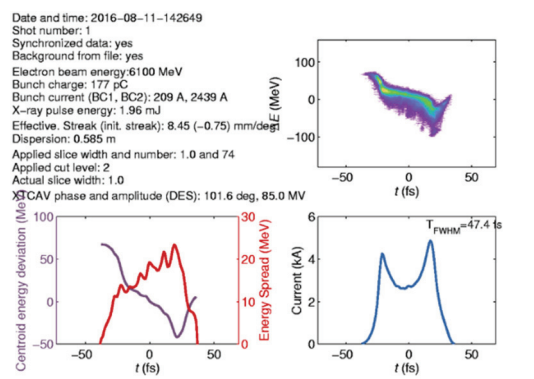

Figure 7: Streaked image (top right), longitudinal charge profile (bottom right) and reconstructed photon profile (bottom left) during SLED operation.

REFERENCES

[1] "Commissioning the New LCLS X-band Transverse Deflecting Cavity with Femtosecond Resolution" P. Krejcik et al, Proceeding Int. Beam Instrumentation Conf. 2013, Oxford 2013.

[2] "Few-femtosecond time-resolved measurements of X-ray free-electron lasers", Behrens, C. et al., Nature Communications, 5. 3762 2014

[3] Flexible control of femtosecond pulse duration and separation using an emittance-spoiling foil in x-ray free-electron lasers Y. Ding (SLAC) et al.. Appl. Phys. Lett. 107, 191104 (2015).

[4] J.W. Wang et al., "R&D of a Super-compact SLED System at SLAC", in Proc. 7th International Particle Accelerator Conference (IPAC'16), Busan, Korea, May 2016, pp. 39-41, ISBN: 978-3-95450-147-2.

ISBN 978-3-95450-177-9

BPM BASED OPTICS CORRECTION OF THE SOLARIS 1.5 GeV STORAGE RING

A. Kisiel*, P. Borowiec, P. P. Goryl, M. Jaglarz, M. Kopeć, A. M. Marendziak, S. Piela, P. Sagało, M. J. Stankiewicz, A. I. Wawrzyniak, Solaris NSRC, Krakow, Poland

Abstract

The Solaris is a novel approach for the third generation synchrotron light sources. The machine consists of 600 MeV linear injector and 1.5 GeV storage ring based on 12 compact Double Bend Achromat (DBA) magnets designed in MAX-IV Laboratory in Sweden. After the commissioning phase of the Solaris storage ring the optimization phase has been started along with the commissioning of the first beamline. An essential part of the beam diagnostics and instrumentation system in the storage ring are Beam Position Monitors (BPMs) based on 36 quarter-wave button BPMs spread along the ring. Proper calibration allowed to measure and correct several beam parameters like closed orbit, tune, chromaticity, dispersion and orbit response matrix. The results of the latest machine optimization including the orbit correction, beam-based alignment and BPM phase advance will be presented.

Table 1: Solaris Storage Ring Design Parameters

Parameter	Value
Energy	1.5 GeV
Beam current	500 mA
Circumference	96 m
Number of bending magnets	12
Main RF frequency	99.931 MHz
Number of bunches	32
Horizontal emittance (bare lattice)	6 nm rad
Tune Q_x, Q_y	11.22, 3.15
Natural chromaticity ξ_x, ξ_y	-22.96, -17.4
Corrected chromaticity ξ_x, ξ_y	+1, +1
Beam size (straight section) σ_x, σ_y	184 µm, 13 µm
Beam size (dipole) σ_x, σ_y	44 µm, 30 µm
Total lifetime	13 h

INTRODUCTION

The first polish third generation light source Solaris is based on the linear accelerator and the storage ring connected with dog-leg transfer line. The linac provides the beam with maximum 600 MeV energy which can be injected to the storage ring and ramped up to the nominal energy 1.5 GeV. A storage ring layout consists of 12 novel highly integrated Double Bend Achromat (DBA) magnets designed by MAX-IV Laboratory in Sweden. One year period of the machine assembling has started in May 2014. Then the commissioning phase started and the process of fine-tuning for reaching the designed parameters is still ongoing. Most important parameters of this 1.5 GeV storage ring are presented in Table 1. A detailed description of the machine and the layout can be found in [1–4].

Recent optimization of linear injector and storage ring allowed to reach 600 mA of injected beam at 525 MeV energy stored in the ring and 400 mA beam ramped to the nominal 1.5 GeV energy. Machine optics, which is described in [5, 6], was corrected closely to the designed values. Sufficiently stable beam along with good reproducibility of beam parameters from injection to injection allowed to start the commissioning of the first beamline — UARPES.

BPM LAYOUT IN SOLARIS

Properly configured Beam Position Monitor (BPM) system is an essential part of the beam diagnostics subsystem for both the linac and the storage ring. The single passing beam in linear structures is monitored in terms of position and stability by 8 stripline BPMs placed along the linac and transfer line. Each quarter-wave directional stripline is 15 cm long and has 50 Ω impedance, what corresponds to the 500 MHz resonant frequency. In order to couple the resonance of the beam with the stripline, mixed-frequency chopper with 500 MHz harmonics will be used.

Storage ring layout includes 36 quarter wave diagonal button BPM sensors distributed evenly along the ring — each DBA is equipped with 3 sensors in two different architectures. The first type of BPM (BPM I) are placed at the ends of each DBA and has button sensors aligned directly along diagonal coordinates, when second type of BPM (BPM II) is placed at the centre of each DBA and has the sensor buttons shifted along the vertical axis on top and bottom of the vessel. BPM made in this architecture is more sensitive to well-centred beam and less sensitive to off-centred beam position, what implies the necessity of separate calibration.

BUTTON BPM CALIBRATION

An electron beam passing the BPM sensors induces on the sensor heads the voltage pulse which magnitude is proportional to the distance between the beam and the sensor head. Comparing the signals from all four BPM channels the position can be calculated as a relative proportion of inducted signals. All position monitors in Solaris are oriented diagonally and horizontal (X) and vertical (Y) positions can be calculated with respect to the formulas:

$$X = K_x \frac{(V_A + V_D) - (V_B + V_C)}{V_A + V_B + V_C + V_D} + X_{off}, \quad (1)$$

$$Y = K_y \frac{(V_A + V_B) - (V_C + V_D)}{V_A + V_B + V_C + V_D} + Y_{off}, \quad (2)$$

* arkadiusz.kisiel@uj.edu.pl

ISBN 978-3-95450-177-9

where $V_{A,B,C,D}$ are magnitudes of signals on each channel, K_x and K_y are scale factors translating the magnitudes into physical distances and X_{off} and Y_{off} are horizontal and vertical offsets from geometrical centre.

Beam Based Alignment

Closed orbit by default indicates an error from geometrical golden orbit, what does not correspond to the real golden orbit delimited by magnetic centres. For the proper beam position offsets calibration the routine named Beam Based Alignment (BBA) supported by Matlab Middle Layer (MML) toolbox is used. The magnetic centres can be estimated by altering the focusing strength of one quadrupole magnet and monitoring the changes of nearest BPM readout. The relative position shift caused by quadrupole strength changes is negligible only when the beam passes the BPM at the magnetic centre of the nearest quadrupole. Figures 1 and 2 present values of vertical and horizontal offsets after few iterations of BBA procedure.

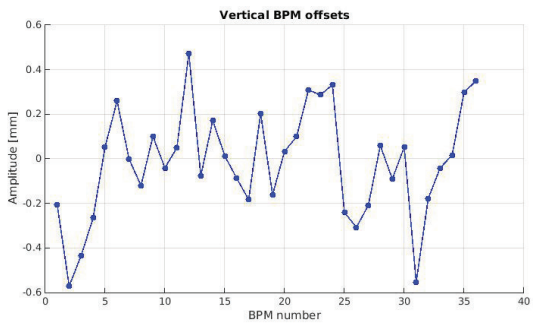

Figure 1: Vertical position offsets.

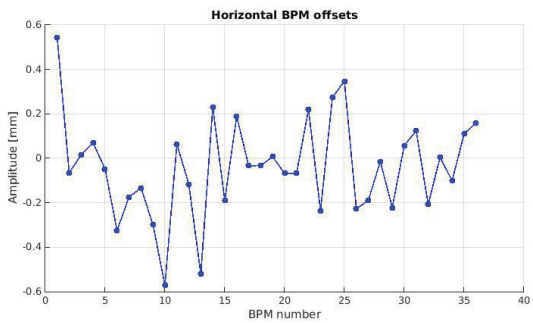

Figure 2: Horizontal position offsets.

Gain Calibration

Second parameters needed for BPM calibration are horizontal and vertical position scale factors — K_x and K_y from equations (1) and (2). Gain factors are independent from the beam behaviour and can be calculated offline in simulations. Using boundary-element method described in [7] the charge distribution around the vessel and induced on buttons can be determined. The simulation results for BPMs in two architectures used in Solaris storage ring are presented in tables 2 and 3

Table 2: BPM I Simulation Results

Parameter	Value
Capacitance	0.56 pF
Power per button	1.4 μW (-28.6 dBm)
Noise power	-121.0 dBm
Estimated resolution X/Y	0.081 μm / 0.22 μm
Loss factor	2.4 mW/pC
H/V sensitivity S_x / S_y	0.149 mm^{-1} / 0.055 mm^{-1}
H/V gain factor K_x / K_y	6.7 mm / 18.0 mm

Table 3: BPM II Simulation Results

Parameter	Value
Capacitance	0.56 pF
Power per button	2.2 μW (-26.5 dBm)
Noise power	-121.0 dBm
Estimated resolution X/Y	0.081 μm / 0.22 μm
Loss factor	3.8 mW/pC
H/V sensitivity S_x / S_y	0.080 mm^{-1} / 0.085 mm^{-1}
H/V gain factor K_x / K_y	12.4 mm / 11.7 mm

OPTICS CORRECTION

The properly calibrated BPM system allows to perform measurements and correction of the storage ring parameters like: dispersion as an orbit shift driven by RF frequency change, betatron tune as a Fourier transform of the transverse excited beam turn-by-turn data and a chromaticity as tune shift dependence on RF frequency change. Additionally, fine-tuning of the optics using LOCO is ongoing issue.

Global Orbit Correction

The most crucial routine affecting directly the injection, accumulation of high currents, lossless ramping and low vacuum levels is global orbit correction. Figure 3 presents the orbit response matrix, which is essential input data for automatic orbit correction.

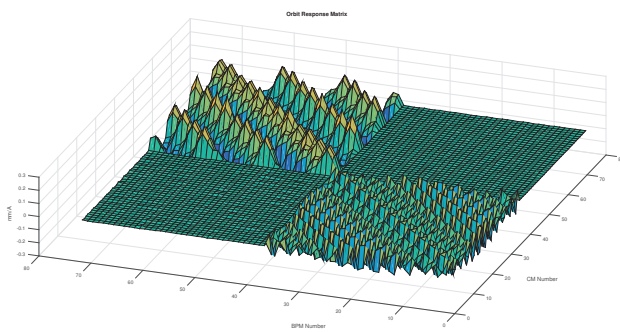

Figure 3: Orbit response matrix.

The corrected closed orbit along with calibrated BPM offsets in BBA procedure reduced the RMS value of the orbit significantly as presented on Figures 4 and 5. Before any corrections the RMS position in the horizontal plane

ISBN 978-3-95450-177-9

was 700 um and 1000 um in the vertical plane. After applying corrections including BPM offsets achieved from BBA routine the horizontal orbit was reduced to 56 um (RMS) whereas the vertical to 45 um (RMS).

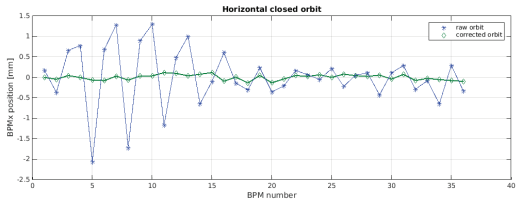

Figure 4: Horizontal closed orbit before (blue) and after (green) corrections.

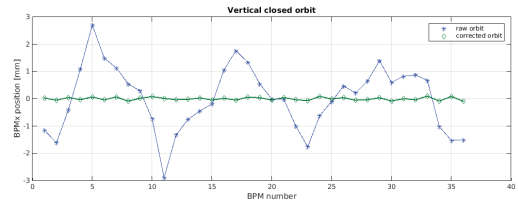

Figure 5: Vertical closed orbit before (blue) and after (green) corrections.

Phase Advance

Turn-by-turn mode of BPM data acquisition is another source of information about the beam characteristics. Exciting the transverse oscillations with kicker magnet, each BPM detects harmonic oscillations described with the function [8]:

$$x_{km} = A_{kx} \cos(2\pi Q_x m + \phi_x), \tag{3}$$

where k — index of BPM, m — number of turn, A_k — measured amplitude, Q_x — horizontal tune and ϕ_x — measured phase.

Two Fourier sums of these oscillations for the large number of turns (N) are approaching the asymptotic values as follows:

$$C_k = \sum_{m=1}^{N} x_{km} \cos(2\pi m Q_x) \overset{N\to\infty}{\to} \frac{A_k N}{2} \cos(\phi_x) \tag{4}$$

$$S_k = \sum_{m=1}^{N} x_{km} \sin(2\pi m Q_x) \overset{N\to\infty}{\to} \frac{A_k N}{2} \sin(\phi_x) \tag{5}$$

The phase of betatron oscillations on k-th BPM can be expressed as:

$$\phi_x = \arctan\left(\frac{S_k}{C_k}\right) \tag{6}$$

Computing the phase for each BPM separately allowed to measure the phase advance between consecutive BPMs along the storage ring. Comparison of measured and model phase advance in horizontal and vertical planes are presented in the Figure 6 and Figure 7.

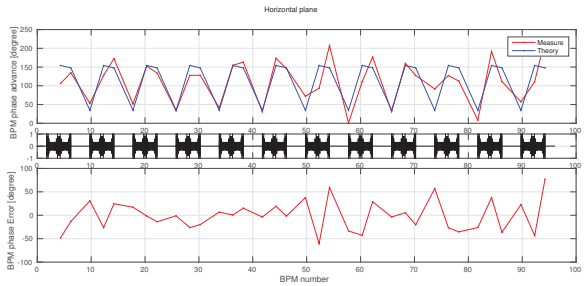

Figure 6: Horizontal phase advance.

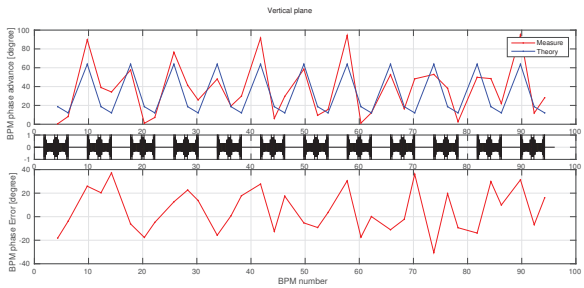

Figure 7: Vertical phase advance.

The measured phase advance values differs from the model at some sections. The origins of this difference are the misalignment and field errors. The main discrepancy is observed at the first, second and twelfth DBAs, which can be the potential source of misalignment errors [5, 9]. Moreover in the second DBA sector also the vacuum chamber was twisted during storage ring installation, which can also affect the middle BPM alignment. Therefore, the BPM reading of this particular BPM can be incorrect. To get the corrected orbit in this region one corrector in the first section always is running close to saturation what also can confirm that there is severe problem with alignment in this region. The other reason of the discrepancy could be the field strength errors between magnets from the same family. At Solaris the magnets are connected in series and potential field errors between them can be eliminated by proper shunting of those magnets. At Solaris the magnets were shunted but still some fine shunting can be needed. This is still under verification. Nevertheless, the optics measurements that has been performed so far has shown that the linear optics is close to the design one which is very good achievement after a year of the Solaris storage ring commissioning.

CONCLUSION

The commissioning of the Solaris 1.5 GeV storage ring requires strong focus on the machine parameters optimization. The BPM subsystem, as an essential part of beam diagnostics, allows to perform both direct and indirect measurements of beam parameters. Nonetheless it requires proper calibration and maintenance. Performance of position monitoring devices was proved by successful optimization parameters like: closed orbit, tune, chromaticity, dispersion. The nearest future should be focused on fine-tuning of the machine

ISBN 978-3-95450-177-9

by implementing LOCO correction and taking additional effort to reduce the disparity between model and measured results revealed in phase advance analysis.

ACKNOWLEDGMENT

Authors would like to thank the MAXIV and Elettra teams and D. Einfeld (ESRF) for providing necessary support during design, installation and commissioning phases. Acknowledgments to F. Perez (ALBA) and G. Rehm (Diamond) for help and fruitful discussions in the Solaris control room. Special thanks to the rest of Solaris team whose role was mandatory and irreplaceable during different stages of this project.

REFERENCES

[1] MAXIV Detailed Design Report `https://www.maxlab.lu.se/node/113`

[2] A. I. Wawrzyniak *et al*, "Injector layout and beam injection into Solaris", Proc. of IPAC2011, San Sebastian, Spain, THPC123, p. 3173 (2011).

[3] M. R. Bartosik *et al.*,"Solaris—National Synchrotron Radiation Centre, project progress, May2012", Radiat. Phys. Chem. **93**, (2013) 4.

[4] A. I. Wawrzyniak, R. Nietubyc et al.,“ Ramping of the Solaris Storage Ring Achromats", Proc. of IPAC2013, Shanghai, China, MOPEA047, p. 184 (2013).

[5] A. I. Wawrzyniak *et al.*, "First results of Solaris synchrotron commissioning", Proc. of IBIC2015, Melbourne, Australia, WEDLA01, p. 602 (2015).

[6] A. I. Wawrzyniak *et al.*, "Solaris Storage Ring Commissioning", IPAC'16, Busan, Korea, WEPOW029.

[7] A. Olmos, F. Perez, G. Rehm, "Matlab code for BPM button geometry computation", Proc. of DIPAC 2007, Venice, Italy, TUPC19, p.186 (2007).

[8] Minty, Michiko G., Zimmermann, Frank, "Measurement and Control of Charged Particle Beams", Springer-Verlag Berlin, Heidelberg, 2003.

[9] J. Wiechecki et al.,“Impact of the DBA blocks alignment on the beam dynamics of the storage ring in Solaris”, IPAC'16, Busan, Korea, WEPOW032.

ISBN 978-3-95450-177-9

TIME-RESOLVED MEASUREMENT OF QUADRUPOLE WAKEFIELDS IN CORRUGATED STRUCTURES*

Chao Lu†[1,2], Feichao Fu[1,2], Shenggunag Liu[1,2], Tao Jiang[1,2], Libing Shi[1,2], Rui Wang[1,2], Dao Xiang‡[1,2], Lingrong Zhao[1,2], Pengfei Zhu[1,2],
[1]Key Laboratory for Laser Plasmas (Ministry of Education), Shanghai Jiao Tong University, Shanghai, China
[2] also at Collaborative Innovation Center of IFSA (CICIFSA), Shanghai Jiao Tong University, Shanghai, China
Zhen Zhang , Department of Engineering Physics, Tsinghua University, Beijing, China

Abstract

Corrugated structures have recently been widely used for manipulating electron beam longitudinal phase space and for producing THz radiation. Here we report on time-resolved measurements of the quadrupole wakefields in planar corrugated structures. It is shown that while the time-dependent quadrupole wakefield produced by a planar corrugated structure causes significant growth in beam transverse emittance, it can be effectively canceled with a second corrugated structure with orthogonal orientation. The strengths of the time-dependent quadrupole wakefields for various corrugated structure gaps are also measured and found to be in good agreement with theories. Our work should forward the applications of corrugated structures in many accelerator based scientific facilities.

INTRODUCTION

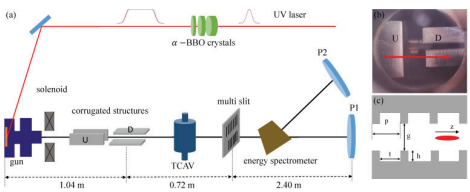

Figure 1: (color online). (a) Schematic layout of the time-resolved measurement of quadrupole wakefields experiment (distances not shown in scale); (b) side view of the CS: upstream CS has a horizontal gap and downstream CS has a vertical gap (the red arrow indicates the beam direction); (c) geometry of the planar CS parameters (the red ellipse represents a beam propagating along the z axis).

When relativistic electron beams pass through metallic pipes or plates with corrugations, electromagnetic waves (wakefields) that propagate with the beams are excited. Such quasi-single frequency radiation on the one hand is a promising candidate for intense THz source (see, for example [1–3]); on the other hand it may be used to manipulate electron beam longitudinal phase space through the interaction between the electron beam and the electromagnetic waves inside the structure (see, for example [4–6]).

* Work supported by the National Natural Science Foundation of China (Grants No. 11327902)
† j.j.lucertainfeel@gmail.com
‡ dxiang@sjtu.edu.cn

EXPERIMENT METHODS TO QUANTIFY QUADRUPOLE WAKEFIELDS

Recently the corrugated structures (CS) have been used to tailor beam longitudinal phase space in three different ways, namely removing linear chirp (correlation between beam's longitudinal position and beam energy), removing quadratic chirp and imprinting energy modulation. For instance, when the electron bunch length is much shorter than the wavelength of the wakefield, the beam sees a deceleration field that increases approximately linearly in longitudinal direction when it passes through a CS. This longitudinal wakefield can be used to "dechirp" the beam after bunch compression to reduce beam global energy spread [4–11]. Alternatively, when the electron bunch length is comparable to the wavelength of the wakefield, the beam sees a longitudinal wake that approximates a sinusoid. This wakefield can be used to compensate for the beam quadratic chirp [12–14] that otherwise increases free-electron laser (FEL) bandwidth in seeded FELs (see, e.g. [15]) and degrades the MeV ultrafast electron microscope (UEM) performance [16, 17]. Yet another scenario is when electron bunch length is much longer than the wavelength of the wakefield. In this regime the longitudinal wakefield can be used to produce energy modulation in beam longitudinal phase space that may be further converted into density modulation for producing THz radiation [18–20].

In this paper the beam emittance and transverse phase space in presence of CS are measured with multi-slit method. We show that the time-dependent focusing or defocusing introduced by quadrupole wakefields mainly results in mis-

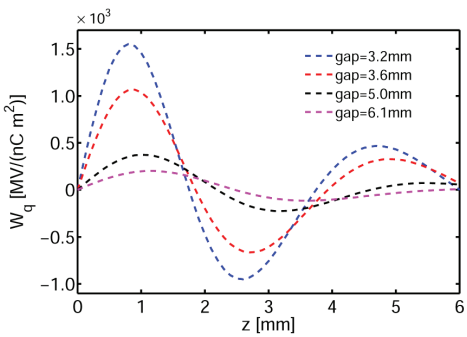

Figure 2: (color online). The point charge quadrupole wake fields at various CS gaps respectively g = 3.2, 3.6, 5.0, 6.1 mm.

ISBN 978-3-95450-177-9

match in beam slice phase space, leading to considerable growth in beam projected emittance. We also provide definitive evidence through measurement of the beam transverse phase space that indeed if the CS is composed of two identical parts with the second half rotated by 90 degrees with respect to the first half, the quadrupole wakes can be canceled. Furthermore, the strengths of the time-dependent quadrupole wakefields for various CS gaps are also measured and found to be in good agreement with theories. We anticipate that our study should forward the applications of CS in many accelerator facilities.

The experiment is conducted at the Center for Ultrafast Diffraction and Microscopy at Shanghai Jiao Tong University [21].The schematic layout of the experiment is shown in Fig. 1(a).The bunch quadrupole wakefield(shown in Fig. 2) $w_\lambda(z)$ is given by the convolution between the point charge quadrupole wake field and the beam longitudinal distribution,

$$w_\lambda(z) = \int_0^\infty W_q(s)\lambda(z-s)\mathrm{d}s \tag{1}$$

The quadrupole wakefield manifests itself as a time-dependent focusing (defocusing) effect and is related to the focal length f as,

$$1/f(z) = w_\lambda(z)L_c/E \tag{2}$$

where L_c is the length of the CS and E is electron beam energy.

In our experiment the quadrupole wakefields are quantified through measurement of the beam phase space in presence of the CS. When a beam passes through a linear Hamiltonian system, its final beam matrix σ_f is connected with its initial beam matrix σ_i as $\sigma_f = R\sigma_i R^T$, where R is the symplectic transfer matrix of the system and R^T is transpose of R. Under the thin-lens approximation, the Twiss parameters of the beam before (α_i, β_i and γ_i) and after (α_f, β_f and γ_f) the CS is connected with the CS focusing effect as (see e.g. [22])

$$\begin{bmatrix}\beta_f\\ \alpha_f\\ \gamma_f\end{bmatrix} = \begin{bmatrix}1 & 0 & 0\\ 1/f & 1 & 0\\ 1/f^2 & 2/f & 1\end{bmatrix}\begin{bmatrix}\beta_i\\ \alpha_i\\ \gamma_i\end{bmatrix} \tag{3}$$

With the beam Twiss parameters measured with the multi-slit method, one obtains the focal length f with Eq. (3). Inserting f into Eq. (2) yields the quadrupole wakefield as

$$w_\lambda(z) = \frac{E}{L_c}\frac{\alpha_f - \alpha_i}{\beta_i} \tag{4}$$

EXPERIMENTAL RESULTS

Cancellation of Time-dependent Quadrupole Wake Fields

With the TCAV on, the streaked beam distributions for various settings of the CS are shown in the top row of Fig. 3, and the corresponding beamlets distributions with the mask inserted are shown in the bottom row of Fig. 3.

Here we give the results for three representative slices (bunch head, bunch center and bunch tail) as indicated by the dashed squares in Fig. 3(a). The phase spaces for the representative slices under various conditions (Fig. 3) are shown in Fig. 4. The slice emittance is about 0.55 μm and the projected emittance is about 0.6 μm when the two CS are widely open (Fig. 4(a)). Because the phase space ellipse for each slice has approximately the same slope, the projected beam emittance is close to the slice emittance. With the gap of the downstream CS reduced to 3.2 mm, it can be clearly seen that slice phase space rotates clockwise from

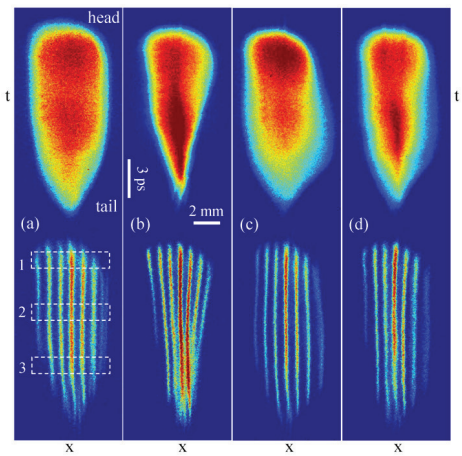

Figure 3: (color online) Time-resolved measurements of beam (top) and beamlets (bottom) distribution on screen P1. Four situations are shown: (a) with two CS widely open; (b) with downstream CS gap set at 3.2 mm; (c) with upstream CS gap set at 3.2 mm; (d) with both CS both gaps set at 3.2 mm. The dashed squares in (a) indicates the three representative slices used for analysis of emittance in Fig. 4.

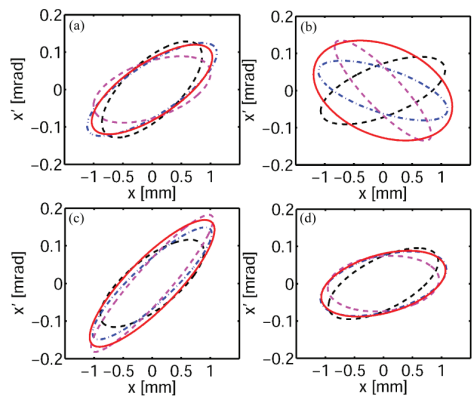

Figure 4: Slice and projected phase space ellipses in four situations respectively: (a) with two CS widely open; (b) with downstream CS gap set at 3.2 mm; (c) with upstream CS gap set at 3.2 mm; (d) with both CS gaps set at 3.2 mm. The phase spaces for the head slice, central slice and tail slice are shown with dashed black line, dotted dashed blue line and dashed magenta line, respectively. The projected phase space is shown with solid red line.

ISBN 978-3-95450-177-9

head to tail (Fig. 4(b)). As a result of this mismatch, the projected beam emittance increases to about 1.0 μm (note, the slice emittance is reduced to about 0.50 μm because a small fraction of the particles (about 15%) with large offset are collimated by the CS).

Similarly, when the gap of the upstream CS is reduced to 3.2 mm, the time-dependent defocusing wake rotates the slice phase space counter clockwise (Fig. 4(c)). It is worth mentioning that in Fig. 4(c) the projected emittance is measured to be about 0.70 μm, smaller than that in Fig. 4(b). This is likely due to the fact that the horizontal beta function is smaller in the upstream CS (beam is diverging) such that the emittance growth is less sensitive to the quadrupole wake [23]. Finally, with the gaps of the two CS both set at 3.2 mm, the slice phase ellipses becomes approximately aligned again as shown in Fig. 4(d). Because of the effective cancellation of quadrupole wakefields, the projected beam emittance is reduced to about 0.60 μm. Note, because of the different beta functions in the upstream and downstream CS, there is still a slight increase of the beam emittance even though the quadrupole wake has essentially the same strength and opposite sign.

In a separate experiment, the gap of the downstream CS was further reduced to about 1.4 mm. In this case a large fraction of the electrons are collimated by the structure and only about 2 pC charge went through. The charge is inferred from the intensity of the beam image at screen P1 where the intensity is calibrated with the Faraday cup without the CS. The streaked beamlets are shown in Fig. 5(a). In this case we used the second mask of which the separation of the slit is 350 μm. At first glance one might think the quadrupole wake focuses the beam at the head and defocuses it at the tail. However, after second thought one realizes that actually the beam is focused by the wake all the way from head to tail because the horizontal beam size is always smaller than that at the bunch head. Because the focusing is strongest in the beam center (the beamlets almost overlap in the beam center), the beamlets finally developed to a curved shape.

To clearly show the relative orientation of the slice phase space ellipses, the beam is divided into 9 slices as indicated in Fig. 5(a). As shown in Fig. 5(b) the front five slice phase ellipses rotate clockwise because the focusing strength increases from the bunch head to the bunch center. After reaching the peak value at the bunch center, the focusing strength of the wakefield decreases from bunch center to bunch tail, and as a result the last five slice phase ellipses rotate counterclockwise as shown in Fig. 5(c). The slice emittance is measured to be about 0.20 μm (primarily due to the reduced charge) and the projected emittance is about 0.40 μm.

It is worth mentioning that the emittance grows here by only a factor of 2 even though the gap is reduced to 1.4 mm. This is because the beam charge is also low in this case (wakefield strength is proportional to beam charge). Furthermore, a mirror symmetry (i.e. the bunch tail is similar to the mirror image of the bunch head with respect to the bunch center) is developed in the final beam distribution because the time-dependent quadrupole wake peaks at the bunch center. This reduces the mismatch of the slice phase space and thus leads to reduced emittance growth (e.g. the phase space ellipses for slice 1 and slice 9 have roughly the same slope; similarly slice 2 and slice 8 are also aligned, etc.).

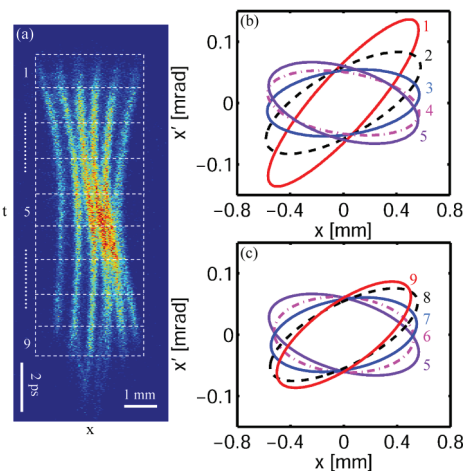

Figure 5: (a) Streaked beam distribution with the gap of the downstream CS reduced to 1.4 mm; (b) Phase space ellipses for the front five slices (from bunch head to bunch center); (c) Phase space ellipses for the latter five slices (from bunch center to bunch tail).

Quadrupole Wake Fields at Various Longitudinal Positions

In addition to studying the effect of quadrupole wakefields on beam emittance growth, here we also present the measurement of the quadruple wakefield strength. By measuring the phase space for various slices one obtains the Twiss parameters of each slice and the quadruple wakefield strengths at various longitudinal positions can be quantified with Eq. (4). It should be pointed out that with the multi-slit method it is the beam phase space at the mask that is measured. In our analysis the beam phase space is back propagated to

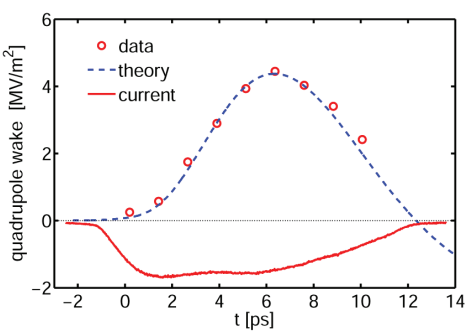

Figure 6: Measured (red circles) and simulated (blue dashed line) time-dependent quadrupole wakefields with the gap of downstream CS set at 3.2 mm. The beam longitudinal distribution is also shown in red solid line.

ISBN 978-3-95450-177-9

the center of the CS to obtain the Twiss parameters at the CS. Specifically, the Twiss parameters at the CS obtained without the CS is taken as those "before" the CS (α_i, β_i and γ_i in Eq. (3)), and the Twiss parameters obtained with the CS is taken as those "after" the CS (α_f, β_f and γ_f in Eq. (3)).

With this method the time-dependent quadrupole wakefield for the beam in Fig. 3(b) is shown in Fig. 6. The simulated quadrupole wakefield obtained by convolving the beam longitudinal distribution (red line in Fig. 6) with the point charge quadrupole wake field is also shown in Fig. 6 with the blue dashed line. To match the experimental results, in the simulation the bunch charge is assumed to be 8 pC which is slightly higher than the measured beam charge. This may be due to the fact that the point wake used for analysis (Fig. 3) only considers the dominate modes of the wakefield, and there might be contributions from other modes [24]. Also there could be considerable uncertainty in measurement of the beam charge with our home-made Faraday cup where secondary electron emission is not minimized. Nevertheless, the overall shape and strength of the quadrupole wakefield is in good agreement with the experimental results.

Quadrupole Wake Fields at Various CS Gaps

To study how the quadrupole wakefield scales with the CS gap, we increased the CS gap to 3.6, 5.0 and 6.1 mm. The measured beamlets are shown in the inset of Fig. 7. The quadrupole wakefield strength at the central slice for various CS gaps are obtained through measurement of the Twiss parameters of the central slice. The beam loss is about 5% for g = 3.6 mm and is negligible for the other two cases, so the beam longitudinal distribution may be assumedd identical. The measured quadrupole wake at various CS gap is normalized to the beam charge (Q = 5 pC as for the g = 3.2 mm case) and shown with red circles in Fig. 7. The theoretical wakefield strength is then similarly obtained by a convolution of the beam distribution (assuming Q = 8 pC)

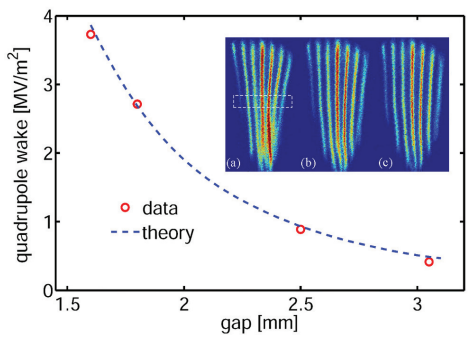

Figure 7: Measured (red circles) and simulated (blue dashed line) quadrupole wakefields of the central slice at various gaps. The streaked beamlets at various CS gaps are shown in the insets [(a) for g = 3.6 mm, (b) for g = 5.0 mm and (c) for g = 6.1 mm].The dashed square indicates the region of the central slice used for analysis .

with the point wake, and is found to be in good agreement with the experimental results.

CONCLUSIONS

In summary, we provided a complete characterization of the quadrupole wakefield in planar CS. It is demonstrated that while the time-dependent quadrupole wakefield produced by a planar CS causes significant growth in beam transverse emittance, it can be effectively canceled with a second CS with orthogonal orientation. Our work should forward the applications of CS in many accelerator based scientific facilities.

REFERENCES

[1] K. Bane *et al.*, *Instrum. Methods Phys. Res.*, A 677, 67–73 (2012).

[2] A.V.Smirnov *et al.*, *Phys. Rev. ST Accel. Beams*, 18, 090703 (2015).

[3] G. Stupakov, *Phys. Rev. ST Accel. Beams*, 18, 030709, 2015.

[4] M. Rosing *et al.*, *ANL Report No.* WF-144, 1990.

[5] P. Craievich, *Phys. Rev. ST Accel. Beams*, 13, 034401 (2010).

[6] K. L. F. Bane *et al.*, *Nucl. Instrum. Methods Phys. Res.*, Sect. A 690, 106 (2012).

[7] M. Harrison, G. Andonian *et al.*, *Proc. of PAC2013*, p.291, Pasadena, USA (2013).

[8] S. Bettoni *et al.*, *Proc. of FEL2013*, p.214, New York, USA (2013).

[9] S. Antipov *et al.*, *Phys. Rev. Lett.* 112, 034801, 2014.

[10] P. Emma et al., *Phys. Rev. Lett.* 112, 034801, 2014.

[11] Z. Zhang, *et al.*, *Proc. of LINAC2012*, p.525, Tel-Aviv, Israel (2012).

[12] Q. Gu *et al.*, *Proc. of LINAC2012*, p.525, Tel-Aviv, Israel (2012).

[13] H. Deng *et al.*, *Phys. Rev. Lett.* 113, 254802 (2014).

[14] F. Fu, *et al.*, *Phys. Rev. Lett.* 114, 114801 (2015).

[15] E. Hemsing *et al.*, *Phys. Rev. ST Accel. Beams*, 17, 070702 (2014).

[16] D. Xiang, *et al.*, *Nucl. Instrum. Methods Phys. Res.*, Sect. A 759, 74 (2014).

[17] R. K. Li *et al.*, *Phys. Rev. Applied,* 2, 024003 (2014).

[18] S. Antipov *et al.*, *Phys. Rev. Lett.* 108, 144801 (2012).

[19] S. Antipov *et al.*, *Phys. Rev. Lett.* 111, 134802 (2013).

[20] F. Lemery and P. Piot, *Phys. Rev. STAccel. Beams,* 17, 112804 (2014).

[21] F. Fu *et al.*, *Rev. Sci. Instrum.* 85, 083701 (2014).

[22] M.G. Minty and F. Zimmermann, *Measurement and control of charged particle beam*, Springer, 2003.

[23] K. Bane and G. Stupakov, SLAC Report No. SLAC-PUB-15852 (2013).

[24] A. Novokhatski, *Phys. Rev. ST Accel. Beams* 18, 104402 (2015).

ISBN 978-3-95450-177-9

OPTICAL EFFECTS IN HIGH RESOLUTION AND HIGH DYNAMIC RANGE BEAM IMAGING SYSTEMS

J. Wolfenden†, R. Fiorito, C.Welsch, University of Liverpool, Liverpool, UK
P. Karataev, K. Kruchinin, JAI at Royal Holloway University of London, Egham, UK
M. Bergamaschi, R. Kieffer, T. Lefevre, S. Mazzoni, CERN, Geneva, CH

Abstract

Optical systems are used to transfer light in beam diagnostics for a variety of imaging applications. The effect of the point spread function (PSF) of these optical systems on the resulting measurements is often approximated or misunderstood. It is imperative that the optical PSF is independently characterised, as this can severely impede the attainable resolution of a diagnostic measurement. A high quality laser and specially chosen optics have been used to generate an intense optical point source in order to accomplish such a characterisation. The point source was used to measure the PSFs of various electron-beam imaging systems. These systems incorporate a digital micro-mirror array, which was used to produce very high ($>10^5$) dynamic range images. The PSF was measured at each intermediary image plane of the optical system; enabling the origin of any perturbations to the PSF to be isolated and potentially mitigated. One of the characterised systems has been used for optical transition radiation (OTR) measurements of an electron beam at KEK-ATF2 (Tsukuba, Japan). This provided an application of this process to actively improve the resolution of the beam imaging system. Presented here are the results of our measurements and complementary simulations carried out using Zemax Optical Studio.

INTRODUCTION

The impact the PSF of an optical system has on a measurement is often ignored as it is usually not the main limiting factor on resolution. When making high resolution measurements this is not true. Any uncertainty can result in a restriction in the precision of the measurement. The imaging systems in use at recent OTR and ODR studies [1, 2, 3] are an example of such a case. The distribution of PSFs usually takes the form of an Airy disc, with the resolution determined by the width. OTR from a single electron is distinct, in that it contains a zero valued central minimum [4]. The detailed shape of the distribution provides a greater effective resolution than its width [1, 2]. The image of OTR from an electron distribution, with a width comparable to the FWHM of the single electron distribution, displays a central minimum but with a finite non-zero value [1, 2]. This convolution with the transverse profile of an electron beam provides a previously unattainable level of resolution on beam size measurements. In practise however the beam size is not the sole contributor to intensity increase found in the centre of the distribution. There are many other effects, all of which restrict the attainable resolution. A prominent example is the PSF of the optical system used to image the OTR. The diffraction and aberration effects of this PSF will broaden the OTR PSF and degrade the resolution of beam size measurements. If the performance of the optics could be independently assessed, then it would be possible to minimise the impact of the optical PSF on the measured OTR profiles. Another limiting factor is the overall intensity of the OTR. For small beam sizes the sensitivity in the centre can be masked by noise and background [1, 2]. If the intensity of the signal could be increased this central value would be lifted away from the background, the rms noise would become statistically less significant, and smaller beam size measurements could be achieved. This intensity increase would also make future studies into high dynamic range (HDR) OTR imaging possible, as this technique currently relies on high signal levels and masking using a digital micro-mirror array (DMD) [5]. It follows that if the low intensity details of the OTR distribution were measured with HDR, this would further increase the resolution of the beam diagnostic measurements utilising OTR. The effect of the DMD on the optical PSF has been investigated previously [3], but the impact on OTR measurements is still to be assessed.

OPTICAL SYSTEM

PSF Measurements

After an investigation into the PSF of an OTR imaging system currently in use [3], an achromatic imaging system with comparable performance has been designed. Figure 1 shows a schematic of this system. The PSF of a similar system was measured following the technique outlined in [3]. This system differed from system in Fig. 1 in that the focal length of the third lens was changed. This was to change the overall magnification of the system from 25 to 10, as this improved the intensity of the OTR signal measured.

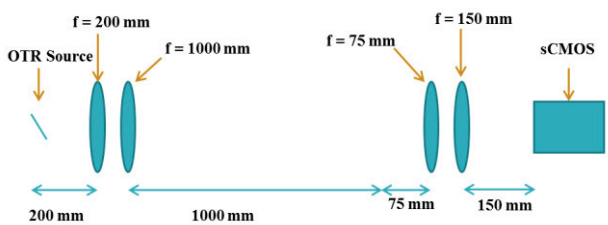

Figure 1: Schematic of OTR imaging system.

As the PSF of an optical system is dominated by the first aperture of the system, the substitution of the third lens for another similar lens would have had a negligible impact on the PSF. The PSF measured is shown in Fig. 2.

† joseph.wolfenden@liverpool.ac.uk

ISBN 978-3-95450-177-9

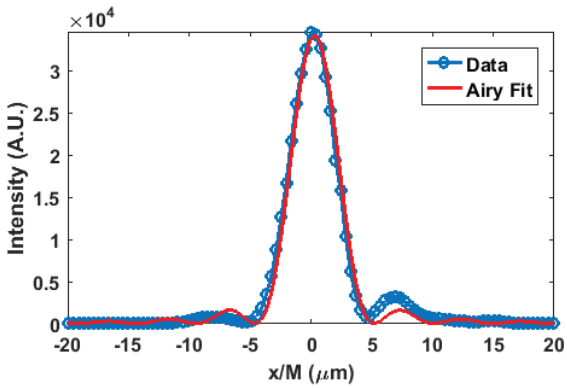

Figure 2: PSF of the OTR imaging system.

The distributions central peak follows that of an Airy distribution. There are slight deviations in the higher order peaks; this may have been caused by aberrations or misalignments, which will be studied further using Zemax [6]. Achromatic lenses provide a more consistent performance with varying wavelengths and, in certain setups, can provide an improved resolution, when compared to a simple singlet lens. It was for these reasons that an achromatic system was implemented. As the lenses are designed to perform best in an infinite conjugate setup [7], the optics were arranged in two confocal pairs. This design also provided a means of investigating the effect of bandpass on the OTR distribution, as images could be taken without the use of interference filters.

OTR MEASUREMENTS

OTR Imaging with No Interference Filter

The measurements were carried out at the ATF2 facility at KEK, Japan. The ability to focus an electron beam down to the micron level made this facility ideal for this type of beam size study. The first measurements were carried out using no interference filter to assess the chromatic performance of the optics. This also provided a baseline signal to noise (S/N) measurement, to which the measurements using an interference filter could be compared. The OTR signal measured from a single-shot is presented in Fig. 3. The transverse profile of the entire beam can be seen. The horizontal size could be acquired here by simply fitting a Gaussian to a horizontal projection of this image. However, the small size in the vertical axis is masked by the OTR distribution as expected.

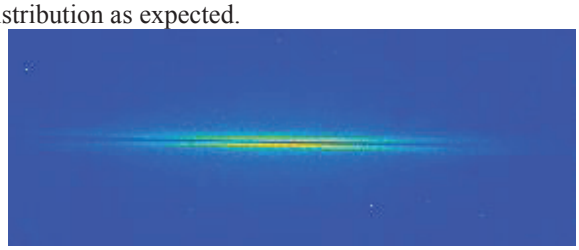

Figure 3: Single-shot OTR with no interference filter.

The vertical projection of Fig. 3 is presented in Fig. 4. The signal has been integrated over 70 pixels across the centre of the image. The window of integration was calculated as described in [1]. Figure 4 has been magnification corrected to provide an OTR source distribution. The peak-to-peak distance of the OTR distribution is indicative of the resolution, and provides a means of direct comparison between different imaging methods. For this distribution this distance is (10.5 ± 0.5) μm. The S/N ratio is 4.6.

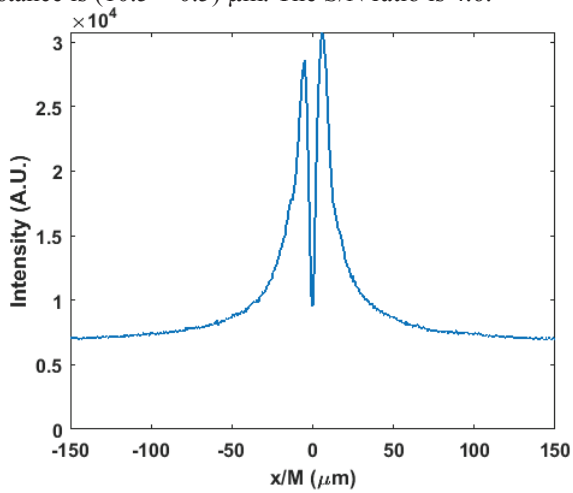

Figure 4: Vertical OTR profile, with a 70 pixel integration window, for unfiltered OTR.

OTR Imaging with an Interference Filter

The measurement process was then repeated for several different interference filters. The best results were found for 650 nm with a 40 nm bandpass, the result of which is displayed in Fig. 5.

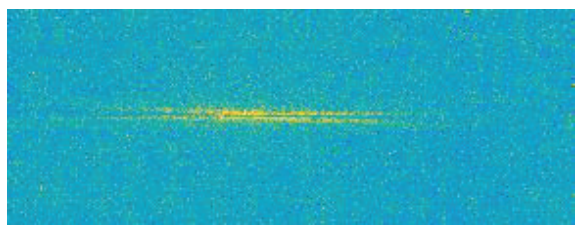

Figure 5: Single-shot OTR with 650(40) nm interference filter.

An integration window of 70 pixels was again calculated using the method outlined in [1]. The resulting profile is presented in Fig. 6. The peak-to-peak distance of this profile is (10.0 ± 0.5) μm, which is comparable to the unfiltered result. The S/N ratio is 1.2, which is a factor of 3.8 less than the unfiltered result.

ISBN 978-3-95450-177-9

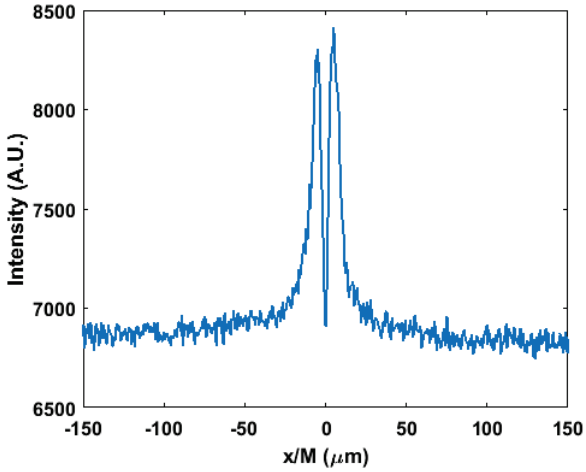

Figure 6: Vertical OTR profile, with a 70 pixel integration window, for filtered OTR.

Conclusions from OTR Measurements

A quadrupole scan was carried out with each setup and the resulting data was analysed as in [1]. This provided a beam size measurement of (1.0 ± 0.5) μm for the filtered light, and a beam size of (2.0 ± 0.5) μm for the unfiltered light. This shows that the lack of a filter causes unwanted intensity to leak into the central minimum and obscure the beam size. However, the S/N ratio found in the unfiltered results was nearly four times better than that of the filtered results. This result points to an optimum bandpass value, which would provide an improved S/N ratio whilst maintaining the resolution of the measurement.

BANDPASS CONVOLUTION STUDIES

The Effect of Bandpass on OTR

As OTR contains an inherent dependence on wavelength, the first step to finding an optimum bandpass must be to understand how a bandpass effects an OTR distribution. The OTR distribution from a single electron was calculated [4], then spatially convolved with a Gaussian with σ = 1 μm. This result simulated what could be theoretically expected from a 1 μm electron beam with no other effects taken into account. The distribution was then convolved with different size Gaussian distributions in the wavelength domain, at a fixed wavelength. This simulated the effect of an interference filter at various bandpasses. Analysis is still underway, but the initial results of these calculations shows that the change from a 40 nm bandpass to a 100 nm bandpass has a minimal effect on the resulting distribution. If analysis continues to show this effect, it would be possible to conclude from these results that the OTR source distribution is not the limiting factor on the bandpass choice for and OTR imaging system.

Other Bandpass Limitations

Another limitation on the bandpass of an OTR imaging system is the wavelength dependence of the response of the camera used. The camera used in the OTR measurements was a pco.edge 4.2LT [8], the response of which is shown is Fig. 7.

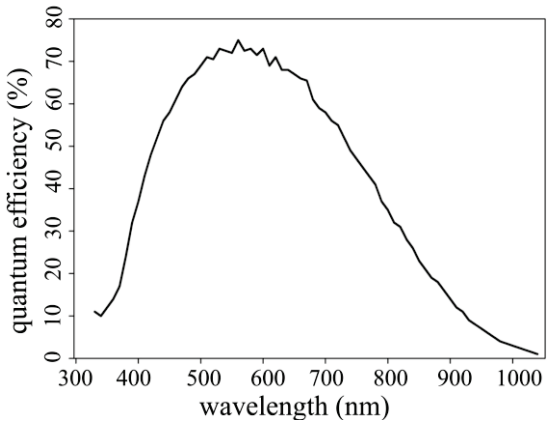

Figure 7: The dependency of quantum efficiency on wavelength of the pco.edge 4.2LT [8].

This wavelength dependence is itself a bandpass filter, and will have acted as such in the unfiltered OTR measurements. By convolving this distribution with the theoretically calculated distribution mentioned previously, a comparison with the unfiltered data can be made. This comparison is presented in Fig. 8.

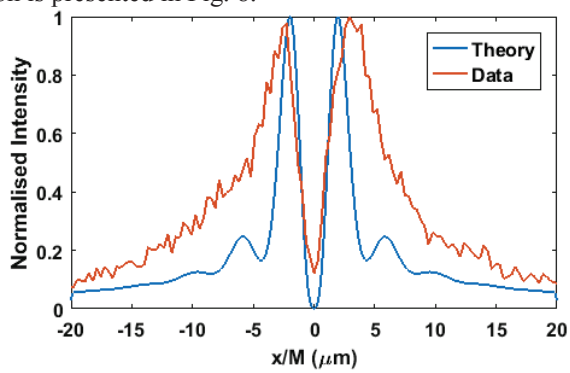

Figure 8: Comparison between the unfiltered OTR data, and the theoretically calculated distribution.

From Fig. 8 it is clear that there is an effect which is not being accounted for and is limiting the resolution of the measurement. The only other effect not being accounted for is the chromatic aberrations of the optics. Although the optics are achromatic, they still have a wavelength dependence. An example wavelength dependence for the type of lens used in the measurements is shown in Fig. 9.

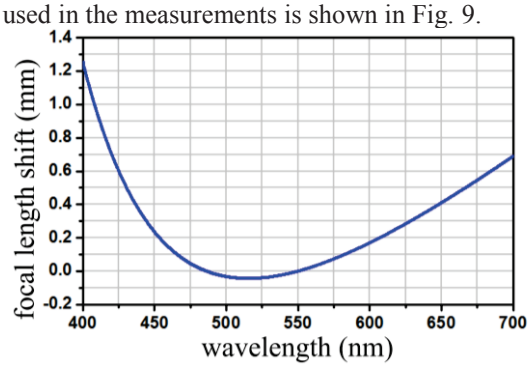

Figure 9: The wavelength dependence of a cemented achromatic doublet from Thorlabs [7].

ISBN 978-3-95450-177-9

It is clear from Fig. 9 that there is still a small wavelength dependency on focal length. This means that for a larger bandpass the optics will begin to introduce a defocussing effect to the OTR image. This will fill in the central minimum and ultimately limit the resolution of the beam size measurement.

CONCLUSION

The measurements taken at ATF2 have led to the conclusion that the defining limitations of this beam size monitoring technique are background light pollution and rms noise. This on-going analysis has begun to direct our attention towards a possible method of combatting these issues; thus improving the resolution of OTR imaging based diagnostics. By optimising the chromatic performance of the optics in the imaging system, a much larger bandpass filter could be used. This would improve the S/N ratio, hereby reducing the impact of rms noise and lifting the value at the centre of the distribution away from the DC background. The achromatic system tested at ATF2 provided a resolution comparable to that of previous measurements [1, 2]. By optimising this system there is potential to increase the resolution to beam size to the sub-micron level. The current plans for this study are to investigate methods of optimising the imaging system via the use of air-spaced doublets, triplets or cylindrical lenses. The next step would be to repeat the OTR measurements at ATF2 with the optimised system. If the sensitivity is indeed increased, then other effects will need to be taken into account. For example, the PSF of the imaging system could no longer be ignored. The effects of diffraction and geometrical aberrations would have to be filtered out of the measurements to improve the resolution further. Measurements to aid in this process have already begun [3]. A systematic analysis of background sources would also help to improve the S/N ratio further.

REFERENCES

[1] K. Kruchinin *et al.*, "Sub-micrometer transverse beam size diagnostics using optical transition radiation", *Jour. of Phys. Conf. Series*, vol. 517, no. 1, p. 012011, May 2014.

[2] B. Bolzon *et al.*, "Very high resolution optical transition radiation imaging system: Comparison between simulation and experiment", *Phys. Rev. ST Accel. Beams*, vol. 18, no. 8, p. 082803, Aug. 2015.

[3] J. Wolfenden *et al*., "High Resolution and Dynamic Range Characterisation of Beam Imaging Systems", in *Proc. 7th Int. Particle Acc. Conf. (IPAC'16)*, Busan, Korea, May 2016, paper MOPMR045, pp. 354-356.

[4] D. Xiang *et al.*, "Theoretical considerations on imaging of micron size electron beam with optical transition radiation", *Nucl. Instr. and Meth. in Phys. Res. A*, vol. 570, no. 3, p. 357-364, Jan. 2007.

[5] H. Zhang *et al.*, "Beam halo imaging with a digital optical mask", *Phys. Rev. ST Accel. Beams*, vol. 15, no. 7, p. 072803, Jul. 2012.

[6] Zemax Optical Studio, optical design and simulation software, URL: http://www.zemax.com

[7] Thorlabs, optical research equipment retailer, URL: http://thorlabs.de

[8] PCO, camera manufacturer and retailer, URL: http://www.pco.de

ISBN 978-3-95450-177-9

PALM CONCEPTS AND CONSIDERATIONS

Pavle Juranić, Rafael Abela, Ishkhan Gorgisyan, Rasmus Ischebeck, Balazs Monoszlai, Luc Patthey, Claude Pradervand, Milan Radović, Volker Schlott, Andrey Stepanov (PSI, Villigen PSI) Rosen Ivanov, Peter Peier (DESY, Hamburg)
Christoph P. Hauri, Leonid Rivkin (EPFL, Lausanne; PSI, Villigen PSI)
Kanade Ogawa, Shigeki Owada, Tadashi Togashi, Makina Yabashi
(RIKEN SPring-8 Center, Sayo-cho, Sayo-gun, Hyogo)
Jia Liu (XFEL.EU, Hamburg)

Abstract

The accurate measurement of the arrival time of a hard x-ray free electron laser (FEL) pulse with respect to a laser is of utmost importance for pump-probe experiments proposed or carried out at FEL facilities around the world. This manuscript presents the Photon Arrival and Length Monitor (PALM), the latest device to meet this challenge, a THz streak camera, and discusses the challenges in its design, use, and analysis of results.

INTRODUCTION

Laser pump, x-ray probe experiments performed at FEL facilities around the world [1, 2, 3, 4, 5] typically want to use short pulse length and intense coherent x-ray radiation to perform experiments with sub-picosecond time resolution. As they go towards improved temporal resolutions, the experiments require accurate measurements of the arrival times of the FEL pulses relative to a laser pump on the sample they are probing. This measurement must also be non-invasive, allowing the experimenters the maximum use of the X-ray beam for their work rather than for diagnostics.

Several methods have been proposed and implemented in the past to meet this diagnostics challenge: transmission/reflectivity spatial and spectral encoding used for soft and hard x-rays at FLASH, SACLA, and LCLS [6, 7, 8, 9], the THz streak camera for soft x-rays at FLASH [10, 11] and other methods [12, 13, 14]. These methods all have their advantages and drawbacks, and the only one that has been attempted for hard x-ray arrival time measurement is the spatial/spectral encoding setup, which has an arrival time accuracy of on the order of 10 fs RMS [6, 9]. The potentially more accurate THz streak camera has not been attempted for use at hard x-ray sources due to the small photoionization cross-section of the gas target and the difficulties in differentiating jitters in the photon energy of the FEL beam from an arrival time signal of the FEL beam by electron spectroscopy. The Photon Arrival and Length Monitor (PALM) prototype chamber [15] developed at the Paul Scherrer Institute (PSI) for the future SwissFEL facility mitigates both of these problems, measuring the pulse length, and the arrival times of hard x-ray FEL pulses relative to a THz pulse and the laser it is generated from.

CONCEPTS

The concept of the THz streak camera has been explained in the past in literature [16, 17, 18], and has shown itself capable of measuring pulse lengths of high-harmonic-generation (HHG) soft x-rays in table-top laser laboratories. The device can also be used to measure the arrival time of the x-ray relative to the THz pulse.

The THz streak camera uses a gas that is photoionized by the x-ray light as an electron emitter. The electrons are then subject to a time-varying vector potential generated by co-propagating THz radiation, the duration of which is longer than the pulse length of the x-ray pulse. A shift in the arrival time of the x-ray pulse translates to a shift in the kinetic energy gained by the electrons in the vector potential. The final kinetic energy of the photoelectrons K_f streaked by the vector potential U_p is

$$K_f = K_0 + 2U_p sin^2(\varphi_0) \pm \sqrt{8K_0U_p}\sin(\varphi_0) \quad (1)$$

where K_0 is the initial kinetic energy of the electrons at the time of ionization, φ_0 is the phase of the vector potential at the time of the ionization, and

$$U_p = \frac{e^2E_{THz}^2(t)}{4m_e\omega_{THz}^2} \quad (2)$$

$E_{THz}(t)$ is the (sinusoidal) THz electric field, e is the electron charge, m_e is the mass of the electron, and ω_{THz} is the frequency of the THz f in radians/s.

The time delay between the external THz field and the FEL pulse is controlled by a translation stage, and time of flight of the electrons under different time delays ise recorded, forming a two dimensional (2D) streaked spectrogram. As shown in Eq.1, the shape of the spectrogram is determined by the THz frequency, initial electron kinetic energy and the vector potential. The time-to-energy map can be extracted by recording the center of mass (COM) kinetic energy of each time delay and shot-to-shot arrival time of the FEL pulses related to the THz pulse are retrieved by recording the single-shot electron kinetic energy when the stage is set at the middle of the time-to-energy slope.

The pulse lengths are measured by looking at the change in spectral width of the kinetic energy of the electrons. A longer pulse will give a longer width, as described in [10, 11].

Since x-ray photoionization cross sections decrease as the x-ray photon energy increases [19], fewer electrons are thus expected to generate from single-shot ionization of the noble gas atoms for hard x-rays. However, the PALM setup

ISBN 978-3-95450-177-9

counterbalanced this effect by using gas from a supersonic pulsed valve [20] that is synchronized to the FEL pulse that increases the sample density in the interaction region, while in the other hand decrease the gas load in the streaking chamber.

SETUP CONSIDERATIONS

The flight path of electrons, and especially low-kinetic-energy electrons, can be affected by magnetic fields, yielding flight times inconsistent with their real kinetic energy. To counteract this issue, the chamber was built out of μ-metal and described in [15]. Two ETF20 Kaesdorf electron time-of-flight (eTOF) spectrometers measured the strength of the streak induced on the photoelectrons by the vector potential of the THz field. This tandem measurement is used to eliminate the photon energy jitter common at FELs from the observed spectra. Furthermore, a third eTOF was placed upstream of the interaction region to measure the non-streaked spectra for single-shot data evaluation of the pulse length. The pressure near the sensor element of the eTOFs, the multi-channel plates (MCPs) should not be on the order of 10^{-6} mbar to prevent sparking and damage to the MCPs. Small pumps are attached to the eTOFs to keep the drift tube under low pressure despite a higher gas load in the chamber. Despite this precaution, the pressure in the main chamber is limited by the tolerance of the MCPs, and should always be checked before the device is started.

The two e-TOF spectrometers in the streaking region, positioned opposite each other, measure exact opposite streaking effects, but measure the same electron kinetic energy shift due to photon energy jitter. The resolution of the eTOFs over the dynamic range of the measurement is controlled by adjusting their drift tube and electrostatic lens settings. By subtracting the average of the two mean kinetic energies from each individual measurement, the photon energy jitter contribution is eliminated, leaving only the clean measurement of the FEL relative pulse arrival time. This calculation can also be achieved by subtracting either of the two streaked eTOFs from the non-streaked eTOF measurement.

The Xe gas is injected into the interaction region by a LaserLab Amsterdam piezo cantilever valve [21] synchronously with the FEL repetition rate. The valve has a 40° conical nozzle with a diameter of 150 μm with a backing pressure of about 3.5 bar above atmospheric pressure. The valve was placed 10 to 12 mm away from the center of the interaction region to deliver the largest amount of gas in the smallest volume possible while not interfering with the flight path of either the THz beam or the FEL pulse. The estimated diameter of the gas target in the interaction region was between 1.2 and 1.5 mm rms. The average pressure in the chamber while the valve was working was 1.1×10^{-5} mbar, with a background pressure of about 3×10^{-7} mbar.

The THz radiation has thus far been generated in a $LiNbO_3$ crystal via the tilted pulse-front pumping method [22] optimized for a high-energy pump [23] by 800 nm laser 5-10 mJ system outside of the chamber and then introduced into vacuum through a z-cut quartz window. The laser intensity should be monitored on a shot-to-shot basis to compensate for the change in the THz field's power in the data analysis. A three inch parabolic mirror focuses the THz radiation 150 mm downstream. Its long focusing distance minimizes the Gouy phase shift [24] effects across the diameter of the gas target. The unfocused x-ray FEL pulses are transmitted though the 3-5 mm hole in the middle of the parabolic mirror and co-propagate with the THz field. High humidity or temperature variations can have an effect on the laser power or the strength of the THz field, so utmost care should be taken to stabilize both in the room the PALM is placed in. A steeper streaking slope gives better results and time resolution.

The setup of the device requires a calibration of the eTOFs to find an accurate electron flight-time to kinetic energy scale. This is best done by either scanning the photon energy of the FEL beam over several hundred electron volts. This process is fairly quick and painless if performed at an FEL with variable gap undulators which can quickly switch to different energies within a few hundred eV of the target energy.

The calibration scan should also record the measured spectral width as a function of the photon energy. The eTOF lensing and retardation systems are usually optimized around one energy—large variations from this sweet spot cause de-focusing effects from the electrostatic lenses, yielding larger measured electron kinetic energy spectral widths than what the FEL delivered. This effect can be corrected for by measuring the response of the spectral width as a function of electron kinetic energy at one photon energy, and then accounted for in analysis later. It is easiest for single-shot evaluations, however, if the sweet spot of the eTOF measurements was made large enough to allow direct comparisons between the streaked and non-streaked spectrum without the need for this additional step. However, since this setup may take a long time, and beam-time at FELs is limited, one must decide whether spending more time on the setup or more time on the data analysis is the best option.

Further tests need to be done to check the accuracy of measurement of the mean kinetic energy of a peak, performed by having to eTOFs measure the same beam at the same time without the THz streak and comparing the variations of the kinetic energies they measure. This measurement is typically accurate to about 0.3-1% of the retarded kinetic energy of the electrons.

ANALYSIS CONSIDERATIONS

There are several effects that have to be accounted for when evaluating the data from a THz streak camera measurement. Some of the most important ones are listed below, along with some suggestions mitigate them.

Spectral width drift and jitter is the tendency of the FEL beam to change the width of its spectrum with time or on a shot-to-shot basis. If a calibration measurement was done

ISBN 978-3-95450-177-9

with one spectral width, and the beam changes this width, the final evaluation for pulse length can be erroneous. The addition of another e-TOF that would measure the non-streaked beam would rectify this problem, seeing any drifts or jitters in the on a shot-by-shot basis.

Space charge is generated in the interaction region as the thousands or millions of atoms are photoionized by the FEL beam. The effect is most easily observed for electrons of low kinetic energies, where even a small space charge can retard the flight of an electron to a measurable degree. High energy electrons, however, are much less sensitive to the space-charge effect, and the few-eV space charge contribution to the streaking strength of a multi-keV electron is negligible.

A large number of electrons flying together through the drift tube of the eTOF have mutual Coulomb repulsions which could distort the original imprint the FEL pulse created at the time of photoionization. This can cause the perceived spectral width to be larger than the real one. However, simulations done with SimION have shown that the contribution from such repulsions for 1000-2000 high-KE electrons flying simultaneously through the drift tube, a number that is typical for a single peak observed by the eTOFs, is small, on the level of a percent or less of the spectral width. The effect is noticeable for low kinetic energy electrons (few eV-10s of eV) since they have more time to separate themselves in the drift tube.

The algorithms for the analysis have to be carefully considered as well. While the measurement of the arrival time is fairly simple, and can be performed by looking at the mean peak energy and its shift from the non-streaked spectra, the width evaluations can be affected by strange timing or spectral features of the FEL pulse. If the FEL pulse is not spectrally Gaussian for some reason, a Gaussian fit becomes very hard. In this case, one can consider using a straight rms evaluation of the data, though one must be very careful in choosing the peak area where the data is evaluated. The area has to be consistent for both the streaked and non-streaked cases, which may be hard as the streaked spectrum is typically broader and lower than the non-streaked one. Typically, this process involves the programming of the algorithm to find minima on either side of the peak that are still above the noise threshold, and then the evaluation of the rms distribution between these two points.

CONCLUSIONS

The PSI-developed PALM device will measure the arrival time and pulse length of hard x-rays at SwissFEL. Because it is a gas-based measurement method, it is also less intrusive than most other methods and allows for the use of the FEL pulse for experiments further downstream with a minimal loss of intensity or wavefront distortion.

REFERENCES

[1] W. Ackermann *et. al.,* "Operation of a Free-Electron Laser from the Extreme Ultraviolet to the Water Window," *Nature Photonics,* vol. 1, p. 336, 2007.

[2] P. Emma *et. al.,* "First Lasing and Operation of an Angstrom-wavelength Free-electron Laser," *Nature Photon,* vol. 4, p. 641, 2010.

[3] D. Pile *et. al.,* "X-rays First Light from SACLA," *Nature Photon,* vol. 5, p. 436, 2011.

[4] E. Allaria *et. al.,* "The FERMI@Elettra Free-electron-laser Source for Coherent X-ray Physics: Photon Properties, Beam Transport System and Applications," *New J. Phys,* vol. 12, p. 075002, 2010.

[5] P. Oberta *et. al.,* "The SwissFEL Facility and its Preliminary Optics Beamline Layout," *Proceedings of SPIE,* vol. 8079, p. 807805, 2011.

[6] M. Bionta *et. al.,* "Spectral Encoding of X-ray/Optical Relative Delay," *Optics Express,* vol. 19, p. 21855, 2011.

[7] M. Beye *et. al.,* "X-ray Pulse Preserving Single-shot Optical Cross-correlation Method for Improved Experimental Temporal Resolution," *Appl. Phys. Lett.,* vol. 100, p. 121108, 2012.

[8] O. Krupin *et. al.,* "Temporal Cross-correlation of X-ray Free Electron and Optical Lasers Using Soft X-ray Pulse Induced Transient Reflectivity," *Optics Express,* vol. 20, p. 11396, 2012.

[9] M. Harmand *et. al.,* "Achieving Few-femtosecondtime-sortingathard X-ray Free-electronlasers," *Nature Photon.,* vol. 7, pp. 215-218, 2013.

[10] I. Grguras et. al., "Utrafast X-ray Pulse Characerization at Free Electron Lasers," *Nature Photon,* vol. 6, p. 852, 2012.

[11] U. Frühling *et. al.,* "Single-Shot Terahertz-Field-Driven X-ray Streak Camera," *Nature Photon,* vol. 3, p. 353, 2009.

[12] F. Tavella *et. al.,* "Few-femtosecond Timing at fourth-generation X-ray Light Sources," *Nature Photon,* vol. 5, p. 162, 2011.

[13] S. Duesterer *et. al.,* "Femtosecond X-ray Pulse Length Characterization at the Linac Coherent Light Source Free-electron Laser," *New J. PHys,* vol. 13, p. 093024, 2011.

ISBN 978-3-95450-177-9

[14] R. Riedel *et. al.,* "Single-shot Pulse Duration Monitor for Exterme Ultraviolet and X-ray Free Electron Lasers," *Nature Comm.,* vol. 4, p. 1731, 2013.

[15] P. Juranic *et. al.,* "A Scheme for a Shot-to-shot, Femtosecond-resolved Pulse Length and Arrival Time Measurement of Free Electron Laser X-ray Pulses that Overcomes The Time Jitter Problem Between the FEL and the Laser," *JINST,* vol. 9, p. P03006, 2014.

[16] M. Hentschel et. al., "Attosecond Metrology," *Nature,* vol. 414, p. 509, 2001.

[17] M. Drescher et. al., "X-ray pulses approaching the attosecond frontier," *Science,* vol. 291, p. 1923, 2001.

[18] M. Uiberecker *et. al.,* "Attosecond Metrology with Controlled Light Waveforms," *Laser Physics,* vol. 15, p. 195, 2005.

[19] B. L. Henke, E. M. Gullikson and J. C. Davis, "X-ray interactions: photoabsorbtion, scattering, transmission, and reflection at E=50-30,000 eV, Z=1-92," *At. Data Nucl. Data Tables,* vol. 54, pp. 181-342, 1993.

[20] G. N. Makarov and A. N. Petin, "Investigation of Atomic and Molecular Clustering in a Pulsed-Gas Dynamic Jet with a Pyroelectric Detector," *Journal of Experimental and Theoretical Physics,* vol. 107, pp. 725-733, 2008.

[21] D. Irimia *et. al.,* "A short pulse (7msFWHM) and high repetition rate (dc-5kHz) cantilever piezovalve for pulsed atomic and molecular beams," *Rev. Sci. Inst.,* vol. 80, p. 113303, 2009.

[22] J. Hebling *et. al.,* "Velocity matching by pulse front tilting for large area THz-pulse generation," *Opt. Express,* vol. 10, pp. 1161-1166, 2002.

[23] A. G. Stepanov *et. al.,* "Mobile Source of High-energy Single-cycle Terahertz Pulses," *Appl. Phys. B,* vol. 101, pp. 11-14, 2010.

[24] A. B. Ruffin *et. al.,* "Direct Observation of the Gouy Phase Shift with Single-Cycle Terahertz Pulses," *Phys. Rev. Lett.,* vol. 17, p. 3410, 1999.

ISBN 978-3-95450-177-9

RECENT DEVELOPMENTS FOR INSTABILITY MONITORING AT THE LHC

T.E. Levens*, K. Łasocha, T. Lefevre, CERN, Geneva, Switzerland

Abstract

A limiting factor on the maximum beam intensity that can be stored in the Large Hadron Collider (LHC) is the growth of transverse beam instabilities. Understanding and mitigating these effects requires a good knowledge of the beam parameters during the instability in order to identify the cause and provide the necessary corrections. This paper presents the suite of beam diagnostics that have been put into operation to monitor these beam instabilities and the development of a trigger system to allow measurements to be made synchronously with multiple instruments as soon as any instability is detected.

INTRODUCTION

The first run of the Large Hadron Collider (LHC), from 2009 to 2013, saw transverse beam instabilities at injection and during physics fills while running with 50 ns bunch spacing at an energy of 3.5 TeV [1]. The second physics run, beginning in 2015, has moved to 25 ns bunch spacing, increasing electron cloud and other collective effects [2]. Other changes, such as tighter collimator settings at 40 cm β^* [3] and strict limits on beam loss at the increased operating energy of 6.5 TeV [4], mean that the mitigation of beam instabilities has continued to be an important consideration.

The availability of diagnostics to characterise beam instabilities is important, both for qualifying experimentally the LHC impedance model [5] and for making the correct adjustments to the machine settings if instabilities occur during operation.

The recently deployed LHC Instability Trigger Network [6], based on White Rabbit technology [7], enables bi-directional trigger distribution between instruments capable of detecting and observing beam instabilities. The first major use of the network has been to trigger the LHC head-tail monitor [8] with a trigger algorithm running on the base-band tune (BBQ) system [9].

HEAD-TAIL MONITOR

A workhorse instrument used for characterising beam instabilities is the LHC head-tail monitor. The system, shown in Fig. 1, is based on the high speed acquisition of a long stripline type beam-position monitor (BPM). A commercial wideband 180° hybrid generates the sum and difference of the BPM electrodes and these signals are directly digitised with a 10 GSPS 8 bit digitizer located close to the beam line in a service gallery.

The head-tail monitor was originally installed in the CERN-SPS for chromaticity measurements by the observation of the phase shift between the head and tail of the bunch [8]. Because of the high bandwidth of the BPM and acquisition system, it can also be used for direct time-domain measurements of intra-bunch motion. Although it can provide direct information about the beam stability, the minimum detectable oscillation amplitude is limited by the dynamic range of the acquisition system. A second limitation is the available acquisition memory and data readout speed. The commercial oscilloscopes used in the LHC are limited to 11 turns for all bunches (1 ms of data) and take approximately 10 seconds to read out. These two factors require that the head-tail monitor be precisely triggered once the oscillation amplitude has reached a sufficient level to be visible, but before significant beam loss leads to a beam abort.

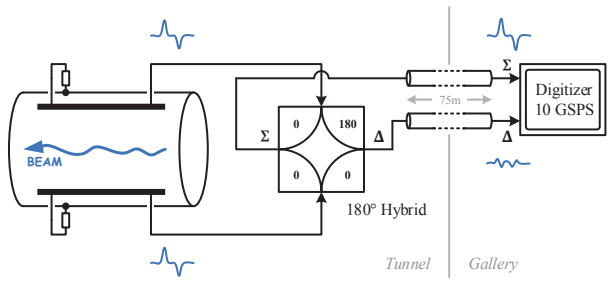

Figure 1: Block diagram of the LHC head-tail monitor.

New digitizers [10] are being tested that feature much larger acquisition memories, capable of storing up to 1.6 s of data. While easing the trigger requirements, the increased data size of up to 64 GB per acquisition poses serious challenges for data storage and processing.

Data Processing

The raw data from the head-tail monitor requires a number of post processing steps in order to obtain useful information about the bunch stability. During the first LHC run, where the head-tail monitor was primarily used for measurements during machine development sessions, the processing was performed manually. In order to understand instabilities that occur during normal operation, the head-tail monitor is now used on a day-to-day basis generating large quantities of data. To help with extracting useful information from these large data sets, an automatic method for determining if an acquisition contains an instability has been developed.

The first step is to determine which, bunch slots are actually filled with beam. For this, a single turn of data from the sum signal of the head-tail pickup is divided into 25 ns intervals. Each of these "bunch slots" is then further subdivided into five 5 ns segments and the maximum signal amplitude in each of these is calculated. For a slot where no

* tom.levens@cern.ch

ISBN 978-3-95450-177-9

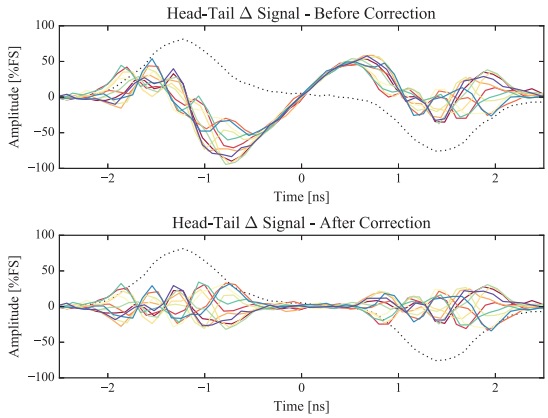

Figure 2: A mode $|m| = 4$ instability, captured by the head-tail monitor, before and after the baseline removal.

bunch is present, all of the 5 ns segments will contain only noise and will therefore be of similar amplitude. For a slot where a bunch is present (LHC bunches are typically 1 ns in length), at least one 5 ns segment will have a data point of much higher amplitude. A simple threshold comparison can therefore be used to determine if a bunch is present or not. The threshold is set such that nominal intensity bunches ($N_b = 1.1 \times 10^{11}$) will be reliably detected while "pilot" bunches ($N_b = 5 \times 10^9$) will be ignored. These threshold settings avoid saving files which only contain low intensity bunches, as the head-tail monitor does not have enough dynamic range to see oscillations of pilot bunches when set up for nominal intensities.

Secondly, the data for each bunch must be aligned over all of the acquired turns. As the sampling rate of the digitizers is constant, the number of samples per turn changes due to variations of the frequency of the LHC RF system. To determine the correct number of samples per turn, the sum signal of a single populated bunch slot is used. An approximate value is taken as a starting point and the overlap of the two turns is changed in steps to search for the best fit. The scan is repeated for both decreasing step sizes and by comparing to more distant turns to obtain the required precision.

Finally, the large, constant, difference signal "baseline", present due to both the beam orbit offset in the head-tail pick-up and non-linearities of the hybrids, needs to be removed. The mean of the corresponding samples in each turn is computed over all turns and this mean is then subtracted from each turn. For example, for a sample a_n in turn t the corrected sample is obtained with:

$$a_n(t) = a_n(t) - \sum_{\tau=1}^{\tau=T} \frac{a_n(\tau)}{T}$$

where T is the number of turns of data acquired. This procedure is complicated by the fact that the number of samples between turns is not an integer number, as the sampling frequency is not linked to the beam's revolution frequency. Before the mean can be calculated, the data from each turn needs to be interpolated, for which a simple linear interpolation is used. The mean value is then re-interpolated to the original sample points of each turn before subtraction.

Finally the amplitude of the instability can be approximated by looking at the ratio of the difference signal amplitude inside and outside the bunch area. The mode number can be determined by searching for the zero-crossing points of the difference signal within the bunch. By automatically processing the head-tail monitor data, "uninteresting" acquisitions, for example those containing no bunches or no visible oscillations, can be removed to limit the amount of data which needs to be evaluated manually.

An example of a mode $|m| = 4$ instability, captured during a 2015 MD session, is shown in Fig. 2, both before and after the baseline removal. The plot overlaps 11 turns of the difference signal from a single bunch such that the stationary nodes within the bunch can be seen. The dotted line shows the corresponding sum signal. Also visible is the characteristic response of the stripline BPM with the first pulse followed by an inverted reflection after twice the length of the stripline. The 40 cm long "BPLX" type BPM, used as the LHC head-tail pickup, is dimensioned to ensure that the two pulses are well separated in time to avoid cancellation.

INSTABILITY TRIGGER

The LHC base-band tune (BBQ) system is based on diode peak detectors that convert the high-frequency signal from the BPM to a low-frequency "oscillation" signal that can be sampled with high resolution audio ADCs [9]. Because of its high dynamic range, the BBQ has the chance to detect the onset of an instability before any other instrument and can serve as a trigger source for less sensitive diagnostics.

Under optimal conditions, a growth in amplitude of the time-domain BBQ signal is a reasonable indication of the appearance of an instability. In this case, the eigenmode of the oscillation becomes the dominant component of the spectrum and gives the biggest contribution to the amplitude of the signal. However, with a high number of bunches and high transverse damper gain, the BBQ signal can be dominated by other noise sources. While still possible to detect, a single bunch becoming unstable then has a much lesser effect on the overall amplitude of the signal.

The first version of an instability trigger algorithm, called the "three-averages" algorithm, was developed in 2013 based on simulated data [11]. For the startup in 2015, the trigger algorithm was deployed on the BBQ to gain experience with its performance under operational beam conditions. Although the algorithm was found to perform well with optimal conditions, during physics fills it proved to be extremely sensitive to small fluctuations resulting in spurious triggers. A second algorithm, called the "increasing-subsequence" algorithm, has been developed using a different principle which attempts to reduce the number of false positives under operational conditions.

ISBN 978-3-95450-177-9

Three-Averages Algorithm

This algorithm computes the average of the standard deviation about the mean of the signal over three different time windows. The window lengths are proportioned so that $W_{short} < W_{med} < W_{long}$. Under stable conditions, it is expected that $\sigma_{short} \approx \sigma_{med} \approx \sigma_{long}$. During an instability, the amplitude of the input signal increases and the averages change with a rate that corresponds to the length of their windows. Then the following inequalities will hold:

$$\sigma_{short} - \alpha\sigma_{med} > 0$$
$$\sigma_{med} - \beta\sigma_{long} > 0$$

where $\alpha, \beta > 1$ are coefficients chosen to reduce the influence of noise. Fulfilling these conditions for many consecutive turns is a clear indicator of a growing instability. To detect this condition a counter (C) is initialised to zero and is incremented on each turn by the normalised difference of each pair of window functions:

$$C = C + w_\alpha \frac{\sigma_{short} - \alpha\sigma_{med}}{\sigma_{short} + \sigma_{med}} + w_\beta \frac{\sigma_{med} - \beta\sigma_{long}}{\sigma_{med} + \sigma_{long}}$$

where w_α, w_β are weighting factors corresponding to the number of turns sufficient to confirm the presence of an instability for this window. Once the counter reaches a threshold value, a trigger is generated and the counter is reset to zero. In order not to generate a large number of consecutive triggers, the counter is held at zero for a short "holdoff" period after each trigger.

Increasing-Subsequence Algorithm

For a given sequence of values (Q) that are oscillating independently around a constant value, for example the steady state amplitude of a stable beam, a subsequence (S) can be defined that consists of the elements that are the maximal ones up to their appearance. In the steady state, it can be shown that the expected length of the subset S is approximately a logarithmic function of the length of Q with a standard deviation lower than the square root of the length [12]. The situation changes dramatically if the values in a sequence correspond to a rapid growth in amplitude, because there is a much higher probability that the current amplitude will be larger than previous one.

A second algorithm for instability detection can then be described by the following procedure. As with the three-averages algorithm, a counter is used to track the instability growth. On each new sample, the maximum value in the last n samples is found. If it is the newest sample, the counter is incremented by one, while if it is the oldest sample, the counter is decremented by a set value. Once the counter reaches a threshold value a trigger is again generated.

In order to reduce the probability of a trigger caused by the large transient seen at beam injection, a further check is made on each sample. If the value is significantly greater than maximum in the last n samples it indicates a transient rather than an instability and can therefore be filtered.

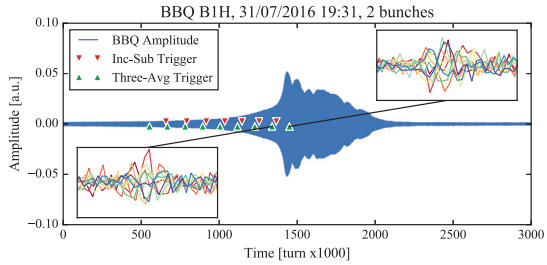

Figure 3: Comparison of the trigger algorithms during an instability with a two nominal bunches with markers indicating the trigger points of each algorithm. The inset plots show the head-tail monitor acquisition for the indicated triggers.

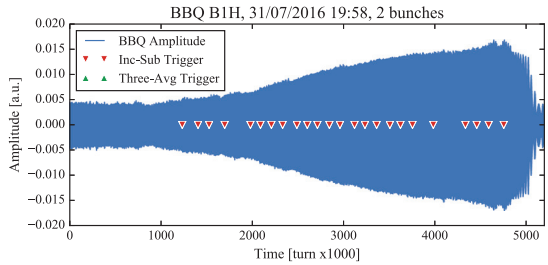

Figure 4: A slower instability, again with two nominal bunches, which is unseen by the three-averages algorithm but is detected by the increasing-subsequence algorithm.

Comparison Between the Algorithms

In order to compare their performance, both algorithms have been simulated during known instability events with various beam conditions where the data from the BBQ and head-tail monitor have been stored.

Figure 3 shows an example of an instability with only two nominal bunches in the machine where both algorithms perform in a similar fashion. However, if the instability rise time is slower, as shown in Fig. 4, the three-averages algorithm does not trigger as all three averages follow the rise in amplitude and their difference is never big enough to generate a trigger. For cases like this, the increasing-subsequence algorithm is a clear improvement as it detects the amplitude increase and generates triggers.

One important requirement for the new algorithm was to avoid triggering on injection transients. The behaviour of the two algorithms to an injection seen by the BBQ is shown in Fig. 5. The three-averages algorithm triggers on the large increase of amplitude caused by the injection event as σ_{short} increases rapidly above σ_{med} and σ_{long} with the counter quickly reaching its threshold. In comparison, the increasing-subsequence algorithm filters the transient and is able to trigger on a subsequent rise in BBQ amplitude which could be indicative of an instability.

For conditions where there are only a small number of bunches in the machine, it is clear that the increasing-subsequence algorithm improves upon the three-averages algorithm, generating triggers for slow instabilities and being

ISBN 978-3-95450-177-9

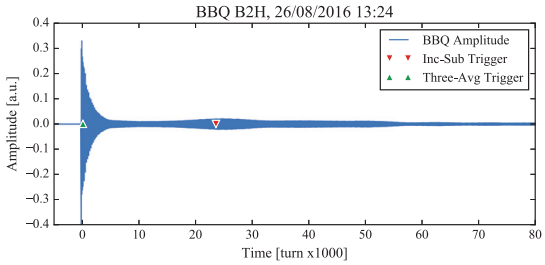

Figure 5: Comparison of the trigger algorithms during the transient caused by an injection.

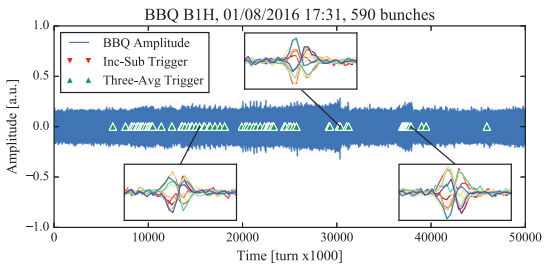

Figure 6: Instabilities with 590 nominal bunches that are seen by the three-averages algorithm but that would not be detected by the increasing-subsequence algorithm.

insensitive to injection transients. However, in cases with a larger number of bunches, the difference in amplitude during the instability can be less prominent on the BBQ if only a small subset of bunches become unstable. A case like this is shown in Fig. 6. As it is very sensitive to changes in amplitude, the three-averages algorithm is able to detect these instabilities while the increasing-subsequence algorithm is not.

FUTURE DEVELOPMENTS

A multi-band instability monitor (MIM) [13] is under development to provide an alternate trigger source and complement the BBQ instability trigger. By looking at the spectral power contained in different frequency bands the MIM can provide information about the instability mode as well as detecting the presence of an instability. The initial version of the MIM splits the signal with a RF filter bank into eight bands from 400 MHz to 3.2 GHz. The acquisition for each band is then performed with diode detectors and high-resolution ADCs, similar to that of the BBQ. Commissioning of the MIM with beam is expected before the end of the 2016.

CONCLUSION

Measurement and mitigation of beam instabilities is an important consideration for the second physics run of the LHC. The head-tail monitor provides a direct measurement of intra-bunch motion and is an important instrument for classifying the type of instability. However, due to the limitations of its high-speed acquisition system, it has to be accurately triggered to catch the oscillation once it reaches a sufficient amplitude. For this, an instability trigger based on the sensitive BBQ system has been developed and two separate algorithms for detection have been tested with various beam conditions. The BBQ is now used to trigger the head-tail monitor regularly during operation for instability analysis. In order to deal with the large amount of data produced by the head-tail monitor, methods to automatically process the data and identify the acquisitions containing unstable bunches have been developed, greatly aiding the subsequent off-line analysis. Finally, to provide additional instability information, a multi-band instability monitor has been installed in the LHC is currently being commissioned.

REFERENCES

[1] E. Métral *et al.*, "Review of the Instabilities Observed During the 2012 Run and Actions Taken" in *LHC Beam Operation Workshop*, Evian, France, 2012.

[2] G. Iadarola *et al.*, "Electron Cloud Effects", in *6th Evian Workshop on LHC Performance*, Evian, France 2015.

[3] A. Mereghetti, "β^*-Reach - IR7 Collimation Hierarchy Limit and Impedance", CERN, Geneva, Switzerland, CERN-ACC-NOTE-2016-0007, Jan. 2016.

[4] A. Lechner *et al.*, "BLM thresholds for post-LS1 LHC operation: UFOs and orbit bumps in the arcs and straight sections", in *Workshop on Beam Induced Quenches*, CERN, Geneva, Switzerland, 2014.

[5] L.R. Carver *et al.*, "Current Status of Instability Threshold Measurements in the LHC at 6.5 TeV", in *7th Int. Particle Accelerator Conf.*, Busan, Korea, 2016.

[6] T. Włostowski *et al.*, "Trigger and RF Distribution Using White Rabbit", in *15th Int. Conf. Accelerator and Large Experimental Control Systems*, Melbourne, Australia, 2015.

[7] J. Serrano *et al.*, "The White Rabbit Project", in *2nd Int. Beam Instrumentation Conf.*, Oxford, UK, 2013.

[8] S. Fartoukh & R. Jones, "Determination of Chromaticity by the Measurement of Head-Tail Phase Shifts: simulations, results from the SPS and a robustness study for the LHC", CERN, Geneva, Switzerland, CERN-LHC-Project-Report-602, Jul. 2002.

[9] M. Gasior, "Faraday Cup Award: High Sensitivity Tune Measurement using Direct Diode Detection", in *Beam Instrumentation Workshop*, Newport News, VA USA, 2012.

[10] Guzik Technical Enterprises, "ADC 6000 Series AXIe Digitizer Modules", Available: `http://www.guzik.com/documents/products/02-107560-04_AXIe_ADC_6000_Series.pdf`

[11] J. Ellis & R.J. Steinhagen "Level-1 Trigger Development for the Multi-Band Instability Monitor", CERN, Geneva, Switzerland, CERN-STUDENTS-Note-2013-103, Aug. 2013.

[12] N. Glick, "Breaking Records and Breaking Boards", American Mathematical Monthly, vol. 85: 2—26, 1978.

[13] R.J. Steinhagen, M.J. Boland & T.G. Lucas, "A Multiband-Instability-Monitor for High-Frequency Intra-Bunch Beam Diagnostics", in *2nd Int. Beam Instrumentation Conf.*, Oxford, UK, 2013.

ISBN 978-3-95450-177-9

MULTI-LASER-WIRE DIAGNOSTIC FOR THE BEAM PROFILE MEASUREMENT OF A NEGATIVE HYDROGEN ION BEAM IN THE J-PARC LINAC *

A. Miura#, K. Okabe, M. Yoshimoto
J-PARC Center, Japan Atomic Energy Agency, Tokai, Ibaraki, Japan
I. Yamane
High Energy Accelerator Research Organization, Tsukuba, Ibaraki, Japan

Abstract

One of the major missions of Japan Proton Accelerator Research Complex (J-PARC) is the establishment of high-brilliance beam operation. For this purpose, transverse profile monitors play crucial roles in obtaining information concerning beam-mismatching factors and emittance evolution for the linac beam tuning. A wire scanner monitor using metallic wire is currently reliably operated in the J-PARC linac. Because the beam loading on a wire increases under high-current beam operation, we focus on using a laser-wire system as a nondestructive monitor. Additionally, we propose the use of a new multi-laser-wire system. In this study, we propose the multi-laser-wire system and its application. Finally we discuss its advantages over the present profile monitoring system.

INTRODUCTION

In the J-PARC linac, the negative hydrogen ion beam is accelerated to 400 MeV. The repetition rate is increased to be from 25 to 50 Hz. Half of the 400-MeV beams are injected into the downstream synchrotron (rapid cycling synchrotron (RCS)), whereas the other half are transported to the planned experimental laboratory of the accelerator-driven transmutation facility.

One of the important issues for high-current, high-brilliance accelerators is the understanding of beam dynamics. A wire scanner monitor (WSM) that employs a thin metallic wire is reliably operated in multiple accelerator facilities around the world to suppress excess beam loss and mitigate beam halo evolution. Because the heat loading on a metallic wire is increased under high-current beam tuning, we focus on using a laser-wire system as the nondestructive beam diagnostic device. In addition, we propose a new multi-laser-wire system [1,2] that uses a pair of concave mirrors with different focal lengths to form multiple laser beam paths, and the beam waists of the laser paths are aligned in principle. In this study, we propose the multi-laser-wire system and its application to beam-profile monitoring.

BEAM SPECIFICATION OF THE J-PARC LINAC

The linac comprises a 50-keV negative hydrogen ion source (IS), a 3-MeV radio frequency quadrupole cavity (RFQ), a 50-MeV drift tube linac (DTL) a 191-MeV separated-type DTL (SDTL), and a 400-MeV annular ring-coupled structure (ACS) [3] as shown in Fig. 1. The ACS-type bunchers are placed between the SDTL and the ACS cavities for longitudinal matching because the operating frequency is 972 MHz for the ACS, which is a threefold frequency jump over that for the SDTL. The ACS downstream is the beam transport line to the RCS.

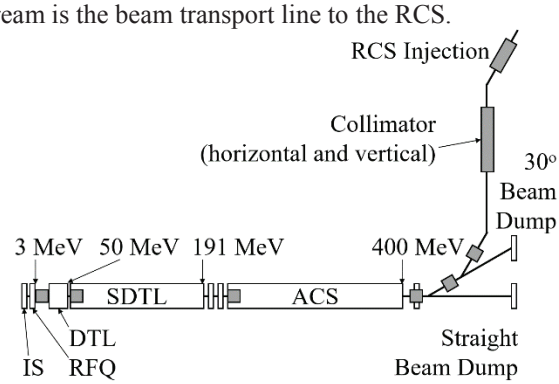

Fig. 1. Beam-line layout of Japan Proton Accelerator Research Complex (J-PARC) linac.

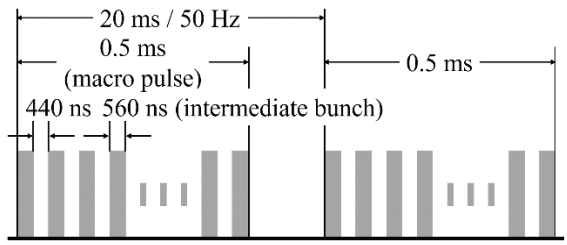

Fig. 2. Time structure of pulsed beam in linac.

The time structure of the pulsed beam in the linac, which is shaped by an RF chopper cavity for RCS injection, is shown in Fig. 2. The beam pulse comprises a 324-MHz micro-bunch, a 560-ns intermediate bunch length, and a 0.5-ms macro-pulse length with 25-Hz repetitions. The shortest pulse duration we can observe occurs during the 3.01-ns micro-pulse.

The metallic wire in a WSM collides with the accelerated beam and destroys a part of it as beam loss. Because it has a high dynamic range in principle [4], we have used it to tune the quadrupole magnets. Tungsten wire has been used due to its high melting point, and its diameter was decided based on the thermal balance and signal gain [4]. However, high beam-current resistance will be required in a device for beam profile measurement. In addition, because the radiation during a high peak current operation should be mitigated, it is important to realize a nondestructive profile monitor based on the laser-wire system.

#akihiko.miura@j-parc.jp

ISBN 978-3-95450-177-9

MULTI-LASER-WIRE DESIGN

Let us consider an optical system, as shown in Fig. 3, which comprises two concave mirrors with different focal lengths of curvature arranged such that both axes and focal points coincide [5]. The focal length of mirror 1 (or 2) is f_1 (or f_2). We refer to confocal point as "a," the points at which the laser beams passes through the plane containing the confocal point and is perpendicular to the axis c_n and the points on mirrors 1 and 2 at which laser beams are reflected at d_n and b_n, respectively.

A laser beam is injected in parallel with the axis of the cavity from the back, and it passes through c_0 just outside of the mirror 2, forming a waist. Then, it is reflected at d_0 on the mirror 1. Since the injected laser beam is in parallel with the axis, the laser beam reflected at d_0 passes through the focal point "a" of mirror 1 and reaches b_1.

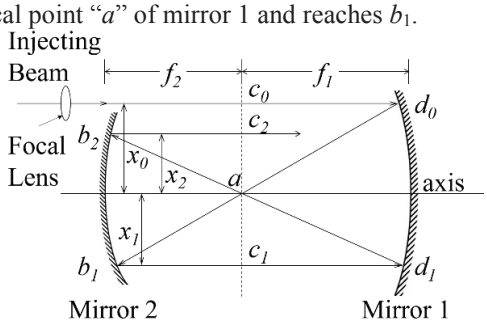

Fig. 3. Asymmetrical confocal cavity and the paths of multiple laser beam.

When the quality of the laser beam is sufficiently high, the intensity distribution is considered to be Gaussian. A Gaussian laser beam is characterized by two parameters; its half-waist size (w), which is defined as the radius where the laser beam intensity is $1/e^2$ of the peak value, and its Rayleigh range (z).

Because "a" is the confocal point of mirrors 1 and 2, the laser beam reflected at b_1 is in parallel with the cavity axis and forms a waist at c_1. Then, the laser beam reflected at d_1 returns to "a" again, forming a waist. Thus, the laser beam repeats triangular paths, and reaches "a" as a waist every time, reducing the separation of the path from the cavity axis with an increase of n.

Here, let us consider the distance between the parallel laser paths. The definition of the distance of the injected laser beam from the axis is x_0, and the first path is formed from b_1 to d_1. The distance of the first path from the axis is assumed to be x_1, and this can be described as follows:

$$x_1 = (f_2/f_1)\, x_0.$$

Then, we estimate the laser-wire position of the nth path using the following equation:

$$x_n = (f_2/f_1)^n\, x_0. \quad (1)$$

When x_0 is negligibly smaller than the distance between mirrors 1 and 2 ($f_1 + f_2$), the distance between c_0 and mirror 1 nearly corresponds to the length f_1. When the Gaussian laser beam is irradiated to the mirror 1 from the back of mirror 2 and the focal lens is set to form a waist at c_0, the waist is also formed at c_1. The beam waist at c_0 is w_0 and that at c_1 is w_1. These are related through the wave length of the laser beam (λ) expressed as follows:

$$w_0 w_1 = \lambda f_1/\pi\,. \quad (2)$$

This relation describes the waist of each laser path. Therefore, the waist radius (w_1) can be expressed as follows:

$$w_1 = (\lambda f_1/\pi)/w_0, \quad (3)$$

Then, we can estimate the waist of the nth laser path (w_n) at c_n using w_0:

$$w_n = (f_2/f_1)^n\, w_0. \quad (4)$$

DEMONSTRATION OF MULTI-LASER-WIRE FORMATION

To examine the formation of the multi-laser wire in a confocal cavity, we assembled the optical setup shown in Fig. 4 using a He–Ne laser with a wavelength of 515 nm. A laser oscillator and a pair of confocal mirrors are set on a guide rail. Because we choose a pair of mirrors with focal lengths of f_1 (435 mm) and f_2 (417 mm), the mirrors are set at a distance of 852 mm. The diameters of the mirrors are the same at 50 mm. We cut an edge of 2.0 mm of mirror 2 for the laser axis to have an offset of 25 mm from the center axis because the beam should be injected from the backside of mirror 2.

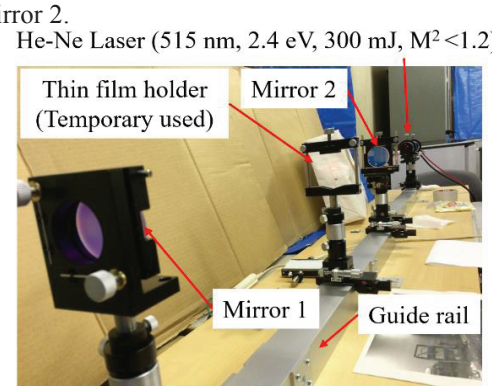

Fig. 4. Optical setup of an asymmetrical confocal cavity.

We set the thin-film target to observe the waist of the multiple laser spots on the guide rail between mirrors 1 and 2, where the film position is adjusted to the line of c_0, c_1, c_2, …, c_n that is perpendicular to the center axis. The aligned multi-laser spots on the target are clearly observed in Fig. 5.

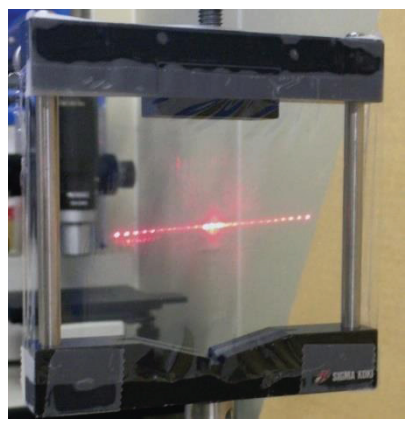

Fig. 5. Laser beam spots of multi-laser wire on a thin-film plane including the confocal point and vertical to the cavity axis.

ISBN 978-3-95450-177-9

The laser beam spots at c_n approach "a" as n increases, and all laser beams reflected by mirror 1 gather at "a" and are stacked up. Eq. (4) suggests the spot size, suggesting that the waist of the laser beam decreases if $f_2 > f_1$.

As a next step, the quantitative measurement of the laser beam intensity distributions on the upper or lower sides of the confocal point are prepared to clarify the extent to which the turns stack up. To compensate the light intensity of each laser wire, we measure the intensity using a photodiode and a micro-mirror, which comprises a golden wire with a ϕ30-mm diameter. The mirror surface is produced via a compression with the optical flat surface (Fig. 6). When the micro-mirror is mechanically scanned with small steps (−0.01 mm), each laser path can be independently reflected.

The intensity measurement result is shown in Fig. 7. A horizontal axis shows the position of the micro-mirror from c_0 to the center of confocal cavity "a." The vertical axis shows the signal gain from the photodiode. Because the diameters of the laser spots decrease from c_0 to "a" in principle, the signal gain relatively increases. We can count over 24 laser spots at the top half of the center axis. As the distance between the spots decreases, spots are overlapped around the center axis.

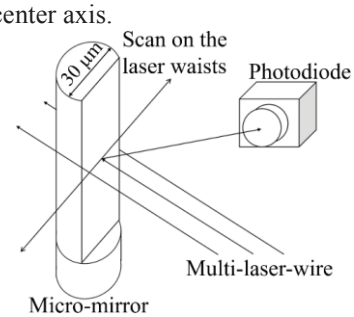

Fig. 6. Image of laser intensity measurement using a micro-mirror.

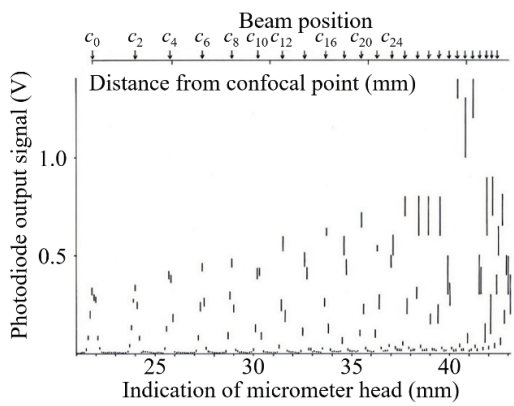

Fig. 7. Position dependence of the multi-laser-wire intensity.

DESIGN OF THE BEAM PROFILE MONITOR USING MULTI-LASER WIRE

When we design the beam profile monitor using the multi-laser wire, we should consider the system configuration in terms of collisions between the laser wires and the accelerated beam bunches to the greatest extent possible. Because the destination of the laser beam is the center axis of the mirrors and the laser wires gather to the center axis, we can use the top half or bottom half of the face aligned on the laser wires shown in Fig. 3. In Fig. 3, the direction of the accelerated beam is perpendicular to the face.

Wavelength of the Laser Beam

When the wavelength of the laser beam matches the ionization cross-section in Fig. 8, we can obtain an electron and a neutral hydrogen atom (H^0) from a negative hydrogen ion. This process is known as photodetachment. When the laser beam with wavelength λ_{LF} collides with the accelerated beam with an energy of βc (where c denotes light velocity) and an incident angle (α), its wavelength (λ_{PRF}) is shifted by the Doppler effect expressed as follows:

$$\lambda_{PRF} = \lambda_{LF}/\gamma(1 + \beta\cos\alpha). \quad (5)$$

The photodetachment cross-section of a negative hydrogen ion on the wavelength of the irradiated laser beam is shown in Fig. 8 [6]. A considerably broad peak is observed to be centered at approximately 800 nm, and the cross-section is approximately 4×10^{-17} cm^2 over a range of ±100 nm around the center. Using visible laser light (λ_{LF} = 380–800 nm), we can obtain a large cross-section with an injection angle α at a beam energy β using Eq. (5).

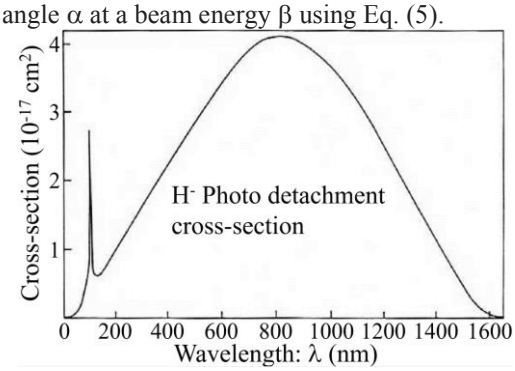

Fig. 8. Photodetachment cross-section of a negative hydrogen ion [6].

Optical Design

When we choose the curvature radius and the focal length of a pair of confocal mirrors, the system configuration of the total length as well as the laser radius and the distances of multiple laser paths are defined by Eqs. (1) and (4). In the J-PARC linac, the smallest transverse beam size is designed upward of the ACS section and the one measured by the WSMs has a root-mean-square (RMS) value of approximately 2.0 mm (Fig. 9). The beam halo is observed in the beam profile measurement under 1/10 of the magnitude of the beam center [7]. The specifications of the beam profile monitor are required to observe the beam halo such that the dynamic range of the laser beam profile monitor should be over two orders of magnitude. Transverse resolution is required to be approximately 0.1–0.5 mm as in the case of the WSM. The top half of the confocal cavity in Fig. 3 is chosen to be used to avoid the focal point "a" which is the laser beam destination. The even-numbered laser path formed by c_0, c_2, c_4, …, c_{2n} is employed for the

ISBN 978-3-95450-177-9

profile monitor, and the laser wire is aligned with a distance of 0.1–0.5 mm. To form a proper span in each laser wire, we should choose appropriate focal lengths as f_1 and f_2 to set the x_0, x_2, x_4, …, x_{2n} values around 0.1 mm. If the ratio of f_2 and f_1 increases ($f_2 > f_1$), we can obtain closer spans.

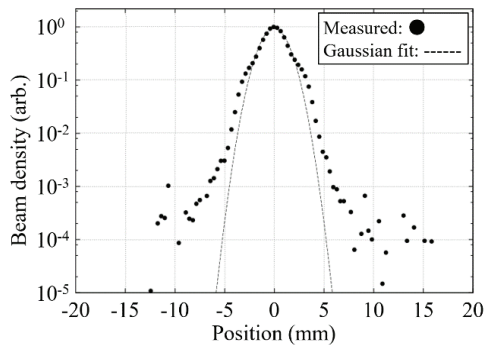

Fig. 9. Minimum transverse profile of linac beam with 191 MeV used by wire scanner monitor.

A pair of mirrors is arranged with a distance L, which is the sum of the focal lengths expressed as follows:

$$L = f_1 + f_2. \quad (6)$$

The laser beam is reflected at mirror 1 and reflected again at mirror 2 with the light velocity in the confocal cavity. The laser path length from c_n to c_{n+2} is approximately $4L$, travel time of the laser beam from c_n to c_{n+2} is $4L/c$. We need to adjust the timing of the laser beam to a frequency of 324 MHz (3.01 ns). In fact, the timing of the laser beam should be "n" times of 324 MHz. Further, we consider the following equation:

$$4L/c = n/(324 \times 10^6). \quad (7)$$

When we define "n" in Eq. (7), the laser path length can be adjusted to the $(n+1)^{th}$ beam bunch and the distance L by Eq. (6). When we chose 3, 4, or 5 as "n," L becomes 69.4, 92.5, or 115.7 cm, respectively. The laser wire interacts with the accelerated beam bunch with intervals of 9.03, 12.04, and 15.05 ns. The signals generated by photodetachment electrons can be obtained by the electron multiplier in each time interval, and the signal height corresponds to the number of detached electrons. Because the time interval corresponds to the path length (L), it can be converted into the transverse position in the geometry. Therefore, the plots of the signal peaks versus time can yield the accelerated beam intensity versus the transverse geometry. When we consider the easy access of the confocal mirrors, we should choose a distance (L), which corresponds to the sum of the focal lengths ($f_1 + f_2$) of approximately 1.0 m.

Detection of Detached Electrons

We can use the detached electrons in the beam profile measurement by employing an electron multiplier. As Yamane reported [8], when a laser beam with a 515-nm wavelength, a full width at half maximum of 1.0 ns, and pulse power of 100 μJ is assumed to be irradiated to the accelerated beam, a number of 10^8 electrons can be estimated. Because this number is sufficiently high for obtaining the signal from the electron multiplier, it is brought to a profile monitor. Because an electron can be bent by a weak magnetic field, electrons are easily separated from the particles with electrons H^0 and H^-. Time structure of electrons is still maintained from the original beam time structure. When the signals have beem highly sampled, the signal waveform can be converted to the beam profile by plotting the peaks of the signals.

CONCLUSION

We proposed a multi-laser-wire profile monitor using the confocal laser cavity proposed by Yamane [2]. Based on the beam profile measurement by the WSM, we set the reqired specifications for the profile measurement system.

When testing the performance of a multi-laser-wire formation, we counted over 20 laser wires in the cavity. Currently, it requires a few minutes to obtain one transverse profile by a WSM; however, this multi-laser-profile monitor only requires one intermediate bunch with several hundres ns. In addition, because we can measure several profiles for each macro-pulse to observe the trend of the accelerated beam profile, it facilitates the evaluation of the RF power stability in a macro-pulse. The system does not require motor-scanning devices; therefore, it uses only a small space and poses low mechanical difficulty compared to a present WSM or a single laser-wire profile monitor. This system offers multiple advantages over the present methods.

We have a 3-MeV linac beam line in the J-PARC as the demonstration beamline. We design and fabricate a multi-laser-wire profile monitor to verify its performance in the beamline. Furthermore, we will apply the system to the 400-MeV linac in the future.

REFERENCES

[1] I. Yamane, et al., "Feasibility Study on Laser Stripping Injection for J-gPARC RCS," J. Particle Accelerator Society of Japan, vol. 13, No. 2, 2016 (in Japanese).
[2] I. Yamane et al.: KEK Report 2009-9, November 2009, A.
[3] Y. Yamazaki ed.: J-PARC Design Report, JAERI-ech 2003-2004, KEK Report 2002-13.
[4] A. Miura et al.: to be published by Journal of Korean Physics Society, (2016).
[5] I. Yamane et al, IPAC10, Kyoto, TUPEA034.
[6] L. M. Branscomb, "Physics of the One-And-Two-Electron Atoms," North-Holland, (1968).
[7] A. Miura, "Progress of beam instrumentation in J-PARC," Procs. of IBIC2012, MOIA02, (2012).
[8] I. Yamane, et al., "Multi-Laser-Wire Profile Monitor for J-PARC 400 MeV H^- Beam," J. Particle Accelerator Society of Japan, to be published in 2016 (in Japanese).

ISBN 978-3-95450-177-9

SiPMs FOR BEAM INSTRUMENTATION. IDEAS FROM HIGH ENERGY PHYSICS

D. Gascon†, D. Ciaglia, G. Fernandez, S. Gomez, R. Graciani, J. Mauricio, N. Rakotonavalona, D. Sanchez, A. Sanuy
Dept. de Física Quàntica i Astrofísica, Institut de Ciències del Cosmos (ICCUB), Universitat de Barcelona (IEEC-UB), Martí Franquès 1, E08028 Barcelona, Spain

Abstract

Silicon Photomultipliers (SiPM) enable fast low-level ight detection and even photon counting with a semiconductor device. Thanks to a now matured technology, SiPMs can be used in a variety of applications like: Medical imaging, fluorescence detection, range-finding and high-energy physics. We present different possible application of SiPMs for beam instrumentation. First, we discuss timing properties of SiPMs, and how to optimize them for high rate environments enabling photon counting. This requires to understand the dependence of SiPM pulse shape on its configuration (total area, cell size, capacitances, etc.) and analyse dedicated front end electronics techniques. Finally, based on the experience of several projects aiming to develop trackers for high-energy physics, we present some ideas to develop beam monitoring instrumentation based on SiPMs.

INTRODUCTION

The two main applications of photo-sensors for the detection of elementary particles are the scintillation detectors and the Cherenkov radiation detectors. Scintillators have been extensively used in calorimeters, and recently also in trackers based on scintillating fibres. Time of flight measurement often requires scintillators detectors as well. The most classical example of Cherenkov detector is the Ring Imaging Cherenkov (RICH), used for particle identification.

The photo-sensor requirements are different according to the specific detector. Usually, RICH detectors require blue and Ultra-Violet (UV) sensitivity and single photon detection. On the contrary, scintillator light yield is much higher and the emission is shifted to the blue/green region of the spectrum. However, calorimeters have large dynamic range, up to 100s or 1000s of photons, whereas scintillating fibre trackers are used for Minimum Ionizing Particle (MIP) signals, producing few photons.

For a long time the main photo-detector for such detection systems was the Photomultiplier Tube (PMT), which was created more than 50 years ago [1]. As alternatives to the PMTs, in the last decade, a new type of photo-detector was developed on the basis of the semiconductor technology, the Silicon Photomultiplier (SiPM) [2].

* † dgascon@fqa.ub.edu

SIPM TECHNOLOGY

The basic element of a SiPM is the Single Photon Avalanche Diode (SPAD) [3], consisting on an Avalanche Photo-Diode (APD) and a quenching element. If the bias voltage of an APD is greater than the junction breakdown voltage (this excess voltage is often called over-voltage), a charge multiplication process occurs and becomes a diverging self-sustaining process (Geiger regime). A quenching resistor, connected in series with the junction, is used to interrupt the avalanche: when the current in the junction is high enough to generate a voltage drop across the resistor close to the applied overvoltage (i.e. the difference between the bias voltage and the breakdown voltage), the current flowing becomes low enough that statistically the avalanche can be quenched and the junction is recharged.

A SiPM ([2], [4], [5], [6]) (also known as Geiger-mode avalanche photodiode, G-APD) is a device obtained by connecting in parallel several miniaturized SPADs (few tens of μm^2) belonging to the same silicon substrate so that the output signal of the SiPM is the sum of the SPADs outputs. The small SPADs in the SiPM are named microcells.

The gain of a SPAD is expressed as the ratio between the charge produced by the avalanche and the primary charge produced by the interaction of the optical photon within the device. Since the avalanche is interrupted when the voltage at the two sides of the micro-cell goes down to the breakdown voltage, the gain at the two sides of the microcell is can be expressed as the product of the SPAD overvoltage and parasitic capacitance.

The output of the SiPM is proportional to the number of cells that fired, provided that the number of incident photons is much smaller than the number of microcells and provided they are uniformly distributed across sensor surface. Since the overvoltage and cell capacitance uniformity can be quite accurate in modern production processes, an excellent separation between peaks in charge spectrum is achieved. This makes possible to count even tens of photons, which is clearly impossible with PMTs.

Photodetection efficiency (PDE) characterizes the probability that a device triggers on an incoming photon [4]. For a SiPM, PDE includes the transmissivity of the coating, the probability to hit the active area versus dead material between microcells (filling factor), and the probabil-

ISBN 978-3-95450-177-9

ity to initiate an electron-hole production, often referred to as quantum efficiency.

SiPMs suffer from three main noise sources: dark counts, afterpulsing and crosstalk ([5], [6]). The noise in SiPM devices is mainly due to the dark count rate: an e/h pair can be thermally generated, triggering an avalanche in a micro-cell without an optical photon impinging on it. The dark noise rate depends on the working temperature and on the overvoltage, and it is directly proportional to the active area of the device. Other noise sources are correlated to other primary events triggered in one cell. Trapping of the carriers and their delayed release in the avalanche region can cause a second avalanche in the junction, named afterpulse [5]: trapped carriers can have a lifetime from tens to hundreds of nanoseconds and the second avalanche can be triggered also after the complete micro-cell recharge, increasing artificially the number of counted events. During the avalanche in a micro-cell, optical photons can be produced, whose interactions in adjacent micro-cells of the SiPM may generate optical crosstalk, introducing an additional noise component. The effect of crosstalk can be prevented with trenches (grooves surrounding each micro-cell), which can have metal-coated sidewalls [4].

SiPM technology has greatly evolved during last 10 years and currently can be considered as mature, although room for improvement still exists. Newest SiPM technologies guarantee a dark count rate of about 100 kHz/mm^2 at room temperature [8]. An optimal device would work with a large PDE (around 50 %), while having a crosstalk typically smaller than 10-20%. Currently, only few Hamamatsu devices achieve these performances [8]. A trade-off exists between PDE and crosstalk, since fill factor and overvoltage should be optimized in opposite directions for each.

A particular concern for particle accelerators and detectors is the radiation damage. It is well known that generating centers are created during irradiation which increase the leakage current. The bulk leakage current is multiplied in avalanche photodiodes (APD) by the gain factor and the resulting pulses are undistinguishable from photon-generated events. Bulk radiation damage in silicon detectors is primarily due to displacing damge. The damage is proportional to the Non-Ionizing Energy Loss (NIEL). Heavier particles produce greater damage. Neutron damage is the major concern for SiPMs. Consequently, an increasing rate of dark pulses as a function of the radiation dose is seen in SiPM [7]. Adverse effects of irradiation on other characteristic parameters of SiPM such as gain uniformity, afterpulsing or optical crosstalk probability would be also detrimental for a detector.

In any case, it is clear that SiPMs can compete with PMTs in nearly all applications. SiPMs are more compact, are not sensitive to magnetic fields, are more robust, are operated at lower voltages, potentially can achieve higher PDE and are better suited for mass production. Nevertheless, PMTs still have some advantages, namely: lower temperature dependence and lower dark count rate. But it is worth to keep in mind that temperature dependence of the SiPM is related to the breakdown voltage temperature dependence and, therefore, can be corrected by smart supply voltage control, as done in some custom and commercial systems.

FRONT END ELECTRONICS

To exploit at best the advantages of SiPMs they need to be read out via a dedicated multi-channel chip. A number of readout ASICs for SiPM readout can be found in the literature [15]. But we can identify some specific functions which a front end electronics for SiPM needs to perform:

- Adapt impedances. SiPM capacitances range from 30 pF to more than 1 nF. That means that low input impedance front end electronics is preferred, particularly for high speed applications.
- Shape the input signal. SiPM pulses typically have a long time constant associated to the recharge of the micro-cell. This may cause saturation or distortion because of pile up. Often, high pass or pole-zero cancellation filters are used to shape the pulse.
- Preamplify to optimize the Signal to Noise Ratio (SNR). Even if “nominal” gain is in the order of 10^6 only a fraction of the charge is used for fast read-out systems using fast shapers.
- Combine (sum) the signal of several SiPMs. In some applications large detection areas have to be covered. Since largest SiPM detection area is about 6x6 mm^2, smaller than largest PMTs, a common solution when large detection is required is to add the signal of several SiPMs. Direct parallel connection of SiPM devices has some drawbacks: extremely large capacitance (introducing limitations in speed and SNR) and difficult equalization of SiPM non-uniformities by overvoltage equalization.
- Equalize overvoltage. The breakdown voltage of SiPMs suffers from process variability, although fabrication processes have improved significantly. The non-uniformity of breakdown voltage is translated mainly in gain non-uniformity when several SiPMs are biased with the same power supply. This is particularly problematic when SiPM signals have to be added. For this reason, some circuits allow DC adjustment of the voltage of the input, which is connected to the SiPM anode or cathode.

An example of circuit implementing all the aforementioned functionalities is the Multiple Use SiPM Integrated Circuit (MUSIC) ASIC [9]. MUSICR1 performs several functionalities using the different output currents from the readout circuit, as depicted in *Figure 1*:

- Channel sum: The sum of the input signals is provided as a dual-gain output in differential mode using the high gain and the low gain currents from the readout circuit.
- Analog channels: 8 individual single ended analog outputs.

ISBN 978-3-95450-177-9

- Digital channels: 8 individual digital outputs are obtained using a discriminator.
- Fast OR signal: A trigger pulse is provided by performing an OR between any selection of digital signals.
- Integrator current: 8 output currents for an external slow integrator.

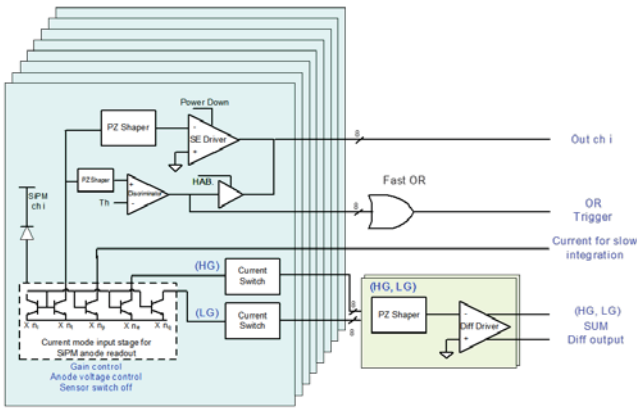

Figure 1: MUSIC block diagram [9].

For each individual channel, the user must select the analog or digital output since both signals share the same output PAD. Moreover, a selectable dual-gain configuration is available for each functionality, the channel sum and the 8 A/D outputs. The Pole-Zero (PZ) cancellation can be used or bypassed in any operation mode.

Other blocks are included to set the correct operation points of the circuit and configure several tunable parameters. For instance, individual SiPM pixel voltage control and switch off is possible by reducing the overvoltage by 4V. It is important to highlight that every block and channel can be disabled (power down mode) with a specific control signal.

Pole-zero cancellation can be applied to any input. Figure 2 shows the PZ cancellation response for a 6x6 mm^2 and 50 µm cell SiPM signal. PZ filter parameters can be adjusted as the pulse shape varies depending on the manufacturer, the SiPM size and microcell (pixel) size.

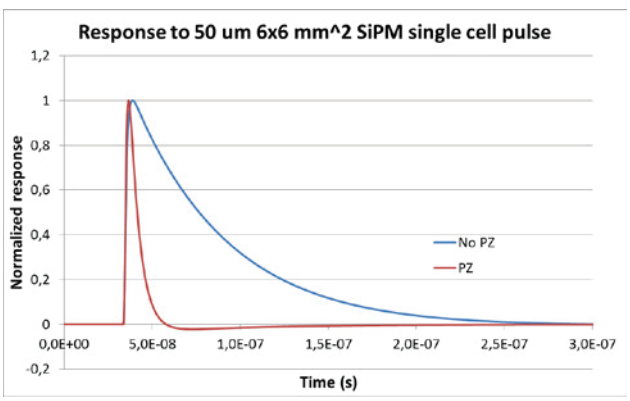

Figure 2: MUSIC Pole-Zero cancellation response for a 6x6 mm^2 and 50 µm cell SiPM signal.

MUSIC achieves excellent SNR, even with PZ cancellation as can be noticed in Figure 3. The SiPM is illuminated with a fast (50 ps FWHM) laser in low light level conditions. The illumination follows a Poisson distribution with an average of few photons. Discrete levels related to the number of fired cell can be easily distinguished in Figure 3. The PZ cancellation narrows down the SIPM pulse to 5 ns FWHM, when the input SiPM pulse FWHM was higher than 100 ns.

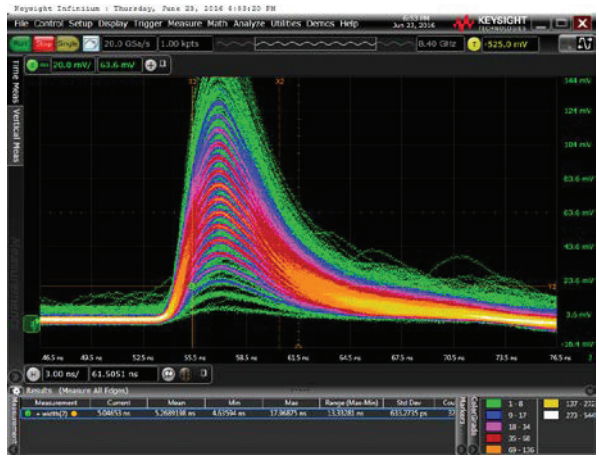

Figure 3: MUSIC analog output with PZ cancellation for low level illumination using a 3x3 mm^2 and 75 µm cell SiPM

MUSIC's low SNR allows clear identification of more than 10 photon peaks in the charge spectrum as shown in Figure 4.

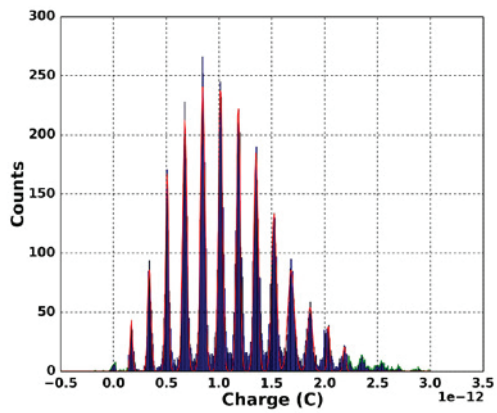

Figure 4: MUSIC charge spectrum with PZ cancellation for low level illumination using a 3x3 mm^2 and 75 µm cell SiPM

As said above, MUSIC individual outputs can provide either analog signal (as above) or a discriminated signal. The later is shown in Figure 5. The high SNR provided by MUSIC allows identifying the number of incident photons looking to the pulse width. The FWHM for a single photon is about 5 ns. The Single Photon Time Resolution (SPTR) of the combination of SiPM and MUSIC can be measured by looking to the RMS spread of the delay between the leading edge of the trigger signal and the leading edge of MUSIC discriminated output. The SPTR of SiPM connected to MUSIC is about 100 ps RMS. SiPMs can provide better time resolution than PMTs, although Micro-Channel Plate (MCP) PMTs can achieved

ISBN 978-3-95450-177-9

SPTR as good as 30 ps. Nevertheless, the cost and fragility of MCP-PMTs limit its use to specific applications.

As a final remark on SiPM and Front End electronics technology, we should consider the so-called digital SiPM or Digital Photon Counter (DPC), which combines the sensor and readout electronics in the same chip [11]. It offers interesting possibilities but the read out is customized to specific applications and lacks from flexibility in many cases.

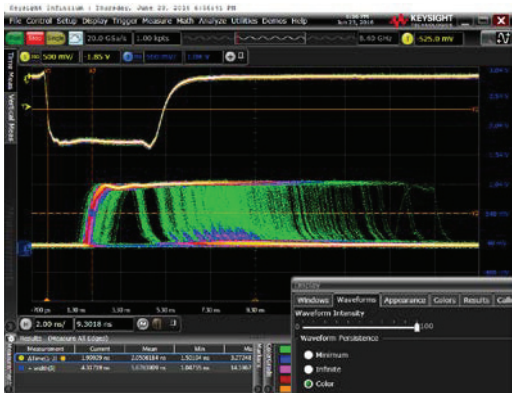

Figure 5: MUSIC discriminated output (bottom) with PZ cancellation for low level illumination using a 3x3 mm^2 and 75 µm cell SiPM. Laser trigger signal on top.

USE CASES IN HIGH ENERGY PHYSICS

Although SiPMs are scarcely used in currently operating detectors, many new projects and upgrades have already chosen SiPMs as baseline detectors.

As a first example we can consider the Scintillating Fiber (SciFi) Tracker, which is being built for the upgrade of LHCb tracking system [12]. The LHCb detector will be upgraded during 2019-2020 in order to collect data from proton-proton collisions at the LHC at higher instantaneous luminosities and to read out the data at 40MHz using a trigger-less read-out system. All front end electronics will be replaced and several subdetectors must be redesigned to cope with the higher occupancy. The current tracking detectors downstream of the LHCb dipole magnet will be replaced by the Scintillating Fibre (SciFi) Tracker. The SciFi Tracker will be constructed using 2.5 m long scintillating fibres and read out by Silicon Photomultipliers (SiPM) located outside the acceptance. The fibres have a diameter of 0.25 mm, are wound into ribbons with 5 or 6 staggered layers of fibres, and will cover a total active area of around 360 m^2. State-of-the-art multi-channel SiPM arrays are being developed to read out the fibres. A custom ASIC, the PACIFIC, will be used to digitise the signals from the SiPMs and additional front end electronics based on FPGAs will be used to reconstruct hit positions. There are a number of challenges involved in the construction of this detector: the radiation hardness of the fibres and the SiPMs; the mechanical precision required while building large active detector components; and the cooling required to mitigate the effects of radiation damage.

It has been seen that scintillating fibres will lose transmission [13] under irradiation. However, the literature describing this particular fibre is limited in the degree of damage in our radiation dose range. Multiple separate irradiation campaigns within the SciFi collaboration were undertaken to investigate the damage, irradiating the fibres with 24 GeV/c protons at the CERN-PS, 23 MeV protons at the Karlsruhe Institute of Technology, in situ LHCb pit irradiation, as well as gamma and x-ray irradiation [12]. The results are shown in Figure 6.

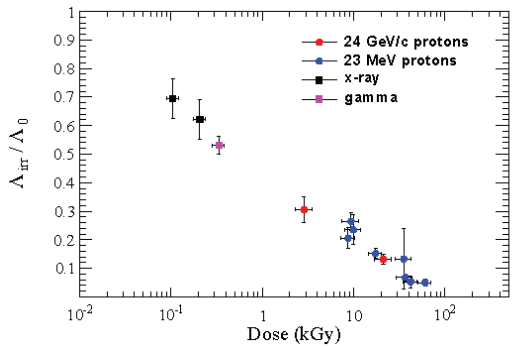

Figure 6: The ratio of attenuation length after irradiation to before as a function of dose for scintillating fibres for multiple source of ionizing radiation [12].

Anyhow, SiPMs are used in many other types of detectors [14]. SiPMs are used in the analog hadronic calorimeter (AHCAL) of CALICE prototypes for an ILC detector. SiPMs are also used in T2K electromagnetic calorimeter, in Belle II endcap detector and in CMS hadronic calorimeter upgrade [14].

APPLICATIONS IN ACCELERATOR BEAM INSTRUMENTATION

As said above, SiPMs could replace PMTs in nearly any possible application:

- For scintillator detectors we know they are used in calorimeters in HEP where a large dynamic range (up to 14-15 bits) is required.
- Cherenkov detectors. A high PDE (near 50 %) and enhanced near Blue/UV sensitivity make SiPMs excellent Cherenkov light photo-sensors.
- Single photon detectors and photon counting. Although the SiPM presents a long time constant related to microcell recharge time, the pulse can be narrowed down below 5ns after by adequate shaping. Moreover, a SiPM readout with a fast electronics presents a SPTR in the order of 100 ps.

Of course, PMTs are still a better choice when very low dark current is required, when the neutron radiation damage might be a concern or when very large photodetection areas must be covered with low pixelation.

An obvious application of SiPMs could be replacing PMTs in beam loss monitors based on Cherenkov light detection. Several works in that direction have been presented in IBIC 2016. A potential limitation in some environments is the SiPM dark count rate. An alternative approach would be to use scintillating fibres in coinci-

ISBN 978-3-95450-177-9

dence, but as discussed above scintillating fibres are quite sensitive to radiation damage. Probably, additional R&D is needed to define the applicability of the SiPMs in beam loss monitoring.

SiPMs could find also an application in transverse profile monitors based on scintillating fibres [16] and similar devices.

Another possible application could be in Time Correlated Single Photon Counting (TCSPC) for beam filling pattern measurements [17]. The technique consists in the measurements of the temporal distribution of the produced synchrotron radiation using Electro-Optical devices, from where the filling pattern is inferred. SiPMs are already outperforming PMT performances [18]. The combination of high-performance SiPM and fast readout as MUSIC [9] reaches SPTR values in the range of 100 ps, lower than current systems based on PMTs.

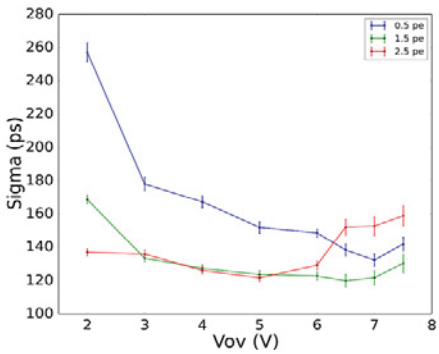

Figure 7: SPTR as function of the overvoltage for a 3x3 mm^2 and 75 µm cell SiPM readout by MUSIC ASIC.

CONCLUSIONS

SiPM technology has reached maturity and combined with adequate readout electronics might be applied in accelerator beam instrumentation. Possible use cases are optical fibre based beam loss monitors and TCSPC measurement of beam filling pattern, among other options.

ACKNOWLEDGEMENT

We would like to thank Chiara Casella (MIB) and Christian Joram (CERN) for providing insight in the state of the art of SiPMs in HEP. Funding for this work was partially provided by the Spanish MINECO under projects FPA2015-69210-C6-2-R and MDM-2014-0369 of ICCUB (Unidad de Excelencia 'María de Maeztu')

REFERENCES

[1] Toshikaza Hakamata et al., "Photomultipliers Tubes, Basics and Applications", Hammamatsu Photonics K.K., Electron Tube Division, Japan, 2006.

[2] V. Saveliev, V. Golovin, "Silicon Avalanche Photodiodes on the basis of Metal-Resistor-Semiconductor (MRS) Structures", Nucl.Instr.Meth.A, 442, 223-229.

[3] S. Cova, A. Longoni, R. Cubeddu, IEEE Journal of Quantum Electronics 19 (4) (1983) 630.

[4] M. Bisogni et al., "Development of analog solid-state photo-detectors for Positron Emission Tomography", Nucl. Instrum. Meth. A 809 (2016) 140.

[5] D. Renker, E. Lorenz, Journal of Instrumentation 4 (2009) P04004.

[6] N. Otte, "SiPM's a very brief review", Proceedings of the International Conference on New Photo-detectors PoS(PhotoDet2015)001, 2015.

[7] S. Sanchez-Majos, "Noise and radiation damage in silicon photomultipliers exposed to electromagnetic and hadronic radiation", Nuclear Instruments and Methods in Physics Research A 602 (2009) 506–510

[8] J. Biteau et al., "Performance of Silicon Photomultipliers for the Dual-Mirror Medium-Sized Telescopes of the Cherenkov Telescope Array". PoS ICRC2015 (2016) 963 arXiv:1508.06245 [astro-ph.IM]

[9] S. Gómez ; D. Gascón; G. Fernández; A. Sanuy; J. Mauricio; R. Graciani; D. Sanchez, "MUSIC: An 8 channel readout ASIC for SiPM arrays", Proceedings of SPIE, Optical Sensing and Detection IV, 98990G (29 April 2016); doi: 10.1117/12.2231095.

[10] T. Gys, L. Castillo García, J. Fopma, R. Forty, C. Frei, R. Gao, N. Harnew, T. Keri, D. Piedigrossi, Performance and lifetime of micro-channel plate tubes for the TORCH detector, NIM A, Vol 766, 2014, Pages 171-172, ISSN 0168-9002, http://dx.doi.org/10.1016/j.nima.2014.04.020

[11] T. Frach, G. Prescher, C. Degenhardt and B. Zwaans, "The digital silicon photomultiplier. System architecture and performance evaluation," Nuclear Science Symposium Conference Record (NSS/MIC), 2010 IEEE, Knoxville, TN, 2010, pp. 1722-1727. doi: 10.1109/NSSMIC.2010.5874069

[12] B. D. Leverington, "LHCb Upgrade – The Scintillating Fibre Tracker", Proceedings of the European Physical Society Conference on High Energy Physics, 22–29 July 2015, Vienna, Austria

[13] C. Zorn, A Pedestrians Guide To Radiation Damage In Plastic Scintillators, Nuclear Physics B (Proc. Suppl.) 32 (1993) 377-383.

[14] E. Garutti, "Silicon photomultipliers for high energy physics detectors", Journal of Instrumentation, Volume 6, October 2011.

[15] W. Kucewicz, "Review of ASIC developments for fast readout electronics, talk at Industry-academia matching event on SiPM and related technologies", http://indico.cern.ch/conferenceDisplay.py?confId=117424, CERN, Geneva Switzerland (2011).

[16] Rojatti et al. "Scintillating fibers used as profile monitors for the CNAO HEBT lines" Proceedings of IPAC2015, Richmond, VA, USA.

[17] L. Torino, U. Iriso, "Filling Pattern Measurements at ALBA using Time Correlated Single Photon Counting", Proceedings of IPAC2014, Dresden, 2014

[18] Martinenghi et al. "Time-resolved single-photon detection module based on silicon photomultiplier: A novel building block for time-correlated measurement systems", Rev. Sci. Instrum. 87, 073101 (2016)

ISBN 978-3-95450-177-9

List of Authors

Bold papercodes indicate primary authors

ISBN 978-3-95450-177-9

ISBN 978-3-95450-177-9

ISBN 978-3-95450-177-9

ISBN 978-3-95450-177-9

— L —

ISBN 978-3-95450-177-9

ISBN 978-3-95450-177-9

ISBN 978-3-95450-177-9

ISBN 978-3-95450-177-9

— T —

ISBN 978-3-95450-177-9

ISBN 978-3-95450-177-9

ISBN 978-3-95450-177-9

ISBN 978-3-95450-177-9

Institutes List

ALBA-CELLS Synchrotron
Cerdanyola del Vallès, Spain
- Alvarez, M.
- Biscari, C.
- Iriso, U.
- Nosych, A.A.
- Pérez, F.
- Torino, L.

Ankara University, Accelerator Technologies Institute
Golbasi / Ankara, Turkey
- Kaya, Ç.

Ankara University, Faculty of Engineering
Tandogan, Ankara, Turkey
- Gundogan, M.T.
- Yavaą, Ö.

ANL
Argonne, Illinois, USA
- Arnold, N.D.
- Brill, A.R.
- Bui, H.
- Carwardine, J.
- Decker, G.
- Deriy, B.
- Dickerson, C.
- DiGiovine, B.
- Emery, L.
- Farnsworth, R.I.
- Fors, T.
- Jaski, Y.
- Keane, R.T.
- Lee, S.H.
- Lenkszus, F.
- Lill, R.M.
- Lin, L.Y.
- Morgan, J.W.
- Paskvan, D.R.
- Pietryla, A.F.
- Ramanathan, M.
- Sereno, N.
- Shang, H.
- Shoaf, S.E.
- Veseli, S.
- Wang, J.
- Westferro, F.
- Xu, S.
- Yang, B.X.

AVS
Elgoibar, Spain
- Carmona, J.M.
- Galipienzo, J.H.
- Noguera Crespo, P.N.G.

Azienda Ospedaliera Papardo
Messina, Italy
- Basile, E.

BARC
Trombay, Mumbai, India
- Bharade, S.K.
- Joshi, G.
- Motiwala, P.D.

BERGOZ Instrumentation
Saint Genis Pouilly, France
- Bergoz, J.F.
- Stulle, F.

BINP SB RAS
Novosibirsk, Russia
- Anchugov, O.
- Borin, V.M.
- Khilchenko, A.D.
- Kotelnikov, A.I.
- Kurkin, G.Y.
- Kvashnin, A.N.
- Meshkov, O.I.
- Petrozhitskii, A.V.
- Schegolev, L.M.
- Shvedov, D.A.
- Zhuravlev, A.N.
- Zinin, E.I.
- Zubarev, P.V.

BINP
Novosibirsk, Russia
- Dorokhov, V.L.

BNL
Upton, Long Island, New York, USA
- Ahrens, L.
- Altinbas, Z.
- Blaskiewicz, M.
- Caracappa, A.
- Cerniglia, P.
- Cheng, W.X.
- Connolly, R.
- Costanzo, M.R.
- Cullen, C.
- Danneil, C.
- Day, N.M.
- Degen, C.
- Della Penna, A.J.
- Drees, K.A.
- Fedotov, A.V.
- Fedurin, M.G.
- Fischer, W.
- Fite, J.M.
- Fliller, R.P.

ISBN 978-3-95450-177-9

- Gassner, D.M.
- Hammons, L.R.
- Harper, C.E.
- Hidaka, Y.
- Hock, J.
- Huang, H.
- Hulsart, R.L.
- Inacker, P.
- Jamilkowski, J.P.
- Kayran, D.
- Kewisch, J.
- Kusche, K.
- Lambiase, R.F.
- Liu, C.
- Marusic, A.
- Mausner, L.F.
- Méot, F.
- Mernick, K.
- Michnoff, R.J.
- Miller, T.A.
- Minty, M.G.
- Montag, C.
- Oddo, P.
- Padrazo, D.
- Paniccia, M.C.
- Pekrul, W.E.
- Pinayev, I.
- Podobedov, B.
- Pogorelsky, I.
- Polyanskiy, M.N.
- Ranjbar, V.H.
- Raparia, D.
- Schoefer, V.
- Seletskiy, S.
- Singh, O.
- Smith, K.S.
- Sorrell, Z.
- Swinson, C.
- Theisen, C.
- Thieberger, P.
- Tuozzolo, J.E.
- Weiss, D.
- Xu, W.
- Zaltsman, A.
- Zhao, Z.

BUTE
Budapest, Hungary
- Dabóczi, T.
- Hajdu, C.F.

CEA/DRF/IRFU
Gif-sur-Yvette, France
- Baudrier, M.

CEA/DSM/IRFU
France
- Bogard, D.
- Harrault, F.
- Luong, M.
- Napoly, O.
- Pottin, B.
- Senée, F.
- Simon, C.
- Tuske, O.
- Uriot, D.

CEA/IRFU
Gif-sur-Yvette, France
- Belloni, F.
- Delbart, A.
- Desforge, D.
- Lahonde-Hamdoun, C.L.H.
- Legou, Ph.
- Marroncle, J.
- Maurice, L.
- Papaevangelou, T.
- Segui, L.
- Tsiledakis, G.

CEA
Gif-sur-Yvette, France
- Bordas, E.
- Leprêtre, F.
- Serruys, Y.

CERN
Geneva, Switzerland
- Aguilera, S.
- Alves, D.
- Andreazza, W.
- Artoos, K.
- Barnes, M.J.
- Barrios Diaz, E.
- Baud, G.
- Belleman, J.M.
- Belohrad, D.
- Belver-Aguilar, C.
- Bergamaschi, M.
- Bett, D.R.
- Betz, M.
- Biskup, B.
- Blas, A.
- Bravin, E.
- Burger, S.
- Calia, A.
- Cantero, E.D.
- Chritin, N.
- Dehning, B.
- Domingues Sousa, F.S.
- Draskovic, D.
- Esperante Pereira, D.
- Fernandes, M.F.
- Fuchsberger, K.
- Gąsior, M.
- Gkotse, B.
- Glaser, M.
- Goldblatt, A.

ISBN 978-3-95450-177-9

- Gras, J-J.
- Hajdu, C.F.
- Hemelsoet, G.H.
- Hofmann, H.
- Hofmann, T.
- Holzer, E.B.
- Hostettler, M.
- Jackson, S.
- Jones, O.R.
- Kastriotou, M.
- Kieffer, R.
- Koettig, T.
- Kolad, B.
- Kral, J.
- Krupa, M.
- Łasocha, K.
- Lees, A.
- Lefèvre, T.
- Levens, T.E.
- Louwerse, R.
- Magagnin, P.
- Matli, E.
- Mazzoni, S.
- Meoli, A.
- Montesano, S.
- Morel, F.N.
- Nebot Del Busto, E.
- Novotny, P.
- Odier, P.
- Olexa, J.
- Oponowicz, E.
- Ortega Ruiz, I.
- Pedersen, S.B.
- Pezzullo, G.
- Raich, U.
- Ravotti, F.
- Roncarolo, F.
- Sadovich, S.
- Scandale, W.
- Schmickler, H.
- Schneider, G.
- Sosa, A.G.
- Spanggaard, J.
- Storey, J.W.
- Tan, J.
- Trad, G.
- Tranquille, G.
- Tshilumba, D.
- Turner, M.
- Valentino, G.
- Veness, R.
- Wendt, M.
- Xu, C.
- Zamantzas, C.
- Zorzetti, S.

CFEL
Hamburg, Germany
- Dornmair, I.
- Kärtner, F.X.
- Kalaydzhyan, A.
- Maier, A.R.
- Mücke, O.D.
- Shafak, K.
- Wang, W.
- Xin, M.

Chiang Mai University, PBP Research Facility
Chiang Mai, Thailand
- Kangrang, N.

Chiang Mai University, Science and Technology Research Institute
Chiang Mai, Thailand
- Wichaisirimongkol, P.

Chiang Mai University
Chiang Mai, Thailand
- Chaisueb, N.
- Kangrang, N.
- Kongmon, E.
- Rimjaem, S.
- Saisa-ard, C.
- Saisut, J.
- Thongbai, C.

CIEMAT
Madrid, Spain
- Abramian, P.
- Brañas, B.
- Calero, J.
- Calvo, P.
- Domínguez, M.A.
- Estévez, E.F.
- García-Tabarés, L.
- Gavela, D.
- Gómez, P.
- Guirao, A.
- Gutiérrez, J.L.
- Ibarra, A.
- Jiménez-Rey, D.
- Lagares, J.I.
- López, D.
- Martínez, L.M.
- Molina Marinas, E.
- Mollá, J.
- Obradors-Campos, D.
- Oliver, C.
- Pérez Morales, J.M.
- Podadera, I.
- Soleto, A.
- Toral, F.
- Varela, R.
- Vázquez, C.

ISBN 978-3-95450-177-9

CIVIDEC Instrumentation
Wien, Austria
- Griesmayer, E.
- Kavrigin, P.
- Weiss, Ch.

CNAO Foundation
Milan, Italy
- Calvi, G.M.A.
- Lanzavecchia, L.
- Parravicini, A.
- Rojatti, E.
- Viviani, C.

Cockcroft Institute
Warrington, Cheshire, United Kingdom
- Fiorito, R.B.
- Kastriotou, M.
- Tzoganis, V.
- Welsch, C.P.
- Widmann, W.
- Zhang, H.D.

Cornell University (CLASSE), Cornell Laboratory for Accelerator-Based Sciences and Education
Ithaca, New York, USA
- Barrett, S.T.
- Billing, M.G.
- Conway, J.V.
- Crittenden, J.A.
- Heltsley, B.K.
- Jones, K.A.
- Li, Y.
- Mikhailichenko, A.A.
- O'Connell, T.I.
- Peterson, D.P.
- Rider, N.T.
- Rubin, D. L.
- Shanks, J.P.
- Sikora, J.P.
- Wang, S.

Czech Technical University
Prague 6, Czech Republic
- Biskup, B.

DESY Zeuthen
Zeuthen, Germany
- Boonpornprasert, P.
- Huck, H.
- Ignatenko, A.
- Jachmann, L.
- Köhler, W.
- Krasilnikov, M.
- Oppelt, A.
- Stephan, F.

DESY
Hamburg, Germany
- Affeldt, A.
- Awwad, A.
- Baboi, N.
- Barret, B.
- Beutner, B.
- Brinker, F.
- Butkowski, Ł.
- Czwalinna, M.K.
- D'Arcy, R.T.P.
- Decking, W.
- Delfs, A.
- Delsim-Hashemi, H.
- Dinter, H.
- Drewitsch, M.
- Flöttmann, K.
- Frank, O.
- Gerth, C.
- Gharibyan, V.
- Hellert, T.
- Hensler, O.
- Hoeptner, M.
- Holz, M.
- Ivanov, R.
- Janas, E.
- Knaack, K.K.
- Krivan, F.
- Krouptchenkov, I.
- Kruse, J.
- Kube, G.
- Lemcke, B.
- Lensch, T.
- Libov, V.
- Liebing, J.
- Limberg, T.
- Lipka, D.
- Lorbeer, B.
- Ludwig, F.
- Lund-Nielsen, J.
- Marchetti, B.
- Mavrič, U.
- Meykopff, S.M.
- Michalek, B.
- Neugebauer, J.
- Neumann, Re.
- Neumann, Ru.
- Nölle, D.
- Osterhoff, J.
- Peier, P.
- Pelzer, M.
- Petrosyan, G.
- Pfeiffer, S.
- Pisarov, Z.
- Pototzki, P.
- Priebe, G.
- Przygoda, K.P.
- Rehlich, K.R.
- Renner, D.
- Rybnikov, V.
- Schlarb, H.

ISBN 978-3-95450-177-9

- Schlesselmann, G.
- Schmidt, Ch.
- Schmidt-Föhre, F.
- Scholz, M.
- Shi, L.
- Smirnov, P.A.
- Sokolinski, H.
- Stechmann, C.
- Steckel, M.
- Steffen, B.
- Susen, R.
- Tiessen, H.
- Vilcins, S.
- Viti, M.
- Wamsat, T.
- Weikum, M.K.
- Wentowski, N.
- Werner, M.
- Wiebers, Ch.
- Wilgen, J.
- Wittenburg, K.
- Zahn, R.
- Ziegler, A.

Dimtel
San Jose, USA
- Teytelman, D.

DLS
Oxfordshire, United Kingdom
- Abbott, M.G.
- Bloomer, C.
- Bobb, L.M.
- Cinque, G.
- Frogley, M.
- Furseman, M.J.
- Gayadeen, S.
- Morgan, A.F.D.
- Rehm, G.

DongHua University
Songjiang, People's Republic of China
- Xu, Y.H.

East China University of Science and Technology
Shanghai, People's Republic of China
- Li, C.L.
- Zhang, W.J.

Electrodynamic
Albuquerque, New Mexico, USA
- Pablo, M.H.
- Roberts, B.F.

Elettra-Sincrotrone Trieste S.C.p.A.
Basovizza, Italy
- Bassanese, S.
- Cautero, G.
- De Monte, R.
- Ferianis, M.
- Penco, G.

ENEA C.R. Frascati
Frascati (Roma), Italy
- Ampollini, A.
- Bazzano, G.
- Nenzi, P.
- Picardi, L.
- Piccinini, M.
- Ronsivalle, C.
- Surrenti, V.
- Trinca, E.
- Vadrucci, M.

ENEA-Bologna
Bologna, Italy
- Castelluccio, D.M.

EPFL
Lausanne, Switzerland
- Aguilera, S.
- Bay, A.
- Gorgisyan, I.
- Haefeli, G.J.
- Hauri, C.P.
- Hofmann, H.
- Rivkin, L.

ESRF
Grenoble, France
- Ewald, F.
- Plouviez, E.
- Scheidt, K.B.
- Uberto, F.

ESS Bilbao
Zamudio, Spain
- Bustinduy, I.
- Ortega, A.
- Rueda, I.
- Varnasseri, S.
- Zugazaga, A.

ESS
Lund, Sweden
- Baron, R.A.
- Galh, T.
- Grandsaert, T.J.
- Hartl, M.A.
- Hassanzadegan, H.
- Jansson, A.
- Kocevar, H.
- Lee, J.H.
- Lee, Y.

ISBN 978-3-95450-177-9

- Serrano, A.
- Shea, T.J.
- Thomas, C.A.

Euclid TechLabs, LLC
Solon, Ohio, USA
- Antipov, S.P.
- Kuzikov, S.V.

Fermilab
Batavia, Illinois, USA
- Thurman-Keup, R.M.

FMB Oxford
Oxford, United Kingdom
- Syme, S.

Forschungszentrum Jülich
Jülich, Germany
- Wuestner, P.

FRIB
East Lansing, USA
- Cogan, S.
- Lidia, S.M.
- Liu, Z.
- Nash, S.
- Shane, R.
- Villari, A.C.C.
- Webber, R.C.
- Yair, O.

FSU Jena
Jena, Germany
- Golm, J.
- Neubert, R.
- Seidel, P.
- Tympel, V.

Fusion for Energy
Garching, Germany
- Cara, P.

FZJ
Jülich, Germany
- Böhme, C.
- Halama, A.J.
- Hinder, F.
- Kamerdzhiev, V.
- Klehr, F.
- Mikirtytchiants, S.
- Shergelashvili, D.
- Soltner, H.
- Srinivasan, S.
- Trinkel, F.
- Trusov, S.
- Valdau, Y.

FZK
Karlsruhe, Germany
- Müller, A.-S.

GANIL
Caen, France
- Andre, T.A.
- Ferdinand, R.
- Jamet, C.
- Le Coz, W.LC.
- Ledu, G.
- Leloir, S.L.
- Loret, S.
- Potier de courcy, C.
- Revenko, R.V.
- Touchard, D.T.
- Vignet, J.L.

Gazi University, Faculty of Arts and Sciences
Teknikokullar, Ankara, Turkey
- Aydin, A.A.
- Kasap, E.

German University in Cairo
New Cairo City, Egypt
- Soliman, E.

GPI
Moscow, Russia
- Gornostaev, P.B.
- Schelev, M.Ya.
- Shashkov, E.V.
- Smirnov, A. V.
- Zarovskii, A.I.

GSI
Darmstadt, Germany
- Fils, J.
- Forck, P.
- Giacomini, T.
- Kester, O.K.
- Kowina, P.
- Kurian, F.
- Lederer, S.
- Lieberwirth, A.
- Reeg, H.
- Sapinski, M.
- Schwickert, M.
- Sieber, T.
- Singh, R.
- Stöhlker, T.
- Udrea, S.
- Vilsmeier, D.M.
- Walasek-Höhne, B.

ISBN 978-3-95450-177-9

Helmholtz-Zentrum Dresden-Rossendorf (HZDR), Institute of Radiation Physics
Dresden, Germany
- Couperus, J.P.
- Irman, A.
- Koehler, A.
- Zarini, O.

HIJ
Jena, Germany
- Geithner, R.
- Golm, J.
- Kurian, F.
- Neubert, R.
- Stöhlker, T.

HIM
Mainz, Germany
- Aulenbacher, K.
- Bruker, M.W.
- Weilbach, T.

HZB
Berlin, Germany
- Falkenstern, F.
- Feikes, J.
- Glock, H.-W.
- Hoffmann, F.
- Kuszynski, J.
- Malyutin, D.
- Matveenko, A.N.
- Ries, M.
- Seiler, I.

HZDR
Dresden, Germany
- Büchner, A.
- Kraemer, J.M.
- Kuntzsch, M.
- Lange, B.
- Lehnert, U.
- Michel, P.
- Schramm, U.
- Schurig, R.
- Steinbrück, R.

I-Tech
Solkan, Slovenia
- Leban, P.

IAP/RAS
Nizhny Novgorod, Russia
- Kuzikov, S.V.
- Vikharev, A.A.

IAP
Frankfurt am Main, Germany
- Forck, P.
- Kester, O.K.
- Udrea, S.

IBS
Daejeon, Republic of Korea
- Boussaid, R.
- Kondrashev, S.A.
- Park, Y.H.

IFIC
Valencia, Spain
- Faus-Golfe, A.
- Fuster-Martínez, N.

IHEP
Beijing, People's Republic of China
- Cao, J.S.
- Geng, H.
- Li, Y.
- Ma, Z.J.
- Meng, C.
- Sui, Y.F.
- Xie, Y.
- Yu, L.
- Yue, J.H.

IKP
Mainz, Germany
- Alexander, I.
- Aulenbacher, K.
- Heidrich, S.
- Hug, F.

INFN-Bologna
Bologna, Italy
- Tosi, N.

INFN-Napoli
Napoli, Italy
- Sabato, L.

INFN-Roma II
Roma, Italy
- Cianchi, A.

INFN-Roma
Roma, Italy
- Addesa, F.M.
- Cavoto, G.
- Iacoangeli, F.
- Marongiu, M.
- Pettinacci, V.
- Valente, P.

ISBN 978-3-95450-177-9

INFN/LNF
Frascati (Roma), Italy
- Alesini, D.
- Anania, M.P.
- Bellaveglia, M.
- Bisesto, F.G.
- Buonomo, B.
- Chiadroni, E.
- Cioeta, F.
- Coiro, O.
- Curcio, A.
- Di Giovenale, D.
- Di Giulio, D.G.C.
- Di Pirro, G.
- Falone, A.
- Ferrario, M.
- Foggetta, L.G.
- Franzini, G.
- Lollo, V.L.
- Pellegrini, D.
- Pellegrino, L.
- Pompili, R.
- Serio, M.
- Shpakov, V.
- Stella, A.
- Vaccarezza, C.
- Variola, A.

IOQ
Jena, Germany
- Geithner, R.
- Kurian, F.
- Neubert, R.
- Stöhlker, T.

IPHT
Jena, Germany
- Schmelz, M.
- Stolz, R.

IPN
Orsay, France
- Ausset, P.
- Ben Abdillah, M.
- Berthelot, S.
- Fournier, F.
- Joly, C.
- Lesrel, J.
- Yaniche, J.-F.

ISIR
Osaka, Japan
- Gohdo, M.
- Kan, K.
- Kondoh, T.
- Nozawa, I.
- Yang, J.
- Yoshida, Y.

ISS
Rome, Italy
- Carloni, A.
- Cisbani, E.
- Colilli, S.
- De Angelis, G.
- Frullani, S.
- Ghio, F.
- Giuliani, F.
- Gricia, M.
- Lucentini, M.
- Notaro, C.
- Santavenere, F.
- Spurio, A.
- Vacca, G.

J-PARC, KEK & JAEA
Ibaraki-ken, Japan
- Kuboki, H.
- Satou, K.
- Toyama, T.

JAEA/J-PARC
Tokai-mura, Japan
- Chishiro, E.
- Harada, H.
- Hayashi, N.
- Hirano, K.
- Kato, Y.
- Kinsho, M.
- Kondo, Y.
- Meigo, S.I.
- Miura, A.
- Morishita, T.
- Oguri, H.
- Okabe, K.
- Takei, H.
- Tsutsumi, K.
- Yamamoto, K.
- Yoshimoto, M.

JAI
Oxford, United Kingdom
- Blaskovic Kraljevic, N.
- Boogert, S.T.
- Bromwich, T.
- Burrows, P.
- Christian, G.B.
- Doucas, G.
- Harrison, H.
- Karataev, P.
- Konoplev, I.V.
- Kruchinin, K.O.
- Lancaster, A.J.
- Lyapin, A.
- Perry, C.
- Ramjiawan, R.L.
- Yamakawa, E.
- Zhang, H.

ISBN 978-3-95450-177-9

JASRI/RIKEN
Hyogo, Japan
- Owada, S.

JASRI
Hyogo, Japan
- Dewa, H.
- Fujita, T.
- Masaki, M.
- Takano, S.

JINR
Dubna, Moscow Region, Russia
- Kalagin, I.V.
- Mitrofanov, S.
- Skuratov, V.A.
- Teterev, Yu.G.

JLab
Newport News, Virginia, USA
- Forman, E.
- Grames, J.M.
- Hannon, F.E.
- Jordan, K.
- Kazimi, R.
- Moore, W.
- Poelker, M.

KACST
Riyadh, Kingdom of Saudi Arabia
- Almalki, M.H.

Karlsruhe Institute of Technology
Eggenstein-Leopoldshafen, Germany
- Holzapfel, B.

Kavli IPMU
Kashiwa, Japan
- Bronner, C.
- Hartz, M.

KEK/JAEA
Ibaraki-Ken, Japan
- Liu, Y.
- Maruta, T.

KEK
Ibaraki, Japan
- Arinaga, M.
- Aryshev, A.
- Flanagan, J.W.
- Friend, M.L.
- Fukuma, H.
- Furuya, T.
- Futatsukawa, K.
- Honda, T.
- Ikeda, H.
- Ishii, H.
- Koseki, T.
- Kubo, K.
- Kuboki, H.
- Mitsuhashi, T.M.
- Miyao, T.
- Mori, K.
- Mulyani, E.
- Nogami, T.
- Obina, T.
- Okada, M.
- Okugi, T.
- Shevelev, M.
- Takai, R.
- Tanimoto, Y.
- Tauchi, T.
- Tejima, M.
- Terunuma, N.
- Tobiyama, M.
- Toyama, T.
- Urakawa, J.
- Yamane, I.

KIT
Eggenstein-Leopoldshafen, Germany
- Ardila Perez, L.E.
- Arndt, M.
- Balzer, B.M.
- Bründermann, E.
- Caselle, M.
- Chilingaryan, S.A.
- Funkner, S.
- Hänisch, J.
- Ilin, K.S.
- Kopmann, A.
- Kuzmin, K.
- Müller, A.-S.
- Nasse, M.J.
- Niehues, G.
- Raasch, J.
- Rota, L.
- Ruprecht, R.
- Schedler, M.
- Schmelzer, T.
- Schmid, A.
- Schuh, M.
- Schwarz, M.
- Schönfeldt, P.
- Siegel, M.
- Smit, B.
- Steinmann, J.L.
- Vogelgesang, M.
- Weber, M.
- Wuensch, S.
- Yan, M.

ISBN 978-3-95450-177-9

Korea University Sejong Campus
Sejong, Republic of Korea
- Jang, S.W.

Kyoto University
Kyoto, Japan
- Ichikawa, A.
- Minamino, A.
- Nakamura, K.G.
- Nakanishi, Y.
- Nakaya, T.

LAL
Orsay, France
- Bambade, P.
- Burmistrov, L.
- Douillet, D.
- Dubos, S.
- Faus-Golfe, A.
- Gamelin, A.R.
- Le Guidec, D.
- Puill, V.
- Scandale, W.
- Stocchi, A.
- Wallon, S.
- Yang, R.J.

LANL
Los Alamos, New Mexico, USA
- Baros, D.
- Martinez, D.
- O'Hara, J.F.
- Rybarcyk, L.
- Sedillo, J.D.
- Valicenti, R.A.
- Watkins, H.A.

LBNL
Berkeley, California, USA
- Leemans, W.
- Nakamura, K.
- Schroeder, C.B.

LLP
Shanghai, People's Republic of China
- Jiang, T.
- Lu, C.
- Shi, L.B.
- Zhao, L.

LNLS
Campinas, Brazil
- Tavares, D.O.

Logicware Inc
New York, USA
- Goncharik, V.

LSU
Baton Rouge, USA
- Santiago-Gonzalez, D.

MAX IV Laboratory, Lund University
Lund, Sweden
- Andersson, Å.
- Breunlin, J.
- Jensen, B.N.
- Lindvall, R.
- Mansten, E.
- Olsson, D.
- Sundberg, J.
- Tavares, P.F.
- Thorin, S.

MEPhI
Moscow, Russia
- Romaniouk, A.
- Sergeeva, D.Yu.
- Strikhanov, M.N.
- Tishchenko, A.A.

MIT
Cambridge, Massachusetts, USA
- Kärtner, F.X.
- Peng, M.Y.
- Xin, M.

Naples University Federico II, Science and Technology Pole
Napoli, Italy
- Arpaia, P.
- Liccardo, A.

NERS-UM
Ann Arbor, Michigan, USA
- Kubley, T.
- Naab, F.U.
- Toader, O.F.
- Uberseder, E.E.

NRC
Moscow, Russia
- Korchuganov, V.
- Kovachev, G.
- Odintsov, D.G.
- Stirin, A.I.
- Tarasov, Yu.F.
- Valentinov, A.G.
- Zabelin, A.V.

ISBN 978-3-95450-177-9

NSRRC
Hsinchu, Taiwan
- Chen, M.L.
- Cheng, Y.-S.
- Chiu, P.C.
- Ho, H.C.
- Hsu, K.H.
- Hsu, K.T.
- Hu, K.H.
- Huang, C.H.
- Huang, D.-G.
- Kuan, C.K.
- Kuo, C.H.
- Lai, W.Y.
- Liao, C.Y.
- Lin, C.J.
- Perng, S.Y.
- Tsai, C.W.
- Tseng, T.C.
- Wang, H.S.

NUAA
Nanjing, People's Republic of China
- Fang, M.H.
- Wang, J.
- Wei, Z.Y.
- Zhu, J.

ODU
Norfolk, Virginia, USA
- Ali, M.M.

Ohio State University
Columbus, Ohio, USA
- Gan, K.K.
- Kagan, H.
- Smith, S.
- Warner, J.D.

ORNL
Oak Ridge, Tennessee, USA
- Aleksandrov, A.V.
- Shishlo, A.P.
- Zhukov, A.P.

PAL
Pohang, Kyungbuk, Republic of Korea
- Baek, S.Y.
- Choi, H. J.
- Hong, J.H.
- Kang, H.-S.
- Kim, C.
- Kim, G.
- Kim, J.H.
- Ko, I.S.
- Lee, S.J.
- Mun, G.
- Oh, B.G.
- Park, B.R.
- Shin, D.C.
- Suh, Y.J.
- Yang, H.

PSI
Villigen PSI, Switzerland
- Abela, R.
- Baldinger, R.
- Bettoni, S.
- Craievich, P.
- Dehler, M.M.
- Ditter, R.
- Divall, M.C.
- Gorgisyan, I.
- Hauri, C.P.
- Hiller, N.
- Hunziker, S.
- Ischebeck, R.
- Juranič, P.N.
- Keil, B.
- Koprek, W.
- Kramert, R.
- Marinkovic, G.
- Monoszlai, B.
- Mozzanica, A.
- Orlandi, G.L.
- Ozkan Loch, C.
- Patthey, L.
- Pedrozzi, M.
- Pradervand, C.
- Prat, E.
- Radović, M.
- Reiche, S.
- Rivkin, L.
- Roggli, M.
- Romann, A.
- Schlott, V.
- Stadler, M.
- Stepanov, A.G.
- Treyer, D.M.
- Trisorio, A.

PTB
Berlin, Germany
- Brandt, G.
- Illemann, J.
- Kapsch, R.-P.
- Klein, R.
- Makowski, C.
- Reichel, T.
- Renner, F.
- Schüller, A.
- Thornagel, R.

ISBN 978-3-95450-177-9

RadiaBeam Systems
Santa Monica, California, USA
- Kutsaev, S.V.
- Murokh, A.Y.
- Ruelas, M.
- To, H.L.

RadiaBeam
Santa Monica, California, USA
- Andonian, G.
- Harrison, M.A.
- Jacobson, B.T.
- O'Shea, F.H.
- Ovodenko, A.G.

RAS/INR
Moscow, Russia
- Kravchuk, L.V.
- Paramonov, V.V.
- Zavadtsev, A.A.

RIKEN SPring-8 Center
Sayo-cho, Sayo-gun, Hyogo, Japan
- Maesaka, H.
- Ogawa, K.
- Takano, S.
- Togashi, T.
- Yabashi, M.

Royal Holloway, University of London
Surrey, United Kingdom
- Arteche, A.
- Boorman, G.E.
- Bosco, A.
- Gibson, S.M.

RWTH
Aachen, Germany
- Hinder, F.

Shanghai Jiao Tong University
Shanghai, People's Republic of China
- Fu, F.
- Liu, S.
- Xiang, D.
- Zhu, P.F.

SINAP
Shanghai, People's Republic of China
- Chen, J.
- Dai, X.L.
- Deng, H.X.
- Lai, L.W.
- Liu, B.
- Liu, M.
- Song, M.
- Wang, D.
- Wang, R.
- Yan, Y.B.
- Yin, C.X.
- Yu, L.Y.
- Yuan, R.X.

SLAC
Menlo Park, California, USA
- Beukers, T.G.
- Bowden, G.B.
- Clarke, C.I.
- Claus, R.
- Colocho, W.S.
- Condamoor, S.
- Corbett, W.J.
- D'Ewart, J.M.
- Decker, F.-J.
- Ding, Y.
- Dolgashev, V.A.
- Eichner, J.P.
- Field, R.C.
- Fisher, A.S.
- Franzi, M.A.
- Frisch, J.C.
- Haase, A.A.
- Haller, G.
- Herbst, R.T.
- Hong, B.
- Huang, X.
- Krejcik, P.
- Legat, U.
- Lewandowski, J.R.
- Lutman, A.A.
- Ma, L.
- Maxwell, T.J.
- McKee, B.D.
- Nicolas, L.Y.
- Olsen, J.J.
- Reese, B.A.
- Ruckman, R.
- Sapozhnikov, L.
- Sebek, J.J.
- Seward, P.
- Sheppard, J.C.
- Smith, S.R.
- Smith, T.J.
- Straumann, T.
- Sullivan, M.K.
- Tantawi, S.G.
- Tian, K.
- Van Winkle, D.
- Vargas, J.L.
- Vásquez, J.A.
- Wang, J.W.
- Weaver, M.
- Williams, E.
- Wu, J.
- Xiao, L.
- Xu, C.
- Young, A.

ISBN 978-3-95450-177-9

SLRI
Nakhon Ratchasima, Thailand
- Klinkhieo, S.
- Klysubun, P.
- Kongtawong, S.
- Krainara, S.
- Pulampong, T.
- Sudmuang, P.
- Suradet, N.

SLSA
Clayton, Australia
- Tan, Y.E.

Sokendai
Ibaraki, Japan
- Kubo, K.
- Mulyani, E.
- Okugi, T.
- Tauchi, T.
- Terunuma, N.

Solaris
Kraków, Poland
- Borowiec, P.B.
- Goryl, P.P.
- Jaglarz, M.B.
- Kisiel, A.
- Kopeć, M.P.
- Marendziak, A.M.
- Piela, S.
- Sagalo, P.S.
- Stankiewicz, M.J.
- Wawrzyniak, A.I.

SOLEIL
Gif-sur-Yvette, France
- El Ajjouri, M.
- Hubert, N.
- Labat, M.
- Loulergue, A.
- Pédeau, D.
- Ribbens, M.
- Sreedharan, R.
- Tordeux, M.-A.

Soreq NRC
Yavne, Israel
- Cohen, A.
- Daniely, E.
- Eliyahu, I.
- Kaizer, B.
- Kreisler, A.
- Perry, A.
- Shor, A.
- Weissman, L.

SSRF
Shanghai, People's Republic of China
- Chen, F.Z.
- Chen, Z.C.
- Lai, L.W.
- Leng, Y.B.
- Yan, Y.B.
- Zhou, W.M.

STFC/DL/ASTeC
Daresbury, Warrington, Cheshire, United Kingdom
- Jamison, S.P.
- Snedden, E.W.
- Walsh, D.A.

STFC/RAL/ISIS
Chilton, Didcot, Oxon, United Kingdom
- Harryman, D.M.
- Jones, B.
- Pertica, A.
- Posthuma de Boer, D.W.
- Wilcox, C.C.
- Williamson, R.E.

Supracon AG
Jena, Germany
- Zakosarenko, V.

The Hebrew University of Jerusalem, The Racah Institute of Physics
Jerusalem, Israel
- Zigler, A.

The University of Liverpool
Liverpool, United Kingdom
- Fernandes, M.F.
- Fiorito, R.B.
- Kastriotou, M.
- Nebot Del Busto, E.
- Tzoganis, V.
- Welsch, C.P.
- Widmann, W.
- Wolfenden, J.
- Zhang, H.D.

The University of Manchester, The Photon Science Institute
Manchester, United Kingdom
- Cliffe, M.J.
- Graham, D.M.
- Jamison, S.P.
- Lake, D.

The University of Melbourne
Melbourne, Victoria, Australia
- Boland, M.J.
- Peake, D.J.

ISBN 978-3-95450-177-9

ThEP Center, Commission on Higher Education
Bangkok, Thailand
- Rhodes, M.W.

TPU
Tomsk, Russia
- Novokshonov, A.I.
- Potylitsyn, A.

TRIUMF, Canada's National Laboratory for Particle and Nuclear Physics
Vancouver, Canada
- Dirksen, P.E.
- Verzilov, V.A.

TU Darmstadt
Darmstadt, Germany
- Bahlo, T.
- Burandt, C.
- Enders, J.
- Ensinger, W.
- Hofmann, K.
- Jürgensen, L.E.
- Kürzeder, T.
- Lederer, S.
- Lieberwirth, A.
- Pietralla, N.
- Wissmann, J.

TUB
Beijing, People's Republic of China
- Zhang, Z.

TUG/ITP
Graz, Austria
- Turner, M.

TUL-DMCS
Łódź, Poland
- Krupa, M.
- Makowski, D.R.
- Mielczarek, A.

U. Sannio
Benevento, Italy
- Sabato, L.

UAB
Barcelona, Spain
- Molas, A.

UB
Barcelona, Spain
- Ciaglia, D.
- Fernàndez, G.
- Gascon, D.
- Graciani, R.
- Gómez, S.
- Mauricio, J.
- Rakotnavalona, N.
- Sanuy, A.
- Sánchez, D.

UCLA
Los Angeles, California, USA
- Curry, E.J.
- Duris, J.P.
- Jarrahi, M.
- Musumeci, P.
- Rosenzweig, J.B.
- Sudar, N.S.
- Yardimci, N.T.

UMAN
Manchester, United Kingdom
- Jones, R.M.
- Joshi, N.Y.
- Shi, L.

UMD
College Park, Maryland, USA
- Shkvarunets, A.G.

United Rocket and Space Corporation, Institute of Space Device Engineering
Moscow, Russia
- Anashin, V.S.

Universita' degli Studi di Milano & INFN
Milano, Italy
- Paroli, B.
- Potenza, M.A.C.
- Siano, M.

Universität Bonn, Helmholtz-Institut für Strahlen- und Kernphysik
Bonn, Germany
- Eltcov, L.

University College West
Trollhätan, Sweden
- Joshi, S.

University of Hamburg, Institut für Experimentalphysik
Hamburg, Germany
- Maier, A.R.

University of Hamburg
Hamburg, Germany
- Dornmair, I.

ISBN 978-3-95450-177-9

University of Hawaii
Honolulu,, USA
- Varner, G.S.

University of Manchester
Manchester, United Kingdom
- Joshi, N.Y.

University of Oslo
Oslo, Norway
- Adli, E.
- Gjersdal, H.
- Jaekel, M.R.
- Rohne, O.

University of Rome "La Sapienza"
Rome, Italy
- Placido, C.

University of Rome La Sapienza
Rome, Italy
- Ciambrella, M.
- Giribono, A.
- Mostacci, A.
- Palumbo, L.
- Tocci, S.

University of Saskatchewan
Saskatoon, Canada
- Zhang, W.J.

University of Trieste
Trieste, Italy
- Brajnik, G.
- Carrato, S.

Università di Pisa
Pisa, Italy
- Fanucci, L.

Universität Bern, Institute of Applied Physics
Bern, Switzerland
- Feurer, T.
- Hayati, M.

UNN
Nizhny Novgorod, Russia
- Kuzikov, S.V.

Uppsala University
Uppsala, Sweden
- Hamberg, M.

Warsaw University of Technology, Institute of Electronic Systems
Warsaw, Poland
- Czuba, K.
- Janas, E.
- Rybaniec, R.

Wayne State University
Detroit, Michigan, USA
- Bonvicini, G.

XFEL. EU
Hamburg, Germany
- Kaukher, A.
- Liu, J.

ISBN 978-3-95450-177-9